

Batteries

2021 Annual Progress Report

Vehicle Technologies Office

(This page intentionally left blank)

Disclaimer

This report was prepared as an account of work sponsored by an agency of the United States government. Neither the United States government nor any agency thereof, nor any of their employees, makes any warranty, express or implied, or assumes any legal liability or responsibility for the accuracy, completeness, or usefulness of any information, apparatus, product, or process disclosed or represents that its use would not infringe privately owned rights. Reference herein to any specific commercial product, process, or service by trade name, trademark, manufacturer, or otherwise does not necessarily constitute or imply its endorsement, recommendation, or favoring by the United States government or any agency thereof. The views and opinions of authors expressed herein do not necessarily state or reflect those of the United States government or any agency thereof.

Acknowledgements

The projects reported in this report were supported through various contracts funded by the U.S. Department of Energy, Vehicle Technologies Office. A list of contributing authors appears in the sections for specific projects in this report.

Acronyms

AABC	Advanced Automotive Batteries Conference
ABF-STEM	Annular bright field (ABF) imaging using aberration-corrected scanning transmission
ABMR	Advanced Battery Materials Research
ABR	Applied Battery research
AC	Alternating current
ACS	American Chemical Society
AEM	Advanced Electrolyte Model
AER	All-electric range
AFM	Atomic force microscopy
AGG	Aggregates
AI	Artificial Intelligence
AIBN	(2,2'-Azobis(2-methylpropionitrile))
AIMD	Ab initio molecular dynamics
AIR	Areal interfacial resistance
ALD	Atomic layer deposition
AMO	Advanced Manufacturing Office
AMR	Annual Merit Review
ANL	Argonne National Laboratory
AOI	Area of Interest
APL	Applied Physics Laboratory
APR	Annual progress report
APS	Advanced Photon Source (laboratory)
ARC	Accelerated rate calorimetry
ARL	Army Research Laboratory
ASI	Area-specific impedance
ASLSB	All solid lithium-sulfur battery
ASR	Area-specific resistance
ASSB	All solid-state battery
ASSLB	All solid-state Li metal batteries
BE	Binding energy
BESS	Battery energy storage system
BET	Brunauer, Emmett, and Teller (surface area analysis)
BEV	Battery electric vehicle
BLI	Beyond Lithium-ion
BM	Black mass
BMF	Battery manufacturing facility
BMR	(Advanced) Battery Materials Research (program)
BMS	Battery management system
BN	Butyronitrile
BNL	Brookhaven National Laboratory
BOL	Beginning of life
BOM	Bill of materials

BOP	Balance of plant
BPTV	Battery Pressure Test Vessel
BTC	Battery Technology Center
BTM	Battery thermal management
BTMS	Behind-the-Meter-Storage
BTO	Building Technologies Office
BYU	Brigham Young University
CAEBAT	Computer-aided engineering of batteries
CAFE	Corporate Average Fuel Economy
CAM	Cathode active materials
CAMP	Cell analysis, modeling, and prototyping (facility)
CB	Carbon black
CBD	Conductive binder domain
CCA	Carbon conductive additive
CCCV	Constant current, constant voltage
CCD	Critical current density
CD	Current density
CDI	Cobalt Development Institute
CE	Coulombic efficiency
CEI	Cathode electrolyte interfaces
CERC	Clean Energy Research Center
CFD	Computational fluid dynamics
CIP	Contact ion pair
CL	Calendar life
CMC	Carboxymethyl cellulose
CMD	Classical molecular dynamics
CNT	Carbon nano-tubes
COP	Critical overpotentials
CP	Co-precipitation
CPE	Constant phase element
CR	Constant risk (protocol)
CSTR	Continuous stirred tank reactor
CV	Cyclic voltammetry
CVD	Chemical Vapor Deposition
CVT	Chemical vapor transport
CWG	Chemical Working Group
CY	Calendar year
DCA	Dicyanamide
DCFC	DC fast charging
DCIR	Direct current inner resistance
DCR	Direct current resistance
DEB	Double-end binding (sites)
DEC	Diethyl carbonate
DEMS	Differential electrochemical mass spectrometry
DFEC	Bis(trifluoroethyl) carbonate (DFEC)

DFT	Density function theory
DHM	Digital Holographic Microscopy
DI	De-ionized (water)
DIW	Direct Ink Writing
DMC	Dimethyl carbonate
DME	Dimethyl ether
DMF	Dimethylformamide
DMSO	Dimethylsulfoxide
DOD	Depth-of-discharge
DOE	Department of Energy
DOL	Dioxolane
DOS	Density of state
DPA	Destructive physical analysis
DPS	Dipropylulfide
DRT	Distribution of relaxation times (analysis)
DRX	Disordered (rocksalt) transition metal oxides
DSC	Differential scanning calorimetry
DST	Dynamic stress test
DTPA	2x molar chelating agent
EADL	Electrochemical Analysis and Diagnostic Laboratory (at ANL)
EBSL	Electron back-scattering diffraction
EC	Ethylene carbonate
ECI	Effective cluster interaction
ECS	Electrochemical Society
EDAX	Energy dispersive x-ray spectroscopy mapping
EDS	Energy dispersive spectroscopy
EDV	Electric Drive Vehicle
EDX	Energy-dispersive x-ray (spectroscopy)
EEI	Electrode/electrolyte interface
EELS	Electron energy loss spectroscopy
EERE	Energy Efficiency and Renewable Energy (DOE Office)
EIA	Energy Information Administration
EIS	Electrochemical impedance spectroscopy
EMC	Ethylmethyl carbonate
EMN	Energy Materials Network
EMS	Energy management system
EO	Ethylene oxide
EOCV	Voltage at the end of charge
EODV	Voltage at the end of discharge
EOL	End of life
EP	Electropolymerization
EPA	Environmental Protection agency
EPR	Electron Paramagnetic Resonance
ESS	Energy storage system
EV	Electric vehicle

EVI	Electric Vehicle Initiative
EVSE	Electric-vehicle supply equipment
EXAFS	Extended X-ray absorption fine structure
FAT	Factory Acceptance Test
FC	Fast-charge
FCAB	Federal Consortium for Advanced Batteries
FCE	First cycle efficiency
FCG	Full concentration-gradient
FCTO	Fuel Cell Technologies Office
FDES	Fluorinated deep eutectic solvent
FDM	Fused Deposition Modeling
FEA	Finite element analysis
FEC	Fluoro ethylene carbonate
FF	Force field
FFT	Fast Fourier-transform
FIB	Focused ion beam
FLHCE	Fluorinated localized high concentration electrolyte
FOA	Federal opportunity announcement
FOME	Figure-of-Merit Energy
FOMP	Figure-of-Merit Power
FRS	Filtered Rayleigh Scattering
FSI	(Lithium) bis(trifluoromethanesulfonyl)imide
FSP	Flame spray pyrolysis
FT-EXAFS	Fourier transformed extended X-ray absorption fine structure
FTIR	Fourier transform infrared spectroscopy
FWHM	Full width at half maximum
FY	Fiscal year
GB	Grain boundary
GBL	Gamma butyrolactone
GC	“generation/collection” (mode)
GCMC	Grand canonical Monte Carlo (simulations)
GDOES	Glow discharge optical emission spectrometry
GF	Glass fiber
GGA	Generalized gradient approximation
GHG	Green-house gases
GITT	Galvanostatic intermittent titration
GIXRD	Grazing incidence X-ray diffraction
GN	Glutaronitrile
GOS	Grain orientation spread
GPE	Gel polymer electrolyte
GREET	Greenhouse gas regulated energy and emissions and transpiration
GROD	Grain reference orientation deviation
GSE	Glassy solid electrolyte
HAADF	High-angle annular dark-field
HAWCS	Hybrid Alternative Wet-Chemical Synthesis

HAXPES	High energy x-ray photoelectron spectroscopy
HCE	High concentration electrolyte
HEBM	High-energy ball-milling
HEHV	High-energy high voltage (protocol)
HELM	High-energy lateral mapping
HEV	Hybrid electric vehicle
HEXRD	High-energy XRD
HF	Hydrofluoric acid
HFE	Hydrocarbon vs. fluoroether
HFTO	Hydrogen and Fuel Cell Technologies Office
HOPG	Highly oriented pyrolytic graphite
HPC	Highly porous carbon
HPLC	High-performance liquid chromatography
HPPC	Hybrid pulse power characterization
HRTEM	High-resolution transmission electron microscopy
HSC	High shear compaction (process)
HT	High temperature
HUB	Heterogeneous unifying battery
HV	High viscosity (slurry)
HVM	High volume manufacturing
HXN	Hard x-ray nanoprobe
IBA	International Battery Materials Association
IC	Incremental capacity
ICE	Internal combustion engine
ICEV	Internal combustion engine vehicle
ICP	Inductively coupled plasma
ICP-MS	Inductively coupled Plasma Mass Spectrometry
ICP-OES	Inductively coupled-plasma optical emission spectroscopy
IEA	International Energy Agency
IEEE	Institute of Electrical and Electronics Engineers
INL	Idaho National Laboratory
IP	Isoprene
IPA	Isopropanol
IPP	Inter primary particle
IR	Infra-red
IZ	Isoxazole
JACS	Journal of the American Chemical Society
KMC	Kinetic Monte Carlo (simulations)
LAGP	$\text{Li}_{1.5}\text{Al}_{0.5}\text{Ge}_{1.5}(\text{PO}_4)_3$
LAM	Loss of active materials
LAMMPS	Large-scale atomic/molecular massively parallel simulator
LATP	$\text{Li}_{1.17}\text{Al}_{0.17}\text{Ti}_{1.83}(\text{PO}_4)_3$
LBCO	$\text{Li}_3\text{BO}_3\text{-Li}_2\text{CO}_3$
LBDC	Lithium butylene dicarbonate
LBNL	Lawrence Berkeley National Laboratory

LBO	Li_3BO_3
LCA	Life cycle analysis
LCFC	Low-cost fast charge (battery)
LCO	Lithium cobalt oxide
LCOC	Levelized Cost of Charging
LCRC	Laboratory Computing Resource Center (at ANL)
LE	Liquid electrolyte
LEC	Lithium ethyl carbonate
LEDC	Lithium ethylene dicarbonate
LEMC	Lithium ethylene monocarbonate
LFP	Li-iron phosphate
LGPS	$\text{Li}_{10}\text{GeP}_2\text{S}_{12}$
LHCE	Localized high concentration electrolyte
LIB	Lithium-ion battery
LIBRA	Lithium Ion Battery Recycling Analysis
LIC	Lithium-ion conducting
LLBZO	Lithium Lanthanum Bismuth Oxide
LLI	Loss of lithium inventory
LLNL	Lawrence Livermore National Laboratory
LLS	Layered-layered spinel
LLZ	$\text{Li}_7\text{La}_3\text{Zr}_2\text{O}_{12}$
LLZO	Lithium lanthanum zirconate
LLZTO	$\text{Li}_{6.75}\text{La}_3\text{Zr}_{1.75}\text{Ta}_{0.25}\text{O}_{12}$
LMA	Lithium metal anode
LMB	Lithium metal battery
LMNOF	Li-Mn-Nb-O-F
LMO	Lithium manganese oxide
LMTOF	Li-Mn-Ti-O-F
LNMO	$\text{LiNi}_{0.5}\text{Mn}_{0.5}\text{O}_2$
LNMTO	$\text{LiNi}_{0.5}\text{Mn}_{1.2}\text{TiO}_{0.3}\text{O}_4$
LNO	Lithium-nickel oxide
LNTMOF	$\text{Li}_{1.15}\text{Ni}_{0.45}\text{Ti}_{0.3}\text{Mo}_{0.1}\text{O}_{1.85}\text{F}_{0.15}$
LOB	Lithium Oxygen Battery
LPAS	Low-temperature plasma assisted separation process
LPC	Large particle cathodes
LPS	Li_3PS_4
LSV	Linear scanning voltammetry
LT	Low-temperature
LTO	Lithium titanate, $\text{Li}_4\text{Ti}_5\text{O}_{12}$
LUMO	Lowest unoccupied molecular orbital (energy level)
LV	Low viscosity
LYC	Li_3YCl_6
LZO	$\text{La}_2\text{Zr}_2\text{O}_7$
MAPE	Mean approximate error
MAS	Magic angle spinning

MC	Monte Carlo (method)
MD	Molecular dynamics
MERF	Materials Engineering Research Facility
METS	Muti-harmonic ElectroThermal Spectroscopy (sensor)
MGF	Mixed glass former (glassy film)
MIBC	Isobutyl carbinol
MILP	Mixed-integer linear programming
ML	Machine learning
MMSR	Modified material-stress reduction (profile)
MNS	$\text{Na}_{0.67}[\text{Mn}_{0.61}\text{Ni}_{0.28}\text{Sb}_{0.11}]\text{O}_2$
MOF	Metal Organic Framework
MOSN	Mixed oxy-sulfide-nitride (glass)
MPC	Model predictive controls
MSD	Mean square displacements
MSR	Material-stress reduction (protocol)
MST	Mass spectrometry titration
MTBE	Methyl tert-butyl ether
MTHF	2-methyl tetrahydrofuran
MWCNT	Multi-walled Carbon Nanotube
NASICON	(Na) Super Ionic CONductor
NBR	Nitrile butadiene rubber
NCA	$\text{LiNi}_{0.8}\text{Co}_{0.15}\text{Al}_{0.05}\text{O}_2$
NCE	No-cost extension
NCM	$\text{Li}_{1+w}[\text{Ni}_x\text{Co}_y\text{Mn}_z]_{1-w}\text{O}_2$
NCW	$\text{Li}[\text{Ni}_{0.9}\text{Co}_{0.09}\text{W}_{0.01}]\text{O}_2$
NEB	Nudged elastic band (method)
NETL	National Energy Technology Laboratory
NFA	$\text{LiNi}_x\text{Fe}_y\text{Al}_z\text{O}_2$
NFM	Layered (sodium) nickel-iron-manganese oxide
NGTK	Newman, Tiedemann, Gu, Kim (model)
NHTSA	National Highway Transportation Safety Administration
NIB	Sodium (Na)-ion battery
NIST	National Institute of Standards and Technology
NLP	Natural language processing
NMA	$\text{LiNi}_{0.9}\text{Mn}_{0.05}\text{Al}_{0.05}\text{O}_2$
NMC	Nickel manganese cobalt (oxide)
NMP	N-methylpyrrolidone
NMR	Nuclear magnetic resonance
NMT	Neometal (battery)
NPDF	Neutron PDF
NR	Neutron reflectometry
NREL	National Renewable Energy Laboratory
NSLSII	National Synchrotron Light Source II
NTI	Negative triple ions
OCV	Open circuit voltage

ODI	Oxygen deficient interphase
OEM	Original equipment manufacturer
OEMS	Online electrochemical Mass Spectrometry
OER	Oxygen evolution reactions
OES	Optical Emission Spectroscopy
OM	Optical microscopy
OPLS	Optimized potentials for liquid simulations
ORNL	Oak Ridge National Laboratory
ORR	Oxygen reduction reaction
OVFE	Oxygen vacancy formation energy
PAA	Polyacrylic Acid
PAD	Polymer Assisted Deposition
PAN	Polyacrylonitrile
PARC	Palo Alto Research Center
PAW	Projected augmented wave
PBDT	Poly-2,2'-disulfonyl-4,4'-benzidine ter-ephthalamide
PBE	Perdew, Burke, and Ernzerhof (parameters)
PC	Propylene carbonate
PCM	Phase change material
PDF	Pair density function
PDMS	Polydimethylsiloxane
PE	Polyethylene
PECVD	Plasma-enhanced chemical vapor deposition
PEDOT	Poly(3,4-ethylenedioxythiophene)
PEEK	Polyetheretherketone
PEGDA	Poly(ethylene glycol) diacrylate
PEO	Polyethyleneoxide
PEV	Plug-in electric vehicle
PFG	Pulsed field gradient
PFIB	Plasma focused ion beam
PG	Gel polymer
PHEV	Plug-in hybrid electric vehicle
PI	Principal investigator
PIP	Polyisoprene
PL	Photoluminescence
PLD	Pulsed laser deposition
PLIF	Planar Laser Induced Fluorescence
PMMA	Poly(Methyl Methacrylate) Microspheres
PMS	Power management system
PNNL	Pacific Northwest National Laboratory
PP	Primary particle
PS	Propane sultone
PSD	Particle size distribution
PST	Partial sintered tape
PSU	Pennsylvania State University

PTF	Post-Test Facility
PTFE	Poly(tetrafluoroethylene) (cathode)
PTI	Positive triple ions
PV	Photovoltaic
PVB	Polyvinyl butyral
PVDF	Poly(vinylidene fluoride)
PXRD	Powder X-ray diffraction
PYR	N-butyl-N-methyl pyrrolidinium
R&D	Research and Development
RAM	Resonant acoustic mixer
RCT	Rate capability test
RDF	Radial distribution functions
RE	Reference electrode
REE	Rare earth element
RIXS	Resonant inelastic x-ray scattering
RM	Redox mediator
RNGC	Realizing Next Generation Cathodes
RNMC	Reaction network-based Monte Carlo
ROI	Return on investment
RP	Red phosphorus
RPA	Random Phase Approximation
RPM	Revolutions per minute
RPT	Reference performance test
RRDE	Rotating ring disk electrode
RS	Rocksalt
RST	Reactive Spray Technology
RT	Room temperature
RTD	Resistance thermal device
SAC	Single-atom catalyst
SAE	Society of Automotive Engineers
SAED	Selected area electrode diffraction
SAM	Self-assembled molecular (film)
SAXS	Small angle X-Ray scattering
SBC	Soluble base content
SBIR	Small Business Innovation Research
SBR	Styrene Butadiene Rubber
SCP	Sulfur containing polymer
SDS	Safety data sheet
SE	Solid electrolyte
SECM	Scanning electrochemical microscope
SEI	Solid electrolyte interphase
SEM	Scanning electron microscopy
SEMS	Scanning electron microscopy
SETO	Solar Energy Technologies Office
SFSP	Slurry Flame Spray Pyrolysis

SHE	Self-healing elastomer
SIB	Sodium-ion battery
SIC	Single-ion-conducting
SIE	Solvation-ion-exchange
SIL	Solvated ionic liquid (electrolyte)
SIMS	Secondary ion mass spectrometry
SLAC	Stanford acceleration laboratory
SLMP	Stabilized lithium metal powder
SLP	Single-layer pouch
SMPS	Scanning mobility particle sizing
SNL	Sandia National Laboratories
SNR	Signal-to-noise ratio
SOA	State of the art
SOC	State of charge
SOH	State of health (for battery)
SP	Spray pyrolysis
SPAN	Sulfurized Polyacrylonitrile
SPC	Small particle cathodes
SPE	Solid polymer electrolyte
SR	Surface reconstruction
SRO	Short-range order
SS	Solid-state
SSB	Solid-state battery
SSE	Solid-state electrolyte
SSP	Slurry Spray Pyrolysis
SSRL	Stanford Synchrotron Radiation Lightsource
STEM	Scanning transmission electron microscopy
STTR	Small Business Technology Transfer Program
SUNY	State University of New York
SWCNT	Single walled carbon nanotube
SXAS	Soft x-ray absorption
SXRD	Surface X-ray diffraction
TAC	Technical Advisory Committee
TAP	Technology assessment program
TARDEC	(U.S. Army) Tank Automotive Research, Development and Engineering Center
TCP	Technology Collaboration Program
TCR	Thermal contact resistance
TEGDME	Tetraethyleneglycoldimethyl
TEM	Transmission electron microscopy
TEMPO	(2,2,6,6-tetramethylpiperidin-1-yl) oxidanyl
TEP	Triethyl phosphate
TES	Tender-energy x-ray absorption spectroscopy
TEY	Total electron yield
TFE	Trifluoroethanol
TFP	Tris(2,2,2-trifluoroethyl) phosphate

TFSI	Bistriflimide (anion)
TGA	Thermal gravimetric analysis
TGC	Titration gas chromatography
THF	Tetrahydrofuran
TM	Transition metal
TMDC	Transition metal dichalcogenide
TMO	Transition metal oxide
TMSPI	Tris(trimethylsilyl) phosphite
TNO	Titanium niobium oxide
TRL	Technology Readiness Level
TTE	Tetrafluoropropyl ether
TVR	Taylor Vortex Reactor
TXM	Transmission X-ray microscopy
UCI	University of California, Irvine
UCL	University College, London
UCSD	University of California, San Diego
UCV	Upper cutoff voltage
UH	University of Houston
UM	University of Michigan
UMD	University of Maryland
UNC	University of North Carolina
URI	University of Rhode Island
USABC	United States Advanced Battery Consortium
USCAR	United States Council for Automotive Research
USCD	University of California, San Diego
USGS	United States Geological Survey
USPTO	United States Patents and Trademarks Office
UTA	University of Texas, Austin
UTK	University of Tennessee, Knoxville
UU	University of Utah
UV	Ultraviolet
UW	University of Washington
UWM	University of Wisconsin, Milwaukee
VASP	Vienna ab initio Simulation Package
VC	Vinylene carbonate
VDW	Van der Waals (force)
VOF	Volume of fluid
VTO	Vehicle Technologies Office
WPI	Worcester Polytechnic Institute
XAFS	X-ray absorption fine structure
XANES	X-ray absorption near edge structure
XAS	X-ray absorption spectroscopy
XCEL	EXtreme Fast Charge Cell Evaluation of Lithium-ion Batteries
XFC	Extreme fast charging
XFM	X-ray fluorescence microscopy

XPD	X-ray powder diffraction
XPEEM	X-ray photoemission electron microscopy
XPS	X-ray photoelectron spectroscopy
XRD	X-ray diffraction
XRF	X-ray fluorescence (microscopy)
XRS	X-ray Raman Spectroscopy

Executive Summary

Introduction

The Vehicle Technologies Office (VTO) of the Department of Energy (DOE) conducts research, development, demonstration, and deployment (RDD&D) on advanced transportation technologies that would reduce the nation's use of imported oil and would also lead to reductions in harmful emissions. Technologies supported by VTO include electric drive components such as advanced energy storage devices (primarily batteries), power electronics and electric drive motors, advanced structural materials, energy efficient mobility systems, and advanced engines and fuels. VTO is focused on funding early-stage high-reward/high-risk research to improve critical components needed for more fuel efficient (and cleaner-operating) vehicles. One of the major VTO objectives is to enable U.S. innovators to rapidly develop the next generation of technologies that achieve the cost, range, and charging infrastructure necessary for the widespread adoption of plug-in electric vehicles (PEVs). An important prerequisite for the electrification of the nation's light duty transportation sector is development of more cost-effective, longer lasting, and more abuse-tolerant PEV batteries. One of the ultimate goals of this research, consistent with the current vehicle electrification trend, is an EV which can provide the full driving performance, convenience, and price of an internal combustion engine (ICE) vehicle. To achieve this, VTO has established the following overarching goal (Source: FY2022 Congressional Budget Justification¹):

...identify new battery chemistry and cell technologies with the potential to reduce the cost of electric vehicle battery packs by more than half, to less than \$100/kWh (ultimate goal is \$60/kWh battery cell cost), increase range to 300 miles, and decrease charge time to 15 minutes or less by 2028.

VTO works with key U.S. automakers through the United States Council for Automotive Research (USCAR) – an umbrella organization for collaborative research consisting of Stellantis, the Ford Motor Company, and General Motors. Collaboration with automakers through the partnership known as U.S. Driving Research and Innovation for Vehicle Efficiency and Energy Sustainability (U.S. DRIVE) attempts to enhance the relevance and the success potential of its research portfolio. VTO competitively selects projects for funding through funding opportunity announcements (FOAs). Directly-funded work at the national laboratories are awarded competitively through a lab-call process. During the past year, VTO continued R&D in support of PEVs. Stakeholders for VTO R&D include universities, national laboratories, other government agencies and industry (including automakers, battery manufacturers, material suppliers, component developers, private research firms, and small businesses).

This document summarizes the progress of VTO battery R&D projects supported during the fiscal year 2021 (FY 2021). In FY 2021, the DOE VTO battery R&D funding was approximately \$115 million. Its R&D focus was on the development of high-energy batteries for EVs as well as very high-power devices for hybrid vehicles. The electrochemical energy storage roadmap (which can be found at the EERE Roadmap web page²) describes ongoing and planned efforts to develop electrochemical storage technologies for EVs. To advance battery technology, which can in turn improve market penetration of PEVs, the program investigates various battery chemistries to overcome specific technical barriers, e.g., battery cost, performance, life (both the calendar life and the cycle life), its tolerance to abusive conditions, and its recyclability/sustainability. VTO R&D has had considerable success, lowering the cost of EV battery packs to \$185/kWh in 2019 (representing more than 80% reduction since 2008) yet even further cost reduction is necessary for EVs to achieve head-to-head cost competitiveness with ICEs (without Federal subsidies). In addition, today's batteries also need improvements in such areas as their ability to accept charging at a high rate, referred to as extreme fast charging (XFC) (15 minute

¹ <https://www.energy.gov/sites/default/files/2021-06/doe-fy2022-budget-volume-3.1-v5.pdf>, Volume 3, Part 1, Page 204.

² <http://energy.gov/eere/vehicles/downloads/us-drive-electrochemical-energy-storage-technical-team-roadmap>.

charge) – to provide a “refueling” convenience similar to ICEs, and the ability to operate adequately at low temperatures. Research into “next-gen lithium-ion” batteries which would provide such functionalities is one of the R&D focus areas. VTO is funding research on both “next gen” chemistries (which employ an alloy anode and/or a high voltage cathode) and beyond lithium-ion (BLI) chemistries (which can, for example, employ a lithium metal anode). Current cycle and calendar lives of next gen and BLI chemistries are well short of goals set for EVs. To quantify the improvements needed to accelerate large-scale adoption of PEVs and HEVs, certain performance and cost targets have been established. Some sample performance and cost targets for EV batteries, both at cell level and at system (pack) level, are shown in Table ES- 1.

Table ES- 1: Subset of EV Requirements for Batteries and Cells

Energy Storage Goals (by characteristic)	Pack Level	Cell Level
Cost @ 100k units/year (kWh = useable energy)	\$100/kWh*	\$75/kWh*
Peak specific discharge power (30s)	470 W/kg	700 W/kg
Peak specific regen power (10s)	200 W/kg	300 W/kg
Useable specific energy (C/3)	235 Wh/kg*	350 Wh/kg*
Calendar life	15 years	15 years
Deep discharge cycle life	1000 cycles	1000 cycles
Low temperature performance	>70% useable energy @C/3 discharge at -20 °C	>70% useable energy @C/3 discharge at -20 °C
	*Current commercial cells and packs not meeting the goal	

The batteries R&D effort includes multiple activities, ranging from focused fundamental materials research to prototype battery cell development and testing. It includes, as mentioned above, R&D on “next-gen” and BLI materials and cell components, as well as on synthesis and design, recycling, and cost reduction. Those activities are organized into mainly two program elements:

- Advanced Battery and Cell R&D
- Advanced Materials R&D.

A short overview of each of those program elements is given below.

Advanced Battery and Cell R&D

The *Advanced Battery and Cell R&D* activity focuses on the development of robust battery cells and modules to significantly reduce battery cost, increase life, and improve performance. This work mainly spans the following general areas:

- United States Advanced Battery Consortium (USABC)-supported battery development & materials R&D (seven projects)
- Processing science and engineering (11 projects)
- Recycling and sustainability (five projects)
- Extreme fast-charging (11 projects)
- Beyond batteries (one project)

- Testing, Analysis, High-Performance Computing, Lab-I4 (eight projects)
- Small business innovative research (SBIR) (multiple Phase I and Phase II projects).

Chapters I through VII of this report describe projects under the *Advanced Battery and Cell R&D* activity. This effort involves close partnership with the automotive industry, through a USABC cooperative agreement. In FY 2021, VTO supported seven USABC cost-shared contracts with developers to further the development of advanced automotive batteries and battery components. The estimated DOE share of those USABC contracts (over the life of the contracts) is approximately \$39M. These include rapid commercialization of high energy anode materials (Nanograf Technologies), fast-charge and low-cost lithium ion batteries for electric vehicle applications (Zenlabs Energy), new high-energy & safe battery technology with extreme fast charging capability for automotive applications (Microvast, Inc.), high energy and power density lithium ion battery based on neocarbonix™ polymer binder-free electrode technology for ev applications (Nanoramic), a low-cost/fast-charging EV project (EnPower), a cell manufacturing – prelithiation project (Applied Materials), and a technology assessment program of Aramid Separators for EV applications (Microvast, Inc.)

In addition to the USABC projects listed above, VTO also supports 11 *processing science and engineering* projects: including one project at UC, Berkeley and 10 projects at the national labs. Most strategies for increasing the performance (and reducing cost) of lithium-ion batteries focus on novel battery chemistries, material loading modifications, and increasing electrode thickness. The latter approach is generally considered useful for increasing energy density (and in turn, the overall cell capacity). However, practical thicknesses are constrained by ionic transport limitations (which limit cell power) and processing issues. Project participants in this area include ANL, BNL, LBNL, and LLNL. The estimated value of those advanced processing projects (over project lifetime) is approximately \$35M.

The *Recycling and Sustainability* activity involves studies of the full life-cycle impacts and costs of lithium-ion battery production/use; cost assessments and impacts of various recycling technologies; and the available material and cost impacts of recycling and secondary use. The participants include ANL, NREL, Farasis Energy, and Worcester Polytechnic Institute and the associated budget is approximately \$10M.

To become truly competitive with the internal combustion engine vehicle (ICEV) refueling experience, EV charging times must also be significantly shorter than at present. A research project to understand/enable extreme fast charging (XFC) in enhanced lithium-ion systems – charging an EV at power rates of up to 400 kW, began in FY 2017. Projects on numerous XFC topics are taking place at multi-lab consortiums, and three universities (the University of Tennessee, the Stony Brook University, and the University of Michigan). In addition, a “behind the meter” storage project is taking place by a team which includes NREL, INL, ORNL, and SNL. This area focuses on novel battery technologies to facilitate the integration of high-rate EV charging, solar power generation technologies, and energy-efficient buildings while minimizing both cost and grid impacts.

The *battery testing, analysis, and high-performance computing* activity develops requirements and test procedures for batteries (to evaluate battery performance, battery life and abuse tolerance). Battery technologies are evaluated according to USABC-stipulated battery test procedures. Benchmark testing of an emerging technology is performed to remain abreast of the latest industry developments. The *battery testing* activity includes performance, life and safety testing, and thermal analysis and characterization. It currently includes four projects based at ANL, INL, SNL, and NREL. The testing activity also supports cell analysis, modeling, and prototyping (CAMP) projects at ANL, which include benchmarking and post-test analysis of lithium-ion battery materials at three labs (ANL, ORNL, and SNL). Projects include testing (for performance, life and abuse tolerance) of cells (for contract, laboratory-developed and university-developed cells), and benchmarking systems from industry; thermal analysis, thermal testing, and modeling; cost modeling; and other battery use and life studies. *Cost assessments and requirements analysis* includes an ANL project on developing the performance and cost model BatPaC. This rigorously peer-reviewed model developed at ANL is used to design automotive lithium-ion batteries to meet the specifications for a given vehicle, and estimate its cost of manufacture. An

analysis using BatPaC compared the estimated costs of cells and packs for different electrode chemistries (Figure ES- 1).

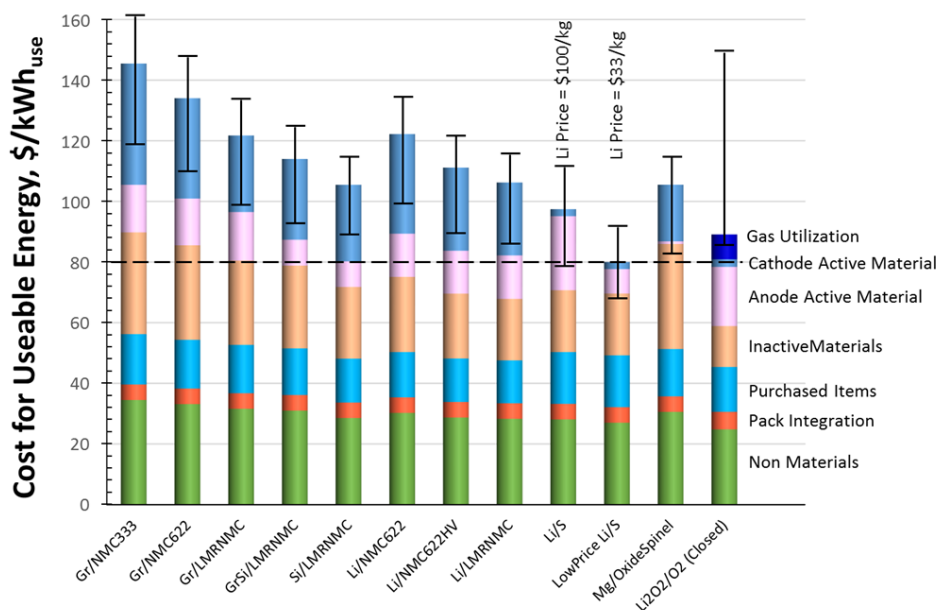


Figure ES- 1. Estimated costs of cells in automotive battery packs with different combination of electrodes. The packs are rated for 100 kWh_{Total} (85 kWh_{Useable}), 300 kW, 315 V, 168 cells, and produced at a plant volume of 100K packs/year

VTO also supports several *small business innovation research* (SBIR) contracts. These SBIR projects focus on development of new battery materials and components and provide a source of new ideas and concepts. The section on SBIR projects includes a short list of recent Phase I and Phase II projects awarded during FY 2019.

Advanced Materials R&D

The *Advanced materials research & development* activity (covered in Chapters VIII to Chapter XX of this report) addresses fundamental issues of materials and electrochemical interactions associated with rechargeable automotive batteries. It develops new/promising materials and makes use of advanced material models to discover them, utilizing scientific diagnostic tools and techniques to gain insight into their failure modes and processes. It is conducted by various national labs, universities, and industry partners. The work is divided into two general areas –“next gen” chemistries (which can, for example, employ an alloy anode and/or a high voltage cathode) and beyond lithium-ion (BLI) chemistries (which can, for example, employ a lithium metal anode). The projects are distributed as follows:

- Next generation (next-gen) lithium-ion battery technologies (42 projects)
 - Advanced anodes (14 projects)
 - Advanced cathodes (six projects)
 - Frontier science at interfaces (six projects)
 - No-cobalt/Low-cobalt cathodes (seven projects)
 - Diagnostics (five projects)
 - Modeling of electrode material (four projects)

- Beyond lithium-ion battery technologies (38 projects)
 - Metallic lithium (five projects)
 - Solid-state batteries (20 projects)
 - Lithium sulfur (five projects)
 - Lithium-air Batteries (three projects)
 - Sodium-ion batteries (four projects)
 - Battery500 Consortium (several keystone projects and seedling projects).

The *next generation lithium-ion battery* R&D area's goal is to advance material performances, designs, and processes to significantly improve performance and reduce the cost of lithium-ion batteries using an alloy or intermetallic anode and/or high voltage cathode. Specific areas of investigation include high-energy anodes (e.g., those containing silicon or tin), high voltage cathodes, high voltage and non-flammable electrolytes, novel processing technologies, high-energy and low-cost electrode designs, and certain other areas. This work spans a range of U.S. DRIVE activities.

- Advanced anodes R&D includes 14 multi-lab collaborative projects – six of them are based in national laboratories (ANL, BNL, NREL, LBNL, SLAC, PNNL), five in industry (Applied Materials, Enovix, Group-14 Technology, Sila Nano, and Solid Power), and three at universities (Stonybrook University, University of Delaware, and University of Maryland).
- Advanced cathodes R&D includes six projects based at three national labs (ANL, LBNL, and PNNL). In addition, there are seven low-cobalt/no-cobalt cathode projects based at two industry partners (Cabot and Nexeris), one national lab (ORNL), and four universities (UCSD, UC Irvine, UTA, and PSU).
- Frontier science at interfaces R&D includes six projects. In one of them, SLAC is developing a molecular-level understanding of cathode-electrolyte interfaces and ANL is working on developing an understanding of the stability of cathode/electrolyte interfaces in high voltage lithium-ion batteries and of fluorinated deep eutectic solvent (FDES)-based electrolytes. In another, LBNL is carrying out interfacial studies of emerging cathode materials.
- Diagnostics R&D includes five projects ranging from interfacial processes to in situ diagnostic techniques and advanced microscopy, thermal diagnostics, and synthesis and characterization. The various researchers for these projects are based at LBNL, BNL, and PNNL.
- Of the four modeling of advanced electrode materials projects, one focuses on novel electrode materials from first principles and another on large-scale ab initio molecular dynamics simulation of liquid and solid electrolytes. Yet another modeling project is concerned with electrode materials design and failure prediction. One modeling project is based at the University of California at Berkeley.

R&D on *beyond lithium-ion battery technologies* includes solid-state technology, lithium metal systems, lithium sulfur, lithium air, and sodium-ion. The main areas of focus include new methods to understand/stabilize lithium metal anodes; lithium polysulfides to enable the use of sulfur cathodes; and developing electrolytes for lithium air and lithium sulfur cells. These systems offer further increases in energy and potentially reduced cost compared to the next-gen lithium-ion batteries. However, they also require additional breakthroughs in materials (often at a fundamental level) before commercial use. VTO is investigating the issues and potential solutions associated with cycling metal anodes. The main research topics include: coatings, novel oxide and sulfide-based glassy electrolytes, and *in situ* diagnostics approaches to characterize and understand Li metal behavior during electrochemical cycling.

- Metallic lithium R&D includes five projects based at four national laboratories (ORNL, LLNL, PNNL, and SLAC).
- Solid state batteries R&D includes 20 projects. These are based at national laboratories (ANL, ORNL), universities (University of California, University of Maryland, College Park, Iowa State University of Science and Technology, University of Michigan, Virginia Polytechnic Institute and State University, Penn State University Park, University of Wisconsin-Milwaukee, University of Houston, Virginia Commonwealth University, and University of Louisville), and industry members (Solid Power, Inc, General Motors LLC, and Wildcat Discovery Technologies).
- Lithium sulfur R&D includes five projects – four of them based at national laboratories (ANL, LBNL, and PNNL) and the one at the University of Wisconsin Milwaukee.
- Additional beyond lithium-ion projects include three on Lithium-Air batteries (one at PNNL and two at ANL) and four on Sodium-ion batteries (based at ANL, BNL, LBNL, and PNNL).

The *Battery500 Innovation Center* is a combined effort by a team of four national labs (PNNL and SLAC) and five universities (University of Texas-Austin, Stanford University, Binghamton University, University of Washington, and University of California, San Diego) with the goal to develop commercially viable lithium battery technologies with a cell level specific energy of 500 Wh/kg while simultaneously achieving 1,000 deep-discharge cycles. The consortium keystone projects focus on innovative electrode and cell designs that enable maximizing the capacity from advanced electrode materials. The consortium works closely with the R&D community, battery/materials manufacturers and end-users/OEMs to ensure that these technologies align well with industry needs and can be transitioned to production.

Recent Highlights

A New Class of Cobalt-free Materials. (ANL)

Due to the wide range of structures and electrochemical properties of manganese (Mn)-oxides, as well as its earth-abundance, Mn has a long history in battery technologies, and new discoveries are showing that Mn may have an important role to play in next-gen cathodes. At Argonne National Laboratory a team of researchers described a novel concept related to lithiated, Mn-spinel oxides as Li-ion cathode materials and demonstrated a high voltage material which delivers a specific energy higher than most NMC811 materials (Figure ES- 2). The spinel framework offers a robust platform to reversibly cycle lithium in and out of its 3D tunneled-structure. However, low capacities (e.g., 130mAh/g for LiMn_2O_4) and/or untenable voltages (e.g., 5V operation in $\text{LiMn}_{1.5}\text{Ni}_{0.5}\text{O}_4$) have hindered the ability of spinel materials to meet practical demands.

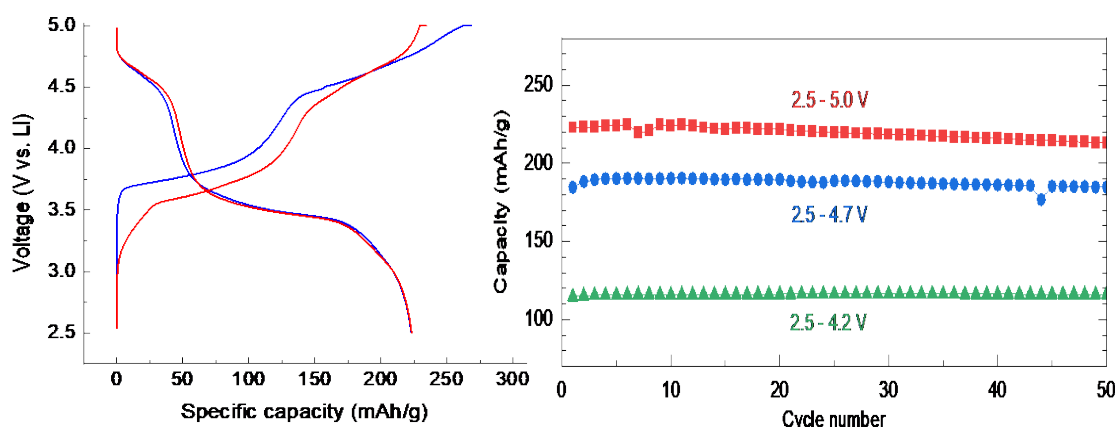


Figure ES- 2. (left) Unique charge/discharge profiles of the novel, lithiated spinel between 5.0-2.5 V. (right) Cycling capacity at three upper cutoff voltages highlighting the stability of the cathode material, electrolyte is 1.2M LiPF_6 EC/EMC 3/7 wt%.

Towards Stable Cycling of Cost-effective DRX Cathodes via Fluorination (LBNL)

Development of new cathode materials with higher performance and lower cost is needed to further enable the commercialization of EVs. Conventional layered oxides are the dominant cathode in commercial lithium-ion batteries for high-energy applications. However, layered cathodes contain a large amount of expensive and scarce transition metals (TM) (i.e., Co, Ni), presenting a challenge to their commercialization. The recently developed Li-excess cation-disordered rock-salts (DRXs) have received significant interest as they are Co/Ni-free and can be made from cost-effective and earth-abundant TMs. The structural flexibility of DRXs substantially lessens the elemental constraints and enables the incorporation of a wide range of TMs as well as fluorine anions (considered enabling for high voltage operation) in the crystal lattice (Figure ES- 3a). Such a large chemical space opens up the opportunities to search for improved and less expensive cathode materials. Researchers at Lawrence Berkeley National Laboratory have synthesized a fluorinated Mn-Ti DRX cathode, $\text{Li}_{1.2}\text{Mn}_{0.6}\text{Ti}_{0.2}\text{O}_{1.8}\text{F}_{0.2}$, via a solid-state reaction. These Mn and Ti TMs present distinct advantages in cost and resource sustainability compared to their counterparts (e.g., Co, Ni) in conventional layered and other DRX analogs (Figure ES- 3b). As shown in Figure ES- 3c, $\text{Li}_{1.2}\text{Mn}_{0.6}\text{Ti}_{0.2}\text{O}_{1.8}\text{F}_{0.2}$ delivers an initial capacity of 233 mAh/g (754 Wh/kg, comparable to NMC 811) when cycled between 4.8 and 1.5 V, using 1M LiPF_6 EC:DMC.

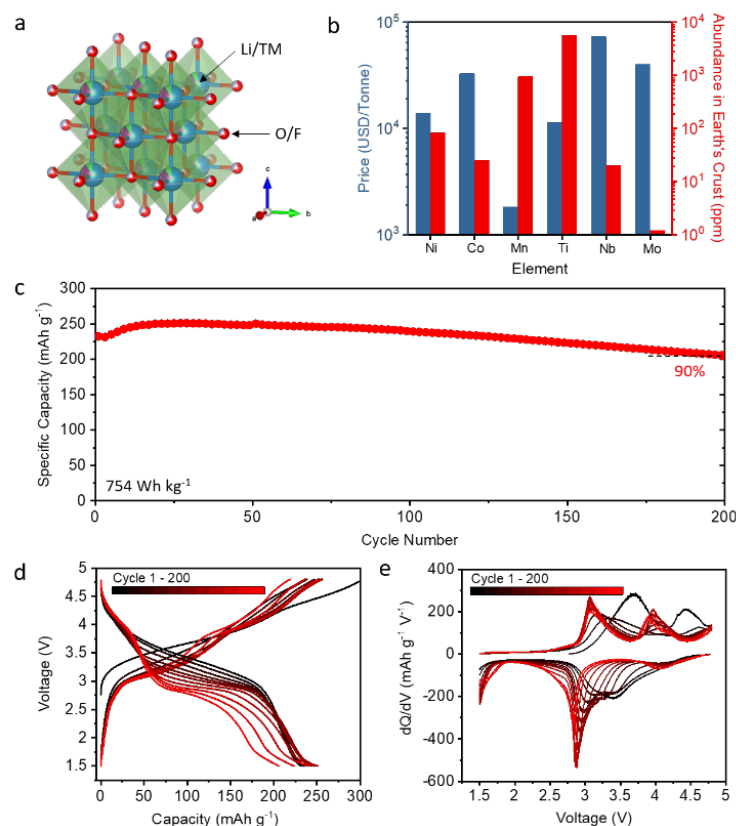


Figure ES- 3. Battery performance of a highly fluorinated DRX, $\text{Li}_{1.2}\text{Mn}_{0.6}\text{Ti}_{0.2}\text{O}_{1.8}\text{F}_{0.2}$. (a) Crystal structure, (b) price and abundance of selected transition metals, (c) specific capacity, (d) voltage profiles, and (e) differential capacity plot. DRX cell is cycled at 16 mA g^{-1} within 4.8 and 1.5 V.

Stable Ni-rich $\text{LiNi}_x\text{Mn}_y\text{Co}_{1-x-y}\text{O}_2$ material synthesized with fast-charge capability (LBNL)

Ni-rich $\text{LiNi}_x\text{Mn}_y\text{Co}_{1-x-y}\text{O}_2$ (NMCs, $x \geq 0.8$) are promising cathode materials for high-energy lithium-ion batteries. Conventional NMCs are polycrystalline (PC) aggregated particles having large number of grains in random orientations. As both Li^+ diffusion and volume expansion/contraction occur anisotropically upon charge/discharge, this causes torturous Li^+ diffusion pathways and nonuniform Li concentration inside the particle, leading to stress and strain and the eventual cracking of the particles. In addition, the newly exposed

surface area from cracking can cause parasitic reactions with the electrolyte. These issues are greatly exacerbated with increasing current density, resulting in rapid capacity fade and impedance rise under fast-charge conditions. Hence, design and development of Ni-rich NMC particles with morphology optimized for the fast-charge application is essential. Previous LBNL studies established fundamental relationships between particle surface properties, particularly surface facets, and cycling stability. This led to the development of single-crystal (SC) NMC cathodes with reduced oxygen release and minimized side reactions under high-voltage operations, enabling excellent performance in high-energy cells. Recently, LBNL prepared Ni-rich NMC single-crystals with morphology and surface orientation optimized for Li transport properties. As an example, studies carried out on $\text{LiNi}_{0.8}\text{Mn}_{0.1}\text{Co}_{0.1}\text{O}_2$ (NMC811) single crystals (referred to as SC811) with $\sim 1\ \mu\text{m}$ size and predominately (104)- surface are shown in Figure ES- 4, along with the comparison with a commercial polycrystalline sample (referred to as PC811).

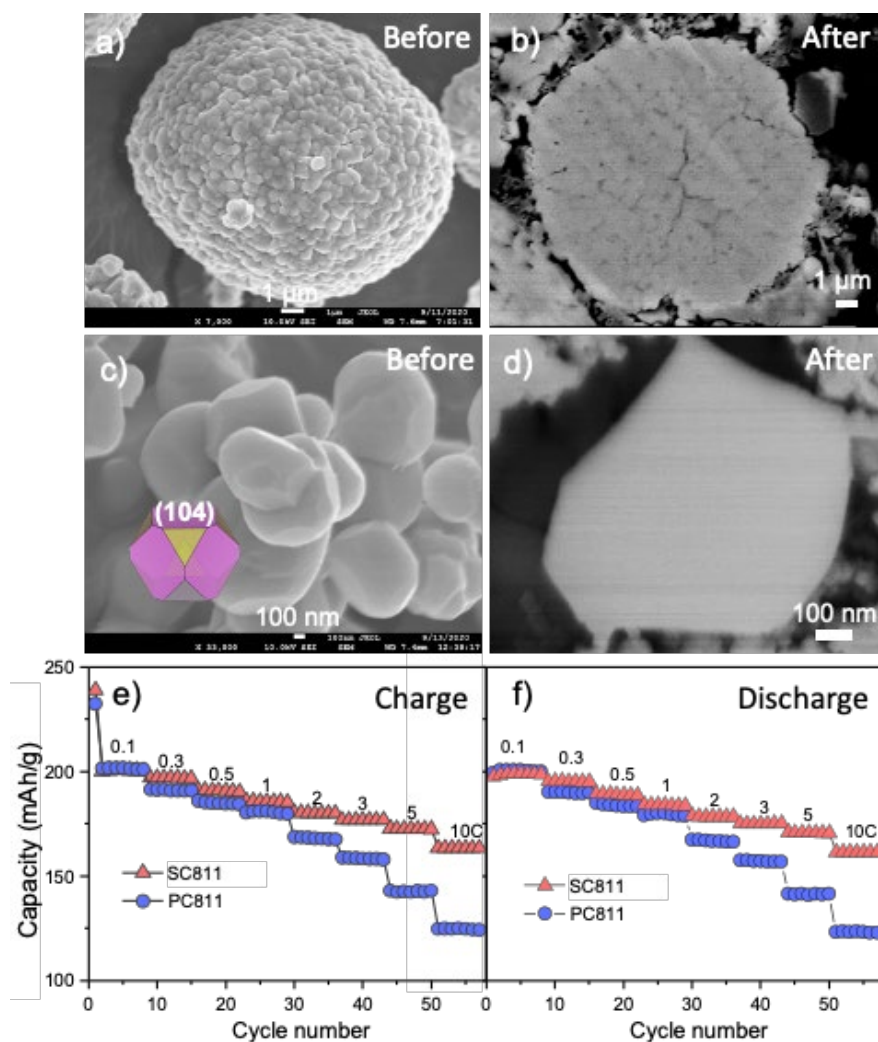


Figure ES- 4. a-d) SEM images of PC (a, b) and SC (c, d) NMC811 before (a, c) and after (b, d) cycling. Enhanced cracking resistance in SC is clearly shown. e-f) Electrochemical testing confirms superior charge and discharge rate capability of SC.

Collaborative Activities

In addition to the above, VTO has in place extensive and comprehensive ongoing coordination efforts in energy storage R&D across all of DOE and with other government agencies. It coordinates efforts on energy storage R&D with both the Office of Science and the Office of Electricity. Coordination and collaboration efforts also include program reviews and technical meetings sponsored by other government agencies and

inviting participation of representatives from other government agencies to contract and program reviews of DOE-sponsored efforts. DOE coordinates such activities with the Army's Advanced Vehicle Power Technology Alliance, the Department of Transportation/National Highway Traffic Safety Administration (DOT/NHTSA), the Environmental Protection Agency (EPA), and the United Nations Working Group on Battery Shipment Requirements. Additional international collaboration occurs through the International Energy Agency's (IEA's) Hybrid Electric Vehicles Technology Collaboration Program (HEV TCP); and bilateral agreements between the U.S. and China.

Organization of this Report

This report covers all the FY 2021 projects as part of the advanced battery R&D (i.e., energy storage R&D) effort in VTO. We are pleased with the progress made during the year and look forward to continued cooperation with our industrial, government, and scientific partners to overcome the remaining challenges to delivering advanced energy storage systems for vehicle applications.



David Howell,
VTO Director (Acting)
Vehicle Technologies Office



Steven Boyd, Program Manager,
B&E Program (Acting)
Vehicle Technologies Office



Tien Q. Duong, Vehicle
Technologies Office



Peter W. Faguy, Vehicle
Technologies Office



Brian Cunningham, Vehicle
Technologies Office



Samm Gillard, Vehicle
Technologies Office



Mallory Clites, Vehicle
Technologies Office



Haiyan Croft, Vehicle
Technologies Office



Simon Thompson, Vehicle
Technologies Office

Table of Contents

Vehicle Technologies Office Overview	1
Annual Progress Report	1
Organization Chart	2
Batteries Program Overview.....	3
Introduction.....	3
Goals	3
State of the Art	4
Battery Technology Barriers	6
Program Organization Matrix	6
Battery Highlights from FY 2021	8
I USABC Battery Development & Materials R&D	19
I.1 Rapid Commercialization of High Energy Anode Materials (NanoGraf Technologies).....	19
I.2 Fast-Charge and Low-Cost Lithium Ion Batteries for Electric Vehicle Applications (Zenlabs Energy)	24
I.3 Low-Cost, High Safety Fast Charge Automotive Cells (Microvast, Inc.).....	32
I.4 High Energy and Power Density Lithium-Ion Battery Based on Neocarbonix™ Polymer Binder-Free Electrode Technology for Electric Vehicle (EV) Applications (Nanoramic).....	37
I.5 Low-cost, Fast-charge Cell Development for EVs (EnPower, Inc.).....	42
I.6 Technology Assessment Program of Aramid Separators for Electric Vehicle Applications (Microvast, Inc.)	46
I.7 Solvent-free Electrode Manufacturing for Low Cost/Fast Charging Batteries (Worcester Polytechnic Institute).....	51
II Processing Science & Engineering	60
II.1 Processing Next Generation Li-ion Battery Cathode Materials (ANL).....	60
II.2 Novel Processing Approaches for LLZO (ANL)	68
II.3 Supercritical Fluid Processing of Battery Cathode Materials (ANL).....	72
II.4 Process R&D and Scale up of Critical Battery Materials (ANL)	78
II.5 Integrated Multiscale Modeling for Design of Robust 3D Solid-State Lithium Batteries (Lawrence Livermore National Laboratory)	85
II.6 Structure-Activity relationships in the optimizing electrode processing streams for LiBs (LBNL)	93

II.7	Fabricate and test solid-state ceramic electrolytes and electrolyte/cathode laminates (LBNL)	99
II.8	Higher Energy Density <i>via</i> Inactive Components and Processing Conditions (LBNL)	104
II.9	Novel data-mining and other AI approaches for synthesis and processing of cathode materials (Lawrence Berkeley National Laboratory)	109
II.10	Minimizing Side-Reactions in Next-Generation Lithium Ion Battery Cathodes Through Structure-Morphology Optimization (ANL)	115
II.11	<i>In Situ</i> Spectroscopies of Processing Next-Generation Cathode Materials (BNL)	125
III	Recycling and Sustainability	133
III.1	Battery and Critical Materials Life Cycle Analysis (ANL)	133
III.2	Lithium-ion Battery Recycling Prize Support (NREL)	138
III.3	Li-ion Battery Recycling R&D Center (ANL)	144
III.4	Development of Advanced Low-Cost/Fast-Charge (LC/FC) Batteries for EV Applications (Farasis Energy)	233
III.5	A Closed Loop Recycling Process for End-of-Life Electric Vehicle Li-ion Batteries-Phase III (Worcester Polytechnic Institute)	237
IV	Extreme Fast Charging (XFC)	244
IV.1	Research on high power, doped titanium-niobium oxide anodes (ORNL)	244
IV.2	Enabling Extreme Fast Charging through Control of Li Deposition Overpotential on Graphite Electrodes (Stony Brook University)	249
IV.3	Detecting Lithium Plating during Fast Charging, and Heterogeneity Effects during Fast Charging (LBNL)	256
IV.4	Novel Electrolyte Development with High Lithium-Ion Transference Number (Hi-LiT) for Extreme Fast Charging (ORNL)	265
IV.5	XCEL R&D: Lithium Detection Thrust	270
IV.6	XCEL: Local Heterogeneity Workgroup	284
IV.7	XCEL R&D: Charge Protocols and Life Assessment for Extreme Fast Charging Thrust	292
IV.8	XCEL R&D: Anode & Electrolyte Thrust	299
IV.9	The Effects of Extreme Fast Charging on Lithium-ion Battery Cathode (Idaho National Laboratory, National Renewable Energy Laboratory, Argonne National Laboratory, Lawrence Berkeley National Laboratory, and SLAC National Accelerator Laboratory)	314
IV.10	XCEL R&D: Heat Generation Thrust	329
IV.11	Highly-Ordered Hierarchical Anodes for Extreme Fast Charging Batteries (University of Michigan, Ann Arbor)	339
V	Beyond Batteries	345

V.1	Behind-the-Meter Storage (NREL, INL, ANL, SNL).....	345
VI	Testing, Analysis, High-Performance Computing, Lab-I4.....	372
VI.1	BatPaC Model Development (Argonne National Laboratory).....	372
VI.2	Battery Performance and Life Testing (Argonne National Laboratory).....	379
VI.3	Battery Safety Testing (Sandia National Laboratories).....	382
VI.4	Battery Thermal Analysis and Characterization Activities (NREL)	387
VI.5	Cell Analysis, Modeling, and Prototyping (CAMP) Facility Research Activities (ANL).....	392
VI.6	Materials Benchmarking Activities for CAMP Facility	403
VI.7	Electrochemical Performance Testing (INL).....	411
VI.8	Machine Learning for Accelerated Life Prediction and Cell Design.....	415
VII	Small Business Innovation Research (SBIR).....	424
VIII	Next Generation Lithium-Ion Materials: Advanced Anodes R&D.....	427
VIII.1	Silicon Consortium Project (Multiple Labs).....	427
VIII.2	Si-Based Li Ion Batteries with Long Cycle Life and Calendar Life (Pacific Northwest National Laboratory)	446
VIII.3	Silicon Anode Seedling Project (ANL)	453
VIII.4	Seedling Project: Two-Dimensional Silicon Nanostructures for Improved Silicon Anode Cycling Stability.....	458
VIII.5	Pre-Lithiation of Silicon Anode for High Energy Li Ion Batteries (Stanford University)	463
VIII.6	Integrated Modeling and Machine Learning of Solid-Electrolyte Interface Reactions of the Si Anode (LBNL)	469
VIII.7	Advanced Anode Manufacturing through Ultra-Thin Li Deposition (Applied Materials, Inc.)	480
VIII.8	Structurally and Electrochemically Stabilized Si-rich Anodes for EV Applications (Enovix Corporation)	486
VIII.9	Rationally Designed Lithium-Ion Batteries Towards Displacing Internal Combustion Engines	494
VIII.10	Ultra-Low Volume Change Silicon-Dominant Nanocomposite Anodes for Long Calendar Life and Cycle Life.....	500
VIII.11	Solid State Li Ion Batteries Using Si Composite Anodes	503
VIII.12	Fully Fluorinated Local High Concentration Electrolytes Enabling High Energy Density Si Anodes.....	505

VIII.13	Devising mechanically compliant and chemically stable synthetic solid-electrolyte interphases on silicon using ex situ electropolymerization for long cycling Si anodes (University of Delaware)	510
VIII.14	Rational Electrolyte Design for Li-ion Batteries with Micro-sized Si Anodes (University of Maryland College Park).....	515
IX	Next-Gen Lithium-Ion: Advanced Cathodes R&D.....	521
IX.1	Design, Synthesis, & Characterization of Low-Cobalt Cathodes (ANL, ORNL, LBNL, NREL, PNNL).....	521
IX.2	Diagnostic Testing and Evaluation (ANL, ORNL, NREL, PNNL)	529
IX.3	Theory and Modeling (ANL, LBNL, PNNL, NREL, ORNL).....	549
IX.4	Design and Synthesis of High Energy, Manganese Rich Oxides for Lithium-Ion Batteries (ANL)	559
IX.5	Disordered RockSalt Structured Cathode Materials: Electrochemistry and Synthesis (LBNL, ORNL, PNNL, UC Santa Barbara).....	568
IX.6	Disordered RockSalt Structured Cathode Materials: Characterization and Modeling (LBNL, ORNL, PNNL, UC Santa Barbara).....	576
X	Next-Gen Lithium-Ion: Frontier Science at Interfaces	583
X.1	Molecular-level Understanding of Cathode-Electrolyte Interfaces (SLAC National Accelerator Laboratory, NREL).....	583
X.2	Stability of cathode/electrolyte interfaces in high voltage Li-ion batteries (ANL)	592
X.3	Interfacial Studies of Emerging Cathode Materials.....	598
X.4	Understanding and Modification of High-Energy Cathodes and their Interfaces with Electrolytes for Next-Generation Li-Ion Batteries (Pacific Northwest National Laboratory)	604
X.5	Fluorinated Deep Eutectic Solvent (FDES)-Based Electrolytes (ANL).....	609
X.6	Developing In situ Microscopies for the Model Cathode / Electrolyte Interface (NREL)	617
XI	Next-Gen Lithium-Ion: Low-Cobalt/No Cobalt Cathodes.....	623
XI.1	Aerosol Manufacturing Technology to Produce Low-Cobalt Li-ion Battery Cathodes (Cabot Corporation)	623
XI.2	Co Free Cathode Materials and Their Novel Architectures (UCSD)	629
XI.3	Novel Lithium Iron and Aluminum Nickelate (NFA) as Cobalt-Free Cathode Materials (ORNL).....	642
XI.4	Enhancing Oxygen Stability in Low-Cobalt Layered Oxide Cathode Materials by Three-Dimensional Targeted Doping (UC Irvine).....	649
XI.5	High-Nickel Cathode Materials for High-Energy, Long-Life, Low-Cost Lithium-Ion Batteries (University of Texas at Austin)	662

XI.6	Cobalt-Free Cathodes for Next Generation Li-Ion Batteries (Nexceris)	670
XI.7	High-Performance Low-Cobalt Cathode Materials for Li-ion Batteries	676
XII	Next-Gen Lithium-Ion: Diagnostics	688
XII.1	Interfacial Processes (LBNL)	688
XII.2	Advanced in situ Diagnostic Techniques for Battery Materials (BNL).....	694
XII.3	Microscopy Investigation on the Fading Mechanism of Electrode Materials (PNNL)	702
XII.4	<i>In-Operando</i> Thermal Diagnostics of Electrochemical Cells (LBNL).....	708
XII.5	High Conductivity, Low Temperature Polymer Electrolytes for Li-Ion Batteries (LBNL) ..	713
XIII	Next-Gen Lithium-Ion: Modeling Advanced Materials	719
XIII.1	Electrode Materials Design and Failure Prediction (Argonne National Laboratory)	719
XIII.2	Characterization and Modeling of Li-Metal Batteries: Model-system Synthesis and Advanced Characterization (LBNL).....	728
XIII.3	Design of High-Energy, High-Voltage Lithium Batteries through First-Principles Modeling (LBNL).....	735
XIII.4	Characterization and modeling of Li-metal batteries: modeling and design of amorphous solid-state Li conductors (LBNL).....	741
XIV	Next-Gen Li-ion: Low Temperature Electrolytes	747
XIV.1	Ethylene Carbonate-Lean Electrolytes for Low Temperature, Safe Li-ion batteries (LBNL) 747	
XIV.2	Fluorinated Solvent-Based Electrolytes for Low Temperature Li-ion Battery (ANL).....	754
XIV.3	Synthesis, screening and characterization of novel low temperature electrolyte for lithium-ion batteries (BNL).....	761
XV	Beyond Li-ion R&D: Metallic Lithium	767
XV.1	Composite Electrolytes to Stabilize Metallic Lithium Anodes (ORNL) (Performing Organization).....	767
XV.2	Lithium Dendrite Prevention for Lithium Batteries (Pacific Northwest National Laboratory)	774
XV.3	Integrated Multiscale Modeling for Design of Robust 3D Solid-State Lithium Batteries (Lawrence Livermore National Laboratory)	780
XV.4	3D Printing of All-Solid-State Lithium Batteries (LLNL)	788
XV.5	Advanced Polymer Materials for Li-ion (SLAC).....	795
XVI	Beyond Li-ion R&D: Solid-State Batteries.....	802
XVI.1	Improving the Stability of Lithium-Metal Anodes and Inorganic-Organic Solid Electrolytes 802	

XVI.2	Lithium Thiophosphate Based Solid Electrolytes and Cathode Interfaces.....	813
XVI.3	Advancing Solid-Solid Interfaces in Li-ion Batteries (Argonne National Laboratory).....	820
XVI.4	Lithium Dendrite-Free Solid Electrolytes for High Energy Lithium Batteries (University of Maryland, College Park).....	827
XVI.5	All Solid-State Batteries Enabled by Multifunctional Electrolyte Materials.....	834
XVI.6	Development of Thin, Robust, Lithium-Impenetrable, High-Conductivity, Electrochemically Stable, Scalable, and Low-Cost Glassy Solid Electrolytes for Solid State Lithium Batteries (Iowa State University of Science and Technology)	836
XVI.7	Physical and Mechano-Electrochemical Phenomena of Thin Film Lithium-Ceramic Electrolyte Constructs (University of Michigan).....	841
XVI.8	Low Impedance Cathode/Electrolyte Interfaces for High Energy Density Solid-State Batteries (University of Maryland, College Park)	846
XVI.9	Molecular Ionic Composites: A New Class of Polymer Electrolytes to Enable All Solid-State and High Voltage Lithium Batteries (Virginia Polytechnic Institute and State University)..	854
XVI.10	Hot Pressing of Reinforced All-solid-state Batteries with Sulfide Glass Electrolyte (General Motors LLC).....	863
XVI.11	Developing Materials for High-Energy-Density Solid State Lithium-Sulfur Batteries (Penn State University, University Park).....	870
XVI.12	Developing an <i>In-situ</i> Formed Dynamic Protection Layer to Mitigate Lithium Interface Shifting: Preventing Dendrite Formation on Metallic Lithium Surface to Facilitate Long Cycle Life of Lithium Solid State Batteries (University of Wisconsin-Milwaukee).....	878
XVI.13	Composite Solid Ion Conductor with Engineered Lithium Interface (Wildcat Discovery Technologies)	884
XVI.14	Fundamental Understanding of Interfacial Phenomena in Solid-State Batteries (General Motors LLC).....	896
XVI.15	Multidimensional Diagnostics of the Interface Evolutions in Solid-State Lithium Batteries (University of Houston).....	903
XVI.16	First-Principles Modeling of Cluster-Based Solid Electrolytes (Virginia Commonwealth University).....	911
XVI.17	Predictive Engineering of Interfaces and Cathodes for High-Performance All Solid-State Lithium-Sulfur Batteries (University of Louisville).....	918
XVI.18	R Design of Strain Free Cathode – Solid State Electrolyte Interfaces Using Chemistry-Informed Deep Learning (ANL).....	927
XVI.19	Enabling continuous production of defect-free, ultrathin sulfide glass electrolytes for next generation solid state lithium metal batteries (Argonne National Laboratory)	933
XVI.20	Scaling-Up and Roll-to-Roll Processing of Highly Conductive Sulfide Solid-State Electrolytes	937

XVII	Beyond Li-Ion R&D: Lithium Sulfur Batteries	943
XVII.1	A Novel Chemistry: Lithium-Selenium and Selenium-Sulfur Couple (ANL)	943
XVII.2	Development of High Energy Lithium-Sulfur Batteries (PNNL).....	952
XVII.3	Nanostructured Design of Sulfur Cathodes for High Energy Lithium-Sulfur Batteries (Stanford University).....	959
XVII.4	Mechanistic Investigation for the Rechargeable Li-Sulfur Batteries.....	964
XVII.5	New electrolyte binder for Lithium sulfur battery (Lawrence Berkeley National Laboratory) 970	
XVIII	Beyond Li-ion R&D: Lithium-Air Batteries	977
XVIII.1	Rechargeable Lithium-Air Batteries (Pacific Northwest National Laboratory)	977
XVIII.2	Lithium-Air Batteries (ANL).....	984
XVIII.3	Lithium Oxygen Battery Design and Predictions (ANL)	990
XIX	Beyond Li-ion R&D: Sodium-Ion Batteries	996
XIX.1	An Exploratory Studies of Novel Sodium-Ion Battery Systems (BNL).....	996
XIX.2	Development of Advanced High-energy and Long-life Sodium-ion Battery (ANL).....	1003
XIX.3	High Capacity, Low Voltage Titanate Anodes for Sodium-Ion Batteries (LBNL).....	1013
XIX.4	Electrolytes and Interfaces for Stable High-Energy Sodium-ion Batteries (PNNL)	1019
XX	Beyond Li-ion R&D: Battery500.....	1026
XX.1	Battery500 Innovation Center (PNNL)	1026

List of Figures

Figure ES- 1. Estimated costs of cells in automotive battery packs with different combination of electrodes. The packs are rated for 100 kWh _{Total} (85 kWh _{Useable}), 300 kW, 315 V, 168 cells, and produced at a plant volume of 100K packs/year	xviii
Figure ES- 2. (left) Unique charge/discharge profiles of the novel, lithiated spinel between 5.0-2.5 V. (right) Cycling capacity at three upper cutoff voltages highlighting the stability of the cathode material, electrolyte is 1.2M LiPF ₆ EC/EMC 3/7 wt%.	xx
Figure ES- 3. Battery performance of a highly fluorinated DRX, Li _{1.2} Mn _{0.6} Ti _{0.2} O _{1.8} F _{0.2} . (a) Crystal structure, (b) price and abundance of selected transition metals, (c) specific capacity, (d) voltage profiles, and (e) differential capacity plot. DRX cell is cycled at 16 mA g ⁻¹ within 4.8 and 1.5 V.	xxi
Figure ES- 4. a-d) SEM images of PC (a, b) and SC (c, d) NMC811 before (a, c) and after (b, d) cycling. Enhanced cracking resistance in SC is clearly shown. e-f) Electrochemical testing confirms superior charge and discharge rate capability of SC.	xxii
Figure 1. Chemistry classes, status, and R&D needs	5
Figure 2. Potential for Future Battery Technology Cost Reductions	5
Figure 3. Battery R&D Program Structure	7
Figure 4. (left) Unique charge/discharge profiles of the novel, lithiated spinel between 5.0-2.5 V. (right) Cycling capacity at three upper cutoff voltages highlighting the stability of the cathode material, electrolyte is 1.2M LiPF ₆ EC/EMC 3/7 wt%.	9
Figure 5. Battery performance of a highly fluorinated DRX, Li _{1.2} Mn _{0.6} Ti _{0.2} O _{1.8} F _{0.2} . (a) Crystal structure, (b) price and abundance of selected transition metals, (c) specific capacity, (d) voltage profiles, and (e) differential capacity plot. DRX cell is cycled at 16 mA g ⁻¹ within 4.8 and 1.5 V.	10
Figure 6. a-d) SEM images of PC (a, b) and SC (c, d) NMC811 before (a, c) and after (b, d) cycling. Enhanced cracking resistance in SC is clearly shown. e-f) Electrochemical testing confirms superior charge and discharge rate capability of SC.	11
Figure 7. Comparison of Gen2 (a) versus B26 (b) electrolytes in cells with NMC 532 cathodes and graphitic anodes (ANL CAMP Pouch cells).	12
Figure 8. 350 Wh/kg pouch cells achieve more than 600 cycles in research from the Battery500 Consortium. (a) Illustration of wet and dry SEI layers in lithium metal anode. (b)-(d) Cycling performances of 350 Wh/kg lithium metal pouch cells using 100, 50 and 20 μm lithium foils as the anodes, respectively. Cathode: LiNi _{0.6} Mn _{0.2} Co _{0.2} O ₂ ; Electrolyte: 1.54 M lithium bis(fluorosulfonyl)imide (LiFSI) in 1,2-dimethoxyethane (DME) and 1,1,2,2-tetrafluoroethyl-2,2,3,3-tetrafluoropropyl ether (TTE).	13
Figure 9. Flowchart of the aqueous sequential separation process to recover cathode films, anode films, copper, and aluminum foils.	14
Figure 10. a. Illustration of the dynamic polarization of i-Li under the electric field. b. Modified charging protocol for Li-metal battery. Specific capacity of c. lithium-metal batteries and d. lithium-ion batteries with/without activation steps.	15
Figure 11. Example of different EC signatures that can be fed	16
Figure 12. (a) Decay of cell energy during cycling. After every 25 cycles, cell was tested at a very slow rate (C/25) producing spikes of higher capacity. For this cell cycled to failure, maps of (b) the local state of charge and (c) the relative abundance of the NMC cathode were collected, allowing three hot spots (1 – 3) with poor performance to be identified.	17
Figure 13. Fast-charge results of prototype single-layer pouch cells (symbols) compared with model predictions (lines).	18

Figure I.1.1 Si anode failure mechanisms (left), NanoGraf graphene-silicon anode architecture (right).....	20
Figure I.1.2 Half-cell electrochemical results for various modified sol-gel reaction conditions.	21
Figure I.1.3 Half-cell electrochemical cycling results for samples A-SG-5 through A-SG-9 with different Li-barrier coating levels.....	21
Figure I.1.4 Half-cell electrochemical cycling results for (Left) samples A-SG-5 and (Right) A-SG-7 with different Li-barrier coating levels.	22
Figure I.1.5 Half-cell coin cell data of SiO _x anode with SiA1 and LiPAA at reduced binder contents of 20%, 15%, and 10%.	22
Figure I.2.1 Projected cell performance progression throughout the program & measured CB#1 & CB#2 values	26
Figure I.2.2 (a) DST Cycling at 0% Fast Charge (FC) vs 100% FC, (b) Calendar life testing at 30, 40, and 50°C	27
Figure I.2.3 The 1C/1C cycling study on cathodes 15, 17, and 18 with two different electrolytes (E4 and E39) on 12 Ah pouch cells	28
Figure I.2.4 The 1C/1C cycling study on cathodes C18 and C19 on 12 Ah pouch cells with E39 electrolyte... ..	28
Figure I.2.5 The 1C/1C cycling of C18 and C19 at 45°C on 12 Ah pouch cell with E39 electrolyte.....	29
Figure I.2.6 1C/1C cycling data of E4, E50 and E51 on coin cells with Cathode 15	30
Figure I.2.7 Gap analysis of CB#1, #2, #3 versus the program targets.....	31
Figure I.3.1 (left) Relative cost of cathode metals, (center) metal fraction of Ni, Mn and Co in cathode compositions, (right) relative cost of metals for various cathode compositions.	33
Figure I.3.2 SEM of project low cobalt FCG particles from kilogram scale batch.....	34
Figure I.3.3 Full cell testing of FCG cathode from 2.7-4.25V, 25°C at 1CCCV/1CD with a C/3 reference cycle	34
Figure I.3.4 (left) Storage test of electrolyte additive from 400g and 1kg batch sizes. (right) Cycling result for additive in electrolyte for 2.6Ah cell cycled from 3–4.25V under 1CCCV/1CD conditions	34
Figure I.3.5 Cycle plot of baseline 38.5 Ah LCFC cell; 3–4.25V, 1CCCV/1CD cycling at room temperature.	35
Figure I.3.6 Capacity and energy density of 38.5 Ah cell fast charged (FC) 0%, 25% and 100% of cycles.....	35
Figure I.4.1 Nanoramic USABC TAP project internal test summary.....	40
Figure I.5.1 Six different iterations of multilayer anode designs from left to right, showing electrode cross sections, porosity profiles (from image analysis), and tortuosity studies from symmetric pouch cell studies ...	43
Figure I.5.2 Between the best- and worst-performing multilayer anode designs, EnPower has demonstrated (a) 10% reduction in DCIR from HPPC tests, (b) 4.6-minute reduction to fastest charge time, and (c) >200 cycle difference in cycles to EOL under aggressive fast-charge cycling.....	44
Figure I.5.3 Between the best- and worst-performing multilayer anode designs, EnPower has demonstrated (a) 10% reduction in DCIR from HPPC tests, (b) 4.6-minute reduction to fastest charge time, and (c) >200 cycle difference in cycles to EOL under aggressive fast-charge cycling.....	44
Figure I.6.1 Dynamic stress test cycle results for aramid separator and ceramic coated PE cells	50
Figure I.6.2 Cycling retention of Li-ion battery module using Aramid separator versus ceramic coated PE.....	50
Figure I.7.1 (a) Experiment measurement (solid lines) vs fitted model prediction (dashed lines) of the charging performance of NMC/graphite cells. (b) Experiment measurement (solid lines) vs fitted model prediction (dashed lines) of the charging voltage curves of dry-printed cells (DC-DA-DL-35%) at different C rates	53

Figure I.7.2 Calculated 3C (a) and 4C (b) charging capacity of different 2-layer electrode configurations with active material loadings of 30 mg/cm ² (NMC) and 15 mg/cm ² (graphite)	53
Figure I.7.3 (a) CC vs CCCV charging capacity of thick NMC cells consisting of different types of electrodes. (b) Final SOC after 4C CC vs CCCV charging as a function of the anode layer porosity near current collector (CC) in NMC cells with uniform cathode and 2-layer graphite anode	54
Figure I.7.4 Two porosity anode and single porosity pouch cell cathode.....	54
Figure I.7.5 (a) 2-sided coated 10 cm x 10 cm cathode sample from batch process (b) observed bending after final rolling to ~40% porosity	55
Figure I.7.6 (a) PVDF coated foil roll (b) cathode materials coated foil roll with target loading collected at the winder after final rolling	56
Figure I.7.7 Microstructure schematics of (a) slurry-cast electrode, (b) dry-printed electrode. Microstructure SEM images of (c) slurry-cast electrode, (d) dry-printed electrode.....	56
Figure I.7.8 Tortuosity of dry-printed and slurry-casted cathode/anode.....	57
Figure I.7.9 Rate comparison of single layer pouch cells made using differing combinations of dry or wet coated electrodes. Single layer pouch cells were tested from 2.7-4.3V with CCCV (CV=15-min)/0.33CD	57
Figure I.7.10 Retention of the single layer pouch cells made using dry or wet electrodes	58
Figure II.1.1 Reproduced Ni(OH) ₂ in 10L TVR displays spherical and dense morphology (left). Top right row SEMs show the morphologies of LNO particles calcined at different temperatures under pure O ₂ atm and bottom row shows the LNO calcined at 665°C under varying O ₂ percentages.	62
Figure II.1.2 Comparison of CSTR vs TVR processing and different calcination furnace applications	64
Figure II.1.3 SEM morphology (left), voltage profiles (middle) and rate tests (right) of LiNi _{0.95} Co _{0.025} Mn _{0.025} O ₂ materials calcined at different temperatures. Electrochemical tests (BAT476) are specific to Deep-Dive program (Half cells, two cells average)	65
Figure II.1.4 Preliminary synthesis results for the Al-doped Li/Mn-rich hydroxide precursor and its cathode. EDS color mapping shows effective Al-incorporation to the structure during co-precipitation process. SEM shows the similar secondary particle morphologies with increasing primary particle sizes as the calcination temperature increases. Electrochemical tests (BAT476) are specific to Deep-Dive program.	65
Figure II.1.5 (a) Morphologies of the Mn-rich NMC hydroxide precursor without Al-doping (left) and its cathode (tube furnace, under O ₂ atm by Dr. Anh Vu) (middle and right). (b) Bulk (left) and cross-sectional (middle and right) morphologies of pretreated hydroxide precursors showing dense interior with ranging levels of particle cracking particularly for the larger particles.....	66
Figure II.2.1 Phase distribution in the immediate product of FSP of NCM811	69
Figure II.2.2 Examples of Slurry Flame Spray Pyrolysis (a) SFSP of P25 titania in acetonitrile/xylene and (b) SFSP of ethanolic nano-milled NCM111	70
Figure II.2.3 Morphology of co-sintered Al-LLZO green powder + NC523	70
Figure II.2.4 Structure and morphology of Spray Pyrolysis produced Lithium Lanthanum Bismuth Zirconium oxide.	71
Figure II.3.1 Particle morphology of polycrystalline NMC96-2-2 and single-crystal NMC96-2-2	73
Figure II.3.2 Synthesized hydrothermal single-crystal precursor with particle size control.....	74
Figure II.3.3 XRD and Coin half-cell evaluation of polycrystalline NMC96-2-2 and single-crystal NMC96-2-2	74
Figure II.3.4 Cross-sectional SEM and FIB SEM of NMC96-2-2 cathode	75

Figure II.3.5 Nanoindentation analysis of single-crystal NMC96-2-2 cathode particle	75
Figure II.3.6 FIB cross-section and elemental mapping of 1wt% Zr/Al-doped NMC96-2-2	76
Figure II.3.7 XPS analysis results of 1wt% Zr/Al-doped NMC96-2-2.....	76
Figure II.3.8 XRD and Coin half-cell evaluation of 1wt% Zr/Al-doped NMC96-2-2	77
Figure II.4.1 Synthesis of Me-FSI	79
Figure II.4.2 Cycling data for Me-FSI cells.....	80
Figure II.4.3 Screening experiments for Me-FSI Synthesis.....	80
Figure II.4.4 Reaction of methyl chloroformate and tetrafluoropropanol.....	80
Figure II.4.5 Calorimetry for the synthesis of MeOC(O)(OCH ₂ CF ₂ CF ₂ H.....	80
Figure II.4.6 Capacity data for Li-DCTA	81
Figure II.4.7 Efficiency data for Li-DCTA.....	81
Figure II.4.8 Chemical structures in the formation of Li-TCl	81
Figure II.4.9 ¹ H NMR and Expanded FTIR spectra showing reaction of 2-amino-4,5-dicyanoimidazole with tert-butyl nitrite.	82
Figure II.4.10 Flow chemistry equipment and expanded view of coil reactor for Li-TCl.....	82
Figure II.4.11 Semi-Batch flow apparatus with expanded view of flow coil.	83
Figure II.4.12 Attempted batch synthesis of TCl.....	83
Figure II.5.1 Histogram of calculated activation energies (in eV) for different Li ⁺ diffusion pathways across the LLZO/LCO interface. Forward and backward diffusion refer to Li ⁺ migration from LLZO to LCO, and from LCO to LLZO, respectively.	87
Figure II.5.2. (a-b) Analysis of MLFF accuracy during a dynamical simulation of disordered LLZO at 3000 K, showing the ability to replicate (a) energies and (b) forces derived from density functional theory (DFT). (c) Li ⁺ diffusivities predicted by MLMD (orange) and AIMD (blue) for amorphous LLZO. (d) Isosurface of Li ⁺ probability density (blue) obtained from MLMD in a LLZO Σ 5(210)/[001] coherent grain boundary model at 2000 K. Magenta and green atoms are Zr and La, respectively, and O atoms are not shown for simplicity.	88
Figure II.5.3. (a) Digital representation of polycrystalline LLZO microstructure; (b) computed von Mises stress profile; (c-d) Li composition profile (c) with and (d) without mechanical stress.	89
Figure II.5.4. (a) 3D porous LLZO microstructure and cross section of LLZO/polymer composite microstructure; (b) computed von Mises stress (top: spatial distribution; bottom: statistics) in the composite microstructure under applied loading; and (c) computed effective elastic modulus of the composite microstructure.	90
Figure II.5.5. Predictions of (a,d) Li ⁺ concentration profile, (b,e) electrical potential profile, and (c,f) EIS for a model 2D LLZO polycrystal, demonstrating the effect of grain boundary Li ⁺ conductivity. Data in (a-c) correspond to the case for which Li ⁺ mobility at the grain boundaries is double that in (d-f).....	91
Figure II.6.1 (Vapor extraction system, K. Higa/LBNL).....	94
Figure II.6.2 (Particle size distribution for Denka black [carbon black] in NMP, Z. Huang and B. Zhang/LBNL)	95
Figure II.6.3 (Particle size distribution for graphite in NMP, Z. Huang and B. Zhang/LBNL).....	95
Figure II.6.4 (Particle size distribution for PVDF in NMP, Z. Huang and B. Zhang/LBNL)	95
Figure II.6.5 (Particle size distribution for component mixtures in NMP, Z. Huang and B. Zhang/LBNL).....	96

Figure II.6.6 (Confocal microscope image of surface of wet battery electrode coating, B. Zhang and K. Higa/LBNL).....	97
Figure II.7.1 Performance of solid state cells with NMC111 cathode including (a) cell impedance, (b) a magnified view of the contribution from the LLZO pellet, (d) cycling performance of the cells and (d) the voltage profiles of a cell with 38 wt% catholyte.....	100
Figure II.7.2 Performance of an LLZO/liquid hybrid cell with NMC111 cathode including (a) cell impedance, (b) cycling performance of the cell at three rates, and (d) the voltage profiles of the cell during several cycles.	101
Figure II.7.3 Performance of a hybrid cell with organic cathode A including (a) cycling performance of the cell at several rates and (b) the voltage profiles of the cell during several cycles.	102
Figure II.7.4 Performance of liquid cells with organic cathode A including (a) cycling performance of the cells at two rates and (b) the voltage profiles of cell 2 during several cycles.	102
Figure II.7.5 LLZO bilayer structure made with porous HSC sheet sintered at 1100°C for 5h. The HSC sheet contained 80 vol% of 63 μm PMMA spheres.....	103
Figure II.8.1 Cycling performance of four electrodes made from the same processing conditions but different fractions of active material to inactive material. The numbers in the legend refer to the wt fraction of active material. 120 C refers to the drying temperature.	105
Figure II.8.2 SEM images of different mixtures of active material (AM), carbon additive (C), and polymer binder (B). Blue highlights are areas of carbon black.....	106
Figure II.8.3 SEMS of the surface of electrodes produced under three different mixing orders. Left, Binder plus carbon black first, then added the active material; center, active material and binder mixed, then added the carbon black; right, carbon black and active materials mixed first, then added polymer.	106
Figure II.8.4 Confocal microscope image of a dried film. Left, just active material and binder mixed; right, active material and carbon mixed then binder added.....	107
Figure II.8.5 Electrodes made with the same amount of inactives but dried at different temperatures. Left, the adhesion and cohesion data measured from peel tests; right, cycling data.	107
Figure II.8.6 Cycling data of two electrodes made with different amounts of solvent. Extra solvent leads to low viscosity (LV) and less solvent leads to a high viscosity slurry (HV).	108
Figure II.9.1 Number of synthesis reactions automatically extracted from all US patents for each element. ..	111
Figure II.9.2 Number of patents for the synthesis of NCM (left) and LiFePO_4 (right) materials in different synthesis types.	112
Figure II.9.3 Earliest years of patents on the synthesis of NCM materials projected in LiNiO_2 - LiCoO_2 - LiMnO_2 phase diagram.	113
Figure II.9.4 Highest synthesis temperatures for LiFePO_4 extracted from patents in different years.....	113
Figure II.10.1 Elucidation of transition metal carbonate precipitation reaction mechanism from the relative amounts of precipitated transition metals in NMC-carbonates. (a) SEM image of the precipitated NMC-carbonates, while maintaining ammonia over transition metal ratio of 40:1. (b) – (d) Distribution of the Mn, Co, and Ni within the precipitate. Uniform distribution of the transition metals indicates similar composition of Mn, Co, and Ni within all the particles. (e) Mass and atomic percentage of Mn, Co, and Ni within the precipitate. It is evident that maximum amount of Mn is deposited, then Co, and very few Ni gets precipitated. It is possible to form transition metal carbonates in two possible ways: i) Precipitation due to reaction between carbonate anions and transition metal ammonia complex, and ii) Direct precipitation due to reaction between metal cations and carbonate anions. (f) Computationally predicted relative amount of free transition metals floating within the solution is plotted with respect to ammonia over transition metal ratio. The experimentally observed relative amount of Mn, Co, and Ni ions within the NMC-carbonate precipitates are demonstrated by	

the symbols. Extremely good correlation between the computational prediction and experimental observation indicates that precipitation of transition metal carbonates occurs due to reaction between the free transition metal cations and carbonate anions. In the present calculations, even though equal amount of Mn, Co and Ni salts were used, very different amount of the three transition metals were precipitated. To obtain equal amount of Mn, Co, and Ni, it is suggested to operate at ammonia over transition metal ratio around 1.0, which is highlighted by the green circle..... 117

Figure II.10.2 Deciphering the primary particle morphology and growth rate of (NMC)CO₃. (a-d) TEM image of the precipitated NMC-carbonate cathode precursors. It is evident that the primary particle size ranges between 5 – 10 nm. These individual primary particles combine with others and form primary aggregates, which are approximately 150 nm long and 30 – 50 nm wide. The X-ray diffraction pattern shown in the inset of (d) indicates a pseudo single crystal nature of these primary aggregates. Usually, growth of surface particles on top of existing ones leads to the formation of pseudo single crystals. Accordingly, we conclude that the primary aggregates are formed by the surface growth mechanism, whereas agglomeration of these primary aggregates leads to the formation of the micron sized secondary particles (as shown in (b)). (e-f) Computationally simulated growth of the NMC-carbonate cathode precursors through the surface growth mechanism. Particle morphology and reactant concentration after 10 mins and 40 mins are shown here. (g) Evolution of the primary particle size (blue curve) and primary aggregate size (black curve) as a function of time. The red curve shows how the reactant concentration within the solution changes over time. It is evident that the particle growth after 1 hours ceases to occur due to the complete depletion of the reactants. Experimentally observed size of the primary aggregates is shown by the black cross symbol. The computational model predictions provide reasonable agreement with the experimental observations. (h) Evolution in (NMC)CO₃ secondary particle size with time as predicted by the Kinetic Monte Carlo (KMC) scheme. Evolution of the secondary particles are expected to occur through the nucleation, growth, and aggregation phenomena. Effect of different transition metal concentration on the secondary particle size is also shown, where increasing the concentration of transition metal salt leads to faster growth and larger secondary particles. The experimentally observed secondary particle size for (NMC)CO₃ with 4.5 mM transition metal is shown by the red cross symbol, which indicates good correlation between computation and experiment. 118

Figure II.10.3 In-situ XRD during calcination of NMC-811}. (a) Temperature profile, (b) square-root of integrated diffraction intensity, and (c) ratios of areas of fitted peaks for (003) and (104) reflections during calcination of layered Ni_{0.8}Mn_{0.1}Co_{0.1}(OH)₂ precursor. (h) Temperature profile, (i) square-root of integrated diffraction intensity, and (j) ratios of areas of fitted peaks for (003) and (104) reflections during calcination of precursor after 350°C pre-annealing. (d–g) Reference patterns for (d) NMC-811, (e) LiOH, (f) NiO, and (g) Li₂CO₃. Dashed lines in (i,j) show maximum (003)/(104) area ratio attained during calcination..... 120

Figure II.10.4 Schematic of NiO lithiation mechanism. (a) Bare NiO surface, LiOH and O₂, (b) oxidation of the surface forms a surface dipole, (c) Ni hopping between surface and bulk sites driven by charge redistribution, (d) Li⁺ ions fill surface sites leading to NiO lithiation and water formation, (e) surface oxidation and water removal, (f) Li–Ni disorder creates a disordered rock salt bulk. The steps will repeat until a LiNiO₂ stoichiometry is reached everywhere. Subsequent Li layering will be favored at high temperature, given the different sizes of Ni³⁺ and Li⁺ ions. 120

Figure II.10.5 Increase in relative density with pressure at elevated temperatures (1000 degree C) as experienced by LLZO. Densification simulations were conducted for 1 hour following the work of Jeff Sakamoto, Univ. of Michigan, Ann Arbor (see Sharafi et al. J. Mater. Chem. A (2017) 5 21491 – 21504). Complete densification is achieved within 60 MPa, which is consistent with the reported experimental results. The final LLZO microstructures obtained by conducting densification at 0 MPa, 40 MPa and 60 MPa are denoted by A, B and C, respectively. The initial average particle size was assumed to be 5 µm..... 121

Figure II.10.6 (a) Phase map between pressure and temperature where blue indicates 50% relative density and yellow denotes complete densification. It is evident that complete densification is possible at high pressure, but complete densification cannot be achieved with only high temperature and lower values of pressure. The sintering simulations were conducted for 1 hour at 1000°C temperature assuming LLZO particles. (b) Phase map between particle size and pressure, where blue indicates 50% relative density and yellow denotes 100% densification. Variation in particle size does not show any significant influence on the pressure induced

densification process. Even with very large particles of size larger than 10 μm , it is possible to obtain complete densification under externally applied pressure of 60 MPa. Without externally applied pressure, it is very difficult to achieve close to 100% relative densities for large sized LLZO particles. 122

Figure II.11.1 Phase progression during solid-state synthesis of NMC811 and LiNiO₂ (LNO) tracked *in situ* by temperature-resolved synchrotron XRD. (a, c) Contour plots of the *in situ* XRD taken during formation of NMC811 and LNO respectively. (b, d) Low-angle characteristic peaks from selected regions (marked with white dashed rectangles). 126

Figure II.11.2 *In situ* PDF analysis of the solid-state synthesis of NMC811 and LNO. (a, b) temperature resolved green function and the calculated c/a, domain size and Li occupancy on 3b site for NMC811 and (c, d) temperature resolved green function and the calculated c/a, domain size and Li occupancy on 3b site for LNO. 127

Figure II.11.3 Real-time tracking of structural evolution in the Nb-coated NMC 811. (a) *In situ* synchrotron XRD patterns of 1.4% Nb-coated NMC 811 at different stages, being illustrated using different colors, namely, initial materials (Black line), during holding at destination temperatures 475°C (Blue), 520°C (Cyan), 560°C (Olive), 600°C (Green), 645°C (Orange), 690°C (Yellow), 730°C (Pink), 770°C (LT Magenta), 815°C (Red) and final cooling down (Dark yellow). Inset: heating profile. (b) Zoom-in view of the diffraction patterns to show the formation of minor Nb-containing phases, as indicated by ♥ for LiNbO₃, ♠ for Li₃NbO₄. (c) Quantitative analysis on the LiNbO₃ and Li₃NbO₄ as a function of time and temperature. Formation of LiAlO₂, arising from Li interaction with cell components at high temperatures (>730°C), was also provided. 128

Figure II.11.4 Quantitative analysis of the kinetics of structural change in the bulk. (a) Intensity ratio of the characteristic peaks, I(003)/I(104); (b-d) Evolution of the lattice parameters a, c, and their ratio c/a during holding (for ~ 50 minutes) at destination temperatures; (e) Ni occupancy on Li site; (f) Particle size (P-size). 129

Figure II.11.5 Operando TXM-XANES spectro-images of local redox reaction within individual single- and poly- crystal NMC811 assembled into a same electrode. (a-i) Representative 2D maps of Ni oxidation states during the charge process up to 4.4 V at 0.15 C. (j) Voltage profile (grey) and quantified Ni⁴⁺ concentration derived by fitting of XANES spectra from ROI 1 (red) and ROI 2 (blue), within single- and poly- crystals, respectively (as labelled in i). (k) Ni⁴⁺ distribution across the single (red)/poly (blue) crystals at the state (i). 130

Figure III.1.1 Potential demand growth for lithium (total) and lithium metal (C. Xu et al., 2020) 135

Figure III.1.2 The GHG emissions associated with NMC LIBs decrease as both energy density and stoichiometric nickel content increase. 136

Figure III.2.1 The Critical Materials Research Plan with three major research areas to address critical materials issues for Li-ion batteries and recovery of materials for re-introduction into the supply chain. 139

Figure III.2.2 Logo of the Lithium-Ion Battery Recycling Prize. 139

Figure III.2.3 The Lithium-ion Battery Recycling Prize consists of three progressive phases from concept through pilot validation for about three years. 140

Figure III.2.4 This illustration shows the timeline of Phase III of the Lithium-ion Battery Recycling Prize, as identified in the Phase III Rules. 142

Figure III.3.1 Basic processing steps associated with direct recycling 145

Figure III.3.2 Process flow diagram for the recovery of manufacturing scrap. 148

Figure III.3.3 Electrochemical discharge capacity of vendor A cathode a) manufacturing scrap and b) comparison of manufacturing scrap and cycled material after reprocessing using a thermal method. 148

Figure III.3.4 Conventional Soxhlet extractor design 149

Figure III.3.5 PVDF binder and cryovap solvent transfer apparatus 151

Figure III.3.6 mapping of NMC 811 electrode scrap.....	152
Figure III.3.7 FTIR spectra of fresh DMF and recovered DMF from vacuum-assisted cryovap process. Inset digital photo shows recovered DMF.....	152
Figure III.3.8 Picture (left) and schematic diagram (right) of the pilot-scale continuous froth column (left) ..	153
Figure III.3.9 NMC111 grade of the recovered froth based on ICP results	155
Figure III.3.10 NMC111 grade of the recovered tailings based on ICP results	155
Figure III.3.11 NMC111 grade as a function of total froth mass (total feed solid: 200g)	156
Figure III.3.12 NMC111 grade as a function of total tailings mass (total feed solid: 200g)	156
Figure III.3.13 Schematic diagrams of the first and second stage froth column operation for 2-step froth flotation.....	157
Figure III.3.14 NMC111 grade of the froth and tailings based on ICP results for the imitated first stage froth column operation	158
Figure III.3.15 NMC111 grade as a function of total mass of froth or tailings for the imitated first stage froth column operation (total mass of feed solids: 250 g)	158
Figure III.3.16 Electrochemical performance of recycled NCA from froth flotation separation at with different conditions.....	159
Figure III.3.17 a) SEM image of NMC111 burned at 200°C b) SEM image of NMC111 burned at 250°C.....	160
Figure III.3.18 XPS analysis of pristine NMC111, collector absorbed NMC111 and thermally treated NMC111.	161
Figure III.3.19 Electrochemical performance of NMC111 from three experimental conditions.....	162
Figure III.3.20 (a) Circuit design of multistage experiment. (b) Recovery and grade of anode materials in tailing after different circuit design experiments. (c) Recovery and grade of cathode materials in concentrate after different circuit design experiments.	163
Figure III.3.21 (a) Electrochemistry of recycled and pristine NMC111 samples, (b) XRD of recycled and pristine NMC111.	164
Figure III.3.22 XRD of pristine NMC622, Solvent Y processed, and relithiated cathode powder	165
Figure III.3.23 Comparison of TGA plots of MSY_ORNL and ReLi NMC 622.....	167
Figure III.3.24 XRD patterns for Pristine NMC622, MSY, and ReLi NMC 622.....	167
Figure III.3.25 Electrochemical cycling performance of relithiated materials (ReLi-NMC622)	168
Figure III.3.26 XRD patterns of cycled NCM622 treated using solvent Y, regenerated NCM622 at 50g scale as well as the standard pattern of pristine NCM622.	169
Figure III.3.27 Voltage profiles (a) and cycling stability (b) of the cycled NCM622, the pristine NCM622 and NCM622 regenerated at 220°C at 50g scale followed by annealing at 850°C (C-NCM622, T-NCM622, HS-NCM622-50g).....	169
Figure III.3.28 Voltage profiles (a) and cycling stability (b) of the cycled NCM622, the pristine NCM622 and NCM622 regenerated at 100°C with green additive followed by annealing at 850°C (C-NCM622, T-NCM622, HS-NCM622-GA).	170
Figure III.3.29 (a) Initial and (b) second charge and discharge voltage profiles of pristine NMC111, De-NMC111, and scaleup relithiated NMC111 powders in 10/30/60 min reaction for half cells.....	171
Figure III.3.30 (a) Initial charge/discharge voltage profiles and (b) cycling performances of pristine NMC111, scaleup_0.5M_10min and scaleup_0.5M_1h for NMC/LTO full cells.	172

Figure III.3.31 (a) Initial and (b) second charge and discharge voltage profiles of pristine NMC111, SolveY_0.5M_2h@64C_air and SolveY_0.5M_2h@64C_O2; (c) Initial and (d) second charge and discharge voltage profiles of pristine NMC111, SolveY_0.5M_24h@65C_air and SolveY_0.5M_24h@65C_O2; (e) XRD patterns of pristine NMC622, Solve Y EOL powder and relithiated SolveY powders.	173
Figure III.3.32 Full parametrization of electrochemically delithiated NMC 111 optimal relithiation protocols with regard to varying the constant current C-rate step, cut-off voltage and scan rate for the scanning voltage step.	174
Figure III.3.33 Relithiation results for commercial NMC 622 EOL material relithiated using slow relithiation protocol in coin cells.	175
Figure III.3.34 XRD of an upcycling product before and after re-annealing to 850°C (left) and expanded view of higher angle peaks (right)	176
Figure III.3.35 SEM images of (a) upcycling products annealed at 720°C and (b) re-annealed at 850°C.	176
Figure III.3.36 Half-cell rate performance for re-annealed upcycling products	177
Figure III.3.37 XRD patterns, ICP results, TGA comparison for Up-NMC-622, P-NMC-622, and D-NMC-111	178
Figure III.3.38 Electrochemical performance tests in half cell of upcycling sample.	179
Figure III.3.39 Electrochemical cycling tests of one upcycling sample	179
Figure III.3.40 SEM image of the Ni(OH) ₂ precursor.	180
Figure III.3.41 SEM image of the NiOOH precursor.	180
Figure III.3.42 XRD patterns of hydrothermal and post annealing upcycled NCM433 using Ni(OH) ₂ and NiOOH as precursor as well as the standard pattern of LiNiO ₂	181
Figure III.3.43 Voltage profiles (a) and cycling stability (b) of hydrothermal and post annealing upcycled NCM433 using Ni(OH) ₂ and NiOOH as precursor and the pristine NCM433.	182
Figure III.3.44 Rate performance of large scale 5g and 100g single-crystal NMC111.	182
Figure III.3.45 SEM images of SC-811 (a,b) and XRD pattern of SC-811 (C). We are exploring the etching method as a universal method to obtain single-crystal NMC811 from polycrystalline NMC811.	183
Figure III.3.46 Rate performance comparison between SC-811 and Commercial811	184
Figure III.3.47 ICP data representing the loss of elements in the solution	184
Figure III.3.48 SEM images of 2h (a), 14h (b) and 25h (c) etching process; XRD patterns comparison between commercial811 and different etching time samples (d).	185
Figure III.3.49 XPS spectra of (a) Na 1s survey scan, (b) F 1s surface and (c) F 1s bulk for cathodes; XPS deconvolution profiles of (d) Ni 2p, (e) Co 2p in surface layer of cathodes; Percentage of (f) Ni ²⁺ , Ni ³⁺ ions and (g) Co ²⁺ , Co ³⁺ ions in surface layer of cathodes.	186
Figure III.3.50 Plot of fitted lines between peak current (I _{p2}) vs. scan rate (v) from CV curves for (a) anodic side and (b) cathodic side; (c) Calculated Li-ion diffusion coefficient D _{Li} , and (d) schematic of Li-ion diffusion in cathode crystals.	187
Figure III.3.51 Electrochemical performance of as-prepared samples. (a) cycle at 0.33C, (b) cycle at 5C, (c) rate to 5C, (d) initial charge-discharge profile, (e) retention after 100 cycles, and (f) retention at specific rate relative to formation cycle (0.05C).	188
Figure III.3.52 Schematic illustration of the impacts on the NCM622 structure caused by fluorine impurity.	189
Figure III.3.53 A laboratory-scale baffled tank used for the stirring experiments for layered component clump liberation	190

Figure III.3.54 Clumps in different sizes used for the stirring experiments	190
Figure III.3.55 Liberation efficiency and mass distribution of different size fractions after stirring clumps at 1290 RPM for 5 minutes with two solid-liquid ratios (50 g/L and 100 g/L).	191
Figure III.3.56 Liberation efficiency and mass distribution of different size fractions after stirring clumps at 1800 RPM and 50 g/L for three stirring times (90 second, 3 minutes and 5 minutes).	191
Figure III.3.57 Liberated clumps after stirring at 1800 RPM at 50 g/L for 3 minutes.....	192
Figure III.3.58 ReCell's pilot-scale, submergible dual-shaft shredder	193
Figure III.3.59 (a) Photos showing the recovery of spent cathode powder using SolveY process in large scale, (b) XRD patterns for the spent cathode before and after SolveY processing, and (c) SEM image showing the morphology of recovered cathode powder, inset picture shows the cathode powder.	194
Figure III.3.60 Photos showing the direct recycling and remanufacturing of anode scraps using the newly invented SolveZ process.	195
Figure III.3.61 XRD patterns for the spent cathode powder, regenerated NMC cathode before and after annealing.....	196
Figure III.3.62 Electrochemical evaluation of regenerated NMC cathode in half coin cell configuration. (a) Voltage profiles for the formation cycles at C/10 rates, (b) charge/discharge curves for the 1 st and 4 th cycles at C/10 rates, and (c) cycle performance at C/3 charge/discharge rates.	196
Figure III.3.63 Electrochemical evaluation of regenerated NMC cathode in full cell configuration paired with graphite anode. (a) Voltage profiles for the formation cycles at C/10 rates, (b) charge/discharge curves for the 1 st and 4 th cycles at C/10 rates, (c) cycle performance at C/3 charge/discharge rates.....	197
Figure III.3.64 Photos showing the size reduction of anode films using (a) Vortex mixer and (b) probe sonicator.....	198
Figure III.3.65 Diagram with photos showing the separation of spent anode and re-processing into new anode.	198
Figure III.3.66 Contact angle measurement. Buffer solution on (a) cathode and (c) aluminum foil, and buffer solution with additive Z on (b) cathode and (d) aluminum foil.	198
Figure III.3.67 Methods of separating anode, cathode, and metal foils.....	199
Figure III.3.68 Manufacturing scrap (top) and shredded pouch cell material (bottom).....	200
Figure III.3.69 Process A separation of shredded pouch cell material using a two-step separation procedure	201
Figure III.3.70 Weight percent of samples after the first (Fraction 1 and 2) and second (Fractions 1.1, 1.2, 2.1, and 2.2) Process A separation steps.....	202
Figure III.3.71 Electrochemical impacts of Al ⁰ ((a), top row) and Cu ⁰ ((b), bottom row) contaminants on NMC-111. First-cycle charge and discharge cycles are shown for samples with 0.1 wt%, 1 wt%, and 5 wt% of each contaminant. Note that samples containing 1 wt% and 5 wt% Cu immediately shorted and showed no discharge capacity. Additional lines (with the same color/linestyle) correspond to coin cell replicates. There is significant variability between replicates for the untreated contaminated cells—probably to do with uneven dispersion of the Al and Cu metal powders in the slurry.	204
Figure III.3.72 Diffraction patterns of pristine and treated simulated BM samples: (a) NMC-111 spiked with 1% Al ⁰ ; (b) NMC-111 spiked with 1% Cu ⁰ . For both (a) and (b), sample designations from top to bottom of the overlaid trace are as follows: Treated, No Extra Wash; Treated, Extra Wash; Untreated; Pristine (i.e., no contaminant).	205
Figure III.3.74 C/10 cycling performance of pristine NMC-111 vs treated simulated BM with 1 wt% Al ⁰ (blue traces) or 1 wt% Cu ⁰ (red traces). The impact of a supplemental DI water rinse is evaluated for simulated BM containing Cu ⁰	206

Figure III.3.75 First-cycle electrochemical performance of practical black mass, with or without purification treatment, as compared to pristine NMC-111.....	208
Figure III.3.76 Equipment that can be used to scale up the rinsing and concentration processes to recover spent electrolyte.	209
Figure III.3.77 ^1H and ^{19}F NMR spectra for a commercial battery that is likely to be utilized for scale up.....	209
Figure III.3.78 a) Raman spectroscopy using a 514 nm laser of the 48% yield graphene sample. b) ICP-OES data on the impurities in the 48% yield graphene sample.....	210
Figure III.3.79 SEM images of H_2 passivated, ultrasonicated and diluted 48% yield graphene sample on an Au/Pd coated silicon substrate.	210
Figure III.3.80 AFM a) phase, height images, and b) height profiles for the 48% yield graphite sample.....	211
Figure III.3.81 Hazardous waste disposal cost payable to state agencies, for a waste volume of 100 tpy, 1,000 tpy, and 10,000 tpy, respectively.	213
Figure III.3.82 Price quotes for hazardous waste disposal from Triumvirate Environmental and Clean Harbors	214
Figure III.3.83 Photos of electrode coatings made from relithiated Solvent Y processed NMC622. Agglomerates in powder resulted in streaking and grit in the electrode coating.	216
Figure III.3.84 XPS results of F1s region from pristine, thermal binder removed, and solvent binder removed NMC622.	218
Figure III.3.85 EBSD data for two hydrothermally upcycled single-crystal samples prepared by UCSD: (a) Grain orientation spread (GOS) for upcycled NMC-433 prepared with NiOOH precursor; (b) Grain reference orientation deviation (GROD) for upcycled NMC-433 prepared with NiOOH precursor; (c) GOS for upcycled NMC-433 prepared with $\text{Ni}(\text{OH})_2$ precursor; (d) GROD for upcycled NMC-433 prepared with $\text{Ni}(\text{OH})_2$ precursor. One representative region is shown for each sample.	219
Figure III.3.86 Superior Graphite/Toda 1520P/NMC-111, 532,622, and 811 heat generation curves for a 2C full discharge (1a - top) and 2C full charge (1b - bottom).	221
Figure III.3.87 BOL and EOL heat efficiency of 1520P/NMC cells under various discharge currents over an SOC range from 100% to 0%.	222
Figure III.3.88 BOL and EOL heat efficiency of a 1520P/NMC811 cell under a 3C discharge current over an SOC range from 100% to 0%.	222
Figure III.3.89 Shredding Simulation results.....	224
Figure III.3.90 Miniature nail penetration tester for low-temperature tests.....	225
Figure III.4.1 C/3 capacity of cathode materials evaluated at different voltages.....	235
Figure III.4.2 Fast charge cycling behavior of a single-layer pouch cell with a graphite anode and a Ni-rich cathode.....	236
Figure III.5.1 SEM images of cathode materials from BRs.....	239
Figure III.5.2 Comparison between the batch of 04092021 and 05122021 in rate performance.....	240
Figure III.5.3 Synthesized 83Ni Precursor with virgin materials	241
Figure III.5.4 83Ni cathode sintered in different batches	241
Figure III.5.5 Rate performance of coin cell with 83Ni cathode powders and reference sample	242
Figure III.5.6 Flow chart of recycling spent Nickel metal hydride battery for feeding to NMC precursor synthesis.....	243

Figure IV.1.1 Voltage profiles and the corresponding background-corrected mass signals $m/z = 44$ (CO_2), 32 (O_2), and 27 (C_2H_4) for a) TNO-Li metal, b) NMC811-Li metal, c) TNO-NMC811, d) coated TNO-NMC811 pouch cells.	245
Figure IV.1.2 Ti 2p, Nb 3d, C 1s XPS spectra of TNO (left) and coated TNO (right) (a) pristine powder; (b) electrode before cycling; (c) electrode at 100% lithiated state (cutoff at 1.0 V); (d) electrode at complete delithiated state (cutoff at 3.0 V); (e) electrode at 100% lithiated state after 2 cycles (cutoff at 1.0 V).....	247
Figure IV.2.1 (a) Areal capacity, and (b) capacity retention for single layer full cells with varying combinations of VENDOR A and BNL produced NMC 622 cathodes and uncoated graphite anodes. Cells were cycled at 30°C under 10-minute charge/ 1C discharge protocol with a C/3 discharge every 50 cycles. Error bars represent one standard deviation from the mean ($n = 3$ cells per configuration).....	250
Figure IV.2.2 (a) areal capacity, and (b) capacity retention for single layer full cells with varying combinations of VENDOR B and BNL produced NMC 622 cathodes and uncoated graphite anodes. Cells were cycled at 30°C under 10-minute charge/ 1C discharge protocol with a C/3 discharge every 50 cycles. Error bars represent one standard deviation from the mean ($n = 3$ cells per configuration).....	251
Figure IV.2.3 (a) Areal discharge capacity, (b) capacity retention, and (c) specific energy for 1 Ah multi-layer full cells with electrolyte to pore volume ratio of 1.5 : 1 (blue), 1.3 : 1 (red), and 1.2:1 (black). A fourth cell with 1.5 : 1 ratio was degassed after formation cycling (green). The cells were cycled at 30°C under 1C charge/ 1C discharge for 200 cycles.....	251
Figure IV.2.4 (a) Areal discharge capacity, (b) capacity retention, and (c) specific energy for 1 Ah multi-layer full cells with electrolyte to pore volume ratio of 1.5 : 1 (red) and 1.3 : 1 (black). Both cells were degassed after formation and cycled under 10-minute charge/ 1C discharge protocol at 40°C with a C/3 discharge every 50 cycles.	252
Figure IV.2.5 Evaluating the influence of upper charge voltage limit (4.2 V vs. 4.3 V) and operating temperature (30°C vs. 40°C) during 10-minute CC/CV charge, 1C discharge protocol: (a) areal capacities, (b) capacity retention values.....	252
Figure IV.2.6 (a) Voltage profiles of first and fourth formation cycles at C/10 rate (b) gravimetric discharge capacity vs. cycle number, and (c) capacity retention vs. cycle number, and (d) 10-minute charge, C/3 discharge voltage profiles for 1 Ah multi-layer full cell with NMC622 cathodes and 20 nm Ni-graphite anodes. The cell was cycled under a 10-minute charge/ 1C discharge protocol with a C/3 discharge every 50 cycles.	253
Figure IV.3.1 Demonstrating the SOC-sweep cycling protocol to quickly detect the onset of plating with coulombic efficiencies in graphite half-cells.	258
Figure IV.3.2 Data analysis to estimate irreversible lithium plating as a function of charge capacity (a,b) and plotting the lithium plating onset as a function of C-rate (c) for Round 2 graphite at 23°C. We define the plating onset as 0.1 mole percent irreversible Li capacity with respect to the capacity of the graphite electrode.	258
Figure IV.3.3 a) 1C charging protocol with pauses for OCV and imaging. b) dOCV indicating the onset of plating after charging to 80 % SOC. c) Volume renderings of a portion of the segmented graphite electrode after 1C intercalation to 80 and 100 % SOC, followed by C/3 deintercalation to 0 % SOC. The graphite is shown in gray, and the mossy lithium is shown in turquoise. d) Areal density of plated lithium across the graphite electrode versus SOC after 1C intercalation (black) and C/3 deintercalation (blue). Total plated lithium given by areal density multiplied by total xy-area of the graphite electrode.	259
Figure IV.3.4 Electrochemical Measurements showing the Li plating onset on edge and basal plane HOPG. (a) Edge plane, galvanostatic. (b) Basal plane, galvanostatic. (c) Basal plane, cyclic voltammetry.....	260
Figure IV.3.5 Galvanostatic lithiation of edge-plane HOPG at different stages of lithiation. Stage IV = LiC_{24} , Stage II = LiC_{12} , Stage I = LiC_6	261
Figure IV.3.6 a) Raw $V_{3\omega}$ data after 1C charging to three different bulk/average SOC's normalized to raw data after 0.1C charging to the same SOC's. b) The k_{anode} profile across the anode. c) The local SOC distribution	

calculated from the measured k_{anode} distribution. D) Cross-section views of pristine (SOC = 0) and lithiated (SOC = 70%) graphite anode show how in the cell charged at 1C, the anode region near the separator has a much higher degree of lithiation (i.e., more gold color) than the regions farther away. Reproduced from [2].262

Figure IV.3.7 (A) Voltage profiles of graphite/Li half cell charged at 4C to different SOC's from 10% to 100% and then discharged at C/5 to 1.5 V. At each SOC, cells are cycled with and without resting after charging; (B) CE of graphite/Li half cells charged to different SOC's and corresponding CE_{w/ resting}/CE_{w/o resting}; (C) dQ/dV curves during discharge after discharged to different SOC's; (D) normalized discharge capacity at different graphite lithiation stages and (E) corresponding difference in normalized discharge capacity between charging w/ resting and w/o resting; SEM images of graphite anodes at (F) pristine state and (G) after charging at 4C to 100% SOC; and (H) CEs of graphite/Li half cells w/ and w/o resting, cells are charged to 100% SOC at 4C.....263

Figure IV.4.1 Illustration of (a) standard coin cell configuration and (b) pouch cell configuration for cyclic voltammetry test.266

Figure IV.4.2 Cyclic voltammograms of the (a) LiFSI (solid lines), and (b) LiPF₆ (dashed lines) electrolyte in coin cells for the first 4 cycles. Cyclic voltammograms of the (c) LiFSI electrolyte in pouch cells with SS foil, and (d) LiFSI and LiPF₆ electrolyte in pouch cells with Al foil as the working electrodes for the first 4 cycles. The picture inset of Figure a showed the black products on cells parts with LiFSI electrolyte.....267

Figure IV.4.3 Tafel polarization curves from the 2nd scanning of SS foil or Al foil in LiFSI or LiPF₆ electrolyte.267

Figure IV.4.4 Photographs of opened pouch cells with LiFSI electrolyte using (a) SS foil and (b) Al foil as the working electrodes. SEM images of (c) pristine Al foil and (d) Al foil after CV test in LiFSI electrolyte.268

Figure IV.4.5 Cycling performance of 1.5 Ah NMC622/graphite pouch cells at different charging/discharging rates with LiFSI electrolyte.....268

Figure IV.5.1 Amount of dead plated Li directly detected by HEXRD as a function of the total amount of plated Li in each cell, as measured via the combination of MST and HEXRD.....271

Figure IV.5.2 (a) Cycle retention of NMC532/graphite cell with fast-charging rate (6C) followed by slow charging rate (C/20). (b) Loss capacity with fast-charging and recovered capacity with followed slow charge rate.272

Figure IV.5.3 Quantification results of plated lithium using ICP-MS.272

Figure IV.5.4 XPS depth profiling results on lithium plating from 50 fast-charged cells. (a) Atomic percent of Li1s, O1s, F1s and C1s. (b) XPS spectra from Li1s region during depth profiling.....273

Figure IV.5.5 (a) Pressure cell (b) Capacity fade over cycle number showing reduce capacity fade in the cell with applied uniform pressure. (c) Preliminary synchrotron XRD peaks showing the presence of Li and Li_xC₆.274

Figure IV.5.6 An overview of Li detection and characterization techniques employed in Li-based batteries. 275

Figure IV.5.7 Cycling data from LFP vs. graphite cells with N/P ratio < 1. a) Coulombic efficiency for a cell cycled at 4C to 50% anode SOC. An amount of Li equal to 4% of the anode capacity was deliberately plated on the Gr on cycle 50 but did not cause major changes in the coulombic efficiency of ensuing cycles. b) Comparison between the initial and final C/20 cycles of the cells in panel a. Cells with N/P ratio < 1 only show capacity fade if anode capacity is lost, which was not the case. c) Coulombic efficiency for a cell cycled at 6C to 80% anode SOC, where Li plating is likely. A dip in coulombic efficiency is observed. d) Comparison between the initial and final C/20 cycles of the cells in panel c, showing loss of accessible anode capacity. .276

Figure IV.5.8 (A) Voltage profiles of graphite/Li half cell charged at 4C to different SOC's from 10% to 100% and then discharged at C/5 to 1.5 V. At each SOC, cells are cycled with and without resting after charging; (B) CE of graphite/Li half cells charged to different SOC's and corresponding CE_{w/ resting}/CE_{w/o resting}; (C) dQ/dV curves during discharge after discharged to different SOC's; (D) normalized discharge capacity at different

graphite lithiation stages and (E) corresponding difference in normalized discharge capacity between charging w/ resting and w/o resting; SEM images of graphite anodes at (F) pristine state and (G) after charging at 4C to 100% SOC; and (H) CE of graphite/Li half cells w/ and w/o resting, cells are charged to 100% SOC at 4C. 277

Figure IV.5.9 Lithium plating reversibility as a function of amount, C-rate, and electrolyte FEC content. a) Protocol to determine lithium plating reversibility in graphite/Li coin cells, which includes a baseline lithiation cycle [C/3 to 0.01V, hold until C/20, and C/5 delithiation to 1.5V] followed by 4-5 overcharge cycles that use an identical sequence with an added lithium plating step with known capacity, P. The total capacity loss in the overcharge cycle (Q_{lost}) is combined with the coulombic efficiency of the baseline cycle (CE) to isolate the capacity loss from irreversible plating, $P(1 - \eta)$, and calculate the Li plating reversibility, η . b) Reversibility values for 4C overcharging with varying amounts of plating as a percent of the total graphite capacity (left), and η for fixed 20% overcharge with varied rates. All electrolytes contain 1.2 M LiPF₆ and the baseline electrolyte is 70:30 EMC:EC, 'Gen 2'. 278

Figure IV.5.10 a) The configuration of operando pressure measurement: the stack contains multilayer pouch cell, metal force-distribution plate, and pressure sensor (load cell) is clamped into a fixed constraint. Zoomed-in schematic of graphite anode illustrating that for the same amount of lithium ions, Li plating induces much higher volume/pressure than intercalation. b) Voltage profiles of NMC-graphite pouch cells at 1C rate and 6C rate. c) Zoomed-in voltage profile during 7th charge step at 6C rate. d) The differential pressure (dP/dQ) profile of the NMC-graphite cell. e) Zoomed-in differential pressure profile during 7th charge step at 6C rate. The black dash line in c) and e) are the upper bound of dP/dQ during intercalation defining the Li plating threshold. 279

Figure IV.5.11 Pressure evolution of NMC-G pouch cells during charging process at (a) 1C rate and (b) 6C rate (1C = 330 mAh cm⁻²). The areal capacity is ~2.2 mAh/cm². 280

Figure IV.5.12 a,b) The corresponding average pressure evolution at different locations. The base pressure at the fully discharged state was set at zero at all locations. The pressure sensor covers the entire pouch cell. c) Optical image of graphite electrode at a fully discharged state. The marked areas match that in a-c figures. 280

Figure IV.5.13 a) A schematic of the measurement setup and thermal contact model. b) Representative raw $V_{3\omega}$ data (normalized to $V_{3\omega}$ at cycle 0), and c) measured TCR as a function of capacity loss. 281

Figure IV.5.14 a) Discharge capacity as a function of cycle number. Fast charging at 6C rate (CCCV) and slow discharging at C/2 rate (CC) (ii)-(vi). b) Area averaged evolution of consumed cathode lithium (y in Li_yNi_{0.5}Mn_{0.3}Co_{0.2}O₂). Open circles indicate metallic plated lithium at charge while closed circles indicate metallic plated lithium at discharge. c) Stripping efficiency is defined as the difference in the percent change in the amount of metallic lithium at charge compared to discharge for the same cycle. Error bars were determined based on the accounting for the set detection limit. 282

Figure IV.5.15 Comparison of Gen2 and B26 electrolytes in terms of discharge capacity achieved with fast charge (6C, CCCV, 3-4.1V) and slow discharge (C/2, CC, 4.1-3V). The cell build was identical for both cells other than the choice of electrolyte. 282

Figure IV.6.1 Round 2 cell negative electrode saturation over time using indicated solvent wetting parameters. Cell wetted from ends and initial saturation at 50%. 285

Figure IV.6.2 Round 2 cell negative electrode after 6C fast charge (left). Saturation distribution of negative electrode assuming gas becomes trapped (right). 286

Figure IV.6.3 – Mapping of local MacMullin number for R2 electrodes for graphite anode (left) and NMC 532 cathode (right). 286

Figure IV.6.4 XRD measured phases in graphite and cathode after 10 fast charge cycles for mapped electrodes. 287

Figure IV.6.5 a) Discharge capacity as a function of cycle number. The initial baseline charge cycle with C/2 rate (i) is followed by fast charging at 6C rate (ii)-(vi). A final baseline charge cycle was performed with C/2 rate following the final fast-charge cycle. b) Comparison of slow charge-rate baseline cycles before fast

charging and after 1255 cycles of fast charging. c) Color maps of lithium plating, scaled to the original cathode lithium, (row 1 and 3), average anode lithiation (row 2 and 4), and irreversible consumption of cathode lithium as fully lithiated graphite at discharge (row 5) at charge and discharge, respectively. x in Li_xC_6 estimated used a four-stage lithiation model corresponding to LiC_6 , LiC_{12} , LiC_{30} , and C_6 . Maps were collected at cycle 0 (i), 3 (ii), 165 (iii), 500 (iv), 665 (v), and 1255 (vi). Note: For (i) the x in Li_xC_6 color range was set from 0.65 to 1 at charge to account for higher lithium intercalation due to slow charging. 288

Figure IV.6.6 (a) The state of lithiation x in Li_xC_6 spatially and temporally measured within the pouch cell during 6C charge (bottom) and 2C discharge (top) alongside the current measured from the potentiostat. (b) Mass fractions of the three lithiation stages during the 6C charge and 2C discharge. 289

Figure IV.6.7 Simulated metallic lithium nucleation and plating kinetics under different charging condition at selected SOC% followed by a C/4 discharge rate. A direct comparison of inactive lithium from titration experiments and simulations for 4C (inset (a)), 4.64C (inset (b)), and 6C (inset (c)) charging and C/4 discharging cycle at various SOC% are in good agreement. 289

Figure IV.7.1 Example of novel fast charge protocols developed to minimize recharge time and prevent lithium plating using P2D models for graphite/NMC cells using a voltage ramping protocol reproduced from Mai et al [3]. 293

Figure IV.7.2 (a) Electrolyte potential sensed by the reference electrode differs from that experienced at the surface of the anode by $\sim iR$, leading to a difference of this same magnitude between the measured potential ϕ and the surface electrode potential η . (b) Charge protocol that maintains the anode at the thermodynamic limit for Li plating. (c) Anode potentials and (d) C-rates during the charging using different ϕ cutoff conditions. In both (c) and (d), the gray, blue, red, and black plots correspond to the CCC ϕ , seesaw ($\phi = 0$), iR corrected seesaw ($\phi = -|iR|$), and 6C corrected seesaw profiles ($\phi = 6C \cdot R$), (Adapted from [7]). 294

Figure IV.7.3 Polarization values extracted from final FY2021 cell deliverables showing an improvement in performance with respect to previous cell deliverables. 295

Figure IV.7.4 Area fraction of the major electrolyte degradation products as a function of apparent molecular weight and charge rate. The error bars represent the area fraction maxima and minima for each component [6]. Copyright © Wiley-GmbH. Reproduced with permission. 295

Figure IV.7.5 Comparison of 10-minute power profiles for several charge protocols after scaling from the cell level to a 65-kWh battery pack. Adapted from data in Ref. [2]. 296

Figure IV.8.1 Electrode composition and design for baseline (“Hero Cell”) pouch cell from Q4 of FY 2020. 301

Figure IV.8.2 (Left) Cell voltage and (right) potential for plating for a 6C-CC charge profile (4.1V, 10 minutes cutoff). 302

Figure IV.8.3 NMC connectivity as function of CBD loading. “III U IV cluster” is the relevant percolation metric for the application, see reference 1 for details. “Wide” (conservative approach) and “thin” (closer to imaging, more likely) separation regions correspond to variants of the CBD numerical generation. 303

Figure IV.8.4 Cathode effective solid conductivity and associated solid tortuosity factor, considering low lithiation (square) and high lithiation (triangle) NMC532 bulk conductivity. Grey vertical area corresponds to the percolation transition region of Figure IV.8.3. 303

Figure IV.8.5 (Left) Model-predicted capacity improvement for “Round 3” cell with laser-ablated electrodes. (Right) Cross-section SEM imaging of laser-ablated electrodes performed with NREL laser system. 304

Figure IV.8.6 (Left) Near-optimal cylindrical channel periodic pattern identified with NREL genetic algorithm. (Right) Cross-section SEM imaging of corresponding laser-ablated electrodes performed with NREL laser system. 304

Figure IV.8.7 Various test results for the HCE13 electrolyte used in coin cells with XCEL R2 NMC 811 + Gr materials: (a) formation capacities, (b) aging over C/2 cycles, and (c) coin cell charge rate capability from 1C to 8C (CC+CV). Note that panel (d) is just for the CC component of charge.	305
Figure IV.8.8 Pouch cell charge rate capability from 1C to 8C for cells having electrolytes Gen2, B26 or “solvent C”. Note that results are just for the CC component of charge. Electrodes are NMC 811 and the new dual-layer graphitic anode.....	306
Figure IV.8.9 Outcomes of INL/NREL collaboration on cell-level modeling involving three different electrolytes for XCEL cells operating at 6C CC after 100s. Salt concentration plots are in panel (a), while various corresponding properties are rendered in panels (b) and (c). Electrolytes are Gen2 (red), B26 (green) and HCE13 (blue). XFC electrolytes B26 and HCE13 show less polarization than Gen2, and hence have better transport performance over the entire cell with correspondingly higher charge acceptance.	307
Figure IV.8.10 Summary of 1C-discharge capacities measured under different charging rates for the electrolyte recipes evaluated in coin-cells at NREL. The voltage window for these tests was set to 2.8-4.1V. Subsequent cycling experiments used a higher end-of-charge voltage. “Round 2” electrodes were used with Celgard 2320 membranes.	308
Figure IV.8.11 Electrodes used in final pouch cell build for FY 2021.	310
Figure IV.8.12 BatPaC Analysis of “Hero Cell” design based on preliminary data of single-layer pouch cells made by the CAMP Facility. See Figure I.4.H.1 for electrode details.....	311
Figure IV.9.1 Cell Polarization and Aging Data. Here, the impedance polarization or overpotential (a) is the immediate (e.g., within ~12 ms) voltage drop during the rest at the end of charge, and transport polarization (b) is the voltage difference between the immediately relaxed state and after a 15-minute rest, a pseudo-equilibrium state, while (c) is the charge acceptance at beginning of life (BOL).....	316
Figure IV.9.2 Cathode aging behavior in coin cells harvested from pouch cells: (a) the capacity fade of NMC811 at C/20; (b) the capacity fade of NMC532 at C/20; (c) the impedance behavior of NMC811; and (d) the impedance behavior of NMC532. Both coin cells had similar configurations. EIS was performed at 3.9V. For areal impedance, a cathode area of 1.27 cm ² was used.....	316
Figure IV.9.3 Representative SEM micrographs for the different XFC cycling conditions at different cycling interval for NMC811 electrodes: (a) Pristine after calendaring; (b) 1C, Cyc 425; (c) 1C, Cyc 600; (d) 4C, Cyc 425; (e) 4C, Cyc 600; (f) 9C, Cyc 425; (g) 6C, Cyc 600; and (h) 9C, Cyc 600. Cumulative cycle-by-cycle throughput at 600 cycles: 1C=10.75 Ah, 4C=10.3 Ah, 6C=9.95 Ah, and 9C=10.16 Ah. See Figure I.1.A.2b for the throughputs. The top of the graphic is the separator, while the bottom of the graphic is the current collector.	318
Figure IV.9.4 Representative SEM micrographs for the 9C- low-voltage conditions after 1000 cycles for NMC811 electrodes: (a) 9C-3.63V; (b) 9C-3.77V; and (c) 9C-3.94V. Cumulative cycle-by-cycle throughput at 1000 cycles: 9C- 9C-3.63V=6.26 Ah, 9C-3.77V= 11.15 Ah, and 9C-3.94V= 13.95 Ah.	319
Figure IV.9.5 TM dissolution of the NMC811 and deposition on the anodes: (a) Ni dissolution; (b) Mn dissolution; and (c) Co dissolution. Normalization was performed by measuring the total anode mass of the cutout section.	319
Figure IV.9.6HR-TEM images of the discharged NMC811 cathodes after different cycle conditions: (a) 1C-4.1V-600 cycles; (b) 9C-4.1V-600 cycles; (c) 9C-3.66V-1000 cycles; and (d) 9C 3.94V-1000 cycles. The marked region in each figure shows the particle surface degradation with different structures of just a rock salt, disorder layer with mixing of a rock salt and layer phase, and a completely layer phase. Corresponding Fast Fourier Transform (FFT) images of the regions were shown in the inset of (a).	320
Figure IV.9.7HR-TEM images of NMC811 cathodes: (a) 1C-4.1V-600 cycles; (b) 9C-4.1V-600 cycles; (c) 9C 3.63V-1000 cycles; and (d) 9C-3.94V-1000 cycles at lower magnification to show the structure of the whole bulk. Corresponding EELS line scans of the O K-edge and L-edges of Mn, Co, and Ni.	320

Figure IV.9.8 (a) Model results showing C/2 discharge capacity with respect to percent volume damaged. Illustrated are the responses for the NMC811 particles and the NMC532 particles, respectively, after 1C and 6C charging. (b) EBSD data from cross-sectioned NMC532 (top) and NMC811 (bottom) particles showing (left) the angles of grains, (middle) the angle between the C-axis of NMC and the radial direction of each grain, and (right) the distribution of those angles in grey relative to a simulated random case in semi-transparent blue. The EBSD slices are assumed to be at the center of the particles. Error bars for the NMC532 particle are the same calculation but for if the slice was for particles were sized at d10 and d90 particle diameters, i.e., that may accrue from parallax error as described in [7]. Due to the characteristic void at the center of the NMC811 particle, it is assumed that the slice is at or near the particle center.....	322
Figure IV.9.9 (a) EBSD of a cross-sectioned NMC532 particles showing (b) the orientations of the grains and (c) the regions within some of the grains with sub-grain misorientation or crystal twins.	323
Figure IV.9.10 Model predicted results using the baseline particle geometry after 25 cycles under 9C CC-CV charging and C/2 discharging: (a) chemo-mechanical displacement u and the continuum-damage D after 25 cycles; (b) damage after formation; (c) damage due to cycling; and (d) intercalation fraction. (a) illustrates the surface of the 3D particle and shows how the particle has shrunk from its initial condition (see gray coloring) due to delithiation. (b) illustrates a cut-plane of the damage variable after formation and shows a significant amount of chemo-mechanical damage occurs before cycling. (c) illustrates the additional damage induced due to charging the particle at 9C for 25 cycles. As illustrated, the additional rate-dependent damage primarily occurs on the particle surface at grain interfaces. (d) illustrates the intercalation fraction. The model predicts red “hotspots” in highly damaged regions where the Li diffusion is extremely hindered.	324
Figure IV.9.11 SEM images of synthesized SC-NMC532 with: (a) Platelet and (b) T-Oct morphologies. (c) Rate comparison of the SC-NMC532 cathodes. (d-f) Cross-sectional SEM images of SC-NMC811 particles collected after 300 cycles at 1C, 6C and 9C rates, respectively. SEM images of PC-NMC532 samples with a secondary particle size of: (g) 20 μm ; (h) 10 μm ; and (i) 5 μm ; respectively. (j) Rate comparison of the PC-NMC532 cathodes.	325
Figure IV.10.1 Cell temperature distributions under immersion cooling versus immersion cooling with external cooling a) Temperature non-uniformity histories; (b) Transient temperature contour for the cell under combined immersion and external cooling.	332
Figure IV.10.2 Maximum and minimum lithium plating potentials within the 40.8 Ah cell under 4C charging with single-sided cooling.	333
Figure IV.10.3 a) Dummy prismatic cell; b) dummy cylindrical cell; the reconstructed heat generation rate compared against the known (imposed) heat generation rate for prismatic (c) prismatic and cylindrical (d) cells. Source: Sean Lubner, LBL.	334
Figure IV.10.4 Internal temperature of the cylindrical dummy cell reconstructed from the heat generation rate measured using the inverse calorimetry approach and the lumped capacitance approach compared against the actual temperature measurement using an embedded thermocouple. The inverse approach can reconstruct the internal temperature more accurately than the traditional lumped capacitance approach. Source: Sean Lubner, LBL.....	335
Figure IV.10.5 a) The raw 3ω data of battery unit cells with different fluids; b) measured effective cell thermal conductivity when filled with fluids or fluid mixtures of varying thermal conductivity; c) measured electrode-separator thermal contact resistance in the unit cell with the same fluids; d) the thermal conductivity of IPA with varying concentrations of alumina nanoparticles added. Source: Sean Lubner, LBL.	336
Figure IV.10.6 Operando Temperature monitoring using RTD in pouch cells (a) schematic image; (b) photo image of the cell; (c) electrochemical performance of the cell vs. RTD responses charging at different rates. Source: Stanford – Fang Liu	337
Figure IV.10.7 (a) Photo image of the data acquisition system and (b) Digital image of the user interface. Source: Stanford – Fang Liu	337

Figure IV.10.8 Photo of (a) 5Ah commercial pouch cell, (b) disassembled pouch cell, (c) pouch cell with RTD sensor inside. Source: Stanford – Fang Liu	337
Figure IV.10.9 DEMS measurements of ethylene (C_2H_4) gas evolution measured via the C_2H_2 fragment ion ($m/z=26$) overlaid with cycling data for Round 2A graphite, Round 2 NMC 811 full cells with B26 (panels a , b) and Gen2 (panels c , d) electrolytes cycled with one C/10 cycle, one C/5 cycle, and three 2C charge-C/5 discharge cycles at room temperature (panels a , c) and 40°C (panels b , d). Source: Eric McShane, UC Berkeley.....	338
Figure IV.11.1 Top-down SEM images of the (a) graphite, (b) Gr-75, (c) Gr-50, (d) Gr-25, and (e) hard carbon anodes [2].....	341
Figure IV.11.2 Normalized discharge capacity vs. cycle number plots during (a) 4C (15-min) and (b) 6C (10-min) fast-charge cycling [2].....	341
Figure IV.11.3 Evolution of the local reaction current density as a function of the position through the thickness of the (a) graphite, (b) Gr-50, and (c) hard carbon anodes during 4C charging. The schematic on the left of panel (a) shows the orientation of the anodes in the evolution plots. The top edge and the bottom edge of each evolution plot correspond to the anode/separator and anode/current collector interfaces, respectively [2].	342
Figure IV.11.4 (a,c) Scanning electron micrographs of the LBCO-coated graphite anodes and (b) of a focused-ion beam cross-section through a coated graphite particle. (d) X-ray photoelectron spectroscopy survey scan and atomic composition of the surface of a coated electrode [6].....	342
Figure IV.11.5. Extended cycling of NMC532/graphite pouch cells with and without LBCO coating. (a) Coulombic efficiency vs. cycle number plot. (b) Discharge capacity for 4C fast-charge cycles only. 80% line is based on initial fast-charge cycle [6].	343
Figure IV.11.6 (a) Voltage profile of the graphite WE during 6C charging; (b – e) Still frames of the WE during 6C charging. Plated Li is circled in (d). The time and the voltage of graphite at each frame is labeled in (a) [5].	343
Figure V.1.1 Overview of BTMS relevance (EVSE: electric vehicle supply equipment).....	347
Figure V.1.2 Decrease in specific and volumetric energy density of ESS from the cell to the rack. Source: NREL	349
Figure V.1.3 Voltage traces for two preliminary cycling regimes conducted on NMC/graphite cells (a) and SOC traces for two refined BTMS cycling regimes (b).....	351
Figure V.1.4 Schematic Depicting the Default Combination of Technologies for BTMS Analysis	352
Figure V.1.5 Representative utility rate structures for FY21 Scenarios	353
Figure V.1.6 Proposed characterization testing for quantification of input variables and model development. Source: NREL.....	355
Figure V.1.7 Illustration of modeling matrix to evaluate thermal management strategies and techniques. Source: NREL.....	356
Figure V.1.8 3D thermal simulation results of a LTO battery module under single-sided cooling: a) Cell temperature rises under 1C discharge; (b) Cell temperature deltas under 1C discharge; (c) Maximum temperature histories of neighboring cells with fins located between cells; (d) Maximum temperature histories of neighboring cells with insulations inserted between cells.	357
Figure V.1.9 Pack flexibility for different modularity levels (5a), pack cost and efficiency for different modularity levels (5b), and layout #5 modular DC-coupled pack configuration (5c). Source: NREL.....	360
Figure V.1.10 Configuration of a 500-kWh battery pack considering 10-Ah LFP/Graphite cells. Source:NREL	361

Figure V.1.11 Discharge energy fade rate for the NMC/graphite cell cycled under two BTMS cycling routines	363
Figure V.1.12 Top-level Results for a Big-Box Grocery Store	365
Figure V.1.13 Building and EV Demand at a Big Box Grocery Store	365
Figure V.1.14 Power Flows Across BTMS System Assuming a Consolidated Edison Utility Rate Structure	366
Figure V.1.15 Power Flows Across BTMS System Assuming a Pacific Gas & Electric Rate Structure	366
Figure V.1.16 Power Flows Across BTMS System Assuming an Xcel Rate Structure	366
Figure V.1.17 LCOC as a Function of PV & Battery Size for a Consolidated Edison Rate Structure	367
Figure V.1.18 LCOC as a Function of PV & Battery Size for a PG&E Rate Structure	367
Figure V.1.19 LCOC as a Function of PV & Battery Size for ae Xcel Energy Rate Structure	368
Figure V.1.20 Screen Capture of the EDGES BTMS Results Dashboard.....	369
Figure V.1.21 Impact of electrochemical prelithiation of the LTO electrode on the long-term cycle performance of LTO/LMO cells.	369
Figure V.1.22 Impact of N/P ratio on the long-term cycle performance of LTO/LMO cells.	370
Figure V.1.23 Formation cycles and rate performance of 2 Ah LTO/LMO pouch cells.	370
Figure VI.1.1 Maximum achievable anode thickness/loading and corresponding cell cost as a function of charging time using the fast-charge model for a set of NMC532/G cells. Dashed red line corresponds to 10 min charging time, whereas the green corresponds to 15 min charging time. Safe charging conditions correspond to $T_{max,lim} = 45^{\circ}\text{C}$, $I_{lim} = 4\text{C-rate}$, $\eta_{PP} = 30\text{ mV}$; moderate charging corresponds to $T_{max,lim} = 55^{\circ}\text{C}$, $I_{lim} = 6\text{C-rate}$, $\eta_{PP} = 10\text{ mV}$; and aggressive charging corresponds to $T_{max,lim} = 60^{\circ}\text{C}$, $I_{lim} = 12\text{C-rate}$, $\eta_{PP} = 0\text{ mV}$. Charging time is determined from 15% to 95% SOC.....	374
Figure VI.1.2 Comparison of ASI calculated from all three methods as a function of SOC for coin-cells with NMC532 cathodes and graphite anodes. State of charge (SOC) is reported with respect to the C/20 capacity, where all cells were assumed to be at 100% SOC at top of charge. The methods are <i>i)</i> average voltage from discharge curves, <i>ii)</i> curve fitting to discharge curves, and <i>iii)</i> hybrid pulse power characterization (HPPC).	375
Figure VI.1.3 Change in the total pack cost for the different plant utilization methodologies.	376
Figure VI.1.4 Comparison of default a) capacities and b) voltages used in old (4.0) and new (5.0) versions of BatPaC. Values for 5.0 were calculated using the N2P calculator that guarantees self-consistency among voltages, capacities, and formation losses. Values for 5.0 assume 1% negative capacity loss, 5% positive capacity loss, and 20 mAh/g _{graphite} SEI losses during formation for all couples with graphite. The LTO couple assumes no negative or SEI losses.	377
Figure VI.1.5 Effect of new estimates for costs of material, labor, capital equipment, floor space, and the depreciation rate. [67 Ah cells, NMC811-Graphite, 5 GWH plant]	377
Figure VI.2.1 C/1 discharge energy vs. cycle count for cells undergoing XCEL charging.	381
Figure VI.3.1 Gas production data of cell collected in BTPV	384
Figure VI.3.2 Historic ARC data summarizing chemistry behaviors published in FY 21.....	384
Figure VI.3.3 Collected analyzed ARC data showing the impact of cell capacity on runaway enthalpy (a) and the impact of specific energy on peak observed runaway temperatures (b).	385
Figure VI.4.1 Efficiency summary of cells tested in NREL's calorimeters. Caption Credits/Source: NREL-Aron Saxon	389
Figure VI.4.2 Calorimeter normalized heat rate for graphite and graphite/Si NMC cells under C/10 charge and discharge. Caption Credits/Source: NREL-Aron Saxon.....	389

Figure VI.4.3 Heat response of cell under fast charge. The calorimeter test temperature was 30°C. Caption Credits/Source: NREL-Aron Saxon.....	390
Figure VI.4.4 Infrared image of lithium battery cell (graphite-silicon/high nickel content NMC) at the end of a C/3 discharge. Caption Credits/Source: NREL- Aron Saxon	391
Figure VI.5.1 Images of the (a) polymer electrolyte [PE] coatings on LTO and graphite electrodes and (b) hybrid composite polymer ceramic electrolyte [CPE] coatings on graphite electrodes. The PE and CPE successfully applied to the electrode via reverse comma and the polymerization was initiated during coating process heat-treatment.	395
Figure VI.5.2 Images of the polymer electrolyte electrode-ceramic (a) LFP cathode and (b) LTO anode slurry coatings using a roll-to-roll reverse comma coater. The material was successfully applied to the carbon-coated Al [cc-Al] foil via reverse comma.	396
Figure VI.5.3 Images of the multifunctional coater during the FAT. The images are of the front end of the coater (left), slot die coating a CAMP Facility-made graphite anode slurry on copper foil (center), and back end of the coater (right).	396
Figure VI.5.4 Sequence of slurry blend process and results for two high pH LNO-based oxide materials. Both materials started in well dispersed carbon, PVDF binder, and NMP blends, as depicted on the right after the fineness gauge test. The center images show slurry conditions after the LNO-based oxide was blended into the prior blend. The images on the right illustrate the resulting electrode coating quality.	398
Figure VI.5.5 Scaled-up batch (200 grams) of $\text{Ni}_{0.9}\text{Mn}_{0.05}\text{Co}_{0.05}$ provided to the CAMP Facility to produce >1.5 Ah pouch cells. Mixing sequence and control of temperature aided in creating a well dispersed slurry dispersion and uniform electrode.	398
Figure VI.5.6 Data from a 5V spinel//Li cell at 30°C, including the voltage profile (a), differential capacity plots in the indicated voltage ranges (b, c) and specific capacity vs specific current (d).	399
Figure VI.5.7 Aging-related changes from a 5V spinel//Gr cell cycled between 3.2 and 4.7 V at 30°C. (a) Voltage profile changes for select cycles, as indicated (b) discharge capacities (left axis) and coulombic efficiencies (right axis), (c) capacity retention (left axis) and capacity fade (right axis), and (d) impedance rise during the cycling. The dotted lines in (b) and (c) are to guide the eye and show the discharge capacity and fade trends during the extended electrochemical cycling.	400
Figure VI.6.1 SEM images of halloysite-derived SiO_2 (left) and Si (right).	405
Figure VI.6.2 Three formation cycles (left) and rate test (right) of Li/Si half-cells.	405
Figure VI.6.3 Schematic illustration of the facile solvent-free process for the preparation of hG/NCM composite cathodes from hG and NCM powder.	406
Figure VI.6.4 (a) SEM and (b) EDS maps of the cross-section of a hG/NCM composite disc with a hG/NCM-90% layer and a neat hG interlayer for improved mechanical robustness and interfacial conductance with current collector. The areal loading values of the layers are shown in (b). (c-h) Higher magnification (c) SEM and EDS maps of (d) C, (e) O, (f) Mn, (g) Co, and (h) Ni elements of the same disc.	407
Figure VI.6.5 Electrochemical performance of Li-NCM batteries with a dry-pressed hG/NCM cathode: cycling performance (in terms of areal capacity at discharge) and the corresponding Coulombic efficiency of identical batteries cycled at 1.2 (blue) and 2.3 mA/cm^2 (red), respectively.	407
Figure VI.6.6 Optical (left) and SEM (middle) images of solid polymer electrolyte containing PEGMA. Optical image of SPE composite electrolyte (right)	408
Figure VI.6.7 Crystal structure of LLZO (left) and flexible thin LLZO solid electrolyte film (right)	409
Figure VI.6.8 Rate (left) and cycle (right) performance of Li/LLZO/LFP cell at 30°C	409
Figure VI.8.1 Observed experimental capacity at RPT 9 (864 cycles) and predicted capacity using 96 cycles (1 month of cycling) [1].	417

Figure VI.8.2 Error percent for RPTs 7-9 for DCFC and delayed DCFC cells both at 30°C. The shift in performance for the delayed DCFC cells is due to a less aggressive calendar aging condition [1].....	417
Figure VI.8.3 Demonstration of AI-Batt toolset on LFP/Gr calendar aging data (Naumann et al., 2018). (a) Visualization of relative discharge capacity for cells stored at 40°C versus time and state-of-charge (SOC). (b) Fitting of a sigmoidal equation, deconvoluting cell- (α_1) and stress-dependent (β_1 , β_2) degradation trends using bilevel regression to simultaneously optimize cell-dependent parameters to the entire data set and stress-dependent parameters to each individual test condition (each line color corresponds to a unique temperature and SOC). (c) Machine-learned model predicting β_2 as a function of temperature and SOC. (d) Example fit of the model after machine-learning with uncertainty bounds using bootstrap resampling. (e) Extrapolation of the calendar aging model to 20 years at 100% SOC and various temperatures.....	418
Figure VI.8.4 Classification of failure mode as either SEI growth or Li plating for cells undergoing several different fast charge protocols [1].....	419
Figure VI.8.5 Validation of the deep learning model using experimental data based on C/20 capacity fade and LLI% (a,e), %LAM _{PE} (b,f), IC curve comparison (c,g). Parts d and h present the trend in primary and secondary IC peaks over the course of cycling [4].	420
Figure VI.8.6 (a) Voltage relaxation after discharge changes non-monotonically with (b) an initial drop in end-of-discharge voltage (EODV) followed by a steady increase in EODV as (dis)charge cycles accumulate. With 5 state-of-health parameters, the p2D model predicts EODV within 20 mV. (c) Comparison of P2D model with raw voltage curves.	421
Figure VIII.1.1 (a) How moiré works with the reference grating labeled 1 and the sample grating labeled 2, (b) cyclic voltammetry of 3 replicates of a successful 50 nm Si, 500 nm Cu foil sample, (c) diagram of house-made in situ cell, and (d) diagram of house-made moiré interferometer. CE = counter electrode, WE = working electrode, RE = reference electrode.	430
Figure VIII.1.2 Schematic of electrode preparation for ultrafast laser quenching process.....	431
Figure VIII.1.3 Schematic of electrode preparation for ultrafast laser quenching process.....	431
Figure VIII.1.4 Representative cycling data for Si/C45/LiPAA cell with 4 μm of Li evaporated on the surface.	433
Figure VIII.1.5 Optical images of annealed SiO powder and concentrated HF solution with (from left to right) increasing amount of surfactant isopropanol (Image Credits – Nathan Neale, NREL)	433
Figure VIII.1.6 (a) Improvements on noise using interferometry, (b) improvement on z-insensitivity using interferometry, and (c) Gaussian beam simulations of the effect of sample tilt. Similar trends were observed experimentally, but with a larger magnitude.	435
Figure VIII.1.7 The capacity loss of commercial graphite-LFP 18650 cells (pictured in inset) measured during calendar aging (either at OCV or a voltage hold at 3.35 V) over 30, 60, or 90 days for (a) traditional OCV-RPT tests, (b) actual capacity loss measured over equivalent voltage hold aging times, and (c) capacity loss during a 90-day voltage hold. To minimize capacity losses due to cycling, each data point of (a) and (b) was collected from a separate cell aged for the indicated time, rather than a single cell aged for the total time with periodic capacity checks. The capacity loss for each cell was calculated from the difference between the capacity measured before and after the aging period. The capacity loss measured during the 90-day long V-hold (c) is $(Q_{\text{hold}}/Q_{\text{norm}}) - Q_{\text{rev}}$, where Q_{hold} is the capacity passed during the voltage hold, Q_{norm} is the capacity measured during the cycle before aging, and Q_{rev} is the increase in SOC during the voltage hold (~22%). The shaded region for each of the data sets is $\pm 20\%$ of the given aging time.	436
Figure VIII.1.8 Comparison of 30-, 60-, and 90-day voltage holds and OCV rests of commercial 1850 Gr-LFP cells. The 4 th cycle is the rest or hold of the length indicated in the legend. The dQ/dV plots are of the lithiation immediately before and delithiation immediately after the rest/hold. The voltage hold resulted in a 22% increase in SOC over that of the OCV rest as is evidenced by the presence of the dQ/dV peak around 3.31 V during delithiation following the voltage hold.....	437

Figure VIII.1.9 Example of inverse polarization technique on a Si composite electrode in a half-cell to separate reversible delithiation (positive current) and parasitic (negative current) processes. Part (a) gives an overview of the protocol where the cell is lithiated, held at 10 mV for 24 hr, OCV for 24 hr, then stepped up to 200 mV and held at that voltage. Part (b) shows the current during the 200 mV voltage hold. Even after 700 hours, the current is still positive, meaning reversible delithiation currents still dominate. This may indicate why it is so difficult to deconvolute reversible and parasitic reactions during a voltage hold.....	438
Figure VIII.1.10 XRD results for parent metals and $\text{Si}_{0.3}\text{Al}_{0.6}\text{Ti}_{0.1}$, $\text{Si}_{0.4}\text{Al}_{0.5}\text{Fe}_{0.1}$, and $\text{Si}_{0.35}\text{Al}_{0.55}\text{Co}_{0.1}$	438
Figure VIII.1.11 Electrochemical performance of $\text{Si}_{0.3}\text{Al}_{0.6}\text{Ti}_{0.1}$, $\text{Si}_{0.4}\text{Al}_{0.5}\text{Fe}_{0.1}$, and $\text{Si}_{0.35}\text{Al}_{0.55}\text{Co}_{0.1}$ and parasitic current measurement result.....	439
Figure VIII.1.12 Cyclic Voltammetry of amorphous a) $\text{Si}_{0.73}\text{Ti}_{0.27}$, b) $\text{Si}_{0.8}\text{Mn}_{0.2}$, c) $\text{Si}_{0.85}\text{Ni}_{0.15}$, d) $\text{Si}_{0.88}\text{Fe}_{0.12}$ electrodes quenched with ultrafast pulsed laser	439
Figure VIII.1.13 a) Parasitic current measurements of amorphous binary Si alloy electrodes quenched with ultrafast pulsed laser. b) Scanning electron microscopy images of the b-i) 50nm a-Si thin film surface b-ii) laser quenched $\text{Si}_{0.88}\text{Fe}_{0.12}$ surface prior and post electrochemical cycling; inserts are macroscopy images of the electrode surfaces.....	439
Figure VIII.1.14 Cycle life testing of various SiO_x cells using two different binders. At 70% loading of the SiO_x electrode material, the blue line highlights the advantage displayed by the use of a P84 binder versus the previous baseline LiPAA binder system in a full cell using electrochemical prelithiation. Cells were aged at a 1C rate, with performance checks at C/10 every 100 cycles.	441
Figure VIII.1.15 Cycle life testing of PECVD Si cells using two different PI binders processing conditions. At approximately 80% loading of the 1:1 Si/C electrode material, the orange data line highlights the advantage displayed by the use of a cured P84 binder versus the uncured P84 binder material.	441
Figure VIII.2.1 (a). Voltage profiles of the cells stored at different temperatures over 33 days. (b). Enlarged voltage profiles corresponding to the region marked by dash lines in (a).	447
Figure VIII.2.2 Discharge resistance of the cells tested at different temperature over time. a) Absolute discharge resistance over time. b) Relative change of discharge resistance over time.	448
Figure VIII.2.3 Formation capacity and recovered capacity after 90 days storage test at different temperatures.	448
Figure VIII.2.4 Experiment design: Re-assembly of EOL SLP components after storage to study the contribution of each cell component.	449
Figure VIII.2.5 Voltage difference of cells reassembled using EOL and fresh cell components.	450
Figure VIII.2.6 Ratio of contributions of individual EOL cell components to the full cell DCR at EOL.	450
Figure VIII.3.1 Fitting the leakage current data collected for SiO at 0.1 V vs. Li^+/Li , using both (a) voids filling model and (b) continuous growth model.	455
Figure VIII.3.2 Fitting the leakage current data collected for SiO at 0.1 V vs. Li^+/Li , using both (a) voids filling model and (b) continuous growth model.	455
Figure VIII.3.3 Mathematic fitting of long term (up to 600hours) leakage current data for SiO anode at 0.1 V vs. Li^+/Li , showing the significant impact of sampling time period on (a) the obtained steady leakage current, and (b) the predicted calendar life.	456
Figure VIII.3.4 Comparison of predicted calendar life of graphite anode and SiO anode.	457
Figure VIII.4.1 Structural characterization of siloxene nanosheets after ultrasonication. (A) HAADF-STEM image. (B) TEM image at low magnification and (C) the corresponding selected area diffraction. (D) TEM images at high magnification and (E) an HRTEM image. (F) AFM at low magnification, (G) AFM at high magnification, and (H) the accompanying thickness measurements.	459

Figure VIII.4.2 Electrochemistry of lithium/siloxene cells with and without 10% FEC. Charge and discharge voltage profiles for cells (A) without FEC and (B) with 10% FEC. (C) Cycling stability at 200 mA/g. (D) Rate capability from 400 to 3200 mA/g. (E) Long-term cycling at 1000 mA/g.	460
Figure VIII.4.3 XPS fitting results of cycles 1 and 3 discharged siloxene electrodes cycled in electrolyte with and without 10% FEC. C 1s spectra of a cycle 1 and 3 discharged electrodes (A-B) without FEC and (C-D) with FEC. O 1s spectra of cycle 1 and cycle 3 discharged electrodes (E-F) without FEC and (G-H) with FEC. F 1s spectra of cycle 1 and cycle 3 discharged electrodes (I-J) without FEC and (K-L) with FEC. P 2p spectra of cycle 1 and cycle 3 discharged electrodes (M-N) without FEC and (O-P) with FEC.	461
Figure VIII.5.1 a, Schematic of the fabrication of ultra-thin lithium foil. b, Cross-sectional SEM images comparing the common thick host before calendaring, and submicron-scale ultra-thin host after controllable calendaring. c, Cross-sectional SEM images of fabricated ultra-thin 1- μ m-thick and 5- μ m-thick hosted lithium films after preliminary calendaring process.....	464
Figure VIII.5.2 a, Schematic of the prelithiation step using Li@eGF films. b, Coulombic efficiencies of prelithiated silicon anodes using different thickness of Li@eGF films in the first cycle. c, Voltage profiles of Si electrodes using different thickness of Li@eGF films in the first cycle.....	465
Figure VIII.5.3 a-b, XPS spectra of the Si anode after Li@eGF prelithiation. Si 2p spectra (a). Li 1s spectra (b). c-d, Top-view SEM images of cycled Si anode without (c) and with (d) Li@eGF prelithiation.....	466
Figure VIII.5.4 a, Galvanostatic cycling of graphite LFP full cells at 0.05 C using different thicknesses of Li@eGF film for prelithiation in the anode. For this graphite LFP full cell, 1C = 150 mA g ⁻¹ . b, Comparisons of the ICE and areal capacity (after five activation cycles) of graphite LFP full cells using different thicknesses of Li@eGF film for anode prelithiation. c, Voltage profiles of graphite LFP full cells at 0.05 C using different thicknesses of Li@eGF film for prelithiation.....	466
Figure VIII.6.1 Visual representation of a molecular dynamics simulation to predict SEI growth. Reactions are added using a template-matching scheme i.e., description of reactants and its proper configuration to react, and products as shown for LEDC formation.	471
Figure VIII.6.2 Thermodynamic pathways of FEC decomposition.....	474
Figure VIII.6.3 Time evolution of SEI film in the EC-based electrolyte during 100 ns. Snapshots of the reaction products every 25 ns. For visualization purposes, bulk EC and LiPF ₆ molecules are not shown.	475
Figure VIII.6.4 (a) Intermediate reaction mechanism, (b) experiment and model fit for total capacity gain consisting of silicon lithiation and irreversible Li consumption during 180-hour voltage-hold of Si half cells at 100 mV and 250 mV, (c) SEI composition evolution at 100 mV Si potential without FEC decomposition reaction, and (d) SEI composition evolution at 250 mV Si potential with FEC decomposition reaction.....	476
Figure VIII.6.5 (a) Current response of Si half-cell predicted by the atomistically informed model, and (b) experimentally measured by the calendar-life team at 100, 125, 175, 200, and 250 mV voltage holds.....	476
Figure VIII.6.6 (a) SEI thickness evolution calibrated from voltage hold experiments, (b) 1C charge performance of NMC532/Si cells with SEI thickness variation. (c) Electrolyte porosity, (d) normal stress, and (e) hydrostatic stress variation with Si anode and SEI thickness.....	477
Figure VIII.7.1 Cell manufacturing steps including pre-lithiation for silicon anodes (source: Applied Materials). A Roll-to-Roll tool (see image above) along with several test-stands (not shown) were designed, installed and are operational at Applied Materials.....	483
Figure VIII.7.2 Examples of controlled Li deposition on SiO _x -C anode on Applied Materials' Sheet-to-Sheet (S2S) R&D tool, without and with CO ₂ passivation (source: Applied Materials). Prelithiated anode and Li on Cu sheets were supplied to project partners for characterization, cell builds and evaluation.	483
Figure VIII.7.3 Pouch cells (4.6Ah, 305Wh/kg) containing Applied Materials' prelithiated SiO _x -C anode and NMC622 cathode reached >700 cycles in 1C-1C cycling (source: Zenlabs).	484

Figure VIII.7.4 Pouch cells (1.5Ah, 300Wh/kg) containing 10 μm Li metal anode generated by Applied Materials, NMC622 cathode and PNNL developed M47 electrolyte reached 288 cycles in C/10-C/3 cycling (source: PNNL). SAFT America built 6.6 Ah multilayer pouch cells using Applied Materials deposited Li anode reached >94% retention after 250 cycles (not shown).	484
Figure VIII.8.1 Capacity Fade Plot for ~300mAh class development cells (Design Type D) in the first Table	489
Figure VIII.8.2 Energy Fade Plot for ~300mAh class development cells (Design Type D) in the first Table.	489
Figure VIII.8.3 Charge Discharge curves for representative cells from budget period 1 builds.	490
Figure VIII.8.4 Representative Reference Performance Test (RPT) profile of a 300 mAh Enovix 3D NMC 622 cell for select cycles.	490
Figure VIII.8.5 (a) Reaction mechanism, (b) normalized irreversible capacity loss from SEI growth for SiO voltage-hold from 100 mV to 250 mV with an SEI electronic conductivity of 0.05 pS/m, (c) SEI composition evolution at 100 mV SiO potential and (d) 300 mV SiO potential.	491
Figure VIII.8.6 (a) Anode hydrostatic stress , (b) Electrode solid phase fraction and (c) anode porosity variation with thickness for NMC-SiO full cells at end of 1C charge to 4.1V. (d) Anode hydrostatic stress , (e) Electrode solid phase fraction and (f) anode porosity variation with thickness for NMC-Si full cells at end of 1C charge to 4.1V.	492
Figure VIII.9.1 Baseline build battery performance (Farasis cycling data).....	496
Figure VIII.9.2 Electrode resistivity for anodes with ~95 wt% SCC55 TM (Cabot Corporation)	497
Figure VIII.9.3 Electron diffraction analysis of SCC55 TM (PNNL)	498
Figure VIII.10.1 Improvements to particle synthesis process enabled higher silicon content and therefore greater volumetric anode capacity.	501
Figure VIII.10.2 Cycle life of automotive loading cells, measured at C/2 and C/5 capacity.....	502
Figure VIII.11.1 A continuous Si anode coating	503
Figure VIII.11.2 Cycle life of the Si anode in a Li half cell: (left) Si anode capacity vs. cycle number; (right) capacity retention vs. cycle number. The anode shows 1500 mAh/g reversible capacity and retains 95% of initial capacity after 100 cycles.....	504
Figure VIII.11.3 Cycle life of a Si-NMC full pouch cell (3 mAh/cm ² loading, C/5–C/5, 100% DOD, 45°C). The cell retains 92% of initial capacity after 500 cycles.	504
Figure VIII.12.1 (A) Viscosity and (B) conductivity of FLHCEs and control electrolyte over a temperature range of 20-50°C. (C-D) Contact angle measurements of FLHCEs and control electrolyte on polyethylene separator over time.....	507
Figure VIII.12.2 Galvanostatic cycling of single layer Si-graphite/NMC622 pouch cells at C/3 rate with fluorinated LHCEs. Data is compared to cells cycled with control electrolyte (1M LiPF ₆ 3/7 EC/DMC). C/3 cycling rate between 3.0 – 4.3 V. (a) Specific capacity, (b) capacity retention, (c) coulombic efficiency. (d-f) Voltage profiles at (d) 100 cycles, (e) 50 cycles, (f) 100 cycles.	507
Figure VIII.12.3 F 1s and S 2p spectra for Si-graphite electrodes cycled 100 \times in full cells containing control and FLHCE #5 electrolyte before (top) and after (bottom) sputtering.	508
Figure VIII.13.1 (a) Electrochemical validation of silicon thin-film model surface produced by sputter-deposition. (b) characterization pipeline established for the R&D of EP-coated synthetic SEIs for silicon anodes.	512
Figure VIII.13.2 Initial facile EP-coating of polystyrene from styrene monomer on silicon thin-film model surface to establish characterization pipeline. 0.2 M LiTFSI in THF is used as supporting electrolyte. (a) Potentiostatic hold at 100 mV to achieve EP-coating of polystyrene on silicon thin-film model surface. (b)	

microscopy image of silicon film surface after EP treatment. (c, d) ATR-FTIR of reference styrene monomer, Unwashed post-EP sample, methanol washed post-EP sample, and control sample from cell without electrochemical treatment. Coupled AFM+NanoIR imaging (e) and IR spectroscopy (f) of water washed post-EP sample. 512

Figure VIII.13.3 (a) Cationic EP-coating of isoprene on silicon thin-film model surface at 4V vs. Li in 0.2 M LiTFSI in THF. (b, c) ATR-FTIR of reference isoprene monomer, methanol washed post-EP sample, and control sample from cell without electrochemical treatment. (d) Co-electropolymerization coating of styrene and isoprene on silicon thin film at 100 mV aimed at exploiting styrene facile initiation to electrodeposit an elastomeric film of polyisoprene on silicon. (e, f) ATR-FTIR of corresponding reference monomers and methanol washed post-EP sample..... 513

Figure VIII.14.1 Electrochemical performances of the LiPF₆-mixTHF-TEFSi electrolyte. (A) Linear scanning voltammetry of 2.0 M LiPF₆ in mixTHF and LiPF₆-mixTHF-TEFSi using stainless steel as working electrode, scan rate = 0.5 mV/sec. (B) Nyquist plots of electrochemical impedance spectrometry (EIS) with Pt blocking electrodes in 2.0 M LiPF₆ -mixTHF and LiPF₆-mixTHF-TEFSi electrolytes at room temperature. The ionic conductivities are referenced and calculated to the standard electrolyte; (C) the cell performance of $\mu\text{Si} \parallel \text{Li}$ half cells in LiPF₆-mixTHF-TEFSi electrolyte between 0.06 and 1V; (D) the initial, 5th, 20th and 30th charge-discharge profiles of the LiPF₆-mixTHF-TEFSi electrolyte. The capacity retention at 30th cycle was calculated by normalizing to capacity at 2nd cycle..... 516

Figure VIII.14.2 Ionic conductivity and high potential performance of the IL electrolyte. (A) Ionic conductivities of the IL electrolyte at different temperatures measured with EIS between 106 Hz to 103 Hz using stainless steel blocking electrodes. Inset shows the MD simulation predictions. (B) Linear scanning voltammetry in IL and commercialized 1.0 M LiPF₆ in ethylene carbonate/ dimethyl carbonate (EC/DMC, v/v = 1:1) using stainless steel as working electrode, scan rate= 1 mV/sec. (C) the charge and discharge curves of NMC 811 \parallel Li cell in the IL operation at 0.3C. (D) Cycling coulombic efficiency and capacity retention of NMC 811 in IL. 517

Figure VIII.14.3 The cycling CE and the capacity retention of (A) the 1.5 mAh/cm² $\mu\text{-Si}$ anode on Cu current collector in IL; (B) the 3 mAh/cm² $\mu\text{-Si}$ anode on conductive carbon coated Cu current collector in IL-Me and (C) the 4.5 mAh/cm² μSi anode on conductive carbon coated Cu current collector in IL-Me. All tests are performed with activation at 0.1C or 0.05C followed by cycling at 0.2 C or 0.1 C, the 80% capacity retention was calculated by taking the first capacity at 0.2 C (for 1.5 mAh/cm² and 3 mAh/cm²) or at 0.1 C (for 4.5 mAh/cm²) as 100%. 518

Figure VIII.14.4 The capacity retention of the 5 mAh/cm² $\mu\text{-Si} \parallel$ 4.5 mAh/cm² NMC811 full cell between 4.2 and 2.7 V with polypropylene and GF separator. 518

Figure VIII.14.5 (a) Composition of different type of Silicon anode. (b) Calendar life test protocol and Qreversible calculation. (c) Current decay versus time during voltage hold of μSi anode and graphite baseline. (d) Capacity loss versus time during voltage hold of μSi and graphite baseline anodes. (e) Summary of CE and stable current during voltage hold of micro-sized silicon and graphite baseline anodes. (f) Current decay versus time during voltage hold of EC/DEC+FEC electrolyte for μSi anode after 20cycles (CE=99.2%) and 50 cycles (CE=98.7%). 519

Figure VIII.14.6 (a)Current decay versus time during voltage hold of silicon anode with different particle size using 2.0 M LiPF₆ mixTHF. (b) Capacity loss versus time during voltage hold of μSi with different particle size using 2.0 M LiPF₆ mixTHF. (c) Current decay versus time during voltage hold of μSi anode at different temperature (IL electrolytes). (d) EIS curve of ionic liquids 40um Si cell before/after the voltage hold at 55°C. 520

Figure IX.1.1 (a)–(c) SEM images of Mn_{0.35}Ni_{0.6}Co_{0.04}Al_{0.01}(OH)₂ precursor with scale bars of 20, 10, and 5 μm , respectively. (d) EDS Al-mapping..... 522

Figure IX.1.2 (a)–(c) SEM images of a Mn_{0.35}Ni_{0.6}Co_{0.04}Al_{0.01}(OH)₂ precursor calcined at 950°C under oxygen with 10% excess Li, scale bars are 20, 10, and 5 μm , respectively. (d) EDS Al-mapping. 523

Figure IX.1.3 (a) Voltage profiles for the first cycle between 4.5-2.5 V (Li/Li⁺) for a baseline NMC-622 and the Mn_{0.35}Ni_{0.6}Co_{0.04}Al_{0.01}(OH)₂ calcined with stoichiometric Li (red, NMCA) and one with a nominal 10% excess Li (blue, NMCA-10%). (b) Discharge rate capability for the samples in (a) between 4.5-2.5 V (Li/Li⁺). Data was collected after similar rate tests (cycles 1-15, not shown) between 4.3-2.5 V. Rates are given in mA/g at the top of each three-cycle test. Electrode loadings were ~10 mg/cm²..... 523

Figure IX.1.4 (a) Schematic diagram of UV Raman system equipped with wavelength-tunable laser sources and a high-temperature in situ Raman cell, and the UV & near IR region Raman spectra of (b) carbonates, (c) hydroxides, and (d) lithium nickel oxide powder samples. 524

Figure IX.1.5 In situ UV Raman spectroscopy experiment: (top) experiment condition indicating the temperature, atmosphere, and sampling timeline points (a)–(e), (bottom) UV Raman spectra of LiNiO₂ collected after exposing at various controlled atmospheres..... 525

Figure IX.1.6 SEM images of LiNiO₂ synthesized under incrementally different oxygen partial pressures; (a) 0.21 atm, (b) 0.6 atm, and (c) 1.0 atm. All were carried out under identical flow rates and temperature. (d) corresponding XRD patterns, (e) voltage profiles at 3rd cycle, and (f) capacity retention..... 526

Figure IX.2.1 Diagnostic tests are conducted at various stages of the oxide development process..... 530

Figure IX.2.2 Effect of test protocol on aging of NMC9055 full-cells using the Gen2 electrolyte. (a) Discharge capacities. (b) Discharge capacity retention as a function of cycle number. c) Capacity retention as a function of total test time. d) Area-specific impedance (ASI), measured from discharge pulses, as a function of cell voltage at various points of the test. Data in different hues represent different cells. The legend in panel a applies to all panels..... 531

Figure IX.2.3 Effect of electrolyte additives on aging behavior of NMC9055 full-cells. (a) Discharge capacities. (b) Discharge capacity retention. (c) ASI vs cell voltage at various points of the test. Data in different hues in the plots represent different cells with the same electrolyte. The legend applies to all panels. 532

Figure IX.2.4 Effect of temperature on performance cycling of NMC9055//graphite coin cells 534

Figure IX.2.5 Area specific impedance (ASI) vs. cell voltage of NMC90-5-5//graphite cells cycled at (a) 30°C, (b) 40°C, (c) 50°C and (d) 60°C. The ASI values increase with aging; higher HPPC Pulse# indicate higher cycle numbers (more aging)..... 534

Figure IX.2.6 Effect of ALF₃ coating on gassing behavior of NMC9055//Gr pouch cells with uncoated (left) and coated (right) cathodes. 535

Figure IX.2.7 Electrochemical performance of LNO//graphite full cells cycled using the HEHV protocol. (a) Cycle retention at 30°C and 45°C. Voltage profiles of cells at 30°C (b) and 45°C (c). 536

Figure IX.2.8 Voltage profiles (C/20 rate, 30°C) of harvested LNO/Li cells compared with C/20 profiles from the corresponding LNO/Gr cells aged at 30°C (a) and 45°C (b). 536

Figure IX.2.9 XPS analysis of the anode SEI (top) and cathode CEI (bottom). The C1s, F1s and O1s spectra were obtained after formation cycling and after 1HEHV protocol at 30°C and 45°C, respectively..... 537

Figure IX.2.10 Ni deposition at the graphite anode harvested from cells aged at 30°C and 45°C. 538

Figure IX.2.11 SEM on cycled LNO electrodes harvested from cells aged at 30°C (a) and at 45°C (b). 538

Figure IX.2.12 Mass Normalized ⁶Li MAS NMR data from pristine (black), cycled (red) and relithiated (blue) LiNiO₂ electrodes. The insets show related electrochemical cycling data..... 539

Figure IX.2.13 Mass Normalized ⁶Li MAS NMR data from LiNiO₂ samples with various Li contents during (a) charge and (b) discharge..... 540

Figure IX.2.14 STEM-HAADF images to illustrate the surface and bulk lattice evolution of LiNiO₂ cathode upon battery cycling. (a) illustrates evolution of the surface reconstruction layer thickness with increasing

cycling number. (b) indicates the bulk lattice structural evolution, featuring a transition from O3 lattice to O2 lattice and disruption of stacking sequences following extended cycling.....	541
Figure IX.2.15 Capacities (a) and coulombic efficiencies (b) of N9M1/Gr full cells cycled to various UCVs.	542
Figure IX.2.16 ASI vs. cell voltage data from HPPC tests on N9M1/Gr cells cycled to UCVs of (a) 4.2 V, (b) 4.3 V and (c) 4.4 V	542
Figure IX.2.17 Voltage profiles of N9M1 cathodes (vs. Li, C/100 rate) extracted from N9M1//Gr cells after formation cycling and after extended cycling with UCVs of 4.2 V (black), 4.3 V (red) and 4.4 V (green).....	543
Figure IX.2.18 (a) Differential capacity plot of NMC9055 half-cells during first cycle from 3.0 to 4.1 V (green), 4.2 V (red) and 4.4 V (black). (b) Specific discharge capacity for the first 10 cycles.	543
Figure IX.2.19 (a) <i>in situ</i> FTIR spectra of NMC9055 during the first 3 cycles with a UCV of 4.4 V. The TM-O stretching modes of the cathode are observed in the energy region of 630-500 cm^{-1} and both the peak intensities and positions shift with cell charging and discharging. The P-F stretching modes of the electrolyte obscure most of the signals below 560 cm^{-1} . (b) Significant differences in reversible behavior of the TM-O ₆ stretching mode intensities are observed with UCVs of 4.1 (green), 4.2 (red) and 4.4 V (black) during the first few cycles, particularly around the H1 \rightarrow M phase transition occurring between 3.6 and 3.8 V.....	544
Figure IX.2.20 Spectral deconvolution of the <i>in situ</i> FTIR spectra separates contributions from the NMC9055 and electrolyte (1.0 M LiClO ₄ in PC) vibrational modes.....	545
Figure IX.2.21 Charge-discharge voltage profiles of Ni _{0.5} Mn _{0.5} (OH) ₂ with and without initial charge process.	546
Figure IX.2.22 Cycling performance and differential capacity plots of Ni _{0.5} Mn _{0.5} (OH) ₂	546
Figure IX.2.23 (a) Mn K-edge XANES, (b) Ni K-edge XANES, (c) XRD and (d) EDS spectra from pristine and cycled Mn _{0.5} Ni _{0.5} (OH) ₂ samples; legends in the plots indicate cycling conditions and electrolytes used.	547
Figure IX.3.1 Representative single TM layer based on the different ordering cases. (b) Total energy comparison of distinctive structures depending on the TM arrangements with varied Li/Ni exchange amount and their populations. Four different Li/Ni exchange rates were applied: 4%, 6%, 8%, and 10%.....	550
Figure IX.3.2 Comparison of experimental and computed NMR spectra after Gaussian broadening process on each configuration (gold: row with 4% Li/Ni exchange, red: row with 10% Li/Ni exchange, blue: zigzag with 10% Li/Ni exchange, and purple: flower). The broadening is employed on the sum of the histogram values obtained from the four structures.	551
Figure IX.3.3 Energy change with c direction expansion for (a) layered and overlithiated spinel LiNiO ₂ (Li ₂ Ni ₂ O ₄) pinned to NMC-111 and layered LiNiO ₂ , (b) layered and overlithiated spinel LiCoO ₂ (Li ₂ Co ₂ O ₄) pinned to NMC-111 (012) surface. (c) Figure 7. Energy change with expansion/contraction in the c direction for layered, spinel-like and real spinel LiNi ₂ O ₄ pinned to the (012) facets of NMC-111 (black-grey) and pinned to LNO (red).	551
Figure IX.3.4 Ball and stick representation of LiMFP absorbed at the (012) surface of a LiNiO ₂ . One fluorine ion from the original LiDFP salt is shown incorporated in the subsurface oxygen lattice. Blue spheres represent F ions, purple spheres represent P ions, grey spheres represent Ni ions, green spheres represent Li ions and grey sticks represent chemical bonds.....	552
Figure IX.3.5 Oxygen vacancy formation energy vs the difference of energy of selected dopants located at bulk and surface of LiNiO ₂ where the oxygen vacancy was taken (a) next to surface dopant in (012) facet, (b) far from dopant in (012) facet, (c) next to surface dopant in (104) facet, (b) far from dopant in (104) facet.	553
Figure IX.3.6 SEM (a-c) and TEM (d-f) images of the pristine SC-LNO samples: (a, d) Cubic, (b, e) Oct and (c, f) T-Poly. Insets in (a-c) show crystal morphologies with dominating surface facets as indexed.....	553

Figure IX.3.7 1st cycle voltage profiles (a-c) and the corresponding dQ/dV plots (d-f) collected at the indicated cycling rate: (a, d) Cubic, (b, e) Oct and (c, f) T-Poly SC-LNO samples. 554

Figure IX.3.8 Voltage profiles of the first 100 cycles: (a) Cubic, (b) Oct and (c) T-poly SC-LNO samples. Cells were cycled between 2.7 and 4.6 V at 0.1C for the first two cycles and then at 0.3C. Data plotted in every 20 cycles except the first cycle at 0.1C and 0.3C. d) Cycling stability shown in discharge capacity as a function of cycle number. 555

Figure IX.3.9 STEM-HAADF images collected on various facets of the pristine (a-e) and cycled (f-j) SC-LNO samples: (a, f) (104) of Cubic, (b, g) (012) of Oct, (c, h) (001) of T-Poly, (d, i) (01-1) of T-Poly and (e, j) (010) of T-Poly. Cycled samples were recovered at discharged state after 100 cycles between 2.7 and 4.6 V. The insets show magnified images of the surface. 555

Figure IX.3.10 XPS analysis of C 1s (a-c), O 1s (d-f) and F 1s (g-i) of SC-LNO samples after 100 cycles: (a, d, g) Cubic, (b, e, h) Oct and (c, f, i) T-Poly. 556

Figure IX.4.1 (a) First-cycle activation of $x\text{Li}_2\text{MnO}_3 \cdot (1-x)\text{LiMn}_{0.5}\text{Ni}_{0.5}\text{O}_2$, with $x = 0.1, 0.3, 0.5$, between 4.6-2.5V in graphite full-cells (30°C, C/20). (b) 4th cycle dQ/dV plots between 4.4-2.5V for the cells in (a), the blue line marks the general onset of impedance rise for all samples at ~3.5V, the inset shows a magnified view of the small process occurring at ~3.0V. (c) ASI values as a function of SOC obtained during the first HPPC cycle (7th cycle) for the cells in (a), blue dots indicate the ~3.5V mark for each cell. 560

Figure IX.4.2 (a) ASI data function of HPPC cycle and voltage and (b) and (c) as a function of HPPC cycle and SOC. HPPC cycles increase from top to bottom (arrow), HPPC 1-5. Figure (b) SOC's are relative to the capacity achieved before each HPPC test during the 120 cycles. Figure (c) SOC's are relative to the initial capacity achieved before the first HPPC test. 561

Figure IX.4.3 (a) ASI data as a function of HPPC cycle and voltage and (b) and (c) as a function of HPPC cycle and SOC. Figure (b) SOC's are relative to the capacity achieved before each HPPC test during the 120 cycles. Figure (c) SOC's are relative to the initial capacity achieved before the first HPPC test. The inset of Figure (c) shows ASI values at a constant 32% SOC (dashed line in Figure) vs cycle number. HPPC cycles can be seen to increase from left to right to (arrow), HPPC 1-5. 561

Figure IX.4.4 Visual representations of the data discussed in the text correlated across (a) ASI as a function of V, (b) dQ/dV over ~120 cycles, and (c) ASI as a function of SOC. The green regions represent fairly good Li insertion behavior expected for layered oxides; the yellow regions indicate lithium contents over which the impedance values drastically increase; and the red regions mark SOC's/capacity that cannot be accessed under the tested protocol. 562

Figure IX.4.5 ASI response over long-term cycling (left) cycle 7-8, (middle) cycle 31-32, and (right) cycle 55-56. The red data sets were collected after charging directly to 3.6V and the blue data set after charging first to 4.5V followed by discharge to 3.6V. Each HPPC was preceded by a 30 min hold at 3.6V. The blue bar line highlights the decrease in ASI at low SOC's over cycling. Delta values listed show the differences in ASI between the data sets at a constant ~23% SOC. 563

Figure IX.4.6 Comparison of the surface-treated $x=0.3$ composition with an industrially prepared NMC-622 under the standardized protocols used for this work using graphite electrodes. The dashed line represents ~80% capacity retention for both electrodes. The inset shows specific energy (Wh/kg_{oxide}) delivered by each cathode-electrode on cycles 10, 118, and 250. 564

Figure IX.4.7 (a) Voltage profiles of Li/LT-LiMn_{0.5}Ni_{0.5}O₂ cells ($i = 15$ mA/g), (b) corresponding differential capacity (dQ/dV) plot (2nd cycle), (c) cycling stability (open = charge, solid = discharge), and (d) synchrotron XRD patterns of LT-LiMn_{0.5}Ni_{0.5}O₂ electrodes at various states of charge (1st cycle). 565

Figure IX.4.8 SEM and (b-d) HAADF-STEM images of LTLiMn_{0.5}Ni_{0.5}O₂. 566

Figure IX.5.1 Electrochemical performances of F10 cathode. a, b) Voltage profiles and corresponding dQ/dV plots at a current density of 10 mA/g. c, d) Comparison of the specific discharge capacity and capacity

retention at various current densities. e) dQ/dV plots at various cycling current densities collected on cycled F10 cathode. f) ASI as a function of the depth of discharge during the 1st and 30th discharge, respectively.... 570

Figure IX.5.2 a) Normalized Mn *K*-edge XANES spectra collected on indicated electrodes. Reference spectra from Mn³⁺/Mn⁴⁺ oxide standards are shown in grey. b) Mn *K*-edge energy position and average Mn valence as compared to the references c) Quantification of Mn valence distribution and the average Mn valence from Mn *L*₃-edge mRIXS-iPFY spectra collected on D1 and D30 electrodes. d) O *K*-edge mRIXS data obtained for the pristine, 1st and 30th charged electrodes. 571

Figure IX.5.3 Local structural analysis for the pristine and cycled F10. a) ⁷Li spin echo MAS NMR spectra (black lines) and pj-MATPASS isotropic spectra (grey shaded areas) recorded at a magnetic field $B_0 = 2.35$ T and a sample spinning frequency of 60 kHz. B) Time-of-flight neutron diffraction data collected on electrodes. c) SAED patterns viewed along [100] zone axis. d) Raman bands for the Mn–O stretching modes. Spectra fitting was carried out using Voigt functions. 572

Figure IX.5.4 Cycling performance of highly fluorinated DRX cathodes. (a) Specific capacity of $M_{0.60}F_{0.60}$ during cycling at different charge cutoff voltages, cells are cycled at C/20; and (b) specific discharge capacity of $M_{0.60}F_{0.60}$ and $M_{0.625}F_{0.675}$ cathodes within 4.5–1.5 V range, cells are cycled at C/20 during the first two cycles and C/3 at Cycle 3–100. 573

Figure IX.5.5 Synthesis and electrochemical performance of $Li_{1.2}Mn_{0.4+z/3}Nb_{0.4-z/3}O_{2-z}F_z$. (a) XRD patterns collected on the samples as labelled; (b) specific discharge capacity; (c) selected voltage profiles during the first 20 cycles; and (d) GITT voltage profiles, yellow areas highlight the relatively large polarization in the high voltage region. Cells are cycled at C/20 between 4.8 and 1.5 V. 573

Figure IX.5.6 a) First cycle charge and discharge voltage curves for three different carbon contents, b) Galvanostatic cycling of LMNOF between 1.8 and either 4.7 V with a constant voltage hold or 4.8 V, c) CV data of LMNOF cathode. After five cycles, the lower cut-off voltage was increased from 1.3 V to 1.8 V. 574

Figure IX.6.1 Calculated surface energies as a function of facet for a broad range of ionic configurations of disordered rocksalt Li_2MnO_2F . The data points are plotted with a small variation along the x-axis to improve readability. 578

Figure IX.6.2 DEMS results for LMNOF series of DRX materials. All three materials were cycled at 0.1 Li hr⁻¹ between 4.8 V and 1.5 V using 1M LiPF₆ in EC-DEC. 578

Figure IX.6.3 Oxygen *K*-edge RIXS maps of 12 different DRX electrodes cycled to fully charged state (4.7–4.8 V). The RIXS maps are plotted with increasing fluorination levels from top (zero fluorination) to bottom (>0.6 fluorination) panels. White grid lines indicate the two fingerprinting features in RIXS on oxidized oxygen in the lattice. 579

Figure IX.6.4 STEM-HAADF images and corresponding EELS maps of nanoscale surface regions to reveal structural evolution with respect to F concentration. (a, b) Comparison of LMNOF₀ at pristine and after 30 cycles. (c, d) Comparison of LMNOF_{0.05} particle at pristine and after 30 cycles. (e, f) Comparison of LMNOF_{0.2} particle at pristine and after 30 cycles. The result shows cycling-induced structural and chemical reconstruction in these cathode particles. 580

Figure X.1.1 Structural evolution of cathode thin-film with/without carbonate-based electrolyte (A) XRR of 10 nm NMC532 films grown on SrTiO₃ substrates with 15 nm SrRuO₃ buffer layers; (B) Off-specular phi-scans of STO {001}, NMC {104}, and NMC {003} of the film; C) SXRD of NMC532 films before and after exposure to EC-EMC solvent and LP57 electrolyte 585

Figure X.1.2 **Transition metal-dependent degradation of NMC cathode in carbonate-based solvent and electrolyte.** Total-reflection X-ray absorption near edge structure (XANES) of NMC thin-films before and after exposure to EC-EMC solvent and LP57 electrolyte at Ni, Co, and Mn *K*-edges 586

Figure X.1.3 **Protonation reaction pathway between cathode and carbonate-based electrolyte.** A) DFT calculation of EC and LiPF₆ salt decomposition reactions and their reaction activation energy on standard cathode $Li_{0.5}NiO_2$ surface; B) Illustration of the possible proton transfer pathways inside layered structure in

cathode; C) Illustration of the interfacial degradation of NMC cathodes through surface protonation due to the deprotonation reaction of EC solvent on cathode surface..... 586

Figure X.1.4 **Solvent effect on cathode degradation and stabilization.** A) Ni L-edge XAS of NMC thin-film before and after exposure to carbonate electrolyte LP57, fluorinated electrolytes 1F and 3F; B) O K-edge XAS of NMC thin-films after exposure to carbonate electrolyte LP57 and fluorinated electrolytes 1F and 3F 587

Figure X.1.5 (A) Electrochemical stability window of carbonate-based LP57 electrolyte and fluorinated electrolytes. (B) Voltage drop of NMC thin-films after charging to 4.2 V in LP57 electrolyte: (C) The leakage current of the NMC532 thin-films during the potential hold at 4.2 V 588

Figure X.1.6 Preliminary TOF-SIMS (A) pristine NMC. (B) charged to 4.2 V and relaxed. (C) charged to 4.5 V and relaxed. (D) and (E) deuterium TOF-SIMS summary..... 588

Figure X.2.1 a) Electrochemical oxidation of EC in 1.1 M LiClO₄/EC. Disk current is shown in blue, ring current, corresponding to the amount of protons created, is shown in red, and their ratio, is shown in orange. OEMS data for CO₂ and CO is depicted by purple and blue dashed curves. b) first step of the reaction mechanism – 3 possible reaction pathways are shown 594

Figure X.2.2 a) Electrochemical oxidation of FEC in 1.1 M LiClO₄/FEC. Disk current is shown in blue, ring current, corresponding to the amount of protons created, is shown in red, and their ratio, is shown in orange. OEMS data for CO₂ and CO is depicted by purple and blue dashed curves. b) Electrochemical oxidation of VC in 1.1 M LiClO₄/VC..... 595

Figure X.2.3 a) Electrochemical oxidation of organic carbonate solvent series. Only disk currents are shown. The order of stability is as follows VC<<DFEC<FEC~PC<EC..... 596

Figure X.2.4 The reactions of protons with a) solvent, b) NMC 622, c) PF6-..... 596

Figure X.3.1 (Left) XRD patterns of Li₄Mn₂O₅ synthesized with various amounts of excess Li₂O and (right) first cycles of these materials..... 599

Figure X.3.2 (Top left) Mn K-edge XAS data for pristine Li₄Mn₂O₅ electrodes and those charged to the indicated potentials, along with reference materials. (Top right) Mn L-edge soft XAS data for pristine and charged electrodes in TEY mode. (Bottom left) O K-edge soft XAS data in TEY mode for pristine and charged electrodes and (bottom right) O K-edge soft XAS data in FY mode..... 600

Figure X.3.3 (Upper left) capacity retention as a function of voltage limits for cells containing Li₄Mn₂O₅. (Upper right) dQ/dV plots showing evidence of structure evolution). (Bottom left) Mn K-edge XAS spectra on pristine and cycled electrodes as a function of voltage limits. (Bottom right) ex situ XRD patterns on pristine and cycled electrodes as a function of voltage limits..... 601

Figure X.3.4 (Left) XRD patterns of Li₄Mn₂O₅ and Li₄Mn₂O₄F. (Right) Hard XAS data on pristine Li₄Mn₂O₄F with reference materials..... 601

Figure X.3.5 (Top left). Voltage profiles of a cell containing Li₄Mn₂O₄F as a function of cycle number. Compare to (top right) data for cell containing Li₄Mn₂O₅. (Bottom left) dQ/dV plots for cell containing Li₄Mn₂O₄F, and (bottom right) capacity as a function of cycle number for cells containing Li₄Mn₂O₄F or Li₄Mn₂O₅ as a function of voltage limits used..... 602

Figure X.4.1 Properties of doped NMC76 single crystals with reduced particle size. (a) Scanning Electron Microscope (SEM) image of downsized NMC76 single crystals with an average size of 2 μm. (b) SEM image of doped NMC76 single crystals after 300 cycles. (c) Comparison of the first charge and discharge curves between undoped and doped NMC76 single crystals. (d) Comparison of long-term cycling stability of undoped and doped NMC76 crystals. The first two cycles are charged and discharged at C/10, while in the subsequent cycling C/3 is applied for charge and discharge. 605

Figure X.4.2 Scheme for *in situ* DEMS, gas analysis and surface morphology evolution of polycrystalline and single crystal NMC76. (a) Illustration of *in situ* DEMS system. (b, c) Gas evolution during the potential stepping procedures as a function of potential applied on the cells consisting of (b) polycrystalline NMC76 and

(c) single crystal NMC76. The cells are firstly charged to 4.3 V. From 4.3 to 4.8 V, the potentials applied on the cells are gradually elevated with a step size of 0.1 V and held for 0.5 hour at each potential. *Upper panels in (b) and (c):* cell voltage vs. time. *central panels in (b) and (c):* CO₂ evolution rate measured by *in situ* DEMS. *lower panels in (b) and (c):* gas evolution rates for O₂, H₂ and CO. (d, e) Microstructural evolution of (d) polycrystalline NMC76 and (e) single crystal NMC76 captured by *in situ* AFM in a functioning electrochemical cell charged to 4.9 V. (f) Summary of gas generation when charging cells consisting of polycrystalline and single crystal NMC76. 607

Figure X.5.1 Chemical stability with lithium metal anode for 1 M and 5 M LiFSI-PMpipFSI electrolyte containing 0.2 M, 1 M, and 2 M H₂O, respectively. (a) Lithium anode in water-containing electrolytes at various period of time; (b) moisture content vs immerse time. 611

Figure X.5.2 Cycling performance and first cycle voltage profiles of NMC532/Li cell with water-containing electrolytes. (a), (c) 1 M LiFSI-PMpipFSI with various H₂O contents and (b), (d) 5 M LiFSI-PMpipFSI with various H₂O contents. 612

Figure X.5.3 Molecular number density profiles along the z-axis normal to the surface of NMC cathode (left panels) and lithium anode (right panels). Center of mass of each molecule is used to calculate molecule distribution. On both electrodes, a tight adsorption layer of H₂O-Li⁺ is followed by an ordered layer of PMpipFSI. The thickness of H₂O-Li⁺ layer on each electrode surface is ~2 Å at all H₂O concentrations studied here. 613

Figure X.5.4 Snapshots of layering of H₂O-Li⁺-IL on NMC cathode surface (a), (c) and Li anode surface (b, d) at concentration of 5 M LiFSI-PMpipFSI with 1 M and 5 M H₂O, respectively. On both electrodes, there is a tight adsorption layer of H₂O-Li⁺ (O, red; Li, green) followed by an ordered layer of IL (cation, cyan; anion, yellow). 613

Figure X.5.5 Water clustering of the H₂O-Li⁺ (green) adsorption layer at anode surface. The FSI anions (yellow), which marginally overlap with the H₂O-Li⁺ adsorption layer is also shown. At concentration of 5 M LiFSI with 1 M H₂O, there is no water clustering; at concentration of 5 M Li salt and 5 M H₂O, strong water clustering is observed; at concentration of 1M Li salt and 1 M H₂O, weak water clustering can be seen. Nearest oxygen-oxygen (O-O) contact distance calculation is used to estimate size of water clusters. The O-O contact is set as 6.0 Å for concentration of 5 M Li salt and 1M H₂O, 4.0 Å for concentration of 5 M Li salt and 5 M H₂O, and 6.0 Å for concentration of 1 M Li salt and 1 M H₂O, respectively. In the above three lithium salt-water concentrations, the most probable size of water cluster is 1, 8 and 4, respectively. 614

Figure X.6.1 Schematic of a typical scanning electrochemical microscopy / Al Hicks, NREL 618

Figure X.6.2 SECM tip voltammograms collected before and after a high voltage hold of a model LMO cathode. Data shown for the 1M LiClO₄:PC electrolyte on the left in PC and on the right in EC. Inset shows photographs of electrolyte samples pre- and post-voltage hold. 619

Figure X.6.3 SECM tip voltammetry collected before and after holding a model LMO substrate at 4.5V for five hours. Inset shows photographs of electrolyte samples pre- and post-voltage hold. 620

Figure X.6.4 SECM tip voltammetry collected before and after holding a PAD-based model cathode (left) and composite cathode (right) at 4.5V. This data was collected using the 1MLiClO₄:PC electrolyte. Inset photograph shows composite electrode after the voltage hold experiment. 621

Figure X.6.5 SECM tip voltammetry collected before and after holding a PAD-based model cathode (left) and composite cathode (right) at 4.5V. This data was collected using the 1MLiPF₆:PC electrolyte. Inset photograph shows composite electrode after the voltage hold experiment. 621

Figure XI.1.1 Picture of (a) the pilot scale slurry making process using RST NCM811, (b) electrode coating using SAFT pilot slot-die system, (c) sample lithium-ion cell delivered to INL and TARDEC 624

Figure XI.1.2 NCM9055 cathode powder made by RST (a) particle size distribution, D50= 5.2mm; (b) half-cell formation cycles: 215 mAh and 91% C.E; and (c) half-cell cycle life, the inset is a NCM9055 SEM image. 625

Figure XI.1.3 Surface coated NCM9055 were used to make full coin cells made with NCM9055 coated with different amounts of fumed alumina (a) rate capability (b) cycling plots showing the advantage of surface coating.....	625
Figure XI.1.4 SEM images for alumina surface coated NCM811 (a) and (b) were coated with FA-1 and (c) with FA-2. A and B is the wt% of fumed alumina used where $B > A$. FA-2 has a higher BET surface area compared to FA-1.	626
Figure XI.1.5 Cycle-life of FA coated NCM811 (commercial core) at 45°C, 1C/1C for coin-cells, 0.5C/1C for pouch cells, using different CCA formulations.	626
Figure XI.1.6 (a) Cell cycle life showing the influence of different CCA wt%, RST NCM811 cathodes (1C/1C, 45°C, 2.8-4.2V). (b) CCA effect on cycle-life of NCM9055 cathode powder made by RST in full coin-cells using 20 mg/cm ² cathodes, 1C-1D, 45°C, 2.8-4.2V cycling conditions.	627
Figure XI.1.7 (a) Full cell cycle life (1C/1C, 45°C) capacity retention using a% BlendA vs. a%CNT-C2 with FA-coated NCM811 (commercial core). (b) DC-IR during cycling of a% BlendA vs. a%CNT-C2.	627
Figure XI.1.8 (a) Interim pouch cell (120 mAh). (b) Plot showing cathode energy retention (left Y-axis) and capacity loss (right Y-axis) are plotted and compared to the project progress cell (PPC) data	628
Figure XI.2.1 Cycling performance of the LNMO-graphite single layer pouch cell.	630
Figure XI.2.2 Schematic of lithium inventory loss in LNMO-graphite cell.	631
Figure XI.2.3 Experimental procedure of calendar life testing. (b) Normalized capacity retention under calendar life testing with various resting time. (c) Reversible (black) and irreversible (red) capacity growth after the first resting time. (inset) Definition of reversible and irreversible capacity loss. Green bars represent full discharge capacity at C/3 before and after the storage cycle, and the yellow and blue bar represents 10% partial discharge before the storage and remaining discharge capacity after the storage during the storage cycle.	632
Figure XI.2.4 Schematic of Li inventory inside LNMO-graphite cell during calendar life test.	633
Figure XI.2.5 (a) STEM image of Fe-doped LNMO and (b) EELS mapping result of the selected area.	634
Figure XI.2.6 (a) Long-term cycling performance of Fe-doped LNMO/ALD-graphite full cell, and (b) average charge/discharge voltage plots with cycle number.	634
Figure XI.2.7 Comparison of the cycling performances of LNMO/pristine-Graphite and LNMO/ALD-Graphite full cells.	635
Figure XI.2.8 TOF-SIMS (a) three-dimensional mapping and (b, c) depth profiles of surface evolution of Graphite and ALD-Graphite electrodes after 300 cycles in full cell.	635
Figure XI.2.9 Discharge capacity and Coulombic efficiency along cycling of 3 mAh/cm ² LNMO/graphite full cells with different electrolytes; the cells were cycled between 3.3-4.85 V with C/3. Data from UCSD team.	637
Figure XI.2.10 Discharge capacity along cycling of 3 mAh/cm ² LNMO/graphite full cells with different electrolytes; the cells were cycled between 3.3-4.85 V with C/3. Data from ARL team.	637
Figure XI.2.11 SEM images of separators after 3 formation cycles in 3 mAh/cm ² LNMO/graphite full cell. (a) Celgard 2400 facing the cathode, (b) Celgard 2400 facing the anode, (c) GF/F glass fiber facing the cathode, (d) GF/F glass fiber facing the anode, (e) Dreamweaver facing the cathode, (f) Dreamweaver facing the anode, (g) C5 coated side facing the cathode, (h) C5 uncoated side facing the anode, (i) C5 uncoated side facing the cathode, (j) C5 coated side facing the anode, (k) C5 coated side facing the cathode, (l) C5 coated side facing the anode.	637
Figure XI.2.12 (a) Formation cycle voltage profile of 3 mAh/cm ² LNMO/graphite full cells using different separators; the cells were cycled between 3.3-4.775 V with C/20. (b) Discharge capacity and Coulombic	

efficiency along cycling of full cells with different separators; the cells were cycled between 3.3-4.85 V with C/3 for the cycling.	638
Figure XI.2.13 (a) Voltage profiles of 1 st C/10 and 1 st C/3 performance of the 3 mAh/cm ² level half-cell and (b) its cycling performance.	638
Figure XI.2.14 (a) Voltage profiles of 1 st C/10 and 1 st C/3 performance as well as the cycling performance of the 4 mAh/cm ² level half-cell. (b) LSV results of bare Al foil, PVDF cast on bare Al foil, and Tesla's carbon-coated Al foil. Inset is the full cell cycling of the 3 mAh/cm ² level Tesla's dry electrode.	639
Figure XI.2.15 (a) Long-term cycling performance and (b) Charge-discharge profile of high mass loading (4 mAh/cm ²) Fe-doped LNMO (dry-coated)/graphite full cell.	639
Figure XI.2.16 Electrochemical performance of 4mAh/cm ² level full cell using ALD graphite including (a) capacity and (b) Coulombic efficiency.	640
Figure XI.3.1 Material and electrochemical characterization of NFA Gen-2 cathode compositional variants: (a) X-Ray diffractogram, (b) Mossbauer spectra, (c) Galvanostatic charge/discharge cycling performance assessment, (d) Galvanostatic charge/discharge cycling performance of the best performing compositional variant under different voltage windows.	644
Figure XI.3.2 Upscaled NFA Gen-2 cathode material: SEM micrographs of (a) cathode precursor, (b) calcined cathode material, (c) EDS compositional maps of the calcined cathode material, (d) X-Ray diffractogram of the calcined cathode material.	645
Figure XI.3.3 Electrochemical performance assessment of upscaled NFA Gen-2 cathode material: (a) Cyclic voltammogram, (b) Galvanostatic charge/discharge profiles, (c) Cycling performance assessment in half coin cells and (d) Cycling performance assessment of 100 mAh NFA Gen-2 full cells.	646
Figure XI.4.1 (a) Experimental set-up for the coprecipitation of UCI Gen2 cathode with a 2-liter batch reactor (the upper panel) and the morphology of the precursor (the middle panel) and secondary particles (the lower panel). (b) DSC profiles of LNO, NMC-811, NMC-622, NMC-532, and UCI Gen2 cathode charged to 4.3 V. (c) Full-cell long-term cycling performance of UCI Gen2 cathode with graphite as an anode. (d) TXM tomography and FIB cross-section of the long-cycled UCI-Gen2 cathode in comparison with NMC-811(100 cycles, 2.5V-4.4V, 1C). (e) Ni-K XANES and FT-EXAFS of UCI-Gen2 and commercial NMC-811 at different cycles.	652
Figure XI.4.2 (a) SEM images of the synthesized single-crystalline NMC-811. (b) HAADF-STEM image and (c) electron diffraction of single-crystalline NMC-811. (d) Charge/discharge profiles, rate capability and impedance tests of the single-crystal NMC-811 in comparison with its polycrystal counterpart. (e) TXM tomography of the single-crystalline NMC-811 cathode after long cycling. (f,g) SEM images showing the morphology of the single-crystalline UCI-Gen2 cathodes synthesized by two different methods.	653
Figure XI.4.3 (a) Schematic of the two-step transformation from O1 phase to rocksalt. (b) 3D imaging of the cracks in LNO with severe oxygen loss. (c) HRTEM image of a crack formed in the doped LNO showing an alternating arrangement of RS and cracks. (d) Atomic-resolution images showing the formation of O1 phase in discharged LNO after cycling. (e) Misfit strain and defect generation at O1/O3 interface.	654
Figure XI.4.4 (a) XRD patterns at different stages of calcination. (b) Evolution of the normalized intensity of the (003) peak and the (104) peak. (c) The intensity ratio of the (003) peak to the (104) peak at different stages of calcination. (d) Neutron diffraction patterns and Rietveld refinement at 600°C and 700°C for 2 h.	655
Figure XI.4.5 (a) Charge/discharge profiles of the cell containing VT Gen 2 cathode at C/10 at 60°C. (b) The comparison of the cycling stability of the cells operated at 22°C and 60°C. (c) Concentration histogram of the Ni deposited on the Li anodes cycled against the VT Gen 2 cathode at different temperatures, the Ni concentration (unit: 10 ⁻⁸ mol cm ⁻²) distribution on the Li anodes cycled at (d) 22°C and (e) 60°C.	656
Figure XI.4.6 Average discharge capacities of (a) Gr NMT SLPCs and (b) Gr NMT DLPCs plotted as the function of cycle number in the voltage range of 2.8-4.4 V and at 25.0°C. The missing data in the figures was caused by the malfunction of the battery tester.	657

Figure XI.4.7 (a) Cycle performances of Gr NMT batteries using Bare NMT and various ratios of PP coated NMT after storage in the dry box for 2 weeks. (b-d) XRD patterns of fresh and stored Bare NMT and PP 0.25%@NMT. (e) XPS F1s spectra of bare NMT and PP@NMT. (f) Cross-sectional SEM images of bare NMT and PP@NMT. (g) The (003) peak from XRD patterns of bare NMT and PP@NMT after cycling at C/3 rate under 25°C of Gr NMT batteries using NMTs after storage in the air for 2 weeks (1C = 200 mA g ⁻¹ or 1.5 mA cm ⁻²).	657
Figure XI.4.8 (a) Cycle performances and (b) Nyquist plots after 500 cycles at C/3 rate under 25°C of Gr NMT cells with the exposed PP@NMT using E-baseline and E-DME-F.	658
Figure XI.4.9 Testing results from cycling at RT and at 45°C	659
Figure XI.4.10 (a) Low temperature discharge testing and (b) thermal stability evaluation.	660
Figure XI.5.1 Full cell cycling data for pristine NMA (P-NMA), ultrathin coated NMA (UTC-NMA), and Ultrathin coated and ball milled NMA (UTC-BM-NMA). The P-NMA and UTC-BM-NMA have the same discharge capacity when charged to 4.4 V and the UTC-BM-NMA retains more of its capacity after 100 cycles.	664
Figure XI.5.2 (a) Ionic conductivity and (b) interfacial resistance of EC-free LiPF ₆ /EMC electrolyte at different concentrations of LiPF ₆ and FEC. EC-containing baseline electrolyte is shown for a reference (1.0 M LiPF ₆ in EC/EMC with a 3:7 weight ratio).	665
Figure XI.5.3 (a) DSC profiles of NMA charged to 4.4 V in different electrolytes. (b) Rate performance of NMA half cells with different electrolytes. Half cells were cycled between 2.8 and 4.4 V at 25°C under various current densities between 0.1C to 5C rates. (c) Long-term cycling performances of NMA/graphite full cells with different electrolytes. The full cells were cycled between 2.5 and 4.2 V at 25°C under 0.5C charge rate and 1C discharge rates. (d) Voltage hysteresis of NMA full cells. Hysteresis is defined as the difference between average charge and discharge operating voltages.	666
Figure XI.5.4 (a) Images of FEC-containing electrolytes stored inside a glovebox for 1 month. (Top row) 1.5 M LiPF ₆ /EMC electrolytes with different FEC concentrations. (Bottom row) Equivalent electrolytes with 1 wt.% LiTDI added. (b) Long-term cycling of NMA/graphite full cells with baseline, FEC, and FEC-LiTDI electrolytes. Cells were cycled between 2.5 to 4.2 V at 25°C under 0.5C charge rate and 1C discharge rate.	667
Figure XI.5.5 (a) Wt. % of Li ₂ CO ₃ measured on NMC, NCA, and NMA after storage in a saturated humidity chamber. (b) SEM images of pristine and stored NMC, NCA, and NMA, showing morphologies of cathode surface and of grown Li ₂ CO ₃ surface species. (c-d) Cycling performance of NMC, NMA, and NCA before and after storage in a saturated humidity chamber. The capacity retention of the stored materials relative the pristine materials is included to aid in comparison.	668
Figure XI.6.1 Schematic of the technical approach for creating high-performance LNMTO Li-ion cathodes.	671
Figure XI.6.2 SEM image of HAWCS synthesized LNMO powder; initial (a), and modified process that achieves larger particle size powder (b).	672
Figure XI.6.3 Single-layer pouch (SLP) full-cell cycle-life at 25 °C comparing LNMO cathodes with different particle sizes. Graphite anode with N/P ratio 1-1.01, Cathode binder LiPAA. Electrolyte 1 M LiPF ₆ in 1:1 wt. EC/EMC (no additive). Cycling conditions: Cycle 1-3: C/10 then C/3.	672
Figure XI.6.4 XRD spectra of LNMO/LNMTO core/shell powders with different shell thicknesses (a), and Cycle performance of coin-cell half-cells (b), comparing LNMTO shell thickness. Electrolyte 1 M LiPF ₆ in 1:1 wt. EC/EMC. Cycling conditions: Cycles 1,2: C/10 then C/3.	673
Figure XI.6.5 SEM images of LNMO powder synthesized through the HAWCS process with different initial precipitating processes (precipitating agent-to-transition metal ratio): 4:1 (standard) (a), 6:1 (b), and 8:1 (c).	673
Figure XI.6.6 Charge/discharge-voltage profiles of LNMO half-cells at 25 °C comparing different precipitating agent-to-transition metal ratios - 4:1 (standard), 6:1, and 8:1. Electrolyte 1 M LiPF ₆ in 1:1 wt. EC/EMC (no additive). Cycling conditions: Cycle 1-2: C/10 then C/3.	673

Figure XI.6.7 Cycle-life of LNMO/LNMTO half-cell coin-cells (a), and SLP-cells with various LNMTO shell compositions (varying Mn-to-Ti ratios). Electrolyte 1 M LiPF ₆ in 1:1 wt. EC/EMC (no additive). Cycling conditions: Cycle 1,2: C/10 then C/3.	674
Figure XI.6.8 Cycle performance of Iteration 1 LNMO/LNMTO single-layer pouch (SLP) full-cells at 25°C: fresh and old LiPAA binder (a) fresh LiPAA binder. Cell configuration: MCMB graphite with N/P ratio 1-1.01, Cathode binder LiPAA. Electrolyte 1 M LiPF ₆ in 1:1 wt. EC/EMC (no additive). Cycling conditions: Cycle 1-3: C/10 then C/3. Comparison of cathode electrodes with different LiPAA binder (b)	674
Figure XI.6.9 Cycle performance of LNMO/LNMTO core/shell SLP full-cells at 25 °C with different LNMTO shell thicknesses and comparing two anode formulations. MCMB graphite anode with N/P ratio 1-1.01, Cathode binder LiPAA. Electrolyte 1 M LiPF ₆ in 1:1 wt. EC/EMC (no additive). Cycling conditions: Cycle 1-3: C/10 then C/3.	675
Figure XI.7.1 a) Capacity retention of the LFP-coated NCM/graphite cells during C/3 cycling at room temperature and 40°C. b) DCR of the LFP-coated NCM/Gr cells during C/3 cycling at room temperature and 40°C.) C/3 capacity retention of the LIBs using different cathode materials during storage at 22°C and 40°C, respectively.	678
Figure XI.7.2 dQ/dV curves at 1 st , 20 th and 50 th cycle for bare and 1% AlPO ₄ coated LiNi _{0.92} Co _{0.055} Mn _{0.025} O ₂	679
Figure XI.7.3 SEM image on cross-section and c-d) XPS spectrum for bare and 1% AlPO ₄ coated LiNi _{0.92} Co _{0.055} Mn _{0.025} O ₂ electrode after 200 cycles, respectively.	679
Figure XI.7.4 XRD patterns of pristine and Mo-coated NMC.	680
Figure XI.7.5 Electrochemical performance of pristine and Mo-coated NMC.	680
Figure XI.7.6 STEM EDS mapping to reveal spatial distribution of W in Li[Ni _{0.9} Co _{0.09} W _{0.01}]O ₂ at pristine and following 1500 cycles. The white dashed lines outline the surface of cathode. (a) HAADF-STEM image of the NCW pristine cathode. (b) The 3D compositional profile of W plotted based on the EDS mapping and corresponding to (a). (c) HAADF-STEM image of the NCW cathode after 1500 cycles. (d) The 3D compositional profile of W based on the EDS mapping and corresponding to (c).	682
Figure XI.7.7 STEM-HAADF and Annular Bright field image to reveal the surface structure of Li[Ni _{0.9} Co _{0.09} W _{0.01}]O ₂ (NCW) at pristine and following 1500 cycles. (a) The HAADF-STEM image of pristine NCW cathodes. (b) The HAADF-STEM image of 1500 cycled NCW cathodes. (c) The ABF-STEM image of cycled NCW cathodes.	682
Figure XI.7.8 Electrochemical performance of W and Zr doped cathode. (a-b) Discharge capacity as a function of cycle number at between 3-4.2 V for Li[Ni _{0.9} Co _{0.09} W _{0.01}]O ₂ , and LiNi _{0.76} Mn _{0.13} Co _{0.10} Zr _{0.01} O ₂ , respectively.	683
Figure XI.7.9 Zr distribution in pristine and cycled NMCZ. The white dashed lines outline the surface of cathode. (a) HAADF-STEM image of the NMCZ pristine cathode. (b) The 3D compositional profile of Zr plotted based on the EDS mapping and corresponding to a. (c) The HAADF-STEM image of pristine NMCZ cathodes. (d) HAADF-STEM image of the NMCZ cathode after 1000 cycles. (e) The 3D compositional profile of Zr based on the EDS mapping and corresponding to d. (f) The HAADF-STEM image of cycled NMCZ cathode, with a thick disordered rocksalt phase developed on surface. (g) The ABF-STEM image of 1000 cycled NMCZ cathodes.	684
Figure XI.7.10 a) SEM image of co-precipitation product LiNi _{0.92} Co _{0.055} Mn _{0.025} O ₂ of 300g batch. b) XRD patterns of co-precipitation product from 150g batch and 300g batch	685
Figure XI.7.11 SEM images of LiNi _{0.92} Co _{0.055} Mn _{0.025} O ₂ precursor mixed with LiOH.H ₂ O at different speeds.	685
Figure XI.7.12 Cycling performance of LiNi _{0.92} Co _{0.055} Mn _{0.025} O ₂ calcined at a) different loading mass and b) different oxygen flow.	686

Figure XII.1.1 Graphene-subsurface Nano-FTIR. (top) schematic of the nano-FTIR experiment. Solid implies either PMMA or mica substrates (bottom) normalized phase of the 2nd harmonic (near field) FTIR signal. Exponential fitting yields a decay constant of ~ 3.6 nm	689
Figure XII.1.2 In situ characterization of the graphene – solid state electrolyte interface and interphase as a function of heating and electrochemical state with scattering-type near-field infrared nanospectroscopy. a) three-dimensional schematic of our experimental setup including metal-coated AFM probe, incident and backscattered infrared light, and cross section of assembled anode free G/SSE/Li cell atop heater element. Inset on the right-hand side is an artistic representation of the tip-sample near-field coupling that enables nanoscale FTIR. b), the electrochemical voltage profile applied to full cell device. Overlaid colored regions with descriptive text describe the state of the device. c), cross sectional illustrations of the device, near the G/SSE interface, for the four electrochemical states characterized.	690
Figure XII.1.3 Characterization of the graphene-solid polymer electrolyte (SPE) interface after Li plating. a) Averaged nano-FTIR absorption from 2 different regions of formed SEI after Li plating b) AFM and IR white light images of the analyzed graphene subsurface c) Venn diagram depicting key similarities and differences between the two predominate SEI regions on the Graphene/Li electrode.	691
Figure XII.1.4 a) 3D schematics and digital photographs of the cell designed for performing nano-FTIR experiments at the liquid electrolytes – graphene interface. b) Cyclic voltammetry of the assembled cell with Li metal and copper electrodes in GEN 2 electrolyte.....	691
Figure XII.1.5 a) ATR-FTIR spectra of Li metal immersed in GEN 2 electrolyte for a different duration b) Raman spectra collected from Li metal flash-dipped in GEN2 electrolyte. Spectra were collected using 2 different lasers on 2 different locations.....	692
Figure XII.2.1 Spectro-microscopic investigation of the LirNMC particles. Panels (a) to (c) are on a pristine particle and panels (d) to (g) are on a charged particle (at 4.8 V in the first charge). Panels (a) and (d) are the 3D visualizations of the pristine and charged particles, with the labeling of different regions of interest on the respective central xz-slices. Panels (b) and (e) are the Mn K-edge x-ray absorption spectroscopic fingerprints over the regions of interest shown in panels (a) and (c), respectively. Panel (c) and (f) are the 3D renderings of the Mn's valence state distribution in the pristine and the charged particles. Panel (g) is a detailed layer-by-layer rendering of the Mn's valence state in the charged particle. Panel (h) is the comparison of the depth profiles of the particles in panels (c) and (f).	696
Figure XII.2.2 (a) XANES and (b) EXAFS spectra of delithiated NMC7611 and sodiation $\text{Na}_x\text{NMC6711}$ for initial discharge (sodiation) and 10 th cycle; (c) fitted local structural information including TM-O bond length (upper panel) and TM-TM/Li/Na disorder reflected by the Debye-Waller (D-W) factor (lower panel).	697
Figure XII.2.3 XANES data of $\text{Na}_x\text{Li}_{1.2-y}\text{Mn}_{0.54}\text{Ni}_{0.13}\text{Co}_{0.13}\text{O}_2$ cathode at K-edges of Mn (c), Co (d), and Ni (e) for the <i>ex situ</i> sample at different charged states. Spectra of reference oxides with known TM valences are also shown for comparison.....	698
Figure XII.2.4 XAS measurements of S (g1) and P (g2) peaks from LGPS after CV scans and holds at 3.2 V in liquid cell (3.2V-L), 3.2 V in solid cell (3.2V-S), and 9.8 V in solid cell (9.8V-S), compared with pristine LGPS. (h): The simulation of P XAS peak changes by applying different	699
Figure XII.3.1 Schematic of Li deposits (a) With commercial carbonate-based electrolyte, the morphology of Li deposits is mainly whisker shape, except for very few particles and some of the whiskers with particle shaped head. Microstructure of Li deposits formed in the different electrolytes. (b-f) Cryo-(S)TEM images of Li deposits formed in the carbonate-based electrolyte: (b) HAADF-STEM image of Li deposits with two typical morphologies; bright-field TEM image of (c) whisker-shaped Li deposit and (d) corresponding high-resolution TEM image; bright-field TEM image of (e) particle-shaped Li deposit and (f) corresponding high-resolution TEM image. Insets: corresponding SAED patterns and enlarged area from Li deposits. (g) Bright-field TEM image of particle head of Li whisker, insets are corresponding high-resolution TEM image and SAED pattern.	703

Figure XII.3.2 Structural features of SEI formed on Li whisker and Li particle that formed in the same coin cell using 1.2 M LiPF₆-EC-EMC with 5wt.% VC. (a and j) Cryo-HADF-STEM image reveals SEI layer and Li deposit. (b and g) Cryo-TEM image shows the crystalline nature of Li deposit and amorphous structure SEI layers (the inset is the Fast Fourier transform (FFT)). (c and h) Filtered image shows the interface between Li-metal and SEI layer. (d and i) Cryo-HRTEM image reveal the interface between Li and SEI. (e and j) FFT of the HRTEM image..... 704

Figure XII.3.3 Cryo-electron energy loss spectroscopy (EELS) map to reveal spatial distribution of different chemical species in the SEI layer. (a and c) Cryo-HAADF-STEM imaging reveals the SEI layer on Li deposit. (b and d) elemental distribution of Li, P, C, O, and F in the SEI layer, indicating different spatial distribution for Li particle and Li whisker. 705

Figure XII.4.1 A METS sensor (a) deposited on glass and (b) deposited on Kapton and attached to a copper current collector 709

Figure XII.4.2 Sensitivity of the thermal response (temperature rise) with frequency at different harmonics of the excitation current 710

Figure XII.4.3 Temperature rise at different harmonics simulated to be measured by the METS sensor 710

Figure XII.4.4 (a) Representative 3ω fitting for one of the cells (Cell 02 at 0 cycles) to extract the thermal interface resistance of the lithium metal-LLZO interface, and (b) summary of the extracted thermal interface resistance as a function of the number of cycles for four different cells 711

Figure XII.6.1 Left panel: a depiction of the electric potential as a function of position throughout a polarized Li-Li symmetric cell with high interfacial impedance and low bulk electrolyte resistance. Right panel: Plot of the SEI and electrolyte contributions to the polarization voltage drop as a function of the interfacial vs bulk electrolyte resistances, where SEI contributions dominate if R_{int}/R_s is greater than 1. Lithium polarization experiments for electrolytes with $R_{int}/R_s > 1$ result in unreliable transference number and thermodynamic factor data because electrolyte potential contributions are orders of magnitude smaller than those from the SEI. 714

Figure XII.6.2. Salt activity coefficient versus concentration as calculated using freezing point depression from DSC for LiPF₆ in DMC. Data from Xin et. al. measured using vapor pressure measurements. 715

Figure XII.6.3. Left panel: The lithium triflimide-appended polystyrene used as the polyelectrolyte in this study. It was selected due to its ability to dissolve and dissociate in 3:7 EC:EMC. Right panel: ⁷Li phase shift (°) versus $g \cdot \delta \cdot \Delta\phi/L$ ($T \cdot s \cdot V \cdot m^2$) measured via electrophoretic NMR with a $\pm 90V$ bias in a 0.5m Li⁺ oligomeric (n=10) triflimide polyanion solution in ethylene carbonate:ethyl methyl carbonate. From the slope of this line the mobility and velocity of the Li⁺ can be calculated. Similar analyses can be used to measure the polymer chain mobility and solvent mobility using ¹H NMR..... 716

Figure XII.6.4 Transference number (pink) and Conductivity (blue) vs. Degree of Polymerization for 0.5m solutions of lithium-triflimide polystyrene in 3:7 EC:EMC. Note for the highest degree of polymerization (n=20) we observe a negative transference number with respect to the electrolyte center of mass, indicating that Li⁺ moves in the opposite direction expected in an applied electric field..... 716

Figure XIII.1.1 (a) Schematic of the computational domain where evolution of the surface void is being investigated. Flow of current and evolution of void space within Li is studied. Nothing is being solved in the electrolyte. (b, c) Snapshot of a void after 5 hours of stripping with ratio of surface over bulk diffusion coefficient being 103 and 104, respectively..... 721

Figure XIII.1.2 Voltage vs. time response during the evolution of a void at the Li/electrolyte interface. Due to higher exchange current densities, the potential drop at interface is minimal. But as the voids start to span the entire domain, the potential starts to increase rapidly. Partially and completely delaminated structures are pointed out by “A” and “B”, which are obtained after Li stripping for 4 and 8.5 hours, respectively. Increasing current density from 1A/m² to 2A/m² quickens the delamination process. Also, the surface diffusion coefficient is assumed to be 5×10^3 times larger than the bulk diffusivity..... 722

- Figure XIII.1.3 (a) Visualization of voids at the Li/LLZO interface using cryo-SEM techniques. (b) Computational simulation of void formation within Li metal. The solid electrolyte is located at the top. Li is being stripped at an applied current density of 1 A/m^2 . (c) Comparison between experimentally observed (red circle) and computationally predicted (blue solid line) depth of voids. It is evident that increasing the current density results in a decrease in pore depth. 722
- Figure XIII.1.4 (a) Voltage vs. time curves obtained at different Li stripping current densities, which shows rapid increase in overpotential when the electrode experiences complete delamination from the solid electrolyte. (b) Comparison between experimentally observed (red squares) and computationally predicted (black solid line) time for failure under different applied current densities. The experimental results are obtained from an article published by the group of Jürgen Janek (*Adv. Ener. Mater.* (2019) 1902568)..... 723
- Figure XIII.1.5 (a) Evolution of a dendritic protrusion during deposition at the bottom electrode. (b) Electrochemical Li dissolution from the bottom electrode shows preferential dissolution of the protrusion. (c) Stress evolution within the polymer electrolyte adjacent to the bottom electrode along vertical direction. 724
- Figure XIII.1.6 (a) Current distribution at the bottom electrode around the dendritic protrusion during the dissolution process. It is evident that current on top of the protrusion is higher than the applied current density, which indicates preferential dissolution of the dendritic protrusion. (b) Ratio of excess current at the tip of the protrusion over the applied (or planar) current observed far away from the protrusion. The computational predictions are compared with experimental observations obtained from Maslyn et al., *JES* 2020 167 100553. 724
- Figure XIII.1.7 (a) Voltage vs. capacity performance curves for NMC/LLZO (black) and NMC/LPSCI (magenta) during the first charge and discharge process. The blue dashed line indicates performance curves without any interfacial delamination. NMC/LPSCI experiences much less detachment, and capacity fade, than NMC/LLZO. (b) Phase map between partial molar volume of lithium within cathodes and Young's modulus of solid electrolytes indicating the domains of stable operation (green) and complete detachment (yellow). Two different stability limits for LLZO and LPSCI are shown. 725
- Figure XIII.1.8 Distribution of potential and concentration within the space charge layer at (a) NMC/LLZO and (b) NMC/LPSCI interface. The solid and dashed lines indicate the space charge layer under fully charged and discharged conditions, respectively. Due to its higher relative permittivity, the space charge layer within LLZO is much thinner than that observed within LPSCI. For both LLZO and LPSCI, the space charge domain in the cathode is substantially thicker under the fully discharged condition..... 725
- Figure XIII.1.9 Influence of the space charge layer on the charge/discharge process is captured through the decrease in exchange current density due to decrease and increase in Li concentration on the electrolyte and cathode, respectively. A strong space charge layer increases the charge transfer resistance between the cathode and electrolytes. (a) Voltage vs. capacity performance curves under applied current density of 4 A/m^2 for NMC cathodes with LLZO and LPSCI. (b) Ratio of space charge layer induced capacity fade over the initial capacity as observed under different applied current densities. Due to its stronger space charge layers, LPSCI experiences more capacity fade than LLZO. 726
- Figure XIII.2.1 SEM images of LIC (a, c, e) and LYC (b, d, f) solid electrolytes: (a, b) are powder samples, (c, d) are top-view and (e, f) are cross-sectional view of the as-prepared pellets. Insets in (c, d) are optical images of the pellets..... 729
- Figure XIII.2.2 *K*-edge XANES spectra of a) In collected on LIC and b) Y collected on LYC pellets. 730
- Figure XIII.2.3 a) Voltage profiles of a Li|LIC|Li symmetrical cell during the step-increase of current density test and b) the corresponding cell resistance. The CD step size is 0.02 mA/cm^2 and the duration of each charge/discharge step is 1 hr. 730
- Figure XIII.2.4 Voltage profiles of a Li|LYC|Li symmetrical cell during the step-increase of current density and b) the corresponding cell resistance. Inset in a) shows the voltage profile during the first 20 hours. The CD step size is 0.02 mA/cm^2 and the duration of each charge/discharge step is 1 hr. 730

Figure XIII.2.5 Nyquist plots of Li LYC Li symmetrical cells after various DC cell testing at the indicated current density (mA/cm^2). AC amplitude was 10 mV and the frequency range was 1 MHz to 0.1 Hz. Inset shows the expanded view of the indicated area on the spectra.	731
Figure XIII.2.6 Initial charge/discharge voltage profiles of ASSB cells assembled with an NMC811/LYC ratio of a) 70:30, b) 85: 15 and c) 90:10 in the composite cathode, respectively. d-e) charge/discharge voltage profiles and cycling stability of an ASSB cell assembled with an NMC/LYC ratio of 85: 15. All cycling rate is 0.1 C. f-g) charge/discharge voltage profiles and rate capability of an ASSB cell assembled with an NMC811/LYC ratio of 85:15.....	731
Figure XIII.2.7 a) Cross-sectional SEM image and b-d) EDX elemental mapping of Y-L, Cl-K, and In-L at the interface.	732
Figure XIII.2.8 Charge and discharge voltage profiles (a, b), discharge capacity retention and coulombic efficiency (c, d) of ASSB cells with a cathode composite consisting of SC-NMC811, LYC and carbon in a 80: 20: 0 weight ratio (a, c) and 57: 40.5: 2.5 weight ratio (b, d).	732
Figure XIII.2.9 a) Nyquist plots from the EIS measurement of a ASSB cell with the cathode containing 2.5 wt.% carbon. (b-d) Cross-sectional SEM images collected at the LYC/Li-In anode interface of the cell before (b) and after (c, d) cycling.....	733
Figure XIII.3.1 a) Molecular dynamics “snapshot” of the solvation structure of a Li cation in the LHCE formulation. b) Molecular dynamics “snapshot” of the solvation structure of a Li cation in the HCE formulation with the fluorinated diluent. Atoms are shown in purple (Li), red (O), white (H), green (F), and orange (P). c) Diffusion coefficients of the various species as a function of concentration. HCE formulations is LiPF ₆ in PC, and HCE + diluent denotes LiPF ₆ in PC and diluent. Vertical lines are for visual ease.	736
Figure XIII.3.2 Framework for generation of amorphous structures. [1]	737
Figure XIII.3.3 The workflow for constructing a reaction network for the Li ⁺ /EC/H ₂ O system and pathfinding to LEMC	739
Figure XIII.4.1 (a) Current density distribution in the void. (b) Evolution of the void boundary as Li deposits inside the void.....	742
Figure XIII.4.2 Schematic illustration of the metal deposition in voids of the SE.	743
Figure XIII.4.3 (a) Total current density at the anode/SE interface. Both the vertical coordinate and the contour plot represent the magnitude of the deposition current. All the length units in the figures are in μm . (b) Distribution of deposition current i_V under applied current i_0 at three different SE electronic conductivities. The ionic conductivity σ_M + is fixed $0.1 \text{ mS}/\text{cm}$, while the electronic conductivity σ_e – varies.	743
Figure XIII.4.4 Diffusion mechanism in Li-stuffed Li ₃ garnet (A) and NASICON (D) by cooperative hopping of Li-ions in activated local environment. Diffusion network of NASICON before (B) and after (C) cooperative migration, diffusion network of garnet before (E) and after (F) cooperative migration are illustrated.	744
Figure XIV.1.1 Low-temperature performance of cell with baseline LP57 electrolyte. A. RCT (charge transfer resistance), RSEI (SEI resistance) and RS (bulk electrolyte resistance) vs temperature at the average voltage for the corresponding temperature. The sum of these resistances is the total cell resistance. Resistance measured via DRT analysis of impedance spectra at the average voltage of the cell. B. Voltage profile during a C/3 discharge (using capacity at 20°C as the reference for C/3 rate) of the cell at different temperatures.	748
Figure XIV.1.2 Left panel: a schematic of a 3-electrode cell that allows deconvolution of interfacial resistance at the anode and cathode. Right panel: the SEI, cathode electrolyte interface (CEI), and charge transfer resistance contributions of a graphite NMC622 cell at various temperatures. Note that the resistance here are different than in Figure XIV.1.1 because of the different cell geometries.....	749
Figure XIV.1.3 Left panel: Total graphite NMC622 cell resistance measured at various temperatures as a function of LiPF ₆ concentration (resistance measured at the average cell voltage). 0.85 M was generally found	

to exhibit the lowest total cell resistance at all temperatures. Right panel: The capacity normalized to 20°C cell capacity as a function of temperature for 2 graphite|NMC622 cells one with LP57 electrolyte (baseline), one with 0.85 M LiPF₆ in 3:7 EC:EMC. C/3 rate was used (using 20°C cell capacity to establish C/3 rate). 749

Figure XIV.1.4 Performance comparisons of lithium-ion cells fabricated with LP57 baseline electrolyte of 1.0M LiPF₆ and additives as a function of temperature. A. Cell energy density at -20°C for cell that contain LP57 (baseline) with various amounts of vinylene carbonate (VC) or propane sultone (PS) added. B. Voltage profiles of 0.5 wt% VC and PS cells compared to LP57 cells. C. Total cell resistance as a function of temperature for cells that contain LP57 and the reported wt% fluoroethylene carbonate (FEC). D. Capacity as a function of temperature of cells comprised of either LP57 or LP57 + 6wt% FEC normalized to their capacity at 20°C. 750

Figure XIV.1.5 EIS of symmetric coin cells comprised of electrodes harvested from pouch cells previously cycled in LP57 electrolyte but transferred to symmetric coin cells with either LP57 or EG12 as the electrolyte. A. Graphite|graphite symmetric cells at -20°C, B. NMC|NMC symmetric cells at -20°C. 751

Figure XIV.1.6 Ion speciation and diffusion trends in 1M LiPF₆ in 3:7 EC/EMC computed from MD simulations. (a) The fraction of lithium ions in each ion speciation state as a function temperature. (b) Schematics representing the ion speciation states depicted in (a): free ions, contact ion pairs (CIP), positive triple ions (PTI), negative triple ions (NTI), and larger aggregates (AGG). Pink spheres represent Li ions, grey clusters represent PF₆⁻ anions, and purple molecules represent solvent species. (c) Self-diffusion coefficients of EC, EMC, PF₆⁻ and Li⁺ in 1M LiPF₆ in 3:7 EC/EMC computed by MD as a function of temperature. 752

Figure XIV.2.1 (a) Theoretical overpotential evolution depending on current density. Limiting factors of electrolytes at low temperatures; (1) ionic conductivity and (2) interfacial resistance. Voltage profiles of (b) graphite and (c) NMC622 half cells with Gen2 at 25oC or -20°C..... 755

Figure XIV.2.2 (a) Ionic conductivity of electrolytes (Gen2, BN/FEC, and BN/EC+FEC) at various temperatures and (b) their activation energies (E_a). 756

Figure XIV.2.3 (a) LUMO levels of BN, EC, and FEC. (b) dQ/dV profiles of 1st charging cycle with different electrolytes. (c) Coordination numbers of electrolytes at 25oC. (d) XPS spectra of C 1s, F 1s, and N 1s branches of graphite electrodes after three C/10 formation cycles with different electrolytes. 757

Figure XIV.2.4 Nyquist plots of cells with (a) Gen2, (b) BN/FEC, and (c) BN/EC+FEC electrolyte at various temperatures. Arrhenius plots of RSEI, RCEI, R_{ct}-anode, R_{ct}-cathode for cells with (d) Gen2, (d) BN/FEC, and (f) BN/EC+FEC electrolyte..... 758

Figure XIV.2.5 Cyclability with electrolytes at (a) 25°C and (b) -40°C. Cyclability and coulombic efficiency of (c) Gen2 and (d) BN/EC+FEC electrolyte with Gen2 or BN/EC+FEC SEI layer at -40°C. 759

Figure XIV.3.1 Electrochemical impedance spectroscopy (EIS) of (a) 1M LiPF₆ in EC/EMC (3/7) (baseline). (b) 1M LiDFOB in isoxazole/FEC (10/1, vol%) electrolytes and (c) comparison of ionic conductivity at different temperature of these two electrolytes. (d) Voltage profiles of Li/graphite cell using 1M LiPF₆ in EC/EMC (3/7) and (e) 1M LiDFOB in isoxazole/FEC (10/1, vol%) at various temperatures at C/10. (f) Cycling performance of Li/graphite cell using 1M DFOB in isoxazole/FEC (10/1, vol%) at 0°C at C/10 rate compared with baseline electrolyte. 763

Figure XIV.3.2 XPS spectra of graphite electrode before (pristine) and after formation cycling using baseline electrolyte (1.2 M LiPF₆ in EC:EMC (3:7 v/v%)) and IZ/FEC electrolyte (1M LiDFOB in IZ/FEC (10/1, vol%)) for (a) C1s, (b) O1s, (c) F1s, (d) B1s and (e) N1s spectra. 764

Figure XIV.3.3 Electrochemical performance of NMC811||Graphite full cells using TTE-based electrolyte. a) The cycling performance of the NMC811||Graphite cell at -20°C; b) The charge-discharge profile of the NMC811||Graphite cell at -40°C with current densities of 0.05C and 0.1C; c) The cycling performance of the NMC811||Li cell at 50°C and d) the rate capability of the NMC811||Li cell at room temperature. 765

Figure XIV.3.4 MD simulations of 2.0 M LiFSI in EMC_{0.5}TTE_{0.5} low temperature electrolyte..... 766

Figure XV.1.1 Gel composite electrolytes consisting of crosslinked PEO (xPEO) matrix, Lithium bis(trifluoromethanesulfonyl)imide (LiTFSI) salt, LICGC particles and TEGDME plasticizer. (a), An scanning electron microscopy (SEM) image of the composite electrolyte with 50 wt% LICGC; inset, a digital photograph of the membrane; (b), Li^+ conductivity of gel electrolyte membranes; (c), A schematic showing the effect of LICGC particles on ion transport; (d,e), Li symmetric cell cycling at room temperature; (e) is a magnification of (d) from 40 to 42 hours of cycling; (f) Half cell cycling using the gel composite electrolyte at room temperature. 769

Figure XV.1.2 Cycling performance of a ~ 140 μm -thick *plasticized* xPEO-LICGC (3-D interconnected) composite electrolyte. a) Li/Li symmetric cell with the *plasticized* composite tape at $25 \mu\text{A}/\text{cm}^2$ and 70°C . b) Schematic illustrating the half-cell assembly procedure with a conventional PVDF-binder based NMC622 cathode and a 3D interconnected LICGC ceramic electrolyte porous tape, *plasticized* with liquid TEGDME plasticizer. c) Cycling performance of the illustrated half-cell at $25 \mu\text{A}/\text{cm}^2$ and 70°C . d) Absolute cell charge and discharge capacity (mAh) of the cell versus cycle number. The cathode loading was $\sim 2 \text{ mAh}/\text{cm}^2$ 770

Figure XV.1.3 Concentration gradients in composites of binary electrolyte (PE) and single ion conductor (LATP). (a) Electrolyte configurations considered in the simulations; (b) From left to right: lithium cation concentration in PE membrane, PE membrane with dense LATP layer in the middle and PE membrane with a CPE layer in the middle; (c) Concentration profiles in PE and PE|LATP|PE with a series of interfacial resistances; (d) Concentration profiles in PE and PE|CPE|PE with a series of interfacial resistances; (e, f) Chronoamperometry monitoring current decay with an applied potential of 10 mV. (e), experimental results; (f) modeling results. 772

Figure XV.2.1 Cycling performance of Li||NMC622 cells using GPE/separator composite electrolyte and HCE (liquid)/separator at C/5 rate in the voltage range of 2.8-4.3 V under 60°C , where $1\text{C} = 1.5 \text{ mA cm}^{-2}$ 775

Figure XV.2.2 (a) Photograph and micrograph of the functional PI separator with regular pore array. (b) Micrograph of PI separator at higher magnification. (c) Photographs of PI ($11 \mu\text{m}$) and PE (7 and $20 \mu\text{m}$) separators before and after heating at 120°C for 1 min. (d) Cycling performance of Li||NMC622 cells using PE and PI/PE composite separators. 776

Figure XV.2.3 (a) Cycling performance of Li||NMC622 cells using the combinations of TMP_a -based LHCE ($\text{LiFSI}:\text{TMP}_a:\text{TTE}=1:1.4:3$ by mol.) and two different separators (PE and PI/PE). (b) Cycling performance of Li||NMC622 cells using the combinations of DME-based LHCE ($\text{LiFSI}:\text{DME}:\text{TTE}=1:1.1:3$ by mol.) and three different separators (PE, PI/PE and PE/PI). 777

Figure XV.2.4 Morphology evolutions of Cu electrodes upon Li deposition by in-situ AFM in (A) E-baseline, (B) E-baseline + 2 wt.% VC, (C) E-baseline + 2 wt.% LiAsF_6 and (D) E-baseline + 2 wt.% VC + 2 wt.% LiAsF_6 777

Figure XV.2.5 (a) Li nuclei density on Cu electrodes as a function of deposition time in $1 \text{ mol L}^{-1} \text{ LiPF}_6$ in EC:EMC=3:7 (by wt.) with different additives. (b) Voltammetry of the in-situ AFM cells using studied electrolytes. (c) Dependence of nuclei size on η^{-1} and (d) dependence of $\ln(\text{surface energy})$ on η^{-2} 778

Figure XV.2.6 Morphologies of deposited Li in $1.2 \text{ M LiPF}_6/\text{EC-EMC}$ (3:7 by wt.) in the presence (a,c) and absence (b,d) of polyolefin separator: (a,b) Top View, (c,d) Cross-section. 778

Figure XV.4.1 Histogram of calculated activation energies (in eV) for different Li^+ diffusion pathways across the LLZO/LCO interface. Forward and backward diffusion refer to Li^+ migration from LLZO to LCO, and from LCO to LLZO, respectively. 782

Figure XV.4.2 (a-b) Analysis of MLFF accuracy during a dynamical simulation of disordered LLZO at 3000 K, showing the ability to replicate (a) energies and (b) forces derived from density functional theory (DFT). (c) Li^+ diffusivities predicted by MLMD (orange) and AIMD (blue) for amorphous LLZO. (d) Isosurface of Li^+ probability density (blue) obtained from MLMD in a LLZO $\Sigma 5(210)/[001]$ coherent grain boundary model at 2000 K. Magenta and green atoms are Zr and La, respectively, and O atoms are not shown for simplicity. 783

- Figure XV.4.3. (a) Digital representation of polycrystalline LLZO microstructure; (b) computed von Mises stress profile; (c-d) Li composition profile (c) with and (d) without mechanical stress. 784
- Figure XV.4.4. (a) 3D porous LLZO microstructure and cross section of LLZO/polymer composite microstructure; (b) computed von Mises stress (top: spatial distribution; bottom: statistics) in the composite microstructure under applied loading; and (c) computed effective elastic modulus of the composite microstructure. 785
- Figure XV.4.5. Predictions of (a,d) Li^+ concentration profile, (b,e) electrical potential profile, and (c,f) EIS for a model 2D LLZO polycrystal, demonstrating the effect of grain boundary Li^+ conductivity. Data in (a-c) correspond to the case for which Li^+ mobility at the grain boundaries is double that in (d-f). 786
- Figure XV.5.1 Optical images of the different 3D-printed LLZTO structures before and after sintering. 790
- Figure XV.5.2 LLZTO films with varying additives after sintering at 1100 °C. 791
- Figure XV.5.3 Sintered LLZTO film filled with solid polymer electrolyte composed of UV cross linked (PEGDA-PEGMA-PEO)/LiTFSI. (a) and (b) SEM morphology. (c) cracks formed in LLZTO during cell assembly. (d) Nyquist plots of SPE and LLZTO/SPE membranes sandwiched between stainless steel electrodes. (e) Charge-discharge capacity curves at 0.1 C-rate using the 3D printed LLZTO-LBO (2 wt%)- SiO_2 (1 wt%) structure infilled with PEGDA/PEGMA/LiTFSI SPE as solid electrolyte, and NMC622/PVDF/CB as cathode. 791
- Figure XV.5.4 (a) Ionic conductivity contour map for the polymer electrolytes made of UV cured PEGDA/PEGMA/PEO/LiTFSI. (b) Increase of ionic conductivity by adding LLZTO powders. 792
- Figure XV.5.5 Battery assembly and testing for a CPE based ASSLB. (a) ASSLB made from infilling of CPE into a 3D printed cathode. (b) EIS before and after testing. (c) charge/discharge curves at 0.8C rate. (d) Rate performance. All tests were conducted at 60°C in coin cell setup. 792
- Figure XV.5.6 (a) Low-binder LLZTO inks printed by direct ink writing (250 μm nozzle). The formulations were as follows for the freestanding and conformal inks, respectively: 94.6 wt% LLZTO / 0.7 wt% PVB / 4.7 wt% BBP in 3:7 wt 1-butanol/alpha terpineol & 95.3 wt% LLZTO / 0.8 wt% PVB / 4.0 wt% BBP in NMP. Cross-section SEM images show the printed films after sintering at 1100 °C for 6h in Ar with mother powder. (b) NMC 622 / LLZTO bilayers printed by direct ink writing (250 μm nozzle) in 2 configurations: 1) cathode on top / electrolyte on bottom; 2) electrolyte on top / cathode on bottom. 793
- Figure XV.5.7 Comparison of EIS results (a) and first cycle charge/discharge voltage profiles at $\sim \text{C}/50$ (b) for different composite cathodes coated on pre-sintered LLZTO pellets and co-sintered at 900°C for 2h in Ar. All were tested at room temperature without extra external pressure. 793
- Figure XV.6.1 **PDMS-Py as the anodic coating for lithium metal batteries.** (A) lithium metal battery with polymer coated anode. (B), the concentrated electric field at vicinity of surface protrusions cause the self-amplifying dendritic deposition of lithium ions. (C), coating on lithium metal anode. During Li^+ deposition, cations in coating remain electrochemically stable and can effectively shield the Li^+ ions, resulting in more flat and homogeneous deposition. (D), chemical structure of the PDMS-PyTFSI coating. 796
- Figure XV.6.2 **Characterization of the PDMS-PyTFSI polymer.** (A) Proton NMR of the PDMS-PyTFSI polymer dissolved in protonated methanol. Each hydrogen containing functionality on the polymer is labeled with number corresponding to the numbering on top of each NMR peak signals. The integration value of the area under each peak is indicated at the bottom of each signal. (B) rheological frequency sweep of the PDMS PyTFSI polymer conducted at room temperature with 1% strain on the polymer. The open symbol stands for loss modulus (G'') and the filled symbol stands for storage modulus (G'). Green: PDMS-PyTFSI with 5% crosslinker, Blue: PDMS-PyTFSI. (C) glass transition (T_g) of the PDMS PyTFSI polymer with and without the crosslinker measured with differential scanning calorimetry (DSC). Green: PDMS-PyTFSI with 5% crosslinker, Blue: PDMS-PyTFSI. 797
- Figure XV.6.3 **The interfacial impedance** measured over 100 hrs on $\text{Li}||\text{Li}$ symmetric cell with 50 μl of electrolytes in between the two electrodes. The carbonate electrolyte is composed of 1M LiPF_6 in EC/DEC and

10% FEC, and the ether electrolyte is composed of 1M LiTFSI and 1 wt% LiNO₃ in DOL/DME. The absolute value of the imaginary part of the interfacial impedance (Z) and the real part of the Z was measured through electrochemical impedance spectroscopy (EIS) and plotted: bare lithium with (A) carbonate electrolyte; (B) ether electrolyte; PDMS PyTFSI coated lithium with (C) carbonate electrolyte; (D) ether electrolyte. 798

Figure XV.6.4 **SEM images of lithium depositing on Cu foil:** (A), bare Cu foil; (B), PDMS-PyTFSI coated Cu foil; size distribution of lithium nuclei under SEM: (C), bare Cu foil, (D) PDMS-PyTFSI coated Cu foil. 799

Figure XV.6.5 Li||Li cycling with polymer coating on the electrodes: the electrolyte composition and cell configurations are marked in the graph..... 800

Figure XVI.1.1 (a) Temperature dependent conductivity κ is shown for three copolymers. (b) The effective conductivity $\kappa\rho^+$ is shown for two polymers with $r = 0.11$ and 0.31 and compared with PEO/LiTFSI, $r = 0.06$ 804

Figure XVI.1.2 (a) Storage modulus of the diblock (red triangle) and triblock (black square) copolymer (b) Creep compliance of the triblock at difference applied stress. Below 12000 Pa the polymers exhibit viscoelastic behavior. At 14000 Pa the slope of compliance increases sharply (c) Yield stress of the copolymers measured from the slope of the creep compliance curve (d) the electrolyte was subjected to 0.15 mA cm^{-2} current and the potential response was observed with time. The cells with diblock copolymer electrolytes failed within 1 h but the cells with triblock copolymer electrolyte was able to sustain the current. All data was collected at 90°C 805

Figure XVI.1.3 (a) Schematic representation of the simultaneous polarization and SAXS experiment. An SEO/LiTFSI electrolyte with randomly oriented grains is sandwiched between two lithium electrodes with current passing parallel to the x -axis. X-rays pass parallel to the z -axis, perpendicular to the current. Scanning the beam along the x -axis allows for spatial resolution between the electrodes. A reference channel filled with electrolyte was placed next to the electrochemical cell. (b) Characteristic 2D SAXS pattern obtained from experiments. The pattern is divided into 16 sectors defined by the azimuthal angle, χ . Scattering data in each sector corresponds to lamellae oriented with the angle between the vector normal to the PEO/PS interfaces and the positive y -axis equal to χ . The cartoons in each sector show the lamellar orientation with normal vectors drawn. 806

Figure XVI.1.4 Results from simultaneous polarization and SAXS experiments at three current densities: (a) The potential drop across the electrolyte, U , versus time, t , is plotted in the top panel of each figure. The dashed line represents the steady state potential (U_{ss}) predicted from concentrated solution theory. In the main panel, the domain spacing, d , is plotted versus normalized cell position, x/L . The color of each data set corresponds with the U versus t plot in the top panel. Purple data sets were obtained at the beginning of polarization ($t = 0 \text{ h}$) and red data sets were obtained at the end of polarization ($t = 46.6 \text{ h}$). 807

Figure XVI.1.5 Orientation dependence of lamellar distortion. The change in domain spacing, Δd , a function of azimuthal angle, χ , is plotted for each cell position for the cell polarized at (a) $iL = 1.96 \mu\text{A cm}^{-1}$ at $t = 46.7 \text{ h}$, (b) $iL = 3.74 \mu\text{A cm}^{-1}$ at $t = 46.7 \text{ h}$, and (c) $iL = 11.1 \mu\text{A cm}^{-1}$ at $t = 60.7 \text{ h}$. Each data set is based on the last scan taken at the end of each polarization. (d) Difference in domain spacing between LAM \perp and LAM \parallel as a function of normalized position, x/L , for the three data sets in (a), (b), and (c). 808

Figure XVI.1.6 a) Volume rendering of a lithium globule at different time intervals. The lithium globule is rendered in dark gray, while the electrolyte is rendered in purple, the bottom lithium in light gray, and the impurity particle in dark red. The top lithium electrode is transparent. Lithium is plated from the top to the bottom electrode. b) yz slice through the 3D reconstruction. The darker gray lithium sandwiches the lighter gray electrolyte. The approximate location of the original electrode-electrolyte interface is marked with the dashed white line. c) Maps of electrolyte thickness, or interelectrode distance, in the xy plane. The first five panels of Figure 1a and 1b were previously published in K. J. Harry, K. Higa, V. Srinivasan, and N. P. Balsara, J. Electrochem. Soc., 163, 2216–2224 (2016). 809

Figure XVI.1.7 Local current density maps for the top and bottom electrode during increasing time of growth for lithium globule on the bottom electrode. Each set of maps is labeled with the time point and normalized globule height corresponding to midway between the start and end points, where the start and end points are the two 3D renderings that were compared to calculate the plotted current density. The colormap indicates the calculated local current density at each x, y position. The plot represents an averaged 3D surface representing the interface between the electrode and electrolyte between the two time points used in the current density calculation. The z dimension represents the location of the interface, if $z = 0$ represents the initial position of the bottom electrode-electrolyte interface at $t = 0$. The plotted surfaces of the two electrodes were separated by an additional 100 μm for clarity. 809

Figure XVI.1.8 Chemical structure of (a) PEO-POSS (b) POSS-PEO-POSS..... 810

Figure XVI.1.9 (a) The voltage (Φ) versus time plot during cycling of the cell for PEO-POSS copolymer electrolyte. (b) Φ versus time plot for POSS-PEO-POSS electrolyte shown up to first 40 cycles. (c) Φ versus time plot for last 3 cycles before failure. The cells were cycled at 0.15 mA cm^{-2} current density for 4h in both positive and negative directions followed by 4h of rest. The cell failure was determined by the abrupt drop in the potential. 810

Figure XVI.1.10 Cross-sections through the cell are represented in the left side panels for (a) POSS-PEO-POSS after 40 cycles and (c) PEO-POSS after failure. Three dimensional (3D) visualizations of the dendrites are represented in the right-side panels, (b) POSS-PEO-POSS and (d) PEO-POSS. The protrusions are represented in grey, and the lithium electrodes are represented in orange..... 811

Figure XVI.2.1 (a) Various P-S polyanionic structures with approximate bond lengths (given in \AA). (b) Neutron pair distribution function (nPDF) for β -Li₃PS₄ and Li₃PS₄ + 1% PEO samples measured at 300K. Vertical lines correspond to expected bond lengths described in (a). Li⁺ conductivity values (σ_{Li^+}) for each sample were measured at room temperature in a blocking cell configuration. 814

Figure XVI.2.2 Hot-pressing equipment inside an Ar-filled glovebox for processing sulfide-based SEs..... 815

Figure XVI.2.3 (a) Open-circuit potential (E°) of a Li_xIn alloy prepared by coulombically titrating In metal in a Li|LPS|In SSB at -79 $\mu\text{A/cm}^2$ at room temperature. (b-c) Electrochemical characterization of SSBs containing an NMC811 cathode, LPS separator, and either a Li metal or Li_{0.169}In anode tested at room temperature with a stack pressure of 5 MPa. (b) Galvanostatic charge/discharge curves for the first 2 cycles and (c) long-term cycling performance. In (b-c), the cathode potential in the Li_xIn-containing SSB was referenced vs. Li/Li⁺ by adding 0.622 V to the measured cell potential. 816

Figure XVI.2.4 Galvanostatic cycling performance of SSBs containing vapor deposited Li metal anodes, LPS separators, and composite NMC cathodes. (a-b) Voltage profiles for cells tested using stack pressures of (a) 5 MPa and (b) 50 MPa. (c) Long-term cycling performance..... 817

Figure XVI.2.5 Electrochemical characterization of SSBs containing a Li anode, LPS separator, and NMC811 cathodes with/without an LNO coating (1 wt.%) showing (a) first cycle charge/discharge curves and (b) capacity and coulombic efficiency over 5 cycles. In (b) open/closed symbols represent charge/discharge capacities, respectively. All cells were cycled at a current density of $\pm 66 \mu\text{A/cm}^2$ 818

Figure XVI.3.1 (XPS measurement of in-situ electrochemical Li deposition) (a) Operando XPS measurements of individual core-level spectra during electrochemical deposition of Li showing their evolution with increasing Li deposition time. All core-level spectra are plotted on the same absolute scale in counts per second except Li 1s spectra, which are magnified by 10 \times for clarity. (b) Zr 3d core-level spectra comparing the extent of Zr⁴⁺ reduction as a function of the deposition technique. 822

Figure XVI.3.2 (a) Simulation cell showing three possible dopant locations in the LLZO near the surface. The optimized dopant locations for Al³⁺ and Ga³⁺ are circled in solid red lines. (b) Density of states for doped and undoped bulk LLZO (left) and Li⁰/LLZO interface (right) shifted to the Fermi level at zero. (c) XPS measurements of Ga-LLZO samples before and after Li metal deposition. (d) Raman spectrum of Ga-LLZO reacted with Li metal. (e) EIS spectra and circuit of Ga-LLZO in a Li||Li symmetric cell at open circuit..... 823

Figure XVI.3.3 (a) Raman mapping of LBO content within an Al-LLZO pellet synthesized with 15 vol % LBO. Dotted lines in the image are drawn to guide the eye around LBO in grain boundaries. (b) EIS spectra of Al-LLZO pellets in Li||Li symmetric cells sintered without and with 15 vol % LBO..... 824

Figure XVI.3.4 (a) Roll-to-roll nanofiber fabrication by electrospinning; XRD pattern showing cubic LLZO fibers; SEM and TEM of nanofibers. (b) Schematics of slot-die coating; inset bench scale coater. (c) Photo and cross-section SEM of slot-die coated LLZO nanofiber-PEO membrane. (d) Symmetric Li||Li cycling of composites with different LLZO loadings at 60°C. (e) EIS spectra of the corresponding cells from (d) before and after cycling..... 825

Figure XVI.4.1 CCD and COP determined by the plating/stripping measurement with step-increased current. Li plating/stripping behaviors for different surface modifications with (a) graphite, (b) Bi and (c) AgF for Li|LLZTO|Li cell and (d) Li|Li6PS5Cl|Li and (e) Li|Li7N2I-LiOH|Li cells at a step-increased current. The determined CCD and COP are listed in the figures. (f) The box chart for the determined CCD and COP of different SSEs. 828

Figure XVI.4.2 Thermodynamic and kinetics analysis for solid state battery. (a) Thermodynamic model of SSE for Li dendrite growth, where σ_i , σ_e are ionic conductivity and electronic conductivity; $\nabla\eta_i$, $\nabla\eta_e$ are electrochemical potential gradients of ions and electrons, δ , ε and ξ (subscripts 1, 2 and 3) represent the areas for near anode, bulk SSE and near cathode. (b) Kinetics of Li dendrite growth in SSEs. Li dendrite growth in stable SSE which is not dense and has different electronic conductivity and interface energy, $PLiSSE$ is the stress of Li nucleation site; $ELiSSE$ is the interface energy of SSE against Li, V_m is the Li molar volume, and A is the interface area, F is the faraday constant. (c-d) 1D battery model near anode and their corresponding spatially dependent potential distribution in (c) stable and (d) unstable SSE. (e) Effects of a potential change on the standard free energy of activation for oxidation and reduction on Li metal (black lines) and SSE (blue lines). At the distance to anode of x , the stress, concentration of species i , and interface energy against Li metal are defined as $P(x)$, $C_i(x)$, and $E_{inter}(x)$ respectively. (f) Li metal diffusion kinetics at different applied current densities simulated by the phase-field model. 829

Figure XVI.4.3 The interface design to reduce surface resistance and suppress Li dendrite in LLZTO electrolyte. (a) Schematic diagram of the bifunctional lithiophilic/lithiophobic interlayer. Cross-section morphology and Sr elemental mapping of the electrode interface with the LLZTO pellet before (b-c) and after (d-e) cycling showing a stable Sr segregation right on the interface. The red dash lines mark the interfaces. (f) Long-term cycling performance of Li-Sr | LLZTO | Li-Sr symmetric cell at 0.5 mA/cm². Inset is the magnification of the voltage profiles of 1-10 cycles and 950-1000 cycles. (g) The Li plating/stripping behavior for the cells at a step-increased current for 0.5 h. (h) The cycle performance for proof-of-concept Li-Sr | LLZTO | LiNi_{0.8}Mn_{0.1}Co_{0.1}O₂ (NMC811) cells at 0.2 C with cathode loading of 0.8 mAh / cm² (0.1 C for the first cycle for activation). 831

Figure XVI.4.4 Li plating/stripping behavior of the Li₇N₂I-5% MWCNT protected Li₇N₂I electrolyte in Li symmetric cell configuration at room temperature. (a) Galvanostatic cycling of the Li symmetric cell at a current density of 0.1 mA cm⁻². (b) Voltage profiles of the cell under step-increased current densities from 0.2 to 4.0 mA cm⁻² for Li plating/stripping with a fixed time of 1h. (c-e) Nyquist plots of the symmetric cell under different conditions: (c) before cycle (d) after activation, and (e) after cycled at 4 mA cm⁻² for 600 cycles. 832

Figure XVI.5.1 The electrolyte development progress: CCD at 70°C and Li ion conductivity at 25°C 835

Figure XVI.5.2 Cycle life of an NMC/Li metal solid state pouch cell with the multifunctional SSE at 25°C. 835

Figure XVI.6.1 Viscosity plot showing expected viscosity behavior of various glass compositions over a range of temperatures above the glass transition temperature with the cutoff point being the crystallization temperature at 1°C/min heating rate. 838

Figure XVI.6.2 Galvanostatic cycling of a 50 μm thin-film LiPO₃ at (A) 60°C (B) 90°C with lower current densities (C) 90°C under a critical current density experiment (D) 90°C with short circuiting exhibited at a current density of 65 μA/cm². Adapted from [2]. 839

Figure XVI.6.3 Preliminary cycling results for (A) a hybrid full cell utilizing a MOS GSE with a Li foil anode and a LiFePO_4 cathode and (B) an all-solid-state full cell utilizing a MOS GSE with a Li foil anode and an LiFePO_4 composite cathode deposited directly onto the surface of the GSE, cycled at 60°C	839
Figure XVI.7.1 Our Perspective1 article accepted in Joule provides insight into the technological status of solid-state batteries and provides a guide for future challenges and opportunities to work with OEMs to advance the technology readiness level (TRL).	842
Figure XVI.7.2 Mechanical strain % vs time plot of Li-LLZO-Li cells consisting of thick (700 micron) and thin (100 micron) Li anodes. When Li was < 100 microns thick, negligible deformation occurred. This behavior suggests that Li-LLZO frictional or adhesion likely created hydrostatic stress in Li, thus limiting deformation when Li is thin (< 100 microns).	843
Figure XVI.8.1 DSC curves of 50/50 w/w mixtures of LLZTO with NMCs of various compositions.	847
Figure XVI.8.2 (a) XRD and (b) DSC curves of 50/50 w/w mixtures of LLZTO (with 10mol% or 40 mol% excess Li) with NMC-111.....	848
Figure XVI.8.3 Heatmaps of chemical stability (Ed) of Li-M-O (M = B, C, N, Al, Si, P, Ti, V, Cr, Zr, Nb, Mo, Zn, Ga, Ge, Ta, or W) with LLZO. Known compounds that are stable with LLZO are marked with blue points.	848
Figure XVI.8.4 Heatmap of the decomposition energy of Li-Al-O compositions with NMC 111.	849
Figure XVI.8.5 Nyquist plot (inset) and DRT Analysis for symmetric NMC622 LLZO NMC622 cells with and without Al_2O_3 coating co-sintered at (a) 700°C and (b) 800°C	850
Figure XVI.8.6 Nyquist plot (inset) and DRT Analysis for symmetric NMC622 LLZO NMC622 cells with and without ZnO coating co-sintered at (a) 700°C and (b) 800°C	850
Figure XVI.8.7 a) Nyquist plot and b) DRT plot for symmetric NMC622 LLZO NMC622 cells co-sintered at 800°C comparing uncoated and Al_2O_3 ALD coated samples.	850
Figure XVI.8.8 a) Nyquist plot and b) DRT plot for symmetric NMC622 LLZO NMC622 cells co-sintered at 800°C comparing samples with and without extra Li from various sources.	851
Figure XVI.8.9 a) Nyquist plot and b) DRT plot for symmetric NMC622 LLZO NMC622 cells co-sintered at 800°C comparing various thicknesses of Al_2O_3 coated samples, all with the same amount of extra Li added.	851
Figure XVI.8.10 a) Nyquist plot and b) DRT plot for symmetric NMC622 LLZO NMC622 cells co-sintered at 800°C comparing samples where the extra Li ratio was increased from 1:3 Li:NMC to 1:1.	852
Figure XVI.9.1 Li/MIC/ LiFePO_4 coin cells demonstrate strong cycling stability over a temperature range from 23°C to 150°C . Li/MIC/ LiFePO_4 cycled at (a) 23°C at C/10, (b) 60°C at C/3, (c) 100°C at 1C, and (d) 150°C at 1C. Inset figures are the voltage profile for selected cycles under each cycling condition.....	855
Figure XVI.9.2 Charge/discharge profiles of the cell built with a spinel LiMn_2O_4 cathode, MIC electrolyte and Li metal anode. The cell was cycled at C/10 in the range 3.0-4.5 V at room temperature. The inset shows the specific capacity as a function of the cycle number.....	856
Figure XVI.9.3 New example composition of MIC electrolytes incorporating the DCA- anion for faster Li^+ transport. The team is also working with the FSI- anion and mixed systems to modulate morphology and phase segregation of different ions.	856
Figure XVI.9.4 New MIC membrane composition and internal structure. The image at upper left shows ion-exchanged electrolyte with iridescent appearance. At lower left are the chemical structures of new ions incorporated via ion exchange. The illustration at right shows liquid crystalline (LC) PBDT grains in blue, which provide a template for and scaffold to support the highly defective and conductive nanocrystalline phase containing LiFSI and LiBF_4	857
Figure XVI.9.5 Solid-state ^7Li and ^{19}F NMR of new MIC-nanocrystal system. (a) ^7Li SSNMR showing that all lithium is found in a single, locally anisotropic environment. The narrow central peak arises from the	

central transition of the spin-3/2 ^7Li energy level structure. The broad peak originates from the NMR quadrupolar satellite transitions, and this peak shape arises from the superposition of an isotropic distribution of crystallite orientations. The 4:6 integration ratio of these two components confirms that only one type of environment for Li^+ exists in this material, and the fact that the broad peak is observed confirms that the local environment is anisotropic, as expected for a nanocrystalline phase. (b) ^{19}F SSNMR identifying the different anions in the material (FSI^- and BF_4^-) and informing on their abundances and phase locations. Peak 1 is mobile BF_4^- found in the PBDT liquid crystalline (LC) phase. Peak 2 is solid-like BF_4^- found in the nanocrystalline grain boundary phase. Peak 3 is FSI^- anion found in both phases and is narrow due to the internal ^{19}F dynamics in this anion, even though $\approx 12\%$ of each anion are in the LC phase and $\approx 88\%$ in the nanocrystalline phase. 858

Figure XVI.9.6 (A) Temperature-dependent diffusion coefficients (via NMR) for the cations and anions in the new $\text{Pyr}_{13}\text{FSI}$ -based MIC (hollow symbols) and original $\text{Pyr}_{14}\text{TFSI}$ -based MIC (filled symbols). These new electrolytes are composed of 10:10:80 wt% PBDT:LiTFSI:IL. Activation energy of diffusion was derived using an Arrhenius fitting, where the measured ions in the $\text{Pyr}_{13}\text{FSI}$ -based MIC have a substantially lower activation energy of diffusion compared to the measured ions in the $\text{Pyr}_{14}\text{TFSI}$ -based MIC. These results are consistent with and support faster Li^+ transport in the $\text{Pyr}_{13}\text{FSI}$ -based MIC. (B) Voltage profile of a symmetric cell cycled at 23°C , with stepwise increases in current density every 10 cycles. Each cycle consisted of charge and discharge times of 0.5 h, respectively. The electrolyte used is composed of a 10:10:80 wt % PBDT:LiTFSI: $\text{Pyr}_{13}\text{FSI}$ MIC membrane. Under these conditions, the limiting current density reaches 0.45 mA/cm^2 . Multiple symmetric cells tested show consistent results. This is an improved limiting current density by at least a factor of 2 from the previous $\text{Pyr}_{14}\text{TFSI}$ -based MIC, which showed a limiting current density below 0.2 mA/cm^2 under the same charge/discharge conditions. This cycling performance is consistent with the lower activation energy and faster diffusion coefficients of this MIC membrane compared to the original composition. 859

Figure XVI.9.7 Synthetic routes to produce Na-PBDT and Li-PBDT from commonly available starting materials. 860

Figure XVI.9.8 (A) Top surface and (B) cross-section of the as-prepared composite cathode with the MIC solid electrolyte as the catholyte. 860

Figure XVI.9.9 Preliminary results of S K-edge XAS data. The EXAFS data has been obtained for the polymer membrane and ionic liquid samples without beam damage. 861

Figure XVI.10.1 NCM microcracking analysis using PFIB and digital image analysis software. a) PFIB SEM image of a NCM85105/ β - Li_3PS_4 cathode composite cross section and b) the corresponding processed image. c) PFIB SEM image of a NCM622/ β - Li_3PS_4 cathode composite cross section and d) the corresponding processed image. The color scheme for the processed images is as follows: white = SSE particle, black = pore, blue = intact NCM particle, and red = damaged NCM particle. 864

Figure XVI.10.2 Cycling data for NCM622/ β - Li_3PS_4 cold-pressed (blue) and hot-pressed (red) cathode composites cycled at 60°C . a) First cycle voltage profiles for cathode composites without carbon black additive. b) First cycle voltage profiles for cathode composites with carbon black additive. c) Cyclic capacity of cathode composites without carbon black additive. d) Cyclic capacity of cathode composites with carbon black additive. 865

Figure XVI.10.3 Pictures of binary and ternary glass samples after hot pressing trials. All samples contained 3 wt.% bulk Kevlar fiber to improve strength and handleability. 866

Figure XVI.10.4 XRD spectra for a) binary and b) ternary glass samples after hot pressing trials. Spectra are indexed to reflections for $\text{Li}_7\text{P}_3\text{S}_{11}$ (red bars, pdf 04-014-8383). 867

Figure XVI.10.5 Solubility of SSEs with glyme-based solvate ionic liquids (SILs). a) Photographic images of as-prepared mixtures of SSE chunks with the liquids ($\text{Li}(\text{G}3)\text{TFSI}$ and $\text{Li}(\text{G}3)_4\text{TFSI}$) and b) after being kept for 7 days. 868

Figure XVI.10.6 UV-Vis molecular absorption spectroscopy results for SSE in a) Li(G3)TFSI and b) Li(G3) ₄ TFSI.....	869
Figure XVI.11.1 The Arrhenius plot and Nyquist impedance plot for (a) cold-pressed and (b) hot-pressed SSE-1 from 25 to 100°C.	871
Figure XVI.11.2 The Arrhenius plot and Nyquist impedance plot for (a) cold-pressed and (b) hot-pressed SSE-1 from 25 to 100°C.	872
Figure XVI.11.3 XRD patterns of SSE-1.	872
Figure XVI.11.4 (a) Cycling of a Li/SSE-1/Li symmetric cell at different current densities under room temperature. (b) Evolution of voltage polarization, total resistance, and interfacial resistance upon cycling. (c-h) XPS spectra of (c-e) original SSE-1 and (f-h) SEI layer on lithium at the Li/SSE-1 interface.	873
Figure XVI.11.5 Electrochemical evaluation of Li-S ASSBs at 60°C. (a) Galvanostatic discharge-charge curves at 0.1 C. (b) Rate performance of Li-S ASSBs. Areal sulfur loading is between 2 and 3 mg cm ⁻² . Li-In alloy is used as the anode.....	874
Figure XVI.11.6 (a) Charge-discharge curves and (b) rate performance of S-C-LPS cathode and S-C-SSE-2 cathode. The cells were tested between 0.8 and 2.5 V at 60°C.....	875
Figure XVI.11.7 Cycling performance of Li-S ASSB using SSE-2 at 60°C.....	875
Figure XVI.11.8 Cycling performance of Li-S ASSB using new sulfur cathode at room temperature.....	876
Figure XVI.11.9 Cycling performance of Li-S ASSB using solid additives (< 3 wt%) in the sulfur cathode. The cell was tested at 60°C.....	876
Figure XVI.12.1 (A) Full cell for full SS battery testing (left); in-situ optical cell (right); (B) comparison of pristine Li and Li anodes with formation of dynamic protective layers.	879
Figure XVI.12.2 Pictures of Li metal pieces and LYCl powder a) before and b) after hand grinding; c) corresponding XRD patterns of the reaction products. Pictures of Li metal pieces and LPSCl powder d) before and e) after grinding; f) corresponding XRD of the reaction products. SEM images of g) LPSCl and h) LYCl powder. i) Ionic conductivity measurement of LYCl pallet and LPSCl/LYCl/LPSCl composite pallet at room temperature. j) Schematic illustration showing the Li/LPSCl/LYCl design (left) and Li/LYCl design (right).880	
Figure XVI.12.3 a) Voltage and current profile of Li/LYCl/Li cell at 0.2 mA cm ⁻² , 0.2 mAh cm ⁻² . b) Corresponding EIS spectra during rest and after 60 h cycling. c) Voltage and current profile of Li/LPSCl/LYCl/LPSCl/Li cell at 0.2 mA cm ⁻² , 0.2 mAh cm ⁻² ; d) the details indicated by the areas marked by the yellow dashes. e) Corresponding EIS spectra during rest and after 60 h cycling.	881
Figure XVI.12.4 a) Charge/discharge profiles of NCM-811/LYCl/Li cell at 0.1 mA cm ⁻² . Electrochemical performance of NCM-811/LYCl/LPSCl/Li cell: b) initial two charge/discharge profiles at 0.1 mA cm ⁻² (corresponding dQ/dV curves shown insert); c) CV profiles at 0.02 mV s ⁻¹ ; d) impedance evolution during one charge/discharge cycle. e) cycling performance at 0.1 mA cm ⁻² ; f) rate capability from 0.1 C to 1 C.....	882
Figure XVI.12.5 Thickness measurement of the cold pressed a) LYCl pallet and b) LPSCl-LYCl pallet before cycling; after cycling: c) cross-sectional SEM image of the LPSCl-LYCl layer, top-view SEM images of d) LYCl surface and e) LPSCl surface; f) cross-sectional SEM image and g-i) elemental mapping analysis of the LYCl/LPSCl interface; j) cross-sectional SEM image and k-m) elemental mapping analysis of the LPSCl/lithium interface.	883
Figure XVI.13.1 A) Linear sweep voltammograms of different polymer based composite electrolytes, and B) ionic conductivity (30°C) results for various HV polymers with increasing salt concentration.	885
Figure XVI.13.2 A) Ionic conductivity (30°C) as a function of increasing PVDF polymer content and B) representative shear modulus plots	886

Figure XVI.13.3 (A) Electrochemical impedance spectroscopy data for different PVDF polymer types in the composite ceramic-polymer electrolyte and (B) Electrochemical impedance spectroscopy data for various ratios for blended PVDF types A and C.	886
Figure XVI.13.4 Screening of various polymer electrolyte using Stainless Steel/Stainless Steel blocking electrode. a) Li salt screening; b) copolymer or filler screening; c) salt concentration screening.	887
Figure XVI.13.5 Synthesis of ultrafine LLZTO powder. a. Flow chart of LLZTO synthesis process. b. XRD pattern of one-step sintered LLZTO, in consistent with standard cubic garnet structure. c. SEM image LLZTO powder, revealing the particle size lower than 2 μ m.	888
Figure XVI.13.6 High lithium salts concentration for polymer electrolyte. a. Impedance spectra and Digital image of prepared free-standing polymer electrolyte with optimized condition. b. Conductivity comparison between polymers with different formula and drying time.	889
Figure XVI.13.7 Composite electrolyte conductivity. a. Flow chart of composite electrolyte film preparation. b. Impedance spectra and digital photo of prepared composite electrolyte film with optimized formulation. c. The effect of LiTFSI/PVDF mass ratio on the room-temperature conductivity. d. The composite electrolyte conductivity under different temperature. e. Arrhenius plot of composites electrolyte, revealing the low activation energy of ~0.11 eV.	890
Figure XVI.13.8 EIS of Li/Li symmetric cells using an SSE composite electrolyte with and without Li metal protection. The cell format is shown in the top right. The average of multiple cells is shown as a colored circle, the average resistance labeled and the black line represents ± 1 standard deviation from the average. The various colors represent various families of additives tested (legend not shown).	891
Figure XVI.13.9 Screening of protected lithium metal anodes using Li/Li symmetric cells. The different colors represent various families of lithium metal protection additives (salts, organics, etc.) and the different shapes represent various types of SSE used in the cell.	892
Figure XVI.13.10 Long-term Li/Li symmetric cell cycling. The protected lithium metal anode (green) shows minimal overpotential with no indication of dendrite formation or soft/hard shorts. The baseline (non-protected) system shows consistent voltage spikes indicative of soft/hard shorts caused by dendrite growth.	892
Figure XVI.13.11 Schematic comparing the structures of cathode and catholyte full cells and the possible extents of their Li ⁺ accessibilities.	893
Figure XVI.13.12 Performance of all-solid-state full cells. (a) Cycle-1 voltage traces of all-solid-state Li//NMC full cells with different PVdF types in the composite SSE. A control cell with an identical catholyte and a liquid electrolyte ("Liquid ELE") is also shown. (b) Specific capacities of the all-solid-state full cells with different PVdFs in SSE for up to 20 cycles.	894
Figure XVI.13.13 Performance of all-solid-state full cells. (a) Cycle life plot of all-solid-state Li//NMC full cells with different SSE types. (b) Voltage traces of Cycles 1, 20, and 60 of all-solid-state full cells with different SSE types.	894
Figure XVI.13.14 Performance of all-solid-state full cells. (a) Cycle life plot of all-solid-state Li//NMC full cells with two different SSE types; Cycling conditions are provided in the inset. (b) Capacity retention plot, (c) Voltage traces of Cycles 1 and 50 of all-solid-state Li//NMC full cells with the two different SSE types.	895
Figure XVI.14.1 a) Voltage & curvature vs. time of the LLZO/quartz electrode. Black and red lines indicate voltage and curvature profile, respectively. b-c) separator and plating side of the LLZO pallet after the experiment. On the plating side, a small crack is observed. d-e) observed crack in the SEM. f) FIB cut on the crack reveals a partial lithium metal penetration through the solid electrolyte. g) EDS mapping of the FIB cut cross-section. Blue, red, and green dots indicate signatures of Oxygen, Zirconium, and Lanthanum, respectively.	897
Figure XVI.14.2 a) Visual representation of the laser orientation angles relative to the crack location after the experiment shown in Figure II.9.N.1a. The data from Figure II.9.N.1a was measured with the laser orientation angle of 0 degrees. b) Measured curvature values vs. laser orientation angle after the experiment shown in	

Figure II.9.N.1a. The curvature values were measured in 45 degrees increment relative to the original laser orientation (0 degrees).....	898
Figure XVI.14.3 KMC simulations of the stripping process. (a) and (c), Under stress bias, $E_p = 0.55$ eV, $\epsilon' = 0.01$) the Li surface during delithiation is smooth at both interfaces. Without the stress, (b) the Li surface is smooth with Li ₂ O layer but (d) has trapped vacancies with LiF layer.....	899
Figure XVI.14.4 Contact resistance vs. time plotted out under various pressure conditions. The initial pressure of 1.81 MPa was applied at time zero.....	900
Figure XVI.14.5 Conceptual diagrams depicting the cross section of lithium and LLZTO interface. The formation of dislocation substructures, and the movement of dislocations after removing the external pressure causing an increase in the contact area with LLZTO.....	900
Figure XVI.14.6 CT scan of the cross-section of Li/LAGP/LiFePO ₄ cell. (a) Li/LAGP/LiFePO ₄ cell with control lithium electrode. (b) Li/LAGP/LiFePO ₄ cell with coated lithium electrode.....	901
Figure XVI.15.1 Charge–discharge profiles of NMC LPSCl Li-In (a) and NMC LPSCl interlayer Li thin cells.....	904
Figure XVI.15.2 Characterization of NMC cathode composites processed with different methods. a and b, SEM images of cathodes containing PTFE (a) and NBR (b) binders processed with dry and wet methods, respectively. c–j, ToF-SIMS mapping (30 μ m * 30 μ m) of F (c, f), transition metals (d, h), Cl (e, i) and the combined view of the three (r, j).....	905
Figure XVI.15.3 Characterization of NMC cathode composites processed with different methods. a and b, SEM images of cathodes containing PTFE (a) and NBR (b) binders processed with dry and wet methods, respectively. c–j, ToF-SIMS mapping (30 μ m * 30 μ m) of F (c, f), transition metals (d, h), Cl (e, i) and the combined view of the three (r, j).....	906
Figure XVI.15.4 (a) Schematic illustration of nano-cell fabrication from the polished thin-cell sample, (b) schematic illustration of the micro-fabricated device for nano-cell testing, (c) optical image of the micro-fabricated device for charging-discharging experiments, (d) optical image of the closed pop-up SEM stub, (e) optical image of an opened pop-up SEM stub, (f) the complete in-operando experimental configuration inside an SEM/FIB system.....	906
Figure XVI.15.5 Nano-cell fabrication process. (a) SEM image of the polished surface of a thin-cell, (b) SEM image of a laminated thin layer prepared by FIB, (c) SEM image of the nano-cell, clearly showing the anode/electrolyte/cathode configuration. (d) SEM image of the nano-cell bridging the gap of two Au electrodes for electrochemical tests.....	907
Figure XVI.15.6 Electrochemical and structural characterization of nano-cells. a and b, Structure (a) and impedance measurement (b) of a Pt LPSCl Pt symmetrical cell. c and d, Structure (c) and cyclic voltammogram (d) of an NMC LPSCl LTO full cell. e and f, In situ observation of the full cell before (e) and after (f) cycling.....	908
Figure XVI.15.7 Structure (a) and in operando morphology characterization (b–d) of an NMC LPSCl Ag–C Li micro-cell during discharge. The imaging area in Figure a is highlighted with a rectangle. A moving structural feature in Figure b–d is highlighted with a circle.....	909
Figure XVI.15.8 In operando morphology characterization of an NMC LPSCl Ag–C Li micro-cell during charge.....	910
Figure XVI.16.1 Studied cluster-based solid electrolytes in the established database.....	914
Figure XVI.16.2 Chemically-mixed and cation-doped cluster-based solid electrolytes in the established database.....	915
Figure XVI.17.1 Structural evolution of cathode/electrolyte interface obtained from AIMD simulations under ambient conditions. The atomic-scale structure of interface between S8(001) (i.e., fully charged cathode) and	

electrolytes with varying P-S motifs (a,b) Li7PS6 (001) (PS4), (c,d) Li2PS3 (001) (PS3), and (e,f) Li4P2S6 (001) (P2S6). Corresponding interfaces with Li2S (001) (i.e., fully discharged cathode) are shown for (g,h) Li7PS6 (001), (i,j) Li2PS3 (001), and (k,l) Li4P2S6 (001). In all panels, Li, P, and S atoms belonging to SSE are depicted as magenta, blue, and tan spheres respectively, while the Li and S in cathode are shown in dark purple and yellow colors. 919

Figure XVI.17.2 Electrochemical performance during cycling of Li-S batteries made up of super P/C-S cathode, Li₆PS₅F_{0.5}Cl_{0.5} SSE and Li anode with 0.04 mL of functionalizing liquid containing (a) 0.6 M of LiTFSI in PYR (b) 2M LiTFSI in PYR:DOL (1:1) using DOL diluent, and (c) 2M LiTFSI in PYR:DOL (1:1) using DOL diluent along with SSE incorporated in the cathode. Note the batteries in panels (a) and (b) do not have any SSE in the cathode. The left axis corresponds to discharge capacity, while the right axis shows the Coulombic efficiency. The batteries are cycles at a rate of C/20. 920

Figure XVI.17.3 Decomposition reactions of (a,b) PYR₁₄-TFSI IL, and (c,d) LiTFSI in DOL-DME near the cathode in its fully discharged state (Li₂S) obtained from ab initio molecular dynamics simulations under ambient conditions. In both panels (a,c), we show the atomic snapshots of the interface in the beginning and end of AIMD trajectory, while the key reactions are summarized in panels (b,d). Note, both Li₂S and Li₆PS₅F_{0.5}Cl_{0.5} are oriented such that their crystallographic [001] directions are aligned normal to the interface. In all cases, TFSI⁻ anion dissociates resulting in Li-F bonds. PYR and DOL do not dissociate as opposed to DME. 921

Figure XVI.17.4 Equilibrated interface structures obtained from ReaxFF-CMD simulations under ambient conditions. (a) Li(001)/LiPS(001), (b) S₈(001)/LiPS(001), and (c) Li₂S(001)/LiPS(001) interfaces. The lithium, sulfur, and phosphorus atoms are shown in red, yellow, and green colors. The PS₄³⁻ tetrahedra are shown in green. Radial distribution functions (RDF) g(r) for selected atom pair types for each interface are shown in the bottom row. The labels (e), (c), (a) identify the atoms that belong to electrolyte, cathode, and anode 922

Figure XVI.17.5 Performance of battery with super-P cathode at high S-loading (4 mg/cm²) functionalized with 40 μ L functionalizing liquid containing 2M LiTFSI in PYR14:DOL (1:1), Li₆PS₅F_{0.5}Cl_{0.5} SSE and Li anode cycled at (a) 30°C, (b) 60°C, and (c) temperatures alternating between 60°C and 30°C. All batteries are cycled at C/20 rate. 923

Figure XVI.17.6 Electrochemical performance of battery consisting of Super P-S cathode with 0.7 mg/cm² loading functionalized with 10 μ L functionalizing liquid containing 2M LiTFSI in PYR14:DOL (1:1), Li₆PS₅F_{0.5}Cl_{0.5} SSE and Li anode (a) without any SSE in cathode, and (b) when SSE is drop casted onto the cathode. 924

Figure XVI.17.7 Performance of battery with CNC-S cathode at high S-loading (4 mg/cm²) functionalized with 40 μ L functionalizing liquid containing 2M LiTFSI in PYR14:DOL (1:1), Li₆PS₅F_{0.5}Cl_{0.5} SSE and Li anode cycled at 60°C at C/20 rate. (a) Charge-discharge curve at 1, 10 and 20 cycles. (b) Charge/discharge capacity (shown in black/red) and Coulombic efficiency (shown in blue) during battery cycling. 924

Figure XVI.18.1 Gibbs free energies for the H3 (O3-rich, in blue) and H3/H4 (O1-rich, in orange) phases for a) 4% Li b) 8% Li c) 12% d) 17% for 4 potentials from the ensemble. 95th confidence intervals are indicated by the shaded region and were determined from a Student's t-distribution fit. 929

Figure XVI.18.2 (a) Sample Li_x(Ni_{0.8}Mn_{0.1}Co_{0.1})O₂ supercell model for x = 0.33 with randomly distributed Li ions in the Li layer. Grey octahedrons represent Ni site, purple octahedrons represent Mn sites, blue octahedron represent Co sites and green spheres represent Li ions. (b) DFT computed Li_x(Ni_{0.8}Mn_{0.1}Co_{0.1})O₂ energy of formation. 930

Figure XVI.18.3 Schematic of workflow to get the lowest energy configurations of fully lithiated doped NMC811 930

Figure XVI.18.4 Representative LiNiO₂-LLZO interface model. Green, grey, red, blue, and purple spheres represent Li, Ni, O, La and Zr respectively. 931

Figure XVI.19.1 Schematic of multimodal synchrotron analysis of sulfide glass samples. 934

- Figure XVI.19.2 Sealed holders mounted at beamline 11-ID-B for PXRD and PDF studies, allowing mapping of the samples. Note that the transparency of the sulfide glass allows for optical characterization of the buried electrode/electrolyte interface in later phases of the project. 934
- Figure XVI.19.3 Data taken from 400 μm -thick sulfide glass from PolyPlus. Data has been corrected for background scatter processes and normalized by atomic scattering factors to get the overall structure factor. Higher q -resolution data collected at low q was used to screen for impurity phases, while data taken to high q was used to compute the PDF of the glass itself. 935
- Figure XVI.19.4 Maps of the glass fraction and deviations from a simple two-phase model of glass and polycarbonate (PC) were constructed from 3600 diffraction patterns for each sample. While the first samples were found to have maps containing $<1\%$ impurities, an example of one point with weak impurity Bragg peaks (labeled “x”) is shown. 935
- Figure XVI.19.5 Examples of real-space PDF data taken from two glass samples (S1 and P1). Peaks due to different chemical bonds are labeled. 936
- Figure XVI.19.6 Preliminary GDOES depth profiling of Li and S species during first 10 sec of sputtering. 936
- Figure XVI.20.1 Electrochemical impedance spectra and SEM images of $\text{Li}_7\text{P}_2\text{S}_8\text{Br}_{0.5}\text{I}_{0.5}$ synthesized with solvent of (a) cyclohexane, (b) toluene, and (c) acetonitrile. 939
- Figure XVI.20.2 (a) XRD patterns and (b) ionic conductivities of $\text{Li}_7\text{P}_2\text{S}_8\text{Br}_{1-x}\text{I}_x$ ($0 \leq x \leq 1$) at 20°C 939
- Figure XVI.20.3 Galvanostatic cycling of the Li-Li cells at step-increased current densities at 20°C with $\text{Li}_7\text{P}_2\text{S}_8\text{Br}_{1-x}\text{I}_x$ ($0 \leq x \leq 1$) electrolytes, where (a) $x = 0$, (b) $x = 0.2$, (c) $x = 0.5$, (d) $x = 0.8$, and (e) $x = 1$. The time for each charge and discharge is 0.5 h. The step size for the current increase is $0.1 \text{ mA}/\text{cm}^2$. (f) The critical current densities versus the composition of the sulfide-based solid-state electrolytes. 940
- Figure XVI.20.4 Nyquist plots of (a) $\text{Li}/\text{Li}_7\text{P}_2\text{S}_8\text{Br}/\text{Li}$, (b) $\text{Li}/\text{Li}_7\text{P}_2\text{S}_8\text{Br}_{0.5}\text{I}_{0.5}/\text{Li}$, and (c) $\text{Li}/\text{Li}_7\text{P}_2\text{S}_8\text{I}/\text{Li}$ cell with equivalent circuit fitting at 20°C . Evolution of overall resistance (d) and areal interfacial resistance (e) of each cell with time at 20°C 941
- Figure XVII.1.1 (a) Cycling performance and (b) charge/discharge curves of Li/Se-S pouch cell with 100 mg Se-S loading at 200 mA g^{-1} with a E/S ratio of 10. (c) The effectiveness of the combination of cathode design, Se doping, and fluorinated electrolyte in achieving a shuttle- and dendrite-free Li/S pouch cell under thick-cathode and low-E/S ratio conditions. (d) Cycling performance and (e) charge/discharge curves of Li/Se-S pouch cell with 50 mg Se-S loading at 200 mA g^{-1} with a E/S ratio of 5. 944
- Figure XVII.1.2 (a,b) TEM images of the 3d-omsh/ ZnS,Co-N-C . (c) High-angle annular dark-field TEM image of the SAC sites (marked by the red circles) inside the 3d-omsh/ ZnS,Co-N-C . (d) TEM image of the polar binding sites inside the 3d-omsh/ ZnS,Co-N-C . (e) Co K-edge EXAFS of the 3d-omsh/ ZnS,Co-N-C with the reference Co foil and Co_3O_4 (top), and the fitting result using the Co-N-C model (bottom), as shown in the inset. χ , absorption coefficient; R , average distance of neighboring atoms from atoms emitting photoelectrons. (f) Zn K-edge EXAFS of the 3d-omsh/ ZnS,Co-N-C with the reference Zn foil (top), and the fitting result using the ZnS model (bottom), as shown in the inset. (g) TEM image of the 3d-omsh/ $\text{ZnS,Co-N-C}/\text{S}$ cathode and the corresponding EDS element mapping of C, N, S, Co and Zn. The scale bars are 200 nm. (h) SAXS simulation on the pore size distributions of 3d-omsh/ ZnS,Co-N-C and 3d-omsh/ $\text{ZnS,Co-N-C}/\text{S}$ using spherical shape model. 946
- Figure XVII.1.3 (a,b) Cycling performance of various sulfur cathodes at 0.2 C (a) and 1.0 C (b). (c) Rate capability of various sulfur cathodes. (d,e) Cycling performance of the 3d-omsh/ $\text{ZnS,Co-N-C}/\text{S}$ cathode with high areal sulfur loading: 4 mg cm^{-2} for 300 cycles at 0.75 C (d) and 6 mg cm^{-2} and 9 mg cm^{-2} for 100 cycles at 0.6 C (e). 1C equals to 1675 mA g^{-1} 948
- Figure XVII.1.4 (a) Optimized configurations of Li_2S_4 , Li_2S_6 and Li_2S_8 absorption on ZnS (a1-a3), the Co-N-C surface (b1-b4) and the ZnS,Co-N-C surface (c1-c4). The yellow, pink, silver, brown, blue and cyan balls denote the S, Li, Zn, Co, N and C atoms, respectively. (b) Relative free energy for the discharging process

from S8 to Li₂S on the bare graphene and Co-N-C surfaces. The optimized structures of the intermediates on the Co-N-C surface are shown as the insets. Same colour coding for atomic structure as in (a)..... 949

Figure XVII.2.1 Electrochemical performances of SPC and LPC Electrodes (4 mg S/cm²) under flooded (E/S ratio=10 μ L/mgs) and lean (E/S ratio=4 μ L/mgs) electrolyte conditions. Capacity retention (a-c) and corresponding discharge/charge curves (d-f) of SPC and LPC under flooded electrolyte condition at 0.1 C (1 C= 1000 mA/g); Capacity retention (g-i) and corresponding discharge/charge curves (j-l) of SPC and LPC under lean electrolyte condition..... 954

Figure XVII.2.2 Simulations of electrolyte infiltration in different electrode structure: (a) initial state and (b) steady state of electrolyte infiltration in LPC and SPC, (c) surface wetting degree and (d) electrolyte absorption degree in LPC and SPC at steady state. 955

Figure XVII.2.3 Electrochemical performances of low-porosity sulfur electrodes with polymer/liquid electrolyte design. (a) Effects of polymer on sulfur utilization rate and cycling stability with electrode porosity of 35% and E/S ratio=4 μ L/mg, (b) charge/discharge curves of polymer integrated electrodes at various porosities and E/S ratio. (c) Cycling performance of 35% porosity electrode and E/S ratio=3 μ L/mg. (d) Cycling performance of 25% porosity electrode at E/S=2.5 μ L/mg. (4 mg s/cm², 0.1C for both charge and discharge)..... 956

Figure XVII.2.4 Preparation of the dense S electrode. (a) Schematic illustration of the preparation process of the G2 electrode. (b) Comparison of electrode density and S content in whole electrode between the G1, G2, and literature results. If electrode density was not directly reported, it was calculated by “S loading/(S content \times electrode thickness)”. (c) Photo of the free-standing G2 electrode. (d-g) Scanning electron microscope (SEM) images of the G2 electrode: (d) surface, (e) cross- section (without milling), and (f, g) high -resolution images of the milled cross-section. 958

Figure XVII.3.1 Polysulfides entrapment in Li₂S@TiS₂ cathodes. (a) Schematic of the setup for in situ optical observation. A thin gap (1–2 mm) between the working electrode and the counter electrode is designed to avoid short-circuiting. (b) Illustration of the electrochemical cell assembled with bare Li₂S working electrode or Li₂S@TiS₂ working electrode, PEO/LiTFSI electrolyte, and lithium metal counter electrode. The entire cell is heated to 60°C. The open circuit voltage of as-prepared cell is 2.5 V. The cell is first charged to 3.8 V at a constant current of 5 μ A and then discharged to 1.6 V at a current of -2 μ A. The in situ OM imaging shows the working electrode/electrolyte interface for (c) bare Li₂S electrode and (d) Li₂S@TiS₂ electrode. 960

Figure XVII.3.2 **TiS₂ enhanced Li₂S oxidation reaction kinetics in all-solid-state Li-S batteries (ASSLSBs).** (a) First cycle charge voltage profiles of Li₂S@TiS₂ and bare Li₂S cathodes. (b) Electrochemical impedance spectra of ASSLSBs using bare Li₂S and Li₂S@TiS₂ cathodes, and the liquid system data adapted from Nat. Commun. 5, 5017 (2014). (c) Cyclic voltammetry (CV) curves and (d) corresponding peak potentials of Li₂S@TiS₂ and bare Li₂S electrode. (e) CV curves of the Li₂S@TiS₂ electrode at various scan rates (0.1 mV s⁻¹, 0.2 mV s⁻¹, 0.3 mV s⁻¹, 0.4 mV s⁻¹, and 0.5 mV s⁻¹). (f) Plots of CV peak current for the anodic oxidation process (peak 3: Li₂S \rightarrow S₈) versus the square root of the scan rates. All the cells are tested at 60 °C. (g) Energy profiles for the oxidation of bare Li₂S and Li₂S on TiS₂. The optimized geometries of TiS₂ with adsorbates (Li₂S*, Li₂S₂*, Li₂S₄*, Li₂S₆*, Li₂S₈*, and S₈*) are shown in the insert (Ti: blue; S: yellow; Li: green). 961

Figure XVII.3.3 **Electrochemical performance of Li₂S@TiS₂ cathodes and bare Li₂S cathodes in ASSLSBs.** (a) Charge-discharge voltage profiles of Li₂S@TiS₂ and bare Li₂S cathodes at 0.2 C at 60°C. (b) Voltage profile and areal capacity of Li₂S@TiS₂ cathode with a high mass loading (4.0 mg·cm⁻²) at a current density of 0.04 mA·cm⁻² at 60°C. (c) Rate performance of Li₂S@TiS₂ and bare Li₂S cathodes at various charging rates, cycled at 60°C, within a potential window of 1.6-2.8 V versus Li⁺/Li. (d) Cycling performance and Coulombic efficiency of Li₂S@TiS₂ cathode at 0.8 C for 150 cycles at 80°C. 962

Figure XVII.4.1 Chemical structure of monomers used in the synthesis 966

Figure XVII.4.2 XRD patterns (A) and DSC curves (B) of elemental sulfur and three sulfur/organic polymers (C) relative abundance of S₈ in the polymeric sulfurs. 967

- Figure XVII.4.3 The discharge/charge profiles and CVs of a Li-Sulfur battery (A), and three Li-Sulfur polymer batteries (B, C, D); The HPLC of dissolved polysulfide distribution in the electrolyte at 20% DoD. 967
- Figure XVII.4.4 The comparison of multiple discharge and recharge curves of S-PAN cathode made with various sulfur to PAN ratios. 968
- Figure XVII.4.5 The comparison of S-PAN cathodes cycled in either and carbonate-based electrolytes. 968
- Figure XVII.4.6 (a)–(h) Structure, (i) polymer- S_4^{2-} interaction energy, and (j) polymer- Li_2S_4 interaction energy of the self-assembled multiple S_4^{2-} , Li^+ and single polymer chain. Columns with heights equal to the value of the interaction energy components are stacked up, where the summation is the total interaction energy corresponding to each polymer. 969
- Figure XVII.5.1 Li-S battery recycling with different amount of DOL added. A. The capacity and coulombic efficiency vs. cycle numbers of the Li-S cell with the DOL additives at 5, 10, 15% by weight. B. The voltage and capacity profile of the Li-S cell at the 25th cycle (of Figure 1A) with the DOL additive at 5, 10, 15% by weight. C. The capacity and coulombic efficiency vs. cycle numbers of the Li-S cell with the DOL additives at 5, 10, 15% by weight, and saturated with LiTFSI salt. D. The voltage and capacity profile of the Li-S cell at the 15th cycle (of Figure 1C) with the DOL additive at 5, 10, 15% by weight, and saturated with LiTFSI salt. 971
- Figure XVII.5.2 0.5M LiTFSI in F_4EO_2/TTE (v/v,1:5) electrolyte: (a) i-t curve of DC polarization process. (b) Impedance of the cell before and after polarization. (c) The transference number of LiTFSI in F_4EO_2/TTE electrolyte as a function of concentration with error bars from multiple tests. 972
- Figure XVII.5.3 The S concentration detected from the supernatant of the electrolyte solution saturated by Li_2S , S, and all types of polysulfides (Li_2S_m , $m = 2, 4, 6, 8$) respectively. The error bar was calculated based on Gaussian distribution analysis. In comparison, the S concentration of 1.0M LiTFSI in DOL is 6.3M based on the literature. 973
- Figure XVII.5.4 (A) Cycling performance of lithium-sulfur cells with different LiTFSI concentrations with 0.6M $LiNO_3$ in DOL/DME (1/1, v/v) and (B) Coulombic efficiency evolution during the cycling test. 974
- Figure XVIII.1.1 (a and b) Cross-sectional images, oxygen- and carbon-EDX maps of Li metal surface with PPG5 (PEO-based gel polymer (PG) coating and electrochemical pre-treatment under O_2) and with PLi (without PG coating but with electrochemical pre-treatment under Ar). (c) Charge/discharge curves of LOBs with different lithium salts and (d) with and without 0.1M TEMPO. (e) EIS of fresh LOBs with different concentration of TEMPO in the LiTFSI based electrolytes. (f) EIS of LOBs with different lithium salts and PPG5 layer before and after pretreatment step. 979
- Figure XVIII.1.2 (a) Cycling stability of pristine Li anode with 0.1 M TEMPO and Li/PS-SEI anodes with different TEMPO concentrations (0.1, 0.15 and 0.2 M) in 1 M LiTf/G4 and (b) schematic illustration of the effect of PS-SEI layer operating with TEMPO as redox mediator. (c) EIS Nyquist plots of the corresponding cells after 10th cycle at a current density of 0.2 mA cm⁻² under a capacity limited protocol of 1.0 mAh cm⁻² in the operation voltage range of 2.0 – 4.5 V operated at 25°C. (d) Charge/discharge curves (110th – 120th) of Li- O_2 batteries with two different lithium salts (LiTf or LiTFSI) in G4 solvent with PS-SEI layer and 0.1 M TEMPO. (e) EIS of fresh Li- O_2 batteries with 0.1 M TEMPO in the LiTFSI based electrolytes and GDL carbon or RuO_2/CNT electrodes. (f) Charge profiles of pristine Li anode in 1 M LiTf/G4 with 0.1 M TEMPO, Li/PS-SEI in 1 M LiTf/G4 with 0.1 M TEMPO, Li/PS-SEI in 1 M LiTFSI/G4 with 0.1 M TEMPO and Li/PS-SEI with RuO_2/CNT electrode in 1 M LiTFSI/G4 with 0.1M TEMPO, respectively. (g) Schematic illustration of the synergy effect of dual-catalysis with PS-SEI layer in Li- O_2 cell. 980
- Figure XVIII.1.3 (a) Schematic illustration of the synergy effect of dual-catalysis with PS-SEI layer in Li- O_2 cell. (b) EIS Nyquist plots (inlet) of fresh Li- O_2 cells with single and dual catalysts and their charge curves during pre-charging to 5 V. (c) Cycling stability of pristine Li anode, Li/mosaic type SEI, Li/PS-SEI with 0.1 M TEMPO and Li/PS-SEI with 0.1 M TEMPO and ruthenium oxide fixed on the SWCNT air electrode at a current density of 0.2 mA cm⁻² under a capacity limited protocol of 1.0 mAh cm⁻² in the operation voltage range of 2 – 5 V operated at 25°C. (d) Schematic illustration of the three-dimensionally ordered macroporous

(3DOM)/SWCNT air electrode with dual-catalyst and PS-SEI layer in Li-O₂ cell. (e) Charge curves of Li-O₂ cells with dual-catalyst/PS-SEI layer and 3DOM/dual catalyst with PS-SEI layer during pre-charging to 5 V. (f) Charge-discharge profiles of Li-O₂ cells with dual-catalyst/PS-SEI and 3DOM/dual-catalyst with PS-SEI layer at a current density of 0.2 mA cm⁻² under a capacity limited protocol of 1.0 mAh cm⁻² in the operation voltage range of 2 – 5 V operated at 25°C..... 981

Figure XVIII.1.4 Top and cross-sectional views of SEM images of (a) Ru/SWCNTs (non-3DOM) and (b) three-dimensionally ordered macroporous (3DOM)-Ru/SWCNTs air electrodes before (fresh) and after 1st discharge at a current density of 0.2 mA cm⁻² under a capacity limited protocol of 1.0 mAh cm⁻² in the operation voltage range of 2.0 – 4.5 V operated at 25°C. EDX line-profiles and spectra scanned through cross-sectional views of (c) Ru/SWCNTs and (d) 3DOM-Ru/SWCNTs air electrodes after 1st discharge, (e) EIS Nyquist plots before (fresh) and after 1st discharge to 2.0 V and (f) cycling stability of Li-O₂ cells with (green) Ru/SWCNTs and (red) 3DOM-Ru/SWCNTs air electrodes at a current density of 0.2 mA cm⁻² under a capacity limited protocol of 1.0 mAh cm⁻² in the operation voltage range of 2.0 – 4.5 V operated at 25°C.... 982

Figure XVIII.2.1 Initial full discharge-charge voltage profiles of CL, CX, CC and CP cathode at a current density of (a) 0.02 mA cm⁻² and (b) 0.2 mA cm⁻²; (c) CV curves of CL, CX, CC and CP electrodes within a voltage window of 2.0-4.5 V at a scanning rate of 1 mV s⁻¹; SEM images of CP cathode after first discharge (d) and charge steps (e) at a current density of 0.02 mA cm⁻²; (f) Raman spectra of CP cathode at different stages: pristine, and after first discharge and charge steps. 985

Figure XVIII.2.2 (a) Nitrogen adsorption-desorption isotherms, (b) pore-size distributions of CL, CX, CC and CP. (c) O 1s and C 1s XPS scan and (d) electric conductivity of CL, CX, CC and CP, respectively. 986

Figure XVIII.2.3 Voltage profiles of Li-O₂ batteries with (a) sample 1, (b) sample 2, and (c) sample 3. SEM images of the discharged cathodes for (d) sample 1, (e) sample 2, and (f) sample 3. The scales are labeled the same for the images. XRD of the discharged cathodes for (g) sample 1, (h) sample 2, and (i) sample 3..... 987

Figure XVIII.2.4 A) Cryogenic transmission electron microscopy of catalytic layer formed in ether-based electrolyte over carbon nanotube. B) Voltage profile of catalytic layer formation process. Rate performance of Li-O₂ assembled using C) pristine carbon paper and D) with catalytic layer formed over the carbon paper. . 988

Figure XVIII.3.1 Li-O₂ battery voltage profiles for cathode based on Cu-THQ) MOF with current densities of 1 A/g (left) and 2 A/g (right)..... 991

Figure XVIII.3.2 Discharge-Charge voltage profile of Li-O₂ battery with Nb_{0.5}Ta_{0.5}S₂ as the cathode catalyst (a-c) current density of 0.1, 0.5 and 1 mAcm⁻², respectively..... 992

Figure XVIII.3.3 (a) DFT simulation of DMSO/IL electrolyte on a Li₂O₂ surface with KMnO₄ shows Li (blue) initially located at interface Li₂O₂; (b) after optimization the Li ion migrates from Li₂O₂ surface to electrolyte without any barrier and the final structure has an energy lower than the initial state by 1.4 eV. 993

Figure XVIII.3.4 Density functional calculations of an Li interface with MnO₂: (a) initial structure of α -MnO₂/Li interface, (b) final structure of the α -MnO₂/Li interface showing LiMnO_x interlayer. The purple, red and green spheres represent the Mn, O and Li atoms, respectively. 994

Figure XIX.1.1 XANES spectra of the a) Mn and b) Ni K-edges of pristine MNS and standard metal oxide references. The two-dimensional (2D) XANES mapping of c) Mn and d) Ni in MNS. The least-square fits of the calculated FT-EXAFS phase and amplitude functions to the experimental EXAFS spectra for Mn e) and Ni f) in MNS..... 998

Figure XIX.1.2 In situ XAS spectra for MNS. a-c) Ni and d-f) Mn K-edge XANES of MNS at various stages during the first charge/discharge and second charge processes, respectively. The edge energy evolution at half edge-step (E0.5) for g) Ni and h) Mn in Na_{0.67}[Mn_{0.61}Ni_{0.28}Sb_{0.11}]O₂ at different states. i) Charge compensation of different elements contribution during charge and discharge..... 999

Figure XIX.1.3 2D-XANES mapping of pristine NaMnFeCoNiO₂ and cyclic voltammetry test. (a) Ni thickness map; (b) Ni²⁺ composition map; (c) Ni XANES integrated from the field of view in (a); (d) Ni³⁺ composition map; (e) CV test for the 1st, 2nd and 3rd electrochemical cycles..... 1000

Figure XIX.1.4 The K-edge X-ray near edge spectrum (XANES) of Mn (a-c) and Fe (d-f) for P2- $\text{Na}_x\text{Mg}_{0.2}[\text{Fe}_{0.2}\text{Mn}_{0.6}\square_{0.2}]\text{O}_2$ (MFM-2) at various charge/discharge states during the first cycle and second charging.	1001
Figure XIX.2.1 (a) Schematic illustration of the structure of hierarchical micro/nanostructured Sbx-RP70-x/C30 composite before and after cycling. (b) High-resolution XRD and (c) PDF data for Sbx-RP70-x/C30 composite. (d) Crystal structure of standard Sb (JCPDS 35-0732) with interatomic Sb-Sb distance index... 1004	1004
Figure XIX.2.2 (a) Charge/discharge curves of $\text{Sb}_7\text{-RP}_{63}/\text{C}_{30}$ anode at C/3. and (b) cycling performance of $\text{Sb}_7\text{-RP}_{63}/\text{C}_{30}$ anode at C/3 and $\text{RP}_{70}/\text{C}_{30}$ anode at C/10. (c) Cycling performance of $\text{Sb}_{35}\text{-RP}_{35}/\text{C}_{30}$ and $\text{Sb}_{70}/\text{C}_{30}$ anode at C/3. (d) Rate performance of $\text{Sb}_7\text{-RP}_{63}/\text{C}_{30}$ and $\text{RP}_{70}/\text{C}_{30}$ anode. Open and solid symbols represent discharge and charge capacities, respectively. (e) The density of states distribution of valence electrons for Na_3P and Sb-doped Na_3P . (f) Estimated cell energy density of sodium-ion batteries with different anode materials using BatPaC.	1005
Figure XIX.2.3 (a) 2D contour plot of In situ HEXRD patterns during solid-state synthesis of O3 $\text{NaNi}_{0.4}\text{Mn}_{0.4}\text{Co}_{0.2}\text{O}_2$. Rietveld refinement of HEXRD patterns of (b) starting material and (c) intermediate product at 350°C.	1006
Figure XIX.2.4 (a) HEXRD patterns of samples with/out quenching. (b) SEM images of O3 $\text{NaNi}_{0.4}\text{Mn}_{0.4}\text{Co}_{0.2}\text{O}_2$. (c) The 1st charge/discharge curve and (d) the corresponding cycling performance of O3 $\text{NaNi}_{0.4}\text{Mn}_{0.4}\text{Co}_{0.2}\text{O}_2$ cathode at C/10.	1007
Figure XIX.2.5 Comparison of performance degradation of Na/NaFeO ₂ cell after resting at the end of 1 st charge for 10 days in (a) 1M NaClO ₄ /PC, (b) 1M NaPF ₆ /PC, and (c) 1M NaPF ₆ /PC with 2% FEC electrolytes. Continuous cycle (C1 – D1) vs. aging cycle (C1 – OCV storage for 10 days – D'1 – C'2 – D'2).	1008
Figure XIX.2.6 The effect of FEC additive on stabilizing the charged $\text{Na}_{1-x}\text{FeO}_2$ electrode in 1M NaPF ₆ /PC electrolyte. (a) SEM morphology (inset image showing the surface of harvested separator), (b) leakage current at 3.8 V, (c) cathode EIS as a function of SOC resting time, (d) ex situ XRD of harvested $\text{Na}_{1-x}\text{FeO}_2$ electrodes.	1009
Figure XIX.2.7 (a-e) Initial voltage profiles and (f) cycle performance of the $\text{NaFe}_x(\text{Ni}_{1/2}\text{Mn}_{1/2})_{1-x}\text{O}_2$ cathodes ($x = 0, 1/3, 1/2, 2/3$, and 0.8). Three formation cycles with 10 mA/g current density were followed by regular cycles with 30 mA/g.	1010
Figure XIX.3.1 a. HRTEM image of a single $\text{Na}_{0.74}\text{Ti}_{1.815}\text{O}_4$ particle, and the corresponding experimental (b) and simulated (c) SAED patterns. Crystal structure model derived from Rietveld refinement of the synchrotron XRD pattern of $\text{Na}_{0.74}\text{Ti}_{1.815}\text{O}_4$ was used in the SAED simulations. d. HRTEM image showing the lattice fringes directing along the zone axis [111]. TEM image (e) and element mapping images for Na (f), Ti (g) and O (h) of a single $\text{Na}_{0.74}\text{Ti}_{1.815}\text{O}_4$ particle. TEM image (i) and element mapping images for Na (j), Ti (k) and O (l) of $\text{Na}_{0.74}\text{Ti}_{1.815}\text{O}_4$ particles. (m) Rietveld refinement of the synchrotron XRD pattern of $\text{Na}_{0.74}\text{Ti}_{1.815}\text{O}_4$, the top panel shows a schematic representation of the crystal structure of $\text{Na}_{0.74}\text{Ti}_{1.815}\text{O}_4$ comprising of TiO ₆ octahedra (blue) and Na ions (yellow spheres).	1014
Figure XIX.3.2 Laboratory X-ray diffraction patterns of $\text{Na}_{0.74}\text{Ti}_{1.815}\text{O}_4$ electrodes in the pristine state and cycled to the annotated voltages in the first electrochemical cycle. b. Magnified plot of the dashed rectangle area in Figure XIX.3.2a. c. <i>Ex-situ</i> Raman spectra of $\text{Na}_{0.74}\text{Ti}_{1.815}\text{O}_4$ electrodes in the pristine state and cycled to the annotated voltages in the first electrochemical cycle.	1015
Figure XIX.3.3 Laboratory X-ray diffraction patterns of $\text{Na}_{0.74}\text{Ti}_{1.815}\text{O}_4$ electrodes collected at the end of discharge for annotated cycles. b. Nyquist plots of a Na/ $\text{Na}_{0.74}\text{Ti}_{1.815}\text{O}_4$ cell showing impedance data at the open circuit voltage (OCV) and at the end of charge for annotated cycles.	1015
Figure XIX.3.4 (a) Ex situ XRD patterns of $\text{Na}_{0.74}\text{Ti}_{1.815}\text{O}_4$ dried to the indicated temperatures, showing evolution into a related layered phase. (b) Second cycle profiles of materials dried to the indicated temperatures.	1016
Figure XIX.3.5 Cycling of sodium half-cells containing $\text{Na}_{0.74}\text{Ti}_{1.815}\text{O}_4$ dried to different temperatures.	1016

Figure XIX.3.6 a) Ti K-edge XAS spectra on heated $\text{Na}_{0.74}\text{Ti}_{1.815}\text{O}_4$ powders and reference materials, b) pre-edge features, c) Fourier-transformed Ti K-edge EXAFS spectra.....	1017
Figure XIX.3.7 a) first cycle of a cell containing $\text{Na}_{0.74}\text{Ti}_{1.815}\text{O}_4$ heated to 60°C with points indicated where data was taken. b) Ti K-edge spectra of discharged electrodes with reference materials included and e) charged electrodes. c) expansion of region showing shifts in the Ti K-edge for discharged electrodes and f) for charged electrodes, d) Fourier-transformed Ti K-edge data.....	1017
Figure XIX.3.8 Cycling profiles of (a) an NVP/Na half cell (b) a NVP/NTO full cell, and (c) a NVP/NTO full cell where the NTO anode was pre-cycled to reduce losses from SEI formation. All the cells were cycled at a current rate of C/10 calculated based on NVP. The capacity is normalized based on NVP. The N/P ratio is ~1.0 -1.04.....	1018
Figure XIX.4.1 (a) 1 st cycle voltage profile and (b) rate performance of PC-4b and AC-4b in sodium half-cell performed in a potential range 5 mV to 2 V with 1 M NaPF_6 in EC/DMC (1:1 in weight) as electrolyte.	1021
Figure XIX.4.2 (a) Voltage profile, (b) Cycling reversible discharge capacity and (c) CE of PC-4b NMC full-cell (N/P=1.01) compared to Kuraray HC NMC full cells (N/P=1.1), using NaFSI-TEP/TTE electrolyte (1:1.5:2 in molar ratio). Both pristine cathode and anode are used without any pretreatment or presodiation. The operating voltage window is 1.2V–3.8V and the 1 st formation C rate is 0.1C and cycling C rate afterward is 0.33C.....	1021
Figure XIX.4.3 Performance of Na NaNMC half-cells using HCE and baseline electrolyte: A) Cycling capacity; B) Coulombic efficiency and C) Voltage profiles.....	1022
Figure XIX.4.4 Performance of HC NaNMC full cell using HCE and baseline electrolyte: A) Cycling stability at 0.2 C; B) Coulombic efficiency, and C) rate capability.....	1022
Figure XIX.4.5 XPS spectra of CEI components on cycled NaNMC surface. a, d) C 1s spectra, b, e) F 1s spectra, c) P 2p spectra and f) S 2p spectra in NaPF_6 -PC electrolyte (a-c) and NaFSI-TEP electrolyte (d-f). g) Atomic composition of CEIs in two electrolytes. h, i) Mn 2p and Ni 3p spectra in two electrolytes.....	1023
Figure XIX.4.6 . XPS spectra of SEI components on cycled hard carbon surface. a, d) C 1s spectra, b, e) F 1s spectra, c, f) P 2p spectra, g) S 2p spectra and h) N 1s spectra in NaPF_6 -PC electrolyte (a-c) and NaFSI-TEP electrolytes (d-h). i) Atom ratios of SEI in two electrolytes.....	1023
Figure XIX.4.7 Electrochemical performance of HC NaNMC full cells: Discharge capacity (a) and CE (b) of HC NaNMC full cells using different electrolytes cycled at 0.2 C in a voltage range 1.2 – 4.2 V after three formation cycles at 0.05 C. The cathode loading is 0.6 mAh cm ⁻²	1024
Figure XX.1.1 Behavior of the new FDMB ether electrolyte, showing (upper) relative to other electrolytes, and (b) for three high Ni NMC cathodes.....	1027
Figure XX.1.2 Impact of a NbO_y treatment of NMC 811. (a) Reduction of 1st cycle loss by surface treatment, 400 and 500°C; (b) Improved rate capability of surface treated material; and (c) bulk treated material shows the highest capacity retention. (a) and (b) charge to 4.6 V; (c) charged to 4.4 V.....	1028
Figure XX.1.3 H_3PO_4 scavenges residual lithium and protects the surface with Li_3PO_4 as revealed by TOF-SIMS with ¹⁸ O labeling. The H_3PO_4 -treated sample (PNC) forms a thinner rock-salt layer (~ 3 nm) than the untreated sample (NC) (~ 15 nm). The purple and green colors in the top of (a) represent, respectively, ¹⁶ O ⁻ and ¹⁸ O ⁻ species, the blue color in the middle of (a) represents $\text{P}^{18}\text{O}_2^-$ species, and the green color in the bottom of (a) represents $\text{Li}_2^{18}\text{O}^+$ species. The scale bar in (a) is 10 μm.	1028
Figure XX.1.4 Cycling of Li LiNi _{0.94} Co _{0.06} O ₂ cells in the prior baseline electrolyte compared with that in LHCE.....	1029
Figure XX.1.5 Operando DSC studies comparing the 2020 carbonate electrolyte with the next generation LiFSI ether-based FDMB and M47 electrolytes.....	1029
Figure XX.1.6 (a) Photo images of Al-NMC811 and LATP-coated Al-NMC811 electrodes. SEM images of (b) Al-NMC811 and (c) LATP-coated Al-NMC811 electrodes. (d) Initial charge–discharge curves and (e) cycling	

performance of pristine and LATP-coated Al-NMC811 electrodes. The dQ/dV curves of (f) the 150th cycle and (g) the 250th cycle of pristine and LATP-coated Al-NMC811 electrodes..... 1030

Figure XX.1.7 Electrochemical performances of cells at different states of charge (SOCs) at 30°C. (a-c) Voltage profiles of the cells during the formation process and rest conditions, (a) the cell rested at fully discharged state (0% SOC), (b) the cell rested at half charged state (50% SOC), and (c) the cell rested at fully charged state (100% SOC). (d-f) Voltage profiles of the cells after different storage periods at different SOC, (d) 0% SOC, (e) 50% SOC, and (f) 100% SOC. 1031

Figure XX.1.8 Electrode-level quantification of the deposited transition metal on Li anode. (a) XRF mapping of the Li anode with spatial resolution around 30 μm . The unit of the color scale bar is $\mu\text{g mm}^{-2}$. (b) Average deposited transition metal mass per unit area for the three transition metals. In both (a) and (b), comparisons are made between the baseline electrolyte and the ‘with additive’ electrolyte. 1032

Figure XX.1.9 Operando DSC measurements (dotted curves for electrochemical test and solid curves for the measured heat flux) of novel ether-based M47, ED2, T3, 1 M LiFSI/FDMB electrolytes and traditional carbonate electrolyte (1M LiPF₆ in EC/DMC (1:1)) for NMC 811 charged to 4.8 V while held at (a) 30°C, (b) 45°C and (c) 60°C isothermally. (d) Summary of total heat release..... 1033

Figure XX.1.10 (a) Cycling performances of lithium-metal pouch cells with LNO cathodes at C/2 charge and 1C discharge rate, with C/3 rate every 50 cycles. (b) Charge-discharge curves of fresh coin cells assembled using the cathodes recovered from the cycled pouch cells. (c) Cross-sectional SEM images of LNO cathodes recovered from cycled pouch cells after 200 cycles in LHCE (top) and carbonate electrolyte (bottom). (d) XPS data of LNO cathodes recovered from cycled pouch cells after 200 cycles in LHCE (top) and carbonate electrolyte (bottom). Spectra were normalized across samples for each element..... 1034

Figure XX.1.11 (a) Voltage profiles of Li metal deposition/stripping in Li||Li symmetric cells (1 mAh cm⁻²) at a current density of 1 mA cm⁻². (b) Schematic illustration and cross-sectional SEM image of DL-3@Cu. (c) Average CEs of Li||Cu cells using bare Li and DL-3@Li. (d) Cycling performances of Li||NMC622 cells (4.2 mAh cm⁻²) at high rate (C/2, 1C = 4.2 mA cm⁻²) in the voltage range of 2.8 – 4.4 V at 25°C. (e) Surface SEM images of bare Li and DL-3@Li after 220 cycles..... 1035

Figure XX.1.12 (a,b) Molecular structures and design logic of FDMB and its analogs. (c) Long cycling CE of Li||Cu half cells. (d) LSV showing the high-voltage stability of developed electrolytes. (e) Anode-free pouch cell performance using the best electrolyte, 1 M LiFSI/1DME/6FDMH. 1036

Figure XX.1.13 STEM EDS mapping of a-d) Pristine SPAN; e-h) 10-cycle discharged SPAN; i-l) 10-cycle charged SPAN 1037

Figure XX.1.14 Electrochemical performances of Li||SPAN batteries with LiPF₆/carbonate and LHCE between 1.0-3.0 V. (a) Cycling stability under 60°C. (b) Cell discharge rate capability tests at 60°C after 3 formation cycles at 25°C, with a constant charge rate of C/5 and different discharge rates from C/5 to 5C. (c, d) Low-temperature discharge tests at C/5 with (c) LiPF₆/carbonate and (d) LHCE, where the operating temperature for all charging process was 25°C while the discharging was conducted at 25, 0, -10, -20, and -30°C, respectively, and then back to 25°C. In all cell tests in (a-d), 1C = 6.0 mA cm⁻². 1038

Figure XX.1.15 (a) SEI XRD of low and high concentration electrolytes using LiFSI as salt and PC, DMC, and DME as solvents. The light grey pattern belongs to SEI-LiF (denoted as LiF_(SEI)). The wavelength used is 0.18323 Å. (b) Rietveld refinement of SEI XRD data of low and high concentration LiFSI in PC. Contributions of individual phase to the XRD pattern are also shown. Open circles, experimental data; black lines, calculated data..... 1039

Figure XX.1.16 (a) the pressure experiment set-up. (b) pressure vs. Coulombic efficiency under various current densities. (c) Optical image of deposited Li under high current density (2mA/cm²), high loading (4 mAh/cm²), and optimized pressure conditions (350 kPa). (d-g) top view and (h-k) cross-section of Li deposited under various pressure at 2 mA/cm² for 1 hour. (d, h) 70 kPa, (e, i) 140 kPa, (f, j) 210 kPa, (g, k) 350 kPa. Scale bar is 2 μ 1040

Figure XX.1.17 Comparative results for electrolyte (a) concentration and (b) potential over 50 cycles for the original model without advective flux (Model 1) and modified model with advective flux (Model 2) at moving interface at $x = 0$ 1041

Figure XX.1.18 a-c) The trend of Li metal corrosion in high concentration “Bisalt” electrolyte: a) the Li^0 mass retention (%) as a function of resting time; The SEM images of the Li morphology b) before and c) after 5 weeks of resting. d-f) The trend of Li metal corrosion in carbonate solvent based “Gen 2” electrolyte (1 M LiPF_6 in EC-EMC): d) the Li^0 mass retention (%) as a function of resting time; The SEM images of the Li morphology e) before and f) after 5 weeks of resting. Total amount of 0.318 mAh of Li is plated at a rate of 0.5 mA cm^{-2} in all samples. 1042

Figure XX.1.19 Comparison of the cycling performance of high areal capacity SPAN electrodes. a) 50% cathode porosity, b) 40% cathode porosity, c) 30% cathode porosity. Voltage profiles of Li||SPAN cells with d) 50% cathode porosity, different binder, e) 40% cathode porosity, different binder, f) 40% cathode porosity, different binder. The mass loading of the SPAN cathode is 10 mg cm^{-2} . The cell was cycled under C/20 rate for two formation cycles and then cycled under C/5 rate. 1043

Figure XX.1.20 Electrochemical Analytic Diagnosis (eCAD) characterizations to analyze cell performance based on cathode active material’s utilization and cell degradation due to Li inventory loss at the Li anode. (a) The NMC622 cathode utilization variations as a function of cycle number among four different cells of design. (b) The capacity retention presented as a function of the ratio of capacity Q vs. capacity ration QR under the same test protocol at C/3. 1044

Figure XX.1.21 IR-free voltage vs SOC profiles derived using the eCAD method to show the OCV vs Li content in the NMC..... 1045

Figure XX.1.22 (a) Cycling performances of Li||NMC811 cells for different electrolytes, operating at 25°C during aging, varied when the temperature during formation cycles was changed from 10°C , 25°C to 45°C ; (b) Raman spectra of ether-based electrolytes (LCE, HCE and LHCE) at different temperatures..... 1046

Figure XX.1.23 Comparison of calendar and cycle life aging for LMBs. 1047

Figure XX.1.24 Electrochemical performances of four types of 350 Wh kg^{-1} Li || NMC622 pouch cells at 2.0 Ah level. **a,b**, Cell-level energy density, cell capacity, CE and charge–discharge curves of the pouch cell with $100 \mu\text{m}$ thick-Li in the anode; the N/P ratio is 5:1. **c,d**, Cycling performance and charge–discharge curves of the $50 \mu\text{m}$ Li pouch cell; the N/P ratio is 2.5:1. **e,f**, Cycling performance and charge–discharge curves of the $20 \mu\text{m}$ thin-Li pouch cell; the N/P ratio is 1:1 and the E/C ratio is 2.4 g Ah^{-1} . **g,h**, Cycling performance and charge–discharge curves of the Li-free-anode pouch cell, Cu || NMC622; the N/P ratio is 0:1. All pouch cells were cycled at 0.1 C for two initial formation cycles, and then charged at 0.1 C (the electric current is $\sim 0.23 \text{ A}$) and discharged at 0.3 C (the electric current is $\sim 0.7 \text{ A}$) in subsequent cycles (1 C equals 4.0 mA cm^{-2} or corresponds to 2.3 A, from 2.7 V to 4.4 V, 25°C). The arrows indicate the voltage changes during the charge–discharge processes. During the long testing of more than 13 months, these pouch cells suffered two power outages and one period of oven maintenance, so some cycling behaviors show fluctuations. Note that the cell energy density is calculated based on the total weight of the whole pouch cell, including all active and inactive parts in the pouch cell. 1048

List of Tables

Table ES- 1: Subset of EV Requirements for Batteries and Cells	xvi
Table 1: Subset of Requirements for Advanced High-Performance EV Batteries and Cells. (Cost and Low Temperature Performance are Critical Requirements).	3
Table 2: Subset of Targets for 12V Start/Stop Micro-hybrid Batteries (Cost and Cold Cranking are Critical Requirements).....	4
Table I.2.1 Electrolyte requirements corresponding to program targets.....	29
Table I.6.1 Summary of physical evaluation of different thickness Aramid separator compared to USABC goal....	48
Table I.6.2 Nail penetration test results for aramid cells versus ceramic coated PE cells	49
Table I.7.1 Comparison of Our Technology to Current Slurry Casting Technology.....	52
Table III.1.1 Location and Capacity of World's Lithium Metal Production (data from USGS)	135
Table III.3.1 Comparison of different Soxhlet extractors.	150
Table III.3.2 Process variables for froth column operation with 8 L feed slurry	154
Table III.3.3 NMC111 grades in froth and tailings based on ICP results and GSAS-II refinement based on XRD results	156
Table III.3.4 Process conditions for the froth column tests with 10 L feed slurry.....	157
Table III.3.5 Surface hydrophobicity tests in 25ml cell.....	160
Table III.3.6 XRD analysis results showing the refinement parameters.....	160
Table III.3.7 Elemental composition and structure of recycled and pristine NMC111 samples.....	163
Table III.3.8 Elemental composition for relithiated NMCs	165
Table III.3.9 Half-cell capacity for relithiated cathodes from solvent Y process	165
Table III.3.10 Scaled up relithiation of MSY in molten salts	166
Table III.3.11 ICP-OES results for ReLi NMC 622.	167
Table III.3.12 Summary of electrochemical capacities of scaleup relithiation process at different reaction time.	171
Table III.3.13 ICP-OES data of pristine NMC111, De-NMC111, and scaleup relithiated NMC111 powders in 10/30/60 min reaction.	172
Table III.3.14 Elemental composition for re-annealed upcycled products measured using GDOES and EDS (values in parentheses).....	176
Table III.3.15 Half-cell data for upcycled products.....	177
Table III.3.16 ICP-OES results for these NMCs.	179
Table III.3.17 Determined composition based on ICP-MS data of Commercial811 and SC-811.	183
Table III.3.18 TGA and ICP results of delaminated powders compared with different stirring conditions	192
Table III.3.19 Cost analysis for recycling graphite anode scraps using different processes. SolveX_IPA and SolveX_H2O stand for SolveX process using IPA and H2O to rinse the residue solvent X, respectively.....	194
Table III.3.20 Cost analysis for recycling NMC622 cathode scraps using different processes. *The modeling assumes that 95% of solvent Y is recycled and reused twice, and that acetone is not reused.	195
Table III.3.21 Purity of electrodes collected in cathode or anode rich fractions from various samples	202

Table III.3.22 Sample information for XPS or SEM study.....	217
Table III.3.23 CAMP cells to be used for thermal characterization—Cathode material was supplied by Toda and anode material was supplied by Superior Graphite.....	220
Table III.3.24 Percentage of capacity remaining after aging the CAMP cells for EOL thermal characterization—Cathode material was supplied by Toda and anode material was supplied by Superior Graphite.	221
Table III.3.25 CAMP cells to be used for thermal Characterization. The cathode material was supplied by Toda and the anode material was supplied by Superior Graphite. Contaminants were added to the slurry before coating the current collectors.	223
Table III.4.1 A comparison in first-cycle efficiency, DCR, discharge rate capability and fast charge capability of single-layer pouch cells among different graphite anode materials.....	235
Table III.5.1 SBC comparison of control, recycled and BRs cathode materials tested by A123 and WPI.....	240
Table III.5.2 Tap density of synthesized 83Ni precursor with virgin materials.....	241
Table III.5.3 Lot number and sample information.....	242
Table V.1.1 Design standards certifications to be used for the rack design (Source: NREL)	349
Table V.1.2 Important design parameters for the advanced rack design (Source: NREL).....	350
Table V.1.3 Representative Climate Locations for FY21 Scenarios	352
Table V.1.4 Key considerations and design variables for thermal management system. Source: NREL.....	354
Table V.1.5 Tasks for fail-safe thermal design for BTMS applications. Source: NREL.....	355
Table V.1.6 Critical parameters for the development of a BMS system. Source: NREL.....	359
Table V.1.7 Final Module/String/Rack/System configuration with different cell chemistries/sizes. Source NREL.....	360
Table V.1.8 Lead Acid Cycle Life Testing Results	364
Table VI.1.1 Reference ASI and activation energies for the 4 methods needed for the Arrhenius equation....	375
Table VI.2.1 Status of Deliverables for Testing	380
Table VI.5.1 Summary of LNO-oxide materials provided to the CAMP Facility.....	397
Table VI.5.2 Summary of Electrode Library Distributions	401
Table VI.6.1 Composition of solid polymer electrolyte	408
Table VI.6.2 Al ₂ O ₃ composite solid polymer electrolyte composition.....	408
Table VI.7.1 Articles Tested for USABC	413
Table VI.7.2 Articles Tested for Benchmark.....	413
Table VI.7.3 Articles Tested for Low Cobalt	414
Table VIII.1.1 (Prelithiation strategies investigated).....	432
Table VIII.1.2 Flash point of isopropanol/water mixtures. Data from reference 1.....	434
Table VIII.1.3 Materials Used in Validation Studies.....	440
Table VIII.2.1 DCR of full cell, cathode, and anode after 30 days storage test at different temperatures measured by Tri-electrode SLPs.....	449
Table VIII.2.2 Comparison of yield and heat generation rate of different experiments	451

Table VIII.7.1 Li Deposition System Manufacturing Target Performance (Measured with respect to established Baseline)	481
Table VIII.7.2 Cell Performance (Minimum Manufacturing Goals)	481
Table VIII.7.3 Project Year-1 Milestones Completion Status	482
Table VIII.8.1 Key cell Energy density models for Enovix 300 mAh development class cells.	488
Table VIII.8.2 Key cell metric summary for Year 1 cell builds.	488
Table VIII.9.1 Electrochemical Objectives for DoE Project – EE0009187.....	494
Table VIII.10.1 Cell Performance Targets.....	500
Table VIII.10.2 Performance in budget period 1 vs go/no-go milestone.....	502
Table VIII.13.1 Summary of program objectives	511
Table IX.2.1 Electrolytes consisting of various additives and solvents for the NMC9055//Gr couple	533
Table X.2.1 Calculated oxidation potential E_{ox} and free energy of proton removal, given relative to EC. Measured E_{ox} are given for comparison.....	595
Table X.5.1 Ionic Conductivity and Viscosity of 1 M and 5 M LiFSI-PMpipFSI Electrolytes with Different H_2O Concentrations (in mol/L and ppm).....	611
Table XI.1.1 Project performance targets for cathode active material and cell made with this material.....	623
Table XI.1.2 RST NCM811 cathode powder quality check values prior to slurry making	624
Table XI.1.3. Summary table showing initial cathode energy densities	628
Table XI.2.1 Summary table of the LNMO-graphite cell lithium inventory after different cycles.	631
Table XI.2.2 Composition and electrochemistry performance of screened novel electrolytes.....	636
Table XI.5.1 Performance Targets.....	663
Table XV.1.1 Porosity and ionic conductivity of partially sintered LICGC tapes as a function of sintering conditions and tape composition.....	771
Table XV.1.2 Composition and interfacial impedance with Li metal of the cross-linked PEO electrolytes evaluated.	771
Table XV.5.1 Composition of LLZTO powders, shrinkage and relative density of sintered LLZTO pellets. .	790
Table XVI.1.1 Composition of the triblock copolymer PEO- <i>b</i> -POSS- <i>r</i> -PSLiTFSI. The compositions of POSS and PSLiTSFI were determined by 1H -NMR spectra. The <i>r</i> values denote the concentration of Li ion in the polymer and is given by $r = [Li]/[EO]$	803
Table XVI.1.2 Comparison of PEO-POSS and POSS-PEO-POSS diblock and triblock copolymers.....	804
Table XVI.2.1 Li^+ conductivity (σ_{Li^+}) and activation energy (E_A) of LPS prepared through solvent-mediated synthesis routes. Samples were pressed at either room temperature or 240°C. Dried samples were rinsed with THF 1-4 times prior to calcinating at 140°C.....	815
Table XVI.6.1 Chemical composition and selected properties of various MOS glasses.....	837
Table XVI.10.1 Summary of process rheology for half-factorial design of experiments.....	866
Table XVI.10.2 Mass of SSEs before and after dissolving in glyme-based solvate ionic liquids (SILs) for 7 days.	868
Table XVII.4.1 Composition of sulfur/organic polymers.....	966
Table XIX.4.1 Effect of synthesis conditions on the physical/electrochemical properties of carbon anode ..	1020

Vehicle Technologies Office Overview

Vehicles move our national economy. Annually, vehicles transport 12 billion tons of freight—more than \$38 billion worth of goods each day³—and move people more than 3 trillion vehicle-miles.⁴ Growing our economy requires transportation, and transportation requires energy. The transportation sector accounts for approximately 27% of total U.S. energy needs,⁵ and the average U.S. household spends over 17% of its total family expenditures on transportation,⁶ making it, as a percentage of spending, the most costly personal expenditure after housing. Transportation is critical to the overall economy, from the movement of goods to providing access to jobs, education, and healthcare.

The Vehicle Technologies Office (VTO) funds research, development, demonstration, and deployment (RDD&D) of new, efficient, and clean mobility options that are affordable for all Americans. VTO leverages the unique capabilities and world-class expertise of the National Laboratory system to develop new innovations in vehicle technologies, including advanced battery technologies (including automated and connected vehicles as well as innovations in efficiency-enhancing connected infrastructure); innovative powertrains to reduce greenhouse gas and criteria emissions from hard-to-decarbonize off-road, maritime, rail, and aviation sectors; and technology integration that helps demonstrate and deploy new technology at the community level. Across these technology areas and in partnership with industry, VTO has established aggressive technology targets to focus RDD&D efforts and ensure there are pathways for technology transfer of federally supported innovations into commercial applications.

VTO is uniquely positioned to accelerate sustainable transportation technologies due to strategic public-private research partnerships with industry (e.g., U.S. DRIVE, 21st Century Truck Partnership) that leverage relevant expertise. These partnerships prevent duplication of effort, focus DOE research on critical RDD&D barriers, and accelerate progress. VTO advances technologies that assure affordable, reliable mobility solutions for people and goods across all economic and social groups; enable and support competitiveness for industry and the economy/workforce; and address local air quality and use of water, land, and domestic resources.

Annual Progress Report

As shown in the organization chart (below), VTO is organized by technology area: Batteries & Electrification R&D, Materials Technology R&D, Advanced Engine & Fuel Technologies R&D, Energy Efficient Mobility Systems, and Technology Integration. Each year, VTO's technology areas prepare an Annual Progress Report (APR) that details progress and accomplishments during the fiscal year. VTO is pleased to submit this APR for Fiscal Year (FY) 2021. The APR presents descriptions of each active project in FY 2021, including funding, objectives, approach, results, and conclusions.

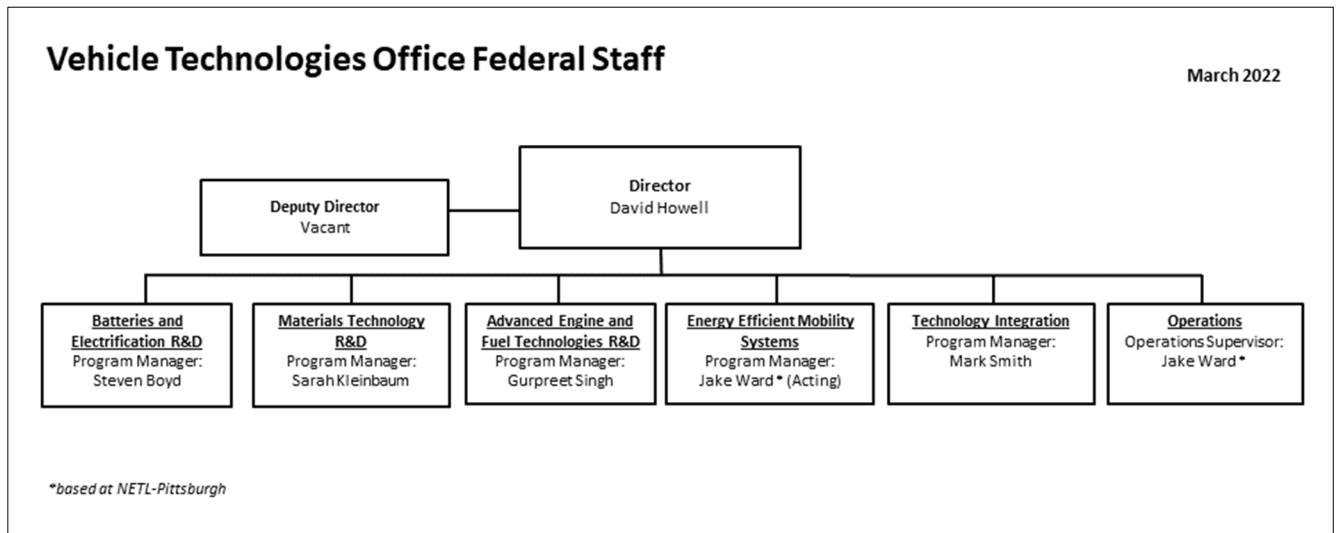
³ U.S. Department of Transportation, Freight Analysis Framework Version 5.0 Data Tabulation Tool.

⁴ U.S. Department of Transportation, March 2022 Traffic Volume Trends, Figure 1.

⁵ U.S. Energy Information Administration. Monthly Energy Review, 2022, <https://www.eia.gov/totalenergy/data/monthly/index.php>.

⁶ Davis, Stacy C., and Robert G. Boundy. Transportation Energy Data Book: Edition 39. Oak Ridge National Laboratory, 2020, <https://doi.org/10.2172/1767864>.

Organization Chart



Batteries Program Overview

Introduction

During the fiscal year 2021 (FY 2021), the Vehicle Technologies Office's (VTO) Batteries program continued research and development (R&D) support of battery technologies for plug-in electric vehicles (PEVs), e.g., plug-in hybrids, extended range electric vehicles, all-electric vehicles, and some hybrid electric vehicles. One objective of this support is to enable U.S. innovators to rapidly develop next generation of technologies that achieve the cost, range, and charging infrastructure necessary for the widespread adoption of PEVs.

Stakeholders involved in VTO R&D activities include universities, national laboratories, other government agencies and industry partners – including automakers, battery manufacturers, material suppliers, component developers, private research firms, and small businesses. VTO works with key U.S. automakers through the United States Council for Automotive Research (USCAR) – an umbrella organization for collaborative research consisting the Ford Motor Company, the General Motors Company, and Stellantis. Collaboration with automakers through the U.S. DRIVE (Driving Research and Innovation for Vehicle Efficiency and Energy Sustainability) partnership enhances the relevance and the success potential of the research platform. An important prerequisite for the electrification of the nation's light duty transportation sector is the development of more cost-effective, longer lasting, and more abuse-tolerant PEV batteries and accordingly, VTO battery R&D is focused on the development of high-energy batteries for PEVs and very high-power devices for hybrid vehicles.

Goals

The goals of this research are to address barriers to EVs reaching the full driving performance, convenience, and price of an internal combustion engine (ICE) vehicle. EVs have the advantage of a very high efficiency compared to other vehicle types, a simplified drive train, and a flexible primary energy source (i.e., the electricity needed to charge an EV can come from coal, natural gas, wind turbines, hydroelectric, solar energy, nuclear, or any other resource). Another current focus is the 12V start/stop (S/S) micro-hybrid architecture, in which the engine is shut down whenever a vehicle stops. Vehicles with the S/S functionality are being deployed worldwide. The 12V battery provides power for auxiliary equipment (e.g., the radio and air conditioning) and then restarts the engine when the vehicle moves. Current 12V S/S batteries, typically lead-acid batteries, have a poor life. Table 1 and Table 2 show a subset of the targets for high-performance EVs and 12V start/stop micro hybrid batteries that have been set by U.S. DRIVE⁸, respectively.

Table 1: Subset of Requirements for Advanced High-Performance EV Batteries and Cells.
(Cost and Low Temperature Performance are Critical Requirements).

Energy Storage Goals (by characteristic)	System Level	Cell Level
Cost @ 100k units/year (kWh = useable energy)	\$125/kWh*	\$100/kWh
Peak specific discharge power (30s)	470 W/kg	700 W/kg
Peak specific regen power (10s)	200 W/kg	300 W/kg
Useable specific energy (C/3)	235 Wh/kg*	350 Wh/kg
Calendar life	15 years	15 years
Deep discharge cycle life	1000 cycles	1000 cycles
Low temperature performance	>70% useable energy @C/3 discharge at -20 °C	>70% useable energy @C/3 discharge at -20 °C

⁸ https://www.uscar.org/guest/article_view.php?articles_id=85

Table 2: Subset of Targets for 12V Start/Stop Micro-hybrid Batteries
(Cost and Cold Cranking are Critical Requirements)

Energy Storage Goals (by characteristic)	Under the hood	Not under the hood
Maximum selling price (@220k units/year)	\$220*	\$180*
Discharge pulse (1s)	6 kW	
Cold cranking power, (-30 °C)	6 kW for 0.5s followed by three 4 kW/4s pulses*	
Available energy (750W acc.)	360 Wh	
Peak recharge rate (10s)	2.2 kW	
Sustained recharge rate	750 W	
Cycle life	450 k	
Calendar life	15 years at 45 °C*	15 years at 30 °C**
Maximum weight	10 kg	
Maximum volume	7 liters	
	*Current commercial cells do not meet this goal **Current cells almost meet this goal	

State of the Art

Battery R&D attempts to advance battery technology to help improve the market penetration of PEVs and hybrid vehicles by overcoming the current barriers. To accomplish this, it focuses on: (1) a significantly reduced battery cost, (2) increased battery performance, e.g., extreme fast charge (XFC) and low temperature performance for enhanced lithium-ion, (3) improved life advanced chemistry cells, (4) increased tolerance to abusive conditions; and (5) more cost-effective recycling and sustainability.

The current status of the broad battery chemistry types (current lithium-ion, next gen, and BLI) is summarized in Figure 1. Battery R&D spans mainly three areas:

- **Current technology (enhanced lithium-ion):** including cells with current materials (graphite anode/transition metal oxide cathode) and features like XFC compatibility, low temperature performance and improved abuse tolerance.
- **Next-gen lithium-ion:** Cells containing an alloy anode, usually silicon-based, and/or a high voltage (>4.5 V) cathode.
- **Beyond lithium-ion (BLI):** Cells containing Li metal anodes.

Over the past 11 years, PEVs have become more commercially viable, with battery costs dropping almost 80% since 2010. Further cost reductions in high-energy batteries for PEVs are always desirable. In addition, although today's batteries approach very attractive cost numbers, they still need the ability to accept extreme fast charging (XFC) and to perform better in low-temperature operations to compete with ICEs in all-weather performance and "refueling" convenience. Research into "enhanced lithium-ion" batteries (which would provide these functionalities) is one of the R&D focus areas. For further gains in energy density and cost reduction, research is needed in both "next gen" chemistries (which employ an alloy anode and/or a high voltage cathode) and BLI chemistries (see Figure 1). Cycle and calendar lives of next-gen and BLI chemistries fall well short of EV goals. Most cells employing a significant amount of silicon provide around 1,000 deep-discharge cycles but with less than two years of calendar life; BLI cells typically provide much less of a cycle life (250 cycles or less). In addition, the requisite low temperature performance and extreme fast charge capability are lacking in all chemistries.

Current Technology Lithium-ion Graphite/NMC	Next Generation Lithium-ion Silicon Composite/High-voltage NMC	Longer-term Battery Technology Lithium Metal
Battery Pack Cost	Battery Pack Cost	Battery Pack Cost
<ul style="list-style-type: none"> Current: \$235/kWh Potential: \$100-160/kWh 	<ul style="list-style-type: none"> Current: \$256/kWh Potential: \$90-125/kWh 	<ul style="list-style-type: none"> Current: ~\$320/kWh Potential: \$70-120/kWh
Large-format EV cells: 20-60 Ah	Large-format EV cells: 20-60 Ah	Large-format EV cells: TBD (Today)
Current cycle life: 1000-5000	Current cycle life: 500-700	Current cycle life: 50-100
Calendar life: 10-15 years	Calendar life: Low	Calendar life: TBD
Mature manufacturing: 	Mature manufacturing: 	Mature manufacturing:
Fast-charge: 	Fast-charge: 	Fast-charge:
R&D Needs	R&D Needs	R&D Needs
<ul style="list-style-type: none"> High-voltage cathode/electrolyte Lower-cost electrode processing Extreme-fast charging 	<ul style="list-style-type: none"> High-voltage cathode/electrolyte Lower-cost electrode processing Durable silicon anode with increased silicon content 	<ul style="list-style-type: none"> High-voltage cathode Lithium protection High-conductive solid electrolyte

Figure 1. Chemistry classes, status, and R&D needs

An overview of the candidate battery technologies and their likely ability to meet the DOE cost goals are shown in Figure 2. Because of the large variation in different battery technologies, battery research also includes multiple activities focused to address remaining high cost areas within the entire battery supply chain.

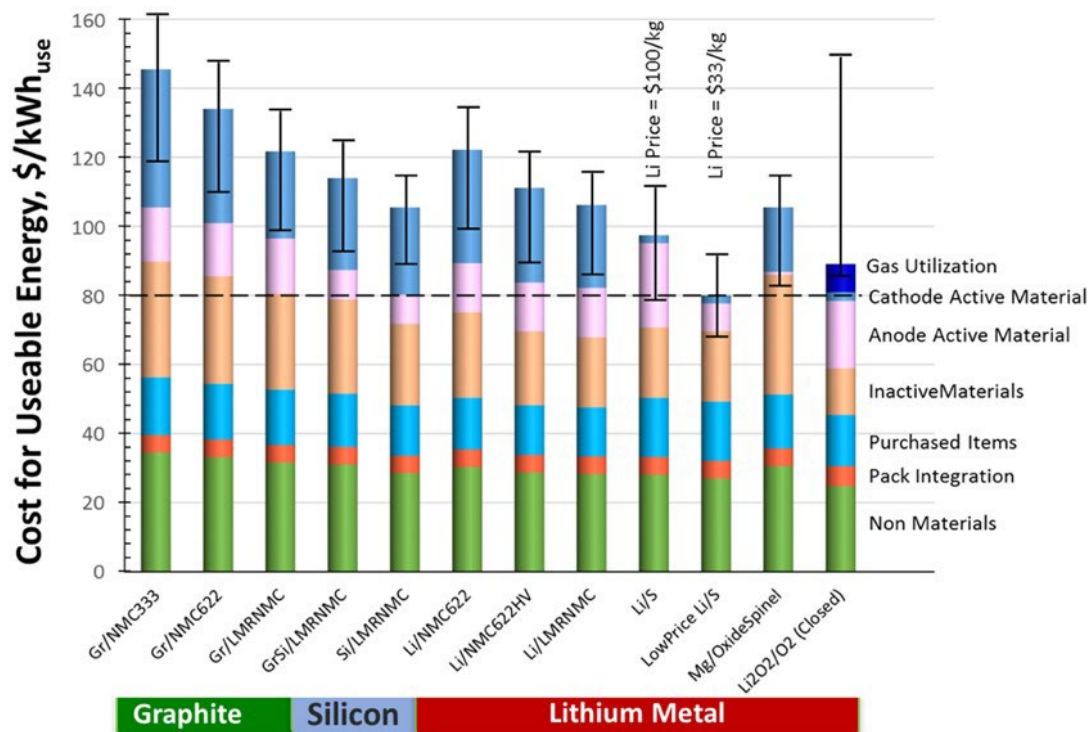


Figure 2. Potential for Future Battery Technology Cost Reductions

Battery Technology Barriers

The major remaining challenges to commercializing batteries for EVs (as well as 12V start-stop micro-hybrid batteries) are as follows:

A. Cost. The current cost of high-energy lithium-ion batteries is approximately \$150 – \$200/kWh (on usable energy basis), a factor of two-three times too high from where it needs to be to be competitive with ICEs. The cost of lithium-ion-based 12V micro-hybrid batteries (which offer significantly better life and higher capacity than conventional lead acid batteries) is approximately 50% higher than lead acid batteries. The main cost drivers are the high cost of raw materials, costs associated with materials processing, the cell and module packaging, and manufacturing.

B. Performance. Historically, a higher energy density was needed to reduce the weight and volume of PEV batteries, but those weight and volume issues have been to a large degree been addressed. The use of higher energy materials is still an effective way to reduce costs further and extend driving range, but cell chemistries that provide higher energy have life and performance issues. Also, existing chemistries (e.g., graphite anodes paired with transition metal oxide cathodes) need improvement in XFC and low temperature performance to compete favorably with gas-powered vehicles in the areas of performance and customer convenience. The main performance issue with lithium-ion 12V start/stop batteries is a challenging “cold start” requirement at -30°C coupled with high or room temperature life.

C. Life. The life issue for mature lithium-ion technologies has mainly been mostly addressed. However, both next-gen and BLI cell technologies still suffer major cycle and calendar life issues. The life of lithium-ion-based 12V start/stop micro-hybrid batteries is relatively good at room temperatures. However, enhancing cold crank performance often shortens battery life at the high temperatures found in the under the hood application.

D. Abuse Tolerance. Many lithium-ion batteries are not intrinsically tolerant to abusive conditions; however, full packs have been engineered by automotive OEMs to mitigate much of the risk. The reactivity of high nickel cathodes and flammability of current lithium-ion electrolytes are areas for possible improvement. The characteristics of next-gen and BLI chemistries to abusive conditions are not well-understood. However, silicon anode cells show very high temperatures during thermal runaway and lithium metal-based batteries have a long history of problematic dendrite growth which can lead to internal shorts and thermal runaway. Thus, research into enhanced abuse tolerance strategies will continue.

E. Recycling and Sustainability. Currently, automotive OEMs pay a relatively large cost (5%-15% of the battery cost) to recycle end of life PEV batteries. The various chemistries used in lithium-ion cells results in variable backend value. Alternatively, unless they get recycled, lithium-ion batteries could lead to a shortage of key materials (lithium, cobalt, and nickel) vital to the technology. Finding ways to decrease the cost of recycling could thus significantly reduce the life cycle cost of PEV batteries, avoid material shortages, lessen the environmental impact of new material production, and potentially provide low-cost active materials for new PEV battery manufacturing.

Program Organization Matrix

VTO's energy storage effort includes multiple activities, ranging from focused fundamental materials research to prototype battery cell development and testing. The R&D activities can involve either shorter-term pre-competitive research by commercial developers or exploratory materials research generally spearheaded by national laboratories and universities. The program elements are organized as shown in Figure 3. Battery R&D activities are organized into the following program elements: Advanced Batteries and Cells R&D, Battery Materials R&D, and the current focus.

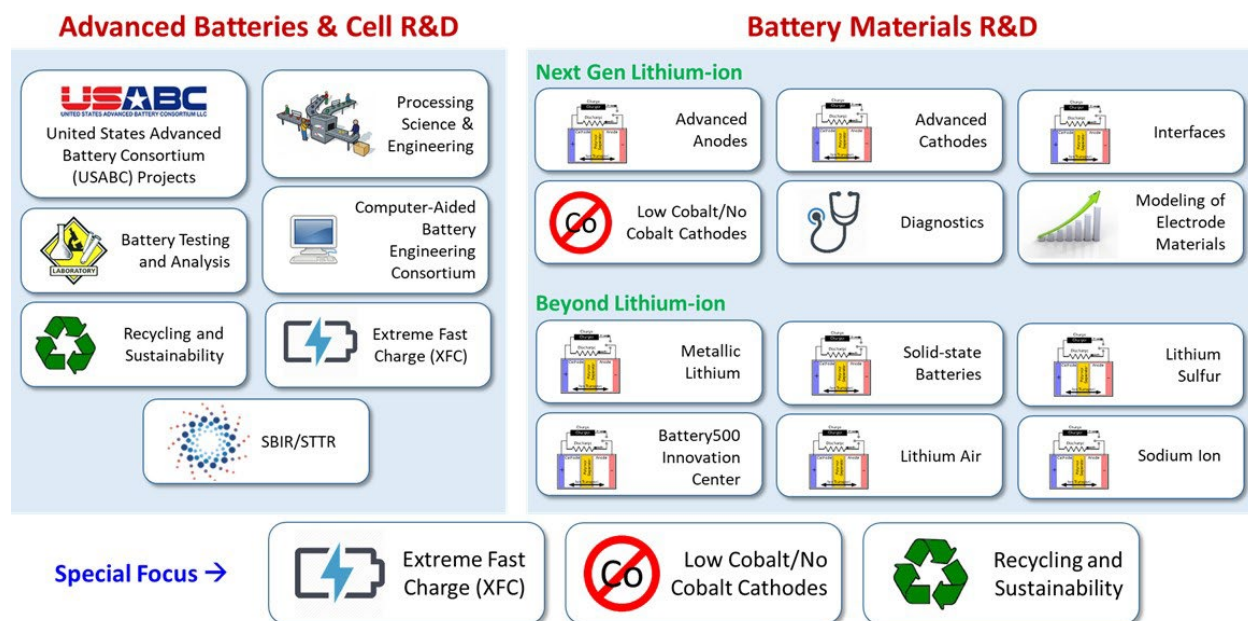


Figure 3. Battery R&D Program Structure

Advanced Cell and Battery Research and Development activity. This activity focuses on the development of robust battery cells and modules to significantly reduce battery cost, increase life, and improve performance. In this report, Part of this effort takes place in close partnership with the automotive industry, through a cooperative agreement with the *United States Advanced Battery Consortium* (USABC). In FY 2021, the USABC supported seven cost-shared contracts with developers to further the development of batteries and battery components for PEVs and HEVs. In addition to the USABC projects, DOE supports battery and material suppliers via contracts administered by the National Energy Technology Laboratory (NETL). Other projects in this area include performance, life and abuse testing of contract deliverables, laboratory- and university-developed cells, and benchmarking new technologies from industry; thermal analysis, thermal testing and modeling; cost modeling; secondary usage and life studies; and recycling studies for core materials. The *processing science & engineering* activity supports the development and scale-up of manufacturing technologies needed to enable market entry of next-generation battery materials and cell components – emphasizing disruptive materials and electrode production technologies that could significantly reduce cost and environmental impact while increasing yield and process control relative to existing production technologies. Several *small business innovation research* (SBIR) projects, also supported by VTO, are focused on the development of new battery materials/components and are the source of new ideas and concepts and are covered in that chapter.

Advanced Materials Research activity. This activity addresses fundamental issues of materials and electrochemical interactions associated with rechargeable automotive batteries. It develops new/promising materials and uses advanced material models to discover them and their failure modes, as well as scientific diagnostic tools and techniques to gain insight into why they fail. This work is carried out by researchers at national labs, at universities, and at commercial facilities. It includes the *next generation lithium-ion* research activity focused on the optimization of next generation, high-energy lithium-ion electro-chemistries that incorporate new battery materials. It emphasizes identifying, diagnosing, and mitigating issues that impact the performance and lifetime of cells constituted of advanced materials. Research continues in the six areas of advanced anodes, advanced cathodes, advanced electrolytes, electrode issues, interfaces, diagnostics, and modeling. The *beyond lithium-ion* (BLI) Technology activity addresses fundamental issues associated with lithium batteries, develops new/promising materials and uses advanced material models to discover such

materials using scientific diagnostic tools/techniques. It includes solid-state battery technologies, lithium metal, lithium sulfur, lithium air, and sodium-ion systems. The newly-started VTO *Battery500* projects are also managed in conjunction with this program element.

Special Focus. The current focus targets three areas of battery research. The first area is concerned with enabling *extreme fast charging* (XFC) in enhanced lithium-ion systems. It started with a 2017 research project to understand XFC, followed by a set of XFC awards (listed in the last year's report). In the second area, recognizing the issues of price volatility and supply reliability with cobalt DOE started several projects to develop and optimize low cobalt cathode materials. The third area consists of a set of *recycling and sustainability* projects, which involve studies of full life-cycle impacts and costs of battery production and use; cost assessments and impacts of various battery recycling technologies; and the material availability for recycling and secondary usage and their cost impacts.

As a further resource, the Electrochemical Energy Storage Roadmap describes ongoing and planned efforts to develop battery technologies for PEVs and can be found at the EERE Roadmap page <http://energy.gov/eere/vehicles/downloads/us-drive-electrochemical-energy-storage-technical-team-roadmap>. VTO also has extensive ongoing *collaboration* efforts in batteries R&D across the DOE and with other government agencies. It coordinates efforts on energy storage with the DOE Office of Science, and the DOE Office of Electricity. Coordination and collaboration efforts include membership and participation in program reviews and technical meetings by other government agencies, and the participation of representatives from other government agencies in the contract and program reviews of DOE-sponsored efforts. DOE also coordinates with the Department of Army's Advanced Vehicle Power Technology Alliance, the Department of Transportation/National Highway Traffic Safety Administration (DOT/NHTSA), the Environmental Protection Agency (EPA), and the United Nations Working Group on Battery Shipment Requirements. Additional international collaboration occurs through a variety of programs and initiatives. These include: the International Energy Agency's (IEA's) Hybrid Electric Vehicles Technology Collaboration Program (HEV TCP); the G8 Energy Ministerial's Electric Vehicle Initiative (EVI); and bilateral agreements between the U.S. and China. The collaborative activities with China under U.S. China CERC.

Battery Highlights from FY 2021

The following are some of the highlights associated with battery R&D funded by VTO (including highlights related to market developments, R&D breakthroughs, and commercial applications).

A New Class of Cobalt-free Materials. (ANL)

Due to the wide range of structures and electrochemical properties of manganese (Mn)-oxides, as well as its earth-abundance, Mn has a long history in battery technologies, and new discoveries are showing that Mn may have an important role to play in next-gen cathodes. At Argonne National Laboratory a team of researchers described a novel concept related to lithiated, Mn-spinel oxides as Li-ion cathode materials and demonstrated a high voltage material which delivers a specific energy higher than most NMC811 materials. The spinel framework offers a robust platform to reversibly cycle lithium in and out of its 3D tunneled-structure. However, low capacities (e.g., 130mAh/g for LiMn_2O_4) and/or untenable voltages (e.g., 5V operation in $\text{LiMn}_{1.5}\text{Ni}_{0.5}\text{O}_4$) have hindered the ability of spinel materials to meet practical demands. The Materials Research Group at Argonne has recently revisited the intriguing concept of lithiated spinels, (e.g., $\text{Li}_2\text{Mn}_2\text{O}_4$), as both stabilizing components of Li-excess cathodes as well as stand-alone, high-capacity electrodes. Using the knowledge from these discoveries, a high-capacity, Co-free composition was targeted utilizing a 50/50 mix of Mn and Nickel (Ni). Again, by controlling atomic-level disorder, within an ordered lithiated spinel framework, the team was able to realize a remarkably stable, high-capacity material. Figure 4 shows charge/discharge profiles between 5.0-2.5V of the MnNi electrode, 5mg/cm². The electrode behaves differently than the high-voltage MnNi spinel, revealing substantial capacity delivered throughout the voltage window (as opposed to the high-voltage material in which a large percentage of the capacity is delivered at 5V). In addition, the new material showed very low expansion/contraction (<3%) during cycling, giving a stable ~225 mAh/g with little structural fatigue. These new findings, along with the large space of relevant

parameters (composition/synthesis/site-order/disorder) reveal exciting new opportunities in the design of next-gen, sustainable cathodes.

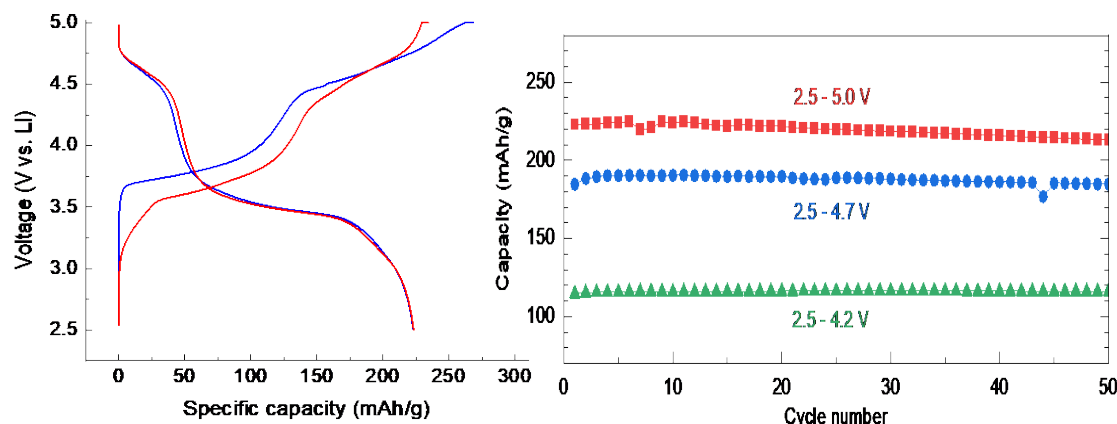


Figure 4. (left) Unique charge/discharge profiles of the novel, lithiated spinel between 5.0-2.5 V. (right) Cycling capacity at three upper cutoff voltages highlighting the stability of the cathode material, electrolyte is 1.2M LiPF₆ EC/EMC 3/7 wt%.

Towards Stable Cycling of Cost-effective DRX Cathodes via Fluorination (LBNL)

Development of new cathode materials with higher performance and lower cost is needed to further enable the commercialization of EVs. Conventional layered oxides are the dominant cathode in commercial lithium-ion batteries for high-energy applications. However, layered cathodes contain a large amount of expensive and scarce transition metals (TM) (i.e., Co, Ni), presenting a challenge to their commercialization. The recently developed Li-excess cation-disordered rock-salts (DRXs) have received significant interest as they are Co/Ni-free and can be made from cost-effective and earth-abundant TMs. The structural flexibility of DRXs substantially lessens the elemental constraints and enables the incorporation of a wide range of TMs as well as fluorine anions (considered enabling for high voltage operation) in the crystal lattice (Figure 5a). Such a large chemical space opens up the opportunities to search for improved and less expensive cathode materials. Researchers at Lawrence Berkeley National Laboratory have synthesized a fluorinated Mn-Ti DRX cathode, Li_{1.2}Mn_{0.6}Ti_{0.2}O_{1.8}F_{0.2}, via a solid-state reaction. These Mn and Ti TMs present distinct advantages in cost and resource sustainability compared to their counterparts (e.g., Co, Ni) in conventional layered and other DRX analogs (Figure 5b). As shown in Figure 5c, Li_{1.2}Mn_{0.6}Ti_{0.2}O_{1.8}F_{0.2} delivers an initial capacity of 233 mAh/g (754 Wh/kg, comparable to NMC 811) when cycled between 4.8 and 1.5 V, using 1M LiPF₆ EC:DMC. Moreover, this material exhibits stable cycling with over 90% capacity retention after 200 cycles. The excellent cycling stability of this DRX cathode is attributed to the partial fluorination of the oxygen lattice, which increases the content of redox-active Mn and facilitates the utilization of more reversible Mn redox during electrochemical cycling. This material experiences a local structural rearrangement during early cycles before exhibiting a stable voltage upon extended cycling (Figure 5d, e). This early change in voltage profile may present an implementation challenge and will be investigated in future studies. These recent advancements demonstrate a great promise to develop cost-effective DRX cathodes with enhanced capacity and retention for high-energy Li-ion batteries.

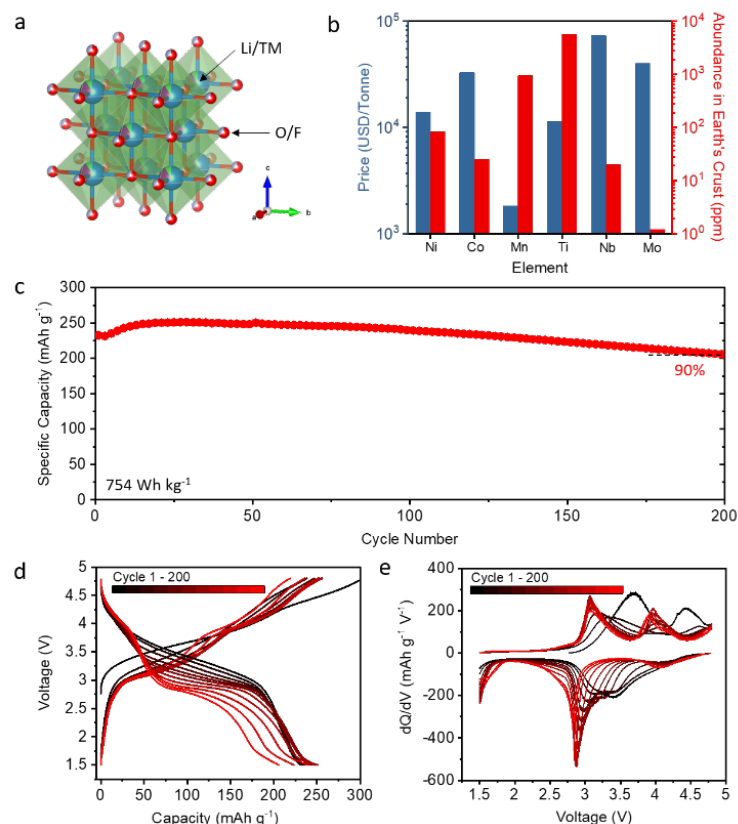


Figure 5. Battery performance of a highly fluorinated DRX, $\text{Li}_{1.2}\text{Mn}_{0.6}\text{Ti}_{0.2}\text{O}_{1.8}\text{F}_{0.2}$. (a) Crystal structure, (b) price and abundance of selected transition metals, (c) specific capacity, (d) voltage profiles, and (e) differential capacity plot. DRX cell is cycled at 16 mA g⁻¹ within 4.8 and 1.5 V.

Stable Ni-rich $\text{LiNi}_x\text{Mn}_y\text{Co}_{1-x-y}\text{O}_2$ material synthesized with fast-charge capability (LBNL)

Ni-rich $\text{LiNi}_x\text{Mn}_y\text{Co}_{1-x-y}\text{O}_2$ (NMCs, $x \geq 0.8$) are promising cathode materials for high-energy lithium-ion batteries. Conventional NMCs are polycrystalline (PC) aggregated particles having large number of grains in random orientations. As both Li^+ diffusion and volume expansion/contraction occur anisotropically upon charge/discharge, this causes torturous Li^+ diffusion pathways and nonuniform Li concentration inside the particle, leading to stress and strain and the eventual cracking of the particles. In addition, the newly exposed surface area from cracking can cause parasitic reactions with the electrolyte. These issues are greatly exacerbated with increasing current density, resulting in rapid capacity fade and impedance rise under fast-charge conditions. Hence, design and development of Ni-rich NMC particles with morphology optimized for the fast-charge application is essential. Previous LBNL studies established fundamental relationships between particle surface properties, particularly surface facets, and cycling stability. This led to the development of single-crystal (SC) NMC cathodes with reduced oxygen release and minimized side reactions under high-voltage operations, enabling excellent performance in high-energy cells. Recently, LBNL prepared Ni-rich NMC single-crystals with morphology and surface orientation optimized for Li transport properties. As an example, studies carried out on $\text{LiNi}_{0.8}\text{Mn}_{0.1}\text{Co}_{0.1}\text{O}_2$ (NMC811) single crystals (referred to as SC811) with $\sim 1 \mu\text{m}$ size and predominately (104)- surface are shown in Figure 6, along with the comparison with a commercial polycrystalline sample (referred to as PC811). After 100 cycles, extensive cracking along the internal grain boundaries is clearly visible in the PC sample, whereas the SC particles remained nearly unchanged morphologically after cycling at 1C or even 6C rate. At the same rate, better cycling stability is achieved on the SC sample. Moreover, while both cathodes delivered similar charge and discharge capacities at 0.1C, the SC cathode significantly outperformed the PC counterpart at higher rates such as 10C. The performance improvement is attributed to the more desirable (104) surface facets for Li transport and better cracking

resistance in the SC sample. Although the SC particles are much smaller than the PC, which can in itself provide significantly better high-rate performance for the SC particles, the same cracking issue has been seen in multiple smaller PC samples and preferentially using the faster 104 facets results in better rate.

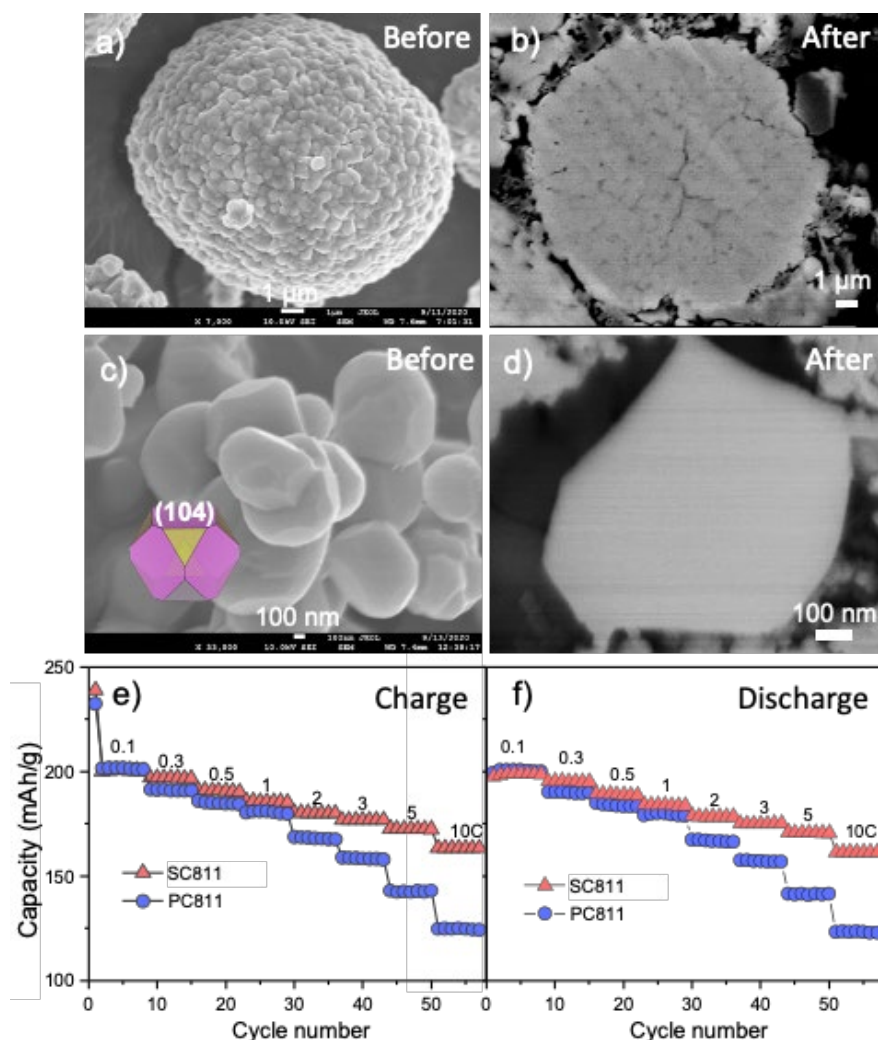


Figure 6. a-d) SEM images of PC (a, b) and SC (c, d) NMC811 before (a, c) and after (b, d) cycling. Enhanced cracking resistance in SC is clearly shown. e-f) Electrochemical testing confirms superior charge and discharge rate capability of SC.

Development of Advanced Electrolyte for Fast-charging (INL)

XCEL researchers are working to advance Li-ion cell design (appropriate for electric vehicle applications) to accomplish a fast-charge (XFC) in 10-minutes or less. Electrolytes are a key component for achieving XFC in Lithium (Li)-ion batteries, while meeting other technical and life goals. Preemptive electrolyte research was conducted using the INL Advanced Electrolyte Model (AEM) to investigate electrolyte metrics that influence cell performance during fast charge, most notably viscosity, conductivity, diffusivity, lithium transference number, Li desolvation energies, activation energies, and other terms related to concentration polarization (which alters local transport properties near electrode surfaces). This led to the identification of a suite of XFC electrolyte candidates for use in XCEL-designed cells having NMC cathodes and graphitic anodes. The electrolytes are designed to achieve improved transport properties (vs the baseline electrolyte) to mitigate concentration polarization effects, decrease lithium plating at the anode, improve permeation of electrolytes through the electrode materials, and stable, low-impedance solid-electrolyte interphase (SEI) films. Based on AEM prescreening, NREL cell modeling determined critical cell performance metrics, concentration

polarization profiles, and whether conditions developed during XFC would likely result in lithium plating. Best electrolyte candidates from this synergistic set of modeling then proceeded to testing cells. Figure 7 (a,b) compares electrolyte B26 (EC: DMC: DEC: EP: PN (20: 40: 10: 15: 15, mass) w/ (3%VC, 3%FEC) + LiPF₆) with the baseline Gen2 (EC-EMC + LiPF₆). B26 sustains a greater fraction of the 6C (10-minute) charge at a constant-current (CC) condition. B26 also produces more consistent cycling performance, indicating less aging compared to Gen2. B26 has also shown less Li metal plating.

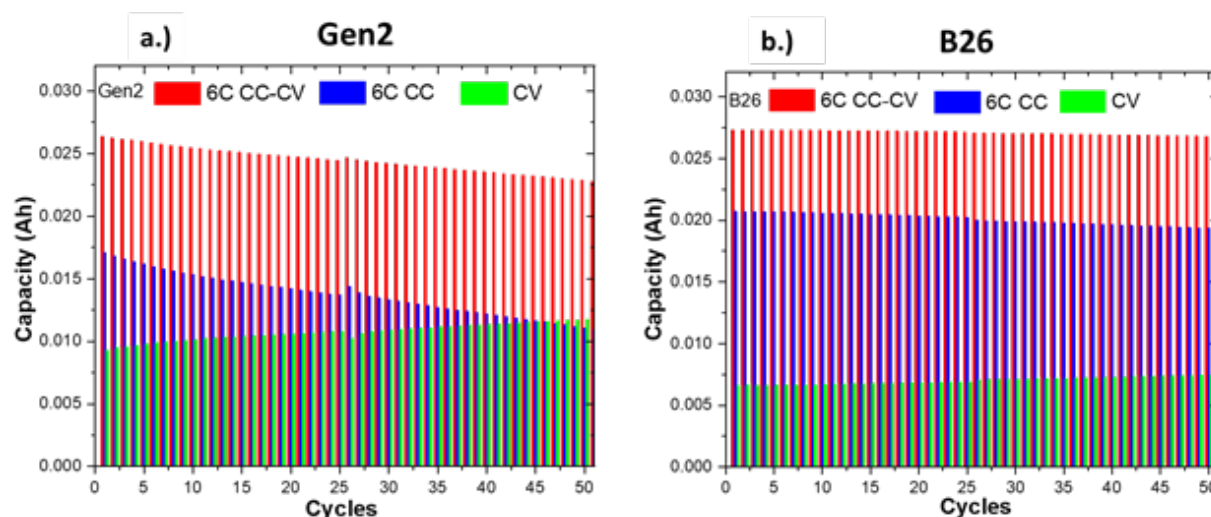


Figure 7. Comparison of Gen2 (a) versus B26 (b) electrolytes in cells with NMC 532 cathodes and graphitic anodes (ANL CAMP Pouch cells).

Balancing interfacial reactions to achieve long cycle life in high-energy lithium metal batteries (PNNL, Battery500)

Lithium (Li) metal cells could enable energy densities significantly higher than today's Li-ion cells. The Battery500 Consortium developed a novel and high-performance electrolyte, an optimized electrode architecture and cell design to balance the electrochemical and chemical (side) reactions in high energy Li metal cells, achieving more than 600-cycles in prototype 350 Wh/kg pouch cells (2 Ah) (Figure 8). Commercial EV cells achieve 220-280Wh/kg. Recently, the Consortium discovered that by reducing the thickness of Li metal foil anodes to 20 μm from 100 μm in 350Wh/kg pouch cells (Figure 8b-Figure 8d), not only is cycle life improved, but the steep capacity drop towards the end of cycle life, due to electrolyte dry out, is also mitigated. When Li metal contacts electrolyte, a passivation film or solid electrolyte interphase (SEI) layer forms due to the high reactivity of Li metal with electrolyte. Ideally, the insulating SEI layer stops further reactions or "corrosion" of Li metal in the electrolyte while still allowing Li⁺ transport. However, the formation of SEI layers consumes electrolyte which is very lean in high-energy cells. To explain this result, the team has theorized that there are two different SEI layers formed within cycled Li anodes, wet and dry. "Wet SEI" (Figure 8a) is formed inside shallow channels or pores of Li metal where contact is retained between the liquid electrolyte and the Li. This wet SEI supports cell cycling. "Dry SEI" (Figure 8a) forms when no liquid electrolyte is left, which is often in the deep and very narrow pores of SEI-covered Li present in thicker strips. These dried out regions subsequently smother further electrochemical reactions, leading to cell death. The thicker the Li metal, the deeper the pores/channels formed. The amount of electrolyte is extremely limited in realistic batteries (20-30 times less than in coin cells) and easily depleted in forming dry SEI layers in those deep pores abundant in thick Li strips. Thus, optimization of Li metal thickness is critical to extend lifespan of Li metal batteries. The team is planning to use ultrasonic imaging to observe the two regions of SEI growth.

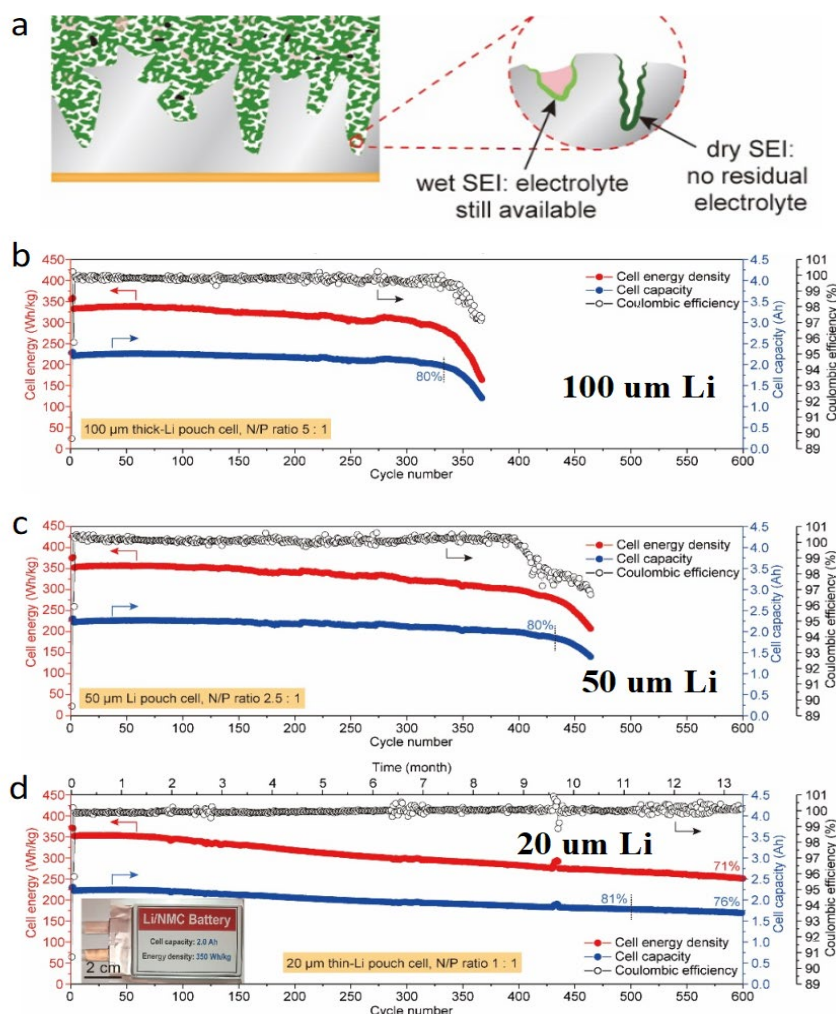


Figure 8. 350 Wh/kg pouch cells achieve more than 600 cycles in research from the Battery500 Consortium. (a) Illustration of wet and dry SEI layers in lithium metal anode. (b)-(d) Cycling performances of 350 Wh/kg lithium metal pouch cells using 100, 50 and 20 μm lithium foils as the anodes, respectively. Cathode: $\text{LiNi}_{0.6}\text{Mn}_{0.2}\text{Co}_{0.2}\text{O}_2$; Electrolyte: 1.54 M lithium bis(fluorosulfonyl)imide (LiFSI) in 1,2-dimethoxyethane (DME) and 1,1,2,2-tetrafluoroethyl-2,2,3,3-tetrafluoropropyl ether (TTE).

Aqueous Sequential Separation of Anodes and Cathodes from Spent Lithium-ion Batteries (ORNL)

Direct recycling of lithium-ion (Li-ion) batteries aims to recover the valuable components in a lithium-ion cell, including black mass (e.g., active cathode materials and graphite), copper (Cu) foils, and aluminum (Al) foil current collectors. Electrode materials are tightly adhered to metal current collectors through binders, increasing the challenge of recovery. The separation challenge is further increased because cathode and anode are mixed after shredding. To reclaim the most valuable active cathode materials with high purity for subsequent regeneration, separation of electrode materials from their current collectors, as well as of anode from cathode, is required. Scientists at Oak Ridge National Laboratory (ORNL), as part of the ReCell program, have developed a low-cost two-step process to recover electrode materials and current collectors from spent Li-ion batteries. During the first step, a solution containing an aqueous potassium phosphate buffer solution with a constant pH at 5.0 is selected to delaminate anode films from copper foils at room temperature and prevent Al from dissolution (Figure 9). At this stage, the graphite is separated while the cathode films stay intact due to the strong adhesion of the binder to the Al foil. In the second step, a surfactant (sodium dodecyl sulfate, Triton™ X-100) is added to the mix of copper foils and cathode electrodes in the presence of the buffer solution to peel off the cathode films from the Al foil by both reducing the surface energy and

weakening the adhesion (Figure 9). Thereafter, the cathode films and current collectors (Al and Cu) are separated due to the difference of density. By avoiding use of complex separation processes, the aqueous sequential separation method alone could fulfill the goal of reclaiming higher-purity materials, making recycling more profitable. Techno-economic analysis with EverBatt modeling developed by Argonne National Laboratory shows that selling recovered metal foils alone could recoup all recycling processing expenses, including those of the developed sequential separation method, suggesting attractive profit motive. After direct regeneration, the cost of recovered cathode materials is about 50% less than that of virgin cathode production. Additionally, this novel process reduces the GHG emission by 60% compared with traditional recycling processes. Overall, the aqueous sequential separation is a potential sustainable electrode recovery process that may advance battery recycling and secures the domestic battery supply chain.

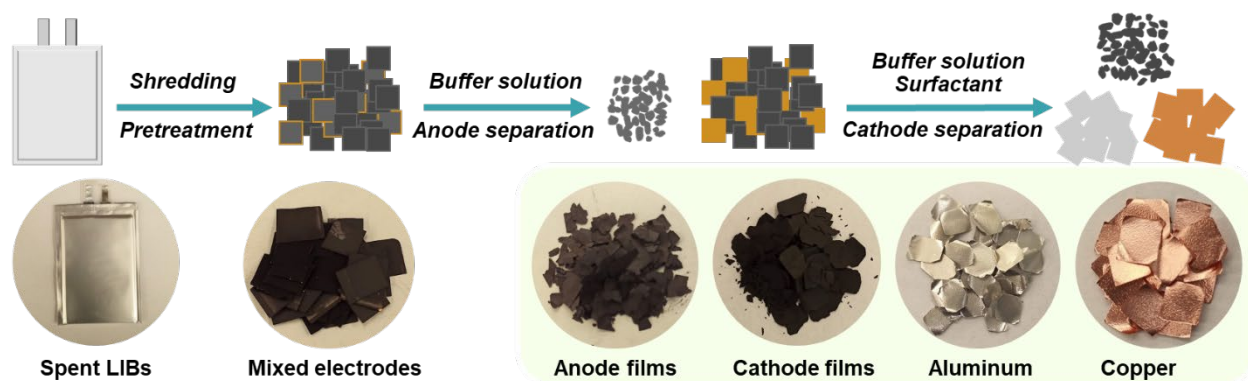


Figure 9. Flowchart of the aqueous sequential separation process to recover cathode films, anode films, copper, and aluminum foils.

Reactivating the Isolated Lithium Metal for Extending Battery Life and Fast Charging (Stanford)

The increasing demand for high-energy batteries has encouraged the development of lithium-(Li) metal batteries. Unfortunately, the current Li anode batteries often exhibit short cycle life due to the continuous generation of solid electrolyte interface and isolated Li (i-Li). The formation of i-Li during cycling leads to a significant capacity loss in Li batteries. Since i-Li loses electrical connection with the current collector, it has been considered electrochemically inactive or “dead” in batteries. Contradictory to this presumption, we discover that i-Li is highly responsive to battery operations because of their dynamic polarization to the electric field in the electrolyte (Figure 10a). Simultaneous Li deposition and dissolution occur on two ends of the i-Li, leading to its spatial progressions toward cathode (anode) during charge (discharge). In the meantime, the migration rate of i-Li is faster under high current densities. To promote the reactivation of i-Li during battery operations (that is, to reconnect it to an electrode), we incorporated a short fast-discharging step after the conventional charging protocol (Figure 10b). During this step, i-Li grows toward Li anode, and some of it can re-establish electrical connection with the electrode, participating in the subsequent electrochemical processes. The benefit of this activation step in Li-metal batteries becomes more pronounced after 30 cycles when the cell without activation starts to exhibit fast capacity fade (Figure 10c). In sharp contrast, the cell with activation maintains stable cycling for more than 40 cycles (vs. 30 cycles) and a much slower degradation process afterward, attributed to the partial recovery of “dead Li.” Moreover, the formation of i-Li also occurs in Li-ion batteries, especially during fast-charging. Graphite/NMC532 cells were charged at 4C, followed by a constant voltage charge until the current decreased to 1C, and discharged at 0.5C at 25 °C. The depth of discharge is 84%. With the modified protocol, the cell can charge to 80% capacity in 15 minutes while losing only 5% of its capacity after 300 cycles (Figure 10d). In comparison, the control cell loses 20% capacity after 300 cycles. In this study, we discovered a mechanism of isolated Li metal filaments in Li-metal batteries and developed a protocol to reactivate them. We

achieved an extended lifetime in Li-metal batteries and found that a similar protocol could also provide fast charging improvement in Li-ion batteries.

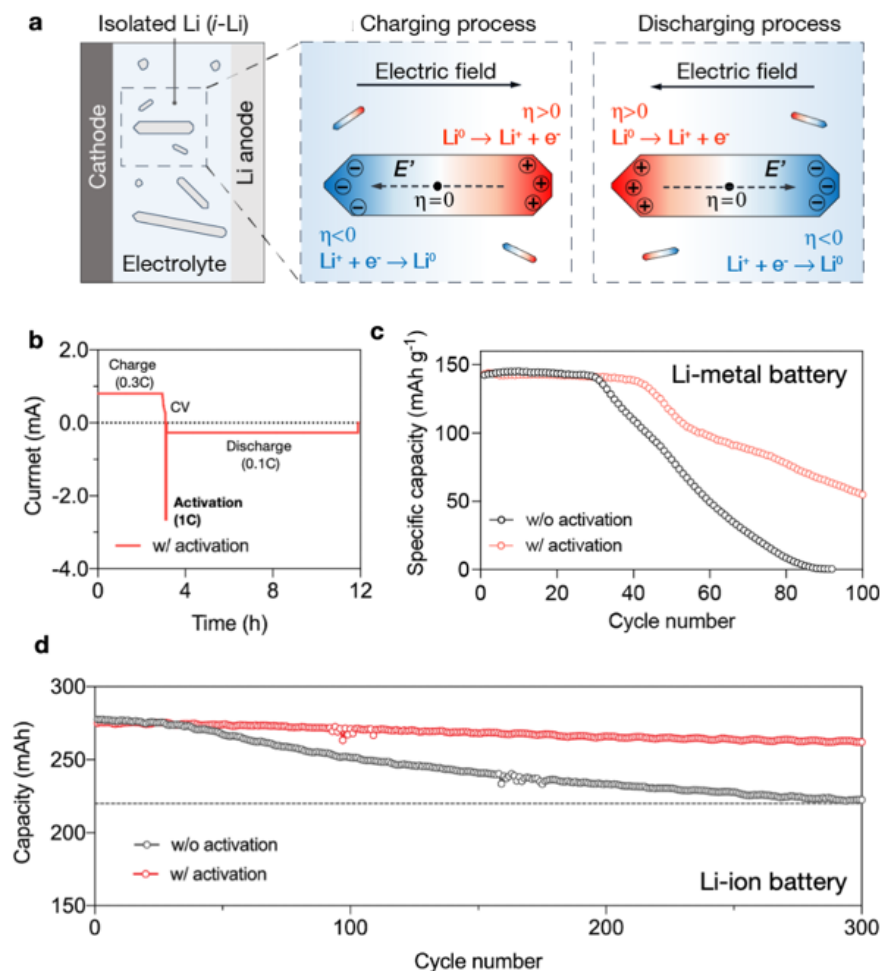


Figure 10. a. Illustration of the dynamic polarization of *i*-Li under the electric field. b. Modified charging protocol for Li-metal battery. Specific capacity of c. lithium-metal batteries and d. lithium-ion batteries with/without activation steps.

Synthetic Data Generation and use for Deep Learning Model Development and Rapid Identification of Failure Modes (INL)

Extreme fast charging (XFC) is a critical advancement for faster adoption of electric vehicles (EVs). For cells undergoing XFC, a critical failure mode is Li plating on the negative electrode. When plating occurs, it can shorten the life of a cell, increase the likelihood of cell-failure and cell-to-cell variability which makes battery management and control more difficult. Recently, a team at INL developed a rapid, machine learning-based classification framework that allows researchers, EV manufacturers and cell developers to rapidly classify if a cell is experiencing Li plating during XFC. The INL team used a combination of electrochemical (EC) signatures obtained from graphite/NMC532 cells during each cycle, including coulombic efficiency, capacity loss, voltage at the end of the rest period after charging, and the differential voltage (dV/dt) signature at rest after charging. Using data collected from the suite of EC signatures made it possible to identify Li plating 4x earlier than a human user. To facilitate the rapid identification of Li plating for multiple charging protocols the team constructed a decision tree, based on logistic elastic net analysis that could identify Li plating for different charging conditions and then verified the presence of Li plating using 30 optical images. Key advantages from this work are that early identification of plated Li shortens several key development and deployment aspects.

First by identifying plating in the first 25 cycles it is possible to evaluate different cell designs and charge protocols more quickly. The framework also allows a streamlined approach that can be used to differentiate between Li plating and more standard solid electrolyte interphase (SEI) growth. (See Figure 11.) The ability to make this distinction early might allow manufacturers to build battery packs with less cell-to-cell variation which enhances overall pack performance. Lastly, early identification of Li plating serves as a key safety feature which can notify consumers or manufacturers early if problems within the battery pack are emerging. This method will be applied to the newly build graphite/NMC811 cells to be studied in the next phase of the fast charge lab program.

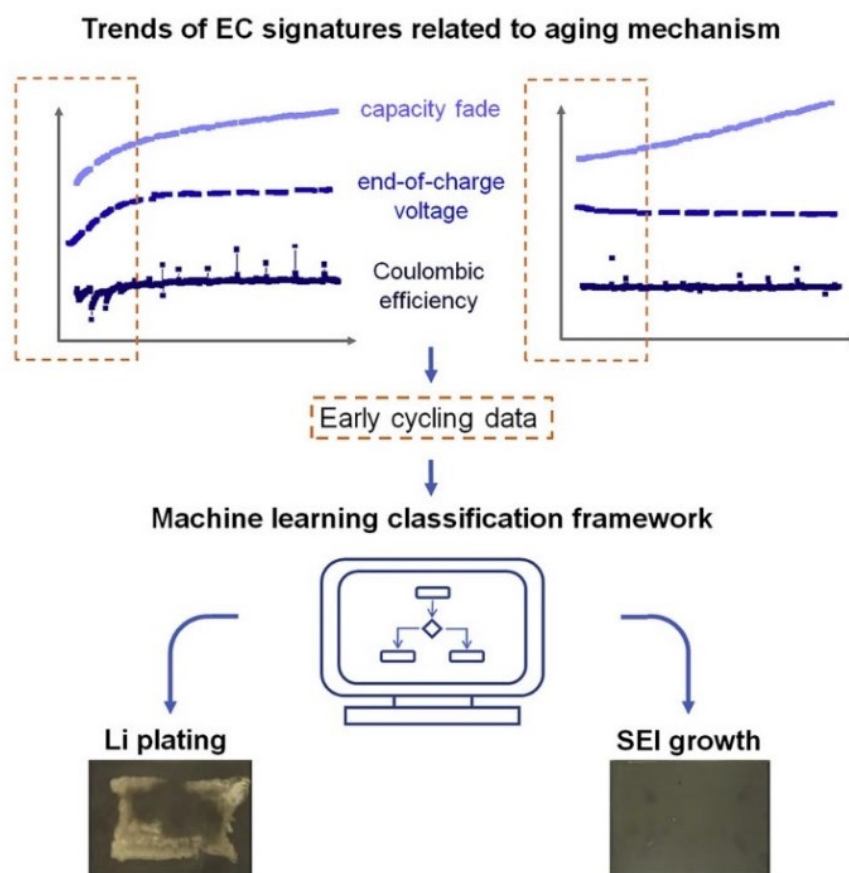


Figure 11. Example of different EC signatures that can be fed

High-energy Lateral Mapping Studies of Inhomogeneity and Failure Mechanisms in Pouch Cells (BNL)

Lithium (Li) metal batteries offer the potential for significant increases in energy density that could enable larger scale adoption of electric vehicles. However, it is not yet possible to build high energy density lithium metal batteries with long lifetimes ($> 1,000$ cycles) due to the reactivity of Li metal with electrolytes. If specific failure mechanisms of Li metal batteries can be identified, this will help in efforts to mitigate them and potentially increase the lifetime of Li metal batteries. While traditional electrochemical testing methods are used for determining when batteries fail, these methods cannot determine what the failure mode is, or where it is occurring. To better understand failure mechanisms, researchers developed new X-ray diffraction methods using the National Synchrotron Light Source II to map position-dependent variations in an end-of-life battery cathode. The high-energy X-rays readily penetrate cells, allowing industrially relevant pouch cells to be studied. As part of research done at BNL, a single cathode layer was extracted from a high-energy density Li metal pouch cell which was subjected to ~ 200 cycles (Figure 12a) and then fully discharged. The cell energy dropped below 80% of its starting value after ~ 175 cycles (corresponding to nominal cell failure), though

much of the lost capacity could be recovered by cycling at a lower rate. In mapping experiments (Figure 12b), three hot spots were found in which the cathode state of charge (SOC) was much higher than average, indicating that these three regions were electrochemically isolated. The non-edge spots formed where the cathode amount was about 5% lower than average, indicating that very small manufacturing problems can lead to early cell failure. Based on the spot sizes, the multi-phase mixtures observed in diffraction patterns, and comparisons with cells designed to fail in a specific manner, it was conclusively determined that cells failed due to depletion of the electrolyte (which can occur through reaction with Li metal) needed to transport ions between the anode and cathode. Further mapping studies on a series of coin cell cathodes allowed the electrochemical signatures of this and two other failure modes (loss of Li inventory and impedance rise), providing a new and facile method to determine how a cell is failing.

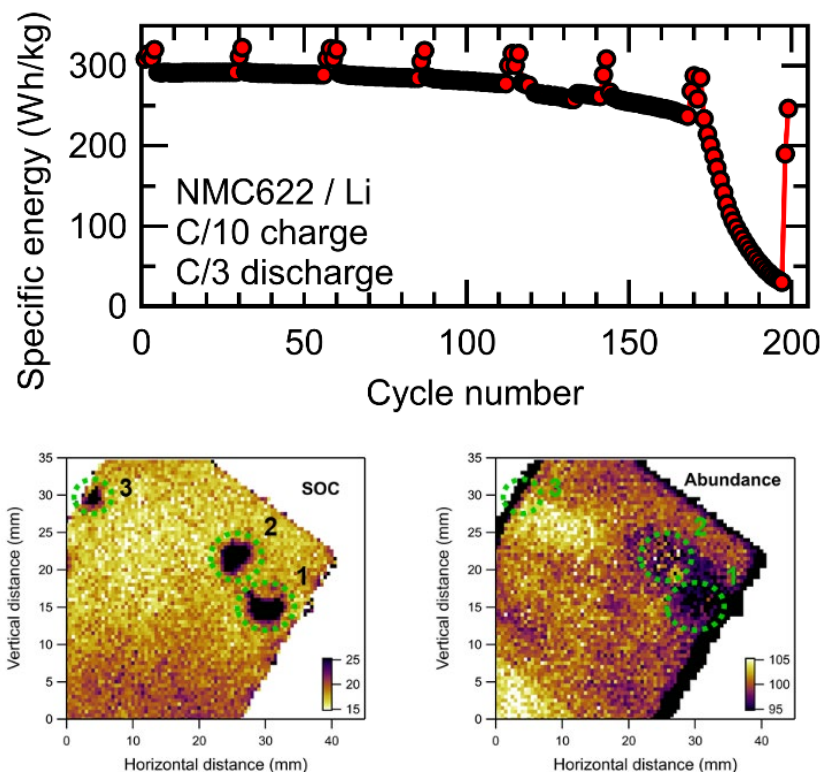


Figure 12. (a) Decay of cell energy during cycling. After every 25 cycles, cell was tested at a very slow rate (C/25) producing spikes of higher capacity. For this cell cycled to failure, maps of (b) the local state of charge and (c) the relative abundance of the NMC cathode were collected, allowing three hot spots (1 – 3) with poor performance to be identified.

Fast-Charging Aging Considerations: Incorporation and Alignment of Cell Design and Material Degradation Pathways (NREL)

Fast-charging of ECVs (in 10-15 minutes) can help increase market adoption. Today's thin-electrode lithium-ion (Li-ion) batteries can be charged in less than 15 minutes, but the cells are 20% less energy-dense and may cost more than thick-electrode cells. Thicker electrode cells, appropriate for EVs, usually struggle to support fast charge and often suffer reduced life when fast charged. DOE's eXtreme Fast Charge Cell Evaluation of Li-ion Batteries (XCEL) program aims to improve the fast-charge performance and cycle life of low-cost thick-electrode (EV) cells. The XCEL team used a combination of prototyping, characterization, diagnostics, and modeling to understand the performance limits and degradation of graphite/nickel-manganese-cobalt cells under fast charging conditions. Multi-scale electrochemical models coupled with testing and diagnostics suggested design improvements. For faster transport of Li^+ ions through the electrode, the team prototyped a dual-layer-anode. Graphite active material is tightly packed into the back of the electrode (near the current collector) to

improve energy density. The front of the electrode is more porous, allowing for fast transport, and uses high-surface-area particles to delay Li plating. Microstructure models were used to optimize the amount of binder and electronic-conductive (CBD) additives in the electrode to provide enough electron conduction without blocking the electrolyte pores. Electrochemical models also guided the selection of a new separator that, despite being thicker, achieved faster electrolyte transport due to its higher porosity. First, the team tested a baseline thin-electrode cell. With low energy density, this cell charges quickly, accepting 79% of its capacity in a 10-minute charge before hitting a 4.1V limit (Figure 13). Next, the team tested a moderately thick electrode cell. This cell exhibited a 30% higher energy density, but its 10-minute charge acceptance dropped to 38%. With the optimized carbon/binder recipe, new separator, and an improved electrolyte formulation developed through a separate modeling effort (B26), the modified cell's charge acceptance increased from 38% to 73% and still maintained 230 Wh/kg, appropriate for EV cells. Finally, the baseline cells plated Li in the first 10 cycles, while the final optimized cell has shown no sign of Li plating after 175 cycles to date. In addition, models optimized the charge protocol by replacing slow-rate constant voltage with a ramped-voltage step that charges faster and avoids Li plating. The physics-based models used here enable fast use of knowledge with different cell designs, chemistries, and protocol constraints. Next, the XCEL team is applying these methods to achieve 10-minute charge acceptance and 1000-cycle lifetime with thick electrode (255 Wh/kg) cells.

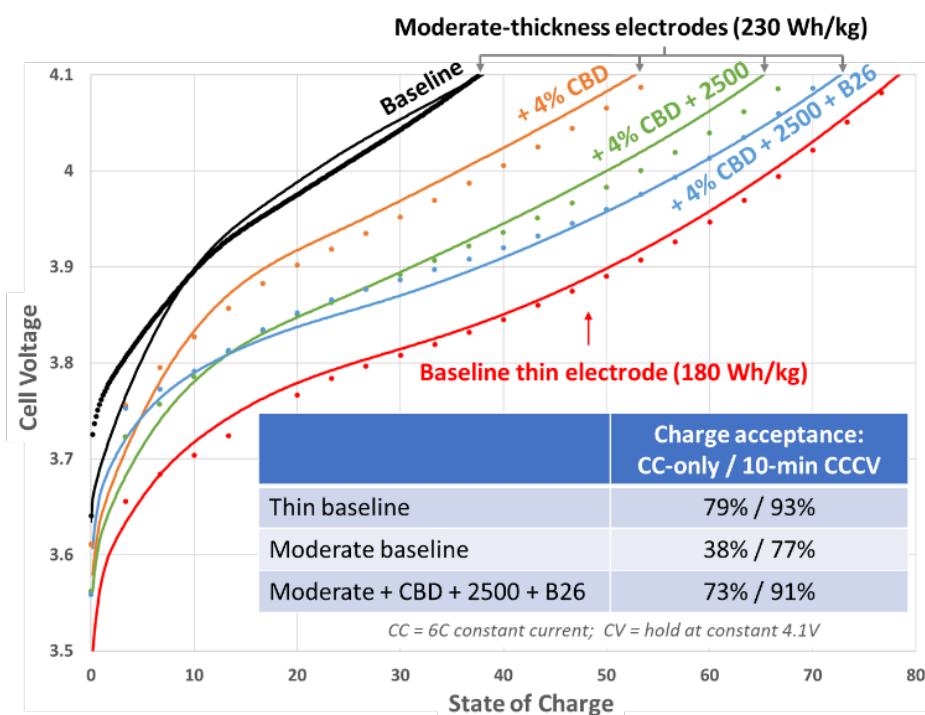


Figure 13. Fast-charge results of prototype single-layer pouch cells (symbols) compared with model predictions (lines).

I USABC Battery Development & Materials R&D

I.1 Rapid Commercialization of High Energy Anode Materials (NanoGraf Technologies)

Francis Wang, Principal Investigator

NanoGraf Corporation
3440 South Dearborn Street, #113N
Chicago, IL 60616
E-mail: francis@nanograf.com

Brian Cunningham, DOE Technology Development Manager

U.S. Department of Energy
E-mail: Brian.Cunningham@ee.doe.gov

Start Date: May 23, 2019	End Date: June 30, 2022	
Project Funding (FY21): \$2,500,000	DOE share: \$1,250,000	Non-DOE share: \$1,250,000

Project Introduction

As global usage of electric vehicles steadily increases, so does the power/energy requirement to meet mainstream needs. Performance trajectories of traditional lithium-ion technology, despite an annual 3-5% improvement in energy density since inception, suggest that long-term electric vehicle needs will not be met without an evolution beyond traditional energy storage materials (i.e., graphitic anodes). NanoGraf Corporation has developed a novel Si-based, negative-electrode material which can enable a quantum leap in battery energy and power density, and significantly impact battery weight and run-times that burden today's electric vehicles.

Objectives

The project entitled "Rapid Commercialization of High Energy Anode Materials" has been established with the aim of extending, benchmarking, and demonstrating the performance of NanoGraf's advanced silicon-based anode materials in battery form factors and designs relevant for electric vehicle applications.

Approach

NanoGraf Corporation has demonstrated a novel high energy density (>1,000 mAh/g) Si-based negative-electrode materials technology with a long-term potential to replace graphitic-based anodes in lithium-ion batteries. NanoGraf's technology uses a proprietary silicon alloy-graphene material architecture to achieve: i) category-leading performance and ii) solutions to long-standing Si anode technical hurdles. The proprietary combination of silicon-based alloys and a flexible 3D graphene network helps to stabilize the active material during charge and discharge by providing an interfacial barrier between the active material and the electrolyte which can accommodate large volumetric changes through a laminar graphene sliding mechanism. The 3D graphene-silicon architecture results in a minimization of capacity losses due to electrical disconnection, significantly improved active utilization (mAh/g), and partial stabilization of the SEI interface with a flexible physical barrier between electrolyte and active material (Figure I.1.1).

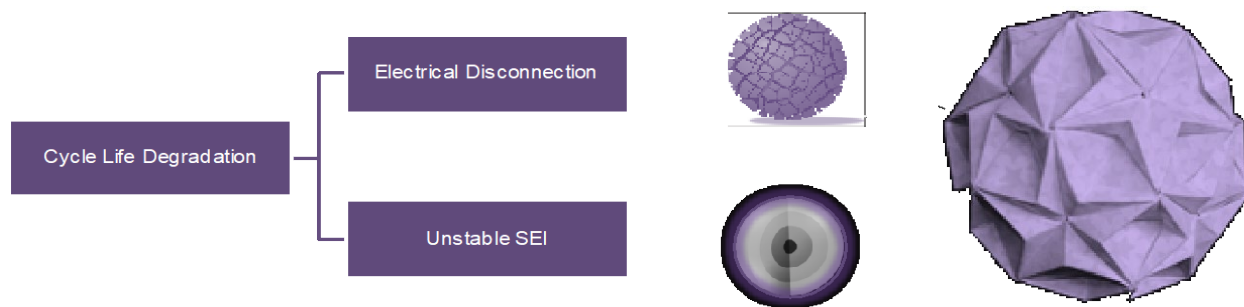


Figure I.1.1.1 Si anode failure mechanisms (left), NanoGraf graphene-silicon anode architecture (right).

NanoGraf continues to make improvements against key USABC advanced electrode metrics over time and has demonstrated a positive trajectory towards USABC advanced electrode goals. The goal of the program is the advancement and commercialization of advanced silicon-based active materials for high energy and high-power EV batteries. Specifically, the program aims to demonstrate that NanoGraf technologies can exceed USABC electric vehicle performance targets in USABC-recognized form factors, be produced at-scale by commercially viable methods, and reach USABC cost targets at scale. To this end, a series of tasks have been developed to address the core technology gaps and their associated barriers: Task 1: Electroactive Synthetic Design & Optimization, 2. Electroactive Barrier Design & Optimization, 3. Anode/Cathode/Electrolyte/Binder Design Optimization, 4. Material Production & Process Development, 5. System Integration & Cell Production and 6. Electrochemical & Safety Testing.

NanoGraf has two strategic partners for this program. A123 Systems works with NanoGraf on Tasks 5 and 6 for the cell deliverables and PPG works with NanoGraf on Task 3 to assist with electrode design and optimization.

Results

NanoGraf made progress in numerous development pathways including active material development (Task 1 & 2), electrode & cell design (Task 3), materials production (Task 4), and prototype performance (Task 5 & 6).

Select project advancements have been highlighted below:

Active Material Development: NanoGraf accelerated development and improvements of the novel synthetic approach to create Si-SiO_x materials that was first introduced in Q6 2020 Review. This modified sol-gel chemistry produces new, composite materials using a bottom-up approach. Thus, it enables more tailorable control over the resulting composite physical and electrochemical properties, including capacity and FCE. After identifying initial promising experimental “whitespace” for synthetic conditions (e.g., catalysts, stirring, reaction temperature, precursors), NanoGraf down-selected a number of successful reaction conditions and siloxane precursors that utilize the most promising acid-catalysts. As shown in Figure I.1.2, multiple samples nearly achieved USABC Year 2 targets for capacity (>1600 mAh/g) and FCE (>82%), although it is expected that cycle life targets will require additional improvements. As can be seen, Samples A-SG-8 through A-SG-10 provided some of the best initial combinations of FCE and capacity. The development of the “doped” SiO_x project in Task 1 was paused, despite the high FCE achievable, since the anode capacity is limited to ~1300 mAh/g, below the requested USABC electrode target of 1800 mAh/g.

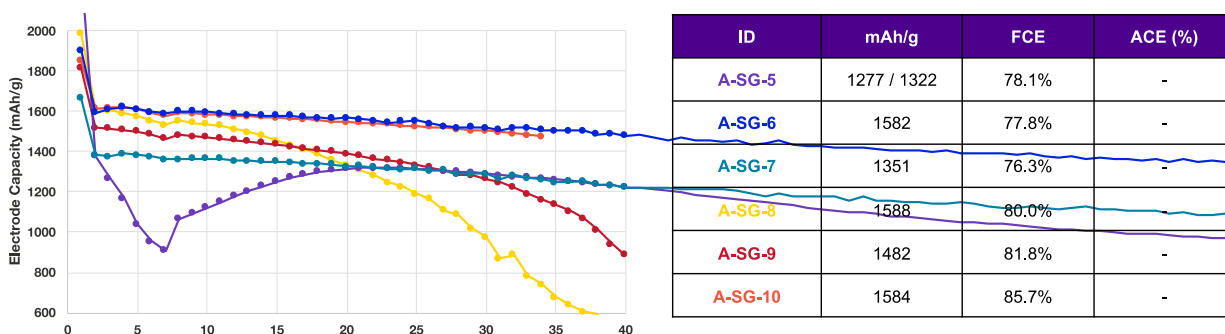


Figure I.1.2 Half-cell electrochemical results for various modified sol-gel reaction conditions.

NanoGraf also focused on applying novel, Li-containing surface barrier coatings to the “bottom-up” material. It was anticipated that such coatings can form artificial SEIs with improved stability to extend cycle life. By modifying reaction conditions and electrochemical formation procedures, NanoGraf was able to overcome resistivity limitations initially encountered with these coatings. It was demonstrated that the coatings not only reduce SEI formation in the first cycle, but they also improved capacity retention compared to non-coated samples. For example, see samples A-SG-7, A-SG-8, and A-SG-9 in Figure I.1.3.

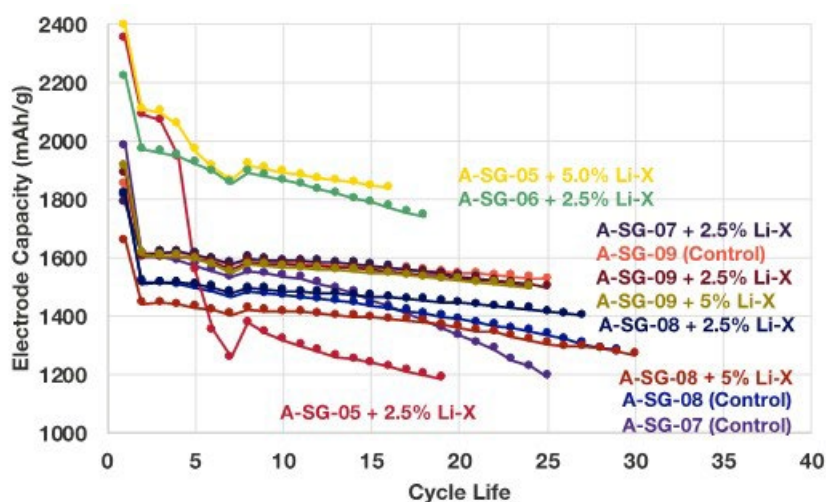


Figure I.1.3 Half-cell electrochemical cycling results for samples A-SG-5 through A-SG-9 with different Li-barrier coating levels

When comparing electrode “sets,” samples A-SG-5 and A-SG-7, for example, showed significant improvements in half cell capacity retention with Li-X barrier coatings through 25 cycles (Figure I.1.4). Overall, it is expected that the Li-X barrier coatings can provide an opportunity to create an artificial SEI that is rich in inorganic lithium species that leads to improved SEI stability and extended cycle life.

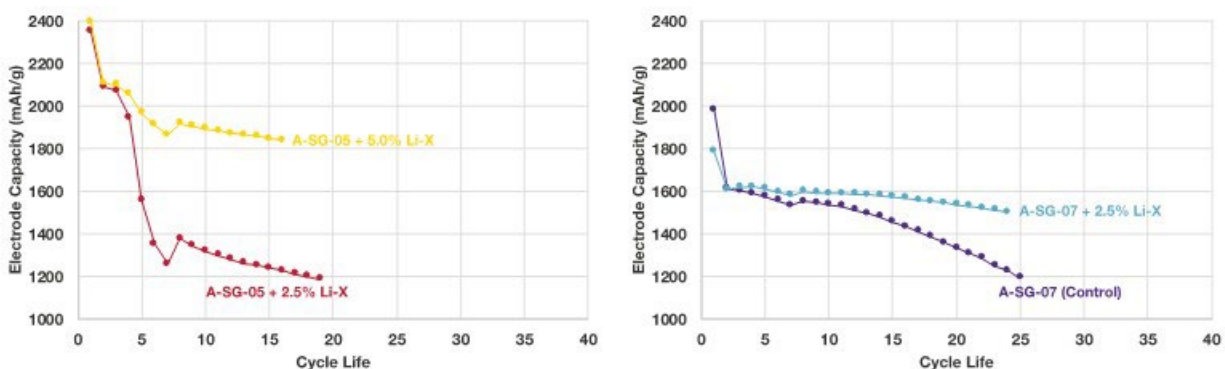


Figure I.1.4 Half-cell electrochemical cycling results for (Left) samples A-SG-5 and (Right) A-SG-7 with different Li-barrier coating levels.

Electrode & Cell Design: PPG continued development of two anode binder formulations (SiA1, SiA2) to improve electrode adhesion in high areal loading formulations (>4 mAh/cm²) and started investigated opportunities to reduce binder content. Specifically, PPG was able to increase the active Si material content by lowering the binder from 20% to 10% and thus, increasing NanoGraf active material from 75% to 85%. Half-cell cycling of electrodes prepared with varying NanoGraf active material content in both LiPAA binder and SiA1 binder is compared in Figure I.1.5. Capacity retention decreases with decreasing binder content, but PPG SiA1 binder had comparatively higher retention over LiPAA at all binder contents, indicating the benefits of PPG SiA1 binder. In addition, PPG binders exhibited higher peel strength than LiPAA at a binder content of 15%, leading to the improved capacity retention observed for PPG electrodes versus LiPAA binder.

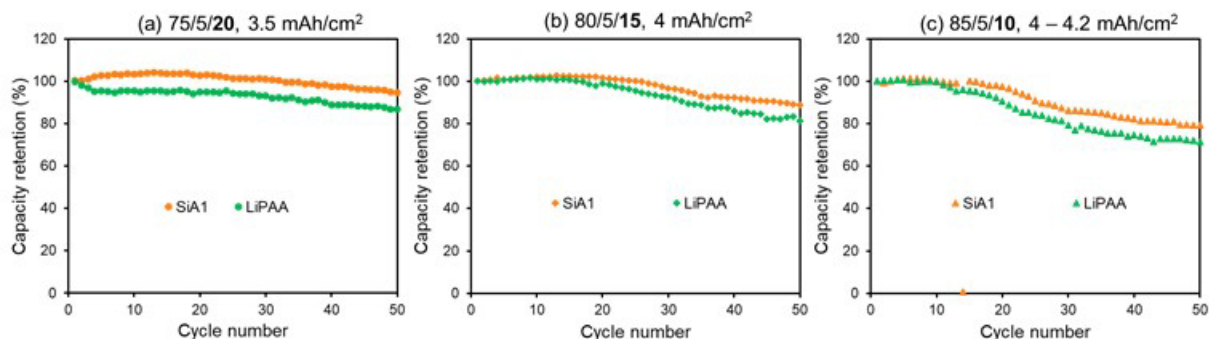


Figure I.1.5 Half-cell coin cell data of SiO_x anode with SiA1 and LiPAA at reduced binder contents of 20%, 15%, and 10%.

Materials Production: NanoGraf made several material and process improvements that will positively impact performance and scalability. For example, alternative graphene dispersants were investigated that do not require high-temperature removal steps. Thus, lower product costs can be achieved using less capital equipment and by reducing energy-expensive thermal processing steps. One new graphene dispersant, CMC, offers a combination of low decomposition temperature and similar electrochemical performance compared to the other surfactant materials tested.

New graphene precursors that are produced through a lower-cost process were also examined. NanoGraf demonstrated good graphene coverage and coating quality on traditional “top-down” silicon active materials using SEM. Future work will seek to better characterize the new graphene material, coating quality using Raman mapping, and electrochemical cycling of the graphene-coated silicon materials.

Prototype Performance: A123 and NanoGraf constructed coin cells and a single-layer pouch (SLP) test plan which will give some insight into material and cell design strategies that can be used to improve the performance of the year 2 builds.

Argonne provided updated electrochemical testing results from the 1 Ah prototype pouch cells that A123 constructed in March 2020. From initial testing results, ANL confirmed the Year 1 cell deliverables were able to achieve 384 cycles (RPT2) before reaching the 80% capacity retention cut-off limit. Calendar life testing is ongoing.

Conclusions

NanoGraf continued to increase the commercial readiness of its composite anode material. Specifically, promising early work produced new silicon materials with increased capacity and cycling stability, especially using the novel “bottom-up” synthesis path. These Si-SiO_x composite materials achieved higher capacity compared to conventional SiO_x anodes and provide a potential pathway to achieving USABC specific capacity targets.

Argonne National Laboratory provided updated electrochemical testing results from the 1 Ah prototype pouch cells and confirmed the Year 1 cell deliverables were able to achieve 384 cycles (RPT2) before reaching the 80% capacity retention cut-off limit, achieving the Year 1 deliverable target. Additionally, progress was made with PPG on new anode and cathode electrode coatings, including the ability to create silicon-dominate anode electrodes with >5 mAh/cm² areal loading and good electrochemical stability.

While challenges associated with energy, cycle life, and calendar life still exist on the path to successfully achieving USABC key metrics, NanoGraf has demonstrated a cadence of innovation and product development throughout the project and looks optimistically towards additional development efforts in 2022.

I.2 Fast-Charge and Low-Cost Lithium Ion Batteries for Electric Vehicle Applications (Zenlabs Energy)

Herman Lopez, Principal Investigator

Zenlabs Energy
3390 Gateway Boulevard
Fremont, CA 94538
E-mail: herman@zenlabsinc.com

Brian Cunningham, DOE Technology Development Manager

U.S. Department of Energy
E-mail: Brian.Cunningham@ee.doe.gov

Start Date: February 01, 2019

End Date: January 31, 2022

Project Funding: \$1,245,738

DOE share: \$622,869

Non-DOE share: \$622,869

Project Introduction

In order to reduce our dependence on fossil fuels and decrease greenhouse gas emissions, electric vehicles (EVs) have received intense attention as a possible solution. Electrification of automobiles is gaining momentum with the main barrier preventing widespread adoption being the lack of available low cost, high energy, fast-charging and safe energy storage solutions. Lithium-ion batteries (LIBs) are presently the best energy storage solution used in current and upcoming EVs. Further improvements to the performance of LIBs by integrating high capacity active materials, novel passive components and unique cell designs will be critical for the success and mass adoption of EVs.

This project has been based on developing novel electrolyte formulations, optimized cell designs and a scalable pre-lithiation solution that enables the use of high-capacity silicon oxide anodes that would result in lithium-ion batteries capable of meeting the Low-Cost and Fast-Charge (LC/FC) USABC goals for advanced EV batteries in CY 2023. High specific capacity anodes containing high amounts of active silicon (>50%), Nickel-rich Ni-Co-Mn (NCM) cathodes and uniquely tailored electrolyte formulations have been integrated in large capacity (10–50 Ah) pouch cells targeting Fast-Charge and Low-Cost energy solutions. During this program, Zenlabs has demonstrated Fast-Charge and Low-Cost LIBs maintaining other performance requirements of EV cells, including energy, power, cycle life, calendar life, and safety.

Objectives

- Develop unique electrolyte formulations integrating commercially available organic solvents, salts and additives that will perform well with Silicon anodes and Ni-rich NCM cathodes.
- Evaluate and support the development of a pre-lithiation solution for high capacity and high percent active silicon anodes addressing manufacturability, reproducibility, cost, and safety.
- Develop optimized cell designs to build and deliver cells that will meet the USABC EV battery goals for commercialization in calendar year 2023.
- Evaluate and integrate cost effective and high performing active and passive materials, processing steps and cell designs to meet the Low-Cost and Fast-Charge targets.
- Build, deliver and test large format (10–50 Ah capacity) pouch cells integrating optimized high-capacity silicon-based anode, NCM cathode, electrolyte, separator and pre-lithiation to meet the USABC fast-charge, low cost, energy, power, cycle life, calendar life, safety and temperature EV goals.

Approach

Zenlabs has utilized a system-level approach to screen, develop and optimize the critical cell components (cathode, anode, electrolyte, separator), pre-lithiation process (process, dose), cell design (N/P ratio, electrode design) and cell formation and testing protocols that would enable meeting the USABC EV cell level goals for the year 2023. The development was based on integrating pre-lithiated silicon-based high-capacity anodes, high-capacity Ni-rich NCM cathodes, high voltage electrolytes and composite separators into large capacity (10-50 Ah) pouch cells. The developed cells were optimized to meet the Low-Cost and Fast-Charge targets along with high energy density and power, good cycle life and calendar life, safety, and low and high temperature performance. During the program, Zenlabs is using three cell build iterations to meet the program targets and deliver cells to the National Laboratories for independent testing. Cells have been tested both at Zenlabs and independently by three National Laboratories: Idaho National Laboratory (INL), Sandia National Laboratory (SNL) and National Renewable Energy Laboratory (NREL).

During the program, Zenlabs leveraged its material, processing and cell design and development expertise to screen, engineer and optimize various electrolytes, pre-lithiation approaches and cell design solutions addressing the challenges associated with meeting the USABC Low-Cost and Fast-Charge cell targets. Zenlabs identified development areas that have been addressed and improved during the program. Significant material and cell development in the areas of electrolyte engineering, pre-lithiation development and cell design engineering have been implemented. Material and cell development typically started at the coin-cell level where initial screening, testing and optimization took place. Zenlabs has extensive experience working with coin-cells ensuring that identical electrode formulations, specifications, cell designs, components, formation, etc. are identical to what is used in the pouch cell designs and therefore ensuring similar results are obtained. Once the critical parameters were optimized at the coin-cell level, results were validated and fine-tuned at the pouch cell level typically in 12 Ah capacity pouch cells.

Zenlabs has shown a path for their silicon-dominant cell technology to meet the USABC program EV cell cost target of 75 \$/kWh. The path to reach the target cell cost is achieved by several approaches. First, the high energy density of the cells increase the kWh of a given system, which reduce the \$/kWh ratio and cost target gap. In addition, by utilizing a high-capacity silicon-based anode, the quantity of active material reduced, and cost decreased. While the current costs for silicon oxide and pre-lithiation are higher compared to graphite-based cells, Zenlabs continues to evaluate and qualify cost effective options and believes that the cost of these important components and processes will continue to decrease significantly in the near future as existing suppliers scale production and additional suppliers come online. Zenlabs has identified and qualified cost-effective silicon suppliers that are projecting similar costs to graphite once manufacturing production levels continue to scale. Zenlabs has also partnered with a cell manufacturing partner and equipment vendors to build pre-lithiation equipment capable of meeting the Low-Cost and manufacturing program targets.

During the duration of this program, Zenlabs has met the majority of the USABC Low-Cost and Fast-Charge cell specifications by integrating silicon-dominant anodes, unique electrolyte formulations and cell designs that have improved fast charging, cycle life and calendar life. The final cell build of the program is anticipated to further improve the calendar life and cost of the cells by integrating an optimized electrolyte formulation and a lower cost pre-lithiation solution, respectively. At the conclusion of the program, Zenlabs will successfully designed and demonstrate cells that will meet the majority of the USABC EV cell goals for the year 2023.

This program consists of 3 cell builds that include a baseline cell build at the beginning of the program (CB#1), a second cell build (CB#2) midpoint in the program and a final cell build (CB#3) at the conclusion of the program. The cell builds were structured in a way that as it progresses, the cell targets increase with respect to specific energy, energy density, cycle life and lower cell cost. Cells from CB#1 and CB#2 were delivered and are independently being tested by the National Laboratories. Figure I.2.1 shows the projected usable BOL (beginning of life) and EOL (end of life) cycle life (a), cell cost (b), specific energy (c) and energy density (d) for the three cell builds. The measured cell parameters and cost for the baseline cells (CB#1) and CB#2 are shown in the figure. Cycle life from CB#1 is already nearing the target 1,000 cycles and anticipate CB#2 and

CB#3 to exceed the cycle life target. Cell cost for CB#2 is similar to CB#1 and higher than anticipated because CB#2 continued to use a costlier pre-lithiation process. CB#3 is anticipated to use a cost effective pre-lithiation process and greatly reduce the cell cost. CB#1 and CB#2 are on track with respect to energy and anticipate CB#3 to also meet the projected energy targets.

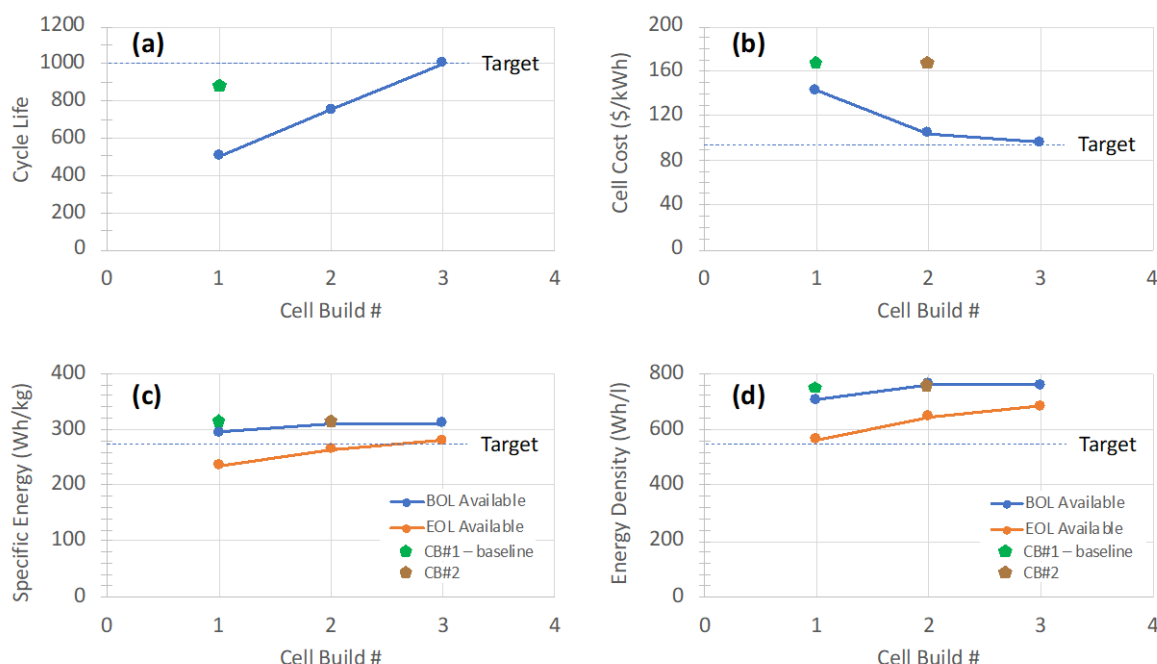


Figure I.2.1 Projected cell performance progression throughout the program & measured CB#1 & CB#2 values

Results

Zenlabs has demonstrated excellent cycling performance and promising calendar life (CL) results from 12 Ah capacity, 315 Wh/Kg specific energy pouch cells integrating a silicon-dominant SiO_x anode and Ni-rich NCM622 cathode. The pouch cells, which are part of Cell Build #1 (CB#1), have exceeded 1,000 cycles maintaining 80% capacity retention both under constant-current and constant-voltage (CC-CV) cycling and under dynamic stress test (DST) cycling. In both cases, the cells have been cycled at 100% of its full state of charge window consisting of 2.5V to 4.3V. Figure I.2.2a shows the DST cycling results measured at Idaho National Laboratory under standard C/3 rate (3 hour) charging labeled 0% FC and under 100% fast-charging 4C rate (15 minute) conditions labeled 100% FC. The cells completed 15 reference performance tests (RPTs), each taken after 112 DST cycles, obtaining 1,680 DST cycles at the standard C/3 rate charging. The cells completed 11 RPTs corresponding to 1,232 DST cycles while maintain a capacity retention greater than 80%. The DST cycling results for the cells cycled under 15 minute 4C rate 100% fast charge conditions, completed 8 RPTs corresponding to 896 DST and still retaining a capacity retention greater than 80%.

Figure I.2.2b shows the calendar life results for the identical CB#1 cells testing under a storage temperature of 30°C, 40°C and 50°C while maintaining the cell at 100% state of charge. A trickle charge was applied to the cells to ensure they are at 100% state of charge during the storage tests. The figure shows very promising CL results for both 30°C and 40°C storage with the cells completing 18 RPTs with each RPT consisting of 32 days of storage. As expected, the capacity degrades faster when the cell that are stored at 50°C, but very promising CL results are obtained when the cells are stored at 30°C. 18 RPTs corresponding to 576 storage days have been completed for the 30°C storage condition and the cells continue to show 94% capacity retention. Each of the data point in the plot is an average of 3 to 4 pouch cells. The calendar life testing continue for the 30°C and 40°C storage conditions.

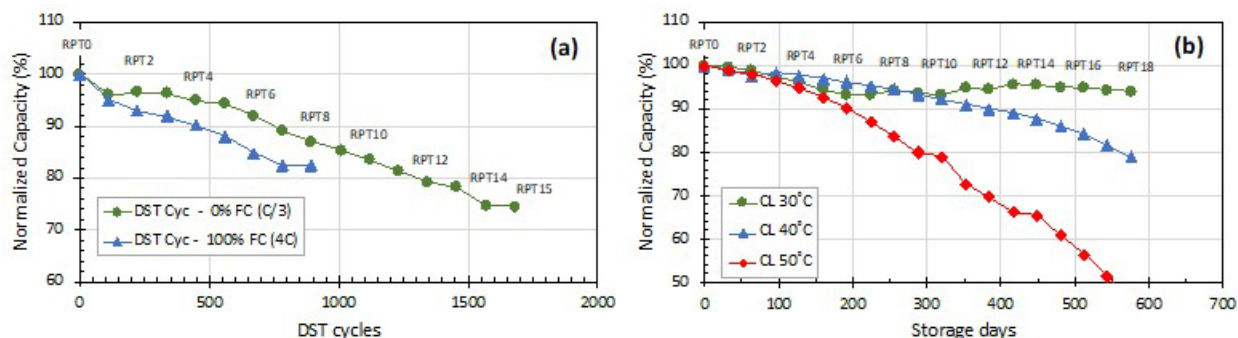


Figure I.2.2 (a) DST Cycling at 0% Fast Charge (FC) vs 100% FC, (b) Calendar life testing at 30, 40, and 50 °C

Zenlabs continues to demonstrate that their high-energy silicon-dominant cell technology consisting of SiO_x anodes and Ni-rich NCM cathodes are able to cycle at full 100% usable window (4.3V to 2.5V) under standard and fast-charging conditions. Cycling results meet the program specifications and have been measured internally at Zenlabs and independently validated by various automotive OEMs and INL. Cycling results suggest that Zenlabs' cell technology is able to compensate and support the large volume expansion of silicon while avoiding fragmentation and pulverization problems. Based on cycle life, fast-charging capability, high energy and power, and calendar life results, this technology is nearly ready from commercialization.

Zenlabs has also delivered 37 (12 Ah pouch cells) CB#2 cells to INL, NREL, and SNL in early Q1 2021. 26 cells were delivered to INL for energy, power, and endurance testing, 3 cells to NREL for thermal characterization and 8 cells to SNL for abuse testing. Results for CB#2 are ongoing and will be reported in a future report.

In 2021 Zenlabs asked for a no cost extension (NCE) that increased the duration of program from 10 quarters to 12 quarters. The additional 2 quarters is enabling Zenlabs to finalize the ongoing tasks and down select the best electrolyte formulation, cathode, cell design and deliver the final cell build of the program. During the last two quarters of the program, most of the cell design parameters have been finalized and by end of December 2021 the remaining cell design parameters will be frozen.

1. Cathode Development

In order to reach the target cell performance as well as the LC/FC program cell targets, 19 different Ni-rich NCM cathodes from different vendors were evaluated. Among the evaluated cathodes, Zenlabs down selected cathode 15, 17, 18, and 19 for pouch cell studies. The 1C/1C studies on these cathodes are shown in the following figures where cathodes 15, 17 and 18 show promising 1C/1C rate CC-CV cycling results from 12 Ah capacity pouch cells when electrolyte formulation E39 was used.

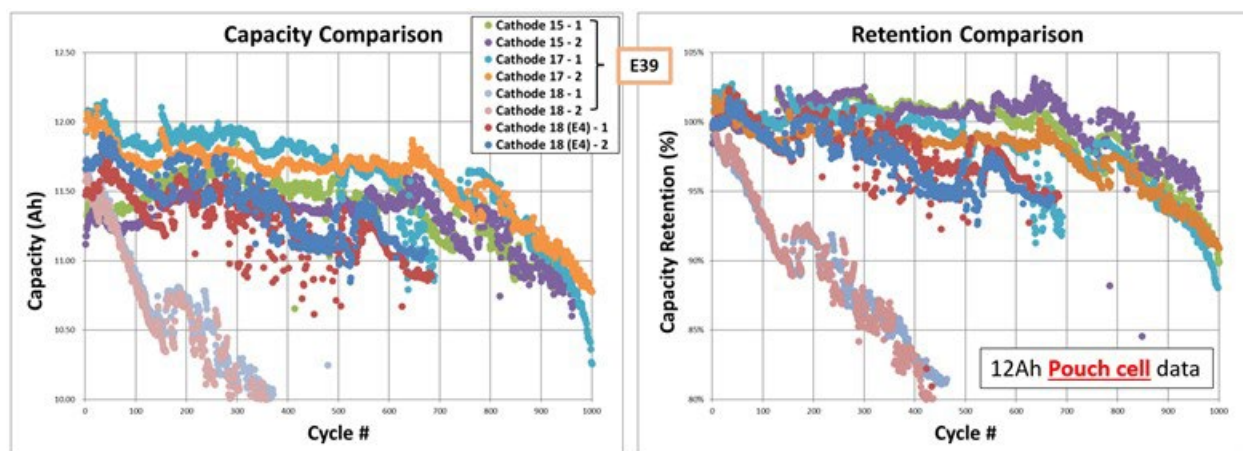


Figure I.2.3 The 1C/1C cycling study on cathodes 15, 17, and 18 with two different electrolytes (E4 and E39) on 12 Ah pouch cells

Based on the results obtained from the down selected cathodes, an upgraded version of Cathode 18 (C18) was developed that is called Cathode 19 (C19). The 1C/1C cycling data from C19 cathode is shown in the following figures. C19 showed improved 1C/1C rate (and 4C/1C rate cycling data, not shown) cycling when paired with electrolyte E39.

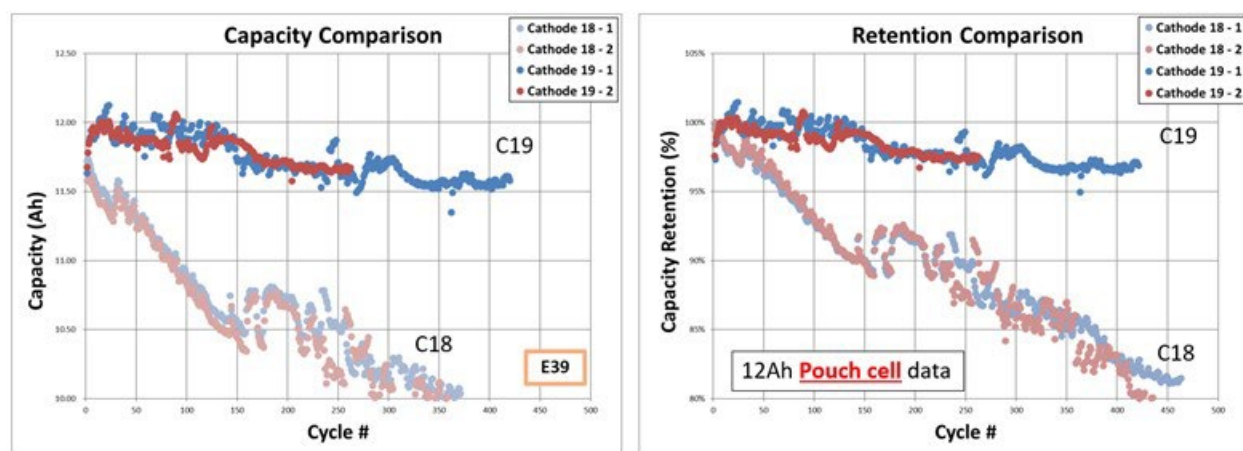


Figure I.2.4 The 1C/1C cycling study on cathodes C18 and C19 on 12 Ah pouch cells with E39 electrolyte

In addition to improved cycling at room temperature, cathode C19 showed superior high temperature (45°C) stability that is shown in the following figure. Based on room temperature 1C/1C rate and 4C/1C rate cycling, and high temperature cycling data, C19 has been selected as the cathode for CB#3. By freezing the anode and cathode design, the final step is to tailor the electrolyte design in order to achieve the program targets.

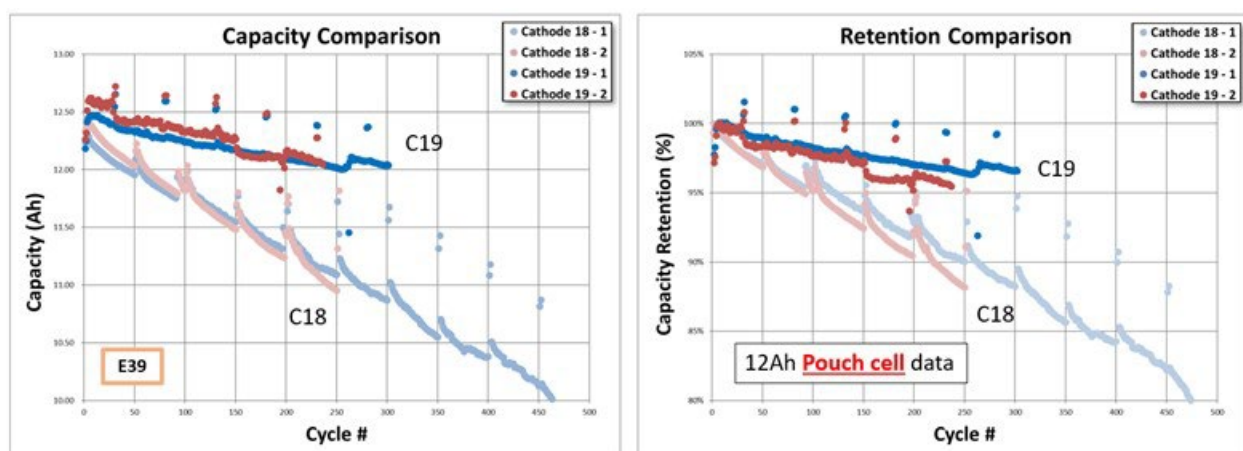


Figure I.2.5 The 1C/1C cycling of C18 and C19 at 45°C on 12 Ah pouch cell with E39 electrolyte

2. Electrolyte Development

Zenlabs considered the electrolyte requirements for achieving each of the program targets. These requirements and their corresponding program targets are summarized in the following table.

Table I.2.1 Electrolyte requirements corresponding to program targets

Program Targets	Electrolyte requirements
Fast Charge	Electrolyte Conductivity SEI Thickness Electrolyte Viscosity Li Ion Transference Number
Low Cost	Commercially Available Electrolyte components
Safety	Less Gas Generation High Temperature Storage Less Side Reactions Electrolyte Boiling Point
Cycle Life	SEI Stability HF Scavenger

Promising electrolyte formulations from E#4 to E39 with anti-gassing, fire-retardant and SEI forming additives have shown promising cycling, calendar life, and gassing results. It was found that E#4 showed excellent cycling and high rate performance, but unfortunately it also suffered from gassing concerns during room temperature cycling and high temperature storage. In order to improve the gassing performance, electrolyte formulation E39 was developed. Currently, Zenlabs is fine tuning the performance of E39 with several additives (E50 and E51) on pouch cells with Cathode 19. The final electrolyte formulation will be used for CB#3. The cycling data on E50 and E51 in coin cells are shown in the following figure.

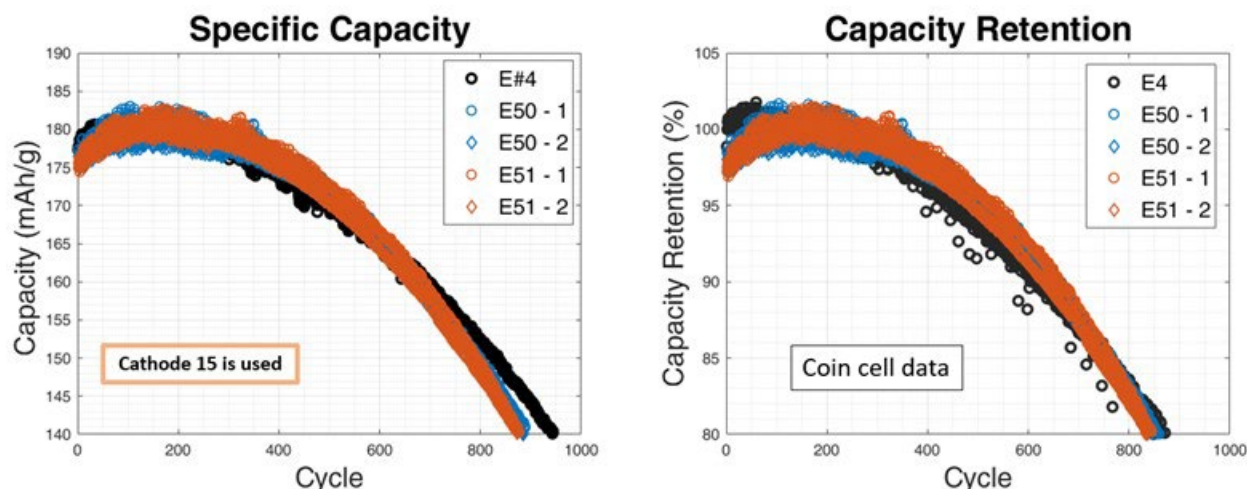


Figure I.2.6 1C/1C cycling data of E4, E50 and E51 on coin cells with Cathode 15

3. Pre-lithiation Process

Zenlabs has been using electrochemical pre-lithiation for their coin cell development and R&D studies. For their pouch cell development, Zenlabs has developed a pre-lithiation process based on lithium metal powder. In order to further reduce the cell cost, as well as improve safety and roll-to-roll manufacturability, Zenlabs is currently evaluating a lithium vapor deposition process and a slurry based lithium metal powder process as a cost effective scalable process to lithiate the anode.

One of the challenges that is being addressed with lithium vapor deposition is the surface passivation after the pre-lithiation process in order to allow for longer storage times. Zenlabs is supporting the lithium vapor deposition development as part of another DOE funded program and anticipates integrating the lithium vapor deposition process in the final CB#3 of the program. Currently, Zenlabs is evaluating the cell performance as a function of various pre-lithiation processes. In parallel, Zenlabs is setting up a second cell prototyping line that will incorporate a roll-to-roll low-cost manufacturable pre-lithiation process capable of building larger footprint high capacity (>50 Ah) pouch cells.

4. Final Cell Build (CB#3)

So far Zenlabs has frozen the design of the cathode (Ni-rich, C19), anode (high SiO_x , EV formulation), separator (composite ceramic separator) and cell footprint (12 Ah and 50 Ah pouch cells). Currently, Zenlabs is on track with finalizing electrolyte (E39, E50, E51) and pre-lithiation process by end of 2021 for CB#3. Zenlabs is planning to finish building and delivering 12 Ah and 50 Ah capacity CB#3 pouch cells to the National Laboratories by end of January 2022 for independent testing.

5. Gap Analysis

Comparison of CB#1, CB#2, and expected CB#3 performance as well as the gap analysis versus the program targets are shown in the following figure. The CB#1 gap analysis is using the data tested by INL and CB#3 values are estimated values based on projected models for the final cell build of the program. The gap analysis shows the anticipated reduction in cell cost for the final CB#3 as a more cost effective lithiation process is used. The gap analysis also projects higher energy for the final cell build as a higher Ni-rich NCM cathode will be used.

Zenlabs Gap Analysis towards Low-Cost / Fast-Charge USABC Advanced EV Battery Goals for CY 2023

#	End of Life (EOL) Characteristics at 30°C	Units	USABC EOL Cell Level Targets	CB#1 (#1) - DST 0% FC		CB#1 (#7) - DST 100% FC		CB#1 (#15) - CL at 30°C		CB#2		CB#3 (Final)	
				BOL (RPT#)	EOL (RPT#)	BOL (RPT#)	EOL (RPT#)	BOL (RPT#)	EOL (RPT#)	BOL (RPT#)	EOL (estimated)**	BOL (estimated)**	EOL (estimated)**
1	Peak Discharge Power Density, 30 s Pulse	W/L	1400	3539*	1053*	3608*	1503*	1313*	2409*	3060*	2448	3000	2400
2	Peak Specific Discharge Power, 30 s Pulse	W/kg	700	1610*	427*	1348*	751*	1310*	1000*	1272	1018	1250	1000
3	Peak Specific Regain Power, 10 s Pulse	W/kg	300	2190*	1660*	2225*	1700*	2610*	1640*	2513	2030	2500	2000
4	Available Energy Density @ C/3 Discharge Rate	Wh/L	550	346*	750*	324*	368*	742*	630*	737	606	800	640
5	Available Specific Energy @ C/3 Discharge Rate	Wh/kg	275	144*	226*	333*	242*	102*	271*	315	232	345	276
6	Available Energy @ C/3 Discharge Rate	kWh	50	50	50	50	50	50	50	50	>50	>50	>50
7	Calendar Life	Years	10						1.4		>1.4		>1.4
8	DST Cycle Life	Cycles	1000				896				>1000		>1000
9	Cost	\$/kWh	75										
10	Normal Recharge Time	Hours	< 7 Hours, J1772	< 7h	< 7h	< 7h	< 7h	< 7h	< 7h	< 7h	< 7h	< 7h	< 7h
11	Fast High Rate Charge	Minutes	80% ASOC in 15 min	< 10	< 10	< 10	< 10	< 10	< 10	< 10	< 10	< 10	< 10
12	Minimum Operating Voltage	V	> 0.55 V max	0.58 V max	0.58 V max	0.58 V max	0.58 V max	0.58 V max	0.58 V max	0.58 V max	0.58 V max	0.60 V max	0.60 V max
13	Unassisted Operating at Low Temperature	%	> 70% E _{usable} @ C/3 Discharge rate at -20°C	70	70	70	70	70	70	70	70	70	70
14	Survival Temperature Range, 24 Hr	°C	-40 to +66	passed	passed	passed	passed	passed	passed	passed	passed	passed	passed
15	Maximum Self-discharge	%/month	< 1	0.32	0.32	0.32	0.32	0.32	0.32	0.32	<1%	<1%	<1%
16	Battery scaling factor (BSF)	# of cells	288 (96s, 3p)	1536 (96s, 16p)	1536 (96s, 16p)	1536 (96s, 16p)	1536 (96s, 16p)	1536 (96s, 16p)	1536 (96s, 16p)	1536 (96s, 16p)	1536 (96s, 16p)	1536 (96s, 16p)	1536 (96s, 16p)
17	Battery capacity	Ah	>40	12	12	12	12	12	12	12	12	12	12

* data is projected by DOE
 ** values are estimated

Figure I.2.7 Gap analysis of CB#1, #2, #3 versus the program targets

Conclusions

Zenlabs' silicon-dominant 12 Ah capacity and 315 Wh/Kg specific energy pouch cells have exceeded the 1,000-cycle life target from USABC and have shown excellent fast charging capability and calendar life results. Results have been independently validated by Idaho National Laboratory where they showed 1,232 and 896 DST cycles completed under C/3 charging and 100% 4C rate fast charging conditions, respectively. The excellent cycling performance under standard and fast-charging conditions, fast charging capability and promising calendar life results (572 storage days) show that the high-energy silicon-dominant cell technology is mature and nearing commercialization.

Zenlabs has successfully frozen the design of the cathode, anode, separator, and cell footprint for the final cell build of the program. Additionally, Zenlabs has delivered CB#2 samples to the National Laboratories for independent testing and evaluation. The final electrolyte formulation is being down-selected from electrolyte formulation E39, E50 and E51 based on pouch cell cycling performance from 12 Ah capacity cells. Zenlabs is on track to down-select the electrolyte formulation and pre-lithiation process by end of December 2021 and build and deliver the final CB#3 cells by end of January 2022.

Key Publications

1. "Fast-Charge and Low-Cost Lithium Ion Batteries for Electric Vehicles", ES247_Lopez_2021_p, US DOE Vehicle Technologies Program Annual Merit Review, AMR, 2021.
2. "Fast-Charge and Low-Cost Lithium Ion Batteries for Electric Vehicles", ES247_Lopez_2020_p, US DOE Vehicle Technologies Program Annual Merit Review, AMR, 2020.

Acknowledgements

Oliver Gross (Fiat Chrysler Automobiles) served as the USABC Program Manager for this project. This work is being performed under the guidance and support from the USABC technical work group which (in addition to Oliver Gross) includes Meng Jiang, Minghong Liu, Jack Deppe, Brian Cunningham, Lee Walker, Aron Saxon and Joshua Lamb.

I.3 Low-Cost, High Safety Fast Charge Automotive Cells (Microvast, Inc.)

Wenjuan Mattis, PhD, Principal Investigator

Microvast, Inc.

3259 Progress Drive, #121

Orlando, FL 32826

E-mail: wenjuanmattis@microvast.com

Brian Cunningham, DOE Technology Development Manager

U.S. Department of Energy

E-mail: Brian.Cunningham@ee.doe.gov

Start Date: January 15, 2020

End Date: January 15, 2023

Project Funding: \$4,500,000

DOE share: \$2,250,000

Non-DOE share: \$2,250,000

Project Introduction

Automakers worldwide have announced plans to begin transitioning from gasoline powered vehicles to ones driven via electricity. To make these bold adoption plans a reality the lithium-ion battery must continue to improve so electric drive trains can become competitive in cost and convenience to a traditional gasoline powered vehicle.

Making the battery cost less is quite challenging, especially for higher energy or higher power cells because raw materials make up a significant portion of the batteries cost; meaning the most significant cost benefits must arise from lowering the material prices. Metals such as Li, Cu, Co, Ni, and Al are heavily used in today's battery cells, with cobalt being the most expensive and least sustainable historically. Therefore, one of the most immediate challenges facing the Li-ion battery community today is how to eliminate the use of cobalt while still having a high-performance material, especially if cost parity to internal combustion engine vehicles is to be achieved.

Fast charge creates additional technical complications that must be overcome, especially in high energy cells. It is well documented that Li plating and dendrite formation can occur; and could lead to performance or safety issues as the cells continue to age.

Objectives

This project is designed to develop low cost (i.e., approaching 75 \$/kWh), high energy (> 310 Wh/kg) fast charge (< 15-minutes) Li-ion battery cells for use in electric vehicles. These three terms have historically not been possible in one cell system, so careful engineering is necessary to prepare a cell capable of meeting the power, energy and cost goals. In addition, the designed cell must consider effects from temperature (hot and cold conditions) as well as safety for the technologies under development to be practically applied in a mainstream product.

Approach

In order to develop a high energy, low-cost, fast charging, and safe battery cell for automotive applications every aspect of the cell's components must be considered. A Li-ion cell is a complex system, and as such each component within the cell can influence the cell's eventual specifications.

One of the most important aspects of this project is to lower the cobalt content in the cathode while simultaneously providing high capacity and durability. Eliminating cobalt is a significant technical challenge, primarily because its use in the cathode does provide positive impact to material performance on matters such as capacity, stability and rate potentially. So, to reduce cobalt without sacrificing performance this the project will employ full concentration gradient (FCG) cathode technology. FCG, as a designer cathode, will allow

cobalt to be minimized and selectively delivered spatially within the cathode material to maximize its utility within the powder particle.

Another unique material approach being explored in this project is the use of a fast charge electrolyte additive that provides dual passivation to the SEI and CEI. A stable interface is important to slow resistance growth, which hinders fast charge. The project will develop a new synthesis process for this compound, which is intended to lower the cost to produce.

The project cell will also integrate a graphite/silicon-based anode blend to help provide energy density for the cell and incorporate Microvast's specialty aramid separator that aids in cell safety since it is significantly more thermally stable than traditional polymer or polymer ceramic coated materials used in automotive cells today. Thru the combination of these advanced materials the project goals for a low cost, fast charge cell will be attained.

Results

Materials for use in the low cost, fast charge cell are critical for the cost and performance objectives to be achieved. To that end, the team has worked to successfully prepare a low cobalt, high nickel FCG cathode material. While metal prices do fluctuate, our estimates show a significant reduction in the cost of metal raw materials for the cathode by our proposed changes, as shown in Figure I.3.1.

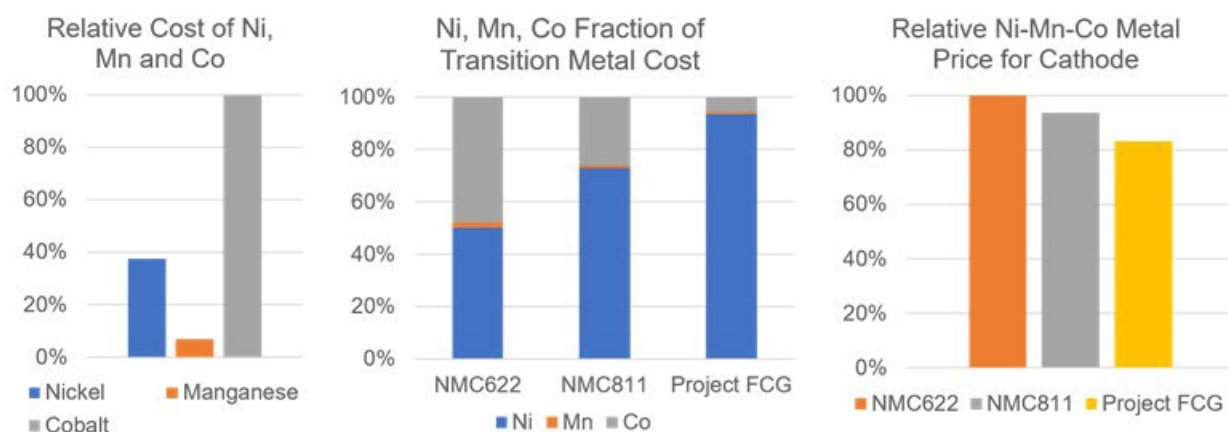


Figure I.3.1 (left) Relative cost of cathode metals, (center) metal fraction of Ni, Mn and Co in cathode compositions, (right) relative cost of metals for various cathode compositions.

This project FCG has less than 1.5 wt.% cobalt in the cathode, which is the major reason it will be more sustainable and less costly than NMC622, for example, which has ~6 wt.% cobalt making it more expensive (on kg and kWh basis) and less sustainable. The project FCG has been produced in the kilogram scale for use in pouch cell evaluation. In Figure I.3.2 an SEM of the particles made is shown, and in Figure I.3.3 the performance of the material, thru 500 cycles in a 5.7 Ah pouch cell with a graphite anode is shown.

In addition to the cathode material, the project team also was able to successfully scale up a new electrolyte additive, arbitrarily labeled WA002, first to 400g and then to 1kg in yield. During this scaling up of the material no difference in performance was observed from the 400g to 1kg batch, meaning the method devised by the team is stable and reproducible.

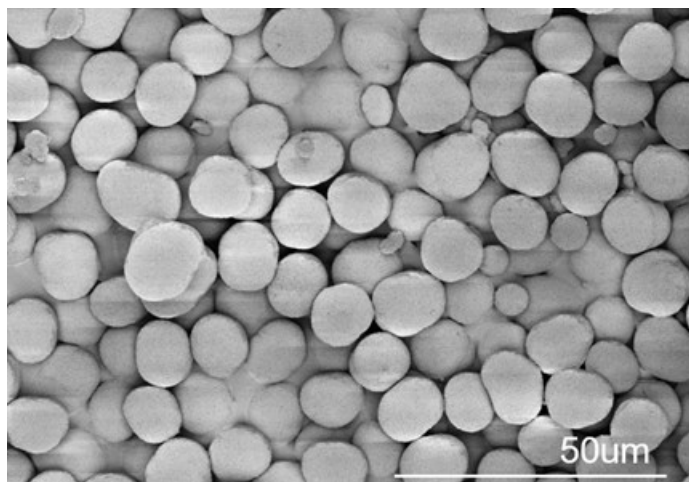


Figure I.3.2 SEM of project low cobalt FCG particles from kilogram scale batch

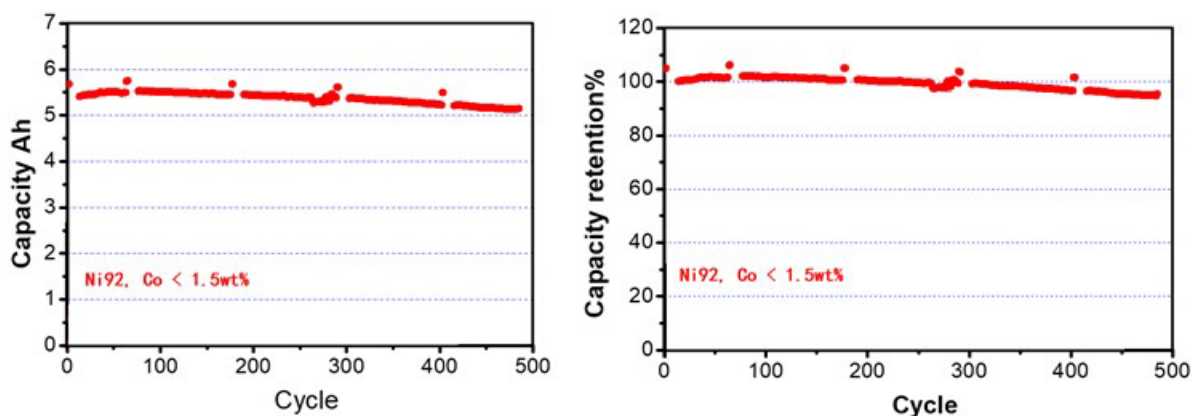


Figure I.3.3 Full cell testing of FCG cathode from 2.7-4.25V, 25°C at 1CCCV/1CD with a C/3 reference cycle

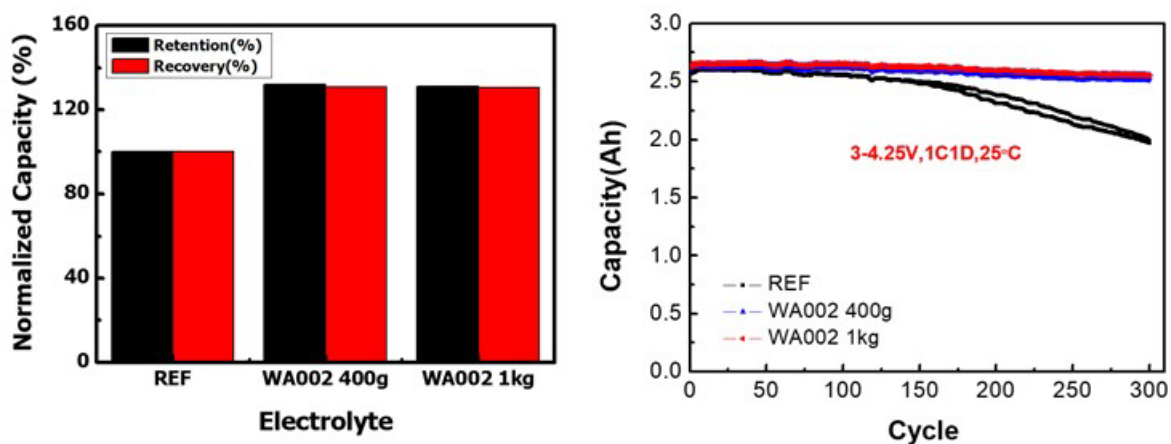


Figure I.3.4 (left) Storage test of electrolyte additive from 400g and 1kg batch sizes. (right) Cycling result for additive in electrolyte for 2.6Ah cell cycled from 3–4.25V under 1CCCV/1CD conditions

In Figure I.3.4 the results of a pouch cell stored at 100% SOC for 7 days is shown. The retention is the delivered C/3 capacity after storage, while the recovery is the C/3 capacity delivered after a few post storage cycles. The results are nearly identical for our 400g and 1 kg material batch, and show significant improvement compared to a cell using the base formulation without the newly synthesized additive. The cycles results after 300 cycles in a 2.6 Ah pouch cell using an NMC811 cathode, graphite anode also show improvement when the additive is present.

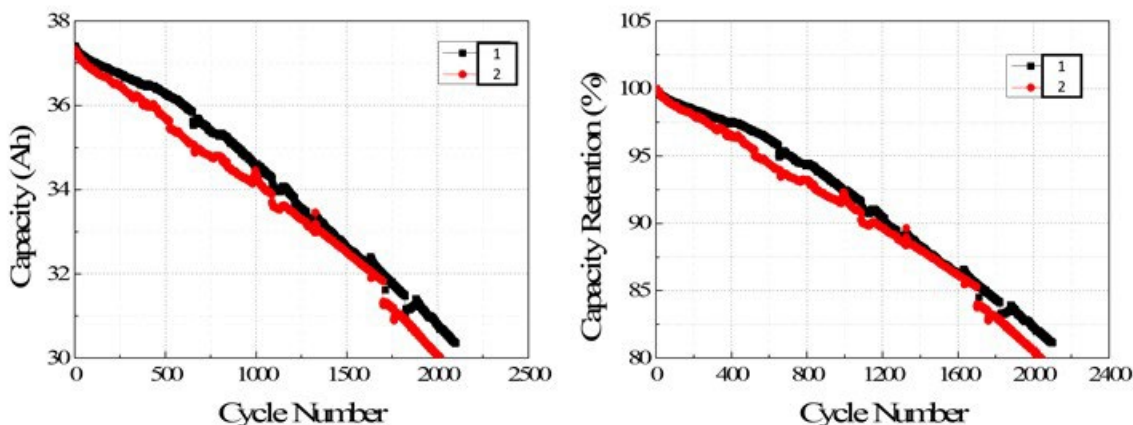


Figure I.3.5 Cycle plot of baseline 38.5 Ah LCFC cell; 3–4.25V, 1CCCV/1CD cycling at room temperature

While the project materials develop, a baseline cell was prepared to benchmark future cell iterations against and to help familiarize the project team with the nuances of USABC testing procedures; particularly the use of useable energy and dynamic stress test (DST) cycling. In Figure I.3.5 the 1CCCV/1CD cycling of the prepared cell is shown. This 260 Wh/kg, 38.5Ah cell can reach over 2000 cycles at room temperature. This cell batch was also evaluated using three DST cycle procedures, 0% fast charge, 25% fast charge and 100% fast charge (see Figure I.3.6). A fast charge was completed in ~13 minutes at beginning of life and is set to never exceed 15-minutes during the test. Since the DST method uses discharge energy, and not a constant capacity, after a fast charge 60% useable energy target was delivered, in part because the capacity on discharge was found to grow as cycling increases which makes it more likely Vmin (a testing end condition) is reached before C/3 retention checks near 80%.

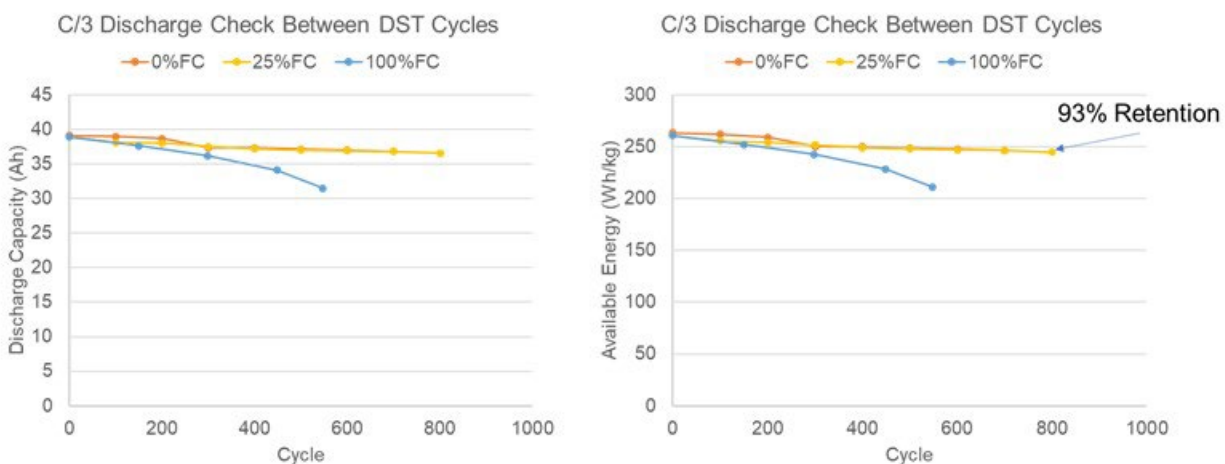


Figure I.3.6 Capacity and energy density of 38.5 Ah cell fast charged (FC) 0%, 25% and 100% of cycles

More recently, work has been focused on developing the low-cost, fast-charge cells energy density thru the integration of a silicon-based anode material, while simultaneously improving the rate possible for fast charging in the 15-minute time limit.

Conclusions

The project team has designed a low cobalt FCG cathode for use in the project, and successfully scaled said material to the kilogram level so it can be incorporated into pouch cells for testing. Concurrently, a new synthesis method for a desired fast charge electrolyte additive has been developed and scaled to 1kg for use in project formulations. The additive shows nearly identical performance as the scale increased for storage and cycling tests compared to a reference solvent. A 38.5 Ah pouch cell was developed and delivered to a DOE national lab for evaluation. In internal testing the cell can cycle over 2,000 times at 1C, and after 800 cycles (roughly 8 months of test) the 0% fast charge and 25% fast charge cells have 93% energy retention.

Key Publications

1. Poster presentation, DOE Annual Merit Review, Washington D.C. June 21-25, 2021

Acknowledgements

Microvast would like to thank project manager Vijay Saharan and the rest of the USABC advisory workgroup to this work for their interest and suggesting in the project. Their support has really helped improve the project.

I.4 High Energy and Power Density Lithium-Ion Battery Based on Neocarbonix™ Polymer Binder-Free Electrode Technology for Electric Vehicle (EV) Applications (Nanoramic)

Dr. Ben Cao, Principal Investigator

Nanoramic Laboratories
21 Dry Dock Avenue, Suite 820E
Boston, MA 02210
E-mail: ben.cao@nanoramic.com

Brian Cunningham, DOE Technology Development Manager

U.S. Department of Energy
E-mail: Brian.Cunningham@ee.doe.gov

Start Date: December 1, 2020

End Date: October 31, 2021

Project Funding: \$732,448

DOE share: \$366,224

Non-DOE share: \$366,224

Project Introduction

Nanoramic has re-invented the way electrodes are manufactured by completely removing high molecular weight polymers such as PVDF and the toxic NMP solvent from the active material layer. This dramatically improves LiB performance while decreasing the cost of manufacturing and the capital expenditures related to mixing, coating, and drying, NMP solvent recovery, and calendaring. In the Neocarbonix™ (NX) electrodes, a 3D nanoscopic carbon matrix works as a mechanical scaffold for the electrode active material and mimics the polymer chain entanglement. Chemical bonds are also present between the surface of the carbon, the active materials, and the current collector promoting adhesion and cohesion. As opposed to polymers, however, the 3D nanoscopic carbon matrix is very electrically conductive, which enables very high power (high C-rates). This scaffold structure is also more suitable for producing thick electrode active material, which is a powerful way to increase the energy density of LiB cells.

Objectives

Nanoramic proposes an EV battery cell capable of meeting or exceeding several critical USABC technical goals targeting high performance EV program. This cell will combine proprietary Neocarbonix cathode and anode technology for the first time in an EV application and is expected to produce benefits including lower cost to manufacture, higher energy density, excellent power density and wide temperature range operation. In this technology assessment program (TAP), Nanoramic will manufacture 36 Neocarbonix electrode technology-based 5 Ah Li-ion battery (LIB) pouch cells and send 18 of them to Idaho National Labs (INL) to evaluate the electrochemical performance and set up a benchmark for future USABC projects. The other 18 LIB pouch cells will be tested at Nanoramic to compare with the test results from INL. The goal of this project is to optimize the electrode manufacturing process of Neocarbonix Ni-rich NMC cathodes and Neocarbonix SiOx-Graphite anodes and optimize a >5Ah cell design using those electrodes. The technical objectives of the 36 identical LIB pouch cells for this TAP project include:

1. High mass loading of Ni-rich NMC cathode Neocarbonix electrodes and their manufacturing method: mass loading = 25–30 mg/cm², specific capacity >210mAh/g.
2. Develop and manufacture SiOx/Graphite anode (SiOx content ≈30 wt.%) based Neocarbonix electrodes and their material synthesis and manufacturing method: mass loading 8–10 mg/cm², reversible specific capacity ≥ 750 mAh/g.
3. Long life performance specially for SiOx/Graphite anode-based Li-ion based electrolyte for battery: from –30 to 60°C.

4. High-energy, high-power density, and long cycle life Ni-rich NMC cathode / SiOx + Graphite/Carbon + based Li-ion battery pouch cells: capacity ≥ 5 Ah, Specific Energy ≥ 350 Wh/kg (based on 5 Ah cell or larger cell format), Energy Density ≥ 800 Wh/L, with a cycle life of more than 500 cycles under 1C-Rate charge-discharge, and ultra-high-power fast charge-discharge C-Rate (15 mins fast charging to achieve 80% of charge capacity at C/3 rate) capabilities.

Approach

Nanoramic's proprietary Neocarbonix™ electrodes are configured with an advanced 3-D nanoscopic carbon binding structure that eliminates the need for polymer binders, providing greater power, energy density (thicker electrodes), and performance in extreme environments compared to traditional battery electrode designs. The high-performance Li-ion battery energy storage devices are designed and manufactured with an optimized capacity ratio design of binder-free cathode/anode electrodes, proprietary anode electrode pre-lithiation method, wide operating temperature electrolyte (-30 to 60 °C), and optimized test formation processes.

Nanoramic has re-invented the way electrodes are manufactured by completely removing high molecular weight polymers such as PVDF and the toxic NMP solvent from the active material layer. This dramatically improves LiB performance while decreasing the cost of manufacturing and the capital expenditures related to mixing, coating, and drying, NMP solvent recovery, and calendaring. In the Neocarbonix™ electrodes, a 3D nanoscopic carbon matrix works as a mechanical scaffold for the electrode active material and mimics the polymer chain entanglement. Chemical bonds are also present between the surface of the carbon, the active materials, and the current collector promoting adhesion and cohesion. As opposed to polymers, however, the 3D nanoscopic carbon matrix is very electrically conductive, which enables very high power (high C-rates). This scaffold structure is also more suitable for producing thick electrode active material, which is a powerful way to increase the energy density of LiB cells.

The Neocarbonix electrode process technology includes the following steps:

- STEP 1: Carbon dispersion and functionalization (see Figure I.4.1)
- STEP 2: Addition of active material and self-assembly occurs (see Figure I.4.2)
- STEP 3: Coating & Drying (see Figure I.4.3)
- STEP 4: Calendaring (see Figure I.4.4)

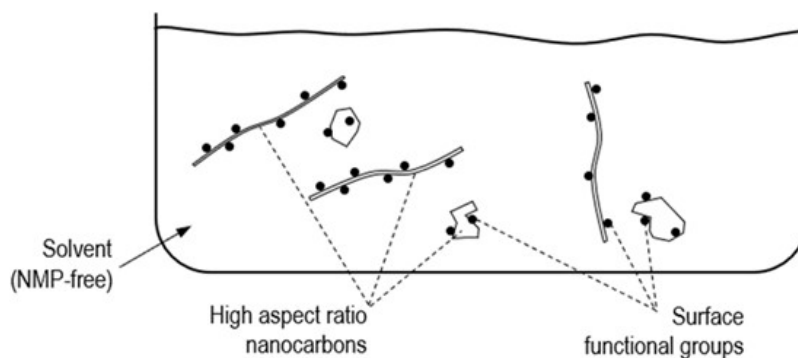


Figure I.4.1 STEP 1: Carbon dispersion and functionalization

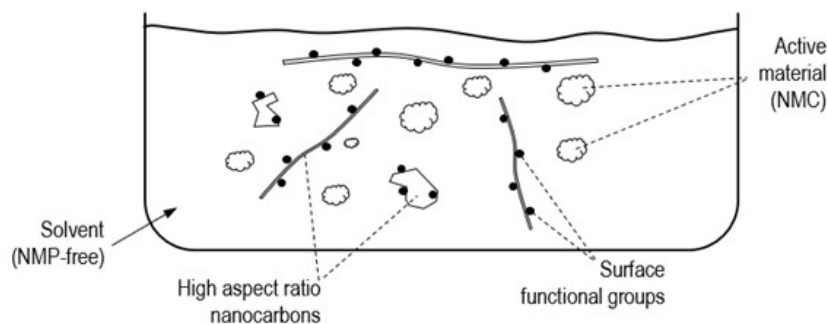


Figure I.4.2 STEP 2: Addition of active material and self-assembly occurs

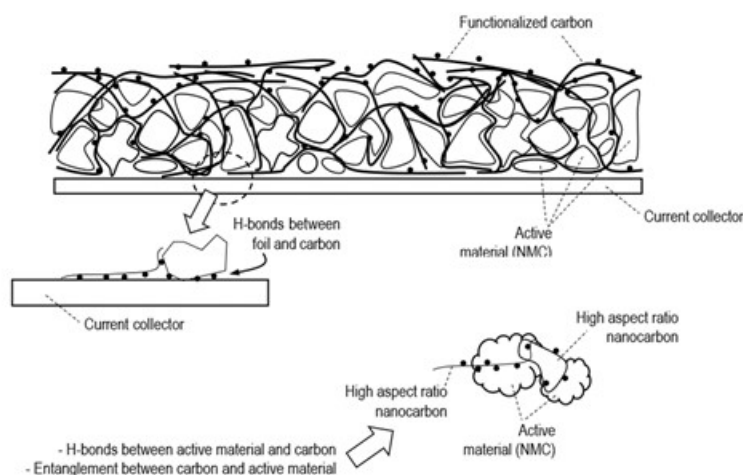


Figure I.4.3 STEP 3: Coating & Drying

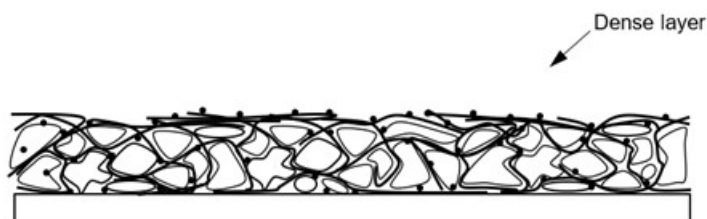


Figure I.4.4 STEP 4: Calendering

Results

Nanoramic has demonstrated the Neocarbonix (NX) battery electrode manufacturing by roll-to-roll (R2R) slot-die coating process during the USABC Technology Assessment Program (TAP) project from December 2020 to August 2021. Figure I.4.5 displays the slot-die coating process for NX NMC811 cathode electrode manufacturing, and a roll of good quality NX NMC811 electrodes, which have been finished. As for the NX Si-C anode, it can be seen from Fig below that there are no issues to use the slot-die to coat the NX Si-C anode slurry, and Nanoramic has also manufactured a good quality roll of NX Si-C anode electrodes.

During the current USABC TAP project from December 2020 to October 2021, Nanoramic Neocarbonix electrode technology has demonstrated the following points as shown in the figure below:

1. Both Neocarbonix NMC811 cathode and Si-C anode battery electrode manufacturing processes have been demonstrated by slot-die R2R coating and calendering processes.

- Neocarbonix battery cell manufacturing process has been demonstrated by standard Li-ion battery pouch cell manufacturing processes.
- With no development / optimization work, Neocarbonix battery electrodes have demonstrated excellent performance in energy density (Wh/L), 1C1C cycle life, and 15 mins 3.5C-Rate CC-CV fast-charging.

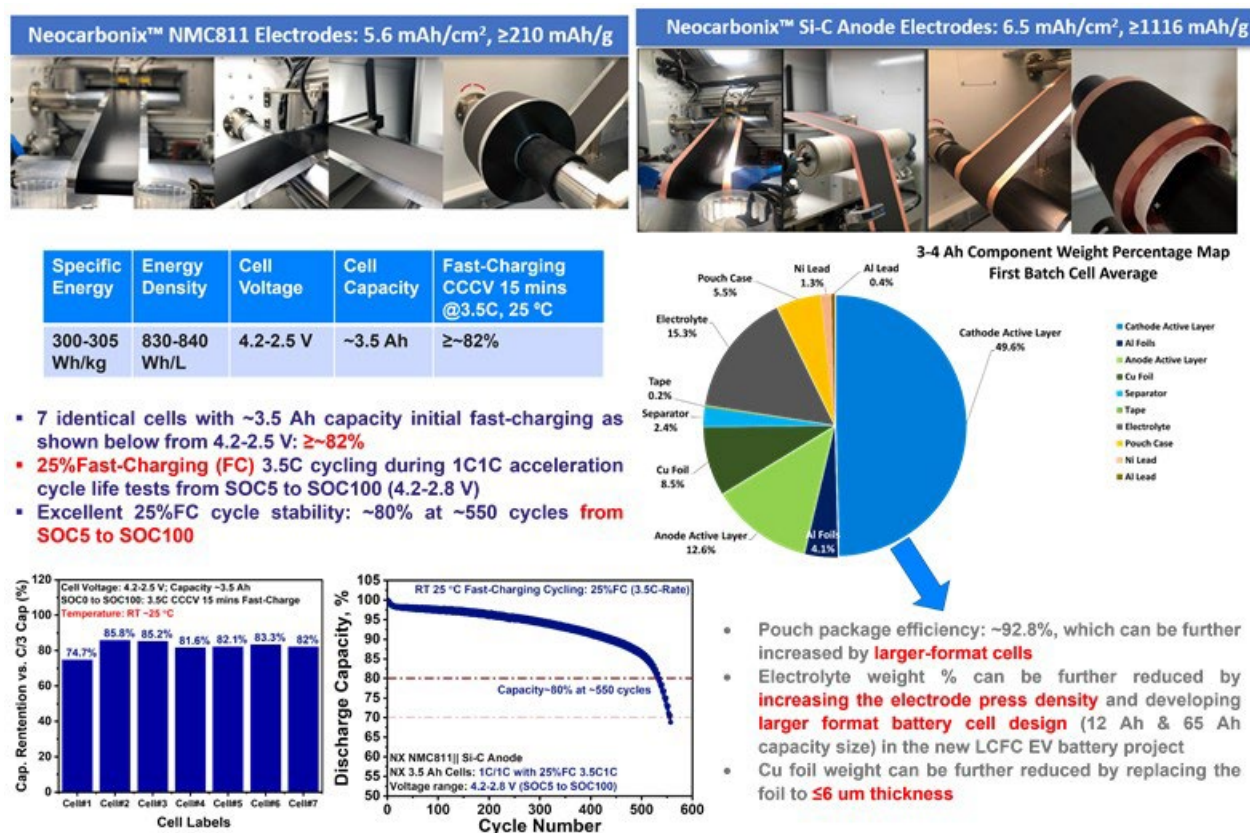


Figure I.4.5 Nanoramic USABC TAP project internal test summary

Conclusions

In summary, during the current USABC TAP project from December 2020 to October 2021, Nanoramic Neocarbonix electrode technology has demonstrated the following points:

- Both Neocarbonix NMC811 cathode and Si-C anode battery electrode manufacturing processes have been demonstrated by slot-die R2R coating and calendering processes.
- Neocarbonix battery cell manufacturing process has been demonstrated by standard Li-ion battery pouch cell manufacturing processes.
- With no development / optimization work, Neocarbonix battery electrodes have demonstrated excellent performance in energy density (Wh/L), 1C1C cycle life, and 15 mins 3.5C-Rate CC-CV fast-charging.

Based on above summarized points, Nanoramic has already demonstrated the solidity of its electrode manufacturing technology side. With this proposed future LCFC-EV battery development project for the next 2.5 years, Nanoramic is confident to bring the Neocarbonix electrode and battery technology to the next level. In the future proposed project, Nanoramic will emphasize the following areas of developments:

1. Li-ion battery low-cost and high-capacity cathode active materials (CAM) NMC811, and NCMA ($\text{Ni}\% \geq 91\%$), and Si anode active materials (cheap \$/kWh and \$/kg) selection development to improve the battery cell energy, fast-charging, and cycle life performance.
2. Increase the Si% content in NX Si anode to increase specific capacity (mAh/g) and lower the Si anode mass loadings (thinner Si anode) to further improve the fast-charging capability.
3. Electrolyte formulations development to further improve the DST cycling performance at RT and high temperature calendar life performance.
4. Large-format LCFC-EV battery cell design development including increasing the packaging efficiency $\geq 95\%$ and cell design modeling and manufacturing process development to further improve the energy density in both Wh/kg and Wh/L.

Acknowledgements

Nanoramic wants to specially thank USABC EV work group including USABC program manager Minghong Liu from Ford, Meng Jiang from GM R&D, Trey Weaver from FCA groups, Matthew G. Shirk from INL, Ahmad Pesaran from NREL, and Maureen LaHote from USCAR for the continuously support and discussions during the whole USABC TAP project.

Nanoramic also wants to specially thank DOE technology development manager Brian Cunningham for the continuously support in this project and thank Haiyan Croft from DOE for attending all the quarterly review meetings and giving Nanoramic precious suggestions and comments.

I.5 Low-cost, Fast-charge Cell Development for EVs (EnPower, Inc.)

Adrian Yao, Principal Investigator

EnPower, Inc.

2155 West Pinnacle Peak Road, Suite 120

Phoenix, AZ 85027

E-mail: adrian@enpowerinc.com

Brian Cunningham, DOE Technology Development Manager

U.S. Department of Energy

E-mail: Brian.Cunningham@ee.doe.gov

Start Date: February 22, 2021

End Date: February 22, 2022

Project Funding: \$367,799

DOE share: \$183,899

Non-DOE share: \$183,900

Project Introduction

As Battery Electric Vehicle (BEV) adoption increases to serve the needs of mainstream consumers, it is ever more critical for battery cell technology to be low-cost with fast-charging capability, all while maintaining a minimum required vehicular range to be practical. However, an inherent tradeoff between energy (range) and power (fast-charge) exists for all Li-ion cells, and current battery cell technology is unable to satisfy both requirements. EnPower addresses this fundamental energy-power tradeoff with its unique and proprietary multilayer electrode architectures that increase the rate capability of thick, high energy density electrodes. By using simultaneous multilayer slot-die coating, EnPower is also able to keep costs low with no detriment to throughput and yield. In this Technology Assessment Program (TAP), EnPower will iterate through multiple designs of multilayer graphite anodes and multilayer NMC811 cathodes to arrive at a semi-optimized cell design. 4.2 Ah Pouch cells incorporating both multilayer anodes and cathodes will be shipped to Idaho National Lab (INL) for final testing upon completion of the TAP.

Objectives

The objective of the project is to demonstrate the feasibility of EnPower's multilayer electrode technology in commercially relevant pouch cell form factors. Cell targets include:

- ≥ 250 Wh/kg (in 4.2Ah pouch cell form factor)
- 80% Δ SOC fast-charge in < 20-mins

Approach

In this TAP, EnPower will first iterate through approximately (6) multilayer graphite anode designs all paired with an identical NMC622 cathode pair to downselect a best-performing design. Subsequently, EnPower will iterate through approximately (6) multilayer NMC811 cathode designs all paired with the previously downselected multilayer anode, again identifying a best-performing architecture. Using this semi-optimized multilayer anode-cathode pair, EnPower will also iterate through several electrolyte formulations tailored for fast-charging capability while keeping component costs in mind. Internal testing will compare cells with multilayer electrode architectures against cells having "homogeneous baseline" electrodes that are chemically- and dimensionally-identical references of their multilayer counterparts. These homogeneous baseline electrodes represent state-of-art conventional electrode architectures. Once a cell stack design (anode, cathode, electrolyte) has been selected, final 4.2 Ah pouch cells will be shipped to INL for third-party testing and validation.

Results

Significant improvements to fast-charge, DC internal resistance (DCIR), and discharge performance have been demonstrated through electrode design and optimization. A best-performing multilayer anode was successfully downselected from six total design iterations, and a best-performing multilayer cathode was similarly downselected from seven design iterations. Significant spread in performance was observed. Between the best- and worst-performing multilayer anode designs, EnPower has demonstrated a 10% spread in DCIR, >20% difference in discharge rate capacity retention at elevated discharge rates, and a ~4.6-minute difference in fastest charge time from 10-80% state-of-charge (SOC), which translates to 0-80% SOC in operating capacity. Figure I.5.1 shows the various multilayer anode design iterations evaluated, whereas Figure I.5.2 summarizes the performance improvements demonstrated.

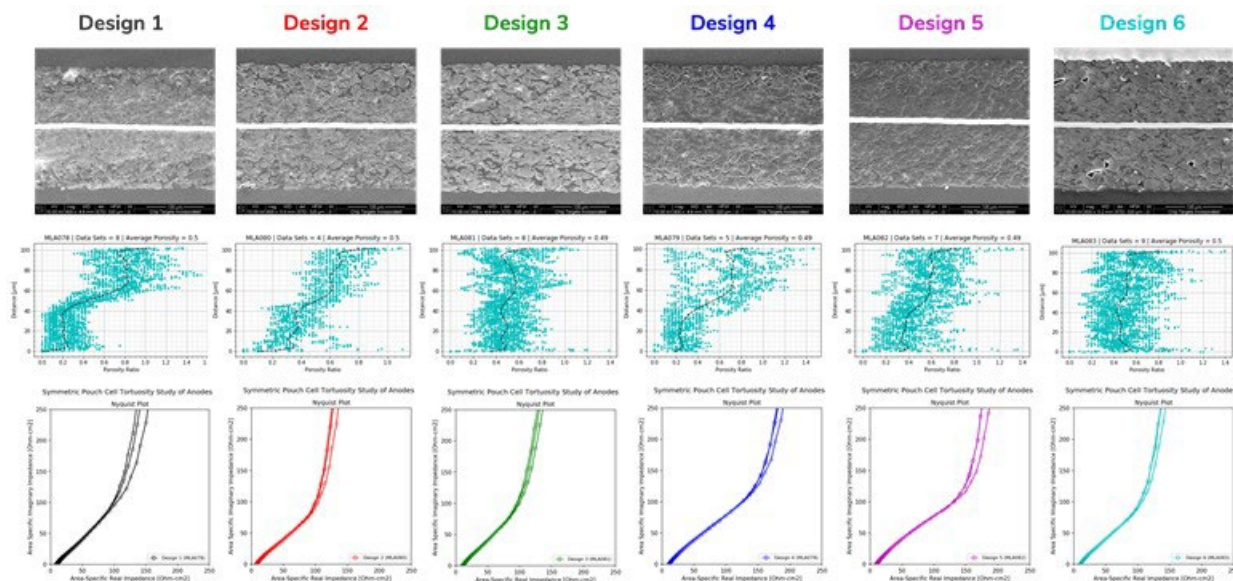


Figure I.5.1 Six different iterations of multilayer anode designs from left to right, showing electrode cross sections, porosity profiles (from image analysis), and tortuosity studies from symmetric pouch cell studies

When the best-performing multilayer anodes are compared with their homogeneous baselines in fast-charge cycling in >4 Ah pouch cells, a significant difference in severity of lithium plating on the anode surface can be observed in post-mortem cell disassembly. These are shown in Figure I.5.3.

Multilayer cathode designs (not shown) also exhibited significant spread, and ~25% improved capacity retention due to continuous discharge was demonstrated. (9) different electrolyte formulations were tested to evaluate fast-charging and low-temperature performance, and a high-power electrolyte was also downselected for the final cell design that demonstrated the ability to delay the onset of lithium plating.

Internal testing of the semi-optimized cell design in 4.2 Ah pouch cells is currently in-progress, and final cells will be shipped to INL at program-end in February 2022.

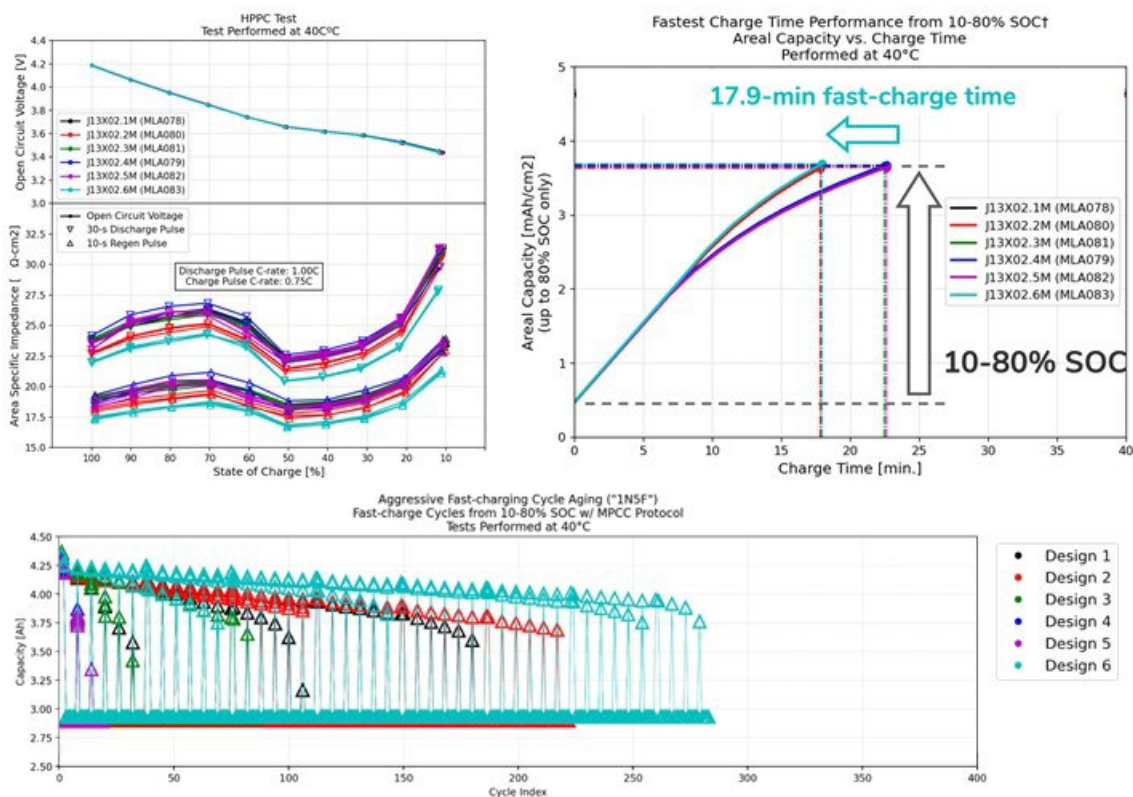


Figure I.5.2 Between the best- and worst-performing multilayer anode designs, EnPower has demonstrated (a) 10% reduction in DCIR from HPPC tests, (b) 4.6-minute reduction to fastest charge time, and (c) >200 cycle difference in cycles to EOL under aggressive fast-charge cycling

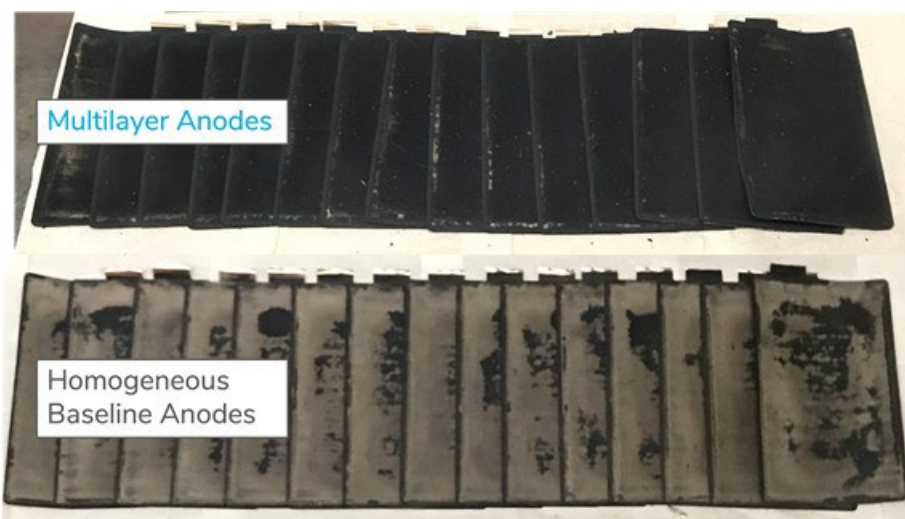


Figure I.5.3 Between the best- and worst-performing multilayer anode designs, EnPower has demonstrated (a) 10% reduction in DCIR from HPPC tests, (b) 4.6-minute reduction to fastest charge time, and (c) >200 cycle difference in cycles to EOL under aggressive fast-charge cycling

Conclusions

EnPower has not only successfully validated the feasibility of the multilayer electrode technology, but also demonstrated its ability to significantly enhance cell performance, especially with respect to fast-charge cycling. By utilizing only graphite-based anode active materials while ensuring drop-in scalability to existing manufacturing infrastructure, EnPower technology can enable low-cost, fast-charge cells for mass-market BEVs.

Acknowledgements

EnPower would like to thank the United States Advanced Battery Consortium (USABC), a subsidiary of the United States Council for Automotive research (USCAR) for support on this project.

I.6 Technology Assessment Program of Aramid Separators for Electric Vehicle Applications (Microvast, Inc.)

Wenjuan Mattis, PhD, Principal Investigator

Microvast, Inc.

3259 Progress Drive, #121

Orlando, FL 32826

E-mail: wenjuanmattis@microvast.com

Brian Cunningham, DOE Technology Development Manager

U.S. Department of Energy

E-mail: Brian.Cunningham@ee.doe.gov

Start Date: June 15, 2020

End Date: September 30, 2021

Project Funding: \$1,045,111

DOE share: \$522,555.50

Non-DOE share: \$522,555.50

Project Introduction

The Aramid Separator is a novel separator that distinguishes itself from traditional polyethylene and polypropylene products by its extraordinary properties. 1) High-temperature resistance; Aramid can withstand high temperature up to 300°C. 2) Inherent flame retardant; Aramid can only be carbonized under the flame but does not catch fire. 3) Excellent wettability and retention of the electrolyte; Composed of polar monomers, Aramid separators have a very high affinity toward the electrolyte solution and tends to retain the electrolyte, which results in a high mobility of lithium ions, as well as a low electrical resistance in the electrolyte-filled separator. 4) High porosity; Aramid separators have a porosity in the range of 50%~60%, which also enables a low electrolyte resistance. 5) Scavenging water molecules; the strong polar Aramid molecules tend to anchor H₂O molecules (introduced during the assembly of the cell from all key materials) by hydrogen bonding. Properties 1 and 2 enables the enhanced abuse tolerance of cells containing Aramid separators. Properties 3 and 4 are fast cell charging enablers, while properties 3 and 5 enable a long cycle life in cells that contain this separator.

The purpose of this program is to assess the properties and performance of Microvast's Aramid separators in cells and modules by comparison with the state-of-art commercial ceramic-coated polyolefin separators.

Objectives

The program objectives are (1) to determine the advantages of Aramid separators at their present development stage over the state-of-art ceramic-coated polyolefin separators, in terms of abuse tolerance and electrochemical performance at both cell and module levels, as well as (2) identify further developments needed for fulfilling the USABC goals for advanced automotive batteries.

Approach

4 samples bare Aramid separator at different thicknesses were prepared by Microvast and delivered to USABC for testing. The same set of bare Aramid separators were tested internally at Microvast. A total 172 cells with 52 Ah capacity and NCM 811 and graphite electrode chemistry were fabricated by Microvast. The main components of the electrolyte are EC, DEC, and LiPF₆. Half of the cells (86 pieces) were made with bare Aramid separators (16 microns thickness), the other half (86 cells) were made with a state-of-the-art commercial ceramic-coated polyolefin separator (16 microns thickness). Moreover, to generate more practical comparison of polyolefin and Aramid separators at the vehicle level, Microvast also fabricated four EV modules, each module being comprised of 12 cells for cycle life testing. The cells from two of the modules had an Aramid separator, while the cells from the other two modules had a state-of-the-art commercial ceramic-coated polyolefin separator.

Results

During the project numerous physical properties were evaluated for the Aramid separator as well as ceramic coated PE for comparison. The findings are described below:

1. **Thickness** – The thickness measurement was conducted on a Millimar C1208M thickness gauge with a precision of 0.1 μm . The diameter of the foot is 5 mm and the pressure used is 0.2 MPa. 4 samples of different thickness have been produced as requested in TAP. The results show that the thickness variation is within $\pm 1 \mu\text{m}$ range, which is comparable to PE separators.
2. **Gurley** – Gurley tests were conducted on an Asahi-Seiko EG01-55-1MR Gurley tester. The sample area is 10 cm^2 . The test pressure is 0.05 MPa with an airflow volume of 100 ml. The results show that all 4 samples have a very narrow distribution of the Gurley value of ± 15 , which indicates a very good uniformity of permeability of aramid separators.
3. **Wettability** – Tests of wettability of electrolyte were carried out on a JC2000C1 contact angle tester. The contact angle of electrolyte on the aramid separator is 22.5 degrees, which is about half of the contact angle of the same electrolyte on the PE separator (43 degrees). The aramid separator demonstrates a much better wettability of electrolyte than the PE separator.
4. **Average Pore Size** – The pore size and pore size distributions of 4 aramid samples were measured on a PMI CFP-1500 pore size analyzer. The average pore size of 4 aramid separator samples is all in the range of 0.08~0.1 μm , with a standard deviation of $\sim 0.04 \mu\text{m}$. In general, the pore size distribution follows a normal distribution, which indicates a very tight pore size distribution of the aramid separators. A narrow distribution of pore sizes is one of the key prerequisites that ensures a uniform permeability of separators.
5. **McMullin Number** – McMullin numbers of 4 aramid separator samples were measured by a home-made electrical resistance tester. All the tests were done in a dry room with controlled room temperature. Separators were first soaked in the electrolyte for at least 30 min to ensure a thorough wetting to minimize the variation and improve the repeatability (2-hour soaking is recommended for PE separators). 4 samples of aramid separator have McMullin numbers ranging from 6.7 to 8.8 with a slight increasing dependence on the thickness. Increasing pore sizes can effectively decrease the McMullin number, however larger pores increase the chance of dendrites growing through separators, which causes serious safety issues.
6. **Shear (Puncture) Strength at Various Thicknesses** – Shear strength of 4 aramid separator samples was measured on a QJ210A Universal Tensile Tester with a testing speed of 250 mm/min and a needle diameter of 1 mm. The puncture strength of aramid separators increases as the average thickness of separators increase, while keeping the same average molecular weight, the same process condition, and the same porosity. The puncture data is greatly affected by the needle diameter and the puncture speed. After normalized to the 3 mm and 0.1mm/s, the puncture value meets USABC requirement.
7. **Tensile Strength** – The tensile strength of 4 aramid separator samples was measured on a QJ210A Universal Tensile Tester with a testing speed of 200 mm/min. All 4 samples show an elastic modulus above 700 MPa, which indicates a $<1\%$ offset at a stress of 1000 psi.
8. **Shutdown Temperature** – Shutdown Temperature of an aramid separator and a ceramic-coated PE separator with a thickness of 14~16 μm were measured by an ARTBRI Hot ER Tester with a heating speed of 20°C/min. Ceramic coated PE separator demonstrates a shutdown peak (an increase of resistance by five orders of magnitude) around 140° and broke down quickly afterward. However, the aramid separator did not present any shutdown sign in the testing range up to 230°C.

- High Voltage Stability – A high voltage (5V) stability test of aramid separator was carried out on a 14~16µm thick aramid separator sample. The separator sample was first dried at 80°C with a vacuum for 12 hrs to remove moisture. With LNMO as the cathode, Li metal as the anode, MV high voltage electrolyte, a coin cell was made to carry out the cyclic voltammetry test at a scanning rate of 0.1 mV/s from 3.5V to 4.9V. All results clearly show that aramid separator is stable under such a high voltage system (5V).

Table I.6.1 Summary of physical evaluation of different thickness Aramid separator compared to USABC goal

Parameter	Units	USABC Goal		7-8 µm	10-12 µm	14-16 µm	18-20 µm
Thickness	Mm	< 25 ± 1		8.02 ± 1.0	12.44 ± 1.0	14.7 ± 1.0	19.2 ± 1.0
Permeability	Gurley #	s /10 cm ³	< 11 (power) 25 (energy)	4.5 ± 1.5	6.7 ± 1.5	8.1 ± 1.5	7.4 ± 1.5
	MacMullin #	non-dimensional	< 4 (power) 8 (energy)	6.73 ± 0.6	8.54 ± 0.6	7.82 ± 0.6	8.78 ± 0.6
Wettability	non-dimensional	wet-out in electrolytes ¹		Y	Y	Y	Y
Functional Life	Years	capable of supporting cell performance for 15 years ²		TBD	TBD	TBD	TBD
Average Pore size	Mm	< 0.2		0.090 ± 0.043	0.085 ± 0.038	0.097 ± 0.049	0.086 ± 0.042
Shear Strength ³	gf / 25.4 µm film	300		903	842	800	681
Thermal Stability ⁴	% shrinkage/90°C ⁵	< 5		< 1%	< 1%	< 1%	< 1%
Uniformity (Defects) ⁶	pinholes/roll	zero throughout roll length		none	none	none	none
Tensile Strength	N/A	<2% offset at 1000 psi		< 1%	< 1%	< 1%	< 1%
Cost	\$/m ²	0.60 @ 10M sqm/yr		< 0.60 @ 10M m ² /yr	< 0.60 @ 10M m ² /yr	< 0.60 @ 10M m ² /yr	< 0.60 @ 10M m ² /yr
Shutdown Temperature (See Section 6.2)	°C	(105 ± 5) °C		None	None	None	None
High Voltage Resistance (See Section 6.2)	V	5.0 V		Y	Y	Y	Y

As summarized in Table I.6.1, the aramid separator shows a low and uniform Gurley value, which results from the high porosity and narrow pore size distribution, and in turn, results in a low and narrow McMullin number. Due to its hydrophilic property, aramid separator has very good wettability toward electrolyte. It can also withstand very high oxidation potential. These properties offer aramid separators excellent permeability and uniformity for lithium ions with a higher voltage limit, which enables fast-charging and long cycle life of cells. Aramid separator also offers very good thermal stability due to aramid's high-temperature resistance property, which greatly improves the safety of the cells. it also shows no shutdown feature below 230°C.

The aramid separator was tested in high energy 52 Ah pouch cells for comparison to identical cells constructed using a ceramic coated PE separator.

- Nail Penetration Test – One set of the nail penetration test were done on three 52Ah cells made with ceramic-coated PE separator and three 52Ah cells made with aramid separator at room temperature with a 3-mm diameter needle at a penetration speed of 0.1 mm/s at 100% SOC. Another set of the nail penetration test was done on three 52Ah cells made with ceramic-coated PE separator and three 52Ah cells made with aramid separator at room temperature with a 3-mm diameter needle at a penetration speed of 0.1 mm/s at 70% SOC. The test results are shown in Table I.6.2. Both 52Ah cells made with ceramic-coated PE separator and Aramid separator failed the first set of tests. But the 52Ah cells made with ceramic-coated PE separator failed at the very beginning of the penetration test, with a penetration depth of only 3 ~ 4 mm. However, two out of three 52Ah cells made with an aramid separator failed after the needle fully penetrating through the cells. 52Ah cells made with ceramic-coated PE separator failed the second set of nail penetration tests with a penetration depth of only 6 ~ 7 mm. However, the 52Ah cells made with an aramid separator successfully passed the second set of tests. These results prove that the aramid separator can provide better safety than the current ceramic-coated PE separator in internal short.

Table I.6.2 Nail penetration test results for aramid cells versus ceramic coated PE cells

No.	Separator	Sample No.	SOC	Depth (mm)	Penetration %	HSL
1	Ceramic-coated PE	02LCE05200202AAP0000113	70%	7.4	64.3%	Flame
2		02LCE05200202AAP0000094	70%	6.4	55.7%	Flame
3		02LCE05200202AAP0000095	70%	6.7	58.3%	Flame
4		02LCE05200202AAP0000109	100%	3.6	31.3%	Flame
5		02LCE05200202AAP0000096	100%	3.7	32.2%	Flame
6		02LCE05200202AAP0000097	100%	4.2	36.5%	Flame
7	Aramid	02LCE05200202AACL0000134	70%	Full	100%	Minor Leakage
8		02LCE05200202AACL0000146	70%	Full	100%	Minor Leakage
9		02LCE05200202AACL0000147	70%	Full	100%	Minor Leakage
10		02LCE05200202AACL0000135	100%	Full (16s after penetration)	100%	Flame
11		02LCE05200202AACL0000149	100%	9.1mm	79.1%	Flame
12		02LCE05200202AACL0000145	100%	Full (464s after penetration)	100%	Flame

- Overcharge Test – The overcharge test was done on three 52Ah cells made with ceramic-coated PE separator and three 52Ah cells made with aramid separator at room temperature with a charging rate of 2 C to 250% SOC. Both 52Ah cells made with ceramic-coated PE separator and Aramid separator failed the overcharge test. The 52Ah cells made with ceramic-coated PE separator failed at HSL=7, but the 52Ah cells made with aramid separator failed at HSL= 6, due to the intrinsic fire-retardant property of aramid.
- Thermal Ramp Test – Thermal ramp tests on cells made with ceramic coated PE separators and Aramid separators at the heating rate of 5°C/min to 250°C. Even though all cells failed the tests, there is a difference. Cells made with ceramic-coated PE separators failed around 150°C, Cells made with Aramid separators failed around 175°C.
- Thermal Performance Test – The thermal performance test has been finished on cells made with ceramic-coated PE separators and cells made with Aramid separators. No obvious performance difference between these two kinds of cells was observed in terms of the available energy, discharge power, and regen power under the temperature of -30°C, -20°C, -10°C, 0°C, and 52°C.
- Survival Temperature Test – The survival temperature test has been finished on cells made with ceramic-coated PE separators and cells made with Aramid separators. No obvious performance difference between these two kinds of cells was observed in terms of the available energy, discharge power (AE target), and regen power @ 99.8% operation capacity under the temperature of -40°C and 66°C.
- Dynamic Stress Test at 30°C – The dynamic stress test at 30°C on 52Ah cells has completed four RPT runs. The result is summarized in Figure I.6.1. No obvious performance difference between two kinds of the cells was observed in the available energy, discharge power, and regen power. The cells made with aramid separator performs as well as the cells made with ceramic-coated PE separator.
- Calendar Life Test – The calendar life tests for 52Ah cells under the temperature of 30°C, 45°C, and 60°C, have completed the four 32-day tests. No obvious performance difference between two kinds of the cells at 30°C, 45°C, and 60°C.

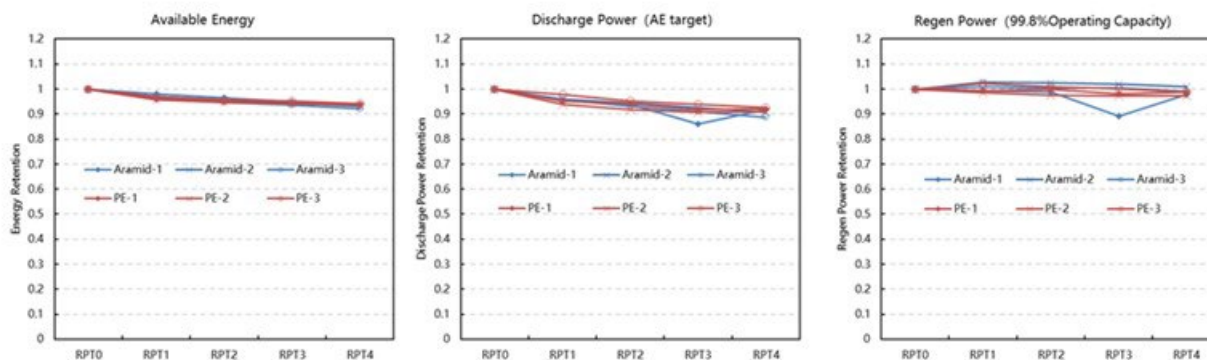


Figure I.6.1 Dynamic stress test cycle results for aramid separator and ceramic coated PE cells

The final comparison test done during the project was a module cycling test. VDA-II Modules made by cells with two different separators (Ceramic-coated PE separators and Aramid Separators) were cycled at 30°C with 0.33 C rate. The results are shown in Figure I.6.2 below. After 500 cycles, no distinct performance difference has been observed. The slightly different of the capacity is within the standard deviation of the VDA-II modules.

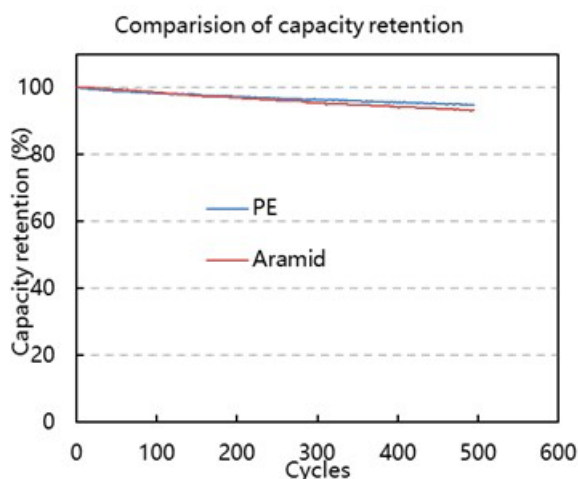


Figure I.6.2 Cycling retention of Li-ion battery module using Aramid separator versus ceramic coated PE

Conclusions

1. Aramid separator meets or exceeds the USABC property requirement for separator in all categories, except for “no shutdown”, which can be further developed.
2. Aramid separator at present development stage greatly improves the safety of the cells at the internal short and thermal stability over the state-of-art ceramic-coated polyolefin separators. With Further ceramic and/or functional coating, the safety margin will be further improved.
3. Aramid separator at present development stage performs at the same level as the state-of-art ceramic-coated PE separator in terms of electrochemical performance at both cell and module levels

Acknowledgements

Microvast would like to thank USABC project manager Ion Halalay and the rest of the technical work group for their useful advice and guidance during this project.

I.7 Solvent-free Electrode Manufacturing for Low Cost/Fast Charging Batteries (Worcester Polytechnic Institute)

Yan Wang, Principal Investigator

Worcester Polytechnic Institute
100 Institute Road
Worcester, MA 01609
E-mail: yanwang@wpi.edu

Brian Cunningham, DOE Technology Development Manager

U.S. Department of Energy
Brian.Cunningham@ee.goe.gov

Start Date: November 19, 2019
Project Funding: \$617,659

End Date: November 18, 2022
DOE share: \$359,252

Non-DOE share: \$258,407

Project Introduction

In conventional lithium-ion batteries, a slurry made of active materials, conductive additive and polymeric binder is cast onto the current collector. The coated electrodes are subsequently dried and calendared. In the slurry casting method, organic solvent (NMP) is used to make the slurry, which contributes significantly to the total cost of lithium ion battery manufacturing (the solvent itself, solvent drying and recovery). In efforts to lower the battery cost associated with the NMP solvent, different approaches have been investigated. Finding a less expensive solvent to replace NMP has been the subject of much research. Water based approaches have been studied and found to compare favorably to organic solvent-based approaches [1], [2], [3]. This approach has achieved significant success on the anode side of Li-ion batteries, and aqueous slurries using Styrene Butadiene Rubber (SBR) as the binder have already been commercialized for graphitic anodes. However, the costly time-consuming and energy-intensive drying step following coating remains part of the fabrication process. In addition, NMP is still being used to dissolve PVDF binder on the cathode side, since binders dissolved in aqueous systems are not chemically or electrochemically stable at the high voltages seen at the positive electrode.

Complete elimination of the solvent is a promising approach to lower both the cost and manufacturing time of Li-ion batteries. Michael Wixom (previously at A123 Systems) at Navitas Systems, who collaborate with Maxwell Technologies, has proposed and developed a solvent-free electrode manufacturing process [4]. In the manufacturing process, the active material, conductive carbon, and Polytetrafluoroethylene (PTFE) binder were pressed onto current collector directly to fabricate the electrode, as a viable approach to fabricate supercapacitors. However, to make Li-ion battery electrodes, the following additional challenges have been identified: (1) PTFE is not electrochemically stable in a lithium battery anode; (2) it is difficult to fabricate thin electrodes, which are essential to provide sufficient power for Li-ion batteries; (3) the electrode is stiff, which complicates or precludes winding for cylindrical cells/prismatic wound cell formats.

Structured electrodes have been demonstrated to improve battery charging rates. For example, experiments [5], [6] reveal that electrolytic transport becomes a major source of cell polarization at conditions of high current and/or large electrode thicknesses, both of which are the case for high rate charging of EV batteries. To enable fast charge, different structured electrodes have been developed [7], [8]. However, previous methods often utilize complex manufacturing processes and are difficult to scale up.

Objectives

The project's objective is to develop low-cost batteries capable of fast charging for EV applications according to the USABC targets. In order to achieve the goal, the team will further develop a solvent-free manufacturing method for hetero-structured electrodes in order to achieve fast charging capability and low cost batteries. The hetero-structure enables fast charging and solvent-free manufacturing allows low cost. It is inherently

challenging to fabricate hetero-structured electrodes using the traditional slurry casting method due to the complicated solvent drying process. In this project, the team will fabricate advanced electrodes with NMC622 and graphite as the cathode and anode materials, respectively.

Approach

Our proposed solvent-free manufacturing could potentially achieve low cost and fast charge concurrently. In this project, solvent-free manufacturing is used to fabricate electrodes with layered structures, whereby layers have varying porosities strategically tuned to enable fast charge batteries. During electrode fabrication, dry mixed powder is directly sprayed onto the current collector. Subsequent hot rolling results in melting of the binder and formation of a strong bond between particles and current collector. In order to enable high rate, electrodes with a multi-porosity hetero-structure will be fabricated. Compared to other methods, such as co-extrusion, to fabricate multi-porosity hetero-structured electrodes, the proposed method does not involve any solvent or complicated hardware and can be easily scaled up. Due to the elimination of solvent, the solvent-free manufactured layered electrodes allow for fast charge (structured electrode), low cost (no solvent and drying), and fast production (no drying step) when compared to the conventional wet processed electrodes. Table I.7.1 is a comparison of our technology to current slurry casting technology to fabricate battery electrodes.

Table I.7.1 Comparison of Our Technology to Current Slurry Casting Technology

	Current technology	Our proposed technology
Material mixing	Wet mixing with solvent	Dry mixing without solvent
Coating	Slurry casting	Dry printing
Dry	Dry step needs	No drying
Solvent recovery	Organic solvent needs to be recovered	No recovery step
Electrode	Uniform porosity electrode	Porosity graded electrode (proposed work)

Results

Modeling

We improved the battery model by fitting model parameters against the rate performance data of single-layer pouch cells of dry-printed electrodes from testing conducted by Microvast. The fitted C-rate curves (dashed lines) show good agreement with the experiments (solid lines) for several types of cells (Figure I.7.1a), and the comparison of charging voltage curves of pouch cells consisting of dry-printed electrodes at different C rates is presented in (Figure I.7.1b). One notable observation from the fitting is that the dry-printed NMC cathode has significantly lower tortuosity than the slurry-casted cathode, which suggests that an added benefit of the dry-printing process is that it could improve the pore alignment and accelerate electrolyte transport on the cathode side. This observation was confirmed by direct tortuosity measurements, which find the tortuosity values of the slurry-casted and dry printed NMC cathodes to be 3.8 and 2.74, respectively. On the other hand, both fitting and direct measurements show that the tortuosities of the dry-printed and slurry-casted graphite anodes are closer to each other (3.28 vs 3.75), which confirms that the improvement in the rate performance of dry-printed 2-layer anodes originates from a more optimal, non-uniform distribution of porosity within the electrode.

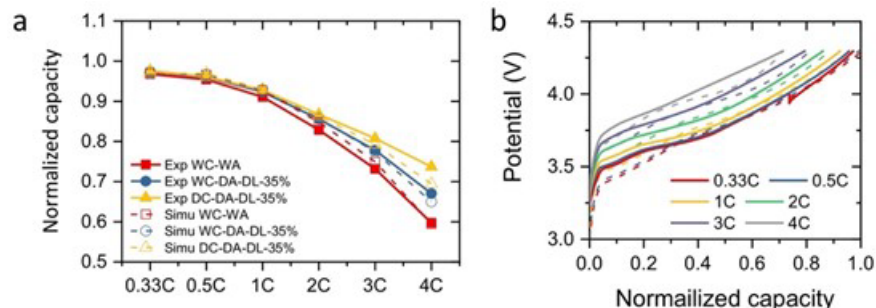


Figure I.7.1 (a) Experiment measurement (solid lines) vs fitted model prediction (dashed lines) of the charging performance of NMC/graphite cells. (b) Experiment measurement (solid lines) vs fitted model prediction (dashed lines) of the charging voltage curves of dry-printed cells (DC-DA-DL-35%) at different C rates

We extended the two-layer electrode design to thicker electrodes with higher active material loadings of ~ 30 mg/cm² for NMC and ~ 15 mg/cm² for graphite. The increased areal capacity increases the electrode thickness from ~ 70 μ m to ~ 110 μ m. We calculated the two-layer electrode performance using cell configurations consistent with the current manufacturing practice, i.e., single porosity NMC cathode, two-porosity graphite anode with equal layer loading and the average porosity between 30% and 40%. Subject to these constraints, we compare the rate performance of different 2-layer anode configurations at 3C and 4C charging, see Figure I.7.2. The 2-layer anode structure could improve the constant current (CC) portion of the charging capacity by 18-32% at 3C and 22-30% at 4C over the baseline single-porosity electrode configurations. However, the CC charging capacity of even the best 2-layer configuration is below the fast-charging target of this project (80%). Therefore, it is necessary to consider the charging capacity achieved during both CC and constant voltage (CV) step in electrode design, and to further alleviate manufacturing constraints such as increasing the porosity contrast between the two layers, etc.

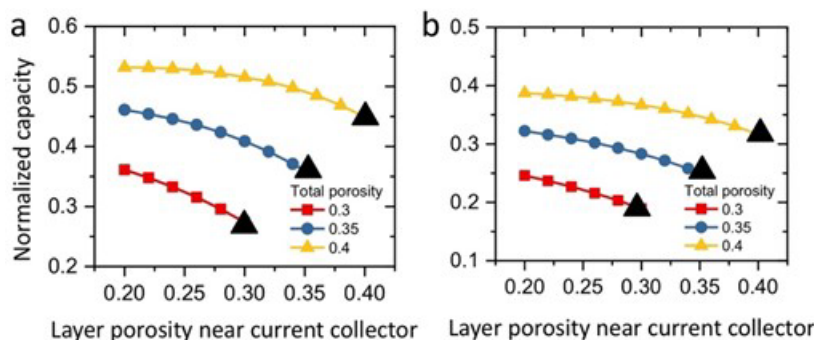


Figure I.7.2 Calculated 3C (a) and 4C (b) charging capacity of different 2-layer electrode configurations with active material loadings of 30 mg/cm² (NMC) and 15 mg/cm² (graphite)

As our previous calculations show that the CC charging capacity of thicker NMC/graphite cells does not meet the fast-charging target, we optimized 2-layer electrode configurations by using the CCCV capacity as the objective function. As shown in Figure I.7.3a, calculations show that the CV step could contribute comparable or even more capacity than the CC step. As a promising sign, the CCCV capacity of the 2-layer dry-printed electrodes at 4C already nears the project target. Figure I.7.3b shows how the CCCV vs CC charging capacities at 4C rate vary with the porosity of the anode layer next to the current collector for full cells with different average anode porosity. The CCCV capacity is less sensitive to the porosity difference between the two anode layers. From the practical point of view, this reduces fabrication challenges as a larger porosity contrast requires harder pressing, which negatively affects the adhesion between the two layers.

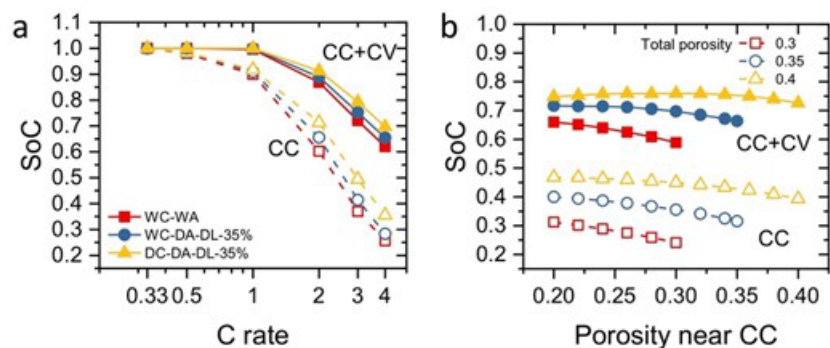


Figure I.7.3 (a) CC vs CCCV charging capacity of thick NMC cells consisting of different types of electrodes. (b) Final SOC after 4C CC vs CCCV charging as a function of the anode layer porosity near current collector (CC) in NMC cells with uniform cathode and 2-layer graphite anode

Electrode fabrication

Electrode manufacturing processes have been developed and refined to fabricate single-porosity cathode and two-porosity anodes for pouch cells testing at Microvast and deliverables. For cathode manufacturing, powder mixing (NMC/C65/PVDF:90/5/5) has been scaled-up and optimized to ensure uniform coating and proper adhesion with the current collector. After improving the adhesion and uniformity, pouch cell size single layer cathodes were fabricated by dry printing method. Carbon coated Al foil was used as the current collector for cathode. Pre-mixed powder was uniformly sprayed to deposit a single layer of cathode material with average area loading of 20 mg/cm²; followed by hot plate annealing of ~1hr in air. After that, a room temperature roller was used to finally press the sample with a uniform porosity of ~35%. The final coated area of the sample is ~5cm x 3.7cm. It also holds an uncoated bare Al tab of ~5cm x 1.27cm at one edge. The loading uniformity has been controlled to be <5%. This method was repeated to manufacture several batches of these cathodes. For two-porosity anode manufacturing, considering the bonding issue between the bottom (denser) and top (porous) layer, it is decided to avoid exceptionally low porosity when fabricating the bottom layer. The bottom layer with loading ~5 mg/cm² and porosity ~40 % was firstly fabricated. Then the second layer with loading ~5 mg/cm² was sprayed followed by hot-rolling process to obtain overall porosity ~35%. The PVDF between the Cu current collector and the first layer is about ~0.05 mg/cm². 100°C hot rolling was applied at the last step for two-porosity anodes. The coated area is 6.2cm x 5.2cm and the tap area is 1.27cm x 6.2cm. Fabricated cathode and anode are shown in Figure I.7.4.

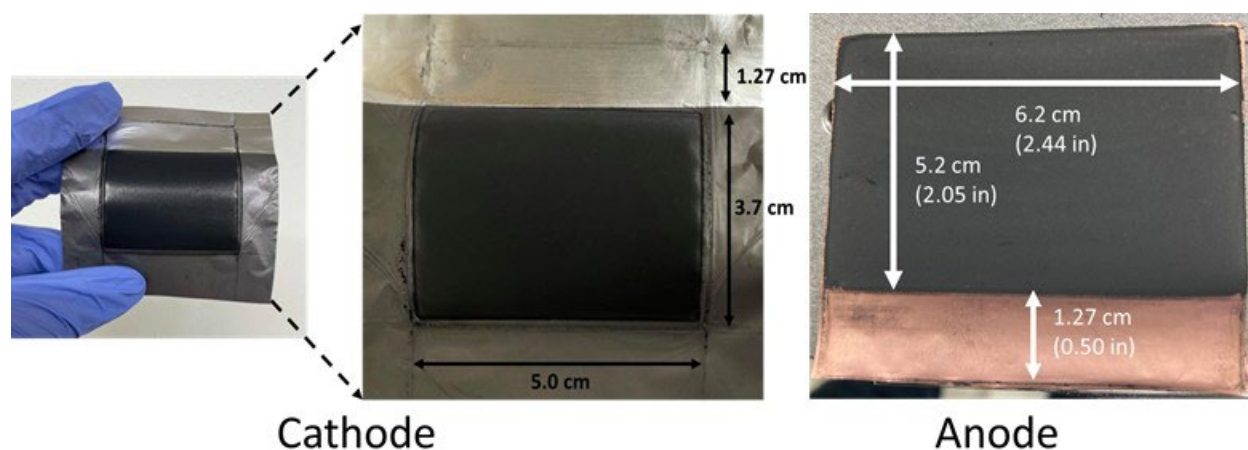


Figure I.7.4 Two porosity anode and single porosity pouch cell cathode

After finalizing the manufacturing processes, 35 pairs of single-porosity cathode and two-porosity anode for pouch cells were fabricated and delivered. For the two-porosity anodes, the first layer loading is 5 mg/cm² and

the second layer loading is 5 mg/cm^2 . Overall porosity is 35%. The PVDF layer between the current collector and the bottom layer is about 0.06 mg/cm^2 . The coated area is $6.20 \text{ cm} \times 3.93 \text{ cm}$ with a tab area of $6.20 \text{ cm} \times 1.27 \text{ cm}$. For cathode, the coated area is $5 \text{ cm} \times 3.8 \text{ cm}$ with an uncoated tab area of $5 \text{ cm} \times 1.27 \text{ cm}$; average area loading was 20 mg/cm^2 and porosity was 35%.

The delivery of 35 pairs of pouch cells meets the milestone of the first year. Then, a batch process was developed and demonstrated for 2-sided coating (30 mg/cm^2 on each side) on a $10 \times 10 \text{ cm}$ current collector. The 2-sided coating was done sequentially. Briefly, PVDF was sprayed on 1st side (0.06 mg/cm^2) followed by a quick annealing step (200° for 2mins) to ensure melting of the PVDF onto the current collector. Then 30 mg/cm^2 of Cathode materials was sprayed on top of the melted PVDF layer and rolled to attain ~53% porosity. The current collector was flipped onto the 2nd side and the PVDF/Cathode spraying was repeated with similar approach (same loading and porosity). Finally, the sample was rolled even more to attain ~40% overall porosity (Figure I.7.5a). The 2-sided coated sample with sequential spraying and rolling was realized with the possibility of roll-to-roll process but the bending of the current collector due to unequal pressing on two sides was observed (Figure I.7.5b) which required further attention.

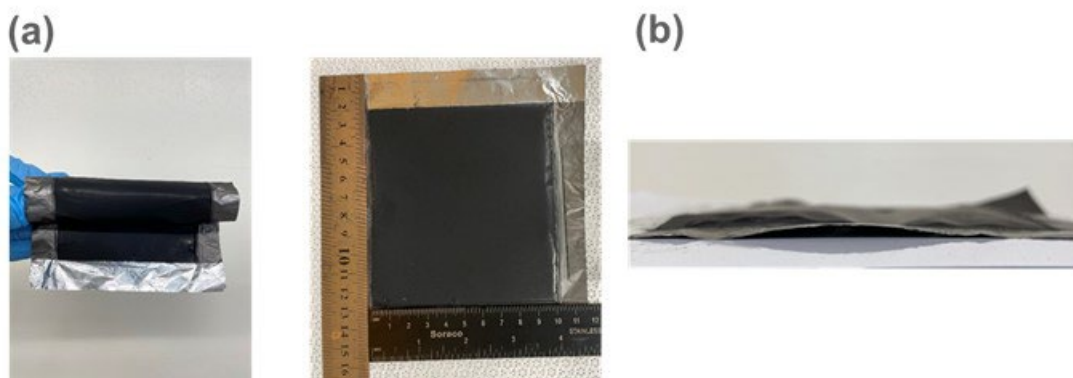


Figure I.7.5 (a) 2-sided coated $10 \text{ cm} \times 10 \text{ cm}$ cathode sample from batch process (b) observed bending after final rolling to ~40% porosity

A roll-to-roll system to achieve 2-sided coating of 2 porosity electrodes was also developed. In an aim to attain this, 30 mg/cm^2 coating (1-sided) on roll-to-roll setup was successfully demonstrated. Briefly, preceded by the unwinding step, PVDF layer was sprayed onto the current collector (Figure I.7.6a). Next, cathode layer of 15 mg/cm^2 was sprayed on top of the PVDF followed by heating (250° for 10mins), rolling and winding step. The foil roll was connected back to the unwinder to spray another layer with 15 mg/cm^2 cathode materials on top of the previously rolled layer. Lastly, the sample undergoes final rolling (~35% porosity) and winding steps and collected on the roll (Figure I.7.6b). This layer-by-layer method to spray and roll cathode materials on the foil roll was needed to ensure good bonding without any wrinkles during rolling. The 2-sided coating with 2 porosities on a roll-to-roll setup is yet to be demonstrated, but the overall success of the 1-sided test on the developed roll-to-roll system provides insight to the possibility of achieving the final target.

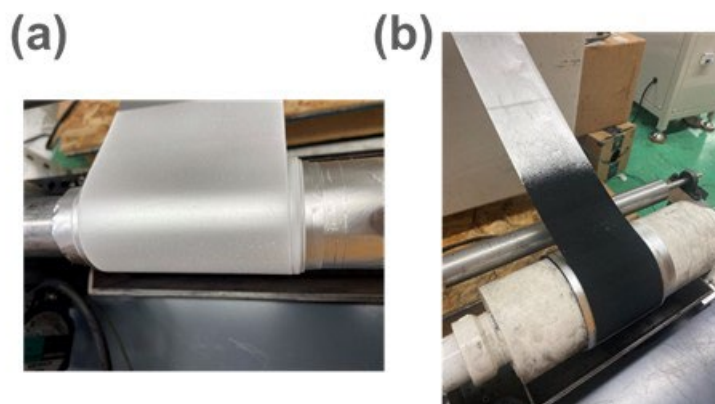


Figure I.7.6 (a) PVDF coated foil roll (b) cathode materials coated foil roll with target loading collected at the winder after final rolling

Electrode testing

Due to the different manufacturing methods, the microstructure of slurry-casted and dry-printed electrodes shows significant difference. The schematics in Figure I.7.7 show that the C65/PVDF agglomerations filled the gap between the active materials in the slurry-casted electrode, which could slow the electrolyte diffusion. In the dry-printed electrode, the bridge-like C65/PVDF clusters can leave a more open interface for electrolyte diffusion and the thin film coating can protect the particle-electrolyte interface. The SEM images could also prove the microstructure morphology models. The coating on the surface of NMC 622 particles could enable a stable materials-electrolyte interface and enhance the cycling stability.

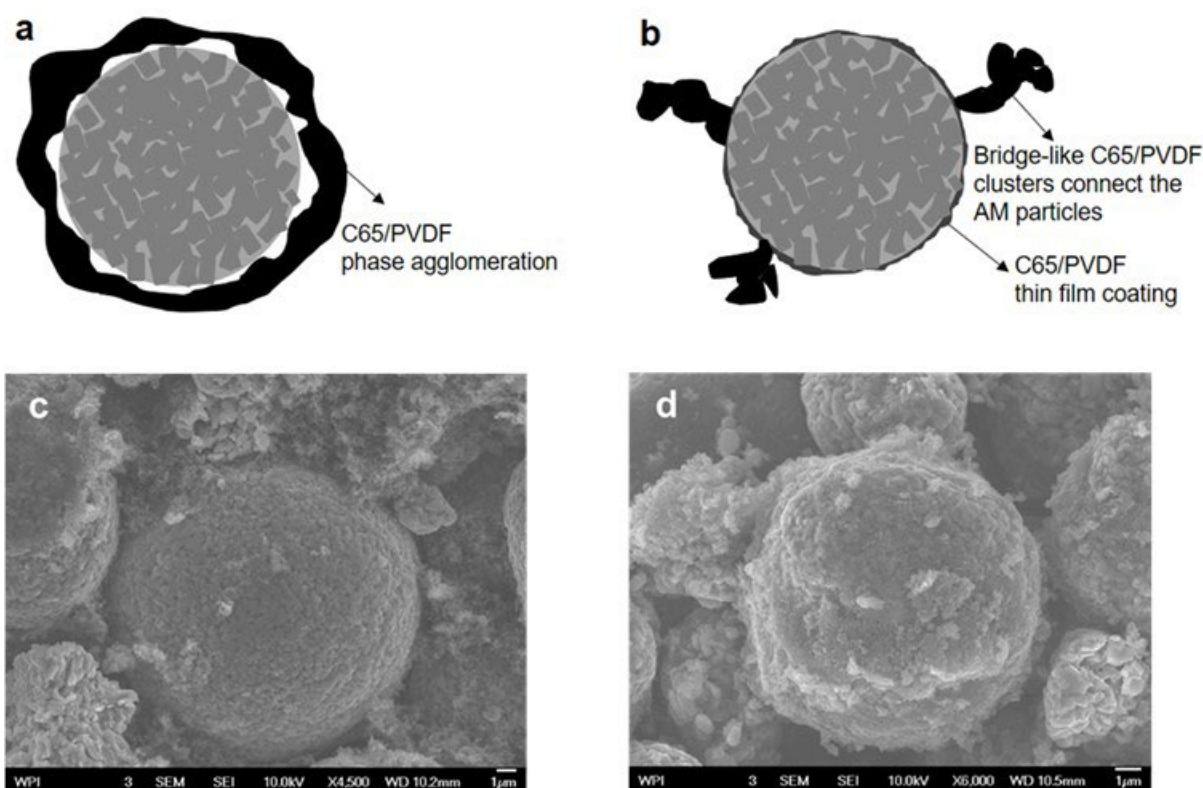


Figure I.7.7 Microstructure schematics of (a) slurry-cast electrode, (b) dry-printed electrode. Microstructure SEM images of (c) slurry-cast electrode, (d) dry-printed electrode

These structural difference enables the electrode level properties. Figure I.7.8 shows the tortuosity of dry-printed and slurry-casted electrodes. The dry-printed cathode has much lower tortuosity than the slurry-casted electrode. The more open pores in the dry-printed electrodes could provide a shorter diffusion path for the electrolyte, which results in much lower tortuosity. The dry-printed anode shows ~12.5% lower tortuosity than the slurry-casted anode. The closer stacking of the plated-like graphite particles could lead to less open pores space than the spherical NMC particles.

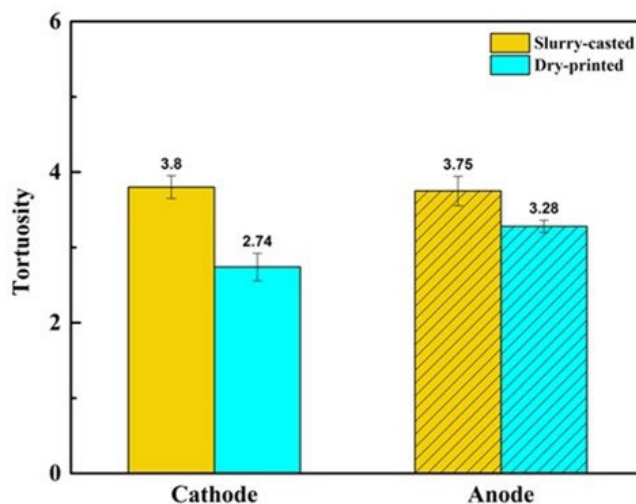


Figure I.7.8 Tortuosity of dry-printed and slurry-casted cathode/anode

Cell fabrication and testing

To evaluate the dry electrodes single layer pouch cells, roughly 45 mAh when graded at C/3, are being used by the project team. To baseline the performance wet electrodes were also prepared with same active material and loadings using a roll-to-roll die coater. By having wet coated electrodes for anode and cathode (noted as wet cathode and wet anode, respectively on figures) it is possible to determine each electrodes benefit individually, and also see how a cell built using only dry coated electrodes fares. In Figure I.7.9 the comparison of the ratio of charge possible before hitting V_{max} in the constant current portion of charge is shown. The results indicate that there is benefit to the dry electrodes in all single layer pouch cell test versions, but the greatest benefit comes from combining a dry coated anode that has 2 layers differing in porosity with a dry coated cathode.

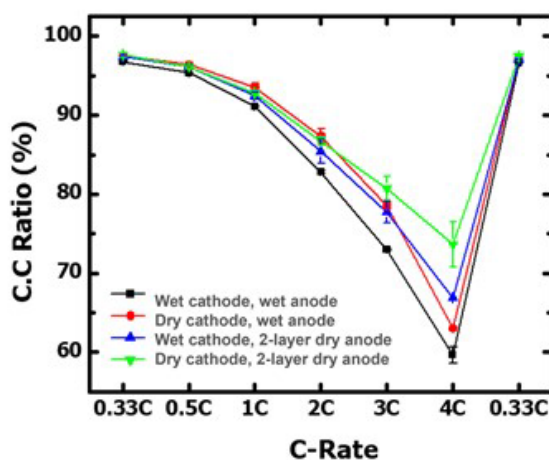


Figure I.7.9 Rate comparison of single layer pouch cells made using differing combinations of dry or wet coated electrodes. Single layer pouch cells were tested from 2.7-4.3V with CCCV (CV=15-min)/0.33CD

The dry electrode batches were also evaluated via cycling of single layer pouch cells under 1CCCV/1CD conditions with a periodic 0.33C reference cycle. From the results it appears cycling is comparable with cells using wet coated electrodes, which is important cause it means the electrode energy storage physics are not drastically changing, nor is the reactivity of the electrode interfaces suddenly different when preparing cells without the use of NMP. In Figure I.7.10 the cycle progress of single layer pouch cells was tested; and retention was similar, even better in some tests, than the wet coating electrode control.

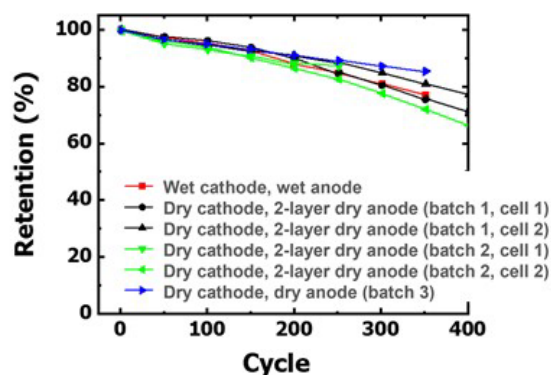


Figure I.7.10 Retention of the single layer pouch cells made using dry or wet electrodes

Conclusions

In summary, guided by modeling, both anode and cathode have been successfully fabricated with dry manufacturing. The electrodes have lower tortuosity compared to slurry casted electrodes, which leads to higher rate performance with single layer pouch cells. The cycle life of single layer pouch cells with dry electrodes are comparable with those with slurry casted electrodes. Detailed SEM images show that a coating is formed on the surface of NMC 622 particles could enable a stable materials-electrolyte interface.

References

1. Bitsch, B., J. Dittmann, M. Schmitt, P. Schaffer, W. Schabel, and N. Willenbacher. 2014. "A novel slurry concept for the fabrication of lithium-ion battery electrodes with beneficial properties." *Journal of Power Sources* no. 265:81–90. doi: 10.1016/j.jpowsour.2014.04.115.
2. Ruffo, R., C. Wessells, R. A. Huggins, and Y. Cui. 2009. "Electrochemical behavior of LiCoO₂ as aqueous lithium-ion battery electrodes." *Electrochemistry Communications* no. 11 (2):247–249. doi: 10.1016/j.elecom.2008.11.015.
3. Doberdo, I., N. Löffler, N. Laszczynski, D. Cericola, N. Penazzi, S. Bodoardo, G. T. Kim, and S. Passerini. 2014. "Enabling aqueous binders for lithium battery cathodes - Carbon coating of aluminum current collector." *Journal of Power Sources* no. 248:1000–1006. doi: 10.1016/j.jpowsour.2013.10.039.
4. Wixom, Michael. 2013. *Dry Process Electrode Fabrication 2013* [cited 13 May 2013]. Available from http://energy.gov/sites/prod/files/2014/03/f13/es134_wixom_2013_p.pdf.
5. Zheng, Honghe, Jing Li, Xiangyun Song, Gao Liu, and Vincent S. Battaglia. 2012. "A comprehensive understanding of electrode thickness effects on the electrochemical performances of Li-ion battery cathodes." *Electrochimica Acta* no. 71:258–265. doi: 10.1016/j.electacta.2012.03.161.
6. Gallagher, K. G., S. E. Trask, C. Bauer, T. Woehrle, S. F. Lux, M. Tschech, P. Lamp, B. J. Polzin, S. Ha, B. Long, Q. L. Wu, W. Q. Lu, D. W. Dees, and A. N. Jansen. 2016. "Optimizing Areal Capacities

through Understanding the Limitations of Lithium-Ion Electrodes." Journal of the Electrochemical Society no. 163 (2):A138–A149.

7. Bae, C. J., C. K. Erdonmez, J. W. Halloran, and Y. M. Chiang. 2013. "Design of battery electrodes with dual-scale porosity to minimize tortuosity and maximize performance." Advanced Materials no. 25 (9):1254–8. doi: 10.1002/adma.201204055.
8. Sander, J. S., R. M. Erb, L. Li, A. Gurijala, and Y. M. Chiang. 2016. "High-performance battery electrodes via magnetic templating." Nature Energy no. 1.

Acknowledgements

The development team (WPI/TAMU/Rice/Microvast) would like to thank the following for all of the help, advice, support and suggestions: USABC program manager Lamuel David (Stellantis) and USABC work group members Renata Arsenault (Ford), Meng Jiang (GM), Brian Cunningham (DOE), and David Robertson (ANL).

COVID-19 Impacts

The progress of the project has been impacted by COVID-19.

II Processing Science & Engineering

II.1 Processing Next Generation Li-ion Battery Cathode Materials (ANL)

Ozge Kahvecioglu, Principal Investigator

Argonne National Laboratory
9700 South Cass Avenue
Lemont, IL 60439
E-mail: okahvecioglu@anl.gov

Peter Faguy, DOE Technology Development Manager

U.S. Department of Energy
E-mail: Peter.Faguy@ee.doe.gov

Start Date: October 1, 2020

End Date: September 30, 2021

Project Funding: \$800,000

DOE share: \$800,000

Non-DOE share: \$0.00

Project Introduction

Nickel-rich cathode materials with low or no cobalt content are critical for the development of less expensive batteries with higher energy densities that meet DOE goals while limit dependences of the country from foreign sources. Although the theoretical capacity of lithium-nickel oxide (LiNiO₂, LNO) is high, the rapid capacity fade makes the material unusable for practical applications. Thermal stability and capacity fade are common issues when the nickel content in the cathode active material increases to 80% or above. The first step to understand the phenomenon and ultimately to solve the problem is to gain an atomic level understanding of the role of nickel substitutes (e.g., cobalt, manganese, aluminum, and the like) in pure LiNiO₂ (LNO) that stabilize the material. Materials of various structures with a variety of percentages and combinations of elements are needed for the study. There are no reliable sources of such materials available to the research community. The availability of hard-to-make, on-demand materials is critical to battery research community to explore and progress toward developing advanced LIBs chemistry. In a close collaboration with other partners in the program, the Process R&D and Scale Up Group at Materials Engineering Research Facility (MERF) at Argonne National Laboratory is utilizing non-traditional, advanced co-precipitation synthesis methods, such as the Taylor Vortex Reactor (TVR), to produce large quantities of uniformly high-quality materials. Samples of the materials are distributed to collaborating research groups for investigation and performance evaluation. By evaluating new precipitation technologies, the Processing Next Generation Li-ion Battery Cathode Materials project is establishing new platforms for scalable and economically feasible manufacturing of advanced cathode materials. The results presented in this report demonstrate that the MERF's developed TVR technology is capable of producing high quality materials with the desired composition and morphology at scale for ultimate deployment in full-scale manufacturing. The development and employment of the TVR platform by the project makes advances in new materials synthesis and deployment faster than ever before.

Objectives

The multifaceted objective of the program is to provide the research community with materials they design and want to investigate and therefore ascertain the key missing link between discovery of advanced active battery materials, evaluation of these materials, and ultimately high-volume manufacturing of the selected targets to reduce the risk associated with their commercialization. We perform systematic process and material engineering research to develop cost-effective customized synthesis and to produce sufficient quantities of high-quality target materials by optimizing process parameters tailored to specific material compositions, evaluating material purity profiles, and applying emerging manufacturing technologies to address challenges associated with manufacturing of advanced materials. The technical targets of this program are the development of customized synthesis

processes for each material selected, scaling up to multi-kilogram quantities with reproducibility under rigorous quality control, and evaluation of emerging manufacturing technologies to assist fundamental research and to reduce the commercialization risk of newly invented active battery materials.

Approach

Over the past three years, the advantages of utilizing an emerging synthesis technology, the Taylor Vortex Reactor (TVR), for the production of cathode precursors for lithium-ion batteries, were demonstrated. This innovative reactor has a cylindrical rotor and tremendous Taylor vortices in the annulus. It produces homogenous micro-mixing, and high mass and heat transfer, enabling a high degree of uniform supersaturation eliminating local concentration and temperature gradient. This results in faster kinetics and denser particles with minimal optimization. The TVR continuously produces spherical precursor particles with a narrow particle size distribution, which is critical to achieve high-quality battery materials, and now it is the preferred platform for rapid production of new chemistries that are not commercially available. While supporting the Cathode Materials for Next Generation Lithium-Ion Batteries program (Deep-Dive: BAT251-253), a total of 10 different cathode chemistries were synthesized at a 1L TVR, more than 300 g scale each. These chemistries were scaled up in 10L TVR, using 1L TVR optimized conditions which showed similar qualities validating the smooth scalability of the TVRs. Some of the more promising candidates were reproduced in 10L TVR to generate kilogram quantity of material.

Within the scope of the project, different scales of TVR operations were used in the reporting period to produce materials in support of basic R&D groups at national laboratories, universities, and startup companies with the new, scaled up or reproduced cathode chemistries from FY19 and FY20, such as LiNiO_2 (LNO), $\text{LiNi}_{0.95}\text{Co}_{0.05}\text{O}_2$, $\text{LiNi}_{0.95}\text{Mn}_{0.05}\text{O}_2$, $\text{LiNi}_{0.95}\text{Mg}_{0.05}\text{O}_2$, $\text{LiNi}_{0.95}\text{Co}_{0.025}\text{Mn}_{0.025}\text{O}_2$ (NMC), $\text{LiNi}_{0.90}\text{Co}_{0.05}\text{Mn}_{0.05}\text{O}_2$ and $\text{LiNi}_{0.60}\text{Co}_{0.20}\text{Mn}_{0.20}\text{O}_2$. Among those, LNO, $\text{LiNi}_{0.90}\text{Co}_{0.05}\text{Mn}_{0.05}\text{O}_2$, and $\text{LiNi}_{0.60}\text{Co}_{0.20}\text{Mn}_{0.20}\text{O}_2$ were reproduced to be used extensively in coating and doping studies within the Deep-Dive program. All LNO-based chemistries were further fabricated into electrodes by the Cell Analysis, Modelling and Prototyping (CAMP) Facility and were distributed internally and externally with other National Laboratories.

Processing related discrepancies for the Ni-based cathode materials using different co-precipitation reactor types as well as different calcination furnaces were also investigated during the last year. In collaboration with the Deep-Dive cathode synthesis subgroup, we investigated the co-precipitation reactions using 1 & 10L TVR (MERF) vs 4L CSTR (subgroup) for the new chemistry, $\text{Ni}_{0.95}\text{Mn}_{0.05}(\text{OH})_2$.

Within the last year, we have also started the synthesis of Mn-rich NMC compositions with and without Al-doping through a hydroxide co-precipitation route.

Continuous support of the “commercially non-available chemistries, morphologies and/or particle sizes” for researchers across the Nation by providing a wide-range of different chemistries, was continued.

Since FY19, MERF has been producing a wide range of LNO-based cathode chemistries using TVRs and has been sharing all these compositions as they become available to the interested parties across the Nation.

Remaining challenges in the manufacturing of the LNO-based chemistries are concentrated around the calcination process, where the Li-ratio, calcination temperature and atmosphere, furnace type, calcination recipe (heating/cooling rates) all need strict adjustment for each chemistry and these parameters are subjected to change for the derivatives of LNO-based chemistries (ranging amounts of Co/Mn). Smaller scale calcinations of LNO-based chemistries showed good performances under the electrochemical tests (Deep-Dive protocols); however, the same performances haven't been obtained when the calcination amounts were increased from 5 g level to ~50-gram levels. This problem was attributed to the decrease of O_2 penetration depths as the bath of loading were increased, affecting the Li-diffusion homogeneity in the bath, where a gas delivery line fixture/mechanism is needed to be designed for the scalable industrial furnaces.

Results

Materials in Support of “Deep-Dive into Next Generation Cathode Materials” (BAT251&BAT252&BAT476&BAT030)

The majority of our efforts were spent on fundamental understanding of calcination challenges for the LNO-based materials. It is fair to say that we have an understanding on how to synthesize the hydroxide precursors of the best performing LNO-based materials. The optimal co-precipitation process parameters, which are specific to the TVR reactions made at MERF, are available to the US battery community. It is also fair to say that the calcination processes and related scale-up challenges for these materials still require extensive studies to be made. Lithium kinetics are strongly dependent on the hydroxide precursor’s physical properties (e.g., porosity, particle size & distribution, density, morphology) for the same composition within. One of MERF’s responsibilities is to consistently provide high quality, hydroxide precursors with a wide range of chemistries while keeping all physical properties similar as the composition changes. This would allow the basic R&D scientists to compare the materials solely based on ranging Ni, Mn and Co ratios.

Effect of calcination temperature and atmosphere

The manufacturing of LNO-based materials are sensitive to processing conditions which can hinder their true performances unless strict process measures are taken. In the past year, different calcination conditions were applied to the TVR made $\text{Ni}(\text{OH})_2$ materials (see Figure II.1.1); where an optimal lower calcination temperature (665°C) with 100% O_2 partial pressure showed the best capacity retention (94% at 100th cycle). This material preserved its spherical morphology and its secondary particle sizes while displaying smaller primaries. The primary particle (PP) growth is known to be closely correlated with the lithium ratio and applied calcination temperature. When the Li-ratio (stoichiometric; $\text{Li}:\text{TM}=1$) and calcination temperature are kept the same, oxygen partial pressure becomes the most effective parameter in the PP growth. In other words, 100% O_2 atmosphere resulted in smaller primaries, perhaps the main reason of higher rate capability and capacity retention when compared to varying O_2 partial pressures.

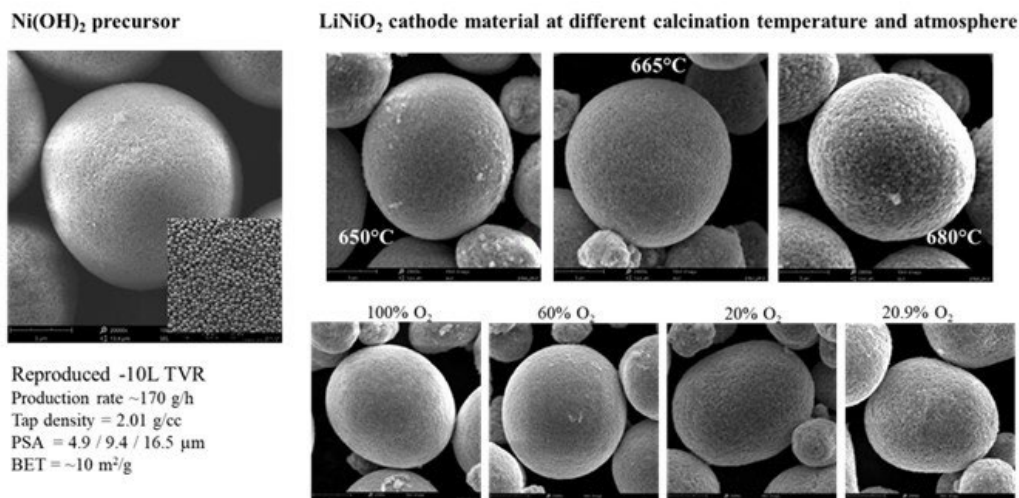


Figure II.1.1 Reproduced $\text{Ni}(\text{OH})_2$ in 10L TVR displays spherical and dense morphology (left). Top right row SEMs show the morphologies of LNO particles calcined at different temperatures under pure O_2 atm and bottom row shows the LNO calcined at 665°C under varying O_2 percentages.

Comparison of different co-precipitation reactors and calcination furnaces

Cathode materials manufacturing is one of the most costly processes, not only because it requires expertise and substantial amounts of critical materials but also it is time-consuming, and it generates lots of waste. There is a great investment in this field for the transitioning to continuous processes to eliminate batch-to-batch variability which also reduces the amount of waste generation. Over the past 6 years, MERF has been utilizing TVRs at different scales to address the most time-consuming step in the cathode manufacturing; the

continuous co-precipitation. Due to its unique flow pattern (Taylor Vortex Flow) inside, these reactors can achieve steady-state conditions faster, which reduces the residence time (and so the reaction time) increasing yield efficiency. In collaboration with the Deep-Dive cathode synthesis subgroup, we investigated the co-precipitation reactions using 1 & 10L TVR (MERF) vs 4L CSTR (subgroup) for the new chemistry, $\text{Ni}_{0.95}\text{Mn}_{0.05}(\text{OH})_2$. While in both TVR reactors the residence time was kept at 4 hours, this was 12 hours for 4L CSTR runs due to the nature of the reactor design. This translates into faster reactions at TVRs vs slower reaction at CSTR; allowing the collection of product sooner and generating less waste for the TVRs. The other reaction parameters, such as temperature, pH, rotation speed, TM: NH_3 ratio and etc., were kept same for all reactors. In our earlier optimization studies (FY19 & FY20) we had shown that the Ni-based hydroxide co-precipitation reactions required high pH conditions ($\text{pH} = 11.7 \sim 12.4$) to obtain the highest possible tapping density with the lowest possible porosities. In this comparison study, low pH conditions ($\text{pH} = 10.9 \sim 11.0$) were used due to the limitation of CSTRs. High pH applications in CSTR require strict adjustments for the rest of the reaction parameters to get spherical and isolated, well-packed secondary particles at/at/above $8\mu\text{m}$; otherwise, the particles are out-of-sphericity and don't pack together, but rather pulverize in the slurry at (sub)-micron sizes when using $\text{pH} \geq 11.5$. The resultant hydroxide precursors from both processes (with identical conditions, except the residence time), were similar in terms of tapping density ($\sim 1.65 \text{ g/cc}$) which were low due to the low pH application discussed above.

The synthesized hydroxide precursors from all reactors were processed into cathode active oxides using a regular laboratory type box furnace and a tube furnace at the same conditions. The results were two-fold: First, all the tube furnace calcinations outperformed the box furnace calcinations. Second, all the TVR-made materials outperformed CSTR-made materials at all identical conditions screened. Some of these results are displayed in Figure II.1.2; where the top row shows the nodular morphologies of a CSTR-made precursor and its cathodes obtained at two different calcination furnaces; and the middle row displays the bi-modal, spherical TVR-made material. Figure also displays the results of the Deep-Dive (RNGC) specific electrochemical protocols and the capacity retention comparison at the bottom row. This study shows the importance of applying optimal processes for each of the major steps in cathode active materials manufacturing, to exploit the true/best performances of one particular chemistry. More diagnostic studies are being reported by the collaborators (BAT251&BAT252&BAT476) for this material.

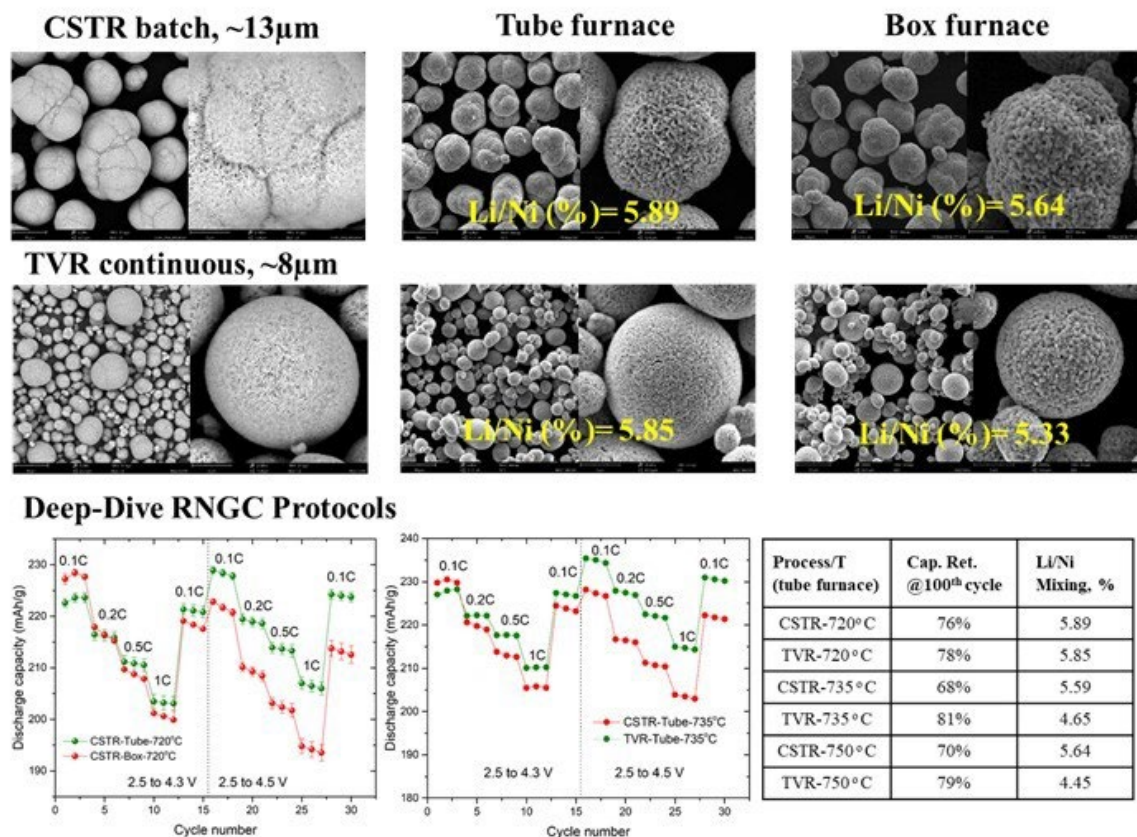


Figure II.1.2 Comparison of CSTR vs TVR processing and different calcination furnace applications

After the preliminary co-precipitation reactions, we have optimized this composition at high pH conditions (pH = 11.9) in the 10L TVR and increased the tapping density of $\text{Ni}_{0.95}\text{Mn}_{0.05}(\text{OH})_2$ from 1.65g/cc (pH = 10.9) to 2.0g/cc (pH = 11.9). Similarly, the surface area of the optimized hydroxide material decreased from 13.1 m²/g to 5.5m²/g, as its tapping density was increased. This material is now under calcination optimization & scale-up and in the queue for the CAMP electrode fabrication.

A similar optimization study was made to the $\text{Ni}_{0.95}\text{Co}_{0.025}\text{Mn}_{0.025}(\text{OH})_2$ material using three different pH conditions (pH = 11, 11.4 and 11.9). An increase in reaction pH resulted in higher tapping densities (~1.7 g/cc → 2 g/cc) and lower surface areas (~15m²/g → 9m²/g) for this composition without compromising the spherical morphology (Fig. I.2.C.3; left). Higher pH conditions also displayed bi-modal particle size distribution, as similar to the other Ni-based compositions that were made in the TVRs. These materials were then calcined at different calcination temperatures (700°C and 730°C) where the lower calcination displayed better capacity retention, especially in the upper cut-off voltage region as shown in Figure II.1.3.

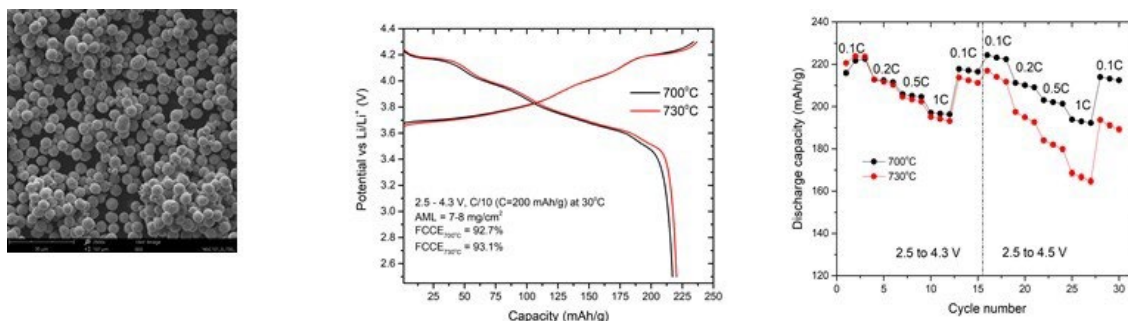


Figure II.1.3 SEM morphology (left), voltage profiles (middle) and rate tests (right) of $\text{LiNi}_{0.95}\text{Co}_{0.025}\text{Mn}_{0.025}\text{O}_2$ materials calcined at different temperatures. Electrochemical tests (BAT476) are specific to Deep-Dive program (Half cells, two cells average)

Preliminary Mn-rich NMC cathode material synthesis

Over the past year, MERF started synthesizing a new composition, $\text{Ni}_{0.60}\text{Mn}_{0.35}\text{Co}_{0.04}\text{Al}_{0.01}(\text{OH})_2$. The detailed recipe of the co-precipitation reaction was retrieved from Dr. Anh Vu and translated to the 1L TVR, without changing the reaction parameters, except the residence time was kept at 4 h (10-12 h for CSTR application). The reaction pH was fixed at 11.2 to simulate the same conditions with the CSTR application. The resultant hydroxide precursor had a nodular morphology with Al effectively being incorporated (Figure II.1.4; top row) having relatively low tapping density valued at ~ 1.6 g/cc. This preliminary material cycled at a lower capacity (Figure II.1.4; bottom right) compared to the optimized CSTR product. One of the reasons was, even if the same conditions (same reactant molarities, TM: NH_3 ratio and etc.) were applied, the Al mol ratio in the TVR-made product was twice the CSTR product. In CSTR applications, it was observed that approximately half of the aluminum is lost in the waste stream in the co-precipitation process while the other half goes into the structure; where the Al-solution molarity is typically increased twice to compensate this Al loss, prior to running the reaction. Using same molarities in TVR, all aluminum was incorporated in the structure making Ni/Al ratio smaller compared to CSTR product. The target composition was thus altered to $\text{Ni}_{0.58}\text{Mn}_{0.36}\text{Co}_{0.04}\text{Al}_{0.02}(\text{OH})_2$.

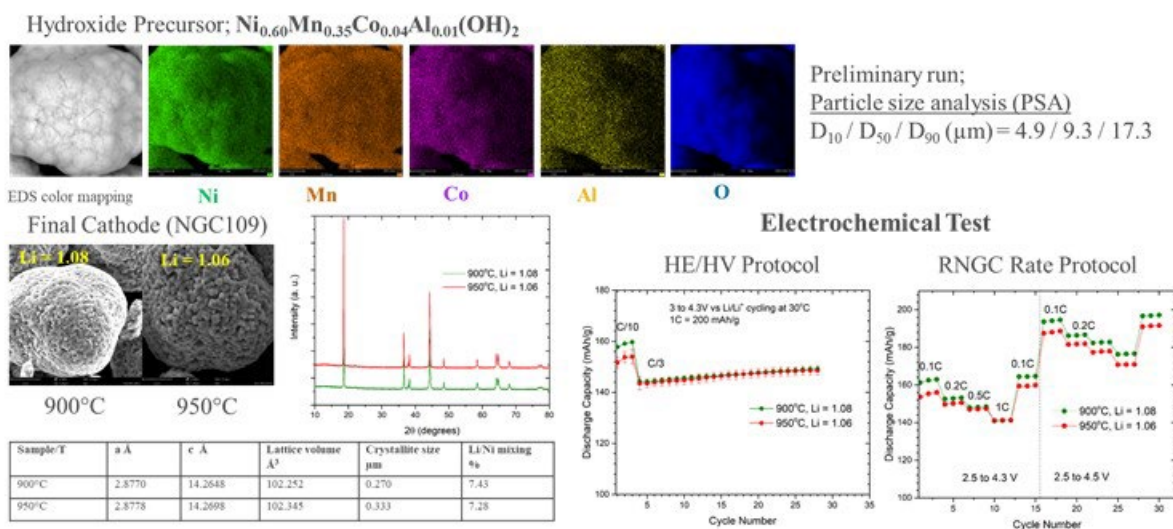


Figure II.1.4 Preliminary synthesis results for the Al-doped Li/Mn-rich hydroxide precursor and its cathode. EDS color mapping shows effective Al-incorporation to the structure during co-precipitation process. SEM shows the similar secondary particle morphologies with increasing primary particle sizes as the calcination temperature increases. Electrochemical tests (BAT476) are specific to Deep-Dive program.

We further applied high pH conditions (11.9) and increased the tapping density of the hydroxide precursor from 1.56 g/cc to 1.88 g/cc and the surface area for the latter was 4.6 m²/g; while keeping the overall PSA

distribution similar to the prior run. However, the morphology wasn't improved to a spherical morphology, rather the nodular morphology was preserved. We believe the aluminum presence in the co-precipitation process was the effective component for this nodular morphology formation due to the fast precipitation of aluminum ions creating tremendous amount of nucleation sites forming irregular particle growth at the high pH conditions.

In an approach to understand this occurrence, we applied the same reaction conditions without Al-doping in the co-precipitation process to observe the morphologies. The morphology of the resultant precursor's morphology was greatly improved having bi-modal PSA (Figure II.1.5 (a)) with increased tap densities to slightly above 2.1 g/cc, while the surface area was decreased at least by twice to 2.09 m²/g compared to the Al-doped version of the same composition. Occasional particle cracking, especially for the larger particles were also observed, which was probably due to the high shear forces as a result of high rotational speed (900 rpm) in the TVR. Further, we have applied a low temperature heat treatment process to convert this hydroxide precursor to oxide (prior to lithiation) and observed the cross-sectional structure of the pretreated precursors (Figure II.1.5 (b)). As commonly observed for the hydroxide precursor pretreatments, the material's surface area was increased by $\sim 10 \times$ (20.5 m²/g) and the tap density was also increased to 2.3 g/cc after the conversion process.

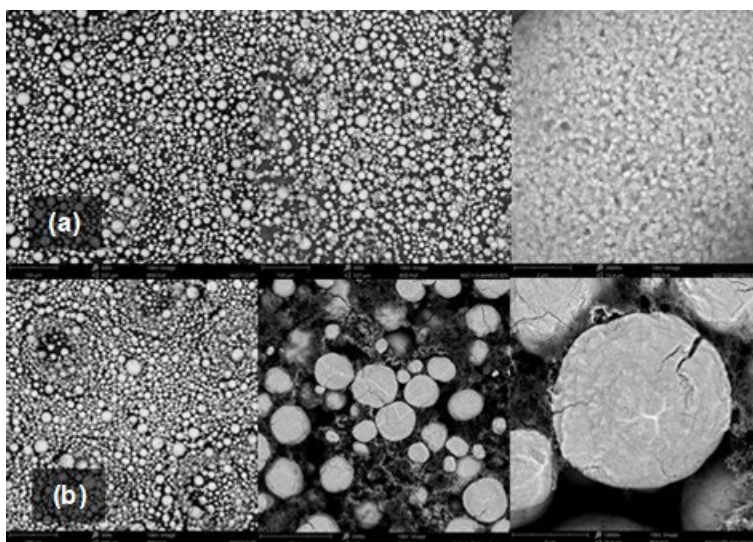


Figure II.1.5 (a) Morphologies of the Mn-rich NMC hydroxide precursor without Al-doping (left) and its cathode (tube furnace, under O₂ atm by Dr. Anh Vu) (middle and right). (b) Bulk (left) and cross-sectional (middle and right) morphologies of pretreated hydroxide precursors showing dense interior with ranging levels of particle cracking particularly for the larger particles.

Materials in Support of DOE-VTO Funded Projects (BAT183&BAT402&BAT377)

We have continued collaborating with Brookhaven National Laboratory (BNL) under the Process Science and Engineering Program focusing on “synthesis by design” (BAT183). In the past year, MERF has provided more materials as needed, such as Ni(OH)₂, and Ni_{0.8}Co_{0.1}Mn_{0.1}(OH)₂ (synthesized at 10L TVR) and shared with the collaborators at BNL for the structural and morphological evolution studies during the sintering process for both chemistries. This collaboration also has the multi-scale simulation effort focusing on lithiation driven morphology evolution (BAT402) where the impact of the initial morphology/porosity are studied for designing the precursor fabrication and sintering processes. Detailed diagnostic studies for the TVR-made materials can be found in BAT183 & BAT402. Future directions for this collaboration include investigating the lithiation process for the Ni-based compositions, such as Ni_{0.95}Co_{0.025}Mn_{0.025}(OH)₂, Ni_{0.95}Mn_{0.05}(OH)₂, Ni_{0.95}Co_{0.05}(OH)₂ as well as Ni(OH)₂ with different particle sizes and porosities.

Last year, MERF provided high quality β -Ni(OH)₂ material that is not commercially available for the RECELL program (BAT377). Upon request, β -Ni(OH)₂ material was synthesized in 10L TVR. This material was used as an intermediate to convert low-Ni cathode into high Ni-cathodes via hydrothermal processing.

Materials in Support of Battery R&D Community

In FY21, we continued supporting researchers at the Northwestern University. Upon request, LiNiO₂ (D_{50} = ~10 μ m) was synthesized using 10L TVR for the proprietary graphene coating methodology (to suppress the O1-O3 stacking faults) that was invented at the Northwestern University. This collaborative work included 8 institutes and 13 researchers' effort which resulted in a journal article published in *Advanced Materials*. Over the past year, MERF also provided Ni_{0.6}Co_{0.2}Mn_{0.2}(OH)₂ and Ni_{0.8}Co_{0.1}Mn_{0.1}(OH)₂ (~500-650 g/each) precursor materials to Chris Johnson (ANL) for his project.

Conclusions

MERF's experimental active cathode materials process R&D and scale-up program assists the battery research community, allows for a comprehensive evaluation of new materials by industrial laboratories, and supports basic research. In fiscal year 2021 the program provided several new and/or reproduced, not commercially available materials. Samples of high, uniform-quality materials were distributed for further evaluation and research. A total of 12 different cathode active material compositions have been synthesized using 1L TVR, and some of the material with higher quantity demand were scaled up in 10L TVR. All the materials produced at MERF were shared with the collaborators either in the form of precursor or active cathode material, ranging from 100 to 1,000 g per sample.

Key Publications

1. Kyu-Young Park, Yizhou Zhu, Carlos, Carlos G. Torres-Castaneda, Hee Joon Jung, Norman S. Luu, Ozge Kahvecioglu, Yisuel Yoo, Jung-Woo T. Seo, Julia R. Downing, Hee-Dae Lim, Michael Bedzyk, Chris Wolverton, Mark C. Hersam, "Realizing high voltage operation of LiNiO₂ cathode for lithium-ion batteries", *Advanced Materials*, Nov 3, 2021 (accepted article), <https://doi.org/10.1002/adma.202106402>
2. Shankar Aryal, Jessica L. Durham, Albert L. Lipson, Krzysztof Z. Pupek, Ozgenur Kahvecioglu, "Roles of Mn and Co in Ni-Rich Layered Oxide Cathodes Synthesized By Utilizing a Taylor Vortex Reactor", *Electrochimica Acta*, Vol 391, Sept 2021, <https://doi.org/10.1016/j.electacta.2021.138929>
3. Shankar Aryal, Jessica L. Durham, Albert L. Lipson, Krzysztof Z. Pupek, Ozgenur Kahvecioglu, "In-situ and Operando Electrochemical Investigation of Cobalt-free, Nickel-rich Layered Oxide Cathode for Next Generation Lithium-Ion Batteries" *2020 MRS Spring/Fall Meeting and Exhibit*, November 27- December 4, 2020, Virtual
4. Shankar Aryal, Krzysztof Pupek, Ozgenur Kahvecioglu, "Emerging Manufacturing Technologies and Characterization of Next Generation LIB Materials" *Battery Congress 2020 Livonia*, September 23-24, 2020, Virtual

Acknowledgements

Dr. Shankar Aryal, Nick Sovronec, Gerald Jeka, Andrew Turczynski, Dr. Carrie Siu and Dr. Kris Pupek are greatly acknowledged for their assistance in the synthesis and characterization studies. Dr. Jason Croy and Dr. Anh Vu are acknowledged for providing the Al-doped Mn-rich NMC composition synthesis recipe and tube furnace calcinations for the TVR-made materials. Dr. Jihyeon Gim and Dr. Jinhyup Han are acknowledged for small scale tube furnace calcinations for the TVR-made Ni-based compositions (LNO) and CSTR application for the Ni_{0.95}Mn_{0.05}(OH)₂ material for comparative studies. We also thank Dr. Adam Tornheim for the electrochemical testing protocols which were used in validating the TVR made materials throughout this report.

II.2 Novel Processing Approaches for LLZO (ANL)

Joseph Libera, Principal Investigator

Argonne National Laboratory
9700 South Cass Avenue
Lemont, IL 60439
E-mail: jlibera@anl.gov

Peter Faguy, Technology Development Manager

U.S. Department of Energy
E-mail: Peter.Faguy@ee.doe.gov

Start Date: October 1, 2020

End Date: September 30, 2021

Project Funding: \$400,000

DOE share: \$400,000

Non-DOE share: \$0

Project Introduction

Aerosol manufacturing technology holds the potential of commodity scale production of energy storage materials in powder form. Reduced liquid chemical waste and suitability for continuous operation are advantages aerosol processing has over competing liquid-based powder synthesis. Aerosol synthesis of powders falls broadly into several categories: (a) spray drying, (b) spray pyrolysis, (c) flame spray pyrolysis and (d) gas combustion synthesis. At the Argonne's MERF aerosol synthesis facility, modalities a–c are now active for materials research into energy storage materials.

Flame spray pyrolysis (FSP) is a materials synthesis technique that uses solution of organic and/or inorganic metal salts in flammable liquids. In the gas-to-particle mode (FSP-GP), the liquid solution is atomized using oxygen and combusted to atomic species from which particles condense and are collected in the exhaust filters. If the available combustion enthalpy is insufficient, particle formation follows the droplet-to-particle modality (FSP-DP), and the produced solids retain some history of the spray droplets.

Spray pyrolysis (SP) starts as in FSP by producing liquid droplets of metal salt solutions but not using combustible solvents. The droplet solvent is removed by evaporation in a tube furnace followed by solid state reaction of the dried particle to produce the desired solid materials. Optional addition of enthalpic components such as ethylene glycol or organic acids allows for exothermic support of the solid-state reactions.

In Spray Drying (SD) the drying of the droplets and subsequent solid-state reactions that characterize Spray Pyrolysis are decoupled and only the dried particles are collected to be separately solid state reacted in calcination furnaces. This technique allows for the exclusion of the spray solvent in the calcination step and enable controlled atmosphere calcination such as inert gas or pure oxygen.

At Argonne's MERF facility, these three modalities are used synergistically to produce a single target materials and thus gain greater understanding of the material apart from the process. In, general FSP-GP produces nano sized powder, while FSP-DP produces micron sized agglomerates of nano-sized primary particles. SP produces micron sized secondary particles consisting of sub-micron primary particles. SD produces micron particles of the constituent metal salts which following a separate calcination retain their particle characteristics. For the FSP and SP techniques we seek to optimize the process to produce ready to use particles in the proper phase purity. However, this can be thermodynamically prohibited by the gaseous environment in the processing reactors requiring separate calcination and or powder refinement. In the industrial setting, even these additional steps are amenable to continuous processing following continuous aerosol powder production.

Objectives

Develop Aerosol Manufacturing Technology as a manufacturing option for Li-ion battery active cathode phase and for solid electrolyte powder for use in conventional and solid state Li-ion batteries for the automotive sector. Obtain economically competitive protocols and recipes using the lowest cost precursor and solvent options. Produce optimized LLZO for separator and catholyte applications. Leverage the advantages of the atomically mixed nano-powder produced by FSP to access otherwise difficult to produce materials.

Approach

Solid state electrolyte (a) aluminum doped lithium lanthanum zirconium oxide Al-LLZO and energy storage materials (b) high Ni cathode active phases are the focus of development using multiple aerosol technologies. Aerosol synthesis is co-optimized with downstream calcination, powder refinement, and validation in battery test cells. Research is focused on the lowest cost precursors available in commodity scales, typically nitrates salts of the metals. Advanced concepts are explored that utilize unique powder morphology available only by aerosol processing.

The ANL MERF FSP reactor has features that allow for convenient and high throughput sample production. A glovebox design filter box allows for collection of nanomaterials and restoration of the filter media within 15 minutes of a run completion allowing for up to 6 generated and collected samples per workday. Material that deposits on the walls of the reactor does not significantly cross-contaminate from sample to sample. On a day-to-day basis, a clean-in-place brushing fixture allows for the combustion tube to be cleaned of wall deposits for changeover to new material systems further assuring no cross contamination between runs.

The ANL FSP facility has been designed to produce powder materials in an industrially relevant way using liquid spray (droplet) combustion which can produce materials at the highest possible rate compared to ultrasonic atomization or gas-fed precursor introduction. In order to best navigate the complexities of spray combustion, the ANL FSP facility has been provided with a suite of in-situ advanced diagnostics: (a) laser diagnostic system for Filtered Rayleigh Scattering (FRS) and Planar Laser Induced Fluorescence (PLIF) imaging of temperature and species distribution respectively, (b) Optical Emission Spectroscopy (OES) of the flame zone, (c) In-situ Raman spectroscopy and (d) particle size analysis using Scanning Mobility Particle Sizing (SMPS). Ex-situ diagnostics are also applied including (a) XRD and temperature programmed XRD, (b) BET-SA, (c) DSC-IR/MS, (d) electrochemical testing and electron microscopy (SEM and TEM).

Results

Progress Towards One-step Synthesis to Layered Phase Using FSP

An ideal outcome of SP or FSP is to directly attain the layered phase of NMC materials in one simple step which would avoid the expensive step of calcination furnaces in conventional cathode manufacture. While it is well known in the aerosol field that the normal behavior in SP or FSP is the formation of a mixture of TM rock salt and lithium hydroxide and/or carbonate, this as-produced material does constitute a useful precursor for layered phase formation following conventional fixed bed calcination in a manner similar to co-precipitation methods. FSP was optimized to maximize the production of the layered phase and a detailed analysis shows that layered phase does occur with the FSP green powders along with spinel and rock salt phases in the proportions provided in Figure II.2.1. The best result was obtained by using the highest available solution enthalpy giving the hottest FSP flames. Further optimization requires moving beyond solution delivered enthalpy and the change in burner designs that could provide high reaction zone temperature.

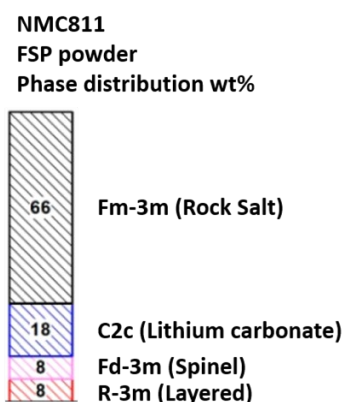


Figure II.2.1 Phase distribution in the immediate product of FSP of NCM811

Slurry Spray Pyrolysis (SSP) and Slurry Flame Spray Pyrolysis (SFSP)

Slurry based aerosol techniques were added to the ANL techniques portfolio. The slurry aerosols are generated by injecting a slurry solution into the conventional two-fluid nozzle of the FSP system using an ISCO slurry syringe pump which uses an active mixer in the syringe pump head to maintain a slurry of solution that is then transport to the nozzle within minutes, avoiding any settling issues. A requirement for good operation is preparing the solid as a nanoparticle suspension. Among the potential applications are (a) respray of FSP nano-green powders, (b) using a lower cost solid as a feed ingredient rather than a more expensive metal-organic compound (c) obtaining large and higher density particulate during droplet-particle modality of SFSP and (d) recycling of cathode powders by milling, blending, and respraying using SSP or SFSP. Preliminary tests were performed using P25 titania which showed that high density particulate from the nano-slurry of P25 in xylene/acetonitrile solvent were obtained as shown in Figure II.2.2(a). Figure II.2.2(b) shows an example of recycled cathode generated using SSP.

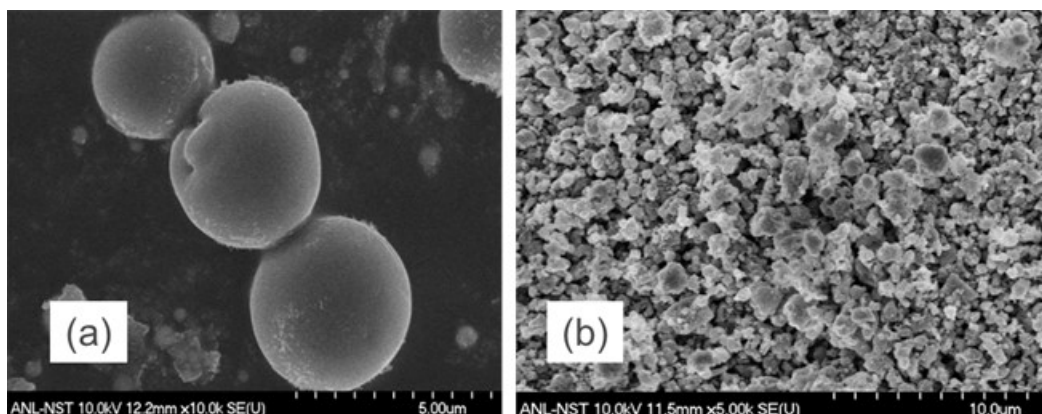


Figure II.2.2 Examples of Slurry Flame Spray Pyrolysis (a) SFSP of P25 titania in acetonitrile/xylene and (b) SFSP of ethanolic nano-milled NCM111

LLZO Green Powder Co-sintering with Cathode Powders

Co-sintering experiments were performed by mixing LLZO green powder and a conventional finished NCM523 cathode powder. The LLZO green powder was used as produced from Spray Pyrolysis and was ultrasonically mixed with the cathode powder at a 1:1 mass ratio. The mixed powders were pressed into pellets and then calcined at 750°C for 12 hours. Cross-sectional EDAX mapping was performed as shown in Figure II.2.3 and shows conformal wetting behavior of the LLZO that formed during the calcination. Xray diffraction analysis shown in Figure II.2.3 shows that LLZO cubic phase was attained and that the layered phase of the cathode was preserved and a minor impurity phases was also formed. Battery cell testing revealed that the LLZO coated cathode could not function as cathode due to the electrically insulating nature of the LLZO overcoat. However, it is expected that as the loading of LLZO is reduced, the electronic impedance will be reduced. Furthermore, the addition of an electronic conducting component to the dry powder mix would alleviate the issue. Altogether this experiment defines a pathway for an all-ceramic cathode that is facilitated by the wetting behavior of the LLZO formed in-situ from LLZO spray pyrolysis green powder.

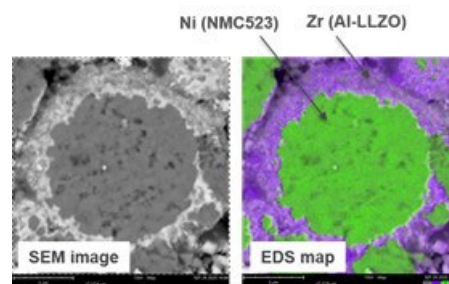


Figure II.2.3 Morphology of co-sintered Al-LLZO green powder + NC523

Synthesis of Lithium Lanthanum Bismuth Oxide (LLBZO) for Polymer Composite SSE

An alternate garnet electrolyte, LLBZO was synthesized using both FSP and SP. The obtained materials behaved very similar to Al-doped LLZO although the cubic phase was more consistently attained and at slightly lower calcination. The materials were milled to a D50 of 100 nm and provided to collaborators for

testing in garnet-PEO composite SE. The milling time required for the LLBZO was about one-half the time to mill similarly prepared Al-LLZO sample. One challenging aspect of the LLBZO materials was the persistence of some LZO from the green powder stage. X-ray diffraction analysis and PSD of the calcined and milled material are shown in Figure II.2.4.

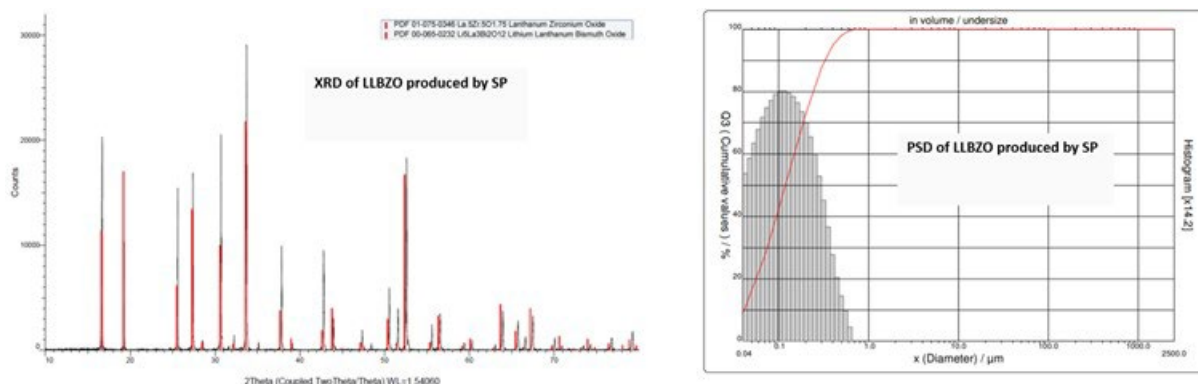


Figure II.2.4 Structure and morphology of Spray Pyrolysis produced Lithium Lanthanum Bismuth Zirconium oxide.

Conclusions

An important process route for one step synthesis to layered phase in FSP was identified and the results published. Exploration of alternate garnet SSE materials was pursued in the form of LLBZO for polymer composite SSE. The techniques portfolio of the ANL aerosol synthesis facility was expanded to include SSP and SFSP and several examples of their operation were performed. A new concept for all ceramic cathode manufacture based on the co-sintering of LLZO green powder and pristine cathode was demonstrated.

Key Publications

1. Villa, A., Verduzco, J.C., Libera, J.A. Marinero, E., “Ionic conductivity optimization of composite polymer electrolytes through filler particle chemical modification”. *Ionics* (2021)
2. Y Liang, K Ku, Y Lin, L Yu, J Wen, E Lee, J Libera, J Lu, “Process Engineering to Increase the Layered Phase Concentration in the Immediate Products of Flame Spray Pyrolysis”, *ACS Applied Materials & Interfaces* (2021).

Acknowledgements

The authors greatly appreciate the continuous support from David Howell and Peter Faguy of the U.S. Department of Energy’s Office of Vehicle Technologies. We also acknowledge the continuing collaboration and advice from Toivo Kodas and Cabot Corporation. We also acknowledge the contributions to this research by Kyojin Ku, E.J. Lee and Yujia Liang. We greatly acknowledge the expertise of Hack-Sung Kim in the development of the custom Raman spectrometer. We also acknowledge the Manufacturing Science and Engineering Initiative at ANL for providing support for the advanced diagnostics for the FSP unit. We also acknowledge the valuable insights for LLZO applications from Marca Doeff, Nancy Dudney and Ernesto Marinero.

II.3 Supercritical Fluid Processing of Battery Cathode Materials (ANL)

Youngho Shin, Principal Investigator

Argonne National Laboratory
9700 South Cass Avenue
Lemont, IL 60439
E-mail: yshin@anl.gov

Peter Faguy, DOE Technology Development Manager

U.S. Department of Energy
E-mail: Peter.Faguy@ee.doe.gov

Start Date: October 1, 2020
Project Funding: \$600,000

End Date: September 30, 2021
DOE share: \$600,000

Non-DOE share: \$0

Project Introduction

The development of rapid and reproducible manufacturing processes for cathode active materials is important for improving performance, increasing lifespan, ensuring safety, and reducing prices of lithium-ion batteries. Supercritical fluids technology, an emerging manufacturing process, can potentially provide materials for a high electrode density due to a robust single crystal without internal void fraction, an improved rate capability due to submicron particle size, cycling stability due to suppressed particle crack and resistance layer, and a facet-controlled particle, thus enabling the production of high-performance battery cathode materials. These material properties are the result of a higher degree of supersaturation and the formation of mono-crystalline oxide particles because of the reduced solubility of metal ions under supercritical hydrothermal conditions. The supercritical hydrothermal reaction is a practical and scalable route for mono-crystalline particle production. The morphology of cathode particles can be customized by changing reactants, solvents, reaction pressure, and reaction temperature. New mono-crystalline active battery materials with tunable particle size, composition distribution, and morphology are synthesized using the installed supercritical hydrothermal reaction system. These advanced battery materials, which are not yet commercially available and not achievable by traditional co-precipitation techniques, are distributed to collaborating research groups for investigation and performance evaluation.

Objectives

The aim of the project is to establish a flexible R&D capability of supercritical fluid reactions as an emerging manufacturing process for active battery materials. It is also one of the key roles to produce and provide mono-crystalline advanced battery materials with the desired particle size, composition distribution, and shape to support basic research. This process is one of the emerging manufacturing technologies with the goal of reducing the risks associated with the discovery of advanced active battery materials, market evaluation of these materials, and their commercialization with mass production. We perform systematic research to develop a cost-effective supercritical fluids process and to produce sufficient quantities of target materials with high quality by optimizing the synthesis parameters and material composition to assist fundamental research. Our effort deepens a basic understanding of the structure-property relationship of the materials and ultimately can contribute to selecting the desired target before the material would be deemed suitable and desirable for large scale manufacturing. This approach will reduce the commercialization risk of advanced battery cathode material and its synthesis process.

Approach

A multipurpose supercritical fluids reaction system was designed and built, and is currently fully operational, allowing the synthesis and surface treatment of battery cathode materials. Using the installed batch-type supercritical hydrothermal reaction system, the synthesis of various battery materials has been optimized, and

materials have been produced in quantities suitable for distribution for a comprehensive investigation. At this stage, the particle shape of the battery materials is controlled by changing reactants, solvents, additives, pH, reaction pressure, reaction temperature, reaction time, and stirring speed. Synthesis and evaluation of various battery materials are performed. The battery material selected for morphology control and optimization of synthesis conditions is nickel-rich NMC96-2-2 cathode material. 3D XRF tomography measurements are performed for the characterization of the synthesized mono-crystalline nickel-rich NMC96-2-2. In addition, research on the use of nano-indentation is conducted to measure particle strength through collaboration. We perform material characterization with particle cross-sectional mapping and Rietveld refinement of powder XRD and evaluate the electrochemical performance of the synthesized cathode particles.

Results

A polycrystalline cathode particle (Figure II.3.1 e) is a secondary particle, composed of primary particles, having a size of several hundred nanometers. This polycrystalline particle structure, commonly prepared via co-precipitation (Figure II.3.1 a) and calcination processes, has been challenged by poor cycle life and cell impedance rise. This is because the anisotropic volume change, during charge and discharge cycles, makes this polycrystalline material intrinsically exposed to grain-boundary fracture, which leads to rapid impedance growth and capacity decay. To mitigate the disadvantages of this polycrystalline particle structure, we successfully installed a hydrothermal batch reactor system (Figure II.3.1 b) and produced single-crystal Ni-rich cathode material (Figure II.3.1 f). This single-crystal cathode materials have many advantages and potential in terms of material structure and electrochemical performance such as micron-sized robust structure without particle cracks, high electrode density without internal void fractions, reduced surface area mitigating side reactions, facet-controlled morphology for faster Li transport, improved surface coating effects, and so on. During FY21, we conducted work to evaluate these potential characteristics of single-crystal NMC96-2-2.

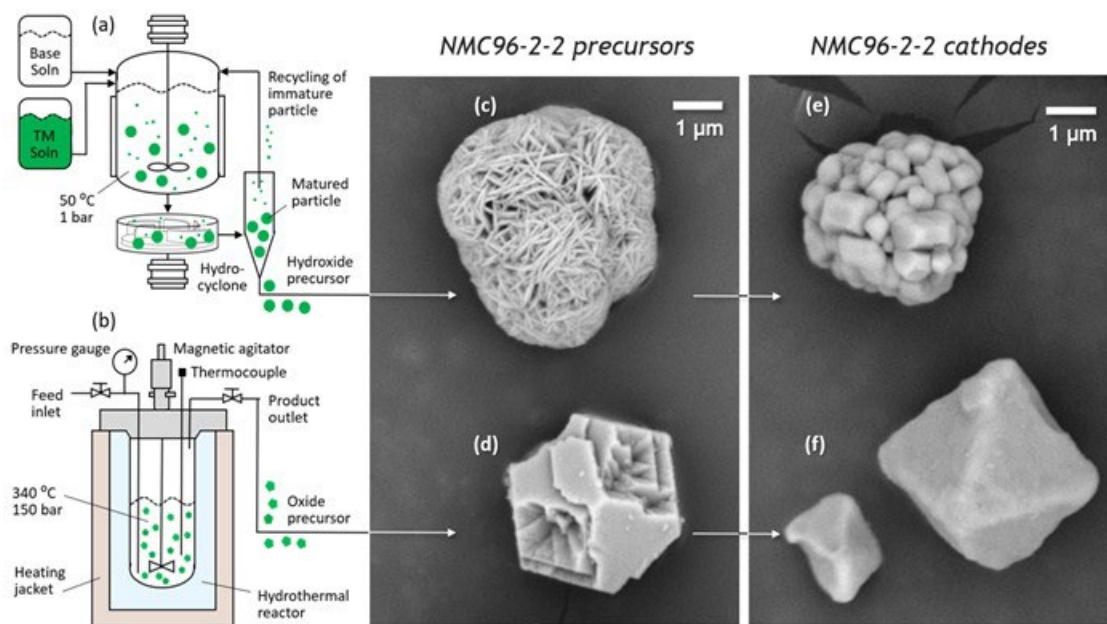


Figure II.3.1 Particle morphology of polycrystalline NMC96-2-2 and single-crystal NMC96-2-2

The hydrothermal single-crystal precursor (Figure II.3.2) was synthesized using a 4 L hydrothermal reactor and lithiated during heat treatment. In particular, we put a lot of effort into optimizing the synthesis process of single-crystal hydrothermal precursors. As a result, single crystals with size ranging from 0.5 μm to 3 μm were produced. A truncated octahedral shape is obtained regardless of size. Particle shape evolution can be controlled by adjusting growth rates along the [100] and [111] facet directions.

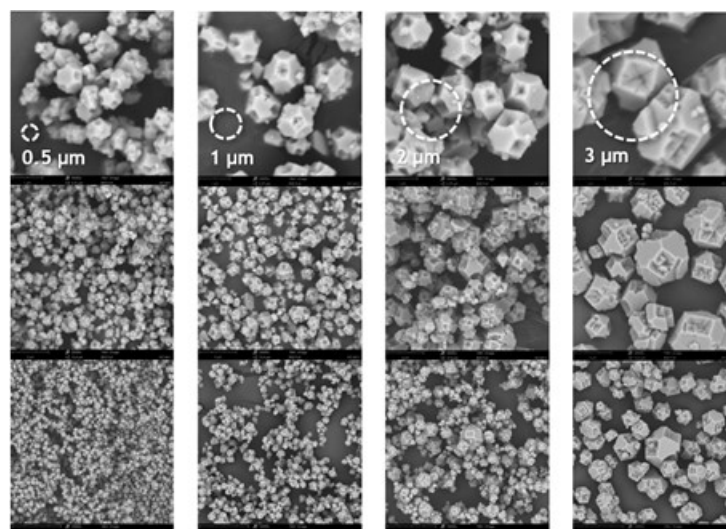


Figure II.3.2 Synthesized hydrothermal single-crystal precursor with particle size control

XRD analysis was performed to characterize the synthesized single-crystal and polycrystalline materials. In Figure II.3.3, the XRD results for the precursor show distinct peaks of the co-precipitated polycrystalline hydroxide precursor and the hydrothermal oxide precursor. However, after heat treatment and lithiation, they have an XRD peak that exactly matches the NMC96-2-2 cathode. The single-crystal material has an initial discharge capacity of 210 mAh/g, while the polycrystalline material has a higher initial discharge capacity of 220 mAh/g. However, in the case of capacity retention, the single-crystal material is more improved.

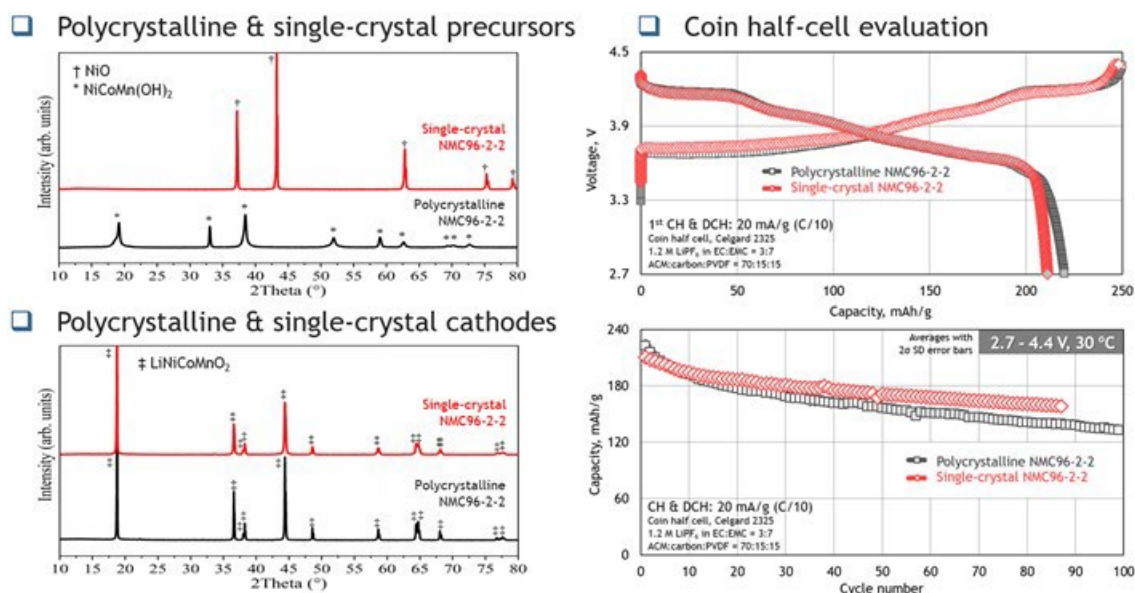


Figure II.3.3 XRD and Coin half-cell evaluation of polycrystalline NMC96-2-2 and single-crystal NMC96-2-2

Single-crystal material has a robust particle structure mitigating particle cracking during cycling (Figure II.3.4). To confirm this, we observed cross-sectional SEM of cathode electrodes before cycling and after cycling. A cross-sectional SEM of a pristine electrode of polycrystalline NMC96-2-2 shows grain boundaries and void fraction inside the particle. After 80 cycles, the particle is destroyed by the volume change during the charge-discharge process. On the other hand, single-crystal NMC96-2-2 particles have no internal grain boundaries, no void fractions, and no particle deformation after 80 cycles. To confirm that the hydrothermally synthesized NMC96-2-2 cathode material is really a single-crystal structure, electron diffraction was measured

through collaboration (Figure II.3.4). This electron-diffraction result clearly shows the single-crystal nature of the large-sized particles.

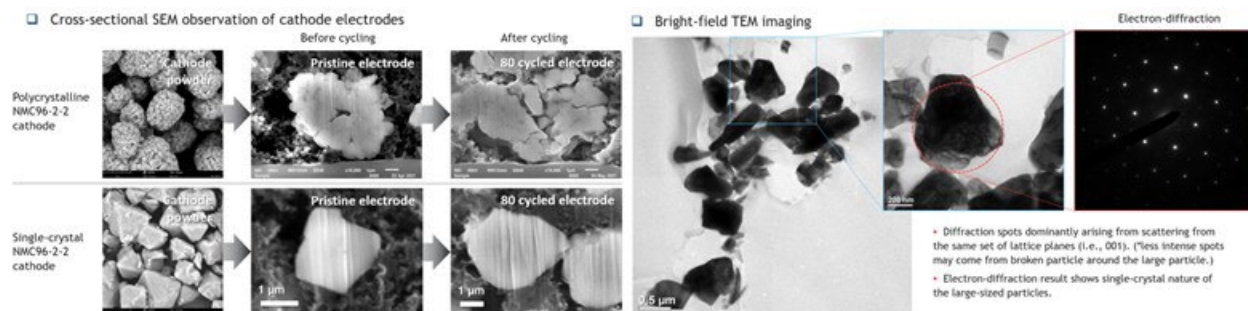


Figure II.3.4 Cross-sectional SEM and FIB SEM of NMC96-2-2 cathode

We conducted nanoindentation analysis to determine the particle strength of polycrystalline and single-crystal materials. Figure II.3.5 shows the indentation of a single-crystal NMC96-2-2 cathode particle. We have tried several indentations on single-crystal materials. However, on the right, as you can see from the behavior of the single crystal taken every second, the single-crystal particle deviates from the center when the single-crystal particle is pressed with the indenter tip. Although we failed to measure the breaking force of the single-crystal particle, its breaking force seems to be quite large. By applying a larger indenter and/or dimpled surface, we will remeasure the breaking force of single-crystal NMC96-2-2 cathode particles.

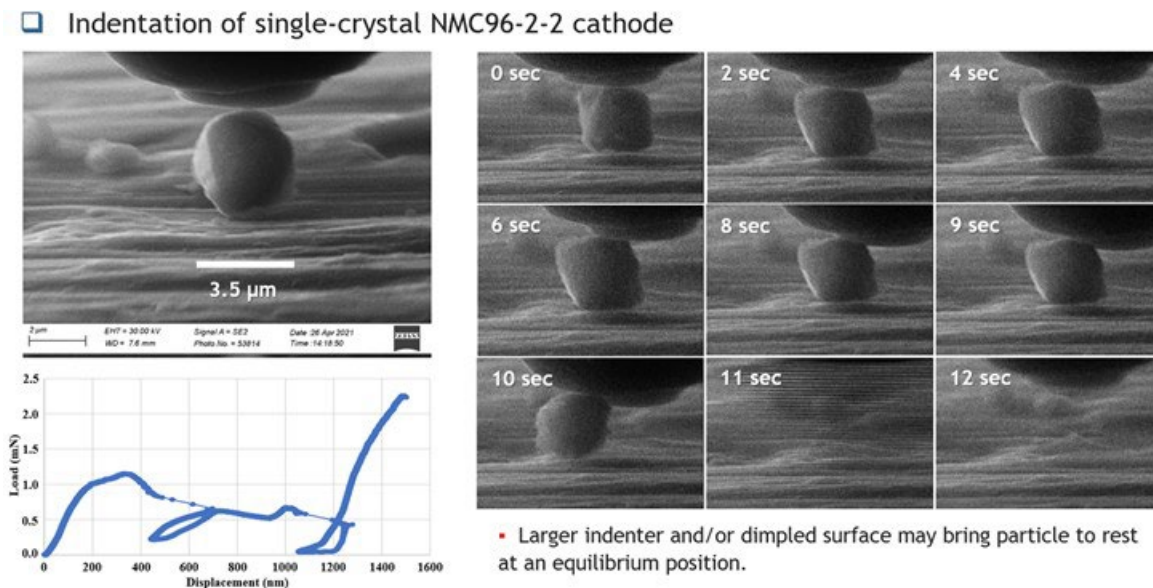


Figure II.3.5 Nanoindentation analysis of single-crystal NMC96-2-2 cathode particle

To improve the electrochemical performance by applying aluminum and zirconium doping to single-crystal material, we synthesized 1% Al and Zr-doped hydrothermal NMC96-2-2 precursors (Figure II.3.6). In order to know how the composition is distributed inside the single-crystal particle, FIB cross-section and elemental mapping were performed through collaboration. Nickel has a uniform distribution throughout the single-crystal particle. Manganese and cobalt show a gradient distribution that decreases in concentration from the center of the particle to the surface. Zirconium is more prevalent on the particle surface. The results of FIB cross-section of 1wt% Al-doped single-crystal NMC96-2-2 precursor reveals that a single-crystal particle with nickel core and NMC96-2-2 shell was obtained. Manganese and cobalt in the particle's shell show a gradient concentration

and aluminum appears to be uniformly distributed throughout the single-crystal particle. So, we obtained 3 micron-sized 1wt% Al-doped nickel cored NMC96-2-2 shelled single-crystal oxide precursor.

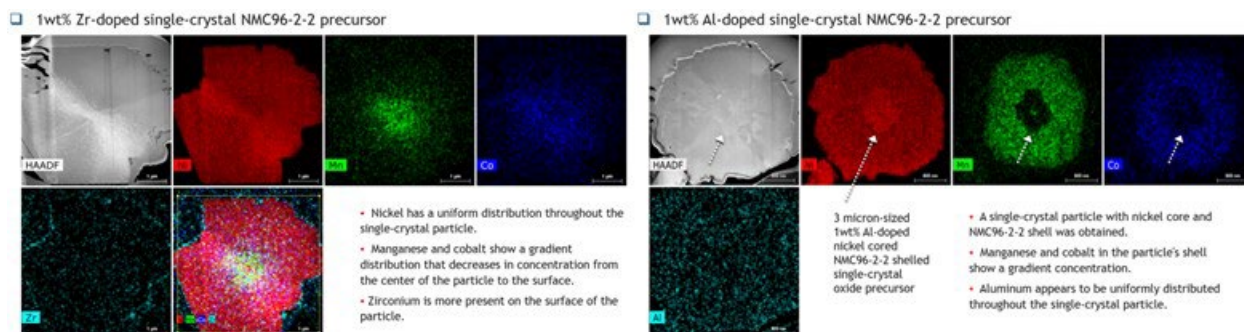


Figure II.3.6 FIB cross-section and elemental mapping of 1wt% Zr/Al-doped NMC96-2-2

XPS analysis (Figure II.3.7) was performed to understand the behavior of zirconium and aluminum on the surface of single-crystal particles before and after calcination. Pure NMC96-2-2 shows a typical XPS spectrum like polycrystalline co-precipitated materials. Zr-doped shows a notable concentration difference after calcination. It is believed that Zr diffuses into the bulk during calcination. On the other hand, aluminum seems to have no significant difference in the concentration distribution before and after calcination. Figure II.3.8 is XRD results of three types of single crystal precursor and cathode materials. Although we could not confirm the peak of aluminum, we confirmed the peaks of Zr oxide in the precursor and lithium zirconium oxide in the cathode. The graph on the right is a coin half-cell cycling result. The capacity reduction of single-crystal NMC96-2-2 is about half of that of polycrystalline NMC96-2-2., 1Wt% Zr/Al-doped materials further suppress the capacity reduction of single-crystal NMC96-2-2 cathode.

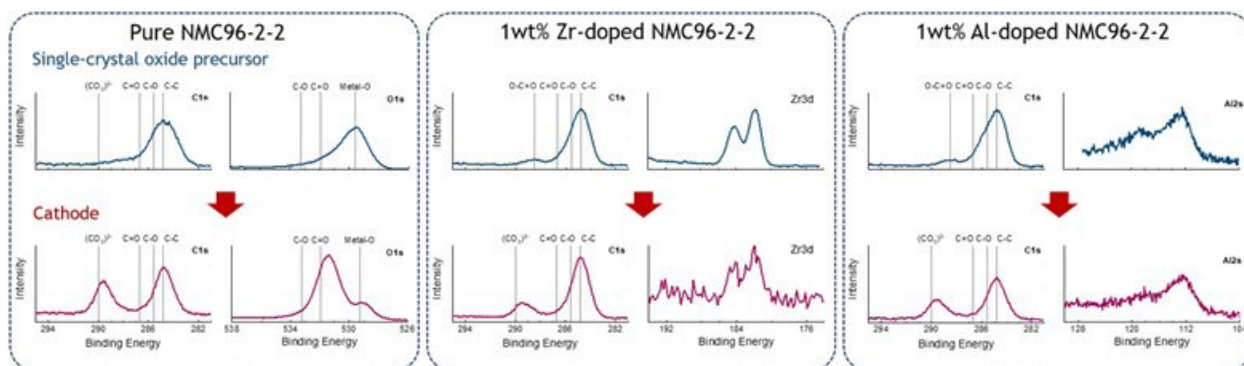


Figure II.3.7 XPS analysis results of 1wt% Zr/Al-doped NMC96-2-2

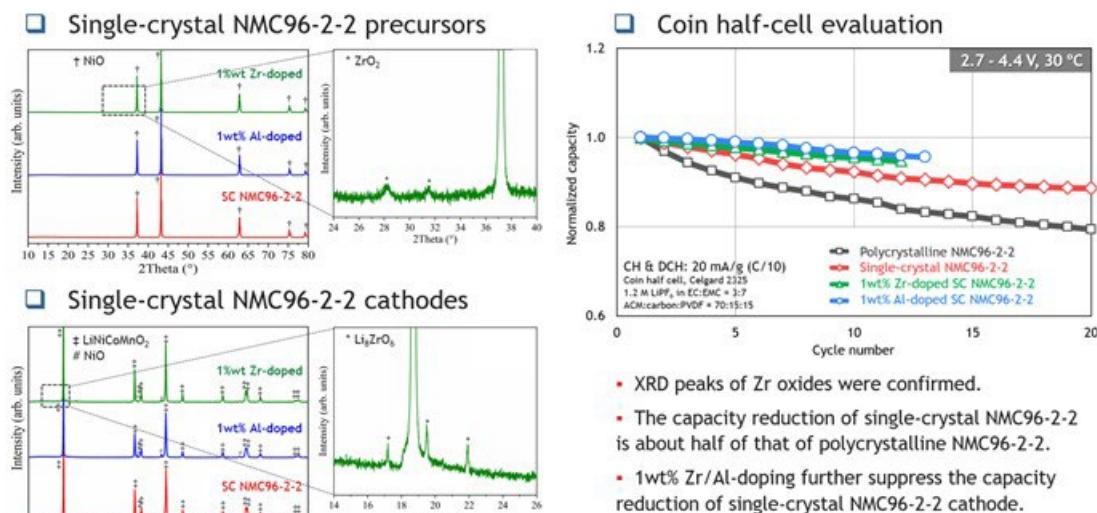


Figure II.3.8 XRD and Coin half-cell evaluation of 1wt% Zr/Al-doped NMC96-2-2

Conclusions

A multi-purpose supercritical hydrothermal reactor system was installed and is being operated, which leads to the establishment of new capabilities to manufacture battery materials with supercritical fluid technology. This supercritical fluid system is a material synthesis platform that is able to produce mono-crystalline cathode materials with a solid structure and unique mechanical and electrochemical properties. This supercritical hydrothermal process is a powerful platform for the synthesis of new single-crystal battery materials with the desired particle size, composition distribution, and morphology which are not commercially available and difficult to produce using other technologies. During FY21, we conducted work to evaluate these potential characteristics of nickel-rich single-crystal NMC96-2-2 prepared using hydrothermal method. We will continue to provide new battery cathode materials that meet the needs of the battery community.

Key Publications

1. Core–Multishell-Structured Digital-Gradient Cathode Materials with Enhanced Mechanical and Electrochemical Durability, Youngho Shin, Sangjin Maeng, Youngmin Chung, Gregory Krumbick and Sangkee Min, *Small*, 2100040 (2021)
2. Hierarchical nickel valence gradient stabilizes high-nickel content layered cathode materials, Ruoqian Lin, Seong-Min Bak, Youngho Shin, Rui Zhang, Chunyang Wang, Kim Kisslinger, Mingyuan Ge, Xiaojing Huang, Zulipiya Shadike, Ajith Pattammattel, Hanfei Yan, Yong Chu, Jinpeng Wu, Wanli Yang, M. Stanley Whittingham, Huolin L. Xin and Xiao-Qing Yang, *Nature communications*, 12, 2350 (2021)

Acknowledgements

Continuous support from David Howell and Peter Faguy of the U.S. Department of Energy's Vehicle Technologies Office is gratefully acknowledged. We gratefully acknowledge the collaboration with Dr. Seongmin Bak (BNL), Dr. Feng Wang (BNL), Dr. Seoung-Bum Son (Argonne Post-Test Facility), Dr. Ira Bloom (Argonne Post-Test Facility), Prof. Huolin Xin (UCI), Prof. Sangkee Min (University of Wisconsin-Madison), and the use of facilities and instrumentation supported by NSF through the University of Wisconsin-Madison Materials Research Science Center (DMR-1720415).

II.4 Process R&D and Scale up of Critical Battery Materials (ANL)

Krzysztof Pupek, Principal Investigator

Argonne National Laboratory
9700 South Cass Avenue
Lemont, IL 60439
E-mail: kpupek@anl.gov

Peter Faguy, Technology Development Manager

U.S. Department of Energy
E-mail: Peter.Faguy@ee.doe.gov

Start Date: October 1, 2020
Project Funding: \$800,000

End Date: September 30, 2021
DOE share: \$800,000

Non-DOE share: \$0

Project Introduction

New experimental materials are constantly invented to improve the safety, energy density, cycle, and calendar life of lithium ion batteries for EV. These materials are typically synthesized in discovery laboratories in small batches providing amounts sufficient only for limited basic evaluation but not in quantities required for full scale validation and prototyping. In addition, bench-scale processes are often un-optimized, not validated, and generate materials with inconsistent purity and yield. This project aims to assist advanced battery research community by enabling access to larger quantities of high quality innovative materials.

Objectives

The objective of this project is to conduct research toward scaling up production of advanced materials for Li-ion batteries originally created in small quantities by discovery scientists at various research organizations. Scaling up the original route used by discovery scientists often requires an extensive modification of the bench-scale chemistry and systematic, science-based process research and development to allow for 1) safe and cost effective production, 2) development of an engineering flow diagram, 3) design of a mini-scale system layout, 4) construction of the experimental system, and 5) validation of the optimized process, all of which are needed for full industrial implementation. The experimental system will be assembled and the materials will be manufactured in quantities sufficient for full scale industrial evaluation and to support further research. The materials produced by the program will be fully characterized to confirm chemical identity and purity. Analytical methods will be developed for quality control. The electrochemical performance of the materials will be validated to confirm that these properties match the original data generated by the discovery scientist. Sample of the materials produced by the project will be available to the advanced lithium ion battery research community to support basic development and large scale performance validation.

Approach

New materials for experimental electrolyte formulations often have complex molecular structure that translates frequently into increased synthesis difficulties and cost. Argonne's Applied Materials Division's Process R&D group, operated in the newly expanded Materials Engineering Research Facility (MERF) is evaluating emerging production technologies to address the challenges. A comprehensive, systematic approach to scale-up of advanced battery materials has been defined. This approach starts with analyzing of the original route the new material was first made in the discovery lab and initial electrochemical evaluation. This determines if the material is to be added to the inventory database, ranked, prioritized and selected for scale up. The Applied Materials Division's Process R&D group at Argonne consults with the DOE technology manager to prioritize new materials based on level of interest, validated performance and scale up feasibility. The new candidate materials for scale up are discuss with DOE for final approval. The Process R&D group evaluates several approaches, including non-standard manufacturing technologies, to determine the best route to scale up of each particular material. One such technology is a Continuous Flow Chemical Reactor that enables the continuous

synthesis of materials from discovery through process development and production scale. Continuous flow reactor technology can be used for rapid screening of reaction conditions to better understand the fundamentals of process kinetics and thermodynamics. The technology offers a cost-effective and safer alternative to traditional batch processes by improving material and energy usage and minimize the environmental impact of the manufacturing operation. At this point, the scale-up process begins with a feasibility study, followed by proof of concept testing, first stage scale-up and, as needed, further scale-up cycles. Several Go/No Go decisions are located after feasibility determination and electrochemical validation testing. For each material, we will develop a scalable manufacturing process, analytical methods and quality control procedures. We also prepare a “technology transfer package” which includes detailed procedures of the revised process for material synthesis, materials balance, analytical methods and results (Specification Sheet) and the SDS for the material. The detailed process description allows for preliminary estimates of production cost, an important factor for decision making in industry. We apply the newly developed process to manufacture kilogram quantities of the material. We fully chemically characterize each material and make samples available for industrial evaluation and to the research community. We also provide feedback to discovery chemists helping to guide future research.

Results

Completing projects from last fiscal year, methyl bis(fluorosulfonyl)imide, or Me-FSI, was scaled to the hundred gram level. This material was targeted as a potential non-flammable electrolyte solvent, but suffered from several technical difficulties in its preparation: notably safety concerns with a large excess of dimethyl sulfate and dioxane, along with significantly exothermic reactions. The existing literature synthesis was strongly, but successfully modified after extensive screening, to remove 1,4-dioxane as a cosolvent and to reduce the required large excess of dimethyl sulfate. The new conditions provide highly pure (>99.9% by GC/MS) material using dimethoxyethane (DME) as a solvent, with 4 molar equivalents of dimethyl sulfate instead of 20 molar equivalents as described previously. Surprisingly, this reaction also works well with lithium bis(fluorosulfonyl)imide (Li-FSI) in ethyl acetate as a solvent.

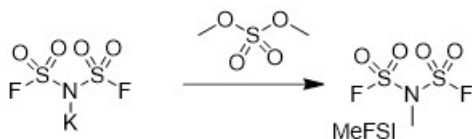


Figure II.4.1 Synthesis of Me-FSI

This material is a useful non-flammable electrolyte solvent, although passivation additives are required to get good cycling. A full cell using NMC622 (C023)/Gr (A002B) cycled well at 4.1 to 3.0 V (1C = 2 mA) using an electrolyte composed of 0.8M LiFSI in Me-FSI:GBL (8:2) + 0.2M LiDFOB, either with or without an addition of 5% VC (Figure II.4.2).

Other routes initially planned to synthesis Me-FSI have not proven reliable, and these efforts have been abandoned.

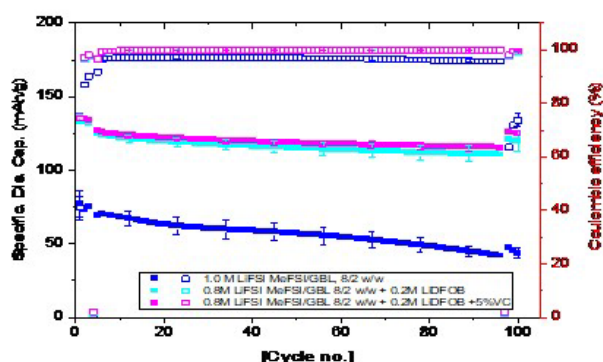


Figure II.4.2 Cycling data for Me-FSI cells

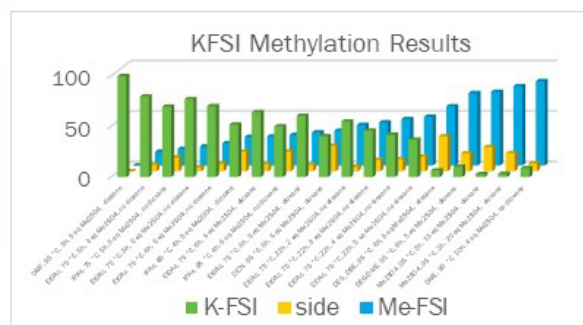


Figure II.4.3 Screening experiments for Me-FSI Synthesis

The synthesis of methyl (tetrafluoropropyl)carbonate was scaled to the 100g level. This is targeted to use in high voltage cells and for extreme temperature use. The material is made in a highly exothermic reaction between methyl chloroformate and tetrafluoropropanol (Figure II.4.4). The calorimetry was investigated and shows a high heat of reaction (210 kJ/mol). There is no induction period in the reaction and the process shows no accumulation (i.e. it reacts as the reagent is added) (Figure II.4.5). This is a good candidate for flow synthesis, although further work is needed to optimize reagents, time and temperature for flow conditions.

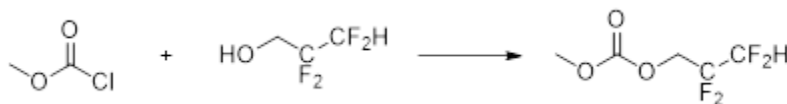
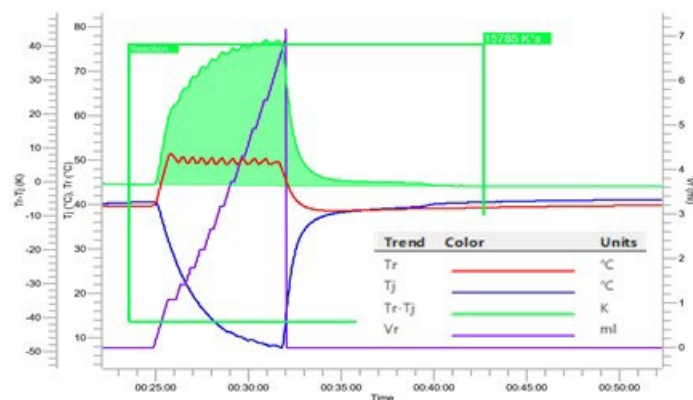


Figure II.4.4 Reaction of methyl chloroformate and tetrafluoropropanol

Figure II.4.5 Calorimetry for the synthesis of MeOC(O)OCH₂CF₂CF₂H

We are currently investigating the synthesis of similar linear fluoroalkyl carbonate structures, including those from pentafluoropropanol. The reactions are showing significant variations from the relatively straightforward tetrafluoropropanol results, hindering the scale-up efforts.

This year, we synthesized a small amount of lithium 4,5-dicyano-1,2,3-triazole (Li-DCTA). This material is reported to be thermally stable, and may be useful in preventing anodic dissolution with high voltage lithium Li-FSI, similar to the reports of lithium trifluorodicyanoimidazole (Li-TDI). In a quick test to check viability of the salt, coin cell cycling showed good efficiency and stable capacity. The 2032 coin cells were prepared from NMC622//Graphite with an electrolyte formulation of 1.0M LiFSI + 0.2M LiDCTA in EC/EMC 3/7.

The cells were cycled at 30°C using a cycling profile of: 1C: 2mA, 3-4.1V, C/20 3X, HPPC, C/3 92X, HPPC, C/20 3X. Scale up of this material is planned for high voltage cell evaluation.

Lithium tricyanoimidazole (Li-TCI) is a new material that has potential to prevent anodic dissolution in LiFSI-based electrolyte, similar to that reported with Li-TDI [2]. We reasoned that both Li-TCI and Li-2-fluoro-4,5-dicyanoimidazole (Li-F-DCI) would show suitable electrochemical behavior. We have made small amounts of both, but now focus on Li-TCI due to a relatively short synthesis. Initial coin cell tests show that the electrochemical cyclability (3.0-4.1V) of cells with electrolyte based on pure LiFSI and LiFSI/LiTCI are similar. More detailed examinations of “corrosion inhibiting” behavior are pending synthesis of suitable amounts of material.

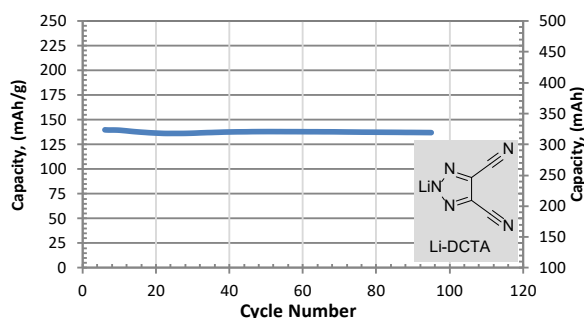


Figure II.4.6 Capacity data for Li-DCTA

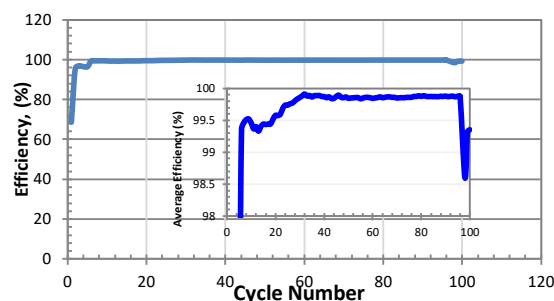


Figure II.4.7 Efficiency data for Li-DCTA

The proposed synthesis of Li-TCI is relatively straightforward. However, the main difficulty are the hazards associated with the diazonium intermediate (Figure II.4.8). This material is frequently cited in the relevant literature as being a potentially explosive compound. This safety concern would stop further scale-up investigations using batch processes, which would involve accumulation of large quantities of the unstable, potentially explosive intermediate. However, one huge advantage of flow chemistry is the ability to make and use only small amounts of material at any one time. This allows the synthesis to be run safely, as the hazardous intermediate is made only in small quantities, and reacted soon after formation. Hazardous quantities are never accumulated, keeping the process safe.



Figure II.4.8 Chemical structures in the formation of Li-TCI

This year, all the main issues with the flow chemistry synthesis were investigated and overcome. The limited solubility of the starting 2-amino-4,5-dicyanoimidazole was solved by using a ternary system of acetonitrile/water/dimethyl sulfoxide. Although adverse effects of pure dmso in these reactions are reported, none were observed in the mixed solvent system. The reaction of this with a solution of tert-butyl nitrite produces an intermediate smoothly with little side reaction as measured by HPLC. However, the optimal time needed could not easily be determined by either visual inspection or by HPLC. In order to optimize this step, investigations were made to determine the time needed in the flow reactor. Both ^1H NMR and FTIR were used to monitor the reaction and determine a reaction time of 5-6 minutes.

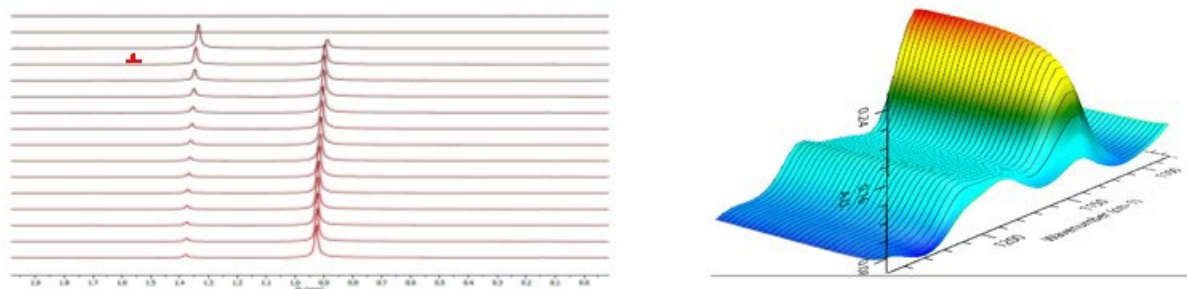


Figure II.4.9 ^1H NMR and Expanded FTIR spectra showing reaction of 2-amino-4,5-dicyanoimidazole with tert-butyl nitrite.

Suitable conditions for a smooth reaction with CuCN and KCN were more difficult. A number of studies were run to arrive at an optimized level of 1.4eq KCN and 0.4eq CuCN. Lower levels lead to decreased reaction, whilst increased amounts had either little effect (KCN) or complicated the workup procedure. It also should be noted that at least a 2:1 ratio of K to Cu is required to form a soluble complex.

A flow system was constructed to evaluate the reaction of the diazo intermediate with the cyanide solution. An all-flow system showed somewhat limited utility. Due to the production of nitrogen gas from the diazo compound, solution mixing was unsystematic, leading to poor reactivity. Addition of a back pressure regulator was ineffective- application of sufficient pressure to limit gas bubble size interfered with the activity of the syringe pumps, causing erratic flow rates. HPLC pumps could be potential replacements of the syringe pumps, but also have reproducibility concerns at low pressure and low flow rates.



Figure II.4.10 Flow chemistry equipment and expanded view of coil reactor for Li-TCl

Ultimately, this was avoided by running a “semi-batch” flow process, whereby the diazo intermediate is formed via flow processes, and then quenched into a large flask of the cyanide complex (Figure II.4.11). A solution of tert-butyl nitrite is mixed with a solution of 2-amino-4,5-dicyanoimidazole to form the diazo intermediate in the coiled tube reactor. The residence time is adjusted to ensure complete reaction, and the intermediate is quenched into a stirred flask containing the copper cyanide/ potassium cyanide mixture. A number of unexpected improvements were made with this setup. It was discovered that by adjusting the pH to ensure basic conditions improved the reaction. Adding an immiscible solvent (first dichloromethane) also helped improve the reaction product quality. There appeared to be a slight benefit to running the process under a nitrogen atmosphere compared to air, but this was slight.

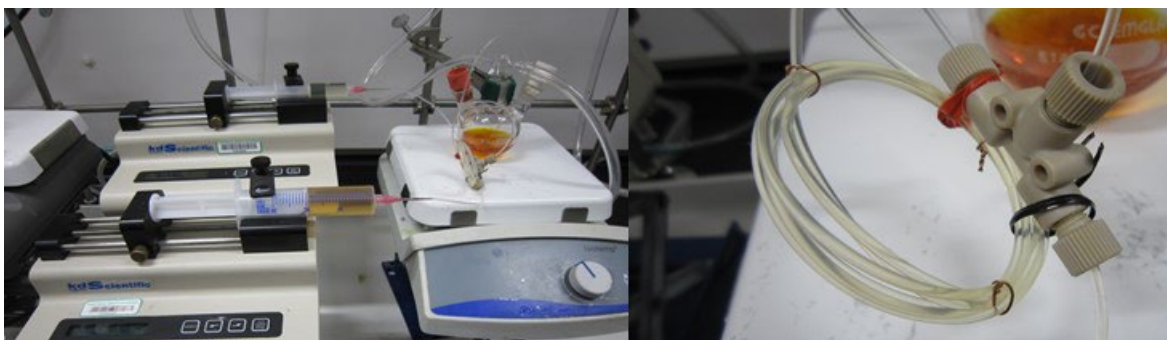


Figure II.4.11 Semi-Batch flow apparatus with expanded view of flow coil.

These adjustments to the reaction conditions improved both the yield and color of the product, as well as removing suspended solids that had previously required a filtration step prior to work up. The lighter color of the product solution improved the visibility of the phase splits in the extractive workup. Finally, it was found that butyl acetate (BuOAc) was unexpectedly good at extracting the product out of the aqueous layer as the potassium salt. Previous work had suggested that an additional cation exchange step was necessary, converting the product to a tetraethylammonium (Et₄N) salt before extracting the Et₄N salt out of water into a suitable organic solvent, typically dichloromethane.

At this point, several hundred grams of K-TCI has been produced via this semi-batch process. Previous development has provided a straightforward process to convert this in good yield to the desired lithium salt. The K salt is dissolved in water and acidified. The protonated TCI is readily extracted into ether solvents such as methyl tert-butyl ether (MTBE) and then dried. The “H-TCI” is lithiated in acetonitrile with lithium carbonate or lithium hydroxide.

Investigations into batch pathways to Li-TCI were made, starting with the bromination of commercial 4,5-dicyanoimidazole. N-methylation gave crystalline material in high yield and purity over the two steps. Debromocyanation was not straightforward. It appeared by HPLC that the reaction worked, and further, that the potassium bromide byproduct demethylated the nitrogen, as anticipated. However, product could not be isolated and appeared to further react upon workup. Given the success in the flow synthesis, this research was then halted.

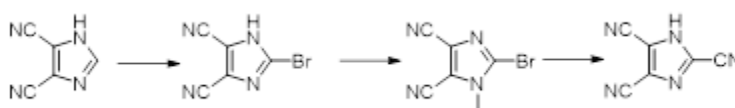


Figure II.4.12 Attempted batch synthesis of TCI.

Conclusions

The Process group’s experimental materials scale-up program assists the battery research community and allows for a comprehensive evaluation of new materials by industrial laboratories as well as supports basic research. In FY20 the program provided several new, not commercially available materials. Samples of high, uniform quality materials were distributed for further evaluation and research. Over 200 samples, ranging from grams to hundreds of grams of experimental battery materials have been provided to researchers since the program inception.

Evaluate emerging manufacturing technologies such as continuous flow reactors, microwave assisted reactions, acoustic mixing, or reactive distillations to improve product quality while lowering manufacturing costs are all under consideration. We utilize our recently acquired, customized Syrris ASIA320 and Corning Advanced-Flow™ continuous flow chemical reactors to develop expedient manufacturing processes for new

electrolyte solvents, salts, and additives by improving safety, minimize waste stream and lower material and energy costs.

Key Publications

1. Dzwiniel, Trevor L.; Pupek, Krzysztof; “Continuous method for preparing carbonate esters” U.S. Patent 11,028,065 B1 June 08, 2021.
2. Yang, Jianzhong; Liu, Qian; Pupek, Krzysztof Z.; Dzwiniel, Trevor L.; Dietz Rago, Nancy L.; Cao, Jiayu; Dandu, Naveen; Curtiss, Larry; Liu, Kewei; Liao, Chen; et al “Molecular Engineering to Enable High-Voltage Lithium-Ion Battery: From Propylene Carbonate to Trifluoropropylene Carbonate” *ACS Energy Letters* (2021), 6(2), 371–378.

References

1. Piotr Jankowski, Orcid, Maciej Dranka, Władysław Wieczorek, and Patrik Johansson “TFSI and TDI Anions: Probes for Solvate Ionic Liquid and Disproportionation-Based Lithium Battery Electrolytes” *Journal of Physical Chemistry Letters* (2017), 8(15), 3678–3682.
2. Ilya A. Shkrob, Orcid, Krzysztof Z. Pupek, James A. Gilbert, Stephen E. Trask, and Daniel P. Abraham “Chemical Stability of Lithium 2-Trifluoromethyl-4,5-dicyanoimidazolid, an Electrolyte Salt for Li-Ion Cells” *Journal of Physical Chemistry C* (2016), 120(50), 28463–28471.
3. An electrolyte additive for extended battery life and fast charging. *Charged Magazine* March 30, 2020.
4. Schmidt, Grégory, Collier, Bertrand, Bonnet, Philippe “Long-Life Lithium-Ion Batteries” World Intellectual Property Organization, WO2015136199 A1.
5. Bitner-Michalska, Anna, Poterała, Marcin, Gajewska, Agnieszka, Kalita, Michał, Żukowska, Grażyna, Piszcz, Michał, Marcinek, Marek, Wieczorek, Władysław, Nolis, Gene “Electrolyte For Metal-Ion Batteries” World Intellectual Property Organization, WO2016203390 A1.

Acknowledgements

Continuous support from David Howell and Peter Faguy of the U.S. Department of Energy’s Vehicle Technologies Office is gratefully acknowledged.

MERF Critical Battery Materials Team: Trevor Dzwiniel, Chia-Wei Hsu, Thomas Do, Amber Tabaka

Argonne's Collaborators: John Zhang, Daniel Abraham, Qian Liu, Wenquan Lu, Bryant Polzin, Steven Trask

II.5 Integrated Multiscale Modeling for Design of Robust 3D Solid-State Lithium Batteries (Lawrence Livermore National Laboratory)

Brandon C. Wood, Principal Investigator

Lawrence Livermore National Laboratory
7000 East Avenue
Livermore, CA 94550
E-mail: wood37@llnl.gov

Tien Q. Duong, DOE Technology Development Manager

U.S. Department of Energy
E-mail: Tien.Duong@ee.doe.gov

Start Date: November 1, 2018
Project Funding: \$1,125,000

End Date: October 31, 2021
DOE share: \$1,125,000

Non-DOE share: \$0

Project Introduction

Architected 3D solid-state batteries have a number of intrinsic performance and safety advantages over conventionally processed 2D batteries based on liquid organic or polymer electrolytes [1]. Functionality and architecture of component materials can be tuned for optimal energy and power density, and the use of solid-state electrolytes offers increased safety and potential compatibility with higher-voltage and higher-energy-density electrodes. Nevertheless, proper design of 3D solid-state batteries remains a formidable challenge. Solid-state batteries tend to suffer from high interfacial resistance arising from poor physical contacts [2], as well as the formation of intermediate phases at the often-unstable interface between the cathode and electrolyte. They also suffer from non-uniform mechanical responses that can promote stress cracking in response to lithium uptake during cycling. For 3D architectures, these issues can become even more problematic, since the complex morphologies tend to introduce additional non-uniformities in electric fields and current densities [3],[4] at the numerous component interfaces. In addition, microstructures that are notoriously difficult to control and vary widely with the specific processing condition.

To realize the ultimate goal of designing and printing optimized 3D solid-state batteries, it is critical to understand the interfacial losses and instabilities that impede performance and promote failure at multiple scales. Validated modeling and simulation have a unique role to play in pursuit of this aim, since they can directly probe structure-property relations and provide guidance for optimizing function of component materials. In general, existing modeling strategies tend to suffer from one of two shortcomings. Some fail to address the multi-physics nature of the various processes active in 3D batteries, which range from electrical to chemical to mechanical responses that are often coupled. Others fail to address the multiscale nature of the battery materials and their integration, ignoring the fact that atomistic, microstructural, and cell-level processes must be considered to understand how processing and architecture affect performance. This project leverages advanced computational models to address these shortcomings and investigate diffusion kinetics limitations in ceramic 3D solid-state battery materials. This can be viewed as a first step towards enabling future optimization of 3D battery designs.

Objectives

This project is developing a multiscale, multi-physics modeling framework for probing the effects of materials microstructure and device architecture on ion transport within 3D ceramic solid-state battery materials, with the goal of enhancing performance and reliability. The project has three primary objectives: (1) integrate multi-physics and multiscale model components; (2) understand interface- and microstructure-derived limitations on ion transport; and (3) derive key structure-performance relations for enabling future optimization.

Approach

The team's approach integrates simulations at three scales to predict ion transport limitations within the ceramic solid-state electrolyte $\text{Li}_{7-x}\text{La}_3\text{Zr}_2\text{O}_{12}$ (LLZO), as well as across the interface between LLZO and LiCoO_2 (LCO) cathodes at composite interfaces in 3D batteries. Classical and *ab initio* molecular dynamics (AIMD) simulations are used to compute fundamental Li-ion diffusion within bulk solid electrolyte and cathode materials, along/across grain boundaries of the electrolyte, and along/across electrolyte/cathode interfaces. Next, phase-field simulations are used to generate digital representation of realistic microstructures of the materials, which are combined with the atomistic simulation results to parameterize mesoscale effective property calculations and to establish microstructure-property relationships for ion transport. Finally, these relationships inform a microstructure-aware model of experimental electrochemical impedance spectroscopy, which connects microscale features to macroscale properties in order to optimize the performance of ceramic 3D solid-state Li batteries based on LLZO solid electrolytes.

Results

Atomistic simulations of Li-ion diffusion across the LLZO/LCO interface

The team utilized high-temperature *ab initio* molecular dynamics (AIMD) to sample the atomic structure of LLZO/LCO interfaces based on several initial electrolyte/cathode orientations and simulated charge states. Multiple snapshots were then randomly chosen from the dynamics trajectories, and possible Li^+ diffusion pathways across the interfaces were identified. Next, the corresponding ensemble of activation energies E_a were computed using the nudged elastic band method. The results are collected and rendered as a histogram in Figure II.5.1. Across all samples, the average E_a is found to be ~ 0.93 eV for forward diffusion of Li^+ from LLZO to LCO—significantly higher than for bulk LLZO or LCO (~ 0.3 eV)—implying orders-of-magnitude slower diffusion across the interface. The Li^+ diffusion pathways were also found to exhibit different values of E_a for forward (LLZO \rightarrow LCO) and backward (LCO \rightarrow LLZO) diffusion, with the latter much more facile (~ 0.32 eV on average). As a result, Li^+ ions that do manage to cross the interface boundary have a high probability of reversing their path, making continuous diffusion across the interface challenging. The findings point to buildup of Li^+ ions in the near-surface regions of LLZO and LCO rather than in the interfacial region. The team further concluded that even for a completely compact interface absent of voids, there is a physical origin for high interfacial impedance that must be considered. Overcoming this limitation may require alternative processing routes or chemical modification strategies, to be explored in future work.

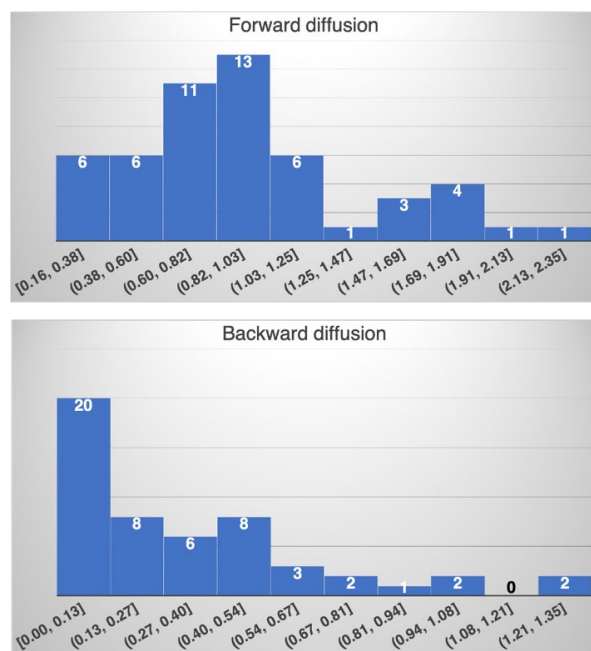


Figure II.5.1 Histogram of calculated activation energies (in eV) for different Li⁺ diffusion pathways across the LLZO/LCO interface. Forward and backward diffusion refer to Li⁺ migration from LLZO to LCO, and from LCO to LLZO, respectively.

Machine-learning interatomic potentials for accelerated atomistic simulations of interfaces

Although the team's primary workhorse for atomistic simulations has been AIMD, obtaining reliable transport coefficients for complex interfaces requires large, long simulations to properly capture the effects of disorder. Because these computations are computationally demanding, they accelerated the simulations by developing machine-learning force fields (MLFFs) that can reproduce quantum accuracy with far less computational expense. The MLFFs were based on an **artificial neural network with a 20-10 hidden-layer architecture and utilized Chebyshev polynomial representations of local atomic environments**. To ensure proper reproduction of disordered and interfacial atomic structures, the team included in the training data a variety of expanded-volume amorphous LLZO structures. The resulting MLFF achieved near-quantum-level accuracy for energies and forces for *NPT* molecular dynamics simulations up to 3000 K, with root-mean-squared errors for energies and forces < 10 meV/atom and < 0.2 eV/Å, respectively (Figure II.5.2a,b). To validate the performance and extract useful parameters for their mesoscale models, the team performed MLFF simulations at various conditions and evaluated radial distribution functions, mechanical properties, Li transport parameters, and atomic vibrational characteristics. Figure II.5.2c shows that the new MLFF approach predicts Li transport parameters close to AIMD for a fully disordered variant, which is a proxy for high-angle grain boundaries. The higher activation energy for the fully disordered variant reflects the blocking effect of grain boundaries, which is known to lead to increased impedance in LLZO. The team also constructed models of specific grain boundaries and interphase boundaries to compute Li⁺ transport. As an illustration, Figure II.5.2d presents the frequented pathways for Li⁺ ions transporting through a LLZO $\Sigma 5(210)/[001]$ grain boundary (GB) model at 2000 K. In addition, analysis of the local environments that promote rapid diffusion or act as diffusion blockers (and hence increased impedance) was aided by the development of new analytical techniques that rely on discretizing jumps and sites to examine spatiotemporal correlation effects, as reported in [5] and [6]. Results from these computations were used to estimate microstructure-dependent transport across both internal (grain boundary) and multiphase interfaces between the cathode and electrolyte.

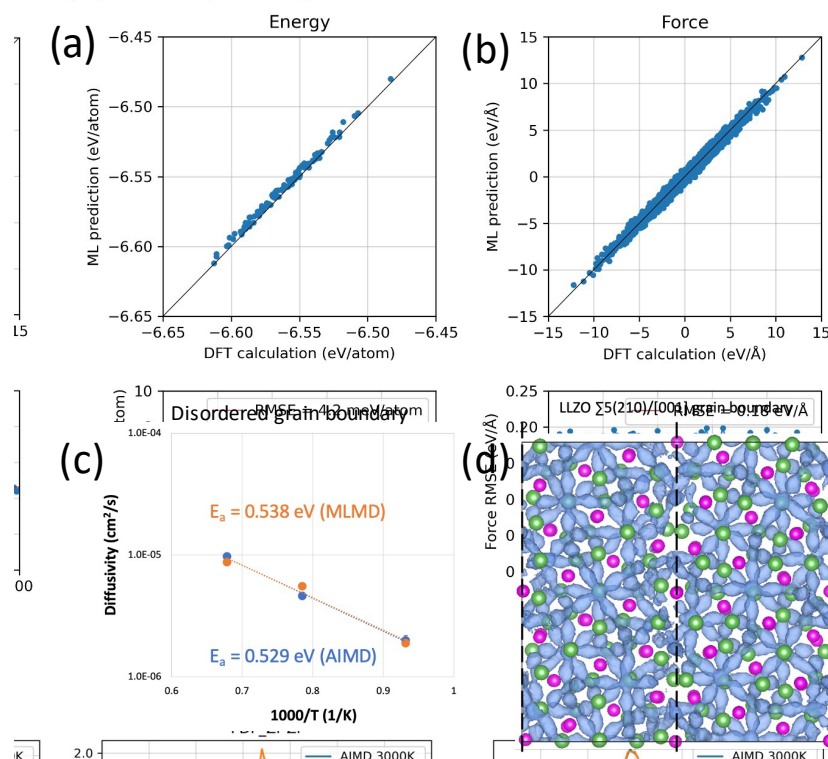


Figure II.5.2. (a-b) Analysis of MLFF accuracy during a dynamical simulation of disordered LLZO at 3000 K, showing the ability to replicate (a) energies and (b) forces derived from density functional theory (DFT). (c) Li^+ diffusivities predicted by MLMD (orange) and AIMD (blue) for amorphous LLZO. (d) Isosurface of Li^+ probability density (blue) obtained from MLMD in a LLZO $\Sigma 5(210)/[001]$ coherent grain boundary model at 2000 K. Magenta and green atoms are Zr and La, respectively, and O atoms are not shown for simplicity.

Mesoscale modeling of microstructural effects on Li transport in polycrystalline LLZO under stress

The team further refined the integration of two mesoscale models for predicting microstructural impacts on 1) Li ion transport and 2) local stress concentrations in LLZO. Within the *MesoMicro* code framework developed at Lawrence Livermore National Laboratory [7], the team successfully combined two numerical schemes for solving the mechanical equilibrium and steady-state diffusion equations in the presence of complex solid electrolyte microstructures. This framework is now capable of naturally incorporating microstructure-aware stress effects on the local Li concentration profile within any polycrystalline microstructure. The team applied the framework to a digital representation of polycrystalline LLZO (Figure II.5.3a) with a microstructure generated by a phase-field simulation. They first verified the ability to predict a nonuniform internal stress profile under applied loading. As shown in Figure II.5.3b, the local von Mises stress profile is affected by local microstructural features, as previously reported. Next, the Li composition profile was analyzed at steady state in the presence of the local stress profile. Figure II.5.3c shows the computed Li composition profile for that scenario. For comparison, the computed Li composition profile without the stress effect is shown in Figure II.5.3d. The simulations confirm that stress concentration can perturb the Li composition profile, inducing segregation or depletion near grain boundaries and junctions. The team proposes use of this formalism to quantify how evolving stresses affect the net ionic conductivity under various operation conditions.

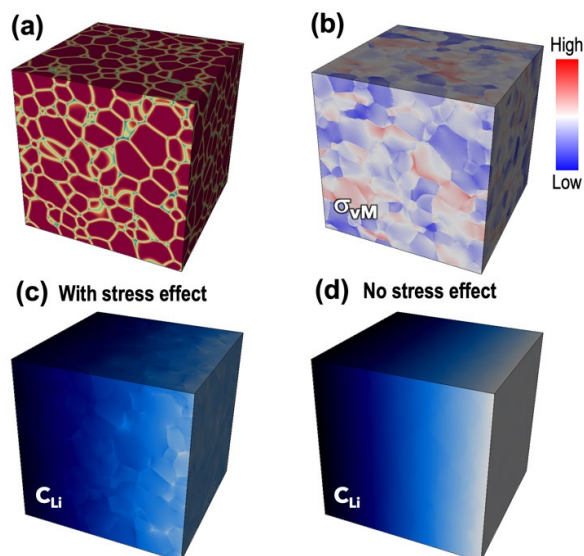


Figure II.5.3. (a) Digital representation of polycrystalline LLZO microstructure; (b) computed von Mises stress profile; (c-d) Li composition profile (c) with and (d) without mechanical stress.

Mesoscale modeling of Li transport and micromechanical response in a polymer/LLZO composite

The team also extended their mesoscale models and their *MesoMicro* code framework to compute properties of polymer/LLZO composites. Figure II.5.4a shows a 3D digital representation of a realistic porous LLZO microstructure filled with a polymer. Mesoscale modeling approaches were applied to compute local mechanical response within the microstructure, the effective elastic modulus, and effective ionic conductivities of both cations (Li^+) and anions (TFSI^-). For input materials parameters, the team combined *ab initio*-derived elastic moduli with experimental ionic conductivities of LLZO and polymer electrolyte constituents. The incorporated composite microstructures exhibit strongly inhomogeneous elasticity and conductivity profiles. Figure II.5.4b shows a simulation result of the local mechanical response (represented by the von Mises stress) within the composite microstructure. The simulation verifies the presence of concentrated mechanical stresses near the polymer/LLZO interfaces, demonstrating the sensitivity of the level of stress concentration to local topological features. Additionally, by applying loads along various normal and shear directions, the team extracted the effective elastic modulus of the composite (Figure II.5.4c), which is expected to be highly sensitive to microstructure and LLZO/polymer phase fraction and has implications for mechanical stability and resistance to Li dendritic growth.

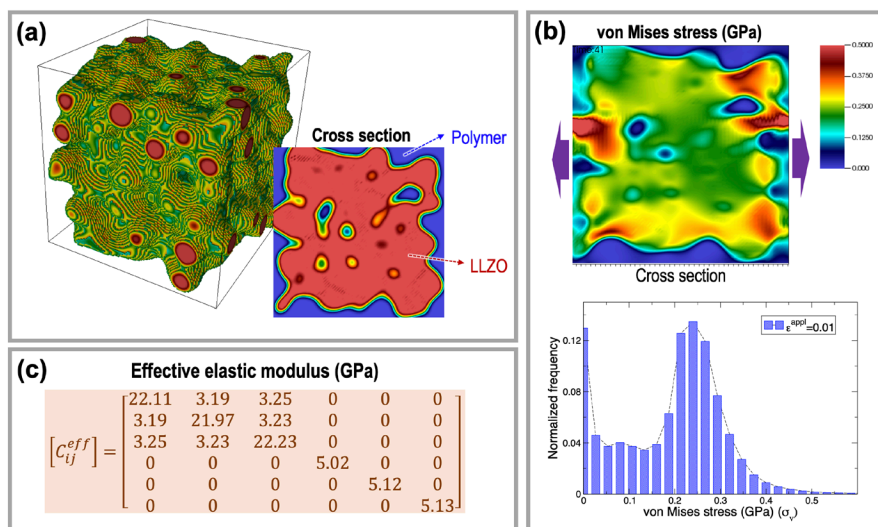


Figure II.5.4. (a) 3D porous LLZO microstructure and cross section of LLZO/polymer composite microstructure; (b) computed von Mises stress (top: spatial distribution; bottom: statistics) in the composite microstructure under applied loading; and (c) computed effective elastic modulus of the composite microstructure.

Modeling of microstructural effects on electrochemical impedance spectra

The team also developed a model to understand impacts of grain boundaries on the electrochemical impedance spectra (EIS) to better connect the simulations to macroscale experiments. This model accounts for Li^+ grain boundary segregation and the corresponding space-charge effects, as well as their collective impacts on electrical potential distributions in polycrystalline solid electrolytes. This framework is being applied within the U.S.-Germany Collaboration on Solid-state Batteries to aid analysis of grain and grain boundary contributions to ionic conductivity as a function of processing conditions. Figure II.5.5 shows the Li^+ ion concentration distribution and the corresponding voltage in a sample polycrystal, along with the effect of grain boundary conductivity on the predicted EIS. Faster grain boundary conductivity (top row) demonstrates higher segregation effects and larger potential gradients across the grain boundary when compared to the slower grain boundary conductivity case (bottom row). The space charge density distribution follows the concentration distribution. Here, the inclusion of space charge segregation in the grain boundary leads to an increase in the overall predicted impedance (specifically the imaginary component). This effort is being performed jointly with the U.S.-Germany CatSE partnership on solid-state battery research, with planned incorporation into device-level models being devised by partner institutions.

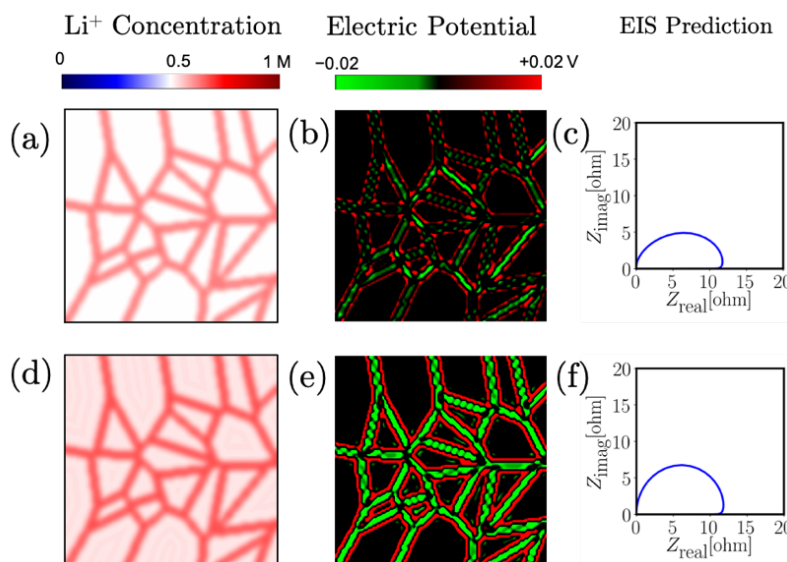


Figure II.5.5. Predictions of (a,d) Li^+ concentration profile, (b,e) electrical potential profile, and (c,f) EIS for a model 2D LLZO polycrystal, demonstrating the effect of grain boundary Li^+ conductivity. Data in (a-c) correspond to the case for which Li^+ mobility at the grain boundaries is double that in (d-f).

Conclusions

The team's activities this year were used to map the range of likely Li^+ mobilities across densified cathode/LLZO interfaces, which illustrated the origins of intrinsic impedance limitations in well-pressed and sintered samples. They also showed that it is possible to access much more complex interfacial systems with near-quantum accuracy by introducing machine learning force fields. These were used to confirm the segregation and transport of Li^+ in specific models of specific grain boundary orientations and generic disordered high-angle grain boundaries. These tools improved the statistical accuracy of the interfacial transport predictions and can be utilized more broadly for analyzing further effects of structure and chemistry on local mobility. At the mesoscale, the team integrated the relationship between local stress and transport into their modeling framework. They showed that stresses concentrate locally at grain junctions, and that these stresses couple to the compositional profile to introduce heterogeneity into the mass transport profile. The team also computed the effect of microstructure on Li^+ transport and micromechanical response in a polymer/LLZO composite, demonstrating the role of highly inhomogeneous and anisotropic transport of individual components on the effective transport. This formalism can in principle be used to optimize microstructures of composites. Finally, the team demonstrated a framework for predicting electrochemical impedance spectra from microstructural features, which can be used to better connect processing to performance and guide future design.

Key Publications

1. T.W. Heo, A. Grieder, B. Wang, M. Wood, S.A. Akhade, L.F. Wan, L.-Q. Chen, N. Adelstein, and B.C. Wood, "Microstructural impacts on ionic conductivity of oxide solid electrolytes from a combined atomistic-mesoscale approach," *npj Comp. Mater.*, in press (2021).
2. B.C. Wood, J.B. Varley, K.E. Kweon, P. Shea, A.T. Hall, A. Grieder, M. Ward, V.P. Aguirre, D. Ringling, E.L. Ventura, C. Stancill, and N. Adelstein, "Paradigms of frustration in superionic solid electrolytes," *Phil. Trans. R. Soc. A* 379, 20190467 (2021).
3. Z. Mehmedovic, V. Wei, A. Grieder, P. Shea, B.C. Wood, and N. Adelstein, "Impacts of vacancy-induced polarization and distortion on diffusion in solid electrolyte Li_3OCl ," *Phil. Trans. R. Soc. A* 379, 20190459 (2021).

4. K. Kim, D. Park, H.-G. Jung, K.Y. Chung, J.H. Shim, B.C. Wood, and S. Yu, “Material design strategy for halide solid electrolytes Li_3MX_6 ($\text{X} = \text{Cl}, \text{Br}, \text{and I}$) for all-solid-state high-voltage Li-ion batteries,” *Chem. Mater.* 33, 3669 (2021).
5. B.C. Wood, “Understanding kinetics of complex interfaces in solid-state batteries from multiscale simulations,” Electrochemical Society PRiME Meeting (Virtual), October 2020.
6. T.W. Heo, A. Grieder, S.A. Akhade, L.F. Wan, N. Adelstein, B.C. Wood, “Integrated modeling framework for investigating multiscale microstructural impacts on the ionic conductivity of garnet solid electrolytes”, Electrochemical Society PRiME Meeting (Virtual), October 2020.
7. L. Wan, A. M. Dive, M. Wood, K. Kim, T. Li and B. C. Wood, “Elucidating interfacial instability in all-solid-state lithium batteries from first-principles simulations”, Materials Research Society 2021 Spring Meeting (virtual), April 2021.

References

1. Arthur, T. S., D. J. Bates, N. Cirigliano, D. C. Johnson, P. Malati, J. M. Mosby, E. Perre, M. T. Rawls, A. L. Prieto, and B. Dunn. 2011. “Three-dimensional electrodes and battery architectures.” *MRS Bulletin* 36 (7):523–531.
2. McOwen Dennis, W., Shaomao Xu, Yunhui Gong, Yang Wen, L. Godbey Griffin, E. Gritton Jack, R. Hamann Tanner, Jiaqi Dai, T. Hitz Gregory, Liangbing Hu, and D. Wachsman Eric. 2018. “3D-Printing Electrolytes for Solid-State Batteries.” *Adv. Mater.* 30 (18):1707132.
3. Hart, R. W., H. S. White, B. Dunn, and D. R. Rolison. 2003. “3-D microbatteries.” *Electrochem. Commun.* 5 (2):120–123.
4. Long, J. W., B. Dunn, D. R. Rolison, and H. S. White. 2004. “Three-dimensional battery architectures.” *Chem. Rev.* 104 (10):4463–4492.
5. Wood, B. C., J. B. Varley, K. E. Kweon, P. Shea, A. T. Hall, A. Grieder, M. Ward, V. P. Aguirre, D. Ringling, E. L. Ventura, C. Stancill, and N. Adelstein. 2021. “Paradigms of frustration in superionic solid electrolytes.” *Phil. Trans. R. Soc. A* 379: 20190467.
6. Mehmedovic, Z., V. Wei, A. Grieder, P. Shea, B. C. Wood, and N. Adelstein. 2021. “Impacts of vacancy-induced polarization and distortion on diffusion in solid electrolyte Li_3OCl .” *Phil. Trans. R. Soc. A* 379: 20190459.
7. Heo, T. W., A. Grieder, B. Wang, M. Wood, S.A. Akhade, L.F. Wan, L.-Q. Chen, N. Adelstein, and B.C. Wood. 2021. “Microstructural impacts on ionic conductivity of oxide solid electrolytes from a combined atomistic-mesoscale approach,” *npj Comp. Mater.*, in press.

Acknowledgements

This work was performed under the auspices of the U.S. Department of Energy by Lawrence Livermore National Laboratory under contract DE-AC52-07NA27344.

II.6 Structure-Activity relationships in the optimizing electrode processing streams for LiBs (LBNL)

Vince Battaglia, Principal Investigator

Lawrence Berkeley National Laboratory
1 Cyclotron Road, MS70R0108B
Berkeley, CA 94720
E-mail: vsbattaglia@lbl.gov

Peter Faguy, DOE Technology Development Manager

U.S. Department of Energy
E-mail: Peter.Faguy@ee.doe.gov

Start Date: October 1, 2020

End Date: September 30, 2021

Project Funding: \$195,000

DOE share: \$195,000

Non-DOE share: \$0

Project Introduction

Despite the maturity of conventional lithium-ion electrode manufacturing, scale-up of manufacturing processes from the lab scale to industrial scale is a time-consuming and costly process that is typically performed by trial-and-error whenever formulations change.

Our project aims to provide a deeper understanding of the relationships among components, processing, and product outcomes. However, academic and government labs rarely have access to full information about proprietary formulations and processes used by manufacturers. To provide maximum value to industry,

our strategy will be to develop experimental strategies and corresponding model frameworks that can be adapted by manufacturers according to their needs. We will perform partially-automated experiments using industrially-relevant materials and use these results to produce models that encapsulate our findings. Others can later perform experiments on reasonably similar systems of interest and adjust our model frameworks accordingly in order to generate new models that are specific to their systems, but which retain the fundamental information encoded in the model frameworks. We expect that such models will help manufacturers to reduce time and cost needed for process optimization.

Objectives

- Contribute to understanding of effects of processing on slurry components during mixing and coating drying.
- Contribute to understanding of interactions among slurry components during mixing and coating drying.
- Contribute to construction of miniature automated coating/drying line (jointly funded by Advanced Manufacturing Office [AMO] and Hydrogen and Fuel Cell Technologies Office [HFTO]).
- Produce experimental procedures and models of mixing and coating drying that are suitable for adaptation to industrial needs.

Approach

Our approach for FY21 was as follows:

- Establish a safe working environment for use of N-methylpyrrolidone (NMP)-based slurries in a laboratory space that had only indirect access to a fume ventilation system.

- Establish an appropriate working space and procure a laser scanning confocal microscope (jointly funded by AMO and HFTO).
- Obtain dynamic particle size distributions for various combinations of components in dilute slurries, using the mixing analysis setup that we constructed in FY20 (jointly funded by AMO).
- Select components for miniature automated coating/drying line that have published interfaces and which are suitable for custom programmatic control.

Results

Our efforts in FY21 have been focused on development of new capabilities for processing investigations. Knowing that we would need to be able to safely work with NMP-based slurries outside of a glove box, our Q1 milestone was to construct a ventilation system that could provide sufficient ventilation for both our automated mixing setup as well as the miniature automated coating/drying system that we would construct this year. The complete ventilation system is shown in Figure II.6.1.



Figure II.6.1 Vapor extraction system (K. Higa/LBNL)

To fulfill the Q2 milestone, we modified the computer-controlled mixing setup for NMP-based solution use and verified the reliability of the experimental system, then obtained dynamic particle size distributions for each of polyvinylidene fluoride (PVDF) (data was expected to be inconclusive if PVDF dissolves well), carbon black, and graphite, dispersed in NMP, each at two dilute concentrations. For the experiments, we changed the mass concentration of carbon black (CB), graphite, and PVDF, for a total of 6 data sets. Results of two different concentrations of CB are shown in Figure II.6.2. We found that even in very dilute solutions, the CB

is not well dispersed in NMP at a mixing speed of 2000 rpm, having a typical agglomerate size peak around 10^{-4} m. The graphite is well-dispersed in NMP, with a peak around 10^{-5} m (Figure II.6.3), in agreement with its expected primary particle size. Figure II.6.4 shows surprising results for PVDF. The measurement at lower concentration (1.5% by weight) shows two different peaks, one around 10^{-4} m, the other around 10^{-5} m. At higher concentration (3% by weight), only one peak around 10^{-4} m was observed.

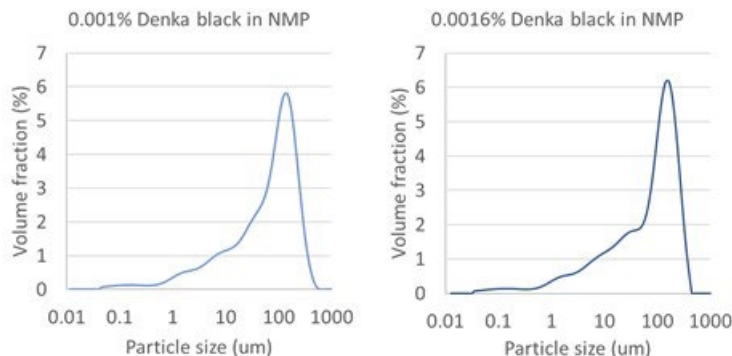


Figure II.6.2 Particle size distribution for Denka black [carbon black] in NMP (Z. Huang and B. Zhang/LBNL)

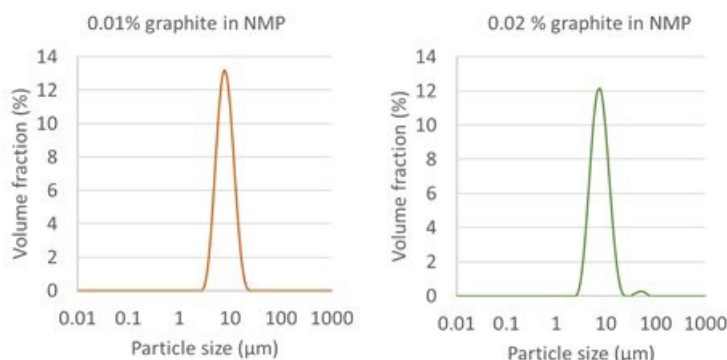


Figure II.6.3 Particle size distribution for graphite in NMP (Z. Huang and B. Zhang/LBNL)

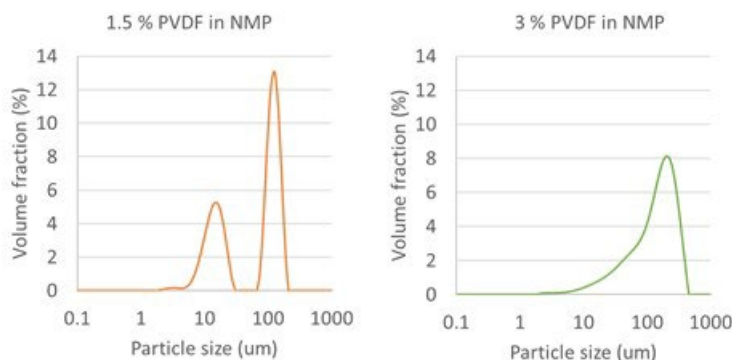


Figure II.6.4 Particle size distribution for PVDF in NMP (Z. Huang and B. Zhang/LBNL)

We continued with this work to fulfill the Q3 milestone. We performed the same mixing observations, but with mixtures containing multiple solid components, as shown in Figure II.6.5.

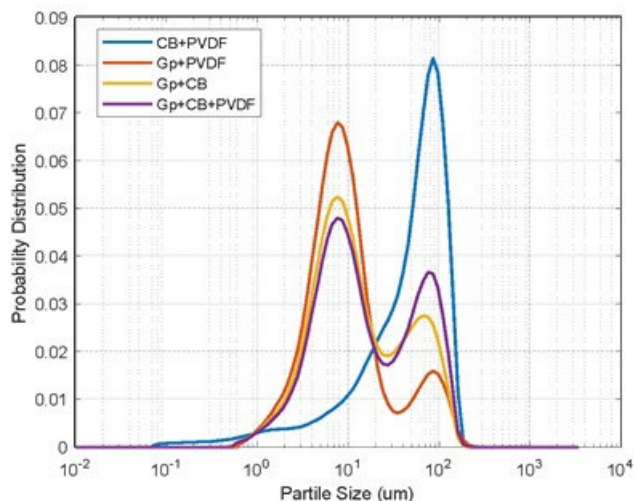


Figure II.6.5 Particle size distribution for component mixtures in NMP (Z. Huang and B. Zhang/LBNL)

In parallel with the earlier milestones, VTO funding has supported the development of our miniature coating/drying line (also jointly funded by AMO and FCTO), with particular focus on remote operation for use of the system in beamline hutches. We have gone from sending low-level USB instructions to motor controllers, to abstracting controls to a human-friendly level in which the coordinated actions of multiple features of the assembly can be described by programs containing only a few lines of Python code.

We have used this new assembly to fulfill our Q4 milestone, by using the assembly to cast an NMP-based slurry on a foil substrate and automatically moving the laminate into position for imaging by a confocal microscope. The floating platform was then engaged by the microscope stage, which then allowed us to capture images of the slurry layer (see Figure II.6.6). In this first attempt, we have allowed the coating to dry under ambient conditions. In future work, we will use the assembly to periodically move the sample between heating modules (presently under construction, jointly funded with AMO) and the microscope to examine the influence of heating.

Finally, in preparation for making our model frameworks publicly available, we have made significant improvements to our open-source Python package for continuum simulation, designed to help domain scientists to set up and solve complicated systems of equations, with limited effort. We likewise updated the documentation and published a paper that provides an overview of the package.

While we met all of our FY21 milestones, operating under COVID-19 pandemic conditions was challenging, producing significant delays which limited the depth to which we could pursue our investigations.

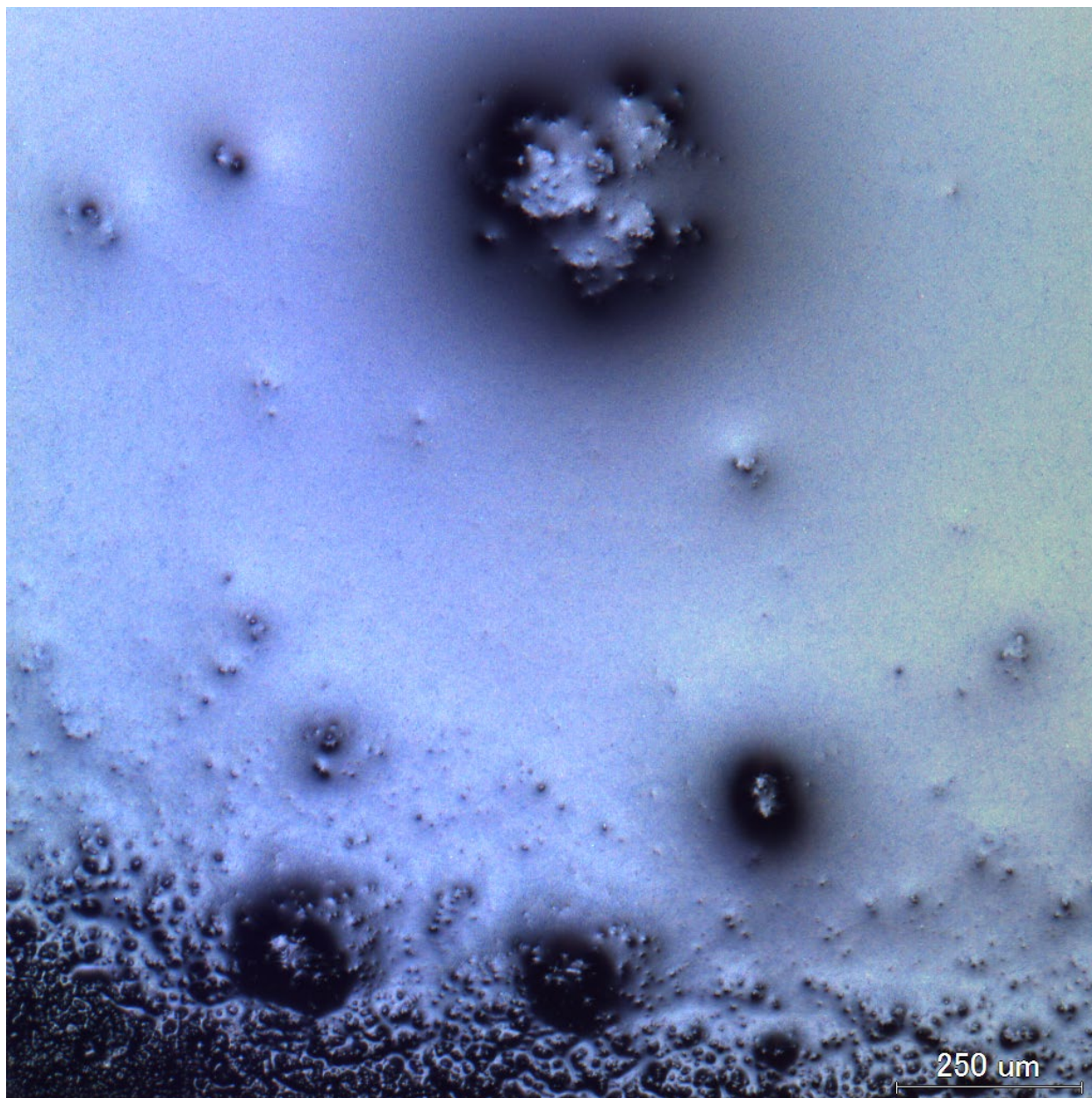


Figure II.6.6 Confocal microscope image of surface of wet battery electrode coating (B. Zhang and K. Higa/LBNL)

Conclusions

From the Q2 and Q3 findings, we infer that the graphite particle size distribution is easily distinguished from that of carbon black and PVDF. The agglomerated carbon black and PVDF, on the other hand, have overlapping distributions. The presence of additional components does not appear to shift the distributions of individual components significantly, which suggests that they do not agglomerate particularly aggressively with each other.

We found that at the high solids concentrations used in industrially-relevant slurries, it is difficult to see through slurry/air interfaces with the confocal microscope. Future work might involve working with diluted slurries in order to study the fundamentals of particle-scale interactions, and/or imaging using the ALS microtomography/radiography beamline, for which slurry density is far less of a limitation.

Key Publications

1. K. Higa, V. Srinivasan, and V. S. Battaglia, (2021). “PyGDH: Python Grid Discretization Helper.” *Journal of Open Source Software*, 6(59), 2744, <https://doi.org/10.21105/joss.02744>

Acknowledgements

Additional contributors to this project include Buyi Zhang (UCB/LBNL graduate student), Zhi Huang and Bei Fan (former LBNL postdocs), Kenneth Higa (LBNL), and Ravi Prasher (UCB/LBNL).

II.7 Fabricate and Test Solid-state Ceramic Electrolytes and Electrolyte/Cathode Laminates (LBNL)

Mike Tucker, Principal Investigator

Lawrence Berkeley National Laboratory
1 Cyclotron Road
Berkeley, CA 94720
E-mail: MCTucker@LBL.gov

Simon Thompson, DOE Technology Development Manager

U.S. Department of Energy
E-mail: Simon.Thompson@ee.doe.gov

Start Date: October 1, 2020

End Date: September 30, 2021

Project Funding: \$200,000

DOE share: \$200,000

Non-DOE share: \$0

Project Introduction

Ceramic solid state battery technology is limited by processing constraints such as Li loss during sintering, reaction between active materials and electrolyte during processing, and non-ideal microstructure and electrochemical/mechanical properties of layers fabricated via conventional processing routes. This project will address these limitations by elucidating behavior of the key materials during processing, including sintering behavior, reactivity, and phase stability. Of particular importance is the fabrication of thin, completely dense electrolyte and thick, highly porous cathode scaffold layers using high-volume, low-cost fabrication processes. Initial work focuses on $\text{Li}_{6.25}\text{Al}_{0.25}\text{La}_3\text{Zr}_2\text{O}_{12}$ (LLZO).

Objectives

The project objectives are: to determine processing methods and conditions that enable high-volume, low-cost production of solid state battery ceramic electrolyte, electrolyte-cathode bilayer structures, and solid state batteries based on these structures; and, demonstrate improved electrochemical and mechanical performance for these structures.

Approach

The impact of processing conditions and precursor properties on layer structure, electrochemical performance, and mechanical properties will be determined. Diagnostic tools such as electrochemical impedance spectroscopy, scanning electron microscopy, and synchrotron techniques will be used to interrogate the relationship between processing and layer quality. Commercially-available LLZO and cathode powders are used for all experiments to eliminate batch variations and ensure experimentally observed processing improvements are not due to variation of powder properties.

Results

Creating and maintaining good interfacial contact between LLZO and cathode material is expected to be one of the more difficult challenges to producing practical solid-state batteries. In order to overcome this issue an ionically conductive polymer is used as part of a composite cathode to act as a flexible, high-contact-area interfacial catholyte material between the LLZO and cathode active material. This is done with low temperature slurry deposition and infiltration methods which eliminates potential interdiffusion from high temperature co-sintering and enables the use of cathodes which are not stable at elevated temperatures.

The viability of the composite cathode strategy was assessed by assembling planar battery cells with the tape cast LLZO sheets developed in the previous reporting period. Two cathode materials were examined: NMC111 which serves as a model for several common oxide-based cathodes and a small-molecule organic cathode labeled Organic Cathode A (OCA). OCA is a naturally derived molecule with a theoretical capacity of 280

mAh/g at an average of 2.3V. Organic cathodes such as OCA generally have high specific capacities but are currently unusable in lithium ion batteries as they are soluble in liquid electrolytes and diffuse across the cell to react with the anode. Planar cells were constructed with both fully solid state cathodes and in a hybrid configuration with a small amount of liquid electrolyte. The anode for both NMC111 and OCA cells was applied by sputtering a gold interfacial layer on to the LLZO surface and applying 10 wt% Mg Li alloy by melting at 200°C.

NMC111 Battery Cells

Solid state cells are fabricated by drop casting a slurry containing the cathode active material, Super P carbon black, PVDF-HFP, succinonitrile, and LiTFSI in NMP solvent directly on to an LLZO pellet. The weight ratio of the PVDF-HFP:SN:LiTFSI catholyte is 1:2.67:1. The impedance and cycling performance of planar solid state NMC111 cells with 9.6 and 38 wt% of catholyte are shown below in Figure II.7.1. While both cells are capable of long term cycling the performance of both cells is poor with the 38 wt% catholyte cell reaching only 10% of its theoretical capacity. Examination of the voltage profile of a 38 wt% catholyte cell (Figure II.7.1, d) demonstrates the cell impedance prevents it from fully charging by the upper cut-off voltage.

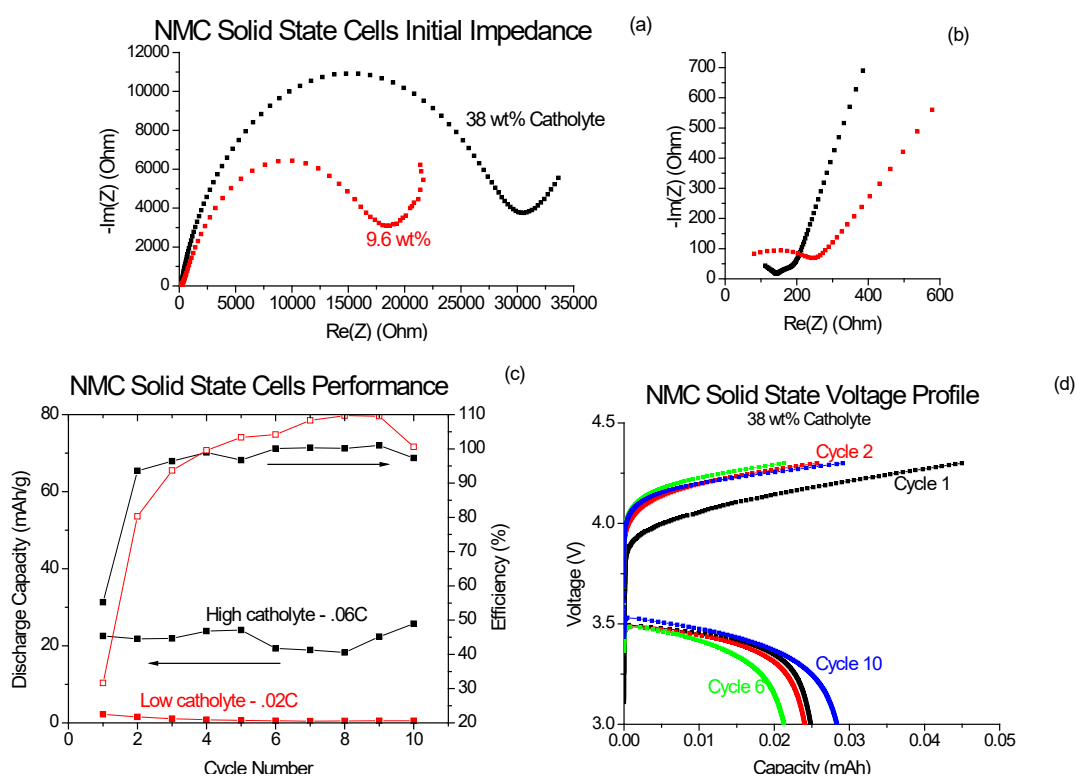


Figure II.7.1 Performance of solid state cells with NMC111 cathode including (a) cell impedance, (b) a magnified view of the contribution from the LLZO pellet, (c) cycling performance of the cells and (d) the voltage profiles of a cell with 38 wt% catholyte.

Performance of a liquid electrolyte hybrid cell (Figure II.7.2) makes it clear that ionic conduction is the main contributor to low performance in the NMC111 solid state cells. LLZO/Liquid electrolyte hybrid cells were assembled by adding a drop of LiPF_6 liquid electrolyte to a dried cathode composite with 38 wt% catholyte before sealing the battery case. Introduction of the liquid electrolyte reduced the cell impedance from $>30\text{k}\Omega$ to approximately $1\text{k}\Omega$. The hybrid cell was capable of cycling to the manufacturer specified cathode capacity (152 mAh/g) at a rate of 0.06C and maintained a capacity of 100 mAh/g at a rate of 0.37 C. These results are promising for future development of planar and scaffold-based LLZO solid state cells as they demonstrate our in-house sintered LLZO is capable of high performance with a good cathode/electrolyte interface.

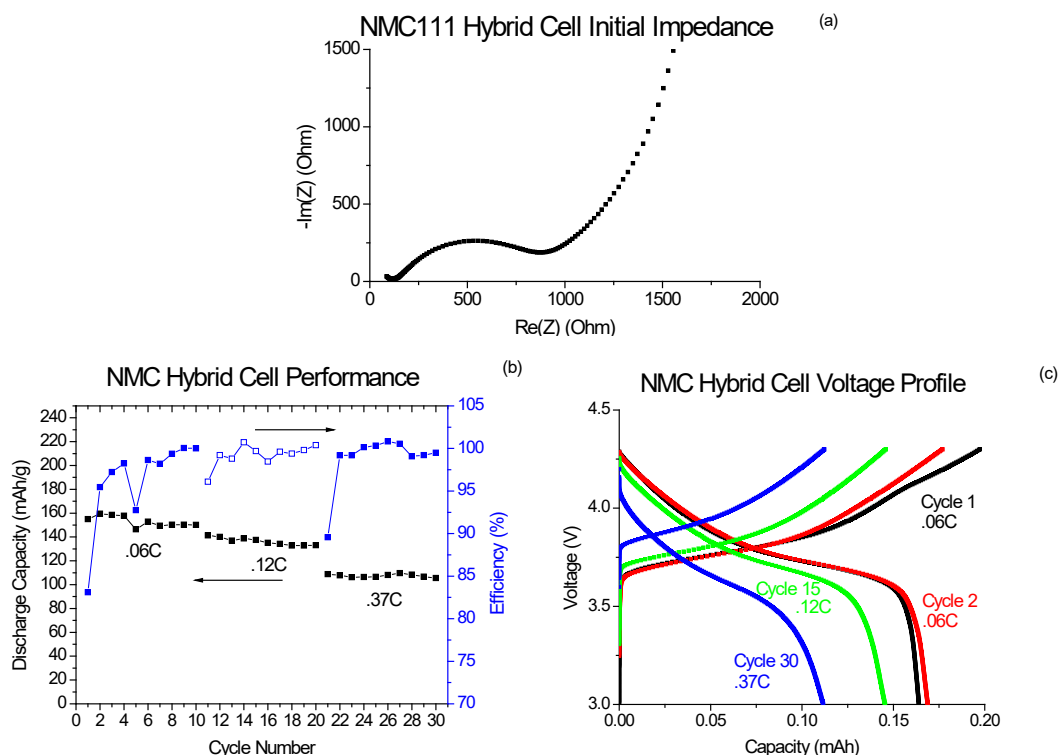


Figure II.7.2 Performance of an LLZO/liquid hybrid cell with NMC111 cathode including (a) cell impedance, (b) cycling performance of the cell at three rates, and (d) the voltage profiles of the cell during several cycles.

Organic Cathode A (OCA) Battery Cells

Solid state OCA cells were fabricated in the same fashion as the NMC111 cells. OCA cells with 48.8 wt% of catholyte had cell impedance in excess of 500 k Ω but were capable of cycling stably at approximately 20 mAh/g after demonstrating a 1st discharge capacity of 75 mAh/g. A notable aspect of the performance of the cells is that they operate at a coulombic efficiency greater than 100%. It is suspected that this is the result of poor Li⁺ transport or electrical conductivity in the cathode material which prevents a full initial discharge cycle and thus “fresh” OCA may be reacted during each subsequent discharge. This may be supported by the very high impedance of the as-assembled OCA cells. Much like the NMC111 solid state cells, if the LLZO/cathode material interface can be improved the OCA cells have promising performance characteristics.

Hybrid cells demonstrate how improved transport impacts cell performance (Figure II.7.3). The addition of the LiPF₆ liquid electrolyte reduced cell impedance from 500 k Ω to 10 k Ω and improved the 1st discharge capacity to 254 mAh/g. This is 91% of the theoretical capacity of the cell, however the voltage profile shows a plateau at 2.8 V during discharge which does not appear in subsequent cycles, indicating that some of this capacity is irreversible. The second discharge, which no longer includes irreversible capacity, was 132 mAh/g (47% of theoretical). Cell capacity fell 20% from the 2nd discharge to the 10th but stabilized on further cycling at higher rates. After 80 cycles the cell retained 75 mAh/g capacity at 0.13 C rate. In comparison OCA cells constructed with liquid electrolyte and a Celgard separator (Figure II.7.4) degrade much more rapidly at lower rates with no LLZO to block transport of dissolved OCA across the cell. Therefore, LLZO can serve as an enabling material for production of lithium batteries with high capacity small molecule organic cathode materials.

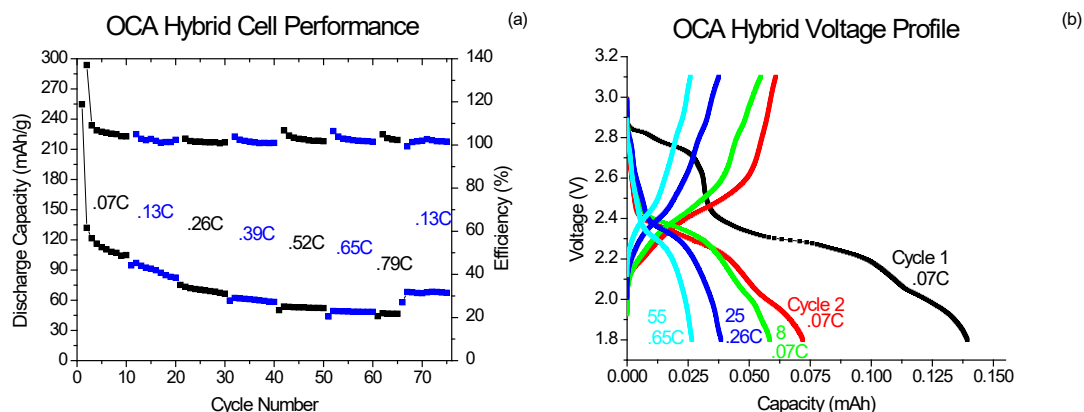


Figure II.7.3 Performance of a hybrid cell with organic cathode A including (a) cycling performance of the cell at several rates and (b) the voltage profiles of the cell during several cycles.

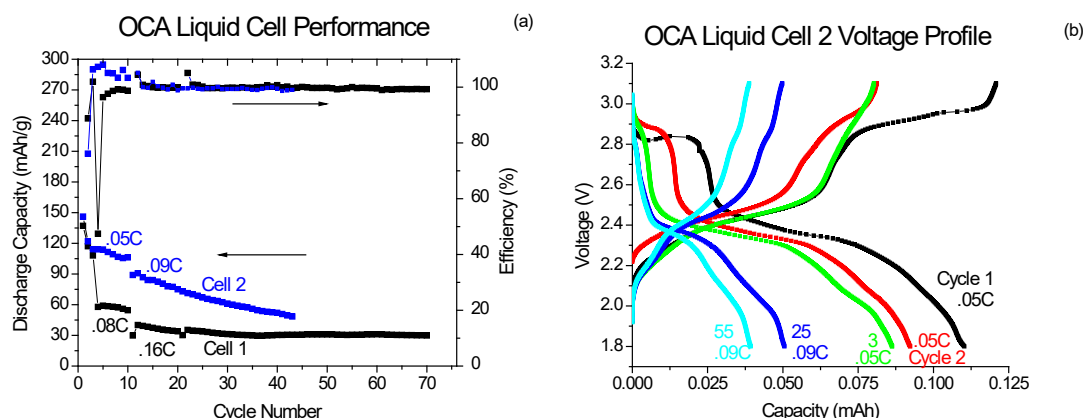


Figure II.7.4 Performance of liquid cells with organic cathode A including (a) cycling performance of the cells at two rates and (b) the voltage profiles of cell 2 during several cycles.

Porous Scaffold and Bilayer Structure Processing

Two methods for producing porous LLZO scaffolds and porous/dense bilayer structures have been investigated. First, tapes were fabricated in-house using the methylcellulose binder system and several pore forming additives including PMMA spheres and biologically-derived particles of starches and cellulose. Second, porous sheets were fabricated by Ragan Technologies with the high shear compaction process (HSC).

In-house tapes cast with PMMA spheres successfully retained their porosity after sintering. However, tapes cast with the biologically-derived pore formers did not retain their expected porosity through the casting, lamination and sintering processes. The porous layers produced with high shear compaction have microstructures much more suitable to cathode infiltration as can be seen in the bilayer displayed Figure II.7.5. This bilayer was made by laminating an HSC sheet with 80 vol% of 63 μm PMMA spheres to a single dense layer. The voids left behind are up to 50 μm in diameter and remain mostly spherical. The void spaces are connected at their contact points by openings 10 μm or larger. Additionally, the surface of the porous layer has large openings that continue deeper into the layer. The LLZO scaffold itself appears to be dense. The HSC porous layers will be used for future experiments creating both symmetric lithium cells and full cells with infiltrated cathode materials.

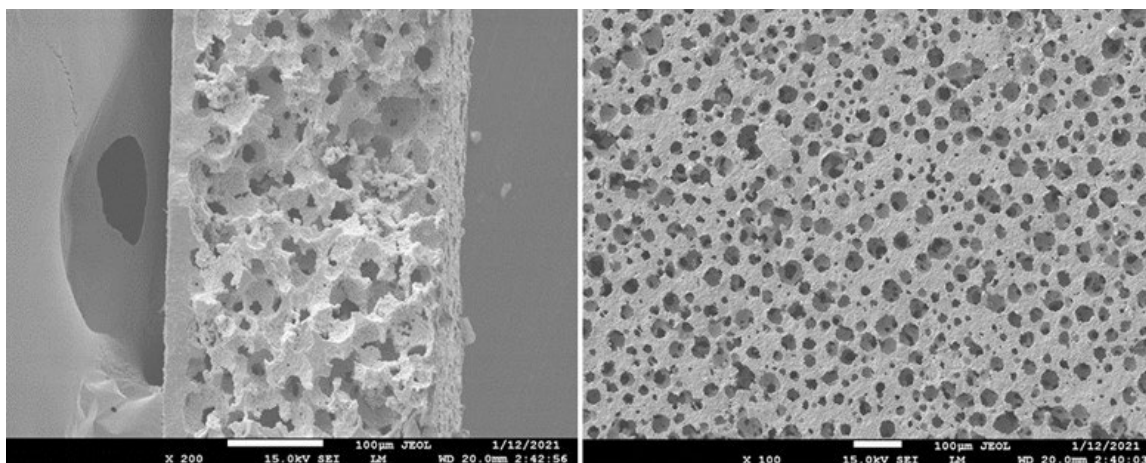


Figure II.7.5 LLZO bilayer structure made with porous HSC sheet sintered at 1100 °C for 5h. The HSC sheet contained 80 vol% of 63 μm PMMA spheres.

Conclusions

This project aims to prepare LLZO-based electrolyte and electrolyte/cathode scaffold structures using scalable processing techniques such as tape casting and furnace sintering. Work in this project period focused on developing a composite cathode which can be deposited on LLZO at low temperature and porous LLZO layers suitable for infiltration by the composite cathode. A catholyte consisting of PVDF-HFP, succinonitrile and LiTFSI was used to produce solid state battery cells with NMC111 and an organic cathode material. These cells suffered from high impedance which limited their performance. Examination of hybrid cells with liquid electrolyte added to the cathode composite identified the catholyte polymer as one of the key inhibitors of battery cell performance. LLZO further demonstrated that it can enable the use of liquid electrolyte soluble organic cathodes in a hybrid configuration where it impedes the transport of dissolved cathode material to the anode of the cell.

Several methods for producing porous LLZO scaffolds were examined. The methycellulose-based tape casting system developed in the previous project period was used in conjunction with several pore forming materials including PMMA spheres, corn starch and cellulose particles. Of those, PMMA is preferred, as the biologically derived starch and cellulose particles did not produce the desired amounts of porosity as they appeared to dissolve in the tape casting slurry. Another process known as high shear compaction used PMMA spheres to produce thick sheets with a high-volume fraction of open porosity that may be suitable for cathode infiltration.

It is recommended that future work focus on improving the performance of the catholyte polymer which has been identified as a critical component of the solid-state cells. This could be either through improvements to the material itself or replacing a large portion of its volume with an LLZO scaffold. Additionally, hybrid LLZO/Liquid electrolyte cells should be studied for their ability to enable cells made with high specific capacity organic cathode materials.

Key Publications

Jonson, Robert A., Eongyu Yi, Fengyu Shen, Michael C. Tucker. 2021. "Optimization of Tape Casting for Fabrication of $\text{Li}_{6.25}\text{Al}_{0.25}\text{La}_3\text{Zr}_2\text{O}_{12}$ Sheets." *Energy Fuels* 35, 10: 8982–8990.
<https://doi.org/10.1021/acs.energyfuels.1c00566>

Acknowledgements

All data presented in this report was generated by Robert Jonson. Thanks to Fengyu Shen for collaboration on porous LLZO layer fabrication and cathode composite optimization.

II.8 Higher Energy Density via Inactive Components and Processing Conditions (LBNL)

Vincent Battaglia, Principal Investigator

Lawrence Berkeley National Laboratory

M.S.70R018B

1 Cyclotron Road

Berkeley, CA 94720

E-mail: vsbattaglia@lbl.gov

Peter Faguy, DOE Technology Development Manager

U.S. Department of Energy

E-mail: Peter.Faguy@ee.doe.gov

Start Date: October 1, 2019

End Date: September 30, 2022

Project Funding (FY21): \$290,000

DOE share: \$290,000

Non-DOE share: \$0

Project Introduction

Li-ion batteries are ubiquitous. Millions of cells are produced every day, mostly in Asia. The manufacturing of Li-ion cells has been figured out. However, the development of new anodes and cathodes has not stopped. These materials are produced on a very small scale and need to be tested such that their performance is fully explored. The problem is that most researchers who produce new active materials do not understand how to properly combine the necessary inactive materials with the active materials nor how much to combine of the inactives to make a highly functional electrode and hence properly test their newly synthesized materials. In other words, what is not fully understood is that more carbon additive and more binder does not make the electrode perform better and can literally, impede performance. In addition, methods by which the materials are mixed and the rate at which the electrodes are dried can greatly impact the relative positions of the components which in turn impacts performance. A larger, perhaps more significant problem we try to address is the lack of manufacturing of Li-ion batteries in the US, which could be overcome with advances in manufacturing.

Objectives

This project is focused understanding the effects that processing conditions have on the configuration of the components used to make a functional Li-ion battery cathode in its final, dried form as an electrode laminate. To add to the challenge, we are trying to understand this in thick electrodes (*c.a.* 5 mAh/cm²) where drying conditions can dictate the degree of relative motion of the components and the final crystallinity of the polymer binder. Through this research we expect to understand processing conditions that lead to good performance and conditions that lead to less than good performance. A second objective of the research is to bring greater understanding as to physically where the inactive components absolutely need to be and the process conditions that lead to that configuration so that US companies can use that information to develop better manufacturing equipment that requires less materials and less energy. In this way, perhaps, the US can claim advanced manufacturing techniques and begin to shift the manufacturing of energy storage systems back to America.

Approach

The approach taken this year was to rely more heavily on the ever increasing focusability of SEMs and a newly acquired confocal microscope. With these tools, we investigated smaller and smaller quantities of the inactive components to the point just short of where the battery is incapable of performing no matter what processing conditions are applied. With our present electrode fabrication set-up, we can make changes to the following: material ratios, mixing order, mixing speed, mixing time; slurry viscosity (*i.e.*, solvent content), laminate casting thickness, and drying temperature and conditions. To assess the physical impact of these conditions, we used state of the art microscopy tools to identify the location and configuration of the inactive

materials relative to the active materials and location to the surface and current collector in a finished electrode to understand that at minimal inactives content what is the configuration needed such that the minimal amount can still lead to performance as good or better as larger fractions of inactives and what were the conditions that brought us there. As there are multiple knobs in the processing conditions and multiple ratios of components, we use a form of machine learning to assess the data and provide correlations that provide clarity and explanation and direction for subsequent experiments.

Results

The results this year build on the results of previous years. In this new direction, initiated this year, of pushing the inactive component content down while keeping the ratio of carbon and binder constant, we fabricated electrodes of four different fractions of active material 92.8, 94.6, 96, and 98%. In the initial experiments, the following process conditions were held constant: electrode loading (5 mAh/cm^2), drying temperature (120°C), mixing conditions (time and speed), and final porosity after calendaring (40%). The results of cycling with regards to normalized capacity *versus* cycle number are provided in Figure II.8.1. It should be noted that under the prescribed processing conditions there was satisfactory mechanical properties in that there was no mud cracking and acceptable adhesion and cohesion. These first results indicated that going all the way to 2% inactives was too far in that the electrode with just 2% showed dramatically more capacity fade than the other three. The cycling of the other three electrodes lies on top of each other through 50 cycles.

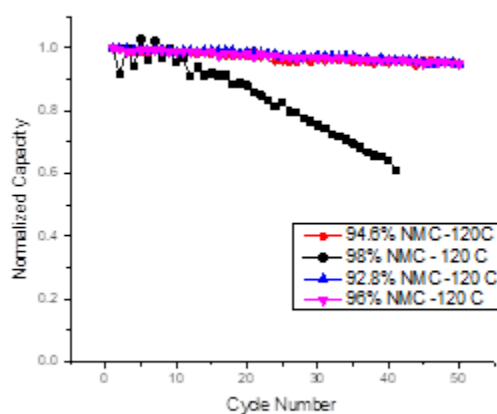


Figure II.8.1 Cycling performance of four electrodes made from the same processing conditions but different fractions of active material to inactive material. The numbers in the legend refer to the wt fraction of active material. 120 C refers to the drying temperature.

The question arises as to can we change our limited processing conditions to produce an electrode that can cycle well at 98% active material. However, before moving on, we wanted to investigate the effect of mixing order on material distribution. In that regard, we mixed carbon and active material, we mixed dissolved binder and active material, and we mixed the carbon and active material and then mixed the two with dissolved binder. The distribution of the materials for these three conditions is provided in Figure II.8.2.

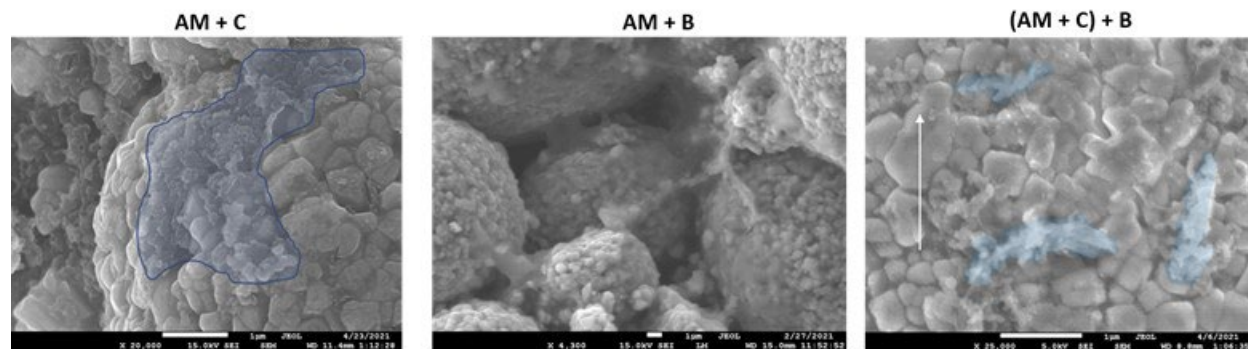


Figure II.8.2 SEM images of different mixtures of active material (AM), carbon additive (C), and polymer binder (B). Blue highlights are areas of carbon black.

What one sees when the carbon and active material are first mixed are thin patches of carbon partially covering the surface of the active material (highlighted in blue in Figure II.8.2, left.) For the mixture of active material and polymer if one looks closely one sees thin transparent sheets between particles and coating everything. When the carbon is first mixed with the carbon and then mixed with the polymer one no longer sees the thin patches of carbon covering the cathode (Figure II.8.2, left) but instead the carbon appears as if has been rolled up into sausages distributed throughout the electrode (Figure II.8.2, right).

We investigated different mixing orders of the three components of carbon black, binder, and active material and cast 5 mAh/cm² electrodes. The SEMs of the surface of the electrodes of different mixing orders are provided in Figure II.8.3. What we see at the surface for the electrodes when binder is mixed with either active material or carbon black first (Figure II.8.3, left and center), is electrodes that charge a bit in the SEM indicating poor electronic conductivity and smaller particles overall as compared to the electrode where the solids were mixed together and then the binder was added (Figure II.8.3, right). Close inspection of the center figure shows lots of carbon black on the surface despite the fact that this electrode charges in the SEM. The electrode where the binder and carbon black were first mixed, one sees on close inspection the binder stretched between active material particles. These observations would suggest that the electrode on the far right should perform better than the other two.

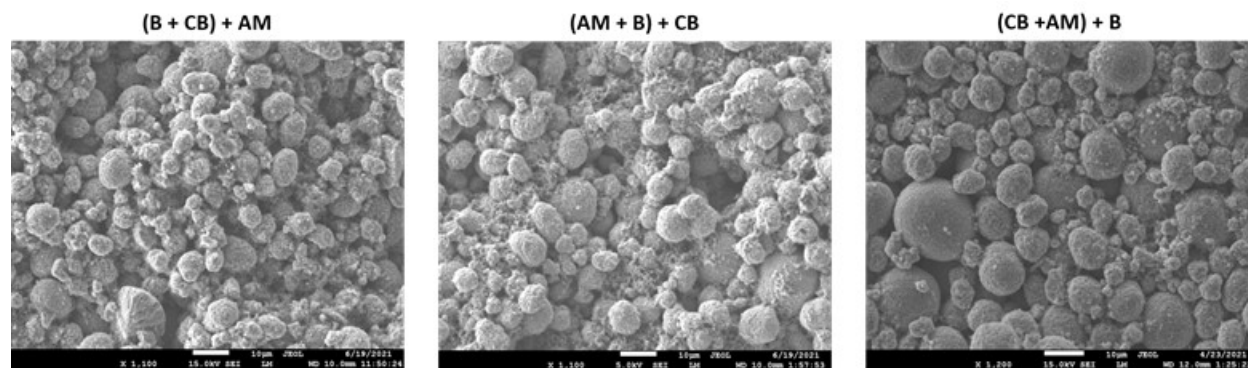


Figure II.8.3 SEMs of the surface of electrodes produced under three different mixing orders. Left, Binder plus carbon black first, then added the active material; center, active material and binder mixed, then added the carbon black; right, carbon black and active materials mixed first, then added polymer.

The confocal microscope was also used to study the electrode surface as the laminate dried. Figure II.8.4 shows the images collected from the microscope when active material and binder are added together and when active material is first mixed with carbon and then the binder is added. From this set of experiments, it appears that the addition of carbon to the active material protects the active material from being broken up upon further mixing with binder.

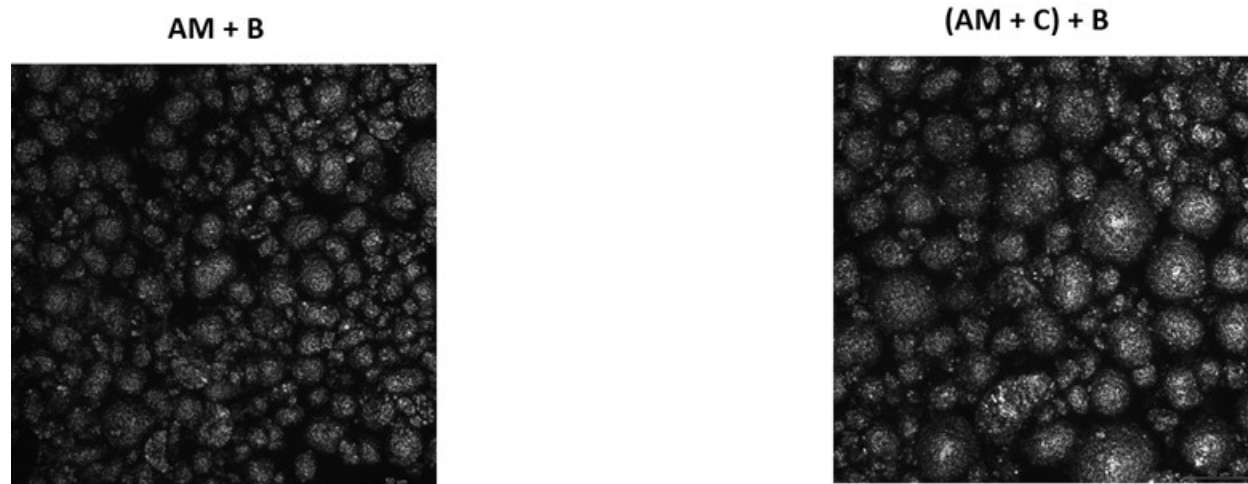


Figure II.8.4 Confocal microscope image of a dried film. Left, just active material and binder mixed; right, active material and carbon mixed then binder added.

We then made a bunch of electrodes with 94.6 % active material and the same carbon to binder ratio of 2.4 to 3 wt % each dried at a different temperature to quantify the influence of temperature on adhesion and cohesion. The results of these tests are provided in Figure II.8.5. Here we see the impact of drying temperature on mechanical properties with a reduction in adhesion as temperature rises until one reaches 180°C, and a steady increase in cohesion with temperature. A closer inspection of the laminate produced at 180°C drying temperature indicated a laminate that appeared to have a thin coating of polymer on the surface. The cycling data indicates that all of the electrodes cycle identically. This suggests that for this amount of inactives, the drying conditions and hence the mechanical properties have little impact on cycleability, which is to say the adhesion may vary but even at its lowest value, it is good enough.

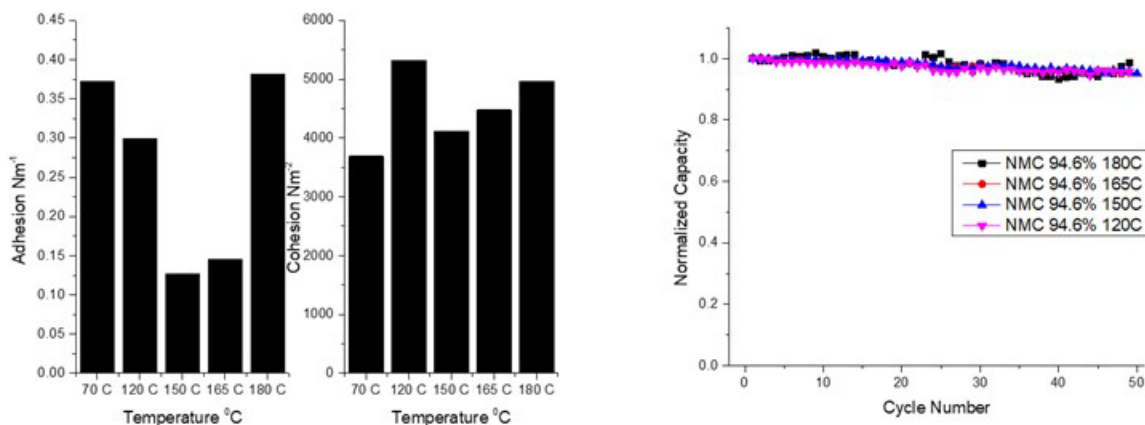


Figure II.8.5 Electrodes made with the same amount of inactives but dried at different temperatures. Left, the adhesion and cohesion data measured from peel tests; right, cycling data.

The last aspect of electrode fabrication investigated in 2021 was the impact of the amount of solvent used in the original slurry, which has a dramatic impact on viscosity and drying time. When we added extra solvent, we found that the laminates produced with 98% active material adhere well to the current collector. When less solvent was added to the slurry than usual, the slurry was more viscous and the resulting laminate showed some delamination but decent cohesion and we were able to make some intact cells. Interestingly, the

electrodes with the good adhesion showed poor cycleability and the electrodes produced with a high viscosity slurry with poor adhesion showed cycleability comparable to other electrodes that cycle well (Figure II.8.6).

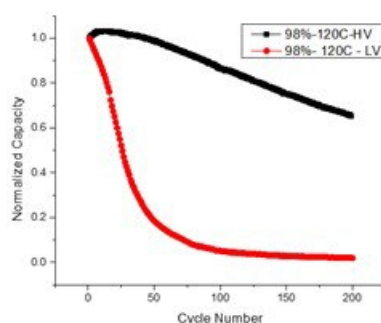


Figure II.8.6 Cycling data of two electrodes made with different amounts of solvent. Extra solvent leads to low viscosity (LV) and less solvent leads to a high viscosity slurry (HV).

Conclusions

This year has led to quite a bit of insight into the electrode fabrication as we have pushed to reduce the sum of the inactive components to 2 %. We found that in our original attempt to make low inactive content cathodes that there appeared to be a limit between 2 and 4 % inactives. For electrodes produced with low inactives we can see the carbon and binder distributions with SEM and that they arrange themselves differently depending on the order of mixing and that this order can impact the electronic conductivity and the size of the particles as the large NCM particles breakdown during mixing without first being mixed with carbon. We've seen that different drying conditions can lead to different mechanical properties but if the adhesion is good enough to allow for the punching of electrodes without flaking, the cyclability is not impacted. We have seen that drying the electrode at 180°C can accelerate the drying time and also lead to improved adhesion. We also see what appears to be a film of melted polymer on the surface when drying at 180°C. It is known in the polymer community that polymer crystallinity improves cohesion but is detrimental to adhesion. To some extent, we have seen this here. With drying above the melt-temperature we are seeing good adhesion to the current collector and good cohesion. This may be the result of low crystallinity leading to good adhesion and a melted polymer film on the surface that promotes good cohesion.

Next year we intend to further study the impact of slurry viscosity on electrode performance, push the inactives content to below 2%, and try to understand a little better the source of capacity fade for electrodes of 5 mAh/cm². We also want to understand a little better the relationship between intrinsic cathode material conductivity and the minimum carbon fraction required and start examining the ratio of carbon and binder and how and if the minimum carbon needed to make an active material powder conductive and the minimum amount of binder needed to make a laminate that is cohesive and adhesive is impacted when all three components are present. Ultimately, we hope to make electrodes with small quantities of binder and carbon and provide explanation as to how one can get to such low concentrations, where the inactives are located in the electrode, and what are the processes required to get there.

Acknowledgements

The majority of this work was performed by Dr. Dilni Koggala Wellalage, post doc. She was provided technical support primarily by Dr. Yanbao Fu and Dr. Kenneth Higa.

II.9 Novel data-mining and other AI approaches for synthesis and processing of cathode materials (Lawrence Berkeley National Laboratory)

Gerbrand Ceder, Principal Investigator

Lawrence Berkeley National Laboratory
One Cyclotron Road, Building 33, Room 142B
Berkeley, CA 94720
E-mail: gceder@lbl.gov

Peter Faguy, DOE Technology Development Manager

U.S. Department of Energy
E-mail: Peter.Faguy@ee.doe.gov

Start Date: January 1, 2019	End Date: September 30, 2022	
Project Funding (FY21): \$200,000	DOE share: \$200,000	Non-DOE share: \$0

Project Introduction

A major obstacle to large-scale manufacturing and utilization of advanced materials arises from the inability to devise synthesis methods for materials in a rational manner. This is an issue for novel predicted materials, which have never been synthesized, as well as for existing materials, which often have to be synthesized with particular precursors, at particular temperatures, or with very targeted composition and structure, in order to achieve optimized behavior and lower cost when producing cathode materials on a large scale.

To bridge the gap between materials prediction and production, this project focusses on the following aspects:

- 1) Create a database of the synthesis of commercial battery materials automatically extracted from patents using advanced natural language processing (NLP) techniques.
- 2) Understand synthesis complexity so that it can be used to guide the synthesis to achieve optimal temperatures, composition, and cost for a given application and performance requirement.

Objectives

Build a comprehensive database of commercial battery materials and learn design principles for the rational synthesis of cathode materials with lower cost and high performance.

Approach

The project will be approached in two aspects.

1. **Automated database construction for the synthesis of commercial battery materials.** Our objective is to extract all known synthesis methods for battery cathode materials from patents, organize them, make them available, and use them for statistical learning of novel synthesis recipes. In order to obtain details of synthesis procedures from patents and convert them into a machine-readable format, we developed a data mining pipeline that uses machine learning techniques to retrieve “codified synthesis recipes” of inorganic compounds from available patents. The most important steps of the pipeline include: i) collecting patents available online using our own web scraper, and parsing the XML text into the plain text; ii) extraction of experimental sections and identification of paragraphs describing materials synthesis in an unsupervised way by using a topics modeling approach; iii) extraction of “codified recipes” for the synthesis procedures which include final product, starting materials, operations and conditions of synthesis, via named entity recognition methods; iv) accumulating all recipes in the database for subsequent data mining.

2. **Understanding of synthesis complexity for cathode materials.** A target material can be potentially synthesized from various recipes, namely, different precursors, different conditions, and even different synthesis types. The selection of recipes depends on both scientific reasons such as bonding, reactivity, and melting point, and anthropogenic reasons such as prior success in the literature, convenience, applications, price of precursors, and human bias. Our approach is to conduct a historical statistical analysis on nearly all the published synthesis recipes for typical cathode materials. By tracking the shift of target composition and synthesis parameters over time, we reveal the influence of anthropogenic factors and their correlation with synthesis parameters.

Results

Automatically extracted database of synthesis recipes for battery materials

To investigate the optimal synthesis method for cathode materials, sufficient data points are necessary. In this project, we focus on the automatic extraction of synthesis data from publicly available patents. Patents may serve as a rich and high-quality data source because (a) R&D institutions and companies are motivated to publish details of synthesis experiments to protect their intellectual property, and (b) patents are usually strictly examined by national patent offices before granted. Hence, a database extracted from patents can potentially provide valuable insights for the synthesis of commercial battery materials.

On top of the work in the last two years, we have further improved our text-mining pipeline and have extracted 5,360 synthesis recipes, covering most commercial battery materials. Starting from the 6.8 million US utility patents granted since 1976, we identified 660,121 patents potentially related to battery studies by looking for the keywords “battery” or “batteries”. By applying a synthesis paragraph classifier [1] on all paragraphs from these patents, we located 7,409 patents that contain synthesis paragraphs. By applying a materials entity recognition model [2] on these synthesis paragraphs, we were able to recognize what materials are targeted and what precursor materials are used to synthesize the cathode materials in these patents. We found 6,126 patents containing precursors and 6,304 patents containing target materials. Finally, by balancing the reactions from precursors to target materials [3], 5,360 chemically meaningful reactions were extracted from 2,475 patents. For each reaction, the corresponding experimental operations and conditions were also extracted using a synthesis operation extractor. Several challenges of applying this pipeline to the patent text have been overcome to achieve high throughput. These problems include but are not limited to: some materials are not well-formatted with special symbols and unnecessary spaces, target materials are not usually mentioned in the same paragraph as precursors, reactions with some precursors are hard to balance because of missing and implied information, and so forth.

In order to verify that the extracted database represents most patents relevant to battery materials, manual inspection and cross-comparison with pertinent studies were conducted. We first compared the estimated fraction of patents with VPS data [4], which is an inventory of patents published by national laboratories all over the US. A selection of lab-identified leading experts across several “hot” technology areas have classified these patents into various categories, such as energy, engineering, and devices. Out of 20,129 issued patents, 196 patents are classified in the “battery” category. We further refined the list into subcategories by manual inspection, including “inorganic synthesis”, “inorganic materials mentioned but no synthesis”, “materials mentioned but no inorganic materials”, and “others”. At last, 46 patents are confirmed to contain synthesis information of inorganic materials for battery applications. Hence, the ratio of patents on battery materials synthesis over all VPS patents is $46/20,129 = 2.3\%$. It is worth noting that this value might overestimate the corresponding ratio for US patents because VPS patents are from academic organizations, which tend to have a larger fraction of materials research than industry. For our data, the fraction of patents on battery materials synthesis over all US patents is $7,409/660,121 = 1.1\%$. The closeness of these two estimated ratios indicates our extracted database is relatively complete. In other words, most patents of interest should have been covered in our database. In addition, we also compared with reports on battery studies. Thackeray and Amine [5] claimed more than 3,300 patents on lithium nickel cobalt manganese oxide (NCM) electrode materials have been published. In our database, 2,984 out of the 7,409 patents contain mentions of NCM materials. Considering our database is focused on synthesis, which is a subset of all materials studies, the agreement on the number of

respectively. The distribution of synthesis types for NCM and LiFePO_4 are displayed in Figure II.9.2. For both NCM and LiFePO_4 , solid-state synthesis and sol-gel synthesis are the most common methods to synthesize them. However, Precipitation synthesis is more frequently used than hydrothermal for NCM, while the order is reversed for LiFePO_4 . The difference occurs due to the chemical difference between oxide and phosphate materials, which will be studied in the following year.

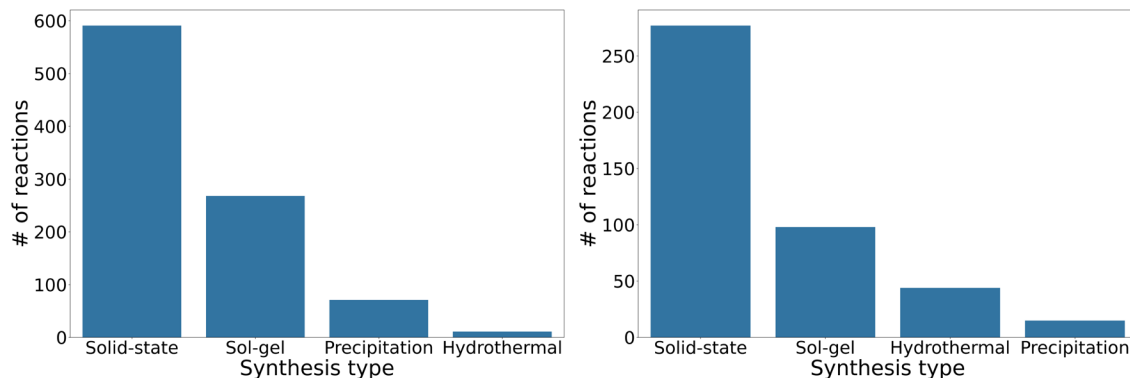


Figure II.9.2 Number of patents for the synthesis of NCM (left) and LiFePO_4 (right) materials in different synthesis types.

For NCM materials, the composition space for the optimization of performance and cost is relatively large. In our database, NCM materials are synthesized as target materials in 1,158 patents. We project these NCM materials into the LiNiO_2 - LiCoO_2 - LiMnO_2 phase diagram (Figure II.9.3) based on the ratio of Ni: Co: Mn. For materials with the same ratio of Ni: Co: Mn, the year of the earliest patent is displayed by color-coding. Many patents before 2010 are around the equimolar region, i.e., the center of the diagram, close to NMC111. However, more recent patents focus on the corners of high Ni and high Mn components. The shift of research interest reflects two branches of mainstream efforts to optimize the composition of NCM materials. One branch is to develop the so-called high-Ni cathode materials. Because of the high cost of raw materials for Co, a higher fraction of Ni is preferred to decrease the use of Co. The other branch is to develop Li-excess cathode materials [6]. Based on the theoretical prediction by Liang et al. [7], stoichiometric NCM materials in the high Mn region are unstable. Indeed, all materials in this region have Li content per formula unit larger than 1. In the following year, we will investigate how the synthesis conditions are varied when pushing the synthesis of these high-Ni and high-Mn NCM materials to success.

For LiFePO_4 , the variation of composition is relatively small but numerous variants of synthesis parameters have been attempted. In our database, 434 reactions for LiFePO_4 were extracted from 218 patents. The highest firing temperature in each synthesis recipe along with the publication year of the patent is displayed in Figure II.9.4. In the years before 2006, few patents existed because the first patent on solid-state synthesis for LiFePO_4 by Goodenough et al. [8] was not issued until 1999. The first data point in the year 2002 in Figure II.9.4 is the divisional version [9] of the patent in 1999. After 2006, more patents were published to diversify precursors and conditions in the synthesis, though solid-state synthesis was still the only method at that time. After 2009, different synthesis types were adopted, including hydrothermal, sol-gel, and precipitation syntheses. Overall, a trend is observed that the lower bound of synthesis temperature is decreasing over years. This is probably related to the practical factor that lower temperature is easier to be achieved in production. Besides, the cost can be reduced by selecting appropriate precursors. In the following year, we will investigate the thermodynamic factors limiting the selection of precursors and synthesis temperature for LiFePO_4 .

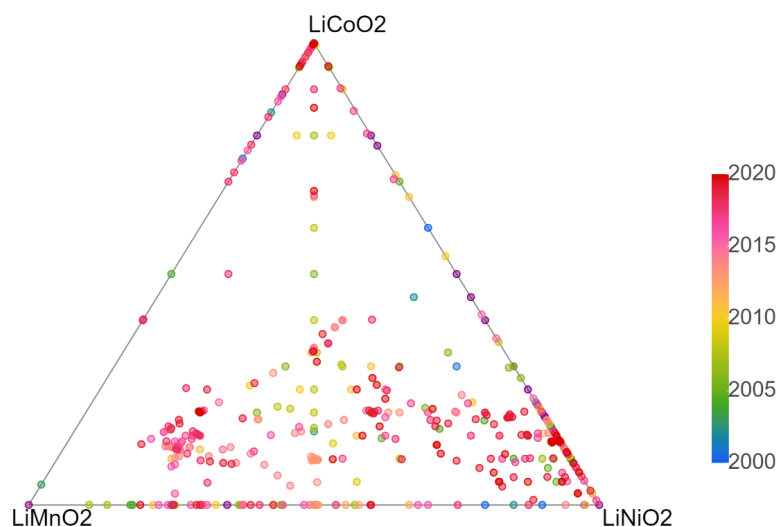


Figure II.9.3 Earliest years of patents on the synthesis of NCM materials projected in LiNiO_2 - LiCoO_2 - LiMnO_2 phase diagram.

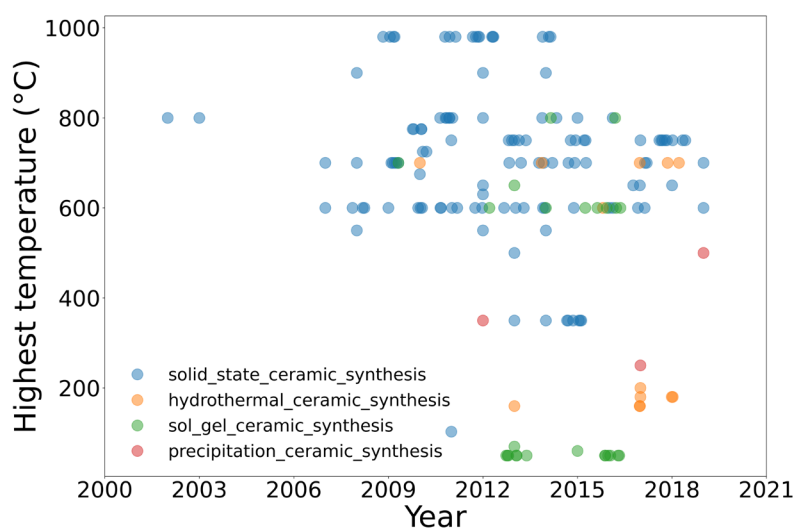


Figure II.9.4 Highest synthesis temperatures for LiFePO_4 extracted from patents in different years.

Conclusions

We have improved our text-mining pipeline and have extracted 5,360 synthesis recipes from US patents, covering most commercial battery materials. The completeness of the extracted database is verified by manual inspection and cross-comparison with pertinent studies. We demonstrate the advantage of our database for large-scale statistical analysis by rediscovering important elements for battery applications. Through case studies on NCM and LiFePO_4 materials, we reveal the shift of research interest on the composition of NCM and synthesis temperature for LiFePO_4 , which also provides clues for our continuing research in the following year.

Key Publications

1. Kononova, Olga, Tanjin He, Haoyan Huo, Amalie Trewartha, Elsa A. Olivetti, and Gerbrand Ceder. "Opportunities and challenges of text mining in materials research." *Iscience* 24, no. 3 (2021).

References

1. Haoyan Huo, Ziqin Rong, Olga Kononova, Wenhao Sun, Tiago Botari, Tanjin He, Vahe Tshitoyan, and Gerbrand Ceder. "Semi-supervised machine-learning classification of materials synthesis procedures." *npj Computational Materials* 5, no. 1 (2019): 1–7.
2. Tanjin He, Wenhao Sun, Haoyan Huo, Olga Kononova, Ziqin Rong, Vahe Tshitoyan, Tiago Botari, and Gerbrand Ceder. "Similarity of precursors in solid-state synthesis as text-mined from scientific literature." *Chemistry of Materials* 32, no. 18 (2020): 7861–7873.
3. Kononova, Olga, Haoyan Huo, Tanjin He, Ziqin Rong, Tiago Botari, Wenhao Sun, Vahe Tshitoyan, and Gerbrand Ceder. "Text-mined dataset of inorganic materials synthesis recipes." *Scientific data* 6, no. 1 (2019): 1–11.
4. Visual Patent Search. Accessed December 3, 2021. <https://vps.labworks.org/>.
5. Thackeray, Michael M., and Khalil Amine. "Layered Li–Ni–Mn–Co oxide cathodes." *Nature Energy* 6, no. 9 (2021): 933–933.
6. Lee, Jinhyuk, Alexander Urban, Xin Li, Dong Su, Geoffroy Hautier, and Gerbrand Ceder. "Unlocking the potential of cation-disordered oxides for rechargeable lithium batteries." *science* 343, no. 6170 (2014): 519–522.
7. Liang, Chaoping, Fantai Kong, Roberto C. Longo, Santosh Kc, Jeom-Soo Kim, SangHoon Jeon, SuAn Choi, and Kyeongjae Cho. "Unraveling the Origin of Instability in Ni-Rich $\text{LiNi}_{1-2x}\text{Co}_x\text{Mn}_x\text{O}_2$ (NCM) Cathode Materials." *The Journal of Physical Chemistry C* 120, no. 12 (2016): 6383–6393.
8. Goodenough, John B., Akshaya K. Padhi, K. S. Nanjundaswamy, and Christian Masquelier. "Cathode materials for secondary (rechargeable) lithium batteries." U.S. Patent 5,910,382, issued June 8, 1999.
9. Goodenough, John B., Akshaya K. Pahdi, K. S. Nanjundaswamy, and Christian Masquelier. "Cathode materials for secondary (rechargeable) lithium batteries." U.S. Patent 6,391,493, issued May 21, 2002.

II.10 Minimizing Side-Reactions in Next-Generation Lithium Ion Battery Cathodes Through Structure-Morphology Optimization (ANL)

Venkat Srinivasan, Principal Investigator

Argonne National Laboratory
9700 South Cass Avenue
Lemont, IL 60439
E-mail: vsrinivasan@anl.gov

Peter Faguy, DOE Technology Development Manager

U.S. Department of Energy
E-mail: Peter.Faguy@ee.doe.gov

Start Date: October 1, 2020

End Date: September 30, 2021

Project Funding (FY21): \$400,000

DOE share: \$400,000

Non-DOE share: \$0.00

Project Introduction

The goal of this project is to improve the performance of next-generation Li-ion battery cathodes by synergistically tuning the structure of the cathode along with its morphology. Understanding the densification behavior of LLZO type oxide based ceramic SSEs, and how that improves its overall conductivity, is another major aim of this project. Improvement in performance will be achieved by developing multi-scale theoretical methods, coupled with *in situ* operando experimentation to create a one-of-a-kind “particles by design” framework. This framework will go beyond the traditional “materials by design” approach used today, wherein the focus is on calculating material crystal structure, by incorporating morphological features to create particles in which the exposed surfaces are tuned to maximize performance. This year, we continued our work on the carbonate based coprecipitation process for making cathode precursors, high temperature calcination process for understanding the lithiation mechanism into Ni-rich NMC hydroxides, and densification of LLZO solid electrolytes. NMC111-carbonate and individual Mn, Ni and Co carbonate were coprecipitated to understand the growth process of these carbonate cathode precursors. To investigate the lithiation of Ni-rich NMC-hydroxide precursors, *in situ* characterization of the high temperature calcination was conducted under both the pre-treated and non-pre-treated conditions. During calcination, extent of lithiation and particle size evolution were extracted from the x-ray diffraction data. For SSEs, influence of external pressure on the overall densification experienced by LLZO have been investigated. Understanding the evolution of microstructure and particle morphology during the synthesis of cathode precursors and SSEs will help to improve the performance of next generation lithium-ion batteries.

Objectives

The overall objectives of this project can be divided into three different parts. The first component deals with the investigation of the impact of solution pH, ammonia content, and transition metal concentration on the size, shape, porosity, tap density and facet dependent reactivity of cathode precursors during the coprecipitation process. As a part of this task, we aim to determine the reaction products under equilibrium conditions while coprecipitating $\text{Ni}_{0.33}\text{Mn}_{0.33}\text{Co}_{0.33}\text{CO}_3$. We also tried to elucidate the impact of thermodynamic and kinetic factors in the growth of primary and secondary particles for NMC-carbonate precursors. The second task involves *in situ* characterization of the calcination of NMC-hydroxide precursors in the presence of LiOH using x-ray diffraction techniques. Extraction of information regarding the extent of lithiation and evolution in particle size is the major aim of this study. Understanding impact of the pre-treatment process in determining the magnitude of lithiation and particle size evolution is also a major objective of this project. In the third task of the project, the main objective is to understand the influence of externally applied pressure on the densification and grain growth observed during the sintering of LLZO pellets. To accomplish this, we developed a phase-field based mesoscale models capable of capturing the sintering process between multiple

LLZO particles under the influence of externally applied pressure. Influence of particle morphology in determining the relative density of LLZO obtained under pressure assisted densification will also be elucidated as part of this research activity.

Approach

To understand how the structure and morphology of cathode and electrolyte particles evolve during the synthesis steps, experimental techniques as well as computational methodologies have been developed. Attempts have been made to establish good correlation between the two for proper elucidation of the physical and chemical phenomena that controls the structure and morphology of these battery particles. The computational approach involves capturing the physical phenomena observed at the atomistic length scale, as well as the mesoscale level.

The atomistic calculations are carried out using spin-polarized Density Functional Theory (DFT) as implemented in the Vienna Ab Initio Simulation Package (VASP). The exchange-correlation potentials are treated by the generalized gradient approximation (GGA) and the interaction between valence electrons and ion cores is described by the projected augmented wave (PAW) method. Moreover, the GGA+U scheme is used for applying the on-site correlation effects among 3d electrons of the transition metal.

For the mesoscale analysis, mass balance equations at the continuum level are solved for the estimation of reaction kinetics as a function of solution pH, ammonia content and concentration of transition metal salt. Phase field-based methodologies are adopted to capture the surface growth of transition metal carbonate particles, which leads to the formation of aggregated nano sized primaries. A continuum-based nucleation, growth and aggregation model have been developed for estimating the secondary particle size of the NMC111 carbonate precursors. Phase field-based methodologies are used to predict the densification and sintering of LLZO particles under externally applied pressure. A combination of volume conserving Cahn-Hilliard equations, and non-conserving Allen-Cahn equations are solved to capture the densification and grain ripening behavior of LLZO particles. Pressure induced deformation of the LLZO particles is captured by solving the stress equilibrium equations.

Experimental measurement of the change in lattice structure and particle morphology during high temperature calcination was conducted using in-situ X-ray characterization. These in-situ X-ray diffraction provided experimental input and verification for the results derived from computational models. In the *in-situ* x-ray diffraction methodology, $\beta\text{-Ni}_{0.8}\text{Mn}_{0.1}\text{Co}_{0.1}(\text{OH})_2$ and $\text{Ni}_{0.8}\text{Mn}_{0.1}\text{Co}_{0.1}\text{O}$ precursors were loaded into separate quartz capillaries along with $\text{LiOH}\cdot\text{H}_2\text{O}$ as a lithium source. X-ray diffraction patterns were collected once per minute during heating to 800°C between 2 to 5°C per minute with a 90-minute temperature hold at 500°C . Diffraction patterns were refined using the Rietveld method to determine the relative phase fractions, unit-cell parameters, and domain sizes.

Results

The results obtained from the research work conducted as part of this project will be divided into three categories. The first one will describe the evolution of NMC carbonate based cathode precursors during the coprecipitation process. The second set of results will elaborate the calcination mechanism of Ni-rich NMC-hydroxides with LiOH as the source of lithium. The third, and final, section will elaborate the influence of external pressure on the densification behavior experienced by LLZO solid electrolytes.

Computational modeling of the co-precipitation of $\text{Ni}_{0.33}\text{Mn}_{0.33}\text{Co}_{0.33}\text{CO}_3$ cathode precursors

Last year a computational model for simulating the coprecipitation of MnCO_3 precursors were developed, which took into account the thermodynamic and kinetic factors of the chemical reaction occurring within a batch reactor. In the present year, the same computational methodology has been extended to capture the coprecipitation of $\text{Ni}_{0.33}\text{Mn}_{0.33}\text{Co}_{0.33}\text{CO}_3$ (NMC-carbonate) under the same conditions. Experimental coprecipitation of the desired cathode precursor was conducted in a batch reactor, where NH_4HCO_3 was used as the source of carbonate anions. The ratio of ammonia (NH_4^+) over transition metal (TM^{2+}) was maintained

at 40:1. The precipitated NMC-carbonate particle morphology is shown in Figure II.10.1(a). Energy dispersive X-ray spectroscopy (EDX) was conducted on top of the precipitates to understand the relative amount of various TMs present within them. Figure II.10.1(b-e) clearly reveals that even though equal amounts of all the three TMs were used at the beginning of the reaction, maximum amount of Mn is precipitated (around 53%), then Co (approximately 37%), and only a small fraction of the Ni actually is precipitated (around 10%). To understand this variability in TM distribution within the precipitated NMC-carbonates, thermodynamic calculations were conducted while considering the solubility of the different hydroxides and carbonates that can precipitate for the different TMs being considered here. By solving mass balance relations for the different TMs (Ni, Mn, Co), bicarbonate anions, and ammonia, while maintaining global charge neutrality within the solution, relative amount of precipitates under equilibrium conditions were estimated. The computationally predicted relative amount of Ni, Co and Mn within the precipitates are shown in Figure II.10.1(f) as a function of ammonia over transition metal ratio. It is evident that increasing the amount of ammonia leads to non-uniform deposition of the TM mostly due to the formation of metal-ammonia complex. The higher solubility of NiCO_3 as compared to Mn and Co-carbonates also contributes to this non-uniformity.

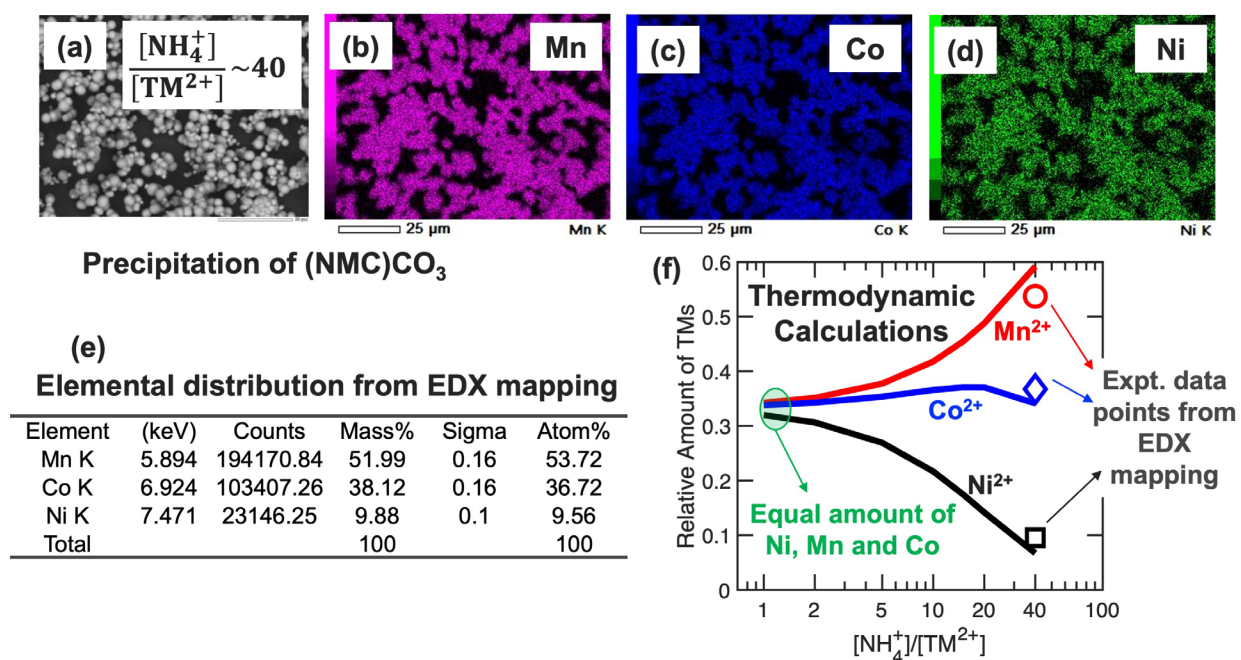


Figure II.10.1 Elucidation of transition metal carbonate precipitation reaction mechanism from the relative amounts of precipitated transition metals in NMC-carbonates. (a) SEM image of the precipitated NMC-carbonates, while maintaining ammonia over transition metal ratio of 40:1. (b) – (d) Distribution of the Mn, Co, and Ni within the precipitate. Uniform distribution of the transition metals indicates similar composition of Mn, Co, and Ni within all the particles. (e) Mass and atomic percentage of Mn, Co, and Ni within the precipitate. It is evident that maximum amount of Mn is deposited, then Co, and very few Ni gets precipitated. It is possible to form transition metal carbonates in two possible ways: i) Precipitation due to reaction between carbonate anions and transition metal ammonia complex, and ii) Direct precipitation due to reaction between metal cations and carbonate anions. (f) Computationally predicted relative amount of free transition metals floating within the solution is plotted with respect to ammonia over transition metal ratio. The experimentally observed relative amount of Mn, Co, and Ni ions within the NMC-carbonate precipitates are demonstrated by the symbols. Extremely good correlation between the computational prediction and experimental observation indicates that precipitation of transition metal carbonates occurs due to reaction between the free transition metal cations and carbonate anions. In the present calculations, even though equal amount of Mn, Co and Ni salts were used, very different amount of the three transition metals were precipitated. To obtain equal amount of Mn, Co, and Ni, it is suggested to operate at ammonia over transition metal ratio around 1.0, which is highlighted by the green circle.

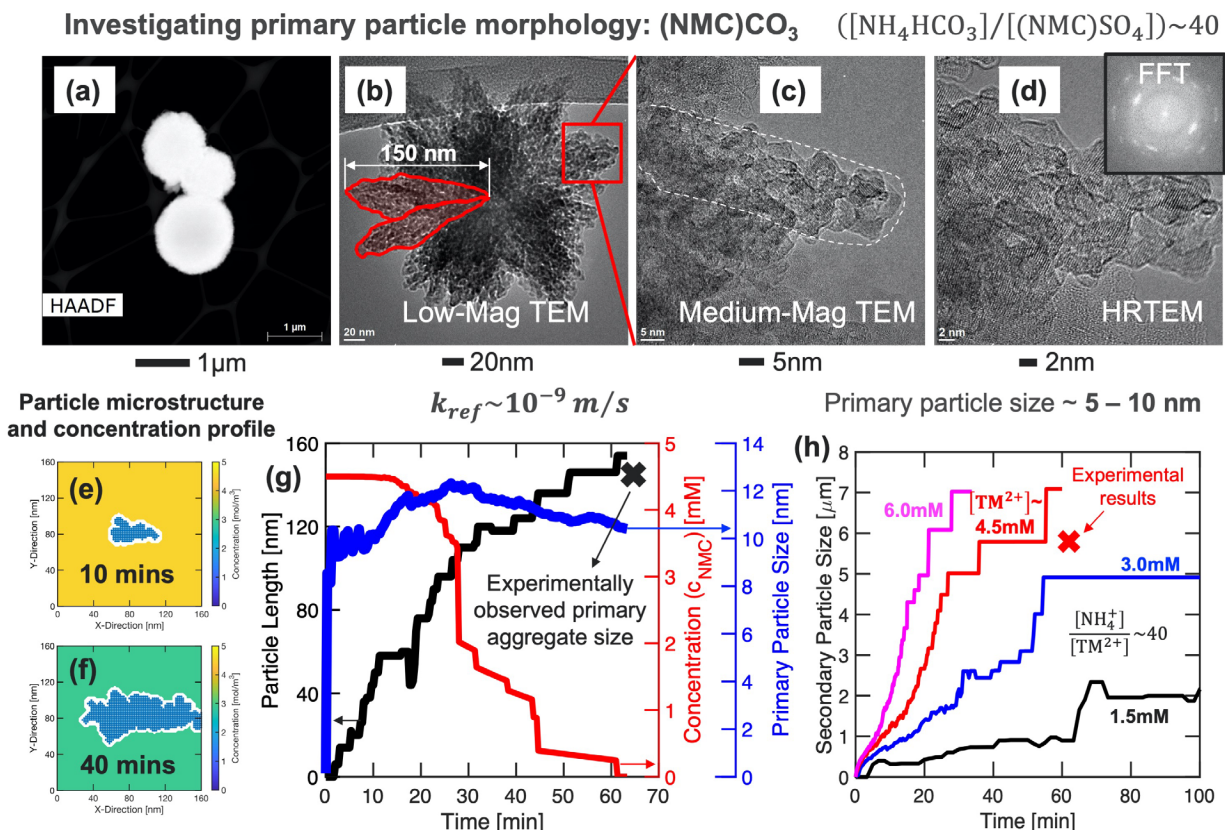


Figure II.10.2 Deciphering the primary particle morphology and growth rate of (NMC)CO₃. (a-d) TEM image of the precipitated NMC-carbonate cathode precursors. It is evident that the primary particle size ranges between 5 – 10 nm. These individual primary particles combine with others and form primary aggregates, which are approximately 150 nm long and 30 – 50 nm wide. The X-ray diffraction pattern shown in the inset of (d) indicates a pseudo single crystal nature of these primary aggregates. Usually, growth of surface particles on top of existing ones leads to the formation of pseudo single crystals. Accordingly, we conclude that the primary aggregates are formed by the surface growth mechanism, whereas agglomeration of these primary aggregates leads to the formation of the micron sized secondary particles (as shown in (b)). (e-f) Computationally simulated growth of the NMC-carbonate cathode precursors through the surface growth mechanism. Particle morphology and reactant concentration after 10 mins and 40 mins are shown here. (g) Evolution of the primary particle size (blue curve) and primary aggregate size (black curve) as a function of time. The red curve shows how the reactant concentration within the solution changes over time. It is evident that the particle growth after 1 hour ceases to occur due to the complete depletion of the reactants. Experimentally observed size of the primary aggregates is shown by the black cross symbol. The computational model predictions provide reasonable agreement with the experimental observations. (h) Evolution in (NMC)CO₃ secondary particle size with time as predicted by the Kinetic Monte Carlo (KMC) scheme. Evolution of the secondary particles are expected to occur through the nucleation, growth, and aggregation phenomena. Effect of different transition metal concentration on the secondary particle size is also shown, where increasing the concentration of transition metal salt leads to faster growth and larger secondary particles. The experimentally observed secondary particle size for (NMC)CO₃ with 4.5 mM transition metal is shown by the red cross symbol, which indicates good correlation between computation and experiment.

Next, the morphology of the primary and secondary particles of the precipitated NMC-carbonate cathode precursors are investigated using SEM and TEM imaging techniques. Figure II.10.2(a-d) clearly indicate that the NMC-carbonate particles consist of nano-sized primaries, with sizes in the range of 5 – 10 nm. These primary particles exist in an aggregated fashion, which forms through the surface growth mechanism evident from the X-ray diffraction pattern demonstrated in the inset of Figure II.10.2(d) reminiscent of pseudo single crystal structures. Agglomeration of the primary aggregates are expected to give rise to the secondary particles usually observed in SEM images. Phase field based computational methodology is developed for capturing the formation of the primary aggregates through the surface growth mechanism. Evolution in particle morphology and reactant concentration profile around the precipitates are shown in Figure II.10.2(e) and (f) after 10 mins and 40 mins, respectively. The reason behind the enhanced growth along a particular direction is still unclear,

which can be attributed to the preferential nucleation of NMC-carbonate particles along certain favorable facets. In the present phase field based framework, this elongated shape has been modeled by allowing more surface nucleation on a desired direction. The black line in Figure II.10.2(g) depicts the increase in primary aggregate size along the direction that demonstrates maximum length. The blue line denotes the variation in the average primary particle size with time. The red line demonstrates the evolution in reactant concentration within the solution around the precipitate. It is evident that the particle growth stops after approximately 1 hour due to complete depletion of reactants. Slight decrease in the average primary particle size at later times can be attributed to the enhanced surface nucleation and slower growth of the individual particles due to lower supersaturation ratio.

To elucidate the growth of the secondary particles, a detailed Kinetic Monte Carlo (KMC) approach is adopted. Nucleation and growth of primary particles are simulated, along with their agglomeration, which leads to the formation of the secondary particles. The primary particle sizes obtained from the KMC scheme is consistent with the primary aggregate size realized in the phase field-based simulations. One major limitation of the KMC methodology is the assumption of spherical shape for both primary and secondary particles. Figure II.10.2(h) denotes the evolution in secondary particle size with time for different TM concentrations ranging from 1.5 mM to 6.0 mM. It is evident that more TM within the solution leads to larger secondary particles due to formation of more primary aggregates, and their agglomeration can eventually form larger secondary particles. The experimentally observed secondary particle size obtained by conducting the co-precipitation reaction under TM concentration of 4.5 mM is denoted by the red cross symbol. Qualitative agreement between the computational predictions and experimental observations help to validate the developed modeling scheme.

Deciphering the calcination mechanism of NMC811 cathode particles along with the influence of atmospheric oxygen

Nanoscale morphology has a direct impact on the performance of materials for electrochemical energy storage, wherein smaller particle sizes result in shorter diffusion lengths and a larger surface area for charge transfer to occur. Despite this importance, little is known about the evolution of primary particle morphology nor its effect on chemical pathways during synthesis. In this work, *operando* characterization is combined with atomic-scale and continuum simulations to clarify the relationship between morphology of cathode primary particles and their lithiation during calcination of $\text{LiNi}_{0.8}\text{Mn}_{0.1}\text{Co}_{0.1}\text{O}_2$ (NMC-811). This combined approach reveals a key role for surface oxygen adsorption in facilitating the lithiation reaction by promoting metal diffusion and oxidation, and simultaneously providing surface sites for lithium insertion. Furthermore, oxygen surface termination is shown to increase the activation energy for sintering, leading to smaller primary particle sizes at intermediate temperatures. Smaller particles provide both shorter diffusion lengths for lithium incorporation and increased surface site density for lithium insertion. These insights provide a foundation for more tailored syntheses of cathode materials with optimized performance characteristics.

To elucidate the mechanism of the calcination reaction, powder X-ray diffraction (XRD) patterns were collected in-situ during synthesis of NMC-811 by calcination of $\text{Ni}_{0.8}\text{Mn}_{0.1}\text{Co}_{0.1}(\text{OH})_2$ and $\text{LiOH} \cdot \text{H}_2\text{O}$, both with and without an initial pre-heating to 350°C in the absence of the lithium salt needed for conversion to lithiated cathode powder. The resulting XRD patterns revealed a series of rich intermediate chemical transformations. The pre-heating step converted the hydroxide starting material to the cubic $\text{Ni}_{0.8}\text{Mn}_{0.1}\text{Co}_{0.1}\text{O}$ observed at intermediate temperatures when using the conventional hydroxide precursor (Figure II.10.3(b)). This pre-conversion step initially produced no difference in terms of particle size or composition, but eventually altered the progress of the subsequent calcination reactions, resulting in more layered cathode (Figure II.10.3(c) and (j)) and smaller particle sizes. To better understand the beneficial effect of pre-heating, these results are combined with atomistic and continuum physics simulations of the conversion from a disordered cubic intermediate to the final layered cathode.

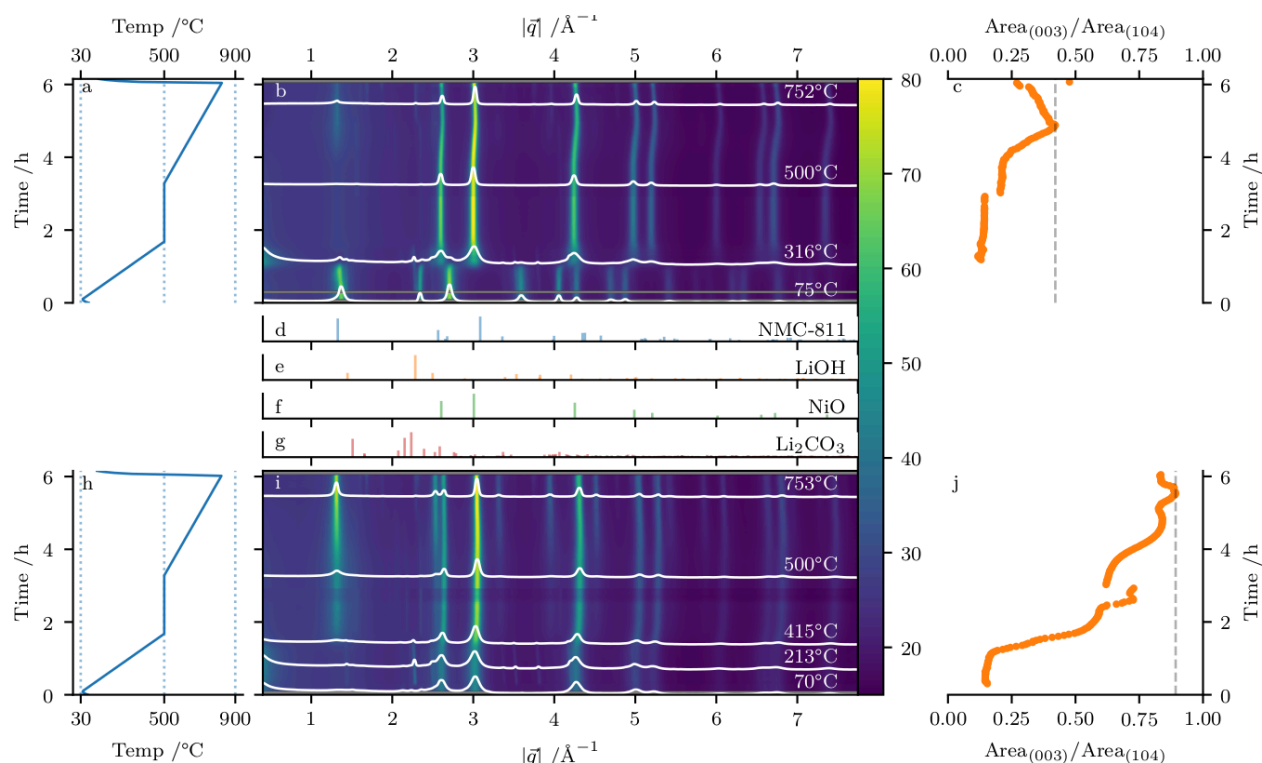


Figure II.10.3 In-situ XRD during calcination of NMC-811. (a) Temperature profile, (b) square-root of integrated diffraction intensity, and (c) ratios of areas of fitted peaks for (003) and (104) reflections during calcination of layered $\text{Ni}_{0.8}\text{Mn}_{0.1}\text{Co}_{0.1}(\text{OH})_2$ precursor. (h) Temperature profile, (i) square-root of integrated diffraction intensity, and (j) ratios of areas of fitted peaks for (003) and (104) reflections during calcination of precursor after 350°C pre-annealing. (d–g) Reference patterns for (d) NMC-811, (e) LiOH, (f) NiO, and (g) Li_2CO_3 . Dashed lines in (i,j) show maximum (003)/(104) area ratio attained during calcination.

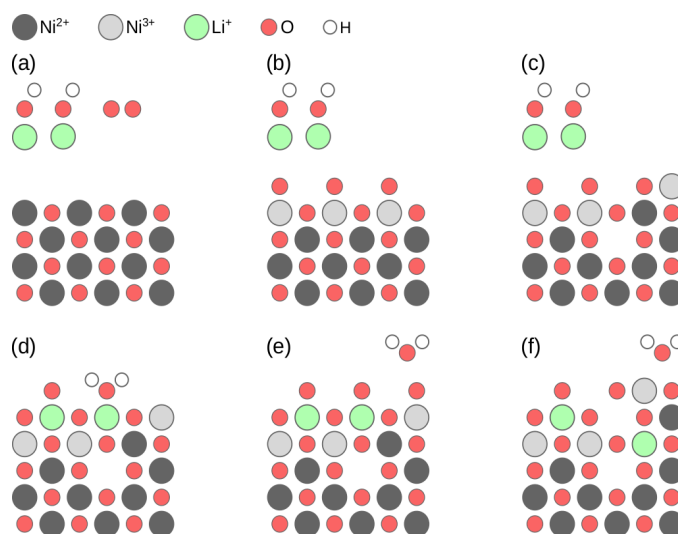


Figure II.10.4 Schematic of NiO lithiation mechanism. (a) Bare NiO surface, LiOH and O_2 , (b) oxidation of the surface forms a surface dipole, (c) Ni hopping between surface and bulk sites driven by charge redistribution, (d) Li^+ ions fill surface sites leading to NiO lithiation and water formation, (e) surface oxidation and water removal, (f) Li–Ni disorder creates a disordered rock salt bulk. The steps will repeat until a LiNiO_2 stoichiometry is reached everywhere. Subsequent Li layering will be favored at high temperature, given the different sizes of Ni^{3+} and Li^+ ions.

Figure II.10.4 summarizes the mechanism of lithiation of NiO particles obtained from molecular dynamics simulations and experimental characterization, starting from a NiO slab in the presence of LiOH and O₂ molecules (Figure II.10.4(a), Mn and Co omitted for tractability). Without O₂ present, no reaction is observed, consistent with experimental results. The first step is the adsorption of oxygen on exposed Ni sites (Figure II.10.4(b)). At low temperature, atmospheric conditions, NiO is often terminated with polar hydroxyl or water species, but these species desorb near 300°C and are replaced by oxygen in the pure O₂ environment needed for calcination. This oxygen adsorption makes the surface polar, leading to Ni surface segregation and bulk cation vacancies that are stabilized by oxidized Co and Mn sites within the lattice (Figure II.10.4(c)). In this oxygen-rich rock salt structure, Li⁺ from molten LiOH can incorporate into surface metal vacancy sites, while simultaneously forming water (Figure II.10.4(d) and (e)). Surface Li sites are quickly terminated by O²⁻ ions leading to a similar termination as the original oxidized NiO surface. Figure II.10.4(f) shows one step further, where Li⁺ ions diffuse deeper into the material and Ni ions diffuse outward toward the surface, creating Ni vacancies that move toward the inner particle. These steps repeat until the lattice is fully lithiated.

Complementing this atomic-scale picture, continuum modeling showed the effect of oxygen coverage on grain sintering. The difference in sintering temperature between oxygen and neutral surface termination is dramatic and highlights the ability of surface oxygen coverage to inhibit particle ripening at intermediate temperatures. Increasing the oxygen concentration produces an associated increase in the sintering activation energy, causing low ion mobility and limited sintering. Only when reaching higher temperatures does the ion diffusion become sufficiently large to permit appreciable sintering.

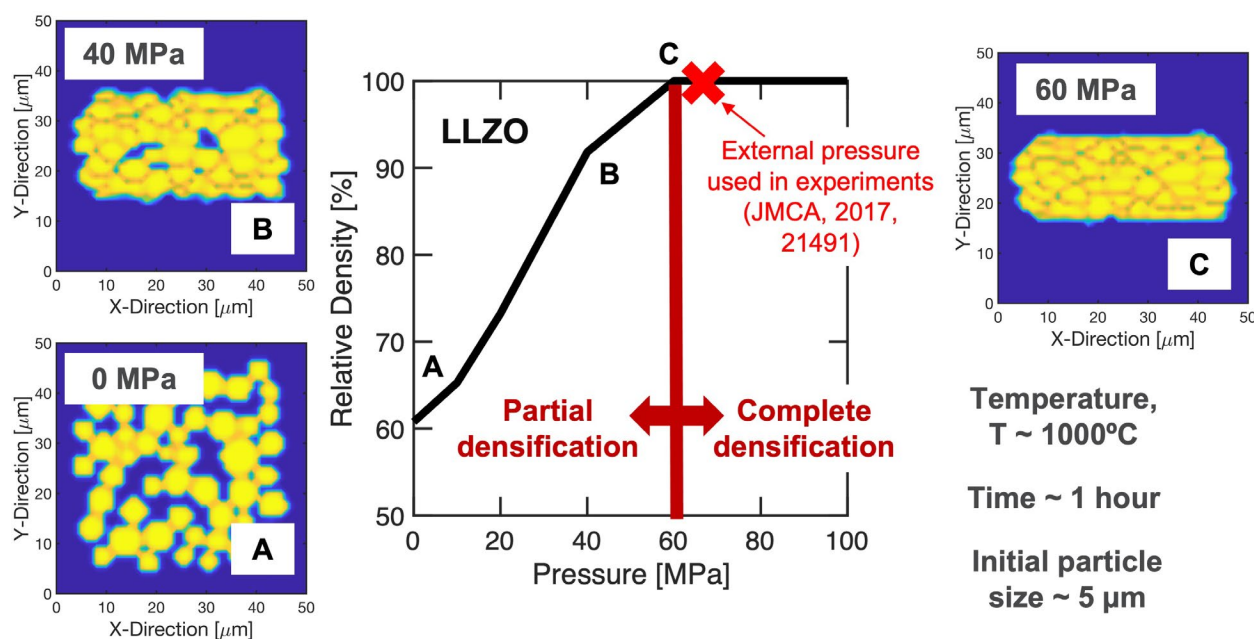


Figure II.10.5 Increase in relative density with pressure at elevated temperatures (1000 degree C) as experienced by LLZO. Densification simulations were conducted for 1 hour following the work of Jeff Sakamoto, Univ. of Michigan, Ann Arbor (see Sharafi et al. J. Mater. Chem. A (2017) 5 21491 – 21504). Complete densification is achieved within 60 MPa, which is consistent with the reported experimental results. The final LLZO microstructures obtained by conducting densification at 0 MPa, 40 MPa and 60 MPa are denoted by A, B and C, respectively. The initial average particle size was assumed to be 5 μm.

Computational modeling of the pressure assisted densification of LLZO solid electrolytes

Last year we investigated the sintering induced densification of LLZO solid electrolytes under elevated temperatures without the application of any external pressure. Several experimental researchers apply external pressure to obtain close to 100% relative densities at much lower temperatures (~ 1000°C). Higher temperatures in the range of 1200°C is necessary for densifying LLZO without any pressure, which can give rise to other issues such as lithium loss from particle surface and formation of non-conductive tetragonal phase.

At present, there does not exist any computational model that successfully captures the pressure induced densification of LLZO. Hence, this year we extended our computational model to capture the influence of externally applied pressure on the overall LLZO densification process. Mechanical equilibrium equation is solved within the phase field framework for capturing the displacement of the individual particles under mechanical load. These deformations are incorporated within the model as a convective motion of the solid media. Along with this rigid body type movement, the usual surface, grain-boundary, and bulk diffusion of material are also simulated through appropriate equations. Viscoplastic motion of the solid LLZO particles are assumed at elevated temperatures. Overall, the computational model predicted very good densification (close to 100%) of the solid electrolytes at 1000°C under pressures higher than 60 MPa, which is in extremely good correlation with the experimental conditions used by Prof Jeff Sakamoto for preparing their LLZO pellets. All these findings are summarized in Figure II.10.5 along with the possible densified LLZO microstructures under 0 MPa, 40 MPa and 60 MPa pressures. Please note that all the densification simulations were run for 1 hour, which is in accordance with the experimental conditions.

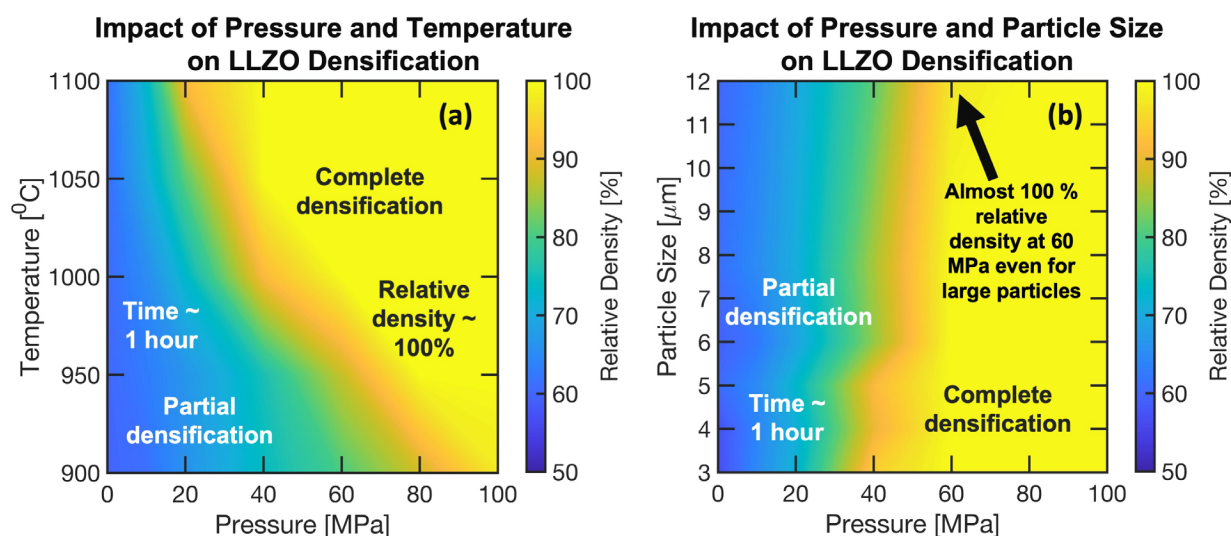


Figure II.10.6 (a) Phase map between pressure and temperature where blue indicates 50% relative density and yellow denotes complete densification. It is evident that complete densification is possible at high pressure, but complete densification cannot be achieved with only high temperature and lower values of pressure. The sintering simulations were conducted for 1 hour at 1000°C temperature assuming LLZO particles. (b) Phase map between particle size and pressure, where blue indicates 50% relative density and yellow denotes 100% densification. Variation in particle size does not show any significant influence on the pressure induced densification process. Even with very large particles of size larger than 10 μm , it is possible to obtain complete densification under externally applied pressure of 60 MPa. Without externally applied pressure, it is very difficult to achieve close to 100% relative densities for large sized LLZO particles.

It is important to note that both temperature and externally applied pressure influence the relative density of LLZO pellets during the densification process. Accordingly, to understand their relative impact a phase map is demonstrated in Figure II.10.6(a) between the applied pressure and temperature while plotting the achievable relative density in 1 hour. It is well known that increasing either pressure or temperature should help to densify the pellets. However, at lower pressure (~ 0 MPa), increasing the temperature from 900°C to 1100°C leads to negligible improvements in the relative density of the pellets. Earlier studies showed that conducting densification even at 1200°C and with small sized particles led to 80% – 85% relative densities. On the contrary, densification even at temperatures as low as 900°C, but under relatively high pressures (around 100 MPa) can lead to complete densification of the pellets. Accordingly, only 40 MPa pressure is needed to achieve 100% relative density at higher temperatures of 1100°C. Hence, it can be concluded that pressure plays a major role in densifying LLZO and may be necessary for making solid electrolytes in the future.

Another advantage of the externally applied pressure on densification is demonstrated in Figure II.10.6(b) where the change in relative density as a function of particle size and pressure is shown in the form of a phase map. The simulation was conducted at 1000°C and continued for 1 hour. The LLZO particle sizes were varied between 3 μm – 12 μm . Interestingly, for almost all the particle microstructures 100% relative density is achieved around 60 MPa pressure. Some minor deviations are observed for very small particles, which can be attributed to the enhanced diffusion effects for smaller particles. However, the overall trend of particle size independent densification of LLZO under external pressure is very different from the heavy particle size dependence observed in pressure less densification of LLZO. It is well known that grain boundaries are a major bottleneck to the lower conductivity experienced by LLZO pellets. Using the concept of pressure assisted densification it is possible to use larger LLZO particles and form pellets with 100% relative density, which can eventually lead to higher conductivities.

Conclusions

In summary, regarding coprecipitation, the existing computational methodology to predict the formation of Mn-carbonate precursors is extended to understand the formation of NMC-carbonate particles. The phase field model used earlier to simulate the growth of primary particles is modified to capture the formation of primary aggregates through the surface nucleation mechanism. For materials with extremely small primary particle growth rate tends to form surface nuclei for quick minimization of the surface energy, which is well reflected in the formation of the primary aggregates in NMC-carbonates. If excess ammonia is present within the reacting solution, enhanced stability of the Ni-ammonia complex leads to NMC precipitates with very small amount of Ni. Finally, a Kinetic Monte Carlo based computational methodology is developed capable of capturing the nucleation, growth, and aggregation of primary particles, and predicting the size evolution of the secondary ones. Good correlation with experiments is demonstrated all throughout the model development process.

The second part of the project deals with understanding the calcination of Ni-rich cathode precursors through in situ experimentation and multiscale modeling activities. The exact mechanism of oxygenation and lithiation experienced by the hydroxide cathode precursors is deciphered and their impact on the overall particle sintering is explained. Impact of pretreatment in air for adsorbing oxygen on top of the particles, and subsequent continuation of the lithiation reaction, is elucidated through detailed atomistic calculations. The insights presented here will aid in the development of more effective energy storage materials, both by elucidating a mechanism for lithiation so that calcination can be better controlled, and by providing a model for particle sintering that can be used to tune particle size and optimize desired performance characteristics in high-nickel cathodes for Li-ion batteries.

The computational simulations of pressure assisted LLZO densification reveals that external pressure exerts substantial impact on the final relative density experienced by the solid electrolytes. It is possible to reach 100% relative density with only 40 MPa – 100 MPa pressure depending on the temperature of operation. It is almost impossible to achieve 100% relative density by conducting the densification of LLZO at very high temperatures without the application of any pressure. Also, external pressure can significantly minimize the particle size effect on the overall densification process. LLZO microstructures with a wide range of particle sizes can be completely densified by applying 60 MPa pressure at 1000°C. Overall, the benefits of external pressure in LLZO densification cannot be neglected and future solid electrolyte fabrication facilities should be equipped with high pressure capabilities.

Key Publications

Publications

1. P. Barai, T. T. Fister, Y. Liang, J. Libera, M. Wolfman, X. Wang, J. C. Garcia, H. H. Iddir, and V. Srinivasan. Investigating the Calcination and Sintering of Li₇La₃Zr₂O₁₂ (LLZO) Solid Electrolytes Using Operando Synchrotron X-ray Characterization and Mesoscale Modeling. *Chemistry of Materials* 33 12 4337–4352 (2021).

2. N. Ngoepe, A. Gutierrez, P. Barai, J. Chen, P. E. Ngoepe, and J. R. Croy. The effects of process parameters on the properties of manganese-rich carbonate precursors: A study of co-precipitation synthesis using semi-batch reactors. *Chemical Engineering Science* 241 116694 (2021).

Presentations

1. M. Wolfman, X. Wang, P. Eng, J. Stubbs, V. De Andrade, P. Barai, J. Garcia, H. Iddir, V. Srinivasan, T. Fister. Unraveling the Role of Primary Particle Size and Morphology During Calcination of Layered NMC Cathodes for Li-Ion Batteries. In: *Materials Research Society Spring Meeting & Exhibit*, April 2021. Best Oral Presentation Award.
2. P. Barai, M. Wolfman, T. T. Fister, X. Wang, J. Garcia, H. Iddir, and V. Srinivasan. Elucidation of Densification Experienced by LLZO Solid Electrolytes. In: *The Electrochemical Society Fall Meeting* October 2020.

Acknowledgements

This research is supported by the Vehicle Technologies Office (VTO), Department of Energy (DOE), USA. Argonne National Laboratory is operated for DOE Office of Science by UChicago Argonne, LLC under the contract number DE-AC02-06CH11357. The authors also acknowledge the computing resources provided by the Laboratory Computing Resource Center (LCRC) at Argonne National Laboratory. Portions of this work were performed at GeoSoilEnviroCARS (The University of Chicago, Sector 13), Advanced Photon Source (APS), Argonne National Laboratory. GeoSoilEnviroCARS is supported by the National Science Foundation – Earth Sciences (EAR – 1634415) and Department of Energy- GeoSciences (DE-FG02-94ER14466). This research used resources of the Advanced Photon Source; a U.S. Department of Energy (DOE) Office of Science User Facility operated for the DOE Office of Science by Argonne National Laboratory under Contract No. DE-AC02-06CH11357.

Regarding the computational and experimental research, the atomistic computations were conducted by Juan Garcia and Hakim Iddir, and the mesoscale level computational modeling and subsequent analysis was carried out by Pallab Barai and Venkat Srinivasan. All the experimental research was conducted by Timothy Fister, Mark Wolfman and Xiaoping Wang. Also, Venkat Srinivasan managed the entire project, and made sure that the project follows the correct direction without deviating much from its primary goal.

II.11 *In Situ* Spectroscopies of Processing Next-Generation Cathode Materials (BNL)

Feng Wang, Principal Investigator

Brookhaven National Lab
Interdisciplinary Science Department
Upton, NY 11973
E-mail: fwang@bnl.gov

Jianming Bai, Principal Investigator

Brookhaven National Lab
National Synchrotron Light Source II
Upton, NY 11973
E-mail: jmbai@bnl.gov

Peter Faguy, DOE Technology Development Manager

U.S. Department of Energy
E-mail: Peter.Faguy@ee.doe.gov

Start Date: October 1, 2020

End Date: September 30, 2021

Project Funding (FY21): \$300,000

DOE share: \$300,000

Non-DOE share: \$0

Project Introduction

The high demand of lightweight, high energy density batteries powering electric vehicles promotes new materials discovery and development. Despite the large number of battery materials being discovered, very few of them have been commercially deployed, mostly bottlenecked by synthesis and processing—namely, making certain phases with the desired structure and properties to meet the multifaceted performance requirements. Under this project, *in situ* spectroscopic techniques are developed and applied to studies of materials processing, to elucidate how the processing parameters affect reaction pathways and, consequently, the target material phases and structural properties. This capability enables probing of reactions and processes during material processing at scales varying from the bulk phases to individual particle, locally down to surface/interfaces. Such studies, in coupling with electrochemical characterization, shed light on the processing-structure-property relationship, thereby providing a science base for process design in materials processing.

In FY21, this project focused on processing of high-Ni cathode materials. New spectroscopic techniques were developed, including the correlated *in situ* X-ray diffraction (XRD)/pair distribution function (PDF) analysis for probing short- and long- range ordering in the same process, and synchrotron X-ray techniques for probing concurrent chemical/structural changes in the surface and bulk of particles. Through *in situ* spectroscopy studies on processing of high-Ni cathode materials, new insights were obtained on the lithiation-driven changes in structure and morphology, compositional dependence of the reaction pathway and the role of Co/Mn in facilitating the Li/O incorporation during crystallization. Guided by those insights, processes were developed for processing high-Ni cathode materials, with improved performance and reduced cost.

Objectives

- Advance electrode performance through process design for materials processing, namely
 - Selectively synthesizing certain phases
 - Intendedly controlling the structure, morphology, and surface properties
- Provide input to theory, modeling, scaling of materials synthesis and processing

Approach

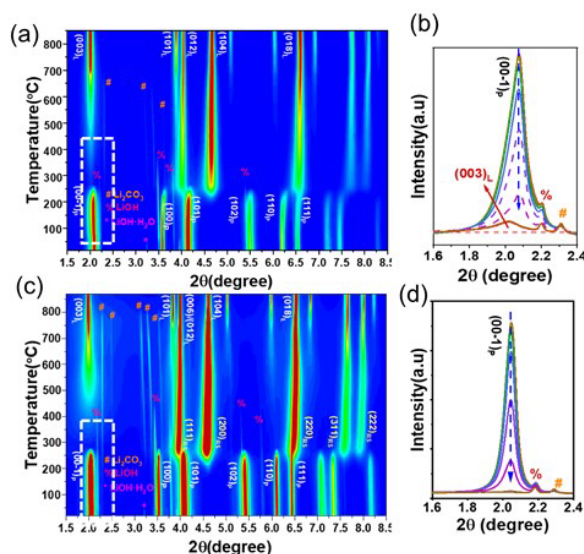
One unique approach taken in this project is to develop mechanistic understanding of materials processing through *in situ* spectroscopy studies using the world-leading facilities at Brookhaven and other national laboratories. Specifically, synchrotron X-ray, neutron-based *in situ* techniques are developed and applied to studies of reaction processes and kinetic pathways during processing of cathode materials. Insights from this study provide a science base for process design in processing of next-generation cathode materials. Some of the results can be used as direct input for theory, modeling, and scaled-up processing through collaborations under the *Processing Science & Engineering* and other VTO programs.

Results

Compositional dependence of structural ordering and crystallization in high-Ni cathodes during synthesis

The majority of *in situ* studies on synthesis/processing have been mostly focusing on structural ordering within the bulk crystalline phases, but less is given to the early stage of the phase nucleation and growth, which often determines the phase morphology of the final products and, consequently, the electrochemical performance. The high X-ray flux of the synchrotron light source allows taking high-quality XRD data as well as the total scattering, with high enough counts in wide angle range, providing great opportunities for real time probing of the early-stage phase formation and crystallization. Under this project, a combination of *in situ* XRD and PDF analysis was applied to tracking structural/chemical evolution at short, intermediate, and long-range ordering of intermediates in preparing LiNiO₂ (LNO) and Li(Ni_{0.8}Mn_{0.1}Co_{0.1})O₂ (NMC811) from hydroxide counterparts.

Figure II.11.1 presents the contour plots of temperature-resolved *in situ* XRD patterns, indicating that the phase transformation went *via* 3 stages in both cases: I) hydroxide precursor phase (P- 3m1); II) transitions through intermediates, involving rocksalt (RS) solid solution and a distorted layered phase ($c/a < 4.899$); III) transition into the normal layered phase. The transition into the RS occurred at very low temperature, upon the decomposition of the hydroxides, as indicated by the appearance of the (200)_{RS} peak. As temperature increases RS continuously grew under the consumption of the hydroxide phase (as shown by the decrease of the (00-1)_p peak). During the heating process, the (200)_{RS} peaks gradually shifted to high angles, indicating the lattice contraction due to the lithiation and Ni oxidation. The formed layered phases at the early stage are nano-sized, as suggested by the diffusive/broadened diffraction peaks. The lattice c/a ratio is unexpectedly small, < 4.899 , different than the normal layered phase, so we call it a distorted layered phase. Compared to LNO, the layered NMC811 formed at a much lower temperature, upon the decomposition of the hydroxides.



The phase nucleation and growth, including both crystalline phase and amorphous phase, was obtained by PDF, with the main results provided in Figure II.11.2. The substitution of Co/Mn to the NMC811 dramatically reduced the temperature for forming the rhombohedral structure, by $\sim 210^\circ\text{C}$ (at 550°C in NMC811 compared to 760°C in LNO). Mn/Co facilitated Li/O incorporation and so the oxidation of Ni, thereby accelerating the nucleation/growth of the layered structure. Therefore, for reaching the same c/a value, the required temperature for forming the layered NMC811 with a shorter-range order of crystalline domains is much reduced. The obvious difference observed in structural ordering between *in situ* XRD and PDF is due to the partial crystallization in materials when undergoing the nucleation process at low temperatures. The total scattering-based PDF analysis samples materials both with long-range order and short-range order. In contrast, XRD only samples materials with long-range order. Therefore, PDF measurements revealed a lithiation threshold for the disorder-order transformation of the rhombohedral layered structure.

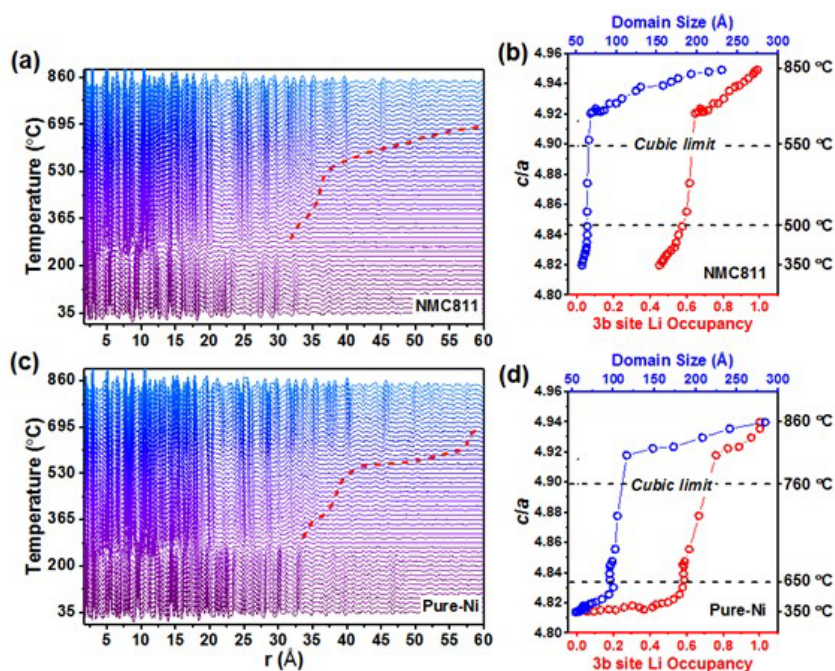


Figure II.11.2 *In situ* PDF analysis of the solid-state synthesis of NMC811 and LNO. (a, b) temperature resolved green function and the calculated c/a , domain size and Li occupancy on 3b site for NMC811 and (c, d) temperature resolved green function and the calculated c/a , domain size and Li occupancy on 3b site for LNO.

Concurrent conditioning of the surface and bulk of high-Ni cathodes with Nb-coating

Surface coating is commonly employed by industries to improve the cycling and thermal stability of high-Ni cathodes in practical use. While the electrochemical performance of the final products varies depending on the post processing. We used *in situ* synchrotron XRD to investigate the kinetic processes and involved structural evolution in Nb-coated NMC811 upon heat treatment. Figure II.11.3 shows the main results by time and temperature-resolved *in situ* synchrotron XRD. Structural evolution of all the involved phases is revealed, both in the bulk of NMC 811 and those Nb-containing minor phases, LiNbO_3 and Li_3NbO_4 . Those Nb compounds came from the reaction of the coating with surface Li residual. Sharp peaks associated with LiNbO_3 were observed quickly at low temperatures, with the amount reaching maximum at around 520° , and by $\sim 690^\circ\text{C}$ LiNbO_3 faded away quickly. The peaks associated with Li_3NbO_4 were initially broad and barely observable at low temperatures, and then became stronger and sharper, indicating enhanced crystallinity.

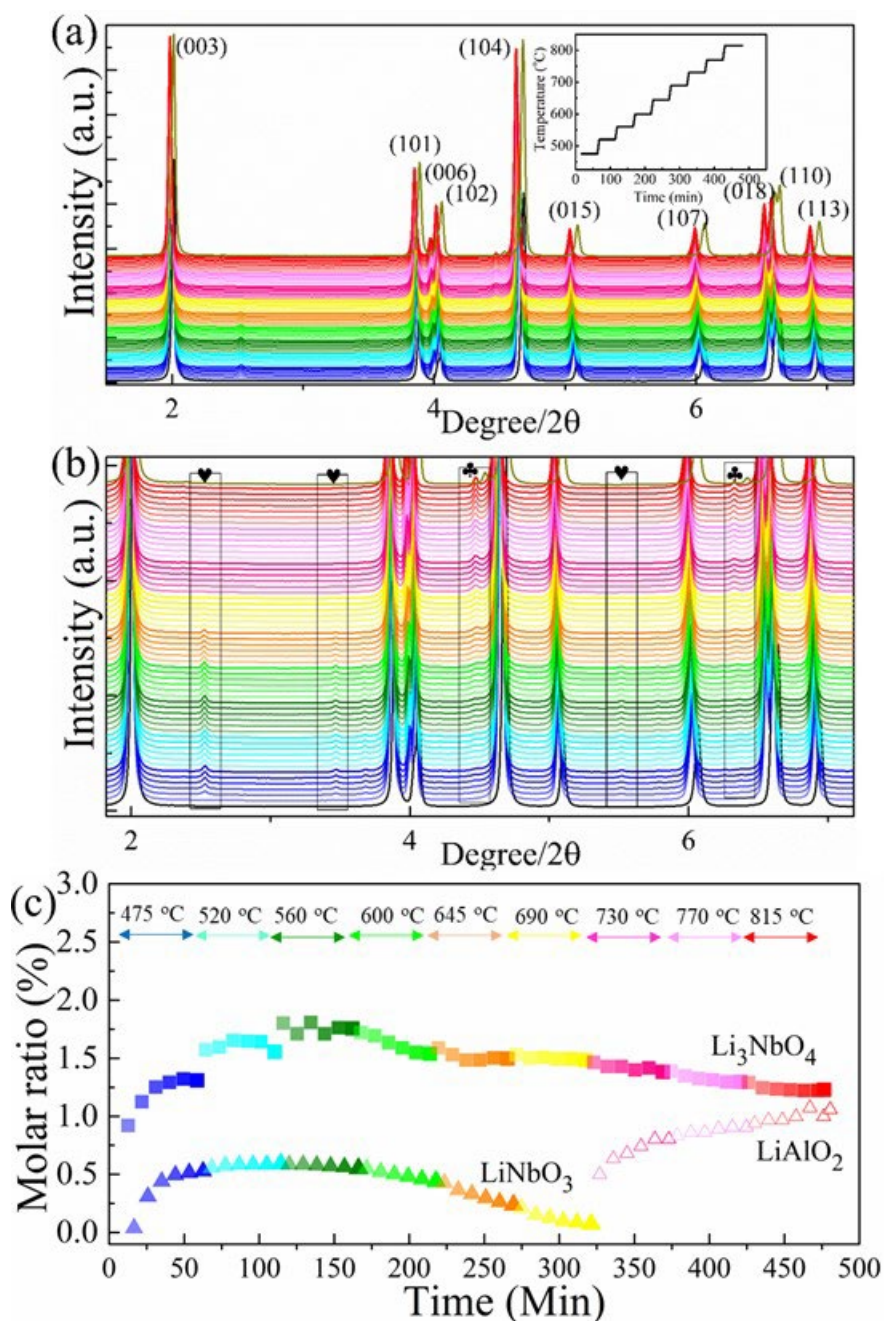


Figure II.11.3 Real-time tracking of structural evolution in the Nb-coated NMC 811. (a) *In situ* synchrotron XRD patterns of 1.4% Nb-coated NMC 811 at different stages, being illustrated using different colors, namely, initial materials (Black line), during holding at destination temperatures 475 °C (Blue), 520 °C (Cyan), 560 °C (Olive), 600 °C (Green), 645 °C (Orange), 690 °C (Yellow), 730 °C (Pink), 770 °C (LT Magenta), 815 °C (Red) and final cooling down (Dark yellow). Inset: heating profile. (b) Zoom-in view of the diffraction patterns to show the formation of minor Nb-containing phases, as indicated by ♥ for LiNbO_3 , ♣ for Li_3NbO_4 . (c) Quantitative analysis on the LiNbO_3 and Li_3NbO_4 as a function of time and temperature. Formation of LiAlO_2 , arising from Li interaction with cell components at high temperatures (>730 °C), was also provided.

In contrast to significant change of the surface coating layer, the change in the bulk is hardly observable from the XRD patterns and so quantitative analysis via refinement was performed, with the main results provided in Figure II.11.4. Nb substitution into the transition metal sites caused cationic disordering, evidenced by the reduced peak intensity ratio, $I(003)/I(104)$. There is a sudden drop of the intensity ratio, $I(003)/I(104)$ by 690 °C, followed by the faster-paced decrease compared to that at low temperatures (illustrated by the slopes of

the linear fitting curves). The lattice parameters a and c increased throughout the heating process, with a much larger amplitude at temperatures above 690°C. The faster change of a and c at temperatures above 690°C was correlated with the cationic disordering, as indicated by the sudden drop of the intensity ratio $I(003)/I(104)$ at the same temperature range and the rapid increase of the Ni occupancy on Li site. Besides structural change, fast particle growth was observed at temperature above 690°C, being facilitated the elemental diffusion.

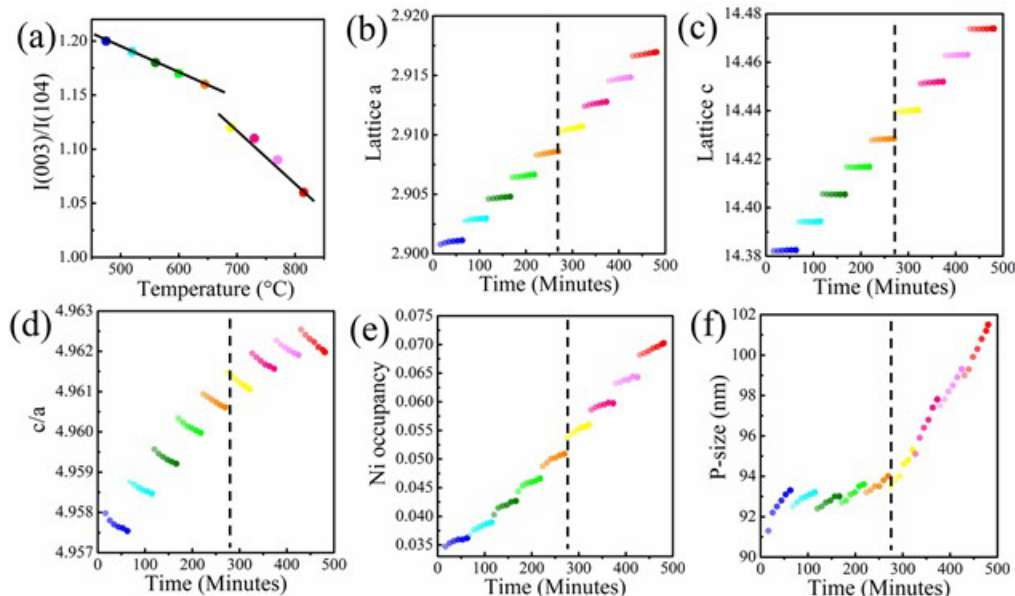


Figure II.11.4 Quantitative analysis of the kinetics of structural change in the bulk. (a) Intensity ratio of the characteristic peaks, $I(003)/I(104)$; (b-d) Evolution of the lattice parameters a , c , and their ratio c/a during holding (for ~ 50 minutes) at destination temperatures; (e) Ni occupancy on Li site; (f) Particle size (P-size).

These observations from *in situ* studies provide important insights into the kinetic processes governing structural/chemical changes, occurred concomitantly in the bulk and surface of the particles. Our findings provide guidance to optimization of the coating and heating processes in tuning the structural and electrochemical properties of high-Ni cathode materials.

Kinetic limitation in single-crystal high-Ni cathodes

In developing high-Ni cathodes, replacing polycrystalline secondary particles with single crystals provides a promising solution to eliminating grain boundaries and inter-granular fracture. In addition, surface parasitic reaction is suppressed due to the smaller specific surface area. However, kinetic limitation, particularly the rate-capacity tradeoff due to the long ion diffusion path in the large-sized crystals has been a major concern. Quantitative assessment was made to the electrochemical kinetics in single-crystal NMC811, in comparison to the polycrystalline counterpart, using *in situ* transmission X-ray microscopy (TXM)/X-ray absorption near-edge structure (XANES) spectromicroscopy. Figure II.11.5 presents the snapshots of Ni oxidation distribution taken every 40 minutes from the initial (green) to fully charged state (red). The gradual color change from green (close to Ni^{3+}) to red (Ni^{4+}) in the oval-shaped polycrystalline particles indicates continuous Li de-intercalation, progressing uniformly within the particle. In contrast, the reaction in another group of particles – an ensemble of single-crystal particles with regular facets did not show significant color change until the late stage, suggesting sluggish Li de-intercalation. The observation of non-uniformity within single-crystal particles, with gradual de-intercalation from the surface of the large crystals, indicates the slow transport kinetics.

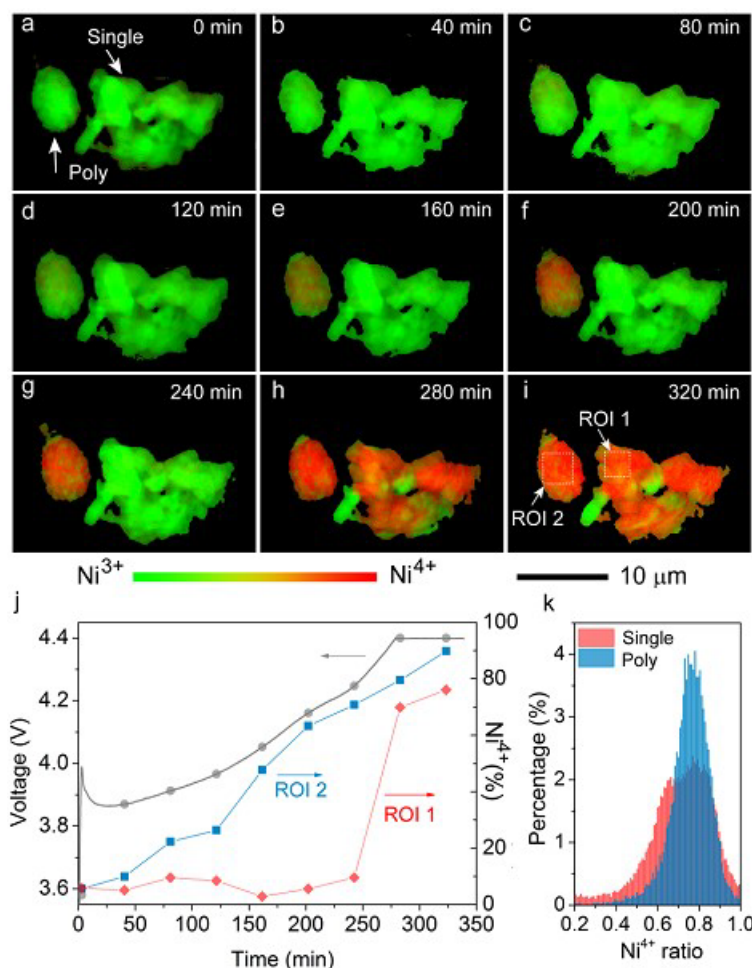


Figure II.11.5 Operando TXM-XANES spectro-images of local redox reaction within individual single- and poly- crystal NMC811 assembled into a same electrode. (a-i) Representative 2D maps of Ni oxidation states during the charge process up to 4.4 V at 0.15 C. (j) Voltage profile (grey) and quantified Ni⁴⁺ concentration derived by fitting of XANES spectra from ROI 1 (red) and ROI 2 (blue), within single- and poly- crystals, respectively (as labelled in i). (k) Ni⁴⁺ distribution across the single (red)/poly (blue) crystals at the state (i).

Results from *in situ* spectromicroscopy studies were corroborated by finite element analysis (FEA) simulation and transport property measurements, indicating that the kinetic limitation is intrinsic to single crystal and may have arisen from the slow ionic transport at low state of charge (SOC), with the value of a few orders lower compared to that at high SOC. The sluggish kinetics may be alleviated through synergistic interaction with polycrystals, or small crystals integrated in a same electrode. The findings from this work, particularly on the mechanistic origin and alleviation of kinetic limitation in single crystals, may inspire new strategies, such as hierarchical electrode design, to enable practical deployment of such materials in lithium-ion batteries.

Conclusions

In FY21, progress was made in the development and application of *in situ* spectroscopic techniques for fundamental understanding and process design of processing high-Ni NMC and other type of cathode materials:

- New *in situ* spectroscopy techniques were developed for studies of processing cathode materials, including correlated *in situ* XRD/PDF for probing short- and long- range ordering, synchrotron X-ray techniques for probing concurrent chemical/structural changes in the surface and bulk.

- Efforts were made on studying the structural and morphological evolution during the calcination process during synthesis of LiNiO₂ and NMC811 as model systems. New insights were obtained about the lithiation-driven structure and morphology changes, in particular the dependence of the reaction pathway on the composition, impact of Co/Mn on Li/O incorporation during structural ordering and crystallization, providing guidance to manipulation of precursors towards targeted structural motifs.
- Synchrotron X-ray diffraction was applied to investigate the kinetic processes and involved structural evolution in Nb-modified NMC811 upon heat treatment. Through this study, we revealed the predominant role of thermo-driven processes in causing concurrent changes in the bulk and surface, in particular, the phase evolution of the coating layer and Nb/transition metal inter-diffusion that facilitates Nb penetration into the bulk and particle growth at the elevated temperatures. Findings from this study, with insights into the kinetic processes of conditioning the bulk and surface of the coated high-Ni cathode materials, provide guidance to the design of coating and post processing for tuning their structural and electrochemical properties.
- Kinetic limitation in single-crystal high-Ni cathodes was identified via *in situ* spectromicroscopy combined with simulation, suggesting that sluggish kinetics in single crystals may be alleviated by synergistic interaction with polycrystals integrated into the same electrode. The findings from this work may inspire new strategies, such as hierarchical electrode design, to enable practical deployment of such materials in next generation lithium-ion batteries.

With the developed *in situ* spectroscopic techniques for probing structural ordering both in the bulk and locally, this project will expand efforts onto processing of high-Ni, low Co/Co-free cathode materials in FY21. New project activities have been initiated on morphology control of high-Ni cathode materials, surface coating/doping and substitution for tuning the structure, morphology, and surface properties of Co-free cathode materials. Aided by *in situ* studies, we will develop new processes for tuning structural and electrochemical properties of Ni-based low Co/Co-free cathode materials.

Key Publications

1. C. Yin, M. Ge, Y. Chung, J. Bai, W-K. Lee, K. Kisslinger, S. Ehrlich, X. Xiao, B. Qiu, Z. Liu, Y. Shin, F. Wang, High-Nickel Cathodes with Local Stoichiometry Control for High-Voltage Operation (*submitted*).
2. F. Wang, J. Bai, Synthesis and Processing of High-Nickel Cathode Materials by Design, Batteries & Supercaps (*Invited review*; DOI: [10.1002/batt.202100174](https://doi.org/10.1002/batt.202100174)).
3. F. Xin, H. Zhou, J. Bai, F. Wang, M.S. Whittingham, Conditioning the Surface and Bulk of High-Nickel Cathodes with a Nb Coating: An *In Situ* X-ray Study, J. Phys. Chem. Lett., 12, 7908 (2021).
4. F. Xin, H. Zhou, Y. Zong, M. Zuba, Y. Chen, N. Chernova, J. Bai, B. Pei, A. Goel, J. Rana, F. Wang, K. An, L. Piper, G. Zhou, M.S. Whittingham, "What is the Role of Nb in Nickel-Rich Layered Oxide Cathodes for Lithium-Ion Batteries?" ACS Energy Lett., 6, 1377 (2021).
5. T.A. Assefa, A. F. Suzana, L. Wu, R.J. Koch, L. Li, W. Cha, R.J. Harder, E.S. Bozin, F. Wang, I.K. Robinson, Imaging the Phase Transformation in Single Particles of the Lithium Titanate Anode for Lithium-Ion Batteries, ACS Appl. Energy Mater. 4, 111 (2021).
6. C Yin, L. Wan, B. Qiu, F. Wang, W. Jiang, H. Cui, J. Bai, S. Ehrlich, Z. Wei, and Z. Liu, Boosting Energy Efficiency of Li-rich Layered Oxide Cathodes by Tuning Oxygen Redox Kinetics and Reversibility. Energy Storage Mater., 35, 388 (2021).

7. M. Ge, S. Wi, X. Liu, J. Bai, S. Ehrlich, D. Lu, W-K. Lee, Z. Chen, F. Wang, Elucidating the Kinetic Limitations in Single-Crystal High-Nickel Cathodes, *Angewandte Chemie*, 2021, 60, 17350.

Acknowledgements

The work was supported by the Energy Efficiency and Renewable Energy, Office of Vehicle Technologies of the U.S. Department of Energy under contract DE-SC0012704. We thank the contribution by the team members, Sizhan Liu, Yusuf Celebi, Sungun Wi, Chong Yin, and by collaborators, Eric Dooryhee, Steve Ehrlich, Mingyuan Ge, Andy Kiss, Wah-Keat Lee, Juergen Thieme (Brookhaven Nat. Lab), Pallab Barai, Zonghai Chen, Ozge Kahvecioglu, Krzysztof Pupek, YoungHo Shin, Venkat Srinivasan, Xiaoping Wang (Argonne National Lab), Gerdbrand Ceder (Berkeley National Lab), Fengxia Xin, Hui Zhou, Stan Whittingham (Binghamton University).

III Recycling and Sustainability

III.1 Battery and Critical Materials Life Cycle Analysis (ANL)

Jarod Kelly, Principal Investigator

Argonne National Laboratory
9700 South Cass Avenue
Lemont, IL 60439
E-mail: jckelly@anl.gov

Michael Wang, Principal Investigator

Argonne National Laboratory
9700 South Cass Avenue
Lemont, IL 60439
E-mail: mqwang@anl.gov

Samm Gillard, DOE Technology Development Manager

U.S. Department of Energy
E-mail: Samuel.Gillard@ee.doe.gov

Start Date: October 1, 2020

End Date: September 30, 2021

Project Funding (FY21): \$240,000

DOE share: \$240,000

Non-DOE share: \$0

Project Introduction

This project examines issues related to automotive battery and critical materials production, from raw material extraction, through processing to usable chemicals, to assembly within battery cells and packs, all the way to potential end of life and recycling stages. This is accomplished using several analytical techniques, including life cycle analysis (LCA), material flow analysis, and supply chains analysis methodologies. Doing so allows for identification of hot spots along the supply chain for batteries and critical materials with respect to energy, greenhouse gases (GHGs) and other environmental burdens. End of life (EoL) treatment, including recycling, of used automotive batteries is also considered in LCA of battery sustainability. We consider battery materials produced for current batteries along with battery assembly and use in battery electric vehicles.

Understanding raw resource recovery processes using life cycle analysis is necessary to evaluate the total energy and environmental burden associated with battery production, since energy and emissions embodied in battery materials are a significant portion of battery LCA energy use and emissions. Additionally, regional aspects of material acquisition and processing can influence total environmental effects of battery production. This ranges from the types of ores from which materials are extracted, resource extraction methods (energy and material inputs), transportation of resources, and local energy input parameters. We evaluate battery materials, production of cathodes, anodes and electrolytes, and battery assembly based on consumed energy and emissions, suitability for PEV applications, and potential advantages relating to economics and scale. While automotive batteries are just beginning to reach their end of life for the early electric vehicle models, it is important to evaluate environmental impacts of the viable processes for end-of-life recycling treatments of such batteries.

This project also investigated future advanced battery challenges, identifying lithium metal as a potential material pathway of environmental interest. This project updated Argonne's Greenhouse gasses Regulated Emissions and Energy use in Technologies (GREET®) model with important material input information for battery materials (lithium from both brine and spodumene ore, and electrolytic manganese) which serves as an important resource to the life cycle analysis community. We expanded the evaluation of automotive battery life cycle, considering different processing locations worldwide thereby improving understanding of vehicle battery burdens. This project also facilitates engagement within the International Energy Agency's (IEAs)

HEV Task 30 and HEV Task 40 projects, which are associated with electric vehicle life cycle analysis, and critical raw materials for electric vehicles, respectively.

Objectives

- Identify and analyze developing and potential material issues affecting automotive lithium-ion batteries (LIB) viability
- Characterize, update, and release LIB LCA module in Argonne's life-cycle analysis model (GREET) to evaluate of battery energy and environmental burdens
- Characterize, implement, and release state-of-knowledge battery material life-cycle analysis data within the GREET battery LCA module to provide up to date information for LCA
- Engage with the international battery community to exchange battery and critical materials production technologies knowledge and advance understanding of battery life cycle
- Evaluate the global supply chain of automotive battery materials and determine environmental variances

Approach

Argonne has developed and maintained the battery LCA module for battery materials and batteries and updated the module with industrial insights and market changes. Argonne updated its life cycle inventory for several materials including manganese and lithium (from both brine and spodumene-ore). For manganese, we focused on electrolytic manganese production while also updating other manganese production pathways. For lithium, we leveraged research funded by lithium producer SQM to update the GREET model's life cycle data for lithium from both brine and ore. That data is based on published information available (Kelly et al., 2021). Life-cycle analysis (LCA) was used to evaluate the environmental burdens of battery production and compare energy savings and emissions reductions LCA was also used to investigate how regional variations in production could affect energy and environmental issues along the global supply chain especially as industry moves toward nickel rich battery cathodes.

Close interactions with stakeholders were sustained to remain engaged in and informed of technological and legislative developments associated with LIB production, and to maintain Argonne's position as the world's leader in battery and critical materials LCA. During FY21, Argonne staff 1) gave invited talks and presentations to government, industry, and academia; 2) interacted with international groups like the IEA and the Faraday institution to coordinate research, 3) improved understanding of the impacts of battery materials production, 4) negotiated materials production modeling studies with global battery material leaders; and 5) responded to countless requests for information.

Results

In FY21, Argonne updated its life cycle inventory data within GREET for lithium and manganese. Argonne worked with lithium producer SQM to develop an LCA of lithium carbonate and lithium hydroxide monohydrate produced from both brine and spodumene-ore resources. The results of this effort yielded a public facing journal article (Kelly et al., 2021) that allowed Argonne to update the data within GREET for lithium chemicals production. For manganese, Argonne developed a detailed production pathway for high purity electrolytic manganese metal, and updated manganese ore quality for other manganese production pathways based on ore grades associated with global production. These updated life cycle inventories allow Argonne's GREET battery LCA module (and its user base) to conduct battery LCA with the latest and most representative data available.

There has been extensive work on lithium availability and potential supply constraints as EV demand grows, as well as LCA of production from brine and hard rock through to lithium chloride, carbonate, and hydroxide. These processes are in large-scale industrial production with the latest technology. However, lithium metal

production is neither well studied nor in place on a scale that will be required if lithium metal anodes achieve significant market penetration. Therefore, we undertook an exploration of the lithium metal landscape, including production volume, location, and technology.

Current world production capacity for lithium metal is shown in Table III.1.1. Total world lithium production was 82,000 T in 2020, and battery-grade lithium metal production is only about 3% of that. Any significant market growth would require massive capacity expansion, creating both a challenge and an opportunity.

Table III.1.1 Location and Capacity of World's Lithium Metal Production (data from USGS)

Company	Location	Li Metal total (t/y)	Battery grade (t/y)
Livent	Bessemer, N.C., US	650	350
Albermarle	King County, N.C. US		200
NCCP	Novosibirsk, Russia		270
Ganfeng Lithium	Xinyu, Jiangxi, China	1500	660
Jianzhong Lithium	Yibin, Sichuan, China	600	300
China Energy Lithium	Tainjin City, China		240
Chongqing Kunyu	Tongilang, China	600	300
Jiangsu Hongwei	Taizhou, Jiangsu, China	100	60
Xinjiang Asia-Europe	Urumqi, Xinjiang, China	400	50
Total			2430

While China is dominant, we see that the US has a significant presence in lithium metal production, with two companies in North Carolina (N.C.) contributing about 20% of world battery-grade lithium metal capacity. Demand for lithium metal could increase dramatically if scenarios projected by the EU come to fruition. Figure III.1.1 shows examples where lithium metal demand exceeds one million tons by 2050 (C. Xu et al., 2020).

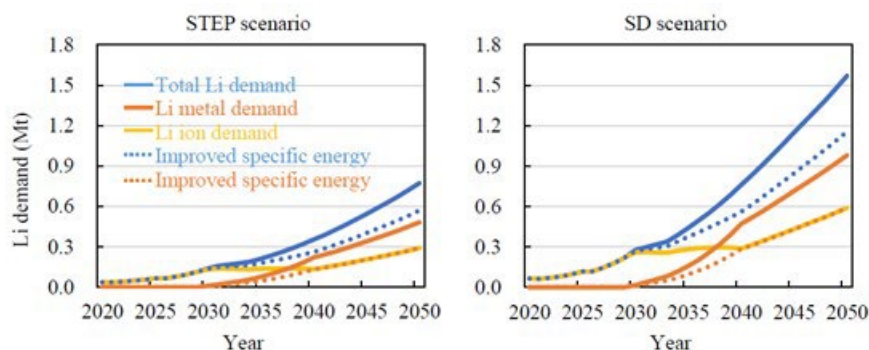


Figure III.1.1 Potential demand growth for lithium (total) and lithium metal (C. Xu et al., 2020)

In the current production process, the purification of LiCl is expensive, energy intensive and uses noxious chemicals, it is also not very efficient. Several technologies have been proposed for cleaner and more efficient production of lithium metal, but none has proven attractive enough to be constructed on large scale. One promising method was published by a US/Chinese collaboration (Yang, 2020). This method produces high-purity electrolytic Li from low-purity LiCl by taking advantage of the high lithium-ion selectivity of the solid electrolyte (LLZTO). This reduces cost, use of energy and chemical reagents. Drawbacks include electrolyte cost and the need to reclaim byproducts. Development of efficient lithium metal production capacity could enable the US to leverage its market presence toward leadership position.

In FY21 Argonne expanded and updated its efforts evaluating the global supply chain of NMC batteries of various stoichiometric variance for their life cycle burdens. The analysis utilized the latest GREET2020 data for battery materials and focused on the effect of locational and stoichiometric differences on sustainability metrics such as energy use, GHG emissions, criteria air pollutants, etc. The findings suggest that the GHG emissions of NMC batteries tend to reduce as energy density increases if battery energy capacity is kept equal (Figure III.1.2). The change in material composition implies that the increase in energy density requires the use of more nickel. Nickel is energy intensive to produce and since it is derived from either sulfide or laterite ores there is a potential environmental tradeoff for nickel from the different sources. Sulfide-based nickel typically require less energy input than laterite-based nickel, but it may be associated with significant SO_x emissions if producers do not manage their refining processes well.

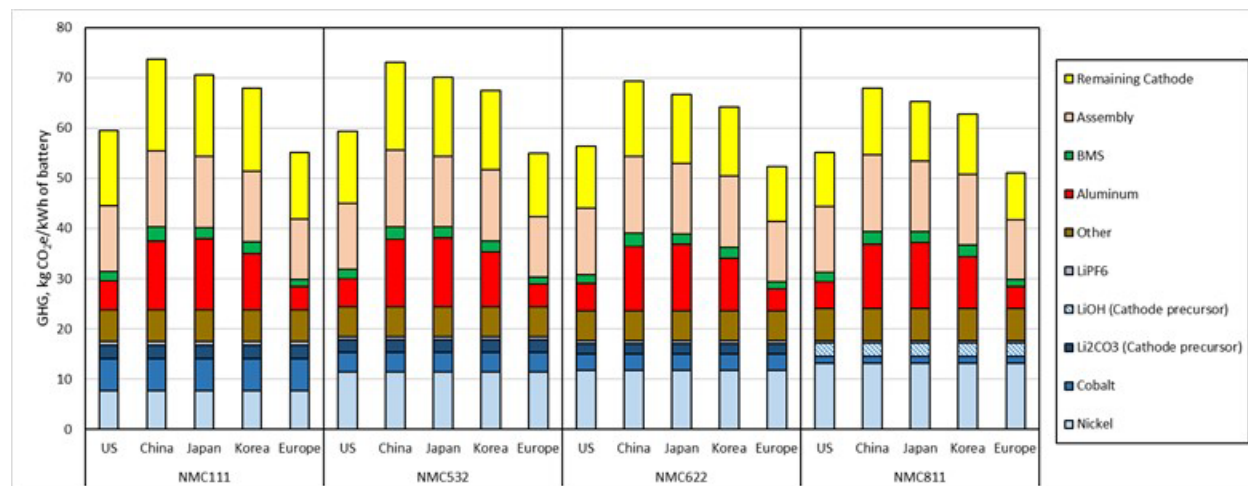


Figure III.1.2 The GHG emissions associated with NMC LIBs decrease as both energy density and stoichiometric nickel content increase.

The IEA Hybrid and Electric vehicles Technology Collaboration Program (HEV TCP) Task Force 30 Working Group held virtual meetings in March and October. The focus of this effort is to better understand the environmental impacts of vehicle electrifications from a life cycle point of view. The meetings included committee members as well as outside guests and invited speakers to discuss and propose extended impact categories of importance beyond greenhouse gases.

The IEA HEV TCP Task Force 40 Working Group held virtual meetings in March and October. This activity especially suffers from lack of in-person meetings because of incompatible time zones and lack of time for impromptu and extended discussions. Despite this challenge, the working group continued to exchange important information and provide key contacts. The October meeting included excellent technical information about nickel supply locations and technologies available for extraction and conversion to battery-grade material. We provided information to the group about the direction of US critical material policy, as detailed in the Blueprint and 100-Day Supply Chain documents. The group continues to develop scenarios to create global critical material demand projections. The group is optimistic about the potential growth rates for production facilities.

Conclusions

As battery technology continues to advance, Argonne continues to examine its environmental burdens. We found that increasing the nickel content of the batteries can lead to reductions in GHG emissions, but that it depends on material sourcing, and that nickel obtained from some sulfidic ores can increase SO_x emissions. Through industry engagement and literature examination Argonne has improved its modeling capabilities of important battery production materials and disseminated that data through publications and technical presentations. Argonne has also investigated lithium metal, finding that future lithium anodes will require

additional lithium metal capacity. The US is already a player in this arena and has its own lithium reserves. Hundreds of 1,000's of tons of lithium metal may be needed (vs. the current 5,000 T market). The US has the potential to lead in the lithium metal industry and control its entire lithium metal supply chain.

Key Publications

1. Paper: Xu, Chengjian, Qiang Dai, Linda Gaines, Mingming Hu, Arnold Tukker and Bernhard Steubing. "Future material demand for automotive lithium-based batteries." *Communications Materials*, Volume 1, Issue 1, pp. 99. December 9, 2020. doi: 10.1038/s43246-020-00095-x.
2. Paper submission: Winjobi, Olumide, Kelly, Jarod, Qiang Dai and Michael Wang. "Globally regional life cycle analysis of automotive lithium-ion nickel manganese cobalt batteries: Transition to higher nickel batteries." submitted to *Sustainable Materials and Technologies*.
3. Presentation: Kelly, Jarod. "Cradle to Grave Lifecycle GHG and Cost Analysis of Current and Future Light Duty Vehicles in the United States", IEA HEV TCP Task 30 Workshop, October 2021.
4. Presentation: Kelly, Jarod, Michael Wang and Qiang Dai. "Issues of Battery critical Materials" Argonne Battery Storage Briefing, January 2021.
5. Presentation: Kelly, Jarod C., and Linda Gaines, 2021. "Challenges and Opportunities Posed by Battery Use of Lithium Metal". 3rd Battery and Energy Storage Conference, October 6–8, 2021.
6. Technical Publication: Winjobi, Olumide and Jarod C. Kelly. "Update of the Manganese pathway in GREET® 2021." Argonne technical memo. September 2021.
7. Invited Lecture: Kelly, Jarod. "Electrified Vehicles and the Batteries they Require: Is this Sustainable?" University of Illinois at Chicago, November 10, 2020.

References

Kelly, Jarod C., Michael Wang, Qiang Dai, and Olumide Winjobi. "Energy, greenhouse gas, and water life cycle analysis of lithium carbonate and lithium hydroxide monohydrate from brine and ore resources and their use in lithium-ion battery cathodes and lithium ion batteries." *Resources, Conservation and Recycling*, Vol. 174 (2021). <https://doi.org/10.1016/j.resconrec.2021.105762>.

Xu, Chengjian, Qiang Dai, Linda Gaines, Mingming Hu, Arnold Tukker and Bernhard Steubing. "Future material demand for automotive lithium-based batteries." *Communications Materials*, Volume 1, Issue 1, pp. 99. December 9, 2020. doi: 10.1038/s43246-020-00095-x.

Yang, Yongan. "Production of lithium metal with ion-selective solid electrolytes." *Green Energy & Environment*, Vol 5, Issue 4, (2020): 382–384., <https://doi.org/10.1016/j.gee.2020.04.011>

III.2 Lithium-ion Battery Recycling Prize Support (NREL)

Lauren Lynch, Principal Investigator

National Renewable Energy Laboratory
15013 Denver West Parkway
Golden, CO 80401
E-mail: lauren.lynch@nrel.gov

Samm Gillard, DOE Technology Development Manager

U.S. Department of Energy
E-mail: Samuel.Gillard@ee.doe.gov

Start Date: October 1, 2020	End Date: September 30, 2021	
Project Funding (FY21): \$1,270,000	DOE share:\$1,270,000	Non-DOE share: \$0

Project Introduction

Lithium-ion (Li-ion) batteries have become the primary choice for portable electronics (smartphones, tablets, and laptops), power tools, and electric vehicles (EV) for personal, commercial, industrial, and military applications. The demand for Li-ion batteries for EVs is expected to grow as manufacturing and materials costs are reduced while performance improves. The U.S. Energy Information Administration (EIA) projects that U.S. light-duty battery EV sales will reach 1.3 million by 2025, and others project even higher sales growth. Global EV sales are expected to reach 30 million by 2030, up from 1.1 million in 2017. This growth in EV sales and increased demand for consumer and stationary uses are expected to double the demand for Li-ion batteries by 2025 and quadruple the demand by 2030.

Demand for the global production of battery materials, such as lithium, cobalt, manganese, nickel, and graphite, will grow at similar rates depending on the future changes in the composition. The growth in demand for Li-ion batteries for EVs is expected to establish EVs as the largest end-user of cobalt and lithium and could create a particularly high supply risk for cobalt as it could be expensive, and its availability depends on foreign sources for production. To address this potential risk, the DOE Vehicle Technologies Office (VTO), within the Office of Energy Efficiency and Renewable Energy (EERE), developed a Research Plan to Reduce, Recycle, and Recover Critical Materials in Li-ion Batteries. A goal identified in the Plan is to reduce the cost of electric vehicle battery packs to less than \$150/kWh with technologies that significantly reduce or eliminate the dependency on critical materials (such as cobalt) and utilize recycled material feedstocks. However, Li-ion batteries are only recycled at a rate of about 5% currently. Analysis has shown that recycled material could potentially provide one-third of United States cathode material needs for Li-ion batteries by 2030. The current recycling supply chain for collecting, sorting, safe storing, and transporting Li-ion batteries and recovering valuable materials is limited, particularly for larger batteries used in EVs and industrial applications. Preventing the Li-ion batteries from ending up at landfills, particularly consumer electronics (as some have caused fires), is important not for the recovery of key materials but for the economy and the environment.

To achieve the above goal and address potential critical materials issues, VTO initiated three key areas of R&D:

1. supporting laboratory, university, and industry research to develop low-cobalt (or no cobalt) active cathode materials for next-generation Li-ion batteries,
2. establishing the ReCell Lithium Battery Recycling R&D Center focused on cost-effective recycling processes to recover lithium battery critical materials, and
3. launching the Lithium-Ion Battery Recycling Prize to incentivize American entrepreneurs to find innovative solutions to solve current challenges associated with **collecting, sorting, storing, and**

transporting discarded Li-ion batteries safely and economically for the eventual recovery of valuable materials for re-introduction to the battery production supply chain.



Figure III.2.1 The Critical Materials Research Plan with three major research areas to address critical materials issues for Li-ion batteries and recovery of materials for re-introduction into the supply chain.

While the first two initiatives focus on creating next-generation cobalt-free Li-ion batteries and conduct research into the recovery of critical materials and re-introduction of these materials in recycled batteries, the \$5.5-million Lithium-Ion Battery Recycling Prize leverages innovative ideas from American entrepreneurs to develop and demonstrate a supply chain that safely transitions spent batteries to specialized battery recycling facilities. The Recycling Prize is a collaboration between VTO and DOE's Advanced Manufacturing Office with \$4.5M funding support from VTO and \$1.0M from AMO.



Figure III.2.2 Logo of the Lithium-Ion Battery Recycling Prize.

The \$5.5 million Prize is designed to be implemented in three progressive phases for three years to bring ideas from concept, to prototype and partnering, through pilot validation. In each phase, expert reviewers will evaluate submissions and a federal consensus panel for recommendation to the DOE selection officials. DOE assigned the administration and execution of the Battery Recycling Prize to National Renewable Energy Laboratory (NREL) to use an already-established framework for American-Made Challenges. Figure 2 provides an overview of the three phases of the contest, the amount awarded, and the number of awards available in each phase.

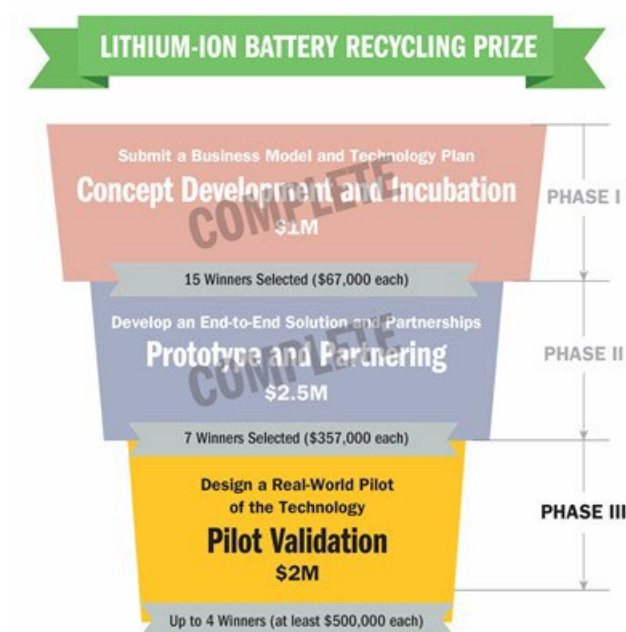


Figure III.2.3 The Lithium-ion Battery Recycling Prize consists of three progressive phases from concept through pilot validation for about three years.

This progress report provides a summary of activities of the Prize for the third year and Phase III “Pilot Validation” with the aim of awarding a \$2M cash prize distributed equally among the Phase III winners.

Objectives

The purpose of the Lithium-Ion Battery Recycling Prize is to incentivize American entrepreneurs to develop and demonstrate processes that, when scaled, have the potential to capture 90% of ALL lithium-based battery technologies in the U.S., covering consumer electronics, stationary, and transportation applications. 90% recycling rate of lithium-based batteries would be a significant achievement compared to today’s 5% recycling rate. It is the goal of this Prize to find innovative solutions to current challenges in safe and economic collecting, sorting, storing, and transporting discarded (or end of life) Li-ion batteries for eventual recycling so the 90% target could be achieved.

The Phase II Final Submissions were due early in FY21. In Phase II, participants were asked to design, simulate, and prototype a proof-of-concept solution—finalists selected in FY21 advanced to the third and final phase of the Lithium-Ion Battery Recycling Prize. In Phase III, participants must substantially advance their end-to-end solutions from proof-of-prototype to a refined pilot of the technology. The Phase III Final Submission could include demonstration and analysis to validate a small-scale pilot prototype focusing on solutions under real-world applications and scenarios for one or multiple applications (consumer electronics, electric vehicles, and stationary storage). The participating teams must demonstrate their ability to recover Li-ion batteries and verify the feasibility of achieving the end-to-end solution’s projected impact when fully scaled.

Approach

Selecting the Phase II Winners

The NREL Prize Administrator began FY21 by coordinating the Phase II Final Submission and judging process for the Lithium-Ion Battery Recycling Prize. A total of 14 teams participated in Phase II of the competition, submitting their final proposals on October 13, 2020, with virtual Participants Day presentations on November 13–14, 2020. NREL organized and hosted Participants Day and coordinated the review of the

submissions by the panel of judges. Each Phase II submission was reviewed and judged by a panel of reviewers representing VTO, AMO, PHMSA, EPA, and NREL. Judges' feedback was compiled and presented to VTO with winning team recommendations. Of the 14 participating teams, seven finalists advanced to Phase III. Phase II winning teams received a \$357,000 cash prize and vouchers of up to \$100,000 to partner with industry experts and DOE's National Laboratories through the American-Made Challenge Network to support their pilot validation.

Once the seven Phase II winning teams were identified, NREL developed the promotion plan to announce the winners publicly. The winner announcement included a press release and e-blast from VTO, an update on the HeroX website, social media, and a short video highlighting each winning team. This announcement took place on December 17, 2020.

Launching Phase III of the Prize

The NREL Prize Administrator worked closely with DOE to develop the structure of Phase III—Pilot Validation. This includes the prize deadlines and events, Phase III Rules, and updated voucher guidelines. The Phase III Rules were released on January 13, 2021, supported by an EERE press release. On January 27, 2021, the NREL Prize Administrator hosted a Phase III Welcome Meeting for all participating teams and the pre-identified voucher service providers. Each team met directly with the Prize Administrator and DOE support to review feedback from their Phase II final submissions in a one-on-one meeting. The Prize Administrator continued to work closely with each team to help develop a statement of works for the use of voucher funds in Phase III.

Continued Outreach and Support in Phase III

After Phase III began, the NREL Prize Administrator provided teams with a comprehensive communications toolkit to elevate their participation in the prize within their media networks. Several teams took advantage of the toolkit, publishing their own blog posts and working with media outlets to elevate their participation in the competition. The NREL Prize Administrator further promoted the Phase III participating teams by sharing brief HeroX updates highlighting each of the participating teams. In addition, the NREL team presented on behalf of the Prize to industry experts at a North Carolina Department of Energy Quality (NC DEQ) webinar.

Mid-way through the calendar year, teams were required to submit a Phase III Progress Update. The NREL Prize Administration Team provided additional guidance on due dates, content requirements, and templates for submitting the information. All seven participating teams submitted their Progress Updates. A panel of four reviewers representing VTO, AMO, and NREL reviewed the Progress Updates and provided feedback to inform the teams' pilot validation development as they work toward the Phase III Final Submission Requirements. The NREL Prize Administration Team worked closely with the review panel to compile and edit feedback that was shared with the participating teams.

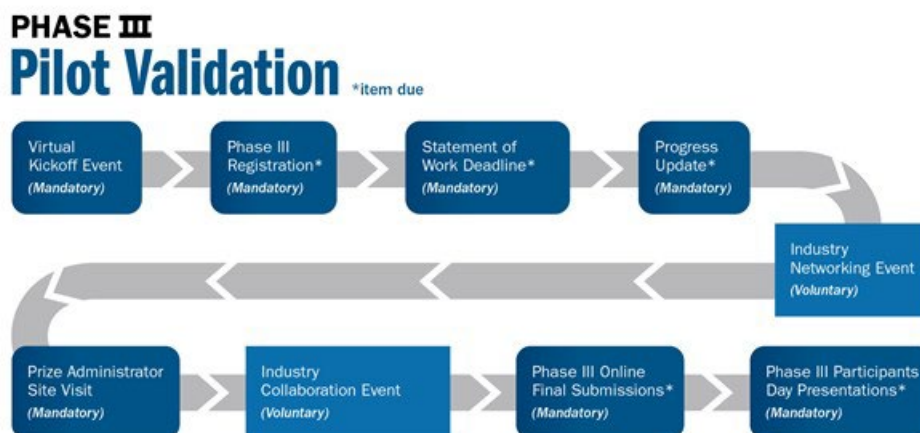


Figure III.2.4 This illustration shows the timeline of Phase III of the Lithium-ion Battery Recycling Prize, as identified in the Phase III Rules.

The final event within FY21 was a voluntary industry networking event coordinated by the NREL Prize Administrator. Teams were invited to present in an additional NC DEQ webinar focused on the Lithium-Ion Battery Recycling Prize. This event encouraged teams to present their concept solutions and receive feedback to inform plans to implement full-scale pilot validation for the Phase III Final Submission. Four of the seven participating teams attended the webinar, recorded, and posted on the HeroX website.

Results and Conclusions

Significant work remains in Phase III of the Lithium-Ion Battery Recycling Prize. Participating teams have until April 8, 2022, to finalize and submit their Phase III Final Submission. Unfortunately, one of the seven participating teams has withdrawn from the competition due to insufficient funding and concerns about the market feasibility of their concept. However, the remaining six teams have shown promising developments to validating their end-to-end concept solutions to recover Li-ion batteries successfully.

- **Li Industries:** Li Industries is developing a machine learning-based, automated Smart Battery Sorting System capable of accurately and efficiently sorting and separating batteries by several characteristics, including chemical composition, size, weight, and packaging type.
- **OnTo Technology:** OnTo's deactivate, identify, sort, and cut (DISC) solution provides safe and efficient end-of-life processing of waste batteries by sorting LIBs by cathode chemistry.
- **Powering the Future:** Claris is leveraging the existing network of collection for lead-acid batteries and applying innovative technologies to handle mixed EOL batteries to identify, separate LIBs from lead-acid, and ultimately optimize the network's value.
- **Renewance:** The Renewance Connect digital platform tracks and manages LIBs throughout their full life cycle by improving access to and utilizing existing infrastructure for decommissioning, collection, warehousing, sorting, transportation, and recycling services.
- **Smartville:** Smartville is deploying distributed heterogeneous unifying battery (HUB) facilities to fully balance conditions and certify LIBs to reduce costs and create value in the reverse logistics supply chain.
- **Titan Advanced Energy Solutions:** Battago is Titan's Battery Market Intelligence platform built to generate, aggregate, and connect battery data to create a transparent marketplace and bridge the gap between battery owners, integrators, and end of life recyclers.

Key Publications

- Phase II Winner Announcement Video (<https://www.youtube.com/watch?v=HpIkXJBjWs8>)
- Phase III Lithium-Ion Battery Recycling Prize Rules
- Updated Voucher Guidelines
- Phase III Rules Welcome Meeting
- Battery Recycling Prize Communications Toolkit
- North Carolina Department of Energy Quality Webinar

References

1. “Department of Energy Battery Recycling Prize – Phase II Winners.” Energy.gov. December 17, 2020. <https://www.energy.gov/eere/amo/departement-energy-battery-recycling-prize-phase-ii-winners>
2. “Battery Recycling Prize Phase III Rules Released.” Energy.gov. January 13, 2021. <https://www.energy.gov/eere/articles/battery-recycling-prize-phase-iii-rules-released>
3. “Renewance, Inc. Receives Battery Recycling Prize from the U.S. Department of Energy.” Business Wire. February 3, 2021. <https://www.businesswire.com/news/home/20210203005757/en/Renewance-Inc.-Receives-Battery-Recycling-Prize-from-the-U.S.-Department-of-Energy>
4. “Lithium-Ion Battery Recycling Prize Drives Recovery of Spent Batteries.” NREL.gov, February 8, 2021. <https://www.nrel.gov/news/program/2021/lithium-ion-battery-recycling-prize-drives-recovery-spent-batteries.html>
5. “Team Portables solution for lithium-ion battery recycling involves incentivizing consumers.” Recycling Today. February 25, 2021, <https://www.recyclingtoday.com/article/everledger-team-portables-lithium-ion-battery-recycling-solution/>
6. “Dept of Energy awards Everledger, HP for blockchain battery recycling app.” Ledger Insights. February 26, 2021. <https://www.ledgerinsights.com/dept-of-energy-awards-everledger-hp-for-blockchain-battery-recycling-app/>

Acknowledgements

DOE Battery Recycling Prize Team

- Connie Bezanson
- Samm Gillard
- Helena Khazdozian

NREL Battery Recycling Prize Team

- Nicholas Langle
- Lauren Lynch
- Sandra Loi
- Rebecca Martineau
- Julie Sodano

III.3 Li-ion Battery Recycling R&D Center (ANL)

Jeff Spangenberg, Principal Investigator

Applied Materials Division
Argonne National Laboratory
9700 South Cass Avenue
Lemont, IL 60439
E-mail: jspangenberg@anl.gov

Samm Gillard, DOE Technology Development Manager

U.S. Department of Energy
E-mail: Samuel.Gillard@ee.doe.gov

Start Date: October 1, 2020
Project Funding: \$5,065,000

End Date: September 30, 2021
DOE share: \$5,065,000

Non-DOE share: \$0

Project Introduction

The use of lithium-ion batteries has steeply risen in recent years, starting with electronics, and expanding into many applications, including the growing electric vehicle (EV) and grid storage industries. But the technologies to optimize recycling of these batteries have not kept pace.

The ReCell Center, U.S. Department of Energy's (DOE) first advanced battery recycling center, will help the United States grow a globally-competitive recycling industry and reduce our reliance on foreign sources of battery materials.

Objectives

DOE sees an opportunity to economically recycle lithium-ion and future batteries and accelerate the growth of a profitable recycling market for spent EV, electronics, and stationary storage batteries. This can be done by developing novel recycling techniques to make lithium-ion recycling cost-effective by using less energy-intensive processing methods and capturing more metals and other high-value materials in forms that make reuse easier.

A profit-driven battery recycling infrastructure will help meet the Vehicle Technology Office's goal of lowering the cost of new batteries and increasing the use of domestic recycled battery materials.

Approach

ReCell is a collaboration of researchers from academia and national laboratories that are working together with industry to develop new recycling processes and battery designs that will enable greater material recovery at end of life. The most promising processes and designs will be demonstrated at pilot scale at the ReCell laboratory facilities based at Argonne. Validated processes and designs will be licensed to industry for commercialization.

The center collaborators will also use modeling and analysis tools to help industry determine how to optimize end of life battery value. Argonne's EverBatt model evaluates the techno-economic and environmental impacts of each stage of a battery's life, including recycling. NREL's LIBRA model provides a birds-eye view of the interconnections between raw material availability, primary manufacture, recycling, and demand.

Despite COVID-19, work in the ReCell laboratories has continued to press forward. As we conclude our third year, we remain on our scheduled path to demonstrate a complete direct recycling process in a small pilot-scale batch operation by the end of the year. A shredder was installed in the facilities at Argonne, and we are starting to generate our own black mass. In FY22, we will work to refine the pilot recycling process and assemble a

more deliberate and continuous system. Figure III.3.1 below depicts the basic operations that need to be accomplished.

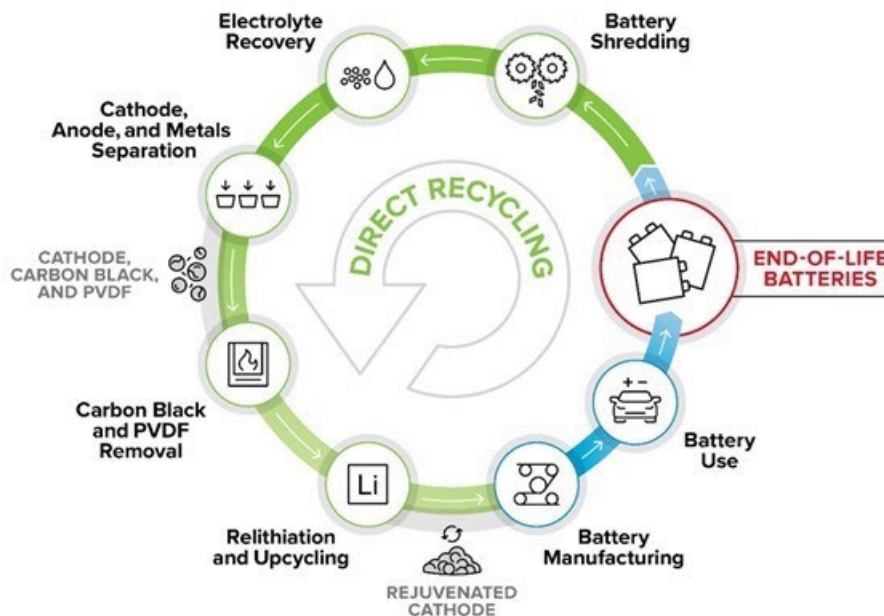


Figure III.3.1 Basic processing steps associated with direct recycling

We are working to determine which of the multiple concepts being evaluated at bench-scale for each recycling process step will be the most viable to scale up. Relithiation is a key step in the direct recycling process, and ReCell currently has five potential techniques under investigation: solid state, hydrothermal, ionothermal, electrochemical, and redox mediated. We are about to complete a comparison of the effectiveness of each of these techniques to process end-of-life cathode materials. Each technique was provided an identical sample to process, and the products are being compared to determine the optimum path forward for the relithiation work.

Work is also underway to demonstrate the feasibility of recycling manufacturing scrap. This represents an early point-of-entry for direct recycling. The benefits of recycling can be realized with fewer steps than needed for end-of-life material recycling. The ReCell team has collected manufacturing scraps and subject it to the processes required to feed the recycled material back into the cell fabrication process. Successful deployment of this concept could enable significant savings on the production of new cells.

As we move into the new quarter, look for ReCell to investigate fresh ideas to cost effectively recover additional materials from end-of-life batteries. We will also continue to improve the front-end processing of batteries to produce cleaner active electrode material, and we will work to combine processes for more efficient results. Lastly, ReCell will be working hard to demonstrate the capability to modernize older cathode chemistry so that it can find a ready market.

To help ensure focus of the work and relevance of projects performed within the ReCell center there are currently four focus areas. They are Direct Cathode Recycling, Recovery of Other Materials, Design for Sustainability, and Modeling and Analysis. Overviews of these focus areas are as follows.

Direct Cathode Recycling

In 2018, global production of lithium-ion batteries (LIB) to meet the world's energy storage needs consumed over 50,000 tons of various transition metals and lithium salts. The consumption of these critical materials is at a scale that it has significant impacts on the business plans for materials and component suppliers, mining

companies, and materials processors. These issues can be clearly seen in the production and supply of the transition metal cobalt, a common active component, where approximately 50% of the world's output is now used to make LIBs. The competition for this limited supply drives up prices, making non-standard materials sources viable for suppliers. The price of cobalt on the open market recently started showing supply and demand correlations. As a by-product of nickel and copper mining, increasing cobalt sourcing also effects the prices of these metals. An alternative to increased mine output and exploration is to utilize recycled end-of-life LIBs as a source of feedstock for new low-cobalt compositions. In this section, we are exploring anode/cathode separation, cathode isolation from the electrode, separation of the various classes of cathode materials from each other, and developing processes to, with minimal input, recover, rejuvenate, and reuse these materials. These cathode materials, most containing cobalt, typically are isolated in a lithium-depleted state due to losses associated with side reactions, salt precipitation, and corrosion. Several paths towards rejuvenating these cathode materials have been evaluated and are being optimized with the EverBatt team, using baseline materials, recovered manufacturing scrap samples, and model black mass.

Within Direct Recycling, there are efforts focused on cathode isolation (anode/cathode separation, binder removal with heat or solvent) and cathode/cathode separation (froth flotation, magnetic separation). The six pathways that address relithiation of the recovered cathode are being evaluated using a down-select process with EverBatt. As we move away from relithiation studies, the effort on cathode upcycling (recycled cathode as feedstock) is being increased, with a focus on solvent choices, mechanisms of cation addition (or subtraction), and electrochemical evaluation. We are also continuing evaluation of the role small levels of impurities (introduced by cathode isolation and processing) play in performance. Advances and new directions will be evaluated with the EverBatt team to identify underlying issues with materials choices and processing variables.

Recovery of Other Materials

A lithium-ion cell is a complex device that contains several valuable materials. Although cathode active material recovery is the main focus of the program, recovery of other materials is also important and offers additional benefits. For the purpose of the project “other materials” are defined as electrolyte components, anode materials, and metals from current collectors. Metals, particularly copper recovered from current collector, provide an additional revenue. By recovering additional materials, the recycling process maximizes the reuse of lithium-ion cell components and therefore tightens the closed loop, driving the overall process to profitability. In addition, costs to dispose of waste are avoided. It is important to design all down-stream processing and material recovery sequences in a way that preserves integrity and assures high salvage rate and quality of all recovered materials.

Cell disassembly and size reduction is the critical first step in LIB recycling. We investigate non-aqueous shredding methods to avoid degradation and to preserve materials to be recovered later in the recycling process. Safety of the process needs to be the top priority. It is also important to explore the effects of size and size distribution of shredded materials on separation efficiency. A shredder selection and procurement are complete. Battery material shredded at Argonne will be distributed and used as a baseline material for the ReCell Center.

Graphite and lithium compounds (electrolyte salt) are two additional high-value materials that are present in cells. These materials are defined as critical due to their limited supply or geographical location of production facilities. By recovering these materials, we will reduce foreign dependence and increase our national security. The Center launched a new project to further develop a University of Virginia process that generates graphene at high yield from cycled anode graphite. This upcycling process can produce high-value material that further improves the economy of battery recycling.

Anode/cathode separation efforts in the ReCell Center focus on separating the anode and cathode shreds while the films of active materials are still attached to copper and aluminum foils, respectively. It was previously demonstrated that delamination (removal of the active material film from current collectors) can be achieved in

“green” organic solvents. Based on this success, the researchers went one step further and attempted delamination and relithiation in the same process. Preliminary data suggest that relithiation in ethylene glycol-based solvents can be achieved at modest conditions. The Center also initiated a project aimed at effective delamination in aqueous solution, with potential to simultaneously separate anode from cathode active material. This would reduce black mass complexity and simplify separation processes further downstream. Ideally, the size-reduced cell components would be processed to remove electrolyte components, followed by dry separation techniques, with the most reasonable option being continuous eddy-current separation. The most effective anode/cathode delamination/separation technique(s) will be chosen and combined with processes for recovering other materials to determine which processes can be easily integrated into a unified battery recycling process.

Black mass resulting from cell shredding is contaminated with sub-micron particles of current collectors (aluminum and copper). The contamination may have a detrimental effect on quality and performance of recovered cathode active material. The Center is working on a process to dissolve solid Al and Cu contaminants under aqueous alkaline conditions without affecting the chemistry and morphology of the cathode material.

Design for Sustainability

Millions of batteries are approaching their end of life and need to be recycled. While many efforts have been focused on recycling the elements and/or compounds from spent cells through various techniques, this project aims to create cell designs that will enable rejuvenation of a spent cell, and/or improve the ease of recycling at the end of life. The ability to regenerate a cell with an electrolyte flush/rejuvenation and restoration of lithium inventory has the potential to extend the life of a lithium-ion battery far beyond its nominal 10-year life. This would reduce the quantity of packs requiring recycling and/or make for easier target material extraction.

Modeling and Analysis

The modeling and analysis focus area is fundamentally different from the other 3 areas, which perform laboratory experiments to develop recycling processes to separate, recover, and upgrade materials from spent batteries. Technical success is not the only hurdle ReCell processes must overcome; processes must also be economically viable, environmentally benign, and avoid exacerbating any material supply constraints. The projects in this focus area evaluate and compare processes developed in the experimental focus areas to make sure that only those that satisfy all of the required conditions are further developed and scaled up. The EverBatt model examines energy and environmental implications, as well as economics, of individual processes and the entire battery lifecycle, to identify the most promising process options. The LIBRA model places battery material supply and demand in a global context.

Results

Binder Removal via Thermal Processing

Once cathode materials are separated to be recycled, the poly(vinylidene difluoride) (PVDF) binder needs to be removed to allow for further processing. This can be done using a large quantity of n-methyl-2-pyrrolidone (NMP), but this is not cost effective. As an alternative to solvent-based methods, thermal decomposition can be used to eliminate the binder. This has the advantage of producing no liquid waste and can be performed at temperatures as low as 500°C. Last year, we demonstrated the binder removal process for NMC622 and began to scale the process using batch rotary kiln processing. The rotary kiln process showed promising scalability but needed further refinement and optimization. This year, this project focuses on transitioning the rotary kiln process to continuous operation and further optimizing it to improve performance.

During this last quarter, we focused on processing cathode recycling scrap material from vendor A with composition close to NMC 622 using the process shown in Figure III.3.2. This material was first shredded using a paper shredder to reduce the size of the electrodes. Then the material was fed into the rotary kiln set to increase temperature slowly up to 500°C. The residence time of the material was approximately 1 h in the kiln. The material was then knocked off the foil by brief acoustical mixing and then sieved to remove the Al foil.

Due to the presence of fluorine in the binder some Li is removed from the structure and it needs to be replaced to restore the material's capacity. This second step was done in either the rotary kiln with a residence time of about 1 hr. or a box furnace with an 8-hr. hold. Both processes occurred at 750°C with 8 wt.% of $\text{LiOH} \cdot \text{H}_2\text{O}$. The last step, a rinsing procedure followed by an anneal at 700°C, removes any excess LiOH or Li_2CO_3 on the surfaces of the cathode.



Figure III.3.2 Process flow diagram for the recovery of manufacturing scrap.

In the previous quarter, the rotary-kiln-processed material showed inferior performance to that processed in the box furnace. It was determined that the likely cause was the shorter residence time in the rotary kiln. To increase the residence time, the tilt of the kiln was reduced from 1° to 0.4° and the rotation rate was reduced from 2 rpm to 1 rpm. This increased the residence time to over 8 h, which significantly improved the performance of the final material, as can be seen in Figure III.3.3a. Both the rate capability and cycle life are improved with similar initial performance.

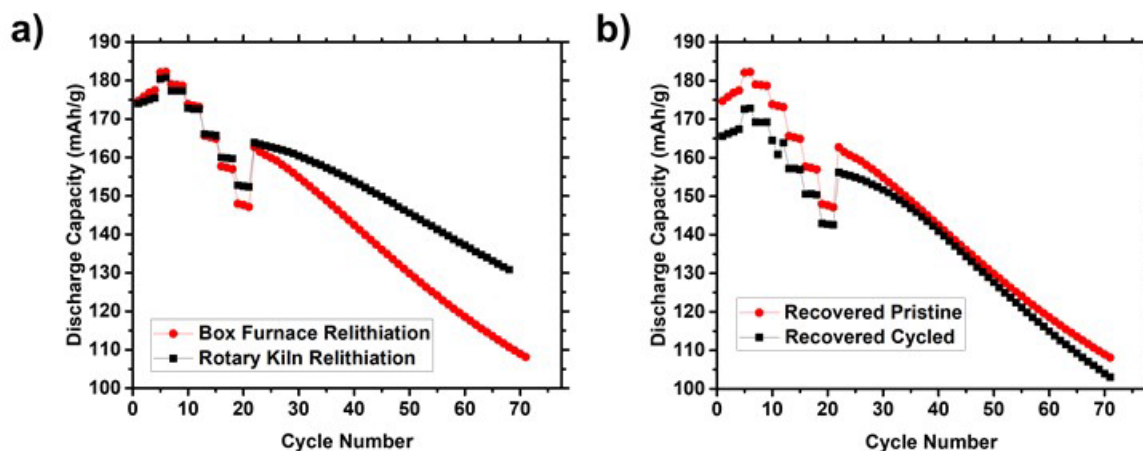


Figure III.3.3 Electrochemical discharge capacity of vendor A cathode a) manufacturing scrap and b) comparison of manufacturing scrap and cycled material after reprocessing using a thermal method.

In addition to recovering manufacturing scrap, cycled material can also be recovered in a similar process, with the amount of Li adjusted to relithiate the cycled material. This cycled material had a Li content of about 0.80, which required about 20 wt.% of $\text{LiOH} \cdot \text{H}_2\text{O}$ to do the relithiation. This recovered material did have slightly reduced performance compared to the manufacturing scrap material, as can be seen in Figure 3b. This difference can probably be reduced or eliminated through further refinement of the recycling process, and by moving from a box furnace to the rotary kiln for the relithiation step.

Binder Removal via Soxhlet Extraction

This project is developing the Soxhlet extraction method to remove and recover the polymer binder (e.g., PVDF) from End-of-Life (EOL) battery cathodes. The electrodes in Li-ion batteries have polymer binders to hold together active materials and conductive carbon additives. However, to recycle EOL battery cathode, it is necessary to remove and/or separate the polymer binder from the electrode. In the ReCell center, thermal decomposition of PVDF has been studied as an option, but not a standard solution method, because the known solution method involves a large quantity of toxic and high-boiling-point solvents (e.g., NMP). It is necessary to minimize the use of organic solvent and environmental impact. In the Soxhlet method, samples are repeatedly extracted with solvent regenerated by distillation through a periodic siphoning process. Therefore, a minimal amount of solvent is required, and fresh solvent is fed via distillation into the sample container every time. This method can be also scaled up to manufacturing scale. In FY21, this project is developing and demonstrating the Soxhlet extraction method for PVDF removal and recovery.

The project ended in the Q3 period. This report mainly summarizes the main activities in this project.

Soxhlet Extraction Process Design

The conventional Soxhlet extractor contains three main components: a percolator, a thimble, and a siphon mechanism (Figure III.3.4). The percolator is used to circulate the solvent. A distillation flask with solvent is placed on the bottom and heated by a heater and a reflux condenser filled with condensed solvent is on the top of main chamber of the Soxhlet extractor. A thimble made of filter paper is placed into the main chamber and used to hold the material that needs to be extracted (here it is cathode material of A-C021). Through the siphon mechanism, the thimble can be emptied in a cyclic fashion.



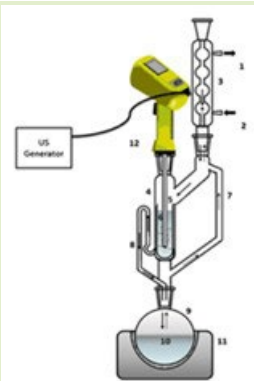


Figure III.3.4 Conventional Soxhlet extractor design

Prior to designing a real Sono-Soxhlet extractor, we made a batch-scale simulated Sono-Soxhlet extractor to evaluate the feasibility of introducing sonication to the Soxhlet process. The ultrasonic source was a handheld ultrasonic homogenizer (Type: UP200Ht from Hielscher Ultrasound Technology). 10 ml solvent with several pieces of cathodes was placed into 30 ml glass vial. With the success of this batch-scale model, a

Sono-Soxhlet imitation reactor was designed, and custom glassware was ordered so we could combine Soxhlet extraction with sonication to facilitate material release from the current collector, as well as more rapid reaction times. Table III.3.1 summarizes the comparison between different Soxhlet extraction designs that were utilized during the course of this project.

Table III.3.1 Comparison of different Soxhlet extractors.

Reactor #	Reactor Description	Reactor Photo	Pros	Cons
1	Conventional Soxhlet Extractor		Minimal solvent needed	Slow reaction time, difficult to remove recycled cathode material from paper filter
2	Sono-Soxhlet Extractor (Batch Scale)		Useful for evaluating the feasibility of Sono-soxhlet imitation extraction	Disabled the solvent reuse functionality
3	Sono-Soxhlet imitation extractor		High efficiency, short reaction time, minimal solvent	Required custom glassware

We also developed and tested a cryovap solvent transfer method to recover PVDF and solvent from a PVDF binder solution. We examined a conventional rotovap technique to evaporate solvent Y from ORNL, but its high boiling point (b.p.) made it difficult to recover the solvent from the solution. To address this issue, we chose a lower b.p. solvent for PVDF. Dimethylformamide (DMF) is a good PVDF solvent and has a b.p. of 152~154°C. Other well-known PVDF solvents are NMP and DMSO, and their b.p.s are 202~204 and 189°C, respectively. Therefore, there is a clear advantage to use DMF for the solvent recovery process. Figure III.3.5 shows a cryovap solvent transfer apparatus. A flask filled with PVDF solution was placed in a water bath and connected to a solvent transfer manifold. The manifold was connected to a liquid nitrogen solvent trap to collect solvent, and also to a Schlenk line to evacuate the whole apparatus. The starting solution in the flask had 5 wt.% PVDF in it. We could use either static or dynamic vacuum for the solvent transfer, and we used a dynamic vacuum by leaving the vacuum valve open to minimize the total process time. First, we started the reaction at room temperature, but it took a long time to notice any changes in the solution level. Therefore, we increased the water bath temperature gradually. After it reached ~50 C, the solvent transfer rate was notably increased, and the transfer reaction was finished within 1 hour. The volume of the recovered DMF solvent was measured, and the apparent volume recovery is ~93%.

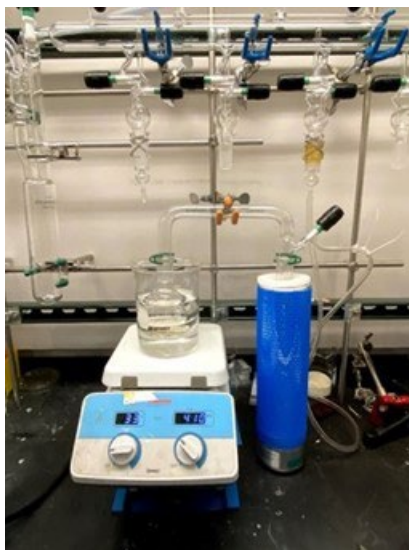


Figure III.3.5 PVDF binder and cryovap solvent transfer apparatus

Once we addressed rapid reaction time through sonication and chose the optimal solvent recovery process with the cryovap solvent transfer apparatus, the last hurdle was finding the optimal thimble, or mesh filter, to collect the NMC particles. Previously, we had tested two types of thimbles for the Soxhlet process: (1) cellulose and (2) porous polypropylene. However, neither of them was promising because of pore-clogging and slow solvent draining problems. Thus, we tested a new custom-made thimble in order to address these problems, made of stainless-steel mesh filters with smooth surface, mono-layer structure, and small pore size (Average pore size of $43\mu\text{m}$, $15\mu\text{m}$ and $5\mu\text{m}$). Prior to applying the filters to the Soxhlet experiment, we performed filtering tests using those stainless-steel mesh screens. Based on filtering tests we conducted with DMF solvent and NMC 111 particles, the $5\mu\text{m}$ stainless-steel mesh filter was chosen and used as thimble in the following Soxhlet process.

Results and Characterization

Once we completed the work above to design the optimal Soxhlet extraction process, we tested the sono-Soxhlet extraction successfully using stainless-steel mesh filters. We characterized recovered NMC 811 powder from ‘vacuum-assisted sono-Soxhlet extraction’ and recovered solvent from the ‘vacuum-assisted cryovap process’. XRD patterns and SEM images of both electrode scrap and recovered powder were taken to confirm that the Soxhlet process had no effect on the crystal structure and morphology of recovered cathode material. After vacuum-assisted sono-Soxhlet process, NMC811 secondary particles are exposed well, and no distinct carbon black/PVDF are detected. A large amount of carbon and fluorine are revealed in the electrode scrap (Figure III.3.6), while the signal of fluorine in the recovered NMC811 powder was reduced significantly. Even though fluorine was not removed completely, the obvious decrease of the fluorine content confirmed the efficient removal of PVDF through the vacuum-assisted sono-Soxhlet extraction process. To minimize solvent usage, the vacuum-assisted cryovap process was introduced to recover and recycle DMF which was used in the sono-Soxhlet process. The recovered DMF was examined by FTIR and compared with fresh DMF, as shown in Figure III.3.7. All peaks of the recovered DMF were indexed to those of the fresh DMF without any impurities. The recovery yield of DMF in the lab-scale experiment was 90.7%, which would be higher in scaled-up experiments. The inset photo in Figure III.3.7 shows the recovered DMF was transparent and visibly the same as fresh DMF solvent. Recovered DMF potentially could be reused as fresh extractant in the continuous sono-Soxhlet extraction to reduce the cost and relieve the environmental burden.

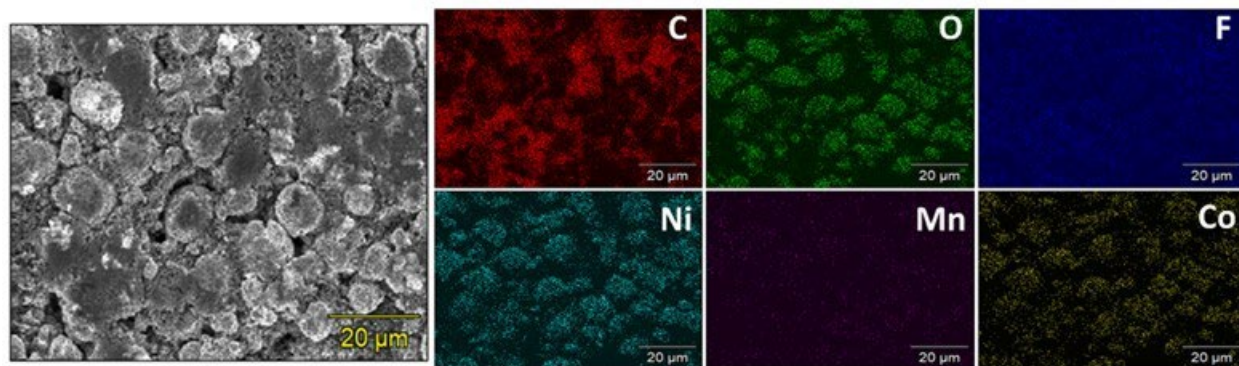


Figure III.3.6 Mapping of NMC 811 electrode scrap

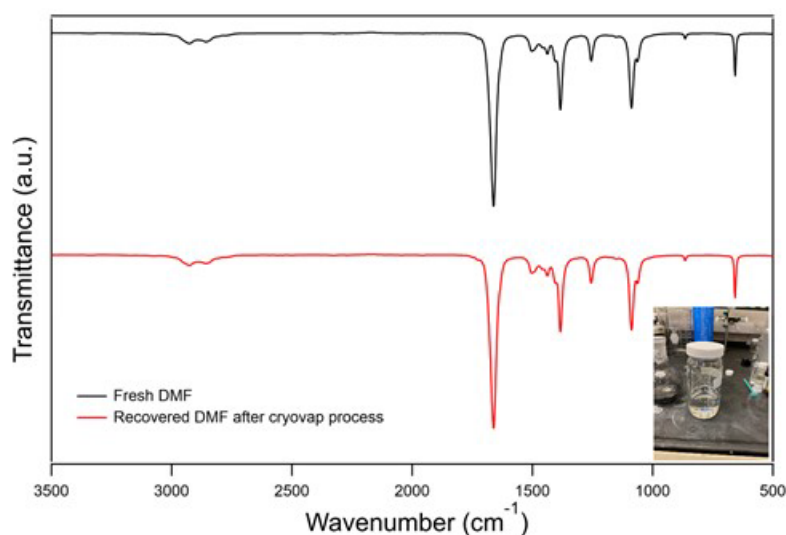


Figure III.3.7 FTIR spectra of fresh DMF and recovered DMF from vacuum-assisted cryovap process. Inset digital photo shows recovered DMF.

Cathode/Cathode Separation Process Development

Most direct recycling operations involve the collection of “black mass,” which is a mixture of anode and cathode powders recovered from shredded cells. Even if cells are presorted before processing, it is still likely that some mixing of cathode materials will occur. Additionally, some cells contain mixtures of different cathode materials, such as lithium manganese oxide (LMO) and lithium nickel manganese cobalt oxide (NMC). While the LMO is unlikely to be reused, the NMC could be used in a modern cell. Direct recycling of lithium-ion batteries will require the ability to effectively separate different cathode chemistries. This work will focus on separation of complex mixtures of virgin cathode powders, as well as those recovered from actual cells. This work has a focus on scale-up of proven techniques, as well as the separation and recovery of complex mixtures of cycled cathode powders.

Continuous Froth Column Flotation

Process Optimization of 1-Step Froth Column Operation

In this quarter, we investigated the separation of lithium nickel manganese cobalt oxide ($\text{LiNi}_{0.33}\text{Mn}_{0.33}\text{Co}_{0.33}\text{O}_2$, NMC111) and lithium manganese oxide (LiMn_2O_4 , LMO) by the pilot-scale continuous froth column. Figure III.3.8 shows a picture of the continuous froth column (left) and a schematic diagram (right).

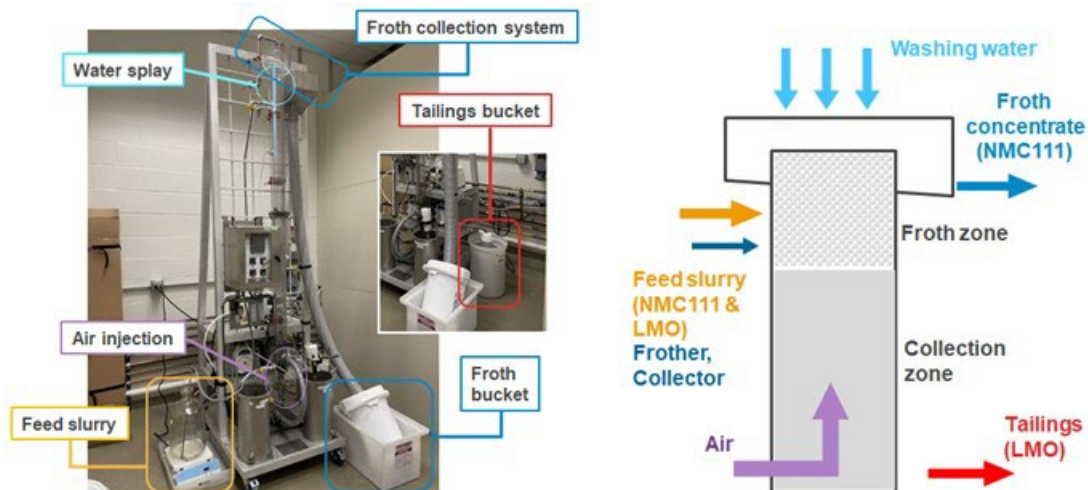


Figure III.3.8 Picture (left) and schematic diagram (right) of the pilot-scale continuous froth column (left)

A feed slurry containing 1:1 mass ratio of pristine NMC111 and LMO powders at 2.5 wt.% solid content was mixed by a magnetic stirrer with Atrac 922 collector and two frother agents (i.e., methyl isobutyl carbinol (MIBC) and polypropylene glycol (PPG400)). Atrac 922 collector adsorbs to the surface NMC111, making the cathode hydrophobic. The hydrophobic surface of NMC111 is attracted to the bubbles in the froth column and ends up concentrated in the froth layer. Before feeding the cathode slurry, 20 ppm MIBC and 2 ppm PPG 400 were added to 10 L of water in the froth column, and the air was introduced through a sparger to create a froth bed. The slurry was fed to the column at 5 RPM feed pump speed and mixed with the air in the collection zone. Wash water was sprayed continuously during the column operation to remove entrained LMO from the froth zone and send it to the tailings. Dilution of frother in the column by washing water was compensated by additional frother to the feed slurry. As the column operates, NMC111 is concentrated in the froth, while LMO is concentrated in the tailings.

Five froth column tests were conducted with 8 L feed slurry at 2.5 wt.% solid content (i.e., 100 g each NMC111 and LMO) to determine the optimum operating condition that concentrates NMC111 and LMO into the froth and tailings, respectively. With the fixed feed slurry solid contents and feeding rate, collector, additional frother, washing water flow rate, and air flow rates were adjusted to optimize the process. Table III.3.2 shows the process variables of conducted tests. Compared to the last quarter, the column pH was increased by adding LiOH solution, at pH 14, in Tests 2 – 5. During column operation, the froth depth was maximized to allow adequate time for impurities in the froth to be removed by wash water.

Table III.3.2 Process variables for froth column operation with 8 L feed slurry

Test #	Feed (8L slurry at 2.5wt% solid)		Washing Water	Air Flow	Column pH Control by pH14 LiOH Solution	Controlled Froth Depth
	Atrac922	MIBC/PPG400				
1	45mg	0.7g / 0.07g	1 Lpm	1.8-2.2 Lpm	None	3"-5"
2	45mg	0.7g / 0.07g	0.3 - 1 Lpm	2.2 Lpm	Added 1mL to column	25"-26"
3	45mg	0.7g / 0.07g	0.6 - 1 Lpm	2 - 2.2 Lpm	Added 1mL to column	45"-55"
4	45mg	0.5g / 0.05g	0.3 Lpm	2 - 2.2 Lpm	Added 1mL to column	28"-33"
5	45mg	0.5g / 0.05g	1 Lpm	2.2 Lpm	Added until pH10	7"-11"

Except for Test 1, the second froth sample was collected 15 minutes after the feed slurry pump was turned on. Figure III.3.9 and Figure III.3.10 show the NMC111 grade (i.e., mass content of NMC111 in the collected solid) of froth and tailings, respectively, based on the results of ICP analysis. Figure III.3.11 and Figure III.3.12 show weighted average NMC111 grades of froth and tailings as a function of the total mass, respectively. Table III.3.3 compares the NMC grades of froth and tailings based on ICP results and GSAS-II refinement based on XRD results. Figure III.3.10 shows that the second froth contained a higher NMC111 content compared to the earlier froth. This is attributed to the thinner, free-flowing froth overflow at the earlier stage of the column operation compared to the thicker froth that would be collected after the later stage, where more solids would be circulating in the collecting zone.

Comparison of Tests in Table III.3.2 clearly shows a big impact of increasing pH in the column on the controlled froth depth. During the operation of Test 2, the amount of froth overflow was dramatically increased compared to Test 1. This resulted in a deeper froth depth which minimized the overflow even after reducing washing water flowrate to reduce the free-flowing nature of the froth. However, reducing washing water to 0.3 L/min resulted in low tailings recovery as shown in Figure III.3.11. Test 2 (with addition of LiOH in the column at the beginning to increase the column pH) had faster froth overflow than Test 1 (without addition of LiOH and the same frother and collector dosage as Test 1). Therefore, to slow down the froth overflow (to avoid overflowing solid without providing enough cleaning time in the froth) as much as possible, the froth depth needed to be increased by lowering the froth/solution interface level. I also reduced washing water in Test 2 to increase solid content in the froth and make the froth thicker, but this resulted in very small amount of tailing recovery. In Test 3, the amount of washing water was increased to 0.6 to 1 L/min. However, it ended up with a huge froth depth, while it did not improve the froth NMC111 grade. Test 4 and Test 5 were conducted with reduced feed frother dosage. The results of Test 4 indicated that washing water flowrate was too small and caused a high contamination in the froth. Test 5 resulted in the highest froth NMC111 grade, achieving 93.9% NMC111 in the second froth. However, it also resulted in a low froth solid recovery and a higher NMC111 contamination in the tailings. Overall, the experiments indicated that the froth NMC111 grade higher than 80% was achieved by the operating conditions with 45 mg collector/100 g NMC111, 0.5 g – 0.7 g MIBC and 0.05 g – 0.07 g PPG400, 1 L/min washing water flowrate and 2.2 L/min air flowrate.

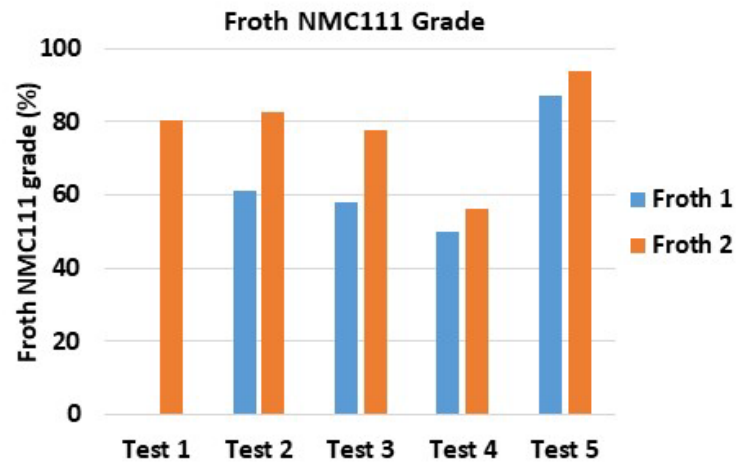


Figure III.3.9 NMC111 grade of the recovered froth based on ICP results

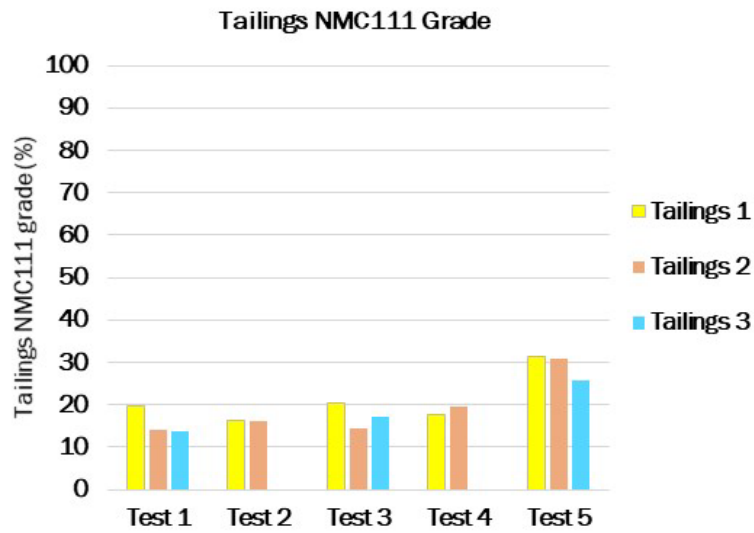


Figure III.3.10 NMC111 grade of the recovered tailings based on ICP results

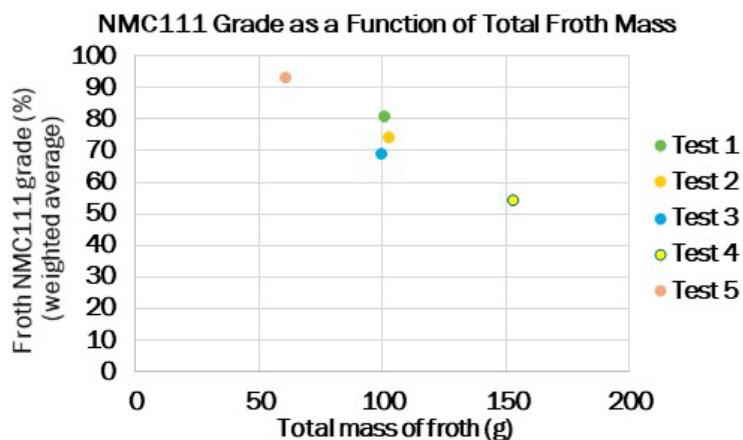


Figure III.3.11 NMC111 grade as a function of total froth mass (total feed solid: 200g)

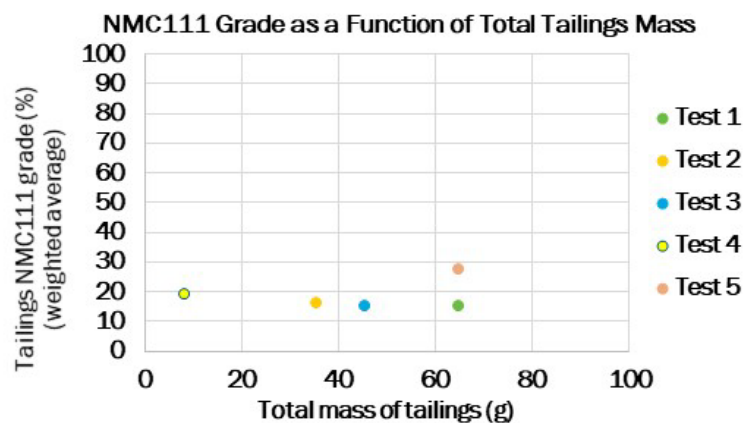


Figure III.3.12 NMC111 grade as a function of total tailings mass (total feed solid: 200g)

Table III.3.3 NMC111 grades in froth and tailings based on ICP results and GSAS-II refinement based on XRD results

Test #	Froth 1 ICP/ [XRD]	Froth 2 ICP/ [XRD]	Tailings 1 ICP/ [XRD]	Tailings 2 ICP/ [XRD]	Tailings 3 ICP/ [XRD]
1	80.5% / [78.5%]		19.7% / [22.7%]	13.9% / [13.7%]	13.6% / [17.9%]
2	61.0% / [57.8%]	82.8% / [80.4%]	16.2% / [17.2%]	16.1% / [15.5%]	
3	57.9% / [51.0%]	77.9% / [78.8%]	20.4% / No data	14.3% / [10.5%]	17.3% / [18.1%]
4	50.0% / No data	56.3% / No data	17.7% / No data	19.5% / No data	
5	87.1% / [84.2%]	93.9% / [92.3%]	31.4% / [34.5%]	30.7% / [34.2%]	25.8% / [30.1%]

Scaled-Up Froth Column Operation for the 1st Stage of 2-Step Froth Flotation

It was determined that multiple-step froth flotation would be beneficial to improve the grades of separated NMC111 and LMO. As only one continuous froth column was available at the laboratory, several batch operations of the froth column would be required to imitate the multiple-step operation. Figure III.3.13 shows the process diagrams of the first batch operation and the second batch operation to imitate 2-step continuous froth column operation. In the first batch, which imitates the first stage of the 2-step froth column operation, NMC111 and LMO from the feed slurry are concentrated as much as possible into the froth and tailings, respectively. The froth with a higher NMC111 content is then fed to the second batch, where a high grade NMC111 is recovered from the froth. In a different second batch operation, the tailing from the first stage is fed to recover a high grade LMO.

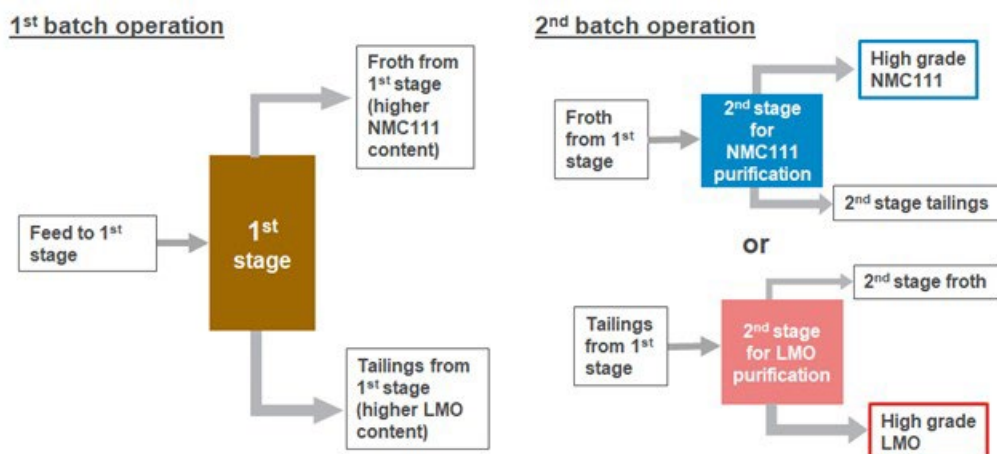


Figure III.3.13 Schematic diagrams of the first and second stage froth column operation for 2-step froth flotation

Three froth column tests were conducted to determine the optimum conditions for the first stage batch operation. Table III.3.4 shows the process condition of these tests. As sufficient solid would be needed to investigate the second stage operation, the feed slurry was scaled up to 10 L with the same solid content and the mass ratio of NMC111 and LMO as the 8 L slurry tests. Test 2-1 was conducted with the collector and frother dosages in the feed slurry equivalent to Test 5 described above. The frother dosage in the feed slurry in Test 2-2 was equivalent to 0.6 g MIBC and 0.06 g PPG400 in 8 L slurry.

Table III.3.4 Process conditions for the froth column tests with 10 L feed slurry

Test #	Feed (10L slurry)		Wash Water	Air Flow	Column pH control by pH14 solution	Observed Froth Depth
	Atrac922	MIBC/PPG400				
2-1	57mg*	0.63g / 0.063g**	1 Lpm	2.2 Lpm	Added until pH11	4" – 11"
2-2	60mg	0.75g / 0.075g	1 Lpm	2.2 Lpm	Added until pH10	28" – 39"
2-3	57mg	0.68g / 0.068g	0.8 – 1 Lpm	2.2 Lpm	Added until pH11	7.5" – 14"

* Corresponding to 45mg Atrac 922 for 100g NMC111.

** Corresponding to 0.5g MIBC/0.05g PPG400 in 8L slurry.

Figure III.3.14 shows NMC111 grades of froth and tailings based on ICP results. Figure III.3.15 shows weighted average NMC111 grades of froth and tailings as a function of total mass. The test numbers corresponding to the results are noted on the graph. As shown in Figure III.3.14, Test 2-1 and Test 2-3

achieved high froth NMC111 grades; both second froth NMC111 grade was above 95%. However, both tests resulted in higher than 30% NMC111 contents in tailings. Figure III.3.15 shows that the froth solid recoveries in Test 2-1 and Test 2-3 were very low despite of the increased feed slurry. Even with a small difference of collector and frother dosages in the feed slurry, it impacted the result of Test 2-2, in which the separation of NMC111 and LMO barely occurred. Although the process conditions of these tests were approximately the scale-up of Test 5, the froth was thinner and overflowed more smoothly compared to the 8 L slurry tests. It was highly likely that the feed slurry system with a magnetic stirrer did not provide sufficient mixing of the 10 L slurry, where the effects of collector and frother were weakened.

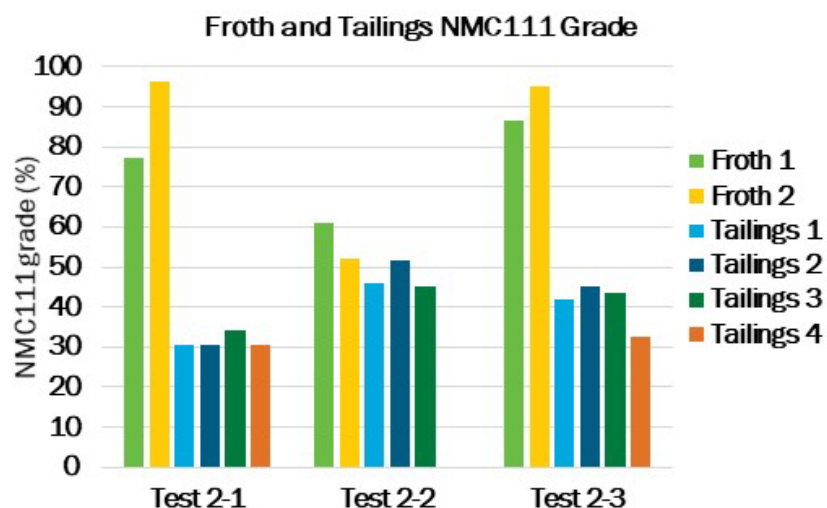


Figure III.3.14 NMC111 grade of the froth and tailings based on ICP results for the imitated first stage froth column operation

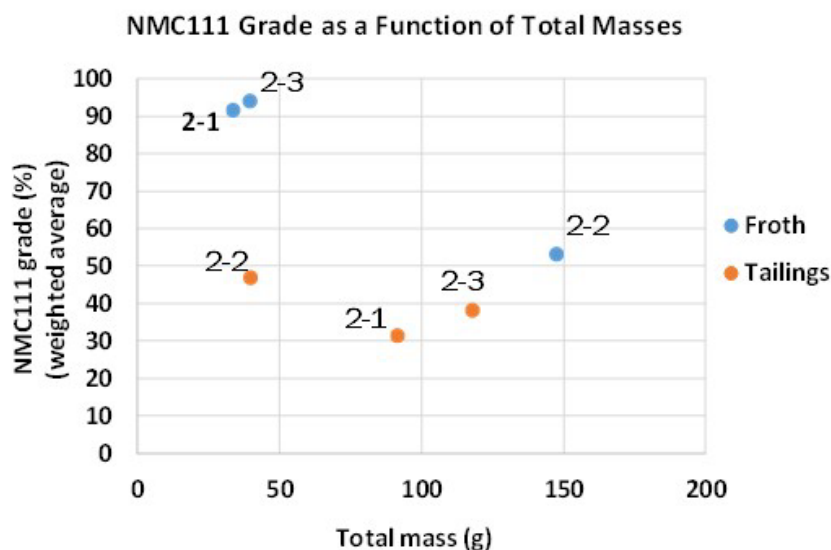


Figure III.3.15 NMC111 grade as a function of total mass of froth or tailings for the imitated first stage froth column operation (total mass of feed solids: 250 g)

In the next year, we will try to improve the separation of NMC111 and LMO by the continuous froth column. Two batch operations of the froth column will be conducted to imitate 2-step continuous froth column operation. The feed slurry system will be modified to provide sufficient mixing of the slurry. Over 95% grade

of NMC111 and LMO in the froth and tailings from the second stage batch operation will be targeted. The process conditions achieving successful result will be incorporated in the EverBatt model.

Cathode-Cathode Separation via Froth Flotation

Li-ion batteries may use multiple cathode compositions in their chemistry. Unlike other recycling processes, direct recycling requires single cathode composition prior to the relithiation and upcycling processes. During this reporting period, we focused on the separation of NCA/ LMO via froth flotation while preserving their functional integrity. The effect of solution chemistry on the separation between NCA and LMO cathode chemistries and their electrochemical performance was investigated. In addition, collector removal experiments were conducted. The results obtained from XRD, SEM, and surface hydrophobicity measurement confirmed complete removal of collector molecules from the surfaces of recovered materials.

Figure III.3.16 shows the effect of LiOH, Li_2CO_3 and solid concentration on the electrochemical performance of the recovered NCA. The result indicates that using 10mM LiOH for the separation of NCA and LMO obtained better electrochemical performance compared to the other conditions tested. Due to the lower grade of the NCA obtained from the 20% solid concentration experiment, the electrochemical performance is lower than the electrochemical performance of NCA obtained from 6% solid slurry. Addition of excess Li_2CO_3 was detrimental to both the rate capacity and cyclability of the NCA materials. The result suggests that LiOH is the ideal solution for preserving the functional integrity of NCA materials.

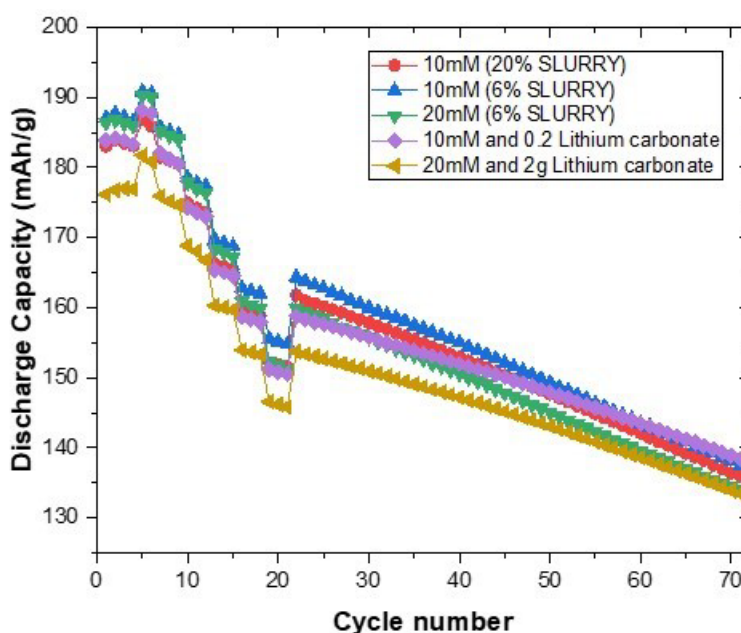


Figure III.3.16 Electrochemical performance of recycled NCA from froth flotation separation at with different conditions.

The floated NMC111 samples by the froth flotation method were heat treated in a box furnace. Different conditions for temperature and duration were investigated. To determine if the collector molecules are present on the surfaces of the recycled NMC111 after a heat treatment, flotation was performed on the heat-treated samples. In the flotation process, the absence of collector was determined by the amount of heat treated NMC111 floated in the froth product. The result showed that no recovery in the froth product means that the collector molecules were decomposed. Table III.3.5 shows the different conditions used for the heat treatment of the floated NMC111 product. The 25ml cell flotation test used as an indicator of surface hydrophobicity of the treated NMC111 determined that samples that were treated at a temperature above 200°C did not float. This suggests that thermally treating the samples above 200°C removes the collector adsorbed on the surface of the recycled NMC111.

Table III.3.5 Surface hydrophobicity tests in 25ml cell.

Temp (oC)	Duration	25ml cell Flotation test	Conclusion
200 °C	60 min	30–40% float	Collector is present
300 °C	90 min	NO recovery	Collector has been burnt off
250 °C	90 min	NO recovery	Collector has been burnt off
200 °C	90 min	NO recovery	Collector has been burnt off

SEM images and XRD refinement confirmed that no significant physical changes were observed. SEM shows similar morphology after heat treatments at different temperatures. XRD refinement results showed similar structural lattice parameters when NMC111 samples from various experimental conditions were compared to pristine NMC111. Figure III.3.17 shows SEM images of NMC111 sample burned at 200°C and 250°C. No significant change in morphology was observed. Table III.3.6 shows the lattice parameters of thermally treated samples as well as the pristine NMC111. The XRD result suggested that negligible changes in crystal structure were found before and after a heat treatment. were very similar to the values obtained for pristine NMC111.

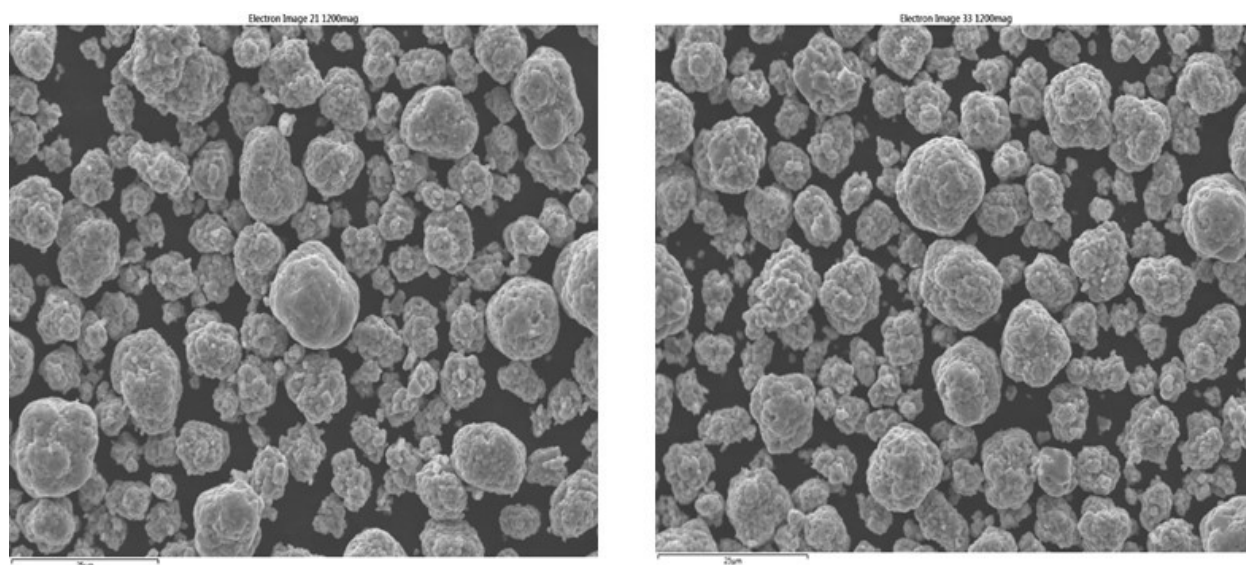


Figure III.3.17 a) SEM image of NMC111 burned at 200 °C b) SEM image of NMC111 burned at 250 °C

Table III.3.6 XRD analysis results showing the refinement parameters

Description	I003/I1004	a (Å)	c (Å)
Pristine NMC111	1.51	2.857	14.223
Collector-treated NMC111	1.50	2.858	14.223
Burned @ 400 °C for 1hr	1.52	2.857	14.220
Burned @ 300 °C for 1hr 30mins	1.51	2.857	14.221
Burned @ 200 °C for 1hr 30mins	1.49	2.857	14.221
Burned @ 250 °C for 1hr 30mins	1.54	2.857	14.223

XPS analysis was conducted to analyze the surface composition of the treated NMC111. In the sample with collector adsorbed on the surface, lithium was not detected on the surface of collector-coated NMC111 due to

a coverage of collector up to 2-3 nm while lithium was detected when the collector was removed by a thermal process.

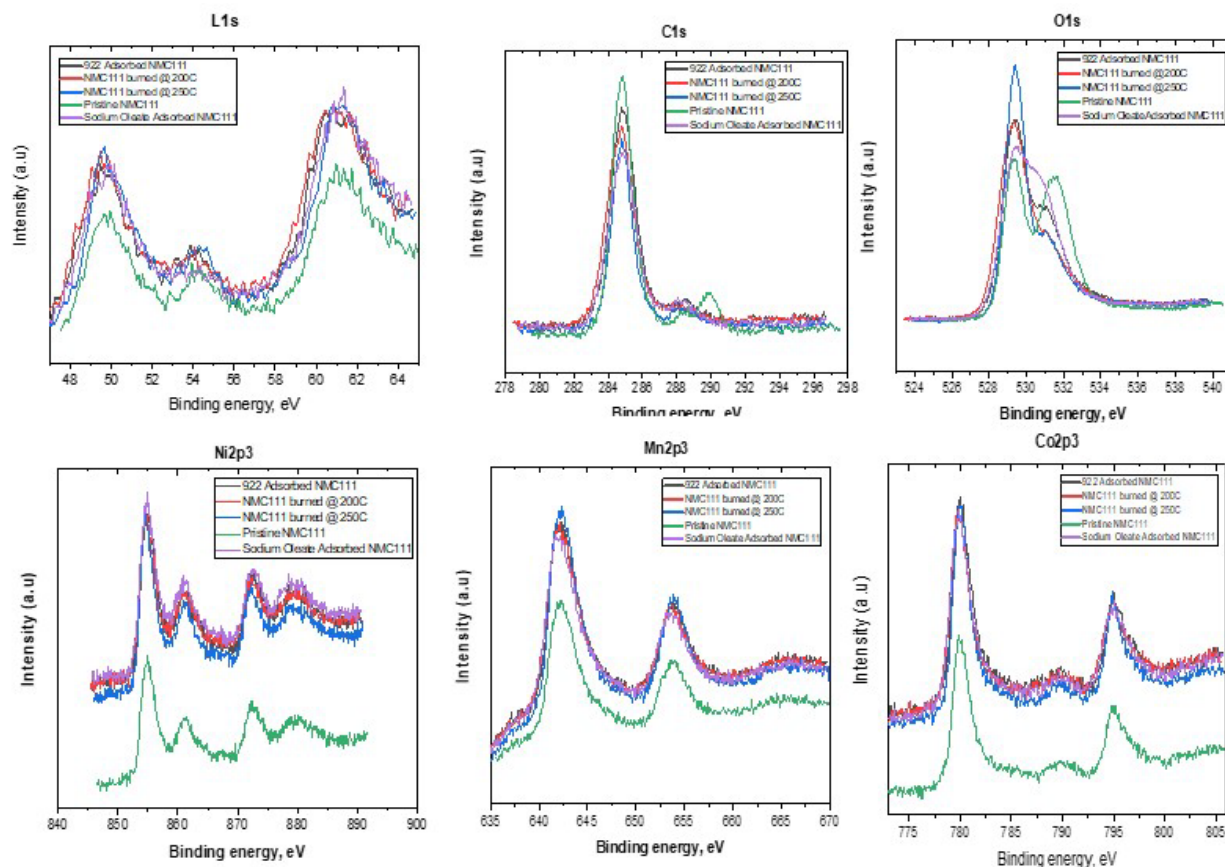


Figure III.3.18 XPS analysis of pristine NMC111, collector adsorbed NMC111 and thermally treated NMC111.

Figure III.3.19 shows the electrochemical performance of three samples, including collector adsorbed NMC111, NMC111 thermally treated at 250°C, and NMC111 thermally treated at 400°C. The collector-adsorbed NMC111 sample exhibited relatively poor electrochemical performance compared to the pristine NMC111, with an initial discharge capacity of 151mAh/g. It also shows that NMC111 sample treated at 400°C had an initial discharge capacity of 155mAh/g, which suggests that the heat treatment at higher temperature was beneficial to restore the initial electrochemical performance of the NMC111.

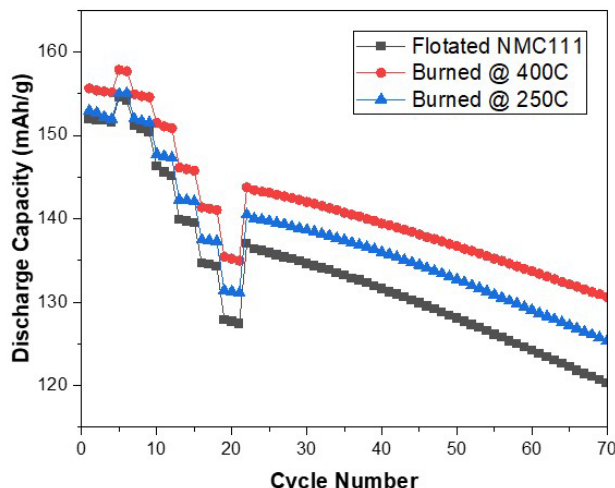


Figure III.3.19 Electrochemical performance of NMC111 from three experimental conditions.

Solvent-based Gravity Separation

This project aims to separate anode and cathode active materials by a centrifugal gravity separation method. In this report, experiments were conducted to further study the effects of centrifugal forces, feed mass, and solid concentrations on separation performance. In addition, multistage separation experiments were performed. The recycled products were found to be of high purity and structurally intact, suitable for follow-up rejuvenation and relithiation.

Results

Figure III.3.20a) shows five typical circuits including rougher, rougher + scavenger, rougher + 2*scavenger, rougher + cleaner, rougher + 2*cleaner. Each circuit produces two products including tailing and concentrate product. Figure III.3.20b and 20c shows both the recovery and grade of graphite in the tailing product, and recovery and grade of NMC111 in the concentrate product, respectively. The feed consisted of 60 wt. % NMC111 and 40 wt. % graphite and mixed with water to prepare a 5% solid slurry. The feed slurry went through two rougher stages in parallel. Overflow slurry was collected as the tailing product, while materials within the concentrator bowl were collected as the concentrate product. The result showed that the percentage of graphite in the tailing product reached ~73% at a 90% yield. In the concentrate product, the percentage of NMC111 reached ~93% with an 80% yield. With one stage of the separation process, a good separation between graphite and NMC111 was achieved. The addition of a scavenger stage enabled an increase in the recovery of NMC111 materials in concentrate product at an expense of grade. In addition, the tailing product from the rougher stage got recleaned by scavenger(s) to obtain a high grade of graphite in the final tailing product. The present result showed that the percentage of graphite in tailing improved from ~73% to 92.5% with additional scavenger stages, while its recovery dropped to ~70% and 42%, separately. Likewise, for rougher coupled with cleaner(s) design, over 98% and 99% of NMC111 in final concentrates were obtained. This result confirmed that high purity of graphite and NMC111 can be obtained after a multistage operation.

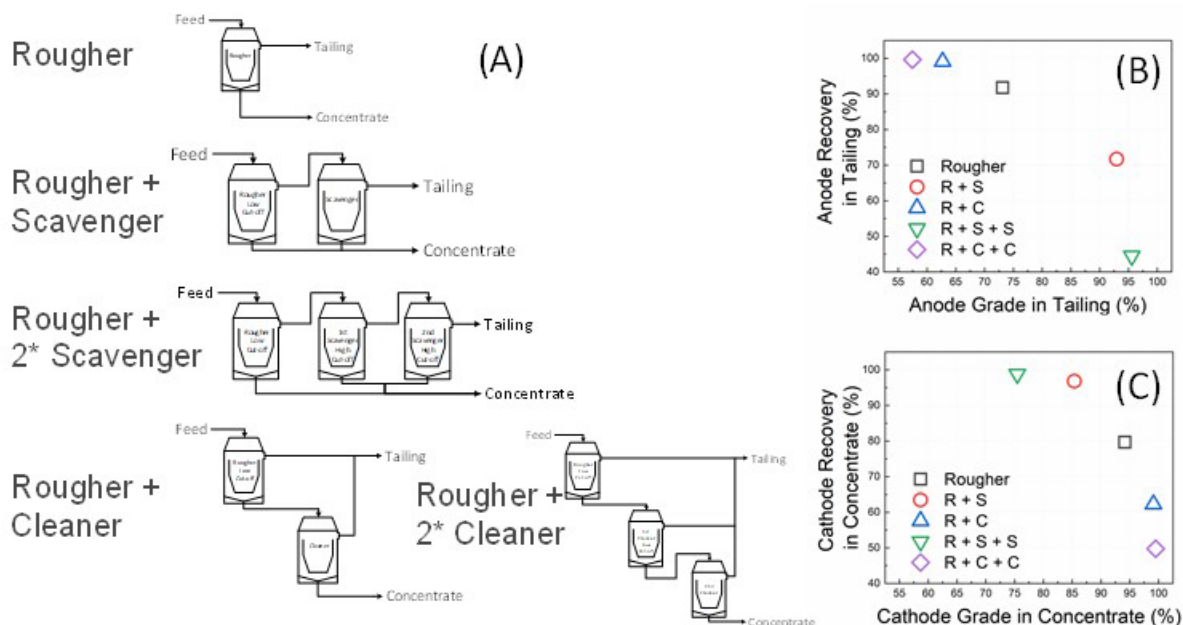


Figure III.3.20 (a) Circuit design of multistage experiment. (b) Recovery and grade of anode materials in tailing after different circuit design experiments. (c) Recovery and grade of cathode materials in concentrate after different circuit design experiments.

Table III.3.7 Elemental composition and structure of recycled and pristine NMC111 samples.

Samples	Li	Mn	Ni	Co	I(003)/I(104)
Recycled NMC in water	1.07	0.33	0.34	0.33	1.98
Recycled NMC in LiOH solutions	1.07	0.33	0.34	0.33	1.95
Pristine NMC111	1.07	0.33	0.34	0.33	2.00

Figure III.3.21a) compares electrochemical performance of recycled NMC111 in DI water and in 10 mM LiOH solutions. Also shown in Figure III.3.21 is the electrochemical performance of pristine NMC111 for a comparison. The discharge capacity of the pristine NMC111 at 1st and 5th cycles were 151 and 155 mAh/g, respectively. The recycled NMC111 in LiOH solutions exhibited comparable rate performance to pristine NMC111. However, the rate performance of the recycled NMC111 in DI water decayed more significantly than the pristine NMC111. In terms of cycling performance, the recycled NMC111 in LiOH solutions exhibited a similar cyclability with pristine NMC111. However, the recycled NMC111 in DI water showed a relatively poorer cycling stability compared to the pristine NMC111. Figure III.3.21b) show the XRD results of these three samples. Table III.3.7 shows the elemental compositions as well as the I(003)/I(104) ratio of these three samples. The result (Table III.3.7) showed that the chemical composition of the NMC111 remained unchanged after recycling in both DI water and 10 mM LiOH solution. However, the I(003)/I(004) ratios of pristine NMC111 was decreased from 2.00 to 1.95 after recycling in DI water, suggesting a possible structural change. This result was consistent with a decreased electrochemical performance, as shown in Figure III.3.21b. Both electrochemical and XRD results suggest a superior performance of the gravity separation process in LiOH solutions in separating pristine anode and cathode active materials for the direct recycling purpose.

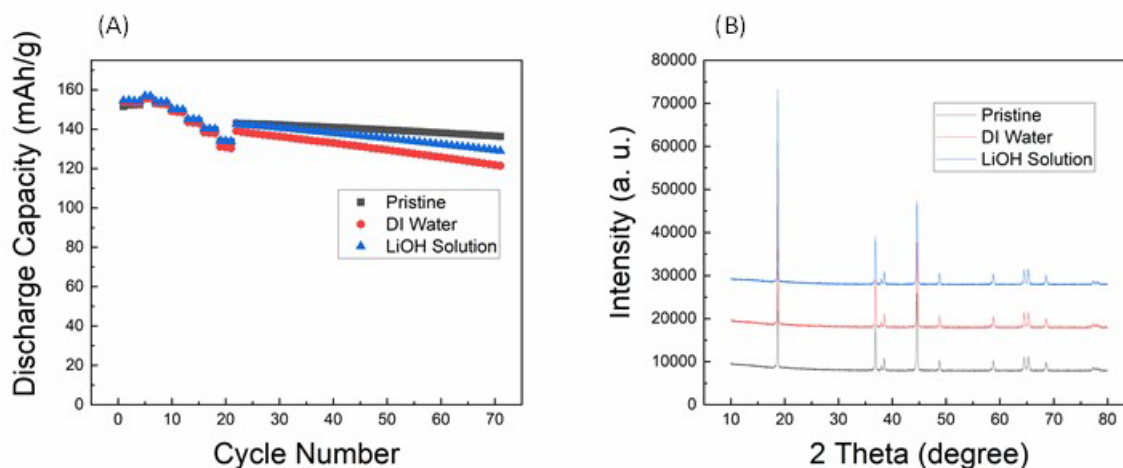


Figure III.3.21 (a) Electrochemistry of recycled and pristine NMC111 samples, (b) XRD of recycled and pristine NMC111.

Chemical Relithiation of NMC Cathodes

Lithium-ion cells made using a recycled cathode are limited in the amount of active lithium they have available to the amount present at initial cell construction. Performance degradation for energy storage materials results from the gradual cycle-to-cycle loss of active lithium from the system by SEI formation, corrosion, and electronic isolation of particles, with the active lithium being irreversibly trapped in a variety of forms that diminish long-term battery performance. On cycling, the amount of lithium trapped and rendered inactive increases at a slow rate (after losses involved in the initial break-in cycling), gradually decreasing the cell's capacity until performance is noticeably affected or the commonly used 80% of initial capacity value is reached. The 80% value (stoichiometry: $\text{Li}_{0.8}(\text{NiMnCo})\text{O}_2$) is associated with rises in impedance, loss of stability, and a decrease in capacity in the standard window (lifetime). The material's structure is a lithium-deficient version of the starting materials, although some further structural changes can be related to the temperature of operation, initial stoichiometry, or processing conditions. Typical structural changes include site mixing of lithium and nickel (due to similar size), oxygen loss, or degradation of the surface layers to similar (but electrochemically less desirable) materials, including various defect spinel or rock-salt structures. In this section we are establishing the conditions required to convert a lithium-deficient NMC cathode material back to a stoichiometric material using chemical relithiation by low- to mid- ($< 400^\circ\text{C}$) temperature annealing in the presence of a lithium source and O_2 -containing atmosphere. Relithiated materials will be characterized and studied for electrochemical activity, extent of anti-site mixing, and sample purity. Data and insights will be provided to the EverBatt team led by Qiang Dai (ANL) and modeled for cost and performance metrics.

This quarter the Vendor A cathode powder recovered using the solvent Y process was selected for moving forward for relithiation benchmarking. This decision was based on the difference in performance from the thermal processed cathode across the relithiation projects observed in the previous quarter. The properties (XRD, TGA) of the scaled-up Solvent Y batch were verified to be consistent with the previous results. The relithiation process tested mixing the delithiated cathode with LiOH in ethanol solution and using the resonant acoustic mixer (RAM). The mixed powder was then annealed at 720°C . Figure III.3.22 shows an overlay of XRD data for a relithiated product with the pristine and solvent Y process powder. The peaks for the relithiated product align with those of the pristine NMC, exhibiting a decreased separation between the 108 and 110 peaks observed in the solvent Y processed sample. GDOES compositional analysis of the relithiated NMCs is shown in Table III.3.8. The Li contents recovered for the ethanol and RAM mixed products were consistent with each other. The amount of LiOH used in the 50 g scale-up was increased slightly and was reflected in the final Li content of the product being near 1.05.

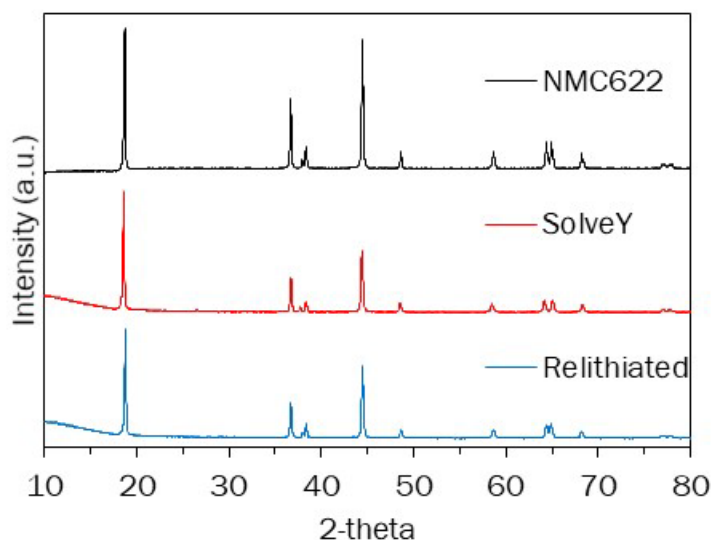


Figure III.3.22 XRD of pristine NMC622, Solvent Y processed, and relithiated cathode powder

Table III.3.8 Elemental composition for relithiated NMCs

	[Li]	[Ni]	[Mn]	[Co]
Ethanol mix	0.992	0.657	0.190	0.153
RAM mix	0.992	0.647	0.202	0.151
RAM mix (50 g)	1.053	0.660	0.187	0.153

Half-cell testing data for the relithiated cathode powders are shown in Table III.3.9. The capacity values for the relithiated cathode using RAM mixing were slightly higher than those from the ethanol mixing. Because of this, RAM mixing was used for the scale-up relithiation. These changes to the relithiation process have been reported to update the EverBatt model and should result in lower costs associated with the solid-state process. The capacity of the scaled-up batch was lower (~5 mAh/g) than that of the smaller scale batch. Bed depth of the powder during the annealing process may have been an issue that contributed to this reduced capacity.

Table III.3.9 Half-cell capacity for relithiated cathodes from solvent Y process

	Ethanol mix	RAM mix	RAM mix (50 g)
1 st Cycle Charge (mAh/g)	201.2	202.5	197.8
1 st Cycle Discharge (mAh/g)	167.1	169.8	163.1
4 th Cycle Charge (mAh/g)	168.2	170.2	167.5
4 th Cycle Discharge (mAh/g)	167.0	170.0	165.2

Direct Regeneration of NMC Cathodes through Ionothermal Lithiation

The objective of this project is to develop a cost-effective ionothermal lithiation process that uses ionic liquids (ILs) to relithiate and/or upgrade spent cathodes at ambient pressure and low temperature. ILs are a family of non-conventional molten salts that offer many advantages, such as negligible vapor pressures, negligible flammability, wide liquidus ranges, good thermal stability, and much synthesis flexibility. The unique solvation environment of these ILs provides new reaction or reactive flux media for controlling the formation of solid-state materials with a minimum perturbation of morphologies. In addition, ILs can be readily recycled and reused after the ionothermal lithiation. During first two years of this project, ionothermal relithiation of chemically delithiated NMC111 (D-NMC111) was extensively investigated under different reaction conditions. The effect of lithium precursor, the type of ionic liquid, different temperatures, and reaction time were studied. The recovered materials were analyzed by various characterization techniques including TGA, XRD, SEM, and ICP-OES, which demonstrate that our ionothermal approaches towards restoring Li into D-NMC111 for direct regeneration of cathode materials are promising and feasible. Large scale lithiation experiments (50 g) have been successfully performed. Preliminary results show no significant difference in thermal stability, morphology, and electrochemical performance for the restored NMC111 in small or large scale ionothermal relithiations using either fresh IL or spent IL. The EverBatt model indicates that the cost of the ionothermal relithiation process is \$21.62/kg, which is less expensive than virgin powder (\$28.83/kg), and comparable to conventional recycling technology (pyro and hydro) costs. During the second quarter of the project's year 3, the upgrade of delithiated NMC111 (D-NMC111) has been studied by Al-doping experiments, providing promising and interesting results. In the rest of year 3, our ionothermal relithiation process will be further optimized.

During FY21 Q3, the ionothermal relithiation of two delithiated NMC622 samples (named MSY and OES) was studied using [C₂mim][NTf₂] or [P₆₆₆₁₄][DEHP] under different experimental conditions. The recovered materials R-NMC622 were characterized by various techniques including TGA, XRD, and ICP-OES, which indicate that the ionothermal approaches restoring Li into these two D-NMC622 for direct regeneration of cathode materials in ionic liquids are not promising.

Based on our earlier results in Q3, we focused on investigating a high-temperature flux relithiation method based on quaternary molten salts flux to relithiate spent NMC622 (MSY_ORNL) as a method to provide 50 g of relithiated material to ANL for performance evaluation. Four batches were created: one 5 grams, two 12 grams, and one 25 grams scale batches were made, and the detailed experimental results are summarized in Table III.3.10. The recovery of black powder is ~95% when molten salts were used as the reaction medium.

Table III.3.10 Scaled up relithiation of MSY in molten salts

Molten salts	Molten salts:MSY (Mass ratio)	Mass of MSY (g)	Black powder recovered (%)
LiCl/NaNO ₃ /NaCl/NaOH	4:1	25	95
LiCl/NaNO ₃ /NaCl/NaOH	4:1	12	92
LiCl/NaNO ₃ /NaCl/NaOH	4:1	5	90

TGA of these samples showed thermal stability of ReLi NMC 622 above 99.7% after calcination, which is much higher than the MSY_ORNL sample as in Figure III.3.23. As shown in the XRD pattern in Figure III.3.24, the peak splitting between (108) and (110) narrowed from 1.05 to 0.55 degree after the flux relithiation process, and the XRD pattern of ReLi NMC 622 is identical to that of pristine NMC 622.

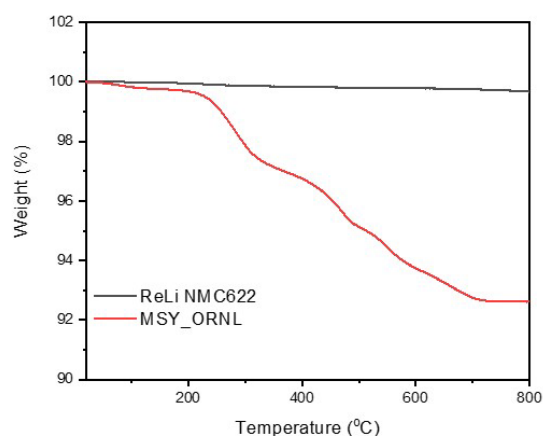


Figure III.3.23 Comparison of TGA plots of MSY_ORNL and ReLi NMC 622.

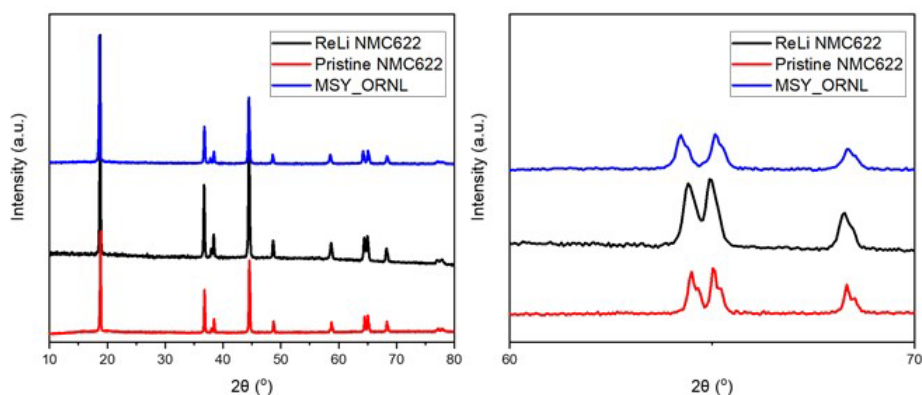


Figure III.3.24 XRD patterns for Pristine NMC622, MSY, and ReLi NMC 622.

The elemental analysis of these samples was performed by inductively coupled-plasma optical emission spectroscopy (ICP-OES) using the Agilent 5110 ICP-OES spectrometer. Results are summarized in Table III.3.11. Note that the Ni, Co, and Mn mole ratios of these samples are similar to the corresponding delithiated samples, and the Li mole ratio is close to that of pristine NMC 622.

Table III.3.11 ICP-OES results for ReLi NMC 622.

	Li (atom)	Co(atom)	Mn(atom)	Ni(atom)
Spent cathode solventY (MSY)	0.85	0.15	0.20	0.65
Pristine NMC 622	1.05	0.19	0.20	0.62
ReLi NMC 622	1.09	0.15	0.20	0.65

The electrochemical cycling performance for ReLi NMC 622 recovered from molten salts was evaluated in half-cell configuration. As illustrated in Figure III.3.25, ReLi NMC 622 (black line) has comparable electrochemical performance to pristine NMC622 (blue line).

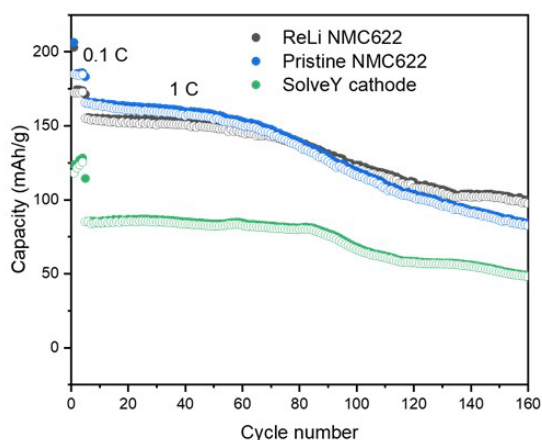


Figure III.3.25 Electrochemical cycling performance of relithiated materials (ReLi-NMC622)

Hydrothermal Relithiation of Cathodes

The direct regeneration method combining hydrothermal relithiation with subsequent short annealing, developed by the UCSD team, can successfully resolve the compositional and structural defects of chemically delithiated NMC111 (D-NMC111). It also recovers the electrochemical performance to the same level as pristine Toda NMC111 (T-NMC111).^{1,2} The process parameters in the hydrothermal and annealing steps, such as temperature, time, and Li-bearing precursor composition, have been extensively explored and optimized. The life cycle analysis indicates the optimized direct recycling method is advantageous in terms of operation cost, greenhouse gas emissions, and energy consumption compared with currently commercialized pyrometallurgical and hydrometallurgical recycling routes. Moreover, the underlying relithiation mechanism has been thoroughly studied with advanced characterization measurements and a density functional theory calculation, which is favorable for designing routes to directly recycle more diverse materials, such as NMC622. To validate the process for practical adoption, the possibility of achieving a larger-scale regeneration must also be explored. In the last quarter, the cathode material regenerated at a 50g-scale was demonstrated to show the same desirable properties as that regenerated at a 1g and 10g- scales. The regeneration scale will be further increased to 100g for validation. Extensive characterization and electrochemical testing will be performed to demonstrate the scalability of the hydrothermal relithiation process.

In FY21, we validated our direct regeneration process for high Ni materials (cycled NCM622 Solvent Y) with 4 M LiOH at 220°C followed by annealing at 850°C at 1g. In Q4 we further scaled up the regeneration process from 1 g to 50 g.

For our initial trial, the 50 g of C-NCM622 was run through the hydrothermal direct regeneration process with 4 M LiOH at 220°C, followed by annealing at 850°C, denoted as HS-NCM622-50g, and side-by-side compared with cycled NCM622 (C-NCM622), and pristine NCM622 (T-NCM622). The crystal structure of HS-NCM622-50g was characterized by X-Ray diffraction (XRD). The patterns of the sample C-NCM622 and T-NCM622 were also collected and are shown in Figure III.3.26 as references. Overall, the diffraction peaks of all the samples matched well with the typical α -NaFeO₂ structure with $R\bar{3}m$ space group, indicating that the bulk structure of NCM622 is not affected by the regeneration process. When the NCM622 is cycled (C-NCM622), the (003) peak shifts to a lower angle, reflecting an increase in c lattice constant. This is due to increased electrostatic repulsion between the oxygen layers along the c direction when Li⁺ is deficient¹. The (003) peak obviously shifts back to the position of pristine T-NCM622 after hydrothermal relithiation and post annealing, which indicates the recovery of the pristine crystal structure.

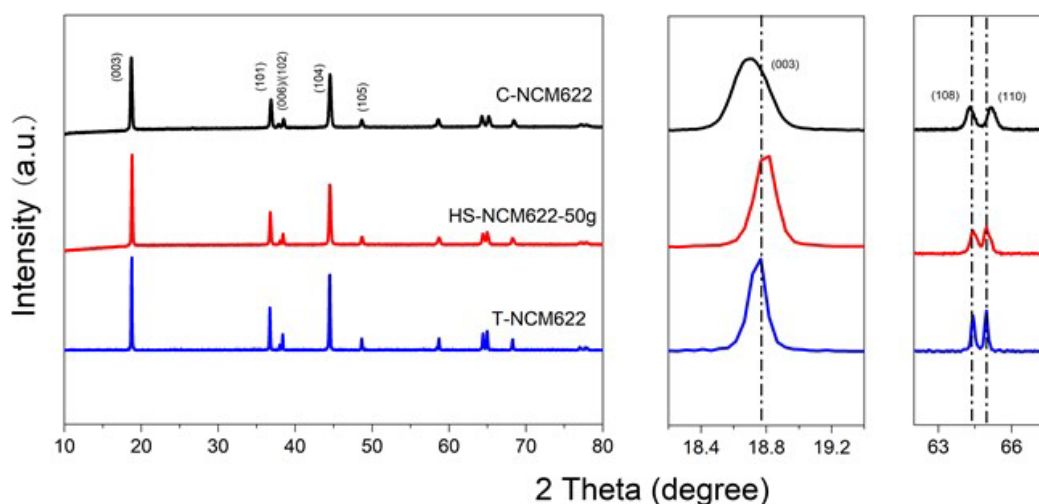


Figure III.3.26 XRD patterns of cycled NCM622 treated using solvent Y, regenerated NCM622 at 50g scale as well as the standard pattern of pristine NCM622.

The electrochemical performance of the regenerated NCM622 regenerated at 50 g scale (HS-NCM622-50g), was examined using coin cells (half-cell) with cathode mass loading of $\sim 10 \text{ mg cm}^{-2}$ and Gen2 (EC/EMC = 3:7) electrolyte and compared with C-NCM622 and T-NCM622. As shown in Figure III.3.27, for cycled materials, C-NCM622 exhibited an initial capacity of only 105.7 mAh/g at the rate of C/3 and remained only 89.1 mAh/g after 45 cycles, for a capacity retention of 84.3%. After regeneration, the initial capacity of HS-NCM622-50g reached 176.3 mAh/g at C/10, and it exhibited an initial capacity of 165.7 mAh/g, retaining 153.8 mAh/g at C/3 even after 45 cycles, for a capacity retention of 92.8%, the same as pristine NCM622. This indicates the cycled NCM622 can be recovered effectively at 50g scale using our hydrothermal treatment method.

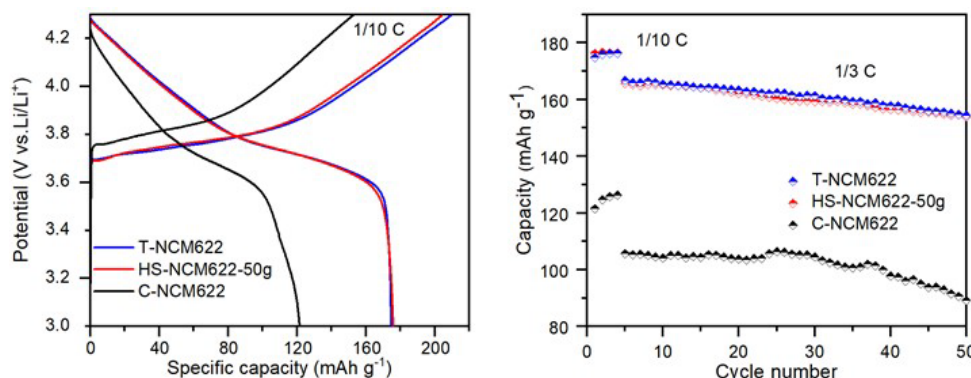


Figure III.3.27 Voltage profiles (a) and cycling stability (b) of the cycled NCM622, the pristine NCM622 and NCM622 regenerated at 220 °C at 50g scale followed by annealing at 850 °C (C-NCM622, T-NCM622, HS-NCM622-50g).

In last quarter, we also demonstrated recovery of the Li in delithiated NCM111 with reduced hydrothermal treatment temperature of 90 and 100 °C at ambient pressure by adding a small quantity of a green additive. This is very helpful to mitigate potential safety concerns for large-scale operation due to the required high-pressure reactor at high temperature.³ In this quarter, we tried to optimize the process for high-Ni materials by adding green additives to reduce the reaction temperature.

For our initial trial, the 1 g of C-NCM622 was subjected to the direct regeneration process with 4 M LiOH at 100°C, with addition of 3% of our green additive, followed by annealing at 850°C for 4h in the pure oxygen atmosphere. The regenerated samples are denoted as ‘HS-NCM622-GA’, compared below with C-NCM622 and T-NCM622.

The electrochemical performance of the NCM622 regenerated at 100°C followed by annealing at 850°C was examined in coin cells (half-cell) with cathode mass loading of $\sim 10 \text{ mg cm}^{-2}$ and Gen2 (EC/EMC = 3:7) electrolyte and comparing with C-NCM622 and T-NCM622. As shown in Figure III.3.28(a), the initial capacity of HS-NCM622-GA reached 176.0 mAh/g at C/10, achieving the same capacity as pristine NCM622. In addition, the cycling stability of HS-NCM622-GA, C-NCM622 and T-NCM622 were evaluated at C/3 rate (Figure III.3.28(b)). The C-NCM622 exhibited an initial capacity of 105.7 mAh/g and dropped to only 89.1 mAh/g after 45 cycles, with the capacity retention of only 84.3%. However, HS-NCM622-GA and T-NCM622 delivered initial capacities of 167.1 mAh/g and 166.7 mAh/g, respectively, and the capacity retentions of HS-NCM622-GA and T-NCM622 achieved 92.8% and 92.6% respectively after 45 cycles. Therefore, the cycled NCM622 can be successfully recovered at 100°C with our improved approach. Further optimization of the process is worth investigating, including trying lower temperature, reducing the reaction time, as well as further scaling up this process to further reduce the cost of regeneration and mitigate potential safety concerns.

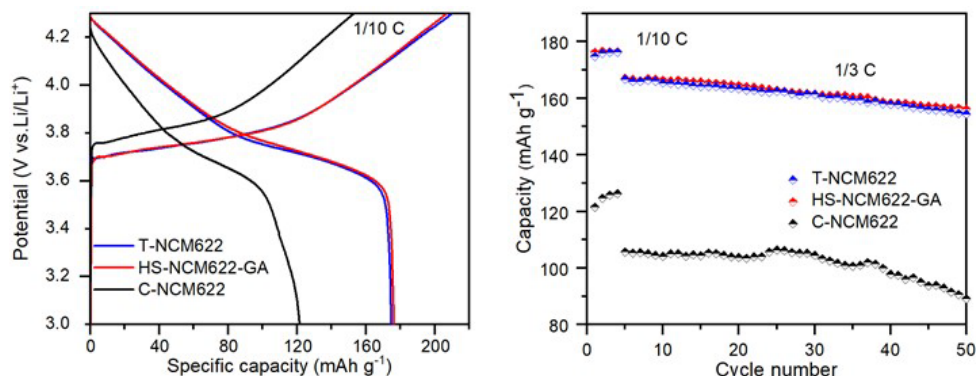


Figure III.3.28 Voltage profiles (a) and cycling stability (b) of the cycled NCM622, the pristine NCM622 and NCM622 regenerated at 100°C with green additive followed by annealing at 850°C (C-NCM622, T-NCM622, HS-NCM622-GA).

Relithiation via Redox Chemistry

The scope of this project is to develop a direct cathode recycling method that utilizes redox mediator chemistry for End-of-Life (EOL) battery cathodes. One of the main characteristics of the EOL cathode is Li deficiencies due to the formation of the irreversible anode SEI layer. In FY20, we demonstrated a room-temperature relithiation process using redox mediators. The redox mediators are reversible charge shuttles in an electrochemical cell that deliver lithium ions and electrons from the anode (e.g., Li metal) to the cathode materials with Li deficiencies. The reaction to relithiate EOL cathode powders is simple, efficient, and fast. In FY21, this project will (1) demonstrate that redox mediators are stable in multi-batch reactions and (2) scale up the cathode relithiation reaction with a large lab-scale reactor.

In this quarter, we tested the large-batch-size relithiation of 10% chemically delithiated NMC111 (De-NMC111). De-NMC111 is used as a model of end-of-life cathode material, provided by CAMP. As instructed by our previous experiment on lab-scale relithiation of De-NMC111, we control redox mediator concentration at 0.5M at various reaction times (10, 30, 60 min, respectively). Continuously stirring the pre-lithiated RM solution as necessary, 50 g of De-NMC111 were mixed with 80 mL pre-lithiated RM solution at room temperature and reacted for 10/30/60 min. After filtering and rinsing, relithiated NMC111 powders are annealed at 850°C for 4 h to obtain final powder. Then half- and full-cells are made to evaluate their electrochemical performance. Cathode compositions used 90 wt.% relithiated powder, 5 wt.% carbon black and 5 wt.% polyvinylidene difluoride (PVDF). Rather than graphite anodes, for cycling stability, an anode composition of 90 wt.% lithium titanate (Li₄Ti₅O₁₂, LTO), 5 wt.% carbon black and 5 wt.% PVDF was created. Both half- and full-cells use Gen II (1.2 M LiPF₆ in EC: EMC at 3:7 by weight) as electrolyte. For half-cells, the first four cycles (C/10 at 3.0–4.3 V vs

Li/Li⁺) are formation evaluation. While in full-cell test, coin cells are charged/discharged at C/10 from 1.0 to 2.8 V vs LTO in the first four cycles and subsequently cycled at 1C (1.0 - 2.7 V vs LTO). Figure III.3.29 shows the initial and second charge/discharge capacities in half-cells. The initial charge capacities of all relithiated powders are over 178 mAh/g, similar to pristine NMC111. Even though 10 min reaction shows a relatively low discharge capacity of 155.93 mAh/g in the initial cycle, its charge and discharge capacities of second cycle reached 157.49 and 156.07 mAh/g, respectively. All three relithiated powders exhibit successful lithium restoration to the delithiated NMC111 cathode material.

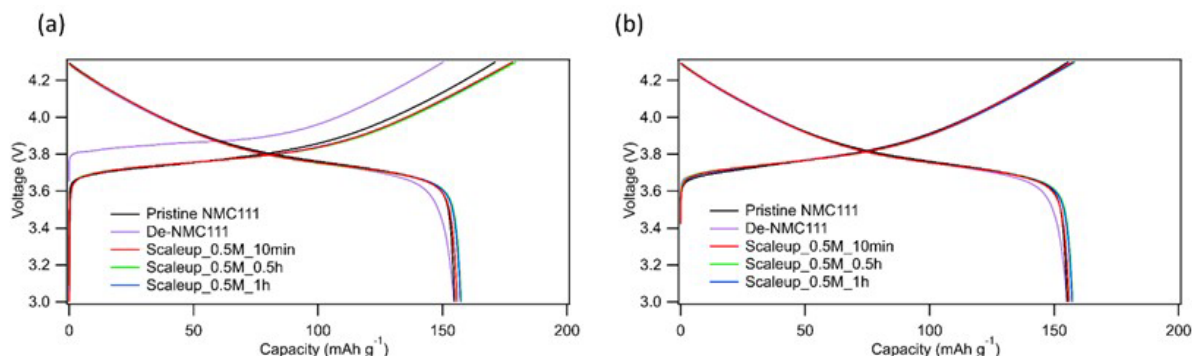


Figure III.3.29 (a) Initial and (b) second charge and discharge voltage profiles of pristine NMC111, De-NMC111, and scaleup relithiated NMC111 powders in 10/30/60 min reaction for half cells.

Table III.3.12 Summary of electrochemical capacities of scaleup relithiation process at different reaction time.

	1st ch cap (mAh/g)	1st dis cap (mAh/g)	1st cycle efficiency (%)	2nd ch cap (mAh/g)	2nd dis cap (mAh/g)	2nd cycle efficiency (%)
Scaleup_0.5M_10min	178.24	155.93	87.5	157.49	156.07	99.1
Scaleup_0.5M_0.5h	179.57	157.43	87.7	158.54	157.45	99.3
Scaleup_0.5M_1h	178.31	157.25	88.2	158.24	157.27	99.4

As shown in Figure III.3.30, the initial charge/discharge capacities of scaleup_0.5M_10min and scaleup_0.5M_1h are 182.48/155.64 and 179.52/157.69 mAh/g respectively, which are consistent with half-cell data and comparable with pristine NMC111. After 100 cycles, scaleup_0.5M_10min decays obviously, however, scaleup_0.5M_1h shows good cyclability, which is as stable as pristine NMC111. Inductively coupled plasma optical emission spectrometry (ICP-OES) determines the actual compositions of relithiated powders (Table III.3.13). Li molar ratios of scaleup relithiated powders are close to pristine NMC111 cathode. With longer reaction time, more Li could be restored to delithiated cathode.

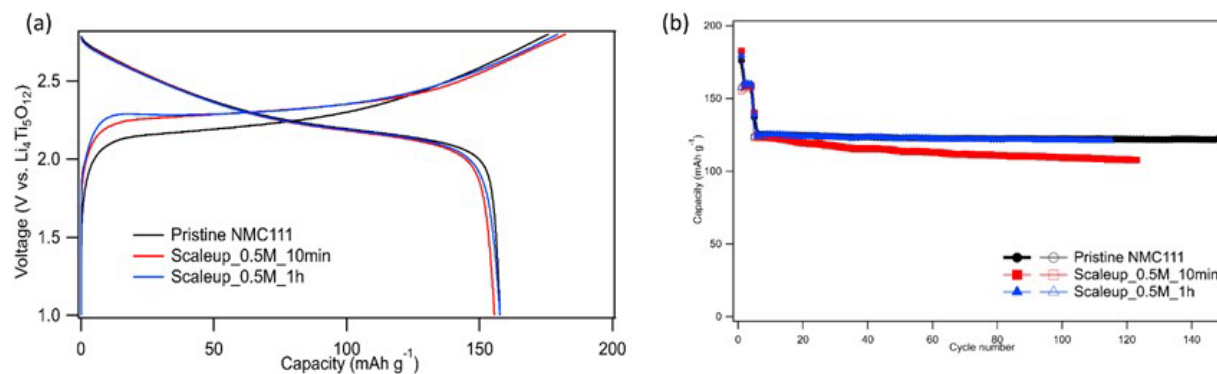


Figure III.3.30 (a) Initial charge/discharge voltage profiles and (b) cycling performances of pristine NMC111, scaleup_0.5M_10min and scaleup_0.5M_1h for NMC//LTO full cells.

Table III.3.13 ICP-OES data of pristine NMC111, De-NMC111, and scaleup relithiated NMC111 powders in 10/30/60 min reaction.

Sample	Li	Ni	Mn	Co
Pristine NMC111	1.089	0.340	0.323	0.336
De-NMC111	0.930	0.342	0.328	0.330
Scaleup_0.5M_10min	1.029	0.344	0.321	0.334
Scaleup_0.5M_0.5h	1.044	0.345	0.320	0.335
Scaleup_0.5M_1h	1.053	0.343	0.325	0.333

We also optimized reaction conditions of solvent Y- treated NMC 622 powder (Solve Y). After investigating multiple parameters (reaction time, reaction temperature, and both), the best charge capacity we could achieve was $\sim 185 \text{ mAh/g}$ at C/10 in a half-cell, which then dropped to $\sim 145 \text{ mAh/g}$ at 1C. Our previous experiments indicated that higher reaction temperature improves capacity. Here, we choose $\sim 65^\circ\text{C}$ as the modified reaction temperature. Considering the high nickel composition of Solve Y powder, we also modified the annealing atmosphere (O_2 vs air) of relithiated powder at different reaction times. In Figure III.3.31a-d, first two charge/discharge voltage profiles are plotted for SolveY_0.5M_2h@64C and SolveY_0.5M_24h@65C annealing in air and oxygen, separately. The initial charge/discharge capacity of SolveY_0.5M_2h@64C_air is 181.06/149 mAh/g, which is slightly lower than those of SolveY_0.5M_2h@64C_ O_2 (185.65/153.47 mAh/g). However, SolveY_0.5M_24h@65C_air exhibits higher performance than powder annealing in O_2 . This inconsistent result is possibly due to the incomplete relithiation of SolveY powder, thereby, the crystal structure is destroyed in the subsequent annealing process (Figure III.3.31e).

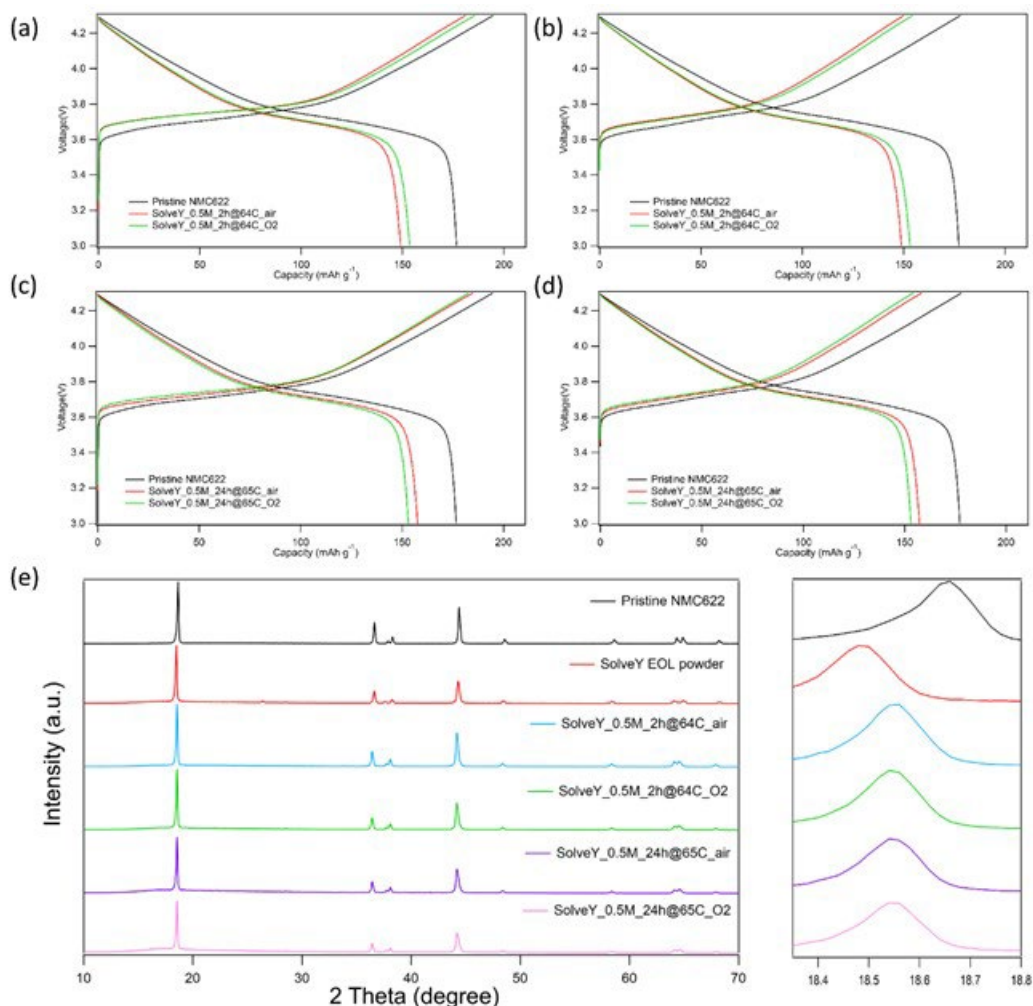


Figure III.3.31 (a) Initial and (b) second charge and discharge voltage profiles of pristine NMC111, SolveY_0.5M_2h@64C_air and SolveY_0.5M_2h@64C_O2; (c) Initial and (d) second charge and discharge voltage profiles of pristine NMC111, SolveY_0.5M_24h@65C_air and SolveY_0.5M_24h@65C_O2; (e) XRD patterns of pristine NMC622, Solve Y EOL powder and relithiated SolveY powders.

Electrochemical Relithiation

The scope of this project is to develop a direct recycling method that utilizes electrochemical relithiation for EOL (End of Life) battery cathodes. The electrochemical relithiation protocol developed by this project is being optimized for application to large-scale direct recycling such as roll-to-roll processes. This means that the electrochemical relithiation must be optimized for rapid relithiation to reduce cost by minimizing the time the EOL cathodes must be in an electrochemical bath. Scanning voltage discharge protocols at elevated temperatures have been identified as promising candidates for rapid relithiation of EOL NMC 111 cathodes that were electrochemically aged in coin cells. In FY21, this project will continue to optimize electrochemical relithiation protocols by incorporating model-driven process parameters and applying them to a wider range of commercial cathode compositions cycle-aged in large format cells. The optimized electrochemical relithiation protocols will be applied in a lab-scale roll-to-roll reactor to assess the scalability of the electrochemical relithiation process.

The focus for electrochemical relithiation in FY21 Q4 was to complete model validation and verify the final optimal relithiation protocol for electrochemically delithiated material as well as participate in the scaling

study that utilized the solvent Y treated end of life NMC 622. In previous quarters, we noted that the optimal protocol for relithiating electrochemically delithiated NMC 111 included a constant current step to a middle cutoff voltage followed by a scanning voltage step to 2.8V. The electrochemical relithiation protocol model was run through a full parametrization set to determine the optimal constant current rate, cut-off voltage and scanning voltage rate for low relithiation time (<30 min) and maximize the capacity restored ($Q > 60$ mAh/g). Figure III.3.32 shows the full parametrization of the electrochemical protocol model including C-rate for the constant current step and scan rate for the scanning voltage step. The black lines mark where the model predicts the protocol will restore greater than 60 mAh/g capacity (red boxes) and where the protocol will take less than 30 minutes to complete (blue boxes). The model was run for four different constant current cut-off voltages. The optimal cut-off voltage and overall protocol was determined to be 2.5C CC to 3.3V followed by a 0.4 mV/s scanning rate. This was confirmed experimentally with reversible capacities of ~ 160 mAh/g achieved for relithiated NMC 111 materials, which is similar to pristine NMC 111.

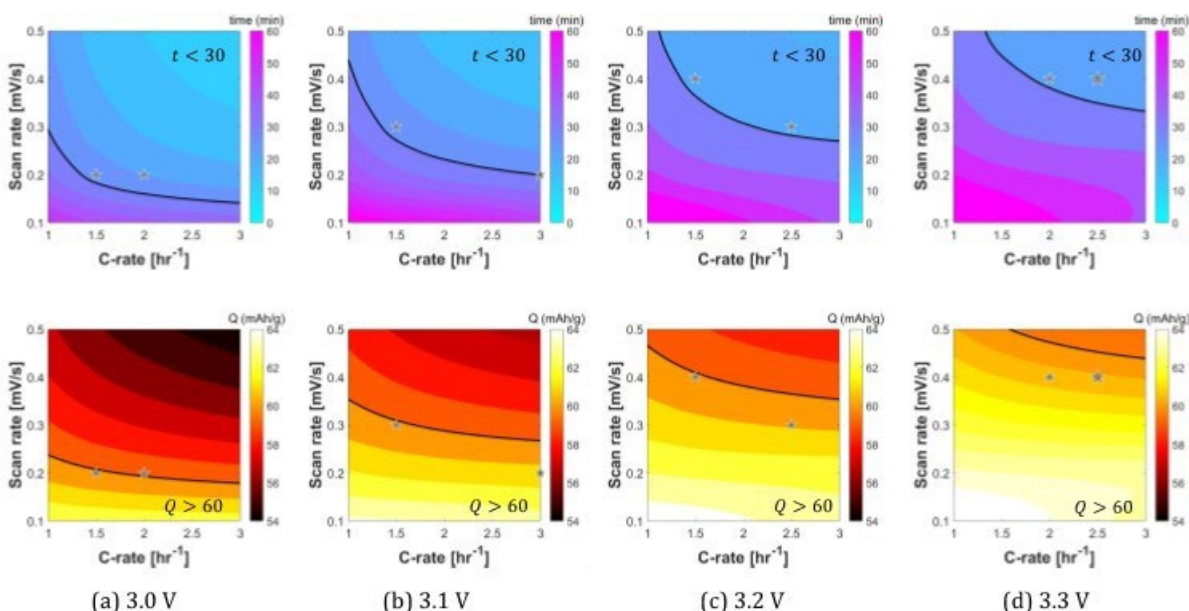


Figure III.3.32 Full parametrization of electrochemically delithiated NMC 111 optimal relithiation protocols with regard to varying the constant current C-rate step, cut-off voltage and scan rate for the scanning voltage step.

We were also provided with cycled NMC622 materials that were treated using the solvent Y process created at ORNL for binder removal. The isolated powders were then recast at ANL to functional electrodes to match the testing criteria for the NREL electrochemical relithiation apparatus. The solvent Y cast NMC622 electrodes were relithiated using the same model-derived protocol as the NMC 111 material but with poor results. A new set of parameters, diffusion coefficients and OCV curves would need to be obtained from the pristine commercial NMC 622 material in order to provide a model-driven protocol with multiple steps and optimized relithiation time. We did not have access to this pristine commercial material, so we attempted large scale relithiation with a much slower protocol to provide the highest relithiation capacity possible for the relithiation task competition. This protocol ended up being a C/20 constant current step to 2.8V followed by a 6-hour voltage hold at 2.8V. Figure III.3.33 shows the results of relithiation attempts for half-cell coin cells with solvent Y cast NMC 622 electrodes provided by CAMP. Both samples had first charge capacities of about 170 mAh/g followed by reversible C/10 half-cell cycling at ~ 140 mAh/g. The expected capacities for pristine NMC 622 are ~ 200 mAh/g for the first charge and ~ 175 mAh/g for reversible C/10 cycling. Scaled up reactions in the model roll to roll reactor yielded similar results. The electrochemical relithiation technique lacks a high-temperature annealing step, which likely limits the usefulness of this technique for more highly degraded materials, such as this commercial NMC 622. However, the coin cell and reactor relithiation results were still comparable for the EOL NMC 622 material, which helps to validate the model reactor.

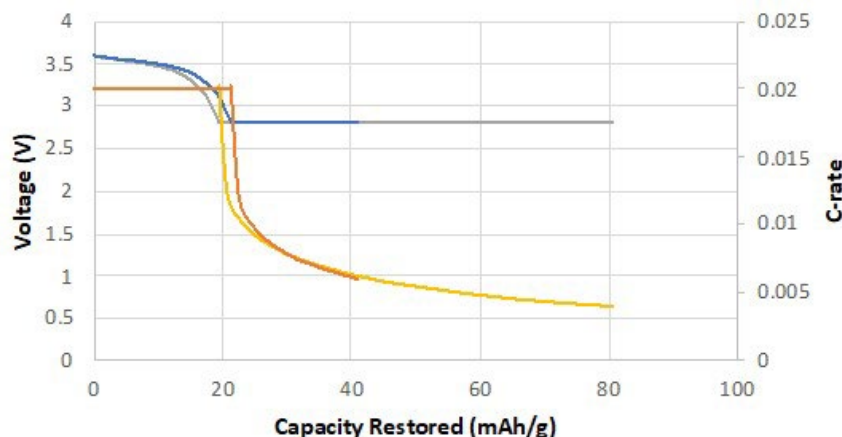


Figure III.3.33 Relithiation results for commercial NMC 622 EOL material relithiated using slow relithiation protocol in coin cells

Solid State Cathode Upcycling

Battery recycling is an overarching process used to recover materials from previous generations of energy storage materials and reverse the effects of degradation, impurity build-up, or having no relevance in the present marketplace to supply new markets, or lower the overall costs of storage. A significant issue in this fast-changing market is that batteries supplied to recyclers reflect chemistries from 5-10 years ago that may not be viable in the present. Recycled materials and materials wanted by the marketplace may not be in sync over time as new chemistries and cell designs drive changes in supply and materials choices. Besides changes in the materials stream available due to material performance improvements and emerging new chemistries, materials from non-transportation sectors may also play a role in adding anomalous materials to the waste stream, for instance LiCoO_2 from consumer electronics. We are designing and evaluating methods to upcycle the metal ratios of recovered cathode materials to convert them to more current cathode formulations. This effort's focus will be on the raw materials, $\text{Li}(\text{NiMnCo})\text{O}_2$ (NMC111) and LiCoO_2 (LCO) and will establish methods to use them as feedstock material to produce other stoichiometries. Initial targets will be NMC622 and $\text{Li}(\text{CoAl})\text{O}_2$, the latter being a variant that has a larger electrochemical window and higher capacity. We are working with cross-cutting teams to employ additional characterization methods to probe the structural changes in the upcycled material.

The work this quarter looked at re-annealing previous upcycled products to higher temperatures with the goal of improving surface and structural properties of the NMC particles. Several products that were originally prepared from 690-820° were mixed with additional LiOH and re-annealed to 850°C under oxygen atmosphere. Figure III.3.34 shows the XRD data for a sample originally prepared at 700°C and the 850°C re-anneal. Notable differences appear at higher angles, where the re-annealed product shows improved separation between the 108 and 110 peaks. The original product also appeared to have an intermediate peak in this region that is no longer present. Similar changes were also observed for the other re-annealed products. The morphology changes upon re-annealing were evaluated using SEM. Following annealing, the primary particles at the surface appeared to be better defined and are larger in size. Compared to the overall particle growth from the starting NMC, there was not further overall particle growth as a result of the second annealing step.

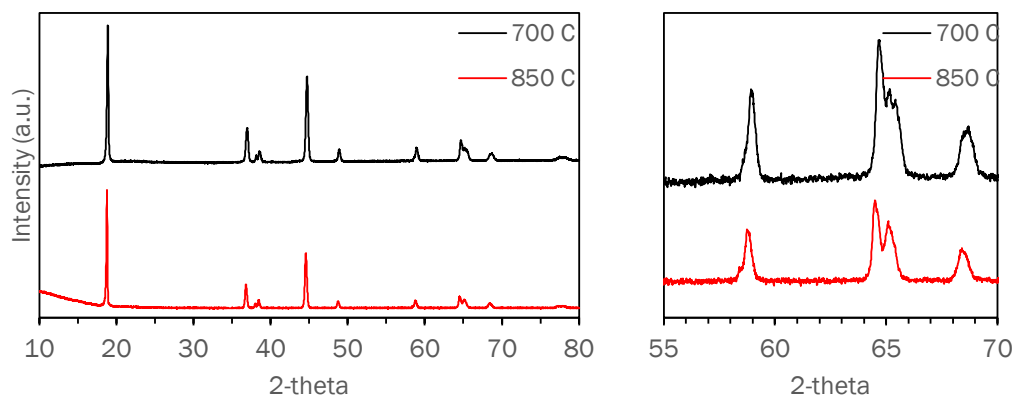


Figure III.3.34 XRD of an upcycling product before and after re-annealing to 850 °C (left) and expanded view of higher angle peaks (right)

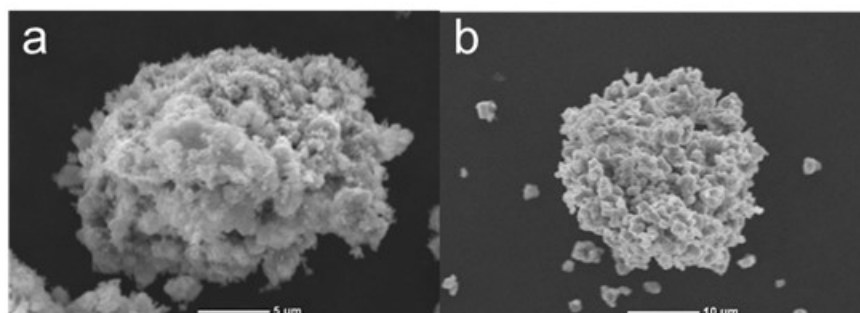


Figure III.3.35 SEM images of (a) upcycling products annealed at 720 °C and (b) re-annealed at 850 °C.

Elemental composition for upcycling products was evaluated using GDOES and EDS (Table III.3.14). The GDOES compositions show lithium contents slightly higher than target values. The amount of lithium added during the re-anneal can be reduced in order to maintain the target content. The transition metal composition remained consistent with the high nickel content from the original annealing. Compared to previous results, there is better agreement in the transition metal contents measure from GDOES and EDS. This may indicate a more uniform elemental distribution than was observed previously.

Table III.3.14 Elemental composition for re-annealed upcycled products measured using GDOES and EDS (values in parentheses)

Original Temperature	[Li]	[Ni]	[Mn]	[Co]
690 °C	1.134	0.622 (0.630)	0.176 (0.185)	0.201 (0.186)
690 °C	1.051	0.597 (0.624)	0.211 (0.193)	0.192 (0.184)
710 °C	1.130	0.623 (0.625)	0.174 (0.179)	0.203 (0.196)
710 °C	1.123	0.597 (0.597)	0.205 (0.219)	0.199 (0.184)
715 °C	1.098	0.539 (0.613)	0.236 (0.198)	0.225 (0.189)
820 °C	1.146	0.617 (0.632)	0.184 (0.188)	0.199 (0.180)

Half-cell testing data for the re-annealed upcycling products are shown in Table III.3.15 and Figure III.3.36. Even though the cathodes used for these tests had all been re-annealed to 850°C, the capacity values ranged from 108-149 mAh/g. The re-anneal of the product originally prepared at 710°C in air had the highest capacity out of these samples. Differences in the capacity performance may still be impacted by slight morphology differences.

Table III.3.15 Half-cell data for upcycled products

Original Temperature	690 C air	690 C O ₂	700 C air	700 C O ₂	710 C air	800 C O ₂	820 C air
1 st Cycle Charge (mAh/g)	173.30	163.84	168.22	177.36	179.39	153.58	165.19
1 st Cycle Discharge (mAh/g)	141.38	129.20	129.25	139.55	149.88	121.16	137.06
4 th Cycle Charge (mAh/g)	139.30	122.70	110.23	136.99	146.84	121.65	137.29
4 th Cycle Discharge (mAh/g)	138.33	121.27	108.48	133.91	145.44	120.91	136.35

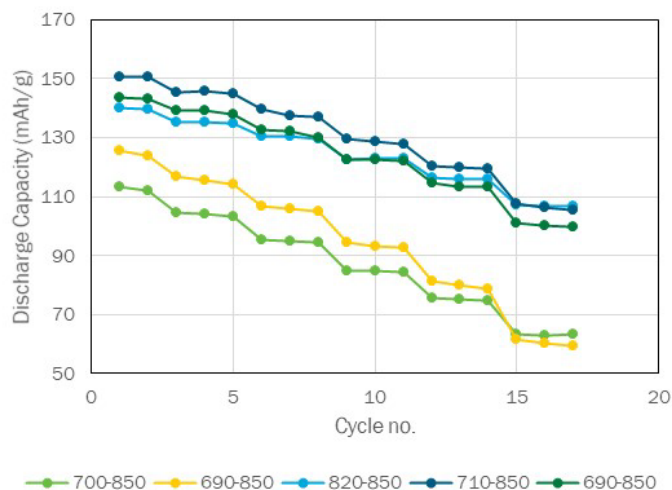


Figure III.3.36 Half-cell rate performance for re-annealed upcycling products

Ionothermal Upcycling of Cathodes

The objective of this project is to develop a cost-effective ionothermal process to upcycle chemically delithiated NMC111(D-NMC111) to NMC 622 in ionic liquids (ILs) at ambient pressure and low temperature. Ionic liquids (ILs) are a family of non-conventional molten salts that offer many unique properties, such as negligible vapor pressures, negligible flammability, wide liquidus ranges, good thermal stability, and much synthesis flexibility. The unique solvation environment of these ILs provides new reaction or reactive flux media for controlling the formation of solid-state materials with a minimum perturbation of morphologies. In addition, ILs can be readily recycled and reused after the ionothermal lithiation process. The key process of upcycling technology is to heal the compositional and structural defects of degraded Li-deficient cathode particles, which can retain the highly added value of cathode particles to the maximum extent. To this end, ionothermal upcycling experiments of D-NMC111 to NMC622 will be extensively investigated under different reaction conditions. The effect of lithium and nickel precursors in different ILs, different temperatures, and reaction time will be studied. The upcycled

materials will be analyzed by various characterization techniques including TGA, XRD, SEM, and ICP-OES, which will indicate if our ionothermal approaches are feasible for not only restoring Li into D-NMC111 but also upcycling D-NMC111 to NMC622. Systematic lab-scale experiments will be performed. If the lab-scale experiments are successful, scale-up experiments (50 g) will be performed. The cost evaluation of the upcycling ionothermal process with ANL's EverBatt will also be performed.

During the last quarter of FY2021, our work has been focused on a molten salts (MS) system that can be used to simultaneously realize the addition of Ni and relithiation in spent NMC 111, where the molten salts (MS) contain two cation species and two anion species. Since the irreversible structure change in spent NMC is mainly caused by irreversible Li loss, the relithiation process is critical and has been achieved by flux methods. Li-containing flux media (eutectic molten salts or ionic liquids) can serve as both Li sources and solvents to restore Li in spent NMC under relatively low temperatures (below 300°C), because the highly charged flux medium favors transporting ionic reactants. For the upcycling of D-NMC 111 to NMC 622, a slurry will form during milling D-NMC 111: molten salts under a specific mass ratio. The slurry is dried under 110°C in a vacuum oven, and heated to 300°C for 5 h, then to 800°C for 5 h in a muffle furnace. The obtained NMC-MS is washed with water to remove MS and reheated to 600°C for 2 h in air to yield the final product (named as Up-NMC 622). The crystal structure and thermal stability of NMCs can be investigated by X-ray diffraction (XRD) patterns and thermogravimetric analysis (TGA) curves, respectively. Both pristine NMC 111 and NMC 622 have the O3-type structure, similar to the layered structure of α -NaFeO₂. Their XRD peaks are indexed according to α -NaFeO₂ (Figure III.3.37A). Though D-NMC 111 maintains the similar O3-type structure to pristine NMC 111 (P-NMC 111), peak shifts can be identified in their XRD patterns. The (108) and (110) diffraction peaks of D-NMC 111 shift away from each other (Figure III.3.37D), and the (003) peak slightly shifts to lower angles compared to those of P-NMC 111 (Figure III.3.37B), TGA investigation of these upcycling materials is shown in Figure 37F. It is clear from Figure 37F, TGA curves of Up-NMC 622 and P-NMC 622 are almost same, indicating their similar thermal stability over 99.5%. However, D-NMC 111 exhibits a weight loss of 2.3% at 800°C in TGA curve (Figure III.3.37F), mainly from the oxygen evolution during surface reconstruction.

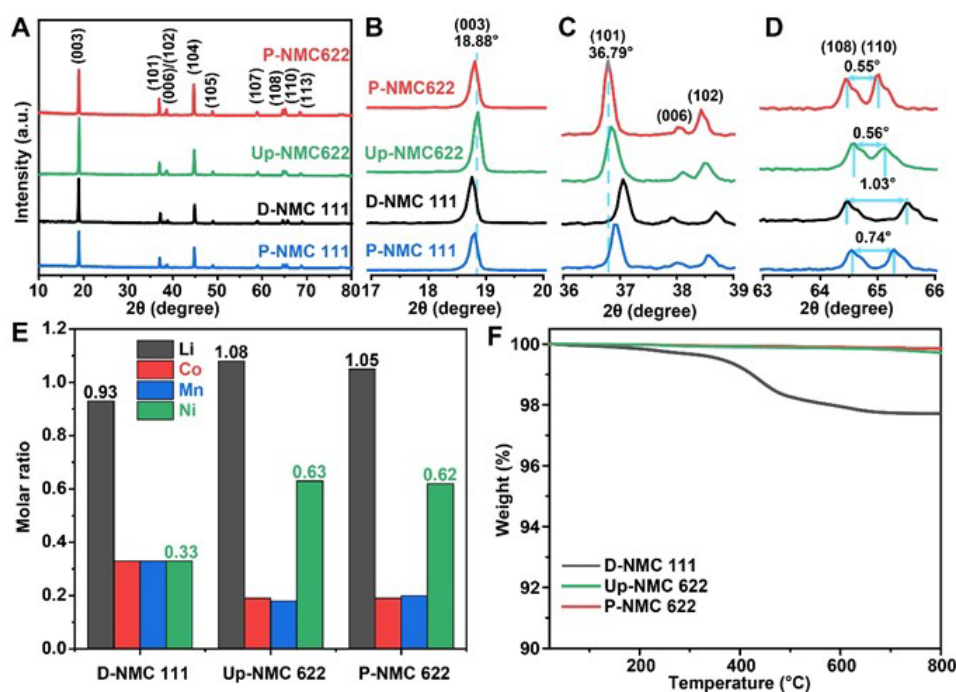


Figure III.3.37 XRD patterns, ICP results, TGA comparison for Up-NMC-622, P-NMC-622, and D-NMC-111

Table III.3.16 ICP-OES results for these NMCs.

Sample ID/Reaction conditions	Mole ratio			
	Li	Ni	Co	Mn
D-NMC 111	0.93	0.33	0.33	0.33
P-NMC 111	1.07	0.33	0.33	0.33
P-NMC 622	1.05	0.62	0.19	0.20
Up-NMC 622	1.08	0.63	0.19	0.18

The elemental analysis of these samples was performed by inductively coupled-plasma optical emission spectroscopy (ICP-OES) using Agilent 5110 ICP-OES spectrometer. Results are summarized in Figure III.3.37E and Table III.3.16 indicating that Up-NMC 622 restored Li mole ratio from 0.93 to ~1.08 and increased Ni contents from 0.33 to ~0.63, indicating success in upcycling from D-NMC111 to NMC622.

The electrochemical performance for these upcycled samples was evaluated in half cell configuration and is shown in Figure III.3.38 and Figure III.3.39. The upcycled sample (blue line) has much better performance than D-NMC111 (black line) but worse than P-NMC622 (red line). Further optimization of these experimental conditions will be performed next quarter.

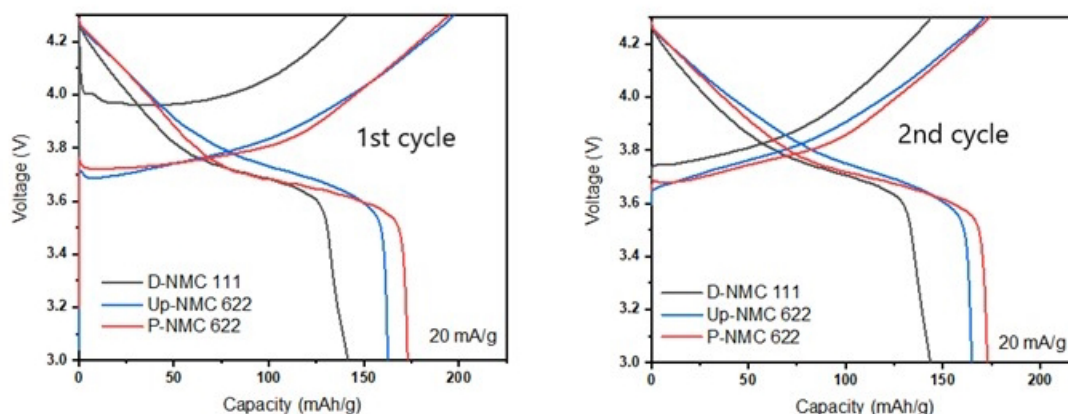


Figure III.3.38 Electrochemical performance tests in half cell of upcycling sample

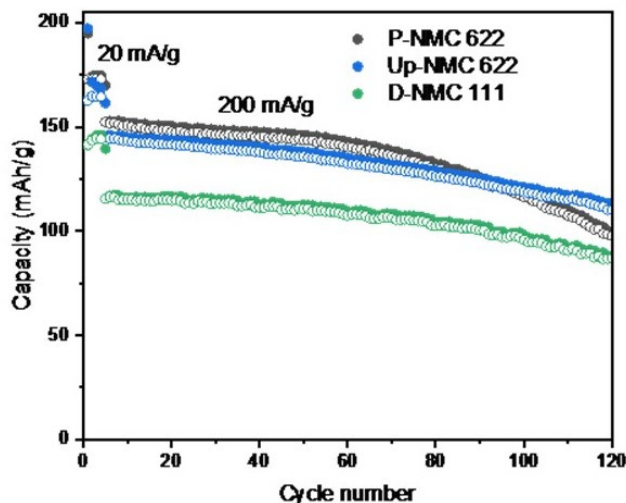


Figure III.3.39 Electrochemical cycling tests of one upcycling sample

Hydrothermal Upcycling of Cathodes

The battery industry is advancing to new cell chemistries to improve the energy density and reduce the cell cost so early cells that used NMC111 as the cathode material may not be usable in large scale in future batteries. Therefore, it is crucial to develop upcycling technology to convert NMC111 cathodes to materials like high-Ni cathodes with comparable performance and cost to the most advanced cathode materials. The direct regeneration method combining hydrothermal relithiation with subsequent short annealing developed by the UCSD team successfully resolves the compositional and structural defects of chemically delithiated NMC111 (D-NMC111). It also recovers the electrochemical performance to the same level as pristine Toda NMC111 (T-NMC111).^{1,2} The process parameters in the hydrothermal and annealing steps, such as temperature, time, and Li-bearing precursor composition, have been extensively explored and optimized. The life cycle analysis indicates the optimized direct recycling method is advantageous in terms of operation cost, greenhouse gas emissions, and energy consumption compared with currently commercialized pyrometallurgical and hydrometallurgical recycling routes. Therefore, besides direct recycling of degraded NMC111, this material will be exploited as a feedstock to produce other cathodes with high Ni content (e.g., NMC622), for upcycling, which can deliver much higher energy density and are more relevant to today's market. This effort will focus on establishing an effective direct upcycling method of D-NMC111 into NMC622 or other high-performance cathodes via the hydrothermal method.

In the past quarter, we tried to minimize the grain size of the Ni source to facilitate Ni diffusion into the delithiated NCM111.¹ Nano-Ni(OH)₂ was synthesized through a precipitation method. Briefly, the transition metal (Ni(II)) solution and a base solution were pumped into the starting solution simultaneously with continuous stirring at 55°C under N₂ protection. The flow rate was controlled at ~2mL/min by a Masterflex peristaltic pump. The mixed solution was set to keep the pH at 11.0 ± 0.2. The precipitate was filtered and dried. A scanning electron microscopy (SEM) image of the homemade Ni(OH)₂ is shown in Figure III.3.40, confirming the nano-sized particles for the homemade Ni(OH)₂.

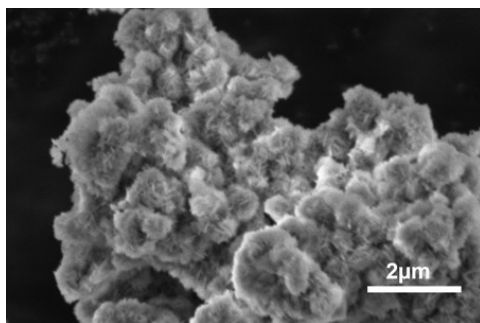


Figure III.3.40 SEM image of the Ni(OH)₂ precursor.

Homemade NiOOH precursor with needle-like nanostructures (Figure III.3.41) was also successfully synthesized in strongly alkaline concentrated sodium hydroxide aqueous solution by oxidizing Ni(OH)₂ precursor, as we reported previously.

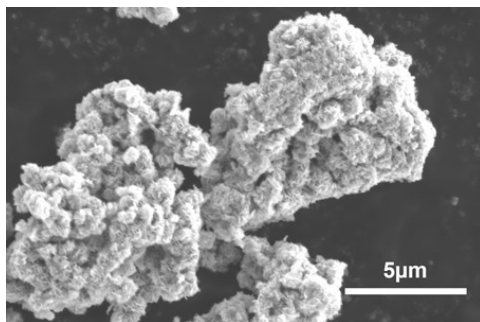


Figure III.3.41 SEM image of the NiOOH precursor.

The direct upcycling of delithiated NCM111 into NCM433 using both $\text{Ni}(\text{OH})_2$ and $\beta\text{-NiOOH}$ as alternative nickel sources via the hydrothermal method and post-annealing was attempted. For the preliminary trials, the $\text{Ni}(\text{OH})_2$ or NiOOH was mixed with D-NMC111 by international PQ-N04 planetary ball milling at 400 rpm for 12h. Afterwards, the ball-milled mixture went through the hydrothermal relithiation process with 4 M LiOH at 220°C, followed by annealing at 850°C in the pure oxygen atmosphere to achieve the hydrothermal upcycling of D-NCM111 into NCM433. The crystal structures of hydrothermal upcycled NCM433 using $\text{Ni}(\text{OH})_2$ (denoted as HTA-NCM433- $\text{Ni}(\text{OH})_2$) and NiOOH (denoted as HTA-NCM433- NiOOH) as precursor were characterized by XRD. Overall, the diffraction peaks of all the samples matched well with the typical $\alpha\text{-NaFeO}_2$ structure with $R\bar{3}m$ space group. No obvious impurity peaks corresponding to LiNiO_2 can be detected for the HTA-NCM433- $\text{Ni}(\text{OH})_2$ and HTA-NCM433- NiOOH (Figure III.3.42).

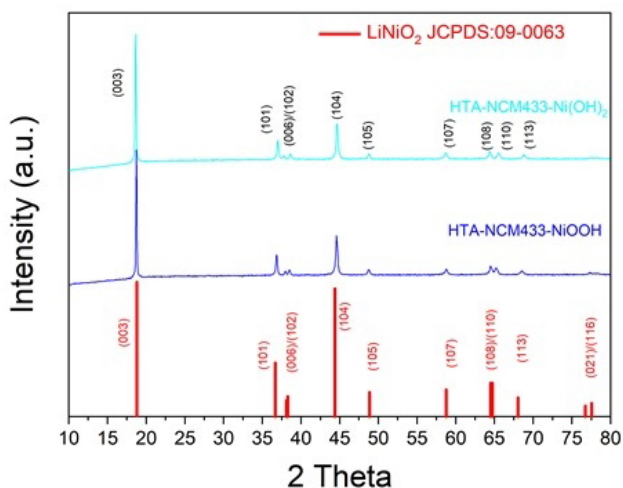


Figure III.3.42 XRD patterns of hydrothermal and post annealing upcycled NCM433 using $\text{Ni}(\text{OH})_2$ and NiOOH as precursor as well as the standard pattern of LiNiO_2 .

The electrochemical performance of NCM433 regenerated at 220°C using $\text{Ni}(\text{OH})_2$ and $\beta\text{-NiOOH}$ as the nickel source respectively were also examined by coin cells (half-cell) with cathode mass loading of $\sim 10 \text{ mg cm}^{-2}$ and Gen2 (EC/EMC = 3:7) electrolyte and compared with T-NCM433. As shown in Figure III.3.43(a), the discharge capacities at the first cycle of C/10 were 163.6 mAh/g (HTA-NCM433- NiOOH) and 161.5 mAh/g (HTA-NCM433- $\text{Ni}(\text{OH})_2$), the same as pristine NCM433 (160.2 mAh/g). Besides, the cycling stability of HTA-NCM433- $\text{Ni}(\text{OH})_2$ and HTA-NCM433- NiOOH were evaluated at C/3 rate (Figure III.3.43(b)). The HTA-NCM433- NiOOH exhibited an initial capacity of 157.0 mAh/g and remained 144.6 mAh/g after 50 cycles, with the capacity retention of only 92.1%, while HTA-NCM433- $\text{Ni}(\text{OH})_2$ and T-NCM433 delivered initial capacities of 152.3 mAh/g and 151.3 mAh/g, respectively, and the capacity retentions reached 93.8% and 93.1%, respectively, after 50 cycles. Therefore, our hydrothermal and annealing methods using nano-sized $\text{Ni}(\text{OH})_2$ or $\beta\text{-NiOOH}$ as the nickel source can be considered as a potential strategy to upcycle spent NCM111 into NCM433 with better electrochemical performance. This suggests the promise of further upcycling of spent NCM to higher Ni content (such as NCM622) with better electrochemical performance.

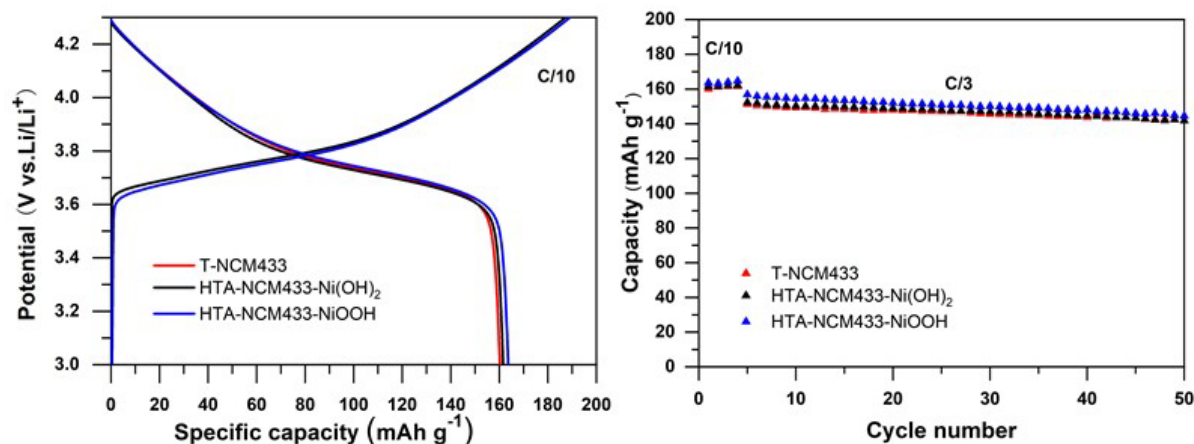


Figure III.3.43 Voltage profiles (a) and cycling stability (b) of hydrothermal and post annealing upcycled NCM433 using Ni(OH)_2 and NiOOH as precursor and the pristine NCM433.

Single Crystal Cathode Production

Lithium-ion batteries, especially cathode materials, are very dynamic. The cathode materials in spent (old) lithium-ion batteries may not find a market even if high quality materials can be recovered. For example, NMC111 is one of the common cathode materials for the EV batteries, however, the industry is moving to high-nickel NMC to increase the energy density and lower the cost. Single-crystal cathode materials hold the promise of better performance in terms of cycle life and rate performance. Conventional cathode materials are secondary particles that include numerous primary particles, which can be the potential single-crystal particles. In this project, the team will develop the methods to upgrade NMC111 polycrystal materials to single crystal NMC111 particles.

We successfully converted polycrystalline NMC111 and NMC622 to single-crystal NMC111 and NMC622 on a bench scale in the past quarter. This quarter, we scaled the experiment up from 1g to 5g and 100g, successfully converting NMC111 to single-crystal NMC111. The rate performance of both larger scale single-crystal NMC111 is comparable to the polycrystalline NMC111 (Figure III.3.44).

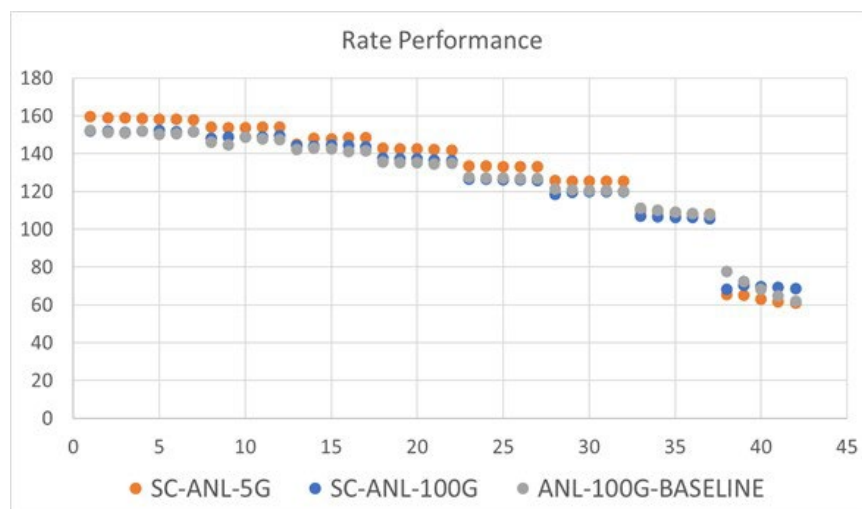


Figure III.3.44 Rate performance of large scale 5g and 100g single-crystal NMC111.

Table III.3.17 Determined composition based on ICP-MS data of Commercial811 and SC-811.

	Li	Mn	Co	Ni
SC-811	1.03	0.12	0.07	0.79
Commercial811	1.02	0.084	0.086	0.83

Thus, we applied the optimized conditions for NMC111 to NMC811 directly. As a result, the Commercial NMC811 (Commercial811) was fully converted to single-crystal NMC811 (SC-811), as seen in Figure III.3.45a and b. The particle size is around 1 μm , which is affected by the primary particle size of secondary particles. Figure III.3.45c shows the structure of obtained SC-811, indicating a perfectly layered structure recovered after the etching and sintering process. However, the interesting thing is that the composition of SC-811 is different from Commercial811 (Table III.3.17). The content of Ni is decreased from 0.83 to 0.79 and the Co from 0.086 to 0.07, while the content of Mn is increased from 0.084 to 0.12. This special composition of SC-811 also contributes to the electrochemical performance.

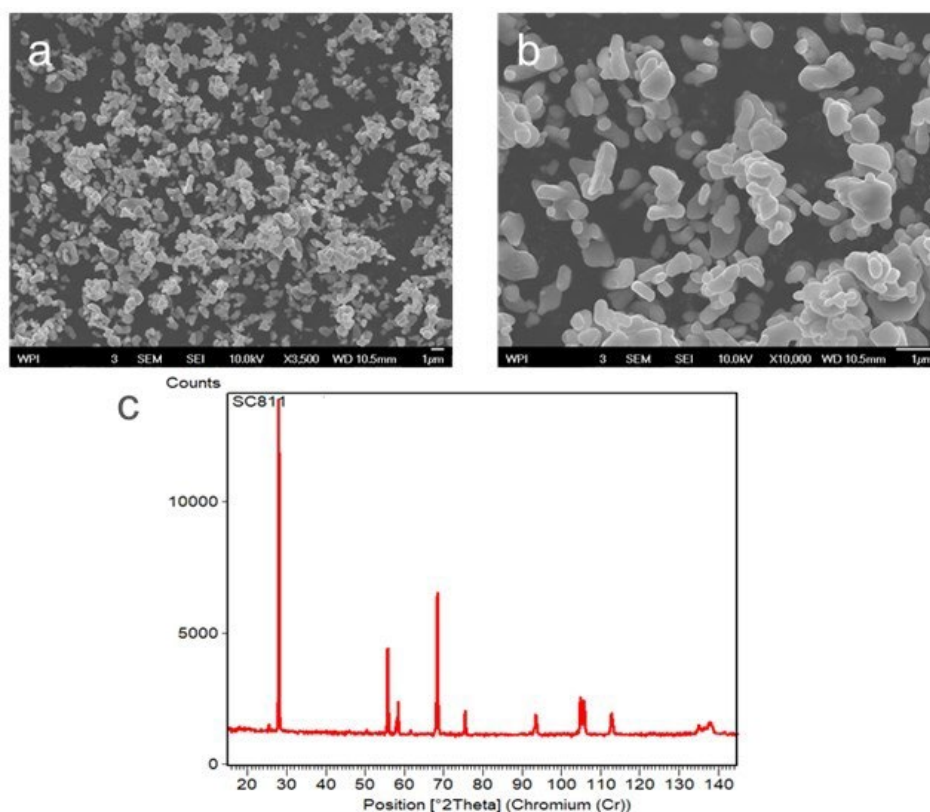


Figure III.3.45 SEM images of SC-811 (a,b) and XRD pattern of SC-811 (C). We are exploring the etching method as a universal method to obtain single-crystal NMC811 from polycrystalline NMC811.

Figure III.3.46a exhibits the comparison of rate performance between Commercial811 and SC-811 from 0.1C to 5C. SC-811 has a slightly lower discharge capacity compared to Commercial811. But the cycle performance of SC-811 is significantly improved (Figure III.3.46b). After 200 cycles, the capacity retention is enhanced by about 30% compared to the Commercial811. With the considerable improvement of cycling performance, the sacrificial rate performance should be acceptable. Moreover, the decreased rate performance is possible because the lower Ni content in SC-811 and the increased Mn content may benefit the enhanced cycle performance.

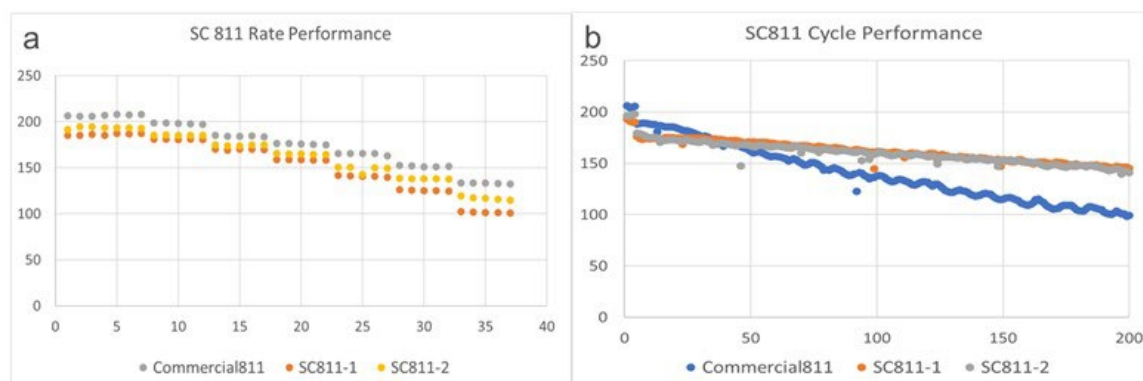


Figure III.3.46 Rate performance comparison between SC-811 and Commercial811

To further confirm the reason for composition change, a systematic comparison of different etching times is investigated. In Figure III.3.47, the ICP results of the etching solution show that Li is dissolved is much more than Ni, Mn and Co, consisting with NMC111 and NMC622. Starting from 2 hours, the amount of dissolved Li is over 50%, which is more than NMC111 and 622. And after 5 hours, the dissolving rate of Li stabilized and increased slightly. Ni and Co have a similar trend as Li, but the dissolution ratio is much lower, about half of Li. Although these results are consistent with NMC111 and NMC622, the dissolution of Mn exhibits an interesting trend. At the first 5 hours, Mn is dissolved in the solution at the same rate as Ni and Co. However, after 5 hours, the concentration of Mn in the solution starts to decrease. And after 20 hours, Mn is disappeared from the solution. It means that Mn is precipitating during the etching process.

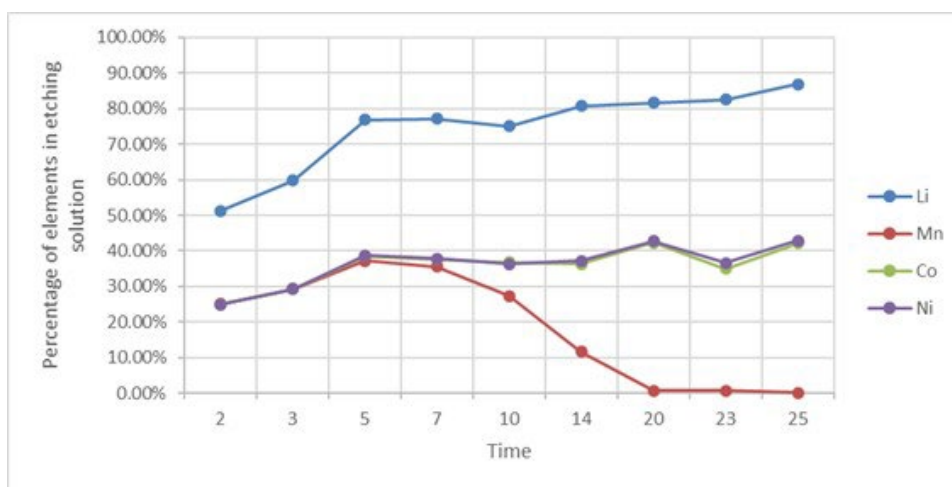


Figure III.3.47 ICP data representing the loss of elements in the solution

Furthermore, we found Commercial811 was breaking starting from 2 hours in Figure III.3.48. All Etched-811-2h, Etched-811-14h and Etched-811-25h are already transferred to a single-crystal structure. And Figure III.3.48d shows the structure change during the etching process. In the beginning, after 2 hours of etching, the intensity decreases, indicating a worse crystal structure. And the (003) peak splits a shoulder peak due to the significant loss of Li. Along with the increase of etching time, peak splitting of the (006)/(012) planes is reduced, whereas the splitting of (018)/(110) planes is extended. This phenomenon is similar to the charging process of layered oxide cathode, where Li ions are removed from the Li layer. It indicates that the structural change is caused by the loss of Li during the etching process.

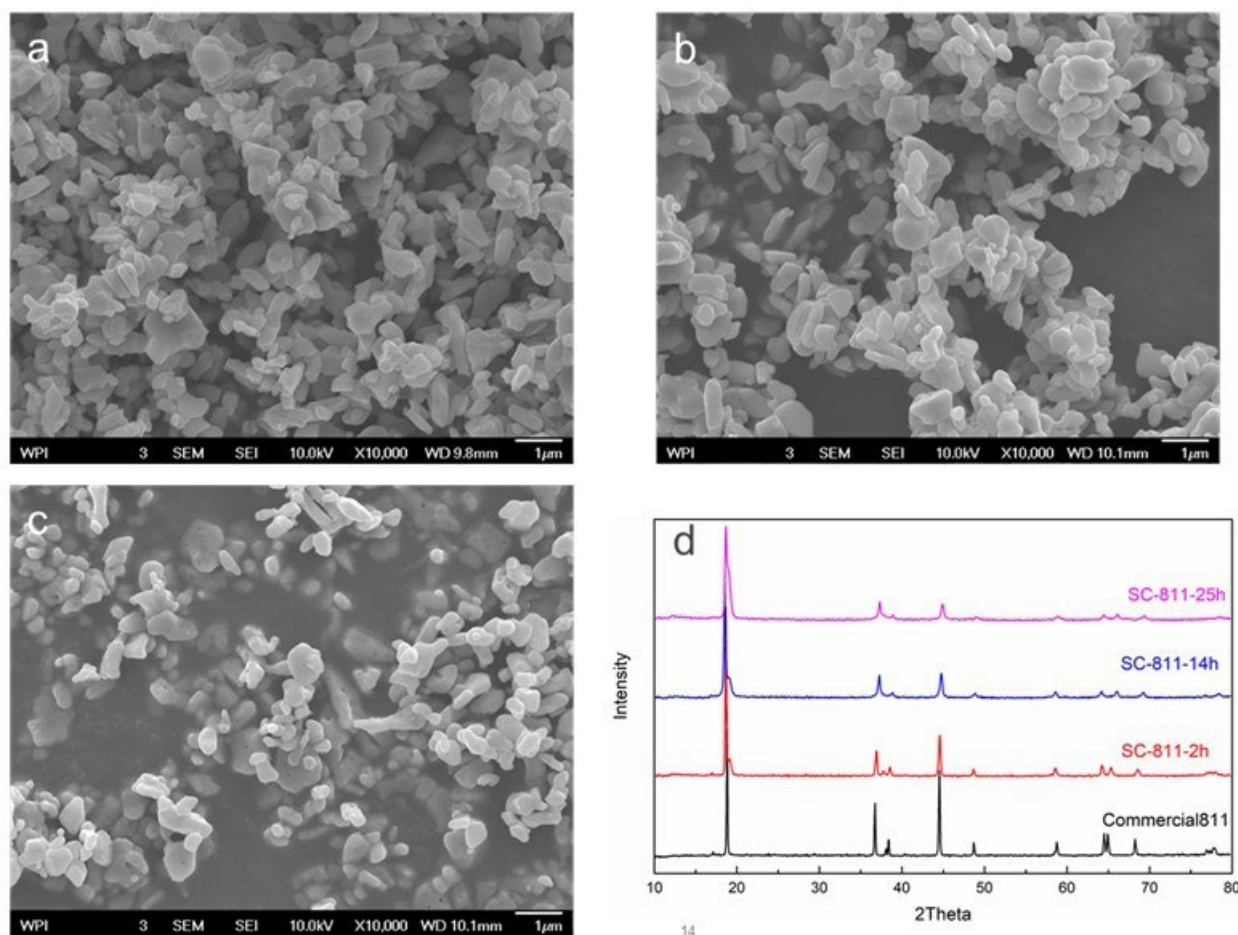


Figure III.3.48 SEM images of 2h (a), 14h (b) and 25h (c) etching process; XRD patterns comparison between commercial811 and different etching time samples (d).

Role of Impurities in Recycled Cathodes

When identifying and developing lithium-ion battery recycling technologies, understanding the role of impurities is always a concern, as they may have an impact on electrochemical performance, material stability, or lifetime. Knowing the wide variety of impurities that may be introduced in the recycling process, the objectives of this project are to determine the possible impurities, their role in structural stability, and their impacts (during synthesis and after synthesis) on the recovered NMC622 precursor and cathode materials. The main impurities in the black mass were determined, including metallic elements (Cu, Al, and Fe) and non-metallic elements (C, F and P). The impact of Cu introduced during precursor synthesis was determined in previous reports. Surprisingly, small amounts of Cu improve the electrochemical performance of synthesized NMC622. The last quarterly report described how Al introduced during precursor synthesis affects the morphology, structure, and electrochemical properties of synthesized NMC622 precursor and cathode powder.

In this quarter, a fluorine impurity (NaF) was added to the metal sulfate solution to synthesize the hydroxide precursor, then sintered with Li_2CO_3 to produce NCM622 cathodes. Previous studies showed that the existence of F ions during the synthesis process had little impact on particle surface morphology but resulted in higher particle porosity. It was speculated that F ions could replace oxygen in the cathode lattice; however, no extra phase was found in 5% F cathodes.

A survey scan on Na 1s in Figure III.3.49a shows no Na in all as-prepared cathodes, which is consistent with the previous ICP-MS results. It ensures that all Na ions within reaction environment are excluded from

recovered products. Any difference between virgin material and impurity-based material is attributed to F ions only. The F 1s spectra of surface and bulk for cathodes are given in Figure III.3.49b&c. A prominent F 1s signal is detected on the surface of FNCM cathodes. On the contrary, there is no fluorine signal in the bulk. It reveals that the F ions prefer to cluster near the surface rather than in the bulk of cathodes. The peak at ~ 685 eV in Figure III.3.49b indicates the M-F (LiF , MF_2) bonds. As the impurity amount increases from 0.2 at% to 5 at%, the peak intensity becomes larger. Therefore, XPS results confirm the inclusion of F ions into cathode materials by replacement of lattice oxygen. And the F ions reside at the particle surface, forming a layer with an elevated ratio of low valence (+2) TM ions.

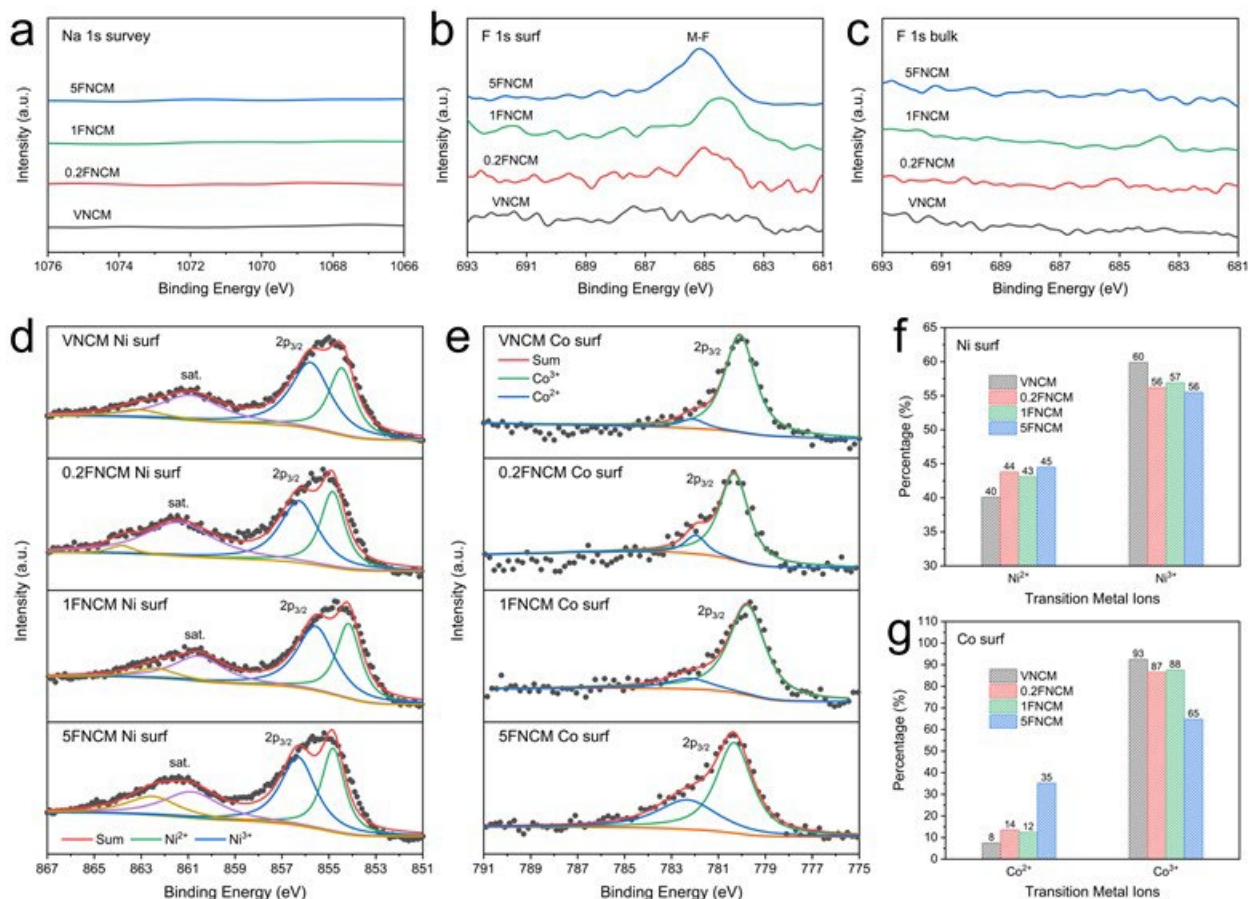


Figure III.3.49 XPS spectra of (a) Na 1s survey scan, (b) F 1s surface and (c) F 1s bulk for cathodes; XPS deconvolution profiles of (d) Ni 2p, (e) Co 2p in surface layer of cathodes; Percentage of (f) Ni²⁺, Ni³⁺ ions and (g) Co²⁺, Co³⁺ ions in surface layer of cathodes.

XPS spectra deconvolution of 2p_{3/2} peak was conducted to determine the ratio of Ni²⁺/Ni³⁺ and Co²⁺/Co³⁺ in cathode materials. The fitted spectra of Ni 2p_{3/2} shown in Figure III.3.49d reveal the presence of Ni²⁺ and Ni³⁺. Based on Figure III.3.49f, the average ratio of Ni²⁺ at FNCM cathode surfaces is about 4% higher than virgin. Figure III.3.49g, shows only a small amount of Co²⁺ at the virgin cathode surface. However, the amount of surface Co²⁺ increases to $\sim 13\%$ for 0.2FNCM and 1FNCM, then continue up to 35% for 5FNCM. The lower oxidation state of Ni and Co ions at the FNCM surface is triggered by the charge compensation effect as a result of F ion incorporation. Note that Ni²⁺ could contribute to a higher reversible capacity as well as a more stable cathode-electrolyte interface during cycling. On the other hand, Co²⁺ is not beneficial for cation order in the cathode crystal. Due to a high surface Co²⁺ concentration, 5FNCM has a poorer cation mixing compared to its counterparts, as verified by previous XRD analysis.

Cyclic voltammetry (CV) tests combined with the Randles-Sevcik equation are used to calculate the lithium bulk diffusivity (D_{Li}) in prepared cathode samples.

$$I_p^2 = (2.69 \times 10^5)^2 n^3 A^2 D_{Li} C^2 \nu$$

In Randles-Sevcik equation, n is the number of electrons transferred during cycling ($n = 1$); A is the surface area of electrode (1.13 cm^2 in this work), and C is the theoretical molar concentration of Li-ion in NCM material (0.05 mol/cm^3). The ratio of the squared peak current (I_p^2) to the scan rate (ν) is proportional to the value of diffusion coefficient (D_{Li}). The relation between I_p^2 vs. ν is depicted in Figure III.3.50a&b, where the slope of fitted lines shows the bulk Li-ion diffusion ability in NCM. The bar chart in Figure III.3.50c gives the value of D_{Li} calculated via Randles-Sevcik equation. The fitted lines in Figure III.3.50a&b reveal a strong correlation between anodic and cathodic diffusivity which represent the Li diffusion during de-lithiation and lithiation respectively. According to the results, both 0.2FNCM and 1FNCM have a better Li-ion diffusivity than virgin cathode, while the value of D_{Li} in 5FNCM is the lowest among all samples. In particular, NCM with 0.2%F has the highest diffusion coefficient: $2 \times 10^{-10} \text{ cm}^2/\text{s}$ (charge) and $4.8 \times 10^{-11} \text{ cm}^2/\text{s}$ (discharge) which are roughly 30% and 14% greater than that of virgin. This implies that small amount of F inclusion could positively influence bulk lithium diffusivity.

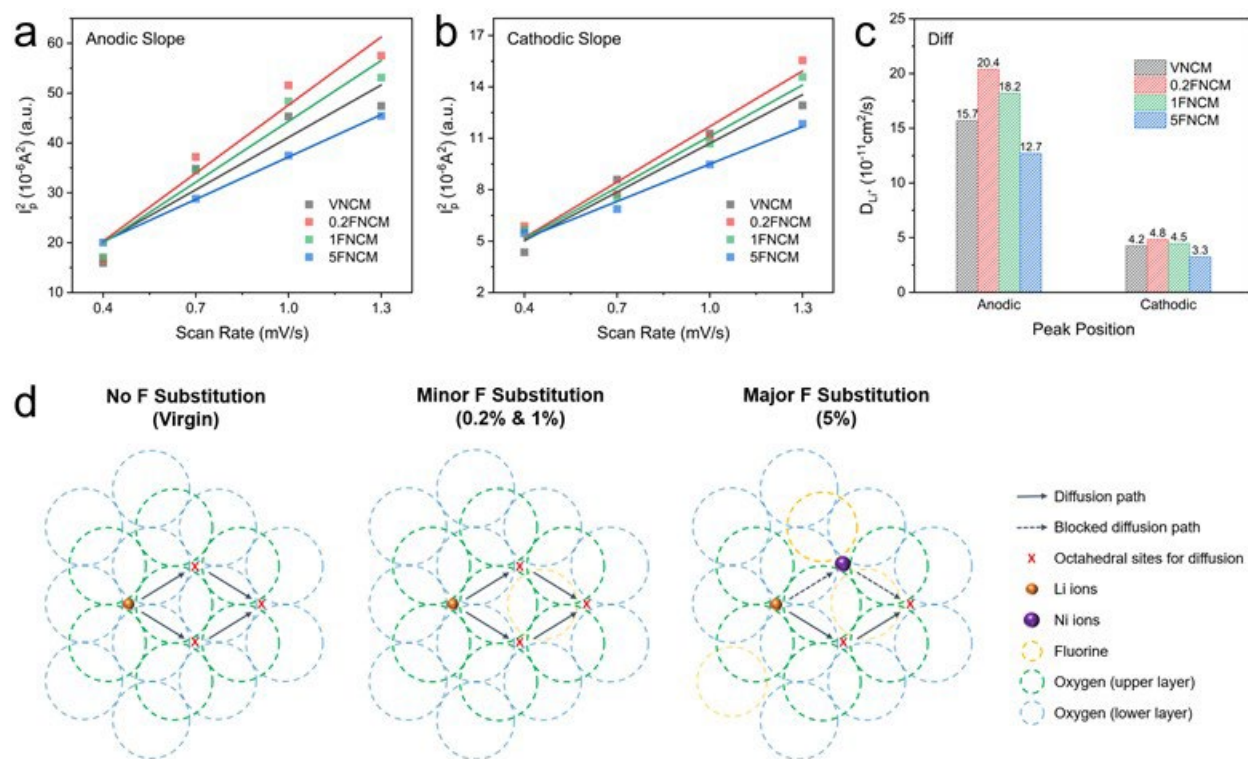


Figure III.3.50 Plot of fitted lines between peak current (I_p) vs. scan rate (ν) from CV curves for (a) anodic side and (b) cathodic side; (c) Calculated Li-ion diffusion coefficient D_{Li} , and (d) schematic of Li-ion diffusion in cathode crystals.

The schematic of the NCM lattice in Figure III.3.50d demonstrates the impacts on bulk Li-ion diffusion under different levels of fluoride incorporation. The red x marks, which refers to the octahedral sites, are essential routes for the movement of Li-ion in materials. When substitution at a low level ($< 1 \text{ at}\%$), the path for diffusion remains available. At the same time, an enlarged interspace and a reduced barrier for diffusion are created due to the smaller size and lower charge status of F ions. In this case, the D_{Li} in 0.2FNCM and 1FNCM is higher than virgin. Nonetheless, excessive F inclusion ($> 5 \text{ at}\%$) could raise the cation mixing degree in the lattice. Mismatched Ni^{2+} ions in the lithium layer block routes, resulting in poor diffusion.

The results of cycling tests at 0.33C and 5C (1C = 175 mAh/g) are given in Figure III.3.51a&b. After 100 cycles at 0.33C, cathodes with low impurity content (< 1 at%) have a discharge capacity of 167 mAh/g, about 8% higher than virgin. Meanwhile, based on Figure III.3.51e, they also possess a superior retention (> 97%) over virgin, which is only 94% after 100 cycles. In a 5C cycling test, both 0.2%F and 1%F cathodes show a better performance as well. In specific, 0.2FNCM has a discharge capacity of 129 mAh/g with 95% retention after 100 cycles at 5C. In contrast, without the boost from fluorine impurity, properties of virgin sample are much poorer (112 mAh/g, 86%).

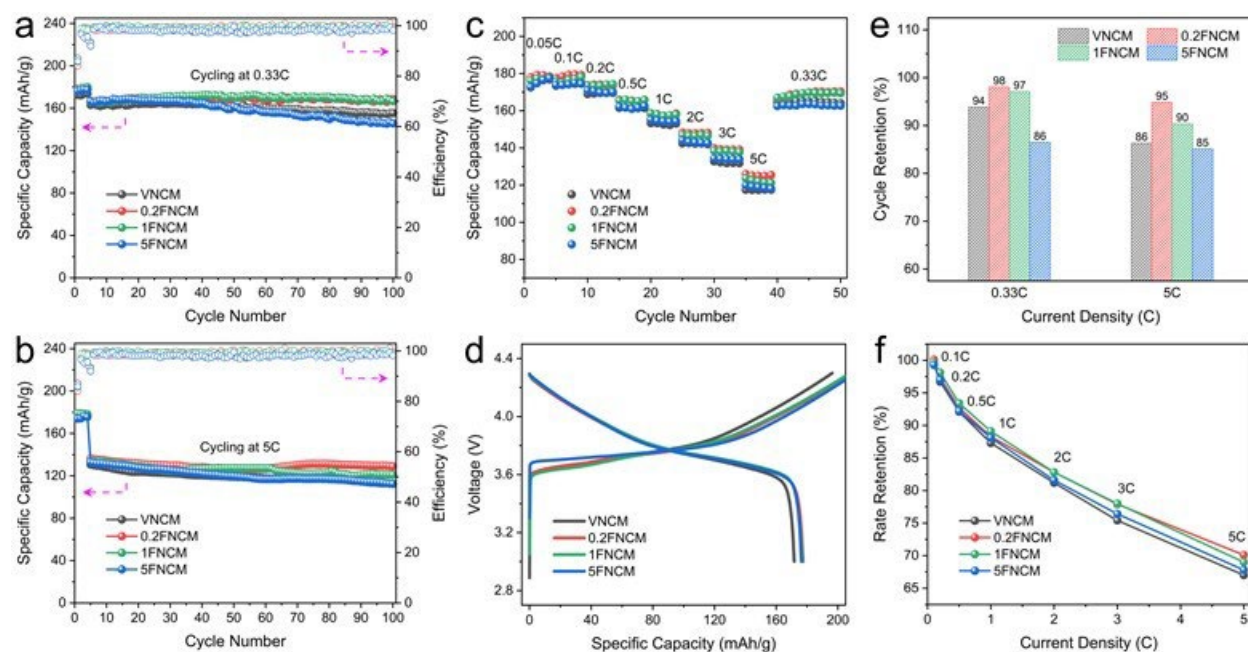


Figure III.3.51 Electrochemical performance of as-prepared samples. (a) cycle at 0.33C, (b) cycle at 5C, (c) rate to 5C, (d) initial charge-discharge profile, (e) retention after 100 cycles, and (f) retention at specific rate relative to formation cycle (0.05C).

As shown in Figure III.3.51c&f, all FNCM cathodes have a higher capacity and retention in rate tests. In addition, the performance gap between FNCM and VNCM is getting wider with the increase of current flow. Apparently, the outstanding cycle and rate performance of FNCM cathodes is attributed to the positive influence from a low-level fluorine impurity. The initial charge-discharge profile at 0.05C is given in Figure III.3.51d. VNCM cathode delivers the lowest capacity of 196 mAh/g and 172 mAh/g in the initial charge and discharge process, respectively. By comparison, FNCM cathodes have an average value of 210 mAh/g and 177 mAh/g during the formation. The boosted initial capacity is caused by the higher surface Ni^{2+} concentration that allows more Li-ion to be activated. Thus, the electrochemical properties of recovered NCM622 cathode could be strongly improved by a fluorine impurity.

Figure III.3.52 illustrates the positive impacts on recovered cathode materials by a fluorine impurity. Firstly, the formation of cavities in cathode particles has positive effects on rate performance and cycle stability. In addition, an increased ratio of Ni^{2+} at the cathode surface, due to F ion incorporation, promotes the reversible capacity and the cathode-electrolyte interface stability. In addition, the bulk Li-ion diffusivity could be improved in FNCM cathodes (< 1 at%). Altogether, impurity F shows a very positive role in the hydrometallurgy process.

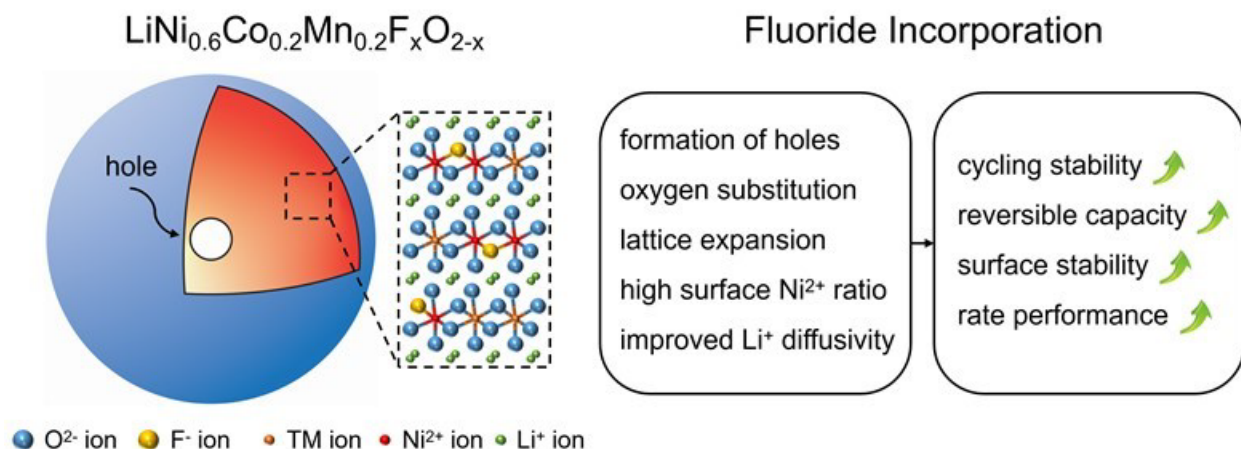


Figure III.3.52 Schematic illustration of the impacts on the NCM622 structure caused by fluorine impurity.

Cell Preprocessing

FY21 marks the second year for the cell pre-processing task in the ReCell center. Pre-processing cells is a critical step in ReCell's direct recycling model. The configuration of battery packs, modules, and cells varies among different electric vehicle models and presents significant challenges for disassembly and material liberation. As a consequence, current commercial methods for battery size reduction used by recyclers create a large amount of contamination and waste. This contamination is of great importance for direct recycling, since a clean black mass is needed to enable recycling to be economically and technically viable. In addition, pre-processing techniques must not adversely affect separation processes further down the line (e.g., we may not want to shred with water because it will cause problems for the recovery of electrolyte salts and degrade cathode materials). Last year, several hammermilling and shredding experiments were conducted. It was determined that the number of shredder shafts (single vs. double), shredder knife configuration, the number and geometry of shredder knife teeth, the size of the hammermill screen, and rotation speed of hammers can have a significant effect on the size and size distribution of shredded material and quantity of fine particles produced. In these experiments, hammermilling generated up to six times more fine particles than shredding. A shredder was selected and ordered to begin shredding manufacturing scrap and cells at Argonne. The shredded electrode laminates will be used as a starting material to recover clean black mass, cathode material, or anode material for use in optimized direct recycling processes within the ReCell Center.

Liberation of Layered Component Clumps

In this quarter, a continued effort was made to investigate liberation of layered component clumps by high-speed stirring. Figure III.3.53 shows pictures of the laboratory-scale baffled tank used for the stirring experiments. A 4 L capacity Pyrex beaker was used as a tank, and an impeller was placed at the center of the beaker. A baffle cage was placed inside the beaker so that vertical circular flow of liquid was created during a mixing. The stirring experiments were conducted by stirring layered component clumps in 1 L deionized water at a high rotation speed (i.e., 1290 RPM and 1800 RPM). Water could be used safely, as the samples did not contain electrolyte (i.e., LiPF_6 containing organic solvent).

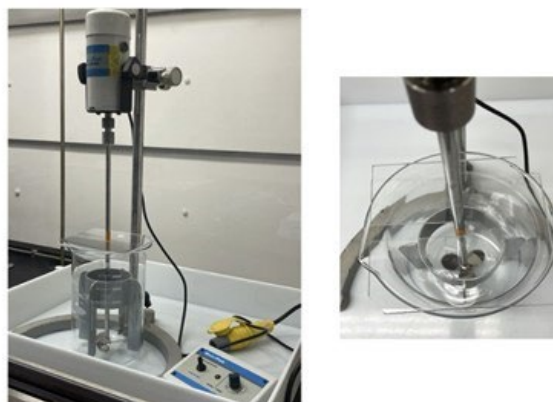


Figure III.3.53 A laboratory-scale baffled tank used for the stirring experiments for layered component clump liberation

Layered component clumps present in different sizes are shown in Figure III.3.54. All the clumps were collected from the >5.6 mm fraction of material (e.g., dry pouch cells) that was shredded by an industrial partner previously. The mass distribution of clump sizes in the sample of each experiment was 24.8% large clumps (>1 cm), 29.2% small clumps (3 mm – 1 cm), 23.7% thin layers (<3 mm) and 22.2% single components. This is the average mass distribution of clump sizes from the size distribution analysis of an 8.5 kg batch of dry pouch cell shreds (see the details in our *ReCell FY21 Q3 report, Cell-Preprocessing*). The single component fraction was composed of fully-coated anode and cathode pieces at 1:1 mass ratio without separator pieces. This is to make the starting sample more consistently between the experiments with different stirring conditions.

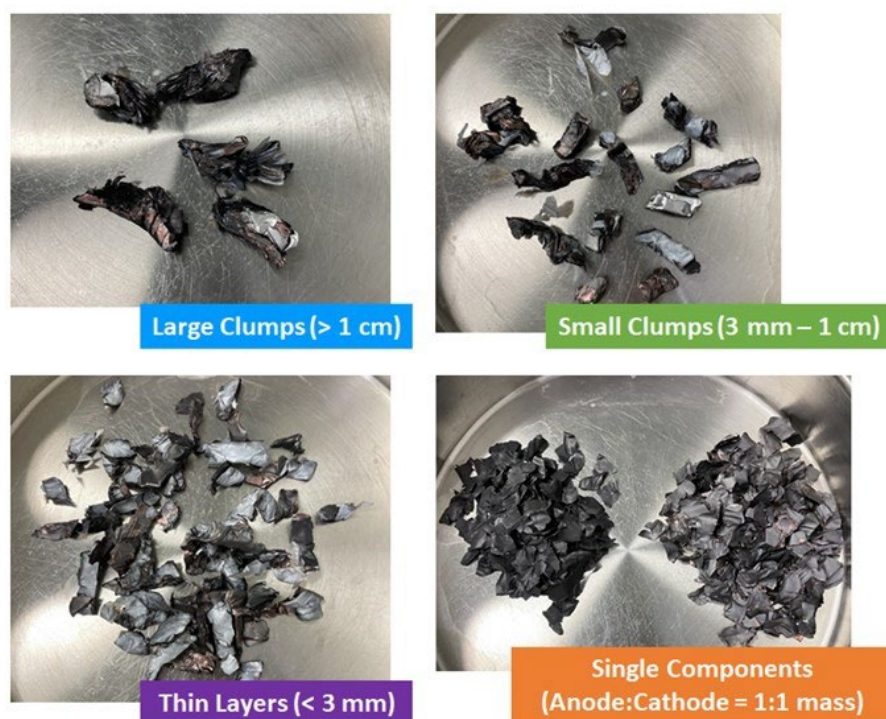


Figure III.3.54 Clumps in different sizes used for the stirring experiments

After the stirring experiments, samples were filtered and dried. Dried samples were sieved with different size screens (i.e., 5.6 mm, 2.8 mm, 1 mm, and 500 μ m), and each size fraction was weighed to analyze size distribution. Remaining clumps (i.e., component layers still bound together) in the >5.6 mm and 2.8 mm – 5.6 mm fractions were

collected and weighed separately. The total mass of remaining clumps divided by the total mass of clumps before stirring (i.e., total mass of large clumps, small clumps and thin layers) was calculated as a liberation efficiency.

Figure III.3.55 shows the results of two stirring experiments conducted at 1290 RPM (i.e., 60% of the maximum stirring speed) for 5 minutes with a solid liquid ratio of 50 g/L and 100 g/L. The liberation efficiency was slightly higher at 83.2% after the stirring at 50 g/L. The graph also shows the size reduction of the sample after the stirring. While stirring, components liberated early in the stirring process were further reduced in size over time. More delaminated powders (i.e., <500 μm fraction) were obtained after stirring at 100 g/L. At the higher solids concentration, more clumps were present during stirring which caused more friction between the pieces. The impact of this effect was more significant with a higher solid-liquid ratio.

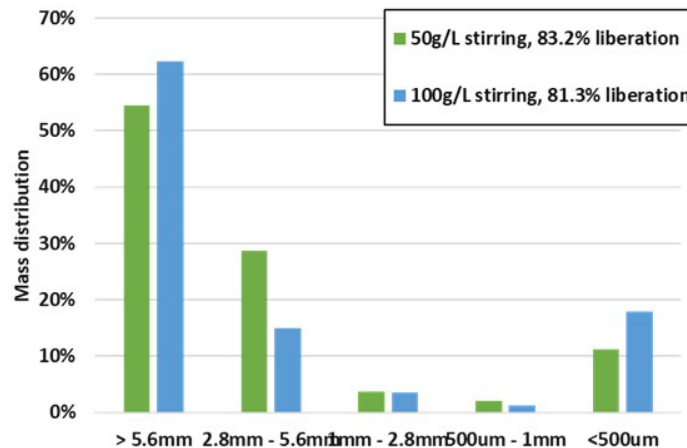


Figure III.3.55 Liberation efficiency and mass distribution of different size fractions after stirring clumps at 1290 RPM for 5 minutes with two solid-liquid ratios (50 g/L and 100 g/L).

Figure III.3.56 shows the results of three stirring experiments conducted at 1800 RPM (i.e., 80% of the maximum stirring speed) at 50 g/L and 100 g/L for 90 seconds, 3 minutes and 5 minutes. The liberation efficiency was only 74.4% after 90 seconds of stirring. The liberation efficiency increased to 94.4% after 3 minutes of stirring. Extending the stirring time to 5 minutes did not affect the liberation efficiency significantly. However, more size reduction of liberated components and delamination of powders occurred with longer stirring time. The <500 μm fraction comprised 15.0% of the sample after 3 minutes stirring and 18.6% after 5 minutes of stirring.

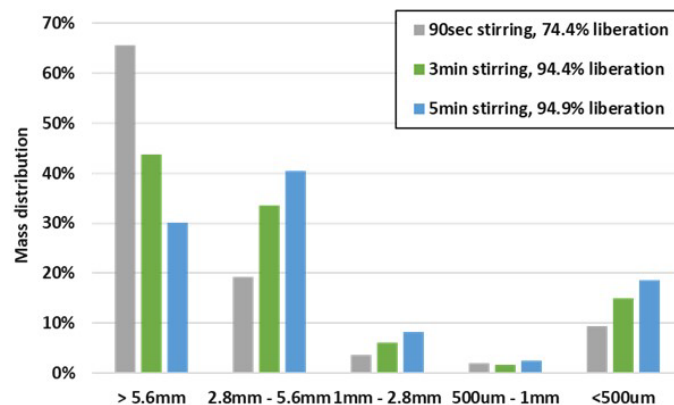


Figure III.3.56 Liberation efficiency and mass distribution of different size fractions after stirring clumps at 1800 RPM and 50 g/L for three stirring times (90 second, 3 minutes and 5 minutes).

Liberated clumps in different size fractions after stirring at 1800 RPM for 3 minutes are shown in Figure III.3.57. Pictures of the >5.6 mm and 2.8 – 5.6 mm fractions clearly show liberated anode, cathode and separator pieces. Exposed copper current collector foils on anode pieces were observed from these photos, while exposed aluminum current collector foils were not observed.

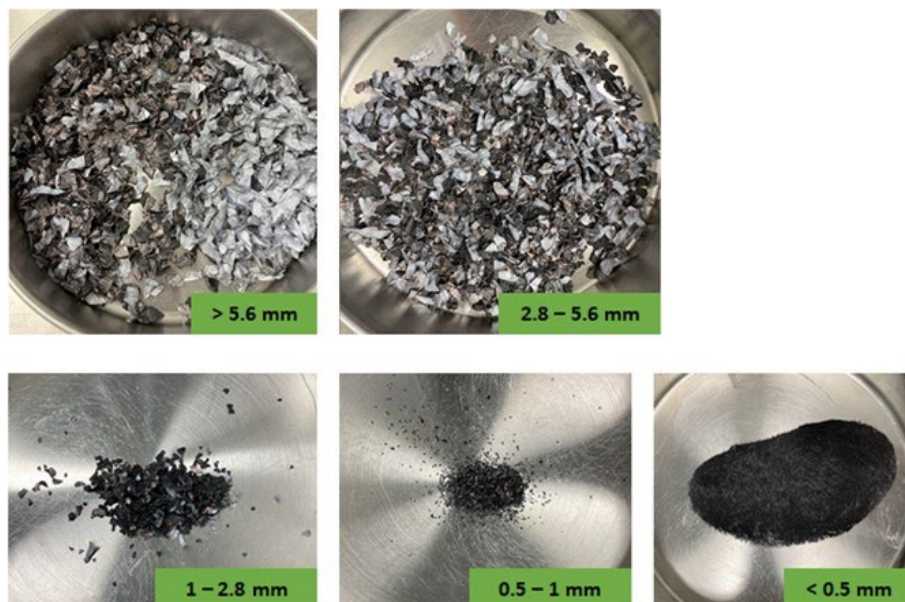


Figure III.3.57 Liberated clumps after stirring at 1800 RPM at 50 g/L for 3 minutes

Table III.3.18 TGA and ICP results of delaminated powders compared with different stirring conditions

Stirring condition	Liberation of clumps	Mass % of <500 μ m powders after stirring	Metal content based on TGA analysis	Molar ratio by ICP analysis					
				Li	Ni	Mn	Co	Al	Cu
1290RPM for 5 min at 50 g/L	83.2%	11.1%	42.5%	0.978	0.382	0.343	0.216	0.043	0.015
1290RPM for 5 min at 100 g/L	81.3%	18.0%	45.1%	0.970	0.378	0.340	0.214	0.054	0.013
1800RPM for 3 min at 50 g/L	94.4%	15.0%	43.0%	1.003	0.392	0.350	0.221	0.024	0.012
1800RPM for 5 min at 50 g/L	94.9%	18.6%	44.0%	0.985	0.384	0.347	0.219	0.039	0.011

Table III.3.18 shows the TGA and ICP results of delaminated powders (i.e., < 500 μ m fraction) compared with the stirring conditions, liberation efficiency and mass fraction of delaminated powders. TGA analysis determined that metal contents in delaminated powders were about 43% - 45% after stirring at 1290 RPM or

1800 RPM. The results indicated that the stirring conditions did not affect delaminated portions of anode and cathode significantly. ICP results showed the consistent molar ratio of Li: Ni: Mn: Co at approximately 1: 0.39: 0.35: 0.22. Aluminum contents were higher compared to copper contents in all the stirring conditions. Aluminum current collector foils likely broke into fine pieces after delamination of cathode powders by stirring, while copper foils retained their shapes.

Future Work

A pilot-scale dual-shaft shredder arrived at Argonne National Laboratory this quarter and is shown in Figure III.3.58. On-going efforts have been made for installation of electrical wiring, the control panel, and a final electrical inspection. The safety plan, which incorporates adequate conditions for safe shredding, will be approved by the Argonne safety team before operation of the shredder. End-of-life lithium-ion battery cells received from an industrial partner will be shredded to provide material for electrolyte recovery, component separation, graphene production, and other up-coming tasks in FY22.



Figure III.3.58 ReCell's pilot-scale, submersible dual-shaft shredder

Ongoing efforts will be made to investigate liberation of layered component clumps. End-of-life batteries containing organic electrolyte should not be stirred in water due to the risk of electrolyte salt decomposition and HF generation. Under a recently approved safety plan, stirring experiments of clumps in organic electrolyte solvent (e.g., diethyl carbonate) will be conducted to investigate the liberation of clumps at the laboratory scale. Other methods, such as rotary milling, will also be investigated as an alternative liberation methods for clumps.

Solvent-based Electrode Recovery

The objective of this project is to develop efficient recovery processes for the separation of black mass from current collectors. The separation processes use green solvents that are inexpensive, nontoxic, do not cause water and/or air pollution, or damage the active materials and current collectors. Recovery of cathodes and anodes from spent Li-ion batteries has high peeling-off efficiency and is cost effective, scalable, energy efficient, and environmentally friendly. The work plan is based on a wet-chemical recovery approach for separating the black mass from metal foils by either dissolving the PVDF binder or weakening its binding with laminates. In FY21, this project continued to optimize separation protocols for the mixture of cathode and anode at a larger scale and to evaluate the electrochemical performance of recovered materials.

SolveX process was applied in the successful recovery and remanufacturing of anode material from scraps. Isopropanol (IPA) was previously used to wash away the residual solvent X in the delaminated anode films before drying. However, cost analysis using EverBatt modeling suggested that IPA was one of the major contributors to the processing cost. Therefore, we optimized the washing step by changing IPA to water to reduce the processing cost, since the graphite anode is stable in water. As a result, the cost to process anode scraps was reduced by ~25%, as shown in Table III.3.19. Additionally, the cost of recovered graphite (battery

grade) was greatly reduced from \$1.47 to \$-0.35 per kg, while the cost of virgin graphite material is \$12.5 per kg. The negative net cost for graphite implies the recycler can fully recoup all their expenses by selling the recovered copper foils. The collaboration between ReCell and industry for the recovery of industrial manufacturing scraps using the SolveX process continued in this quarter. Several batches of recovered electrode materials, including both cathode and anode films, were provided to the industry for further re-coating and electrochemical evaluation.

Table III.3.19 Cost analysis for recycling graphite anode scraps using different processes. SolveX_IPA and SolveX_H2O stand for SolveX process using IPA and H2O to rinse the residue solvent X, respectively.

Recycling graphite anode scraps	SolveX_IPA	SolveX_H2O	Pyro	Hydro	Virgin
Cost (\$/kg material processed)	3.49	2.62	2.81	0.95	
Revenue (\$/kg material processed)	8.75	8.75	2.51	2.59	
Cost (\$/kg graphite)	1.47	-0.35	N/A	N/A	12.5

The SolveY process was selected as a separation strategy to recover spent cathode powder for the relithiation benchmarking project. Spent cathode from large format pouch cells was obtained from Argonne National Laboratory (Figure III.3.59a). Those large cathode coatings were cut into small pieces (~1 cm²) in the dry room, followed by washing in diethyl carbonate to remove electrolyte salt. The dry cathode pieces were then treated in the solvent Y in large scale (100 g of spent cathode in 500 mL of solvent Y) at 150°C. More than 550 g of spent cathode powder was separated and recovered from the spent electrode (Figure III.3.59a). Recovered cathode powder was characterized by XRD, SEM, and ICP-OES. XRD patterns in Figure 59b show no impurity phases for the recovered cathode powder when compared with the spent cathode, suggesting that SolveY process does not alter the cathode structure. Figure III.3.59c shows the morphology of recovered cathode powder with isolated NMC particles and small aggregates of particles in the matrix of carbon and binder. The lithium amount was determined by ICP-OES and found to be ~0.82, indicating a ~20% lithium loss that is typical for end-of-life EV batteries.

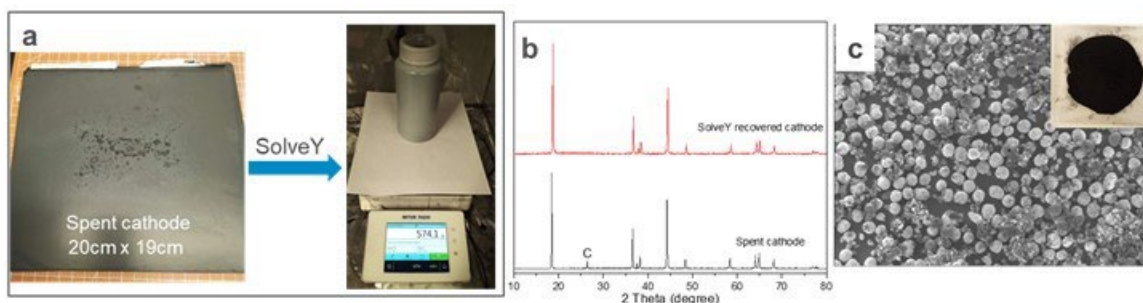


Figure III.3.59 (a) Photos showing the recovery of spent cathode powder using SolveY process in large scale, (b) XRD patterns for the spent cathode before and after SolveY processing, and (c) SEM image showing the morphology of recovered cathode powder, inset picture shows the cathode powder.

Process cost for recovering materials through the SolveY process was preliminarily evaluated by the EverBatt model. Cathode scraps of NMC622 were selected as a model system. As shown in Table III.3.20, recovering materials directly from manufacturing scraps using our SolveY process can greatly reduce the material cost. Compared with pyro- and hydro-metallurgical processes, SolveY recovered NMC622 was found to be much cheaper. Cost of recovered NMC622 is ~\$15.60 per kg, which is 24.3% less than the cost of virgin material. Guided by the EverBatt model, the cost can be further reduced by recycling and reusing solvent Y and acetone.

Table III.3.20 Cost analysis for recycling NMC622 cathode scraps using different processes. *The modeling assumes that 95% of solvent Y is recycled and reused twice, and that acetone is not reused.

Recycling NMC622 cathode scraps	SolveY*	Pyro	Hydro	Virgin
Cost (\$/kg material processed)	12.31	3.54	2.92	NA
Revenue (\$/kg material processed)	16.17	8.54	9.04	NA
Cost (\$/kg NMC622)	15.60	21.25	19.61	20.60

In addition to the efficient SolveX and SolveY processes, we recently developed a SolveZ process targeting on the direct recycling and remanufacturing of anode scraps. This process utilizes a green and cost-effective solvent Z to delaminate anode coatings (PVDF as binder) from copper current collector with 100% peeling off efficiency. SolveZ process takes only a minute to fully delaminate the anode films. As shown in Figure III.3.60, recovered anode films can be directly reprocessed into new anode for new cell production.



Figure III.3.60 Photos showing the direct recycling and remanufacturing of anode scraps using the newly invented SolveZ process.

Solvent-based Dual Process for Material Recovery

Both delamination of cathode materials from aluminum foil and subsequent direct regeneration of active cathode materials are of great importance, as cathode represents one of the most valuable components in a lithium-ion cell. It is desirable to develop a process with dual functionality that can separate and simultaneously restore lithium in the same solvent system. This means that the targeted solution should act as a delamination as well as a relithiation medium. The objective of this project is to accomplish both separation and regeneration of cathode materials through a solvent-based dual process. This approach eliminates complicated processes, making recycling scalable and more profitable. Furthermore, the process is completed in a green solvent at a relatively low temperature and ambient pressure, which will both reduce energy consumption and alleviate environmental impact. In FY21, this project identified the optimal solvent and lithium precursors for the cathode delamination/relithiation. It also determined process conditions to separate and regenerate cathode materials with desirable electrochemical performance.

We previously demonstrated that chemically delithiated NMC111 can be directly regenerated through a solvent-based relithiation process using lithium hydroxide as the lithium precursor. Various characterizations like XRD, ICP-OES, and electrochemical evaluation in both half and full cells confirmed the successful relithiation. We also demonstrated initially the solvent-based dual process for the separation of delithiated NMC111 coating from Al foil and its direct relithiation in the same solvent system. In addition to the relithiation of chemically delithiated NMC111, we shifted our focus in this quarter on the direct regeneration of spent cathode from end-of-life commercial lithium-ion cells. Spent NMC cathode powder was obtained through the SolveY process. Compositional analysis using ICP-OES confirmed the lithium ratio in the spent cathode powder to be ~0.82, suggesting a lithium loss of ~20% in the spent cathode.

Spent cathode powder was treated via the solvent-based relithiation process using LiOH as the lithium precursor. Specifically, spent cathode material of NMC was dispersed in the solvent with the addition of LiOH, followed by heating at 120°C under ambient pressure for 2 h. After filtration, washing, and drying, the obtained powder (ReLi) was then calcined at 600°C in air for 2 h to produce a thermally relithiated NMC sample (ReLi_600). The crystal structure for the NMC cathode materials before and after relithiation was

characterized by XRD (Figure III.3.61). As shown in Figure III.3.61a, no impurity phases were detected after relithiation, and all the diffraction peaks can be indexed to the layered rhombohedral structure of α -NaFeO₂. The relithiation is also proved by the (003) diffraction peak shift that represents the changes in the interslab distance of a layered structure (Figure III.3.61b). In addition, relithiated NMC showed a reduced peak splitting between (108) and (110) from 0.89 to 0.51 degree. The Li/TM ratio obtained from the ICP analysis showed an increase from 0.82 to 1.02 after the solvent-based relithiation process, suggesting the successful restoring of Li.

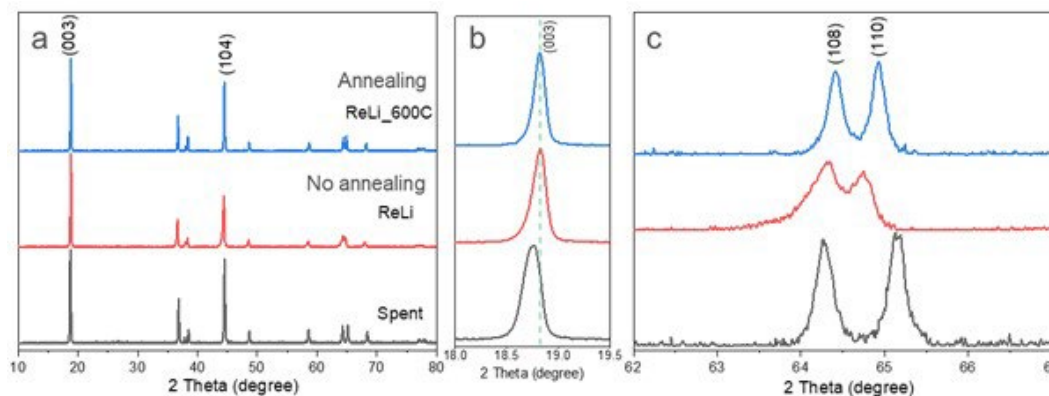


Figure III.3.61 XRD patterns for the spent cathode powder, regenerated NMC cathode before and after annealing.

The electrochemical performance of the thermally relithiated NMC (ReLi_600) was evaluated in half coin cells, as plotted in Figure III.3.62. The high first charge capacity (~ 200 mAh/g) confirms the successful restoring of lithium. As shown in Figure III.3.62b, the reversible discharge capacity is ~ 178 mAh/g at C/10 rates. Figure III.3.62c showed the cycle performance of regenerated NMC at C/3 charge/discharge rates. The regenerated NMC showed a capacity retention of 90.2% after 50 cycles. Future work needs to compare the regenerated NMC with the spent and pristine samples.

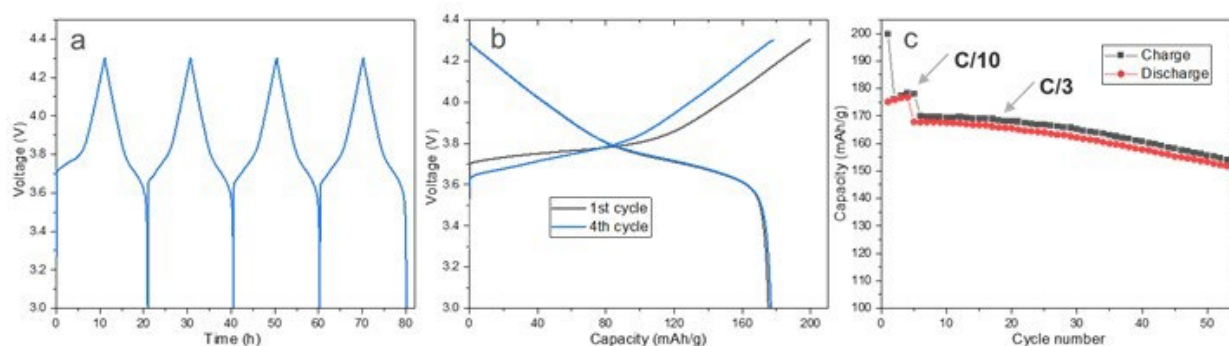


Figure III.3.62 Electrochemical evaluation of regenerated NMC cathode in half coin cell configuration. (a) Voltage profiles for the formation cycles at C/10 rates, (b) charge/discharge curves for the 1st and 4th cycles at C/10 rates, and (c) cycle performance at C/3 charge/discharge rates.

In addition to half-cell test, full cells paired with graphite anode (N/P ratio of ~ 1.1) were fabricated to further evaluate the relithiated NMC cathode. As shown in Figure III.3.63b, the relithiated sample showed a high 1st charge capacity of ~ 188 mAh/g and a reversible capacity of ~ 164 mAh/g at C/10 charge/discharge rates. Stable cycle performance was achieved for relithiated NMC with nearly no degradation after 40 cycles.

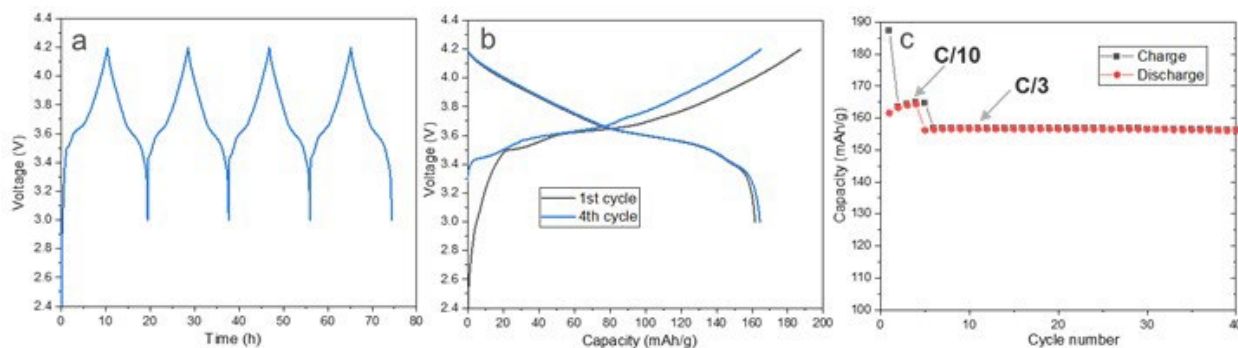


Figure III.3.63 Electrochemical evaluation of regenerated NMC cathode in full cell configuration paired with graphite anode. (a) Voltage profiles for the formation cycles at C/10 rates, (b) charge/discharge curves for the 1st and 4th cycles at C/10 rates, (c) cycle performance at C/3 charge/discharge rates.

Aqueous Sequential Separation of Anode and Cathode Materials

After shredding, a feedstock of anode and cathode on their current collectors is generated. This feedstock contains the most valuable components in a lithium-ion cell, including black mass (e.g., active cathode materials and graphite), Cu foils, and Al foils. To reclaim active cathode materials with high purity for direct regeneration, separation of electrode materials from their current collectors as well as of anodes from cathodes is required. It is extremely important to develop a simple and cost-effective separation process to efficiently recover high-purity cathode materials as well as other materials so that different concentrated feedstocks are provided for further direct recovery and regeneration processes. The objective of this project is to develop an aqueous separation process to sequentially separate anode/cathode and electrode/current collectors to recover cathode films, anode films and metal foils. By simplifying a complex set of separation processes, the aqueous sequential separation method alone could fulfill the goal of reclaiming higher-purity materials and making recycling more profitable. The designed aqueous medium neither damages the active cathode materials nor corrodes the metal foils. In addition, this process enables room-temperature separation in a low-priced water solution, reducing energy consumption and processing costs. In FY21, this project identified the optimal composition of the aqueous solution and determined separation conditions to obtain higher-purity cathode materials.

We previously demonstrated that spent anode coatings can be easily delaminated from copper current collector in a water or buffer-based solution. This process is accompanied by heat and hydrogen gas generation. It is also found that the delamination of spent anode coatings in water is independent of the binder system, meaning that the separation process works for both PVDF and CMC/SBR binder-based spent anodes. Spent anodes from both commercial and house-made pouch cells have been demonstrated to be separable in water. The following study used spent anode from a house-made NMC622/graphite pouch cell that was charge/discharged for 1000 cycles at 1C rates. It is worth mentioning that the anode was based on the PVDF binder.

One of the goals for the aqueous sequential separation process is to separate anode coatings from copper and cathode so that anode/cathode separation can be realized. As the anode coating is delaminated from the copper foil as a whole piece, it is necessary to reduce the size of delaminated anode films so that they can be separated from both copper foil and spent cathode by sieving. As a continuous process, it is preferred that anode films were separated under wet condition. In this regard, we investigated the size reduction process by using a Vortex mixer and probe sonicator. Figure III.3.64a and Figure III.3.64b compare the results of two size reduction methods. It is found that Vortex shaking easily broke the delaminated anode films, while probe sonication was less effective in size reduction. As shown in Figure III.3.64b, there are still many large pieces of anode films that were not broken down. Therefore, Vortex shaking is more efficient in size reduction.

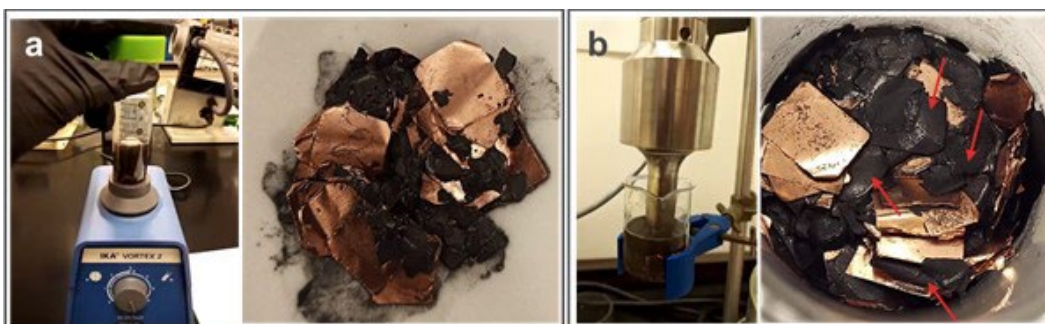


Figure III.3.64 Photos showing the size reduction of anode films using (a) Vortex mixer and (b) probe sonicator.

In addition to size reduction of anode films, we also investigated the possibility of re-processing the separated anode films into new anode for new cell manufacturing. After delamination in buffer solution, anode films were washed with water and dried. As the anode was based on PVDF binder, NMP was added to the dry anode films to form a slurry. However, it is hard to dissolve the PVDF binder from the spent anode films to form a good slurry, as shown in Figure III.3.65. It may be due to changes in MW or a loss of consistency in particle size of the recovered product. Therefore, it is necessary to remove the binder to directly regenerate the graphite anode so that the recovered graphite can be introduced into a new loop of cell manufacturing.

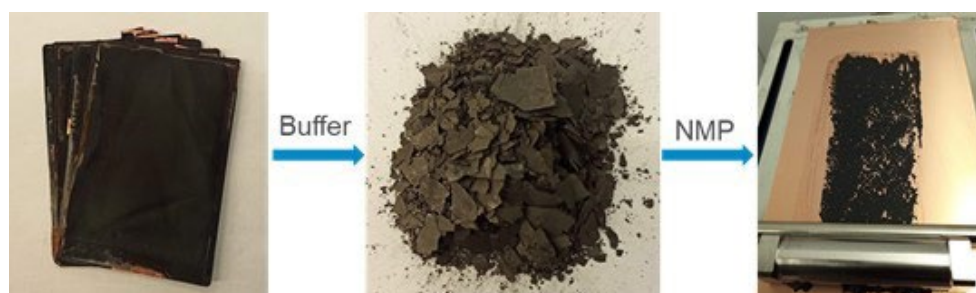


Figure III.3.65 Diagram with photos showing the separation of spent anode and re-processing into new anode.

It was previously found that the delamination of cathode required the addition of additive Z in a buffer solution. We found several useful additives that show similar performance as additive Z in the separation of cathode films from aluminum foils. In addition, we also investigated the separation mechanism for the delamination of cathode with additive Z. Contact angles on both cathode and aluminum foil were measured for both buffer solution and buffer solution with additive Z. As shown in Figure III.3.66, contact angles are greatly reduced after adding additive Z, suggesting that buffer solution with additive Z can greatly enhance the wetting behavior on both cathode and aluminum foils. Good wetting can introduce more solution in between cathode coating and aluminum foil, facilitating the delamination.

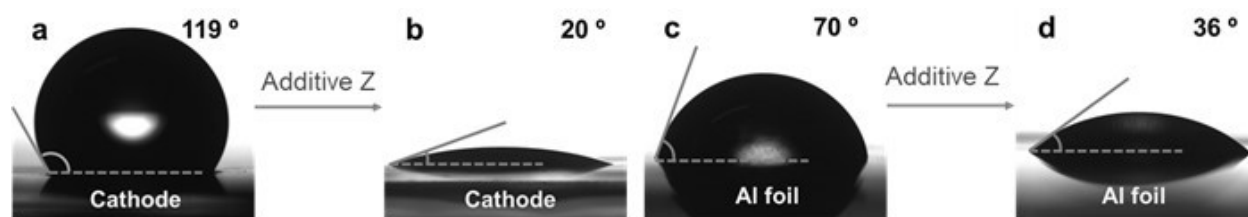


Figure III.3.66 Contact angle measurement. Buffer solution on (a) cathode and (c) aluminum foil, and buffer solution with additive Z on (b) cathode and (d) aluminum foil.

Anode/Cathode Separation and Purification

After size reduction (cell shredding), electrolyte recovery, and component separation (i.e., plastics, cell casing, ferrous metals) we are left with electrode fragments that include anode on copper foil and cathode on aluminum foil. Separation of the anode and cathode is a critical step in the direct recycling process to purify black mass. Efficiently production of multiple clean streams of material (cathode, anode, and Al/Cu foil) would make direct recycling more profitable. The separation of anode, cathode, and metals can be achieved in 2 different ways (Figure III.3.67). First, delamination and binder removal (i.e., via thermal binder removal or a solvent-based delamination and binder removal process) can be performed on the anode/cathode mixture to yield one product stream consisting of mixed Al/Cu foils sieved and another comprised of combined anode/cathode powders. The mixed anode/cathode powders and metals would each have to undergo additional separation processes. The second method would produce more clean streams of product by first separating the anode and cathode laminates (still attached to foils) prior to delamination and binder removal. The products would be one that contains cathode powder on Al foil and another containing anode on Cu foil. Binder removal would be performed on the two batches to produce separate streams of Al foil, Cu foil, anode powder, and cathode powder. The presence of four separate product streams after a simple anode/cathode separation would reduce black mass complexity and significantly streamline subsequent steps in the direct recycling process.

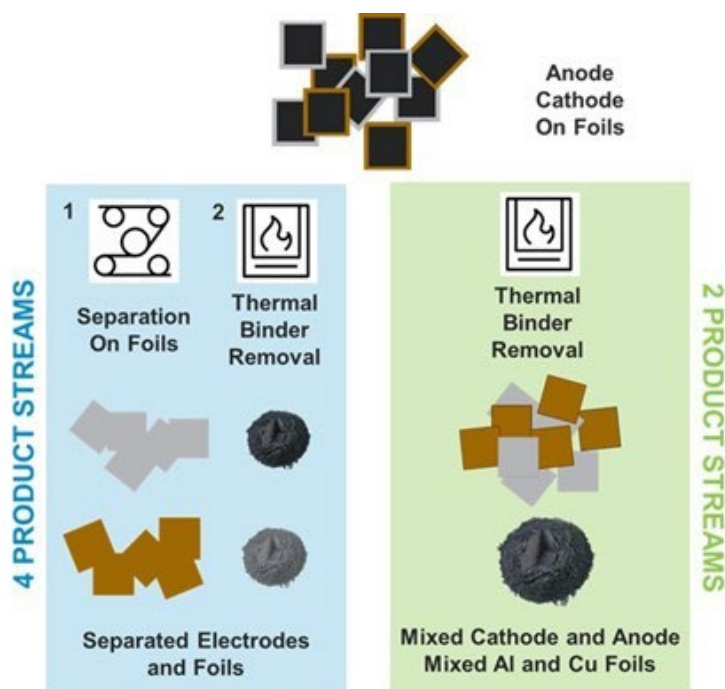


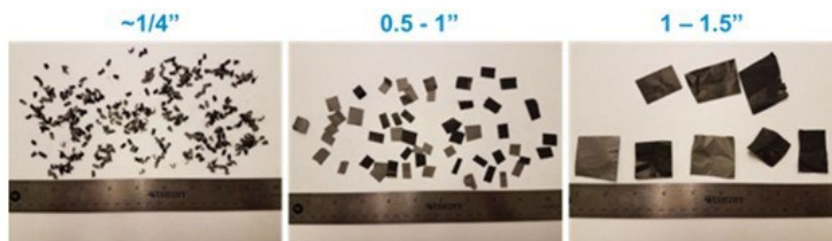
Figure III.3.67 Methods of separating anode, cathode, and metal foils

Last year, dry fluidized magnetic separation of powders with PVDF binder, density-based flotation experiments of laminates in a variety of solvents, froth flotation, and magnetic separation of aqueous slurries were performed using anode/cathode mixtures. In FY21, dry separation techniques will be explored, such as magnetic, eddy current, and forced-air separation, to separate anode and cathode laminates. The most effective anode/cathode separation technique will be chosen and combined with processes for recovering other materials to determine which processes can be best integrated into a battery recycling process chain.

Separation of Manufacturing Scrap and Shredded Pouch Cell Material Using Process A

A separation technique, which will be referred to as “Process A”, has been used to separate manufacturing scrap (various sizes including 1/4”, 0.5–1”, and 1–1.5”) and shredded pouch cell material. Manufacturing scrap was cut into various size pieces by hand and a batch of dry pouch cells was shredded by an industry partner

using a dual-shaft shredder, as shown in Figure III.3.68. The Process A experiments were conducted by another industrial partner. The purpose of Process A is to separate cathode electrodes from anode electrodes. Separation results from Process A have been shown in the previous *ReCell FY21 Q2 report* and *ReCell FY21 Q3 report for Anode/Cathode Separation and Purification*.



Various Sized Electrodes



Shredded Pouch Cell Material

Figure III.3.68 Manufacturing scrap (top) and shredded pouch cell material (bottom)

To separate manufacturing scrap and shredded material using Process A, the materials underwent two separation steps. An example process flow for shredded pouch cell material is shown in Figure III.3.69. After the first separation step, two fractions are produced. One fraction is rich in cathode/Al foil while the second fraction is rich in anode/Cu foil. In a second separation step, Fractions 1 and 2 are further purified using Process A to produce Fractions 1.1, 1.2, 2.1, and 2.2. Fractions ending in .1 have higher purities of cathode/Al foil while .2 fractions contain higher concentrations of anode/Cu foil.

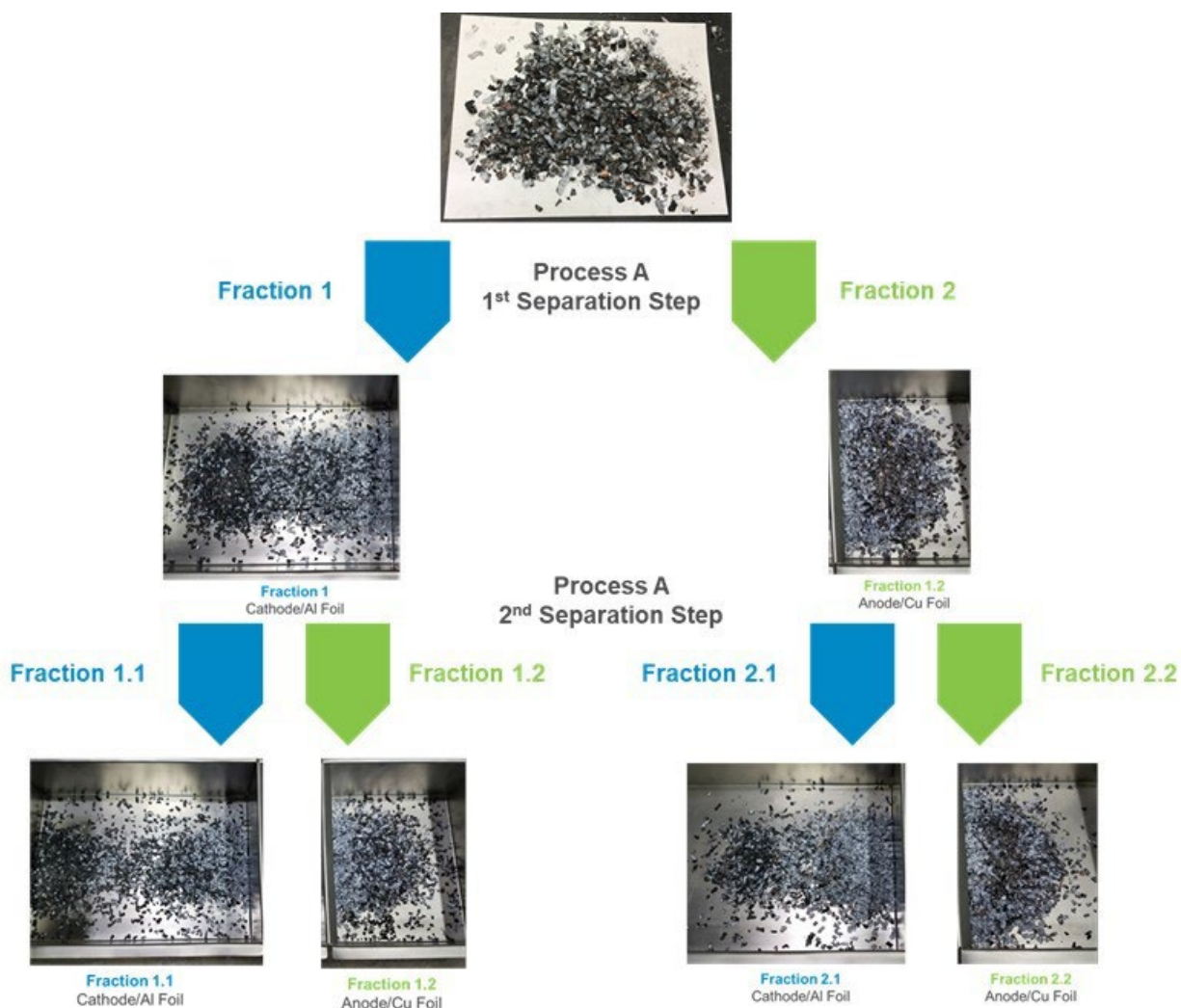


Figure III.3.69 Process A separation of shredded pouch cell material using a two-step separation procedure

After the Process A separation process, both the weight percent and purities of material in various fractions were analyzed. The mass distribution of fractions is shown in Figure III.3.70. As described in a previous report, the 1–1.5” material only underwent one separation step due to the electrode pieces being too large for the lab-scale equipment used. The equipment will need to be sized appropriately to the electrode pieces to achieve efficient separation. The weight percent of fractions collected after the first separation step is typically around 40–55% and demonstrates that one fraction is rich in cathode/Al foil while the other fraction contains concentrated anode/Cu foil. The second separation step was used to further purify the electrodes collected from the first step. The weight percents for a simple 1:1 mixture of electrodes by weight show that little material (< 5%) is removed after the second step, suggesting that the material from the first step is fairly pure to begin with. However, the more complex mixture of components in the shredded pouch cell material decreases separation efficiency. There is still a significant quantity of material, approximately 25-35%, removed from various fractions after the second separation step. To determine the purity of electrodes collected in each fraction, materials (0.5–1”, 1–1.5”, and shreds) were hand sorted. The quarter inch pieces were very small and not selected for hand sorting. Purities from Fractions 1 and 2 could not be determined because the samples (0.5–1” and shreds) were further separated into Fraction x.1 and x.2 by our industrial partner.

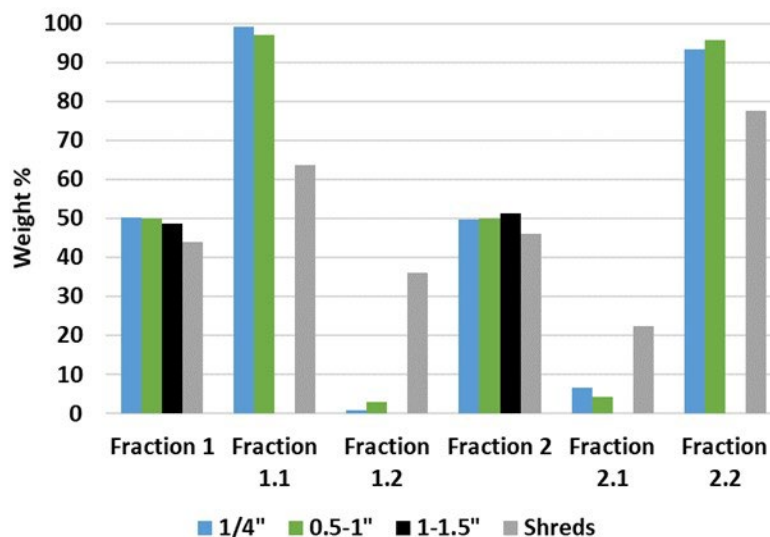


Figure III.3.70 Weight percent of samples after the first (Fraction 1 and 2) and second (Fractions 1.1, 1.2, 2.1, and 2.2) Process A separation steps

The purity of electrodes collected from Process A separation is shown in Table III.3.21. As mentioned previously, the 1–1.5” pieces were oversized for the lab-scale equipment and showed poor separation efficiency. The poor separation can be further seen after purity analysis, where only about 82–83% purity of electrodes was achieved. The 0.5–1” pieces showed much higher separation efficiency using Process A. Cathode and anode purities of 99.5% and 99.8%, respectively, were achieved after separation. Considering this was only two passes of manufacturing scrap through Process A, it is encouraging to see that such high purities can be achieved. Shredded material, which is similar in size to the 0.5–1” scrap, showed lower purities in both the cathode rich (90.2%) and anode rich (89.5%) fractions. The results suggest that the process for shredded material can be further optimized to improve electrode purity. Two ways to do this could include removing additional components (e.g., separator and pouch cell material) prior to Process A separation or subjecting shredded material to more passes through Process A.

Table III.3.21 Purity of electrodes collected in cathode or anode rich fractions from various samples

Sample	Purity of Cathode Electrode in Cathode/Al Rich Fraction	Purity of Anode Electrode in Anode/Cu Foil Rich Fraction
0.5-1"	99.5% (Fraction 1.1)	99.8% (Fraction 2.2)
1-1.5"	83.7% (Fraction 1)	82.3% (Fraction 2)
Shreds	90.2% (Fraction 1.1)	89.5% (Fraction 2.2)

Future Work

Argonne has received lab-scale equipment to conduct Process A separation. This equipment is currently being safety approved and will be used to further improve the separation of shredded pouch cell material. In FY22, efforts will also be made to separate end-of-life materials using Process A.

Black Mass Purification

Obtaining high-purity material outputs from recycling is crucial to the viability of the process and to industry acceptance of recycled products. Within ReCell, electrochemical and thermal studies conducted on “contaminated” cathode material (i.e., cathode material containing small fractions of other metals) have suggested that certain contaminants may inhibit cell performance. In particular, trace levels of Al and Cu from the electrode current collectors are anticipated following mechanical shredding, and there is no process in place to address removal of these contaminants. Thus, purification of shredded black mass (BM) to eliminate undesired metals is a critical issue to investigate in the context of direct recycling.

Dissolution of Al and Cu contaminants from solid to ionic form can enable effective purification of NMC via physical filtration, while not incurring damage to the NMC itself. Further, the Al and Cu may be separately recaptured in purified form, adding revenue to the value stream of the recycling process. Thus, this fiscal year, we began development of a process combining these two approaches. Specifically, we are optimizing an aqueous dissolution process to ionize solid Al and Cu, which will operate in conjunction with a reversible and tunable adsorbent filter to recover these ionized metals from solution. This will allow for effective removal of trace-level contaminants from the BM and will improve the circularity of the direct recycling process through enhanced component recovery. Work on this project will be broken into two primary sub-tasks:

1. Developing optimized methods for Al and Cu corrosion, where suitability of conditions is contingent on both effectively ionizing the target metals and avoiding damage to NMC;
2. Synthesizing a functionalized adsorbent material to bind ionized Al and Cu and selectively recover these metals with high purity.

Work this quarter has emphasized the application of the optimized Al⁰ and Cu⁰ corrosion protocols established in Q1-Q3 to practically relevant contaminated NMC. Specifically, the black mass purification process has been evaluated on both simulated black mass (pristine NMC spiked with known concentrations of Al⁰ and Cu⁰ contaminants) and black mass obtained from an industrial partner. Efficacy of treatment has been measured via structural and electrochemical analysis, and additional chemical analysis is underway.

Treatment of Al⁰-Contaminated NMC

Simulated black mass was prepared by spiking pristine NMC-111 with practically relevant concentrations of Al⁰ contaminant (0.1 wt%, 1 wt%, and 5 wt%). As shown in Figure III.3.71(a), the presence of Al⁰ contaminant significantly reduced cell capacity, primarily through kinetic losses. The observed reduction in initial charge resistance for 1 and 5 wt% Al⁰ suggests that Al⁰ may function as a conductive dopant; this is consistent with previous findings. However, the overall impact of Al⁰ contamination is detrimental to cell performance.

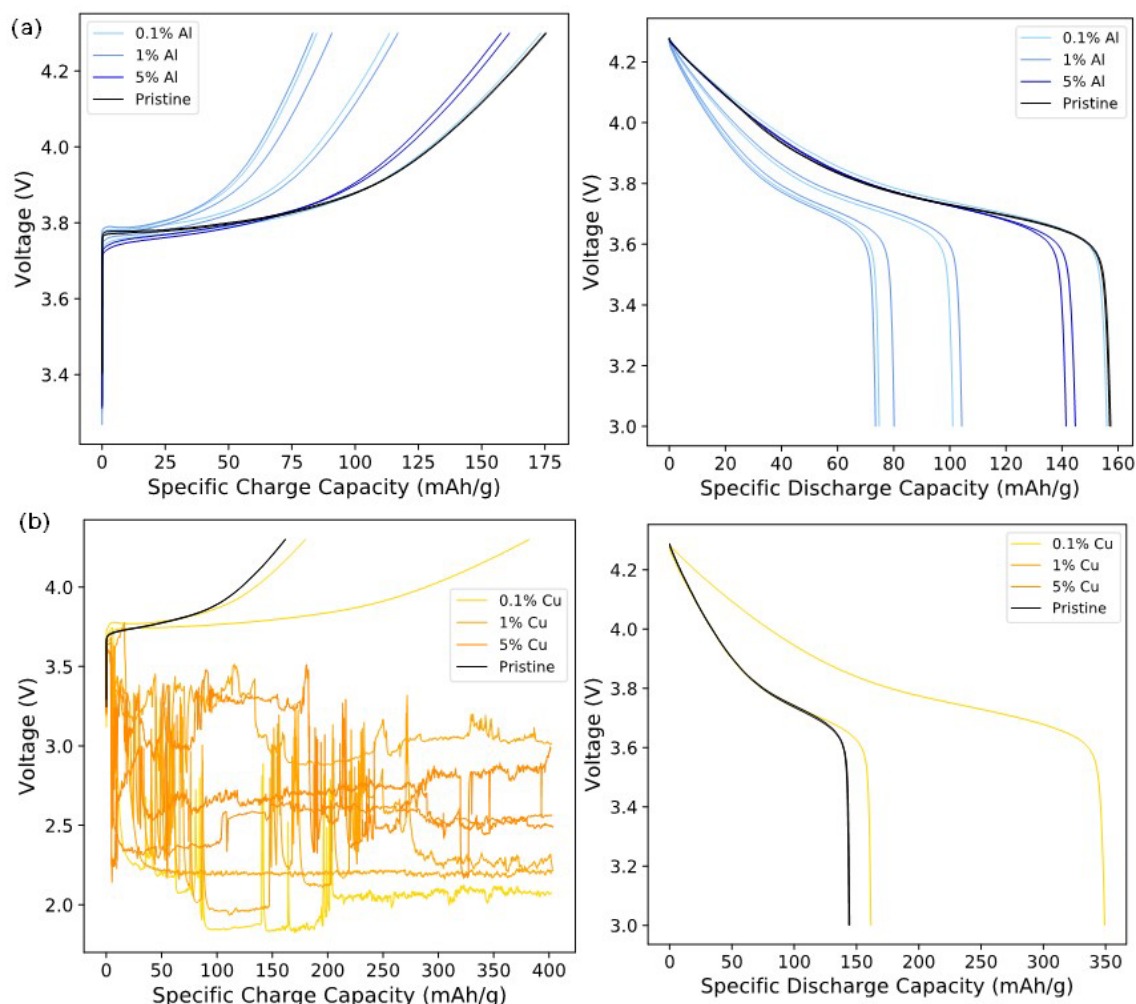


Figure III.3.71 Electrochemical impacts of Al^0 ((a), top row) and Cu^0 ((b), bottom row) contaminants on NMC-111. First-cycle charge and discharge cycles are shown for samples with 0.1 wt%, 1 wt%, and 5 wt% of each contaminant. Note that samples containing 1 wt% and 5 wt% Cu immediately shorted and showed no discharge capacity. Additional lines (with the same color/linestyle) correspond to coin cell replicates. There is significant variability between replicates for the untreated contaminated cells—probably to do with uneven dispersion of the Al and Cu metal powders in the slurry.

To evaluate the efficacy of treatment, a sample of simulated BM containing 1 wt% Al^0 contaminant was processed under optimized corrosion conditions (pH 13; 60°C; overhead stirring + sonication; 2.5 hr. exposure). Following purification, samples were either filtered and immediately dried (“No Extra Rinse” condition) or subject to a supplemental wash with deionized (DI) water to remove any residual salt (“Extra Rinse” condition) prior to drying.

Structural analysis (powder X-ray diffraction; PXRD) was performed to evaluate the impacts of both the contaminant spike and subsequent treatment on the structure of the simulated BM. At a 1 wt% contamination level, the phase associated with metallic Al is not well-resolved (Figure III.3.72(a)). This is anticipated, as the detection limit for PXRD is typically a few percent crystallinity. Importantly, however, PXRD and associated Rietveld refinement suggest no impact of the treatment conditions on cation mixing or lattice parameters. suggests no bulk Li loss, even when the material is briefly processed in neutral deionized water.

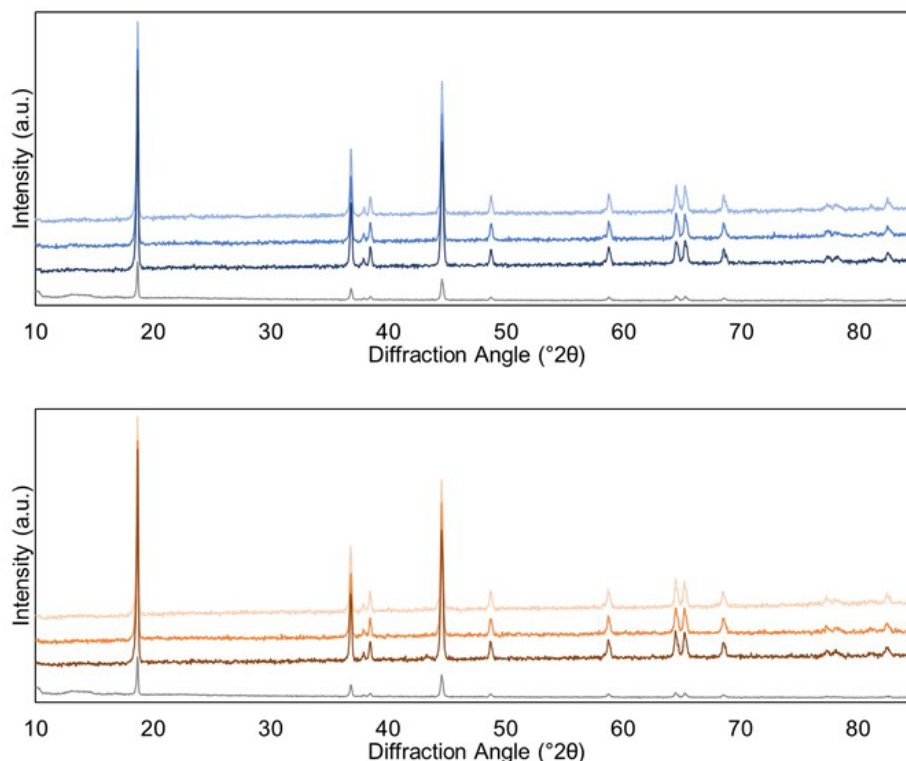


Figure III.3.72 Diffraction patterns of pristine and treated simulated BM samples: (a) NMC-111 spiked with 1% Al⁰; (b) NMC-111 spiked with 1% Cu⁰. For both (a) and (b), sample designations from top to bottom of the overlaid trace are as follows: Treated, No Extra Wash; Treated, Extra Wash; Untreated; Pristine (i.e., no contaminant).

This suggests no bulk Li loss, even when the material is briefly processed in neutral deionized water. There is some evidence of a spinel-phase transformation in the treated material, as compared to the material with 1% Al⁰ spike, but this may be the result of improper indexing of the Al⁰ impurity phase. Note that the difference in intensity between pristine material and simulated BM signals is the result of a detector change between samples; the pristine sample will be reanalyzed using the new detector for consistency.

Further, the optimized purification process is found to successfully restore the electrochemical performance of Al⁰-contaminated NMC in half-cell testing (Figure III.3.73(a); Figure III.3.74). Slightly higher impedance is observed at the beginning of the first charge cycle for treated material (Figure III.3.73(a)), which may be the result of remaining residual salt. However, this impedance is comparable with the pristine material by the second charge cycle and does not appear to significantly impact subsequent cycling. As shown in Figure III.3.74, the purified simulated BM with Al⁰ contamination has comparable half-cell performance to pristine NMC-111, with capacity of the simulated BM restored to pristine levels during formation cycles and initial C/10 cycling after treatment. This suggests successful nondestructive purification, whereby the undesired contamination has been removed without adversely impacting the performance of the NMC. Validation of performance in full cells is underway.

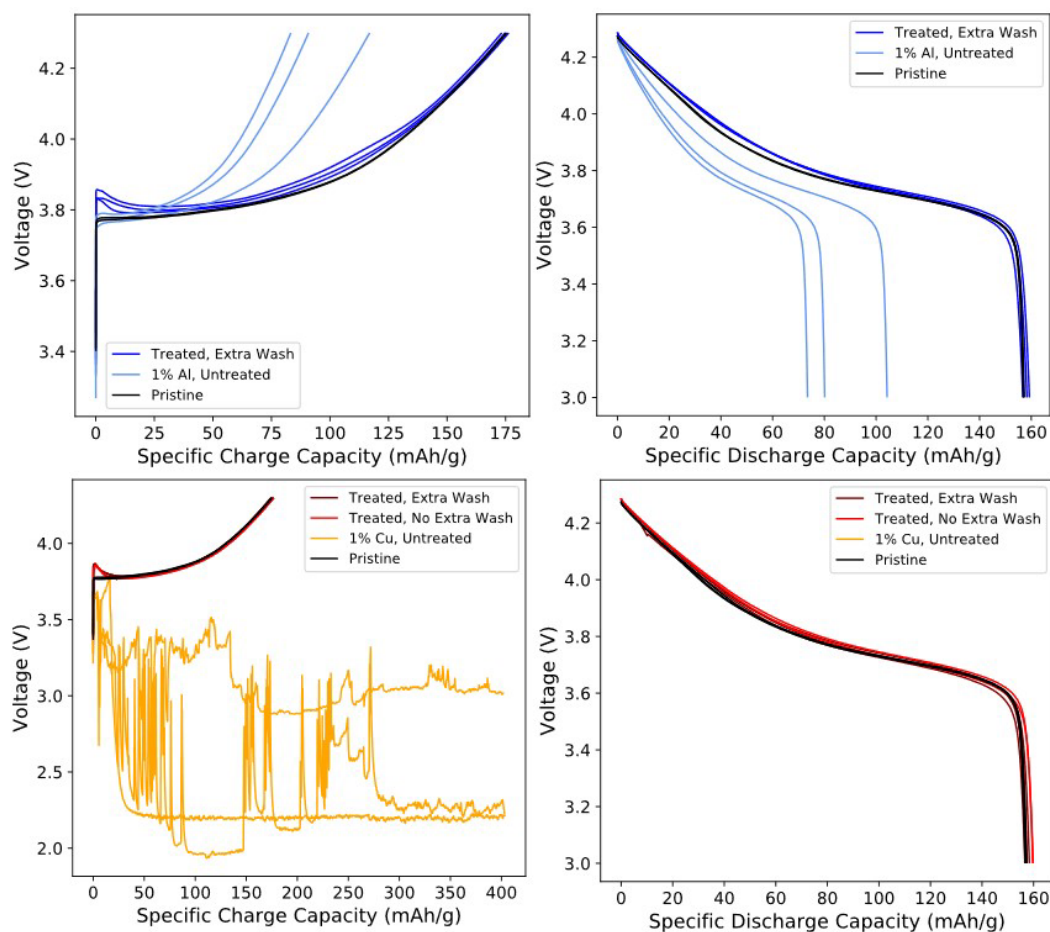


Figure III.3.73 First-cycle charge and discharge cycles for treated samples of simulated BM containing (a), top: 1 wt% Al; (b), bottom: 1 wt% Cu. The impact of an additional rinse with DI water is assessed for simulated BM containing Cu^0 contaminant (corresponding data for material prepared without a supplemental rinse for simulated BM containing Al^0 contaminant is pending).

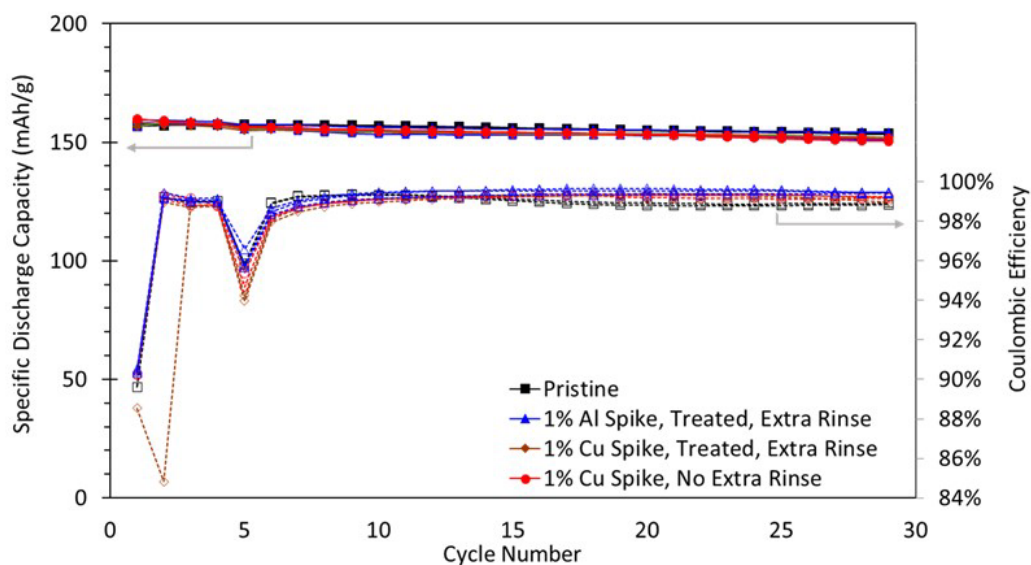


Figure III.3.74 C/10 cycling performance of pristine NMC-111 vs treated simulated BM with 1 wt% Al^0 (blue traces) or 1 wt% Cu^0 (red traces). The impact of a supplemental DI water rinse is evaluated for simulated BM containing Cu^0 .

Treatment of Cu⁰-Contaminated NMC

In an analogous manner, separate samples of simulated BM were prepared by spiking pristine NMC-111 with 0.1 wt%, 1 wt%, and 5 wt% Cu⁰. The impact of the Cu⁰ impurity on electrochemical performance is even more significant than for the Al⁰ contaminant: Specifically, at a practically relevant contamination level of 1 wt% Cu⁰, the cell immediately shorts (Figure III.3.71(b)). This highlights the importance of a purification process that can effectively remove Cu⁰ contamination, as even trace levels of Cu⁰ impurity in recycled material will be detrimental to viability.

For the simulated BM containing Cu⁰, optimized processing conditions were similar to that earlier described (pH 13; 60°C; overhead stirring + sonication; 2.5 hr. exposure); however, the system also contained 2x molar chelating agent (DTPA). These samples were also either filtered and immediately dried (“No Extra Rinse”) or subject to a supplemental wash with deionized water (“Extra Rinse”) prior to drying.

PXRD analysis of the treated simulated BM containing Cu⁰ also revealed no significant impact of treatment on the bulk structural properties of NMC (Figure III.3.72(b)). This implies that the addition of DTPA to the system did not induce bulk Li leaching from the NMC or otherwise disrupt the NMC structure. As previously described, the apparent increase in spinel phase for the treated material, as compared to the Cu⁰-spiked material, may be an artifact of improper indexing of the Cu impurity phase.

Figure III.3.73(b) demonstrates that the pristine capacity is also restored for Cu⁰-contaminated NMC following treatment, and that the supplemental rinse in DI water does not significantly impact the cell’s voltage response (i.e., no indication of structural rearrangement associated with Li loss). An increase in first-cycle initial impedance is again observed, which resolves by the second charge cycle. Stable cycling performance is observed for the treated Cu⁰-containing simulated BM, with capacity comparable to pristine material (Figure III.3.74).

Taken together, the above results demonstrate the successful purification of a standardized BM (i.e., NMC with known concentrations of Al⁰ and Cu⁰ contaminants). This represents completion of a crucial milestone in the present work.

Purification of Practical BM

A sample of industrial black mass was obtained from ANL for preliminary evaluation of the BM purification process on a representative feedstock. This product had unknown composition and unknown impurity content but was believed to primarily contain manufacturing scrap. Additionally, this sample had previously been subjected to both froth flotation and binder burnout. PXRD analysis suggested that this material contained a mixture of several stoichiometries of NMC (refinement suggested a blend of low-nickel and high-nickel materials) and perhaps an additional transition-metal phase, which was not fully indexed. Treatment did not appear to significantly impact the material’s structure, although imperfect refinement made direct evaluation of lattice parameters challenging.

The practical BM was subjected to the treatment conditions optimized for Cu⁰ corrosion (i.e., included the use of DTPA), and was evaluated in half cells. As shown in Figure III.3.75, treatment was not sufficient to restore the capacity of pristine NMC-111—and in fact, treatment appeared to have a negative impact on this material’s performance. Given the extremely high initial impedance observed for the treated material, we anticipate that the poor performance is associated with a side reaction between the treatment matrix and a surface impurity (possibly from the froth flotation process) or changes to the NMC surface chemistry occurring during the binder burnout. This finding highlights the need to evaluate direct recycling processes in the context of the whole direct recycling line, i.e., assessing the impacts of upstream processes on subsequent downstream processes. Further evaluation of practical BM materials will be ongoing in FY22.

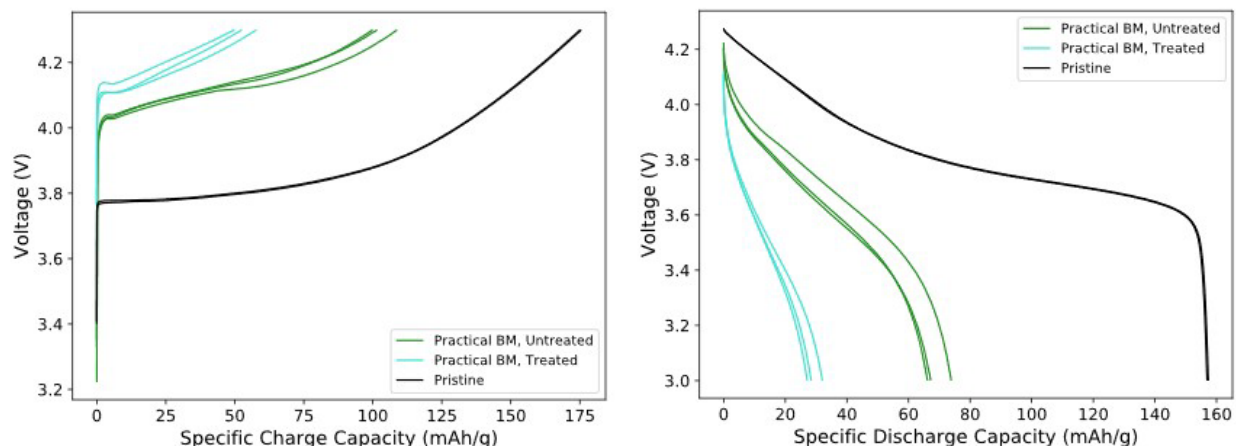


Figure III.3.75 First-cycle electrochemical performance of practical black mass, with or without purification treatment, as compared to pristine NMC-111.

Electrolyte Component Removal and Recovery

Electrolyte must be removed during the recycling process to allow for further processing of the remaining components. This can be done in several ways, including supercritical CO₂ extraction, thermal drying, water washing, and solvent extraction. Of these, only supercritical CO₂ with added co-solvent or solvent extraction can recover the LiPF₆, which is the most valuable component of the electrolyte. We have demonstrated that the electrolyte can be extracted by diethyl carbonate and then reconstituted, with cycling performance exceeding that of 1.2 M LiPF₆ in 3:7 EC:EMC electrolyte. This process was demonstrated at 0.5 L scale, and the washed anode materials are being utilized for the graphite-to-graphene project. We have also attempted several different methods for purification of the concentrated extract, but more work is needed to find an optimal process. We also plan to scale the process to supply cleaned cycled materials to downstream processes.

During this quarter, we worked on plans to scale up as larger quantities of shredded material becomes available. We currently have available and approved for use the equipment shown in Figure III.3.76. This includes various sizes of tank reactors with mixers from 4 L to 100 L. Some of these reactors have integrated filtration capability, allowing us to remove the solvents from the solids while they are still in the reactor. Other mechanisms can also be used to filter the material depending on how it behaves. Once the rinse liquid is separated from the material, this liquid will be transferred to a rotary evaporator. This will allow for the material to be heated while the pressure is reduced to facilitate concentration of the electrolyte. The concentrated electrolyte can then be transferred to a glovebox or dry room for reconstitution and reuse in cells. As might be clear from the pictures and description, this equipment is not currently in a dry room. As part of the scale-up process we intend to determine how this brief air exposure effects the electrolyte and see if it results in significant HF generation. As a first step towards this scale-up process, we analyzed the electrolyte from a variety of manufacturers, including the one shown in Figure III.3.77, which is likely to be utilized for the initial scale up. As is typical for recovered electrolytes, the NMR shows the materials we added to do the analysis (diethyl carbonate (DEC), trifluoroethanol (TFE), and acetonitrile (ACN)), along with LiPF₆ and ethylene carbonate (EC). There is also a very small quantity of other volatile carbonates (dimethyl carbonate (DMC)) and a likely decomposition product of EC. The composition of this electrolyte is similar to those we successfully reused previously, and so it is likely to be recyclable as well.



Figure III.3.76 Equipment that can be used to scale up the rinsing and concentration processes to recover spent electrolyte.

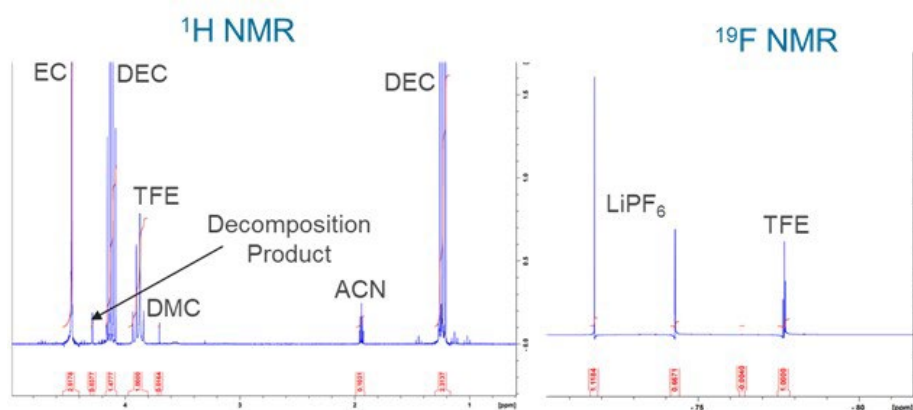


Figure III.3.77 ^1H and ^{19}F NMR spectra for a commercial battery that is likely to be utilized for scale up.

We are also beginning to consider whether these processes can be combined with other cell preprocessing steps. Can separations be performed simultaneously with the rinsing process? Removal of the fines from shredding may be an obvious target that we can explore. Furthermore, we are identifying the equipment that can be used to run this process industrially. This includes the washing equipment, concentration equipment with solvent recovery, filtration, and drying of the shred. Each component has multiple possible options for how the material is treated.

Cycled Graphite to Graphene

Maximizing the revenue that can be generated from all the components of the battery can greatly improve the profitability of Li-ion battery recycling. Currently, it is a challenge to recycle the graphite anode because the product has relatively low value. It has been previously published that cycled anode graphite can be more easily exfoliated into graphene than other graphite sources. If this process can be scaled, the graphene produced would have a much higher selling price than graphite, resulting in substantial revenue gains. The challenge in scaling this process has two parts. The first is finding a method to simply create graphite feedstocks for this process. The second is finding the best exfoliation method, additives, and conditioning steps to improve yield and throughput. We will test traditional and innovative processes to determine the optimal conditions and then determine the cost metrics for these processes using the EverBatt model.

This quarter we focused on understanding the quality of the graphene produced via long-term shear mixing of spent anode material. This material was double acid treated and had an additive included to improve

exfoliation. The Raman spectrum of this material is shown in Figure III.3.78a. This spectrum is similar to that from graphene produced via solution exfoliation methods. It is indicative of relatively small flakes with a variety of thicknesses, from single layer to many layers. Contamination by various metals is also important to users of these materials. The most likely contaminants will come from shredding the materials: Al and Cu flakes in addition to cathode material. The double acid treatment will significantly reduce the quantity of these materials, as confirmed by inductively coupled plasma optical emission spectroscopy (ICP-OES). These results, shown in Figure III.3.78b, indicate that the graphene purity is about 99.7% with these metals being the only impurities considered. Copper is the largest constituent, as these were hand processed electrodes and only the copper foil was cut. Copper is also more resistant to corrosion by sulfuric acid than the other metals.

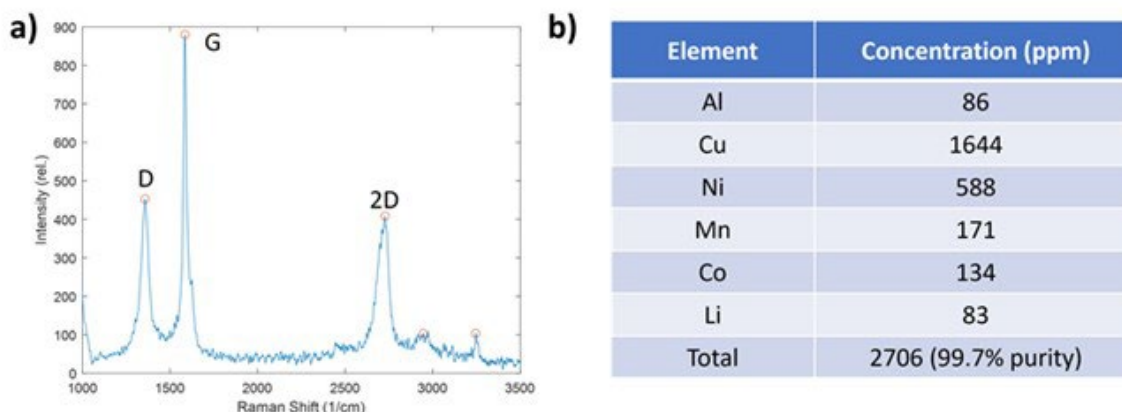


Figure III.3.78 a) Raman spectroscopy using a 514 nm laser of the 48% yield graphene sample. b) ICP-OES data on the impurities in the 48% yield graphene sample.

To gain a better idea of the morphology of this material, a combination of scanning electron microscopy (SEM) and atom force microscopy (AFM) was used. The SEM shown in Figure III.3.79 shows the graphene flakes on an Au/Pd coated silicon substrate. The single layer graphene can be seen to blur the texture of the Au/Pd film. This graphene was passivated with hydrogen, diluted, and ultrasonicated in the attempt to disperse it better. However, some agglomeration is still seen. Despite some agglomeration, evidence of what appears to be single-layer graphene is present, with a mixture of bilayer and multilayered graphene as well. The flakes are in the range of 100 nm to about 500 nm in size.

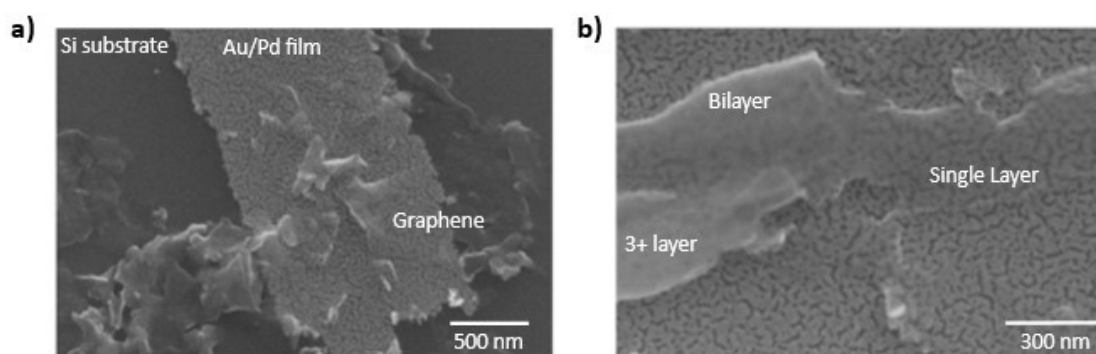


Figure III.3.79 SEM images of H₂ passivated, ultrasonicated and diluted 48% yield graphene sample on an Au/Pd coated silicon substrate.

The AFM images and height profiles of this sample are shown in Figure III.3.80. There are some larger flakes present that are clearly multilayer graphene. In addition, smaller flakes that have an oblong structure with aspect ratios close to 3:1 are present. These flakes have a height of about 1 nm, which is indicative of single layer graphene or bilayer at most.

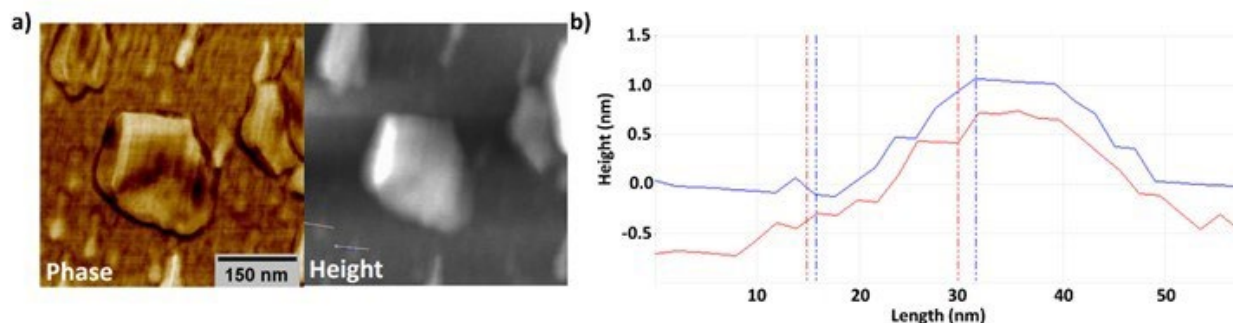


Figure III.3.80 AFM a) phase, height images, and b) height profiles for the 48% yield graphite sample.

Cell Design

Current lithium-ion batteries are manufactured without much consideration of recycling. Developing a new cell design that allows for cell maintenance could be of great interest, as it can extend cycle life. As a result, the number of batteries to be recycled can be significantly reduced, which alleviates the demand on battery materials and pressure on battery recyclers. In FY19 and FY20 we developed new cell configurations with external ports on both cylindrical and pouch cells at Argonne and Oak Ridge National Laboratories. We also used the battery techno-economic model BatPaC to estimate the energy densities in the new designs. Depending on the cell and pack design, there would be 1-13% reduction in energy density in the new designs to accommodate the ports and tubing. We explored numerous solvents and protocols to flush the spent cells and demonstrated capacity recovery in some appropriate protocols. Adverse effects were observed when flushing the cells outside of a confined fixture. In addition, we investigated dynamic process mechanisms that contribute to solid electrolyte interphase buildup and lithium dendrite formation in three-electrode pouch cells. In FY21, we continued exploring the rinsing protocol and Li restoration to spent cathodes to realize extended cycle life.

The project ended in the Q4 period. This report summarizes the main activities in this project.

Demonstrating benefits in rinsed spent electrodes in coin cells

Pouch cells were assembled consisting of $\text{LiNi}_{0.6}\text{Mn}_{0.2}\text{Co}_{0.2}\text{O}_2$ (NMC622) and superior 1520T graphite electrodes and cycled at C/3 to generate spent electrodes (~20% capacity fade). The pouch cells were disassembled inside a glovebox filled with Ar gas. The spent electrodes were rinsed with dimethyl carbonate (DMC), isopropanol (IPA), or ethanol (EtOH) before being reassembled into full cells and cycled with same protocol. Higher capacity was observed from the cells with rinsed electrodes, showing the benefit of rejuvenation. However, the capacity degradation was much faster, and the recovered capacity only lasted for a short term. It was unclear whether the fast capacity fade was due to the rinsing process or the cell disassembly and reassembly process. Thus, rejuvenation in pouch cells was planned and performed subsequently.

Designing pouch cells with ports to facilitate rejuvenation

To enable rejuvenation in pouch cells, multiple designs were evaluated to integrate ports that allowed rinsing spent cells and injecting fresh electrolyte. Challenges occurred in choosing the tubing with appropriate diameter and sealing the tubes to the pouch cells without leakage. Solvent was flushed through the ports and cell pressure recorded as a function of feeding rate. Simulation was performed to evaluate the pressure and flow velocity distribution within a pouch cell, and the distribution was not uniform. Electrolyte showed a higher velocity through the graphite anode, followed by the cathode. The electrolyte velocity in the separator was much slower, especially in the in-plane direction. Experimentally, electrolyte could flow through the gap between the pouch and electrodes under pressure.

Demonstrating benefits in rinsed spent electrodes in pouch cells

Three-electrode pouch cells were first assembly to understand electrochemical potential changes before and after electrode rinsing without disassembling the cells. To avoid any potential sealing issues with ports, the

pouch cells were cycled without the ports and opened to rinse the electrodes. Similar results as those in coin cells were observed. Capacity increased after rejuvenation, but only lasted for a limited numbers of cycles. The electrochemical potential of the rinsed graphite anode increased, showing the solid electrolyte interphase (SEI) was at least partially removed during rinsing. The compositions of the effluent were characterized by Mass Spectroscopy (MS). POF_3 , $\text{C}_5\text{H}_{10}\text{O}_3$, $\text{C}_7\text{H}_{14}\text{O}_5$, and $\text{C}_8\text{H}_{14}\text{O}_6$ were present in both the rinsed cathode and anode solutions, regardless of the solvents. $\text{C}_2\text{H}_6\text{O}$ was also detected in the anode solution but not the cathode one.

Eventually, 1-Ah pouch cells with ports were successfully assembled and sealed under vacuum. The cells demonstrated good capacity in the first formation cycles at C/10. However, significant capacity fade started afterwards in some cells due to leakage in the sealing region. The cells didn't last very long before reaching 20% capacity fade.

We are wrapping up this task and no extensive experimental work is planned. However, some future activities could include exploring different materials to wrap the tube and seal with the pouch materials. The tubing material also needs further screening, as it will be exposed to electrolyte all the time. It needs to be sealed to the pouch material but not to itself so that electrolyte or solvent can still go through during the subsequent rejuvenation process.

EverBatt: Cost and Environmental Impacts Modeling

Recycling has the potential to reduce the cost and environmental footprint of lithium-ion batteries (LIBs). Argonne has developed the EverBatt model to estimate the cost and environmental impacts associated with closed-loop recycling of LIBs. We use the model to evaluate the recycling processes and design-for-recycling (DfR) strategies developed under the ReCell Center, and to help inform and direct the R&D efforts. Specifically, we will

1. Expand EverBatt to include unit processes proposed for direct cathode recycling and recovery of other battery components;
2. Increase the granularity of the battery manufacturing module and the recycling module in EverBatt to enable evaluation of DfR strategies; and
3. Develop customized versions of EverBatt for specific recycling techniques to identify cost/environmental hotspots and barriers to commercialization.

In Q4FY2021, we continued working with ReCell researchers to analyze their processes and developed a version of EverBatt for the solvent-based dual process, the results of which are discussed in detail in the milestone report. In Q4FY2021, we also looked at costs for hazardous waste disposal that could be applicable to battery recycling.

Hazardous wastes are wastes that exhibit any one of the following characteristic properties: ignitability, corrosivity, reactivity, and toxicity. Examples of hazardous wastes include fluorine compounds and electrolyte solvents in the battery, and possibly also some of the materials (additives, solvents, etc.) used in the recycling processes. In the U.S., the EPA regulates hazardous waste disposal, but each state can set their own fee schedule. Nevertheless, hazardous waste disposal charges by state agencies normally consist of a generator fee, a permit fee for storage if applicable, and a disposal fee. The generator fee is charged to the waste generator (battery recycler) and can vary with the volume of wastes generated per month/year. If a waste generator (battery recycler) needs to store wastes on-site, a permit may be required, and the permit fee will also vary with the volume of wastes stored. Finally, the disposal fee is charged at the disposal facility that accepts the wastes from the generator (battery recycler).

In Figure III.3.81 we show the costs charged by state agencies for a few states that 1) are close to big battery manufacturing plants and/or big electric vehicles markets (i.e., potential locations for battery recycling plants), and 2) have an existing commercial hazardous waste landfill. We also show how the costs vary when the waste

volume increases from 100 metric tons per year (tpy) to 10,000 tpy. The results show that the storage permit/facility fee dominates the total charge when the volume is low, but disposal fee becomes the biggest contributor as the volume increases.

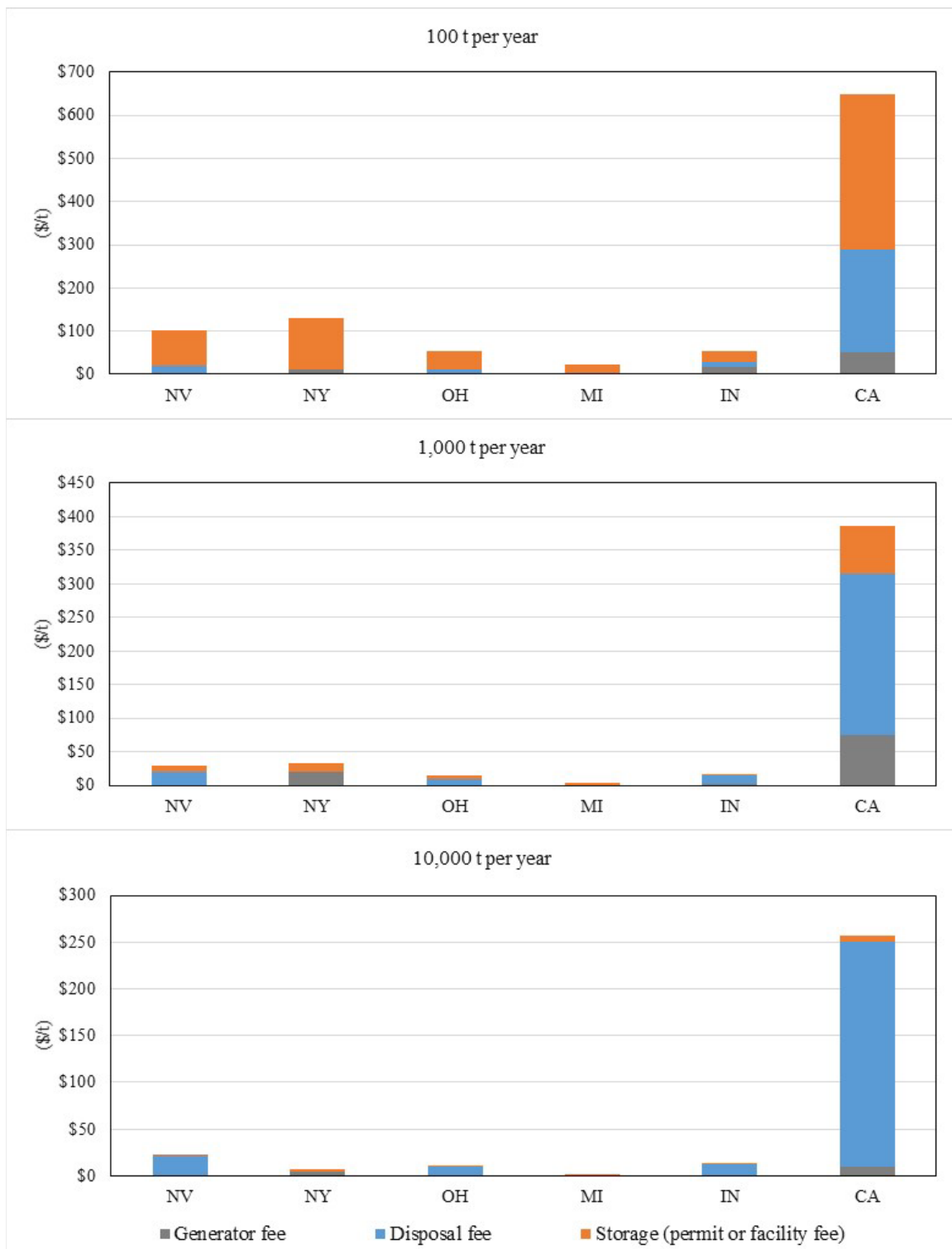


Figure III.3.81 Hazardous waste disposal cost payable to state agencies, for a waste volume of 100 tpy, 1,000 tpy, and 10,000 tpy, respectively.

In addition to fees payable to state agencies, the total cost of hazardous waste disposal should also include logistics cost and operating cost of the landfill. We were not able to find good information for the latter, but we did find quotes for hazardous waste disposal from two service providers, which can serve as a proxy for the sum of logistics and operating costs. The price quotes are shown in Figure III.3.82. In summary, a battery recycler may need to pay \$0.30-\$650 to state agencies, and \$460-\$1,300 to service providers, per metric ton of hazardous wastes generated.

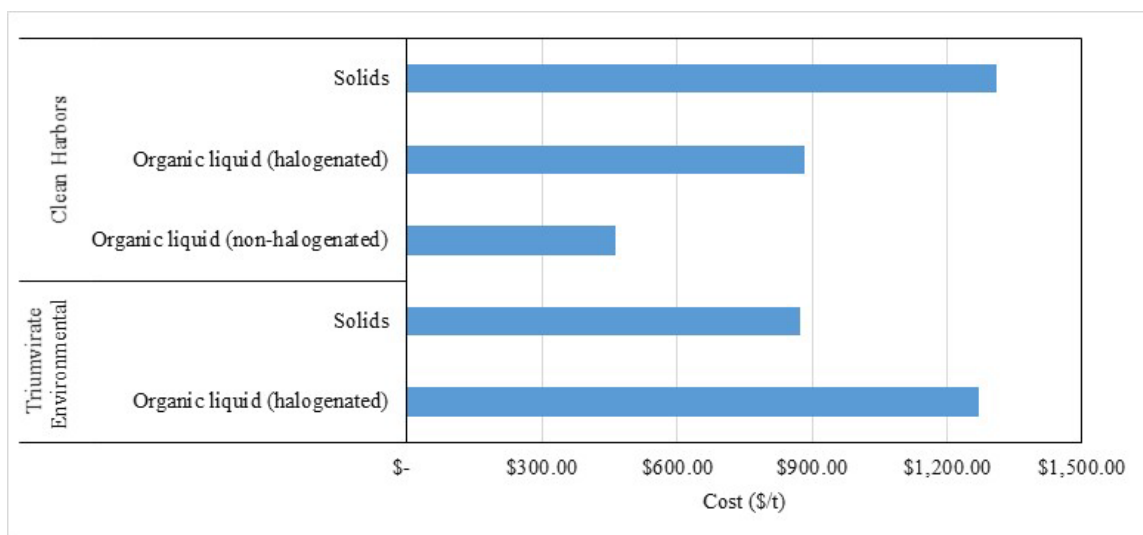


Figure III.3.82 Price quotes for hazardous waste disposal from Triumvirate Environmental and Clean Harbors

Analysis of Supply Chain Challenges for Battery Recycling

NREL has developed LIBRA (Lithium-Ion Battery Resource Analysis), a systems dynamics model, to explore impacts related to the interlinking global and regional supply chains associated with battery manufacturing and recycling. Electrification of the transportation and energy storage markets is projected to result in explosive growth in the demand for batteries. In response to concern over raw material supply, increased emphasis is being placed on battery recycling capacity expansion. While some resulting impacts are anticipated, such as the shift in manufacturing costs and raw material prices, the inter-connectiveness of multiple markets, new manufacturing investments, operations, and policies could have unanticipated impacts on the success of electrification efforts.

LIBRA analyzes the technological and market feedback and feed-forward signals that could affect global supply chains for raw materials, new and recycled batteries, and electric vehicles. Included in these analyses are the potential build-out of these industries. The objective of this project is to help answer critical supply chain questions regarding the opportunities and challenges of lithium-ion battery recycling, including insights into the impact that R&D achievements can have on the successful development of recycling capabilities, and how evolving global supply chains are affecting the projections of EV deployment.

In fiscal year 2021, analysis in several areas was accomplished:

- LIBRA sensitivity analyses results
 - Importance of recycling consumer electronics
 - Changing battery chemistry on the economics of recycling technologies
 - Importance of piloting or other investment for technology development
 - Effect of capital vs. operating improvements on technology deployment

- LIBRA Improvements
 - Cathode powder manufacturing (based on independent NREL analysis)
 - Cell and pack manufacturing (based on EverBatt 2.0)
 - Battery sorting
 - Scrap recycling
 - Updating of assumptions to 2021 values and incorporating all vehicle types
- Calculations and technical support for DOE's response to the Department of Energy's 100-Day Reviews under Executive Order 14017 "America's Supply Chains" for the Vehicle Technologies Office
- Macro-economic analyses and the development of input/output model for battery manufacturing and recycling supply chain
 - Assessment of economic impacts (Jobs/GDP) for domestic supply chain by segment
 - Development of capital costs by cost area for domestic mining, refining, cathode powder production, cell and packs, and recycling

Additionally, the following activities were completed:

- LIBRA Deployment and Branding
 - Website available: <https://www.nrel.gov/transportation/libra.html>
- Draft report "Economic Analysis for Domestic LIB Supply Chain 2025-2040"
- HQ presentation materials
- Evaluation of Impact of GM Full EV Production
- Other analyses and updates as requested
- Outreach and Collaboration
 - Recycling Prize Projects
 - Li-Industries – Smart Battery Sorting System
 - Renewance – Battery Reuse Value Estimator

CAMP Facility Support

Numerous recycled battery materials created in the ReCell Program will need to be validated in prototype electrodes and pouch cells. The Cell Analysis, Modeling, and Prototyping (CAMP) Facility at Argonne will validate these materials (active cathode powders, graphite, electrolytes, etc.) and compare their electrochemical performance to baseline electrodes (and electrolyte). Validating the electrochemical performance of recycled battery materials will be critical to establishing their market viability.

The CAMP Facility will use pristine NMC111 cathode material and SLC1520P graphite as the baseline materials to use in capacity-matched electrodes and cells. All future recycled NMC111 cathode materials will be compared against this baseline electrochemical performance data, as well as other recycled battery materials

that are of interest to the ReCell Center. All electrodes will first be tested in coin cells for initial validation and then tested in single-layer pouch cells for rate performance, HPPC impedance, and cycle life, if warranted.

Expansion of Mixing Capabilities to Improve Recycled Material Electrodes - Updated

The CAMP Facility has occasionally observed incomplete mixing with a few of the recycled active materials over the last couple of years. A search for a solution was conducted that focused on mixing systems with internal screening mechanisms to break up agglomerates. The Filmix Model 56-L mixer from Primix Corporation was identified as an ideal mixer that would improve the quality of coatings using recycled materials and other materials that tend to form agglomerates. This mixing unit has a unique system to eliminate agglomerates/aggregates in the slurry, and additionally, it can be set up with one of our current mixers as an add-on unit. An order was placed for the Filmix mixer, which arrived in late September 2021.

Relithiation Processes Benchmarking Pouch Cell Builds

Electrode and pouch cell fabrication plans were made for testing NMC622 powder recovered from ORNL's Solvent Y processed electrode material. The cathodes used for this work were harvested from industrial End-of-Life (EOL) cells from an industrial collaborator. This recovered NMC622 material (500 g) was sent from ORNL to Argonne where it was then divided into 50 g portions and sent to the ReCell relithiation projects (five in total) to be relithiated and sent back to CAMP. The same industrial vendor also sent pristine NMC622 powder, which the CAMP Facility used to make a baseline electrode. One of the five portions of Solvent Y-recovered NMC622 was retained by CAMP Facility and made into an electrode and then sent to NREL for electrochemical relithiation of the electrode (eChem). Both the pristine NMC622 powder and Solvent Y-recovered NMC622 powder blended well in the slurry process and yielded good quality electrodes.

The CAMP Facility received all four relithiated NMC622 powders from the four relithiation teams (Hydrothermal, Ionothermal, Solid State, and Redox) in mid-September. The pH was measured for the pristine NMC622 powders, the Solvent Y-processed NMC622, and the four relithiated NMC622 powders. The Solvent Y-processed NMC had a pH of 11.02, which is lower than the pristine powder (pH 11.71). Whereas the four relithiated Solvent Y-NMC powders had increases in pH (between 11.80 to 12.19). All four relithiated powders were coated, but the coating quality was marginal although still useable. The relithiated powders did not blend well in their slurries, resulting in poor coating quality, which made hitting the desired coating loading very difficult. The slurry preparation and fineness gauge observations suggest that the powders had large "hard" agglomerates/aggregates (that may have formed during sintering). Additional aggressive mixing (rotor-stator) was attempted to break up these agglomerates, with little success. The agglomerates caused severe streaking in the electrode coating, as can be seen in Figure III.3.83. This issue also resulted in substantial variations for the coating loading/thickness, both across and throughout these electrodes. It is unlikely these are "soft" agglomerates, because gelation behavior was not observed in the slurry; rotor-stator would have for the most part broken up "soft" agglomerates.

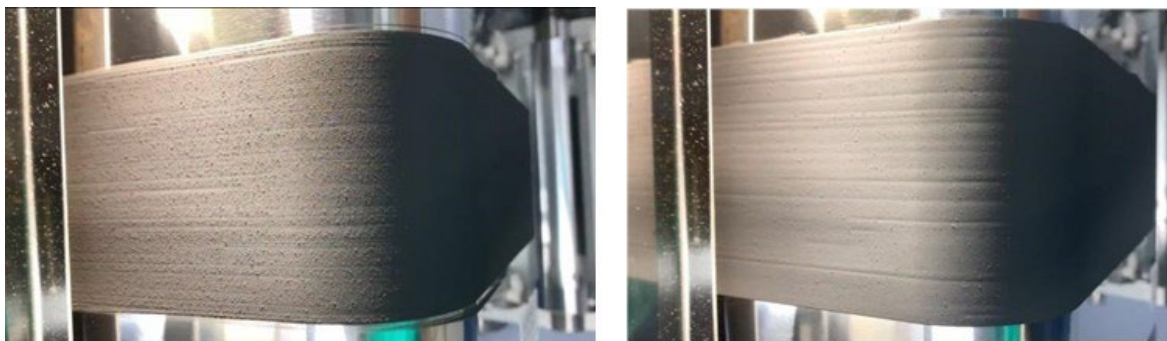


Figure III.3.83 Photos of electrode coatings made from relithiated Solvent Y processed NMC622. Agglomerates in powder resulted in streaking and grit in the electrode coating.

All six NMC622 powders were coated by the CAMP Facility to match an anode (A005B, SLC1520P Graphite) from the Electrode Library. Electrodes were punched from these electrodes to make single layer pouch cells in the xx3450 format, with the exception of the eChem relithiated electrodes, which are being shipped from NREL.

Post-Test Facility Support

The Post-Test Facility at Argonne performs a supporting role in the ReCell Program. Post-test diagnostics of aged batteries can provide additional information regarding the cause of performance degradation, which previously could be only inferred. The facility combines microscopy, spectroscopy, and chromatography in a controlled-atmosphere glove box to characterize materials without air exposure. These results will help us identify issues in the recycled materials, such as how well a given recycling process separates an initial mixture of cathode, anode, supporting foils, and casing materials.

In the Q4 of FY2021, we continued to help different groups understand the key parameters in various recycling processes. We characterized the samples given in Table III.3.22 by a combination of scanning-electron microscopy and X-ray photoelectron spectroscopy. Our contributions to the work are summarized below.

- **WPI:** We worked together on the manuscript focusing on the F impurity study and have it ready for submission. We characterized powder samples to study the effect of the concentration of phosphorus impurities on the surface and the bulk TM properties of NMC622 cathodes by XPS depth profiling measurements. Unlike F impurity which mainly stays on the powder surface, P tends to be mixed in both surface and bulk.
- **CAMP:** We characterized the NMC 622 powder and electrode samples by XPS. The surface information including Ni^{2+/3+}, Ni/Co/Mn content, and possible surface impurity species e.g., F was evaluated to study the effect of different binder removal processes.

We have already shared the results with the owners and are working together on the data analysis for potential publications.

Table III.3.22 Sample information for XPS or SEM study

Institutions	Sample description
WPI (Impurity study)	1. Pristine NMC 622 powder
	2. 0.2% Phosphorus doped NMC 622 powder
	3. 1.0% Phosphorus doped NMC 622 powder
	4. 5.0% Phosphorus doped NMC 622 powder
	5. Pristine NMC 622 precursor
	6. 5.0% Phosphorus doped NMC 622 precursor
CAMP (Binder removal)	7. NMC 622 Pristine powder
	8. NMC 622 Pristine electrode
	9. NMC 622 cycled electrode
	10. Recovered NMC 622 powder after thermal binder removal
	11. Recovered NMC 622 powder after solvent binder removal

Figure III.3.84 summarizes the XPS results of pristine NMC622 and NMC622 retrieved using the thermal and solvent binder removal processes. In our XPS study, we mainly focused on F1s since CF₂ (at 688 eV) is a

characteristic peak for the binder (polyvinylidene fluoride, PVDF). In addition, Ar-ion sputtering is used to obtain XPS data from beneath the surface. The sputtering time was fixed to 1 minute (1kV). In pristine NMC622, no prominent peak was observed in F1s region, as expected. However, both thermal and solvent binder removal samples showed noticeable peak intensity in F1s region. The peaks observed from both samples can be assigned to either LiF (~685 eV) or Li_xPyF_z (~687.5 eV). Given that the PVDF binder shows a strong peak at 688 eV, it can be concluded that both thermal and solvent binder removal processes remove the PVDF binder but remaining fluorine in the sample forms impurities, such as LiF or Li_xPyF_z on the surface of NMC622.

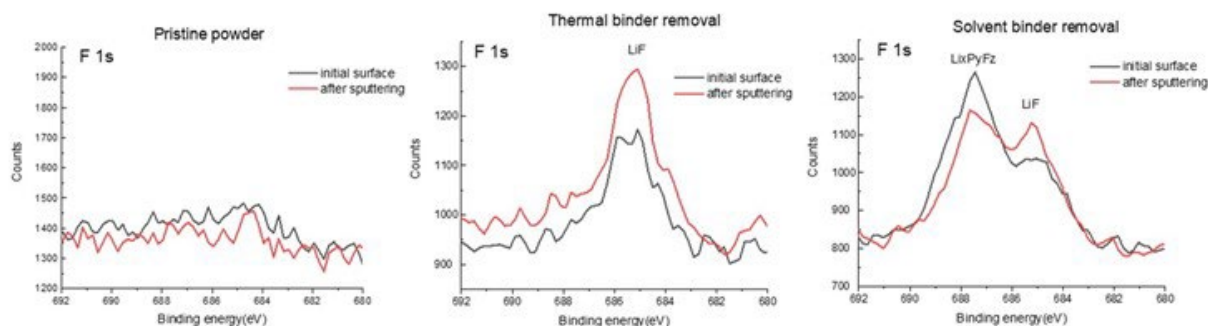


Figure III.3.84 XPS results of F1s region from pristine, thermal binder removed, and solvent binder removed NMC622.

Diagnostics of Aged Materials

Within the battery community, characterization of cathode material typically involves multiple disparate techniques, including detailed measurement of particle size distribution, tap density, reversible capacity, first cycle efficiency, specific surface area, ash content, etc. In the context of a direct recycling line, such characterization may be applied both upstream (i.e., sorting material feedstocks) and downstream (i.e., evaluating the output of a recycling process). While thorough characterization is essential to process viability, the standard practice of relying on numerous techniques to gain particle-scale information may be impractical and cost-prohibitive.

Thus, we have developed and optimized a streamlined advanced characterization method coupling electron backscatter diffraction (EBSD) with electron dispersive spectroscopy (EDS). The combination of EBSD and EDS is particularly powerful, as it yields simultaneous structural (EBSD) and chemical (EDS) signatures. High data quality and spatial resolution at both the particle and electrode scale have been achieved. As a crosscutting technique, this analysis method may be utilized both to analyze degraded material and to assess particle-scale changes resulting from recycling methods. EBSD/EDS data collected at a statistical scale can inform metrics enabling batteries from different life histories to be distinguished in a mixed recycling stream. This technique may also be applied to materials undergoing novel recycling processes (separation, purification, upcycling, etc.) to track impacts to NMC chemistry and structure. Data from new samples analyzed via EBSD/EDS may be compared to the extensive database of material parameters collected in previous quarters.

The EBSD/EDS diagnostic techniques developed and optimized in FY19 and FY20 continue to be available in support of the ReCell sub-tasks. In Q4, we completed analysis of two hydrothermally upcycled samples prepared by the UCSD team under different conditions. Specifically, comparisons in the distribution of intra-grain misorientation were analyzed for upcycled single-crystal NMC-433 prepared with two different precursors (NiOOH and $\text{Ni}(\text{OH})_2$). Differences between the two samples were readily evident, as shown in Figure III.3.85. The sample prepared with NiOOH precursor experienced higher average misorientation (Grain Orientation Spread (GOS); Figure III.3.85(a)), and also showed a particle-scale gradient in misorientation (Grain Reference Orientation (GROD); Figure III.3.85(b)), whereby the outer edge of the particle had higher misorientation values than the interior of the particle. The sample prepared with $\text{Ni}(\text{OH})_2$ precursor showed improved uniformity in GROD across the particle (Figure III.3.85(d)), and also showed reduced GOS as compared to the sample with NiOOH precursor (Figure III.3.85(c)). These data have been reviewed with the

USCD team and, when paired with electrochemical data, can inform improvements in optimal conditions for hydrothermal upcycling.

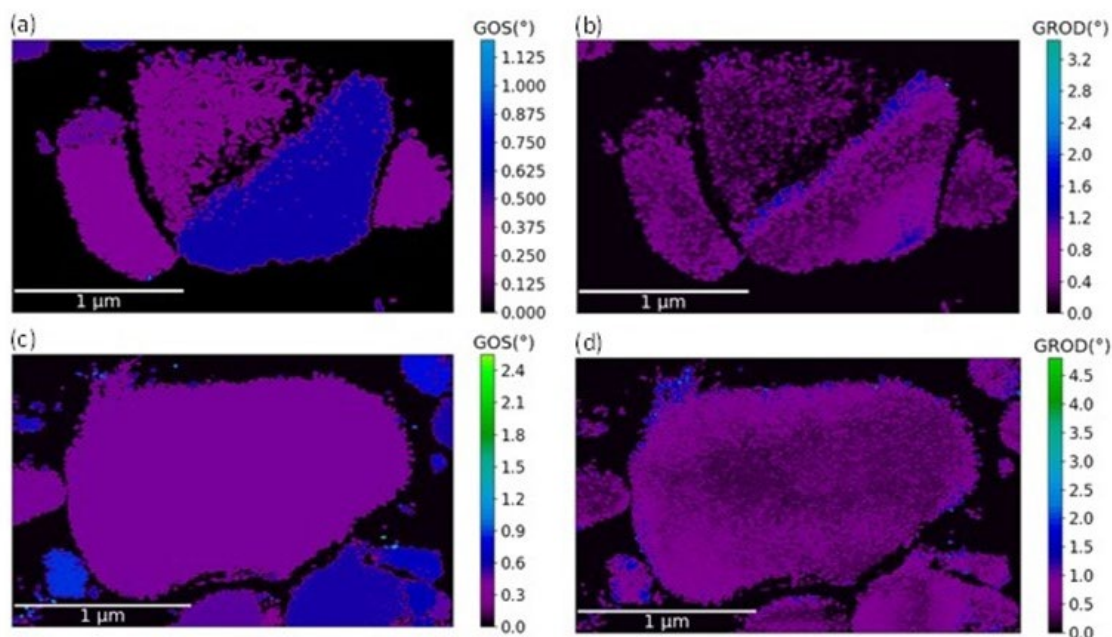


Figure III.3.85 EBSD data for two hydrothermally upcycled single-crystal samples prepared by UCSD: (a) Grain orientation spread (GOS) for upcycled NMC-433 prepared with NiOOH precursor; (b) Grain reference orientation deviation (GROD) for upcycled NMC-433 prepared with NiOOH precursor; (c) GOS for upcycled NMC-433 prepared with Ni(OH)₂ precursor; (d) GROD for upcycled NMC-433 prepared with Ni(OH)₂ precursor. One representative region is shown for each sample.

Additional upcycled samples have been received and are in various stages of analysis and data processing. These include samples from the solid-state upcycling team (ANL) and the ionothermal upcycling team (ORNL). Analysis needs have been discussed individually with each team, and the characterization approaches has been tailored accordingly. For the ionothermally upcycled material, emphasis is being placed on particle-scale compositional mapping (EDS) to reveal any gradients in Ni content from the edge to the center of the particle; for the solid-state upcycled material, gradients in both misorientation and composition across the secondary particle will be evaluated to assess the efficacy of new treatment protocols.

During the past quarter, we have also submitted revisions for the manuscript submitted in Q3, where EBSD has been applied to evaluate electrode-scale and sub-grain-scale structural changes associated with cell cycling.

Analysis of additional samples from the ReCell subtasks will continue as they are received.

Microcalorimetry on Recycled Materials

The chemistries of advanced energy storage devices are very sensitive to operating temperature. High temperatures degrade batteries faster, while low temperatures reduce their power and capacity. NREL's equipment is sensitive enough to determine how changing the design of cell components affects the overall performance of the cell. We will use our isothermal calorimeters to develop an understanding of the life cycle effects on heat generation and determine if the recycling processes being developed under the ReCell program have a deleterious effect on cell performance. In particular, NREL will investigate the following:

1. Thermally characterize existing NMC cathode compositions to understand how the thermal signature of a battery changes from the beginning of life to the end of life. The data will be used to assess the quality of the recycled material being produced under the ReCell program.
2. Thermally characterize NMC/graphite cells with a known contaminant. For instance, we want to understand how much copper material can be tolerated in the cathode without having a negative effect on heat generation and efficiency.
3. Match the extent and type of thermal degradation to target recycling methods, based on load profiles, cycling windows, and cost metrics.

Heat Generation Summary: NREL received ANL CAMP cells for thermal characterization. A comprehensive list of materials evaluated is given in Table III.3.23. The cells supplied by CAMP were a combination of NMC and graphite—standard materials used in electric vehicles today.

Table III.3.23 CAMP cells to be used for thermal characterization—Cathode material was supplied by Toda and anode material was supplied by Superior Graphite

Cathode Material	Anode Material	Number of Cells
NMC - 111	1506T	4
NMC - 532	1506T	4
NMC - 622	1506T	4
NMC - 811	1506T	4
NMC - 111	1520P	4
NMC - 532	1520P	4
NMC - 622	1520P	4
NMC - 811	1520P	4

NREL measured the heat generation of two of each of the pristine/fresh 1520P/NMC cell versions (NMC - 111, 532, 622, and 811). Figure III.3.86a shows the measured beginning-of-life (BOL) heat generation of the four types of cells under a 2C constant current discharge. As expected, the heat generation is at a maximum at the end of the discharge – typical for graphite-based cells. Unexpectedly, the 2C heat generation was the highest for the 1520P/NMC-111 and the lowest for the 1520P/NMC-811 for a given SOC at BOL. The heat generation difference between the two cells varied by as much as 200% over the discharge curve. Since both cells use the same anode, the heat generation difference between the test runs is attributed to the cathode. Figure III.3.86b shows the heat generation of the four variants of cells under a 2C constant current charge. The difference in heat generation between the four different types of cells under charge was less than that for the discharge over the entire SOC range. Finally, the heat generation trend reversed under charge as expected – in general, the 1520P/NMC-111 produced the least amount of heat for a given SOC and the 1520P/NMC-811 produced the most.

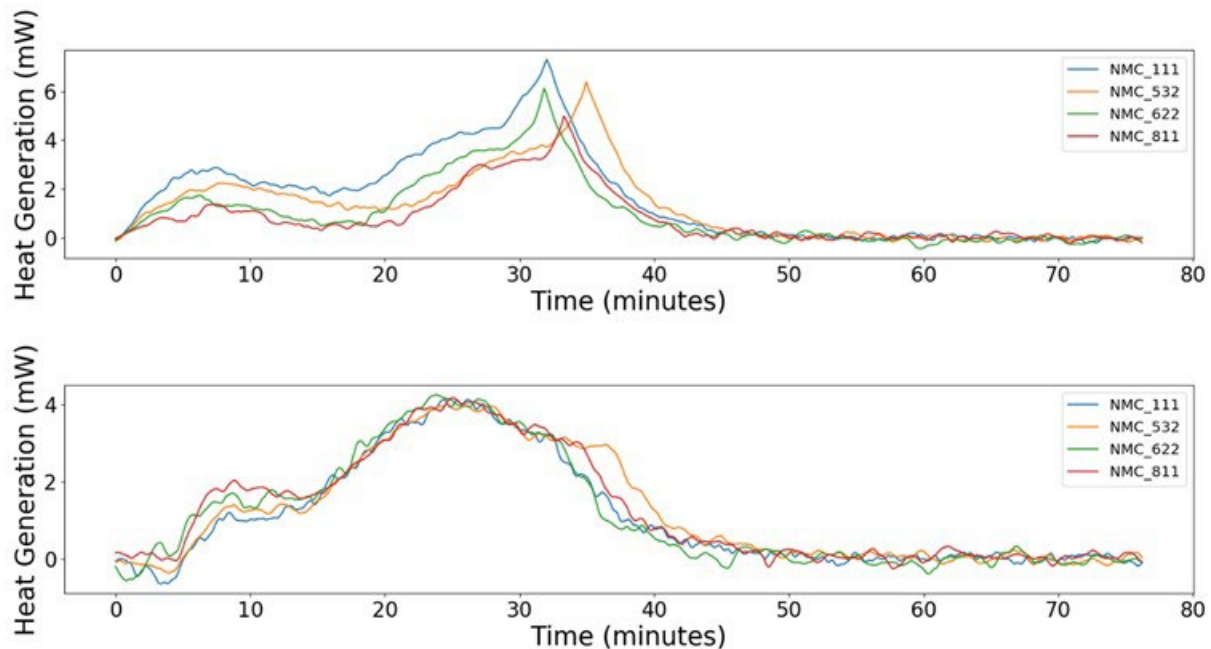


Figure III.3.86 Superior Graphite/Toda 1520P/NMC-111, 532,622, and 811 heat generation curves for a 2C full discharge (1a - top) and 2C full charge (1b - bottom).

Over the past year, NREL has cycled the graphite/NMC cells versions until 80% of the initial capacity remains at End of Life (EOL). We wanted to measure the heat generation and efficiency at the EOL and use the BOL and EOL data to bracket the performance of graphite/NMC cells. The data will be used to determine the efficacy of future recycled material and processes. We aged the cells by applying a C/1 charge/discharge profile until the cells reached 80% of their initial capacity. Table III.3.24 shows the percent capacity that remains as compared to the beginning of life for each of the cells. Unfortunately, the graphite/NMC811 cells aged/degraded much faster than the other cells and its EOL heat generation and efficiency tests are biased due to the increased capacity loss

Table III.3.24 Percentage of capacity remaining after aging the CAMP cells for EOL thermal characterization—Cathode material was supplied by Toda and anode material was supplied by Superior Graphite.

Cathode Material	% of BOL Capacity	Number of cycles to reach EOL
NMC – 111	79.0	1602
NMC – 532	78.4	1411
NMC – 622	80.4	2447
NMC – 811	63.8	799

NREL also measured the heat generation and efficiency of the four types of cells at various charge and discharge currents over several SOC ranges. The data shown in Figure III.3.87 is for a constant current discharge from 4.1 V to 3.0V – discharging the cells from 100% to 0% SOC. As expected, the heat efficiency decreases as the discharge rate is increased. Furthermore, the heat efficiency of the 111, 532, and 622 cathodes are similar in magnitude and decrease the most under a 3C discharge current, the maximum discharge current used for this study. Finally, the 811-cathode cell showed the largest decrease in efficiency from BOL to EOL, since it was aged to around 64% of its initial capacity.

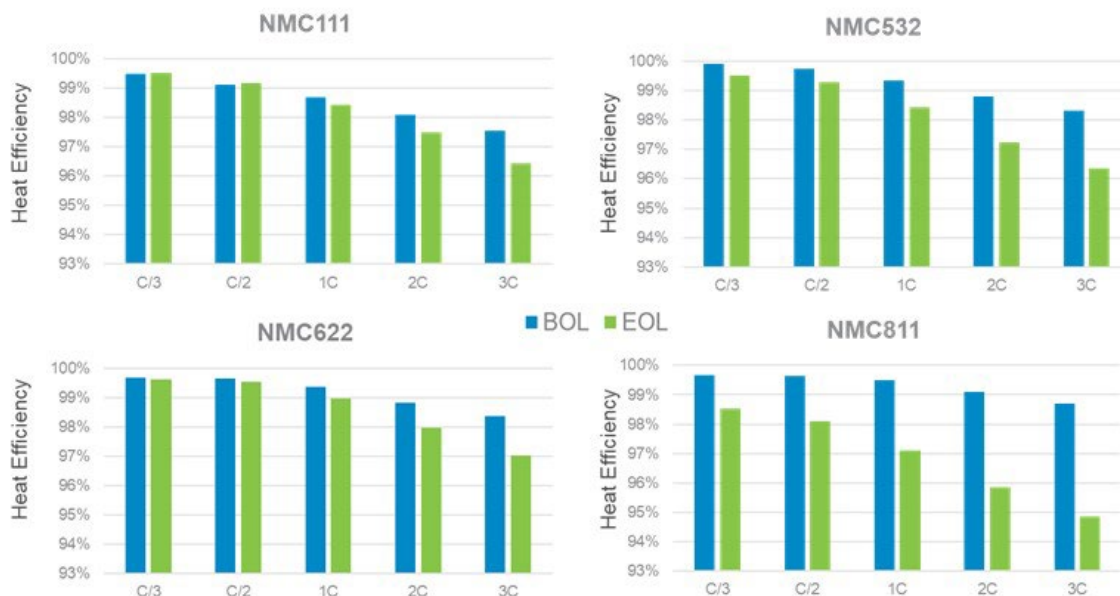


Figure III.3.87 BOL and EOL heat efficiency of 1520P/NMC cells under various discharge currents over an SOC range from 100% to 0%.

The microcalorimeter developed by NREL has been designed to measure the heat generation from both the cathode and anode when a single pair of electrodes is used—typical for coin cells but also for the pouch cells provided to NREL by CAMP. Figure III.3.88 compares the BOL and EOL heat generation of a NMC811 cell over a 3C full discharge from 100% to 0% SOC. Figure III.3.88 shows that the heat generation from the anode was greater than the heat from the cathode at the beginning of life. However, after the cell was aged, the heat from the cathode was much greater than that of the anode. The increased heat generation from the cathode at end of life can probably be attributed to cathode cracking, a known failure mechanism of NMC811 material, and will be verified with EBSD in the future.

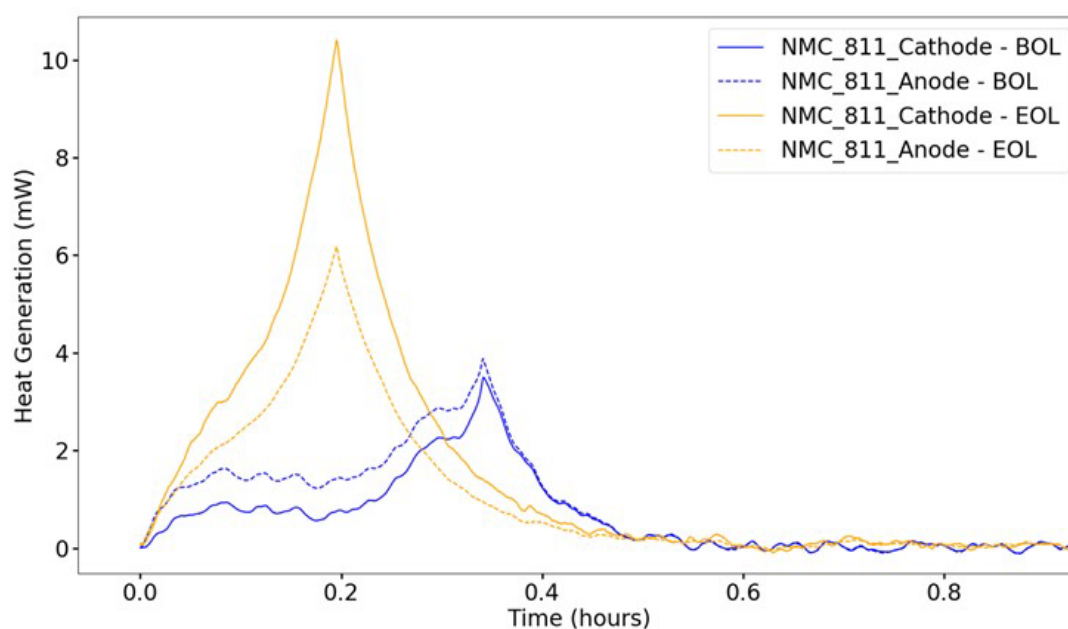


Figure III.3.88 BOL and EOL heat efficiency of a 1520P/NMC811 cell under a 3C discharge current over an SOC range from 100% to 0%.

Contaminant Summary: NREL received cells from Argonne National Laboratory (ANL) that had a known contaminant added to the cathode or anode. The entire list of compositions is given in Table III.3.25. The batteries supplied by CAMP are a combination of NMC-111 and graphite—a typical chemistry used in electric vehicles today. The contaminant was added to the slurry of the cathode or anode during the coating process—the contaminants added were either iron, copper, silicon, magnesium, and aluminum at a 1% by mass ratio.

Table III.3.25 CAMP cells to be used for thermal Characterization. The cathode material was supplied by Toda and the anode material was supplied by Superior Graphite. Contaminants were added to the slurry before coating the current collectors.

Cell	Cathode Material	Cathode Impurity	Anode Material	Anode Impurity
1	NMC111 (90%)	NA	Graphite 1520P (91.83%)	NA
2	NMC111 (89%)	Cu 1%	Graphite 1520P (91.83%)	NA
3	NMC111 (89%)	Fe 1%	Graphite 1520P (91.83%)	NA
4	NMC111 (89%)	Al 1%	Graphite 1520P (91.83%)	NA
5	NMC111 (89%)	Mg 1%	Graphite 1520P (91.83%)	NA
6	NMC111 (89%)	Si 1%	Graphite 1520P (91.83%)	NA
7	NMC111 (90%)	NA	Graphite 1520P (90.83%)	Fe 1%
8	NMC111 (90%)	NA	Graphite 1520P (90.83%)	Al 1%
9	NMC111 (90%)	NA	Graphite 1520P (90.83%)	Mg 1%
10	NMC111 (90%)	NA	Graphite 1520P (90.83%)	Cu 1%

CAMP shipped the cells to NREL dry and sealed as we anticipated that the heat generation would be most visible during the formation process. After receiving the cells from CAMP, NREL filled and resealed the pouch material and then placed the cells within our microcalorimeter for thermal testing. During the last quarter, NREL and ANL collaborated on a paper detailing how thermal and electrochemical measurements can be used to identify contaminants introduced into cells through the direct recycling process. Following is the abstract of the paper.

Low-Temperature Cell Analysis

The goal of this project is to elucidate and quantify any hazards of mechanically shredding lithium-ion batteries at extremely low temperatures. End-of-life batteries are expected to arrive at recycling facilities with varying electrolyte chemistries, capacities, SOC, and SOH, to possibly be chilled and shredded *en masse*. While the passivating effects of low temperatures on lithium-ion batteries are well-known and documented, the scope of the work has thus far not expanded to include destructive testing. Even at sufficiently low temperatures to all but arrest lithium-ion movement, the shredding process will inevitably release heat in the form of mechanical friction and possibly electronic discharge. As such, the realistic potential for electrolyte evaporation, and corresponding health and fire hazards, must be addressed.

Additionally, the effects of low temperatures on the individual battery components must be examined. At the temperatures needed to prevent ion transport between electrodes, the integrity of the materials, especially polymer separators and binders, will be in question. Binder failure may produce non-risk consequences such as active material disintegration or delamination from the current collectors, which may be helpful to know for separation processes further down-line from the shredder. A tear in the battery separator, however, may cause a cascading thermal runaway event upstream of the shredder. To properly implement preventative measures for such an event, the relationship between cell temperature and the rate of self-heating must be understood.

The outcome from this project will include:

1. Quantifying the relationship between initial cell temperature and external short circuit response (heat release, fire hazard, etc.)
2. Determining the effects of extreme cold on battery components, and their reversibility
3. Identifying the dependence of the above factors on cell SOH and SOC.

With multiple factors delaying cryogenic nail penetration testing (including an inability to prepare cells), Q4 was devoted to other activities. First among them was a set of tests conducted to aid in safety approval for battery shredding experiments at ANL, which shall henceforth be referred to as shredding simulations. The intended samples for the shredding experiments at ANL are cells of low capacity at 0% SOC. As such, it was decided upon (in collaboration with Jessica Durham at ANL) to run nail penetration tests on three cells at low states of charge for the shredding simulations. The samples selected were commercial, 10 Ah Li-polymer cells. One was discharged to 0% SOC with a 1h voltage hold, the next was similarly discharged without the voltage hold, and the last cell was discharged to 25% SOC with a 1h voltage hold. Each cell was enclosed in a layer of insulation, and then subjected to nail penetration at room temperature. The temperature of the 25% SOC sample rose to nearly 80°C, and the temperatures of the 0% SOC samples both remained below 50°C and were not significantly different (although, as expected, the sample without the voltage hold had a marginally higher temperature). Overall, the shredding simulations served to demonstrate the relatively low risk of shredding discharged batteries, as well as an inherent factor of safety. Even the cell at 25% SOC did not generate enough heat to start a fire. As such, so long as the shredding experiments are performed at low SOC and in an inert atmosphere, the risk of fire will be negligible.

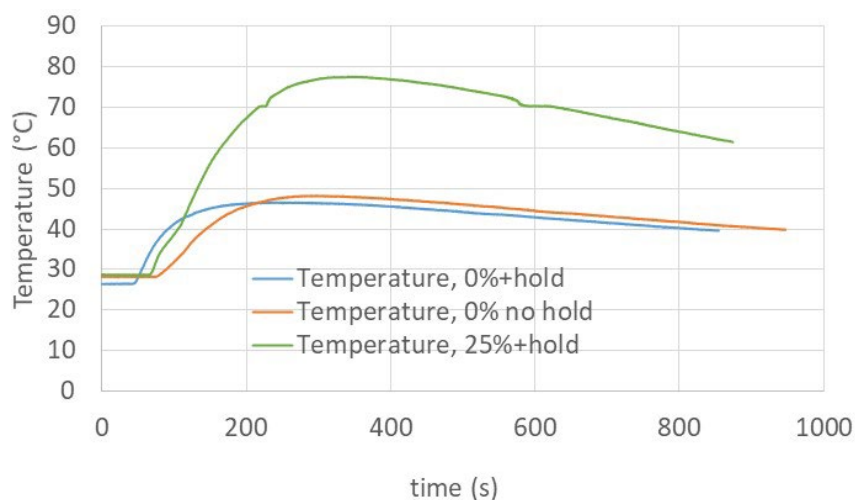


Figure III.3.89 Shredding Simulation results.

When at last cells could again be made for low-temperature testing, the nail penetration chamber had unfortunately become occupied for the foreseeable future. As such, Q4 efforts included the construction (and safety validation) of a dedicated nail penetration tester for the low-temperature work. As prescribed in the original test plan for this project, nail penetration tests will be conducted on cells at 100% SOC, at a variety of starting temperatures. Previous cryogenic nail penetration tests have demonstrated that thermal runaway will occur in cells that are penetrated while submerged in LN₂ and allowed to thaw. The question remains of what would happen in cells that are allowed to thaw to an extent that the voltage has recovered, but the electrolyte is still frozen. The singular low-temperature nail penetration test in Q4 was conducted on a cell in such a state, and the cell did not experience a thermal runaway event. Further testing is needed to determine if this result is repeatable. As of FY22 week 1, the cryogenic nail penetration experiments have been authorized, and shall begin posthaste.



Figure III.3.90 Miniature nail penetration tester for low-temperature tests.

Conclusions

Binder Removal via Thermal Processing

Further improvements were made to the process for recovering NMC 622 manufacturing scrap and cycled materials. For the manufacturing scrap, it was shown that when the rotary kiln had a residence time was increased to be similar to that in the box furnace, the material performance improved, so that both the rate performance and the cycle life are better for the rotary-kiln-processed material. The last step of this process also can be transitioned to rotary-kiln processing, enabling this process to run completely continuously. Cycled material can also be processed this way, but so far, the initial capacity is about 5% below that for the manufacturing scrap material. Further improvements to the processing conditions should be able to reduce this gap. Large quantities of material will soon be available allowing these processes to be further optimized and scaled up.

Binder Removal via Soxhlet Extraction

During the course of this work, we identified an optimal solvent, introduced a vacuum-assisted cryo-vap process, and evaluated various Soxhlet designs for low temperature scalable binder removal from end-of-life NMC cathodes. However, the NMC particle yield, even after introducing steel mesh, was still relatively low, and the process does not control against fluorine contamination of the recovered NMC materials. We are wrapping up this task, and no extensive experimental work is planned. Should this work ever continue, future activities would include attempting to prevent fluorination of the NMC surface and designing a more efficient thimble for NMC recovery.

Cathode/Cathode Separation Process Development

Process optimization of the froth column operation was conducted to determine the process condition that could be used for the first stage of the 2-step froth flotation. To imitate the 2-step continuous froth column operation, two batch operations of the existing froth column would be needed. Froth column tests with 8 L feed slurry demonstrated over 80% froth NMC111 grade within the investigated process conditions. Increasing pH in the column resulted in more froth, while the recovery of froth solid with high NMC111 grade was low. Scaled-up froth column tests with 10 L slurry resulted in significantly low froth recovery and high contamination in the tailings. The feed slurry system will be modified to provide sufficient mixing of the larger quantity of slurry to conduct imitated 2-step froth column operation.

Cathode-Cathode Separation via Froth Flotation

We found that Li_2CO_3 is detrimental to the electrochemical performance of recycled NCA. Heat treatment was demonstrated to be an effective method to remove collector chemicals from the surface of the recycled NMC111. The electrochemistry data showed that electrochemical performance improves after a heat treatment.

Solvent-based Gravity Separation

Separation between the pristine anode and cathode active materials was investigated using different circuit designs. The result showed that multiple stages of separation processes are required to produce high-grade cathode and anode materials in the separated products. Both the electrochemistry and structural analysis of the recycled products were conducted and compared for direct recycling application. The results showed that recycling in LiOH-rich solutions helps preserve electrochemical performance for the cathode active materials.

Chemical Relithiation of NMC Cathodes

Relithiation of the cycled commercial cathode powder focused on material recovered using the solvent Y process. Ethanol coating and resonant acoustic mixing were both used as methods for mixing LiOH with the cathode prior to annealing. Characterization results and electrochemical performance appeared consistent between the two methods. Proceeding using the RAM allows easier scalability and reduces waste associated with the relithiation process. The 50 g batch of relithiated powder was submitted to CAMP for pouch cell fabrication and testing to be reported in the future.

Direct Regeneration of NMC Cathodes through Ionothermal Lithiation

The large scale relithiation of spent MSY_ORNL in molten salts has been investigated at different scales. The recovered materials ReLi-NMC622 was characterized by various techniques, including TGA, XRD, and ICP-OES, which indicate that the ionothermal flux approaches for restoring Li are successful. Further optimization of experimental conditions will continue in next quarter.

Hydrothermal Relithiation of Cathodes

For the past quarter, we validated our regeneration process to recover cycled NCM622. We also showed that the direct regeneration process with a green additive can be successfully used to regenerate C-NCM622 at reduced temperature and pressure (100°C and nearly at ambient pressure). Pushing the temperature and pressure lower for high-Ni materials, reducing the reaction time, as well as further scaling up our regeneration process to lower the overall regeneration costs will be verified in the next step.

Relithiation Via Redox Chemistry

We finished the scaleup experiment of delithiated NMC111 and made relative characterizations. Relithiated NMC111 in a large batch experiment also shows promising results, encouraging the possibility of large-scale application. We also continued to optimize the Solve Y EOL powder, with minor improvements. In the next quarter, we will try to determine the effect of cathode surface characteristics on redox kinetics and explore new quinone-based redox mediators and solvent candidates to reduce the overall process cost and improve the efficiency.

Electrochemical Relithiation

Scaled up reactions were completed for end-of-life commercial NMC 622 materials in the roll-to-roll reactor and coin cells with results indicating that a new model-driven protocol or annealing step would need to be developed to fully recover this material to pristine performance using the electrochemical relithiation method. Full model parametrization and experimental validation were completed for electrochemically aged NMC 111 materials, and a manuscript is in progress.

Solid State Cathode Upcycling

Previous upcycled cathode samples were re-annealed to higher temperature with the goal of improving morphology and homogeneity. Bulk and surface elemental analysis indicates that the composition is more uniform after re-annealing than previous samples were. The increase in lithium content indicates that less

additional LiOH is needed to compensate for potential lithium loss at the high temperature re-anneal. Additional samples have been submitted for analysis using EBSD to further evaluate the upcycled NMC particles and homogeneity. Future work is looking into dilute acid treatment to etch the particles of the upcycled products.

Ionothermal Upcycling of Cathodes

Upcycling via the ionothermal flux method using molten salts as the reaction medium was investigated in detailed this quarter. The recovered materials Up-NMC622 were characterized by various techniques including TGA, XRD, and ICP-OES. The electrochemical performance in a half cell was tested and promising results were obtained. Experimental conditions will be further optimized during the next quarter. Electrochemical performance of the upcycled materials will also be evaluated in a full-cell configuration next quarter.

Hydrothermal Upcycling of Cathodes

We demonstrated a simple yet efficient cathode upcycling strategy to convert spent NCM111 particles into NCM433 particles using nano-sized precursors. The direct upcycling of D-NCM111 into NCM622 will be our next step. This work paves a new pathway toward recycling LIB spent materials at low cost and with good efficiency to accommodate many modern chemistries for NCM cells.

Single Crystal Cathode Production

The etching method can effectively convert NMC cathode materials to the single-crystal structure without introducing any impurities. NMC111, NMC622 and NMC811 have been evaluated, all showing that the performance of upgraded single-crystal cathode materials is improved. And the process has been scaled up. Next, the scaled-up process will be further optimized and the process for NMC811 will be further investigated.

Role of Impurities in Recycled Cathodes

It has been shown that low levels of fluorine impurity bring positive effects on the recovered cathode materials, improving the performance of prepared NCM622 cathodes. F removal from the leaching solution during hydrometallurgy recycling may not be required. On the contrary, we believe that by adding fluorine additives into the reaction, it is feasible to use the hydrometallurgical method to produce NCM-based cathodes with enhanced properties in the near future.

Cell Preprocessing

In this quarter, continuing effort was made in the investigation of layered component clumps liberation by stirring in water. 94.4% liberation efficiency was achieved by stirring the clumps at 50 g/L and 1800 RPM for 3 minutes. Sufficient liberation was not achieved at lower stirring speed and shorter stirring time. Increase in a solid-liquid ratio and stirring time resulted in more delamination of electrode powders. Analysis of delaminated powders indicated that both anode and cathode powders were delaminated, while cathode but not anode current collector foils were subjected to breakdown into fine pieces.

In FY22, the pilot-scale dual shaft shredder will be operated to provide end-of-life battery materials for the downstream direct recycling processes. Electrical work, inspection, and finalization of the safety plan are underway for the safe operation of the shredder. After the safety approval of the shredder, liberation of clumps from end-of-life batteries by stirring will be investigated using organic electrolyte solvent.

Solvent-based Electrode Recovery

In summary, the SolveX process has been successfully applied for the recovery of industrial electrode scraps. Processing cost was greatly reduced by optimizing the washing step using water to replace IPA. Large quantities of spent cathode powder have been recovered through the SolveY process and supplied to relithiation groups for relithiation benchmarking study. Besides SolveX and SolveY processes, an efficient and cost-effective SolveZ process has been demonstrated for the direct recycling and re-manufacturing of anode scraps.

Solvent-based Dual Process for Material Recovery

In addition to the direct regeneration of chemically delithiated NMC111, spent NMC cathode from electrochemically degraded commercial cells has been directly regenerated via a solvent-based thermal relithiation process. Characterizations like XRD and ICP analysis demonstrated the successful restoring of Li. Additionally, the relithiated NMC showed high charge/discharge capacities as well as stable cycle performance. Optimization of the relithiation process as well as evaluation of the electrochemical performance will be the focus in the future.

Aqueous Sequential Separation of Anode and Cathode Materials

In summary, two size-reduction methods were investigated for breaking down the delaminated anode films. It was found that Vortex shaking is more efficient than probe sonication in size reduction. Additionally, reprocessing the separated anode films into new anode was found not practical, as good slurry cannot be formed, possibly due to the SEI layer. Contact angle was measured to explain the separation mechanism for the cathode delamination.

Anode/Cathode Separation and Purification

Process A was able to separate the shredded pouch cell material, however, with lower electrode purities than manufacturing scrap after two passes. As seen here and previous quarters' reports, Process A is effective for recycling manufacturing scrap that contains a mixture of cathode and anode electrodes and can generate material with purities over 99.5%.

Black Mass Purification

The optimized purification methods developed in Q1-Q3 FY21 have been applied to simulated BM containing a known and practically relevant concentration of Al₂O₃ and CuO impurity. In Q4 FY21, we demonstrated that this purification process successfully restores the pristine capacity of simulated BM, with no associated adverse impact on NMC structure or electrochemical performance. The inclusion of a supplemental rinse with neutral DI water does not appear to significantly impact electrochemical behavior, but the effect on Li inventory needs to be evaluated in full-cell format. Finally, we have conducted initial evaluation of BM purification methods on a sample of industrial BM, obtained from ANL after undergoing both froth flotation and binder burnout. This particular batch of treated material shows increased impedance following treatment, which is attributed to side reactions due to unknown surface impurities. Further study of industrial BM will continue throughout FY22, with purification method optimization ongoing. This work was presented at the American Chemical Society Fall 2021 conference (virtual presentation).

Electrolyte Component Removal and Recovery

Equipment and safety approvals are in place to run the scale up of the electrolyte recovery process up to about 10 kg scale per batch. We have analyzed several different commercial manufacturer's electrolytes. Recycling of the electrolyte from the planned cells for scale up appears straightforward. The initial scale-up will be a batch process, but the final industrial process should be continuous. We are developing equipment designs for this continuous process and considering how it might incorporate some separation steps to reduce overall processing cost.

Cycled Graphite to Graphene

Characterization of the high-yielding graphene specimen indicates that it contains graphene with quality similar to other solution-processed graphene. There is a mixture of single, bilayer, and multilayer graphene, with sizes around a few hundred nanometers. It is expected that, based on these data, this graphene should perform similarly to many graphene materials that are currently produced industrially. Going forward, we would like to determine the economics and improve the speed of production of the graphene. In addition, we plan to test these materials in various applications, including composite materials to prove that they perform as well or better than current graphene materials.

Cell Design

In this project, proof-of-concept on rejuvenation of a lithium-ion battery was demonstrated. However, there were challenges in attaching the ports to the pouch cells without leakage and incompatibility with electrolyte. As a result, the benefit of rejuvenating a cell was only demonstrated for a short time.

EverBatt: Cost and Environmental Impacts Modeling

We evaluated in EverBatt the solvent-based dual process for spent battery recycling. We also estimated the cost to dispose of hazardous wastes that could be generated from battery recycling. The preliminary results show that hazardous waste disposal is quite expensive, and the cost varies with the waste volume, waste type, and geographic region. The high cost of hazardous waste disposal highlights the need to track waste streams generated from battery recycling processes, including their sources, compositions, and volumes. It also provides an incentive to develop processes to recycle/neutralize materials that may be of little economic value but can end up as hazardous wastes, to reduce the total cost of battery recycling.

CAMP Facility Support

The CAMP Facility actively supports the efforts of the ReCell Center by providing baseline materials, fabricating trial electrodes and baseline electrodes, fabricating and testing coin cells, and fabricating single-layer pouch cells. These electrodes are evaluated for their electrochemical performance using test protocols that were developed in FY 2019-2020. Test protocols and the testing results are routinely uploaded to the ReCell Center website as they become available for the general public's use. In this quarter, the new mixer from Primix Corporation was received and is being installed in the CAMP Facility. This new mixer should improve the electrode coating quality by breaking up active material agglomerates.

Four relithiated NMC622 powders recovered from EOL cells via the Solvent Y process were received from relithiation teams and made into electrodes by CAMP Facility. However, hard agglomerates in these powders resulted in marginal quality electrodes. If not previously performed, sieving the powders prior to delivering to CAMP Facility will most likely help improve the issues with coating quality, uniformity, and ability to hit a target coating loading. NREL's eChem relithiated electrode is expected in early Q1 of FY22 and will be made into pouch cells rapidly to minimize any concerns related to air sensitivity. Plans are to begin testing all six pouch cell sets (baseline plus five relithiated electrodes) at the same time in November 2021.

Post-Test Facility Support

The Post-Test Facility will continue to provide support for ReCell projects, providing characterization expertise where needed. The future work planned includes characterizing recycled materials that were produced as part of this project. As the recycling processes mature, cells will be constructed from the materials. Cells containing these materials will be sent to Post-Test for additional characterization data regarding causes of loss of performance.

Diagnostics of Aged Materials

Optimized EBSD/EDS techniques continue to be employed in support of the ReCell program. This quarter, two hydrothermally upcycled samples prepared by UCSD were evaluated for trends in particle-scale misorientation. Analysis of GOS and GROD suggests improved particle-scale uniformity in misorientation – and reduced average misorientation – for samples prepared with Ni(OH)₂ precursor, as compared to samples prepared with NiOOH precursor. Collaboration with several additional upcycling tasks is underway, with tailored EBSD/EDS analysis planned to validate structural and chemical changes induced by upcycling treatment conditions. The manuscript summarizing the results from the EBSD task in FY20 and incorporating novel data analysis techniques has been revised and re-submitted this quarter.

Microcalorimetry on Recycled Materials

NREL has submitted the electrochemical/thermal contamination studies to a journal, and we hope to have the data published by the end of 2021. We are presently working on a second journal article outlining the calorimeter tests used to assess the performance of future recycled material and processes. The article will

bookend beginning of life and end of life, the efficiency and heat generation performance of pristine materials to understand the efficacy of future recycled material and processes.

Low-Temperature Cell Analysis

Conclusions have yet to be drawn from low-temperature nail penetration testing. For shredding experiments, it can reasonably be concluded that shredding individual cells of low capacity at 0% SOC under an inert atmosphere is not likely to start a fire.

Key Publications

1. Jianlin Li; Accelerating Battery Manufacturing and Recycling; Trends in Chemistry, 2021, 3 (9), 689-690
2. Ruiting Zhan, Zhenzhen Yang, Ira Bloom, and Lei Pan; Significance of Solid Electrolyte Interphase on Separation of Anode and Cathode Materials from Spent Li-ion Batteries by Froth Flotation; ACS Sustainable Chemistry and Engineering, 2021, 9(1), 531-540
3. Tinu-Oloade Folayan, Albert Lipson, Jessica Durham, Haruka Pinegar, Donghao Liu, Lei Pan; Direct Recycling of Blended Cathode Material by Froth Flotation; Energy Technology, 2021, <https://doi.org/10.1002/ente.202100468>
4. Kae Fink, Paul Gasper, Jaclyn Coyle, Nathaniel Sunderlin, Shriram Santhanagopalan; Impacts of Solvent Washing on the Electrochemical Remediation of Commercial End-Of-Life Cathodes; ACS Applied Energy Materials, 2020, 3(12), 12212-12229
5. Panpan Xu, Qiang Dai, Hongpeng Gao, Haodong Liu, Minghao Zhang, Yan Chen, Ke An, Ying Shirley Meng, Ping Liu, Yanran Li, Jeffrey S. Spangenberg, Linda Gaines, Jun Lu, Zheng Chen; Efficient direct recycling of lithium-ion battery cathodes by targeted healing; Joule, 2020, 4(12), 2609-2626
6. Panpan Xu, Zhenzhen Yang, Xiaolu Yu, John Holoubek, Hongpeng Gao, Mingqian Li, Guorui Cai, Ira Bloom, Haodong Liu, Yan Chen, Ke An, Krzysztof Z. Pupek, Ping Liu, Zheng Chen; Design and optimization of direct recycling of spent Li-ion batteries cathode materials; ACS Sustainable Chemistry & Engineering, 2021, 9(12), 4543-4553
7. Ruihan Zhang, Zifei Meng, Xiaotu Ma, Mengyuan Chen, Bin Chen, Yadong Zheng, Zeyi Yao, Panawan Vanaphuti, Sungyool Bong, Zhenzhen Yang, Yan Wang; Understanding the fundamental effects of Cu impurity in different forms for recovered LiNi_{0.6}Co_{0.2}Mn_{0.2}O₂ cathode materials; Nano Energy, 2020, 78, 105214
8. Ruihan Zhang, Yadong Zheng, Panawan Vanaphuti, Yangtao Liu, Jinzhao Fu, Zeyi Yao, Xiaotu Ma, Mengyuan Chen, Zhenzhen Yang, Yulin Lin, Jianguo Wen, and Yan Wang; Valence Effects of Fe Impurity for Recovered LiNi_{0.6}Co_{0.2}Mn_{0.2}O₂ Cathode Materials; ACS Applied Energy Materials; 2021, 4(9), 10356-10367
9. Yadong Zheng, Ruihan Zhang, Zhenzhen Yang, Yan Wang; Unveiling the Influence of Carbon Impurity on Recovered NCM622 Cathode Material; ACS Sustainable Chemistry & Engineering, 2021, 9(17), 6087-6096
10. Xiaotu Ma, Panawan Vanaphuti, Jinzhao Fu, Jiahui Hou, Yangtao Liu, Ruihan Zhang, Sungyool Bong, Zeyi Yao, Zhenzhen Yang, and Yan Wang; A Universal Etching Method for Synthesizing High Performance Single Crystal Cathode Materials; Nano Energy, 2021, 87, 106194

11. Kyusung Park, Jiuling Yu, Jaclyn Coyle, Qiang Dai, Sarah Frisco, Meng Zhou, and Anthony Burrell; Direct Cathode Recycling of End-Of-Life Li-Ion Batteries Enabled by Redox Mediation; ACS Sustainable Chemistry and Engineering, 2021, 9(24), 8214-8221
12. G. Harper, R. Sommerville, E. Kendrick, L. Driscoll, P. Slater, R. Stolkin, A. Walton, P. Christensen, O. Heidrich, S. Lambert, A. Abbott, K. Ryder, L. Gaines & P. Anderson; Recycling lithium-ion batteries from electric vehicles; Nature, 2019, 575, 75-86
13. Linda Gaines, Qiang Dai, John T. Vaughey, and Samm Gillard; Direct Recycling R&D at the ReCell Center Recycling; Special Issue on Recycling of Lithium-Ion Batteries and Other Next Generation Materials, 2021,6
14. Linda Gaines and Yan Wang; How to Maximize the Value Recovered from Li-Ion Batteries: hydrometallurgical or Direct Recycling; ECS Interface, 2021, Fall, 66-70
15. Yaocai Bai, Nitin Muralidharan, Yang-Kook Sun, Stefano Passerini, M. Stanley Whittingham, Ilias Belharouak; Energy and Environmental Aspects in Recycling Lithium-ion Batteries: Concept of Battery Identity Global Passport; Materials Today, 2020, 41, 304-315
16. Bai, Yaocai; Essehli, Rachid; Jafta, Charl; Livingston, Kelsey; Belharouak, Ilias; Recovery of Cathode Materials and Aluminum Foil Using a Green Solvent; ACS Sustainable Chemistry & Engineering, 2021, 9(17), 6048-6055

References

For Hydrothermal Relithiation of Cathodes

1. Shi, Y., Chen, G., & Chen, Z. (2018). Effective regeneration of LiCoO₂ from spent lithium-ion batteries: a direct approach towards high-performance active particles. Green Chemistry, 20(4), 851–862.
2. Shi, Y., Chen, G., Liu, F., Yue, X., & Chen, Z. (2018). Resolving the Compositional and Structural Defects of Degraded Li_{1-x}Ni_xCo_{1-y}Mn_yO₂ Particles to Directly Regenerate High-Performance Lithium-Ion Battery Cathodes. ACS Energy Letters, 3(7), 1683–1692.
3. Shi, Y., Zhang, M., Meng, Y. S., & Chen, Z. (2019). Ambient-pressure relithiation of degraded Li_{1-x}Ni_xCo_{1-y}Mn_yO₂ (0 < x < 1) via eutectic solutions for direct regeneration of lithium-ion battery cathodes. Advanced Energy Materials, 9(20), 1900454.
4. Noh, H. J., Youn, S., Yoon, C. S., & Sun, Y. K. (2013). Comparison of the structural and electrochemical properties of layered Li [Ni_xCo_yMn_{1-x-y}]O₂ (x= 1/3, 0.5, 0.6, 0.7, 0.8 and 0.85) cathode material for lithium-ion batteries. Journal of power sources, 233, 121–130.

For Hydrothermal Upcycling of Cathodes:

1. Zhu, J.; Chen, G., Single-crystal based studies for correlating the properties and high-voltage performance of Li [Ni_x Mn_y Co_{1-x-y}] O₂ cathodes. Journal of Materials Chemistry A 2019, 7 (10), 5463-5474.
2. Chen, K.-S.; Xu, R.; Luu, N. S.; Secor, E. B.; Hamamoto, K.; Li, Q.; Kim, S.; Sangwan, V. K.; Balla, I.; Guiney, L. M.; Seo, J.-W. T.; Yu, X.; Liu, W.; Wu, J.; Wolverton, C.; Dravid, V. P.; Barnett, S. A.; Lu, J.; Amine, K.; Hersam, M. C., Comprehensive Enhancement of Nanostructured Lithium-Ion Battery Cathode Materials via Conformal Graphene Dispersion. Nano Letters 2017, 17 (4), 2539—2546.

For Black Mass Contamination:

1. Fink, K.E.; Polzin, B.J.; Vaughey, J.T.; Major, J.J.; Dunlop, A.R.; Trask, S.E.; Jeka, G.T.; Spangenberg, J.S.; Keyser, M.A. Influence of Metallic Contaminants on the Electrochemical and Thermal Behavior of Li-Ion Electrodes (submitted)

Acknowledgements

The following individuals worked as individual task leaders/members for the tasks described in this project: Michael LeResche, Haruka Pinegar, Jessica L. Durham, Peyton Melin, Albert L. Lipson (ANL) on Binder Removal via Thermal Processing; Jaclyn Coyle, Jiuling Yu, Kyusung Park (NREL) on Binder Removal via Soxhlet Extraction; Haruka Pinegar, Mike LeResche, Peyton Melin, Kristen Chismudy, Albert Lipson, Jessica Durham (ANL) on Cathode/Cathode Separation Process Development; Lei Pan, Tinu Folayan (Michigan Technological University) on Cathode/Cathode Separation via Froth Flotation; Lei Pan, Ruiting Zhan (Michigan Technological University) on Solvent-based Gravity Separation; Tony Montoya, Jack Vaughey (ANL) on Chemical Relithiation of NMC Cathodes; Sheng Dai, Huimin Luo, Tao Wang, Yaocai Bai, Jianlin Li, Ilias Belharouak (ORNL) on Direct Regeneration of NMC Cathodes through Ionothermal Lithiation; Xiaolu Yu, Zheng Chen (UC San Diego) on Hydrothermal Relithiation of Cathodes; Jiuling Yu, Jaclyn Coyle, Kyusung Park (NREL) on Relithiation via Redox Chemistry; Jaclyn Coyle, Ankit Verma, Nathaniel Sunderlin, Andrew Colclasure, Matt Keyser (NREL) on Electrochemical Relithiation; Jack Vaughey, Tony Montoya (ANL) on Cathode Upcycling; Sheng Dai, Huimin Luo, Tao Wang, Yaocai Bai, Jianlin Li, Ilias Belharouak (ORNL) on Ionothermal Upcycling of Cathodes; Xiaolu Yu, Hongpeng Gao, Zheng Chen (UC San Diego) on Hydrothermal Upcycling of Cathodes; Yan Wang (WPI) on Single Crystal Cathode Production; Yan Wang (WPI) on Role of Impurities in Recycled Cathodes; Jessica Durham, Haruka Pinegar (ANL) on Cell Preprocessing; Ilias Belharouak, Yaocai Bai, Jianlin Li, Rachid Essehli, Huimin Luo, Sheng Dai (ORNL) on Solvent-based Electrode Recovery; Ilias Belharouak, Yaocai Bai, Rachid Essehli, Jianlin Li, Huimin Luo, Sheng Dai (ORNL) on Solvent-based Dual Process for Material Recovery; Ilias Belharouak, Yaocai Bai, Rachid Essehli, Jianlin Li, Huimin Luo, Sheng Dai (ORNL) on Aqueous Sequential Separation of Anode and Cathode Materials; Jessica Durham, Albert Lipson, Haruka Pinegar (ANL) on Anode/Cathode Separation and Purification; Kae Fink, Andrew Colclasure, Joshua Major (NREL) on Black Mass Purification; Donghao Liu, Albert L. Lipson (ANL) on Electrolyte Component Removal and Recovery; Michael LeResche, Haruka Pinegar, Albert L. Lipson (Argonne National Laboratory) on Cycled Graphite to Graphene; Jianlin Li, Yaocai Bai, Sergiy Kalnus (ORNL) on Cell Design; Qiang Dai (ANL) on EverBatt: Cost and Environmental Impacts Modeling; Margaret Mann, Vicky Putsche, Dustin Weigl, Daniel Inman (NREL) on Analysis of Supply Chain Challenges for Battery Recycling; Alison R. Dunlop, Andrew N. Jansen (PI), Bryant J. Polzin, Stephen E. Trask (ANL) on CAMP Facility Support; Zhenzhen Yang, Ira Bloom (ANL) on Post-test Facility Support; Kae Fink, Helio Moutinho, Patrick Walker, Shriram Santhanagopalan (NREL) on Diagnostics of Aged Materials; and Matthew Keyser, Josh Major, Kae Fink, Shriram Santhanagopalan (NREL) on Microcalorimetry on Recycled Materials; Nathaniel Sunderlin (NREL) on Low-Temperature Cell Analysis

III.4 Development of Advanced Low-Cost/Fast-Charge (LC/FC) Batteries for EV Applications (Farasis Energy)

Madhuri Thakur, Principal Investigator

Farasis Energy
21363 Cabot Boulevard
Hayward, CA 94545
E-mail: mthakur@farasis.com

Brian Cunningham, DOE Technology Development Manager

U.S. Department of Energy
E-mail: Brian.Cunningham@ee.goe.gov

Start Date: February 1, 2021	End Date: February 28, 2024	
Total Project Cost: \$4,060,000	DOE share: \$2,030,000	Non-DOE share: \$2,030,000

Project Introduction

The goal of this project is to develop a low cost/ fast charge lithium-ion cell technology that meets the USABC goals for Advanced Low-Cost/Fast-Charge (LC/FC) batteries for EV's applications. Farasis headed the development effort which will bring together technical contributions from many leaders in the Li-ion technology industry including Umicore, BASF, Talga, Imerys, Celgard, Zeon and Solvay, etc. The 36-month development effort will be iterative, with an intermediate Go/No Go Milestone based on cell performance goals and progress tracked against the USABC goals for Advanced Low-Cost/Fast-Charge (LC/FC) Batteries. The major objective of this project is to develop cell technology capable of providing 275 Wh/kg after 1000 cycles at a cost target of \$75/kWh and with having charge time of 15 min for the 80% of the capacity. Key technologies that be developed and integrated into cells include a low-cost cathode, high surface area anode, and electrolyte additives, etc. As a large volume battery manufacturer, a major goal of the project will be to help accelerate production and enable the commercialization of several novel cell component technologies (including low cobalt NCM, Mn-rich NCM, electrolytes, coated graphite as well as high surface area natural graphite) by supporting scale-up and providing a commercialization path. Deliverables will include large pouch cells produced at our manufacturing facility in China/Europe/US with parallel performance and safety testing done at Farasis, cost models associated with the deliverable technology, and a production roadmap to commercialization comprising all components of the cell. The project's total budget will be ~ \$4.05 M with Farasis covering 50% of the cost.

The key barriers for this project include fast charging without Li plating, low cost, and energy density. Fast charging is a crucial enabler of the mainstream adoption of electric vehicles (EVs) to make them competitive to the IC engine cars. None of today's EVs can withstand fast charging due to the risk of lithium plating. Efforts to enable fast charging hampered by the trade-off nature of a lithium-ion battery. The implementation of the fast charge can lead to sacrificing cell durability. Compromise is required between fast charge capability and cell durability, especially for energy-dense cells. To achieve the target of energy density of the cells, high-voltage and high-capacity cathodes are desired. However, the selection of such cathodes will be limited by the cost target.

Objectives

- Develop an EV cell technology of providing 275 Wh/kg after 1000 cycles at a cost target of \$0.075/Wh.
- Develop a fast charge cell having charge time of 15 min for the 80% of the capacity.

- Develop low-cost, high-capacity cathodes such as Mn-rich, Ni-rich cathodes or their blended composite cathode.
- Develop high surface area graphite anodes with fast charge capability.
- Develop and optimize electrolytes and conductive additives to stabilize Mn-rich / Ni-rich cathodes and improve the safety.
- Optimize the negative/positive electrode formulation for maximum energy density and cycle life, and fast charging capability.

Approach

Phase I of the project, which lasted for approximately 15 months, will be focused on the development and characterization of materials and the development of negative/positive electrode technology. Initial sets of single-layer pouch (SLP) cells (ca. 0.1-0.5 Ah) were used to evaluate different positive/negative electrode composites and material combinations in an iterative manner. The specific plan includes: (1) to evaluate the capacity and first-cycle efficiency of different low-cost cathode materials using coin cell builds, (2) to identify a graphite candidate with excellent fast charge capability as the anode material, and (3) to down-select low-cost, high-capacity cathodes while having good cycling stability. Several types of graphite materials with different size, surface area and morphology were evaluated using SLP cell builds. Three criteria including cell resistance, discharge rate capability and fast charge capability were used for the screening of graphite anode materials. The cathode materials were down-selected using SLP cell builds among a wide range of materials including Ni-rich NCM, stabilized Mn-rich cathode materials, zero-Co cathode materials, and their blended composites. Three criteria including cell resistance, discharge rate capability and cycling stability were also used for the screening of low-cost high-capacity cathode materials. A second iteration leads to narrow down the range of electrode designs, introduce materials improvements. The electrolyte development effort was conducted in parallel with the cell optimization work. The electrolyte work will focus on evaluating and optimizing electrolyte formula with additives to meet the requirement of the graphite anodes and the down-selected low-cost, high-capacity cathodes. A combination of device level testing and fundamental electrochemical measurements will be used to guide the development of large form factor cells for Phase II of the project. In the middle of Phase I, baseline cells with a capacity of ca. 73 Ah using Farasis “next-generation” cell chemistry have been built and delivered to national labs for evaluation and testing.

Phase II of the project is scheduled for approximately 17 months and shifts to manufacturing and testing of larger format pouch cells using a refined subset of cell chemistries developed in Phase I. Some ongoing chemistry developments will continue at this stage to address specific issues identified in Phase I builds and to pursue further optimization of cell level performance. To achieve the targeted energy density of 300 Wh/kg we need to evaluate the Mn-rich and the Ni rich cathode with a capacity in between 210–240mAh/g. Other cell components such as foil, separators, electrolyte, conductive additives, and pouch materials is also get evaluated for fast charge cell development. This will occur in two iterations starting with ca. 70 Ah form factor cells (Gen1 cells) for the intermediate evaluation and progressing to the final deliverable cells (Gen 2 cells) based on a larger pouch cell form factor, which will be ca. 87Ah using the optimized high-energy cell chemistry with achieving a cost target of 75 Wh/kg and a charge time of 15 min for the 80% of the capacity. Phase II of the program will also include testing to guide system development in future applications; these tests will characterize cells in small groups to efficiently evaluate their behavior on a large scale where thermal management, cycling-induced gradients, and failure isolation become important.

Results

Cathode materials evaluation: We have evaluated the capacity, first-cycle efficiency and cycling stability of 2 Mn-rich, 3 Ni-rich, 1 zero-Co cathode materials and 3 blended cathode materials consisting of Mn-rich and Ni-rich cathode materials with different compositions. Figure III.4.1 shows the C/3 capacity of cathode

materials evaluated at different voltages. 2 Mn-rich (C2 and C4) and 1 Ni-rich (C1) cathode materials can achieve a C/3 capacity of 200–220 mAh/g, while 1 Ni-rich cathode materials (C3) and blended cathode materials with C3 and C4 Mn-rich materials can achieve a C/3 capacity of 185–200 mAh/g. 1 Ni-rich (C5) and 1 zero-Co (C6) cathode materials achieves a lower C/3 capacity. However, for this project, we will down select cathode materials based on compromising the C/3 capacity, cost and cycling stability of the cathode materials evaluated.

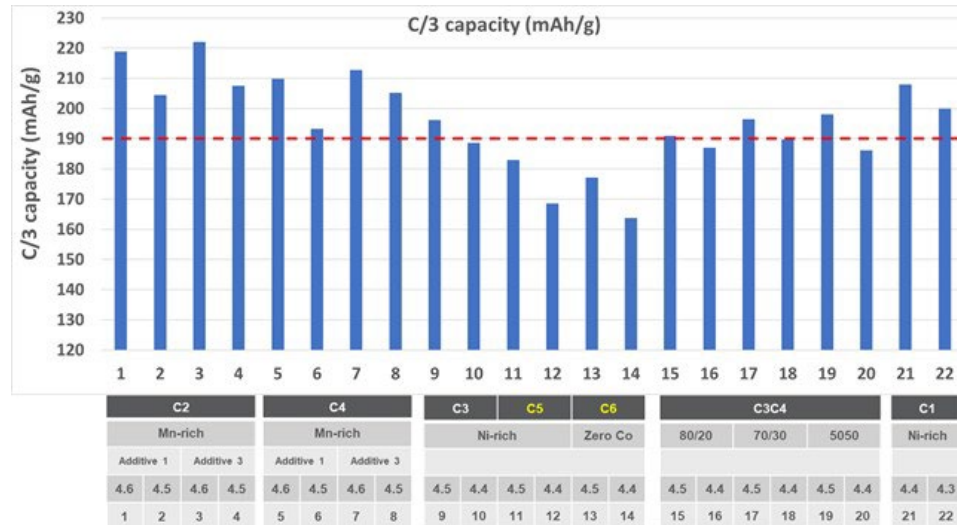


Figure III.4.1 C/3 capacity of cathode materials evaluated at different voltages

Negative electrode development: A set of single-layer pouch cells have been built and evaluated with a fixed cathode and different graphite anodes. The graphite anode materials vary with particle size, surface area and morphology. Three criteria were used to narrow the graphite anode materials for future cell builds: direct current resistance (DCR), discharge rate capability (for example, the ratio of 3C to C/5 discharge capacity) and fast charge capability (for example, maximum SoC for 3C charging to without Li plating). Table III.4.1 shows first-cycle efficiency, cell DCR, discharge rate capacity and fast charge capacity of single-layer pouch cells with different anode materials. It is found that the pouch cells with A1 type of graphite anodes shows low cell resistance and high ratio of 3C to C/5 discharge capacity. Very importantly, the cells can be charged to 80 % SoC at 3C rate while there is no Li plating during fast charge. Therefore, A1 graphite anode material is a good candidate for future cell builds to narrow cathode materials and fast charge cell development.

Table III.4.1 A comparison in first-cycle efficiency, DCR, discharge rate capability and fast charge capability of single-layer pouch cells among different graphite anode materials

Graphite Anode	First-cycle efficiency (%)	DCR_discharge (ohm)	Rate_discharge (ratio of 3C to C/5)	Rate_3C charge (max SoC*)
A1	84.7	0.55–0.88 (@ 54–57 % DoD)	84.7–89.0 %	> 80 %
A2	87.6	0.61–0.62 (@ 51 % DoD)	71.9–72.0 %	54–59 %
A3	89.0	0.58–0.69 (@ 54–57 % DoD)	85.4–87.0 %	67–72 %
A4	88.1	0.58–0.59 (@ 53–54 % DoD)	72.2–77.0 %	55–61 %
A5	89.4	0.62–0.75 (@ 51–52 % DoD)	84.3–86.2 %	68–72 %

* Maximum SoC for being charged to at 3C rate while there is no Li plating during fast charge.

Fast charge cell development: Figure III.4.2 shows fast charge cycling performance of a single-layer pouch (SLP) cell with a graphite anode and a Ni-rich cathode. A comparison in cycling performance between fast charge and regular C-rate ($C/2$) cycling is also shown in the figure. The cell can be charged to 80 % SoC using multiple charge steps within 15 min. From the voltage profile during rest period after fast charging, the voltage plateau related to the stripping of deposited Li isn't observed, showing that there is no Li plating during fast charge step. The cell can achieve ~250 and ~500 fast charge cycles at a capacity retention of 80 % and 70 %, respectively. However, the cell decays faster during fast charge than regular C-rate (such as $C/2$) cycling, which may be due to local Li plating during fast charge cycling. Farasis will continue fast charge cell development and improve fast charge cycling performance of SLP cells with low-cost and high-capacity cathodes.

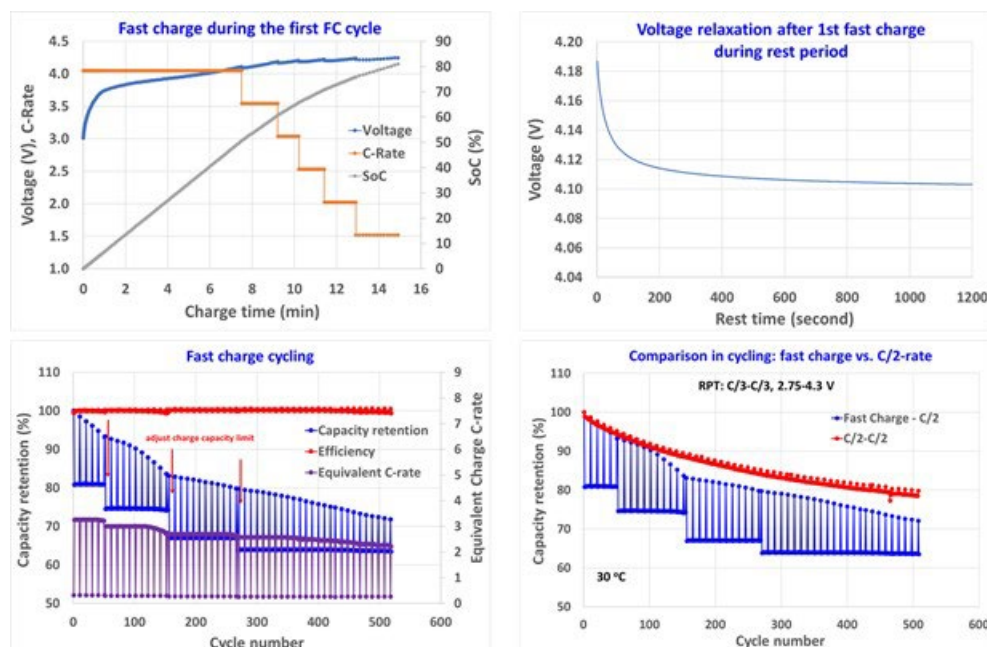


Figure III.4.2 Fast charge cycling behavior of a single-layer pouch cell with a graphite anode and a Ni-rich cathode

Conclusions

Farasis has shown ~250 and ~500 fast charge cycles in a single-layer pouch cell with a graphite anode and a Ni-rich cathode before reaching 80 % and 70 % capacity retention, respectively. Farasis has identified a graphite candidate with excellent fast charge capability as anode material from several types of graphite materials. The down-selection of cathode materials with low cost and high capacity is ongoing. Farasis will build ~70 Ah capacity Gen 1 cells with optimized chemistry with an energy density of ~272 Wh/kg and a charge time of 15 min for the 80% of the capacity. The Gen 1 cells will be also delivered to national labs for related performance evaluation and tests.

Acknowledgements

Meng Jiang, GM R&D Center, Battery Systems Group CMS, served as the USABC Program Manager for this project.

III.5 A Closed Loop Recycling Process for End-of-Life Electric Vehicle Li-ion Batteries-Phase III (Worcester Polytechnic Institute)

Yan Wang, Principal Investigator

Worcester Polytechnic Institute

100 Institute Road

Worcester, MA 01609

E-mail: yanwang@wpi.edu

Brian Cunningham, DOE Technology Development Manager

U.S. Department of Energy

E-mail: Brian.Cunningham@ee.goe.gov

Start Date: March 10, 2021

End Date: March 09, 2024

Project Funding: \$66,793

DOE share: \$53,820

Non-DOE share: \$12,793

Project Introduction

The U.S. Department of Energy (DOE) has established aggressive goals to lower the cost of lithium-ion batteries for EVs. Therefore, in the Phase III program, the team will target lowering the cathode cost by 30% (relative to commercial equivalent) by significantly increasing the amount of recycled materials (>80%) in the synthesized cathode materials. In the WPI/BRs recycling process, virgin materials (CoSO₄, NiSO₄ and MnSO₄) must be added to the leaching solution in order to reach the target ratio of Ni, Mn and Co. Earlier generation spent EV batteries use mostly NMC111 or mixed NMC111 and LMO or NMC622 as the cathode materials, and the leaching solution has more Mn than Co and Ni. However, in order to increase the energy density and lower the cost, high nickel cathode materials (for example NMC622 or above) are preferred by the EV industry. Therefore, in order to transform the Mn-rich leaching solution into a Ni-rich metal sulfate solution, supplemental virgin materials CoSO₄ and NiSO₄ are needed. In the BRs' cost model, the virgin materials currently account for 45% of the bill of materials (BOM) cost, since 0.36 kg of virgin materials are added to the leaching solution per kg of NMC622 cathode output. Therefore, in order to further reduce the cathode cost by 30%, which will help reach the DOE cost target (less than \$100/kWh, ultimately \$80/kWh) [1], the team will increase the use of recycled materials to >80%.

In addition, the lithium-ion battery (LIB) industry is a dynamic field with ongoing innovations and continually evolving materials delivering ever improving performance. It is critical that recycling technologies keep pace with state-of-the-art LIB technologies. LiNi_xMn_yCo_zAl_{1-x-y-z}O₂ (x≥0.8) has the potential to be used in the next generation of lithium-ion batteries [2]. The specific capacity of LiNi_xMn_yCo_zAl_{1-x-y-z}O₂ is >200mAh/g. Al can be introduced as dopant and/or coating to stabilize the materials. Therefore, it is critical to be able to synthesize such high nickel cathode materials from spent lithium-ion batteries in order to remain competitive in the cathode supplier space.

Finally, the team will further improve the performance of recovered NMC622 from spent lithium-ion batteries. Compared to A123 control NMC622, the recycled materials have inferior cycle performance and elevated gas generation. The reduced cycle life is likely because the stabilizing alumina coating developed rapidly in Phase II cannot fully protect the NMC622. The gas generation is likely because the soluble base content on recovered NMC622 is higher than that of control powder. It is expected that the process improvement from this task will equally benefit the higher nickel work streams.

During this 3-year program, ≥300-coin cells, 40 1Ah cells and 20 10Ah large format cells will be produced from recycled automotive lithium-ion batteries and 20 1Ah cells and 20 10Ah large format cells from control materials will be produced. 36 1Ah cells and 24 10Ah cells will be delivered to Argonne National Laboratory for testing using EV application USABC test methods. The cost of the proposed program is \$1,996,180, which

includes a 50% cost share by WPI, A123 and Battery Resourcers. At the end of program, the team expects to be able to lower the cathode cost by 30%, produce high quality NMCA and solve the cycle life and gas generation issues observed with the recycled NMC622. Achieving these targets is challenging, but necessary in order to offer a product with low cost, high quality and high energy, and to remain aligned with market trends.

Objectives

The overall objective of phase III program is: 1) to lower the cathode cost by >30% relative to commercial equivalent material through increasing the recycled content of the metal sulfate solution to >80% (<20% virgin materials); 2) to develop $\text{LiNi}_x\text{Mn}_y\text{Co}_z\text{Al}_a\text{O}_2$ ($x \geq 0.8$) from the spent EV batteries; 3) to improve the performance of the recovered NMC622 (solve the gas generation and improve the cycle life) in order to be comparable with commercial material.

Approach

High-quality NMC111&NMC622 have been successfully synthesized using WPI's closed loop recycling process for end-of-life xEV Li-ion batteries. Although much knowledge has been gained from this experience, technical challenges remain in obtaining additional Ni and Mn from other recycling streams in order to further lower the cathode cost, synthesizing NMCA precursor and cathode powder by co-precipitation and solid-state reaction. In addition, the recovered NMC622 has worse cycle life and gas generation compared to control powder, which also need to be addressed.

Recovering Ni from Ni/MH will be studied in order to reduce the amount of the virgin metal sulfate and lower the cost of the recovered cathode materials. In typical Ni/MH batteries, Ni accounts for 17.9wt% [3]. According to Inside EVs [4], ~60,000 tons Ni/MH batteries (Toyota Prius HEVs) were sold in 2013. Assuming that HEVs with Ni/MH batteries have 8~10 years life, there are 60,000 tons of spent Ni/MH batteries in U.S, which have over 10,000 tons of Nickel. In Ni/MH batteries, the cathode is $\text{Ni}(\text{OH})_2$ coated on Nickel foam. The anode is hydrogen absorbing alloys coated on steel. Although there is a high content of Ni in Ni/MH batteries, obtaining high concentration of pure Ni solution can be challenging. Impurities will significantly degrade the performance of recovered cathode materials. If the concentration of obtained solution is not high enough, a high amount of virgin chemicals will still need to be added in order to reach target concentrations. In addition to Ni/MH batteries, the team will also investigate other recycling streams for Ni that can be readily incorporated into the existing process.

High Nickel $\text{LiNi}_x\text{Mn}_y\text{Co}_z\text{Al}_a\text{O}_2$ ($x \geq 0.8$) has the advantages of high capacity and safety and is considered a promising next generation cathode material for lithium-ion batteries which could enable a driving range of 300 miles. However, the ultra-high nickel amount will also increase issues related to capacity fade. Therefore, we would expect technical challenges related to the precursor synthesis and cathode sintering steps. Although our previous research on NMC111 and NMC622 should provide good guidance, the optimum synthesis conditions for NMCA precursor need to be determined. It will thus be necessary to thoroughly investigate the effects of various factors on the key properties (e.g., morphology, tap density etc.) of resultant precursor, and experimentally determine the ideal combination of pH, temperature, reactant concentrations and flowrates, residence time, stirring speed, etc.

The high Ni content also has implications on the preparation of NMCA by high temperature calcination of precursor and the Li source. For good electrochemical performances of NMCA, the calcination needs to occur in an oxygen environment, unlike static (closed reactor) air atmosphere for NMC111, and flowing air for NMC622. This seems to be attributed to the difficulty of oxidizing Ni^{2+} . Therefore, it is essential to examine effects of oxygen partial pressure on resultant cathode properties. Moreover, compared to the calcination temperature and calcination time required for NMC111 and NMC622, the temperature and calcination time for NMCA are expected to be lower and shorter in order to minimize undesired cation mixing. It is thus critical to optimize the calcination temperature and furnace residence time in order to produce high quality NMCA cathode powder.

Aluminum incorporation in the NMCA needs to be carefully studied. There are the following three possible ways to add Al in NMCA. We will study these different approaches separately and a combination of these approaches to determine how to improve the cycle life.

1. During precursor synthesis. $\text{Al}_2(\text{SO}_4)_3$ can be added into metal sulfate solution. Then Al^{3+} will be co-precipitated with Ni^{2+} , Mn^{2+} and Co^{2+} as $\text{NiMnCoAl}(\text{OH})_2$ precursor.
2. During sintering. $\text{Al}(\text{OH})_3$ is mixed with $\text{NiMnCo}(\text{OH})_2$ precursor and Li source (LiOH) for sintering.
3. After sintering. Al_2O_3 can be coated onto LiNiMnCoO_2 surface by dry or wet methods.

Therefore, a detailed study needs to be conducted to determine the best way to dope or coat Al. In addition, the amount of Al doping or coating needs to be determined.

Another technical challenge is to improve the cycle life and reduce the gas generation of recovered NMC622 developed in the Phase II program. It is expected that improvement strategies found to be effective for this will also enhance and inform results for Phase III chemistry.

Results

NMC622

Figure III.5.1 shows synthesized NMC622 spherical secondary particle with nano size primary particles and the tap density is 2.51 g/cm^3 . The soluble base content (SBC) of different batches of powder is shown in Table III.5.1. The cathode materials from BRs exhibits the lower SBC compared to control and recycled cathode material from WPI. The powder has been delivered to A123 for further analysis. Because there are lots of broken particles in the previous batch of 04092021, BRs sintered another batch (05122021) of NMC622.

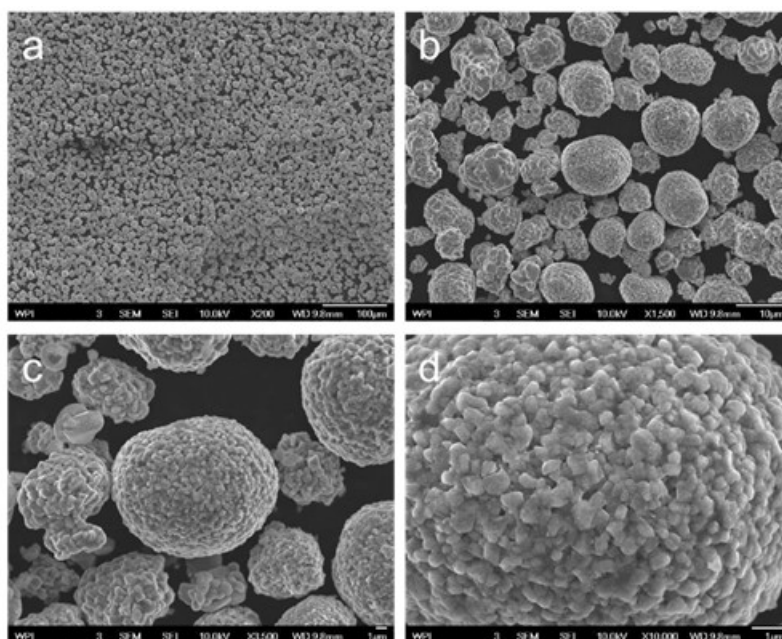


Figure III.5.1 SEM images of cathode materials from BRs

Table III.5.1 SBC comparison of control, recycled and BRs cathode materials tested by A123 and WPI

Sample Name	Residual Lithium			Free Lithium (ppm)	Free Lithium (wt.%)
	Li ₂ CO ₃ (ppm)	LiOH (ppm)*	Total (ppm)		
Control (Test by WPI)	3284.04	2128.89	5414.93	1233.78	0.123
Control (Tested by A123)	3511.263	2179.029	5690.292	1291.228	0.129
WPI 08192019 coated – 1Ah (Tested by WPI)	5277.929	3152.602	8430.531	1904.959	0.190
WPI 02212020 uncoated – 10Ah (Tested by WPI)	4597.662	4004.972	8602.63	2024.17	0.202
WPI 02212020 coated – 10Ah (Tested by WPI)	3776.651	4164.639	7941.29	1916.21	0.192
BRs cathode-04092021 (Tested by WPI)	3366.146	632.3111	4922.896	1083.411	0.108
BRs cathode-05122021 (Tested by WPI)	3530.348	2235.333	5765.681	1310.889	0.131

A123 has tested the tap density, particle size distribution and electrochemical properties with coin cells). Based on the results from A123, the tap density of these two batches NMC622 are close, which is consistent with the result from WPI. These two batches NMC622 cathode have similar electrochemical performance, and the new batch (05122021) is slightly better than the last batch (04092021) in rate performance (Figure III.5.2). To deliver 2 kg NMC622 cathode powder to A123 for gas generation test, the precursor from Battery Resources was used to synthesize the NMC622 cathode. The synthesized NMC622 cathode material is dense. The tap density is 2.48 g/cc, and the SBC is 0.106 wt.% before coating and 0.087 wt.% after coating, which is lower than the control. The 2kg recycled NMC622 has been delivered to A123 for further testing.

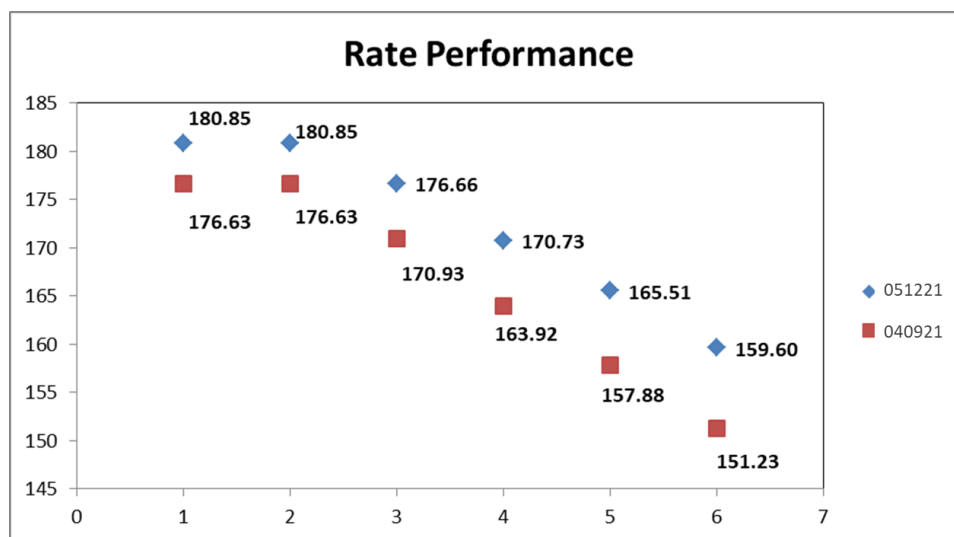
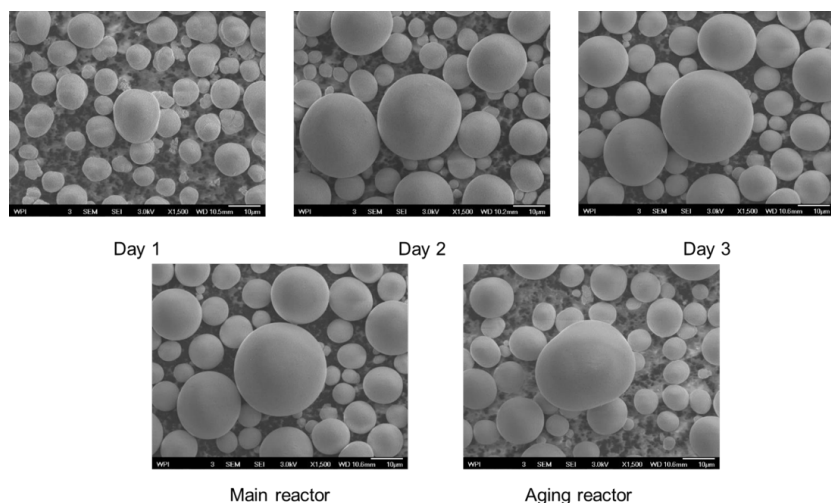


Figure III.5.2 Comparison between the batch of 04092021 and 05122021 in rate performance

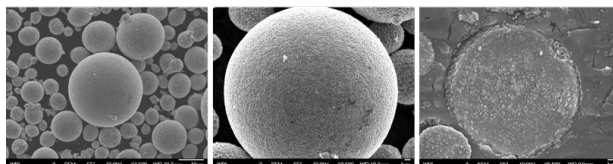
High Nickel NMC (83% Ni)

In order to determine the parameters for high Nickel NMC (83% Ni) precursor and cathode materials, WPI first used virgin materials for the experiments. Figure III.5.3 shows precursor collected at different days. From the figure, the particles become larger and denser with the increased time. The particles are spherical in shape and dense. Table III.5.2 shows tap density of the precursor collected at different time. Then, day 3 precursor was used to prepare the cathode materials (Figure III.5.4) with LiOH using a tube furnace with an oxygen atmosphere.

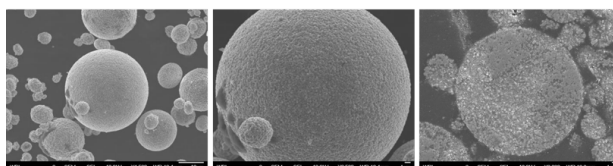
Figure III.5.3 Synthesized ^{83}Ni Precursor with virgin materialsTable III.5.2 Tap density of synthesized ^{83}Ni precursor with virgin materials

Time	Tap Density (g/mL)	Weight (g)
Day1	1.79	338.4
Day2	1.82	667.4
Day3	1.96	910.4
Main	1.91	195.5
Aging	1.92	125.5

05242021 (2.38g/ml; 20g)



05312021 (2.34g/ml; 50g)

Figure III.5.4 ^{83}Ni cathode sintered in different batches

In addition to determine the precursor synthesis parameters, we further determine the condition of sintering and washing steps. Firstly, the precursor was sintered with different amounts of LiOH (1 mol.%, 3 mol.% and 5mol.% LiOH excess) at different temperatures (at 775°C and 800°C). All synthesized ^{83}Ni cathode materials show better morphology than the control. Obtained ^{83}Ni cathode materials have a more spherical shape.

However, the SBC of all synthesized ^{83}Ni cathode materials is much higher than the control. The SBC of control is 0.138 wt.%, and it is over 0.4 wt.% for the sample sintered with 5 mol.% excess LiOH. Although reducing Li amount can decrease the SBC number, it is still higher than the control. On a small scale, particles

will start to break after 3 mins. The SBC of the washed samples is lower than the control. Then two 50g batches are delivered for the electrochemical performance test. It is worth mentioning that when the amount of powder is increased, the SBC drop is lower than that of a small-scale experiment, and the particles will not be broken as much as the small-scale experiment. Moreover, we washed a sample with 10 mins of hand stirring. Because of the long-time washing, particles break a lot. This batch powder was delivered to A123 to confirm if the washing step would affect the performance.

A123 tested WPI synthesized 83Ni and control (reference) powder. The lot number and sample information are in Table III.5.3. And the coin cell test results are shown in Figure III.5.5, which shows the comparison of rate performance between WPI synthesized samples and reference sample. 20210906 has the lowest capacity under all current rates and 20210818 has the highest capacity, possibly caused by broken particles.

Table III.5.3 Lot number and sample information

	Sintering condition	Wash condition
Reference	Control/commercial powder	
20210524	450 °C 5hrs, 775 °C 10hrs; 20g	Unwashed
20210531	450 °C 5hrs, 775 °C 10hrs; 50g	Unwashed
20210818	450 °C 5hrs, 775 °C 10hrs; 50g	Washed with hand stirring
20210906	450 °C 5hrs, 800 °C 10hrs; 50g	Unwashed

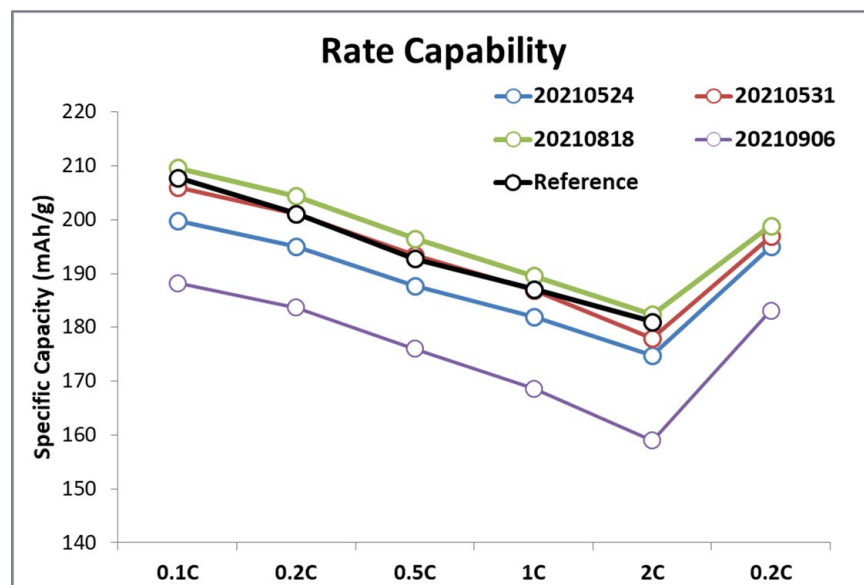


Figure III.5.5 Rate performance of coin cell with 83Ni cathode powders and reference sample

Ni source from Ni/MH batteries

BR starts to recycle spent Ni/MH batteries in order to obtain Ni source. The flowchart is shown in Figure III.5.6. After leaching process, according to the ICP result, there are some rare earth elements (REE) in the leaching solution. When the pH was adjusted to 5.3, all of the metal impurities including REE were removed from the leaching solution. The ICP results suggested that a separate REE removal step is still necessary. Efforts will continue to focus on optimization of leaching efficiency, REE separation, impurity removal pH ranges and recovery method development for nickel and cobalt into precursor syntheses.

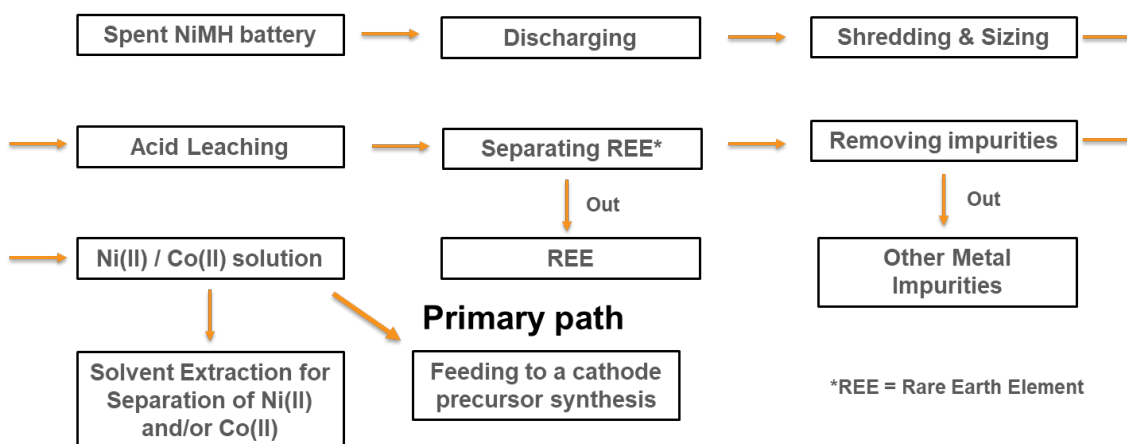


Figure III.5.6 Flow chart of recycling spent Nickel metal hydride battery for feeding to NMC precursor synthesis

Conclusions

In this USABC Phase III project, the team has successfully lowered SBC of NMC622 powder through washing method developed by BR. In addition, multiple batches of high Nickel NMC has been synthesized. The precursor particles are spheric, dense and have the right composition. The Cathode particles have been prepared and delivered to A123 Systems for capacity checking and their capacity is ~200mAh/g. Currently, the team is developing approach to lower the SBC for high Nickel NMC. Finally, initial work has been conducted to recovered Ni from Ni/MH batteries.

Key Publications

1. Xiaotu Ma, Mengyuan Chen, Zhangfeng Zheng, Dennis Bullen, Jun Wang, Chloe Harrison, Eric Gratz, Yulin Lin, Zhenzhen Yang, Youtian Zhang, Fan Wang, David Robertson, Seoung-Bum Son, Ira Bloom, Jianguo Wen, Mingyuan Ge, Xianghui Xiao, Wah-Keat Lee, Ming Tang, Qiang Wang, Jinzhao Fu, Yubin Zhang, Bryer C. Sousa, Renata Arsenault, Peter Karlson, Nakia Simon, Yan Wang,* (2021), Recycled Cathode Materials Enabled Superior Performance for Lithium-Ion Batteries, *Joule*, DOI:10.1016/j.joule.2021.09.005

References

1. <https://www.energy.gov/eere/vehicles/batteries>.
2. Kim, U.-H.; Kuo, L.-Y.; Kaghazchi, P.; Yoon, C. S.; Sun, Y.-K., Quaternary Layered Ni-Rich NCMA Cathode for Lithium-Ion Batteries. *ACS Energy Letters* 2019, 4 (2), 576–582.
3. Lin, S.-L.; Huang, K.-L.; Wang, I.-C.; Chou, I.-C.; Kuo, Y.-M.; Hung, C.-H.; Lin, C., Characterization of spent nickel–metal hydride batteries and a preliminary economic evaluation of the recovery processes. *Journal of the Air & Waste Management Association* 2016, 66 (3), 296–306.
4. <https://insideevs.com>.

Acknowledgements

The development team (WPI/A123/BRs) would like to thank the following for all of the help, advice, support and suggestions: USABC program manager Renata Arsenault (Ford) and USABC work group members Nakia Simon (Stellantis), Kely Markley (GM), Brian Cunningham (DOE), and David Robertson (ANL).

IV Extreme Fast Charging (XFC)

IV.1 Research on high power, doped titanium-niobium oxide anodes (ORNL)

Sheng Dai, Principal Investigator

University of Tennessee
354/502 Buehler Hall
1416 Circle Drive
Knoxville, TN 37996
E-mail: sdai@utk.edu

Brian Cunningham, DOE Technology Development Manager

U.S. Department of Energy
E-mail: Brian.Cunningham@ee.doe.gov

Start Date: July 1, 2018
Project Funding: \$800,000

End Date: June 30, 2021
DOE share: \$720,000

Non-DOE share: \$80,000

Project Introduction

Commercial lithium-ion batteries (LIBs) using graphite as the anode material can easily result in lithium plating during extreme fast charging or abuse conditions, leading to fast capacity fading and safety issues. To eliminate the lithium plating issue in LIBs during extremely fast charging, we proposed to use doped titanium niobium oxide (TNO) as anode, which has not only an operation voltage of 1.66 V vs. Li/Li⁺ that is far from the lithium plating but also a high theoretical capacity of 387 mA h g⁻¹.

Objectives

The main objective of this project is to synthesize titanium niobium oxide (TNO) that has a nanoporous structure with porous channels for rapid lithium diffusion, enabling extreme fast charging (XFC). The focus of this project is to improve the electronic conductivity and ion diffusion coefficient in TNO to achieve high capacities under extreme fast charge conditions. In addition, electrolytes with additives will be formulated to promote stable interphase formation on the NMC cathode surface to improve long cycling stability.

Approach

- Enhance rate capability by formation of nanostructures.
- Improve electronic conductivity by doping and surface coating with carbon.
- Synthesize large scale TNO with low-cost precursors.
- Evaluate rate performance and long term cyclability of coin cells with high loading TNO.
- Improve long term cyclability of coin full cells using functional additives.
- Evaluate rate performance and long term cyclability of pouch full cells.

Results

In the past period, one of our focuses was to synthesize enough TNO materials for fabrication of 18 2Ah pouch cells for evaluation at ANL. At the same time, we have also tried to find out the origin of gassing issue in NMC/TNO pouch cells that we have noticed in previous investigations. Although there is less gas generated during the initial formation cycles in the TNO based full cells, it will be continually generated during the

following cycles, which will significantly affect the long cycle stability of full cells, particularly under fast charge conditions.

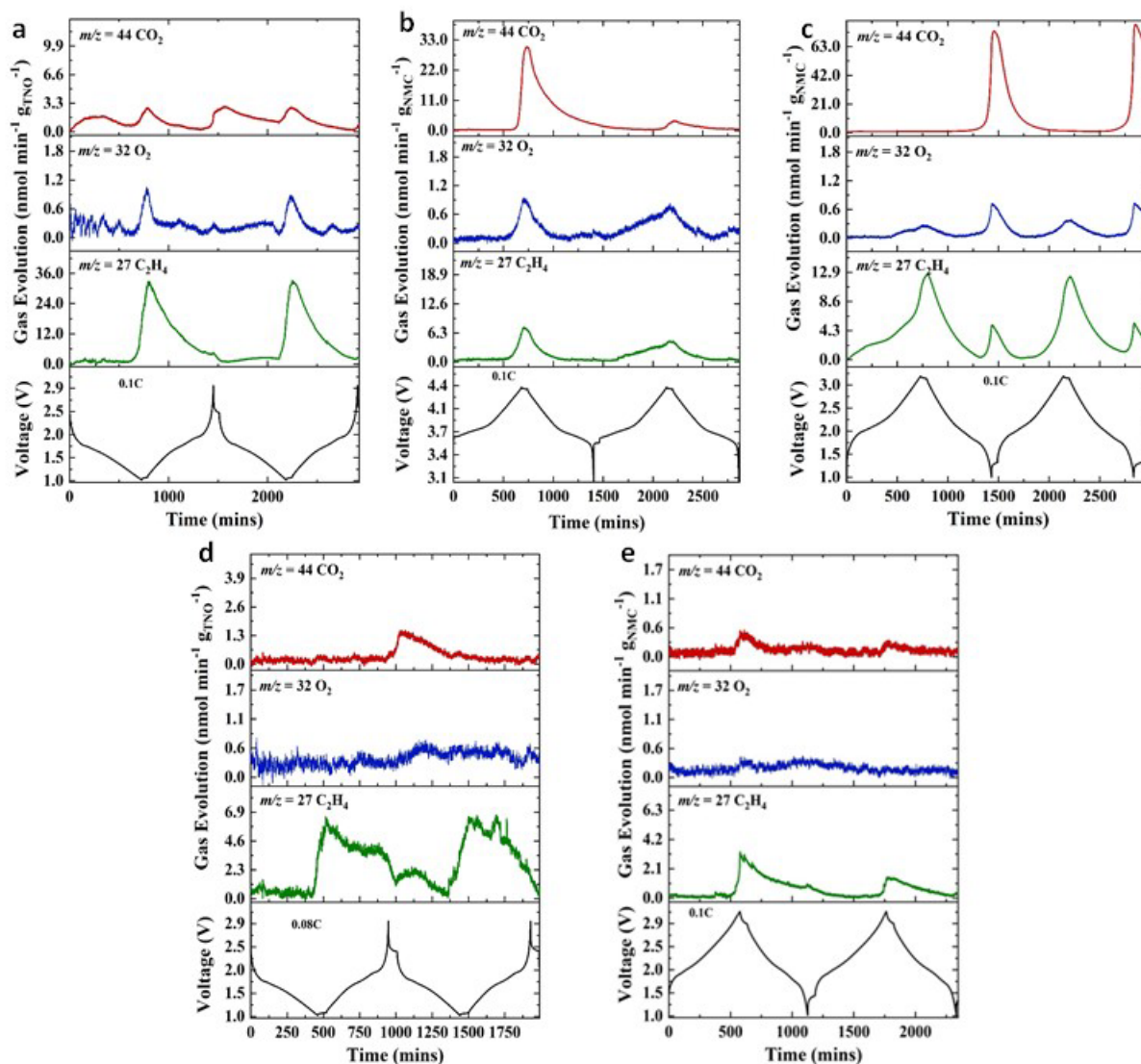


Figure IV.1.1 Voltage profiles and the corresponding background-corrected mass signals $m/z = 44$ (CO_2), 32 (O_2), and 27 (C_2H_4) for a) TNO-Li metal, b) NMC811-Li metal, c) TNO-NMC811, d) coated TNO-NMC811 pouch cells.

A commercial mass spectroscopy instrument was directly connected to the pouch cells *via* a glass capillary tube without any stationary phase on the inner wall, which was first sealed in the pouch cell using hot melt adhesive, and then the other end of the capillary tube was connected to the MS. This setup is advantageous as it does not require a special cell for the in-situ study and testing can be done with higher sensitivity as no carrier gas is required during the measurements. [1] As shown in Figure IV.1.1a for the TNO-Li metal pouch cell, the intensity of CO_2 increases from 0 to $\sim 1.8 \text{ nmol min}^{-1} \text{ g}_{\text{TNO}}^{-1}$ as the voltage drops from its open circuit voltage (OCV = 3.18 V) to ~ 1.6 V. The intensity of CO_2 falls back to $0.6 \text{ nmol min}^{-1} \text{ g}_{\text{TNO}}^{-1}$ as the discharge process completes and the voltage reaches 1.0 V. This behavior might be ascribed to some interfacial side reaction at the anode during the lithiation process. Another peak for CO_2 is observed along with the onset of C_2H_4 and O_2 formation as the cell voltage reaches close to 1.15 V towards the end of the discharge process (lithiation). All the three gaseous species, C_2H_4 , O_2 , and CO_2 peak towards the end of the discharge process and voltage relaxation with a maximum gas evolution of 32.8 , 0.98 and $2.8 \text{ nmol min}^{-1} \text{ g}_{\text{TNO}}^{-1}$, respectively.

Similar trends in C_2H_4 , O_2 , and CO_2 evolution are observed during the second cycle at 0.1C. C_2H_4 generation is the highest among all gases during this lithium insertion process (discharge cycle), which can be attributed to the decomposition of EC component in the electrolyte.

Figure IV.1.1b shows the voltage profile and gas composition for NMC-Li metal pouch cell. The on-set potential for CO_2 , C_2H_4 , and O_2 evolution is ~ 4.2 V during the delithiation process. The CO_2 generation rate is $\sim 0.1 \text{ nmol min}^{-1} \text{ g}_{\text{NMC}}^{-1}$ at 4.2 V, while a dramatic rise in the CO_2 concentration ($\sim 4.5 \text{ nmol min}^{-1} \text{ g}_{\text{NMC}}^{-1}$) is observed once the cell reaches a cut-off voltage of 4.4 V towards the end of the charging process. It is observed that CO_2 generation rate of NMC electrodes was significantly influenced by the cut-off voltage, where CO_2 concentration increased dramatically when the voltage increased from 4.2 to 4.4 V while O_2 generation was not as sensitive as CO_2 to the cut-off voltage. The gas concentration of O_2 and C_2H_4 peaks at approximately 0.22 and $1.75 \text{ nmol min}^{-1} \text{ g}_{\text{NMC}}^{-1}$ towards the beginning of the voltage relaxation (4.4 V), respectively. We could rule out the possibility of lattice oxygen release because the cut-off voltage is limited to 4.4 V, and lattice oxygen evolves at >4.6 V for NMC. Hence, the O_2 and C_2H_4 generation at 4.4 V is mainly due to the decomposition of impurities and electrolyte solvent.

Figure IV.1.1c shows the gas evolution and voltage profiles of the TNO-NMC full cell. The C_2H_4 generation is the highest among all the gases during the charging process when the cell potential reaches 3.2 V. Small amounts of O_2 and CO_2 are generated during this process. During the discharge process towards the cell potential of 1.0 V, CO_2 generation is significantly higher than other gases with little quantities of O_2 and C_2H_4 . As lithium ions move towards the TNO anode during the charging process, C_2H_4 generation begins and peaks at the end of voltage relaxation process after the cell potential reaches the cut-off voltage of 3.2 V. Approximately $12.55 \text{ nmol min}^{-1} \text{ g}_{\text{NMC}}^{-1}$ of C_2H_4 and $0.25 \text{ nmol min}^{-1} \text{ g}_{\text{NMC}}^{-1}$ of O_2 are generated by the end of voltage relaxation period, suggesting the electrolyte decomposition takes place during the charging process at low currents. Likewise, a dramatic rise in CO_2 generation ($\sim 74.33 \text{ nmol min}^{-1} \text{ g}_{\text{NMC}}^{-1}$) is observed during the start of the voltage relaxation period after the discharge process. The O_2 generation is almost three times higher than the charge process, close to $0.69 \text{ nmol min}^{-1} \text{ g}_{\text{NMC}}^{-1}$. C_2H_4 evolution peaks to $\sim 5.06 \text{ nmol min}^{-1} \text{ g}_{\text{NMC}}^{-1}$ at the beginning of the voltage relaxation period after the discharge process, suggesting further electrolyte decomposition on the cathode side, leading to formation of cathode electrolyte interface (CEI).

To mitigate the gassing issue, we have developed a protective polyimide coating on the TNO particles following a US patent procedure. [2] Figure IV.1.1d shows the CO_2 , O_2 and C_2H_4 gas evolution decreases significantly once the protective polyimide coating is applied to the TNO particles. At 0.08C, CO_2 evolution begins at the end of the charge cycle (delithiation process), and peaks to $\sim 1.45 \text{ nmol min}^{-1} \text{ g}_{\text{TNO}}^{-1}$ at the end of voltage relaxation. Whereas C_2H_4 evolution begins at the end of the discharge cycle (lithiation process) as the voltage drops close to 1.1 V, and peaks to $\sim 6.8 \text{ nmol min}^{-1} \text{ g}_{\text{TNO}}^{-1}$ at the end of the voltage relaxation process. O_2 generation was almost constant throughout the cycling process, close to $0.6 \text{ nmol min}^{-1} \text{ g}_{\text{TNO}}^{-1}$. With the protective polyimide coating on TNO particles, the rate of CO_2 and C_2H_4 evolution dropped by almost 2 and 5 times, respectively, as compared to the pristine TNO-Li pouch cell in Figure 1a. This dramatic reduction in gas evolution suggests that the rate of side reactions relating to the electrolyte decomposition on the TNO anode surface decreases significantly with the help of the protective polyimide coating.

In case of the coated TNO-NMC full cell, a drastic drop in CO_2 , O_2 and C_2H_4 gas generation rate is also observed as shown in Figure IV.1.1e. The CO_2 , O_2 and C_2H_4 gas evolution begins from the end of the first low current (0.1C) charge cycle, and peaks at 0.52, 0.31, and $3.45 \text{ nmol min}^{-1} \text{ g}_{\text{NMC}}^{-1}$, respectively, by the end of the voltage relaxation period. It is noted that the CO_2 and C_2H_4 generation rates decreased by $\sim 99\%$ and $\sim 72\%$, respectively, suggesting a major reduction in electrolyte decomposition at the anode side. The application of the protective polyimide coating on TNO particles is a significant step to improve TNO based anodes as the next generation lithium-ion batteries for achieving extreme fast charging.

Surface analysis of pristine and coated TNO were investigated by XPS, exhibiting similar behaviors as illustrated in Figure IV.1.2. The Ti 2p spectra shows two peaks at 459 eV and 465 eV, which is in good

agreement with Ti 2p_{1/2} and Ti 2p_{3/2} of Ti⁴⁺ ions in TNO, respectively (curve a and b). At fully lithiated state (curve c), the peaks almost disappear with a slight hump at 456 eV during the first cycle. The peaks completely disappear at fully lithiated state after two cycles (curve e). A similar behavior is observed with the Nb 3d spectra where the peak disappears at fully lithiated state after 2 cycles. This indicates that a layer, i.e., SEI, was formed during lithiation which reduced the intensity of Ti and Nb from the bulk. This layer grows with cycles and completely blocks the signal from the bulk after two cycles. Based on the XPS analysis, the spectra of Ti, Nb and C (curve d) are almost identical to the as-coated electrode after complete delithiation. This suggests that the preformed SEI layer during lithiation step becomes thinner if not completely disappeared at 3.0 V. The formation and dissolution of the SEI indicates a more dynamic process for TNO during lithiation and delithiation compared to a more stable one for the graphite counterpart. For the C 1s XPS profile, bonds of C-C from carbon black and C-F from PVDF are observed at 284 eV and 292 eV, respectively for curve b. During the first cycle after full lithiation (curve c), the C=O double bonds appear at 287 eV and 289 eV, corresponding to LiCO₃ and RCOOLi, respectively, which are common components of SEI. The C-F bond from PVDF disappears in curve c confirming an SEI layer forms and covers the surface of TNO electrode. Likewise, at the delithiation state (curve d), the C-F bonds reappear and the SEI related peaks disappear. The SEI related peaks at 287 eV and 289 eV appear again at 100% lithiation state after two cycles, indicating dynamic evolution of a reversible SEI is observed on the TNO surface even at a high operating voltage (1.0 V).

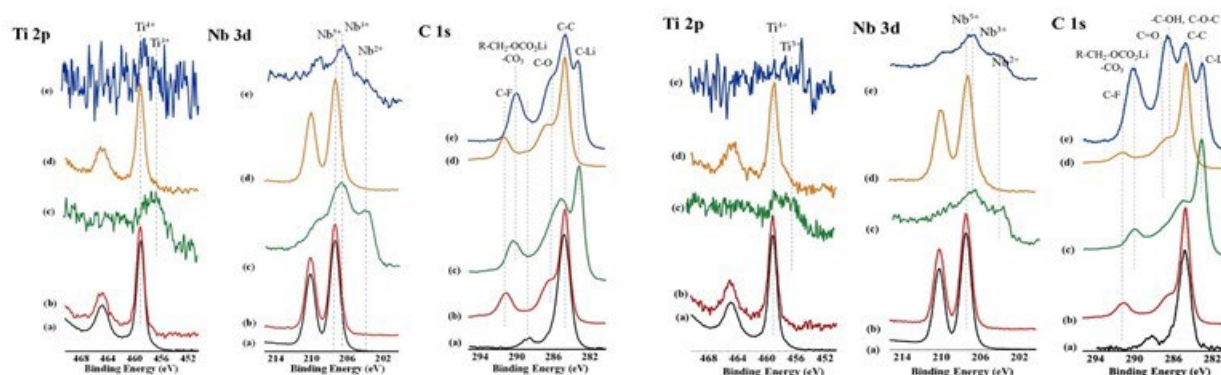


Figure IV.1.2 Ti 2p, Nb 3d, C 1s XPS spectra of TNO (left) and coated TNO (right) (a) pristine powder; (b) electrode before cycling; (c) electrode at 100% lithiated state (cutoff at 1.0 V); (d) electrode at complete delithiated state (cutoff at 3.0 V); (e) electrode at 100% lithiated state after 2 cycles (cutoff at 1.0 V).

Conclusions

The nature of gas evolution during the cycling of TNO based anodes (half-cell and full-cell configuration) was investigated *via* operando mass spectrometry analysis. The main detected gases generated during the cycling process were C₂H₄, O₂, and CO₂. The evolution of C₂H₄ is attributed to the decomposition of EC component of electrolyte on the TNO surface, leading to formation of a reversible SEI film. Unlike a stable SEI on the graphite counterpart, the SEI on TNO dissolved during the lithium extraction process, as confirmed by XPS. The gas evolution was dramatically suppressed by coating a protective layer on the TNO particles, reducing the CO₂ and C₂H₄ evolution by almost 2 and 5 times respectively. The reduction on gas generation in full cells was even more pronounced. The surface coating of TNO electrode provide an effective way to improve its cycling stability.

Key Publications

1. D. Parikh, L. X. Geng, H. L. Lyu, H. S. Liu, X. G. Sun, S. Dai, J. L. Li, In-situ Analysis of Gas Evolution in TiNb₂O₇ (TNO) based Anodes for Advanced High Energy Lithium-Ion Batteries under Extreme Fast Charging Conditions, *ACS Appl. Mater. Interfaces*, 2021, in press.

References

1. L. Geng, D. L. Wood, S. A. Lewis, R. M. Connatser, M. Li, C. J. Jafta, I. Belharouak, High accuracy in-situ direct gas analysis of Li-ion batteries. *J. Power Sources* **2020**, 466, 228211.
2. H. Liu, X. Lin, Talostech LLC, 2019. Polyimide coated lithium titanate particles and use thereof in a lithium-ion battery. U.S. Patent 10,381,648.

Acknowledgements

U.S. DOE Office of Energy Efficiency and Renewable Energy (EERE) Vehicle Technologies Office (VTO)

Program Managers: Adrienne L. Riggi, Brian Cunningham, David Howell

ORNL Contributors: Xiao-Guang Sun, Jianlin Li

UTK Contributors: Hailong Lyu

IV.2 Enabling Extreme Fast Charging through Control of Li Deposition Overpotential on Graphite Electrodes (Stony Brook University)

Esther Takeuchi, Principal Investigator

Stony Brook University
100 Nicolls Road, 675 Chemistry
Stony Brook, NY 11790
E-mail: esther.takeuchi@stonybrook.edu

Brian Cunningham, DOE Technology Development Manager

U.S. Department of Energy
E-mail: Brian.Cunningham@ee.doe.gov

Start Date: July 1, 2018
Project Funding: \$892,496

End Date: August 31, 2021
DOE share: \$800,000

Non-DOE share: \$92,496

Project Introduction

A major barrier facing the adoption of electric vehicles (EVs) is that currently utilized Li-ion batteries take significantly longer to recharge compared to the time necessary to refuel vehicles powered by internal combustion engines. Thus, the need to develop Li-ion batteries which can be charged in approximately 10 minutes (6 C rate) without sacrificing range, cost, or cycle life is critical for the widespread implementation of EVs. Fast charging capability of state-of-the-art Li-ion batteries is limited by the occurrence of Li plating at the graphite anode. At fast charge rates the graphite anode is polarized below 0V, causing Li plating that results in capacity loss, increased resistance, and internal short circuits. To suppress Li plating, multiple strategies have been demonstrated with only limited effectiveness, and new approaches are needed to enable cycling at extreme fast charging rates.

Objectives

The objective of the project is to research, develop, design, fabricate, and demonstrate 2 Ah XFC cells, with an energy density ≥ 200 Wh/kg, capable of a 10-minute fast charge protocol at ≥ 6 C charging rate, cost of $\leq \$150$ /KWh, and 500 cycles with $< 20\%$ fade in specific energy.

Approach

The technological approach is to deliberately increase the overpotential for Li metal deposition at the graphite anode surface, thereby inhibiting Li metal deposition. This is accomplished by coating graphite electrodes with nanometer scale coatings of Cu or Ni metal, which have high overpotentials unfavorable for lithium deposition. During battery charging, the overpotentials for Li deposition on the metal coated electrode surface are greater in magnitude than the overpotential for intercalation into graphite, resulting in preferred lithiation of graphite and inhibited Li plating. The nanometer scale thickness of the metal coatings enables the function of the graphite electrode to be maintained and preserve state of the art energy density. The program represents an entirely novel and potentially transformative strategy for Li plating suppression.

Results

1. Identification of Vendor for Electrodes Used in Multi-layer Cell Fabrication

Work in this fiscal year was focused on fabrication of multi-layer cells with the fast-charging technology for delivery to DOE for evaluation. One of the tasks associated with the multilayer cell build was to identify a suitable vendor for procurement of electrodes to be used in the cells. An initial batch of single and double sided NMC622 and graphite electrodes was procured from vendor A. Graphite electrodes were prepared with composition of 90% SLC 1506T natural graphite, 3% carbon black, and 7% KF-9300 Kureha PVDF binder,

with 8.6 mg cm^{-2} graphite loading. NMC622 cathodes were prepared with 90% NMC622, 5% carbon black, 5% PVDF with 16.8 mg/cm^2 NMC622 loading. The VENDOR A produced electrodes were tested relative to the BNL produced electrodes with respect to capacity and retention where a 2×2 ‘design of experiment’ matrix of BNL graphite vs. VENDOR A graphite and BNL NMC vs. VENDOR A NMC was used, with triplicate single layer pouch cells for each condition. The single layer pouch cells were filled with a 1M LiPF₆ 30:70 ethylene carbonate (EC): dimethyl carbonate (DMC) electrolyte with 2% wt. of vinylene carbonate (VC) electrolyte. All cell testing was performed at 30°C. A cell formation protocol of 4 cycles at C/10 rate between 3 V – 4.3 V was utilized prior to further testing. The cells were then fully discharged at C/10, and charged under a 10-minute charge protocol, where the fast charge protocol consisted of a 6C constant current step followed by a constant voltage step at 4.3V for the remainder of the 10-minute segment. The cells were then discharged at C/3 rate to 3.0 V to determine the initial discharge capacity after a 10-minute charge. Further cycling was then performed under 10-minute charge/ 1C discharge, where every 50 cycles the cells underwent the fast charge protocol followed by discharge at C/3 rate.

Plots of areal capacity and capacity retention are shown in Figure IV.2.1 The BNL fabricated graphite and NMC electrodes had superior capacity retention when compared with the VENDOR A fabricated electrodes. After 300 cycles, the areal capacity retention values were $36.4 \pm 2.6 \%$, $61.4 \pm 4.0 \%$, $49.2 \pm 2.4 \%$, and $73.3 \pm 0.8 \%$ for VENDOR A graphite—VENDOR A NMC, VENDOR A graphite—BNL NMC, BNL graphite—VENDOR A NMC, and BNL graphite—BNL NMC cells respectively. Discussions with the VENDOR A prototyping facility took place to attempt to improve the electrode performance and a second batch of electrodes was purchased and tested. The second batch of electrodes exhibited no significant improvement in capacity retention after 300 fast charge cycles (44% retention).

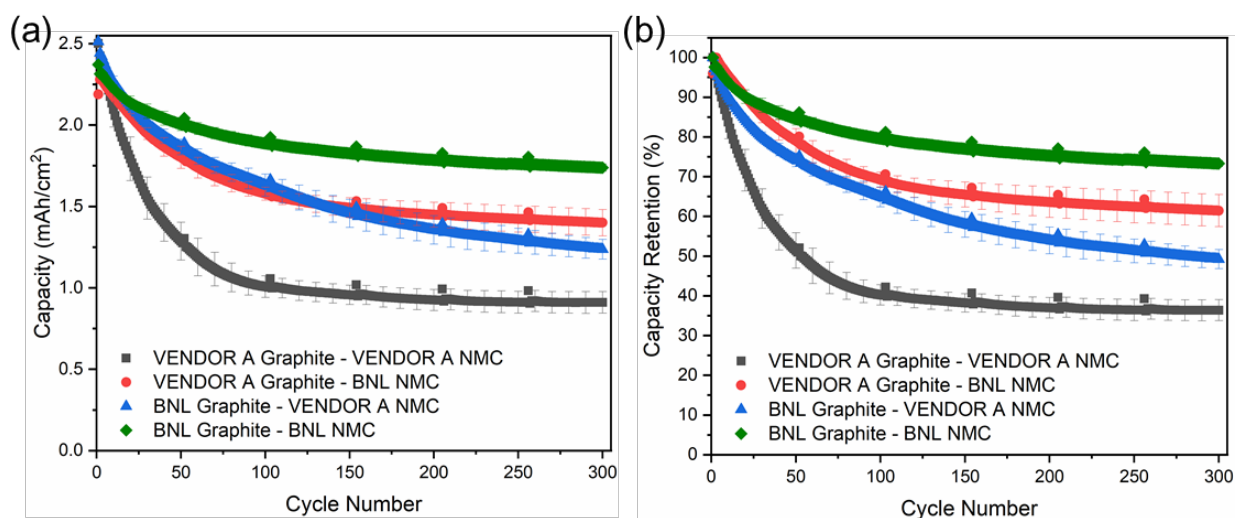


Figure IV.2.1 (a) Areal capacity, and (b) capacity retention for single layer full cells with varying combinations of VENDOR A and BNL produced NMC 622 cathodes and uncoated graphite anodes. Cells were cycled at 30 °C under 10-minute charge/ 1C discharge protocol with a C/3 discharge every 50 cycles. Error bars represent one standard deviation from the mean (n = 3 cells per configuration).

Due to the continued poor performance of electrodes procured from VENDOR A, new electrodes were obtained from a different vendor—VENDOR B—using the same materials and compositions as described previously. A 2×2 ‘design of experiment’ matrix of BNL graphite vs. VENDOR B graphite and BNL NMC vs. VENDOR B NMC was tested, with triplicate single layer pouch cells for each condition (Figure IV.2.2). Cells were tested under a 10-minute charge (6C CC, CV at 4.3 V) protocol for 300 cycles. Cells containing the VENDOR B electrodes were comparable to those containing BNL electrodes in both initial capacity after fast charge (VENDOR B: 2.25 mAh/cm^2 vs. BNL: 2.42 mAh/cm^2) and retention after 300 cycles (VENDOR B:

88% vs. BNL: 78%). Based on these promising results, VENDOR B was selected as the vendor for single- and double-sided electrodes for the final multilayer cell build.

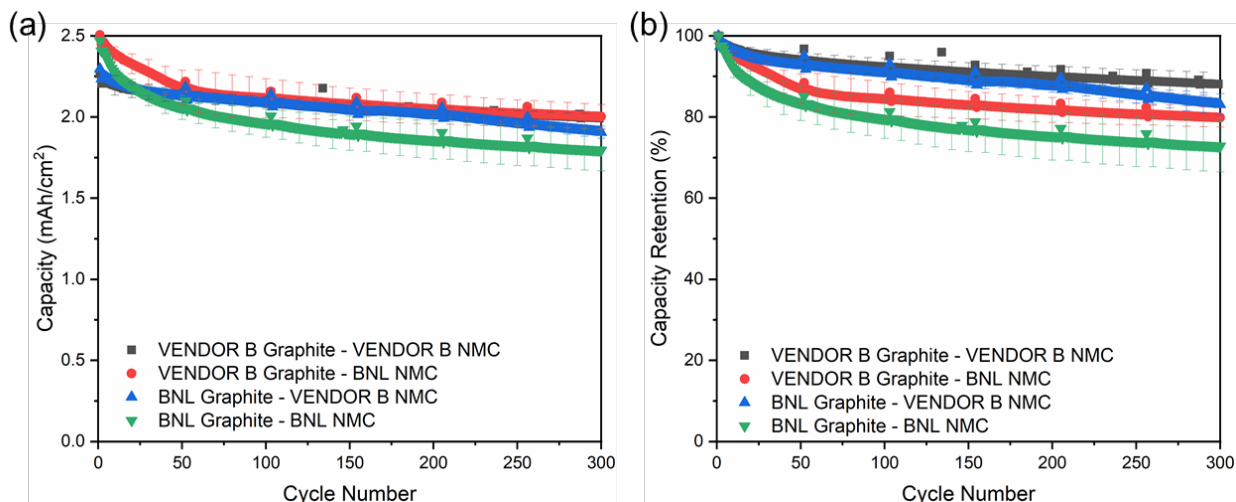


Figure IV.2.2 (a) areal capacity, and (b) capacity retention for single layer full cells with varying combinations of VENDOR B and BNL produced NMC 622 cathodes and uncoated graphite anodes. Cells were cycled at 30 °C under 10-minute charge/ 1C discharge protocol with a C/3 discharge every 50 cycles. Error bars represent one standard deviation from the mean (n = 3 cells per configuration).

2. Optimization of Electrolyte Loading and Charging Protocol

The influence of electrolyte loading in multi-layer cells was also evaluated with the goal of improving the cell specific energy. This task was performed using 1 Ah cells fabricated with the pouch cell pilot line at BNL. The effect of electrolyte volume to pore volume ratio was studied, with 1.5 : 1 and 1.3 : 1, and 1.2 : 1 ratios tested. A fourth cell with 1.5 : 1 ratio was cut open and resealed after formation to release any gaseous degradation products produced during SEI formation. The cells were cycled at 30 °C under 1C charge/ 1C discharge protocol for 200 cycles (Figure IV.2.3). When comparing the performance of electrolyte ratios at 1C, the 1.3 : 1 ratio resulted in the highest specific energy and capacity retention. Use of the degassed cell was found to significantly improve the specific energy, with the value of 180 Wh/kg achieved.

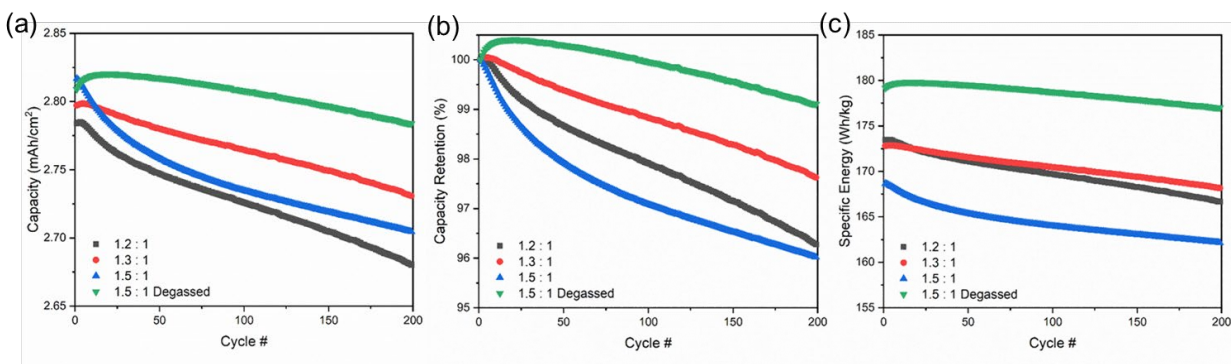


Figure IV.2.3 (a) Areal discharge capacity, (b) capacity retention, and (c) specific energy for 1 Ah multi-layer full cells with electrolyte to pore volume ratio of 1.5 : 1 (blue), 1.3 : 1 (red), and 1.2:1 (black). A fourth cell with 1.5 : 1 ratio was degassed after formation cycling (green). The cells were cycled at 30 °C under 1C charge/ 1C discharge for 200 cycles.

Based on the promising results cells utilizing the 1.3 : 1 electrolyte to pore volume ratio and the degassed 1.5 : 1 ratio cell, two additional degassed cells were fabricated with 1.3 : 1 and 1.5 : 1 electrolyte : pore volume ratios. The cells were charged under 10-minute fast charge conditions at 40 °C (Figure IV.2.4) with a 6C

constant current step followed by a constant voltage step at 4.3V for the remainder of the 10-minute segment. A C/3 discharge was performed every 50 cycles. The cell with the 1.5 : 1 pore ratio delivered significantly higher specific energy (2.6 mAh/cm² vs. 2.4 mAh/cm²) and capacity retention (67% vs. 32%) under the fast-charging conditions. The results clearly indicated that the electrolyte to pore volume ratio of 1.5 : 1 was superior for enhanced capacity retention under XFC charging.

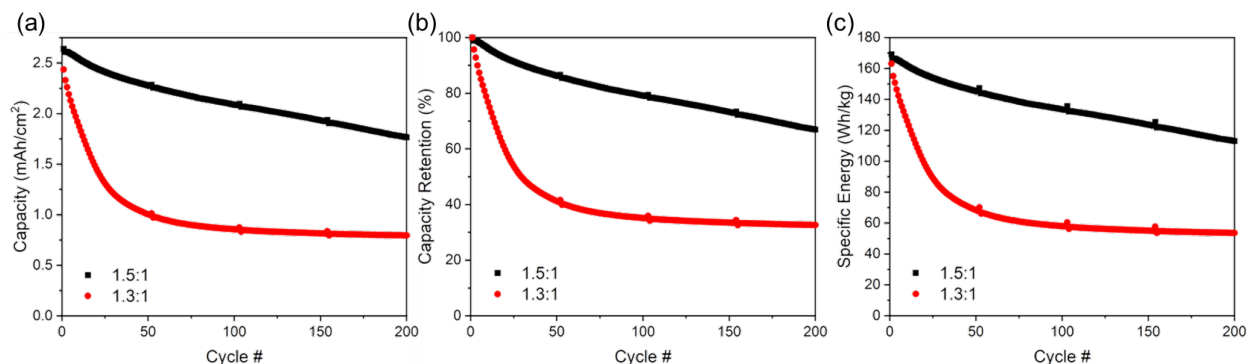


Figure IV.2.4 (a) Areal discharge capacity, (b) capacity retention, and (c) specific energy for 1 Ah multi-layer full cells with electrolyte to pore volume ratio of 1.5 : 1 (red) and 1.3 : 1 (black). Both cells were degassed after formation and cycled under 10-minute charge/ 1C discharge protocol at 40 °C with a C/3 discharge every 50 cycles.

The influence of charging voltage limit and operating temperature was also evaluated. Testing was performed in single layer full pouch cells where the graphite electrodes were sputtered with 20 nm Ni. A 2 x 2 design of experiments matrix of 4.2 V vs. 4.3 V upper charging voltage and 5C V vs. 6C constant current was tested, with triplicate cells for each condition (Figure IV.2.5). A test temperature of 40 °C was used for all cells. The 4.3 V, 6C condition resulted in the highest initial delivered capacity after first fast charge (2.54 ± 0.02 mAh/cm²), and capacity retention of 78% after 500 fast charge cycles. The other test conditions resulted in improved capacity retention values 89% or above, but at the expense of lower delivered capacity (< 2.4 mAh/cm²) during the first cycle.

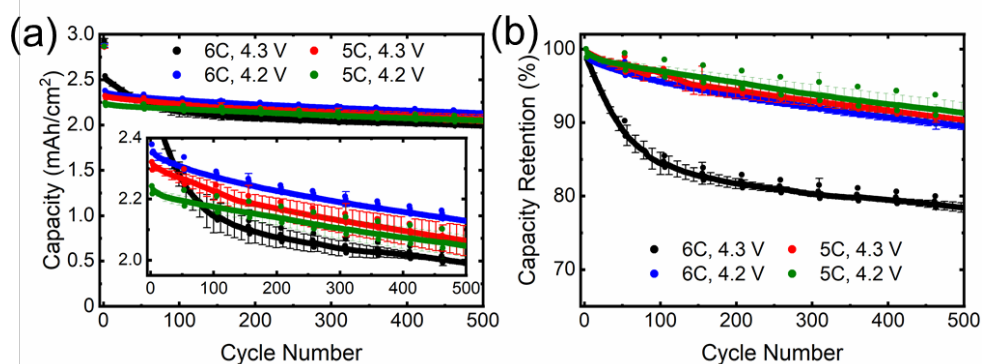


Figure IV.2.5 Evaluating the influence of upper charge voltage limit (4.2 V vs. 4.3 V) and operating temperature (30 °C vs. 40 °C) during 10-minute CC/CV charge, 1C discharge protocol: (a) areal capacities, (b) capacity retention values.

3. Final Delivery of 1 Ah Cells to DOE

Eighteen multilayer 1 Ah cells were fabricated and delivered to a DOE test lab. The deliverable was achieved using 1 Ah cells fabricated with the pouch cell pilot line at BNL. The 1 Ah cells utilized single and double sided NMC622 and graphite electrodes. Graphite electrodes had composition of 90% SLC 1506T natural graphite, 3% carbon black, and 7% PVDF binder with average electrode loading of 8 mg cm⁻² graphite. Of the 18 cells sent to DOE, 12 of the cells utilized graphite electrodes which were sputter coated with 20 nm of Ni as the fast charge technology. The graphite electrodes were paired with NMC622 cathodes (90% NMC622, 5%

carbon black, 5% PVDF, 15.8 mg/cm² NMC622 loading) with average N : P ratio of 1.16 : 1. The 1 Ah cells were fabricated with 1M LiPF₆ 30:70 ethylene carbonate (EC): dimethyl carbonate (DMC) electrolyte with 2% wt. of vinylene carbonate (VC). An electrolyte: pore volume ratio of 1.5:1 was used. Cell formation cycling was performed consisting of 4 cycles at C/10 rate between 3.0 – 4.3 V at a temperature of 30°C. Post formation cycling, the cells were cut open and resealed to release any gaseous degradation products produced during SEI formation. The cells were then discharged to 3.7 V (50% SOC) for shipping.

A cell containing the final fast charge technology, i.e., containing 20 nm Ni-graphite coated anodes, was cycled under a 10-minute fast charging protocol, consisting of a 6C constant current step followed by a constant voltage step at 4.3V for the remainder of the 10-minute segment, with testing performed at 40°C. A C/3 discharge was performed every 50 cycles. Figure IV.2.6 shows the first and fourth formation cycles at C/10 rate, as well as the cycling data under the fast charge protocol. At C/10 rate the 1 Ah cell delivered 177 mAh/g or 2.75 mAh/cm². Under the 10-minute fast charge protocol, when modeled to a 50 Ah cell design, this corresponds to a 180 Wh/kg specific energy. After 500 cycles, the capacity retention was 80% when discharged at the C/3 rate.

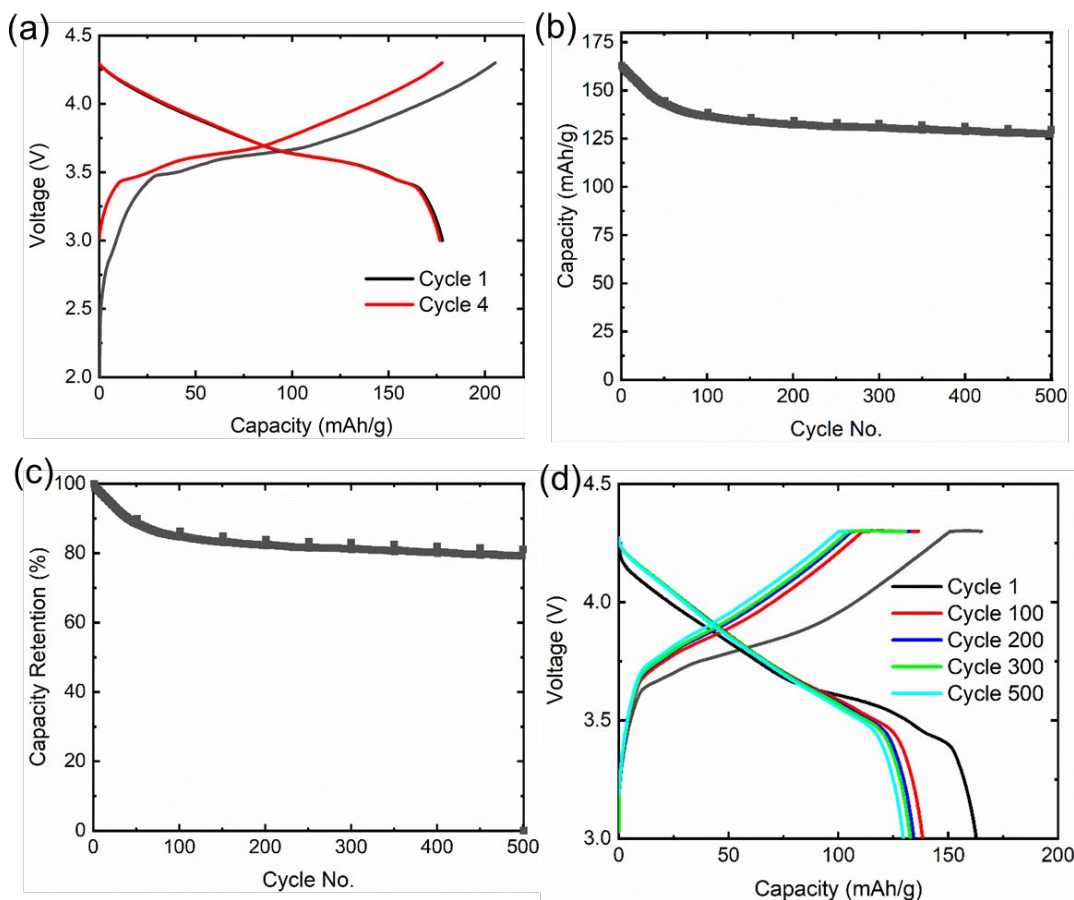


Figure IV.2.6 (a) Voltage profiles of first and fourth formation cycles at C/10 rate (b) gravimetric discharge capacity vs. cycle number, and (c) capacity retention vs. cycle number, and (d) 10-minute charge, C/3 discharge voltage profiles for 1 Ah multi-layer full cell with NMC622 cathodes and 20 nm Ni-graphite anodes. The cell was cycled under a 10-minute charge/ 1C discharge protocol with a C/3 discharge every 50 cycles.

Conclusions

Work during the past year focused on the development and fabrication of multi-layer Ah scale pouch cells with metal coated electrodes under a 12-month no-cost extension. Performance of electrodes procured from two different vendors were evaluated for use in the multi-layer cells. Single layer cells utilizing electrodes

fabricated by VENDOR B Corporation had initial delivered capacities and capacity retention comparable to cells fabricated utilizing electrodes fabricated at BNL; the VENDOR B fabricated electrodes were used for the multi-layer cell build. The influence of electrolyte loading in multi-layer cells was also evaluated. An electrolyte volume to pore volume ratio of 1.5 to 1 was identified as the optimal loading to achieve high energy density and capacity retention. Based on the development work, 18 multi-layer cells with nominal 1 Ah capacity were fabricated using the BNL pilot pouch cell line (12 cells with optimized Ni-coated anodes, 6 control cells with uncoated anodes) and delivered to a DOE test lab for evaluation. Under the 10-minute fast charge protocol, when modeled to a 50 Ah cell design, 180 Wh/kg specific energy was achieved. After 500 cycles, the capacity retention was 80% when discharged at the C/3 rate.

Key Publications

Publications

1. Tallman, Killian R.; Zhang, Bingjie; Wang, Lei; Yan, Shan; Thompson, Katherine; Tong, Xiao; Thieme, Juergen; Kiss, Andrew; Marschilok, Amy C.; Takeuchi, Kenneth J.; Bock, David C.; Takeuchi, Esther S. "Anode Overpotential Control via Surface Treatment: Inhibition of Lithium Plating." *ACS Appl. Mater. Inter.* 2019, 11, 50, 46864–46874.
2. Tallman, Killian R.; Yan, Shan; Quilty, Calvin D.; Abraham, Alyson; McCarthy, Alison H.; Marschilok, Amy C.; Takeuchi, Kenneth J.; Takeuchi, Esther S.; Bock, David C. "Improved Capacity Retention of Lithium-Ion Batteries under Fast Charge via Metal-coated Graphite Anodes." *J. Electrochem. Soc.* 2020, 167, 16, 160503.

Patents

1. Takeuchi, Esther S.; Takeuchi, Kenneth J.; Marschilok, Amy C.; Bock, David C. Device and Method for Fast Charge of Batteries. Provisional Patent Application No.: 62/618,116 (2018). (filed prior to program start).

Presentations

1. Takeuchi, Esther S.; Takeuchi, Kenneth J.; Marschilok, Amy C.; Bock, David C., "Enabling Extreme Fast Charging Through Control of Li Deposition Overpotential," Poster Presentation at 2019 Vehicle Technologies Office Annual Merit Review, Arlington, VA, June 2019.
2. Takeuchi, Esther S.; Takeuchi, Kenneth J.; Marschilok, Amy C.; Bock, David C., "Enabling Extreme Fast Charging Through Control of Li Deposition Overpotential," Oral Presentation at U.S. Drive XFC Meeting, Lemont, IL, August 2019.
3. Takeuchi, Esther S.; Takeuchi, Kenneth J.; Marschilok, Amy C.; Bock, David C., "bat 396: Enabling Extreme Fast Charging Through Control of Li Deposition Overpotential," 2020 Vehicles Technologies Annual Merit Review, virtual, June 2020.
4. Takeuchi, Esther S.; "From Medical Applications to the Environment: The Important Role of Energy Storage, Cary Lecture, Ga Tech University, Atlanta, GA, March 2020, *invited*.
5. Takeuchi, Esther S.; "Parasitic Reactions and Their Impact on Electrochemistry, Battery Gordon Conference, Ventura, CA, February 2020, *invited*.
6. Bock, D. C., "Enabling Extreme Fast Charging through Anode Modification" 2021 Society of Vacuum Coaters Virtual Technical Conference, virtual, May 2021.
7. Bock, D. C., "Enabling Extreme Fast Charging through Control of Li Deposition Overpotential" 3rd Battery and Energy Storage Conference, virtual, October 2021.

8. Bock, D. C., “Improved Capacity Retention of Lithium-Ion Batteries Under Fast Charge Via Metal-Coated Electrodes” 240th Electrochemical Society Meeting, virtual, October 2021.

Acknowledgements

The co-PIs for this project include Kenneth J. Takeuchi (Stony Brook University and Brookhaven National Laboratory), Amy C. Marschlok (Stony Brook University and Brookhaven National Laboratory) and David C. Bock (Brookhaven National Laboratory).

IV.3 Detecting Lithium Plating during Fast Charging, and Heterogeneity Effects during Fast Charging (LBNL)

Dr. Nitash P. Balsara, Principal Investigator

Department of Materials Sciences
Lawrence Berkeley National Lab
University of California, Berkeley
Berkeley, CA 94720
E-mail: nbalsara@berkeley.edu

Dr. Guoying Chen, Principal Investigator

Lawrence Berkeley National Lab
Berkeley, CA 94720
E-mail: gchen@lbl.gov

Dr. Bryan McCloskey, Principal Investigator

Lawrence Berkeley National Lab
Berkeley, CA 94720
E-mail: bmcclosk@berkeley.edu

Dr. Robert Kostecki, Principal Investigator

Lawrence Berkeley National Lab
Berkeley, CA 94720
E-mail: r_kostecki@lbl.gov

Dr. Ravi Prasner, Principal Investigator

Lawrence Berkeley National Lab
Berkeley, CA 94720
E-mail: rsprasher@lbl.gov

Dr. Wei Tong, Principal Investigator

Lawrence Berkeley National Lab
Berkeley, CA 94720
E-mail: weitong@lbl.gov

Brian Cunningham, DOE Technology Development Manager

U.S. Department of Energy
E-mail: Brian.Cunningham@ee.doe.gov

Start Date: October 1, 2020

End Date: September 30, 2021

Project Funding (FY21): \$900,000

DOE share: \$900,000

Non-DOE share: \$0

Project Introduction

The U.S. Department of Energy's Office of Energy Efficiency and Renewable Energy (DOE-EERE) has identified fast charging—with a goal of 15-min recharge time—as a critical challenge to pursue in ensuring mass adoption of electric vehicles. Present-day high-energy cells with graphite anodes and transition metal cathodes in a liquid electrolyte are unable to achieve this metric without negatively affecting battery performance. There are numerous challenges that limit such extreme fast charging at the cell level, including Li plating, lithiation heterogeneity, rapid temperature rise, and possible particle cracking. Of these, Li plating is thought to be the primary reason for limiting charging rates in lithium batteries.

Objectives

The primary goal of this project is to detect the initial nucleation event using data available in typical battery management systems. Identifying the initial onset of Li plating during fast charging is a multi-faceted, challenging “needle-in-a-haystack” problem. First, there may be a barely perceptible chemical signature of this event. For example, the presence of lithium may lead to the sudden formation of a small amount of gases due to irreversible reactions between the plated lithium and the electrolyte-soaked solid electrolyte interphase (SEI). Second, identifying the particular particle where the overlithiation and Li plating occurs can be challenging at the immediate onset of Li plating. Clearly, the particular particle that is overlithiated first will depend on the state-of-charge of the electrode, as it will be governed by the amount of lithium intercalated at that time and the lithium concentration in the surrounding liquid electrolyte. The third and final challenge is identifying electrical signatures of the overlithiation event so that our work can be used in practical battery management systems. We note here that the signatures may be different at different states-of-charge and that the electrical signature may be inherently non-linear, and thus not clearly evident in standard electrochemical measurements. Our objective is to address all three challenges.

Improved fast charging performance of lithium-ion batteries requires an accurate understanding of the lithium insertion and lithium plating process at the graphite surface. In practical graphite anodes characterization of these processes is complicated by the three-dimensional porous composite nature of the anode, and the mixed edge/basal nature of the graphite surfaces in it. The goal of our work is to determine some of the fundamental factors at play by performing experiments using planar, highly oriented pyrolytic graphite (HOPG) samples.

To perform thermal analysis of lithiation and lithium plating in graphite anodes, we are developing an anode-side 3ω sensor for *operando* measurements of anode thermal conductivity (k_{anode}). As Li^+ ions intercalate into the graphite anode, the anode thermal conductivity varies with the associated lattice change. With k_{anode} vs. state of charge (SOC) calibrated at a slow charge rate, the measured local thermal conductivity across the anode can thus be related to the local lithium distribution including for very fast charge rates. Therefore, our sensors, which live on the outside of the battery, can non-invasively measure *operando* the spatial distribution of Li ion concentration across the thickness of the anode, including during extreme fast charging.

Approach

A wide variety of methods have been utilized to address the problems mentioned earlier. Titrations with *ex situ* differential electrochemical mass spectrometry was performed on lithium plated graphite electrodes. Optical and X-ray tomography cells are being developed to study lithiation and plating *in situ*. Thermal sensors were developed for *operando* measurements of thermal resistances during fast charging. Cycling protocols have been developed that use coulombic efficiencies to estimate the evolving amount of irreversible Li plating during a single fast charge in graphite/lithium cells. Electrochemical techniques were applied to detect the onset of plating, to investigate rate limitations of NMC and graphite electrodes, and to compare the edge and basal plans of pristine HOPG and different stages of HOPG. A mounting and polishing procedure was developed to conveniently study edge plane samples of known area. Stage IV HOPG (LiC_{24}) was prepared electrochemically, and stage I and II HOPG (LiC_6 , LiC_{12}) were prepared using immersion in molten Li. Gas desorption measurements were used to determine the edge and basal plane proportions in battery grade graphite powders. A 3ω sensor was developed for *operando* measurements of anode thermal conductivity.

Results

Estimation of Li plating onset using incremental state-of-charge (SOC) coulombic efficiency measurements. A constant-current fast charge is conducted until a capacity cutoff is reached corresponding to an average electrode SOC, at which point the graphite is then fully delithiated at C/5 rate. Each subsequent cycle has a longer fast charging time incremented to deliver an additional 5% SOC. Plotting the efficiencies for each cycle as a function of the capacity cutoff provides a method to compare fast charged cells to controls in which no Li plating is expected, and this information can be used to estimate the onset of Li plating. Figure IV.3.1 demonstrates the SOC-sweep cycling protocol that can estimate the lithium plating onset from only a single cell. Efficiencies for each cycle are plotted in Figure IV.3.1, right, showing that the longer charges have

decreasing efficiencies due to the formation of inactive lithium, nearly all of which is plated lithium that becomes electronically isolated from the electrode.

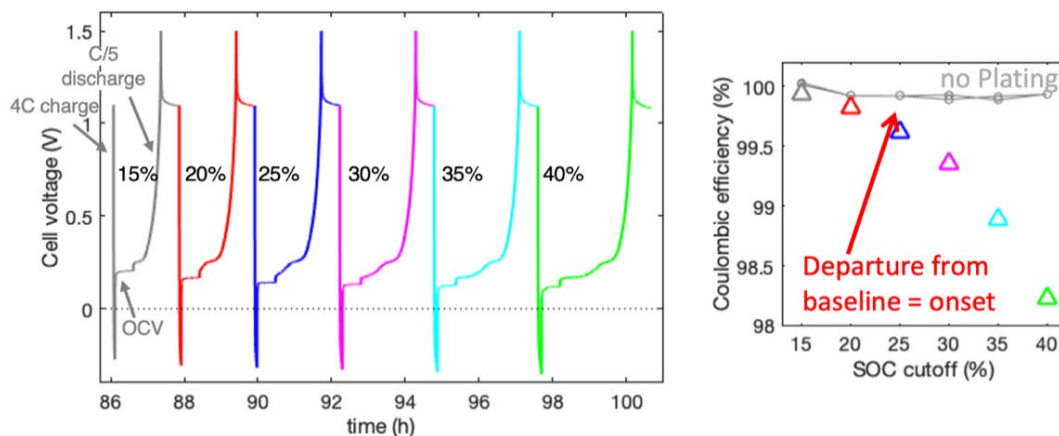


Figure IV.3.1 Demonstrating the SOC-sweep cycling protocol to quickly detect the onset of plating with coulombic efficiencies in graphite half-cells.

Figure IV.3.2 shows how this technique can be applied to estimate the onset of Li plating at various C-rates for the Round 2 graphite electrodes at 23°C. The CE% data as a function of the capacity cutoff are plotted in Figure IV.3.2a for 14-coin cells and color-coded by C-rate. In Figure IV.3.2b, the CE% data has been used to calculate an inefficiency from Li plating which is then used to estimate a capacity of irreversibly plated lithium. That amount is normalized to the total graphite electrode capacity—about 5.5 mAh for the 15 mm diameter—and shown on the y-axis. The solid lines represent averages, and the shaded regions represent 1 standard deviation from the averages. By defining 0.1% of the graphite capacity of irreversible lithium plating as a threshold, we identify plating onset as the intersection of the dotted line with the colored curves. Figure IV.3.2c summarizes this information plotted as a function of C-rate. We have collected this type of plating onset data for over 50 coin cells with varying electrode thicknesses (R1 and R2 electrodes), temperatures (23, 35, 45°C), and C-rates (3–6C) and are collaborating with Andrew Colclasure and Ankit Verma from NREL to provide a continuum scale understanding of the underlying phenomena that result in Li plating at the SOC onsets that we observe.

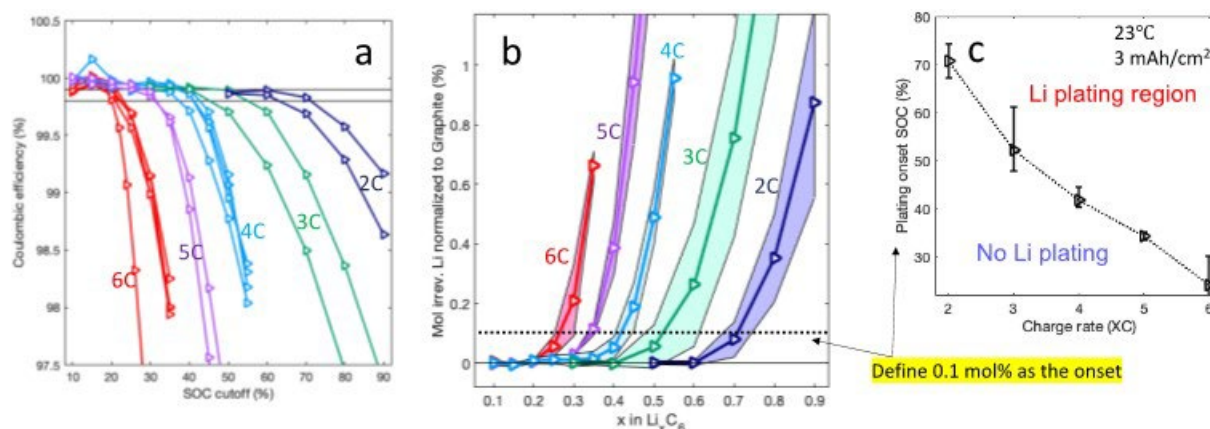


Figure IV.3.2 Data analysis to estimate irreversible lithium plating as a function of charge capacity (a,b) and plotting the lithium plating onset as a function of C-rate (c) for Round 2 graphite at 23°C. We define the plating onset as 0.1 mole percent irreversible Li capacity with respect to the capacity of the graphite electrode.

Cross-validating lithium plating onset detection by dOCV and reversibility measurements by titration with *in situ* X-ray tomography. The Balsara group has performed *in situ* X-ray tomography on Li metal/101 μm

Superior graphite SLC1520P ($D_{50} = 16.94 \mu\text{m}$) microtomography cells with a Celgard 2500 separator wetted with 1.2 M LiPF_6 3:7 wt% EC:EMC. Previously, a graphite half-cell was charged at 1C to 100% SOC, resulting in a thick layer of mossy lithium plating at the graphite surface nearest the separator. A region of poor lithiation was found by digital volume correlation to lie underneath the region of mossy, indicating a “shadow effect”.

To follow up this work, which has been published as reference [11], a half-cell was lithiated at 1C in 20 % SOC pulses to determine the onset of the plating. Figure IV.3.3a shows the charging and imaging protocol, where after each pulse the cell was allowed rest at OCV for 15 minutes, following by imaging with X-ray tomography. Figure IV.3.3b shows the emergence of a peak feature in the voltage derivative occurring after lithiating to 80 % SOC. Figure IV.3.3c shows three-dimensional volume renderings of the segmented graphite particles (gray) and plated lithium (turquoise) in a $0.5 \text{ mm} \times 0.5 \text{ mm}$ area of the electrode after lithiating to various SOC. No lithium plating is detected until after lithiating to 80 % SOC (Figure IV.3.3c, left), in agreement with the peak feature in Figure IV.3.3b. The onset of plating thus occurs between 60 to 80 % SOC for this cell configuration and charging protocol. Lithium plates further after lithiating to 100 % SOC (Figure IV.3.3c, middle). After delithiating at C/3 to 0 % SOC, the plated lithium is partially stripped, leaving the inactive lithium (Figure IV.3.3c, right). Figure IV.3.3d shows the areal capacity of plated lithium as a function of SOC, where the segmented volume of lithium plating is converted to capacity and normalized by the xy -area of the graphite. Total plated lithium in the electrode is estimated by multiplying the areal capacity by, $4\pi \text{ mm}^2$, the xy -area of the whole graphite electrode. The amount dead lithium measured this way is $7.7 \mu\text{Ah}$, corresponding to a stripping efficiency of 73 %. Within an hour after the X-ray tomography experiment, the cell was disassembled in an argon-filled glovebox, and graphite electrode was put under vacuum for 10 minutes. Mass spectrometry titration (MST) performed on this sample by the McCloskey group found $7.5 \mu\text{Ah}$ of inactive lithium in the electrode. Quantitative agreement between X-ray tomography and MST and qualitative agreement between X-ray tomography and dOCV cross-validates three techniques for detecting lithium plating.

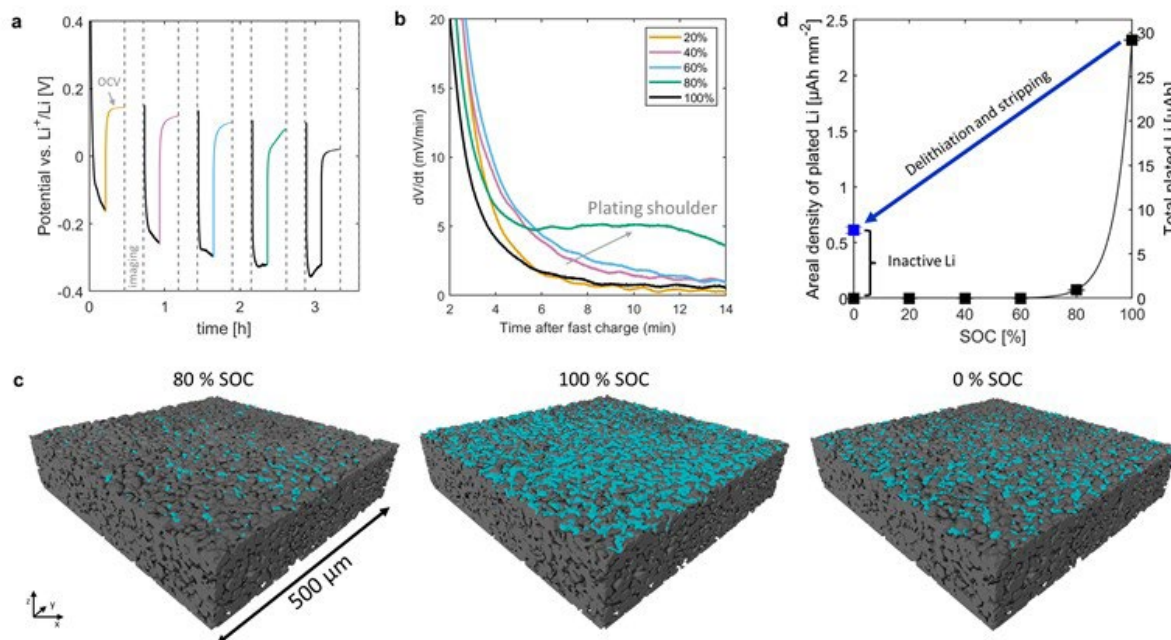


Figure IV.3.3 a) 1C charging protocol with pauses for OCV and imaging. b) dOCV indicating the onset of plating after charging to 80 % SOC. c) Volume renderings of a portion of the segmented graphite electrode after 1C intercalation to 80 and 100 % SOC, followed by C/3 deintercalation to 0 % SOC. The graphite is shown in gray, and the mossy lithium is shown in turquoise. d) Areal density of plated lithium across the graphite electrode versus SOC after 1C intercalation (black) and C/3 deintercalation (blue). Total plated lithium given by areal density multiplied by total xy -area of the graphite electrode.

Robert Kostecki's group developed approaches to study Li intercalation and plating in a 1D geometry using HOPG. It was reported previously that lithium insertion occurs exclusively at edge planes, but plating could occur on either. Figure IV.3.4 shows the region about 0 V (vs Li/Li⁺) of galvanostatic edge plane lithiation (a), galvanostatic basal plane lithiation (b), and cyclic voltammetry on a basal plane (c). Both (a) and (b) exhibit a local minimum followed by a plateau, which corresponds to the nucleation and growth of plated Li.

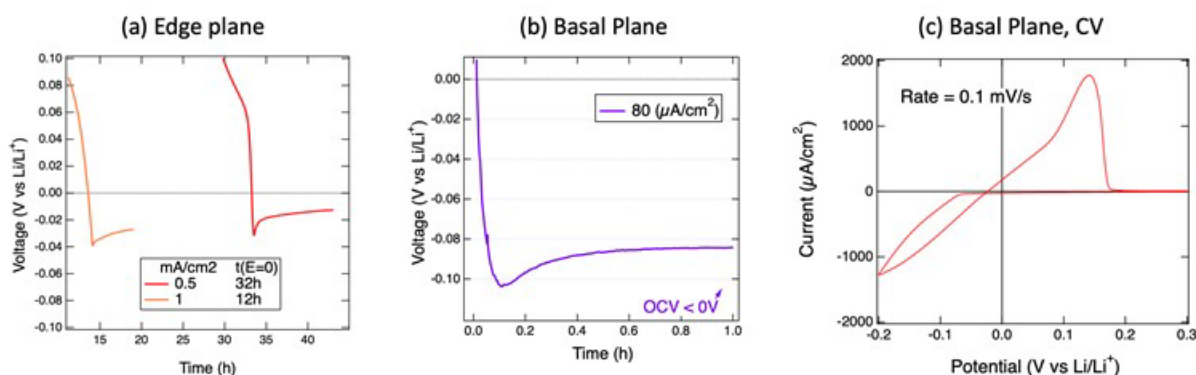


Figure IV.3.4 Electrochemical Measurements showing the Li plating onset on edge and basal plane HOPG. (a) Edge plane, galvanostatic. (b) Basal plane, galvanostatic. (c) Basal plane, cyclic voltammetry.

On the basal plane, a more negative voltage is required to initiate plating, suggesting that in the case of a graphite powder with a mixed edge/basal surface, plating would occur on edge planes first. This is reasonable since edge planes are defective by definition and indicates that plated Li would directly interfere with the intercalation process. Nevertheless, Figure IV.3.4(c) shows that given sufficiently low potentials, Li can be plated onto basal planes at a rate of mA/cm², which is 2–3 orders of magnitude greater than the parasitic current observed on basal planes at positive potentials.

On edge planes, the kinetics can reasonably be expected to vary with the Li_xC₆ stage present (or state of charge). To investigate this, galvanostatic lithiation experiments were conducted on pristine edge plane HOPG, on stage IV (prepared electrochemically) and stage I and II (prepared by molten Li immersion). The results are shown in Figure IV.3.5. It can be seen that within the 15 minute or so time window that is of interest for fast charging, pristine HOPG can be charged at 6 mA/cm², stage IV can be charged at 2 mA/cm², and stage II can be charged at 0.24 mA/cm², while remaining at positive voltages. Stage I represents fully lithiated graphite, and it can be seen that any further galvanostatic lithiation pushes the potential to negative voltages within milliseconds.

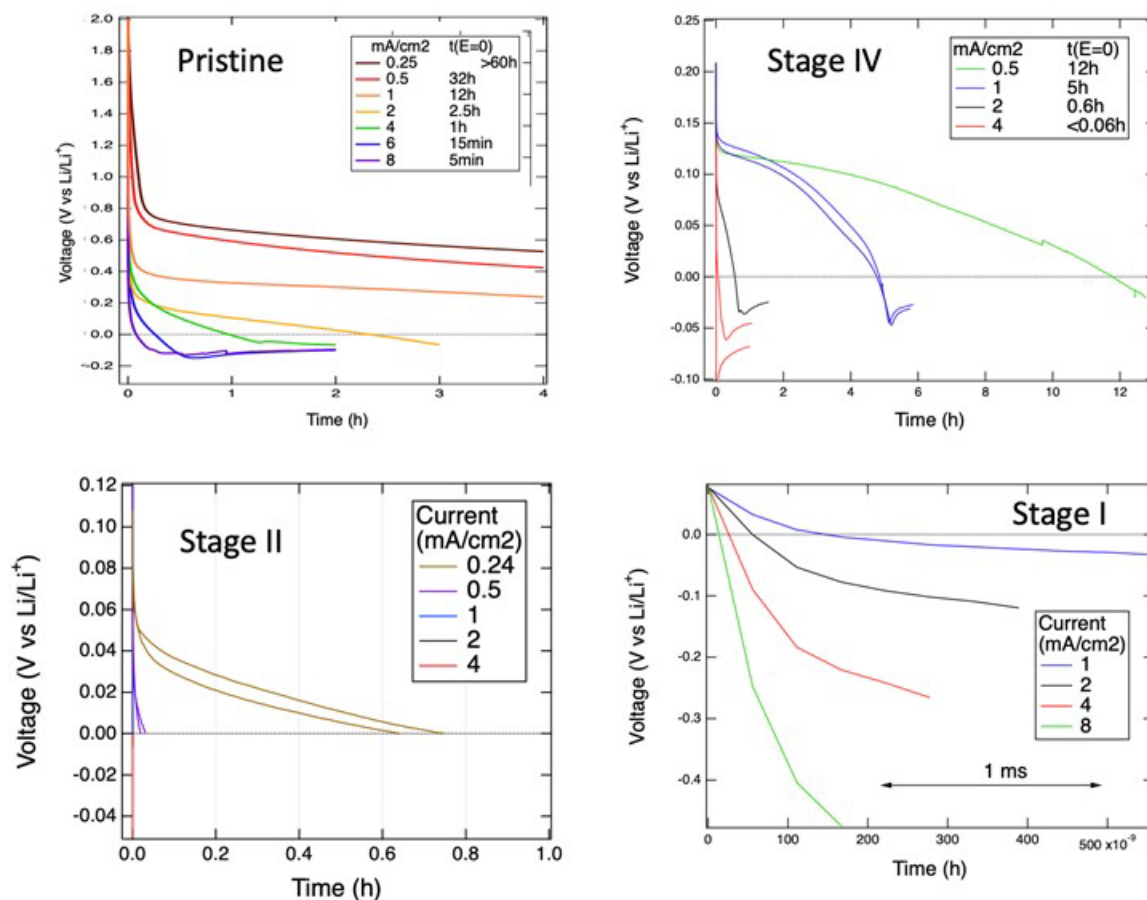


Figure IV.3.5 Galvanostatic lithiation of edge-plane HOPG at different stages of lithiation. Stage IV = LiC₂₄, Stage II = LiC₁₂, Stage I = LiC₆.

Having determined threshold currents for different stages of HOPG, it is of interest to convert these to relevant values for composite electrodes. R2 graphite anodes studied within this project have about 100 cm² of BET surface area per cm² of electrode area. Oxygen desorption measurements conducted on different but similar battery grade graphite showed that about 5% of the BET surface area is edge-plane area. The edge area of R2 anodes is therefore likely to be 5x greater than the geometric area, and it is known that their capacity is 3 mAh/cm². This yields the following maximum C-rates that maintain positive potentials for at least 15 minutes: 10C for pristine HOPG, 3.3C for stage IV, and 0.4C for stage II. The data on pristine HOPG and stage IV are broadly in agreement with the C-rates found to be workable experimentally and indicate that synthesizing graphite with a greater proportion of edge-plane area would improve fast charging performance. In the extreme case of 100% edge area, the limiting C-rates would be 20 times higher, 8C for stage II and greater for lower stages, making fast-charging straightforward from a graphite surface standpoint.

Quantification of lithium distribution across the graphite anode by 3 ω sensor. Ravi Prasher's group developed an anode side 3 ω sensor to quantify the lithium distribution across the graphite anode under XFC. The 3 ω sensor can map the cross-plane thermal conductivity of graphite anodes by varying the penetration depth with different frequencies. A calibration of k_{anode} vs. SOC was performed at a slow charge rate when lithium ions are uniformly intercalated into graphite anodes. With the calibrated relationship, the local SOC can be back calculated from the measured local electrode thermal conductivity (Figure IV.3.6). A proof-of-concept study was conducted in graphite anodes at 0.1C for calibration and 1C for distribution measurement, respectively. To verify the measurement, optical images of the cross-section view of graphite anodes at different SOC's and with

different C rates were taken as a qualitative proof. The anode region near the separator has a higher degree of lithiation (i.e., more gold color) than the regions farther away, similar as the quantitative results by our method.

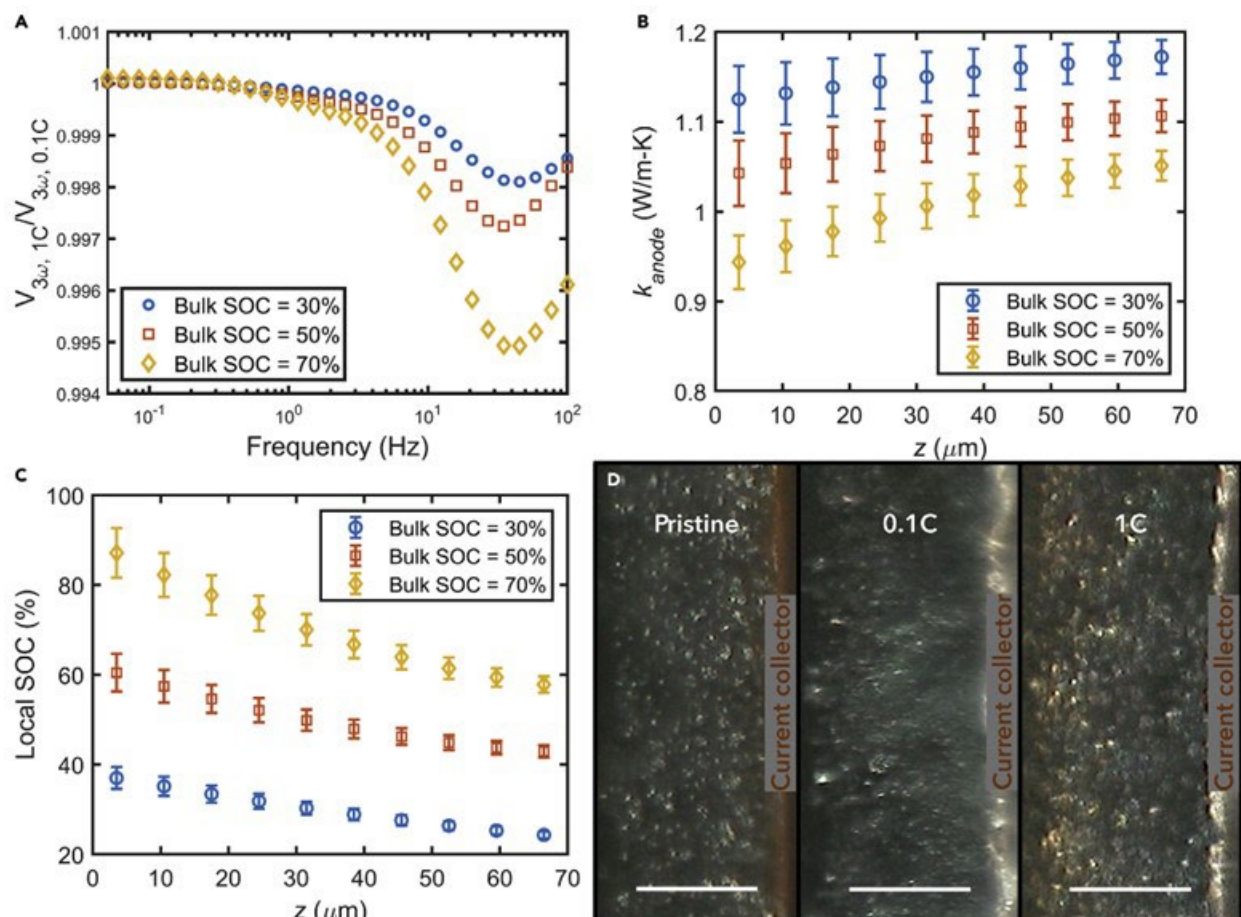


Figure IV.3.6 a) Raw $V_{3\omega}$ data after 1C charging to three different bulk/average SOC's normalized to raw data after 0.1C charging to the same SOC's. b) The k_{anode} profile across the anode. c) The local SOC distribution calculated from the measured k_{anode} distribution. D) Cross-section views of pristine (SOC = 0) and lithiated (SOC = 70%) graphite anode show how in the cell charged at 1C, the anode region near the separator has a much higher degree of lithiation (i.e., more gold color) than the regions farther away. Reproduced from [2].

Understanding the cycling behavior of plated Li and its effect on graphite cell performance. Wei Tong's group studied the properties of deposited Li and its effect on cyclability of graphite anode. Two testing protocols with (w/) and without (w/o) resting after charging were designed (Figure IV.3.7A) to investigate the reversibility behavior of deposited Li. The graphite/Li half cell was charged at 4C to different SOC's from 10% to 100% and then slowly discharged to 1.5 V at C/5. CE typically decreases at higher SOC's because of Li plating. By comparing the CEs at different SOC's in both cases with and without resting (Figure IV.3.7B), we noticed that when SOC increases above 30%, the value of $CE_{w/resting}/CE_{w/o resting}$ starts to decrease. Note that once Li plating occurs during fast charge, the plated Li is either irreversible by reacting with electrolyte and forming "dead" Li or reversible through Li stripping during discharge or reacting with partially lithiated graphite, while lower CE is expected if plated Li becomes irreversible. Therefore, the decrease in $CE_{w/resting}/CE_{w/o resting}$ suggests the deposited Li at the SOC higher than 30% is partially irreversible, meaning reactions with electrolyte and formation of dead Li. This hypothesis is further confirmed by the differential discharge capacity curves (Figure IV.3.7C). Without resting, the delithiation peak for Li metal was observed at a discharge potential below 0.1 V at the SOC higher than 30%. In sharp contrast, it became invisible in the discharge profiles when the cells are rested after charging. Correspondingly, the lithiated degree of graphite anode exhibited a slight

increase with resting (Figure IV.3.7D, E), which is in good agreement with the reaction between deposited Li and non-fully lithiated graphite. Compared to the graphite anode in a pristine state (Figure IV.3.7F), massive growth of Li dendrites was observed on the graphite anode after charging to 100% SOC at 4C (Figure IV.3.7G). To investigate the cyclability of the deposited Li, graphite/Li half cells with or without resting after charging were assembled for cycling tests. As shown in Figure IV.3.7H, both cells show a gradual decrease in CE with cycling, due to the cumulative dead Li. Moreover, the cell cycled without resting exhibits a higher CE than that with resting, which confirms the formation of dead Li during resting. These results suggest that the deposited Li undergoes complex chemical and electrochemical reactions, which gradually degrades the cycling performance of graphite anodes.

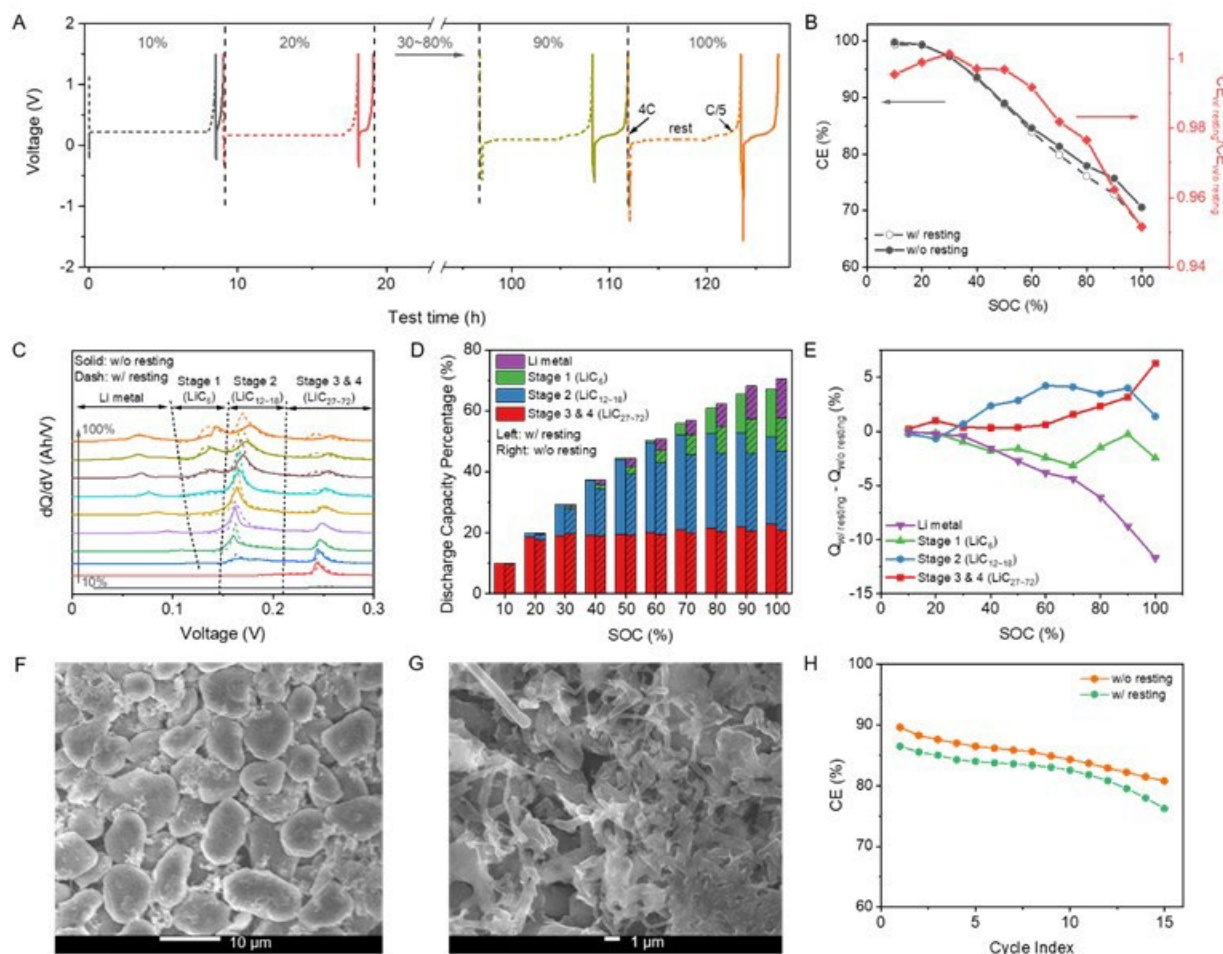


Figure IV.3.7 (A) Voltage profiles of graphite/Li half cell charged at 4C to different SOC levels from 10% to 100% and then discharged at C/5 to 1.5 V. At each SOC, cells are cycled with and without resting after charging; (B) CE of graphite/Li half cells charged to different SOC levels and corresponding CE_{w/ resting}/CE_{w/o resting}; (C) dQ/dV curves during discharge after discharged to different SOC levels; (D) normalized discharge capacity at different graphite lithiation stages and (E) corresponding difference in normalized discharge capacity between charging w/ resting and w/o resting; SEM images of graphite anodes at (F) pristine state and (G) after charging at 4C to 100% SOC; and (H) CEs of graphite/Li half cells w/ and w/o resting, cells are charged to 100% SOC at 4C.

Work conducted by Guoying Chen and Marca Doeff at LBNL has been included in the Cathode and Anode reports of XCEL, respectively.

Conclusions

In the present research, detecting lithium plating during fast charging, heterogeneity effects, and graphite anodes with directional pores have been investigated. The major conclusions are summarized below:

1. A straightforward Li plating protocol based on coulombic efficiency measurements was developed to identify the state-of-charge at which Li plating commences as a function of electrode composition, electrolyte composition, temperature, and C-rate.
2. The onset and reversibility of lithium plating were measured by X-ray tomography. Results were cross-validated by dOCV and mass spectrometry titration.
3. Studies on HOPG showed that Li plating occurs on edge planes first but can occur at substantial current densities on basal planes if the potential is sufficiently negative (below -0.1V). This indicates that potential inhomogeneities in the electrode should be kept below this value of fast charging to high SOC with negligible plating is desired. Furthermore, limiting fast charge current densities were measured for different stages of edge plane graphite. These predict reasonable limiting C-rates for R2 anodes given a measured value of 5% edge plane area and indicates that synthesis of graphite with a greater share of edge plane surfaces would greatly facilitate fast charging.
4. Thermal wave sensing, based on the k_{anode} vs. SOC relationship, was developed for studying the lithium concentration during fast charge, which may lead to much cheaper and faster sensing techniques compared with synchrotron-based techniques.
5. The deposited Li undergoes both chemical and electrochemical reactions, which gradually degrades the cycling performance of graphite anodes.

Key Publications

1. Brown, D. E.; McShane, E. J.; Konz, Z. M.; Knudsen, K. B.; McCloskey, B. D. "Detecting the onset of Li plating during fast charging of Li-ion batteries using operando electrochemical impedance spectroscopy." *Cell Reports Physical Science* (2021) 2(10), 100589.
2. Paul, P. P.; McShane, E. J.; Nelson Weker, J. et al. "A review of existing and emerging methods for lithium detection and characterization in Li-ion and Li-metal batteries." *Advanced Energy Materials* (2021) 2100372.
3. Ho, A. S.; Parkinson, D. Y.; Finegan, D. P.; Trask, S. E.; Jansen, A. N.; Tong, W.; Balsara, N. P. "3D Detection of Lithiation and Lithium Plating in Graphite Anodes during Fast Charging. *ACS Nano* (2021), 15 (6), 10480–10487.
4. Zeng, Yuqiang, et al. "Operando spatial mapping of lithium concentration using thermal-wave sensing." *Joule* 5.8 (2021): 2195–2210.

References

1. Ho, A. S.; Parkinson, D. Y.; Finegan, D. P.; Trask, S. E.; Jansen, A. N.; Tong, W.; Balsara, N. P. "3D Detection of Lithiation and Lithium Plating in Graphite Anodes during Fast Charging. *ACS Nano* (2021), 15 (6), 10480–10487.
2. Zeng, Yuqiang, et al. "Operando spatial mapping of lithium concentration using thermal-wave sensing." *Joule* 5.8 (2021): 2195–2210.

IV.4 Novel Electrolyte Development with High Lithium-Ion Transference Number (Hi-LiT) for Extreme Fast Charging (ORNL)

Zhijia Du, Principal Investigator

Oak Ridge National Laboratory
One Bethel Valley Road
Oak Ridge, TN 37830
E-mail: duz1@ornl.gov

Brian Cunningham, DOE Technology Development Manager

U.S. Department of Energy
E-mail: Brian.Cunningham@ee.doe.gov

Start Date: August 15, 2018	End Date: July 15, 2021	
Project Funding (FY21): \$1,000,000	DOE share: \$900,000	Non-DOE share: \$100,000

Project Introduction

This project focuses on development of novel electrolyte to address AOI 2 (Batteries for Extreme Fast Charging (XFC)) in DE-FOA-0001808. The DOE has ultimate goals for EV batteries, which include reducing the production cost of a BEV cell to \$80/kWh, increasing the range of BEVs to 300 miles, and decreasing the charging time to 15 minutes or less. Increasing electrode thickness is an effective way to achieve these goals; however, thicker electrodes present several barriers to fast charging. This project is to implement a novel high-Li-ion-transport (Hi-LiT) electrolyte and enable a 10-minute charge of 180 Wh/kg energy density with less than 20% fade after 500 cycles (144 Wh/kg). The targeted improvements in the Hi-LiT electrolyte will be increasing Li ion transference number from 0.363 to 0.7-0.75 while maintaining a relatively high conductivity of 4-10 mS/cm. The improvement in electrolyte formulation will suppress the Li plating issue during cycling. This electrolyte will be implemented into high energy density Li-ion cells.

Objectives

The objective of this project is the increase of Li ion transference number while maintaining high conductivity of non-aqueous electrolyte through novel Li salt synthesis, anion receptors additives screening and solvent systems optimization, which will significantly increase the Li ion mass transport from cathode to anode during XFC to avoid abrupt end of charging and Li plating/dendrite growth. The implementation of this novel non-aqueous electrolyte system in high energy density Li-ion cells meet the battery performance goal of delivering 180 Wh/kg of stored energy to the cell in 10-minute charging at the beginning of life and achieving less than 20% fade in specific energy after 500 cycles (144 Wh/kg).

Approach

1. Innovative Li salts to improve Li ion mobility and increase Li ion transference number.
2. Formulations with multiple solvent systems to provide better Li ion mobility and suppress Li plating.
3. Anion receptor additives to further immobilize anions and dissociate cations in electrolyte.

Results

Corrosion test was performed to ensure the use of LiFSI salt for fast charging without Al corrosion issue. Cyclic voltammetry was performed at 0.1 mV/s with different voltage windows using a VSP potentiostat (Bio-logic). The measurement was carried out in two different cell formats: 2032 coin cell and pouch cell. The working electrodes were made from Al or SS foils. The coin cell and pouch cell configurations are illustrated

in Figure IV.4.1. In the standard coin cell configuration, Al foil was used as the working electrode while the cell parts (can, spacer, spring, and cap) are made from SS. In the pouch cell configuration, the pouch bag was made from Al laminated film with polypropylene as the inner layer (in contact with the “jelly roll”). Al foil and SS foil were used as the working electrodes in pouch cell for the CV test. Tafel polarization test was performed at the same condition. The corrosion current and potential were determined by using Tafel-extrapolation method in EC-lab software (Bio-logic). Extrapolation involves extending a known sequence of linear values within a Tafel plot to determine these parameters.

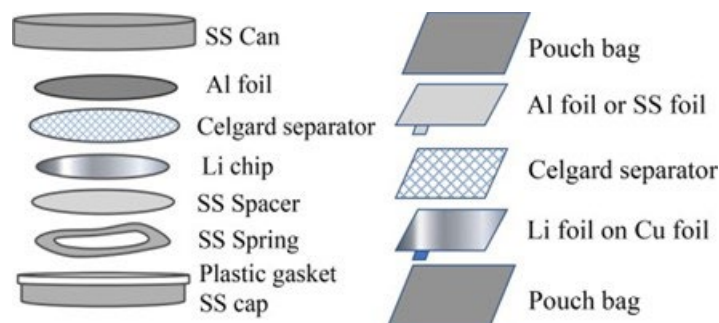


Figure IV.4.1 Illustration of (a) standard coin cell configuration and (b) pouch cell configuration for cyclic voltammetry test.

CV was carried out in the standard coin cell setup with Al foil as the working electrode and Li foil as the counter electrode. The cells were filled with either LiFSI or LiPF₆ electrolyte. Karl Fischer titration showed both electrolytes have a water content <25 ppm. Figure IV.4.2 shows the CV profiles of the first 4 cycles with two different electrolytes. For LiFSI electrolyte, significant oxidation current was observed above 4.0 V in the 1st cycle. This can be ascribed to pitting corrosion behavior. This current corresponding to corrosion even increases in the following cycles. The voltage where the current starts to increase also shifts to lower voltages. This indicates the LiFSI electrolyte could not passivate the metal in the coin cells. Contrarily, LiPF₆ electrolyte shows the typical passivation behavior with the anodic current much lower than that obtained in LiFSI electrolyte. It is noticed that the current for the reverse cathodic scan is lower than the upward anodic scan. The responding current also becomes smaller in the following cycles.

However, there are two different metals in the coin cell setup that can be possible corrosion sources. Both Al and SS have been found to corrode in Li-ion cell environment. After the CV testing, coin cells with LiFSI electrolyte were opened in Ar-filled glove box. As shown in the inset of Figure IV.4.2, black product was observed on SS cell parts, instead of Al foil. Therefore, the SS might be the source that leads to the corrosion current. To distinguish the two metals in corrosion study, the pouch cell setup was used for CV study. In this case, cells parts in direct contact with electrolyte was made of polypropylene, instead of SS. Figure IV.4.2c and d shows the CV test results with pouch cells setup with SS foil or Al foil as the working electrodes. For LiFSI electrolyte with SS foil, similar behavior is observed compared to Figure IV.4.2a. A large hysteresis loop is indicative of corrosion phenomenon occurring with cathodic current greater than the anodic current. The magnitude of the current also increases with cycle numbers, indicating corrosion becomes more serious in following cycles. Noticeably, the current response of CV test is orders of magnitude lower when Al foil is used to replace SS foil as the working electrode in LiFSI electrolyte. In Figure IV.4.2d, the responding current decreases significantly with the increase of cycle number. The magnitudes of current in CV is similar to each other when LiFSI electrolyte and LiPF₆ electrolyte are used. It indicates LiFSI electrolyte can effectively passivate Al and thus prevent it from corrosion in further cycling.

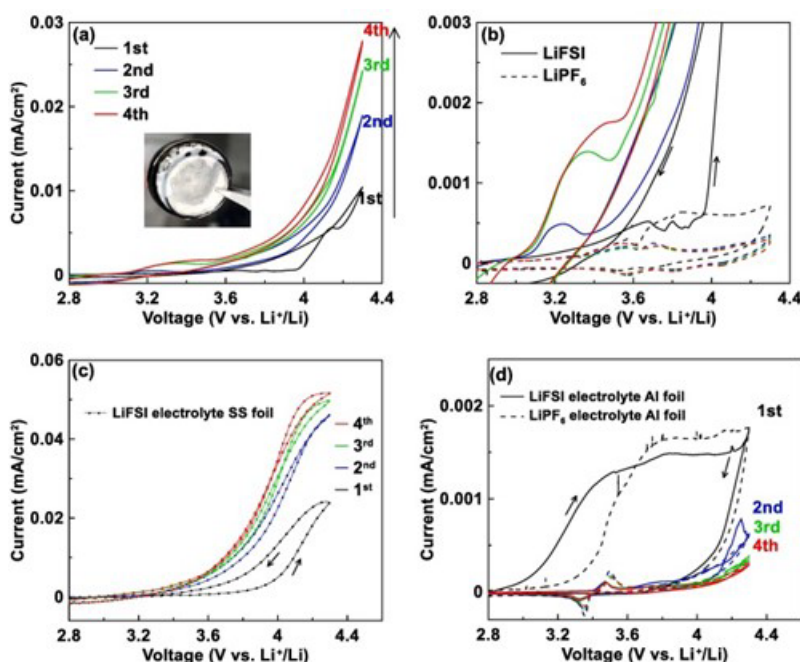


Figure IV.4.2 Cyclic voltammograms of the (a) LiFSI (solid lines), and (b) LiPF₆ (dashed lines) electrolyte in coin cells for the first 4 cycles. Cyclic voltammograms of the (c) LiFSI electrolyte in pouch cells with SS foil, and (d) LiFSI and LiPF₆ electrolyte in pouch cells with Al foil as the working electrodes for the first 4 cycles. The picture inset of Figure a showed the black products on cells parts with LiFSI electrolyte.

Tafel polarization result is shown in Figure IV.4.3 to provide the accurate corrosion potential and corrosion current density. The corrosion potential of SS foil and Al foil in LiFSI electrolyte is 3.21 V and 3.96 V, respectively. Al foil corrosion potential in LiFSI electrolyte is very close to that in LiPF₆ electrolyte at 4.10 V. The corrosion current density for SS foil in LiFSI electrolyte is 7.35 $\mu\text{A}/\text{cm}^2$, which is significantly greater than Al foils in LiFSI (0.033 $\mu\text{A}/\text{cm}^2$) and LiPF₆ (0.049 $\mu\text{A}/\text{cm}^2$) electrolyte. These result shows that LiFSI electrolyte can corrode SS foils while effectively suppress the corrosion of Al foil.

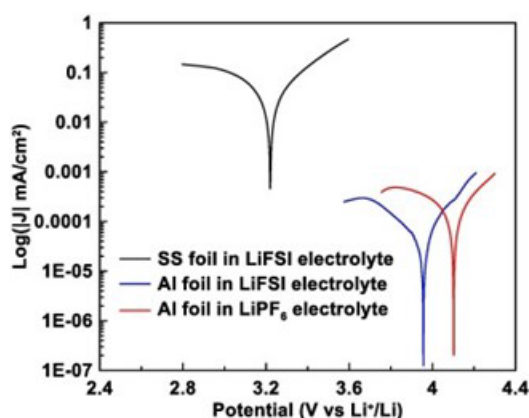


Figure IV.4.3 Tafel polarization curves from the 2nd scanning of SS foil or Al foil in LiFSI or LiPF₆ electrolyte.

Figure IV.4.4 shows the photographs of opened pouch cells with LiFSI electrolyte using SS foil and Al foil as working electrodes after cycles of CV in Figure IV.4.2. The top parts of photos show the anode side (Li foil on Cu current collector), with the semi-transparent wet separators covering the SS foil or Al foil on the bottom parts of the photos. For pouch cell with Al foil as the cathode, all the parts are clean as shown in Figure IV.4.4b, indicating that a satisfactory passivation is achieved. This is further confirmed by the SEM images in Figure IV.4.4c and d. Compared to the pristine Al foil, there is no pitting holes or other corrosion signs in

Figure IV.4.4d after CV testing in LiFSI electrolyte. It is surprising to note the black product is observed in Figure IV.4.4a in pouch cells with SS foil. We speculate the surface of SS foil may be attacked and the electrolyte may thus have dissolution products of Cr and Fe ions. The Cr/Fe ions can migrate and deposit on anode surface from the electric field during CV scanning. Then the electrolyte decomposition is accelerated, corresponding to the large current response in CV test in Figure IV.4.2c.

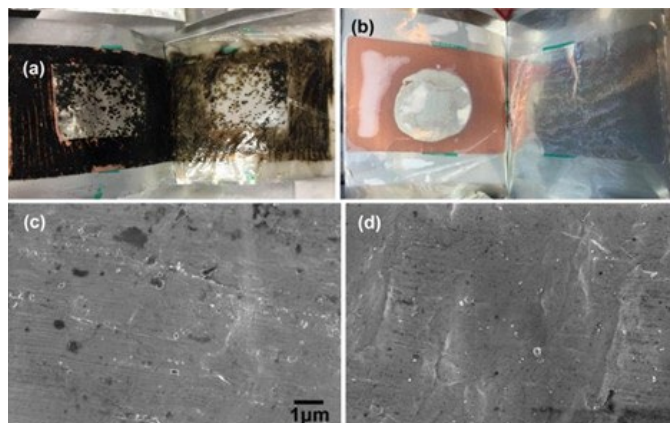


Figure IV.4.4 Photographs of opened pouch cells with LiFSI electrolyte using (a) SS foil and (b) Al foil as the working electrodes. SEM images of (c) pristine Al foil and (d) Al foil after CV test in LiFSI electrolyte.

With the elucidation of the corrosion behavior of the LiFSI electrolyte on Al and SS, the electrochemical performance of NMC622/graphite cells is evaluated with LiFSI electrolyte using 1.5 Ah pouch cells. Figure IV.4.5 shows the cycling performance and voltage curves at different charging rates. The initial capacity is 181, 175 and 130 mAh/g for $\pm C/3$, $\pm 1C$ and XFC, respectively. At low or moderate cycling rates, the cells show 93% after 400 cycles at $\pm C/3$, and 88.5% after 1000 cycles of $\pm 1C$. The excellent cycling performance demonstrates the feasibility of using LiFSI electrolyte for Li-ion cells. It has been proved that LiFSI electrolyte has higher conductivity and Li ion transference number, which is suitable for fast charging. The cell with LiFSI electrolyte has 89% capacity retained after 500 XFC cycles, which is better than the targeted goal (80% after 500 cycles). Continued cycling of the cells shows 80% capacity retention after 1000 cycles. This demonstrates the excellent performance of Li-ion cell using LiFSI electrolyte formulation for XFC capability.

18 2-Ah Li-ion pouch cells have also been delivered to Argonne National Lab for testing, and similar excellent results were obtained for XFC cycling.

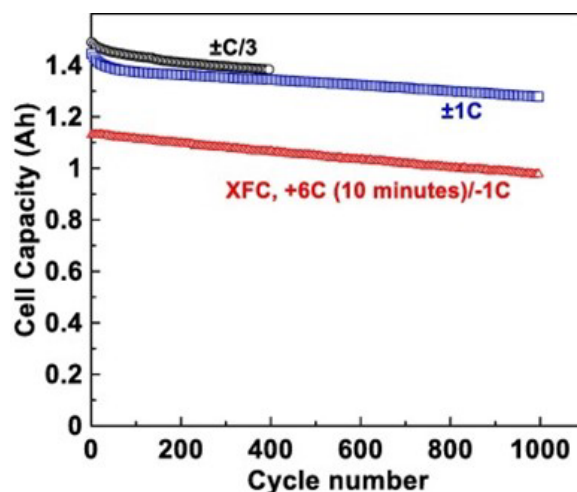


Figure IV.4.5 Cycling performance of 1.5 Ah NMC622/graphite pouch cells at different charging/discharging rates with LiFSI electrolyte.

Conclusions

Electrolytes with LiFSI salt was demonstrated to have passivation towards Al current collector, which showed similar current response behavior in CV test compared to LiPF₆ electrolyte. In contrary, huge current response was observed in CV test of LiFSI electrolyte when SS parts/electrodes were present in the cell. Black reaction product was observed inside the cells with SS parts/electrodes. XPS results confirmed the composition of the black product is from the decomposition of electrolyte. The probable explanation is that the Fe/Cr ions from corrosion reaction deposited on anode surface and then accelerated the decomposition of electrolyte. 1.5 Ah pouch cells were used to test the suitability of LiFSI electrolyte for NMC622/graphite cells. Good cycling performance was demonstrated with 93% capacity retention after 400 cycles at C/3, 88.5% after 1000 cycles at 1C, and 80% after 1000 cycles at XFC rates. The results indicated that LiFSI based electrolyte is feasible for Li-ion cells when SS cell parts are absent.

Key Publications

1. Wu, Xianyang, and Zhijia Du. "Study of the corrosion behavior of LiFSI based electrolyte for Li-ion cells." *Electrochemistry Communications* 129 (2021): 107088.
2. Wu, X., Song, B., Chien, P. H., Everett, S. M., Zhao, K., Liu, J., & Du, Z. (2021). Structural Evolution and Transition Dynamics in Lithium-Ion Battery under Fast Charging: An Operando Neutron Diffraction Investigation. *Advanced Science*, 2102318.

Acknowledgements

This research at Oak Ridge National Laboratory (ORNL), managed by UT Battelle, LLC, for the U.S. Department of Energy under contract DE-AC05-00OR22725, was sponsored by the Office of Energy Efficiency and Renewable Energy Vehicle Technologies Office (VTO) (Technology Managers: Brian Cunningham).

IV.5 XCEL R&D: Lithium Detection Thrust

Venkat Srinivasan, Principal Investigator

Argonne National Laboratory
9700 South Cass Avenue
Lemont, IL 60439
E-mail: vsrinivasan@anl.gov

Samm Gillard, DOE Technology Development Manager

U.S. Department of Energy
E-mail: Samuel.Gillard@ee.doe.gov

Start Date: October 1, 2020	End Date: September 30, 2021	
Project Funding (FY21): \$800,000	DOE share: \$800,000	Non-DOE share: \$0

Project Introduction

Detecting the onset of Li metal plating and quantifying its presences during extreme fast charging (XFC) is fundamental in understanding the role of Li plating in the degradation of cells at such high charging rates. Additionally, understanding the conditions under which Li plating occurs during fast charging is critical to taking steps to avoid plating and extend the life-time of Li ion cells. Our approach was to utilize the different detection techniques we had identified to link the onset of Li plating with cell performance and aging.

Approach

Milestone 1 was to use a combination of at least two of the Li detection methods explored last fiscal year to determine where the lost Li inventory is trapped. The second milestone was to submit a perspective on Li detection technique outlining each technique in terms of detection accuracy and correlations between multiple techniques. The third milestone was to connect “dead Li” to cycling age and determine if the presence of dead Li accelerates additional Li plating. Namely, we intentionally plated Li metal in the first few cycles to test how it affected future capacity fade during standard CCCV cycling. Milestone 4 was to identify if and what are the early warning signs of Li plating for different detection techniques and to identify which techniques could be incorporated on a vehicle. The final milestone was to determine if the “hero” cell plated less Li or at time points later in life or at later state of charge (SOC) compared to the Round 2 cells.

Results

Milestone 1: Trapped Li Inventory

SEI species

As part of the focus of the Li detection thrust, we explored the use of multimodal experimental techniques to better detect Li plating, by leveraging advantages of complementary experimental techniques. In particular, we show how the use of high-energy X-ray diffraction (HEXRD) from SLAC with mass spectrometry titration (MST) from UC Berkeley. These techniques have been extensively used individually to detect Li in the XCEL program. [1],[2],[3] HEXRX has been extensively used to detect Li, as well as the amount of dead Li_xC_6 . However, due to the weak scattering of Li compared to the other cell components as well as non-detectability of nanocrystalline/amorphous deposits of Li, quantification of plated Li with HEXRD is challenging. MST, on the other hand, is extremely sensitive to Li deposits (can detect nanomoles of Li) but cannot differentiate between plated Li and dead Li_xC_6 . Thus, by combining the two techniques, the amount of plated Li can be accurately determined, by Equation 1.

$$(\text{Dead Li})_{\text{MST}} - (\text{Dead Li}_x\text{C}_6)_{\text{HEXRD}} = \text{Plated Li} \quad (1)$$

Figure IV.5.1 shows the amount of plated Li detected by HEXRD, as a function of the total plated Li measured by Equation 1. We see that HEXRD detects ~80% of the total amount of plated Li, irrespective of the total

amount of plated Li in the cell. This result is important given the increasing appeal in using HEXRD available at synchrotron sources to quantify degradation through Li plating in LIBs. The non-destructive nature of characterization allows for *in-situ* and operando studies, which is an invaluable tool. This multimodal analysis allows to quantify the challenges associated with the detection of Li using HEXRD, in particular how much of the total Li we miss in such analyses.

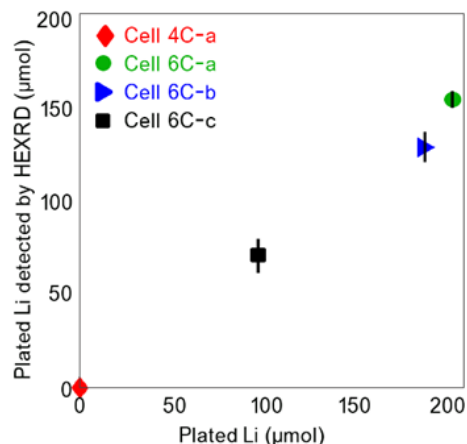


Figure IV.5.1 Amount of dead plated Li directly detected by HEXRD as a function of the total amount of plated Li in each cell, as measured via the combination of MST and HEXRD.

Irreversible behavior of fast-charge driven lithium plating

Object of this work from ANL is to understand the irreversible behavior of lithium plating on the anode during fast-charging rate. The conducted study in this report will provide the insight to understand following questions: i) how plated lithium affects the following cycles?, ii) how much irreversible lithium present on the graphite after fast-charging?, and iii) what and where is the irreversible lithium present on the graphite.

Figure IV.5.2a shows the capacity retention of cells cycled at the 6C followed by C/20 charging rates. The cells achieved around 150 mAh g⁻¹ in formation cycles then shows gradual capacity decrease with fast-charging rates. The lower capacity retention in fast-charging rate is due to the kinetic limitations and the lithium plating on the anode surface. Number of cycles counts with fast-charging rate is controlled to 1, 5, 10, 20 and 50 then all cells were subjected to continuous C/20 rate charging rate for 10 cycle counts. It was observed that considerable amount of capacity is recovered with slow charging rate cycles. The recovered capacity with slow rate should be the one limited during fast-charging cycles. However, the amount of recovered capacity with C/20 rate is different based on the fast-charged cycle numbers of each cells indicating presence of another factor that constrains capacity deliveries even with slow charging rate. Given that previous studies, different amount of lithium plating is present on the graphite in the function of fast-charging cycle counts and limits the capacity recovery.

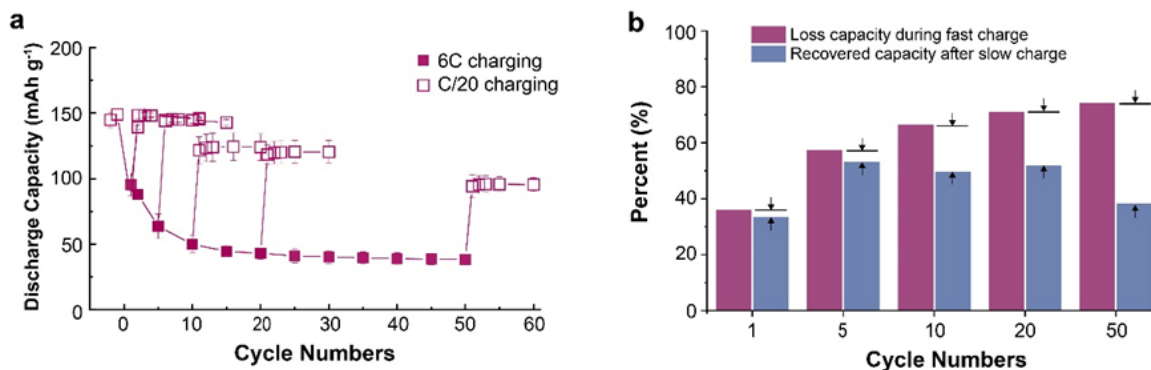


Figure IV.5.2 (a) Cycle retention of NMC532/graphite cell with fast-charging rate (6C) followed by slow charging rate (C/20). (b) Loss capacity with fast-charging and recovered capacity with followed slow charge rate.

Figure IV.5.2b further details the discovery in Figure IV.5.2a. The bar in red and blue indicates loss capacity during fast charge and recovered capacity with slow rate, respectively. The capacity percent is based on the capacity achieved in 2nd formation cycle. The percent of loss capacity is gradually increase with cycle counts increases, while the percent of recovered capacity with slow rate does not show clear trend with cycle counts. However, it should be noticed that the difference between loss capacity and recovered capacity indicated by arrows gradually increases with cycle counts. The difference between these two can be regarded as an amount of the capacity that cannot be recovered. Therefore, it can be concluded that more numbers of fast-charging to the cells bring about more capacity loss in the cells.

To understand the amount of plated lithium after fast charging as well as after followed slow charge, ICP-MS analysis was conducted as displayed in Figure IV.5.3. ICP-MS results of initial cycles were not collected as cells do not show noticeable lithium plating. In Figure IV.5.3, red bars indicate the lithium amount on the graphite anode after each fast-charge cycle numbers (i.e., fast-charge only) and blue bars indicate that lithium amount after 10 slow charge cycles after each fast charge cycle numbers (i.e., fast-charge followed by slow charge). Amount of the lithium plating after only fast-charge gradually increase with cycle counts, as expected. Then amount of the lithium after fast-charge followed by slow charge shows similar or slightly higher amount of lithium compared to fast-charge only. Although this is *ex-situ* experiment but results in Figure 3 do not show clear evidence of lithium amount decrease after slow charge cycles suggesting plated lithium barely intercalate back to cathode after 10 continuous fast charging cycles. In other words, fast-charge driven plated lithium on the graphite is barely reversible even with continuous slow rate cycles.

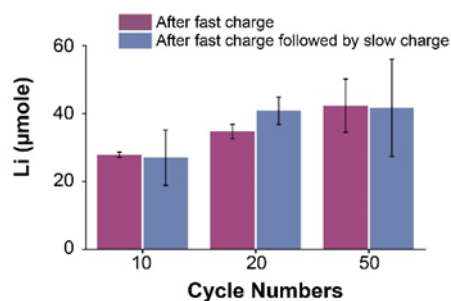


Figure IV.5.3 Quantification results of plated lithium using ICP-MS.

The XPS depth profiles analysis has been performed to investigate the composition and chemistry of lithium plating with depth information. For the study, NMC532/graphite coin-cell was fast-charged for 50 cycles at 30c then disassembled. Then harvested graphite anode with lithium plating is loaded to the XPS without any air exposure. Figure IV.5.4a shows the atomic percent of lithium, oxygen, fluorine, and carbon versus sputter

time. As sputter time increases, it gets close to the graphite surface and XPS information comes from near graphite surface as well. In Figure IV.5.4a, it was observed that atomic percent of the Li1s increases as sputter time increases while atomic percent of the C1s decreases. Atomic percent of O1s (~35 at. %) and F1s (~10 at. %) do not change much from top surface to interface with the graphite. This result tells that lithium plating is a composite of various elements including oxygen, fluorine and carbon and its composition changes from surface to bulk.

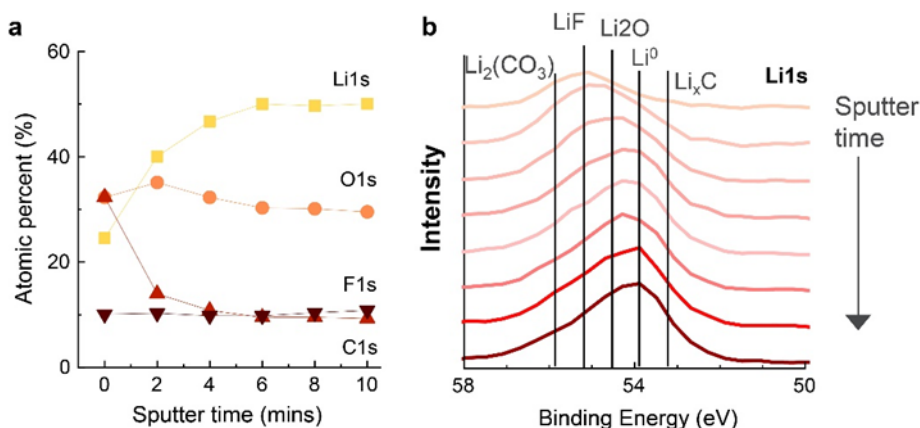


Figure IV.5.4 XPS depth profiling results on lithium plating from 50 fast-charged cells. (a) Atomic percent of Li1s, O1s, F1s and C1s. (b) XPS spectra from Li1s region during depth profiling.

The XPS spectrum of Li1s in Figure IV.5.4b further details the lithium related chemistry changes during depth profiling. In Li1s region, compounds of Li₂(CO₃), LiF, Li₂O, lithium metal and LiC_x were mainly observed. The Li1s spectra gradually shifts from higher binding energy (BE) to the lower BE as spectra gets close to the graphite surface suggesting lithium plating contains more lithium metal and LiC_x closes to the graphite surface. Among these compounds, only lithium in lithium metal and LiC_x can intercalate back to the cathode. However, as we have seen in ICP-MS results in Figure IV.5.3, these reversible lithium in lithium metal and lithium carbides are sitting on the anode and do not intercalate back to the cathode. As unveiled with XPS depth profile, the lithium plating is a composite material including elements of oxygen, fluorine and carbon forming Li₂(CO₃), LiF and Li₂O which are irreversible. As the lithium metal and LiC_x are blended with or isolated by those irreversible forms of lithium, lithium conduction along with the lithium plating could be highly disturbed. Therefore, although lithium plating partially contains the reversible form of lithium, it is mostly irreversible due to the ambient compounds which are irreversible and barely lithium-ionic conductive.

In summary, irreversible behavior of fast-charge driven lithium plating was investigated by means of electrochemical performance, ICP-MS and XPS depth profiling analysis. Although plated lithium partially contains reversible form of lithium such as lithium metal and LiC_x, lithium plating seems barely reversible based on results from electrochemical performance and ICP-MS. The results from XPS depth profiling provide that lithium plating also contains irreversible form of lithium including Li₂(CO₃), LiF and Li₂O. Continuous fast-charging the cells could cause isolation of the lithium metal and LiC_x in the lithium plating and results in irreversible lithium plating.

Influence of external pressure on Li plating

External stack pressure can improve electrical contact, minimize delamination, and an understanding of the impact of pressure on capacity fade can provide insight into the degradation mechanisms. [4],[5] This year, we have investigated the effect of uniform pressure applied to cells charged in the extreme fast charging (XFC) regime. We continue to investigate cell degradation and parasitic Li plating using single-layer pouch cells with graphite anodes, LiNi_{0.5}Mn_{0.3}Co_{0.2}O₂ (NMC532) cathodes, and 1.2 M LiPF₆ in 3:7 weight % ethylene carbonate and diethyl carbonate. Cells are tested between 10 – 150 psi, and the cells cycled at higher pressures

show a strong reduction in capacity fading after 20 cycles (shown in Figure IV.5.5b), further studies are being conducted at higher cycle counts. To study this, we designed a novel pressure (Figure IV.5.5a) cell to study Li plating, parasitic reactions, and Li intercalation into graphite under controlled, uniform pressure that allows *operando* measurements in the future. We performed synchrotron radiation-based *in situ* XRD at APS on beamline 5-BM-C at 25 keV. The data is being analyzed to create 2D XRD intensity maps of Li and Li_xC_6 to understand the effect of heterogeneity under uniform pressure; preliminary XRD patterns are shown in Figure IV.5.5c. This will be complemented with *ex situ* XPS to study the composition of parasitic reaction products and corrosion to correlate local Li plating to pressure and heterogeneity. Our data reveals the emergence of Li_xC_6 and Li metal during cycling at XFC, with a reduction in plated parasitic Li at elevated pressure. These results show that the observed improvement on performance is due to more homogenous reaction conditions across the anode and less polarization through the electrode thickness. We emphasize the importance of electrode stack pressure in XFC batteries and quantify Li plating and intercalation yielding critical insight into the degradation mechanisms that cause capacity fade for better battery engineering.

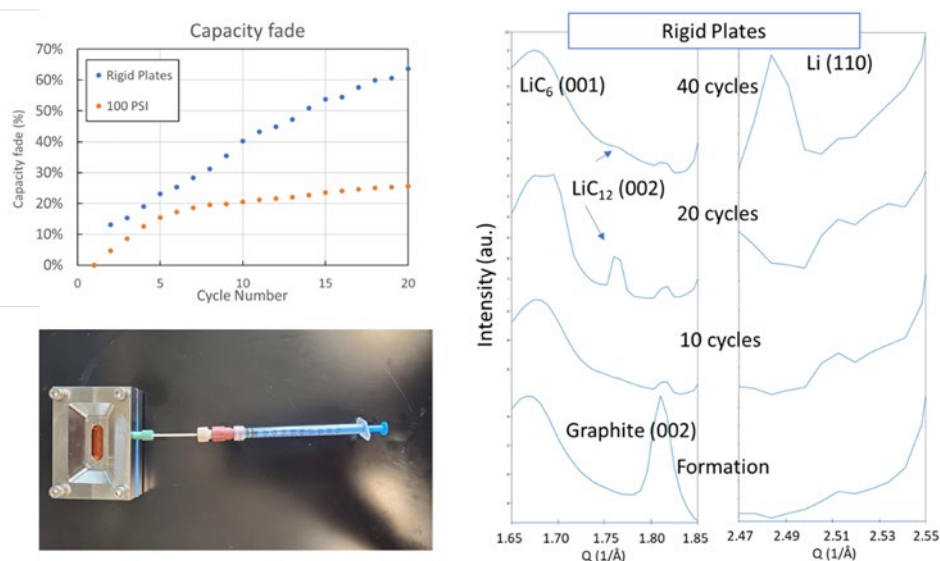


Figure IV.5.5 (a) Pressure cell (b) Capacity fade over cycle number showing reduce capacity fade in the cell with applied uniform pressure. (c) Preliminary synchrotron XRD peaks showing the presence of Li and Li_xC_6 .

Milestone 2: Perspective on Li detection techniques

As part of the Q1 deliverables, we wrote a review paper, now published in *Advanced Energy Materials*, on an overview of existing and emerging methods for Li detection in Li-based batteries. [6] This review covered a majority of Li detection and characterization techniques employed in the XCEL project (Figure IV.5.6). The methods were broadly classified into: (i) *ex situ* detection methods, such as mass spectrometry titration and electrochemical analyses (electrochemical impedance spectroscopy, dQ/dV analyses, calorimetry); (ii) *in situ* characterization techniques, such as x-ray and neutron-based methods; and (iii) *operando* detection/characterization methods, such as x-ray diffraction and electron microscopy). Numerical modeling methods were also broadly reviewed in this work to help connect underlying mechanisms such as Li plating leading to poor cell performance. Finally, the applicability of electrochemical techniques as part of battery management systems for predicting the life and performance of the battery pack on-board electric vehicles was discussed.

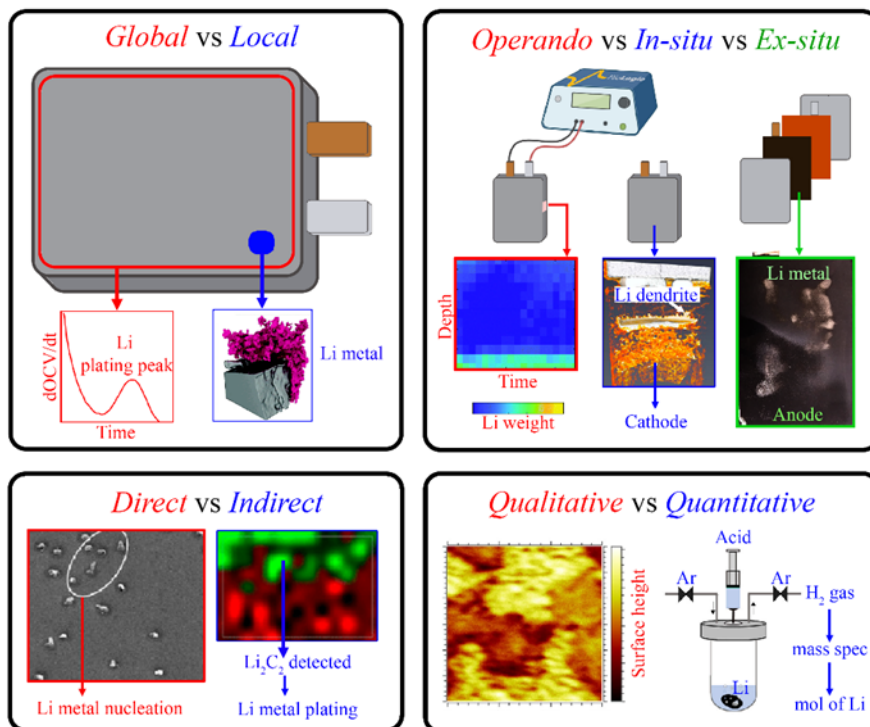


Figure IV.5.6 An overview of Li detection and characterization techniques employed in Li-based batteries.

Milestone 3: Connect “dead Li” to accelerated aging

LFP/Graphite full-cell testing

Work from ANL focused on trying to understand how the occurrence of Li plating affects the future cell behavior during fast charging. To that end, we used graphite anodes paired with LFP cathodes at a N/P ratio < 1, so the excess Li^+ inventory in the cell enables repeated cycling of the cell to a same *anode* SOC. By exploring various cycling conditions, the main observations were:

- After deliberately plating lithium at the anode, resuming fast charging under conditions that were originally not conducive to plating did not lead to additional Li plating (Figure IV.5.7a);
- Repeatedly cycling the cell under conditions that are conducive to Li plating led to a decay in coulombic efficiency (Figure IV.5.7c);
- Decreases in coulombic efficiency were correlated with losses of accessible anode capacity (Figure IV.5.7d).

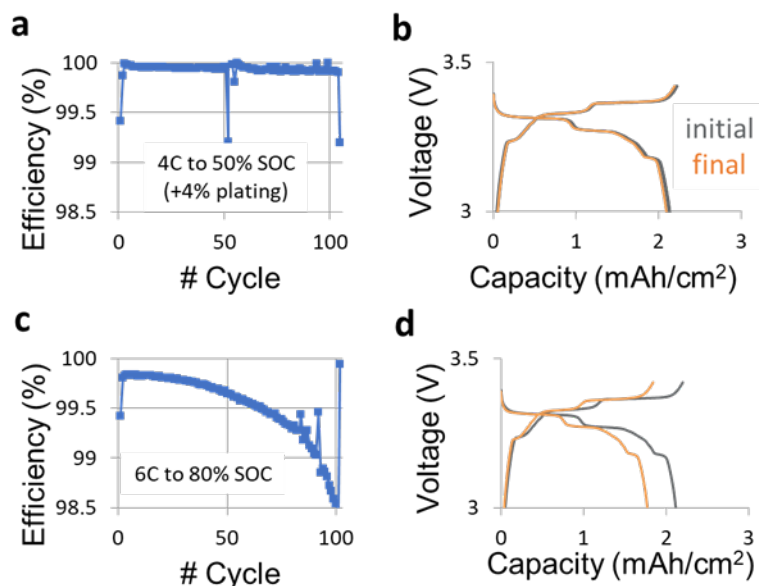


Figure IV.5.7 Cycling data from LFP vs. graphite cells with N/P ratio < 1. a) Coulombic efficiency for a cell cycled at 4C to 50% anode SOC. An amount of Li equal to 4% of the anode capacity was deliberately plated on the Gr on cycle 50 but did not cause major changes in the coulombic efficiency of ensuing cycles. b) Comparison between the initial and final C/20 cycles of the cells in panel a. Cells with N/P ratio < 1 only show capacity fade if anode capacity is lost, which was not the case. c) Coulombic efficiency for a cell cycled at 6C to 80% anode SOC, where Li plating is likely. A dip in coulombic efficiency is observed. d) Comparison between the initial and final C/20 cycles of the cells in panel c, showing loss of accessible anode capacity.

In summary, our experiments appear to indicate that cumulative Li plating could slowly block domains of the anode, facilitating additional Li plating. However, if the amount of plating is small (such as during accidental exposure of the cell to lower temperatures during charging) and if the charge protocol is conservative, pre-existence of plated Li is unlikely to favor additional Li deposition. The balance between these two scenarios is dynamic and depends essentially on the relative effect of Li deposition on the Li^+ inventory and the accessible anode capacity: future Li plating becomes more likely only when losses of anode capacity are larger than that of Li^+ inventory.

Reversibility of Li plating

In this year at LBNL, we propose to study the properties of deposited Li and its effect on cyclability of graphite anode. Two testing protocols with (w/) and without (w/o) resting after charging are designed (Figure IV.5.8A) to investigate the reversibility behavior of deposited Li. The graphite/Li half cell is charged at 4C to different SOC from 10% to 100% and then slowly discharged to 1.5 V at C/5. CE typically decreases at higher SOC because of Li plating. By comparing the CEs at different SOC in both cases with and without resting (Figure IV.5.8B), we notice that when SOC increases above 30%, the value of $\text{CE}_{\text{w/ resting}}/\text{CE}_{\text{w/o resting}}$ starts to decrease. Note that once Li plating occurs during fast charge, the plated Li is either irreversible by reacting with electrolyte and forming “dead” Li or reversible through Li stripping during discharge or reacting with partially lithiated graphite, while lower CE is expected if plated Li becomes irreversible. Therefore, the decrease in $\text{CE}_{\text{w/ resting}}/\text{CE}_{\text{w/o resting}}$ suggests the deposited Li at the SOC higher than 30% is partially irreversible, meaning reactions with electrolyte and formation of “dead” Li. This hypothesis is further confirmed by the differential discharge capacity curves (Figure IV.5.8C). Without resting, the delithiation peak for Li metal is observed at a discharge potential below 0.1 V at the SOC higher than 30%, in sharp contrast, it becomes invisible in the discharge profiles when the cells are rested after charging. Correspondingly, the lithiated degree of graphite anode exhibits a slight increase with resting (Figure IV.5.8D, E), which is in good agreement with the reaction between deposited Li and non-fully lithiated graphite. Compared to graphite anode at pristine state (Figure IV.5.8F), massive growth of Li dendrite is observed on graphite anode after charging to

100% SOC at 4C (Figure IV.5.8G). To investigate the cyclability of the deposited Li, graphite/Li half cells with or without resting after charging are assembled for cycling test. As shown in Figure IV.5.1H, both cells show a gradual decrease in CE with cycling, due to the cumulative “dead” Li. Moreover, the cell cycled without resting exhibits a higher CE than that with resting, which confirms the formation of “dead” Li during resting. These results suggest that the deposited Li undergo complex chemical and electrochemical reactions, which gradually degrades the cycling performance of graphite anode.

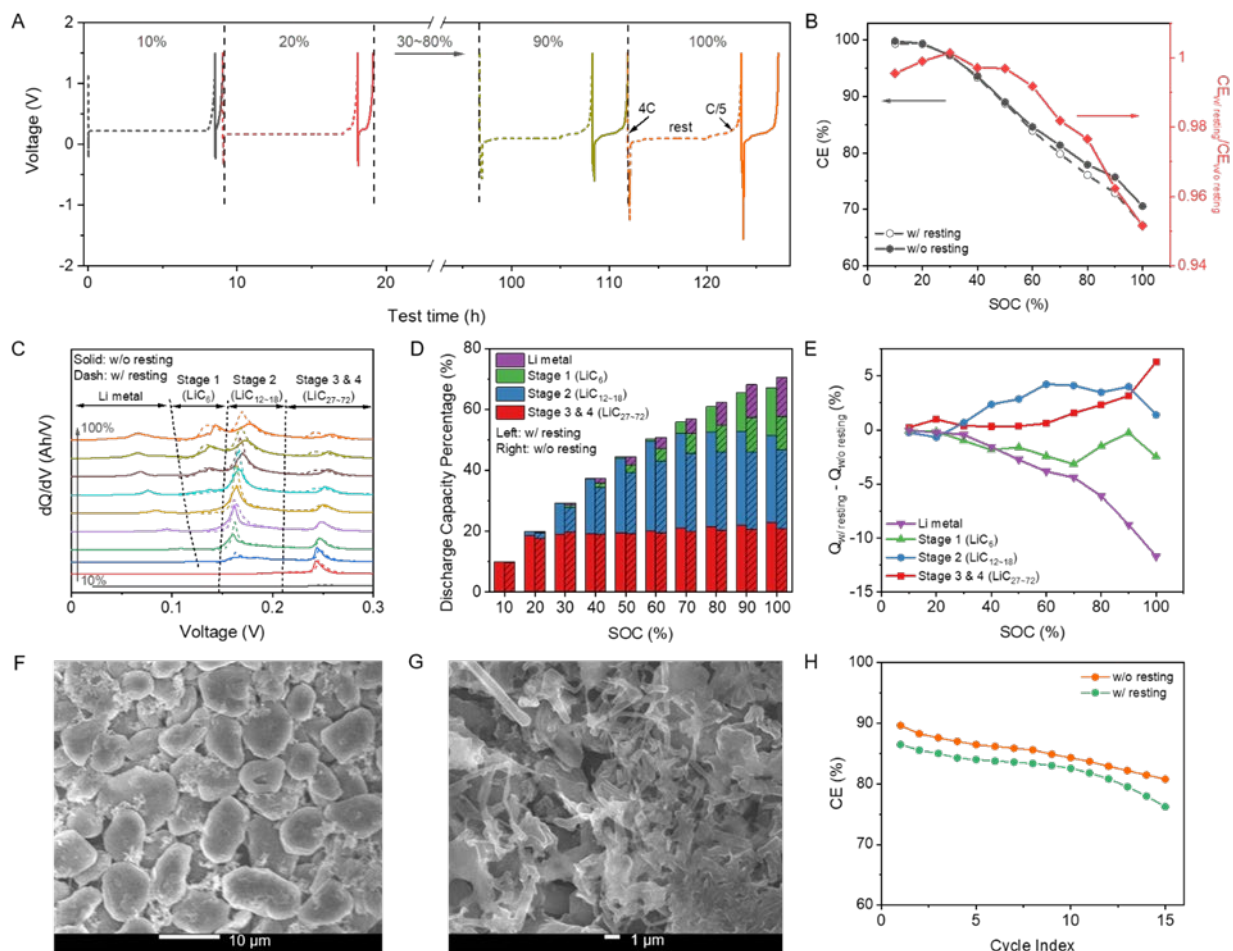


Figure IV.5.8 (A) Voltage profiles of graphite/Li half cell charged at 4C to different SOC from 10% to 100% and then discharged at C/5 to 1.5 V. At each SOC, cells are cycled with and without resting after charging; (B) CE of graphite/Li half cells charged to different SOC and corresponding $CE_{w/\text{resting}}/CE_{w/o\text{resting}}$; (C) dQ/dV curves during discharge after charged to different SOC; (D) normalized discharge capacity at different graphite lithiation stages and (E) corresponding difference in normalized discharge capacity between charging w/ resting and w/o resting; SEM images of graphite anodes at (F) pristine state and (G) after charging at 4C to 100% SOC; and (H) CEs of graphite/Li half cells w/ and w/o resting, cells are charged to 100% SOC at 4C.

The McCloskey Lab at UC Berkeley has developed cycling protocols to rigorously estimate the reversibility of lithium plating induced by overcharging in graphite half-cells. Figure IV.5.9a summarizes the cycling procedure and equation used to calculate the lithium plating reversibility, η . The first step is to estimate the coulombic efficiency for complete lithiation of graphite without lithium plating (CE) at C/3 intercalation rate with a 0.01 V hold prior to C/5 deintercalation to 1.5 V. Next, that same cycle is repeated with an added overcharge step to induce a known capacity of lithium plating, P (Figure IV.5.9a, right). The capacity loss from the intercalation process, $(1-CE)(Q_i+E)$, determined from the baseline cycle, where Q_i+E is the total charge capacity including intercalation (Q_i) and electrolyte degradation (E), is then subtracted from the total capacity loss during the overcharge cycle (Q_{lost}) to isolate the capacity lost due to irreversible lithium plating,

$P(1-\eta)$, which allows the calculation of η . Four to five repeat overcharge cycles on the same cell gives reproducible calculated reversibility values, further increasing our confidence in the technique.

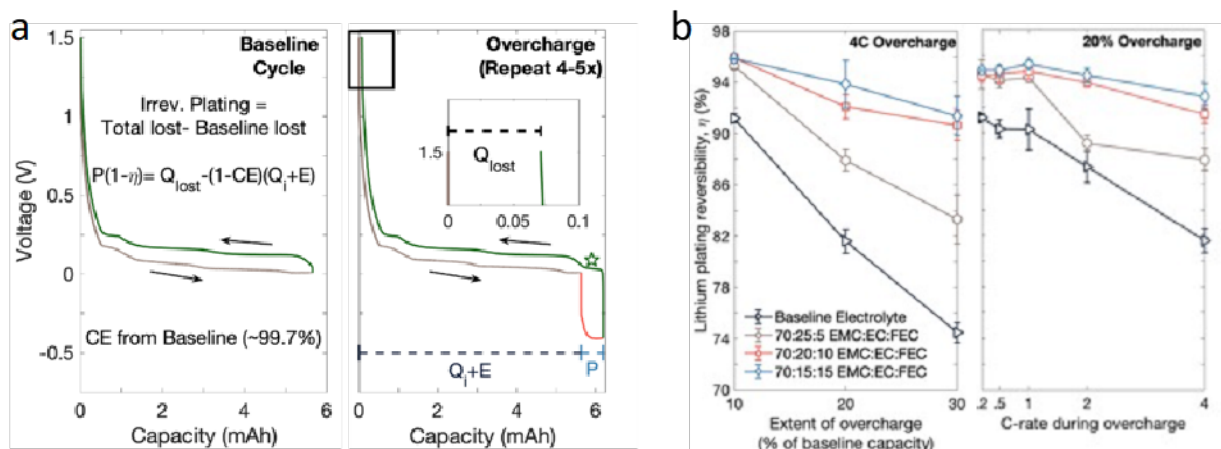


Figure IV.5.9 Lithium plating reversibility as a function of amount, C-rate, and electrolyte FEC content. a) Protocol to determine lithium plating reversibility in graphite/Li coin cells, which includes a baseline lithiation cycle [C/3 to 0.01V, hold until C/20, and C/5 delithiation to 1.5V] followed by 4-5 overcharge cycles that use an identical sequence with an added lithium plating step with known capacity, P . The total capacity loss in the overcharge cycle (Q_{lost}) is combined with the coulombic efficiency of the baseline cycle (CE) to isolate the capacity loss from irreversible plating, $P(1-\eta)$, and calculate the Li plating reversibility, η . b) Reversibility values for 4C overcharging with varying amounts of plating as a percent of the total graphite capacity (left), and η for fixed 20% overcharge with varied rates. All electrolytes contain 1.2 M LiPF_6 and the baseline electrolyte is 70:30 EMC:EC, 'Gen 2'.

This method was then applied to understand the effect of electrolyte fluoroethylene carbonate (FEC) content on lithium plating reversibility as a possible solution to irreversible plating losses during fast charge. FEC was selected for its known benefits to plating reversibility on other substrates for Li metal anode development. In Figure IV.5.9b we show η as a function of electrolyte composition, plating amount (left), and overcharge rate (right) for the CAMP R2a graphite electrodes (3.0 mAh/cm^2). We first observe that for a fixed 4C overcharge rate (Figure IV.5.9b, left), increasing the overcharge amount from 10% to 30% of the baseline capacity negatively affects η , with the effect most prominent for the Baseline Gen 2 electrolyte without FEC. With a fixed overcharge capacity of 20% (Figure IV.5.9b, right), increasing the rate of lithium plating from C/5 to 1C does not affect η , but further increasing the rate from 1C to 4C decreases the reversibility, η .

There are a few important conclusions and future directions resulting from this work. The first is that FEC-containing electrolytes exhibit higher η than the Gen 2 electrolyte for all compositions and charging conditions. This performance improvement is most drastic for the 10% FEC case at extreme overcharge conditions of 4C plating rate at 20-30% extent of overcharge, in which $\eta > 90\%$ are observed compared with $< 80\%$ for the Gen 2 electrolyte. While only a 10% difference in efficiency, this would mean a 2x difference in irreversible lithium formed for the same amount of lithium plating. The second conclusion is that this data confirms the speculated high variability of lithium plating reversibility with local plating rate and plating amount. We are incorporating these variable plating reversibilities into fast charging models from NREL. We are also relating these observations to fast charging performance and plating that occurs on graphite electrodes that are only partially lithiated in contrast to these overlithiation studies.

Milestone 4: Early warning signs and onboard Li detection

Differential pressure sensing

In 2020, the Cui group at Stanford developed an operando detection of Li-plating technique based on differential pressure sensing (DPS) which measures the pressure change per unit of charge on multilayer pouch cells (Figure IV.5.10a). We showed in previous reports that this technique can identify the Li-plating as early as nucleation stage and serve as on-board dynamic regulating system to avoid Li-plating at 1C rate at 30°C and

0°C. In 2021, we employed DPS system to elucidate the occurrence of Li-plating under extreme fast charging conditions (up to 6C rate) and we upgraded the DPS system with an advanced pressure mapping system to achieve an even lower detection limit.

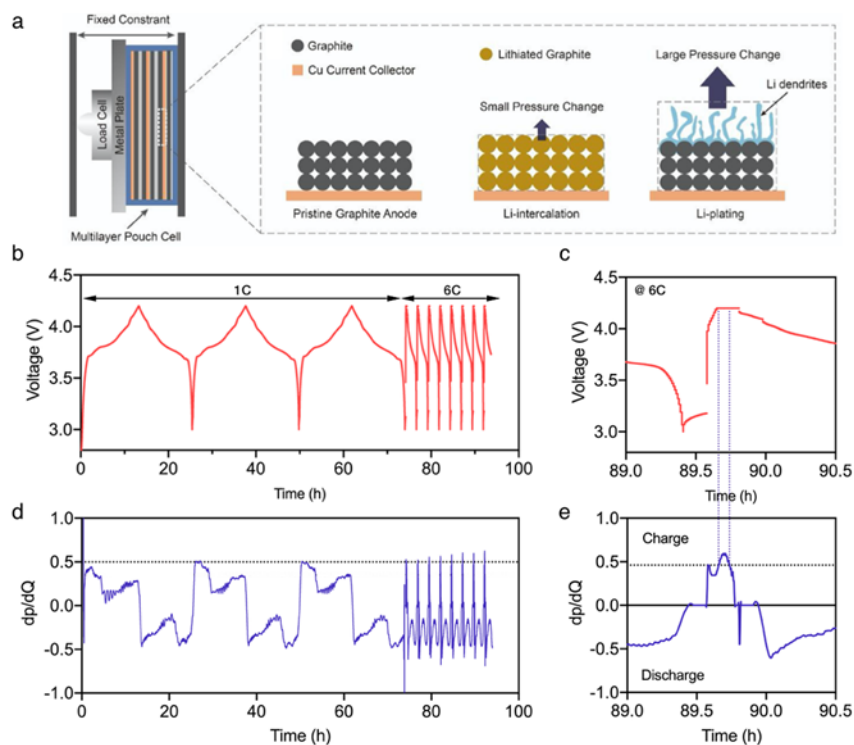


Figure IV.5.10 a) The configuration of operando pressure measurement: the stack contains multilayer pouch cell, metal force-distribution plate, and pressure sensor (load cell) is clamped into a fixed constraint. Zoomed-in schematic of graphite anode illustrating that for the same amount of lithium ions, Li plating induces much higher volume/pressure than intercalation. b) Voltage profiles of NMC-graphite pouch cells at 1C rate and 6C rate. c) Zoomed-in voltage profile during 7th charge step at 6C rate. d) The differential pressure (dp/dQ) profile of the NMC-graphite cell. e) Zoomed-in differential pressure profile during 7th charge step at 6C rate. The black dash line in c) and e) are the upper bound of dp/dQ during intercalation defining the Li plating threshold.

Here we employed the DPS system to a multi-layer commercial NMC-graphite cell with a capacity around 200 mAh and monitored its pressure evolution at 1C and 6C rates (Figure IV.5.10b-c). Under 1C charging, no Li deposition was observed and the maximum dp/dQ under this condition was used to define the Li deposition threshold (Figure IV.5.10d). In contrast, we observed a significant amount of Li deposition during 6C charging and the dp/dQ curve most of initial Li-plating occurred during constant voltage charging step at 4.2 V (Figure IV.5.10e).

To further decrease the detection limit of the pressure sensor, we upgraded the DPS system with an advanced pressure mapping system with a spatial resolution of 0.3 mm². First, we measured the pressure distribution and evolution of the commercial NMC-G pouch cell during charge at 1C rate and 6C rate (1C = 330 mAh), respectively. During the constant current charging at 1C rate, the average pressure gradually increases, and the pressure distribution is relatively uniform (Figure IV.5.11a). The average pressure at fully charged state (100% SOC) is ~40 psi with a standard deviation of 17 psi. In contrast, under a fast-charging condition (6C), the pressure evolution is much more pronounced, especially during constant voltage charging (Figure IV.5.11b). At the fully charged state, the average pressure reaches ~65 psi with a large standard deviation of 26 psi. Such evolution can be attributed to Li-plating during the fast-charging process.

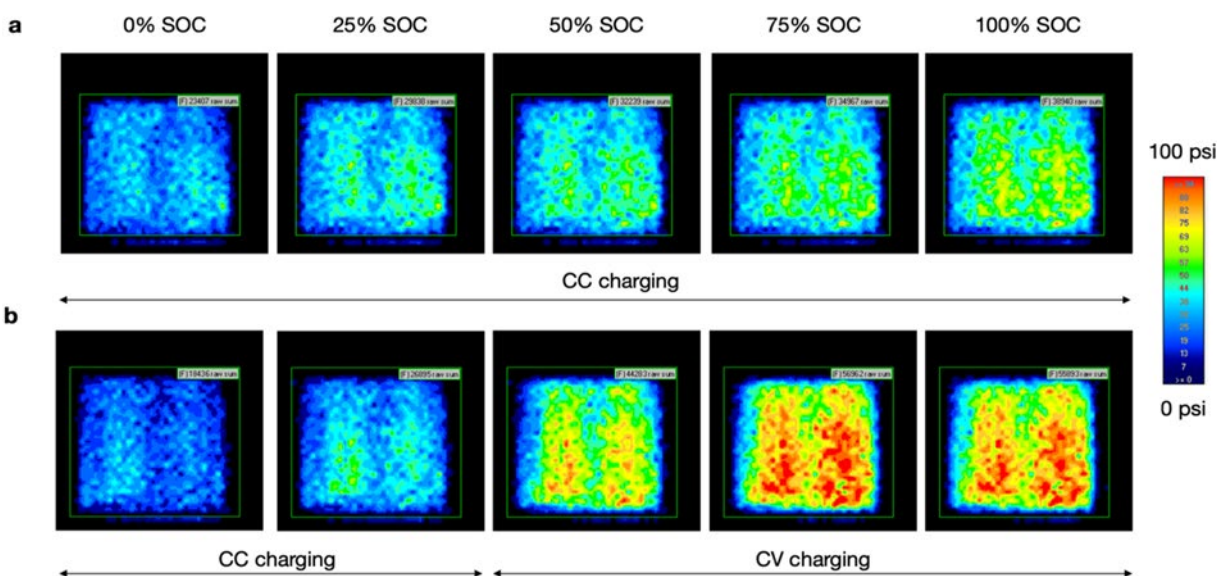


Figure IV.5.11 Pressure evolution of NMC-G pouch cells during charging process at (a) 1C rate and (b) 6C rate (1C = 330 mAh cm⁻²). The areal capacity is ~2.2 mAh/cm².

Later, we tested a multi-layer NMC-graphite cell (Round 2 electrodes) under fast charging conditions (6C rate) and analyzed the pressure evolution at a global scale, as well as individual locations (Figure IV.5.12a). We found that pronounced pressure evolution correlates well with “dead Li” formation (Figure IV.5.12b,c). A threshold of irreversible Li deposition can be defined with their fast rate of pressure evolution during fast charging process.

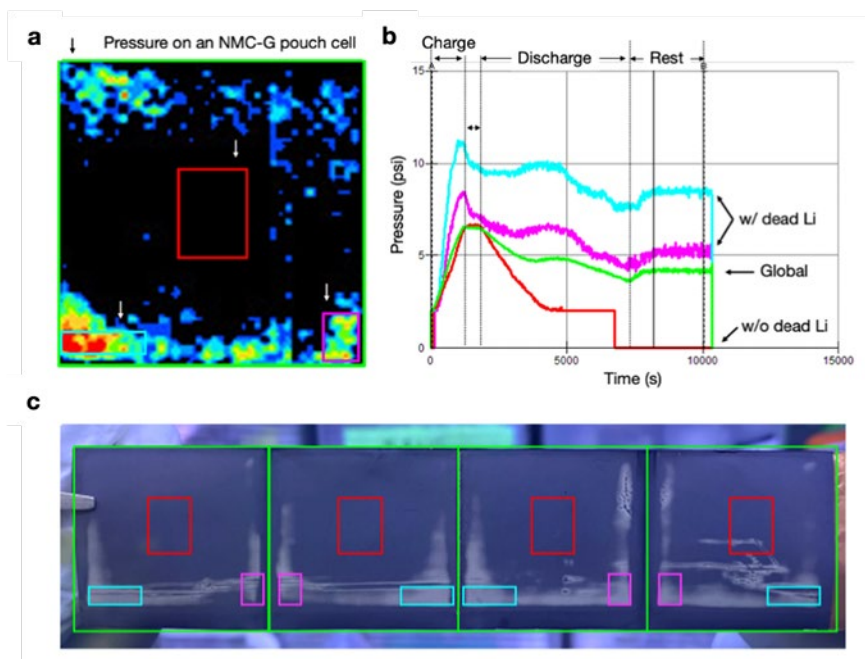


Figure IV.5.12 a,b) The corresponding average pressure evolution at different locations. The base pressure at the fully discharged state was set at zero at all locations. The pressure sensor covers the entire pouch cell. c) Optical image of graphite electrode at a fully discharged state. The marked areas match that in a-c figures.

Thermal wave sensors

The Prasher group at LBNL has developed thermal wave sensing for lithium detection. We initially used a thermal sensor inside pouch cells for detecting local lithium concentration distributions through the thickness of graphite anodes. More recently, we attached our thermal sensor outside batteries and measured battery thermal resistance during XFC (Figure IV.5.13a). Our preliminary data supported that significant capacity loss at XFC causes a decrease of V_{3w} (Figure IV.5.13b) and battery thermal resistance (Figure IV.5.13c). From post-mortem studies in the literature, the k of electrode and separator layers does not change much with battery cycling. Thus, the increase of measured k_{eff} should be attributed to the decreased thermal contact resistance (TCR) between layers. Based on our thermal contact model, lithium with a high thermal conductivity can be a high- k filler between graphite particles and separator and improve the effective contact area and thus the thermal contact.

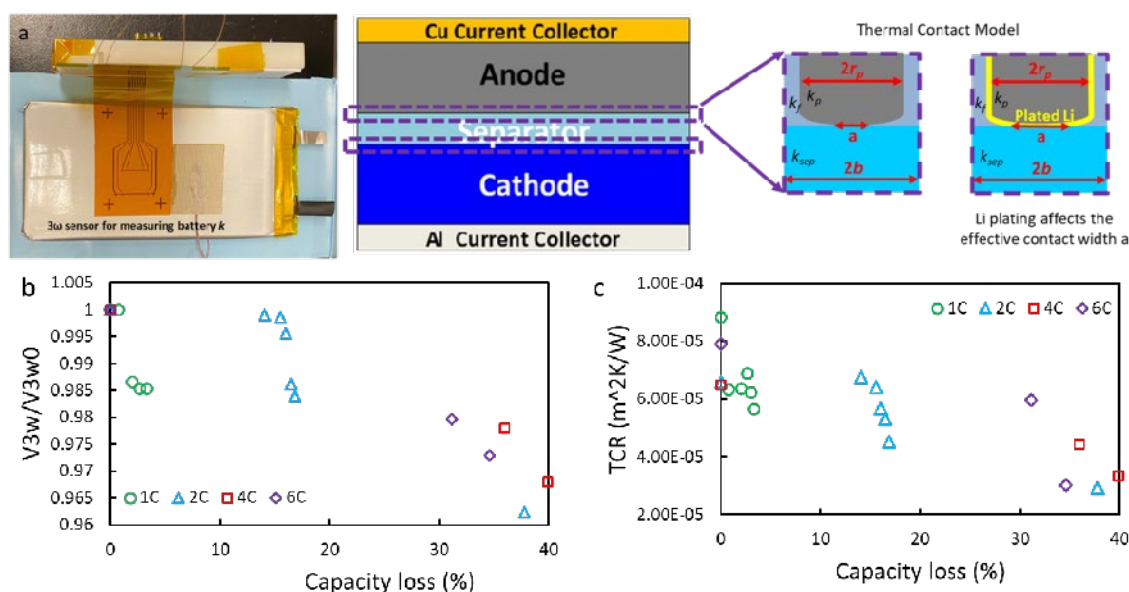


Figure IV.5.13 a) A schematic of the measurement setup and thermal contact model. b) Representative raw V_{3w} data (normalized to V_{3w} at cycle 0), and c) measured TCR as a function of capacity loss.

Milestone 5: Characterize “Hero” cell

Round 2, high loading electrodes with NMC532 cathodes cycled with limited specific capacity, 80-90 mAh/g, and significant lithium plating, ~6% of total lithium by the end of cycle life (Figure IV.5.14). As a result, numerous changes have been made to each component to create a new cell build referred to as the March cell build: the cathode (NMC532 to NMC811, lowering of CBD to 3%), anode (reduction in porosity), separator (2320 to 2500) and electrolyte (Gen2 to B26). Two cells were cycled using both Gen2 and B26 as a comparison. Initial testing with periodic XRD mapping at ANL indicates little evidence for plating. The onset of plating appears to have been delayed significantly by the new cell build with no sign of plating for the B26 cell after 391 cycles and very little sign of plating for the Gen2 cell after 386 cycles based on XRD mapping. Both cells achieved similar capacities and capacity fade through the first 500 fast charge cycles (Figure IV.5.15). B26 electrolyte may further prevent lithium plating, the other changes to the cell build may also significantly delay or prevent plating.

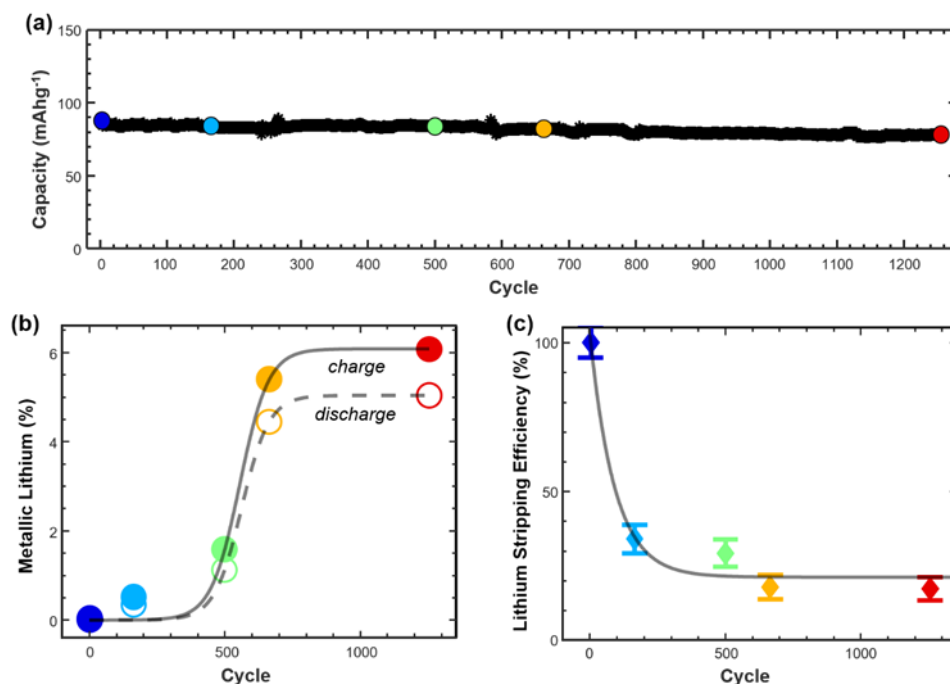


Figure IV.5.14 a) Discharge capacity as a function of cycle number. Fast charging at 6C rate (CCCV) and slow discharging at C/2 rate (CC) (ii)-(vi). b) Area averaged evolution of consumed cathode lithium (y in $\text{Li}_y\text{Ni}_{0.5}\text{Mn}_{0.3}\text{Co}_{0.2}\text{O}_2$). Open circles indicate metallic plated lithium at charge while closed circles indicate metallic plated lithium at discharge. c) Stripping efficiency is defined as the difference in the percent change in the amount of metallic lithium at charge compared to discharge for the same cycle. Error bars were determined based on the accounting for the set detection limit.

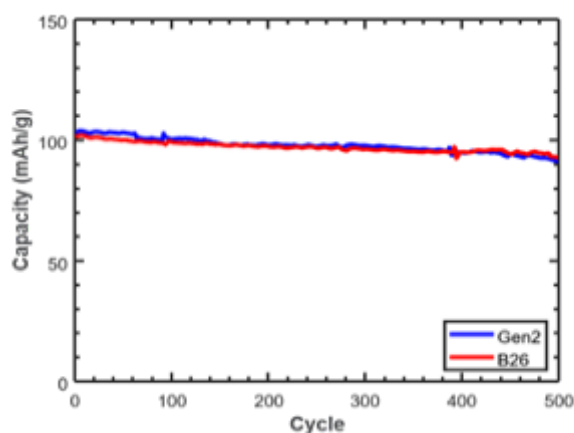


Figure IV.5.15 Comparison of Gen2 and B26 electrolytes in terms of discharge capacity achieved with fast charge (6C, CCCV, 3-4.1V) and slow discharge (C/2, CC, 4.1-3V). The cell build was identical for both cells other than the choice of electrolyte.

References

1. Paul, P. P., *et al.* Quantification of heterogeneous, irreversible lithium plating in extreme fast charging of lithium-ion batteries. *Energy & Environmental Science*, 2021 14(9), 4979–4988.
2. Charalambous, H., *et al.* Comprehensive Insights into Nucleation, Autocatalytic Growth, and Stripping Efficiency for Lithium Plating in Full Cells. *ACS Energy Letters*, 2021 6, 3725–3733.

3. McShane, E. J., Colclasure, A. M., Brown, D. E., Konz, Z. M., Smith, K., & McCloskey, B. D. (2020). Quantification of Inactive Lithium and Solid–Electrolyte Interphase Species on Graphite Electrodes after Fast Charging. *ACS Energy Letters*, 5(6), 2045–2051.
4. C. Cao *et al.* Influence of Controlled Pressure on Fast-Charging Li-ion Batteries (in preparation)
5. J. Cannarella and C. B. Arnold, *J. Power Source*, 2014, 245, 745–751.
6. P. Paul, *et al.* A review of existing and emerging techniques for lithium detection and characterization in Li-ion and Li-metal batteries, *Advanced Energy Materials*, 2021, 2100372

Publications

1. Paul, Thampy, Cao, Steinrück, Tanim, Dunlop, Dufek, Trask, Jansen, Toney, Nelson Weker, Quantification of heterogeneous, irreversible lithium plating in extreme fast charging of lithium-ion batteries. *Energy & Environmental Science*, 2021 14(9), 4979–4988.
2. Rodrigues, Son, Colclasure, Shkrob, Trask, Bloom, Abraham, How Fast Can a Li-Ion Battery Be Charged? Determination of Limiting Fast Charging Conditions. *ACS Applied Energy Materials* 2021, 4 (2), 1063–1068.
3. Paul, McShane, Colclasure, Balsara, Brown, Cao, Chen, Chinnam, Cui, Dufek, Finegan, Gillard, Huang, Konz, Kosteki, Liu, Lubner, Prasher, Preefer, Qian, Rodrigues, Schnabel, Son, Srinivasan, Steinrück, Tanim, Toney, Tong, Usseglio-Viretta, Wan, Yusuf, McCloskey, Nelson Weker, A Review of Existing and Emerging Methods for Lithium Detection and Characterization in Li-Ion and Li-Metal Batteries. *Advanced Energy Materials* 2021, 11 (17), 2100372.
4. Paul, Cao, Thampy, Steinrück, Tanim, Dunlop, Trask, Jansen, Dufek, Nelson Weker, Toney, Using *in-Situ* X-ray Diffraction to Quantify Electrode Behavior of Lithium-Ion Batteries from Extreme Fast Charging, *ACS Applied Energy Materials* 2021, 4, 10, 11590–11598.
5. Gao, Kim, Chinnam, Dufek, Colclasure, Jansen, Son, Bloom, Dunlop, Trask, Gering, Methodologies for Design, Characterization and Testing of Electrolytes that Enable Extreme Fast Charging of Lithium-ion Cells. *Energy Storage Materials* 2022, 44, 296–312.
6. Brown, McShane, Konz, Knudsen, McCloskey, Detecting the onset of Li plating during fast charging of Li-ion batteries using operando electrochemical impedance spectroscopy. *Cell Reports Physical Science* 2021 2(10), 100589.

Publications in preparation

1. Chinnam, Parameswara; Tanim, Tanvir; Dufek, Eric; Dickerson, Charles; Li, Meng, "Sensitivity and Reliability of Key Electrochemical Markers for Detecting Lithium Plating during Extreme Fast Charging" (submitted)
2. C. Cao *et al.* Influence of Controlled Pressure on Fast-Charging Li-ion Batteries (in preparation)
3. Monasterial *et al.* "Quantifying the heterogeneous response of graphite to fast charging conditions in pouch cells"

IV.6 XCEL: Local Heterogeneity Workgroup

Venkat Srinivasan, Principal Investigator

Argonne National Laboratory
9700 South Cass Avenue
Lemont, IL 60439
E-mail: vsrinivasan@anl.gov

Andrew Colclasure, Principal Investigator

National Renewable Energy Laboratory
Energy Conversion and Storage Systems Center
15031 Denver West Parkway
Golden, CO 80401
E-mail: Andrew.colclasure@nrel.gov

Samm Gillard, DOE Technology Development Manager

U.S. Department of Energy
E-mail: Samuel.Gillard@ee.doe.gov

Start Date: October 1, 2020

End Date: September 30, 2021

Project Funding (FY21): \$225,000

DOE share: \$225,000

Non-DOE share: \$0

Project Introduction

A 2017 DOE technology gap assessment report [1] established goals for next-generation electric vehicle (EV) batteries, namely battery cost of \$80/kWh, energy density of 275 Wh/kg and 550 Wh/L, vehicle range of 300 miles, and charge time of 80% ΔSOC in 15 minutes. Compared to thin electrodes, thick electrodes are preferred due to less inert material, higher energy density and lower cost. Unfortunately, today's thick electrodes cannot tolerate fast charge rates. The thick electrodes have increased distance for ionic transport through the liquid electrolyte. Thin electrode batteries are capable of fast charge, however they come at an almost 2x increase in cell cost (from \$103/kWh to \$196/kWh) and have around 20% less energy density (180Wh/kg vs. 220 Wh/kg) [1]. In addition to polarization and low capacity, electrolyte transport limitations can lead to lithium plating, a side reaction with degradation and safety consequences. It is uncertain what graphite materials can best tolerate fast charge and why. At the system level, fast charging presents thermal management challenges to remove the heat generated during charging.

Objectives

The goal of this workgroup is to quantify how local heterogeneities result in early onset of lithium plating during extreme fast charging (XFC). Local heterogeneities being investigated scan length scales from nm (graphite crystallographic orientation of edge vs. basal plane) to mm (changes in local electrode microstructure properties such as porosity, tortuosity, and conductivity). A major objective is to determine if local lithium plating is driven by local changes in ionic transport properties. Another objective is to understand the effective of electrolyte wetting/trapped gas on variation in local SOC and lithium plating. Further, more accurate models for lithium plating and graphite lithiation are needed to better understand fast charge performance/limitations. In the second year of this thrust, the major goal is to move to a more quantitative understanding of the impact of heterogeneities resulting in early onset of lithium plating and limiting fast charge capacity. Including determining which heterogeneities dominate performance/plating.

Approach

The team has used a combination of novel experimental techniques/characterization and theoretical modeling to understand the effects of heterogeneity at many different length scales. Experimental techniques include:

- Local mapping of MacMullin number (ionic resistance) and electrical resistivity of electrodes using novel probe/EIS – BYU
- High-energy, in-situ XRD to monitor local SOC and lithium plating in-situ resting (APS) and operando (NREL)

Further many modeling efforts have helped interpret experimental measurements and suggest methods to improve fast charge performance:

- Advanced lithium plating model with nucleation and growth principles from ORNL
- Electrolyte wetting modeling from ANL
- Microstructure electrochemical model to study heterogeneity at different length scales – NREL

Results

Model predictions for heterogeneity driven by incomplete electrolyte wetting

This effort was initiated by obtaining wetting studies on Round 2 electrodes and separator with ethyl methyl carbonate (EMC) and octane to establish the cell wetting characteristics with a solvent close to the electrolyte characteristics. All standard contact porosimetry studies were conducted by MPM&P Research Inc. As in the earlier simulations, the electrolyte density, surface tension, and viscosity were provided by Kevin Gering's Advanced Electrolyte Model. The solvent mixture in the Round 2 cell electrolyte contains 70% by weight EMC. Octane is considered a universal solvent (i.e., wetting angle is zero for all materials). This porosimetry technique not only gives key information needed to determine the J-function for the wetting model, but also is very useful in establishing the overall pore volume, pore size distribution, and internal surface area important for estimating the permeability of the components.

Most notably, a comparison between the octane and EMC results indicates that the binder in the electrodes absorbs the EMC and significantly changes the pore size distribution within the electrodes resulting in a much lower estimate of the permeability, as estimated by the Kozeny-Carman equation. Electrode permeabilities based on EMC studies are a factor of five lower for the anode and a factor of seven lower for the cathode compared to the octane derived values, which significantly slows all pouch cell wetting processes. The initial portion of the pouch cell wetting process, where electrolyte is worked between the layers and the components are wetted from the face is slower, but still very quick (i.e., tenths of seconds). A direct comparison of the pouch cell wetting simulations, where the edge of the cell is partially wetted, is given in Figure IV.6.1 for the negative electrode saturation. For the octane-based parameters, the negative electrode reaches 90% saturation in 1.5 hours. For EMC, it takes the negative electrode about 11.8 hours to reach 90% saturation (i.e., more than a factor of seven slower).

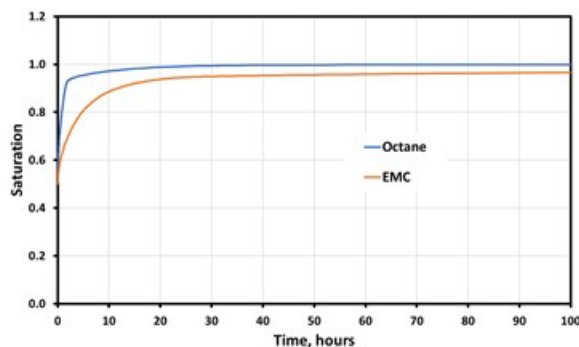


Figure IV.6.1 Round 2 cell negative electrode saturation over time using indicated solvent wetting parameters. Cell wetted from ends and initial saturation at 50%.

As previously discussed, there is a tendency for electrolyte to saturate all edges first, which combined with the higher saturation level of the separator, tends to cause gas to be trapped in the electrode layers. The model predicts full saturation can take weeks but goes to completion providing there is an adequate quantity of electrolyte in contact with the cell edges and the gas has a path to escape. However, the longer time constant for full saturation suggests that the wetting process can extend far past the formation process. Finally, at any point where the gas cannot escape, the wetting process will effectively stop. Figure IV.6.2 gives a typical plating pattern for the Round 2 pouch cells compared to the electrolyte saturation distribution for a partially wetted edge where the gas has become trapped. Electrochemical simulations indicate that for a 6C charge the saturation distribution can generate 10s of millivolts potential difference between the center and the edge.

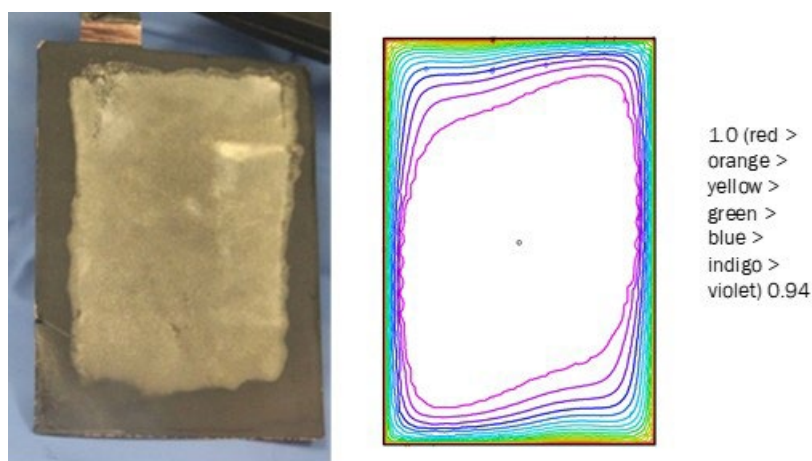


Figure IV.6.2 Round 2 cell negative electrode after 6C fast charge (left). Saturation distribution of negative electrode assuming gas becomes trapped (right).

Investigating if local SOC heterogeneity is driven by variations in microstructure properties

Figure IV.6.3 shows results for microstructure mapping at BYU of a full-size R2 anode and cathode, respectively, before being delivered back to ANL for assembly into a pouch cell and x-ray scanning after initial fast charge cycling. The maps show variation of MacMullin number for an anode (left) and cathode (right). Interestingly, the scans show a striped horizontal pattern in the ionic properties of the anode and a localized high-resistance region of the cathode that may be due to the electrode fabrication process. These anomalies are not visible in optical pictures of the electrodes. The high and low MacMullin numbers on some edges of the maps are due to edge effects and will be corrected after adjustments are made to the model. The striped horizontal pattern has not been prominently observed in XRD patterns.

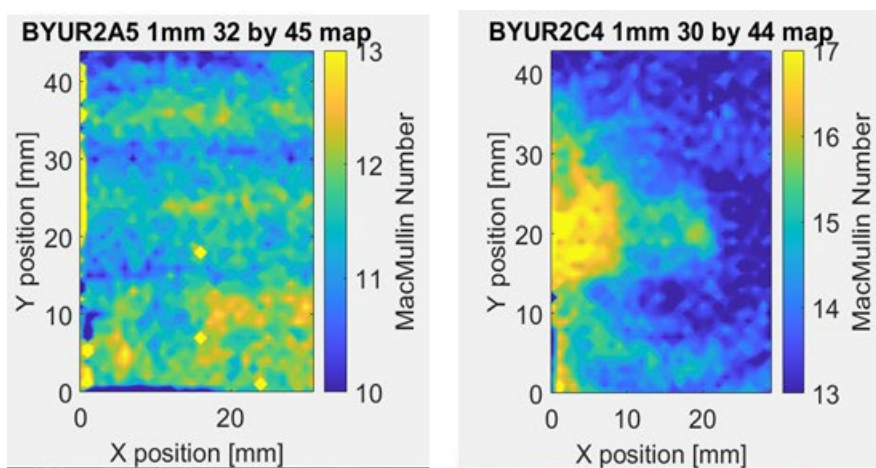


Figure IV.6.3 – Mapping of local MacMullin number for R2 electrodes for graphite anode (left) and NMC 532 cathode (right).

his set of anode and cathode round 2 electrodes measured by BYU was built into a single layer pouch cell, formed, and cycled under fast charge 6C-CCCV conditions for 10 cycles at CAMP. The cell was then handed over to the APS group at a discharged state (3V CC) and mapped using the X-ray beam with 1 mm separation between measurements as shown in Figure IV.6.4. Although plating was not observed at such an early stage of cycle life, interesting findings about the heterogeneity in performance in the cell may point to future plating that can be observed in a future map after extended cycling. The graphite anode, Li_xC_6 staging was quantified using the (0 0 *l*) Miller index relative intensities and the NMC cathode c/a lattice parameter ratio was also mapped concurrently, with higher c/a ratio corresponding to more delithiation as c-axis expansion and a-axis contraction are characteristic of layered oxide cathode delithiation. **Based on studies performed to date, the local SOC on mm length scale measured by XRD during rest does not seem to be correlated with variations in local microstructure properties.**

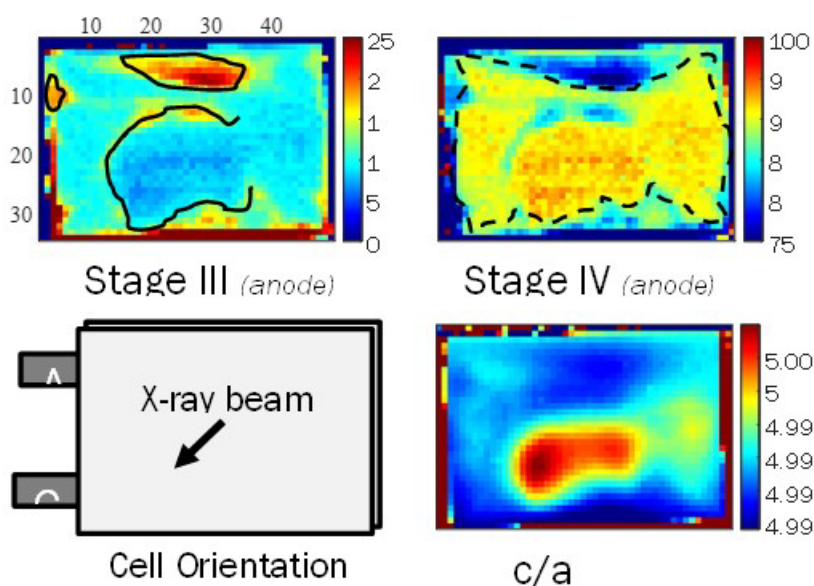


Figure IV.6.4 XRD measured phases in graphite and cathode after 10 fast charge cycles for mapped electrodes.

Heterogeneity in Lithium Plating

A recent publication by this group elucidated the causes of heterogeneity in lithium ion pouch cells, indicating that fast charging induces significant lateral heterogeneities in Round 1 cells at any stage of cycle life. A systematic study of a high loading Round 2 cell was performed to detect the heterogeneity of lithium plating. Round 2, high loading electrodes with NMC532 cathodes cycled with limited specific capacity, 80-90 mAh/g, and significant lithium plating, ~6% of total lithium by the end of cycle life (Figure IV.6.5). XRD mapping was used to determine the onset and growth of plating and how it relates to heterogeneity in the cell. Lateral lithium heterogeneity was studied in the anode both preceding plating as well as following plating.² Lithium plating was found to occur initially at isolated nucleation sites and then to grow in total concentration according to an “S-shaped” curve following the Finke-Watzky model, predicting two-step nucleation and autocatalytic growth of lithium deposits. Trapped LiC_6 (fully intercalated graphite at discharge) was observed with regions of plating highly correlated to regions of trapped LiC_6 .

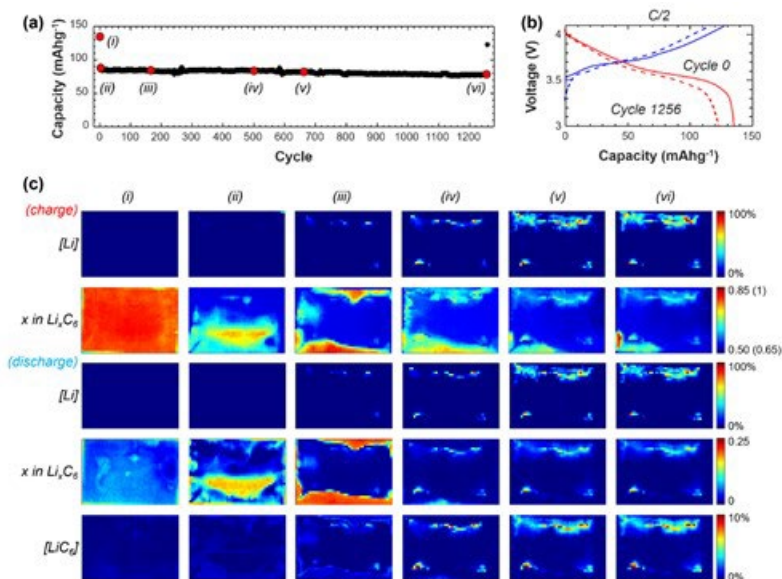


Figure IV.6.5 a) Discharge capacity as a function of cycle number. The initial baseline charge cycle with C/2 rate (i) is followed by fast charging at 6C rate (ii)-(vi). A final baseline charge cycle was performed with C/2 rate following the final fast-charge cycle. b) Comparison of slow charge-rate baseline cycles before fast charging and after 1255 cycles of fast charging. c) Color maps of lithium plating, scaled to the original cathode lithium, (row 1 and 3), average anode lithiation (row 2 and 4), and irreversible consumption of cathode lithium as fully lithiated graphite at discharge (row 5) at charge and discharge, respectively. x in Li_xC_6 estimated used a four-stage lithiation model corresponding to LiC_6 , LiC_{12} , LiC_{30} , and C_6 . Maps were collected at cycle 0 (i), 3 (ii), 165 (iii), 500 (iv), 665 (v), and 1255 (vi). Note: For (i) the x in Li_xC_6 color range was set from 0.65 to 1 at charge to account for higher lithium intercalation due to slow charging.

Novel high-energy, high-speed operando XRD measurements of fast charging pouch cells

In this work high-speed operando XRD is applied laterally across a pouch cell contain electrodes of approximately 100 μm thick in Gen 2 electrolyte from CAMP to quantify the spatial response of graphite to fast charging conditions. 46-point measurements 1 mm apart were taken laterally at the top and bottom of the cell. The cell was cycled between 2.8 V and 4.2 V for 2 consecutive cycles at 6C CC charge followed by CV for 25 mins and a 2C CC discharge followed by CV for 25 mins. The lithiation state as a function of position and time is shown in Figure IV.6.6a where nearing the end of the charge step, the graphite exhibited a difference in state of charge (SOC) of 0.1 across the measured region, between an SOC of 0.6 and 0.7. The rate of divergence of SOC was greatest after the cell reached an average SOC of 0.4. This is likely to have been influenced by the free energy barrier associated with the transition from Stage II (LiC_{12}) to Stage I (LiC_6). The color maps in Figure IV.6.6b show that the local evolution of mass fractions of Stage III/IV, Stage II, and Stage I during lithiation and delithiation of the graphite. During charge, graphite transitions from Stage III/IV to Stage II and to Stage I, as seen by the appearance and disappearance of Stage III/IV, then Stage II, and finally the appearance of Stage I. The final mass fraction of Stage I reached around 0.8 indicating that most of the graphite reached full lithiation.

On discharge, the inverse stage sequence was observed, starting with Stage I, and progressing through Stage II and Stage III/IV towards graphite. While Stages II and III/IV reached close to 0% mass fraction by 1800 s, residual Stage I amounting to a mass fraction of around 0.3 remained, which may also have been associated with Li plating and was seen in other work by NREL, SLAC, and ANL.

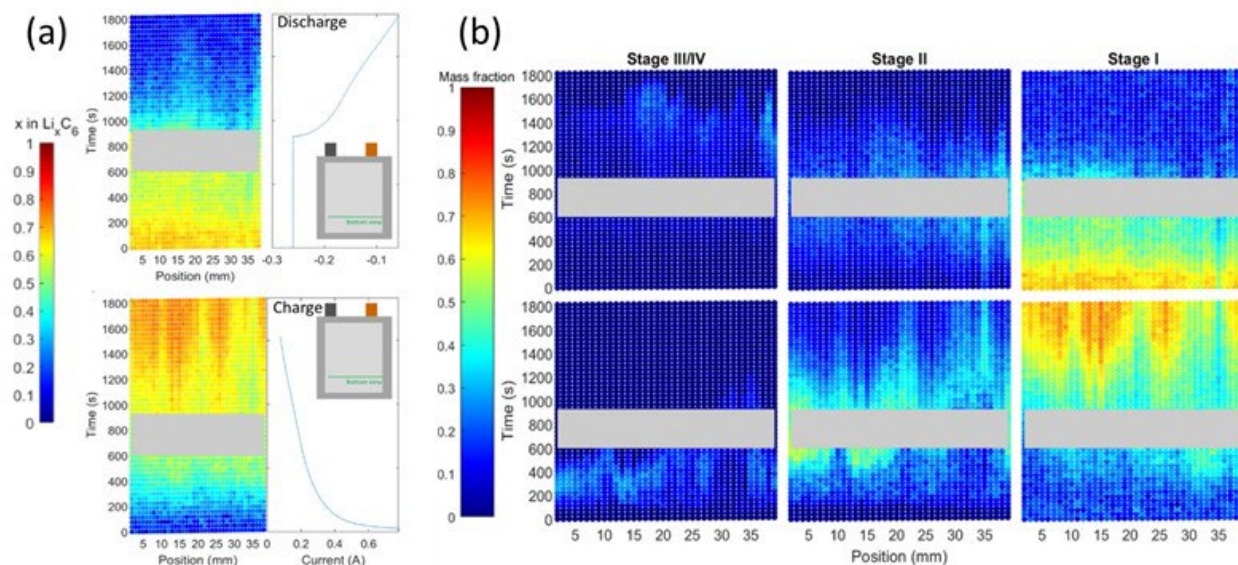


Figure IV.6.6 (a) The state of lithiation x in Li_xC_6 spatially and temporally measured within the pouch cell during 6C charge (bottom) and 2C discharge (top) alongside the current measured from the potentiostat. (b) Mass fractions of the three lithiation stages during the 6C charge and 2C discharge.

Nucleation and growth model for lithium plating compared with gas titration quantification – ORNL

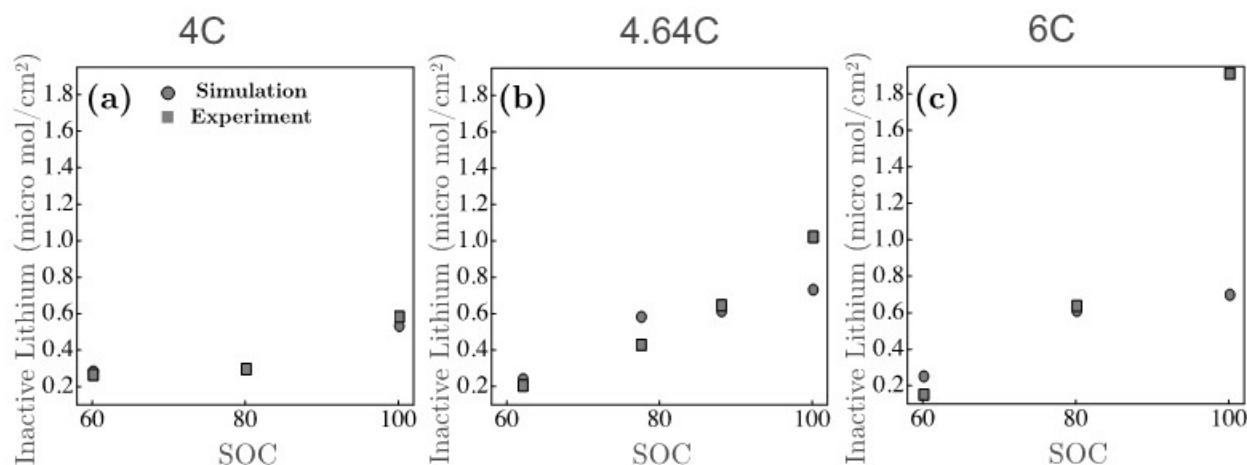


Figure IV.6.7 Simulated metallic lithium nucleation and plating kinetics under different charging condition at selected SOC% followed by a C/4 discharge rate. A direct comparison of inactive lithium from titration experiments and simulations for 4C (inset (a)), 4.64C (inset (b)), and 6C (inset (c)) charging and C/4 discharging cycle at various SOC% are in good agreement.

ORNL extended the previously presented lithium nucleation and plating formulation by incorporating the electrolyte/lithium metal interfacial electrochemical reaction. In collaboration with LBNL & NREL, the results from the mass spec/titration experiments were used to validate the studies conducted for inactive lithium after fast charging conditions. Figure IV.6.7 demonstrates a direct comparison of inactive lithium measured using titration technique against calculated inactive lithium via lithium plating model at different SOC for various C-rates, i.e., 4C (inset (a)), 4.64C (inset (b)), and 6C (inset (c)). At 4C charging, the simulation results demonstrate that nucleation is initiated at 60% average SOC, and the lithium plating and growth increases with SOC. During C/4 discharge, most of the plated lithium is stripped back into electrolyte for 60% & 80% SOC. However, some plated lithium is left behind for 100% SOC. The overall inactive lithium, i.e., in the graphite

particle and metallic lithium is calculated from simulations are compared against the titration experiments, which show a good agreement. The amount of inactive lithium increases with the increase in C-Rates to 4.64C and 6C. Inactive lithium calculations for 60%-90% SOC for various C-Rates are in good agreement. However, for 6C, large C-Rate, the inactive lithium from simulation results at 100%SOC is underpredicting when compared against the titrations. The large inactive lithium at high C-Rates can be predicted by considering the SEI effects, other side chemical reactions in the current framework.

Conclusions

A combination of novel characterization and modeling is used to better understand the early onset of lithium plating during extreme fast charging. The electrolyte wetting model by ANL has shown complete electrolyte wetting can take several days to weeks. Further, gas may become isolated and trapped in the center of electrodes leading to early onset of lithium plating. Novel measurements of local microstructure properties and XRD have shown local resting SOC doesn't seem to be correlated to changes in local ionic or electronic conductivity. In-situ, high-speed, high-energy XRD measurements have shown the local SOC can vary as much as 10% during 6C charging. Lithium plating was found to occur initially at isolated nucleation sites and then to grow in total concentration according to an "S-shaped" curve. Lithium inventory tends to move to edges of the cells over continued cycling.

Key Publications

1. D.P. Finegan, A. Quinn, D.S. Wragg, A.M. Colclasure, X. Lu, C. Tan, T.M.M. Heenan, R. Jarvis, D.J.L. Brett, S. Das, T. Gao, D.A. Cogswell, M.Z. Bazant, M.D. Michiel, S. Checchia, P.R. Shearing, K. Smith, "Spatial dynamics of lithiation and lithium plating during high-rate operation of graphite electrodes," *Energy Environ. Sci.*, 13:2570–2584 (2020).
2. EJ McShane, AM Colclasure, DE Brown, ZM Konz, K Smith, BD McCloskey, "Quantification of Inactive Lithium and Solid Electrolyte Interphase (SEI) Species on Graphite Electrodes After Fast Charging." *ACS Energy Letters*, 5: 2045–2051 (2020).
3. Juan C. Garcia, Ira Bloom, Christopher Johnson, Dennis Dees, Hakim Iddir. "Graphite Lithiation under Fast Charging Conditions: Atomistic Modeling Insights," *Phys. Chem. C* 124, 8162–8169 (2020).
4. F. Usseglio-Viretta, D. P. Finegan, A. Colclasure, T. M. M. Heenan, D. Abraham, and K. Smith, Quantitative relationships between pore tortuosity, pore topology, and solid particle morphology using a novel discrete particle size algorithm, *J. Electrochem. Soc.*, 167 100513 (2020).
5. J. Allen, J. Chang, F. Usseglio-Viretta, P. Graf, and K. Smith, "A Segregated Approach for Modeling the Electrochemistry in the 3-D Microstructure of Li-Ion Batteries and its Acceleration Using Block Preconditioners," submitted to *Journal Scientific Computing*
6. H. Xu, F. Usseglio-Viretta, S. Kench, S. J. Cooper, and D. P. Finegan, Microstructure reconstruction of battery polymer separators by fusing 2D and 3D image data for transport property analysis, *J. Power Sources*, 480 229101 (2020).
7. "Quantification of heterogeneous, irreversible lithium plating in extreme fast charging of lithium-ion batteries", P.P. Paula, V. Thampy, C. Cao, H.-G. Steinrück, T.R. Tanim, A.R. Dunlop, E.J. Dufek, S.E. Trask, A.N. Jansen, M.F. Toney, J. Nelson Weker, *Energy Environ. Sci.* 14, 4979–4988 (2021). 10.1039/D1EE01216A
8. "Using In Situ High-Energy X-ray Diffraction to Quantify Electrode Behavior of Li-Ion Batteries from Extreme Fast Charging", PP Paul, C Cao, V Thampy, H-G Steinrück, TR Tanim, AR Dunlop, SE Trask, AN Jansen, EJ Dufek, J Nelson Weker, MF Toney, *ACS Appl. Ener. Mater.* 4, 11590–11598 (2021). 10.1021/acsaem.1c02348

9. “Conformal Pressure and Fast-Charging Li-ion Batteries” Chuntian Cao, Hans-Georg Steinrück, Partha P. Paul, Alison R. Dunlop, Andrew N. Jansen, Robert M. Kasse, Vivek Thampy, Maha Yusuf, Johanna Nelson Weker, Badri Shyam, Ram Subbaraman, Kelly Davis, Christina M Johnston, Christopher J. Takacs, Michael F. Toney, submitted to J Power Sources.
10. H. Charalambous, O.J. Borkiewicz, A.M. Colclasure, A.R. Dunlop, S.E. Trask, A.N. Jansen, Z. Yang, I.D. Bloom, U. Ruett, K.M. Wiaderek, Y. Ren. Quantifying the evolution of heterogeneous lithium plating and stripping during fast charging. ACS Energy Letters. 2021, 6, 3725–3733
11. Harry Charalambous, Daniel P Abraham, Alison R Dunlop, Stephen E Trask, Andrew N Jansen, Tanvir R Tanim, Parameshwara R Chinnam, Andrew M Colclasure, Wenqian Xu, Andrey A Yakovenko, Olaf J Borkiewicz, Leighanne C Gallington, Uta Ruett, Kamila M Wiaderek, Yang Ren. Revealing causes of macroscale heterogeneity in lithium-ion pouch cells via synchrotron X-ray diffraction. J. Power Sources. 507, 230253 (2021).

Acknowledgements

This work was performed by a large consortium of several people from many national labs and universities.

NREL: Andrew Colclasure, Francois Usseglio-Viretta, Jeffrey Allen, Donal Finegan, Kandler Smith

SLAC/Stanford: Che-Ning Yeh, William Chueh, Maha Yusuf, Michael Toney, Johanna Nelson Weker, Partha Paul, Zhelong Jiang

LBNL/Berkeley: Alec Ho, Nitash Balsara, Manual Schnabel, Robert Kostecki

ANL/APS: Dennis Dees, Hakim Iddir, Juan Garcia, Harry Charalambous, Kamila Wiaderek, Yang Ren

ORNL: Srikanth Allu, Karra

BYU: Dean Wheeler

IV.7 XCEL R&D: Charge Protocols and Life Assessment for Extreme Fast Charging Thrust

Eric Dufek, Principal Investigator

Idaho National Laboratory
2525 Fremont Avenue
Idaho Falls, ID 83415
E-mail: eric.dufek@inl.gov

Samm Gillard, DOE Technology Development Manager

U.S. Department of Energy
E-mail: Samuel.Gillard@ee.doe.gov

Start Date: October 1, 2020

End Date: September 30, 2021

Project Funding (FY21): \$600,000

DOE share: \$600,000

Non-DOE share: \$0

Project Introduction

Extreme fast charging (XFC) of Li-ion batteries can create life and safety issues [1]. With respect to performance loss one of the key complications is plating of Li metal on the negative electrode during fast charging. When this occurs, there is a pronounced loss of Li inventory and subsequent enhanced electrolyte degradation due to the reaction of electrolyte molecules with Li metal. Additional degradation modes including cathode aging can complicate analysis as new charging protocols are developed. As part of this thrust a team consisting of researchers at Idaho National Laboratory (INL), the National Renewable Energy Laboratory (NREL) and Argonne National Laboratory (Argonne) looked to develop methods to both more clearly understand life and failure mode analysis for cells undergoing fast charge and to use understanding of cell design to develop new fast charge protocols. Using a combination of experimental and physics-based models the team was able to develop methods and validate performance which showed a 25% increase in charge acceptance in a 10 min charge and a 3x improvement in charge acceptance for charging segments that did not include a constant voltage component.

Objectives

Key objectives during FY21 were to continue to increase knowledge on the limitations of fast charge using graphite-based Li-ion batteries and to use that knowledge to provide improvements in performance. Overall objectives were to increase charge acceptance in cells with a fixed charge time of 10 minutes, identification of failure modes and development of means to facilitate early identification of failure modes using electrochemical signatures. The team also looked to verify the efficacy of different modes of improving charge acceptance including the use of different temperatures or cell design aspects.

Approach

Using existing and expanding knowledge the team developed advanced charging algorithms using both experimental work and physics-based models. Both 3-electrode and pseudo-2D (P2D) model outputs provided understanding on when possible issues with Li metal plating could emerge in the cells. Using this knowledge specific protocols were developed that limited Li plating. Using the protocols researchers validated performance using single layer pouch cells. The electrochemical data from those cells was used for advanced cell analysis on overall performance and key failure modes were validated using post-test characterization including analysis of the electrolyte, optical imaging and advanced characterization using different user facilities. The electrochemical data was also used to scale charge protocols to understand how different protocols could impact the power requirements of electric vehicle service equipment.

Results

Within the Charge Protocol and Life Assessment thrust in FY21 several activities were performed spanning the development of protocols, validation of performance and verification of failure modes. Below highlights from some of these activities are provided.

Charge Protocol Development

Electrochemical P2D models provide the opportunity to understand how different protocols impact the probability of Li plating. Different protocols were developed which used either multiple current steps or which used a constant current to a fixed voltage after which point a voltage ramp was applied for the remainder of the 10 min charge (Figure IV.7.1) [3]. These advanced protocols have shown the ability to increase charge acceptance during a fixed time during and have also shown the ability to be modified based on changes in electrolyte, electrode/cell design and active material. Since their initial development in FY2020 the protocols have been demonstrated experimentally and can be readily adapted as cell design and electrolytes are changed. During FY2021 over 10 variation of the voltage ramp profile were developed for cells with different anode and cathode materials and different electrolytes. The P2D models while informing on the optimal charge protocols to minimize plating were also applied to reducing the stress on cathode particles and also can provide information on how aging and changes to the electrodes changes the overpotential at both the positive and negative electrodes [4].

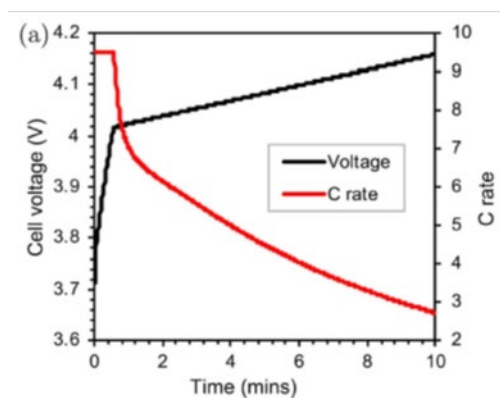


Figure IV.7.1 Example of novel fast charge protocols developed to minimize recharge time and prevent lithium plating using P2D models for graphite/NMC cells using a voltage ramping protocol reproduced from Mai et al [3].

In addition to the use of P2D models, 3-electrode experiments were used to understand potential at the different electrodes and also to develop new charge protocols (Figure IV.7.2). For thick electrodes new protocols, such as the seesaw charging, are needed to enable a 10-minute charge. The seesaw profile which was developed uses an initial constant current charge and then the current is periodically reduced in order to keep the measured potential (ϕ) below a fixed value [7]. The team effectively demonstrated how this approach could be developed in a 3-electrode cell and then modified and deployed in both 2-electrode coin cells and 2-electrode single layer pouch cells. By adjusting where ϕ is fixed and the initial charge rate it was also demonstrated that the total charge acceptance could be modified to reduce aging as a function of cycling.

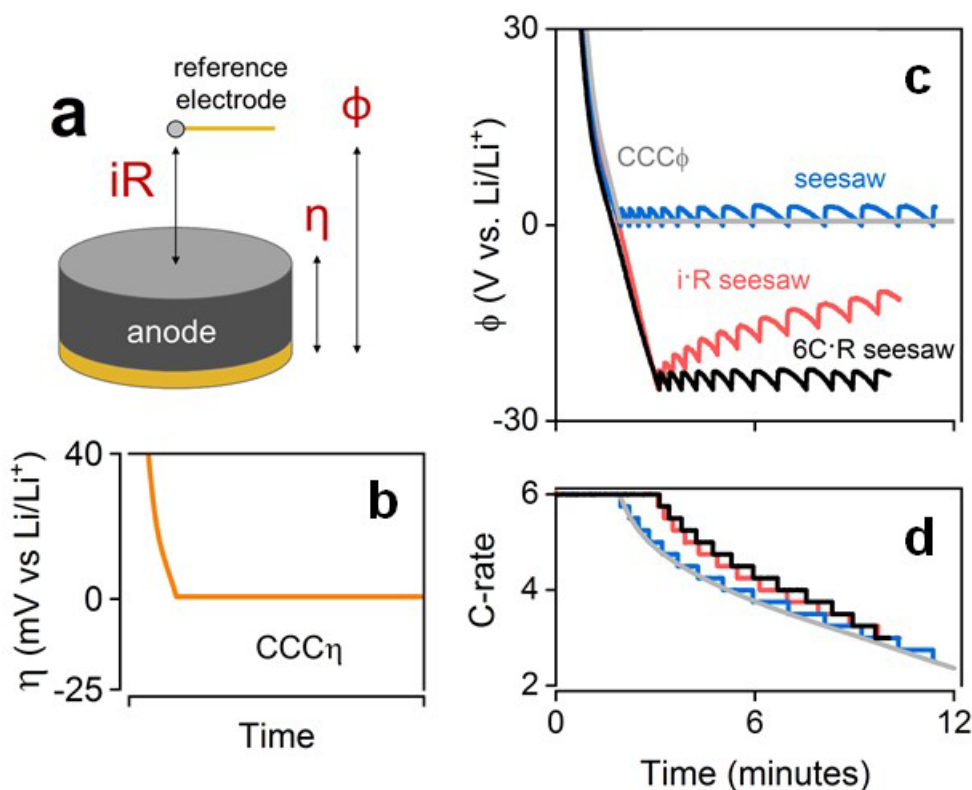


Figure IV.7.2 (a) Electrolyte potential sensed by the reference electrode differs from that experienced at the surface of the anode by $\sim iR$, leading to a difference of this same magnitude between the measured potential ϕ and the surface electrode potential η . (b) Charge protocol that maintains the anode at the thermodynamic limit for Li plating. (c) Anode potentials and (d) C-rates during the charging using different ϕ cutoff conditions. In both (c) and (d), the gray, blue, red, and black plots correspond to the $CCC\phi$, seesaw ($\phi = 0$), iR corrected seesaw ($\phi = -|iR|$), and $6C$ corrected seesaw profiles ($\phi = 6C \cdot R$), (Adapted from [7]).

The Charge Protocol and Life Assessment Thrust also evaluated the benefit of different cell modifications incorporated by other thrusts in the XCEL project. In Figure IV.7.3 the transportation polarization as determined at the end of a rest period for several different cell builds and with different electrolytes. As seen in Figure IV.7.3 the final deliverables from FY21 had significant reduction in transport overvoltage as a function of different rates leading to significant improvements in the amount of charge that could be accepted in a 10-minute charge window. The advances in both design and the use of different protocols, including the voltage ramp described above, have led to a 25% increase in charge acceptance during the course of the XCEL program and a 3x increase in charge acceptance prior to cells moving to a constant voltage portion of charge. In line with the improvement in charge acceptance both the new protocols and cell improvements have also removed Li plating as a key failure mode for protocols which can reasonably charge a cell in 10 min.

How failure modes vary based on cell design was a key finding of work by Chinnam et al. In their work they found that altering design can shift key failure modes from cathode related losses which equate to loss of active material (LAM) to loss of lithium inventory (LLI) [4]. These losses largely align with shifts in the electrode structure and how Li can effectively transport between electrodes during fast charge. The work also identified that as little as a 3% change in electrode porosity during charging can result in an increased probability of Li plating.

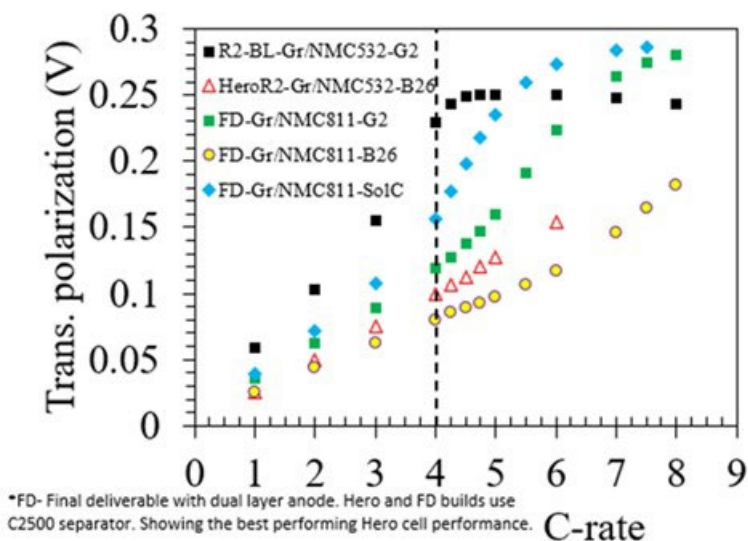


Figure IV.7.3 Polarization values extracted from final FY2021 cell deliverables showing an improvement in performance with respect to previous cell deliverables.

Verification of Electrolyte Degradation

Few studies have been reported on electrolyte changes which occur during XFC. Those that do exist mainly focus on the solid electrolyte interphase (SEI) [6]. During FY21 work within the thrust by Yang, et al showed that, when using graphite//Li(Ni_{0.5}Mn_{0.3}Co_{0.2})O₂ and Gen 2 (1.2 M LiPF₆ in 3:7 EC:EMC) electrolyte, there was no change in the relative amounts of electrolyte decomposition products, Figure IV.7.4. In the work, three components, C₁₁H₂₂O₇PF₆, C₁₄H₃₃O₁₅P₃, and C₁₆H₃₇O₁₅P₃ corresponding to m/e values of 317, 535 and 563 Da were tracked with aging [8]. These results suggest that minimal impact to electrolyte composition should occur during fast charge and that most shifts in Li transport will be driven by changes in electrode structure including pore blockage or cathode particle fracturing.

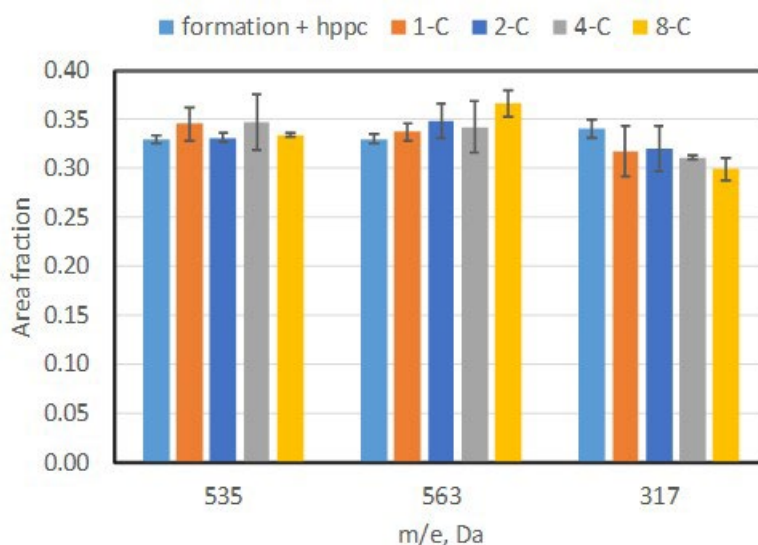


Figure IV.7.4 Area fraction of the major electrolyte degradation products as a function of apparent molecular weight and charge rate. The error bars represent the area fraction maxima and minima for each component [6]. Copyright © Wiley-GmbH. Reproduced with permission.

Thermal Performance Analysis

How temperature and porosity affect Li plating during XFC was recently reported by Robertson, et al. In that work, two sets of cells (26% and 47% porosity) were charged at the 6-C rate and discharged at C/2 rate at temperatures ranging from 20 to 50°C. During cycling cells from each group were analyzed and imaged to identify the presence of Li plating. In most cases direct evidence was readily observed, however at the higher temperatures plating was mitigated. The study also found that temperature played a larger role in reducing plating than porosity did [5]. While advantageous to minimizing Li plating, the cells at higher temperature experienced both elevated capacity fade and increased resistance growth. To mitigate the aging impacts of elevated temperature the team developed test procedures which would more closely mimic EV battery pack thermal management systems which can both allow for increased temperature during charge as well as cooling during discharge and rest. This was done to understand how different thermal management schemes may play a role in minimizing aging while also facilitating XFC.

Protocol Scaling

Within the thrust team the protocols developed were also used to develop insight into how different charge protocols would scale and impact needed EV service equipment (EVSE). Figure IV.7.5 shows how three different protocols would scale for a 65-kWh battery pack that could accept 20 miles per minute of range replacement. The scaling was based on vehicle profiles incorporated into the DirectXFC project and experimental data captured from the FY2020 and mid-year FY2021 cell deliverables. Scaling provides the ability to better optimize protocols that can increase cell level charge acceptance while also ensuring that the power remains reasonable for future EVSE.

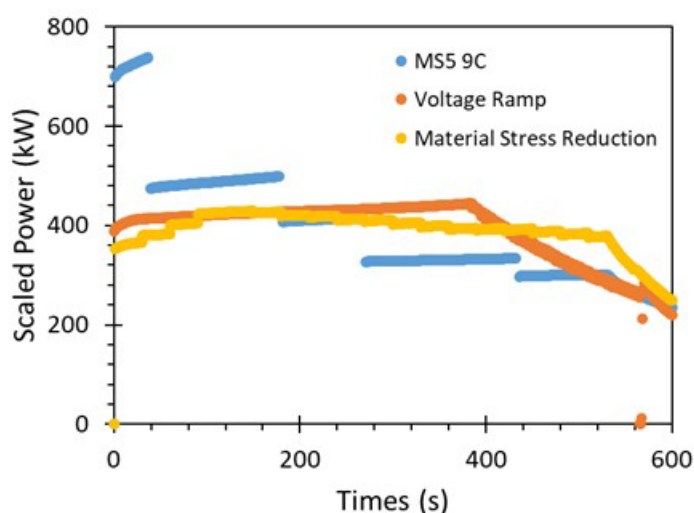


Figure IV.7.5 Comparison of 10-minute power profiles for several charge protocols after scaling from the cell level to a 65-kWh battery pack. Adapted from data in Ref. [2]

Conclusions

Charge protocols and impacts to battery life as a result of extreme fast charging (XFC) have been investigated. Using P2D models and 3-electrode experimental cells it has become possible to increase charge acceptance during a 10-minute charge by over 25% while also mitigating Li plating. By looking at different degradation modes which occur during XFC it has been identified that shifts in pathway are observed as cell design changes and that a shift from LAM at the cathode is replaced by LLI as thicker electrodes are used. During FY2021 it was also found that while changes to active material aging impact the cell performance there is little if any change to the composition of the electrolyte in a cell. Lastly, using experimental results and projections for different vehicle types it was possible to scale charge protocols to understand future EVSE needs.

Key Publications

1. N. Gao, S. Kim, P. Chinnam, E.J. Dufek, A.M. Colclasure, A. Jansen, S.-B. Son, I. Bloom, A. Dunlop, S. Trask, K.L. Gering, Methodologies for Design, Characterization and Testing of Electrolytes that Enable Extreme Fast Charging of Lithium-ion Cells, *Energy Storage Materials*. (2021). <https://doi.org/10.1016/j.ensm.2021.10.011>.
2. M. T. F. Rodrigues, S.-B. Son, A. M. Colclasure, I. A. Shkrob, S. E. Trask, I. D. Bloom, D. P. Abraham, How Fast Can a Li-Ion Battery Be Charged? Determination of Limiting Fast Charging Conditions, *ACS Applied Energy Materials*. 4 (2021) 1063–1068. <https://doi.org/10.1021/acsaem.0c03114>.
3. P. R. Chinnam, A. M. Colclasure, B.-R. Chen, T. R. Tanim, E. J. Dufek, K. Smith, M. C. Evans, A. R. Dunlop, S. E. Trask, B. J. Polzin, A. N. Jansen, Fast-Charging Aging Considerations: Incorporation and Alignment of Cell Design and Material Degradation Pathways, *ACS Applied Energy Materials*. 0 (2021). <https://doi.org/10.1021/acsaem.1c01398>.
4. D.C. Robertson, L. Flores, A.R. Dunlop, S.E. Trask, F.L.E. Usseglio-Viretta, A.M. Colclasure, Z. Yang, I. Bloom, Effect of anode porosity and temperature on the performance and lithium plating during fast-charging of lithium-ion cells, *Energy Technology*. (2020) 2000666.
5. P.P. Paul, V. Thampy, C. Cao, H.-G. Steinrück, T.R. Tanim, A.R. Dunlop, E.J. Dufek, S.E. Trask, A.N. Jansen, M.F. Toney, J. Nelson Weker, Quantification of heterogeneous, irreversible lithium plating in extreme fast charging of lithium-ion batteries, *Energy & Environmental Science*. 14 (2021). <https://doi.org/10.1039/D1EE01216A>.
6. P.P. Paul, E.J. McShane, A.M. Colclasure, N. Balsara, D.E. Brown, C. Cao, B.R. Chen, P.R. Chinnam, Y. Cui, E.J. Dufek, D.P. Finegan, S. Gillard, W. Huang, Z.M. Konz, R. Kostecki, F. Liu, S. Lubner, R. Prasher, M.B. Preefer, J. Qian, M.T.F. Rodrigues, M. Schnabel, S.B. Son, V. Srinivasan, H.G. Steinrück, T.R. Tanim, M.F. Toney, W. Tong, F. Usseglio-Viretta, J. Wan, M. Yusuf, B.D. McCloskey, J. Nelson Weker, A Review of Existing and Emerging Methods for Lithium Detection and Characterization in Li-Ion and Li-Metal Batteries, *Advanced Energy Materials*. 11 (2021). <https://doi.org/10.1002/aenm.202100372>.
7. Z. Yang, J.W. Morrisette, Q. Meisner, S.-B. Son, S.E. Trask, Y. Tsai, S. Lopykinski, S. Naik, I. Bloom, , Extreme Fast-Charging of Lithium-Ion Cells: Effect on Anode and Electrolyte, *Energy Technology*. (2020) 2000696.

References

1. Ahmed, S., I. Bloom, A.N. Jansen, T. Tanim, E.J. Dufek, A. Pesaran, A. Burnham, et al. 2017. “Enabling Fast Charging – A Battery Technology Gap Assessment.” *Journal of Power Sources* 367. <https://doi.org/10.1016/j.jpowsour.2017.06.055>.
2. Kim, S., T.R. Tanim, E.J. Dufek, D. Scofield, T.D. Pennington, K.L. Gering, A.M. Colclasure, W. Mai, A. Meintz, and J. Bennett. n.d. “Projecting Recent Advancements in Battery Technology to next Generation Electric Vehicles.” Submitted.
3. Mai, Weijie, Andrew M. Colclasure, and Kandler Smith. 2020. “Model-Instructed Design of Novel Charging Protocols for the Extreme Fast Charging of Lithium-Ion Batteries Without Lithium Plating.” *Journal of The Electrochemical Society* 167 (8): 080517. <https://doi.org/10.1149/1945-7111/ab8c84>.
4. R. Chinnam, Parameswara, Andrew M. Colclasure, Bor-Rong Chen, Tanvir R. Tanim, Eric J. Dufek, Kandler Smith, Michael C. Evans, et al. 2021. “Fast-Charging Aging Considerations: Incorporation

and Alignment of Cell Design and Material Degradation Pathways.” ACS Applied Energy Materials 0 (0). <https://doi.org/10.1021/acsaem.1c01398>.

5. Robertson, D.C., L. Flores, A.R. Dunlop, S.E. Trask, F.L.E. Usseglio-Viretta, A.M. Colclasure, Z. Yang, and I. Bloom. 2020. “Effect of Anode Porosity and Temperature on the Performance and Lithium Plating during Fast-Charging of Lithium-Ion Cells.” *Energy Technology*, 2000666.
6. Somerville, L., J. Bareno, S. Trask, P. Jennings, A. McGordon, C. Lyness, and I. Bloom. 2016. “The Effect of Charging Rate on the Graphite Electrode of Commercial Lithium-Ion Cells: A Post-Mortem Study.” *Journal of Power Sources* 335: 189–96.
7. T. F. Rodrigues, Marco, Seoung-Bum Son, Andrew M. Colclasure, Ilya A. Shkrob, Stephen E. Trask, Ira D. Bloom, and Daniel P. Abraham. 2021. “How Fast Can a Li-Ion Battery Be Charged? Determination of Limiting Fast Charging Conditions.” *ACS Applied Energy Materials* 4 (2): 1063–68. <https://doi.org/10.1021/acsaem.0c03114>.
8. Yang, Z., J.W. Morrisette, Q. Meisner, S.-B. Son, S.E. Trask, Y. Tsai, S. Lopykinski, S. Naik, and I. Bloom. 2020. “, Extreme Fast-Charging of Lithium-Ion Cells: Effect on Anode and Electrolyte.” *Energy Technology*, 2000696.

Acknowledgements

The activities described were a collaborative effort utilizing the capabilities of many researchers. Key contributors across the different national laboratories include Daniel P. Abraham, Ira Bloom, Bor-Rong Chen, Parameswara R. Chinnam, Andrew M. Colclasure, Kevin L. Gering, Matthew Keyser, Sangwook Kim, Weijie Mai, David Robertson, Marco-Tulio F. Rodrigues, Kandler Smith, Tanvir R. Tanim, Francois L. E. Usseglio-Viretta, and Peter Weddle.

IV.8 XCEL R&D: Anode & Electrolyte Thrust

Venkat Srinivasan, Principal Investigator

Argonne National Laboratory
9700 South Cass Avenue, Building 200
Lemont, IL 60440
E-mail: vsrinivasan@anl.gov

Andrew N. Jansen, Principal Investigator

Argonne National Laboratory
Chemical Sciences & Engineering Division
9700 South Cass Avenue, CSE-200
Lemont, IL 60440
E-mail: Jansen@anl.gov

Samm Gillard, DOE Technology Development Manager

U.S. Department of Energy
E-mail: Samuel.Gillard@ee.doe.gov

Start Date: October 1, 2020	End Date: September 30, 2021	
Project Funding (FY21): \$1,400,000	DOE share: \$1,400,000	Non-DOE share: \$0

Project Introduction

The focus of the XCEL Program in FY 2018-2019 centered on the influence of areal capacity loading on lithium plating during extreme fast charging (XFC). Two sets of capacity-matched electrodes were designed and fabricated by the Cell Analysis, Modeling, and Prototyping (CAMP) Facility with identical compositions – only the capacity loading was changed. The low loading electrode set (Round 1) utilized a 2 mAh/cm² graphite loading and the higher loading set utilized a 3.0 mAh/cm² graphite loading. Numerous pouch cells were fabricated and delivered to the national laboratory and university teams. These two cell builds are the early baselines for the XCEL Program. It became clear after extensive testing that lithium plating is rare on the Round 1 anodes, but is abundant on the Round 2 anodes during 6C charging. In FY 2020, a multi-thrust approach was formed to solve the problems related to XFC, the chief of which is lithium plating. This section summarizes the activities of the XCEL-Electrode & Electrolyte Thrust for FY 2021 where focus was directed to determine impact of carbon and binder domains in the positive and negative electrodes, and the impact of improved electrolyte compositions. A pouch cell build (nicknamed “Hero Cell”) was completed at the end of Q4 in FY 2020 with lower carbon and binder content in each electrode and a new candidate electrolyte. This “Hero Cell” build was based on the same baseline active materials (SLC1506T graphite vs. NMC532 cathode).

Objectives

The goal of the XCEL Electrode & Electrolyte Thrust in FY 2021 was to develop higher Ni-content NMC (e.g. NMC811) cathodes with low carbon and binder content, new electrode architectures (e.g., dual layer), and improved electrolyte compositions. It is anticipated that these combined tasks will result in a cell system with over 3.5 mAh/cm² loading (anode) that can achieve >600 cycles at 6C charge with no lithium-plating. It is expected that modifications of the electrode architecture to lower the tortuosity will enable fast lithium-ion transport to and from the active material closest to the current collector, while maintaining low porosity to maintain high energy density. New electrolyte systems were targeted to have higher ionic conductivity with lithium transference numbers closer to 1, while also maintaining a robust solid electrolyte interface (SEI) on the anode (and cathode to a lesser extent).

Approach

There were several approaches in electrode architecture as well as in electrolyte development. Both of these areas involved coordinated efforts between several national labs.

1. NREL used its suite of electrochemical models and microstructure analysis tools to investigate advanced electrode architectures to improve fast charge performance and prevent lithium plating. The key to improving fast charge performance is to lower the ionic transport resistance through the entire cell including anode, separator, and cathode to prevent preferential utilization of electrodes near separator. Detailed modeling indicated three promising strategies to improve ionic transport are: reducing the amount of carbon/binder in electrodes, introduction of a secondary pore network, and dual-layer electrodes.
2. It was then up to the electrode fabrication teams to design and build electrodes that mimic the model-predicted ideal electrode architectures. These fabrication teams are centered at Argonne's CAMP Facility, which relies on traditional coating equipment, and LBNL, which has developed freeze-cast techniques.
3. Model predictions of ideal electrolyte systems rely heavily on the Advanced Electrolyte Model (AEM) developed at INL, which was used here to investigate premier electrolyte metrics that have influence on cell performance during XFC, most notably viscosity, conductivity, diffusivity (all species), lithium transference number, lithium desolvation energies, and other terms.
4. Meanwhile, the NREL team assembled electrolyte formulations using solvents screened from high throughput calculation results, evaluated stability of these formulations across the usable electrochemical window, and measured cell-level performance.

The new benchmark cell design for the start of FY 2021 was the “Hero Cell”, which is described in Figure IV.8.1. The baseline electrolyte was the “Gen2” electrolyte, which is 1.2 M LiPF_6 in EC:EMC (3:7 wt%, from Tomiyama), while the best candidate electrolyte system was “B26” from INL, which is (LiPF_6 in EC:DMC:DEC:EP:PN (20:40:10:15:15) with 3% VC & 3% FEC). Changes were made in the separator, with the new separator being Celgard 2500 (PP), which has higher porosity. The “Hero Cell” pouch cells consisted of 14.1 cm^2 single-sided cathodes and 14.9 cm^2 single-sided graphite anodes (SLC1506T from Superior Graphite) using Celgard 2320 separator (20 μm , PP/PE/PP) or Celgard 2500 (PP) separator, and 0.59 mL of “Gen2” electrolyte for Celgard 2320 (0.65 mL for Celgard 2500). The n:p ratio was between 1.13 to 1.23 for this voltage window (3.0 to 4.1 V), and the nominal C/2 capacity is 30 mAh. In FY 2021, the cathode was developed further using NMC811 and low carbon and binder content to increase the energy density (and reduce the thickness of the cathode). On the anode side, a dual-layer electrode was developed with relatively larger graphite (~8 micron) near the copper current collector and smaller graphite (~3 micron) near the separator.

Anode: LN3237-70-2

(single-sided)

95.83 wt% Superior Graphite SLC1506T

0.5 wt% Timcal C45 carbon

3.5 wt% Kureha 9300 PVDF Binder

0.17 wt% Oxalic Acid

XCEL, Trial coating as part of electrode compositional study

Targeted Round 2 areal capacity: SLC1506T Lot#: 573-824

"SS" = single sided -> **CALENDERED**Cu Foil Thickness: 10 μm Total Electrode Thickness: 80 μm SS Coating Thickness: 70 μm

Porosity: 37.4 %

Total SS Coating Loading: 9.57 mg/cm²Total SS Coating Density: 1.37 g/cm³Estimated SS Areal Capacity: 3.03 mAh/cm²

[Based on rev. C/10 of 330 mAh/g for 0.005 to 1.5 V vs. Li]

Made by CAMP Facility

Cathode: LN3237-78-4

(single-sided)

96 wt% Toda NMC532

2 wt% Timcal C45

2 wt% Solvay 5130 PVDF Binder

XCEL, Coating used in FY20 Q4 SLP Hero Cells

Targeted Round 2 areal capacity, Prod: NCM-04ST, Lot#: 7720301

"SS" = single sided -> **CALENDERED**Al Foil Thickness: 20 μm Total Electrode Thickness: 80 μm SS Coating Thickness: 60 μm

Porosity: 34.9 %

Total SS Coating Loading: 17.24 mg/cm²Total SS Coating Density: 2.87 g/cm³Estimated SS Areal Capacity: 2.65 mAh/cm²

[Based on rev. C/10 of 160 mAh/g for 3.0 to 4.2 V vs. Li]

Made by CAMP Facility

Figure IV.8.1 Electrode composition and design for baseline ("Hero Cell") pouch cell from Q4 of FY 2020.

New electrolyte formulations using solvents screened from calculation results were evaluated for their stability across the usable electrochemical window within the cell using the Round 2 baseline electrodes. For candidates that appeared suitable for fast charging, pouch cells were built with the Round-2 baseline electrodes by CAMP and subjected to long-term cycling according to standard protocols established for the XCEL program. Detailed characterization of the degradation mechanism, and integration of these results into INL's Advanced Electrolyte Model (AEM) provided additional insights into electrolyte and interfacial properties that enable fast charge.

Coin cells and pouch cells were assembled with selected electrode pair and selected electrolytes and evaluated for electrochemical performance. Efforts were also directed to developing formation processes with the new electrodes and electrolytes to create a robust SEI while preventing lithium-plating during cycling. A mid-term and final pouch cell builds were fabricated in FY2021 and distributed to the testing labs for electrochemical performance under fast charges. (Many of these lab activities were shortened due to the on-going COVID19 pandemic impact on laboratory time.) Comparisons were made to the benchmark (Round 2 pouch cells). The techno-economic model BatPaC was used to determine the cost implications of the new fast charge cell system.

Results

Model Prediction of Ideal Electrode Architecture (NREL Focus)

NREL used its multiscale modeling to update transport properties of Hero cell taking into consideration modified porosity and carbon-binder loading. Given the uncertainty of the carbon-binder domain (CBD) spatial location, two approaches have been used: (i) assuming a uniform distribution of CBD within the pore domain, thus with a high CBD nano-porosity, and (ii) assuming an heterogeneous distribution with preferential location of the CBD between adjacent particles, effectively bridging particles, with a 47% literature image-based CBD nano-porosity. **Model indicates that a 6% and 12% Bruggeman exponent reduction can be achieved by reducing the CBD loading from 10 to 4%, and from 8 to 4%, respectively, for the cathode and the anode.** As deduced transport coefficients have been then used in NREL macroscale electrochemical models, considering Celgard 2500 separator and B26 electrolyte. Good agreement between experimental measurements and model predictions has been achieved at 6C CC with "Hero Cell" voltage and lithium plating close to the much thinner Round 1 cell, consequence of the ionic transport overall improvement due to the cumulative impact of reduced CBD loading, separator porosity increase/tortuosity reduction, and enhanced electrolyte, cf. Figure IV.8.2. By combining all improvements readily available to the team, macro-model predicts a charge capacity of ~80% can be obtained in 10 minutes with minimal plating for a cell with an EV

relevant loading of 3.5 mAh.cm^{-2} cathode/cell and 4.2 mAh.cm^{-2} anode. Thus, we suggest a final cell loading of close to $4 \text{ mAh.cm}^{-2}/100 \text{ microns thick}$ at the anode side is possible.

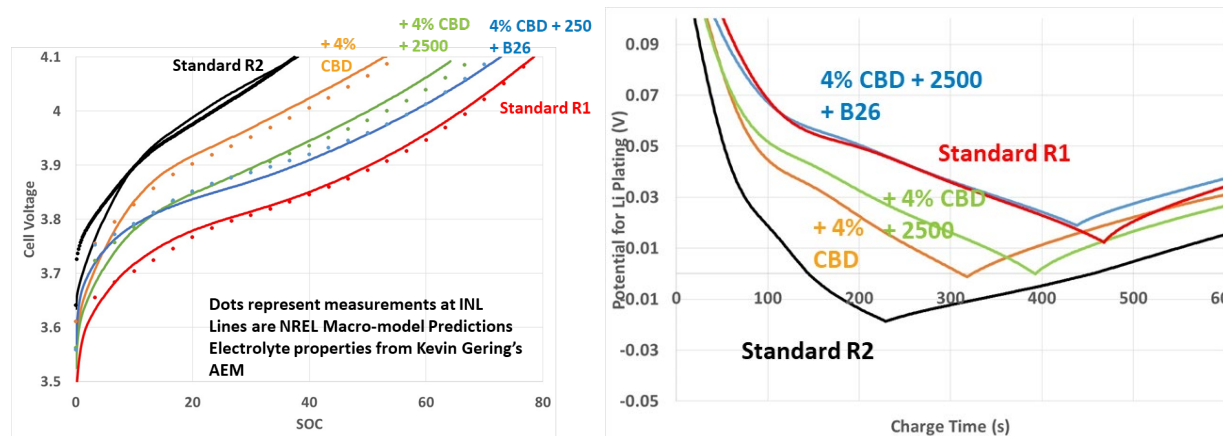


Figure IV.8.2 (Left) Cell voltage and (right) potential for plating for a 6C-CC charge profile (4.1V, 10 minutes cutoff).

While a reduced CBD loading is beneficial for ionic transport, it may adversely impact the electronic conduction, especially for the NMC cathode which relies on the conductive carbon black for electron transport. NREL has performed a connectivity analysis to determine a CBD loading threshold for which model predicts electron transport is provided by the CBD above it, and by the NMC below it. The percolation transition region for the NMC particles is $0.028 \leq \epsilon_{\text{CBD}} \leq 0.058$ depending on the CBD representation, cf. Figure IV.8.3. **The baseline volume fraction (0.138) is then unnecessarily high to achieve the percolation objective.** The optimal CBD volume fraction is set within the upper range of the percolation threshold to be conservative, at $\epsilon_{\text{CBD}} \approx 0.052$, that corresponds to a CBD weight ratio of 4%. It suggests a CBD loading lower than the one used for the hero cell is not recommended, considering the assumptions used in the microstructure model. The associated effective cathode solid conductivity for the different CBD loadings has been also calculated through homogenization calculation, cf. Figure IV.8.4. Due to the NMC bulk conductivity significant variation with its state of charge (SOC), **the impact of CBD percolation on the effective solid conductivity is mostly visible for the end of discharge.** This analysis has been made possible by combining different NREL tools built upon the past four years: particle identification², particle connectivity³, and CBD numerical generation¹ – all included in the NREL open-source toolbox.

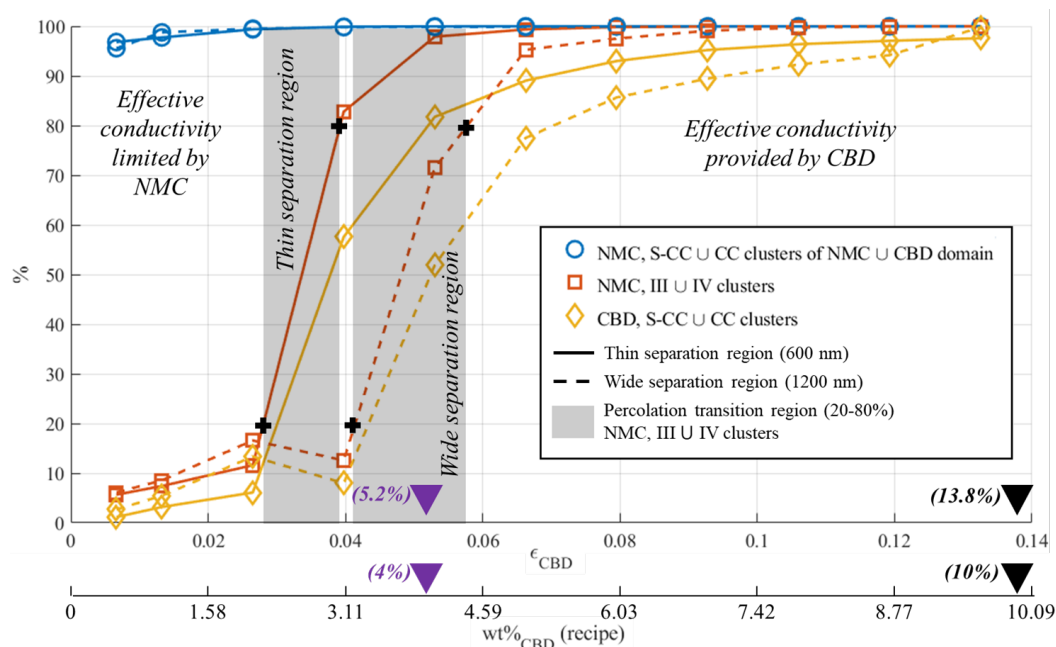


Figure IV.8.3 NMC connectivity as function of CBD loading. “III ∪ IV cluster” is the relevant percolation metric for the application, see reference 1 for details. “Wide” (conservative approach) and “thin” (closer to imaging, more likely) separation regions correspond to variants of the CBD numerical generation.

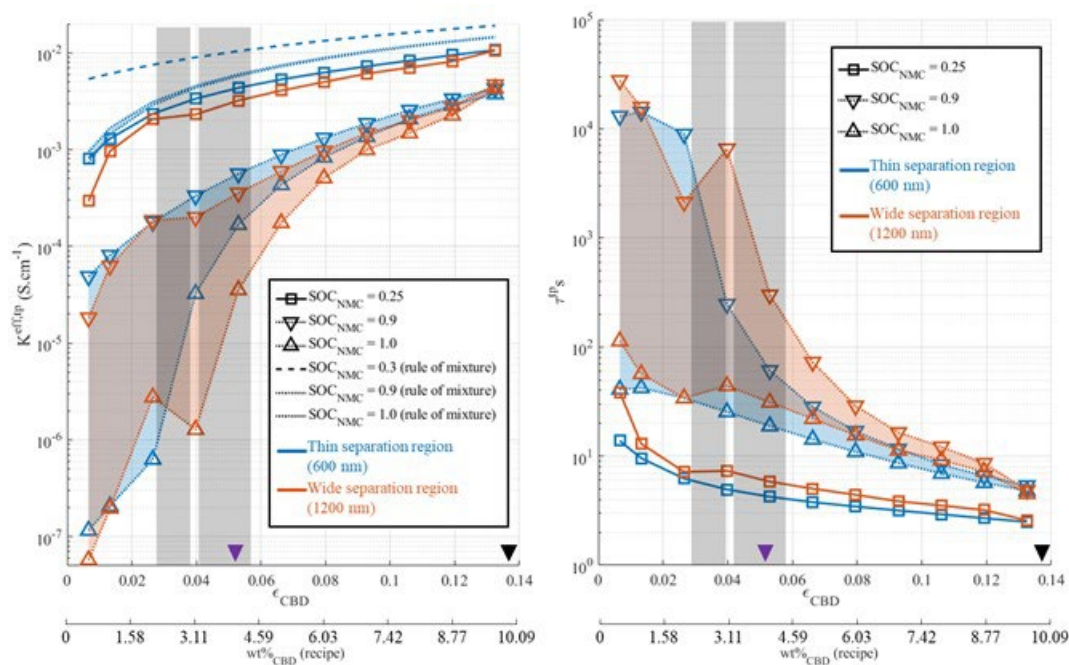


Figure IV.8.4 Cathode effective solid conductivity and associated solid tortuosity factor, considering low lithiation (square) and high lithiation (triangle) NMC532 bulk conductivity. Grey vertical area corresponds to the percolation transition region of Figure IV.8.3.

NREL has provided design recommendations on secondary pore network architecture for the “Round 3” loading, considering design constraints specific to laser ablation system, using NREL electrochemical 2D COMSOL model. This model was validated on unstructured cells for charge rates from 0.5 to 6C. Model predicts a **+12% 6C-CC capacity improvement with a 45 μm channel spacing (edge-to-edge), a 55 μm anode-side and a 33.6 μm cathode-side channel depth**, with both electrodes’ channel roughly contributing

equally to the capacity improvement (cf. Figure IV.8.5). Model predicted channels are significantly reducing lithium-plating as well (10 times), with most improvement due to the anode-side channels. Capacity improvement is likely underestimated as the model does not consider the negative impact of lithium plating and the difference in electrolyte wetting between the baseline and structured electrodes. **One-dimensional groove channels, while providing some capacity improvement are, however, over-removing active materials for their benefits.** 3D patterns have been investigated considering cylindrical channels and an optimal geometry, periodic regular hexagon, have been identified using an in-house genetic algorithm (cf. Figure IV.8.6). COMSOL modeling is on-going but has already demonstrated this architecture is providing better volume loss-capacity improvement trade off compared with the previous one-dimensional grooves.

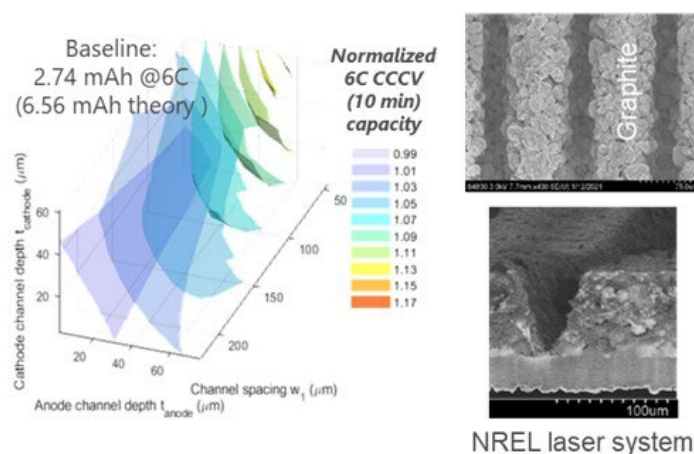


Figure IV.8.5 (Left) Model-predicted capacity improvement for “Round 3” cell with laser-ablated electrodes. (Right) Cross-section SEM imaging of laser-ablated electrodes performed with NREL laser system.

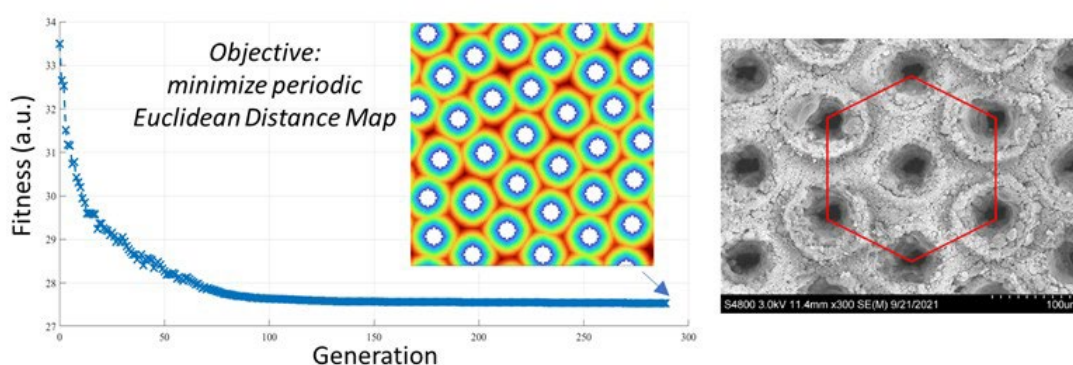


Figure IV.8.6 (Left) Near-optimal cylindrical channel periodic pattern identified with NREL genetic algorithm. (Right) Cross-section SEM imaging of corresponding laser-ablated electrodes performed with NREL laser system.

XFC Electrolyte Development through INL Advanced Electrolyte Model; Cell Testing (INL Focus)

INL supported the XCEL Electrode & Electrolyte Thrust area in terms of electrolyte modeling (characterization and screening) and cell testing to identify and validate candidate electrolyte systems compatible with extreme fast-charge (XFC) conditions. Preemptive electrolyte research is gained through the INL Advanced Electrolyte Model (AEM) to investigate foremost electrolyte metrics that influence cell performance during fast charge, most notably viscosity, conductivity, diffusivity (all species), lithium transference number, lithium desolvation energies, activation energies of these properties, and other terms related to concentration polarization (which alters local transport properties and behavior nearby electrode surfaces). This has led to feasible XFC electrolyte candidates for use in XCEL-designed cells. Our XFC

electrolytes are designed to achieve improved transport properties (past the Gen2 baseline) to mitigate concentration polarization effects, decreased lithium plating at the anode, improved permeation of electrolytes through the electrode materials, and stable, low-impedance SEI films. For FY 2021, laboratory activities and cell testing at INL focused on support of the “Hero Cell” milestones, newer cell chemistries from CAMP, and successful investigation of highly-concentrated electrolyte (HCE) systems. Coordination for this task area involved Argonne, INL, and NREL. Highlights and summary of tasks:

- Based on AEM prescreening, NREL cell modeling, and cell testing, a new series of HCE were identified that show impressive rate capability and life, with some cases showing improvement past B26. Through AEM, HCE systems were identified with less variance of activation energies over salt concentration. Cell tests demonstrated that our HCE systems satisfy many of the attributes needed for use in Li-ion cells used for fast-charge applications. Some HCE show benefit in the proximity of 3 molal LiPF₆ in preference over typical 1–1.2 molal conditions.
- Early studies were performed on cell formation parameters and their impact on capacity and early aging trends, using B26 with the NMC532/graphite electrode couple. Our studies indicate that it is beneficial to extend the rest periods between formation cycles. Another study investigated the impact of having a pre-formation electrolyte soak period at elevated temperature to aid in electrolyte permeation, a foreseen step when utilizing HCE systems.
- Electrolyte B26 was used with the new electrode materials developed at CAMP in FY21 and showed improved charge rate capabilities and reduced lithium plating, compared to the Gen2 electrolyte.
- Collaborated with NREL to understand transport properties for new compounds envisioned for XCEL applications, such as 7-oxabicyclo[2.2.1]heptane-2-carbonitrile and its mixtures with Gen2 electrolyte.

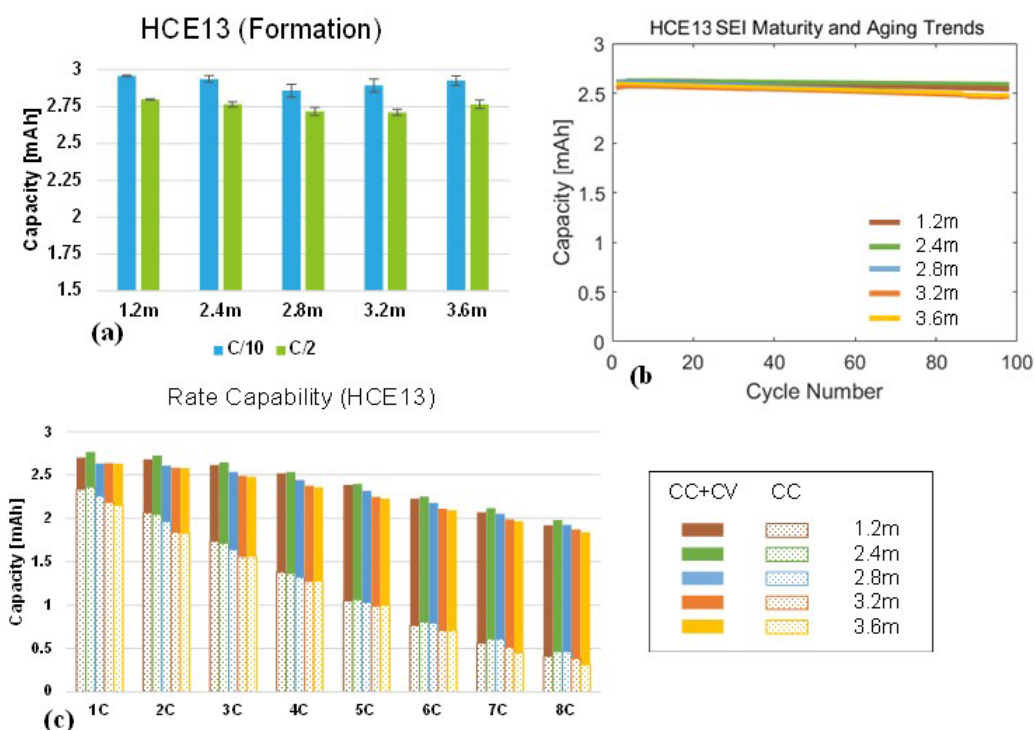


Figure IV.8.7 Various test results for the HCE13 electrolyte used in coin cells with XCEL R2 NMC 811 + Gr materials: (a) formation capacities, (b) aging over C/2 cycles, and (c) coin cell charge rate capability from 1C to 8C (CC+CV). Note that panel (d) is just for the CC component of charge.

Based on AEM-guided formulations, eight HCEs were tested in CR2032-type coin cells, each with differing amounts of salt as high as 4 molal.

Most testing was done using the XCEL “Round 2” SLC1506T and NMC811 electrode materials. The electrolytes were systems comprised of multiple solvents, the salt LiPF_6 and additives VC and FEC. For brevity’s sake, selected testing results for the systems B26 and HCE13 are shown below. Figure IV.8.7 shows (a) post-formation capacities at C/10 and C/2 rates, (b) aging trends at C/2 cycling, and (c) charging rate capability for HCE13. Formation capacities remain high over the entire range of salt, with all cases showing competitive values at the high salt concentration of 3.6 molal. It is seen that HCE13 has exceptional life retention over all the salt concentrations. Charging rate capability for HCE13 shows at least 80% charge acceptance at 6C conditions (vs 1C). In all these metrics, HCE13 has superior performance over the Gen2 baseline. Figure IV.8.8 shows rate capability test results for electrolytes Gen2, B26 and “Solvent C” in cells with an NMC811 cathode and the new dual-layer graphitic anode (all “Round 2” loadings); note that results are just for the CC component of charge.

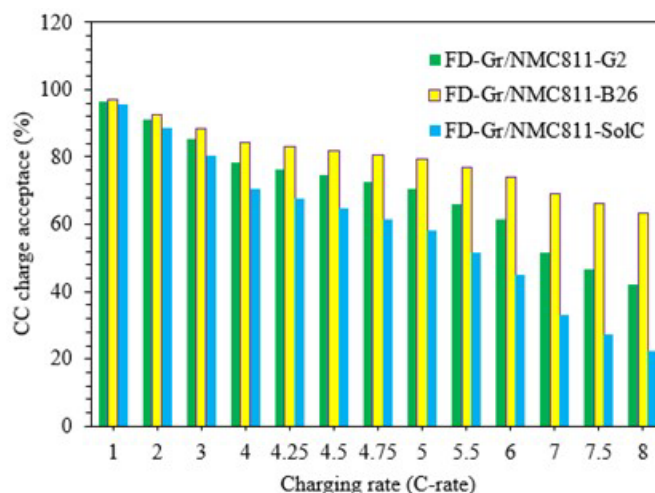


Figure IV.8.8 Pouch cell charge rate capability from 1C to 8C for cells having electrolytes Gen2, B26 or “solvent C”. Note that results are just for the CC component of charge. Electrodes are NMC 811 and the new dual-layer graphitic anode.

Modeling work continued in FY 2021 based on AEM simulations at INL and cell-level modeling at NREL. Detailed property reports from AEM are passed to the Newman-type cell model to support accurate rendering of concentration polarization (CP) effects across the cell. Once CP profiles are obtained, corresponding property profiles can be produced that show how properties undergo profound spatial variance during fast-charge conditions. Figure IV.8.9 shows this type of analysis starting with (a) electrolyte concentration profiles during a 6C charge of XCEL R2 materials, with various property profiles (b) and (c) after 100s of 6C CC charging. In panels (b) and (c), the following electrolytes (starting at 1.2 m bulk) are compared: Gen2 (red), B26 (green) and HCE13 (blue). This type of analysis is highly useful to identify regions within the cell that suffer the most profound consequences during XFC. Here, the cathode side experiences local high viscosity that impacts local transport.

The results above demonstrate that INL, NREL, and Argonne have formed an effective team to identify, screen, characterize, simulate, and test XFC electrolytes, with selected candidates showing appreciable improvements past the Gen2 baseline system. Other laboratory test results and modeling/simulation outcomes were accomplished in FY 2021, but for the sake of brevity were not included herein.

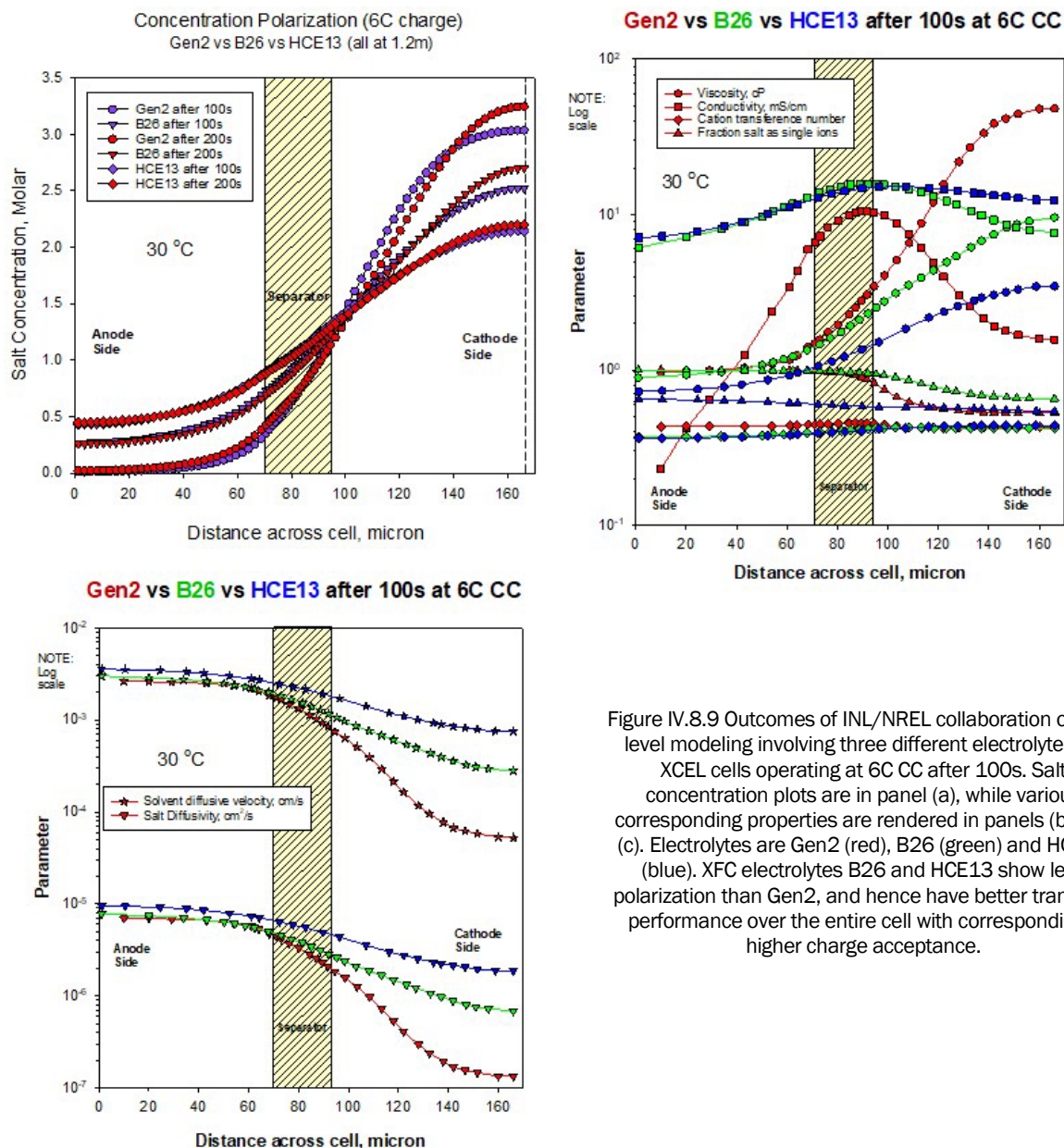


Figure IV.8.9 Outcomes of INL/NREL collaboration on cell-level modeling involving three different electrolytes for XCEL cells operating at 6C CC after 100s. Salt concentration plots are in panel (a), while various corresponding properties are rendered in panels (b) and (c). Electrolytes are Gen2 (red), B26 (green) and HCE13 (blue). XFC electrolytes B26 and HCE13 show less polarization than Gen2, and hence have better transport performance over the entire cell with correspondingly higher charge acceptance.

Electrolyte Predictions using Database of Electrolyte Properties (NREL Focus)

The NREL team evaluated multiple electrolyte recipes with different weight fractions of additives identified from previous year efforts in coin-cell and pouch cell formats. Three formulations that were stable up to 4.3V in half-cell studies against the “Round 2” were short-listed and one batch of pouch cells were built in the latest round of ‘Hero Cell’ builds for evaluation at INL.

Based on solvation-shell structure calculations that show easier dissociation of Li^+ at higher local salt concentrations (which are bound to happen under ultra-high fast charging rates), “Solvent C” was used to replace 10% of the ethylene carbonate in the baseline Gen2 recipe (3:7 ethylene carbonate to ethyl methyl carbonate containing 1.2 M LiPF_6). This formulation was named Electrolyte 1. Further modifications to this recipe were based on initial evaluation of the cycling performance. The second batch (Electrolyte 2) comprised of addition of 2% fluorinated ethylene carbonate (FEC) which was shown to maintain good cycling performance on the baseline electrolyte. It is not clear yet, if “Solvent C” can be fluorinated directly instead of adding FEC separately. Results from Electrolyte 2 still showed higher surface impedance, to combat which the

FEC content was lowered to 1% and the rest was substituted with 1% vinylene carbonate, a known additive deployed to lower impedance at the anode surface (Electrolyte 3). Capacities measured for these recipes are shown in Figure IV.8.10 below.

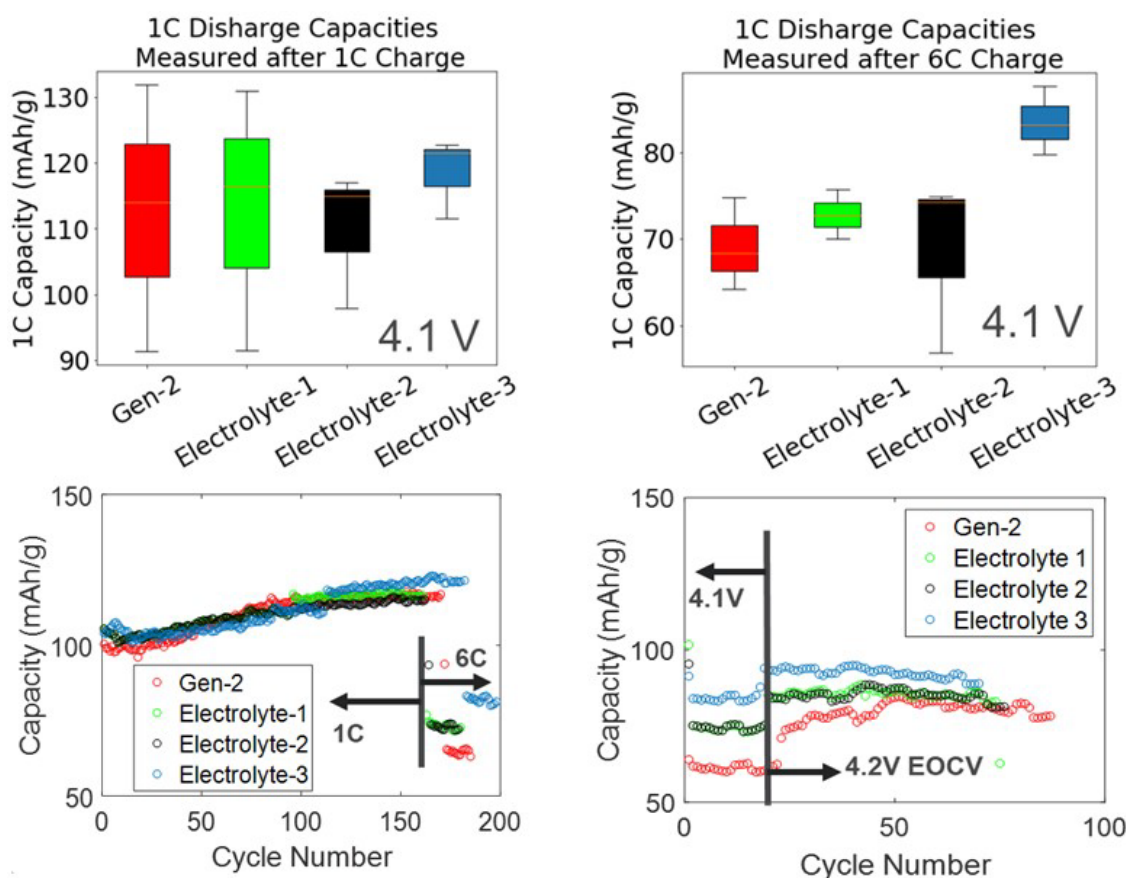


Figure IV.8.10 Summary of 1C-discharge capacities measured under different charging rates for the electrolyte recipes evaluated in coin-cells at NREL. The voltage window for these tests was set to 2.8-4.1V. Subsequent cycling experiments used a higher end-of-charge voltage. "Round 2" electrodes were used with Celgard 2320 membranes.

Several of the formulations showed stable cycling at 4.2V in the full cell configuration. Electrolyte 3 retained ~70% of the 1C capacity when charged at the 6C rate at 4.1V and ~77% at the 4.2V. Evaluation of these recipes in the pouch cell format is currently underway. As expected, the formulation, as well as formation conditions need to be optimized for different cell formats and/or chemistries. In addition to these, we will also explore thermal properties of different electrolytes and how these can be fine-tuned to minimize cell impedance when operating at different ambient temperatures.

Fabrication of Mid-Term Pouch Cells for March Deliverable (Argonne-CAMP Focus)

Testing data from the "Hero Cell" indicated a significant gain was achieved in enabling fast charge cycling simply by reducing the carbon and binder content – as predicted by the NREL model. Decreasing the amount of inert materials in the electrodes increased the energy density of the electrodes, but also decreased the thickness of the positive electrode because the density of the inert additives is well under half the density of the NMC cathode. The calendered thickness of the NMC532 cathode electrode was reduced from 70 microns to 60 microns when the active material (NMC532) content was increased from 90 wt.% to 96 wt.%. This increased the cell's energy density by reducing the amounts of inert additives in the cathode and reducing the amount of electrolyte needed to cover the extra inert materials. It also increased the power capability by decreasing the distance the lithium ions must transverse between electrode foils. However, on the negative electrode side,

there was little change in electrode thickness when increasing the graphite content because the binder, carbon, and graphite materials have similar densities.

In FY 2021 efforts were centered on making further improvements on the positive electrode by increasing the specific capacity of the NMC cathode via replacing the NMC532 with NMC811, and by increasing the active material content beyond 96 wt.%. Electrodes were made with 97 wt.% NMC811 at the “Round 2” loadings with 1.5 wt.% Timcal C45 carbon additive and 1.5 wt.% Solvay 5130 PVDF. A matching uni-layer graphite (SLC1506T) was also made but with the original baseline composition of 91.6 wt.% graphite (delamination was eventually observed in the “Hero Cell” anodes after 100 cycles, which used 96 wt.% graphite). The mid-term (“March”) cell build consisted of 42 single-layer pouch cells using these matching electrodes with the B26 electrolyte and Celgard 2500 separator. These cells were formed and then shipped to INL, NREL, and Argonne for testing under various protocols, which are described in other XCEL sections of this annual report.

Fabrication of Final Pouch Cell Build Using Structured Electrodes (LBNL & Argonne-CAMP Focus)

The effort in dual-layer anode development was paused in FY 2020 due to lack of graphite particles in the 3-micron diameter region. Meanwhile, discussions were held with a domestic source of battery grade graphite (American Energy Technologies Co, AETC) to determine if they could make a pilot-scale batch of graphite with smaller diameter. They agreed to try modifying their process to target under 4 microns diameter (D50). Success was achieved in early FY 2021, and they shipped 1 kg of graphite to Argonne. The CAMP Facility made trial coatings with this powder to determine its electrochemical performance (specific capacity and cycle life), and then used it to develop a dual-layer anode (SLC1506T on foil, AETC graphite near separator) for the final cell build.

Structured anodes were also developed at LBNL using an alternative method of freeze-tape-cast graphite layer on top of a tape-cast graphite to make a dual layer graphite electrode. Earlier approach of direct freeze-tape-casting on tape-cast electrode has been problematic due to non-uniform ice growth directions resulting in vertical as well as parallel ice growth (pore) domains. In order to simplify and decouple the two processes, freeze-tape-cast electrodes were produced separately and detached from the substrate prior to freeze-drying in order to obtain free-standing electrodes. These electrodes were then attached to a tape-cast electrode by placing them on a cast slurry after tape-casting. The two layers bonded well. While this method of making dual-layer anodes with ideal structure is appealing, it was not scaled enough to produce the needed amount of anode for the final pouch cell build.

Early results from the mid-term pouch cell testing indicated that these cells had higher than expected impedance (1 kHz) and less charge acceptance at the 6C rate. It was suspected that the carbon additive and binder content was too low (see early discussion on NREL electrode model). The active content of the NMC811 was then lowered from 97 down to 96 wt.% active content. The electrodes used in the final single-layer pouch cell build are summarized in Figure IV.8.11. The cells used Celgard 2500 separator and were then divided into three lots. One lot of 7 cells used Gen2 electrolyte, 10 cells used B26 electrolyte from INL, and 7 cells used “Solvent C” (7-Oxabicyclo[2.2.1]heptane-2-carbonitrile) electrolyte from NREL. These cells were formed and then shipped to INL for testing under various protocols, which are described in other XCEL sections of this annual report.

Anode: LN210035-(16-5)&(21-3)**91.83 wt% Superior Graphite SLC1506T**• 1st layer (on foil), ~1.5 mAh/cm²**AETC LM2803 graphite**• 2nd layer (on calendared 1st layer), ~1.5 mAh/cm²**2 wt% Timcal C-45****6 wt% Kureha 9300 PVDF Binder****0.17wt% Oxalic Acid***2021 XCEL Final Cell Build, **Dual Layer Anode**,

SLC1506T Lot#: 573-824; American Energy Technologies Company (AETC) LM2803 graphite Lot#: GN201125008 -> D50 = 3.07 µm, "SS" = single sided

1st layer calendared to ~25% porosity, then 2nd layer coated and calendared to ~45% porosity. *Oxalic acid only used for 1st layer slurry.

Cu Foil Thickness: 10 µm

Total Electrode Thickness: 82 µm

SS Coating Thickness: 72 µm

Porosity: 35.1 %

Total SS Coating Loading: 10.11 mg/cm²Total SS Coating Density: 1.40 g/cm³Expected SS Areal Capacity: 3.07 mAh/cm²

[Based on rev. C/10 of ~325 mAh/g for 0.005 to 1.5 V vs. Li]

Made by CAMP Facility**Cathode: LN210035-33-3 "Round 2"**
(single-sided)**96 wt% Targray NMC811****2 wt% Timcal C-45****2 wt% Solvay 5130 PVDF Binder**

2021 XCEL Final Cell Build, Low CBD Cathode,

Designed for full cell 3.0 to 4.1 V window

Product: SNMC03004, Lot#: 12846

"SS" = single sided -> CALENDERED

Al Foil Thickness: 20 µm

Total Electrode Thickness: 73 µm

SS Coating Thickness: 53 µm

Porosity: 35.2 %

Total SS Coating Loading: 15.35 mg/cm²Total SS Coating Density: 2.90 g/cm³Expected SS Areal Capacity: 2.71 mAh/cm²

[Based on rev. C/10 of ~185 mAh/g for 3.0 to 4.2 V vs. Li]

Made by CAMP Facility

Figure IV.8.11 Electrodes used in final pouch cell build for FY 2021.

BatPaC Analysis of "Hero Cell" (Argonne-BatPaC Focus)

The Battery Performance and Cost (BatPaC) techno-economic model was used to assess the impact of modifications to battery designs that enable extreme fast charge (XFC). With the new developments in cell designs that led to the "Hero Cell", it was time to benchmark the cost of an XFC Li-ion battery. Several properties were defined from BatPaC (version 4.0), CAMP Facility, XCEL partners, and literature. These include:

- Fast Charge = 80% capacity (15 to 95% SOC) recharged in 15 min.
- Adiabatic operation during charging
- Charging Protocol
 - Initially, constant power
 - C-rate adjusted to avoid lithium plating potential
 - C-rate adjusted to avoid maximum allowable temperature (35, 40, 45 °C) at end of charge
 - Constant voltage hold till SOC limit is reached

The results from this analysis are summarized in Figure IV.8.12, where the anode thickness and cell cost are aligned as a function of charge time for the "Hero Cell" design with maximum allowed temperature rise limitations (35, 40, and 45°C). Important to note is that "Hero Cell" costs are lower if the cell is allowed to reach 45°C (instead of 35°C) during adiabatic charging. For example, the cost of a "Hero Cell" capable of a 15 minute charge is \$130/kWh (total energy), with an anode thickness 42 microns, if the cell is allowed to heat up to 45°C during adiabatic charging. If a 40°C limit is used, the anode thickness must be reduced to 30 microns, which increases the cost to \$155/kWh. Whereas, a cell with a 70-micron anode without fast charging (>30 min) costs \$111/kWh (45°C temperature limit). Other scenarios will be explored in the future, particularly on when the heat removal should begin (*i.e.*, non-adiabatic charging – active cooling).

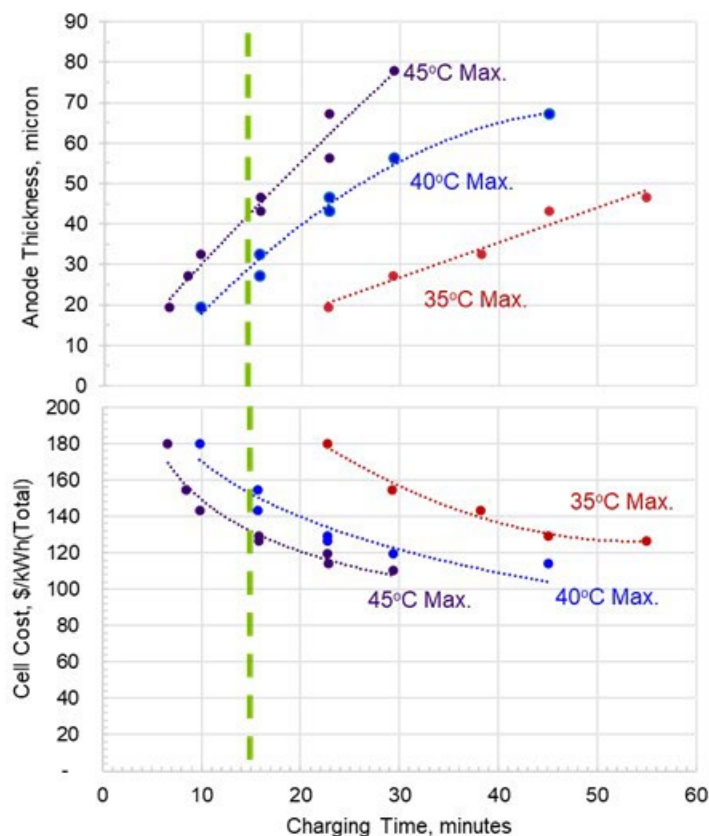


Figure IV.8.12 BatPaC Analysis of “Hero Cell” design based on preliminary data of single-layer pouch cells made by the CAMP Facility. See Figure I.4.H.1 for electrode details.

Conclusions

The Electrode & Electrolyte Thrust of the XCEL Program successfully coordinated its efforts in developing the ideal structured electrode and electrolyte to enable fast charging with minimal lithium plating.

- A suite of electrochemical and microstructure tools was developed at NREL to investigate the effect of advanced electrode architectures on fast charge performance. NREL used its multiscale modeling to update transport properties of the “Hero Cell” taking into consideration modified porosity and carbon-binder loading. It was predicted that a capacity loading near 4 mAh/cm² at the anode side is possible with minimal lithium plating under 6C charging.
- Positive electrodes for the Mid-term and Final pouch cell builds were fabricated at Argonne’s CAMP Facility using NMC811 with lower carbon and binder content.
- Dual-layer negative electrode for the Final pouch cell build was developed at Argonne’s CAMP Facility.
- Electrodes were used by CAMP Facility in single-layer pouch cells for several Deliverables.
- Freeze tape-cast efforts at LBNL focused on developing an alternative path to construct freeze-tape-cast / tape-cast dual-layer graphite electrodes.
- Further studies of the B26 electrolyte were conducted that showed good compatibility with NMC811. This electrolyte was predicted by INL using their Advanced Electrolyte Model (AEM).

- The NREL electrolyte team focused on electrolyte solutions containing “Solvent C” for detailed experimental characterization. Electrolytes containing various amounts of salt and solvent concentrations were built for measuring transport properties.
- BatPaC analysis was conducted using the electrode and cell design parameters of the “Hero Cell” from October of 2020. In this work, the anode thickness and cell cost are aligned as a function of charge time with maximum allowed temperature rise limitations (35, 40, and 45°C). The cell costs are lower if the cell is allowed to reach 45°C (instead of 35°C) during adiabatic charging.

Key Publications and References

1. F. L. E. Usseglio-Viretta, A. M. Colclasure, A. Dunlop, S. E. Trask, A. Jansen, D. Abraham, M.-T. Fonseca Rodrigues, E. Dufek, T. Tanim, K. Smith, “Carbon-binder weight loading optimization for improved lithium-ion battery rate capability”, in redaction
2. F. Usseglio-Viretta, D. P. Finegan, A. Colclasure, T. M. M. Heenan, D. Abraham, P. Shearing, K. Smith, “Quantitative Relationships Between Pore Tortuosity, Pore Topology, and Solid Particle Morphology Using a Novel Discrete Particle Size Algorithm”, *Journal of The Electrochemical Society*, 167 100513 (2020)
3. F. Usseglio-Viretta, K. Smith, “Quantitative Microstructure Characterization of a NMC Electrode”, *ECS Transaction*, 77(11), 1095–1118 (2017)
4. F. L. E. Usseglio-Viretta, P. Patel, E. Bernhardt, A. Mistry, P. P. Mukherjee, J. Allen, S. J. Cooper, K. Smith, “MATBOX: an open-source microstructure analysis toolbox for microstructure generation, segmentation, characterization, visualization, correlation, and meshing”, submitted to SoftwareX, https://github.com/NREL/MATBOX_Microstructure_analysis_toolbox.
5. N. Dunlap, D. B. Sulas-Kerna, B. J. Tremolet de Villers, P. J. Weddle, F. L. E. Usseglio-Viretta, A. M. Colclasure, K. Smith, D. P. Finegan, “Capacity improvement for laser-structured thick lithium-ion battery cell”, in redaction
6. F. L. E. Usseglio-Viretta, P. J. Weddle, D. P. Finegan, B. J. Tremolet de Villers, N. Dunlap, D. B. Sulas-Kern, K. Smith, “Secondary Pore Network for Lithium-Ion Batteries, Part I: Optimal Periodic Pattern Identified with a Genetic Algorithm”, in redaction
7. N. Gao, S. Kim, P. Chinnam, E. Dufek, A. Colclasure, A. Jansen, S.-B. Son, I. Bloom, A. Dunlop, S. Trask, and K. Gering, “Methodologies for Design, Characterization and Testing of Electrolytes that Enable Fast Charging of Lithium-ion Cells”, *Energy Storage Materials* **44** 296–312 (2022).
8. D. C. Robertson, L. Flores, A. R. Dunlop, S. E. Trask, F. L. E. Usseglio-Viretta, A. M. Colclasure, Z. Yang, and I. Bloom, “Effect of anode porosity and temperature on performance and lithium plating during fast-charging of lithium-ion cells,” *submitted*
9. Mallarapu, V. Bharadwaj and S. Santhanagopalan, “Understanding extreme fast charge limitations in carbonate mixtures”, *J. Mater. Chem. A* **9** 4858–4869 (2021).
10. L. Meyer, D. Curran, R. Brow, S. Santhanagopalan, J. Porter, “Operando Measurements of Electrolyte Li-ion Concentration during fast charging with FTIR/ATR”, *J. Electrochem. Soc.*, 168, 090502, 2021.
11. S. Santhanagopalan and R. Brow, “Electrolyte Components for Charging of Batteries”, Application No. 63/166,338.
12. Donakowski, R. Brow, K. Steirer, S. Santhanagopalan, “Degradation Products of Solvents under Extreme Fast Charging”, CCAC Annual Summit, August 2021.

Acknowledgements***Argonne***

Shabbir Ahmed, Alison Dunlop, Andrew Jansen (Thrust Lead), Joseph Kubal, Zhe Liu, Paul Nelson, Bryant Polzin, Juhyun Song, Steve Trask, and Zhenzhen Yang

INL

Parameswara Chinnam, Eric Dufek, Michael Evans, Ningshengjie Gao, Kevin Gering (INL point of contact), and Sangwook Kim

LBNL

Marca Doeff, Eongyu Yi

NREL

Vivek Bharadwaj, Ryan Brow, Andrew Colclasure, Nathan Dunlap, Donal Finegan, Anudeep Mallarapu, Shriram Santhanagopalan, Kandler Smith, Dana B. Sulas-Kern, Bertrand J. Tremolet de Villers, Francois Usseglio-Viretta, and Peter Weddle

IV.9 The Effects of Extreme Fast Charging on Lithium-ion Battery Cathode (INL, NREL, ANL, LBNL, SLAC)

Tanvir R. Tanim, Principal Investigator

Idaho National Laboratory
1955 Fremont Avenue
Idaho Falls, ID 83415
E-mail: Tanvir.Tanim@inl.gov

Samm Gillard, DOE Technology Development Manager

U.S. Department of Energy
E-mail: Samuel.Gillard@ee.doe.gov

Start Date: October 1, 2020	End Date: September 30, 2021	
Project Funding (FY21): \$600,000	DOE share: \$600,000	Non-DOE share: \$0

Project Introduction

Extreme fast charging (XFC) of Li-ion batteries (LiBs) can create a host of life and safety issues. The eXtreme Fast Charge Cell Evaluation of Lithium-ion Batteries (XCEL) Program has worked on identifying the key bottlenecks of enabling XFC during Phase I. Collaborative research has found that besides Li plating, there could be a significant impact of XFC on battery cathode performance. In some instances, the fade associated with cathode aging could exceed losses due to Li plating. Key objectives of the cathode thrust include gaining a better understanding of the cathode issues and their dynamics with XFC cycling, identification, and quantification of different cathode aging mechanisms including cracking by combining experimental, operando, and modeling efforts. The program shifted its focus from $\text{LiNi}_{0.5}\text{Mn}_{0.3}\text{Co}_{0.2}\text{O}_2$ (NMC532) to $\text{LiNi}_{0.8}\text{Mn}_{0.1}\text{Co}_{0.1}\text{O}_2$ (NMC811) in the final year. Therefore, the team primarily focused on NMC811, and compared its cycle life performance to NMC532 for extended XFC cycling up to 9C. The findings of this activity are deemed to be crucial for a comprehensive understanding of the extent of cathode issues and identifying key research and development (R&D) efforts required to resolve those issues for enabling XFC. The cathode thrust team is composed of members from Idaho National Laboratory (INL), the National Renewable Energy Laboratory (NREL), Argonne National Laboratory (Argonne), SLAC National Accelerator Laboratory, and Lawrence Berkeley National Laboratory (LBNL).

Objectives

The key objectives of this work are to enable a better scientific understanding of the cathode aging modes and mechanisms during XFC conditions. Earlier studies have suggested that a major cause of capacity fade within a Li-ion cell is the cracking of polycrystalline nickel manganese cobalt (NMC) particles [1]. The cathode thrust aimed to understand the impact of charging rate and voltage on polycrystalline cathode cracking in NMC532 and NMC811 and how that evolves with cycling. In particular, the thrust is focused on gaining a better understanding on whether cracking triggers additional aging mechanisms (e.g., transition metal [TM] dissolution, rock salt formation, cracking, etc.). Gaining a better understanding of the impact of reaction heterogeneity that typically arises during XFC conditions and its correlation with cracking is another aim. Other objectives include developing tools to better classify aging, including mapping polycrystalline architectures of NMC particles in 3D and the implementation of mapped architectures in multi-physics models to better capture particle-grain interactions that may limit performance and induce aging. The final objective looks to evaluate innovative particle architectures (e.g., particle size, microstructure, crystal type, etc.) under XFC conditions and identify performance improvements.

Approach

To achieve the cathode thrust objectives, the team used a combination of experimental (including post-testing), in-operando x-ray powder diffraction (XRD), and modeling. Researchers at INL performed extensive

experimental tests on 60+ single layer pouch cells (SLPCs) assembled at Argonne's Cell Analysis, Modeling, and Prototyping (CAMP) Facility. INL tested the cells at different charging rates (i.e., 1C, 4C, 6C, and 9C) and upper charge cutoff voltages (i.e., 4.1V-100% state of charge [SOC], 3.94V- 80% SOC, 3.78V-60% SOC, and 3.66V- 35% SOC). INL identified the dominating aging modes using reference performance test (RPT) and cycle-by-cycle electrochemical data. Argonne researchers performed a comprehensive post-test characterization on a subset of INL cells for mechanism verification/confirmation. Researchers at the Advanced Photon Source (APS) at Argonne performed in-operando studies using high energy XRD. At NREL, researchers identified, and quantified sub-particle architectures of the cathode materials using electron backscatter diffraction (EBSD) and then extended them to 3D through the application of focused-ion beam (FIB) EBSD. NREL also developed a chemo-mechanical model incorporating strain-induced damage to study the effects of particle size, grain size, and charge rate on capacity fade. Finally, LBNL researchers evaluated the effects of XFC on particles and microstructures, identify improvement needs, and explore synthesis approaches to produce cathode particles with different microstructures.

Across the labs, cathode thrust research primarily focused on the use of Round 1 cells, which include a graphite anode ($\sim 1.93 \text{ mAh cm}^{-2}$) and either NMC532 or NMC811 cathode ($\sim 1.65 \text{ mAh cm}^{-2}$). Tools and learnings from the work using NMC532 were transferred over to the NMC811 system, and the key issues associated with NMC811 during XFC have been identified in FY21.

Results

Identifying the Key Aging Modes and Mechanisms and Their Relative Extent

Figure IV.9.1 compares experimental, and pseudo two-dimensional (P2D)-modeled polarization results extracted from rate capability test (RCT) and cell-level charging currents for Gr/NMC811 and Gr/NMC532. The impedance polarization increases with charging rate and some slight improvement for NMC811 cells as compared to NMC532 cells at comparable charging rates. The reduced impedance polarization in the NMC811 cells is primarily due to a thinner electrode and an improved electron conductivity of NMC811, as observed in Figure IV.9.1a. The transport polarization in the NMC811 cell shows more of a distinct improvement without showing any transport-related plateau, primarily because of the one order higher magnitude of solid-state diffusion of NMC811 as compared to NMC532 [2] (also verified with P2D modeling). Figure IV.9.1c shows the first cycle charge acceptance for different C-rates for the Gr/NMC811 cells. Overall, the NMC811 cells show very good charge acceptance ranging from 99.6% ($158.8 \text{ mAhg}_{\text{NMC}}^{-1}$) to 93.6% ($149.5 \text{ mAhg}_{\text{NMC}}^{-1}$) for C-rates between 1C to 9C when the charge cutoff voltage was set to 4.1V. The charge acceptance for the NMC811 cells at comparable rates is superior to the NMC532 cells due to better polarization behavior already discussed, as provided in Figure IV.9.1a. For instance, the NMC811 cells outperformed the charge acceptance of the NMC532 cells by 3.3% ($22.7 \text{ mAhg}_{\text{NMC}}^{-1}$), 2.4% ($20.8 \text{ mAhg}_{\text{NMC}}^{-1}$), 3.2% ($21.2 \text{ mAhg}_{\text{NMC}}^{-1}$), and 1.7% ($19.4 \text{ mAhg}_{\text{NMC}}^{-1}$), respectively, at 1C, 4C, 6C, and 9C, respectively, reaching very close to full acceptance. The conditions where voltage was constrained to lower than 4.1V also show a high charge acceptance at 9C [i.e., 34.6% ($54.2 \text{ mAhg}_{\text{NMC}}^{-1}$) at 3.63V, 62% ($98.5 \text{ mAhg}_{\text{NMC}}^{-1}$) at 3.77V, and 82.5% ($129.8 \text{ mAhg}_{\text{NMC}}^{-1}$) at 3.94V].

Therefore, from the observations in Figure IV.9.1a through Figure IV.9.1c, it can be concluded that the improved material properties of NMC811 is primarily responsible for the superior polarization and charge acceptance.

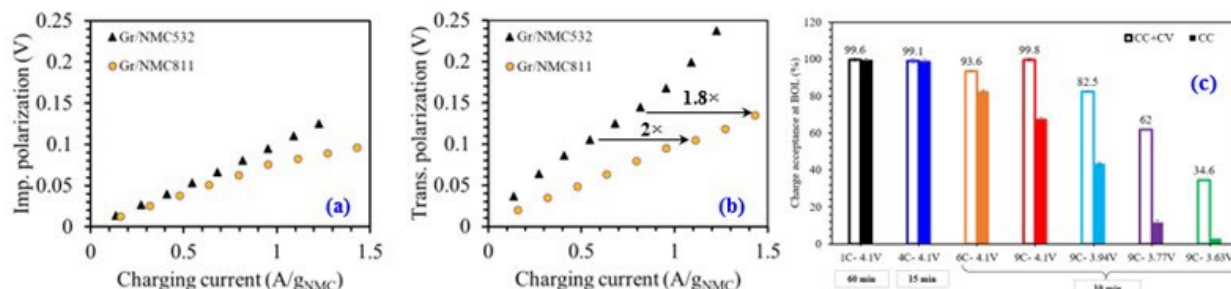


Figure IV.9.1 Cell Polarization and Aging Data. Here, the impedance polarization or overpotential (a) is the immediate (e.g., within ~ 12 ms) voltage drop during the rest at the end of charge, and transport polarization (b) is the voltage difference between the immediately relaxed state and after a 15-minute rest, a pseudo-equilibrium state, while (c) is the charge acceptance at beginning of life (BOL).

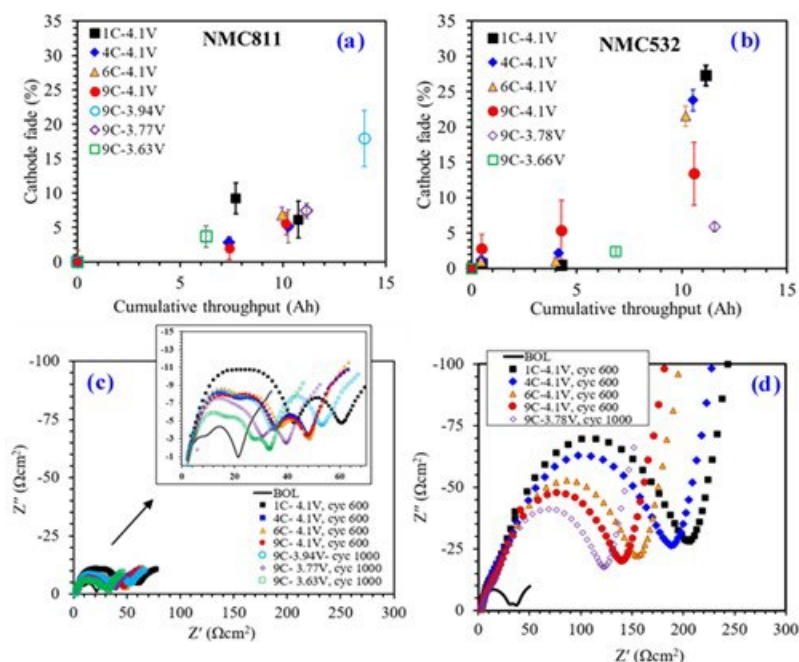


Figure IV.9.2 Cathode aging behavior in coin cells harvested from pouch cells: (a) the capacity fade of NMC811 at C/20; (b) the capacity fade of NMC532 at C/20; (c) the impedance behavior of NMC811; and (d) the impedance behavior of NMC532. Both coin cells had similar configurations. EIS was performed at 3.9V. For areal impedance, a cathode area of 1.27 cm^2 was used.

Figure IV.9.2a and Figure IV.9.2c present the aging evolution for the NMC811 cathode with respect to cycle-by-cycle cumulative throughput in the Li/NMC811 coin cells that were harvested from the SLPCs after retiring cells at specific cycling intervals (i.e., cycle 425, 600, and 1000). Figure IV.9.2b and Figure IV.9.2d show the aging behavior for the NMC532 cathodes in comparable cycling conditions with a similarly built coin for comparison. Note in Figure IV.9.2c, NMC811 has a distinctly better impedance behavior than NMC532, which is shown in Figure IV.9.2d, at BOL. After 425 cycles (≈ 7.5 Ah throughput), the average NMC811 fade remains between 2 to 9%, with an order of $1\text{C} > 4\text{C} \geq 9\text{C}$, as shown in Figure IV.9.2a. At 600 cycles (≈ 11 Ah throughput), the capacity fade falls between 5.1% to 6.8% for the 4.1V fast-charge conditions irrespective of C-rate (e.g., between 5.1% to 5.5% for 4C and 9C, and 6.1% to 6.8% for 1C and 6C conditions, respectively, as observed in Figure IV.9.2a). The half-cell electrochemical impedance spectroscopy (EIS) data for NMC811 are in-line with full-cell $R_{\text{CEI}+\text{CT}}$ at the end of cycling and remain tightly packed except for the cell cycled at 1C, which shows a slightly higher impedance at 600 cycles (≈ 11 Ah), as shown in Figure IV.9.2c. The 9C low-voltage conditions—particularly the 3.63V and 3.77V conditions—show much lower aging effects even after 1000 cycles, as observed in Figure IV.9.2a and Figure IV.9.2c. The 9C-3.94V (80% SOC) that

accumulated the highest throughput (≈ 14 Ah), as seen in Figure I.1.A.2a, shows the most cathode fade (18%) and a higher impedance growth after 1000 cycles, which is seen in Figure IV.9.2a and Figure IV.9.2c.

Unlike the NMC532, the NMC811 sample experiences a gradual and much less severe capacity fade. After 600 cycles (≈ 11 Ah throughput), the capacity fade of NMC532 for 4C and 6C conditions were at 23.8% and 21.5%, respectively. The NMC811 at the same cycling conditions and aging stage incurred only between a 5–7% fade (e.g., a $4.6\times$ and $3.15\times$ reductions at 4C and 6C, respectively). Moreover, comparatively the NMC532 samples in general experience a distinctly lower increase in impedance with no drastic increase in later cycling, as observed in Figure IV.9.2c and Figure IV.9.2d, respectively. INL's electrochemical and incremental capacity (IC) analyses confirmed that similar to NMC532 cells, the cell capacity fade in NMC811 cells were also dominated by the loss of lithium inventory (LLI), while cathode loss of active material is a silent aging mode [3].

Post-testing Characterization

To gain a better understanding of the aging mechanisms, INL sent cells to different institutions at different aging states. The results are summarized below.

Cathode Cracking Identification by Cross-section Scanning Electron Microscopy (SEM)

SEM analysis was used to evaluate the extent of mechanical damage within the secondary particles. Figure IV.9.3a shows the SEM micrographs of the pristine NMC811 electrode after calendaring, while Figure IV.9.3b, Figure IV.9.3d, and Figure IV.9.3f, and Figure IV.9.3c, Figure IV.9.3e, Figure IV.9.3g, and Figure IV.9.3h, present the SEM micrographs at 425 and 600 cycles, respectively, for the different XFC conditions cycled with a 4.1V charge cutoff. The pristine samples in Figure IV.9.3a do not show any distinct inter primary particle (IPP) grain boundaries. The cycled samples after 425 cycles show some IPP grain boundaries in all particles, irrespective of C-rate, concomitant with cracking in the larger particles, as observed in Figure IV.9.3b, Figure IV.9.3d, and Figure IV.9.3f. The extent of IPP cracking in the 1C condition is higher than that seen in the 4C and 9C conditions. The SEM images included in Figure IV.9.3c, Figure IV.9.3e, Figure IV.9.3g, and Figure IV.9.3h at 600 cycles show more and wider IPP grain separation in the smaller particles, as well as more distinct cracking in the larger particles.

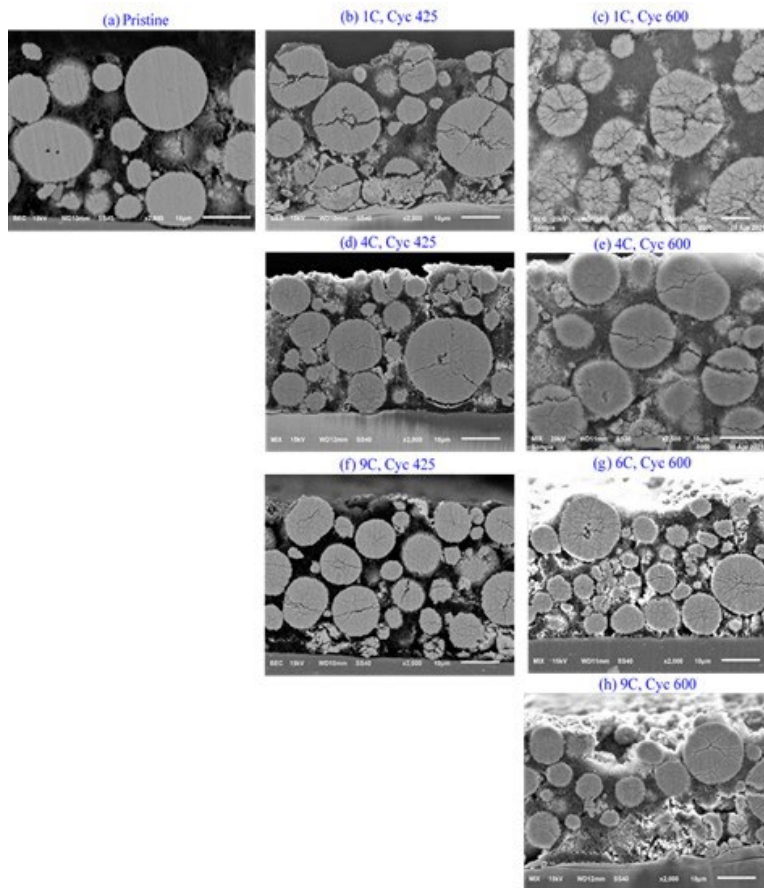


Figure IV.9.3 Representative SEM micrographs for the different XFC cycling conditions at different cycling interval for NMC811 electrodes: (a) Pristine after calendaring; (b) 1C, Cyc 425; (c) 1C, Cyc 600; (d) 4C, Cyc 425; (e) 4C, Cyc 600; (f) 9C, Cyc 425; (g) 6C, Cyc 600; and (h) 9C, Cyc 600. Cumulative cycle-by-cycle throughput at 600 cycles: 1C=10.75 Ah, 4C=10.3 Ah, 6C=9.95 Ah, and 9C=10.16 Ah. See Figure I.1.A.2b for the throughputs. The top of the graphic is the separator, while the bottom of the graphic is the current collector.

Figure IV.9.4 shows the NMC811 SEM images after 1000 cycles for the 9C low-voltage conditions. A correlation between damage, voltage cutoff, and/or throughput can be observed where the 9C-3.63V sample with 6.26 Ah throughput has kept the particle structure nearly intact, the 9C-3.77V specimen with 11.15 Ah throughput has distinct IPP grain boundaries, and the 9C-3.94V with 13.95 Ah throughput sample has the worst damage. The 9C-3.77V condition after 1000 cycles, as observed in Figure IV.9.4b, with comparable throughput and fade, as observed in Figure IV.9.2a, to the 9C-4.1V condition at 600 cycles shows more severe particle damage. These observations imply that besides the initial charging rates, upper cutoff, or average voltage, NMC particle damage is also sensitive to cycle numbers.

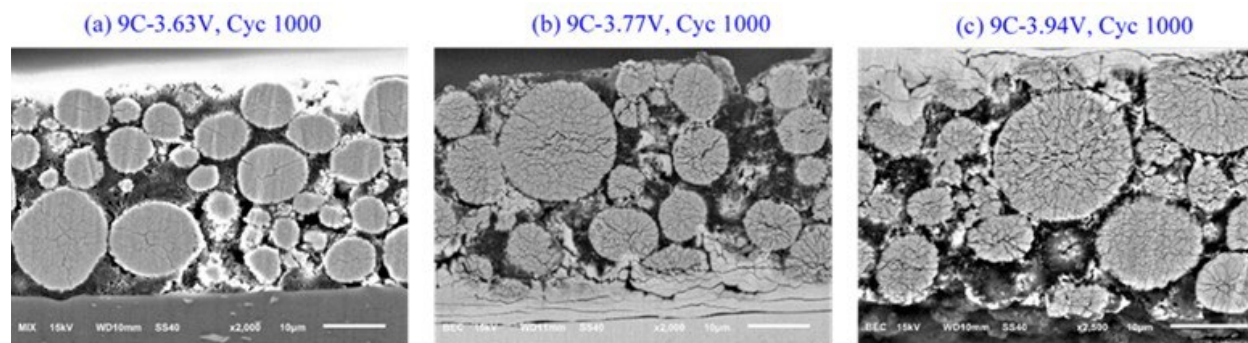


Figure IV.9.4 Representative SEM micrographs for the 9C- low-voltage conditions after 1000 cycles for NMC811 electrodes: (a) 9C-3.63V; (b) 9C-3.77V; and (c) 9C-3.94V. Cumulative cycle-by-cycle throughput at 1000 cycles: 9C- 9C-3.63V=6.26 Ah, 9C-3.77V= 11.15 Ah, and 9C-3.94V= 13.95 Ah.

TM Dissolution, Deposition, and Li on Anodes by Inductively Coupled Plasma Mass Spectrometry (ICP-MS)

ICP-MS data in Figure IV.9.5 maps out the extent of TM (e.g., Ni, Co, Mn) that migrated from NMC811 to the anode for different XFC conditions at different cycles. TM dissolution in NMC chemistry has been reported to happen predominantly at a higher voltage (e.g., > 4.3V) [4],[5] contributing to capacity fade and impedance rise. Here, the primary goal was to investigate whether different XFC conditions (e.g., 1C to 9C) with a lower charge voltage (e.g., ≤ 4.1V) would lead to any distinctly different TM dissolution, and if so, how that would affect the electrochemical data. Among the three TM metals, irrespective of charging conditions, Co migrated the least amount, followed by Mn and then Ni, as shown in Figure IV.9.5. For the 4.1V charge cutoffs, Co and Mn dissolution remain comparable irrespective of C-rate, as shown in Figure IV.9.5b and Figure IV.9.5c. An increase in Ni dissolution is more distinct for the different C-rate conditions with a 4.1V charge cutoff between 425 and 600 cycles; however, it remains within the error bound, except for the 6C-4.1V condition, which shows a slightly lower Ni dissolution. The 9C-constrained voltage conditions show a slightly lower extent of TM dissolution, which was also observed for NMC532 [3]. Similar to NMC532, the comparable extent of TM dissolution for the different XFC conditions with a 4.1V voltage cutoff conclude that fast charging between 1C-9C do not distinctly impact TM dissolution in the NMC811 cathode.

The closely packed electrochemical cathode aging data in Figure IV.9.2a and Figure IV.9.2c is another indication that the extent of TM dissolution in Figure IV.9.5 is not strongly contributing to cathode aging.

Surface Phase Transformation of Degraded Cathodes by HR-TEM

The crystal structure of the reconstruction layer of the NMC811 particles were evaluated using HR-TEM, as shown in Figure IV.9.6, and electron energy loss spectroscopy (EELS), as shown in Figure IV.9.7. In general, the particle surface primarily consists of a rock salt structure at the outermost surface with some atomic layers of mixed structure as a “bridge” between the layered structure and the rock salt structure, as observed in Figure IV.9.6. The thickness of the reconstructed layer is greatly influenced by fast charge cycling conditions. The 9C-4.1V condition leads to a thicker surface reconstruction layer than the 1C-4.1V condition with comparable

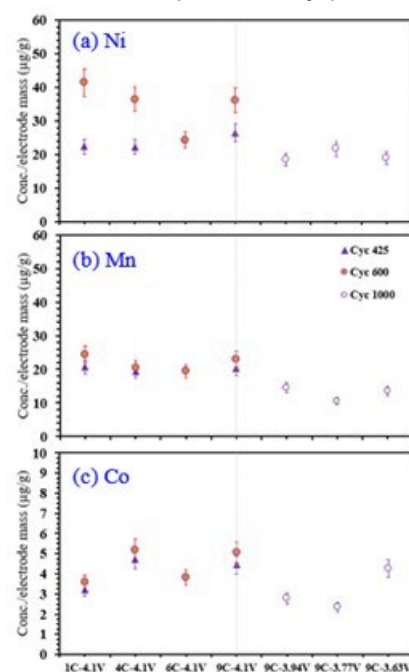


Figure IV.9.5 TM dissolution of the NMC811 and deposition on the anodes: (a) Ni dissolution; (b) Mn dissolution; and (c) Co dissolution. Normalization was performed by measuring the total anode mass of the cutout section.

throughput after 600 cycles. The 9C-3.63V condition after 1000 cycles, and with half the throughput of 1C and/or 9C-4.1V conditions, show distinct surface deterioration (i.e., 9C-3.63V samples have developed by $5.5\times$ and by $2\times$ thicker rock salt layer than with the 1C-4.1V and 9C-4.1V conditions, respectively). The 9C-3.94V condition after 1000 cycles, and with $\sim 1.3\times$ throughput of 1C-4.1V or 9C-4.1V, shows the most severe surface degradation in Figure IV.9.7d.

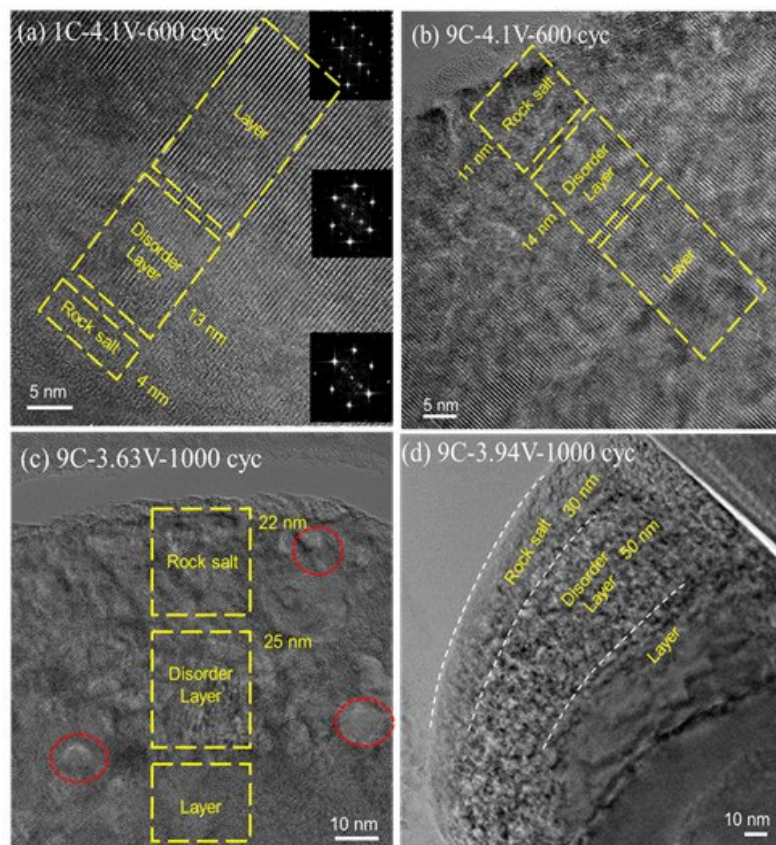


Figure IV.9.6 HR-TEM images of the discharged NMC811 cathodes after different cycle conditions: (a) 1C-4.1V-600 cycles; (b) 9C-4.1V-600 cycles; (c) 9C-3.63V-1000 cycles; and (d) 9C-3.94V-1000 cycles. The marked region in each figure shows the particle surface degradation with different structures of just a rock salt, disorder layer with mixing of a rock salt and layer phase, and a completely layer phase. Corresponding Fast Fourier Transform (FFT) images of the regions were shown in the inset of (a).

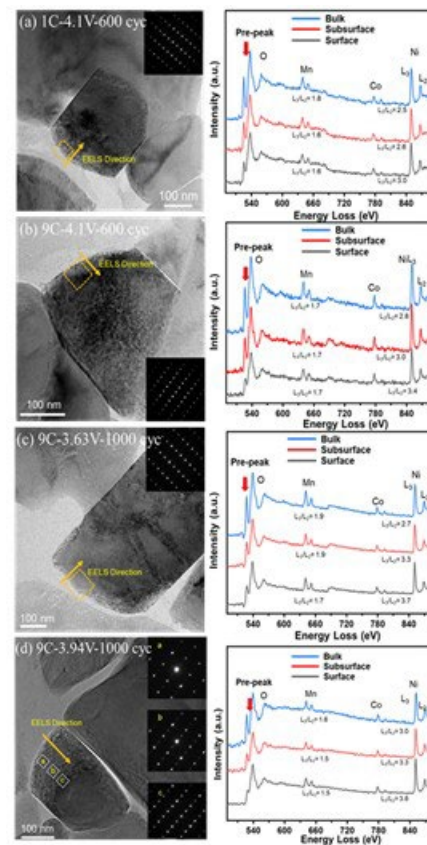


Figure IV.9.7 HR-TEM images of NMC811 cathodes: (a) 1C-4.1V-600 cycles; (b) 9C-4.1V-600 cycles; (c) 9C-3.63V-1000 cycles; and (d) 9C-3.94V-1000 cycles at lower magnification to show the structure of the whole bulk. Corresponding EELS line scans of the O K-edge and L-edges of Mn, Co, and Ni.

Comparing the value of L_3/L_2 of Ni at the surface for each sample, the trend of 1C-4.1V-600 cycles < 9C-4.1V-600 cycles < 9C-3.63V-1000 cycles < 9C-3.94V-1000 cycles can be seen in Figure IV.9.7, which indicates that the Ni oxidation state is getting lower as a cycle rate and a cycle life increased. A significantly reduced state of Ni^{2+} probably produced NiO or any other reduced form at the primary particle surface [3],[4],[5]. If Ni ions at the surface are reduced, either the other TMs should be oxidized, or the oxygen ions should leave the structure to satisfy charge neutrality. As seen in Figure IV.9.7, the slightly lower L_3/L_2 ratio of Mn implies that Mn ions are oxidized to compensate for the charge imbalance during Ni reduction at the surface. But the variation of Mn electronic structure is small because the L_3/L_2 ratio relative change is small from the surface layer to the inner layer; therefore, the stabilization effect of Mn is very limited. Thus, oxygen has to leave the structure, which is also evident by the reduced pre-peak intensity of the O K-edge in Figure IV.9.7, as well as to compensate for the charge imbalance. Such oxygen release is more clearly manifested as

nanovoids in the 9C low-voltage conditions that went through 1000 cycles and experienced the most surface reconstruction.

The extent of surface reconstruction in Figure IV.9.6, respectively, as well as the corresponding chemical changes in Figure IV.9.7 for the selected XFC conditions, conclude that cycle life has a more dominant impact on particle surface than C-rate or SOC. Earlier non-XFC studies on NMC have showed that distinct surface, interphase, and oxygen release-driven aging effects do not become dominant until above 4.3 V vs. Li/Li+ [4],[5],[6]. The XFC conditions evaluated in this study cycled up to only 4.1V. As a result, despite evidence of degraded surface and interphase, as observed in Figure IV.9.6 and Figure IV.9.6, respectively, there is minimal impact to the electrochemical performance, as presented in Figure IV.9.2a and Figure IV.9.2c, respectively.

EBSD of Particle Architectures and Continuum-level Modeling

Additional sub-particle information and 3D continuum modeling simulations were used to further rationalize as to why the performance of NMC811 is superior to NMC532. A 3D continuum-level damage model was constructed using realistic particle architecture derived from the experimental data as described previously [7]. For this case study, the same particle geometry and random grain orientations are used for the two chemistries. The NMC532 response in Figure IV.9.8a illustrates that as more of the particle is damaged, less capacity is reached. Furthermore, less capacity is realized at high rates (e.g., 6C) as compared to low rates (e.g., 1C) with a 4.1V charge cutoff. For NMC811, these responses are significantly different. Even at reasonably high damage percentages (i.e., ~40%), the NMC811 particle retains near 100% capacity. The high resilience of the NMC811 particle to damage is consistent with the SEM, as shown in Figure IV.9.3 and Figure IV.9.4, and the half-cell capacity measurements, as shown in Figure IV.9.2. The high-capacity retention, despite the significant damage (i.e., cracking), is mainly due to a high solid phase Li diffusion coefficient in the NMC811. Besides improved solid-phase diffusion, NMC811 also possesses a higher electrical conductivity than NMC532 because of the higher Ni content. The higher electrical conductivity of NMC811 effectively retained a better electrical pathway than the NMC532, thereby resulting in a significantly lower impedance growth, as shown in Figure IV.9.2.

There may also have been an influence of the particle architectural properties, such as the grain sizes and orientations, on the post-cycling impedance behavior. Particles from both the NMC523 and NMC811 samples were cross-sectioned and imaged with EBSD. For layered materials, the transport of lithium will be in the radial direction if the c-axis is at 90° to the radial line. In Figure IV.9.8b, plots of the r-orientation distribution (i.e., the angle between the radial line and the c-axis of NMC) for both the NMC532 and NMC811 are shown. The closer to 90°, the more radially aligned the grains for fast Li-transport into the particle. For reference, a semi-transparent blue region illustrates the shape of a distribution that would be associated with random orientations. NMC532 displayed random orientations, which are shown as the close to semi-transparent blue curve, while the NMC811 shows a strong preference for radial alignment. This preferential grain orientation could be one reason for better performance of NMC811 than NMC532, since radially aligned grains are less likely to become ionically isolated from each other in the case of radially directed cracking.

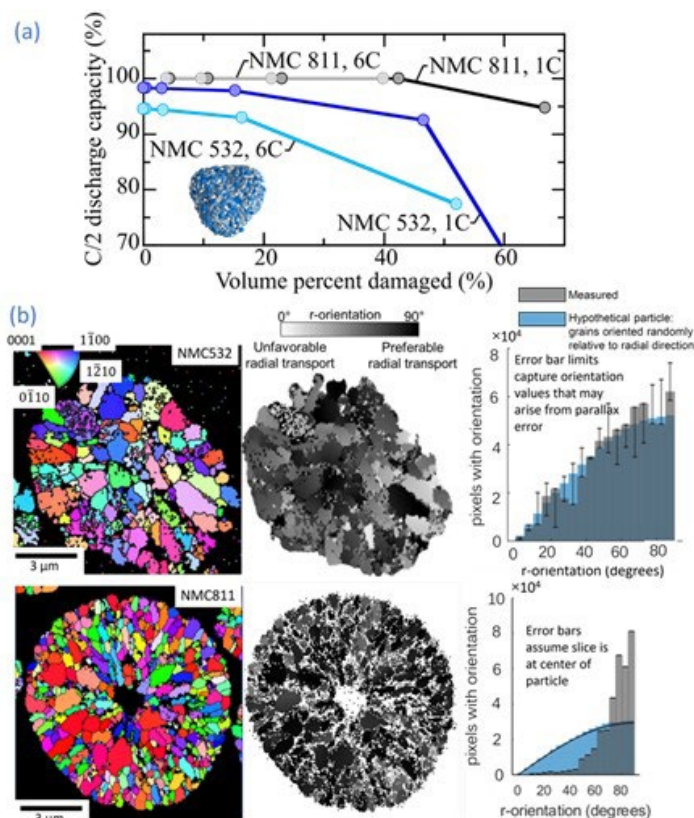


Figure IV.9.8 (a) Model results showing C/2 discharge capacity with respect to percent volume damaged. Illustrated are the responses for the NMC811 particles and the NMC532 particles, respectively, after 1C and 6C charging. (b) EBSD data from cross-sectioned NMC532 (top) and NMC811 (bottom) particles showing (left) the angles of grains, (middle) the angle between the C-axis of NMC and the radial direction of each grain, and (right) the distribution of those angles in grey relative to a simulated random case in semi-transparent blue. The EBSD slices are assumed to be at the center of the particles. Error bars for the NMC532 particle are the same calculation but for if the slice was for particles were sized at d10 and d90 particle diameters, i.e., that may accrue from parallax error as described in [7]. Due to the characteristic void at the center of the NMC811 particle, it is assumed that the slice is at or near the particle center.

In-situ and Operando Investigation of High Rate NMC532 Performance

In FY-20, group members used operando XRD mapping in NMC532 cells and found that fast charging induces significant in-plane variability in lithiation as compared to slow rate charging. Furthermore, heterogeneous cathode utilization resulted in over-lithiated and under-lithiated regions. In FY-21, the cathode active material has been changed from NMC532 to NMC811. Furthermore, the active material loading was increased from 90% to 97%, which allows for further reduction in the loading thickness. Advanced B26 electrolyte (LiPF₆ in EC:DMC:DEX:EP:PN (20:40:10:15:15) with 3% VC & 3% FEC) is compared to the original Gen2 electrolyte (1M LiPF₆ in 3:7 wt% EC:EMC). Comparable specific capacities were achieved with both electrolytes, suggesting that no differences in cathode performance due to electrolyte composition in early cycle life. The team plans to perform operando XRD mapping in mid-year and final build cells upon completion of cycling and compare their performance to baseline NMC532 builds.

Understanding the Cause of Cracking in NMC Particles and Crack Modeling

Developing EBSD as a technique for quantifying sub-particle architectures first required demonstration in 2D, which is shown in Figure IV.9.9a. The grain boundaries and orientation of individual grains were quantified with a high degree of confidence and software was developed to segment and distinctly label the grains. The technique was then extended to 3D through the application of FIB EBSD and, with help from collaborators at University of Ulm, the images were aligned and segmented using machine learning approaches before reconstructing the particle architecture in 3D, as shown in Figure IV.9.9b.

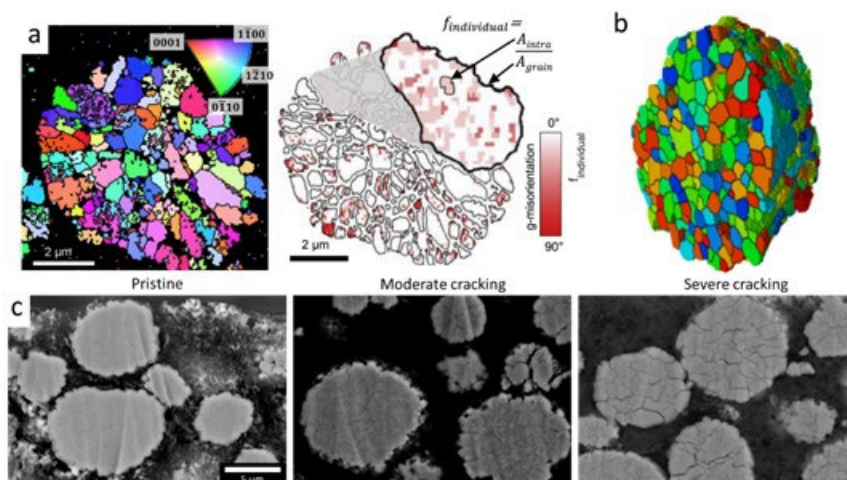


Figure IV.9.9 (a) EBSD of a cross-sectioned NMC532 particles showing (b) the orientations of the grains and (c) the regions within some of the grains with sub-grain misorientation or crystal twins.

The random orientations are expected to lead to a sub-particle tortuosity for lithium transport since transport in the layered materials like NMC occurs perpendicularly to the c-axis of the crystal lattice, as previously modeled and presented in Figure IV.9.8. Additionally, the random orientations combined with the anisotropic expansion/contraction of the lattice during operation is expected to create a complex spatial distribution of strain within the particle, with the potential of high strain concentration regions leading to the formation of cracks between the grains, as observed in Figure IV.9.9c. This mechanism of cracking along grain boundaries is in addition to cracks that can nucleate from defects within the individual crystals, such as by strain fields propagating from the lattice dislocations [8]. However, to date, crack evolution within electrodes has evaded quantification. This stems from cracks ranging in size from nanometers to micrometers, and their heterogeneous nature requiring a large field of view for statistical significance. Techniques like SEM are useful for qualitative observation of crack growth but have yet to achieve quantitative results. In collaboration with the University of Ulm, NREL has shown that cracks can be identified and segmented from cross-sectional SEM images. Initially, the team quantified the crack density (i.e., the ratio of crack area to active material area) for large cracks only. However, the team did not quantify the smaller and less obvious micro-separations along the grain boundaries, which are likely to contribute to performance loss by increasing interfacial resistance between grains and potentially being the source of nucleation in the larger cracks. These fine, poorly resolved micro-separations, are challenging to segment, but are important to accurately quantify mechanical damage to particles.

SLAC is performing extensive data analysis to use image segmentation on microCT reconstructions of thousands of particles in NMC electrodes cycled at 1C, 6C, and 9C after 225 and 600 cycles. This segmentation method is being used to understand how volume and sphericity change trends scale with rate. NanoCT data gives insight into the 3D internal cracking propagation with cycling in individual particles. More cracking or primary particle separation is evident with increasing cycle number at 6C, which is contextualized by the microCT data.

Although intraparticle cathode fracture is observed experimentally, it is not well understood how these chemo-mechanically induced stresses influence overall cathode performance. Furthermore, little is known on how design parameters (e.g., charging procedures, cathode-particle-level design) influence cathode mechanical damage. In this work, a 3D continuum-damage model is used to: (1) determine chemo-mechanically induced damage in realistic cathode particles during cycling; (2) identify how mechanical failure influences overall cathode capacity loss; and (3) determine cathode-particle design criteria that reduce mechanical failure. The model is used to simulate both NMC532 and NMC 811 chemistries. Some results are presented in Figure IV.9.8.

The model predicts that mismatched strain near the grain boundaries during Li (de)intercalation can result in mechanical damage that negatively impacts Li solid diffusion. The severe reduction in effective solid-diffusion results in reduced cathode capacity. The model is initially simulated on NMC532 representative geometries. The model predicted capacity loss after 25 cycles is validated against experiments measured NMC532 capacity fade measurements, as observed in Figure IV.9.10. The model is later extended to NMC811 chemistry, as seen in Figure IV.9.8.

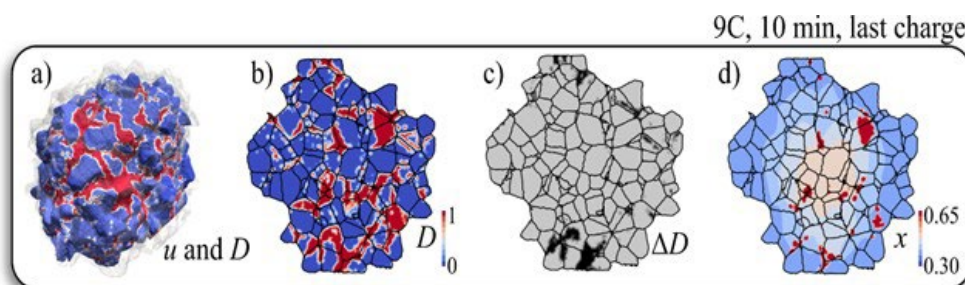


Figure IV.9.10 Model predicted results using the baseline particle geometry after 25 cycles under 9C CC-CV charging and C/2 discharging: (a) chemo-mechanical displacement u and the continuum-damage D after 25 cycles; (b) damage after formation; (c) damage due to cycling; and (d) intercalation fraction. (a) illustrates the surface of the 3D particle and shows how the particle has shrunk from its initial condition (see gray coloring) due to delithiation. (b) illustrates a cut-plane of the damage variable after formation and shows a significant amount of chemo-mechanical damage occurs before cycling. (c) illustrates the additional damage induced due to charging the particle at 9C for 25 cycles. As illustrated, the additional rate-dependent damage primarily occurs on the particle surface at grain interfaces. (d) illustrates the intercalation fraction. The model predicts red “hotspots” in highly damaged regions where the Li diffusion is extremely hindered.

NREL previously developed and validated a P2D electrochemical model for the XCEL 2.6 mAh cm⁻² (Round 2) cells with NMC532 cathode. The model captures all charge/discharge physics, as well as the Li plating degradation mechanism. In FY-21, NREL incorporated electrode particle stress/strain physics into the model and validated its responses for the Round 2 cell at various C-rates. The model is used to predict NMC532 and NMC811 Li plating and cathode-stress responses for standard charging protocols, such as CC-CV, as well as more sophisticated protocols that seek to avoid Li plating, minimize cathode stress, and thus extend life. Using the new P2D electrochemical model, simulations of INL’s material-stress reduction (MSR) multi-step protocol showed that MSR reduces cathode stresses: 10% reduction in maximum cathode stress (MSR 80%) and 18% reduction in maximum cathode stress (MSR 70%). Based on these insights, the modeling study identified a new “modified material-stress reduction” (MMSR) profile that reduces both Li plating and cathode stress. For achieving 70% Δ SOC in 10 minutes, MMSR reduces cathode stress by 18% as compared to the previous MSR protocol and avoids Li plating as well. The team hopes to validate these results in Phase II of the XCEL Program.

Evaluate XFC Effects on Particles and Microstructures, Identify Improvement Needs, and Explore Synthesis Approaches

The surface of the polycrystalline (PC)-NMC secondary particles could terminate with a variety of crystalline facets that are not optimized for Li-transport, causing prolonged Li⁺ diffusion pathways and non-uniform Li concentration inside the secondary particles. There could be several ways to minimize the stress and strain. Here, LBNL experimentally evaluates two approaches to address these issues in fast charging NMC cathodes: (1) developing SC-NMCs with optimized surface to eliminate intergranular cracking and facilitate charge transport; and (2) optimizing the microstructure and surface of PC-NMCs to minimize strain/stress and cracking and improve Li⁺ diffusion.

An example of how single crystal (SC) surface design can impact cathode rate capability is demonstrated. SC-NMC532 samples were prepared using a molten-salt method. Figure IV.9.11a and Figure IV.9.11b show two particle morphologies typically obtained, platelet shaped—shown in Figure I.1.A.11a—and truncated-octahedron (T-Oct) shaped—shown in Figure IV.9.11b. Both samples have the same particle size of ~ 200 nm.

While the platelet sample has a predominating (001)-family surface, the T-Oct sample has a predominating (012)-family surface. Figure IV.9.11c compares their rate capability when cycled between 3–4.3 V in a coin cell half-cell with a Gen2 electrolyte. The delivered capacities were similar at a low current density of C/10; however, the T-Oct sample showed much better performance at higher rates. The improvement provides direct evidence on the importance of surface engineering. As (001) facets in the layered oxides are Li impermeable, reducing their presence on the surface is critical to achieve fast charging.

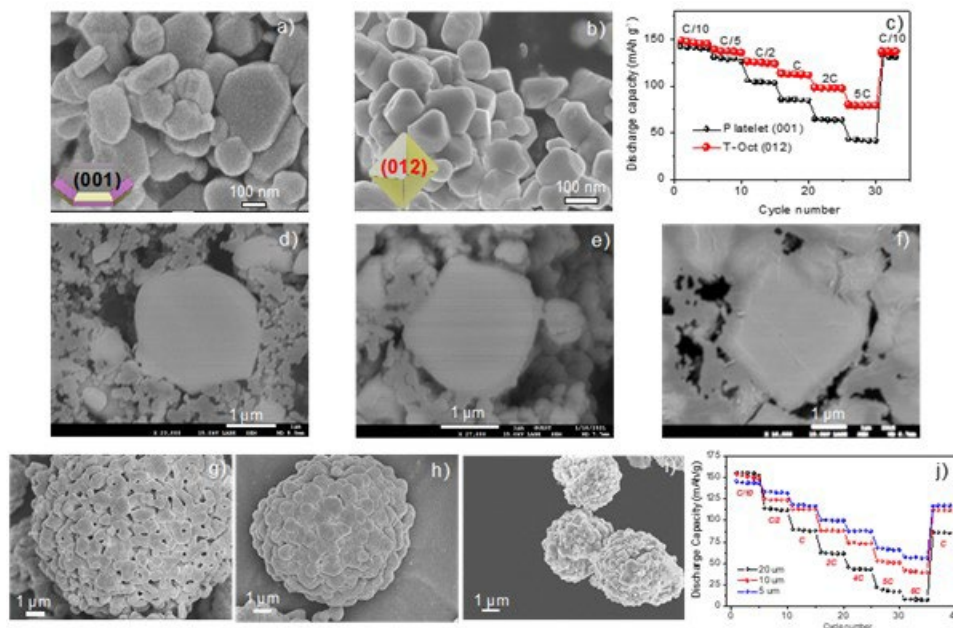


Figure IV.9.11 SEM images of synthesized SC-NMC532 with: (a) Platelet and (b) T-Oct morphologies. (c) Rate comparison of the SC-NMC532 cathodes. (d-f) Cross-sectional SEM images of SC-NMC811 particles collected after 300 cycles at 1C, 6C and 9C rates, respectively. SEM images of PC-NMC532 samples with a secondary particle size of: (g) 20 μm ; (h) 10 μm ; and (i) 5 μm ; respectively. (j) Rate comparison of the PC-NMC532 cathodes.

In the second approach, particle size, morphology, and surface at both primary and secondary particle levels are optimized to minimize strain/stress and cracking, and to improve Li^+ diffusion in PC-NMCs. As an example, we show how the size of PC secondary particles can impact fast-charge performance. A series of PC-NMC532 samples were obtained by first preparing the $\text{Ni}_{0.8}\text{Co}_{0.1}\text{Mn}_{0.1}(\text{CO}_3)_2$ intermediates using a hydrothermal method and then annealing them with a Li precursor at an elevated temperature. The size of final NMC secondary particles was mostly controlled by that of the intermediate, which can be tuned by changing the solvent ratio during the hydrothermal synthesis. Three representative PC-NMC532 samples with a particle size of 20, 10, and 5 μm are shown in Figure IV.9.11g through Figure IV.9.11i, respectively. All particles adopted a spherical shape, with the size and shape of the primary particles mostly maintained in the 20 and 10 μm -sized samples. In comparison, the size of the primary particles are relatively smaller in the 5 μm -sized samples. Figure IV.9.11j compares the rate capability when cycled between 3–4.3 V in a coin cell half-cell. Although the 5 μm -sized sample does not show obvious advantage at low current rate of C/10, it exhibits significant higher reversible capacities upon increasing current rates from C/2 to 6C. Meanwhile, when the rate is reduced back to 1C, the 5 μm particle cathode regained the high-capacity at the low C-rate, indicating excellent electrochemical stability. The improved electrochemical performance is likely a result of the decreased particle size, which not only better accommodates volume expansion/contraction, but also shortens the length for Li^+ solid phase diffusion and electron transport. The study suggests that modifying the microstructure in PC particles is a viable way to achieve a faster charging rate, as well as a longer cycle life, as observed in the microscopy image in Figure IV.9.11b. This new process effectively eliminates the need of using a molten-salt flux in our previous synthesis approach and reduces the manufacturing cost of SC-NMC cathodes.

Conclusions

During FY-21, the team of researchers at different national labs made several advances in understanding the implication of XFC on NMC cathodes (i.e., NMC532 and NMC811). In summary, two primary issues for the NMC cathodes under XFC conditions up to 9C are identified when the upper charge cutoff voltage is limited to 4.1V. They are particle cracking and surface-interphase issues. Between these two aging mechanisms, cracking is found to be more dominant. Higher surface-interphase issues at higher rates and cycles did not show a profoundly negative effect on performance, primarily because of limiting the charge voltage to 4.1V. The extent of those two aging mechanisms manifest differently for different variants of NMCs because of their inherent materials properties. The NMC532 showed distinct cathode aging in later cycling, whereas NMC811 was less affected by those aging mechanisms despite having a greater extent. Reducing charge cutoff voltage (e.g., 60 to 80% SOC), even at aggressive rates of 9C, were shown to have a beneficial effect on cell and cathode aging. Several pathways to further improve cathode performance have been identified. Among those, electrode composition optimization, particle size and microstructure optimization, alternate electrolyte, and cathode aging agnostic charging protocol could provide the most benefit in minimizing cell and cathode issues. As different solution pathways emerge that will enable exceeding 4.1V charge cutoff without lithium plating, the cathode aging issues should be re-evaluate as higher voltage would distinctly aggravate both cracking and surface issues. Bringing additional characterization and modeling techniques, as well as refining the existing ones developed in Phase I, would continue to play a key role in providing fundamental insights into the overall aging phenomena of LiB and its building blocks.

Key Publications

1. T.R.Tanim, P.J. Weddle, Z. Yang, A. Colclasure, H. Charalambous, D. P. Finegan, Y. Lu, M. Preefer, S. Kim, J. M. Allen, F. L. E. Usseglio-Viretta, P. R. Chinnam, I. Bloom, E. J. Dufek, K. Smith, G. Chen, K. M. Wiaderek, J. Nelson Weker, and Y. Ren, Enabling Extreme Fast-Charging: Challenges at the Cathode and Mitigation Strategies, in prep.
2. Z. Yang, H. Charalambous, Y. Lin, S. E. Trask, L. Yu, J. Wen, A. N. Jansen, Y. Tsai, K. M. Wiaderek, Y. Ren, and I. Bloom, Extreme fast charge aging. I-Correlation between electrode scale and heterogeneous degradation from bulk to surface in Ni-rich layered cathodes, in prep.
3. L. E. Usseglio-Viretta, A.M. Colclasure, A. Dunlop, S. E. Trask, A.N. Jansen, D. P. Abraham, M. F. Rodrigues, E. J. Dufek, T. R. Tanim, K. Smith, Carbon-binder weight loading optimization for improved lithium-ion battery rate capability, in prep.
4. E. McShane, P. Paul, T.R. Tanim, C. Cao, A. R. Dunlop, A.N. Jansen, E. J. Dufek, M. F. Toney, J. Nelson Weker, and B. McCloskey, Multimodal insights into degradation pathways during extreme fast charging of lithium-ion batteries, in prep.
5. O. Furat, D. P. Finegan, Z. Yang, T. Kirstein, V. Schmidt, Super-resolving microscopy images of Li-ion electrodes for fine-feature quantification using generative adversarial networks, under review (2021).
6. T. R. Tanim, Z. Yang, D.P. Finegan, P. R. Chinnam, Y. Lin, P. Weddle, I. Bloom, A. M. Colclasure, E. J. Dufek, J. Wen, Y. Tsai, M. C. Evans, K. Smith, J. M. Allen, C. C. Dickerson, A. Quinn, A. R. Dunlop, S. E. Trask, and A. N. Jansen, A comprehensive understanding of the aging effects of extreme fast charging on high Ni NMC cathode, submitted (2021)
7. Y. Lu, T. Zhu, E. McShane, B. D. McCloskey and G. Chen, Single-Crystal $\text{LiNi}_x\text{Mn}_y\text{Co}_{1-x-y}\text{O}_2$ Cathodes for Extreme Fast Charging, under review (2021).
8. K. Smith, P. Gasper, A.M. Colclasure, Y. Shimonishi, S. Yoshida, Lithium-Ion Battery Life Model with Electrode Cracking and Early-Life Break-in Processes, J. Echem. Soc., 168 (2021) 100530

9. T. R. Tanim, Z. Yang, A. M. Colclasure, P. R. Chinnam, P. Gasper, S. Son, P. J. Weddle, E. J. Dufek, I. Bloom, K. Smith, C. C. Dickerson, M. C. Evans, A. R. Dunlop, S. E. Trask, B. J. Polzin, A. N. Jansen, Extended cycle life implications of fast charging for lithium-ion battery cathode, *Energy Storage Materials*, 41 (2021) 656-666. DOI: 10.1016/j.ensm.2021.07.001
10. P.R. Chinnam, A.M. Colclasure, B.-R. Chen, T. R. Tanim, E. J. Dufek, K. Smith, M. C. Evans, A. R. Dunlop, S. E. Trask, B. J. Polzin, and A. N. Jansen, Fast-Charging Aging Considerations: Incorporation and Alignment of Cell Design and Material Degradation Pathways, *ACS Appl. Energy Mater.* 9 (2021) 9133-9143
11. A. Quinn, H. Moutinho, F. Usseglio-Viretta, A. Verma, K. Smith, M. Keyser, and D.P. Finegan, Electron backscatter diffraction for investigating lithium-ion electrode particle architectures, *Cell Reports Physical Science*, 1(8) (2020) 100137
12. O. Furat, D.P. Finegan, D. Diercks, F. Usseglio-Viretta, K. Smith, and V. Schmidt, Mapping the architecture of single electrode particles in 3D using electron backscatter diffraction and machine learning segmentation, *J Power Sources*, 483 (2021) 229148
13. J.M. Allen, P.J. Weddle, A. Verma, A. Mallarapu, F. Usseglio-Viretta, D.P. Finegan, A.M. Colclasure, W. Mai, V. Schmidt, O. Furat, D. Diercks, T.R. Tanim, and K. Smith, Quantifying the influence of charge rate and cathode-particle architectures on degradation of Li-ion cells through 3D continuum-level damage models, *J Power Sources*, 512 (2021) 230415
14. H. Charalambous, D.P. Abraham, A.R. Dunlop, S.E. Trask, A.N. Jansen, T.R. Tanim, P.R. Chinnam, A.M. Colclasure, W. Xu, A.A. Yakovenko, O.J. Borkiewicz, L.C. Gallington, U. Ruett, K.M. Wiaderek, and Y. Ren, Revealing causes of macroscale heterogeneity in lithium-ion pouch cells via synchrotron X-ray diffraction, *J Power Sources*, 507 (2021) 230253
15. P.P. Paul, V. Thampy, C. Cao, H.-G. Steinrück, T.R. Tanim, A.R. Dunlop, E.J. Dufek, S.E. Trask, A.N. Jansen, M.F. Toney, and J. Nelson Welker, Quantification of heterogeneous, irreversible lithium plating in extreme fast charging of lithium-ion batteries, *Energy and Environmental Science*, 14 (2021) 4979–4988

References

1. T.R. Tanim, E.J. Dufek, M. Evans, C. Dickerson, A.N. Jansen, B.J. Polzin, A.R. Dunlop, S.E. Trask, R. Jackman, I. Bloom, Z. Yang, E. Lee, Extreme Fast Charge Challenges for Lithium-Ion Battery: Variability and Positive Electrode Issues, *J. Electrochem. Soc.* 166 (2019) A1926–A1938.
2. H.-J. Noh, S. Youn, C.S. Yoon, Y.-K. Sun, Comparison of the structural and electrochemical properties of layered Li[NixCoyMnz]O2 ($x = 1/3, 0.5, 0.6, 0.7, 0.8$ and 0.85) cathode material for lithium-ion batteries, *J. Power Sources*. 233 (2013) 121–130.
3. T.R. Tanim, Z. Yang, A.M. Colclasure, P.R. Chinnam, P. Gasper, Y. Lin, L. Yu, P.J. Weddle, J. Wen, E.J. Dufek, I. Bloom, K. Smith, C.C. Dickerson, M.C. Evans, Y. Tsai, A.R. Dunlop, S.E. Trask, B.J. Polzin, A.N. Jansen, Extended cycle life implications of fast charging for lithium-ion battery cathode, *Energy Storage Mater.* 41 (2021) 656–666. <https://doi.org/10.1016/j.ensm.2021.07.001>.
4. W. Li, X. Liu, Q. Xie, Y. You, M. Chi, A. Manthiram, Long-Term Cyclability of NCM-811 at High Voltages in Lithium-Ion Batteries: an In-Depth Diagnostic Study, *Chem. Mater.* 32 (2020) 7796–7804.

5. S.-K. Jung, H. Gwon, J. Hong, K.-Y. Park, D.-H. Seo, H. Kim, J. Hyun, W. Yang, K. Kang, Understanding the Degradation Mechanisms of $\text{LiNi}_{0.5}\text{Co}_{0.2}\text{Mn}_{0.3}\text{O}_2$ Cathode Material in Lithium-Ion Batteries, *Adv. Energy Mater.* 4 (2014) 1300787.
6. R. Jung, M. Metzger, F. Maglia, C. Stinner, H.A. Gasteiger, Oxygen Release and Its Effect on the Cycling Stability of $\text{LiNi}_x\text{Mn}_y\text{Co}_z\text{O}_2$ (NMC) Cathode Materials for Li-Ion Batteries, *J. Electrochem. Soc.* 164 (2017) A1361–A1377.
7. O. Furat, L. Petrich, D.P. Finegan, D. Diercks, F. Usseglio-Viretta, K. Smith, V. Schmidt, Artificial generation of representative single Li-ion electrode particle architectures from microscopy data, *Npj Comput. Mater.* 7 (2021) 105.
8. P. Yan, J. Zheng, M. Gu, J. Xiao, J.-G. Zhang, C.-M. Wang, Intragranular cracking as a critical barrier for high-voltage usage of layer-structured cathode for lithium-ion batteries, *Nat. Commun.* 8 (2017) 14101.

Acknowledgements

This work was supported by efforts of the following individuals: Andrew N. Jansen, Bryant J. Polzin, Alison R. Dunlop, Stephen E. Trask, Zhenzhen Yang, Ira Bloom, Harry Charalambous, Kamila Wiaderek, Yang Ren, Uta Ruett, Kandler Smith, Donal Finegan, David Diercks, Orkun Furat, Volker Schmidt, Jeffrey Allen, Ankit Verma, Peter Weddle, Anudeep Mallarapu, Francois Usseglio-Viretta, Andrew Colclasure, Paul Gasper, Johanna Nelson Weker, Molleigh Preefer, Partha P. Paul, Michael Toney, Guoying Chen, Tanvir R. Tanim, Bor-Rong Chen, Parameswara R. Chinnam, Sangwook Kim, Eric J. Dufek, Michael F. Evans, and Charles C. Dickerson.

We gratefully acknowledge support from the U.S. Department of Energy—Office of Energy Efficiency and Renewable Energy (DOE-EERE), Vehicle Technologies Office (VTO).

IV.10 XCEL R&D: Heat Generation Thrust

Matthew Keyser, Principal Investigator

National Renewable Energy Laboratory
15013 Denver West Parkway
Golden, CO 80401
E-mail: Matthew.Keyser@nrel.gov

Samm Gillard, DOE Technology Development Manager

U.S. Department of Energy
E-mail: Samuel.Gillard@ee.doe.gov

Start Date: October 1, 2020
Project Funding (FY21): \$225,000

End Date: September 30, 2021
DOE share: \$225,000

Non-DOE share: \$0

Project Introduction

The 2022 U.S. Department of Energy's (DOE's) battery goals of 350 Wh/kg, 1,000 Wh/L, and \$150/kWh_(useable) require battery packs that have higher energy densities, resulting in a very compact system. To meet the specific energy goal, the electrode thickness of the battery will need to increase while decreasing the thickness of the current collectors. Furthermore, the amount of electrochemically inactive material, such as binders, will need to decrease. All of these factors will have a deleterious effect on the thermal performance of the cell. Furthermore, many of the advanced chemistries being developed to attain these goals, such as silicon and lithium metal anodes along with high-energy cathodes, have heretofore suffered from low efficiencies at low to moderate charge and discharge rates. Even if the energy efficiency of the next generation of batteries increases, more heat is being generated per unit volume with a smaller heat transfer area because of the compactness of these batteries. Thus, combining the heat transfer limitations associated with advanced chemistries with XFC will challenge the battery designers to keep the battery temperatures in the "Goldilocks" zone that prevents acceleration of the aging mechanisms within the battery while limiting the cycle life cost. Our working group is working to identify the critical parameters associated with heat generation and developing techniques to quantify temperature gradients within the cell.

Objectives

The battery thermal performance is critical to the life, cost, performance, and safety of energy storage systems. As such, the objectives of this workgroup are:

- Provide feedback to DOE on the battery thermal challenges associated with XFC.
- Understand temperature nonuniformity within cell during XFC.
- Develop techniques for operando interior temperature measurements.
- Identify limitations of using high specific energy density cells.
- Identify thermal areas of concern with existing battery systems.
- Identify how changes to the battery chemistry and cell design affect the cells' efficiency and performance.
- Identify state-of-the-art thermal management strategies and how these can be applied to future battery electric vehicles.

Approach

Develop a 1D/3D model capable of assessing heterogeneities, heat transport, and strategies to mitigate temperature rise under XFC conditions. We developed a 1-D model to explore the critical parameters associated with heat generation within a representative pouch cell for an EV. The study performed was not exhaustive, but an executive summary of the major findings is given below.

- A 100-kW-hr battery would produce 50 kW of heat during 10-minute charge, with significant amount of heat being from li-ion transport/conduction within electrolyte phase using current Gen2 formulation.
- For every 1.0 kW of heat generated during a 10-minute charge, the adiabatic temperature of the cell will rise a corresponding 1.3°C.
- If the allowable temperature rise of the cell is 20°C during charge, then 35 kW of heat must be removed to prevent the cell from exceeding the maximum operational temperature of the cell. A thermal management system of this size is substantially larger than what is in present EVs.
- Temperature difference from top to bottom of a pouch cell is proportional to the number of layers squared (N^2).
- If cooling is only available from one face side, then capacity is likely limited to ~30 Ah.
- If cooling is available on both sides of the pouch cell, then 50–60 Ah cells could be used.
- Large amounts of heat can be removed via tab cooling. However, the temperature difference between the center and edge of layers becomes large when >20% of heat is removed through tabs.
- Voltage drop across cell from lateral current conduction is proportional to the square of the cell length (L^2).
- Using existing 10- and 15-micron copper and aluminum foils, respectively, would limit cell length to 15 cm to prevent a large temperature spread/voltage change across the cell.
- Cells up to 23 cm in length could be made if the current collector thickness was doubled. However, the cell energy density would be reduced from 230 to 210 Wh/kg.

The 1-D model gave us direction but not the required fidelity. Thus, we utilized an ANSYS/Fluent modeling framework developed under the DOE computer aided engineering for battery (CAEBAT) program. The semi-empirical Newman, Tiedemann, Gu, Kim (NGTK) electrochemical model is suitable for thermal modeling of battery cells under constant current charge/discharge conditions. The high computational efficiency of the model allowed us to vary the numerous cell parameters to assess the temperature differences within a cell and module. The model was used to investigate temperature heterogeneities for:

- Various cooling strategies—air, liquid, and active.
- Different tab designs—opposing tabs, large/small, “standard” tab.
- Alternative electrolytes proposed by the XCEL electrolyte team to increase heat transport and ionic conductivity while limiting lithium plating.
- Cell sizes between 20 and 60 Ah with an areal capacity of greater than 3.5 mAh/cm² for the anode.
- Various cell length/width ratios.
- Impact on cell life/degradation.

Finally, temperature inhomogeneity is often hypothesized to be a culprit in observed inhomogeneous degradation such as local Li plating, local state-of-charge variation, local and solid electrolyte interphase (SEI) thickness variation. Thus, the workgroup has focused on the following techniques to assess the internal temperature of a battery and understand the methods to improve the thermal performance under extreme fast charging conditions.

- Place a resistance thermal device (RTD) into an electrochemically active cell.
- Use differential electrochemical mass spectrometry to assess the performance of XCEL developed electrolytes at higher temperatures.
- Use an inverse calorimetry measurement technique to assess the internal temperature of a battery.
- Experimented with additives to improve the thermal conductivity of the electrolyte to remove heat generated during extreme fast charging.

Results

Develop a 3D model that is capable of evaluating heterogeneities, heat transport, and strategies to control temperature rise under XFC conditions. (NREL)

In FY21, NREL's efforts have been focused on cooling techniques to mitigate heterogeneity and inhomogeneous lithium plating and understanding how battery size amplifies these conditions. For large EV cells, multiple-sided or immersion cooling demonstrate effectiveness of significant heterogeneity reduction. Fast charge differences between small Round 2 32 mAh Cells and 25 Ah and 40.8 Ah large cells used in vehicles was elucidated by incorporating electrochemistry into a 3D cell model. NREL's validated 1D fast charge control model was upscaled to 3D to address nonhomogeneous lithium plating with a large size cell. The model predicts that uneven cell cooling during fast charging may trigger early onset of lithium plating in the lower temperature regions of the cell.

To suppress temperature and charge heterogeneity, multiple-sided cooling with cold plates and liquid immersion cooling were evaluated using a semi-empirical electrochemical-thermal model. Compared with bottom cooling, cooling at both bottom and top surfaces reduced temperature and SOC differences within a 3P2S module by about 10°C and 4%, respectively, at the end of 6C fast charging. With additional tab cooling, the SOC difference was further reduced by 3%. This is because the maximum temperature difference occurred between active materials close to tab and active materials close to bottom cooling surfaces. Tab cooling works as spot cooling, directly control temperature of electrode close to the tab.

Liquid immersion cooling is also effective to mitigate cell temperature heterogeneity. Modeling of this cooling using 3M Novec 7500 engineering fluid was carried out by integrating the electrochemical-thermal model with computational fluid dynamic models. With natural convection immersion cooling, SOC and temperature difference of the 25 Ah cell maintained less than 5% and 5°C, respectively, during 6C charging. By combining this passive approach with external single-sided bottom cooling, cell temperature heterogeneity was not provoked, as shown in Figure IV.10.1. This indicates the hybrid cooling approach promising for both temperature rise and heterogeneity control. Similar control results can be achieved with forced convection immersion cooling. Its performance is however affected by a few design factors, such as liquid inlet temperature, direction, and cell-to-cell spacing, etc.

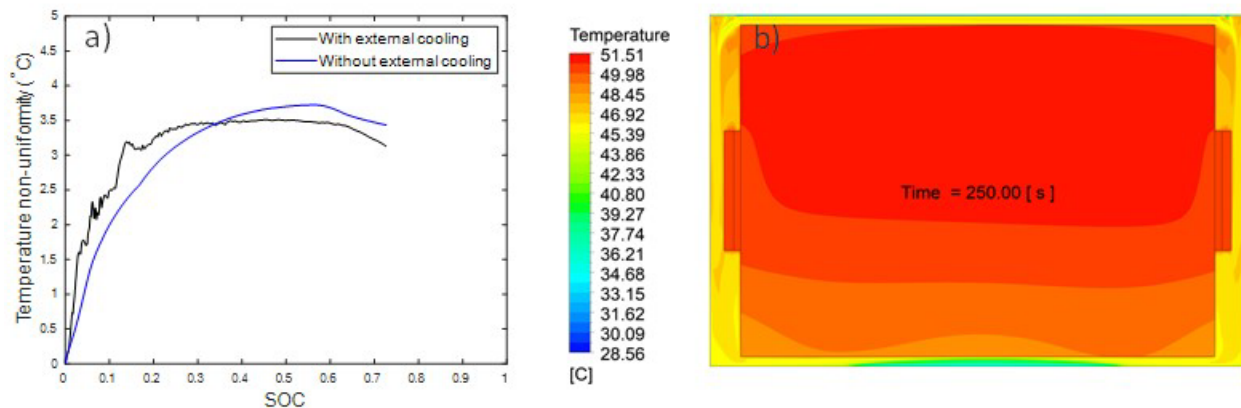


Figure IV.10.1 Cell temperature distributions under immersion cooling versus immersion cooling with external cooling a) Temperature non-uniformity histories; (b) Transient temperature contour for the cell under combined immersion and external cooling.

To address the effects of cell sizes on cell temperature heterogeneity, a larger size pouch cell, having a capacity of 40.8 Ah, was compared to the 25 Ah cell used in previous simulations. Like the 25 Ah cells, charge heterogeneity of the 40.8 Ah cell was negligible along cell thickness direction. However, charge heterogeneity was considerably provoked in plane because of longer tab distances and larger temperature non-uniformity. Further simulations confirm that multiple-sided cooling is also effective to mitigate temperature and charge heterogeneities for this larger size pouch cell. Furthermore, a round 2 32 mAh cell was compared with the 40.8 Ah cell to understand differences between small test cells and large cells used in vehicles. Under adiabatic conditions, the temperature of the small cell under test was maintained nearly constant and exhibited negligible temperature and SOC difference because of heat absorption by large thermal mass of testing accessories. As a result, cell was charged less than 20% with a 6C rate at 20°C. Charge performance of a large 40.8 Ah cell was significantly improved due to self-heating. Though thermal mass of its packaging components is less than that of the small testing cell, they create considerable temperature and charge differences within the cell. Considering overcooling at early stage of fast charging may provoke cell heterogeneity, it is worthwhile to encourage self-heating at early stage of fast charging and introduce limited EV cooling subsequently.

To address effects of temperature and charge heterogeneities on cell life and safety, a fast charge P2D model validated with Round 2 Graphite/NMC532 cells was upscaled to 3D for spatial estimation of lithium plating in the 40.8 Ah cell. Due to the large computational burden of 3D P2D modeling, cell mesh size was limited to be around 100 elements. As such, mesh grids were distributed directionally to capture cell non-uniformity. By comparing 4C charge with and without single-sided surface cooling, the 3D model confirmed that low cell temperature could lead to lithium plating before the cell reached the charge cut off voltage. Additionally, lithium plating occurred first at lower temperature areas of the cell, as illustrated in Figure IV.10.2. Cooler areas have lower electrolyte concentrations, resulting in lower charge acceptance and earlier lithium plating.

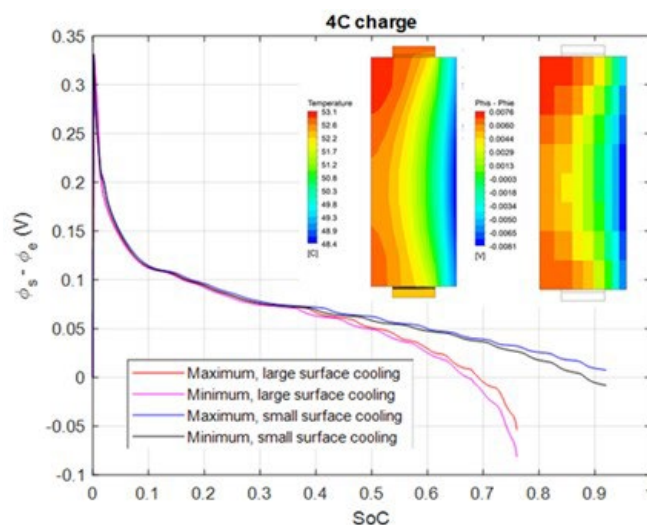


Figure IV.10.2 Maximum and minimum lithium plating potentials within the 40.8 Ah cell under 4C charging with single-sided cooling.

Inverse Calorimetry (LBL)

Prasher group has developed an iterative inverse calorimetry approach based on thermal properties (thermal conductivity and specific heat), boundary temperature, and heat flux measurements to reconstruct the real time heat generation rate during the operation of a battery. This method corrects for the thermal lag due to the poor thermal conduction across the battery and improves upon previous calorimetry approaches such as the lumped capacitance (uniform temperature) approach to give a more accurate time resolved heat generation information, especially significant in high energy density batteries.

The inverse calorimetry approach uses an iterative scheme to solve the heat generation rate and the temperature field simultaneously based on the boundary temperature and heat flux measurement. To verify the approach, we assembled two dummy cells (one cylindrical and one prismatic) with resistive heating elements to create a known heat generation rate according to a known time varying current. We measured the heat flux and the boundary temperature for both dummy cells and reconstructed the heat generation rate using the inverse approach and the more traditional lumped capacitance calorimetry approach.

As seen from Figure IV.10.3 (c) and (d), results show that the inverse approach can recover the original heat generation rate while traditional calorimetry approaches that rely on surface heat flux and temperature measurement underpredict the heat generation rate.

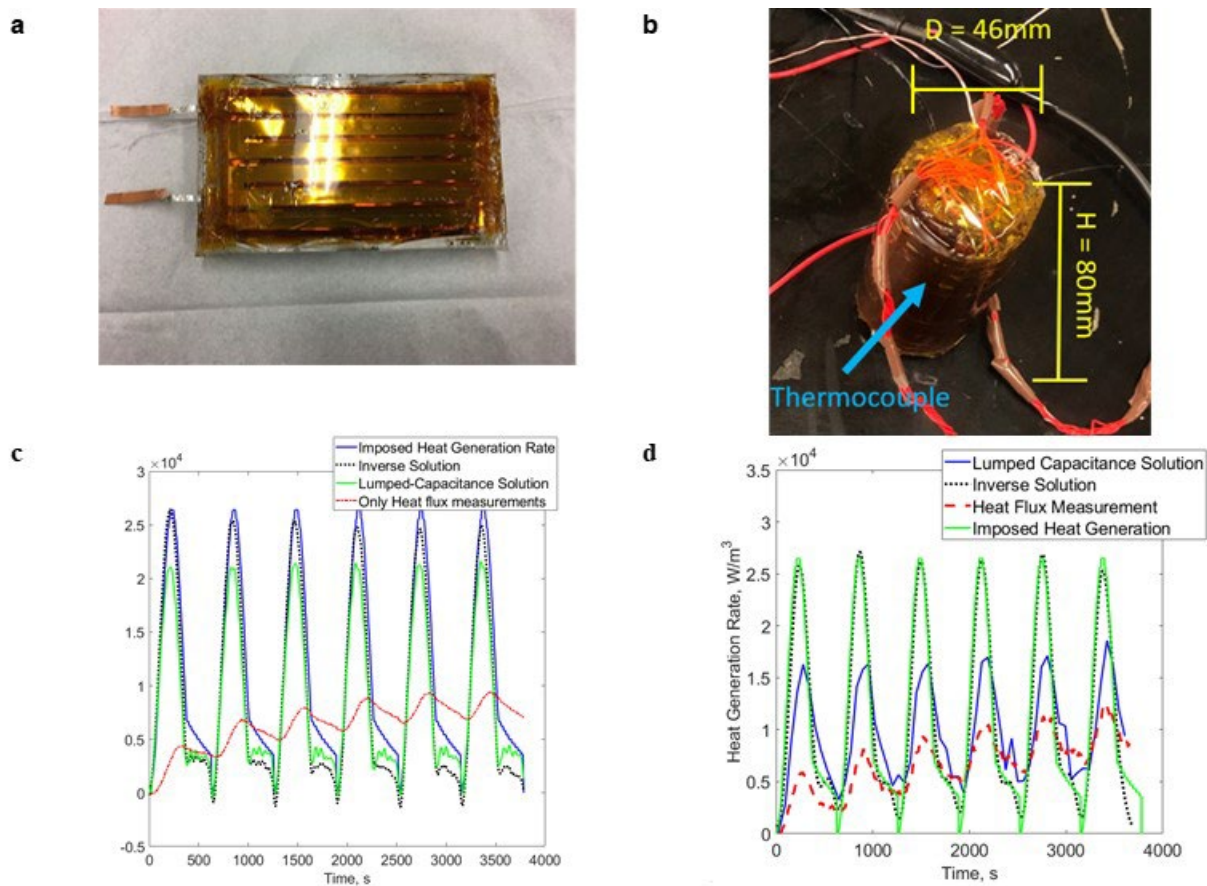


Figure IV.10.3 **a)** Dummy prismatic cell; **b)** dummy cylindrical cell; the reconstructed heat generation rate compared against the known (imposed) heat generation rate for prismatic **(c)** prismatic and cylindrical **(d)** cells. Source: Sean Lubner, LBL.

Additionally, the cylindrical dummy cell also had a thermocouple embedded in the center of the cell. While passing the time varying current, we measured the temperature with the embedded thermocouple and compared it against the internal temperature reconstructed from the heat generation rate given by different calorimetry approaches. As shown in Figure IV.10.4, using the heat generation rate from the inverse calorimetry, we were able to reconstruct the internal temperature more accurately than that from the lumped capacitance method, emphasizing the importance of accurate calorimetry for accurate internal temperature prediction.

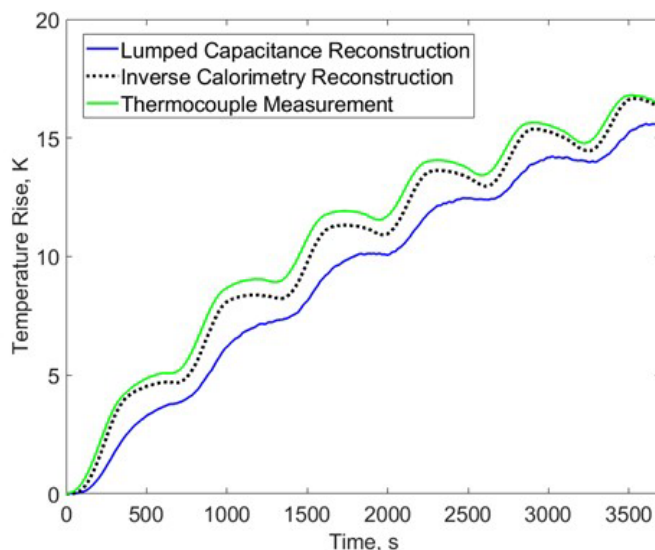


Figure IV.10.4 Internal temperature of the cylindrical dummy cell reconstructed from the heat generation rate measured using the inverse calorimetry approach and the lumped capacitance approach compared against the actual temperature measurement using an embedded thermocouple. The inverse approach can reconstruct the internal temperature more accurately than the traditional lumped capacitance approach. Source: Sean Lubner, LBL.

In summary, we have developed a method to reconstruct the real time battery heat generation rate during XFC. Our approach corrects for the thermal lag due to the poor thermal conduction across the battery and improves upon previous calorimetry methods such as the lumped capacitance (uniform temperature) approach to give a more accurate time resolved heat generation information, especially significant in high energy density batteries during XFC.

Improving the electrolyte thermal conductivity for efficient heat transfer inside batteries

Prasher group performed 3ω measurements to quantify the impact of the thermal conductivity of electrolyte on the effective thermal conductivity of batteries. We studied the effective thermal conductivity of battery unit cells with different fluids, *i.e.*, air, IPA, and the mixture of water and IPA (1:1 based on volume). These fluids were chosen for a proof of principle study because they vary significantly in k , while fully wetting the porous battery layers. Figure IV.10.5a shows the raw data of our 3ω measurements for the unit cells. As the thermal conductivity of the liquid increases, the effective thermal conductivity of the unit cell increases significantly (see Figure IV.10.5b), *e.g.*, 0.19 W/m-K for the dry unit cell and 0.37 W/m-K for the unit cell with the mixture of water and IPA. The enhanced effective thermal conductivity was attributed to the significant decrease of the thermal contact resistance between the electrodes and separator along with the increased fluid thermal conductivity (see Figure IV.10.5c). Our experimental study suggests an effective approach to improve the effective thermal conductivity of batteries using the electrolyte with a high thermal conductivity. From the literature, it is possible to improve the thermal conductivity of fluids using nanoparticle additives. We measured the thermal conductivity of alumina-based nanofluids using hot disk. Figure IV.10.5d demonstrates no statistically significant enhancement to the thermal conductivity of IPA with alumina nanoparticle additives. As our study highlights the role of the electrolyte thermal conductivity in improving the battery thermal conductivity, it is worth exploring other approaches to improve the electrolyte thermal conductivity and thus the effective thermal conductivity of batteries.

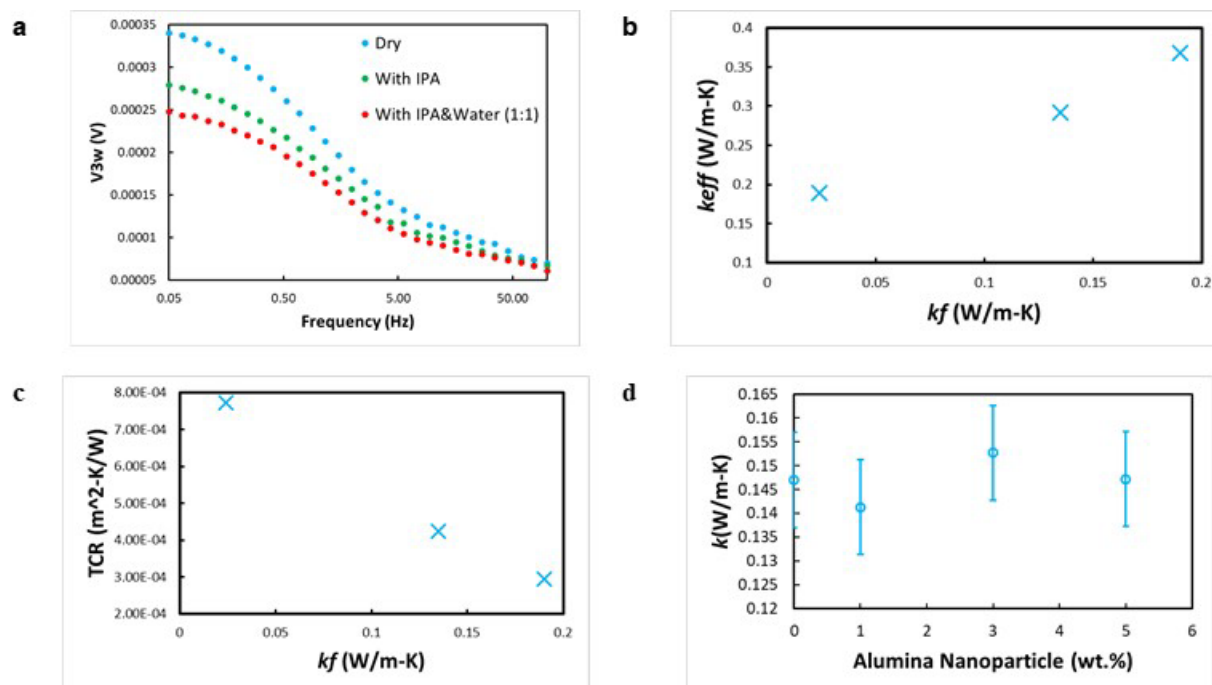


Figure IV.10.5 a) The raw 3ω data of battery unit cells with different fluids; b) measured effective cell thermal conductivity when filled with fluids or fluid mixtures of varying thermal conductivity; c) measured electrode-separator thermal contact resistance in the unit cell with the same fluids; d) the thermal conductivity of IPA with varying concentrations of alumina nanoparticles added. Source: Sean Lubner, LBL.

We have investigated the role of the electrolyte thermal conductivity in the effective thermal conductivity of batteries. Our results indicate that the effective thermal conductivity of batteries can be significantly enhanced using high thermal conductivity electrolyte. However, we found that alumina nanoparticle additives did not effectively enhance the thermal conductivity of liquids with similar k as electrolytes. Improving the electrolyte thermal conductivity can enhance battery heat transfer and achieve a more uniform temperature distribution across the battery.

Battery Diagnostic with RTDs under Extreme Fast Charging Conditions (Stanford)

In 2020, we developed a single resistive temperature detector (RTD) to monitor the temperature on LIBs under extreme fast charging conditions. The challenge of this project is the stabilization of RTDs in the nonaqueous electrolyte environment within a relative wide temperature range. We built a pouch cell with RTD sensors both inside and outside the cell (Figure IV.10.6a,b). The battery was then cycled at different charge/discharge rates, while both electrochemical performance (Figure IV.10.6c, upper and middle panel) and RTD response (Figure IV.10.6c lower panel) are recorded. We were able to use the RTD for operando temperature measurements in batteries. While limited temperature responses can be observed at 0.5C rate with rather flat current response, significant resistance change can already be observed at 2C rate (both black and red curve in Figure IV.10.6c lower panel). However, we did not observe significant temperature difference between the inside and outside the cell even at 2C rate, due to the limited capacity (200 mAh) and fast heat dissipation of the cell.

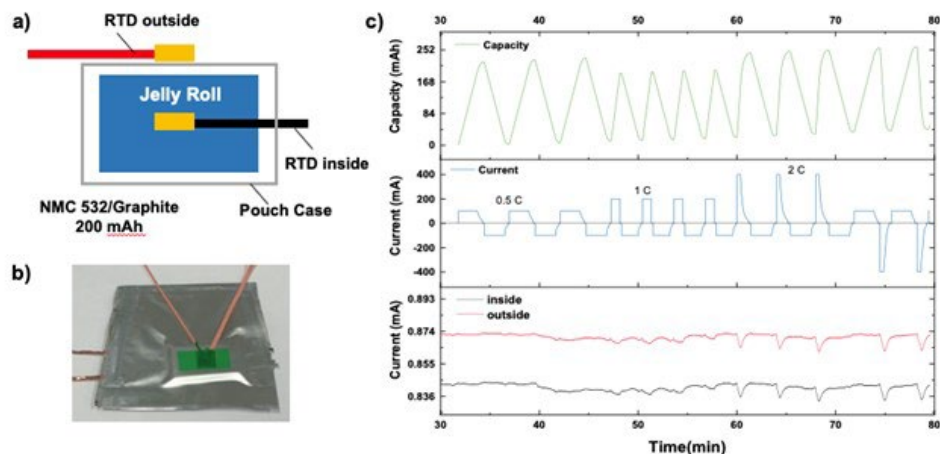


Figure IV.10.6 Operando Temperature monitoring using RTD in pouch cells (a) schematic image; (b) photo image of the cell; (c) electrochemical performance of the cell vs. RTD responses charging at different rates. Source: Stanford – Fang Liu

In 2021, we have been focused on the development of RTD arrays and their applications in 5 Ah large pouch cells under fast charging conditions. We customized a RTD array with 15 individual sensors with a resolution of 36 mm² (Figure IV.10.7a) and developed a software program to monitor their independent temperature and resistance change over time (Figure IV.10.7b). The RTD array can operate in a non-aqueous electrolyte environment at a temperature range of 20°C to 60°C.

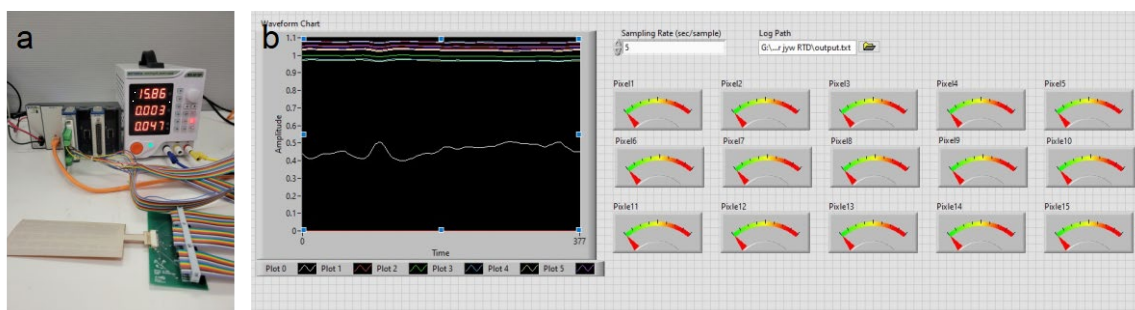


Figure IV.10.7 (a) Photo image of the data acquisition system and (b) Digital image of the user interface. Source: Stanford – Fang Liu

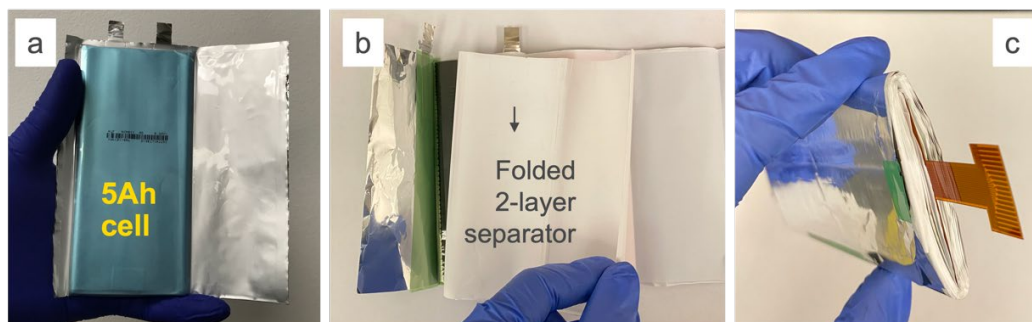


Figure IV.10.8 Photo of (a) 5Ah commercial pouch cell, (b) disassembled pouch cell, (c) pouch cell with RTD sensor inside. Source: Stanford – Fang Liu

During the last quarter, we have integrated the RTD arrays with a 5Ah NMC-G pouch cell (Figure IV.10.8a) to monitor its temperature evolution and distribution during extreme fast charging process. The flexible RTD array has been put in the middle of the pouch cell, sandwiched between 2-layers of separator (Figure IV.10.8b,c). Due to safety concerns, the electrochemical testing process are conducted in an inert gas

environment. To summarize, we have developed a RTD array for the onboard monitoring of temperature evolution and distribution of lithium-ion batteries under fast charging conditions. This device and associated software can be readily adopted by practical applications.

Operando Temperature Measurements in Pouch Cells (UC Berkeley)

The UC Berkeley group (Eric McShane and Bryan McCloskey) performed operando gassing measurements using differential electrochemical mass spectrometry (DEMS) at room temperature and at elevated temperature (40°C) to assess the effect of temperature on ethylene (C_2H_4) outgassing within the cell. C_2H_4 evolution is generally thought to coincide with ethylene carbonate (EC) reduction, which in turn deposits lithium ethylene dicarbonate (LiEDC) in the solid-electrolyte interphase (SEI) on graphite. The results of the DEMS study are summarized in Figure IV.10.9. Comparing Figure IV.10.9a and Figure IV.10.9c, one notices that at room temperature, there is less C_2H_4 gas evolved (measured via the C_2H_2 fragment ion, $m/z=26$) for the B26 electrolyte compared to the standard Gen2 electrolyte. This is likely because the fluoroethylene carbonate and vinylene carbonate additives used in the B26 formulation are reduced before EC during the initial C/10 formation cycle, creating a stable SEI that prevents substantial EC reduction. Additionally, comparing Figure IV.10.9b and Figure IV.10.9d, we observe increased C_2H_4 evolution at elevated temperature for the Gen2 electrolyte, but little change in the amount of C_2H_4 evolution is observed at elevated temperature for the B26 electrolyte. This suggests that the B26 electrolyte may be well-suited for elevated temperature applications, as the LiEDC layer thickness on the graphite electrode remains a consistently low even at elevated temperature, while the LiEDC layer grows significantly at elevated temperature when using the standard Gen2 electrolyte.

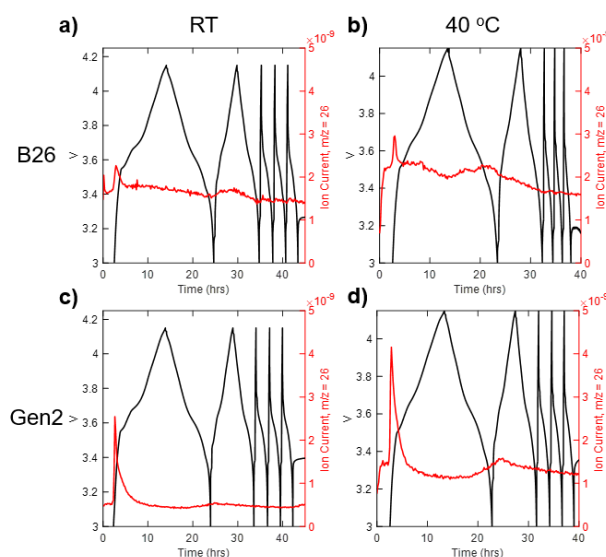


Figure IV.10.9 DEMS measurements of ethylene (C_2H_4) gas evolution measured via the C_2H_2 fragment ion ($m/z=26$) overlaid with cycling data for Round 2A graphite, Round 2 NMC 811 full cells with B26 (panels **a**, **b**) and Gen2 (panels **c**, **d**) electrolytes cycled with one C/10 cycle, one C/5 cycle, and three 2C charge-C/5 discharge cycles at room temperature (panels **a**, **c**) and 40 °C (panels **b**, **d**). Source: Eric McShane, UC Berkeley.

Conclusions

The heat generation workgroup has made significant progress towards understanding the crucial parameters that affect heat generation and how to measure temperature within a cell. During FY21, we used the pseudo 3D ANSYS/Fluent model to assess the temperature heterogeneities for different cell geometries and electrolytes. Furthermore, we successfully fabricated and tested the third generation RTD in a working 200 mAh cell. We also performed differential electrochemical mass spectrometry experiments to assess the gas generation of the electrolytes developed under the XCEL program. Finally, we developed an inverse calorimetry measurement technique to assess the internal temperature of a battery and we experimented with improving the thermal conductivity of the electrolyte to remove heat generated during extreme fast charging.

IV.11 Highly-Ordered Hierarchical Anodes for Extreme Fast Charging Batteries (University of Michigan, Ann Arbor)

Neil Dasgupta, Principal Investigator

University of Michigan, Ann Arbor
2350 Hayward Street
Ann Arbor, MI 48109
E-mail: ndasgupt@umich.edu

Jeff Sakamoto, Principal Investigator

University of Michigan, Ann Arbor
2350 Hayward Street
Ann Arbor, MI 48109
E-mail: jeffsaka@umich.edu

Katsuyo Thornton, Principal Investigator

University of Michigan, Ann Arbor
2300 Hayward Street
Ann Arbor, MI 48109
E-mail: kthorn@umich.edu

Jyoti Mazumder, Principal Investigator

University of Michigan, Ann Arbor
2350 Hayward Street
Ann Arbor, MI 48109
E-mail: mazumder@umich.edu

Mohan Karulkar, Principal Investigator

Sandia National Laboratories
1515 Eubank Drive SE, M/S 0613
Albuquerque, NM 87185
E-mail: mpkarul@sandia.gov

Brian Cunningham, DOE Technology Development Manager

U.S. Department of Energy
E-mail: Brian.Cunningham@ee.doe.gov

Start Date: July 1, 2018

End Date: June 20, 2021

Project Funding: \$1,667,000

DOE share: \$1,500,000

Non-DOE share: \$167,000

Project Introduction

The rapidly expanding electric vehicle (EV) market drives a strong need for fast charging capability of Li-ion batteries without sacrificing their power or energy density. Specifically, the capability of extreme fast charging (XFC) in <10 min is crucial for the batteries to be compatible with 400 kW charging stations [1]. XFC remains challenging for high energy density battery cells, because several fundamental challenges exist as the charging rate increases, including 1) electrolyte concentration gradients 2) kinetic overpotentials 3) metallic Li plating 4) excess heat generation and 5) accelerated electrolyte decomposition and capacity fade. In this way, it is necessary to innovate the design rules for XFC anode performance.

Objectives

The objective of the project is to enable XFC using on Li-ion cells in commercially relevant cell format. This is achieved via a combination of 1) rational design and manufacturing of hierarchically structured anode architectures; 2) computational modeling of coupled transport, kinetic, and electrochemical phenomena; and 3) improved fundamental understanding of lithium plating through electrochemical analysis. The unique facilities at the University of Michigan and Sandia National Lab are leveraged to manufacture, prototype, and characterize commercially relevant $> 2\text{Ah}$ and $> 180\text{ Wh/kg}$ cells with a target of charging at 6C rates with $< 20\%$ capacity fade over 500 cycles.

Approach

1. Overcoming the energy/power density tradeoff of anode active material by blending graphite/hard carbon into a bulk hybrid anode.
 - Tune the material composition of the hybrid anodes and characterize electrochemical performance.
 - Demonstrate scale-up of hybrid anodes to $> 2\text{ Ah}$ pouch cells.
 - Perform electrochemical dynamics simulations of hard carbon anodes during fast charging.
2. Engineering artificial solid-electrolyte interphase (SEI) coating with reduced interphase impedance.
 - Coat a single-ion conducting solid electrolyte ($\text{Li}_3\text{BO}_3\text{-Li}_2\text{CO}_3$) onto post-calendered graphite electrodes via atomic layer deposition (ALD).
 - Demonstrate 80% capacity retention under 15 minute (4C) fast-charging conditions after 500 cycles.
3. Improved fundamental understanding of lithium plating through *operando* video microscopy analysis.

Results

To study the effects on fast charging performance when blending graphite and hard carbon, five graphite/hard carbon blend ratios were investigated, namely, graphite/hard carbon = 100/0, 75/25, 50/50, 25/75, and 0/100 (weight ratios) [2]. The resulting hybrid anodes are described below as graphite, Gr-75, Gr-50, Gr-25, and hard carbon, respectively. For all studies described in this report, the anodes, including graphite and hybrid, have a capacity loading of 3 mAh cm^{-2} and a calendered porosity of 31–33%.

Scanning electron microscopy (SEM) was performed to examine the morphology of the prepared hybrid anodes. Figure IV.11.1 Top-down SEM images of the (a) graphite, (b) Gr-75, (c) Gr-50, (d) Gr-25, and (e) hard carbon anodes [2]. Figure IV.11.1a shows a top-down image of a graphite anode. The graphite particles have an ellipsoidal shape with an average particle size of $7.8\text{ }\mu\text{m}$. Figure IV.11.1e shows an image of the hard carbon anode. Compared to the graphite, hard carbon particles have a more isotropic shape. The hard carbon also displays a smaller average particle size of $3.3\text{ }\mu\text{m}$. For Gr-75 (Figure IV.11.1b), Gr-50 (Figure IV.11.1c), and Gr-25 (Figure IV.11.1d) hybrid anodes, the SEM images show that both graphite and hard carbon particles were homogeneously distributed.

To evaluate the fast-charge capability of composite anodes, a CC-CV charge protocol with a charge time cutoff was used. Pouch cells were first charged at a constant current (CC) 4C rate until reaching the upper voltage cutoff (4.2V), then charged at constant voltage (CV) until a total charge time (CC+CV) of 15 minute was reached. For the 6C charging protocol, the applied current was 6C and the total charge time was limited to 10 minutes. Throughout the fast-charge cycling, the discharge rate was fixed at 1C with a 2.7 V voltage cutoff and without any CV hold.

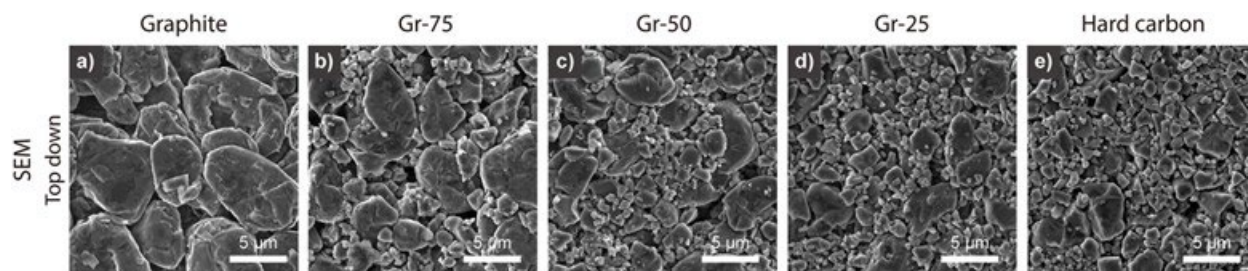


Figure IV.11.1 Top-down SEM images of the (a) graphite, (b) Gr-75, (c) Gr-50, (d) Gr-25, and (e) hard carbon anodes [2].

Figure IV.11.2a-b show the normalized capacity vs. cycle number plots at 4C (15-min) charge and 6C (10-min) charge, respectively. The y-axis is normalized to the first-cycle discharge capacity to facilitate a direct comparison of capacity fade among all pouch cells. During 4C fast-charge cycling (Figure IV.11.2a), the Graphite cell exhibits a significant capacity fade within the first 40 cycles. After 100 cycles, the capacity retention is only 66% (34% capacity fade). This decrease in cell capacity can be attributed to severe Li plating during fast charging. Gr-75 cell also displays a similar initial capacity fade (though to a smaller extent) during fast-charge cycling. The corresponding capacity retention after 100 cycles is 85% (15% capacity fade). In contrast, the Gr-50, Gr-25, and Hard carbon cells exhibit stable fast-charge cycling throughout the test. There is no capacity drop associated with Li plating during initial cycles, and the capacity retention after 100 cycles is as high as 96% (only 4% capacity fade). This result suggests that composite anodes with hard carbon content > 50 wt.% can effectively suppress Li plating during fast charging.

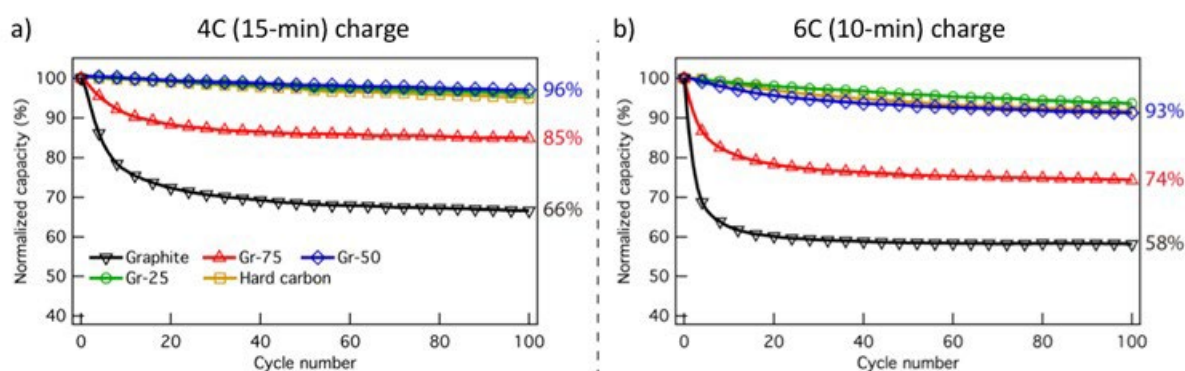


Figure IV.11.2 Normalized discharge capacity vs. cycle number plots during (a) 4C (15-min) and (b) 6C (10-min) fast-charge cycling [2].

Continuum-scale simulations were conducted to gain mechanistic insights for the improvement in rate performance of the hybrid anodes. Galvanostatic charging of the graphite, Gr-50, and hard carbon anodes at 4C charging were simulated (Figure IV.11.3). For the graphite anode (Figure IV.11.3a), it can be observed that the current density distribution becomes highly inhomogeneous after ~20 s of charging, with most of the reaction taking place in the region near the anode/separator interface. A highly inhomogeneous current distribution results in a large anode overpotential, thereby resulting in an earlier termination of the simulation. In contrast, the distribution of the reaction current density is much more uniform in the hard carbon anode during 4C charging (Figure IV.11.3c). This results in a smaller overpotential in the anode, which allows it to maintain current at a potential higher than 0 V for a longer time. By blending graphite and hard carbon, the resulting Gr-50 hybrid anode exhibits a significant improvement in the homogeneity of the current density distribution (Figure IV.11.3b), as compared to the graphite anode. For the graphite component, most of the reaction takes place in the region near the anode/separator interface, while for the hard carbon component, the reaction is distributed more uniformly. The hard carbon component contributes a large fraction of the current throughout the charging, and, as a result, reduces the load on the graphite component.

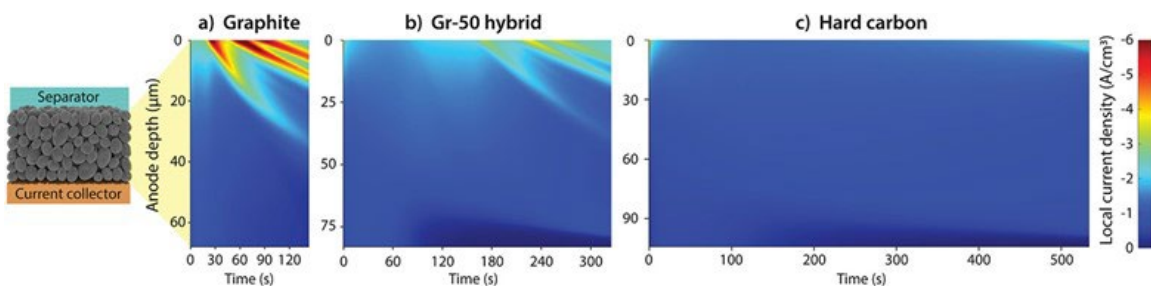


Figure IV.11.3 Evolution of the local reaction current density as a function of the position through the thickness of the (a) graphite, (b) Gr-50, and (c) hard carbon anodes during 4C charging. The schematic on the left of panel (a) shows the orientation of the anodes in the evolution plots. The top edge and the bottom edge of each evolution plot correspond to the anode/separator and anode/current collector interfaces, respectively [2].

Besides creating graphite-hard carbon hybrid electrode, we also studied the effect of applying an artificial SEI (a-SEI) layer on graphite electrodes for improving its fast charge performance [6]. In this study, ALD of $\text{Li}_3\text{BO}_3\text{-Li}_2\text{CO}_3$ (LBCO) was applied as the a-SEI, because it exhibits promising properties, including: 1) high ionic conductivity and low electronic conductivity; 2) homogeneous chemical composition; and 3) a wide electrochemical stability window [3].

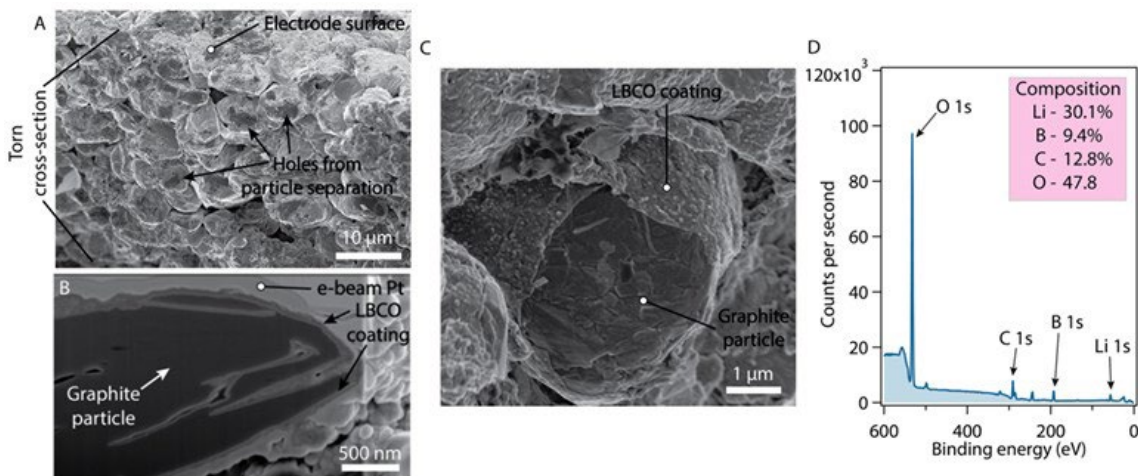


Figure IV.11.4 (a,c) Scanning electron micrographs of the LBCO-coated graphite anodes and (b) of a focused-ion beam cross-section through a coated graphite particle. (d) X-ray photoelectron spectroscopy survey scan and atomic composition of the surface of a coated electrode [6].

After deposition, the morphology and composition of the coating were characterized by SEM and X-ray photoelectron spectroscopy (XPS), respectively. SEM shows that the film conformally coats the graphite particles within the volume of the composite electrode (Figure IV.11.4 a and b). XPS result confirms that the composition indicates that the film is similar to the composition expected from our previous work [3]. Importantly, when the electrode was torn to create the SEM cross section shown in Figure IV.11.4 a and c, no film was observed at the exposed contact points between graphite particles. This reveals that particle-particle contact remains after deposition, which allows for electronic conduction through the thickness of the electrode.

Extended cycling with 4C fast charging was performed, where CC charging was applied until the cell voltage reached 4.2 V, followed by a CV hold until 15 minutes total time for the charging step had been reached. The remaining capacity at C/3 charge rate was checked every 50 cycles. Pouch cell performance data with uncoated graphite anodes (Control) and LBCO coated graphite anodes (LBCO) are shown in Figure IV.11.5. The Control cell exhibits rapid capacity fading in the first 20 cycles before stabilizing to a more linear capacity decline. The Coulombic efficiency (CE) of the Control cell also shows a dip during the first 10 cycles (Figure IV.11.5a). The

low CE during the first several cycles is attributed to Li plating during fast charging. This leads to a capacity retention of just 67.3% after 50 cycles of 4C charging. In comparison, the LBCO 250x retains more than 80% capacity throughout the 500-cycle test. This represents a greater than 40-fold increase in cycle life.

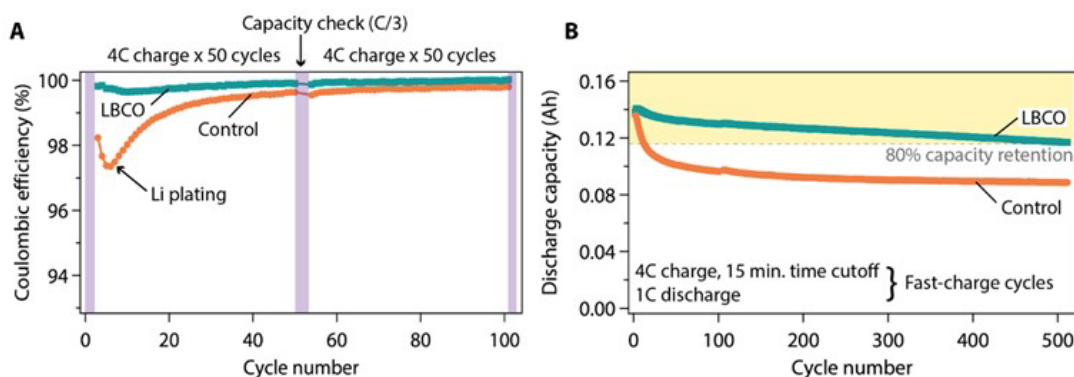


Figure IV.11.5. Extended cycling of NMC532/graphite pouch cells with and without LBCO coating. (a) Coulombic efficiency vs. cycle number plot. (b) Discharge capacity for 4C fast-charge cycles only. 80% line is based on initial fast-charge cycle [6].

Finally, in order to gain a mechanistic understanding of Li plating during fast charging, *operando* video microscopy was performed on a graphite electrode during 6C galvanostatic charging [5]. Before charging, the graphite potential was 0.4 V vs Li/Li^+ (Figure IV.11.6a and b). CC charging was performed until reaching a specific charge of 85 mAh g^{-1} . After the initiation of charging, the potential of the graphite WE dropped below 0V vs. Li/Li^+ at a time of $t = 8.5 \text{ s}$ (4.3 mAh g^{-1}). Furthermore, the potential continued to drop until $t = 104 \text{ s}$ (52 mAh g^{-1}) as the color of the graphite evolved from gray to blue and then to gold (Figure IV.11.6b-d).

Spatial heterogeneity was observed across the graphite surface during 6C charging. After 63 s (32 mAh g^{-1}), distinct blue (LiC_{18}), red (LiC_{12}) and gold (LiC_6) regions can all be observed on the electrode surface (Figure IV.11.6c). This demonstrates that individual particles lithiate at different rates, which could be caused by differences in crystallographic orientation, morphology, interfacial resistance, and size. The anode potential reached a minimum at 104s (52 mAh g^{-1}), and Li nucleation was observed in the first frame after this voltage minimum (Figure IV.11.6d). Li plating nucleates on the particles that turned gold first, even after adjacent particles have experienced an increase in their surface Li^+ concentration. This demonstrates that the particles associated with the lowest initial impedance for lithiation are also associated with the lowest impedance for nucleation. The Li deposits continue to grow during the remainder of the 6C charge (Figure IV.11.6e).

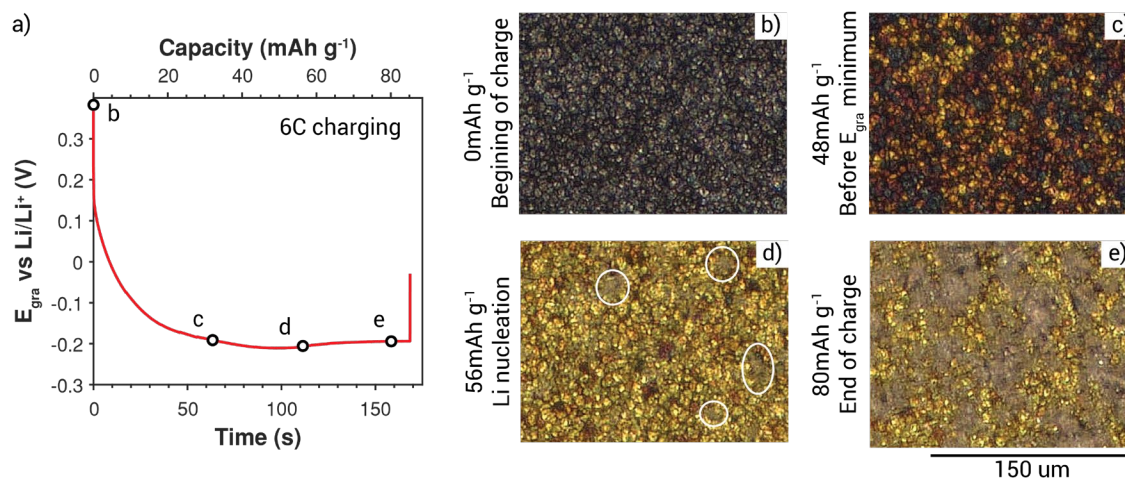


Figure IV.11.6 (a) Voltage profile of the graphite WE during 6C charging; (b – e) Still frames of the WE during 6C charging. Plated Li is circled in (d). The time and the voltage of graphite at each frame is labeled in (a) [5].

Conclusions

We demonstrated >4C fast charging of hybrid graphite/hard carbon anodes in industrially relevant multi-layer pouch cells (>1 Ah) with high-capacity loading (3 mAh cm⁻²). The graphite/hard carbon blending ratio was tuned to achieve the high-energy density while reducing Li plating. Using the Gr-50 anode, we have achieved pouch cell with 87% and 82% specific energy retention after 500 cycles of 4C and 6C fast-charge cycling, compared to 61% and 48% for cells using graphite anodes under the same conditions. Continuum-scale electrochemical simulations identified the origin of the enhanced fast-charge performance to be the improved homogeneity in reaction current distribution throughout the hybrid anode volume.

Furthermore, ALD of LBCO was used as an a-SEI on graphite, which led to a significant improvement in fast-charging performance without sacrificing the energy density. Multimodal characterization proved the conformality and the desired stoichiometry of the a-SEI. Pouch cell cycling result shows that the a-SEI led to a significant improvement in cycle-life to 80% capacity retention with a 4C (15-min.) charging protocol (500 cycles, compared to just 12 for the uncoated control).

Lastly, *operando* video microscopy was performed on calendared 3 mAh cm⁻² graphite electrodes to study the dynamic evolution of local state-of-charge (SoC) and Li plating during 6C fast charging. Visualization of the spatial heterogeneity of SoC and the nucleation and growth of Li filament shows that (1) Li plating preferentially nucleates on the graphite particles that lithiate fastest during fast charging; and (2) the onset of Li plating correlates with the local minimum of the graphite electrode potential.

Key Publications

1. K. H. Chen et al., *J. Power Sources*, **471**, 228475 (2020).
2. K. H. Chen et al., *Adv. Energy Mater.*, **11**, 200336 (2020).
3. Y. Chen et al., *J. Mater. Chem. A*, **9**, 23522–23536 (2021).
4. E. Kazyak, et al., *Adv. Energy Mater.*, **12**, 2102618 (2022).

References

1. S. Ahmed et al., *J. Power Sources*, **367**, 250–262 (2017).
2. K. H. Chen et al., *Adv. Energy Mater.*, **11**, 200336 (2020).
3. E. Kazyak et al., *J. Mater. Chem. A*, **6**, 19425–19437 (2018).
4. C. Fear et al., *ACS Appl. Mater. Interfaces*, **12**, 30438–30448 (2020).
5. Y. Chen et al., *J. Mater. Chem. A*, **9**, 23522–23536 (2021).
6. E. Kazyak, et al., *Adv. Energy Mater.*, **12**, 2102618 (2022).

V Beyond Batteries

V.1 Behind-the-Meter Storage (NREL, INL, ANL, SNL)

Anthony Burrell, Principal Investigator

National Renewable Energy Laboratory
15013 Denver West Parkway
Golden, CO, 80401
E-mail: anthony.burrell@nrel.gov

Samm Gillard, DOE Technology Development Manager

U.S. Department of Energy
E-mail: Samuel.Gillard@ee.doe.gov

Start Date: October 1, 2018	End Date: September 30, 2022	
Project Funding (FY21): \$2,400,000	DOE share: \$2,400,000	Non-DOE share: \$0

Project Introduction

This initiative, referred to as Behind-the-Meter Storage (BTMS), focuses on novel critical-materials-free battery technologies to facilitate the integration of electric vehicle (EV) charging, solar power-generation technologies, and energy-efficient buildings while minimizing both costs and grid impacts. For extreme fast-charging at levels of 650 kW or higher, novel approaches are required to avoid significant negative cost and resiliency impacts. However, it is reasonable to assume that BTMS solutions would be applicable to other intermittent renewable energy generation sources or short-duration, high-power-demand electric loads.

BTMS research is targeted at developing innovative energy-storage technology specifically optimized for stationary applications below 10 MWh that will minimize the need for significant grid upgrades. Additionally, avoiding excessive high-power draws will eliminate excess demand charges that would be incurred during 350-kW fast charging using current technologies. The key to achieving this is to leverage battery-storage solutions that can discharge at high power but be recharged at standard lower-power rates, acting as a power reservoir to bridge to the grid and other on-site energy-generation technologies such as solar photovoltaics (PV), thereby minimizing costs and grid impacts. To be successful, new and innovative integration treatments must be developed for seamless interaction between stationary storage, PV generation, building systems, and the electric grid.

Key components of BTMS address early-stage research into new energy-generation and building-integration concepts, critical-materials-free battery energy-storage chemistries, and energy-storage designs with a focus on new stationary energy-storage strategies that will balance performance and costs for expanded fast-charging networks while minimizing the need for grid improvements.

Objectives

A cohesive multidisciplinary research effort is being undertaken to create a cost-effective, critical-materials-free solution to BTMS by employing a whole-systems approach. The focus of this initiative is to develop innovative battery energy-storage technologies with abundant materials applicable to EVs and high-power charging systems. Solutions in the 1–10-MWh range will eliminate potential grid impacts of high-power EV charging systems as well as lower installation costs and costs to the consumer.

Although many lessons learned from EV battery development may be applied to the BTMS program, the requirements for BTMS systems are unique—carrying their own calendar-life, cycle-life, and cost challenges. For example, EV energy-storage systems need to meet very rigorous energy-density and volume requirements to meet consumer transportation needs. Despite that, current stationary-storage systems use batteries designed

for EVs due to high volumes that drive down costs. This creates another market demand for EV batteries, further straining the EV battery supply chain and critical-material demand.

By considering BTMS electrochemical solutions optimized for these applications with less focus on energy density in mass and volume, the potential for novel battery solutions is very appealing. Furthermore, the balance-of-plant (BOP) cost for a BTMS battery system—the cost of everything minus the battery cells—is thought to be upwards of 60% of the total energy-storage system cost. In contrast, the BOP costs of EVs make up roughly 30% of the total battery cost. Therefore, to realize desired cost targets, BTMS will also need to focus on reducing BOP cost through system optimization.

Design parameters are needed to optimize the BTMS system for performance, reliability, resilience, safety, and cost.

The objectives of the project are to:

- Produce behind-the-meter battery solutions that can be deployed at scale and meet the functional requirement of high-power EV charging
- Use a total-systems approach for battery storage to develop and identify the specific functional requirements for BTMS battery solutions that will provide novel battery systems in the 1–10-MWh range at \$100/kWh installed cost, and that are able to cycle twice per day, discharging for at least 4 hours, with a lifetime of roughly 20 years or at least 8,000 cycles.

Approach

A cohesive multidisciplinary research effort—involving the National Renewable Energy Laboratory (NREL), Idaho National Laboratory (INL), Sandia National Laboratories (SNL), and Argonne National Laboratory (ANL)—will create a cost-effective, critical-materials-free solution to BTMS by employing a whole-systems approach. The focus of this initiative is to develop innovative battery energy-storage technologies with abundant materials applicable to PV energy generation, building energy-storage systems, EVs, and high-power charging systems. Solutions in the 1–10-MWh range will enable optimal integration of PV generation from a DC-DC connection, increase energy efficiency of buildings, eliminate potential grid impacts of high-power EV charging systems, and lower installation costs and costs to the consumer.

Many lessons learned from EV battery development may be applied to the BTMS program, but the requirements for BTMS systems are unique—carrying their own calendar-life, cycle-life, and cost challenges. For example, EV energy-storage systems need to meet very rigorous energy-density and volume requirements to meet consumer transportation needs. Despite that, current stationary-storage systems use batteries designed for EVs due to high volumes that drive down the costs. This creates another market demand for EV batteries, further straining the EV battery supply chain and critical-material demand.

By considering BTMS electrochemical solutions optimized for these applications with less focus on energy density in mass and volume, the potential for novel battery solutions is very appealing. Furthermore, the BOP cost for a BTMS battery system, or the cost of everything minus the battery cells, is thought to be upwards of 60% of the total energy-storage system cost. In contrast, the BOP costs for EVs make up roughly 30% of the total battery cost. Therefore, BTMS will also need to focus on reducing BOP cost through system optimization to realize desired cost targets.

Integration of battery storage with PV generation, energy-efficient buildings, charging stations, and the electric grid will enable new and innovative control strategies (see Figure V.1.1). Design parameters are needed to optimize the BTMS system for performance, reliability, resilience, safety, and cost.

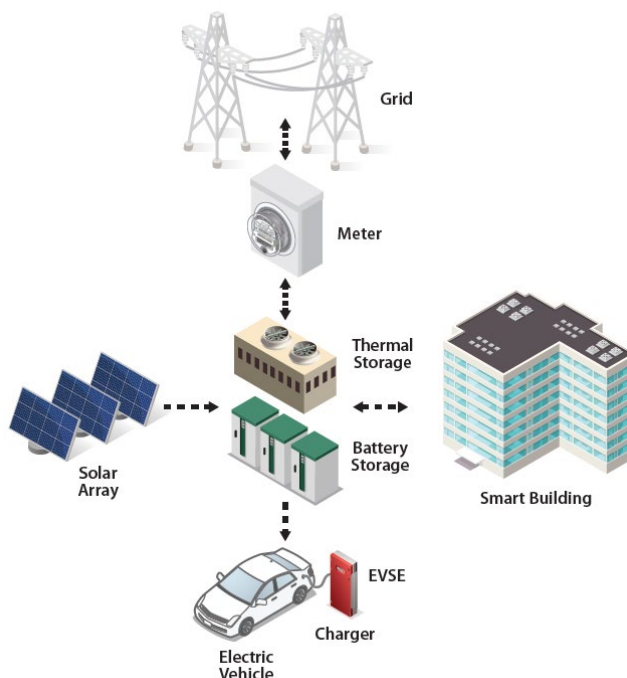


Figure V.1.1 Overview of BTMS relevance (EVSE: electric vehicle supply equipment)

The Fiscal Year (FY) 2021 Milestones for this project are as follows:

- Milestone A: Define critical parameters for enabling an advanced rack and battery management system design incorporating new sensors, controls, electronics, and thermal control strategies for BTMS storage chemistries
- Milestone B: Report on the degradation of cells under two cycling regimes and delineate the aging effects induced by the two protocols
- Milestone C: NREL will use the EnStore Model to evaluate the economic feasibility of BTMS with cobalt-free battery chemistries using testing data from BTMS chemistries at a representative fulfilment center for package deliveries using medium-duty vehicles.
- Milestone D: Have critical-material-free pouch cells (2 Ah) prepared and on test using BTMS protocols.

To complete those milestones, a set of activities have been taking place during FY21 as listed below:

- Enabling Technologies for an Advanced Rack Design
- Report on the degradation of cells under two cycling regimes
- Use the EnStore Model to evaluate the economic feasibility of BTMS with cobalt-free battery chemistries
- Have critical-material-free pouch cells (2 Ah) prepared and on test using BTMS protocols.

Each of those activities are described below in greater detail.

Enabling Technologies for an Advanced Rack Design

The main objective is to develop a strategy to enable a fail-safe rack design over a three-year period. “Fail-safe” is defined as preventing cell to cell propagation in a best-case scenario and preventing rack to rack propagation in a worst-case scenario.

In 2017, Bloomberg estimated that 94MWh of grid storage were affected by lithium-ion battery fires in South Korea. After a thorough review, the Korean Ministry of Trade, Industry and Energy (MOTIE) determined that the four primary causes of the fires were:

1. **Insufficient battery protection systems against electric shock** – Systems were not able to properly protect against electrical hazards due to ground faults or short circuits. Existing fusing for the energy storage system (ESS) was not able to interrupt large electrical surges which led to catastrophic failure of the contactors. The short circuit current allowed the failures to cascade to the bus bar which resulted in fires inside the ESS.
2. **Inadequate management of operating environment** – Of the 23 fire incidents that occurred, 18 were installed in harsh conditions - the mountains or coastal areas. It was concluded that these environments resulted in conditions including large temperature swings, high humidity and elevated levels of dust and particulates which ultimately led to failure modes resulting in fires.
3. **Faulty Installations** – Human error during installations led to system faults resulting in ESS fires.
4. **ESS System Integration** – The integrated protection and management systems were found to be insufficient with the ESS installation. The committee indicated that there were gaps in the energy management system (EMS), integration of the battery management system (BMS), and power management system (PMS) leading to the potential for fires.

More recently, South Korea experienced five ESS fires in 2019 and MOTIE determined that the fires originated due to internal defects within the batteries in combination with high charging rates at high states of charge. The committee attributed the defects to foreign matter in the cathode and lithium plating on the separator and anode after performing a physical analysis of the batteries. Due to similar concerns associated with lithium-ion ESS, the BTMS program is assuming that existing and future quality control measures at battery manufacturing facilities will not eliminate all single cell thermal runaway events and that improvements are needed to the EMS, BMS, and PMS systems. Thus, BTMS formed a team, Enabling Technologies for Advanced Rack Design, that has developed a four-pronged approach to mitigate the hazards associated with BTMS systems:

1. **Advanced Cell, Module, and Rack Thermal Design:** Battery thermal management techniques will be investigated to regulate battery systems under normal temperature ranges to minimize temperature differences and achieve optimum performance and life. These thermal management strategies will further be optimized to mitigate/prevent thermal runaway propagation that might occur in a battery system.
2. **Advanced Battery Management Systems (BMS):** Develop advanced BMS systems capable of cell balancing, state of health estimation, regulating temperature gradients between cells, and monitoring the health of individual cells and the pack.
3. **Advanced Sensors and Controls:** Advances in battery management sensing and controls will be investigated in the interest of maximizing life, performance, and safety of large battery systems.
4. **System Safety:** Reduce, isolate or eliminate the combustible products/potential within the cell and system design.

As expected, there are several standards and certification guidelines available, and the Team will be using them to inform the “fail-safe” design. The following specifications in Table V.1.1 will help guide the development of technologies engineered under this task. Even though this is not a comprehensive list, the specifications outlined below are commonly used within the grid storage industry.

Table V.1.1 Design standards certifications to be used for the rack design (Source: NREL)

Safety	Description
UL 9540	Safety for energy storage systems and equipment.
UL 1973	Batteries for use in light electric rail applications and stationary applications. ¹
NFPA 70E	Standard for electrical safety in the workplace.
UL 1642	Standard for lithium batteries. ²
IEC 61508	Functional safety of electrical/electronic/programmable electronic safety-related systems. ³

¹ Applicable to battery modules and racks only.

² Applicable to battery cells only.

³ Evaluation of battery management system only, in support of UL 1973, UL 9540, and IEC 62619 certification.

The technologies contributing to a safe rack design involve a very complicated design space. To limit the number of design considerations, we will only be considering three cathode/anode combinations: lithium manganese oxide (LMO)/lithium titanate oxide (LTO), lithium iron phosphate (LFP)/lithium titanate oxide, and lithium iron phosphate/graphite. The chemistries were chosen due to their lack of critical materials and excellent safety record. It is understood that the specific and volumetric energy densities of these battery systems is lower than those used for transportation and consumer electronics, but we are assuming that weight and space restrictions will not be as severe for behind-the-meter-storage applications. Furthermore, our focus will be to develop a system primarily focused on the volumetric energy density as this is considered a more critical/important parameter. Figure V.1.2 shows graphically how the specific and volumetric energy densities will be affected from the cell to rack level – our target will be developing a rack system with 36% of the cell’s specific energy density and 30% of the cell’s volumetric energy density.

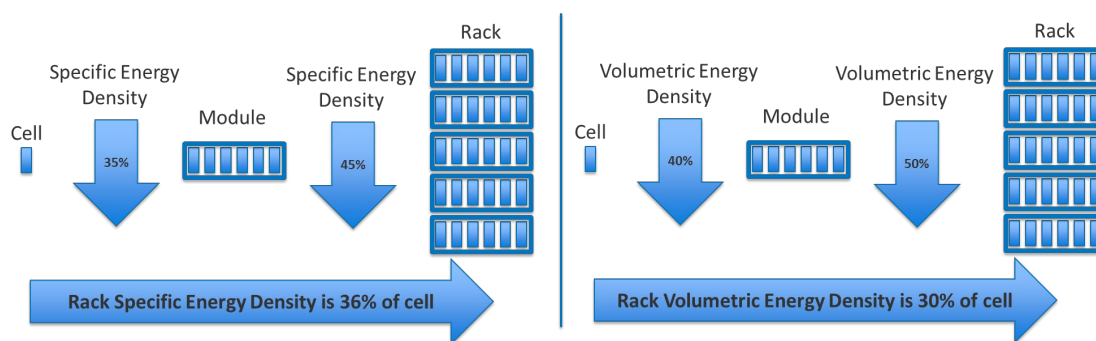


Figure V.1.2 Decrease in specific and volumetric energy density of ESS from the cell to the rack. Source: NREL

Another important aspect of the study will be to limit the battery discharge capacities to 10 Ah, 50 Ah, and 100 Ah. Even though some existing grid storage systems are using cells greater than 250 Ah, cell-to-cell propagation is difficult to limit or prevent in larger cells if a cell enters thermal runaway. As such, part of the study will investigate the positives/negatives of various series and parallel connected systems to achieve the appropriate fail-safe design and overall energy metrics for the system. Finally, temperature is critical to the lifetime and safety of the system. Initial, design specifications will be to limit the temperature of the batteries

to between 20°C and 45°C and limit the temperature spread across the cells in the rack to 3°C. Table V.1.2 summarizes the important design parameters for our study. However, it should be noted each of the four efforts under this task will have additional design variables such as overvoltage, undervoltage, overcurrent, balancing requirements, etc... and these will be covered in the subsequent sections of this report.

Table V.1.2 Important design parameters for the advanced rack design (Source: NREL)

Design Parameter	Units	
Rack Specific Energy Density	Wh/kg	> 36% of Cell Specific Energy Density
Rack Volumetric Energy Density	Wh/liter	> 30% of Cell Volumetric Energy Density
Rack Power Density	W/kg	> 40% of Cell Power Density
Rack Design Cost – (Cells, Modules, Racks, and BMS)	\$/kWh	210
Power Conversion Cost (Inverter, Electrical BOS)	\$/kW	240
Maximum Temperature ¹	°C	45
Minimum Temperature ¹	°C	20
Temperature Delta across Rack	°C	3

¹ TBD by cell development team.

As previously indicated, we envision this effort to occur over the next three years. A generic timeline of the activities is given below.

- Year 1: Simulation and Design – the first year’s effort will focus on modeling and designing
- Year 2: Bench scale prototypes/verification
- Year 3: System integration and characterization.

Report on the degradation of cells under two cycling regimes

Last year a simplified BTMS peak-shaving system providing support for twenty-four daily XFC events at peak power was designed as a basis for energy storage device life cycling and performance testing. XFC event timing, as expected under real-world conditions, can vary significantly, which in turn would affect the power profile demanded from the BTMS system. The effect of varied timing of the charge and discharge cycle on life and performance of several cell types was sought to help elucidate the need for multiple variations of BTMS test cycles. A second quarter milestone was established to report on the degradation of cells under two cycling regimes and delineate the aging effects induced by the two protocols. Discussion of BTMS testing work in this report is limited to that performed in support of completing the Q2 milestone.

Two timing scenarios were identified that bookend the range of vehicle arrivals at an XFC station designed to support twenty-four peak fast charges per day, with the capacity for twelve events in a row. This design can result in up to two cycles per day. The first scenario considered back-to-back fast charge events being conducted, discharging the BTMS continuously for two hours twice per day. This reflects a situation where there is a high demand for fast charging during two daily rush-hour periods. The second case considered evenly spaced vehicle arrivals throughout the day, totaling four hours of gross discharge time, with intermittent partial recharging throughout a 14-hour period. This reflects the operation of a depot-type charging station. The two respective cycling routines are referred to herein as continuous and intermittent routines.

First, accelerated cell aging using continuous and intermittent constant-power discharge protocols with faster recharge periods than the BTMS specific cycle was conducted on NMC-graphite cells as a surrogate in

advance of obtaining critical-materials free cells. These profiles are shown in subfigure A in Figure 3 below. Both cycles utilized constant-power charging at a 0.33E rate, and constant-power discharging at a 0.4E rate. The resulting maximum current, which was reached at the discharge voltage limit, was maintained below 0.6C. Next, the effects of the two BTMS specific cycling routines were investigated by applying them to different critical material free cell chemistries and designs. Several varieties of lead-acid, and one nickel-zinc design were cycled using the refined continuous and intermittent cycling routines. The refined profile corresponding to two BTMS cycles per day, with 24 XFC events is shown in subfigure B in Figure V.1.3. These profiles varied in their E-rates among cell types because the optimal energy margin at beginning-of-life varied by cell type. Each discharge, though, provided for two-hours of continuous, or gross discharge at the targeted discharge power. Cells reached end-of-life when they were unable to provide their target discharge power throughout the routine.

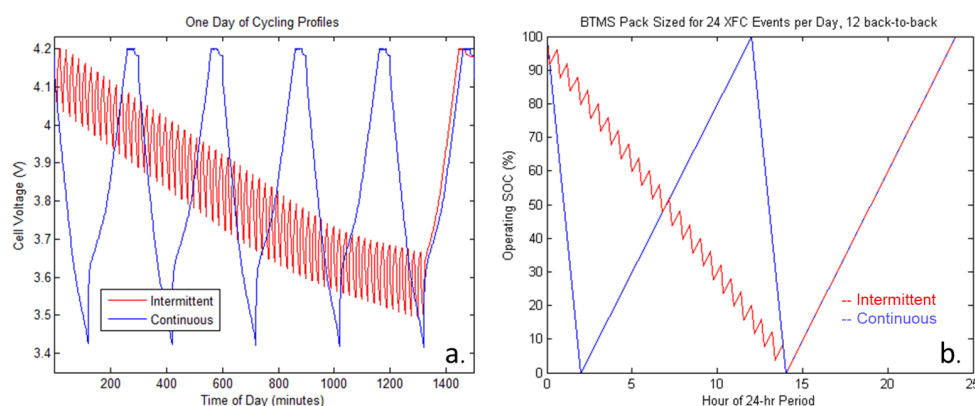


Figure V.1.3 Voltage traces for two preliminary cycling regimes conducted on NMC/graphite cells (a) and SOC traces for two refined BTMS cycling regimes (b).

Use of the EnStore Model to evaluate the economic feasibility of BTMS with cobalt-free battery chemistries

The Behind the Meter Storage (BTMS) Analysis project is funded by the Buildings Technologies Office (BTO), the Vehicle Technologies Office (VTO), and the Solar Energy Technologies Office (SETO) within the Department of Energy (DOE) Office of Energy Efficiency and Renewable Energy (EERE), whose mission is to create and sustain American leadership in the transition to a global clean energy economy. Electric vehicle (EV) adoption is expected to grow significantly over the coming years, and could have a significant, and potentially negative, effect on grid infrastructure due to large and irregular demands. Additionally, the rapid penetration of solar photovoltaic (PV) generation installed on buildings is leading to new challenges for the electric grid. In response to these changes, utilities are evaluating multiple options for managing dynamic loads, including time-of-use pricing and demand charges. Buildings, as well as EV charging stations, can leverage energy storage, including battery and thermal energy storage (TES), coupled with on-site generation to manage energy costs as well as provide resiliency and reliability for EV charging and building energy loads. While each of these technologies can make contributions to the U.S. economy, integrating them in ways that optimize cost and energy flows for varying energy demand and climate conditions across the country can lead to multiple benefits. BTMS research is targeted at developing innovative modeling approaches to optimize energy storage and PV system designs and energy flows for grid-interactive energy-efficient building and extreme EV fast charging loads.

The key question in this project is the following: what are the optimal system designs and energy flows for thermal and electrochemical energy storage systems at sites with on-site photovoltaic (PV) generation and electric vehicle (EV) charging, and how do solutions vary with climate, building type, and utility rate structure?

The primary objective function for most analyses in this project will be Levelized Cost of Charging (LCOC). This metric, measured in \$/kWh, is the minimum price that EV station owners would need to charge users in order to “break even”, or to pay back all capital and operating expenses over the lifetime of the system. Financial metrics including LCOC are crucial to determining how various details of the BTMS system affect the whole and assess the economic value and attractiveness of BTMS. A high-level schematic depicting the various behind-the-meter systems, including stationary battery, solar PV, electric vehicle supply equipment (EVSE), and TES, is shown in Figure V.1.4.

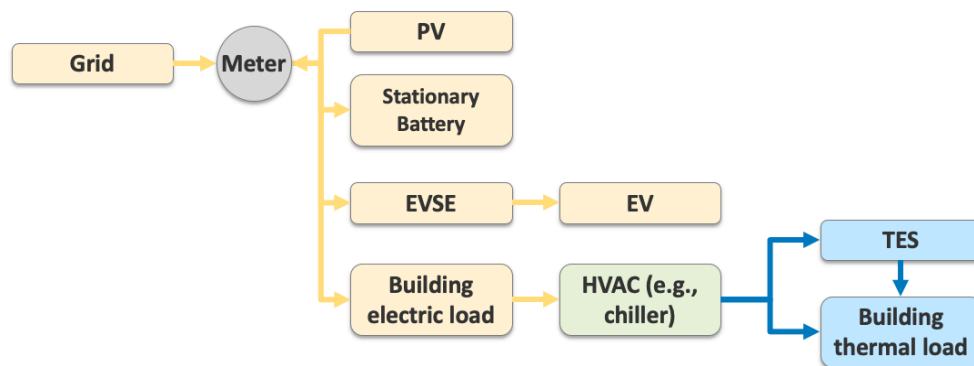


Figure V.1.4 Schematic Depicting the Default Combination of Technologies for BTMS Analysis

The BTMS Analysis team has developed the EVI-EDGES Model, short for Electric Vehicle Infrastructure - Enabling Distributed Generation Energy Storage, to capture performance characteristics and interactions between disparate technologies with high fidelity. Public-facing information about this model can be found at <https://www.nrel.gov/transportation/evi-edges.html>.

Work in FY21 was focused on increasing simulation capability of the EDGES Model, increasing simulation time, particularly with regard to the thermal energy storage (TES) module, and evaluating results across the project scenarios. Simulations were run across four representative climates (Table V.1.3), three representative utility rate structures (Figure V.1.5), and five building types: corner charging station, retail big-box grocery store, fleet vehicle depot, commercial office building, and multi-family residential. For each building type, numerous electric vehicle (EV) load profiles were developed using the EVI-EnSite Model (<https://www.nrel.gov/transportation/evi-ensite.html>) to span multiple charging port counts, port utilization, and voltage levels. A library of EV load profiles has been compiled to allow for access by the BTMS Analysis team and other projects funded by VTO. Energy storage in stationary batteries and as thermal energy for building use was included in the EDGES Model, and co-optimized within the predictive model controls algorithm developed for the project. Solar PV was varied in size and modeled for the solar irradiance available at each location.

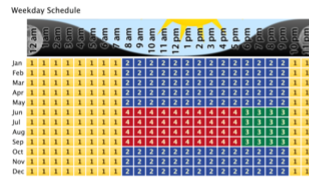
Table V.1.3 Representative Climate Locations for FY21 Scenarios

Climate Zone	Climate	Location
2a	Hot & Humid	Tampa, Florida
4b	Mixed Dry	Albuquerque, New Mexico
5b	Cool & Dry	Aurora, Colorado
7	Very Cold	International Falls, Minnesota

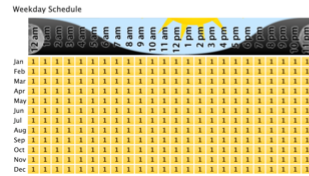
CONED

Consolidated Edison: monthly demand charges that range **5.36 - 16.7 \$/kW** and **TOU** demand charges up to **23.89 \$/kW**; flat energy rates

Demand Charge Schedule



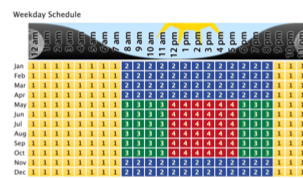
Energy Charge Schedule



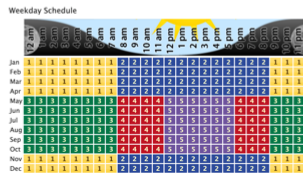
PGE

Pacific Gas & Electric: flat demand charges of **15.97 \$/kW** and **TOU** demand charges up to **20.62 \$/kW**; **TOU** energy charges

Demand Charge Schedule



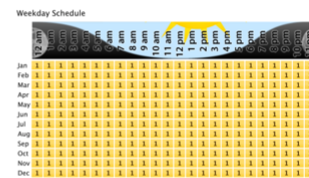
Energy Charge Schedule



XCEL

Xcel Energy: constant demand charges at **5.63 \$/kW**, but energy charges vary much more than those of CONED

Demand Charge Schedule



Energy Charge Schedule

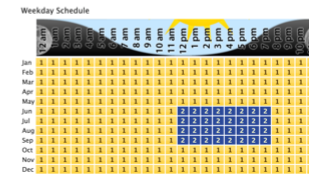


Figure V.1.5 Representative utility rate structures for FY21 Scenarios

BTMS Materials Development

The main objective is to establish the cell design of the 2 Ah pouch cells. Specifically:

- Fabricate LTO and LMO electrodes with the highest possible capacity while maintaining good utilization at 1C current rate
- Determine the optimal negative-to-positive (N/P) ratio that enables long cycle life
- Develop safety-enhanced electrolytes, factoring in the choice of separator and operating temperature

LTO/LMO cells were evaluated using Gen2 (1.2 M LiPF₆ in EC/EMC (3:7, w/w)) and EC (1 M LiPF₆ in EC) electrolytes, the former being a conventional Li-ion battery electrolyte and the latter being BTMS-targeted electrolyte with enhanced safety by eliminating the flammable linear carbonate. To mitigate the capacity fade due to loss of Li inventory, two different approaches were taken—electrochemical prelithiation of the LTO electrode and oversizing the LMO electrode areal capacity. While both methods successfully enhanced the capacity retention, the latter method was selected (i.e., making N/P<1 cells) to avoid additional prelithiation steps. LTO and LMO electrodes with 3.35 mAh/cm² and 3.94 mAh/cm² areal capacities, respectively, were selected as the final electrodes for the 2 Ah pouch cell deliverable.

Results

Enabling Technologies for an Advanced Rack Design

Advanced Cell, Module, and Rack Thermal Design

The essential objective of thermal design is to enable fail-safety design for battery systems under abusive conditions, such as thermal runaway. To prevent cascading thermal runaway failures, temperatures of neighboring cells or modules must be sufficiently low to break the thermal runaway propagation chain. Thermal management is also essential to maximize the performance and life of battery systems for behind-the-meter energy storage, which can be achieved through optimizing operating temperature range, minimizing temperature differences, and reducing cell heterogeneity. An ideal thermal design needs to meet the temperature control goal and includes features such as compactness, lightweight, and low-cost design.

Table V.1.4 Key considerations and design variables for thermal management system. Source: NREL

Key Considerations	Design Variables
Control goal	Optimal operating temperature range, temperature difference among cells, thermal runaway onset temperature
Thermal control strategy	Cooling and insulation, passive and active control
Thermal management material	Air, liquid, PCM, Insulation material
Cooling technique	Natural convection or forced convection, cold plate cooling, direct liquid cooling, busbar cooling, tab cooling
Battery cell	Chemistry, battery size, form factor, energy efficiency, thermal runaway heat, thermal runaway heat release rate
Electrical configuration	Cell-to-cell connection, rack-to-rack connection, fusing feature-parallel/series connections, modular design
Environmental condition	Corrosion, condensation

Thermal design requirements are affected by the entire battery rack system. Table V.1.4 summarizes design considerations that are crucial to thermal management strategies. Thermal hazard caused by single cell failure is not only determined by individual cells, but the failure trigger modes that are tightly related with system electrical configuration and environmental conditions.

Under abusive conditions, key input variables include volumetric-thermal-runaway heat and heat release rate. Volumetric-thermal-runaway heat is a product of thermal runaway enthalpy in kJ/Ah and cell energy density in Ah/m³. Based on ARC testing of 18650, recent research reveals that the total thermal runaway enthalpy is comparable cells with different cathode materials though thermal runaway onset temperature and self-heating rates are tightly related with cell chemistries.

Fail-safe design requires appropriate thermal design strategies. Ideally, mitigation approaches to prevent or postpone thermal runaway propagation should be implemented at cell level. Passive thermal management is preferred for worst-case thermal scenarios, i.e., thermal runaway events. Active thermal management may be ineffective because of the rapid evolution nature of thermal runaway events. Another key consideration is the dissipation or isolation of thermal runaway heat by initially failed cells, which can be used to control temperatures of neighboring cells. Heat dissipation to ambient or cooling system is challenging because of insufficient cooling power designed for battery nominal operation and high thermal heat rate that is hard to achieve. Heat isolation slows down thermal runaway heat transfer to neighboring cells. It however negatively affects thermal performance of the system at normal operating conditions.

It is also worthwhile to investigate cooling techniques for battery energy storage systems (BESS). State-of-the-art strategies are to heat or cool batteries externally through battery surface. Air, liquid, and phase change materials (PCM) are typical medias for BTMS. Compared to air, liquid systems provide better thermal control and are relatively compact. Their disadvantages include higher weight and cost. Except active control using air and liquid, PCM is also employed as a passive BTM solution. A PCM controls maximum temperatures of a battery system can be reached by utilizing its large latent heat of fusion. Usually, it has a low thermal conductivity, which has been problematic when battery cooling or preheating is needed. In the past decade, several new techniques have been proposed for battery thermal management, such as immersion cooling as one of direct liquid cooling methods, heat pipe, and thermoelectric element cooling. Except of cooling techniques mentioned above, novel thermal management materials have been developed for battery thermal/flame protection by companies including 3M, DuPont, and Rogers Corporation, etc.

Table V.1.5 Tasks for fail-safe thermal design for BTMS applications. Source: NREL

Tasks	Task Description
1. Cell-level analysis	<ul style="list-style-type: none"> Determine temperature control goals Identify constraints and flexibility of thermal management Thermal runaway characterization and thermal hazard analysis of individual cells Evaluate thermal management design variables Develop fail-safe concept at multi-cell scale
2. Module design and validation	<ul style="list-style-type: none"> Propose thermal control strategies for module design Thermal hazard analysis for battery modules Estimate module performance along its service life Validate fail-safe designs at module level with modeling Proof-of-concept testing of small-scale module
3. System integration	<ul style="list-style-type: none"> Estimate heterogeneous behaviors battery racks Validate fail-safe designs at multi-module level Integrate and optimize thermal management system Early detection and rapid response of management system to thermal runaway failure

With a bottom-up design and development approach, three tasks were proposed, as listed in Table V.1.5. In Task 1, the goal is to propose fail-safe concepts based on cell-level evaluations of design constraints, input variables and thermal management options. Task 2 aims to validate fail-safe designs with multi-physics modeling and proof-of-concept testing. The performance of the module incorporated the thermal design along its service life will be estimated. Studies at multi-module level will be carried out under Task 3. Combined with fail-safe designs for other components, such as battery management system, safety performance at multi-module levels will be investigated.

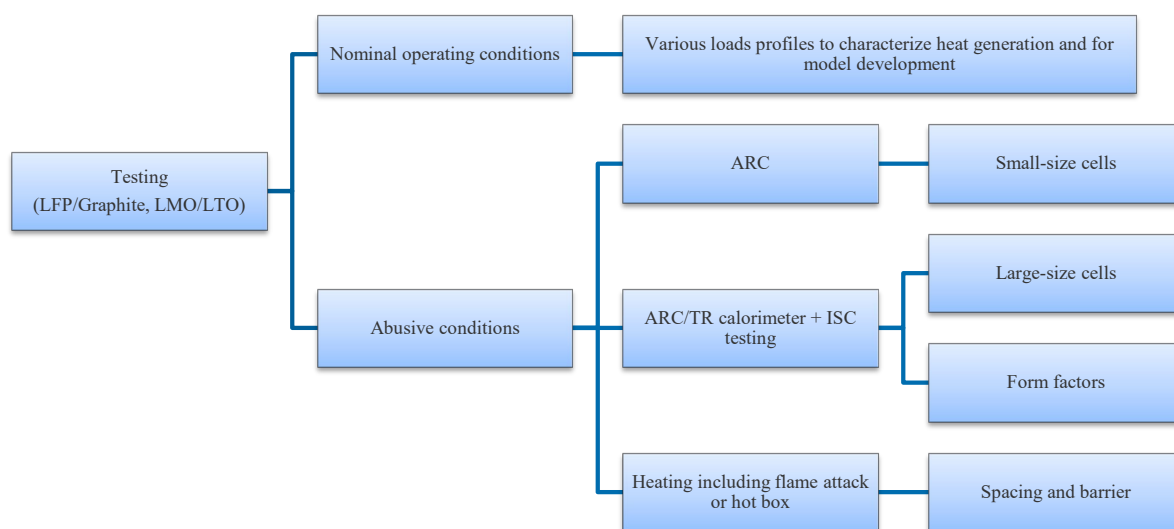


Figure V.1.6 Proposed characterization testing for quantification of input variables and model development. Source: NREL

A combined experimental and numerical approach is proposed to accomplish these tasks and enable fail-safe design even for worst-case scenarios. Figure V.1.6 and Figure V.1.7 illustrate the testing and modeling plans, respectively. The characterization testing shown in Figure V.1.6 is primarily designed to assist model

development through quantifying input design variables including thermal loads and thermal hazard of battery cells, which likely vary with cell sizes and form factors.

Modeling is an effective approach to evaluate thermal management options. Shown in Figure V.1.7, module level is the appropriate scale for the implementation of different management strategies. A bulk cooling approach for modules is preferred rather than cooling for individual battery cells for stationary energy storage systems. As such, external cooling of battery modules is preferable. Within battery modules, insulation techniques with air gaps or flame-retardant materials and heat dissipation through conduction may be effective for the battery chemistry identified. With this strategy, packaging efficiency at module level can be significantly improved. To compare against BESS on the market, air cooling will be investigated first. Considering the battery loads proposed in this study, air cooling may be sufficient for temperature control of battery modules under nominal operating conditions. If not, liquid cooling such as liquid-cooled cold plate will be investigated. In this case, fail-safe design at cell level is impractical, and we will examine the possibility of preventing module-to-module propagation through insulation.

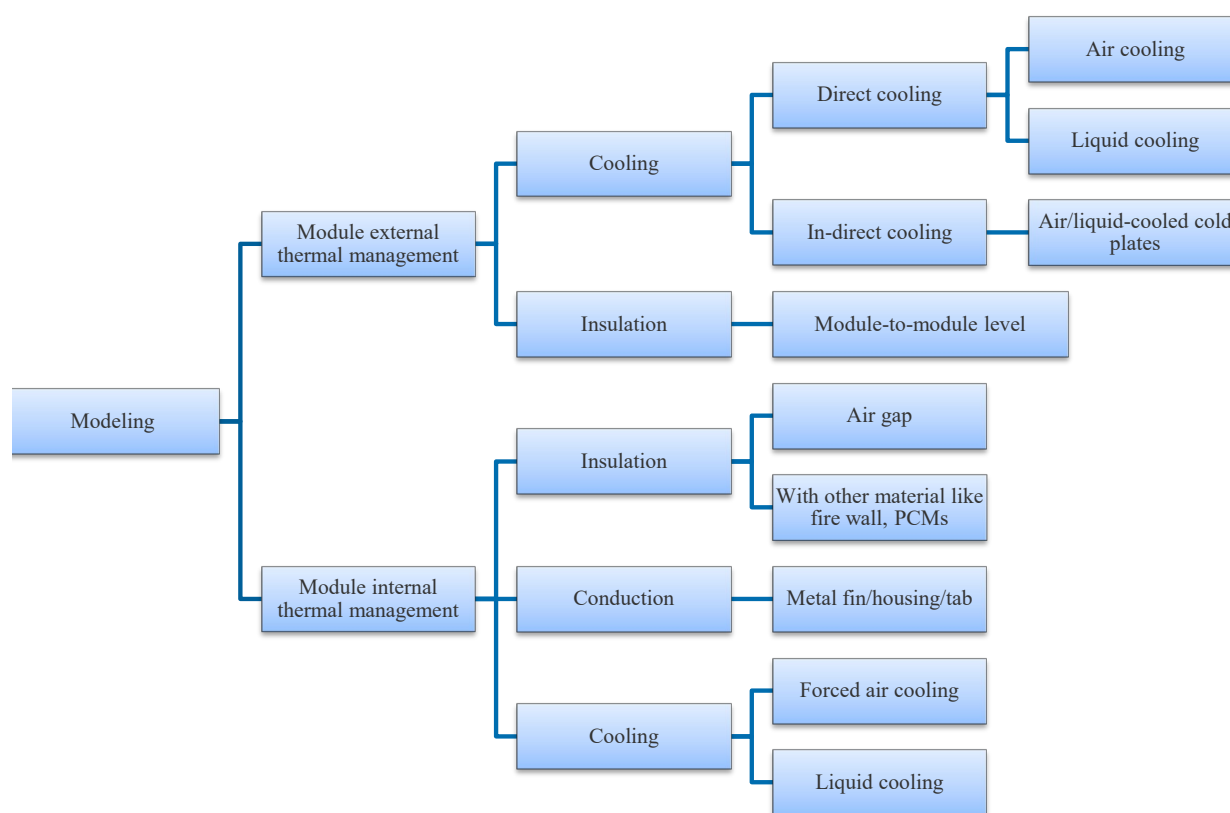


Figure V.1.7 Illustration of modeling matrix to evaluate thermal management strategies and techniques. Source: NREL

Advanced Cell, Module, and Rack Thermal Design Technical Progress

Based on heat generation measurements of 20 Ah LFP/Graphite and LCO/Graphite cells with NREL's isothermal battery calorimeter, lumped-capacitance calculations indicate adiabatic temperature rises of LFP and LCO are about 17°C and 11°C, respectively, after C/1 full discharge. As estimated with a 3D thermal model, cell temperature rise can be controlled with single-sided cooling, shown in Figure V.1.8a. More importantly, results plotted in Figure V.1.8b shows no considerable temperature heterogeneities are developed within the prismatic LTO cells under various cooling conditions. Even with effective cooling (i.e., 300 Wm⁻²K⁻¹), the cell temperature

delta remains less than 1°C. Sufficient single-sided cooling allows thermal insulation between cells for thermal runaway management.

Thermal runaway propagation may be triggered by conductive heat transfer through cell casing or heat distributed by cell ejecta. To limit conduction of thermal runaway heat through cell casing, three scenarios were addressed including direct contact for the baseline case, insulation foams, or aluminum fins inserted between cells. In the baseline case, the 3D thermal model predicts temperature migration in neighboring cells under realistic thermal conductivity scenarios. The resulting peak temperature in adjacent cells are around 200°C and may damage the separators of these cells leading to cascading thermal runaway. With fins between adjacent cells, thermal shock remains but with reduced peak temperatures, as illustrated in Figure V.1.8c. Further simulations suggest increasing fin thickness is not effective to remove the temperature migration. However, propagation can be limited with 1 mm thick foam insulation assuming it is thermally stable up to 420°C. With foam insulation, neighboring cells exhibit a gradual rise in temperature until reaching thermal equilibrium. As plotted in Figure V.1.8d, neighboring cell temperatures can be further controlled with single-sided cooling. The model predicts the insulating approach works for both 20 Ah and 50 Ah LTO prismatic cells.

Furthermore, a computational fluid dynamic (CFD) model has been built to identify thermal management requirements to protect neighboring cells from failure cell ejecta. The next step is to fine-tune modeling parameters describing ejection thermal hazards characterized with accelerating calorimeter testing.

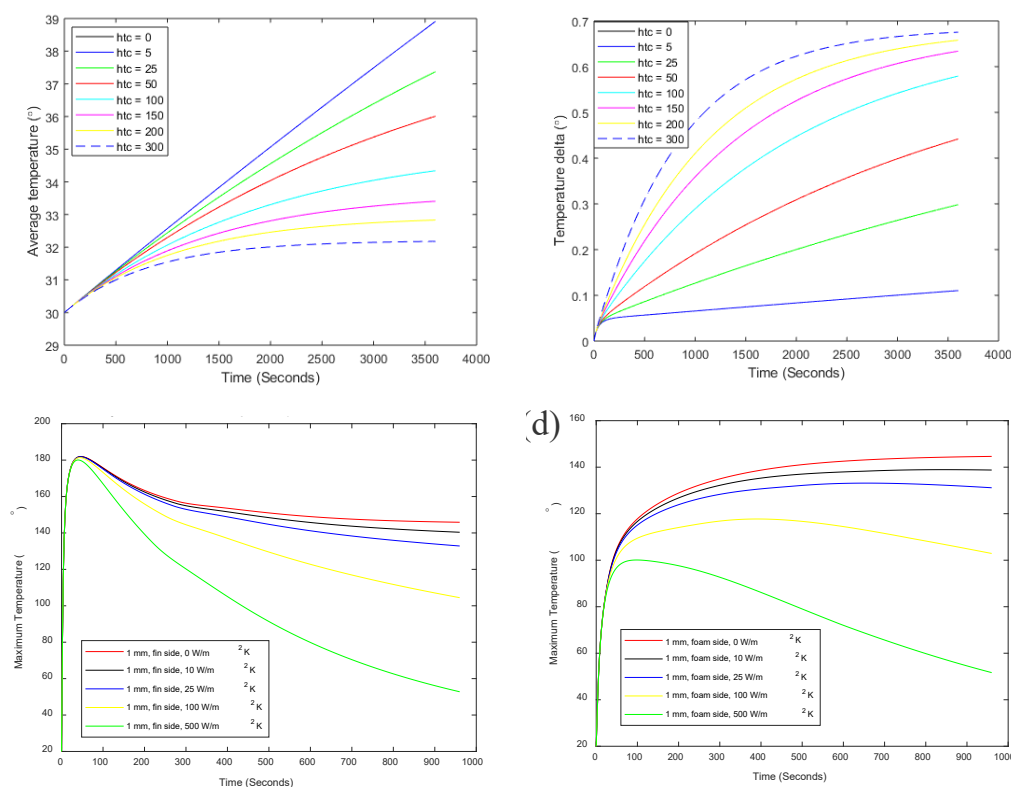


Figure V.1.8 3D thermal simulation results of a LTO battery module under single-sided cooling: a) Cell temperature rises under 1C discharge; b) Cell temperature deltas under 1C discharge; c) Maximum temperature histories of neighboring cells with fins located between cells; d) Maximum temperature histories of neighboring cells with insulations inserted between cells.

Advanced Battery Management System (BMS)

The essential objective of battery management design is to enable fail-safety design for battery systems through by providing mechanisms to balance individual cell differences to create a more homogenous system. However,

behind-the-meter applications will need to have significantly higher energy than for existing batteries in vehicle systems. Improvements in the thermal and cell design will for the rack system will help balance differences but the larger capacity design and continuous operating window will require a better understand of how battery management systems (BMS) should also evolve. The primary functions of a BMS are:

- a. Cell balancing to keep series connected cells at similar state of charge (SOC)
- b. State estimation for to prevent over/under charge of the cells
- c. State estimation for power limits to prevent under/over-voltage during transient condition
- d. Regulate temperature gradient between cells and temperature rise in balancing system
- e. Monitor the health individual cells and the pack to update state estimation for power (resistance) and capacity changes throughout life.

Traditionally the design of battery management systems has achieved these functions through string level control of the power flow to and from the battery, with thermal systems that try to limit the difference of temperature across the string, with system identification techniques to understand the variation in state across the string, and with passive cell balancing to bleed off excess energy from cells with higher SOC.

The thermal design and system identification efforts will be addressed in (a) the Advanced Cell, Module, and Rack Design and (b) the Sensors and Controls tasks of the project. In the Advanced BMS effort the goal will be to investigate advanced balancing techniques that incorporate power conversion with the objective of controlling the power flow within the string level. This will improve the ability to manage larger variations in within the battery system to reduce power from those cells battery pack that are aged while maintaining predictable performance across the battery system. The tasks that are envisioned for advanced BMS design for BTMS battery systems are described below:

Evaluate Various passive and active balancing schemes in simulation domain

There are various cell balancing topologies in the literature that will be evaluated in simulation domain for their performance and complexity. These topologies include passive balancing schemes such as fixed resistor, switched resistor, single switched capacitor, modularized switched capacitor, single switched inductor, single winding transformer and multi winding transformer. Some power electronics-based topologies such as buck converter, buck-boost converter, and flyback converter, and SEPIC converter have also been proposed. These topologies will be evaluated in the simulation domain for large format cell designs considering BTMS pack utilization profiles under various temperature gradients for common aged cells. Further analysis to understand performance with mixed-aged cells will then be consider. Then 1-2 topologies will be selected for design to be tested with the battery pack that will be designed by BTMS research group.

The evaluation of passive and active balancing in the simulation domain will support identification of critical parameters for the development of an advanced BMS for BTMS as included in Table V.1.6.

Table V.1.6 Critical parameters for the development of a BMS system. Source: NREL

Parameter	Description
Balancing Current	<ul style="list-style-type: none"> The applicability of active versus passive strategies are dependent on the required balancing current. Imbalance in the string is depends on the size of the string, cell to cell variation in resistance, and the operational/load profile.
Cell-to-Cell Resistance	<ul style="list-style-type: none"> Variations in the cell-to-cell resistance is the primary driver in balancing current for the balancing system. Resistance variation depends on manufacturing practices, temperature gradients in the system, and inconsistent aging.
Modularity (Cell-to-Module-to-Rack Capacity)	<ul style="list-style-type: none"> The decision about whether to move power conversion from a system-level or rack (string) level to a module level is dependent on the relationship between the cell and system capacity. A “fail-safe” design and a 20-year life imply the need to easily swap out cells in the system due to failures to maintain performance, however, maintaining matched cells for repair and replacement may be a significant challenge. Defining the appropriate modularity for the BTMS will influence the design of the balancing and power conversion system

Design, Construct, and Evaluate the BMS system

Based on the evaluation performed in year 1, a BMS topology will be selected and designed to regulate the battery pack designed in-house as part of the BTMS project. The BMS will be designed to match the size of the battery pack and ratings of the cells. A BMS designed through a PCB layout will have the topology in circuit configuration along with sensors and other components as part of the BMS. The BMS will be evaluated for the in-house designed battery pack will be used under cycling test to determine how well it performs in various temperature and state of pack unbalance conditions with new cells.

Power management between battery strings/modules of different age

The BMS would be evaluated with cells of different ages. It should be able to regulate the balancing and depending on the converter topology regulate the power flow within the battery system to reduce power from those cells battery pack that are aged while maintaining predictable performance across the battery system.

Technical Progress for Battery Management Systems

- This task focuses on defining a 500-kWh pack system configuration, including how cells/modules are connected to form a pack, power conversion system, and cell balancing system.
- Five battery pack layouts (considering different grid interface and modularity level) and two balancing schemes (passive and active) are explored and compared in terms of flexibility/reliability, cost, and efficiency.
 - Layout #1** [AC-coupled with LF isolation (conventional)]: a battery pack is integrated to a 480-V AC feeder through a single inverter and LF transformer.
 - Layout #2** [AC-coupled with isolated converter]: a battery pack is integrated to a 480-V AC feeder through a single inverter and an isolated DC-DC converter (one per pack).
 - Layout #3** [Modular AC-coupled]: a battery pack is integrated to a 480-V AC feeder through a single inverter and multiple isolated DC-DC converters (a converter per string).
 - Layout #4** [DC-coupled with isolated converter per pack]: a battery pack is integrated to a 1000-V DC feeder through a single isolated DC-DC converter (one per pack).

- **Layout #5** [DC-coupled with isolated converter per string]: a battery pack consists of several parallel strings and each string is integrated to a 1000-V DC feeder through a single isolated DC-DC converter.
- Each layout was evaluated with a) cell balancing (active and passive), b) cell chemistries (K2 LFP/Graphite, LMO/LTO, and LFP/LTO), c) cell capacities (10 Ah, 50 Ah, and 100 Ah), and d) modularity level represented by number of modules in series per string.

Key Findings

- Layouts with multiple converters (#3 and #5) show the highest flexibility (Figure V.1.9a).
- DC-coupled layouts (#4 and #5) show the highest efficiency and lowest cost (Figure V.1.9b).
- Modular DC-coupled layout (#5), in Figure V.1.9c, with 5–7 modules in series shows a good balance between flexibility, efficiency, and cost.
- Active balancing increases the system complexity and cost, and decreases reliability, however, it is expected to be more effective and efficient for large cells.
- Considering the modular DC-coupled layout, the final module/string/rack/system configuration with different cell chemistries and sizes is summarized in Table V.1.7.
- As an example, Figure V.1.10 shows how to get to a 500-kWh battery system using 10-Ah LFP/Graphite cells.

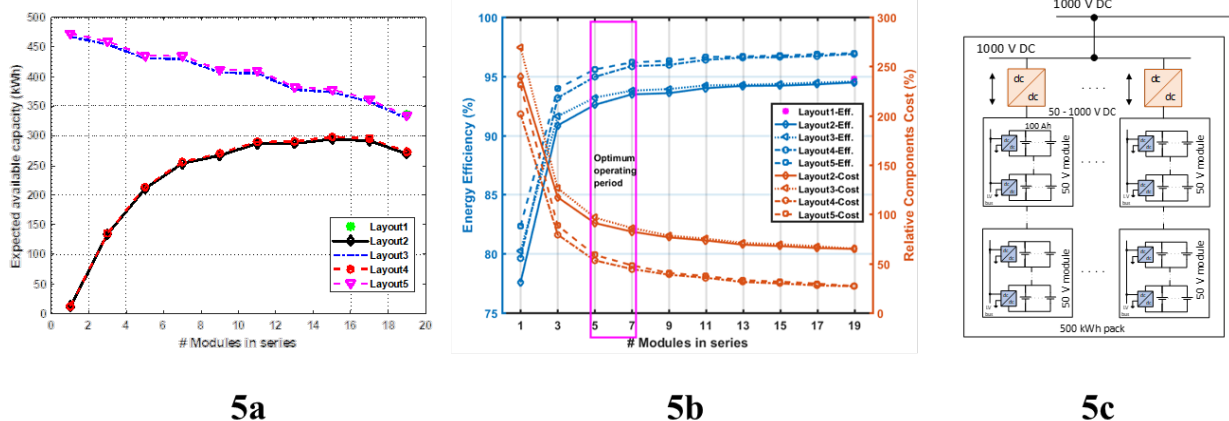


Figure V.1.9 Pack flexibility for different modularity levels (5a), pack cost and efficiency for different modularity levels (5b), and layout #5 modular DC-coupled pack configuration (5c). Source: NREL

Table V.1.7 Final Module/String/Rack/System configuration with different cell chemistries/sizes.
Source NREL.

	Module configuration	Module kWh	String config.	String kWh	Rack config.	Rack kWh	System config.	System kWh	# converters / System	# balancing / System
Cell capacity	10 Ah	50 Ah	100 Ah							
LFP/Graphite	14s10p	14s2p	14s1p	4.3	5s1p	21.5	1s2p	43	1s12p	516
LMO/LTO	18s10p	18s2p	18s1p	3.96	6s1p	23.76	1s2p	47.52	1s11p	522.7
LFP/LTO	20s10p	20s2p	20s1p	3.7	6s1p	22.2	1s2p	44.4	1s12p	532.8

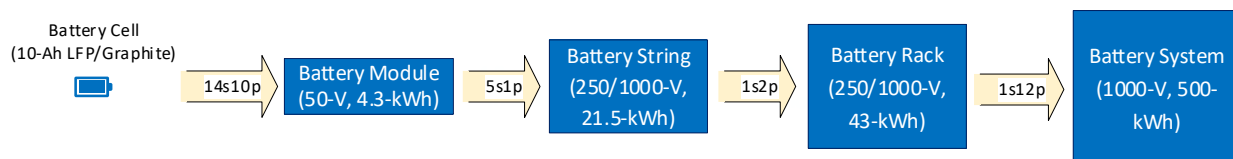


Figure V.1.10 Configuration of a 500-kWh battery pack considering 10-Ah LFP/Graphite cells. Source:NREL

Advanced Systems and Controls

Traditional battery pack management systems calculate a system state-of-health parameter based on cell resistance rise and capacity loss determined from voltage, current, and temperature sensing at the system and cell level. They also must track the state-of-charge of the system and provide the power and energy available back to the systems that interface with the battery controller. New techniques are being developed to use such in-situ data to expand beyond the traditional SOC and SOH determination, and to evaluate not only the effective loss of performance throughout use, but to attribute such losses to specific degradation mechanisms. The intent of incorporating these diagnostic techniques into an energy storage system is to rapidly identify the occurrence of degradation that is proceeding faster than expected, and to watch for signatures of degradation mechanisms that, left unchecked, could evolve beyond premature system end-of-life into an unsafe operating condition. Examples of off-normal conditions that present a safety concern could include cell internal short circuits, or lithium plating.

Currently, electrochemical signature-based degradation mechanism identification and quantification methods are being investigated using single cell per test channel on high-fidelity test equipment with frequent calibration and smaller measurement error. Large amounts of data are being collected from these testers and the computational resources available to process and analyze the data are large compared to typical embedded systems. To apply the diagnostic methods being developed to large arrays of cells in an energy storage system, several considerations must be taken into account to balance the cost and feasibility when designed for use in production systems. First, the architecture of the system, including the number, location, and accuracy of the sensors employed should be designed to balance cost and performance. The data collected from the sensors may need to be stored either directly or processed into summary parameters to document the progression of degradation through time and usage. Either of these methods will require memory and computational resources, which also will need to be designed to result in a reasonable balance of system cost and fidelity of the resulting information.

Another aspect of translating from lab-based data to field data is the shift from scripted routines to unscripted field data based on variable customer demands on the system. The power conversion system architecture could provide the ability to run transparent module tests by shuttling energy within the storage system to conduct charge and discharge pulses, or to provide scripted rest periods to groups of energy storage devices behind the minimum lowest level of power conversion.

The timeline for this work aligns with the overall project timeline, where the first year will include the progression of the single-cell diagnostic techniques, with subsequent years' work scaling the methodology to arrays of cells while using sensing hardware designed to a minimum cost to support functionality. The final year would result in demonstration in a multi-module rack system.

Advanced Systems and Controls Technical Progress

Forty-eight (48) LMO/LTO cells began accelerated aging and performance testing to serve, among other things, as a data set for the investigation of advanced sensing techniques to improve safety and utility of a large battery system. Cells were grouped into 9 different combinations of SOC, rate, and temperature for cycling, and 7 different combinations of SOC and temperature for calendar aging. Aging was accelerated relative to expected BTMS conditions for some cells by cycling using increased rates, SOC windows and storage points, and temperatures. While the data was fit to a semi-empirical life estimation model, investigation into the degradation modes was started using incremental capacity techniques, and sigmoidal rate expressions. These

efforts will feed into machine learning algorithms using, in part, synthetic data sets, to quantify the probability of the extent of three dominant degradation modes throughout aging (LLI, LAM-PE, LAM-NE). Once this characterization is complete, the large data set collected during operation of each cell throughout cycling, storage, and aging, can be analyzed using machine learning techniques to search for in-operando signatures that might signal both silent and performance-limiting degradation modes.

System Safety Progress

Our first task in this effort was to define critical parameters for enabling an advanced rack and battery management system design incorporating new sensors, controls, electronics, and thermal control strategies for BTMS storage chemistries. From a safety perspective we defined “fail-safe” as preventing cell to cell propagation in a best-case scenario and preventing rack to rack propagation in a worst-case scenario. The program is assuming the risk that a single cell thermal runaway event is unavoidable. The critical parameters/controls from a safety perspective were defined as reducing, isolating, or eliminating the combustible products/potential within the cell and system design. The final design will most likely include aspects of all three areas. The first control is reduction of the hazard. One possible way to achieve this will be implementing intrinsically safe chemistries. LTO anodes and LFP cathodes are considerably less exothermic in thermal runaway scenarios when compared to the standard graphite NMC systems so employing those chemistries in the BTMS system mitigates the runaway hazard. Another avenue to limit the effects of thermal runaway is to develop nonflammable electrolytes or electrolyte additives. By using a nonflammable electrolytes or electrolyte additives the other exothermic heat source is eliminated from thermal runaway which will aid in preventing cell to cell propagation. Anode, cathode and electrolyte development work are currently being performed in the BTMS program, so these potential solutions are actively being worked. The second control will be thermal management. Managing the heat generated from a thermal runaway event is critical in preventing cell to cell propagation. There are two strategies for thermal management: isolation where the heat generated from a cell is isolated to that cell, and conduction where the heat generated from the cell is removed from the cell. Isolation can be achieved by either physical separation or housing a cell in a phase change material. Conduction can be achieved by housing a cell in a material with high thermal transport properties and coupling that with an active cooling system. The final control will be direct monitoring of the cells or rack via a battery management system. Strategy using voltage and temperature data collected directly from the cells or rack in real time can provide state of health checks. These state of health checks when coupled with the machine learning efforts currently taking place can provide early warning diagnostics alerting the user to a potential runaway event and preventing it before it happens. The challenge in this effort is to balance both the cost and efficiency of the battery management system by only using the proper type and number of sensors. Should the above cell propagation controls fail the most effective way in preventing rack to rack failure is with an active fire protection system. All of the above options will be evaluated to minimize cost, maximize energy density, and pack efficiency in the final system.

Two safety briefings were presented to the team to help advance the design effort and solicit feedback. The first briefing focused on the basics and challenges of thermal runaway. The key takeaways from this briefing were that when normalizing for energy density, peak runaway temperatures tend to be linearly proportional to the cell specific energy. Additionally, the heat released is also linearly proportional to the stored energy. This briefing sparked the conversation on how to effectively manage thermal runaway. Different thermal management strategies are being investigated as well as concepts such as thermal peak shaving are being evaluated with the goal to prevent propagation. This effort also aligns directly with the sensing effort as symptoms of thermal runaway can be used in the BMS to electrically isolate the cell or remove energy from the string to make the event less energetic. The second briefing revolved around the two major driving regulations for large energy storage systems NFPA 855 and UL9540A. The key take away NFPA 855 is that there are several moving targets as well as gray area for each requirement with the final decision being held by the Authority having Jurisdiction which can adopt any all or none of these regulations. As a result of this briefing the energy storage size limitations and safety regulations were incorporated into the final design concept from the Advanced Power Conversion and Battery Management Systems effort. Upon completion of the briefing of 9540A Standard for Safety: Test Method for Evaluating Thermal Runaway Fire Propagation in

Battery ESS it was decided that the goal for the rack effort would be to stop propagation at the module level as a cell runaway event is unavoidable.

Finally, abuse testing was performed on commercial LTO/LMO cells in an effort to characterize the response of this new chemistry. Gas sampling analysis was performed cells that were cycled and significantly aged and compared to fresh cells in an attempt to quantify the impacts of cycling on the abuse behavior of the cell. Results show that peak temperatures observed for graphite/NMC are much higher than LTO/LMO (700°C vs. ~350°C) which has implications for the advanced rack design effort. Less heat released is easier to manage. There is a slight difference in heat released between aged LTO/LMO and fresh LTO/LMO. This could be from loss of capacity or cell to cell variation. Gas sampling analysis shows by in large combustion products of electrolyte. Quantities observed somewhat consistent with graphite/NMC CO₂ being dominate species observed. This information can be leveraged for the sensing effort as an early indication of thermal runaway. In summary, the key difference between LTO/LMO and graphite/NMC is the evolution of hydrogen and water and no significant difference observed between aged cells and fresh cells.

Report on the degradation of cells under two cycling regimes

The preliminary cycling method resulted in very rapid energy fade for the continuous routine cycled NMC/graphite cell, as illustrated in Figure V.1.11 Discharge energy fade rate for the NMC/graphite cell cycled under two BTMS cycling routines. While the cell was maintained well within its specified voltage and current limits, the continuous constant-power discharge resulted in rapid capacity loss compared to the cell intermittently discharged and charged at the same rates. This clearly showed a need to perform testing on additional cells to quantify their sensitivity to the different cycling protocols.

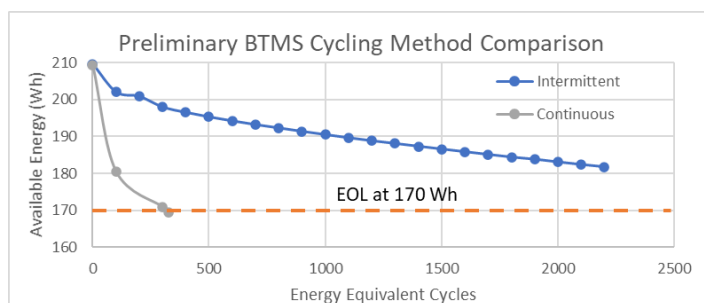


Figure V.1.11 Discharge energy fade rate for the NMC/graphite cell cycled under two BTMS cycling routines

The nickel-zinc cells tested were able to maintain the intermittent cycling routine for approximately twice as many cycles as the continuous discharged cells, yielding approximately 600 and 300 cycles respectively. Despite the appearance of slower capacity fade for the intermittent cycle cells, based on their ability to perform the cycling routine for a longer period, both groups lost capacity at similar rates. It was determined that the charging efficiency varied greatly across the SOC range for those cells, with the mid- and low-SOC partial recharges returning more capacity than was anticipated based on the average relationship between energy charged and capacity returned during a full, continuous charge. That resulted in less depth of discharge for the intermittent cycled cell when the gross discharge energy target was reached. This was verified by analyzing the rest voltage at the end of the discharge cycle, because these cells' low and variable coulombic efficiency precluded coulomb counting as a good method for estimating state-of-charge for the intermittently charged cells.

Several lead acid technologies were cycled under both routines as well, and generally the devices cycled under the intermittent routine maintained higher capacity through life. The results of the cycle life testing is captured in Table V.1.8 below. It is likely that the intermittent routine resulted in the devices reaching a less deeply discharged state at the completion of the routine. Generally, lower depth of discharge can prolong cycle life in lead acid systems.

Table V.1.8 Lead Acid Cycle Life Testing Results

Lead Acid Technology	BTMS Cycles	Continuous Cycle Relative Capacity (%)	Intermittent Cycle Relative Capacity (%)	EOL Capacity (%)
High Carbon AGM	700	78	83	70
Flat Plate Gel	300	60 (EOL)	81	60
Thin Plate Pure Lead	400	50 (EOL)	73	50
Quasi-Bipolar	500	100	98	30
Bipolar	400	50 (EOL)	58	50

Use of the EnStore Model to evaluate the economic feasibility of BTMS with cobalt-free battery chemistries

2. Sensitivity Analysis

The EDGES Model was run on the NREL High Performance Supercomputer (HPC) Eagle, across a full factorial of multiple variables. Sensitivity analysis is critical for understanding important cost levers and determining optimal configurations to meet the project objectives. The primary variables evaluated include the following:

- Climate: building energy use, battery conditioning, battery lifetime, efficiency of EVs
- Utility rate structures: demand and time-of-use charges, cost of energy
- Connection to the grid: infrastructure improvement costs (and can BTMS help reduce or defer these costs)
- Building type energy demand profiles, space limitations, population served
- Capital costs – batteries, thermal energy storage (TES), EVSEs, PV, power electronics
- Controls algorithm – when to dispatch stationary battery and TES; EnStore now uses supervisory model predictive controls (MPC)
- Storage operation – battery and TES state-of-charge, discharge/charge rate, temperature

Thousands of simulations were run, advanced visualization techniques and the development of an online tool to explore the results space.

3. Example Results – Big Box Grocery Store

Example results from simulations on a big-box grocery store are presented in this section. Each case assumes 350 kW fast EV charging at a 6-port station with 12 and 20 events per day. Figure V.1.12 provides the minimum LCOC, PV size, and battery size for the least-cost design for each case. In these cases, the utility rate structure has a significant impact on LCOC, PV size, and battery size. Location (climate), while important, has a smaller impact because EV charging demand dominates costs. With less EV demand, climate differences result in different building energy use and have a larger impact on LCOC. For the cases shown, the following assumptions were made: battery cost = \$120/kWh, \$ 540/kW; PV Cost = \$1600/kW, and EVSE cost per port = \$185,000.

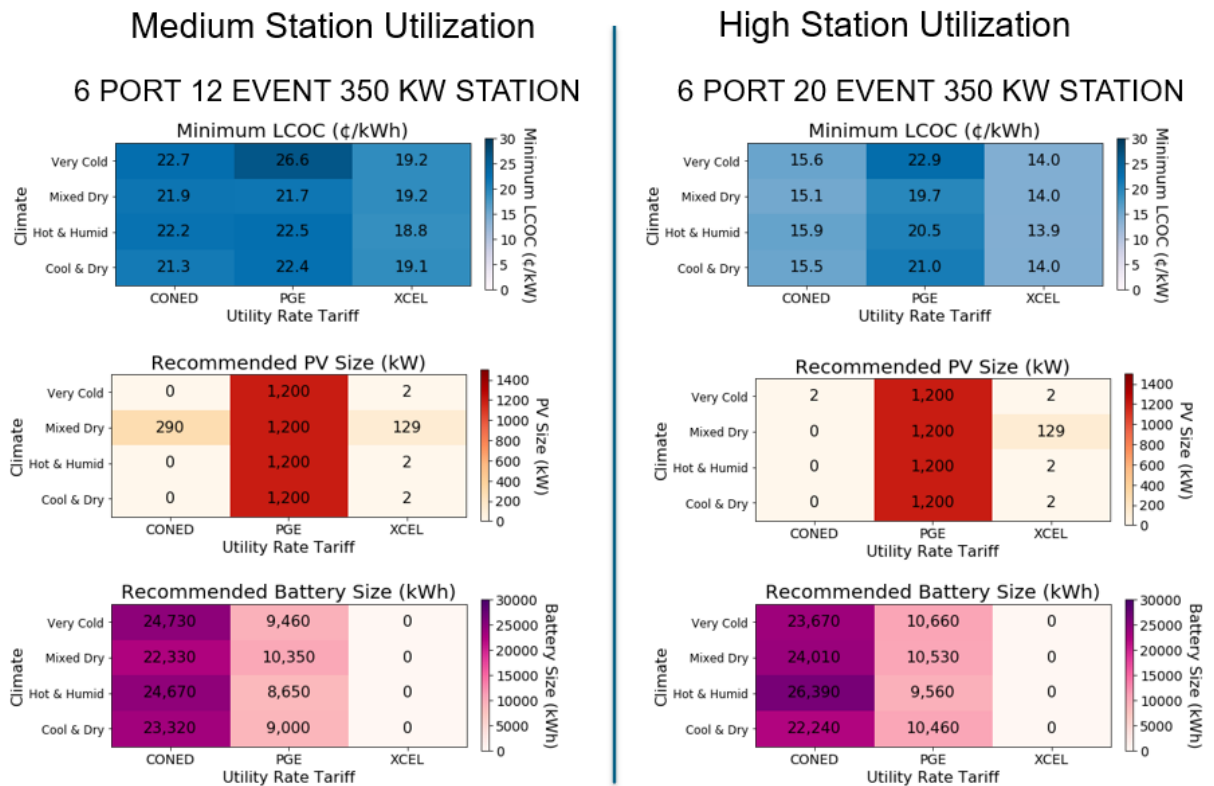


Figure V.1.12 Top-level Results for a Big-Box Grocery Store

The building and EV demand for the case assuming high-port utilization (20 events per port per day) are shown in Figure V.1.13.

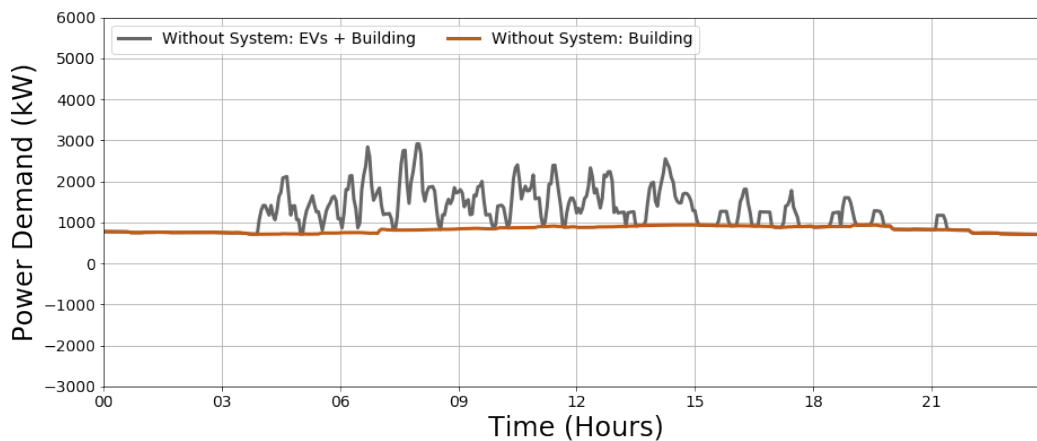


Figure V.1.13 Building and EV Demand at a Big Box Grocery Store

Figure V.1.14-Figure V.1.16 show an example day of 5-minute average power flows demonstrating the variation in dispatch of the battery for optimizing the BTMS system in a hot and humid location with different representative utility rate structures. In the Consolidated Edison case (Figure V.1.14), the battery mostly follows EV charging demand, but some electricity is purchased from the grid to supplement. For this scenario, it's cheaper to buy electricity than to install PV, although sensitivity analyses show that PV can be installed with very little impact to LCOC. In the PG&E case (Figure V.1.15), the battery is dispatched to mostly follows

EV charging demand but has strong support from PV during the sunny hours and some purchased grid electricity. In the Xcel Energy case (Figure V.1.16), a behind-the-meter battery is not recommended, as this utility rate structure has very few time-of-use energy charges and no demand charges.

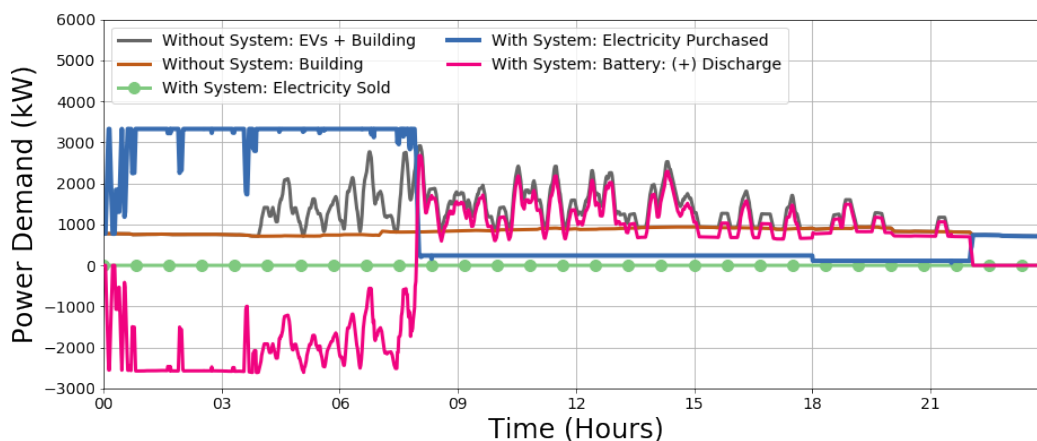


Figure V.1.14 Power Flows Across BTMS System Assuming a Consolidated Edison Utility Rate Structure

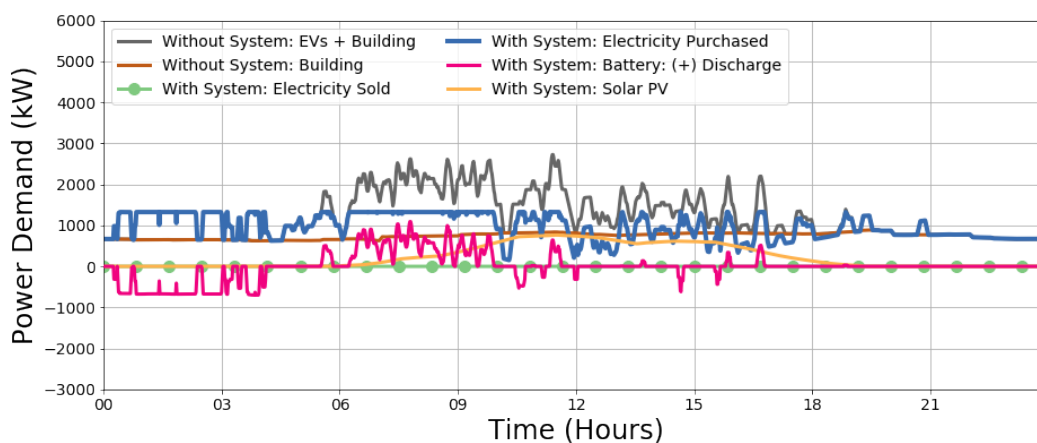


Figure V.1.15 Power Flows Across BTMS System Assuming a Pacific Gas & Electric Rate Structure

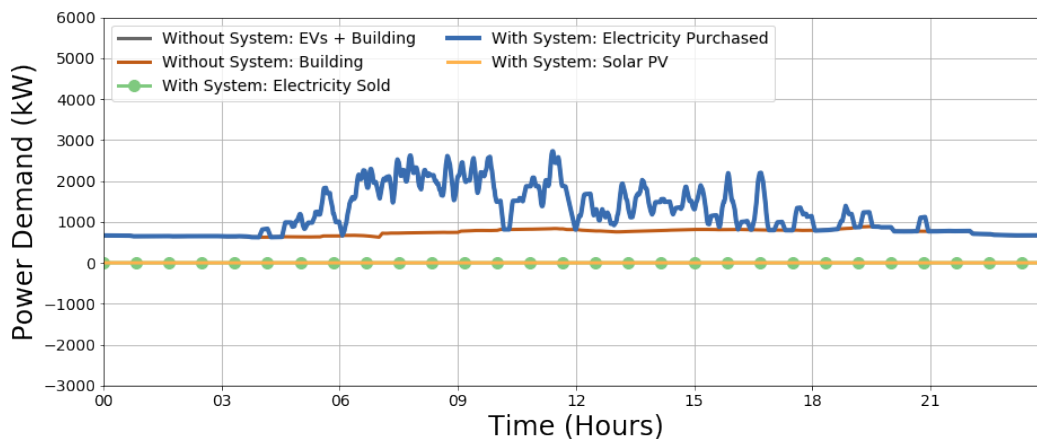


Figure V.1.16 Power Flows Across BTMS System Assuming an Xcel Rate Structure

The minimum LCOC in ¢/kWh as a function of PV and battery sizes, and the variation in LCOC as a function of battery and PV size are shown in Figure V.1.17-Figure V.1.19 for each of the three representative utility rates. The optimized design for each case is highlighted with a circle, while the LCOC without BTMS is highlighted with a square. The addition of a stationary battery and PV results in a 42% reduction in LCOC for the Consolidated Edison case, and a 29% reduction in LCOC for the PG&E case. No change in LCOC is shown in the Xcel Energy case (Figure V.1.19), because a behind-the-meter battery was not recommended.

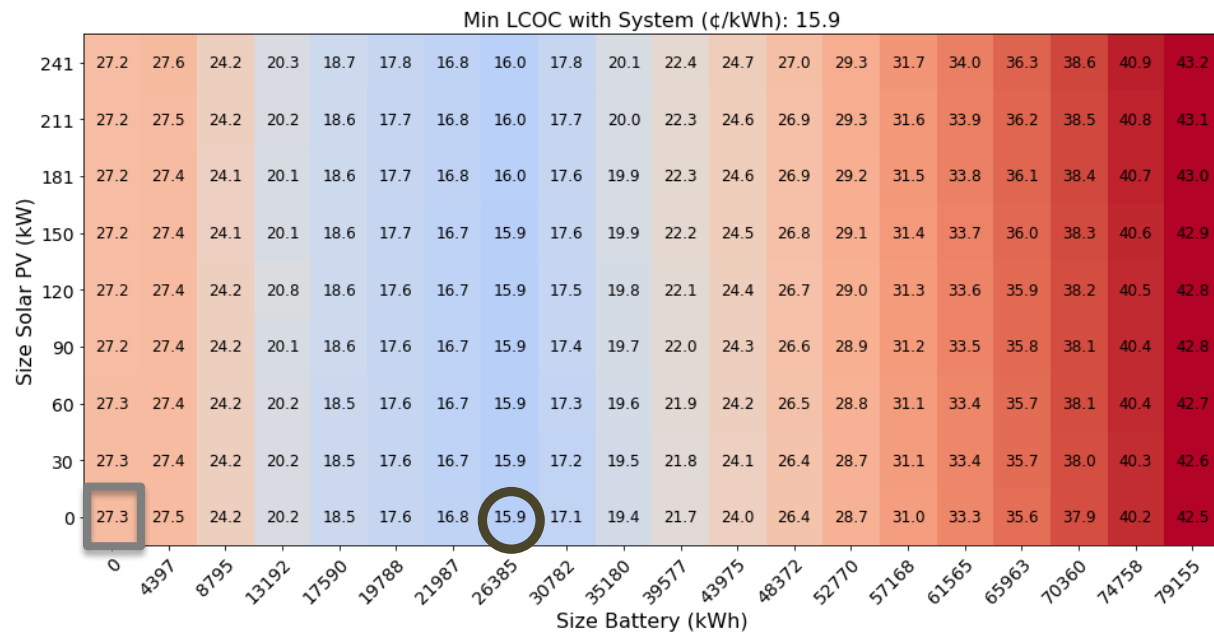


Figure V.1.17 LCOC as a Function of PV & Battery Size for a Consolidated Edison Rate Structure

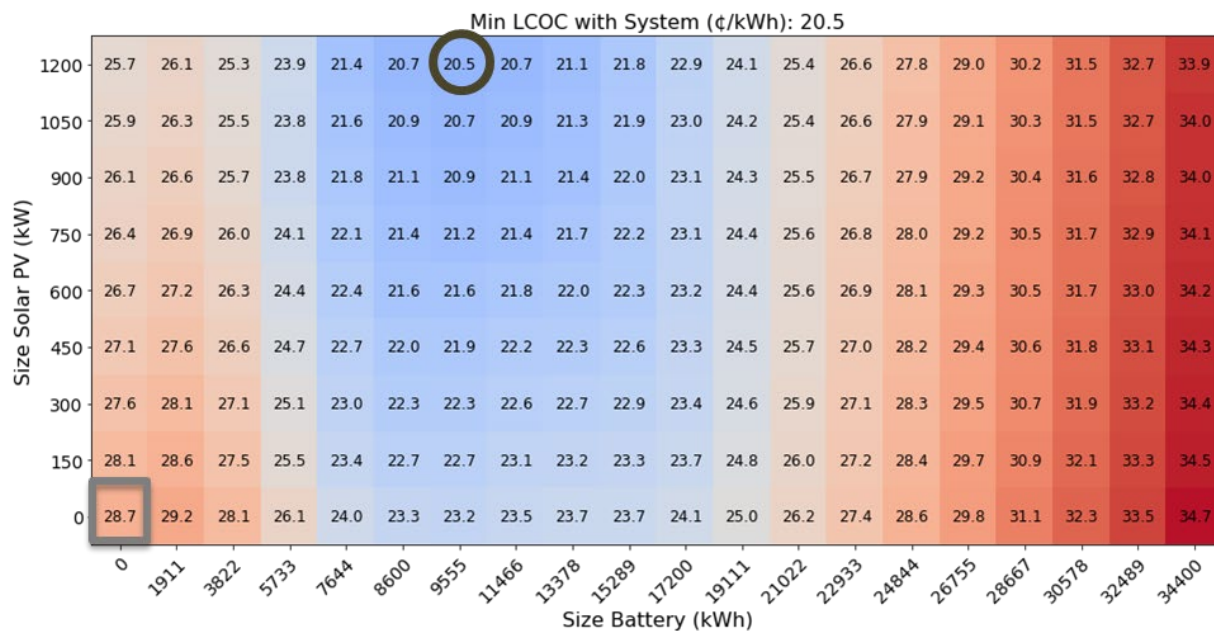


Figure V.1.18 LCOC as a Function of PV & Battery Size for a PG&E Rate Structure

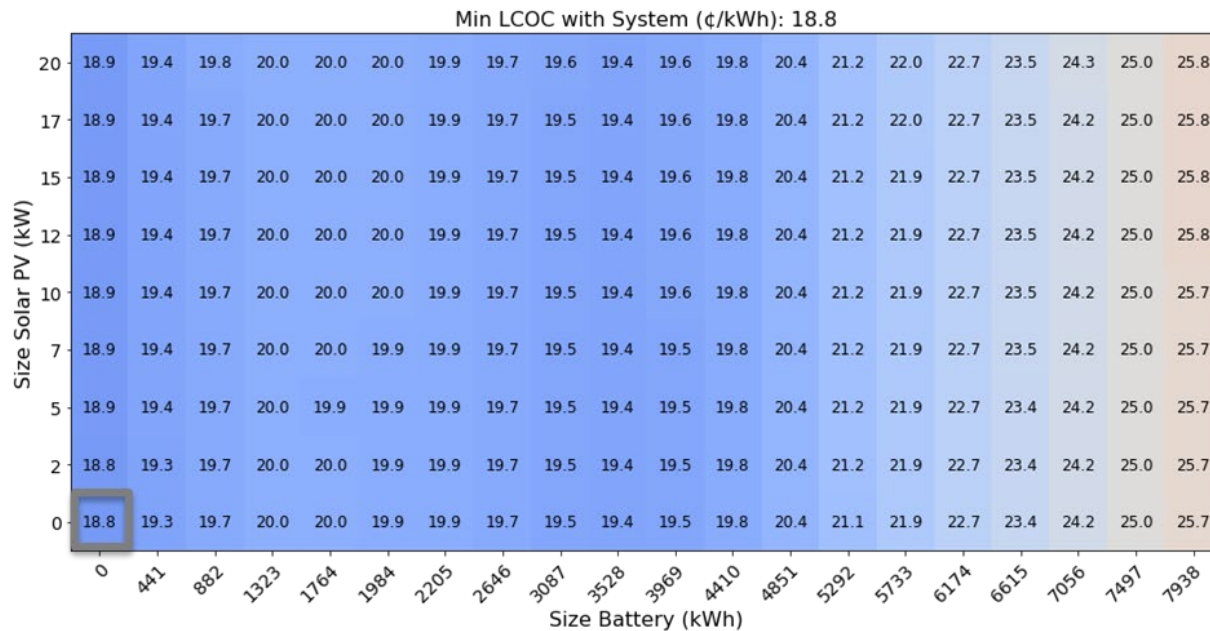


Figure V.1.19 LCOC as a Function of PV & Battery Size for ae Xcel Energy Rate Structure

4. Visualization of Results

The fourth quarterly milestone for this project was to develop an interactive visualization tools for scenario exploration by audiences outside of project team such as DOE and industry advisors. A dashboard for interactively exploring the results of the thousands of scenarios run in the EDGES Model was developed using Plotly, which is an open-source front-end platform that wraps JavaScript visualization libraries so they can be used in Python, R, or Julia. The project used the Python bindings to connect to results on the HPC; visualizations are deployed on a website using Flask. (<https://plotly.com>). The primary heatmaps, similar to those shown in Figure V.1.12, summarize the data results. Filters can be applied to By selecting a cell in the primary heat map, the user can examine results similar to those in Figure V.1.14–Figure V.1.19. A screen capture of the EDGES dashboard is shown in Figure V.1.20. Use of the dashboard is very intuitive and zoomable online. For a copy of credentials to use the dashboard, please contact Monte Lunacek at monte.lunacek@nrel.gov.



Figure V.1.20 Screen Capture of the EDGES BTMS Results Dashboard

BTMS Materials Development

Figure V.1.21 shows the long-term cycle performance (>5000 cycles) of LTO/LMO coin cells fabricated with and without electrochemical prelithiation of the LTO anode. As the absence of linear carbonate in the EC electrolyte impedes Li^+ ion transport, the cells were tested at 45°C. Dreamweaver Gold 20 and Celgard 2325 separators were used for EC and Gen2 electrolytes, respectively, since cyclic carbonate-only electrolytes cannot wet polyolefin separators. PrelithEC cell, which contains electrochemically prelithiated (0.42 mAh/cm²) LTO electrode, exhibits negligible capacity fade up to ~3500 cycles, and then the capacity starts to decrease with a similar slope as the non-prelithiated cell. The non-prelithiated EC cell shows 0.42 mAh/cm² fade by ~3500 cycle, indicating the capacity fade rate remains similar regardless of the prelithiation. Gen2 electrolyte shows faster capacity fade compared to the EC electrolyte.

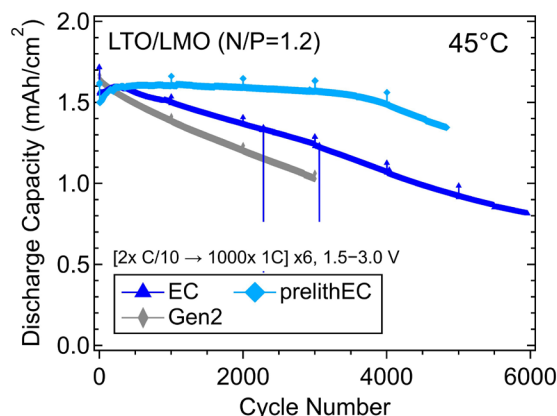


Figure V.1.21 Impact of electrochemical prelithiation of the LTO electrode on the long-term cycle performance of LTO/LMO cells.

Figure V.1.22 shows the impact of N/P ratio on the cycle performance of LTO/LMO coin cells. Three different N/P ratios ($N/P > 1$, $N/P = 1$, $N/P < 1$) were tested by fixing the LTO electrode to 3.35 mAh/cm² and varying the LMO electrode loadings. Comparing EC and Gen2 electrolytes at 45°C, EC electrolyte shows lower discharge capacity due to limited Li^+ ion transport and poor electrode utilization. However, EC cells exhibit better

capacity retention than the Gen2 cells upon long-term cycling, which agrees with the trend observed from thinner electrodes (Figure V.1.21). For both electrolytes, $N/P < 1$ cells show higher discharge capacity and better capacity retention than $N/P = 1$ cells. While an elevated operating temperature of 45°C is necessary for the EC electrolyte, Gen2 electrolyte shows good rate capability and stable performance at 30°C for all N/P ratios. Specifically, the $N/P < 1$ cells exhibit negligible capacity fade up to 1500 cycles.

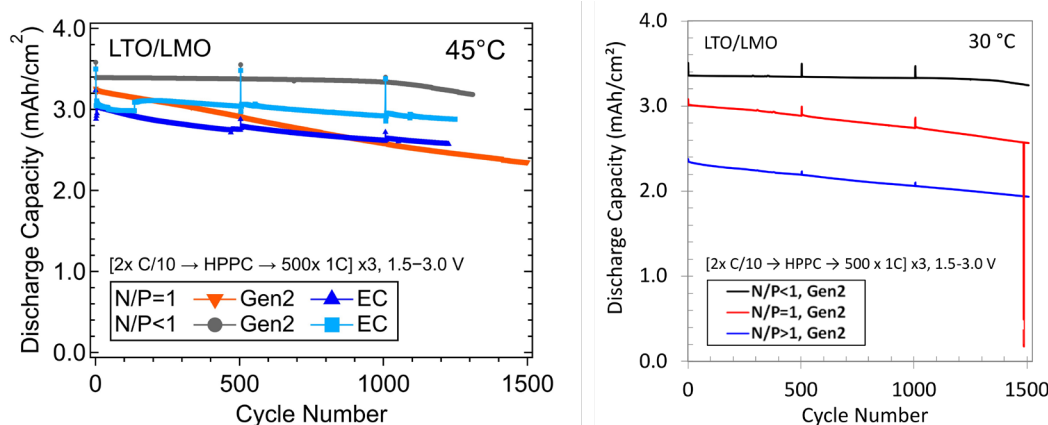


Figure V.1.22 Impact of N/P ratio on the long-term cycle performance of LTO/LMO cells.

Based on these results, 2 Ah pouch cells were fabricated using LTO and LMO electrodes with $3.35 \text{ mAh}/\text{cm}^2$ and $3.94 \text{ mAh}/\text{cm}^2$ areal capacities, respectively, to have an N/P ratio of 0.90 based on total anode area (785.6 cm^2) and cathode area (740.8 cm^2) for xx6395 build design. Two different sets of cells were examined: (1) Gen2 electrolyte and Celgard 2500 separator tested at 30°C ; and (2) EC electrolyte and Dreamweaver Gold 20 separator tested at 45°C . The Celgard 2500 cells were dried at 60°C in a vacuum oven, filled with Gen2 electrolyte and vacuum sealed in the dry room like typical. On the other hand, due to the hydrophilic nature of the Dreamweaver Gold 20 separator, these cells were dried to 100°C , filled with the EC electrolyte, and vacuum sealed in an argon gas glovebox. In addition, during the degassing step, it was noticed that the EC electrolyte crystallized at room temperature, so the cells were degassed while still warm and placed directly back in the 45°C oven. After forming and degassing, both sets of cells were then put back onto a rate test as shown in Figure V.1.23. Notably, EC electrolyte shows better rate capability in pouch cells compared to the coin cell results (Figure V.1.22), potentially due to enhanced wetting in pouch cells with vacuum sealing. The cells were degassed again due to all the gassing that occurred during the rate test and are currently under long-term cycle testing.

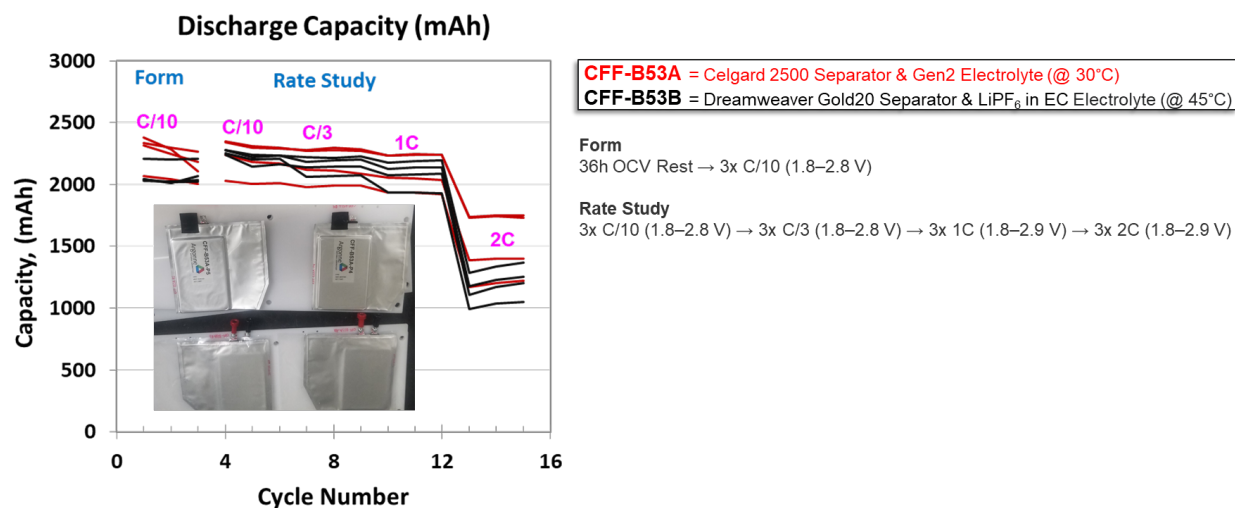


Figure V.1.23 Formation cycles and rate performance of 2 Ah LTO/LMO pouch cells.

Conclusions

Enabling Technologies for an Advanced Rack Design

In FY21, we identified the critical parameters needed to prevent thermal propagation within an advanced rack design.

Report on the degradation of cells under two cycling regimes

For some chemistries and cell designs, it is clear that there can be a significant impact on aging based on the methods used to simplify real-world scenarios into cycling tests that can be consistently executed in the lab. Therefore, it is important that the cycling protocols capture more than simply average rate, throughput, and depth of discharge; the timing of power demand and recharging must also be representative of the system in which the cells are being qualified to perform.

BTMS Materials Development

In FY21, we obtained thorough understandings of the LTO/LMO system and leveraged the findings to successfully design and deliver 2 Ah pouch cells. Moving forward, we will begin the development of BTMS chemistry version two by examining low- or no cobalt-containing cathodes (e.g., $\text{LiNi}_{0.9}\text{Mn}_{0.1}\text{O}_2$, $\text{LiNi}_{0.9}\text{Mn}_{0.05}\text{Co}_{0.05}\text{O}_2$, $\text{LiNi}_{0.95}\text{Co}_{0.05}\text{O}_2$) paired with LTO anode.

Key Publications

BTMS Materials Development

1. Ha, Yeyoung, Steven P. Harvey, Glenn Teeter, Andrew M. Colclasure, Stephen E. Trask, Andrew N. Jansen, Anthony Burrell, and Kyusung Park. 2021. "Long-term cyclability of $\text{Li}_4\text{Ti}_5\text{O}_{12}/\text{LiMn}_2\text{O}_4$ cells using carbonate-based electrolytes for behind-the-meter storage applications." *Energy Storage Materials* 38:581–589. doi: <https://doi.org/10.1016/j.ensm.2021.03.036>.
2. Ha, Yeyoung, Andrew M. Colclasure, Stephen E. Trask, Shabbir Ahmed, Kevin L. Gering, Andrew N. Jansen, Anthony Burrell, and Kyusung Park. 2021. "Impact of electrode thickness and temperature on the rate capability of $\text{Li}_4\text{Ti}_5\text{O}_{12}/\text{LiMn}_2\text{O}_4$ cells." *Journal of the Electrochemical Society*. doi: <https://doi.org/10.1149/1945-7111/ac3781>.

VI Testing, Analysis, High-Performance Computing, Lab-I4

VI.1 BatPaC Model Development (Argonne National Laboratory)

Shabbir Ahmed, Principal Investigator

Argonne National Laboratory
9700 South Cass Avenue
Argonne IL 60439
E-mail: Shabbir.Ahmed@anl.gov

Brian Cunningham, DOE Technology Development Manager

U.S. Department of Energy
E-mail: Brian.Cunningham@ee.doe.gov

Start Date: October 1, 2020	End Date: September 30, 2023	
Project Funding (FY21): \$900,000	DOE share: \$900,000	Non-DOE share: \$0

Project Introduction

A performance and cost model (BatPaC [2]) was developed at Argonne to design automotive Li-ion batteries that can meet the specification of a given vehicle, and then to estimate the cost of manufacturing such batteries. It is the product of long-term research and development at Argonne through sponsorship by the U.S. Department of Energy.

Over a decade, Argonne has developed methods to design Li-ion batteries for electric-drive vehicles based on modeling with Microsoft® Office Excel spreadsheets. These design models provided all the data needed to estimate the annual materials requirements for manufacturing the batteries being designed. This facilitated the next step, which was to extend the effort to include modeling of the manufacturing costs of the batteries.

The BatPaC model has been peer reviewed and is available on the web [1]. It captures the interplay between design and cost of Li-ion batteries for transportation applications. BatPaC helps estimate the impact of R&D advances on the mass, volume, and cost of lithium-ion cells and battery packs. Moreover, BatPaC is the basis for the quantification of battery costs in U.S. EPA and NHTSA 2017-2025 Light-Duty Vehicle Technical Assessment. This assessment is used to determine what mileage (i.e., CAFE) and CO₂ emission standards are optimal from a cost-benefit analysis.

Objectives

To develop and utilize efficient simulation and design tools for lithium-ion batteries to predict:

- Overall and component mass and dimensions
- Cost and performance characteristics when manufactured in large volume
 - Specific Energy (Wh/kg), Energy Density (Wh/L)
 - Cost to achieve fast charge time and power needs
 - Inventory of key materials that are available for recycle

Approach

The battery pack design and cost calculated in BatPaC represent projections for a specified level of annual battery production (10,000–500,000). As the goal is to predict the future (~5 years) cost of manufacturing batteries, a mature manufacturing process is assumed. The model designs a manufacturing plant with the sole purpose of producing the battery being modeled. The assumed battery design and manufacturing facility are based on common practice today but also assume some problems have been solved to result in a more efficient production process and a more energy dense battery. The proposed solutions do not have to be the same methods used in the future by industry. It is assumed the leading battery manufacturers, those having successful operations in the near future, will reach these ends by some means.

For a selected battery chemistry, BatPaC solves the governing equations to determine the size of each layer, cell, and module that make up the battery pack that can meet the desired requirements for power and energy. This allows the calculation of the mass of each material, the volume of the components, and the heat removal needed during discharge. The cost of the pack is then estimated based on a predefined manufacturing process.

Current effort is directed at

- Improving the design capability by including correlations derived from continuum modeling and updating the default material properties to reflect recent experimental and industrial performance data
- Reducing the uncertainty of model predictions by setting up independent models of the manufacturing processes
- Validating the results through discussions with manufacturers and component developers
- Updating the cost of materials used in BatPaC calculations

Results

Key Accomplishments

- Developed an electrochemical + thermal model to simulate fast charge capabilities
- Developed a tool to correlate area specific impedance (ASI) to temperature
- Developed a tool to validate the active material specific capacities, the cell voltages, and the negative to positive capacity ratio
- Used BatPaC in a study of total cost of ownership between electric vehicles and internal combustion engine vehicles
- Conducted a plant design study to compare and update BatPaC cost parameters

Fast Charging a Cell

The current version of BatPaC (4.0) uses three current (C-rate) ramp rates to compute the required thickness for a given charging time. While this method has reasonable fidelity, it can overshoot several possible safety limits—*i.e.*, lithium plating, cell temperature, and charger limits. To understand the practical limits of how fast a cell can be charged, an external electrochemical + thermal model was developed and used to simulate charging under controlled risk conditions. Results of the simulations are being implemented into the next iteration of BatPaC (5.0). They provide reasonable estimates for minimum achievable charge times based on electrode thickness and operational limits during charging.

The model was used to study the limits of fast charging under thermal and electrical considerations by controlling the charging current and the coolant flow based on the trajectory of the lithium plating overpotential and the cell temperature. To control the charging current, a constant risk (CR) charging protocol

was introduced that maximizes the current within pre-defined, operational limits that minimize the risk of degradation. These limits are set for the following design variables: *i*) the maximum allowable C-rate to prevent particle fracturing (I_{lim}), *ii*) the maximum allowable temperature to prevent electrolyte decomposition ($T_{max,lim}$), and *iii*) the minimum allowable overpotential to protect against lithium plating in the anode (η_{PP}). The current is reduced when the cell voltage approaches η_{PP} ; the coolant flow is started when the temperature approaches $T_{max,lim}$. Each simulation provides the minimum charge time within the operational limits. Correlations from these results are being implemented into the next version of BatPaC (5.0), which will allow users to understand how changes in charging conditions influence the design constraints on the cell. For instance, allowing a higher $T_{max,lim}$ permits operating at higher sustained currents and allows for thicker electrodes. Thicker electrodes reduce the cell cost by reducing the fraction of inactive materials (current collectors, separators, etc.). The figure below highlights simulation results and demonstrates how changing the charging conditions impacts the allowable electrode thickness and cell cost for a target charging time.

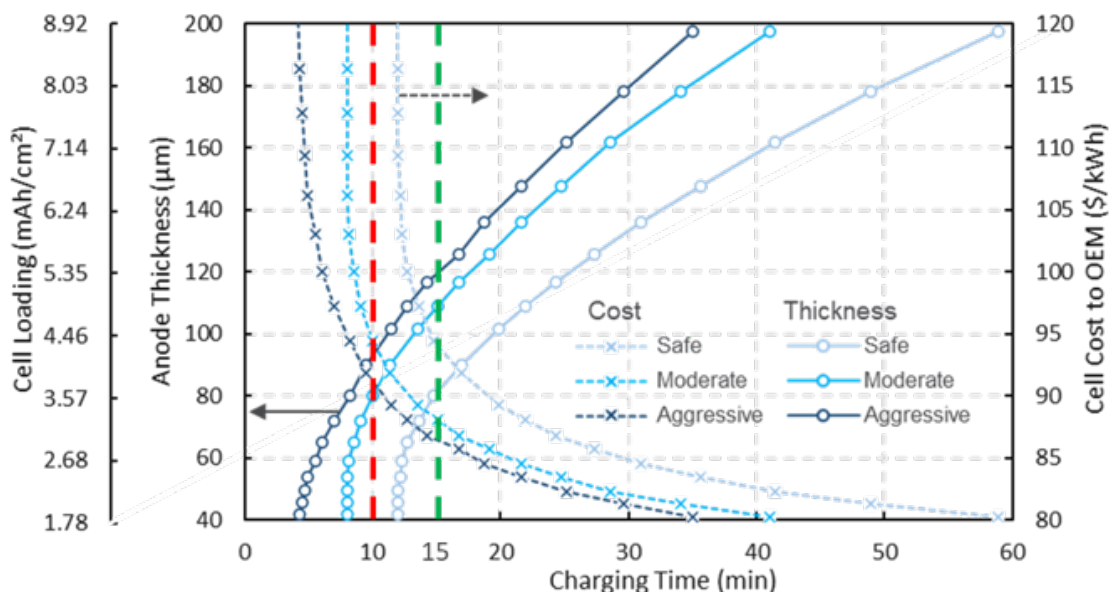


Figure VI.1.1 Maximum achievable anode thickness/loading and corresponding cell cost as a function of charging time using the fast-charge model for a set of NMC532/G cells. Dashed red line corresponds to 10 min charging time, whereas the green corresponds to 15 min charging time. Safe charging conditions correspond to $T_{max,lim} = 45^\circ\text{C}$, $I_{lim} = 4\text{C-rate}$, $\eta_{PP} = 30\text{ mV}$; moderate charging corresponds to $T_{max,lim} = 55^\circ\text{C}$, $I_{lim} = 6\text{C-rate}$, $\eta_{PP} = 10\text{ mV}$; and aggressive charging corresponds to $T_{max,lim} = 60^\circ\text{C}$, $I_{lim} = 12\text{C-rate}$, $\eta_{PP} = 0\text{ mV}$. Charging time is determined from 15% to 95% SOC.

ASI Dependence on Temperature and Cycle Life

The current version of BatPaC (4.0) does not include the influence of operating temperature on the area specific resistance (ASI), which is a major performance parameter used in the design of the battery. Understanding the ASI/temperature relationship is important for the standard operation and for fast charge applications where the temperature rises at the high applied currents. Thus, a comprehensive study was conducted which examined the electrochemical behavior of lithium-ion batteries containing five different cathode materials (one NCA and four NMC), all with graphite anodes, as a function of temperature from -20 to 40°C . ASI values were obtained using three different DC methodologies: *i*) average voltage from discharge curves, *ii*) curve fitting to discharge curves, and *iii*) hybrid pulse power characterization (HPPC). Pre-factors and activation energies for Arrhenius expressions of the ASI for all five cells (calculated using all three DC methods) were obtained with the equation described below.

$$ASI(T) = R_{ASI,0} \cdot \exp \left[\frac{E_a}{R} \left(\frac{1}{T_{ref}} - \frac{1}{T} \right) \right]$$

The rationale for comparing these different methods to compute the ASI is that BatPaC examines numerous electrode couples. The experimental data for each couple can be gathered from different sources and suppliers; testing protocols are not always consistent between these groups. Thus, having values for the ASI from several methods allows for comparisons across multiple sources and helps in the selection of consistent baseline values. Figure VI.1.2 highlights the differences among these methods for a NMC532/graphite couple.

Table VI.1.1 Reference ASI and activation energies for the 4 methods needed for the Arrhenius equation

Cathode	Fit to V_{avg} vs. I		Curve Fitting ^a		HPPC, 2 s ^a		HPPC, 10 s ^a	
	$R_{ASI,0}$ ($\Omega \text{ cm}^2$)	E_a (kJ/mol)	$R_{ASI,0}$ ($\Omega \text{ cm}^2$)	E_a (kJ/mol)	$R_{ASI,0}$ ($\Omega \text{ cm}^2$)	E_a (kJ/mol)	$R_{ASI,0}$ ($\Omega \text{ cm}^2$)	E_a (kJ/mol)
NMC111	41	-21	37	-23	30	-23	34	-22
NMC532	27	-27	26	-30	20	-30	24	-28
NMC622	31	-30	30	-30	20	-30	25	-28
NMC811	30	-31	30	-27	20	-29	25	-27
NMC111	41	-21	37	-23	30	-23	34	-22

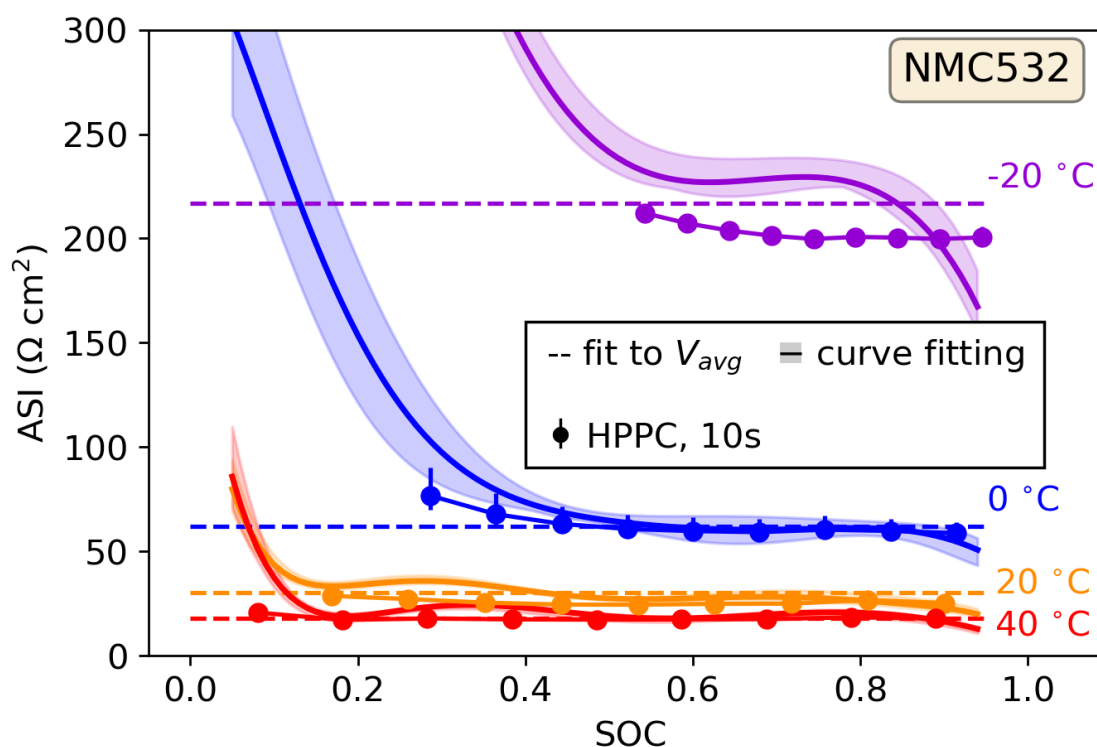


Figure VI.1.2 Comparison of ASI calculated from all three methods as a function of SOC for coin-cells with NMC532 cathodes and graphite anodes. State of charge (SOC) is reported with respect to the C/20 capacity, where all cells were assumed to be at 100% SOC at top of charge. The methods are i) average voltage from discharge curves, ii) curve fitting to discharge curves, and iii) hybrid pulse power characterization (HPPC).

Effect of Plant Utilization

BatPaC 4.0 assumes that the plant always produces at the design capacity. However, many battery-manufacturing plants are designed for larger future demands and go into production to meet current demands. The method in which they start production affects the cost of the product based on how these plants are set up.

A short study was conducted to compare the effects of the operating methods, by looking at the effect of the plant utilization. The three methods are described below.

- Method 1: The default case where the plant production rate is at full capacity
- Method 2: Equipment is provided only for the initial part-production level, but the space is provided for full-scale production
- Method 3: The plant is built for full capacity, but operated at part-capacity

Figure VI.1.3 shows how the plant utilization can alter the price of the pack. The idled extra production capacity incurs a cost which leads to a higher pack price. The cost of under-utilization is highest when the plant (space + equipment) is built for full capacity (Method 3). The new version of BatPaC (5.0) will allow the user to distinguish between the three methods to better understand the effect of plant overdesign on pack cost.

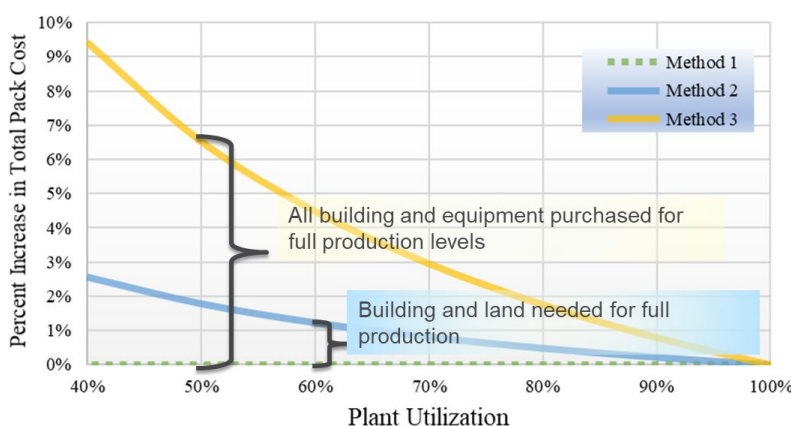


Figure VI.1.3 Change in the total pack cost for the different plant utilization methodologies.

Negative-to-Positive Capacity Ratio (N2P)

A new tool has been developed that enables a cross-check between the active material specific capacities, the cell voltage window, and the minimum negative-to-positive capacity ratio. The tool ensures that the three parameters are self-consistent and that the full capacity of the positive electrode, which is typically the limiting component, is available for use. The tool provides a self-consistent method for determining the capacities (mAh/g) of the active materials and the voltage of the cell based on the desired negative-to-positive (N2P) capacity ratio in the cell. For a given electrode couple, the calculation allows the user to input a desired N2P ratio after formation, expected capacity losses during formation, and target cell voltage at 100% state-of-charge. This information is combined with capacity vs. voltage relationships for each electrode from the literature/experiments to calculate the specific capacities of both electrode materials and the voltage vs. state-of-charge for the cell. The calculation is an improvement over BatPaC 4.0 because it guarantees self-consistency between the N2P ratio, capacities, and voltages when over-riding the baseline assumptions for a given electrode couple. It also allows the user to study the influence of N2P ratio, formation losses, and allowable voltage on the design of the pack. Figure VI.1.4 shows how the specific capacities of the materials and voltages from the default electrode couples change using this tool. Slight modifications are observed for most parameters. The largest changes are associated with increases in the default NMC capacities in Figure VI.1.4a).

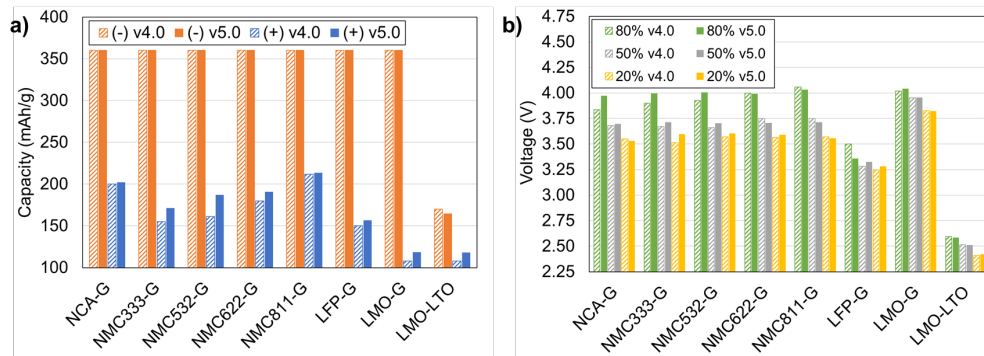


Figure VI.1.4 Comparison of default a) capacities and b) voltages used in old (4.0) and new (5.0) versions of BatPaC. Values for 5.0 were calculated using the N2P calculator that guarantees self-consistency among voltages, capacities, and formation losses. Values for 5.0 assume 1% negative capacity loss, 5% positive capacity loss, and 20 mAh/g_{graphite} SEI losses during formation for all couples with graphite. The LTO couple assumes no negative or SEI losses.

Plant Design Study

A plant design exercise was conducted with the help of an industrial collaborator, Top Materials Inc. The objective was to do a preliminary design of a large volume (5-50 GWh) lithium-ion battery manufacturing plant starting production in 3-7 years. The data generated are being reviewed to update the cost factors in BatPaC. The plant design included an assessment of the labor, the capital equipment, the floor space, and the utilities required for each of the processing steps. The cost of the capital equipment is converted to installed cost and the floor space is multiplied by a cost factor (\$3,000/m²) to represent cost of building, infrastructure, and utilities. BatPaC assumes an average labor rate of \$24/hr.

For a 5 GWh plant producing EV cells, the generated data (for material prices, labor requirement, the capital equipment, and the floor space) were applied to BatPaC to illustrate the effect on the cell cost estimate. Figure VI.1.4 shows that the baseline cost of the cell estimated from the default parameters of BatPaC is \$95/kWh. Progressively applying the new values from the study shows that the material prices have the biggest impact, followed by the capital investment, and depreciation rate. The BatPaC default of depreciation rate of 16.67% was changed to 10% per year. The final cost upon applying the new parameter values is \$79.5/kWh. The presented comparison is for a 100-kWh pack built from 67 Ah cells, using NMC811 and graphite as the active materials.

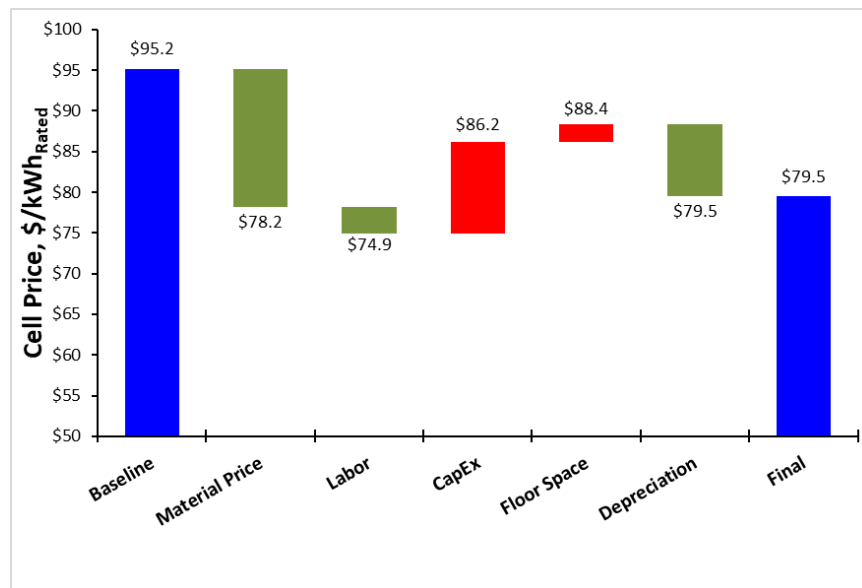


Figure VI.1.5 Effect of new estimates for costs of material, labor, capital equipment, floor space, and the depreciation rate. [67 Ah cells, NMC811-Graphite, 5 GWh plant]

Conclusions

- An electrochemical-thermal model provided design constraints for electrode thickness and charge time with respect to fast charging conditions (maximum temperature, maximum C-rate, minimum overpotential for lithium plating).
- Measured activation energies between -30 and -20 kJ/mol were implemented in BatPaC to account for temperature effects on area specific impedance (ASI).
- BatPaC now allows for studying the cost implications of under-utilizing a manufacturing plant. Under-utilizing the plant (equipment + building) by 50% can increase the full pack cost by ~6.5%.
- A new tool provided self-consistent capacity and voltage values for the default battery couples, which changed the capacities and voltages by -3 to 16% and -4 to 4%, respectively, from the previous version of BatPaC.
- Results of a new plant design study reduced the cell cost by ~16% due to decreases in the assumed material prices and depreciation time.

Key Publications

1. Ehsan Islam, Shabbir Ahmed, Aymeric Rousseau, “Future Battery Material Demand Analysis Based on U.S. Department of Energy R&D Targets,” *World Electric Vehicle Journal*, 2021, 12, 90. [<https://doi.org/10.3390/wevj12030090>]
2. Zhe Liu, Juhyun Song, Joseph Kubal, Naresh Susarla, Kevin W. Knehr, Ehsan Islam, Paul Nelson, Shabbir Ahmed, “Comparing total cost of ownership of battery electric vehicles and internal combustion engine vehicles,” *Energy Policy*, 158 (2021) 112564, [<https://doi.org/10.1016/j.enpol.2021.112564>]

References

1. Chemical Sciences and Engineering Division, A. N. (2021). BatPaC Model Software. (Chemical Science and Engineering Division, Argonne National Laboratory) Retrieved from ANL.GOV/CSE: <https://www.anl.gov/cse/batpac-model-software>
2. Nelson, P., Ahmed, S., Gallagher, K., & Dees, D. (2019). Modeling the Performance and Cost of Lithium-Ion Batteries for Electric-Drive Vehicles, ANL/CSE-19/2, DOI:10.2172/1503280. Argonne National Laboratory.

Acknowledgements

K. Knehr, J. Kubal, P. Nelson, D. Dees, Z. Liu, J. Song, H.-K. Kim, Cell Analysis Modeling and Prototyping Facility (CAMP), D. Robertson, E. Islam, G. Henriksen, R.W. Jin (TopMaterials, Inc).

VI.2 Battery Performance and Life Testing (Argonne National Laboratory)

Ira Bloom, Principal Investigator

Argonne National Laboratory
9700 South Cass Avenue
Lemont, IL 60439
E-mail: ira.bloom@anl.gov

Samm Gillard, DOE Technology Development Manager

U.S. Department of Energy
E-mail: Samuel.Gillard@ee.doe.gov

Start Date: October 1, 2020

End Date: September 20, 2021

Project Funding (FY21): \$850,000

DOE share: \$850,000

Non-DOE share: \$0

Project Introduction

Batteries are evaluated using standard tests and protocols that are transparent to technology. These protocols are based on those developed by the USABC [\[1\]](#), [\[2\]](#), [\[3\]](#), [\[4\]](#).

Objectives

- Provide DOE, USABC, and battery developers with reliable, independent, and unbiased performance and life evaluations of cells, modules, and battery packs.
- Benchmark battery technologies that were not developed with DOE/USABC funding to ascertain their level of maturity.

Approach

The batteries are evaluated using standardized and unbiased protocols, allowing a direct comparison of performance within a technology and across technologies. For those tested using the USABC methods, the performance of small cells can be compared to that of larger cells and full-sized pack by means of a battery scaling factor [\[1\]](#), [\[2\]](#).

Results

Batteries, which were fabricated during programs with developers, are sent to Argonne for evaluation. Here, the purpose of evaluation is two-fold: to provide confirmation of other test information and to provide an independent assessment of the state of the given battery technology, that is, how does it compare to the USABC [\[1\]](#), [\[2\]](#), [\[3\]](#), [\[4\]](#) and/or project goals. A list of program deliverables associated with Argonne during fiscal year 2020-21 is given in Table VI.2.1, along with their status.

Table VI.2.1 Status of Deliverables for Testing

Developer	Sponsor	Quantity x System Level	Application	Status
WPI	USABC	24 x 1 Ah cells	Recycling/EV	On-going
WPI	USABC	24 x 10 Ah cells	Recycling/EV	On-going
SiNode	USABC	24 x 8.9 Ah cells	EV	Complete
NanoGraf	USABC	24 x 1 Ah cells	EV	On-going
WPI/Microvast	USABC	52 x 0.045 Ah cells	LCFC	On-going
Microvast	DOE	18 x 35 Ah cells	XFC	On-going
ORNL	DOE	18 x 2 Ah cells	XFC	Complete
UT ORNL	DOE	9 x 2 Ah cells	XFC	Complete
UT ORNL	DOE	16 x 2 Ah cells	XFC	Complete
Stonybrook	DOE	18 x 1.01 Ah cells	XFC	On-going
UMich	DOE	18 x 2.9 Ah cells	XFC	On-going
Group14	DOE	16 x 0.4 Ah cells	EV	On-going
LG	DOE	18 x 58.4 Ah cells	EV/comparison testing	Complete
ANL CAMP	DOE	18 x 0.03 Ah cells	XFC	On-going
Si Consortium Project	DOE	24 x 1 Ah cells	Voltage-hold confirmation	Complete
24M	USABC	18 x 52 Ah cells	EV	Complete
SiNode	USABC	24 x 1 Ah cells	EV	Complete

Refilling an automobile with gasoline typically takes ten minutes or less. Decreasing the charging time of a battery to something that today's drivers are accustomed represents a technical challenge. To do this, the battery must be charged at very high rates. Here, not only does the technology have to avoid lithium deposition at the high charge rate, but the technology must also avoid life-shortening degradation caused by i^2R heating from the high current/power. There are, in principle, many ways to do this, including increasing the pack voltage so that the current at high power is relatively low. This is an engineering solution. Perhaps, a better way to overcome these issues is to develop or adapt lithium-ion technology to tolerate or avoid the problems.

There were many different solutions proposed to the fast-charge problem under the XCEL Project. The target for the project is to be able to discharge 180 Wh/kg after a 10 min charge at the beginning of life and not exhibit more than 20% energy loss after 500 cycles. Some results from one of these projects is shown in Figure VI.2.1.

Figure VI.2.1 shows that, after 10 cycles, the C/1 discharge energy for this group of cells met the beginning-of-life goal of 180 Wh/kg. Indeed, with continued cycling, the average energy fade was 2.7% after 500 cycles, clearly exceeding the project goal. The cells did not reach the end-of-life metric until after more than 1700 cycles were accrued. These results indicate that solutions to the XFC are possible and that project goals can be met (and, in some cases, exceeded).

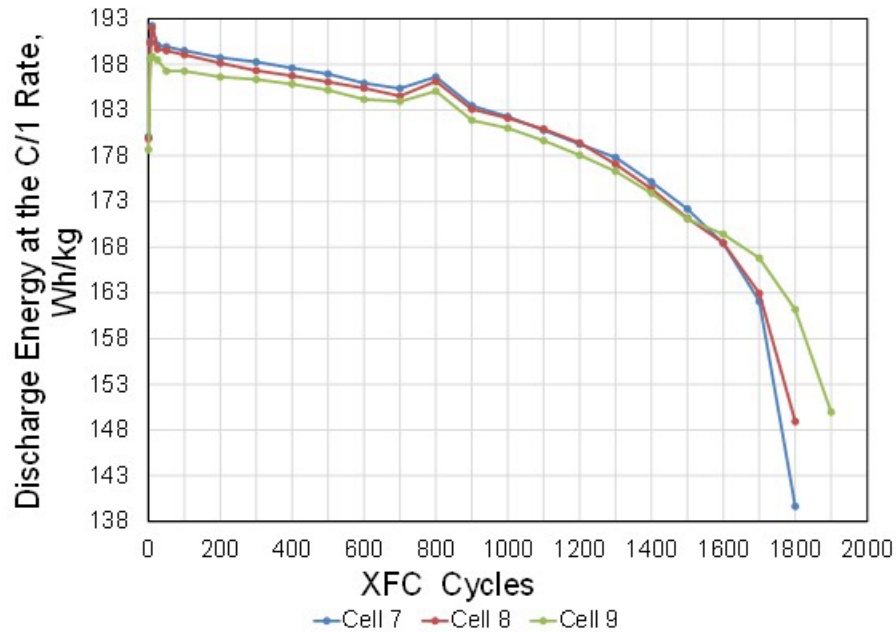


Figure VI.2.1 C/1 discharge energy vs. cycle count for cells undergoing XCEL charging.

Conclusions

We will continue to support DOE's and the USABC's cell development efforts by providing unbiased evaluation of cell performance. In the case cited above, there appears to be at least one solution to the general fast-charging problem.

Acknowledgments

David Robertson and LeRoy Flores contributed significantly to this project.

References

1. FreedomCAR Battery Test Manual for Power-Assist Hybrid Electric Vehicles, DOE/ID-11069, October 2003.
2. FreedomCAR Battery Test Manual for Plug-In Hybrid Electric Vehicles, June 2010.
3. Electric Vehicle Battery Test Procedures Manual, Revision 3.1, October 2020.
4. Battery Test Manual for 12 Volt Start/Stop Vehicles, Rev. 1, May 2015, INL/EXT-12026503.

Abbreviations

USABC: United States Advanced Battery Consortium

HPPC: hybrid pulse power characterization test

PHEV-20: plug-in hybrid electric vehicle, 20-mi electric range

12-V S/S: 12-V start/stop

XCEL, XFC: extreme fast charging

EV: electric vehicle

VI.3 Battery Safety Testing (SNL)

Joshua Lamb, Principal Investigator

Sandia National Laboratories
1515 Eubank Drive SE, M/S 0613
Albuquerque, NM 87185
E-mail: jlamb@sandia.gov

Brian Cunningham, DOE Technology Development Manager

U.S. Department of Energy
E-mail: Brian.Cunningham@ee.doe.gov

Start Date: October 1, 2020	End Date: September 30, 2021	
Project Funding (FY21): \$350,000	DOE share: \$350,000	Non-DOE share: \$0

Project Introduction

Abuse tests are designed to determine the safe operating limits of HEV/PHEV energy storage devices. Testing is intended to achieve certain worst-case scenarios to yield quantitative data on cell/module/pack response, allowing for failure mode determination and guiding developers toward improved materials and designs. Standard abuse tests with defined start and end conditions are performed on all devices to provide comparison between technologies. New tests and protocols are developed and evaluated to more closely simulate real-world failure conditions. While robust mechanical models for vehicles and vehicle components exist, there is a gap for mechanical modeling of EV batteries. The challenge with developing a mechanical model for a battery is the heterogeneous nature of the materials and components (polymers, metals, metal oxides, liquids).

Materials characterization to better understand batteries that have undergone abusive conditions is of interest. Our partnerships with Argonne National Lab (ANL) and Oakridge National Lab (ORNL) through the Post Test Analysis Program for ABR, spans the building of cells with known materials (ORNL), overcharge testing to various states (SNL), and the posttest analysis of the cells (ANL). Abuse testing of advanced high energy materials has also revealed limits of existing test hardware, particularly regarding the maximum observed temperatures during thermal runaway. Continuous development of capabilities is necessary to ensure the most relevant data is collected. This has included the stand up of a small number of high temperature thermocouples that are able to detect these extreme temperatures.

Sandia has a record of a wide variety of Accelerating Rate Calorimetry (ARC) data that have been used to evaluate the relative safety of various materials. A key publication generated in FY21 provided a comparison of different chemistries, sizes, and cell formats previously tested. This has found that thermal runaway risk may be heavily tied to the specific energy of a battery system and should be factored in any safety evaluation.

Objectives

- Provide independent abuse testing support for DOE and USABC.
- Abuse testing of all deliverables in accordance with the USABC testing procedures.
- Provide battery safety testing support for DOE VTO programs.

Accomplishments

- Completed testing of USABC deliverables and reported results to the USABC TAC.
- Provided support to Behind the Meter Storage Program using tools developed as part of this testing program.

- Accelerating rate calorimetry data from programs at SNL were collected into a study covering the impact of increasing capacity and energy density. Publication released in FY21.
- Provided testing support for the Lithium-ion recycling prize through the voucher program.
- Capabilities developed in the battery abuse laboratory were used to support extreme fast charging research led by University of Michigan.

Approach

Abuse tolerance tests evaluate the response to expected abuse conditions. The goals of abuse and safety testing include a) testing to failure of energy storage devices and documentation of conditions that caused failure, b) systematic evaluation of failure modes and abuse conditions using destructive physical analysis (DPA), c) provide quantitative measurements of cell/module response, d) document improvements in abuse response, and e) develop new abuse test procedures that more accurately determine cell performance under most probable abuse conditions. Electrical (overcharge/overvoltage, short circuit, over discharge/voltage reversal, and partial short circuit), mechanical (controlled crush, penetration, blunt rod, drop, water immersion, laser induced short circuit, mechanical shock and vibration) and thermal abuse (thermal stability, simulated fuel fire, elevated temperature storage, rapid charge/discharge, and thermal shock cycling) cover the main categories of possible conditions evaluated. These techniques are applied to USABC deliverables, and the results reported to DOE and USABC.

Accelerating rate calorimetry was used to evaluate the impact of cell chemistry, state of charge, cell capacity, and ultimately cell energy density on the total energy release and peak heating rates observed during thermal runaway of Li-ion batteries. While the traditional focus has been using calorimetry to compare different chemistries in cells of similar sizes, this work seeks to better understand how applicable small cell data is to understand the thermal runaway behavior of large cells as well as determine if thermal runaway behaviors can be more generally tied to aspects of lithium-ion cells such as total stored energy and specific energy.

Results

Testing of deliverables was performed for USABC development programs, including testing deliverables from Farasis, Microvast, Gotion, and Zenlabs. Test results have been reported to the USABC Technical Assessment Committee. Sandia continues to make functional improvements to battery testing to enable the testing of new high energy materials. Sandia has also participated in a working group to prepare a revised test manual for USABC battery abuse testing. The test procedures used in the new manual were developed by the USABC Abuse test working group and prepared at Sandia. The revised manual is expected to be released by early CY 2022.

The development and maintenance of Battery Safety and Abuse Testing at Sandia has also allowed support for other DOE VTO programs. This has included support of the Behind the Meter Storage (BTMS) program performing testing of cells of interest for the program and support of the Lithium-Ion Battery Recycling Prize voucher program. The Battery Pressure Test Vessel (BPTV) previously developed as part of this program was used to determine the total gas production and composition information for cells of interest to the program. An example of the gas production data is shown in Figure 6.C.1, showing both gas release during an initial vent as well as gas release.

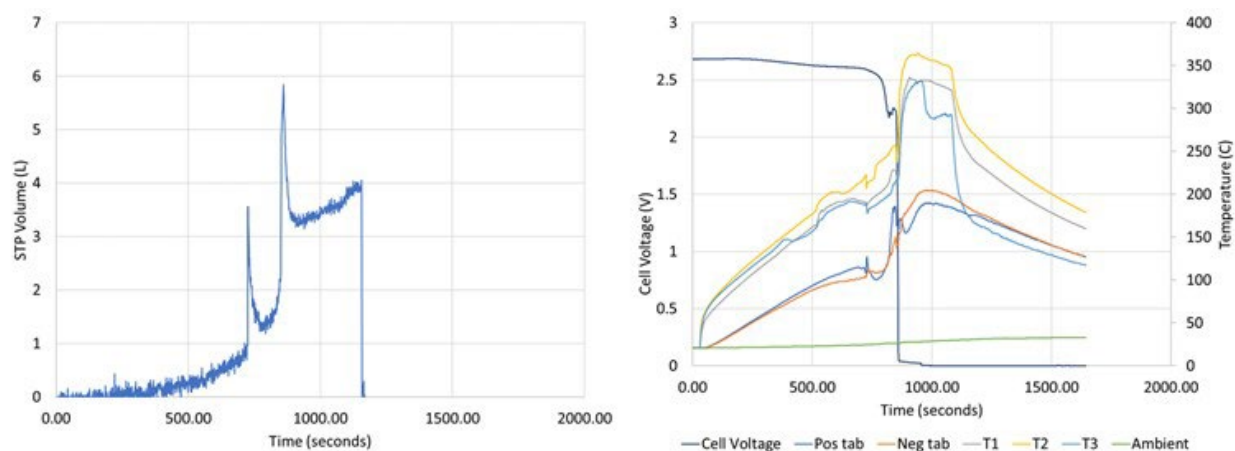


Figure VI.3.1 Gas production data of cell collected in BTPV

Sandia National Laboratories has long used ARC to compare the energetics of new chemistries. This has typically been done by constructing 18650-format cells of ~1 Ah with the materials in question for test. A collection of these data taken in the ES ARC in sealed sample holders is presented in Figure 6.C.2, taken from a publication this year by Lamb et al. This shows a broad array of the thermal runaway behavior of several widely used battery chemistries. Even a cursory glance will note the high runaway kinetics of NCA and LCO cathodes compared to an LFP cathode. The collection of this data has been a long-standing goal of this battery safety test program, but this publication represents a broad-based comparison of the data collected released in a peer-reviewed forum.

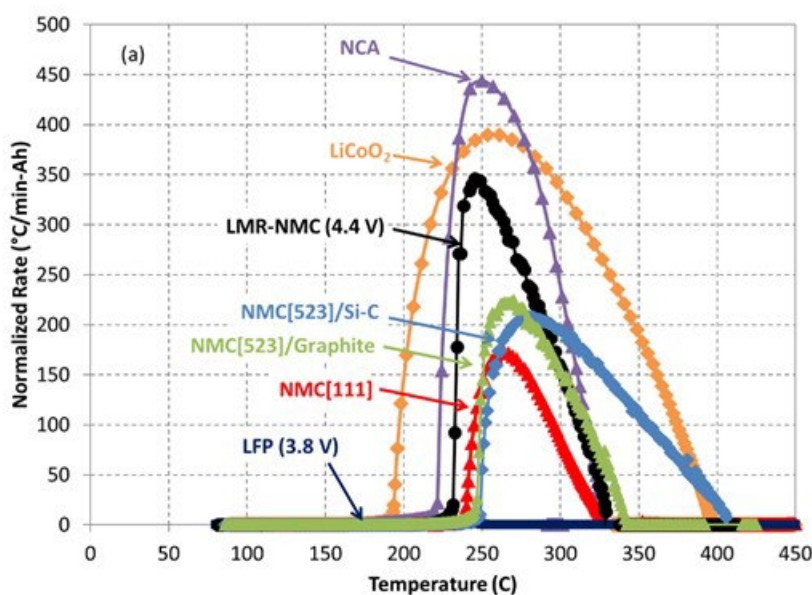


Figure VI.3.2 Historic ARC data summarizing chemistry behaviors published in FY 21.

Figure 6.C.3 shows peak heating rate as a function of the stored energy in J normalized to the heat capacity of cell and constraint. This results in a pseudo-temperature potentially suitable for comparing activation energies. A more full description of this process was provided in key publication 1 below. This presents a potential means to evaluate the activation energies of thermal runaway at the full cell level, experimentally accounting for the multitude of reactions that can occur during a full-cell thermal runaway process.

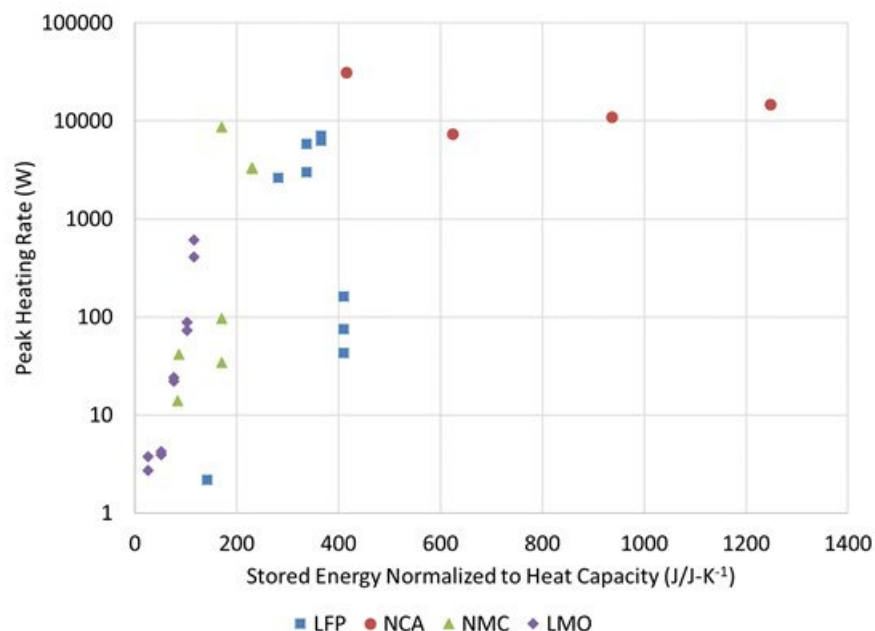


Figure VI.3.3 Collected analyzed ARC data showing the impact of cell capacity on runaway enthalpy (a) and the impact of specific energy on peak observed runaway temperatures (b).

Conclusions

Development and testing of higher energy, larger format cells and modules continues for USABC developers in hopes to meet the EV Everywhere goals. We provide a means to field the most inherently safe chemistries and designs to help address the challenges in scaling up lithium-ion technologies of interest. This has required careful control and monitoring of tests with the potential of high energy release as well as standing up a larger facility at SNL to support module level testing this FY. This has provided critical information to cell developers to aid in the development of increasingly abuse tolerant cell chemistries and module designs. This independent testing is also necessary to perform objective evaluations of these various designs and chemistries by the DOE and US automobile manufacturers.

An evaluation of ARC data presented here, when normalizing for energy density, indicates that peak runaway temperatures in adiabatic environments tend to be linearly proportional to the cell specific energy. These data cover four cathode chemistries, multiple form factors, and stored energy ranging from 3.5 to 122 Wh. This follows from ARC measurements that show the heat released is also linearly proportional to the stored energy. More importantly, perhaps, ARC measurements of the heat-release rate suggest that the kinetics of cell failure display an exponential relationship with increasing energy density. This compares well to a materials level analysis of oxygen release presented for layered metal oxide cathodes.

In a practical scenario, thermal runaway occurs when the self-heating rate of a battery failure event exceeds the heat loss rate in its current environment or installation. The logical next step is that increasing energy density will lead to increased consequences of thermal runaway occurring. With exponentially faster heat release at higher energy density, it will be easier for the thermal runaway to exceed any heat dissipation to the environment, likely leading to more severe consequences in terms of further damage or cascading failure. This would be considered intuitive if discussing chemical energy storage, but is a concept often avoided when considering electrochemical energy. As new technologies are developed with increased energy in mind, increasing attention will need to be paid to designing mitigation into systems that minimize consequences.

SNL continues to provide safety testing support to DOE programs as needed. The capabilities developed as part of this battery safety testing program currently support work done as part of the Behind the Meter Storage program and the Lithium-ion Recycling program.

Key Publications

1. Lamb J, Torres-Castro L, Hewson JC, Shurtz RC, Preger Y. Investigating the Role of Energy Density in Thermal Runaway of Lithium-Ion Batteries with Accelerating Rate Calorimetry. *Journal of The Electrochemical Society*. 2021;**168**(6):060516.
2. Torres-Castro, L., et al., Passive Mitigation of Cascading Propagation in Multi-Cell Lithium-Ion Batteries. *Journal of the Electrochemical Society*, 2020. **167**(9): p. 9.
3. Rago, N.D., et al., Effect of binder on the overcharge response in LiFePO₄-containing cells. *Journal of Power Sources*, 2020. **450**.
4. Rago, N.D., et al., Effect of overcharge on Li(Ni_{0.5}Mn_{0.3}Co_{0.2})O₂/Graphite cells-effect of binder. *Journal of Power Sources*, 2020. **448**.
5. Deichmann, E., et al., Investigating the Effects of Lithium Deposition on the Abuse Response of Lithium-Ion Batteries. *Journal of the Electrochemical Society*, 2020. **167**(9).

Acknowledgements

Sandia Contributors

Loraine Torres-Castro

Eric Deichmann

Christopher Grosso

Kyle Fenton

Lucas Gray

National Lab and Industry Partners

USABC TAC Team

Shriram Santhanagopalan (NREL)

Ira Bloom (ANL)

Eric Dufek (INL)

Matt Keyser (NREL)

Lee Walker (INL)

Sandia National Laboratories is a multi-mission laboratory managed and operated by National Technology and Engineering Solutions of Sandia, LLC., a wholly owned subsidiary of Honeywell International, Inc., for the U.S. Department of Energy's National Nuclear Security Administration under contract DE-NA0003525.

VI.4 Battery Thermal Analysis and Characterization Activities (NREL)

Matthew Keyser, Principal Investigator

National Renewable Energy Laboratory
15013 Denver West Parkway
Golden, CO 80401
E-mail: Matthew.Keyser@nrel.gov

Samm Gillard, DOE Technology Development Manager

U.S. Department of Energy
E-mail: Samuel.Gillard@ee.doe.gov

Start Date: October 1, 2020

End Date: September 30, 2022

Project Funding (FY21): \$500,000

DOE share: \$500,000

Non-DOE share: \$0

Project Introduction

While EDVs promise to curb America's need for imported oil, designing high-performance, cost-effective, safe, and affordable energy-storage systems for these cars can present challenges, especially in the critical area of battery thermal control. As manufacturers strive to make batteries more compact and powerful, knowing how and where heat is generated becomes even more essential to the design of effective thermal-management systems. NREL's thermal characterization activities provide developers, manufacturers, and OEMs with the knowledge necessary to assure that batteries are designed to perform strongly, last a long time, and operate at maximum efficiency.

The Vehicle Technologies Office has a goal to reduce the cost of electric vehicle battery packs by 2030 to less than \$65/kWh with technologies that significantly reduce or eliminate the dependency on critical materials (such as cobalt) and utilize recycled material feedstocks [1]. To meet these metrics, the battery packs will need to have higher energy densities resulting in a very compact system. Even if the energy efficiency of the next generation of batteries increases, because of the compactness of these batteries more heat is being generated per unit volume with less heat transfer area. Thus, more advanced heat rejection systems are needed to keep the battery temperatures in the "goldilocks" zone that prevents acceleration of the aging mechanisms within the battery.

The chemistries of advanced energy-storage devices—such as lithium-based batteries—are very sensitive to operating temperature. High temperatures degrade batteries faster while low temperatures decrease their power and capacity, affecting vehicle range, performance, and cost. Understanding heat generation in battery systems—from the individual cells within a module, to the inter-connects between the cells, and across the entire battery system—is imperative for designing effective thermal-management systems and battery packs.

Inadequate or inaccurate knowledge of the thermal characteristics of batteries makes it difficult to design effective thermal-control systems. This can negatively affect lifespan, safety, and cost, ultimately resulting in negative consumer perception and reduced marketability. In 2012, Nissan had to address problems with the battery for its Leaf fully electric vehicle (EV) losing capacity in the hot Arizona climate. Many attributed this issue to inadequate battery-thermal management.

Accurately measuring battery thermal performance under various electrical loads and boundary conditions makes it possible for battery-system engineers to design effective thermal-management systems. NREL, with the funding from DOE VTO, has developed unique capabilities to measure the thermal properties of cells and evaluate thermal performance of active, air, and liquid cooled battery packs. Researchers also use electro-thermal finite element models to analyze the thermal performance of battery systems in order to aid battery developers with improved thermal designs. In addition, our lumped capacitance multi-node battery-vehicle-ambient model can predict the temporal temperature of batteries as a function drive cycle, ambient

temperature, and solar radiation. These one-of-a-kind tools allow NREL to work with the battery manufacturers and OEMs to meet stringent EDV life, performance, cost, and safety goals

Objectives

- Thermally characterize battery cells and evaluate thermal performance of battery packs provided by USABC developers.
- Provide technical assistance and modeling support to USDRIVE/USABC and developers to improve thermal design and performance of energy storage systems.
- Evaluate extreme fast charging effects on battery thermal performance.
- Quantify the impact of temperature and duty-cycle on energy storage system life and cost.
- Address high energy storage cost due to battery packaging and integration costs
- Reduce the cost, size, complexity, and energy consumption of thermal management systems
- Optimize the design of passive/active thermal management systems—explore new cooling strategies to extend the life of the battery pack.

Approach

NREL has measured the thermal properties of the cells and batteries with many different chemistries (lead acid, NiMH, and many versions of lithium cells) through heat generation, heat capacity, and infrared thermal imaging; conducted performance thermal testing of battery and ultracapacitor modules and packs; analyzed the thermal performance of cells and modules; and developed thermal models. Researchers perform thermal testing, analysis, and modeling (1) to assist DOE/USABC battery developers in designing cells/modules/packs for improved thermal performance, and (2) to evaluate and validate the thermal performance of cell/module/pack deliverables from DOE/USABC battery developers and suppliers.

NREL's equipment can benchmark how changing the design of the cell using a different cathode, anode, current collector, electrolyte, additive, or separator affects the overall performance of the cell. The information garnered from these tests helps battery and advanced vehicle manufacturers improve their designs, while providing critical data for the development of thermal management systems that will reduce the life-cycle cost of battery systems. Using NREL's unique R&D 100 Award-winning calorimeters and infrared thermal imaging equipment, we obtain thermal characteristics of batteries and ultracapacitors developed by USABC battery developers and other industry partners. NREL supports the Energy Storage Technical Team by participating in various work groups such as the Zenlabs, Farasis, and USABC Electric Vehicle Cell Development Working Groups.

Results

Calorimeter Testing

Figure VI.4.1 shows the efficiency of cells tested in FY20/FY21 at NREL at a calorimeter temperature of 30°C. The lithium-ion cells were fully discharged from 100% SOC to 0% SOC under a C/2, C/1, and 2C currents. The cells in this figure have been developed under the HPEV and LCFC programs within USABC. These cells are designed for mainly high energy applications (the LCFC program maintains aggressive energy level targets). It should be noted that as the specific energy of these graphite systems increases, the efficiency decreases. This is primarily due to the impact of thicker electrodes have on the thermal performance. In contrast, the efficiency of the silicon blend cells is increasing due to chemistry optimization. Silicon containing cells can maintain high energy content with lower electrode thickness due to the much greater material energy potential when compared to graphite. However, the general trend still shows that silicon containing systems still need improvement in performance to reach the heat efficiency of graphite cells with similar electrode thickness. DOE and USABC are investigating both graphite and silicon to improve energy density, power

density, cycle life and/or cost benefits. NREL's calorimeters provide the fundamental understanding of whether the inefficiencies shown below are due to chemistry or cell design.

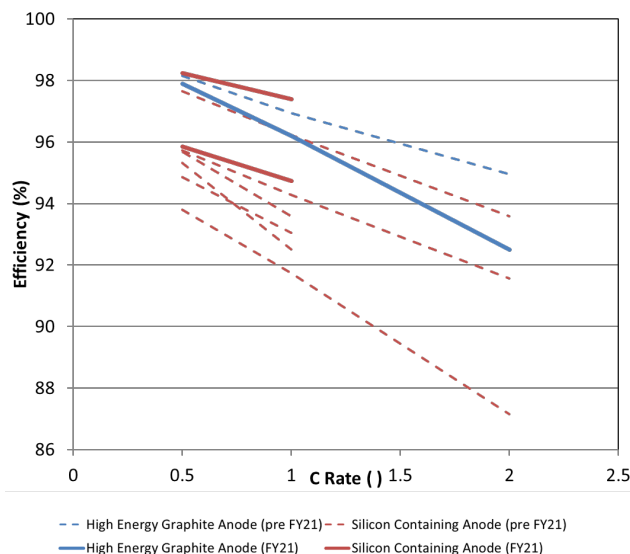


Figure VI.4.1 Efficiency summary of cells tested in NREL's calorimeters.
Caption Credits/Source: NREL-Aron Saxon

NREL's calorimeters were designed to be accurate enough to measure the electrochemical response from batteries under test—this capability allows NREL to understand benefits associated with design and chemistry changes to the cell. Figure VI.4.2 shows the entropic heat generation rates normalized to the Ah capacity of two cells—one cell has a graphite anode and the other has a graphite/Si anode—under a C/10 charge and discharge at 30°C. The cells in this figure were cycled over their entire state-of-charge range—minimizing the current decreases the joule heating of the cell and allows for the entropic heat signature to be assessed. From the figure, we can observe how the entropic response changes by introducing increasing amounts of Si. The response flattens out and the magnitude of peaks and valleys prevalent in graphite due to phase changes are reduced. The entropic response in cells has been a historic indicator of understanding material processes without deconstructing the full cell and how these processes impact cell performance.

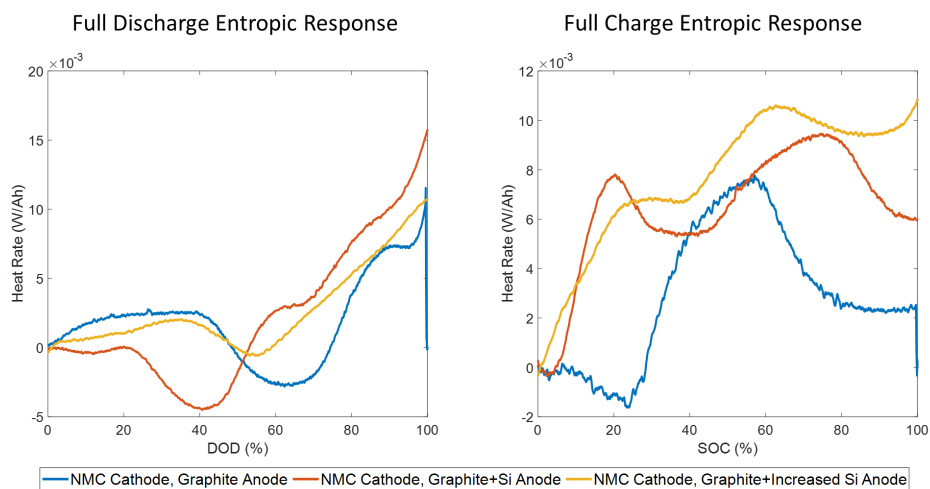


Figure VI.4.2 Calorimeter normalized heat rate for graphite and graphite/Si NMC cells under C/10 charge and discharge.
Caption Credits/Source: NREL-Aron Saxon

NREL has also been involved with testing cells under fast charge conditions. The USABC test procedure consists of a fifteen-minute fast charge from the minimum operational voltage to the maximum operational voltage. If the maximum operational voltage is reached during the charge, then the current is tapered to complete the charge. Figure VI.4.3 illustrates the heat generation results of a cell that was tested at NREL under this condition under three different charge rate— $(X-n)C$, XC , and $(X+n)C$. The results indicate that both the XC and $(X+n)C$ cases returned the same amount of usable capacity into the cell. The XC rate however, produced the least amount of heat per energy inserted. This case provides evidence that charge algorithm optimization is needed in addition to chemistry optimization to provide the most return for fast charge cases. NREL is continuing research into charge algorithm optimization to lessen the burden of fast charging on the cells lifetime while minimizing the thermal management system.

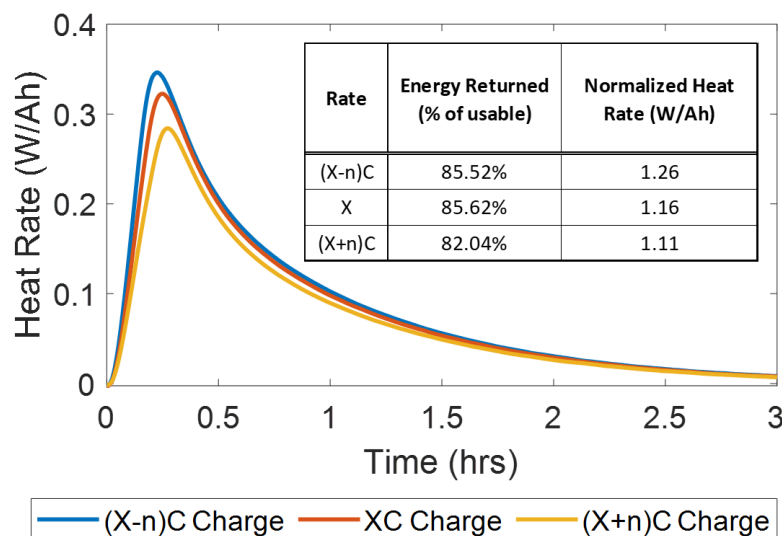


Figure VI.4.3 Heat response of cell under fast charge. The calorimeter test temperature was 30°C. Caption Credits/Source: NREL-Aron Saxon

Infrared Imaging of Cells

NREL performs infrared (IR) thermal imaging of battery manufacturer's cells to determine areas of thermal concern. We conduct IR thermal imaging under a set of prescribed procedures and environments to minimize the error from different sources such as reflective cell surfaces, radiation from surrounding surfaces, and cooling from the power cables attached to the cell. NREL combines the IR imaging equipment with a battery cyclor to place the cells under various drive cycles, such as a US06 charge depleting cycle for a PHEV, to understand the temperature differences within the cell. We then make recommendations to the battery manufacturers and USABC on how to improve the thermal design of the cell to increase its cycle life and safety.

Figure VI.4.4 shows a lithium battery (High Nickel Content NMC/Graphite+SiX) at the end of a high-rate discharge. Each IR image has a temperature spread associated with it – by decreasing the temperature spread a visual reference can be used to determine where the heat is preferentially being generated within the cell. For this cell, the heat generation is uniform across the surface of the battery. The cell's highest temperature point is in the center of the cell. This indicates that there is not a bias towards either the positive or negative tab. When the cell temperature is not uniform and consistent or symmetrical, individual cells within modules and packs age differently affecting the cycle life of the module. NREL is working with battery developers to understand how temperature non-uniformities affect the efficiency and cost of the cell over its life.

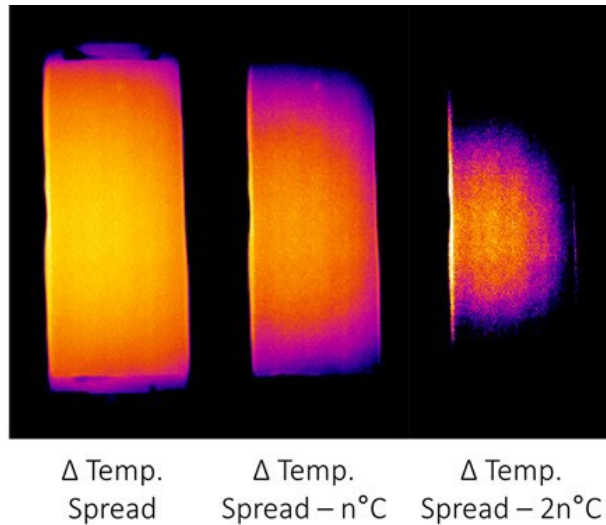


Figure VI.4.4 Infrared image of lithium battery cell (graphite-silicon/high nickel content NMC) at the end of a C/3 discharge.
Caption Credits/Source: NREL- Aron Saxon

Conclusions

NREL has thermally tested cells and modules from Zenlabs and Farasis during FY21 across multiple USABC programs. We have provided critical data to the battery manufacturers and OEMs that can be used to improve the thermal design of the cell, module, pack, and their respective thermal management systems. The data included heat generation of cells under typical profiles for HEV, PHEV, and EV applications, which is essential for designing the appropriately sized battery thermal management system. In FY22, NREL will continue to thermally characterize cells and modules for USABC, DOE, and our industry partners but the focus will shift to fast charging applications and the heat generation differences between advanced battery chemistries.

References

1. Steven Boyd, Overview: Batteries and Electrification R&D, Annual Merit Review, Washington DC, 2021

Acknowledgements

We wish to acknowledge Samm Gillard, Brian Cunningham, Haiyan Croft and DOE for sponsoring these efforts. We would also like to acknowledge Aron Saxon-the co-author of this report-and Tom Bethel for program support.

VI.5 Cell Analysis, Modeling, and Prototyping (CAMP) Facility Research Activities (ANL)

Andrew N. Jansen, Principal Investigator

Argonne National Laboratory
9700 South Cass Avenue CSE-200
Lemont, IL 60439
E-mail: Jansen@anl.gov

Stephen E. Trask, Principal Investigator

Argonne National Laboratory
9700 South Cass Avenue CSE-200
Lemont, IL 60439
E-mail: STrask@anl.gov

Peter Faguy, DOE Technology Development Manager

U.S. Department of Energy
E-mail: Peter.Faguy@ee.doe.gov

Start Date: October 1, 2018

End Date: September 30, 2022

Project Funding (FY21): \$800,000

DOE share: \$800,000

Non-DOE share: \$0

Project Introduction

The “valley of death” is a phrase often used to describe the path a new discovery must traverse to become a commercial product. This is especially true for novel battery materials invented in research laboratories around the world. Often researchers are resource limited and are only able to make gram quantities of their new material. The CAMP Facility is appropriately sized to enable the design, fabrication, and characterization of high-quality prototype cells using just a few hundred grams of the latest discoveries involving high energy battery materials. Prototype cells made in the CAMP Facility generally have 400-mAh capacity, which straddles the gap between coin cells and industrially-sized cells nicely—two orders of magnitude from each end point. Thus, a realistic and consistent evaluation of candidate chemistries is enabled in a time-effective manner with practical quantities of novel materials in cell formats commonly used in industry.

The CAMP Facility is an integrated team effort designed to support the production of prototype electrodes and cells, and includes activities in materials validation (benchmarking), modeling, and diagnostics. It is not the aim of this facility to become a small battery manufacturer, but instead to be a laboratory research facility with cell production capabilities that adequately evaluate the merits and limitations of new lithium-ion chemistries in a close-to-realistic industrial format. The source of these materials (anodes, cathodes, electrolytes, additives, separators, and binders) may originate from DOE Battery Programs, as well as from other domestic and foreign organizations such as universities, national labs, and industrial vendors. Electrochemical couples with high power and energy density are given extra priority.

The CAMP Facility has the capability to make three prototype cell formats in their 150 m² dry room: pouch cells (xx3450 format, with capacity around 0.5 Ah; and xx6395, with capacity around 2 Ah) and 18650 cells (with capacity around 2 Ah). Pouch cells are generally easier to assemble and are a useful indicator of gassing problems in a cell during cell aging and cycling. Central to this effort is a pilot-scale coating machine that operates with slurry sizes that range from 20 mL to 2 L. These key features of the CAMP Facility enable a professional evaluation of both novel materials (typically limited quantities) and commercial materials for benchmarking. In addition, the Materials Engineering Research Facility (MERF) is available for scaling up materials for these prototype cell builds.

Objectives

The objective of this core-funded effort is to design, fabricate, and characterize high-quality prototype electrodes and cells that are based on the latest discoveries involving high energy anode and cathode battery materials. Using this multi-disciplined facility, analytical diagnostic results can be correlated with the electrochemical performance of advanced lithium-ion battery technologies for electric vehicle (EV) applications.

- Link experimental efforts through electrochemical modeling studies.
- Identify performance limitations and aging mechanisms.
- Support lithium-ion battery projects within the DOE-EERE-VTO

In FY21, the CAMP Facility milestone objectives were to:

- Develop methods to coat hybrid ceramic polymer composites with reverse comma coater in dry room conditions. (also refer to efforts described in [VI.6](#))
 - Produce 5 meter of coating without major pinholes.
- Develop methods to coat electrode-ceramic structures using reverse comma coating methods. (also refer to efforts described in [VI.6](#))
 - Produce 10 meter of electrode-ceramic on foil with at least 3 mAh/cm² loading.
- Maintain supply of advanced prototype electrodes in Electrode Library.
 - Add at least 100 meters total of needed anode and cathode electrodes to support various DOE battery programs.
- Complete installation of multifunctional coater in dry room and begin training on its operation.
 - Confirm coater meets specifications of original order.

Approach

The general approach used in this effort is to start small and grow large in terms of cell size and amount of resources devoted to each novel battery material. At various points in the development process, decisions are made to either advance, modify, or terminate studies to maximize utilization of available resources.

Coin cells (2032 size) are used for materials validation purposes with initial studies performed at 30°C. After formation cycles, the coin cells go through rate capability testing, HPPC testing, and limited cycle life testing. Additional temperatures and test conditions are employed, if warranted.

Using the results obtained by the materials validation of promising materials (also refer to [VI.6](#)), single-sided electrodes are fabricated on the larger dry-room coater for diagnostic study. The new cell chemistries are studied in detail using advanced electrochemical and analytical techniques, including the employment of micro-reference electrode cells. Factors are identified that determine cell performance and performance degradation (capacity fade, impedance rise) on storage and on extensive deep-discharge cycling. The results of these tests are used to formulate data-driven recommendations to improve the electrochemical performance/life of materials and electrodes that will be incorporated in the prototype cells that are later fabricated in the dry room. This information also lays the foundation for electrochemical modeling focused on correlating the electrochemical and analytical studies, in order to identify performance limitations and aging mechanisms.

If the results from diagnostics and modeling still look promising, full cell builds are conducted using double-sided electrodes. The electrodes are then either punched (in the case of pouch cells) or slit (in the case of 18650 cells) and assembled into full cells in the dry room using semi-automated cell assembly equipment. Formation procedures are conducted on the cells to encourage electrolyte wetting and uniform solid-electrolyte-interface (SEI) formation. These cells undergo rigorous electrochemical evaluation and aging studies under the combined effort of the CAMP Facility team and Argonne's Electrochemical Analysis and Diagnostic Laboratory (EADL). After testing, select cells are destructively examined by the Post-Test Facility to elucidate failure mechanisms. This information is then used to further improve the new chemistry, as well as future electrode and cell builds.

Results

The CAMP Facility is designed to work closely with materials researchers across the many electrochemical energy storage programs throughout the DOE-EERE-VTO. In addition to its own yearly R&D tasks, it actively coordinates its efforts to provide support to other national lab team Programs such as: Realizing Next Generation Cathodes (RNGC), Silicon Consortium Project (SCP), ReCell Advanced Battery Recycling Center, eXtreme Fast Charge Cell Evaluation of Lithium-Ion Batteries (XCEL), and Behind-the-Meter-Storage (BTMS), and Liquid Electrolyte Projects. The Materials Benchmarking Activities (Section I.6.F) is a segment of the CAMP Facility. The CAMP Facility also complements the capabilities of other DOE support facilities such as: Materials Engineering Research Facility (MERF - Argonne), Post-Test Facility (PTF - Argonne), Battery Abuse Testing Lab (BATLab - SNL), and Battery Manufacturing Facility (BMF - ORNL). More information about these programs can be found in the relevant chapters and sections of this annual report. The remainder of this CAMP Facility section will discuss the results of the CAMP Facility deliverables and related topics for FY21.

Develop Methods to Coat Hybrid Ceramic Polymer Composites with Reverse Comma Coater

In continuation of themes related to prior FY20 advancements, the CAMP Facility pursued developments in methods to coat specialty films onto electrodes using a reverse comma coater. Specifically, solid polymer electrolytes which offer significant advantages by avoiding a high temperature sinter step, able to be applied with roll-to-roll processes, flexibility in formulation design, and can incorporate ceramics such aluminum oxide (Al_2O_3) and LLZO. Initial material identification and composition development information used in this section is further described in [VI.6](#).

As Figure VI.5.1 highlights, the CAMP Facility successfully produced 5 meters of roll-to-roll polymer-ceramic electrolyte coatings without major pinholes using PEGDA (Poly(ethylene glycol) diacrylate), AIBN (2,2'-Azobis(2-methylpropionitrile)), LiTFSI (lithium bis-trifluoromethanesulfonimide), GN (Glutaronitrile), and Al_2O_3 ($\text{D}_{50} \leq 10 \mu\text{m}$). It was found that uncalendered electrodes had improved wetting behavior with the PE and CPE materials, compared to calendered electrodes. The coating process provided ~5 minutes of heat treatment to initiate polymerization. A final curing step was completed in convection oven following the roll-to-roll initiation.



Figure VI.5.1 Images of the (a) polymer electrolyte [PE] coatings on LTO and graphite electrodes and (b) hybrid composite polymer ceramic electrolyte [CPE] coatings on graphite electrodes. The PE and CPE successfully applied to the electrode via reverse comma and the polymerization was initiated during coating process heat-treatment.

Develop Methods to Coat Electrode-Ceramic Structures using Reverse Comma Coating Methods

Experience gained in the overcoating methods was critical in the electrode-ceramic structure coating development, which resulted in >10 meters of electrode-ceramic films on foil, with loading targets ranging between 1 to 3 mAh/cm². The material was successfully applied to the carbon-coated Al foil via reverse comma without major pinholes and the polymerization was initiated during 5-minute heat-treatment (Figure VI.5.2). Additional information about the polymer electrolyte composition development used in this section is further described in [VI.6](#).

The CAMP Facility has made progress in improving reverse comma overcoatings on existing electrodes and coating of electrode-ceramic structures on substrates. However, the expansion of coating capabilities with the new multifunctional coater will provide new tools well suited for coating these novel electrochemical energy storage systems by enabling uniform thin ceramic coatings and electrolyte membranes.

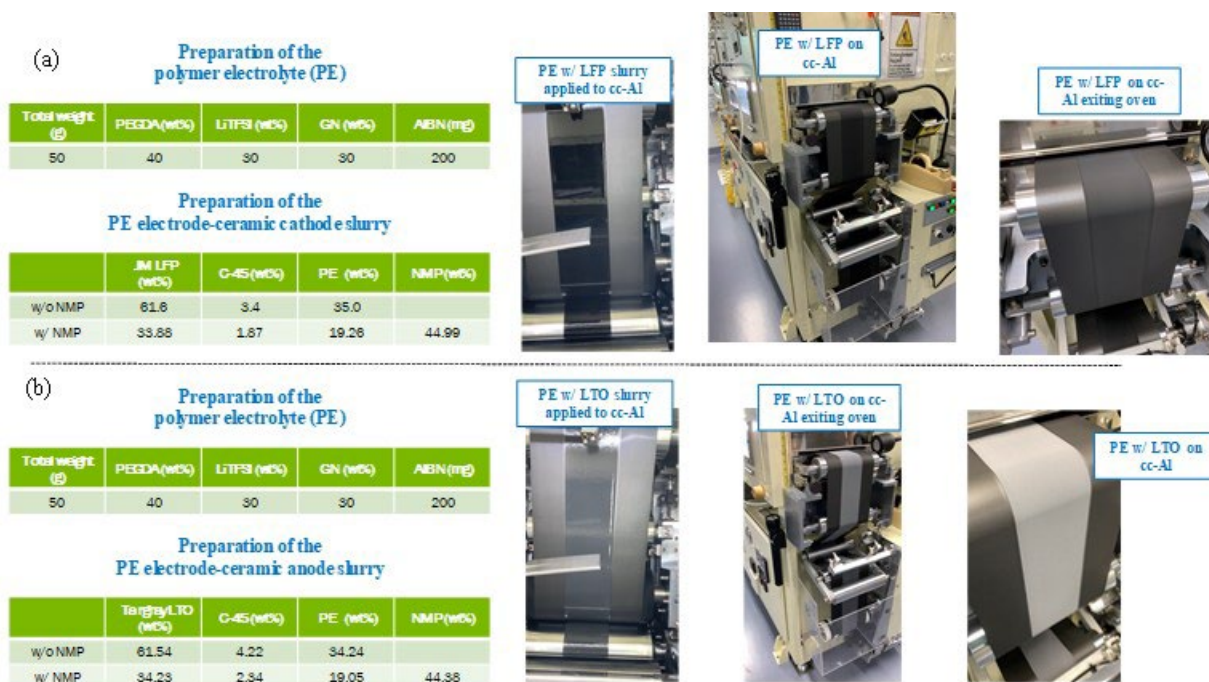


Figure VI.5.2 Images of the polymer electrolyte electrode-ceramic (a) LFP cathode and (b) LTO anode slurry coatings using a roll-to-roll reverse comma coater. The material was successfully applied to the carbon-coated Al [cc-Al] foil via reverse comma.

Multifunctional Coater Specifications Confirmed during Factory Acceptance Test

The new multifunctional roll-to-roll coater has met the specifications of the original order with Frontier. This was determined during an on-site Factory Acceptance Test (FAT) in FY21. The FAT demonstrated the required features of allowing interchangeable coating heads, gravure coating, single-slot die coating, the progressive cavity pump, corona treatment of substrates, and utilizing the IR drying zone (Figure VI.5.3).



Figure VI.5.3 Images of the multifunctional coater during the FAT. The images are of the front end of the coater (left), slot die coating a CAMP Facility-made graphite anode slurry on copper foil (center), and back end of the coater (right).

The FAT also provided an opportunity for CAMP Facility team members to develop familiarity of the unit, receive initial training on its proper operation, verify quality of various samples, provide feedback to the company, and identify any periphery materials needed to be procured in advance of the unit arrival to Argonne.

The CAMP Facility dry room lab logistics (power, ventilation, space) have been accounted for and modified for the arrival of the new coating system. Delivery of the equipment is scheduled for the end of the calendar year 2021.

Support of Realizing Next Generation Cathodes (RNGC)

Numerous prototype electrodes made in support of systematic LNO-based oxide studies for RNGC. The study aims to explore materials that have low/no cobalt, thus being more sustainable. Most materials provided to the CAMP Facility for electrode fabrication were MERF-made precursors that were calcined by RNGC team members. CAMP Facility received between 30-to-200-gram calcined samples for each material in Table VI.5.1. The provided powder quantities yielded between 2 to 7 meters of single-side electrodes. Each electrode was designed for proper capacity matching against a ~2 mAh/cm² baseline graphite anode in the CAMP Facility Electrode Library.

Table VI.5.1 Summary of LNO-oxide materials provided to the CAMP Facility

Composition	mg Co / Wh	Wh / kg	pH value
Ni _{0.6} Mn _{0.2} Co _{0.2}	179	680	12.41 (12.06*)
Ni _{0.94} Co _{0.06}	42	861	12.63
Ni _{0.92} Co _{0.06} Al _{0.02}	41	882	12.83
Ni _{0.90} Mn _{0.05} Co _{0.05}	37	825	12.65
Ni _{0.95} Co _{0.05}	34	881	12.7
Ni _{0.95} Mn _{0.025} Co _{0.025}	16	921	12.71
Ni _{0.9} Mn _{0.1}	0	824	12.7
Ni _{0.95} Mn _{0.05}	0	830	12.75
LNO	0	942	12.65

*represents the measured pH value from a commercial powder.

Table VI.5.1 depicts the impact of low/no cobalt materials on the measured pH value. In general, pH values <12 are desirable for slurry preparation (PVDF- NMP- based) and electrode coating, due to common gelation issues observed for powders with higher pH values (>12). There are slurry preparation methods to help minimize gelation, however these methods are not necessarily guaranteed to address the issue for all materials.

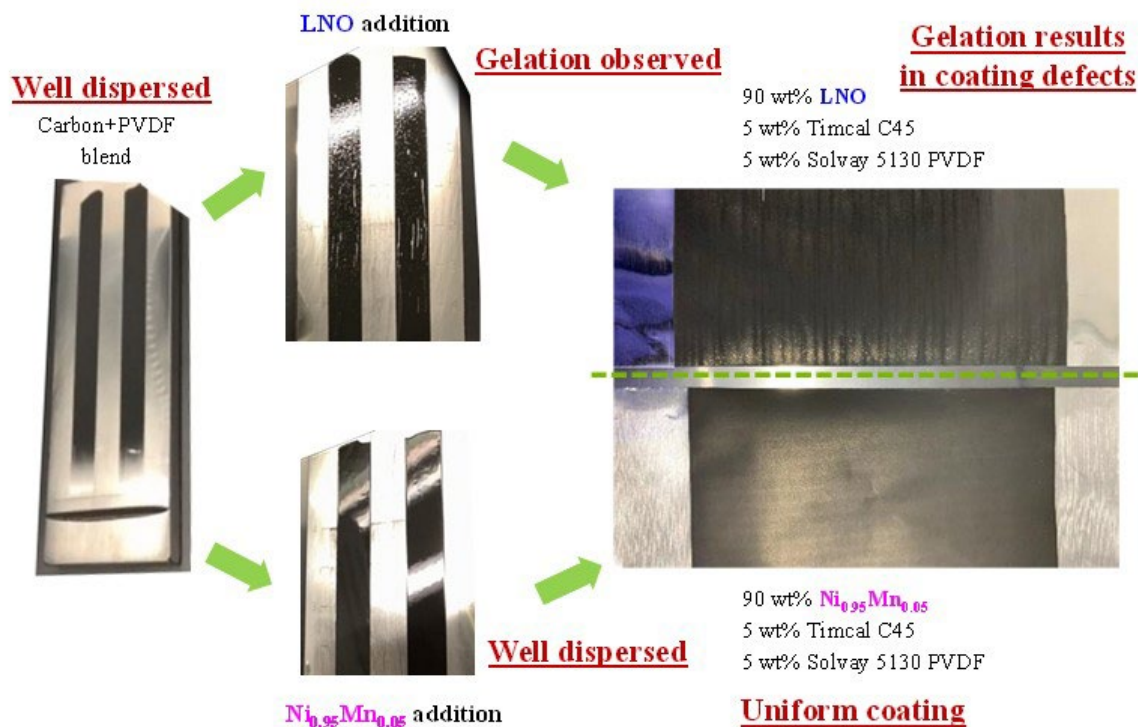


Figure VI.5.4 Sequence of slurry blend process and results for two high pH LNO-based oxide materials. Both materials started in well dispersed carbon, PVDF binder, and NMP blends, as depicted on the right after the fineness gauge test. The center images show slurry conditions after the LNO-based oxide was blended into the prior blend. The images on the right illustrate the resulting electrode coating quality.

In this study, there was an interesting exception to the expectation that gelation would occur due to the powder having a high pH. The $\text{Ni}_{0.95}\text{Mn}_{0.05}$ oxide powder had a pH value of 12.75, the second highest pH value in this study. Figure VI.5.4 shows this material blended well into the slurry and yielded a quality electrode, whereas the LNO with a lower pH value had gelation issues. All other materials in the study showed a tendency to have gelation (except for $\text{Ni}_{0.6}\text{Mn}_{0.2}\text{Co}_{0.2}$). The result suggests that pH is a helpful indicator that there likely will be gelation issues, but not necessarily solely predict this behavior.



Figure VI.5.5 Scaled-up batch (200 grams) of $\text{Ni}_{0.9}\text{Mn}_{0.05}\text{Co}_{0.05}$ provided to the CAMP Facility to produce >1.5 Ah pouch cells. Mixing sequence and control of temperature aided in creating a well dispersed slurry dispersion and uniform electrode.

The RNGC team provided the CAMP Facility with 200 grams of a promising material, $\text{Ni}_{0.9}\text{Mn}_{0.05}\text{Co}_{0.05}$, in order to fabricate electrodes and assemble >1.5 Ah pouch cells for further demonstration. Learned approaches of controlling the slurry temperature were applied and resulted in minimal/no gelation. The absence of the gelation resulted in the ability to achieve a uniform coating, as shown in Figure VI.5.5. Cell assembly and testing is planned for early FY22.

Examining electrochemical characteristics of cells with 5V spinel electrodes Abraham et al.

The 5V spinel oxide ($\text{LiMn}_{1.5}\text{Ni}_{0.5}\text{O}_4$) is a promising cathode material because it can deliver an energy density of ~ 650 Wh/kg and has the potential for superior rate capability because the spinel structure has 3-D ionic channels for Li^+ ion diffusion. Furthermore, it is reported to have better thermal stability and it is considered more sustainable than the typical NMC oxides because it does not contain cobalt. Hence, this spinel oxide is being considered as a candidate for the CAMP library of electrode materials.

Here we report half and full cell data on cells containing a 5V spinel oxide purchased from Targray. The positive electrode in these cells has a $61\text{ }\mu\text{m}$ thick coating, containing 90% $\text{LiMn}_{1.5}\text{Ni}_{0.5}\text{O}_4$ (Haldor-Topsoe), 6 wt% C45 carbon (Timcal) and 4 wt% PVdF binder (Solvay 5130), on a $20\text{ }\mu\text{m}$ thick Al current collector; the electrode has 38.2% porosity and a spinel loading of 13.2 mg/cm^2 . In the full cells, the negative electrode has a $43\text{ }\mu\text{m}$ thick coating, containing $\sim 92\%$ CGP-A12 graphite (Conoco-Phillips), 2 wt% C45 carbon (Timcal) and 6 wt% PVdF binder (Kureha KF-9300), on a $10\text{ }\mu\text{m}$ thick Cu current collector; the electrode has 34.9% porosity and a graphite loading of 5.6 mg/cm^2 . In addition to the electrodes, the cells contain Celgard 2320 separator and the 5V spinel baseline electrolyte (5VS-BL) which is 1.0 M lithium hexafluorophosphate salt (LiPF_6) in a 1:9 v/v solvent mixture of ethylene carbonate (EC) and ethyl methyl carbonate (EMC).

Results from a 5V spinel//Li cell are shown in Figure VI.5.6. The voltage profile (Figure VI.5.6a) is typical of the material. The differential capacity plots during charge show a minor peak at $\sim 4.04\text{ V}$ (Figure VI.5.6b) and the main peaks at 4.69 and 4.74 V vs. Li/Li^+ (Figure VI.5.6c). During discharge, the main peaks are at 4.71 and 4.66 V and the minor peaks are at ~ 4.16 and 3.98 V vs. Li/Li^+ . These data indicate the voltage hysteresis of the material during the charge-discharge cycle. The specific capacity of the material at C/25 rate is 135 mAh/g, but it decreases at higher currents. The estimated C/1 capacity of the electrode is 99 mAh/g. The decrease in specific capacity at high specific currents (Figure VI.5.6d) reflects the electrode impedance.

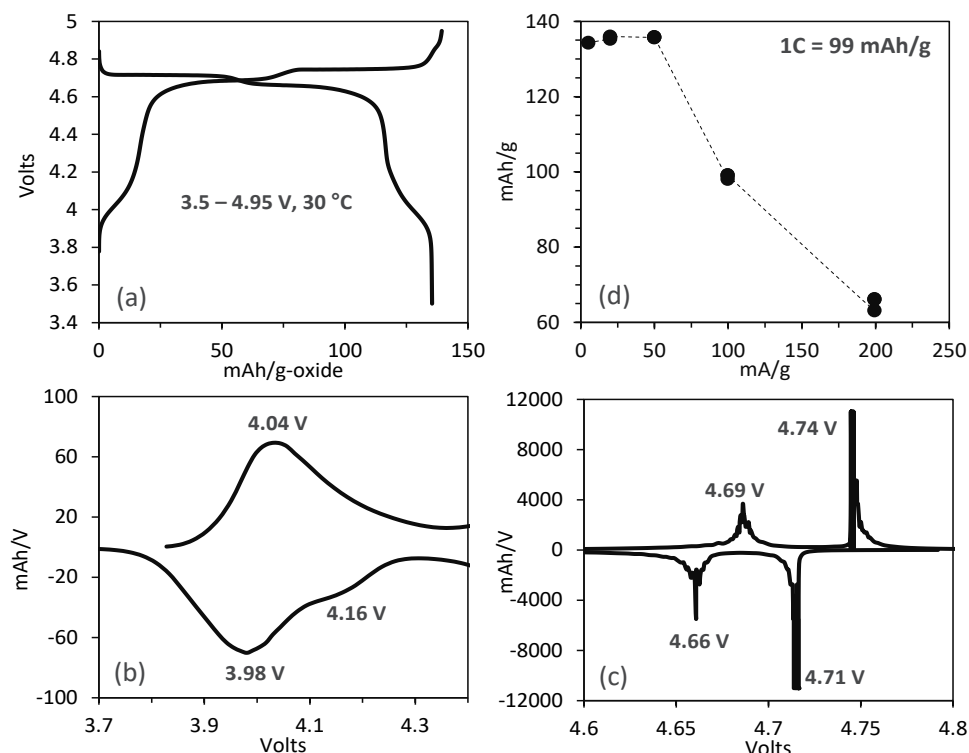


Figure VI.5.6 Data from a 5V spinel//Li cell at $30\text{ }^\circ\text{C}$, including the voltage profile (a), differential capacity plots in the indicated voltage ranges (b, c) and specific capacity vs specific current (d).

Representative results during cycling of a 5V spinel//Gr cell are shown in Figure VI.5.7. In each 100 cycles of the protocol, cycles 1–3 and 98–100 are at C/20 rate, cycles 4 and 97 contain the HPPC test and cycles 4–96 are at a C/2 rate. This series of steps is repeated to determine longer-term aging performance of the cells. Figure VI.5.7a shows the voltage profiles as the cell ages. The shift and shape of the profiles reflect cell performance changes. The C/20 discharge capacity (Figure VI.5.7b) decreases from ~110 mAh/g at cycle 2 to ~70 mAh/g at cycle 300. The calculated capacity capacity fade (Figure VI.5.7c) shows that the cell loses ~34% capacity (determined at the C/20 rate) after 300 cycles.

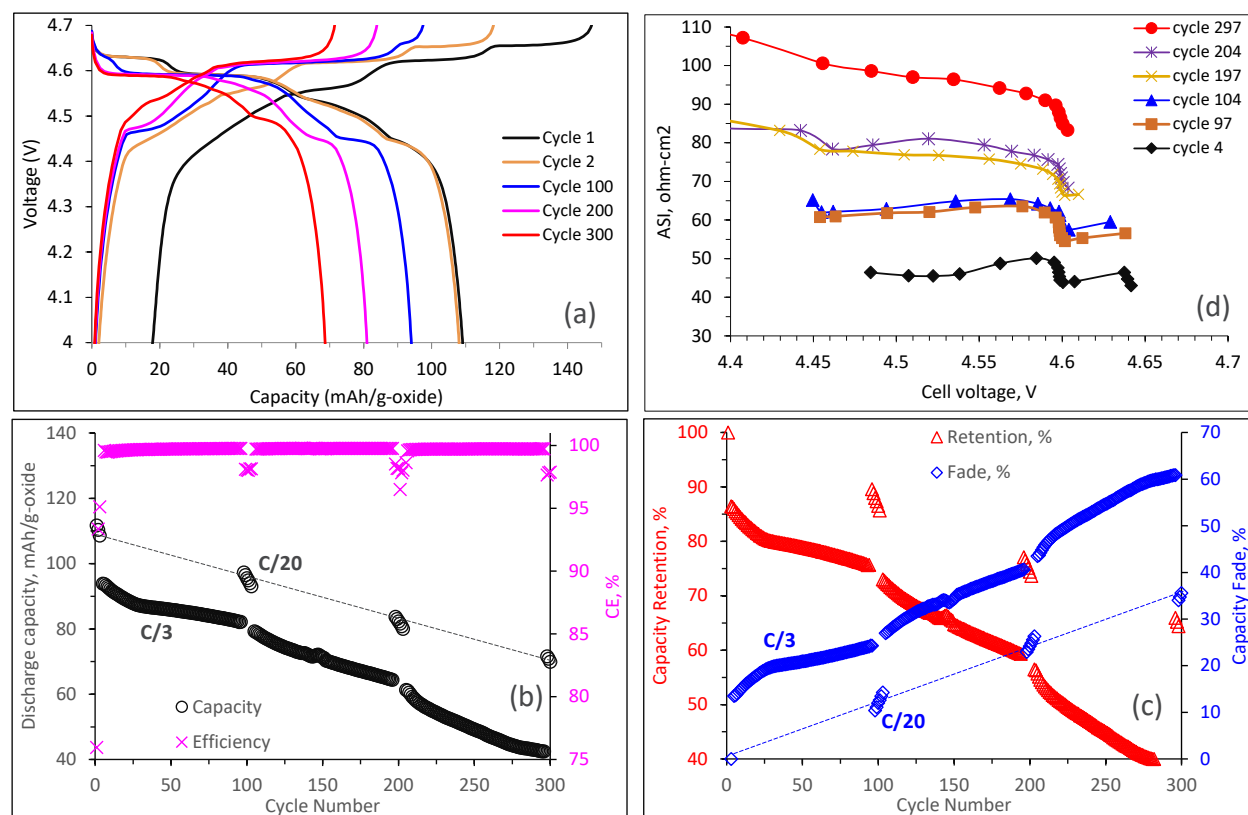


Figure VI.5.7 Aging-related changes from a 5V spinel//Gr cell cycled between 3.2 and 4.7 V at 30 °C. (a) Voltage profile changes for select cycles, as indicated (b) discharge capacities (left axis) and coulombic efficiencies (right axis), (c) capacity retention (left axis) and capacity fade (right axis), and (d) impedance rise during the cycling. The dotted lines in (b) and (c) are to guide the eye and show the discharge capacity and fade trends during the extended electrochemical cycling.

The coulombic efficiency (Figure VI.5.7b) increases from ~76% at cycle 1 to ~99.8 during the C/3 cycles; the value is lower (~98%) during the slower cycles, which could be an indication of electrolyte oxidation because of the longer times spent at high-voltage during these C/20 cycles. Note that this electrolyte oxidation can increase charge capacity by injecting electrons into the oxide electrode; the obvious consequence of this oxidation is electrolyte depletion which would be deleterious in a electrolyte-starved cell. Cell impedance (Figure VI.5.7d) indicate an increase during the cycling. At ~4.55 V, the impedance values at cycle 4 and cycle 297 are ~46 and ~96 ohm-cm² respectively. This impedance rise may arise at both the positive and negative electrode; electrolyte changes could also contribute to this rise.

In summary, although the high-voltage spinel offers the multiple advantages listed earlier, it displays performance degradation during the electrochemical cycling, which includes capacity fade and impedance rise. Factors that contribute to this degradation could include electrolyte decomposition due to the high cell operating voltage, degradation at the electrode-electrolyte interfaces and structural changes in the 5V spinel material. Detailed diagnostic studies will be needed to pinpoint the actual degradation mechanisms. Identifying

these mechanisms will allow the targeted development of electrode and electrolyte materials needed to enhance long-term performance of the 5V spinel/graphite cells.

Lithium Metal Electrodeposition Samples Tested at the CAMP Facility

The CAMP Facility dry room has been utilized in the development of a new lithium metal electrodeposition process that can produce a sub-20-micrometer thin lithium metal anode. Recently, coin cell studies using one- & two- compartment deposition substrates have been tested versus a CAMP Facility NMC electrode.

Summary of Electrode Library Activities

Table VI.5.2 highlights the distribution of electrodes from the Electrode Library, which is maintained by the CAMP Facility. The Electrode Library serves as a supply of standard electrode samples that are designed to be interchangeable with one another (capacity matched). Electrodes can be made with as little as 50 g of experimental material and can be made to match an existing counter electrode. From October 1, 2020, to September 30, 2021, 1807 sheets of electrode were fabricated and distributed by the CAMP Facility, which is >40 square meters of electrodes. These electrodes were supplied by the CAMP Facility in support of DOE's numerous activities in advanced battery R&D (11 labs, 33 universities, and 13 companies). In addition to these electrodes, the CAMP Facility fabricated ~265 pouch cells for DOE projects (consisting of many unique combinations of electrodes, electrolytes, and separators).

Table VI.5.2 Summary of Electrode Library Distributions

Electrodes Delivered	FY18		FY19		FY20		FY21	
Argonne	140	14 %	160	15 %	245	25 %	302	17 %
Other National Labs	172	18 %	224	21 %	299	30 %	354	20 %
Universities	175	18 %	296	28 %	333	33 %	426	23 %
Industry	495	50 %	388	36 %	121	12 %	725	40 %
Total:	982		1068		998		1807	

Conclusions

The CAMP Facility developed methods to coat hybrid ceramic polymer composites with a roll-to-roll reverse comma coater in the dry room and produced >5 meters of these advanced films. These learned methods were critical in the electrode-ceramic structure coating development, which resulted in >10 meters of electrode-ceramic films on foil, with loading targets ranging from 1 to 3 mAh/cm².

Overcoating with a ceramic-hybrid-composite polymer electrolyte and/or polymer electrolyte, as well as coating electrode-ceramic structures, will be greatly enhanced with the new multi-functional coating system. The multi-functional coating system will provide coating method flexibility (i.e., gravure, single-slot die, dual slot die, gravure, knife-over-roll), enhancing our ability to create uniform solid-state-electrolyte and ceramic separator films/coatings onto electrodes. The coating system was inspected and confirmed to have met the specifications of the original order in FY20. Delivery of the equipment is scheduled for the end of calendar year 2021.

Controlling temperature has aided in minimizing gelation from high pH (>12) cathode powders and specialty coatings in PVDF/NMP slurry blends. However, depending on the material process parameters and characteristics of the final powder, some level of gelation may persist with this approach. Thus, the CAMP Facility continually works to identify and resolve non-ideal rheological slurry/coating behavior for specific materials and blends that exhibit gelation, phase separation, agglomerates, aggregates, etc.

The CAMP Facility continued its support of numerous DOE programs, much of which was performed through the CAMP Facility's Electrode Library. Numerous prototype electrodes (>100 meters) and pouch cells were fabricated and delivered to DOE-EERE programs.

Diagnostic studies of 5V spinel oxide ($\text{LiMn}_{1.5}\text{Ni}_{0.5}\text{O}_4$) electrochemical characteristics were performed. While the high-voltage spinel has the potential to offer multiple advantages (sustainability, thermal stability, high energy density and rate capability), it displays performance degradation during the electrochemical cycling, which includes capacity fade and impedance rise. Aspects that contribute to this degradation could include electrolyte decomposition due to the high cell operating voltage, degradation at the electrode-electrolyte interfaces and structural changes in the 5V spinel material. Systematic diagnostic studies are necessary to identify the actual degradation mechanisms. Distinguishing these mechanisms will allow the targeted development of electrode and electrolyte materials needed to enhance long-term performance of the 5V spinel/graphite cells.

It should be noted that several of the planned tasks for FY21 were modified or delayed because of reduced laboratory time due to the COVID19 pandemic.

Key Publications

1. Stoichiometric irreversibility of aged garnet electrolytes. J. Cai, B. Polzin, L. Fan, L. Yin, Y. Liang, X. Li, Q. Liu, S.E. Trask, Y. Liu, Y. Ren, X. Meng, Z. Chen. *Materials Today Energy*. Volume 20 (2021). <https://doi.org/10.1016/j.mtener.2021.100669>
2. Synthesis as a design variable for oxide materials. Jack Vaughey, Steve Trask, Ken Poeppelmeier. *Electrochem. Soc. Interface* 30 53 (2021). <https://doi.org/10.1149/2.F08211IF>
3. Spatially-resolved lithiation dynamics from operando X-ray diffraction and electrochemical modeling of lithium-ion cells. Abhi Raj, Ilya A. Shkrob, John S. Okasinski, Marco-Tulio Fonseca Rodrigues, Andrew C. Chuang, Xiang Huang, Daniel P. Abraham. *Journal of Power Sources*, Volume 484, 229247 (2021). <https://doi.org/10.1016/j.jpowsour.2020.229247>
4. Apparent Increasing Lithium Diffusion Coefficient with Applied Current in Graphite. Dennis W. Dees, Marco-Tulio F. Rodrigues, Kaushik Kalaga, Stephen E. Trask, Ilya A. Shkrob, Daniel P. Abraham, Andrew N. Jansen. *J. Electrochem. Soc.* 167 120528 (2020). <https://doi.org/10.1149/1945-7111/abaf9f>

Acknowledgements

Key contributors to this work: Daniel Abraham, Shabbir Ahmed, Eva Allen, Ira Bloom, Jiyu Cai, Zonghai Chen, Dennis Dees, Nancy Dietz-Rago, Alison Dunlop, James Gilbert, Jihyeon Gim, Ozge Kahvecioglu, Donghyeon Kang, Hyun Woo Kim, Yejing Li, Chen Liao, Kewei Liu, Wenquan Lu, Bryant Polzin, Yan Qin, Andressa Prado Rodrigues, Marco-Tulio Fonseca Rodrigues, Seoung-Bum Son, Steve Trask, Jack Vaughey, Zhenzhen Yang, and Sanpei Zhang.

VI.6 Materials Benchmarking Activities for CAMP Facility

Wenquan Lu, Principal Investigator

Argonne National Laboratory
9700 South Cass Avenue
Lemont, IL 60439
E-mail: luw@anl.gov

Andrew N. Jansen, Principal Investigator

Argonne National Laboratory
9700 South Cass Avenue
Lemont, IL 60439
E-mail: jansen@anl.gov

Peter Faguy, DOE Technology Development Manager

U.S. Department of Energy
E-mail: Peter.Faguy@ee.doe.gov

Start Date: October 1, 2018

End Date: September 30, 2022

Project Funding (FY21): \$400,000

DOE share: \$400,000

Non-DOE share: \$0

Project Introduction

High energy density electrode materials are required in order to achieve the requirements for electric vehicle (EV) application within the weight and volume constraints established by DOE and the USABC. One would need a combination of anode and cathode materials that provide 420 mAh/g and 220 mAh/g, respectively, as predicted by Argonne's battery design model (BatPaC), if one uses a 20% margin for energy fade over the life of the battery assuming an average cell voltage of 3.6 volts. Therefore, the search for new high energy density materials for lithium-ion batteries (LIB) is the focus of this material benchmarking project. In addition to electrode materials, other cell components, such as separators, binders, current collectors, etc., are evaluated to establish their impact on electrochemical performance, thermal abuse, and cost.

This benchmarking effort is conducted as part of the Cell Analysis, Modeling, and Prototyping (CAMP) Facility (Refer to [Chapter VI.5](#)) to identify and support promising new materials and components across the "valley of death", which happens when pushing a new discovery towards a commercial product. The CAMP Facility is appropriately sized to enable the design, fabrication, and characterization of high-quality prototype cells, which can enable a realistic and consistent evaluation of candidate chemistries in a time-effective manner. However, the CAMP Facility is more than an arrangement of equipment, it is an integrated team effort designed to support the production of prototypes electrodes and cells. In order to utilize the facility more efficiently and economically, cell chemistries are validated internally using coin type cells to determine if they warrant further consideration. In addition, the bench marking will advance the fundamental understanding of cell materials and facilitate advance the technology development.

Objectives

- The primary objective is to identify and evaluate low-cost materials and cell chemistries that can simultaneously meet the life, performance, and abuse tolerance goals for batteries used in EV applications.
- The secondary objective is to enhance the understanding of the impact of advanced cell components and their processing on the electrochemical performance and safety of lithium-ion batteries.
- This project also provides the support to the CAMP Facility for prototyping cell and electrode library development, and the MERF facility for material scale up.

Approach

Though there are an overwhelming number of materials being marketed by vendors for lithium-ion batteries, there are no commercially available high energy materials that can meet all the requirements for all-electric-range (AER) vehicle within the weight, volume, cost, and safety constraints established for EVs by DOE and the USABC. Identification of new high-energy electrode materials is one of the challenges for this project.

Under materials benchmarking activities, we constantly reach out to, or are approached by, material developers to seek opportunities to test their advanced or newly released products. By leveraging Argonne's expertise in electrode design and cell testing, we can provide not only a subjective third opinion to material suppliers, but also deeper understanding on their materials, which can aid their material development. This deep understanding becomes even more important when the material developers are small companies or new players, who often overlook overall requirements of battery materials.

In addition to industrial partners, we also work closely with scientists from various research institutes, such as universities and research laboratories. They often come up with novel materials with advanced electrochemical performance, but small quantities, which is only enough for validation purpose. These test results help us to determine how much effort should be expanded to explore the material potential.

In general, we will validate any potential cell material, which has impact on the cell performance, mainly in terms of electrochemical performance, electrode optimization, and thermal stability. The electrochemical performance is the centerpiece of the materials benchmarking activities, which will be tested using 2032-sized coin-type cells under test protocols derived from USABC PHEV 40 requirements [Battery Test Manual for Plug-In Hybrid Electric Vehicles, Idaho National Laboratory]. The freshly made coin cells will undergo three formation cycles at a C/10 rate. The cells are then tested for the rate performance. For the rate test, the charging rate is set at C/5, while the discharge rate varies from C/5, C/3, C/2, 1C to 2C. Three cycles are performed for each discharge rate. After the rate test, the cells then undergo cycling test at C/3 rate. During the cycling test, we change the current rate to C/10 every 10th cycle to check the rate effect. Also, Hybrid Pulse Power Characterization (HPPC) is conducted every 10th cycle, which will be used to calculate the Area Specific Impedance (ASI).

This fiscal year, we have investigated various battery materials, such as cathode, anode, conductive additives, and solid-state electrolyte. In this report, selective work, including SiO anode and electrode optimization using single-wall carbon nano-tube, nickel-rich cathode material, and lithium lanthanum zirconium oxide (LLZO) solid-state electrolyte, will be presented.

Results

Si from halloysite: Nano-structured silicon is one of the most promising materials to replace the current most common anode material, graphite, due to its high theoretical capacity. The use of high-capacity silicon, which decreases the anode thickness and charge carrier (ion) transport distance, is also favorable for the fast-charging process. However, the downsizing of Si to the nanoscale dimension is often impeded by complicated and expensive methods.

Halloysite, with a stoichiometric composition of $\text{Al}_2\text{Si}_2\text{O}_5(\text{OH})_4 \cdot n\text{H}_2\text{O}$, is a naturally abundant material in USA. Owing to its existing nano-cylindrical shape, the silicon that is made from halloysite may preserve the nano structure and make it a promising anode material for lithium-ion batteries. Decreasing the cost and resolving the volume expansion issue of Si derived from halloysite have potential to facilitate the commercial application of Si-based anode material. Halloysite in this work was obtained from Applied Minerals and processed at Brigham Young University (BYU). Halloysite was first turned to SiO_2 after acid washing. The intermediate product SiO_2 derived from halloysite kept the tubular shape (Figure VI.6.1). Si was obtained after SiO_2 reduction, and the nanofiber feature of the final Si product was observed in SEM (Figure VI.6.1).

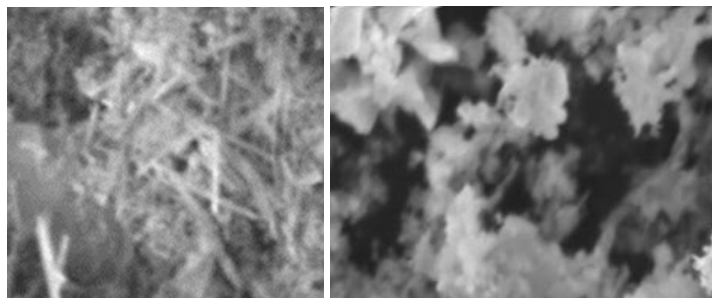


Figure VI.6.1 SEM images of halloysite-derived SiO₂ (left) and Si (right).

The Si powder derived from halloysite was made into electrode with 70 wt.% Si, 10 wt.% C45, and 20 wt.% LiPAA binder. The Si electrode was put into half cells using lithium metal as counter electrode and Celgard 2325 as separator. The electrolyte was 1.2 M LiPF₆ in EC/EMC (3/7) with 10wt.% FEC. The lithium half cells were tested between 10 mV and 1.5 V for 3 formation cycles and followed by rate testing. Three formation cycles were tested using C/10 charge and discharge current. Five different rates were applied during rate test including C/5, C/3, C/2, 1C, and 2C. Three cycles were applied for each rate. During the rate test, the lithiation rate was kept constant to be C/5.

Figure VI.6.2 show the formation performance of Si electrode. The reversible capacity of this Si electrode is above 1800 mAh/g with as high as 85% 1st cycle coulombic efficiency. At 2C rate, the Si electrode can deliver around 1450 mAh/g capacity, which is 86% of discharge capacity at C/5 rate. This result suggests the good rate performance of Si from halloysite.

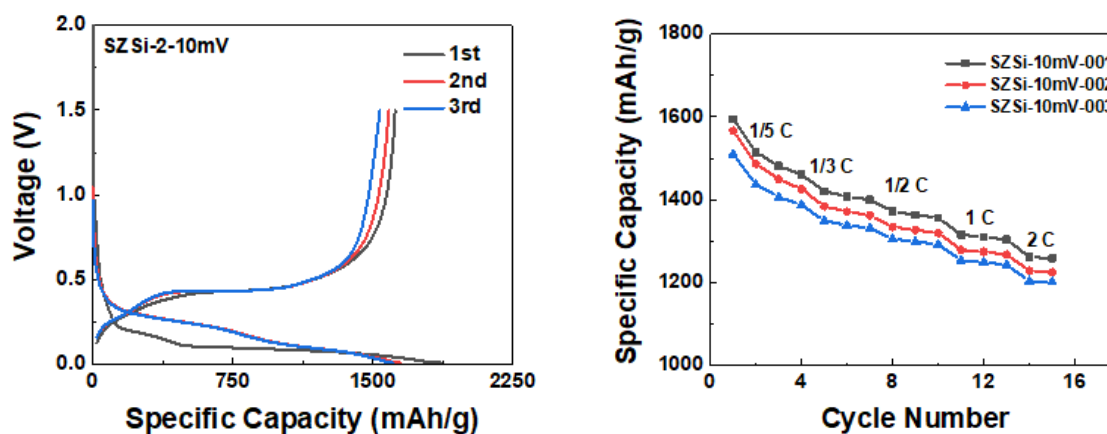


Figure VI.6.2 Three formation cycles (left) and rate test (right) of Li/Si half-cells.

Dry pressed holey graphene (hG) hosted electrode: There is an increasing demand for electric vehicle batteries with higher energy densities that can be manufactured with low cost utilizing environmentally friendly processes. These electrodes are typically fabricated using environmentally hazardous, energy intensive, and time-consuming solvent-based slurry casting processes. Polymeric binders, also required for cathode preparation, add weight and can undergo parasitic reactions during battery cycling. Here we report a facile, solvent-free, binder-free, and rapid cold-press electrode fabrication process to prepare high mass loading LiNi_{0.5}Co_{0.2}Mn_{0.3}O₂ (NCM523) cathodes within minutes. This process is enabled by the use of holey graphene (hG), a unique lightweight, compressible carbon nanomaterial that serves as both a binder and an electrically conductive matrix.

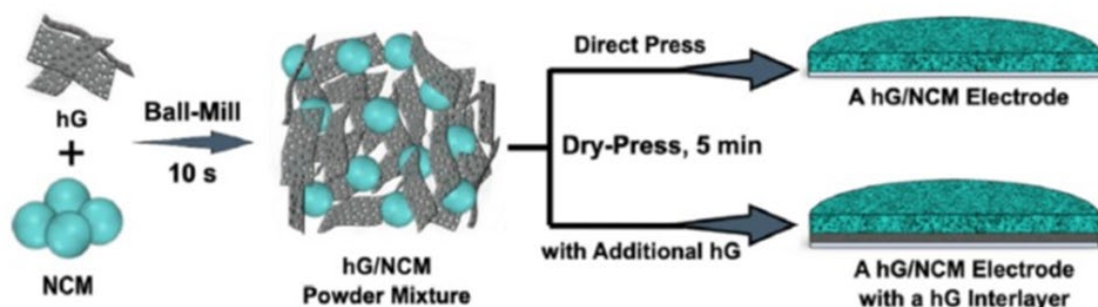


Figure VI.6.3 Schematic illustration of the facile solvent-free process for the preparation of hG/NCM composite cathodes from hG and NCM powder.

Dry pressed holey graphene (hG) hosted NCM523 (hG/NCM) composite cathodes were prepared in a facile solvent-free and binder-free procedure, as illustrated in Figure VI.6.3. More specifically, lightweight hG powder (tap density $\sim 5.7 \times 10^{-3} \text{ g/cm}^3$) and dense NCM powder (tap density $\sim 2.2 \text{ g/cm}^3$) were mixed at the desired weight ratio (in the range of 1:1 to 1:9) using a ball-mill. Due to the significant tap density difference, the lightweight hG powder is of much larger volume (~ 400 times larger volume at the same weight) and can therefore effectively serve as a conductive host scaffold for the denser NCM material even with a small weight fraction. A very short mixing duration of 10 sec was used and turned out to be sufficiently effective to mix the components. This mixture with known NCM content (10–90 wt%) was then readily compressed at a relatively low hydraulic pressure of ~ 20 – 25 MPa to form composite discs. To improve the mechanical robustness, a lightweight “interlayer” of hG is typically added in between the Al current collector and the composite structure (Figure VI.6.3). Besides the mechanical benefit, the interlayer of hG can also be considered as a “three-dimensional current collector” that significantly improves the interfacial and thus the electrical contact between the active material and the Al current collector.

The morphology and microscopic distribution of hG sheets and NCM particles within a composite disc were evaluated with SEM coupled with EDS mapping of the disc cross-section. Using a hG/NCM-90% disc with a hG interlayer as an example (Figure VI.6.4), the hG/NCM-90% composite layer at a total mass loading of 17.3 mg/cm^2 in the cross-section exhibited a thickness of $\sim 90 \mu\text{m}$, while the lightweight hG interlayer, with a mass loading of 3 mg/cm^2 that is a content of $<15\%$ of the total weight, exhibited a thickness of $\sim 45 \mu\text{m}$. In future improvements, the interlayer thickness should be further decreased to improve overall cathode gravimetric and volumetric performance. Nevertheless, NCM particles, on the order of 8 – $10 \mu\text{m}$, are densely packed in the composite layer (Figure VI.6.4 a & b). At a higher magnification (Figure VI.6.4 c), the carbon elements, i.e., hG sheets, can be seen surrounding all NCM particles and fill the inter-particle spaces, exhibiting excellent contact with each of the adjacent NCM particles. This feature shows that the rapid mixing and dry-press processes were sufficient to provide a continuous percolation of the carbon matrix to ensure the conductivity of the hG/NCM cathodes. Unless otherwise specified, all hG/NCM composite cathodes in subsequent sections are of hG/NCM-90% composition with a NCM mass loading of 15.6 mg/cm^2 and a 3 mg/cm^2 hG interlayer.

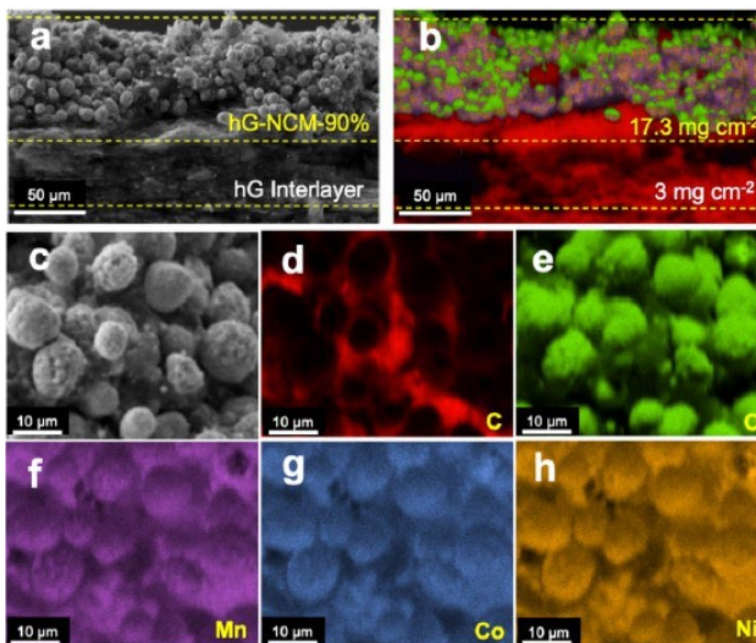


Figure VI.6.4 (a) SEM and (b) EDS maps of the cross-section of a hG/NCM composite disc with a hG/NCM-90% layer and a neat hG interlayer for improved mechanical robustness and interfacial conductance with current collector. The areal loading values of the layers are shown in (b). (c-h) Higher magnification (c) SEM and EDS maps of (d) C, (e) O, (f) Mn, (g) Co, and (h) Ni elements of the same disc.

The typical discharge and charge performance were measured for an identical battery with the same hG/NCM cathode in the voltage range of 3–4.3 V. These Li-NCM batteries were subjected to long term cycling at currents of 1.2 and 2.3 mA/cm² and remained relatively stable for over 200 cycles (Figure VI.6.5 e), with Coulombic efficiencies consistently above 95% and 91%, respectively.

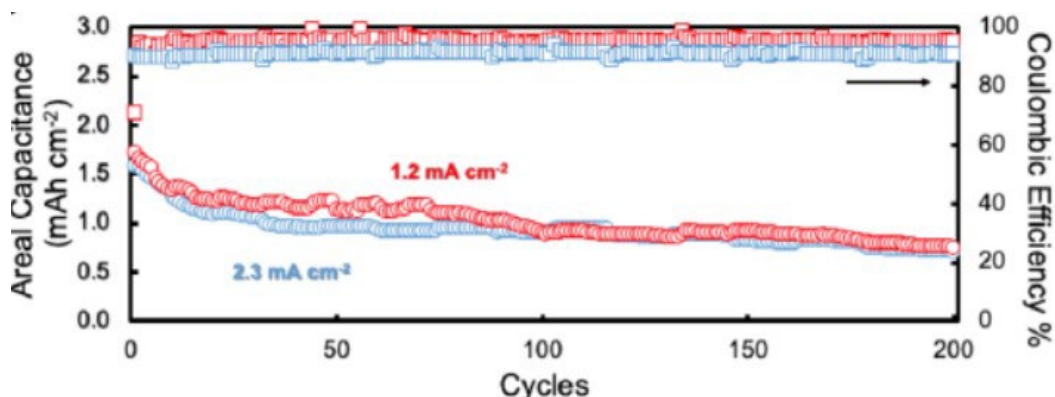


Figure VI.6.5 Electrochemical performance of Li-NCM batteries with a dry-pressed hG/NCM cathode: cycling performance (in terms of areal capacity at discharge) and the corresponding Coulombic efficiency of identical batteries cycled at 1.2 (blue) and 2.3 mA/cm² (red), respectively.

Organic solid state electrolyte processing development: Poly (ethylene glycol) diacrylate (PEGDA) has been used as a cross-linking agent to copolymerize with other monomers in the application of solid polymer electrolytes (SPE). Instead of UV curing, PEGDA based SPE were prepared through an in-situ thermal polymerization method of a blended precursor solution in liquid electrolyte.

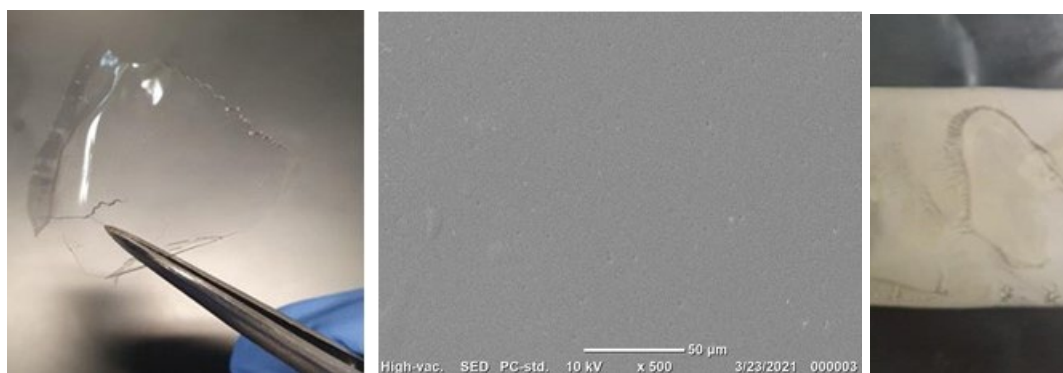


Figure VI.6.6 Optical (left) and SEM (middle) images of solid polymer electrolyte containing PEGMA. Optical image of SPE composite electrolyte (right)

Two approaches were attempted to process SPE thin film, stand-alone thin film and direct-casting SPE on electrode fabrication. Figure VI.6.6 shows the stand-alone SPE film prepared in the lab. LiTFSI was dissolved in a mixture of PEGDA monomer and glutaronitrile (GN) plasticizer under stirring for 1-3 hours. 2,2-Azobis (2-methylpropionitrile (AIBN) heat initiator was then added into the system and the solution was stirred under room temperature for another 1 hour. The detail SPE composition is shown in Table VI.6.1. For the heat-initiated polymerization, the solution was placed on the hot plate at 90°C for 2 hours. Transparent free-standing SPE was obtained with thickness around 0.11~0.16 mm. SEM image in Figure VI.6.6 suggests uniform component distribution. Lithium ionic conductivity from ac impedance was determined to be around 0.1 mS/cm.

Table VI.6.1 Composition of solid polymer electrolyte

Total weight (g)	PEGDA (wt%)	LiTFSI (wt%)	GN (wt%)	AIBN (mg)
2g	40	30	30	8

AIBN: 2,2-Azobis(2-methylpropionitrile), GN: Glutaronitrile

Using same composition and procedure, SPE was directly coated and cured on LTO electrode. The direct-casting approach will wet the electrode and improve the electrode conductivity. Various amounts of ceramic particles (Al_2O_3) were introduced into the polymer electrolyte solution Table VI.6.2. The composite Al-SPE was directly coated and cured on LTO electrode, as shown in Figure VI.6.6. Large scale thin polymer electrolyte coating was achieved by the CAMP facility (See [VI.5](#)).

Table VI.6.2 Al_2O_3 composite solid polymer electrolyte composition

Total weight (g)	PEGDA (wt%)	LiTFSI (wt%)	GN (wt%)	AIBN (mg)
10	36	27	27	8
20	32	24	24	8
30	28	21	21	8
40	24	18	18	8
50	20	15	15	8

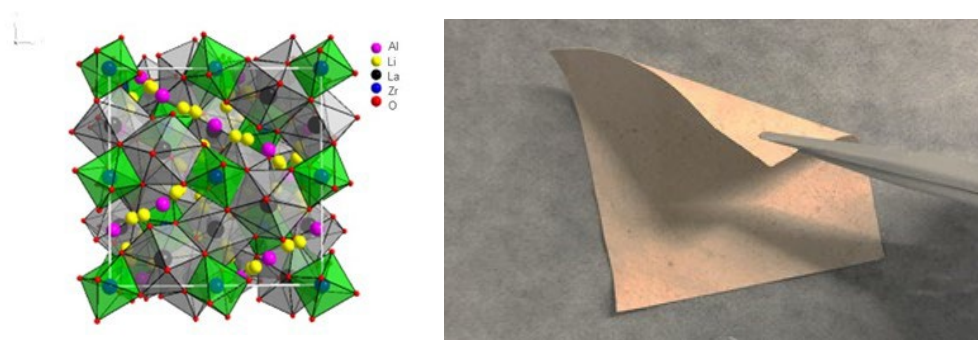


Figure VI.6.7 Crystal structure of LLZO (left) and flexible thin LLZO solid electrolyte film (right)

SPE is easy to synthesize, and compatible with large-scale manufacturing processes. However, polymer chains locked in a crystal lattice hinder the motion of cations, making it a low ionic conductivity electrolyte. *Solid inorganic electrolytes* (SIE), such as LLZO (Figure VI.6.7), have high ionic conductivity. However, LLZO has issues of manufacturing difficulties, poor interfacial charge transport, and the risk of metal dendrite growth. By combining the best merits of SIE and SPE, we attempted to develop LLZO/LiTFSI/PVDF composite solid-state electrolyte. Simple mixing LLZO, LiTFSI, and PVDF/NMP solution, thin and flexible stand-alone composite film (80 μm) was fabricated in the lab as shown in Figure VI.6.7.

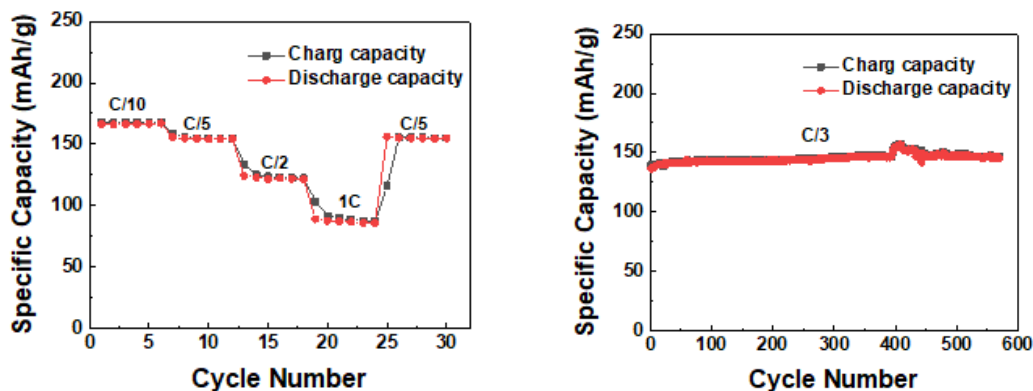


Figure VI.6.8 Rate (left) and cycle (right) performance of Li/LLZO/LFP cell at 30°C

The electrochemical performance of flexible solid-state electrolyte was investigated using LiFePO_4 (LFP) electrode, which consisted of the same LLZO electrolyte. Li/LLZO/LFP 2032 coin cells were fabricated in a dry room and tested at 30°C. The all-solid-state battery (ASSB) were cycled between 2.6V and 3.8V. During formation cycle with C/10 rate charge and discharge, the LFP electrode delivered theoretical capacity, 170 mAh/g as shown in Figure VI.6.8. The cells also went through rate testing with C/5, C/2, and 1C (charge = discharge). At 1C rate, the cell can still deliver around 100 mAh/g capacity. Finally, the cycling performance of the ASSB was conducted at C/3 (charge = discharge). As shown in Figure VI.6.8, there is almost no capacity fading after 500 cycles.

Conclusions

In the report, we investigated halloysite derived Si anode, holey-graphene enabled binder and solvent free cathode, and solid-state electrolyte processing development.

First, the Si electrode derived from halloysite demonstrated good electrochemical performance, including high 1st cycle coulombic efficiency, high reversible capacity, and reasonable rate performance. We will continue to work with Applied Minerals and Brigham Young University to further develop this promising domestic Si materials.

Second, high mass loading Li-ion battery cathodes utilizing NCM523 hosted by hG were fabricated using a facile, scalable, solvent-free, and binder-free method. This method cannot be achieved by using any other carbon material but only enabled by the unique dry compressibility of hG. While the dry-press method is very attractive from the viewpoint of electrode fabrication, several issues such as irreversible capacity loss, low active material utilization, and volumetric performance related to the disc density and porosity will need to be carefully addressed and optimized in future studies.

Last, processing of solid polymer and solid inorganic electrolytes were explored. As for solid polymer electrolyte, a thermal curing method was developed to cross link the polymer. Both stand-alone electrolyte film and direct coating on electrode were successfully demonstrated. As for solid inorganic electrolyte, a flexible thin LLZO electrolyte film was fabricated, which showed excellent electrochemical performance using LiFePO_4 electrode.

Key Publications

1. Dry-Pressed, High Mass Loading, Lithium Nickel Cobalt Manganese Oxide (NCM) Cathodes Enabled by Holey Graphene Host, Brandon A Walker; Christian O Plaza-Rivera, Sam-Shajing Sun, Wenquan Lu, John W Connell, Yi Lin, *Electrochimica Acta*, Vol 362 (2020), 137129.
2. Electrode Prototyping Activities in ANL's Cell Analysis, Modeling and Prototyping (CAMP) Facility, Steve Trask, Daniel Abraham, Shabbir Ahmed, Eva Allen, Zonghai Chen, Alison Dunlop, James Gilbert, Hyun Woo Kim, Yejing Li, Chen Liao, Kewei Liu, Wenquan Lu, Bryant Polzin, Andressa Prado, Yan Qin, Marco Rodrigues, Sanpei Zhang, and Andrew Jansen, 2021 DOE Vehicle Technology Office Annual Merit Review and Peer Evaluation Meeting, Washington D.C., 06/21/2020
3. Materials Benchmarking Activities For Cell Analysis, Modeling, and Prototyping (CAMP) Facility, Wenquan Lu, Sanpei Zhang, Hyun-Woo Kim, Yejing Li, Yan Qin, Steve Trask, Alison Dunlop, Bryant Polzin, Kewei, Liu, Chen Liao, and Andrew Jansen, 2021 DOE Vehicle Technology Office Annual Merit Review and Peer Evaluation Meeting, Washington D.C., 06/21/2020
4. Estimating the diffusion coefficient of lithium in graphite: Extremely fast charging and a comparison of data analysis techniques, Minkyu Kim, David C. Robertson, Dennis W. Dees, Koffi Pierre Yao, Wenquan Lu, Stephen E. Trask, Joel T. Kirner, and Ira Bloom, *J. Electrochem. Soc.*, 168 (2021), 070506.
5. Unlocking the Electrochemical-Mechanical Coupling Behaviors of Dendrite Growth and Crack Propagation in All-Solid-State Batteries, Chunhao Yuan, Wenquan Lu, Jun Xu, *Advanced Energy Materials*. 2021, 2101807.
6. High adhesive Polyimide binder for silicon anodes of lithium-ion batteries, Sanpei Zhang, Stephen E. Trask, Alison Dunlop, Bryant Polzin, Yan Qin, Andrew N. Jansen and Wenquan Lu, 2021 Meet. Abstr. MA2021-01 130.
7. Direct casted LLZO-LiTFSI composites solid state electrolyte lithium-ion batteries by direct casting method, Sanpei Zhang, Andrew Jansen, and Wenquan Lu, 2021 Meet. Abstr. MA2021-01 431.

Acknowledgements

First, contributions from Sanpei Zhang, Hyun-Woo Kim, Steve Trask, Yan Qin, Alison Dunlop, Yejing Li, and Bryant Polzin are gratefully acknowledged. We would also like to acknowledge the contribution from Applied Minerals and Brigham Young University for providing their halloysite silicon powders. At last, I want to thank Dr. Yi Lin from National Institute of Aerospace for his contribution to the holey graphene work.

VI.7 Electrochemical Performance Testing (INL)

Lee Walker, Principal Investigator

Idaho National Laboratory

2525 Fremont Avenue

Idaho Falls, ID 83402

E-mail: lee.walker@inl.gov

Samm Gillard, DOE Technology Development Manager

U.S. Department of Energy

E-mail: Samuel.Gillard@ee.doe.gov

Start Date: October 1, 2020

End Date: September 30, 2021

Project Funding (FY21): \$3,275,000

DOE share: \$3,275,000

Non-DOE share: \$0

Project Introduction

The advancement of battery technologies that can meet the emerging demands for vehicle electrification requires in-depth understanding of the performance of early-stage pre-commercial batteries, state-of-the-art commercial cells and the ability to adapt evaluation methods as mobility needs change. The Battery Test Center (BTC) at Idaho National Laboratory (INL) has been supporting the evolution of electrified transportation through high-quality, independent testing of electrical energy storage systems for more than 30 years. Independent testing provides data for quantitative assessment of the fundamental technology gaps that exist in early-stage battery development. Test methods and techniques are continuously improved to offer data on relevant metrics as vehicle applications evolve and as new core gaps are identified. Advancing electrified powertrain transportation including understanding both high-energy battery chemistries and high power, extreme fast charging needs, is a top priority in advancing how people and goods are transported in the United States. As a designated core capability and lead test facility for the Vehicle Technologies Office (VTO), the BTC at INL directly supports the US Advanced Battery Consortium (USABC) and other VTO programs by providing discrete information on failure modes, mechanisms and shortfalls in emerging technologies. Gaps in performance relative to targets are used as a metric to guide future R&D priorities.

The development and deployment of batteries in new, diverse applications requires both that the batteries function in the necessary environment as well as a deep understanding of their performance, life and expected failure mechanisms. In the past the primary means to advance knowledge on performance and life was to test batteries for extended periods of time under a range of different scenarios. Testing of batteries in this manner can take upwards of a year to make reasonable estimations of life and to clearly identify failure modes and rates. The need to shorten the design and testing cycle is critical to bringing new battery chemistries and cell designs into emerging applications such as in stationary energy storage to support electric vehicle charging stations capable of extreme fast charging.

Objectives

The activities at the INL BTC are focused on providing high fidelity, science-based performance and life testing, analysis, modeling, and reporting. To ensure the alignment with future industry and government needs, it is a key objective to update test and analysis procedures as new concepts and design space become achievable. Refined procedures help identify promising future research paths and identify key fundamental gaps that need to be addressed.

Approach

With 20,000 square feet of laboratory space, the INL BTC is equipped with over 800 test channels for advanced energy storage testing at the cell-level (e.g., up to 7V, 300A), module-level (e.g., up to 65V, 1200A),

and pack-level (e.g., 500–1000V, 500A). Test equipment is programmed to perform distinct test profiles while simultaneously monitoring for compliance with operating limits such as voltage, current and temperature. The output from such tests enables principles-based analysis to be performed that can aid in identification of key technology gaps.

To ensure high quality, repeatable and dependable data is used for analysis, batteries and other energy storage devices are typically subjected to specific test sequences while housed inside precision thermal chambers. To enhance performance testing across a wide range of thermal conditions, driven by automotive usage scenarios, the thermal chambers can be operated across a broad temperature range (e.g., -70 to 200°C). This temperature range enables key information to be extracted by modifying the chemical kinetic degradation rates within the evaluated items and enables accelerated aging analysis.

Successful performance testing and accurate life modeling are highly dependent on the fidelity of the acquired test data. The INL BTC has developed advanced calibration verification and uncertainty analysis methodologies to ensure that voltage, current, and temperature measurements are within the tolerance specified by the test equipment manufacturer (e.g., 0.02% of the full scale). These measured test parameters are subsequently used in various mathematical combinations to determine performance capability (e.g., resistance, energy, power, etc.). INL has also quantified the error associated with these derived parameters using the accuracy and precision of the relevant measured parameter (e.g., voltage) to ensure high-quality and repeatable results and meaningful presentation.

The INL BTC is also equipped with facilities that enable the characterization of batteries in aggressive use cases. One such use case is vibration that mimics what would be seen over the life of a battery in a typical automotive setting. Analysis of vibration on batteries at INL utilizes a high-capacity vibration table to perform non-destructive tests to understand reliability and safety of new cell topologies to mechanical vibration and shock. Emerging cell designs that vary from current state of the art cell designs are the focus of mechanical vibration and shock testing at INL.

Adjacent to the vibration table are two fire-rated isolation rooms that can be used for tests that push the known limits of battery operation. These aggressive use cases include extreme fast charging, subtle over- or under-charging, high-temperature thermal characterization for under-hood systems, among many others. The isolation rooms allow for safe testing of emerging cell technologies at or near the design limits and help characterize future use cases. The rooms also enable identification of key changes in performance fade that may emerge in aggressive use cases that can directly inform future rounds of early-stage material and cell development activities. These complimentary non-destructive evaluation capabilities comprise INL's Non-Destructive Battery Evaluation Laboratory.

Results

The INL BTC continues to test articles of various sizes and configurations using standardized test protocols developed by INL with industry partnerships for different electric drive vehicle application. Table VI.7.1 and Table VI.7.2 summarize the testing activities under the USABC and Benchmarking programs, respectively, for FY-21. Technologies developed through USABC contracts are aged and tested against the appropriate application target (HP-EV, LC/FC-EV, HEV, PHEV, 12V S/S, 48V HEV) and, where applicable, they are compared to previous generations of test articles from the same developer. 284 articles were tested for USABC in FY-21, including 2 modules and 282 cells. The purpose of the Benchmark program is to evaluate device technologies that are of interest to VTO within DOE but are not deliverables developed under a contract. In some cases, Benchmark devices are used to validate newly developed test procedures and analysis methodologies. Benchmark activities also are used to understand which gaps need to be fundamentally addressed to improve cell performance. 104 cells were tested for the Benchmark program in FY-21. A new testing program was started in FY-20 to evaluate deliverables from the VTO Low Cobalt FOA programs. Testing of the first round of deliverable cells was continued into FY-21. The purpose of the program is to find

Li-Ion battery chemistries that have little to no cobalt content. 96 cells were tested for the Low Cobalt program in FY-21.

Analysis was performed for all articles tested, and results were presented regularly at quarterly review meetings and USABC Technical Advisory Committee (TAC) meetings to USABC representatives from different automotive manufacturers, DOE VTO representatives, developers, and national laboratory staff. INL worked with the USABC test methods committee to develop the methodology and update the manual for testing EV batteries.

Table VI.7.1 Articles Tested for USABC

Developer	Application	System	Number of Articles Tested	Status at Year End
Amprius	HP-EV	Cell	13	Completed
Farasis	Recycle	Cell	18	Completed
PPG	HP-EV	Cell	18	Completed
Zenlabs	HP-EV	Cell	17	Completed
Benchmark	LC/FC-EV	Cell	30	Ongoing
Farasis	HP-EV	Cell	15	Ongoing
Farasis	Recycle	Cell	12	Ongoing
Farasis	Recycle	Cell	12	Ongoing
Farasis	Recycle	Cell	12	Ongoing
Farasis	LC/FC-EV	Cell	12	Ongoing
Microvast	LC/FC-EV	Cell	24	Ongoing
Microvast	HP-EV	Cell	36	Ongoing
Microvast	HP-EV	Module	2	Ongoing
Saft	HEV	Cell	13	Ongoing
Zenlabs	LC/FC-EV	Cell	23	Ongoing
Zenlabs	LC/FC-EV	Cell	27	Ongoing

Table VI.7.2 Articles Tested for Benchmark

Developer	Application	System	Number of Articles Tested	Status at Year End
LG/CPI	EV	Cell	15	Completed
Microvast	EV	Cell	6	Completed
Microvast	EV	Cell	6	Completed
PPG	EV	Cell	18	Completed
PARC	EV	Cell	13	Completed
Daikin	EV	Cell	22	Completed
Daikin	EV	Cell	24	Ongoing

Table VI.7.3 Articles Tested for Low Cobalt

Developer	Application	System	Number of Articles Tested	Status at Year End
Nextech-Nexceris	Low Cobalt	Cell	12	Completed
ORNL	Low Cobalt	Cell	12	Completed
UC – San Diego	Low Cobalt	Cell	12	Completed
Cabot	Low Cobalt	Cell	12	Ongoing
ORNL	Low Cobalt	Cell	12	Ongoing
Penn State	Low Cobalt	Cell	12	Ongoing
UT – Austin	Low Cobalt	Cell	12	Ongoing
UC - Irvine	Low Cobalt	Cell	12	Ongoing

Collaborative work continued in FY-21 between the 21st Century Truck Partnership (21CTP) and INL. This work has focused on developing battery specifications for commercial trucks with electric drives. Targets were finalized for class-8 line-haul battery electric trucks, class-6 battery electric box truck, and class-4 battery electric step vans. 21CTP consists of OEM companies across the commercial vehicle market, DOE-VTO, and National Labs.

In addition to providing high-fidelity test results the INL team also prepared a pre-application Battery test manual for the Federal Consortium for Advanced Batteries (FCAB). The FCAB battery test manual provides guidance on key tests which can provide early information to federal stakeholders on battery performance.

Conclusions

The ability to perform discrete performance and life evaluation of emerging technologies in an independent, reliable manner is a direct aid to the identification of key technology gaps. Over the course of FY-21, the INL BTC was able to directly support many different endeavors within VTO with a keen focus on advancing battery technologies for emerging trends in electrified transportation. As a core capability in performance and life analysis for VTO, INL has identified key performance fade modes that exist in cells and has advanced the understanding of performance and evaluation protocols for multiple programs funded by VTO and USABC. 484 devices were tested in FY-21. The work also continues to develop the update of the USABC EV test manual and the submission/acceptance of 2 peer reviewed manuscripts. In FY-22, INL plans to continue this level of support for multiple programs with broad support for the USABC and Benchmark programs. INL will also continue developing and refining standard test protocols and analysis procedures in collaboration with USABC and on providing information on core fundamental performance gaps that need to be addressed across VTO programs. Also, in FY-22, INL will continue to work with the 21st Century Truck Partnership to build battery targets for next generation electric commercial vehicles and publication of their electrification roadmap for commercial vehicles.

Key Publications

1. Federal Consortium for Advanced Batteries Pre-application Battery Test Manual
<https://cet.inl.gov/ArticleDocuments/FCABManualRev1Final.pdf>

Acknowledgements

The following staff at INL supported this work Matthew Shirk, Tanvir Tanim, Sergiy Sazhin, Eric Dufek, Randy Bewley, Charles Dickerson, Chinh Ho, Jordan Todd, Kevin Meudt, Michael Evans,

VI.8 Machine Learning for Accelerated Life Prediction and Cell Design

Eric Dufek, Principal Investigator

Idaho National Laboratory
2525 Fremont Avenue
Idaho Falls, ID 83415
E-mail: eric.dufek@inl.gov

Kandler Smith, Principal Investigator

National Renewable Energy Laboratory
15013 Denver West Parkway
Golden, CO 80401
E-mail: kandler.smith@nrel.gov

Simon Thompson, DOE Technology Development Manager

U.S. Department of Energy
E-mail: Simon.Thompson@ee.doe.gov

Start Date: October 1, 2019	End Date: December 31, 2024	
Project Funding (FY21): \$1,200,000	DOE share: \$1,200,000	Non-DOE share: \$0

Project Introduction

The development and deployment of batteries in new, diverse applications requires both that the batteries function in the necessary environment as well as a deep understanding of their performance, life and expected failure mechanisms. In the past the primary means to advance knowledge on performance and life was to test batteries for extended periods of time under a range of different scenarios. Testing of batteries in this manner can take upwards of a year to make reasonable estimations of life and to clearly identify failure modes and rates. The need to shorten the design and testing cycle is critical to bringing new battery chemistries and cell designs into emerging applications such as in stationary energy storage to support electric vehicle charging stations capable of extreme fast charging and the use of batteries in an assortment of different emerging areas of mobility. Connection of physics-based life models and machine learning (ML) provides the opportunity to enable more robust assessment of battery aging, failure mechanism identification and understanding as new use case scenarios are proposed. The current project is focused on means to apply ML to enhance the estimation of life while also identifying key failure pathways. During the first portion of the project existing data sets will be used for both training and validation of ML approaches to better characterize expected battery life. The work also looks to link ML with existing physics-based life models at INL and NREL.

Work in this project is focused on clearly aligning physics-based models with experimental data, synthetic data as generated from different electrochemical models and advanced data analysis methods. As a combined set of efforts, it is envisioned that the time needed for validation of both performance and key failure modes will be significantly reduced. The project also aims to develop tools that will help in the design space to more quickly align different materials and design considerations with application-specific needs. The combined set of tools are targeting a robust experimental-modeling-analysis framework which will provide more discrete information to stakeholders and battery developers to enable technology innovation with rapid turn-around.

Key contributions from this work during FY21 included the ability to predict performance and failure mode to within 2% for multiple types of cells and use conditions, the auto-identification of battery life models using ML and the generation of over 26,000 synthetic data sets that enabled high-throughput identification,

classification, and quantification of failure modes. The team also initiated development of a data hub for sharing DOE-internal research data.

Objectives

Key objectives during FY21 were aligned with expanded development of the tool architecture, demonstration of the ability to not just predict and validate performance at a fixed point in aging, but also the prediction of failure mode and failure mode extent and initiating the creation of a centralized datahub. These outcomes and objectives were achieved through the direct linkage of physics-based life models with electrochemical models and targeted experimental characterization. The use of statistical, machine learning and deep learning methods complemented the other activities.

Approach

To achieve the project objectives the team has taken an approach that blends the use of physical data acquisition, synthetic data generation using electrochemical models and battery life models. The bulk of activities focused on the use of single layer pouch cells with a graphite/NMC532 chemistry that had undergone different types of fast-charging characterization. Additional analysis used data sourced from the literature and previously collected data as part of a charging study on Nissan Leaf cells. Cells were characterized across different rates with post-test analysis for targeted confirmation of failure modes and extent of failure modes. Synthetic data was generated using a combination of incremental capacity (IC) models and electrochemical models based on a pseudo-2D (p2D) framework. Both sets of models incorporate key elements of the cell design including chemistry and electrode details and also aspects of failure modes including loss of lithium inventory (LLI), loss of active materials at the positive (LAM_{PE}) and negative (LAM_{NE}) electrodes. The p2D model further included changes in transport and kinetic properties with aging for diagnosis of high-rate data.

Advanced analysis used a combination of techniques including a suite of machine and deep learning frameworks, algebraic life models and targeted data extraction were used to analyze critical data for predictions. To maintain the link with physicality, analysis focused on using key electrochemical and environmental data points that inform both on how and why a cell is performing in a specific manner. For more complete details on each of the different tool used please refer to citations [\[1\]](#),[\[2\]](#),[\[3\]](#),[\[4\]](#),[\[5\]](#).

Results

Early prediction of performance was one of the first areas tackled as part of this project. Typically, standard life and performance testing takes a minimum of 9-15 months to predict life of a new cell design. New chemistries can take even longer to establish a firm framework for analysis. Two approaches were used during early efforts including the development of an ARIMA-based machine learning architecture that used a set of cells undergoing either AC Level 2 (ACL2) or DC fast charging (DCFC). Using the combination of features built from different voltages during the charge and rest periods, charge capacity and cell temperature it was possible to construct a model for prediction purposes. This model was then used to predict performance for 2 mixed-use-case data sets that used either a delayed direct-current fast charge (DCFC) or a combination of (alternating-current level 2) ACL2 and DCFC cycles. As shown in Figure VI.8.1 there was close alignment between the predicted and observed performance for capacity at reference performance test (RPT 9, 864 cycles) when using just the first 96 cycles of data (2 weeks of testing). Sensitivity analysis on the number of cycles needed to make a prediction of less than 1.5% mean approximate error (MAPE) determined that only 45 cycles (2 weeks of cycling data) were needed, a significant reduction in time compared to traditional life and performance evaluation methods.

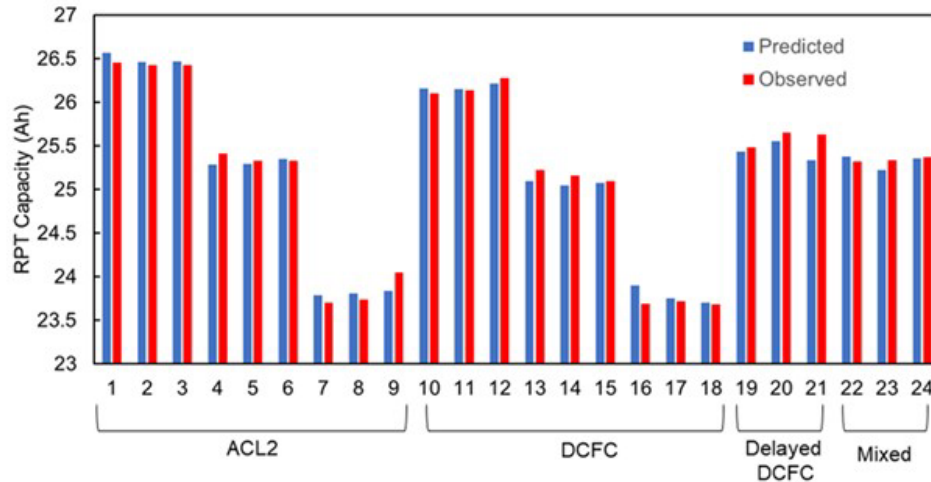


Figure VI.8.1 Observed experimental capacity at RPT 9 (864 cycles) and predicted capacity using 96 cycles (1 month of cycling) [1].

While low error was observed across the different conditions, when looking at the predictions for the delayed and mixed-use case conditions for RPTs 7–9 it was identified. Between the RPTs the prediction progressively underpredicted performance (Figure VI.8.2). This underprediction at long times is significant as it arises due to the less aggressive calendar aging that the delayed DCFC cells underwent. Based on their cycling procedure they were held for a longer period at a low state-of-charge which reduced their aging extent and thus led to the underprediction in performance. Thus, a key finding of this study was that while straight cycle life analysis is beneficial there also needs to be consideration of calendar aging aspects.

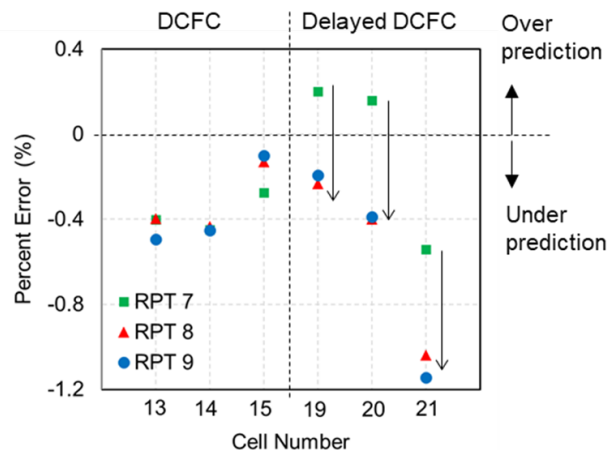


Figure VI.8.2 Error percent for RPTs 7-9 for DCFC and delayed DCFC cells both at 30°C. The shift in performance for the delayed DCFC cells is due to a less aggressive calendar aging condition [1].

The second method used to facilitate early life prediction capitalized on algebraic battery life models identified using newly developed ML techniques. The team developed AI-Batt (Autonomous Identification of Battery Lifetime Models), a toolkit for machine-learning-driven battery lifetime model identification and simulation [3]. The automated AI-Batt toolkit eliminates approximately one month of human-expert labor required to identify life-predictive models. It also reduces model error by approximately half compared to human-expert models [2],[3] (Gasper, in preparation, 2022). Features of AI-Batt include:

- Visualization of multi-dimensional timeseries data from accelerated calendar and cycling aging.
- A library of reduced-order equations derived from physically informed modeling of chemical and electrochemical systems to fit to observed degradation trends.
- Deconvolution of cell- and stress-dependent modeling parameters using bilevel regression.
- Machine-learning of parsimonious relationships between stress-dependent parameters and experimental stress conditions using a symbolic regression approach that searches through tens of millions of possible models using penalized regression or compressed-sensing algorithms.
- Uncertainty quantification via bootstrap resampling to determine confidence intervals on parameter values and extrapolate uncertainty into predictions of future aging.

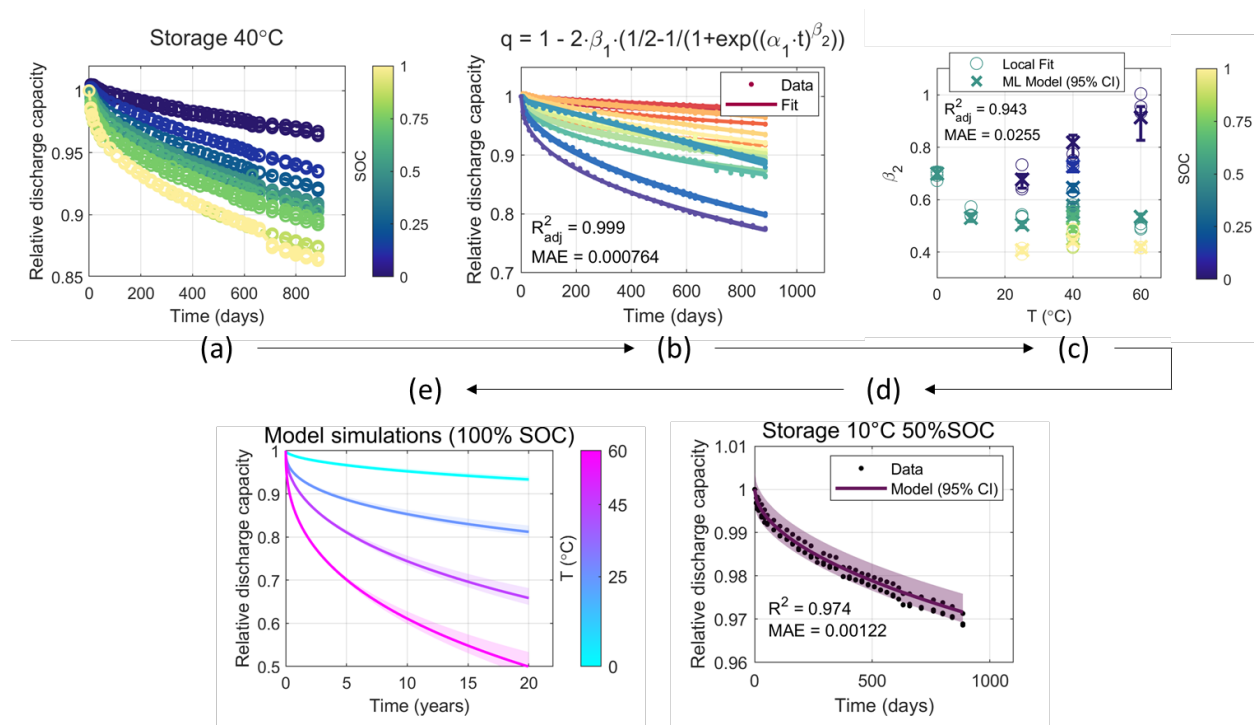


Figure VI.8.3 Demonstration of AI-Batt toolset on LFP/Gr calendar aging data (Naumann et al., 2018). (a) Visualization of relative discharge capacity for cells stored at 40 °C versus time and state-of-charge (SOC). (b) Fitting of a sigmoidal equation, deconvoluting cell- (α_1) and stress-dependent (β_1 , β_2) degradation trends using bilevel regression to simultaneously optimize cell-dependent parameters to the entire data set and stress-dependent parameters to each individual test condition (each line color corresponds to a unique temperature and SOC). (c) Machine-learned model predicting β_2 as a function of temperature and SOC. (d) Example fit of the model after machine-learning with uncertainty bounds using bootstrap resampling. (e) Extrapolation of the calendar aging model to 20 years at 100% SOC and various temperatures.

AI-Batt has been used to develop several battery life models, including models for NMC/Gr, LFP/Gr (Figure VI.8.3) and LMO/LTO lithium-ion battery chemistries. These models have been incorporated into several key publications and also implemented elsewhere. LFP/Gr and LMO/LTO models have been incorporated into the DOE BTMS-funded EVI-EDGES techno-economic model; these models are also incorporated into NREL's open-source energy generation and storage analysis software, SAM, enabling a wide variety of users to make better predictions of energy storage system lifetime and costs. The LFP/Gr aging model has also been incorporated into SimSES, an open-source technoeconomic analysis tool for energy storage systems developed at Tech. Univ. of Munich (TUM), which will be reported in upcoming publications (Collath et al., 2022; Gasper, in preparation, 2022). NMC/Gr and LFP/Gr aging models have also been used to analyze the potential battery capacity of the future electric vehicle fleet, in partnership with U. Leiden (Xu et al., 2022).

The automated model search procedure implemented in AI-Batt empowers research into difficult modeling questions. One key question is the relationship between input data and resulting models: how much data, both in terms of test time and number of aging conditions, is required to safely extrapolate models to real-world use? Because the model search process is automated, this question can be addressed in an apples-to-apples manner, rather than relying on a human researcher to find model equations via trial-and-error. In a key publication this year, analysis of calendar fade data from LFP/Gr cells showed that only 6 calendar fade aging conditions studied for approximately 6 months is enough data to identify a calendar fade model that accurately extrapolates to new conditions [2]. Analysis of LMO/LTO aging data has shown that after only 120 days of testing, cell resistance growth can likely be extrapolated safely to end-of-life, but that more data is required to extrapolate the observed capacity fade because the capacity fade is small and degradation trends are more complex. These efforts help accelerate the model identification process, reducing the cost of aging studies, and can help to design new experiments.

Predicting life was only one of the objectives during FY21 for this work. The second was on identification and classification of failure modes. In order to classify failure modes, it is often necessary to use several different sets of complementary electrochemical signals. Using a combination of capacity fade, coulombic efficiency, and the relaxation of voltage at the end of charge (EOCV) and end of discharge (EODV) it was possible to construct a decision tree that clearly classified LLI as either due to Li plating during fast charge or due to standard solid electrolyte interphase (SEI) growth. Using a similar elastic net as was used in the study above it was possible to classify cells which had gone through several different fast charge procedures using only the first 25 cycles. This number of cycles is $\sim 4\times$ less than what was needed for a human determination of Li plating [1]. Overall, the ability to classify was successful with only 2 classifications which were uncertain as seen in Figure VI.8.4.

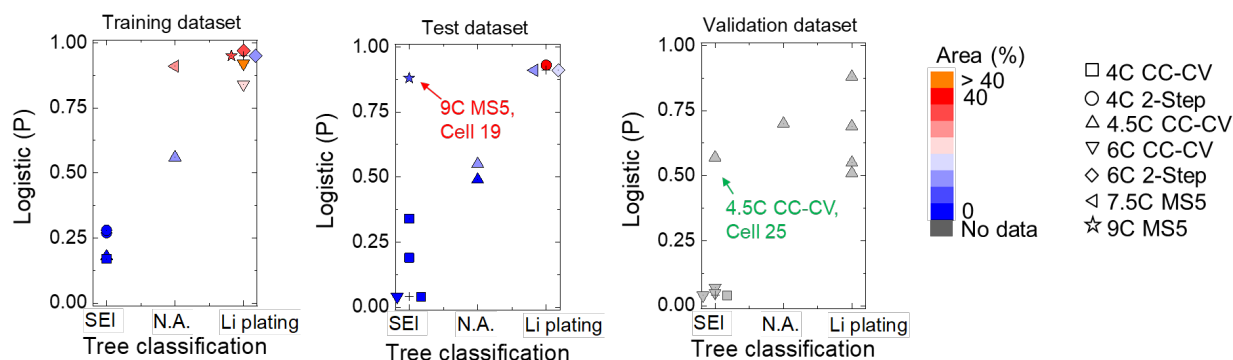


Figure VI.8.4 Classification of failure mode as either SEI growth or Li plating for cells undergoing several different fast charge protocols [1].

Building on classification the team next focused on quantifying both performance predictions and failure modes. This required a slight shift in approach due to the sparse experimental data. To account for this limitation the team utilized an incremental capacity (IC) model which was used to generate extensive synthetic data sets (26,000). Using these and a deep learning approach it was possible to quantify failure mode (LLI and LAM) and predict capacity fade across several different conditions and use cases (Figure VI.8.5). This use of synthetic data significantly reduced the number of experimental resources needed and allowed both rapid prediction and quantification of failure modes [4]. Extensions of this work were able to additionally predict and quantify failure mode at 400+ cycles using as little as 100 cycles.

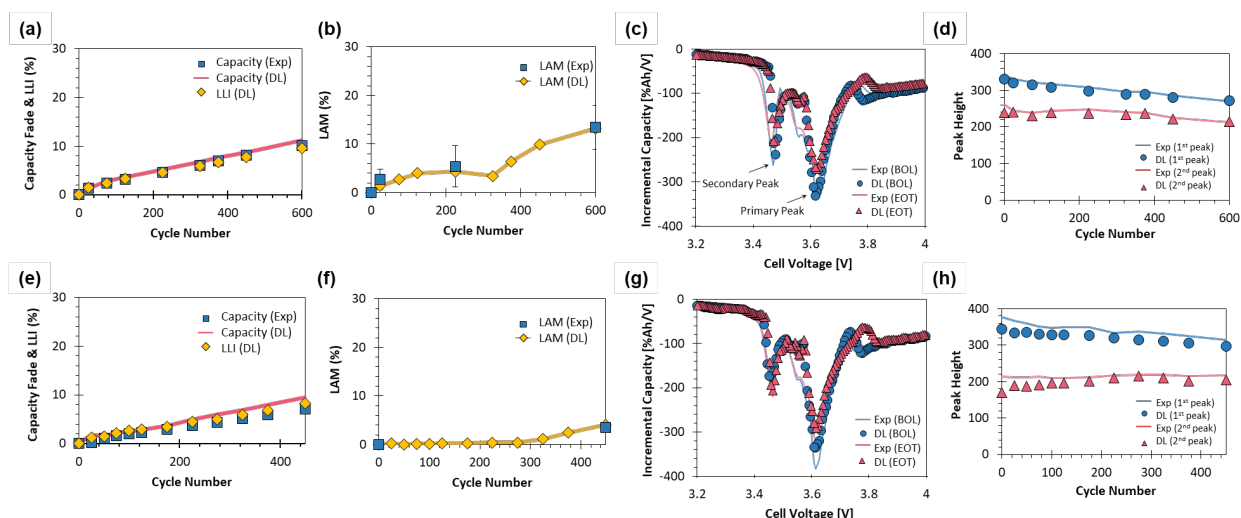


Figure VI.8.5 Validation of the deep learning model using experimental data based on C/20 capacity fade and LLI% (a,e), %LAM_{PE} (b,f), IC curve comparison (c,g). Parts d and h present the trend in primary and secondary IC peaks over the course of cycling [4].

While incremental capacity analysis is highly useful for tracking LLI and LAM, this thermodynamic analysis can only be applied to low-rate capacity data (\sim C/20) that is infrequently measured by interrupting aging tests (each \sim 100 cycles). Valuable early-prediction information is available in high-rate data; however, a more sophisticated analysis method is needed that incorporates transport and kinetic degradation mechanisms. To this end, the team developed a physically based p2D battery model and validated it against initial performance and aging behavior observed from XCEL-program cells with two different electrode loadings. The model was then used to generate a synthetic dataset that, in FY22, will be used to train a DL algorithm to diagnose failure mechanisms from high-rate raw cycling data.

The p2D model incorporated five aging parameters identified from experiments: LAM_{PE}, LLI, τ Ds PE, R_{ct}, and R _{Ω} . LAM_{PE} and LLI were obtained from afore-mentioned incremental capacity analysis. Changes in positive electrode diffusivity, attributed to NMC particle fracture, were obtained by fitting an exponential-relaxation model—with time constant τ Ds PE—to cycle-by-cycle EODV data. Charge-transfer and ohmic resistance changes, respectively Δ R_{ct}, and Δ R _{Ω} , were obtained from EIS measurements. The resulting p2D model compares favorably to voltage dynamics for all charge/discharge aging cycles throughout life. With some outliers, the model generally reproduces EOCV data within 25 mV and EODV within 50 mV for both cell loadings across separate aging tests conducted at 1C, 4C, 6C, and 9C charge rates. Sensitivity analysis shows LAM_{PE} and LLI account for the majority of aging trends, with resistance and diffusivity parameters further improving the fit.

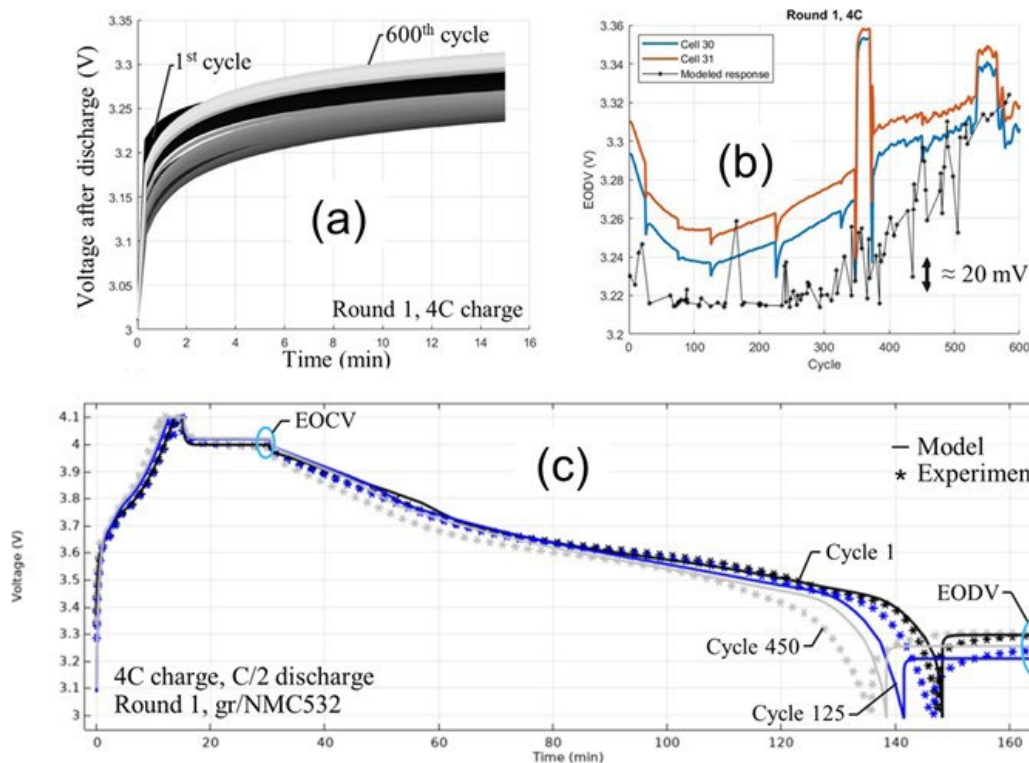


Figure VI.8.6 (a) Voltage relaxation after discharge changes non-monotonically with (b) an initial drop in end-of-discharge voltage (EODV) followed by a steady increase in EODV as (dis)charge cycles accumulate. With 5 state-of-health parameters, the p2D model predicts EODV within 20 mV. (c) Comparison of P2D model with raw voltage curves.

Figure VI.8.6 compares aging data and the p2D model. With 5 state-of-health parameters extracted from IC analysis, EODV relaxation behavior, and EIS, the p2D model reasonably tracks the raw voltage data, including features such as non-monotonic changes in EODV. Compared to EOCV which changes much less, EODV is sensitive to previous charge, rest, and discharge response (much harder to predict). The validated p2D model is now being exercised to generate synthetic data for a DL algorithm that will identify degradation modes directly from cycle-by-cycle data, offering a path to physics-based early life prediction.

A goal of the project is to accelerate DOE battery R&D using novel ML algorithms. Also supporting this goal, in parallel, the team is building a web-based data hub and standardizing the way that data is stored. The data hub will enable secure data storage, data search and retrieval capabilities, as well as research collaboration across DOE research projects. The data hub application will leverage existing and approved infrastructure currently utilized throughout other DOE Energy Materials Network (EMN) and non-EMN data hubs; Supporting secure authentication and access mechanisms, the front end will enable data categorization into hierarchical structures to best support research requirements. Accomplishments thus far include but are not limited to completed scoping of development for timely completion, obtained approval and finalization of <https://batterydata.energy.gov> domain name, defined and formalized metadata in JSON format, and created front-end wireframe.

Conclusions

Leveraging methods developed in FY21 the ability to make performance, failure mode and life predictions using significantly less data has been demonstrated. Using less than one month of data it was possible to predict performance to within 1.2% for cells undergoing a mixed-use scenario using a machine learning framework based off a logistic elastic net. Using a similar framework and a decision tree, a 4x reduction in time needed to classify Li plating vs standard SEI growth was developed and demonstrated. This significant improvement allows researchers to use as little as 25 cycles to make an analysis of new protocols or use cases.

Where experimental data is sparse two different methods were developed and implemented to enable use of deep learning methods and to facilitate advanced predictions. The synthetic data generated using either an IC or a p2D model framework allow specific electrochemical signatures to be readily extracted and used to make more robust data sets for prediction purposes. When incorporated into a deep learning framework the synthetic data allows rapid identification and quantification of both LLI and LAM in addition to cell performance over life.

AI-Batt, a battery lifetime model identification toolkit empowered by machine-learning, has helped accelerate the analysis of battery lifetime aging trends and identify models that have approximately half the error of human-expert models. Various battery lifetime models identified using AI-Batt (NMC/Gr aging data from NREL, LFP/Gr aging data from TUM, and LMO/LTO aging data from INL) have been implemented in a variety of projects, including the open-source energy storage systems and analysis tools SAM (NREL) and SimSES (TUM), and have supported the development of the DOE BTMS funded EVI-EDGES.

The data hub, Batterydata.energy.gov was initiated in FY21 with production expected at end of FY22.

Key Publications

1. Chen, B. R., Kunz, M. R., Tanim, T. R., & Dufek, E. J. (2021). A machine learning framework for early detection of lithium plating combining multiple physics-based electrochemical signatures. *Cell Reports Physical Science*, 2(3). <https://doi.org/10.1016/j.xcrp.2021.100352>
2. Collath, Nils, P. Gasper, A. Jossen, K. Smith, and H. Hesse. 2022. *The Economic Impact of Battery Degradation Modeling Uncertainty*. Submitted to the 2022 IEEE Power & Energy Society General Meeting (PESGM).
3. Gasper, P., Gering, K., Dufek, E., & Smith, K. (2021). Challenging Practices of Algebraic Battery Life Models through Statistical Validation and Model Identification via Machine-Learning. *Journal of the Electrochemical Society*, 168(2). <https://doi.org/10.1149/1945-7111/abddel>
4. Gasper, Paul, Collath, N., H. Hesse, A. Jossen, and K. Smith. 2022. *Machine-Learning Battery Lifetime Equations with Uncertainty for Simulating Extended Aging and Real-World Use*. In preparation
5. Kim, S., Yi, Z., Chen, B.-R., Tanim, T. R., & Dufek, E. J. (2021). Rapid Failure Mode Classification and Quantification in Batteries: A Deep Learning Modeling Framework. *Energy Storage Materials*. <https://doi.org/10.1016/j.ensm.2021.07.016>
6. Kunz, M. R., Dufek, E. J., Yi, Z., Gering, K. L., Shirk, M. G., Smith, K., Chen, B., Wang, Q., Gasper, P., Bewley, R. L., & Tanim, T. R. (2021). Early Battery Performance Prediction for Mixed Use Charging Profiles Using Hierarchical Machine Learning. *Batteries & Supercaps*, 4(7). <https://doi.org/10.1002/batt.202100079>
7. Tanim, Tanvir R., Z. Yang, A.M. Colclasure, P.R. Chinnam, P. Gasper, Y. Lin, L. Yu, P. Weddle, J. Wen, E. Dufek, I. Bloom, K. Smith, C.C. Dickerson, M.C. Evans, Y. Tsai, A.R. Dunlop, S.E. Trask, B.J. Polzin, and A.N. Jansen. 2021. *Extended Cycle Life Implications of Fast Charging for Lithium-Ion Battery Cathode*. *Energy Storage Materials*, 41 p.656-666, DOI: 10.1016/j.ensm.2021.07.001.
8. Ward, L., Babinec, S., Dufek, E. J., Howey, D. A., Viswanathan, V., Aykol, M., Beck, D. A. C., Blaiszk, B., Chen, B.-R., Crabtree, G., de Angelis, V., Dechent, P., Dubarry, M., Eggleton, E. E., Finegan, D. P., Foster, I., Gopal, C., Herring, P., Hu, V. W., ... Tao, L. (2021). *Principles of the Battery Data Genome*. <http://arxiv.org/abs/2109.07278>

9. Xu, Chengjian, P. Gasper, K. Smith, M. Hu, A. Tukker, and B. Steubing. 2022. *Future Flexible Energy Storage Capacity from Automotive Lithium-Ion Batteries*. In preparation

References

1. Chen, B. R., Kunz, M. R., Tanim, T. R., & Dufek, E. J. (2021). A machine learning framework for early detection of lithium plating combining multiple physics-based electrochemical signatures. *Cell Reports Physical Science*, 2(3). <https://doi.org/10.1016/j.xcrp.2021.100352>
2. Gasper, P., Gering, K., Dufek, E., & Smith, K. (2021). Challenging Practices of Algebraic Battery Life Models through Statistical Validation and Model Identification via Machine-Learning. *Journal of the Electrochemical Society*, 168(2). <https://doi.org/10.1149/1945-7111/abddel>
3. Gasper, Paul, Kandler Smith, and USDOE Office of Energy Efficiency and Renewable Energy. AI-BATT-OS (Autonomous Identification of Battery Life Models – Open Source). August 24, 2021. DOI: 10.11578/dc.20210915.3. Available online: <https://github.com/NREL/AI-Batt-OS>.
4. Kim, S., Yi, Z., Chen, B.-R., Tanim, T. R., & Dufek, E. J. (2021). Rapid Failure Mode Classification and Quantification in Batteries: A Deep Learning Modeling Framework. *Energy Storage Materials*. <https://doi.org/10.1016/j.ensm.2021.07.016>
5. Kunz, M. R., Dufek, E. J., Yi, Z., Gering, K. L., Shirk, M. G., Smith, K., Chen, B., Wang, Q., Gasper, P., Bewley, R. L., & Tanim, T. R. (2021). Early Battery Performance Prediction for Mixed Use Charging Profiles Using Hierarchical Machine Learning. *Batteries & Supercaps*, 4(7). <https://doi.org/10.1002/batt.202100079>
6. Naumann, Maik, M. Schimpe, P. Keil, H.C. Hesse, and A. Jossen. 2018. *Analysis and Modeling of Calendar Aging of a Commercial LiFePO₄/Graphite Cell*. *Journal of Energy Storage* 17 p.153–169. DOI: 10.1016/j.est.2018.01.019.
7. Smith, Kandler, P. Gasper, A.M. Colclasure, Y. Shimonishi, S. Yoshida. 2021. *Lithium-Ion Battery Life Model with Electrode Cracking and Early-Life Break-in Processes*. *Journal of the Electrochemical Society*, 168 100530. DOI: 10.1149/1945-7111/ac2ebd.

Acknowledgements

The activities described were a collaborative effort utilizing the capabilities of many researchers. Key contributors across the different national laboratories include Bor-Rong Chen, Parameswara R. Chinnam, Andrew M. Colclasure, Paul Gasper, Kevin L. Gering, Rachel Hurst, Ross Kunz, Sangwook Kim, Tanvir R. Tanim, and Peter Weddle and Zonggen Yi. This work was also aided by collaboration with the XCEL and BTMS programs run by Venkat Srinivasan and Anthony Burrell.

VII Small Business Innovation Research (SBIR)

Simon Thompson, DOE Technology Development Manager

U.S. Department of Energy

E-mail: Simon.Thompson@ee.doe.gov

Project Introduction

The advanced batteries effort of the Vehicle Technologies Office supports small businesses through two focused programs: Small Business Innovation Research (SBIR) and Small Business Technology Transfer (STTR). Both programs are established by law and administered by the Small Business Administration. Grants under these programs are funded by set aside resources from all Extramural R&D budgets; 3.0% of these budgets are allocated for SBIR programs while 0.45% for STTR grants. These programs are administered for all of DOE by the SBIR Office within the Office of Science. Grants under these programs are awarded in two phases: a 6-9 month Phase I with a maximum award of \$200K and a 2 year Phase II with a maximum award of \$1.1M. Both Phase I and Phase II awards are made through a competitive solicitation and review process.

Objectives

Use the resources available through the Small Business Innovation Research (SBIR) and Small Business Technology Transfer (STTR) programs to conduct research and development of benefit to the advanced batteries effort within the Vehicle Technologies Office.

Approach

The advanced batteries team participates in this process by writing a topic which is released as part of the general DOE solicitation. Starting in FY12, the advanced batteries team decided to broaden its applicant pool by removing specific subtopics and allowing businesses to apply if their technology could help advance the state of the art by improving specific electric drive vehicle platform goals developed by the DOE with close collaboration with the United States Advanced Battery Consortium.

Results

The advanced batteries team participates in this process by writing a topic which is released as part of the general DOE solicitation. Starting in FY12, the advanced batteries team decided to broaden its applicant pool by removing specific subtopics and allowing businesses to apply if their technology could help advance the state of the art by improving specific electric drive vehicle platform goals developed by the DOE with close collaboration with the United States Advanced Battery Consortium.

Phase II Awards Made in FY 2021

Under the SBIR/STTR process, companies with Phase I awards made in FY 2020 were eligible to apply for a Phase II award in FY 2021. The following three Phase II grants were awarded:

A high-energy-density vehicle battery with drop-in lithium anode enabled by a stable liquid electrolyte (Automat Solutions, Inc., Fremont, CA)

In this project, a novel class of high-energy-density batteries will be developed by dropping lithium metal anode into conventional lithium-ion battery, enabled by an advanced liquid electrolyte. The development process employs a closed-loop machine learning and high-throughput robotic experimentation workflow, which allows for an efficient search of the vast chemical and material space for possible electrolytes. This interdisciplinary approach will produce advanced liquid electrolytes offering longer cycle life and lower cost in a more efficient manner than the currently employed *Edisonian* processes.

Tailored Cathode Chemistry for Next-Generation Lithium-ion Batteries (Nexceris, LLC, Lewis Center, OH)

The technology that Nexceris and The Ohio State University (OSU) are working to develop focuses on the enormous market opportunity for new materials innovations that address these safety and cycle-life challenges that are slowing the roll-out of nickel-rich NMC cathodes. In Phase I Nexceris and OSU demonstrated two extremely promising product concepts that significantly improve the capacity and cycle life of nickel-rich cathodes. In the Phase II effort, the commercial readiness of these product concepts will be advanced, and the performance enhancement demonstrated in large 2-Ah cells. This project aims to advance the commercial adoption of electric vehicles by improving battery performance. A new coating strategy will be developed to accelerate new batteries to increase electric vehicle adoption.

Direct sorting, purification and regeneration of cathode materials for aged lithium-ion batteries using a novel low-temperature plasma assisted separation process (LPAS) (Princeton NuEnergy Incorporation, Princeton, NJ)

This technology will enable the regeneration of cathode materials without complete breakdown of the underlying chemical compounds, which will significantly reduce energy and chemical consumption compared to current industrial processes. Direct regeneration of cathode materials using the proposed technology will increase the commercial viability of lithium-ion batteries (LIBs) and reduce the cost of batteries, thus accelerating the electrification of transportation and large-scale energy storage for renewable energy in the near future. Moreover, the direct upgrading technology is transformative. If successful, it will create a new manufacturing process for LIB cathode materials from recycled batteries and establish the leadership of U.S. manufacturing of LIBs. Along with Princeton NuEnergy-developed purification and separation processes, this direct upgrading technology offers systematic advantages in costs, energy efficiency, and environmental protection by reusing, recycling, and reproducing lithium ion batteries within an optimized system. This invention brings new opportunities to recycle batteries with high energy efficiency and low environmental impact.

Phase I Awards Made in FY 2021

Nine Phase I grants were awarded in the Summer of FY 2021.

Conformal Graphene-Based Coatings for No-Cobalt, High-Performance Lithium-Ion Batteries (Volexion, Inc., Wilmette, IL)

The increasing energy storage demands of electric vehicles require next-generation, high energy density lithium-ion battery materials, which have continued need for improved cycle life and safety performance for wide commercial adoption. Volexion, Inc. proposes a comprehensive protective coating technology to stabilize these emerging materials, thereby enhancing the battery life and safety while simultaneously improving driving range and minimizing weight.

Real-time Electromagnetic Characterization of Thermal Runaway Conditions in Li-ion Modules (Parthian Energy LLC, Pasadena, CA)

A real-time module screening detection technology to reduce increase safety and reduce cost Parthian Energy is developing a rapid battery diagnosis product, PES, which can detect internal short circuits in a few minutes, either during manufacturing or during use.

High-Throughput Manufacturing of Lithium Dendrite Suppression Membranes for High-Energy Density Anodeless Lithium Metal Batteries (Ampcera Inc., Tucson, AZ)

Ampcera Inc. is developing a high-energy anodeless lithium battery to enhance electric vehicle (EV) safety and driving range. A scalable manufacturing method is used to reduce battery cost, making EV more economical. The technology will enable widespread EV implementation helping to reach net zero carbon emissions by 2050.

Domestic Halloysite-Derived Silicon as a Low-Cost High-Performance Anode Material for Li-Ion Batteries (Applied Minerals Inc, Eureka, UT)

To enable the widespread adoption of electric vehicles, the cost of lithium-ion battery electrode materials must be reduced. This project will enable commercial production of high-performance, low-cost battery electrode material through an innovative process derived from a unique domestic mineral resource found in Utah.

Taming Ultrahigh Energy Cathodes with Stabilizing Coatings: Harnessing Atomic Layer Deposition to Employ High-Nickel, Cobalt-Free Cathodes in Electric Vehicles (TexPower, Austin, TX)

Electric vehicles are a pivotal piece of a new energy economy with less pollution and greater energy independence, but a critical component of state-of-the-art batteries, cobalt, has a vulnerable supply chain. This project applies chemical innovations to the battery to eliminate cobalt while increasing stored energy at lower cost.

Solution-based Organic Coating for the Stabilization of Si Electrodes (Coreshell Technologies Incorporated, Berkeley, CA)

Coreshell and CU Boulder have identified new coatings that prevent mechanical failure and instability of high-capacity silicon-anode lithium-ion batteries. These stable, silicon-containing anodes will significantly reduce lithium-ion battery costs, increase capacity, and accelerate the widespread adoption of zero-emission electric vehicles.

FAST (Flame-Assisted Spray Pyrolysis Technology) Direct Recycling of EV Battery Electrode Materials (Storagenenergy Technologies, Inc., Salt Lake City, UT)

This technology will enable low-cost battery materials recycling with high recycling rate making it extremely attractive for implementation in both portable power and EV batteries industries.

Novel Composite Membrane Electrolyte Based Batteries for Electrical Vehicles (Giner, Inc., Newton, MA)

Conventional lithium-ion batteries using liquid electrolytes face some major challenges such as battery safety and low energy density, for electrical vehicle applications. This project aims to develop an alternative solid electrolyte battery technology that will address these barriers, and the success of this project will significantly facilitate the commercialization of electrical vehicles.

Optimizing the Silicon anode interfacial stability to achieve high energy, fast charge Li-ion EV batteries at scale (Graphenix Development Inc, Rochester, NY)

Graphenix Development Inc (GDI) is creating high-energy and high-power silicon-based anodes for lithium-ion batteries

VIII Next Generation Lithium-Ion Materials: Advanced Anodes R&D

VIII.1 Silicon Consortium Project (ANL, LBNL, SNL, ORNL, PNNL, NREL)

Anthony K. Burrell, Principal Investigator

National Renewable Energy Laboratory
15013 Denver West Parkway
Golden, CO 80401
E-mail: Anthony.Burrell@nrel.gov

Brian Cunningham, DOE Technology Development Manager

U.S. Department of Energy
E-mail: Brian.Cunningham@ee.doe.gov

Start Date: October 1, 2020	End Date: September 30, 2025	
Project Funding (FY21): \$7,950,000	DOE share: \$7,950,000	Non-DOE share: \$0

Introduction

The current energy-storage roadmap for transportation has identified next-generation anodes as key components leading to the development of electric vehicle battery packs costing less than \$100/kWh by 2028. While the cycle life of silicon (Si)-based cells and the overall capacity have improved significantly, calendar life achieves only ~10% of the target. Historically, Si anode research has focused on the large crystallographic expansion (~320%) that Si experiences upon lithiation to form Li_xSi . However, it has become clear that other failure mechanisms are also present. Specifically, the limited calendar life of Si cells demonstrates that a passivating solid electrolyte interphase (SEI) does not form on the Si anode. This will remove the barriers associated with the development of advanced lithium-ion negative electrodes based upon Si as the active material, with a specific focus on understanding the formation and evolution of the SEI on Si to solve the calendar life challenge. The targets for this project detailed in the lab call require the delivery of >2-Ah full cells, with Si-based anodes, that deliver 1,000 cycles at C/3, have useable energy of >375 Wh/kg, energy density of >750 Wh/L, and a calendar life >10 years. Meeting all these requirements in a single cell will require a comprehensive program to understand the limits of Si SEI stability and cell design.

For FY21 the milestones were:

- Establish a Pre-lithiation protocol that can be utilized by all partners Q1.
- Go/no-go on HF etching of Silicon Oxide-silicon as viable route to silicon Q2.
- Go/No go on the Moire spectroscopy at as a method of probing the calendar life of the silicon SEI? Q3.
- Produce 20 grams of next generation silicon's with at least two different coatings, at least one of which exhibits enhanced calendar life over the baseline commercial silicon.
- Advanced version of the calendar life protocols that quantifies calendar life in silicon-based anodes within 20% of the "real" calendar life predictions of calendar life.
- Synthesis and testing of 5 different metallic glasses with theoretical capacities > 1000 mAh/g.

- Identify active cell components and cell designs to achieve stable calendar life electrode performance with a cell build demonstrating 300 cycles with <20% capacity fade.

Information associated with individual milestones is provided below.

Go/no-go on HF etching of Silicon Oxide-silicon as viable route to silicon

This project targeted the Silicon Consortium Project (SCP) FY21 Q2 Milestone: Go/no-go on HF etching of Silicon Oxide-silicon as viable route to silicon. Jiguang (Jason) Zhang and colleagues at PNNL have pioneered a novel route to a porous Si/C active material that has shown promising performance in full-cell cycling studies (anode specific capacity >1000 mAh/g, >99.9% CE and 78% capacity retention over 400 cycles against NMC532 and with Gen2 + 10 wt% FEC electrolyte). Note: These data are from the state-of-the-art in early FY22. Additional performance above and beyond these values have been established by PNNL in FY22 in their Seedling Project.

The PNNL porous Si/C synthesis process relies on HF etching of Si nanoparticles (NPs) embedded in a silica (SiO_x) matrix. Commercial SiO from Osaka is annealed under inert gas to cause a disproportion reaction, where the thermodynamic driving force of forming SiO_2 causes Si NPs to precipitate out in the oxide matrix. Subsequently, the annealed SiO powder (Si NPs in SiO_x where $x \approx 2$), is treated with hydrofluoric acid (HF) and a surfactant, and the liberated Si NPs are collected via filtration and then coated with carbon. The porous Si/C material has been characterized by PNNL to contain: (1) <5nm primary Si particle size, (2) ~5 μm secondary particle size, (3) < 10 m^2/g surface area, and (4) sealed porosity to mitigate particle swelling.

Go/No-Go on Moiré Interferometry (Sandia National Laboratories)

Silicon is a promising candidate as a next generation anode to replace or complement graphite electrodes due to its high energy density and low lithiation potential. When silicon is lithiated, it experiences over 300% expansion, which stresses the silicon as well as its solid electrolyte interphase (SEI), leading to poor performance. The use of nano-sized silicon has helped to mitigate volume expansion and stress in the silicon, yet the silicon SEI is still both mechanically and chemically unstable.¹ Identifying the mechanical failure mechanisms of the SEI will help enhance calendar and cycle life performance through improved SEI design.

Si Calendar Life Estimation from Electrochemical Testing Protocols

Calendar testing of batteries is a highly time intensive process, often taking months to years to acquire sufficient data to accurately predict calendar life. Therefore, it is highly desirable to only take promising materials through a long-term test protocol after estimating calendar life performance via a short-term test. An initial two week-long voltage hold protocol developed in late FY20 proved useful as a qualitative stage-gate to screen new materials. This year, the feasibility of extending this shortened test to quantitative predictions of calendar life was explored. Due to several complicating factors, discussed herein, it was determined that the current voltage hold protocol is not quantitative.

Synthesis and testing of 5 different metallic glasses with theoretical capacities > 1000 mAh/g

The goal of this project is to develop amorphous Si-based metallic glass anodes for Li-ion batteries using rapid quenching approaches. Such anodes combine Si with non-alloying elements and can provide improved interfacial stability and capacity retention, while maintaining the volumetric energy density of Si electrodes. Rapid quenching approaches include as an ultrafast laser quenching as a high-throughput Si-based glass anode screening tool, and splat quenching as a first step towards scale-up.

Objectives

Go/no-go on HF etching of Silicon Oxide-silicon as viable route to silicon

The objective of this project is to establish the scalability of the porous Si/C active material synthesis as a potential option as a new baseline active material within the SCP.

Go/No-Go on Moiré Interferometry (Sandia National Laboratories)

In order to identify the mechanical failure mechanisms of the SEI, *in situ* moiré interferometry was investigated to track the in-plane strain in the SEI and silicon electrode for this purpose. Moiré can detect on the order of 10 nm changes in displacement and is therefore a useful tool in the measurement of strain.² Despite the fact that measuring in-plane strain should be possible, the resolution of moiré spectroscopy was anticipated to be near the limit of what would be needed, making it a high-risk activity. Because of the high risk, the activity was intentionally bounded in time by setting a Go/No-Go milestone in quarter three to evaluate whether Moiré spectroscopy could be used for probing the calendar life of the silicon SEI.

Q4 Milestone. Si Calendar Life Estimation from Electrochemical Testing Protocols

The milestone to be achieved by Q4 in FY21 was to develop an advanced version of the calendar life protocols that quantifies calendar life in silicon-based anodes within 20% of the “real” calendar life predictions of calendar life.

Synthesis and testing of 5 different metallic glasses with theoretical capacities > 1000 mAh/g

The objective for this year has been to synthesis and test of 5 different Si-based metallic glasses with theoretical capacities > 1000 mAh/g with pulsed laser and splat quenching. The associated FY21 milestone was met.

Approach***Go/no-go on HF etching of Silicon Oxide-silicon as viable route to silicon***

Our approach was to mimic the PNNL lab-scale process and test whether it is amenable to scale-up at the several hundred-g to kg-scale required for the SCP. We coordinated with PNNL staff members to understand their process and repeat it exactly at small scale and devised a work plan to gradually scale the process from g-scale to well beyond.

Go/No-Go on Moiré Interferometry (Sandia National Laboratories)

Moiré spectroscopy can measure strain because, as the sample undergoes small deformations, large changes in the moiré fringe allow for measurements of displacement below the diffraction limit of light. Figure VIII.1.1(a) shows how the moiré fringe changes as the sample grating deforms. As the sample contracts or expands, the frequency of the moiré fringe changes, and this change is proportional to the strain in the sample.

Model thin foil electrodes were fabricated by spin-coating photoresist on a silicon wafer and then evaporating 50 nm of SiO₂, 50 nm of Si, and 500 nm of Cu on the top of the wafer. Si gratings with a 4 μm period were patterned on the Cu. The in-plane strain is very small due to constraint from the copper current collector on the silicon thin film, so the current collector was made as thin as possible without losing structural integrity. The foils were released by dissolving the photoresist using acetone. The free foils were then adhered to stainless steel washers as mechanical supports using silver epoxy. The SiO₂ layer served as a protective layer between the silicon and photoresist. The samples were cleaned by O₂ plasma and then the SiO₂ layer was removed using 1% v/v HF. The cyclic voltammogram of a successful electrode is shown in Figure VIII.1.1(b). The electrodes were used in a house-made *in situ* cell for strain measurements, as shown in Figure VIII.1.1(c).

The moiré interferometer was built in-house. Both geometric (reference grating projected onto the sample) and interferometric Moiré (interference of light used to generate the reference grating) were explored. The moiré interferometer is shown schematically in Figure VIII.1.1(d).

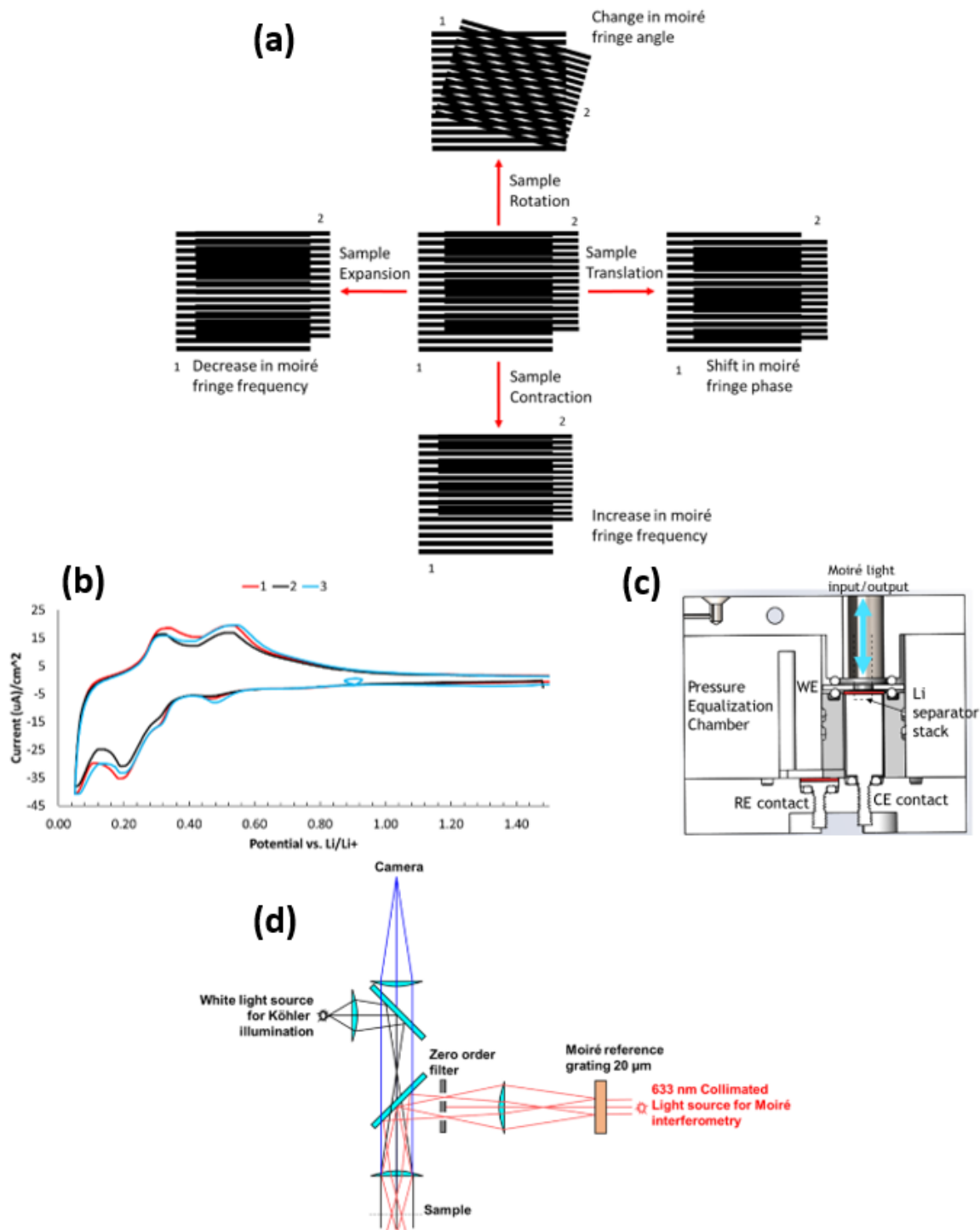


Figure VIII.1.1 (a) How moiré works with the reference grating labeled 1 and the sample grating labeled 2, (b) cyclic voltammetry of 3 replicates of a successful 50 nm Si, 500 nm Cu foil sample, (c) diagram of house-made in situ cell, and (d) diagram of house-made moiré interferometer. CE = counter electrode, WE = working electrode, RE = reference electrode.

Q4 Milestone. Si Calendar Life Estimation from Electrochemical Testing Protocols

A voltage hold is one potential option for an accelerated calendar lifetime test, because it could allow measuring, fitting, and extrapolating the time dependency of parasitic lithium inventory consuming reactions that are a significant contributor to calendar aging. However, any accelerated testing protocol must be carefully

designed to maintain relevant conditions and must be representative of or able to predict the aging that would occur under normal conditions. In this approach, a validation is necessary in order to see if the predictive capability is possible. We decided to validate the voltage hold protocol through testing of commercial graphite/LFP 18650 cells. Since it is well known that graphite/LFP commercial cells are well understood, and have proved to possess exceedingly long calendar life, this test should be indicative of proving robust and predictive long calendar life battery cell chemistry.

Synthesis and testing of 5 different metallic glasses with theoretical capacities > 1000 mAh/g

Si-based metallic glass anodes were fabricated using two distinct rapid quenching approaches, splat quenching and ultrafast laser quenching. These approaches are detailed below.

Splat Quenching

Ternary Si alloys [Si-Al-M (Ti, Fe, Co)] were prepared by an arc melter, followed by splat quenching (Figure VIII.1.2). This system quenches molten alloys using Cu metal surfaces at a rate of 10^5 – 10^6 K/s to produce amorphous metallic glass thin foils. Alloy elements were uniformly distributed in the metallic glass thin foil, as verified by SEM and X-ray diffraction.

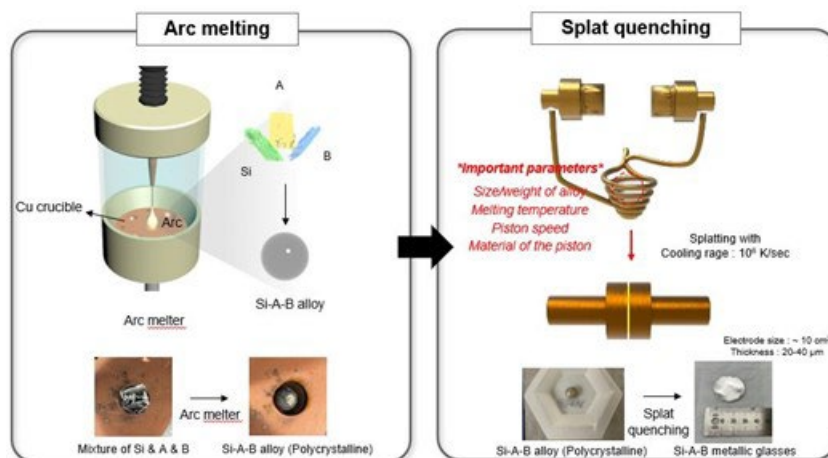


Figure VIII.1.2 Schematic of electrode preparation for ultrafast laser quenching process

Ultrafast Laser Quenching

A thin layer (~50nm) of binary Si alloy [Si-M (M=Fe, Ni, Mn, Cu, Ti)] was co-sputtered onto copper coated fused silica wafers (Figure VIII.1.3). Ultrafast laser quenching was performed with our automated femtosecond (fs) laser experimental system under Nitrogen gas flow. The electrodes were scanned on the top surface line-by-line with a 515nm femtosecond (fs) laser. The laser power and the scanning speed was optimized for each alloy system to form an amorphous and uniform surface. The amorphous phase of the electrode material was verified with micro-Raman spectroscopy and grazing incidence X-ray diffraction (GIXRD).

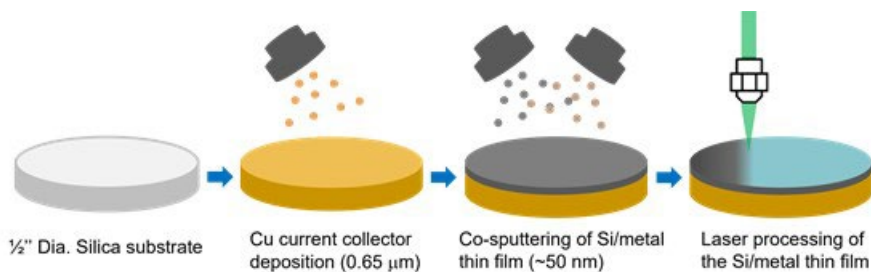


Figure VIII.1.3 Schematic of electrode preparation for ultrafast laser quenching process

Following splat quenching or ultrafast laser quenching fabrication (as described above), the electrochemical performance of the electrodes was characterized in a half-cell configuration through cyclic voltammetry (CV) and parasitic current measurements. Electrodes were assembled into 3-electrode Swagelok T-cells, with Li metal being the reference and counter electrodes. CV was performed at a sweep rate of 0.1mV/s between 0.05-1.5V vs. Li/Li⁺. The parasitic current was measured when applying a voltage hold at 0.05V for 12 hours.

Results

Prelithiation Protocols Across Consortium Partners

In anticipation for the requirement to prelithiate silicon electrodes a programmatic milestone was developed to evaluate processes and facilities across consortium member labs. Key to this milestone was to need to (1) develop a uniform standard for a method/methods to prelithiate silicon composite electrodes, and (2) ensure that all consortium members could reproduce the process. Table VIII.1.1 lists the various processes that were investigated and the results of the study.

Table VIII.1.1 (Prelithiation strategies investigated)

Method	Description	Comment
Redox Shuttle	Expose Si electrode to organic	Did not lithiate electrodes
Li ₅ FeO ₄ /Li ₂ O/Li ₃ N	Add excess Li to cathode through	Challenge casting electrode due to gelling
Lithium metal pushed on	Squeeze Li onto silicon electrode and	Incomplete lithiation on irregular surface
Li-Stearate	Lithium additive to surface	Did not lithiate electrode
Alloy Li with Si powder	Thermal mixing of Li metal and	Powder passivated and did not cycle
Milling Li+Si into powder	Mechanically mill silicon and Li to	Powder passivated and did not cycle
Electrochemical Lithiation	Assemble half cell and lithiate	Applicable to most electrodes: challenge
SLMP	Mix powder on surface of electrode	Requires administrative action
Li-evaporation	Thermally evaporate Li onto the	Applicable to most electrodes; challenge

For these experiments the cells were cycled using standard protocols developed by the SCP. Through the process we identified a process (electrochemical prelithiation) that could be easily applied, a second method that looked most promising (evaporation), and a third reserve mechanism with stabilized lithium metal powder that would require administrative action for using across the consortia.

Electrochemical Process – For the electrochemical testing composite electrodes made from two different silicon materials (G18 Paraclete Si and Osaka SiOx) were mixed with C45 and PI binder with a mass ratio of 70:10:20. The laminated process was carried out on the pilot coating machine at the CAMP Facility. The typical loading of active materials is ~1 mg/cm². After calendaring, the electrode sheets were heat treated at 350°C for 1 h in Ar atmosphere at a ramping rate of 10 °C/min for the polymerization process. The heat-treated electrodes were fabricated into 2032 coin-type cell or pouch cell using Li metal anode as counter electrode. The electrolyte consists of 1.2 M LiPF₆ in EC/EMC (3/7), plus 10% FEC additive. The cut-off voltages were explored between 10 mV and 100 mV to vary the extent of lithiation. The electrodes were disassembled in a desired lithiated state and combined with a fresh 622 cathode and were able to operate for 1100+ cycles and hit performance milestones for the year. There were challenges associated with this process. Specifically, the extent of lithiation to match losses during SEI formation; too much lithiation limits the effective utilization of the silicon due to cathode capacity limitations while too little lithiation results in excessive losses of lithium from the cathode.

Lithium evaporation – Thermal evaporation of lithium showed significant promise. In this method lithium was thermally evaporated onto a composite electrode surface. The lithium deposits with enough thermal energy to induce Li-Si alloy formation with a small amount of residual Li metal. The electrochemical potential

of the electrode can be adjusted depending on the extent of lithiation and matches the open circuit voltage of known Li-Si alloys at 0.43, 0.28, and 0.10 V (vs. Li/Li⁺). The first discharge capacity (half-cell) is a measure of the excess Li added during the electrochemical cycling. The amount of material deposited, less the material removed during the first discharge reaction, is reflective of the concentration of Li lost during SEI formation reaction. It was observed that 4 μm of Li on the A018 electrodes nearly all reacted with the electrolyte to form the SEI, Figure VIII.1.4. Further, these cells cycled hundreds of cycles with high coulombic efficiency. The thermal evaporation offers several advantages. First it is scalable in a roll-to-roll process. Second, a sacrificial electrolyte can be added to form the SEI before cell fabrication. In this way a more stable SEI could be formed that would allow effective cycling with the standard GEN2-3% FEC electrolyte. Third, the extent of lithiation can be accurately controlled by adjusting the deposition time and rate.

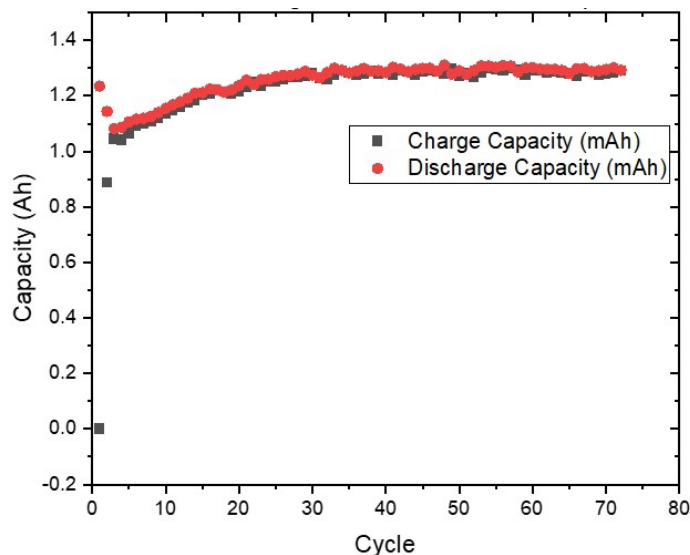


Figure VIII.1.4 Representative cycling data for Si/C45/LiPAA cell with 4 μm of Li evaporated on the surface.

Go/no-go on HF etching of Silicon Oxide-silicon as viable route to silicon

Results of small-scale HF etching experiments are shown in Figure VIII.1.5. Annealed SiO powder (4 g) was added to 60 mL concentrated (49 wt%) HF solution and increasing amounts of isopropanol were added to achieve dispersion (complete wetting) of the annealed SiO powder. Dispersion is important to ensure a homogeneous etching rate for the material (per PNNL). We found incomplete wetting at 5 vol% isopropanol, and complete dispersion was achieved at 33 vol% isopropanol (far right image, Figure 5). Further optimization likely would yield satisfactory dispersion between these values.

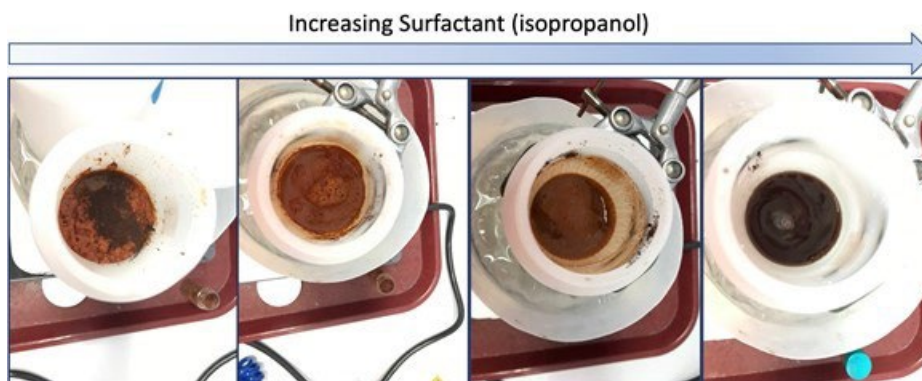


Figure VIII.1.5 Optical images of annealed SiO powder and concentrated HF solution with (from left to right) increasing amount of surfactant isopropanol (Image Credits – Nathan Neale, NREL)

During etching, we also found that the HF/isopropanol solution heated rapidly, and a temperature of 40–50°C could be maintained only through slow addition of the annealed SiO powder over several minutes (i.e., ~1 g/min) and cooling the HF/isopropanol solution in an ice bath. Investigation of the flash point—the lowest temperature at which a volatile substance evaporates to form an ignitable mixture with air in the presence of an igneous source—of the isopropanol surfactant/aqueous HF mixture required to achieve dispersion (>5 vol% and up to 33 vol% isopropanol) exceeds the flash point of isopropanol/water mixtures (approx. 20–40°C; Table VIII.1.2).

Table VIII.1.2 Flash point of isopropanol/water mixtures. Data from reference 1.

Vol% isopropanol	0.92	2.15	3.12	4.96	10.0	18.1	25.2	39.7	50.5	74.9	100
Flash point (°C) of mixture	56.5	43.0	38.0	31.3	26.0	24.0	21.0	20.0	18.5	16.3	12.0

The SCP team members discussed these results and provided several alternative, non-flammable surfactant options to Jiguang (Jason) Zhang at PNNL so that they can re-optimize their process to one compatible with scaling. Suggested alternative surfactants included Tween®, TRITON™, cetyltrimethylammonium bromide, sodium cholate, and sodium dodecyl sulfate. Alternatively, it was suggested that the etching process may be conducted under an oxygen-free environment where flammability is no longer a concern.

Go/No-Go on Moiré Interferometry (Sandia National Laboratories)

Initial experiments using geometric moiré seemed promising as there was a change in the perceived strain as a function of voltage. However, it was determined that the measurement was convoluted by changes in height of the foil relative to the objective. The setup was then changed to a moiré interferometer to achieve a more uniform fringe pattern with changes in height. Despite achieving more consistent measurements with changes in height and a decrease in static noise (Figure VIII.1.6(a) and Figure VIII.1.6(b), respectively), *in situ* variability continued. Through Gaussian beam simulations, it was determined that this was due to sensitivity to tip and tilt of the sample. With perfect alignment, the change in tilt caused a large change in perceived strain behavior making a systematic tilt correct difficult, as shown in Figure VIII.1.6(c). An auto collimator was built and used to make the sample perpendicular to the objective. However, this became infeasible with the foils *in situ*. The thin foils were used to enhance strain resolution required because of the confinement of the Si from the Cu, but they also made it nearly impossible to maintain a sufficiently flat surface. Because of these limitations, it was determined that moiré interferometry would be very difficult to use as an *in situ* method for measuring strain at the resolution needed for this project.

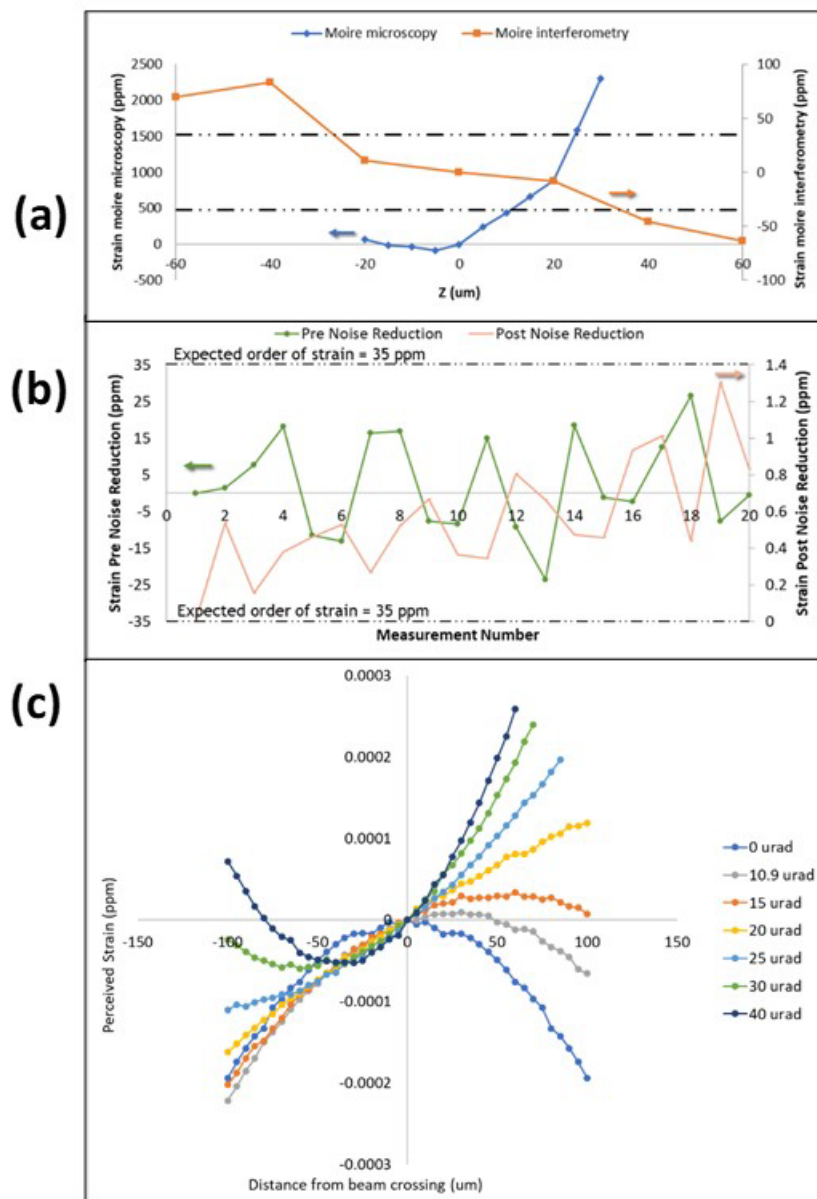


Figure VIII.1.6 (a) Improvements on noise using interferometry, (b) improvement on z-insensitivity using interferometry, and (c) Gaussian beam simulations of the effect of sample tilt. Similar trends were observed experimentally, but with a larger magnitude.

Produce 20 grams of next generation silicon's

The Silicon Consortium Program (SCP) milestone was established to “Identify active cell components and cell designs to achieve stable calendar life electrode performance with a cell build demonstrating 300 cycles with <20% capacity fade”. One of the key issues was ensuring that there were sufficient materials produces to adequately assess calendar life of proposed systems while also understanding the factors that influence performance. The Q4 milestone that enabled these studies was: Produce 20 grams of next generation silicon's with at least two different coatings, at least one of which exhibits enhanced calendar life over the baseline commercial silicon.

The materials of prime interest where those prepared using plasma-enhanced chemical vapor deposition (PECVD). Materials where prepared in batches of 2–5g and then were treated using both thermal carbon coatings and chemical modification using polyethylene oxides. Other materials have also been prepared using

silicon milling and modification of commercial silicon oxide samples. The data from full cells related to these materials are shown in outcomes of other milestones, for example Figure VIII.1.4.

Q4 Milestone. Si Calendar Life Estimation from Electrochemical Testing Protocols

Figure VIII.1.7 summarizes the reasons why the current V-hold protocol cannot be used to quantitatively predict calendar lifetime within 20%. While this figure compares datasets of well-behaved commercial graphite-LFP 18650 cells, we believe that the same issues will be present, and sometimes exacerbated, in Si containing cells. In Figure VIII.1.7(a) represents the “real” calendar lifetime of these cells as determined by traditional calendar aging at OCV. In Figure VIII.1.7(b) is the actual capacity loss that is measured over equivalent voltage hold aging times, while (c) represents the capacity loss measured during the voltage hold that would be used to try and quantitatively predict the real calendar lifetime. With no overlap of the shaded regions representing $\pm 20\%$ of the aging times in Figure VIII.1.7, the trend exhibited by (c) grossly overestimates the trend exhibited by the real lifetime (a). We attribute this discrepancy to two main reasons:

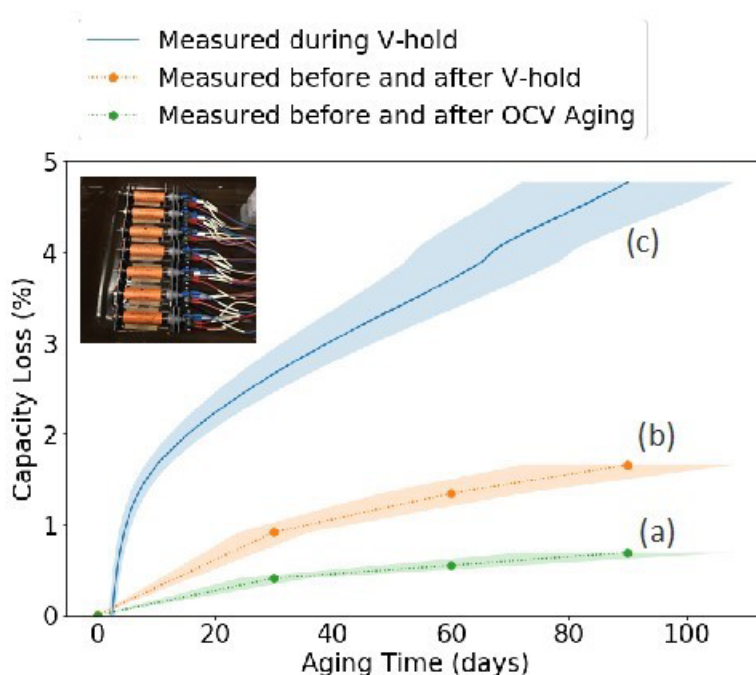


Figure VIII.1.7 The capacity loss of commercial graphite-LFP 18650 cells (pictured in inset) measured during calendar aging (either at OCV or a voltage hold at 3.35 V) over 30, 60, or 90 days for (a) traditional OCV-RPT tests, (b) actual capacity loss measured over equivalent voltage hold aging times, and (c) capacity loss during a 90-day voltage hold. To minimize capacity losses due to cycling, each data point of (a) and (b) was collected from a separate cell aged for the indicated time, rather than a single cell aged for the total time with periodic capacity checks. The capacity loss for each cell was calculated from the difference between the capacity measured before and after the aging period. The capacity loss measured during the 90-day long V-hold (c) is $(Q_{\text{hold}}/Q_{\text{norm}}) - Q_{\text{rev}}$, where Q_{hold} is the capacity passed during the voltage hold, Q_{norm} is the capacity measured during the cycle before aging, and Q_{rev} is the increase in SOC during the voltage hold ($\sim 22\%$). The shaded region for each of the data sets is $\pm 20\%$ of the given aging time.

First, the SOC of the electrode typically increases during voltage hold aging, while it stays the same or decreases slightly during OCV aging. A higher SOC is generally known to accelerate calendar aging rates, and this effect is demonstrated in Figure VIII.1.7 by the voltage hold aging (b) being more than twice that of the OCV aging (a). This increase in SOC during a voltage hold is shown in Figure VIII.1.8 where the dQ/dV plots are given before an OCV rest and voltage hold of the same length. The voltage hold resulted in $\sim 22\%$ higher SOC than the OCV, as evidenced by the delithiation peak around 3.31 V that is only present in Gr-LFP cells that underwent the voltage hold. Due to their large lithiation overpotentials, silicon electrodes will exhibit significant increases in SOC during a voltage hold at any chosen potential, making relevant comparisons between systems difficult due to differences in the state of charge at the same relative potential.

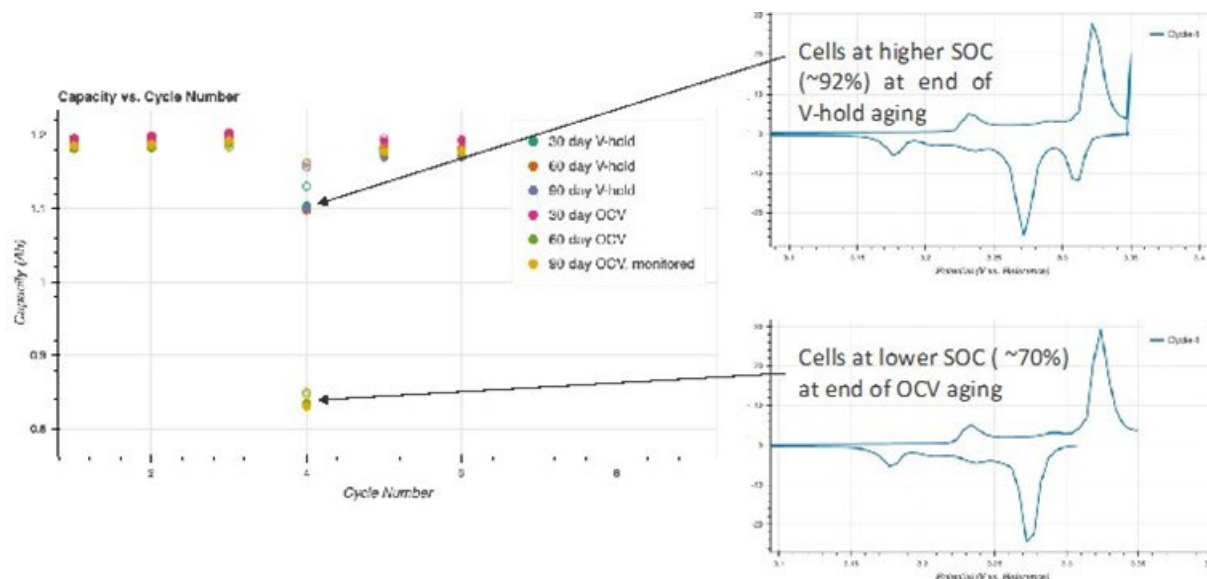


Figure VIII.1.8 Comparison of 30-, 60-, and 90-day voltage holds and OCV rests of commercial 1850 Gr-LFP cells. The 4th cycle is the rest or hold of the length indicated in the legend. The dQ/dV plots are of the lithiation immediately before and delithiation immediately after the rest/hold. The voltage hold resulted in a 22% increase in SOC over that of the OCV rest as is evidenced by the presence of the dQ/dV peak around 3.31 V during delithiation following the voltage hold.

Second, the reversible (lithiation) contributions to the capacity measured can remain significant over the duration of the voltage hold, causing the irreversible (parasitic) contributions responsible for calendar aging to be overestimated. This is one of, but possibly not the only reason, for the Figure VIII.1.7 aging trend of (c) to far exceed its actual aging trend (b). For silicon electrodes, the amount of time for parasitic processes to dominate over lithiation can take a month or more. The inverse polarization technique (Figure VIII.1.9) is a way to understand the parallel processes of reversible and parasitic reactions. In this experiment, the voltage hold is approached in the delithiation direction, so that relaxation of the electrode involves delithiation rather than lithiation and the reversible relaxation current has the opposite sign of parasitic current. The sum of the lithiation and parasitic currents is the measured current, therefore, a change in sign of the measured current from positive to negative represents a change from reversible current dominating to parasitic current dominating. As can be seen in Figure VIII.1.9, even after 700 hours of holding at a constant potential, the reversible current is still dominating for a Si composite electrode in a half-cell. Although delithiation kinetics may not be exactly the same as lithiation kinetics, this technique gives an initial measure of how long relaxation processes take for a given electrode. Due to silicon's sloped voltage profile, delayed relaxation of reversible reactions is likely true at all potentials of interest. Predictions from time periods where reversible lithiation is dominating may result in large underestimates of calendar life.

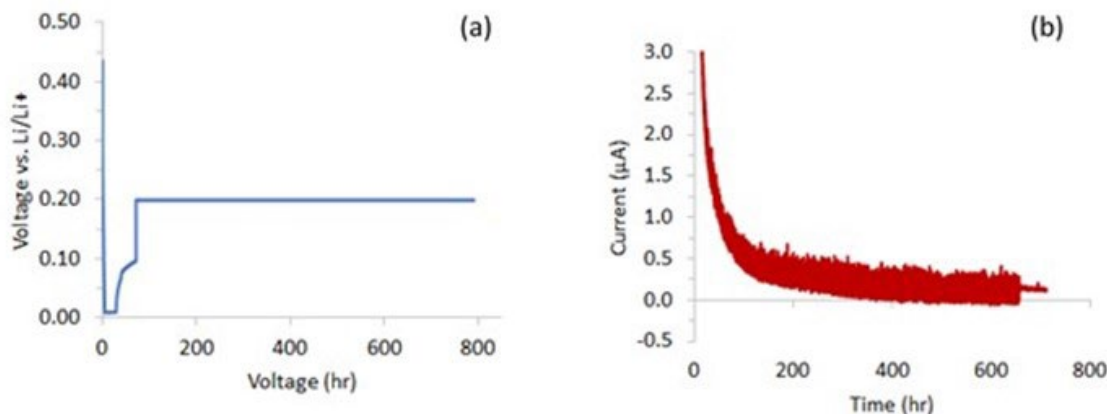


Figure VIII.1.9 Example of inverse polarization technique on a Si composite electrode in a half-cell to separate reversible delithiation (positive current) and parasitic (negative current) processes. Part (a) gives an overview of the protocol where the cell is lithiated, held at 10 mV for 24 hr, OCV for 24 hr, then stepped up to 200 mV and held at that voltage. Part (b) shows the current during the 200 mV voltage hold. Even after 700 hours, the current is still positive, meaning reversible delithiation currents still dominate. This may indicate why it is so difficult to deconvolute reversible and parasitic reactions during a voltage hold.

Synthesis and testing of 5 different metallic glasses with theoretical capacities > 1000 mAh/g

We tested a variety of Si-based metallic glass systems and compositions with splat quenching and laser quenching, across a multidimensional parameter space. Through this process and down-selected 7 distinct metallic glass systems that combined: (1) theoretical and practical capacity > 1000 mAh/g, (2) improved parasitic currents as compared to a-Si, and (3) amorphous phase.

Splat Quenching

We synthesized $\text{Si}_{0.3}\text{Al}_{0.6}\text{Ti}_{0.1}$, $\text{Si}_{0.4}\text{Al}_{0.5}\text{Fe}_{0.1}$, and $\text{Si}_{0.35}\text{Al}_{0.55}\text{Co}_{0.1}$, using splat quenching. All samples showed amorphous phase with a broad Si peak (Figure VIII.1.10). The thickness of the splat quenched samples was 20–40 μm and these electrodes demonstrated high areal capacity of $\sim 10 \text{ mAh/cm}^2$. The foils showed both theoretical and practical capacity > 1000 mAh/g. Despite the thickness, of the foils, their Li-ion diffusion kinetics are much better compared to 500 nm Si thin film, confirmed by GITT measurements. Furthermore, the splat quenched samples demonstrated significantly reduced parasitic currents. Specifically, on average, metallic glass thin foil showed a 50% reduction in parasitic current compared to Si thin films (Figure VIII.1.11).

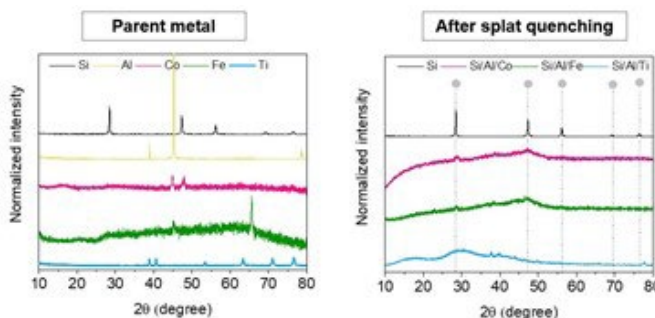


Figure VIII.1.10 XRD results for parent metals and $\text{Si}_{0.3}\text{Al}_{0.6}\text{Ti}_{0.1}$, $\text{Si}_{0.4}\text{Al}_{0.5}\text{Fe}_{0.1}$, and $\text{Si}_{0.35}\text{Al}_{0.55}\text{Co}_{0.1}$

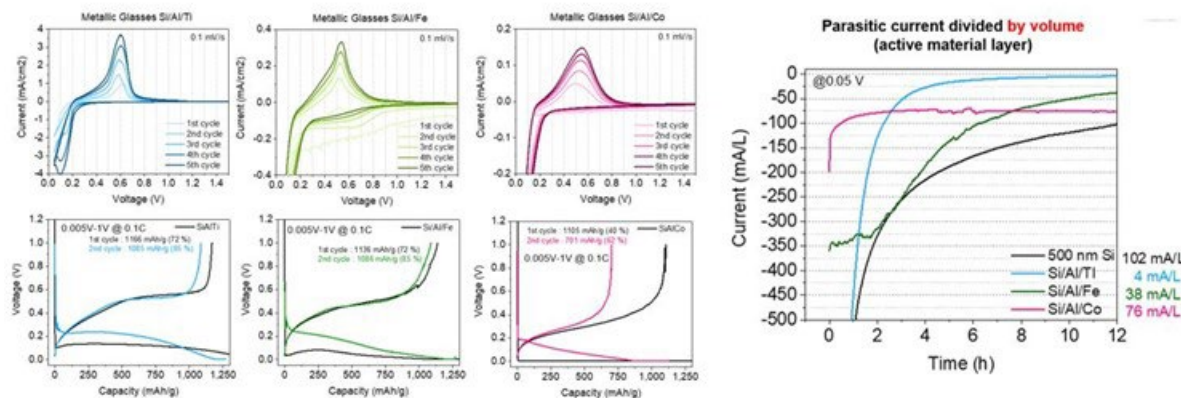


Figure VIII.1.11 Electrochemical performance of $\text{Si}_{0.3}\text{Al}_{0.6}\text{Ti}_{0.1}$, $\text{Si}_{0.4}\text{Al}_{0.5}\text{Fe}_{0.1}$, and $\text{Si}_{0.35}\text{Al}_{0.55}\text{Co}_{0.1}$ and parasitic current measurement result

Ultrafast Laser Quenching

Using high-throughput laser quenching, we synthesized a variety of Si-based metallic glass chemistries, and down-selected 4 thin-film metallic glass systems that combined the capacity, parasitic current, and amorphous phase criteria listed in the beginning of this section. The corresponding metallic glass chemistries were $\text{Si}_{0.73}\text{Ti}_{0.27}$, $\text{Si}_{0.80}\text{Mn}_{0.20}$, $\text{Si}_{0.85}\text{Ni}_{0.15}$, and $\text{Si}_{0.88}\text{Fe}_{0.12}$. The practical specific capacity (calculated from CV plots) of the laser quenched metallic glass systems ranged between 1250–1865 mAh/g (Figure VIII.1.12). Parasitic current measurements of these Si-based metallic glasses were compared to that of an a-Si thin film anode. The laser quenched Si-M thin-film metallic glasses demonstrated on average a 76% drop in parasitic currents compared to that of the a-Si thin film anode, strongly suggesting an improvement of the interfacial stability of the metallic glass anode materials (Figure VIII.1.13a).

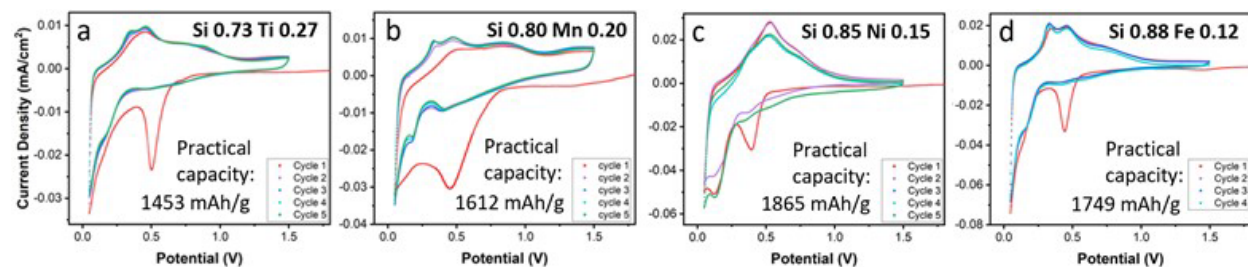


Figure VIII.1.12 Cyclic Voltammetry of amorphous a) $\text{Si}_{0.73}\text{Ti}_{0.27}$, b) $\text{Si}_{0.80}\text{Mn}_{0.20}$, c) $\text{Si}_{0.85}\text{Ni}_{0.15}$, d) $\text{Si}_{0.88}\text{Fe}_{0.12}$ electrodes quenched with ultrafast pulsed laser

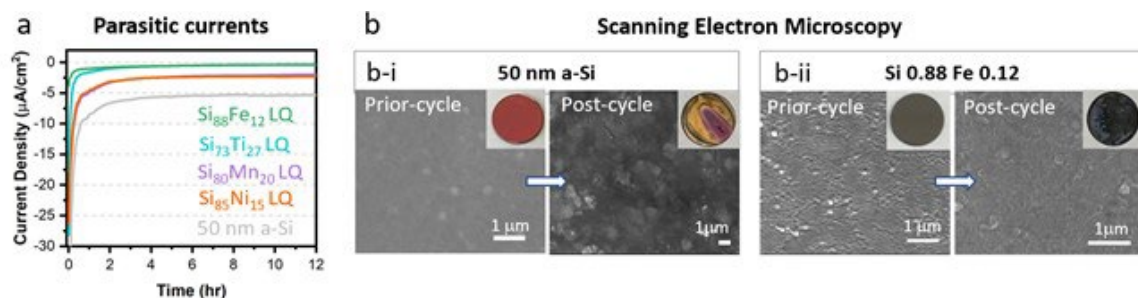


Figure VIII.1.13 a) Parasitic current measurements of amorphous binary Si alloy electrodes quenched with ultrafast pulsed laser. b) Scanning electron microscopy images of the b-i) 50 nm a-Si thin film surface b-ii) laser quenched $\text{Si}_{0.88}\text{Fe}_{0.12}$ surface prior and post electrochemical cycling; inserts are macroscopy images of the electrode surfaces.

Preliminary analyses of the post-cycling surface morphology and composition were performed on a Si-Fe electrode. White light interferometry of the formed Solid-Electrolyte Interphase (SEI) showed that while non-quenched a-Si electrode experienced a 313% surface roughness increase with cycling, the roughness increase in Si metallic glass electrodes was limited to 144% (Figure VIII.1.13b). The combination of SEI morphological studies and improved parasitic parents points to significant differences in the SEI morphology and thickness, which merit additional characterization with surface-sensitive techniques to understand the origins of improved interfacial stability.

Identify active cell components and cell designs to achieve stable calendar life electrode performance with a cell build demonstrating 300 cycles with <20% capacity fade.

The Silicon Consortium Program (SCP) milestone was established to “Identify active cell components and cell designs to achieve stable calendar life electrode performance with a cell build demonstrating 300 cycles with <20% capacity fade”. For this effort we focused on a series of materials detailed in Table VIII.1.3.

Table VIII.1.3 Materials Used in Validation Studies

Materials		
Silicon	SiO _x (Osaka, CAMP)	Coated 6nm CVD-Si (NREL)
Binders	Polyimide (P84)	Lithiated polyacrylate (LiPAA)
Conductive Additives	Carbon, C45	Carbon, C65
Electrolytes	Gen2 + 3% FEC	

The studies, performed in support of our Q4 milestone, were focused on identifying cell components (silicon, binder, conductive additives) and are detailed in Table 1. Initial choices for silicon were (1) SiO_x – a commercially available nanoscale mixture of elemental silicon and silicon dioxide procured by CAMP and (2) a nanoscale silicon produced from silane gas at NREL. The SCP has initiated investigations of a bulk coated silicon nanopowder produced at ORNL that will be evaluated as our baseline silicon in FY22.

For our SiO_x based efforts, initial tests have focused on the need for prelithiation, active material loading, binder choice, and electrochemical window. Distinct advantages for prelithiation were identified, especially with SiO_x-based silicon sources and they are discussed in more detail for our Q1 milestone. Several electrode compositions (60% to 92.5% SiO_x) and areal loadings (1.3 mAh/cm² to 4.5 mAh/cm²) were investigated. Rapid capacity fade was observed for weight% > 85% due to insufficient binder and conductive additive content. Lower areal loadings had more stable performance but at the price of overall capacity. Based on these data many of the studies were done using a 70 wt% SiO_x electrode. BatPaC modeling (Kubal) indicated that this composition could meet programmatic goals of 350 Wh/kg, if fabricated at 4.6 mAh/cm² and 35% porosity.

The performance of cells containing 70 wt% SiO_x using two different binders was investigated, as shown in Figure VIII.1.14. The binders were a poly-imide (P84) and a lithiated poly-acrylic acid (LiPAA) system. For this study the SiO_x anodes were initially prelithiated electrochemically using lithium metal in a different cell; then, the prelithiated anodes were harvested and used in single layer pouch cells with a NMC622 cathode and Gen2/4FEC electrolyte. The data highlights that cells built with the P84 binder showed significantly higher stability and cycle life than those constructed with LiPAA. For the LiPAA cells, while the higher loading cell initially had about 30% higher capacity, both cells converged to roughly the same cycling capacity after approximately 400 cycles at C/10 (~700 mAh/g Si + C45). *Data from these series indicate that cells using P84 binder do achieve the cell cycling requirements of milestone 07, presenting less than 20% capacity fade for nearly 800 cycles.* Additional studies focused on identifying the desirable electrochemical window for testing electrodes with high SiO_x content. These tests showed that attempts to increase the utilization of the Si domains in the SiO_x composite ultimately led to a decrease in long-term stability of the electrode, resulting in the recommendation of not taking the anode below 50mV.

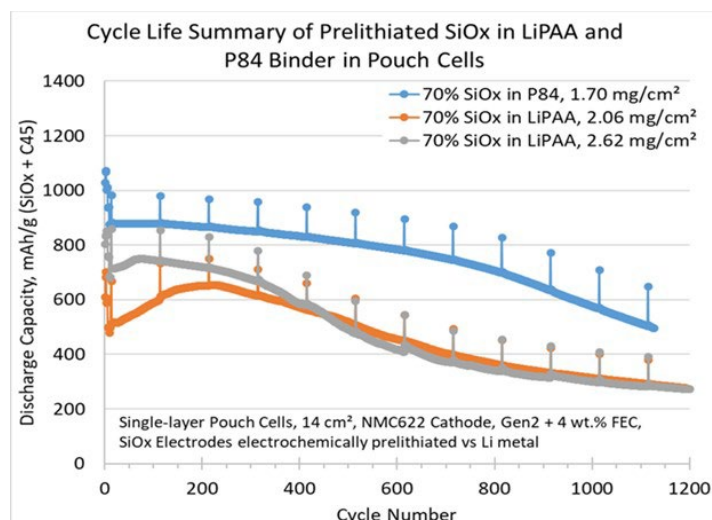


Figure VIII.1.14 Cycle life testing of various SiOx cells using two different binders. At 70% loading of the SiOx electrode material, the blue line highlights the advantage displayed by the use of a P84 binder versus the previous baseline LiPAA binder system in a full cell using electrochemical prelithiation. Cells were aged at a 1C rate, with performance checks at C/10 every 100 cycles.

For our PECVD-Si materials, the synthesis and production of the materials at NREL is detailed in Milestone 4. We evaluated several PECVD-Si materials that achieved the Milestone 7, and here we highlight one such example with a carbon coating derived from petroleum pitch, a carbon precursor additive. In these studies, PECVD silicon has an active material particle size of approximately 6nm. These particles are then coated with the pitch (primarily [a]benzopyrene) using a solution-phase coating process and heated to produce a carbon-coated pitch active material. For these electrode studies, the materials are then built into an electrode (80% active, 10% C65, 10% P84 (PI) binder). Initial studies indicated *the electrode produced achieved the FY21 300 cycles with less than 20% capacity fade requirement*. Further analysis on the changes that occur near 400 cycles were analyzed in collaboration between CAMP and ORNL. Analysis of the thermal properties of the PI binder indicated that near 350 C the PI binder undergoes a coupling reaction and becomes a more stable electrode binder. Using the PECVD material, a notable improvement in performance is noted (Figure VIII.1.15) based on the newly cured electrode binder, achieving over 800cycles under the conditions required.

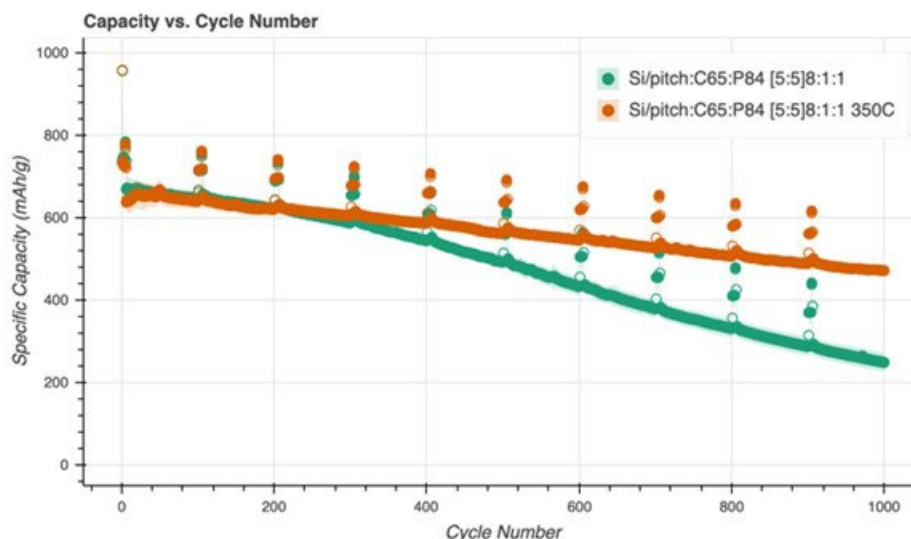


Figure VIII.1.15 Cycle life testing of PECVD Si cells using two different PI binders processing conditions. At approximately 80% loading of the 1:1 Si/C electrode material, the orange data line highlights the advantage displayed by the use of a cured P84 binder versus the uncured P84 binder material.

Conclusions

Prelithiation Protocols Across Consortium Partners

Thermal evaporation is a critical area to investigate as it offers the opportunity to tune the SEI in ways that electrochemical processes cannot. Further, the process allows one to precisely control the amount of Li added to a cell to balance the cell chemistry with the losses due to SEI formation and capacity of the cathode.

Go/no-go on HF etching of Silicon Oxide-silicon as viable route to silicon

In conclusion, we determined that the porous Si/C material developed by PNNL for Li-ion battery anodes is incompatible with scaling, and thus the current material is a No-Go. Alternative synthesis using non-flammable methods are required to achieve a safe process at the several hundred-g to kg-scale.

Go/No-Go on Moiré Interferometry (Sandia National Laboratories)

The project had a Go/No-Go decision in quarter three to decide if moiré could probe calendar life in the silicon SEI. The first step to achieving this goal is the ability to measure strain, which could then have been correlated with SEI mechanical failure and the resulting impact on calendar life. Because robust strain measurements in the SEI were deemed unlikely, a No-Go decision was made on using this technique in the rest of the project.

Produce 20 grams of next generation silicon's

Materials supply for FY21 based upon this milestone as completed and provided silicon of sufficient quantity and quality for the project.

Q4 Milestone. Si Calendar Life Estimation from Electrochemical Testing Protocols

The project had a Go/No-Go decision in quarter four to decide if voltage hold can give a quantitative prediction of Si-containing battery calendar life. A voltage hold protocol can be a useful tool, but due to the above complications its use as a calendar life performance metric is not straightforward. Based on current data in 18650 and coin cell format, its main utility would possibly be qualitative comparisons at long (at least one month) times, and can be used as a stage gate test, but not in quantitative prediction of calendar life. A No-Go decision was made on using this technique as a predictor of calendar life but useful in research as a predictor of SEI stability under dynamic electrochemical conditions.

Synthesis and testing of 5 different metallic glasses with theoretical capacities > 1000 mAh/g

We performed high-throughput testing of more than 150 fabrication parameters and down-selected 7 promising Si-based metallic glass chemistries with theoretical and practical capacity > 1000 mAh/g, developed by laser quenching and splat quenching. All metallic glass chemistries showed improved parasitic current, which indicates high interfacial stability.

Next steps will focus on experimentally expanding the amorphous glass chemistries for binary and ternary Si-based metallic alloys with theoretical and practical capacities > 1000 mAh/g. This research will be based on splat quenching and ultrafast laser quenching technologies as tools for accelerated material/composition discovery. The discovery process will be followed by scaled-up fabrication of the best-performing electrodes using quenching techniques operating at industrial-relevant scales, such as melt spinning.

Identify active cell components and cell designs to achieve stable calendar life electrode performance with a cell build demonstrating 300 cycles with <20% capacity fade.

Single layer pouch cells using 70% SiO_x can achieve 800 cycles with 80% capacity retention.

CAMP has developed the capability to perform large-scale processing of polyimide-based electrodes by curing the binder at 350°C.

Rate capability is maintained with 70% SiO_x as areal loading increases, even at lower porosities.

The sequence of processing steps matter, and electrodes must be calendared before the binder is cured

BatPaC identified that 350 Wh/kg can be theoretically achieved with 70% SiOx if porosity < 40% and areal loading > 4.5 mAh/cm².

Small levels of electrochemical activity in the P84 system may add small amounts of capacity to the system.

While C45 and C65 are both electrochemically active, the actual choice was not found to significantly change the cycling performance although its activity should be included in cell capacity calculations.

Cells based on PECVD silicon achieved the FY21 performance goals and showed significant improvements with advances in binder curing.

Key Publications

Go/No-Go on Moiré Interferometry (Sandia National Laboratories)

1. McBrayer, Josefine D., Christopher A. Apblett, Katharine L. Harrison, Kyle R. Fenton, and Shelley D. Minter. "Mechanical studies of the solid electrolyte interphase on anodes in lithium and lithium-ion batteries." *Nanotechnology* 32, no. 50 (2021): 502005.
2. McBrayer, Josefine D., Marco-Tulio F. Rodrigues, Maxwell C. Schulze, Daniel P. Abraham, Christopher A. Apblett, Ira Bloom, Gerard Michael Carroll et al. "Calendar aging of silicon-containing batteries." *Nature Energy* 6, no. 9 (2021): 866–872.
3. Arnot, David, Eric Allcorn, and Katharine Harrison. "Effect of Temperature and FEC on Silicon Anode Heat Generation Measured by Isothermal Microcalorimetry." *Journal of The Electrochemical Society* (2021).

Q4 Milestone. Si Calendar Life Estimation from Electrochemical Testing Protocols

1. McBrayer, Josefine D., Marco-Tulio F. Rodrigues, Maxwell C. Schulze, Daniel P. Abraham, Christopher A. Apblett, Ira Bloom, Gerard Michael Carroll et al. "Calendar aging of silicon-containing batteries." *Nature Energy* 6, No. 9 (2021): 866–872.

Synthesis and testing of 5 different metallic glasses with theoretical capacities > 1000 mAh/g

Title : Stable SEI Formation on Al-Si-Mn Metallic Glass Li-ion Anode

Publication : Journal of The Electrochemical Society, 2021, 168, 100521

Abstract : Alloying anodes such as silicon are of great interest for lithium-ion batteries due to their high lithium-ion storage capacities but have only seen minimal commercial deployment due to their limited calendar life. This has been attributed to an intrinsically unstable solid electrolyte interphase (SEI) that is aggravated by mechanical failure. An amorphous structure can mitigate lithiation strains, and amorphous alloys, or metallic glasses, often exhibit exceptional fracture toughness. Additional elements can be added to metallic glasses to improve passivation. Splat quenching was utilized to prepare an amorphous Al₆₄Si₂₅Mn₁₁ Li-ion anode with a specific capacity >900 mAh g⁻¹ that remains amorphous upon cycling. On this metallic glass electrode, parasitic electrolyte reduction is found to be much reduced in comparison to pure Si or Al, and comparable to that on Cu. The SEI is much thinner, more stable, and richer in fluorinated inorganic phases than the SEI formed on Si, while organic carbonate compounds such as lithium ethylene decarbonate (LiEDC) are notably absent. This study indicates that metallic glasses can become a viable new class of Li-ion anode materials with improved surface passivity.

Identify active cell components and cell designs to achieve stable calendar life electrode performance with a cell build demonstrating 300 cycles with <20% capacity fade.

1. McBrayer, et al., "Calendar aging of silicon-containing batteries" *NATURE ENERGY*, 6(9) 866–872 (2021) DOI: 10.1038/s41560-021-00883-w

2. Prado, AYR, et al., “Electrochemical Dilatometry of Si-Bearing Electrodes: Dimensional Changes and Experiment Design” *Journal of the Electrochemical Society*, 167(16), 160551 (2020) DOI: 10.1149/1945-7111/abd465
3. Rodrigues, M. et al., “Modulating electrode utilization in lithium-ion cells with silicon-bearing anodes” *J. Power Sources*, 477, 229029 (2020). DOI: 10.1016/j.jpowsour.2020.229029
4. Rodrigues, M., et al., “Insights on the cycling behavior of a highly-prelithiated silicon-graphite electrode in lithium-ion cells” *J. Phys Energy* 2(2), 024002 (2020) DOI: 10.1088/2515-7655/ab6b3a
5. Martin, T. et al., “Understanding why poly(acrylic acid) works: decarbonylation and cross-linking provide an ionically conductive passivation layer in silicon anodes” *J. Mat Chem A*, 9, 21929–21938 (2021) DOI: 10.1039/d1ta04319f

References

Go/no-go on HF etching of Silicon Oxide-silicon as viable route to silicon

1. “Flash point determination of binary mixtures of alcohols, ketones and water,” P.J. Martínez, E. Rus and J.M. Compañía, report from AICHE.
<https://engage.aiche.org/HigherLogic/System/DownloadDocumentFile.ashx?DocumentFileKey=e53a8ccc-48b1-4e3b-b59f-bb579cc5132b&ssopc=1>

Go/No-Go on Moiré Interferometry (Sandia National Laboratories)

1. Zhang, Wei, Truong H. Cai, and Brian W. Sheldon. “The impact of initial SEI formation conditions on strain-induced capacity losses in silicon electrodes.” *Advanced Energy Materials* 9, no. 5 (2019): 1803066.
2. Post, Daniel, Bongtae Han, and Peter Ifju. *High sensitivity moiré: experimental analysis for mechanics and materials*. Springer Science & Business Media, 1997.

Acknowledgements

Go/no-go on HF etching of Silicon Oxide-silicon as viable route to silicon

1. Ryan Pekarek (NREL, now at TexPower) and Nathan Neale (NREL) executed this project in consultation with Jiguang (Jason) Zhang, Xiaolin Li, and Jie Xiao (PNNL) and members of the SCP.

Go/No-Go on Moiré Interferometry (Sandia National Laboratories)

1. The work for the Q3 milestone was performed by Josephine McBrayer, Christopher Applett, Shelley Minter, Darwin Serkland, Katharine Harrison, Eric Allcorn, David Arnot, Chad Sherwood, Kyle Fenton, and Katharine Harrison.
2. Sandia National Laboratories is a multimission Laboratory managed and operated by National Technology & Engineering Solutions of Sandia, LLC, a wholly owned subsidiary of Honeywell International Inc., for the U.S. Department of Energy’s National Nuclear Security Administration under contract DE-NA0003525.

Q4 Milestone. Si Calendar Life Estimation from Electrochemical Testing Protocols

1. The work for the Q4 milestone was performed by the calendar life team members consisting of Max Schulze (NREL), Marco Fonseca Rodrigues (ANL), Josey McBrayer (SNL), Ankit Verma (NREL), Daniel Abraham (ANL), Ira Bloom (ANL), Andrew Colclasure (NREL), Chen Fang (LBNL), Gao Liu (LBNL), Nathan Neale (NREL), Gabriel Veith (ORNL), and Christopher Johnson (ANL)

Identify active cell components and cell designs to achieve stable calendar life electrode performance with a cell build demonstrating 300 cycles with <20% capacity fade.

1. The team would like to thank the BatPaC team led by Dr. Shabbir Ahmed and specifically Dr. Joseph Kubal for helpful discussion with regards to silicon electrode construction.

VIII.2 Si-Based Li-ion Batteries with Long Cycle Life and Calendar Life (PNNL)

Ji-Guang Zhang, Principal Investigator

Pacific Northwest National Laboratory
902 Battelle Boulevard, Richland, WA 99354
E-mail: jiguang.zhang@pnnl.gov

Ran Yi, Principal Investigator

Pacific Northwest National Laboratory
902 Battelle Boulevard, Richland, WA 99354
E-mail: ran.yi@pnnl.gov

Brian Cunningham, DOE Technology Development Manager

U.S. Department of Energy
E-mail: Brian.Cunningham@ee.doe.gov

Start Date: October 1, 2020

End Date: September 30, 2023

Project Funding (FY21): \$400,000

DOE share: \$400,000

Non-DOE share: \$0

Project Introduction

Silicon (Si) has been regarded as one of the most promising anode materials for next generation lithium-ion batteries (LIBs) because it has 10 times higher theoretical specific capacity (4200 mAh/g) than that of graphite. However, severe volume change (~300%) of Si during lithiation and delithiation hinders the practical application of Si anode. In the last decade, significant progresses have been made on the specific energy and cycle life of Si based LIBs. However, calendar-life of these batteries is still less than two years which is far less than 10-year target required by DOE.

Objectives

In this project, we will investigate the mechanisms of short calendar life of Si based LIBs and extend their cycle life using porous Si materials and localized high concentration electrolytes (LHCEs) tailored to improve the stability of SEI layer on the surface of Si particles. The scalability of the production process of the porous Si materials will also be studied in order to reach the goals required by DOE's EV program.

Approach

- Investigate the mechanisms of short calendar life of Si based LIBs through post-mortem analysis of the cathode, Si-based anode, and electrolyte after storage to identify the main factors affecting calendar life of Si based LIBs. Detailed characterizations will be carried out to study the structure and composition evolution of both cathode and anode after calendar life test, especially SEI/CEI layers.
- Study crosstalk effect on calendar life in Si based LIBs by storing cathode and anode electrode separately.
- Tailor Localized High Concentration Electrolytes (LHCEs) to improve the stability of SEI layer on the surface of Si particles. SEI layers formed in LHCEs is rich in inorganic components such as LiF and Li₂O. These SEIs have a much better mechanical stability and can tolerate large volume expansion of Si particle without break down and expose Si directly to electrolyte, therefore largely minimize the continuous growth of high impedance SEI layers.

Results

1. Investigate the mechanisms of short calendar life of Si based LIBs

We investigated the mechanisms of calendar life degradation of porous Si anode using single layer pouch (SLP) cells (~64 mAh) following the USABC calendar life test protocol. PNNL developed carbon coated porous Si with a reversible capacity of ~1000 mAh g⁻¹ was used as anode. NMC622 with a loading of 3.3 mAh/cm² was used as cathode. A LHCE (LiFSI-DMC-TTE with EC and FEC additive) is used as the electrolyte. The cells are stored at 100% SOC at 30, 40, 47.5 and 55°C after formation. Note that the Si anode is lithiated before the test. The cells are discharged at 1C for 30 second every day to check the voltage drop and impedance change, then a taper charge is applied daily to charge the cells back to 100% SOC. The voltage of cells is monitored throughout the test period. Figure VIII.2.1 shows voltage change of the cells tested at different temperatures over 33 days. It is found that the voltage drop at 1C discharge pulse is related to storage temperature and duration of storage (Figure VIII.2.1a). In general, the voltage drop increases over time, and higher storage temperature leads to larger voltage drop. However, the voltage drop change is slow when storage temperature is below 40 °C, while more significant voltage drop is observed at above 47.5 °C. Figure VIII.2.1b shows more details on the voltage drop occurred during the 24 hours rest period, which could be used as an indicator of leakage current. The leakage current has been found to increase with increasing storage temperature. This accelerated degradation may come from the high temperature instability of electrolytes, active materials and/or interphase layers (SEI and CEI) as well as the inter talk between cathode and anode.

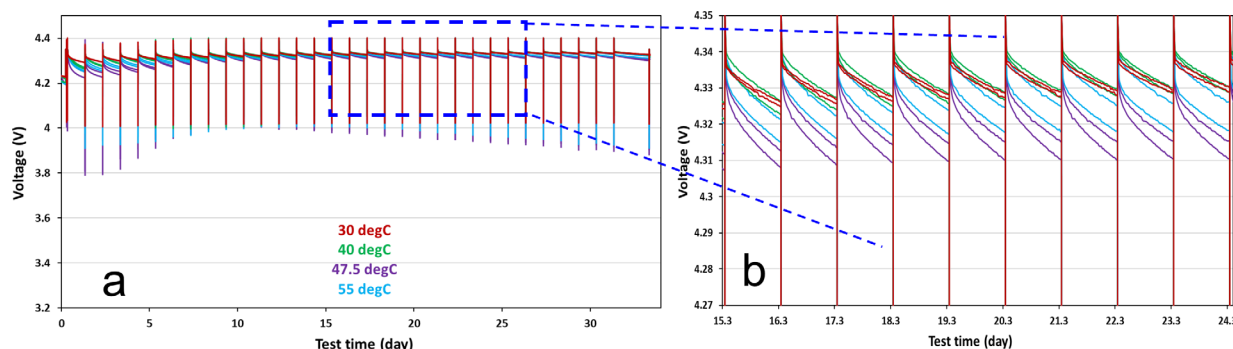


Figure VIII.2.1 (a) Voltage profiles of the cells stored at different temperatures over 33 days. (b) Enlarged voltage profiles corresponding to the region marked by dash lines in (a).

Figure VIII.2.2 show the absolute (a) and relative (b) changes of discharge resistances (DCR) as a function of time (days), respectively. The absolute DCR is calculated by taking the differences between the initial voltages prior to the pulse and the voltages at the end of the pulse divided by the constant current. It is clear that DCR increases over time, and higher storage temperature leads to larger DCR increases. The DCR increases slowly with time when storage temperature is below 40°C but increase dramatically at higher temperature. The discharge resistance increases by ~22% at 30°C and ~200% at 55°C after 95 days. This again suggests more pronounced impact of high temperature to cell properties.

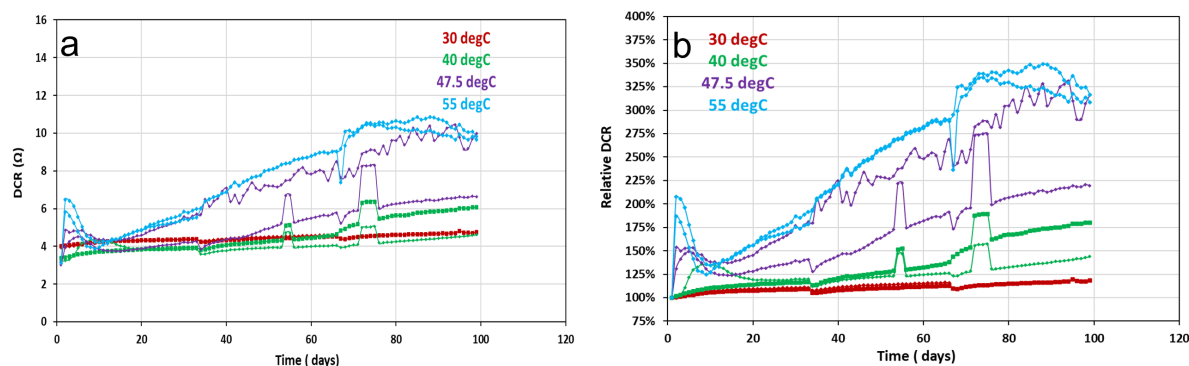


Figure VIII.2.2 Discharge resistance of the cells tested at different temperature over time. a) Absolute discharge resistance over time. b) Relative change of discharge resistance over time.

The capacity of the cells is checked after 90 days storage to investigate the influence of temperature on reversible capacity. Figure VIII.2.3 shows the capacity of cells checked at 0.1C at different time and temperatures. Higher temperature is found to lead to lower reversible capacity. Discharge capacity retention is higher than 90% for cells stored at 30°C for 90 days; however, only about 45% of original capacity is recovered for cells stored at 55°C for 90 days. The accelerated degradation can be attributed to continuous increase in impedance and irreversible consumption of Li source from both cathode and anode due to growth of CEI and SEI that accelerated at higher temperature. Further characterization will be carried out to verify this assumption.

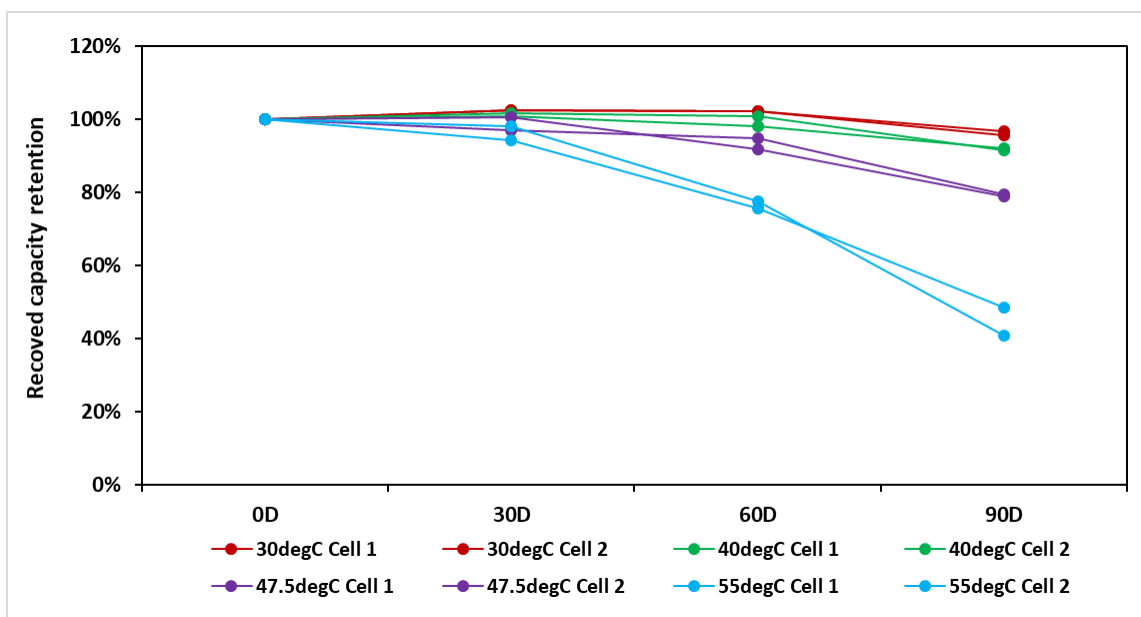


Figure VIII.2.3 Formation capacity and recovered capacity after 90 days storage test at different temperatures.

Table VIII.2.1 shows DCR of full cell, cathode and anode after 30 days storage at different temperatures based on tri-electrode SLP study. In general, DCR of both anode and cathode increases after 30 days at different temperatures. In particular, increase in DCR at temperature higher than 40°C is more significant. Compared to anode, cathode has a larger increase in DCR at 40 and 55°C. The portion of cathode contribution to the overall full cell DCR is in the range of 70–80% (calculated by cathode DCR divided by full cell DCR). We suspect that the large contribution from cathode DCR is from oxidation of electrolyte at high voltage (4.35V) and high

temperature. Both cathode and anode will be harvested for further characterization of particle level degradation and interphase evolution.

Table VIII.2.1 DCR of full cell, cathode, and anode after 30 days storage test at different temperatures measured by Tri-electrode SLPs

Tri-electrode SLP			0 day									DCR		
			The initial voltage prior to the pulse(1C-30s)			The voltage at the end of the pulse(1C-30s)			Voltage difference			The difference voltage divided by the constant current		
			Cathode/V	Anode/V	Full cell/V	Cathode/V	Anode/V	Full cell/V	Cathode/V	Anode/V	Full cell/V	Cathode/V	Anode/V	Full cell/V
2	30degC	Cell 1	4.41	0.08	4.34	4.31	0.23	4.07	0.11	0.16	0.26	1.55	2.23	3.78
22		Cell 2	4.41	0.07	4.34	4.28	0.21	4.07	0.13	0.13	0.26	1.81	1.92	3.74
12	40degC	Cell 1	4.42	0.08	4.34	4.30	0.24	4.06	0.12	0.16	0.27	1.65	2.28	3.93
29		Cell 2	4.41	0.07	4.34	4.29	0.21	4.08	0.12	0.14	0.25	1.69	1.94	3.63
11	47.5degC	Cell 1	4.42	0.08	4.34	4.31	0.23	4.08	0.11	0.15	0.26	1.55	2.13	3.68
30		Cell 2	4.41	0.08	4.34	4.28	0.20	4.07	0.14	0.13	0.26	1.96	1.82	3.78
17	55degC	Cell 1	4.40	0.06	4.34	4.28	0.20	4.09	0.12	0.14	0.25	1.65	1.94	3.59
20		Cell 2	4.40	0.06	4.34	4.28	0.20	4.08	0.12	0.14	0.25	1.69	1.95	3.64

Tri-electrode SLP			30 days									DCR		
			The initial voltage prior to the pulse(1C-30s)			The voltage at the end of the pulse(1C-30s)			Voltage difference			The difference voltage divided by the constant current		
			Cathode/V	Anode/V	Full cell/V	Cathode/V	Anode/V	Full cell/V	Cathode/V	Anode/V	Full cell/V	Cathode/V	Anode/V	Full cell/V
2	30degC	Cell 1	4.42	0.09	4.33	4.29	0.24	4.06	0.13	0.15	0.28	1.86	2.11	3.98
22		Cell 2	4.42	0.09	4.34	4.28	0.21	4.07	0.14	0.13	0.26	1.96	1.81	3.77
12	40degC	Cell 1	4.42	0.08	4.33	4.23	0.21	4.02	0.19	0.13	0.31	2.65	1.80	4.45
29		Cell 2	4.42	0.09	4.33	4.27	0.22	4.04	0.16	0.13	0.29	2.24	1.90	4.14
11	47.5degC	Cell 1	4.43	0.10	4.33	4.25	0.23	4.01	0.18	0.14	0.32	2.60	1.97	4.57
30		Cell 2	4.43	0.10	4.33	4.18	0.22	3.96	0.25	0.12	0.37	3.53	1.69	5.22
17	55degC	Cell 1	4.42	0.09	4.33	4.13	0.21	3.92	0.29	0.12	0.41	4.11	1.69	5.80
20		Cell 2	4.41	0.08	4.33	4.06	0.19	3.87	0.35	0.11	0.45	4.94	1.53	6.46

We further investigated the failure mechanism of short calendar life of porous Si anode based SLP cells by post mortal analysis and reassembled cells using the cell components retrieved from the SLP cells at the end of life (EOL). Figure VIII.2.4 shows the experiment design to study the contribution of each cell component to overall cell impedance growth. SLPs after 66- and 132-days storage at 55°C were disassembled and four components (cathode, anode, electrolyte, and separator) were harvested. Each end-of-life (EOL) component was matched with three fresh components to make new cells for impedance analysis, based on which contribution from individual component can be clearly distinguished.

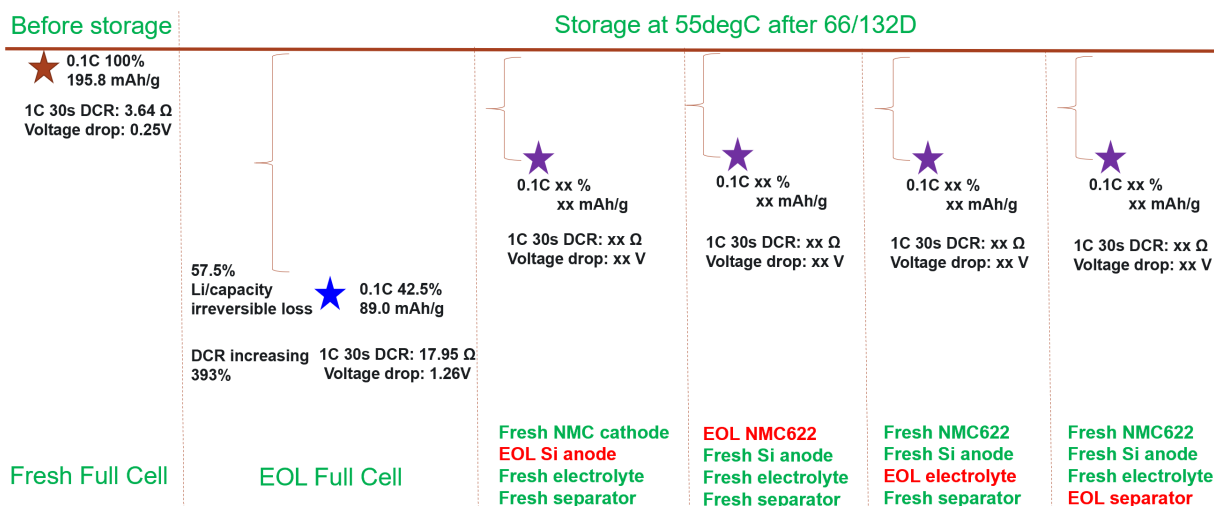


Figure VIII.2.4 Experiment design: Re-assembly of EOL SLP components after storage to study the contribution of each cell component.

As shown in Figure VIII.2.5 it is clear that DCR increases over time and the contribution of each cell component varies significantly. While there is little change in DCR from EOL anode, electrolyte and separator, EOL cathode makes major contribution to the DCR increase of full cell at EOL. It should be noted that it is still unclear that if the cathode DCR growth is caused by crosstalk between anode and cathode in full cells or because of electrolyte degradation during high temperature storage. This will be one of our focuses in FY22 work.

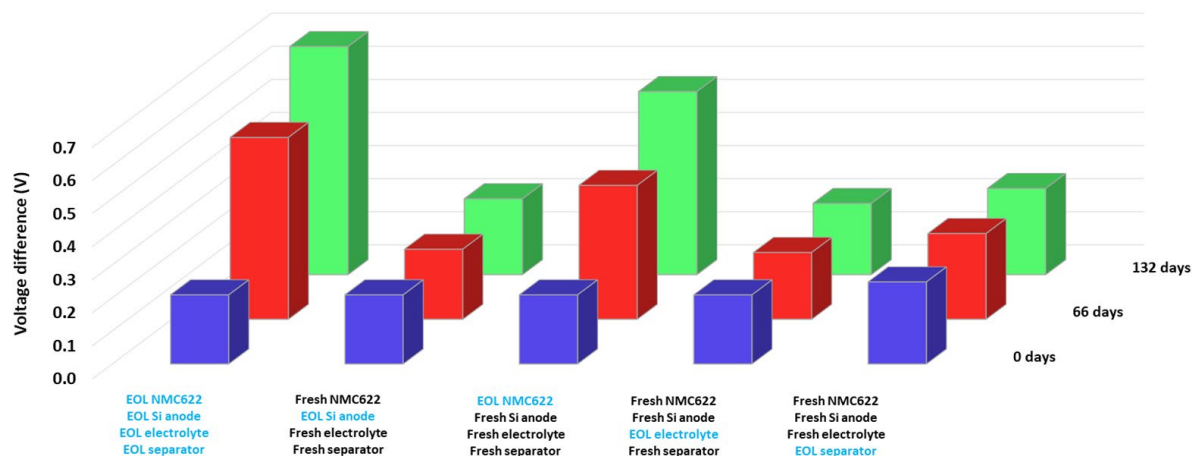


Figure VIII.2.5 Voltage difference of cells reassembled using EOL and fresh cell components.

Figure VIII.2.6 shows the ratio of contribution to full cell DCR from each EOL cell component. It was found that the EOL cathode contributes about 72% while EOL anode, electrolyte and separator make negligible contributions to the increase of DCR in the full cell. Note that there is a difference of 21% between the total EOL DCR increase measured in the coin cells using all components from EOL pouch cells and the sum of the DCR measured in the four coin cells using individual component from EOL pouch cells matched with fresh components. This difference may be caused by variation of components harvested from EOL pouch cell after long term storage. However, this does not change the conclusion that the major contribution to the DCR increase in the end of life of full cell is from EOL cathode.

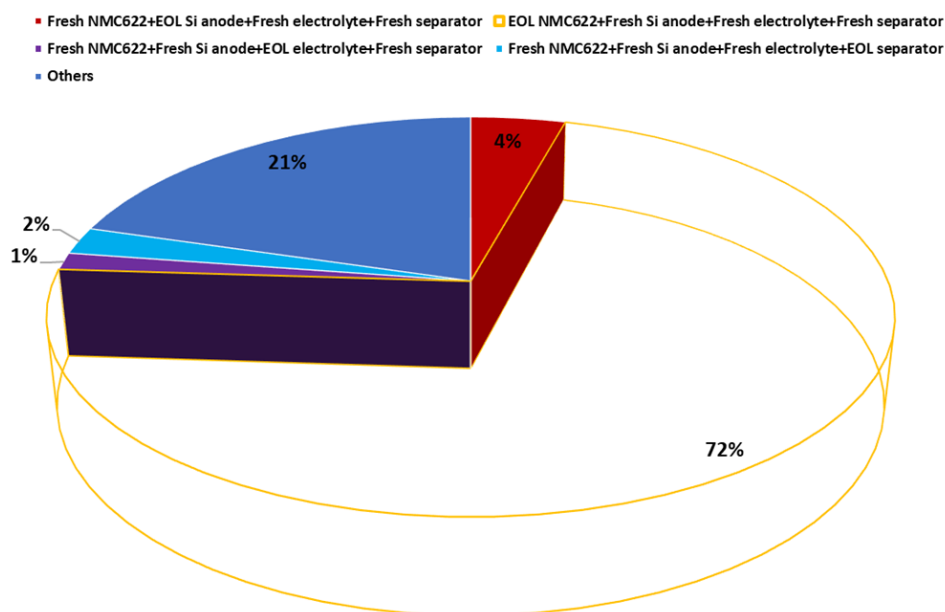


Figure VIII.2.6 Ratio of contributions of individual EOL cell components to the full cell DCR at EOL.

2. Develop a scalable process for etching of SiO_2 to produce porous Si

A new etching etchant system has been developed consisting of 1) organic solvents that are not miscible with water and cannot oxidize Si, 2) etchants that can be mixed with the organic solvents and 3) a reservoir of etchants that can be transferred to the organic solvents. Because the organic solvents cannot oxidize Si to

produce SiO_x and it is not miscible with water, the etching is only limited to original SiO_x in the Si/SiO_x matrix formed after disproportionation reaction of SiO precursor at 850°C . As a result, a mild etching reaction rate can be achieved without over-etching of Si , leading to a higher Si yield and a process with lower heat generation rate that is easy to handle. The theoretical yield from Si/SiO_x precursor to Si is 31.8 wt% ($2\text{SiO} \rightarrow \text{Si} + \text{SiO}_2$) assuming disproportionation reaction is complete during heat treatment and there is no material loss during sample collection after etching. As shown in Table 1, using aqueous etching system alone (experiment 1-3) leads to a yield much lower than the theoretical value, indicating significant over-etching. Over-etching is also evidenced by decreased yield with longer etching duration. The etching process also generates a noticeable amount of heat which may lead to safety hazard due to bubbling/spilling of etching agent which requires the use of external cooling to avoid overheating/spilling of the etching solution. Table VIII.2.2 shows comparison of etching yield and heat generation rate of different experiments using different etching agents. In comparison, a yield close to the theoretical value is obtained by using the new etchant system (experiment 4 and 6). In addition, the yield does not change with different etching duration, which suggests that the new etchant system does not attack Si . The heat generation is also very mild. Experiment 5 shows that the etching is not complete after 10 mins. In contrast, Si is over-etched in just 10 mins using the conventional etchant agent as shown in experiment 2. This is a clear evidence that the etching process in experiment 5 with the new etching system is much slower than that in experiment 2 with the conventional etching system.

Table VIII.2.2 Comparison of yield and heat generation rate of different experiments

Experiment	Etching agent	Etching time	Yield (weight)	Heat generation rate
1	48% HF in water	1 hour	20%	High
2	48% HF in water	10 minutes	22%	High
3	48% HF in water	2 hours	18%	High
4	48% HF in water/benzene	1 hour	28%	Low
5	48% HF in water/benzene	10 minutes	200%	Low
6	48% HF in water/benzene	2 hours	28%	Low

Conclusions

- The calendar life of the single layer pouch cells using PNNL's carbon coated porous Si anode and NMC622 cathode have been investigated. It is found that higher storage temperature leads to 1) larger voltage drop, 2) higher discharge resistance and 3) higher leakage current. All these parameters increase with increasing storage time.
- It has been found that cathode DCR contributes to more than 70% of the overall DCR of full cells at EOL. Different cell formats also affect the overall DCR. This observation is different with the previous assumption that the main reason for shortened calendar life in Si -based LIBs is due to faster anode degradation. Therefore, this work point to a new direction to address the challenges on the limited calendar life of Si -based LIBs. The possible crosstalk between anode and cathode in full cells will be further investigated during high temperature storage.
- A method has been developed to control the etching rate and safety of materials to produce porous Si . Compared to conventional aqueous based etchants, this method leads to mild reaction with low heat generation rate and avoids the safety hazard associated with bubbling/spilling occurred in the conventional etching process. It also increased yield of porous Si by preventing over-etching of Si . In addition, the etching agent used in this etchant system is easy to be separated and recycles/reused so the total cost of etching process is largely reduced.

Key Publications

1. Sujong Chae, Yaobin Xu, Ran Yi, Hyung-Seok Lim, Dusan Velickovic, Xiaolin Li, Qiuyan Li, Chongmin Wang, and Ji-Guang Zhang, Micron-Sized Silicon/Carbon Composite Anode Synthesized by Impregnation of Petroleum Pitch in Nano-Porous Silicon, *Advanced Materials*, 2021, 33, 2103095.
2. Ran Yi and Ji-Guang Zhang. A Method to Control the Etching Rate of Materials, U.S. patent application filled.

Acknowledgements

Key contributors include Qiuyan Li, Yaobin Xu.

VIII.3 Silicon Anode Seedling Project (ANL)

Zonghai Chen, Principal Investigator

Argonne National Laboratory
9700 South Cass Avenue
Lemont, IL 60439
E-mail: Zonghai.chen@anl.gov

Brian Cunningham, DOE Technology Development Manager

U.S. Department of Energy
E-mail: Brian.Cunningham@ee.doe.gov

Start Date: October 1, 2020

End Date: September 30, 2023

Project Funding (FY21): \$150,000

DOE share: \$150,000

Non-DOE share: \$0

Project Introduction

The silicon anode has recently attracted substantial attention primarily due to its significantly high specific capacity that is 10 times higher than the graphitic counterpart. However, the deployment of silicon anode has been hindered by its insufficient calendar life performance. Major progress has been made to mitigate the detrimental impact of volumetric changes during charge/discharge cycles by size and morphology control. However, aggressive parasitic reactions between lithiated silicon and the non-aqueous electrolytes remain a big challenge that limits the calendar life of batteries using silicon anode. Stabilizing silicon/electrolyte interface has been one of the top challenges to enable its application in high energy density electric vehicle batteries. Here, we propose to develop an accurate calendar life model, based on the high precision leakage current measurement, in order to predict the calendar life of silicon-based batteries. High precision leakage current measurement provides an accurate determination of the Si SEI stability for a charged cell hold, and the associated physical characteristics occurring in the battery.

Objectives

The objective of this project is two-fold. The first objective is to establish an accurate model to predict the calendar life of electric vehicle batteries using silicon anode from leakage current measurements. The second objective is to collaborate with the Si consortium team to support determination of chemical/electrochemical phenomena occurring in the Si anode and provide a decoupling mechanism between Li inventory issues versus active material electrical isolation. The resulting model will be used to accelerate the down selection of Si anodes, surface coating technologies, and electrolyte additives for long calendar life silicon-based automobile batteries.

Approach

The fundamental assumption of this project is that the parasitic reaction at the silicone/electrolyte interface is the root of the performance loss of the silicone anode, and that the precise measurement of the rate of parasitic reaction can provide the fundamental base for predicting the calendar life of silicone anode. Following are details of the approaches adopted for this project.

1. Precise measurement of parasitic current

The quality of the calendar predicting model heavily depends on the availability of high quality parasitic current data that mimics the parasitic reactions during the storage of the batteries at high state of the charge (SOC). In this project, a home-developed high precision leakage current (HpLC) measurement system is deployed for accurately measuring the evolution of leakage current as a function of storage time.

2. Mathematic modeling the parasitic reactions

Mathematic descriptors of parasitic reactions will be developed based on physical model of solid/electrolyte interphase (SEI) growing model. The descriptors are then parameterized using the high-quality parasitic current data collected using HpLC system.

3. Assisting development of high-performance silicone-based chemistries

The ultimate goal of this project is to utilize the knowledge obtained from the calendar life prediction to assist the develop of the advanced silicone anode chemistry with extended life. It is also our goal to investigate the impact of surface chemistry, binder, as well as electrolyte composition on the parasitic current and the life of the silicone anode, and to accelerate the development of long-life silicone-based lithium-ion chemistry.

Results

Figure II.1.C.1a shows the picture of a 16-channel home developed high precision leakage current (HpLC) system that was used to accurately measure the evolution of parasitic current of silicone anodes. During the measurement, a high precision source meter (Keithley 2401) was used to constant-voltage discharge of half cells comprising silicone anode at a specific potential for extended period of time, up to 140 hours (see Figure II.1.C.1b for a measuring principle). Figure II.1.C.1c shows a typical data obtained from the constant-voltage hold for a SiO electrode at 0.15 V vs. Li⁺/Li up to 140 hours. It can be clearly seen that the measured current decayed, roughly, exponentially with the experimental time. The initial rapid decay of the current was mostly contributed from the relaxation process that eliminates the concentration gradient of Li⁺ inside the cell, which step generally takes up to several hours for graphite anodes. Figure II.1.C.1c also shows that that the measurement stays almost constant, but significantly above 0, after 100 hours. This portion of the measured current is dominated by neither the lithiation/delithiation of the anode nor the relaxation of Li⁺ concentration gradient, but the continuous parasitic reactions between the lithiated anode and the non-aqueous electrolyte (schematically shown in Figure II.1.C.1b). In other word, the measured leakage current is a direct measurement of rate the charge transfer reaction across the interface during the storage period, therefore, it can be used to quantitatively model the loss of charge/performance of the anode materials during storage period.

Ideally, if the parasitic current measured is able to model with a mathematic descriptor $f(t)$, then the integration of the descriptor $f(t)$ over time will easily predict the loss of the charge during the storage period as shown in Equation II.1.C.1.

$$\int_0^{T_{cal}} \frac{1}{Q} f(t) dt = 0.8 \quad (\text{II.1.C.1})$$

In Equation II.1.C.1, Q is the reversible capacity of the silicone anode, and T_{cal} is the time it takes to consume 20% of charge stored in the silicone anode (Q). To achieve a good approximation to the real parasitic reactions at silicone anode, two different types of SEI growth models were evaluated. The fundamental assumption of the voids filling model is that the constant current charging/discharging before the constant voltage hold will irreversibly cause damage to the SEI layer, creating voids in the SEI layer. The continuous parasitic current is attributed to the parasitic reactions to fill the voids, proving needed protection to silicone anode. In this regard, the time-dependent leakage current will exponentially decay function. On the other hand, after extensive constant-voltage hold, the possible voids can be completed filled, and a continuous film growth model will dominate the parasitic reactions, in which model the increase of SEI thickness will impede the charge transfer between the silicone anode and the electrolyte, causing the leakage current to decay with square root of holding time ($1/\sqrt{t}$). Figure VIII.3.2 compares the fitting of the leakage current of SiO collected at 0.1 V using both the voids filling model and the continuous growth model. Visually, both models can fit the experimental data well. However, the continuous growth model predicts a negative stead leakage current (see Figure VIII.3.2b for a negative y_0), which underestimate the possible parasitic current. In other word, the voids filling model still plays a crucial role even after being constant-voltage held for up to 140 hours. Disregarding the potential underestimation of the continuous growth model, both models were used to estimate the calendar life of the SiO anode electrode using Equation II.1.C.1, and prediction are 270 hours, and 300 hours, respectively.

The result implies that both models can give a consistent prediction and that the parasitic reactions will consume 20% of charge stored in silicon anode in 270-300 hours. Apparently, the predicted numbers are far below the expected calendar life of SiO anode.

Figure VIII.3.1(a) Picture of the home-developed high precision leakage current (HpLC) measurement system; (b) schematics showing the principle of measuring parasitic current for silicone anode; (c) a typical time-dependent leakage current measured at 0.15 V of SiO anode.

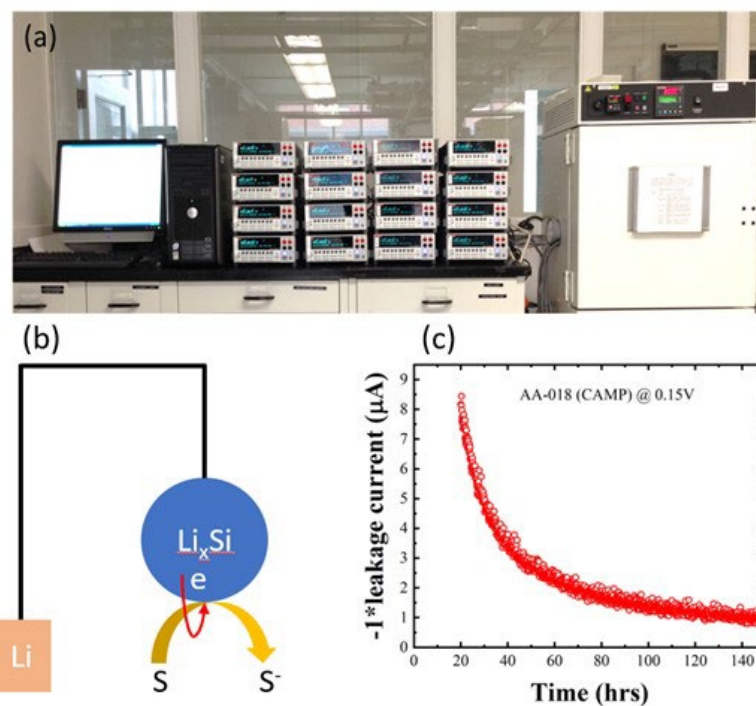


Figure VIII.3.1 Fitting the leakage current data collected for SiO at 0.1 V vs. Li⁺/Li, using both (a) voids filling model and (b) continuous growth model.

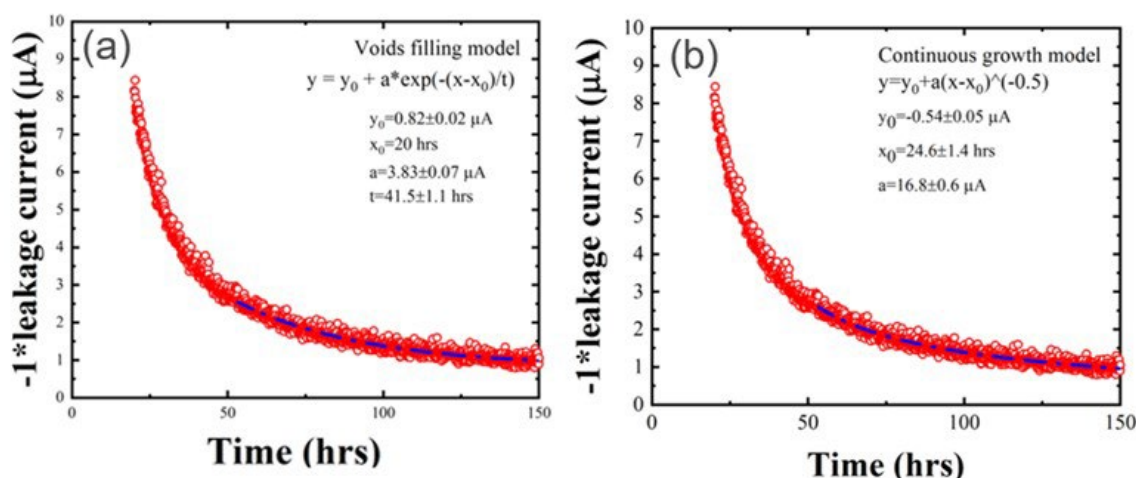


Figure VIII.3.2 Fitting the leakage current data collected for SiO at 0.1 V vs. Li⁺/Li, using both (a) voids filling model and (b) continuous growth model.

To further investigate the cause on underestimation of the calendar life prediction, new cells were assembled and similar measurement was conducted except to collect the leakage current data for longer period, up to 600 hours. In this run of exercise, the collected leakage current were chopped into different segments based on sampling time as shown in X axis of Figure VIII.3.3a. The segmentized data were then fitted with both the voids filling model and continuous growth model to predict its steady leakage current. Figure II.1.C.3a clearly shows that the fitting results strongly depends on the sampling time of the experimental data. Modeling the early-stage leakage current, collected between 20 hours and 40 hours, generates very rough results. The continuous growth model predicts a very negative leakage current of about $-5.7 \mu\text{A}$. At the same, the fitting results using both models also show a big error bar, indicating a big discrepancy between the ideal models and the reality. Significant improvements on the results were observed by modeling experimental data collected at a later stage. These improvements include: (1) the reduce of the error bar in fitting the experimental data with the models, (2) continuous reduce of discrepancy between two SEI growth models, and (3) continuous reduce on the underestimation of steady leakage current by the continuous growth model. Particularly, when the data collected between 320 hours and 600 hours were used for modeling, the predicted steady leakage current by the continuous growth model finally agrees with the prediction from the voids filling model. Similarly, a steady increase on the predicted calendar life was also observed by modeling the leakage current data collected at a later stage. The predicted number stabilized at about 1400 hours when data within range between 320 hours and 600 hours are used. This exercise clearly indicates that there is a kinetically very slow process associated with the SiO anode, hypothetically a slow diffusion kinetics of Li^+ in lithiated silicone (Li_xSi), which significantly complicates the electrochemical measurement procedure to collect clean leakage current. This complicated coupling between the parasitic reaction and the low reaction kinetics in SiO raises a technical need to long sampling of clean leakage current up to 600 hours.

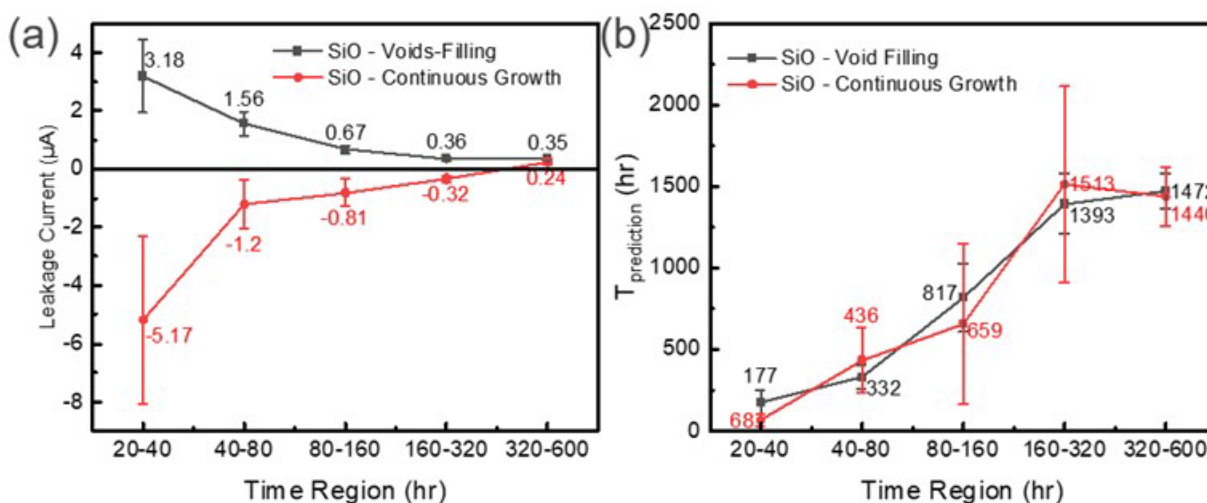


Figure VIII.3.3 Mathematic fitting of long term (up to 600hours) leakage current data for SiO anode at 0.1 V vs. Li^+/Li , showing the significant impact of sampling time period on (a) the obtained steady leakage current, and (b) the predicted calendar life.

Keeping the long sampling period up to 600 hours as the current gold procedure, the data collection protocol and modeling approach was also applied to benchmark the data on a graphite anode. The comparison on the predicted results on both SiO anode and graphite is shown in Figure VIII.3.4. Encouraging result is shown that both models predict that the graphite will have about twice the calendar life of SiO anode, which is well expected. However, the actual predicted calendar life (2500–3000 hours for graphite) is still far below the expectation. A systematic understanding on the physical root of this discrepancy is crucial for further improvement of the calendar life prediction model.

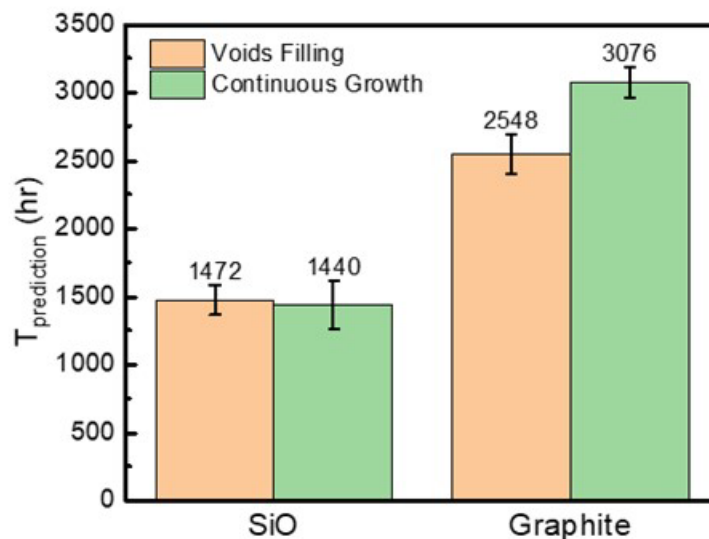


Figure VIII.3.4 Comparison of predicted calendar life of graphite anode and SiO anode.

Conclusions

A working sampling protocol to collect clean leakage data for silicone anode has been established. Two mathematic models based on the different SEI growth mechanisms were developed. A consistent modeling results were obtained for both models on modelling both SiO anode and graphite anode. At the current stage, the relative difference on the calendar life of different chemistries can be reasonably predicted. The developed method can be used as high through put characterization to assist the development o high performance silicone anode chemistry. However, more effort is still needed to understand the connection between the parasitic current and the loss of calendar life.

Acknowledgements

This report is coauthored by Dr. Jiyu Cai, and Dr. Guiliang Xu. We also wish to thank Bryant Polzin and Steve Trask of ANL-CAMP facility in providing standard SiO electrode, graphite electrode and standard electrolyte for this project.

VIII.4 Seedling Project: Two-Dimensional Silicon Nanostructures for Improved Silicon Anode Cycling Stability (BNL)

Amy C. Marschilok, Principal Investigator

Brookhaven National Laboratory
Interdisciplinary Science Department, Building 734
Upton, NY 11973
E-mail: amarschilok@bnl.gov

Lei Wang, Principal Investigator

Brookhaven National Laboratory
Interdisciplinary Science Department, Building 734
Upton, NY 11973
E-mail: lwang@bnl.gov

Kenneth J. Takeuchi, Principal Investigator

Stony Brook University
1000 Innovation Road
Stony Brook, NY 11794
E-mail: kenneth.takeuchi.1@stonybrook.edu

Brian Cunningham, DOE Technology Development Manager

U.S. Department of Energy
E-mail: Brian.Cunningham@ee.doe.gov

Start Date: October 1, 2020

End Date: September 30, 2023

Project Funding (FY21): \$200,000

DOE share: \$200,000

Non-DOE share: \$0

Project Introduction

The high specific capacity of Si (3579 mAh/g) is unobtainable, especially after extended cycling due to: ~300% volume expansion on lithiation, resulting in particle cracking/fracture¹ and active material loss, and continual formation of a heterogeneous solid electrolyte interphase layer, resulting in electrolyte depletion and impedance increase.² Decreasing crystallite size of silicon can improve cycling stability by dissipating effects of mechanical stress. However, decreasing size increases surface area, which can promote parasitic electrolyte degradation reactions. The approach for this project is to investigate two-dimensional silicon to gain additional benefit beyond surface area increase (nanosizing), recognizing that two-dimensional silicon may show additional advantage over its spherical counterparts due to higher mechanical strength,³ improved transversal flexibility,⁴ conductivity,⁴ and ion transport⁵ properties.

Objectives

The project objectives are to:

1. Identify appropriate two-dimensional material alternatives to silicon.
2. Develop and investigate synthesis approaches.
3. Characterize materials properties.
4. Evaluate electrochemical function.

Approach

This project will emphasize development and investigation of synthesis approaches that are tunable, scalable, and repeatable/reliable for generation of 2D silicon materials. We will characterize physical properties of the materials (i.e., surface area, morphology, crystallinity), process them into battery electrodes, and determine electrochemical function under conditions relevant to vehicle battery technology use.

Results

2D siloxene nanosheets were prepared via a topotactic reaction. The as-prepared materials were characterized via electron microscopy and atomic force microscopy (Figure VIII.4.1). TEM revealed a layered structure with a typical thickness of around 10 layers. HRTEM showed a clear lattice pattern of $d = 3.22 \text{ \AA}$ for the (110) phase. AFM showed some very thin layers with a thickness of 3–4 nm corresponding to ~5–7 layers of siloxene, however, the majority of the nanosheets have thicknesses ~13 nm, and some show thickness of ~70 nm. X-ray photoelectron spectroscopy was used to probe the surface oxidation level of siloxene. The O/Si ratio for our siloxene samples was found to be 0.69 from the XPS analysis, which is much lower than previously reported siloxene work with O/Si ratios of 1.55⁶ or 1.39⁷.

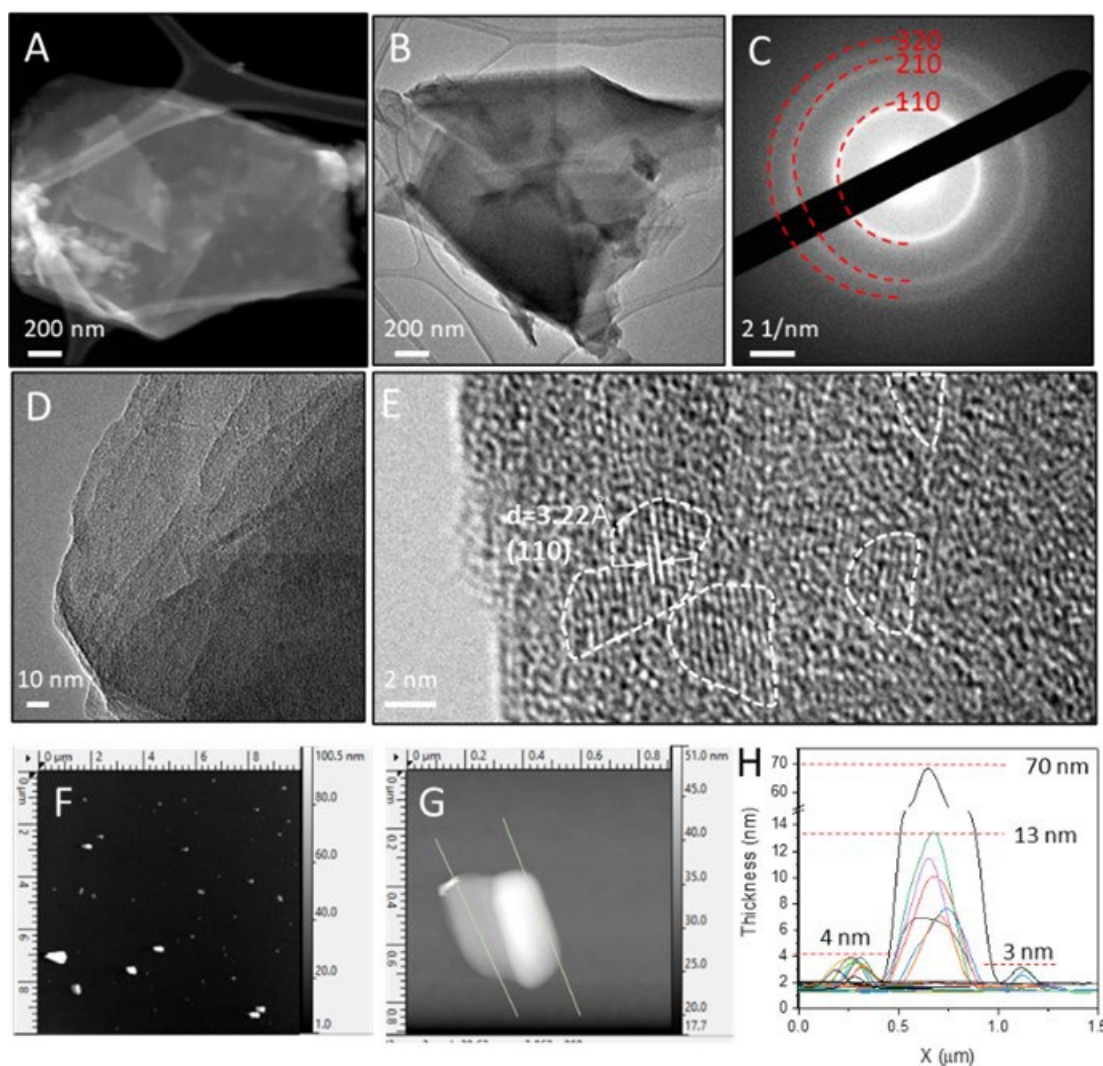


Figure VIII.4.1 Structural characterization of siloxene nanosheets after ultrasonication. (A) HAADF-STEM image. (B) TEM image at low magnification and (C) the corresponding selected area diffraction. (D) TEM images at high magnification and (E) an HRTEM image. (F) AFM at low magnification, (G) AFM at high magnification, and (H) the accompanying thickness measurements.

To investigate the efficacy of the synthesized 2D siloxene nanosheets as potential Li-ion anodes, coin cells were assembled with Li metal counter electrodes. Cells were made with and without 10 wt.% fluoroethylene carbonate (FEC) to determine the effect of the electrolyte additive. The voltage profiles for select cycles with and without FEC at a 200 mA/g rate are shown (Figure VIII.4.2, Parts A, B). In the first discharge (lithiation), a plateau is observed at 0.2 V followed by a sloping profile, while a second plateau at 0.5 V appears for the second discharge. The 0.5 V plateau decreases and disappears by cycle 30 in electrolyte without FEC but remains for the electrolyte with 10% FEC. Without FEC, the siloxene delivers cycle 1 discharge and charge (delithiation) capacities of 2180 mAh/g and 1110 mAh/g respectively, with coulombic efficiency of 50.9%. The siloxene in electrolyte with 10% FEC first discharges a capacity of 2100 mAh/g and charges 980 mAh/g with a coulombic efficiency of 46.5%. In the FEC electrolyte, the initial capacity and coulombic efficiency is lower, but the capacity increases to 1310 mAh/g after 10 cycles compared to a maximum of 1250 mAh/g for the non-FEC electrolyte. Similar phenomena have been observed for cells using a-Si thin films cycled at C/2 current where cells with no FEC in the electrolyte showed higher initial capacity than the cell with FEC electrolyte⁸. The discharge capacity retention from cycle 2 to 100 was 82% for the electrolyte with 10% FEC compared to 62% for the non-FEC electrolyte (Figure VIII.4.2, Part C). The rate capability testing (Figure VIII.4.2, Part D) shows similar performance for cells with and without 10% FEC at discharge rates of 400, 800, 1600, 3200 mA/g and back to 400 mA/g with a constant charge rate at 400 mA/g. A high capacity of 935 mAh/g at 3200 mA/g was obtained as well as high reversibility when the discharge rate was returned to 400 mA/g. Due to the strong rate performance, the cycling stability was tested at 1000 mA/g for cells with both electrolytes. For these high-rate tests, the siloxene was first cycled three times at 200 mA/g as a formation step. After 200 cycles, the siloxene delivers a capacity of 750 mAh/g and capacity retention of 77% with 10% FEC versus a capacity of 200 mAh/g and capacity retention of 13% without FEC (Figure VIII.4.2, Part E).

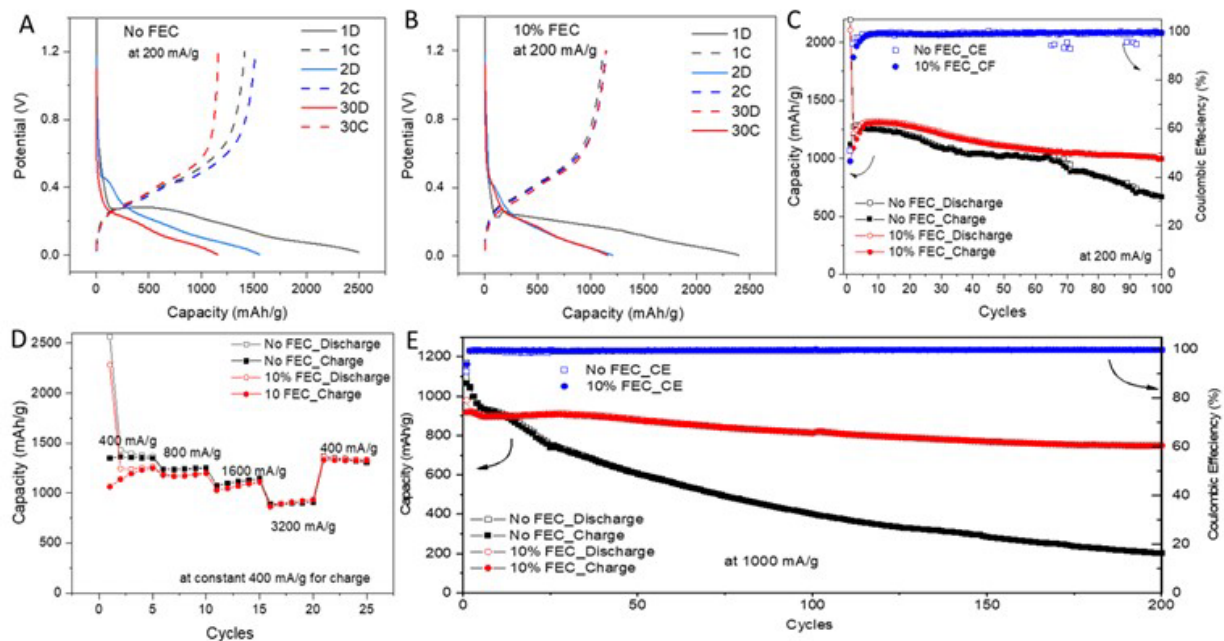


Figure VIII.4.2 Electrochemistry of lithium/siloxene cells with and without 10% FEC. Charge and discharge voltage profiles for cells (A) without FEC and (B) with 10% FEC. (C) Cycling stability at 200 mA/g. (D) Rate capability from 400 to 3200 mA/g. (E) Long-term cycling at 1000 mA/g.

Pristine siloxene electrodes were analyzed with XPS to identify features in the C 1s, Si 2p, and O 1s spectral regions. XPS was also performed on cycled siloxene electrodes in the discharged state of cycles 1 and 3 in electrolyte with and without 10% FEC to investigate differences in SEI composition (Figure VIII.4.3). The XPS shows electrodes cycled with FEC electrolyte have a higher concentration of LiF and that $\text{Li}_x\text{PO}_y\text{F}_z$ was formed in situ on the surface of the electrodes. This is consistent with the electrochemical behavior of our

siloxene cells cycled at 1000 mA/g where capacity retention was 77% for cells with FEC versus 13% for cells without FEC.

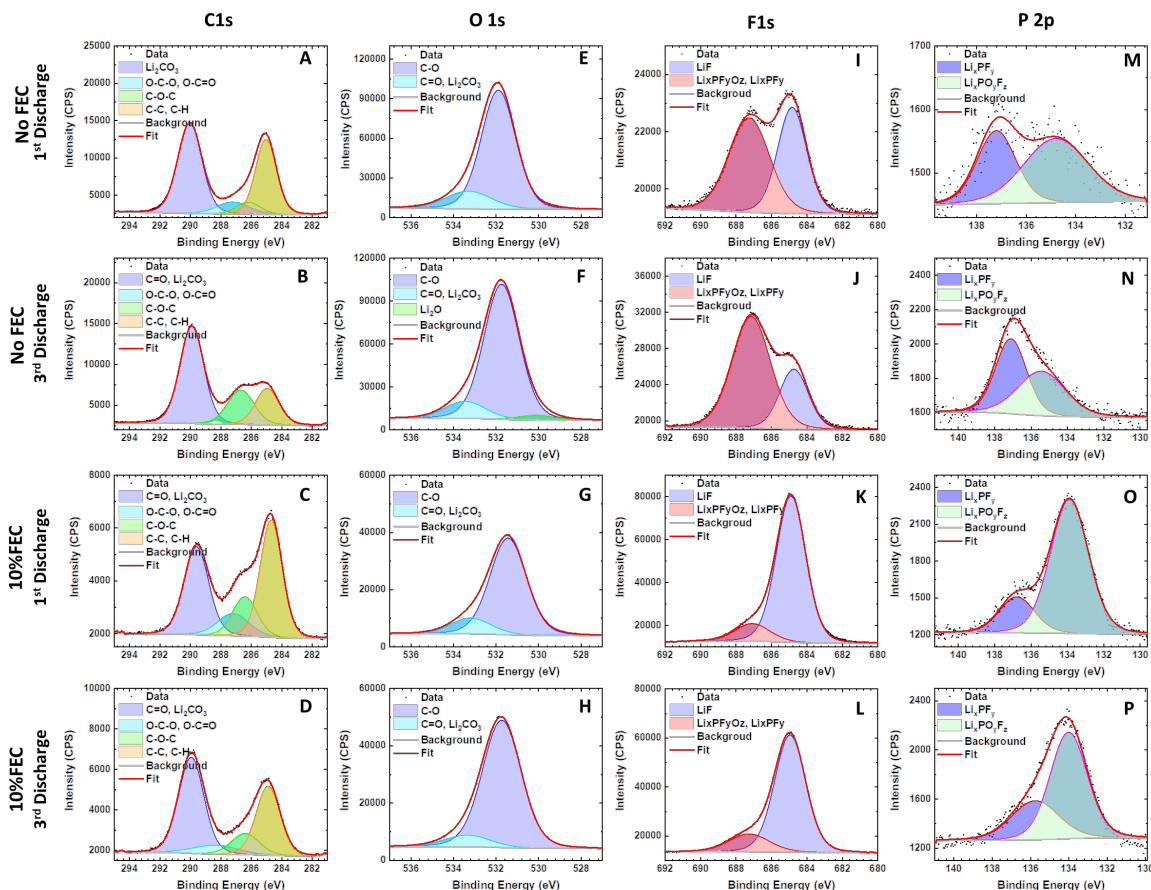


Figure VIII.4.3 XPS fitting results of cycles 1 and 3 discharged siloxene electrodes cycled in electrolyte with and without 10% FEC. C 1s spectra of a cycle 1 and 3 discharged electrodes (A-B) without FEC and (C-D) with FEC. O 1s spectra of cycle 1 and cycle 3 discharged electrodes (E-F) without FEC and (G-H) with FEC. F 1s spectra of cycle 1 and cycle 3 discharged electrodes (I-J) without FEC and (K-L) with FEC. P 2p spectra of cycle 1 and cycle 3 discharged electrodes (M-N) without FEC and (O-P) with FEC.

Conclusions

The 2D siloxene nanosheets showed low oxidation with only 15% Si-oxide. The siloxene nanosheets were tested for reversible lithium storage in lithium half cells with a focus on the effects of FEC as an electrode additive. The cells exhibited good rate capability with a lithiation capacity of 935 mAh/g at 3200 mA/g and high coulombic efficiency. We found that the addition of 10% FEC to the electrolyte greatly increased the capacity retention for the siloxene sheets, especially at a high-rate of 1000 mA/g. Cells with FEC containing electrolyte delivered 750 mAh/g at cycle 200 with 77% capacity retention compared to 200 mAh/g and 13% capacity retention for cells without FEC. The ex-situ XPS and Raman of the electrodes from cells with 10% FEC additive showed a high concentration of LiF/LiPOyFz in the SEI layer on the surface of the siloxene electrodes, which likely contributed to the enhanced cycling stability observed in the presence of FEC.

Key Publications

- David J. Arnot, Wenzao Li, David C. Bock, Chavis A. Stackhouse, Xiao Tong, Ashley R. Head, Esther S. Takeuchi, Kenneth J. Takeuchi, Shan Yan*, Lei Wang *, Amy C. Marschilok*. "Low-oxidized siloxene nanosheets with high capacity, capacity retention and rate capability in lithium-based batteries." *Revision under Review*.

References

1. T. Yoon, C. X. Xiao, J. Liu, Y.K. Wang, S. Son, A. Burrell, C.M. Ban, J. Power Sources, 2019, 425, 44–49.
2. I. Hasa, A.M. Haregewoin, L. Zhang, W.Y. Tsai, J.H. Guo, G.M. Veith, P.N. Ross, R. Kostecki, ACS Appl. Mater. Interfac., 2020, 12(36), 40879–40890.
3. Q. Peng, X. Wen, S. De, RSC Adv., 2013, 3, 13772.
4. L.C. Lew Yan Voon, J. Zhu, U. Schwingenschlögl, Appl. Phys. Rev. 2016, 3 (4), 040802.
5. J. Setiadi, M.D. Arnold, M.J. Ford, ACS Appl. Mater. Interfaces, 2013, 5, 10690.
6. S. Li, H. Wang, D. Li, X. Zhang, Y. Wang, J. Xie, J. Wang, Y. Tian, W. Ni, Y. Xie, Journal of Materials Chemistry A 2016, 4, 15841.
7. K. Krishnamoorthy, P. Pazhamalai, S.-J. Kim, Energy & Environmental Science 2018, 11, 1595.
8. K. Schroder, J. Alvarado, T. A. Yersak, J. Li, N. Dudney, L. J. Webb, Y. S. Meng, K. J. Stevenson, Chemistry of Materials 2015, 27, 5531.

Acknowledgements

Xiao Tong and Ashley R. Head are acknowledged for support with XPS measurements. Electron microscopy, AFM, and XPS instrumentation and support were provided by the Center for Functional Nanomaterials, a U.S. DOE Office of Science Facility, at Brookhaven National Laboratory under Contract No. DE-SC0012704.

VIII.5 Pre-Lithiation of Silicon Anode for High Energy Li-ion Batteries (Stanford University)

Yi Cui, Principal Investigator

Stanford University

Department of Materials Science and Engineering, Stanford University
Stanford, CA 94305

E-mail: yicui@stanford.edu

Tien Q. Duong, DOE Technology Development Manager

U.S. Department of Energy

E-mail: Tien.Duong@ee.doe.gov

Start Date: October 1, 2019

End Date: September 30, 2021

Project Funding (FY21): \$500,000

DOE share: \$500,000

Non-DOE share: 0

Project Introduction

Lithium-Ion Batteries (LIBs) offer superior performance among all rechargeable battery technologies and are the main power sources for portable electronic devices and electric vehicles. Silicon is a high-performance anode material for next generation lithium-ion batteries, with an order of magnitude higher capacity than traditional graphite anode. In our lab, challenges of Si anode materials associated with large volume change (>300%) during lithium insertion and extraction are largely addressed by well-designed nanostructures [1]. However, the common issue associated with these anode materials is the increased solid electrolyte interphase (SEI) formation on high-surface-area nanostructures during the first cycle. The process consumes an appreciable amount of lithium, resulting in irreversible loss of capacity and low 1st CE (50–80%) [2], while a value of at least 90% is needed for real applications. Such capacity loss is usually compensated by additional loading of cathode materials in commercial lithium-ion batteries. However, the lithium metal oxide cathodes have much lower specific capacity than the anodes. The excessive loading of cathode material causes appreciable reduction of battery energy density. It is therefore highly desirable to suppress such loss and consequently increase the 1st CE through prelithiation. In addition, pre-storing lithium inside anodes enable the opportunity to pair with Li-free cathodes such as sulfur and oxygen cathodes. This project's success will make high-energy-density Li ion batteries for EVs.

Objectives

Prelithiation of high-capacity electrode materials is an important means to enable those materials in high-energy batteries. This study pursues three main directions: (1) developing facile and practical methods to increase 1st cycle CE of anodes, (2) synthesizing fully lithiated anode to pair with high-capacity Li free cathode materials, and (3) prelithiation from the cathode side. The challenge associated with the anode prelithiation is the high chemical reactivity of prelithiation materials, which are hard to survive multiple processing steps (exposure to air and solvent, slurry mixing, coating, and baking) during battery electrode fabrication. A protective coating is therefore needed. Different passivation coatings have been used to increase the dry-air and solvent stability of prelithiation reagents. At the end of battery assembly, the coatings are activated to ensure quick lithium ions diffusion for prelithiation. The passivation coatings can improve the dry-air stability of prelithiation materials to a certain extent, but much study is still needed to improve solvent stability to better compatible with practical battery fabrication. We plan to explore a new solvent-free dry method for anode prelithiation through in situ prelithiation. Prelithiation reagents are added to the battery in the assembly step, to avoid the concern of solvent compatibility. We also plan to design prelithiation reagents for this solvent-free method, and accurately control the prelithiation amount of anode materials to pair with different-capacities cathode materials.

Approach

Three main approaches have been developed for prelithiation: 1) Synthesizing lithium alloying Li_xM particles as novel prelithiation reagents to provide a low-cost and general strategy for prelithiation. The synthesized Li-rich compounds should be able to mix with various anode or cathode materials during slurry process and serve as prelithiation reagents. 2) Developing new prelithiation process based-on pressure-induced prelithiation. By direct contact with Li and Si under pressure, heat-free and solvent-free prelithiation can be achieved without the concern of solvent compatibility. Also, prelithiation amount is controllable through contact time and pressure. 3) Developing new in-situ prelithiation process based on shorting-mechanism. A layer of thin lithium is inserted above Si anode in cell fabrication to achieve in-situ prelithiation during battery resting period. Prelithiation reagents need to carefully design for this approach to control prelithiation amount and avoid excessive Li. Besides prelithiation step, a series of morphological and chemical composition characterizations including SEM, TEM, XPS, Raman spectroscopy, XRD, etc. and electrochemical testing are conducted for performance characterization.

Results

In-situ prelithiation is a promising dry one-step prelithiation strategy without the concern of cell reassembly and solvent compatibility. This prelithiation approach takes one step to insert lithium mesh above Si anode in fabrication and allows prelithiation in-situ take place in battery resting period based on shorting mechanism. Due to no extraction of lithium out of the cell after prelithiation, the inserted Li amount requires to be carefully controlled to match the desired prelithiation amount. Here, we present rGO-hosted ultra-thin Li (Li@eGF) foils as a new type of prelithiation reagent promising for facile and controllable in-situ prelithiation.

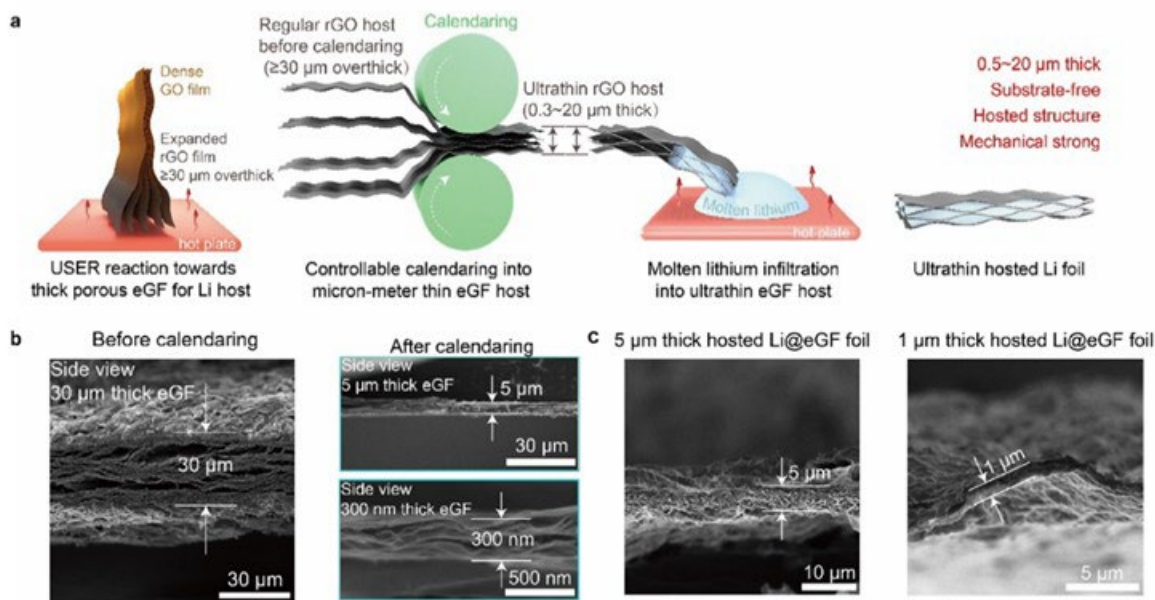


Figure VIII.5.1 a, Schematic of the fabrication of ultra-thin lithium foil. b, Cross-sectional SEM images comparing the common thick host before calendaring, and submicron-scale ultra-thin host after controllable calendaring. c, Cross-sectional SEM images of fabricated ultra-thin 1- μm -thick and 5- μm -thick hosted lithium films after preliminary calendaring process.

In industry, the existing extrusion-based fabrication technologies are only capable of producing Li metal foil with thickness of 20 to several hundreds of microns. Extruding free-standing Li metal foil less than 20 micron thick presents the challenge of mechanical fragility. Here, we develop a process that generates a microns-thin, free-standing, and hosted Li metal foil down to sub-micron in thickness. First, we use a tunable calendaring process to decrease the thickness of a porous reduced graphene oxide (rGO) host to a thickness of 0.3 to 20 μm (Figure VIII.5.1 a-b). GO film is chosen here because it makes the process scalable and has good mechanical strength. Edge-contacting molten Li to the ultra-thin rGO host loads metallic Li inside its internal channels

while retaining the similar micron-scale thickness. As a result, we fabricate a robust, free-standing, scalable, and flexible Li metal film thicknesses ranging 0.5 to 20 μm (corresponding to ultra-low areal capacities of 1 to 4 mAh cm^{-2}) (Figure VIII.5.1c). This procedure fabricates a micron-scale thin Li foil that overcomes the thinness limitations of presently available Li films (20 to 750 μm thick, 4 to 150 mAh cm^{-2} capacity). Besides, the embedded graphene host provides strong mechanical support to the free-standing ultra-thin Li metal foil. The tunable and ultralow capacity of this Li metal film makes it promising for prelithiation for a wide-range of anode choices with different amount of initial active Li loss.

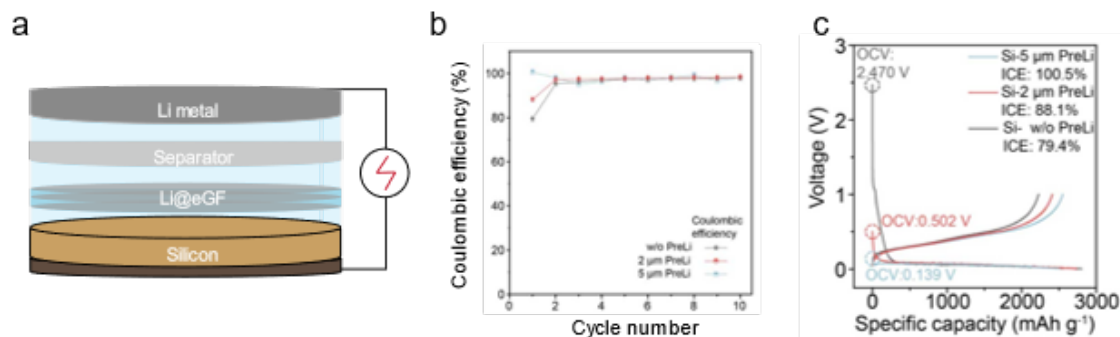


Figure VIII.5.2 a, Schematic of the prelithiation step using Li@eGF films. b, Coulombic efficiencies of prelithiated silicon anodes using different thickness of Li@eGF films in the first cycle. c, Voltage profiles of Si electrodes using different thickness of Li@eGF films in the first cycle.

Prelithiation was carried out as the schematic shows in Figure VIII.5.2a. Li@eGF foil was inserted between silicon anode and separator in the cell assembly process. With electrolyte immersed, silicon was lithiated through electrochemical reaction between silicon and lithium. The mass loading of silicon electrodes was controlled around 1.2 mg cm^{-2} . Two different thickness of Li@eGF foils of 2 μm and 5 μm were applied for prelithiation, which exhibited capacities of 0.4 mAh cm^{-2} and 1 mAh cm^{-2} , respectively. Shown in Figure VIII.5.2b, 2- μm -Li@eGF foil improves the initial CE of silicon from ~80% to 88.1% and 5- μm -Li@eGF foil successfully improves the initial CE of silicon to the nearly ideal 100%. Noticeably, considering the initial CE of 80% of pristine Si, the theoretical initial capacity loss in silicon anode is around 1 mAh cm^{-2} . Therefore, 5- μm -Li@eGF foil, exhibiting capacity of 1 mAh cm^{-2} , both theoretically and experimentally fully compensated the irreversible capacity loss in silicon. This result indicates that Li@eGF foil is promising for precise prelithiation through thickness tuning to match its stored capacity with the theoretically desired prelithiation capacity. Figure VIII.5.2c further shows the delithiation capacity improvement after prelithiation. While the lithiation capacity remain similar, silicon without prelithiation has the lowest delithiation capacity and 5- μm -Li@eGF lithiated silicon anode has the highest delithiation capacity. This increase further supports that Li@eGF prelithiation has successfully compensates the initial capacity loss. The decreased OCVs indicate increased prelithiation level with more lithium applied for prelithiation. In sum, Li@eGF with its unique tunable thickness and ultra-thin properties, was demonstrated to be an ideal prelithiation reagent. The tunable thickness makes Li@eGF facilitate control the prelithiation amount and the ultra-thin thickness provides Li@eGF appropriate capacity for prelithiation without the safety and stability concern of excessive lithium.

To fundamentally understand the reactions in Li@eGF-based prelithiation, we continue to investigate the chemical and morphological evolution of Si anode with Li@eGF prelithiation. We first investigated chemical evolution of Si anode after Li@eGF prelithiation through X-ray photoelectron spectroscopy (XPS). High resolution Si 2p spectra (Figure VIII.5.3a-b) can be differentiated into three peaks, Li_xSiO_y at ~102 eV, Si peak at ~99.2 eV, and Li_xSi peak at around ~98.2 eV. The appearance of Li_xSiO_y peak and Li_xSi peak indicates prelithiated status of Si, where Li_xSiO_y comes from lithiated surface oxides on Si particles. Interestingly, Si peak remains after prelithiation, indicating partial lithiation of Si particles. This phenomenon raises the assumption that in the 100 nm Si particles used in this project, the outer surface of the particles is lithiated, while the core of the particles remains in pristine state. The slow prelithiation of Si core can be possibly explained by the low diffusion coefficient of Li ions in Si (~10-12 cm^2/s) and the limited prelithiation

time of 10 hours. Figure VIII.5.3b further shows the appearance of Li 1s peak after prelithiation, confirming the prelithiated status of Si. LiF and ROLi signals possibly come from the reduction product of electrolyte.

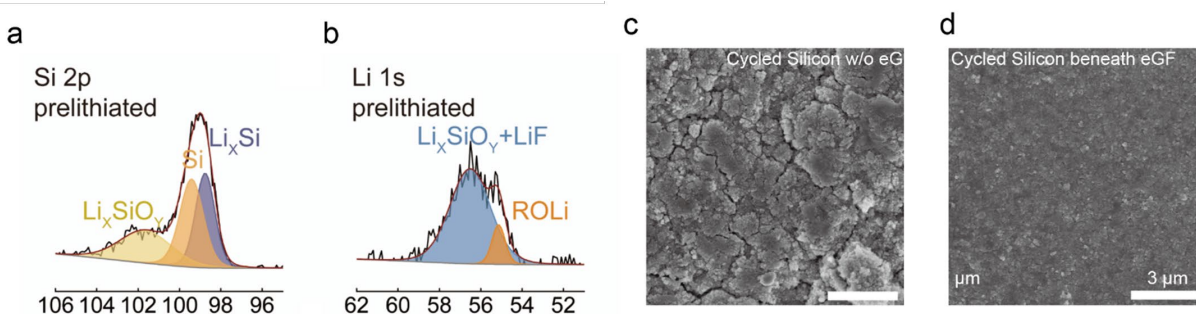


Figure VIII.5.3 a-b, XPS spectra of the Si anode after Li@eGF prelithiation. Si 2p spectra (a). Li 1s spectra (b). c-d, Top-view SEM images of cycled Si anode without (c) and with (d) Li@eGF prelithiation.

Besides chemical evolution of Si anode after Li@eGF prelithiation, we further explore the morphological evolution of Si anode with and without Li@eGF prelithiation after cycling. Li@eGF has a unique advantage in prelithiation is that it leaves a conductive layer of reduced graphene (eGF) film above Si anode after prelithiation. This eGF film acts both as a secondary current collector to enhance the conductivity between Si particles, and as a protective layer to tightly hold the Si particles together to reduce cracks. As shown in the SEM images, Si anode cycled without Li@eGF prelithiation is not protected by eGF film during cycling, thus leading to amounts of cracks after cycling (Figure VIII.5.3c). In comparison, Si anode cycled with Li@eGF prelithiation shows a smooth surface without obvious cracks (Figure VIII.5.3d), benefited from the condensation role of eGF film. These results well support that Li@eGF provide strong protection of Si anode during cycling.

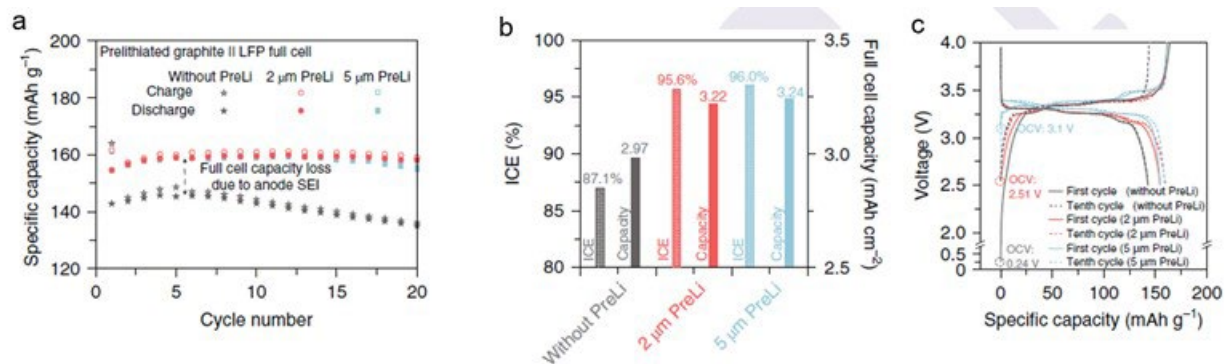


Figure VIII.5.4 a, Galvanostatic cycling of graphite || LFP full cells at 0.05 C using different thicknesses of Li@eGF film for prelithiation in the anode. For this graphite || LFP full cell, 1C = 150 mA g⁻¹. b, Comparisons of the ICE and areal capacity (after five activation cycles) of graphite || LFP full cells using different thicknesses of Li@eGF film for anode prelithiation. c, Voltage profiles of graphite || LFP full cells at 0.05 C using different thicknesses of Li@eGF film for prelithiation.

We further use graphite || LFP full cells as a model to investigate Li@eGF prelithiation in full cells. Similar to silicon, graphite meets the same problem of relatively low initial CE of around 93%, suggesting ~7% of the battery capacity is lost after initial cycle. In our demonstration, graphite anodes with designed capacity of 3.22 mAh cm⁻² are paired with LFP cathodes with designed capacity of 3.22 mAh cm⁻². Therefore, the constructed battery has a theoretical capacity of 3.22 mAh cm⁻². However, without prelithiation, the first discharge capacity of the cell is only ~2.97 mAh cm⁻². The initial loss of 7% of battery capacity is mainly due to the initial SEI formation on the anode and leads to irreversible battery capacity degradation (Figure VIII.5.4a). To address this problem, we apply Li@eGF prelithiation to the graphite anodes to compensate the initial capacity loss. We coat a 2-μm-thick and a 5-μm-thick Li@eGF film, respectively, on a graphite anode. In both cases, the full-cell

ICE improves from 87% to around 96% (Figure VIII.5.4b). Correspondingly, the capacities of Li-ion full cells are fully recovered and stabilized at the theoretical capacity (around 3.22 mAh cm⁻²). This result illustrates that this prelithiation function significantly improves the cell capacity and compensates for the initial loss of Li in the anode. In addition, appropriate prelithiation amount is important to avoid excessive Li deposition on the anodes, which prevents poor battery performance and safety hazards. Prelithiation with 5- μ m-thick Li@eGF (0.853 mAh cm⁻²) exceeds the initial Li loss amount of the graphite anode (0.25 mAh cm⁻²). Expectedly, the full cell suffers from metallic Li plating, because the graphite cannot accommodate all Li ions from the cathode during cell charging. Shown in Figure VIII.5.1c, this plating induces higher-voltage plateaus (Figure VIII.5.4c), presenting metallic Li deposition. By contrast, the graphite || LFP full cell prelithiated with 2- μ m-thick Li@eGF has similar voltage profiles compared to the cell without prelithiation, showing no evidence of metallic Li plating. These results demonstrate the importance of tunable thickness in Li@eGF, to well match the prelithiation capacity with initial capacity loss.

Conclusions

In the past year, we have developed ultra-thin lithium foils (Li@eGF) as a new dry prelithiation reagent promising for facile and controllable prelithiation. Through a tunable calendaring process and an edge-contacting molten Li infusion, Li@eGF foils with varied thickness of 0.5 to 20 μ m were fabricated, breaking the thickness limit of the commercialized Li foils. Our Li@eGF foils have capacities of 0.1 to 4 mAh cm⁻², and these capacity amounts can promisingly compensate the irreversible capacity loss in the first cycle of various anode materials. We have further applied Li@eGF foils for Si anode prelithiation and achieve initial CE improvement from ~80% to ~100% when matching Li@eGF capacity with the desired prelithiation amount. XPS study shows appearance of Li_xSiO_y peak and Li_xSi peak after prelithiation, indicating prelithiated status of Si. Interestingly, Si peak remains in the prelithiated sample, rising the future interest to investigate prelithiation kinetics within the electrodes. SEM shows reduced cracks in cycled Si electrodes with Li@eGF prelithiation. This finding supports the dual-function of our designed prelithiation reagent. Besides providing tunable prelithiation capacity, Li@eGF also acts as a protection layer for Si cycling stabilization by its conductive nature. Moreover, we use graphite || LFP full cells as a model to investigate Li@eGF prelithiation in full cells, showing the capacities of Li-ion full cells are fully recovered and stabilized at the theoretical capacity when applying Li@eGF as prelithiation reagents. All these results demonstrate that our designed Li@eGF is a promising prelithiation reagent towards applicable high-energy-density anode electrodes.

Key Publications

1. Zhao, Jie, Zhenda Lu, Nian Liu, Hyun-Wook Lee, Matthew T. McDowell, and Yi Cui. "Dry-air-stable lithium silicide–lithium oxide core–shell nanoparticles as high-capacity prelithiation reagents." *Nature communications* 5, no. 1 (2014): 1–8.
2. Zhao, Jie, Zhenda Lu, Haotian Wang, Wei Liu, Hyun-Wook Lee, Kai Yan, Denys Zhuo, Dingchang Lin, Nian Liu, and Yi Cui. "Artificial solid electrolyte interphase-protected Li_xSi nanoparticles: an efficient and stable prelithiation reagent for lithium-ion batteries." *Journal of the American Chemical Society* 137, no. 26 (2015): 8372–8375.
3. Zhao, Jie, Hyun-Wook Lee, Jie Sun, Kai Yan, Yayuan Liu, Wei Liu, Zhenda Lu, Dingchang Lin, Guangmin Zhou, and Yi Cui. "Metallurgically lithiated SiO_x anode with high capacity and ambient air compatibility." *Proceedings of the National Academy of Sciences* 113, no. 27 (2016): 7408–7413.
4. Sun, Yongming, Hyun-Wook Lee, Zhi Wei Seh, Nian Liu, Jie Sun, Yuzhang Li, and Yi Cui. "High-capacity battery cathode prelithiation to offset initial lithium loss." *Nature Energy* 1, no. 1 (2016): 1–7.
5. Sun, Yongming, Hyun-Wook Lee, Guangyuan Zheng, Zhi Wei Seh, Jie Sun, Yanbin Li, and Yi Cui. "In situ chemical synthesis of lithium fluoride/metal nanocomposite for high capacity prelithiation of cathodes." *Nano letters* 16, no. 2 (2016): 1497–1501.

6. Sun, Yongming, Hyun-Wook Lee, Zhi Wei Seh, Guangyuan Zheng, Jie Sun, Yanbin Li, and Yi Cui. "Lithium Sulfide/Metal Nanocomposite as a High-Capacity Cathode Prelithiation Material." *Advanced Energy Materials* 6, no. 12 (2016): 1600154.
7. Sun, Yongming, Yanbin Li, Jie Sun, Yuzhang Li, Allen Pei, and Yi Cui. "Stabilized Li₃N for efficient battery cathode prelithiation." *Energy Storage Materials* 6 (2017): 119–124.
8. Zhao, Jie, Jie Sun, Allen Pei, Guangmin Zhou, Kai Yan, Yayuan Liu, Dingchang Lin, and Yi Cui. "A general prelithiation approach for group IV elements and corresponding oxides." *Energy Storage Materials* 10 (2018): 275–281.
9. Chen, Hao, Yufei Yang, David T. Boyle, You Kyeong Jeong, Rong Xu, Luiz Scalco de Vasconcelos, Zhuojun Huang et al. "Free-standing ultrathin lithium metal–graphene oxide host foils with controllable thickness for lithium batteries." *Nature Energy* (2021): 1–9.

References

1. Liu, Yayuan, Guangmin Zhou, Kai Liu, and Yi Cui. "Design of complex nanomaterials for energy storage: past success and future opportunity." *Accounts of chemical research* 50, no. 12 (2017): 2895–2905.
2. Zhao, Jie, Zhenda Lu, Nian Liu, Hyun-Wook Lee, Matthew T. McDowell, and Yi Cui. "Dry-air-stable lithium silicide–lithium oxide core–shell nanoparticles as high-capacity prelithiation reagents." *Nature communications* 5, no. 1 (2014): 1–8.

VIII.6 Integrated Modeling and Machine Learning of Solid-Electrolyte Interface Reactions of the Si Anode (LBNL)

Kristin A. Persson, Principal Investigator

Lawrence Berkeley National Laboratory
1 Cyclotron Road
Berkeley, CA 94720
E-mail: kapersson@lbl.gov

Jean-Luc Fattebert, Principal Investigator

Computational Sciences and Engineering Department
Oak Ridge National Laboratory
One Bethel Valley Road
Oak Ridge, TN 37831
E-mail: fattebertj@ornl.gov

Andrew Colclasure, Principal Investigator

National Renewable Energy Laboratory
Center for Integrated Mobility Sciences
Golden, CO 80401
E-mail: andrew.colclasure@nrel.gov

Brian Cunningham, DOE Technology Development Manager

U.S. Department of Energy
E-mail: Brian.Cunningham@ee.doe.gov

Start Date: October 1, 2019	End Date: September 30, 2022	
Project Funding (FY21): \$650,000	DOE share: \$650,000	Non-DOE share: \$0

Project Introduction

Silicon anode batteries have the potential of meeting future energy storage demands thanks to the high theoretical Si capacity of 3500 mAh/g. However, major issues exist before Si anodes can be put into practical use, including the formation mechanism of key components of the solid electrolyte interface (SEI), cracking of the SEI due to its large volume change, and instability of the electrolyte which continues reducing at the cracked SEI. In this effort, we aim to leverage the DOE high-performance computing (HPC) facilities and apply multiscale computational approaches (from first-principles density functional theory, classical molecular dynamics, continuum modeling, to machine learning) to capture the species and chemical reaction paths of SEI growth on Si, coupled together with the Si anode's surface and phase structure evolution with cycling. The resulting electrolyte stability insights, SEI phase evolution, and microstructure analysis will provide valuable data for feedback and close integration with the existing DOE Si Consortium program to ultimately advance our understanding of the Si anode reactivity and the development of novel Si electrolyte.

Objectives

With the overall goal of understanding the underlying instability of the SEI formed on silicon-based anodes to identify strategies to improve stability and thus cycling lifetimes, the LBNL, ORNL, and NREL teams pursue three distinct and complementary objectives.

The LBNL team seeks to use a first-principles data-driven approach, leveraging both high-throughput workflows and machine learning models of reactivity, to construct and analyze massive chemical reaction networks. The reaction networks include all the thousands of species and millions of reactions that may participate in the SEI formation cascade, and we aim to identify the reaction paths most likely to form key SEI

species with minimal imposed bias. The thermodynamics and kinetics of the identified pathways are provided to the ORNL and NREL teams.

The ORNL team seeks to simulate atomistically the SEI growth on a Si anode. By supplementing classical molecular dynamics (MD) simulations with the most important reactions identified by the LBNL team or via experimental feedback, ORNL aims to capture approximate ab initio reactivity on much longer timescales that are intractable for fully ab initio MD while accounting for atomistic interphase growth, SEI spatial composition and molecular diffusion to obtain novel atomistic insight.

The NREL team is actively developing and refining continuum-level models to (1) upscale atomistically informed electrolyte decomposition and SEI formation mechanisms, (2) predict Si particle-level chemo-mechanically induced active surface area dynamics, and (3) predict electrode-level stress, strains, pore closures, and electrode thickness dynamics from Si-particle expansion/contraction on cycling. The continuum-level models developed for this project seek to explain experimentally observed non-passivating SEI formation and chemo-mechanically induced failure of Si anodes. The continuum-level models are well suited to address Si-anode design criteria on electrode-level length scales and order hours/days timescales.

Approach

LBNL

To construct massive chemical reaction networks that include all possible species and reactions that may participate in the SEI formation cascade, we have developed two foundational tools: (1) a reaction network-based Monte Carlo (RNMC) model to handle massive number of reactions, and (2) a graph neural network machine learning model to leverage unlabeled chemical reaction data for the prediction of reaction kinetics.

Combining the reaction network we developed in the previous year and a shortest-path algorithm, we have identified optimal pathways to two key SEI products, lithium ethylene dicarbonate (LEDC) [1] and lithium ethylene monocarbonate (LEMC) [2]. However, network construction is still significantly limited by the poor scaling of shortest-path algorithms, which severely constrains the number of species as well as the number and type of reactions can be included. To address this limitation, we have developed a new RNMC approach. By using extensible filters, rather than prescriptive templates, we eliminate reactions based on physical or practical criteria without relying heavily on human chemical intuition. By filtering, the massive set of all stoichiometrically valid reactions in a chemical space is reduced to a still massive but computationally tractable set of chemically reasonable - though potentially unintuitive - reactions. To overcome the scaling limitations of graph-based pathfinding, we use a Monte Carlo-based approach, where the reactive space is sampled using reaction thermodynamics.

The RNMC approach is based solely on thermodynamics. To get a full picture, we need to incorporate kinetics (determined by the reaction activation barrier) into it. Due to the size of the reaction space, we cannot afford to compute them all via density function theory, and thus we aim to build a machine learning model for fast estimation of activation barriers and remove pathways that robustly exhibits large activation barriers. Recently, we developed the BonDNet graph neural network model [3] for the prediction of bond dissociation energy which we will adapt to allow changing the training target from bond dissociation energies to activation barriers. We note the challenge in generating a large enough training set of activation barriers. To address this, we have developed a transfer learning approach for graph neural networks, where we first pretrain the model on a large number of unlabeled reactions without activation barriers using self-supervised contrastive learning, and then fine-tune the model with a limited supply of labels. This pretraining will distill general knowledge of chemical reactions into the model to help it improve on the target task, i.e., activation energy prediction.

ORNL

To model the SEI formation at the atomistic level and properly bridge the timescale from femtoseconds (to model atom vibrations in MD simulations) to nano/microseconds (for the SEI growth), we simulate chemical reactions in classical molecular dynamics. While classical MD simulations do not account for reactive events

such as bond breaking or bond formation, it is possible to modify the atomic potential of each atom in a reactant molecule with the atomic potential of the product by identifying if two molecules are in a likely configuration for a pre-defined chemical reaction to occur. To do that, each reaction requires the specification of a reactant and product template describing the geometry, atomic charges and atomical potential parameters. This capability exists as *bond/react* [4] in the open-source molecular dynamics code LAMMPS (<https://lammps.sandia.gov>) used for our simulations. Other parameters to control the reaction such as the probability can be tuned in our simulations to favor one reaction over another. In our simulations, we choose these reactions rates close to 1, thus much higher than the actual rates, which leads to an accelerate simulation of the chemistry happening in the system.

The SEI formation was studied using the above framework in an EC/LiPF₆ electrolyte in an all-atom simulation. We included a set of reactions and first-principles data for the EC decomposition provided by the LBNL team, combined with a PF₆⁻ decomposition reaction found in the literature. All the atomic potential parameters (bonded and nonbonded) were obtained from the commonly used optimized potentials for liquid simulations (OPLS) force field. In Figure VIII.6.1 we highlight one reaction to form LEDC (the reactants geometry, product geometry, and atoms involved in bond breaking/formation) and the time evolution. Our simulations can model the formation of SEI components by specifying the reaction topologies for all the reactions happening near the Si anode. As the rate at which reactions occur is accelerated, the Li⁺ diffusion is also accelerated by an external force in the direction perpendicular to the anode to ensure enough Li⁺ ions are present to feed those reactions.

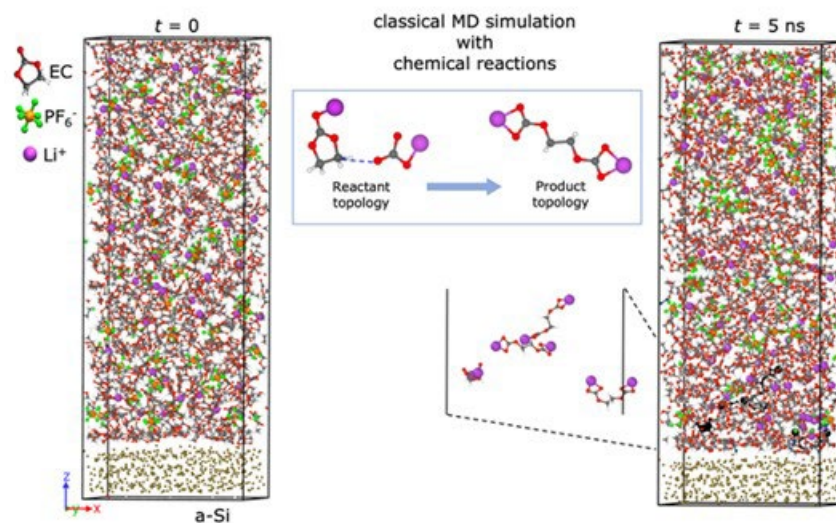


Figure VIII.6.1 Visual representation of a molecular dynamics simulation to predict SEI growth. Reactions are added using a template-matching scheme i.e., description of reactants and its proper configuration to react, and products as shown for LEDC formation.

Current simulations allow hundreds of reactions in a 100 ns period for a small system, enough to observe with atomistic detail the first stages of the SEI, however, film growth and microstructure formation is still far. To achieve even longer timescales within the same total computing time, this framework is being extended by combining coarse grain simulations with all-atom reactive MD.

NREL

NREL is developing several continuum-level models to explain experimentally observed failure mechanisms in Si anodes. These models can be separated into two categories: chemically complex particle-level models, and chemo-mechanics models. The chemically complex models capture SEI formation dynamics at different

voltage-holds and during cycling. The chemo-mechanics models capture stress/strain dynamics induced by the large Si expansion/contraction on cycling.

SEI modeling

We develop two models to explain Si SEI formation. The “intermediate” mechanism model implements $\cong 10$ electrolyte decomposition/SEI deposition irreversible global reactions informed by the literature [5],[6]. The intermediate-mechanism model is calibrated to the current responses from voltage-hold experiments and has been shown to predict voltage-dependent SEI electrical conductivity, and the expected dual-layer structure. The dual-layer consists of an inorganic rich inner-layer and an organic-rich outer layer. The intermediate mechanism proposes reaction pathways to form common SEI species such as Li_2EDC , Li_2CO_3 , LiMC , Li_2O , and LiF . The “atomistically informed” mechanism model implements the EC ring-opening, decomposition pathways developed by the LBNL team to form Li_2CO_3 and Li_2EDC . It implements $\cong 25$ reversible electrolyte decomposition reactions and is currently being enhanced to include SEI solid-phase deposition/dissolution reactions. The SEI models solve conservation equations that resolve:

- Heterogeneous electrochemical reactions and homogeneous chemical reactions throughout SEI volume
- Electrolyte (ions and solvent) transport through the SEI pore-phase
- Ionic transport through the SEI solid phase
- Charge transport through the SEI and electrolyte

The governing conservation equations are discretized using the finite volume method. The open-source software CANTERA is used to handle species thermodynamics and kinetics [7]. The flexibility of CANTERA allows for incorporation of additional species and reactions without modifying the underlying code. The purpose of the SEI modeling is to develop fundamental insights into SEI formation and ideally passivation of the electrochemically unstable Si-electrolyte interface. The insights developed on SEI formation will help inform the Si consortium on deleterious electrolyte reduction reactions and provide possible mitigation strategies to reduce continual SEI formation during calendar aging.

Chemo-mechanics modeling

Furthermore, we also develop models to explain the stress/strain Si dynamics and the resulting electrochemical consequences. The particle-level chemo-mechanics model predicts the dynamic solid-electrolyte surface area increase/decrease when Si is lithated/delithiated, respectively. For example, a stress-free 300% volume expansion of a Si spherical particle during lithiation results in an increased surface area of $32/3 \cong 200\%$ for intercalation reactions (good) and electrolyte decomposition reactions (bad). The particle-level model is well-suited to couple particle-level chemo-mechanics with the complex SEI reaction mechanism models. The finite-strain electrode-level chemo-mechanics model predicts full-cell electrochemical and stress/strain consequences to large Si volume expansion. The electrode-level model is a reformulation of the standard pseudo-2D model [8], that can predict electrode thickness changes, dynamic pore closure (and induced overpotential increases due to increased Li^+ transport resistances), and stresses that can lead to electrode delamination or “shredding” of the anode current collector.

The chemo-mechanics models will inform the consortium on electrode design requirements to achieve a high-loading NMC/Si-graphite cell. These design requirements include (1) optimal initial electrode porosities, (2) maximum particle diameters, (3) external pressure constraints, (4) carbon-binder loading requirements, (5) charge protocol requirements/limits, and (6) suggested composite material properties (e.g., Young’s modulus). The electrode-level chemo-mechanics model is expected to accelerate high-loading electrode development by considering not only electrochemical and transport overpotentials, but also the strongly coupled influences of chemo-mechanics.

Validation

There are several sources of model validation available within the consortium. For the SEI models, the leakage current measured in the calendar-life capacity-fade measurements are used to evaluate reasonable reduction reaction kinetic rates. Additionally, the voltage-dependent SEI electrical conductivity needed in the intermediate mechanism to describe the leakage current dynamics is also seen in experimental Si-consortium data. In the next fiscal year, additional species/atom sensitive techniques, such as X-ray Photoelectron Spectroscopy (XPS) and Neutron Reflectometry (NR), can be used to validate the model-predict species concentrations, SEI thickness, and potentially the species distributions (i.e., inorganic inner layer/organic outer layer).

In summary, for FY21, NREL implemented a multi-species SEI model onto planar/stationary surface to predict film composition and thickness during cycling at different current rates and open circuit conditions at different states of charge (SOC). Intermediate ($\cong 10$ global reactions) mechanism is utilized to generate well-known solid-phase SEI reaction products including Li_2EDC , Li_2CO_3 , Li_2O , LiF , LiMC . Furthermore, atomistic ($\cong 25$ elementary reactions) mechanism forming Li_2EDC and Li_2CO_3 are upscaled to the continuum-level utilizing species thermodynamic and kinetic data provided by LBNL. The SEI model is validated against current-decay data from voltage hold experiments at multiple SOC from the Calendar Life subgroup of the Silicon Consortium which measures the total current contributing to silicon lithiation and irreversible SEI growth. Finally, the SEI model is implemented into an electrode-scale macro-model with large deformation mechanics capable of handling pore-closure and Si electrode expansion to delineate the impact of SEI growth and Si swelling on performance.

Results

LBNL

Using the RNMC approach, over 300 million reactions were generated to search for thermodynamically favorable formation pathways to LiF from FEC and LiPF_6 . We have identified unexpected pathways for FEC decomposition without the presence of H_2O , leading to LiF , lithium ethyl carbonate (LEC), vinylene carbonate (VC), hydrogen fluoride (HF), and vinoxy radical, among others. These species are important because they may strongly promote further reactivity. HF is generally reactive, and both vinoxy radical and VC can participate in polymerization [9]. These pathways, as shown in Figure VIII.6.2, are all thermodynamically favorable, indicating their plausibility. Notably, fluorine from FEC can be abstracted to form PF_6^- from PF_5^- . In addition, both vinylene carbonate (VC) and vinoxy radical—both known to be involved in polymerization—can be formed from thermodynamically favorable mechanisms.

We have also interrogated the decomposition pathways of LiPF_6 with and without the presence of H_2O . Thus far, our analysis of LiPF_6 has indicated no thermodynamically viable decomposition pathways in the absence of H_2O (or possibly an explicit surface), suggesting that H_2O plays a necessary role in PF_6^- reactivity. However, we note that further work is needed to rule out the possibility of non-water-assisted or surface-dependent decomposition. To investigate the pathways with the presence of H_2O , we have generated a large set of more than 6500 recombinant molecules relevant to $\text{LiPF}_6/\text{H}_2\text{O}$ reactivity and allow them to form new reactions in addition to the 300 million existing ones. We are still in the process of analyzing whether thermodynamically favorable decomposition pathways of LiPF_6 exist when H_2O is present.

As to the transfer learning approach to pretrain the graph neural network model for activation energy prediction, we are still in the process of computing a set of reference activation barriers. Nevertheless, as a proof of concept, we have applied this approach to a reaction type classification problem. The results show that the number of labelled data to train the model can be significantly reduced: with only 16 labeled reactions per type, the reactions can be well separated, achieving a classification F1 score higher than 0.9. This gives strong evidence that the approach could work for the activation energy prediction task.

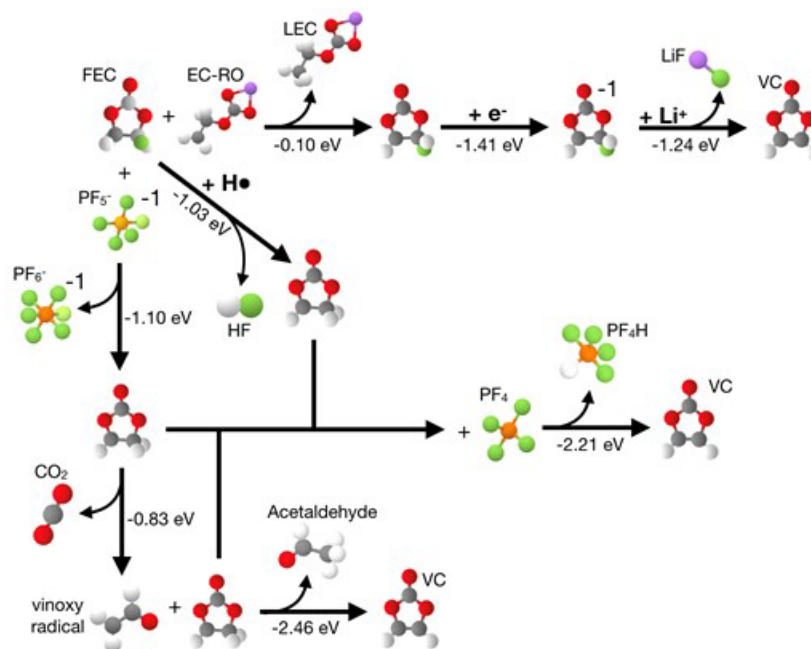


Figure VIII.6.2 Thermodynamic pathways of FEC decomposition.

ORNL

Simulations to predict SEI on a 1M LiPF₆ EC electrolyte have been carried out with a total of 12 key reactions. During the 100 ns, constant production of open-ring LiEC complexes, by reduction of EC-Li⁺, allow the formation of LEDC, LBDC and Li₂CO₃ molecules. PF₆⁻ decomposes following a three-step reaction mechanism that leads to the formation of 3LiF and a PF₃ molecule.

Our simulations reveal that the majority of LiEC complexes undergo to a second reduction forming LiCO₃⁻ molecules that can either react to produce Li₂CO₃ or LEDC, accompanied by the production of ethylene gases, which dissolve into the electrolyte as simulation evolves, but deposit as well in the SEI/anode interface. The formation of LEDC and LBDC via polymerization of two open-ring LiEC molecules is rarely seen. We found that more than 80% of LEDC molecules are produced by the two-electron reduction mechanism, in agreement with previous theoretical studies. During the first 10 to 25 nanoseconds most of the EC-derived product LiCO₃⁻ reacts to form LEDC, whereas between 25 and 50 ns it reacts to form the inorganic compound Li₂CO₃. LiF formation from the decomposition of PF₆⁻ is steady during the first 50 ns but increases rapidly after 80 ns due to the reaction of PF₅⁻ and PF₄⁻ molecules left unreacted near the anode, the PF₃ molecules diffuse in the electrolyte.

In Figure VIII.6.3 we show the SEI formation process as it evolves every 25 ns of MD simulation. At 100 ns, it can be observed that the SEI film is mostly homogeneous in composition with an approximated thickness of 3 nm. Structural trends such as the deposition of few LBDC molecules and some LEDC in the outer region of the SEI, are consistent with the proposed double-layer model. Initial products formed on the SEI are LiF and LEDC in agreement with experimental results.

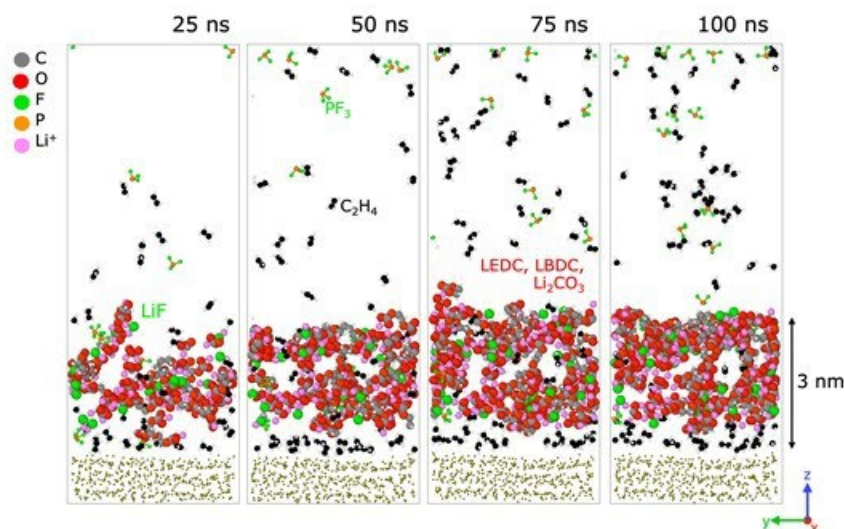


Figure VIII.6.3 Time evolution of SEI film in the EC-based electrolyte during 100 ns. Snapshots of the reaction products every 25 ns. For visualization purposes, bulk EC and LiPF_6 molecules are not shown.

NREL

Figure VIII.6.4 reports results from our planar, multi-species silicon-SEI model to predict film composition at open circuit at different states of charge (SOC) of the silicon with a five-reaction intermediate reaction mechanism. Experimental voltage hold data from 100 mV to 250 mV for $\text{Li}|\text{Si}$ half-cell with silicon composite electrodes is collected. A nonlinear function fit model is developed to split the capacity data into reversible lithiation and irreversible SEI components. Subsequently, the detailed multiphase-multispecies SEI model is used to validate with capacity data, and it showcased varying conductivities of the SEI at different voltages ranging from 8 pS/m to 0.07 pS/m from 100 mV to 250 mV respectively (Figure VIII.6.4 (b)). The SEI composition map without FEC (in electrolyte) in Figure VIII.6.4 (c) shows the formation of a bi-layer SEI with an inorganic rich inner layer consisting of Li_2O and Li_2CO_3 and an organic rich outer layer consisting of Li_2EDC . With the incorporation of the FEC decomposition reaction, LiF is observed to form throughout the inner and outer layer of the SEI (Figure VIII.6.4 (d)). This illustrates that the chemical composition of the SEI is highly sensitive to the electrolyte constituents and modeling can provide pathways towards electrolyte additive screening that can form favored SEI products.

Figure VIII.6.5 illustrates the leakage current predicted by the atomistically informed SEI model (a) and the experimentally measured total current consisting of silicon lithiation and irreversible Li consumption (b) at several voltage holds. As illustrated, the model predicts similar current decay trajectories as measured experimentally. Additionally, the model predicts lower leakage currents at higher voltage holds, which is consistent with the leakage current measured at 250 mV (Figure VIII.6.5 (b)). However, currently the model predicts higher currents than the measurements. Additionally, the model over-predicts the current sensitivity to the voltage at low (100–175 mV) voltage holds and under-predicts the current sensitivity at high voltages (i.e., 250 mV). These dynamics indicate that the current model requires an extra passivation mechanism. These passivation mechanisms may include (1) implementing electron thermodynamics in the SEI phase, (2) SEI deposition/dissolution reactions, or (3) transport limitations. In the next fiscal year, these additional physics will be explored/adopted in the model to improve the model predictions. The intent of developing this physically complex, atomistically informed, SEI growth model is to provide a bridge between fundamental modeling at LBNL and experimentally observed phenomena.

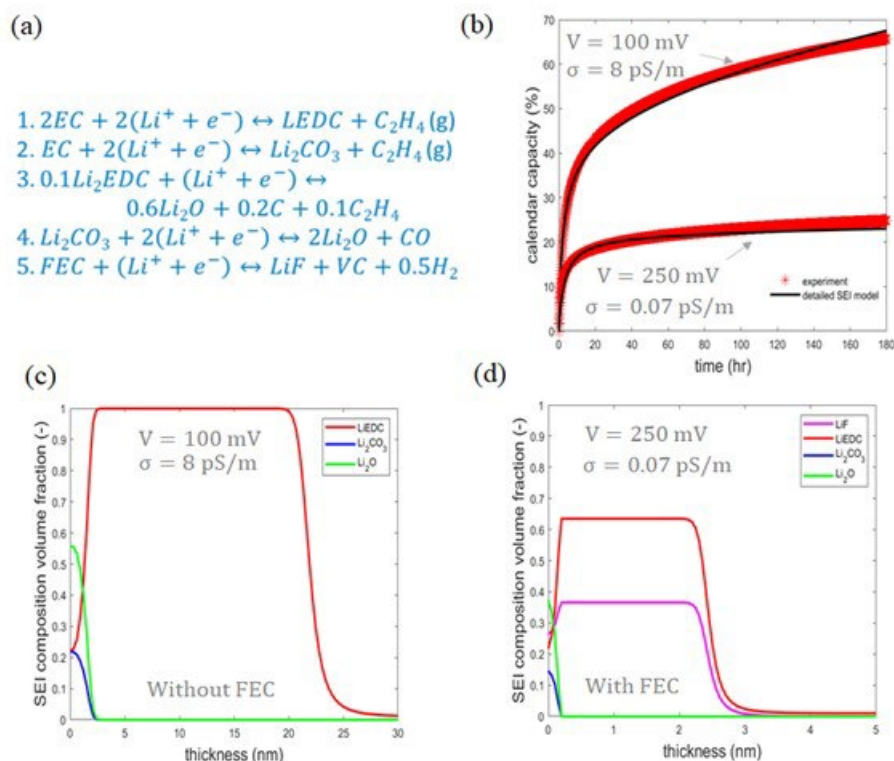


Figure VIII.6.4 (a) Intermediate reaction mechanism, (b) experiment and model fit for total capacity gain consisting of silicon lithiation and irreversible Li consumption during 180-hour voltage-hold of Si half cells at 100 mV and 250 mV, (c) SEI composition evolution at 100 mV Si potential without FEC decomposition reaction, and (d) SEI composition evolution at 250 mV Si potential with FEC decomposition reaction.

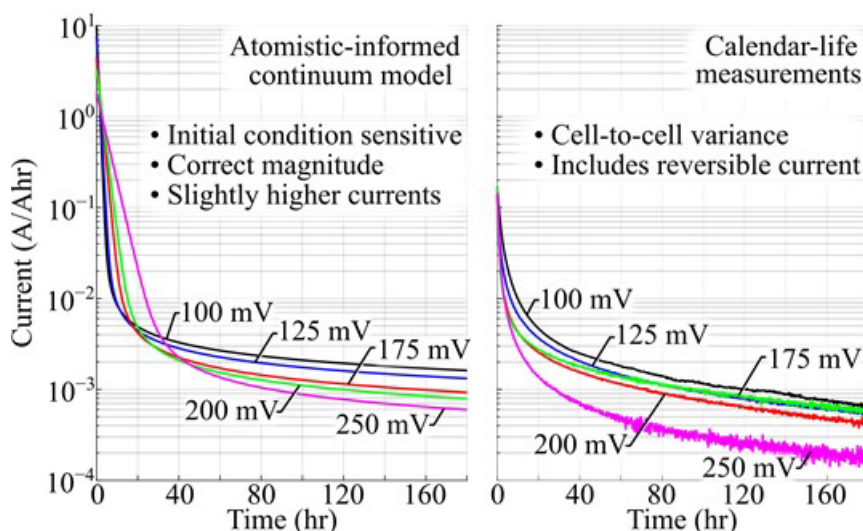


Figure VIII.6.5 (a) Current response of Si half-cell predicted by the atomistically informed model, and (b) experimentally measured by the calendar-life team at 100, 125, 175, 200, and 250 mV voltage holds.

Furthermore, the detailed multiphase-multispecies SEI model is incorporated in an electrode scale model with large deformation mechanics. An empirical expression for SEI film growth as a function of the SEI thickness and anode potential (Figure VIII.6.6 (a)) is provided to the finite-strain electrode scale model that can predict electrode level stresses, simulate SEI growth, capture SEI stretching on particle surfaces and predict electrolyte pore closure from Si expansion and SEI growth. Figure VIII.6.6 (b) shows 1C charge performance of a

NMC532/Si full cell from 3.0 to 4.1V with an initial particle radius of 100 nm in a rigid cell setup. The charge performance of Si|NMC full cells is adversely impacted from SEI growth; SEI thickness increase from 1 nm to 10 nm increases electrolyte transport limitations through pore closure. Figure VIII.6.6 (c) shows the anode porosity variation. Si is preferentially lithiated near the separator resulting in significant porosity decrease near the separator with increasing SEI thickness. Large normal and hydrostatic stresses develop inside the Si anode (see Figure VIII.6.6 (c) and (d)). Internal stresses are predicted to be near copper fracture strength; hence the model could be used to develop strategies to prevent copper tearing and improve poor rate capability, which has been observed for Si manufacturing team especially at higher loadings. Further, the model will be used to optimize initial porosity to maximize rate capability and energy density.

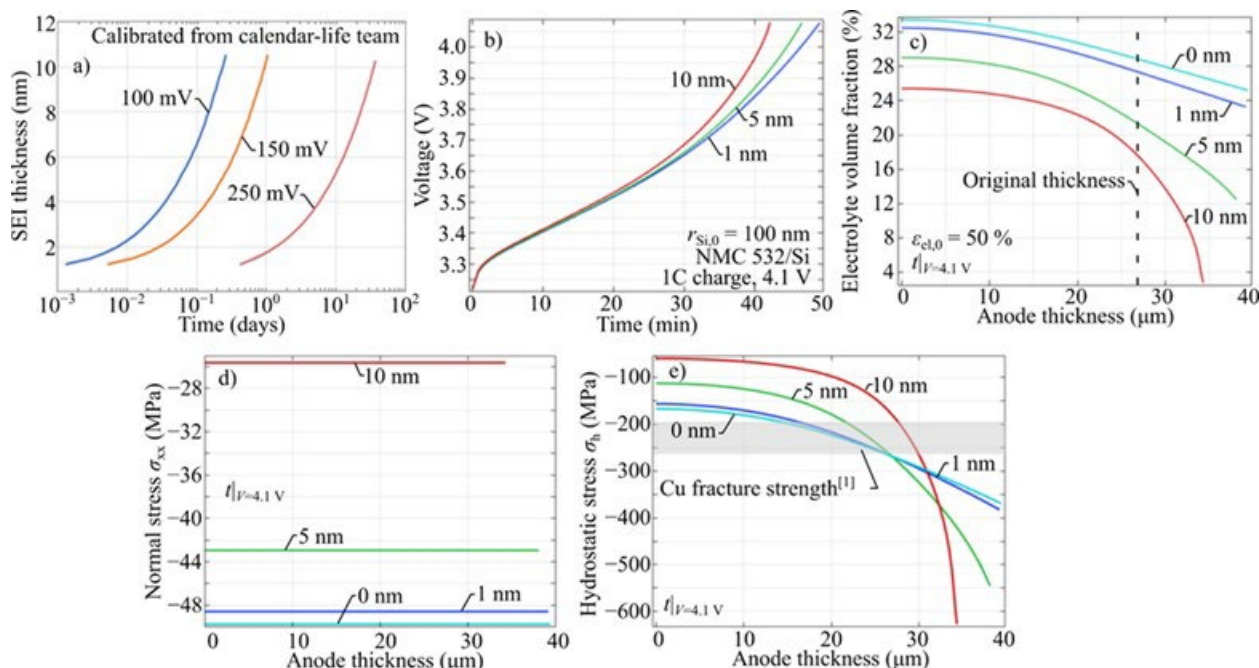


Figure VIII.6.6 (a) SEI thickness evolution calibrated from voltage hold experiments, (b) 1C charge performance of NMC532/Si cells with SEI thickness variation. (c) Electrolyte porosity, (d) normal stress, and (e) hydrostatic stress variation with Si anode and SEI thickness.

Conclusions

LBNL

- Developed a RNMC model to handle even larger reaction networks without the need of shortest-path algorithms and a transfer learning strategy to pretrain chemical reactions for the estimation of activation barriers.
- Applied the RNMC model to study the decomposition pathways of LiPF₆ and FEC to form LiF and other products. Thermodynamically favorable pathways from FEC to LiF are identified, and thermodynamically favorable pathways without the presence of H₂O are – so far - not discovered.

ORNL

- Assembled reactive molecular dynamics simulations of the Si anode and electrolyte, including reactions that describe EC and PF₆- decomposition. We continue working with LBNL to add more reactive complexity and make our simulations more quantitative kinetics using reaction energy barriers.
- Current simulations up to 100 ns predict the SEI formation at an early stage, where LiF and LEDC products are initially formed near the anode. LEDC products form by a two-electron reduction

mechanism. The SEI microstructure remains unclear and longer timescales are required. Efforts are underway to further extend timescale of MD simulations.

NREL

- Developed continuum scale electrochemical SEI model framework incorporating intermediate and atomistic reaction mechanisms, and particle/electrode level finite deformation model framework for silicon anode systems.
- Validated SEI model with calendar life voltage hold experiments, and bridged SEI model with electrode model to delineate the impact of SEI growth on Si anode performance.
- In the coming year, the continuum SEI model will be validated with elemental composition profiles from electron energy loss spectroscopy (EELS) and XPS. The coupling between SEI and electrode model will help provide suggestions for improving SEI stability during calendar and cycling aging.

Key Publications

LBNL

1. Xie, Xiaowei, Evan Walter Clark Spotte-Smith, Mingjian Wen, Hetal D. Patel, Samuel M. Blau and Kristin A. Persson. "Data-driven prediction of formation mechanisms of lithium ethylene monocarbonate with an automated reaction network." *J. Am. Chem. Soc.* 143 (2021), 13245–13258.
2. Barter, Daniel, Evan Walter Clark Spotte-Smith, Nikita S. Redkar, Shyam Dwaraknath, Kristin A. Persson, and Samuel M. Blau "Template-free reaction networks enable predictive and automated analysis of complex electrochemical reaction cascades." *Under review*.
3. Wen, Mingjian, Samuel M. Blau, Xiaowei Xie, Shyam Dwaraknath, and Kristin A. Persson. "Improving machine learning performance on small chemical reaction data with unsupervised contrastive pretraining." *Under review*.

ORNL

1. Alzate-Vargas, Lorena, Samuel M. Blau, Evan Walter Clark Spotte-Smith, Srikanth Allu, Kristin A. Persson, and Jean-Luc Fattebert. "Insight into SEI growth in Li-ion batteries using molecular dynamics and accelerated chemical reactions." *J. Phys. Chem. C* 125 (2021): 18588–18596.

NREL

1. Ha, Yeyoung, Donal P. Finegan, Andrew M. Colclasure, Stephen E. Trask, and Matthew Keyser. "Evaluating temperature dependent degradation mechanisms of silicon-graphite electrodes and the effect of fluoroethylene carbonate electrolyte additive." *Electrochim. Acta* 394 (2021): 139097.
2. McBrayer, Josefine D., Marco-Tulio F. Rodrigues, Maxwell C. Schulze, Daniel P. Abraham, Christopher A. Apblett, Ira Bloom, Gerard Michael Carroll, Andrew M. Colclasure, Chen Fang, Katharine L. Harrison, Gao Liu, Shelley D. Minter, Nathan R. Neale, Gabriel M. Veith, Christopher S. Johnson, John T. Vaughey,
3. Anthony K. Burrell & Brian Cunningham. "Calendar aging of silicon-containing batteries." *Nat. Energy* 6 (2021): 866–872.

References

1. Blau, Samuel M., Hetal D. Patel, Evan Walter Clark Spotte-Smith, Xiaowei Xie, Shyam Dwaraknath, and Kristin A. Persson. "A chemically consistent graph architecture for massive reaction networks applied to solid-electrolyte interphase formation." *Chem. Sci.* 12 (2021): 4931–4939.

2. Xie, Xiaowei, Evan Walter Clark Spotte-Smith, Mingjian Wen, Hetal D. Patel, Samuel M. Blau and Kristin A. Persson. "Data-driven prediction of formation mechanisms of lithium ethylene monocarbonate with an automated reaction network." *J. Am. Chem. Soc.* 143 (2021), 13245–13258.
3. Wen, Mingjian, Samuel M. Blau, Evan Walter Clark Spotte-Smith, Shyam Dwaraknath, and Kristin A. Persson. "BonDNet: a graph neural network for the prediction of bond dissociation energies for charged molecules." *Chem. Sci.* 12 (2021): 1858–1868.
4. Gissinger, Jacob R., Benjamin D. Jensen, and Kristopher E. Wise. "Modeling chemical reactions in classical molecular dynamics simulations." *Polymer* 128 (2017): 211–217.
5. Single, Fabian, Birger Horstmann, and Arnulf Latz. "Revealing SEI Morphology: In-Depth Analysis of a Modeling Approach." *J. Electrochem. Soc.* 164 (2017): E3132.
6. Single, Fabian, Birger Horstmann, and Arnulf Latz. "Dynamics and morphology of solid electrolyte interphase (SEI)." *Phys. Chem. Chem. Phys.* 18 (2016): 17810–17814.
7. Goodwin, David G., Raymond L. Speth, Harry K. Moffat, and Bryan W. Weber. "Cantera: An object-oriented software toolkit for chemical kinetics, thermodynamics, and transport processes." www.cantera.org. Caltech, Pasadena, CA (2009).
8. Mai, Weijie, Andrew Colclasure, and Kandler Smith. "A Reformulation of the Pseudo2D Battery Model Coupling Large Electrochemical-Mechanical Deformations at Particle and Electrode Levels" *J. Electrochem. Soc.* 166 (2019): A1330.
9. Jin, Yanting, Nis-Julian H. Kneusels, Pieter CMM Magusin, Gunwoo Kim, Elizabeth Castillo-Martínez, Lauren E. Marbella, Rachel N. Kerber et al. "Identifying the structural basis for the increased stability of the solid electrolyte interphase formed on silicon with the additive fluoroethylene carbonate." *J. Am. Chem. Soc.* 139 (2017): 14992–15004.

Acknowledgements

LBNL: Samuel M. Blau, Mingjian Wen, Hetal D. Patel, Evan Walter Clark Spotte Smith, Xiaowei Xie

ORNL: Lorena Alzate Vargas

NREL: Ankit Verma, Peter Weddle, Kandler Smith, Steven DeCaluwe, Jake Atkins

VIII.7 Advanced Anode Manufacturing through Ultra-Thin Li Deposition (Applied Materials, Inc.)

Subra Herle, Ph.D., Principal Investigator

Applied Materials, Inc.
3225 Oakmead Village Drive
Santa Clara, CA 95054
E-mail: Subra_Herle@amat.com

Brian Cunningham, DOE Technology Development Manager

U.S. Department of Energy
E-mail: Brian.Cunningham@ee.doe.gov

Start Date: May 25, 2020
Project Funding: \$7,277,087

End Date: September 30, 2021
DOE share: \$3,143,848

Non-DOE share: \$4,133,239

Project Introduction

Much of the doubling in Li-ion battery energy density over the past 30 years has been achieved through cathode material improvement. To increase anode capacity cell manufacturers are investigating silicon-blended graphite anodes. Improvements in anode energy density have languished, partly due to integration and manufacturing challenges with new anode materials. Si/SiO_x blended with graphite has shown significant improvements in the anode capacity as well as enabling fast charge EV cells. These gains, however, are offset by a first-cycle irreversible loss of lithium which can degrade performance up to 30% or more and Li inventory loss per cycle over long cycle life. Additionally, not all the lithium that enters the Si/SiO_x-Gr anode is active as some of the lithium is consumed during the solid electrolyte interface (SEI) cell formation cycle. Continual buildup of SEI layers upon subsequent cell cycling further decreases energy density causing gradual cell degradation.

Pre-lithiation, the practice of providing additional lithium to the anode offers a path to compensate for the Li losses during the first cycle and SEI formation. Apart from SEI losses, volume change associated with Si anode particle could be minimized with additional buffer of Li, providing long cycle performance. With pre-lithiation, the energy density increases of >10-30% over equivalent graphite-based cells can be realized by recovering the various Li losses [1], [2]. *However, none of the many different approaches tried to date meet high volume manufacturing (HVM) requirements for lithiation*, including ease of integration with existing Li-ion battery process flows, defect-free lithium films, scalable in thickness and to industry-standard widths, at low cost, in a safe environment (low TRL level).

In this project, Applied Materials proposes to leverage its extensive knowledge base and expertise in Materials Engineering, Vacuum Deposition and Roll-to-Roll (R2R) processing to develop and validate an HVM-capable Li deposition tool for prelithiation and Li metal anode applications. In collaboration with the industry and National Laboratory partners, the objective of the program is to fully optimize the vacuum based prelithiation process on Applied's Roll-to-Roll (R2R) platform to meet DOE goals for high volume production of cost-effective, high-energy density Si/SiO_x based Li-ion batteries.

Objectives

The objective of the project is to develop and validate a cost effective ultra-thin Li deposition system for advanced anode high volume manufacturing (HVM) and demonstrate the following:

Objective 1: Advance batteries with pre-lithiated SiO_x-C anodes with energy density >337Wh/kg from TRL 5 to TRL 7

Objective 2: Advance batteries with Li-metal anode with energy density >375Wh/kg from TRL 4 to TRL 6

Objective 3: Develop a Li deposition system to meet high volume mfg. (HVM) requirements from TRL 4 to TRL 8.

Table VIII.7.1 Li Deposition System Manufacturing Target Performance (Measured with respect to established Baseline)

Parameter	Measure (Minimum Manufacturing Goals)	End of Program Performance Goals (10 μ m Li deposition)
Mechanical System Throughput, Web Speed Increase	$\geq 100\%$	>20m/min
Substrate Width Increase	$\geq 100\%$	800 mm
Uniformity Increase	$\geq 50\%$	+/- 7.5%
Uptime Increase	$\geq 50\%$	Roll-to-Roll Baseline TBD

The ultra-thin Li deposition system will be validated with the following cell performance:

Table VIII.7.2 Cell Performance (Minimum Manufacturing Goals)

Parameter	Pouch Cells (Pre-lithiated Silicon Anodes)	Pouch Cells (Lithium Metal Anodes)
Energy Density	≥ 337 Wh/kg	≥ 375 Wh/kg
Cycle Life	1100 Cycles	300 Cycles
Fast Charge	80% in ≤ 15 minutes	N/A

Approach

With funding support from DoE and working closely with leading U.S. battery makers Zenlabs Energy, Inc. (pre-lithiated SiOx-C anode) and Saft America, Inc. (Li metal anode), and leveraging advanced battery research capabilities of key National Laboratories (PNNL, LBNL, ANL), Applied Materials proposes accelerating the time to market of a high productivity, Roll-to-Roll (R2R) lithiation solution for both SiOx-C anodes and Li-metal anodes. In this three-year project, Applied Materials will accelerate the development of its current R&D R2R Lithium deposition system based on Applied's production proven SmartWeb™ platform. Li-coated anodes will be fabricated and shared with project partners: Zenlabs (SiOx-C prelithiation), Saft America, PNNL and LBNL for characterization and for integration into cells. The deposition equipment and processes will be optimized to achieve volume manufacturing performance targets while meeting the battery performance and cost targets, as validated by the project collaborators. Zenlabs will focus on high silicon content SiOx-C based batteries and Saft & Pacific Northwest National Laboratory (PNNL) on high energy density Li-metal batteries. Lawrence Berkeley National Laboratory (LBNL) will be responsible for investigation polymers for prelithiated SiOx-C binder and lithium metal surface protection and interface properties, stabilization, and provide metrology services for the program. The partners will work with Argonne National Laboratory (ANL) to update the techno-economic BatPac models to incorporate battery architectures that use prelithiated Si/SiOx-C and Li metal anode based batteries.

Budget Period 1 (BP-1): Hardware and Process Baseline and Pathfinding

In Budget Period 1 of the project, the team will design, procure and operationalize hardware for Li deposition and Surface protection. Hardware and Process baseline will be established and deposited samples generated for pathfinding and initial cell testing.

Budget Period 2 (BP-2): Roll-to-Roll (R2R) HVM Test Preparations

In Budget Period 2, the team will complete scale up design for the Li deposition and protection equipment, procure and operationalize scaled up components and continue to further optimize hardware and process. Cell testing will move to large format cells to meet or exceed interim performance goals towards high volume manufacturing (HVM).

Budget Period 3 (BP-3): R2R HVM Validation

In Budget Period 3, the team will focus on validating the Li deposition and protection hardware and process to meet the equipment and cell performance goals for high volume manufacturing (HVM). The team will also establish a cell and pack level technoeconomic model incorporating these advanced anodes.

Results

Year-1 activities focused on hardware design, procurement of the various deposition tools and test-stands. Equipment was installed, operationalized and initial Li deposition process baseline developed. Graphite and SiO_x-Graphite anodes provided by project partners were prelithiated, and samples without and with CO₂ passivation were provided for further characterization and initial cell-building. Sheets of Li metal deposited on Cu were generated for Li-metal anode evaluation. All Budget Period-1 Milestones were completed successfully, and Year-1 performance targets achieved. Preparations were started towards meeting Budget Period-2 objectives.

The Year-1 Milestones progress status is summarized in the Table VIII.7.3 below:

Table VIII.7.3 Project Year-1 Milestones Completion Status

Milestone	Type	Description	Status as of 09/30/2021
Gen2 Lithium Deposition Source Design Completed	Technical	Complete Design of Gen2 lithium deposition source	Design Completed. HW procured and installed, key features tested and validated on R2R tool (Figure VIII.7.1)
Test Stand for Lithium Deposition Source Design Completed	Technical	Complete Design Test Stand for lithium deposition source	Design Completed. Test-stand installed in dry-room, first samples generated and provided to project partners for evaluation.
Protective Layer Hardware Design Completed	Technical	Complete design of protection layer hardware for Sheet to Sheet (S2S) testing	Design Completed. HW procured and upgrade completed.
Polymer selected	Technical	Selection of a polymer for testing subsequent tasks.	Completed in PQ3. Leading high temperature binder candidates were evaluated and two candidates down-selected for evaluation in PQ4 and BP-2
Go/No Go Decision	Go/No Go	S2S tool fabricated planned samples for program	Completed in PQ3. S2S tool installed. HW & process validation in progress - Li/Cu and prelithiated anode samples generated for testing from the S2S tool provided to partners for building and testing cells (Figure VIII.7.2)
	Go/No Go	R2R signed off by AMAT safety	Safety Sign-off Completed. AMAT safety approved R2R operation. R2R operations continue

	Go/No Go	SiO _x -C anode: Meet R&D Demonstration cell performance (300Wh/kg and 700 Cycles @ 80%)	Met in PQ3. R&D Demonstration pouch cells, 4.6Ah, 305Wh/kg, reached >700 cycles (Figure VIII.7.3)
	Go/No Go	Li-metal anode: Meet R&D Demonstration cell performance. (300Wh/kg), (80% after 200 cycles)	Met in PQ4. Achieved >200 cycles for both coin and single layer R&D demonstration pouch cell. Achieved >200 cycles with capacity retention of 87.4%, exceeding the goal set for BP1 (Figure VIII.7.4)

Green box indicates successful completion



To illustrate the Milestones progress, some key results are shown in Figure VIII.7.1 – Figure VIII.7.4

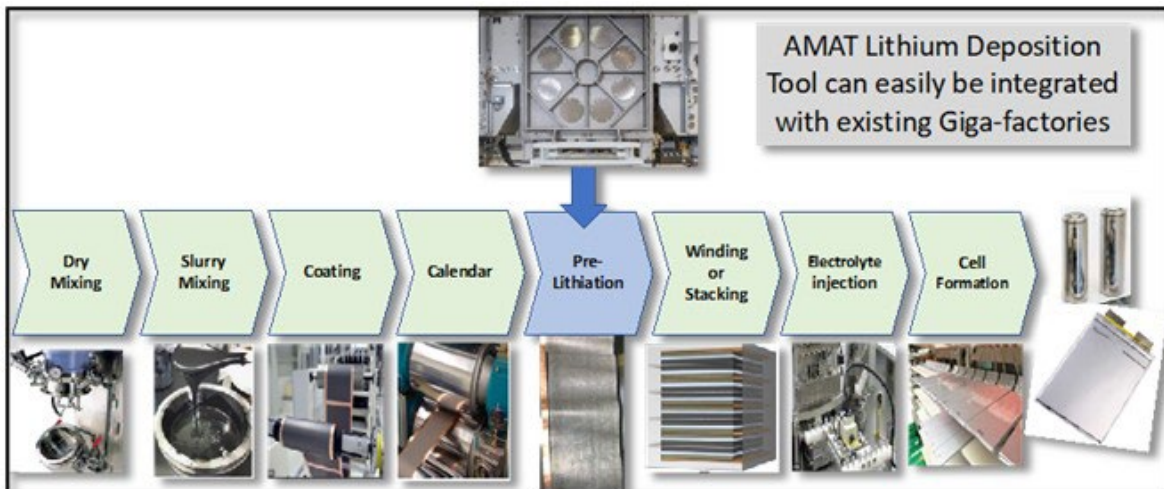


Figure VIII.7.1 Cell manufacturing steps including pre-lithiation for silicon anodes (source: Applied Materials). A Roll-to-Roll tool (see image above) along with several test-stands (not shown) were designed, installed and are operational at Applied Materials.

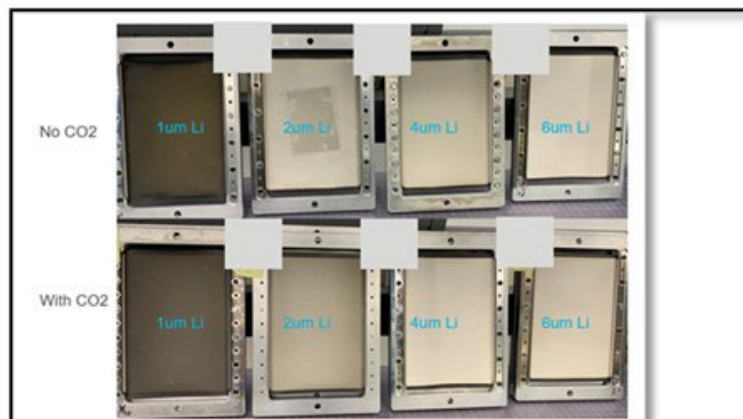


Figure VIII.7.2 Examples of controlled Li deposition on SiO_x-C anode on Applied Materials' Sheet-to-Sheet (S2S) R&D tool, without and with CO₂ passivation (source: Applied Materials). Prelithiated anode and Li on Cu sheets were supplied to project partners for characterization, cell builds and evaluation.

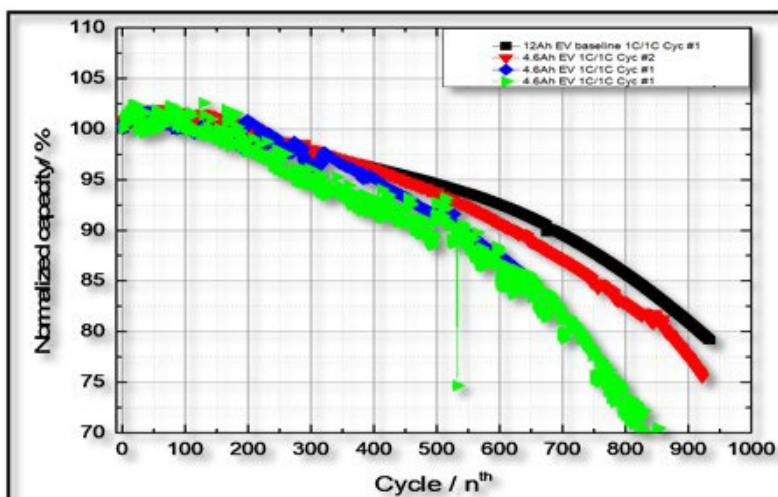


Figure VIII.7.3 Pouch cells (4.6Ah, 305Wh/kg) containing Applied Materials' prelithiated SiO_x-C anode and NMC622 cathode reached >700 cycles in 1C-1C cycling (source: Zenlabs).

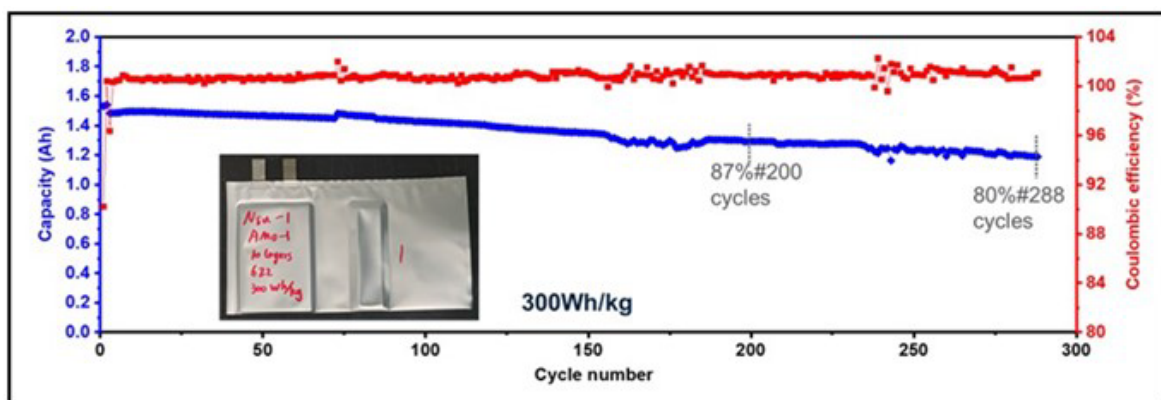


Figure VIII.7.4 Pouch cells (1.5Ah, 300Wh/kg) containing 10 μ m Li metal anode generated by Applied Materials, NMC622 cathode and PNNL developed M47 electrolyte reached 288 cycles in C/10-C/3 cycling (source: PNNL). SAFT America built 6.6 Ah multilayer pouch cells using Applied Materials deposited Li anode reached >94% retention after 250 cycles (not shown).

Conclusions

In 2021, the Applied Materials-led team consisting of Zenlabs, Saft America, LBNL, and PNNL successfully completed all Year-1 milestones and deliverables and made significant progress towards Year-2 objectives.

Key Publications

A poster summarizing Budget Period-1 results was presented virtually at the 2021 EERE VTO Annual Merit Review in June.

1. 2021 Vehicle Technologies Annual Merit Review (Project ID: Bat 495)

References

1. Zhao, *et al.* Nano Lett. 14 (2014) 6704–6710
2. K. H. Kim, *et al.* Journal of Power Sources 459 (2020) 228066

Acknowledgements

Ajey M. Joshi, Ph.D. (Applied Materials, Inc.) served as the Program Director for this project.

This material is based upon work supported by the U.S. Department of Energy's Office of Energy Efficiency and Renewable Energy (EERE) Award Number DE-EE0009093. Applied Materials team thanks Brian Cunningham—our EERE-Vehicle Technologies Office (VTO) Technology Manager for technical guidance, and Kimberly Nuhfer at NETL for helping navigate the contracting aspects. We greatly appreciate active participation of the broader VTO team, including Tien Duong, Haiyan Croft, Jack Deppe and others who regularly attend the Quarterly Review meetings and offer valuable insights. Finally, the progress reported here would not be possible without the diligent efforts, persistence and contributions of engineers and colleagues from Applied Materials and our project partners at Zenlabs Energy Inc., Saft America Inc., Lawrence Berkeley National Laboratory (LBNL), Pacific Northwest National Laboratory (PNNL) and Argonne National Laboratory (ANL).

VIII.8 Structurally and Electrochemically Stabilized Si-rich Anodes for EV Applications (Enovix Corporation, NREL)

Murali Ramasubramanian, Principal Investigator

Enovix Corporation
3501 West Warren Avenue
Fremont, CA 94538
E-mail: murali@enovix.com

Andrew Colclasure, Principal Investigator

National Renewable Energy Laboratory
Center for Integrated Mobility Sciences
Golden, CO 80401
E-mail: andrew.colclasure@nrel.gov

Brian Cunningham, DOE Technology Development Manager

U.S. Department of Energy
E-mail: Brian.Cunningham@ee.doe.gov

Start Date: October 1, 2020
Project Funding: \$3,156,600

End Date: December 31, 2023
DOE share: \$1,548,878

Non-DOE share: \$1,608,722

Project Introduction

Silicon has long been heralded as the next important anode material in lithium-ion batteries. Silicon anodes can theoretically store more than twice as much lithium than the graphite anode used in nearly all lithium-ion batteries today (1800mAh/cm³ vs. 800mAh/cm³). However, to successfully commercialize a practical high energy silicon anode lithium-ion battery, four significant technical problems need to be solved:

- **Formation expansion:** When fully charged, a silicon anode can more than double in thickness, resulting in significant swelling that can physically damage the battery, causing failure.
- **Formation efficiency:** When first charged, a silicon anode can absorb and permanently trap as much as 50%–60% of the original lithium in the battery, reducing the battery's capacity by 50%–60% unless a pre-lithiation solution is implemented.
- **Cycle swelling:** A silicon anode will swell and shrink when the battery is charged and discharged, respectively, causing damage to both the package and the silicon particles in the anode, which can crack, and further trap lithium on the fresh silicon surfaces exposed by the cracks.
- **Cycle and calendar life:** Silicon particles can become electrically disconnected from the electrode when the silicon anode is in its shrunken state and can crack when the silicon anode is swollen, both of which can lower cycle life. In addition, when silicon particles become disconnected from the electrode, they are no longer able to accept lithium and neighboring particles must absorb the excess, causing over charging and further opportunities for physical damage. Electrolyte continuously reacts with Si surface and unlike graphite does not form a well passivating surface.

These four problems have limited the practical application of silicon anodes in conventional lithium-ion battery cells. Enovix has developed a 3D cell architecture and manufacturing process that uniquely solves these four technical problems to enable 100% active silicon anodes. While Enovix technology has been well vetted and proven in the consumer space, its significant potential to improve the state of the art in electric vehicle (EV) batteries remains largely unexplored. This project is intended to study the effect of Enovix's unique cell architecture against the automotive performance requirements of high energy density (achieved by using a silicon anode) coupled with high cycle and calendar life.

Objectives

The objective of this project is to build and deliver cells using the Enovix architecture with an optimized silicon anode, automotive class cathode, and electrolyte formulation that can achieve the following performance and long-term stability targets required for EV applications:

- 750 Wh/L energy density,
- 350 Wh/kg specific energy,
- <20% energy fade after 1000 C/3 cycles, and
- 10-year calendar life.

Approach

Enovix

We are working towards accomplishing the above targets by utilizing the cell design and manufacturing capabilities of Enovix, the modeling and fundamental understanding of expertise of National Renewable Energy Laboratory (NREL), and the electrolyte development know-how of Mitsubishi Chemical Corporation (MCC). Baseline cells with automotive cathodes will be built in Year 1 to demonstrate current capability and performance. Using an iterative approach, we will screen new electrolyte formulations for their ability to stabilize the silicon electrode-electrolyte interface. Formulations that show significant improvement will be characterized post-mortem to understand the underlying physical structure of the solid electrolyte interphase (SEI) on the anode and the resulting structure modelled. These results will then be used to guide additional modification to the electrolyte and testing repeated. Various sources of silicon (particle sizes, shapes) will also be screened in combination with electrolytes for their performance. Cells will be built with improved anode material-electrolyte combinations in Year 2. Effect of internal stack pressure on cell performance will be determined by modifying cell designs to provide various levels of stack pressure. ~3Ah cells with optimized anode-electrolyte-stack pressure will be built and performance tested in Year 3.

NREL

NREL is developing continuum-level models to aid electrolyte and electrode design for silicon-based (Si and SiO_x) anode formulations. A detailed multiphase-multispecies solid electrolyte interphase (SEI) model implements $\cong 5$ electrolyte decomposition/ deposition irreversible global reactions informed by the literature and provides fundamental insights into associated capacity fade and SEI composition [1],[2]. The model captures bi-layer (inorganic-organic) SEI features, electronic conduction limited growth and can be leveraged to aid electrolyte additive design forming favorable SEI compounds with sluggish electron conduction. Furthermore, chemo-mechanic models incorporating Si particle expansion, SEI growth are developed which capture pore closure and expansion at the electrode level and can provide electrode design inputs for optimal transport and stress [3]. These design requirements can include initial electrode porosities, particle size, stack pressure, current protocol limits etc. This model will accelerate high-loading electrode development by considering not only electrochemical and transport overpotentials, but also the strongly coupled influences of chemo-mechanics.

Results

Enovix

NMC Electrode Formulation Definition. Coin cells were run with various formulations of NMC-622, binder, and conductive aids. Discharge capacity, rate capability, and electrode integrity were used as the primary screening metrics used to determine the positive electrode formulation for cell builds.

Cell Design Definition. The initial cell design proposal was intended to achieve a high energy density cell (like the ones that are being built for consumer electronics) with the Enovix architecture and an NMC cathode. However, upon further discussion with the collaborators and the DOE technology development manager, it

was decided that the best course of action would be to build baseline cells for Year 1 using an established positive electrode material and a cell design that shows that a silicon anode in the Enovix architecture can achieve the cycle life and calendar life goals. To this effect, the cell design D in Table VIII.8.1 below was used for Year 1 builds. Higher electrode loading cells that result in higher energy density (Cell designs B and C) will be part of the Year 2 cell builds.

Table VIII.8.1 Key cell Energy density models for Enovix 300 mAh development class cells.

Parameter	Unit	300 mAh-class Development Cell			
		Cell Type			
		LCO Cathode	NMC622 Cathode		
Dimensions (x * y * z)	mm	28.72 * 17.34 * 3.39			
Design Code		A	B	C	D
Cathode Design Type		High Loading High Energy	High Loading High Energy	High Loading Conservative	Low Loading Conservative
Cathode Active Material		LCO	NMC622	NMC622	NMC622
Cathode Specific Capacity	mAh/g	177	198	198	177
Voltage Range	V	2.7-4.35	2.5-4.35	2.5-4.35	2.5-4.2
Cell Capacity	Ah	0.337	0.343	0.307	0.263
Volumetric Energy Density	Wh/L	722	695	632	533
Gravimetric Energy Density	Wh/kg	257	261	235	197

Electrolyte Definition. The Year 1 deliverable cells were built with the Enovix baseline electrolyte. Electrolyte optimization studies are being conducted on test vehicles by varying the composition in collaboration with Mitsubishi Chemical Corporation.

300mAh class cell performance. Table VIII.8.2 summarizes the metrics for cells that have been built and are being tested for cycle life, calendar life, and voltage hold tests. Similar cells are also being built for delivering to the DOE for testing in Q4'2021.

After formation, the cells were subjected to a diagnostic testing protocol to measure the DC-IR as a function of State of Charge (SOC) as well as the rate capability at 25°C, then 25 cycles at C/3 at 30°C. >250 cycles had been completed by the end of Q3 and show good capacity and energy retention projected to exceed 1000 cycles to 80% of initial energy.

Table VIII.8.2 Key cell metric summary for Year 1 cell builds.

Quantity	Unit	Value	stdev
x length	mm	29.76	± 0.22
y length	mm	17.04	± 0.06
z length	mm	3.46	± 0.07
Cell weight	g	4.43	± 0.09
Capacity	mAh	266.1	± 0.1
Energy	Wh	0.922	± 0.005
Volumetric energy density	Wh/L	526	± 13
Gravimetric energy density	Wh/kg	208	± 4

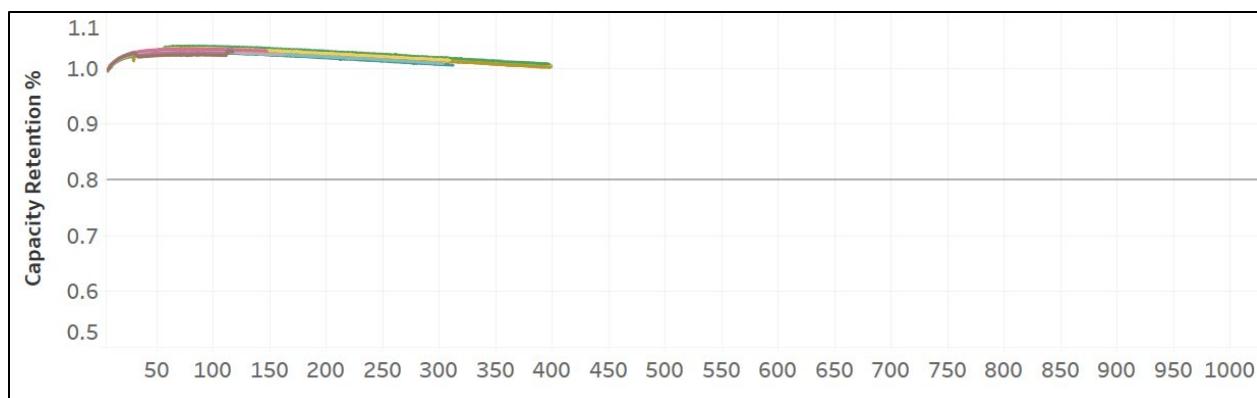


Figure VIII.8.1 Capacity Fade Plot for ~300mAh class development cells (Design Type D) in the first Table

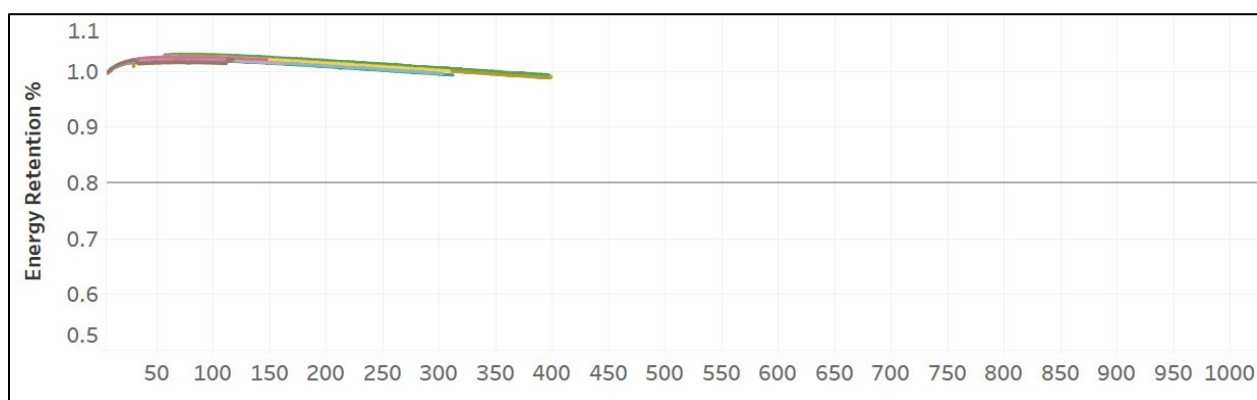


Figure VIII.8.2 Energy Fade Plot for ~300mAh class development cells (Design Type D) in the first Table

Figure VIII.8.1 and Figure VIII.8.2 show the capacity and energy fade of the baseline 3D cells built using the parameters for Design Type D in Table VIII.8.1. Both the capacity and energy fade are past 400 cycles and are on a trajectory of >1000 cycles to 20% fade.

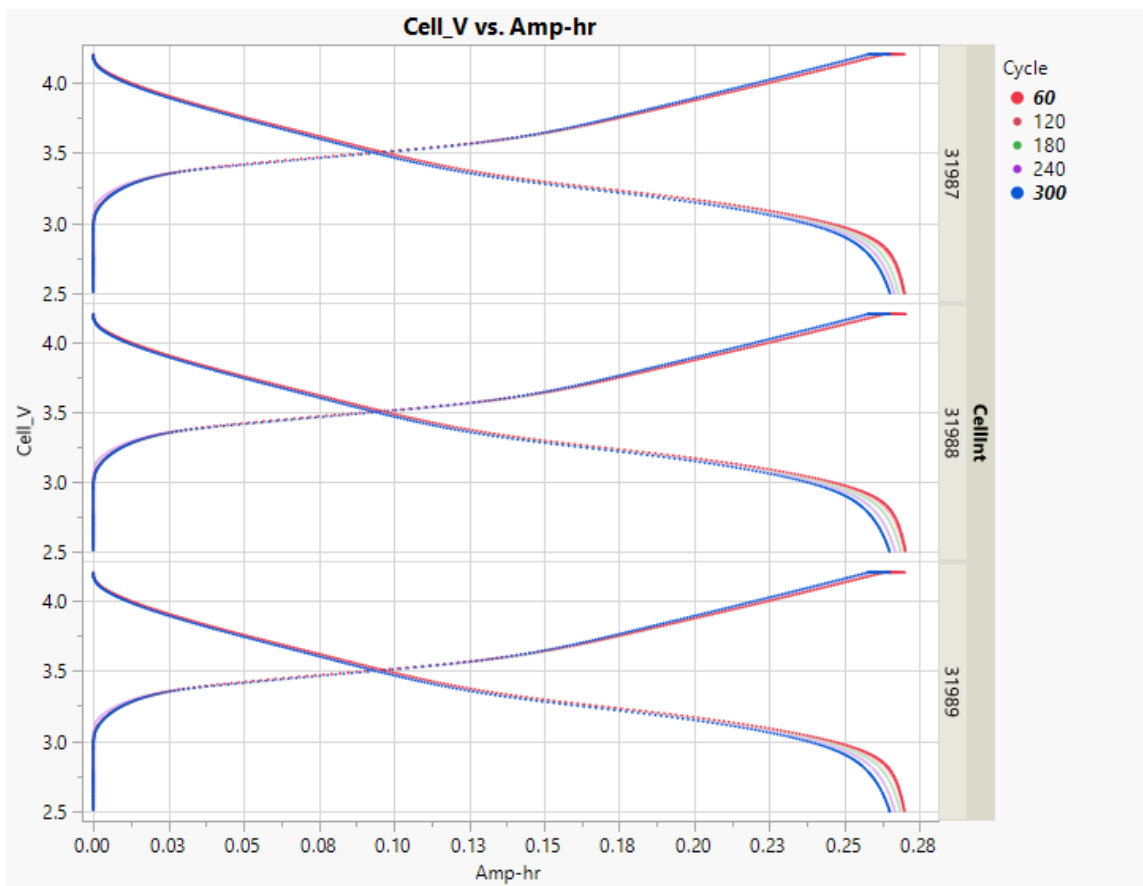


Figure VIII.8.3 Charge Discharge curves for representative cells from budget period 1 builds.

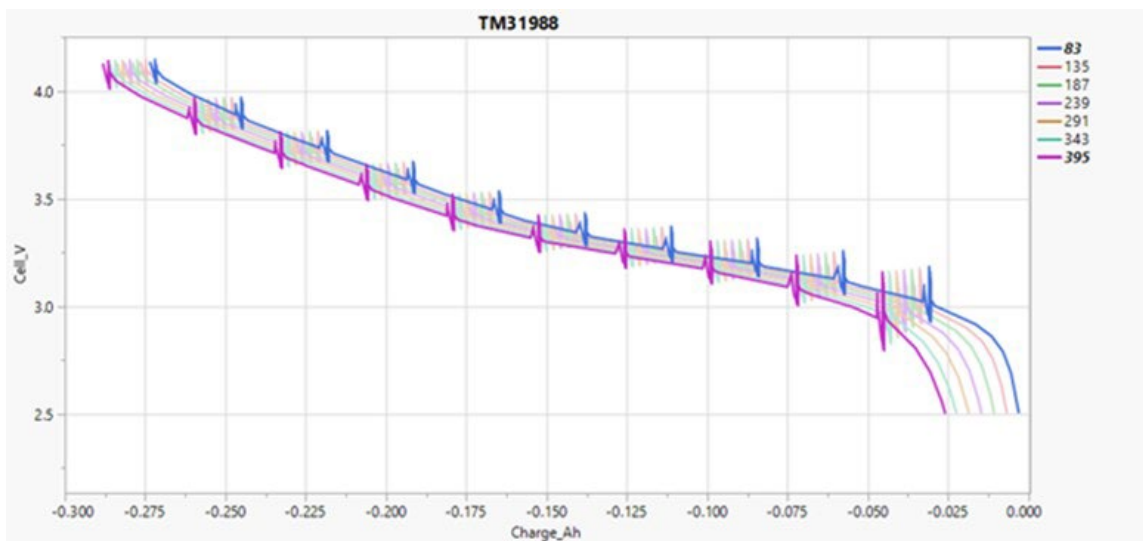


Figure VIII.8.4 Representative Reference Performance Test (RPT) profile of a 300 mAh Enovix 3D NMC 622 cell for select cycles.

Figure VIII.8.3 shows charge discharge curves as a function of cycle for three representative cells. Figure VIII.8.4 shows representative RPT profiles of the 3D NMC 622 cell at various cycles. The low-current HPPC profile consists of a 30-s discharge pulse at 1C, a 40-s rest, and a 10-s regen pulse at 0.75C.

The 300 mAh Enovix 3D NMC 622 cells were subjected to calendar life testing at target temperatures of 30°C, 40°C, 50°C, 60°C and 70°C. The interval between RPTs for cells at 30°C, 40°C and 50°C is 32 days, and that for cells at 60°C and 70°C is 16 days as cells at higher temperatures are likely to degrade faster. The calendar life analysis will be conducted when long-term data are collected in the upcoming months.

NREL

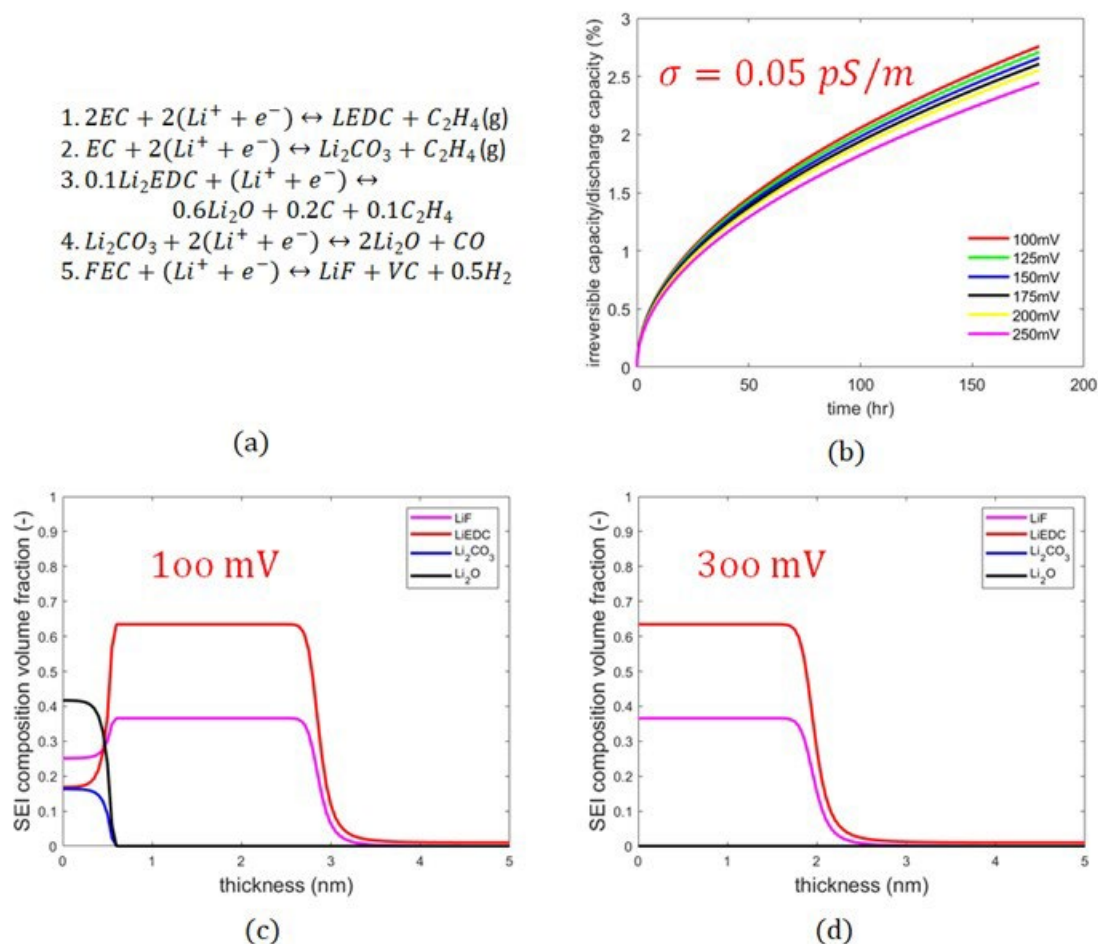


Figure VIII.8.5 (a) Reaction mechanism, (b) normalized irreversible capacity loss from SEI growth for SiO voltage-hold from 100 mV to 250 mV with an SEI electronic conductivity of 0.05 pS/m, (c) SEI composition evolution at 100 mV SiO potential and (d) 300 mV SiO potential.

Figure VIII.8.5 report results from a planar, multi-species SEI model to predict irreversible capacity loss and film composition at different states of charge (SOC) of SiO with a five-reaction intermediate reaction mechanism. Irreversible capacity loss due to SEI growth with an average electronic conductivity of 0.05 pS/m at voltage holds ranging from 100 mV to 250 mV is showcased in Figure VIII.8.5 (b). Low anode voltage holds (high SiO state of charge) lead to more driving force for SEI formation, leading to higher parasitic currents and consequently, larger parasitic capacity losses. Furthermore, the SEI chemical composition varies as a function of anode voltage, with a heterogeneous bilayer (inner) inorganic- (outer) organic SEI seen at 100 mV. Li_2CO_3 , Li_2O and LiF are the primary inorganic and Li_2EDC is the dominant organic constituent of the SEI. Beyond 300mV, only FEC and EC decomposition to LiF and Li_2EDC are activated, resulting in a relatively homogeneous SEI. This model will aid development of strategies resulting in favorable SEI decomposition products with favorable electronic conductivities, for example, electrolyte salt/solvent screening and electrochemical formation protocols for desirable SEI.

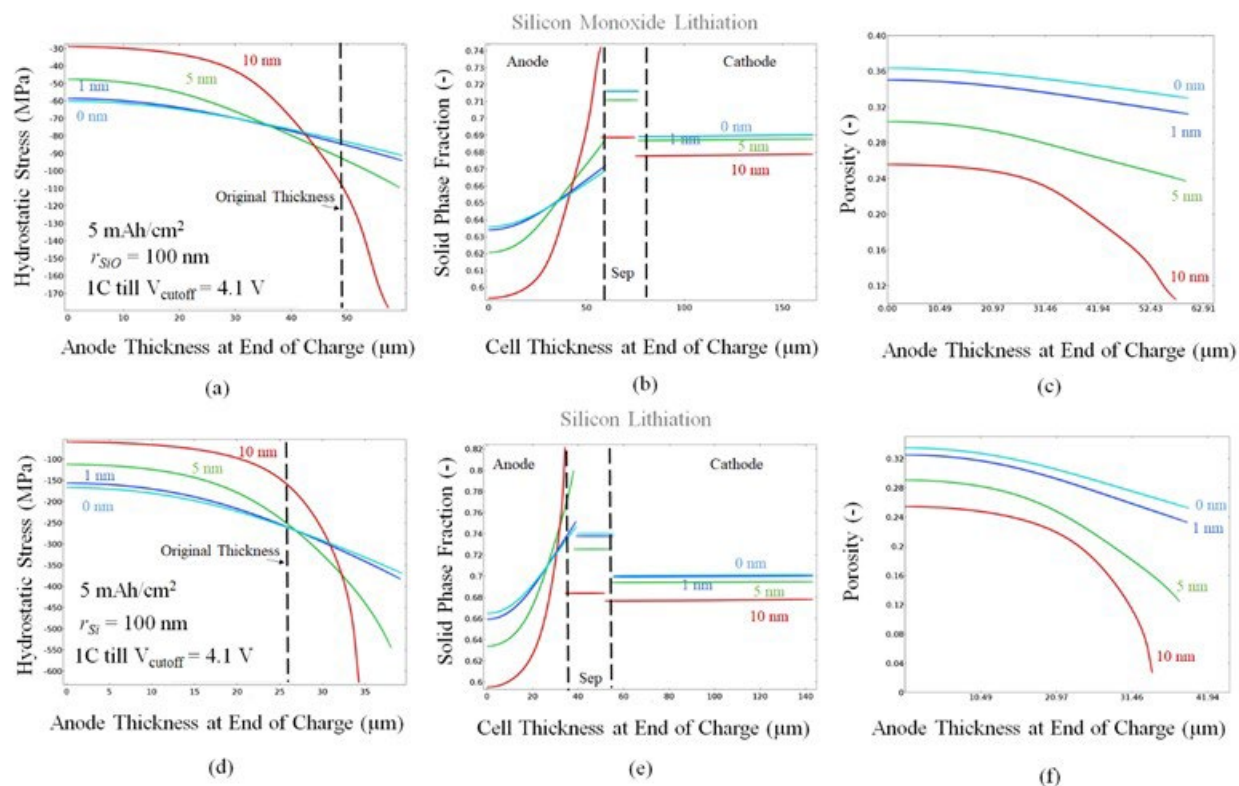


Figure VIII.8.6 (a) Anode hydrostatic stress , (b) Electrode solid phase fraction and (c) anode porosity variation with thickness for NMC-SiO full cells at end of 1C charge to 4.1V. (d) Anode hydrostatic stress , (e) Electrode solid phase fraction and (f) anode porosity variation with thickness for NMC-Si full cells at end of 1C charge to 4.1V.

Furthermore, an electrode level large-deformation chemo-mechanics model accounting for SEI growth, SiO_x expansion and pore closure is developed which can predict the cell performance and stress distributions within the system. Figure VIII.8.6 (a-c) shows the anode hydrostatic stress, electrode solid phase fraction and anode porosity variation with thickness for 1C charge of a NMC532-SiO full cell from 3.0 to 4.1 V with an initial particle radius of 100 nm and varying SEI thicknesses of 0, 1, 5 and 10 nm in a fully rigid cell setup, while Figure VIII.8.6 (d-f) show the corresponding results for a NMC532-Si full cell with same parameters. The cell capacities are kept constant at 5.0 mAh/cm² for both the silicon monoxide and silicon cells. The theoretical capacity of SiO is smaller as compared to Si (2280 mAh/g vs 3800 mAh/g), correspondingly, we ensure capacity matching by using a larger initial thickness anode for silicon oxide as compared to silicon with an initial porosity of 50% for both systems. Correspondingly, thickness of the SiO electrode ~50 μm while the Si anode thickness is ~27 μm at the beginning of charge. The rigid cell setup mimics the condition of no overall cell expansion i.e., expansion of the anode results in compression of separator and the cathode such that the full cell thickness is the same. Larger expansion of Si anode as compared to SiO anode results in considerably higher compressive hydrostatic stress generation in Si. Higher SEI thicknesses also lead to exacerbated transport limitations due to pore closure and large compressive stresses throughout the anode. Anode expansion and SEI thickness increase compresses the separator and cathode as well resulting in an increase in their solid phase fractions from porosity reduction. The largest porosity reductions are observed near the anode-separator interface, and this can lead to large ohmic overpotentials decreasing performance. This model will be used to develop optimal electrode porosity/thicknesses to maximize rate capability, energy density and minimize stress. External pressure based mechanical conditions can be simulated as well to mimic cell swelling with lithiation and will be useful for delineation of optimal stack pressures for Si anode systems.

Conclusions

300mAh class cells have been built with NMC cathode, and are in cycling, calendar life testing, and are starting TOC voltage hold testing. These cells have achieved the designed energy density and specific energy, have excellent BOL performance, and are on track to achieve >1000 cycles to 20% energy fade. Calendar life testing is progressing as planned and initial results should be available in Q4 2021. NREL has developed a detailed chemical SEI model predicting irreversible capacity loss, thickness growth, compositional variation and an electrode level large deformation chemo-mechanics model predicting cell-level performance and stress generation with SiO and Si expansion and SEI growth. The above models will be leveraged for SEI and electrode design towards reaching performance metrics for EV applications.

Key Publications

NREL

1. Ha, Yeyoung, Donal P. Finegan, Andrew M. Colclasure, Stephen E. Trask, and Matthew Keyser. "Evaluating temperature dependent degradation mechanisms of silicon-graphite electrodes and the effect of fluoroethylene carbonate electrolyte additive." *Electrochimica Acta* 394 (2021): 139097.
2. McBrayer, Josefine D., Marco-Tulio F. Rodrigues, Maxwell C. Schulze, Daniel P. Abraham, Christopher A. Apple, Ira Bloom, Gerard Michael Carroll, Andrew M. Colclasure, Chen Fang, Katharine L. Harrison, Gao Liu, Shelley D. Minter, Nathan R. Neale, Gabriel M. Veith, Christopher S. Johnson, John T. Vaughey, Anthony K. Burrell & Brian Cunningham. "Calendar aging of silicon-containing batteries." *Nature Energy* 6, no. 9 (2021): 866–872.

References

1. Single, Fabian, Birger Horstmann, and Arnulf Latz. "Revealing SEI Morphology: In-Depth Analysis of a Modeling Approach." *J. Electrochem. Soc.* 164 no. 11 (2017): E3132.
2. Single, Fabian, Birger Horstmann, and Arnulf Latz. "Dynamics and morphology of solid electrolyte interphase (SEI)." *Phys. Chem. Chem. Phys.* 18 no. 27 (2016): 17810–17814.
3. Mai, Weijie, Andrew Colclasure, and Kandler Smith. "A Reformulation of the Pseudo2D Battery Model Coupling Large Electrochemical-Mechanical Deformations at Particle and Electrode Levels" *J. Electrochem. Soc.* 166 no. 8 (2019): A1330.

Acknowledgements

Enovix: John S. Thorne, Ashok Lahiri, James Wilcox, Rajeswari Chandrasekaran, Wang Xu, Kang Yao, Chaojun Shi

NREL: Ankit Verma, Shriram Santhanagopalan, Ahmad Pesaran

VIII.9 Rationally Designed Lithium-Ion Batteries Towards Displacing Internal Combustion Engines (Group14)

Henry R. Costantino, Principal Investigator

Group14 Technologies, Inc.
8502 Maltby Road
Woodinville WA 98072
E-mail: rcostantino@group14.technology

Brian Cunningham, DOE Technology Development Manager

U.S. Department of Energy
E-mail: Brian.Cunningham@ee.doe.gov

Start Date: October 1, 2020 End Date: December 31, 2021
Project Funding: \$2,272,060 DOE share: \$1,789,064 Non-DOE share: \$482,996

Project Introduction

Group14 Technologies is leading a world-class team composed of Cabot Corporation, Silatronix, Arkema, Pacific Northwest National Laboratories, and Farasis Energy to research, fabricate, test and demonstrate lithium ion batteries (LIB) implementing $\geq 30\%$ silicon-carbon (Si-C) composite anodes achieving aggressive next generation automotive energy targets. The project's centerpiece technology is Group14's high performing Si-C composite anode material already proven to provide 35% increased energy density at 12% composite blended with graphite, >1000 cycle stability, and a projected cell cost of $< \$125/\text{kWh}$ in conventional LIBs under a prior DOE VTO award (DE-EE0001201). This project advances this baseline by taking a holistic approach to increase silicon content for higher energy density and to improve calendar and cycle life through the optimization and incorporation of carbon additives, surface coatings and binders for the anode along with high performance co-solvent electrolyte additives. These anode improvements are being paired with high-nickel, low-cobalt, commercially available cathode to achieve the project's performance targets.

Objectives

This three year project will culminate in a $\geq 0.4\text{Ah}$ pouch cell which demonstrates targets of $>350 \text{ Wh/kg}$, $>750 \text{ Wh/L}$, ≥ 1000 cycle stability, and >10 year calendar life. This target will be achieved incrementally each year of the project with a LIB build achieving the baseline, interim and final cell targets listed below:

Table VIII.9.1 Electrochemical Objectives for DoE Project – EE0009187

Objective	Metric	Baseline	Interim	Final
Useable Specific Energy at 30°C and C/3	Wh/kg	>340	>350	>350
Useable Energy Density at 30°C and C/3	Wh/L	>750	>750	>750
Calendar Life	Years to 20% fade	>3	>5	>10
Cycle Life (C/3 deep discharge to 350 Wh/kg)	Cycles to 20% fade	≥ 300	≥ 600	≥ 1000

Approach

Our approach is to leverage Group14 Technologies' carbon and Si-C composite expertise in conjunction with our partnering organizations' expertise to holistically improve the performance of a LIB as measured by our yearly electrochemical targets. Within this collaboration, each of our partners contribute a unique approach toward improving the battery:

- **Group14 Technologies:** Our core technology is to create a composite material that accounts for and overcomes the failings of traditional silicon-based anode material solutions. The basis for Group14 Si-C's superior performance is its rationally designed structure. At its foundation is an amorphous carbon scaffold, with its porosity fine-tuned for promoting intra-particle growth of the desired type and size of silicon. The resulting Si-C composite includes internal void space to buffer expansion, nano-silicon to prevent particle fracture with cycling, and a carbon scaffold to enhance conductivity and particle integrity while minimizing exposed silicon surface area. Our approach for this project is to further optimize both the carbon scaffold and to modify the resulting Si-C in order to protect the surface from adverse interactions that may negatively impact cell performance.
- **Cabot Corporation:** Global leader in nanoengineered conductive carbon additives for LIBs. Their role in the project is: (1) to assist Group14 in characterization of carbon and resulting Si-C and (2) to optimize the carbon additive type and loading to maximize performance.
- **Silatronix:** Producers of organosilicon co-solvent additives that improve LIB cycle and calendar stability. Silatronix pioneered industrial relevant analytical methods for investigating silicon-electrolyte interactions, including quantitative gassing analysis and identification of degradation mechanisms. Leveraging their expertise, they will produce an optimized electrolyte formulation that will synergize with Group14 Si-C to extend battery life by controlling degradation mechanisms.
- **Arkema:** A specialty chemicals and advanced materials developer and supplier that successfully commercialized several electrode binders and separators coating resins, especially for high-energy, high-voltage LIBs. Their role in the project is to develop an optimized binder solution to maximize cohesion of Group14's Si-C composite with other anode components and to promote the long-term cycling and calendar performance of the battery.
- **Farasis Energy:** A leading U.S. developer and supplier of LIBs for EVs. Farasis has designed and built its own Li-ion cell and battery system manufacturing plant and has been in high volume production since 2010 with fully automated production capability of 4 GWh/y. By leveraging Farasis' battery production research and experience the best design and form factor of LIB will be utilized to promote high energy density and increase cycle life.
- **Pacific Northwest National Lab (PNNL):** World-renown experts in energy storage research. PNNL lead in mechanistic investigations regarding LIB materials and assure the guidance to the project towards success. PNNL provides critical advanced materials characterization support toward synergizing the team's optimization efforts.

Results

The two primary project objectives for FY21 were: (1) to establish a baseline set of LIBs to use as benchmarks for future cell builds and (2) to down-select a materials approach for the FY22 interim battery build to meet or exceed all of the interim build's performance targets. As discussed with the Department of Energy (DoE) during the regular quarterly project meetings, both of these objectives have been satisfactorily completed. The project's current focus is combining these down-selected material approaches in full cell pouch cells in order to refine the composition and material ratios for the interim build.

The key milestone and deliverable in FY21 were the design, development, production and finally the delivery of baseline devices to Argonne National Lab. These cells are being tested at Argonne National Lab to serve as a benchmark for future builds in the project. The intent of the baseline build is to combine Group14's non-modified Si-C (SCC55™) and commercially available electrode materials to achieve key baseline build metrics: >340 projected Wh/kg and ≥300 cycle life stability. In order to successfully accomplish this goal, the first step of the process was to determine the appropriate percentage of Si-C and graphite in the anode. Through energy density modeling and observed electrochemical data it was determined to use a 35% SCC55™ blend in combination with graphite. This loading ensured the ability to achieve a projected 340 Wh/kg, balance

cycle life and allow for an appropriate ratio of the other anode components. When selecting the non-active materials for the anode formulation such as the binder, conductive additive, graphite and electrolyte, only commercially relevant materials were selected. For each of these additives, we used recommendations from Farasis Energy based on their commercial experience. This decision was to ensure that the benchmark cells provide for an anode and LIB approach with commercial relevance for electric vehicle use, concomitant with the commercialization of SCC55™.

The LIBs made for the baseline build met all performance metrics. The finalized baseline LIBs contained anodes which were comprised of a 35wt. % Si-C and graphite blend using an electrode formulation of 94% active material, 4% binder and 2% carbon additive and were paired with high nickel cathodes. Testing at Farasis demonstrated that these cells would attain a projected >340 Wh/kg energy density when scaled to a fully optimized battery. These cells achieved well over 300 cycles to 80% capacity retention at a C/2 rate conducted at 30C. Sixteen of these cells were then delivered to Argonne National Lab where they are currently testing on three calendar life profiles at 30C, 40C and 50C as well as a cycle life test regime. Cycle life performance data reported by Farasis is shown in Figure VIII.9.1 and demonstrates approximately 600 cycle stability, corresponding to double the minimum target.

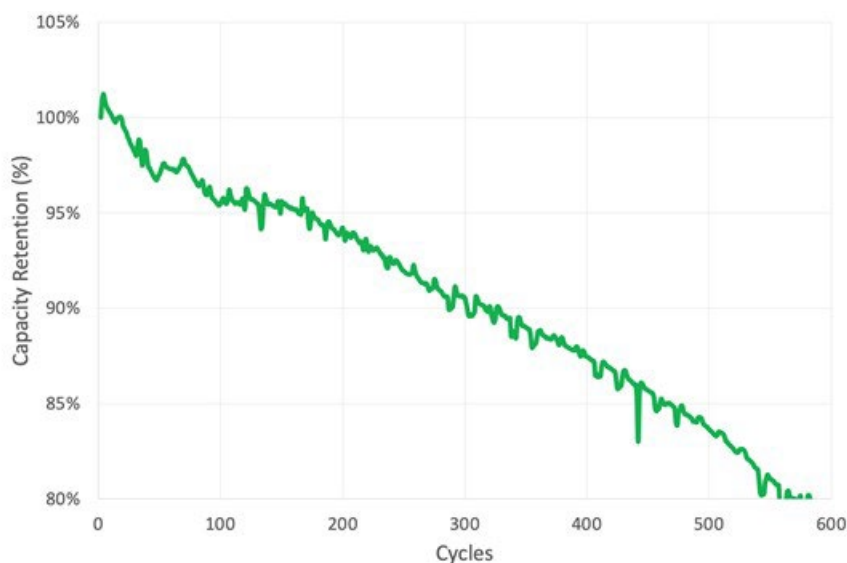


Figure VIII.9.1 Baseline build battery performance (Farasis cycling data)

The second key objective for FY21 was to optimize each of the anode materials to be used in FY22's interim battery build. This objective was highly multifaceted and involved strong collaboration and communication among each of the project partners. Group14 took the lead on the optimization coordination but primarily focused on SCC55™. To this end, Group14 fine-tuned: (1) The carbon scaffold and (2) the Si-C composite. With regards to the carbon scaffold, the fine tuning efforts included material and processing modifications. The resulting carbon scaffold materials were processed into composites and subsequently tested in half-cells to assess the effects. With regards to the Si-C composite, the fine tuning efforts included material and processing modifications. Each composite was then used to determine the effects on electrochemical performance in half-cells. These results were discussed with the DoE and resulted in the agreement of a down-selected approach for the interim build.

Over 70 different modifications of scaffold and composite were assessed within this project. Through physiochemical and electrochemical analysis three Si-C modifications were down-selected as candidates for use in the interim build. One such modified Si-C was delivered to Farasis for full cell analysis. By using this modified Si-C composite two notable positive impacts in full cell performance were observed: (1) an average increase in cycle life and (2) better rate capability with significantly lower DCIR. Group14 has now produced a

Si-C using a combination of both carbon scaffold and Si-C modifications. In half-cell testing at Group14, this combined approach Si-C composite demonstrated a significant increase in average stable coulombic efficiency, an increase in first cycle efficiency while maintaining a high gravimetric and volumetric capacity. This Si-C composite is currently being tested in full cell pouch cells at Farasis in assessment for use in the interim build in FY22. Indications from correlations made between Group14 and Farasis electrochemical data suggest that this material can exceed the ≥ 600 cycle stability target.

In parallel to the work being done at Group14 to improve the Si-C composite performance, each of our partners have optimized the other anode materials to synergize with Group14 Si-C. The carbon additive, binder and electrolyte optimization are being conducted at Cabot, Arkema and Silatronix respectively. As lead, Group14 moderates these material improvements and has conducted several experiments combining our partner's modifications in half-cell coin cells. This step has been used as a filter before recommending these materials be tested in full cell pouch cells at Farasis.

To begin carbon additive optimization, Cabot characterized the conductivity of several commercial carbon additives, Cabot commercial additives and Cabot experimental additives in a 95% SCC55™ electrode. Several types of carbon additives were explored including single-walled carbon nanotubes, multi-walled carbon nanotubes, carbon nano-structures and colloidal carbons including the commonly used Super C45 as an additive benchmark. The electrode sheet resistance data as a function of carbon additive concentration are shown in Figure VIII.9.2. One of the experimental Cabot materials, Enhancer 1, showed the best performance in terms of loading and conductivity. This Cabot additive is a non-commercialized carbon nano-structure: A highly branched network of carbon nanotubes. SEM analysis of electrodes with Group14's Si-C and Cabot's carbon nano-structure reveal a high degree of connectivity between the particles demonstrating that the carbon nano-structures completely entangle the Si-C particles to one another. This additive was put into several coin cell design of experiments at both Group14 and Cabot. The results of these experiments show significant increases in rate capability, conductivity, and cycle life over other commercially available additives.

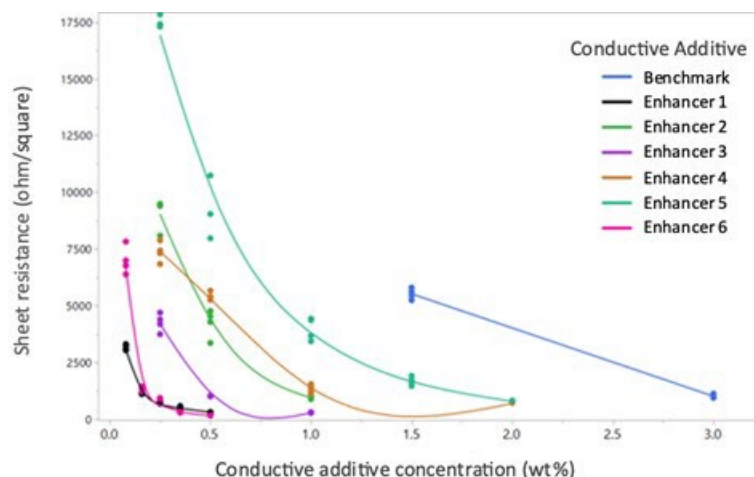


Figure VIII.9.2 Electrode resistivity for anodes with ~95 wt% SCC55™ (Cabot Corporation)

The binder is one of the most critical materials to promote stability in a high silicon containing anode. An ideal binder not only needs to have good cohesion and adhesion but also needs to allow for the natural expansion and contraction of a silicon containing material during cycling. Binder screening experiments were conducted at both Group14 and Arkema and focused on both physical and electrochemical characterization. Binder candidates were incorporated into electrodes that were tested for adhesion, cohesion, electrical conductivity and homogeneity. Once electrodes demonstrated suitable physical properties, they were tested electrochemically at both room temperature and elevated temperatures to determine differences in binder stability. Through these experiments a PAA based binder was down-selected. This binder, when combined

with Group14's Si-C and the down-selected carbon nano-structures show improvement in capacity retention and coulombic efficiency in half-cell coin cells over a traditional SBR/CMC binder system.

The LIB electrolyte needs to fulfil several roles in a high silicon anode containing system. It needs to continuously provide lithium ions to the anode while at the same time mitigate or even completely prevent side reactions that can starve the electrode of lithium. Silatronix' organosilicon additives have previously shown to work well with silicon containing anode materials. This additive scavenges cell degradation byproducts and hinders gas evolution during cycling. This organosilicon containing electrolyte is currently being electrochemically tested against to two other electrolytes in Farasis full cells to determine suitability for the interim build. All of the candidate electrolytes are being characterized using a multi-pronged cell testing approach: 30C cycle life, 45C calendar life and an aggressive 60C calendar life test.

Finally, PNNL has provided crucial support for this project. They fill two prominent analytical roles: Si-C composite characterization and electrode characterization. Using advanced characterization techniques like XPS, HRTEM and electron diffraction, we assessed the material characteristics of the Si-C before and after various modifications. In FY22 PNNL will continue their important role including post-mortem characterization of electrodes after cycling and calendar life testing. Furthermore, novel techniques such as in-situ TEM lithiation will be utilized to determine the expansion and contraction properties of the material once modifications have been made to both the carbon scaffold and the resulting Si-C.

In Figure VIII.9.3 an example of PNNL's material characterization support is shown. These images show the electron diffraction analysis of a 4-5 μ m Si-C particle. This particular analysis reveals information about the physical state of silicon and carbon within the composite. According to PNNL's experts the data shown here are consistent with amorphous silicon dispersed throughout an amorphous carbon. Such analysis will be critical to guide down-selections for the next stages of the project.

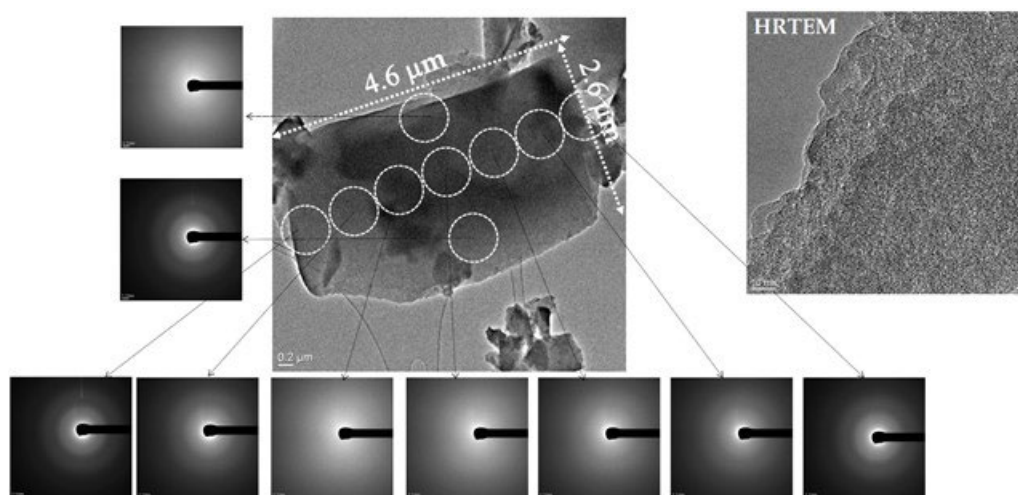


Figure VIII.9.3 Electron diffraction analysis of SCC55™ (PNNL)

Conclusions

Two primary project goals have been accomplished in FY21: (1) Producing and testing baseline LIBs containing Group14 Si-C to achieve baseline targets and (2) Down-selecting key anode components for an interim LIB build in FY22. The baseline build was highly successful, demonstrating a projected >340 Wh/kg and cycle life of ≥ 300 cycles. Furthermore, sixteen of these ~ 0.4 Ah cells were delivered to and tested at Argonne National Lab. Through independent cycling tests at Argonne National Lab, the Farasis cycle life result was confirmed, showing that the baseline LIBs achieve a cycle life of approximately 600 cycles.

Over the course of FY21, Group14, Cabot, Farasis, Arkema, Silatronix and PNNL have collaborated towards significant optimization of each of the functional materials that comprise the anode. Group14 has down-selected a Si-C using a combination of both carbon scaffold and Si-C modifications. In full cell pouch cells, the down-selected Si-C alone has already demonstrated an increase in cycle life, an increase in rate capability and a dramatic reduction in DCIR. Further optimizations in half-cell screening at Group14 have resulted in very high first cycle and stable coulombic efficiencies. These optimizations have advanced into pouch cell full cell testing at Farasis and are on track toward down-selection for the interim build.

Each of our project partners contributed to the down-selection of the carbon-additive, binder, and electrolyte to be used in the final build. For a conductive additive we have selected a carbon nano-structure which has shown to be highly synergistic with Group14's Si-C. For a binder we have selected a highly robust PAA based binder which performs well at both room temperatures and elevated temperature. Finally, for the electrolyte we are currently characterizing organosilicon compounds from Silatronix to help to increase the longevity of our LIBs. Each of these down-selected components are actively being investigated together in half-cells and full cells in order to fine tune material ratios in order to successfully achieve the interim build milestones in FY22.

Acknowledgements

The PI thanks Adam Strong for managing the project and Avery Sakshaug, Dr. Abirami Dhanabalan, Dr. Nate Phillip and Dr. Rajan Patel (Group14 Technologies) for their critical contributions to the project. The PI would also like to thank Cabot, Arkema, Farasis and Silatronix for their work on the project using their excellent domain expertise. Finally, the PI would like to thank Dr. Chongmin Wang of PNNL for his many contributions to the characterization of key materials throughout the project.

VIII.10 Ultra-Low Volume Change Silicon-Dominant Nanocomposite Anodes for Long Calendar Life and Cycle Life (Sila Nanotechnologies)

Naoki Nitta, Principal Investigator

Sila Nanotechnologies
2470 Mariner Square Loop
Alameda, CA 94501
E-mail: nnitta@silanano.com

John Tannaci, Principal Investigator

Sila Nanotechnologies
2470 Mariner Square Loop
Alameda, CA 94501
E-mail: jtannaci@silanano.com

Brian Cunningham, DOE Technology Development Manager

U.S. Department of Energy
E-mail: Brian.Cunningham@ee.doe.gov

Start Date: October 1, 2020
Project Funding: \$4,600,000

End Date: December 31, 2023
DOE share: \$3,600,000

Non-DOE share: \$1,000,000

Project Introduction

Today's state-of-the-art Li-ion battery cells use a small fraction of silicon in the anode to boost cell energy density. Anode silicon content is kept low because higher amounts would cause massive volume change, resulting in undesirable electrolyte reactions which have detrimental effects on both calendar and cycle life. Batteries for automotive applications have particularly stringent calendar and cycle life requirements, posing a challenging problem for high energy density cell development. However, higher energy density cells are able to deliver more energy storage per cell and therefore open a path to achieving lower cost.

Sila's silicon-dominant anode material technology is manufactured with scalable processes and inputs, and has ultra-low volume change, enabling high-capacity anodes to achieve both long calendar and cycle life. Sila Nanotechnologies has already begun commercial sales of its silicon anode material for consumer applications, starting with wearable electronics, and is scaling up production to enter larger battery markets. This project applies Sila's anode technology to research, develop, fabricate, and validate high energy density silicon-dominant Li-ion battery cells meeting automotive cycle life and calendar life requirements.

Objectives

The objective is to research, fabricate, and test lithium battery cells that implement $\geq 30\%$ silicon content electrodes with commercially available cathode technology and achieve cell performance identified in Table VIII.10.1 below.

Table VIII.10.1 Cell Performance Targets.

Beginning of Life Characteristics at 25°C	Cell Level
Usable Specific Energy @ C/3	>350 Wh/kg
Usable Energy Density @ C/3	>750 Wh/L
Calendar Life (<20% energy fade)	>10 Years
Cycle Life (C/3 deep discharge to 350 Wh/kg, <20% energy fade)	>1,500

Approach

Sila's nano-engineered particles enable ultra-low volume change silicon-dominant anodes and are the most promising candidate for silicon-based electric vehicle Li-ion batteries. This project utilizes Sila's proprietary particles and know-how for its application in standard Li-ion battery manufacturing processes. Both the bulk and surface properties of the particle are engineered for improved performance, and the electrode construction process is optimized around the adjustments made to the particle, as are electrolyte formulations. Sila's state of the art analysis techniques are also employed, and new methods are developed to understand how material and process changes impact cell performance.

In addition, Sila has partnered with ARL to simulate electrolyte reaction mechanisms and reveal the causes of cell performance differences between formulations with different electrolyte components. Sila has also partnered with PNNL to develop Localized High Concentration Electrolytes for higher automotive commercial readiness and achieve even better performance with Sila's anode material.

Results

The particle and the electrode slurry were optimized to stabilize higher silicon content particles, which in turn improved the anode volumetric capacity by 30% (Figure VIII.10.1). This increase in capacity was achieved alongside a cycle life of >900 cycles (Figure VIII.10.2) in a silicon-dominant anode. At C/3, the cell level energy density achieved was 275 Wh/kg and 950 Wh/L, meeting all go/no-go milestones for 2021 (Table VIII.10.2). Cycle life improvements were also achieved by utilizing Sila's proprietary electrolyte solvents. However, these improvements were not yet incorporated into the cells that achieved the go/no-go milestones.

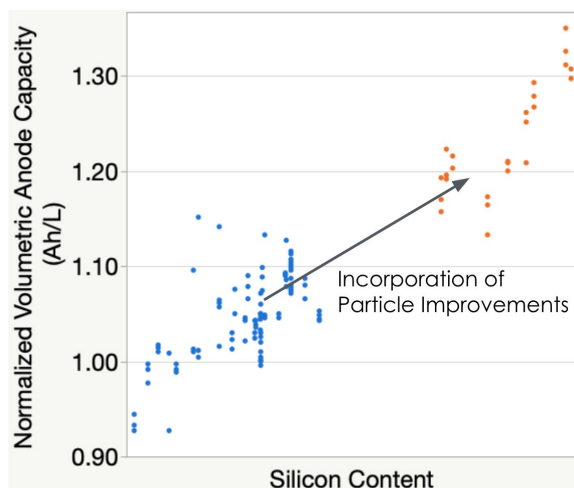


Figure VIII.10.1 Improvements to particle synthesis process enabled higher silicon content and therefore greater volumetric anode capacity.

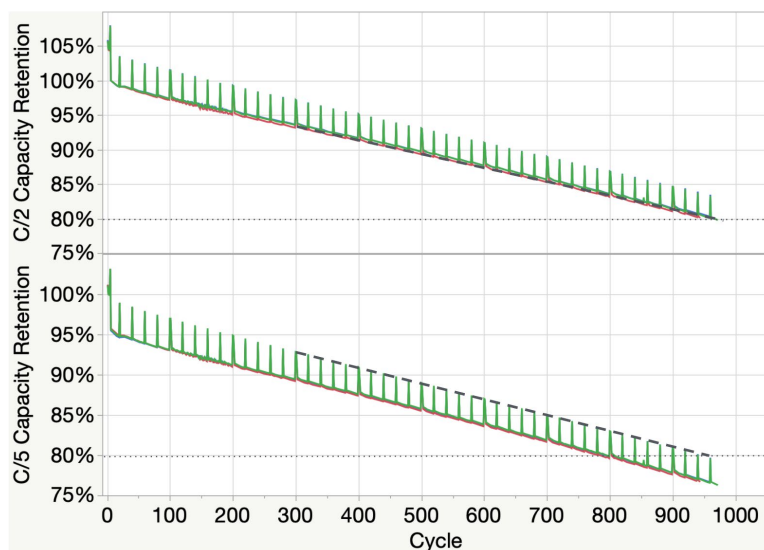


Figure VIII.10.2 Cycle life of automotive loading cells, measured at C/2 and C/5 capacity.

Table VIII.10.2 Performance in budget period 1 vs go/no-go milestone.

Metric	Go/No-Go Milestone	Achieved
Wh/L (C/3)	750+	950
Wh/kg (C/3)	250+	275
Cycles to 80% Capacity	750+ Projected	~950 @ C/2 & C/5

Conclusions

Sila has achieved all go/no-go milestones for 2021, reaching 950 Wh/L and 275 Wh/kg at the cell level, while also reaching >900 cycles to 80% capacity in the same cells through a combination of improvements to the particle and electrode.

VIII.11 Solid State Li-Ion Batteries Using Si Composite Anodes (Solid Power, Inc.)

Pu Zhang, Principal Investigator

Solid Power Inc.
486 South Pierce Avenue, Suite E
Louisville, CO 80027
E-mail: pu.zhang@solidpowerbattery.com

Brian Cunningham, DOE Technology Development Manager

U.S. Department of Energy
E-mail: Brian.Cunningham@ee.doe.gov

Start Date: October 1, 2020
Project Funding: \$1,649,849

End Date: December 31, 2023
DOE share: \$1,319,883 Non-DOE share: \$329,966

Project Introduction

Solid Power is teaming with Argonne National Laboratory (Dr. Wenquan Lu) to develop an all-solid-state lithium-ion battery (ASSB) that will achieve high energy, long cycle life, and long calendar life. It is based on a high-capacity solid-state Si composite anode. The project will enable scalable production of large format all-solid-state batteries required by the vehicle market

Objectives

The project objective is to develop all-solid-state Li ion batteries that implement high energy silicon anodes for EV application. The all-solid-state battery (ASSB) cell will be able to deliver > 350 Wh/kg specific energy, > 750 Wh/L energy density, > 1000 cycle life, and > 10 years calendar life.

Approach

The project will develop a solid-state electrolyte (SSE) for Si anode and synthesize a Si-SSE composite anode. The solid-state electrolyte system addresses the calendar life challenge of the Si anode batteries by forming highly stable SEI. A high-Ni content NMC cathode will be selected to match the Si anode. The all-solid-state cell will be assembled by scalable roll-to-roll processes developed by Solid Power.

Results

1. Si composite anode development

The Si composite was synthesized by integrating a Si powder and a Solid Power's sulfide solid state electrolyte (SSE). The Si-SSE composite material was mixed with a binder, a conductive carbon additive and a solvent to form an anode slurry. The slurry was then coated to Cu foil to form an electrode. A roll-to-roll process has been developed to coat the Si anode. Figure VIII.11.1 shows a Si anode coated by a slot-die coater.

The Si anode has demonstrated a capacity of 1500 mAh/g at electrode level, 92% first cycle efficiency (FCE), and stable cycle life in a Si-Li half cell (Figure VIII.11.2). The cell was tested at C/5 – C/5, 0.05 – 1.0V with the anode loading at 3 mAh/cm².



Figure VIII.11.1 A continuous Si anode coating

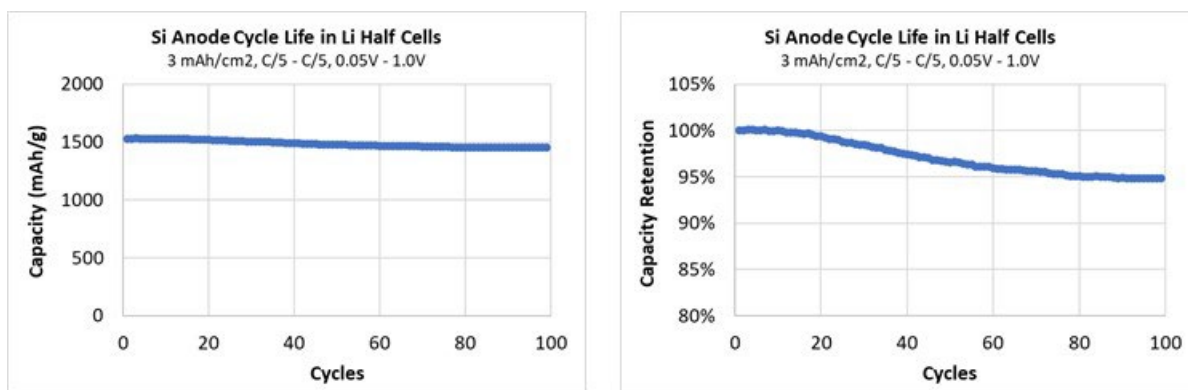


Figure VIII.11.2 Cycle life of the Si anode in a Li half cell: (left) Si anode capacity vs. cycle number; (right) capacity retention vs. cycle number. The anode shows 1500 mAh/g reversible capacity and retains 95% of initial capacity after 100 cycles.

2. Full cell demonstration

An NMC622 cathode was selected to match the anode to form a full pouch cell. The solid state pouch cell was assembled with the NMC cathode, an SSE separator, and the Si composite anode. When cycled at C/5 – C/5., 100% DOD, and 45°C, the cell shows 90% first cycle efficiency and retains 92% capacity after 500 cycles (as in Figure VIII.11.3).

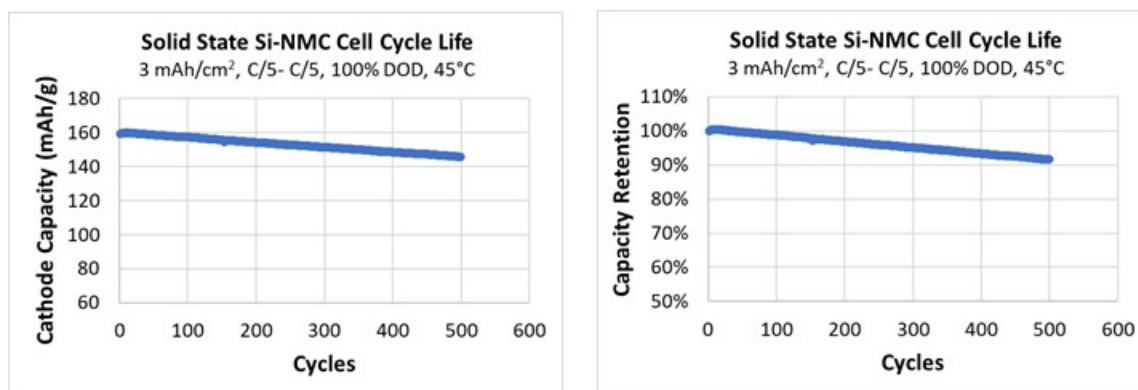


Figure VIII.11.3 Cycle life of a Si-NMC full pouch cell (3 mAh/cm² loading, C/5–C/5, 100% DOD, 45 °C). The cell retains 92% of initial capacity after 500 cycles.

Conclusions

Si-SSE composite materials have been developed with a specific capacity of 1500 mAh/g (at electrode level). A Si anode with the loading of 3 mAh/cm² was coated by using a roll-to-roll process. All-solid-state NMC-Si pouch cells have been assembled and tested. The cycle life of > 500 at 100% DOD has been demonstrated in all-solid-state Si-NMC pouch cells.

VIII.12 Fully Fluorinated Local High Concentration Electrolytes Enabling High Energy Density Si Anodes (Stony Brook U, BNL)

Amy C. Marschilok, Principal Investigator

Stony Brook University
1000 Innovation Road
Stony Brook, NY 11794-6044
E-mail: amy.marschilok@stonybrook.edu

Esther S. Takeuchi, Principal Investigator

Stony Brook University
1000 Innovation Road
Stony Brook, NY 11794-6044
E-mail: esther.takeuchi@stonybrook.edu

Kenneth J. Takeuchi, Principal Investigator

Stony Brook University
1000 Innovation Road
Stony Brook, NY 11794-6044
E-mail: kenneth.takeuchi.1@stonybrook.edu

David C. Bock, Principal Investigator

Brookhaven National Laboratory
Interdisciplinary Science Department, Building 734
Upton, NY 11973
E-mail: dbock@bnl.gov

Brian Cunningham, DOE Technology Development Manager

U.S. Department of Energy
E-mail: Brian.Cunningham@ee.doe.gov

Start Date: September 25, 2020	End Date: December 31, 2023	
Project Funding (FY21): \$280,000	DOE share: \$280,000	Non-DOE share: \$0

Project Introduction

Si-based anodes are promising for Li-ion batteries given their high specific capacity and low operating potential, yet they suffer from extreme volume changes during (de)lithiation that lead to continual growth of the solid electrolyte interface (SEI) layer. The extreme volume change (> 300%) in each (de)lithiation cycle causes dynamic growth of the SEI layer, which incrementally consumes electrolyte while causing loss of electrical connection between active material particles, which results in severe capacity fading. [1] As a result, current Li-ion automotive cells which incorporate Si as an anode component contain only a low percentage (5–10%). [2] Strategies for improving the electrochemical performance of Si to enable high Si anode content can be defined broadly in three categories: (1) engineering of the Si material/electrode structure for mitigating volume changes, [3] (2) use of electrically conductive and mechanically strong polymeric binders to improve electrode integrity, [4], [5] and (3) tailoring the electrolyte to optimize the properties of the SEI layer. [6], [7], [8] While (1) and (2) can temper the effects of volume change and may ultimately play a role in future Si-anode technology, they cannot prevent the dynamic rupture/reformation of the SEI in each cycle. Thus, development of electrolytes that can construct a mechanically stable SEI on Si particles to mitigate the volume effects is critical for enabling practical anodes with high Si content.

Objectives

The project objectives are to:

1. Identify appropriate fluorinated localized high concentration electrolyte (FLHCE) chemistries.
2. Prepare LHCE and evaluate physical properties.
3. Identify appropriate concentration ranges for LHCEs.
4. Evaluate electrochemical function.

Approach

The technological approach is to use fluorinated localized high concentration electrolytes, where each component of the electrolyte contains at least one fluorine in its structure, to construct a functional SEI on Si based anodes. The approach combines the SEI modification strategies of fluorinated carbonate solvents and local high concentration electrolytes. The resulting synergy of anion and fluorinated solvent decomposition will form a mechanically robust, fluorinated SEI that enables extended cycling with high-capacity retention. Diluting the LiFSI/fluorinated carbonate concentrated electrolyte with inert hydrofluoroethers will reduce viscosity and increase wettability while preserving the coordination environment of the concentrated electrolyte. The strong electron withdrawing fluorine substituents on the solvents will enable high oxidative stability, permitting the Si-based anode to be paired with state-of-the-art NMC811 cathodes.

Results

FLHCEs were prepared and their physical properties (viscosity, wettability) were characterized through viscometer and contact angle measurements of the electrolytes (Figure VIII.12.1). The control electrolyte had the highest initial average contact angle. In contrast, the FLHCEs had lower average contact angles, indicating favorable wetting properties for the FLHCEs relative to the control.

Extended cycling of the electrolytes was performed in Si-graphite/NMC622 full cells using a single layer pouch cell configuration (20 cm² cathode area), where loading of the Si-graphite and NMC622 electrodes were 2.5 mg/cm² and 18.5 mg/cm² respectively. Cycling was performed at C/3 rate between 3.0 – 4.3 V for 100 cycles (Figure VIII.12.2) after formation cycling under the same voltage limits at a lower current of C/10. Although the initial capacity of the cells with control electrolyte was higher than that of cells utilizing the FLHCE electrolytes, the control cells exhibited rapid capacity fade and low coulombic efficiency, with capacity dropping to below 20 mAh/g after 100 cycles. Notably, FLHCEs #2 and #5 which have the greatest salt concentrations, high viscosity, and high conductivity, resulted in the greatest improvement in delivered capacity after 100 cycles, at 88 mAh/g and 81 mAh/g, respectively.

Post-mortem SEM analysis of the cycled anodes highlighted the ability of the FLHCEs to stabilize the Si-graphite electrodes against extreme mechanical failure, which was observed for the control electrolyte sample. XPS showed electrodes cycled with the FLHCEs to have substantial amounts of LiF in their SEI layers as compared to the control electrolyte (Figure VIII.12.3), which can explain the poor cycling performance and mechanical electrode failure in the control sample. XPS data also revealed the lithiation depth was limited to the outer SiO₂ layer for the electrode cycled in control electrolyte, while the electrodes cycled with the FLHCEs indicated lithiation into the core Si layer of the active particles.

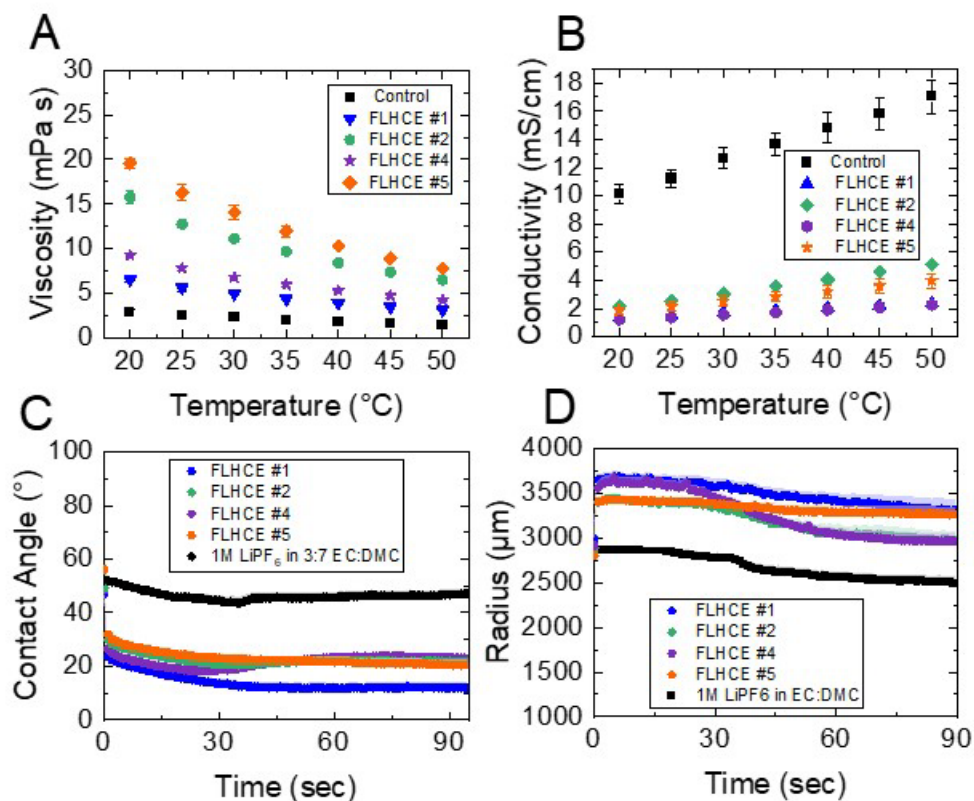


Figure VIII.12.1 (A) Viscosity and (B) conductivity of FLHCEs and control electrolyte over a temperature range of 20-50 °C. (C-D) Contact angle measurements of FLHCEs and control electrolyte on polyethylene separator over time.

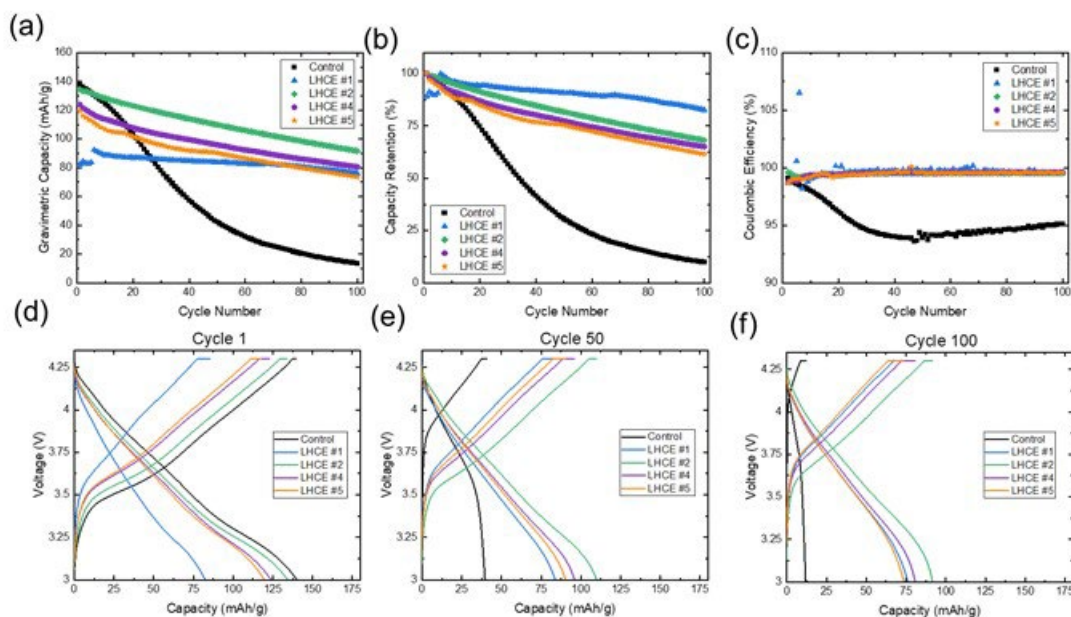


Figure VIII.12.2 Galvanostatic cycling of single layer Si-graphite/NMC622 pouch cells at C/3 rate with fluorinated LHCEs. Data is compared to cells cycled with control electrolyte (1M LiPF₆ 3/7 EC/DMC). C/3 cycling rate between 3.0 – 4.3 V. (a) Specific capacity, (b) capacity retention, (c) coulombic efficiency. (d-f) Voltage profiles at (d) 100 cycles, (e) 50 cycles, (f) 100 cycles.

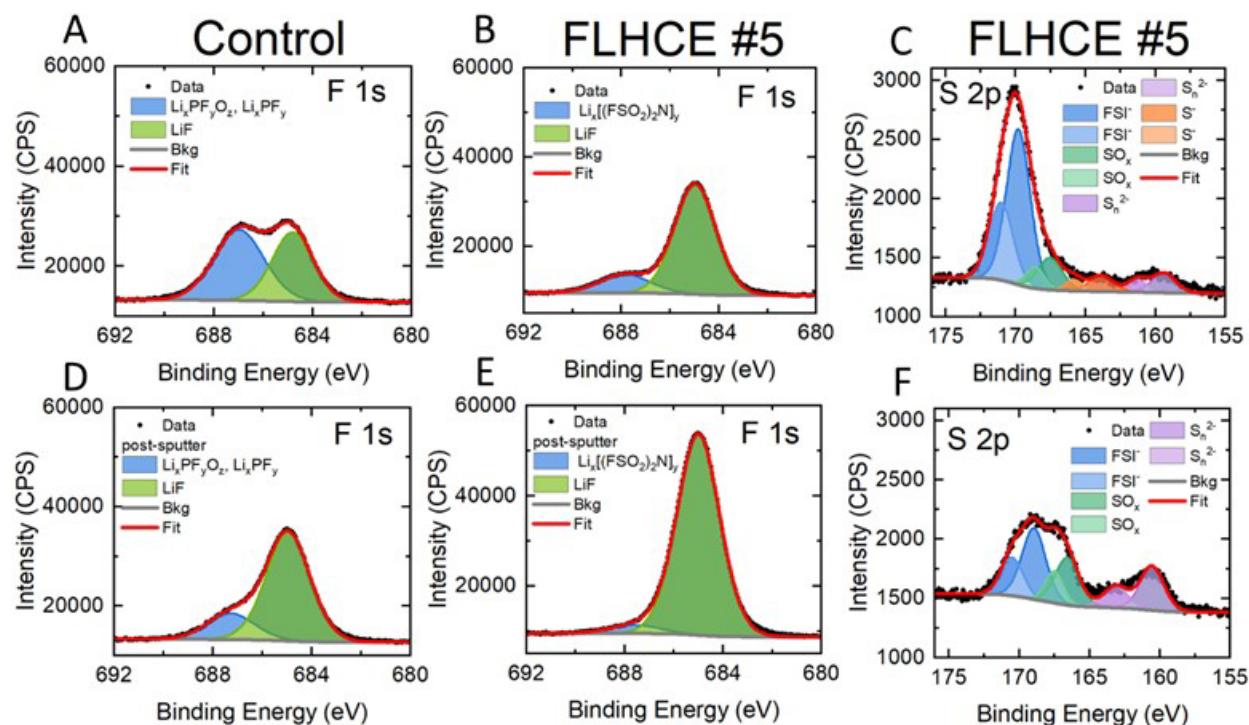


Figure VIII.12.3 F 1s and S 2p spectra for Si-graphite electrodes cycled 100× in full cells containing control and FLHCE #5 electrolyte before (top) and after (bottom) sputtering.

Conclusions

We have made progress in the successful development and characterization of novel FLHCEs containing fluorinated carbonate co-solvents and a fluorinated ether diluent. Work over the past year ultimately gave rise to four stable electrolyte formulations. Electrolyte properties such as viscosity, contact angle, and conductivity were largely influenced by final salt concentration. All LHCEs also benefited from high voltage stability up to 5 V. Overall, the FLHCEs outperformed the control electrolyte in full cell cycling tests, evincing higher capacity and capacity retention despite having lower conductivity. These results indicate that a robust LiF-rich and sulfur-containing SEI formed on electrodes cycled with the FLHCEs could accommodate the volume change of Si, stabilize the structural integrity of the Si electrode over extended cycling, and lead to facile Li⁺ conductivity through the SEI layer to the active particle.

Key Publications

1. Diana M. Lutz[†], Alison H. McCarthy[†], Steven T. King, Gurpreet Singh, Chavis A. Stackhouse, Lei Wang, Calvin D. Quilty, Killian R. Tallman, Ashley R. Head, Xiao Tong, Kenneth J. Takeuchi, Esther S. Takeuchi, David C. Bock*, Amy C. Marschilok*, *In preparation*.

References

1. Veith, G. M.; Doucet, M.; Sacci, R. L.; Vacaliuc, B.; Baldwin, J. K.; Browning, J. F., Determination of the Solid Electrolyte Interphase Structure Grown on a Silicon Electrode Using a Fluoroethylene Carbonate Additive. *Scientific Reports* 2017, 7 (1), 6326.
2. Shan, J.; Yang, X.; Yan, C.; Chen, L.; Zhao, F.; Ju, Y., Promoting Si-graphite composite anodes with SWCNT additives for half and NCM811 full lithium-ion batteries and assessment criteria from an industrial perspective. *Frontiers in Energy* 2019, 13 (4), 626–635.
3. Jia, H.; Li, X.; Song, J.; Zhang, X.; Luo, L.; He, Y.; Li, B.; Cai, Y.; Hu, S.; Xiao, X.; Wang, C.; Rosso, K. M.; Yi, R.; Patel, R.; Zhang, J.-G., Hierarchical porous silicon structures with extraordinary

mechanical strength as high-performance lithium-ion battery anodes. *Nature Communications* 2020, 11 (1), 1474.

4. Choi, S.; Kwon, T.-w.; Coskun, A.; Choi, J. W., Highly elastic binders integrating polyrotaxanes for silicon microparticle anodes in lithium-ion batteries. *Science* 2017, 357 (6348), 279–283.
5. Park, S.-J.; Zhao, H.; Ai, G.; Wang, C.; Song, X.; Yuca, N.; Battaglia, V. S.; Yang, W.; Liu, G., Side-Chain Conducting and Phase-Separated Polymeric Binders for High-Performance Silicon Anodes in Lithium-Ion Batteries. *Journal of the American Chemical Society* 2015, 137 (7), 2565–2571.
6. Hu, Z.; Zhao, L.; Jiang, T.; Liu, J.; Rashid, A.; Sun, P.; Wang, G.; Yan, C.; Zhang, L., Trifluoropropylene Carbonate-Driven Interface Regulation Enabling Greatly Enhanced Lithium Storage Durability of Silicon-Based Anodes. *Advanced Functional Materials* 2019, 29 (45), 1906548.
7. Eshetu, G. G.; Figgemeier, E., Confronting the Challenges of Next-Generation Silicon Anode-Based Lithium-Ion Batteries: Role of Designer Electrolyte Additives and Polymeric Binders. *ChemSusChem* 2019, 12 (12), 2515–2539.
8. Xu, Z.; Yang, J.; Li, H.; Nuli, Y.; Wang, J., Electrolytes for advanced lithium-ion batteries using silicon-based anodes. *Journal of Materials Chemistry A* 2019, 7 (16), 9432–9446.

Acknowledgements

Xiao Tong and Ashley R. Head are acknowledged for support with XPS measurements. XPS instrumentation and support were provided by the Center for Functional Nanomaterials, a U.S. DOE Office of Science Facility, at Brookhaven National Laboratory under Contract No. DE-SC0012704.

VIII.13 Devising mechanically compliant and chemically stable synthetic solid-electrolyte interphases on silicon using *ex situ* electropolymerization for long cycling Si anodes (University of Delaware)

Koffi Pierre Yao, Principal Investigator

University of Delaware
210 South College Avenue
Newark, DE 19716
E-mail: claver@udel.edu

Ajay K. Prasad, Principal Investigator

University of Delaware
210 South College Avenue
Newark, DE 19716
E-mail: prasad@udel.edu

Thomas Epps, Principal Investigator

University of Delaware
210 South College Avenue
Newark, DE 19716
E-mail: thepps@udel.edu

Daniel Abraham, Principal Investigator

Argonne National Laboratory
9700 South Cass Avenue
Lemont, IL 60439
E-mail: abraham@anl.gov

Brian Cunningham, DOE Technology Development Manager

U.S. Department of Energy
E-mail: Brian.Cunningham@ee.doe.gov

Start Date: September 26, 2020

End Date: December 31, 2021

Project Funding (FY21): \$367,823

DOE share: \$367,823

Non-DOE share: \$0

Project Introduction

Silicon (Si) as an earth-abundant material could enable near tenfold (> 3500 mAh/g) increase in the anode capacity of Li-Ion batteries which currently are almost universally based on graphite (372 mAh/g). A major issue halting the widespread use of silicon in Li-Ion batteries is the reactive surface combined with the 350% expansion and contraction of silicon nanoparticles during electrochemical cycling. The expansion and contraction of silicon nanoparticles in the anode results in the cyclical cracking of the solid electrolyte interphase (SEI) and its subsequent reformation through reductive decomposition of the battery cell electrolyte. This irreversible and continuous decomposition of the electrolyte into formation of new SEI products results in the consumption of the electrolyte, loss of lithium inventory, densification of the electrode, and loss of electrical contact of Si particles in the electrode. As a consequence, current Si-based electrodes are routinely unable to achieve more than 100 cycles in a battery and only limited loading (<15 weight%) in blended graphite-silicon electrodes are somewhat reliably useable.

Objectives

The program aims to produce cells based on Si anodes paired with existing transition metal oxide cathodes capable of achieving greater than 350 Wh/kg, 750 Wh/L at the cell level with a target calendar life of 10 years and cycle life of 1000 cycles (Table VIII.13.1).

Table VIII.13.1 Summary of program objectives

Beginning of Life Characteristics at 30 °C	Cell Level
Useable Specific Energy @ C/3	>350 Wh/kg
Useable Energy Density @ C/3	>750 Wh/L
Calendar Life (<20% energy fade)	>10 Years
Cycle Life (C/3 deep discharge to 350Wh/kg, <20% energy fade)	>1,000

Our project objective is to remedy the continuous electrolyte electro-decomposition on Si surfaces by devising a coating capable of containing the expansion and contraction of Si particles without film breakage. We have three specific goals in this pursuit: (1) Spectroscopically benchmark and optimize the film growth, quality, chemistry, stability, and electrochemical properties during electrodeposition; (2) utilize electropolymerization to coat nanometer-thin elastomeric and ionically conductive SEIs on Si allowing for fabrication of Si-anodes with over 30% Si loading; (3) validate, in an industrially representative pouch cell, the long-term stable cycling of anodes equipped our electrocoated Si.

Approach

The approach presented herein seeks to employ electropolymerization (EP) *ex situ* of a battery to form an elastomeric coating on the surface of silicon nanoparticles. The externalization of the SEI application process is intended to enable the use of a wider range of monomeric precursors in order to achieve a synthetic SEI coating with the requisite strain resistance to withstand the ~350% expansion/contraction of silicon during electrochemical cycling. Thus, created elastomeric SEI is targeted towards containing the expansion of silicon nanoparticles while retaining the integrity of the surface film in order to shield the electrolyte against cyclical reduction whence particles are integrated into a functional battery. A shielded cell electrolyte enables the use of high silicon loading (up to 70 wt.%) anodes towards achieving the desired 750 Wh/kg and 1000 cycles.

As justified by the novelty of the approach, fundamental benchmarking is undertaken in budget period one of the project wherein silicon thin films are used for model studies of the EP-coating of silicon in presence of selected monomers aimed at producing an elastomeric synthetic SEI coating. Translation of successful and optimized elastomeric EP-coating to nanoparticles coating will follow this benchmarking effort cumulating in testing with coin cells and pouch cells targeting the cell-level performance listed Table VIII.13.1.

Results

Covid-19 Impact

Our project kicked off in September 2020 amidst COVID-19 closures which impacted several aspects of the project execution including international personnel approval timelines as well as supplies acquisitions through June 2021. Supply acquisition including PPEs (disposable gloves), basic research supplies through University of Delaware's suppliers, and shared laboratory instrumentation use was significantly limited until approximately June 2021. Efforts to acquire research supplies such as electrolysis cells, lithium foil, electrolyte salts and solvents met with unusually extended timelines in Q1, Q2, and Q3. Shared laboratory instrumentation for research purposes such as the FTIR and AFM used extensively in our project were restricted on the University of Delaware campus to guard against the spread of COVID; unrestricted access was granted in

April 2021 (Q3). Personnel-wise, a key full-time researcher, citing COVID-19 and its psychological impact elected not to pursue a Ph.D. This researcher left in May 2021 resulting in difficulty recruiting a replacement through summer 2021. COVID-19 has had a measurable impact on the planned progress for the budget period both through tangible barriers such as restricted lab occupancies and research supply and instrumentation delays as well as intangible setbacks such as COVID-driven unforeseen personnel change.

We established a characterization pipeline suited to the identification and imaging of the nanometric synthetic SEI film to be deposited by electropolymerization on Si thin-film model surface (Si-film, picture and cell cycling shown in Figure VIII.13.1a). This characterization pipeline, illustrated in Figure VIII.13.1b, consists of (1) the electrochemical treatment for electrodeposition of corresponding polymers from various monomers, (2) retrieval of thus EP-treated Si-film, (3) rapid identification of the deposited film via Attenuated Total Reflection Fourier Transform Infrared spectroscopy (ATR-FTIR), (4) spatially-resolved imaging and spectroscopy using Atomic Force Microscopy (AFM) coupled with AFM-tip IR (NanoIR), and (5) X-ray photo-electron spectroscopy (XPS). All EP-coatings presented were carried out with 0.2 M Lithium bis(trifluoromethanesulfonyl)imide salt (LiTFSI) in tetrahydrofuran (THF) as the supporting electrolyte.

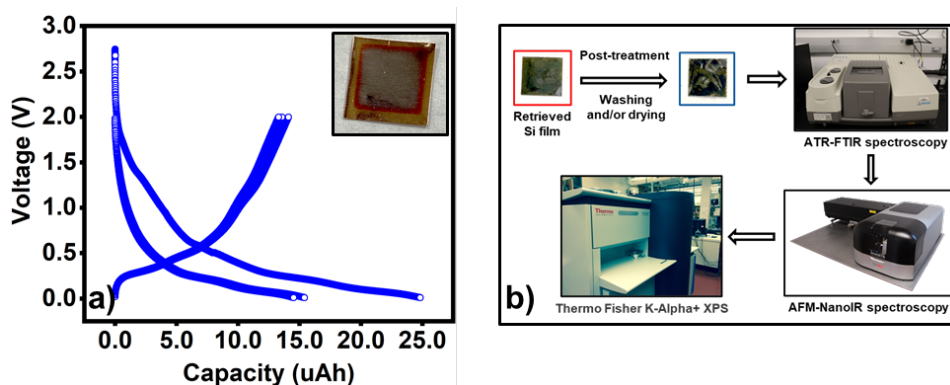


Figure VIII.13.1 (a) Electrochemical validation of silicon thin-film model surface produced by sputter-deposition. (b) characterization pipeline established for the R&D of EP-coated synthetic SEIs for silicon anodes.

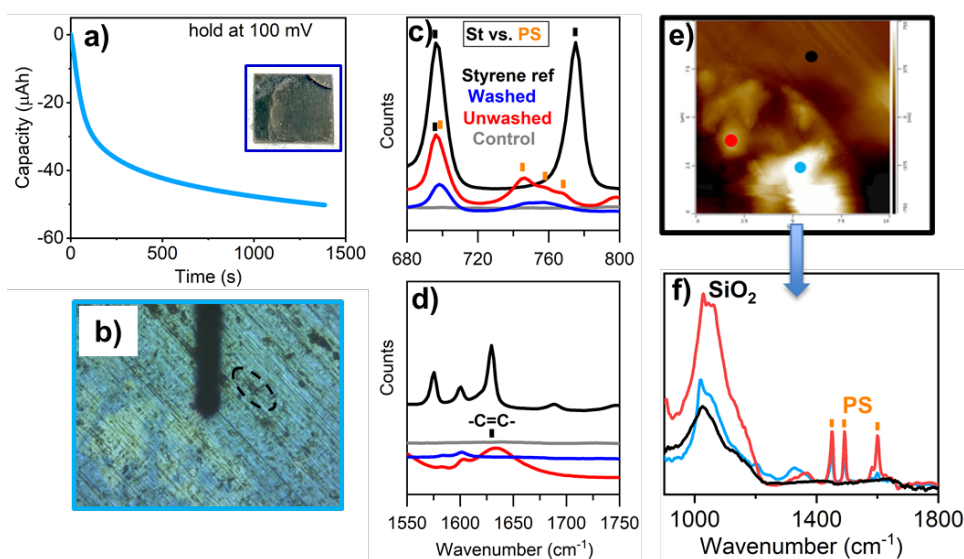


Figure VIII.13.2 Initial facile EP-coating of polystyrene from styrene monomer on silicon thin-film model surface to establish characterization pipeline. 0.2 M LiTFSI in THF is used as supporting electrolyte. (a) Potentiostatic hold at 100 mV to achieve EP-coating of polystyrene on silicon thin-film model surface. (b) microscopy image of silicon film surface after EP treatment. (c, d) ATR-FTIR of reference styrene monomer, Unwashed post-EP sample, methanol washed post-EP sample, and control sample from cell without electrochemical treatment. Coupled AFM+NanoIR imaging (e) and IR spectroscopy (f) of water washed post-EP sample.

The facile electropolymerization of heterocyclic styrene [1] due to its ability to accept or donate electrons through the π system of its aromatic ring was an opportune entry to investigating the EP-coating of Si. We successfully demonstrated the EP-coating of silicon surfaces with polystyrene (PS) starting from styrene monomer at 100 mV versus lithium (Li) (Figure VIII.13.1). The presence of PS is verified by presence of characteristic FTIR peaks at 746 and 757 cm^{-1} and the absence of the vinyl $\text{C}=\text{C}$ stretch at 1630 cm^{-1} present in its monomer (Figure VIII.13.2c and Figure VIII.13.2d). Morphological imaging using AFM shows nodular deposits which are ascertained to be PS using integrated spatially-resolved NanoIR (Figure VIII.13.2f). Nonetheless, with its failure strain of $\sim 4\%$, PS is unsatisfactory for compliant containment of silicon with its 350% volumetric electrochemical expansion.

In pursuit of more elastomeric synthetic SEI-coatings, we investigate the EP-coating of Si-films with polyisoprene (PIP) and derivative films from electropolymerization of isoprene (IP). Electropolymerization of IP to PIP is achieved on Si-films at 4V vs. Li (Figure VIII.13.3a, Figure VIII.13.3b, and Figure VIII.13.3c); conversely, at 100 mV, no evidence of PIP was observed on the surface by FTIR (not shown for brevity). Electropolymerization of IP is known to proceed via the initial formation of a carbocation leading to cationic chain growth. [2] At the oxidative potential of 4V, likely electron withdrawal from IP molecules resulted in the EP-deposition of PIP as shown by the presence of characteristic peaks at 1033, 1044, 1140, 1150, 1325, ~ 1660 cm^{-1} in FTIR (Figure VIII.13.3b, and Figure VIII.13.3c). Most notably, the absence of $-\text{C}=\text{CH}_2$ stretch at ~ 887 cm^{-1} in the methanol washed sample post EP-treatment in Figure VIII.13.3b versus the presence of this characteristic FTIR peak in the IP monomer reference spectrum conclusively indicates the formation of polyisoprene.

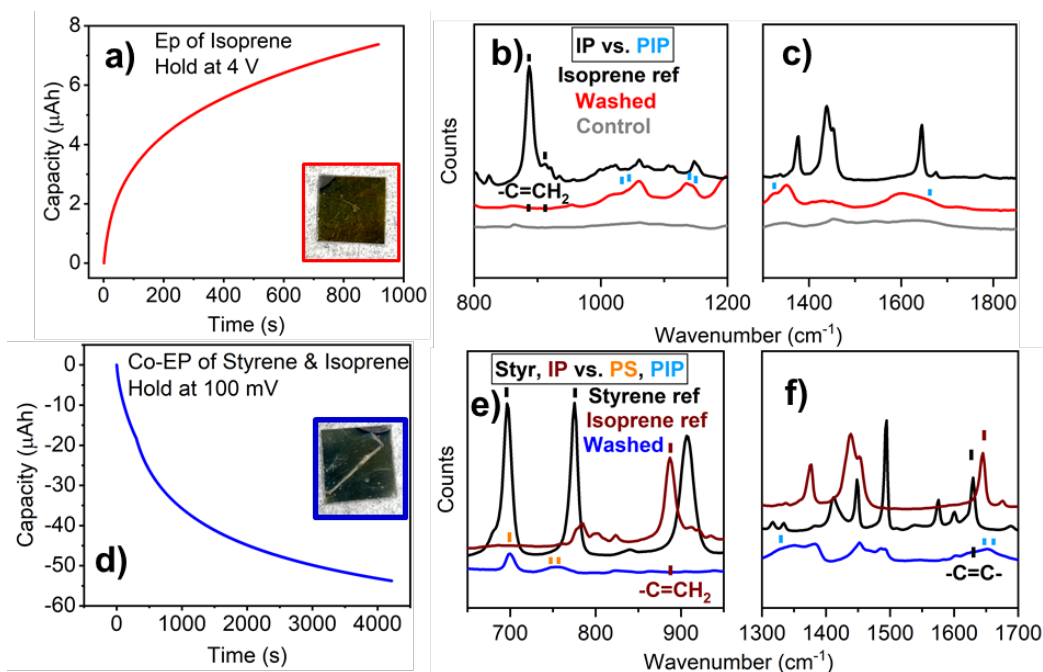


Figure VIII.13.3 (a) Cationic EP-coating of isoprene on silicon thin-film model surface at 4V vs. Li in 0.2 M LiTFSI in THF. (b, c) ATR-FTIR of reference isoprene monomer, methanol washed post-EP sample, and control sample from cell without electrochemical treatment. (d) Co-electropolymerization coating of styrene and isoprene on silicon thin film at 100 mV aimed at exploiting styrene facile initiation to electrodeposit an elastomeric film of polyisoprene on silicon. (e, f) ATR-FTIR of corresponding reference monomers and methanol washed post-EP sample.

Considering the possible instability of anodic silicon at high potentials (4V) in lithium-electrolyte, we investigate the co-electropolymerization of isoprene with styrene at low potentials (100 mV). At 100 mV, we anticipate the reductive initiation of co-polymerization through the formation of styrene carbanions. The same presence and absence of peaks revealing the EP-deposition of polystyrene (Figure VIII.13.2c and Figure

VIII.13.2d) and polyisoprene (Figure VIII.13.3b and Figure VIII.13.3c) in single monomer electrodeposition are observed after the co-electropolymerization treatment (Figure VIII.13.3e and Figure VIII.13.3f). It is likely that the co-electropolymerization yields an isoprene-styrene block copolymer [3] on the surface of Si-films upon electrochemical treatment at 100 mV. PIP (natural rubber) is an elastomer with yield strain above 500%. Consequently, achieving a PIP-based film on silicon with a template of ionically conductive salt products such as LiF and Li_2CO_3 would offer a pathway to contain the expansion and contraction of silicon anode nanoparticles and thereby shield the electrolyte in a cell.

Conclusions

In budget period one, we have developed a research and development pipeline for the benchmarking of the ex-situ EP-coating of silicon with elastomeric synthetic SEIs. Using Si-films as silicon model surfaces, we have achieved the low potential EP-deposition of polystyrene (yield-strain $\approx 4\%$) as well as polyisoprene (yield-strain $> 500\%$) through co-polymerization in presence of styrene. Future effort in this direction will involve tuning of the electropolymerization precursor and acidic surface treatment towards achieving conformal thin films of synthetic SEIs for silicon anodes. Transfer of the optimized EP-coating process to Si-nanoparticles coating is planned in our continued efforts to produce high-loading Si-based cells with stable cycling.

References

1. Darafarin, M., Eslami, H. & Raoufian, E. “Electropolymerization of styrene in alcoholic solution and preparation of its bilayer with polyacrylamide.” *Polym. Bull.* 76, 3003–3016 (2019). doi: 10.1007/s00289-018-2514-8
2. Kostjuk, S. V et al. “Carbocationic Polymerization of Isoprene Co-initiated by $\text{B}(\text{C}_6\text{F}_5)_3$: An Alternative Route Toward Natural Rubber Polymer Analogues?” *Macromolecules* 44, 1372–1384 (2011). doi: 10.1021/ma1027966
3. Zhang, H., Luo, Y. & Hou, Z. “Scandium-Catalyzed Syndiospecific Copolymerization of Styrene with Isoprene.” *Macromolecules* 41, 1064–1066 (2008). doi: 10.1021/ma7027006

Acknowledgements

The P.Is acknowledge the research efforts of graduate student researchers Rownak Jahan Mou, Shane Shearman, and Mengying Yang. The P.Is also thank Brian Cunningham and Adrienne Riggi for productive technical discussions and invaluable assistance in the management on the project.

VIII.14 Rational Electrolyte Design for Li-ion Batteries with Micro-sized Si Anodes (University of Maryland College Park, ARL)

Chunsheng Wang, Professor, Principal Investigator

Department of Chemical & Biomolecular Engineering
University of Maryland
College Park, MD 20742
E-mail: cswang@umd.edu

Oleg Borodin, Scientist, Principal Investigator

Energy Storage Branch, Sensor and Electron Devices Directorate
U.S. Army Combat Capabilities Development Command
Army Research Laboratory
2800 Powder Mill Road
Adelphi, MD 20783
E-mail: oleg.a.borodin.civ@mail.mil

Brian Cunningham, DOE Technology Development Manager

U.S. Department of Energy
E-mail: Brian.Cunningham@ee.doe.gov

Start Date: October 1, 2019	End Date: March 31, 2021 (extended to September 30, 2021)
Project Funding (FY21): \$200,000	DOE share: \$200,000 Non-DOE share: \$0

Project Introduction

The success of micro-sized graphite (10 μm) anodes in carbonate electrolyte for Li-ion batteries is attributed to the formation of organic-inorganic solid electrolyte interphase (SEI) through simultaneous reduction of LiPF_6 salt and carbonate solvents at $\sim 0.8\text{V}$ (vs. Li/Li^+). The organic-inorganic SEI can accommodate the small volume change of graphite during lithiation/delithiation without cracking, ensuring a high Coulombic efficiency (CE) of $>99.98\%$ and cycle life of >1000 . Si anodes are the most promising anode materials for next-generation Li-ion batteries (LIBs) due to favorable average potentials (0.3 V vs Li^+/Li) and 10 times higher capacities than graphite anodes. However, since both Si particles and the SEI undergo larger volume changes during cycling, the SEI is more prone to be damaged and cannot effectively prevent the side reactions between Si and the electrolyte, resulting in SEI thickening and pulverization of the Si particles. Thus, the Si-based Li-ion batteries usually demonstrate rapid capacity decay and low coulombic efficiency (CE). Extensive efforts have been devoted to suppressing the Si and SEI cracking during charge/discharge cycling, and the battery community has reached a consensus that the carbon coated nano-sized Si and fluoroethylene carbonate (FEC)-contained electrolytes is the best combination to enable high-capacity Si anodes. However, the technique still suffers from high cost, low $i\text{CE}$ and low volumetric energy density, which limits the practical applications.

Objectives

Large ($>10\ \mu\text{m}$) Si microparticles (μSi) are especially attractive due to their low production cost. The objectives of this project are (1) to research, fabricate and test lithium-ion batteries that implement $\geq 30\%$ silicon content electrodes with commercially available cathode and (2) to achieve cell level energy density of $>350\ \text{Wh/Kg}$ (C/3) for 1000 cycle life with $< 20\%$ energy fade. The main task is to screen, select and investigate the solvation structures and properties of a variety of electrolytes for the μSi anode. The tasks for the first budget period are: (1) screen and select inorganic salts solvents to promote LiF SEI formation on Si and LiF CEI on NCA and NCM cathodes; (2) theoretically and experimentally investigate the solvation structures and properties the developed electrolytes.

Approach

To reduce the deformation of SEI layer, it is desirable to form an SEI layer with a low affinity to the lithiated Si particles, so that the lithiated Si can slip at the interface during volume change without damaging the SEI. Among the known components in the SEI, lithium fluoride (LiF) possesses the highest interfacial energy with $\text{Li}_x\text{Si}/\text{Si}$. In addition, the wide bandgap and highly insulated LiF also significantly reduces the thickness of the LiF SEI (increasing the $i\text{CE}$). The PIs have conducted preliminary studies and identified that 2.0 M LiPF_6 in 1:1 v/v mixture of tetrahydrofuran (THF) and 2-methyl tetrahydrofuran (MTHF) electrolyte (mixTHF electrolyte) can efficiently form LiF SEI on μSi . The mixTHF has electrochemical stability window of 4.2 V and enables μSi electrodes to provide 2800 mAh g^{-1} capacity with cycling life of >400, $i\text{CE}$ of >90% and $c\text{CE}$ of >99.9% without any pre-treatment. The mixTHF electrolyte also enables $\text{LiNi}_{0.8}\text{Co}_{0.15}\text{Al}_{0.05}\text{O}_2$ (NCA)/Si and $\text{LiFePO}_4/\text{Si}$ full cells to stably charge/discharge up to 100 cycles. A highly fluorinated LiPF_6 and cathodic stable THF-MTHF solvents were selected to enlarge reduction potential gap between salt and solvent, which ensures the formation of LiF SEI on Si at >1.1 V and avoid formation of the organic polymer until the end of lithiation process. Based on the preliminary results, we propose to extend the anodic stability of mixTHF electrolyte using inorganic additives and fluorinated anti-solvents. Other potential chemistries that demonstrate the tendency to form inorganic and LiF-rich SEI are also explored.

Results

1. Electrochemical Performance of $\mu\text{Si} \parallel \text{Li}$ Cells with modified mix-THF Electrolytes

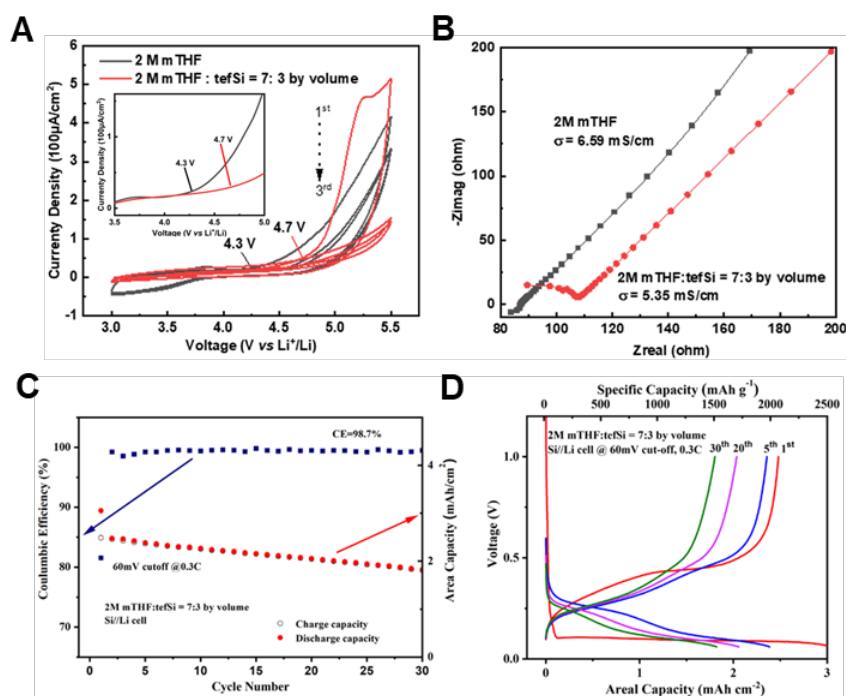


Figure VIII.14.1 Electrochemical performances of the LiPF_6 -mixTHF-TEFSi electrolyte. (A) Linear scanning voltammetry of 2.0 M LiPF_6 in mixTHF and LiPF_6 -mixTHF-TEFSi using stainless steel as working electrode, scan rate = 0.5 mV/sec. (B) Nyquist plots of electrochemical impedance spectrometry (EIS) with Pt blocking electrodes in 2.0 M LiPF_6 -mixTHF and LiPF_6 -mixTHF-TEFSi electrolytes at room temperature. The ionic conductivities are referenced and calculated to the standard electrolyte; (C) the cell performance of $\mu\text{Si} \parallel \text{Li}$ half cells in LiPF_6 -mixTHF-TEFSi electrolyte between 0.06 and 1V; (D) the initial, 5th, 20th and 30th charge-discharge profiles of the LiPF_6 -mixTHF-TEFSi electrolyte. The capacity retention at 30th cycle was calculated by normalizing to capacity at 2nd cycle.

Our study with mixTHF electrolyte has demonstrated that inorganic-rich SEI is essential to maintain stable cycle of μSi anode in Si/LFP full cell. To further extend the anodic stability of the electrolyte to pair with high voltage layered oxide cathode, inorganic additives and fluorinated anti-solvents were systematically investigated. Particularly, triethoxyfluorosilane (TEFSi) demonstrates the most noticeable enhance of anodic

stability from 4.3 V to 4.7 V (Figure VIII.14.1A) with minimum reduction in ionic conductivity from 6.59 to 5.35 mS/cm (Figure VIII.14.1B). The mixTHF-TEFSi electrolyte also demonstrates favorable initial coulombic efficiency (*i*CE) of 81.3% and cycling coulombic efficiency (*c*CE) of 98.7% in μ -Si || Li cell with a capacity retention of 73.3% at the 30th cycle (Figure VIII.14.1C and Figure VIII.14.1D). The test conditions and the additives/anti-solvents will be tuned pivoting LiF-rich SEI for highly reversible μ -Si based batteries.

2. Solvent-free ionic liquid electrolyte

Another strategy to improve the anodic stability of the electrolyte is to avoid using the reductive THF as electrolyte solvent. We developed ionic liquid (IL) electrolyte that efficiently forms dense and ceramic-based SEI on lithium metal. The IL electrolyte demonstrates the ionic conductivity of 4.07 mS/cm (Figure VIII.14.2A) and an anodic stability of 4.5 V vs. Li^+/Li (Figure VIII.14.2B). The IL also supports reversible NMC 811 cathodes with negligible variation of potential and stable capacity retention over 100 cycles (Figure VIII.14.2C and Figure VIII.14.2D). The compatibility between IL and μ -Si anode was evaluated in μ -Si || Li half-cells and the *i*CE is around 93% and the *c*CE is 99.8% (Figure VIII.14.3A and Figure VIII.14.3B). Despite relatively high *c*CE, the capacity gradually faded (Figure VIII.14.3B), which is possibly caused by loss of electronic and ionic contact of the Si particles. And it was mitigated by enhancing the adhesion between Si and the current collector as well as using a less viscous version of the IL electrolyte (denoted as IL-Me) for better wettability (Figure VIII.14.3C). The same performance was observed when the electrode areal loading increases from 3.0 mAh/cm² to 4.5 mAh/cm² (Figure VIII.14.3D).

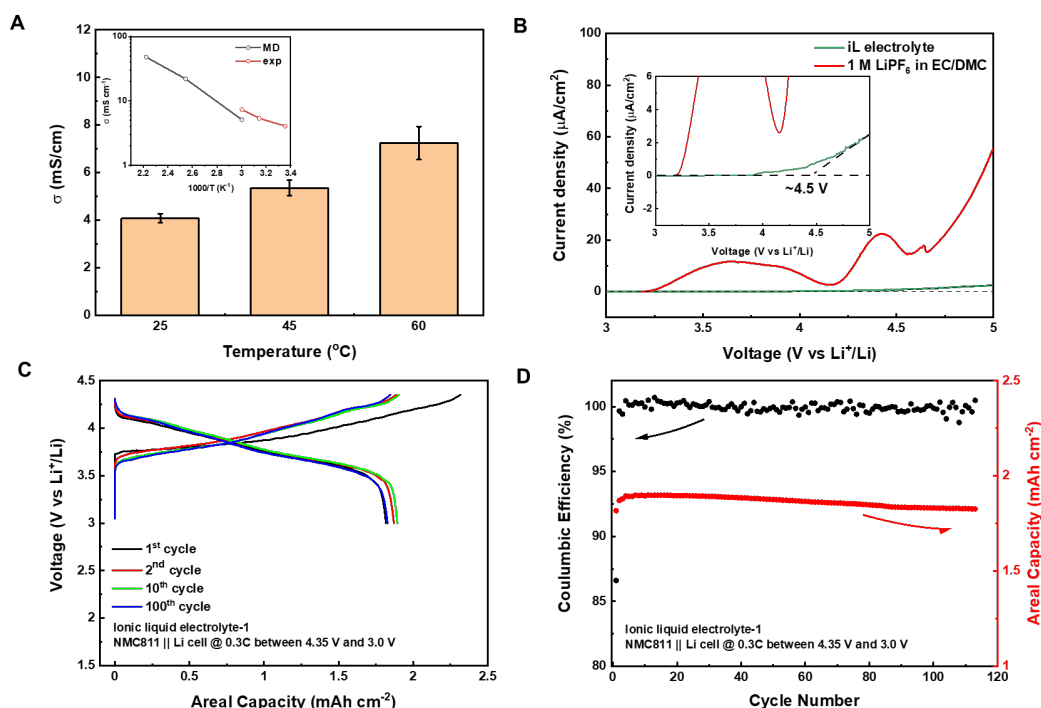


Figure VIII.14.2 Ionic conductivity and high potential performance of the IL electrolyte. (A) Ionic conductivities of the IL electrolyte at different temperatures measured with EIS between 106 Hz to 103 Hz using stainless steel blocking electrodes. Inset shows the MD simulation predictions. (B) Linear scanning voltammetry in IL and commercialized 1.0 M LiPF₆ in ethylene carbonate/dimethyl carbonate (EC/DMC, v/v = 1:1) using stainless steel as working electrode, scan rate = 1 mV/sec. (C) the charge and discharge curves of NMC 811 || Li cell in the IL operation at 0.3C. (D) Cycling coulombic efficiency and capacity retention of NMC 811 in IL.

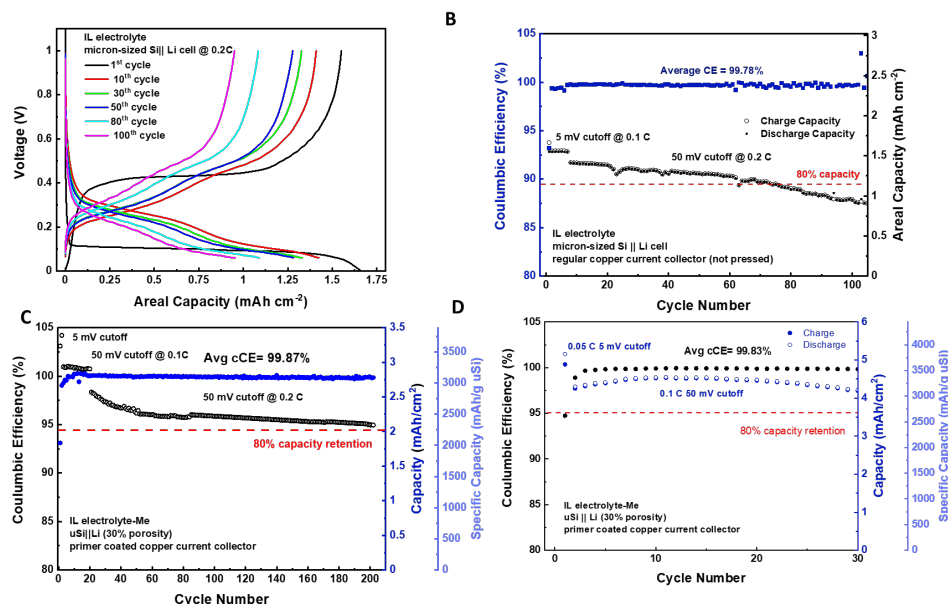


Figure VIII.14.3 The cycling CE and the capacity retention of (A) the 1.5 mAh/cm² μ -Si anode on Cu current collector in IL; (B) the 3 mAh/cm² μ -Si anode on conductive carbon coated Cu current collector in IL-Me and (C) the 4.5 mAh/cm² μ -Si anode on conductive carbon coated Cu current collector in IL-Me. All tests are performed with activation at 0.1C or 0.05C followed by cycling at 0.2 C or 0.1 C, the 80% capacity retention was calculated by taking the first capacity at 0.2 C (for 1.5 mAh/cm² and 3 mAh/cm²) or at 0.1 C (for 4.5 mAh/cm²) as 100%.

The most noticeable differences of a rigid NMC 811 in the full cell compared to the soft Li metal in half-cells is the stress applied to Si anode upon volume expansion, which demonstrated as only 50% capacity utilization from the beginning in a 4.5 mAh/cm² full cell. When cathode and anode were cushion by the compressible glass fiber separator (GF), the capacity loss was alleviated (Figure VIII.14.4).

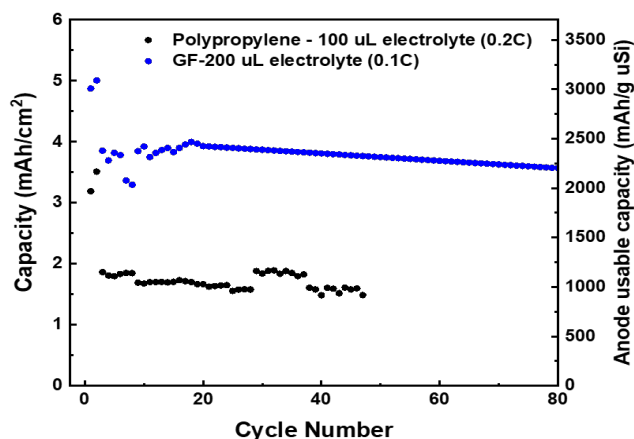


Figure VIII.14.4 The capacity retention of the 5 mAh/cm² μ -Si || 4.5 mAh/cm² NMC811 full cell between 4.2 and 2.7 V with polypropylene and GF separator.

3. Calendar life of micro-sized Si anode with LiF-rich SEI

The calendar aging of silicon anodes is critical for practical use, and it is mainly due to the Li inventory losses from parasitic reactions. There are two strategies to reduce calendar aging: a stable and electronic insulating SEI, and reduced electrode surface area. Among the known SEI components, LiF is one of the most chemically stable insulating components toward lithiated Si. Therefore, the combination of LiF-rich SEI and μ Si with small surface area is promising in reducing the calendar aging.

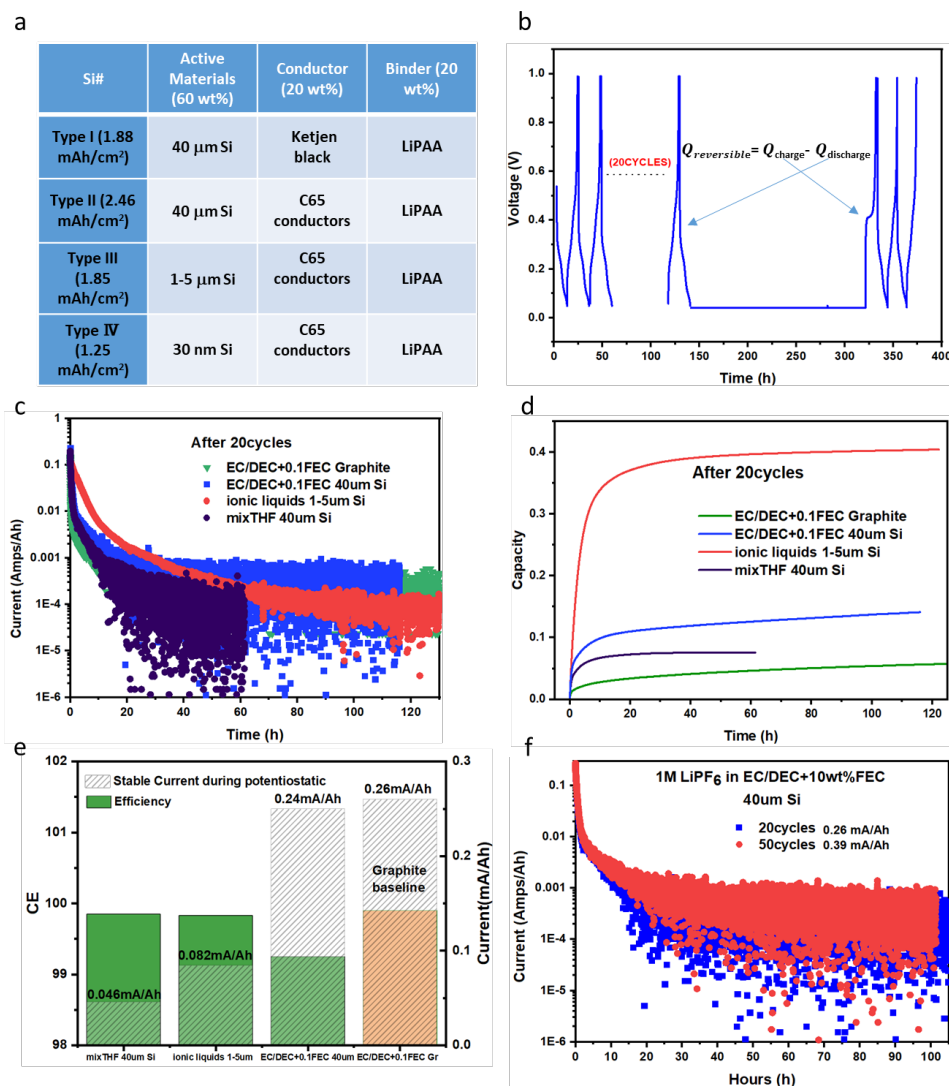


Figure VIII.14.5 (a) Composition of different type of Silicon anode. (b) Calendar life test protocol and $Q_{\text{reversible}}$ calculation. (c) Current decay versus time during voltage hold of μ Si anode and graphite baseline. (d) Capacity loss versus time during voltage hold of μ Si and graphite baseline anodes. (e) Summary of CE and stable current during voltage hold of micro-sized silicon and graphite baseline anodes. (f) Current decay versus time during voltage hold of EC/DEC+FEC electrolyte for μ Si anode after 20cycles (CE=99.2%) and 50 cycles (CE=98.7%).

To simulate the process of calendar aging, we measure the leakage currents in Si || Li cells (the types of Si anode used are listed in Figure VIII.14.5A) held at 60 mV (10 mV for graphite || Li cells) after pre-cycling the cells for stable CE (Figure VIII.14.5B). The leakage current of Type I Si anode in mixTHF electrolyte is 0.046mA/Ah, and that in carbonate electrolyte is 0.24 mA/Ah, both of which are lower than the that of graphite anode in commercial carbonate electrolyte (0.26mA/Ah) (Figure VIII.14.5C). The low leakage current suggests the side reaction rate is low thus beneficial for long-term storage. The lower slope value of capacity faded versus time also confirm the better calendar life (Figure VIII.14.5D). We also identified that the cCE is positively related to the calendar life (Figure VIII.14.5E), since cCE reflects the stability and integrity of the SEI. And the SEI stability on Si is dynamic, in which the leakage currents of Type I Si anode in commercial carbonate electrolyte after 20 and 50 cycles increase from 0.26 mA/Ah to 0.39 mA/Ah (Figure VIII.14.5F).

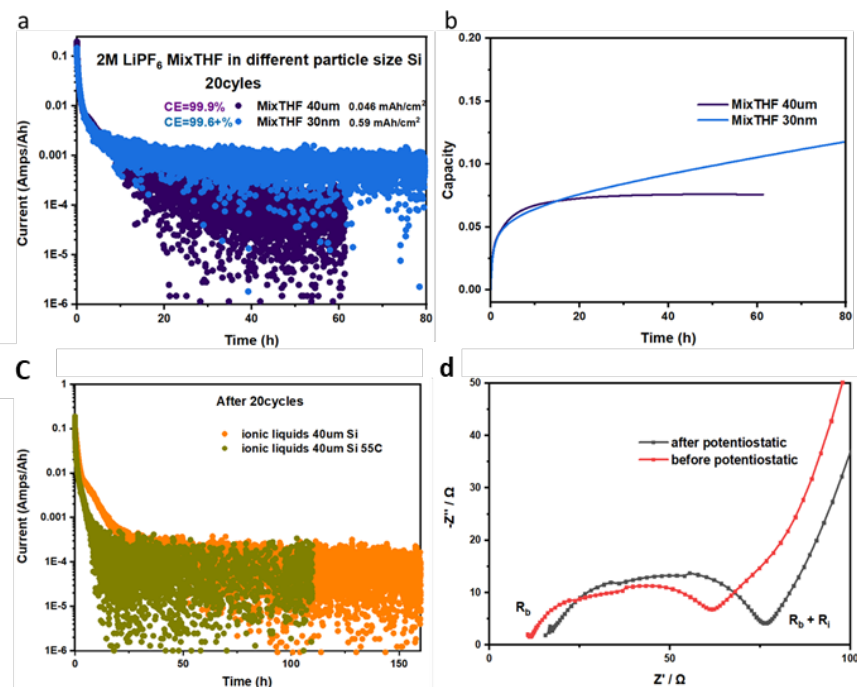


Figure VIII.14.6 (a) Current decay versus time during voltage hold of silicon anode with different particle size using 2.0 M LiPF₆ mixTHF. (b) Capacity loss versus time during voltage hold of μ Si with different particle size using 2.0 M LiPF₆ mixTHF. (c) Current decay versus time during voltage hold of μ Si anode at different temperature (IL electrolytes). (d) EIS curve of ionic liquids 40um Si cell before/after the voltage hold at 55°C.

The particle size also plays a critical role in the leakage current. The *c*CE of Type IV Si is comparable to Type I Si in mixTHF electrolyte (99.6+% versus 99.9%) yet Type IV Si demonstrates much higher leakage currents (0.59 mAh/Ah versus 0.046 mAh/Ah) (Figure VIII.14.6A) and the cumulative capacity loss (Figure VIII.14.6B) because of the higher surface area of nano-Si particle. When the particle size is at the same level, the SEI stability controls the calendar life, which is mainly impacted by ratio of ionic to electronic conductivity (passivation ability) of SEI as well as SEI solubility in the electrolyte (need to repair the dissolved part of SEI). In this case, we tested the 40 μ m silicon cell in ionic liquids at high temperatures, where the SEI are much easier to dissolve. As shown in Figure VIII.14.6C, even at 55°C, the leakage current is still very low, which is due to the superior passivation ability of the inorganic-rich SEI formed between the IL electrolytes and silicon anodes. The small increase in resistance before and after 180 h of voltage hold at 100% state of charge (Figure VIII.14.6D) also further confirm low SEI growth with inorganic-rich SEI even at high temperatures.

Conclusions

In summary, to make stable Si-NMC 811 cell, we used anti-solvents to extend the anodic stability of mix-THF electrolyte originally proposed. The addition of TEFSi anti-solvent demonstrates the most promising behavior in terms of both Si anode stability, ionic conductivity, and anodic stability. Alternatively, we also have demonstrated that modified IL electrolyte with a reduced viscosity can form inorganic SEI on Si, enabling 80% of capacity retention at 200th cycle in μ Si|| Li half-cell. The μ Si/ NMC 811 full cells in the IL electrolyte demonstrated a super cycling stability when the cathode and anode are cushioned by a compressive glass fiber (GF) separator. Further optimization of the electrolytes and operating conditions will be performed in the next fiscal year, targeting high CE and cycling capacity retention for the μ Si-NMC full cell. Calendar aging of the Si anodes was also investigated through monitoring the leakage current. Our result shows that larger particle size and stable SEI could significantly enhance the calendar life problem of silicon anode.

Acknowledgements

We sincerely acknowledge Ms. Kimberly R. Nuhfer's strong support.

IX Next-Gen Lithium-Ion: Advanced Cathodes R&D

IX.1 Design, Synthesis, & Characterization of Low-Cobalt Cathodes (ANL, ORNL, LBNL, NREL, PNNL)

Jason R. Croy, Principal Investigator

Argonne National Laboratory
9700 South Cass Avenue
Lemont, IL 46039
E-mail: croy@anl.gov

Peter Faguy, DOE Technology Development Manager

U.S. Department of Energy
E-mail: Peter.Faguy@ee.doe.gov

Start Date: October 1, 2018	End Date: September 30, 2022	
Project Funding (FY21): \$4,700,000	DOE share: \$4,700,000	Non-DOE share: \$0

Project Introduction

State-of-the-art Li-ion batteries (LIBs) for transportation applications contain transition metal (TM) oxide cathodes consisting of $\text{Li}_{1+x}\text{Ni}_a\text{Co}_b\text{Al}_c\text{O}_2$ (NCA) or $\text{Li}_{1+x}\text{Ni}_a\text{Mn}_b\text{Co}_c\text{O}_2$ (NMC-abc) oxides, where $x = \sim 0-0.05$ and $a+b+c = 1$. Both oxide chemistries contain Co, which has been recognized over many years of research as an important component in terms of structure, stability, and electrochemical performance. Currently, however, geopolitical concerns associated with Co mining, availability, and cost have caused the LIB community to pursue the development of low- to no-cobalt layered oxides as next-generation cathodes. The goal of this work is to show progress towards the realization of low/no-cobalt oxides having acceptable performance (energy/power densities), safety, and cycle/calendar life by way of new insights into cathode design and synthesis as they pertain to the critical roles of Co in layered oxides.

Objectives

- Understanding of local ordering as a function of Co and dopant/substitution content.
- Synthesis of new, low- to no-cobalt cathodes showing promise with respect to an NMC-622 baseline.
- Synthesis and understanding of LiNiO_2 -based oxides with low- to no-cobalt compositions.
- Atomic-scale characterization, understanding, design, and synthesis of NiMn-based cathodes.

Approach

- Advanced characterization of Ni-rich, low- and no-cobalt cathodes including synchrotron techniques, solid-state NMR, electron microscopy, and theory/modeling.
- Advanced characterization of MnNi-based, low- and no-cobalt cathodes including synchrotron techniques, solid-state NMR, electron microscopy, and theory/modeling.
- Development of novel surface modifications for low/no-cobalt oxides.
- Large batch co-precipitation synthesis of model and new compositions for practical evaluation.
- Synthesis of standardized materials for distribution and study across multiple teams.

Results

Lowering the cobalt and nickel content of NMC – Cathode-oxides with >80% Ni content are being heavily developed with good success. However, cathode materials that contain less Ni and can deliver performance with very low-to-no Co contents are of significance, as it is now clear that future markets will rely heavily on Ni. This project has pursued the design of novel cathodes with the goal of lowering Co *and* Ni contents while incorporating higher Mn contents and delivering performance that is better, or on par, with state-of-the-art NMC-622. The Co-free $\text{LiMn}_{0.5}\text{Ni}_{0.5}\text{O}_2$, known to have severe Li/Ni exchange issues, was used as a model oxide for these designs with the goal of achieving highly-layered oxides with < 5% cobalt. Substantial progress has been made on the design of such oxides within the program, revealing that an understanding of atomic ordering can lead to layered-oxides with high performance. [1] Notably, very low Co (~5%) can be used to facilitate layering, while allowing higher Mn contents and some excess Li, without forming substantial Li/Mn ordering (i.e., LiMn_6). Extensive compositional studies within the program [2] have found that oxides derived from $\text{Mn}_{0.35}\text{Ni}_{0.6}\text{Co}_{0.04}\text{Al}_{0.01}(\text{OH})_2$ precursors show promise in meeting the goals noted above. This FY, efforts were focused on an understanding of how the synthesis of such compositions can be scaled, via co-precipitation, utilizing continuous stirred tank (CSTR) and Taylor vortex (TVR) reactors. TVR studies were conducted in collaboration with ANL's Materials Engineering Research Facility (MERF), the details of which can be found in section I.2.C of this report.

One of the main challenges with the synthesis of $\text{Mn}_{0.35}\text{Ni}_{0.6}\text{Co}_{0.04}\text{Al}_{0.01}(\text{OH})_2$ is controlling the Al content and distribution within the hydroxide precursor. Solid state reactions, sol-gel synthesis, and dry coating can all be effective but typically achieve best results (e.g., uniform distribution) at very low levels of Al (~ppm). In addition, the composition of the oxide can play a significant role where Al more readily incorporates into high Co/Ni content oxides but tends to segregate in the presence of Mn. [3] In order to facilitate more intimate mixing, incorporation of Al at the precursor stage (i.e., during co-precipitation) would be advantageous. However, co-precipitation of Al^{3+} in the same reactor with Ni^{2+} , Mn^{2+} , and Co^{2+} is very challenging because of the vast differences between the product constants of these metal hydroxides. Al^{3+} also does not form a strong complex with NH_3 and $\text{Al}(\text{OH})_3$ is often precipitated at an uncontrollable rate, resulting in low-density, needle-shaped, and phase separated precursor particles. Therefore, the coprecipitation of $\text{Al}(\text{OH})_3$ must be controlled. To achieve this goal, Al^{3+} was first converted to $\text{Al}(\text{OH})_4^-$ by dissolving $\text{Al}_2(\text{SO}_4)_3$ in NaOH utilizing the amphoteric characteristic of Al. The $\text{Al}(\text{OH})_4^-$ complex can be converted back to $\text{Al}(\text{OH})_3$ at a lower pH in the reactor at reasonably slow rates where it is then incorporated with other NMC hydroxides. Because the $\text{Al}(\text{OH})_4^-$ solution has a very high pH compared to the NMC sulfate solution, the $\text{Al}(\text{OH})_4^-$ and NMC sulfate solutions must be injected into the reactor separately at precisely controlled flow rates.

Figure IX.1.1(a)–(d) show scanning electron microscopy (SEM) images of $\text{Mn}_{0.35}\text{Ni}_{0.6}\text{Co}_{0.04}\text{Al}_{0.01}(\text{OH})_2$ precursors synthesized by the method described. The particles showed a bimodal size distribution with larger particles between 5–8 μm and smaller particles between 1–3 μm . The Al-doped particles were not as rounded as undoped particles (not shown) but the needle-like shape, indicative of uncontrolled precipitation, is not observed, revealing that the method can control $\text{Al}(\text{OH})_3$ precipitation. Energy-dispersive X-ray spectroscopy (EDS) mapping of Al, Figure IX.1.1(d), shows that Al is homogeneously distributed on the surface of particles, implying that it is also well incorporated inside the particles due to the diffusion-controlled mechanism of particle growth.

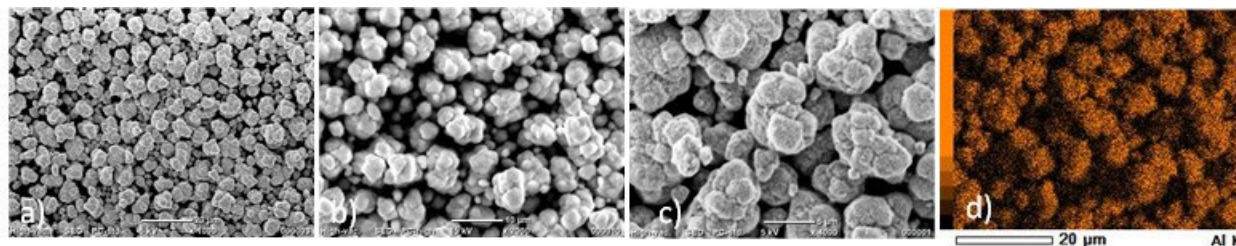


Figure IX.1.1 (a)–(c) SEM images of $\text{Mn}_{0.35}\text{Ni}_{0.6}\text{Co}_{0.04}\text{Al}_{0.01}(\text{OH})_2$ precursor with scale bars of 20, 10, and 5 μm , respectively. (d) EDS Al-mapping.

Figure IX.1.2(a)-(d) show SEM images of the particles after calcination at 950°C under oxygen. We note here that samples prepared at ~800°C showed similar performance to those at 950°C. This is in contrast to Ni-rich NMCs where higher temperatures typically lead to poor performance. However, higher temperatures can be advantageous in producing dense particles and the lower Ni, and higher Mn, content of this composition facilitates a wide range of calcination temperatures. An O₂ environment during calcination was also found to improve electrochemical performance. Preliminary data on this process show that these materials perform as well or better than NMC-622. Work is now ongoing to further optimize scale-up of large batches (~kg).

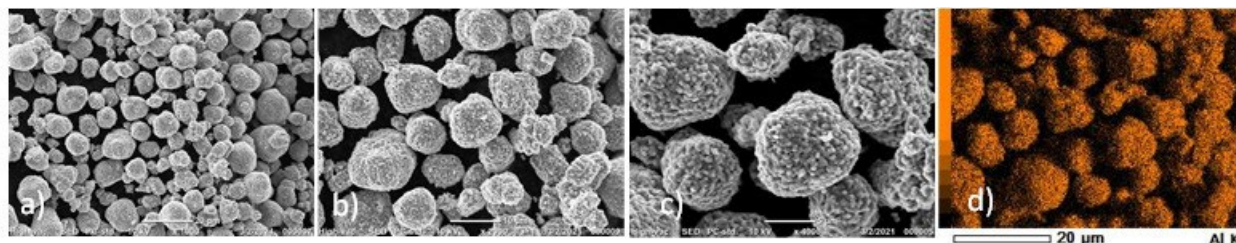


Figure IX.1.2 (a)–(c) SEM images of a $\text{Mn}_{0.35}\text{Ni}_{0.6}\text{Co}_{0.04}\text{Al}_{0.01}(\text{OH})_2$ precursor calcined at 950°C under oxygen with 10% excess Li, scale bars are 20, 10, and 5 μm, respectively. (d) EDS Al-mapping.

Figure IX.1.3(a) shows the voltage profiles for the first cycle between 4.5–2.5 V (Li/Li⁺) of the projects baseline $\text{LiMn}_{0.35}\text{Ni}_{0.6}\text{Co}_{0.04}\text{Al}_{0.01}\text{O}_2$ calcined with stoichiometric Li (red, NMCA) and the same precursors calcined with a nominal 10% excess Li (blue, NMCA-10%, particles shown in Figure IX.1.2) compared to NMC-622. As can be observed, the Al-doped NMCA achieves similar capacity as the NMC-622 but with slightly higher voltage.

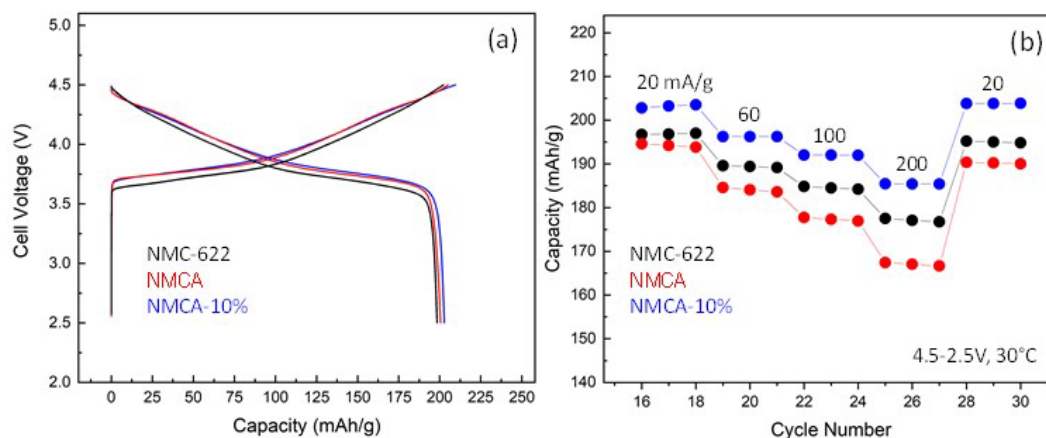


Figure IX.1.3 (a) Voltage profiles for the first cycle between 4.5–2.5 V (Li/Li⁺) for a baseline NMC-622 and the $\text{Mn}_{0.35}\text{Ni}_{0.6}\text{Co}_{0.04}\text{Al}_{0.01}(\text{OH})_2$ calcined with stoichiometric Li (red, NMCA) and one with a nominal 10% excess Li (blue, NMCA-10%). (b) Discharge rate capability for the samples in (a) between 4.5–2.5 V (Li/Li⁺). Data was collected after similar rate tests (cycles 1–15, not shown) between 4.3–2.5 V. Rates are given in mA/g at the top of each three-cycle test. Electrode loadings were ~10 mg/cm².

Figure IX.1.3(b) shows the discharge rate capability of the samples in (a). As expected from the material design, the excess lithium in this composition improves the performance at the electrode level and the material delivers higher discharge capacities at all rates than the NMC-622. The performance of this cathode is achieved with a remarkable 80% less Co than NMC-622 and a Mn content of ~35%, and achieves the goals of this program of delivering on-par performance with state-of-the-art NMC-622 with less than 5% Co. The NMCA-10% oxide is being optimized under the new synthesis methods described above for larger-scale testing.

Synthesis of LiNiO₂ – Another important thrust within the program is focused on very high Ni-content ($\geq 90\%$) oxide-cathodes. In particular, pure LiNiO₂ has been extensively studied under the program as a physiochemical baseline towards enabling stable, low/no-Co, Ni-rich cathodes.

Formation mechanism of residual Li – The residual lithium species (such as LiOH•H₂O and Li₂CO₃) on the surface of Ni-rich NMC cathodes significantly affect cell performance. However, reliable analysis of residual lithium has been challenging because of the difficulty in the detection of the poorly crystalline, surface impurity levels of LiOH•H₂O and Li₂CO₃. Acid-base titration has been widely used to estimate the residual lithium content on NMC cathodes, but the technique, which analyzes the concentration of dissolved LiOH•H₂O and Li₂CO₃ species in filtered water solution, only provides indirect information about the original LiOH•H₂O/Li₂CO₃ concentrations in the dry cathode powder, and the quality of the data is largely dependent on the sampling methods. X-ray photoelectron spectroscopy (XPS) can directly probe the dry cathode powder sample, but it should be performed in a vacuum condition which might alter the nature of the impurity species and more importantly, XPS cannot effectively distinguish LiOH•H₂O from Li₂CO₃. In comparison, the vibrations of lithium hydroxide, carbonate, and oxides are intense and distinct in Raman spectroscopy and can thus be probed sensitively and selectively when they form as surface impurities on oxide particles. Raman spectroscopy doesn't require a vacuum and the signal acquisition can be done in any controlled atmosphere, making it ideal for in situ analysis. Moreover, the vibration signals of LiOH•H₂O and Li₂CO₃ can be further enhanced when UV lasers are used for excitation instead of commonly-used visible light lasers. [4] Therefore, Raman spectroscopy is an exceptional technique for sensitive, quantitative, and in situ probing of the residual Li species on cathodes. In this fiscal year, this program has employed Argonne's unique capability of UV & visible Raman spectroscopy, Figure IX.1.4(a), to investigate the formation mechanisms of residual Li species on LiNiO₂, under controlled synthesis and storage environments, which has not yet been fully understood. Particularly, the origin of the Li₂CO₃ impurities is not clear, although they are frequently observed, even in samples that are prepared by a theoretically carbon-free process using hydroxide precursors and pure oxygen gas streams.

Figure IX.1.4(b) and (c) show Raman spectra of lithium/nickel carbonates and hydroxides materials. All the reference materials are clearly discerned with sharp and strong Raman peaks. The enhanced intensity of the deep UV resonance Raman signal for LiOH, in Figure IX.1.4(c), further confirms that LiOH•H₂O and Li₂CO₃ can be probed with high sensitivity and selectivity by tuning the excitation wavelength. Raman spectra of commercial (Sigma-Aldrich) and ANL-prepared LiNiO₂ powder samples are also compared in Figure IX.1.4(d). A strong Li₂CO₃ peak is shown in the commercial sample and the corresponding impurity concentration was estimated to be ~ 110 ppm. The ANL-LiNiO₂ sample that was prepared with careful synthesis controls shows no Li₂CO₃ or LiOH•H₂O signals at ~ 1100 and ~ 3670 cm⁻¹, respectively. More interestingly, these high-quality UV Raman data clearly indicate the Li-O vibration of LiNiO₂ at ~ 370 cm⁻¹, which was predicted by theory but has never been experimentally observed, as the vibration band is greatly enhanced by the UV resonance effect. [5]

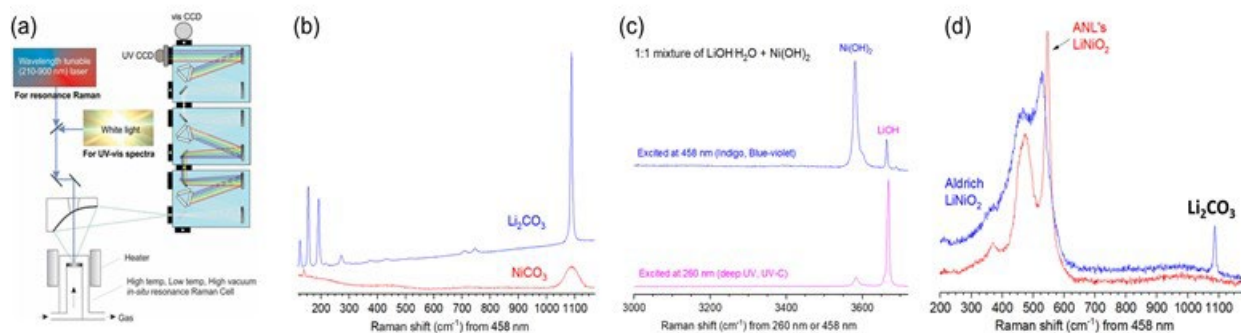


Figure IX.1.4 (a) Schematic diagram of UV Raman system equipped with wavelength-tunable laser sources and a high-temperature in situ Raman cell, and the UV & near IR region Raman spectra of (b) carbonates, (c) hydroxides, and (d) lithium nickel oxide powder samples.

For *in situ* analysis of $\text{LiOH}\cdot\text{H}_2\text{O}$ and Li_2CO_3 formation dynamics, a surface-pure LiNiO_2 cathode powder was first synthesized by directly heating the $\text{LiOH}\cdot\text{H}_2\text{O}$ and $\text{Ni}(\text{OH})_2$ precursor mixture to a target synthesis temperature in an O_2 flowing Raman cell. The Raman cell was used as both the synthesis and characterization vessel so that the as-synthesized, surface-pure LiNiO_2 powder was never exposed to the ambient atmosphere. UV Raman measurements revealed the presence of a Li_2CO_3 impurity in the $\text{LiOH}\cdot\text{H}_2\text{O}$ precursor material. The Li_2CO_3 impurity remained up to 647°C (data not shown) and only disappeared when the sample was calcined at 688°C , Figure IX.1.5(a). The final LiNiO_2 product shows no $\text{LiOH}\cdot\text{H}_2\text{O}$ / Li_2CO_3 impurity. After confirming the synthesis of impurity-free LiNiO_2 , O_2 gas was removed by pulling a vacuum and dry CO_2 was purged into the Raman cell. As shown in Figure IX.1.5(b), the LiNiO_2 surface remained intact without any impurity species such as Li_2CO_3 even after five days of exposure to an excessive CO_2 atmosphere (7.7 Torr, ~ 25 times higher than $p\text{CO}_2$ of ambient air). This result suggests that Li_2CO_3 does not form directly with dry CO_2 , rejecting the single-step reaction mechanism such as: $\text{LiNiO}_2 + x\text{CO}_2 \rightarrow \text{Li}_{1-2x}\text{NiO}_{2-x} + x\text{Li}_2\text{CO}_3$. In the next step, CO_2 was removed, and DI water was vaporized into the Raman cell under vacuum to create a moisture-only atmosphere (13.5 Torr; note that $p\text{H}_2\text{O}$ for typical ambient and humid air are 3.8 Torr and 47 Torr respectively). The corresponding UV Raman spectrum in Figure IX.1.5(c) exhibits the formation of $\text{LiOH}\cdot\text{H}_2\text{O}$ species after 18 hours of exposure. The $\text{LiOH}\cdot\text{H}_2\text{O}$ was then completely converted to Li_2CO_3 in the next step when CO_2 was introduced to the moisture atmosphere, Figure IX.1.5(d). It is interesting to observe that Li_2CO_3 also can be reversely converted back to $\text{LiOH}\cdot\text{H}_2\text{O}$ when the moisture level is increased. In Figure IX.1.5(e), the $\text{LiOH}\cdot\text{H}_2\text{O}$ peak reappears at the expense of the Li_2CO_3 signal intensity, while the Li-O intensity at $\sim 370\text{ cm}^{-1}$ remains unchanged. This result strongly suggests that the source of Li in the newly formed $\text{LiOH}\cdot\text{H}_2\text{O}$, in (e), is Li_2CO_3 rather than the LiNiO_2 substrate. Therefore, our *in situ* UV Raman spectroscopy data convincingly support the two-step mechanism for the formation of residual lithium species on the surface of LiNiO_2 :

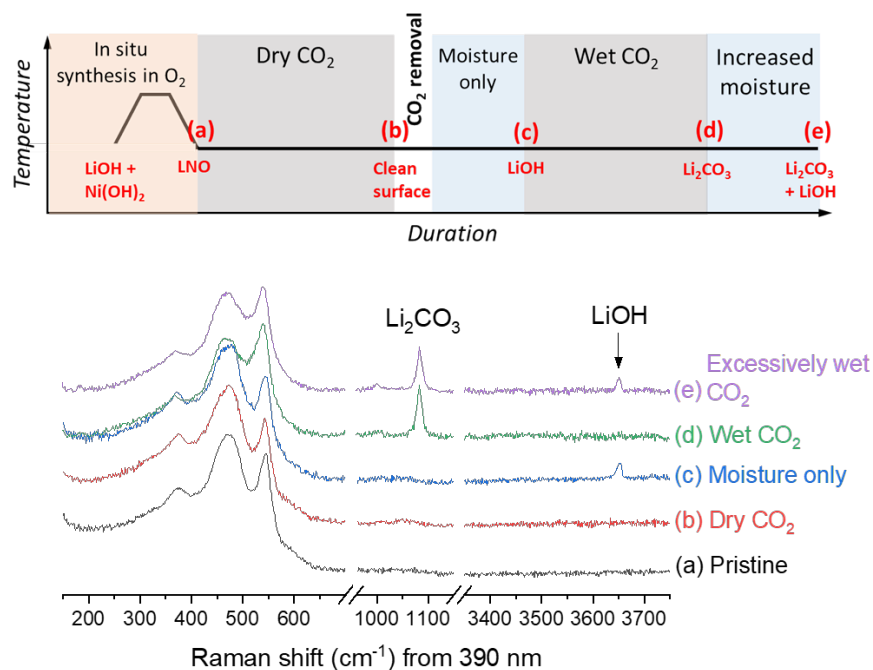
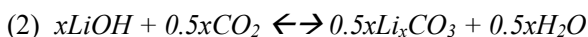
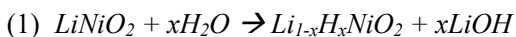


Figure IX.1.5 *In situ* UV Raman spectroscopy experiment: (top) experiment condition indicating the temperature, atmosphere, and sampling timeline points (a)–(e), (bottom) UV Raman spectra of LiNiO_2 collected after exposing at various controlled atmospheres.

The effect of oxygen partial pressure for LiNiO₂ synthesis – It is well known that the synthesis process for pure LNO is complicated and challenging due to a significantly narrow phase diagram of the stoichiometric LNO. [6] Several groups have studied the importance of calcination atmosphere where it is now generally accepted that high oxygen partial pressures are necessary to achieve good performance. [7], [8] It is reasonable to conclude that higher oxygen pressures during the calcination enables stabilization of higher Ni³⁺ content, resulting in more ordered structures. This is especially critical when the calcination is carried out at high temperatures (> 700°C). However, the driving force towards oxygen non-stoichiometry decreases at low temperatures, where the oxygen chemical potential is higher, and so too the requirement for the high oxygen partial pressures during calcination.

Based on previous studies within the program on optimizing highly-layered and high-performing LNO, a series of experiments was carried out to study the effect of oxygen partial pressure under optimum conditions. LNO was synthesized at 665°C under different oxygen partial pressure from 0.21 to 1.00 atm, labeled as LNO-*p*O₂-0.21 atm, LNO-*p*O₂-0.60 atm, and LNO-*p*O₂-1.00 atm, Figure IX.1.6. Note that *p*O₂-0.21 atm refers to dry air, the *p*O₂-0.60 is a mixed gas balanced by nitrogen, and *p*O₂-1.00 utilized ultra-pure oxygen gas. Figure IX.1.6(a)-(c) shows SEM images revealing the resultant particle morphologies where a trend of decreasing primary particle size is observed with increasing *p*O₂. Although there is no obvious difference in the XRD patterns of these samples in terms of peak positions and ratios, Figure IX.1.6(d), the full-width at half maximum (FWHM) values indicate that crystallite size decreases as the oxygen partial pressure increases, inset of Figure IX.1.6(d), consistent with SEM results. This observation is further supported by our continuum model simulation results that exhibit suppressed grain growth under higher *p*O₂ (data not shown).

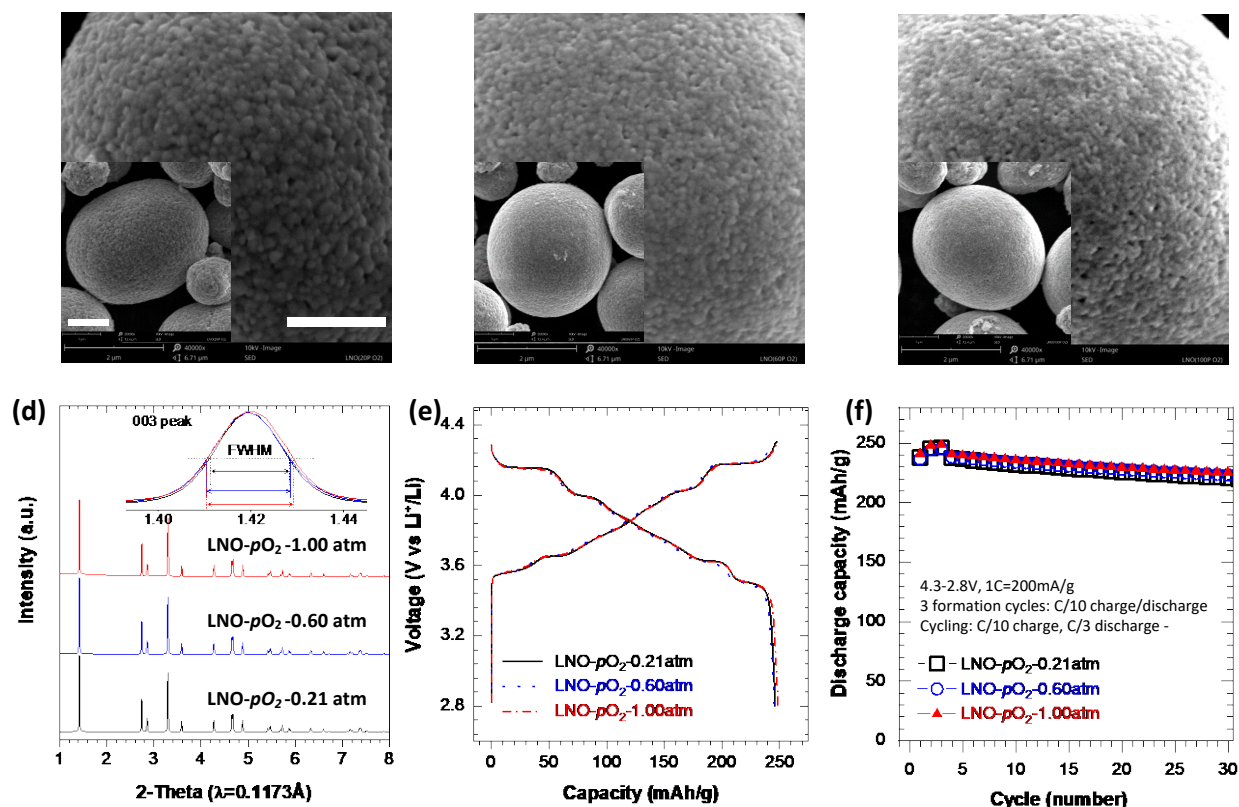


Figure IX.1.6 SEM images of LiNiO₂ synthesized under incrementally different oxygen partial pressures; (a) 0.21 atm, (b) 0.6 atm, and (c) 1.0 atm. All were carried out under identical flow rates and temperature. (d) corresponding XRD patterns, (e) voltage profiles at 3rd cycle, and (f) capacity retention.

Figure IX.1.6(e) and (f) shows the electrochemical performance of the LNO- pO_2 -0.21/0.60/1.00 atm cathode-electrodes. Electrodes were cycled against Li metal anodes in coin-cells as noted in plot (f). The voltage profiles of all cells, after 3 formation cycles at C/10, were identical and there was virtually no difference in capacity retention within the 30 cycles tested. The results here are somewhat contradictory to the accepted understanding of utilizing high oxygen partial pressures. The data presented show that highly-layered, stable, pure LiNiO₂ can be synthesized within a wide range of oxygen partial pressures, even as low as 0.2 atm, if temperatures remain low (< ~700°C). Full-cell tests with graphite anodes (not shown) are ongoing and will be reported at a later date, however, correspondingly excellent performance has so far been achieved.

Conclusions

The program has successfully designed and tested a novel composition consisting of just 4% Co that incorporates ~35% Mn. Electrochemical testing shows that this composition can perform on par with commercial NMC-622 despite utilizing ~80% less Co. In addition, a scale-up process was developed and proven whereby Al substitution can be controlled at the precursor level during co-precipitation. This material achieves the goal of the program by delivering performance at the level of NMC-622 with less than 5% Co.

Detailed studies were also continued in order to gain insights on the synthesis and mechanisms of Ni-rich and pure LiNiO₂ oxides. A two-step mechanism for the formation of LiOH•H₂O and Li₂CO₃ impurities on the surface of LiNiO₂ has been elucidated by a novel, in situ UV Raman experiment. The results clearly indicate the importance of moisture control in processing the LiNiO₂-based cathode oxides. LiOH•H₂O is a reaction intermediate for the formation of Li₂CO₃, and it is not the main residual Li species in a typical ambient atmosphere as the conversion to Li₂CO₃ is facile on the LiNiO₂. The high concentration of LiOH•H₂O species commonly observed in acid-base titration results is probably due to the reverse conversion of Li₂CO₃ to LiOH•H₂O in the aqueous solution. In addition, detailed studies on the synthesis of Pure LiNiO₂ have revealed important trends related to oxygen partial pressure, temperature, and electrochemical performance. In contrast to general belief, the data herein suggest that high oxygen partial pressures may not be necessary when other conditions, such as temperature, are truly optimized.

References

1. J. R. Croy, B. R. Long, M. Balasubramanian, A Path Towards Cobalt Free Lithium-Ion Cathodes, *J. Power Sources*, 440, 227113 (2019).
2. J.R. Croy, Realizing the Potential of Layered TM Oxides, *VTO annual merit review*, BAT375 (2019).
3. B. Han, B. Key, S.H. Lapidus, J.C. Garcia, H. Iddir, J.T. Vaughey, F. Dogan, *ACS Appl. Mater. Interfaces*, 9, 47, 41291 (2017).
4. H. Kim, K. M. Kosuda, R. P. V. Duyne, and P. C. Stair, Resonance Raman and Surface- and Tip-enhanced Raman Spectroscopy Methods to Study Solid Catalysts and Heterogeneous Catalytic Reactions, *Chem. Soc. Rev.* 39, 4820 (2010).
5. T. Du, B. Xu, M. Wu, G. Liu, and C. Ouyang, Insight into the Vibrational and Thermodynamic Properties of Layered Lithium Transition-Metal Oxides LiMO₂ (M = Co, Ni, Mn): A First-Principles Study, *J. Phys. Chem. C*, 120, 11, 5876 (2016).
6. E. Cho, S.-W. Seo, and K. Min, Theoretical Prediction of Surface Stability and Morphology of LiNiO₂ Cathode for Li Ion Batteries, *ACS Appl. Mater. Interfaces* 9, 33257 (2017).
7. T. Ohzuku, A. Ueda, and M. Nagayama, Electrochemistry and Structural Chemistry of LiNiO₂ (R3-m) for 4 Volt Secondary Lithium cells, *J. Electrochem. Soc.* 140, (1993) 1862.
8. G.X. Wang, S. Zhong, D.H. Bradhurst, S.X. Dou, and H.K. Liu, Synthesis and characterization of LiNiO₂ compounds as cathodes for rechargeable lithium batteries, *J. Power Sources* 76, 141 (1998).

Acknowledgements

Anh Vu, Jihyeon Gim, Jinhyup Han, Eungje Lee, Hacksung Kim, Ozge Kahvecioglu, Chongmin Wang, Peng Zou, Jason R. Croy. Support from the U.S. Department of Energy's Vehicle Technologies Program, specifically from Peter Faguy and Dave Howell, is gratefully acknowledged.

IX.2 Diagnostic Testing and Evaluation (ANL, ORNL, NREL, PNNL)

Daniel P. Abraham, Principal Investigator

Argonne National Laboratory
9700 South Cass Avenue
Lemont, IL 46039
E-mail: abraham@anl.gov

Peter Faguy, DOE Technology Development Manager

U.S. Department of Energy
E-mail: Peter.Faguy@ee.doe.gov

Start Date: October 1, 2019	End Date: September 30, 2022	
Project Funding (FY21): \$3,500,000	DOE share: \$3,500,000	Non-DOE share: \$0

Project Introduction

State-of-the-art lithium-ion batteries (LIBs) being developed for transportation applications contain a transition metal (TM) oxide cathode and a graphite anode; both serve as host-matrices to house lithium ions during battery operation. The cathode typically contains $\text{Li}_{1+x}\text{Ni}_a\text{Co}_b\text{Al}_c\text{O}_2$ (NCA) or $\text{Li}_{1+x}\text{Ni}_a\text{Mn}_b\text{Co}_c\text{O}_2$ (NMC) oxides, where $x \sim 0-0.05$ and $a+b+c = 1$. Both oxide chemistries contain Co, which is known to preserve the layered structure during lithium extraction/insertion reactions. However, the possibility of a global Co shortage and soaring costs has galvanized the LIB community to seek explore layered oxides with lower Co contents and eventually develop Co-free cathodes, while maintaining cell performance (energy/power densities), safety and cycle/calendar life. The goal of the diagnostic testing and evaluation team is to identify constituents and mechanisms responsible for cell performance, performance degradation and safety. Various diagnostic tools (electrochemical, physicochemical, mechanical, etc.) are used to characterize the behavior of materials (both active and inactive) contained in the electrodes and cells; this characterization may be conducted before, during, and after electrochemical cycling. Understanding the fundamental mechanisms allows the development of rational solutions to minimize performance degradation and thermal instability in the materials and electrodes, leading to safer and long-life and battery cells.

Objectives

- Evaluate the long-term aging behavior of a cathode with 90% Ni in full-cells, exploring the influence of cycling conditions and electrolyte composition on performance retention.
- Identify electrolyte compositions, which can mitigate performance degradation of full cells containing low-cobalt cathodes.
- Elucidate effect of temperature on performance of Li-ion full cells with high nickel cathodes.
- Investigate effect of coatings on the gas generation behavior of Li-ion cells with high nickel cathodes.
- Determine effect of temperature on performance of full cells with LiNiO_2 electrodes using a combination of microscopy, spectroscopy and chemical analysis techniques.
- Apply solid state NMR techniques to directly observe bulk and surface lithium environments within the LiNiO_2 oxide and to determine structure changes that occur during electrochemical cycling.
- Utilize scanning transmission electron microscopy to probe the bulk and surface structure evolution of the LiNiO_2 oxide during electrochemical cycling.

- Probe performance of full cells with the $\text{LiNi}_{0.9}\text{Mn}_{0.1}\text{O}_2$ (N9M1) cathode at specific energies comparable to those of cells with the LiNiO_2 cathode.
- Utilize in-situ spectroscopic techniques to examine transition metal redox chemistry, formation and evolution of the cathode-electrolyte interphase (CEI) and electrolyte solution structures on high-Ni cathodes.
- Determine proton extraction mechanisms from layered transition metal hydroxides at high voltages.

Approach

The approach pursued to meet the above objectives is summarized in Figure IX.2.1 (below).

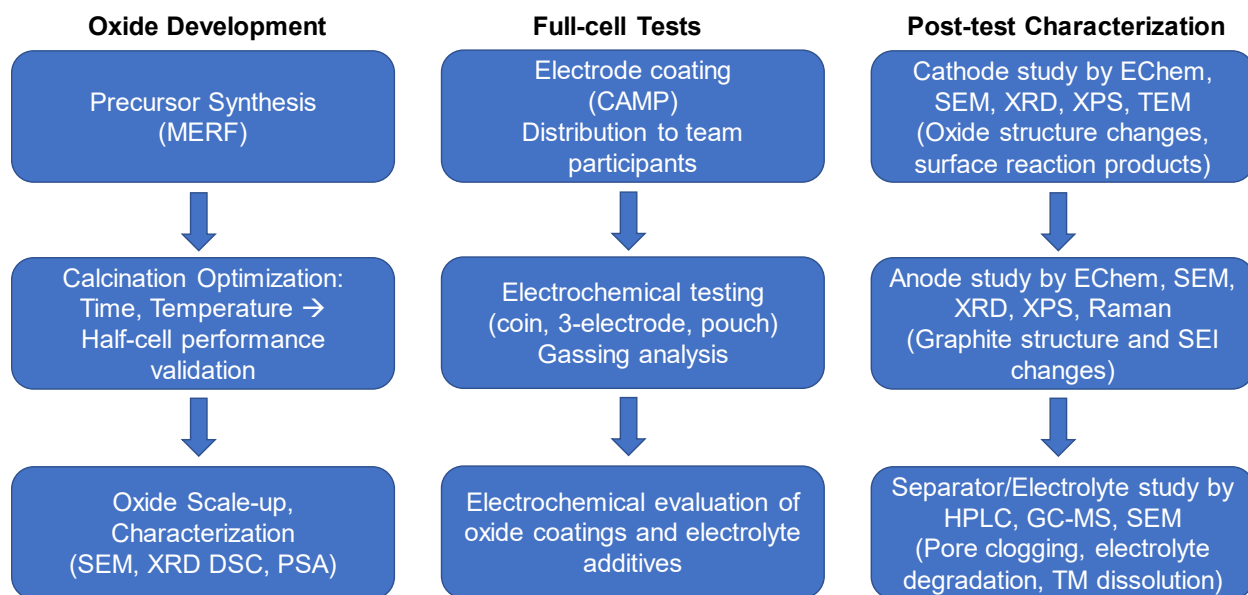


Figure IX.2.1 Diagnostic tests are conducted at various stages of the oxide development process.

Results

Studies on cells with $\text{LiNi}_{0.90}\text{Mn}_{0.05}\text{Co}_{0.05}\text{O}_2$ (NMC9055) electrodes: *Marco Rodrigues et al., ANL*

Electrochemical tests were conducted in cells with the oxide cathode and graphite anode. The cathode contained 90 wt% NMC9055, 5 wt% C45 carbon and 5 wt% PVdF binder. The anode contained ~92 wt% Superior Graphite SLC1506T, 2 wt% C45 carbon and 6 wt% PVdF. Coin cells were assembled using Celgard 2325 separator and 40 μL electrolyte. The baseline electrolyte (denoted “Gen2”) contained 1.2 M LiPF_6 in a 3:7 w/w mixture of ethylene carbonate (EC) and ethyl methyl carbonate (EMC). Some cells used electrolytes that contained either 2 wt% vinylene carbonate (VC) or a mixture of 2 wt% VC, 2 wt% ethylene sulfite (ES) and 2 wt% tris(trimethylsilyl) phosphite (TMSPI) as additives to the Gen2 electrolyte. The test protocol (HEHV) consists of a combination of aging blocks and reference performance tests (RPTs). The RPTs included a full cycle at a C/25 rate (3 – 4.2 V) and pulse-based tests for impedance measurements. Aging was performed using either constant current (CC) cycles at C/3 or CC cycles followed by a 3-hour hold at 4.2 V at every charge half-cycle (CCCV). RPTs were obtained every 50 cycles for the former, and 19 cycles for the latter. Prior to aging, all cells were conditioned using ten CC cycles at C/25 rate.

Many of the electrochemical tests within the RNGC program use protocols like the CCCV detailed above to accelerate cell aging. One apparent shortcoming of such protocols is that materials can be incorrectly perceived as underperforming if directly compared with the more common CC experiments that are typically reported in the literature. To examine the effect of protocol, Figure IX.2.2 compares the behavior of NMC90-5-5 cells

using Gen2 electrolyte tested under both CC and CCCV protocols. Figure IX.2.2a shows that, in general, CCCV cells display higher capacities than the CC cells early on during the test. The fact that this remains true for the slow RPT cycles (without a hold at 4.2 V) suggests that slight oxidation of the electrolyte at high voltages can artificially increase the number of cyclable electrons in CCCV cells, increasing cell capacity. Despite this additional capacity, the CCCV protocol generally leads to faster capacity fade, ~20% loss after 350 cycles; in comparison, CC cells present this same level of retention after over 500 cycles (Figure IX.2.2b).

A key difference between these two protocols is *time*: a single charge takes ~3 hours in the CC protocol, but ~6 hours in the CCCV. Interestingly, when capacity retention is represented as a function as total test time (Figure IX.2.2c), both protocols present similar rates of performance loss, with 20% fade being achieved ~150 days into cycling. Such behavior can be rationalized by considering that capacity loss is mainly caused by Li^+ trapping at the anode SEI, and that additional processes at the cathode at high voltage (transition metal loss, for example) do not significantly affect the rate of SEI reactions. Hence, as CCCV tests take longer to complete a given number of cycles, the rate of capacity fade appears higher (vs. cycle number) than in CC tests, even though the underlying processes are not accelerated. Though the evolution of capacity fade in time is nearly unaffected by the high-voltage holds of CCCV tests, impedance rise is markedly accelerated at this protocol (Figure IX.2.2d). The utility of CCCV protocols is that it allows for the faster identification of electrolyte additives that can mitigate the processes responsible for this impedance rise.

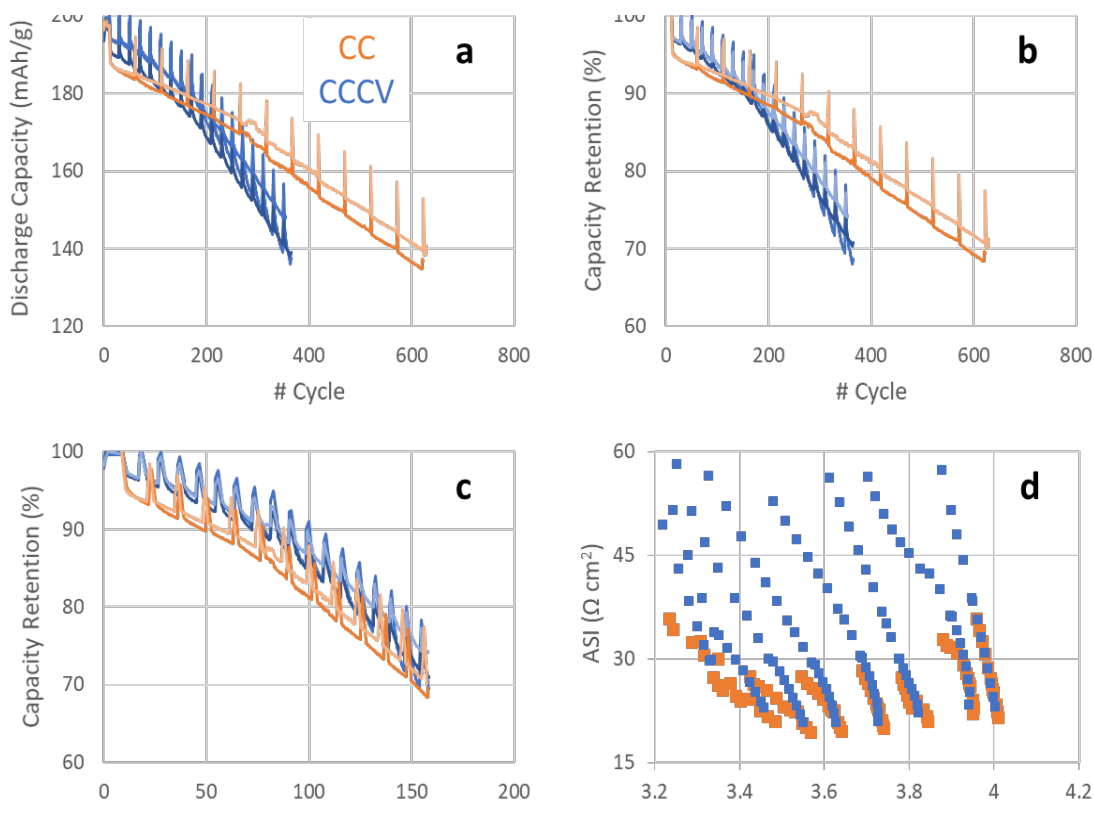


Figure IX.2.2 Effect of test protocol on aging of NMC9055 full-cells using the Gen2 electrolyte. (a) Discharge capacities. (b) Discharge capacity retention as a function of cycle number. (c) Capacity retention as a function of total test time. (d) Area-specific impedance (ASI), measured from discharge pulses, as a function of cell voltage at various points of the test. Data in different hues represent different cells. The legend in panel a applies to all panels.

The behavior of cells tested using the CCCV protocol varies widely in the presence of electrolyte additives (Figure IX.2.3). Addition of 2 wt% VC has a dramatic effect on capacity retention: Gen2 cells lose ~20% of their initial capacity after ~350 cycles, while cells using VC lose only ~10% capacity in as many cycles. This improved stability appears to come at the expense of the Li^+ inventory, as VC cells display lower discharge

capacity values for almost 200 cycles; the additive helps construct a better SEI but requires more charge to be consumed in the process. Adding ES and TMSPI to the electrolyte is counter-productive, as some of the improvement derived from VC disappears. The electrolyte additives also have little effect on impedance rise (Figure IX.2.3c), which is only ~4% smaller than that observed with Gen2, on average. All in all, the additives appear to improve stability of the anode interface, without bestowing additional stability on the cathode side. Nevertheless, differential voltage analysis of this data (*not shown here*) indicates that the simultaneous addition of VC, ES and TMSPI to the electrolyte appears to slow down the rate of cathode capacity loss, although this does not translate into capacity retention gains because the latter is dominated by Li^+ losses to the anode SEI.

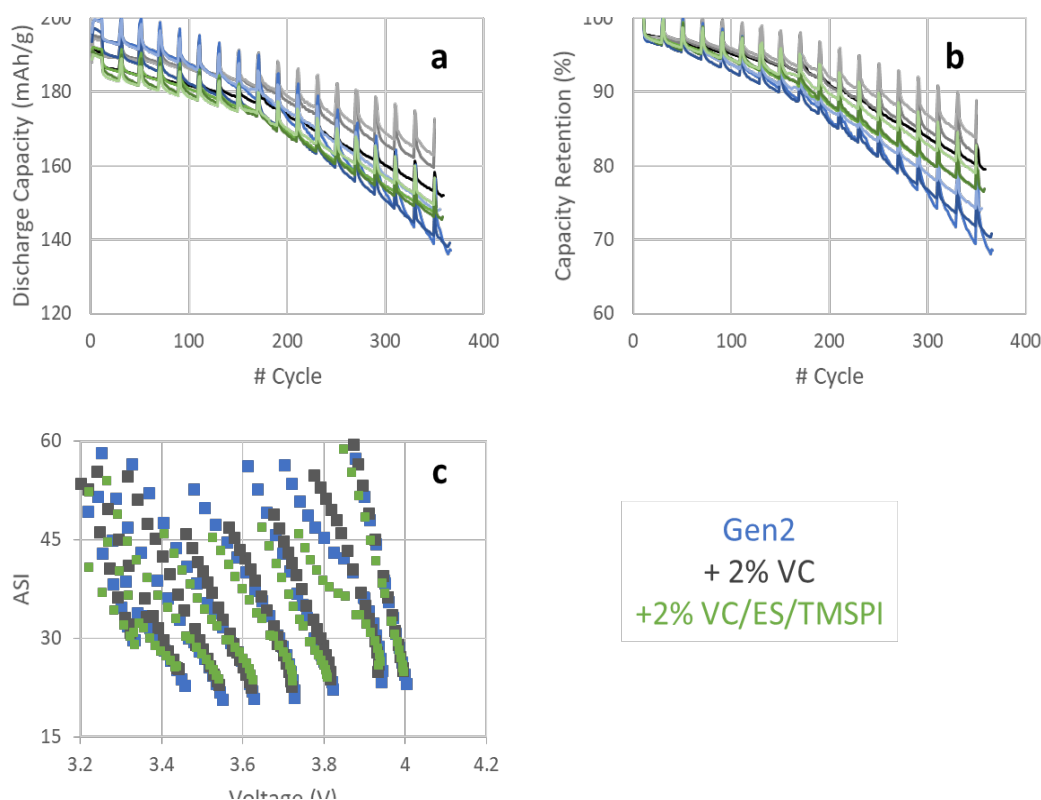


Figure IX.2.3 Effect of electrolyte additives on aging behavior of NMC9055 full-cells. (a) Discharge capacities. (b) Discharge capacity retention. (c) ASI vs cell voltage at various points of the test. Data in different hues in the plots represent different cells with the same electrolyte. The legend applies to all panels.

Development and implementation of novel electrolyte additives: *Chen Liao et al. ANL*

In the past year, our focus has been on developing electrolytes for full cells with the NMC9055 cathodes. For this we applied the following approaches: (1) Using anode and cathode additives in the Gen2 electrolyte. (2) Using dual-salt electrolytes containing LiPF_6 and LiPO_2F_2 (LiDFP) in various ratios. (3) Altering the EC/EMC solvent ratio. The acronyms of the electrolyte components and their full names are as follows: VC (vinylene carbonate), PES (prop-1,3-sultone), MS (lithium tetrafluoromalonate phosphate), LiDFP (lithium difluorooxyphosphate), PyDMA (dimethylamine pyrrole), TAP (triallyl phosphate), EC (ethylene carbonate), and EMC (ethyl methyl carbonate).

Table IX.2.1 lists a series of additives and solvents combinations tested for NMC9055 cathodes and their Figure-of-Merit Energy (FOME) and Figure-of-Merit Power (FOMP) values. Cells with the Gen2 electrolyte have an initial energy density of 748 Wh/kg and an initial power density of 142 (mW/cm²) at 80% SOC. For these cells the FOME and FOMP, which is the number of cycles required to reach 80% of the initial energy density and power density are 447 and 63 cycles, respectively. Among the additives tested, the only one that

outperforms the Gen2 electrolyte is entry **4** in Table IX.2.1, 1% MS in Gen2. For the dual salts, two electrolytes, entries **13** and **15** in Table IX.2.1 outperform the baseline electrolyte: impedance rise is also lower for these electrolytes, suggesting enhanced cathode protection. Regarding solvents, the EC:EMC (1:9) is marginally better than the baseline, which indicates that 10% EC content in the electrolyte is sufficient to form a stable anode SEI.

Table IX.2.1 Electrolytes consisting of various additives and solvents for the NMC9055//Gr couple

	Entry	Electrolyte composition	FOME	FOMP
	1	Gen 2	447	63
Additives	2	2wt% VC+ 1wt% LiDFP in Gen 2	324	161
	3	2 wt% VC+ 1 wt% PyDMA in Gen 2	308	21
	4	1 wt% MS in Gen 2	474	422
	5	2wt% PES+ 1wt% PyDMA in Gen 2	162	0
	6	0.1 wt% LDF in Gen 2	286	59
	7	0.2 % PES + 0.2 % TAP in Gen 2	441	109
	8	2% VC+1 wt% MS EC/EMC 1/9	166	12
	9	1% MS in 1.0 M LiPF ₆ EC/EMC 1/9	281	n/a
Dual Salts	10	0.9M LiPF ₆ 0.3M LiDFP EC/EMC 3/7	223	46
	11	1.0M LiPF ₆ 0.2M LiDFP EC/EMC 3/7	350	304
	12	1.1M LiPF ₆ 0.1M LiDFP EC/EMC 3/7	182	14
	13	1.15M LiPF ₆ 0.05M LiDFP EC/EMC 3/7	560	441
	14	0.8M LiPF ₆ 0.2M LiDFP EC/EMC 1/9	346	19
	15	0.9M LiPF ₆ 0.1M LiDFP EC/EMC 1/9	564	901
Solvents	16	1.0 M LiPF ₆ EC/EMC 4/6	330	7
	17	1.0 M LiPF ₆ EC/EMC 3/7	290	8
	18	1.0 M LiPF ₆ EC/EMC 2/8	402	2
	19	1.0 M LiPF ₆ EC/EMC 1/9	527	57
	20	1.0 M LiPF ₆ EMC	157	1
	21	1.2 M LiPF ₆ EC/EMC 3/7	300	55

Evaluating effect of temperature on performance of NMC9055 full cells: Linxiao Geng et al., ORNL

Coin cells with NMC9055 and graphite electrodes from Argonne's CAMP facility were assembled in Battery Manufacturing Facility (BMF) at ORNL and tested using Argonne's HEHV protocol at temperatures from 30°C to 60°C. The protocol included HPPC evaluations at regular cycling intervals. Figure IX.2.4 exhibits the discharge capacity and Coulombic efficiency (CE) as a function of cycle number. As the operating temperature is increased, the capacity retention decreased. In particular, the cell cycled at 60°C showed significant capacity fade. Accordingly, CE of the cell cycled at 60°C was also lower than the cells cycled at lower temperature (30°C, 40°C, and 50°C). The cycle-to-cycle variation in CE was small for cells measured at all temperatures.

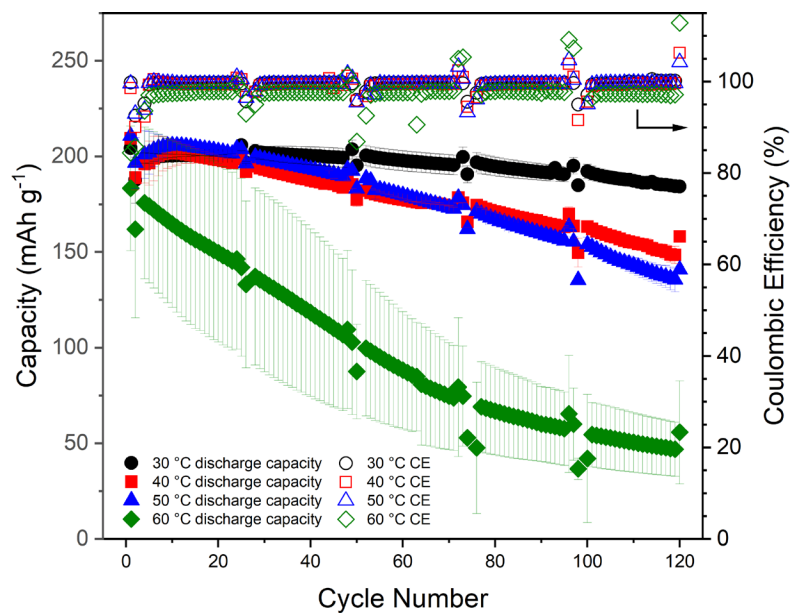


Figure IX.2.4 Effect of temperature on performance cycling of NMC9055/graphite coin cells

Figure IX.2.5 shows area specific impedance (ASI) as a function of cell voltage derived from HPPC data. At all temperatures, the ASI during the early HPPC cycle (labeled #1) is in the 2–40 $\Omega \cdot \text{cm}^2$ range. As cycling progresses (HPPC cycles —5), there is systematic and gradual increase in the ASI. In particular, the cells cycled at 50°C and 60°C show significant increase in the ASI. At elevated temperatures, the cells polarize significantly on extended cycling and exhibit relatively poor performance. This study establishes the baseline (control) for future studies that will aim to understand potential correlations between ASI, temperature, and gas evolution characteristics of cells with electrodes subjected to surface treatments and electrolyte additives.

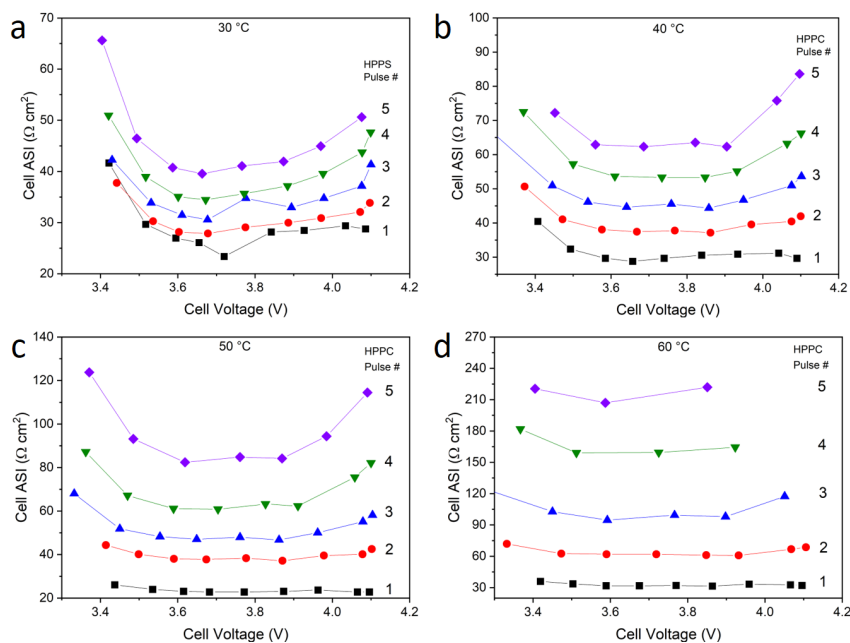


Figure IX.2.5 Area specific impedance (ASI) vs. cell voltage of NMC90-5-5/graphite cells cycled at (a) 30 °C, (b) 40 °C, (c) 50 °C and (d) 60 °C. The ASI values increase with aging; higher HPPC Pulse# indicate higher cycle numbers (more aging).

Evaluating effect of ALD-coating of NMC9055 electrodes on gas generation: Linxiao Geng et al., ORNL

Electrode laminates of NMC9055 fabricated at CAMP were AlF_3 -coated using an atomic layer deposition (ALD) technique at Argonne. Pouch cells containing uncoated and AlF_3 -coated cathodes and graphite anodes (from CAMP) were assembled at the BMF. Gas generation was monitored operando during first two cycles using a cycling protocol established previously. Figure IX.2.6 compares gas generation behavior of the cells. There is copious CO_2 generation in the cell with the uncoated cathode. On the other hand, CO_2 generation is largely suppressed by the AlF_3 coating in the pouch cells with coated cathodes.

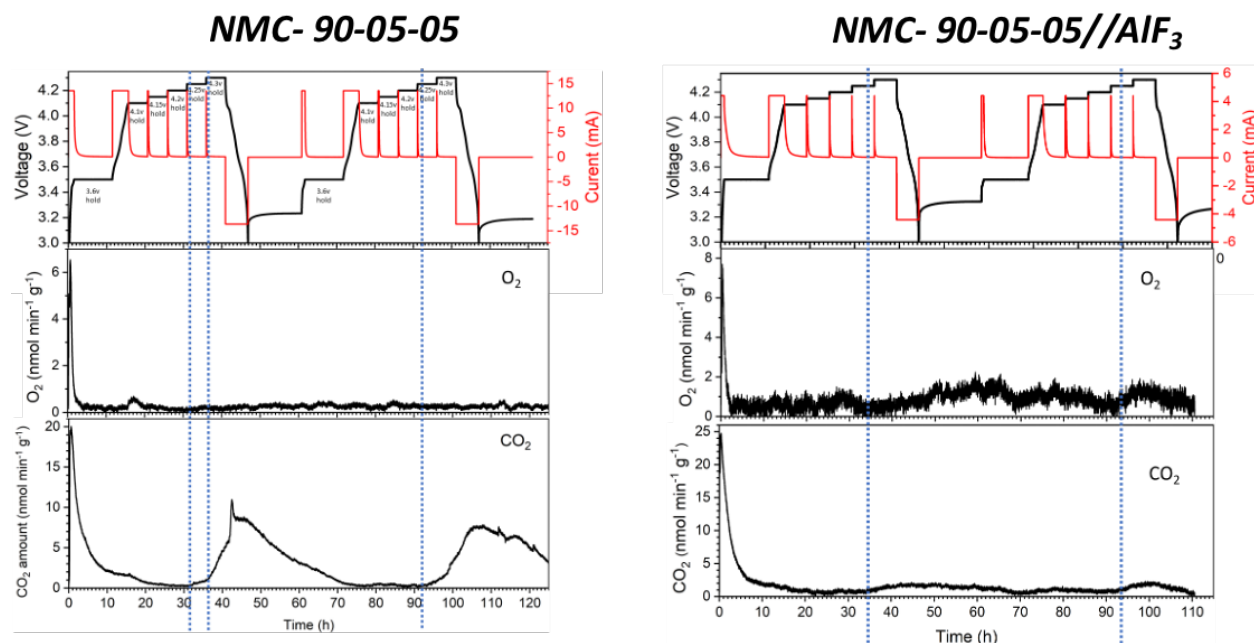


Figure IX.2.6 Effect of AlF_3 coating on gassing behavior of NMC9055//Gr pouch cells with uncoated (left) and coated (right) cathodes.

Diagnostic studies at the post-test facility: Seoung-Bum Son et al., ANL

The diagnostic studies conducted at Argonne's post-test facility aim to provide an in-depth understanding of the performance and degradation of oxide materials developed in the RNGC project. In FY21, a major focus was to determine the effect of temperature on full cell performance. In this report, we show results from cells with the LiNiO_2 (LNO) electrode. The LNO oxide was synthesized at Argonne and the electrodes were fabricated at the CAMP facility. The electrochemical tests were performed on 2032-type coin-cells containing the LNO cathode, graphite anode and Gen2 electrolyte. After cycling, the cells were disassembled for post-test analysis, which included scanning electron microscopy (SEM), Raman spectroscopy, X-ray photoelectron spectroscopy (XPS) and high-performance liquid chromatography (HPLC).

Galvanostatic cycling of the full cells was performed to characterize how electrochemical behavior changes with the test temperature. Figure IX.2.7 shows the cycle retention and voltage profiles of cells examined at 30°C and 45°C. In Figure IX.2.7a, the cells show an initial charge capacity of 230 and 253 mAh/g at 30°C and 45°C, respectively. Both cells show similar retention till around the 25th cycle, then cells tested at 45°C show faster degradation than the cells at 30°C. At the end of testing (1 HEHV protocol), the cells showed capacity retention of 83% and 63% at 30°C and 45°C, respectively. In the voltage profiles, the cells cycled at 30°C (Figure IX.2.7b) show the upper voltage plateau at ~4.1 V, corresponding to H2 to H3 phase transition in the oxide. In contrast, this plateau is not seen for the 45°C cells (Figure IX.2.7c) after ~50 cycles. The hindered 4.1 V phase transition leads to loss of available capacity from the LNO. This capacity loss could be due to changes in the oxide bulk structure, surface structure and/or changes at the oxide-electrolyte interfaces.

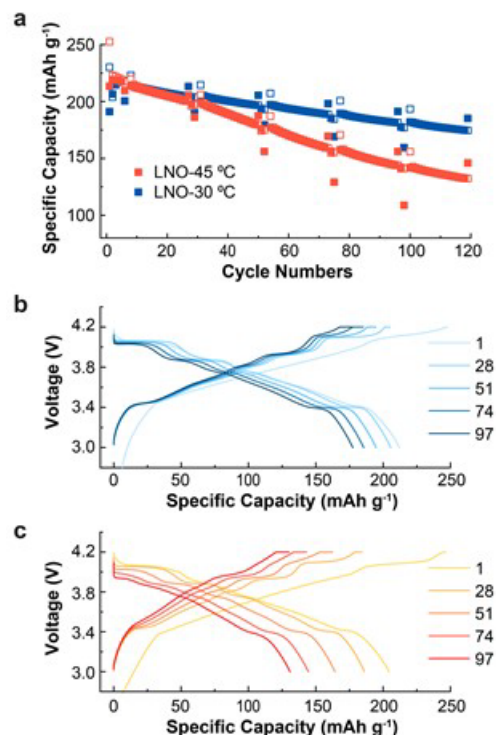


Figure IX.2.7 Electrochemical performance of LNO//graphite full cells cycled using the HEHV protocol. (a) Cycle retention at 30 °C and 45 °C. Voltage profiles of cells at 30 °C (b) and 45 °C (c).

After the full cell tests were complete, the LNO electrodes were harvested and cycled (C/20, 30 °C) in cells vs. Li metal (Figure IX.2.8). The data were compared with the final cycle (C/20) data conducted on the LNO/graphite full cells. Figure IX.2.8 shows that the LNO harvested from the 30 °C aged cell recovers ~25 mAh/g capacity. In contrast, the LNO electrode harvested from the 45 °C aged cell shows no recovered capacity. The results indicate greater LNO degradation at 45 °C than at 30 °C.

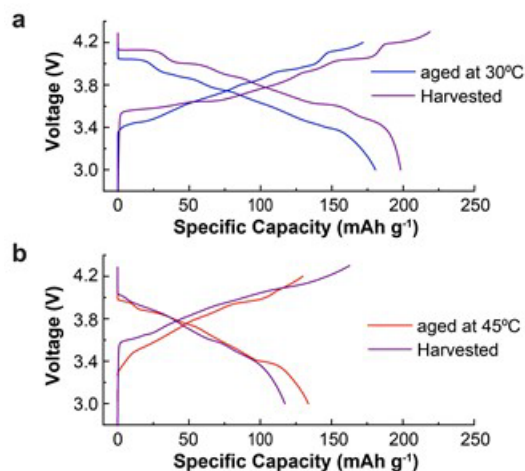


Figure IX.2.8 Voltage profiles (C/20 rate, 30 °C) of harvested LNO/Li cells compared with C/20 profiles from the corresponding LNO/Gr cells aged at 30 °C (a) and 45 °C (b).

To investigate reasons for the LNO degradation, various characterization studies were performed. First, XPS analysis was performed to investigate surface chemistry evolution of electrodes after aging (Figure IX.2.9).

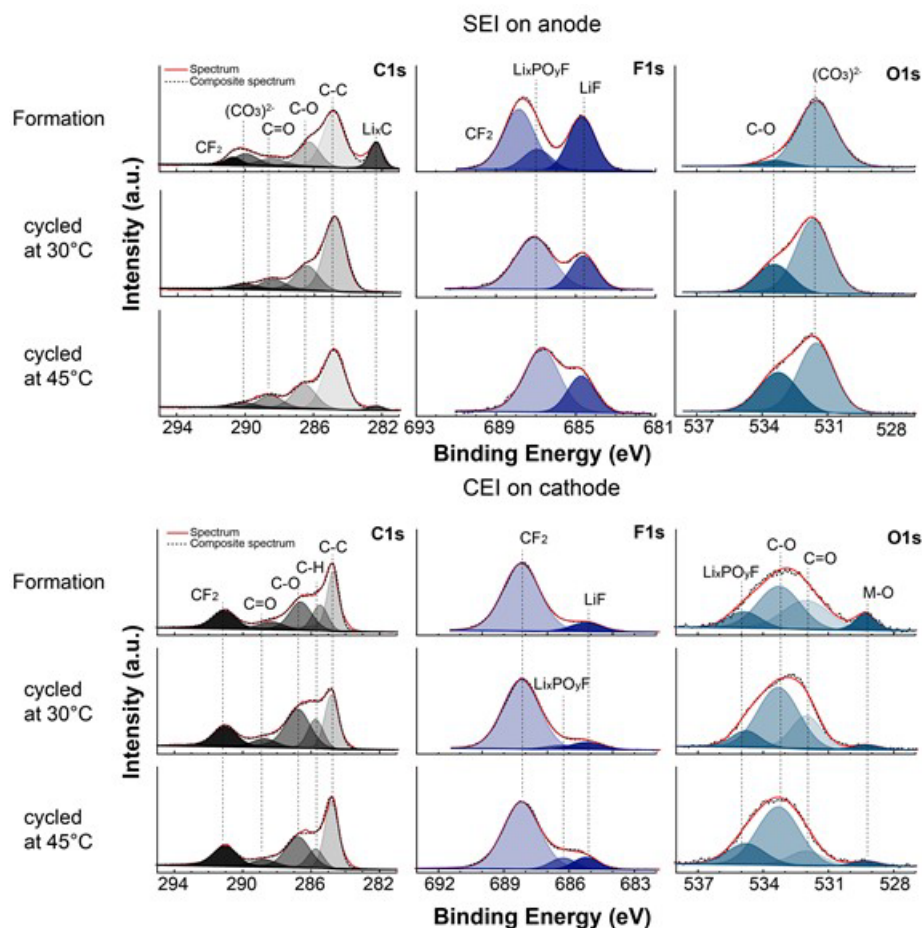


Figure IX.2.9 XPS analysis of the anode SEI (top) and cathode CEI (bottom). The C1s, F1s and O1s spectra were obtained after formation cycling and after 1HEHV protocol at 30 °C and 45 °C, respectively.

Figure IX.2.9 shows XPS spectra from the LNO cathodes (cathode electrolyte interphase, CEI) and graphite anodes (solid electrolyte interphase, SEI). The C1s, O1s, and F1s spectra were obtained on electrodes harvested from cells that underwent formation cycling and 1HEHV test at 30 °C or 45 °C. The SEI chemistry is shown in the top portion of Figure IX.2.9. Here, in the C1s region, peaks for C-C, C-O, C=O, $(\text{CO}_3)^{2-}$, CF_2 and Li_xC are observed. The peaks for C-O, C=O and $(\text{CO}_3)^{2-}$ are likely from lithium ethylene dicarbonate (LEDC), which is one of the main reduction products of EC. The CF_2 peak from the PVDF binder is observed only for the formation sample; it is probably buried under other reduction (and decomposition) products after aging. In the F1s spectra, intensity of the $\text{Li}_x\text{PO}_y\text{F}$ peak increases after aging. Furthermore, the ratio of $\text{Li}_x\text{PO}_y\text{F}$ to LiF is higher for the 45 °C sample, indicating more reductive decomposition of the electrolyte during the electrochemical cycling.

The CEI chemistry is shown in the bottom portion of Figure IX.2.9. In the C1s spectra, peaks for C-C, C-H, C-O, C=O and CF_2 are observed. The C-C and CF_2 peaks are from the PVDF binder, while the C-O and C=O peaks likely originate from electrolyte solvent oxidation. The CF_2 peaks are clearly seen both for the formation and aged samples, which indicates that the CEI layer is relatively thin compared to the SEI layer. No obvious changes were observed in the C1s spectra, as a consequence of aging, at both temperatures. In the F1s spectra, the main peaks are from CF_2 and LiF. The LiF peak, which arises from LiPF_6 decomposition, persists after the HEHV aging cycles. A $\text{Li}_x\text{PO}_y\text{F}$ peak is observed after aging; intensity of this peak is higher for the sample from the 45 °C cell, which is similar to that seen for the SEI. In O1s spectra, metal (M)-O, C=O, C-O and $\text{Li}_x\text{PO}_y\text{F}$ peaks are observed. The M-O peak is from the Ni-O bond of LNO; intensity of this peak is lower for

the aged electrodes indicating that it is partially covered by electrolyte decomposition products that build-up during aging.

The ICP-MS technique was used to determine Ni dissolution from the oxide that deposits on the graphite anode. This determination is important as Ni dissolution leads to the loss of active LNO, which would cause cell capacity fade. Figure IX.2.10 shows that notable amounts of Ni are detected on the anode surface for both the 30°C and 45°C samples. Interestingly, more Ni is seen for the 30°C electrode than for the 45°C electrode, even though the latter cell shows greater capacity loss. The data suggest that the Ni deposition is influenced more by SOC and aging time than by the test temperature. Additional studies are needed to examine the factors that affect these Ni dissolution and deposition reactions.

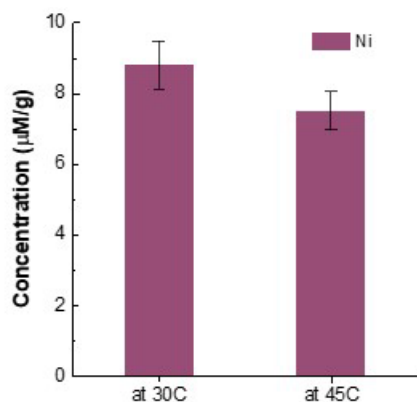


Figure IX.2.10 Ni deposition at the graphite anode harvested from cells aged at 30 °C and 45 °C.

Figure IX.2.11 shows cross-section SEM observations on cycled LNO electrodes. It is believed that cracks in the oxide particles contribute to capacity degradation in the Ni-rich cathodes; these cracks interfere with Li^+ diffusion inside the particles and isolate particles from the electronic conduction network. We did not observe cracking in the oxide particles; the loss of Li^+ from the oxides apparently does not cause severe crack initiation in the LNO during cycling. We expect to conduct detailed crack initiation and propagation studies in the LNO oxide particles in the upcoming year to determine the effect of SOC and extended cycling.

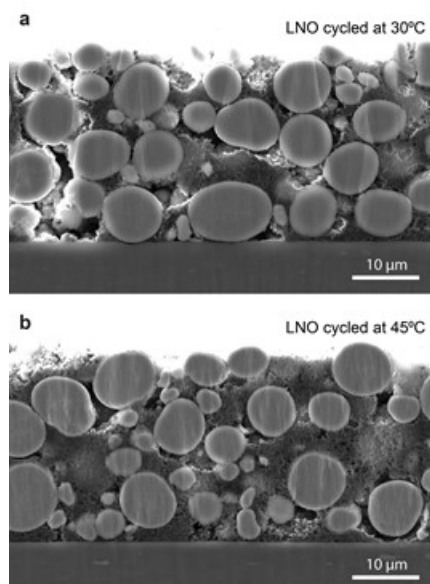


Figure IX.2.11 SEM on cycled LNO electrodes harvested from cells aged at 30 °C (a) and at 45 °C (b).

Solid state NMR characterization of LiNiO₂ cathodes: Fulya Dogan et al., ANL

The goal of solid-state NMR characterization studies has been to understand the atomic-level structural changes in various oxide compositions and local structural changes as a result of electrochemical cycling. In the past year the work focused on LiNiO₂ cathodes. The objectives were to study (i) lithium local structures, in the oxide at different states of charge/discharge during the 1st cycle, that result from phase transitions; (ii) irreversible structural changes that result from extended cycling in order to correlate capacity loss with lithium local environment changes within the oxide bulk and surface.

The approach was to use ⁶Li Solid State Nuclear Magnetic Resonance (NMR) spectroscopy, which is an effective local probe to study lithium local environments and coordination in lithium-ion battery oxides. The ⁶Li NMR shifts, caused by the surrounding paramagnetic transition metal (TM) ions, are generally large and dominated by hyperfine shift (Fermi contact shift), which is a measure of unpaired electron spin density transfer from the TM ion to Li through oxygen. The magnitude of the shifts is determined by the Li coordination, bond angle and bond length whereas the sign of the shift is determined by nature of TMs and their oxidation state. Diamagnetic lithium environments give NMR peaks around 0 ppm.

Figure IX.2.12 shows comparison of ⁶Li MAS NMR data from LiNiO₂ samples; the data are from pristine, after 240 cycles, and relithiated after 240 cycles, electrodes. The pristine sample shows a symmetric peak centered around 700 ppm for bulk Li environments coordinated to Ni³⁺ in 1st and 2nd coordination shell. The pristine sample also shows a small peak at ~450 ppm which can be assigned to Li vacancies, defects and/or a rock salt phase, as presence of these features would shift the hyperfine shift to lower ppm values. This peak accounts for ~8% of the total bulk Li environment. A peak at 0 ppm is also observed, which is due to surface impurities (such as Li₂CO₃) that remain from the oxide synthesis process.

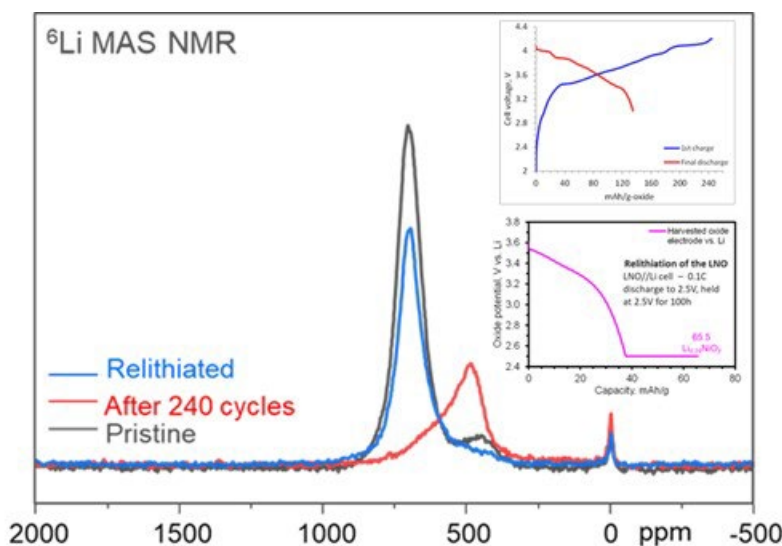


Figure IX.2.12 Mass Normalized ⁶Li MAS NMR data from pristine (black), cycled (red) and relithiated (blue) LiNiO₂ electrodes. The insets show related electrochemical cycling data.

After 240 cycles, the main Li peak completely disappears and a new asymmetric peak forms at ~490 ppm with a shoulder at ~600 ppm with roughly 2 to 1 ratio. These peaks can be assigned as Li⁺ with Ni³⁺ and Ni⁴⁺/lithium vacancy in the first and coordination shell, as Ni⁴⁺ and/or vacancies increase the peak shifts to lower frequencies. Following the heuristic rules for the Li-O-Ni³⁺ per bond Fermi shift values, the Li-O-Ni 180° coordination mostly remains and Li loss is mainly from loss in the Li-O-Ni 90° coordination. Any reordering in the structure, such as formation of spinel or rock salt phase, should also show itself as new peaks at lower frequencies. Quantification of the data with respect to pristine ⁶Li peak shows that there is ~46% Li

left in the structure after the extended cycling. Overall, the peaks observed at lower frequencies are due to Li reordering in the bulk, presence of vacancies, and/or diamagnetic Ni^{+4} in the oxide.

In order to study the reversible/irreversible local structure changes upon cycling, ^6Li MAS NMR was also performed on a relithiated sample after extended cycling. As seen in Figure IX.2.12, the main NMR peak of the relithiated sample is mostly restored, with a symmetric main peak at ~ 700 ppm. The data suggest that the layered structure is mostly restored by relithiation and that the changes induced by the electrochemical cycling are mostly reversible. The main difference observed between the cycled and relithiated samples is the intensity decrease of the 450-ppm peak after cycling (by $\sim 50\%$). Although the bulk structure remains the same, quantification of these NMR data reveals that only $\sim 24\%$ Li is put back into the structure and that the relithiated sample only has $\sim 70\%$ Li in the oxide bulk, when compared to the pristine sample. These NMR quantitations are consistent with the electrochemistry data, which also showed similar values.

In an effort to correlate the above peak shifts and changes with Li content and/or irreversible bulk structure changes, samples with different Li contents were prepared after electrochemical cycling and studied by ^6Li MAS NMR. Figure IX.2.13 shows ^6Li MAS NMR data for LiNiO_2 samples with different lithium contents from the first charge and discharge cycle. The Li contents were chosen to be similar to the cycled and relithiated samples ($\sim 73\%$ Li and $\sim 48\%$ Li) discussed in Figure IX.2.12, as well as $\sim 30\%$ Li to capture phase transitions, and $\sim 17\%$ Li to capture local structure near the top of charge (mostly delithiated oxide).

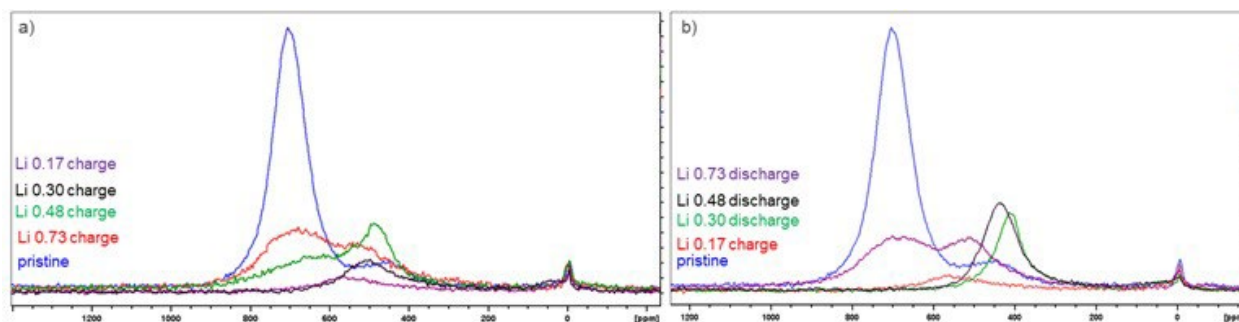


Figure IX.2.13 Mass Normalized ^6Li MAS NMR data from LiNiO_2 samples with various Li contents during (a) charge and (b) discharge

As seen in Figure IX.2.13a, as Li is removed during the first charge, there is a gradual decrease in the main peak (700 ppm) and a new peak forms at ~ 520 ppm due to Li vacancies and/or diamagnetic $\text{Ni}^{+4}/\text{Ni}^{+3}$ ordering around the remaining Li environments. When the Li content is $\sim 17\%$ (~ 226 mAh/g) both peaks disappear and a new, single peak forms at ~ 550 ppm. These are the remaining, thermodynamically stable Li environments within the structure. Comparison of the 70% Li (charge) sample data with that of the relithiated sample (Figure IX.2.12) indicates that the latter has the same Li ordering and local structure as the pristine structure with possible densified reconstruction of Ni_xO_y composition on the surface hindering lithium reinsertion during relithiation. Comparison of the $\sim 40\%$ Li (charge) sample data with the 240 cycle sample data shows similar NMR peak positions with differences only in the relative intensities of peaks, suggesting that there is no significant irreversible change in Li ordering caused by aging and that the new peaks observed in the ^6Li NMR data are due to the presence of vacancies and diamagnetic Ni^{+4} .

Within the first cycle, studying differences in NMR data of samples with the same Li content provides important insights. In Figure IX.2.13, for $\text{Li}0.70$ samples, even though there are differences in relative intensities of the peaks, the peak positions remain unchanged suggesting that the local Li environments and Li occupancies follow the same order during delithiation and relithiation. However, there is considerable difference in peak positions, peak shapes, and widths for $<50\%$ Li samples during charge (delithiation) and discharge (relithiation), showing clear structural hysteresis. These differences in the Li peaks could be due to phase transitions, reordering, and/or Li^+ mobility/diffusion differences in the oxide structure; additional NMR theory/modeling studies are needed to pinpoint the actual reasons for the observed differences.

Analytical electron microscopy studies of LiNiO₂: Chongmin Wang et al., PNNL.

Structural and chemical rearrangements at oxide surfaces determine the way in which the cathode interacts with its surrounding environment. In layered oxides with α -NaFeO₂ structure ($R\bar{3}m$ space group), the transition metal (TM) atoms can migrate into the Li layers, a phenomenon termed “cation mixing”. Cation mixing at surfaces of the layered oxides can cause local phase transformation, from the layered structure to spinel-like ($Fd\bar{3}m$ space group) or rocksalt ($Fm\bar{3}m$ space group) structures. The reconstructed surfaces are often observed in as-synthesized materials but evolves and growth during the charge-discharge cycles. This surface reconstruction layer is believed to contribute to the capacity fade and poor rate performance of the layered oxide cathodes.

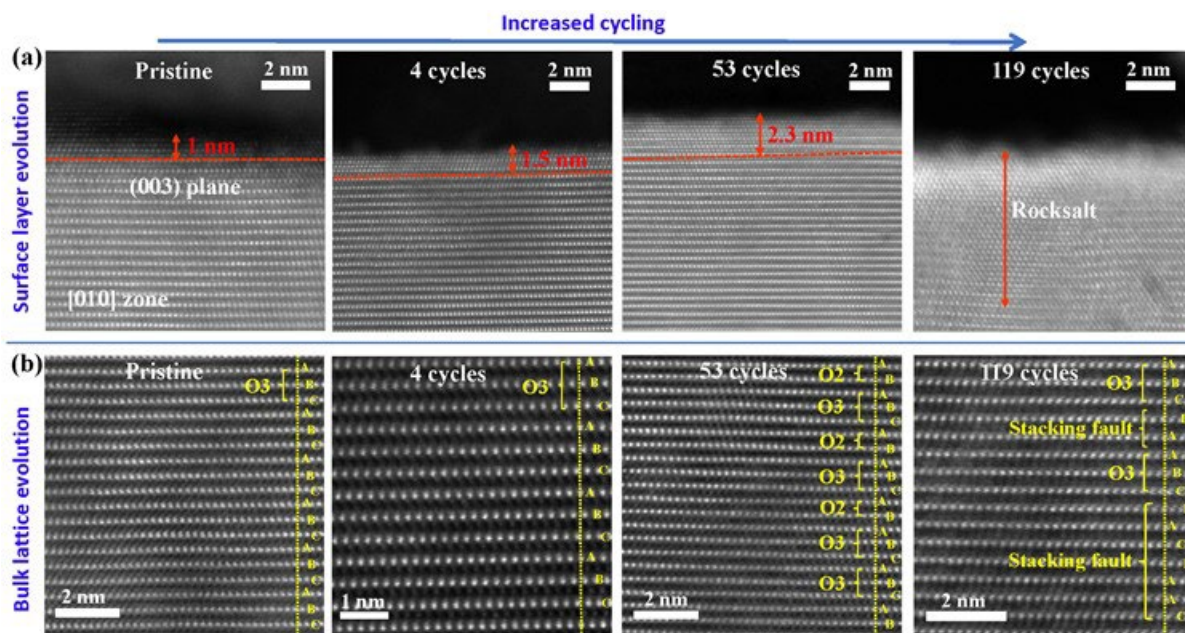


Figure IX.2.14 STEM-HAADF images to illustrate the surface and bulk lattice evolution of LiNiO₂ cathode upon battery cycling. (a) illustrates evolution of the surface reconstruction layer thickness with increasing cycling number. (b) indicates the bulk lattice structural evolution, featuring a transition from O3 lattice to O2 lattice and disruption of stacking sequences following extended cycling.

The structural evolution of LiNiO₂ upon battery cycling is not fully understood. We used scanning transmission electron microscopy (STEM) high angle annular dark field (HAADF) imaging to probe the structural evolution of LiNiO₂ from the point of view of both oxide surface and the bulk lattice. In the pristine state, the surface reconstruction layer on the LiNiO₂ particle is ~1 nm in thickness as shown in Figure IX.2.14a. With cycling, the thickness of this surface reconstruction layer increases gradually; representative values are ~1.5 nm after 4 cycles and ~2.3 nm after 53 cycles. After 119 cycles, this surface reconstruction feature is no longer a uniform layer; instead, it shows patchy features that penetrate into the bulk lattice. Evolution of this surface reconstruction layer is a consequence of the direct interaction of the cathode with liquid electrolyte. It is known that the formation of oxygen vacancies will facilitate the migration of Ni to the Li layer. A gradual increase of the surface reconstruction layer with cycling likely indicates continued removal of oxygen from the surface region, therefore thickening the reconstruction layer. It is apparent that these disordered (non-layered) regions can impede Li⁺ extraction and insertion during electrochemical cycling.

Another prominent feature is the bulk lattice structural evolution with cycling (Figure IX.2.14b). From STEM-HAADF images we observe that in the pristine state, LiNiO₂ possesses the O3 structure. Upon cycling, the bulk lattice appears to maintain the O3 structure in the first 4 cycles. After 53 cycles, part of the O3 structure converts into the O2 structure. On extended cycling (119 cycles), stacking sequences in portions of the oxide are completely disrupted. The formation of stacking faults during cycling appears to be related to “layer

invariant sliding”, which has been reported for NMC811 single crystals with a dimension of several micrometers. Such sliding induced stacking faults have not been reported previously for LiNiO₂ materials. Additional work is needed to fully understand the sliding process and its implications for the voltage profile evolution and performance/degradation of the LiNiO₂ cathode.

Performance of full cells with the LiNi_{0.9}Mn_{0.1}O₂ (N9M1) cathode: Adam Tornheim et al., ANL

The objective of this work was to probe the performance of the N9M1 cathode at specific energies comparable to those of the LiNiO₂ (LNO) cathode. Our approach was to increase the upper-cutoff voltage (UCV) of the test protocol from 4.2 V to 4.3 and 4.4 V to achieve higher energies. Figure IX.2.15 shows discharge capacities and coulombic efficiencies (CEs) of N9M1//Gr full cells cycled at the 3 UCVs. As expected, the initial capacities increased with increasing UCV. During cycling, cells with the 4.3 V and 4.4 V UCV showed significant capacity decay, with the 4.4 V UCV cells showing faster performance degradation. This trend is also seen in the CE data, with 4.4 V UCV CE significantly below CEs for the other UCVs. Interestingly, the final discharge capacity is the same for both 4.2 V and 4.3 V UCVs, although the difference in initial discharge capacity leads to different capacity retentions over the course of the test.

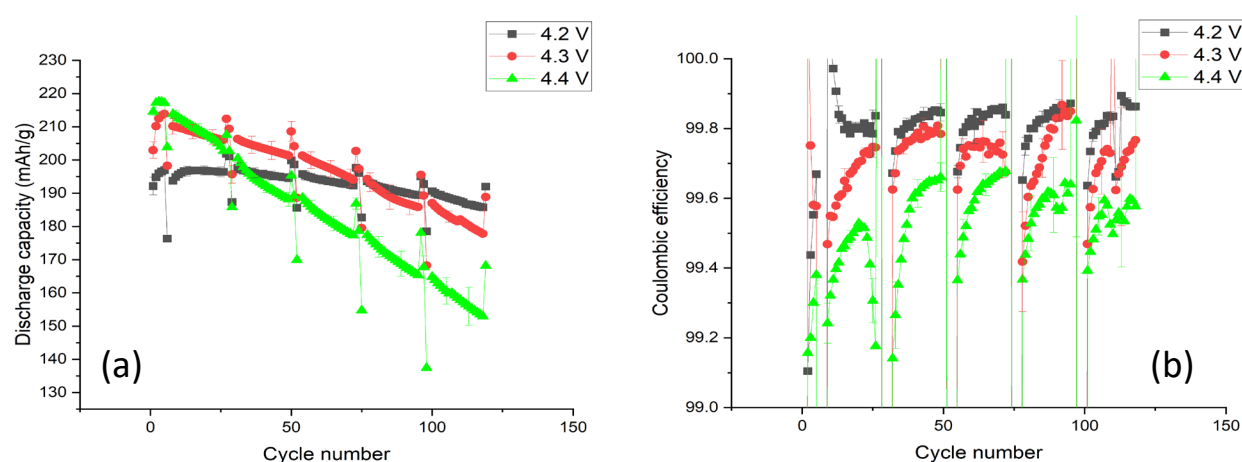


Figure IX.2.15 Capacities (a) and coulombic efficiencies (b) of N9M1/Gr full cells cycled to various UCVs.

Interspersed throughout the protocol, C/10 diagnostic cycles and HPPC cycles are used for further evaluation of cell performance. Examination of dQ/dV profiles showed negligible changes for the 4.2 V UCV cell. For the 4.3 V UCV cell, the capacity loss correlated with decreases in the peaks at 4.12 V and 3.65 V. For the 4.4 V UCV cell, most peaks in the dQ/dV profiles were greatly diminished, with the significant peak separation suggesting higher cell impedance. The HPPC tests confirm these impedance rise trends (Figure IX.2.16).

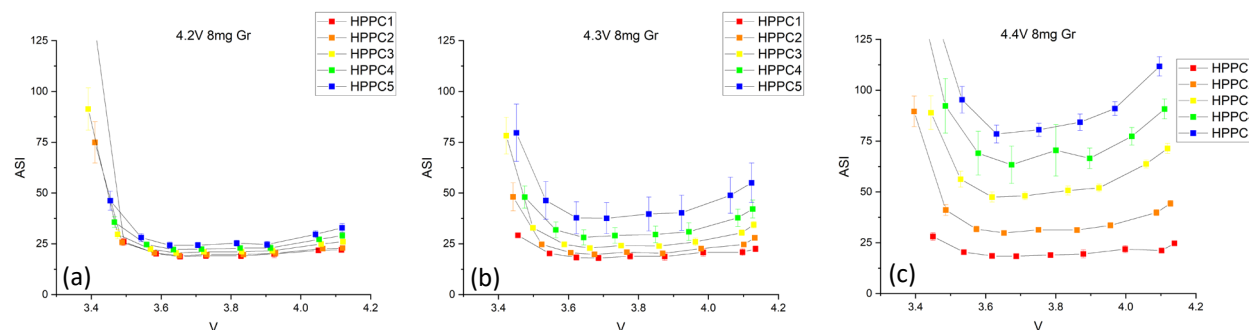


Figure IX.2.16 ASI vs. cell voltage data from HPPC tests on N9M1/Gr cells cycled to UCVs of (a) 4.2 V, (b) 4.3 V and (c) 4.4 V

At the completion of the test protocol, one cell from each UCV was disassembled and recombined into half cells to check for active material changes and losses. The resulting voltage profiles are shown in Figure

IX.2.17, along with a N9M1 cathode extracted from a cell that was formed (4 C/10 cycles). In the figure, cells with the formed and 4.2 V UCV electrodes have the same profile and capacity. The 4.3 V UCV electrodes show ~5% capacity loss, while the 4.4 V UCV cathode show ~15% capacity loss. These data indicate that while the capacity retention and impedance rise of the 4.3 V UCV cell are moderate, that cathode is mostly intact, which points to impedance rise and Li-trapping as the main drivers for performance loss. However, in the 4.4 V UCV cell, cathode damage is a likely contributor to performance loss.

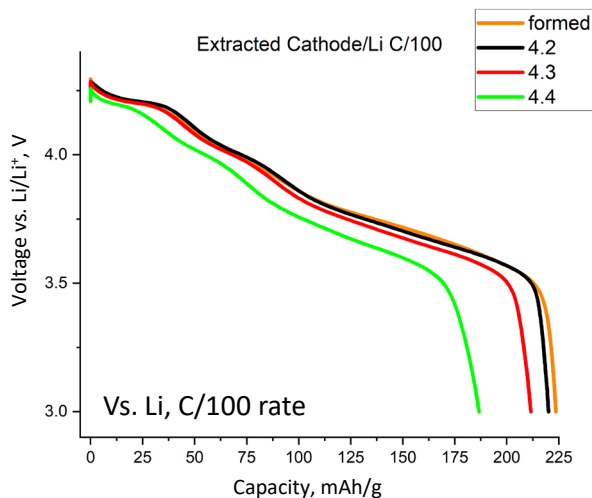


Figure IX.2.17 Voltage profiles of N9M1 cathodes (vs. Li, C/100 rate) extracted from N9M1//Gr cells after formation cycling and after extended cycling with UCVs of 4.2 V (black), 4.3 V (red) and 4.4 V (green).

***In situ* spectroscopic analysis of the cathode-electrolyte interface: Sang-Don Han et al., NREL**

In prior reports, we have shown how *in situ* ATR-FTIR can be used to investigate the cathode-electrolyte interfacial region during electrochemical cycling of a $\text{LiNi}_{0.6}\text{Mn}_{0.2}\text{Co}_{0.2}\text{O}_2$ (NMC622) cathode. Here, we show how the upper cutoff voltage (UCV) during cycling affects electrode aging behaviors in the high-Ni cathode $\text{LiNi}_{0.9}\text{Mn}_{0.5}\text{Co}_{0.5}\text{O}_2$ (NMC9055) to better understand how the transition metal redox chemistry and corresponding structure changes (e.g., local and long-range order) dictate the electrochemical performance.

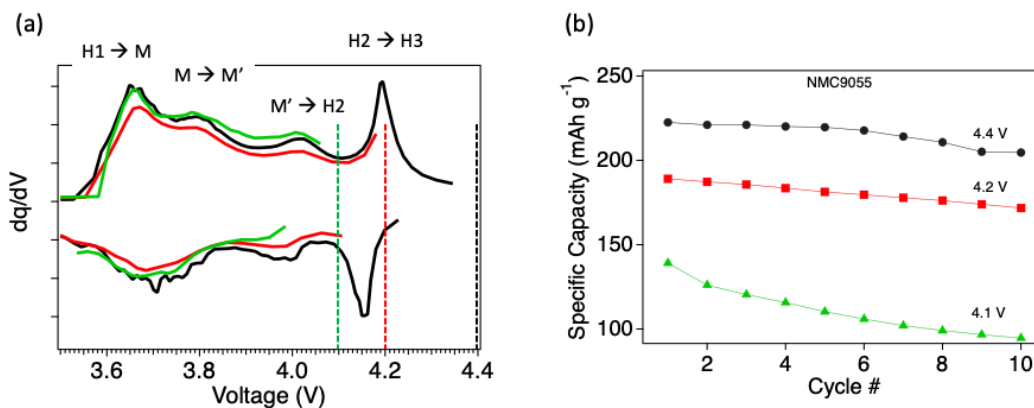


Figure IX.2.18 (a) Differential capacity plot of NMC9055 half-cells during first cycle from 3.0 to 4.1 V (green), 4.2 V (red) and 4.4 V (black). (b) Specific discharge capacity for the first 10 cycles.

A custom spectroelectrochemical cell was designed and built for *in situ* collection of ATR-FTIR spectra while enabling reliable electrochemical battery cycling. This cell was used to investigate NMC9055 during galvanostatic charging and discharging between 3.0 to UCVs of 4.1, 4.2, and 4.4 V (vs. Li/Li^+). In these

studies, we used the Gen2 electrolyte. The UCVs in this study were chosen around specific known phase transitions that occur in the NMC9055 structure as a function of voltage (Figure IX.2.18a), particularly the Hexagonal 2 to Hexagonal 3 transition ($H2 \rightarrow H3$) between 4.15–4.3 V that has been shown to result in irreversible volume changes in the NMC9055 lattice structure contributing to cell degradation. While UCVs > 4.3 V have shown greater capacity fade up to 100 cycles, our study finds that early performance degradation within the first few cycles likely stems from something else, and that the lowest UCV used (4.1 V) shows the worst early capacity fade (Figure IX.2.18b).

In situ FTIR spectra (taken every ~10 mins during cycling) provide a useful probe of the voltage-induced changes to the cathode. The vibrational absorptions in the energy region between 630–500 cm^{-1} include transition-metal (TM)–oxygen stretching and bending modes. The TM–O bond vibrations, and therefore corresponding FTIR absorption peak positions and peak intensities, are sensitive to the changes in oxidation states of the TMs during lithiation and de-lithiation (Figure IX.2.19a). Surprisingly, we found significant differences with UCVs in the reversible behavior of the TM–O₆ stretching mode intensities during the first few cycles (Figure IX.2.19b), particularly around the Hexagonal 1 to Monoclinic phase transition ($H1 \rightarrow M$) occurring between 3.6 and 3.8 V. This transition is mainly associated with the Ni oxidation from Ni^{2+} to Ni^{3+} and the Ni^{3+} -rich monoclinic phase shows higher intensity vibrational absorption. Notably, when the UCV is only 4.1 V (Figure IX.2.19b, green), there is a “hysteresis” with voltage of the TM–O₆ vibrational intensity. This behavior is not observed when the UCV is 4.4 V. Two conclusions from these observations are that the reversibility of the NMC9055 bonding structure at lower voltages (<4.0 V) can be affected by cathode behavior at higher voltages (>4.0 V) and that the *in situ* FTIR intensities of the NMC9055 vibrational modes can indicate cell capacity behavior.

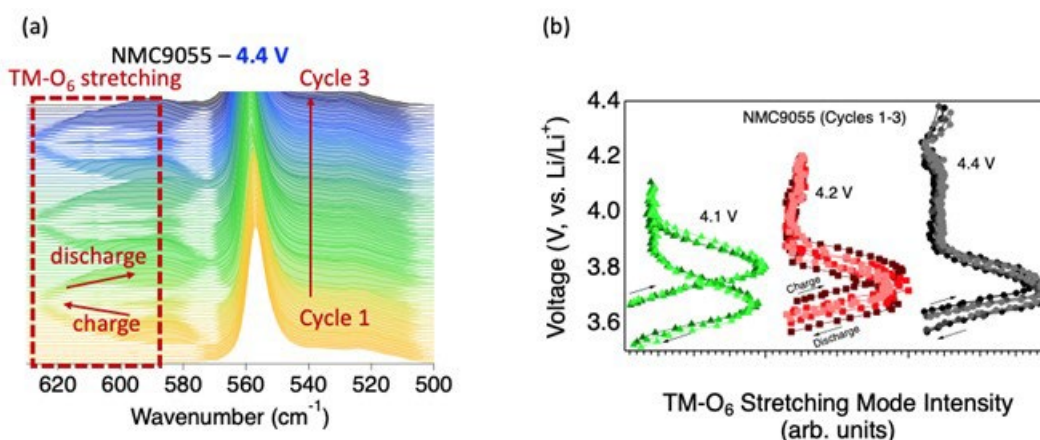


Figure IX.2.19 (a) *in situ* FTIR spectra of NMC9055 during the first 3 cycles with a UCV of 4.4 V. The TM–O stretching modes of the cathode are observed in the energy region of 630–500 cm^{-1} and both the peak intensities and positions shift with cell charging and discharging. The P–F stretching modes of the electrolyte obscure most of the signals below 560 cm^{-1} . (b) Significant differences in reversible behavior of the TM–O₆ stretching mode intensities are observed with UCVs of 4.1 (green), 4.2 (red) and 4.4 V (black) during the first few cycles, particularly around the $H1 \rightarrow M$ phase transition occurring between 3.6 and 3.8 V.

While the Gen2 electrolyte is the most commonly used one for studying state-of-the-art LiB materials, very strong FTIR absorption of the P–F stretching modes centered around 558 cm^{-1} obscure some of the NMC9055 cathode vibrations in the same region. Therefore, we have explored alternative electrolytes for the *in situ* FTIR studies. We have found that 1.0 M lithium perchlorate (LiClO_4) in propylene carbonate (PC) provides equally good electrochemical performance for the first 10 cycles in our spectroelectrochemical cells. The advantage of using this electrolyte is that it simplifies the FTIR spectral deconvolution in the areas of interest for tracking changes of the TM–O stretching and bending vibration modes. We have developed methods to fit and deconvolute the FTIR spectra such that NMC9055 and electrolyte absorptions can be separated (Figure IX.2.20). This deconvolution should enable analysis of the TM–O–TM bending modes changes with voltage

occurring between $560\text{--}500\text{ cm}^{-1}$, which we hope to correlate to the observed TM-O stretching and the electrochemical cell performance.

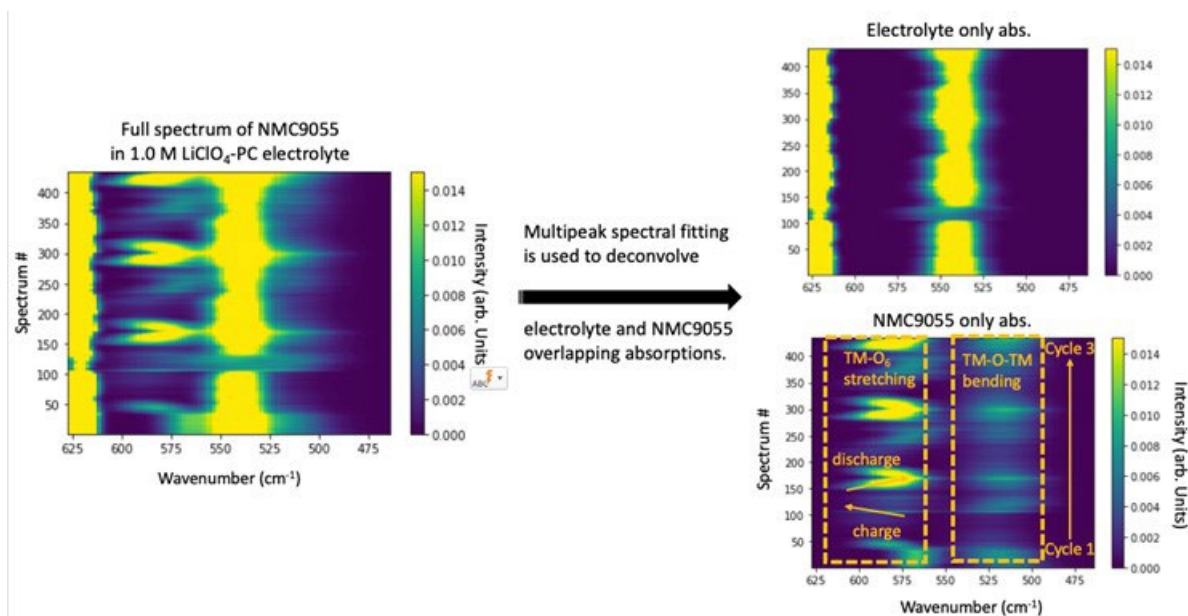


Figure IX.2.20 Spectral deconvolution of the in situ FTIR spectra separates contributions from the NMC9055 and electrolyte (1.0 M LiClO₄ in PC) vibrational modes.

Proton extraction mechanism in layered transition metal hydroxides: Sang-Don Han et al., NREL

Increasing cell operating voltage is a realistic strategy to enhance the energy density of LiBs with next-generation materials. However, it is inevitably accompanied by oxidative electrolyte decompositions and irreversible phase transitions in the cathode that result in battery failure. At high operating voltages ($>4.5\text{ V vs. Li/Li}^+$) we should consider another potential detrimental factor—proton extraction from layered transition metal hydroxides and its adverse effect on electrochemical performance. Experimental observations and computational simulations indicate that proton extraction from the structure is transition metal dependent and a kinetically-limited behavior.

$\text{Mn}_{0.5}\text{Ni}_{0.5}(\text{OH})_2$ —as a simple model structure without lithium—demonstrates significant amount of charge capacity ($\sim 252\text{ mAh/g}$) and subsequent discharge capacity of around 109 mAh/g , but only a limited discharge capacity ($\sim 15\text{ mAh/g}$) was obtained when $\text{Mn}_{0.5}\text{Ni}_{0.5}(\text{OH})_2$ was discharged first (Figure IX.2.21). The unexpectedly high initial charge capacity is attributed to both bulk structural changes possibly induced by proton extraction and oxidative electrolyte decomposition at high voltages. We think protons (instead of Li^+) play a role as charge carrier ions for the initial cycle. On the other hand, both $\text{Ni}(\text{OH})_2$ and $\text{Co}(\text{OH})_2$ show abnormal charge behaviors indicating that the proton extraction does not occur in both of these materials, which supports the hypothesis that proton extraction is a transition-metal dependent phenomenon and occurs in Mn-O-H bonding environments. In addition, density functional theory (DFT) calculation results indicate that hydrogen atoms could be relatively easily extracted from $\text{Mn}_{27}\text{O}_{54}\text{H}_{54}$ compared to $\text{Co}_{27}\text{O}_{54}\text{H}_{54}$ and $\text{Ni}_{27}\text{O}_{54}\text{H}_{54}$. The Mn system, however, shows a broader angular distribution than the Co and Ni systems at the same dehydrogenation level, implying that the Mn-based system possesses a largely distorted structure upon hydrogenation.

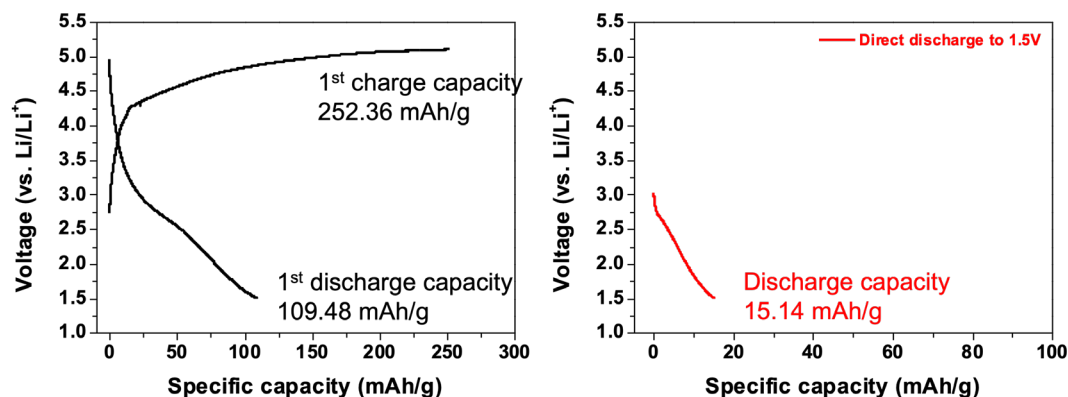


Figure IX.2.21 Charge-discharge voltage profiles of $\text{Ni}_{0.5}\text{Mn}_{0.5}(\text{OH})_2$ with and without initial charge process.

The proton extraction is a kinetically unfavored reaction (based on applied current density dependent electrochemical performance of $\text{Mn}_{0.5}\text{Ni}_{0.5}(\text{OH})_2$ data showing decrease in reversible capacity with increase of current density, not shown), so all protons may not be extracted during the 1st charge process and electrochemical substitution of protons by Li^+ ions occurs over many cycles (Figure IX.2.22). Distinct plateaus around 3.25 V for charge curves and around 3.0 and 3.5 V for discharge curves with initial overpotential decrease were observed in the charge-discharge curves of $\text{Mn}_{0.5}\text{Ni}_{0.5}(\text{OH})_2$ at different cycle numbers. Based on the redox voltage region of around 3.0 – 3.5 V, it can be concluded that Mn may dominantly play a role as a redox center rather than Ni in $\text{Mn}_{0.5}\text{Ni}_{0.5}(\text{OH})_2$, which supports electrochemically inactive characteristics of $\text{Ni}(\text{OH})_2$ and $\text{Co}(\text{OH})_2$ for the initial charge process.

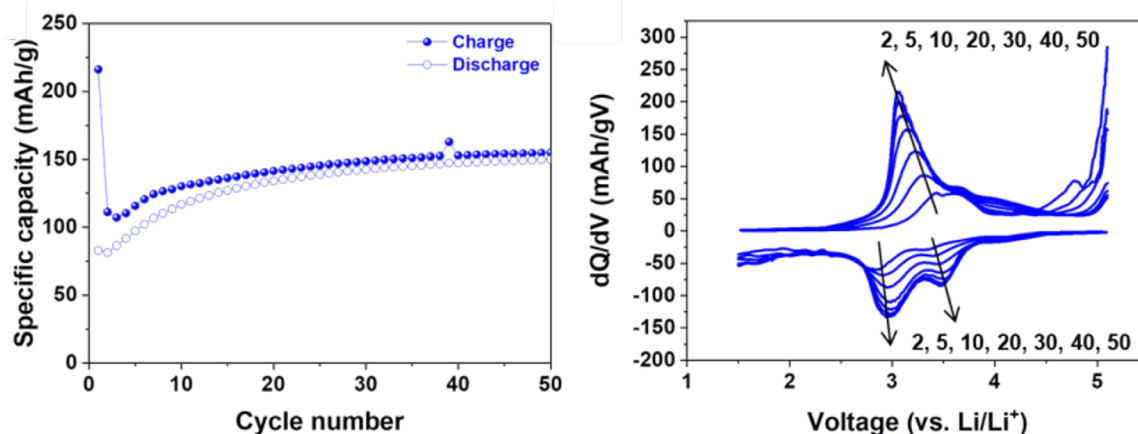


Figure IX.2.22 Cycling performance and differential capacity plots of $\text{Ni}_{0.5}\text{Mn}_{0.5}(\text{OH})_2$.

Ex situ Mn K-edge and Ni K-edge XANES spectra revealed that Mn is the dominant redox center in the material, as shown in Figure IX.2.23a and Figure IX.2.23b. In XRD analysis (Figure IX.2.23c), the (001) peaks of discharged states for the 1st, 2nd and 5th cycles gradually shifts toward lower two-theta angle compared with the pristine state of fully protonated $\text{Mn}_{0.5}\text{Ni}_{0.5}(\text{OH})_2$, indicating that the interlayer spacing is gradually expanded. In addition, the peak intensity decrease and FWHM value increase over cycles are attributed to gradual structural disorder due to co-presence of Li^+ and H^+ ions (not shown). The cycled and washed Li metal in a Gen2 electrolyte displays a drastic discoloration with strong attachment to the separator after the 1st charging (not shown). In Figure IX.2.23d, the F, O, P and C elemental signals from the Li metal cycled in the Gen2 electrolyte could have originated from the SEI layers formed from the reduction of electrolyte components. The signals of Ni and Mn might come from the transition metals dissolution in the $\text{Mn}_{0.5}\text{Ni}_{0.5}(\text{OH})_2$ electrode by proton extraction and subsequent highly corrosive HF formation and transferred by cross-talk between the electrodes.

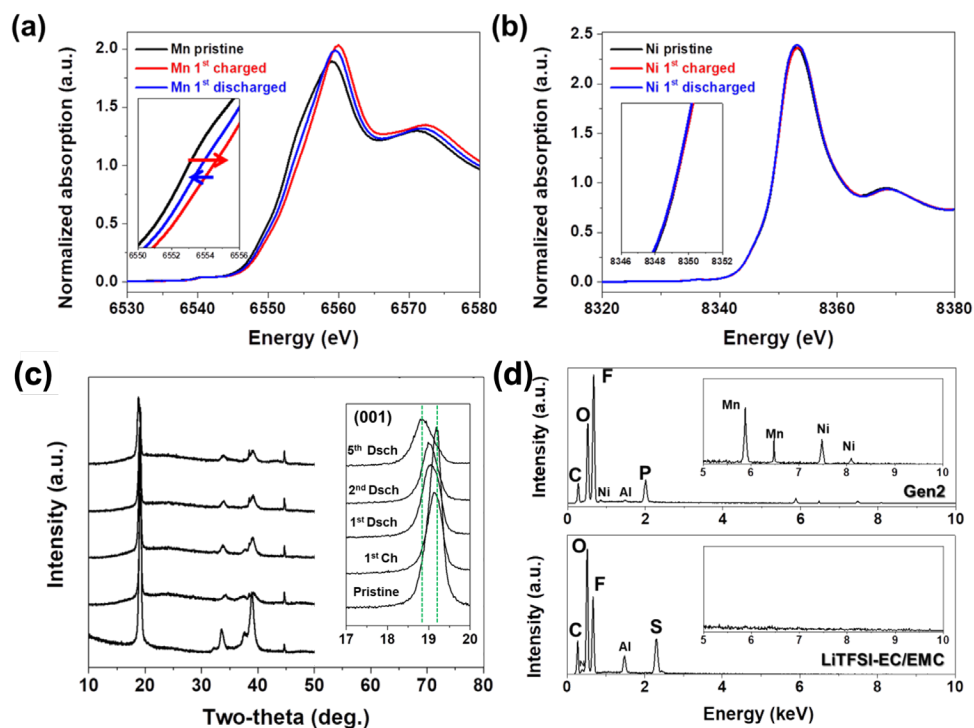


Figure IX.2.23 (a) Mn K-edge XANES, (b) Ni K-edge XANES, (c) XRD and (d) EDS spectra from pristine and cycled $\text{Mn}_{0.5}\text{Ni}_{0.5}(\text{OH})_2$ samples; legends in the plots indicate cycling conditions and electrolytes used.

Conclusions

- For $\text{LiNi}_{0.90}\text{Mn}_{0.05}\text{Co}_{0.05}\text{O}_2$ //Graphite cells, the CCCV protocol leads to faster capacity fade and higher impedance rise than the CC protocol. Addition of 2 wt% of VC to the Gen2 electrolyte improves capacity retention but has minimal effect on cell impedance rise. Adding 1% MS (lithium tetrafluoromalonate phosphate) to the Gen2 electrolyte also improves cell performance.
- New dual-salt ($\text{LiPF}_6 + \text{LiPO}_2\text{F}_2$) electrolyte compositions show promise for improving capacity and power retention in cells with high-Ni oxide cathodes.
- Extended cycling at elevated temperatures leads to faster capacity fade and impedance rise in $\text{LiNi}_{0.90}\text{Mn}_{0.05}\text{Co}_{0.05}\text{O}_2$ //Graphite cells; performance loss is especially severe at 60°C.
- Operando GCMS studies show that ALD-based AlF_3 coatings on NMC9055 electrodes suppress gas generation at high voltages.
- Performance degradation in LiNiO_2 //Gr full cells is more severe during cycling at 45°C than at 30°C. XPS analysis of electrodes from these cells reveal that both CEI and SEI layers contain more $\text{Li}_x\text{PO}_y\text{F}$ species at 45°C as a result of electrolyte decomposition.
- ^6Li Solid State NMR data show that although there is 52% Li^+ loss after extended cycling (240 cycles), and only 24% of the Li^+ can be restored after relithiation, the bulk Li^+ ordering remains the same as in the pristine LiNiO_2 oxide, suggesting that there is no significant irreversible change in the bulk Li local structure during extended cycling.
- STEM studies show that the surface reconstruction layer on LiNiO_2 particle gets thicker on cycling. On extended cycling, this surface reconstruction feature is no longer a uniform layer, but manifests as patchy regions that penetrate into the bulk lattice.

- Studies on full cells with the Co-free LiNi_{0.9}Mn_{0.1}O₂ cathodes show that electrode capacity increases when the cells are cycled at higher voltages. However, cell capacity loss and impedance rise are also higher for the higher voltage cycling.
- Using an in situ ATR-FTIR cell, vibrational absorption spectra of NMC9055 were obtained during cycling to different UCVs. The transition metal-oxygen vibrational characteristics of NMC905 display hysteresis below 4.2 V, indicating the importance of the oxide's hexagonal II to hexagonal III phase transition between 4.15 – 4.3 V.
- Mechanistic studies reveal that proton extraction from layered transition metal hydroxides at high voltages (>4.5 V vs. Li/Li⁺) is transition metal dependent and kinetically limited. The extracted protons could form HF in a LiPF₆-based electrolyte, which could accelerate transition metal dissolution and cross-talk between the electrodes, ultimately contributing to battery failure.

Key Publications

1. J. Yang, M.-T.F. Rodrigues, S.-B. Son, J.C. Garcia, K. Liu, J. Gim, H. Iddir, D.P. Abraham, Z. Zhang, C. Liao, "Dual-Salt Electrolytes to Effectively Reduce Impedance Rise of High-Nickel Lithium-Ion Batteries", *ACS Appl. Mater. Interfaces* 2021, 13, 40502.
2. M.-T.F. Rodrigues, A. Tornheim, J. Gim, J. Yang, J. Croy, S.E. Trask, C. Liao, D.P. Abraham "Performance loss mechanisms in lithium-ion cells with nickel-dominant oxide cathodes", 239th ECS Meeting, Chicago, May 30 – June 3, 2021.
3. C. Liao, J. Yang, S.-B. Son, M.-T.F. Rodrigues, D.P. Abraham, "Electrolyte with New Composition for High Nickel Lithium-Ion Batteries", 239th ECS Meeting, Chicago, May 30 – June 3, 2021.
4. S.-B. Son, D. Robertson, Y. Tsai, S. Trask, A. Dunlop, I. Bloom, "Systematic Study of the Cathode Compositional Dependency of Cross-talk Behavior in Li-ion Battery" *J. Electrochem. Soc.* 2020, 167, 160508.
5. Tornheim, D.C. O'Hanlon, *J. Electrochem. Soc.* 167 (2020) 110520.
6. J. Tremolet de Villers, J. Yang, S.-M. Bak and S.-D. Han, "In Situ ATR-FTIR Study of Cathode-Electrolyte Interphase: Electrolyte Solution Structure, Transition Metal Redox, and Surface Layer Evolution," *Batter. Supercaps* 2021, 4, 778–784.
7. Huang, C. Engtrakul, S. Nanayakkara, D. W. Mulder, S.-D. Han, M. Zhou, H. Luo and R. C. Tenent, "Understanding Degradation at the Lithium-Ion Battery Cathode/Electrolyte Interface: Connecting Transition-Metal Dissolution Mechanisms to Electrolyte Composition," *ACS Appl. Mater. Interfaces* 2021, 13, 11930-11939.
8. B. J. Tremolet de Villers, K. Fink, J. Yang, J. Palmer and S.-D. Han, "In Situ Analytical and Spectroscopic Characterizations of the Electrode-Electrolyte Interfacial Chemistry in Lithium-Ion Batteries with Next-Generation Electrodes," Oral presentation, 239th ECS Meeting, Digital Meeting (2021).

Acknowledgements

Support from the U.S. Department of Energy's Vehicle Technologies Program, specifically from Peter Faguy and Dave Howell, is gratefully acknowledged. We acknowledge contributions from the following individuals: S.-M. Bak, M. Balasubramanian, I. Belharouak, I. Bloom, A.N. Jansen, F. Dogan, C. Engtrakul, S.-D. Han, D. Huang, J. Kim, S. Lee, C. Liao, H. Luo, D.W. Mulder, S. Nanayakkara, E. Paek, S. Park, B.J. Polzin, M.-T.F. Rodrigues, J. Sharma, S.-B. Son, R.C. Tenent, A. Tornheim, S.E. Trask, Y. Tsai, B.J. Tremolet de Villers, C. Wang, J. Yang, M. Zhou, L. Zou.

IX.3 Theory and Modeling (ANL, LBNL, PNNL, NREL, ORNL)

Hakim Iddir, Principal Investigator

Argonne National Laboratory
9700 South Cass Avenue
Lemont, IL 60439
E-mail: Iddir@anl.gov

Guoying Chen, Principal Investigator

Lawrence Berkeley National Laboratory
1 Cyclotron Road
Berkeley, CA 94720
E-mail: gchen@lbl.gov

Peter Faguy, DOE Technology Development Manager

U.S. Department of Energy
E-mail: Peter.Faguy@ee.doe.gov

Start Date: October 1, 2018

End Date: September 30, 2021

Project Funding (FY21): \$3,500,000

DOE share: \$3,500,000

Non-DOE share: \$0

Project Introduction

Geopolitical concerns over critical resources, and in particular cobalt, as well as market demand have instigated new efforts to improve the sustainability of lithium-ion cathode technologies. This project will use first-principles modeling applied to prototypical cobalt free cathode oxides including LiNiO_2 (LNO), $\text{LiNi}_{0.5}\text{Mn}_{0.5}\text{O}_2$, and newly developed derivatives thereof in order to advance cathode design in accord with DOE targets for cost, performance, and sustainability.

Objectives

- Identify promising surface and bulk dopant elements and provide a fundamental understanding of their efficacy in modifying the properties of low/no cobalt oxides with respect to cobalt as a counterpart.
- Improve cathode design by understanding and elucidating the mechanisms and tendencies of facet-dependent degradation, stability, and dopant segregation.
- Narrow the gap in understanding between structure-property relationships by elucidating the effects that local phenomena (e.g., cation ordering) have on measured, physical and electrochemical data.

Approach

Atomistic modeling

The calculations required to accomplish the project goals were performed within the spin polarized density functional theory (DFT) methodology as implemented in the Vienna Ab Initio Simulation Package (VASP) [1], [2]. The generalized gradient approximation (GGA) is used to model the exchange-correlation potentials as developed by Perdew, Burke, and Ernzerhof (PBE) [3]. The interaction between valence electrons and ion cores is described by the projected augmented wave (PAW) method [4]. Furthermore, the GGA+U scheme is used for applying the on-site correlation effects among 3d electrons of the transition metals, where the parameter of (U–J) is set to 5.96, 5.00, and 4.84 eV for Ni, Co, and Mn, respectively [5]. The magnetization was used to assign the oxidation state of the ions. Therefore, in order to get a better representation of the electronic structure, a single point calculation with a screened hybrid functional (HSE06) is performed after each geometry optimization [6]. Total energy and hyperfine shift calculations were accomplished using the

Vienna Ab initio Simulation Package (VASP) under the projector augmented wave (PAW) pseudopotentials with the generalized gradient approximation (GGA) of the Perdew-Burke-Ernzerhof (PBE) exchange-correlation function.

Model systems

Combining single-crystal model systems with controlled physical properties (composition, size, morphology, surface orientation etc.) and single-particle-based diagnostic techniques to enable better understanding of composition-structure-property-performance correlations at the intrinsic material's level.

Results

Atomistic modeling

Understanding Lithium Local Environments in $\text{LiMn}_{0.5}\text{Ni}_{0.5}\text{O}_2$ Cathodes: A DFT-supported ^6Li Solid-state NMR Study

$\text{LiMn}_{0.5}\text{Ni}_{0.5}\text{O}_2$ has been plagued by the structural failure driven by the irreversible phase change upon subsequent cycling and the structural degradation caused by the seemingly unavoidable Li/Ni exchange. To understand the nature and change in lithium local structures, we use DFT to assist the experimental ^6Li solid-state magic angle spinning (MAS) nuclear magnetic resonance (NMR) spectroscopy. To correlate the NMR peak changes after different synthesis conditions we calculated the NMR spectra of representative low-energy model configurations of $\text{LiMn}_{0.5}\text{Ni}_{0.5}\text{O}_2$: zigzag, row, and flower structures and the influence of Ni/Mn and Li/Ni ordering on each spectrum. As expected, the zigzag configuration exhibited the most thermodynamically stable structure with a formation energy of -23.19 eV per formula unit (f.u.), while the flower was only 0.02 eV/f.u. higher than the zigzag, and the row configuration is 0.08 eV/f.u. higher (Figure IX.3.1). For all TM ordering models, Li/Ni exchange in general increases the energy of the system. Special configurations of extended defects resulting from concerted Li/Ni exchange show a different behavior, with a minimum energy around 3-4%. However, the energy deviation between the pristine and optimum Li/Ni exchange is less than 0.02 eV/f.u., hence configurations easily within reach at the elevated synthesis and annealing temperatures (900°C).

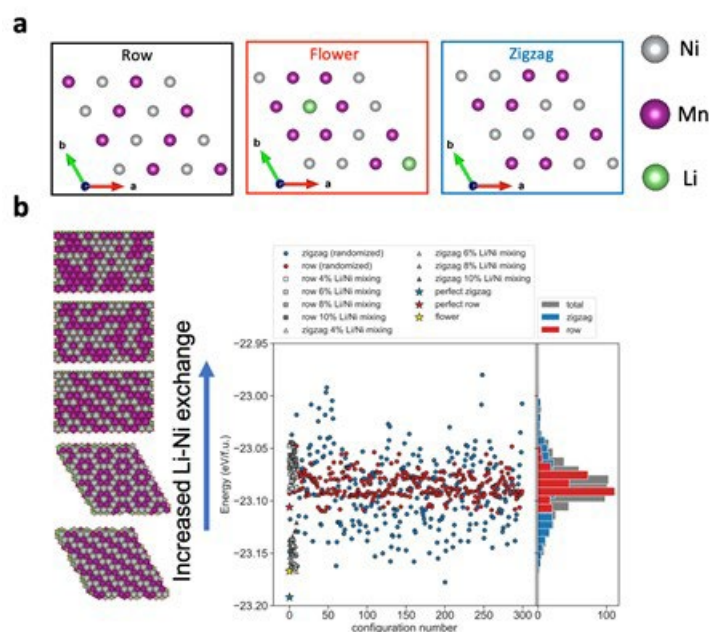


Figure IX.3.1 Representative single TM layer based on the different ordering cases. (b) Total energy comparison of distinctive structures depending on the TM arrangements with varied Li/Ni exchange amount and their populations. Four different Li/Ni exchange rates were applied: 4%, 6%, 8%, and 10%.

Figure IX.3.2 shows the computed NMR spectrum for each configuration exhibiting its characteristic curve. In particular, the flower model is responsible for spectrum at 500 ppm and 1000 ppm, the zigzag with 10% Li/Ni exchange accounts for the intensity near 880 ppm, and the row with 10% swap mainly contributes to peaks around 620 ppm, 900 ppm, and 1500 ppm. The most notable feature is the reduction in the peak widths and intensities around 200 ppm, 600 ppm, and 1300 ppm in 216 hour annealed sample, which now can be attributed to more defined orderings within the $\text{LiMn}_{0.5}\text{Ni}_{0.5}\text{O}_2$ structure in general, and less Li/Ni exchange, consistent with the DFT results. To be specific, the reduced intensity of the shoulder peaks around 500 ~ 680 ppm, where the shoulder peaks are, associated with Li/Ni exchange for configurations based off row models. The peak reduction at 200 ~ 300 ppm cannot be indexed to a particular TM ordering; however, we can claim that the configuration belong to this range could be row/zigzag ordering with high Li/Ni exchanged structures. Thus, we can argue that the long annealing at 900 °C improves local ordering and domain structures that are kinetically accessible and reduces Li/Ni exchange rate from row and zigzag-based configurations.

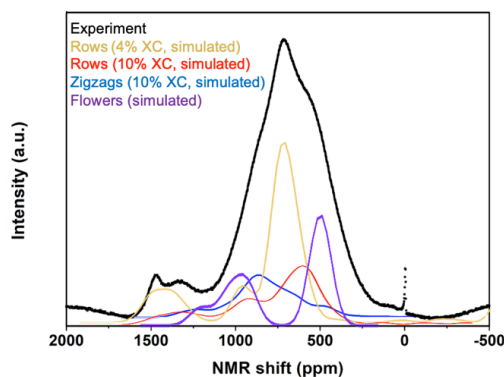


Figure IX.3.2 Comparison of experimental and computed NMR spectra after Gaussian broadening process on each configuration (gold: row with 4% Li/Ni exchange, red: row with 10% Li/Ni exchange, blue: zigzag with 10% Li/Ni exchange, and purple: flower). The broadening is employed on the sum of the histogram values obtained from the four structures.

Strain-driven surface reconstruction and cation segregation in layered cathode materials

The composition, structure and phase transformations occurring on cathode surfaces greatly affect the performance of Li-ion batteries. Li-ion diffusion and surface-electrolyte interaction are two major phenomena that impact the capacity and cell impedance. We used DFT calculations to investigate the processes taking place during surface segregation and reconstruction. Facet dependent segregation was found in NMC cathodes. Specifically, Co tends to segregate to the (104) surface of the primary particles within the transition metal layer, while Ni ions tend to segregate to the (012) surface in the Li layer, forming a surface reconstruction (SR) layer. Experimental evidence shows the SR to be epitaxial with the bulk of the as-synthesized material, the new SR phase is pinned to the NMC unit cell leading to a strained SR. Here, we show that strain can stabilize a spinel structure of the SR layers. Figure IX.3.3 shows how the energy of the surface model changes with strain, favoring the formation of a spinel-like phase only for Ni-rich surfaces.

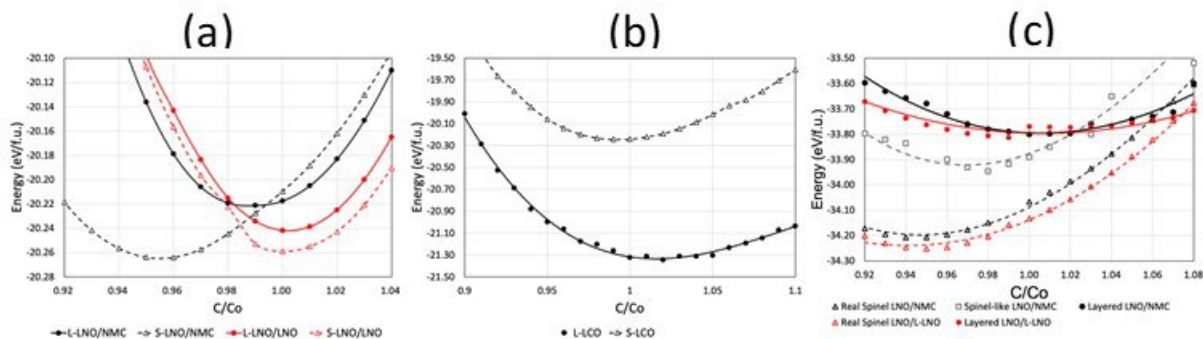


Figure IX.3.3 Energy change with c direction expansion for (a) layered and overlithiated spinel LiNiO_2 ($\text{Li}_2\text{Ni}_2\text{O}_4$) pinned to NMC-111 and layered LiNiO_2 , (b) layered and overlithiated spinel LiCoO_2 ($\text{Li}_2\text{Co}_2\text{O}_4$) pinned to NMC-111 (012) surface. (c) Figure 7. Energy change with expansion/contraction in the c direction for layered, spinel-like and real spinel LiNiO_4 pinned to the (012) facets of NMC-111 (black-grey) and pinned to LNO (red).

In summary, a complex mechanism for Ni segregation is put forward, where we show the presence of a thermodynamic driving force for the segregation of Ni to the surface via Li-Ni exchange near the (012) surface, and strain-driven stabilization of the LiNi_2O_4 spinel thin film pinned to NMC and LiNiO_2 lattices. The elemental segregation and SR layer formation are intimately linked and facet dependent phenomena. The global composition and strain affect the nature and the thickness of the SR, which impacts the impedance and the chemical stability of the cathode/electrolyte interface as well.

Theoretical insights on dual-Salts Electrolyte to Effectively Reduce Impedance Rise of High-Nickel Lithium-Ion Batteries

Dual-salts electrolytes play a role in modifying the cathode surface. We performed DFT calculations to study the interaction of LiDFP with the surface of a Ni-rich cathode. A slab surface of pure LiNiO_2 is used to represent Ni-rich compositions, such as $\text{Ni}_{94}\text{Co}_{06}$. We used the (012) facet as the prototype surface in all our calculations [5], and ab-initio molecular dynamics to explore the configuration space of the molecules over the surfaces. The results indicate a favorable and barrierless chemical transformation of the salt at the cathode surface, where LiDFP is converted to lithium monofluorophosphate (LiMFP). The final state (Figure IX.3.4) shows an exchange between one of the fluorine ions originally in the LiDFP molecule and a sub-surface oxygen atom from the LiNiO_2 lattice. This configuration is stabilized by the electrostatic interaction created by the negatively charged LiMFP group and the F-doped oxygen lattice. The stability of this system could explain the improved electrochemical performance of the dual salt system, with the LiMFP playing the role of a passivating agent, by preventing further surface reactions. The interchange between F from the LiDFP and O from the cathode surface, also works as surface F-doping mechanism that would reduce further surface reactivity.

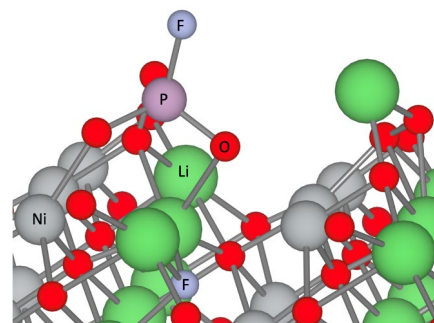


Figure IX.3.4 Ball and stick representation of LiMFP absorbed at the (012) surface of a LiNiO_2 . One fluorine ion from the original LiDFP salt is shown incorporated in the subsurface oxygen lattice. Blue spheres represent F ions, purple spheres represent P ions, grey spheres represent Ni ions, green spheres represent Li ions and grey sticks represent chemical bonds.

The role of dopants in Ni-rich cathode materials

Oxygen vacancy formation energy (OVFE) can be used as a proxy for reactivity. The harder to form an oxygen vacancy the harder is to reduce the surface. Generally, a negative OVFE indicates a thermodynamically favorable release of oxygen and hence would happen spontaneously. Figure IX.3.5 shows the OVFE for doped (012) and (104) surfaces as a function of the difference in energy between the dopant located at the bulk and the surface ($\Delta E = E_{\text{bulk}} - E_{\text{surf}}$). A positive ΔE means that the dopant prefers to be at the surface. The results show that surface reactivity increases upon delithiation and there is a threshold for spontaneous oxygen evolution. This threshold is affected by the facet and the nature of dopant. The threshold for the evolution of a second oxygen vacancy after the initial reduction of the surface is pushed to higher states of charge. The details of such calculations will be presented in an upcoming paper currently in preparation.

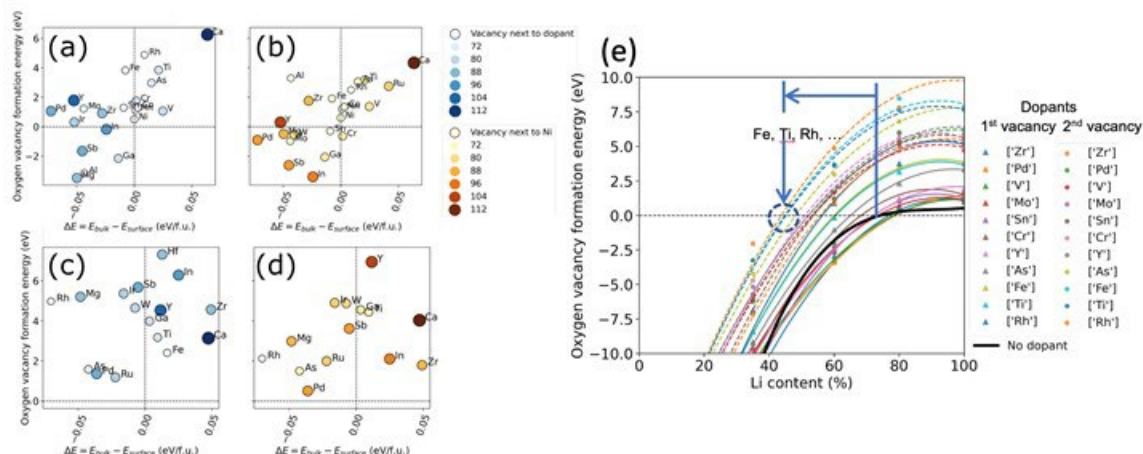


Figure IX.3.5 Oxygen vacancy formation energy vs the difference of energy of selected dopants located at bulk and surface of LiNiO_2 where the oxygen vacancy was taken (a) next to surface dopant in (012) facet, (b) far from dopant in (012) facet, (c) next to surface dopant in (104) facet, (d) far from dopant in (104) facet.

Model systems

Impact of particle morphology and surface on LiNiO_2 cathode performance

To enable successful development of Ni-rich $\text{Li}[\text{Ni}_x\text{Mn}_y\text{Co}_{1-x-y}]\text{O}_2$ (NMC, $x \geq 0.9$) and other LiNiO_2 (LNO)-based cathodes, fundamental understanding in the synthesis-property-performance relationships of LNO parent phase is needed. Here, three well-formed single-crystal (SC) LNO samples were synthesized by using a molten-salt method. [7] As shown in the scanning electron microscopy (SEM) images in Figure IX.3.6a-c, all SC-LNOs have the same average particle size of $\sim 1 \mu\text{m}$ while the morphology varies from cubic, octahedron and truncated-polyhedron (hereafter referred to as Cubic-SC-LNO, Oct-SC-LNO and T-poly-SC-LNO, respectively). Combined with focused ion beam (FIB) sectioning, cross sectional scanning transmission electron microscopy (STEM) high angle annular dark field (HAADF) imaging and electron diffraction analysis were used to determine the dominant surface facets, which are (104)-family and (012)-family for Cubic and Oct, respectively. A mix of (001), (012), (104), (010) and (011) families are present on T-poly-SC-LNO surface (Figure IX.3.6d-f).

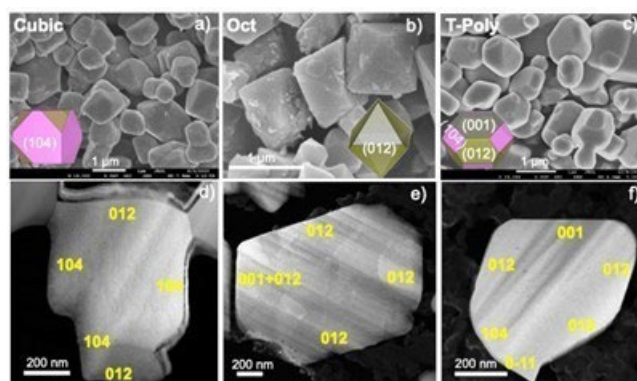


Figure IX.3.6 SEM (a-c) and TEM (d-f) images of the pristine SC-LNO samples: (a, d) Cubic, (b, e) Oct and (c, f) T-Poly. Insets in (a-c) show crystal morphologies with dominating surface facets as indexed.

Electrochemical properties of the as-synthesized single crystals were evaluated in half-cell coin cells with a Gen 2 electrolyte (1.2M LiPF_6 in EC/EMC 3:7). SC-LNO composite cathodes were prepared with a polyvinylidene difluoride (PVDF) binder and carbon following a standard procedure. Figure IX.3.7 compares the 1st cycle voltage profiles and the corresponding differential capacity versus voltage plots (dQ/dV) at various rates. At C/100, all three cathodes showed similar voltage profiles with a discharge capacity of ~ 235

mAh/g and a coulombic efficiency of $\sim 90\%$. A discharge plateau at ~ 3.5 V is clearly shown in all samples. Upon increasing the rate to C/50, the discharge capacity decreased to ~ 215 mAh/g. While the 3.5 V plateau disappeared in the cells with the Cubic (Figure IX.3.7a and d) and T-Poly (Figure IX.3.7c and f) cathodes, it largely remained in the cell with the Oct-SC-LNO (Figure IX.3.7b and e). Further increasing the rate to C/10 reduces the discharge capacity to ~ 210 mAh/g, along with the disappearance of the 3.5 V plateau in all samples. Although the redox reactions occurring at the 3.5 V plateau is currently not well understood, earlier studies indicate a kinetically sluggish process that greatly enhances LNO capacity when utilized. [8] Our results reveal that Oct-SC-LNO with the (012) surface has better ability in extracting the capacity from the 3.5 V region, demonstrating the importance of morphology and surface design in achieving improved kinetic properties.

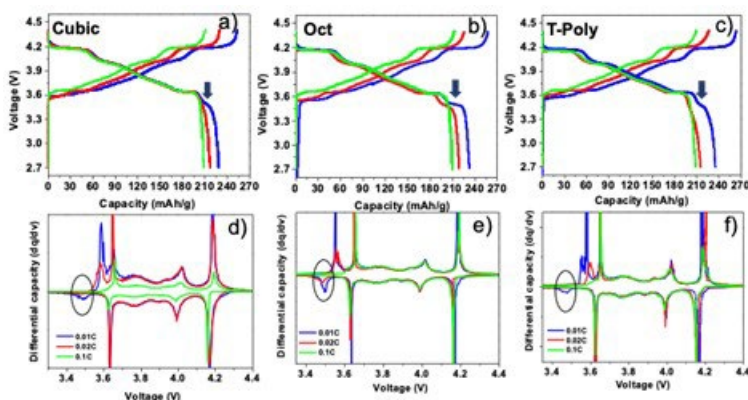


Figure IX.3.7 1st cycle voltage profiles (a-c) and the corresponding dQ/dV plots (d-f) collected at the indicated cycling rate: (a, d) Cubic, (b, e) Oct and (c, f) T-Poly SC-LNO samples.

Figure IX.3.8 compares the cycling stability of the SC-LNO cathodes, carried out at 0.1C for the first two cycles and then 0.3C charge/discharge in the voltage window of 2.7–4.6 V. The initial discharge capacities were similar at ~ 210 mAh/g for 0.1C and ~ 200 mAh/g for 0.3C. After 100 cycles at 0.3C, the discharge capacity was reduced to 130, 102 and 87 mAh/g for Cubic, Oct and T-poly respectively, corresponding to a capacity retention of $\sim 65\%$, 51% and 43% . The superior cycling stability of Cubic-SC-LNO with the (104) surface is clearly demonstrated. Further comparison of the voltage profiles shows reduced polarization on the Cubic sample, suggesting that side reactivities on the cathode surface likely play an important role in the observed performance differences. We then evaluated the changes on SC-LNO surface before and after cycling by using STEM-HAADF imaging. These images provide brightness contrast that is proportional to the atomic number of the atoms present, enabling the differentiation of heavy atoms (such as transition metals) from light atoms (such as Li). The technique is widely used to monitor surface reconstruction (SR) in layered oxide cathodes where the appearance of brightness in the Li layers increases upon structural transformation from the layered to spinel-like or rocksalt-type. [9] Figure II.2.C.9 compares the STEM-HAADF images collected on the various facets of the pristine and discharged SC-LNO particles after 100 cycles. For the pristine series (Figure IX.3.9a-e), while bright spots are not observed in the lithium layers in the bulk, their presence is clearly seen on the top few atomic layers of all surface facets, indicating SR on as-synthesized SC-LNO particle surface. After cycling, a varying degree of further surface reconstruction was observed on all facets, leading to SR thickness increase to 2.5, 2.6, 2.1, 5.1 and 7.0 nm on (104), (012), (001), (01-1) and (010), respectively. Among the three samples, Cubic-SC-LNO with the dominating (104) surface experienced the least surface reconstruction during cycling, consistent with the best stability observed in the series.

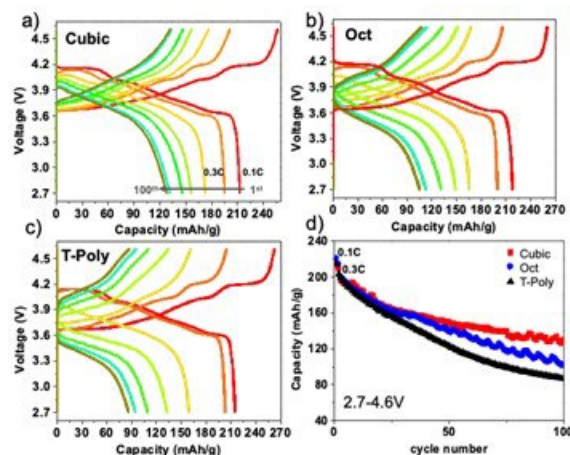


Figure IX.3.8 Voltage profiles of the first 100 cycles: (a) Cubic, (b) Oct and (c) T-poly SC-LNO samples. Cells were cycled between 2.7 and 4.6 V at 0.1C for the first two cycles and then at 0.3C. Data plotted in every 20 cycles except the first cycle at 0.1C and 0.3C. d) Cycling stability shown in discharge capacity as a function of cycle number.

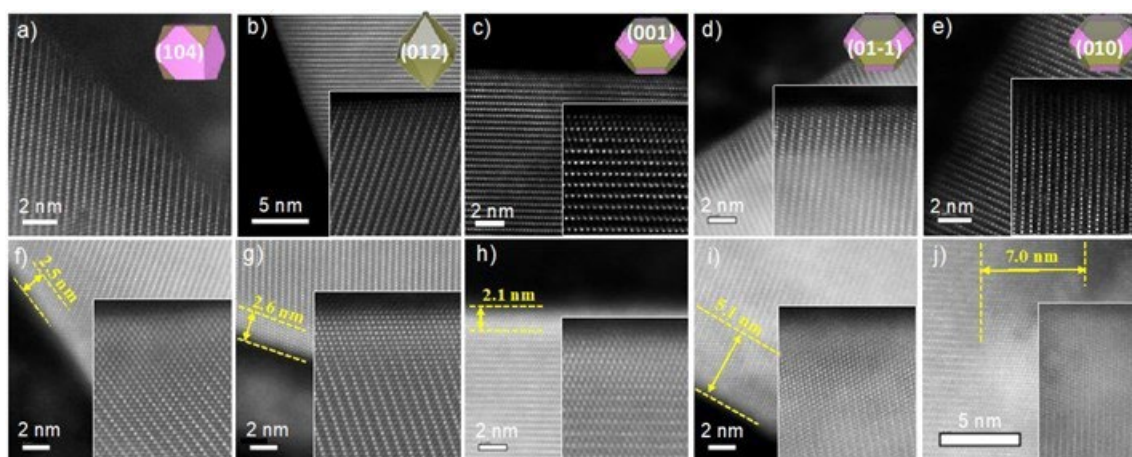


Figure IX.3.9 STEM-HAADF images collected on various facets of the pristine (a-e) and cycled (f-j) SC-LNO samples: (a, f) (104) of Cubic, (b, g) (012) of Oct, (c, h) (001) of T-Poly, (d, i) (01-1) of T-Poly and (e, j) (010) of T-Poly. Cycled samples were recovered at discharged state after 100 cycles between 2.7 and 4.6 V. The insets show magnified images of the surface.

Further analysis on surface changes was performed using X-ray photoelectron spectroscopy (XPS). As Li is extracted during charge, the Fermi level of LNO facets typically moves closer to that of electrolyte, leading to side reactions with the electrolyte and deposition of various organic and inorganic decomposition products. Figure IX.3.10 compares C 1s, O 1s and F 1s spectra collected on the discharged SC-LNO samples after 100 cycles. All samples showed similar carbon spectra with the presence of peaks attributed to C-C, C-O, C=O, O-C=O and $(\text{CO}_3)^{2-}/\text{CF}_2$ (Figure IX.3.10a-c). For O 1s, peaks at 529.5, 532.4 and 534.1 eV are attributed to Ni-O (lattice oxygen), C=O and C-O bonding, respectively (Figure IX.3.10d-f). In Ni-rich layered oxides, the intensity of O 1s peak from lattice oxygen often decreases with cycling due to the shielding effect from the surface decomposition products. Compared to that in Oct and T-Poly (Figure II.2.C.10e and f), the O 1s peak from Ni-O is noticeably stronger in the cycled Cubic sample (Figure IX.3.10d), suggesting reduced presence of side reaction products. Significant differences are observed on the F 1s spectra where peaks at 685.2, 686.2, and 688.0 eV are attributed to LiF, $\text{Li}_x\text{PO}_y\text{F}_z$ and $\text{CF}_2/\text{LiPF}_6$, respectively (Figure IX.3.10g-i). Much higher LiF peak intensity was found on Cubic-SC-LNO cathode (Figure IX.3.10i), suggesting preferential formation of LiF product on the (104) surface. The presence of LiF-rich cathode-electrolyte interphase has previously been shown to provide surface protection against HF and other free radical compounds in the electrolyte [10].

leading to enhanced cathode stability. Our results further demonstrate the importance of morphology and surface design in achieving better cycling performance.

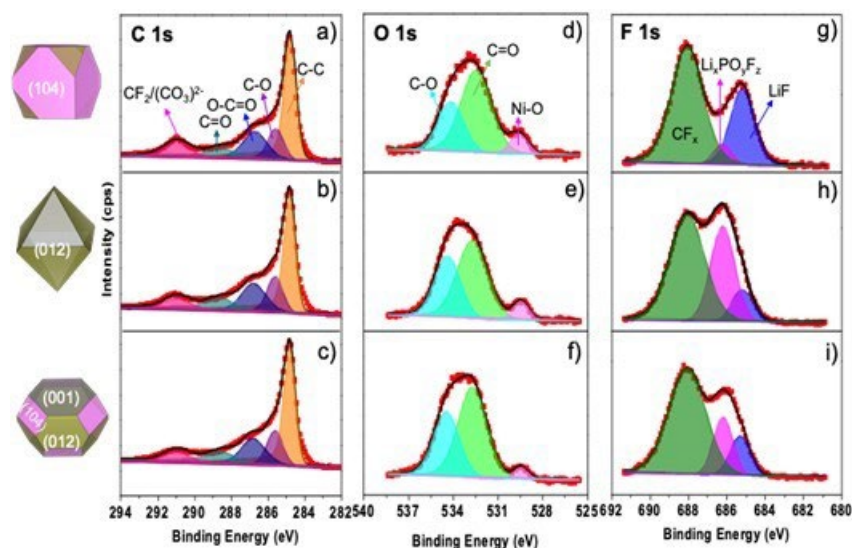


Figure IX.3.10 XPS analysis of C 1s (a-c), O 1s (d-f) and F 1s (g-i) of SC-LNO samples after 100 cycles: (a, d, g) Cubic, (b, e, h) Oct and (c, f, i) T-Poly.

Conclusions

Model systems

Synthesis methods were developed to prepare LNO single-crystal samples with the same particle size but three different morphologies. The dominating surface facets were determined to be (104)-family and (012)-family for Cubic and Oct samples, respectively, whereas T-poly consists of a mixture of surface facets including (001), (012), (104), (010) and (0 $\bar{1}1$). Particle morphology and surface were found to play critical roles in cathode kinetics and stability. Oct-SC-LNO with the (012) surface shows better rate capability and improved ability in utilizing the kinetically slow process in the 3.5 V region. On the other hand, Cubic-SC-LNO with the (104) surface shows superior cycling stability, especially upon cycling with a high upper cutoff voltage of 4.6 V. Improvement in cycling stability was corrected to reduced surface reconstruction and enhanced LiF formation from the electrolyte decomposition reactions on (104) surface. Our study demonstrates the importance of surface design and provides critical insights for future development of LNO-based cathodes with improved performance.

Atomistic modeling

- $\text{LiMn}_{0.5}\text{Ni}_{0.5}\text{O}_2$ cathodes configurations contributing to the experimental spectra are in fact composed of a blend of configurations higher in energy than the classical well-ordered ground state structures.
- The extended annealing of $\text{LiMn}_{0.5}\text{Ni}_{0.5}\text{O}_2$ slightly enhances Ni/Mn and Li/Mn orderings while reducing the Li/Ni mixing ratio.
- NMR shifts near 1400 ppm, for $\text{LiMn}_{0.5}\text{Ni}_{0.5}\text{O}_2$ cathodes, do not emanate from Li in the transition metal layer but could result from configurations of Li in the Li layer.
- The global cathode composition and strain on Ni-rich cathodes affect the nature and the thickness of the surface reconstruction layer, which impacts the impedance and the chemical stability of the cathode/electrolyte interface.

- The dual-salts electrolyte with optimal ratios can improve the electrochemical performance of LIBs and effectively suppress the impedance rise of cells during aging via the formation of a stable cathode interface and mitigate the structural damage to cathode particles.
- The facet dependent distribution of dopant in Ni-rich materials and the nature of the dopant play a critical role in the reactivity of the surfaces.

Key Publications

1. C. Garcia, J.; Bareño, J.; Chen, G.; R. Croy, J.; Iddir, H. Strain-Driven Surface Reconstruction and Cation Segregation in Layered $\text{Li}(\text{Ni}_{1-x-y}\text{Mn}_x\text{Co}_y)\text{O}_2$ (NMC) Cathode Materials. *Physical Chemistry Chemical Physics* **2020**, 22 (42), 24490–24497.
2. Yang, J.; Fonseca Rodrigues, M.-T.; Son, S.-B.; Garcia, J. C.; Liu, K.; Gim, J.; Iddir, H.; Abraham, D. P.; Zhang, Z.; Liao, C. Dual-Salt Electrolytes to Effectively Reduce Impedance Rise of High-Nickel Lithium-Ion Batteries. *ACS Appl. Mater. Interfaces* **2021**, 13 (34), 40502–40512.
3. M. Kim, J. Zhu, L. Li, C. Wang and G. Chen, “Understanding Reactivities of Ni-rich $\text{Li}[\text{Ni}_x\text{Mn}_y\text{Co}_{1-x-y}]\text{O}_2$ Single-Crystal Cathode Materials,” *ACS Applied Energy Materials* **3**(12) 12238 (2020). DOI: 10.1021/acsaem.0c02278
4. Y. Lu, T. Zhu, E. McShane, B. D. McCloskey and G. Chen, “Single-Crystal $\text{LiNi}_x\text{Mn}_y\text{Co}_{1-x-y}\text{O}_2$ Cathodes for Extreme Fast Charging,” under review (2021).

Patents and Invention Disclosures

1. “Methods of Synthesizing Single-Crystal $\text{LiNi}_x\text{Mn}_y\text{Co}_{1-x-y}\text{O}_2$ Cathode Materials,” Y. Lu and G. Chen, U.S. Patent Application Ser. No: 63/210,335, June 2021.

References

1. G. Kresse and J. Furthmüller. Efficiency of ab-initio total energy calculations for metals and semiconductors using a plane-wave basis set. *Comput. Mater. Sci.*, 1996, 6, 1, 15–50.
2. G. Kresse and J. Hafner. Ab Initio molecular dynamics for liquid metals. *Phys. Rev. B*, 1993, 47, 1, 558–561.
3. J. P. Perdew, K. Burke, and M. Ernzerhof, “Generalized Gradient Approximation Made Simple,” *Phys. Rev. Lett.*, vol. 77, no. 18, pp. 3865–3868, Oct. 1996, doi: 10.1103/PhysRevLett.77.3865.
4. P. E. Blöchl. Projector augmented-wave method. *Phys. Rev. B*, 1994, 50, 24, 17953–17979.
5. J. C. Garcia et al., “Surface Structure, Morphology, and Stability of $\text{Li}(\text{Ni}_{1/3}\text{Mn}_{1/3}\text{Co}_{1/3})\text{O}_2$ Cathode Material,” *J. Phys. Chem. C*, vol. 121, no. 15, pp. 8290–8299, Apr. 2017, doi: 10.1021/acs.jpcc.7b00896.
6. V. Krukau, O. A. Vydrov, A. F. Izmaylov, and G. E. Scuseria. Influence of the exchange screening parameter on the performance of screened hybrid functionals. *J. Chem. Phys.*, 2016, 125, no. 22, 224106.
7. Zhu, J.; Chen, G., Single-crystal based studies for correlating the properties and high-voltage performance of $\text{Li}[\text{Ni}_x\text{Mn}_y\text{Co}_{1-x-y}]\text{O}_2$ cathodes. *Journal of Materials Chemistry A* 2019, 7 (10), 5463–5474.
8. Bae, C.; Dupre, N.; Kang, B., Further Improving Coulombic Efficiency and Discharge Capacity in LiNiO_2 Material by Activating Sluggish approximately 3.5 V Discharge Reaction. *ACS Appl Mater Interfaces* 2021, 13 (20), 23760–23770.

9. Lin, F.; Markus, I. M.; Nordlund, D.; Weng, T.-C.; Asta, M. D.; Xin, H. L.; Doeff, M. M., Surface reconstruction and chemical evolution of stoichiometric layered cathode materials for lithium-ion batteries. *Nat. Commun.* 2014, 5, 3529.
10. Deng, T.; Fang, X. L.; Cao, L. S.; Chen, J.; Hou, S. Y.; Ji, X.; Chen, L.; Li, S.; Zhou, X. Q.; Hu, E. Y.; Su, D.; Yang, X. Q.; Wang, C. S., Designing In-Situ-Formed Interphases Enables Highly Reversible Cobalt-Free LiNiO₂ Cathode for Li-ion and Li-metal Batteries. *Joule* 2019, 3 (10), 2550–2564.

Acknowledgements

Juan Garcia, Fulya Dogan, Anh Vu, Woonchul Shin, Jason Croy, Chen Liao, Javier Bareno, Minkyung Kim, Faxing Wang, Yanying Lu, Lianfeng Zou, Seoung-Bum Son, Ira D. Bloom and Chongmin Wang. Support from the U.S. Department of Energy's Vehicle Technologies Program, specifically from Peter Faguy and Dave Howell, is gratefully acknowledged.

IX.4 Design and Synthesis of High Energy, Manganese Rich Oxides for Lithium-Ion Batteries (ANL)

Jason R. Croy, Principal Investigator

Argonne National Laboratory
9700 South Cass Avenue
Lemont, IL 46039
E-mail: croy@anl.gov

Peter Faguy, DOE Technology Development Manager

U.S. Department of Energy
E-mail: Peter.Faguy@ee.doe.gov

Start Date: October 1, 2018

End Date: September 30, 2021

Project Funding (FY21): \$670,000

DOE share: \$670,000

Non-DOE share: \$0

Project Introduction

Recent concerns over the growing dependence of energy storage technologies on critical materials such as cobalt has led to significant efforts in the development of low-cobalt, high-nickel cathode oxides for lithium-ion batteries, notably for electric vehicle applications. And, while these efforts are proving successful, similar concerns are being raised over greater dependence on Ni and the related issues of supply and demand as well as sustainability. This project seeks to expand the available portfolio of cathode oxides by utilizing earth-abundant manganese as the majority component. Successful development of earth-abundant cathodes would help to simultaneously address issues related to cost, supply, and sustainability while alleviating the burden future markets will likely place on other battery-critical materials such as cobalt and nickel.

Objectives

- Develop low-cost, Co-free, Mn-oxide-based cathodes for electric vehicle applications.
- Improve the design, composition, and performance of advanced electrodes with stable architectures and surfaces, facilitated by an atomic-scale understanding of electrochemical/degradation processes.
- Research and development of new synthesis and processing methods that can enable a higher degree of control over the physiochemical properties of Mn-based oxide cathodes.
- Development of new and novel Mn-based oxides enabled by cumulative project results.

Approach

1. A bottom-up approach to fabricate Mn-rich cathodes with ~50% or more Mn is taken whereby
 - The extent of Li/Mn ordering is limited (i.e., $x < 0.30$) and, therefore, the damaging effects (e.g., voltage fade) of the electrochemical activation process and subsequent cycling.
 - Introducing novel spinel-type domains (especially at surfaces) to help improve rate capability, stability, and cyclable capacity through improved first-cycle efficiencies enabled by vacant sites within integrated spinel domains.
2. Explore novel spinel-based materials with unique local structures as a new class of cathodes and as stabilizing components of LLS electrode materials.

- Explore new materials and processes for stabilization of Mn-rich cathode surfaces under extended electrochemical cycling with verification in graphite cells under standardized electrochemical protocols.

Results

Mechanisms of Low SOC Impedance

Impedance rise with cycling and high impedance at low SOC that inhibit useable energy at high rates are both of concern for Li/Mn rich oxides in terms of practical implementation. As with other unique traits of these materials, the impedance at low SOC is likely linked to the local environments that make up the oxide structure. However, unlike phenomena such as oxygen redox, TM migration, voltage fade and hysteresis, low SOC impedance has received relatively little attention in terms of mechanistic studies. Furthermore, no studies exist which propose possible solutions. In FY21, a main objective of this project was to benchmark and understand the impedance response of Li/Mn rich electrodes as a function of excess Li/Mn content, surface vs bulk contributions, cycle life, and cycling protocols. Such an understanding is critical to moving forward in the design of advanced Li/Mn-rich electrodes.

Figure IX.4.1 shows area specific impedance (ASI) values from a series of $x\text{Li}_2\text{MnO}_3 \cdot (1-x)\text{LiMn}_{0.5}\text{Ni}_{0.5}\text{O}_2$ electrodes, with $x = 0.1, 0.3, 0.5$, derived from the protocols reported in [1]. The data show that as excess Li/Mn is increased in the initial composition, the capacity achieved below $\sim 3.5\text{V}$ [blue line in (b)] increases after the first-cycle activation process and utilization of the excess Li. Figure IX.4.1 (c) shows that the ASI increases significantly below $\sim 3.5\text{V}$ [blue dots in (c)] and the point of ASI rise shifts to higher SOC as the capacity in the lower voltage region increases with x . The same trends can be observed when considering each composition individually, where activating the $x=0.3$ composition (for example) to higher SOC during the first cycle gives similar results, indicating an activation/vacancy-dependent response. These data show that the origin of the rising ASI at lower voltages/SOCs is rooted in the activation mechanisms (O activity, M-O bond breaking, cation migration) that take place during the first-cycle charge to high voltage and lead to low-voltage Li sites (voltage fade). As the activation process and subsequent mechanisms of voltage fade are not surface only properties, but occur throughout the bulk of particles, it is of interest to follow the ASI response over long-term cycling with respect to the correlated and vacancy-dependent mechanisms of voltage fade and voltage hysteresis.

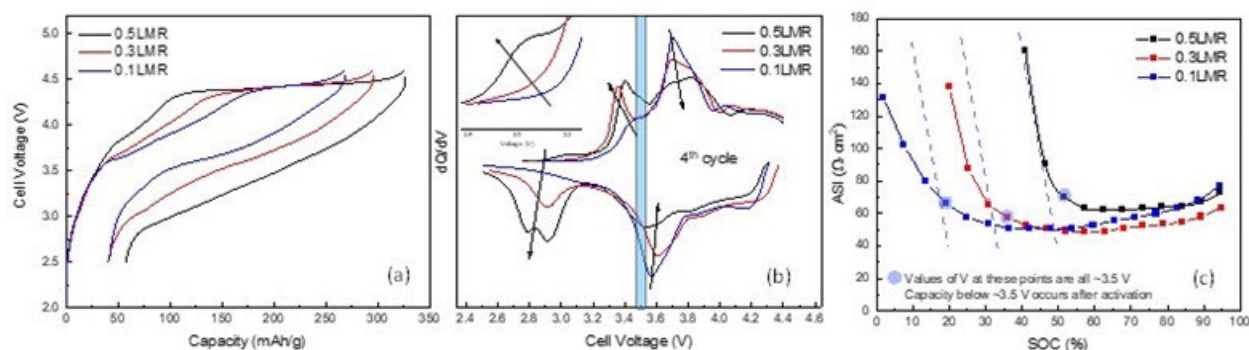


Figure IX.4.1 (a) First-cycle activation of $x\text{Li}_2\text{MnO}_3 \cdot (1-x)\text{LiMn}_{0.5}\text{Ni}_{0.5}\text{O}_2$, with $x = 0.1, 0.3, 0.5$, between 4.6-2.5V in graphite full-cells (30°C , $\text{C}/20$). (b) 4th cycle dQ/dV plots between 4.4-2.5V for the cells in (a), the blue line marks the general onset of impedance rise for all samples at $\sim 3.5\text{V}$, the inset shows a magnified view of the small process occurring at $\sim 3.0\text{V}$. (c) ASI values as a function of SOC obtained during the first HPPC cycle (7th cycle) for the cells in (a), blue dots indicate the $\sim 3.5\text{V}$ mark for each cell.

Figure IX.4.2 shows ASI data obtained every ~ 20 cycles over ~ 120 cycles on test for the $x=0.3$ composition. Immediately apparent is the overall impedance rise that occurs with cycling. Of note is that the protocols used [1] have a three-hour hold at the top of each charge (4.4V vs graphite) during ageing cycles and the cathode spends considerable time at high voltage/SOCs. The impedance rise observed in the data are a result of surface/electrolyte interactions accompanied by manganese dissolution from the cathode. Clearly, the low SOC

impedance response becomes lost, and its behavior over long-term cycling is difficult to monitor. This presents a challenge not yet addressed in the literature when considering the low SOC impedance response of this class of electrodes. This project has previously developed robust surface treatments for Mn-rich electrodes which can considerably mitigate metal dissolution and extend cycle-life of Li/Mn-rich electrodes [2].

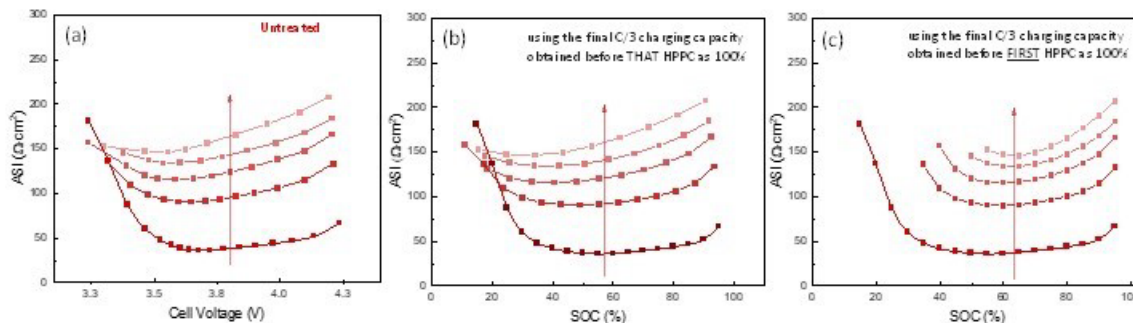


Figure IX.4.2 (a) ASI data function of HPPC cycle and voltage and (b) and (c) as a function of HPPC cycle and SOC. HPPC cycles increase from top to bottom (arrow), HPPC 1-5. Figure (b) SOC is relative to the capacity achieved before each HPPC test during the 120 cycles. Figure (c) SOC is relative to the initial capacity achieved before the first HPPC test.

Figure IX.4.3 shows ASI data of the $x=0.3$ electrodes (as collected in Figure IX.4.2) after a surface-treatment/additive combination has been applied [2]. The surface treatment is able to eliminate impedance rise due to electrolyte interactions and the ASI response is remarkably stable over ~ 120 high-voltage cycles. As shown in Figure IX.4.3a, the low SOC ASI response is constant over the ~ 120 cycles as a function of voltage, rising sharply in the region below ~ 3.5 V where the activation/voltage fade processes create new, low-voltage sites (Figure IX.4.1). However, as shown in Figure IX.4.3b, the point at which the ASI rises shifts with increasing cycle number when plotted as a function of SOC. This data shows that as the material evolves on cycling (e.g., voltage fade/disorder), it becomes harder to insert the same amount of lithium at a given SOC. As an example, Figure IX.4.3c shows how the ASI value at 32% SOC rises as a function of cycle number. Clearly, the low ASI response can be directly correlated with voltage fade sites, triggered by the activation processes, and the disorder induced over long-term cycling. It is important to note here that these electrodes lose only $\sim 7\%$ of the initial capacity over the time on test. In addition, under the protocols used to collect this ASI data (e.g., 1.5C discharge pulses), no capacity below ~ 3.3 V can be utilized (blue circle in Figure IX.4.3a), revealing that the low-voltage sites represent a significant barrier to lithium insertion at high rates.

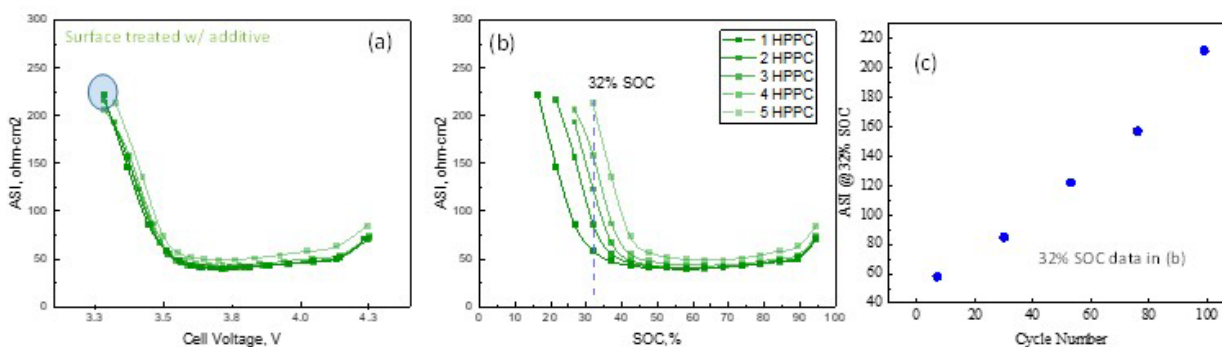


Figure IX.4.3 (a) ASI data as a function of HPPC cycle and voltage and (b) and (c) as a function of HPPC cycle and SOC. Figure (b) SOC is relative to the capacity achieved before each HPPC test during the 120 cycles. Figure (c) SOC is relative to the initial capacity achieved before the first HPPC test. The inset of Figure (c) shows ASI values at a constant 32% SOC (dashed line in Figure) vs cycle number. HPPC cycles can be seen to increase from left to right (arrow), HPPC 1-5.

Figure IX.4.4 shows a visual representation of the ASI response with respect to the data discussed above. The green regions at higher SOC represent good Li insertion into high-voltage, layered-type sites, largely unaffected by voltage fade. The yellow regions indicate lithium contents over which the impedance values drastically increase in a linear fashion as a function of SOC. This region is very narrow, spanning a voltage window of just $\sim 0.2\text{V}$ from $\sim 3.5 - 3.3\text{V}$ when using 1.5C pulses for the ASI measurements. The ASI increases so rapidly here that none of the lower-voltage sites ($< 3.3\text{V}$) can be utilized under these tests, represented by the area marked in red, and implies a kinetic limitation associated with the almost full, layered-type network of Li sites. The yellow region marks the transition from layered-type sites into the sites created by voltage fade and shows that an extreme barrier to Li diffusion into these sites exists. As such, the yellow region might be thought of as representing typical behavior expected of the layered component (e.g., LiMO_2 , $\text{M}=\text{Mn, Ni}$) nearing the end of Ni redox at low SOC due to the extreme diffusion barrier presented by the lower voltage sites.

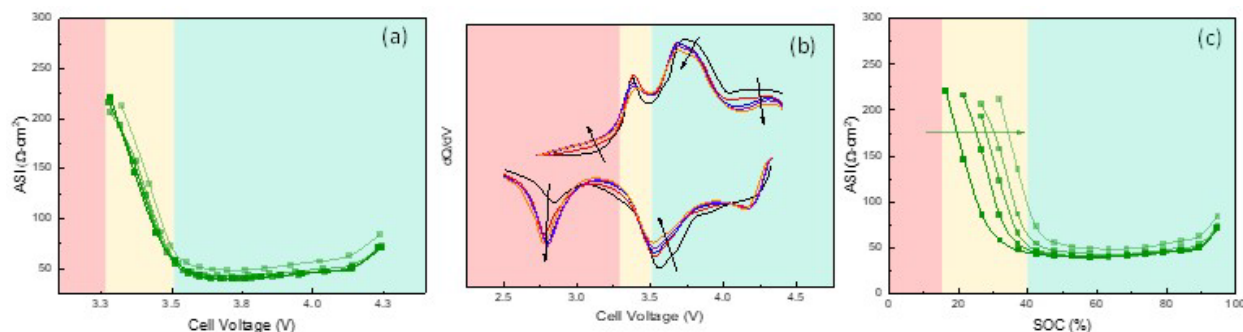


Figure IX.4.4 Visual representations of the data discussed in the text correlated across (a) ASI as a function of V, (b) dQ/dV over ~ 120 cycles, and (c) ASI as a function of SOC. The green regions represent fairly good Li insertion behavior expected for layered oxides; the yellow regions indicate lithium contents over which the impedance values drastically increase; and the red regions mark SOC/capacity that cannot be accessed under the tested protocol.

The data above show that the low SOC response is correlated to the mechanisms of voltage fade, which are not surface-only processes, further corroborated by robust surface treatments enabling negligible overall impedance rise over long-term, high-voltage cycling. Because of the negligible impedance rise, the ASI response as a function of voltage hysteresis, a correlated mechanism of voltage fade involving partially reversible cation migration, can also be probed.

Figure IX.4.5a-c show how the low SOC ASI evolves over cycling when probed with respect to voltage hysteresis. Specifically, the red curves are discharge ASI values taken after a charge to just 3.6V , representing SOC where hysteresis is not yet activated. The blue ASI values are measured after a charge to high voltage/SOCs (4.5V) where vacancy concentrations induce cation migrations. Here it can be seen that the ASI response itself shows a hysteresis in the presence of voltage hysteresis, revealing that cation migrations play a role in lithium insertion mechanisms. As expected, the red curves slowly shift to higher SOC in response to voltage fade as shown above. Of interest, however, is that the blue curves shift between the first (left) and second (middle) ASI tests but stop by the third (right) and shift to slightly lower SOC. The path-dependent hysteresis gap at $\sim 150\ \Omega\cdot\text{cm}^2$ is $\sim 15\%$ SOC on ASI test 1 (cycle 7) and decreases to $\sim 10\%$ SOC on ASI test 3 (cycle 55). These data agree with our previous models of voltage fade/hysteresis where it was first proposed that partially reversible migrations slowly subside over cycling at the expense of creating low-voltage sites (voltage fade) [3].

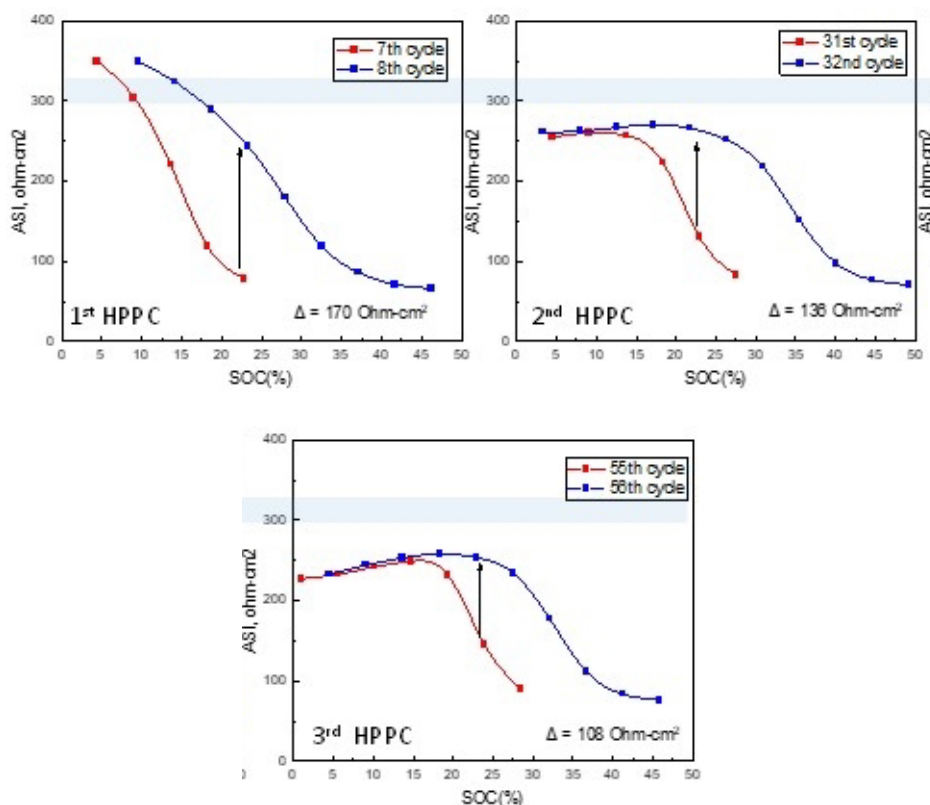


Figure IX.4.5 ASI response over long-term cycling (left) cycle 7-8, (middle) cycle 31-32, and (right) cycle 55-56. The red data sets were collected after charging directly to 3.6V and the blue data set after charging first to 4.5V followed by discharge to 3.6V. Each HPPC was preceded by a 30 min hold at 3.6V. The blue bar line highlights the decrease in ASI at low SOC over cycling. Delta values listed show the differences in ASI between the data sets at a constant $\sim 23\%$ SOC.

Many more details and experiments of this comprehensive study can be found in ref. [1]. The results show that these materials, upon activation and instigation of voltage fade/hysteresis, can be thought of as a percolating network of higher-voltage, layered-type sites having facile Li diffusion. Interspersed throughout this network are lower-voltage, disordered sites that represent a significant barrier to lithium insertion. As voltage fade/hysteresis are governed by the local structures that form in these oxides (e.g., Li/Mn ordering), optimization of Li/Mn content along with efforts to rationally engineer both surface and bulk, nano-domain and local structures, including the extent (e.g., domain size) and type of ordering, appear to be viable paths for improving impedance performance.

Despite the remaining challenges, Mn-rich materials still represent some of the highest TRL options for low/no cobalt and low Ni cathode oxides. The robust surface treatment highlighted herein shows that impedance rise and capacity fade can be greatly mitigated. In addition, rate performance over much of the SOC range is still quite good for optimized compositions. Figure IX.4.6 shows the cobalt-free, $x=0.3$ composition of this study with the applied surface treatment. Electrodes were cycled under standardized VTO protocols and compared to a commercially available NMC-622. The Mn-rich electrode delivers higher capacity and specific energy over longer cycles than the NMC-622. These results are encouraging and certainly warrant continued development of this class of electrodes.

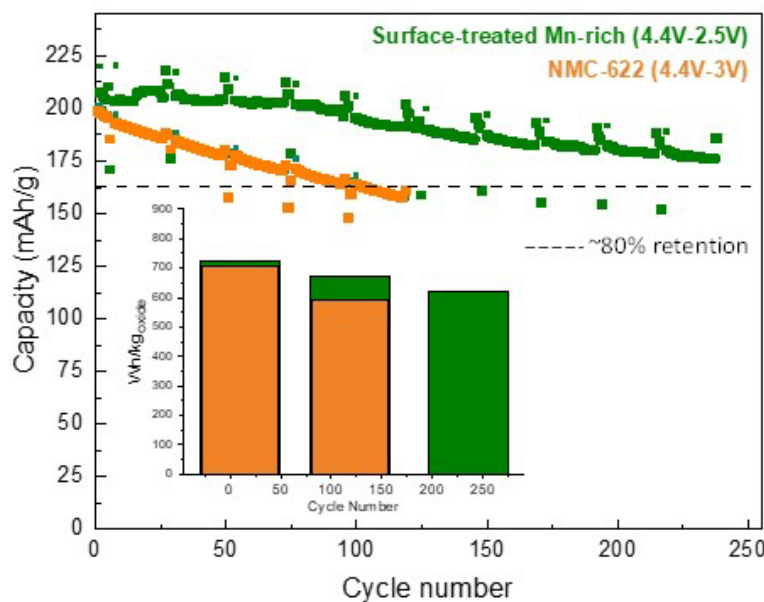


Figure IX.4.6 Comparison of the surface-treated $x=0.3$ composition with an industrially prepared NMC-622 under the standardized protocols used for this work using graphite electrodes. The dashed line represents ~80% capacity retention for both electrodes. The inset shows specific energy (Wh/kg_{oxide}) delivered by each cathode-electrode on cycles 10, 118, and 250.

New Discoveries: Cobalt-free lithiated spinel

Lithium transition-metal (TM) spinels, such as LiMn_2O_4 , $\text{Li}_4\text{Mn}_5\text{O}_{12}$, $\text{LiMn}_{1.5}\text{Ni}_{0.5}\text{O}_4$, and $\text{Li}_4\text{Ti}_5\text{O}_{12}$, have been extensively studied as cathode-electrodes. Their cubic structural frameworks, with 3D lithium diffusion channels, provide stable and facile lithium insertion and extraction up to high SOC. However, the low lithium content in the pristine compounds limits the specific capacity (~140 mAh/g) of this family of materials. Early works by Thackeray et al. showed that synthesis of high-capacity, lithiated-spinels ($\text{Li}_2\text{M}_2\text{O}_4$, $\text{M}=\text{Co}, \text{Ni}$) was possible. However, these materials did not show markedly improved performance and were mostly forgotten in favor of layered oxides such as LCO, NCA, and NMCs. Focused again on the potential advantages of high lithium contents, 3D cubic frameworks, and the possibility of tuning voltage profiles by way of substitutions, lithiated spinel $\text{Li}_2\text{Co}_{2-x}\text{M}_x\text{O}_4$ materials were revisited by this project as potential, integrated components in Li-rich oxides [4]. Despite their historically, poor electrochemical performance, new discoveries under this project have shown that Al-substitution dramatically improves the cycling stability of $\text{Li}_2\text{Co}_{2-x}\text{Al}_x\text{O}_4$ ($0 < x < 1$) [4]. Furthermore, the electrochemical signatures of these materials exhibited single-phase, zero-strain behavior on lithium extraction. Structural refinements connected this phenomenon to a small amount of cation disorder between octahedral lithium and TM ions.

Based on in-depth synthesis studies and structural analyses of the Co-based $\text{Li}_2\text{Co}_{2-x}\text{Al}_x\text{O}_2$ materials, a low-temperature polymorph of layered $\text{LiMn}_{0.5}\text{Ni}_{0.5}\text{O}_2$ was developed to create a Co-free, $\text{Li}_2\text{MnNiO}_4$ cathode-oxide (LT- $\text{LiMn}_{0.5}\text{Ni}_{0.5}\text{O}_2$). Unlike earlier materials, this novel spinel cathode shows excellent capacities (~225 mAh/g between 2.5-5.0V) with remarkable stability of the cathode structure and capacity over 50 charge/discharge cycles (Figure IX.4.7a-c).

Synchrotron XRD patterns, collected ex situ at different SOC, reveal that the (111) peak shifts reversibly during cycling, Figure IX.4.7d, and that the close-packed oxygen array of the structure maintains its cubic symmetry. In addition, the unit cell volume contracts and expands by only 2.7% over the wide compositional range of $0 \leq x \leq 2$. This is significantly less than the volume change observed in the spinel electrode, $\text{Li}_x\text{Mn}_{1.5}\text{Ni}_{0.5}\text{O}_4$ (12%). Note that the (113) and (222) peaks, Figure IX.4.7d, show reversible changes, not only in their 2θ positions but also in their peak intensities, indicating reversible atomic rearrangements within the structure.

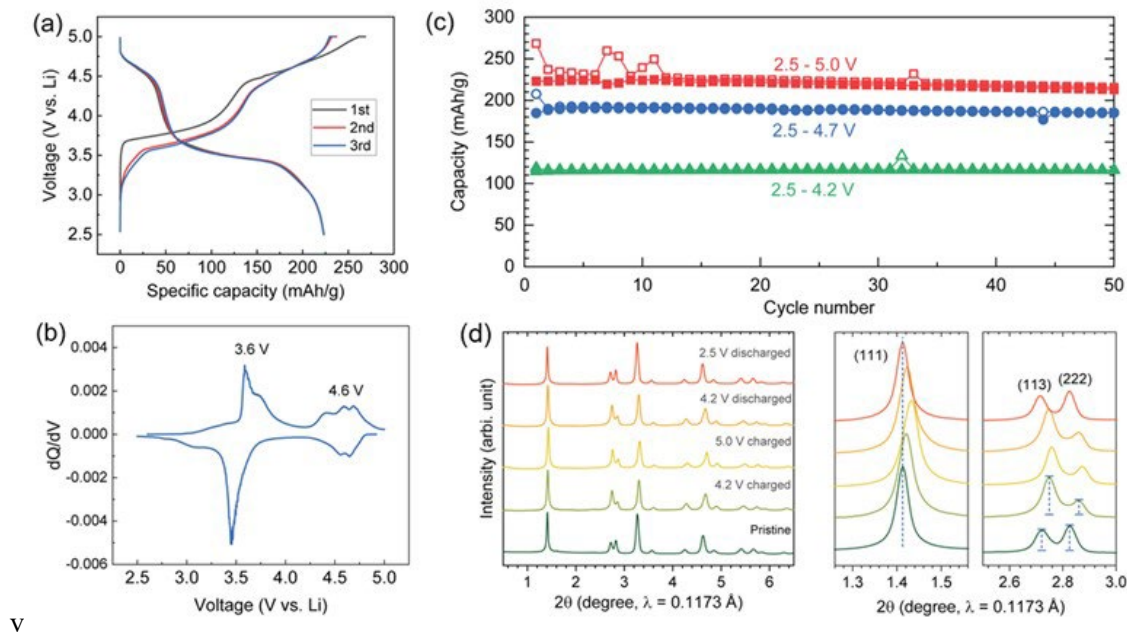


Figure IX.4.7 (a) Voltage profiles of Li/LT-LiMn_{0.5}Ni_{0.5}O₂ cells ($i = 15$ mA/g), (b) corresponding differential capacity (dQ/dV) plot (2nd cycle), (c) cycling stability (open = charge, solid = discharge), and (d) synchrotron XRD patterns of LT-LiMn_{0.5}Ni_{0.5}O₂ electrodes at various states of charge (1st cycle).

The remarkable electrochemical properties of this material are enabled by its unique and complex structure. Refinements of synchrotron XRD data reveal good fits using a cubic lithiated-spinel model, $\text{Li}_2^{(16c)}\text{M}_2^{(16d)}\text{O}_4$ ($\text{M}=\text{Mn}, \text{Ni}$; space group $\text{Fd-}3\text{m}$), in which 16.6% ($\sim 1/6$) of the Li ions on the 16c sites were exchanged with Mn/Ni ions on the 16d sites, yielding a disordered, layered-like configuration with strong lithiated-spinel character, $(\text{Li}_{0.83}\text{M}_{0.17})_2^{(16c)}[\text{Li}_{0.17}\text{M}_{0.83}]_2^{(16d)}\text{O}_4$. The particle morphologies and internal atomic structure of particles can be seen in the SEM and HAADF-STEM images of Figure IX.4.8. The atomic arrangements are consistent with the $[110]$ zone axis of a lithiated-spinel structure. Multiple images revealed localized domains that could be assigned predominantly to lithiated-spinel and disordered, layered atomic arrangements, but also to some more highly disordered rock salt regions (c and d).

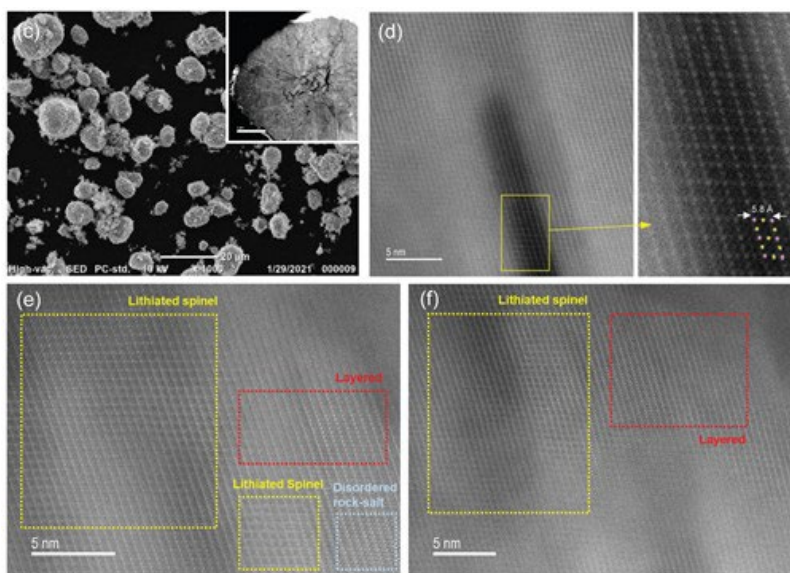


Figure IX.4.8 SEM and (b-d) HAADF-STEM images of LTLiMn_{0.5}Ni_{0.5}O₂.

In light of structural data, the electrochemical processes of Figure IX.4.7 can be assigned. The ‘low-voltage’ (LV) plateau is associated with two processes at 3.5 and 3.6V attributed to lithium extraction from octahedral sites and nickel oxidation in the delithiated spinel and layered-like regions, respectively. The ‘high-voltage’ (HV) plateau is associated with three distinct processes, the first of which at ~4.5V is attributed to lithium extraction from tetrahedral sites and nickel oxidation in the spinel domains while the two reactions observed in the dQ/dV plot between 4.6 and 4.7V are attributed, tentatively, to further nickel oxidation and the possible participation of oxygen ions in the electrochemical reaction, as alluded to by preliminary ex situ X-ray absorption spectroscopy (not shown).

The XRD data, electrochemical profile, dQ/dV plot, and HAADF-STEM images support a complex structural model for LT-LiMn_{0.5}Ni_{0.5}O₂ with predominant, partially-disordered, lithiated-spinel character, which coexists with disordered layered-like domains. The high, accessible capacity (225 mAh/g), likely reflects cation ordering, rather than a random disorder, revealing some “order within the disorder” that helps to give these materials their unique properties; a stable structural framework with facile lithium transport pathways and unique electrochemical features enable by atomic disorder. The discovery of this new class of materials opens new possibilities for tailoring the properties of next-gen electrodes based in earth-abundant manganese. More details related to materials and experiments discussed here can be found in refs. [4], [5].

Conclusions

Mn-rich electrodes represent some of the best options for enabling low-cost, safe, earth-abundant electrode materials for lithium-ion applications. Progress in this project has elucidated the mechanisms of low SOC impedance in the class of Li/Mn-rich electrodes. This phenomenon represents a key barrier to larger implementation and the information gained should help to guide future advancements. In addition, optimized compositions and novel surface-treatment strategies, developed within this project, have been shown to enable oxide-specific energies and cycle-life that outperform commercial NMC-622 under standardized, full-cell protocols. Furthermore, continued work by this project on the concept of utilizing stabilizing spinel components has led to an exciting discovery of a new class of cobalt-free, Mn-rich, lithiated spinel oxides. These cathode materials consist of complex, integrated structures built on a lithiated-spinel framework that can accommodate a moderate degree of disorder. The ability to modify this disorder within the overall framework suggests new avenues for tailoring electrode properties such as stability and rate.

Key Publications

1. Chen, J.; Gutierrez, A.; Tomadoni Saray, M.; Shahbazian Yassar, R.; Balasubramanian, M.; Wang, Y.; Croy, J.R. Critical Barriers to Successful Implementation of Earth-Abundant, Mn-rich Cathodes for Vehicle Applications and Beyond: A Detailed Study of Low SOC Impedance, *J. Electrochem. Soc.* **168**, (2021) 080506.
2. Ngoepe, N.; Gutierrez, A.; Barai, P.; Chen, J.; Noguepe, P.E.; Croy, J.R. the effects of process parameters on the properties of manganese-rich carbonate precursors: A study of co-precipitation synthesis using semi-batch reactors, *Chem. Eng. Sci.* **241** (2021) 116694.
3. Shi, B.; Gim, J.; Li, L.; Wang, C.; Vu, A.; Croy, J.R.; Thackeray, M.M.; Lee, E. LT-LiMn_{0.5}Ni_{0.5}O₂: A Unique Co-Free Cathode for High Energy Li-Ion Cells, *Chem. Comm.* **57** (2021) 11009.

References

1. Chen, J.; Gutierrez, A.; Tomadoni Saray, M.; Shahbazian Yassar, R.; Balasubramanian, M.; Wang, Y.; Croy, J.R. Critical Barriers to Successful Implementation of Earth-Abundant, Mn-rich Cathodes for Vehicle Applications and Beyond: A Detailed Study of Low SOC Impedance, *J. Electrochem. Soc.* **168** (2021) 080506.
2. Gutierrez, A.; He, M. N.; Yonemoto, B. T.; Yang, Z. Z.; Wang, J.; Meyer, H. M.; Thackeray, M. M.; Croy, J. R. Advancing Lithium- and Manganese-Rich Cathodes through a Combined Electrolyte Additive/Surface Treatment Strategy. *J. Electrochem. Soc.* **166** (2019) A3896.
3. Gallagher, K. G.; Croy, J. R.; Balasubramanian, M.; Bettge, M.; Abraham, D. P.; Burrell, A. K.; Thackeray, M. M. Correlating hysteresis and voltage fade in lithium- and manganese-rich layered transition-metal oxide electrodes. *Electrochem. Commun.* **33** (2013) 96.
4. Lee, E.; Blauwkamp, J.; Castro, F. C.; Wu, J.; Dravid, V. P.; Yan, P.; Wang, C.; Kim, S.; Wolverton, C.; Benedek, R.; Dogan, F.; Park, J. S.; Croy, J. R.; Thackeray, M. M. Exploring Lithium-Cobalt-Nickel Oxide Spinel Electrodes for ≥ 3.5 V Li-Ion Cells. *ACS Appl. Mater. Inter.* **8**, (2016) 27720.
5. Shi, B.; Gim, J.; Li, L.; Wang, C.; Vu, A.; Croy, J.R.; Thackeray, M.M.; Lee, E. LT-LiMn_{0.5}Ni_{0.5}O₂: A Unique Co-Free Cathode for High Energy Li-Ion Cells, *Chem. Comm.* **57** (2021) 11009.

Acknowledgements

Support from the U.S. Department of Energy's Vehicle Technologies Program, specifically from Peter Faguy and Dave Howell, is gratefully acknowledged.

IX.5 Disordered RockSalt Structured Cathode Materials: Electrochemistry and Synthesis (LBNL, ORNL, PNNL, UC Santa Barbara)

Guoying Chen, Principal Investigator

Lawrence Berkeley National Laboratory
1 Cyclotron Road
Berkeley, CA 94720
E-mail: GChen@lbl.gov

Peter Faguy, DOE Technology Development Manager

U.S. Department of Energy
E-mail: Peter.Faguy@ee.doe.gov

Start Date: October 1, 2018
Project Funding: \$1,940,000

End Date: September 30, 2021
DOE share: \$1,940,000

Non-DOE share: \$0

Project Introduction

The projected growth of Li-ion battery (LIB) production towards multiple TWh/year will require several million tons of Co/Ni combined, which constitutes a very sizeable fraction of the annual production of these metals. The recent development of Li-excess cation-disordered rocksalts (DRX) provides an alternative to develop high energy density LIB cathodes that use more abundant and less expensive elements and can respond to the industry need for lower cost, less resource intensive cathode materials. DRX materials have been shown to deliver energy densities over 1000 Wh/kg, and its cation disordered nature allowing for a wide range of chemistry free of Co and/or Ni. The ability to substitute some of the oxygen by fluorine in locally Li-rich environments provides an extra handle to optimize performance through increasing transition-metal (TM) redox capacity. As this class of cathodes are relatively new, further materials design and development are needed in order to properly evaluate their promises and challenges towards eventual commercialization. To do so, fundamental understanding of what controls DRX performance characteristics, particularly rate capability, cycling stability and voltage slope, is critical. This project has assembled necessary research expertise in modeling, synthesis, electrochemistry and characterization to tackle these challenges. The current chapter reports on the Synthesis and Electrochemistry components of the project and it has a companion report on Modeling and Characterization of the materials.

Objectives

The goals of this project are as follows:

- Understand the factors that control DRX cycling stability, particularly to what extent cycle life is controlled by impedance growth on the surface and by bulk changes in the material.
- Understand what controls the rate capability of DRX materials, particularly rate limitation posed by bulk transport and surface processes.
- Investigate the root of voltage profile slope in DRX.
- Develop Co-free high energy density DRX cathodes.

Approach

This project originally focused on three representative baseline systems and their analogues: 1) Mn-redox based $\text{Li}_{1.2}\text{Mn}_{0.625}\text{Nb}_{0.175}\text{O}_{1.95}\text{F}_{0.05}$ (LMNOF), 2) Ni-redox based $\text{Li}_{1.15}\text{Ni}_{0.45}\text{Ti}_{0.3}\text{Mo}_{0.1}\text{O}_{1.85}\text{F}_{0.15}$ (LNTMOF), and 3) a high F-content $\text{Li}_2\text{Mn}_{1/2}\text{Ti}_{1/2}\text{O}_2\text{F}$ (LMTOF) that utilizes the $2e^- \text{Mn}^{2+}/\text{Mn}^{4+}$ redox couple. The team operates in six thrust areas representing the challenges and opportunities in DRX materials:

1. Characterization of the local and global structures of the bulk material before, during and after cycling, including detailed characterization of TM and O redox processes in the bulk and on the surface.
2. Characterization and manipulation of short-range cation ordering (SRO) to enhance rate capability.
3. Characterization and modeling of the DRX surface chemistry and processes during cycling to high voltages
4. Electrolyte/cathode interface issues and impedance growth due to surface processes
5. Fluorine solubility limits and synthesis of highly fluorinated compounds with scalable methods
6. Electrochemistry and testing in coin and pouch cells.
7. The current report focuses on items (5–6) whereas items (1–4) are discussed in the companion report.

Results

1. Development of Mn-rich DRX oxyfluorides based on Mn^{3+}/Mn^{4+} redox

To improve DRX cycling stability, increasing capacity contribution from Mn redox at the expense of that from O-based redox processes is an effective strategy, as the former is inherently more reversible than the latter. F substitution into the O anionic sublattice lowers the overall anionic valence and enables a higher amount of Mn to be incorporated into the material. In FY21, scalable synthesis approaches were explored to prepare phase-pure Mn^{3+}/Mn^{4+} -based DRX oxyfluorides with the maximum Mn and F contents incorporated. Here we use $Li_{1.2}Mn_{0.7}Nb_{0.1}O_{1.8}F_{0.2}$ (F10) as an example to demonstrate the unique properties of this class of materials which experience capacity increase upon cycling as opposed to capacity decrease in traditional LIB cathodes.

F10 was synthesized by using a solid-state synthesis method with inexpensive poly(tetrafluoroethylene) (PTFE) as a F precursor, which has a lower melting point of 327°C than LiF (m.p. = 848.2°C). The cubic rocksalt crystal structure with a $Fm\bar{3}m$ space group was confirmed by both neutron and X-ray diffraction (XRD), whereas ~ 10% lattice F incorporation was confirmed by 7Li and ^{19}F solid-state nuclear magnetic resonance (NMR). Composite cathodes were prepared by mixing the as-synthesized F10 powder with carbon (in a weight ratio of 8:2) *via* high-energy ball milling prior to adding the polyvinylidene difluoride (PVdF) binder. Figure 1a and b show the electrochemical performance when cycled between 1.5 and 4.8 V at 10 mA/g. The 1st cycle voltage profile displays a sloping curve upon both charge and discharge and a single redox feature in the differential capacity versus voltage plot (dQ/dV , Figure IX.5.1b), corresponding to a solid-solution dominated process. As the number of cycles increases, the voltage regions around 3.0, 4.0 and 4.6 V on charge and 4.0, 3.0 and 1.5 V on discharge become flatter, implying changes in the material's chemistry and/or crystal structure that affect the Gibbs free energy and Li chemical potential. As a result, the discharge capacity increases from 207 mAh/g (1st cycle) to over 258 mAh/g after 30 cycles, a net gain of ~ 25%. A similar trend was observed at a higher current density of 20, 30 or 100 mA/g (Figure IX.5.1c–d). Figure IX.5.1e shows the evolution of dQ/dV profile as a function of charge/discharge current density, collected on F10 after 30 cycles. With an increase in current density, the charge capacity in the voltage region A decreases while that of region B increases, indicating that the redox process in region A is more rate limiting. On discharge, a majority of the capacity is obtained from region (E) at all current densities, with its contribution increasing with current densities. This suggests that the redox process around 3 V has better kinetics. Figure IX.5.1f compares area specific impedance (ASI) as a function of depth of discharge (DOD) during the 1st and 30th cycle, obtained by using a hybrid pulse power characterization (HPPC) method. The ASI is generally lower during the 30th discharge process compared to that of the 1st, suggesting improvement in cathode kinetics after extensive cycling. Relatively lower impedance values are recorded at the beginning of discharge around 4 V, which then reaches the minimum during the second flatter voltage region around 3 V where the cathodic peak (E) in Figure 1e is located. The results further confirm that the process occurring in the 3 V-region improves Li transport kinetics.

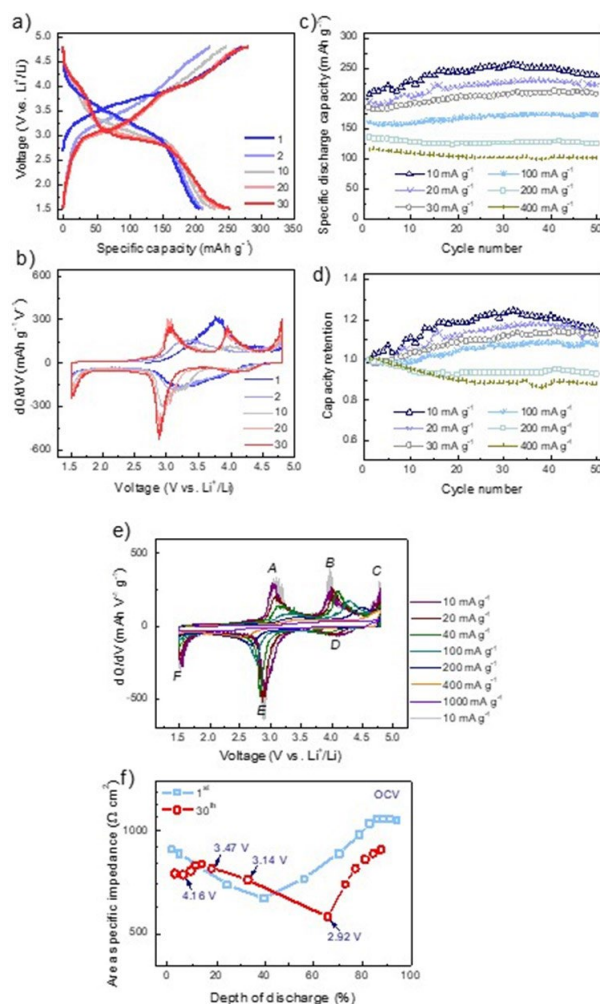


Figure IX.5.1 Electrochemical performances of F10 cathode. a, b) Voltage profiles and corresponding dQ/dV plots at a current density of 10 mA/g. c, d) Comparison of the specific discharge capacity and capacity retention at various current densities. e) dQ/dV plots at various cycling current densities collected on cycled F10 cathode. f) ASI as a function of the depth of discharge during the 1st and 30th discharge, respectively.

To understand the origin of this unique electrochemical behavior, Mn and O redox chemistry evolution was evaluated by *ex situ* hard X-ray absorption spectroscopy (hXAS) and soft X-ray mapping of resonant inelastic X-ray scattering (mRIXS) measurements. The samples examined include the pristine cathode (P) and cycled cathodes recovered at the end of 1st charge (C1), 1st discharge (D1), 30th charge (C30) and 30th discharge (D30), with an upper voltage cutoff of 4.8 V for charge and a lower voltage cutoff of 1.5 V for discharge, respectively. On the X-ray absorption near-edge structure (XANES) spectra collected on the P, D1 and D30 samples, Mn *K*-edge energy position is close to that of the Mn_2O_3 standard containing Mn(III) (Figure IX.5.2a). As expected, the *K*-edge position shifts to a higher energy near that of MnO_2 (Mn(IV)) upon charge (C1 and C30, Figure IX.5.2b) confirming an overall $\text{Mn}^{3+}/\text{Mn}^{4+}$ redox process in the bulk. Figure IX.5.2c shows the changes in Mn valence near particle subsurface and surface regions, probed by Mn *L*-edge mRIXS measurements in inverse partial fluorescence yield (iPFY) and total fluorescence yield (TEY) mode, respectively. Both discharged cathodes (D1 and D30) primarily consist of Mn^{3+} . After the 30th discharge, the average oxidation state of subsurface Mn remains close to 3+ while that of the surface Mn is significantly lower ($\sim 2.6+$). The relatively higher Mn^{2+} content in the latter is consistent with previous reports on surface Mn reduction during cycling of similar compounds. In the O *K*-edge two-dimensional mRIXS data, the signal at the excitation energy of 531 eV and the emission energy of ~ 524 eV is often used as a fingerprint for

oxidized oxygen (O^{2-}) species. The characteristic features are not easily discernable for the P, C1 or C30 electrode samples (Figure 2d), however, semi-quantitative analysis by comparing the RIXS cut at 531 eV (dotted line in Figure IX.5.2d) with the shoulder peak at ~ 524 eV showed that a significant portion of O oxidation takes place near the end of charge. While the presence of oxidized oxygen species is clear even after 30 cycles, its intensity decreases after the 1st charge. The observed capacity increase with cycling, therefore, is unlikely a result of additional O redox contribution in later cycles.

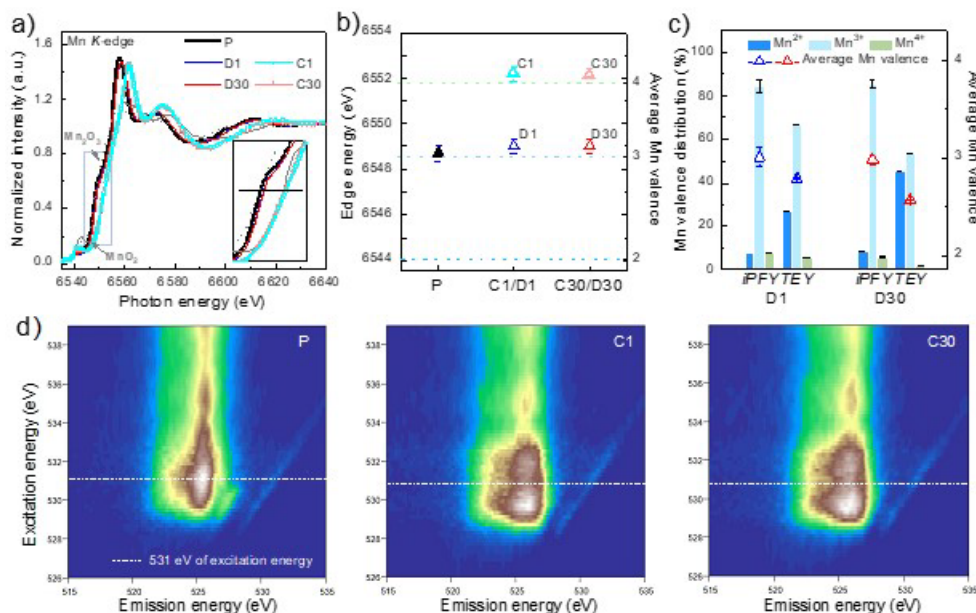


Figure IX.5.2 a) Normalized Mn K-edge XANES spectra collected on indicated electrodes. Reference spectra from Mn^{3+}/Mn^{4+} oxide standards are shown in grey. b) Mn K-edge energy position and average Mn valence as compared to the references c) Quantification of Mn valence distribution and the average Mn valence from Mn L_{3} -edge mRIXS-iPFY spectra collected on D1 and D30 electrodes. d) O K-edge mRIXS data obtained for the pristine, 1st and 30th charged electrodes.

The analysis on local structure evolution upon F10 cycling is shown in Figure IX.5.3. The average 7Li chemical shift in 7Li solid-state NMR spectrum for the pristine sample is about 290 ppm, which increases to about 500 ppm after 30 cycles (Figure IX.5.3a). The latter value is commonly observed in cubic-structured spinel-type phases where Li cations occupy the tetrahedral (T_d) 8a sites, suggesting likely involvement of partial Li relocation and formation of spinel-like domains during F10 cycling. Li site migration to T_d sites is further supported by the time-of-flight neutron diffraction pattern refinement, although additional diffraction peaks are not observed after cycling (Figure IX.5.3b). A comparison of the selected area electron diffraction (SAED) patterns (Figure IX.5.3c, region I and II) clearly illustrates partial transition-metal presence in the T_d sites and the appearance of local features consistent with spinel-type structures after cycling. On the Raman spectra (Figure IX.5.3d), while a predominant A_{1g} symmetric stretching band centered around 625 cm^{-1} is observed at the pristine state, a new peak (~ 665 cm^{-1}) associated with A_{2u} asymmetric stretching vibration of MnO_6 octahedron in off-stoichiometry Li-Mn-O spinel phases, is also observed after cycling. These combined results confirm that local structural rearrangements in the form of Li and TM site migration initiates during the 1st cycle and continues through the subsequent cycles. The process enables a broad integration of off-stoichiometry local domains into the cation-disordered cubic rocksalt framework. This arrangement creates excellent percolation pathways of Li migration channels, leading to better material utilization at a given current density and increased capacity retention with cycling. We believe a combination of high F content in the oxygen anionic sublattice, the random distribution of cations, the vast presence of Mn and its high mobility in Mn-rich DRX oxyfluorides are responsible for the unique electrochemistry in this class of cathode materials.

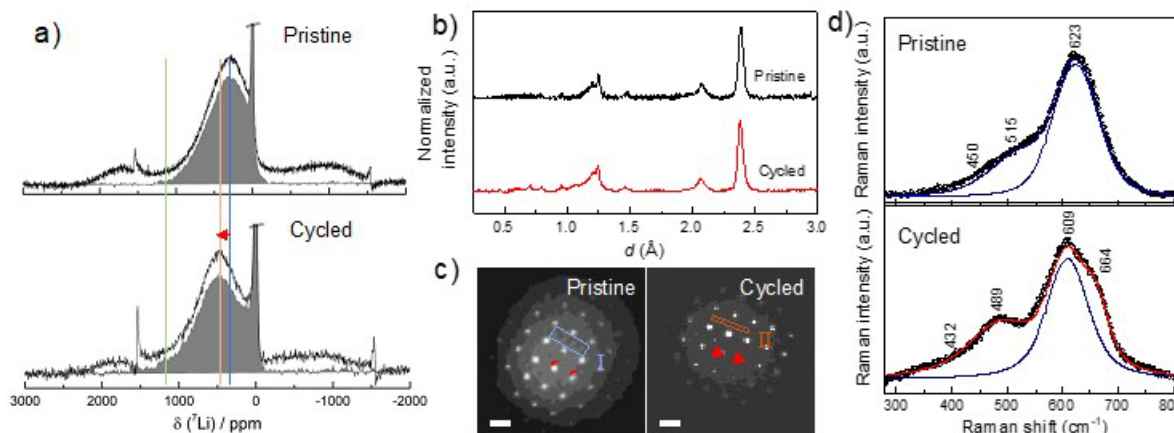


Figure IX.5.3 Local structural analysis for the pristine and cycled F10. a) ^7Li spin echo MAS NMR spectra (black lines) and pJ-MATPASS isotropic spectra (grey shaded areas) recorded at a magnetic field $B_0 = 2.35$ T and a sample spinning frequency of 60 kHz. b) Time-of-flight neutron diffraction data collected on electrodes. c) SAED patterns viewed along $[100]$ zone axis. d) Raman bands for the Mn–O stretching modes. Spectra fitting was carried out using Voigt functions.

2. Synthesis and electrochemistry of $2e^- \text{Mn}^{2+}/\text{Mn}^{4+}$ -redox based DRX

To further increase F content, mechanochemical reactions were explored to prepare phase-pure highly fluorinated DRX samples based on $\text{Mn}^{2+}/\text{Mn}^{4+}$ redox couple. A series of $\text{Li-Mn}^{2+}\text{-Nb}^{5+}\text{-O-F}$ DRX compositions, $\text{Li}_{1.2}\text{Mn}_{0.4+z/3}\text{Nb}_{0.4-z/3}\text{O}_{2-z}\text{F}_z$, with Li content fixed at 1.2 per formula unit, F content ranges from 0.15 to 0.3, 0.45, 0.6, and 0.675, and the corresponding Mn^{2+} content at 0.45, 0.5, 0.55, 0.6 and 0.625, were synthesized. The optimal milling time is 10, 12, 15, 18 and 20 h, respectively, and the resulting samples are labelled by Mn and F content. For example, $\text{M}_{0.45}\text{F}_{0.15}$ represents $\text{Li}_{1.2}\text{Mn}_{0.45}\text{Nb}_{0.35}\text{O}_{1.85}\text{F}_{0.15}$. The XRD patterns (Figure IX.5.4a) of the final products share the common cubic rocksalt features of $Fm\bar{3}m$. The as-synthesized DRX samples were subjected to galvanostatic charge and discharge cycling tests. All the DRX samples deliver a reversible capacity of 250 – 300 mAh g^{-1} , corresponding to 0.9 – 1 Li^+ per formula unit (Figure 4b, c). With increasing F and Mn^{2+} contents, the plateau around 4.5 V diminishes (Figure IX.5.4c), which is in good accordance with the excellent cyclability of the highly fluorinated DRX sample (Figure IX.5.4b). In comparison, $\text{Li}_{1.2}\text{Mn}_{0.625}\text{Nb}_{0.175}\text{O}_{1.325}\text{F}_{0.675}$ ($\text{M}_{0.625}\text{F}_{0.675}$) displays an initial discharge capacity of 258 mAh g^{-1} , with 242 mAh g^{-1} maintained after 20 cycles, corresponding to 93.8% capacity retention. While at a lower F content, $\text{Li}_{1.2}\text{Mn}_{0.45}\text{Nb}_{0.35}\text{O}_{1.85}\text{F}_{0.15}$ ($\text{M}_{0.45}\text{F}_{0.15}$) delivers a discharge capacity of 294 and 166 mAh g^{-1} during the 1st and 20th cycle, respectively, corresponding to a capacity retention of 56.5%. Upon cycling, the capacity decay in less fluorinated samples is consistent with the loss of the high-voltage charge plateau and polarization buildup (Figure IX.5.4c). The hysteresis and kinetics are examined by galvanostatic intermittent titration technique (GITT). The charge profiles of the less fluorinated samples display the high-voltage plateau with an overpotential of ~180 – 260 mV, which is greater than that (<100 mV) in the low-voltage sloping region (Figure IX.5.4d). High fluorination alters the high-voltage O reactions above 4.5 V, leading to improved kinetics (overpotential <180 mV) and suppressed hysteresis (symmetric profiles). On the other hand, the less fluorinated samples (e.g., $\text{M}_{0.45}\text{F}_{0.15}$ and $\text{M}_{0.5}\text{F}_{0.3}$) exhibit higher overpotentials than the highly fluorinated ones during discharge. The results confirm the design principle of incorporating more F^- anion and Mn^{2+} cation is effective in enhancing cyclability while maintaining a reasonably high reversible capacity.

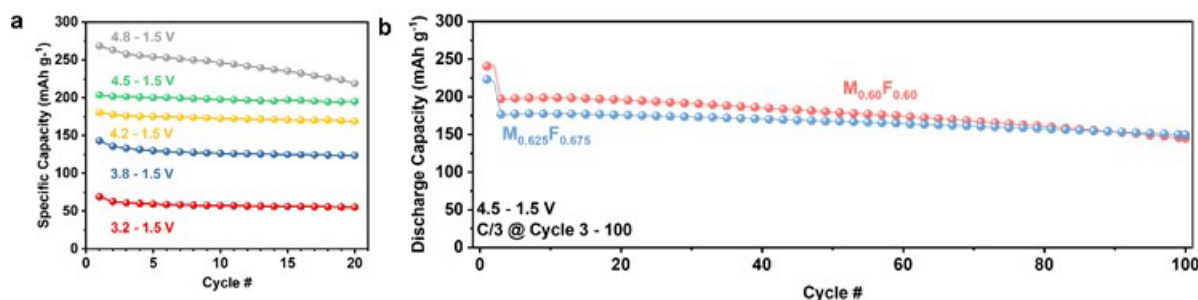


Figure IX.5.4 Cycling performance of highly fluorinated DRX cathodes. (a) Specific capacity of $M_{0.60}F_{0.60}$ during cycling at different charge cutoff voltages, cells are cycled at C/20; and (b) specific discharge capacity of $M_{0.60}F_{0.60}$ and $M_{0.625}F_{0.675}$ cathodes within 4.5–1.5 V range, cells are cycled at C/20 during the first two cycles and C/3 at Cycle 3–100.

To further examine the reversibility of redox processes upon cycling, the highly fluorinated $M_{0.60}F_{0.60}$ cathode is charged to different cutoff potentials (Figure IX.5.5a). At the charge cutoff voltage below 4.5 V, the charge and discharge processes mostly remain unchanged. When increasing the cutoff voltage to 4.8 V, a gradual decrease in capacity is observed, due to the challenge of electrolyte stability at high voltages. $M_{0.60}F_{0.60}$ and $M_{0.625}F_{0.675}$ are then subjected to long-term cycling test within the range of 4.5 – 1.5 V at a high rate of C/3, following the full activation of all redox processes between 4.8 and 1.5 V during the first two cycles. At a current density of 100 mA g^{-1} , $M_{0.60}F_{0.60}$ sample exhibit an initial capacity of 197 mAh g^{-1} , with a capacity retention of 73.5% after 100 cycles (Figure IX.5.5b). In comparison, $M_{0.625}F_{0.675}$ sample demonstrates quite stable cycling with a capacity of $\sim 170 \text{ mAh g}^{-1}$ at a high rate of C/3 (100 mA g^{-1}), suggesting the excellent rate capability of the DRX cathode.

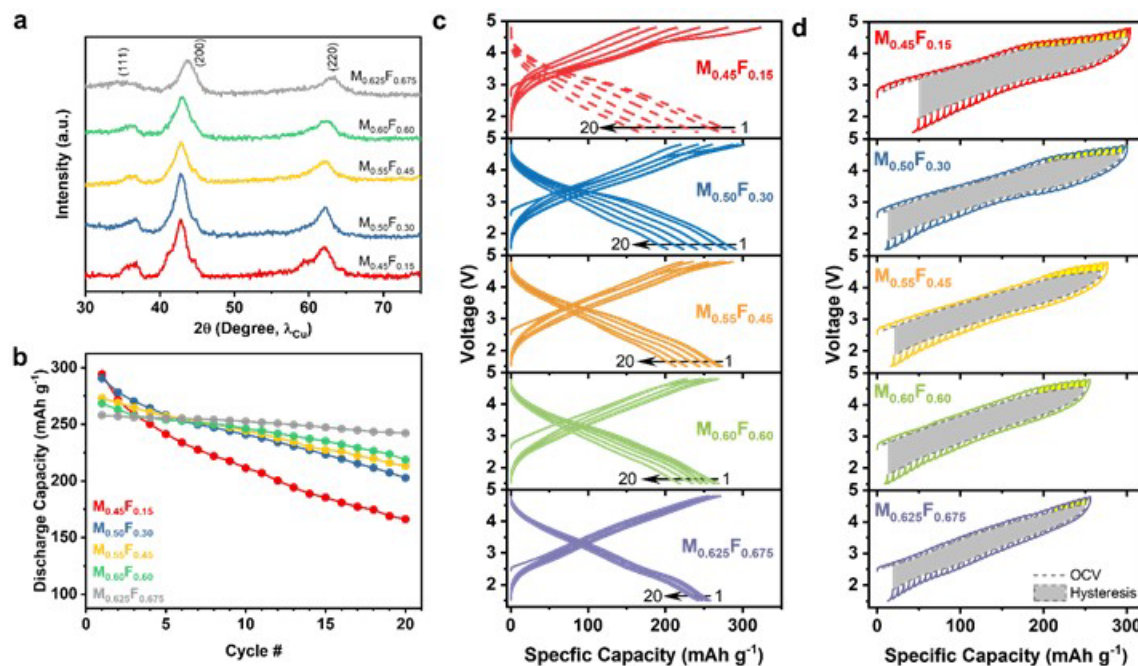


Figure IX.5.5 Synthesis and electrochemical performance of $\text{Li}_{1.2}\text{Mn}_{0.4+z/3}\text{Nb}_{0.4-z/3}\text{O}_{2-z}\text{F}_z$. (a) XRD patterns collected on the samples as labelled; (b) specific discharge capacity; (c) selected voltage profiles during the first 20 cycles; and (d) GITT voltage profiles, yellow areas highlight the relatively large polarization in the high voltage region. Cells are cycled at C/20 between 4.8 and 1.5 V.

3. Evaluation of electrode formulation and testing protocols

In FY21, we continue to develop proper electrode fabrication and testing protocols for DRX cathodes. Early in the year we investigated the impact of adding carbon to the electrode formulation. We found that additional

carbon leads to higher capacity at C/10 and less capacity fade. Electrochemical impedance spectroscopy (EIS) analysis indicates that the added carbon reduces interfacial impedance, whereas its impact on hysteresis in the charge/discharge voltage curves is minimal (Figure IX.5.6a). We also found that the side reaction rate increased by 50% as the carbon increased from 25 to 34%. Overall, carbon appears to slightly reduce the impedance of the electrode but its main impact with regard to capacity and capacity fade is the increase in the rate of side reactions, which essentially extends the charge time and acts like a constant voltage hold at the top of charge, allowing additional time for full charge of the cathode.

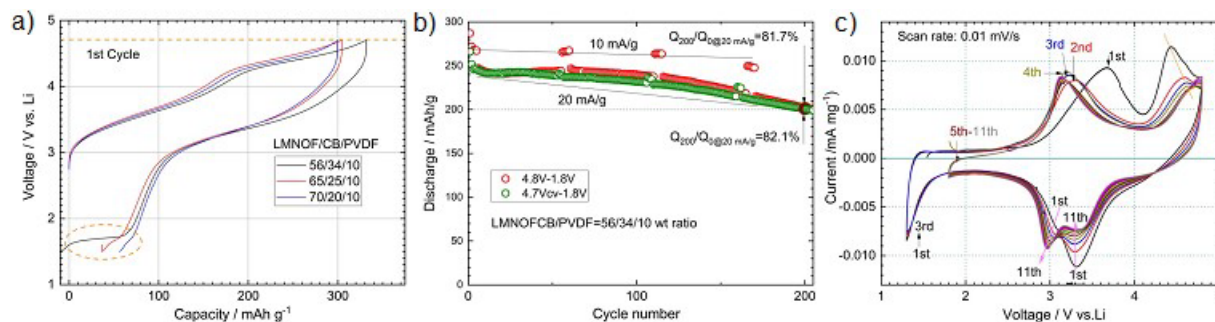


Figure IX.5.6 a) First cycle charge and discharge voltage curves for three different carbon contents, b) Galvanostatic cycling of LMNOF between 1.8 and either 4.7 V with a constant voltage hold or 4.8 V, c) CV data of LMNOF cathode. After five cycles, the lower cut-off voltage was increased from 1.3 V to 1.8 V.

The long-term cycling stability of LMNOF was investigated using cyclic voltammetry with changes to the upper and lower cutoff voltage limits. Figure IX.5.6b is an example of cycling performance of LMNOF for the voltage limits 1.8 V and either 4.7 V with a constant voltage hold or 4.8 V. One sees that the capacity and capacity fade are similar for the two limits, both achieved a retention of ~82% after more than 200 cycles. To better understand the mechanism of capacity fade and source of capacity in the cathode material, we cycled the cathode in a half cell under cyclic voltammetry conditions with a lower cutoff voltage of 1.3 V which, after 4 cycles, was switched to 1.8 V (Figure IX.5.6c). The results suggest that: 1) the cathodic capacity below 1.8 V is very repeatable, 2) as a result of moving the cutoff voltage to avoid this capacity, there is a corresponding reduction in anodic capacity between 3.15 and 4 V, suggesting large hysteresis peak, 3) there is another anodic peak between 4.1 V and 4.7 V which is shrinking and moving to higher voltage with cycling, 4) another peak is growing in between 4.6 and 4.8 V with cycling, 5) the reduction in capacity at high voltage is matched with a reduction of capacity between 4.3 and 3.1 V, another large hysteresis peak, 6) another reduction peak is identified at 3.2 V that shifts to lower voltage and gets higher with cycling. The reversible, low-voltage reduction peak is believed to be over-lithiation of the cathode material. The high voltage anodic peak between 4.1 and 4.7 V is believed to be oxygen redox which lessens and becomes more difficult with cycling. The mid-peak is believed to be the reversible Mn³⁺ oxidation peak that is growing with cycling and moving to a lower voltage. The very high oxidation peak above 4.6 V is believed to be the result of side reactions that is growing with time. Thus, the overall loss of capacity with cycling appears to come from a loss of the redox capacity that becomes more difficult to activate, with less capacity that may be cut short by the upper cutoff voltage. Other data, not shown, indicates that the low-voltage over-lithiation peak diminishes with cycling without the presence of impedance rise.

Conclusions

DRX are energy dense and Co-free cathode materials with a wide range of chemistry, offering attractive alternatives to today's commercialized LIB cathodes. In FY21, the synthesis and electrochemistry part of the "deep-dive" program focused on developing high-energy Mn-based DRX oxyfluorides for low cost and sustainable lithium-ion technologies. Solid-state synthesis was successfully used to prepare phase-pure Mn³⁺/Mn⁴⁺-based DRX that maximizes Mn and F contents. This class of materials was found to deliver increased capacity over cycling, as opposed to capacity decay often observed in traditional LIB cathodes. We reveal the source of this unique electrochemical behavior is short-range structural rearrangements, which leads to a broad

integration of off-stoichiometry short-range ordered domains within the cubic disordered rocksalt framework. The arrangement promotes better Li diffusion and improves material utilization. Mechanochemical synthesis method was developed to prepare phase-pure highly fluorinated DRX samples utilizing the $2e^- \text{Mn}^{2+}/\text{Mn}^{4+}$ redox couple. Simultaneously increasing F anion and Mn^{2+} cation content was found to be an effective strategy in enhancing cyclability while achieving high capacity in these compounds. Electrode engineering approaches and cycling protocol optimization were further investigated. The role of carbon was better understood which facilitates future work on DRX electrode formulation.

Key Publications

1. J. Ahn, Y. Ha, R. Satish, R. Giovine, L. Li, J. Liu, C. Wang, R. J. Clement, R. Kostecki, W. Yang and G. Chen, "Exceptional Cycling Performance Enabled by Local Structural Rearrangements in Disordered Rocksalt Cathodes," submitted (2021).
2. D. Chen, J. Zhang, Z. Jiang, C. Wei, J. Burns, L. Li, C. Wang, K. Persson, Y. Liu and G. Chen, "Role of Fluorine in Chemomechanics of Cation-Disordered Rocksalt Cathodes," *Chemistry of Materials* (2021). DOI: 10.1021/acs.chemmater.1c02118
3. Y. Zhang, E. Self, B. Thapaliya, R. Giovine, L. Li, Y. Yue, D. Chen, H. Meyer, R. Clément, W. Tong, G. Chen, C. Wang, S. Dai, J. Nanda, "Formation of LiF Surface Layer During Direct Fluorination of High-Capacity Co-Free Disordered Rock-Salt Cathodes," *ACS Applied Materials & Interfaces*, 13(32), 38221-38228 (2021). DOI: 10.1021/acsami.1c07882
4. D. Chen, J. Ahn and G. Chen, "An Overview of Cation-Disordered Lithium-Excess Rocksalt Cathodes," *ACS Energy Lett.* 6, 1358-1376 (2021). DOI: 10.1021/acsenenergylett.1c00203
5. D. Chen, J. Ahn, E. Self, J. Nanda and G. Chen, "Understanding Cation-Disordered Rocksalt Oxyfluoride Cathodes," *J. Mater. Chem. A* 9, 7826 (2021). DOI: 10.1039/d0ta12179g
6. Y. Yue, Y. Ha, T.-Y. Huang, N. Li, L. Li, Q. Li, J. Feng, C. Wang, B. D. McCloskey, W. Yang, and W. Tong, "Interplay between Cation and Anion Redox in Ni-Based Disordered Rocksalt Cathodes", *ACS Nano*, 2021, 15, 8, 13360–13369.
7. N. Li, M. Sun, W. H. Kan, Z. Zhuo, S. Hwang, S. E. Renfrew, M. Avdeev, A. Huq, B. D. McCloskey, D. Su, W. Yang and W. Tong, "Layered-Rocksalt Intergrown Cathode for High-Capacity Zero-Strain Battery Operation," *Nature Communications*, 12, 2348 (2021).
8. Y. Yue, N. Li, Y. Ha, M. Crafton, B. D. McCloskey, W. Yang, and W. Tong, "Tailoring the Redox Reactions for High-Capacity Cycling of Cation-Disordered Rocksalt Cathodes", *Advanced Functional Materials*, 2021, 2008696.

Acknowledgements

Juhyeon Ahn, Oxana Andriuc, Vincent Battaglia, Tyler Bennet, Jordan Burns, Zijian Cai, Dongchang Chen, Guoying Chen, Jianli Cheng, Raphaela Juliette Clement, Matthew Crafton, Emily Foley, Yanbao Fu, Raynald Giovine, Yang Ha, Kenny Higa, Mathew Horton, Tzu-Yang Huang, Huiwen Ji, Robert Kostecki, Linze Li, Zhengyan Lun, Bryan McCloskey, Jagjit Nanda, Bin Ouyang, Kristin Persson, Rohit Satish, Ethan C. Self, Martin Siron, Wei Tong, Chongmin Wang, Ruoxi Yang, Wanli Yang, Yuan Yue, Yiman Zhang, Peichen Zhong

IX.6 Disordered RockSalt Structured Cathode Materials: Characterization and Modeling (LBNL, ORNL, PNNL, UC Santa Barbara)

Gerbrand Ceder, Principal Investigator

Lawrence Berkeley National Laboratory
1 Cyclotron Road
Berkeley, CA 94720
E-mail: gceder@berkeley.edu

Peter Faguy, DOE Technology Development Manager

U.S. Department of Energy
E-mail: Peter.Faguy@ee.doe.gov

Start Date: October 1, 2018
Project Funding: \$4,810,000

End Date: September 30, 2021
DOE share: \$4,810,000

Non-DOE share: \$0

Project Introduction

The projected growth of Li-ion battery (LIB) production towards multiple TWh/year will require several million tons of Co/Ni combined, which constitutes a very sizeable fraction of the annual production of these metals. The recent development of Li-excess cation-disordered rocksalts (DRX) provides an alternative to develop high energy density LIB cathodes that use more abundant and less expensive elements and can respond to the industry need for lower cost, less resource intensive cathode materials. DRX materials have been shown to deliver energy densities over 1000 Wh/kg, and its cation disordered nature allowing for a wide range of chemistry free of Co and/or Ni. The ability to substitute some of the oxygen by fluorine in locally Li-rich environments provides an extra handle to optimize performance through increasing transition-metal (TM) redox capacity. As this class of cathodes are relatively new, further materials design and development are needed in order to properly evaluate their promises and challenges towards eventual commercialization. To do so, fundamental understanding of what controls DRX performance characteristics, particularly rate capability, cycling stability and voltage slope, is critical. This project has assembled necessary research expertise in modeling, synthesis, electrochemistry and characterization to tackle these challenges. The current chapter reports on the Modeling and Characterization components of the project and it has a companion report on Synthesis and Electrochemistry of the materials.

Objectives

The goals of this project are as follows:

- Understand the factors that control DRX cycling stability, particularly to what extent cycle life is controlled by impedance growth on the surface and by bulk changes in the material.
- Understand what controls the rate capability of DRX materials, particularly rate limitation posed by bulk transport and surface processes.
- Investigate the root of voltage profile slope in DRX.
- Develop Co-free high energy density DRX cathodes.

Approach

This project originally focused on three representative baseline systems and their analogues: 1) Mn-redox based $\text{Li}_{1.2}\text{Mn}_{0.625}\text{Nb}_{0.175}\text{O}_{1.95}\text{F}_{0.05}$ (LMNOF), 2) Ni-redox based $\text{Li}_{1.15}\text{Ni}_{0.45}\text{Ti}_{0.3}\text{Mo}_{0.1}\text{O}_{1.85}\text{F}_{0.15}$ (LNTMOF), and 3) a high F-content $\text{Li}_2\text{Mn}_{1/2}\text{Ti}_{1/2}\text{O}_2\text{F}$ (LMTOF) that utilizes the $2e^- \text{Mn}^{2+}/\text{Mn}^{4+}$ redox couple. The team operates in six thrust areas representing the challenges and opportunities in DRX materials:

1. Characterization of the local and global structures of the bulk material before, during and after cycling, including detailed characterization of TM and O redox processes in the bulk and on the surface.
2. Characterization and manipulation of short-range cation ordering (SRO) to enhance rate capability.
3. Characterization and modeling of the DRX surface chemistry and processes during cycling to high voltages.
4. Electrolyte/cathode interface issues and impedance growth due to surface processes.
5. Fluorine solubility limits and synthesis of highly fluorinated compounds with scalable methods
6. Electrochemistry and testing in coin and pouch cells.
7. The current report focuses on items (1–4) whereas items (5–6) are discussed in the companion report.

Results

1. Understanding the role of cation short-range order on the rate capability of DRX cathode materials.

Short-range cation order influences the Li-transport through its effect on the amount and organization of the 0-TM channels which are the low barrier pathways through which Li diffuses. We previously showed that typical short-range cation order enhances the mixing of transition metals and lithium on tetrahedra, thereby reducing the fraction of 0-TM configurations. In FY21 we developed multiple approaches to reduce the SRO: a) Using ideas from the high-entropy alloy field we showed that SRO can be reduced, and rate performance increased, by mixing more metals into the DRX. A DRX with six metal components enabled very high charge/discharge rates up to 2A/g-cathode. b) In a second approach, we improved the rate capability near the top of charge by adding a small amount of Cr to a Mn-Ti-based DRX, enabling charge/discharge rates up to 1000 mA/g. Cr functions by selectively migrating to the tetrahedral site upon oxidation thereby freeing up transport channels for Li. c) We also investigated the effect of materials processing on the formation of SRO. By using in-situ diffraction during synthesis of a DRX material, we found that the cation disordered rocksalt phase forms early in the synthesis process with almost no SRO present. After several hours at 1000°C cations slowly reorganized and SRO was observed to form. Using these insights, we were able to improve rate capability by optimizing the synthesis time. These systematic rate improvements stem directly from the team's detailed modeling and characterization of SRO on multiple DRX, providing the insights needed to derive multiple rate optimization methods.

2. Understanding surface chemistry and interfacial reactions

In FY21, detailed investigation on DRX surface chemistry and the reactions occurring between cathode surface and the electrolyte were carried out. A combination of modeling and characterization tools, including nuclear magnetic resonance (NMR), scanning transmission electron microscopy - high angle annular dark field (STEM-HAADF), electron energy loss spectroscopy (EELS), differential electrochemical mass spectrometry (DEMS) and X-ray absorption spectroscopy (XAS), were used to compare the materials before and after cycling and correlate it to electrochemical performance. In modeling, surface energies were obtained from bulk and slab calculations of {100}, {110}, {111} and {111} type facets of various disordered configurations of pristine $\text{Li}_2\text{MnO}_2\text{F}$, resulting in 236 data points. Figure IX.6.1 shows the spread of calculated surface energies for different ionic configurations for each crystal facet. {100} type surfaces exhibit the lowest energies followed by {110} type surfaces. A simplified Boltzmann weighting was used to obtain a single surface energy for each facet which were then used to create an equilibrium particle shape. In agreement with the distributions of energies in

Figure IX.6.1, the dominant facets are of type $\{100\}$. The Boltzmann weighted surface energy for the $\{100\}$ type facet is significantly lower than the others, which results in a $\{100\}$ -dominated cube equilibrium particle shape.

To investigate the preferred surface chemistry, bootstrapping and linear regression were used to estimate the relationship between the surface concentration of particular atoms and surface energy. It was found that increasing surface manganese increases the predicted surface energy, while increasing surface fluorine content decreases the predicted surface energy. This indicates that surface enrichment of lithium and fluorine are generally energetically favorable. Experimental work in the literature report DRX materials exposing $\{100\}$ and $\{110\}$ type facets, in good agreement with our computational results [1],[2]. The thermodynamic driving force for oxygen release on each of the $\{100\}$, $\{110\}$, $\{111\}$ and $\{112\}$ type facets as a function of lithiation state is currently underway, which will elucidate the facets that are most robust to oxygen loss and help optimize DRX particle design against oxygen loss.

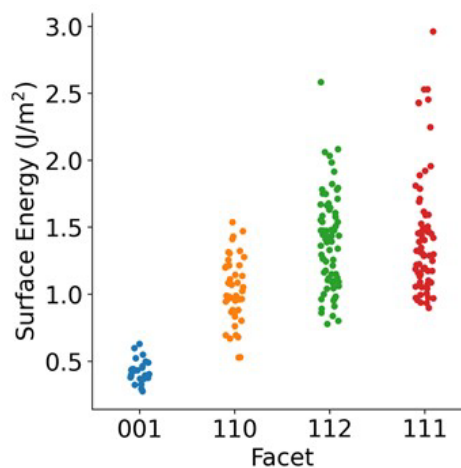


Figure IX.6.1 Calculated surface energies as a function of facet for a broad range of ionic configurations of disordered rocksalt $\text{Li}_2\text{MnO}_2\text{F}$. The data points are plotted with a small variation along the x-axis to improve readability.

The surface chemistry can be further modified by sample storage conditions, exposure history and pre-treatment processes. To this end, we investigated the changes in electrode-electrolyte interactions and their effect on cathode performance upon prolonged exposure of pristine $\text{Li}_{1.2}\text{Mn}_{0.625}\text{Nb}_{0.175}\text{O}_{1.95}\text{F}_{0.05}$ to a Gen 2 electrolyte (1.2M LiPF_6 3:7 EC: EMC by wt.) at 60°C . Compared to the untreated counterparts, electrodes constructed with this pre-treated powder showed a 10 % improvement in capacity retention. A combination of XAS, EELS, STEM-HAADF, NMR and DEMS analysis results indicate that the exposure to electrolyte leads to i) removal of an amorphous layer on the surface of the cathode, exposing fresh crystalline facets for Li (de)intercalation, ii) reduction of the amount of cation short-range ordering in the material, and iii) extraction of a fraction of Li from the bulk DRX lattice.

The removal of a native TM-F rich layer from the pristine surface enables facile Li insertion/extraction, and the surface changes also lead to suppression of O_2 gas evolution during cycling. The results suggest the importance of electrolyte exposure history and the need to tailor the exposure process according to the nature of both cathode and electrolyte.

To characterize the reactions occurring at the surface of DRX materials during cycling to high voltages, we used *in-situ* DEMS to monitor and quantify the products of parasitic outgassing reactions. The materials used in this study are named LMNOF-4515 ($\text{Li}_{1.2}\text{Mn}_{0.45}\text{Nb}_{0.35}\text{O}_{1.85}\text{F}_{0.15}$), LMNOF-6060 ($\text{Li}_{1.2}\text{Mn}_{0.6}\text{Nb}_{0.2}\text{O}_{1.4}\text{F}_{0.2}$), and LMNOF-6368 ($\text{Li}_{1.2}\text{Mn}_{0.625}\text{Nb}_{0.175}\text{O}_{1.325}\text{F}_{0.675}$). As shown in Figure IX.6.2, all three materials exhibit CO_2 evolution during cycling. In the case of LMNOF-4515, CO_2 evolution during the first charge occurs in two separate peaks, the first occurring around

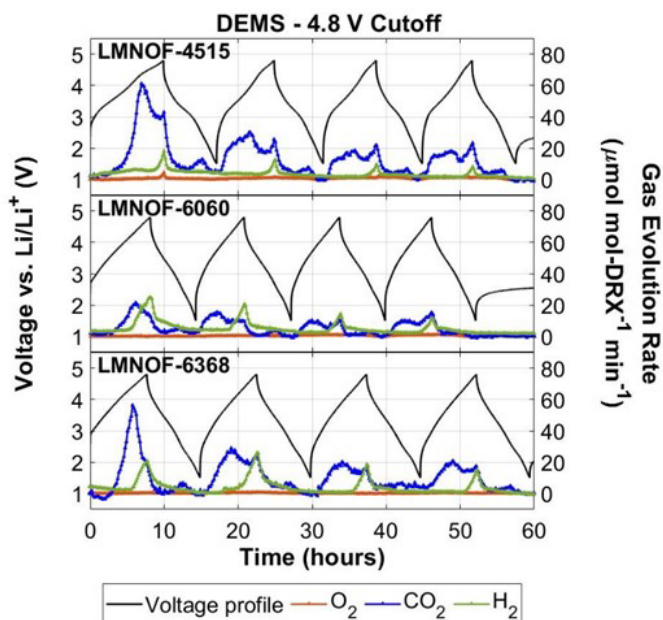


Figure IX.6.2 DEMS results for LMNOF series of DRX materials. All three materials were cycled at 0.1 Li hr^{-1} between 4.8 V and 1.5 V using 1M LiPF_6 in EC-DEC.

4.4 V and the second occurring at 4.8 V. In the cases of LMNOF-6060 and LMNOF-6368, on the other hand, only the first peak of CO₂ evolution at 4.4 V is observed. By quantifying the amount of surface carbonate species present throughout the first charge using *ex-situ* acid titrations, we expect that the CO₂ evolution peak at 4.4 V is caused by electrolyte degradation while the secondary CO₂ evolution peak from LMNOF-4515 at 4.8 V is caused by surface carbonate oxidation. On subsequent cycles, the CO₂ evolution profiles for all three materials exhibit a broad peak around 4.4 V and a sharp peak around 4.8 V. This pattern indicates that the CO₂ evolution on subsequent cycles for each material is driven by lower-voltage (~4.4 V) electrolyte degradation and higher-voltage (~4.8 V) surface carbonate oxidation. Furthermore, the total amount of CO₂ evolved from each material decreases from cycle to cycle, suggesting that the cathode surface becomes passivated towards electrolyte degradation.

Unlike CO₂ evolution, O₂ evolution is only observed to a minor extent at the end of the first charge of LMNOF-4515. The lack of O₂ evolution from LMNOF-6060 and LMNOF-6368 indicates that increasing fluorine content suppresses O₂ evolution, a finding that is consistent with those of previous studies.[3],[4] Furthermore, the lack of O₂ evolution from LMNOF-4515 on subsequent cycles indicates that the surface of the material becomes passivated towards additional O₂ evolution.

All three DRX materials exhibit similar extents of H₂ evolution at potentials above 4 V throughout cycling. Significant H₂ evolution is not common during comparable cycling of other DRX materials with the same electrolyte, eliminating the possibility that H₂ evolution occurs due to moisture in the electrolyte.[4] Instead, H₂ evolution is expected to arise from a multi-step process in which high-voltage electrolyte oxidation at the DRX surface forms protic degradation products which subsequently diffuse to the anode where they are reduced to form H₂. [5],[6],[7],[8] Given that H₂ evolution is not observed for other DRX materials, something characteristic to the materials studied herein must lead to elevated interfacial reactivity that drives this degradation process. The materials studied in this work were synthesized *via* high energy ball milling, giving rise to a high specific surface area and surface damage. It is likely that the morphology of the ball-milled materials leads to an elevated interfacial reactivity, driving the electrolyte degradation processes underlying high voltage H₂ evolution. These results highlight the importance of material synthesis and particle morphology. Finally, the attenuation of H₂ evolution from cycle to cycle for each material supports the conclusion that cathode surface becomes less reactive towards the electrolyte during cycling.

Considering the effects of the observed degradation provides insight into the manner in which performance decay occurs in DRX cells. O₂ evolution is expected to leave behind an oxygen-depleted, cation-densified outer layer that cannot be re-intercalated and instead creates a barrier to Li transport into the bulk of the material. Furthermore, the electrolyte degradation process resulting in CO₂ evolution inevitably leads to impedance rise from deposition of insulating degradation products and depletion of the electrolyte. Finally, the additional electrolyte degradation that ultimately leads to H₂ evolution is likely to deplete the electrolyte and form reactive electrolyte degradation products that may degrade other cell components.

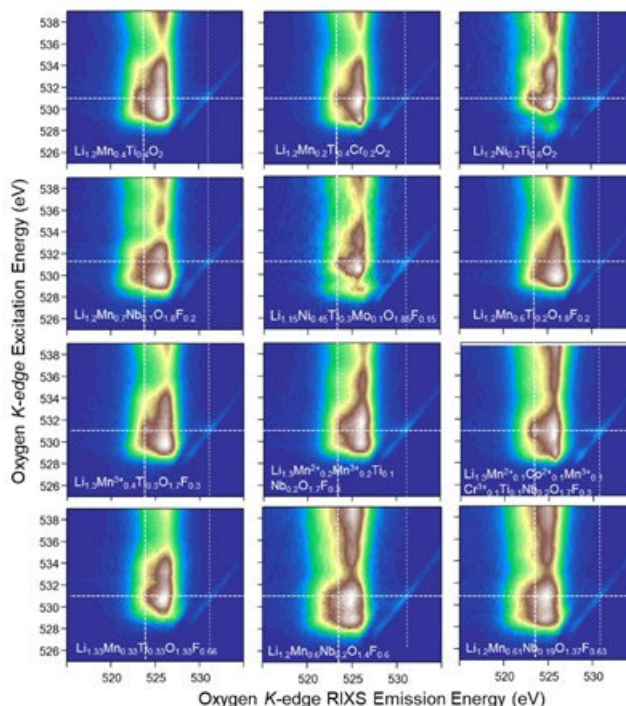


Figure IX.6.3 Oxygen K-edge RIXS maps of 12 different DRX electrodes cycled to fully charged state (4.7-4.8 V). The RIXS maps are plotted with increasing fluorination levels from top (zero fluorination) to bottom (>0.6 fluorination) panels. White grid lines indicate the two fingerprinting features in RIXS on oxidized oxygen in the lattice.

3. Characterization of F solubility and its impact

Partial fluorine substitution for oxygen allows significant performance improvements for DRX cathodes. Increasing fluorination level leads to a much-suppressed oxidized oxygen state compared with other systems. This could be seen from the overall but systematically decreased oxidized oxygen fingerprint feature in fully charged (4.7–4.8 V) DRX electrodes upon increasing fluorination (Figure IX.6.3). However, the configuration of the TMs also plays an important role in the oxygen activities, which leads to distinct oxygen behaviors of some DRX electrodes even with the same fluorination level, e.g., materials with F content of 0.2 display different levels of oxygen activities at the high-voltage charged state.

To reveal the underlying microscopic mechanism of fluorination-level effect, STEM-HAADF and EELS analysis were used to investigate nanoscale structural and chemical changes during cycling of a series of Mn-based DRX cathodes, $\text{Li}_{1.2}\text{Mn}_{(0.6+x)}\text{Nb}_{(0.2-x)}\text{O}_{2.0-x}\text{F}_x$ (LMNOF_x, $x = 0, 0.05$, and 0.2), where the F concentration is systematically increased. For the pristine LMNOF₀ particle (Figure IX.6.4a), the STEM-HAADF image and EELS maps indicate that the cations and anions are uniformly distributed in the particle, except with a loss of a small amount of Li near the particle surface. In comparison, for the cycled (after 30 cycles) LMNOF₀ particle, a high density of black-dot-like nanoregions are observed in the STEM-HAADF image (Figure IX.6.4b). The corresponding EELS elemental maps show that these black-dot-like nanoregions are voids. The voids formation is associated with surface O vacancy injection due to the high-level of O redox process. Loss of a significant amount of Li is observed at the voids and at local nanoregions near the voids (Figure IX.6.4b), which should deteriorate Li transport from the surface area to the bulk, leading the capacity drop upon cycling. For the LMNOF_{0.05} cathode particles, the pristine and cycled (after 30 cycles) particles (Figure IX.6.4c and d) show similar characteristics as observed for LMNOF₀ particles. These characteristics include uniform elemental distribution in the pristine LMNOF_{0.05} particle (Figure IX.6.4c), and formation of nanoscale voids in the cycled LMNOF_{0.05} particle (Figure IX.6.4d). Further increasing the F concentration to a high level in the DRX lattice can improve the structural stability dramatically, which is demonstrated by the characteristics of the LMNOF_{0.2} cathode particles (Figure IX.6.4e and f). The STEM-HAADF images and corresponding EELS maps in Figure IX.6.4e and f indicate that the uniform elemental distribution is maintained in the LMNOF_{0.2} cathode particle after 30 cycles. Apparently, the well-preserved Li distribution can ensure facile Li-ion diffusion at the surface of the LMNOF_{0.2} cathode upon cycling. These findings demonstrate the critical role of high-level fluorination in the DRX cathode for the enhanced structural stability and chemical homogeneity during cycling.

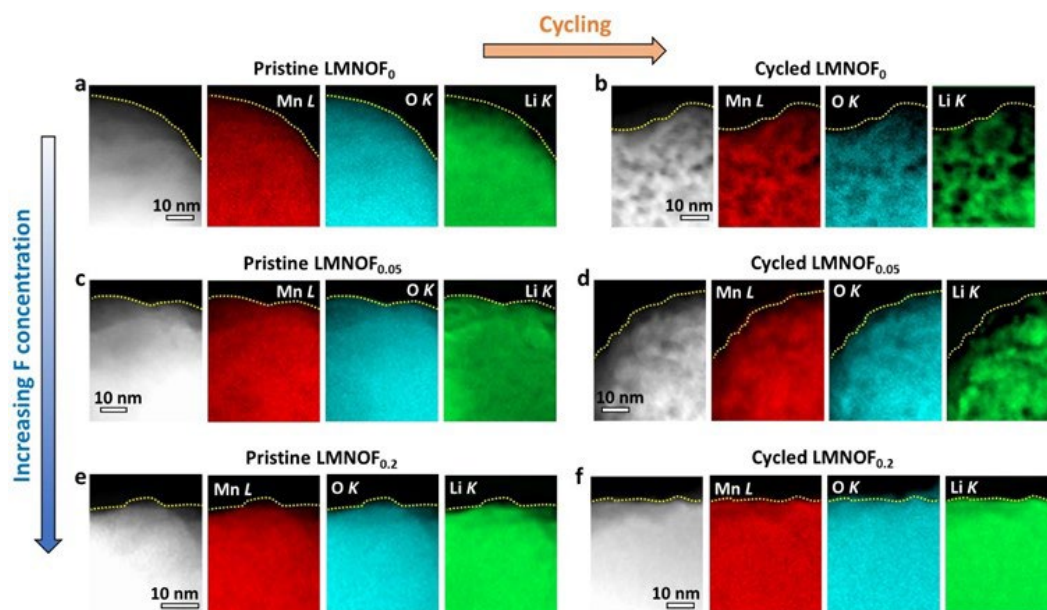


Figure IX.6.4 STEM-HAADF images and corresponding EELS maps of nanoscale surface regions to reveal structural evolution with respect to F concentration. (a, b) Comparison of LMNOF₀ at pristine and after 30 cycles. (c, d) Comparison of LMNOF_{0.05} particle at pristine and after 30 cycles. (e, f) Comparison of LMNOF_{0.2} particle at pristine and after 30 cycles. The result shows cycling-induced structural and chemical reconstruction in these cathode particles.

Further optimization of DRX compositions requires accurate determination of the actual fluorine content incorporated into the DRX matrix, yet this part of work remains challenging. In FY21, we continued to develop methodologies to: (i) assess the solubility of fluorine in DRX compounds quantitatively, and (ii) determine the impact of residual LiF, Li₂CO₃ and other potential impurities on the electrochemical performance. A washing procedure that partially removes impurities at the surface of DRX particles was established.

Conclusions

DRX are energy dense, Co-free cathode materials with flexible cation and anion chemistry. Many of the promising compositions are also free of Ni, providing an inexpensive and resource-unconstrained path towards growth of Li-ion technology. This part of the “deep-dive” program has assembled the technical strengths in theory as well as bulk, local and surface characterizations to investigate the key issues in DRX cathodes. SRO has been found to be a key factor in controlling rate capability and several improvement strategies have been devised. Capacity degradation has been attributed to several factors. Electrolyte degradation issues, resulting from the high voltage charging, have been clearly identified. Additionally, low-F content materials have also been observed to undergo surface degradation due to O-loss. Adequate fluorine content seems to stop this last mechanism.

Key Publications

1. R. Satish, L. Wichmann, M. J. Crafton, J. Ahn, L. Li, B. McCloskey, G. Chen, C. Wang, Y. Yu, W. Tong and R. Kostecki, “Exposure History and Its Effect Towards Stabilizing Li Exchange Across Disordered Rock Salt Interfaces,” *ChemElectroChem* (2021).
2. L. Li, J. Ahn, Y. Yue, W. Tong, G. Chen and C. Wang, “Mechanistic Understanding of Surface Stability Enabled by Fluorination in Disordered Rocksalt Cathodes,” under review (2021).
3. L. Li, Z. Lun, D. Chen, Y. Yue, W. Tong, G. Chen, G. Ceder, C. Wang, “Fluorination-Enhanced Surface Stability of Cation-Disordered Rocksalt Cathodes for Li-Ion Batteries,” *Advanced Functional Materials*, 2101888 (2021). DOI: 10.1002/adfm.202101888.
4. J. Huang, P. Zhong, Y. Ha, D.-H. Kwon, M.J. Crafton, Y. Tian, M. Balasubramanian, B.D. McCloskey, W. Yang, G. Ceder, *Non-topotactic reactions enable high-rate capability in Li-rich cathode materials*, *Nat Energy*, 6, 706-714 (2021), DOI: 10.1038/s41560-021-00817-6 (2021)
5. P. Zhong, Z. Cai, Y. Zhang, R. Giovine, B. Ouyang, G. Zeng, Y. Chen, R. Clement, Z. Lun, G. Ceder, *Increasing Capacity in Disordered Rocksalt Cathodes by Mg Doping*, *Chem. Mater.* 2020 32, 24, 10728-10736, DOI: 10.1021/acs.chemmater.0c04109 (2020)
6. Z. Lun, B. Ouyang, D.-H. Kwon, Y. Ha, E.E. Foley, T.-Y. Huang, Z. Cai, H. Kim, M. Balasubramanian, Y. Sun, J. Huang, Y. Tian, H. Kim, B.D. McCloskey, W. Yang, R. J. Clément, H. Ji, G. Ceder, *Cation-disordered rocksalt-type high-entropy cathodes for Li-ion batteries*, *Nat. Mater.* 20, 214-221, DOI: 10.1038/s41563-020-00816-0 (2020)

References

1. Deok Hwang Kwon, Jinhyuk Lee, Nongnuch Artrith, Hyunchul Kim, Li-jun Wu, Zhengyan Lun, Yaosen Tian, Yimei Zhu, and Gerbrand Ceder. The Impact of Surface Structure Transformations on the Performance of Li-Excess Cation-Disordered Rocksalt Cathodes. *Cell Reports Physical Science*, 1(9):100187, 2020.
2. Dongchang Chen, Jin Zhang, Zhisen Jiang, Chenxi Wei, Jordan Burns, Linze Li, Chongmin Wang, Kristin Persson, Yijin Liu, and Guoying Chen. Role of Fluorine in Chemomechanics of Cation-Disordered Rocksalt Cathodes. *Chemistry of Materials*, 33(17):7028–7038, 2021.

3. Lun, Z., Ouyang, B., Kitchaev, D. A., Clément, R. J., Papp, J. K., Balasubramanian, M., Tian, Y., Lei, T., Shi, T., McCloskey, B. D., Lee, J., Ceder, G. *Adv. Energy Mater.* 2019, 9, 1802959.
4. Crafton, M. J., Yue, Y., Huang, T. Y., Tong, W., McCloskey, B. D. *Adv. Energy Mater.* 2020, 10, 1–12.
5. Metzger, M., Strehle, B., Solchenbach, S., Gasteiger, H. A. *J. Electrochem. Soc.* 2016, 163, A798–A809.
6. Yu, Y., Karayaylali, P., Katayama, Y., Giordano, L., Gauthier, M., Maglia, F., Jung, R., Lund, I., Shao-Horn, Y. *J. Phys. Chem. C* 2018, 122, 27368–27382.
7. Freiberg, A. T. S., Sicklinger, J., Solchenbach, S., Gasteiger, H. A. *Electrochim. Acta* 2020, 346, 136271.
8. Zhang, Y., Katayama, Y., Tatara, R., Giordano, L., Yu, Y., Fraggadakis, D., Sun, J. G., Maglia, F., Jung, R., Bazant, M. Z., Shao-Horn, Y. *Energy Environ. Sci.* 2020, 13, 183–199.

Acknowledgements

Juhyeon Ahn, Oxana Andriuc, Vincent Battaglia, Tyler Bennet, Jordan Burns, Zijian Cai, Dongchang Chen, Guoying Chen, Jianli Cheng, Raphaele Juliette Clement, Matthew Crafton, Emily Foley, Yanbao Fu, Raynald Giovine, Yang Ha, Kenny Higa, Mathew Horton, Tzu-Yang Huang, Huiwen Ji, Robert Kostecki, Linze Li, Zhengyan Lun, Bryan McCloskey, Jagjit Nanda, Bin Ouyang, Kristin Persson, Rohit Satish, Ethan C. Self, Martin Siron, Wei Tong, Chongmin Wang, Ruoxi Yang, Wanli Yang, Yuan Yue, Yiman Zhang, Peichen Zhong

X Next-Gen Lithium-Ion Materials: Frontier Science at Interfaces

X.1 Molecular-level Understanding of Cathode-Electrolyte Interfaces (SLAC National Accelerator Laboratory, NREL)

Michael F. Toney, Principal Investigator

SLAC National Accelerator Laboratory
2575 Sand Hill Rd
Menlo Park, CA 94025
E-mail: michael.toney@colorado.edu

Peter Faguy, DOE Technology Development Manager

U.S. Department of Energy
E-mail: Peter.Faguy@ee.doe.gov

Start Date: October 1, 2018

End Date: September 31, 2022

Project Funding (FY21): \$450,000

DOE share: \$450,000

Non-DOE share: \$0

Project Introduction

Understanding the underlying reaction mechanisms accounting for cathode-electrolyte interphase formation is crucial to overcome present limitations and to develop stabilization strategies for next-generation lithium-ion batteries (NG-LIBs). To tackle this challenge, we combine theoretical modeling with X-ray surface scattering and spectroscopic studies along with electrochemical characterization using model thin-film cathode electrodes and high purity electrolytes. The collaboration team consists of researchers from SLAC National Accelerator Laboratory, U.S. Army Research Laboratory (ARL), the University of Colorado Boulder, and Oregon State University (OSU). Molecular-level modeling of cathode-electrolyte reactions are combined with diagnostics of cathode interphase evolution. This approach allows in-depth theoretical modeling and experimental probes to develop the necessary level of understanding into the interface degradation mechanisms and cathode stabilization strategies and it builds on our past success in related interfacial research [1]–[8]. To achieve our goals, we have employed high-voltage epitaxial thin film cathodes and carbonate-based and advanced fluorinated electrolytes. We have conducted synchrotron x-ray scattering and spectroscopy along with ion spectroscopies to elucidate underlying mechanisms of interfacial degradation of cathode surfaces and rationalization of cathode stabilization strategies through electrolyte design. Our approach will provide fundamental knowledge about how electrode surface and electrolyte design dictate interfacial reaction pathways and will help enable stabilization strategies for cathode interface.

Objectives

High-energy NG-LiB electrochemistry requires the utilization of high capacity and high voltage metal-oxide cathode materials. Their full potential has to date been hampered by the paucity of understanding the underlying chemistry and physics on the cathode-electrolyte reaction and the directed interphase. In particular, the practical implementation of NG-LIBs is to a large extent obstructed by the lack of a suitable electrolyte. While typical carbonate-based electrolytes have been reliable in commercial LiBs, there is degradation of electrolyte at high potentials. In combination with the highly reactive cathode metal oxide surface and surface defects, this creates an unstable cathode-electrolyte interface, which results in gas evolution, transition metal dissolution, active material consumption, and increased interfacial impedance. This is more problematic at elevated temperatures and/or during fast charging. Significant progress in mitigating these issues has been reported by using different electrolytes, such as nitriles [9], sulfones [10],[11], ionic liquids, and fluorinated carbonates [12]. However, stabilization of high voltage cathode-electrolyte interface (CEI) is unresolved due to a lack in mechanistic understanding of the degradation and stabilization strategy [13]–[14]. Our objective is to

provide a detailed understanding of the interfacial reaction between the cathode and electrolyte. This includes an elucidation of the interphase evolution pathway and the changes on cathode structure and composition. We anticipate that our results will fill the gap in current understanding of the underlying chemistry and physics of cathode-electrolyte reactions and will be disseminated through impactful publications. This knowledge can be utilized to guide the design of advanced electrolytes and the development of cathode stabilization strategies and will help to accelerate the development and deployment of NG-LIBs for various applications.

Approach

Our approach is to combine density functional theory (DFT) calculations and molecular dynamics (MD) simulations with advanced x-ray studies and precision electrochemical characterization using model thin-film electrodes. It starts with the purification of electrolytes and the controlled growth of low-Co, transition metal oxide thin films by Pulsed Laser Deposition (PLD). The reactivity and stability of cathode in electrolytes are probed by synchrotron-based X-ray scattering and spectroscopy studies. PLD-derived epitaxial lithium nickel-manganese-cobalt-oxide (NMC) thin-film are used as well-defined, high voltage cathode materials. Utilization of epitaxial NMC532 thin films as model systems enables high resolution x-ray experiments and well-controlled electrochemical experiments that only contain contributions from the cathode rather than the parasitic reactions from the conductive additive or binder material. In order to achieve our objectives to identify the key cathode-electrolyte reactions, we plan a multimodal surface-sensitive probes, involving synchrotron-based x-ray scattering techniques (x-ray reflectivity or XRR and surface X-ray diffraction or SXRD, as well as x-ray spectroscopy (x-ray absorption spectroscopy or XAS) measurements. XRR and SXRD will yield information on the structural transformation of NMC thin film cathodes when they react with the electrolyte. XAS will unravel complementary chemical information and composition on cathode interphase. The obtained experimental results are compared with the molecular-scale modelling on the cathode-electrolyte interfacial reactions.

Results

In general, progress was dramatically slowed due to the covid-19 restrictions and lab-based research and access to synchrotron sources. This delayed many experiments at the Advanced Photon Source and the Stanford Synchrotron Radiation Lightsource and limited access to labs at SLAC, OSU, CU Boulder and the ARL. It was impossible to conduct in situ experiments at either SSRL or APS, as site access was eliminated for most user. From the experimental side, we focused on data analysis, some remote experiments and planning.

We first focus on the reactivity and stability of cathode thin-films in carbonate-based electrolyte. Here, NMC532 thin films with controlled surface structure and film thickness have been developed through PLD growth. Surface X-ray characterization showed that single-crystal 10 nm $\text{LiNi}_{0.5}\text{Mn}_{0.3}\text{Co}_{0.2}\text{O}_2$ (NMC532) thin-films have been successfully deposited on SrTiO_3 substrate with 15 nm SrRuO_3 as conductive buffer layer (Figure X.1.1A). Non-specular phi scans confirmed the epitaxial relationship between NMC film and SrTiO_3 substrate (Figure X.1.1B). In order to probe the chemical reaction between cathode and carbonate-based electrolyte, the thin-film is subject to the solvent of ethylene carbonate (EC) - ethyl methyl carbonate (EMC) and electrolyte LP57 (1 M LiPF_6 in EC-EMC) for chemical soaking in glovebox for 2 hours. There are almost no changes on the SXRD peak position and profile of NMC films before compared to after chemical soaking (Figure X.1.1C), indicating negligible influence of chemical soaking on the out-of-plane structure of the NMC thin films.

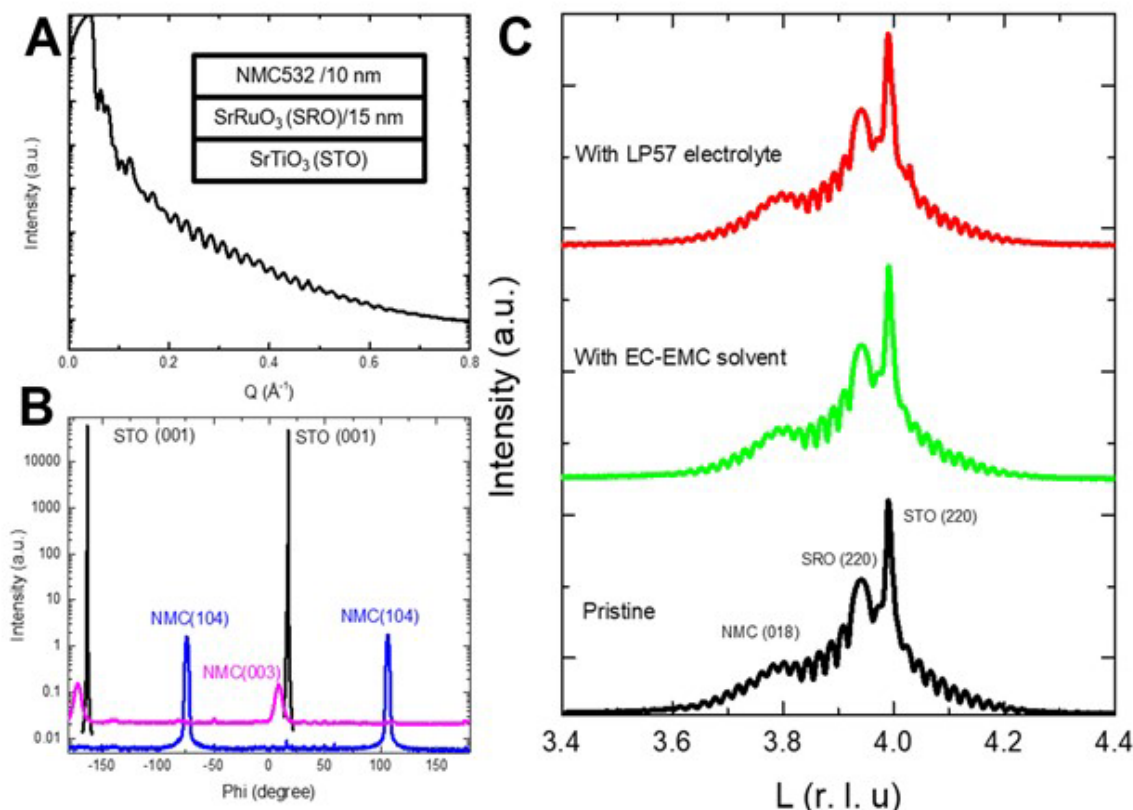


Figure X.1.1 Structural evolution of cathode thin-film with/without carbonate-based electrolyte (A) XRR of 10 nm NMC532 films grown on SrTiO_3 substrates with 15 nm SrRuO_3 buffer layers; (B) Off-specular ϕ -scans of STO {001}, NMC {104}, and NMC {003} of the film; (C) SXRD of NMC532 films before and after exposure to EC-EMC solvent and LP57 electrolyte

Although there are negligible structural transformations of NMC films upon chemical soaking, there are significant chemical transformations of NMC thin films. Total-reflection X-ray absorption near edge structure (XANES) of NMC thin-films has been utilized as a surface-sensitive probe to study the valence evolution of transition metals before and after the exposure to EC-EMC solvent and LP57 electrolyte. Ni K-edge XANES showed that compared to the pristine films, there are significant negative shifts of spectra toward lower energy after exposure to LP57 electrolyte (Figure X.1.2A). This indicated a dramatic reduction of Ni sites in NMC thin films after soaking in carbonate electrolyte. Such reduction phenomena can be also evidenced using EC-EMC solvent. After EC-EMC solvent soaking, the NMC thin-films showed similar spectra shifts at Ni K-edges, indicating the main contribution from carbonate solvent for Ni reduction, showing the LiPF_6 salt is plays a negligible role. Solvent-induced transition metal reduction is further evidenced in Co sites in NMC thin-films by the peak shifts after chemical soaking of NMC thin-films in EC-EMC solvent and LP57 electrolyte, while the peak shifts are smaller than Ni sites, indicating a decreased reduction degree for Co. Interestingly, there are negligible changes on the absorption peak position for Mn sites after the exposure to LP57 electrolyte and EC-EMC solvent under the same condition. Therefore, this shows the transition-metal-dependent degradation of NMC thin-films in carbonate-based electrolyte, and the EC-EMC solvent is believed to play a dominant role. Observation of different behaviors for transition metal reduction in carbonate-electrolyte is found to be consistent with the current understanding of the key contribution from Ni redox and partial contribution from Co redox in NMC cathode capacity, while Mn sites are believed to play a stabilization effect.

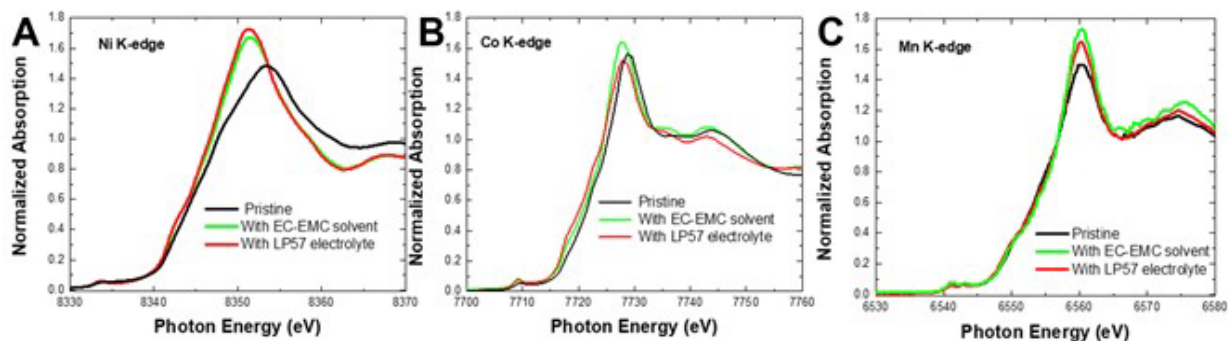


Figure X.1.2 **Transition metal-dependent degradation of NMC cathode in carbonate-based solvent and electrolyte.** Total-reflection X-ray absorption near edge structure (XANES) of NMC thin-films before and after exposure to EC-EMC solvent and LP57 electrolyte at Ni, Co, and Mn K-edges

To understand the chemical reaction between the cathode and carbonate-based electrolyte, density functional theory (DFT) calculations have been conducted using the Li_xNiO_2 model cathode surface at different stages of lithiation that mimics different battery state of charge. The LiFSI and LiPF_6 salts decomposed on the LiNiO_2 surface forming LiF [15],[16]. Carbonate solvents EC, EMC, fluoroethylene carbonate (FEC), propylene carbonate (PC) and additives 3,5-bis(trifluoromethyl)-1H-pyrazole, 1-methyl-3,5-bis(trifluoromethyl)-1H-pyrazole underwent H-transfer from solvent to the oxygen of Li_xNiO_2 surface [16],[17]. Solvent fluorination, complexation of the solvent with a Li^+ and increasing lithiation of Li_xNiO_2 cathode surface made this H-transfer reaction less favorable (Figure X.1.3). Cyclic carbonates undergo ring opening reaction after H-transfer and evolve CO_2 . Further DFT calculation showed the possible proton transport pathways in layered structure.

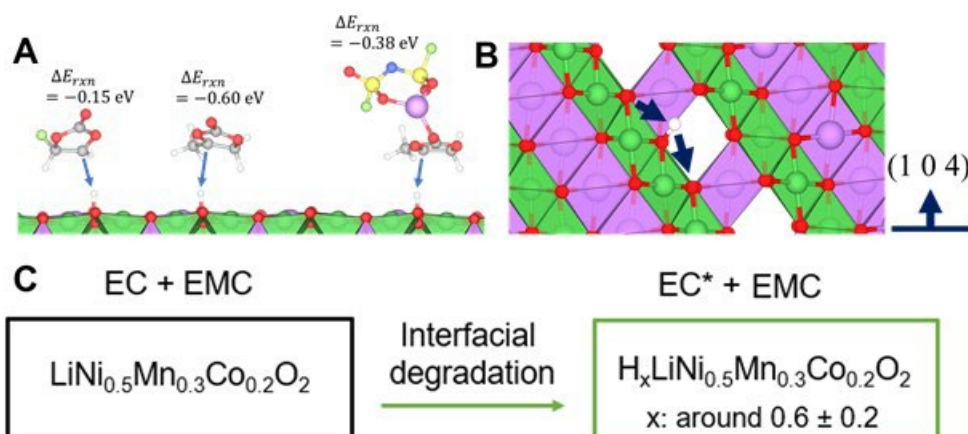


Figure X.1.3 **Protonation reaction pathway between cathode and carbonate-based electrolyte.** A) DFT calculation of EC and LiPF_6 salt decomposition reactions and their reaction activation energy on standard cathode $\text{Li}_{0.5}\text{NiO}_2$ surface; B) Illustration of the possible proton transfer pathways inside layered structure in cathode; C) Illustration of the interfacial degradation of NMC cathodes through surface protonation due to the deprotonation reaction of EC solvent on cathode surface

Therefore, when NMC thin-films are subject to a carbonate-based electrolyte, there are interfacial protonation reactions accounting for the degradation of cathode surface. The deprotonation of EC solvent at cathode can produce protons which would be transported in layered cathode, therefore reducing both Ni and Co sites, and generating radicals. Such a hypothesis is found to be consistent with our x-ray studies on the chemical transformation of NMC thin-films in carbonate-based electrolyte. Due to a fact that the proton is small, there are expected to be negligible changes on the out-of-plane structure in layered NMC. However, because of the positive charge that proton carries, the charge compensation mechanism will lead to significant reduction of Ni and Co sites. Therefore, SXRD showed negligible structural changes after chemical soaking of NMC thin film in carbonate electrolyte and solvent, however, significant chemical transformation of both Ni and Co sites have

been evidenced by XAS. Since Ni and Co reduction origins from proton trapping, an estimation of proton numbers in the NMC thin film has been conducted through a quantification of Ni and Co reduction degree (Figure X.1.3). More importantly, our hypothesis on the protonation degradation in NMC is found to be consistent with early theoretical prediction on the possibility of layered cathode hydrogenation [18],[19].

Such a hypothesis is further supported by a solvent fluorination effect on cathode stabilization. Based on the physical chemistry understanding, the fluorination of carbonate solvent leads to advanced solvent and electrolyte with enhanced chemical stability, therefore this can suppress the deprotonation reactions. NMC thin-film is then subject to carbonate-based solvent (EMC) and electrolyte (LP57), and the fluorinated electrolytes 1 M LiPF₆ in fluoroethylene carbonate (FEC)-EMC (labeled as 1F electrolyte) and 1 M LiPF₆ in fluoroethylene carbonate/3,3,3-fluoroethylmethyl carbonate/1,1,2,2-tetrafluoroethyl-2, 2, 2'-trifluoroethyl ether (FEC:FEMC:HFE, 2:6:2 by weight, labeled as 3F electrolyte) and HFE solvent. Soft-XAS collected in total electron yield with high surface sensitivity has been utilized to study the oxidation state of Ni and electronic properties of O when NMC thin-film is subject to different solvent and electrolyte (Figure II.3.A 4). As evidenced in Ni L₃-edge XAS, as compared to pristine sample, there is negative shift of spectra toward lower energy after NMC is exposed to LP57 electrolyte (1 M LiPF₆ in EC-EMC solvent), indicating a Ni reduction (Figure X.1.4A). However, such reduction is absent in NMC thin films after soaking in EMC solvent, indicating that the main deprotonation source comes from EC solvent. This result is found to be consistent with our theoretical modelling on EC deprotonation on cathode surface (Figure X.1.3A). Besides EMC, fluorinated solvent (HFE) and electrolytes (1F and 3F) are also found to be able to stabilize Ni sites in NMC, indicating the key contribution from solvent fluorination on cathode stabilization. The effect of solvent on cathode reactivity is further confirmed by O K-edge soft-XAS (Figure X.1.3B). The pre-edge peaks in O K-edge soft-XAS are a good indicator of transition metal oxidation states in NMC cathode since this comes from the hybrid orbital of transition metal 3d orbital and oxygen 2p orbital. As clearly shown, as compared to NMC films exposure to the fully fluorinated electrolyte 3F, there is slightly decreased intensity for pre-edge peak located around 530.2 eV for NMC films exposure to half-fluorinated 1F electrolyte, while the carbonate-based electrolyte LP57 leads to significant weakening in pre-edge peak intensity. This demonstrates that carbonate-based electrolyte tended to lead to NMC reduction, while the fluorinated solvents help to stabilize the cathode surface. The soft-XAS studies further support our hypothesis on interfacial degradation of NMC cathode by EC deprotonation reaction, since a replacement of hydrogen in solvent molecule by fluorine leads to fluorinated solvent with enhanced chemical stability toward deprotonation. Therefore, with an absence of solvent deprotonation, the stability of NMC cathode in electrolyte is enhanced.

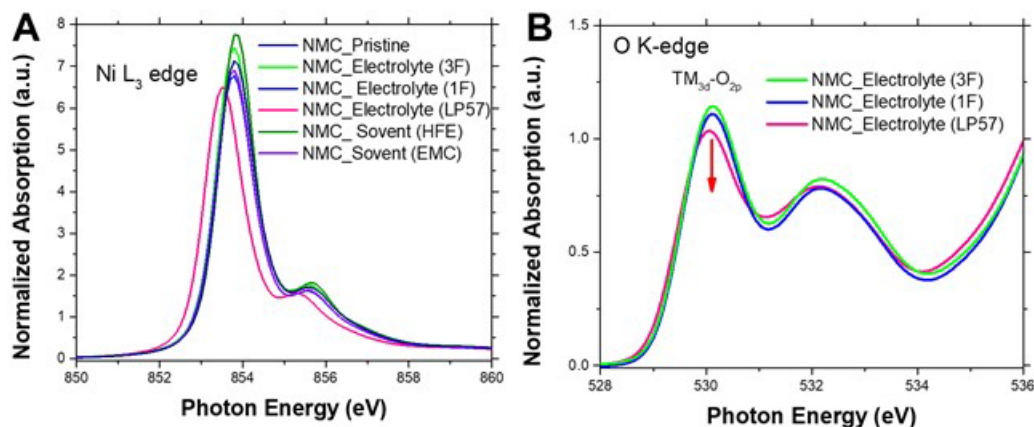


Figure X.1.4 **Solvent effect on cathode degradation and stabilization.** A) Ni L₃-edge XAS of NMC thin-film before and after exposure to carbonate electrolyte LP57, fluorinated electrolytes 1F and 3F; B) O K-edge XAS of NMC thin-films after exposure to carbonate electrolyte LP57 and fluorinated electrolytes 1F and 3F

We have further investigated the self-discharge properties of the NMC532 thin film electrodes. Figure X.1.5 shows the stability of the electrolyte (A), the self-discharge, as observed from the potential drop after cathode

charge to 4.2 V (B), and the leakage current flow to the cathode charged to 4.2 V (C). This shows a strong self-discharge that we hypothesize is related to the deprotonation of the carbonate electrolyte at high potential and the proton insertion into the NMC532 metal-oxide cathode.

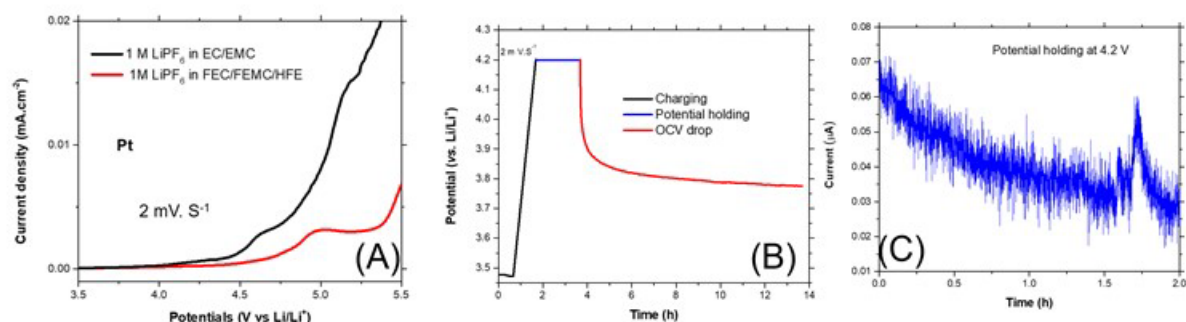


Figure X.1.5 (A) Electrochemical stability window of carbonate-based LP57 electrolyte and fluorinated electrolytes. (B) Voltage drop of NMC thin-films after charging to 4.2 V in LP57 electrolyte; (C) The leakage current of the NMC532 thin-films during the potential hold at 4.2 V

To confirm the presence of protons in the transition metal cathodes, we turn to time-of-flight secondary ion mass spectrometry (TOF-SIMS) performed at NREL (Steve Harvey). The electrodes were charged in deuterated EC:DMC with 1 M LiPF₆. These preliminary and not yet analyzed results are shown in Figure X.1.6 for NMC532 thin films cathode for pristine (A), charged to 4.2 V and relaxed to 4.15 V (B) and charged to 4.5 V and relaxed to 4.46 V (C). This suggests loss of Li near the surface for higher state of charge. Figure X.1.6(D) shows the deuterium signals and suggested more deuterium in the higher charge states, which will be confirmed. These compositional results are consistent with our model.

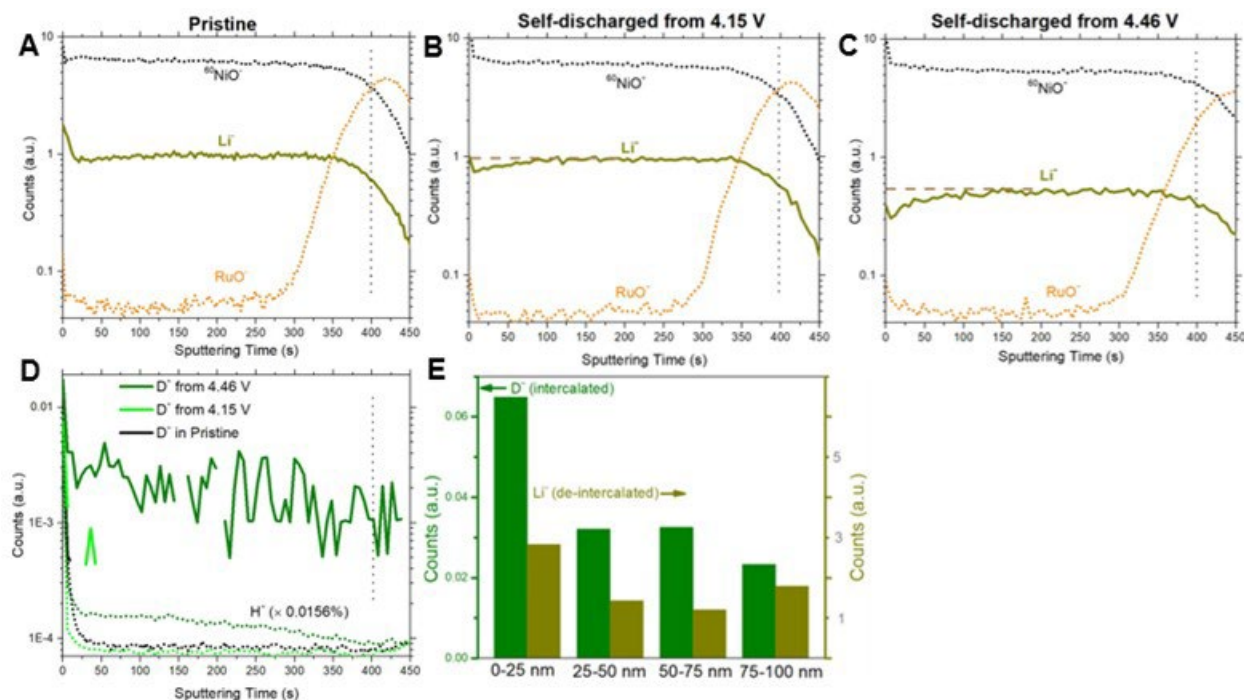


Figure X.1.6 Preliminary TOF-SIMS (A) pristine NMC. (B) charged to 4.2 V and relaxed. (C) charged to 4.5 V and relaxed. (D) and (E) deuterium TOF-SIMS summary.

Conclusions

In summary, we have combined advanced x-ray surface scattering and x-ray spectroscopy studies with molecular modelling, we showed that the protonation reaction is the key to understanding the cathode-electrolyte reaction. The degradation of NMC cathode shows transition-metal dependent reduction behaviors in carbonate-based electrolyte, where the deprotonation from the solvent EC on cathode surface is believed to play a dominant role. We further show the rationalization for advanced electrolyte design to suppress such deprotonation reactions, therefore offering molecular-level insights into the degradation mechanisms of cathode in carbonate-based electrolytes and providing fundamental understanding for the development of cathode stabilization strategies.

Understanding the evolution and stabilization of the cathode interphase in electrolyte is of great significance for the development of NG-LiBs. In this project, we conducted surface X-ray scattering and spectroscopy studies using model epitaxial thin film cathodes in conjunction with theoretical modeling to probe key interfacial chemistry between thin-film cathodes and electrolytes. The structural and chemical evolutions of NMC cathode thin film in electrolytes has been experimentally and theoretically explored. As revealed by surface X-ray scattering and different x-ray spectroscopy probes, NMC thin films show transition metal dependent degradation behaviors in carbonate-based electrolyte and solvent, which we attribute to the interfacial protonation reaction between cathode and EC solvent. We further provide the molecular-level rationalization for advanced electrolyte design to suppress solvent deprotonation on cathode surface. We anticipate that our combined x-ray, electrochemistry, and molecular scale modeling approach will provide scalable insights into the understanding of the chemical and electrochemical stability of cathode surface in electrolyte, therefore promoting the rational design of advanced high-energy batteries.

Key Publications

1. Cho, S.-J.; Yu, D.-E.; Pollard, T. P.; Moon, H.; Jang, M.; Borodin, O.; Lee, S.-Y., Nonflammable Lithium Metal Full Cells with Ultra-high Energy Density Based on Coordinated Carbonate Electrolytes. *iScience* 2020, 23, 100844–100855.
2. Von Aspern, N.; Grünebaum, M.; Diddens, D.; Pollard, T.; Wölke, C.; Borodin, O.; Winter, M.; Cekic-Laskovic, I., Methyl-group functionalization of pyrazole-based additives for advanced lithium ion battery electrolytes. *J. Power Sources*. 2020, 461, 228159–228169.
3. Ko, J. S.; Paul, P. P.; Wan, G.; Seitzman, N.; DeBlock, R. H.; Dunn, B. S.; Toney, M. F.; Nelson Weker, J., NASICON $\text{Na}_3\text{V}_2(\text{PO}_4)_3$ Enables Quasi-Two-Stage Na^+ and Zn^{2+} Intercalation for Multivalent Zinc Batteries. *Chem. Mater.* 2020, 32, 3028–3035.

References

1. Cao, C., H. G. Steinruck, B. Shyam, K. H. Stone, and M. F. Toney. "In Situ Study of Silicon Electrode Lithiation with X-Ray Reflectivity." *Nano. Lett.* 16, no. 12 (Dec 14, 2016): 7394–401. <https://doi.org/10.1021/acs.nanolett.6b02926>.
2. Cao, C. T., H. G. Steinruck, B. Shyam, and M. F. Toney. "The Atomic Scale Electrochemical Lithiation and Delithiation Process of Silicon." *Adv. Mater. Inter.* 4, no. 22 (Nov 23, 2017): 1700771. <https://doi.org/ARTN 1700771>.
3. Horowitz, Y., H. G. Steinruck, H. L. Han, C. Cao, Abate, II, Y. Tsao, M. F. Toney, and G. A. Somorjai. "Fluoroethylene Carbonate Induces Ordered Electrolyte Interface on Silicon and Sapphire Surfaces as Revealed by Sum Frequency Generation Vibrational Spectroscopy and X-Ray Reflectivity." *Nano. Lett.* 18, no. 3 (Mar 14, 2018): 2105–11. <https://doi.org/10.1021/acs.nanolett.8b00298>.

4. Steinrück, Hans-Georg, Chuntian Cao, Yuchi Tsao, Christopher J. Takacs, Oleg Kononov, Jenel Vatamanu, Oleg Borodin, and Michael F. Toney. "The Nanoscale Structure of the Electrolyte–Metal Oxide Interface." *Ener. Environm. Sci.* 11, no. 3 (2018): 594–602. <https://doi.org/10.1039/c7ee02724a>.
5. Franklin, J. B., B. Zou, P. Petrov, D. W. McComb, M. P. Ryan, and M. A. McLachlan. "Optimised Pulsed Laser Deposition of ZnO Thin Films on Transparent Conducting Substrates." *J. Mater. Chem.* 21, no. 22 (2011): 8178–82. <https://doi.org/10.1039/c1jm10658a>.
6. Hartung, S., N. Bucher, J. B. Franklin, A. M. Wise, L. Y. Lim, H. Y. Chen, J. N. Weker, *et al.* "Mechanism of Na⁺ Insertion in Alkali Vanadates and Its Influence on Battery Performance." *Adv. Ener. Mater.* 6, no. 9 (May 11, 2016): 1502336. https://doi.org/ARTN_1502336
[10.1002/aenm.201502336](https://doi.org/10.1002/aenm.201502336).
7. Wang, H. W., Y. Zhang, H. X. Ang, Y. Q. Zhang, H. T. Tan, Y. F. Zhang, Y. Y. Guo, *et al.* "A High-Energy Lithium-Ion Capacitor by Integration of a 3d Interconnected Titanium Carbide Nanoparticle Chain Anode with a Pyridine-Derived Porous Nitrogen-Doped Carbon Cathode." *Adv. Funct. Mater.* 26, no. 18 (May 10 2016): 3082–93.
8. Gauthier, M., T. J. Carney, A. Grimaud, L. Giordano, N. Pour, H. H. Chang, D. P. Fenning, *et al.* "Electrode-Electrolyte Interface in Li-Ion Batteries: Current Understanding and New Insights." *J Phys. Chem. Lett.* 6, no. 22 (Nov 19, 2015): 4653–72. <https://doi.org/10.1021/acs.jpcclett.5b01727>.
9. Zhi, H., L. Xing, X. Zheng, K. Xu, and W. Li. "Understanding How Nitriles Stabilize Electrolyte/Electrode Interface at High Voltage." *J Phys. Chem. Let.* 8, no. 24 (Dec 21, 2017): 6048–52. <https://doi.org/10.1021/acs.jpcclett.7b02734>.
10. Alvarado, J., M. A. Schroeder, M. H. Zhang, O. Borodin, E. Gobrogge, M. Olguin, M. S. Ding, *et al.* "A Carbonate-Free, Sulfone-Based Electrolyte for High-Voltage Li-Ion Batteries." *Mater. Today* 21, no. 4 (May 2018): 341–53. <https://doi.org/10.1016/j.mattod.2018.02.005>.
11. Su, Chi-Cheung, Meinan He, Paul Redfern, Larry A. Curtiss, Chen Liao, Lu Zhang, Anthony K. Burrell, and Zhengcheng Zhang. "Alkyl Substitution Effect on Oxidation Stability of Sulfone-Based Electrolytes." *ChemElectroChem* 3, no. 5 (2016): 790–97. <https://doi.org/doi:10.1002/celec.201500550>.
12. Suo, L., W. Xue, M. Gobet, S. G. Greenbaum, C. Wang, Y. Chen, W. Yang, Y. Li, and J. Li. "Fluorine-Donating Electrolytes Enable Highly Reversible 5-V-Class Li Metal Batteries." *Proc. Natl. Acad. Sci. U. S. A.* 115, no. 6 (Feb 6 2018): 1156–61. <https://doi.org/10.1073/pnas.1712895115>.
13. Borodin, O., and D. Bedrov. "Interfacial Structure and Dynamics of the Lithium Alkyl Dicarboxate Sei Components in Contact with the Lithium Battery Electrolyte." *J. Phys. Chem. C* 118, no. 32 (Aug 14, 2014): 18362–71. <https://doi.org/10.1021/jp504598n>.
14. Borodin, O., Guorong V. Zhuang, Philip N. Ross, and Kang Xu. "Molecular Dynamics Simulations and Experimental Study of Lithium-Ion Transport in Dilithium Ethylene Dicarboxate." *J. Phys. Chem. C* 117, no. 15 (April 18, 2013): 7433–44. <https://doi.org/10.1021/jp4000494>.
15. Cho, S. J., D. E. Yu, T. P. Pollard, H. Moon, M. Jang, O. Borodin, and S. Y. Lee. "Nonflammable Lithium Metal Full Cells with Ultra-High Energy Density Based on Coordinated Carbonate Electrolytes." *iScience* 23, no. 2 (Feb 21, 2020): 100844. <https://doi.org/10.1016/j.isci.2020.100844>.
16. Huang, Q., T. P. Pollard, X. Ren, D. Kim, A. Magasinski, O. Borodin, and G. Yushin. "Fading Mechanisms and Voltage Hysteresis in FeF₂-NiF₂ Solid Solution Cathodes for Lithium and Lithium-Ion Batteries." *Small* 15, no. 6 (Feb 2019): e1804670. <https://doi.org/10.1002/smll.201804670>.

17. Von Aspern, Natascha, Mariano Grünebaum, Diddo Diddens, Travis Pollard, Christian Wölke, Oleg Borodin, Martin Winter, and Isidora Cekic-Laskovic. "Methyl-Group Functionalization of Pyrazole-Based Additives for Advanced Lithium-Ion Battery Electrolytes." *Journal of Power Sources* 461, (461 (2020/06/15/ 2020): 228159. <https://doi.org/10.1016/j.jpowsour.2020.228159>.
18. Benedek, R., M. M. Thackeray, and A. van de Walle. "Free Energy for Protonation Reaction in Lithium-Ion Battery Cathode Materials." *Chem. Mater.* 20, no. 17 (Sep 9 2008): 5485–90. <https://doi.org/10.1021/cm703042r>.
19. Fang, C. M., and G. A. de Wijs. "Local Structure and Chemical Bonding of Protonated $\text{Li}_x\text{Mn}_2\text{O}_4$ Spinels from First Principles." *Chem. Mater.* 18, no. 5 (March 1 2006): 1169–73. <https://doi.org/10.1021/cm051564a>.

Acknowledgements

Co-PIs, Oleg Borodin and Marshall Schroeder, conducted the DFT and MD and purified electrolytes, respectively. Co-PI, Zhenxing Feng growth PLD films. Use of the Stanford Synchrotron Radiation Lightsource, SLAC National Accelerator Laboratory, is supported by the U.S. Department of Energy, Office of Science, Office of Basic Energy Sciences under Contract No. DE-AC02-76SF00515. This research used resources of the Advanced Photon Source; a U.S. Department of Energy (DOE) Office of Science User Facility operated for the DOE Office of Science by Argonne National Laboratory under Contract No. DE-AC02-06CH11357.

X.2 Stability of cathode/electrolyte interfaces in high voltage Li-ion batteries (ANL)

Dusan Strmcnik, Principal Investigator

Argonne National Laboratory
9700 South Cass Avenue
Lemont, IL 60439
E-mail: strmcnik@anl.gov

Peter Faguy, DOE Technology Development Manager

U.S. Department of Energy
E-mail: Peter.Faguy@ee.doe.gov

Start Date: October 1, 2020

End Date: September 30, 2021

Project Funding (FY21): \$350,000

DOE share: \$350,000

Non-DOE share: \$0

Project Introduction

Li-ion batteries have become very important in the last two decades and represent the power source of choice for most portable electronic devices. However, an improvement of this technology is still necessary to be durably introduced onto new markets such as electric vehicles (EVs) and hybrid electric vehicles (HEVs). One of the viable options to meet the high energy density demands of the new Li-ion technology are the high voltage Li-ion batteries, which utilize the cathode materials that can operate at voltages higher than 4.5 V vs. Li/Li⁺. A major problem with these high voltage cathode materials is the incompatibility with “conventional” Li-ion electrolytes, which commonly consist of a combination of lithium hexafluorophosphate (LiPF₆) salt with a binary solvent mixture of cyclic and linear alkyl carbonates such as ethylene carbonate (EC) and ethyl methyl carbonate (EMC). These electrolytes undergo severe degradation at high voltages which is often remedied by cathode passivation additives. Another approach is to develop new solvents which are intrinsically stable at high voltages. Both approaches, however, demand a much better fundamental understanding of the underlying degradation mechanisms of the Li-ion cathode/electrolyte interfaces, which would be on par with understanding of aqueous electrochemical interfaces.

Objectives

The main goal of this proposal is to establish fundamental mechanistic understanding of the principles that govern the decomposition and properties of cathode/electrolyte interfaces and relate them to the performance of high voltage Li-ion cells.

In order to achieve this goal, we will divide our work into five objectives:

- Investigate the chemistries of individual electrolyte components of a Li-ion battery on a variety of materials, from well-defined metal single crystals to realistic TMO samples at high potentials, relevant for high voltage LiB. These individual components will range from different solvents, electrolyte salts to impurities that can either be present in the electrolyte from the beginning or contaminate the system during battery operation (e.g., metals from the cathode side).
- Investigate how the experimental conditions influence these individual chemistries or how they enhance or diminish individual processes in the case of overlapping chemistries.
- By utilizing both theoretical as well as experimental tools, establish thermodynamic and kinetic windows of stability of individual components. Furthermore, an attempt will be made to include mass transport effects into the understanding of the interface stability in various electrochemical environments.

- Combine the thermodynamic, kinetic and mass transport properties of a certain chemistry under specific experimental conditions to build an EEI with specific properties.
- Test the performance of the EEI in coin cells.

Approach

The number one priority of this proposal is to extend the state of the art of understanding how individual components of the cathode/electrolyte interface behave at potentials relevant for high-voltage Li-ion batteries and how these individual components interact with each other. A long-term goal, however, is to implement this knowledge into next generation high-voltage cathode materials and electrolytes. While there are many studies available in the literature exploring the electrolyte as well as cathode material decomposition, most of the attempts focused on real materials in real cells. Although such complex phenomena can be ‘tested’ in real systems, the only way to resolve, apply and connect the underlying fundamental processes with real cell performance would be possible with unique experimental-computational approach. To the best of our knowledge, a deeper fundamental understanding about the structure and properties of cathode side electrode-electrolyte-interphase at the atomic/molecular level is still lacking and would be of high importance for the development of next generation LIBs.

Our approach differs significantly from the well-established testing approach, incorporating three critical steps: (i) utilization of model well-defined systems to assess fundamental descriptors for the decomposition of the electrolyte as well as cathode components; (ii) probing more complex electrolytes and electrode materials with different morphologies; and (iii) exploring the properties of cathode materials that are currently, or are potential candidates, to be used in LIB.

Results

Covid-19 Impact

Due to the pandemic, Argonne National Laboratory has been in limited operations mode, i.e., 60% working capacity. Our output has been affected and we are experiencing delays in reaching our milestones.

The mechanism of oxidation of cyclic organic carbonates

The first steps in the electrooxidation of the carbonate solvents is the removal of the electron with concomitant or subsequent abstraction of the proton, as schematically depicted for the case of EC molecule in Figure X.2.1. Either of these steps can potentially be rate determining. Three possible reaction paths are shown in Figure X.2.1: (i) Path A leads to the formation of radical cation through a rate-limiting electron transfer at oxidation potential E_{ox} . The radical cation itself is most likely an unstable species decomposing further into CO and other fragments. (ii) Path B suggests simultaneous removal of electron with E_{ox} and proton with the free energy of proton removal ΔG_{H-S} , either of which can be rate determining, to obtain a radical species, which further decomposes into CO₂ and other fragments. (iii) Finally, path C leads to the formation of a carbocation through a transfer of two electrons and a removal of one proton. Based on our DFT calculations, the carbocation can be stabilized with the electrolyte anions, giving it higher stability than the forementioned radicals.

An oxidation stability of a series of cyclic carbonates was tested, including EC, PC, VC, FEC and DFEC. The fluorinated carbonates were provided to us by John Zhang’s group. We employed a combination of RRDE and OEMS to get insight into the reaction mechanisms. The results are summarized in Figure X.2.1, Figure X.2.2 and Figure X.2.3 as well as in Table X.2.1. Several observations are noteworthy. (i) the oxidation of individual solvents is characterized by a sharp, ignition-like increase in the positive current, preceded by a potential region with lower, diffusion controlled current, most likely originating from solvent impurities. (ii) The oxidation potentials for the investigated series of solvents give the following trend: VC << DFEC < FEC < PC < EC (Figure X.2.3). Based on calculated E_{ox} and ΔG_{H-S} (Table X.2.1) VC is the only solvent with strongly indicated electron transfer as the rate determining step, the rest lean more toward the rate limiting proton abstraction. (iii) Based on RRDE data 1 proton is created per 2 electrons for all carbonates apart from VC, where that ratio is 1:4. This suggests reaction path A for VC oxidation and reaction path C for oxidation of other carbonates. The

OEMS data tracking CO₂ and CO production, at least qualitatively, confirm the suggested reaction paths, with low initial gas evolution observed for PC, EC, FEC and DFEC, indicative of path C, while a substantially higher (5-10x) higher gas evolution with a significant CO presence is observed for VC, indicative of path A. Alternatively, a combination of path A and B can also explain the observed proton:electron ratio. A more detailed quantification of the data will be performed to provide further insight into the mechanisms. (iv) The premises of using fluorinated solvents is based on their supposed higher stability towards electrooxidation. DFT suggests 0.2 V and 0.5 V higher E_{ox} for FEC and DFEC vs EC, respectively. Experimentally, however, we observe no stabilization effect in fluorinated solvents. The main electroreduction process (high current densities) actually commences at 0.1 and 0.2 V lower potentials for FEC and DEFC compared to EC. This suggests that the deprotonation (ΔG_{H-S}) and not the electron transfer (E_{ox}) is rate determining. A possible explanation for beneficial effects of the fluorinated solvents might be in the low current density potential range (more relevant for LIB operation), where we see very small amount of protons created compared to other solvents.

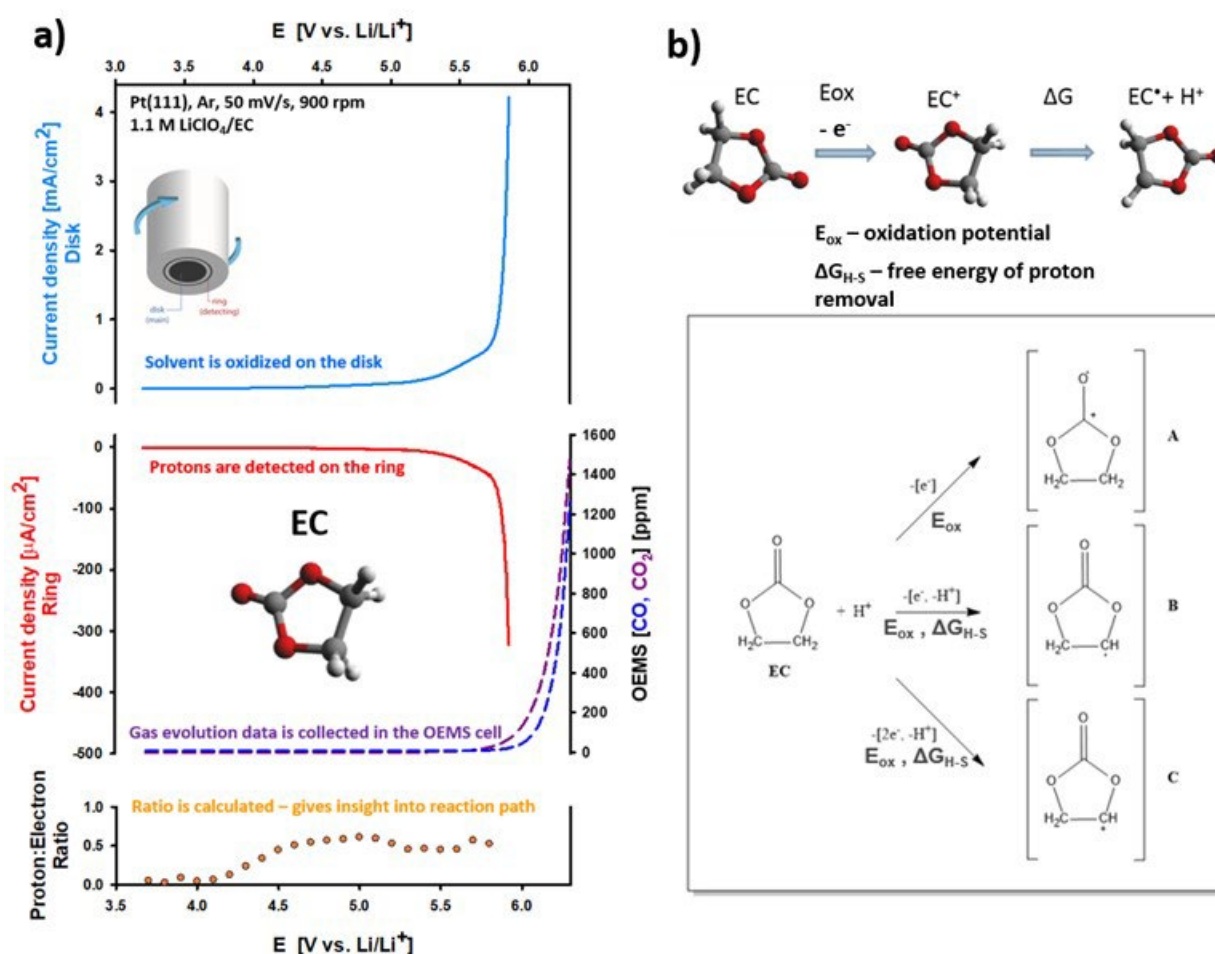


Figure X.2.1 a) Electrochemical oxidation of EC in 1.1 M LiClO₄/EC. Disk current is shown in blue, ring current, corresponding to the amount of protons created, is shown in red, and their ratio, is shown in orange. OEMS data for CO₂ and CO is depicted by purple and blue dashed curves. b) first step of the reaction mechanism – 3 possible reaction pathways are shown

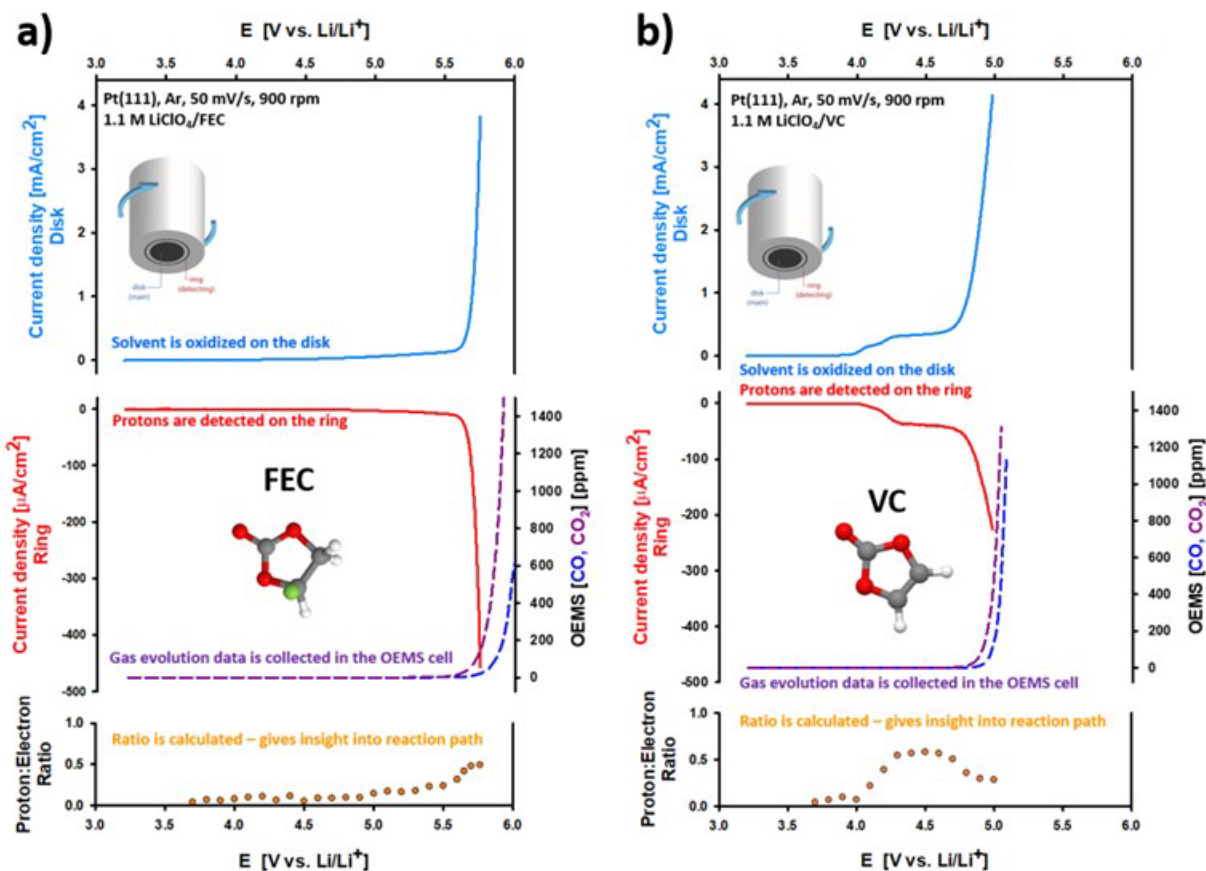


Figure X.2.2 a) Electrochemical oxidation of FEC in 1.1 M LiClO₄/FEC. Disk current is shown in blue, ring current, corresponding to the amount of protons created, is shown in red, and their ratio, is shown in orange. OEMS data for CO₂ and CO is depicted by purple and blue dashed curves. b) Electrochemical oxidation of VC in 1.1 M LiClO₄/VC.

Table X.2.1 Calculated oxidation potential E_{ox} and free energy of proton removal, given relative to EC. Measured E_{ox} are given for comparison.

Solvent	ΔE_{ox}	$\Delta GH-S$	E_{ox} @ 3.5 mA/cm ² experiment
EC	0.0 V	0.0 eV	5.85 V
1FEC	0.2 V	-0.1 eV	5.75 V
2FEC	0.5 V	-0.4 eV	5.65 V
VC	-1.5 V	2.7 eV	4.9 V
PC	-0.2 V	0.2 eV	5.75 V

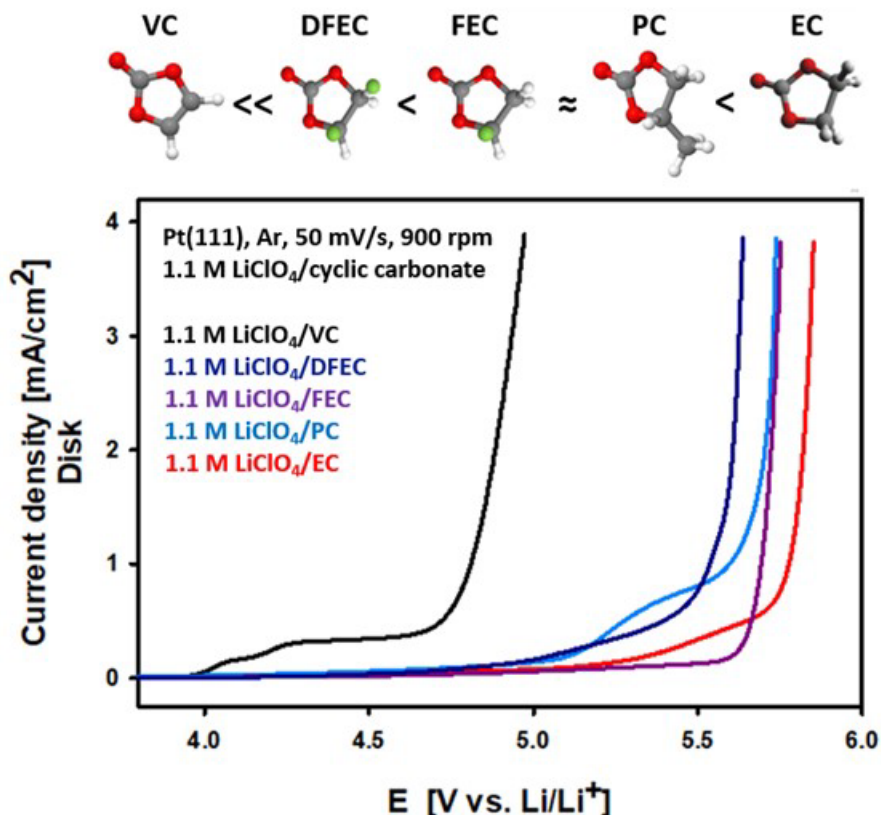


Figure X.2.3 a) Electrochemical oxidation of organic carbonate solvent series. Only disk currents are shown. The order of stability is as follows $VC \ll DFEC < FEC \approx PC < EC$.

The life of a proton, created via solvent oxidation:

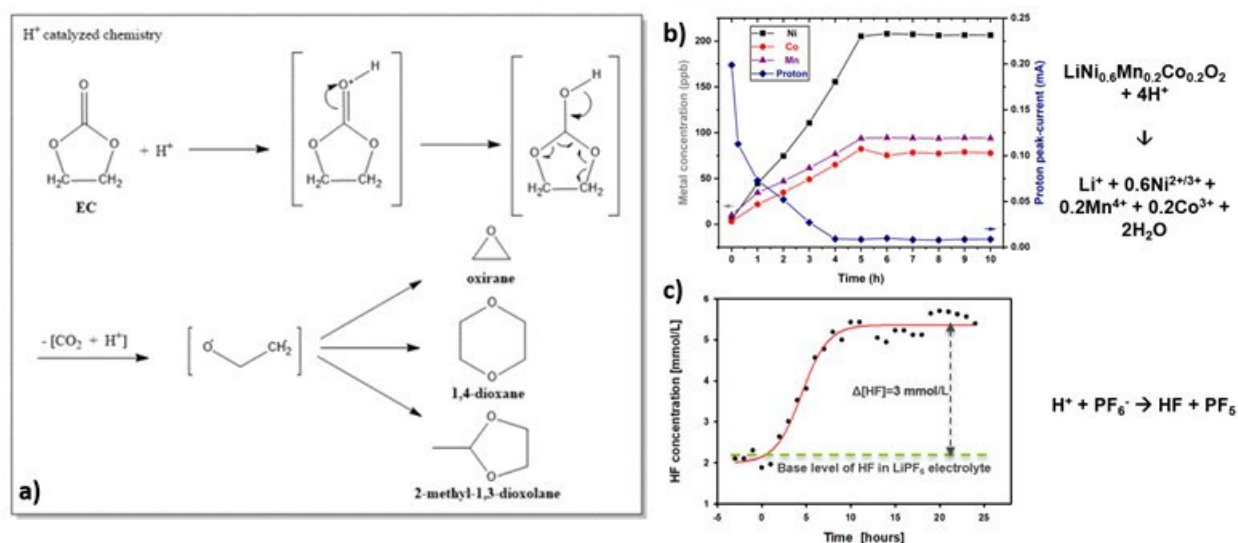


Figure X.2.4 The reactions of protons with a) solvent, b) NMC 622, c) PF₆⁻

Proton is by far the most detrimental species in LiB. It is the product of solvent oxidation which can occur as early as 4 V vs. Li/Li⁺. By developing a method for proton detection, we have been able to quantify the amount

of protons, created during solvent oxidation, and follow their reaction with the solvent, electrolyte and cathode material. We have identified and followed 3 different reactions: (i) The reaction of the proton with the solvent (EC) initiates the opening of the ring with concomitant evolution of CO_2 . The remaining part of the molecule can form several products, including ethylene oxide, dioxane and methyl-dioxolane. The mechanism for this reaction is given in Figure X.2.4a. The rate constant was determined by following the CO_2 production with time and was determined to be $1.3 \times 10^{-5} \text{ s}^{-1}$. (ii) The dissolution of NMC 622, caused by the reaction with proton was followed by means of ICP-MS with time and the rate constant was determined to be $1.7 \times 10^{-5} \text{ s}^{-1}$ (Figure X.2.4b) (iii) The reaction of the proton with the electrolyte anion PF_6^- produces HF. The amount of produced HF was quantified and monitored with time (Figure X.2.4c). The rate constant for this process was calculated to be $4.3 \times 10^{-5} \text{ s}^{-1}$. Considering the same order of magnitude of the rate constants none of the processes can be neglected.

Conclusions

In the last funding cycle, we were able to advance our knowledge of the reaction mechanism for carbonate solvent oxidation. A series of cyclic organic carbonates was investigated with RRDE, OEMS and DFT calculations. We identified two possible rate determining steps in the oxidation process, i.e., first electron transfer and proton abstraction, and proposed 3 different reaction pathways. Most solvents seem to follow the two-electron pathway with a concomitant abstraction of one H^+ , with the abstraction of H^+ as rate determining step. Interestingly, experimentally, we do not find a fundamental reason for higher stability of fluorinated solvents. The order of stability is $\text{VC} \ll \text{DFEC} < \text{FEC} \approx \text{PC} < \text{EC}$.

Furthermore, we continued the investigation of the chemical reaction of the formed protons with the solvent and electrolyte. When proton reacts with EC, it initiates the opening of the ring with concomitant evolution of CO_2 . The remaining part of the molecule can form several products, including ethylene oxide, dioxane and methyl-dioxolane. In LiPF_6 containing electrolytes, proton reacts with the anion, producing HF and PF_5 . We also confirmed the reaction of the proton with NMC 622 producing significant concentrations of transition metals cations and water. The reaction products of all three reactions were quantified and reaction rates calculated. In addition, electrochemically produced protons can enter the reaction with oxide electrode materials. Due to the same order of magnitude of these rate constants, none of the three decomposition processes can be neglected.

X.3 Interfacial Studies of Emerging Cathode Materials

Marca Doeff, Principal Investigator

Lawrence Berkeley National Laboratory
1 Cyclotron Road
Berkeley, CA 94720
E-mail: mmdoeff@lbl.gov

Peter Faguy, DOE Technology Development Manager

U.S. Department of Energy
E-mail: Peter.Faguy@ee.doe.gov

Start Date: October 1, 2018

End Date: September 30, 2021

Project Funding (FY21): \$300,000

DOE share: \$300,000

Non-DOE share: \$0

Project Introduction

Recently, the discovery that reversible or partly reversible oxygen redox processes can occur in a variety of structures has opened up a new design space for cathode materials, with the tantalizing possibility of attaining capacities well beyond the 280 mAh/g theoretical limit of traditional intercalation layered oxides. Materials of interest include Li_2MnO_3 , [1] lithium and manganese rich NMCs (LMR-NMCs) [2] and Co-free analogs, [3] other types of lithium-rich layered oxides with structures similar to Li_2MnO_3 [4] and cation-disordered rock salts (DRX materials) [5]. Many of these materials exhibit capacities of 300 mAh/g or more, but suffer from poor rate capability, voltage hysteresis, and capacity fading [6]. In these cases, irreversible oxygen loss, [7] morphological [8] and structural changes [9] are to blame for the performance issues. Strategies such as partial fluorine substitution for oxygen [10], [11] appear to mitigate irreversible oxygen loss and result in improved behavior. For this work, we use an array of surface-sensitive and bulk techniques to understand what gives rise to processes that result in their degradation and attempt to mitigate them in selected materials.

Objectives

Reports of oxygen redox activity in materials with unusually high capacities are intriguing, but fairly little is known about how these materials actually work. There are a number of unanswered questions to which the work proposed here is designed to answer. First, how deep into the bulk does oxygen redox occur? Is it primarily a surface reaction? When does oxygen release occur, as opposed to reversible redox? Does the oxygen redox or oxygen release contribute to the structural instability that is often seen, and can this be prevented by, e.g., cationic or anionic substitutions, coatings, or other strategies? How do the surfaces of particles of charged or partially charged materials interact with the electrolytic solutions, and how does this contribute to capacity fading, rate limitations, and other performance issues? Once these questions are answered, strategies such as substitutions, coatings and particle morphology/size engineering can be considered to ensure robust cycling.

Approach

To answer the above questions, we will synthesize materials with differing particle sizes/surface areas, subject them to electrochemical charge, discharge, and cycling or chemical delithiation, and study them using an array of surface and bulk sensitive techniques including synchrotron X-ray absorption spectroscopy (XAS), X-ray photoelectron spectroscopy (XPS), transmission X-ray microscopy (TXM), X-ray Raman (XRS), and microscopy. For FY21, we focused on $\text{Li}_4\text{Mn}_2\text{O}_5$ [12].

Results

Access to the synchrotron beam lines we needed to carry out this work was still severely restricted by circumstances surrounding the pandemic in FY21. For this reason, we focused on synthesis and electrochemistry of $\text{Li}_4\text{Mn}_2\text{O}_5$, with plans to finish characterization as access to the Stanford Synchrotron

Radiation Lightsource gradually improves. Mail-in services for some beam lines were available in FY21, but generally only for ex situ work. As of this writing, users are beginning to be allowed back on site under carefully controlled conditions.

The discharge capacity of $\text{Li}_4\text{Mn}_2\text{O}_5$ (Figure X.3.1) is well in excess of what is expected for complete oxidation of Mn to the tetravalent state. X-ray Raman spectroscopy carried out in prior years shows no evidence of formation of pentavalent Mn during charge. Thus, the excess capacity seen on discharge is due to oxygen redox, while the excess on charge is a combination of this and electrochemical decomposition of lithia or lithium carbonate. The effect of changing the amount of lithia used during synthesis on the electrochemical properties of $\text{Li}_4\text{Mn}_2\text{O}_5$ is also shown in Figure X.3.2. The greater the excess amount of Li_2O used, the higher the initial charge capacity, but similar discharge profiles are seen for all samples.

Mn K-edge hard XAS ex situ data for pristine and charged $\text{Li}_4\text{Mn}_2\text{O}_5$ electrodes are shown in Figure X.3.2 along with MnO , Mn_2O_3 , and MnO_2 reference materials. This pristine material has an oxidation state close to +3. For the charged materials, there is a shift to higher energy, similar to that found for MnO_2 , indicating

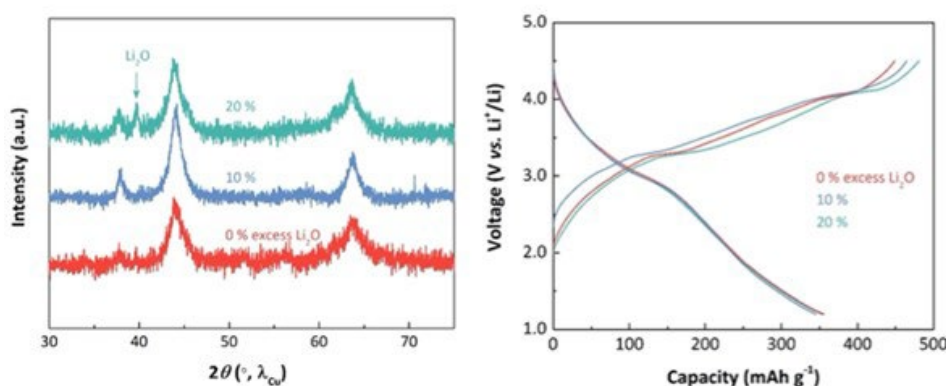


Figure X.3.1 (Left) XRD patterns of $\text{Li}_4\text{Mn}_2\text{O}_5$ synthesized with various amounts of excess Li_2O and (right) first cycles of these materials.

oxidation to the tetravalent state. There is very little difference between the data for the electrode charged to 4.5V and the one charged to 4.8V, indicating that redox processes involving Mn are completed in cells by 4.5V, if not sooner. Above this potential, other processes add to the capacity that is observed.

Also shown in Figure X.3.2 are the Mn L-edge and O K-edge data for pristine electrodes and those charged to various points, in either TEY (sensitive to about 5 nm into the sample) or FY mode (sensitive to about 100 nm into the sample). While the Mn L-edge TEY results show that Mn on the surface is oxidized initially, there is a shift back to lower energy upon charge to 4.8V, indicating some reduction of Mn on the surface at this high state-of-charge. Li_2O is evident in the pristine material in the O K-edge TEY data, and, to a lesser extent in the FY data, but the signal diminishes in the charged electrodes, and disappears entirely for the electrode charged to 4.8V. In the fully charged electrode, a signal due to Li_2CO_3 is observed in both the TEY and FY data for the fully charged electrode. This is consistent with electrochemically induced decomposition of Li_2O and possible reaction with the electrolytic solution at high voltages to form Li_2CO_3 .

The effect of changing voltage limits on the electrochemical performance of cells containing $\text{Li}_4\text{Mn}_2\text{O}_5$ was studied (Figure X.3.3). Much better cycling performance is observed if the upper voltage limit is restricted to 3.5V rather than 4.5V, although this reduces the capacity to about 200 mAh/g initially. Higher voltage cutoffs also result in increased hysteresis between charge and discharge curves. Extended cycling to 4.5V results in changes to the voltage profile consistent with formation of spinel. New features near 4 and 2V grow in as the cells are cycled, apparent in the dQ/dV plot. The effect of changing the lower voltage cutoff was also examined (not shown). As the cutoff potential is decreased, there is an intensification of the 4V feature (i.e.,

spinel formation is more pronounced). Likewise, the feature near 2V appears to be related to the upper voltage cutoff with higher voltages resulting in more rapid increases of this feature. Hard XAS results (Figure X.3.3) indicate that Mn is reduced to below 3+ after ten cycles between 1.5–4.5V in the bulk, while remaining almost unchanged when the charge cutoff voltage is lowered. Ex situ synchrotron XRD results on pristine and cycled electrodes as a function of voltage largely concur with the results of the electrochemical and XAS experiments, showing that lithia decomposes during initial charge. The rock salt structure is largely maintained upon initial charge to 4.5V, but changes after discharge to 1.5V.

Fluorination has been shown to improve the electrochemical properties of DRX electrode materials by ameliorating oxygen release. $\text{Li}_4\text{Mn}_2\text{O}_4\text{F}$ was synthesized by mechanochemical synthesis. Figure X.3.4 shows the XRD pattern and hard XAS data. These indicate that the rock salt structure is similar to that of the parent compound, although the average oxidation state of Mn is between +2 and +3, as expected from the chemical formula. While the fluorinated material yields a lower capacity than $\text{Li}_4\text{Mn}_2\text{O}_5$ initially in half-cells, it appears to cycle somewhat better. The evolution of the voltage profile to that of a spinel is much less pronounced (Figure X.3.5) although there is some development of the 2V and 4V features evident in the dQ/dV plot.

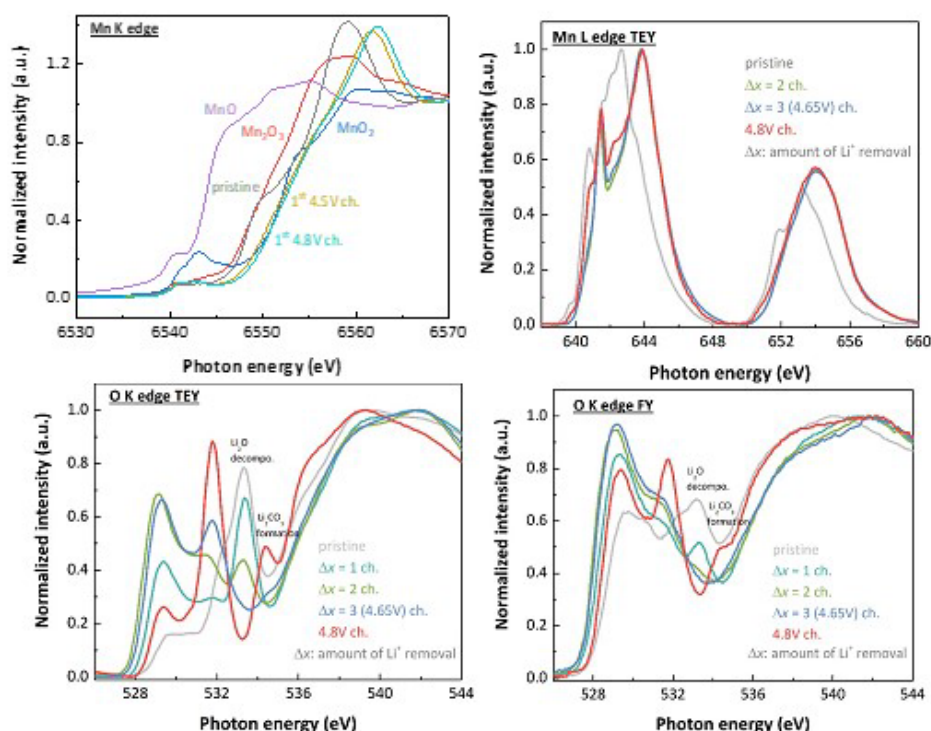


Figure X.3.2 (Top left) Mn K-edge XAS data for pristine $\text{Li}_4\text{Mn}_2\text{O}_5$ electrodes and those charged to the indicated potentials, along with reference materials. (Top right) Mn L-edge soft XAS data for pristine and charged electrodes in TEY mode. (Bottom left) O K-edge soft XAS data in TEY mode for pristine and charged electrodes and (bottom right) O K-edge soft XAS data in FY mode.

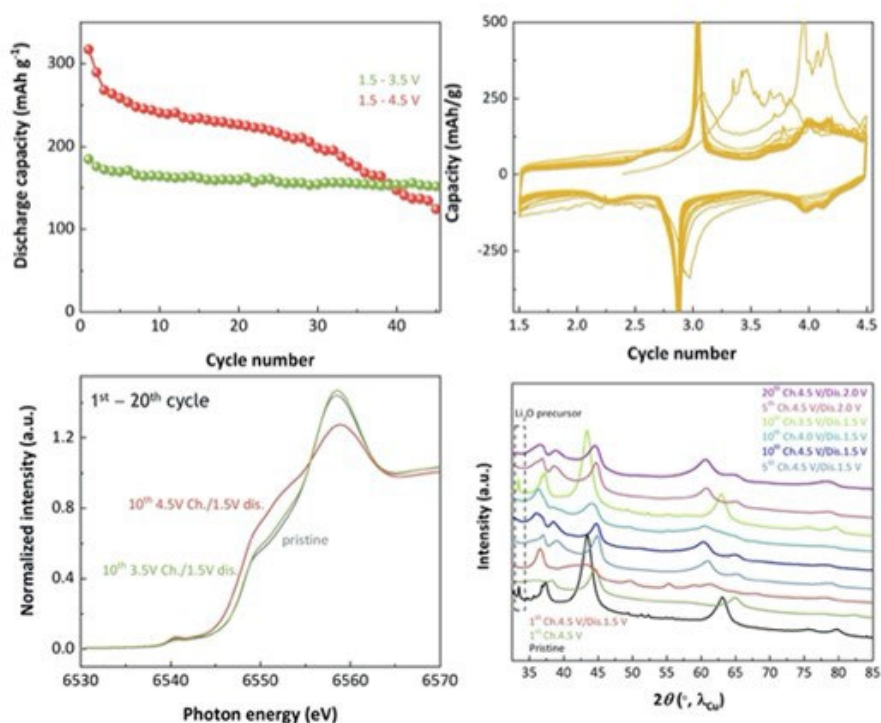


Figure X.3.3 (Upper left) capacity retention as a function of voltage limits for cells containing $\text{Li}_4\text{Mn}_2\text{O}_5$. (Upper right) dQ/dV plots showing evidence of structure evolution). (Bottom left) Mn K-edge XAS spectra on pristine and cycled electrodes as a function of voltage limits. (Bottom right) ex situ XRD patterns on pristine and cycled electrodes as a function of voltage limits.

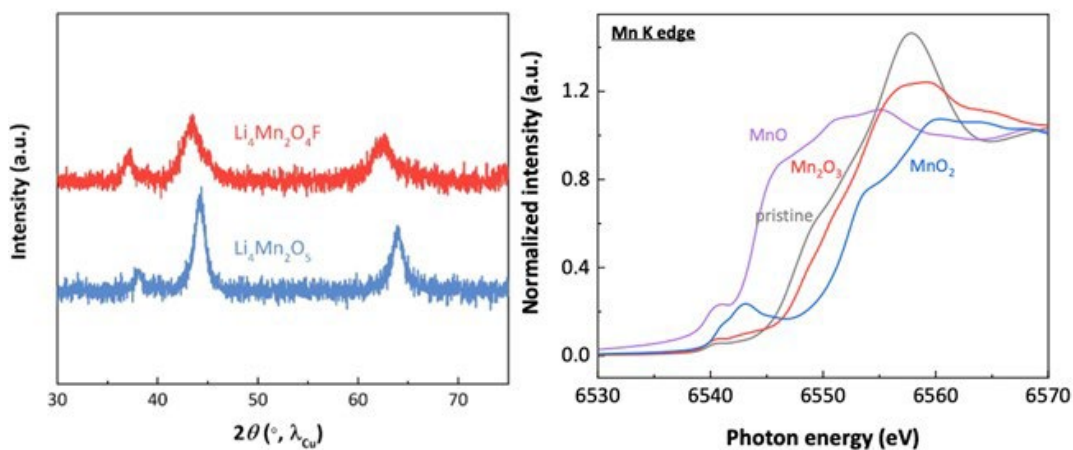


Figure X.3.4 (Left) XRD patterns of $\text{Li}_4\text{Mn}_2\text{O}_5$ and $\text{Li}_4\text{Mn}_2\text{O}_4\text{F}$. (Right) Hard XAS data on pristine $\text{Li}_4\text{Mn}_2\text{O}_4\text{F}$ with reference materials.

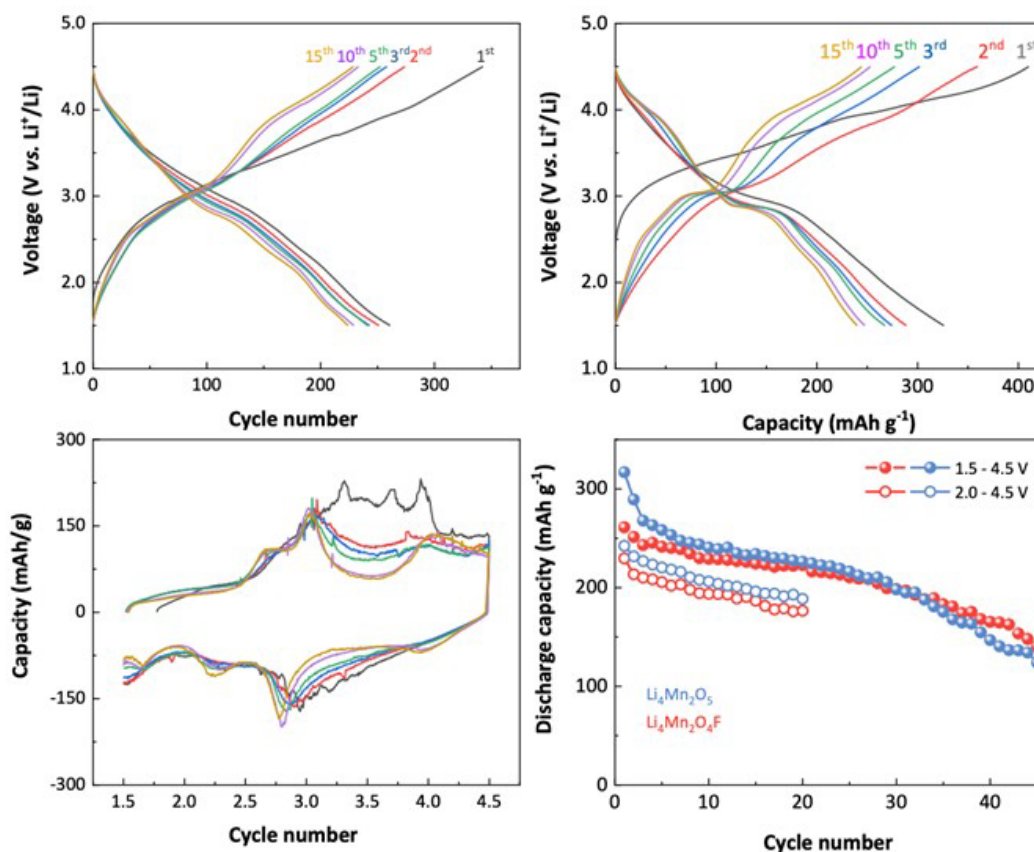


Figure X.3.5 (Top left). Voltage profiles of a cell containing $\text{Li}_4\text{Mn}_2\text{O}_4\text{F}$ as a function of cycle number. Compare to (top right) data for cell containing $\text{Li}_4\text{Mn}_2\text{O}_5$. (Bottom left) dQ/dV plots for cell containing $\text{Li}_4\text{Mn}_2\text{O}_4\text{F}$, and (bottom right) capacity as a function of cycle number for cells containing $\text{Li}_4\text{Mn}_2\text{O}_4\text{F}$ or $\text{Li}_4\text{Mn}_2\text{O}_5$ as a function of voltage limits used.

Conclusions

$\text{Li}_4\text{Mn}_2\text{O}_5$ undergoes a number of surface and bulk structural changes that result in capacity fade upon cycling. These include oxygen loss, reaction with electrolyte to form Li_2CO_3 , and reduction of manganese on particle surfaces and in the bulk. The bulk structural change to spinel appears to be mitigated somewhat by partial fluorine substitution for oxygen, although some changes in the voltage profile are still observed for the substituted material.

Key Publications

1. Besli M. M., Usabelli C., Subbaraman A., Safaei, R. F. P., Bone S., Johnston C., Schneider G., Beauchaud F., Ravi N., Christensen J., Doeff M., Metzger, M., and Kuppan S., “Location Dependent Cobalt Deposition in Smartphone Cells Upon Long-Term Fast-Charging Visualized by Synchrotron X-ray Fluorescence” *Chem. Mater.* 33 (2021): 6318–6328.
2. Lee R.-C., Tian C., Doeff M., Nordlund D., Franklin, J. and Kostecki R., “The Origin of Impedance Rise in Ni-Rich Cathodes for Lithium-Ion Batteries” *J. Power Sources* 498, (2021): 229885.
3. Besli, M. M., Subbaraman A., Safaei R.F. P., Johnston C., Schneider G., Ravi N., Christensen J., Liu Y., Doeff, M. M., Metzger M., and Kuppan S. “A Study of Model-based Protective Fast-charging and Associated Degradation in Commercial Smartphone Cells: Insights on Cathode Degradation as a Result of Lithium Depositions on the Anode”, *Adv. Energy Mater.* (2021): 2003019.

References

1. Chen, H., and Islam, M. S., "Lithium Extraction Mechanism in Li-Rich Li_2MnO_3 Involving Oxygen Hole Formation and Dimerization" *Chem. Mater.* 28, (2016): 6656–6663.
2. Croy, J. R., Balasubramanian, M., Gallagher, K. G., and Burrell, A. K., "Review of the U.S. Department of Energy's "Deep Dive" Effort to Understand Voltage Fade in Li- and Mn-Rich Cathodes" *Acc. Chem. Res.* 48, (2015): 2813–21.
3. Luo, K., Roberts, M. R., Guerrini, N., Tapia-Ruiz, N., Hao, R., Massel, F., Pickup, D. M., Ramos, S., Liu, Y. S., Guo, J., Chadwick, A. V., Duda, L. C., and Bruce, P. G., "Anion Redox Chemistry in the Cobalt Free 3d Transition Metal Oxide Intercalation Electrode $\text{Li}[\text{Li}_{0.2}\text{Ni}_{0.2}\text{Mn}_{0.6}]\text{O}_2$ " *J. Am. Chem. Soc.* 138, (2016): 11211–11218.
4. Sathiya, M., Rousse, G., Ramesha, K., Laisa, C. P., Vezin, H., Sougrati, M. T., Doublet, M. L., Foix, D., Gonbeau, D., Walker, W., Prakash, A. S., Ben Hassine, M., Dupont, L., and Tarascon, J. M., "Reversible Anionic Redox Chemistry in High-capacity Layered-oxide Electrodes" *Nature Mater.* 12 (2013): 827–835.
5. Seo, D. H., Lee, J., Urban, A., Malik, R., Kang, S., and Ceder, G., "The Structural and Chemical Origin of the Oxygen Redox Activity in Layered and Cation-disordered Li-excess Cathode Materials" *Nature Chem.* 8 (2016): 692–697.
6. Assat, G., Delacourt, C., Corte, D. A. D., and Tarascon, J.-M., "Practical Assessment of Anionic Redox in Li-Rich Layered Oxide Cathodes: A Mixed Blessing for High Energy Li-Ion Batteries" *J. Electrochem. Soc.* 163, (2016): A2965–A2976.
7. Xu, J., Sun, M., Qiao, R., Renfrew, S. E., Ma, L., Wu, T., Hwang, S., Nordlund, D., Su, D., Amine, K., Lu, J., McCloskey, B. D., Yang, W., and Tong, W., "Elucidating Anionic Oxygen Activity in Lithium-rich Layered Oxides" *Nature Commun.* 9, (2018): article no. 947.
8. Kan, W. H., Chen, D., Papp, J. K., Shukla, A. K., Huq, A., Brown, C. M., McCloskey, B. D., and Chen, G., "Unravelling Solid-State Redox Chemistry in $\text{Li}_{1.3}\text{Nb}_{0.3}\text{Mn}_{0.4}\text{O}_2$ Single-Crystal Cathode Material" *Chem. Mater.* 30, (2018): 1655–1666.
9. Mikhailova, D., Karakulina, O. M., Batuk, D., Hadermann, J., Abakumov, A. M., Herklotz, M., Tsirlin, A., Oswald, S., Giebeler, L., Schmidt, M., Eckert, J., Knapp, M., and Ehrenberg, H., "Layered-to-Tunnel Structure Transformation and Oxygen Redox Chemistry in LiRhO_2 upon Li Extraction and Insertion" *Inorg. Chem.* 55, (2016): 7079–7089.
10. Gent, W. E., Lim, K., Liang, Y., Li, Q., Barnes, T., Ahn, S. J., Stone, K. H., McIntire, M., Hong, J., Song, J. H., Li, Y., Mehta, A., Ermon, S., Tylliszczak, T., Kilcoyne, D., Vine, D., Park, J. H., Doo, S. K., Toney, M. F., Yang, W., Prendergast, D., and Chueh, W. C., "Coupling between Oxygen Redox and Cation Migration Explains Unusual Electrochemistry in Lithium-rich Layered Oxides" *Nature Commun.* 8, (2017): article no. 2091.
11. Lee, J., Papp, J. K., Clement, R. J., Sallis, S., Kwon, D. H., Shi, T., Yang, W., McCloskey, B. D., and Ceder, G., "Mitigating Oxygen Loss to Improve the Cycling Performance of High-Capacity Cation Disordered Cathode Materials" *Nature Communications* 8, (2017): article no. 981.
12. Freire, M., Kosova, N. V., Jordy, C., Chateigner, D., Lebedev, O. I., Maignan, A., and Pralong, V., "A New Active Li-Mn-O Compound for High Energy Density Li-Ion Batteries" *Nature Mater.* 15, (2016): 173–177.

X.4 Understanding and Modification of High-Energy Cathodes and their Interfaces with Electrolytes for Next-Generation Li-Ion Batteries (PNNL)

Jie Xiao, Principal Investigator

Pacific Northwest National Laboratory
902 Battelle Boulevard
Richland, WA 99352
E-mail: jie.xiao@pnnl.gov

Ji-Guang Zhang, Principal Investigator

Pacific Northwest National Laboratory
902 Battelle Boulevard
Richland, WA 99352
E-mail: jiguang.zhang@pnnl.gov

Peter Faguy, DOE Technology Development Manager

U.S. Department of Energy
E-mail: Peter.Faguy@ee.doe.gov

Start Date: October 1, 2020

End Date: September 30, 2021

Project Funding (FY21): \$350,000

DOE share: \$350,000

Non-DOE share: \$0

Project Introduction

Traditional $\text{LiNi}_{1/3}\text{Mn}_{1/3}\text{Co}_{1/3}\text{O}_2$ (NMC) cathodes are prepared using a co-precipitation method which yields agglomerated nanosized NMC particles. [1],[2] This aggregated particle structure shortens the diffusion length of the primary particles and increases the number of pores and grain boundaries within the secondary particles, which accelerates the electrochemical reaction and improves the rate capability of NMC. However, particle pulverization along the “weak” internal grain boundaries is generally observed after cycling. This intragranular cracking exposes more surfaces to electrolyte inducing more side reactions on those newly exposed surfaces. Accordingly, cell degradation is accelerated once cracks form within secondary NMC particles. More importantly, as Ni content increases, Ni-rich NMC, e.g., NMC811 becomes very sensitive to moisture, which creates challenges for storing and transporting the Ni-rich NMC. [3] During extensive cycling, gas generation is commonly observed in Ni-rich NMC and raises safety concern. All these aforementioned challenges are rooted in the phase boundaries within polycrystalline Ni-rich NMC particles. The application of micron sized single crystal Ni-rich NMC could potentially overcome the roadblocks present in polycrystalline NMC because of the significantly reduced number of phase boundaries in single crystals.

In FY20, PNNL reported high-performance single crystal $\text{LiNi}_{0.76}\text{Mn}_{0.14}\text{Co}_{0.1}\text{O}_2$ (NMC76) and validated its electrochemical performances in full cells. The team also discovered the reversible gliding and microcracking phenomena observed in single crystal NMC76 charged to above 4.3 V (vs. Li/Li⁺). [4] A critical crystal size of 3.5 μm was predicted below which gliding will be eliminated. This year we successfully reduced particle size of NMC76 single crystal to 2 μm and proved the hypothesis of the critical crystal size. A detailed comparison of gas generation from single crystal and polycrystalline NMC76 is also investigated and reported here.

Objectives

- Mitigate gliding and microcracking in single crystal Ni-rich NMC76.
- Side-by-side comparison of gas generation in single crystal and polycrystalline NMC76.
- Optimize synthesis procedure of single crystal Ni-rich NMC with IP protection (application #: 31837).

Approach

- Reduce single crystal size of NMC76 to 2 μm through synthesis modification.
- Validate the performances of downsized single crystals in full cell testing.
- Apply in situ differential electrochemical mass spectrometry (DEMS) to analyze and quantify gases generated from single crystal and polycrystalline NMC76.

Results

Through appropriate synthesis modification and element doping, the particle size of single crystal NMC76 has been reduced to ca. 2 μm with a drum-like morphology (Figure X.4.1a). After 300 cycles between 2.7 and 4.4 V (vs. Graphite) in full cells, downsized NMC76 single crystals remain intact (Figure X.4.1b) without obvious detection of cracking that was observed in our previously reported single crystals (data not shown here). Note that the single crystal cathodes are charged to 4.4 V vs. graphite which equals to 4.5 V vs. Li/Li^+ . High stress will be generated accompanied by large strain energies at such a high voltage. The absence of cracking after 300 cycles proves our earlier prediction on the critical size of single crystals at $\sim 3.5 \mu\text{m}$, below which cracks can be considered stable inside of the particle. Due to element doping, the first discharge capacity (Figure X.4.1c) of doped single crystal NMC76 is 191 mAh/g, slightly less than that of undoped crystals. Improved cycling stability at high cutoff voltage (4.4 V) is observed in downsized doped single crystals. The capacity retention of undoped and doped single crystal NMC76 after 300 cycles are 73.3% and 62.8% (Figure X.4.1d), respectively. The electrochemical evaluations in Figure X.4.1d are tested in graphite||NMC76 full cells with mass loadings of ca. 20 mg/cm^2 for NMC76 to ensure the results are still applicable in realistic batteries.

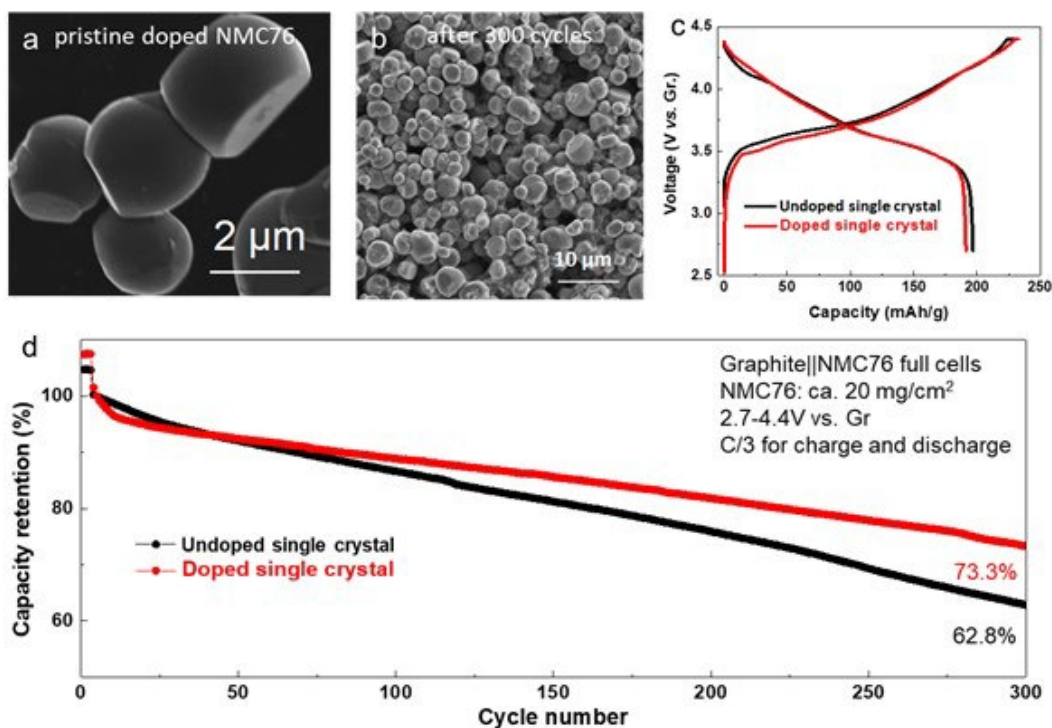


Figure X.4.1 Properties of doped NMC76 single crystals with reduced particle size. (a) Scanning Electron Microscope (SEM) image of downsized NMC76 single crystals with an average size of 2 μm . (b) SEM image of doped NMC76 single crystals after 300 cycles. (c) Comparison of the first charge and discharge curves between undoped and doped NMC76 single crystals. (d) Comparison of long-term cycling stability of undoped and doped NMC76 crystals. The first two cycles are charged and discharged at C/10, while in the subsequent cycling C/3 is applied for charge and discharge.

One of the important attributes of single crystal Ni-rich NMC is that gas generation issue, commonly observed in Ni-rich cathode, is expected to be mitigated given the largely reduced phase boundaries and therefore stable structures during repeated cycling. Figure X.4.2a illustrates the *in situ* Differential Electrochemical Mass Spectrometry (DEMS) system used for gas analysis. Polycrystalline and single crystal NMC76 in contact of the same electrolyte (1M LiPF₆ in EC/EMC) are firstly charged to 4.3 V. From 4.3 to 4.8 V, the potentials applied on the cell are gradually elevated with a step size of 0.1 V (Figure X.4.2b,c). Four different gases, i.e., CO₂, O₂, H₂ and CO, have been detected in both cases during charge. For polycrystalline NMC76, the onset voltages of CO₂, CO, O₂, and H₂ evolution are 3.95 V, 4.4 V, 4.5 V and 4.7 V, respectively (Figure X.4.2b). Compared to polycrystalline NMC76, single crystal NMC76 displays higher onset voltages for each individual gas. For example, O₂ does not show up until 4.7 V (Figure X.4.2c) in single crystals, while it is detected at 4.5 V for polycrystals. CO₂ is always the first gas detected in both cases. Before 4.0 V, CO₂ detected is assigned to the residual surface carbonate salts that is from materials synthesis and/or during storage. A substantial increase of CO₂ content is found when the electrodes are further polarized, which is due to the accelerated reaction between electrolyte and the released oxygen from NMC76 lattice. For polycrystalline NMC76, CO₂ induced by the interfacial side reaction occurs at as early as ca. 4.25 V (vs. Li/Li⁺), much lower than that of single crystal NMC76 (after 4.4 V). Even for single crystals, there is a sharp increase of CO₂ generation rate beyond 4.4 V. In both cases, a trace amount of CO is also detected, which is accompanied by the generation of CO₂ and aligns well with the trend of CO₂ evolution (Figure X.4.2b,c). The almost simultaneous evolution of CO₂/CO is a good indicator of O release from lattice which chemically reacts with the electrolyte producing CO₂ and CO concurrently. [5] O₂ is also found to evolve at 4.5 V and 4.7 V, for polycrystalline and single crystal NMC76, respectively, indicating that part of O escaped from NMC76 lattice recombines to O₂ gas. The signal of H₂ is ignorable in the background noise until beyond 4.7 V (for polycrystalline NMC76) or 4.8 V (for single crystal NMC76). During charge, solvent such as ethylene carbonate is vigorously oxidized to produce protic species R-H⁺, which are reduced on the anode side promoting H₂ evolution. [6]

The morphological changes of polycrystalline and single crystal NMC76 after the first charge are probed by using Atomic Force Microscope (AFM). As potential increases to 4.5 V, new phase boundaries are immediately found among primary particles of polycrystalline NMC76 (dotted line in Figure X.4.2d), while single crystal NMC76 shows almost no change (Figure X.4.2e). But at a high voltage e.g., 4.9 V, gliding within individual single crystal is seen. Because most practical cells will not go beyond 4.5 V, single crystal NMC76 will have minimum increase of new phase boundaries or surface areas within the regular electrochemical window. Figure X.4.2f summarizes gas generation from two different NMC76 crystals. A higher electrochemical driving force is generally needed for gas generation in cells consisting of single crystals, compared to those with polycrystalline NMC76, suggesting the enhanced safety nature of single crystal Ni-rich NMC cathode.

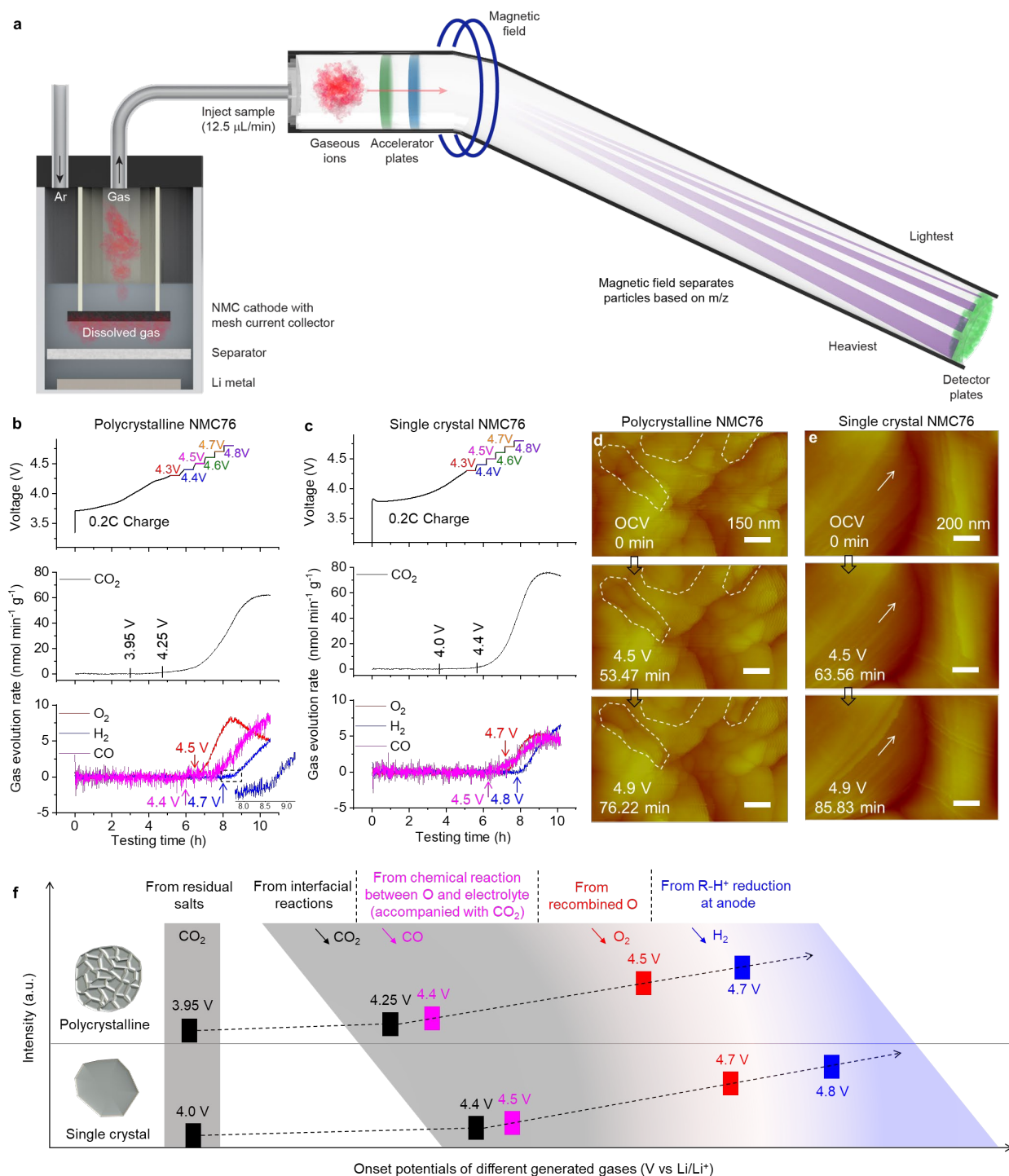


Figure X.4.2 Scheme for *in situ* DEMS, gas analysis and surface morphology evolution of polycrystalline and single crystal NMC76. (a) Illustration of *in situ* DEMS system. (b, c) Gas evolution during the potential stepping procedures as a function of potential applied on the cells consisting of (b) polycrystalline NMC76 and (c) single crystal NMC76. The cells are firstly charged to 4.3 V. From 4.3 to 4.8 V, the potentials applied on the cells are gradually elevated with a step size of 0.1 V and held for 0.5 hour at each potential. Upper panels in (b) and (c): cell voltage vs. time. central panels in (b) and (c): CO_2 evolution rate measured by *in situ* DEMS. lower panels in (b) and (c): gas evolution rates for O_2 , H_2 and CO . (d, e) Microstructural evolution of (d) polycrystalline NMC76 and (e) single crystal NMC76 captured by *in situ* AFM in a functioning electrochemical cell charged to 4.9 V. (f) Summary of gas generation when charging cells consisting of polycrystalline and single crystal NMC76.

Conclusions

The particle size of single crystal NMC76 has been successfully reduced to ca. 2 μm through synthesis modification and element doping. The gliding and microcracking issue, found in the single crystals reported earlier, has been largely eliminated in the downsized single crystals that demonstrate enhanced cycling stability. After 300 cycles, a capacity retention of 73.3% has been displayed in full cells consisting of high mass loading single crystal NMC76. A quantifiable comparison has been conducted to understand the origin and evolution of different gases, i.e., CO_2 , CO , O_2 , and H_2 , generated from cells consisting of polycrystalline and single crystal Ni-rich NMC. A higher electrochemical driving force is always needed to trigger gas generation from single crystals than from polycrystalline NMC76. The drastically reduced number of phase boundaries and oxygen deficiency in single crystals alleviates interfacial side reactions, mitigates gas generation and extends stable cycling of Ni-rich NMC cathode materials.

Key Publications

1. J. Hu, B. Wu, S. Chae, J. Lochala, Y. Bi, J. Xiao, "Achieving highly reproducible results in graphite-based Li-ion full coin cells", *Joule*, **2021**, 5, 1–5.
2. J. Hu, L. Li, E. Hu, S. Chae, H. Jia, T. Liu, B. Wu, Y. Bi, K. Amine, C. Wang, J.-G. Zhang, J. Tao, J. Xiao, "Mesoscale-architecture-based crack evolution dictating cycling stability of advanced lithium ion batteries", *Nano Energy*, **2021**, 79, 105420.

References

1. Bommel, Andrew van, and J. R. Dahn. 2009. "Synthesis of Spherical and Dense Particles of the Pure Hydroxide Phase $\text{Ni}_{1/3}\text{Mn}_{1/3}\text{Co}_{1/3}(\text{OH})_2$." *Journal of The Electrochemical Society* 156 (5). doi: 10.1149/1.3079366.
2. Lee, M. H., Y. J. Kang, S. T. Myung, and Y. K. Sun. 2004. "Synthetic optimization of $\text{Li}[\text{Ni}_{1/3}\text{Co}_{1/3}\text{Mn}_{1/3}]\text{O}_2$ via co-precipitation." *Electrochimica Acta* 50 (4):939–948. doi: <https://doi.org/10.1016/j.electacta.2004.07.038>.
3. Jung, Roland, Robert Morasch, Pinar Karayaylali, Katherine Phillips, Filippo Maglia, Christoph Stinner, Yang Shao-Horn, and Hubert A. Gasteiger. 2018. "Effect of Ambient Storage on the Degradation of Ni-Rich Positive Electrode Materials (NMC811) for Li-Ion Batteries." *Journal of The Electrochemical Society* 165 (2):A132–A141. doi: 10.1149/2.0401802jes.
4. Bi, Yujing, Jinhui Tao, Yuqin Wu, Linze Li, Yaobin Xu, Enyuan Hu, Bingbin Wu, Jiangtao Hu, Chongmin Wang, Ji-Guang Zhang, Yue Qi, and Jie Xiao. 2020. "Reversible planar gliding and microcracking in a single-crystalline Ni-rich cathode." *Science* 370:1313–1317. doi: 10.1126/science.abc3167.
5. Wandt, Johannes, Anna T. S. Freiberg, Alexander Ogrodnik, and Hubert A. Gasteiger. 2018. "Singlet oxygen evolution from layered transition metal oxide cathode materials and its implications for lithium-ion batteries." *Materials Today* 21 (8):825–833. doi: 10.1016/j.mattod.2018.03.037.
6. Metzger, Michael, Benjamin Strehle, Sophie Solchenbach, and Hubert A. Gasteiger. 2016. "Origin of H_2 evolution in LIBs: H_2O reduction vs. electrolyte oxidation." *Journal of The Electrochemical Society* 163 (5):A798–A809. doi: 10.1149/2.1151605jes.

Acknowledgements

We thank Dr. Jiangtao Hu and Dr. Yujing Bi for their contributions to this project.

X.5 Fluorinated Deep Eutectic Solvent (FDES)-Based Electrolytes (ANL)

Zhengcheng (John) Zhang, Principal Investigator

Argonne National Laboratory
9700 South Cass Avenue, B200
Lemont, IL 60439
E-mail: zzhang@anl.gov

Peter Faguy, DOE Technology Development Manager

U.S. Department of Energy
E-mail: Peter.Faguy@ee.doe.gov

Start Date: October 1, 2019

End Date: September 30, 2023

Project Funding (FY21): \$400,000

DOE share: \$400,000

Non-DOE share: \$0

Project Introduction

The lithium-ion battery (LIB) is widely used in the devices supporting our digital and mobile lives; however, the LIB's adoption in electric vehicles (EVs) and more strategically smart grid applications has been limited by its energy density, high cost, and safety concerns. [1],[2],[3],[4] Battery electrode materials with high theoretical capacity and high voltage are critical components and always desired for advancing the technology, and such battery materials for next-generation applications in electric vehicles have been reported in recent years. [5],[6],[7] However, new challenges arise from the non-aqueous electrolytes because the carbonate-based electrolytes are thermodynamically instable on charged cathode at voltages higher than 4.3 V vs Li⁺/Li, [8],[9],[10] and these electrolytes are extremely reactive with the conversion-type, high-capacity anode such as silicon (Si), which leads to rapid deterioration in battery cycling performance. [11],[12],[13] Furthermore, there is severe safety concern of this highly flammable electrolyte due to the presence of highly volatile organic carbonate solvents. Due to its many advantages such as high conductivity, high electrochemical stability, and good passivation of the Al current collector, lithium hexafluorophosphate (LiPF₆) is still the dominating electrolyte salt in state-of-the-art electrolytes despite its thermal and chemical instability. Transition metal (TM) dissolution in the electrolyte and crosstalk with the anode have been widely reported for the high-voltage system; the reasons for these to occur have been ascribed to the cathode surface structure transformation and reconstruction. Nevertheless, even the pristine oxide cathode is in contact with the electrolyte, TM ions, for example Mn²⁺ dissolves simultaneously in the electrolyte due to the reaction of the weak acid HF, the hydrolysis product of LiPF₆ with a trace amount of moisture in the electrolyte, with oxide surface layer. [14],[15],[16],[17],[18] In both cases, diffusion and deposition of TM (mainly Mn²⁺) on the anode side catalyzes the parasitic reactions, leading to active lithium loss and rapid capacity fade of the cell. [17],[19],[20],[21] Therefore, demand is great for a new electrolyte that could enable the reversible and rapid positive/negative redox reactions and thus advance next-generation, high-voltage, high-energy LIB technology.

Objectives

The objective of this project is to develop fluorinated deep eutectic solvent (FDES, also called fluorinated ionic liquid-based aprotic electrolytes)-based electrolytes as new high voltage electrolytes to address the high reactivity of conventional organic electrolyte at the surface of the charged cathode and the safety concern associated with the organic electrolyte. The FDES are designed to provide thermodynamic stability on the charged cathode surface affording a stabilized cathode/electrolyte interface and should be highly compatible with anode including graphite and Si. The FDES is a new room-temperature molten salt comprising of new fluorinated organic cations and new fluorinated organic anions with a wide liquid window. FDES has superior thermal stability with no vapor pressure even heated to 300–400°C, and excellent fluidity at temperature lower

than -20°C . Not only high performance, the FDES are non-flammable with significantly enhanced safety characteristic.

Approach

To solve the low conductivity and high viscosity issue of FDES electrolyte, an aqueous-organic hybrid electrolyte containing an ionic liquid N-methyl-N-propyl-piperidinium bis(fluorosulfonyl)imide was developed. Due to its tolerance to moisture and environment, the use of this electrolyte eliminates the critical environmental control employed for the state-of-the-art (SOA) electrolyte, electrode and cell fabrication thus reduces the cost of the battery mass production. Furthermore, this electrolyte addresses the most critical technical challenges associated with the EV batteries *i.e.*, low energy density, safety, and high cost. In this paper, the benefits of this hybrid electrolyte were demonstrated for the first time in a high energy cell comprising a Ni-rich $\text{LiNi}_{0.5}\text{Mn}_{0.3}\text{Co}_{0.2}\text{O}_2$ (NMC532) as cathode coupled with a low potential lithium metal as anode.

Moreover, the physical and electrochemical properties could be systematically tuned by changing the structures of cations or anions. We have synthesized and evaluated two new ILs with fluorine and fluorinated alkyl functionalized cations, *i.e.*, 1-methyl-1-propyl-3-fluoropyrrolidinium bis(fluorosulfonyl)imide (PMpyr-FSI) and 1-methyl-1-(2,2,3,3,3-pentafluoropropyl)pyrrolidinium bis(fluorosulfonyl)imide (P₅FMPyr-FSI). Solvent purity is also critical for good cycling performance of Li-ion batteries. Different from the traditional synthesis method for ionic liquid, a facile one-step route was adopted for the FDES synthesis, which affords these materials with extremely high purity.

Results

Room temperature ionic liquids (IL) comprising a bis(sulfonyl)imide anion, *i.e.*, bis(trifluoromethanesulfonyl)imide (TFSI-) or bis(fluorosulfonyl)imide (FSI-) and an organic cation, *i.e.*, ammonium, pyrrolidinium and imidazolium have been widely studied as alternative liquid electrolytes for SOA carbonate/LiPF₆ electrolyte. Addition of trace amount of H₂O into LiPF₆-based electrolyte could readily hydrolyze and form HF. Although there is report showing the HF could lead to LiF-rich SEI on Li metal surface and thus suppress Li dendrite, the etching of transition oxide from HF could be detrimental. Differing from the labile P-F bond in PF₆⁻ anion, the C-F and S-F bonds in TFSI- and FSI- anions are more resistive to hydrolyzation in the presence of water, and thus eliminate the side impact caused by the LiPF₆ hydrolysis making it an ideal water-tolerate electrolyte. A few recent studies reported that addition of H₂O into IL electrolytes didn't interfere with Li or Na metal stripping and deposition process. However, no in-depth understanding on how the water molecules could be stabilized in the IL bulk and its dynamic distribution on the metal surface; no demonstration of the practicality of the reported electrolytes in a $\text{Li}_{1-x-y-z}\text{Ni}_x\text{Mn}_y\text{Co}_z\text{O}_2$ /lithium metal cell.

Table X.5.1 Ionic Conductivity and Viscosity of 1 M and 5 M LiFSI-PMpipFSI Electrolytes with Different H₂O Concentrations (in mol/L and ppm).

1 M LiFSI-PMpipFSI ^a				5 M LiFSI-PMpipFSI ^a			
H ₂ O Concentration		Conductivity ^b (S cm ⁻¹)	Viscosity (cP @ RT)	H ₂ O Concentration		Conductivity ^b (S cm ⁻¹)	Viscosity (cP @ RT)
[mol/L]	ppm ^c			[mol/L]	ppm ^c		
5 M	56,279	8.58 x10 ⁻³	35.6	5 M	38,339	1.73 x10 ⁻³	170.4
2 M	23,298	3.36 x10 ⁻³	67.3	2 M	15697	0.81 x10 ⁻³	373.3
1 M	11,787	3.21 x10 ⁻³	92.5	1 M	7,911	0.61 x10 ⁻³	589.6
0.2 M	2,380	2.45 x10 ⁻³	121.8	0.2 M	1592	0.51 x10 ⁻³	811.0
0 M	-	2.24 x10 ⁻³	133.5	0 M	-	0.35 x10 ⁻³	936.6

Same as SOA carbonate/LiPF₆ electrolyte, N-methyl-N-propyl-piperidinium bis(fluorosulfonyl)imide (PMpipFSI)-LiFSI electrolyte is highly hygroscopic and readily absorbs 20,000 ppm moisture when exposed to air for 12 hours with relative low humidity. To precisely control the absorbed water amount, various amount of water was added to the 1 M and 5 M LiFSI-PMpipFSI electrolyte. Table X.5.1 summarizes the physical properties of these water-containing electrolytes. The viscosity of 1 M LiFSI-PMpipFSI significantly decreases from 133.5 cP to 92.5 cP when 1.0 M water is present, and conductivity increases with increasing amount of water by a less degree. Similar trend is observed for the 5 M electrolyte. 5 M LiFSI-PMpipFSI electrolyte achieves a maximum conductivity of $1.73 \times 10^{-3} \text{ S cm}^{-1}$ when 5.0 M water is added, a five-time increase from the water free sample. The viscosity decreases 5.5 times to 170.4 cP with 5.0 M H₂O and 1.6 times to 589.6 cP with 1.0 M H₂O. Figure X.5.1 summarizes the conductivity dependence on temperature. It is manifest that presence of water helps reduce the viscosity and improve the conductivity, one of the major technical barriers preventing the practical application of PMpipFSI electrolyte.

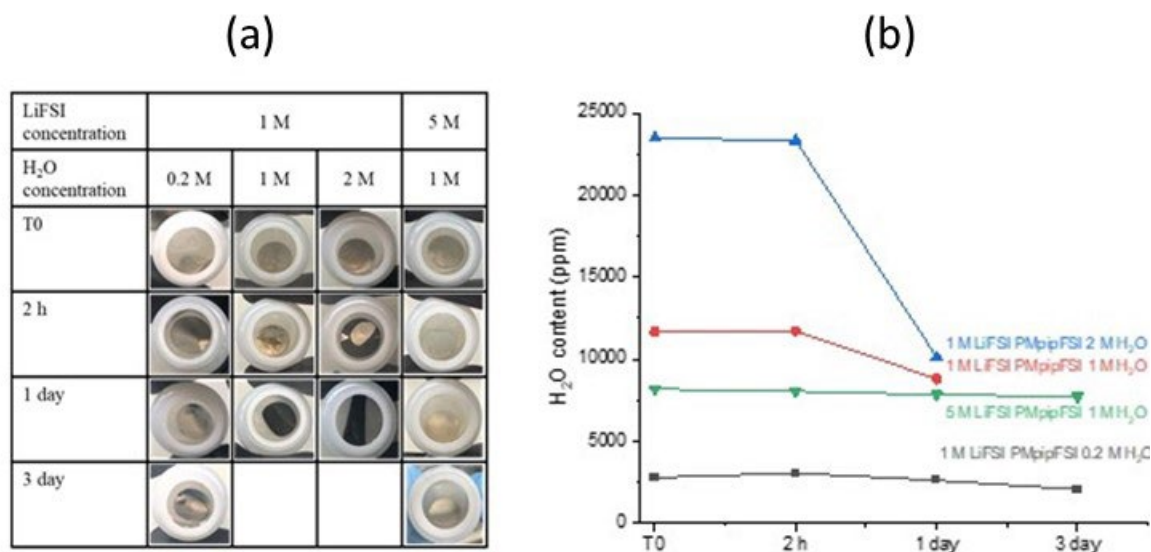


Figure X.5.1 Chemical stability with lithium metal anode for 1 M and 5 M LiFSI-PMpipFSI electrolyte containing 0.2 M, 1 M, and 2 M H₂O, respectively. (a) Lithium anode in water-containing electrolytes at various period of time; (b) moisture content vs immerse time.

Chemical stability of water-containing electrolytes was evaluated by immersing a piece of Li metal into the electrolytes. The changes of Li anode surface and remaining H₂O content was monitored over time. As shown in Figure X.5.1, for 1 M LiFSI electrolytes, with low H₂O amount of 0.2 M, the Li surface remains unchanged over 3 days and the H₂O amount slightly decrease suggesting slow reaction between H₂O with Li metal. As H₂O concentration increases from 0.2 M to 1 M and 2 M, the dark Li surface was readily observed after only 2 h and Li turned to completely black over 24 h, along with a sudden decrease in H₂O amount of the electrolyte (Figure X.5.1b). In contrast, when Li metal is immersed in high concentration 5 M LiFSI-PMpipFSI with 1 M H₂O, it doesn't show any sign of darkness over an extended period of time and no substantial H₂O decrease was measured, suggesting high Li salt concentration stabilizes the lithium with at least 1 M H₂O in the electrolyte.

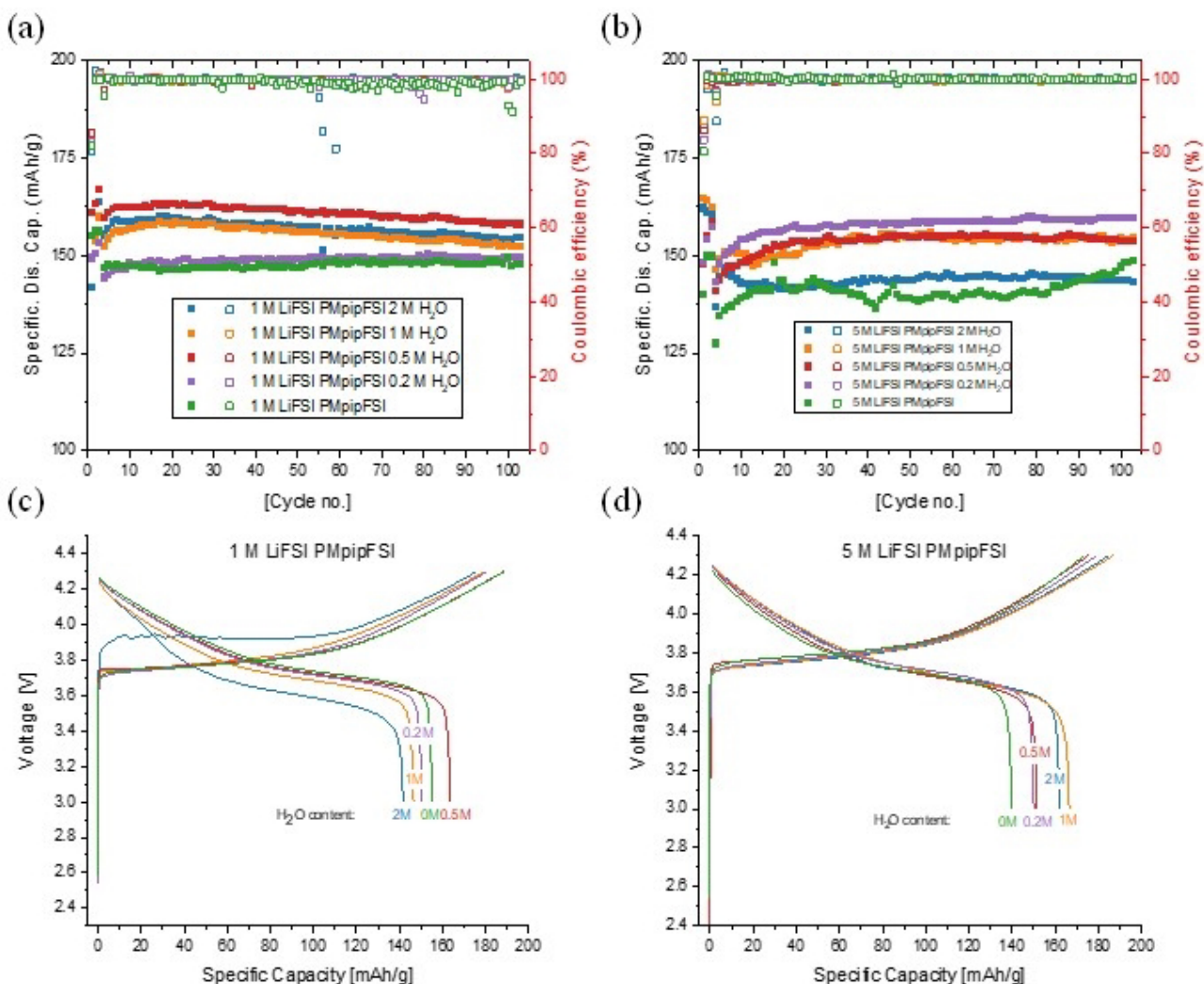


Figure X.5.2 Cycling performance and first cycle voltage profiles of NMC532/Li cell with water-containing electrolytes. (a), (c) 1 M LiFSI-PMpipFSI with various H₂O contents and (b), (d) 5 M LiFSI-PMpipFSI with various H₂O contents.

Electrochemical performance of the water-containing electrolytes was evaluated in NMC532/Li cell with a cutoff voltage of 4.3–3.0 V. Water-free 1 M LiFSI-PMpipFSI shows stable cycling performance with no capacity fade in 100 cycles as shown in Figure X.5.2a. When water was added, the cell capacity was elevated due to the low viscosity and high conductivity of the electrolytes. Electrolyte with 0.2 M H₂O (2380 ppm) showed no difference in capacity and retention compared with water-free one. Further increase H₂O

concentration from 0.2 M to 1.0 M (11,787 ppm) afforded an even higher initial capacity due to its higher conductivity without performance deterioration. Note that with the same 1 M water content, the cell using the SOA electrolyte fails rapidly. For super concentrated 5 M LiFSI-PMpipFSI, low concentration H₂O, *i.e.*, 0.2 M and 0.5 M didn't show difference in cycling performance compared with 1 M LiFSI-PMpipFSI with same amount of water. However, with higher amount 1.0 M H₂O, the cell achieved the highest 1st cycle Coulombic efficiency of 89.1%, a value that is even higher than that of the water-free cell, and capacity retention (Figure X.5.2b). Further increase water concentration to a tremendously high level of 2 M, the cell still didn't show degradation until an extremely high level of 5 M H₂O where the cell started to fail, indicating the excess water is not stable which participates the parasitic reaction at the electrode surface. Figure X.5.2c and Figure X.5.2d show the 1st cycle cell voltage profile for various water-containing electrolytes.

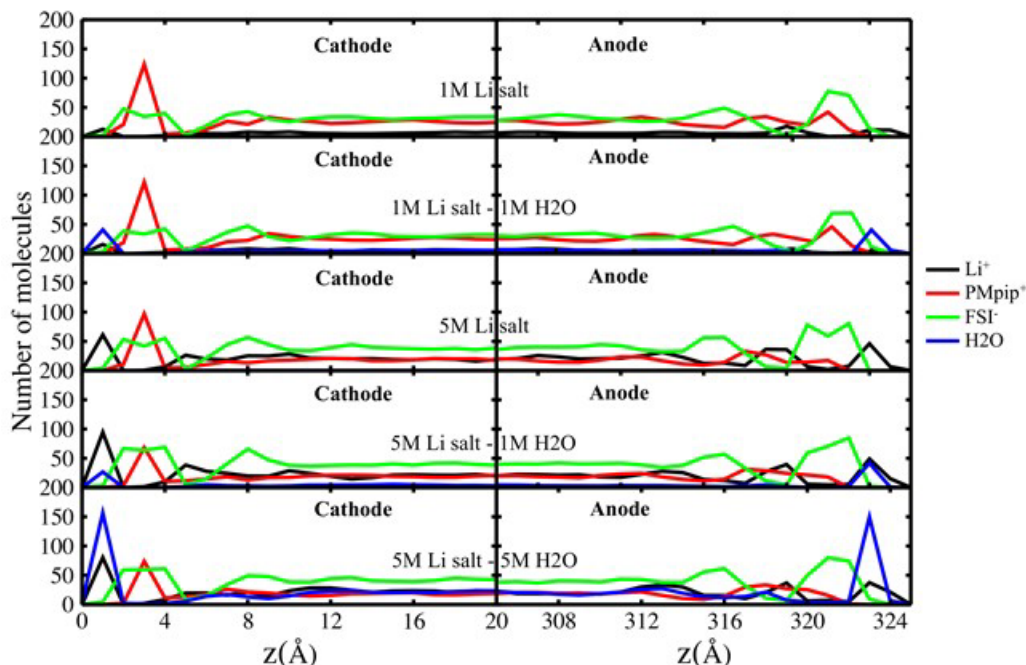


Figure X.5.3 Molecular number density profiles along the z -axis normal to the surface of NMC cathode (left panels) and lithium anode (right panels). Center of mass of each molecule is used to calculate molecule distribution. On both electrodes, a tight adsorption layer of H₂O-Li⁺ is followed by an ordered layer of PMpipFSI. The thickness of H₂O-Li⁺ layer on each electrode surface is ~ 2 Å at all H₂O concentrations studied here.

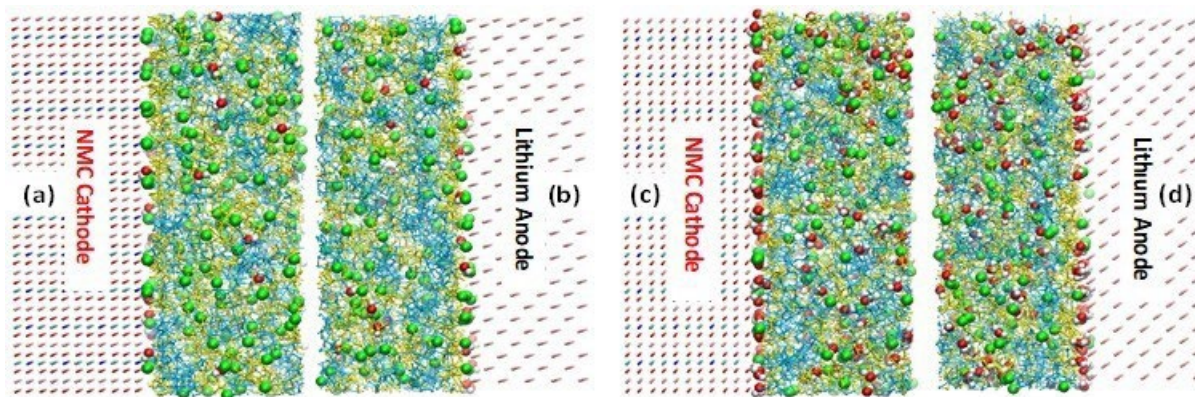


Figure X.5.4 Snapshots of layering of H₂O-Li⁺-IL on NMC cathode surface (a), (c) and Li anode surface (b, d) at concentration of 5 M LiFSI-PMpipFSI with 1 M and 5 M H₂O, respectively. On both electrodes, there is a tight adsorption layer of H₂O-Li⁺ (O, red; Li, green) followed by an ordered layer of IL (cation, cyan; anion, yellow).

Figure X.5.3 illustrates a monolayer of $\text{H}_2\text{O}-\text{Li}^+$ adsorbed on both electrode surfaces followed by IL layer for 5 M LiFSI-PMpipFSI with 1 M and 5 M H_2O . It is manifest that for 1 M H_2O , Li^+ ions dominate the $\text{H}_2\text{O}-\text{Li}^+$ adsorption layer at electrode surfaces, while for 5 M H_2O , H_2O molecules dominate the adsorption layer. As shown in Figure X.5.4, the 1 M H_2O significantly boost Li^+ distribution at high concentration 5 M LiFSI at NMC532 surface (no considerable impact at anode) compared to H_2O free electrolyte, offering another perspective to investigate Li^+ transport enhancement. At the cathode surface the cation-anion of PMpipFSI exhibits strong ordering, which yields dense molecular packing and high energy barrier for Li^+ transport and interprets the vanishing Li^+ density at the layer of 2 – 4 Å above the cathode surface. Likewise, at lithium anode surface the strong ordering of FSI⁻ also results in a layer of ~2 – 4 Å with vanishing Li^+ density. 1 M H_2O content considerably weakens the PMpip⁺ ordering and therefore lowers kinetic barrier for Li^+ transport between cathode surface and electrolyte bulk. In charging phase, as the source of charge carrier transport, higher Li^+ density at cathode interface indicates enhanced carrier flux through electrolyte bulk. Likewise, in discharging phase, dense Li^+ assembly at cathode surface facilitates ion intercalation. The above analysis exhibits a qualitative picture for Li^+ transport at electrode interface, while a quantitative investigation for the kinetic behavior of Li^+ at electrode interface is our ongoing research.

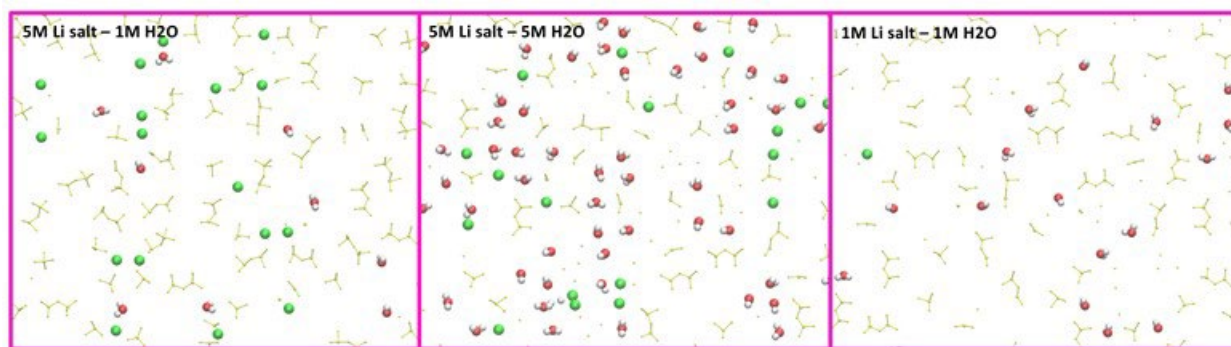


Figure X.5.5 Water clustering of the $\text{H}_2\text{O}-\text{Li}^+$ (green) adsorption layer at anode surface. The FSI anions (yellow), which marginally overlap with the $\text{H}_2\text{O}-\text{Li}^+$ adsorption layer is also shown. At concentration of 5 M LiFSI with 1 M H_2O , there is no water clustering; at concentration of 5 M Li salt and 5 M H_2O , strong water clustering is observed; at concentration of 1M Li salt and 1 M H_2O , weak water clustering can be seen. Nearest oxygen-oxygen (O-O) contact distance calculation is used to estimate size of water clusters.

The O-O contact is set as 6.0 Å for concentration of 5 M Li salt and 1 M H_2O , 4.0 Å for concentration of 5 M Li salt and 5 M H_2O , and 6.0 Å for concentration of 1 M Li salt and 1 M H_2O , respectively. In the above three lithium salt-water concentrations, the most probable size of water cluster is 1, 8 and 4, respectively.

However, it is recognized that excessive adsorption H_2O molecules at electrode surface tend to induce eruptive reaction with its dissociation and solvation ability. H_2O dissociation involves one hydronium ion (essentially one water molecule attached with a proton) and one hydroxide in hydrogen bond distance (2 Å). The associated H_2O molecules provide solvation shell of catalysis while the hydroxides can directly participate reactions, and therefore surface H_2O clustering needs to be quantified to correlate water structure with electrode/electrolyte interface stability. Water cluster analysis based on MD trajectories indicates that high concentration lithium salts effectively inhibit the dissociation of surface water at low concentration, by disrupting water clustering of the adsorption layer. Due to the strong electrostatic interactions with high concentration (5 M) Li^+ , there is no water cluster observed when 1 M H_2O is present, as illustrated in Figure X.5.5. Such ‘isolated’ water molecule is not reactive and has no solvation ability either, and applies negligible perturbation to the Li^+ -FSI-PMpip⁺ layering structure at interface. However, with 5 M H_2O concentration, strong water clustering can be seen, indicating a reactive surface water layer that can induce severe instability at electrode/electrolyte interface.

Conclusions

Moisture is prohibited in the SOA carbonate/ LiPF_6 electrolyte due to its adverse effect on the battery performance. In this work, we demonstrated that piperidinium-based ionic liquid electrolytes can accommodate large content of water (up to 1 M) and showed exceptional stability on both NMC cathode and

lithium metal anode. The hybrid electrolyte is immune to the environment/moisture which eliminates the stringent control for electrolyte formulation, storage, and transportation. It also facilitates the mass production process and reduces the cost of the battery. MD simulations shed light on the underpinned mechanism that with high LiFSI concentration, low H₂O content (≤ 1 M) is essentially stabilized at electrode interfaces and electrolyte bulk due to the tight interaction with Li⁺; while at low Li salt concentration the H₂O molecules readily form large clusters in the bulk and yields a reactive surface water layer that induces severe instability of electrode/electrolyte interface. Simulations results also confirm that for the high LiFSI salt, low concentration H₂O significantly enhances Li⁺ distribution at NMC surface while decreases the ordering of IL and therefore facilitates charge carrier transport at cathode/electrolyte interface, explaining the high-rate capability of the water-containing electrolyte.

Key Publications

1. **Liu, Q.;** Jiang, W.; Yang, Z. Z.; Zhang, Z. C. “An Environmentally Benign Electrolyte for High Energy Lithium Metal Batteries” *ACS Appl. Mater. Interfaces*. 2021, in press.
2. **Liu, Q.;** Hsu, C. W.; Dzwiniel, T. L.; Pupek, K. Z.; Zhang, Z. C. “A fluorine-substituted pyrrolidinium-based ionic liquid for high-voltage Li-ion battery” *Chem. Comm.* 2020, 56, 7317–7320.
3. **Liu, Q.;** Jiang, W.; Piernas-Muñoz, M. J.; Liu, Y. Z.; Yang, Z. Z.; Bloom, I.; Dzwiniel, T. L.; Li, Y.; Pupek, K. Z.; Zhang, Z. C. “Stabilized Electrode/Electrolyte Interphase by a Saturated Ionic Liquid Electrolyte for High-Voltage NMC532/Si-Graphite Cells” *ACS Appl. Mater. Interfaces*. 2020, 12, 23035.

References

1. Armand, M.; Tarascon, J. M., Building Better Batteries. *Nature* 2008, 451 (7179), 652–657.
2. Goodenough, J. B.; Park, K.-S., The Li-Ion Rechargeable Battery: A Perspective. *J. Am. Chem. Soc.* 2013, 135 (4), 1167–1176.
3. Nitta, N.; Wu, F.; Lee, J. T.; Yushin, G., Li-Ion Battery Materials: Present and Future. *Mater. Today* 2015, 18 (5), 252–264.
4. Li, M.; Lu, J.; Chen, Z.; Amine, K., 30 Years of Lithium-Ion Batteries. *Adv. Mater.* 2018, 30 (33), 1800561.
5. Tarascon, J. M.; Armand, M., Issues and Challenges Facing Rechargeable Lithium Batteries. *Nature* 2001, 414 (6861), 359–367.
6. Thackeray, M. M.; Wolverton, C.; Isaacs, E. D., Electrical Energy Storage for Transportation—Approaching the Limits of, and Going Beyond, Lithium-Ion Batteries. *Energy Environ. Sci.* 2012, 5 (7), 7854–7863.
7. Chen, S.; Wen, K.; Fan, J.; Bando, Y.; Golberg, D., Progress and Future Prospects of High-Voltage and High-Safety Electrolytes in Advanced Lithium Batteries: From Liquid to Solid Electrolytes. *J. Mater. Chem. A* 2018, 6 (25), 11631–11663.
8. Li, Q.; Chen, J.; Fan, L.; Kong, X.; Lu, Y., Progress in Electrolytes for Rechargeable Li-Based Batteries and Beyond. *Green Energy & Environment* 2016, 1 (1), 18–42.
9. Yang, H.; Zhuang, G. V.; Ross, P. N., Thermal Stability of Lipf6 Salt and Li-Ion Battery Electrolytes Containing Lipf6. *J. Power Sources* 2006, 161 (1), 573–579.
10. Campion, C. L.; Li, W.; Lucht, B. L., Thermal Decomposition of Lipf6-Based Electrolytes for Lithium-Ion Batteries. *J. Electrochem. Soc.* 2005, 152 (12), A2327.

11. Plakhotnyk, A. V.; Ernst, L.; Schmutzler, R., Hydrolysis in the System Lipf6—Propylene Carbonate—Dimethyl Carbonate—H₂O. *J. Fluorine Chem.* 2005, 126 (1), 27–31.
12. Kim, J.; Lee, J. G.; Kim, H.-s.; Lee, T. J.; Park, H.; Ryu, J. H.; Oh, S. M., Thermal Degradation of Solid Electrolyte Interphase (Sei) Layers by Phosphorus Pentafluoride (P_f5) Attack. *J. Electrochem. Soc.* 2017, 164 (12), A2418–A2425.
13. Wilken, S.; Treskow, M.; Scheers, J.; Johansson, P.; Jacobsson, P., Initial Stages of Thermal Decomposition of Lipf6-Based Lithium-Ion Battery Electrolytes by Detailed Raman and Nmr Spectroscopy. *RSC Adv.* 2013, 3 (37), 16359–16364.
14. Campion, C. L.; Li, W.; Lucht, B. L., Thermal Decomposition of Lipf[Sub 6]-Based Electrolytes for Lithium-Ion Batteries. *J. Electrochem. Soc.* 2005, 152 (12), A2327.
15. Zhan, C.; Wu, T.; Lu, J.; Amine, K., Dissolution, Migration, and Deposition of Transition Metal Ions in Li-Ion Batteries Exemplified by Mn-Based Cathodes – a Critical Review. *Energy Environ. Sci.* 2018, 11 (2), 243–257.
16. Vetter, J.; Novák, P.; Wagner, M. R.; Veit, C.; Möller, K. C.; Besenhard, J. O.; Winter, M.; Wohlfahrt-Mehrens, M.; Vogler, C.; Hammouche, A., Ageing Mechanisms in Lithium-Ion Batteries. *J. Power Sources* 2005, 147 (1), 269–281.
17. Gilbert, J. A.; Shkrob, I. A.; Abraham, D. P., Transition Metal Dissolution, Ion Migration, Electrocatalytic Reduction and Capacity Loss in Lithium-Ion Full Cells. *J. Electrochem. Soc.* 2017, 164, A389.
18. Banerjee, A.; Shilina, Y.; Ziv, B.; Ziegelbauer, J. M.; Luski, S.; Aurbach, D.; Halalay, I. C., On the Oxidation State of Manganese Ions in Li-Ion Battery Electrolyte Solutions. *J. Am. Chem. Soc.* 2017, 139, 1738.
19. Zheng, L.-Q.; Li, S.-J.; Lin, H.-J.; Miao, Y.-Y.; Zhu, L.; Zhang, Z.-J., Effects of Water Contamination on the Electrical Properties of 18650 Lithium-Ion Batteries. *Russ. J. Electrochem.* 2014, 50 (9), 904–907.
20. Wu, X.; Ruan, D.; Tan, S.; Feng, M.; Li, B.; Hu, G., Effect of Stirring Environment Humidity on Electrochemical Performance of Nickel-Rich Cathode Materials as Lithium-Ion Batteries. *Ionics* 2020, 26 (11), 5427–5434.
21. Li, J.; Daniel, C.; An, S. J.; Wood, D., Evaluation Residual Moisture in Lithium-Ion Battery Electrodes and Its Effect on Electrode Performance. *MRS Advances* 2016, 1 (15), 1029–1035.

Acknowledgements

Support from Peter Faguy, Mallory Clites and David Howell at Vehicle Technologies Office (VTO), Office of Energy Efficiency and Renewable Energy, U.S. Department of Energy is gratefully acknowledged. Argonne, a U.S. Department of Energy laboratory, is operated by UChicago Argonne, LLC under contract DE-AC02-06CH11357.

X.6 Developing *In situ* Microscopies for the Model Cathode/Electrolyte Interface (NREL)

Robert C. Tenent, Principal Investigator

National Renewable Energy Laboratory
16253 Denver West Parkway
Golden, CO 80401
E-mail: robert.tenent@nrel.gov

Peter Faguy, DOE Technology Development Manager

U.S. Department of Energy
E-mail: Peter.Faguy@ee.doe.gov

Start Date: October 1, 2018

End Date: September 30, 2022

Project Funding (FY21): \$336,000

DOE share: \$336,000

Non-DOE share: \$0

Project Introduction

The work presented here focuses on the development of new diagnostic techniques based on the scanning electrochemical microscope (SECM) to examine cell degradation processes occurring at the cathode/electrolyte interface. While lithium-ion batteries have developed significant market traction, key issues remain to be resolved for more broad adoption including developing a better understanding of degradation processes that limit cell life. Many commonly used cathode materials are known to degrade through various processes (transition metal dissolution and oxygen evolution, as examples). Products of this degradation are also known to diffuse through the cell and deposit at the anode SEI leading to performance loss. While these processes are known to occur, many open questions remain regarding the exact mechanisms by which they take place. As an example, while dissolution of manganese from cathode materials has been extensively studied, debate remains even regarding the oxidation state of Mn generated in the dissolution process. [1] This effort focuses on using the SECM format paired with complementary analytical techniques to detect and characterize cathode degradation products at and near to an active cathode/electrolyte interface

Objectives

This project seeks to employ SECM paired with complementary analytical techniques to study degradation processes occurring at the cathode/electrolyte interface. Specifically, we study degradation products evolving from a model LiMn_2O_4 (LMO) cathode. We examine the impact of varied parameters on the degradation process as well as the properties of the resulting products. This will help develop understanding not only of how these degradation processes occur, but how degradation products may react elsewhere in the cell driving overall performance degradation.

Approach

The SECM is a scanning probe microscope which uses a small electrode to conduct electrochemical experiments near an active electrode/electrolyte interface. Figure X.6.1 shows a schematic of a typical SECM instrument which includes two working electrodes consisting of the small “tip” electrode as well as the underlying substrate sample. In the case of this work, the substrate would be a model cathode material under study. All electrodes are contained in an active electrochemical cell containing an electrolyte of interest. The tip and substrate electrode voltages are controlled by a bi-potentiostat using the same reference and counter electrodes. This configuration allows independent control of electrode voltages for both the substrate sample and the “sensing” tip electrode. This allows the tip to be used to conduct a variety of electrochemical experiments either in bulk electrolyte or near the substrate which can be held at a variety of voltages. A three-axis positioning system is used to place the tip electrode at various locations in the cell and across the substrate surface for measurements as required.

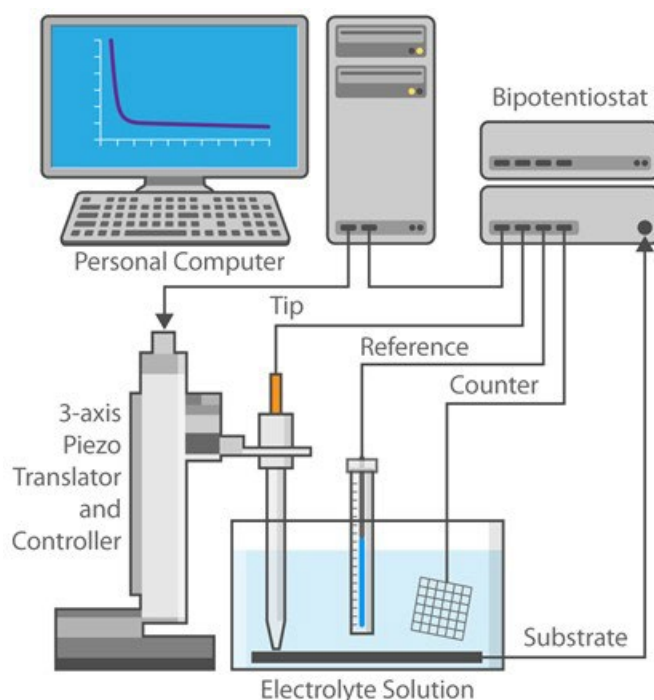


Figure X.6.1 Schematic of a typical scanning electrochemical microscopy / Al Hicks, NREL

The SECM can be employed in a variety of so-called “modes” which can be categorized broadly as imaging modes (as implied by the name of the technique) or as measurement modes. The work here focuses on applying SECM measurement modes to better understand cathode degradation products and their reactivity. In our case, we work with the “generation/collection” (GC) mode of SECM in which species generated at the substrate are detected or “collected” at the tip electrode. This approach is conceptually similar to the rotating ring disk electrode (RRDE) method commonly used in electrochemical characterization in which a species is generated at a disk electrode and then hydrodynamically driven to a surrounding ring electrode for detection and characterization. The key differentiator between the GC-SECM and RRDE methods is increased flexibility in the experimental conditions that can be used for detection at the tip electrode. In the case of this work, we employ cyclic voltammetry measurements made at the tip to characterize the electrochemical properties of cathode degradation products occurring both near the active cathode/electrolyte interface as well as in bulk electrolyte.

In addition to SECM, we have also employed companion analysis using Inductively Coupled Plasma (ICP) and Electron Paramagnetic Resonance (EPR) spectroscopies to study the concentration and oxidation state of transition metal dissolution products, respectively. We use this combination of techniques to focus on developing a better understanding of the chemistry and electrochemistry associated with Mn dissolution from a model LMO cathode material. This allowed us to study cathode degradation without the complication of conductive additives or binder systems.

Results

Results reported in FY20 were focused on examining the impact of the electrolyte ion on cathode degradation products. This work appeared to show that electrolyte anions with the potential to generate acid in the cell (i.e., ClO_4^- and PF_6^-) led to increased degradation. ICP and EPR studies focused on understanding Mn dissolution in these systems and found increased Mn dissolution with these two anions as compared to the TFSI^- anion which is not expected to lead to acid generation. Furthermore, it appeared that the identity of the anion also correlated to the oxidation state of Mn found following dissolution. Specifically, for the acid generating anions, Mn^{2+} was

detected in the electrolyte after degradation while we appeared to observe Mn^{3+} when studying the TFSI⁻ anion. [2]

In FY21, focus moved toward examining the impact of the carbonate solvents used in the electrolytes. The earlier studies used propylene carbonate (PC) as the electrolyte solvent, in this work we compare to ethylene carbonate (EC). Recent studies have shown a strong interaction between the Mn^{2+} ion and EC as well as the PF_6^- anion. [3] This work appeared to show that the complexes formed by Mn^{2+} , EC and PF_6^- led to a continuous electrolyte degradation process occurring in the cell. We have chosen to explore EC because of those earlier studies as well as EC's common inclusion in present state of the art electrolyte systems. Our experimental work used methods that have been reported previously as a part of this effort and focused on the use of generation/collection scanning electrochemical microscopy (G/C SECM). All studies discussed focus on the LiMn_2O_4 (LMO) system as has been the focus throughout the previous studies also. In the G/C SECM format, a tip electrode, which consisted of either a 10 μm or 25 μm dia. disk ultramicroelectrode embedded in glass, was placed in the SECM cell with a LMO coated stainless steel model cathode material as the substrate. All work was conducted using lithium metal as a quasi-reference as well as counter electrode to mimic a half cell configuration. Upon cell assembly, a cyclic voltammogram (CV) was collected at the tip electrode in the fresh electrolyte. Following this, the LMO substrate was held at 4.5V for various lengths of time after which an additional CV was collected at the tip electrode. The periodic CV data was used to track the electrochemical signature of any species being generated from the LMO degradation process.

Figure X.6.2 shows G/C SECM voltammograms collected in fresh electrolyte as well as after holding the LMO substrate at 4.5V for a total of 5 hours. The figure to the left shows data collected in 1M LiClO_4 in PC while the figure to the right shows data for the same electrolyte salt in EC. The black trace shows initial data collected in fresh electrolyte and the blue trace shows data collected after a five-hour voltage hold. The inset photographs show samples of the electrolyte before and after the voltage hold. Note that features observed in both the EC and PC based electrolytes are similar. The oxidation process observed at $\sim 3.4\text{V}$ is present in both systems and shows a pronounced asymmetry between the oxidation peaks and likely associated reduction peaks. The origin of this asymmetry is still under study presently. There is also a second apparent electron transfer reaction occurring at $\sim 4.5\text{V}$ in both systems. The inset photos show a significant color change following the voltage hold indicating the presence of degradation products. It is noteworthy that the EC sample appears darker and hence likely indicates either an accelerated or a different degradation process compared to the PC system. Further analysis of these post voltage hold electrolytes is pending.

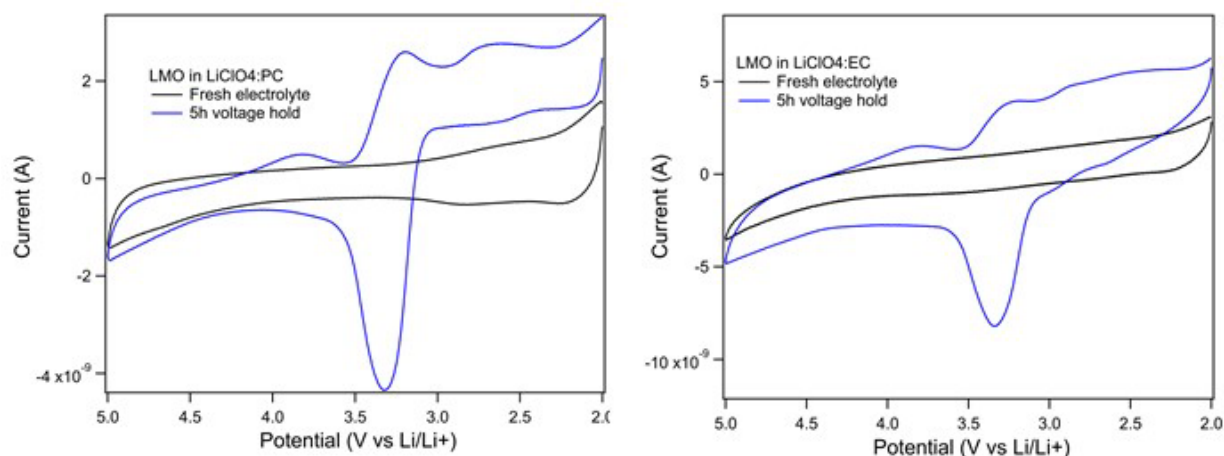


Figure X.6.2 SECM tip voltammograms collected before and after a high voltage hold of a model LMO cathode. Data shown for the 1M LiClO_4 :PC electrolyte on the left in PC and on the right in EC. Inset shows photographs of electrolyte samples pre- and post-voltage hold.

Figure X.6.3 shows the results of the same experimental protocol as above applied to the 1M LiPF₆ in EC system. As before, the black trace shows the initial background scan collected in the fresh electrolyte while the blue trace shows the post voltage hold data. Note that the black trace shows an electron transfer reaction occurring at ~3V with significant peak separation indicating sluggish electron transfer. Through other studies this species was shown to be related to the presence of the PF₆⁻ anion. Due to this interferent, earlier studies incorporating PF₆⁻ were only conducted at tip potentials between 3V and 5V. When those conditions were applied to the PF₆⁻:EC system, no electrochemical signatures for degradation products were observed (i.e., background and post voltage hold CVs were identical). This was despite the significant color change observed in the electrolyte (see inset). However, when CV data was collected over the wider range including the known background process, a substantial increase in current was observed between 2V and 3V as shown in the blue trace. This increase is expected to be due to LMO degradation products in solution. The fact that the process overlaps with the reduction process associated with the PF₆⁻ anion may be tied to the predicted strong interaction between both the PF₆⁻ anion and EC. While in earlier data, what we believe is the oxidation of Mn²⁺ to Mn³⁺, no such signal is observed here. It is possible that the interactions of PF₆⁻ and EC with Mn²⁺ significantly shifts the electrochemical signature to the point that it overlaps with the larger background signal. This possibility is under further study. If our hypothesis is correct, this data likely indicates that LMO degradation products in the presence of both PF₆⁻ and EC react quite differently throughout the cell than those generated from degradation products in the presence of ClO₄⁻, PC and PF₆⁻ in the absence of EC.

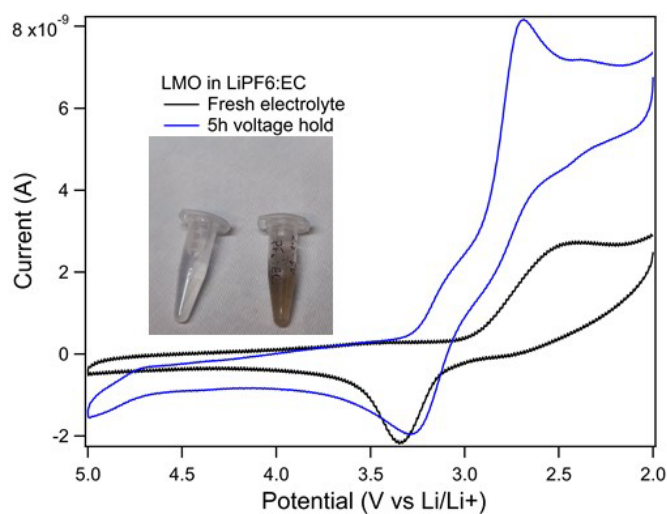


Figure X.6.3 SECM tip voltammetry collected before and after holding a model LMO substrate at 4.5V for five hours. Inset shows photographs of electrolyte samples pre- and post-voltage hold.

Additional focus in FY21 was also placed on comparing our earlier results from model cathode materials with results using full composite cathodes (including conductive additive and binder). G/C SECM experiments were performed as discussed above with the model LMO substrates replaced by a composite cathode that was affixed to a stainless-steel sample using a conductive carbon tape. Figure X.6.4 shows identical data sets collected with both our PAD-based model LMO materials and a composite LMO electrode in a 1M LiClO₄:PC electrolyte. The same voltage hold protocol as described earlier was applied and tip electrode voltammetry data was collected in fresh electrolyte as well as after holding the cathode materials at 4.5V for a total of 4 hours.

As has been seen previously with the LiClO₄:PC system, similar features are observed in both cases with some nuanced differences. The oxidation at 3.4V is still observed as well as a process observed at ~4.5V. This appears to indicate that the degradation process occurring in the LiClO₄:PC system is relatively insensitive to both to electrolyte components as well as the addition of conductive additive and binder. It should be noted, however, that a physical deformation of the composite cathode was observed after the 4.5V hold. While less impactful in this study, this may present a problem for SECM imaging analysis of degradation processes on this cathode with this electrolyte.

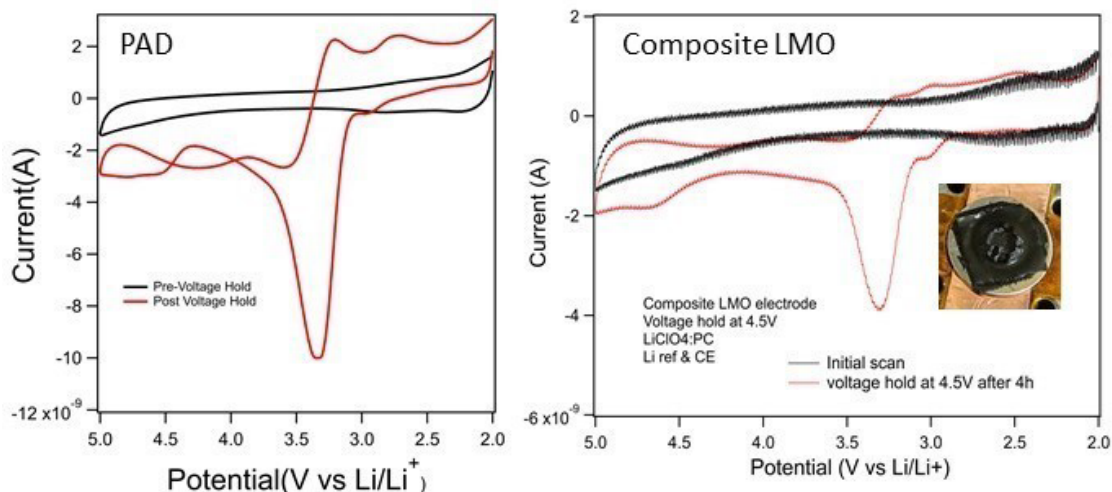


Figure X.6.4 SECM tip voltammetry collected before and after holding a PAD-based model cathode (left) and composite cathode (right) at 4.5V. This data was collected using the 1M LiClO₄:PC electrolyte. Inset photograph shows composite electrode after the voltage hold experiment.

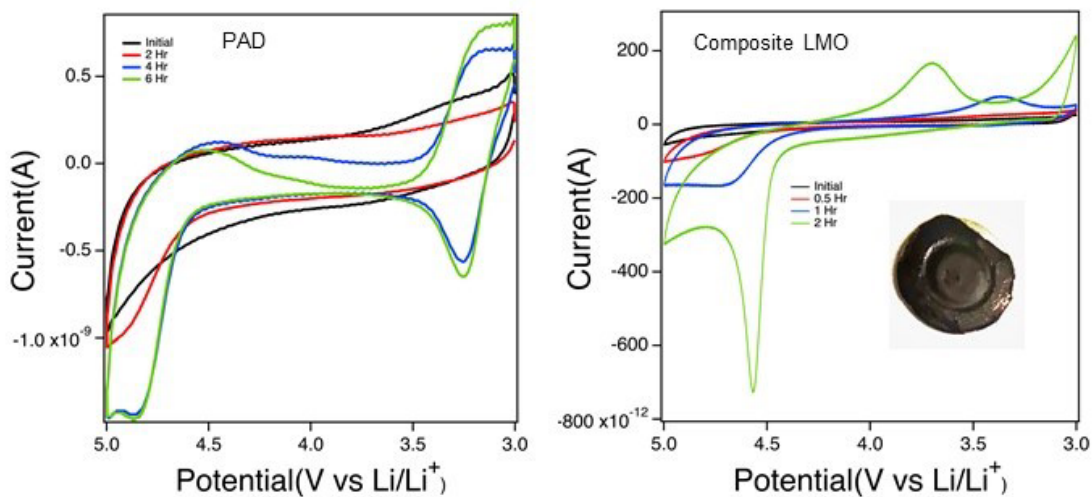


Figure X.6.5 SECM tip voltammetry collected before and after holding a PAD-based model cathode (left) and composite cathode (right) at 4.5V. This data was collected using the 1M LiPF₆:PC electrolyte. Inset photograph shows composite electrode after the voltage hold experiment.

Figure X.6.5 shows the results of a similar experiment conducted using the 1M LiPF₆:PC system. While similar observations were made following the high voltage hold in the 1M LiClO₄:PC system for both the model PAD cathode film and the composite electrode, this is not the case here. The data shown to the left was collected following the high voltage hold at a model PAD film while the plot to the right was for the composite cathode. For the PAD system, there are similarities to what was observed earlier for the 1M LiClO₄:PC system. Specifically, an oxidation process is observed between 3V and 3.5V with an associated reduction process. A second oxidation process is observed between 4.5V and 5V. In the case of the composite cathode, we no longer see an oxidation between 3V and 3.5V, however a similar oxidation process is observed between 4.5V and 5V. Also note that degradation products are evident in the CV results at shorter times for the voltage hold with the composite cathode as compared to the model PAD film. This observation is consistent with the hypothesis that conductive additives may play a role in accelerating cathode degradation. While still presently not understood, it is worth noting that no physical deformation of the composite cathode was observed after the high voltage hold in the 1M LiPF₆:PC electrolyte (see inset photo). This likely indicates that SECM imaging experiments may be feasible in this electrolyte system with a composite electrode.

Conclusions

In FY21, this project focused in two main areas. The first being to gain a better understanding of the role that carbonate solvents may play in the observed electrochemical properties of cathode degradation products. The second focus was comparison of earlier results collected with model systems to full composite cathode materials to judge the impact of additional electrode components. We appear to have found that cathode degradation products observed in the LiClO_4 based electrolytes (in both PC and EC) are relatively insensitive to both changes in electrolyte solvent as well as additional composite cathode components. However, the story appears to be dramatically different when considering the 1M LiPF_6 salt. In particular, the combination of both the PF_6^- anion and EC may show a dramatic shift in the redox potential of cathode degradation products such that they overlap with already existing background processes due to the PF_6^- anion itself, although this hypothesis is under further study. When comparing degradation of composite cathode materials to earlier model studies, we found that, again the LiClO_4 :PC system was relatively insensitive to the change in cathode sample while the 1M LiPF_6 :PC system appears to be quite sensitive to this change. While substantial further work remains to be conducted, it appears that the PF_6^- anion in combination with the presence of EC in LIB electrolytes play a very significant role in determining the electrochemical properties of cathode degradation products. These systems will be studied further in future work as this project begins to conduct work on more industrially relevant systems.

Key Publications

1. Di Huang, Chaiwat Engtrakul, Sanjini Nanayakkara, David W. Mulder, Sang-Don Han, Meng Zhou, Hongmei Luo and Robert C. Tenent; Understanding Degradation at the Lithium-Ion Battery Cathode/Electrolyte Interface: Connecting Transition Metal Dissolution Mechanisms to Electrolyte Composition; (2021) *ACS Applied Materials and Interfaces*, 13(10), 11930–11939.

References

1. Banerjee, A.; Shilina, Y.; Ziv, B.; Ziegelbauer, J. M.; Luski, S.; Aurbach, D.; Halalay, I. C., On the Oxidation State of Manganese Ions in Li-Ion Battery Electrolyte Solutions. *J. Am. Chem. Soc.* **2017**, 139 (5), 1738–1741.
2. Huang, D.; Engtrakul, C.; Nanayakkara, S.; Mulder, D.W., Han, S-D.; Zhou, M.; Luo, H.; Tenent, R.C. Understanding Degradation at the Lithium-Ion Battery Cathode/Electrolyte Interface: Connecting Transition Metal Dissolution Mechanisms to Electrolyte Composition; (2021) *ACS Applied Materials and Interfaces*, 13(10), 11930–11939.
3. Wang, C.; Xing, L.; Vatamanu, J.; Chen, Z.; Lan, G.; Li, W.; Xu, K. Overlooked Electrolyte Destabilization by Manganese (II) in Lithium-ion Batteries; *Nature Communications* **2019**, 10, 3423.

Acknowledgements

This work was authored in part by the National Renewable Energy Laboratory, operated by Alliance for Sustainable Energy, LLC, for the U.S. Department of Energy (DOE) under Contract No. DE-AC36-08GO28308. Funding provided by the U.S. Department of Energy Office of Energy Efficiency and Renewable Energy Vehicles Technologies Office. The views expressed in the article do not necessarily represent the views of the DOE or the U.S. Government. The U.S. Government retains and the publisher, by accepting the article for publication, acknowledges that the U.S. Government retains a nonexclusive, paid-up, irrevocable, worldwide license to publish or reproduce the published form of this work, or allow others to do so, for U.S. Government purposes. The authors would like to thank Peter Faguy and David Howell of the U.S. Department of Energy Office of Energy Efficiency and Renewable Energy Vehicles Technologies office for their continued support of this work. The authors would also like to thank Alfred Hicks in the NREL communications department for generating many of the graphics in this manuscript.

XI Next Generation Lithium-Ion Materials: Low-Cobalt/No Cobalt Cathodes

XI.1 Aerosol Manufacturing Technology to Produce Low-Cobalt Li-ion Battery Cathodes (Cabot Corporation)

Toivo Kudas, Principal Investigator

Cabot Corporation
157 Concord Road
Billerica, MA 01821
E-mail: Toivo.Kudas@cabotcorp.com

Peter Faguy, DOE Technology Development Manager

U.S. Department of Energy
E-mail: Peter.Faguy@ee.doe.gov

Start Date: October 1, 2018

End Date: June 30, 2021

Project Funding : \$2,749,057

DOE share: \$1,989,057

Non-DOE share: \$760,000

Project Introduction

Although considerable progress has been made with battery materials over the last 5-10 years, the cathode remains a major performance-limiting material in Li-ion battery (LIB) technology. New materials and battery chemistries will overcome some of the remaining challenges, but cathode materials must also be manufactured at a lower cost and with a smaller environmental footprint using new processes that can also enable improved control over stoichiometry, morphology, and compositional homogeneity. Cabot, Argonne National Laboratory and SAFT research teams are combining their extensive expertise in particle synthesis, battery materials and cell design to develop a low-cost, flexible aerosol manufacturing technology for production of high-performance Li-ion battery cathodes. This project will develop low-Co cathode materials via Reactive Spray Technology (RST) and Flame Spray Pyrolysis (FSP) to reach performance targets of < 50 mg Cobalt/Wh.

Objectives

The objective of this project is to research, develop, and demonstrate RST and FSP for production of low-Cobalt cathode active materials (CAM) for use in next-generation LIBs capable of the following:

Table XI.1.1 Project performance targets for cathode active material and cell made with this material

Beginning of Life Characteristics at 30 °C	Cell Level	Cathode Level
Useable Specific Energy @ C/3	---	≥60 Wh/kg
Calendar Life (< energy fade)	15 years	---
Cycle Life (C/3 deep discharge with <20% energy fade)	1,000	---
Cobalt Loading	<50 mg/Wh	---
Cost	≤\$100/kWh	---

Approach

To achieve the above targets, we are working towards demonstrating the production of low-Cobalt particle compositions. Cabot has shown the feasibility of $\text{LiNi}_{0.8}\text{Mn}_{0.1}\text{Co}_{0.1}\text{O}_2$ (NMC811) by RST; for this project we are extending this to even lower Co amounts. This requires us to identify approaches to solve key problems of

phase stability, water sensitivity, interface degradation and others. The team is exploring particle doping, coating, morphology, and size control on a robust platform that can be extended to other material configurations. We are leveraging the flexibility of RST and FSP to produce key low-Co cathode compositions relevant for achieving a scale up pathway. Cabot and ANL are identifying the most suitable aerosol platform and process conditions to synthesize low-Co cathode active material compositions. The optimization of low-Co electrodes includes new conductive additive formulations and improved low-Co cathode pastes that ensure percolation and mechanical stability of the film.

The performance goals in Table XI.1.1 drive us to new compositions, lower Cobalt than NCM811 (such as $\text{LiNi}_{0.9}\text{Co}_{0.05}\text{Mn}_{0.05}$ and $\text{Ni}_{0.9-x}\text{Co}_{0.06}\text{Al}_x$ $x=0.005-0.03$), along with other materials systems comprising fluorine (Li-excess disordered rock salt, LxDRS). Composition must be optimized for performance, cycling, stability and operation, among others. Our proposed RST/FSP route will address these issues and allow doping, coating, gradients, and novel particle morphologies which can solve these problems.

Results

Project Progress Cell (PPC) Build and Test

Due to the implication of the COVID19 pandemic the fabrication and delivery PPCs was delayed to the beginning of FY21. Our team at ANL utilized the RST system to synthesize > 4kg of NCM811, followed by powder post processing (calcination, milling/ washing processes to remove surface contaminants). Table XI.1.2 summarizes impurity measurement and other physical properties of the RST NCM811 powder used to make PPCs. Particle size distribution (PSD) and tap density were $D_{10}=1\mu\text{m}$, $D_{50}=4.8\mu\text{m}$, $D_{90}=9\mu\text{m}$ and 2.02 mg/cm^3 respectively. Besides surface contaminant removal, the NCM811 particles were not further modified (i.e., surface coating). The positive electrode (cathode) composition was set to be 94%/3%/3% for NCM811/CCA/Binder respectively. The binder content was adjusted to consider the higher powder surface area ($3.8\text{ m}^2/\text{g}$) of the RST NCM811 compared to commercial cathode materials ($<1.0\text{ m}^2/\text{g}$). The negative electrode (anode) composition was 97%/1.5%/1.5% of graphite/CMC/SBR respectively.

Table XI.1.2 RST NCM811 cathode powder quality check values prior to slurry making

Sample	pH value	Li_2CO_3	LiOH	Particle D50 (mm)	Moisture after drying (ppm)
RST NCM811	11.4	0.17%	0.14%	3.3	6.7
Reference	11.2	0.05%	0.16%	8.6	5.6

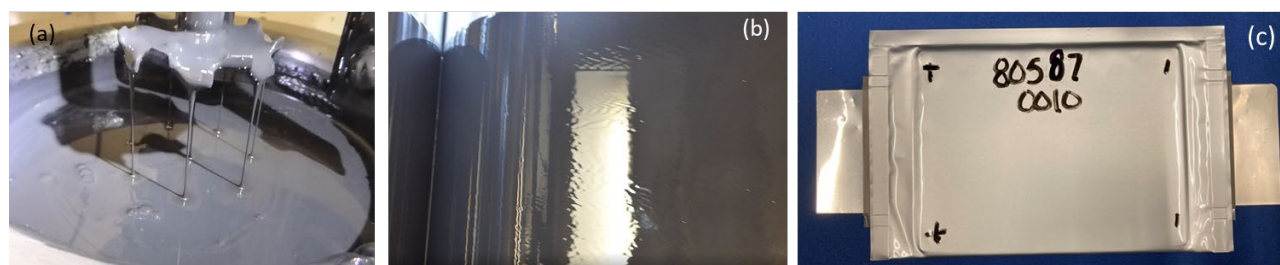


Figure XI.1.1 Picture of (a) the pilot scale slurry making process using RST NCM811, (b) electrode coating using SAFT pilot slot-die system, (c) sample lithium-ion cell delivered to INL and TARDEC

SAFT successfully mixed and coated electrodes with pilot scale equipment using RST NCM811. The slurry (Figure XI.1.1a and b), yielded 100 meters of double side electrodes with a mass loading of 10 mg/cm^2 . A total of 45 PPCs were assembled and formed ($>2\text{Ah}$) using USABC protocols, before shipping them to Idaho National Lab (INL) and TARDEC for further testing. Ten cells were kept at SAFT for parallel cycle life testing, the results are presented in Figure XI.1.8 and Table XI.1.3. SAFT results showed that PCCs retained 80% of their initial capacity after 300 cycles. The cells sent to INL are still under cycle and calendar life testing, showing 73% and 68% capacity retention after 600 and 900 cycles (30°C at C/3) respectively.

Hi-Ni NCM made by RST for interim pouch cells

ANL scientists continued working to improve the synthesis process to prepared interim NCM material. The team focused on optimizing post processing conditions (calcination, milling and powder washing). Based experimental data (ICP composition analysis, particle size distribution and BET surface area) we selected a two-step calcination/milling process. This approach allows us to obtain the most suitable cathode material (regarding particle size, surface area, and electrochemical capacity) for interim pouch cells. The particle size (D50) was 4–5 μm with a surface area of 3.5 m^2/g . The NCM9055 initial discharge capacity (before surface modification) was 215 mAh/g as shown in Figure XI.1.2(b) and (c). As expected, the cycle life of the NCM9055 was not as good as the NCM811 indicating the need for surface coating.

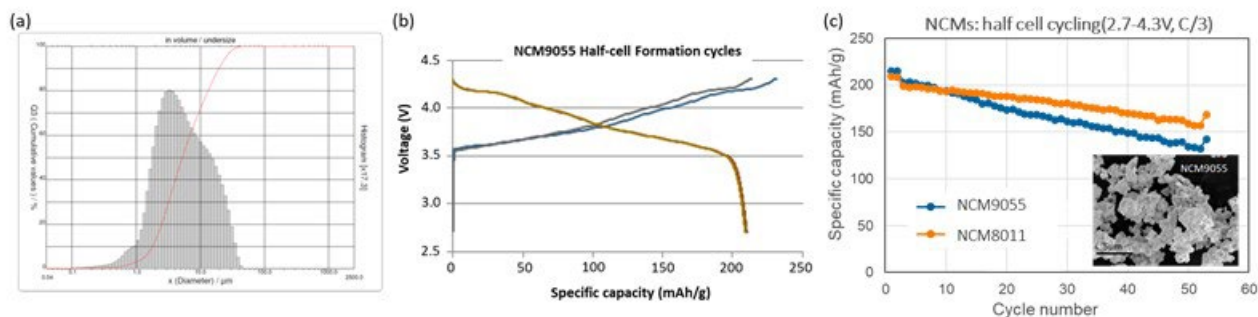


Figure XI.1.2 NCM9055 cathode powder made by RST (a) particle size distribution, D50= 5.2 μm ; (b) half-cell formation cycles: 215 mAh and 91% C.E; and (c) half-cell cycle life, the inset is a NCM9055 SEM image.

Cathode surface modification

During FY20 we studied cathode surface coating using fumed alumina and commercially available NCM811 core. These learnings were applied to RST made NCM9055. Thanks to our communication and characterization experiments with ANL, we learned that changing cathode composition (from NCM811 to 9055) and their compatibility with alumina influence the electrochemical performance of the coated particle. In addition, heat treatment conditions (second step for dry surface coating) determine coating layer composition and thickness. While core particle coverage depends on coating particle surface area and weight percent. We focused on selecting and optimizing some of these parameters to obtain the most desirable surface coating for NCM9055. Figure XI.1.3 shows rate capability and cycling data for cells (full cell with a graphite anode, 3.2 mAh/cm^2 , 2.7–4.2V, 1C/1C cycling) made with FA coated NCM9055. Electrochemical results using full coin cells clearly shows that particle surface coating enhances electrode performance while reducing impedance growth during cycle life testing. This formulation was used to make NCM9055 interim material for pouch cells.

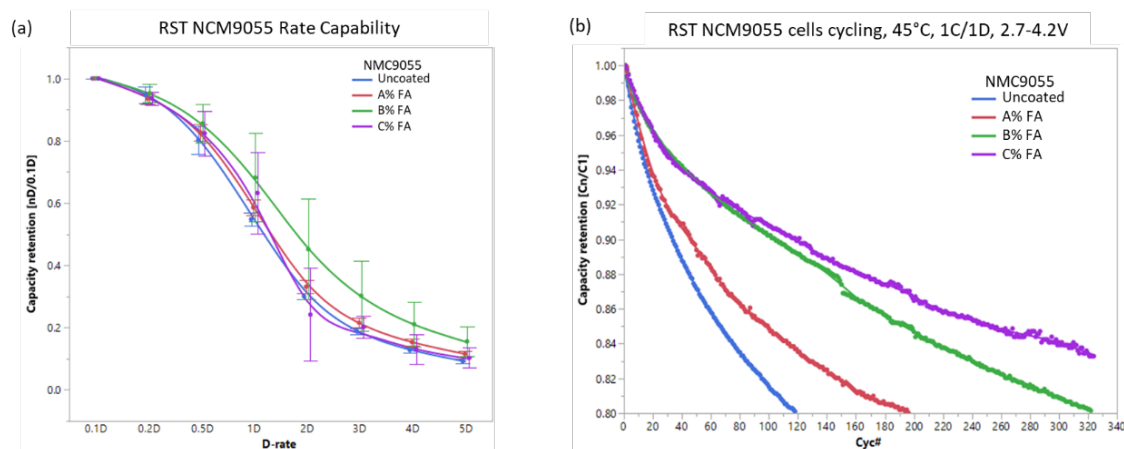


Figure XI.1.3 Surface coated NCM9055 were used to make full coin cells made with NCM9055 coated with different amounts of fumed alumina (a) rate capability (b) cycling plots showing the advantage of surface coating.

Cabot has continue working to further improve CAM surface coating properties using different fumed alumina and nano scale lithium metal oxides. Related to the studies with fumed alumina, we have added two more coating particles with smaller particle size and higher surface areas ($> 100 \text{ m}^2/\text{g}$). The idea is to explore the effectiveness of higher surface area alumina on NCM particle coverage. SEM images (Figure XI.1.4) shows that the higher BET area alumina gives better core particle surface coverage (BET: FA-2 $>$ FA-1) than our baseline fumed alumina (FA-1). Additionally, initial results suggest that FA-2 can provide similar coating coverage with less amount of material to FA-1. This is particularly advantageous because it will limit the initial capacity reduction due to reaction of lithium with Al_2O_3 . In addition, we are studying the influence of thermal treatment parameters on coating layer composition and cathode particle stability. Electrochemical testing is ongoing and will be presented next reporting period.

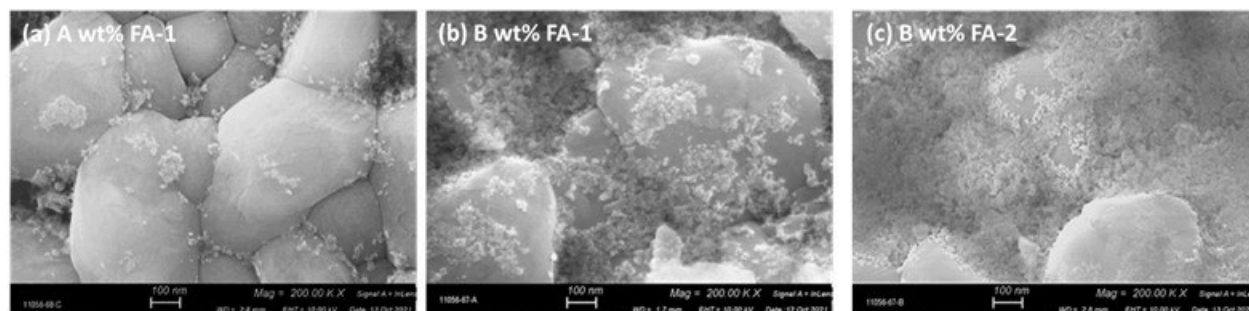


Figure XI.1.4 SEM images for alumina surface coated NCM811 (a) and (b) were coated with FA-1 and (c) with FA-2. A and B is the wt% of fumed alumina used where $B > A$. FA-2 has a higher BET surface area compared to FA-1.

Carbon Conductive Additives for Hi-Ni NCMs

Carbon conductive additive (CCA) experiments continued to address issues with the lower conductivity of Hi-Ni CAMs. Earlier results indicated that blends of carbon black (CB) and carbon nanotubes (CNTs) are very synergistic enhancing cell cycle-life. We have used commercially made NCM811 ($0.5 \text{ m}^2/\text{g}$ BET surface area) with fumed alumina coating as model to optimize CB + CNT blends. Cell cycling results, both in coin-cell and pouch cells, indicated that best cycle-life is achieved with CNT-rich 'Blend A', which outperforms pure CNTs (CNT-C1), or CB-rich 'Blend B' (Figure XI.1.5).

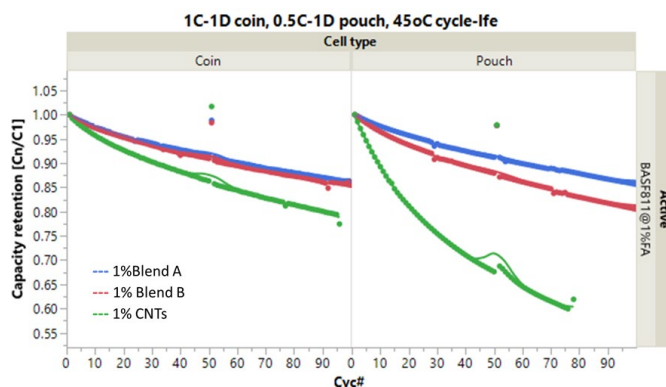


Figure XI.1.5 Cycle-life of FA coated NCM811 (commercial core) at 45°C , 1C/1C for coin-cells, 0.5C/1C for pouch cells, using different CCA formulations.

We also demonstrated the importance of adjusting overall CCA amount to the active material surface area. Since CAMs prepared by RST ($2\text{--}5 \text{ m}^2/\text{g}$) have higher BET than the ones produced by co-precipitation ($0.5 \text{ m}^2/\text{g}$). As seen in Figure XI.1.6 (a), the RST made NCM811 having a BET SA of $3.4 \text{ m}^2/\text{g}$ needs more CCA to achieve longer cycle life, b wt.% CCA was necessary to achieve over 300 cycles (where $b > a > 1 \text{ w}\%$). Figure XI.1.6 (b) shows full coin cells made with surface modified NCM9055 and blends A & B conductive additive. It is very clear that the optimized blend of Cabot's carbon black and CNTs further enhances cycle performance. Based on the results we used Blend A (CNT-C1 + CB) to fabricate interim pouch cells.

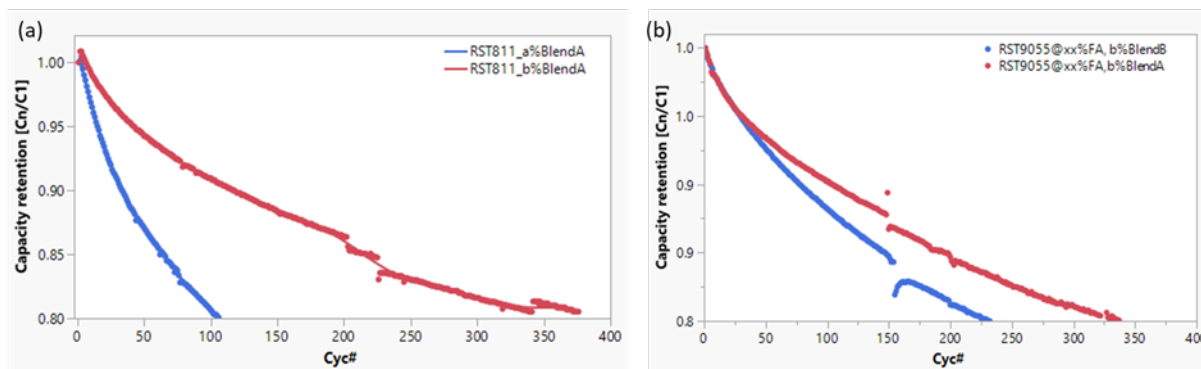


Figure XI.1.6 (a) Cell cycle life showing the influence of different CCA wt%, RST NCM811 cathodes (1C/1C, 45 °C, 2.8-4.2V). (b) CCA effect on cycle-life of NCM9055 cathode powder made by RST in full coin-cells using 20 mg/cm² cathodes, 1C-1D, 45 °C, 2.8-4.2V cycling conditions.

Cabot has continued investigating other CNTs and CB blends to further improve Hi-Ni NCM electrode performance. In this study we have added CNTs (CNT-C2) with smaller average diameter and higher conductivity and blended them with Cabot's battery grade carbon black. In the case of blends with carbon black, we previously found that CNT-C1 blended with CB resulted in cycle-life improvement over CNT-C1 alone. However, in the case of CNT-C2, it was found that a%CNT-C2 alone resulted in the best cycle-life (Figure XI.1.7.a). It also resulted in the lowest DC-IR during cycling (Figure XI.1.7.b), and therefore will be our new recommendation for maximizing cycle-life of FA coated High Ni NCM future builds

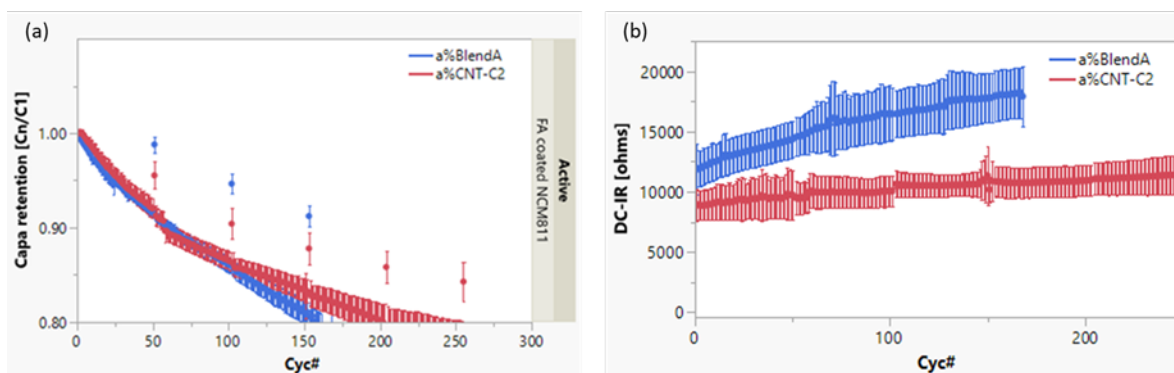


Figure XI.1.7 (a) Full cell cycle life (1C/1C, 45 °C) capacity retention using a% BlendA vs. a%CNT-C2 with FA-coated NCM811 (commercial core). (b) DC-IR during cycling of a% BlendA vs. a%CNT-C2.

Interim pouch cell fabrication and testing

During Q3FY21, SAFT worked to fabricate interim pouch cells. Prior to slurry making, the RST-made NCM9055 (with FA coating) powder was dispersed in water to measure pH and surface contaminants. The values obtained were pH = 11.6, Li₂CO₃ 0.34wt% and LiOH 0.14 wt%, which are within the range of SAFT's baseline material. The slurry was processed in SAFT's dry room using conventional R&D equipment. SAFT assembled 20 double layer pouch cells (120 mAh). All cells were formed using USABC protocols. Twelve cells were tested at SAFT (at 30°C, C/3 and 1C) and 6 at Cabot (at 45°C, C/3 and 1C). Figure XI.1.8 shows cycle life comparison between the interim pouch cells and the project progress cells (PPC, 2Ah) at 30°C. PPCs were made with RST NCM811(without surface coating) and tested at Idaho national laboratory. The capacity retention for both cells were very similar after 300 cycles, noting that the NCM9055 cathode particles were surface coated with alumina. Table XI.1.3 summarizes cathode energy densities for these cells at C/10 and C/3. The initial energy density of the interim cells were 710Wh/kg and they retained 80% of it after 300 cycles.

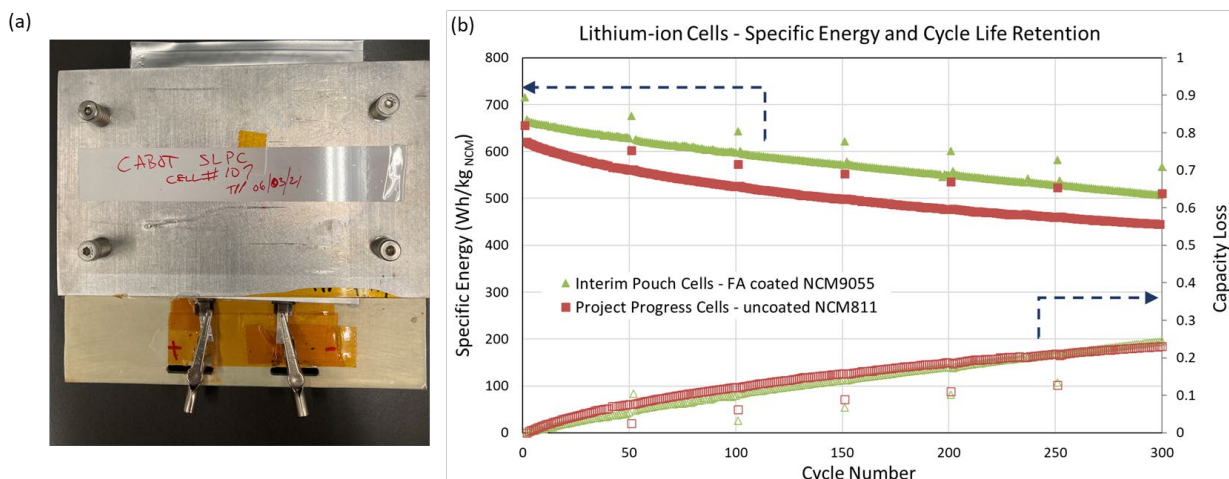


Figure XI.1.8 (a) Interim pouch cell (120 mAh). (b) Plot showing cathode energy retention (left Y-axis) and capacity loss (right Y-axis) are plotted and compared to the project progress cell (PPC) data

Table XI.1.3. Summary table showing initial cathode energy densities

Active material	Cathode Energy Density (Wh/kg)			
	Initial		After 300 cycles (C/3)	
	0.1C	0.33C	0.1C	0.33C
PPC: uncoated NCM811	650	610	515	450
Interim: FA coated NCM9055	710	670	570	515

Conclusions

In FY2021, we increased spray pyrolysis synthesis yield to produce NCM811, which was used to fabricate project progress cells. These batteries were delivered to INL and TARDEC for cycle and calendar life testing. PPCs cycling at SAFT showed an initial energy of 650 Wh/kg and 80% capacity retention after 300 cycles. To meet the Co amount ($\text{mg}_{\text{Co}}/\text{Wh}$) target, we use RST to produce CAMs with higher Ni content. After initial experimentation, NCM9055 was selected as active material for interim pouch cells. The NCM9055 particles were surface modified using fumed alumina particles, and the electrodes were made with CB + CNT blends to reduce cell impedance and enhance cycle life. These cells showed an initial capacity of 710 Wh/kg, reaching 570 Wh/kg after 300 cycles. To further increase cycle life and meet end-project goals, we are working to reduce CAM surface area, utilize better surface coating materials, and design an improved carbon conductive additive formulation.

Key Publications

1. “Aerosol Manufacturing Technology to Produce Low-Cobalt Li-ion Battery Cathodes”, BAT411_Kodas_2020_o, US DOE Vehicle Technologies Office Annual Merit Review, AMR, 2020.

Acknowledgements

We would like to acknowledge Dr. Joseph Libera and Dr. Eungje Lee at ANL; Mrs. Carine Steinway, Mrs. Serena Peterson, and Dr. Joong Sun Park at SAFT for their valuable contribution to this project.

XI.2 Cobalt-free Cathode Materials and their Novel Architectures (UCSD)

Ying Shirley Meng, Principal Investigator

University of California, San Diego
9500 Gilman Drive
La Jolla, CA 92093
E-mail: shmeng@ucsd.edu

Peter Faguy, DOE Technology Development Manager

U.S. Department of Energy
E-mail: Peter.Faguy@ee.doe.gov

Start Date: October 1, 2020
Project Funding: \$1,043,000

End Date: September 30, 2021
DOE share: \$834,000

Non-DOE share: \$209,000

Project Introduction

Since its discovery [1], $\text{LiNi}_{0.5}\text{Mn}_{1.5}\text{O}_4$ (LNMO) spinel-type cathode materials have long intrigued the transportation industry due to their high operating voltage (4.7 V) and capability to handle high charging rates. More recently, the strong desire to eliminate cobalt in cathode materials has sparked a renewed interest in this class of oxides. Various attempts to create LNMO/graphite batteries that exhibit high voltage, relatively high energy density, and high charging capabilities have been carried out worldwide, but they all have suffered from excessive degradation and short cycle life, especially when stored or cycled at elevated temperatures (55°C or higher) [2]. Our proposed work will solve the long-standing issues by 1) novel architecture of LNMO thick electrodes to enable 4-6 mAh/cm² loading, 2) new electrolyte formulation to suppress degradation in LNMO/Gr full cells, and 3) close collaboration among university-national lab-industry to demonstrate the feasibility of a Co free Li-ion cell with energy density exceeding 600 Wh/kg at cathode level. The main focus of this research is to solve the structural stability of LNMO and the interphase problems with electrolytes, including adopting an appropriate surface coating for the cathode; the development of a novel electrolyte (electrolyte additive, sulfone-based electrolyte); and the advancement of a new dry electrode processing method. In the past five years, our research team has made great progress on developing innovative synthesis techniques of high tap density cathode materials; conformal coating methods on powder samples; advanced characterization techniques on the atomic scale, electrode scale, and at the cell level; we have also made significant inroads on thick-electrode-architecture cell prototyping. **UT Austin** has extensive experience in the co-precipitation synthesis of LNMO cathode materials with a batch tank reactor at above the kilogram scale. **UCSD** has achieved conformal coatings on cathode particles through polymer assisted deposition. **UCSD** has also demonstrated that cryo-(S)TEM is crucial for interphase studies as it can effectively preserve cathode electrolyte interphase (CEI) structure/chemistry from beam damage. **LBNL** has effective diagnostic methods for full cells at both the coin cell and pouch cell level. **Tesla, Inc.** possesses a unique dry battery electrode coating technology that offers extraordinary ionic and electronic conductivity for extremely thick electrodes. It is through these successful experiences and fundamental understanding of these high voltage cathode materials that we can successfully formulate strategies to optimize LNMO-based battery system.

Objectives

The proposed research aims to deliver a Co free Li-ion battery with energy density exceeding 600Wh/kg at the cathode active material level. More specifically, the main goal of this project is to develop a high-performance and low-cost spinel-type $\text{LiNi}_{0.5}\text{Mn}_{1.5}\text{O}_4$ electrode and novel electrolyte formulation to suppress full cell degradation at high voltage and temperature. The best combination of high voltage electrode and electrolyte will achieve higher cell energy density, better safety performance, longer battery life, and greatly reduce the overall cost of the battery. The critical success factors in achieving that goal include:

1. Electrolyte stability and compatibility for both the cathode and anode materials under high charge and discharge voltage.
2. LNMO bulk and surface stability at high working temperature 55–60°C.
3. High areal cathode loading with new polymer binder and a dry-processing method to ensure adequate electronic and ionic transport for fast rates.

Approach

The main focus of this research is to solve the structural stability of LNMO and the interphase problems with electrolytes, including adopting an appropriate surface coating for the cathode; the development of a novel electrolyte (electrolyte additive, sulfone-based electrolyte); and the advancement of a new dry electrode processing method. In addition, to guide our research to determine which electrolyte system is more stable and compatible for LNMO electrode materials under high voltage cycling, we will develop a series of characterization techniques such as ex-situ X-ray photoelectron spectroscopy (XPS), ex-situ cryogenic transmission electron microscopy (cryo-TEM), ex-situ cryogenic focused ion beam microscope (cryo-FIB), in-situ Fourier-transform infrared spectroscopy (FTIR) and in-situ time-of-flight secondary-ion mass spectrometry (TOF-SIMS).

Results

The following progress has been achieved in FY21:

Active lithium quantification on 2 mAh/cm² LNMO-graphite single layer pouch cell

Single-layer pouch cells with 2 mAh/cm² level were prepared using LNMO as the cathode and graphite as the anode, Gen2 (1M LiPF₆ in EC: EMC = 3:7 wt.%) as the electrolyte. The cycling performance of the cell is shown in Figure XI.2.1. The LNMO-graphite cells were stopped after 140 cycles, and the capacity retention was 82%. As for the lithium quantification, we first set up the methodologies for the cathode, electrolyte, and anode, respectively. XRD was applied for the cathode Li quantification. Several half cells were performed with identical cell configurations for the methodology setup and were stopped at different depths of discharge (DOD) controlled by the discharge capacity. And then, the LNMO materials were collected from each cell for establishing XRD relation between (111) peak position and remaining capacity of each sample. The XRD data of LNMO collected from pouch cells with different cycling numbers, together with the pristine, the fully charged, and the fully discharged LNMO materials were then analyzed. The peak position was extracted, and the remained capacity was calculated based on the previously fitted equation. The delivered capacities are obtained from the cycler, while the remained capacities are calculated by the fitted equation, and the trapped capacities are the difference between delivered and remained capacities. The LNMO has a 10 mAh/g trapped capacity at the beginning of cycling due to the kinetics limitation. The trapped capacity increases to 16 mAh/g after long-term cycling, which might be due to the impedance growth. The increasing amount of trapped lithium amount is around 6 mAh/g at the cathode side after 140 cycles. Considering that the total delivered capacity loss is 24.41 mAh/g, nearly one-fourth of the capacity lost is due to the cathode trapped lithium.

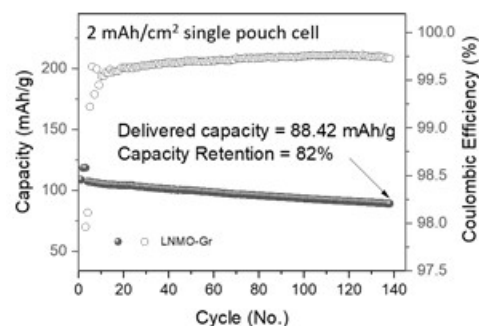


Figure XI.2.1 Cycling performance of the LNMO-graphite single layer pouch cell.

The amount of trapped active lithium in the graphite anode was also investigated by a Titration gas chromatography (TGC) method. It is noted that the amount of trapped active lithium decreases after long-term cycling, which implies the instability of the anode interphase. The lithium amount in the electrolyte was

monitored by ICP-MS. It is found that the lithium concentration has not changed obviously before and after long term cycling (Li concentration of Gen2: 1 mol/L).

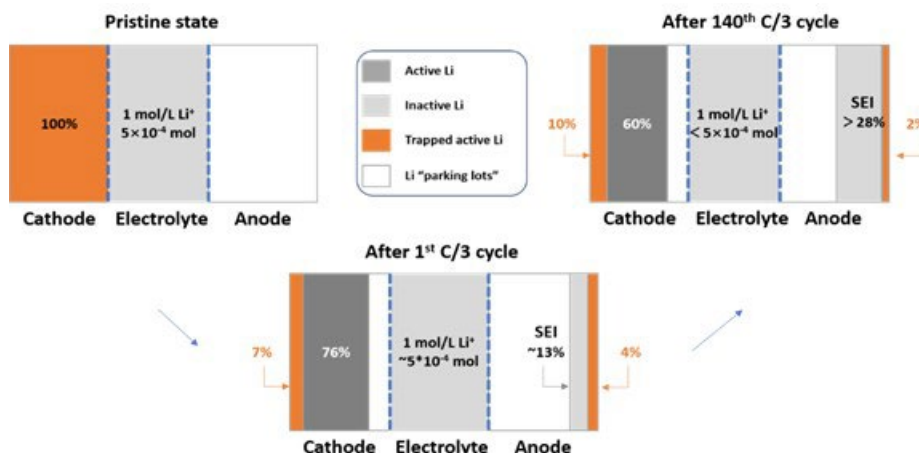


Figure XI.2.2 Schematic of lithium inventory loss in LNMO-graphite cell.

Table XI.2.1 Summary table of the LNMO-graphite cell lithium inventory after different cycles.

*Interphase Li = Total Li (cathode + electrolyte) – Active Li in cathode – Li trapped in cathode – Li trapped in anode – Electrolyte Li

Sample	Active Li in cathode (mAh/g)	Li trapped in cathode (mAh/g)	Li trapped in anode (mAh/g)	Electrolyte Li amount	Interphase Li* (inactive Li) (mAh/g)
After 1 cycle	112.83	10	5.7	$\sim 5 \times 10^{-4}$ mol	~ 18.5
After 140 cycles	88.4	16	3.3	$< 5 \times 10^{-4}$ mol	> 39.3

All the related lithium inventory data are summarized in Table XI.2.1. From this study, we conclude that the major reason for lithium inventory loss is excessive interphase formation. This finding is consistent with our previous electrolyte decomposition study, where acidity level increases due to the electrolyte decomposition on the cathode side. These by-products may corrode the cathode surface, causing transition metal dissolution, and transfer to the anode side and then corrode interphase of lithiated graphite. Therefore, active lithium is consumed to build up the new interphase. The detailed changes along with the cycling are summarized in Figure XI.2.2.

Calendar life and storage testing for 2 mAh/cm² LNMO/graphite full cell at room temperature

Calendar life testing was conducted in LNMO/graphite full cells (~ 2.0 mAh/cm²) with different storage time. The testing procedure is shown in Figure XI.2.3. In this study, cells were cycled at C/10 for the first two formation cycles and C/3 for the subsequent three cycles. In the 6th cycle, the cells were fully charged to 4.85 V and then discharged with a 10% depth of discharge (DOD). Then, the cells were stored at OCV with various storage time and discharged to 3.3 V. The time intervals include one day, three days, and ten days. The cycling and storage testing was repeated, and all the procedures were conducted at room temperature.

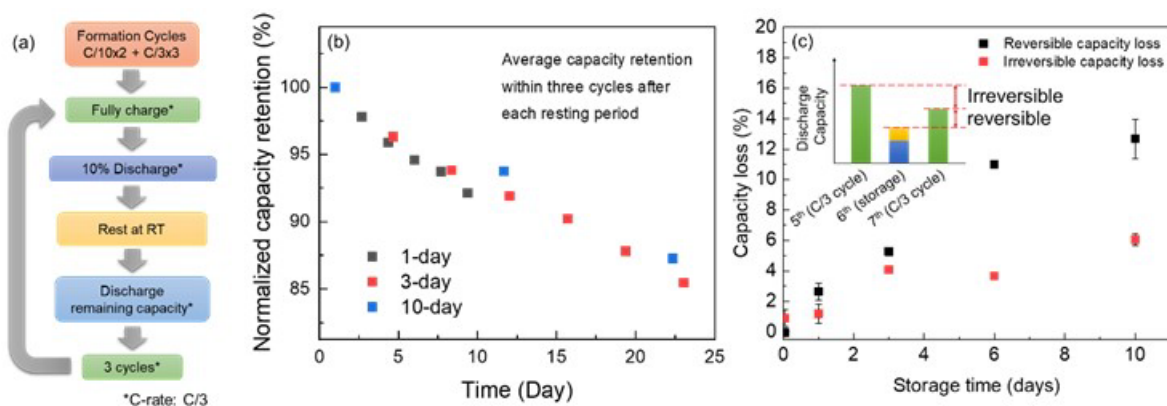


Figure XI.2.3 Experimental procedure of calendar life testing. (b) Normalized capacity retention under calendar life testing with various resting time. (c) Reversible (black) and irreversible (red) capacity growth after the first resting time. (inset) Definition of reversible and irreversible capacity loss. Green bars represent full discharge capacity at C/3 before and after the storage cycle, and the yellow and blue bar represents 10% partial discharge before the storage and remaining discharge capacity after the storage during the storage cycle.

Normalized capacity retention (regarding the 5th cycle discharge capacity as 100%) under the various storage days is shown in Figure XI.2.3b. Each data point indicates average discharge capacity over three cycles after each resting period. The capacity decay with various storage time shows a similar trend, suggesting that the high voltage storage time should be the main reason for capacity. Moreover, the 1-day storage process has a slightly steeper slope than the 10-day storage process, implying that continuous electrochemical cycling also influences capacity retention. Figure XI.2.3c shows reversible and irreversible capacity loss after the 1st resting process. The reversible capacity loss is defined as the subtraction of 6th cycle storage capacity (i.e., 10% DOD before storage + remaining discharge capacity after storage) from 7th cycle discharge capacity, whereas the irreversible capacity loss is defined as the subtraction of 7th cycle discharge capacity from 5th cycle discharge capacity. As seen in the Figure, both capacity losses grow faster in the early storage period, especially within 3 days of storage. Then the irreversible capacity loss slowed down while the reversible part kept growing till the 6th days, which might be attributed to the system's equilibrium.

To elucidate effects due to the storage, it is necessary to track Li distribution inside cells. Thus, A titration gas chromatography (TGC) method was employed to quantify Li inventory in an anode. TGC method provides Li amount in the form of Li_xC_6 in graphite anode by measuring H_2 amount, which is a product when Li_xC_6 reacts with sulfuric acid. The measured Li amount by TGC is compared with estimated capacity before storage and capacity after storage measured by electrochemistry (EC). Both TGC and EC measured results are less than the estimated capacity without any storage time, indicating that the graphite anode would lose capacity during the storage period. This result is consistent with our previous view that the graphite anode suffered degradation due to the electrolyte decomposition byproducts. Another characteristic feature is that capacity measured by EC is larger than that by TGC in the short storage period while they are almost the same after long time storage. Since TGC measures Li amount inserted into graphite (Li^0) whereas EC measures Li amount actively discharged after storage, it is possible that some of Li is stored in either Li^+ in the electrolyte or solid electrolyte interphase, which can contribute to the discharge capacity. Li amount in the cathode with different storage time was quantified by X-ray diffraction (XRD). Since the crystal structure expands as more Li is contained in LNMO, the XRD peak shift correlates with the lithiation state. Therefore, by analyzing peak position, the Li amount inside LNMO is uniquely identified. A detailed study was demonstrated in the previous quarterly report. XRD results of LNMO after 1 hour, 1 day, 10 days storage are compared. The 1-hour sample is considered a short time for the cells to reach equilibrium to be regarded as the cell without any storage. The Li amount in the cathode obviously increased after storage and could quickly be stabilized after 1 day. The identical Li amount between 1 day and 10 days samples indicates that Li insertion to LNMO during storage occurs in the initial storage period but stops after 1 day.

To summarize the discussion above, a storage model is depicted in Figure XI.2.4. TGC results show that the Li_xC_6 amount in the anode keeps decreasing while the LNMO cathode does not gain Li amount after 1 day based on XRD results. These Li that are released from anode but not inserted into cathode are still electrochemically active for short time storage of up to 3 days, contributing to discharge capacity. After a long time of storage, they become electrochemically inactive, which suggests that those Li are consumed as a part of SEI or become inactive in the electrolyte. The calendar life evaluation indicates the robustness of the LNMO cathode and the vulnerable graphite anode. Modifications such as surface coating and novel electrolyte design should be performed to improve LNMO and graphite cell calendar life. Meanwhile, further characterizations such as nuclear magnetic resonance (NMR) and Fourier transform infrared spectroscopy (FTIR) can be conducted to fully understand the electrolyte change during storage time.

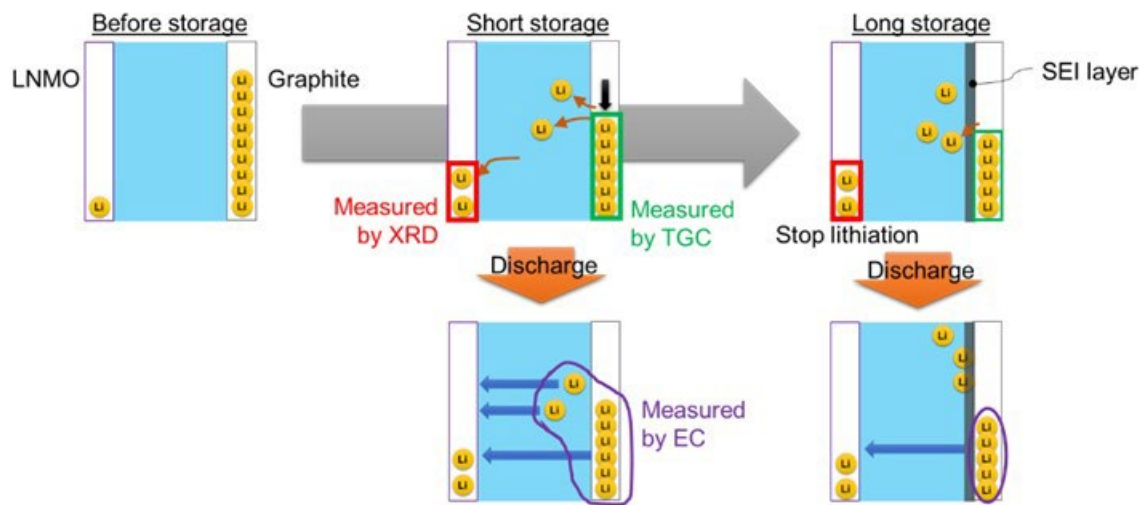


Figure XI.2.4 Schematic of Li inventory inside LNMO-graphite cell during calendar life test.

Investigation of Fe-doping effect on the stability of LNMO cathode at 3 mAh/cm² level

Following our previous findings, the Fe-doped LNMO shows much-improved cycling stability compared to the undoped sample. The XPS results indicate that the lithium salt decomposition is alleviated in the Fe-doped LNMO. It is obvious that the cathode surface reactivity with electrolyte changes upon Fe doping. A transmission electron microscopy (TEM) study was carried out to assess its microstructure. As shown in Figure XI.2.5, the Fe-doped Mn-rich LNMO shows a typical atomic arrangement of the spinel structure. Electron energy loss spectroscopy (EELS) mapping results demonstrate that a ~ 2 nm thick Fe-concentrated layer is formed on the surface of the primary particles. It is consistent with the finding made a few years ago by UT-Austin team [3]. Since the capacity degradation of LNMO/Li cell mainly originates from severe electrolyte oxidation on the cathode surface, it is highly possible that the Fe-concentrated surface alters the reactivity between the electrode and the electrolyte, thus alleviating electrolyte decomposition, helping to stabilize the CEI, and suppressing metal dissolution.

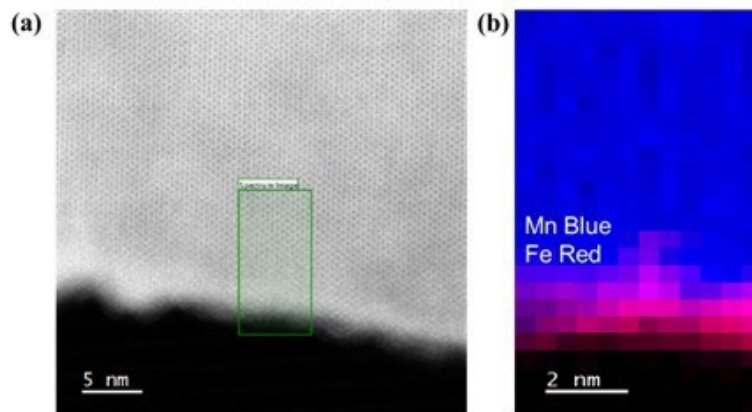


Figure XI.2.5 (a) STEM image of Fe-doped LNMO and (b) EELS mapping result of the selected area.

As demonstrated, a stable CEI can be formed on the Fe-doped Mn-rich LNMO during the cycling process, and the ALD-graphite shows apparent advantages in suppressing the lithium salt decomposition. Therefore, a good cycle performance can be expected with Fe-doped Mn-rich LNMO/ALD-graphite full cells, as shown in Figure XI.2.6. Fe-doped LNMO cathode with an areal capacity of 2.6 mAh/cm^2 and ALD-graphite anode with an areal capacity of 3.1 mAh/cm^2 were utilized to build a full cell. 90% capacity retention can be achieved after 300 cycles, and no noticeable cell impedance growth can be observed as the average charge/discharge voltage plots maintain stability during cycling.

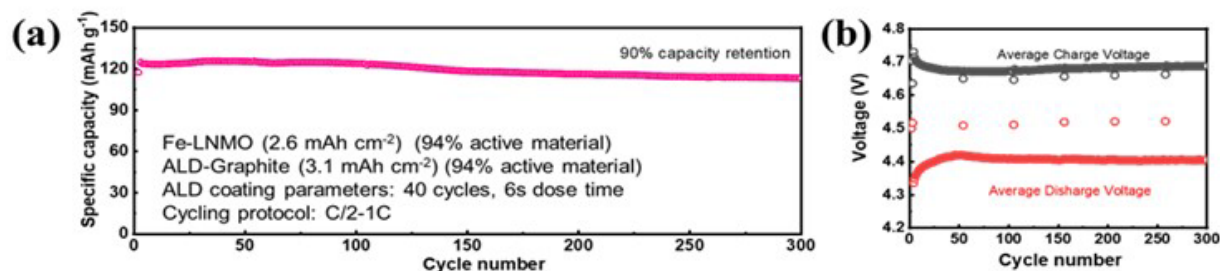


Figure XI.2.6 (a) Long-term cycling performance of Fe-doped LNMO/ALD-graphite full cell, and (b) average charge/discharge voltage plots with cycle number.

Graphite coating with Al_2O_3 via ALD for improving 3 mAh/cm^2 level full coin cell cycling stability

A 4 nm thick Al_2O_3 layer was coated onto the graphite electrode via atomic layer deposition (ALD), and the obtained Al_2O_3 -coated graphite was paired with an LNMO cathode. As shown in Figure XI.2.7, both the reversible capacity and cycling stability of LNMO||ALD-Graphite full cell is significantly enhanced compared to those obtained with the full cell assembled with pristine graphite. Specifically, the LNMO||ALD-Graphite full cell displays capacity retention of 98.6% over 300 cycles. In contrast, LNMO||pristine-Graphite shows fast capacity degradation with only 57.7% capacity retention.

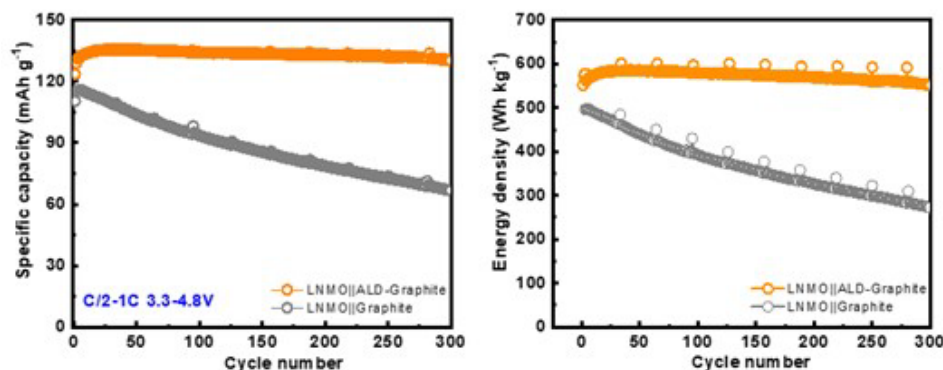


Figure XI.2.7 Comparison of the cycling performances of LNMO/pristine-Graphite and LNMO/ALD-Graphite full cells.

We also collected the interface evolution on graphite anode and A

D-graphite anode after 300 cycles and analyzed the CEI and SEI components through TOF-SIMS. Figure XI.2.8 presents the 3D distribution images and TOF-SIMS depth profiles of a series of fragments collected from graphite electrodes after 300 cycles. Much higher Mn^+ , Fe^+ , and Cr^+ can be detected in the graphite electrode than the ALD-Graphite electrode. It should be noted that the intensive Al^+ observed in the ALD-Graphite is due to the dissolution of Al_2O_3 coating layer. All these metal ions should be generated by the acidic corrosion of the cathode and coin cell cases. It can be observed that all the metal ions (Al^+ , Mn^+ , Fe^+ , Cr^+) are concentrated on the surface of the graphite electrode while mainly exist around 60 nm beneath the surface of ALD-Graphite. This is because the metal ions prefer to be deposited on carbonaceous materials instead of oxides. Also, it can be noticed that the lithium salt decomposition (represented by LiF_2^-) and graphite fluorination (represented by C_2F^-) are much more pronounced in the graphite electrode compared to the ALD-Graphite electrode.

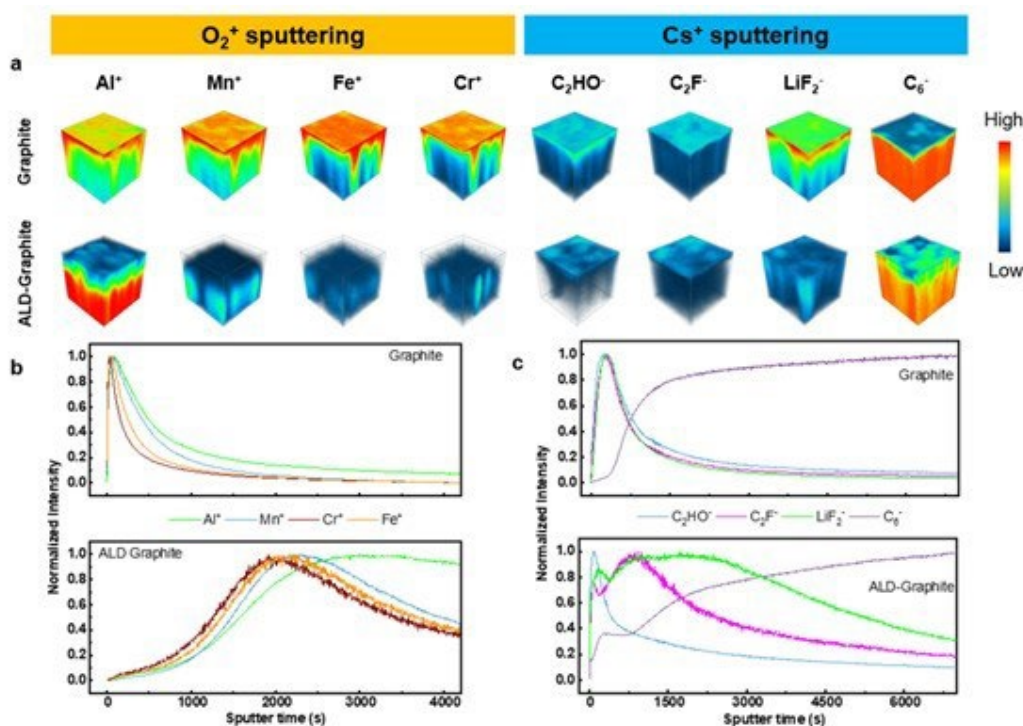


Figure XI.2.8 TOF-SIMS (a) three-dimensional mapping and (b, c) depth profiles of surface evolution of Graphite and ALD-Graphite electrodes after 300 cycles in full cell.

The SEI of graphite electrode, represented by C_2HO^+ , shows a single layer structure with a thickness of ca. 14.4 nm (480 s Cs^+ sputtering time). Notably, the SEI of ALD-Graphite presents a two-layer structure: the first layer with a thickness of ca. 4.05 nm (135 s Cs^+ sputtering time) could arise from the solvent decomposition on the surface of the Al_2O_3 coating layer. The second layer, which shows a wide range with much lower intensity, could be due to the solvent decomposition on the exposed graphite surface. This may be because Al_2O_3 can be etched by the acidic species generated by the lithium salt decomposition during the repeatedly charge-discharge process and the electrolyte can penetrate through the cracks and get in touch with fresh graphite surface and form SEI there. All the above-mentioned results demonstrate that the Al_2O_3 coating layer can separate the graphite from the electrolyte, alleviating the lithium salt decomposition, stabilizing the interface, and extending the service life of the LNMO/graphite full cell.

Novel electrolyte optimization in LNMO 3 mAh/cm² thick electrode full cell

Besides previously identified FECTMB electrolyte, more novel electrolytes are screened in the LNMO/graphite system in UCSD, focusing on the fluorinated solvents and more electrolyte additives. Table XI.2.2 lists the detailed composition for the screened electrolytes and their performance details in the electrochemistry testing. The corresponding capacity and Coulombic efficiency changes during cycling are also shown in Figure XI.2.9. All the newly screened cells are tested with Al-clad CR2032 cases and Dreamweaver separator under 3.3–4.85V with 2 cycles of C/10 and then C/3 for the long-term cycling (1C = 147 mA/g). While all the cells show similar initial discharge capacities, the capacity retention of the cells after 50 cycles already exhibits large difference. In the new batch of electrolyte screening, FEC/FEMC electrolyte gives the most promising performance with 124.7 mAh/g initial capacity, 87.7% initial Coulombic efficiency, and 94.1% capacity retention after 50 cycles. The capacity retention in FEC/FEMC is even higher than the previously identified best performer— FECTMB electrolyte (91.6% after 50 cycles). Other than FEC/FEMC, Gen2-TMSP-LiDFOB electrolyte also shows promising cycling results, which is 90.7% retention after 50 cycles. The promising cycling performance in the FEC/FEMC electrolyte may be attributed to its highest oxidation stability at high voltage

Table XI.2.2 Composition and electrochemistry performance of screened novel electrolytes

Cell	Electrolyte	1st Dch Cap. (mAh/g)	1st CE (%)	50th Retention (%)
#1	Gen2	126.9	89.0	87.2
#2	Gen2-LiDFOB	124.3	84.9	88.2
#3	Gen2-TMSP-LiDFOB	125.1	87.0	90.7
#4	FEC/EMC	127.1	88.5	87.0
#5	FEC/FEMC	124.7	87.7	94.1
#6	Gen2 (Previous)	128.0	86.7	87.9
#7	FECTMB (Previous)	125.7	87.8	91.6

ARL team also conducted similar electrolyte screening experiments in coordinated with UCSD team. In the initial tests this quarter, ARL used a standard galvanostatic protocol to compare two of the previous baseline electrolytes (Gen II and 1m $LiPF_6$ in FEC/DMC (1/4 wt.%) + 0.25 wt.% TMB) with a new baseline proposed by the UCSD team (1m $LiPF_6$ in FEC/FEMC (3/7 wt.%)). ARL's results in Figure XI.2.10 showed that the new baseline consistently exhibited the best 1st cycle CE (82.69%) and the best 10 cycle average CE (97.3%) among the cells tested. There was some variability in initial capacity, but cell B for the new baseline (shown in light green) exhibited a significantly higher capacity (~10 mAh/g) than any of the other baseline cells. These results will need to be confirmed in future experiments, but the initial results are promising and confirm the UCSD observation regarding this formulation.

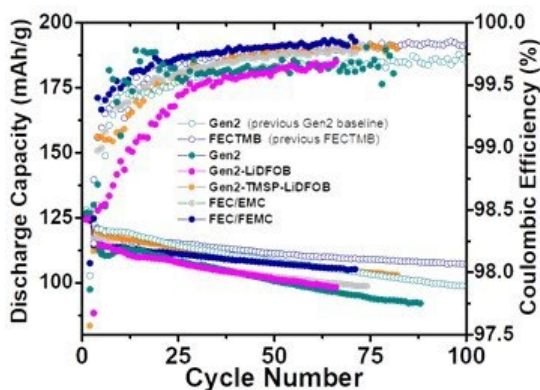


Figure XI.2.9 Discharge capacity and Coulombic efficiency along cycling of 3 mAh/cm² LNMO/graphite full cells with different electrolytes; the cells were cycled between 3.3–4.85 V with C/3. Data from UCSD team.

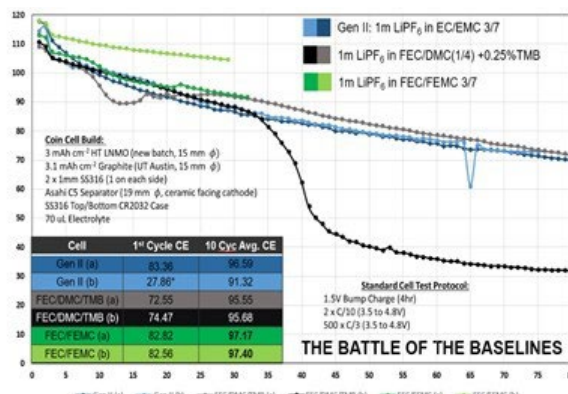


Figure XI.2.10 Discharge capacity along cycling of 3 mAh/cm² LNMO/graphite full cells with different electrolytes; the cells were cycled between 3.3–4.85 V with C/3. Data from ARL team.

Separator clogging issue investigation and optimization with 3 mAh/cm² LNMO/graphite full cell

In previous study, the clogging issues of the Celgard separator was identified in the 3 mAh/cm² LNMO/graphite full cells after cycling. Thus, different separators were screened in the full cell with baseline Gen2 electrolyte to identify a separator with larger pore size and to avoid clogging. Figure XI.2.11 compares the SEM image of the two sides of different separators after 3 formation cycles in 3 mAh/cm² LNMO/graphite cell under 3.3–4.775 V and C/20 (1C=147 mA/g). For the cycled Celgard 2400 (monolayer PE) separator, the porous structure was maintained on the surface facing the cathode side, but large number of residues can be seen on the separator surface facing the anode side, blocking many pores of the separator. For C5 separators, no matter the uncoated or coated side facing the anode, residues were also formed on the surface. Both GF/F glass fiber and polyaramid Dreamweaver separator has much larger pore size (around 400–700 nm) compared to Celgard. After cycling, the glass fiber and Dreamweaver surface facing the anode also had residues. However, since the pore size is much larger, the residues did not block the pores.

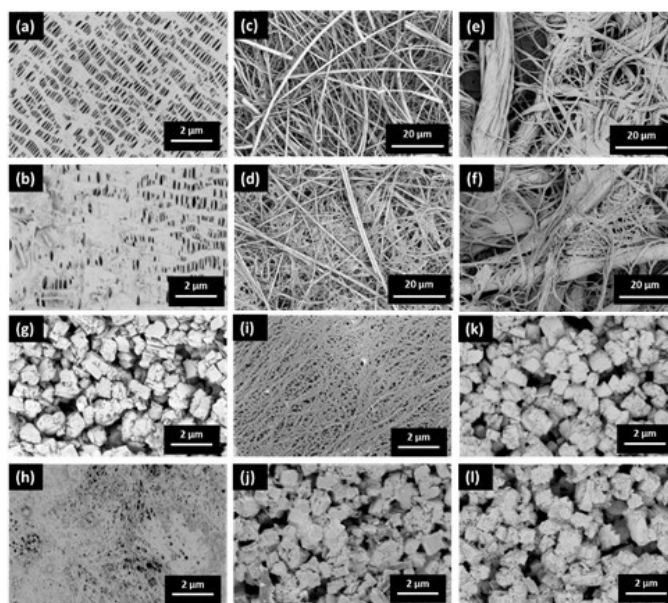


Figure XI.2.11 SEM images of separators after 3 formation cycles in 3 mAh/cm² LNMO/graphite full cell. (a) Celgard 2400 facing the cathode, (b) Celgard 2400 facing the anode, (c) GF/F glass fiber facing the cathode, (d) GF/F glass fiber facing the anode, (e) Dreamweaver facing the cathode, (f) Dreamweaver facing the anode, (g) C5 coated side facing the cathode, (h) C5 uncoated side facing the anode, (i) C5 uncoated side facing the cathode, (j) C5 coated side facing the anode, (k) C5 coated side facing the cathode, (l) C5 coated side facing the anode.

The first cycle voltage profile and the long-term cycling performance of 3 mAh/cm² LNMO/graphite full cells using different separators are shown in Figure XI.2.12. All cells were cycled with SS304 CR2032 case and Gen2 electrolyte. With different separators, all cells deliver about 125 mAh/g initial discharge capacity. However, after long-term cycling, the capacity retention is much higher in the Dreamweaver cell, which is around 86.1% after 75 cycles and 78.5% after 150 cycles. The relatively more stable cycling performance in the Dreamweaver separator may come from its ability to avoid clogging during cycling. The Dreamweaver separator was also used in the following novel electrolyte screening.

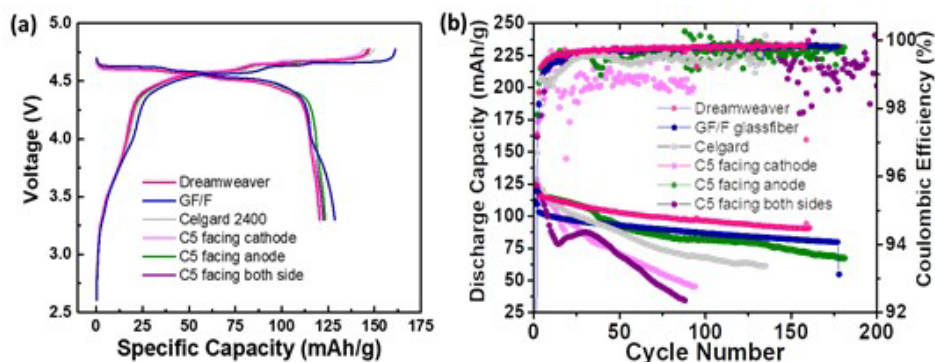


Figure XI.2.12 (a) Formation cycle voltage profile of 3 mAh/cm² LNMO/graphite full cells using different separators; the cells were cycled between 3.3–4.775 V with C/20. (b) Discharge capacity and Coulombic efficiency along cycling of full cells with different separators; the cells were cycled between 3.3–4.85 V with C/3 for the cycling.

Dry coated LNMO thick electrode (3~4 mAh/cm²) performance

For dry-coated electrodes, a new batch of 3 and 4 mAh/cm² level dry LNMO electrodes were fabricated by Tesla using the LNMO (from Haldor Topsoe) and Super C65 conductive carbon (from MTI). Both 3 and 4 mAh/cm² level (~22.5 mg/cm² and ~30.4 mg/cm² respectively) were made to evaluate the performance. Figure XI.2.13 shows both voltage profiles of cycling performance in the half cells. Glassfiber was used as the separator, and 150 μ L of Gen2 electrolyte was injected. Figure XI.2.13a shows typical LNMO voltage profile in both C/10 and C/3 rates. With glassfiber as the separator, there is not much impedance growth when the C-rate was switched due to more electrolyte and probably an optimum internal stack pressure within the cell. This can also be seen in Figure XI.2.13b, which shows a relatively stable cycling performance. The half cell at >20 mg/cm² level loading did not experience severe failure after ~14 cycles since there was still electrolyte to be consumed.

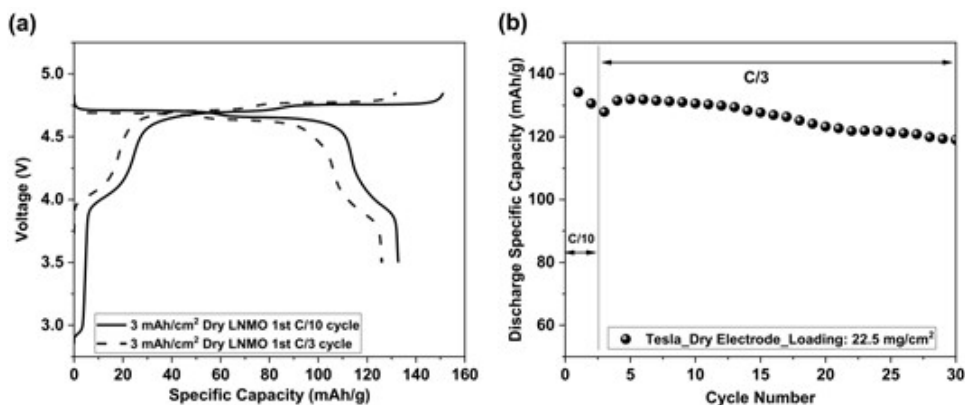


Figure XI.2.13 (a) Voltage profiles of 1st C/10 and 1st C/3 performance of the 3 mAh/cm² level half-cell and (b) its cycling performance.

When the loading increases to $\sim 30.4 \text{ mg/cm}^2$, which corresponds to $\sim 4 \text{ mAh/cm}^2$ level, we can see the 1st C/10 and 1st C/3 performance are still comparable with the 3 mAh/cm^2 level with the same testing conditions shown in Figure XI.2.14. However, the cycling performance is no longer comparable since the plating/stripping rate of Li^+ on the Li metal counter electrode becomes much larger (from 1.1 mA/cm^2 to 1.5 mA/cm^2), which accelerates the electrolyte consumption rate. More importantly, based on the linear sweep voltammetry (LSV) results shown in Figure XI.2.14b, carbon coating will vigorously react with electrolyte as seen from the leakage current jump when the voltage is greater than 4.5 V and 5 V . On the other hand, conventional PVDF binder has minimum impact on the electrolyte decomposition, as seen from its low and smooth leakage current trend. The peak at 4.2 V is the self-passivation of the Al foil. Recovery of the leakage current from 4.2 V to 5 V also indicates Al foil itself has negligible impact on the electrolyte decomposition. The effect from carbon coating is also clearly shown in the 3 mAh/cm^2 level LNMO/graphite full cell cycling in Figure XI.2.14b. After 100 cycles, the CE% only has $\sim 99.5\%$, and the capacity retention is $\sim 68\%$. Li inventory was consumed due to the excessive side reactions between carbon coating and electrolyte, leading to low CE% and poor capacity retention.

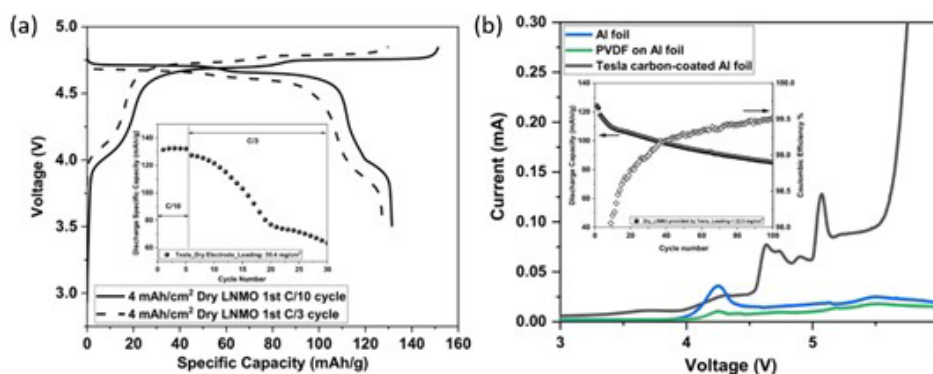


Figure XI.2.14 (a) Voltage profiles of 1st C/10 and 1st C/3 performance as well as the cycling performance of the 4 mAh/cm^2 level half-cell. (b) LSV results of bare Al foil, PVDF cast on bare Al foil, and Tesla's carbon-coated Al foil. Inset is the full cell cycling of the 3 mAh/cm^2 level Tesla's dry electrode.

Evaluation of Fe-doped LNMO and ALD-coated graphite electrode with high areal capacity (4 mAh/cm^2)

Fe-doped LNMO electrode with an areal capacity of 4 mAh/cm^2 (calculated with a capacity of 140 mAh g^{-1}) was fabricated. The electrode was prepared via dry-coating technology, and the ratio of active material, carbon, and binder is 93: 5: 2. The graphite electrode was prepared at UT Austin via a traditional wet-coating method. Note that the graphite here is not ALD-coated. The areal capacity is $\sim 5 \text{ mAh/cm}^2$, the mass ratio of

graphite, carbon, and binder (CMC+SBR) is 94 : 1 : 5. The full cells were fabricated, and the results are shown in Figure XI.2.15. As displayed, both full cells deliver an initial capacity of 119 mAh g^{-1} at C/10 rate and the capacity retention after 100 cycles is 87.4 %. Notably, no obvious cell impedance growth can be observed from the charge-discharge profiles, indicating the lithium salt decomposition on the graphite is suppressed. This might be benefited from the dry-coating technology. Further investigation is ongoing.

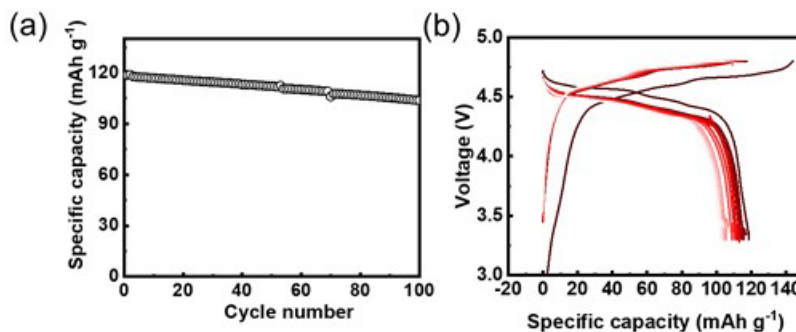


Figure XI.2.15 (a) Long-term cycling performance and (b) Charge-discharge profile of high mass loading (4 mAh/cm^2) Fe-doped LNMO (dry-coated)/graphite full cell.

ALD coating was also carried in another 4 mAh/cm² graphite electrode and paired with unmodified LNMO material (HT-LNMO). Full cells were fabricated and evaluated, and the results are shown in Figure XI.2.16. When cycled at a C/3 rate, the full cell can deliver a capacity of around 3.3 mAh, which equals a specific capacity of 106 mAh/g.

Meanwhile, the average coulombic efficiency is 99.2%. The capacity retention after 80 cycles is 88%. It can be noticed that capacity degradation is slowing down upon cycling. There is only a 2.2% capacity loss from the 54th cycle to the 82nd cycle. Further investigation is ongoing to assemble full cells with both Fe-doped LNMO and ALD-coated graphite.

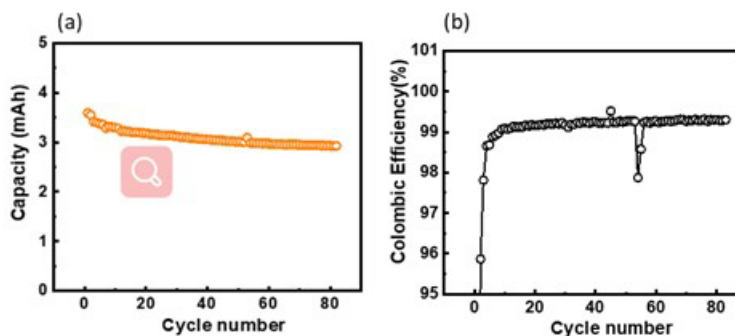


Figure XI.2.16 Electrochemical performance of 4mAh/cm² level full cell using ALD graphite including (a) capacity and (b) Coulombic efficiency.

Conclusions

Fundamental study was conducted in 2 mAh/cm² LNMO/graphite system. Through the lithium inventory quantification, we conclude that the major reason for lithium inventory loss is excessive interphase formation. The calendar life evaluation indicates the robustness of the LNMO cathode and the vulnerable graphite anode. Modifications such as surface coating and novel electrolyte design may improve LNMO and graphite cell calendar life. Optimization for different cell parts were conducted in 3 mAh/cm² LNMO/graphite full cells to achieve better cycling stability. First, Fe-doped LNMO cathode shows 90% capacity retention after 300 cycles without noticeable cell impedance growth. Secondly, an Al₂O₃ layer was coated onto the graphite electrode via atomic layer deposition (ALD), the LNMO||ALD-Graphite full cell displays capacity retention of 98.6% over 300 cycles. Thirdly, the full cell with FEC/FEMC novel electrolyte shows FEC/FEMC electrolyte gives the most promising performance with 124.7 mAh/g initial capacity, 87.7% initial Coulombic efficiency, and 94.1% capacity retention after 50 cycles. The increased cycling retention may be attributed to the oxidative stability of fluorinated solvents. Lastly, different separators were investigated to improve long-term cycling stability as the Celgard separator shows severe clogging issue after cycling due to its small pore size (50~100 nm). In this screening, the Dreamweaver separator shows the best cycling stability among all the separators due to its large pore size (400~700 nm). Furthermore, LNMO/graphite cell at 4 mAh/cm² level was investigated in this year. It has been identified that carbon coating on the current collector will vigorously react with electrolyte at high voltage, thus reducing carbon content or finding alternative is needed. Fe-doped LNMO electrode (4 mAh/cm²) was then prepared with dry coating method and then paired with bare graphite, the full cell delivers an initial capacity of 119 mAh g⁻¹ at C/10 rate and the capacity retention after 100 cycles is 87.4 %. Further investigation is ongoing to assemble full cells with both Fe-doped LNMO and ALD-coated graphite.

Key Publications

1. F. Zou, A. Manthiram, et al., Long-life LiNi_{0.5}Mn_{1.5}O₄/graphite lithium-ion cells with an artificial graphite-electrolyte interface. *Energy Storage Materials* 43 (2021): 499–508.
2. F. Zou, A. Manthiram, et al., Long-Term Cycling of a Mn-Rich High-Voltage Spinel Cathode by Stabilizing the Surface with a Small Dose of Iron. *ACS Applied Energy Materials* (2021), in press, DOI: 10.1021/acsaem.1c02903
3. W. Li, M. Zhang, Y.S. Meng, et al., Artificial Cathode Electrolyte Interphase for Improving High Voltage Cycling Stability of Thick Electrode with Co-Free 5 V Spinel Oxides. Submitted to *ACS Energy Letters*.

References

1. Ohzuku, T.; Takeda, S.; Iwanaga, M. Solid-State Redox Potentials for $\text{Li}[\text{Me}_{1/2}\text{Mn}_{3/2}]\text{O}_4$ (Me: 3d-Transition Metal) Having Spinel-Framework Structures: A Series of 5 Volt Materials for Advanced Lithium-Ion Batteries. *J. Power Sources* **1999**, 81-82, 90–94.
2. Lu, J.; Lee, K. S. Spinel Cathodes for Advanced Lithium Ion Batteries: A Review of Challenges and Recent Progress. *Mater. Technol.* **2016**, 31 (11), 628–641.
3. Shin, Dong Wook, Craig A. Bridges, Ashfia Huq, M. Parans Paranthaman, and Arumugam Manthiram. Role of Cation Ordering and Surface Segregation in High-Voltage Spinel $\text{LiMn}_{1-x}\text{Ni}_x\text{O}_4$ (M= Cr, Fe, and Ga) Cathodes for Lithium-Ion Batteries. *Chemistry of Materials* **2012**, 24(19) 3720–3731.

Acknowledgements

The following individuals partnered on this project: Arumugam Manthiram (the University of Texas at Austin), Hieu Duong (Tesla, Inc.), Vince Battaglia (Lawrence Berkeley National Laboratory), Kang Xu (Army Research Laboratory), and Marshall Schroeder (Army Research Laboratory). We also thank Dr. Aaron D. Yocum (NETL manager), Dr. Yi Ding (TARDEC manager), Dr. Ahmad Pesaran (NREL manager), Dr. Jack Deppe (INL manager) for supporting our work.

XI.3 Novel Lithium Iron and Aluminum Nickelate (NFA) as Cobalt-Free Cathode Materials (ORNL)

Ilias Belharouak, Principal Investigator

Oak Ridge National Laboratory
2370 Cherahala Boulevard
Knoxville, TN 37932
E-mail: belharouaki@ornl.gov

Peter Faguy, DOE Technology Development Manager

U.S. Department of Energy
E-mail: Peter.Faguy@ee.doe.gov

Start Date: October 1, 2018
Project Funding: \$2,130,000

End Date: September 30, 2021
DOE share: \$2,130,000

Non-DOE share: \$0

Project Introduction

United States Department of Energy (US DOE) has set ultimate goals for cost and performance metrics of electric vehicles (EV) which includes: (i) reducing the cost of EV batteries to \$80/kWh, (ii) increasing EV range to over 300 miles and (iii) decreasing EV charging times to less than 15 minutes. Realizing this cost target requires refocusing modern day battery research and development towards reducing one of the most expensive component of EV batteries—cobalt, in battery cathodes to less than 50 mg/wh at the cell level.[1] Mainstream cathode materials such as $\text{LiNi}_x\text{Mn}_y\text{Co}_z\text{O}_2$ (NMC) and $\text{LiNi}_{0.8}\text{Co}_{0.15}\text{Al}_{0.05}\text{O}_2$ (NCA), have considerable amounts of cobalt in their compositions thus posing a major hurdle towards achieving the desired battery cost targets. Moreover, cobalt prices have been rapidly rising in the past decade with prices nearly tripling in recent years. Additionally, the Cobalt Development Institute (CDI) recently reported that almost 58% of cobalt production across the globe is directed towards critical military and industrial applications such as manufacturing of catalysts, pigments, super alloys, magnets, etc.,[2] leaving only a little over 40% for the battery sector. Most companies engaged in these critical sectors can sustain higher cobalt prices even when there are severe supply shortages as cobalt only constitutes a negligible part of their raw material costs. However, for battery industries which are organized based on economies of scale driven by tight profit margins, price fluctuations of one of the most expensive battery raw material becomes unsustainable. Moreover, as EV markets are poised for an exponential growth with projections of number of EVs on road by 2050 exceeding hundreds of millions, a sustainable solution to the cobalt problem is the need of the hour. In the quest for an economically viable alternative to this looming cobalt threat to EV batteries, this project provides a paradigm shifting approach that aims to replace cobalt with alternative cost-effective elements without compromising battery performance. The primary objective of this work is to develop and upscale a novel class of battery cathode material analogous to the mainstream NCAs and NCMs but without cobalt. This new cobalt-free class of cathode—the lithium, iron, and aluminum nickelate, $\text{LiNi}_x\text{Fe}_y\text{Al}_z\text{O}_2$ (NFA: Ni, Fe, Al), replaces cobalt with cost-effective alternatives such as iron and aluminum. Moreover, this new cathode material with properties similar to that of mainstream cobalt containing cathodes, is expected to be integrated into the battery manufacturing industry in a seamless manner with minimal entry barriers.

Objectives

The overall objective of this project is to implement $\text{LiNi}_{0.8(0.9)}\text{Fe}_{0.2(0.1)-x}\text{Al}_x\text{O}_2$ (NFA) as novel cobalt-free cathodes in large format Li-ion cells achieving the following performance and cost targets:

1. Zero (0) cobalt loading as NFA cathodes only have nickel (80–90%), and the balance (10–20%) is a combination of iron and aluminum.
2. 650–750 Wh/kg usable specific energy at C/3 rate at the material level at the beginning of life.

3. Thousand (1000) deep charge and discharge cycles at the C/3 rate with less than 20% capacity fade in 2.3 Ah cells.
4. Less than \$100 per kWh at the cell level.

Approach

Three major approaches at the material level will be implemented in this work:

1. Optimization of the amounts of Al^{3+} which favors the stabilization of nickel in the 3+ oxidation state, which ensures the dual dimensionality and oxygen stability in the cathodes. (*good for reversibility and cycle life*).
2. Introduction of controlled amounts of Fe^{3+} (equal or less than 10%) to improve the electronic conductivity in the Ni-Al slab. (*good for power*).
3. Fine-tuning of the synthesis conditions and processes to yield highly-ordered layered NFA cathodes with higher packing densities to achieve higher energy densities without compromising cycling performance. (*good for translating the material properties and performance from bench scale to pilot scale*).

Results

Technical accomplishments for the previous two budget periods include successful development, scale-up and electrochemical evaluation of cobalt free batteries using NFA Gen-1 cathode material ($\geq 80\%$ nickel), $\text{LiNi}_{0.8}\text{Fe}_x\text{Al}_y\text{O}_2$ ($x+y=0.2$). During this budget year, the project objective was to develop NFA Gen-2 cathode material with $\geq 90\%$ nickel content, $\text{LiNi}_{0.9}\text{Fe}_x\text{Al}_y\text{O}_2$ ($x+y=0.1$) followed by upscaling and electrochemical evaluation of cobalt-free lithium-ion batteries enabled by NFA Gen-2 cathode material. Compositional variants of the NFA Gen-2 class were initially synthesized using a bench scale sol-gel process to identify and down select the best performing variant for further upscaling using the coprecipitation process in continuous stirred tank reactors (CSTR). Three compositional variants (A, B and C) with varying amounts of iron and aluminum in the cathode compositions were assessed during this study. For the sol-gel process, Ni, Fe, Al, and Li reagents in appropriate molar concentrations were initially dissolved in DI water with citric acid. The solution was then heated and continuously stirred at 60°C to obtain a clear gel. This gel was then completely evaporated to obtain the precursor powders which were then subjected to heat treatment followed by calcination in oxygen atmospheres at temperatures $>700^\circ\text{C}$ to obtain the final cathode powders. The crystallographic characteristics of the various compositional variants of the NFA Gen-2 system is shown in Figure XI.3.1 (a). The diffractograms revealed that the obtained materials had good phase purities and well-ordered crystal structures belonging to the R-3m space group, consistent with the layered pure phase $\alpha\text{-NaFeO}_2$ [3]. Due to the size similarities between Ni^{2+} ions and Li^+ ions, these nickel rich systems may sometimes suffer from cation mixing between the transition metal and the lithium layers. This intermixing results in ion migration bottlenecks which hampers the electrochemical performance of these cathode materials. [4] The extent of cation mixing can be assessed using the ratio between the intensities of (003) and (104) peaks. From the diffractograms it was observed that these materials had high (003)/(104) ratio (>1.5) which indicates minimal cation mixing. Mossbauer spectroscopy (Figure XI.3.1 (b)) was also performed on these materials due to the presence of iron. Analysis of the obtained spectra revealed that iron in these materials is in +3 oxidation state in an asymmetric octahedral site. Electrochemical performance assessment using galvanostatic charge/discharge cycling tests conducted in half cell configurations for the NFA Gen-2 compositional variants is provided in Figure XI.3.1 (c). These materials showed high capacities >190 mAh/g and reasonable cycling stabilities at C/3 between the voltage window 3V-4.5V. Based on the electrochemical performance data, the best performing compositional variant was identified and down selected for further upscaling. Scale-up of the best performing NFA Gen-2 compositional variant was performed using coprecipitation process in a CSTR.

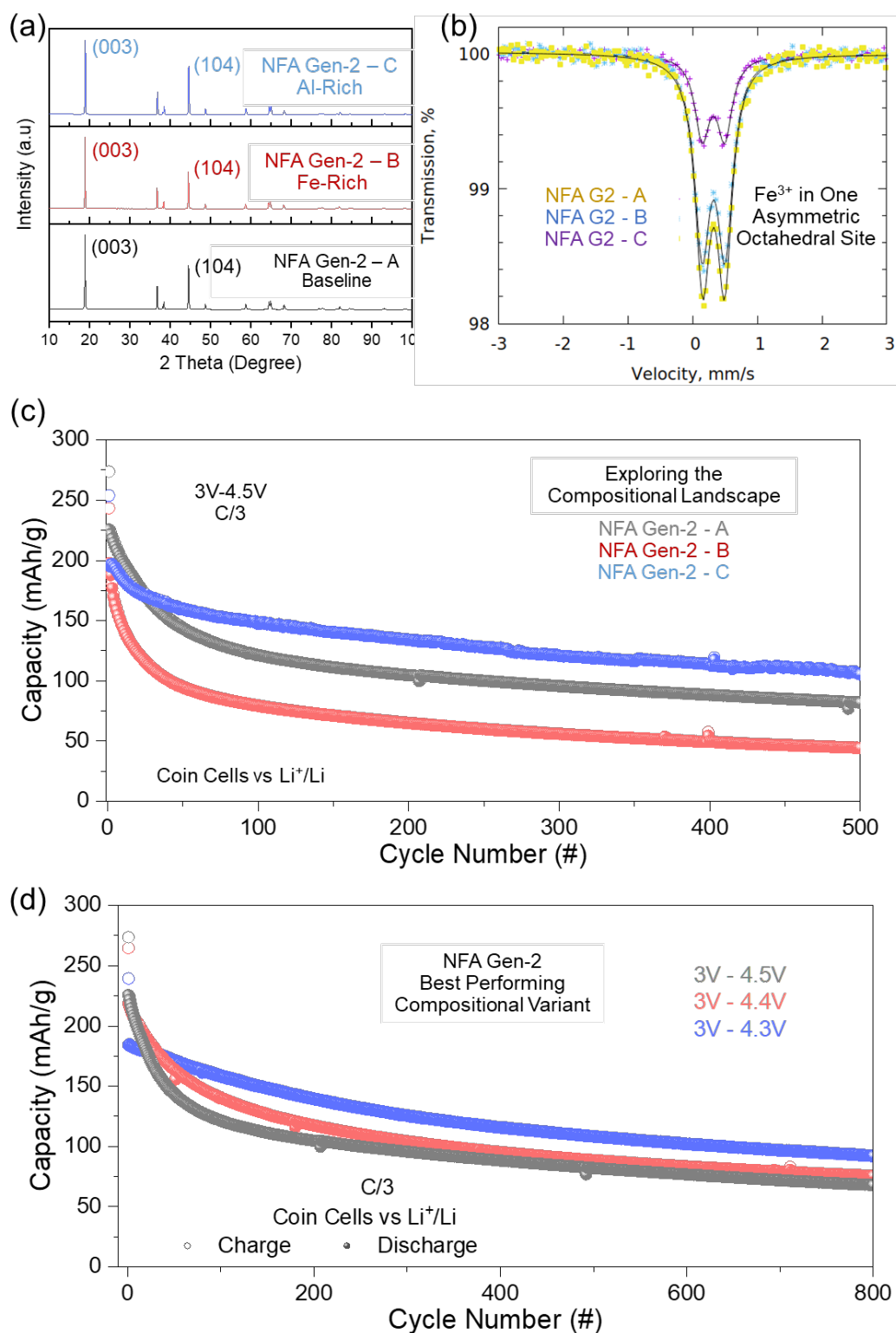


Figure XI.3.1 Material and electrochemical characterization of NFA Gen-2 cathode compositional variants: (a) X-Ray diffractogram, (b) Mossbauer spectra, (c) Galvanostatic charge/discharge cycling performance assessment, (d) Galvanostatic charge/discharge cycling performance of the best performing compositional variant under different voltage windows.

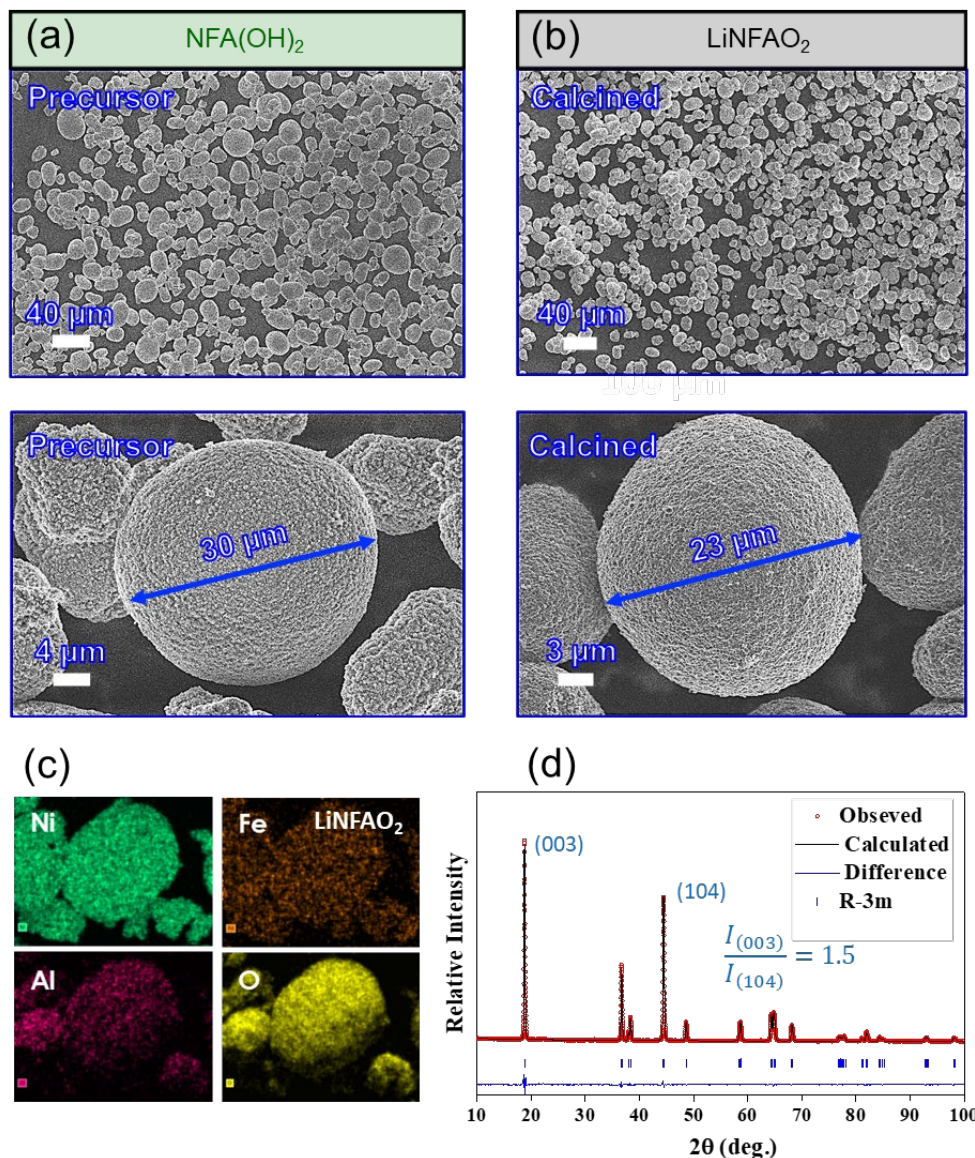


Figure XI.3.2 Upscaled NFA Gen-2 cathode material: SEM micrographs of (a) cathode precursor, (b) calcined cathode material, (c) EDS compositional maps of the calcined cathode material, (d) X-Ray diffractogram of the calcined cathode material.

For the coprecipitation process, the transition metal reagents were pumped into the CSTR reaction vessel at a fixed flow rate. The pH inside the reactor was maintained >11 along with a fixed stirring rate to facilitate optimal precipitation of the metal hydroxide precursor. The obtained precursors were then washed thoroughly, dried and mixed with appropriate amount of a suitable lithium source followed by heat treatment and calcination at temperatures $>700^\circ\text{C}$. The calcined powders were then subjected to material and electrochemical characterization. SEM micrographs of the precursor and calcined NFA gen-2 powders are shown in Figure XI.3.2 (a) and (b). These micrographs indicate that the spherical morphology of the precursor and cathode material were maintained after the calcination process. EDS elemental mapping was also performed on the calcined cathode material which indicate that the constituent elements have been successful incorporated in the spherical cathode particles. X-Ray diffractogram of the calcined powder indicates that the coprecipitation synthesized upscaled NFA Gen-2 material has good phase purity and minimal cation mixing inferred from a high (003)/(104) ratio ~ 1.5 .

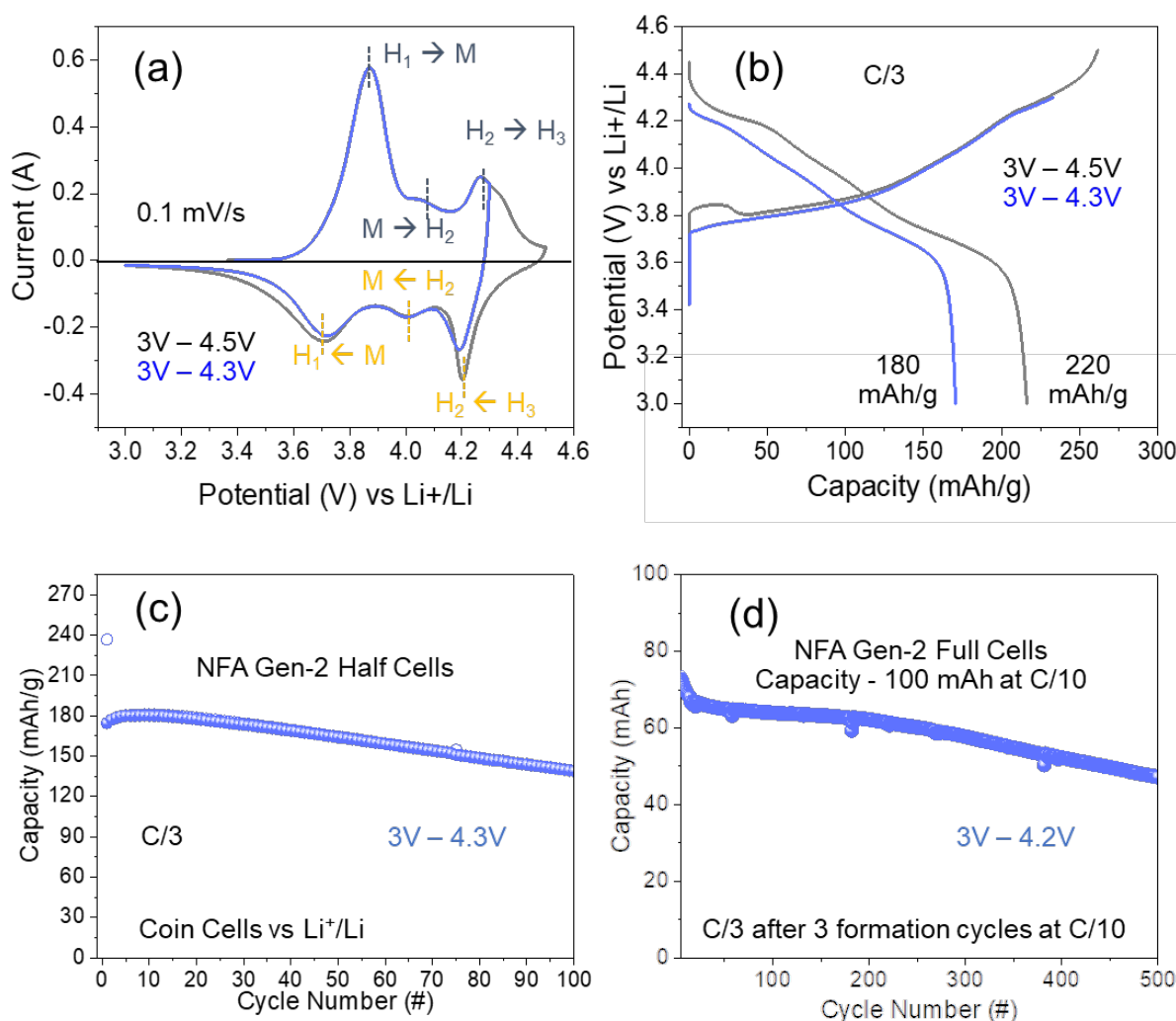


Figure XI.3.3 Electrochemical performance assessment of upscaled NFA Gen-2 cathode material: (a) Cyclic voltammogram, (b) Galvanostatic charge/discharge profiles, (c) Cycling performance assessment in half coin cells and (d) Cycling performance assessment of 100 mAh NFA Gen-2 full cells.

Following material optimization, the NFA Gen-2 cathode material with the desired morphology and composition was subjected to electrochemical performance assessment initially in half cells and then followed by evaluations in full single layer pouch cells and 2 Ah pouch cells. Figure XI.3.3 (a) shows the cyclic voltammogram of the NFA Gen-2 cathode material at a scan rate of 0.1 mV/s between the voltage windows 3V–4.3 and 4.5V. The cobalt-free NFA system shows electrochemical characteristics similar to that of cobalt containing NCM and NCA type materials. Galvanostatic charge/discharge profiles of the NFA Gen-2 material in the two voltage windows at a rate of C/3 is shown in Figure XI.3.3 (b). These materials delivered a high capacity of 220 mAh/g and 180 mAh/g in the voltage windows 3V–4.3V and 3V–4.5V respectively. Cycling stability tests at C/3 for an upper cut off voltage of 4.3V in half coin cells indicate that the material shows reasonable capacity retention after 100 charge/discharge cycles (Figure XI.3.3 (c)). 100 mAh single layer pouch cells were also fabricated and subjected to electrochemical cycling performance assessment. The cobalt-free batteries enabled by NFA Gen-2 cathode materials showed reasonable cycling stabilities with good capacity retention even after 500 continuous cycles. Following this, 2Ah pouch cells were also fabricated and delivered for independent evaluation and performance validation. Overall, these results highlight the potential of the NFA system towards the development of next generation batteries for electric vehicle applications.

Conclusions

In conclusion, this R&D effort was aimed at the successful development and implementation of the novel NFA class of cobalt-free cathode materials as a promising step towards the US DOE's EV battery performance and cost targets. Overall technical accomplishments include the successful synthesis, material characterization, identification and down selection of the best compositional variants, upscaling, battery fabrication and electrochemical performance evaluation of cobalt-free lithium-ion batteries enabled by NFA Gen-1 (Ni 80%) and Gen-2 (Ni 90%) cathodes. These novel cathode materials delivered high capacities (>200 mAh/g) while demonstrating good cycling stabilities. These promising results indicate that the NFA system is an ideal candidate for meeting the overall project objectives. Broadly, the systematic investigations and approaches undertaken as part of this effort provides key insights on the NFA class of cobalt-free materials which shows great potential for developing next-generation LIBs for electric vehicle applications.

Key Publications

1. Muralidharan, Nitin, Rachid Essehli, Raphael P. Hermann, Anand Parejiya, Ruhul Amin, Yaocai Bai, Zhijia Du, and Ilias Belharouak. "LiNixFeyAlzO2, a new cobalt-free layered cathode material for advanced Li-ion batteries." *Journal of Power Sources* 471 (2020): 228389.
2. Muralidharan, Nitin, Rachid Essehli, Raphael P. Hermann, Ruhul Amin, Charl Jafta, Junjie Zhang, Jue Liu et al. "Lithium Iron Aluminum Nickelate, LiNixFeyAlzO2—New Sustainable Cathodes for Next-Generation Cobalt-Free Li-Ion Batteries." *Advanced Materials* 32, no. 34 (2020): 2002960.
3. Belharouak, Ilias, Marissa Wood, Chengyu Mao, Jianlin Li, Jagjit Nanda, and Nitin Muralidharan. "Cobalt-free layered oxide cathodes." U.S. Patent Application 16/750,171, filed July 23, 2020.
4. Belharouak, Ilias, and Nitin Muralidharan. "Battery Materials Scale-up and Processes." U.S. Patent Application 16/781,063, filed August 6, 2020.
5. Muralidharan, Nitin, Rachid Essehli, Ethan Craig Self, Jagjit Nanda, and Ilias Belharouak. "Investigating the Origin of Cation Mixing in Nickel Rich Cathodes." In 236th ECS Meeting (October 13-17, 2019). ECS, 2019.
6. Muralidharan, Nitin; Essehli, Rachid; Amin, Ruhul and Belharouak, Ilias. "Recent Advances in Cobalt-Free Nickel-rich Li-ion Battery Cathode Materials for Next Generation Electric Vehicles." 2021 Meet. Abstr. MA2021-02, 357.
7. Muralidharan, Nitin; Self, Ethan; Nanda, Jagjit and Belharouak, Ilias. "Next-Generation Cobalt-Free Cathodes – A Prospective Solution to The Battery Industry's Cobalt Problem." Accepted Book Chapter – Wiley 2021
8. Muralidharan, Nitin; Self, Ethan; Dixit, Marm; Essehli, Rachid; Amin, Ruhul; Nanda, Jagjit and Belharouak, Ilias. "Next-Generation Cobalt-Free Cathodes – A Prospective Solution to The Battery Industry's Cobalt Problem." Accepted Manuscript – *Advanced Energy Materials*, 2021.

References

1. D. Howell, Vehicle Technologies Office Merit Review 2017: Overview of the DOE VTO Advanced Battery R&D Program, <https://www.energy.gov/eere/vehicles/downloads/vehicle-technologies-office-merit-review-2017-overview-doe-vto-advanced>
2. Sebastien Gandon, No cobalt, no Tesla?, <https://techcrunch.com/2017/01/01/no-cobalt-no-tesla/>
3. Muralidharan, Nitin, Rachid Essehli, Raphael P. Hermann, Ruhul Amin, Charl Jafta, Junjie Zhang, Jue Liu et al. "Lithium Iron Aluminum Nickelate, LiNixFeyAlzO2—New Sustainable Cathodes for Next-Generation Cobalt-Free Li-Ion Batteries." *Advanced Materials* 32, no. 34 (2020): 2002960.

4. Myung, Seung-Taek, Filippo Maglia, Kang-Joon Park, Chong Seung Yoon, Peter Lamp, Sung-Jin Kim, and Yang-Kook Sun. "Nickel-rich layered cathode materials for automotive lithium-ion batteries: achievements and perspectives." *ACS Energy Letters* 2, no. 1 (2016): 196–223.

Acknowledgements

We would like to acknowledge Dr. Nitin Muralidharan, Dr. Rachid Essehli, Dr. Ruhul Amin, Dr. Sergiy Sazhin and Dr. Raphael Hermann for their involvement with the synthesis, characterization, and useful discussions regarding this work.

XI.4 Enhancing Oxygen Stability in Low-Cobalt Layered Oxide Cathode Materials by Three-Dimensional Targeted Doping (UC Irvine)

Huolin Xin, Principal Investigator

University of California, Irvine
4129 Frederick Reines Hall
Irvine, CA 92697
E-mail: huolin.xin@uci.edu

Feng Lin, Principal Investigator

Virginia Tech
Department of Chemistry
Blacksburg, VA 24061
E-mail: fenglin@vt.edu

Kristin Persson, Principal Investigator

University of California Berkeley
210 Hearst Mining Building
Berkeley, CA 94720
E-mail: kristinpersson@berkeley.edu

Wu Xu, Principal Investigator

Pacific Northwest National Laboratory
902 Battelle Boulevard
Richland, WA 99354
E-mail: wu.xu@pnnl.gov

Jiang Fan, Principal Investigator

American Lithium Energy Corporation
2261 Rutherford Road
Carlsbad, CA 92008
E-mail: jfan@americanlithiumenergy.com

Peter Faguy, DOE Technology Development Manager

U.S. Department of Energy
E-mail: Peter.Faguy@ee.doe.gov

Start Date: October 1, 2018

End Date: December 31, 2021

Project Funding: \$1,210,000

DOE share: \$970,000

Non-DOE share: \$243,000

Project Introduction

In this project, we propose to develop a new concept and a generic platform that can lead to the greatly enhanced stabilization of all high-energy cathode materials, and in particular high-nickel (Ni) and low-cobalt (Co) oxides. The new concept is a 3D doping technology that hierarchically combines surface and bulk doping. We will use surface doping to stabilize the surface of primary particles and also introduce dopants in the bulk to further enhance oxygen stability, conductivity, and structural stability in low-Co oxides under high voltage and deep discharging operating conditions. This new concept not only will deliver a low-cost, high-energy cathode but also will provide a generic method that can stabilize all high-energy cathodes. The proposed novel 3D doping approach is poised to resolve some longstanding challenges in fundamental doping effects on

battery materials as well as to reduce Li-ion batteries' cost and improve their safety, energy density, and lifetime.

To tackle this problem, we have formed a highly complementary multi-university/national labs/industry team to enable a doping-central and systematic investigation of low-Co materials and create a knowledge base for many electrode materials to be used in advanced electric vehicles. The successful execution of the proposed project relies on five components that can be carried out by the complementary team members: (1) a theoretical investigation of the surface and bulk stabilizing dopants (Persson), (2) a precise synthesis of materials with targeted doping (Lin and Xin), (3) development of electrolytes for high-Ni low-Co oxides (Xu), (4) multi-scale characterization of the structures and their interfaces by scanning transmission electron microscopy (SEM) and synchrotron X-ray imaging and spectroscopy tools (Xin and Lin), and (5) pouch cell-level integration (Fan). The UCI-led project will enable a doping-central and systematic investigation of low-Co materials and create a knowledge base for many electrode materials to be used in advanced electric vehicles.

Objectives

The primary objectives of this project are:

- Displace Co while maintaining high-Ni content and high energy density: Cobalt concentration < 50 mg/Wh or No-Co, Energy density > 750 Wh/kg (C/3, 2.5–4.4 V) at cathode level, Cost ≤ \$100/kWh.
- Improve cycle and calendar life by retaining oxygen through a 3D doping technology: Capacity retention > 80% at 1,000 cycles, energy retention > 80% at 1,000 cycles, calendar life: 15 years.
- Deliver a theoretical model: High-throughput DFT calculations that rationalize the selection of oxygen-retraining surface and bulk dopants.
- Develop electrolytes with functional additives to form high-quality surface protection layers on both high-Ni/low-Co layered oxides and graphite anode to help the whole project achieve the proposed energy and capacity retention target, i.e., >80% at 1,000 cycles. The FY19 work will focus on electrolyte formulating for NMC811 baseline cathode and graphite anode.
- Offer a knowledge base by performing proactive studies of thermal stability, oxygen loss, and the degradation of the cathode/electrolyte interfaces.

Approach

- We utilize a three-dimensional (3D) doping technology that is a hierarchical combination of surface and bulk doping: (1) Surface doping stabilizes the interface between the primary particles and the electrolyte. (2) Introduction of dopants to the bulk enhances oxygen stability, conductivity, and structural stability in low-Co oxides under high voltage and deep discharging operating conditions. (3) A composition controlled, and thermodynamics driven synthesis will be used to accurately achieve the desired 3D doping structures.
- Using first-principle calculations to predict surface dopants for oxygen retention at surface of LiNiO₂ and rationalize the effectiveness of dopants.
- Formulate new electrolytes that stabilize the cathode/electrolyte interfaces at deep charging conditions: (1) Coin cell testing of commercial baseline materials. Perform coin cell electrochemical studies of baseline commercial NMC811 cathode and graphite (Gr) anode using the baseline electrolyte to establish coin cell-level benchmarks. (2) Coin cell testing of NMC-D. Evaluate the capacity and cycle life of the synthesized 3D doped cathode materials at the coin cell level using the baseline electrolyte. The results will be compared with the commercial NMC811 baseline. (3) Electrolyte formulating. Formulate functional localized high-concentration electrolytes (LHCEs) to

improve cycle life and safety of baseline commercial NMC811 cathode and Gr anode at the coin cell level, optimize electrolyte formulation for NMC-D-90532, and compare with electrolyte baseline for >200 cycles in Gr||NMC full cells at a 4.4 V cutoff.

- Advanced computational and characterization techniques are developed to study: (1) dopant environment and chemistry. (2) thermal stability, oxygen loss, and the degradation of the cathode/electrolyte interfaces.

Results

1. Synthesis optimization, full-cell-level long-term cycling performance and the mechanistic study of UCI Gen2 cathode

In FY21, the UCI team has optimized the synthesis of UCI Gen2 cathode, performed thermal stability tests and full-cell-level long-term cycling tests of UCI Gen2 cathode at different cut-off voltages. Figure XI.4.1a presents the experimental set-up for the coprecipitation and representative SEM images showing the morphology of the precursor and secondary particles of UCI Gen2 cathode. To evaluate the thermal stability of UCI Gen2 cathode, differential scanning calorimetry (DSC) was performed on UCI Gen2 cathode and a series of Ni-rich cathodes including NMC-811, NMC-622, NMC-532, and LNO. The results (Figure XI.4.1b) show that for the conventional Ni-rich cathodes, the maximum heat flow and thereby the thermal stability of the cathode monotonically decreases with the increase of Ni content. However, for the UCI Gen2 cathode which has exactly the same Ni-content (80%) as that in NMC-811, it delivers a maximum heat flow at 286°C, remarkably higher than the 230°C of NMC-811 and even approaching the 292°C of NMC-532. That is to say, our Co-free chemistry (UCI Gen2) cathode breaks the trade-off between Ni content and thermal stability of the Ni-rich cathodes. Figure XI.4.1c shows the capacity retention and Coulombic efficiency of the UCI-Gen2 cathode at different cut-off voltages. The results show that after 100 cycles, 99.5% capacity retention was achieved within 2.5–4.2V, and 98.9% capacity retention was obtained within 2.5–4.3V. The structural stability of the UCI-Gen2 cathode was evaluated by TXM tomography at the secondary-particle level. Figure XI.4.1d shows the 3D reconstructions and analyses of a representative long-term-cycled NMC-811 and UCI-Gen2 secondary particle, respectively. The results show that after cycling, substantial intergranular cracks (indicated by the arrows) formed inside the NMC-811 cathode, while no obvious cracks are observed in the UCI-Gen2 cathode. SEM cross-section results are in good agreement with the TXM tomography results. We have also performed mechanistic study of the UCI-Gen2 cathode by XANES and EXAFS. Figure XI.4.1e shows the Ni-K XANES and FT-EXAFS of UCI-Gen2 and commercial NMC-811 at different cycles. The Ni-K XANES curve of the cycled sample overlays well with that of the pristine sample, showing that the UCI-Gen2 has excellent local stability during cycling. In contrast, for the commercial NMC-811, the Ni-K absorption edge of the cycled electrode moves to higher energy slightly, indicating that oxidization occurred during the cycling. FT-EXAFS results show that the Ni-TM coordination length in UCI-Gen2 remains stable after cycling, while for NMC-811, the Ni-TM coordination length shrinks after long cycles.

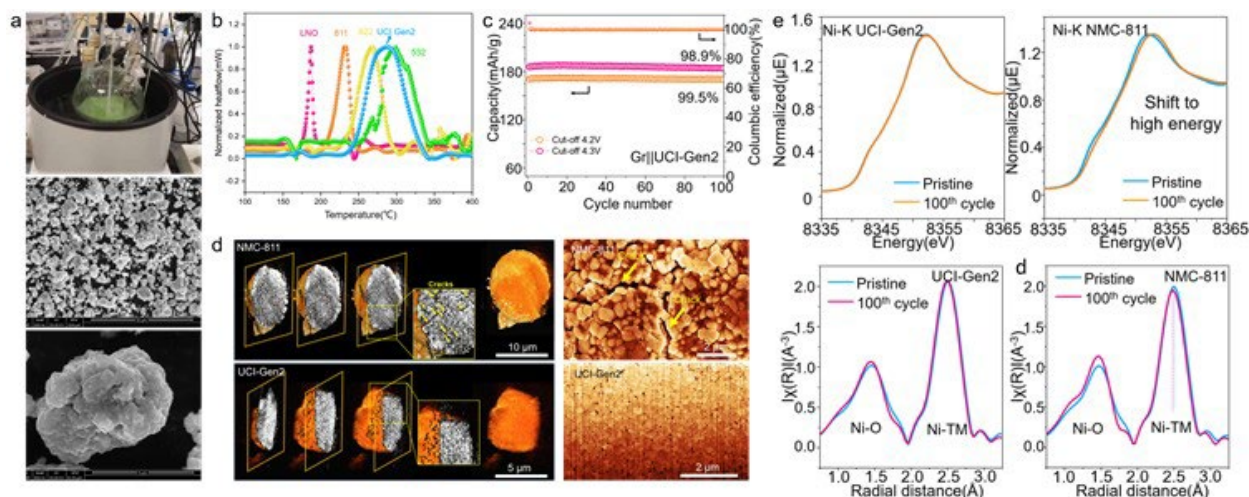


Figure XI.4.1 (a) Experimental set-up for the coprecipitation of UCI Gen2 cathode with a 2-liter batch reactor (the upper panel) and the morphology of the precursor (the middle panel) and secondary particles (the lower panel). (b) DSC profiles of LNO, NMC-811, NMC-622, NMC-532, and UCI Gen2 cathode charged to 4.3 V. (c) Full-cell long-term cycling performance of UCI Gen2 cathode with graphite as an anode. (d) TXM tomography and FIB cross-section of the long-cycled UCI-Gen2 cathode in comparison with NMC-811(100 cycles, 2.5V-4.4V, 1C). (e) Ni-K XANES and FT-EXAFS of UCI-Gen2 and commercial NMC-811 at different cycles.

2. Synthesis, electrochemical tests, and the mechanistic study of single-crystalline NMC-811 and UCI Gen2 cathodes

In FY21, the UCI team has performed a pathfinder test synthesis of single-crystalline NMC-811 cathodes, detailed structural characterization, and electrochemical evaluations. SEM images (Figure XI.4.2a) of the synthesized NMC-811 single-crystalline cathode show that the particles have uniform morphology and an average diameter of ~ 2 μm . Atomic-resolution HAADF-STEM image (Figure XI.4.2b) and electron diffraction (Figure XI.4.2c) show that the single-crystalline cathode has a well-defined layered structure. Electrochemical tests (Figure XI.4.2d) show that the cathode exhibits an excellent discharge capacity of ~ 210 mAh/g, comparable to that of the polycrystal NMC-811. Rate capability tests show that the capacity of the single-crystalline NMC-811 is worse than its polycrystalline counterpart particularly at a high rate, which is in accordance with expectations. EIS curves of the half-cells containing single-crystalline and polycrystalline NMC-811 before and after the formation step show that the impedance in the single-crystalline cathode is much lower than that in its polycrystalline counterpart, indicating less surface reconstruction in the former. TXM tomography (Figure XI.4.2e) was performed on the long cycled single-crystalline NMC-811. Different from the cracking behavior widely observed in the secondary particles of polycrystalline cathodes, the single-crystalline NMC-811 particles remain intact as cracks are not observed in the tomographic reconstruction. Based on the optimized synthesis conditions used for the single-crystalline NMC-811, the UCI team synthesized single-crystalline cathodes using the UCI-Gen2 chemistry. Figure XI.4.2f presents representative SEM images showing the morphology of the calcinated cathodes using two different methods. The cathodes synthesized by method 1 still show secondary particle morphology composed of polycrystals. As for the cathodes synthesized by method 2, although a certain amount of single crystals are formed, bunches of polycrystalline particles decorated on the single-crystalline particles are also identified. The calcination condition will be further optimized to get better single-crystalline UCI-Gen2 cathodes.

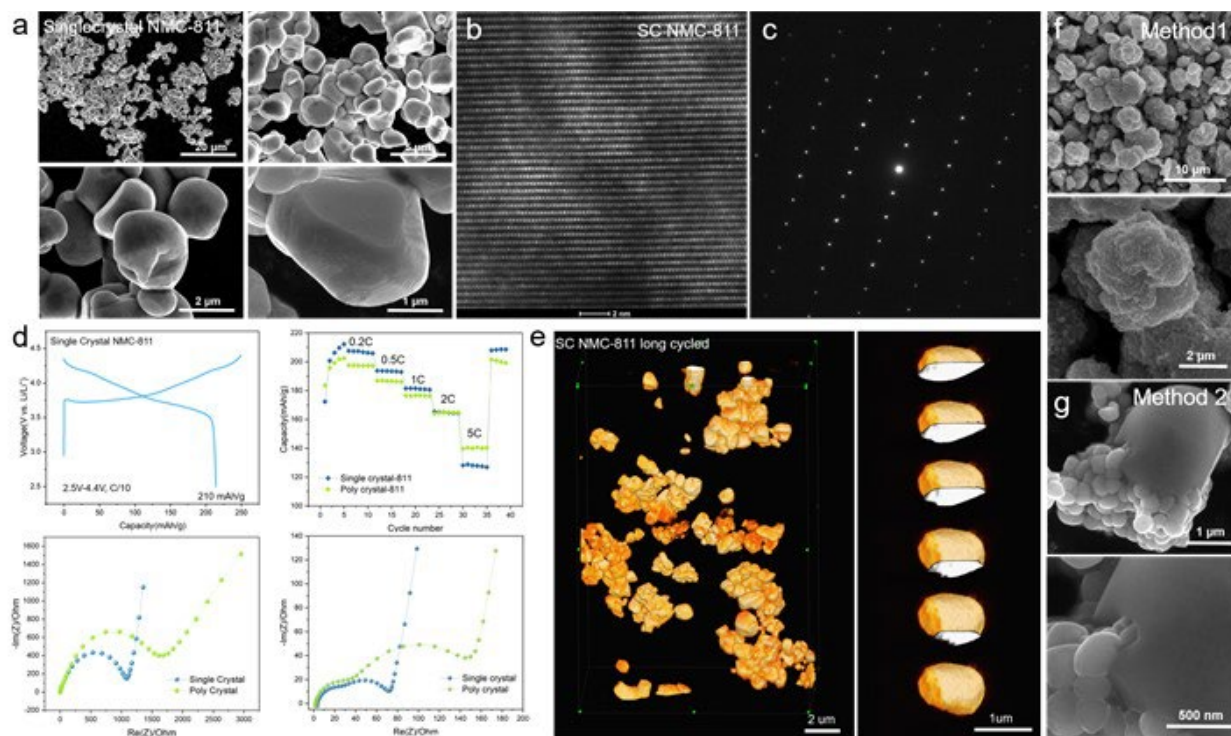


Figure XI.4.2 (a) SEM images of the synthesized single-crystalline NMC-811. (b) HAADF-STEM image and (c) electron diffraction of single-crystalline NMC-811. (d) Charge/discharge profiles, rate capability and impedance tests of the single-crystal NMC-811 in comparison with its polycrystal counterpart. (e) TXM tomography of the single-crystalline NMC-811 cathode after long cycling. (f,g) SEM images showing the morphology of the single-crystalline UCI-Gen2 cathodes synthesized by two different methods.

3. Mechanistic study on the chemomechanical degradation of LNO and VT Gen 2 cathode

The chemomechanical degradation mechanisms of LNO and VT Gen 2 cathode were comparatively studied by the UCI team. By combining in-situ electron microscopy and first-principles calculations, we elucidate the atomic-level chemomechanical degradation pathway of LiNiO₂-derived cathodes. We uncover that O1 phase formed at high voltages acts as preferential sites for rock-salt transformation via a two-step pathway involving cation-mixing and shear along (003) planes (Figure XI.4.3a). Moreover, electron tomography (Figure XI.4.3b) reveals that planar cracks nucleated simultaneously from particle interior and surface propagate along [100] direction on (003) planes, accompanied by concurrent structural degradation in a discrete manner (Figure XI.4.3c). Our results provide in-depth understanding of the degradation mechanism of LNO-derived cathodes, pointing out the direction that suppressing the O1 phase as well as oxygen loss is the key in stabilizing LNO for developing next-generation high-energy cathode materials. Several useful guidelines could be gained from the above findings. Firstly, the O1 phase which forms in a deep delithiation state should be suppressed to mitigate oxygen loss and rock salt transformation. Secondly, efforts on protecting only the surface of primary particles will not be sufficient to improve the mechanical stability of primary particles regarding prohibiting cracks formation and propagation. To achieve that, both surface and bulk of primary particles need to be protected, e.g., through concurrent 3D bulk and surface doping as demonstrated in Ti/Mg co-doped LNO. We also performed a detailed analysis on the structure of LNO cycled at an ultrahigh voltage (4.7 V). We found that after extensive cycling, a layer of rock salt-structured material is formed on the particle surface due to severe surface oxygen loss, while aside from that, substantial amounts of O1 phase or O1+O3 mixture (Figure XI.4.3d) are identified near the particle surface. Because a large part of the particle interior remains in the O1 phase even after discharge, it is likely that the penetration depth of lithiation is limited due to the high energy barrier for Li⁺ intercalating back to the O1 faulted phase. The contraction of the *c* axis (perpendicular to the (003) plane) of the O1 phase compared with that of the O3 phase results in a misfit strain along the *c* axis at the O1/O3 interface. Consequently, misfit dislocations (Figure XI.4.3e) are formed and cation mixing was observed in the dislocation core, resulting in the development of a rock salt embryo. In the meantime, a

considerable lattice expansion is identified in the interfacial O3 phase adjacent to the dislocation core, which could act as a nucleus for pore or crack initiation. The result implies that the strained O1/O3 interface possibly provides a highway for oxygen loss, rocksalt transformation, and intragranular cracking.

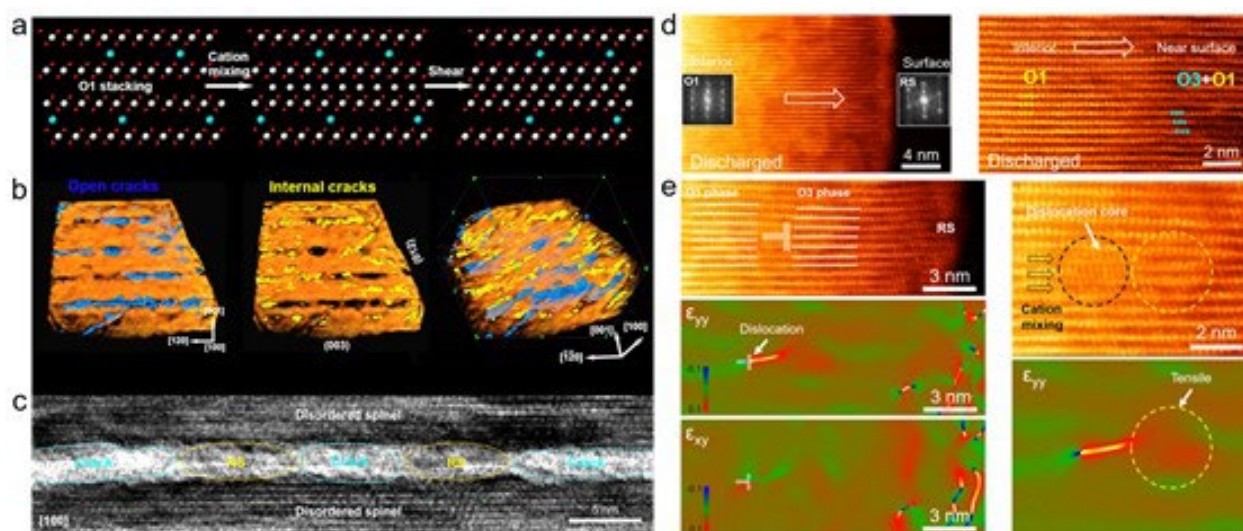


Figure XI.4.3 (a) Schematic of the two-step transformation from O1 phase to rocksalt. (b) 3D imaging of the cracks in LNO with severe oxygen loss. (c) HRTEM image of a crack formed in the doped LNO showing an alternating arrangement of RS and cracks. (d) Atomic-resolution images showing the formation of O1 phase in discharged LNO after cycling. (e) Misfit strain and defect generation at O1/O3 interface.

4. Structural change and phase transformation at different stages of the synthesis of VT Gen 2 material

The VT Group has performed synchrotron XRD at different stages of calcination to study the structural change and phase transformation (Figure XI.4.4a). The mixed metal hydroxide and LiOH are thoroughly mixed to prepare the precursor before calcination. Ni hydroxide predominates the metal hydroxide and the effect of Mg/Ti dopants on the diffraction pattern is trivial due to the low content. A mixture of LiOH phase and $\text{Ni}(\text{OH})_2$ phase is observed from the diffraction peaks. As the temperature reaches 300°C , the bi-phase gradually transforms to an intermediate phase X, where $\text{Ni}(\text{OH})_2$ and LiOH characteristic peaks diminish and the rock-salt NiO-like characteristic peaks appear. When the temperature reaches 700°C , several diffraction peaks of LiNiO_2 start to grow, which indicates the formation of a new phase named as L. As the temperature is held at 700°C for a longer time, the intensity of LiNiO_2 diffraction peaks further increases, and the peaks become narrower due to the overall increased crystallinity and particle growth. The appearance of the (003) peak implies the formation of the layered structure. The overall increased intensity of (003) and (104) peaks and the (003)/(104) intensity ratio reveal less Ni/Li cation mixing and a better-defined layered structure (Figure XI.4.4b,c). Moreover, the (220) peak in the rock-salt NiO converts to the (108) peak and (110) peak in the layered LiNiO_2 also suggests the formation of the layered structure. The neutron diffraction patterns imply the co-existence of three phases at high temperatures, i.e., layered $(\text{Li}_{1-x}\text{Ni}_x)(\text{Ni}_{0.96-x}\text{Li}_x\text{Mg}_{0.02}\text{Ti}_{0.02})\text{O}_2$ phase, monoclinic Li-rich phase, and Li_2CO_3 phase (Figure XI.4.4d). From 600°C to the 700°C holding stage, the fraction of the layered oxide phase increases while the monoclinic Li-rich phase diminishes and almost disappears at 700°C . Both Mg and Ti remain on the Ni site after 600°C until the formation of the cathode product (Figure XI.4.4d). The XRD result further confirms that the metal hydroxide phase is still present at the temperature (below 300°C) when Mg/Ti dopants diffuse into the matrix. In brief, phase transformation takes place from the mixed hydroxide bi-phase to the layered L phase through an intermediate metal oxide-like X phase, and dopants diffuse into the metal hydroxide matrix below 300°C .

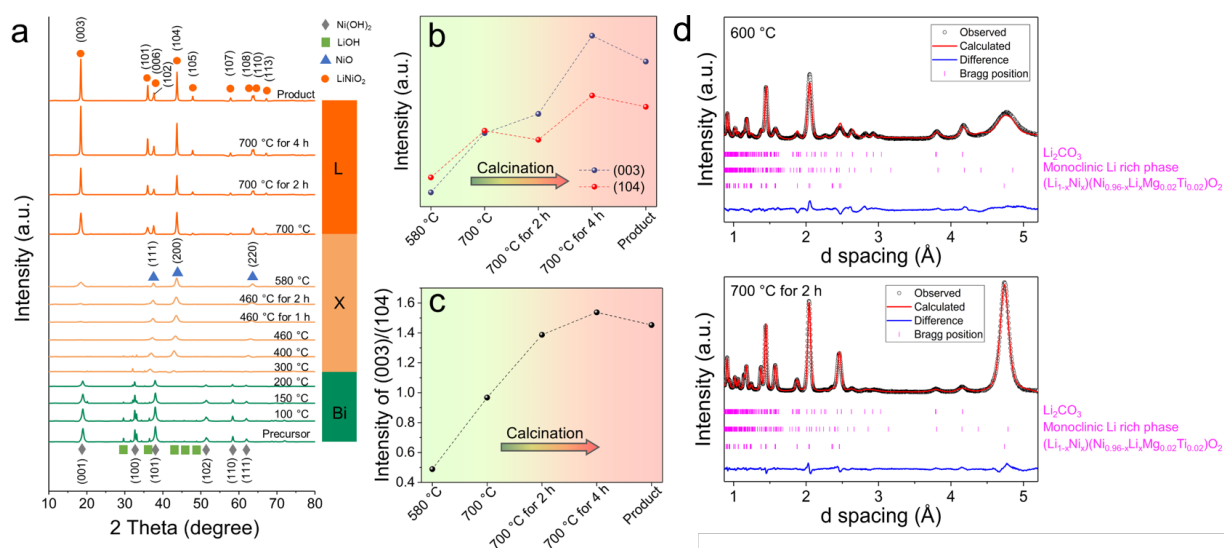


Figure XI.4.4 (a) XRD patterns at different stages of calcination. (b) Evolution of the normalized intensity of the (003) peak and the (104) peak. (c) The intensity ratio of the (003) peak to the (104) peak at different stages of calcination. (d) Neutron diffraction patterns and Rietveld refinement at 600 °C and 700 °C for 2 h.

5. Performance evaluation of the VT Gen 2 cathode at the temperatures of 22 °C and 60 °C

The surface instability of Co-free Ni-rich layered cathodes can become more severe at elevated temperatures through accelerating chemical/electrochemical reactions. Thus, we evaluated and compared the cycling performance of the VT Gen 2 cathode material at the temperatures of 22 and 60 °C. The elevated temperature facilitated the reversible capacity, indicated by the slightly higher discharge capacity of $\sim 220 \text{ mAh g}^{-1}$ at C/10 (Figure XI.4.5a) compared to the cell cycled at 22 °C with a discharge capacity of $\sim 208 \text{ mAh g}^{-1}$. However, the lower initial Coulombic efficiency of $\sim 70\%$ ($\sim 86\%$ for the cells at 22 °C) suggests the combination of accelerated side reactions and electrolyte decomposition. The charge/discharge profiles in the initial 10 cycles overlapped well. At the current rate of C/3, the capacity retention at 60 °C was much lower than that at 22 °C after 100 cycles (Figure XI.4.5b, the capacity retentions were 72% and 93% of the cells cycled at 60 °C and 22 °C, respectively). These results present the challenge that the LiNiO_2 based materials face at elevated temperatures. Metal dissolution (nickel in this case), representing one aspect of surface instability, can be studied through performing X-ray fluorescence microscopy (XFM) measurements on the cycled anodes to quantitatively analyze the Ni dissolution at different temperatures. The Ni concentrations (Figure XI.4.5c) on the counter Li anodes distributed within 0–5 and 10–28 nmol cm^{-2} , giving an average concentration of 3.12 and 18.16 nmol cm^{-2} at 22 °C and 60 °C, respectively. The concentration of nickel deposited on the lithium anode at 60 °C was roughly six times higher than that at 22 °C. Additionally, we found that the Ni distribution on the Li anodes was highly inhomogeneous for both cases (Figure XI.4.5d, e). The observation may be associated with the inhomogeneous solid electrolyte interface (SEI) formation. The cathode–electrolyte interface (CEI) can be easily disrupted at elevated temperature, which exposes freshly reactive surfaces that subsequently undergo continuously interfacial reactions, accelerating the degradation process. The multiplied nickel concentration on the anode side is one consequence of the unstable CEI at 60 °C.

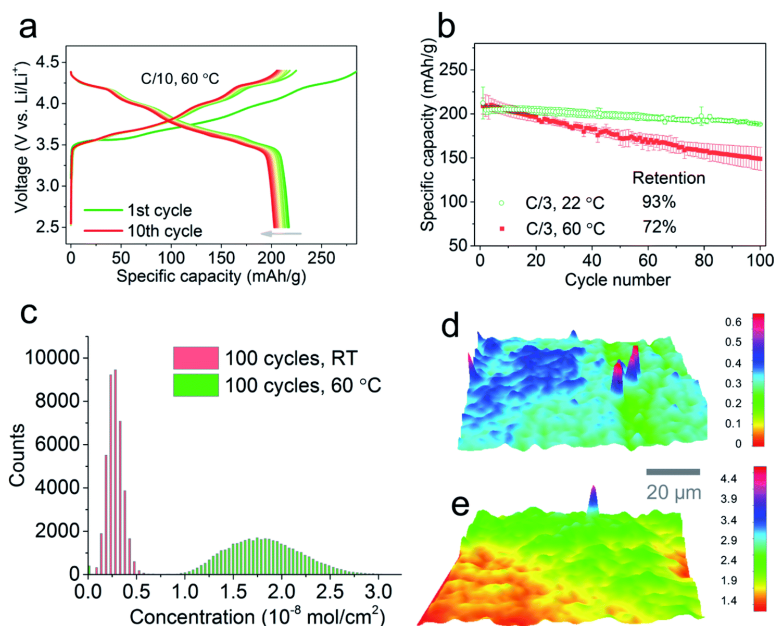


Figure XI.4.5 (a) Charge/discharge profiles of the cell containing VT Gen 2 cathode at C/10 at 60 °C. (b) The comparison of the cycling stability of the cells operated at 22 °C and 60 °C. (c) Concentration histogram of the Ni deposited on the Li anodes cycled against the VT Gen 2 cathode at different temperatures, the Ni concentration (unit: $10^{-8} \text{ mol cm}^{-2}$) distribution on the Li anodes cycled at (d) 22 °C and (e) 60 °C.

6. Calculation of the phase diagrams of pristine and doped LiNiO_2

In FY21, we explored various doping elements with different ionic radii and valent states. For doped $\text{LiNi}_{1-y}\text{M}_y\text{O}_2$ (M is the doping element), we consider three different phases: O3, O1-3 and O1, and use Gibbs formation energy (G_f) to determine the phase stability as a function of Li content. We use Canonical Monte Carlo (CMC) simulations to obtain the ground states and the phase diagrams. Here, we take Li_xNiO_2 and $\text{Li}_{1-x}\text{Ni}_{0.98}\text{M}_{0.02}\text{O}_2$ as examples and discuss their calculated Gibbs formation energy convex hull and phase transitions.

We find that in Li_xNiO_2 O3 is stable for $x \leq 0.75$. A two-phase region consisting of O3 and O1-3 appears between $0.75 < x < 1$. On the other hand, in $\text{Li}_{1-x}\text{Ni}_{0.98}\text{M}_{0.02}\text{O}_2$ O3 is stable for $x \leq 0.5$. A two-phase region consisting of O3 and O1 appears between $0.5 < x < 0.75$. Upon further delithiation, an O1+O1-3 two-phase region appears. The widths of the two-phase regions may be smaller than is shown, as we find that in our pristine and doped LiNiO_2 systems the G_f differences are relatively small across the three phases near the phase boundaries, e.g., less than 3 meV/f.u. The calculated phase diagrams are obtained using fixed Li chemical potentials and varying temperature trajectories. We are currently exploring grand canonical Monte Carlo (GCMC) simulations to generate the phase diagrams using fixed temperature and varying Li chemical potentials trajectories. Based on the phase diagrams calculated by CMC simulations, we find a correlation between the effectiveness of doping elements on mitigating phase transitions and their ionic radii and valent states. We will compare the phase diagrams generated by CMC and GCMC and validate our conclusions in the phase stability of pristine and doped LiNiO_2 .

Similar to the CMC approach, we start by constructing cluster expansions for O3, O1-3, and O1 phases. From the fitted cluster expansions, we can extract the effective cluster interaction (ECI) values, which are expansion coefficients describing the dependence of the energy of the crystal on different configurations. The positive ECI indicates a Li-Li repulsion, whereas the negative value indicates an attraction. We find that the ECI corresponding to the first-nearest neighbor pair cluster is the largest, and quickly decays with cluster radius. In O3 phase, there exists a non-negligible attractive interaction between Li ions in different planes, which results from the coupling of the Li ions with the Jahn-Teller distortion of Ni^{3+} centers.

7. Evaluation of NMT performance in pouch cells

In FY21, the NMT electrode sheets were successfully tuned to the required areal capacity loadings (1.5 mAh cm^{-2} and 3.0 mAh cm^{-2}), and the Gr||NMT pouch cells were assembled with two electrolytes – one baseline electrolyte and another DME-based LHCE. The NMT cathode with the areal capacity of 1.5 mAh cm^{-2} was coupled with ANL 1.84 mAh cm^{-2} Gr electrode to make single layer pouch cells (SLPCs), while the NMT cathode with the areal capacity of 3.0 mAh cm^{-2} was coupled with ALE 3.5 mAh cm^{-2} Gr electrode to make double layer pouch cells (DLPCs). These Gr||NMT pouch cells were conducted formation cycles at C/10 rate and then cycling at C/3 charge and C/3 discharge in the voltage range of 2.5-4.4 V at 25°C (Figure XI.4.6). It is seen that the cells using the DME-based LHCE achieved significantly improved capacity retentions compared with those using E-baseline. After 500 cycles, the capacity retentions of SLPCs and DLPCs using DME-based LHCE amounted to 79.4% and 70.9%, respectively, while those of SLPCs and DLPCs using E-baseline were merely 57.2% and 59.8%, respectively. Based on the results, it can be concluded that the DME-based LHCE is a highly favorable electrolyte for the Gr||NMT cell chemistry.

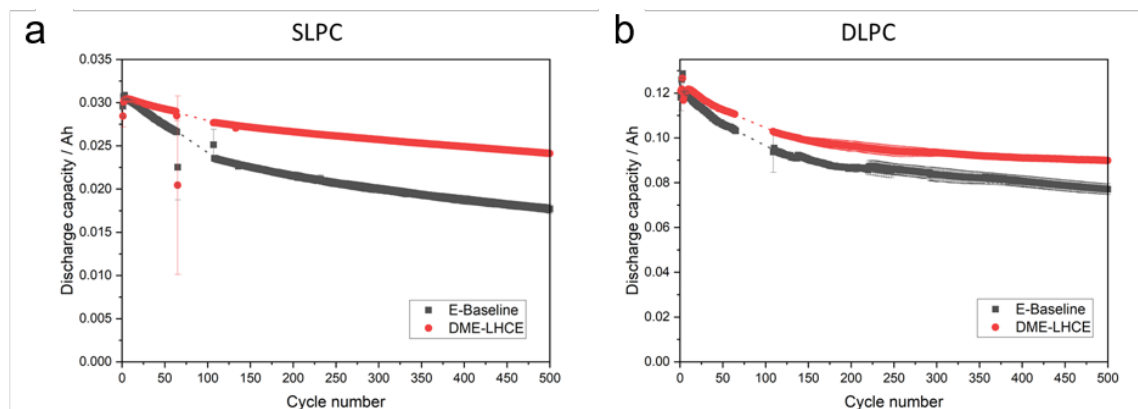


Figure XI.4.6 Average discharge capacities of (a) Gr||NMT SLPCs and (b) Gr||NMT DLPCs plotted as the function of cycle number in the voltage range of 2.8-4.4 V and at 25.0°C . The missing data in the figures was caused by the malfunction of the battery tester.

8. Evaluation of polymer coating layer protected NMT particles

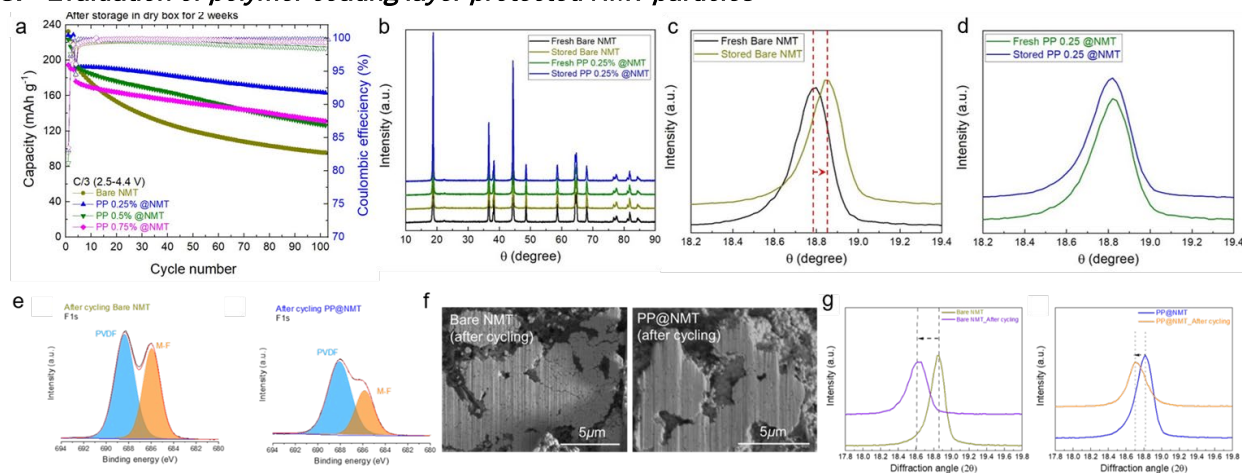


Figure XI.4.7 (a) Cycle performances of Gr||NMT batteries using Bare NMT and various ratios of PP coated NMT after storage in the dry box for 2 weeks. (b-d) XRD patterns of fresh and stored Bare NMT and PP 0.25%@NMT. (e) XPS F1s spectra of bare NMT and PP@NMT. (f) Cross-sectional SEM images of bare NMT and PP@NMT. (g) The (003) peak from XRD patterns of bare NMT and PP@NMT after cycling at C/3 rate under 25°C of Gr||NMT batteries using NMTs after storage in the air for 2 weeks ($1\text{C} = 200 \text{ mA g}^{-1}$ or 1.5 mA cm^{-2}).

The exposure of NMT to air and moisture generates residual Li compounds such as Li_2CO_3 and LiOH on the NMT surface and these surface contaminations trigger the increase in internal resistance and degradation of cell performance. To suppress this issue, we conducted the surface coating on NMT particles to protect the NMT materials in FY21. A protective polymer coating layer (abbreviated as PP) was successfully coated on NMT particles with various thicknesses. To demonstrate the protection effect, the bare and PP-coated NMT active materials were stored in a dry box for two weeks before measuring the cell performance. The cycling performances of Gr||NMT batteries (Figure XI.4.7a) show that among various coating amounts, PP 0.25wt.% coated NMT (referred to as PP 0.25%@NMT) shows the best cell performance. This indicates that the 0.25wt.% of PP coating layer may serve optimum coverage to prevent contamination. To further verify the role of the PP coating layer, X-ray powder diffraction (XRD) results (Figure XI.4.7b–d) show that after storage in a dry box for 2 weeks, the (003) peak of the bare NMT shifts to a higher angle indicating the structure shrinkage along c-axis, which should be caused by the loss of Li ion from the NMT during the surface reaction with moisture. While the PP 0.25%@NMT presents no structure change after storage. These results demonstrate that the PP coating layer could effectively prevent the generation of residual compounds on the surface. To understand the enhanced cycle performance, XPS F1s spectra were employed to characterize the cycled NMT cathodes. After 100 cycles, the bare NMT shows a strong metal (M)-F peak (685.2 eV, F1s in Figure XI.4.7e), which should originate from the HF attack in the LiPF_6 /carbonate electrolyte. However, the PP@NMT has a lower M-F peak than Bare NMT, demonstrating the PP layer serves the protection against the side reactions and the suppression of generation of byproducts such as NiF between cathode surface and electrolyte. SEM results (Figure XI.4.7f) show that the cycled bare NMT cathodes suffer from cracks while the cycled PP@NMT cathodes remain intact. XRD patterns show that the (003) peak of bare NMT cathode shifts to a lower angle, indicating destruction of the layered characteristic compared to PP@NMT (Figure XI.4.7g). These results indicate the PP coating layer could effectively prevent not only the generation of the residual compounds on the surface but also the side reactions during cycling, resulting in an improvement of battery performance.

9. Advanced Gr||NMT batteries test using localized high-concentration electrolyte

To achieve further improvement in cell performance of the Gr||NMT batteries using the exposed PP@NMT cathode, the E-DME-F, which can form a stable SEI layer, was selected among various LHCE candidates. The Gr||NMT cell using the exposed PP@NMT cathode and E-DME-F shows high-capacity retention of 86.7% after 500 cycles at room temperature (Figure XI.4.8a). In comparison, the capacity retention of the Gr||NMT cell using E-baseline (1M LiPF_6 in EC:EMC (3:7 w/w) + 2% VC) presents only 63.2% after 500 cycles. The enhanced capacity retention of the E-DME-F cell was further verified by the AC impedance spectra after cycling (Figure XI.4.8b). The charge-transfer resistance is considerably suppressed in the cell using the E-DME-F after 500 cycles. These results demonstrate that the combination of coating strategy and advanced electrolyte can significantly enhance the lifespan of batteries using NMT even after its exposure to moisture and air.

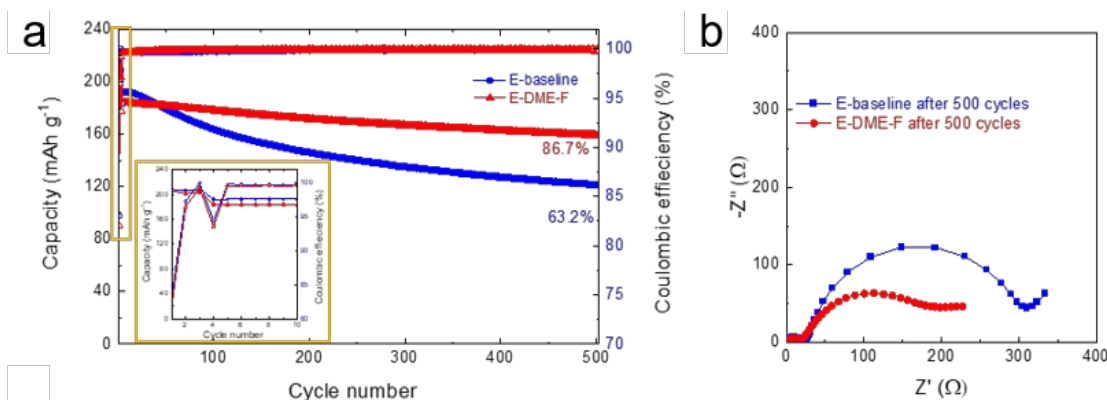


Figure XI.4.8 (a) Cycle performances and (b) Nyquist plots after 500 cycles at C/3 rate under 25 °C of Gr||NMT cells with the exposed PP@NMT using E-baseline and E-DME-F.

10. Cell assembly and testing of PNNL electrolytes

In FY21, we have performed cell assembly and testing of the PNNL electrolytes, i.e., AE-003 (carbonate-based) and ALE-01 (ether-based), in comparison to the baseline PPC cells. All cell materials except the electrolyte were the same for both batches of cells. Formation and testing procedures were also kept the same for both batches. Cells with the three electrolytes were cycled at room temperature (Figure XI.4.9a) and at 45°C (Figure XI.4.9b). Cells were charged galvanostatically to 4.4 V at 1 A (C/3) and then potentiostatically at 4.4 V until the current was below 150 mA (C/20). The cells were then galvanostatically discharged at 1 A (C/3) to 2.5 V to complete one cycle. After approximately 60 cycles, the baseline cell capacity decreased from 3.089 Ah to 2.443 Ah, a loss of 20.9%. By comparison, the cell with carbonate-based electrolyte, AE-003, had an initial capacity of 3.092 Ah and, after 60 cycles, the capacity decreased to 2.681 Ah, a loss of 13.3% and nearly half the loss of the cell with the baseline electrolyte. Interestingly, the failure modes of the electrolytes are very different. The baseline electrolyte initially shows a remarkably high Coulombic efficiency of 99.9%, which gradually decreases as cycling progresses. By contrast, the carbonate-based LHCE shows lower Coulombic efficiency that gradually increases to 99.7%. This indicates the baseline cell may not be fully passivated and electrolyte consumption may be ongoing, while the carbonate-based LHCE may have some initial issues with wetting, but as cycling progresses the SEI/CEI is more stable. The cycle performance of the ether-based LHCE was the poorest. The cell had an initial capacity of 3.102 Ah and after 60 cycles the capacity decreased to 2.294 Ah, a loss of 26.0%. Towards the end of cycling, Coulombic efficiency begins to drop precipitously indicating the onset of Li plating and soft-shortening within the cell. Cycle life data at 45°C is still immature, and no concrete conclusions can be drawn. Still, it appears the baseline cell is losing capacity the fastest. Indeed, the baseline cell also has the lowest average Coulombic efficiency.

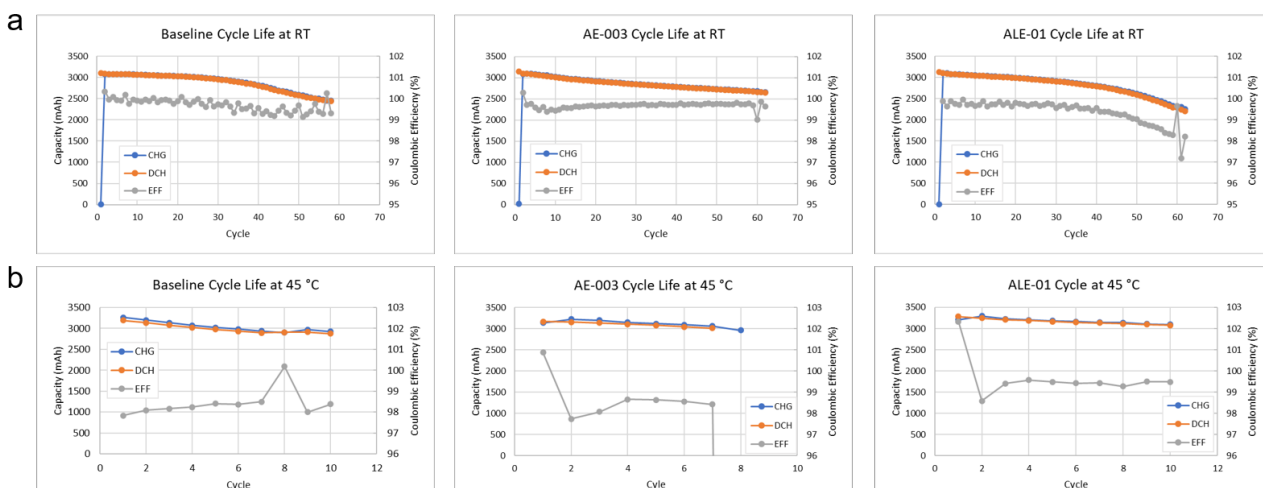


Figure XI.4.9 Testing results from cycling at RT and at 45 °C

The cells were also evaluated for their low-temperature performance (Figure XI.4.10a). Cells were charged to 4.4V at room temperature using the same charging profile as described in cycle life. Cells were then placed in an environmental chamber and cooled to the test temperature. Following thermal equilibration, cells were discharged at 1 A (C/3) to 2.5 V. The baseline cell and the AE-003 cell performed nearly identically, with very similar capacity activation down to -30°C. The ALE-01 cell capacity retention falls off below 0°C. To evaluate the thermal stability of the electrolyte, cells were also fully charged using the procedure described in the cycle life section. They were then placed in an oven at 60 C for 1 week to age the cells. After 1 week, a discharge rate test was performed by galvanostatically discharging the cells at various currents from C/5 to 3C. After storage, the baseline cell only activated 94.7% of its initial (before storage) capacity at C/3 and activated 72.9% of its initial capacity at 3C when compared to discharge rate capability testing results before storage, indicating both capacity and power loss (Figure XI.4.10b). The AE-003 cell activated 97.3% of its initial C/3 capacity and 69.1% of its initial 3C capacity, indicating power loss is the primary performance degradation. The ALE-01 cell activated 98.3% of its initial C/3 capacity and 77.8% of its 3C capacity. For this test, the

ALE-01 cell had the least performance degradation, which correlates well to the calendar life test, which was also performed at elevated temperatures. These two tests will both be reevaluated in future work.

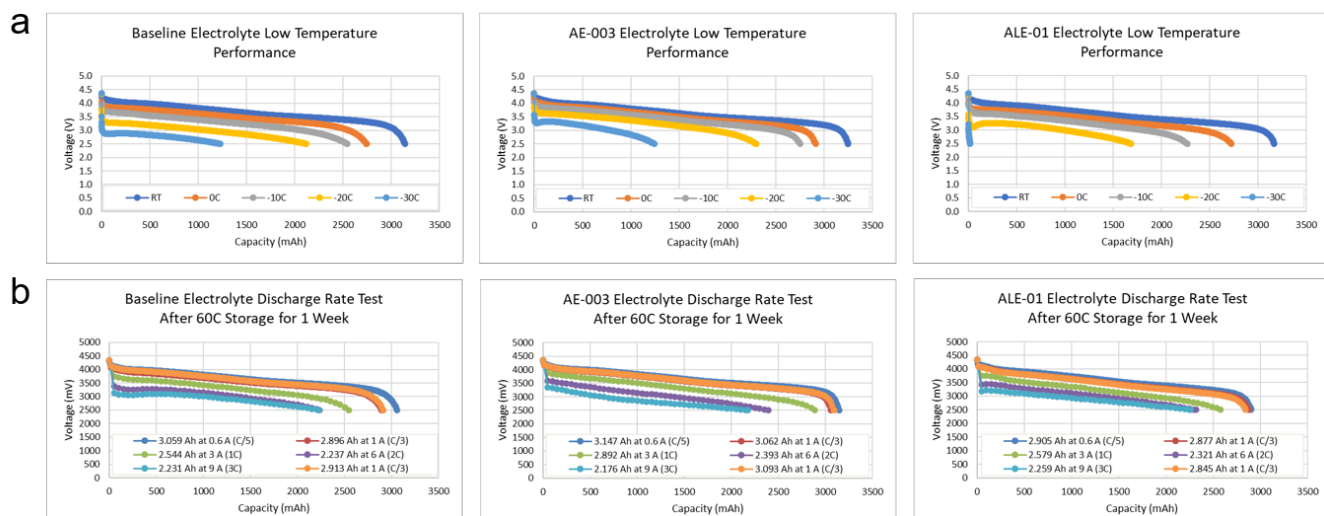


Figure XI.4.10 (a) Low temperature discharge testing and (b) thermal stability evaluation.

Conclusions

- We optimized the synthesis of UCI Gen2 cathode, performed thermal stability tests and full-cell-level long-term cycling tests.
- We performed a pathfinder test synthesis of single-crystalline NMC-811 cathodes and conducted detailed structural characterization and electrochemical evaluations. The synthesis of single-crystalline cathode with UCI-Gen2 chemistry was explored and the calcination condition needs to be further optimized.
- A mechanistic study on the chemomechanical degradation of LNO and VT Gen 2 cathode was performed. We elucidated the phase transformation at different stages of the synthesis of VT Gen2 material.
- Using CMC simulations, we calculated the phase diagrams for various doped LiNiO₂ systems. We find a correlation between the effectiveness of doping elements on mitigating phase transitions and their ionic radii and valent states.
- We evaluated the NMT performance in pouch cells and demonstrated that the capacity retentions of SLPCs and DLPCs using DME-based LHCE amounted to 79.4% and 70.9%, respectively, suggesting that the DME-based LHCE is a highly favorable electrolyte for the Gr||NMT cell chemistry.
- We show that the polymer coating strategy could effectively prevent not only the residual surface compounds but also the side reactions during cycling.
- We improved the cell performance of the Gr||NMT batteries using the exposed PP@NMT cathode, the E-DME-F The Gr||NMT cell using the exposed PP@NMT cathode and E-DME-F shows high-capacity retention of 86.7% after 500 cycles at room temperature.
- We performed cell assembly and testing of the PNNL electrolytes, i.e., AE-003 (carbonate-based) and ALE-01 (ether-based), in comparison to the baseline PPC cells.

Key Publications

1. Yang, Z.; Mu, L.; Hou, D.; Rahman, M. M.; Xu, Z.; Liu, J.; Nordlund, D.; Sun, C. J.; Xiao, X.; Lin, F.* Probing Dopant Redistribution, Phase Propagation, and Local Chemical Changes in the Synthesis of Layered Oxide Battery Cathodes. *Advanced Energy Materials*, 2021, 11(1): 2002719.
2. C.Y. Wang, L.L. Han, R. Zhang, H. Cheng, L.Q. Mu, K. Kisslinger, P.C. Zou, Y. Ren, P.H. Cao, F. Lin, H.L. Xin*. Resolving atomic-scale phase transformation and oxygen loss mechanism in ultrahigh-nickel layered cathodes for cobalt-free lithium-ion batteries. *Matter*, 4(6), 2013–2026 (2021)
3. C.Y. Wang, R. Zhang, K. Kisslinger, H.L. Xin*. Atomic-Scale Observation of O1 Faulted Phase-Induced Deactivation of LiNiO₂ at High Voltage. *Nano Letters*, 21(8), 3657–3663 (2021)
4. R. Lin, S. Bak, Y. Shin, R. Zhang, C. Wang, K. Kisslinger, M. Ge, X. Huang, Z. Shadike, A. Pattammattel, H. Yan, Y. Chu, J. Wu, W. Yang, M. S. Whittingham, H. L. Xin*, Xiao-Qing Yang. Hierarchical nickel valence gradient stabilizes high-nickel content layered cathode materials. *Nature Communications*, 2021, 12(1): 1–10.
5. Yang, Z., **Lin, F.*** Heterogeneous, Defect-Rich Battery Particles and Electrodes: Why Do They Matter, and How Can One Leverage Them?. *The Journal of Physical Chemistry C*, 2021, 125(18): 9618–9629.
6. X. Zhang#, H. Jia#, L. Zou, Y. Xu, L. Mu, Z. Yang, M. H. Engelhard, B. E. Matthews, C. Niu, C. Wang, H. L. Xin, F. Lin, W. Xu*, “Electrolyte Regulating towards Stabilization of Cobalt-Free Ultrahigh-Nickel Layered Oxide Cathode in Lithium-Ion Batteries”, *ACS Energy Letters*, 2021, 6, 1324–1332.
7. H. Jia, Y. Xu, X. Zhang, S. Burton, P. Gao, B. E. Matthews, M. H. Engelhard, K. Han, L. Zhong, C. Wang, W. Xu*, “Advanced low-flammable electrolytes for stable operation of high-voltage lithium-ion batteries”, *Angewandte Chemie*, 2021, 133(23): 13109–13116.
8. H. Jia#, X. Zhang#, Y. Xu, L. Zou, J.-M. Kim, P. Gao, M. H. Engelhard, Q. Li, C. Niu, B. E. Matthews, T. L. Lemmon, J. Hu, C. Wang, W. Xu*, “Towards practical use of cobalt-free lithium-ion batteries by an advanced ether-based electrolyte”, *ACS Appl. Mater. Interfaces*, 2021, 13 (37), 44339–44347.
9. C.Y. Wang, R. Zhang, C. Siu, M.Y. Ge, K. Kisslinger, Y. Shin, H. L. Xin. Chemomechanically Stable Ultrahigh-Ni Single-Crystalline Cathodes with Improved Oxygen Retention and Delayed Phase Degradations. *Nano Letters*, 21(22), 9797–9804 (2021)

Acknowledgements

This material is based upon work supported by the U.S. Department of Energy’s Office of Energy Efficiency and Renewable Energy (EERE) under the Award Number: DE-EE0008444.

XI.5 High-Nickel Cathode Materials for High-Energy, Long-Life, Low-Cost Lithium-Ion Batteries (University of Texas at Austin)

Arumugam Manthiram, Principal Investigator

University of Texas at Austin
Texas Materials Institute, University of Texas at Austin
Austin, TX 78712
E-mail: manth@austin.utexas.edu

Shriram Santhanagopalan, Principal Investigator

National Renewable Energy Laboratory
Golden, CO 80401
E-mail: Shriram.santhanagopalan@nrel.gov

Peter Faguy, DOE Technology Development Manager

U.S. Department of Energy
E-mail: Peter.Faguy@ee.doe.gov

Start Date: October 1, 2018
Project Funding: \$3,000,000

End Date: March 31, 2022
DOE share: \$2,400,000

Non-DOE share: \$600,000

Project Introduction

Despite the success with lithium-ion technology, energy and cost requirements are extremely stringent, especially for electric vehicle (EV) applications. Therefore, there is a need to further enhance the energy density of layered oxide cathodes ($\text{Li}[\text{Ni}_a\text{Co}_b\text{Mn}_c]\text{O}_2$ with $a + b + c = 1$, denoted as NCM-*abc* and $\text{Li}[\text{Ni}_{1-x-y}\text{Co}_x\text{Al}_y]\text{O}_2$, denoted as NCA). Moreover, the substantial dependence on the scarce and costly cobalt in these cathodes (e.g., 12 wt.% Co in NCM-622) needs to be lowered for sustained mass market penetration of EVs. With the currently employed cathode formulations, demand for Co could outstrip supply by 2030 with surging global EV production, setting the stage for far higher prices. Although Co-free cathodes, such as LiFePO_4 and LiMn_2O_4 exist, their energy density cannot meet the requirements of next-generation EVs.

This project is focused on developing low-cobalt and cobalt-free, high-nickel layered $\text{LiNi}_{1-x}\text{M}_x\text{O}_2$ ($\text{M} = \text{Mn}, \text{Al}, \text{Mg}, \text{Zr}, \text{Ta}, \text{etc.}$ and $x \leq 0.15$) oxide cathode materials for lithium-ion batteries for EVs. With these high-nickel cathodes, high energy, high power, long lifetime over a wide temperature range, as well as excellent safety under abuse can be prioritized for varying market needs through careful compositional tuning. These efforts will also reduce or even eliminate the dependence of lithium-ion batteries on cobalt, thus leading to more secure supply chains, lower cost, and less adverse impacts on the environment. The cathode materials and understanding developed in this project will contribute to advancing the designs of low-cobalt or cobalt-free, high-energy-density lithium-ion batteries.

Objectives

The overall goal of this project is to achieve low-cobalt or cobalt-free lithium-ion cells with the following performance targets:

Table XI.5.1 Performance Targets

Beginning of Life Characteristics at 30 °C	Cell Level	Cathode Level
Useable Specific Energy @ C/3		≥ 600 Wh/kg
Calendar Life (<. energy fade)	15 Years	
Cycle Life (C/3 deep discharge with < 20% energy fade)	1,000	
Cobalt Loading		≤ 50mg/Whr
Cost	≤ \$100/kWh	

Approach

Low-cobalt and cobalt-free high-nickel layered $\text{LiNi}_{1-x-y}\text{M}_x\text{Co}_y\text{O}_2$ ($x \leq 0.15$, $y < 0.06$, $M = \text{Mn, Al, Mg, Zr, Ta, etc.}$) oxides are developed and assessed as cathodes in lithium-ion batteries with graphite anode. The materials are synthesized by hydroxide co-precipitation and lithiation annealing to maintain good thermal and cycling stability while achieving the 600 Wh kg^{-1} energy goal. Selected compositions are also subjected to atomic layer deposition (ALD) coatings at NREL and assessed with compatible ethylene carbonate (EC)-free electrolyte systems. Based on the results, an optimal cathode is selected to produce twenty-one 2 Ah pouch cells to deliver to DOE for independent evaluation/validation. Detailed experimental approaches for Year 3 are below:

1. ALD Coating Survey: Further evaluation and validation of ALD coatings on best-performing $\text{LiNi}_{1-x-y}\text{M}_x\text{Co}_y\text{O}_2$ ($x \leq 0.15$, $y \leq 0.05$, and $M = \text{Mn, Al, Mg, and more}$).
2. Electrolyte Study: A survey of electrolyte additives on best-performing $\text{LiNi}_{1-x-y}\text{M}_x\text{Co}_y\text{O}_2$ ($x \leq 0.15$, $y \leq 0.05$, and $M = \text{Mn, Al, Mg, and more}$) in EC-free electrolytes.
3. Air-Storage Stability Study: Exploration of methods to improve air-storage stability of $\text{LiNi}_{1-x}\text{M}_x\text{O}_2$ ($x \leq 0.15$, and $M = \text{Mn, Al, Mg, and more}$), such as chemical coating, doping, and *in-situ* formed surface layers.

Results

High-nickel cathode materials are slated to become the next commercial cathode for electric vehicles, but their long-term cycle life retention and air stability remain a barrier. Surface reactivity and mechanical degradation, especially at high voltage, remain as issues that impede their commercialization. While surface treatments have shown great promise in reducing surface reactivity, mechanical degradation or “cathode cracking” persists. We have combined two mitigation strategies to limit particle fracture and surface degradation caused by air instability. First, the cobalt-free $\text{LiNi}_{0.9}\text{Mn}_{0.05}\text{Al}_{0.05}\text{O}_2$ (NMA) cathode was ball-milled to effectively “pre-crack” the secondary particles into their primary constituents or single crystallites. Then, these primary particles were coated with lithium phosphate using a manufacturing friendly, solution-based chemistry to protect the primary particles from detrimental side reactions as a consequence of its high surface-to-volume ratio. These pre-cracked cathode powders have a higher volumetric energy density and greater high voltage and air stability, with double the cycle life retention in full cells cycled at high voltage (Figure XI.5.1).

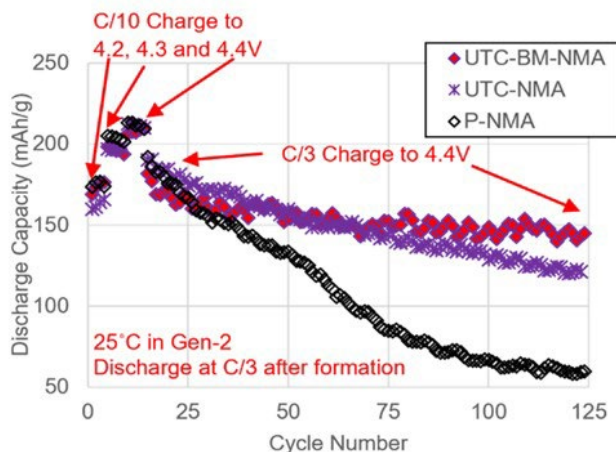


Figure XI.5.1 Full cell cycling data for pristine NMA (P-NMA), ultrathin coated NMA (UTC-NMA), and Ultrathin coated and ball milled NMA (UTC-BM-NMA). The P-NMA and UTC-BM-NMA have the same discharge capacity when charged to 4.4 V and the UTC-BM-NMA retains more of its capacity after 100 cycles.

We focused on identifying additives to enable ethylene carbonate (EC)-free electrolytes for improved cycling and thermal stability of high-Ni, Co-free cathode materials. Preliminary results pointed to fluoroethylene carbonate (FEC) as a promising additive for EC-free electrolytes. In EC-containing LiPF_6 -based electrolytes, FEC has been shown to aid in the formation of stable solid electrolyte interphases. FEC brings about these benefits by altering the Li^+ solvation structure and reduction behavior of the electrolyte without substantially affecting transport properties. None of these mechanisms are specific to EC, so the stabilizing benefits of FEC are likely to be found in EC-free electrolytes as well. FEC is explored as an additive in EC-free, ethyl methyl carbonate (EMC)-based electrolytes. Figure XI.5.2 displays the ionic conductivity and interfacial resistance of LiPF_6 /EMC electrolytes at different concentrations of LiPF_6 and FEC. These EC-free electrolytes were compared against the EC-containing baseline of 1.0 M LiPF_6 in EC/EMC (EC : EMC ratio is 3 : 7 by weight). Removing EC from the electrolyte causes a severe drop in conductivity and a rise in resistance at all concentrations of LiPF_6 . The inclusion of FEC, however, substantially reduces interfacial resistance while also improving conductivity. Across all levels of FEC inclusion, 1.5 M LiPF_6 exhibits the highest conductivity and was used as the conducting salt concentration for the remainder of the study. While both conductivity and resistance are improved with higher inclusions of FEC, FTIR analysis indicates that there is no change in the FEC solvent coordination beyond 20 wt.%. As such, 5 wt.% and 20 wt.% FEC in 1.5 M LiPF_6 /EMC were selected for further study. The samples will be referred to hereafter as 5F1.5M and 20F1.5M, respectively, for the 5 wt.% and 20 wt.% FEC electrolyte formulations.

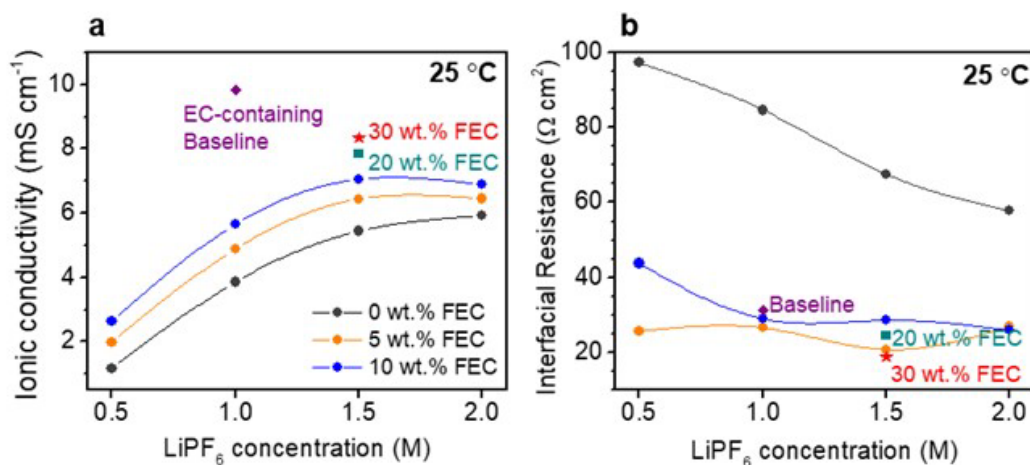


Figure XI.5.2 (a) Ionic conductivity and (b) interfacial resistance of EC-free LiPF₆/EMC electrolyte at different concentrations of LiPF₆ and FEC. EC-containing baseline electrolyte is shown for a reference (1.0 M LiPF₆ in EC/EMC with a 3:7 weight ratio).

The cobalt-free LiNi_{0.9}Mn_{0.05}Al_{0.05}O₂ (NMA) cathodes were used to examine the efficacy of the FEC-containing electrolytes during electrochemical operation with high-Ni, Co-free cathode materials. Both half cell (paired with Li) and full cell (paired with graphite) coin cells were tested to determine the effect of FEC on the EC-free electrolyte. Figure XI.5.3 presents the thermal and electrochemical stability of the different electrolyte formulations in various NMA cells. While the onset temperature of the thermal decomposition reaction is not substantially changed (Figure XI.5.3a), the EC-free electrolytes exhibit much lower overall and peak heat evolution, with 20F1.5M showing the lowest level of heat generation. This indicates that removing EC from the electrolyte improves the thermal stability, and inclusion of FEC improves thermal abuse tolerance even further. Further benefits are seen in the rate performance of NMA half cells, shown in Figure XI.5.3b. The 20 wt.% FEC electrolyte shows a substantial improvement in rate capability at the high discharge rate of 5C. This is likely due to the significantly lower interfacial resistance of the EC-free electrolyte, enabling facile charge transfer at the cathode interface even at high rates. It also suggests that the FEC may be inducing a thinner cathode electrolyte interphase (CEI) layer to form, further reducing the charge-transfer resistance. The FEC electrolytes also outperformed the EC-containing baseline in long-term cycling tests of NMA full cells (Figure XI.5.3c-d). Both FEC electrolytes exhibited superior capacity retention and substantially reduced voltage hysteresis, further supporting that the FEC improves the cathode surface stability.

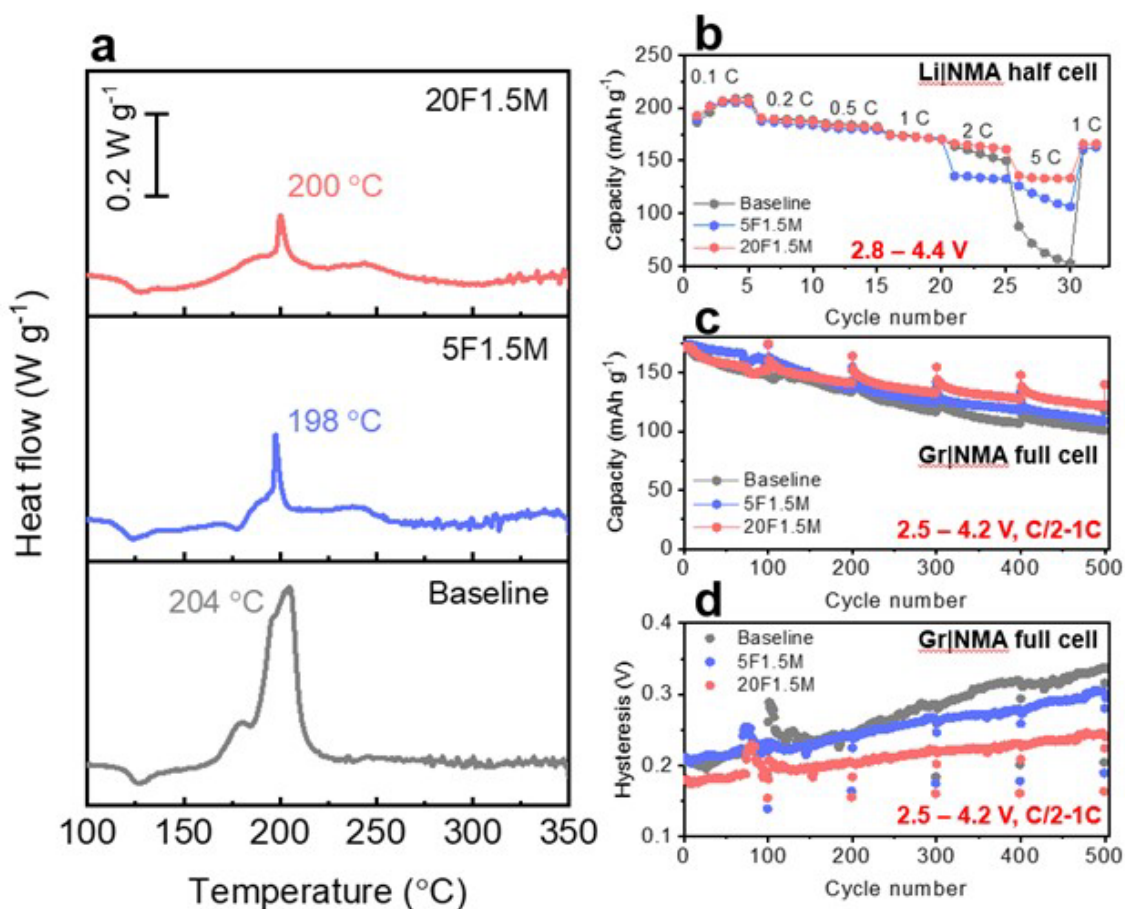


Figure XI.5.3 (a) DSC profiles of NMA charged to 4.4 V in different electrolytes. (b) Rate performance of NMA half cells with different electrolytes. Half cells were cycled between 2.8 and 4.4 V at 25°C under various current densities between 0.1C to 5C rates. (c) Long-term cycling performances of NMA/graphite full cells with different electrolytes. The full cells were cycled between 2.5 and 4.2 V at 25°C under 0.5C charge rate and 1C discharge rates. (d) Voltage hysteresis of NMA full cells. Hysteresis is defined as the difference between average charge and discharge operating voltages.

One issue with FEC is that it is incredibly moisture sensitive and degrades very quickly even when stored inside an argon-filled glovebox. Figure XI.5.4 presents images showing the degradation of FEC-containing electrolytes after 1 month storage under argon. Despite being kept inside a glovebox, trace amounts of moisture cause rapid degradation of FEC-containing electrolytes, as evidenced by the brown color of the solutions. This occurs due to FEC polymerization enabled by the decomposition products of LiPF_6 in the presence of trace moisture. To combat FEC degradation, $1 \text{ wt.}\%$ of LiTDI (lithium 4,5-dicyano-2-(trifluoromethyl)imidazole) was added to the electrolytes. LiTDI is a fluorinated, nitrogenous aromatic molecule that has shown success as a moisture-scavenging electrolyte additive. As can be seen in the bottom row of Figure XI.5.4a, the LiTDI-containing electrolytes show no signs of FEC degradation. The stabilized FEC-LiTDI electrolyte was further tested in NMA/graphite full cells to determine any impact LiTDI has on electrochemical performance (Figure XI.5.4b). Impressively, the addition of LiTDI further improves the performance of EC-free electrolyte beyond that of the baseline. The moisture-scavenging properties of LiTDI likely reduce the formation of HF inside the cell, further protecting the cathode surface against acid attack.

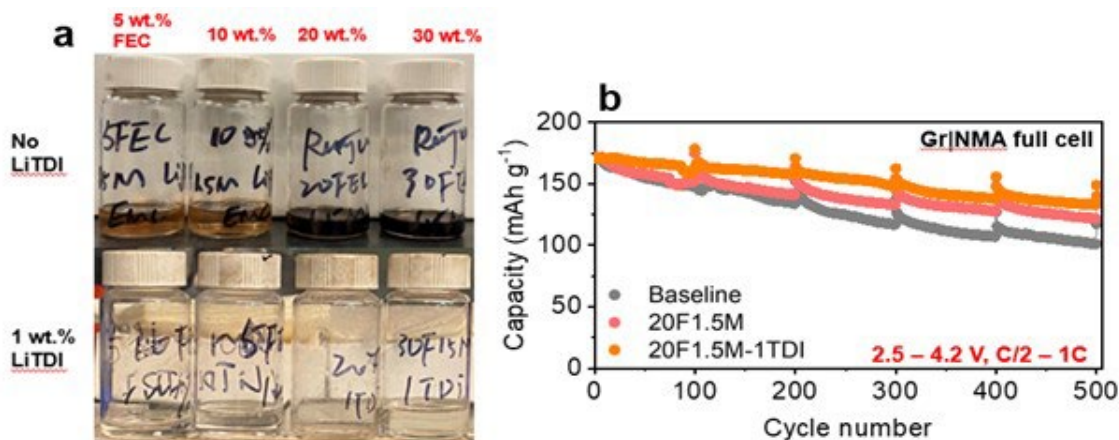


Figure XI.5.4 (a) Images of FEC-containing electrolytes stored inside a glovebox for 1 month. (Top row) 1.5 M LiPF₆/EMC electrolytes with different FEC concentrations. (Bottom row) Equivalent electrolytes with 1 wt.% LiTDI added. (b) Long-term cycling of NMA/graphite full cells with baseline, FEC, and FEC-LiTDI electrolytes. Cells were cycled between 2.5 to 4.2 V at 25 °C under 0.5C charge rate and 1C discharge rate.

We further focused on understanding and improving the air-storage capability of high-Ni layered oxides. To begin, an investigation of the effects of transition metal dopant composition was performed to better understand the influencing factors of surface residual lithium formation. To evaluate the effects of moisture and air exposure on the different cathode compositions, LiNi_{0.90}Mn_{0.05}Co_{0.05}O₂ (NMC), LiNi_{0.90}Mn_{0.05}Al_{0.05}O₂ (NMA), and LiNi_{0.90}Co_{0.05}Al_{0.05}O₂ (NCA) were stored in a saturated humidity chamber for 10 days. Accumulation of surface residual lithium species, namely Li₂CO₃, was measured with an acid-base titration with dilute HCl, which was performed on each material periodically throughout storage. The residual lithium contents are included in Figure XI.5.5a. In the pristine materials, NMC and NMA both contain roughly equivalent amounts of Li₂CO₃, while NCA contains over twice that. NMA and NMC experience a slightly higher growth rate of surface residual lithium (300% over 10 days) compared to NCA (200% over 10 days), though we expect this largely to be the result of lower lithium availability in the NCA surface layers due to depletion from the initial Li₂CO₃ growth. Further evidence of Li₂CO₃ growth is seen in the SEM images in Figure XI.5.5b. The pristine materials all exhibit similar surface morphology, with perhaps a slightly visible smattering of amorphous regions on the NCA surface, consistent with the high initial residual lithium content. After five days, large platelets of Li₂CO₃ are visible on NCA, and a semi-continuous amorphous coating is visible on all materials after 10 days. The above results suggest that Mn plays a key role in mitigating the formation of surface residual lithium species. This may be due to a lithium scavenging effect, a tendency to segregate to the surface and form a stabilizing Mn-rich layer, or an alteration of the other transition-metal oxidation states, which slows the surface reconstruction that accompanies residual lithium formation. While the specific mechanisms are currently uncertain, work is ongoing to better understand the influence of Mn on residual lithium formation.

The cycling performances of the pristine and stored materials were tested in coin half-cells, the results of which are displayed in Figure XI.5.5c-d. As expected, the stored materials deliver a substantially lowered initial capacity. Interestingly, there seems to be no correlation between the amount of residual lithium after storage and the decrease in initial capacity delivered by the materials. All three materials retained 86 – 88% of initial capacity after storage. Also surprising was that the cyclability of the stored materials remained relatively unchanged compared to the pristine materials. Aside from the initial loss of capacity, the materials cycled fairly well despite the large growth of detrimental surface lithium species. This is in stark contradiction to numerous examples in the literature that even brief air-storage severely impacts both the capacity and cyclability; this may be due to the heavy calendaring applied to our cathodes. We have found that sufficient calendaring pulverizes the cathode particles, revealing previously unexposed surface area. In calendaring the stored cathodes, the rock salt surface region that accumulates in response to residual lithium formation may

have been disrupted and exposed fresh surface for lithium de/intercalation. In this way, lithium diffusion pathways may have formed, which bypass the rock salt layers, negating the reduction to lithiation kinetics that normally occurs. Further work is being carried out to examine the phases present before and after calendaring of the stored materials.

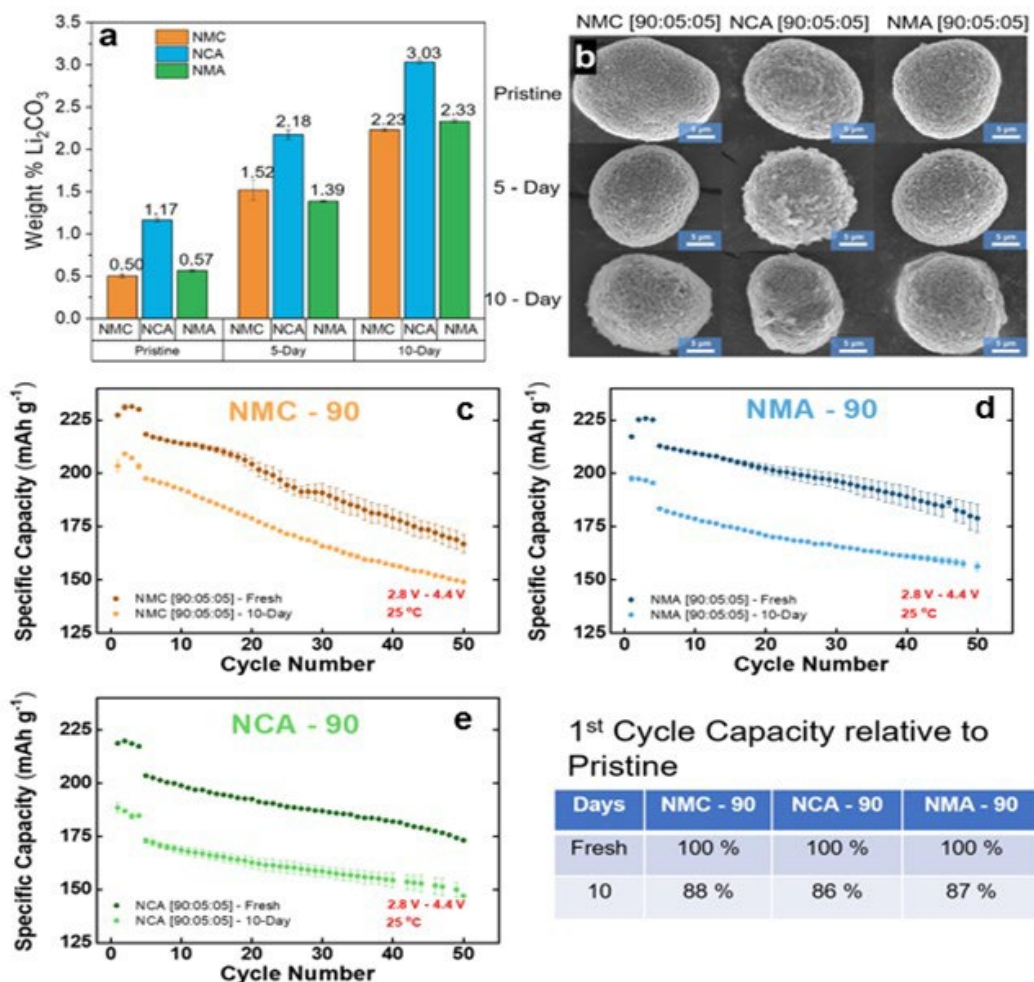


Figure XI.5.5 (a) Wt. % of Li_2CO_3 measured on NMC, NCA, and NMA after storage in a saturated humidity chamber. (b) SEM images of pristine and stored NMC, NCA, and NMA, showing morphologies of cathode surface and of grown Li_2CO_3 surface species. (c-d) Cycling performance of NMC, NMA, and NCA before and after storage in a saturated humidity chamber. The capacity retention of the stored materials relative the pristine materials is included to aid in comparison.

Conclusions

In this year, UT Austin and NREL have explored various pathways to improve the performance and storage capability of high-nickel layered oxide cathodes. ALD and wet-chemical coating at both the primary and secondary particle levels was found to improve the surface stability and mechanical robustness of the cathode material. In addition, we have developed EC-free electrolytes that improve both cell longevity and thermal stability, enabling better performance in addition to greater safety. Finally, we explored the effects of transition metal dopant composition on the air-storage stability of the high-nickel layered oxides. The ability of manganese to limit the formation of residual lithium species, as well as the surprising effect of calendaring to break up surface rock salt regions, will greatly benefit the processing and handling of materials moving forward. These results have built a strong foundation for our continuing efforts towards the development of low-cobalt and cobalt-free, high-nickel layered oxide cathodes for automotive batteries throughout this project.

Key Publications

Reports

Four quarterly reports have been submitted to the DOE (one at the end of each quarter).

Publications

1. W. M. Seong, Y. Kim, and A. Manthiram, “Impact of Residual Lithium on the Adoption of High-nickel Layered Oxide Cathodes for Lithium-ion Batteries,” *Chemistry of Materials* **32**, 9479–9489 (2020).
2. H. Park, A. Mesnier, S. Lee, K. Jarvis, J. H. Warner, and A. Manthiram, “Intrinsic Li Distribution in Layered Transition-Metal Oxides Using Low-Dose Scanning Transmission Electron Microscopy and Spectroscopy,” *Chemistry of Materials* **33**, 4638–4650 (2021).
3. S. Lee, W. Li, A. Dolocan, H. Celio, H. Park, J. H. Warner, and A. Manthiram, “In-depth Analysis of the Degradation Mechanisms of High-Nickel, Low/No-Cobalt Layered Oxide Cathodes for Lithium-ion Batteries,” *Advanced Energy Materials* <https://doi.org/10.1002/aenm.202100858> (2021).

XI.6 Cobalt-Free Cathodes for Next Generation Li-ion Batteries (Nexceris)

Neil Kidner, Principal Investigator

Nexceris
404 Enterprise Drive
Lewis Center, OH 43035
E-mail: n.kidner@nexceris.com

Peter Faguy, DOE Technology Development Manager

E-mail: Peter.Faguy@ee.doe.gov

Start Date: October 1, 2018

End Date: March 31, 2022

Project Funding: \$3,083,213

DOE share: \$2,466,547

Non-DOE share: \$616,666

Project Introduction

This is a disruptive period for global automakers. Economic, political, and ecological pressures have hastened the global transition from internal combustion engine (ICE) to electric vehicles (EVs). In response, automakers are investing over \$300 billion to accelerate the launch of EVs. However, to realize mass-market adoption of EVs, Li-ion battery costs must fall ($< \$100/\text{kWh}$), and performance must improve to alleviate customer concerns over driving range and lifetime. Today's commercial, state-of-the-art Li-ion batteries for EVs are based on high-energy-density layered oxides, and require cobalt, a metal of limited resources and subject to price speculation. There is, therefore, a need for new high-potential, and high-capacity cathode materials that are less reliant on critical materials to secure the supply chain and sustain rapid electrification of the U.S. transportation sector.

The spinel formulation $\text{LiNi}_{0.5}\text{Mn}_{1.5}\text{O}_4$ (LNMO) is a very promising candidate based on its high specific energy (650 Wh/kg-cathode level) and cobalt-free formulation. Unfortunately, the adoption of this material has been limited by its poor cycle life, caused by oxidative decomposition of the electrolyte and a series of parasitic reactions occurring at the electrode-electrolyte interface, which prevents its commercial adoption.

[1],[2]

Objectives

The project goal is to develop a next-generation Li-ion battery based on a LNMO high-voltage spinel cathode material. LNMO is an attractive candidate cathode material, which already satisfies two of the project specifications, a usable specific energy (cathode level) of at least 600 Wh/kg, and a low-cobalt formulation that is compatible with a cell cost of less than \$100/kWh

The goal of this project is to develop and validate a stabilized Ti-substituted lithium manganese nickel-oxide, $\text{LiNi}_{0.5}\text{Mn}_{1-x}\text{Ti}_x\text{O}_4$ (LNMTO) with improved cycle and calendar life. The cell chemistry, including electrode and electrolyte formulations, will be optimized for stable performance under aggressive high-voltage operating conditions. Technical feasibility will be demonstrated through the fabrication and testing of 2 Ah-cells.

Approach

The proposed project approach is shown schematically in Figure XI.6.1. The cycle and calendar life of high-voltage cathodes will be improved by developing a novel core-shell microstructure that enables the formation of a solid-electrolyte interface that effectively passivates the cathode surface. The microstructural enhancements of the cathode material focus on preferentially enriching the surface with titanium^[3]. In parallel, new, optimized LiPAA electrode binder and electrolyte chemistries will be incorporated to address degradation mechanisms associated with high-voltage systems.

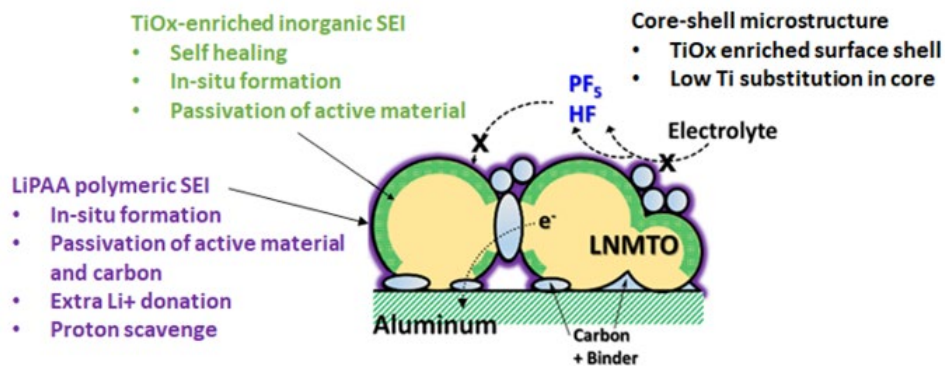


Figure XI.6.1 Schematic of the technical approach for creating high-performance LNMTO Li-ion cathodes.

In the first budget period (FY19) the project team focused on producing LNMTO (and LNMO) powders by conventional solid-state synthesis methods, and fabricating LiB cells using these cathode materials, and test these cells to establish baseline performance levels. Analytical and testing protocols have been established that will be used throughout the project. Multiple large (2-Ah) cells were successfully manufactured and fifteen of these Project Progress Cells (PPCs) delivered to Idaho National Laboratory (INL) for performance testing.

In the second budget period (FY20) the project team built on the Year 1 results and continued to improve the performance of the LNMTO based cells. An alternative, low-cost powder synthesis approach was developed and integrated to produce core-shell LNMO/LNMTO cathode microstructures. The project team continued electrolyte development to identify a complementary electrolyte formulation to pair with this high-voltage cathode. This budget period culminated with a set of down-select 2-Ah cells that enabled an assessment of progress towards the overall project goals and identification of gaps to be addressed.

In the third budget period, post-mortem characterization of the intermediate 2-Ah cells has been used to refine the development plan, which is divided into a series of down-select powder iterations for single-layer pouch cell and 2-Ah cell testing. This approach, of frequent large-format testing of down-select LNMO/LNMTO core-shell powders has enabled scale-up challenges to be addressed, mitigates technical risk, and builds confidence in the eventual Project Completion Cells (PCCs).

Results

Nexceris' two-step *Hybrid Alternative Wet-Chemical Synthesis* (HAWCS) process, developed in the second budget period enables excellent compositional and particle morphology homogeneity using a modified precipitation process that does not require the strict process controls associated with other synthesis approaches. The improved LNMO powder microstructure resulted in a significant performance improvement compared to the original solid-state LNMO powder. Nexceris has continued to focus on optimization of the HAWCS LNMO core powder and integration with the core/shell process to produce a high-performance LNMO/LNMTO core-shell powder. Process modifications have been evaluated and three down-select powder iterations produced in large batch sizes for single-layer pouch (SLP) and 2-Ah cell fabrication and testing.

The initial HAWCS process produced a small particle size ($d_{50} \sim 2\text{-}5\ \mu\text{m}$) LNMO powder. This is undesirable, the high surface-area-to-volume ratio results in more significant, detrimental electrode-electrolyte interfacial interactions. Nexceris has therefore worked to increase the LNMO particle. The effect on particle-size of different process-parameters have been investigated and the particle-size of the LNMO powder successfully controlled through modification of the initial precipitation parameters. A modified HAWCS process, incorporating a combination of slower addition of the precipitation agent and stir speed during the initial precipitation reaction was down-selected that increases the median LNMO particle size (d_{50}) from $\sim 2\text{-}5$ to $20\text{-}30\ \mu\text{m}$ as shown in Figure XI.6.2.

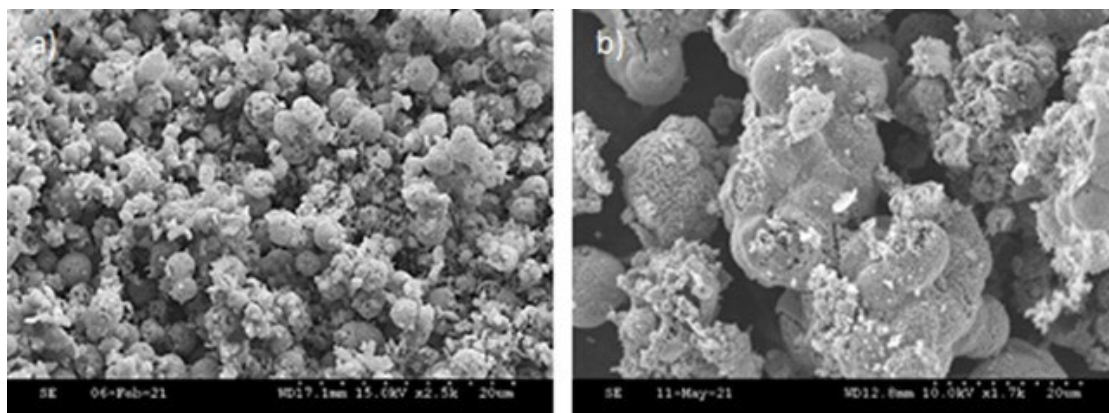


Figure XI.6.2 SEM image of HAWCS synthesized LNMO powder; initial (a), and modified process that achieves larger particle size powder (b).

To determine whether increasing the particle size of the LNMO cathode, improves the cycle-life behavior, SLP cells were fabricated from cathodes with different LNMO particle-sizes. Figure XI.6.3 compares the cycle-life of SLP cells with down-select (large particle size, $d_{50} = 30 \mu\text{m}$), and the initial ($d_{50} \sim 3\text{--}5 \mu\text{m}$) LNMO powder. Increasing the LNMO particle-size results in a significantly improvement in cycle-life and indicates the importance of optimizing the LNMO powder to minimize detrimental interfacial interactions.

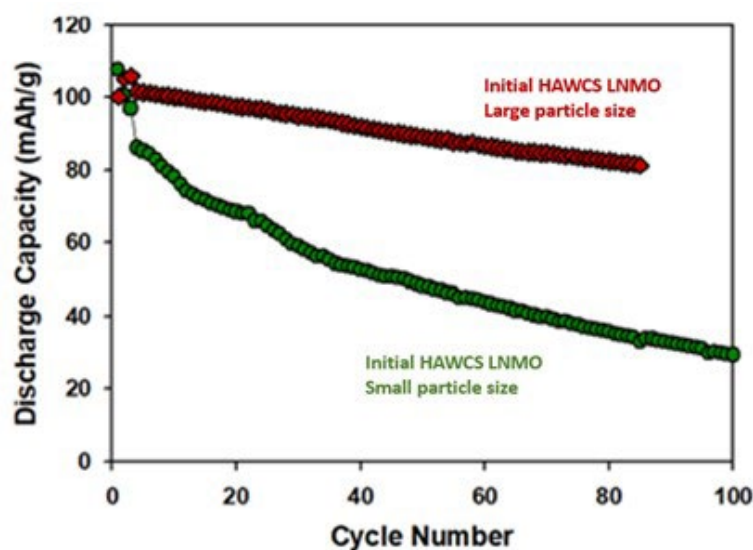


Figure XI.6.3 Single-layer pouch (SLP) full-cell cycle-life at 25 °C comparing LNMO cathodes with different particle sizes. Graphite anode with N/P ratio 1-1.01, Cathode binder LiPAA. Electrolyte 1 M LiPF_6 in 1:1 wt. EC/EMC (no additive). Cycling conditions: Cycle 1-3: C/10 then C/3.

The larger LNMO core powder down-select required re-targeting of the LNMTTO shell thickness. A systematic study (shell thickness $0.25 \mu\text{m} - 5 \mu\text{m}$) has been completed to identify the optimal LNMTTO shell thickness to pair with the larger LNMO core. Figure XI.6.4 shows the XRD spectra and the half-cell coin-cell cycle life of LNMO/LNMTTO core-shell powders with different shell thicknesses. For thin shell thickness ($< 1.5 \mu\text{m}$), the XRD spectra are the same as the LNMO control sample, but for powders with thicker (2 and $5 \mu\text{m}$) shell thicknesses impurity phases are present. Except for the extremely thick $5 \mu\text{m}$ shell, which causes a breakdown in the powder microstructure all the core-shell samples show higher initial discharge capacity than the LNMO control. Based on a combination of microstructural analysis (XRD, SEM) and half-cell testing core-shell powders with LNMTTO shell thicknesses between 0.5 and $1 \mu\text{m}$ were down-selected for full-cell coin-cell and SLP testing and resulted in a shell thickness of $0.75 \mu\text{m}$ being down-selected.

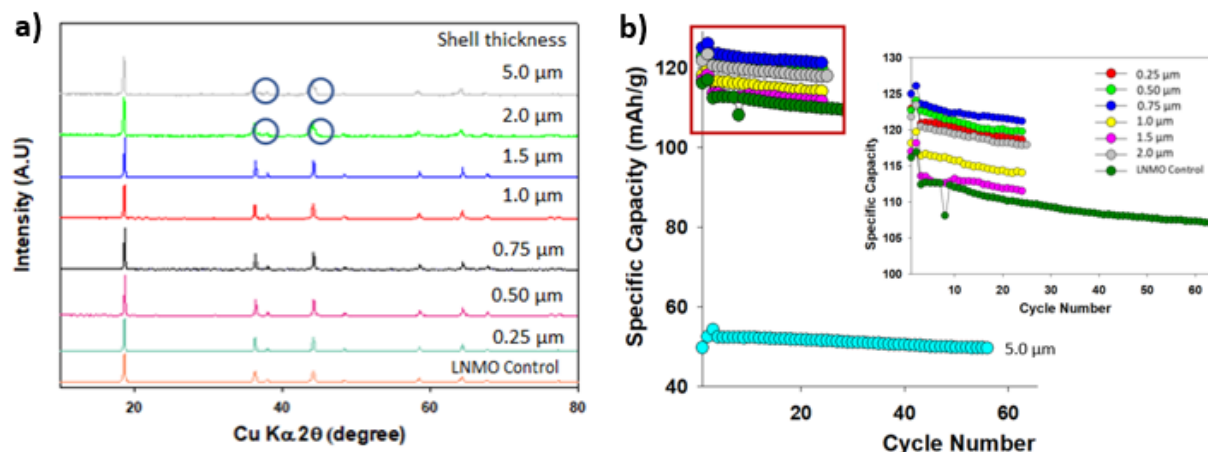


Figure XI.6.4 XRD spectra of LNMO/LNMTMO core/shell powders with different shell thicknesses (a), and Cycle performance of coin-cell half-cells (b), comparing LNMTMO shell thickness. Electrolyte 1 M LiPF₆ in 1:1 wt. EC/EMC. Cycling conditions: Cycles 1,2: C/10 then C/3.

Further process modifications to the initial *HAWCS* precipitation step have been implemented. ICP analysis of the supernatant detected transition metal ions (Ni and Mn), indicating incomplete precipitation and a non-stoichiometric (Ni deficient) LNMO powder. To achieve complete precipitation the ratio of sodium bicarbonate (precipitating agent) to transition metal was increased. Figure XI.6.5 shows SEM images of LNMO powder and Figure XI.6.6 initial half-cell charge/discharge voltage profiles for different precipitation ratios. As the ratio increases the average particle size of the LNMO powder increases, however, the spherical powder morphology is preserved. More importantly the more complete precipitation reaction minimizes transition metal loss and produces an improved more stoichiometric LNMO powder with higher capacity.

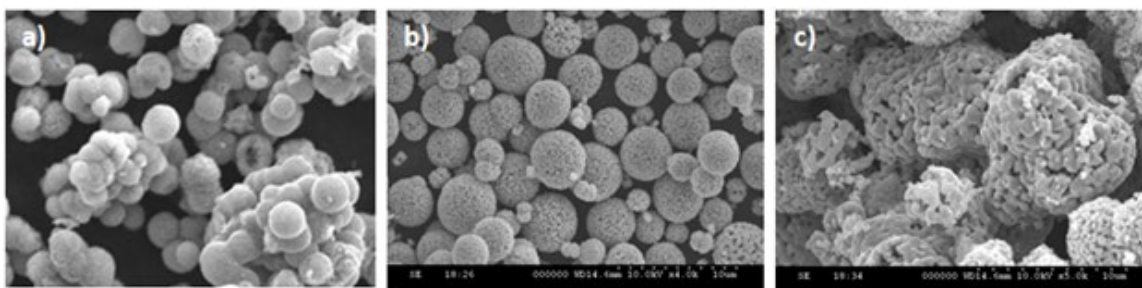


Figure XI.6.5 SEM images of LNMO powder synthesized through the *HAWCS* process with different initial precipitating processes (precipitating agent-to-transition metal ratio): 4:1 (standard) (a), 6:1 (b), and 8:1 (c).

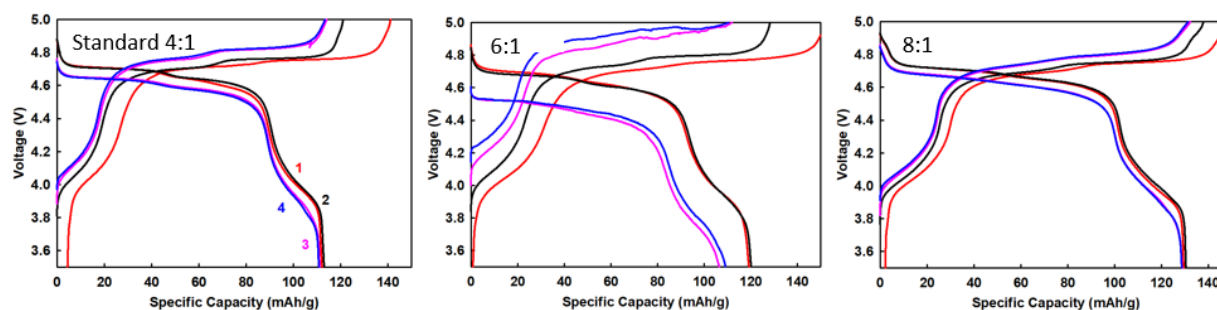


Figure XI.6.6 Charge/discharge-voltage profiles of LNMO half-cells at 25 °C comparing different precipitating agent-to-transition metal ratios - 4:1 (standard), 6:1, and 8:1. Electrolyte 1 M LiPF₆ in 1:1 wt. EC/EMC (no additive). Cycling conditions: Cycle 1-2: C/10 then C/3.

The Ti concentration in the LNMTO shell has also been studied to see whether increasing the Ti concentration can provide additional cycle life improvements. Half-cells with different LNMTO shell compositions, Figure XI.6.7(a) show that all core-shell powders provide enhance the specific capacity compared to the LNMO core. Single-layer pouch cells, Figure XI.6.7(b) are on-test to determine the effect on cycle-life and will be used to down-select the LNMTO shell composition for the PCCs.

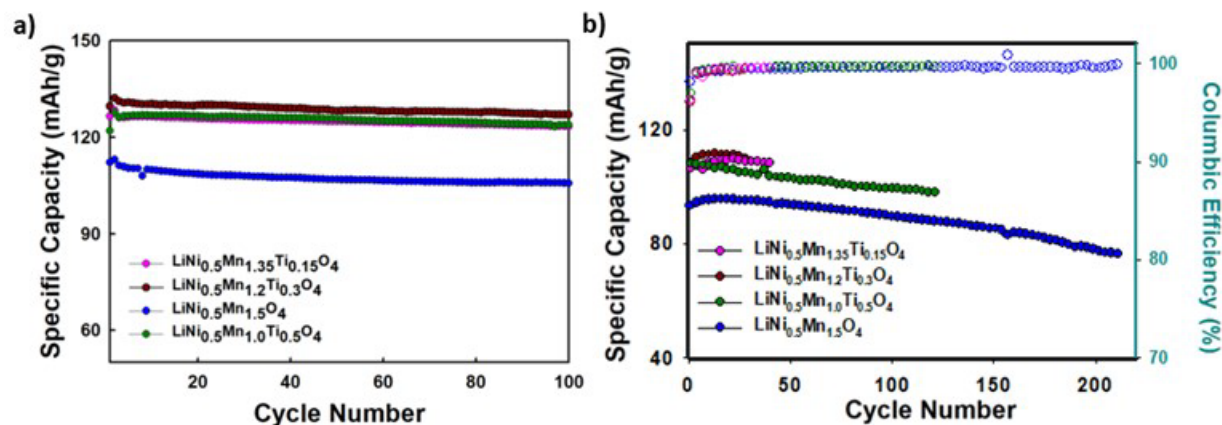


Figure XI.6.7 Cycle-life of LNMO/LNMTO half-cell coin-cells (a), and SLP-cells with various LNMTO shell compositions (varying Mn-to-Ti ratios). Electrolyte 1 M LiPF₆ in 1:1 wt. EC/EMC (no additive). Cycling conditions: Cycle 1,2: C/10 then C/3.

Delivering multiple power iterations for integration into the same cell manufacturing processes as the 2-Ah PCCs has enabled potential discrepancies in fabrication and testing to be resolved. Two potential issues that have been successfully addressed are LiPAA binder shelf-life, and the importance of electrode porosity. Figure XI.6.8(a) shows the cycle-life behavior of Iteration 1 LNMO/LNMTO SLPs fabricated with fresh and aged LiPAA binder. Segmentation of the electrode fabrication process identified that the LiPAA binder has a very short shelf-life and using old LiPAA binder degrades cathode electrode quality, causing cracks in the electrode as highlighted in Figure XI.6.8(b) that strong effect on cell cycle-life behavior. Procedures have been implemented to ensure that fresh LiPAA binder is used in the future. The results could also explain why a composite LiPAA sodium-alginate binder has shown promising results since it may be less susceptible to shelf-life degradation.

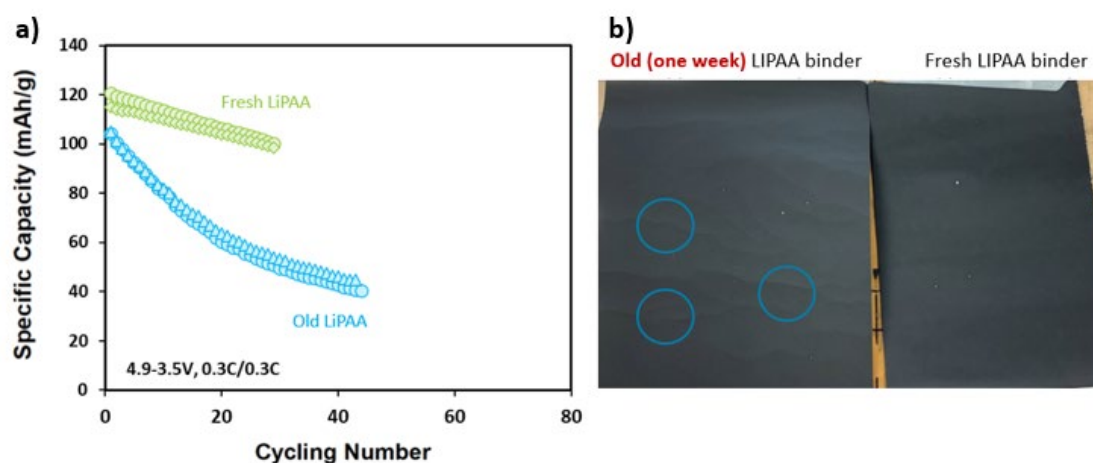


Figure XI.6.8 Cycle performance of Iteration 1 LNMO/LNMTO single-layer pouch (SLP) full-cells at 25 °C: fresh and old LiPAA binder (a) fresh LiPAA binder. Cell configuration: MCMB graphite with N/P ratio 1-1.01, Cathode binder LiPAA. Electrolyte 1 M LiPF₆ in 1:1 wt. EC/EMC (no additive). Cycling conditions: Cycle 1-3: C/10 then C/3. Comparison of cathode electrodes with different LiPAA binder (b)

While evaluating the LNMT0 shell-thickness multiple SLP cells were fabricated. Figure XI.6.9 shows the cycle-life behavior of the SLP cells fabricated with two different anode formulations. Although the initial capacities of the SLP cells are similar, the cells made with anode 2 show significantly higher capacity fade and degrade relatively quickly. In comparison, the SLP cells made with anode 1 show very good cycle-life behavior. Both anode formulations were made from MCMB graphite. The team is carefully analyzing differences in the formulation (conductive carbon content) and microstructure (porosity) between the two anodes to identify the best anode to use for the final PCCs.

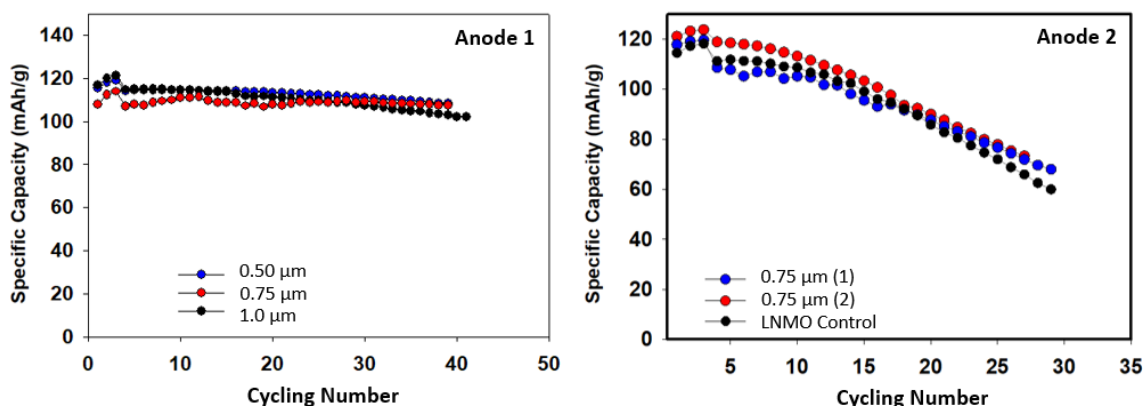


Figure XI.6.9 Cycle performance of LNMO/LNMT0 core/shell SLP full-cells at 25 °C with different LNMT0 shell thicknesses and comparing two anode formulations. MCMB graphite anode with N/P ratio 1-1.01, Cathode binder LiPAA. Electrolyte 1 M LiPF₆ in 1:1 wt. EC/EMC (no additive). Cycling conditions: Cycle 1-3: C/10 then C/3.

Conclusions

Nexceris has focused on optimizing the LNMO/LNMT0 core-shell cathode powder through a series of down-select powder iterations that incorporate a range of process modifications. Large-batches of down-select powders have been synthesized and provided for single-layer pouch cell and 2-Ah large-format cell fabrication and testing. This has enabled potential issues with the LiPAA binder and anode electrode microstructure to be identified and resolved and is anticipated to mitigate the technical risks with the end of project 2-Ah Project Completion cells (PCCs).

The LNMO core powder has been re-targeted to a large particle-size to minimize detrimental surface iterations through modification of the initial *HAWCS* precipitation process parameters. This has resulted in a significant enhancement in the LNMO cycle-life behavior. The precipitation and washing step have been further improved to prevent incomplete precipitation and address powder non-stoichiometry. The LNMT0 shell has been optimized to pair with the larger LNMO core powder.

References

1. J.-H. Kim, N.P.W. Pieczonka, Z. Li, Y. Wu, S. Harris, B.R. Powell, Understanding the capacity fading mechanism in LiNi_{0.5}Mn_{1.5}O₄/graphite Li-ion batteries, *Electrochimica Acta*. 90 (2013) 556–562.
2. J.-H. Kim, N.P.W. Pieczonka, L. Yang, Challenges and Approaches for High-Voltage Spinel Lithium-Ion Batteries, *ChemPhysChem*. 15 (2014) 1940–1954.

Acknowledgements

Nexceris would like to acknowledge the support of their project partners, Dr. Jung-Hyun Kim at The Ohio State University, and Dr. James Dong at Navitas Systems. Dr. Kim's team has provided excellent technical guidance and support for cell chemistry development and cell testing. Navitas Systems has provided feedback on the large-format cell manufacturing and testing.

Nexceris would also like to thank the project's NETL manager, Adrienne Riggi for her project support and management, and Dr. Jack Deppe and Dr. Ahmad Pesaran for their technical guidance.

XI.7 High-Performance Low-Cobalt Cathode Materials for Li-ion Batteries

Donghai Wang, Principal Investigator

Department of Mechanical Engineering
The Pennsylvania State University
University Park, PA 16802
E-mail: dwang@psu.edu

Chao-Yang Wang, Principal Investigator

Department of Mechanical Engineering
The Pennsylvania State University
University Park, PA 16802
E-mail: cxw31@psu.edu

Jagjit Nanda, Principal Investigator

Chemical Sciences Division
Oak Ridge National Laboratory
Oak Ridge, TN 37831
E-mail: nandaj@ornl.gov

Chongmin Wang, Principal Investigator

Environmental Molecular Sciences Laboratory
Pacific Northwest National Laboratory
Richland, WA 99352
E-mail: chongmin.wang@pnnl.gov

Peter Faguy, DOE Technology Development Manager

U.S. Department of Energy
E-mail: Peter.Faguy@ee.doe.gov

Start Date: January 1, 2021
Project Funding: \$739,259

End Date: December 31, 2021
DOE share: \$591,407

Non-DOE share: \$147,852

Project Introduction

The layer-structured $\text{Li}[\text{Ni}_x\text{Co}_y\text{Mn}_{1-x-y}]\text{O}_2$ (NCM) cathode materials have been the best choice for increasing the driving distance per charge of electric vehicles. [1],[2],[3] The high Ni layered oxide represents successfully commercialized NCM cathodes (such as NCM622 [4] and NCA [5]) in lithium-ion batteries (LIBs) for EV applications due to their high energy density and acceptable cycling stability. The price of cobalt, a key element within LIBs for stability, has nearly tripled over the past few years due to increased demand from the cell phone industry, current materials shortage, increased adoption of electrical vehicle, and speculation for a future global shortage, [6],[7],[8] as mentioned in the DOE Funding Opportunity Announcement. To meet the requirement and sustainability of the next-generation long-range and low cost EVs, developing cathode materials with very low Co content to achieve higher energy density and lower cost is both essential and urgent.

Objectives

The overarching objective of this proposed work is to develop stabilized NCM cathode materials with low Co content (namely $\text{LiNi}_x\text{Co}_y\text{Mn}_{1-x-y}\text{O}_2$, $y \leq 0.04$) so as to meet DOE's goal of reducing Co loading to below 50 mg Wh^{-1} , while maintaining energy density greater than 600 Wh kg^{-1} based on cathode material. The obtained

NCM cathode paired with graphite anode shall deliver batteries with a high initial specific energy density of over 240 Wh kg⁻¹ and low capacity fading rate of less than 20% in 1000 cycles under C/3 discharge rate.

Approach

To accomplish this goal, a multidisciplinary team with several co-investigators has been formed from three organizations: The Pennsylvania State University (PSU), Oak Ridge National Laboratory (ORNL), and Pacific Northwest National Laboratory (PNNL). The PI and co-investigators are Dr. Donghai Wang (PI) from PSU with expertise on synthesis of nanostructured materials and manipulation of interfacial properties of electrochemically active materials, Dr. Jagjit Nanda with substantial knowledge of and expertise in state-of-the-art cathodes from ORNL, Dr. Chao-Yang Wang with significant experience in advanced cell design and fabrication and cell diagnostics from PSU, and Dr. Chongmin Wang with world-wide known expertise of advance atomic scale characterization of electrode materials from PNNL. Furthermore, this project will leverage off and synergistically work with the current DOE-funded programs on battery materials at PSU and ORNL, and electrode materials characterization at PNNL.

Results

1. LFP-coated NCM811 cathode

In this year, we continued to cycle the 2.5Ah pouch cells consisted of NCM811 cathode coated with 10wt% LFP and graphite anode, with the cathode loading of 17.5 mg/cm² and the N/P ratio of 1.1. These cells are cycled at 40°C as well as room temperature, as shown in Figure XI.7.1a. The cycling conditions are: C/3 CCCV to 4.2V till C/5, and aged cells are characterized at RPT condition every 200 cycles, i.e., C/3 CCCV to 4.2V till C/20. It can be seen that LFP coated NCM811 is very stable at room temperature, with the capacity retention at C/3 of 76.7% after 2413 cycles. At 40°C, the cell achieves 67.3% capacity retention after 1609 cycles. High temperature also leads to fast increase of DCR, as shown in Figure XI.7.1b. The cell's capacity fade at elevated temperature is much faster than that at room temperature. That's due to low stability of cathode material at high temperature.

The stability of LFP coated NCM811 is further investigated in calendar life tests, as shown in Figure XI.7.1c. At 22°C and at 100% SOC (fully charged), LFP coated NCM811 is much stable than NCM622 at initial calendar aging test. C/3 capacity retention for LFP coated NCM811 becomes less than the NCM622 after testing for 240 days. Moreover, LFP coated NCM811 shows fast capacity fade at an elevated temperature, as evidenced by a 65.3% capacity retention during storage at 40°C for 120 days. The result of calendar life tests agrees well with the cycle life test at different temperatures.

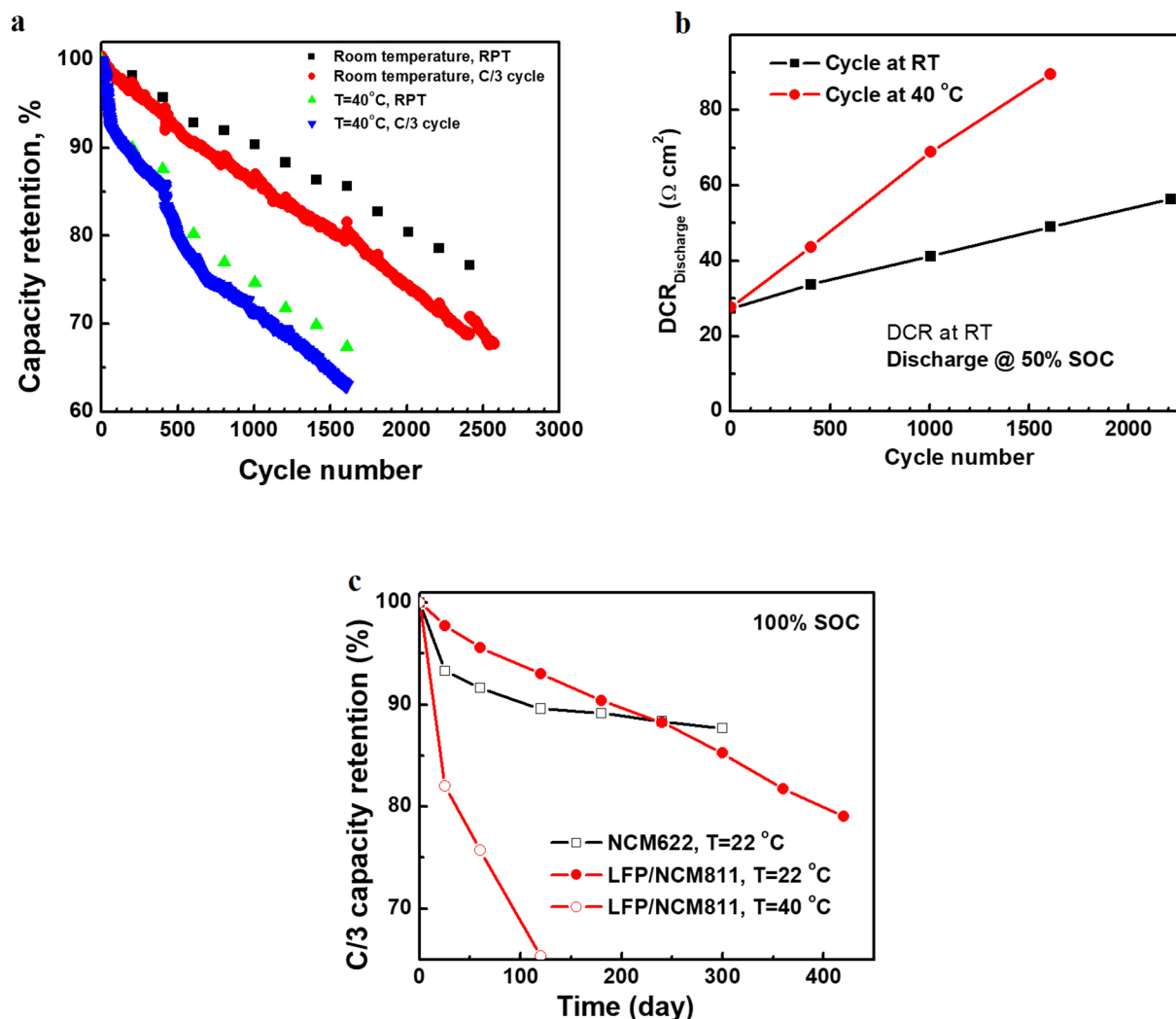


Figure XI.7.1 a) Capacity retention of the LFP-coated NCM/graphite cells during C/3 cycling at room temperature and 40 °C. b) DCR of the LFP-coated NCM/Gr cells during C/3 cycling at room temperature and 40 °C. c) C/3 capacity retention of the LIBs using different cathode materials during storage at 22 °C and 40 °C, respectively.

2. Phosphate coating on $\text{LiNi}_{0.92}\text{Co}_{0.055}\text{Mn}_{0.025}\text{O}_2$

In continuation of last year, we worked on characterizations to explore the effect of phosphate/metaphosphate compounds coating on $\text{LiNi}_{0.92}\text{Co}_{0.055}\text{Mn}_{0.025}\text{O}_2$. To understand how dry coating of AlPO_4 nanoparticles can enhance better cycling performance of high-nickel cathode, dQ/dV curves of 1st, 20th and 50th cycles between bare and coated cathode are compared on Figure XI.7.2. For the bare sample, gradual delays in peak position are observed for all redox peaks, while the last peak from charging curve at around 4.2V, which is assigned for H2 to H3 phase transformation [1], is totally disappeared after 50 cycles of charging-discharging, suggesting the irreversible property of crystal structure during cycling. After coating of AlPO_4 at 1% ratio, the peak position evolution is negligible, while the H2 to H3 is still clearly observed after 50th cycle. The coating layer has preserved the crystal structure during cycling.

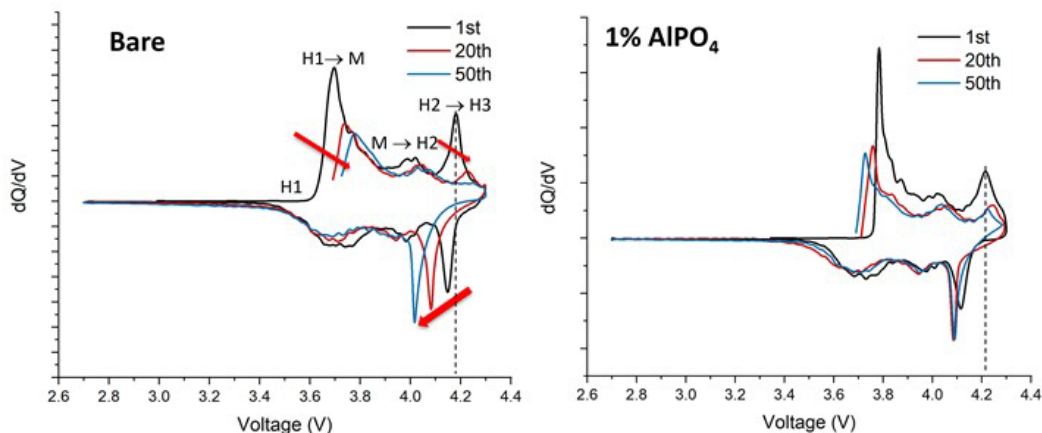


Figure XI.7.2 dQ/dV curves at 1st, 20th and 50th cycle for bare and 1% AlPO₄ coated LiNi_{0.92}Co_{0.055}Mn_{0.025}O₂

After 200 cycles of cycling, coin cells were disassembled, and electrodes were washed then dried for post-cycling characterizations. Cross-section of electrodes on Figure XI.7.3a-b show significant improvement in particle morphology after coating. The bare sample shows distinct cracks from the center toward surface of particles, while the coated particles remain intact and no visible cracking is observed. To further understand the mechanism of coating layer protection, XPS was performed, and results is shown on Figure XI.7.3c-d. On the surface of bare sample, there is a noticeable amount of Li-CO₂⁻, the product from decomposition of carbonate electrolyte after charging at high voltage from Li 1s spectrum. This peak is remarkable reduced for coated sample. While comparing the F 1s spectrum between bare and coated sample, the LiF component is increased after coating, supporting the mechanism of PO₄³⁻ protection layer, where it can react with acidic components from decomposition of electrolyte to become LiF and protect transition metals from dissolution into electrolyte. [2],[3]

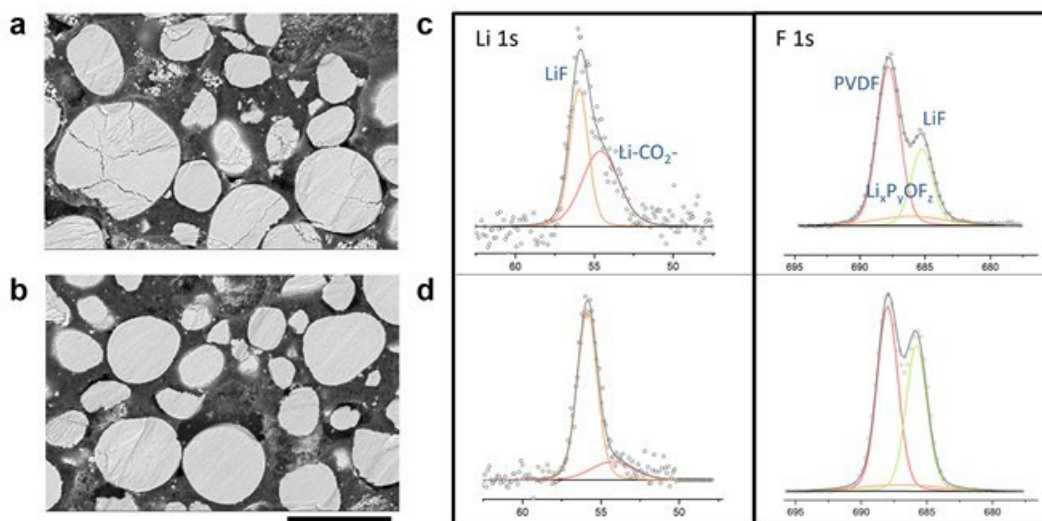


Figure XI.7.3 SEM image on cross-section and c-d) XPS spectrum for bare and 1% AlPO₄ coated LiNi_{0.92}Co_{0.055}Mn_{0.025}O₂ electrode after 200 cycles, respectively.

3. LiNi_{0.92}Co_{0.055}Mn_{0.025}O₂ coated with Mo compound

Other than phosphate compounds, we are developing new coating compounds in order to further improve the structural and electrochemical stability of the high-nickel cathode material. Mo compound is considered as one of the most promising coating materials to mitigate surface oxygen evolution and exhibit strong tendency to segregate to the surface region. [4]

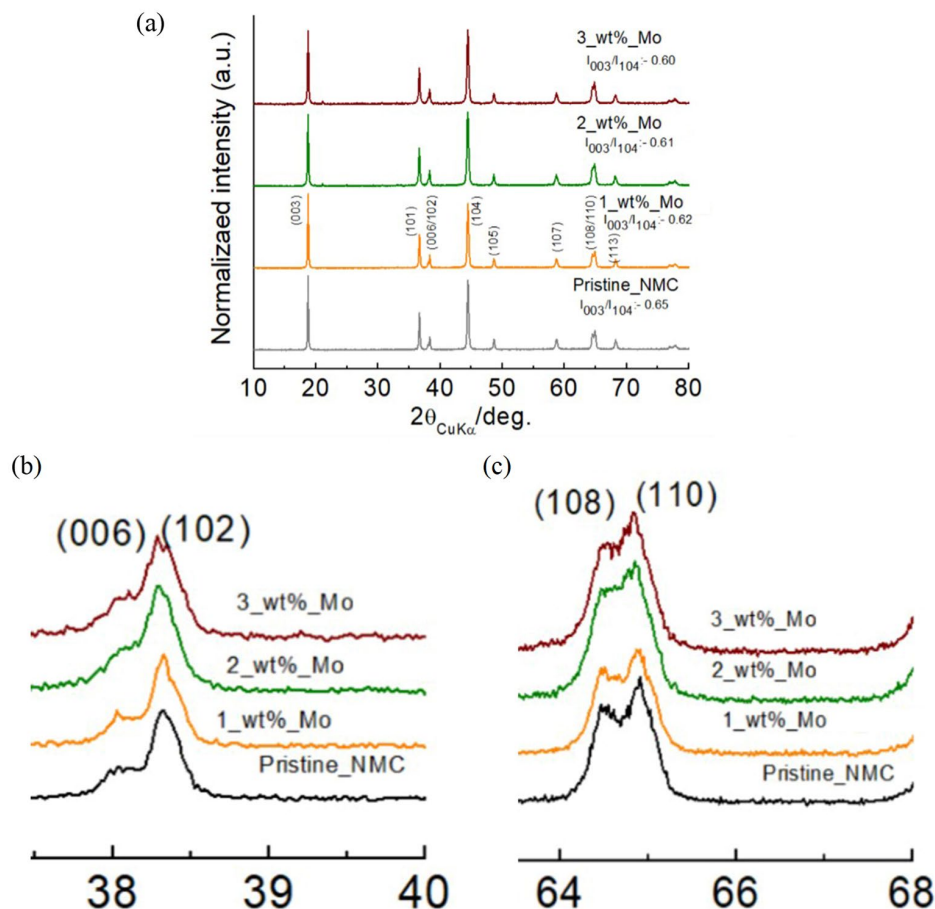


Figure XI.7.4 XRD patterns of pristine and Mo-coated NMC.

Figure XI.7.4 shows XRD patterns of LiNi_{0.92}Mn_{0.025}Co_{0.055}O₂ powders with and without Mo coating. All shows α -NaFeO₂ layered structures ($R\bar{3}m$ space group). Li₂MoO₄ impurities were formed for 2 and 3 wt.% Mo-coated NMC (Figure XI.7.4a). The characteristics of layered structure is known from XRD peaks split at $\sim 38^\circ$, $\sim 65^\circ$ and it was observed minimal splitting for 2 and 3 wt.% Mo because of impurities. For 1 wt.% Mo coating, the layered structure seems to be well preserved.

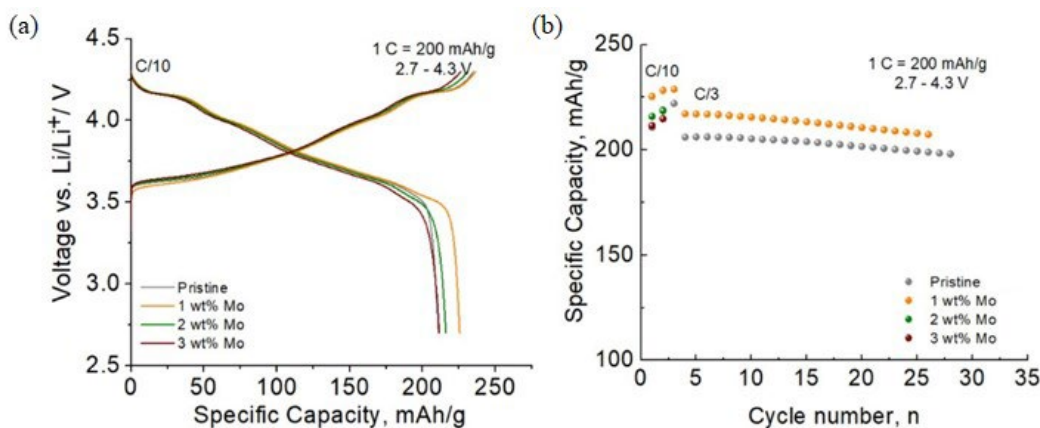


Figure XI.7.5 Electrochemical performance of pristine and Mo-coated NMC.

Consistent with XRD patterns, the 1 wt.% Mo coated sample exhibits better electrochemical performance compared with 2 and 3 wt.% Mo coated ones (Figure XI.7.5). NMC, 1-3 wt.% Mo coated NMC cathode represents initial capacity of 210, 225, 215 and 211 mAh/g, respectively. The cycling performance is still under investigation.

4. W-doped high-nickel $\text{Li}[\text{Ni}_{0.9}\text{Co}_{0.09}\text{W}_{0.01}]\text{O}_2$ and Zr-doped $\text{Li}[\text{Ni}_{0.76}\text{Mn}_{0.13}\text{Co}_{0.10}\text{Zr}_{0.01}]\text{O}_2$ cathode material

For NMC cathode, different strategies have been established for enhancing the oxygen stabilities towards better electrochemical performance. Cationic doping is one of the most prevalent approaches and the general guideline is to introduce dopants that bond with oxygen more strongly than the native transition metals. Based on the scheme, many dopants, such as Zr[5], W[6], Al[7], Mg[8], Mo[4], Na[9], are found to be effective for enhancing the thermal and structural stability upon cycling, which is perceived to be associated with the discretely and uniformly dispersed dopants that limit the oxygen depletion. Indeed, a strong dopant-oxygen interaction anchors the neighboring oxygens that are directly bonded with the dopants. However, given the intrinsically low concentration of doping species, the majority of lattice oxygens fails to bond directly with the dopants and are thus beyond the protection of the dopants. Therefore, the conventional scheme of “uniform” dopants distribution leaves out many puzzles for understanding the enhanced cycling stability through doping.

Here we reveal the “non-uniform” scheme, in contrast to the traditional “uniform” scheme, that enables the trace dopants to enhance the performance of layered cathode materials without requiring to fix individual oxygen. We choose W to reveal the non-uniform distribution resultant successive dopant-oxygen network that governs the battery performance. The W doped sample has the formula of $\text{Li}[\text{Ni}_{0.9}\text{Co}_{0.09}\text{W}_{0.01}]\text{O}_2$ (termed as NCW).

W concentration shows fluctuation at near surface regions that leads to the evident non-uniform distribution and develops a successive dopants wall at the NCW surface (Figure XI.7.6). The characteristic non-uniform distribution of W is firstly captured by the high-angle annular dark-field scanning transmission electron microscopy (HAADF-STEM). Because the HAADF-STEM is a “Z contrast” imaging technique whose intensity scales with atomic number square (Z^2), it shines the heavy elements. In the NCW, the W possesses a much higher atomic number relative to the TMs (Ni and Co) in the host structure, therefore, the much brighter contrast appears on surfaces is very likely related to the W aggregations. The visualization in the HAADF-STEM imaging is further supported by the EDS quantifications, in which the W concentration at surface increases by eight fold (8at.%) relative to the average doping amount. More critically, the W is seen to cover the entire surface, without leaving undoped gaps for the oxygen flowing out. In the cycled NCW, the brighter contrast that registers to the W segregation is repeatedly observed in the HAADF-STEM imaging. Meanwhile, the EDS mapping agrees well with HAADF-STEM imaging, in which W enriched columns are seen to occupy the entire surface and display a concentration of 10at.%-13at.%.

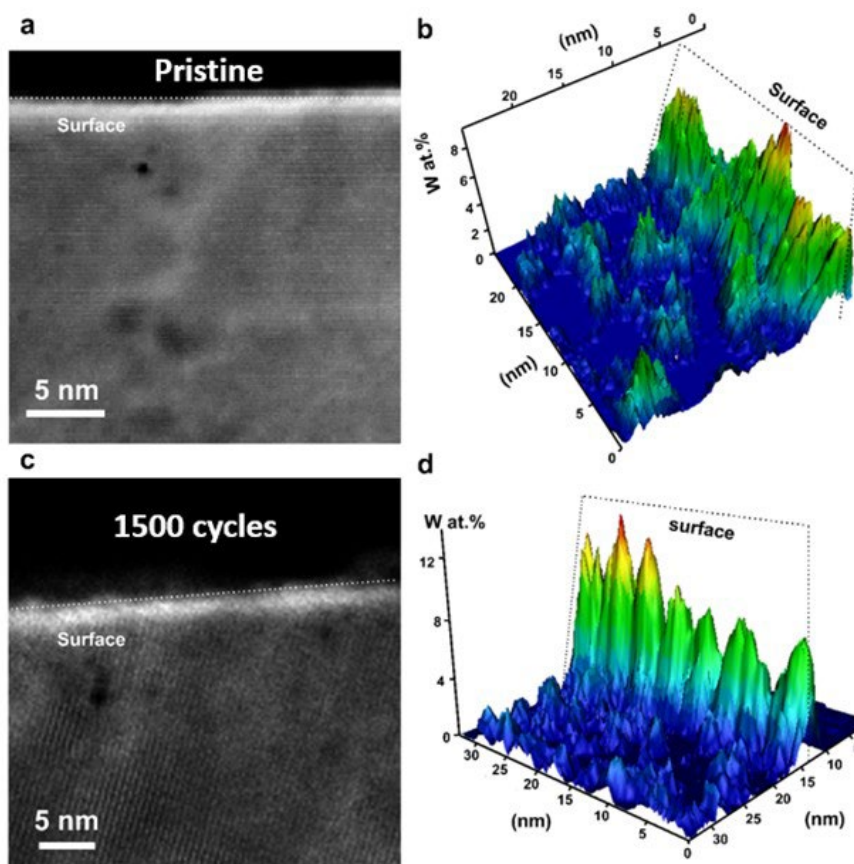


Figure XI.7.6 STEM EDS mapping to reveal spatial distribution of W in $\text{Li}[\text{Ni}_{0.9}\text{Co}_{0.09}\text{W}_{0.01}]\text{O}_2$ at pristine and following 1500 cycles. The white dashed lines outline the surface of cathode. (a) HAADF-STEM image of the NCW pristine cathode. (b) The 3D compositional profile of W plotted based on the EDS mapping and corresponding to (a). (c) HAADF-STEM image of the NCW cathode after 1500 cycles. (d) The 3D compositional profile of W based on the EDS mapping and corresponding to (c).

The dopant can possibly alter the cathode electronic structure and trigger the formation of cathode electrolyte interphase (CEI) layers that prevent the structural evolutions, therefore, the properties of CEI layers in NCW are examined. The ABF-STEM imaging shows that a continuous thin film, with a thickness of $\sim 2\text{nm}$, forms on NCW surface, which is absent in the system without doping, suggesting the W has effectively triggered the formation of the CEI layers (Figure XI.7.7).

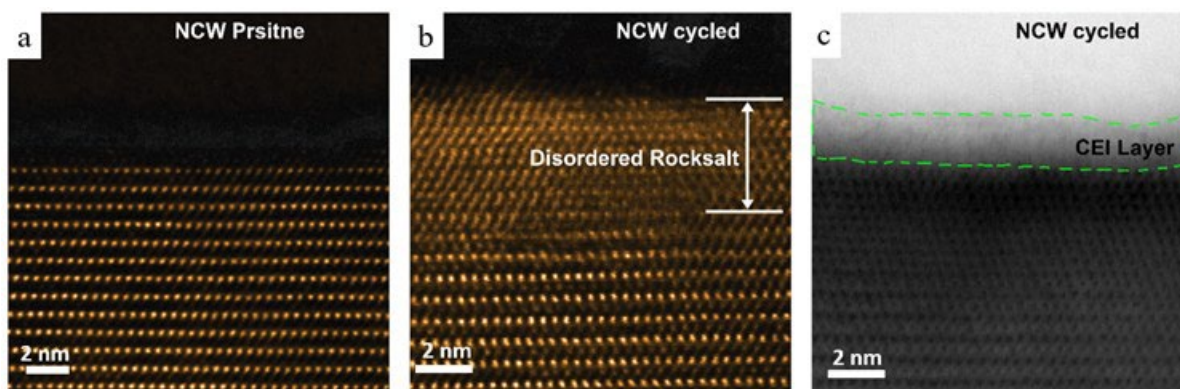


Figure XI.7.7 STEM-HAADF and Annular Bright field image to reveal the surface structure of $\text{Li}[\text{Ni}_{0.9}\text{Co}_{0.09}\text{W}_{0.01}]\text{O}_2$ (NCW) at pristine and following 1500 cycles. (a) The HAADF-STEM image of pristine NCW cathodes. (b) The HAADF-STEM image of 1500 cycled NCW cathodes. (c) The ABF-STEM image of cycled NCW cathodes.

The beneficial effects relevant to non-uniform dopants distribution in mitigating the cathode degradations are identified by the HAADF-STEM imaging. In the W doped samples, the thickness of the surface reconstruction layer is reduced to 2.8 nm even after 1500 cycles. This indicates that the cycling induced amorphous CEI layers may be insufficient to sustain the prolonged cycling, while the dual protection, CEI layers plus W-oxygen network, provides a more desirable protection against the interfacial degradation. The outcome of the distinct interface stability is in accordance with the electrochemical performance, in which the capacity retention is 94.3% for NCW after 1000 cycles.

In comparison with W as a doping element, we investigate the doping effect of Zr for the low Co NMC. The overall composition of the cathode is: $\text{LiNi}_{0.76}\text{Mn}_{0.13}\text{Co}_{0.10}\text{Zr}_{0.01}\text{O}_2$ (NMCZ). As shown in Figure XI.7.8, as similarly with the case of W doped sample, the Zr doped NMC shows stable cycling up to 1000 cycles.

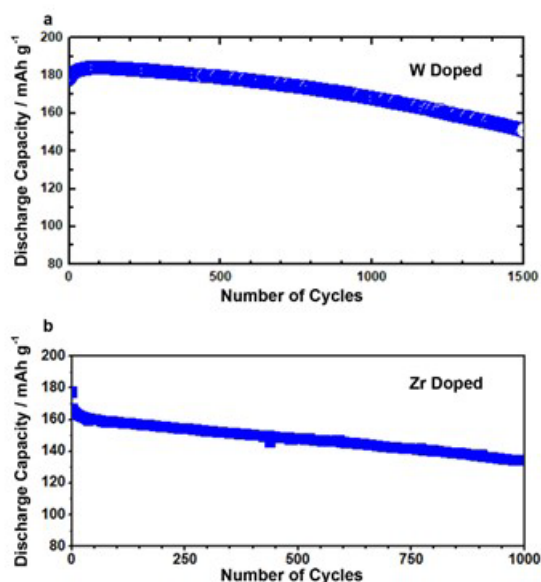


Figure XI.7.8 Electrochemical performance of W and Zr doped cathode. (a-b) Discharge capacity as a function of cycle number at between 3-4.2 V for $\text{Li}[\text{Ni}_{0.9}\text{Co}_{0.09}\text{W}_{0.01}]\text{O}_2$, and $\text{LiNi}_{0.76}\text{Mn}_{0.13}\text{Co}_{0.10}\text{Zr}_{0.01}\text{O}_2$, respectively.

STEM-EDS elemental mapping indicates the Zr atoms spread over the entire sample. However, due to the limited amount (1at.%), the Zr is presented on part of cathode sites only and renders a non-uniform distribution in the pristine NMCZ: The peaks represent the Zr-enriched zones; the valleys outline the Zr-depleted regions. With less concentration of Zr, the oxygens fail to bond with Zr. The quantitative analysis based on the EDS mapping captures the concentration oscillation that ranges from 2 at.% to 3 at.% for the Zr-enrich zones (Figure XI.7.9), suggesting the slight fluctuation of Zr (relative to the overall 1 at.% doping) at the atomic scale.

Upon electrochemical cycling, the Zr in the host cathode maintains the similar spatial distribution, as evidenced by the three-dimensional STEM-EDS mapping that displays similar scattered peaks over entire regions (Figure XI.7.9). The quantitative analysis based on the EDS results again reveals the small fluctuation of Zr at the dopants enriched regions with the concentration oscillating at between 2 at.% and 3.5 at.%.

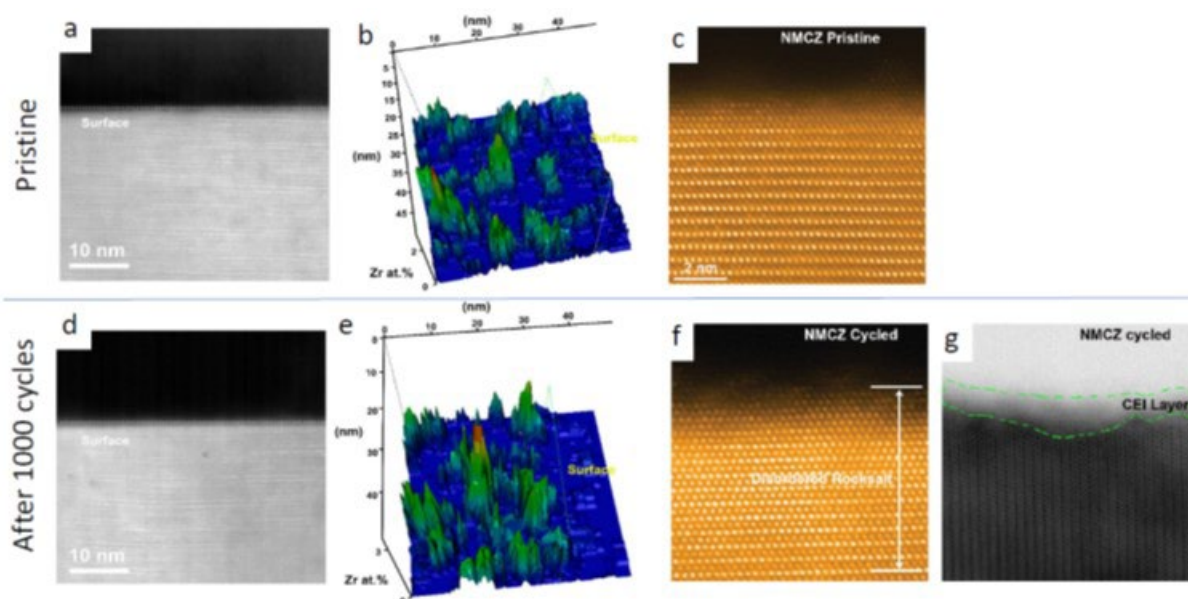


Figure XI.7.9 Zr distribution in pristine and cycled NMCZ. The white dashed lines outline the surface of cathode. (a) HAADF-STEM image of the NMCZ pristine cathode. (b) The 3D compositional profile of Zr plotted based on the EDS mapping and corresponding to a. (c) The HAADF-STEM image of pristine NMCZ cathodes. (d) HAADF-STEM image of the NMCZ cathode after 1000 cycles. (e) The 3D compositional profile of Zr based on the EDS mapping and corresponding to d. (f) The HAADF-STEM image of cycled NMCZ cathode, with a thick disordered rocksalt phase developed on surface. (g) The ABF-STEM image of 1000 cycled NMCZ cathodes.

The beneficial effects associated with the non-uniform dopants distribution in mitigating the cathode degradations are identified by the HAADF-STEM imaging. In the Zr doped samples, despite the continuous cathode electrolyte interface (CEI) layers that mitigate the interfacial side reactions, a surface region of ~ 6.8 nm in thickness is observed to transit into the disordered rocksalt structure after 1000 cycles, which is significantly thicker than that of W doped case.

By combining advanced electron microscopy and density-functional theory calculation, we reveal the critical role of dopant spatial distribution, rationalizing a dopant non-uniform spatial distribution scheme for enhancing the lattice stability of cathode. The scenario is exemplified by the Zr doped and W doped Ni-rich cathodes: despite the same dopant concentration and similar dopant-oxygen bonding strength, the W doped cathode significantly outperforms the Zr doped cathode, which is proved to arise from the non-uniform distribution of W, leading to a conformal W-O wall that is adjacent to the cathode particle surface. Moreover, we reveal that the surface reconstruction layer, though detrimental to the Li transport, is beneficial in fixing oxygen. The results provide new insights for the lattice oxygen retention and establish a distinct guideline for the dopant engineering towards optimized battery performance.

5. Scaling up of high-nickel cathode material production

In our previous works, we have reported our efforts on exploring different coating and doping strategy that showed improvement in prolonging cycle life of cathode materials. In this year, we also start to work on scaling up production of high-nickel cathode material, along with coating method on large scale production for pouch cell delivery.

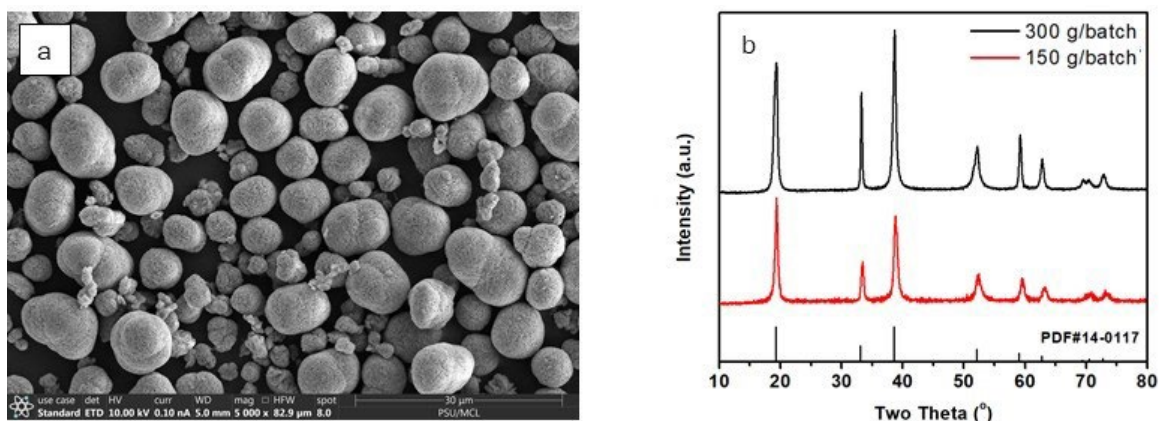


Figure XI.7.10 a) SEM image of co-precipitation product $\text{LiNi}_{0.92}\text{Co}_{0.055}\text{Mn}_{0.025}\text{O}_2$ of 300g batch. b) XRD patterns of co-precipitation product from 150g batch and 300g batch

Figure XI.7.10 shows the morphology of co-precipitation product $[\text{Ni}_{0.92}\text{Co}_{0.055}\text{Mn}_{0.025}](\text{OH})_2$ on large scale production of 300g/batch. Most particles are at 10-15 μm size range, with small amount of newly nucleated particles. The XRD patterns comparison on product of 150g batch and 300g batch shows similarity in peak positions and no impurities are detected.

The precursor then needs to be mixed with $\text{LiOH}\cdot\text{H}_2\text{O}$ for later lithiation. We use a 9-speed blender as the mixer, and blending parameters were optimized. As shown on Figure XI.7.11, 1 speed cannot break the $\text{LiOH}\cdot\text{H}_2\text{O}$ particles, leaving big chunks $\text{LiOH}\cdot\text{H}_2\text{O}$ remained. On the other hand, the 9 speed can break both $\text{LiOH}\cdot\text{H}_2\text{O}$ and precursor particles, as hemispheres of broken precursors are observed on SEM image. For 5 speed trial, there is no big $\text{LiOH}\cdot\text{H}_2\text{O}$ particle is observed and only an adequate amount of broken hemispheres of broken particles is visible. A dry mixer is already purchased to further preserve the particle morphology and enhance better mixing. For the time being, the 5 speed is then chosen for further optimization of scaling up experiment.

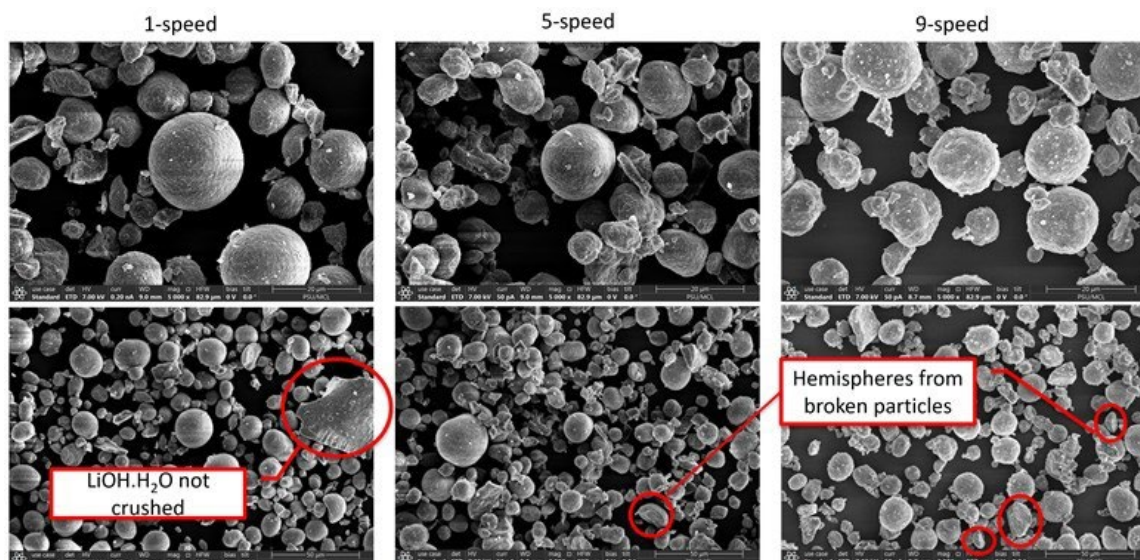


Figure XI.7.11 SEM images of $\text{LiNi}_{0.92}\text{Co}_{0.055}\text{Mn}_{0.025}\text{O}_2$ precursor mixed with $\text{LiOH}\cdot\text{H}_2\text{O}$ at different speeds.

For calcination process, a big tube furnace was used to calcine larger amount of material at the same time. Mass loading effect on cycling performance was explored and shown on Figure XI.7.12a. Different loading does not have effect on initial capacity but can impact the cycling performance. Lower loading at 15g/crucible

clearly enhanced better capacity retention of 89% after 40 cycles, in comparison with 85% for 30g/crucible and 83% for 40g/crucible. A reasonable explanation for this behavior is the difference in contact surface for oxygen during calcination. For large loading of material on a same crucible, surface area for material to be in contact with oxygen flow is limited and the ratio of material cannot be in contact with oxygen is higher compared to low loading sample. Therefore, the oxidation reaction of material with oxygen is the rate limited step for lithiation process of precursor. To enhance better rate for this reaction, higher partial pressure of oxygen should be the key factor. Different oxygen flow is then investigated to confirm this assumption. Figure XI.7.12b shows that increasing oxygen flow significantly increases the capacity retention. When 0.75L/h flow is used, capacity retention after 40 cycles improves to 92%. Further optimizations are in progress to enhance even better performance.

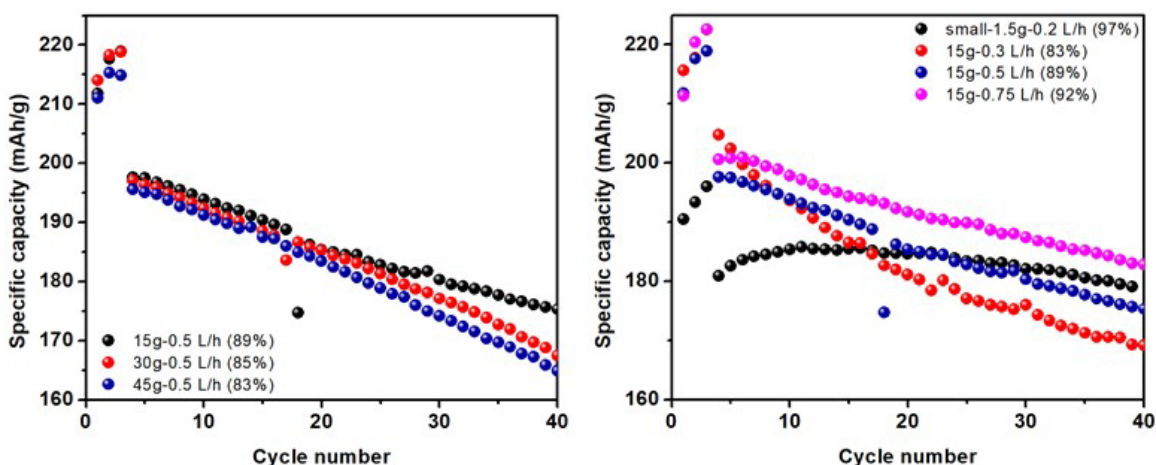


Figure XI.7.12 Cycling performance of $\text{LiNi}_{0.92}\text{Co}_{0.055}\text{Mn}_{0.025}\text{O}_2$ calcined at a) different loading mass and b) different oxygen flow.

Conclusions

In conclusion, this year we have worked on NCM811 and $\text{LiNi}_{0.92}\text{Co}_{0.055}\text{Mn}_{0.025}\text{O}_2$. We mainly focused on the optimization by coating/doping, and also deeply explored the structural reconstruction at the surface and subsurface of the particles.

The 2.5 Ah LFP-coated NCM/graphite cells is ultra-stable with the capacity retention at C/3 of 76.7% after 2413 cycles. At 40°C, the cell remains 67.3% capacity retention after 1609 cycles.

For $\text{LiNi}_{0.92}\text{Co}_{0.055}\text{Mn}_{0.025}\text{O}_2$, we have found that Al doping can reduce H2-H3 phase transition upon cycling and inhibit the growth of cavities and intergranular cracks inside the secondary particles, and thus greatly improve the cycling stability. On the other hand, phosphate coating can greatly inhibit penetration of acidic components from decomposition of electrolyte and trace water, which in turn improves the cycling performance of high-nickel cathode material. In addition, Mo-doped $\text{LiNi}_{0.92}\text{Co}_{0.055}\text{Mn}_{0.025}\text{O}_2$ also exhibited superior cycling stability compared with the undoped one.

By combing advanced electron microscopy and density-functional theory calculation, the role of dopant spatial distributions is revealed, as W and Zr are chosen as representatives. Despite the same doping concentration and similar bonding strength between dopant and oxygen, W doped cathode significantly surpass Zr doped cathode in cycling performance, suggesting that the non-uniform distribution of W can become a wall-protection on the cathode surface. This work rationalizes a dopant non-uniform spatial distribution scheme for improving battery performance works in the future.

High-nickel $\text{LiNi}_{0.92}\text{Co}_{0.055}\text{Mn}_{0.025}\text{O}_2$ cathode material is successfully synthesized at large scale. Cycling performance of cathode materials synthesized at different loading mass and oxygen flow reveal that oxygen

contact surface is the key component for optimization of scaling up of calcination step. Further optimizing works will be conducted.

References

1. Chen, Jie, Huiping Yang, Tianhao Li, Chaoyang Liu, Hui Tong, Jiaxin Chen, Zengsheng Liu, et al. "The Effects of Reversibility of H₂-H₃ Phase Transition on Ni-Rich Layered Oxide Cathode for High-Energy Lithium-Ion Batteries." *Frontiers in Chemistry* 7 (July 16, 2019): 500. <https://doi.org/10.3389/fchem.2019.00500>.
2. Hua, Weibo, Jibin Zhang, Zhuo Zheng, Wenyuan Liu, Xihao Peng, Xiao-Dong Guo, Benhe Zhong, Yan-Jie Wang, and Xinlong Wang. "Na-Doped Ni-Rich LiNi_{0.5}Co_{0.2}Mn_{0.3}O₂ Cathode Material with Both High Rate Capability and High Tap Density for Lithium Ion Batteries." *Dalton Trans.* 43, no. 39 (August 6, 2014): 14824–32. <https://doi.org/10.1039/C4DT01611D>.
3. Huang, Zhenjun, Zhixing Wang, Xiaobo Zheng, Huajun Guo, Xinhai Li, Qun Jing, and Zhihua Yang. "Structural and Electrochemical Properties of Mg-Doped Nickel Based Cathode Materials LiNi_{0.6}Co_{0.2}Mn_{0.2-x}Mg_xO₂ for Lithium-Ion Batteries." *RSC Advances* 5, no. 108 (2015): 88773–79. <https://doi.org/10.1039/C5RA16633K>.
4. Li, Jianyu, Wangda Li, Shanyu Wang, Karalee Jarvis, Jihui Yang, and Arumugam Manthiram. "Facilitating the Operation of Lithium-Ion Cells with High-Nickel Layered Oxide Cathodes with a Small Dose of Aluminum." *Chemistry of Materials* 30, no. 9 (May 8, 2018): 3101–9. <https://doi.org/10.1021/acs.chemmater.8b01077>.
5. Li, Wei, Lishan Yang, Yunjiao Li, Yongxiang Chen, Jia Guo, Jie Zhu, Hao Pan, and Xiaoming Xi. "Ultra-Thin AlPO₄ Layer Coated LiNi_{0.7}Co_{0.15}Mn_{0.15}O₂ Cathodes with Enhanced High-Voltage and High-Temperature Performance for Lithium-Ion Half/Full Batteries." *Frontiers in Chemistry* 8 (July 16, 2020). <https://doi.org/10.3389/fchem.2020.00597>.
6. Ma, Xiaoling, Chiwei Wang, Xiaoyan Han, and Jutang Sun. "Effect of AlPO₄ Coating on the Electrochemical Properties of LiNi_{0.8}Co_{0.2}O₂ Cathode Material." *Journal of Alloys and Compounds* 453, no. 1–2 (April 2008): 352–55. <https://doi.org/10.1016/j.jallcom.2006.11.087>.
7. Park, Kwangjin, Dong Jin Ham, Seong Yong Park, Ji Hyun Jang, Dong-Hee Yeon, San Moon, and Sung Jin Ahn. "High-Ni Cathode Material Improved with Zr for Stable Cycling of Li-Ion Rechargeable Batteries." *RSC Advances* 10, no. 45 (2020): 26756–64. <https://doi.org/10.1039/D0RA01543A>.
8. Sattar, Tahir, Seung-Hwan Lee, Bong-Soo Jin, and Hyun-Soo Kim. "Influence of Mo Addition on the Structural and Electrochemical Performance of Ni-Rich Cathode Material for Lithium-Ion Batteries." *Scientific Reports* 10, no. 1 (December 2020): 8562. <https://doi.org/10.1038/s41598-020-64546-8>.
9. Zhao, Zaowen, Bao Zhang, Lei Cheng, Zihang Liu, Jingtian Zou, Jiafeng Zhang, and Bin Huang. "Enabling Ultra-Fast Charging for Ni-Rich LiNi_{0.88}Co_{0.09}Mn_{0.03}O₂ Cathode by Bulk W-Doping." *Materials Letters* 308 (February 2022): 131043. <https://doi.org/10.1016/j.matlet.2021.131043>.

Acknowledgements

The work was supported by the Department of Energy, Office of Energy Efficiency and Renewable Energy (EERE), Vehicle Technologies Office, under Award Number DE-EE0008447. We appreciated the support from NETL manager, Colleen Butcher, at National Energy Technology Laboratory.

XII Next Generation Lithium-Ion Materials: Diagnostics

XII.1 Interfacial Processes (LBNL)

Robert Kostecki, Principal Investigator

Lawrence Berkeley National Laboratory
1 Cyclotron Road
Berkeley, CA 94720
E-mail: r_kostecki@lbl.gov

Tien Q. Duong, DOE Technology Development Manager

U.S. Department of Energy
E-mail: Tien.Duong@ee.doe.gov

Start Date: October 1, 2020

End Date: September 30, 2021

Project Funding (FY21): \$440,000

DOE share: \$440,000

Non-DOE share: \$0

Project Introduction

Li-based batteries are inherently complex and dynamic systems. Although often viewed as simple devices, their successful operation relies heavily on a series of complex mechanisms, involving thermodynamic instability in many parts of the charge/discharge cycle and the formation of metastable phases. This paradigm of Li-battery system operation usually drives the battery toward irreversible physical and chemical conditions that lead to battery degradation and failure.

The requirements for long-term stability of Li batteries are extremely stringent and necessitate control of the chemistry at a wide variety of temporal and structural length scales. Progress towards identifying the most efficient mechanisms for electrical energy storage and the ideal material depends on a fundamental understanding of how battery materials function and what structural/electronic properties limit their performance. This in turn necessitates the development and use of new characterization tools to monitor these processes.

The design of the next generation of Li batteries requires a fundamental understanding of the physical and chemical processes that govern these complex systems. Although some significant advances have been made to prepare and utilize new materials efforts towards the understanding of their operation mechanisms and degradation modes have been insufficient and/or unsuccessful.

Instability and/or high resistance at the interface of battery electrodes limit electrochemical performance of high-energy density batteries. A better understanding of the underlying principles that govern these phenomena is inextricably linked with successful implementation of high energy density materials in Li-based cells for PHEVs and EVs. Pristine and cycled composite and thin film model electrodes are investigated using a variety of state-of-the-art techniques to identify, characterize and monitor changes in materials structure and composition that take place during battery operation and/or storage. This project constitutes an integral part of the concerted effort within the BMR Program, and it supports development of new electrode materials for high-energy Li-metal based rechargeable cells.

Objectives

This collaborative project involves the development and application of advanced experimental methodologies to study and understand the mechanism of operation and degradation of high-capacity materials for rechargeable cells for PHEV and EV applications. The main objective of this task is to establish specific design rules toward the next generation of low impedance Li-metal rechargeable batteries that are capable of performing 1000 deep discharge cycles at CE > 99.9% and suppress lithium dendrites formation at high current densities (> 2 mA/cm²). This project aims at the following:

1. Apply far- and near-field optical multifunctional probes and synchrotron-based x-ray techniques to obtain detailed insight into the composition, structure, and mechanism of reactions at Li/electrolyte interfaces at an adequate spatial and temporal resolution.
2. Design new *in situ* diagnostic techniques and experimental methodologies that are capable of unveiling the function and operation of hidden or buried interfaces and interphases that determine material, electrode and battery cell electrochemical performance and failure modes.
3. Understand the mechanism of operation and degradation of high energy density materials for rechargeable Li-metal batteries for PHEV and EV applications.
4. Propose effective remedies to address inadequate Li-metal rechargeable batteries calendar/cycle performance for PHV and EV applications.

The other goal is development and application of far- and near-field optical probes and synchrotron-based advanced X-ray techniques to obtain insight into the mechanism of Li^+ transport and interfacial reactions in lithium/liquid model systems. Through an integrated synthesis, characterization, and electrochemistry effort, this project aims to develop a better understanding of lithium / liquid electrolyte interface so that rational decisions can be made as to their further development into commercially viable Li-metal cells.

Approach

- The pristine and cycled composite electrode and model thin-film electrodes were probed using various surface- and bulk-sensitive techniques, including FTIR, ATR-FTIR, near-field IR and Raman spectroscopy/microscopy, and SPM to identify and characterize changes in materials structure and composition.
- Novel *in situ* / *ex situ* far- and near-field optical multi-functional probes in combination with standard electrochemical and analytical techniques are developed to unveil the structure and reactivity at interfaces and interphases that determine materials electrochemical performance and failure modes.

Results

Extreme reactivity of lithium toward organic and inorganic-based liquid and solid electrolytes constitutes a key challenge to enable metallic Li-metal anodes in rechargeable batteries for transportation applications. In order to overcome this challenge, it is paramount to understand the composition of the interface of lithium and electrolytes. The SEI layer chemistry is known to be highly complex and heterogeneous at sub-nanometer scale, the exact function of its constituents remains poorly understood. With the advancement of spectroscopic techniques, it is possible to probe chemical composition on nanometer scale, breaking the diffraction limit of optical methods. We employed a new methodology that enables studies of the molecular structure of graphene-liquid interfaces with nanoscale spatial resolution. A monolayer graphene sheet was used as a working electrode and optical window for nano-FTIR probe characterization. The infrared transparency of graphene enables IR spectroscopy studies of its interface with liquids and solids *in situ*.

Before moving to *in-situ* experiments, it is important to understand how does graphene affect the near-field FTIR signal. In particular, we investigated 2 questions: a) How does the near-(electric) field, that drives dipole oscillations in nanoscopic spatial regions of

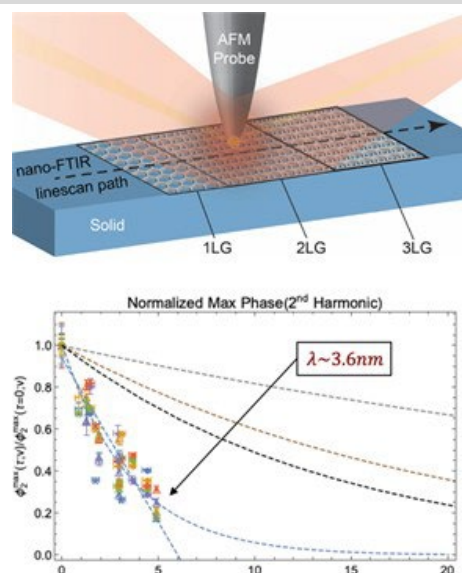


Figure XII.1.1 Graphene-subsurface Nano-FTIR. (top) schematic of the nano-FTIR experiment. Solid implies either PMMA or mica substrates (bottom) normalized phase of the 2nd harmonic (near field) FTIR signal. Exponential fitting yields a decay constant of ~ 3.6 nm

interest, decay subsurface? b) How do near-field infrared nano spectroscopy absorption spectra of buried chemistries change as a function of subsurface depth?

To answer those questions, we investigated the decay of the signal from the substrate depending on a different number of deposited graphene layers. We chose 2 substrates of interest: mica and PMMA. Both offer a flat, clean surface that provides the nano-FTIR signal. We deposited the mono- to few-layer graphene *via* the scotch-tape method from highly oriented pyrolytic graphite (HOPG). This method provides a clean surface with the least contamination, which is essential for studying the interfaces. We observed the decay of the intensity of the nano-FTIR signal from both mica and PMMA substrates dependent on the number of graphene layers. To extract the correlation parameters, we collected hundreds of nano-FTIR spectra through 1 to 4 layers of graphene on both substrates and performed fitting of the decaying signal. For PMMA substrate we investigated 5 vibrations (1155 cm^{-1} , 1196 cm^{-1} , 1242 cm^{-1} , 1267 cm^{-1} and 1736 cm^{-1}), whereas for mica we investigated 4 vibrations (933 cm^{-1} , 998 cm^{-1} , 1042 cm^{-1} and 1100 cm^{-1}).

As a result, we determined that nano-FTIR signals from known graphene-subsurface vibrational modes exponentially decay with increasing graphene thickness. The decay constant of $\lambda \sim 3.6\text{ nm}$ was obtained after performed fitting. This systematic study will allow us to better interpret results that would be obtained from the in-situ measurements.

For lithium-solid electrolyte interface investigation, we chose a solid-state model battery system consisting of Li/LiTFSI-PEO/C (graphene). The developed in-situ cell was measured during electrochemical cycling by nano-FTIR in a nitrogen-filled glovebox. After Li plating process, a morphological and chemical changes at the graphene/Li-electrolyte (SSE) interface were probed through the graphene window at nanoscale resolution. The dry nitrogen atmosphere prohibited any interference from oxygen and moisture and allowed us to obtain high quality nano-FTIR spectra. In this work, we do just that (Figure XII.1.2a), utilizing a fully functional solid-state device comprised of graphene (G) as an infrared transparent model carbon anode, a solid state electrolyte (SSE) of PEO/LiTFSI (EO:Li ratio 10:1), and a counter/reference electrode of lithium (Li). The full cell device is brought through one full electrochemical process (Figure XII.1.2b) in which Li is galvanostatically ($45\text{ }\mu\text{A cm}^{-2}$) plated (stripped) to (from) the model carbon anode at an elevated temperature of 45°C . The electrochemical process is stopped at four states – pristine, heated, plated, and stripped – at which points AFM, sSNOM, nano-FTIR, and attenuated total reflection Fourier transform infrared spectroscopy (ATR-FTIR) are all

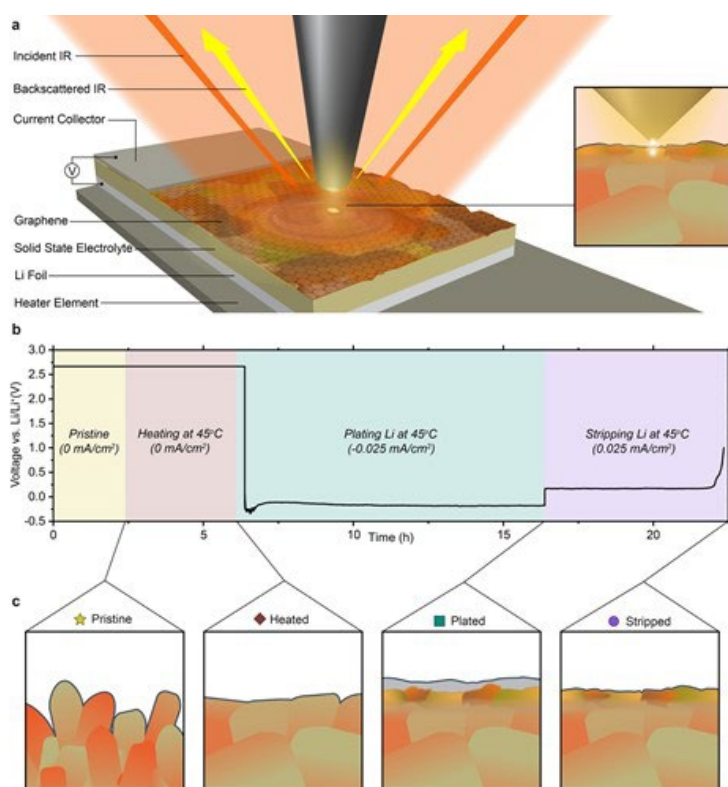


Figure XII.1.2 In situ characterization of the graphene – solid state electrolyte interface and interphase as a function of heating and electrochemical state with scattering-type near-field infrared nanospectroscopy. a) three-dimensional schematic of our experimental setup including metal-coated AFM probe, incident and backscattered infrared light, and cross section of assembled anode free G/SSE/Li cell atop heater element. Inset on the right-hand side is an artistic representation of the tip-sample near-field coupling that enables nanoscale FTIR. b), the electrochemical voltage profile applied to full cell device. Overlaid colored regions with descriptive text describe the state of the device. c), cross sectional illustrations of the device, near the G/SSE interface, for the four electrochemical states characterized.

conducted, at room temperature. Comparison of the nano-FTIR and ATR-FTIR is particularly useful in delineating absorption signals that originate from the interface verses the bulk. This is because the lion's share of spectral signal acquired in ATR-FTIR is attributable to absorption events occurring within 10's of microns subsurface, while in nano-FTIR, 10's of nanometers.

Figure XII.1.2c conveys some key findings. The pristine SSE has a rough surface in comparison to the heated surface and chemical inhomogeneity at the nanoscale (depicted by red-to-tan color gradients within grains). Heating improves these, but a flat and chemically homogeneous interface isn't reached. After plating protocols, we find plating is non-uniform (both at the microscale and nanoscale), that an electrochemically induced SEI layer with a chemically diverse mosaic structure has grown, and that PEO within the SEI layer undergoes a phase transition from a crystalline state to an amorphous state, which increases ionic conductivity.

During *in-situ* investigation we have observed non-uniform Li plating on graphene electrodes at the solid polymer electrolyte (SPE) interface using near-field Fourier transform infrared nano-spectroscopy (nano-FTIR). With the resolution, provided by nano-FTIR, we were able to observe 2 distinct regions of Li plated on a graphene electrode. We found that the structural properties of the polymer (chain orientation) and chemical composition (polymer/salt ratio) directly influence local Li^+ transport properties which then give rise to inhomogeneous SEI formation on a congruent spatial scale—triggering and continuously aggravating nonuniform current distribution and non-uniform Li plating and at the electrode/SEI interphase in following cycles.

As for the investigation of non-homogeneity at the liquid electrolyte interface, we have optimized the *in situ* electrochemical cell that will allow performing *in-situ* studies *via* nano-FTIR. We have addressed the issues with the previous design such as wetting of the electrodes, more room for the AFM cantilever in nano-FTIR. The cell must allow having graphene window to analyze subsurface interfaces. The proposed cell design and a digital photograph of machined parts are presented in Figure XII.1.4.

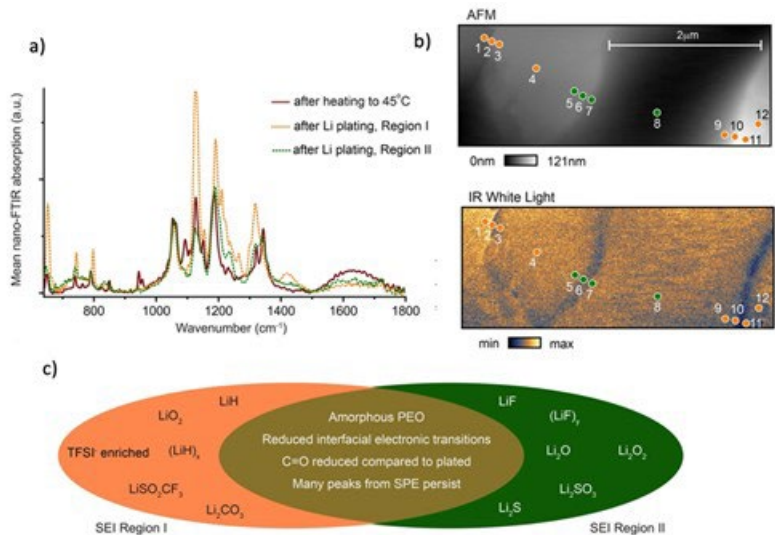


Figure XII.1.3 Characterization of the graphene-solid polymer electrolyte (SPE) interface after Li plating. a) Averaged nano-FTIR absorption from 2 different regions of formed SEI after Li plating b) AFM and IR white light images of the analyzed graphene subsurface c) Venn diagram depicting key similarities and differences between the two predominate SEI regions on the Graphene/Li electrode.

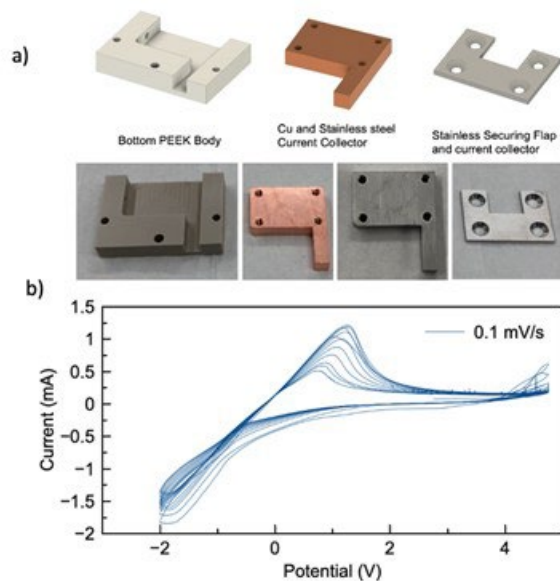


Figure XII.1.4 a) 3D schematics and digital photographs of the cell designed for performing nano-FTIR experiments at the liquid electrolytes – graphene interface. b) Cyclic voltammetry of the assembled cell with Li metal and copper electrodes in GEN 2 electrolyte

The 2-electrode electrochemical cell is machined from PEEK and is compatible with both liquid and solid electrolytes. Copper current collector can accommodate Li metal electrode, while stainless steel current collector is designed to accommodate lithium iron phosphate (LFP) electrode. The slurry of LFP will be drop casted and dried on stainless steel current collector. The choice of LFP as a cathode material is explained by the wide plateau of de-lithiation of LFP in GEN 2 electrolyte, which allows controlled plating of Li without change of the cell potential in 2-electrode cell configuration. Figure 4b shows electrochemical data obtained from the assembled electrochemical cell with Li metal and copper electrodes in GEN 2 electrolyte. The cyclic voltammetry shows 2 peaks corresponding to Li plating (negative current) and Li stripping (positive current). Further testing will be done using LFP slurry drop casted on stainless steel current collector.

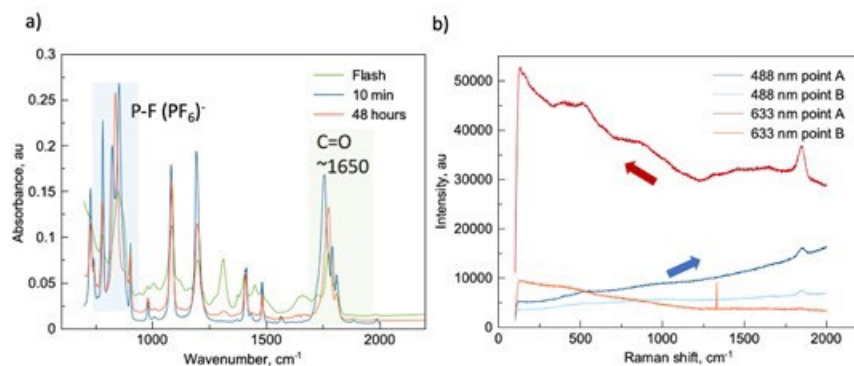


Figure XII.1.5 a) ATR-FTIR spectra of Li metal immersed in GEN 2 electrolyte for a different duration b) Raman spectra collected from Li metal flash-dipped in GEN2 electrolyte. Spectra were collected using 2 different lasers on 2 different locations.

It is known that the composition of the SEI layer is very diverse, therefore it is important to establish key components expected to appear on the subsurface of the graphene layer when the lithium will be plated during an in-situ experiment. The formation of the SEI layer, or passivation, happens the moment the lithium surface comes in contact with the electrolyte. Therefore, we collected bulk Attenuated Total Reflection (ATR)-

FTIR (Figure XII.1.5a), and Raman (Figure XII.1.5b) spectra of Li metal cleaned and dipped in GEN. ATR-FTIR spectroscopy was performed on Lithium samples immersed in GEN 2 electrolyte for a different amount of time: from flash-dipping till 2 days. Afterward, spectra were collected under a dry N₂ atmosphere. We observed the evolution of P-F stretching vibration as well as carbonyl group with a time of Li contact with the electrolyte. Interestingly, splitting of carbonyl peak is an indication of Li interaction with the carbonyl group, and the difference in peak position corresponds to the difference in composition of Li solvation shell. Raman spectroscopy was performed on a sample contained in the Ar atmosphere. A clear indication of photoluminescence (PL) is observed: the PL peak is expected to be observed between 488 nm and 633 nm. These preliminary results constitute the proof of concept and foundation for future in situ studies of SEI layer in organic liquid electrolytes

Conclusions

- Investigated Li/SSE interface at nanometer resolution using in situ near-field IR spectroscopy
 - Developed an effective strategy for in-situ electrochemical characterization of SEI layer through graphene window
 - Showed nanometer-scale inhomogeneities, namely polymer chain orientation and polymer/salt ratio distribution at graphene-polymer electrolyte interface
- Pioneered in situ near-field IR experiments to investigate Li/carbonate-based liquid electrolyte interface at nanometer resolution
 - Developed in-situ cell compatible with liquid electrolytes and LFP as a source of Li for investigation via near-field IR spectroscopy

Key Publications

1. He, Xin, Dominic Bresser, Stefano Passerini, Florian Baakes, Ulrike Krewer, Jeffrey Lopez, Christopher Thomas Mallia et al. “The passivity of lithium electrodes in liquid electrolytes for secondary batteries.” *Nature Reviews Materials* (2021): 1–17. <https://doi.org/10.1038/s41578-021-00345-5>
2. Paul, Partha P., Eric J. McShane, Andrew M. Colclasure, Nitash Balsara, David E. Brown, Chuntian Cao, Bor-Rong Chen et al. “A Review of Existing and Emerging Methods for Lithium Detection and Characterization in Li-Ion and Li-Metal Batteries.” *Advanced Energy Materials* 11, no. 17 (2021): 2100372. <https://doi.org/10.1002/aenm.202100372>
3. Horstmann, Birger, Jiayan Shi, Rachid Amine, Martin Werres, Xin He, Hao Jia, Florian Hausen et al. “Strategies towards enabling lithium metal in batteries: interphases and electrodes.” *Energy & Environmental Science* 14, no. 10 (2021): 5289–5314. DOI: [10.1039/D1EE00767J](https://doi.org/10.1039/D1EE00767J)

Acknowledgements

This work has been performed in close collaboration with:

- ABMR Research Groups
 - ANL, LBNL, SUNY, UP, HQ, NREL, URI, UM and UU
 - G. Chen, V. Battaglia, M. Doeff, K. Persson, V. Zorba, W. Yang, C. Martin, C. Ban, B. McCloskey
 - ALS, H. Bechtel, E. Crumlin
- UCL (UK), P. Shearing
- University of Liverpool (UK). L. Hardwick
- Central Laser Facility, Research Complex at Harwell (UK)
- Umicore, Farasis Energy, Inc.
- MEET (Germany), J. Li, M. Winter
- ESRF (France).

XII.2 Advanced *in situ* Diagnostic Techniques for Battery Materials (BNL)

Xiao-Qing Yang, Principal Investigator

Chemistry division, Brookhaven National laboratory
Bldg. 555, Brookhaven National Laboratory
Upton, NY 11973
E-mail: xyang@bnl.gov

Enyuan Hu, Principal Investigator

Chemistry division, Brookhaven National laboratory
Bldg. 555, Brookhaven National Laboratory
Upton, NY 11973
E-mail: enhu@bnl.gov

Tien Q. Duong, DOE Technology Development Manager

U.S. Department of Energy
E-mail: Tien.Duong@ee.doe.gov

Start Date: October 1, 2020

End Date: September 30, 2021

Project Funding (FY21): \$350,000

DOE share: \$350,000

Non-DOE share: \$0

Project Introduction

This project is focused on the development of advanced diagnostic characterization techniques for the following issues: obtaining in-depth fundamental understanding of the mechanisms governing the relationship between the structure and the performance of battery materials; providing guidance and approaches to improve the properties of battery materials. The approach of this project is the development and application of combined synchrotron based *in situ* X-ray techniques such as x-ray diffraction (XRD), pair distribution function (PDF), hard and soft x-ray absorption (XAS and SXAS), together with other imaging and spectroscopic tools such as transmission electron microscopy (TEM), scanning transmission electron microscopy (STEM), mass spectroscopy (MS), X-Ray fluorescence microscopy (XRF) and transmission x-ray microscopy (TXM), as well as neutron-based techniques, such as neutron diffraction and neutron PDF (NPDF). For advanced Li-ion battery technologies, the revolutionary approaches using new generation of materials for cathode, anode, electrolyte, and separator are in the horizon. The new generation of cathode materials such as Li-rich high energy density $\text{Li}_{1+x}(\text{NiMnCo})\text{O}_2$ (NMC) composite materials, high Ni content, NMC cathode materials, and high energy density S-based cathode materials, together with high energy density lithium metal anode materials will significantly increase the energy density of the advanced Li-ion and beyond lithium-ion battery systems. However, many technical barriers must be overcome before the large-scale commercialization of these new materials can be realized. This project uses the time-resolved x-ray diffraction TR-XRD and absorption (TR-XAS) developed at BNL to study the kinetic properties of these materials with structural sensitivity (TR-XRD) and elemental selectivity (TR-XAS). This project develops and applies the HRTEM, TXM and PDF techniques, as well as neutron diffraction and neutron PDF to study the mechanisms of capacity and performance fading of cathode and anode materials. Another important issue is the thermal stability of new cathode materials which is closely related to the safety of the batteries. This problem has been studied using the combined TR-XRD, TR-XAS with mass spectroscopy (MS). This project also develops a novel *in situ* and *ex situ* X-ray fluorescence (XRF) microscopy combined with X-ray absorption spectroscopy (XAS) technique, which will enable us to track the morphology and chemical state changes of the electrode materials during cycling. In summary, this project supports the goals of VTO, the Battery and Electric Drive Technologies, and BMR program by developing new diagnostic technologies and applying them to the

advanced Li-ion as well as beyond lithium-ion (such as Li-metal, Na-ion, and Li-S) battery systems and by providing guidance for new material development.

Objectives

The primary objective of this project is to develop new advanced in situ material characterization techniques and to apply these techniques to support the development of new cathode, anode, and electrolyte materials with high energy and power density, low cost, good abuse tolerance, and long calendar and cycle life for the next generation of lithium-ion batteries (LIBs) and beyond Li-ion batteries (Li-metal, Na-ion, and Li-S) to power plug-in hybrid electric vehicles (PHEV) and electric vehicles (EV). The diagnostic studies have been focused on issues relating to capacity retention, thermal stability; cycle life and rate capability of advanced Li-ion and beyond Li-ion batteries

Approach

- Develop and apply advanced diagnostic techniques to study and improve the performance of high energy density LIBs and Li/S batteries.
- Using nano-probe beamline at NSLSII to study the elemental distribution of new solid electrolyte materials for Li-ion and Na-ion batteries.
- Using hard X-ray fluorescence (XRF) imaging on the concentration gradient Ni-rich NCM cathode particles in a noninvasive manner with 3D reconstructed images through tomography scans to study the 3D Ni, Co, and Mn elemental distribution from surface to the bulk.
- Using transmission X-ray Microscopy (TXM) studies on the concentration gradient Ni-rich NCM cathode particles with 3D reconstructed images through tomography scans.
- Using the S K-edge XRF imaging and XAS studies with examination of the reaction products on the sulfur cathode and Li-metal anode in high energy density Li/S cell.

Results

In FY2021, BNL has been focused on the development of new diagnostic techniques to study and improve the performance of high energy density LIBs. In collaboration with Dr. Yijin Liu at SLAC, the spectro-tomography technique has been applied to study the Li-rich NMC (LirNMC), which could spatially resolve the local valence state of the element of interest in 3D. Such capability is achieved by conducting tomographic scans at several different energy levels across the absorption edge of the targeted element of interest. This technique is first applied to Mn, the most abundant transition metal in LirNMC. Two particles at the pristine and the charged (to 4.8 V in the initial cycle, at the fully charged state) states are scanned. As shown in Figure XII.2.1a, Figure XII.2.1d, the particle morphology is similar and their Mn K-edge spectroscopic fingerprints over different regions (see labeling in the virtual slices through the center of the particle) are shown in Figure XII.2.1b and Figure XII.2.1e, respectively. The pristine particle appears to be relatively homogeneous in the Mn's valence state as indicated by the depth-dependent Mn XANES plots in Figure XII.2.1b and the 3D rendering of the Mn K-edge energy distribution in Figure XII.2.1c. On the other hand, the charged particle clearly shows a depth-dependent Mn redox variation (see Figure XII.2.1e, Figure XII.2.1f, Figure XII.2.1g). The core and the surface layer of the charged LirNMC particle exhibits high Mn valence state at 4+, while the Mn cations in the transition layers appear to be relatively reduced. These visual assessments of the pristine and the charged particles are further confirmed by the depth profile of Mn's K-edge energy shown in Figure XII.2.1h. While the relative homogeneity of the Mn valence state distribution in the pristine particle is anticipated, the observed depth-dependent Mn valence in the charged LirNMC particle is somewhat a surprise, specifically because of its non-monotonicity. This observation motivates a more systematic study of all the transition metal cations (Mn, Co, and Ni) in the LirNMC particle in a correlative manner.

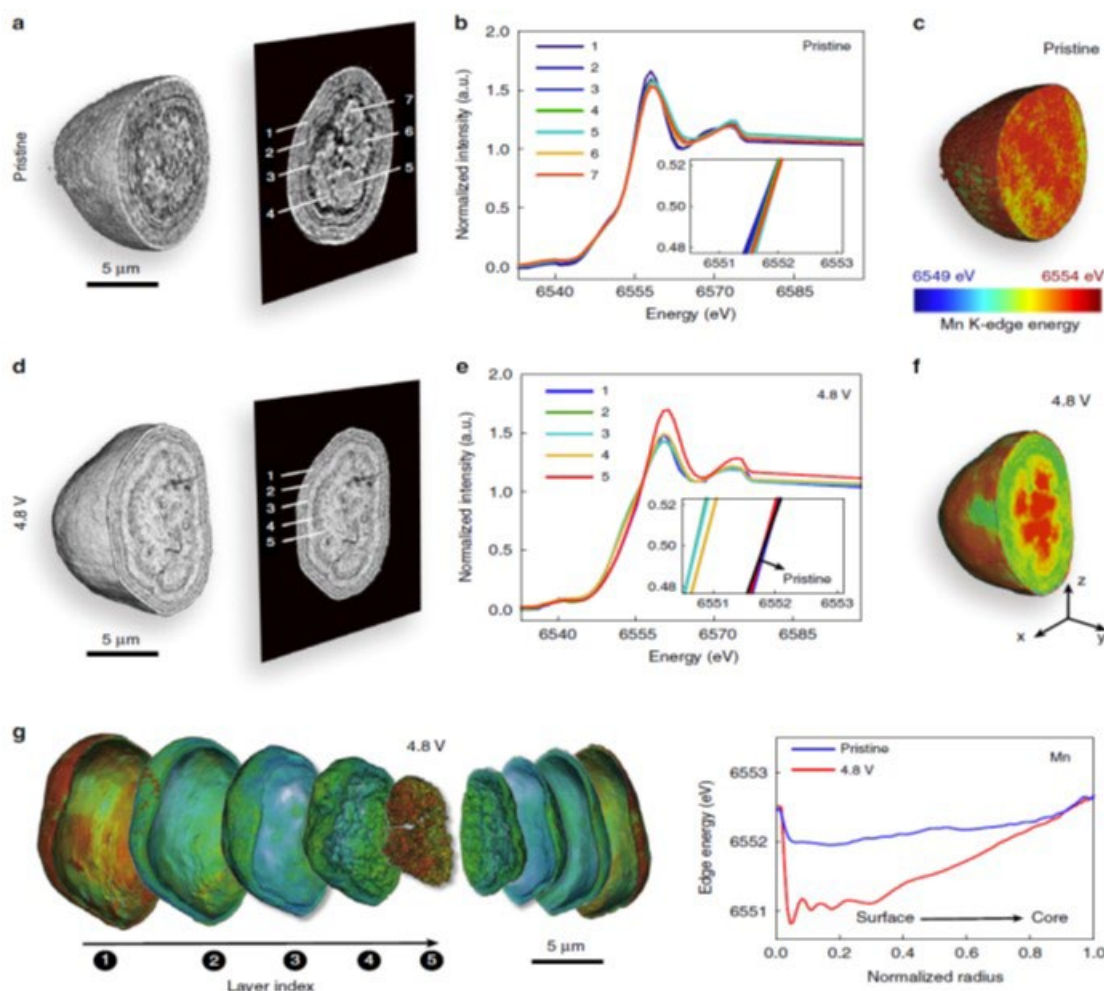


Figure XII.2.1 Spectro-microscopic investigation of the LirNMC particles. Panels (a) to (c) are on a pristine particle and panels (d) to (g) are on a charged particle (at 4.8 V in the first charge). Panels (a) and (d) are the 3D visualizations of the pristine and charged particles, with the labeling of different regions of interest on the respective central xz-slices. Panels (b) and (e) are the Mn K-edge x-ray absorption spectroscopic fingerprints over the regions of interest shown in panels (a) and (c), respectively. Panel (c) and (f) are the 3D renderings of the Mn's valence state distribution in the pristine and the charged particles. Panel (g) is a detailed layer-by-layer rendering of the Mn's valence state in the charged particle. Panel (h) is the comparison of the depth profiles of the particles in panels (c) and (f).

Developing single-crystal cathode material is one of efficient strategies to suppress the anisotropic volume changes during ion extraction/insertion which makes the materials intrinsically vulnerable to grain-boundary (inter-granular) fracture leading to rapid impedance increase and capacity decay. Scientists at PNNL led by Dr. Phung Le used single crystal $\text{LiNi}_{0.76}\text{Mn}_{0.14}\text{Co}_{0.1}\text{O}_2$ (NMC7611) to synthesize the analogue Na-ion cathode material $\text{Na}_z\text{Ni}_{0.76}\text{Mn}_{0.24}\text{Co}_{0.1}\text{O}_2$ (Na_zNMC) by inserting sodium into delithiated phase of Li_yNMC . The micro sized single-crystal Ni-rich sodium layered oxide Na_zNMC was obtained. In collaboration with PNNL scientists, BNL team carried out the characterization studies on the structural evolution of this material using synchrotron-based X-ray absorption techniques during the first sodiation and after multiple cycles. Results of ex-situ XAS including the X-ray absorption near edge structure (XANES) and extended X-ray absorption fine structure (EXAFS) for delithiated NMC7611 and sodiation Na_xNMC 7611 after initial discharge (sodiation) and 10th cycle are shown in Figure XII.2.2. Figure XII.2.2a shows that Ni^{3+} was oxidized to Ni^{4+} after delithiation and the 1st sodiation reduces Ni back to Ni^{3+} , while Mn and Co show little spectra changes. Figure XII.2.2b shows the ex situ EXAFS data of NMC7611 cathode. In all cases, the EXAFS of Ni, Mn, and Co have shifts from delithiation state to sodiation state, suggesting the change of bond lengths between transition

metal cation and their neighboring atoms. Quantitative local structural features are obtained through fitting the Fourier transformed EXAFS data against the layered model structure and the results are shown in Figure XII.2.2c. The results indicate that the bond lengths between transition metals and oxygen increase from delithiation to sodiation. Such change is obvious for Ni. The Debye-Waller (D-W) factor for the transition metal—transition metal/Li/Na scattering path generally increases from delithiation to sodiation, suggesting that introducing Na into an originally Li-based structure induces some local structural disorder. Upon cycling, such disorder may be relaxed as seen from the decreased D-W factor from the 1st cycle to the 10th cycle.

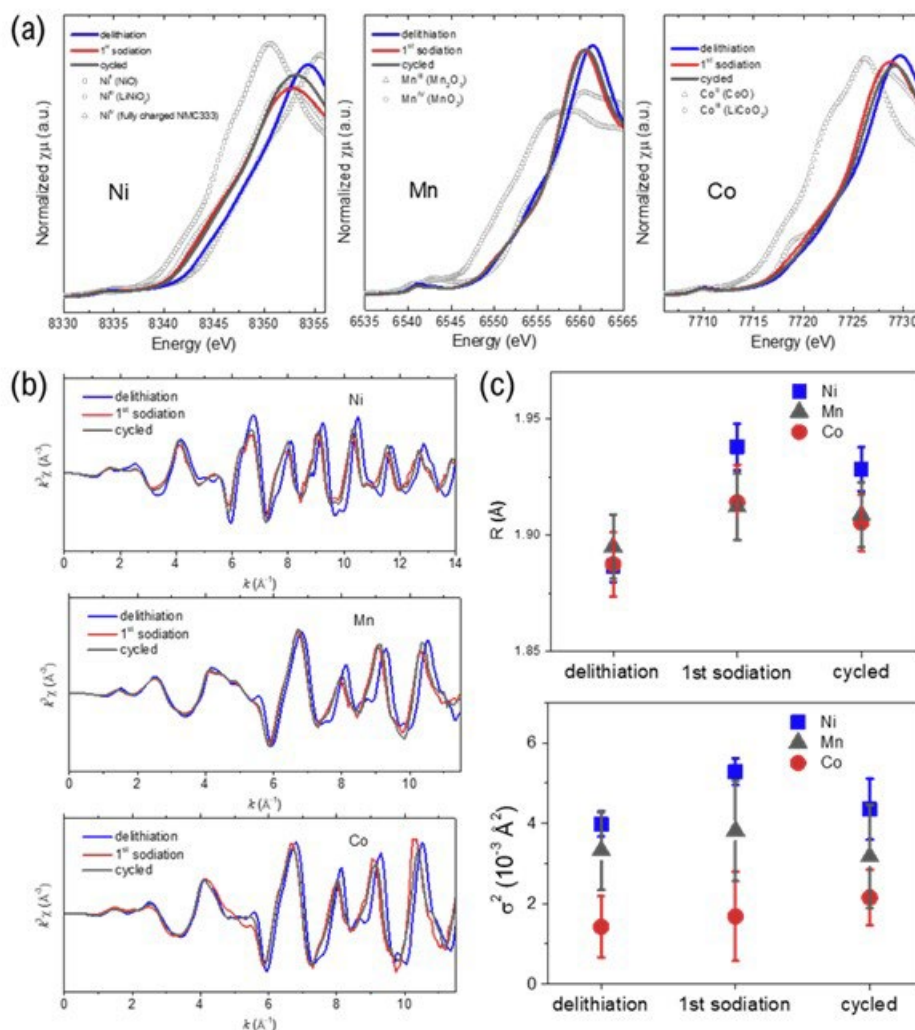


Figure XII.2.2 (a) XANES and (b) EXAFS spectra of delithiated NMC7611 and sodiation Na_xNMC6711 for initial discharge (sodiation) and 10th cycle; (c) fitted local structural information including TM-O bond length (upper panel) and TM-TM/Li/Na disorder reflected by the Debye-Waller (D-W) factor (lower panel).

Na-ion batteries with gravimetric energy density potentially comparable to some Li-ion batteries and the raw materials widely available, have been pursued persistently for grid energy storage and low speed vehicles. Mn-rich (Mn >50%) layered oxide with high energy density and low-cost have been explored extensively in Li-ion batteries and also in Na-ion battery cathode development. The large size of Na-ions affects the stacking of layers and hence further complicates the structure of these layered Na-ion materials. X-ray absorption near edge structure (XANES) can clearly reveal the TM cation valence and is commonly used to study charge compensation mechanism for battery materials. In collaboration with Dr. Xiaolin Li at PNNL and Prof. Xin Li at Harvard University, ex situ Mn, Co, Ni K-edge XANES studies were carried out on Na_xLi_{1.2}-

$\text{Mn}_{0.54}\text{Ni}_{0.13}\text{Co}_{0.13}\text{O}_2$ at fully sodiated, charged to 3V and charged to 3.8V states, along with some reference metal oxides with results shown Figure XII.2.3c-Figure XII.2.3e. The Mn K edge XANES in Figure 1c reveals that Mn does not show obvious valence change upon charging and stays at 4+ all the time. Co K edge XANES in Figure XII.2.3d shows that minor oxidation has taken place when charged to 3.8V. The Ni K edge XANES, however, displays very drastic change, as shown in Figure XII.2.1, Figure XII.2.3e. The fully sodiated $\text{Na}_x\text{Li}_{1.2-y}\text{Mn}_{0.54}\text{Ni}_{0.13}\text{Co}_{0.13}\text{O}_2$ has very close Ni valence to that of pristine $\text{Na}_x\text{Li}_{1.2-y}\text{Mn}_{0.54}\text{Ni}_{0.13}\text{Co}_{0.13}\text{O}_2$, which is between 2+ and 3+. When charged to 3.0V, the valence becomes close to that of LiNiO_2 with 3+ valence state. Further charging to 3.8V shows continuous shift to higher energy position located between LiNiO_2 (3+) and charged $\text{LiNi}_{1/3}\text{Co}_{1/3}\text{Mn}_{1/3}\text{O}_2$ (4+). The XANES results demonstrate that Ni is the major element that contributes to the capacity within the voltage range of 2-3.8 V.

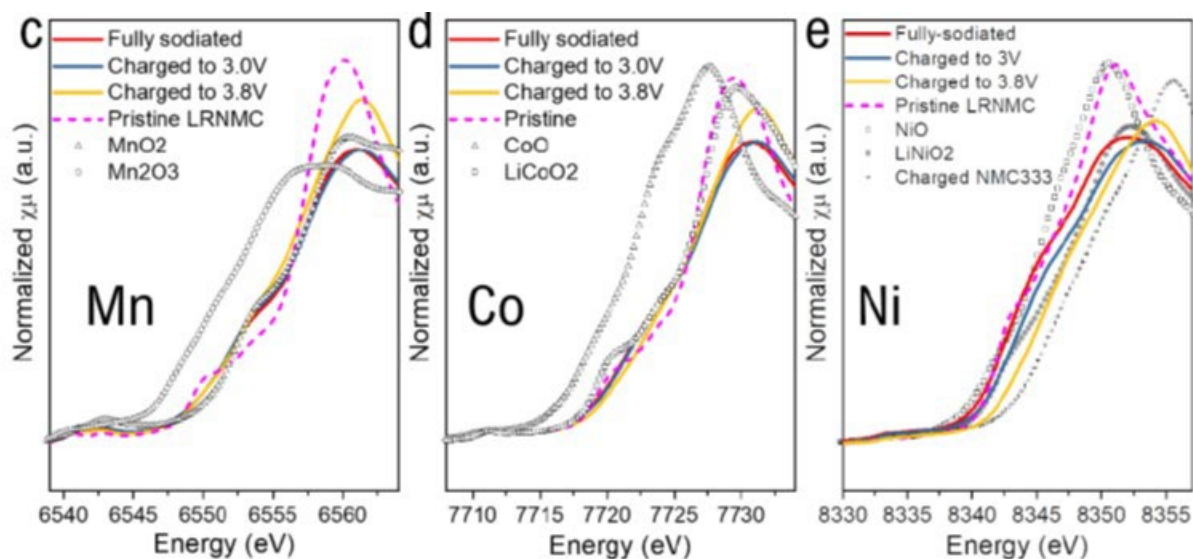


Figure XII.2.3 XANES data of $\text{Na}_x\text{Li}_{1.2-y}\text{Mn}_{0.54}\text{Ni}_{0.13}\text{Co}_{0.13}\text{O}_2$ cathode at K-edges of Mn (c), Co (d), and Ni (e) for the ex situ sample at different charged states. Spectra of reference oxides with known TM valences are also shown for comparison.

Solid-state electrolyte is the key component of solid-state batteries. Sulfur based ceramic solid-state electrolytes have spurred great interest due to their high ionic conductivity. Amongst them, ceramic sulfide solid electrolytes were reported with conductivities of 12 - 25 mS/cm, which is similar to or even higher than traditional liquid electrolytes. Unfortunately, the intrinsic voltage window of ceramic sulfide solid electrolytes is narrow (1.7-2.1 V). However, previous works have reported that $\text{Li}_{10}\text{GeP}_2\text{S}_{12}$ (LGPS) based batteries can be stable up to 5 V. These seemingly contradictory results remain one of the most pressing issues facing the solid-electrolyte field. It has been reported that the stability window of ceramic sulfides can be controlled, and substantially widened, using mechanical constraints to induce metastabilities and understanding the mechanism of this will provide valuable information for developing high voltage solid-state electrolytes. X-ray absorption spectroscopy (XAS) technique was applied to this study in collaboration with Prof. Xin Li at Harvard University. Figure XII.2.4g shows the P and S XAS peaks of pristine LGPS compared with the ones after CV scan up to 3.2V and 9.8V in liquid or solid-state batteries. In the conditions of no mechanical constraint in the liquid battery (denoted as 3.2V-L), both P and S show obvious peak shift toward the high energy and the shape change, indicating significant global oxidation reaction and rearrangement of local atomic environment in LGPS. In contrast, the P and S peaks don't show obvious sign of oxidation in solid state batteries, as no peak shift is observed. However, it is noticeable that the shoulder intensity increases at 2470 eV and 2149 eV in P and S spectra, respectively. An *ab initio* multiple scattering simulation of the P XAS peak from LGPS with various strain applied to the unit cell is shown in Figure XII.2.4h. A comparison between experiment and simulation suggests that the increase of shoulder intensity in XAS here might be caused by the negative strain, i.e., the compression experienced by crystalline LGPS after CV scan and holding at high voltages. If we connect the strain broadening in XRD with the shoulder intensity increase in XAS, and

simultaneously considering that no obvious decomposition current was observed in the CV test up to 10V, a physical picture emerges about the small local decomposition induced compression to nearby crystalline LGPS.

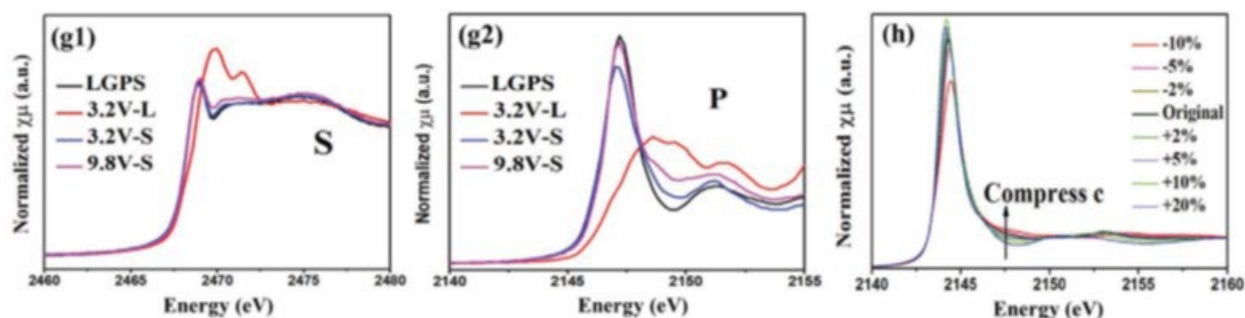


Figure XII.2.4 XAS measurements of S (g1) and P (g2) peaks from LGPS after CV scans and holds at 3.2 V in liquid cell (3.2V-L), 3.2 V in solid cell (3.2V-S), and 9.8 V in solid cell (9.8V-S), compared with pristine LGPS. (h): The simulation of P XAS peak changes by applying different

Conclusions

This project, Advanced in situ Diagnostic Techniques for Battery Materials (BNL), has been successfully completed in FY2021. All milestones have been completed. The publication records are very good. Extensive collaboration with other national labs, US universities and international research institutions were established.

Key Publications

Publications

1. Maria R. Lukatskaya,* Dawei Feng, Seong-Min Bak, John W.F. To, Xiao-Qing Yang, Yi Cui, Jeremy I. Feldblyum, and Zhenan Bao*, “Understanding the Mechanism of High Capacitance in Nickel Hexaaminobenzene Based Conductive Metal–Organic Frameworks in Aqueous Electrolytes” *ACS Nano*, 2020, 14, 11, 15919–15925, DOI: 10.1021/acsnano.0c07292, Publication Date: November 9, 2020
2. Si-Yu Yang, Ding-Ren Shi, Tian Wang, Xin-Yang Yue, Lei Zheng, Qing-Hua Zhang, Lin Gu, Xiao-Qing Yang, Zulipiya Shadike,* Hong Li,* Zheng-Wen Fu*, “High-rate cathode CrSSe based on anion reactions for lithium-ion batteries”, *J. Mater. Chem. A*, 2020, 8, 25739-25745, DOI: 10.1039/D0TA08012H, Publication Date: November 9th, 2020.
3. Longsheng Cao, Dan Li, Enyuan Hu, Jijian Xu, Tao Deng, Lin Ma, Yi Wang, Xiao-Qing Yang, and Chunsheng Wang*, “Solvation Structure Design for Aqueous Zn Metal Batteries”, *J. Am. Chem. Soc.* 2020, 142, 51, 21404–21409, DOI: 10.1021/jacs.0c09794, Publication Date: December 08, 2020.
4. Bi, Y., Tao, J., Wu, Y., Li, L., Xu, Y., Hu, E., Wu, B., Hu, J., Wang, C., Zhang, J.G. and Qi, Y., 2020. Reversible planar gliding and microcracking in a single-crystalline Ni-rich cathode. *Science*, (2020), Vol. 370, Issue 6522, pp. 1313-1317, DOI: 10.1126/science.abc3167, Publication Date: December 11, 2020.
5. Xiaoxiao Liu, Tongchao Liu, Rui Wang, Zhao Cai, Wenyu Wang, Yifei Yuan, Reza Shahbazian-Yassar, Xiaocheng Li, Songru Wang, Enyuan Hu, Xiao-Qing Yang, Yinguo Xiao, Khalil Amine, Jun Lu,* and Yongming Sun*, “Prelithiated Li-Enriched Gradient Interphase toward Practical High-Energy NMC–Silicon Full Cell”, *ACS Energy Letter*, 2021, 6, XXX, 320–328, DOI: 10.1021/acsenenergylett.0c02487, Publication Date: December 31, 2020.
6. Jin Zhang, Qinchao Wang, Shaofeng Li, Zhisen Jiang, Sha Tan, Xuelong Wang, Kai Zhang, Qingxi Yuan, Sang-Jun Lee, Charles J. Titus, Kent D. Irwin, Dennis Nordlund, Jun-Sik Lee, Piero Pianetta,

- Xiqian Yu, Xianghui Xiao, Xiao-Qing Yang, Enyuan Hu*, and Yijin Liu*, “Depth-dependent valence stratification driven by oxygen redox in lithium-rich layered oxide”, *Nature Communications* volume 11, Article number: 6342 (2020), DOI: 10.1038/s41467-020-20198-w, Publication Date: December 11, 2020. (This paper was published in Q1 of FY2021, but not listed in FY2021Q1 report)
7. Jiangtao Hu, Qinchao Wang, Bingbin Wu, Sha Tan, Zulipiya Shadike, Yujing Bi, M. Stanley Whittingham, Jie Xiao,* Xiao-Qing Yang,* and Enyuan Hu*, “Fundamental Linkage Between Structure, Electrochemical Properties, and Chemical Compositions of $\text{LiNi}_{1-x-y}\text{Mn}_x\text{Co}_y\text{O}_2$ Cathode Materials”, *ACS Appl. Mater. Interfaces* 2021, DOI: 10.1021/acsami.0c18942, Publication Date: January 07, 2021.
 8. Zulipiya Shadike, Hongkyung Lee, Oleg Borodin, Xia Cao, Xiulin Fan, Xuelong Wang, Ruqian Lin, Seong-Min Bak, Sanjit Ghose, Kang Xu, Chunsheng Wang, Jun Liu, Jie Xiao*, Xiao-Qing Yang* and Enyuan Hu*, “Identification of LiH and nanocrystalline LiF in the solid–electrolyte interphase of lithium metal anodes”. *Nat. Nanotechnol.* (2021). DOI: 10.1038/s41565-020-00845-5, Publication Date (web): January 28, 2021.
 9. Enyuan Hu, Qinghao Li, Xuelong Wang, Fanqi Meng, Jue Liu, Jie-Nan Zhang, Katharine Page, Wenqian Xu, Lin Gu, Ruijuan Xiao, Hong Li, Xuejie Huang, Liquan Chen, Wanli Yang*, Xiqian Yu*, and Xiao-Qing Yang*, “Oxygen-redox reactions in LiCoO_2 cathode without O–O bonding during charge-discharge”, *Joule*, Volume 5, Issue 3, Pages 720–736, DOI: 10.1016/j.joule.2021.01.006. Publication date: March 17, 2021.
 10. Zhao Cai, Yangtao Ou, Bao Zhang, Jindi Wang, Lin Fu, Mintao Wan, Guocheng Li, Wenyu Wang, Li Wang, Jianjun Jiang, Zhi Wei Seh, Enyuan Hu, Xiao-Qing Yang, Yi Cui,* and Yongming Sun*, “A Replacement Reaction Enabled Interdigitated Metal/Solid Electrolyte Architecture for Battery Cycling at 20 mA cm⁻² and 20 mAh cm⁻²”, *J. Am. Chem. Soc.* 2021, 143, 8, 3143–3152, DOI: 10.1021/jacs.0c11753, Publication Date (web): February 17, 2021.
 11. Ruqian Lin, Rui Zhang, Chunyang Wang, Xiao-Qing Yang & Huolin L. Xin*, “TEM mageNet training library and AtomSegNet deep-learning models for high-precision atom segmentation, localization, denoising, and deblurring of atomic-resolution images”, *Scientific Report*, 11, Article number: 5386 (2021), DOI: 10.1038/s41598-021-84499-w. Publication Date (web): March 08, 2021
 12. Ruqian Lin*, Seongmin Bak*, Youngho Shin, Rui Zhang, Chunyang Wang, Kim Kisslinger, Mingyuan Ge, Xiaojing Huang, Zulipiya Shadike, Ajith Pattammattel, Hanfei Yan, Yong Chu, Jinpeng Wu, Wanli Yang, M. Stanley Whittingham, Huolin L. Xin*, Xiao-Qing Yang*, “Hierarchical nickel valence gradient stabilizes high-nickel content layered cathode materials”, *Nature Communications*, 12, Article number: 2350 (2021), DOI: 10.1038/s41467-021-22635-w, Publication date: April 20, 2021.
 13. Shuang Li, Zulipiya Shadike, Gihan Kwon, Xiao-Qing Yang, Ji Hoon Lee,* and Sooyeon Hwang*, “Asymmetric Reaction Pathways of Conversion-Type Electrodes for Lithium-Ion Batteries”, *Chem. Mater.* 2021, 33, 3515–3523, DOI: 10.1021/acs.chemmater.0c04466, Publication date: April 27, 2021.
 14. Longsheng Cao, Dan Li, Travis Pollard, Tao Deng, Bao Zhang, Chongyin Yang, Long Chen, Jenel Vatamanu, Enyuan Hu, Matt J. Hourwitz, Lin Ma, Michael Ding, Qin Li, Singyuk Hou, Karen Gaskell, John T. Fourkas, Xiao-Qing Yang, Kang Xu*, Oleg Borodin* & Chunsheng Wang*, “Fluorinated interphase enables reversible aqueous zinc battery chemistries” *Nat. Nanotechnol.* 2021, DOI: 10.1038/s41565-021-00905-4, Publication Date: May 10, 2021.
 15. Longsheng Cao, Dan Li, Fernando A. Soto, Victor Ponce, Bao Zhang, Lu Ma, Tao Deng, Jorge M. Seminario, Enyuan Hu, Xiao-Qing Yang, Perla B. Balbuena*, Chunsheng Wang*, “Highly Reversible

Aqueous Zinc Batteries enabled by Zincophilic–Zincophobic Interfacial Layers and Interrupted Hydrogen-Bond Electrolytes”, *Angew. Chem. Int. Ed.* 2021, DOI: 10.1002/anie.202107378, Publication date: July 1, 2021.

16. Zhaohui Wu, Seong-Min Bak*, Zulipiya Shadike, Sicen Yu, Enyuan Hu, Xing Xing, Yonghua Du, Xiao-Qing Yang, Haodong Liu*, and Ping Liu, “Understanding the Roles of the Electrode/Electrolyte Interface for Enabling Stable Li||Sulfurized Polyacrylonitrile Batteries”. *ACS Appl. Mater. Interfaces* 2021, 13, 31733–31740, Publication date: July 2, 2021.

XII.3 Microscopy Investigation on the Fading Mechanism of Electrode Materials (PNNL)

Chongmin Wang, Principal Investigator

Pacific Northwest National Laboratory
902 Battelle Boulevard, Mail Stop K8-93
Richland, WA 99352
E-mail: Chongmin.wang@pnnl.gov

Tien Q. Duong, DOE Technology Development Manager

U.S. Department of Energy
E-mail: Tien.Duong@ee.doe.gov

Start Date: October 1, 2019

End Date: September 30, 2022

Project Funding (FY21): \$250,000

DOE share: \$250,000

Non-DOE share: \$0

Project Introduction

The aim of the proposed project is to establish the structure and property relationships for rechargeable batteries of both solid-state and liquid electrolytes. We will focus on addressing the challenges related to the stability of Li metal anode, lithium nickel-manganese-cobalt oxide cathode, sulfur based solid electrolyte and interfaces defined by these active components in rechargeable batteries. The project will gain critical insights regarding the structural and chemical evolution of interfaces and their effect on electrode stability, which will form the foundation for addressing the key challenges of rechargeable batteries. The outcome of the proposed study will feed back to the battery materials fabrication group to aid in designing better materials with enhanced battery performance.

Objectives

The main objective of the proposed research is to explore interfacial phenomena in rechargeable Li-ion batteries of both solid state and liquid electrolyte configuration, to identify the critical parameters that control the stability of interface and the electrodes as well as solid electrolyte. The outcome of the work will be establishing correlations between structural-chemical evolution of active components of batteries and their properties. These correlations will provide insight and guidance to the battery materials development groups for developing high performance battery materials. Success of this project will advance the research and development effort of next generation rechargeable batteries and therefore accelerate market penetration of EVs required by DOE's EV Everywhere program.

Approach

We will use integrated advanced microscopic and spectroscopic techniques, including in-situ S/TEM, ex-situ S/TEM, environmental S/TEM, cryo-electron microscopy, and in-situ liquid SIMS to directly probe the structural and chemical information during Li deposition and stripping. Cryo-S/TEM with analytical tools, such as EDS and EELS, will be used to gain chemical and electronic structural information at the interface between Li metal and electrolyte of both solid state and liquid, which will allow the direct correlation between the morphology and the chemistry. STEM-HAADF atomic level imaging and EDS and EELS will be used to probe the interface and bulk lattice stability. The work will be in close collaboration with the battery development group within the BMR and US-Germany Collaboration on Energy Storage.

Results

Revealing the structural nature of Li particle and Li whisker formed in the same coin cell

Li deposition morphology critically controls the performance of Li metal battery. One of the fundamental challenges for using Li metal is the dendritic Li deposition. Existing knowledge indicates that the morphologies of Li deposits are affected by a range of factors, such as pressure, temperature, current density,

electrolyte composition, and physical/chemical properties of the solid electrolyte interphase (SEI). Although remarkable progress has been achieved in stabilizing Li electrodeposition, an in-depth and comprehensive understanding of the underlying mechanisms of Li dendrites growth still remains unclear. It has been realized that within the same battery cell, both Li particle and Li whisker can be formed. Probing into the details of the structural and chemical features of Li particle and Li whisker lead to insights on intrinsic factors that govern Li deposition.

The electrolytes of 1.2 M LiPF₆ in ethylene carbonate (EC)/ethyl methyl carbonate (EMC) (3:7 by wt.) with 5wt.% VC was used to electrochemically deposit Li on Cu TEM grids at the current density of 0.1 mA cm⁻².

a 1.2 M LiPF₆-EC-EMC (3:7 by wt.) + 5 wt.% VC (traditional electrolyte)

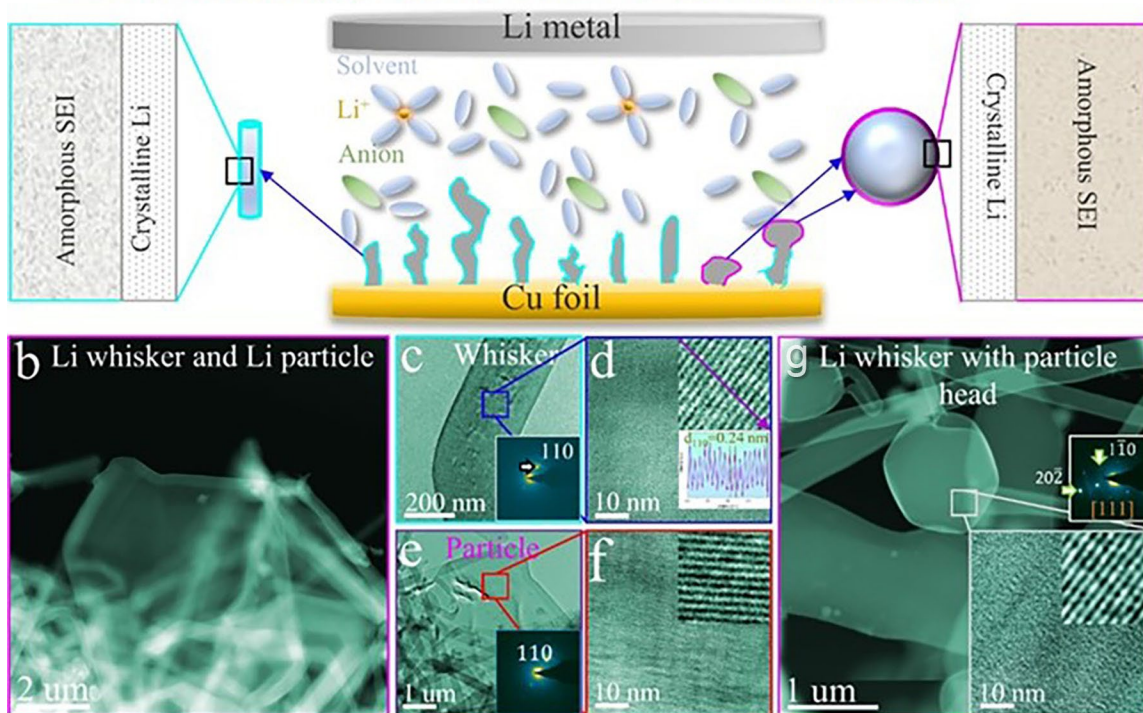


Figure XII.3.1 Schematic of Li deposits (a) With commercial carbonate-based electrolyte, the morphology of Li deposits is mainly whisker shape, except for very few particles and some of the whiskers with particle shaped head. Microstructure of Li deposits formed in the different electrolytes. (b-f) Cryo-(S)TEM images of Li deposits formed in the carbonate-based electrolyte: (b) HAADF-STEM image of Li deposits with two typical morphologies; bright-field TEM image of (c) whisker-shaped Li deposit and (d) corresponding high-resolution TEM image; bright-field TEM image of (e) particle-shaped Li deposit and (f) corresponding high-resolution TEM image. Insets: corresponding SAED patterns and enlarged area from Li deposits. (g) Bright-field TEM image of particle head of Li whisker, insets are corresponding high-resolution TEM image and SAED pattern.

This system primarily leads to the formation of Li whiskers, while still with certain fraction of Li particle (Figure XII.3.1a). Most of the Li whiskers have a diameter (non-uniform) of a few hundred nanometers as shown in Figure XII.3.1. Select area electron diffraction (SAED) pattern (inset of Figure XII.3.1c) acquired from the EDLi (blue color-coded area in Figure XII.3.1c) indicates that the EDLi is crystalline Li metal, which is further substantiated by the high-resolution image that taken at cryogenic temperature as shown in Figure XII.3.1d. Except for Li whiskers, particle-shaped EDLi is also formed, providing a clean system to investigate the difference between Li whisker and Li particle. Similar with Li whisker, as shown in Figure XII.3.1e and f, the particle-shaped Li deposit is single-crystalline Li metal. It has been reported that Li particle formed at low current density (0.2 mA cm⁻² and 1 mA cm⁻²) is mostly amorphous. The possible reason for the difference is the different current density, time duration, and electrolyte for the deposition. In other words, the morphology and structure of Li deposit are very sensitive to the current density, deposition time, and electrolyte chemistry, which indicate the complexity of the electrochemical behaviors of Li deposition. We also notice that some Li whiskers have a

particle-shaped head as shown in Figure XII.3.1g, featuring a hexagonal-shaped particle of single-crystalline Li metal. The facets of this type of particle are the $\{110\}$ surfaces (insets of Figure XII.3.1g). In the body-centered cubic (BCC) crystal structure, the $\{110\}$ family of planes are the most densely packed and thus has the lowest-energy surface according to the broken bond model. The results are consistent with the previous *in-situ* TEM results, by which the Li particle head is associated with the nucleation stage of Li whisker.

Delineating the microstructure of SEI layer on Li whisker and Li particle that were formed in the same coin cell

The co-existence of Li whisker and Li particle in the same coin cell provides the opportunity to unequivocally explore the SEI features on Li whisker and Li particle. We reveal that the SEI layer on the Li whisker has a smooth surface (Figure XII.3.2a), with a thickness of ~ 20 nm, as shown by the atomically resolved cryo-TEM image in Figure XII.3.2b. High-resolution TEM image (Figure XII.3.2b) and corresponding FFT pattern (Figure XII.3.2e) indicate its amorphous structure. The interface between electrochemical deposited Li (EDLi) and SEI is atomically sharp (Figure XII.3.2d). Similarly, the SEI layer on the Li particle shows amorphous structure, which is thicker than that on the Li whisker as shown in Figure XII.3.2f-j. Cryo-electron energy loss spectroscopy (Cryo-EELS) is used to reveal the fine structures of SEI layers on the Li particle and Li whisker. Figure XII.3.2 illustrates the EELS elemental maps, showing the spatial distribution of elements in SEI layers on the Li whisker and Li particle. As shown in Figure XII.3.2b, C, O, and Li within the SEI on Li whisker are uniformly distributed. For the Li particle (Figure XII.3.2d), O is distributed uniformly across the SEI, while C, P and F have a higher concentration in the outer layer of the SEI. Li shows non-uniform distribution across the SEI layer.

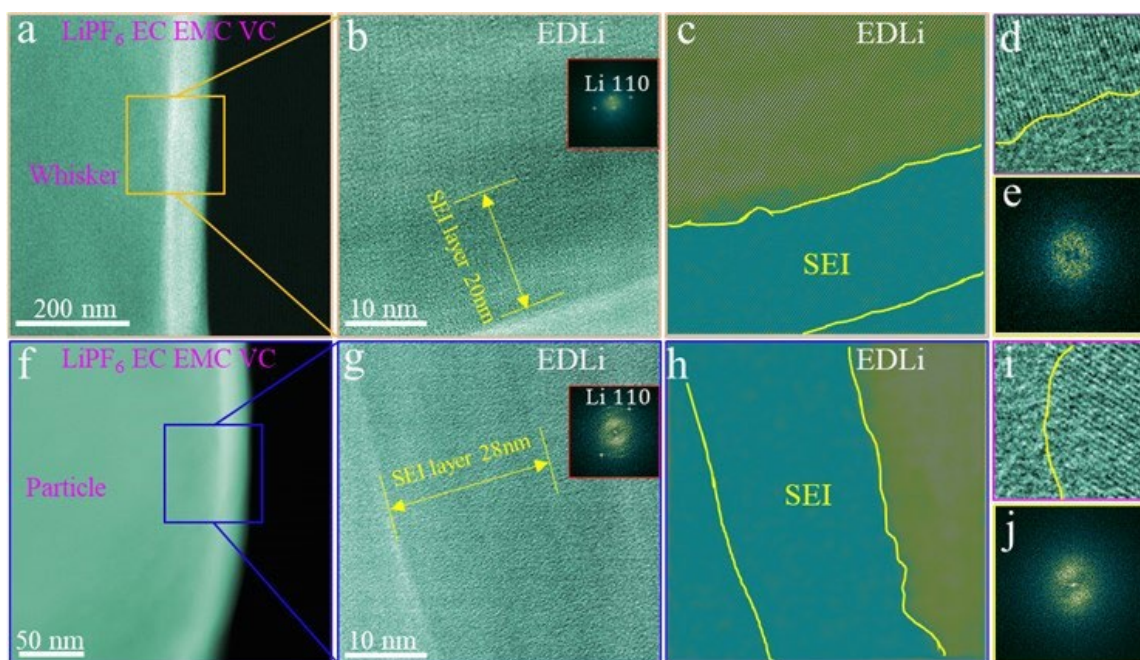


Figure XII.3.2 Structural features of SEI formed on Li whisker and Li particle that formed in the same coin cell using 1.2 M LiPF_6 -EC-EMC with 5wt.% VC. (a and f) Cryo-HADF-STEM image reveals SEI layer and Li deposit. (b and g) Cryo-TEM image shows the crystalline nature of Li deposit and amorphous structure SEI layers (the inset is the Fast Fourier transform (FFT)). (c and h) Filtered image shows the interface between Li-metal and SEI layer. (d and i) Cryo-HRTEM image reveal the interface between Li and SEI. (e and j) FFT of the HRTEM image.

Revealing the composition and elemental spatial distribution in SEI layer on Li whisker and Li particle formed in the same coin cell

Compositionally, EDS elemental maps indicate that the SEI on Li whisker, Li particle, and particle head of Li whisker is similarly composed of O, C, F, and P, with O and C as the dominant components. However, the relative ratio of O and C is different for the case of the SEI layer on the Li whisker, Li particles, particle head

of Li whisker, and tip of Li whisker. SEI layer on Li particle, head particle of Li whisker, and tip of Li whisker is enriched with O and mean with C, while SEI layer on Li whisker is enriched with C and O. In addition, F is also relatively rich in the SEI layer on the Li particle. The significant difference of SEI compositions on the Li whisker, particle, whisker head, and tip of Li whisker indicate the direct correlation of SEI with the morphological features of the deposited Li, even though those SEI layers were formed at the same electrochemical conditions.

Electron energy loss spectroscopy (EELS) can yield element spatial distribution with high spatial resolution. Figure XII.3.3 illustrates the EELS elemental maps, showing the spatial distribution of elements in SEI layers on the Li whisker and Li particle. As shown in Figure XII.3.3b, C, O, and Li within the SEI on Li whisker are uniformly distributed. For the Li particle (Figure XII.3.3d), O is distributed uniformly across the SEI, while C, P and F have a higher concentration in the outer layer of the SEI. Li shows non-uniform distribution across the SEI layer. The corresponding C K-edge and O K-edge spectrums acquired from Li particle and the SEI layer further confirm these observations.

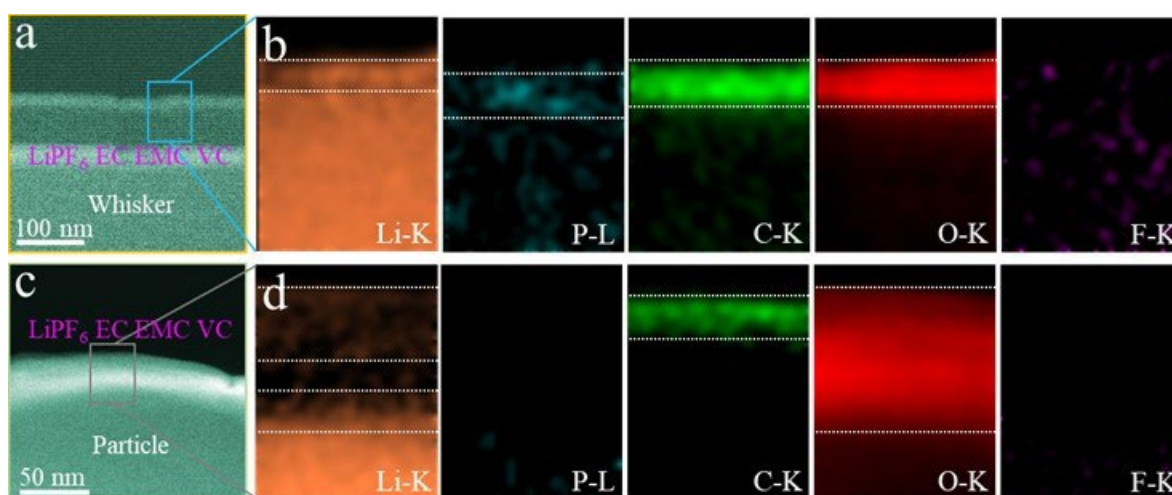


Figure XII.3.3 Cryo-electron energy loss spectroscopy (EELS) map to reveal spatial distribution of different chemical species in the SEI layer. (a and c) Cryo-HAADF-STEM imaging reveals the SEI layer on Li deposit. (b and d) elemental distribution of Li, P, C, O, and F in the SEI layer, indicating different spatial distribution for Li particle and Li whisker.

General discussion on the correlation of SEI layer features with Li deposition morphology

The morphology of Li electrodeposits has been noticed to show a strong dependence on the operating conditions of the battery cell, such as current density, temperature, and stack pressure, which are all mutually correlated to the structure and local chemistry of the electrode/electrolyte interface. The distinctive difference of composition and spatial distribution of chemical species within the SEI layer on Li whisker and Li particle formed in the same battery cell as observed here provides clues for correlating SEI feature with Li deposition morphology. The high content of C and low content of F in the SEI layer of Li whisker indicate that the SEI layer on the Li whisker is mainly from the electrolyte solvent. Especially, the high content of C indicates enrichment of organic species inside the SEI. Lithium ethylene dicarbonate (LEDC), as the main component of SEI formed in the carbonate-based electrolyte, is almost an ionic insulator. In other words, SEI layer on the Li whisker is highly ionic resistive, which is consistent with the general observation that carbonate-based electrolyte is prone to promote Li whisker formation. In addition, this amorphous organic species based SEI also exhibit low mechanical strength compared with inorganic species based SEI.

On the contrary, the SEI layers on the Li particle and the head of Li whisker is featured by a low C and high F contents, indicating more anions (PF_6^-) participated in the SEI formation process in non-dissociated $(\text{EC})_n\text{-Li}^+\text{-PF}_6^-$ form. This kind of SEI component could enhance Li^+ ion conductivity and homogenizes Li^+ ion flux. Similarly, SEI on the tip region of Li whisker exhibit higher ionic conduction than that at the whisker stem

region. In addition, the LiF is proven to possess much higher γE of 4761 eV/Å² MPa, which is larger than that of Li₂O and Li₂CO₃, showing the fluorinated interphase has the most outstanding dendrite suppression ability.

Conclusions

- Using cryo-TEM, EDS, and EELS revealed detailed nanostructure and chemical features of Li whisker and Li particle that were formed in the same coin cell in the carbonate-based electrolyte.
- SEI layers on both Li whisker and Li particle are similarly exhibiting monolithic amorphous structure, but different in chemical composition.
- The SEI layer on Li whisker has a high content of C, while the SEI layer on Li particle has low concentration of C but including F.
- The SEI on Li-particle is mostly derived from the salt of the electrolyte, while SEI on the Li whisker is mostly derived from the solvent of the electrolyte.
- The SEI on the Li whisker has a poor Li⁺ ion conductivity, while the SEI on Li particle has a high Li⁺ ion conductivity.

Key Publications

1. Yaobin Xu, Haiping Wu, Hao Jia, Ji-Guang Zhang, Wu Xu, and Chongmin Wang, “Current Density Regulated Atomic to Nanoscale Process on Li Deposition and Solid Electrolyte Interphase Revealed by Cryogenic Transmission Electron Microscopy”, *ACS Nano* 14, 8766–8775(2020).
2. Haiping Wu, Hao Jia, Chongmin Wang, Ji-Guang Zhang, and Wu Xu, “Recent Progress in Understanding Solid Electrolyte Interphase on Lithium Metal Anodes”, *Adv. Energy Mater.* 2003092(2020).
3. Xiaodi Ren, Peiyuan Gao, Lianfeng Zou, Shuhong Jiao, Xia Cao, Xianhui Zhang, Hao Jia, Mark H. Engelhard, Bethany E. Matthews, Haiping Wu, Hongkyung Lee, Chaojiang Niu, Chongmin Wang, Bruce W. Arey, Jie Xiao, Jun Liu, Ji-Guang Zhang, and Wu Xu, “Role of inner solvation sheath within salt–solvent complexes in tailoring electrode/electrolyte interphases for lithium metal batteries”, *PNAS*, 117, 28603–28613 (2020).
4. Yang He, Lin Jiang, Tianwu Chen, Yaobin Xu, Haiping Jia, Ran Yi, Dingchuan Xue, Miao Song, Arda Genc, Cedric Bouchet-Marquis, Lee Pullan, Ted Tessner, Jinkyong Yoo, Xiaolin Li, Ji-Guang Zhang, Sulin Zhang and Chongmin Wang, “Progressive growth of the solid-electrolyte interphase towards the Si anode interior causes capacity fading”, *Nature Nanotech.* 16, 1113–1120 (2021).
5. Jaegeon Ryu, Taesoo Bok, Se Hun Joo, Seokkeun Yoo, Gyujin Song, Su Hwan Kim, Sungho Choi, Hu Young Jeong, Min Gyu Kim, Seok Ju Kang, Chongmin Wang, Sang Kyu Kwak, Soojin Park, “Electrochemical scissoring of disordered silicon-carbon composites for high-performance lithium storage”, *Energy Storage Mater.* 36 139–146(2021).
6. Hui Yang, Muhammad Abdullah, Joseph Bright, Weiguo Hu, Kevin Kittilstved, Yaobin Xu, Chongmin Wang, Xiangwu Zhang, Nianqiang Wu, “Polymer-ceramic composite electrolytes for all-solid-state lithium batteries: Ionic conductivity and chemical interaction enhanced by oxygen vacancy in ceramic nanofibers”, *J. Power Sources*, 495, 229796 (2021).
7. X. H. Zhang, L. F. Zou, Z. H. Cui, H. Jia, M. H. Engelhard, B. E. Matthews, X. Cao, Q. Xie, C. M. Wang, A. Manthiram, J.-G. Zhang, W. Xu. “Stabilizing Ultrahigh-Nickel Layered Oxide Cathodes for High-Voltage Lithium Betal Batteries.” *Mater. Today* 44, 15–24 (2021).

8. H. Jia, Y. B. Xu, X. H. Zhang, S. D. Burton, P. Y. Gao, B. E. Matthews, M. H. Engelhard, K. S. Han, L. R. Zhong, C.M. Wang, Wu Xu. “Advanced Low-Flammable Electrolytes for Stable Operation of High-Voltage Lithium-Ion Batteries.” *Angew. Chemie Inter. Ed.* 133, 13109–13116 (2021).
9. H. Jia, X. H. Zhang, Y. B. Xu, L. F. Zou, J.-M. Ki, P. Y. Gao, M. H. Engelhard, Q. Y. Li, C. J. Niu, B. E. Matthews, T. L. Lemmon, J. T. Hu, C. M. Wang, W. Xu. Towards Practical Use of Cobalt-Free Lithium-Ion Batteries by an Advanced Ether-Based Electrolyte. *ACS Appl. Mater. Interf.* 13, 44339–444347 (2021).
10. S. Chae, Y. B. Xu, R. Yi, H.-S. Lim, D. Velickovic, X. L. Li, C. M. Wang, J.-G. Zhang. Micron-Sized Silicon/Carbon Composite Anode Synthesized by Impregnation of Pitch in Nano-Porous Silicon. *Adv. Mater.* 33, 2103095 (2021).
11. X. Han, S. Y. Wang, Y. B. Xu, G. M. Zhong, Y. Zhou, B. Liu, X. Y. Jiang, X. Wang, Y. Li, Z. Q. Zhang, S. Y. Chen, C. M. Wang, Y. Yang, W. Q. Zhang, J. L. Wang, J. Liu, J. H. Yang. All Solid Thick Oxide Cathodes Based on Low Temperature Sintering for High Energy Solid Batteries. ***Energy Environ. Sci.* 14, 5044 (2021).**

Acknowledgements

Support from the U. S. Department of Energy (DOE), Vehicle Technologies Office, specifically from Tien Duong and David Howell is gratefully acknowledged.

XII.4 *In-Operando* Thermal Diagnostics of Electrochemical Cells (LBNL)

Ravi Prasher, Principal Investigator

Lawrence Berkeley National Lab
1 Cyclotron Road
Berkeley, CA 94720
E-mail: RSPrasher@lbl.gov

Tien Q. Duong, DOE Technology Development Manager

U.S. Department of Energy
E-mail: Tien.Duong@ee.doe.gov

Start Date: October 1, 2019

End Date: September 30, 2022

Project Funding (FY21): \$180,000

DOE share: \$180,000

Non-DOE share: \$0

Project Introduction

Characterizing electrochemical processes in Li-metal cells such as lithium deposition and dendrite growth at interfaces is of great significance for understanding and enhancing their electrochemical performance and reliability. In situ and operando 3-omega micro thermal sensors can provide significant information regarding the impact of buried interfaces as a function of time, material, voltage, current, and temperature, etc. Therefore, it is important to develop operando 3-omega micro thermal sensors and develop models relating those signals to electrochemical performance for beyond lithium-ion cells. The physics-based model relating thermal and electrochemical properties based on these measurements can facilitate future design of Li metal batteries.

Objectives

Transport at various interfaces in beyond lithium-ion cells will play a major role in electrochemical performance and reliability. It has not yet been possible to thermally profile a Li-metal cell during operation to provide a spatially resolved map of thermal transport properties throughout the cell. The objective of this research is to create a metrology capable of spatially resolved in operando thermal property profiling, and then relate thermal property to the quality of electrodes and interfaces and use the developed thermal metrology to understand electrochemical processes in Li-metal batteries such as dendrite growth, interface kinetics, and ionic transport.

Approach

To accomplish project goals, the team will utilize an in-house adapted 3-omega technique to probe thermal properties of a Li-metal cell while it is in operation, without affecting the operation of the cell. The 3 omega sensors will be deposited and fabricated on Li-metal cells based on previous learning on 3-omega sensor fabrication. The characteristic depth of the thermally probed region is defined by the wave's "thermal penetration depth, $\delta = \sqrt{D/2\omega}$, where D is the sample's thermal diffusivity, and 2ω is the heating frequency of the thermal wave (Lubner et al. 2020). By depositing the project's 3ω sensors on the battery's outer surface and adjusting ω , the team controls δ to span the full range from the top to the bottom layer, thereby noninvasively probing the thermal transport in subsurface layers and interfaces within the bulk of the battery. Thermal transport can be related to quality of the interface. By doing concurrent thermal transport and electrochemical performance measurements, the team plans to relate thermal transport to electrochemical performance. As frequency based thermal measurement techniques provide excellent spatial resolution within the cell, the team also plans to study heat generation at the electrolyte–Li-metal interface and relate the thermal signals to the interface kinetics and ionic transport. The frequency dependence of heat generated due to transport resistance is different from that due to kinetic resistance. The team plans to utilize this difference to separate the contributions of kinetic and transport resistance at the interface, which will enable understanding of interface kinetics and transport at the Li-metal–SSE interface.

Results

The Prasher group is building operando 3ω micro thermal sensors and developing models relating thermal signals to electrochemical performance for beyond lithium-ion cells. The anode-side 3ω sensor will be used to probe thermal properties of Li metal anodes and related interfaces. The group is also developing a general frequency based thermal metrology to probe the interface kinetics and transport. Last year, we described our approach of studying thermal signatures of the heat generated at multiple harmonics of the excitation current to extract the electrochemical properties of buried interfaces and named the method Multi-harmonic ElectroThermal Spectroscopy (METS). We also presented a prototype design for a METS sensor and laid out an experimental plan for the verification of METS by comparing the electrochemical properties obtained from METS to those obtained from Electrochemical Impedance Spectroscopy (EIS).

In Q1, we worked on integrating the METS sensor on the Li-symmetric cell. We deposited the sensor on two different substrates (glass slide and Kapton film) with e-beam deposition of Platinum through a shadow-mask. The sensors on glass and Kapton are shown in Figure XII.4.1 (a) and (b). We also worked on reducing the maximum noise amplitude for 1ω , 2ω and 4ω signals. The noise amplitude for the signals at all three harmonics was obtained to be less than 100nV corresponding to a temperature fluctuation of less than 50 μ K, while the METS signal is expected to be of the order of micro-Volts (μ V), which makes the signal-to-noise ratio greater than 10.

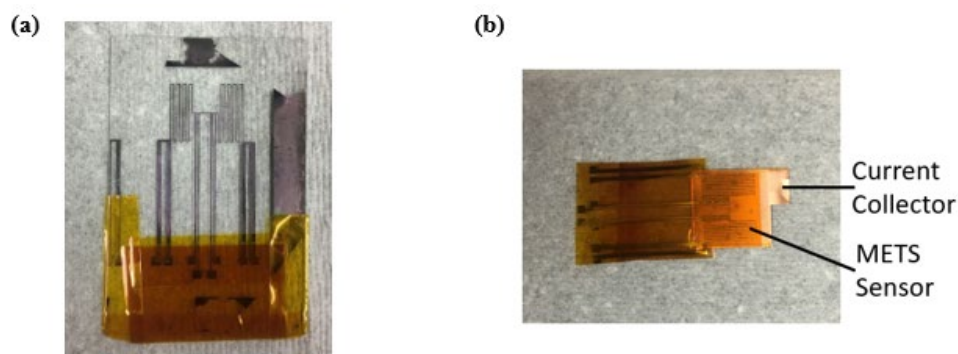


Figure XII.4.1 A METS sensor (a) deposited on glass and (b) deposited on Kapton and attached to a copper current collector

In Q2, we started assembling lithium symmetric cells with 3ω sensors and carry out 3ω measurements to isolate the thermal interface resistance to the lithium morphology at the lithium-solid state electrolyte interface. The symmetric cell consisted of LLZO electrolyte with 100 μ m Li foil on both sides, followed by 50 μ m thick current collectors. One of the current collectors was coated with an electrical insulation layer consisting of 500 nm Alumina, 400nm Parylene and 200nm Alumina, and a 3ω sensor is deposited on top of the Alumina layer. This recipe for the insulation layer was followed in all our works in the subsequent quarters as the performance of the insulation layer was consistent. In Q3, we performed the sensitivity analysis to extract the electrochemical parameters, namely the exchange current density, interface transport resistance, electrolyte transport resistance and the entropic coefficient using Multi-harmonic ElectroThermal Spectroscopy (METS). We also worked on determining the appropriate method for micro-Kelvin temperature sensing needed for the thermal signal measurement. Figure XII.4.2 shows the result of the sensitivity analysis at different harmonics of the AC frequency of the current passed through the cell and Figure XII.4.3 shows the temperature rise as a function of frequency at the different harmonics. In the first harmonic (1ω), the signal is the most sensitive to the reaction entropy for all the frequencies of interest. Similarly, the second harmonic (2ω) thermal signature, which relates to the transport losses, is the most sensitive to the electrolyte transport resistance. Similarly, the fourth harmonic (4ω) thermal signature is the most sensitive to the exchange current density, a measure of the reaction kinetics at the interface.

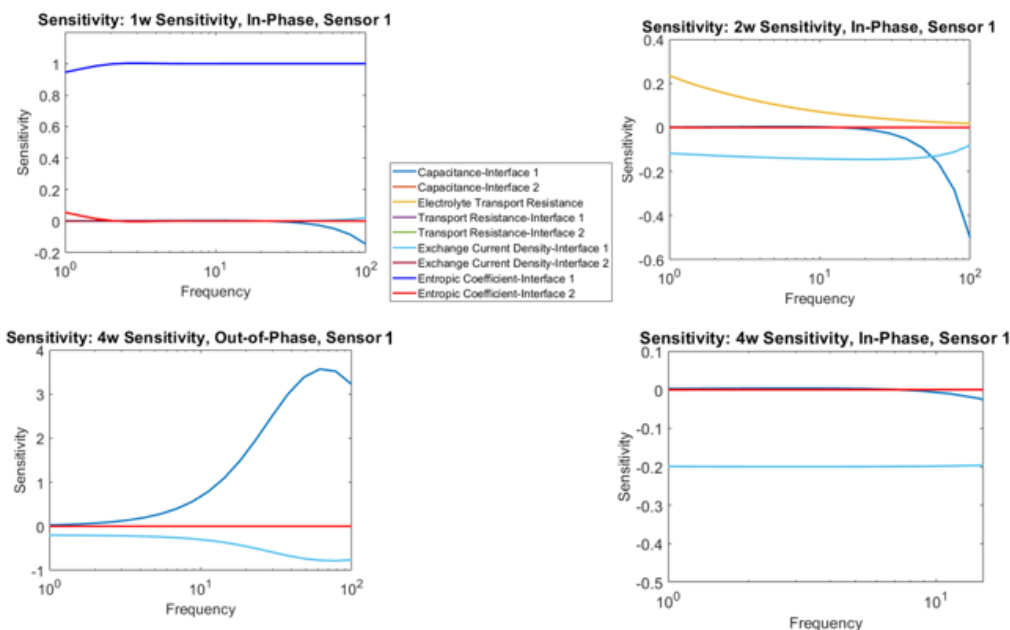


Figure XII.4.2 Sensitivity of the thermal response (temperature rise) with frequency at different harmonics of the excitation current

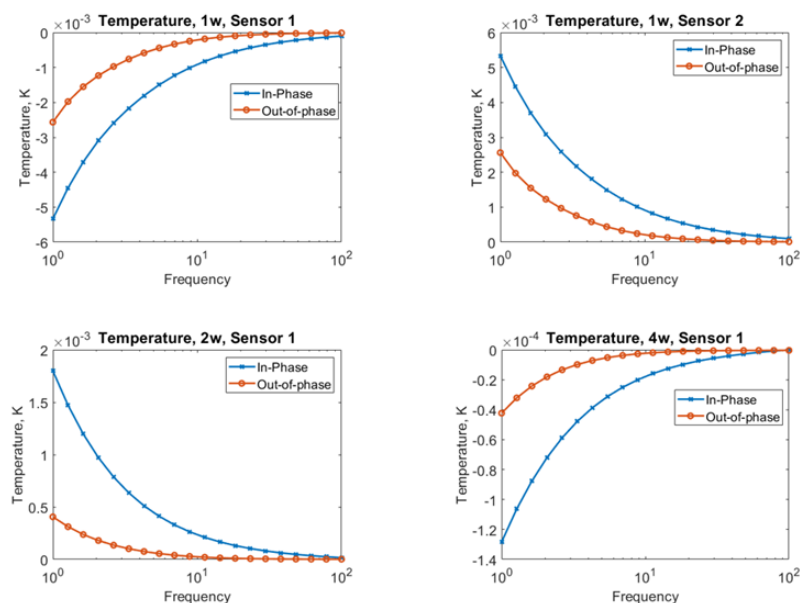


Figure XII.4.3 Temperature rise at different harmonics simulated to be measured by the METS sensor

As seen in Figure XII.4.3, the temperature rise in each harmonic is in the order of milliKelvins. Therefore, we need a temperature sensing technique that can resolve such small temperature oscillations. We have identified a scheme developed by Chen et al. (Chen et al. 2013) to be the appropriate technique for the temperature detection for our purposes. In addition to the lock-in temperature sensing that is commonly employed in 3-omega measurements, this method also employs a noise cancellation scheme to cancel the effects of the ambient temperature fluctuations. Additionally, we also use a Keithley 6221 current source, which is capable of shot-noise suppression, to minimize the noise due to current fluctuations in the sensor. By adopting this scheme, we were able to achieve a temperature resolution of 50 micro-Kelvins, which is sensitive enough for the temperature rise we expect to measure.

In Q4, we assembled and cycled symmetric lithium-LLZO cells and performed simultaneous Impedance Spectroscopy and 3ω measurements as a function of the number of cycles for up to 3 cycles, until failure due to shorting. The cells were cycled maintaining a constant current of $20 \mu\text{A}/\text{cm}^2$ and to a capacity of $400 \mu\text{Ah}$. Figure XII.4.4 (a) shows a representative 3ω fitting to extract the lithium metal-LLZO thermal interface, and Figure XII.4.4 (b) shows the extracted thermal interface resistance for four different cells as a function of the number of cycles. We make two important observations from the extracted thermal interface resistance. First, the interface resistance value is of the order of $10^{-4} \text{ m}^2\text{K}/\text{W}$, which is significantly high for a solid-solid contact. We are currently working on explaining this observation with a theoretical model. Additionally, we also observe that the interface resistance for all the cells improves after the first cycle and gets worse upon further cycling. To explain this behavior, we hypothesize that initially during the cell assembly (0 cycles), some voids are formed, which is mitigated during plating in the first cycle, thus improving the resistance after one cycle. Upon further cycling, there are new interfacial voids formed due to uneven plating and stripping, which increases the thermal interface resistance. Once we have the theoretical model to explain the thermal contact resistance and understand how microscopic voids play a role in the determining the interface resistance, we will work on confirming this hypothesis.

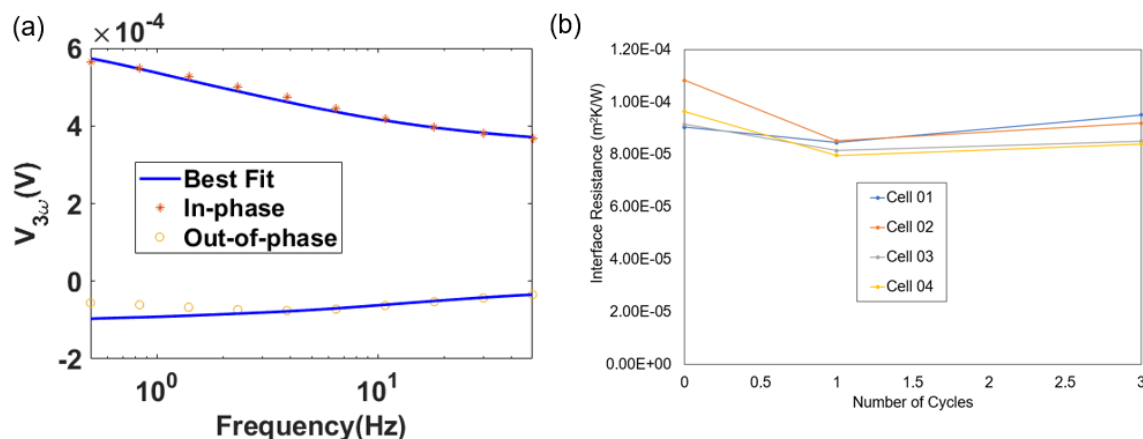


Figure XII.4.4 (a) Representative 3ω fitting for one of the cells (Cell 02 at 0 cycles) to extract the thermal interface resistance of the lithium metal-LLZO interface, and (b) summary of the extracted thermal interface resistance as a function of the number of cycles for four different cells

Conclusions

In summary, we are working on operando diagnostics of the lithium-solid state electrolyte interface in beyond lithium-ion cells using thermal metrology. We are using the 3ω method to study the interface morphology and developing a new method, Multi-harmonic ElectroThermal Spectroscopy (METS), to understand transport and kinetics phenomena at the interface through thermal signatures.

This year, we were able to devise a recipe to fabricate thermal sensors with an electrical insulation layer on the current collector of the cells. Additionally, we carried out the sensitivity analysis for METS and determined the acceptable noise level to obtain a high signal-to-noise ratio (SNR). We also designed a noise cancellation scheme that was able to reduce the thermal noise to less than $50 \mu\text{K}$, which was enough for obtaining a SNR greater than 10.

Further, we assembled symmetric lithium-LLZO cells with 3ω sensors to extract the thermal interface resistance. We were able to cycle the cells up to 3 cycles and track the evolution of the thermal interface resistance as a function of the number of cycles. We observed that the thermal interface resistance was, in general, very high (order of $10^{-4} \text{ m}^2\text{K}/\text{W}$) and that it decreased during the first cycle and increased upon further cycling.

Next year, we will work on explaining the high thermal interface resistance and relate the changes in the interface resistance with the interface morphology. We will also assemble cells to perform METS measurements to extract the properties associated with ion transport and charge transfer kinetics at the lithium metal-LLZO interface.

References

1. Lubner, Sean D., Sumanjeet Kaur, Yanbao Fu, Vince Battaglia, and Ravi Prasher. 2020. "Identification and Characterization of the Dominant Thermal Resistance in Lithium-Ion Batteries Using Operando 3-Omega Sensors." *Journal of Applied Physics* 127 (10). <https://doi.org/10.1063/1.5134459>.
2. Jianlin Zheng, Matthew C. Wingert, Edward Dechaumphai, and Renkun Chen. 2013. "Sub-picowatt/kelvin resistive thermometry for probing nanoscale thermal transport" *Review of Scientific Instruments* 84 (11). <https://doi.org/10.1063/1.4826493>.

Acknowledgements

We thank Divya Chalise, Dr. Yuqiang Zeng, Dr. Sean Lubner, Dr. Suman Kaur, Dr. Yanbau Fu, Dr. Vince Battaglia, Dr. Rob Jonson and Dr. Michael Tucker for their help in carrying out the research in this project.

XII.5 High Conductivity, Low Temperature Polymer Electrolytes for Li-Ion Batteries (LBNL)

Bryan D. McCloskey, Principal Investigator

Lawrence Berkeley National Laboratory and University of California, Berkeley
201-D Gilman Hall
Berkeley, CA 94720
E-mail: bmcclosk@berkeley.edu

Tien Q. Duong, DOE Technology Development Manager

U.S. Department of Energy
E-mail: Tien.Duong@ee.doe.gov

Start Date: October 1, 2019

End Date: September 30, 2021

Project Funding: \$225,000

DOE share: \$225,000

Non-DOE share: \$0

Project Introduction

Nonaqueous polyelectrolyte solutions, in which anion motion is slowed through their covalent attachment to a polymer chain, have attracted recent interest as potential high Li^+ transference number (t_+) electrolytes, which have been theorized to improve the efficiency of Li metal stripping and plating. However, fully characterizing transport liquid electrolyte properties (not just polyelectrolytes, but also traditional binary salt electrolytes) has been challenging from an experimental standpoint for reasons that are not entirely clear. Such transport characterization will be critical to develop an understanding of the influence of electrolyte properties on Li metal stripping/plating performance. In FY21, we focused on understanding the limitations of liquid electrolyte transport characterization using electrochemical methods, as well as developing alternative transport characterization methods that circumvent these challenges. We additionally completed our molecular simulation studies to understand ion correlations in polyelectrolyte solutions and how they impact their Li^+ transference number. Ultimately, we would like to optimize these transport properties (e.g., create a high conductivity, high t_+ number electrolyte) to enable long-life Li metal batteries. We will continue to develop the aforementioned alternative transport characterization techniques, including electrophoretic nuclear magnetic resonance (eNMR, to measure ion mobilities in an electric field, and hence a transference number), small volume Hittorff cells (an electroanalytical method to measure the transference number independently from eNMR), and Raman microfluidic cells (to measure salt diffusion coefficients), as part of our new VTO project starting in FY22.

Objectives

In FY21, our objectives were:

1. To understand the cause of large error in electrochemical measurements of the Li^+ transference number for concentrated liquid electrolytes.
2. To develop new capabilities to improve accuracy and precision of the transference number and activity measurements.
3. Develop a complete understanding of how correlated ion motion impacts Li^+ transference numbers in polyelectrolyte solutions by confirming prior simulation results that predict a decreasing transference number with increasing polyelectrolyte chain length.

Approach

To understand various aspects of lithium plating and ion transport in polyelectrolyte solutions and binary salt electrolytes, we developed various diagnostic and computational modeling techniques. Model polyelectrolytes,

based on a styrenic triflimide chemistry, were used as polyanions given their ability to fully dissociate in many nonaqueous solvents. Solution parameters that can be varied for both polyelectrolyte solutions and concentrated electrolytes included solvent and salt composition and additive inclusion, all of which can have a profound impact on electrostatic interactions between charged species in solution, as well as interfacial stability and reaction kinetics of the lithium electrode. We developed capabilities that allow an understanding of how molecular-level ion dynamics in these electrolytes impact macroscale transport properties and Li-metal plating and stripping. We optimized electrochemical methods for these electrolytes to evaluate relevant transport properties under the Newman Concentrated Solution Theory framework. Briefly, we use concentration cells to help quantify the thermodynamic factor, restricted diffusion in a Li-Li symmetric cell to measure the diffusion coefficient, polarization in a Li-Li symmetric cells to measure the so-called current fraction (steady-state current divided by current immediately upon initiation of an applied voltage bias), and a simple conductivity measurement through a conductivity probe. We use 1M LiPF₆ in ethylene carbonate:ethyl methyl carbonate (EC:EMC) as a typical model liquid electrolyte to compare our results. ¹H and ¹⁹F nuclear magnetic resonance (NMR) diffusometry were also used to measure single-ion self-diffusion coefficients without an applied electric field, and electrophoretic NMR to measure ion mobilities in an applied electric field.

Results

Interfacial Effects on Transport Coefficient Measurements in Li-ion Battery Electrolytes. We had originally hoped to use exclusively electrochemical techniques to study ion transport in our polyelectrolyte systems. Specifically, using Newman's Concentrated Solution Theory, one can measure the 3 independent transport coefficients and thermodynamic factor (activity as a function of concentration) needed to fully characterize transport of a binary salt electrolyte by analyzing data from 4 independent measurements: a conductivity probe, a Li-Li symmetric concentration cell, a Li-Li symmetric cell polarization measurement, and voltage relaxation measurement after polarization of a Li-Li symmetric cell (restricted diffusion). However, for electrolyte systems where the electrolyte resistance (R_s) is smaller than the Li metal interfacial (solid electrolyte interface) resistance (R_{int}), we demonstrated that techniques that rely on lithium plating and stripping, such as the polarization measurement listed above, do not yield reliable transport properties (see Figure XII.5.1, which is the TOC Figure from our publication, *J. Electrochem. Soc.* (2021) 168, 060543). Instead, such measurements appear to probe both interfacial and transport phenomena that cannot easily be deconvoluted. Essentially all liquid electrolytes have the characteristics of high interface impedance and low bulk resistance (a typical value range for 1M LiPF₆ in EC:EMC, as measured in our laboratories and consistent with other reported values, is shown in Figure XII.5.1). As a result, we concluded that in order to accurately measure transference numbers and activity measurements, both of which rely on the polarization measurement, other measures of each are required.

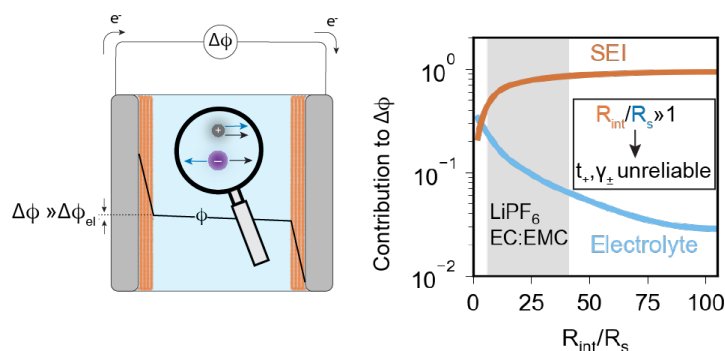


Figure XII.5.1 Left panel: a depiction of the electric potential as a function of position throughout a polarized Li-Li symmetric cell with high interfacial impedance and low bulk electrolyte resistance. Right panel: Plot of the SEI and electrolyte contributions to the polarization voltage drop as a function of the interfacial vs bulk electrolyte resistances, where SEI contributions dominate if R_{int}/R_s is greater than 1. Lithium polarization experiments for electrolytes with $R_{int}/R_s > 1$ result in unreliable transference number and thermodynamic factor data because electrolyte potential contributions are orders of magnitude smaller than those from the SEI.

Freezing point depression as a method to calculate activity coefficients. We developed alternative non-electrochemical methods to measuring the activity coefficients of electrolytes in order to potentially enable transference number measurements from lithium concentration cells, which were found to be substantially more precise than polarization measurements. Specifically, we focused on using freezing point depression measurements from differential scanning calorimetry to determine salt activity coefficients, γ_{\pm} . In order to validate the method on single salt in solvent systems we measured the freezing point of LiPF₆ in DMC for concentrations ranging from neat DMC to 1 molal LiPF₆. This electrolyte was chosen due to the availability of high-quality activity coefficient measured in a vapor pressure manometer setup (Xin et al. J. Chem. Thermodyn. 2018). We found for a single solvent system we can accurately predict activity of the salt using freezing point depression (see Figure XII.5.2). While we note that there is some deviation in the predicted salt activity coefficient because part of the process of converting osmotic coefficients to activity coefficients allows shifting of the activity coefficient by an arbitrary constant, for electrolyte transport measurements we only need the slope of the activity coefficient as a function of concentration to determine the thermodynamic factor. We see excellent agreement between our thermodynamic factor calculated from DSC to those in the literature.

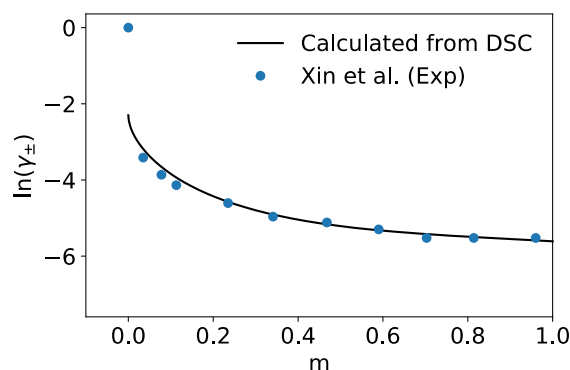


Figure XII.5.2. Salt activity coefficient versus concentration as calculated using freezing point depression from DSC for LiPF₆ in DMC. Data from Xin et. al. measured using vapor pressure measurements.

The development of eNMR and Hitorff cells to enable more accurate transference number measurements. In collaboration with colleagues in Prof. Nitash Balsara and Jeff Reimer's laboratories, we have established protocol for measuring ion mobilities, which in turn provides a straightforward calculation of the Li⁺ transference number, in liquid electrolytes using electrophoretic nuclear magnetic resonance spectroscopy (eNMR). We measured the self-diffusion coefficients, conductivity and transference number for an oligomeric 10-repeat unit (n=10) lithium triflimide appended polystyrene (see Figure XII.5.3). We first confirmed that in a 3:7 EC-EMC mixture we measure a conductivity of 1.08 mS/cm at 0.5 molal Li⁺ as measured by a conductivity probe. Using pulsed field gradient NMR, in which we measure self-diffusion coefficients without the presence of an applied electric field, we measure self-diffusion coefficients of $1.2 \times 10^{-6} \text{ cm}^2/\text{s}$ and $9.0 \times 10^{-7} \text{ cm}^2/\text{s}$ for the Li-ion and anionic backbone, respectively, resulting in an ideal NMR transport number (t_{NMR}^+) of 0.57. However, this technique simply measures the movement of ions due to Brownian motion and does not take into consideration any correlated ion-ion motion. Using eNMR, where an applied electric field via two platinum electrodes integrated into the NMR tube provides a directional driving force for ion movement, we were able to measure the electrophoretic mobilities of the Li⁺, backbone and solvent molecules through an applied electric field (see Figure XII.5.3). We measured mobilities of $3.3 \times 10^{-10} \text{ m}^2/\text{Vs}$ for the Li⁺ ion and $1.75 \times 10^{-9} \text{ m}^2/\text{Vs}$ for the oligomer backbone, yielding a true transference number of 0.16 and a conductivity of 1.08 mS/cm, in remarkable agreement with our conductivity probe measurements. We observed small deviations in mobilities measured at high electric field strengths which is likely indicative of small amounts of convection and have noted this as an area for technique optimization. The large difference between the true transference number (0.16) and the ideal NMR transference number (0.57) is likely due to significant anion-anion correlation along the polymer backbone, in agreement with molecular dynamics simulations performed previously in this project (see, for example, *Macromolecules* (2020) 53, 9503).

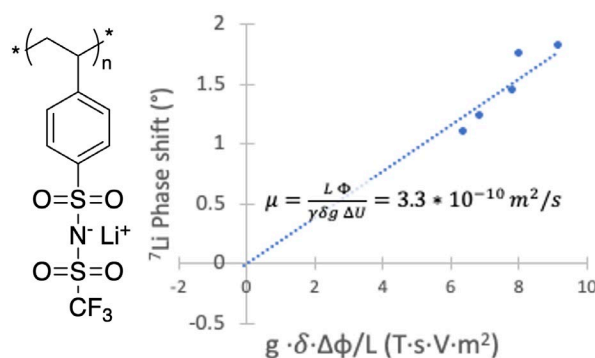


Figure XII.5.3. Left panel: The lithium triflimide-appended polystyrene used as the polyelectrolyte in this study. It was selected due to its ability to dissolve and dissociate in 3:7 EC:EMC. Right panel: ⁷Li phase shift (°) versus $g \cdot \delta \cdot \Delta \phi / L$ (T·s·V·m²) measured via electrophoretic NMR with a ± 90 V bias in a 0.5m Li⁺ oligomeric (n=10) triflimide polyanion solution in ethylene carbonate:ethyl methyl carbonate. From the slope of this line the mobility and velocity of the Li⁺ can be calculated. Similar analyses can be used to measure the polymer chain mobility and solvent mobility using ¹H NMR.

After our initial studies on the 10-repeat unit triflimide polyelectrolyte to confirm the reliability of the eNMR measurements, we scaled up synthesis of our polyelectrolytes, synthesizing a 10-repeat unit, 20-repeat unit, and 40-repeat unit lithium triflimide appended polystyrene in 5g batches. We finalized our initial transport characterization of these polyions in carbonate solutions at a single Li⁺ molality (0.5m). We successfully measured the electrophoretic mobilities (via eNMR) and conductivity (via a conductivity probe) of the lithium-triflimide styrene monomer (n=1 in Figure XII.5.3), as well as 10- and 20-repeat unit lithium triflimide appended polystyrene. We measured mobilities of 1.2×10^{-9} m²/Vs for the Li⁺ ion and 2.63×10^{-9} m²/Vs for the anionic monomer yielding a true transference number of 0.32 and a conductivity of 2.01 mS/cm. The transference number of the monomeric system is notably higher than that of the 10-repeat unit oligomeric system, which has a true transference number of 0.16. This again agrees with the theory that our group has developed that predicts increasing anion-anion correlation with polymer chain length will decrease the true transference number (*Macromolecules* (2020) 53, 9503). This theory predicts that at long chain lengths and low concentrations eventually the transference number will become negative with respect to the center of mass, meaning that lithium is dragged in multi-ion clusters in the “wrong-direction” in the applied electric field. We have recently completed measurements on a 0.5 molal 20-repeat unit polyelectrolyte in EC:EMC system which indicate a negative transference number of -0.15 with respect to center of mass. We believe this is the first known observation of a negative true transference number in non-aqueous polyelectrolyte systems using electrophoretic methods.

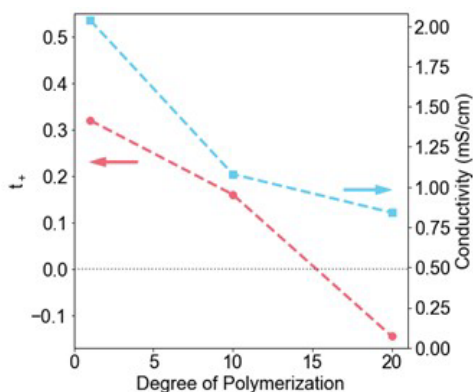


Figure XII.5.4 Transference number (pink) and Conductivity (blue) vs. Degree of Polymerization for 0.5m solutions of lithium-triflimide polystyrene in 3:7 EC:EMC. Note for the highest degree of polymerization (n=20) we observe a negative transference number with respect to the electrolyte center of mass, indicating that Li⁺ moves in the opposite direction expected in an applied electric field.

In addition to progress on eNMR measurements, we made progress on developing small volume Hittorf Cells as an alternative electrochemical method for measuring Li^+ electrolyte transference number. We designed and fabricated a custom low-volume Hittorf cell out of PTFE. Given that we synthesize only small, ~gram batches of our polyanions, we desire a low-volume system to reduce the total material necessary for these measurements. The design is straightforward, with two lithium electrodes placed in separate chambers, each of which is connected by a longer chamber. Valves are also in place to allow each chamber to be isolated. The entire cell is filled with electrolyte, and the total cell volume is roughly 3 mL. After passing a known amount of current between two lithium electrodes, we extract the solutions from each chamber of the 3-chamber cell and measure salt concentration using ^7Li NMR, which then can be used to calculate a transference number. Initial studies using lithium electrodes and a model system of LiPF_6 in EC:EMC were challenging because of significant instability in the measurements due to the highly reactive nature of lithium metal. In many solutions we observed lithium particles and debris floating in the cathodic chamber. To address this, we experimented with eliminating all lithium metal from our Hittorf design, instead using intercalation electrodes (graphite, lithium titanate, NMC, and LFP) as the Li^+ sources and sinks. We observe significantly more stable and repeatable electrochemistry with all of these electrodes compared to Li metal. We are currently completing validation studies using LiPF_6 in EC:EMC but so far have measured transference numbers of $\sim 0.4 - 0.5$ for 1M LiPF_6 in EC:EMC using this method, in agreement with other published studies. We hope to achieve better accuracy through better calibration of the NMR, and by inducing larger concentration gradients using higher current densities. We have started to apply this method to the polyelectrolyte system and hope to be able to validate our electrophoretic NMR transference number methods using the Hittorf method as part of our new VTO project starting in FY22.

Conclusions

The key conclusions from our research this year are:

1. Electrochemical measurements of liquid electrolyte transport coefficients are limited by the large interfacial impedance that exists at Li metal electrodes in contact with the electrolyte. The interfacial resistance severely impedes the accuracy of correcting the potential drop across the electrolyte phase when applying a voltage bias between two electrodes.
2. Salt activity coefficients can be accurately measured using freezing point depression in single component solvent electrolyte systems.
3. Electrophoretic NMR can be used to more accurately measure transference numbers in liquid electrolytes, circumventing aforementioned issues with Li-Li symmetric cell polarization measurements.
4. As measured by eNMR, the Li^+ transference number in polyanionic electrolyte solutions decreases with increasing molecular weight, which is counterintuitive because appending more anions together should result in a slowing of their motion, making Li^+ transport faster in comparison. In fact, a negative transference number is observed when using our highest repeat unit polymer chain ($n=20$). These results confirm our prior molecular dynamics simulations that predicted both the molecular weight dependence and the negative transference number. Future work should focus on higher molecular weight polymers that could reach an entangled regime and result in higher transference numbers.

Key Publications

1. Bergstrom, H. K.; Fong, K. D.; McCloskey, B. D. "Interfacial effects on transport coefficient measurements in Li-ion battery electrolytes." *Journal of the Electrochemical Society* (2021) 168, 060543.
2. Fong, K. D.; Self, J.; McCloskey, B. D.; Persson, K. A. "Ion correlations and their impact on transport in polymer-based electrolytes." *Macromolecules* (2021) 54(6), 2575–2591.

3. Fong, K. D.; Self, J.; McCloskey, B. D.; Persson, K. A. “Onsager Transport Coefficients and Transference Numbers in Polyelectrolyte Solutions and Polymerized Ionic Liquids.” *Macromolecules* (2020) 53, 9503.
4. “Molecular Dynamics Characterization of Onsager Transport Coefficients and Transference Number in Polyelectrolyte Solutions.” American Institute of Chemical Engineers (virtual), November 2020, Kara Fong presenting.
5. “Ion Correlations in Li-Ion Battery Electrolytes.” Women Excelling in Computational Modeling Engineering Seminar Series (virtual, invited), April 2021, Kara Fong presenting.
6. “The Onsager Framework for Transport Phenomena in Electrolyte Solutions.” Young Investigator Lecture Series, Electrochemical Society San Francisco Section (virtual), November 2021, Kara Fong presenting.
7. “Ion Transport and Ion-Correlation in Non-Aqueous Lithium-Ion Polyelectrolyte Solutions.” American Institute of Chemical Engineers, November 2021, Helen Bergstrom presenting.
8. “Bridging Length Scales in Electrolyte Transport Theory Via the Onsager Framework.” American Institute of Chemical Engineers, November 2021, Kara Fong presenting.
9. “Understanding Electrochemical Systems across Length and Time Scales.” American Institute of Chemical Engineers (poster), November 2021, Kara Fong presenting.

Acknowledgements

B.D.M. gratefully acknowledges his colleagues- Kara Fong, and Helen Bergstrom- who performed this work, as well as the fruitful computational collaboration with Prof. Kristin Persson, theory collaboration with Kranthi K. Mandadapu, and NMR collaboration with Jeffrey Reimer and Nitash Balsara.

XIII Next-Gen Lithium-Ion: Modeling Advanced Materials

XIII.1 Electrode Materials Design and Failure Prediction (Argonne National Laboratory)

Venkat Srinivasan, Principal Investigator

Argonne National Laboratory
9700 South Cass Avenue
Lemont, IL 60439
E-mail: vsrinivasan@anl.gov

Tien Q. Duong, DOE Technology Development Manager

U.S. Department of Energy
E-mail: Tien.Duong@ee.doe.gov

Start Date: October 1, 2016
Project Funding: \$3,475,000

End Date: September 30, 2021
DOE share: \$3,475,000

Non-DOE share: \$0

Project Introduction

To enhance the energy density of next generation lithium ion batteries it is very important to use lithium metal based anodes. Solving the issues of unstable deposition of lithium metal during the charging process might require usage of solid state electrolytes. It is hypothesized that solid electrolytes can possibly prevent dendrite growth by creating a mechanical stress field around the lithium protrusion. However, usage of ceramic based solid electrolytes (such as, LLZO oxides and LPS sulfides) comes with an additional drawback associated with the formation of voids during the stripping process. This is very different from the pits observed during lithium stripping with liquid electrolytes. The major difference comes from the fact that the liquid electrolytes are always in contact with the non-uniform lithium metal anodes. However, solid electrolytes loose contact with the lithium metal electrode as soon as a void initiates at the interface. We believe that apart from the bulk diffusion of lithium within the metal electrode, surface diffusion of lithium also contributes to the formation of these porous lithium interfaces. These interfacial pores are also responsible for a decrease in the electrochemically active surface area, which can substantially increase the cell resistance. Along with that, porous surface of the lithium metal anodes also leads to current focusing and possibility of dendrite growth during the subsequent lithium deposition process. To better understand the formation of these interfacial void spaces within the lithium metal anodes, a phase field based computational methodology is developed, which help us better understand the impact of various operating and material parameters that leads to the abovementioned porous microstructures. Propensity of externally applied pressure to prevent the formation of these voids during the stripping process will also be investigated.

Apart from the ceramic type electrolytes, dry polymer based solid electrolytes have also been investigated for enabling lithium metal anodes. PEO have not been very successful in preventing the growth of lithium dendrites. However, cross linking PEO chains with polystyrene (PS) can help to enhance the mechanical rigidity of the solid electrolyte, which shows substantial decrease in dendrite growth velocity. Interestingly, during the stripping process in SEO (block co-polymer electrolytes constructed as a combination of PS and PEO) electrolytes, the dendritic protrusions tend to dissolve first. Enhanced lithium dissolution from a protrusion can be attributed to two aspects: a) The first one being closeness to the counter electrode, b) The second one is the influence of mechanical stress on the anodic reaction current density. Regions under higher pressure experience less deposition and faster dissolution. Impact of these two aspects in the early dissolution of the dendritic protrusions in SEO (PS-PEO) solid electrolytes will be investigated.

Along with helping to suppress lithium dendrite growth in the metallic anode, transition from liquid to solid electrolytes substantially influence the cathode/solid-electrolyte interface as the electrochemically active

surface area decreases substantially for the all-solid-state system. Performance of the ceramic solid electrolytes with oxide based cathodes will be discussed in terms of their interfacial delamination and surface charge layer formation. Two types of solid electrolytes are considered, mechanically stiff oxide based LLZO, and sulfide based soft LPSCI. Apart from their difference in elastic modulus, LLZO and LPSCI demonstrates different fracture energies with oxide based cathodes. Also, differences in their relative permittivity result in variations in space charge layers and subsequent charge transfer resistance at the cathode electrolyte interface. In the present context, a mesoscale level computational methodology is developed to understand the formation of the space charge layers experienced by LLZO and LPSCI electrolytes and their influence on the overall cell performance, resistance growth and capacity fade.

Objectives

The main project objective is to develop computational models for understanding the various degradation mechanisms for next-generation Li-ion batteries. This year's goal is to use the continuum-based mathematical model to investigate interfacial stability between Li-metal electrodes and solid electrolytes during deposition and dissolution of lithium under externally applied currents. Both soft polymer and hard ceramic type electrolytes will be investigated. The team also aims to develop a computational model for understanding the space charge layer formation at the cathode/solid-electrolyte interface, and its impact on the interfacial charge transfer resistance. Ceramic-based solid electrolytes are expected to enable high-energy-density and liquid-free, safe, next-generation Li-ion batteries. Li-metal anodes should be incorporated due to their substantially larger volumetric and specific capacity, as compared to present day graphite-based anodes. During charge, lithium dendrites are observed through the solid electrolytes, which are supposed to occur because of the non-uniform current distribution at the Li/electrolyte interface. Interfacial detachment between the lithium electrode and solid electrolyte has been observed during electrochemical dissolution of lithium (or, the stripping process), which can lead to nonhomogeneous contact and substantially higher charge transfer resistance between the electrode and electrolytes. Similar issues have also been observed at the Li/polymer-electrolyte interface during lithium stripping, which will also be investigated thoroughly. On the cathode side, formation of a space charge layer at the cathode/solid-electrolyte interface, along with delamination between cathode and solid electrolytes, leads to increased interfacial resistance. The space charge layer formation between cathodes and solid electrolytes is a bigger issue for the sulfides as compared to the oxide-based ceramics, whereas the delamination is supposed to be more dominant within the oxides. The developed computational model will be used to investigate the impact of physicochemical and transport properties of the solid electrolytes on the overall interfacial degradation observed at both the cathode and anode sides. The main focus will be to elucidate interfacial issues and devise strategies to enable successful implementation of solid electrolytes in next-generation Li-ion batteries.

Approach

To capture the formation of the pore space at the Li/solid-electrolyte interface, a phase field based computational methodology is developed that can predict the charge and mass transport process through the lithium metal electrodes. A new parameter, the surface diffusion coefficient, is introduced to simulate the formation and propagation of the micron sized voids. Butler-Volmer prescribed reaction current densities are applied at the interface between lithium electrode and the solid electrolyte. No current is assumed to flow through the pores. To investigate the impact of external pressure on the void formation, creep flow of the metallic lithium is also taken into consideration. Influence of the external temperature on the mass transport processes are considered through the Arrhenius relationship. Comparison with experimental results have been conducted to extract relevant parameters and validate the developed computational model.

Propensity of electrochemical dissolution of lithium from a dendritic protrusion within SEO solid polymer electrolytes is predicted using a finite element based computational framework. Both the plated and stripped Li electrodes are modeled here, along with the SEO electrolyte in between. Flow of current within the Li metal occurs through the transport of electrons. The potential distribution associated with electron flow can be successfully captured by solving the Poisson's equation. In contrast, Li^+ ions carry current within the electrolyte through both migration and diffusion, which requires the solution of a relatively more complicated

set of partial differential equations obtained from the concentrated solution theory considerations. The conductivity and diffusivity of the electrolyte salt within the SEO polymer electrolyte depends on the local electrolyte salt concentration. However, a constant value of the transference number is taken into consideration to simplify the governing differential equation for mass transport within the electrolyte. The growth of the lithium protrusion leads to unequal deformation of the stripped and plated Li electrodes, which eventually generates stress within the electrodes and the SEO electrolyte. The evolution of mechanical stress is estimated by solving the equilibrium equations. Both elastic and plastic deformation of Li metal and the SEO polymer electrolyte is taken into account. The reaction current density at the electrode/electrolyte interface is given by a modified version of the Butler-Volmer equation that considers not only the effect of local electrolyte salt concentration, but also the mechanical stress distribution at the interface.

The interfacial delamination between the cathode and solid-electrolytes are modeled using a combination of lattice spring method and finite volume method, that can capture the evolution of potential field and mechanical deformation within the system. Butler-Volmer based reaction current have been assumed at the electrode/electrolyte interface. On the other hand, formation of the space charge layer is tricky and relies on the development of a two-scale approach, where the regular charge-discharge curves are simulated using the global model. The local model focuses closer to the cathode/solid-electrolyte interface, where the length scale is proportional to the Debye length. Instead of an abrupt jump observed in the global scale, the local model assumes continuity of potential at the interface, and corresponding rearrangement of the mobile ions lead to the formation of the space charge layers. The space charge layer is visualized as a decrease in lithium ion concentration on the solid-electrolyte side and an increase in the lithium atom concentration on the cathode side. This variation in surface concentration enhances the charge transfer resistance at the cathode and solid electrolytes, which finally leads to a decrease in observable capacity of the cell.

Results

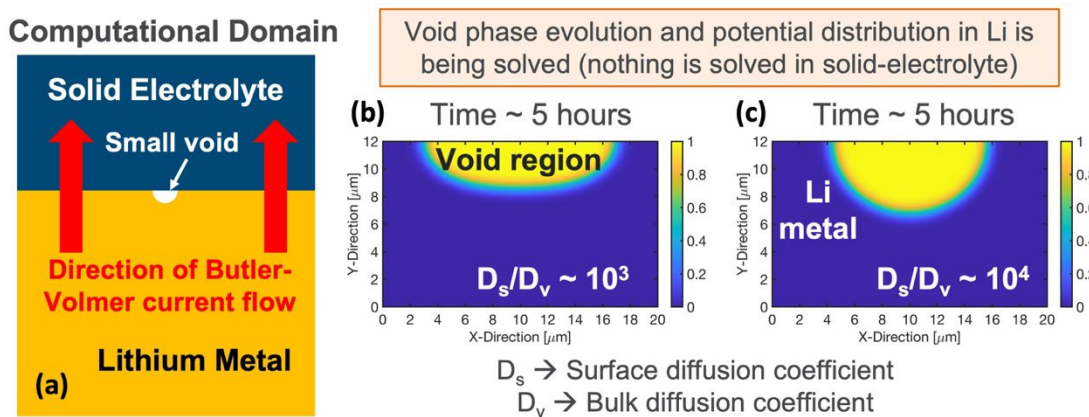


Figure XIII.1.1 (a) Schematic of the computational domain where evolution of the surface void is being investigated. Flow of current and evolution of void space within Li is studied. Nothing is being solved in the electrolyte. (b, c) Snapshot of a void after 5 hours of stripping with ratio of surface over bulk diffusion coefficient being 103 and 104, respectively.

Development of a mesoscale model to capture the void formation at the Li/LLZO interface during dissolution: It has been experimentally observed that voids evolve at the Li/LLZO interface during the electrochemical dissolution process. These voids are observed even if extremely good interfacial contact is developed between the electrode and the electrolyte prior to stripping. It is hypothesized that any form of surface heterogeneity, either pre-existing surface roughness, or heterogeneous reaction kinetics arising from grain/grain-boundary microstructure of the solid electrolytes, leads to non-uniform current distribution. This eventually results in excessive Li stripping at certain places, and forms surface voids. Generation of voids brings in a new transport mechanism into picture, the “surface diffusion” of Li, along with the conventional bulk diffusion process. This extra surface diffusion phenomena helps to understand the formation and evolution of pores at the Li/LLZO interface. In the present context, a computational model is developed that takes into consideration the surface

diffusion of Li and can capture the growth of surface voids and complete delamination of cathode and ceramic solid-electrolytes. A Cahn-Hilliard type equation is solved with both bulk and surface diffusion phenomena. A sink term is incorporated at the electrode electrolyte interface which captures the non-uniformity in current distribution and drives void formation. Butler-Volmer reaction kinetics is adopted at the Li/solid-electrolyte interface. Figure XIII.1.1(a) schematically demonstrates the computational domain along with the solid electrolyte where nothing is being simulated. Figure XIII.1.1(b) and Figure XIII.1.1(c) demonstrates the evolution of the void region for different magnitudes of the surface diffusivities, where the bulk diffusivities are kept constant. It is evident that increasing the surface diffusion coefficient helps to give the void a more circular shape. Please note that all these simulations started with a small pre-existing pore at the Li/electrolyte interface, as shown in Figure XIII.1.1(a).

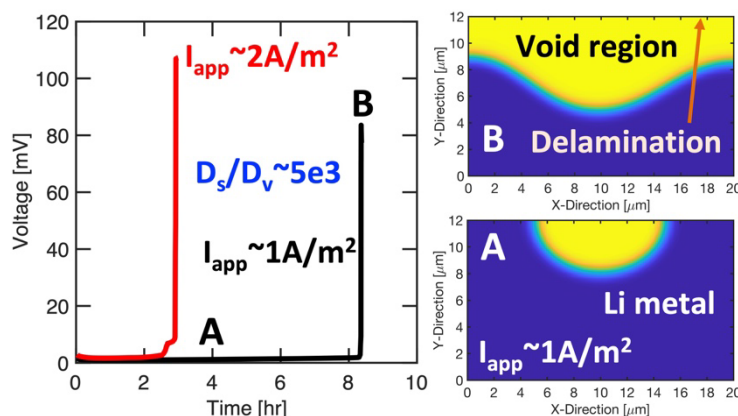


Figure XIII.1.2 Voltage vs. time response during the evolution of a void at the Li/electrolyte interface. Due to higher exchange current densities, the potential drop at interface is minimal. But as the voids start to span the entire domain, the potential starts to increase rapidly. Partially and completely delaminated structures are pointed out by “A” and “B”, which are obtained after Li stripping for 4 and 8.5 hours, respectively. Increasing current density from 1 A/m^2 to 2 A/m^2 quickens the delamination process. Also, the surface diffusion coefficient is assumed to be 5×10^3 times larger than the bulk diffusivity.

Influence of void formation on the cell potential is plotted in Figure XIII.1.2, which increases rapidly once the void starts to span across the entire domain. Increasing the current density aggravates the propagation of voids, and much earlier delamination is observed. Development of this mesoscale model, capable of capturing the formation and evolution of pores at Li/electrolyte interface, successfully deciphers the physical mechanism responsible for the interfacial delamination during the lithium stripping process.

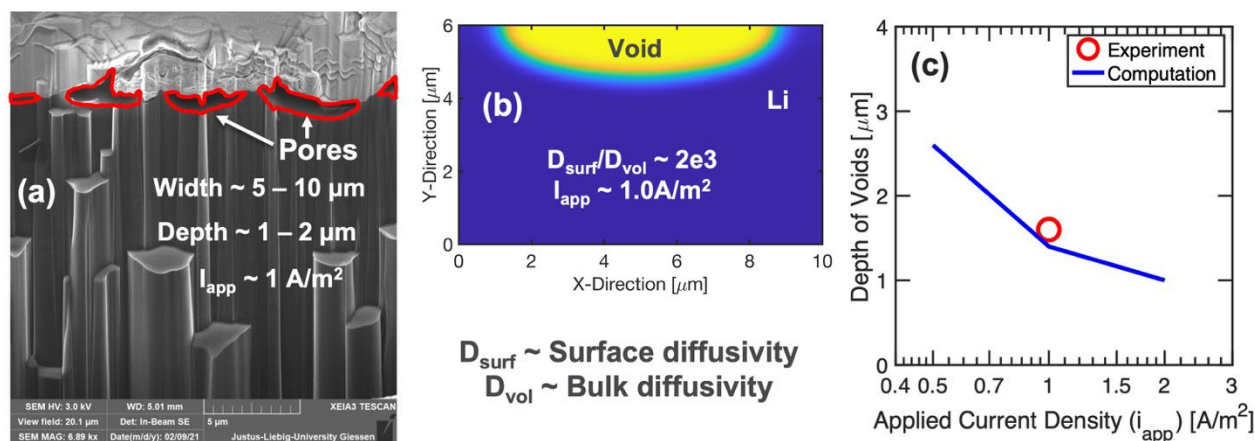


Figure XIII.1.3 (a) Visualization of voids at the Li/LLZO interface using cryo-SEM techniques. (b) Computational simulation of void formation within Li metal. The solid electrolyte is located at the top. Li is being stripped at an applied current density of 1 A/m^2 . (c) Comparison between experimentally observed (red circle) and computationally predicted (blue solid line) depth of voids. It is evident that increasing the current density results in a decrease in pore depth.

Comparison of the lithium dissolution results as predicted by the mesoscale computations (conducted at ANL) with the experimental results obtained from the German (Jürgen Janek, Giessen) group: The mesoscale level computational model developed in the previous section capable of capturing the formation of voids within the lithium electrode at the Li/LLZO interface is used here. Surface diffusion of atoms is a key factor controlling the evolution of pores at the interface between Li electrode and the solid electrolyte, which eventually leads to delamination and significant impedance rise. Experiments conducted by the group of Prof. Jürgen Janek (Giessen, Germany) clearly shows the evolution of surface voids at the Li/LLZO interface. The German research group looked at the pore morphology using Cryo-SEM techniques, and investigated the influence of applied current density, external pressure, etc. on the overall void formation process. In the present section, comparison between the experimental results with that obtained from the mesoscale level computational models is conducted. In order to obtain a better understanding of the pore morphology that evolves during the Li stripping process, cryo-SEM imaging of the electrode/electrolyte cross section is conducted by the group of Jürgen Janek. Their results are shown in Figure XIII.1.3(a), which clearly depicts that the pores can be of 5 – 10 μm in width and 1 – 2 μm in depth. These imaged voids are generated under an applied current density of $1\text{A}/\text{m}^2$. Computational simulations with a Li surface diffusivity 2000 times larger than the Li volume diffusivity leads to the generation of similar void microstructures under equivalent current densities, which is shown in Figure XIII.1.3(b). Comparison between the depth of voids obtained at different current densities using the computational simulations are shown in Figure XIII.1.3(c), which compares well with the experimental observations.

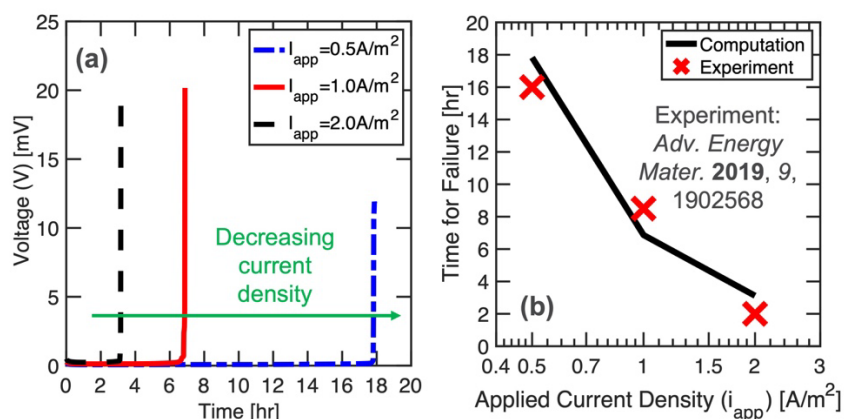


Figure XIII.1.4 (a) Voltage vs. time curves obtained at different Li stripping current densities, which shows rapid increase in overpotential when the electrode experiences complete delamination from the solid electrolyte. (b) Comparison between experimentally observed (red squares) and computationally predicted (black solid line) time for failure under different applied current densities. The experimental results are obtained from an article published by the group of Jürgen Janek (Adv. Ener. Mater. (2019) 1902568).

Time required to completely delaminate the Li electrode from the LLZO solid electrolyte under different applied current densities are shown in the Figure XIII.1.4(a). Comparison with experimental results regarding “time for failure” obtained by the group of Jürgen Janek is shown in Figure XIII.1.4(b). A good comparison between computational models and experimental observations successfully validates the developed phase field based computational model.

Understanding current distribution around a dendritic protrusion during lithium dissolution: Lithium metal electrodes are necessary for next generation batteries because of the possibility of enhancement in energy density. Dendrite growth during the charge, or lithium deposition process, is a major bottleneck preventing widespread implementation of lithium metal anodes. Solid electrolytes are being actively considered for their capability to prevent the growth of dendritic protrusions. Due to the generation of mechanical stress field at the tip of the protrusion, shape and size of the lithium dendrites observed within solid electrolytes are very different than that in liquid electrolytes. Evolution of the globular morphology of Li deposits within SEO solid electrolytes are attributed to the current focusing associated with concentration and potential gradients within

the solid electrolyte, and influence of stress induced electrochemical potential on the Butler-Volmer reaction current density. Generation of compressive stress is expected to slow down the Li deposition process at the tip of the protrusion but cannot prevent it completely. Dissolution of dendritic protrusions is also a very interesting aspect. Experimentally it has been observed that during discharge, or electrochemical dissolution of Li, the dendritic protrusions tend to dissolve quickly (see Maslyn et al., “Preferential Stripping of a Lithium Protrusion Resulting in Recovery of a Planar Electrode” *Journal of the Electrochemical Society* 2020 167 100553). It is indeed true that the dendritic protrusion is closer to the counter electrode, and should experience larger magnitudes of anodic current, which should lead to its early dissolution. Whether the mechanical stress field around the globule demonstrates any impact or not, needs to be studied. Accordingly, we simulated the dissolution of a Li dendritic protrusion within SEO electrolyte with dimensions same as that reported in the experimental article (see Maslyn et al., *JES* 2020 167 100553). Change in protrusion dimension during the dissolution process is shown in Figure XIII.1.5(a) and Figure XIII.1.5(b). Evolution of stress within the solid electrolyte adjacent to the bottom electrode is shown in Figure XIII.1.5(c) as a function of the distance from the tip of the protrusion. Compressive stress prevails within the solid electrolyte.

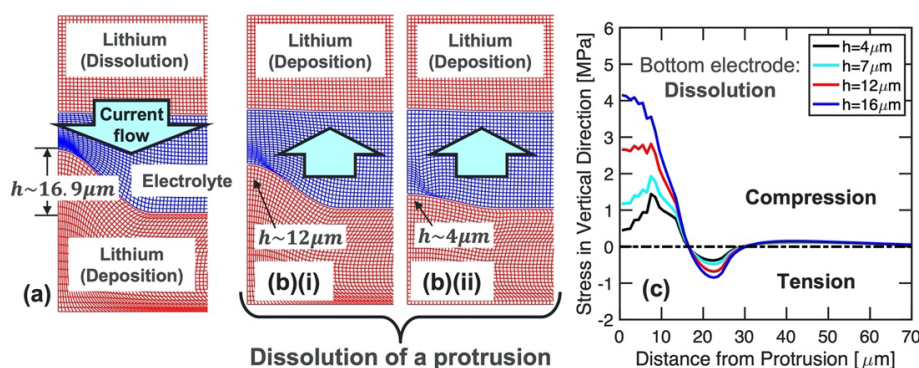


Figure XIII.1.5 (a) Evolution of a dendritic protrusion during deposition at the bottom electrode. (b) Electro-chemical Li dissolution from the bottom electrode shows preferential dissolution of the protrusion. (c) Stress evolution within the polymer electrolyte adjacent to the bottom electrode along vertical direction.

Compressive stress helps to increase the anodic component of reaction current, which leads to faster dissolution of Li in regions under higher compression. Dissolution current density at the tip for different heights of the dendritic protrusions are shown in Figure XIII.1.6(a). The ratio of excess current at the tip of the protrusion over the applied current density is shown in Figure XIII.1.6(b) for different heights of the globule and compared with experiments, which shows good qualitative correlation.

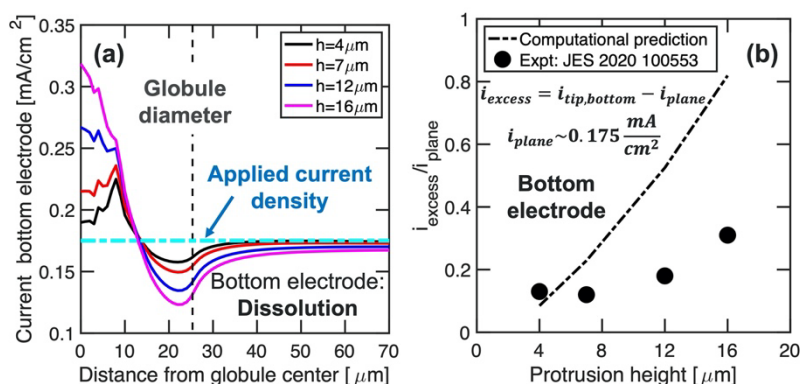


Figure XIII.1.6 (a) Current distribution at the bottom electrode around the dendritic protrusion during the dissolution process. It is evident that current on top of the protrusion is higher than the applied current density, which indicates preferential dissolution of the dendritic protrusion. (b) Ratio of excess current at the tip of the protrusion over the applied (or planar) current observed far away from the protrusion. The computational predictions are compared with experimental observations obtained from Maslyn et al., *JES* 2020 167 100553.

Develop computational model for sulfide electrolytes: A computational model, in the continuum level, is developed in the present section for capturing the interfacial delamination and space charge layers that form at the interface between sulfide electrolytes and oxide cathodes. Capacity fade experienced by sulfides due to these above-mentioned issues are compared with that of LLZO. It is well known that sulfide based solid electrolytes (Young's modulus ~ 20 GPa) are much softer than garnet type LLZO (Young's modulus ~ 150 GPa), and the fracture energy between sulfides and cathodes (~ 0.8 J/m²) have been reported to be slightly smaller than that between cathode and LLZO (~ 2.0 J/m²). Figure XIII.1.7(a) demonstrates the voltage vs. capacity curves during the charge and discharge processes for NMC cathodes with LLZO (black) and LPSCI (magenta) solid electrolytes. The blue dashed line indicates discharge capacity without any interfacial delamination. The extent of detachment at NMC/LLZO interface is 73% and at NMC/LPSCI interface is much less, only 45%. Hence, the delamination induced capacity fade experienced by LPSCI is smaller than LLZO. Extent of interfacial detachment depends on the partial molar volume of Li within the cathode particles and elastic modulus of the solid electrolytes. Accordingly, a phase map is demonstrated in Figure XIII.1.7(b) for various cathode and solid electrolyte materials. The stability limits for LLZO and LPSCI based solid electrolytes are clearly demonstrated, where the difference can be attributed to the mismatch in their fracture energies. The green and yellow regions within the phase map indicates stable operation and complete detachment, respectively.

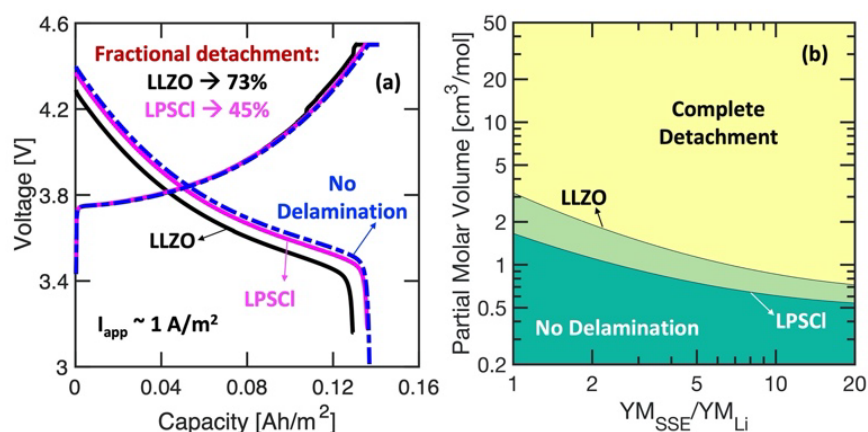


Figure XIII.1.7 (a) Voltage vs. capacity performance curves for NMC/LLZO (black) and NMC/LPSCI (magenta) during the first charge and discharge process. The blue dashed line indicates performance curves without any interfacial delamination. NMC/LPSCI experiences much less detachment, and capacity fade, than NMC/LLZO. (b) Phase map between partial molar volume of lithium within cathodes and Young's modulus of solid electrolytes indicating the domains of stable operation (green) and complete detachment (yellow). Two different stability limits for LLZO and LPSCI are shown.

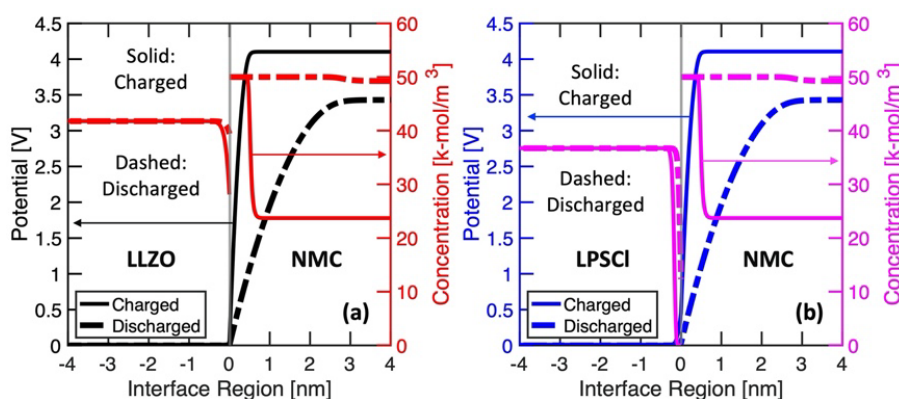


Figure XIII.1.8 Distribution of potential and concentration within the space charge layer at (a) NMC/LLZO and (b) NMC/LPSCI interface. The solid and dashed lines indicate the space charge layer under fully charged and discharged conditions, respectively. Due to its higher relative permittivity, the space charge layer within LLZO is much thinner than that observed within LPSCI. For both LLZO and LPSCI, the space charge domain in the cathode is substantially thicker under the fully discharged condition.

Evolution of a space charge layer between cathode and solid electrolyte is also modeled. Difference in relative permittivity of NMC cathode, LLZO and LPSCI solid electrolytes dictates the extent of space charge layers at the charged and discharged state. Evolution of potential and concentration at the NMC/LLZO and NMC/LPSCI interfaces are demonstrated in Figure XIII.1.8(a) and Figure XIII.1.8(b).

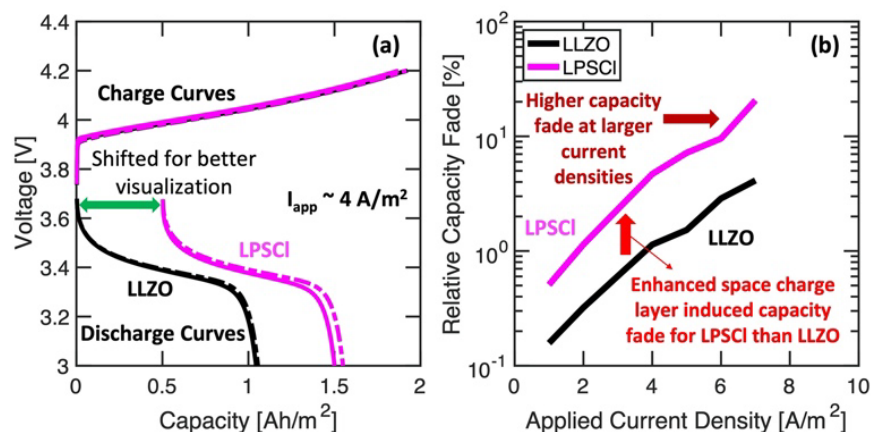


Figure XIII.1.9 Influence of the space charge layer on the charge/discharge process is captured through the decrease in exchange current density due to decrease and increase in Li concentration on the electrolyte and cathode, respectively. A strong space charge layer increases the charge transfer resistance between the cathode and electrolytes. (a) Voltage vs. capacity performance curves under applied current density of 4 A/m^2 for NMC cathodes with LLZO and LPSCI. (b) Ratio of space charge layer induced capacity fade over the initial capacity as observed under different applied current densities. Due to its stronger space charge layers, LPSCI experiences more capacity fade than LLZO.

Discharge capacity fade due to the space charge layer is shown in Figure XIII.1.9(a) and Figure XIII.1.9(b). This computational model development for sulfide electrolytes successfully captures both the delamination as well as space charge layer induced resistance growth and capacity fade.

Conclusions

Lithium dendrite growth within polymer and ceramic based solid electrolytes were studied thoroughly in the past. Growth of dendritic protrusions are expected to occur during the lithium deposition process. Along with lithium deposition, lithium dissolution during electrochemical stripping process may also lead to interfacial issues. Hence, lithium dissolution in both ceramic and polymer based solid electrolytes are investigated here. It is evident that ceramic electrolytes tend to form voids at the metallic-anode/electrolyte interface, which can lead to a substantial decrease in the electrochemically active surface area and an increase in cell overpotential. On the contrary, even though adoption of SEO based dry solid polymer electrolytes lead to formation and propagation of dendritic protrusions, they dissolve completely during the subsequent dissolution process. This particular beneficial behavior can be attributed to the compressive mechanical stress field around the dendritic protrusion, which enhances the anodic reaction current. From the analysis of the lithium stripping behavior, block co-polymer solid electrolytes appear to perform better than ceramics in a lithium metal cell.

At the cathode solid electrolyte interface, softer sulfide-based ceramics are not necessarily beneficial than the LLZO type oxides. Even though the sulfide electrolytes experience smaller delamination than the oxides, the stronger space charge layer observed in LPSCI can lead to an increase in interfacial charge transfer resistance. Apart from that, sulfides also demonstrate smaller chemical stability against high voltage cathode particles. Hence, implementation of interphase layers between the cathode and solid electrolytes are necessary for successful implementation of solid electrolytes within next generation lithium-ion batteries.

Key Publications

1. Pallab Barai, Tomas Rojas, Badri Narayanan, Anh Ngo, Larry A Curtiss, Venkat Srinivasan. Investigation of delamination-induced performance decay at the cathode/LLZO interface. *Chemistry of Materials* **33** 14 5527–5541 (2021).

2. Alec S. Ho, Pallab Barai, Jacqueline A. Maslyn, Louise Frenck, Whitney S. Loo, Dilworth Y. Parkinson, Venkat Srinivasan and Nitash P. Balsara. Uncovering the relationship between diameter and height of electrodeposited lithium protrusions in a rigid electrolyte. *ACS Applied Energy Materials* **3** 10 9645–9655 (2020).

Acknowledgements

This research is supported by the Vehicle Technologies Office (VTO), Department of Energy (DOE), USA, through the Battery Materials Research (BMR) program. Argonne National Laboratory is operated for DOE Office of Science by UChicago Argonne, LLC under the contract number DE-AC02-06CH11357. The project contributors also thank the US-German collaboration with the group of Prof. Jürgen Janek from the Justus Leibig University, Giessen, Germany.

XIII.2 Characterization and Modeling of Li-Metal Batteries: Model-system Synthesis and Advanced Characterization (LBNL)

Guoying Chen, Principal Investigator

Lawrence Berkeley National Laboratory
1 Cyclotron Road
Berkeley, CA 94720
E-mail: GChen@lbl.gov

Tien Q. Duong, DOE Technology Development Manager

U.S. Department of Energy
E-mail: Tien.Duong@ee.doe.gov

Start Date: October 1, 2019

End Date: September 30, 2022

Project Funding: \$500,000

DOE share: \$500,000

Non-DOE share: \$0

Project Introduction

Development of mitigating approaches and the ability to rationally design advanced functional materials require a better understanding of the relationships among structure, properties and function. For Li-metal batteries employing a solid-state electrolyte (SSE), significant challenges, both at the materials level and systems level, prevent them from practical applications. It is well recognized that fundamental knowledge on the role of SSE microstructure in solid-state ion conduction and Li dendrite formation/propagation, performance-limiting processes and phase transition mechanisms in SSEs, and the dynamic evolution of the SSE/electrode interfaces are key to the development of high-energy Li-metal batteries with improved commercial viability. This project addresses these challenges in a systematic way, by synthesizing well-controlled SSE model systems and SSE/electrode model interfaces, obtaining new insights into the model materials and interfaces utilizing state-of-the-art analytical techniques, and subsequently establishing the correlations between specific property and function. The goal is to use these findings to rationally design and synthesize advanced SSE materials and SSE/electrode interfaces with improved performance.

Objectives

This project will use a rational, non-empirical approach to design and develop SSE materials and interfaces for the next-generation Li-metal batteries. Combining a suite of advanced diagnostic techniques with well-controlled model-system samples, the project will perform systematic studies to achieve the following goals: 1) obtain understanding on the role of SSE grain and grain boundaries on Li ion conduction and dendrite formation, 2) obtain fundamental knowledge on rate- and stability-limiting properties and processes in SSEs when used in Li-metal batteries, 3) investigate the reactivities between SSE and electrodes and gain insights on the dynamic evolution of the interfaces, and 4) design and synthesize improved SSE materials and interfaces for safer and more stable high-energy Li-metal batteries.

Approach

The project will combine model-system synthesis and advanced diagnostic studies to investigate ion conduction and interfacial chemistry of SSE in Li-metal batteries. Single crystalline, polycrystalline and amorphous model samples with various grain and grain boundary properties will be synthesized. Model interfaces between the SSE and electrodes with controlled properties will also be developed. Both bulk-level and single-grain level characterization will be performed. Global properties and performance of the samples will be established from the bulk analysis, while the single-grain-based studies will utilize time- and spatially-resolved analytical techniques to probe the intrinsic redox transformation processes and failure mechanisms under Li-metal battery operating conditions.

Results

Halide SSEs with a general formula of Li_3MX_6 ($\text{M} = \text{Sc}, \text{Y}, \text{In}, \text{Er}$ etc., $\text{X} = \text{Cl}, \text{Br}$) have been shown to have a high room-temperature ionic conductivity of up to 10^{-2} S/cm, a wide electrochemical stability window of up to 6 V, and excellent stability towards the 4 V-class oxide cathode materials. Previous theory work indicated reactivities between halides and Li metal at the anode, however, the exact reaction pathways and kinetics as well as their implication on cycling stability and rate capability remain unclear. Here we synthesized two of the halide SSEs, Li_3InCl_6 (LIC) and Li_3YCl_6 (LYC), to evaluate their reactivities at the interfaces with Li metal anode. Figure XIII.2.1a and b show the SEM images of as-prepared LIC and LYC powder, respectively, synthesized after extensive ball milling at room temperature. The samples have a similar average secondary particle size of several microns, although the LIC particles appear more fused than those of LYC. SSE pellets were prepared by cold sintering of approximately 80–100 mg of the halide powder, using an external pressure of 200 MPa at room temperature. Figure 1c-f show SEM images of the planar (Figure XIII.2.1c and d) and cross-sectional (Figure XIII.2.1e and f) views of the pellets. The optical images are also shown in Figure XIII.2.1c and d insets. Both pellets displayed an off-white color with relatively smooth and dense surfaces and cross sections. The overall thickness and diameter were ~ 500 μm and 10 mm, respectively. The calculated densities were 2.22 and 2.44 g/cm^3 , corresponding to a relative density of $\sim 82\%$ and 81% for LIC and LYC pellets, respectively. These values are similar to what was reported on other soft SSE pellets in the literature.

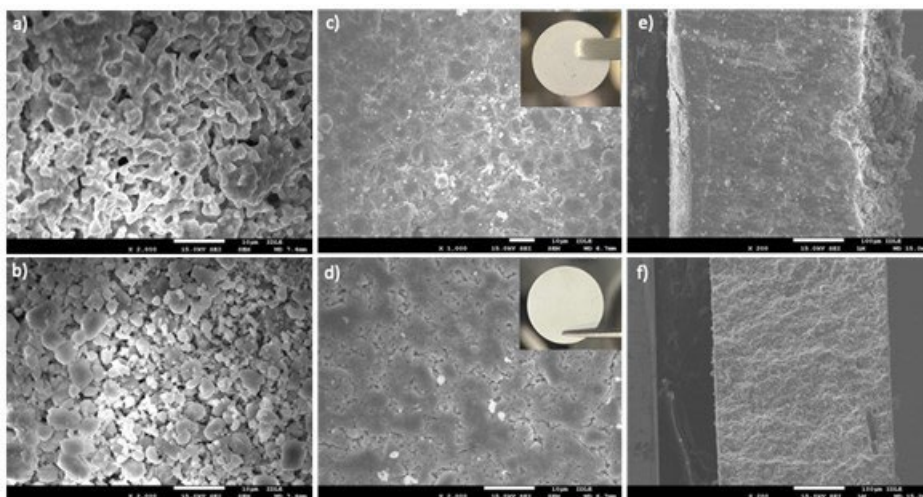


Figure XIII.2.1 SEM images of LIC (a, c, e) and LYC (b, d, f) solid electrolytes: (a, b) are powder samples, (c, d) are top-view and (e, f) are cross-sectional view of the as-prepared pellets. Insets in (c, d) are optical images of the pellets.

To investigate the chemical reactivities at the interface between Li metal and the halide SSEs, intimate contact was achieved by pressing the prepared pellet together with a piece of lithium foil under an external pressure of 200 MPa. The assemble was then removed from the pressure jig and left inside the glovebox. After a varying amount of time, the SSE pellet was removed and analyzed by hard X-ray absorption spectroscopy (XAS) at Stanford Synchrotron Radiation Lightsource (SSRL). Figure XIII.2.2 compares In and Y K -edge X-ray absorption near edge structure (XANES) spectra collected on the pristine and recovered LIC (Figure XIII.2.2a) and LYC (Figure XIII.2.2b) pellets after 2 days or 30 days. The K -edge absorption energy, determined by the normalized intensity at 0.5, is traditionally used to monitor the changes in metal oxidation state. As shown in Figure XIII.2.2a, the absorption edge energy for pristine LIC was at ~ 27.94 KeV, consistent with In at 3+ oxidation state. While the edge remained at the same energy after 2 days in contact with Li metal, a significant low-energy shift occurred after 30 days, suggesting extensive reduction of In after prolonged exposure to Li metal. On the other hand, the Y K -edge energy in LYC remained unchanged at ~ 17.045 KeV, even after 30 days. These results indicate superior chemical stability of LYC against Li metal.

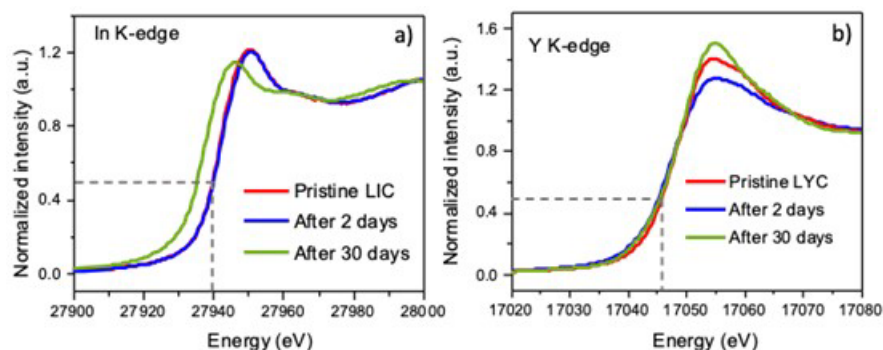


Figure XIII.2.2 K-edge XANES spectra of a) In collected on LIC and b) Y collected on LYC pellets.

Further comparison on interfacial reactivities were obtained by using electrochemical analytical methods. Figure XIII.2.3a shows the voltage profiles of a Li|LIC|Li symmetrical cell when the current density (CD) gradually increased at a step size of 0.02 mA/cm^2 . At a low CD (up to 0.04 mA/cm^2), the voltage response is largely constant, demonstrating a flat profile consistent with ohmic-dominating behavior. As the CD increases, cell polarization also increases, and the voltage profile becomes more slopy. Significant voltage fluctuation occurs when the CD is raised above 0.08 mA/cm^2 . Assuming the cell remains in the ohmic regime, the evolution of cell resistance determined by the ratio between cell voltage and current is shown in Figure XIII.2.3b. The overall resistance of LIC symmetrical cell is rather high, in the range of 10^3 - 10^4 Ohm . Cell hard-shorting was detected at a CD above 0.1 mA/cm^2 , signaling extensive formation and propagation of electronically-conducting species, likely Li metal dendrites.

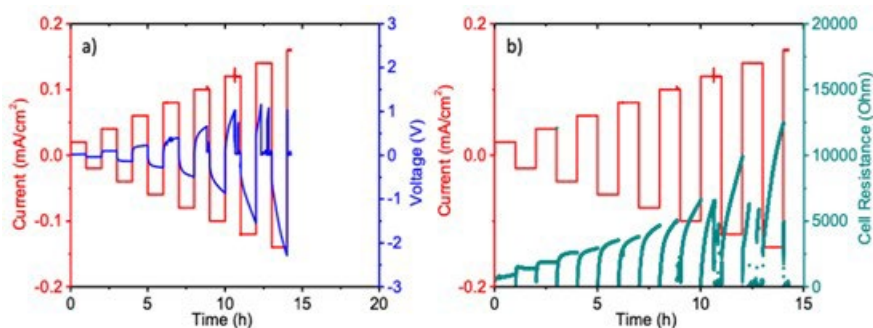


Figure XIII.2.3 a) Voltage profiles of a Li|LIC|Li symmetrical cell during the step-increase of current density test and b) the corresponding cell resistance. The CD step size is 0.02 mA/cm^2 and the duration of each charge/discharge step is 1 hr.

The voltage profiles and cell resistance of a Li|LYC|Li symmetrical cell during a similar test are shown in Figure XIII.2.4a and Figure XIII.2.4b, respectively. The deviation from the ohmic regime occurred when the CD is greater than 0.12 mA/cm^2 , much higher than that in the LIC cell. The cell resistance is also significantly lower, in the range of 10^2 Ohm .

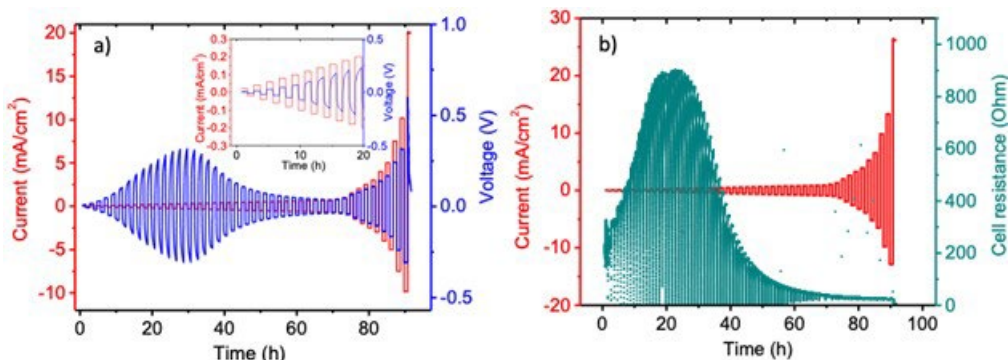


Figure XIII.2.4 Voltage profiles of a Li|LYC|Li symmetrical cell during the step-increase of current density and b) the corresponding cell resistance. Inset in a) shows the voltage profile during the first 20 hours. The CD step size is 0.02 mA/cm^2 and the duration of each charge/discharge step is 1 hr.

At a critical current density of 0.28 mA/cm^2 , the cell resistance began to decrease, suggesting cell soft-shortening, likely through the formation of electronically-conducting “tunnels”. Decrease in resistance continues with the further increase in CD, however, cell hard-shortening was not observed until the CD reaches a very high value of 20 mA/cm^2 . The results suggest that the LYC/Li interface has better electrochemical stability than that of LIC/Li. Although LYC and LIC belong to the same family of halide SSEs with In and Y sharing the same oxidation state of +3, the observed differences suggest the critical role of metal center in halide SSE behavior and the need for its optimization in future development.

Electrochemical impedance spectroscopy (EIS) measurements were also carried out on the Li|LYC|Li cell after each DC cycling step. Figure XIII.2.5 shows the results collected on the cell at the as-assembled state as well as after DC testing at 1, 5 and 20 mA/cm^2 . Before cycling, the Nyquist profile obtained on the symmetric cell shows the typical profile where the intercept at the real axis corresponds to the total bulk electronic/ionic conductivity and the low-frequency region corresponds to charge transfer at the LYC/Li interface. Overall, DC cycling leads to a reduction in cell resistance. After cycling at 1 mA/cm^2 , cell bulk resistance was reduced by more than half, from 80 to 30 ohm. Further decrease was observed after 5 mA/cm^2 cycling, however, significant changes on the EIS profile was only found after cycling at 20 mA/cm^2 . The results are consistent with what was obtained from the symmetrical cell cycling, confirming that low CD cycling leads to very limited reactions at the LYC/Li interface. Damaging electronic conduction pathways through the SSE is only established after cycling at a very high current density.

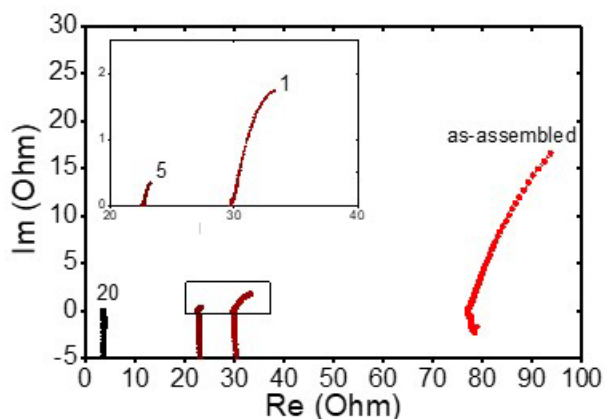


Figure XIII.2.5 Nyquist plots of Li|LYC|Li symmetrical cells after various DC cell testing at the indicated current density (mA/cm^2). AC amplitude was 10 mV and the frequency range was 1 MHz to 0.1 Hz. Inset shows the expanded view of the indicated area on the spectra.

All solid-state battery (ASSB) cells with a $\text{LiNi}_{0.8}\text{Co}_{0.1}\text{Mn}_{0.1}\text{O}_2$ (NMC811)/LYC composite cathode, LYC SSE separator and a Li-In alloy anode were then assembled and evaluated. To prepare the composite cathode, conventional NMC811 secondary particles and LYC particles were mixed in various weight ratios and pressed into a pellet under external pressure. Figure XIII.2.6a-c shows the effect of

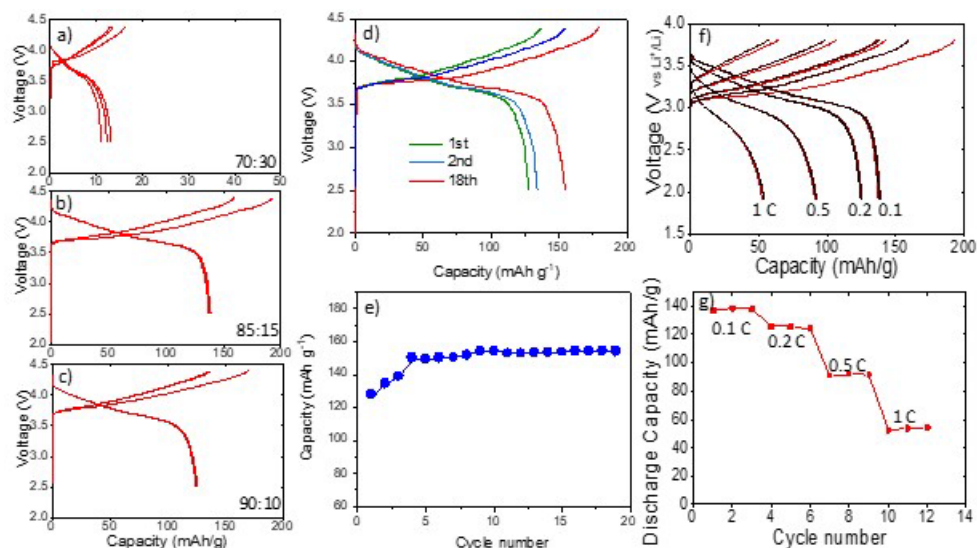


Figure XIII.2.6 Initial charge/discharge voltage profiles of ASSB cells assembled with an NMC811/LYC ratio of a) 70:30, b) 85: 15 and c) 90:10 in the composite cathode, respectively. d-e) charge/discharge voltage profiles and cycling stability of an ASSB cell assembled with an NMC/LYC ratio of 85: 15. All cycling rate is 0.1 C. f-g) charge/discharge voltage profiles and rate capability of an ASSB cell assembled with an NMC811/LYC ratio of 85:15.

the ratio on voltage profiles as well as capacity of the ASSB full cell. All cycling was carried out at 0.1 C between 2.5 and 4.4 V (vs. Li^+/Li). While a low NMC811/LYC ratio of 70:30 delivered very small capacity, a high ratio of 90:10 also diminishes the cycling performance somewhat. This suggests that establishing effective conduction pathways through proper particle distribution in composite cathode is essential for ASSB cycling. The optimal ratio was found to be 85:15 where a reversible initial discharge capacity of ~ 140 mAh/g was obtained. The capacity increases during the first few cycles but stabilizes after 4 cycles, reaching ~ 160 mAh/g. Stable cycling was achieved afterwards, with the cell delivering performance near the level of what is typically obtained in a liquid cell (Figure XIII.2.6d-e). Figure XIII.2.6f-g shows the voltage profiles and rate capability of the same cell. Significant capacity loss was observed upon increasing the rate from 0.1 C to 0.5 C, suggesting large cell impedance and the need in further optimization of ionic and electronic conduction in the composite cathode as well as the interfaces.

The ASSB cell was disassembled after cycling and the components were recovered for analysis. Figure XIII.2.7a shows the cross-sectional SEM image collected at the interface between LYC and Li-In anode. While cracking was observed on the LYC separator, the physical contact at the interface mostly maintained. The phase boundary between LYC and Li-In metal, however, became less even, with growth of additional small features clearly seen. Figure XIII.2.7b-d shows the energy dispersive X-ray spectroscopy (EDX) elemental mapping for Y, Cl and In, respectively. Indium was detected in the observed small features, suggesting that these are likely Li dendrites with the inclusion of In metal. The results show the dynamic nature of the SSE/anode interface.

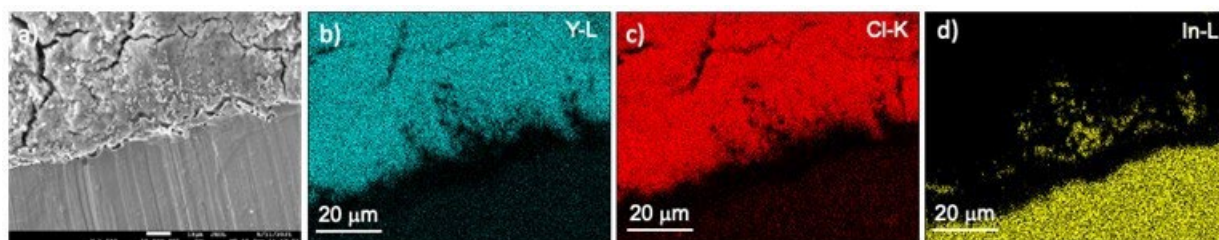


Figure XIII.2.7 a) Cross-sectional SEM image and b-d) EDX elemental mapping of Y-L, Cl-K, and In-L at the interface.

To gather further understanding on cycling-induced changes, we then evaluated the long-term cycling stability of the ASSB cells cycled between 3.0 and 4.3 V. To eliminate intergranular cracking associated with volume expansion/contraction of conventional NMC secondary particles, single-crystalline (SC) NMC811 was used in this study. The composite cathodes were prepared by combining SC-NMC811, LYC and carbon in a weight ratio of either 80: 20: 0 (without carbon) or 57: 40.5: 2.5 (with 2.5 wt.% carbon). Figure XIII.2.8 compares the electrochemical performance of both cells cycled at 0.2 C. The 1st cycle voltage profiles (Figure XIII.2.8a and Figure XIII.2.8b) show large irreversible capacity

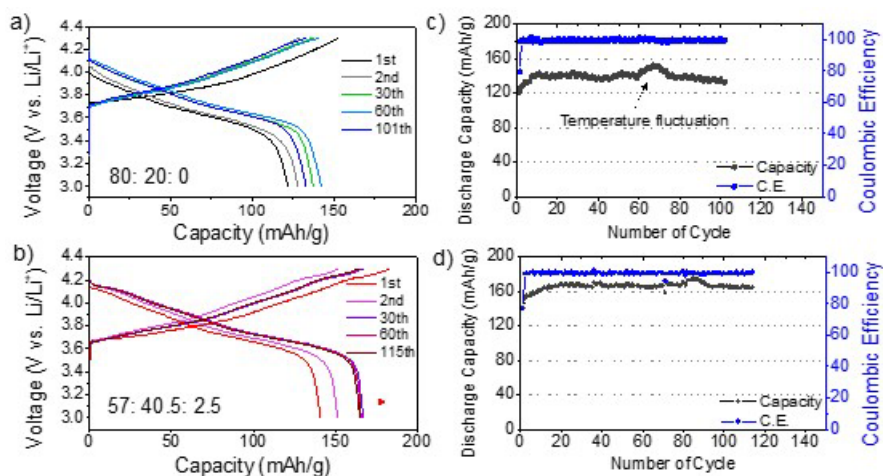


Figure XIII.2.8 Charge and discharge voltage profiles (a, b), discharge capacity retention and coulombic efficiency (c, d) of ASSB cells with a cathode composite consisting of SC-NMC811, LYC and carbon in a 80: 20: 0 weight ratio (a, c) and 57: 40.5: 2.5 weight ratio (b, d).

Figure XIII.2.8 compares the electrochemical performance of both cells cycled at 0.2 C. The 1st cycle voltage profiles (Figure XIII.2.8a and Figure XIII.2.8b) show large irreversible capacity

loss, indicating side reactions upon initial charge and discharge. The reversibility drastically improved in the following cycle, with both cells achieving excellent coulombic efficiency of $\sim 99\%$ over 100 cycles. Figure XIII.2.8c and Figure XIII.2.8d further compare the discharge capacity as a function of cycle number. While the cell without carbon delivered ~ 140 mAh/g, a discharge capacity of ~ 170 mAh/g was obtained on the cell with 2.5 wt.% carbon. The results show the positive effect of introducing carbon on cathode active material utilization, demonstrating the importance of better-connected electronic pathways and improved conductivities in ASSB performance.

EIS was used to monitor the impedance evolution in the cell with a cathode composite containing SC-NMC811, LYC and carbon in a weight ratio of 57: 40.5: 2.5. The data was collected at the charged state of the indicated cycle number, each after 2 h rest at the open circuit voltage (Figure XIII.2.9a). There is a small impedance increase during the initial cycles, however, the cell largely stabilizes upon further cycling, suggesting possible formation of passivation layer(s) at the SE/electrode interfaces. The SEM cross-sectional images collected at LYC/Li-In anode interface before and after cycling are compared in Figure 9b-d. The pristine interface (Figure XIII.2.9b) shows a clean boundary between LYC and Li-In anode. After 115 cycles, a distinct interlayer with a thickness of $\sim 3\text{--}5$ μm is clearly seen between the separator and the anode. The chemical nature, its dynamic evolution as well as the role of this interlayer in ASSB cycling are under further investigation.

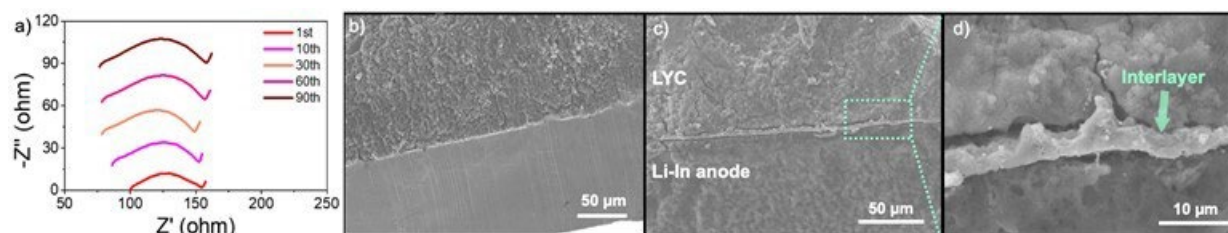


Figure XIII.2.9 a) Nyquist plots from the EIS measurement of a ASSB cell with the cathode containing 2.5 wt.% carbon. (b-d) Cross-sectional SEM images collected at the LYC/Li-In anode interface of the cell before (b) and after (c, d) cycling.

Conclusions

Li-metal based ASSBs are currently facing a number of challenges. Among them are oxidative instability of SSE in the composite cathode, cracking and grain isolation associated with volume changes in cathode active materials as well as chemical, electrochemical and mechanical instabilities at the SSE/electrode interfaces. Here we employed halide SSEs that are stable against 4 V class NMC cathodes and single-crystal NMCs that eliminates intergranular cracking upon cycling. We demonstrate excellent cycling stability and coulombic efficiency for over 100 cycles in an ASSB cell consisting of a SC-NMC811/LYC composite cathode, LYC SSE separator and a Li-In alloy anode. Carbon was found to be critical in establish conduction pathways in the composite cathode and improving active material utilization. The metal center in halide SSEs plays a critical role as LYC with Y^{3+} was found to be significantly more stable against Li metal than LIC with In^{3+} . Halide SSE/anode interface evolves dynamically over cycling, and a distinct interlayer of $\sim 3\text{--}5$ μm thickness was detected in the cycled cells. Our study suggests that proper chemistry design of halide SSEs and their interface engineering are likely to lead to high-energy lithium-metal batteries with much improved performance.

Key Publications

1. D. Chen, J. Ahn and G. Chen, "An Overview of Cation-Disordered Lithium-Excess Rocksalt Cathodes," *ACS Energy Letters* **6**, 1358–1376 (2021). DOI: 10.1021/acsenerylett.1c00203
2. D. Chen, J. Ahn, E. Self, J. Nanda and G. Chen, "Understanding Cation-Disordered Rocksalt Oxyfluoride Cathodes," *Journal of Materials Chemistry A* **9**, 7826 (2021). DOI: 10.1039/d0ta12179g

3. D. Chen, J. Zhang, Z. Jiang, C. Wei, J. Burns, L. Li, C. Wang, K. Persson, Y. Liu and G. Chen, "Role of Fluorine in Chemomechanics of Cation-Disordered Rocksalt Cathodes," *Chemistry of Materials* (2021). DOI: 10.1021/acs.chemmater.1c02118

Patents and Invention Disclosures

1. S. Kim, Y. Lu and G. Chen, "High-energy and high-power composite cathodes for all solid-state batteries," LBNL ROI 2021-176, September 2021.
2. E. Yi, M. M. Doeff, G. Chen and S. Sofie "All-Solid-State Battery Including a Solid Electrolyte and Methods of Making Thereof," U.S. Patent Application Ser. No. 17/095,483, November 2020.
3. J. Ahn, D. Chen and G. Chen, "Fluorinated Cation-Disordered Rocksalt Materials and Methods of Making Thereof," U.S. U.S. Patent Application Ser. No. 17/502,491, October 2021.

Acknowledgements

This work was conducted by Dongchang Chen, Yanying Lu and SeYoung Kim at LBNL. We acknowledge the support from the Vehicle Technologies Office of U. S. Department of Energy.

XIII.3 Design of High-Energy, High-Voltage Lithium Batteries through First-Principles Modeling (LBNL)

Kristin A. Persson, Principal Investigator

Lawrence Berkeley National Laboratory
1 Cyclotron Road
Berkeley, CA 94720
E-mail: kapersson@lbl.gov

Tien Q. Duong, DOE Technology Development Manager

U.S. Department of Energy
E-mail: Tien.Duong@ee.doe.gov

Start Date: October 1, 2019
Project Funding: \$500,000

End Date: September 30, 2021
DOE share: \$500,000

Non-DOE share: \$0

Project Introduction

This project supports VTO programmatic goals by developing next-generation, high-energy cathode materials and enabling stable cathode operation at high voltages through target particle morphology design, functional coatings, and rational design of electrolytes. We aim to provide fundamental insights into the atomistic mechanisms underlying surface reactivity and performance of Li-ion cathode materials and electrolytes with the ultimate goal to suggest improvement strategies, such as coatings, surface protection, novel electrolyte formulations, and particle morphology design. Transport modes as a function of solvent and salt concentrations will be clarified, and a data-driven reaction network framework will be designed and implemented to predict early SEI formation on lithium metal.

Objectives

The end-of-project goals include the following:

- Understanding of the factors that govern charge transport in nonaqueous, superconcentrated LEs.
- Critical surface and coating design and optimization strategies that will improve cycling of Li-ion battery cathodes by reducing cathode degradation from oxygen loss.
- Simulation and ML of the early formation of the SEI on Li-metal electrodes.

Approach

- First-principles calculations, both static and dynamic approaches, are used to model SSE material thermodynamics and kinetics. LEs are modeled through coupled classical MD and first-principles methods to accurately capture solvation structure as well as reactivity of the liquid system.
- Examine different transport models to study the electron and ion mobility through the amorphous coating layer.
- The reaction network is built on large-scale first-principles data, using graph theory and machine learning (ML) models.

Results

The superconcentrated liquid electrolyte (LE) project within the BMR aims at understanding and identifying which LE formulations using high salt concentrations may allow for improved electrochemical performance. One particular focus is the use of co-solvents to improve transport properties, one case study involves the use of co-solvents for LiPF₆ in propylene carbonate (PC) electrolytes. LiPF₆ in PC is a previously investigated and

characterized system (see Self, Fong and Persson, ACS Energy Letters, 2019). In the work here, the co-solvent is a “diluent” which is chosen for reducing viscosity while avoiding direct coordination with the electroactive cation (see Cao et al, PNAS, 2021).

In order to investigate such a system, one particular fluorinated diluent was chosen, and added to PC-LiPF₆ for two concentrations: one which would allow a high concentration electrolyte (approximately 3 M of salt, ratio of Li:PC:diluent 1:2:0.3) and one which could potentially allow the “localized high concentration electrolyte” (LHCE, ratio Li:PC:diluent 1:3:3), at 1 M (see Ren et al., Chem, 2018). To this end, classical molecular dynamics simulations were employed in order to investigate the change in solvation structure and transport resulting from the addition of the diluent co-solvent (methods following to Self, Fong and Persson, ACS Energy Letters, 2019).

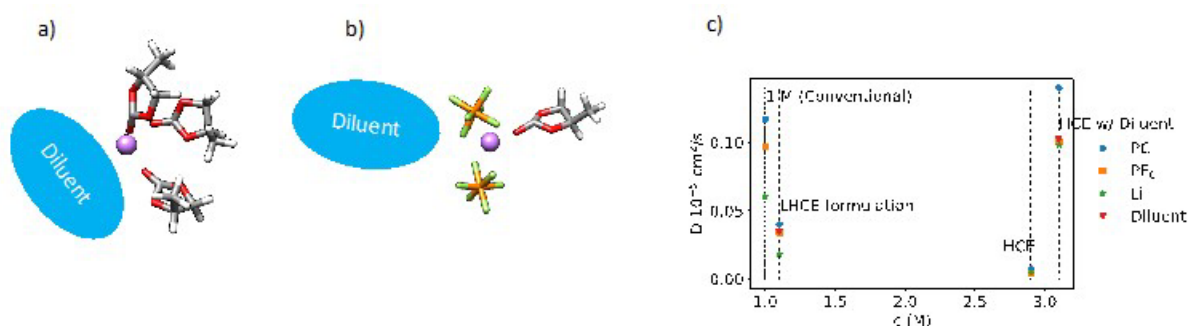


Figure XIII.3.1 a) Molecular dynamics “snapshot” of the solvation structure of a Li cation in the LHCE formulation. b) Molecular dynamics “snapshot” of the solvation structure of a Li cation in the HCE formulation with the fluorinated diluent. Atoms are shown in purple (Li), red (O), white (H), green (F), and orange (P). c) Diffusion coefficients of the various species as a function of concentration. HCE formulations is LiPF₆ in PC, and HCE + diluent denotes LiPF₆ in PC and diluent. Vertical lines are for visual ease.

Figure XIII.3.1 a) and b) show snapshots of solvation structures of the Li cation for the two studied concentrations (LHCE and HCE, respectively). It is found that in the LHCE concentration, the true LHCE regime is not in fact attained. More specifically, the diluent co-solvent is found in the first solvation shell of the electroactive cation. This indicates that this particular diluent is more-so a conventional co-solvent than a non-coordinating species in this case. In addition, this suggests that the success of the LHCE strategy is likely system-specific and may not work for polar carbonate electrolyte solvents such as PC. In fact, the diffusion constants of the various species were not improved for the LHCE formulation, as shown in Figure XIII.3.1 c), where they decrease from the formulation at a similar concentration without the diluent. In the case of the HCE with the diluent, the Li cation is less often directly solvated by the diluent. Moreover, the diffusion constants of the various species are greatly increased Figure XIII.3.1 c), suggesting success of the chosen diluent as viscosity reducing co-solvent. Further characterization, both in silico and experimental, is planned.

The second goal of the BMR is to improve cathode performance by reducing degradation from oxygen loss using novel coating materials. Prior to evaluating the Li and O transport through amorphous films, we first simulate amorphous structures using AIMD. The amorphous structures are generated by implementing a “liquid-quench” process, in which heating, equilibration, and quenching are done through an AIMD workflow. To generate a liquid phase of the amorphous structure, the structure is “heated” at a temperature that is higher than the material’s melting point. A sequence of 4 ps AIMD simulations in the NVT ensemble are employed to equilibrate the external pressure, wherein the cell volume is rescaled according to the average external pressure before the next AIMD simulation until the averaged external pressure was below 5 kbar in a 2 ps duration. The energy equilibration was achieved when the difference between the averaged energy per atom in a 2 ps duration and the averaged energy per atom in a 4 ps duration is smaller than 1 meV/atom. Next, the liquid phases were simulated for additional 10 ps, from which 10 independent configurations were selected and

quenched to 0 K, via direct DFT structure optimization, to obtain the ground-state atomic positions in the amorphous structures. The entire framework can be seen in Figure XIII.3.2.

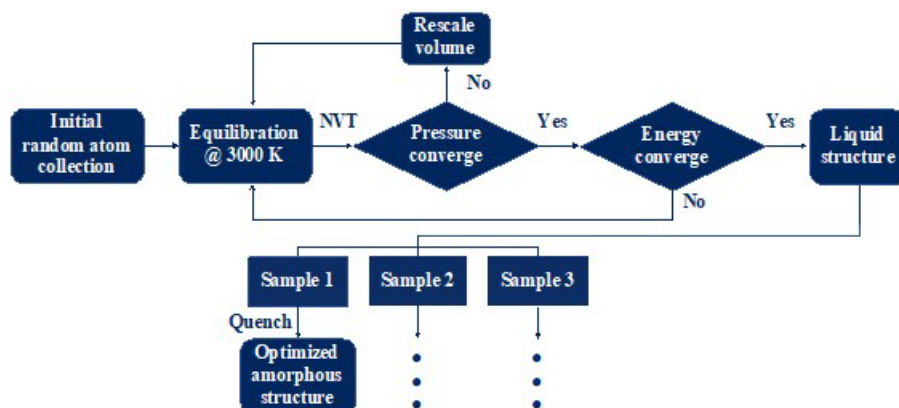


Figure XIII.3.2 Framework for generation of amorphous structures. [1]

Unlike in crystalline materials, direct comparison to experimental structures is not possible, however we have compared the radial distribution functions (rdfs) and local structure within our amorphous structures to experimental data and found reasonable agreement. The comparison of the rdf of amorphous Al_2O_3 generated through our liquid-quench process and experimental data obtained through x-ray and neutron diffraction is presented in Figure XIII.3.3. The rdfs for each element pair agrees well with the amorphous Al_2O_3 prepared by anodic oxidation of aluminum foils.

We reported a computation scheme to evaluate Li^+ and O^{2-} ion transport in amorphous cathode coating. A cathode coating layer can increase the resistance and capacity loss at higher C-rates due to its large overpotentials at higher currents. Thus, we estimate the overpotential, ΔV , on the cathode surface because of coating. The relation between ΔV and Li^+ diffusivity D^{Li} is:

$$\Delta V = \frac{JLk_B T}{D^{\text{Li}} c^{\text{Li}} q^2} \quad (1)$$

where L is the coating thickness, k_B is the Boltzmann constant, T is the temperature, c^{Li} is the Li^+ concentration in the coating, q is the electron charge, and J is the electric current density through the cathode coating, which can be approximated as:

$$J = \frac{\rho V C}{S t} = \frac{\rho r C}{3 t} \quad (2)$$

Where ρ is the cathode density, V is the particle volume, S is the particle surface area, r is the particle radius, C is the cathode capacity, and t is the charging/discharging time. Combining Eq. (1) and (2), ΔV can be expressed as:

$$\Delta V = \frac{\rho r C}{3 t} \frac{L k_B T}{D^{\text{Li}} c^{\text{Li}} q^2} \quad (3)$$

In this study, we choose LiNiO_2 as the relevant cathode material, with $\rho = 4.78 \text{ g/cm}^3$. To avoid detrimental phase transitions and oxygen evolution, we consider that LiNiO_2 can only be charged to 65% of its theoretical capacity with $C = 180 \text{ mAh/g}$. Eq. (3) shows that a smaller ΔV can be realized by reducing cathode particle size and coating thickness and selecting a coating with high Li^+ diffusivity D^{Li} and concentration c^{Li} . By assuming an $r = 1 \text{ }\mu\text{m}$ LiNiO_2 primary particle and a 1C rate current density through the coating, J is estimated to be 0.03 mA/cm^2 . In our previous work, we estimated that Li^+ diffusivity in amorphous Al_2O_3 is $10^{-16} \text{ cm}^2/\text{s}$, therefore we estimate $\Delta V = 0.17 \text{ V}$ for a 1 nm thick coating.

To evaluate the effectiveness of the amorphous cathode coating in blocking O^{2-} transport, we estimate the O^{2-} flux J^0 and the time t required for O^{2-} to diffuse through the coating. We assume the oxygen loss induced surface rocksalt layer mainly consists of NiO phase, which is densified from the layered NiO_2 . Let c_{\max}^0 denote the upper value of the O^{2-} concentration in NiO_2 , and t can be expressed as:

$$t = \frac{0.5Vc_{\max}^0}{AJ^0} \quad (4)$$

where V and A are the shell volume of the surface rocksalt phase and surface area of the coated $LiNiO_2$, respectively. To estimate J^0 under the driving force of the chemical potential gradient across the coating layer, we applied the Onsager transport equation:

$$J^0 = -L^{00}\nabla\mu^0 \quad (5)$$

where L^{00} and $\nabla\mu^0$ are the Onsager transport coefficient, and oxygen chemical potential gradient, respectively. Assuming steady-state conditions, we can reasonably approximate the chemical potential gradient $\nabla\mu^0$ to be a constant throughout the coating, which renders the above equation as

$$J^0 = L^{00} \frac{\mu_c^0 - \mu_e^0}{l_c} \quad (6)$$

where μ_c^0 and μ_e^0 are the chemical potentials at the cathode and electrolyte sides, respectively. Combining Eq. (4) and (6), t can be expressed as:

$$t = \frac{r^3 - (r - l_s)^3}{6(r + l_c)^2} \frac{c_{\max}^0 l_c}{L^{00}(\mu_c^0 - \mu_e^0)} \quad (7)$$

μ_c^0 can be estimated from the cathode densification reaction consistent with the phase diagram. For example, at 4.3 V, layered NiO_2 would densify to rocksalt NiO , with oxygen being released at $\mu_c^0 = -4.95$ eV. μ_e^0 can be estimated using the condition where oxygen loses electrons to the carbon network and is released as O_2 (at $\mu_e^0 = -5.24$ eV at room temperature and $P_{e^{O_2}} = 0.21$ atm). We set the thickness of the surface rocksalt phase to be $l_s = 2$ nm. Therefore, the time t required for the surface NiO_2 to lose 50% of its oxygen is estimated to be 1.6 hrs.

The third goal of the current BMR project is aimed toward using a data-driven reaction network approach to identify reaction pathways responsible for the formation of important SEI component species. One goal of interest is identifying the formation mechanisms of lithium ethylene monocarbonate (LEMC), which has recently been proposed to be the major component of the Li-anode SEI rather than lithium ethylene dicarbonate (LEDC). To that end, the team first improved the following two aspects of the reaction network. The entire workflow is shown in Figure XIII.3.3. They proposed a systematic way of sampling the relevant molecular species to be included, for example, a fragmentation and ML-assisted recombination procedure. They generated the fragments of the starting materials (Li^+ , EC, and water) and recombinant molecules through connecting one bond between any two fragments. Subsequently, all the recombinant molecules that are predicted to be exergonic on recombination by ML model BonDNet were included in the reaction network. The team utilized a mixed-integer linear programming (MILP) scheme to incorporate concerted reactions (reactions involving multiple bond changes at the same time) with up to five bond changes to account for complicated hydrolysis mechanisms. Following this procedure, they constructed a reaction network with 570 species and close to nine million reactions.

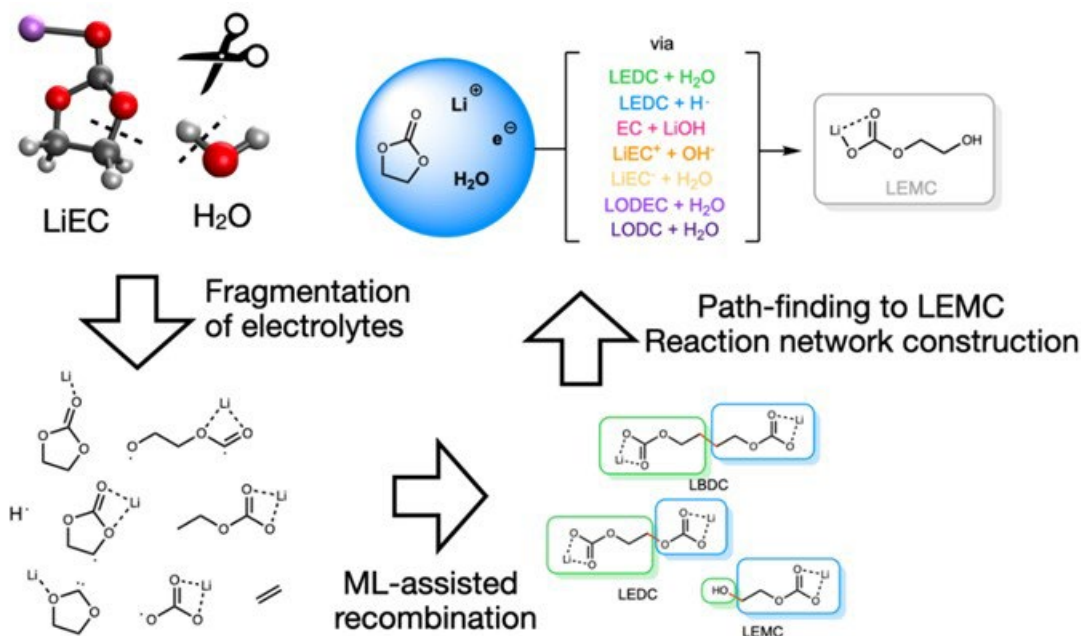


Figure XIII.3.3 The workflow for constructing a reaction network for the $\text{Li}^+/\text{EC}/\text{H}_2\text{O}$ system and pathfinding to LEMC

Analyzing 30,000 top-ranking LEMC formation pathways as identified by the reaction network, the team (1) successfully recovered, automatically, two literature-proposed mechanisms, namely EC hydrolysis and LEDC hydrolysis pathways, and (2) found that nearly all feasible routes to LEMC involve water and/or LEDC participation. This condition severely limits the amount of LEMC that can form in the first cycles, as compared to LEDC, in well-dried commercial Li-ion electrolytes.

Conclusions

- Benchmarked workflow for sampling of amorphous structures and computed Li and O diffusivity in various amorphous oxide films.
- Established a computational scheme to evaluate Li^+ and O_2^- ion transport in amorphous cathode coatings.
- Found that the success of the LHCE strategy is system-specific and may not work for polar carbonate electrolyte solvents. For the system studied, the diffusivity was not improved for the LHCE formulation.
- Use ML-assisted recombination to identify recombinant molecules for incorporation into the reaction network. Recovered two literature-proposed mechanisms for EC and LEDC hydrolysis using the improved reaction network. Additionally, found that all feasible routes to LEMC involve water or LEDC.

Key Publications

1. Predicting and Understanding Novel Electrode Materials from First-Principles, poster presentation, Kristin A. Persson, AMR 2021, virtual format
2. Blau, Samuel M., Hetal D. Patel, Evan Walter Clark Spotte-Smith, Xiaowei Xie, Shyam Dwaraknath, and Kristin A. Persson. "A chemically consistent graph architecture for massive reaction networks applied to solid-electrolyte interphase formation." *Chem. Sci.* 12 (2021): 4931–4939.

3. Xie, Xiaowei, Evan Walter Clark Spotte-Smith, Mingjian Wen, Hetal D. Patel, Samuel M. Blau and Kristin A. Persson. "Data-driven prediction of formation mechanisms of lithium ethylene monocarbonate with an automated reaction network." *J. Am. Chem. Soc.* 143 (2021), 13245–13258.
4. Wen, Mingjian, Samuel M. Blau, Evan Walter Clark Spotte-Smith, Shyam Dwaraknath, and Kristin A. Persson. "BonDNet: a graph neural network for the prediction of bond dissociation energies for charged molecules." *Chem. Sci.* 12 (2021): 1858–1868.
5. Spotte-Smith, E.W.C., Blau, S.M., Xie, X. *et al.* Quantum chemical calculations of lithium-ion battery electrolyte and interphase species. *Sci Data* 8, 203 (2021). <https://doi.org/10.1038/s41597-021-00986-9>
6. Ion Correlations and Their Impact on Transport in Polymer-Based Electrolytes, Kara D. Fong, Julian Self, Bryan D. McCloskey, and Kristin A. Persson, *Macromolecules* **2021** 54 (6), 2575–2591, DOI: 10.1021/acs.macromol.0c02545

References

1. Aykol, M.; Persson, K. A., Oxidation Protection with Amorphous Surface Oxides: Thermodynamic Insights from Ab Initio Simulations on Aluminum. *ACS Applied Materials & Interfaces* 2018, 10 (3), 3039–3045.
2. Aykol, M., Dwaraknath, S. S., Sun, W. & Persson, K. A. Thermodynamic limit for synthesis of metastable inorganic materials. *Sci. Adv.* 4, eaaq0148 (2018).

Acknowledgements

This work was intellectually led by the Battery Materials Research (BMR) program under the Assistant Secretary for Energy Efficiency and Renewable Energy, Office of Vehicle Technologies of the U.S. Department of Energy, Contract DE-AC02-05CH11231. This research used resources of the National Energy Research Scientific Computing Center, a DOE Office of Science User Facility supported by the Office of Science of the U.S. Department of Energy under Contract No. DE-AC02-05CH11231. This research also used the Lawrence computational cluster resource provided by the IT Division at the Lawrence Berkeley National Laboratory (Supported by the Director, Office of Science, Office of Basic Energy Sciences, of the U.S. Department of Energy under Contract No. DE-AC02-05CH11231)

XIII.4 Characterization and modeling of Li-metal batteries: modeling and design of amorphous solid-state Li conductors (LBNL)

Gerbrand Ceder, Principal Investigator

Lawrence Berkeley National Laboratory
1 Cyclotron Road, MS: 33-146
Berkeley, CA 94720
E-mail: gceder@berkeley.edu

Tien Q. Duong, DOE Technology Development Manager

U.S. Department of Energy
E-mail: Tien.Duong@ee.doe.gov

Start Date: October 1, 2020
Project Funding: \$460,000

End Date: September 30, 2021
DOE share: \$460,000

Non-DOE share: \$0

Project Introduction

Solid electrolytes (SEs) that are made of lithium superionic conductors (SICs) are the essential component of lithium solid-state batteries [1],[2]. Metal penetration in SEs is one of the challenging problems facing the development of solid-state batteries [3],[4],[5],[6]. Previously, various mechanisms are proposed to be responsible for metal propagation in SEs, including low diffusivity of mobile cations at grain boundaries [7], low relative density of SEs [8], pre-existing microstructural defects on the surface of and in bulk SEs [9], inhomogeneous plating resulting from contact loss between metal anodes and SEs [10], and enhanced electronic conductivity in SEs resulting from vacancy generation during cycling [5]. In this part of the BMR program, we investigate the conditions for high ionic conductivity in solid electrolytes, and the mechanisms by which Li metal can propagate through them.

Objectives

Solid-state batteries are promising to achieve high energy density. The project objective is to determine the design principles needed to create SSEs with high Li-ion conductivity while also achieving stability against common Li-ion cathodes and Li-metal anodes.

Approach

Ab-initio computations are used to screen suitable solid electrolyte with high electrochemical stability and high ionic conductivity. The Nudged Elastic Band (NEB) and an AIMD method are used to evaluate Li-ion mobility. Meanwhile, DFT is used to calculate bulk elastic constants of materials, surface energies, and interface decohesion energies of GBs. Thermodynamic interface stability is assessed from ab initio computed grand potential phase diagrams in which the lithium voltage can be controlled. Kinetic limits for solid electrolyte decomposition are assessed by topotactic lithium insertion and removal from the solid electrolyte. Continuum modeling has been used to model stress, macroscopic transport, and fracture resistance.

Results

Investigating metal propagation in solid electrolytes

Li metal can be deposited within voids inside the SE when both electronic current and ionic current can reach the location of the voids, and the plating potential is large enough for the Li deposition reaction. Figure XIII.4.1a shows the deposition current density at the surface of the void in the SE that is close to the anode. At the start of charging ($t = 0$), the part of the surface in yellow color, indicating the largest current, is oriented towards the anode. At time $t = 0$, Li metal is plated on the surface of the void as the deposition is limited by the electronic current. However, the deposition current changes as more Li metal is deposited ($t > 0$). This is

because plating of metal on the inside of the void changes the electronic current thereby modifying where the plating potential is largest.

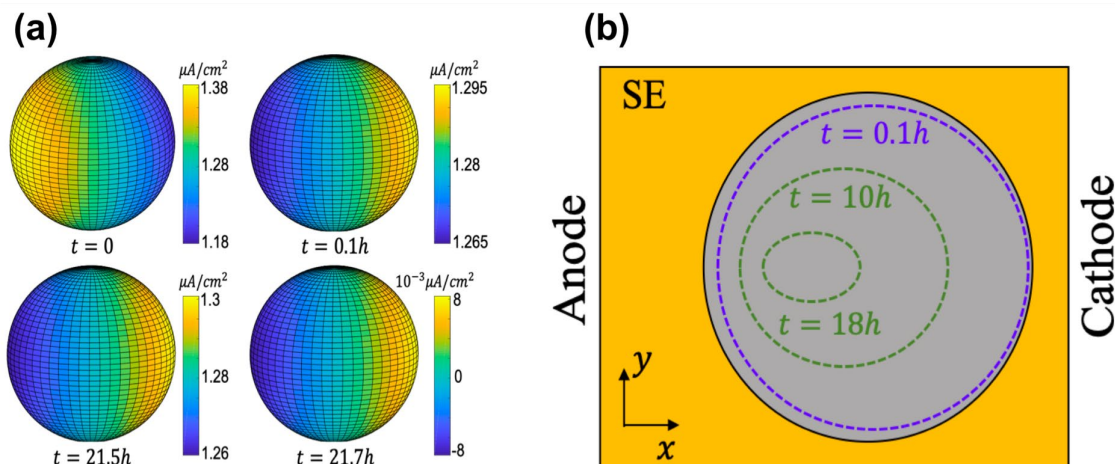


Figure XIII.4.1 (a) Current density distribution in the void. (b) Evolution of the void boundary as Li deposits inside the void.

Figure XIII.4.1b shows the evolution of the metal boundary in the void under the applied deposition current density described in Figure XIII.4.1a. After about 0.1 hours, the total deposited thickness of *Li* metal is approximately 1 nm, as indicated by the blue dashed ellipse. Meanwhile, the thickness of deposited metal on the left tip is larger than that on the right tip (blue dashed ellipses). After around 10 hours of *Li* deposition, the total deposited thickness of *Li* metal reaches approximately 100 nm. Due to the larger current density at the cathode side ($t > 0.1$ hours in Figure XIII.4.1), the thickness of *Li* metal on the cathode side increases faster than that on the anode side, pushing the *Li* metal boundary toward the anode side (two green ellipses).

The existence of electronic conductivity in SEs is believed to be one of the reasons for metal penetration in SSB cells. The key issue to prevent *Li* metal propagation through the electrolyte is to prohibit initiation of metal plating in the vulnerable region near the anode, as illustrated schematically in Figure XIII.4.2. The fraction of the SE that sees a negative plating potential (a_0/L) is approximately the ratio of the anode surface overpotential (η_A) and the cell voltage $V_C - V_A$. This area increases with current density because η_A increases as can be seen from the linearized Butler Volmer equation ($\eta_A \approx i_0 R_A$). The relevant current density is the local current density, which may be very different from the average current density due to inhomogeneous contact at the interface. From this analysis, three strategies to reduce *Li* plating in the SE become apparent: 1) Creating a dense layer between the metal anode and porous SE either by introducing a coating between the anode and SE or by densification to obtain a thin “void-free” layer near the SE surface; 2) Decreasing the *M* chemical potential in the anode; 3) Improve contact between the anode and the SE to reduce the local current density, as a lower current density reduces the depth of the SE that is susceptible to plating. The first two solutions are schematically shown in Figure XIII.4.2b and Figure XIII.4.2c.

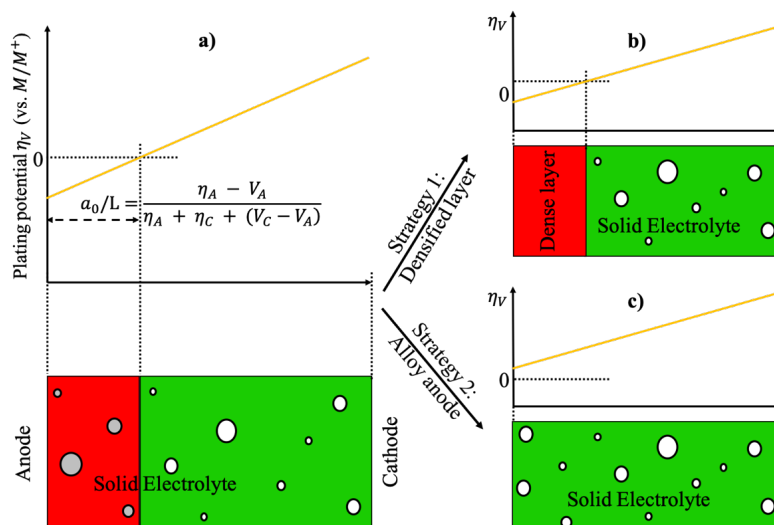


Figure XIII.4.2 Schematic illustration of the metal deposition in voids of the SE.

The internal metal deposition only leads to metal penetration in the SE as well as causing inhomogeneous plating at the electrode/SE interfaces. This is called “shadowing effect”. Figure XIII.4.3a indicates the shadowing effect due to the presence of metal deposition in the void. The vertical coordinate shows the magnitude of the total current density going into the anode. Shadowing by the void reduces the current by 0.5% at the point ($x = y = z = 0$) but the total current converges to the applied value (i_0) far enough from the center. The shadowing effect rapidly increases as the void approaches the interface. Therefore, the total current distribution is not only affected by the electrode/SE interface but also by internal deposition within the SE.

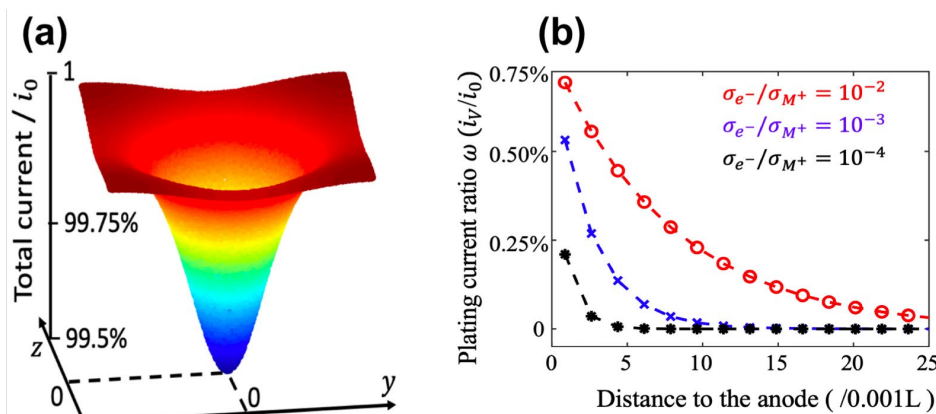


Figure XIII.4.3 (a) Total current density at the anode/SE interface. Both the vertical coordinate and the contour plot represent the magnitude of the deposition current. All the length units in the figures are in μm . (b) Distribution of deposition current i_V under applied current i_0 at three different SE electronic conductivities. The ionic conductivity σ_{M^+} is fixed 0.1 mS/cm , while the electronic conductivity σ_{e^-} varies.

Figure XIII.4.3b shows the average deposition current (\bar{i}_V) of the voids in the SE under an applied current i_0 . The deposition current decreases rapidly as voids are positioned deeper within the SE. This is because both the electrochemical potential of electrons ($\tilde{\mu}_{e^-}$) and the deposition overpotential ($-e\eta_V = \tilde{\mu}_{M^+} + \tilde{\mu}_{e^-}$) decrease rapidly. For SE materials with higher electronic conductivities (σ_{e^-}), the average deposition current is larger and decays much slower. However, the value still decays to a negligibly small value for voids located deeper than $0.02L$ (L is the SE thickness). Therefore, preparing a sufficiently void-free surface of the SE at the anode side can be an efficient way to prevent M metal deposition in the voids of the SE.

Lithium Oxide Superionic Conductors

Experimental^[11] and theoretical^[12] work indicated that the interaction between Li ions is an important factor for having high Li ionic conductivity in superionic conductors. However, the mechanism behind this effect has not been clearly investigated. By observing the diffusion network of garnet and NASICON frameworks, a common pattern of an activated diffusion network” has been discovered. The presence of a 3-D percolation network, a short distance between occupied Li sites, and the homogeneity of the transport path are three topological features of the diffusion network that we identified as being beneficial for fast Li migration. Figure XIII.4.4 shows that in garnet and NASICON frameworks, these three features allow 3-D percolation of the activated local environment resulting in their superionic conductivities.

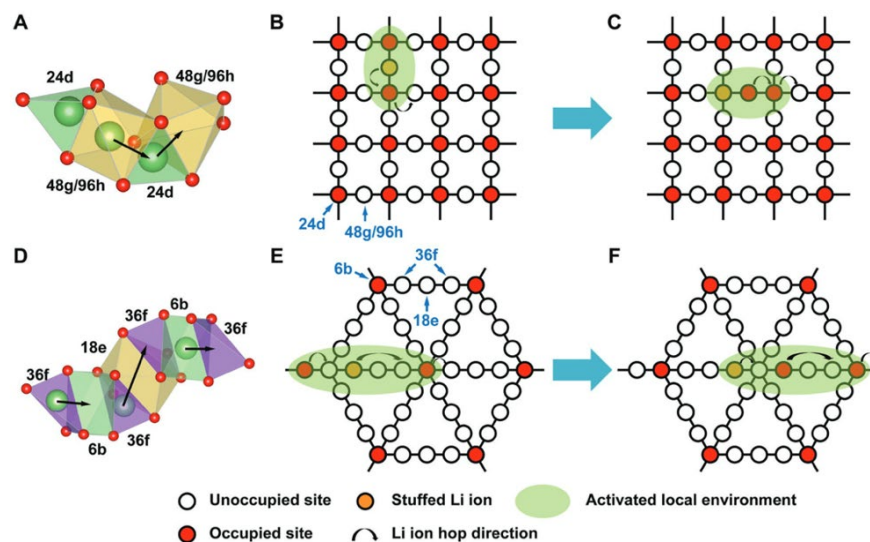


Figure XIII.4.4 Diffusion mechanism in Li-stuffed Li_3 garnet (A) and NASICON (D) by cooperative hopping of Li-ions in activated local environment. Diffusion network of NASICON before (B) and after (C) cooperative migration, diffusion network of garnet before (E) and after (F) cooperative migration are illustrated.

The activated diffusion network and its three key features can be directly used as screening criteria to discover novel oxide superionic conductors. By performing high-throughput screening on the Materials Project database^[13], seven novel frameworks that have high ionic conductivity have been found. Ab-initio molecular dynamics simulation results show that these materials exhibit 0.1 mS/cm or higher at 300K. One example of the predicted candidate is Li_2TeO_4 with a distorted inverse spinel structure. While the activation energy of the stoichiometric structure is 1.13 eV^[14], upon Li stuffing by doping Nb^{5+} into Te^{6+} site, face-sharing tet-oct environments form which can lower the activation energy to 0.21 eV, allowing high ionic conductivity of 3.2 mS/cm at 300K. This result clarifies how the interaction between Li ions within close proximity can drastically enhance the ionic conductivity.

Conclusions

The existence of electronic conductivity in SEs is believed to be one of the reasons for metal penetration in SSB cells. We show that a small amount of electronic conductivity is sufficient to trigger metal propagation in the SE whenever porosity is present near the anode. Our work also showed that creating a densified layer on the SE near the anode, or alloying the metal anode are two strategies to prevent/alleviate the metal deposition in the SE.

We also identified an “activated diffusion network” as a structural feature by which novel conductors can be found.

Key Publications

1. Cai, Zijian, Huiwen Ji, Yang Ha, Jue Liu, Deok-Hwang Kwon, Yaqian Zhang, Alexander Urban et al. "Realizing continuous cation order-to-disorder tuning in a class of high-energy spinel-type Li-ion cathodes." *Matter* (2021).
2. Tu, Qingsong, Tan Shi, Srinath Chakravarthy, and Gerbrand Ceder. "Understanding metal propagation in solid electrolytes due to mixed ionic-electronic conduction." *Matter* 4, no. 10 (2021): 3248–3268.
3. Xiao, Yihan, KyuJung Jun, Yan Wang, Lincoln J. Miara, Qingsong Tu, and Gerbrand Ceder. "Lithium oxide superionic conductors inspired by garnet and NASICON structures." *Advanced Energy Materials* 11, no. 37 (2021): 2101437.
4. Blanc, Lauren, Christopher J. Bartel, Haegyeom Kim, Yaosen Tian, Hyunchul Kim, Akira Miura, Gerbrand Ceder, and Linda F. Nazar. "Toward the Development of a High-Voltage Mg Cathode Using a Chromium Sulfide Host." *ACS Materials Letters* 3, no. 8 (2021): 1213–1220.
5. Yang, Julia H., Haegyeom Kim, and Gerbrand Ceder. "Insights into Layered Oxide Cathodes for Rechargeable Batteries." *Molecules* 26, no. 11 (2021): 3173.
6. Huang, Jianping, Peichen Zhong, Yang Ha, Deok-Hwang Kwon, Matthew J. Crafton, Yaosen Tian, Mahalingam Balasubramanian, Bryan D. McCloskey, Wanli Yang, and Gerbrand Ceder. "Non-topotactic reactions enable high-rate capability in Li-rich cathode materials." *Nature Energy* (2021): 1–9.

References

1. Janek, Jürgen, and Wolfgang G. Zeier. "A solid future for battery development." *Nature Energy* 1, no. 9 (2016): 1–4.
2. Bachman, John Christopher, Sokseiha Muy, Alexis Grimaud, Hao-Hsun Chang, Nir Pour, Simon F. Lux, Odysseas Paschos et al. "Inorganic solid-state electrolytes for lithium batteries: mechanisms and properties governing ion conduction." *Chemical reviews* 116, no. 1 (2016): 140–162.
3. Han, Fudong, Jie Yue, Xiangyang Zhu, and Chunsheng Wang. "Suppressing Li dendrite formation in Li₂S-P₂S₅ solid electrolyte by LiI incorporation." *Advanced Energy Materials* 8, no. 18 (2018): 1703644.
4. Taylor, Nathan J., Sandra Stangeland-Molo, Catherine G. Haslam, Asma Sharafi, Travis Thompson, Michael Wang, Regina Garcia-Mendez, and Jeff Sakamoto. "Demonstration of high current densities and extended cycling in the garnet Li₇La₃Zr₂O₁₂ solid electrolyte." *Journal of Power Sources* 396 (2018): 314–318.
5. De Jonghe, Lutgard C., Leslie Feldman, and Andrew Beuchele. "Slow degradation and electron conduction in sodium/beta-aluminas." *Journal of Materials Science* 16, no. 3 (1981): 780–786.
6. De Jonghe, Lutgard C. "Transport number gradients and solid electrolyte degradation." *Journal of the Electrochemical Society* 129, no. 4 (1982): 752.
7. Sudo, R., Y. Nakata, K. Ishiguro, M. Matsui, A. Hirano, Y. Takeda, O. Yamamoto, and N. Imanishi. "Interface behavior between garnet-type lithium-conducting solid electrolyte and lithium metal." *Solid State Ionics* 262 (2014): 151–154.
8. Tsai, Chih-Long, Vladimir Roddatis, C. Vinod Chandran, Qianli Ma, Sven Uhlenbruck, Martin Bram, Paul Heitjans, and Olivier Guillon. "Li₇La₃Zr₂O₁₂ interface modification for Li dendrite prevention." *ACS applied materials & interfaces* 8, no. 16 (2016): 10617–10626.

9. Porz, L., Swamy, T., Sheldon, B. W., Rettenwander, D., Frömling, T., Thaman, H. L., ... & Chiang, Y. M. (2017). Mechanism of lithium metal penetration through inorganic solid electrolytes. *Advanced Energy Materials*, 7(20), 1701003.
10. Sharafi, Asma, Eric Kazyak, Andrew L. Davis, Seungho Yu, Travis Thompson, Donald J. Siegel, Neil P. Dasgupta, and Jeff Sakamoto. "Surface chemistry mechanism of ultra-low interfacial resistance in the solid-state electrolyte $\text{Li}_7\text{La}_3\text{Zr}_2\text{O}_{12}$." *Chemistry of Materials* 29, no. 18 (2017): 7961–7968.
11. Arbi, K., S. Mandal, J. M. Rojo, and J. Sanz. "Dependence of Ionic Conductivity on Composition of Fast Ionic Conductors $\text{Li}_{1+x}\text{Ti}_{2-x}\text{Al}_x(\text{PO}_4)_3$, $0 \leq x \leq 0.7$. A Parallel NMR and Electric Impedance Study." *Chemistry of materials* 14, no. 3 (2002): 1091–1097.
12. Xu, Ming, Min Sik Park, Jae Myung Lee, Tae Young Kim, Young Sin Park, and Evan Ma. "Mechanisms of Li^+ transport in garnet-type cubic $\text{Li}_{3+x}\text{La}_3\text{M}_2\text{O}_{12}$ ($\text{M} = \text{Te}, \text{Nb}, \text{Zr}$)." *Physical Review B* 85, no. 5 (2012): 052301.
13. ain, Anubhav, Shyue Ping Ong, Geoffroy Hautier, Wei Chen, William Davidson Richards, Stephen Dacek, Shreyas Cholia et al. "Commentary: The Materials Project: A materials genome approach to accelerating materials innovation." *APL materials* 1, no. 1 (2013): 011002.
14. González, C., M. L. López, M. Gaitán, M. L. Veiga, and C. Pico. "Relationship between crystal structure and electric properties for lithium-containing spinels." *Materials research bulletin* 29, no. 8 (1994): 903–910.

XIV Next-Gen Li-ion: Low Temperature Electrolytes

XIV.1 Ethylene Carbonate-Lean Electrolytes for Low Temperature, Safe Li-ion batteries (LBNL)

Bryan D. McCloskey, Principal Investigator

Lawrence Berkeley National Laboratory and University of California, Berkeley
201-D Gilman Hall
Berkeley, CA 94720
E-mail: bmcclosk@berkeley.edu

Mallory Clites, DOE Technology Development Manager

U.S. Department of Energy
E-mail: Mallory.Clites@ee.doe.gov

Start Date: October 1, 2019

End Date: September 30, 2022

Project Funding: \$650,000

DOE share: \$650,000

Non-DOE share: \$0

Project Introduction

Li-ion batteries suffer from performance limitations at low temperatures (sub- 0°C) due to a large rise in overall cell impedance. In the first year of this project, we identified the charge transfer resistance—an interfacial process—as the dominant limitation for low temperature battery performance. In the second year of this project (FY21), we aim to understand how the anode and cathode contribute to the charge transfer resistance, and how charge transfer as a function of temperature is impacted by electrolyte composition.

Objectives

The overall 3-year project goal is to develop an electrolyte that provides optimal transport and interfacial properties to enable high capacity (70% of room temperature capacity) at modest rates (C/3) during low temperature discharge (-20°C) of graphite|NMC622 cells. Specific objectives of our project are:

- To understand the origins of poor low temperature energy density in Li-ion batteries.
- To understand the role of electrolyte composition (salt concentration, additives, and solvent composition) on total cell resistance at various temperatures.
- Applying results obtained in Li|graphite half cells and coin cell sized graphite|NMC622 full cells to select an optimized electrolyte composition.

Approach

We will use a systematic approach in which we characterize the transport and interfacial effects of incorporating a moderate to large fraction of low viscosity, low melting point linear ester solvents into the electrolyte. GBL-rich electrolytes will also be studied given GBL's high dielectric constant, wide liquid temperature range, and relatively low viscosity compared to EC. We will use the numerous capabilities developed by the project PI's at LBNL to guide selection of optimal additive and solvent composition. Of particular interest for this year, we use impedance spectroscopy coupled with distribution of relaxation times (DRT) analysis, which allows straightforward deconvolution of processes that occur on similar time scales. We have found the DRT method to be important to deconvolute resistances associated with interfacial processes (specifically charge transfer resistance and solid electrolyte interface resistance) at low temperatures. We study coin cells with ~3 mAh total capacity but will move to larger cells as our understanding of the optimal electrolyte properties improves. Both full graphite|NMC622 cells and graphite|Li cells will be used to ensure validity of our data analysis. Li|Li symmetric cells will be used in the analysis of electrolyte transport

properties. In FY21, we focused on completing our initial studies on low temperature behavior of our baseline electrolyte, 1 M LiPF₆ in 3:7 wt ethylene carbonate:ethyl methyl carbonate (LP57), with graphite and Li(Ni_{0.6}Co_{0.2}Mn_{0.2})O₂ (NMC622) electrodes provided by the Cell Analysis, Prototyping, and Modelling (CAMP) facility at Argonne National Laboratory. We have also targeted 3 important solvent parameters this year and will use knowledge gained in these initial studies to guide further development later in the project: **1.** Varying additive composition (2–3 wt. % fluoroethylene carbonate (FEC), vinylene carbonate (VC), and propane sultone (PS)) in an EC:EMC electrolyte, and **2.** Varying LiPF₆ concentration in 3:7 EC:EMC electrolyte, and **3.** Varying EC/GBL content with 2-3 wt.% added FEC.

Results

Charge transfer resistance dominates at low temperatures. We completed our studies on the various contributions to total cell resistance as a function of temperature when using graphite|NMC622 coin cells (2032) with LP57 baseline electrolyte. We studied cell discharge performance at temperatures below 30°C, with discharges being performed at a given temperature (20°C to -30°C), but always charging the cell at 30°C between discharges. Our results of baseline characterization are provided in Figure XIV.1.1. Here, the cell capacity and impedance were measured during the discharge at each of the temperatures. Each cell was discharged at a rate of C/3 from 4.1 to 3.0V. The obtained resistances were deconvoluted into bulk and interfacial resistances (solid electrolyte interface and charge transfer) using distribution of relaxation times (DRT) analysis. It was found that as the temperature is lowered, the total resistance of the cell increases (Figure XIV.1.1A) while the capacity and average cell voltage decrease (Figure XIV.1.1B). This is expected, because higher resistances from sluggish kinetics and transport at low temperatures cause the cut-off voltage to be reached at much lower capacities. The increase in resistance is particularly steep below 0°C. The charge-transfer resistance, and not the bulk electrolyte resistance associated with ion transport, is primarily responsible for the increase in total resistance at lower temperatures (Figure XIV.1.1). To further deconvolute the anode and cathode contributions to the SEI and charge transfer resistances, we turn to a custom-built 3-electrode Swagelok cell, which allows us to collect impedance at both the anode and cathode versus a AuLi reference electrode (Figure XIV.1.2). Here, we see that at room temperature (20°C), the cathode impedance dominates over the anode impedance. However, at -20°C, the total resistance contribution from the anode, particularly the charge transfer resistance, dramatically increases, such that impedances at both the anode and cathode become large and important. Therefore, strategies to lower the charge transfer impedance at either electrode would provide good routes to improve low temperature battery performance.

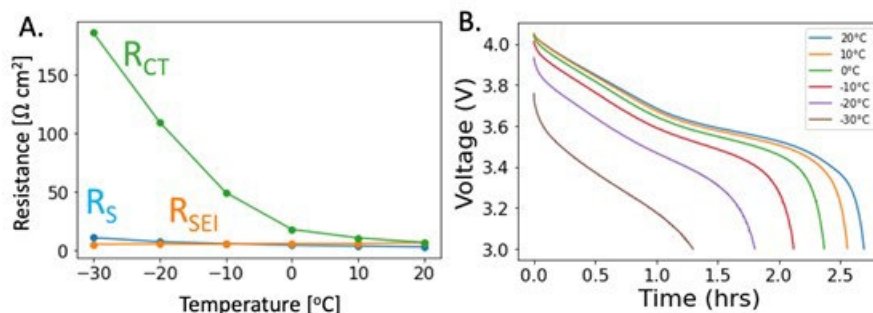


Figure XIV.1.1 Low-temperature performance of cell with baseline LP57 electrolyte. A. RCT (charge transfer resistance), RSEI (SEI resistance) and RS (bulk electrolyte resistance) vs temperature at the average voltage for the corresponding temperature. The sum of these resistances is the total cell resistance. Resistance measured via DRT analysis of impedance spectra at the average voltage of the cell. B. Voltage profile during a C/3 discharge (using capacity at 20 °C as the reference for C/3 rate) of the cell at different temperatures.

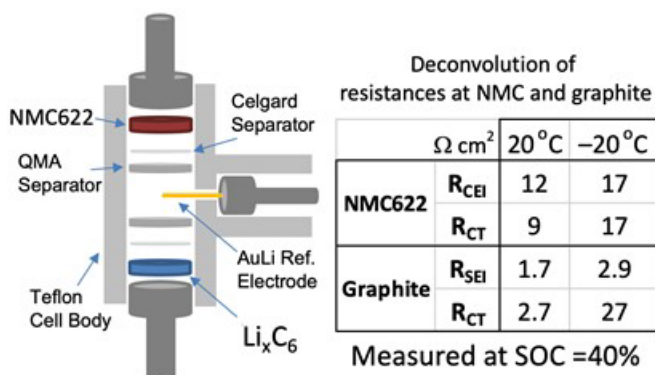


Figure XIV.1.2 Left panel: a schematic of a 3-electrode cell that allows deconvolution of interfacial resistance at the anode and cathode. Right panel: the SEI, cathode electrolyte interface (CEI), and charge transfer resistance contributions of a graphite|NMC622 cell at various temperatures. Note that the resistance here are different than in Figure XIV.1.1 because of the different cell geometries.

Electrolyte concentration dependence. The solvation environment of Li^+ can affect the charge-transfer kinetics and interfacial resistance, so we varied the LiPF_6 salt concentration in our 3:7 EC:EMC solvent system to understand how the EC to Li^+ ratio impacted the measured cell resistances as a function of temperature. The concentration of the salt was varied between 0.35 M and 2.0 M keeping the same EC:EMC ratio. The impedance was recorded during the discharge of cells containing each of the different concentration electrolytes at each of the different temperatures. It was found that varying the salt concentration has a modest effect on both the total resistance and the capacity (Figure XIV.1.3). The electrolyte with salt concentration of 0.85 M showed optimal performance at all temperatures with minimum total resistance and highest capacity. Noted here in passing, the charge transfer resistance (compared to the SEI or bulk electrolyte resistance) changes the most with concentration, with R_{CT} decreasing from $109 \Omega \text{ cm}^2$ at 1 M LiPF_6 to $74 \Omega \text{ cm}^2$ at 0.85 M LiPF_6 . When considering why 0.85M LiPF_6 provided the lowest resistance, we note that the EC/ Li^+ ratio at 0.85 M is 4.2. We reason that the decrease in resistance from 2.0 M to 0.85 M can be explained by the better solvation of Li as the number of EC molecules per Li approaches 4. EC has a very high dielectric constant (~ 90 at 25°C), as compared to EMC (~ 2.9 at 25°C). During discharge, the Li^+ in the graphite passes through the SEI and enters the solvent where it is solvated by the solvent molecules. As the number of EC per Li approaches 4, sufficient EC is available to better solvate the Li^+ than EMC in the solvation shell.

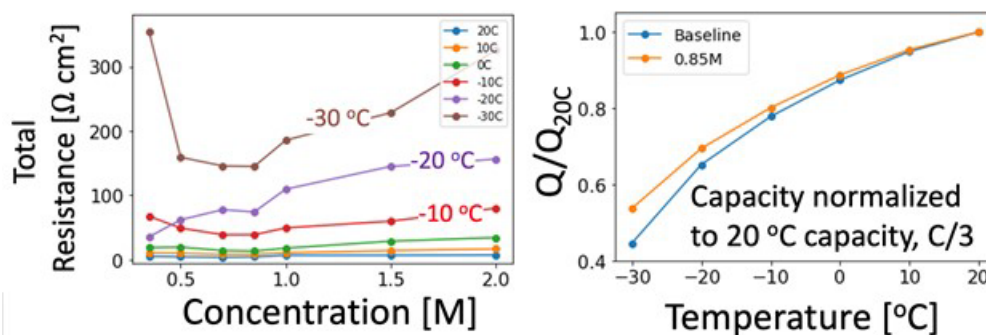


Figure XIV.1.3 Left panel: Total graphite|NMC622 cell resistance measured at various temperatures as a function of LiPF_6 concentration (resistance measured at the average cell voltage). 0.85 M was generally found to exhibit the lowest total cell resistance at all temperatures. Right panel: The capacity normalized to 20 °C cell capacity as a function of temperature for 2 graphite|NMC622 cells one with LP57 electrolyte (baseline), one with 0.85 M LiPF_6 in 3:7 EC:EMC. C/3 rate was used (using 20 °C cell capacity to establish C/3 rate).

Low temperature performance with additive incorporation. Overall, electrolyte design affects low temperature performance primarily by determining the makeup of Li-ion solvation shells—the breakup of which requires the greatest energy input out of all simultaneous processes during operation [Li, ACS Appl. Mater. Interfaces,

2017]. However, given that the charge transfer process very likely occurs at the electrode-SEI/CEI interface (rather than the SEI/CEI-electrolyte interface), the solvation environment of Li^+ within the SEI likely has an impact on the overall cell resistances. Therefore, electrolyte additives, which are typically used to impact SEI/CEI composition, play a role to enhance low temperature performance in addition to larger electrolyte composition effects.

A few additives were incorporated into the LP57 baseline electrolyte and tested in 2032 coin cells as shown in Figure XIV.1.4. Both vinylencarbonate (VC) and propane sultone (PS) show some promising results in enhancing low temperature performance of the cells (Figure XIV.1.4 A and B). However, the overall effect is fairly moderate at a low additive amount of 0.5%. The largest enhancement for these additives is about a 5% capacity-retention gain at -20°C compared to the capacity of baseline electrolyte when compared at the same temperature. Additionally, further increasing the additives amount to 2% in the electrolyte do not improve but degrade low temperature performance. On the other hand, we found that adding 6 wt% fluoro ethylene carbonate (FEC) to our baseline electrolyte resulted in minimum resistance at lower temperatures (Figure XIV.1.4C), thereby improving the capacity of cells at lower temperatures (Figure XIV.1.4D). As we go from 2 wt% FEC to 10 wt% FEC, we see an initial decrease in resistance, a minimum at 6 wt% FEC, followed by an increase. It is the charge transfer resistance that changes the most with changing FEC concentrations (109 vs $82\ \Omega\ \text{cm}^2$ for LP57 and LP57 + 6% FEC, respectively). We anticipate that the FEC improves the overall resistance because of the composition of the graphite SEI becomes more rich in LiF and Li_2CO_3 , which together are known to form an SEI which is more conductive than an SEI consisting of only the individual components.

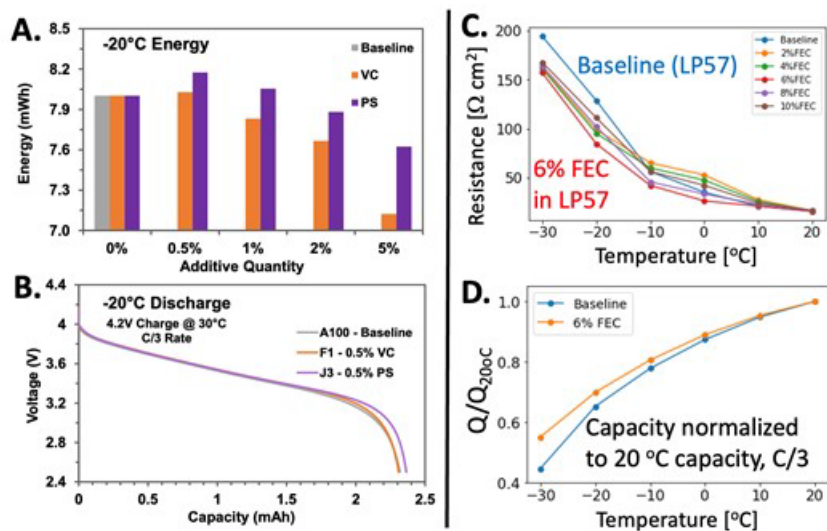


Figure XIV.1.4 Performance comparisons of lithium-ion cells fabricated with LP57 baseline electrolyte of 1.0M LiPF_6 and additives as a function of temperature. A. Cell energy density at -20°C for cell that contain LP57 (baseline) with various amounts of vinylene carbonate (VC) or propane sultone (PS) added. B. Voltage profiles of 0.5 wt% VC and PS cells compared to LP57 cells. C. Total cell resistance as a function of temperature for cells that contain LP57 and the reported wt% fluoroethylene carbonate (FEC). D. Capacity as a function of temperature of cells comprised of either LP57 or LP57 + 6wt% FEC normalized to their capacity at 20°C .

Changing the electrolyte solvent. Gamma butyrolactone (GBL)-substitution for EC was initially studied in this project due to GBL's high dielectric constant, wide liquid temperature range, and relatively low viscosity compared to EC, perhaps making electrolyte comprised of GBL better suited for low temperature performance. However, we found that electrolytes that contained GBL had substantially worse capacity fade and interfacial resistance at the graphite anode than LP57 at all temperatures. Nevertheless, we surprisingly found that GBL-rich electrolytes actually reduce the interfacial resistance at the NMC cathode. To investigate the impact of electrolyte on cycled cells, we made symmetric cells of cathodes and anodes extracted from full cells cycled with LP57 electrolyte. The symmetric cells (Gr|Gr and NMC|NMC) were prepared with either LP57 or 1M

LiPF₆ in EC/GBL/EMC 1/2/7 wt. (EG12), which allowed a comparison of how each electrolyte impacted the cycled electrodes. At 30°C, the resistance of the symmetric cycled cells is very similar for the cathode symmetric cells when LP57 and EG12 electrolyte are added to the reconstructed symmetric cells, with the total cell resistance of the EG12 cell (25 Ωcm²) being slightly lower than that of the LP57 cell (30 Ωcm²). However, at -20°C, the charge transfer resistance of LP57 (4000 Ωcm²) is almost four times greater than that of the EG12 cell (Figure XIV.1.5B). For the anode symmetric cells, the charge transfer resistance of LP57 is roughly half of the EG12 cell, but the EG12 cell is only has a charge transfer resistance of 200 Ωcm² (Figure XIV.1.5A). Since the cathode symmetric cell charge transfer resistance is over 10 times that of anode symmetric cell resistance, we reconfirmed that the cathode resistance is the dominant resistance in full cells at -20°C. It is possible that although the cathode charge transfer resistance is improved with EG12, the electrolyte conductivity and diffusion transport is worse, and this is limiting the access to capacity in EG12 cells. Therefore, EG12 may be good for pulse power but no sufficient for steady removal of energy.

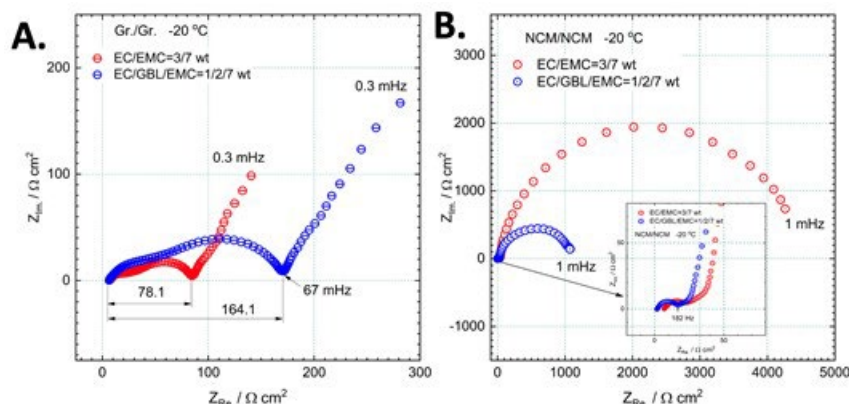


Figure XIV.1.5 EIS of symmetric coin cells comprised of electrodes harvested from pouch cells previously cycled in LP57 electrolyte but transferred to symmetric coin cells with either LP57 or EG12 as the electrolyte. A. Graphite|graphite symmetric cells at -20°C, B. NMC|NMC symmetric cells at -20°C.

Molecular dynamics simulations to understand ion solvation and dynamics. In FY21, we completed our studies to understand how ion dynamics and ion solvation are impacted by temperature and solvent choice, ultimately publishing this work in the Journal of the Electrochemical Society (*J. Electrochemical Society* (2021) 168, 080501). We used classical molecular dynamics (MD) simulations to probe the solvation and transport properties of the LP57 electrolyte, allowing us to decouple the transport and thermodynamic phenomena impacting low temperature performance. Broadly speaking, ionic conductivity is influenced by two factors: the concentration of free charge carriers and the speed at which free charge carriers migrate in solution. These factors are in turn influenced by the extent of ion association, the solvent dielectric constant, the size and shape of the charge-carrying species, and the solvent viscosity, some of which may be dependent on temperature. We have sought to identify the molecular processes influencing low temperature ionic conductivity and evaluate existing hypotheses in the literature.

The number of free charge carriers in solution is dictated by the ion association behavior of the electrolyte. However, predicting the dependence of ion association on temperature is not straightforward, and contradictory arguments have been presented in the literature. While ion association is very difficult to quantitatively assess from experiment, molecular dynamics simulations are well-suited to answer these questions. Our results suggest that ion pairing decreases as temperature decreases (Figure XIV.1.6), most likely due to the higher solvent dielectric constant at low temperatures. Furthermore, we find no evidence of an increased fraction of negative triple ions at low temperatures. Previous experimental work has hypothesized that these negatively charged aggregates may contribute toward a negative cation transference number in this systems. Our simulations, however, yield a transference number which is positive and roughly independent of temperature. We thus conclude that solvent viscosity, not ion association, is the dominant factor contributing to poor ion transport at low temperature. We demonstrate based on experimental data that the solvent diffusion

coefficient (Figure XIV.1.6C) can be used as a reasonable proxy for solvent viscosity in these systems. As temperature decreases, the self-diffusion coefficient of all species declines significantly. Notably, EMC exhibits the fastest self-diffusion, followed by the second solvent component, EC. This may be a consequence of the lower viscosity of neat EMC compared to EC and the relatively larger fraction of EMC that exists within the bulk solvent. Since EMC is in much larger abundance than EC, a greater proportion of EMC molecules are not involved in Li ion solvation, which is expected to increase the average self-diffusivity of EMC.

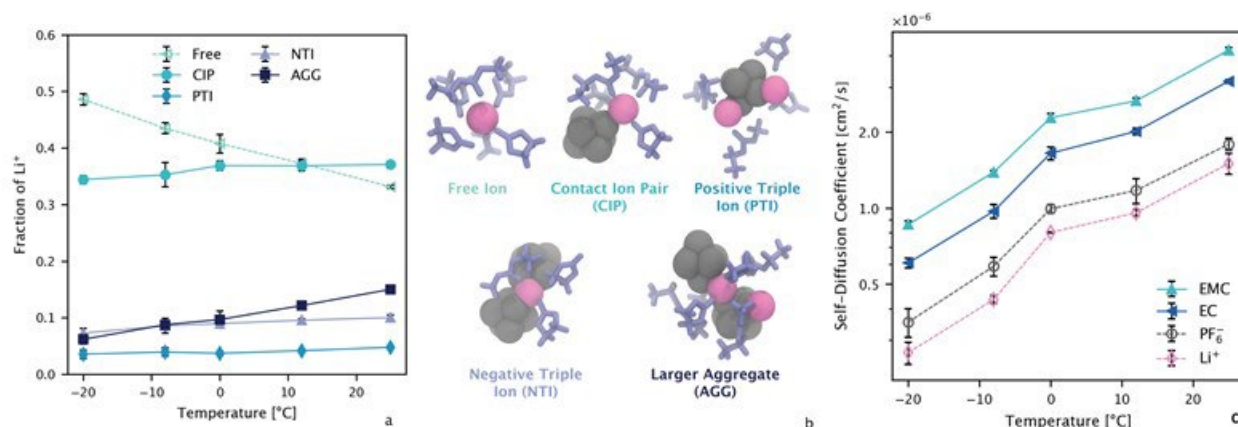


Figure XIV.1.6 Ion speciation and diffusion trends in 1M LiPF_6 in 3:7 EC/EMC computed from MD simulations. (a) The fraction of lithium ions in each ion speciation state as a function temperature. (b) Schematics representing the ion speciation states depicted in (a): free ions, contact ion pairs (CIP), positive triple ions (PTI), negative triple ions (NTI), and larger aggregates (AGG). Pink spheres represent Li ions, grey clusters represent PF_6^- anions, and purple molecules represent solvent species. (c) Self-diffusion coefficients of EC, EMC, PF_6^- and Li^+ in 1M LiPF_6 in 3:7 EC/EMC computed by MD as a function of temperature.

We have additionally explored the implications and viability of using γ -butyrolactone (GBL) as a co-solvent to create novel, EC-lean electrolytes. Via computation of static and dynamic transport properties, we find that while GBL reduces solvent viscosity, it promotes greater ion aggregation within the electrolyte. The competition of these two factors results in ionic conductivity values comparable to that of the baseline electrolyte. We further observe that GBL does not shift Li ion transport mechanisms towards more structural diffusion, and we suggest that co-solvents with more dissimilar chemistry to EC may enable a shift to faster diffusion modes. We expect that the molecular underpinnings of low temperature transport phenomena clarified in the present work will inform the development of superior low temperature electrolytes in future milestones.

Conclusions

The key conclusions from our research this year are:

1. Charge transfer resistance at low temperatures originates from both the graphite anode and NMC cathode, with the anode charge transfer resistance dramatically increasing from room temperature to -20°C.
2. The optimal concentration for LiPF_6 in 3:7 EC:EMC for reduced interfacial resistance is 0.85M, which provides close to a 4 EC/ Li^+ ratio, implying that this concentration provides an optimal solvation shell around the Li^+ for charge transfer.
3. While VC and PS provide only minor improvements in energy density at low temperatures when used as additives, FEC as an additive provides a sizable boost in capacity due to a reduction in charge transfer resistance when it is employed.

4. GBL as a co-solvent generally reduces cell performance compared to LP57 due to a large interfacial resistance at the graphite anode. However, it also reduces interfacial resistance at the NMC cathode, the cause of which we will pursue in FY22.
5. Conductivity decreases as a result of increasing solvent viscosity rather than increased ion pairing, which counterintuitively decreases with decreasing temperature.

Key Publications

1. Ringsby, A. J.; Fong, K. D.; Self, J.; Bergstrom, H. K.; McCloskey, B. D.; Persson, K. A. "Transport phenomena in low temperature lithium-ion battery electrolytes." *Journal of the Electrochemical Society* (2021) 168, 080501.
2. Hubble, D.; Brown, D. E.; Lau, J.; McCloskey, B. D.; Liu, G. "Liquid electrolyte development for low-temperature lithium-ion batteries." *Energy & Environmental Science*, accepted (2021).

Acknowledgements

This section was coauthored by co-PIs Kristin Persson, Gao Liu, Nitash Balsara, Vincent Battaglia, Robert Kostecki, and Wei Tong, as well as Kara Fong, Alexandra Ringsby, David Brown, Dion Hubble, Yanbao Fu, and Triesha Singh. We also thank Bryant Polzin, Andrew Jansen, and their CAMP Facility colleagues for providing the graphite and NMC622 electrodes used in our studies.

XIV.2 Fluorinated Solvent-Based Electrolytes for Low Temperature Li-ion Battery (ANL)

Zhengcheng (John) Zhang, Principal Investigator

Argonne National Laboratory
9700 South Cass Avenue
Lemont, IL 60439
E-mail: zzhang@anl.gov

Mallory Clites, DOE Technology Development Manager

U.S. Department of Energy
E-mail: Mallory.Clites@ee.doe.gov

Start Date: October 1, 2019
Project Funding: \$400,000

End Date: September 30, 2023
DOE share: \$400,000

Non-DOE share: \$0

Project Introduction

Electric vehicles require Li-ion batteries (LIB) that not only have high energy/power densities at low cost, but also can achieve superior performances at low temperature (LT) environment ($< 0^{\circ}\text{C}$). However, current battery technology has not yet met the satisfactory LT performance requirement, in large part due to the limitation in the electrolyte and the electrolyte-derived electrode/electrolyte interfaces. Particularly at LT, the electrolyte ionic conductivity is significantly reduced and the interface impedances are significantly increased, [1] severely limiting the energy/power of LIB and potentially causing undesired lithium plating. This project aims to improve the electrolyte performances at LT using fluorinated solvents.

Objectives

The objective is to develop electrolytes that enable LIB to deliver $> 70\%$ of usable energy at -20°C compared to the normal battery operating temperature (30°C) at C/3 rate, and to achieve excellent cycling performances and calendar life at high temperatures ($40\sim 60^{\circ}\text{C}$).

Approach

Our first approach is to use fluorinated carbonates as co-solvents for the state-of-the-art (SOA) electrolyte. Due to the weaker polar-polar interaction in fluorine-containing groups, fluorinated carbonates are anticipated to show lower melting points than their non-fluorinated counterparts, which can be beneficial for LT application. Moreover, our previous studies demonstrated that fluorinated carbonates can significantly improve high temperature cycling performances of LIB. [2],[3],[4] Thus, incorporating fluorinated carbonates into the SOA electrolyte can potentially improve the performances of LIB at both low and high temperature.

Our second approach is to use fluorinated carboxylate esters as single solvents with solid-electrolyte interphases (SEI)-forming additives. Carboxylate esters generally have very low melting points, good dielectric constants, and low viscosities; thus, it is anticipated that carboxylate esters and its fluorinated derivatives can likely maintain excellent ionic conductivities at LT. Previous studies have reported the use of carboxylate esters or fluorinated carboxylate esters as co-solvents in the SOA electrolyte for LIB; [5],[6] however, their use as single solvents is less explored. The major challenge of using carboxylate esters is that carboxylate esters cannot form stable graphite SEI, and thus SEI-forming additives are required.

Results

During the normal operation of a lithium-ion battery, electrode reaction kinetics are retarded by various factors, and among them there are three main overpotentials: 1) activation overpotential (η_{act}), 2) concentration overpotential (η_{conc}), and 3) Ohmic resistance. Since ohmic resistance is largely dominated by the ionic conductivity of electrolyte and not the electrodes, we only considered the activation overpotential and

concentration overpotential which directly affect the kinetics on electrochemical reaction in lithium-ion battery system. Figure XIV.2.1a shows the evolution of theoretical overpotential with current density. Activation overpotential can be expressed by the classical Butler-Volmer equation. Furthermore, we further identified that the interface of graphite electrode affects more sensitively to performance than that of $\text{LiNi}_{0.6}\text{Mn}_{0.2}\text{Co}_{0.2}\text{O}_2$ (NMC622) electrode, supported by the fact that graphite half-cell with Gen2 retained only 7% of capacity at -20°C with respect to that at 25°C , while NMC622 half-cell showed a relatively high capacity retention of 64% Figure XIV.2.1b and Figure XIV.2.1c).

To validate the above theory, we selected a nitrile-based electrolyte due to their high ionic conductivities. 18-19 Butyronitrile (BN) containing electrolytes: BN/FEC (1M LiPF_6 in BN/FEC (75/25 v/v)) and BN/EC+FEC (1M LiPF_6 in BN/EC (75/25 v/v) + 5 wt% FEC) were studied and compared with the conventional electrolyte Gen 2 which is 1.2 M LiPF_6 EC/EMC (3/7 w/w). Figure XIV.2.2a shows the ionic conductivities of these electrolytes at various temperatures. While Gen 2 had the lowest ionic conductivity of $7.5 \times 10^{-3} \text{ Scm}^{-1}$ at 20°C , BN/FEC and BN/EC+FEC showed much higher ionic conductivity of 13×10^{-3} and $11.6 \times 10^{-3} \text{ Scm}^{-1}$ at 20°C , respectively, due to the high dielectric constant and the low viscosity BN present in the electrolytes. In addition, the activation energy (E_a) was calculated from the Arrhenius plots and shown in Figure 2a. Compared to a high activation energy of 6.3 kJ mol^{-1} for Gen 2, BN/FEC and BN/EC+FEC electrolytes showed low activation energy of 4.5 kJ mol^{-1} , indicating both can maintain high ionic conductivity at further low temperatures. The high ionic conductivity and low activation energy of BN-based electrolytes result in a low concentration overpotential at low temperatures.

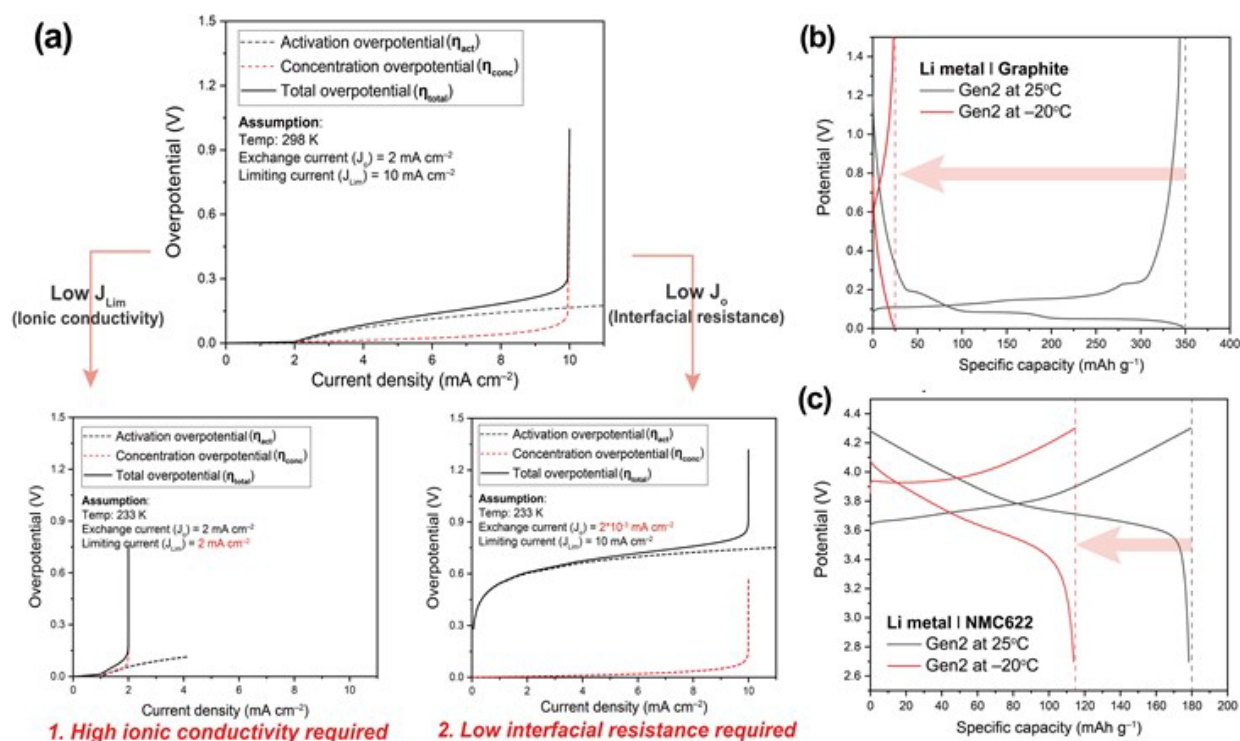


Figure XIV.2.1 (a) Theoretical overpotential evolution depending on current density. Limiting factors of electrolytes at low temperatures; (1) ionic conductivity and (2) interfacial resistance. Voltage profiles of (b) graphite and (c) NMC622 half cells with Gen2 at 25°C or -20°C .

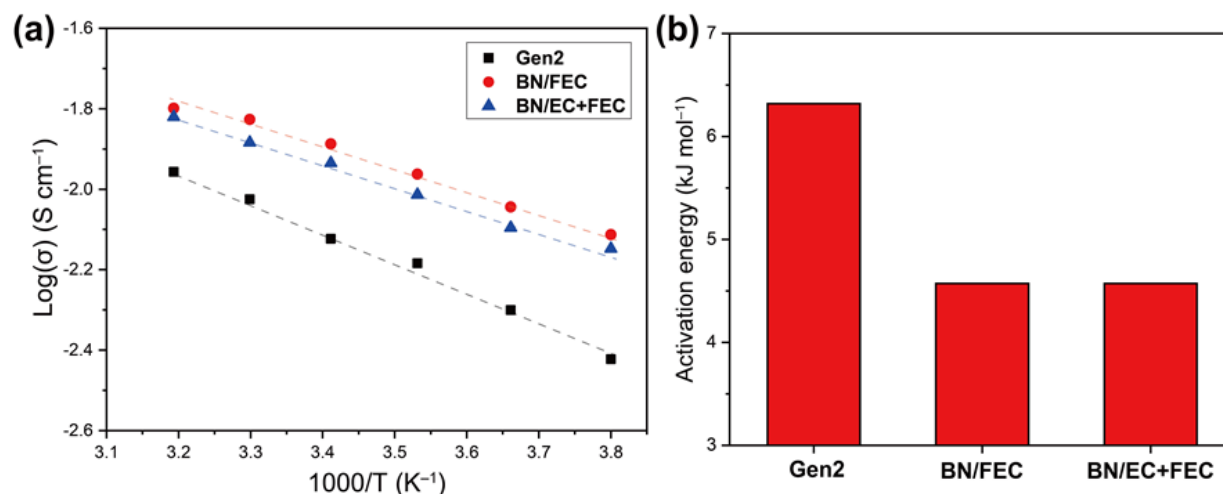


Figure XIV.2.2 (a) Ionic conductivity of electrolytes (Gen2, BN/FEC, and BN/EC+FEC) at various temperatures and (b) their activation energies (E_a).

Since interfacial resistance is largely determined by solid-electrolyte-interface (SEI), we analyzed the formation of SEI by various characterizations (Figure XIV.2.3). The lowest unoccupied molecular orbital (LUMO) energy level correlates to the thermodynamics of the electrochemical reduction on the anode surface, and calculated reduction potentials based on LUMO energy levels of BN, EC, FEC were calculated to -0.244, -0.313 and -0.386 eV, respectively. This trend in reduction potentials is well matched with the reduction peak at 3.1, 3.0, and 2.65 V in the dQ/dV plots of NMC622/graphite full-cells during the first charging cycle as shown in Figure XIV.2.3b. It is worth to note that BN solvent itself could not form a stable SEI layer, and BN/EC (75/25 v/v) co-solvent also showed a low initial Coulombic efficiency (CE) due to the close reduction potential EC and BN. However, the robust SEI layer can be formed by adding 5 wt% FEC as additive to BN/EC solvent electrolyte. Large contribution of EC to SEI layer formation is still convinced by the fact that coordination number of EC (0.55) is much higher than FEC (0.03) in BN/EC+FEC electrolyte (Figure XIV.2.3c).

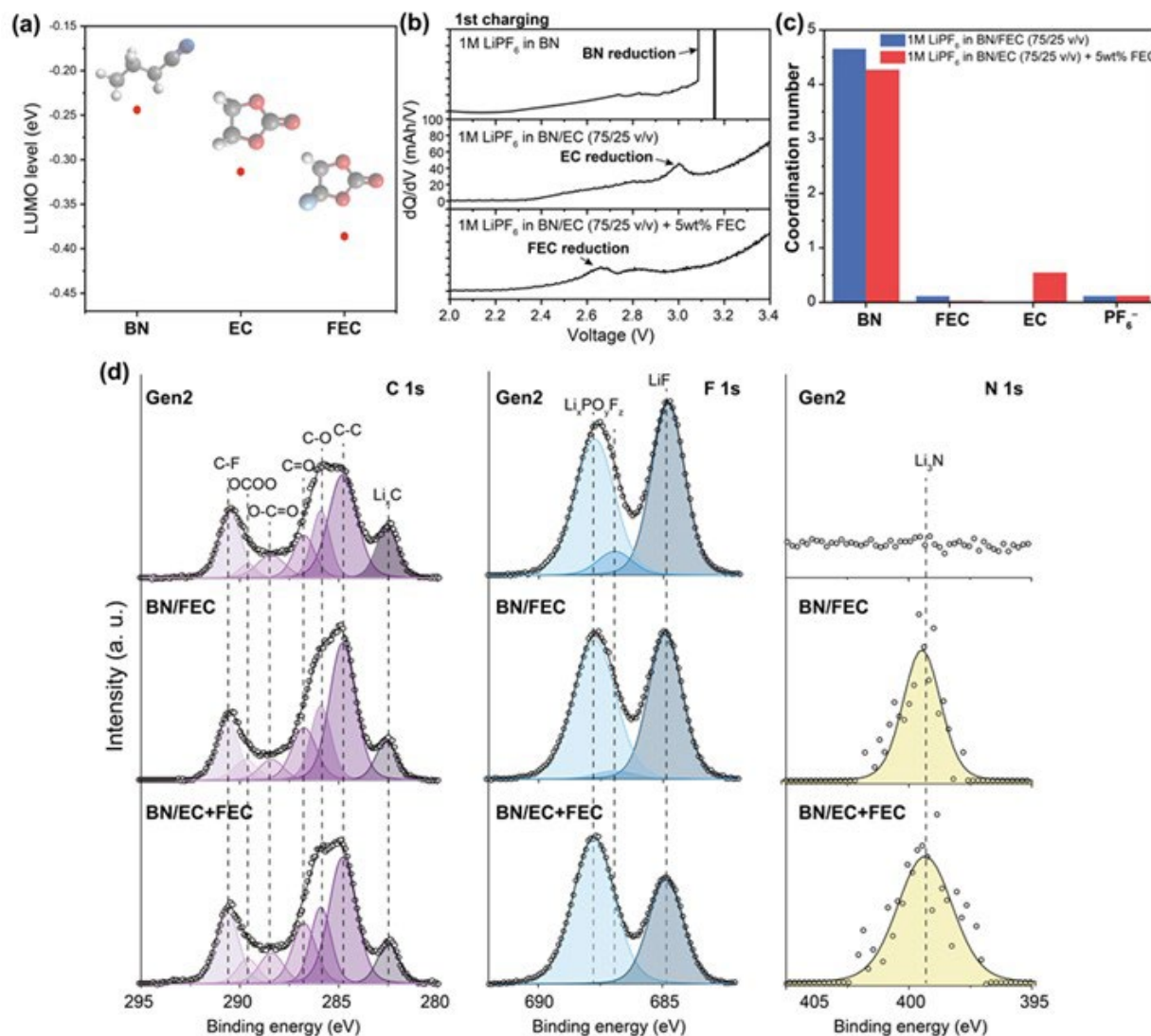


Figure XIV.2.3 (a) LUMO levels of BN, EC, and FEC. (b) dQ/dV profiles of 1st charging cycle with different electrolytes. (c) Coordination numbers of electrolytes at 25°C. (d) XPS spectra of C 1s, F 1s, and N 1s branches of graphite electrodes after three C/10 formation cycles with different electrolytes.

The effect of the electrolytes on the chemical compositions of SEI layers was examined by X-ray photoelectron spectroscopy (XPS) after three formation cycles (Figure XIV.2.3d). The peaks in C 1s branch at 289.6, 288.4, 286.8, 285.8, and 284.8 eV are assigned to OCOO, O=C=O, C=O, C-O-C, and C-C, respectively, and are attributed to the decomposition of carbonates such as EC or FEC. There was no significant difference between Gen2, BN/FEC, and BN/EC+FEC in C 1s branch, sharing the high portion of carbonate-derived functional groups. In the case of F 1s and N 1s branches, the peaks at 687.8, 684.7, and 399 eV are assigned to Li_xPO_yF_z, LiF, and Li₃N, respectively. Compared to Gen2, the SEI layer with BN/FEC and BN/EC+FEC included Li₃N which is known to have a high ionic conductivity. In addition, BN/EC+FEC showed a lower portion of LiF in SEI layer than BN/FEC.

In order to measure the interface resistance of electrolytes, we carried out electrochemical impedance spectroscopy (EIS) analysis depending on various temperatures (Figure XIV.2.4). We measured EIS of each cell charged to 3.7 V at 50% state of charge (SOC) after three formation cycles. As temperature decreases, the total resistance increases due to the lower thermal energy for electrochemical reaction. To separate each

resistance contribution to the performance, we deconvoluted the measured data with an equivalent circuit of one resistor and four resistors with constant phase elements which are bulk electrolyte (R_{elect}), SEI layer (R_{SEI}), CEI layer (R_{CEI}), charge-transfer at anode ($R_{\text{ct-anode}}$) and cathode ($R_{\text{ct-cathode}}$). We matched the frequencies of each resistance component by using anode and cathode symmetric cells. EIS data of electrolytes were well fitted with the equivalent circuit at -15°C verifying the fitting model.

In Figure XIV.2.4a-c, BN/FEC and BN/EC+FEC showed significantly smaller total resistances compared to Gen2 at all temperatures, indicating their lower interfacial resistance and overpotential during operating. When it comes to each resistance contribution, BN/EC+FEC had a much smaller $R_{\text{ct-anode}}$ than BN/FEC due to the modified SEI layer with a lower portion of LiF. We further analyzed the temperature effect on each resistance component by the Arrhenius plots (Figure XIV.2.4d-f). In the plots of $\text{Log } R$ vs. $1000/T$, the slope indicates an activation energy for the reaction, meaning the temperature dependence of the reaction. As the activation energy is higher, the reaction is slower, and the resistance becomes higher at low temperature. In the case of Gen2, the activation energies of R_{SEI} , R_{CEI} , $R_{\text{ct-anode}}$ and $R_{\text{ct-cathode}}$ are 0.8, 11.3, 24.4 and 25.3 kJ mol^{-1} , respectively, showing that charge-transfer resistance becomes a main limiting factor at low temperature. While BN/FEC has a similar $R_{\text{ct-anode}}$ activation energy of 24.3 kJ mol^{-1} with Gen2, BN/EC+FEC has a lower activation energy of 22.1 kJ mol^{-1} . Considering that the overpotential on graphite is a limiting factor at low temperature, the significantly lower $R_{\text{ct-anode}}$ activation energy of BN/EC+FEC enables it to exhibit superior rate capabilities at low temperature, confirming the effect of modified SEI layer.

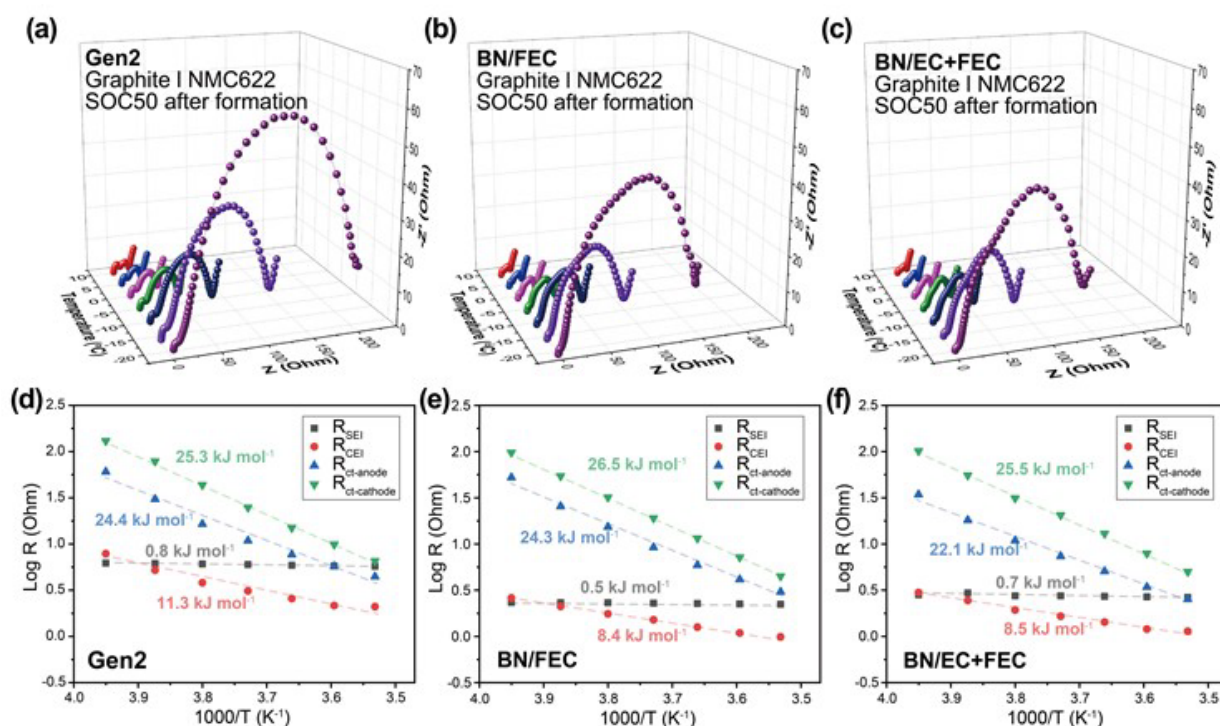


Figure XIV.2.4 Nyquist plots of cells with (a) Gen2, (b) BN/FEC, and (c) BN/EC+FEC electrolyte at various temperatures. Arrhenius plots of R_{SEI} , R_{CEI} , $R_{\text{ct-anode}}$, $R_{\text{ct-cathode}}$ for cells with (d) Gen2, (e) BN/FEC, and (f) BN/EC+FEC electrolyte.

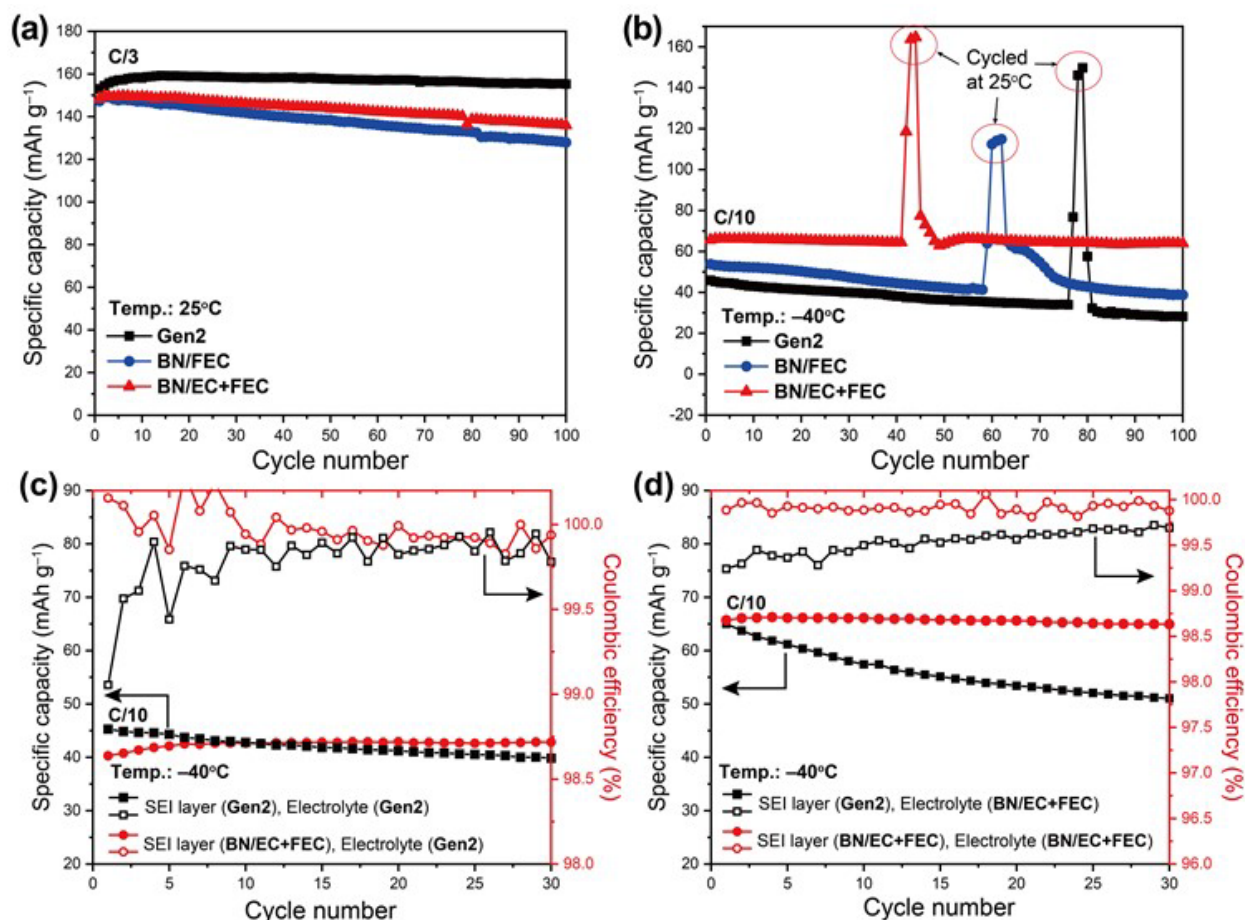


Figure XIV.2.5 Cyclability with electrolytes at (a) 25 °C and (b) -40 °C. Cyclability and coulombic efficiency of (c) Gen2 and (d) BN/EC+FEC electrolyte with Gen2 or BN/EC+FEC SEI layer at -40 °C.

When the cells were subjected to galvanostatic cycling tests at a rate of C/3 at room temperature (Figure XIV.2.5a), while Gen2 showed stable cyclability retaining 98% of its initial capacity after 100 cycles, BN/FEC and BN/EC+FEC exhibited a slight decaying only maintaining 86 and 91%, respectively, due to the continuous BN reduction during cycling. It is also supported by the lower CEs of BN/FEC and BN/EC+FEC compared to that of Gen2. However, when C/10 was applied at -40°C (Figure XIV.2.5b), BN/EC+FEC exhibited a remarkably high capacity retention of 97% after 100 cycles, whereas Gen2 exhibited only 61% after 100 cycles. Considering that a large overpotential at anode causes Li plating lowering CEs and capacity retention, the low interfacial resistance of BN/EC+FEC enabled it to stably operate at low temperature compared to Gen2.

In order to prove the relation of SEI layer and cyclability, we tested cells with preformed SEI layer by different electrolytes of Gen2 and BN/EC+FEC (Figure XIV.2.5c, d). To note, after three formation cycles at room temperature, the cells were reassembled with different electrolytes and cycled at -40°C. In the case of Gen2 electrolytes (Figure XIV.2.5c), while the cell with SEI layer by Gen2 showed a slight degradation maintaining 87% of initial capacity during 30 cycles, the cell with SEI layer by BN/EC+FEC didn't show any capacity decay. In the case of BN/EC+FEC electrolytes (Figure XIV.2.5d), both cells showed a high initial capacity of 66 mAhg⁻¹ compared to 45 mAhg⁻¹ of Gen2. While the cell with SEI layer by Gen2 exhibited a severe decaying with 77% of capacity retention over 30 cycles, the cell with SEI layer by BN/EC+FEC displayed a high capacity retention of 98% with a high average CE close to 100%, proving the improved stability of SEI layer at low temperature is higher than that of Gen 2 electrolyte (67%). These results suggest that using carboxylate esters as the solvent can be highly beneficial for LT application, especially below -40°C.

Fluorinated carboxylate esters-based electrolyte suffers from low capacities/energies, the cause of which is currently under investigation.

Conclusions

In conclusion, we have revealed that the overpotential of graphite limits the performance at low temperature due to its close electrochemical reaction potential to cut-off voltage and Li plating. We demonstrated the importance of interface modification by employing nitrile-based electrolytes. Importantly, the SEI layer with presence of Li₃N and less portion of LiF significantly lowers the anode charge-transfer resistance with a low activation energy, resulting in superior rate capability and cyclability even at -40°C. This investigation provides a useful insight in designing electrolytes for high performance Li-ion batteries at low temperature.

References

1. Choi, J. W.; Aurbach, D., Promise and reality of post-lithium-ion batteries with high energy densities. *Nature Reviews Materials* 2016, 1 (4), 16013.
2. Etacheri, V.; Marom, R.; Elazari, R.; Salitra, G.; Aurbach, D., Challenges in the development of advanced Li-ion batteries: a review. *Energy & Environmental Science* 2011, 4 (9), 3243–3262.
3. Dunn, B.; Kamath, H.; Tarascon, J.-M., Electrical Energy Storage for the Grid: A Battery of Choices. *Science* 2011, 334 (6058), 928–935.
4. Bandhauer, T. M.; Garimella, S.; Fuller, T. F., A Critical Review of Thermal Issues in Lithium-Ion Batteries. *Journal of The Electrochemical Society* 2011, 158 (3), R1.
5. Gupta, A.; Manthiram, A., Designing advanced lithium-based batteries for low-temperature Conditions. *Advanced energy materials* 2020, 10 (38), 2001972.
6. Jow, T. R.; Delp, S. A.; Allen, J. L.; Jones, J.-P.; Smart, M. C., Factors Limiting Li⁺ Charge Transfer Kinetics in Li-Ion Batteries. *Journal of The Electrochemical Society* 2018, 165 (2), A361–A367.
7. Rodrigues, M.-T. F.; Babu, G.; Gullapalli, H.; Kalaga, K.; Sayed, F. N.; Kato, K.; Joyner, J.; Ajayan, P. M., A materials perspective on Li-ion batteries at extreme temperatures. *Nature Energy* 2017, 2 (8), 17108.
8. Ren, D.; Smith, K.; Guo, D.; Han, X.; Feng, X.; Lu, L.; Ouyang, M.; Li, J., Investigation of Lithium Plating-Stripping Process in Li-Ion Batteries at Low Temperature Using an Electrochemical Model. *Journal of The Electrochemical Society* 2018, 165 (10), A2167–A2178.

Acknowledgements

Support from Peter Faguy, Mallory Clites, and David Howell at Vehicle Technologies Office (VTO), Office of Energy Efficiency and Renewable Energy, U.S. Department of Energy is gratefully acknowledged. Argonne, a U.S. Department of Energy laboratory, is operated by UChicago Argonne, LLC under contract DE-AC02-06CH11357.

XIV.3 Synthesis, screening and characterization of novel low temperature electrolyte for lithium-ion batteries (BNL)

Xiao-Qing Yang, Principal Investigator

Brookhaven National Laboratory
Bldg. 555, Brookhaven National Laboratory
Upton, NY 11973
E-mail: xyang@bnl.gov

Enyuan Hu, Principal Investigator

Brookhaven National Laboratory
Bldg. 555, Brookhaven National Laboratory
Upton, NY 11973
E-mail: enhu@bnl.gov

Mallory Clites, DOE Technology Development Manager

U.S. Department of Energy
E-mail: Mallory.Clites@ee.doe.gov

Start Date: October 1, 2020

End Date: September 30, 2021

Project Funding: \$1,000,000

DOE share: \$1,000,000

Non-DOE share: \$0

Project Introduction

While the energy density and cost of batteries powering electric vehicles are becoming competitive with internal combustion engines, there are still several critical issues that need to be addressed. The low temperature performance of the batteries and the fast charge capability are two of them. Current lithium-ion batteries (LIB) experience a significant capacity drop down to about one fifth of its room temperature capacity at -30°C. Current LIB electrolyte is almost exclusively based on ethylene carbonate (EC) as a major solvent component due to the high dielectric constant and formation of an excellent solid-electrolyte-interphase (SEI) on the graphite anode. Unfortunately, EC has a rather high melting point (37°C), leading to significantly increased viscosity and severely decreased Li⁺ conductivity at low temperatures. LIB also has high impedance at low temperature due to the sluggish Li⁺ transport through SEI. These issues result in the much-decreased capacity and poor cyclability at low temperature. Therefore, to improve the low temperature performance of LIB, it is critical to develop new electrolyte system that is low in viscosity, high in Li⁺ conductivity, and is able to form stable and low-impedance interphase on both anode and cathode. This consortium, with team members of Brookhaven National Laboratory (BNL), Army Research Laboratory (ARL), University of Maryland (UMD), and University of Rhode Island (URI), address the low temperature electrolyte challenge through integrated approaches of theoretical calculation, electrolyte components design, synthesis, and testing, as well as advanced characterization.

Objectives

The project objective is to develop next generation electrolyte formulations that enable the Li-ion batteries to deliver >70% of room temperature energy at -20°C, while still meeting the United States Advanced Battery Consortium (USABC) Operating Environment Conditions (-30 to +52°C), fast charge capability, calendar life testing at 30, 40, 50, and 60°C.

Approach

Up to date, most low temperature electrolyte development efforts have been focused on adjusting the combination of different commercially available solvents only, and a decent low-temperature performance can only be achieved by sacrificing other properties such as high-temperature and high voltage performance. Keeping the goals of automobile application in mind, to achieve the desired low temperature performance

while maintaining other performance, we need to design new electrolyte systems using an integrated approach starting from theoretical calculations of the new electrolytes, understanding the electrolyte-electrode interphases, to the synthesis of new solvents, salts, and additives, as well as advanced characterizations of the electrolyte systems in actual battery environments. Theoretical calculations have been used to predict the transport property, electronic structure and SEI formation mechanism to propose possible candidates that have high Li^+ conductivity, good stability, as well as low-impedance SEI. These candidates have been or will be synthesized and purified for experimental validation. The new electrolyte system is subject to a series of electrochemical testing and diagnostic studies for performance evaluation and mechanistic studies. These knowledges provide feedback to the theoretical model for better understanding and more accurate predictions.

Solvent candidates to be explored include but are not limited to ethers, esters, nitriles and their fluorine-substituted derivatives. Salt candidates include lithium tetrafluoroborate (LiBF_4), lithium hexafluorophosphate (LiPF_6), lithium bis(fluorosulfonyl) imide (LiFSI), lithium bis(trifluoromethanesulfonyl) imide (LiTFSI), lithium bis(oxalato) borate (LiBOB), and lithium difluoro(oxalato)borate (LiDFOB) etc. Additive candidates include vinylene carbonate (VC), fluoro ethylene carbonate (FEC), phosphites, phosphates, sulfones, sultones, and sulfates.

New electrolyte systems are subject to a series of characterizations and theoretical calculations such as Infrared and Raman spectroscopies as well as x-ray and neutron pair distribution function (xPDF and nPDF) analysis. The results have been analyzed together with molecular dynamic (MD) calculations to understand the structure of the electrolyte. The SEI and cathode-electrolyte-interphase (CEI) components are subject to characterizations such as high energy x-ray photoelectron spectroscopy (HAXPES), resonant inelastic x-ray scattering (RIXS), x-ray absorption spectroscopy (XAS), x-ray photoemission electron microscopy (XPEEM), as well as cryo transmission electron microscopy (TEM) to obtain information such as structure, depth-profiling, and chemical distribution.

Results

In FY2021, significant progress has been made by this consortium. Different electrolyte systems with new solvents, new salts, and new additives have been designed, tested, and characterizes. Several systems have been selected which show very promising electrochemical performance at a wide temperature range, especially at -20°C . Two research papers have been published (on *ACS Applied Materials and Interface* and *Journal of Electrochemical Society*) in FY2021. More research papers and one review paper about low temperature electrolyte are under preparation for publication.

1. Low-temperature electrolytes development at BNL

At **BNL**, isoxazole (IZ) is identified to be a promising solvent for low temperature application. As shown in Figure XIV.3.1a, Figure XIV.3.1b and Figure XIV.3.1c, the ionic conductivity of IZ based electrolyte was more than doubled comparing to the baseline electrolyte using ethylene carbonate-ethyl methyl carbonate (EC-EMC) in a temperature range between -20°C to 20°C . As shown in Figure XIV.3.1d, Figure XIV.3.1e, and Figure XIV.3.1f, the new IZ based electrolyte using Lithium difluoro(oxalato)borate (LiDFOB) salt and fluoroethylene carbonate (FEC) additive can form stable solid electrolyte interphase (SEI) on the surface of graphite anode and cells using new electrolyte with 1M LiDFOB in FEC:IZ (1:10, vol%) solvents demonstrated very high 187.5 mAhg^{-1} reversable capacity at -20°C while the baseline electrolyte (1M LiPF_6 in EC/EMC(3/7)) only delivered 23.1 mAhg^{-1} reversible capacity.

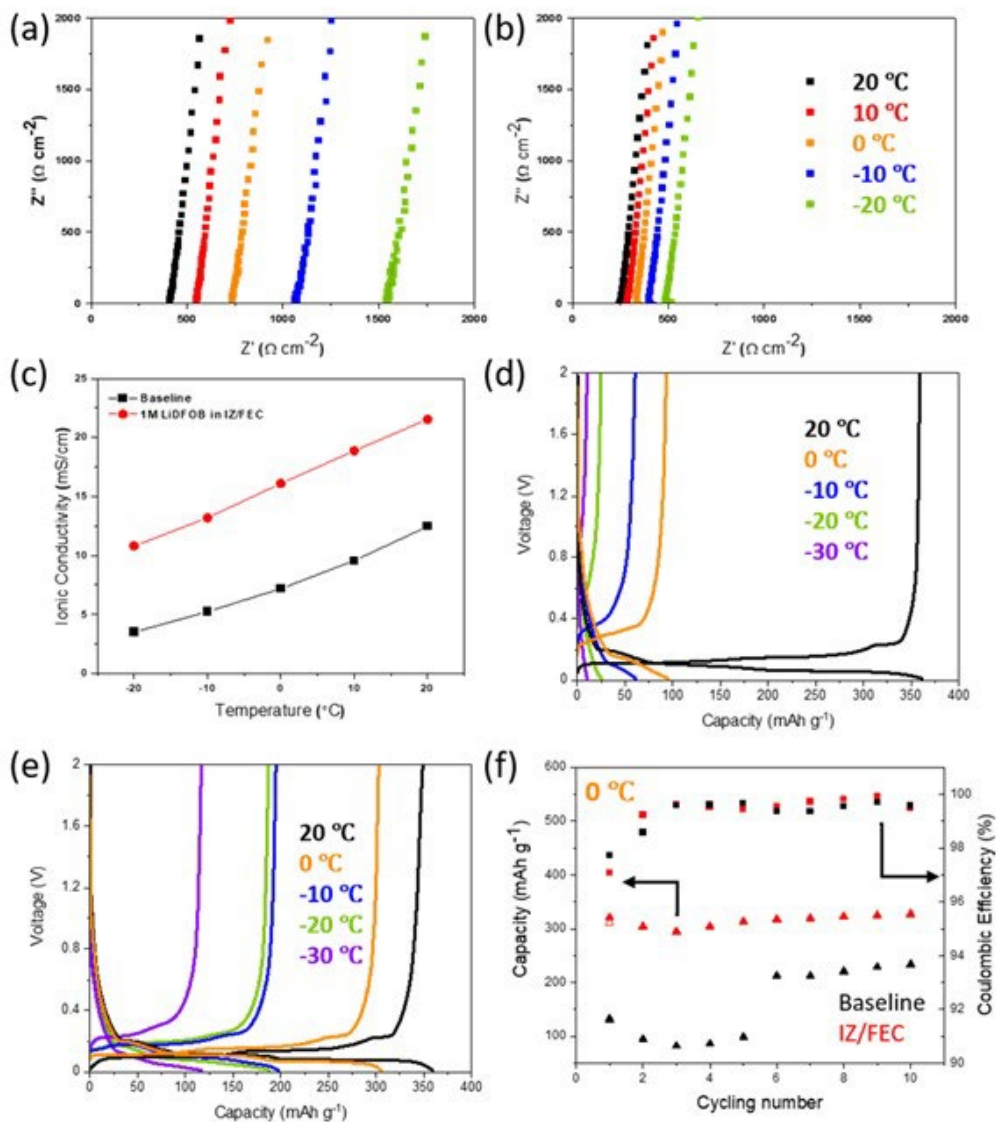


Figure XIV.3.1 Electrochemical impedance spectroscopy (EIS) of (a) 1M LiPF₆ in EC/EMC (3/7) (baseline). (b) 1M LiDFOB in isoxazole/FEC (10/1, vol%) electrolytes and (c) comparison of ionic conductivity at different temperature of these two electrolytes. (d) Voltage profiles of Li/graphite cell using 1M LiPF₆ in EC/EMC (3/7) and (e) 1M LiDFOB in isoxazole/FEC (10/1, vol%) at various temperatures at C/10. (f) Cycling performance of Li/graphite cell using 1M DFOB in isoxazole/FEC (10/1, vol%) at 0 °C at C/10 rate compared with baseline electrolyte.

2. SEI characterization at URI

Aimed to understand the improved cycling performance of IZ based electrolytes using LiDFOB salt and FEC additive, surface film on graphite electrodes before and after formation cycling at room temperature was investigated by X-ray Photoelectron Spectroscopy (XPS). C1s, O1s, F1s and B1s spectra of graphite surface film formed in cells containing 1.2 M LiPF₆ in EC:EMC (3:7 v/v%) (Baseline), 1M LiDFOB in FEC:IZ (1:9 v/v%) are shown in Figure XIV.3.2. The XPS spectra of the surface of the anodes cycled with LiDFOB electrolytes are significantly different from the XPS spectra observed for the cells cycled in baseline electrolyte. The C1s, O1s, F1s, B1s and N1s XPS spectra of the pristine graphite and electrodes cycled using baseline and 1M LiDFOB in IZ/FEC (10/1, vol%) electrolytes show that the formation of an oxalates rich SEI in IZ-based electrolytes might be the main contributor to the enhanced SEI stability and improved cycling performance of the IZ based electrolyte.

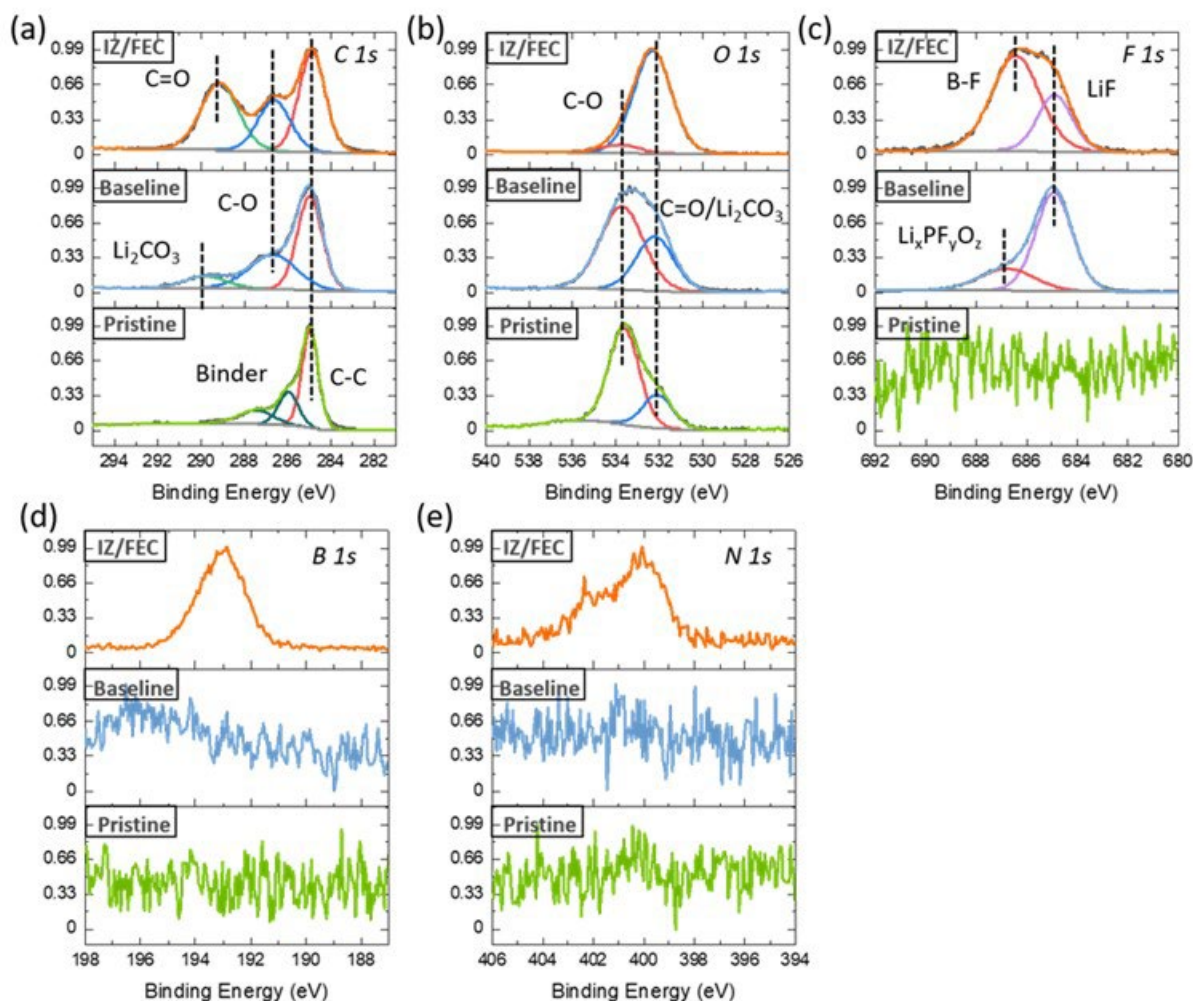


Figure XIV.3.2 XPS spectra of graphite electrode before (pristine) and after formation cycling using baseline electrolyte (1.2 M LiPF₆ in EC:EMC (3:7 v/v)) and IZ/FEC electrolyte (1M LiDFOB in IZ/FEC (10/1, vol%)) for (a) C1s, (b) O1s, (c) F1s, (d) B1s and (e) N1s spectra.

3. New low temperature electrolytes developed at UMD using LiFSI salt in EMC-TTE co-solvents

UMD team developed a new low temperature electrolyte using LiFSI in EMC-TTE co-solvents (TTE-based electrolyte) and compared it with standard electrolyte (1M LiPF₆ in EC_{0.5}-DMC_{0.5}, SE) in NMC811||Graphite full cells. As shown in Figure XIV.3.3, the NMC811||Graphite cell can maintain 75.4% of its initial capacity while the capacity of the cell using standard electrolyte (SE) quickly decays to only 58.9% of its initial capacity after 200 cycles at room temperature at a current density of 1/3C (Figure XIV.3.3a). When the NMC811||Graphite with TTE-based electrolyte is charged/discharged at -20°C with the same current density, ~77% of its room-temperature capacity could be delivered. The capacity retention of the cell remains over 50% at a higher current density of 2/3C at the same temperature (Figure XIV.3.3b). Figure XIV.3.3c show that NMC811||Graphite can remain 91.1 mA h g⁻¹ capacity after 100 cycles at a current density of 1/3C at 50°C. At -40°C, the cell using TTE-based electrolyte can deliver ~54.5% and 78.0% of its room-temperature capacity at a current density of 1/10C and 1/20C, respectively (Figure XIV.3.3d). Therefore, the TTE-based electrolyte enables NMC811||Graphite work at -20°C with a large capacity retention, while keeping good battery performance in a wider temperature range between -40°C +50°C.

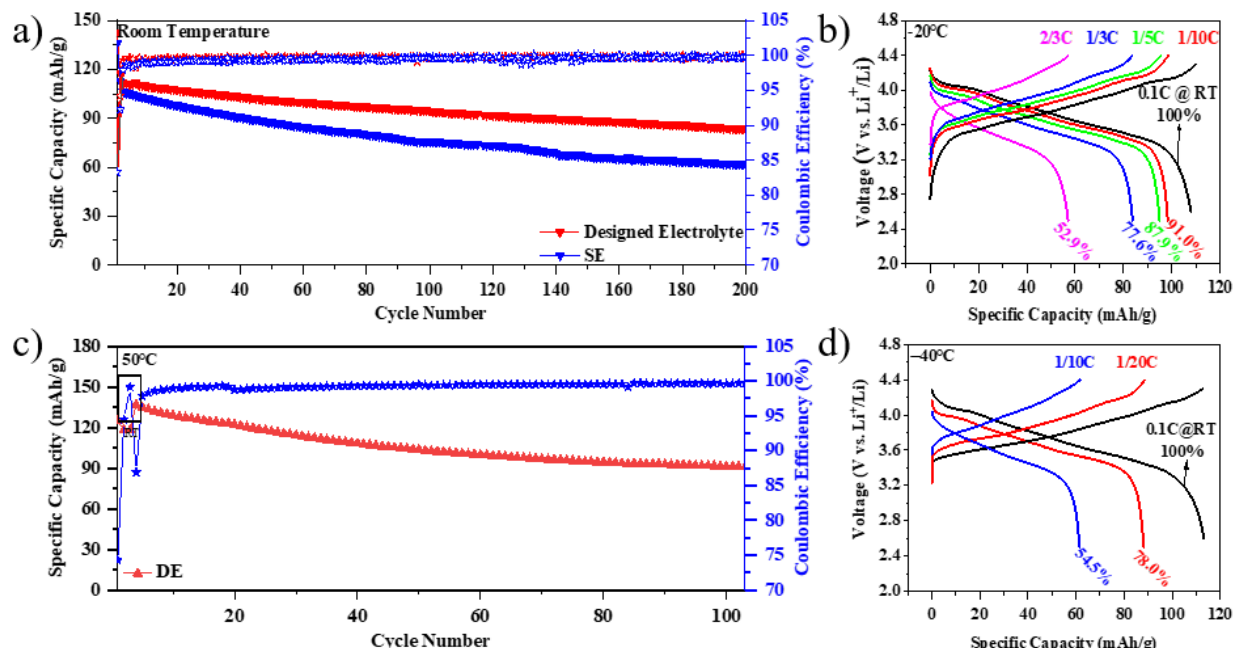


Figure XIV.3.3 Electrochemical performance of NMC811 | Graphite full cells using TTE-based electrolyte. a) The cycling performance of the NMC811 | Graphite cell at -20°C; b) The charge-discharge profile of the NMC811 | Graphite cell at -40°C with current densities of 0.05C and 0.1C; c) The cycling performance of the NMC811 | Li cell at 50°C and d) the rate capability of the NMC811 | Li cell at room temperature.

4. Molecular dynamics (MD) simulation work at ARL

Molecular modeling efforts at ARL are aimed at understanding the electrolyte structure, transport and initial stages of the SEI formation. Many-body polarizable force field (APPLE&P) was chosen for molecular dynamics (MD) simulations because it allows direct parameterization based upon quantum chemistry calculations and unlike the non-polarizable force fields does not require any empirical scaling of charges to match ion transport. Quantum chemistry (QC) calculations were performed on the TTE, TTE/Li⁺, FEC/Li⁺, LiFSI and EC/DMC/Li⁺/PF₆⁻ to validate ability of MD simulations predict baseline properties where ample experimental data are available for validation. Figure XIV.3.4 demonstrates an excellent ability of MD simulations using the revised APPLE&P force field to predict the Li⁺ solvation shell composition, diffusion coefficients of all species and temperature dependence of conductivity. MD simulations of the LiFSI-EMC_{0.5}-TTE_{0.5}-based electrolytes have been carried out based upon the optimization performed by UMD.

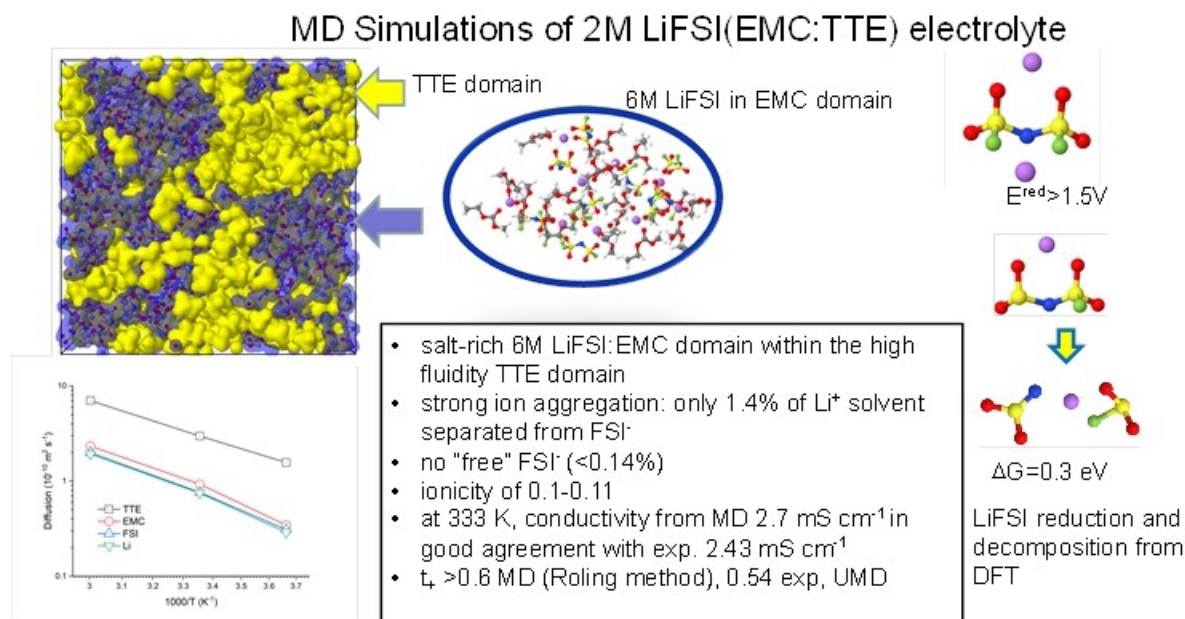


Figure XIV.3.4 MD simulations of 2.0 M LiFSI in $\text{EMC}_{0.5}\text{TTE}_{0.5}$ low temperature electrolyte

Conclusions

This project, “Synthesis, screening and characterization of novel low temperature electrolyte for lithium-ion batteries (BNL)”, has been successfully completed in FY2021. All milestones have been completed and publication record is very good.

Key Publications

1. Sha Tan, U. Nuwanthi D. Rodrigo, Zulipiya Shadike, Brett Lucht*, Kang Xu, Chunsheng Wang, Xiao-Qing Yang*, and Enyuan Hu*, “Novel Low-Temperature Electrolyte Using Isoxazole as the Main Solvent for Lithium-Ion Batteries”, *ACS Appl. Mater. Interfaces* 2021, 13, 24995–25001. DOI: 10.1021/acsami.1c05894, Publication date: May19, 2021.
2. Nuwanthi D. Rodrigo*, Sha Tan, Zulipiya Shadike, Enyuan Hu, Xiao-Qing Yang, Brett L. Lucht*, “Improved Low Temperature Performance of Graphite/Li Cells Using Isoxazole as a Novel Cosolvent in Electrolytes”, *Journal of Electrochemical Society.*, 2021, 168, 070527, DOI: 10.1149/1945-7111/ac11a6, Publication date: July 14, 2021.

XV Beyond Li-ion R&D: Metallic Lithium

XV.1 Composite Electrolytes to Stabilize Metallic Lithium Anodes (ORNL)

Xi (Chelsea) Chen, Principal Investigator

Oak Ridge National Laboratory
PO Box 2008, MS6124
Oak Ridge, TN 37830
E-mail: chenx@ornl.gov

Nancy Dudney, Principal Investigator

Oak Ridge National Laboratory
PO Box 2008, MS6124
Oak Ridge, TN, 37830
E-mail: ncdudney@gmail.com

Tien Q. Duong, DOE Technology Development Manager

U.S. Department of Energy
E-mail: Tien.Duong@ee.doe.gov

Start Date: October 1, 2018	End Date: September 30, 2021	
Project Funding (FY21): \$1,300,000	DOE share: \$1,300,000	Non-DOE share: \$0

Project Introduction

A stable lithium anode is critical to achieve high energy density batteries with excellent safety, lifetime and cycling efficiency. This study will identify the key design strategies that should be used to prepare composite electrolytes to meet the challenging combination of mechanical and chemical and manufacturing requirements to protect and stabilize the lithium metal anode for advanced batteries. The composites are composed of two solid electrolytes, a ceramic component for high ionic conductivity and high elastic modulus plus a small volume fraction of a polymer electrolyte to provide processability of a very thin, light weight and flexible electrolyte membrane. Success in this program will enable these specific DOE technical targets: 500–700Wh/kg, 3000–5000 deep discharge cycles, robust operation.

Objectives

The overall objective of this program is to prepare composites of polymer and ceramic electrolyte materials as thin membranes which have the unique combination of electrochemical and mechanical properties required to stabilize the metallic lithium anode while providing for good power performance and long cycle life. If successful, this composite electrolyte will help eliminate failure mechanisms including the formation of lithium dendrites, delamination of the lithium or cathode electrodes, and the gradual consumption of lithium due to side reactions or physical isolation.

Approach

Our earlier approach was to spray coat a slurry containing the ceramic powder along with a Li salt and dissolved polyethylene oxide (PEO). This was subsequently dried and pressed to densify the film into a homogeneous membrane with high ceramic loading of discrete particles with polymer filling the interstices. Composites were also formed by hot-pressing the dry mixtures of the ceramic, Li salt and PEO as this provided a more rapid sample fabrication to shape. For either processing route, only when the PEO was plasticized with a small organic molecule was the ceramic-polymer interface sufficiently conductive for the composite to achieve our goal for an acceptable Li ion conductivity. The interface properties were carefully

confirmed by using ideal laminated structures of the same materials used in the composites. Clearly other materials and methods were needed to further improve the composite electrolyte.

Alternatives for both the ceramic and the polymer phase are being explored with goals to: improve the percolated connectivity of ceramic, improve the Li ion conduction across polymer-ceramic interface, and enhance the Li ion transference number and conductivity in polymer. Various polymer materials were synthesized and tested, including cross-linked and gelled polymer electrolytes and single ion conducting polymers with anions bound to the polymer structure. Impedance spectroscopy together with a host of other characterizations methods are used to determine the ion associations and polymer dynamics as they affect the Li⁺ conductivity in both the neat polymer phase and in the ceramic composites. For ceramic phase, the processing methods and performance of thin sintered membranes is explored, initially with glass-ceramic LATP-based powders from Ohara Corporation, LICGCTM, then with alternatives including the garnet LLZO. The sintering process is intended to ensure a fully 3D connected pathway of the ceramic phase across and along the membrane. The porosity in the ceramic membrane will then be filled with the polymer electrolyte. If Li⁺ ion transport between the ceramic and polymer was facile, this would improve the overall homogeneity of Li ion current across the separator membrane. X-ray tomography and electron microscopy are used to determine the microstructure, and various dynamic and stress-strain tests to determine mechanical properties.

While the scientific goals are focused on addressing the composite electrolyte and interfaces, fabricating and cycling electrochemical cells is an important way to characterize the stability with Li and mechanical integrity of the electrolyte. We are seeking to identify practical processing routes to fabricate full batteries using the composite electrolytes with a composite cathode and thin lithium metal anode. The addition of a very thin single ion conducting layer, such for Lipon, may play an important role to eliminate the salt concentration polarization and provide a smooth interface for the lithium anode. These studies increase the complexity of the program but are practical approaches to improve performance and advance our appreciation for challenges to come with implementation of the solid electrolyte and Li anode technology.

Results

Results are summarized for three topics: 1. Gel composite electrolytes with improved Li⁺ transference number and cycling performance. 2. Development of a three-dimensional interconnected polymer/ceramic composite as a thin film solid electrolyte. 3. Concentration gradients in composites of binary electrolyte and single ion conductor.

1. Gel composite electrolytes with improved Li⁺ transference number and cycling performance.

In this FY we completed the gel composite electrolyte work started in 2019. We fabricated a gel composite electrolyte by incorporating a lithium aluminum titanium phosphate (LATP)-type ceramic, LICGCTM, into crosslinked polyethylene oxide (PEO)-based gel electrolyte membrane plasticized with tetraethylene glycol dimethyl ether (TEGDME). The morphology and physical appearance of the composite electrolyte prior to plasticizing is shown in Figure XV.1.1a. The effects of LICGC particles in the gel composite membrane are twofold: 1) LICGC serves as an anion receptor and immobilizes the anion TFSI⁻ in the crosslinked PEO matrix, leading to more than 2-fold increase in the Li⁺ transference number from 0.2 to 0.44 (with 50 wt% LICGC); simultaneously, it promotes Li⁺ dissociation and enhances Li⁺ mobility due to increased plasticizer to Li⁺, causing a 2-fold increase in Li⁺ conductivity (Figure XV.1.1b). A schematic of the effects of LICGC particle is shown in Figure XV.1.1c.

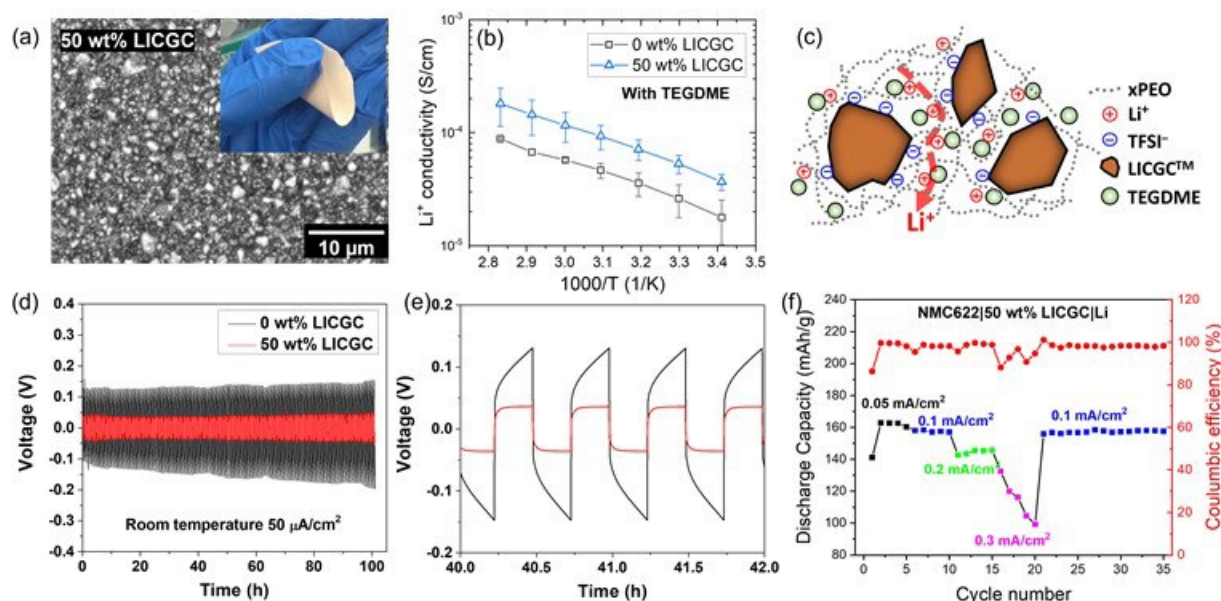


Figure XV.1.1 Gel composite electrolytes consisting of crosslinked PEO (xPEO) matrix, Lithium bis(trifluoromethanesulfonyl)imide (LiTFSI) salt, LICGC particles and TEGDME plasticizer. (a), An scanning electron microscopy (SEM) image of the composite electrolyte with 50 wt% LICGC; inset, a digital photograph of the membrane; (b), Li⁺ conductivity of gel electrolyte membranes; (c), A schematic showing the effect of LICGC particles on ion transport; (d,e), Li symmetric cell cycling at room temperature; (e) is a magnification of (d) from 40 to 42 hours of cycling; (f) Half cell cycling using the gel composite electrolyte at room temperature.

Due to the positive effects of LICGC particle on ion transport, the composite electrolyte with 50 wt% ceramic exhibited superior cycling performance against Li metal, showing lower interfacial impedance, lower overpotential and higher rate capability (Figure XV.1.1d). A close examination of the cycling profile revealed a much smaller concentration gradient in the composite electrolyte compared to the polymer electrolyte, as the former reached plateau much more quickly (Figure XV.1.1e). Half cell cycling using the composite electrolyte showed much better rate capability (0.2 mA/cm², Figure XV.1.1f) than the polymer electrolyte (0.05 mA/cm²). The transport enhancement was achieved without sacrificing the mechanical properties of the membrane, as the volume fraction of TEGDME in the composite and polymer electrolytes was relatively constant. Rather, the composite electrolyte showed significantly improved handleability.

2. Development of a three-dimensional interconnected polymer/ceramic composite as a thin film solid electrolyte.

In this FY, main efforts were focused on the integration of the 3D-interconnected composite into cells and optimize performance. Figure XV.1.2b illustrates ‘in-essence’ the half-cell assembly procedure, where the partially sintered porous ceramic tape was placed on top of a conventional PVDF-based NMC622 cathode and then infiltrated with the crosslinked PEO (xPEO) liquid precursor. This layered stack was cured together and used in the cell assembly. Plasticizer was used to soften the membrane and prevent any reaction at the Li//PE interface (not shown in schematic). Figure XV.1.2a shows stripping/plating voltage profile of Li//Li symmetric cell containing this membrane, where a constant current of 25 μA/cm² was applied for a period of 20h during each half cycle (to pass a capacity of 1 mAh/cm²). The inset photograph shows the composite electrolyte membrane after plasticization, where its flexible nature can be observed in its folds (before plasticization the membrane was flat and brittle). Figure XV.1.2c shows the charge/discharge voltage profile as the cell was cycled galvanostatically at 25 μA/cm² and 70 °C. The corresponding charge and discharge capacity in mAh are plotted in Figure 2d.

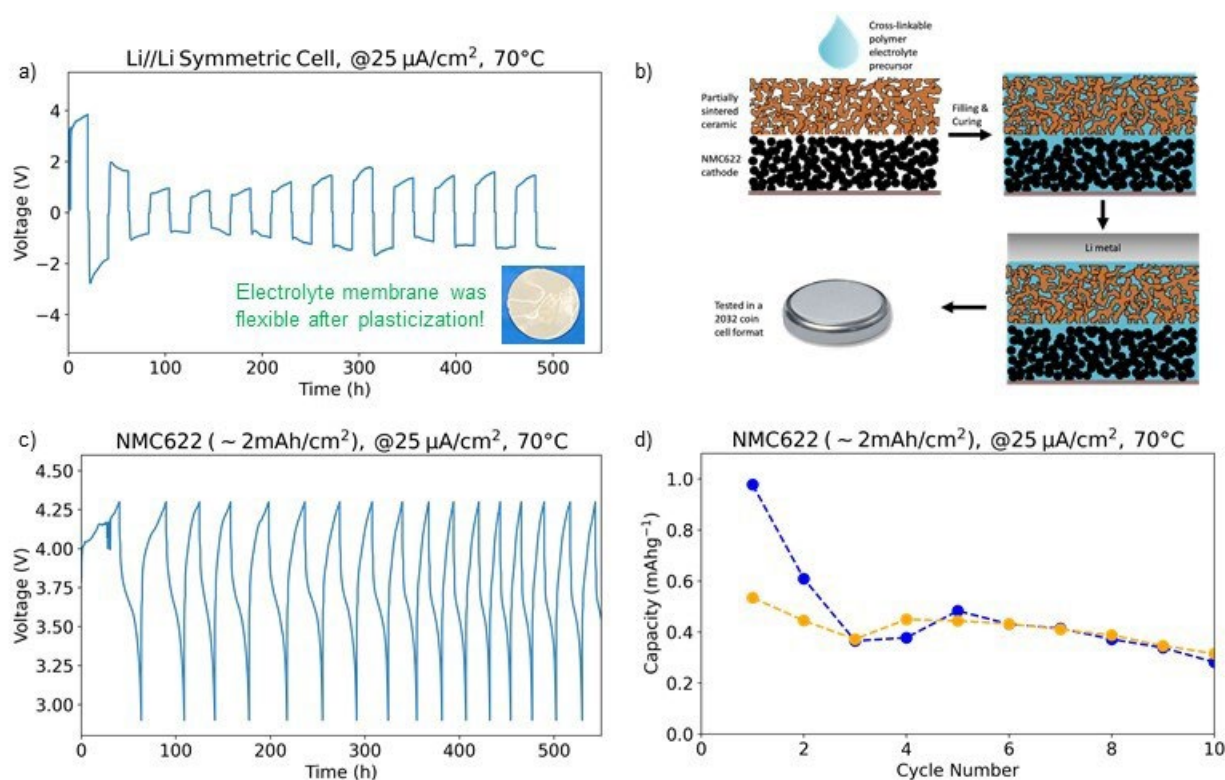


Figure XV.1.2 Cycling performance of a $\sim 140\text{ }\mu\text{m}$ -thick *plasticized* xPEO-LICGC (3-D interconnected) composite electrolyte. a) Li//Li symmetric cell with the *plasticized* composite tape at $25\text{ }\mu\text{A}/\text{cm}^2$ and $70\text{ }^\circ\text{C}$. b) Schematic illustrating the half-cell assembly procedure with a conventional PVDF-binder based NMC622 cathode and a 3D interconnected LICGC ceramic electrolyte porous tape, *plasticized* with liquid TEGDME plasticizer. c) Cycling performance of the illustrated half-cell at $25\text{ }\mu\text{A}/\text{cm}^2$ and $70\text{ }^\circ\text{C}$. d) Absolute cell charge and discharge capacity (mAh) of the cell versus cycle number. The cathode loading was $\sim 2\text{ mAh}/\text{cm}^2$.

As shown in Figure XV.1.2, the initial lithium symmetric cell showed high overpotential and the half cell showed relatively low capacity. For the rest of the FY21 we focused on optimizing the free-standing 3D interconnected composite on two aspects: 1) conductivity of the partial sintered tape (PST) and 2) minimizing interfacial resistance with Li.

We tried at least 10 sintering conditions of PSTs containing $1\text{ }\mu\text{m}$ size LICGC particles. Ionic conductivity of partially sintered tapes (PSTs) as a function of sintering conditions is shown in Table XV.1.1. The initial conditions we tried all showed either relatively low ionic conductivity or loss of the desired structure (PST_01 to 09). By increasing the ceramic content slurry from 30% to 40%, and altering the packing density in the cast tape, we were able to achieve very good conductivity ($1.2 \times 10^{-5}\text{ S}/\text{cm}$), similar to partially sintered thick pellet (LICGC_Pellet).

Table XV.1.1 Porosity and ionic conductivity of partially sintered LICGC tapes as a function of sintering conditions and tape composition

Sample ID	Sintering Conditions	Vol. % of porosity in PSTs	Wt. % of ceramic if all porosity is filled with xPEO	Ionic Conductivity of PSTs (S/cm)
PST_01	600 °C for 2 h, 1000 °C for 3 h (baseline sintering protocol)	52.4 %	66.5 %	2.6 x 10 ⁻⁶
PST_02	600 °C for 2 h, 1000 °C for 6 h	48.9 %	69.5 %	7.9 x 10 ⁻⁶
PST_03	600 °C for 2 h, 1000 °C for 9 h	51.1 %	67.5 %	4.1 x 10 ⁻⁶
PST_04	600 °C for 2 h, 1100 °C for 3 h	9.3 %	90.7 %	4.8 x 10 ⁻⁵
PST_05	600 °C for 2 h, 1050 °C for 2 h	35.9 %	79.6 %	Could not be measured
PST_08	200 °C for 1 h, 300 °C for 1 h, 200 °C for 1 h, 350 °C for 1 h, 450 °C for 1 h, 500 °C for 1 h, 1000 °C for 3 h (slow burn-off of binder)	52.3 %	66.5 %	4.3 x 10 ⁻⁶
PST_09	600 °C for 2 h, 1000 °C for 3 h (buried in mother powder)	Not measured	-	4.0 x 10 ⁻⁶
PST_10	600 °C for 2 h, 1000 °C for 3 h (higher solid loading tape)			1.2 x 10 ⁻⁵
LICGC_Pellet	200 °C for 1 h, 300 °C for 1 h, 200 °C for 1 h, 350 °C for 1 h, 450 °C for 1 h, 500 °C for 1 h, 1000 °C for 3 h (slow burn-off of binder)	44.9 %	72.8 %	1.8 x 10 ⁻⁵
LICGC_Dense plate	From supplier	No porosity	-	2.9 x 10 ⁻⁴

Second, we also optimized the formulation of cross-linked PEO used for filling the PSTs. Changing the molecular weight of one of the precursor molecules (Jeffamine) from 900 to 2000 (Table XV.1.2) led to significantly lowered interfacial resistance and overpotentials during cycling of Li//Li symmetric cells made with purely polymer electrolyte membranes (no ceramic).

Table XV.1.2 Composition and interfacial impedance with Li metal of the cross-linked PEO electrolytes evaluated.

Sample ID	PEGDGE M.W. (g/mol)	Jeffamine M.W. (g/mol)	[EO + PO] : LiTFSi	Initial Li//Li Interfacial resistance at 70 °C (Ω·cm ²)
xPEO-previous	500	900	16.0	230
xPEO-current	500	2000	16.0	55

3. Concentration gradients in composites of binary electrolyte and single ion conductor

We used numerical modeling to study the influence of introducing single-ion-conducting ceramic (LATP) to PEO-LiTFSi binary polymer electrolyte (PE) on the concentration gradients in the polymer phase. Three electrolyte configurations were studied (Figure XV.1.3a): single layer PE, two layers of PE with a dense LATP layer in the middle, and two layers of PE with a layer of composite polymer electrolyte (CPE) in the middle where ceramic particles are dispersed within.

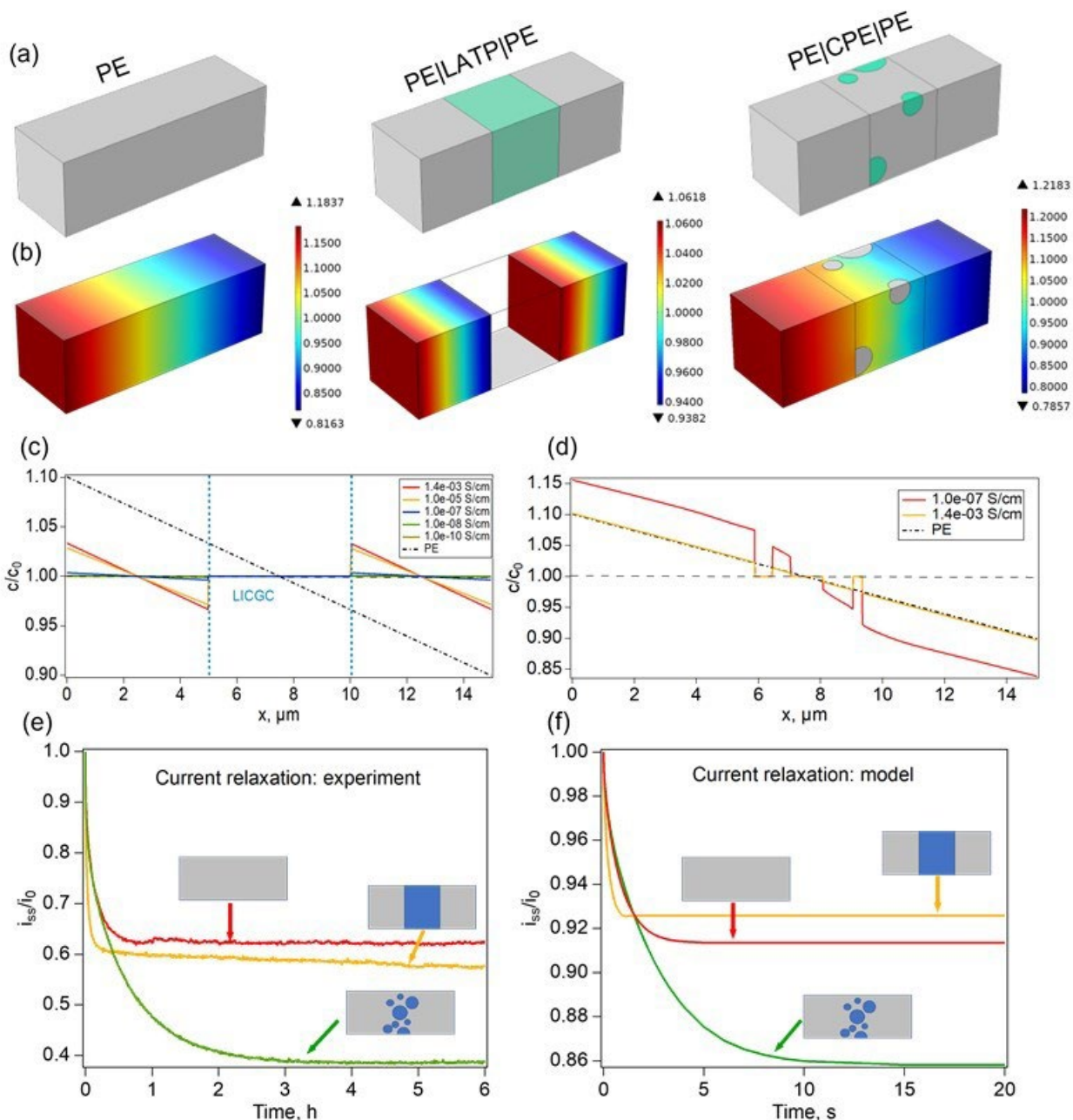


Figure XV.1.3 Concentration gradients in composites of binary electrolyte (PE) and single ion conductor (LATP). (a) Electrolyte configurations considered in the simulations; (b) From left to right: lithium cation concentration in PE membrane, PE membrane with dense LATP layer in the middle and PE membrane with a CPE layer in the middle; (c) Concentration profiles in PE and PE|LATP|PE with a series of interfacial resistances; (d) Concentration profiles in PE and PE|CPE|PE with a series of interfacial resistances; (e, f) Chronoamperometry monitoring current decay with an applied potential of 10 mV. (e), experimental results; (f) modeling results.

Nernst-Planck equations were solved in the 3D geometry to obtain concentration of ions at each time step. The plots in Figure XV.1.3b show the concentration of lithium cations in PE normalized to the initial concentration with the interface conductivity equal to $1 \times 10^{-7} \text{ S/cm}$. It is evident that the placement of single-ion-conducting (SIC) particles increases the concentration gradient in the binary polymer electrolyte, while the placement of SIC membrane (impenetrable to the anions) leads to lower concentration gradient in steady state. It is worth mentioning that in these simulations, the interaction between the TFSI⁻ anion and the surface of LATP particle was not taken into account.

The effect of interfacial resistance between PE and LATP on the concentration gradients in PE|LATP|PE and PE|CPE|PE is shown in Figure XV.1.3c and d. With the decrease in conductivity of the interface between LATP and PE, the concentration gradient further decreases in PE|LATP|PE (Figure XV.1.3c). On the contrary, the concentration gradient becomes more severe in PE|CPE|PE since the LATP particle is not participating in ionic transport and higher current is forced through the PE (Figure XV.1.3d). We further modeled the transient behavior (current decay to steady state with applied potential) of the three electrolyte configurations and qualitatively compared the results with the experimental measurements (Figure XV.1.3e and f). The modeling results follow the experimentally measured current trends. It can be seen that in the case of trilayer arrangement with the fully dense LATP plate, the steady state is reached faster than in other scenarios, as the developed concentration gradients are minimal.

Conclusions

1. We fabricated a gel composite electrolyte by incorporating an LATP-type ceramic, LICGC™, into crosslinked PEO-based gel electrolyte membrane plasticized with TEGDME. The composite electrolyte with 50 wt% ceramic exhibited superior cycling performance against Li metal, showing lower interfacial impedance, lower overpotential and higher rate capability. The root cause of the performance improvement is thoroughly investigated.
2. In the development of free-standing 3D interconnected composites, we discovered that the porosity and ionic conductivity of the partially sintered tapes are very sensitive to sintering condition and composition of the tape casting slurry. We achieved good room temperature ionic conductivity (1.2×10^{-5} S/cm) while maintaining the 3D interconnected structure by increasing solid content in the casting slurry.
3. Modeling of adding single-ion-conducting particles into a binary polymer electrolyte indicates that SIC particles does not help mitigating the concentration gradient across the PE membrane, given that there is no surface interaction between the SIC and the ions in the binary electrolyte. On the other hand, inserting a dense SIC plate in the middle of PE decreases the concentration gradient by 50%.

Key Publications

Publications

1. Chen, X. C.; Zhang, Y. M.; Merrill, L. C.; Soulen, C.; Lehmann, M. L.; Schaefer, J. L.; Du, Z. J.; Saito, T.; Dudney, N. J., Gel composite electrolyte—an effective way to utilize ceramic fillers in lithium batteries. *Journal of Materials Chemistry A* **2021**, 9 (10), 6555-6566.
2. Kalnaus, S.; Asp, L. E.; Li, J.; Veith, G. M.; Nanda, J.; Daniel, C.; Chen, X. C.; Westover, A.; Dudney, N. J., Multifunctional approaches for safe structural batteries. *Journal of Energy Storage* **2021**, 40, 102747.

Patents

1. “Method of Manufacturing a Thin Film Composite Solid Electrolyte”, U.S. Patent Application 17/497,023, Filed October 8, 2021.

Acknowledgements

These researchers provided important insight and assistance with the program:

Drs. Sergiy Kalnaus, Ritu Sahore, Beth Armstrong and Sergiy Kalnaus, staff members at Oak Ridge National Laboratory

Dr. Joseph Libera, MERF, Argonne National Laboratory

Professor Yanyan Hu and Michael Deck, Florida State University

XV.2 Lithium Dendrite Prevention for Lithium Batteries (Pacific Northwest National Laboratory)

Wu Xu, Principal Investigator

Pacific Northwest National Laboratory
902 Battelle Boulevard
Richland, WA 99354
E-mail: wu.xu@pnnl.gov

Ji-Guang Zhang, Principal Investigator

Pacific Northwest National Laboratory
902 Battelle Boulevard
Richland, WA 99354
E-mail: jiguang.zhang@pnnl.gov

Tien Q. Duong, DOE Technology Development Manager

U.S. Department of Energy
E-mail: Tien.Duong@ee.doe.gov

Start Date: October 1, 2020

End Date: September 30, 2021

Project Funding (FY21): \$275,000

DOE share: \$275,000

Non-DOE share: \$0

Project Introduction

Lithium (Li) metal is an ideal anode material for high-energy-density rechargeable batteries. However, the application of Li metal anode is hindered by safety concerns and short cycle life. The safety concerns of Li metal batteries mainly arise from Li dendrite growth and electrolyte flammability, while the short cycle life is related to low Li Coulombic efficiency (CE). Although much progress has been achieved in suppressing Li dendrites and increasing Li CE in liquid electrolytes, most liquid electrolytes are flammable and may pose safety hazards in case of extreme conditions. Therefore, development of electrolytes with improved safety for advanced battery chemistry is imperative. An ideal electrolyte for Li metal anode should not only suppress Li dendrite growth and have high CE, but also be intrinsically nonflammable. In FY20, we developed polymer electrolytes and studied the effects of polymer electrolytes on oxidation stability, ionic conductivity, Li CE, Li anode morphology, battery performance and compatibility with $\text{LiNi}_x\text{Mn}_y\text{Co}_z\text{O}_2$ (NMC) cathodes. The ex-situ protective coating for Li metal anode was also studied. In FY21, we further developed nonflammable polymer composite electrolytes (NPCEs) and high thermal-stability separators that have high Li CE, suppress Li dendrites, and are stable with high-voltage cathodes.

Objectives

The objective of this project is to enable Li metal to be used as an effective anode in rechargeable Li metal batteries with good stability and high safety. The investigation in this fiscal year will focus on two aspects. First, develop NPCEs and investigate effects of various flame-retardant solvents and polymers on ionic conductivity, Li CE, Li anode morphology, flammability, and battery performances in terms of long-term cycling stability and rate capability at various temperatures. Second, establish correlation of morphologies of SEI layer and deposited Li with electrolyte formulation, current density, and Li deposition/stripping process.

Approach

The approach has encompassed the following areas: (1) develop NPCEs that can enable long-term cycling with significantly improved safety features of Li metal batteries, (2) develop current collectors with 3D structure for Li metal anode to suppress Li dendrite growth, increase Li utilization, and extend cycle life of Li metal batteries, and (3) conduct mechanistic studies on Li deposition behavior to lay groundwork for future improvement of electrolytes (salts, solvents, and additives) for Li metal batteries.

Results

1. Evaluation of nonflammable composite gel polymer electrolyte (GPE)

To improve the mechanical strength of the nonflammable gel polymer electrolyte (GPE) based on a nonflammable high concentration electrolyte (HCE) of lithium bis(fluorosulfonyl)imide and trimethyl phosphate (LiFSI-TMP_a, 1:1.4 by mol.) and a nonflammable polymer matrix developed in last quarter of FY20, the nonflammable GPE was combined with a separator before being applied to Li metal batteries. Due to the relatively low ionic conductivity of the HCE-based GPE at room temperature, the cycling performance tests of the Li||NMC622 cells were carried out at 60°C. Figure XV.2.1 shows that the cells using the GPE-separator composite exhibit a continuous capacity decay after ~30 cycles (the black square symbol). As a comparison, the Li||NMC622 cells using the liquid TMP_a-based HCE exhibit even faster capacity decay (the red dot symbol). These results indicate that the TMP_a-based HCE is not compatible with the Li||NMC622 cell chemistry at high temperatures.

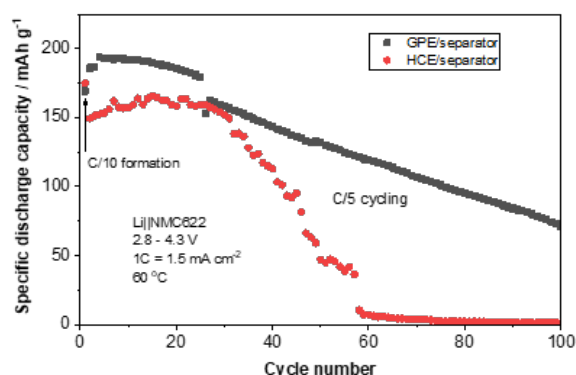


Figure XV.2.1 Cycling performance of Li||NMC622 cells using GPE/separators composite electrolyte and HCE (liquid)/separator at C/5 rate in the voltage range of 2.8-4.3 V under 60°C, where 1C = 1.5 mA cm⁻².

2. Safe composite separator based on polyimide and polyethylene

The high service temperature of 221–241°C of polyimide (PI) enables it maintaining its structural integrity upon overheating. Moreover, PI is intrinsically non-flammable. Therefore, it is expected to protect the cell from internal short circuiting during thermal runaway. The porous PI membrane was prepared by mixing the PI solution with Al₂O₃ nanoparticles of regular size. After obtaining the PI-Al₂O₃ composite membrane, the Al₂O₃ was removed by acid etching, leaving a PI membrane with highly regular pores arrays. The regularity of the PI membrane is considered to regulate the Li⁺ flux and achieve better Li deposition morphology. Figure XV.2.2a and Figure XV.2.2b show the photograph and micrograph of the PI separator. Regular pores with the diameter of 400–500 nm and the thickness of PI membranes can be controlled at 11–20 μm. As shown in Figure XV.2.2c, when the three-dimensional (3D) microporous PI membranes and the conventional polyethylene (PE) separators were stored in an oven of 120°C for 1 min, the PI membrane can well maintain its dimensions while the PE separators shrank significantly, demonstrating the excellent thermal stability of the 3D microporous PI membranes.

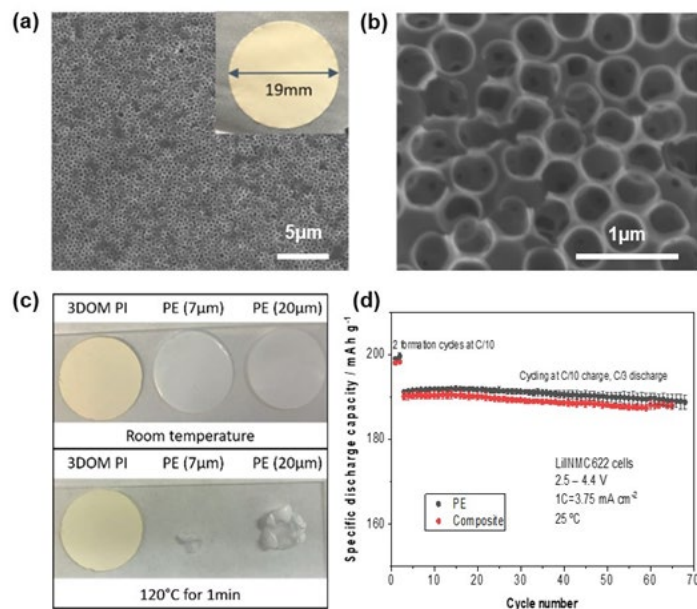


Figure XV.2.2 (a) Photograph and micrograph of the functional PI separator with regular pore array. (b) Micrograph of PI separator at higher magnification. (c) Photographs of PI (11 μm) and PE (7 and 20 μm) separators before and after heating at 120 °C for 1 min. (d) Cycling performance of Li||NMC622 cells using PE and PI/PE composite separators.

These 3D microporous PI membranes were then evaluated as a separator in Li metal batteries. However, it is found that the PI separator alone can easily lead to short circuit due to the penetration by Li dendrites. Therefore, the PI membrane was combined with a very thin layer (7 μm thick) of PE separator to construct the dual separator. The cycling performances of Li||NMC622 cells with the PI/PE composite separator (where PI layer contacts Li directly) and the single PE separator were first evaluated and compared by using a localized high-concentration electrolyte (LHCE) comprising of LiFSI, 1,2-dimethoxyethane (DME) and 1,1,2,2-tetrafluoro-2,2,3,3-tetrafluoropropyl ether (TTE) at a molar ratio of 1:1.2:3. As shown in Figure II.8.B.2d, the cells using the PI/PE composite separator (total thickness 18 μm) exhibit comparable cycling performance to those comprising single PE separator with similar thickness (20 μm).

Next, the influence of the separators was evaluated with the TMP_a-based LHCE of LiFSI-1.4TMP_a-3TTE. As shown in Figure XV.2.3a, although the cell with the PI/PE composite separator, where the PI membrane directly contacts Li metal, exhibits a lower specific capacity than the cell using the single layer PE separator, it shows higher capacity than the single layer PE cell after 85 cycles since the cell using the single layer PE suffers rapid capacity loss starting at about the 70th cycle. However, both cells exhibit relatively fast capacity fading, which could be due to the intrinsic incompatibility between the TMP_a-LHCE and the Li||NMC622 cell chemistry. Therefore, the influence of the separators on the cycling performance of Li||NMC622 cells was further evaluated with the DME-based LHCE. The cells contained 50 μm thick Li, 4.2 mAh cm⁻¹ NMC622, 75 μL electrolyte, and were cycled in 2.5–4.4 V at C/10 charge and C/5 discharge after three formation cycles at C/10, where 1C = 4.2 mA cm⁻². As shown in Figure XV.2.3b, the cell using PE/PI composite separator (where PE layer contacts Li directly) exhibits excellent cycling stability in both discharge capacity and CE. After 350 cycles, the capacity retention of PE/PI based cell can reach 83.5%, whereas those of single layer PE and PI/PE composite separator only reach 49.3% and 1.9%, respectively. The PE/PI based cell maintains a CE of 99.8% at 350th cycle. The cell based on single PE shows slightly lower and decreased CE with cycling. In contrast, the cell based on PI/PE composite separator exhibits large fluctuation in CE after about 150 cycles. The cell with PI/PE separator exhibits the worst cycling performance, mainly due to the reactivity between Li and PI.

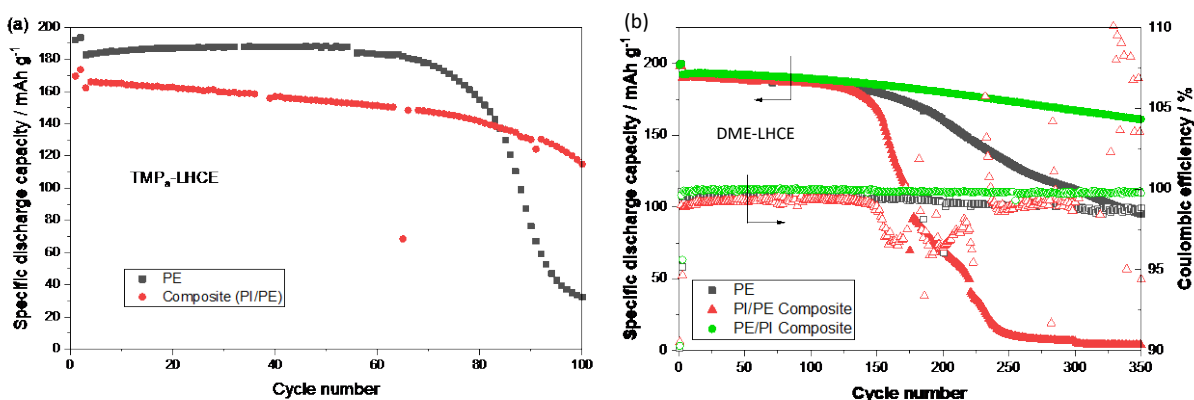


Figure XV.2.3 (a) Cycling performance of Li | NMC622 cells using the combinations of TMP_a-based LHCE (LiFSI:TMP_a:TTE=1:1.4:3 by mol.) and two different separators (PE and PI/PE). (b) Cycling performance of Li | NMC622 cells using the combinations of DME-based LHCE (LiFSI:DME:TTE=1:1.1:3 by mol.) and three different separators (PE, PI/PE and PE/PI).

3. Influences of electrolyte additives on the deposition behavior of metallic Li via in-situ AFM

The deposition behaviors of Li on copper (Cu) substrate in conventional electrolytes with various additives were systematically studied by in-situ atomic force microscope (AFM). Figure XV.2.4 reveals the morphology evolution of Li deposited on Cu over time. 1.0 M LiPF₆ in EC-EMC (3:7 by wt.) (hereinafter, E-baseline) was selected as the benchmark electrolyte for the evaluations (Figure XV.2.4A). On the basis of E-baseline, three additional electrolytes with different additives, vinylene carbonate (VC) (Figure XV.2.4B), LiAsF₆ (Figure XV.2.4C) and VC + LiAsF₆ (Figure XV.2.4D) were evaluated.

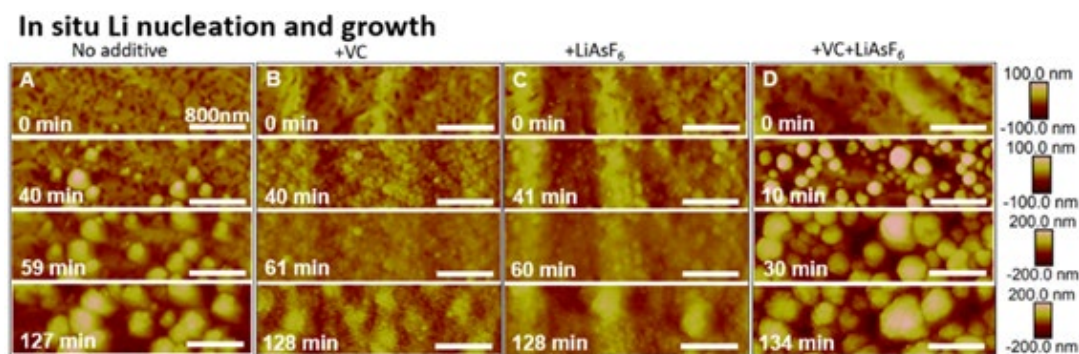


Figure XV.2.4 Morphology evolutions of Cu electrodes upon Li deposition by in-situ AFM in (A) E-baseline, (B) E-baseline + 2 wt.% VC, (C) E-baseline + 2 wt.% LiAsF₆ and (D) E-baseline + 2 wt.% VC + 2 wt.% LiAsF₆.

As indicated by the in-situ AFM results, the electrolyte additives have significant influence over the Li deposition behavior. The introduction of VC postpones the formation of Li nuclei, while the introduction of LiAsF₆ increases the nucleation density. Based on the in-situ AFM results, the growth kinetics can be obtained. As shown in Figure XV.2.5a, the introduction of different additives has a substantial influence over the nucleation density in the early stage of Li deposition. Figure XV.2.5b shows the voltammetry of the in-situ AFM cells during the Li deposition process, from which the overpotential, η , can be obtained. The dependence of particle size over η^{-1} and the natural logarithm of surface energy over η^{-2} can also be obtained (Figure XV.2.5c and Figure XV.2.5d, respectively). The interpretations of these dependences will be further analyzed.

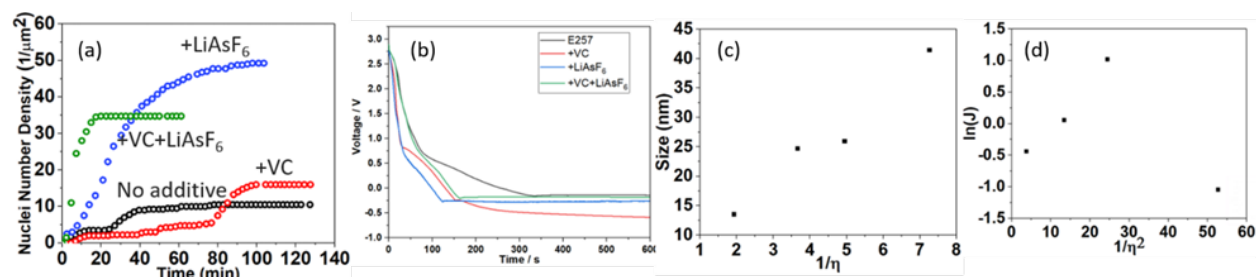


Figure XV.2.5 (a) Li nuclei density on Cu electrodes as a function of deposition time in 1 mol L⁻¹ LiPF₆ in EC:EMC=3:7 (by wt.) with different additives. (b) Voltammetry of the in-situ AFM cells using studied electrolytes. (c) Dependence of nuclei size on η^{-1} and (d) dependence of $\ln(\text{surface energy})$ on η^{-2} .

4. Influence of separator on Li deposition behavior

In a separate effort, the influence of PE separator on Li deposition behavior was investigated. Figure XV.2.6 shows the morphologies of Li deposited on Cu substrates in a conventional electrolyte in coin cell with a PE separator and the electrochemical cell without separator. As shown in Figure XV.2.6a,c, the Li deposited in the conventional coin cells exhibits a highly irregular morphology. Whisker-like and flake-like Li deposits can be observed. In the absence of PE separator, the deposited Li exhibits a rod-array morphology (Figure XV.2.6b,d), being much more regular than that in coin cell. The difference between these two morphologies could be assigned to either the uneven Li⁺ flux induced by the polyolefin separator or the mechanical pressure in the coin cell. More investigations are needed to understand how the separators influence the Li deposition morphology.

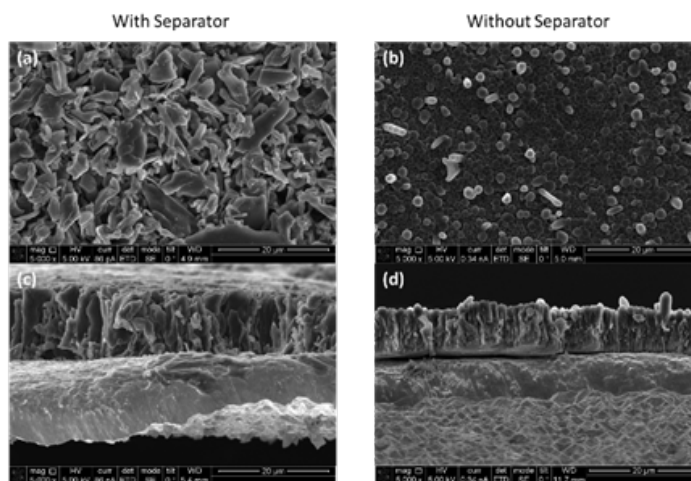


Figure XV.2.6 Morphologies of deposited Li in 1.2 M LiPF₆/EC-EMC (3:7 by wt.) in the presence (a,c) and absence (b,d) of polyolefin separator: (a,b) Top View, (c,d) Cross-section.

Conclusions

- 3D microporous PI membranes with highly regular pores arrays were successfully fabricated via template method. Such PI membranes demonstrate excellent thermal stability while the conventional polyolefin separators show poor dimension stability under heat.
- The combination of PE/PI dual separator (with PE contacting Li metal) greatly enhances the long-term cycling stability of Li metal batteries with Ni-rich cathodes compared to the single PE separator and the PI/PE dual separator (with PI contacting Li).

- In-situ AFM results indicate that electrolyte additives have significant influence on Li deposition behavior. The introduction of VC postpones the formation of Li nuclei, while the introduction of LiAsF6 increases the nucleation density.

Key Publications

1. H. Jia, X. Cao, J.-G. Zhang, W. Xu*, “Electrolytes for Lithium-Ion and Lithium Metal Batteries”, in *Encyclopedia of Energy Storage*, 2021, DOI:[10.1016/B978-0-12-819723-3.00106-2](https://doi.org/10.1016/B978-0-12-819723-3.00106-2). Publisher: Elsevier Inc.
2. H. Jia, W. Xu*, “Nonflammable Nonaqueous Electrolytes for Lithium Batteries”, *Current Opinion in Electrochemistry*, 2021, **30**, 100781. In a theme issue on Energy Storage, edited by Yi-Chun Lu. DOI:[10.1016/j.coelec.2021.100781](https://doi.org/10.1016/j.coelec.2021.100781) (Invited)
3. H. Wu[#], P. Gao[#], H. Jia, L. Zou, L. Zhang, X. Cao, M. H. Engelhard, M. E. Bowden, M. S. Ding, D. Hu, S. D. Burton, K. Xu, C. Wang, J.-G. Zhang*, W. Xu*, “A polymer-in-salt electrolyte with enhanced oxidative stability for lithium metal polymer batteries”, *ACS Applied Materials & Interfaces*, 2021, **13** (27), 31583–31593. DOI:[10.1021/acsami.1c04637](https://doi.org/10.1021/acsami.1c04637)
4. P. Gao[#], H. Wu[#], X. Zhang, H. Jia, J.-M. Kim, M. H. Engelhard, C. Niu, Z. Xu, J.-G. Zhang, W. Xu*, “Optimization of Magnesium-Doped Lithium Metal Anode for High Performance Lithium Metal Batteries through Modeling and Experiment”, *Angewandte Chemie International Edition*, 2021, **133** (30), 16642–16649. DOI:[10.1002/anie.202103344](https://doi.org/10.1002/anie.202103344)
5. B. Horstmann[#], J. Shi[#], R. Amine[#], M. Werres[#], X. He, H. Jia, F. Hausen, I. Cekic-Laskovic, S. Wiemers-Meyer, J. Lopez, D. Galvez-Aranda, F. Baakes, D. Bresser, Dominic; C.-C. Su, Y. Xu, W. Xu, P. Jakes, R.-A. Eichel, E. Figgemeier, U. Krewer, J. M. Seminario, P. B. Balbuena, C. Wang, S. Passerini, Y. Shao-Horn, M. Winter, K. Amine*, R. Kostecki*, A. Latz*, “Strategies towards enabling lithium metal in batteries: interphases and electrodes”, *Energy & Environmental Science*, 2021, **14** (10), 5289–5314. DOI:[10.1039/d1ee00767j](https://doi.org/10.1039/d1ee00767j).
6. X. He[#], D. Bresser[#], S. Passerini, F. Baakes, U. Krewer, J. Lopez, C.T. Mallia, Y. Shao-Horn, I. Cekic-Laskovic, S. Wiemers-Meyer, F. A. Soto, V. Ponce, J. M. Seminario, P. B. Balbuena, H. Jia, W. Xu, Y. Xu, C. Wang, B. Horstmann, R. Amine, C.-C. Su, J. Shi, K. Amine, M. Winter, A. Latz*, R. Kostecki*, “The passivity of lithium electrodes in liquid electrolytes for secondary batteries”, *Nature Reviews Materials*, 2021, **6** (11), 1036–1052. DOI:[10.1038/s41578-021-00345-5](https://doi.org/10.1038/s41578-021-00345-5)
7. H. Wu[#], H. Jia[#], C. Wang, J.-G. Zhang, W. Xu*. “Recent Progress in Understanding Solid Electrolyte Interphase on Lithium Metal Anodes”, *Advanced Energy Materials*, 2020, **11** (5), 2003092. DOI:[10.1002/aenm.202003092](https://doi.org/10.1002/aenm.202003092)

Acknowledgements

Key contributors: Drs. Hao Jia, Hyung-Seok Lim, Peiyuan Gao, Jinhui Tao, Mark H. Engelhard, Chongmin Wang and Yaobin Xu.

XV.3 Integrated Multiscale Modeling for Design of Robust 3D Solid-State Lithium Batteries (Lawrence Livermore National Laboratory)

Brandon C. Wood, Principal Investigator

Lawrence Livermore National Laboratory
7000 East Avenue
Livermore, CA 94550
E-mail: wood37@llnl.gov

Tien Q. Duong, DOE Technology Development Manager

U.S. Department of Energy
E-mail: Tien.Duong@ee.doe.gov

Start Date: November 1, 2018	End Date: October 31, 2021	
Project Funding (FY21): \$1,125,000	DOE share: \$1,125,000	Non-DOE share: \$0

Project Introduction

Architected 3D solid-state batteries have a number of intrinsic performance and safety advantages over conventionally processed 2D batteries based on liquid organic or polymer electrolytes [1]. Functionality and architecture of component materials can be tuned for optimal energy and power density, and the use of solid-state electrolytes offers increased safety and potential compatibility with higher-voltage and higher-energy-density electrodes. Nevertheless, proper design of 3D solid-state batteries remains a formidable challenge. Solid-state batteries tend to suffer from high interfacial resistance arising from poor physical contacts [2], as well as the formation of intermediate phases at the often-unstable interface between the cathode and electrolyte. They also suffer from non-uniform mechanical responses that can promote stress cracking in response to lithium uptake during cycling. For 3D architectures, these issues can become even more problematic, since the complex morphologies tend to introduce additional non-uniformities in electric fields and current densities [3],[4] at the numerous component interfaces. In addition, microstructures that are notoriously difficult to control and vary widely with the specific processing condition.

To realize the ultimate goal of designing and printing optimized 3D solid-state batteries, it is critical to understand the interfacial losses and instabilities that impede performance and promote failure at multiple scales. Validated modeling and simulation have a unique role to play in pursuit of this aim, since they can directly probe structure-property relations and provide guidance for optimizing function of component materials. In general, existing modeling strategies tend to suffer from one of two shortcomings. Some fail to address the multi-physics nature of the various processes active in 3D batteries, which range from electrical to chemical to mechanical responses that are often coupled. Others fail to address the multiscale nature of the battery materials and their integration, ignoring the fact that atomistic, microstructural, and cell-level processes must be considered to understand how processing and architecture affect performance. This project leverages advanced computational models to address these shortcomings and investigate diffusion kinetics limitations in ceramic 3D solid-state battery materials. This can be viewed as a first step towards enabling future optimization of 3D battery designs.

Objectives

This project is developing a multiscale, multi-physics modeling framework for probing the effects of materials microstructure and device architecture on ion transport within 3D ceramic solid-state battery materials, with the goal of enhancing performance and reliability. The project has three primary objectives: (1) integrate multi-physics and multiscale model components; (2) understand interface- and microstructure-derived limitations on ion transport; and (3) derive key structure-performance relations for enabling future optimization.

Approach

The team's approach integrates simulations at three scales to predict ion transport limitations within the ceramic solid-state electrolyte $\text{Li}_{7-x}\text{La}_3\text{Zr}_2\text{O}_{12}$ (LLZO), as well as across the interface between LLZO and LiCoO_2 (LCO) cathodes at composite interfaces in 3D batteries. Classical and *ab initio* molecular dynamics (AIMD) simulations are used to compute fundamental Li-ion diffusion within bulk solid electrolyte and cathode materials, along/across grain boundaries of the electrolyte, and along/across electrolyte/cathode interfaces. Next, phase-field simulations are used to generate digital representation of realistic microstructures of the materials, which are combined with the atomistic simulation results to parameterize mesoscale effective property calculations and to establish microstructure-property relationships for ion transport. Finally, these relationships inform a microstructure-aware model of experimental electrochemical impedance spectroscopy, which connects microscale features to macroscale properties in order to optimize the performance of ceramic 3D solid-state Li batteries based on LLZO solid electrolytes.

Results

Atomistic simulations of Li-ion diffusion across the LLZO/LCO interface

The team utilized high-temperature *ab initio* molecular dynamics (AIMD) to sample the atomic structure of LLZO/LCO interfaces based on several initial electrolyte/cathode orientations and simulated charge states. Multiple snapshots were then randomly chosen from the dynamics trajectories, and possible Li^+ diffusion pathways across the interfaces were identified. Next, the corresponding ensemble of activation energies E_a were computed using the nudged elastic band method. The results are collected and rendered as a histogram in Figure XV.3.1. Across all samples, the average E_a is found to be ~ 0.93 eV for forward diffusion of Li^+ from LLZO to LCO—significantly higher than for bulk LLZO or LCO (~ 0.3 eV)—implying orders-of-magnitude slower diffusion across the interface. The Li^+ diffusion pathways were also found to exhibit different values of E_a for forward (LLZO \rightarrow LCO) and backward (LCO \rightarrow LLZO) diffusion, with the latter much more facile (~ 0.32 eV on average). As a result, Li^+ ions that do manage to cross the interface boundary have a high probability of reversing their path, making continuous diffusion across the interface challenging. The findings point to buildup of Li^+ ions in the near-surface regions of LLZO and LCO rather than in the interfacial region. The team further concluded that even for a completely compact interface absent of voids, there is a physical origin for high interfacial impedance that must be considered. Overcoming this limitation may require alternative processing routes or chemical modification strategies, to be explored in future work.

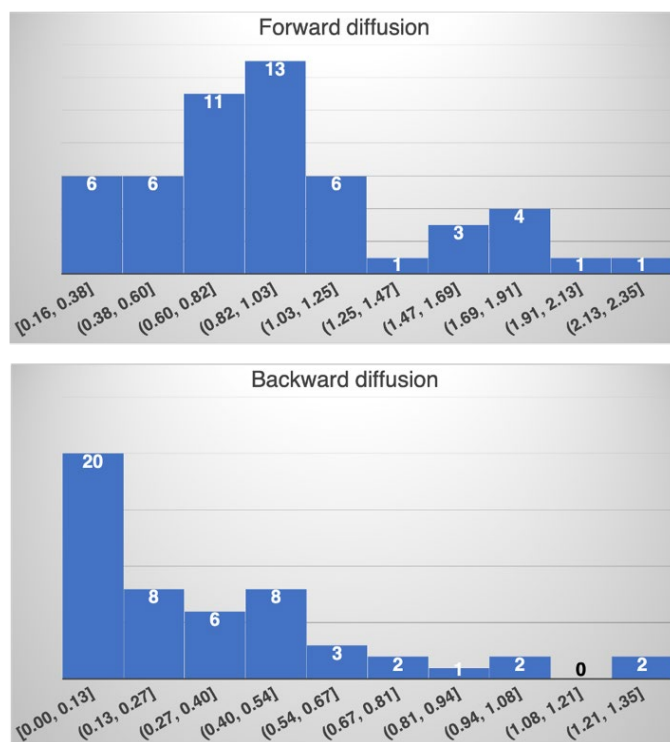


Figure XV.3.1 Histogram of calculated activation energies (in eV) for different Li⁺ diffusion pathways across the LLZO/LCO interface. Forward and backward diffusion refer to Li⁺ migration from LLZO to LCO, and from LCO to LLZO, respectively.

Machine-learning interatomic potentials for accelerated atomistic simulations of interfaces

Although the team's primary workhorse for atomistic simulations has been AIMD, obtaining reliable transport coefficients for complex interfaces requires large, long simulations to properly capture the effects of disorder. Because these computations are computationally demanding, they accelerated the simulations by developing machine-learning force fields (MLFFs) that can reproduce quantum accuracy with far less computational expense. The MLFFs were based on an **artificial neural network with a 20–10 hidden-layer architecture and utilized Chebyshev polynomial representations of local atomic environments**. To ensure proper reproduction of disordered and interfacial atomic structures, the team included in the training data a variety of expanded-volume amorphous LLZO structures. The resulting MLFF achieved near-quantum-level accuracy for energies and forces for *NPT* molecular dynamics simulations up to 3000 K, with root-mean-squared errors for energies and forces < 10 meV/atom and < 0.2 eV/Å, respectively (Figure XV.3.2a,b). To validate the performance and extract useful parameters for their mesoscale models, the team performed MLFF simulations at various conditions and evaluated radial distribution functions, mechanical properties, Li transport parameters, and atomic vibrational characteristics. Figure XV.3.2c shows that the new MLFF approach predicts Li transport parameters close to AIMD for a fully disordered variant, which is a proxy for high-angle grain boundaries. The higher activation energy for the fully disordered variant reflects the blocking effect of grain boundaries, which is known to lead to increased impedance in LLZO. The team also constructed models of specific grain boundaries and interphase boundaries to compute Li⁺ transport. As an illustration, Figure XV.3.2d presents the frequented pathways for Li⁺ ions transporting through a LLZO $\Sigma 5(210)/[001]$ grain boundary (GB) model at 2000 K. In addition, analysis of the local environments that promote rapid diffusion or act as diffusion blockers (and hence increased impedance) was aided by the development of new analytical techniques that rely on discretizing jumps and sites to examine spatiotemporal correlation effects, as reported in [5] and [6]. Results from these computations were used to estimate microstructure-dependent transport across both internal (grain boundary) and multiphase interfaces between the cathode and electrolyte.

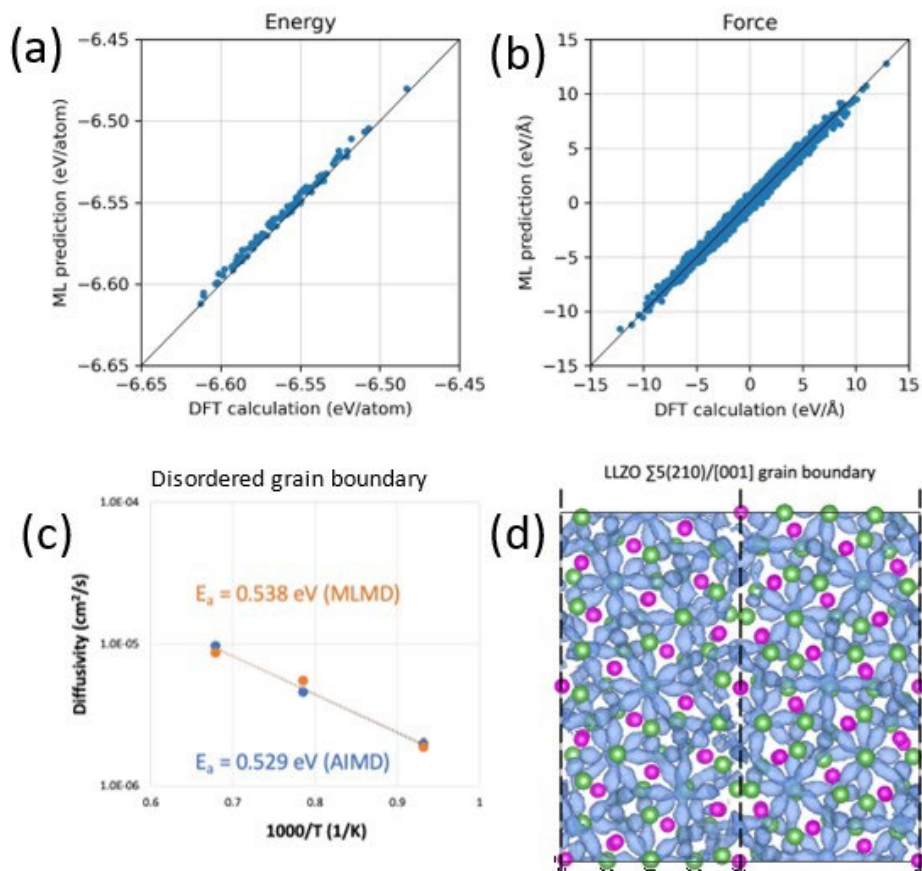


Figure XV.3.2 (a-b) Analysis of MLFF accuracy during a dynamical simulation of disordered LLZO at 3000 K, showing the ability to replicate (a) energies and (b) forces derived from density functional theory (DFT). (c) Li^+ diffusivities predicted by MLMD (orange) and AIMD (blue) for amorphous LLZO. (d) Isosurface of Li^+ probability density (blue) obtained from MLMD in a LLZO $\Sigma 5(210)/[001]$ coherent grain boundary model at 2000 K. Magenta and green atoms are Zr and La, respectively, and O atoms are not shown for simplicity.

Mesoscale modeling of microstructural effects on Li transport in polycrystalline LLZO under stress

The team further refined the integration of two mesoscale models for predicting microstructural impacts on 1) Li ion transport and 2) local stress concentrations in LLZO. Within the *MesoMicro* code framework developed at Lawrence Livermore National Laboratory [7], the team successfully combined two numerical schemes for solving the mechanical equilibrium and steady-state diffusion equations in the presence of complex solid electrolyte microstructures. This framework is now capable of naturally incorporating microstructure-aware stress effects on the local Li concentration profile within any polycrystalline microstructure. The team applied the framework to a digital representation of polycrystalline LLZO (Figure XV.3.3a) with a microstructure generated by a phase-field simulation. They first verified the ability to predict a nonuniform internal stress profile under applied loading. As shown in Figure XV.3.3b, the local von Mises stress profile is affected by local microstructural features, as previously reported. Next, the Li composition profile was analyzed at steady state in the presence of the local stress profile. Figure XV.3.3c shows the computed Li composition profile for that scenario. For comparison, the computed Li composition profile without the stress effect is shown in Figure XV.3.3d. The simulations confirm that stress concentration can perturb the Li composition profile, inducing segregation or depletion near grain boundaries and junctions. The team proposes use of this formalism to quantify how evolving stresses affect the net ionic conductivity under various operation conditions.

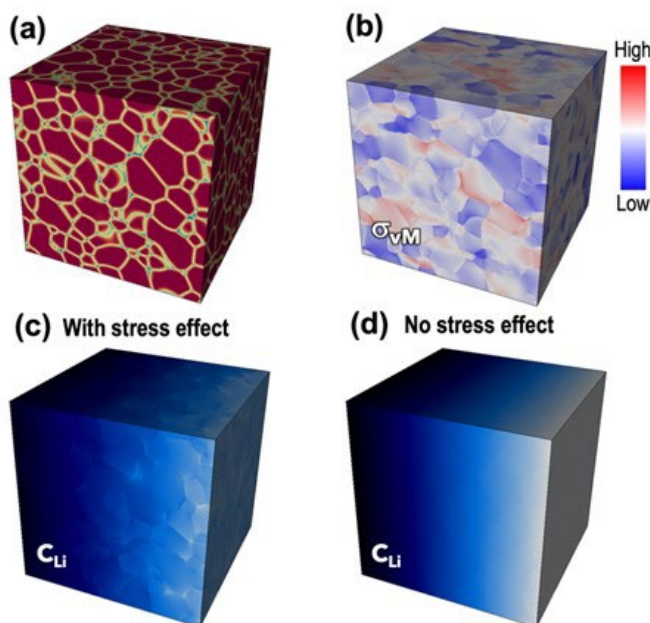


Figure XV.3.3. (a) Digital representation of polycrystalline LLZO microstructure; (b) computed von Mises stress profile; (c-d) Li composition profile (c) with and (d) without mechanical stress.

Mesoscale modeling of Li transport and micromechanical response in a polymer/LLZO composite

The team also extended their mesoscale models and their *MesoMicro* code framework to compute properties of polymer/LLZO composites. Figure XV.3.4a shows a 3D digital representation of a realistic porous LLZO microstructure filled with a polymer. Mesoscale modeling approaches were applied to compute local mechanical response within the microstructure, the effective elastic modulus, and effective ionic conductivities of both cations (Li^+) and anions (TFSI^-). For input materials parameters, the team combined *ab initio*-derived elastic moduli with experimental ionic conductivities of LLZO and polymer electrolyte constituents. The incorporated composite microstructures exhibit strongly inhomogeneous elasticity and conductivity profiles. Figure XV.3.4b shows a simulation result of the local mechanical response (represented by the von Mises stress) within the composite microstructure. The simulation verifies the presence of concentrated mechanical stresses near the polymer/LLZO interfaces, demonstrating the sensitivity of the level of stress concentration to local topological features. Additionally, by applying loads along various normal and shear directions, the team extracted the effective elastic modulus of the composite (Figure XV.3.4c), which is expected to be highly sensitive to microstructure and LLZO/polymer phase fraction and has implications for mechanical stability and resistance to Li dendritic growth.

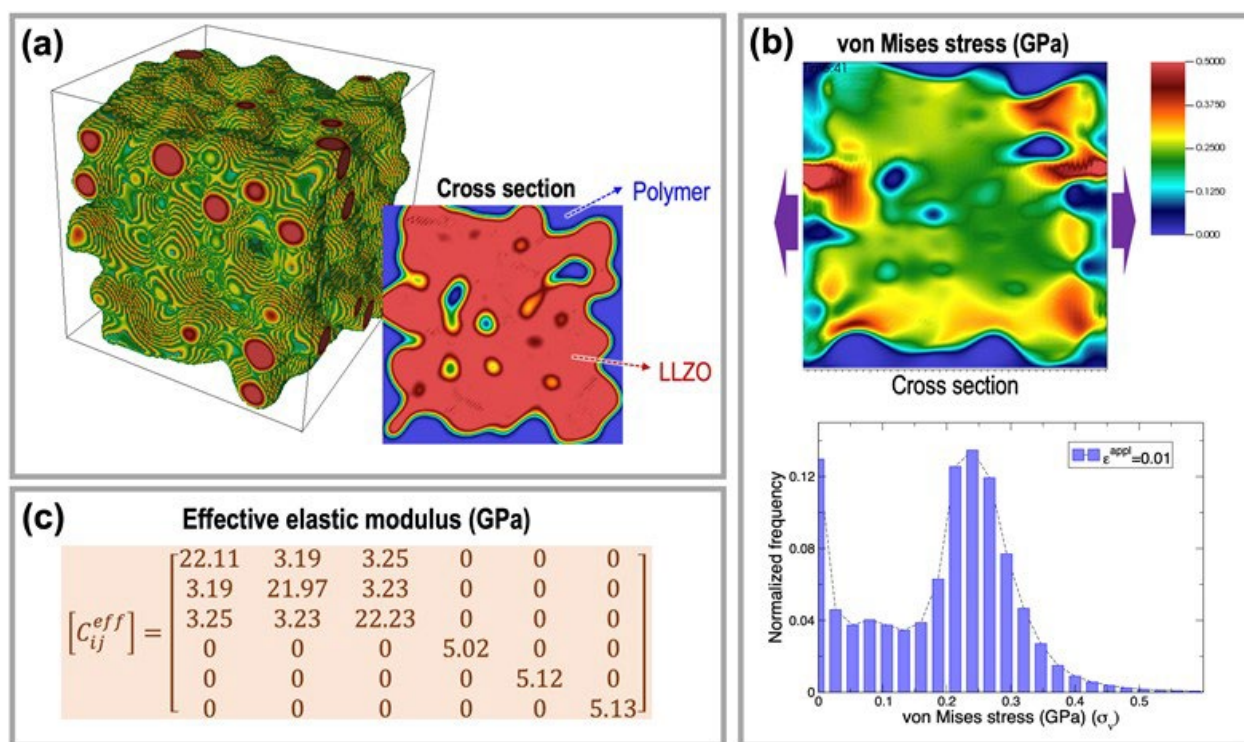


Figure XV.3.4. (a) 3D porous LLZO microstructure and cross section of LLZO/polymer composite microstructure; (b) computed von Mises stress (top: spatial distribution; bottom: statistics) in the composite microstructure under applied loading; and (c) computed effective elastic modulus of the composite microstructure.

Modeling of microstructural effects on electrochemical impedance spectra

The team also developed a model to understand impacts of grain boundaries on the electrochemical impedance spectra (EIS) to better connect the simulations to macroscale experiments. This model accounts for Li^+ grain boundary segregation and the corresponding space-charge effects, as well as their collective impacts on electrical potential distributions in polycrystalline solid electrolytes. This framework is being applied within the U.S.-Germany Collaboration on Solid-state Batteries to aid analysis of grain and grain boundary contributions to ionic conductivity as a function of processing conditions. Figure XV.3.5 shows the Li^+ ion concentration distribution and the corresponding voltage in a sample polycrystal, along with the effect of grain boundary conductivity on the predicted EIS. Faster grain boundary conductivity (top row) demonstrates higher segregation effects and larger potential gradients across the grain boundary when compared to the slower grain boundary conductivity case (bottom row). The space charge density distribution follows the concentration distribution. Here, the inclusion of space charge segregation in the grain boundary leads to an increase in the overall predicted impedance (specifically the imaginary component). This effort is being performed jointly with the U.S.-Germany CatSE partnership on solid-state battery research, with planned incorporation into device-level models being devised by partner institutions.

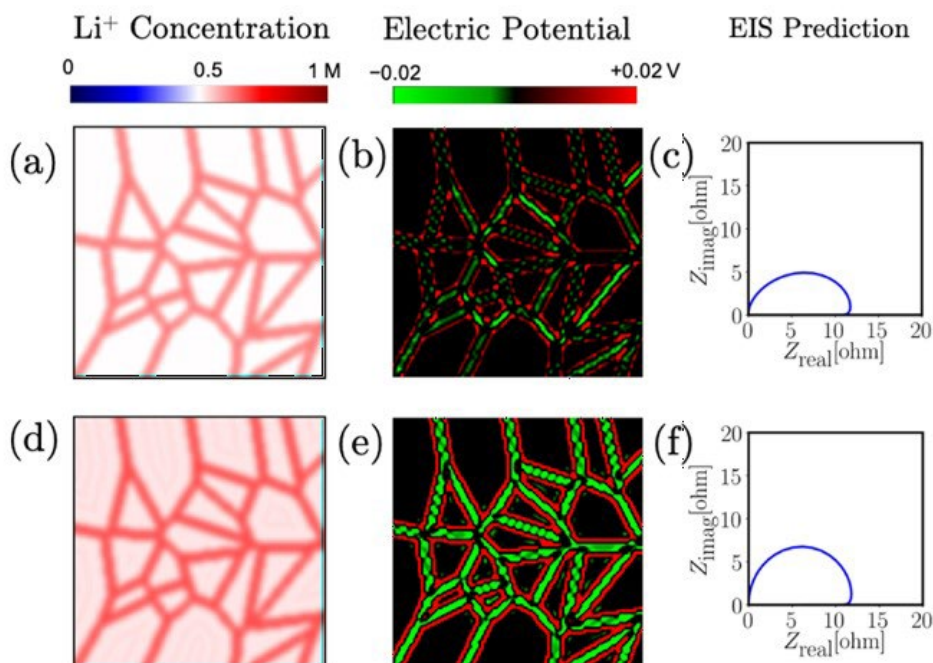


Figure XV.3.5. Predictions of (a,d) Li^+ concentration profile, (b,e) electrical potential profile, and (c,f) EIS for a model 2D LLZO polycrystal, demonstrating the effect of grain boundary Li^+ conductivity. Data in (a-c) correspond to the case for which Li^+ mobility at the grain boundaries is double that in (d-f).

Conclusions

The team's activities this year were used to map the range of likely Li^+ mobilities across densified cathode/LLZO interfaces, which illustrated the origins of intrinsic impedance limitations in well-pressed and sintered samples. They also showed that it is possible to access much more complex interfacial systems with near-quantum accuracy by introducing machine learning force fields. These were used to confirm the segregation and transport of Li^+ in specific models of specific grain boundary orientations and generic disordered high-angle grain boundaries. These tools improved the statistical accuracy of the interfacial transport predictions and can be utilized more broadly for analyzing further effects of structure and chemistry on local mobility. At the mesoscale, the team integrated the relationship between local stress and transport into their modeling framework. They showed that stresses concentrate locally at grain junctions, and that these stresses couple to the compositional profile to introduce heterogeneity into the mass transport profile. The team also computed the effect of microstructure on Li^+ transport and micromechanical response in a polymer/LLZO composite, demonstrating the role of highly inhomogeneous and anisotropic transport of individual components on the effective transport. This formalism can in principle be used to optimize microstructures of composites. Finally, the team demonstrated a framework for predicting electrochemical impedance spectra from microstructural features, which can be used to better connect processing to performance and guide future design.

Key Publications

1. T.W. Heo, A. Grieder, B. Wang, M. Wood, S.A. Akhade, L.F. Wan, L.-Q. Chen, N. Adelstein, and B.C. Wood, "Microstructural impacts on ionic conductivity of oxide solid electrolytes from a combined atomistic-mesoscale approach," *npj Comp. Mater.*, in press (2021).
2. B.C. Wood, J.B. Varley, K.E. Kweon, P. Shea, A.T. Hall, A. Grieder, M. Ward, V.P. Aguirre, D. Ringling, E.L. Ventura, C. Stancill, and N. Adelstein, "Paradigms of frustration in superionic solid electrolytes," *Phil. Trans. R. Soc. A* **379**, 20190467 (2021).

3. Z. Mehmedovic, V. Wei, A. Grieder, P. Shea, B.C. Wood, and N. Adelstein, "Impacts of vacancy-induced polarization and distortion on diffusion in solid electrolyte Li_3OCl ," *Phil. Trans. R. Soc. A* **379**, 20190459 (2021).
4. K. Kim, D. Park, H.-G. Jung, K.Y. Chung, J.H. Shim, B.C. Wood, and S. Yu, "Material design strategy for halide solid electrolytes Li_3MX_6 (X = Cl, Br, and I) for all-solid-state high-voltage Li-ion batteries," *Chem. Mater.* **33**, 3669 (2021).
5. B.C. Wood, "Understanding kinetics of complex interfaces in solid-state batteries from multiscale simulations," Electrochemical Society PRiME Meeting (Virtual), October 2020.
6. T.W. Heo, A. Grieder, S.A. Akhade, L.F. Wan, N. Adelstein, B.C. Wood, "Integrated modeling framework for investigating multiscale microstructural impacts on the ionic conductivity of garnet solid electrolytes", Electrochemical Society PRiME Meeting (Virtual), October 2020.
7. L. Wan, A. M. Dive, M. Wood, K. Kim, T. Li and B. C. Wood, "Elucidating interfacial instability in all-solid-state lithium batteries from first-principles simulations", Materials Research Society 2021 Spring Meeting (virtual), April 2021.

References

1. Arthur, T. S., D. J. Bates, N. Cirigliano, D. C. Johnson, P. Malati, J. M. Mosby, E. Perre, M. T. Rawls, A. L. Prieto, and B. Dunn. 2011. "Three-dimensional electrodes and battery architectures." *MRS Bulletin* 36 (7):523-531.
2. McOwen Dennis, W., Shaomao Xu, Yunhui Gong, Yang Wen, L. Godbey Griffin, E. Gritton Jack, R. Hamann Tanner, Jiaqi Dai, T. Hitz Gregory, Liangbing Hu, and D. Wachsman Eric. 2018. "3D-Printing Electrolytes for Solid-State Batteries." *Adv. Mater.* 30 (18):1707132.
3. Hart, R. W., H. S. White, B. Dunn, and D. R. Rolison. 2003. "3-D microbatteries." *Electrochem. Commun.* 5 (2):120-123.
4. Long, J. W., B. Dunn, D. R. Rolison, and H. S. White. 2004. "Three-dimensional battery architectures." *Chem. Rev.* 104 (10):4463-4492.
5. Wood, B. C., J. B. Varley, K. E. Kweon, P. Shea, A. T. Hall, A. Grieder, M. Ward, V. P. Aguirre, D. Ringling, E. L. Ventura, C. Stancill, and N. Adelstein. 2021. "Paradigms of frustration in superionic solid electrolytes." *Phil. Trans. R. Soc. A* 379: 20190467.
6. Mehmedovic, Z., V. Wei, A. Grieder, P. Shea, B. C. Wood, and N. Adelstein. 2021. "Impacts of vacancy-induced polarization and distortion on diffusion in solid electrolyte Li_3OCl ." *Phil. Trans. R. Soc. A* 379: 20190459.
7. Heo, T. W., A. Grieder, B. Wang, M. Wood, S.A. Akhade, L.F. Wan, L.-Q. Chen, N. Adelstein, and B.C. Wood. 2021. "Microstructural impacts on ionic conductivity of oxide solid electrolytes from a combined atomistic-mesoscale approach," *npj Comp. Mater.*, in press.

Acknowledgements

This work was performed under the auspices of the U.S. Department of Energy by Lawrence Livermore National Laboratory under contract DE-AC52-07NA27344.

XV.4 3D Printing of All-Solid-State Lithium Batteries (LLNL)

Jianchao Ye, Principal Investigator

Lawrence Livermore National Laboratory
7000 East Avenue
Livermore, CA 94550
E-mail: ye3@llnl.gov

Tien Q. Duong, DOE Technology Development Manager

U.S. Department of Energy
E-mail: Tien.Duong@ee.doe.gov

Start Date: October 1, 2020

End Date: September 30, 2021

Project Funding (FY21): \$350,000

DOE share: \$350,000

Non-DOE share: \$0

Project Introduction

Traditional batteries are composed of two-dimensional films that are stacked and/or rolled. Thin film batteries display high power density while their thick film counterparts show good energy density, but it has proven difficult to concurrently achieve both within these planar form factors. In addition, conventional Li-ion batteries based on liquid organic electrolytes or gel polymer electrolytes have raised severe safety concerns due to the intrinsic flammable properties of the organic electrolytes. They are also not ideal for the use of high energy density metallic lithium (Li) anodes due to Li dendrite growth, or sulfur cathodes due to shuttling effects that result in fast capacity fade. There is an urgent need to develop safe, high-performance solid-state batteries (SSBs) with advanced electrolyte and separator technologies. Although in recent years a series of superionic conductors have been developed for electrolytes and separators [1],[2],[3], their performance does not satisfy demanding criteria due to large impedance from poor solid electrolyte-electrode contact and questionable electrochemical and mechanical stability. Unlike the well-established roll-to-roll fabrication of conventional Li-ion batteries, the processing of SSBs is unique due to the brittleness of solid-state electrolytes (SSEs). The commercially available or lab-developed SSE discs are usually very thick (hundreds of micrometers to millimeters) to overcome their brittle nature, which unfortunately increases the cell impedance and accounts for the majority of the overall cell weight and volume, leading to dramatically decreased power and energy densities. [4]

In this project, we will investigate 3D printing techniques to overcome safety, fabrication, mechanical, and electrochemical issues in SSBs. 3D printing builds complex structures in a layer-by-layer fashion, which allows rapid production of hierarchical architectures, gradient and multi-material structures, and multi-component assemblies. 3D printing is an emerging area that could fundamentally transform energy storage devices. For example, 3D printing can produce batteries with arbitrary form factors to fit a product's specific volume requirements and can create interwoven electrode arrangements over a wide range of length scales to improve transport and increase power density for a given energy density. For SSBs, 3D printing may dramatically reduce the separator thickness from ~1 mm (by hydraulic pressing) to tens of micrometers or less. In addition, the interfacial contact area between the electrolyte and the electrode may be increased via 3D interdigitated designs. Hence, we expect a significant reduction of the overall cell impedance and enhancement of both energy and power densities of SSBs by harnessing an array of 3D printing technologies being developed at Lawrence Livermore National Laboratory (LLNL).

The major R&D challenge in 3D printing of batteries is to develop a fabrication scheme that exhibits good printability, processability, and compatibility while achieving the ideal 3D layouts and feature resolution necessary to improve properties and performance. Batteries are complex systems that typically involve assembly of multiple components—for example, active materials (anode and cathode), electrolyte, separator, electrically conductive additives, binders, current collectors, and packaging. To be economically viable, the

assembled system must meet many stringent requirements, such as high weight percentage of active materials, high ionic and electronic conductivities, and good mechanical and thermal properties. To print a battery, the feedstocks (e.g., inks, resins, powders, suspensions, etc.) must also meet certain process requirements, such as exhibiting proper flow characteristics (or rheology), being stable and predictable, or perhaps even being photocurable for some specific 3D printing approaches. In addition, the multi-material nature of batteries is a nontrivial problem for 3D printing, and aspects such as varied particle morphologies and surface chemistry place increased importance on properly tuning the feedstock properties. For the case of SSBs, the solid-state electrolyte (SSE) is included in three battery components, the anode, cathode, and separator, which increases the difficulty in the feedstock development as multiple interactions between different solid components (e.g., solid electrolyte, conductive filler, and active materials) need to be considered. In the case of extrusion-based 3D printing processes, such as Direct Ink Writing (DIW) and Fused Deposition Modeling (FDM), particle aggregation or agglomeration in the ink can limit the minimum feature size that can be achieved due to jamming and nozzle clogging, which hinders the enhancement of power characteristics in 3D batteries. To realize the full potential of 3D printing, feedstocks for each component must be created that are suitable for the particular printing approach, multi-material printing methods must be developed, and material compatibility during post-processing steps must be addressed. With respect to the latter, sintering is a typical post-processing method used to improve the ionic conductivity of SSE separators. Yet, co-sintering with active materials could facilitate undesired reactions that may increase the interfacial impedance. [5],[6] Furthermore, stresses that develop during post-processing due to dimensional changes and volume reductions could lead to cracking and fracturing. We aim to solve these materials, manufacturing, and processing challenges to create 3D multi-material batteries and will first focus on the printing of SSEs. In addition, we will strive to develop materials and 3D printing approaches for SSBs that eliminate the need for sintering steps.

Objectives

- Objective 1: Tuning microstructures of 3D printed SSE separators.
- Objective 2: Process compatibility with cathode printing.
- Objective 3: 3D printing of sinter-free SSE separators.

Approach

The project will focus on 3D printing the solid-state electrolyte to tackle materials, manufacturing and processing challenges. In the first year, we will develop feedstock materials based upon state-of-the-art Li-ion conductors for SSBs. Next, we will explore a range of LLNL 3D printing methods to determine feedstock compatibility, complexity of 3D structure, and minimal feature size. We will focus on DIW, but other AM techniques will also be explored throughout the three-year timeline as long as budget allows. We will consider the scalability of these approaches and strive to develop high throughput methods that could be economically viable. In addition, material and processing compatibilities will be considered throughout the project. For example, we will verify the compatibility of our printed SSEs with typical SSB cathode materials during post-processing, specifically during sintering. Recognizing that sintering could be a limiting factor, both from a technological but also from a business standpoint, we will develop sintering-free feedstocks and 3D printing techniques to eliminate the possible compatibility issues during post-processing.

Results

In FY21, we evaluated new $\text{Li}_{6.4}\text{Ta}_3\text{Zr}_{1.4}\text{Ta}_{0.6}\text{O}_{12}$ (LLZTO) powders from four vendors and selected one for further studies. The 3D LLZTO structures were printed by Direct Ink Writing. Li loss issue was solved by add extra amount of Li_2CO_3 . Relative density was tuned by sintering temperatures and ink recipes. Co-sintering stability with printed/casted NMC cathode was evaluated. Solid polymer electrolytes based on PEGDA/PEGMA/PEO/LiTFSI were studied and conductivity was further improved by adding LLZTO powders. We developed three approaches for potential battery assembly using similar chemistries: 1) sintering-free approach using composite polymer electrolytes and 3D printed cathode; 2) hybrid electrolytes using SPE infilled 3D printed porous LLZTO; 3) co-sintered LLZTO/NMC-LLZTO bilayers. Preliminary battery tests

were conducted, and benefits and issues from each approach were identified for future performance optimization.

New powder evaluation

Due to the discontinuation of the $\text{Li}_{6.4}\text{Ta}_3\text{Zr}_{1.4}\text{Ta}_{0.6}\text{O}_{12}$ (LLZTO) powder product from previous vendor (vendor 1), we switched to new vendors. In FY21 Q1, new LLZTO powders from four manufacturers were received and evaluated. SEM, XRD, ICP-OES, and density measurements were conducted, and the results were compared with previous powders. It was found that only the LLZTO pellets from Vendor 2 can be densified as well as the original ones from Vendor 1. The other two form $\text{La}_2\text{Zr}_2\text{O}_7$ or LaO_9Ta_3 phases after sintering. ICP-OES (Table XV.4.1) suggests that the lower content of Li in the pristine powders might be the origin of secondary phase formation during sintering. Although the vendor 3 powder with low Li and Ta doping cannot be sintered well by itself, we found that adding a few percent of SiO_2 as a sintering agent can stabilize cubic LLZTO phase and accelerate the densification process.

Table XV.4.1 Composition of LLZTO powders, shrinkage and relative density of sintered LLZTO pellets.

Manufacturer	ICP-OES analysis	Shrinkage (%) and Relative density (%) of sintered pellets @ 1100 °C 6h
Vendor 1	$\text{Li}_{7.10}\text{La}_{3.00}\text{Zr}_{1.39}\text{Ta}_{0.61}\text{O}_x$	~13% and 93%
Vendor 2	$\text{Li}_{6.84}\text{La}_{3.00}\text{Zr}_{1.38}\text{Ta}_{0.60}\text{O}_x$	31.02% and 92%
Vendor 3	$\text{Li}_{6.53}\text{La}_{3.00}\text{Zr}_{1.46}\text{Ta}_{0.50}\text{O}_x$	1.42% and 60%
Vendor 4	$\text{Li}_{6.26}\text{La}_{3.00}\text{Zr}_{1.53}\text{Ta}_{0.67}\text{O}_x$	2.49% and 75%

Porous LLZTO films and infilling of polymer electrolytes

We used the powders from Vendor 2 to continue the Direct Ink Writing (DIW) and post sintering of LLZTO structures. As shown in Figure XV.4.1, the LLZTO/PEGDA inks with various sinter agents can be printed successfully. However, the high-temperature sintering of the films leads to stronger Li loss than pressed pellets. We solved this issue by adding extra amount of Li_2CO_3 in the ink preparation. Figure XV.4.2 shows the effects of Li_2CO_3 addition to the morphologies of LLZTO films. Relative dense films were obtained for the one sintered at 1100°C with the addition of Li_2CO_3 , SiO_2 and LBO; while highly porous films were obtained in ones without LBO addition or ones sintered at lower temperatures.

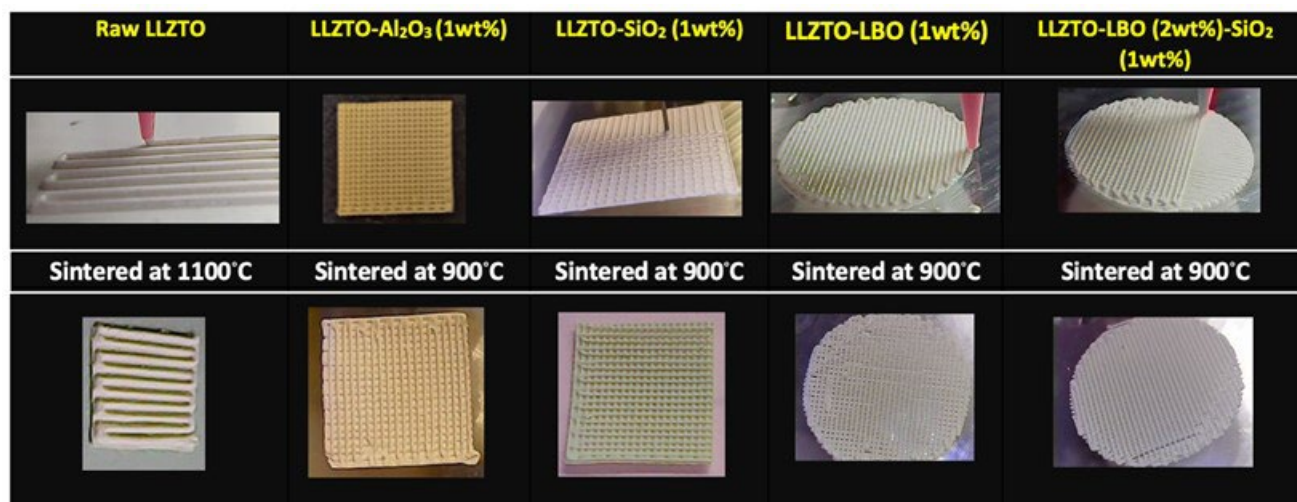


Figure XV.4.1 Optical images of the different 3D-printed LLZTO structures before and after sintering

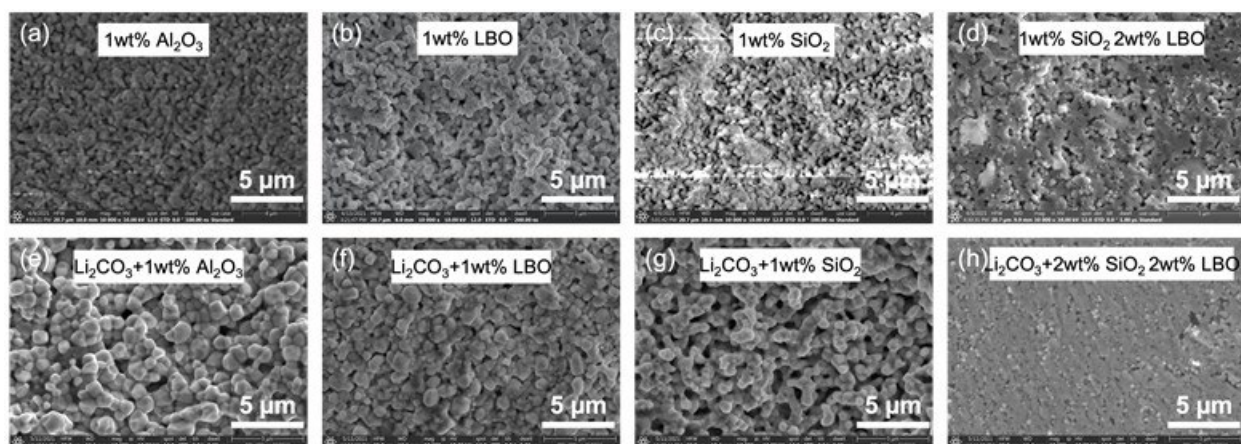


Figure XV.4.2 LLZTO films with varying additives after sintering at 1100 °C.

Based on the porous LLZTO backbone, we further infilled solid polymer electrolytes into it to improve the mechanical robustness and ionic conductivity (Figure XV.4.3). UV curable solid polymer electrolytes (SPEs) were utilized for the infilling purpose. Although the LLZTO film still cracked after cell assembly, the SPE phase may prevent the shorting. Depending on the curing condition, an ionic conductivity up to 10^{-4} S/cm can be obtained (Figure XV.4.3(d)). To demonstrate a full-cell battery using the 3D printed LLZTO structure, a NMC622 cathode ink with PVDF and carbon black additives was prepared and applied on the patterned side of porous LLZTO structure. After drying, PEGDA/PEGMA/LiTFSI solution was infilled, and UV cured to make a full battery against metallic Li. The performance was evaluated and shown in Figure XV.4.3(e). The cell can be cycled although with low capacity. The performance could be improved by tuning the compositions and integration procedures in the future work.

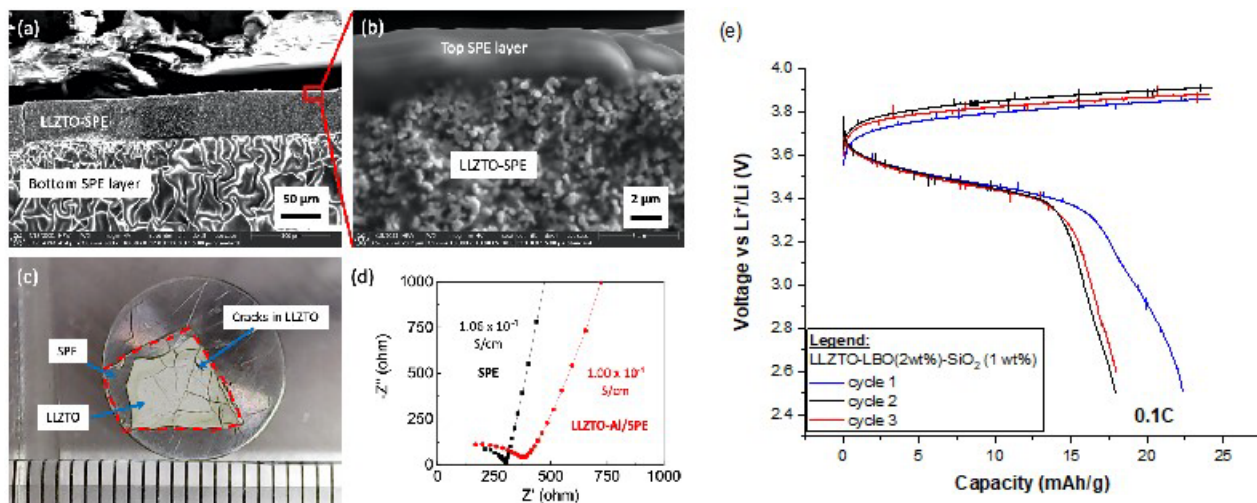


Figure XV.4.3 Sintered LLZTO film filled with solid polymer electrolyte composed of UV cross linked (PEGDA-PEGMA-PEO)/LiTFSI. (a) and (b) SEM morphology. (c) cracks formed in LLZTO during cell assembly. (d) Nyquist plots of SPE and LLZTO/SPE membranes sandwiched between stainless steel electrodes. (e) Charge-discharge capacity curves at 0.1 C-rate using the 3D printed LLZTO-LBO (2 wt%)-SiO₂ (1 wt%) structure infilled with PEGDA/PEGMA/LiTFSI SPE as solid electrolyte, and NMC622/PVDF/CB as cathode.

Composite polymer electrolytes

15 different PEGDA/PEGMA/PEO based solid polymer electrolytes (SPEs) were prepared to screen the optimized composition for best conductivity. The ionic conductivity was increased by adding more PEGMA, although the mechanical stiffness was decreased (Figure XV.4.4(a)).

To improve the ionic conductivity as well as mechanical properties, composite polymer electrolytes were further developed by adding ball milled LLZTO nano powders, as shown in Figure XV.4.4(b). A 13wt% LLZTO in 1:8:1 PEGDA/PEGMA/PEO CPE shows 5.6×10^{-5} S/cm ionic conductivity, about 3.7 times of the SPE without LLZTO. Further increasing LLZTO content to 18wt% seems to show less improvement (3.2×10^{-5} S/cm), which is consistent with the trend found in many literatures.

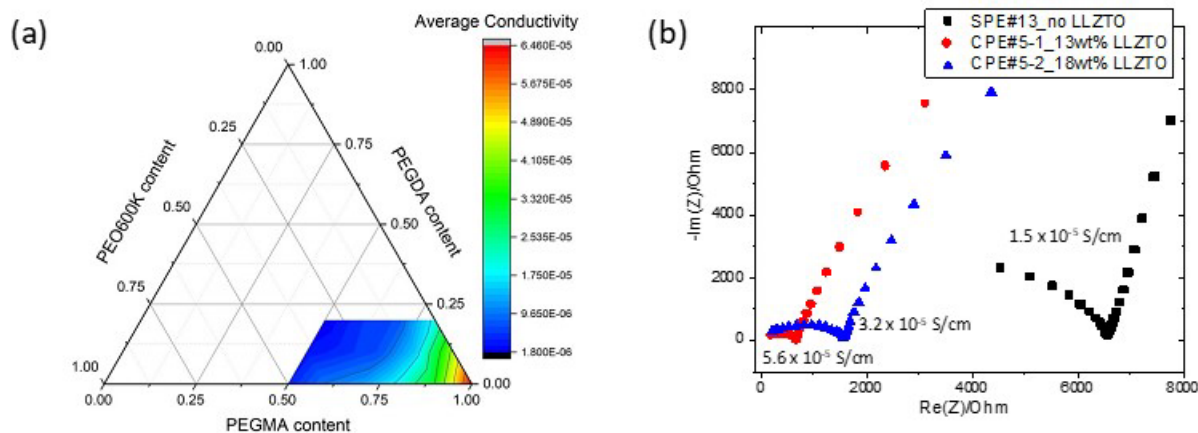


Figure XV.4.4 (a) Ionic conductivity contour map for the polymer electrolytes made of UV cured PEGDA/PEGMA/PEO/LiTFSI. (b) Increase of ionic conductivity by adding LLZTO powders.

To evaluate a full battery performance based on the developed CPEs, 3D LFP cathodes were printed on Al foil. A CPE ink with 30wt% LLZTO in 1:8:1 PEGDA/PEGMA/PEO compositions was infilled into the LFP structure. Metallic lithium was pressed against the CPE layer to make a full cell. The cell could be cycled at 60°C with reasonable capacities (Figure XV.4.5). However, fast capacity decay and low coulombic efficiency are to be resolved in future studies.

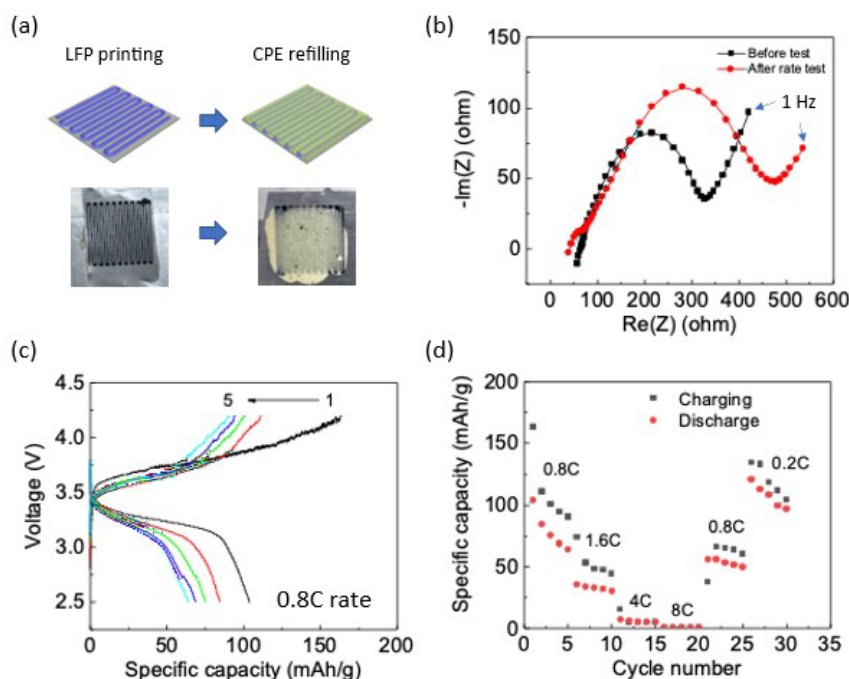


Figure XV.4.5 Battery assembly and testing for a CPE based ASSLB. (a) ASSLB made from infilling of CPE into a 3D printed cathode. (b) EIS before and after testing. (c) charge/discharge curves at 0.8C rate. (d) Rate performance. All tests were conducted at 60°C in coin cell setup.

Co-sintering compatibility

We continue evaluating the process compatibility with cathode printing especially under co-sintering conditions. Besides the UV curable PEGDA based LLZTO inks, we also developed low-binder ink formulations to accelerate the densification of the LLZTO layer. Over 40 different LLZTO ink formulations were evaluated as part of the development of a low-binder ink for 3D printing. Excellent densification was obtained in two recipes: 1) 94.6 wt% LLZTO / 0.7 wt% PVB / 4.7 wt% BBP in 3:7 wt 1-butanol/alpha terpineol (freestanding); 2) 95.3 wt% LLZTO / 0.8 wt% PVB / 4.0 wt% BBP in NMP (conformal). Bilayer printing was demonstrated to obtain LLZTO/(NMC-LLZTO) structure for our ultimate goal of co-printing and co-sintering.

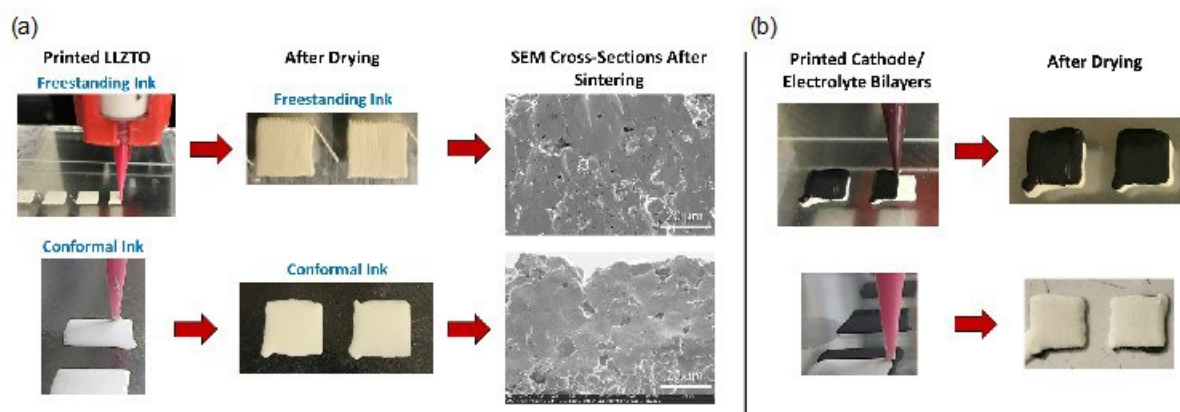


Figure XV.4.6 (a) Low-binder LLZTO inks printed by direct ink writing (250 μm nozzle). The formulations were as follows for the freestanding and conformal inks, respectively: 94.6 wt% LLZTO / 0.7 wt% PVB / 4.7 wt% BBP in 3:7 wt 1-butanol/alpha terpineol & 95.3 wt% LLZTO / 0.8 wt% PVB / 4.0 wt% BBP in NMP. Cross-section SEM images show the printed films after sintering at 1100 $^{\circ}\text{C}$ for 6h in Ar with mother powder. (b) NMC 622 / LLZTO bilayers printed by direct ink writing (250 μm nozzle) in 2 configurations: 1) cathode on top / electrolyte on bottom; 2) electrolyte on top / cathode on bottom.

To evaluate co-sintering stability of the two layered structure, we first used the NMC/LLZTO composite slurry to coat on a pre-sintered LLZTO pellet and co-sintered it at 900 $^{\circ}\text{C}$ for 2h in Ar. The obtained bilayer structure was then assembled into a cell using metallic Li as anode and graphite foil as cathode current collector. EIS and battery cycling were measured, and data are shown in Figure XV.4.7. It was found that the cathode made of 75 wt% NMC with 25wt% LLZTO and additional LBO and SiO₂ sintering agents behaved the best. Adding carbon black or ITO led to much worse performance. The compatibility of LLZTO and NMC with electrically conductive additives must be addressed in the future to further improve the battery performance. The poor cycling stability may also arise from the interface fracture that leads to contact degradation and shall be investigated in depth.

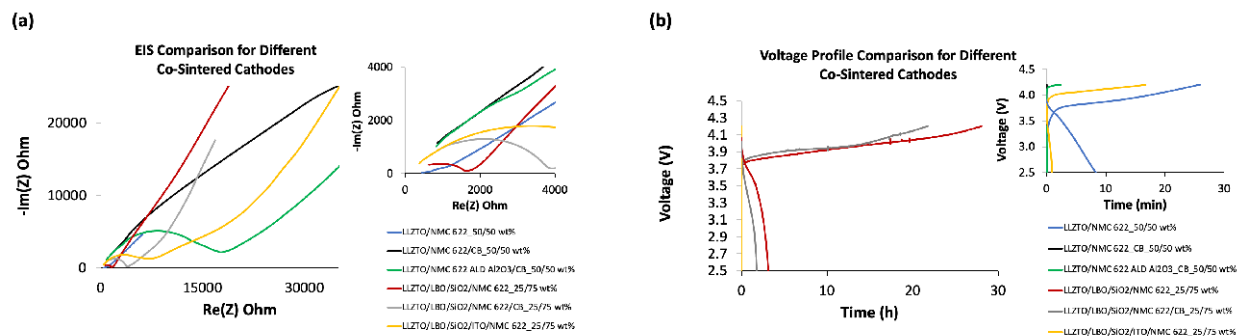


Figure XV.4.7 Comparison of EIS results (a) and first cycle charge/discharge voltage profiles at $\sim \text{C}/50$ (b) for different composite cathodes coated on pre-sintered LLZTO pellets and co-sintered at 900 $^{\circ}\text{C}$ for 2h in Ar. All were tested at room temperature without extra external pressure.

Conclusions

In FY21, we have down selected LLZTO powders from new vendors, and fabricated sintered films and 3D structures with different porosities. We have obtained ionic conductivity of composite polymer electrolytes and SPE infilled LLZTO films, and determined the co-sintering compatibility between LLZTO and NMC and with various additives. We also evaluated the performance of full batteries from the three approaches (CPEs, hybrid, and co-sintering) and identified future directions for optimization.

Key Publications

1. M. Wood, X. Gao, R. Shi, T.W. Heo, J.A. Espitia, E.B. Duoss, B.C. Wood, J. Ye, Exploring the relationship between solvent-assisted ball milling, particle size, and sintering temperature in garnet-type solid electrolytes, *Journal of Power Sources* 484 (2021) 229252.
2. Joshua A. Hammons, J. Ali Espitia, Erika Ramos, Rongpei Shi, Frederick Meisenkothen, Marissa Wood, Maira R. Cerón, and Jianchao Ye. Pore and Grain Chemistry during sintering of garnet-type $\text{Li}_{6.4}\text{La}_3\text{Zr}_{1.4}\text{Ta}_{0.6}\text{O}_{12}$ solid-state electrolytes. Submitted.

References

1. N. Kamaya, K. Homma, Y. Yamakawa, M. Hirayama, R. Kanno, M. Yonemura, T. Kamiyama, Y. Kato, S. Hama, K. Kawamoto, A. Mitsui, A lithium superionic conductor, *Nature Materials* 10(9) (2011) 682–686.
2. W.S. Tang, A. Unemoto, W. Zhou, V. Stavila, M. Matsuo, H. Wu, S. Orimo, T.J. Udovic, Unparalleled lithium and sodium superionic conduction in solid electrolytes with large monovalent cage-like anions, *Energy & Environmental Science* 8(12) (2015) 3637–3645.
3. Y. Wang, W.D. Richards, S.P. Ong, L.J. Miara, J.C. Kim, Y.F. Mo, G. Ceder, Design principles for solid-state lithium superionic conductors, *Nature Materials* 14(10) (2015) 1026–1032.
4. Y. Kato, S. Hori, T. Saito, K. Suzuki, M. Hirayama, A. Mitsui, M. Yonemura, H. Iba, R. Kanno, High-power all-solid-state batteries using sulfide superionic conductors, *Nature Energy* 1 (2016) 1–7.
5. Y.Y. Ren, T. Liu, Y. Shen, Y.H. Lin, C.W. Nan, Chemical compatibility between garnet-like solid state electrolyte $\text{Li}_{6.75}\text{La}_3\text{Zr}_{1.75}\text{Ta}_{0.25}\text{O}_{12}$ and major commercial lithium battery cathode materials, *Journal of Materiomics* 2(3) (2016) 256–264.
6. L. Miara, A. Windmüller, C.-L. Tsai, W.D. Richards, Q. Ma, S. Uhlenbruck, O. Guillon, G. Ceder, About the compatibility between high voltage spinel cathode materials and solid oxide electrolytes as a function of temperature, *ACS applied materials & interfaces* 8(40) (2016) 26842–26850.

Acknowledgements

I would like to acknowledge our team members including Erika Ramos, Marissa Wood, Siwei Liang, Joshua Hammons, for their great contributions to the project. We also express our thanks to Brandon Wood, Rongpei Shi, Tae Wook Heo, Marcus Worsley and Tony Van Buuren for helpful discussions. This work was performed under the auspices of the U.S. Department of Energy by Lawrence Livermore National Laboratory under Contract DE-AC52-07NA27344.

XV.5 Advanced Polymer Materials for Li-ion (SLAC)

Zhenan Bao, Principal Investigator

Stanford University
Department of Chemical Engineering, Stanford University
Stanford, CA 94305
E-mail: zbao@stanford.edu

Yi Cui, Principal Investigator

Stanford University
Department of Materials Science and Engineering, Stanford University
Stanford, CA 94305
E-mail: yicui@stanford.edu

Tien Q. Duong, DOE Technology Development Manager

U.S. Department of Energy
E-mail: Tien.Duong@ee.doe.gov

Start Date: October 1, 2020

End Date: September 30, 2021

Project Funding: \$450,000

DOE share: \$450,000

Non-DOE share: \$0

Project Introduction

These lithium metal batteries (LMB), which are considered as the “Holy Grail” of future Li-based batteries, have limited success in commercialization due to battery short-circuits and poor cycle life. These issues are rooted in the unstable interface between lithium metal anode and the electrolyte. By introducing a layer of polymer coating to the lithium metal surface with tunable mechanical properties, electrostatic interaction, and salt-solvent interaction, we aim to promote stable lithium metal deposition morphology and prolong the cycle life of lithium metal batteries.

Objectives

This project will develop new polymer materials for batteries. The team will develop polymer coatings with specific mechanical properties that can accommodate the volume expansion and contraction of the Li-metal anode associated with deposition and stripping (charging and discharging). The cycling stability and Coulombic efficiency (CE) of Li-metal electrodes will be increased by implementation of a polymer based protective layer that functions as an artificial SEI with desired properties. The improved performance will enable further development toward practical utilization of Li-metal anodes with higher cycling efficiency and less susceptibility to dendrite-based failure.

Approach

The project uses soft polymer coatings with dynamic crosslinking to give the resulting polymers liquid-like rheological properties and stretchable and self-healing properties. In previous work, the project has shown that such coatings resulted in uniform deposition/stripping of lithium metal and improved cycling stability of Li-metal electrodes. To understand the design rules for effective polymer coatings, the team chose a few representative polymers to systematically understand structure property relationships. Here, the team investigates the correlation between surface energy of the polymer and exchange current for lithium deposition.

Results

We hypothesize that an effective method to address the lithium anodic interfacial instability is to fundamentally alter the lithium-ion deposition pathways by electrostatically blocking the heterogenous surface regions that concentrate lithium ions due to high electric field. This can be experimentally implemented using

electro-inactive cations at the interface that can ‘shield’ the inhomogeneous protrusion on the electrode surface to neutralize the electric field landscape. However, this strategy can be successful only when it is ensured that these electro-inactive cations do not undergo reduction during lithium deposition process. In other words, their reduction potential need to be even lower than that of Li^+ ions that already has the lowest intrinsic reduction potentials among metallic cations. Previously Ding et al. pointed out that Cs^+ can achieve lower reduction potential than Li^+ by tuning its concentration based on Nernst Equation. [1] Furthermore, it was shown that addition of Cs^+ ions in electrolyte resulted in improved lithium deposition morphology and battery operation. However, the concentration dependent electrochemical stability of Cs^+ ions can be undermined by their localized aggregation at the electrode surface, resulting in the reduction of Cs^+ .

Instead of using free cations, here we propose to tether the electroactive cations (Pyrrolidinium Py^+) onto a flexible and stable polymer backbone (Polydimethylsiloxane PDMS) to form a PDMS based poly (ionic liquid) (PDMS-Py) coating which would homogenize the electric field distribution on the electrode surface and promoting uniform lithium deposition. Based on previous study, Py^+ was selected based on its lower reduction potential comparing to Li^+ , and its chemical stability with the lithium metal anode. Incorporation of Py^+ in a polymer coating on the lithium anode is a facile method that doesn’t alter existing manufacturing capabilities and limit their interaction with other battery components. Building on previous studies on anodic coating using polymers (PEO, Nafion, PVDF), and drawing on our previous knowledge on designing cation-tethered polymeric coating on anode surface, [2] this work, the interfacial material, in this work, is designed on economically viable chemistry, chemically and electrochemically inert with lithium metal, possessing conducting pathway for lithium conduction, and mechanically robust for adapting to rapid volume changes.

The schematic of Figure XV.5.1A illustrates lithium anode coated with PDMS-PyTFSI containing electro-inactive cations and its counter anion TFSI. In absence of any coating, the concentrated electric field at surface protrusion triggers self-amplified surface roughening process of lithium deposition (Figure XV.5.1B). The presence of cations is hypothesized to neutralize the radiating electric field and helps to homogenize lithium deposition pathways. Figure XV.5.1C showcases the ‘cationic shielding’ phenomenon where the presence of the PDMS-PyTFSI coating results in re-distribution of Li^+ ions away from the surface protrusions leading to a more uniform topology. The physio-chemical prerequisites of the PDMS-Py polymer coating for the cationic shielding mechanism are following: (1) the cations in PDMS-PyTFSI backbone should have a lower reduction potential than that of Li^+ , (2) sufficient mobility of the polymer chains is essential for electric-field based response of the cations. In the previous work, we utilized a system of random co-polymer on poly(acrylic) backbone: one of the co-polymer side chain contains the Py^+ (pyrrolidinium) cation units, and the other side chain is perfluoroalkyl as an inert component that can also lower the glass transition of the final co-polymer and introduce mobility to the polymer chains.

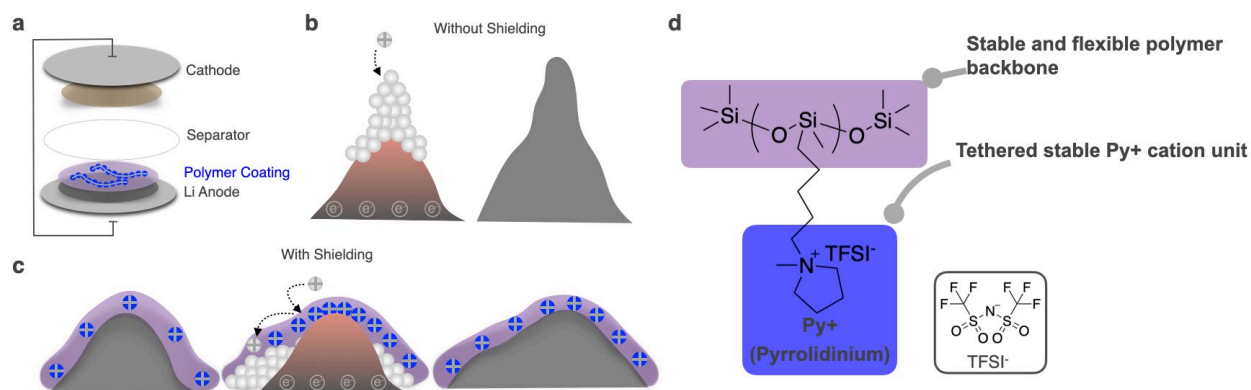


Figure XV.5.1 **PDMS-Py as the anodic coating for lithium metal batteries.** (A) lithium metal battery with polymer coated anode. (B), the concentrated electric field at vicinity of surface protrusions cause the self-amplifying dendritic deposition of lithium ions. (C), coating on lithium metal anode. During Li^+ deposition, cations in coating remain electrochemically stable and can effectively shield the Li^+ ions, resulting in more flat and homogeneous deposition. (D), chemical structure of the PDMS-PyTFSI coating.

The PDMS-PyTFSI polymer was synthesized by tethering the Py^+ side chain to purchased PDMS backbone, which has controlled molecular weight with an average of 30 monomer unit per polymer chain. After the polymer was synthesized, its chemical structure was confirmed with proton NMR. As shown in Figure XV.5.2A, hydrogen containing functionality on the polymer structure are numerically numbered, corresponding to the peak signals on the NMR spectrum. The integration value of area under each peak represents the amount of hydrogen atoms for each signal peak. Through comparing the ratio among the peak integration value and the stoichiometric ratio of the hydrogen atoms at each unique chemical environment on the polymer, we concluded that the PDMS polymer with Py^+ side chain tethered was correctly synthesized. Other than linear polymer, we also synthesized crosslinked PDMS-PyTFSI polymer using short chain siloxane crosslinking agent. 5% (molar of crosslinking agent: molar of monomer units) of crosslinker was added to the polymer during polymer synthesis and the result polymers' mechanical properties and glass transition temperatures were compared. The mechanical properties were measured with rheology frequency sweep measurements, where the polymer samples were placed under oscillatory 1% strain, and both the storage and loss moduli of the samples were measured at multiple frequencies. (Figure XV.5.2B) Upon crosslinking, both the storage and loss moduli of the polymer increased: as indicated on the plot, the storage modulus measured at 1 Hz frequency increases by an order. The storage and loss moduli from the rheological measurement are also indication of the solid/ liquid state of the materials: when the storage modulus is higher than the loss modulus, the material exhibit solid-like behavior, and vice versa. When there was no crosslinker, the measured polymer's loss modulus is lower than its storage modulus, indicating that the polymer was a viscous elastic liquid in the measured frequency range. Upon addition of the crosslinker, the polymer exhibited solid-like behavior with its storage modulus at lower frequency range, with its storage modulus higher than the loss modulus. Beyond mechanical properties, the glass transition temperatures (T_g) of the crosslinked and linear polymer were also characterized with differential scanning calorimetry (DSC), and we found the T_g of the polymer increased from -29.8°C to -2.2°C (Figure XV.5.2C). After crosslinking, the polymer's T_g was still below room temperature (25°C), indicating that the resulting polymer still has sufficient chain mobility at room temperature. Both the rheological and DSC measurements showcased that the mechanical and molecular dynamic of the PDMS-PyTFSI polymer can be tuned with minimal effect on the overall polymer chemistry through controlled crosslinking. We believe, the polymer design reported in this work based on PDMS chemistry, provided a synthetically accessible, economically viable, and mechanically tunable solution to the unstable lithium metal deposition at the anode/ electrolyte interface.

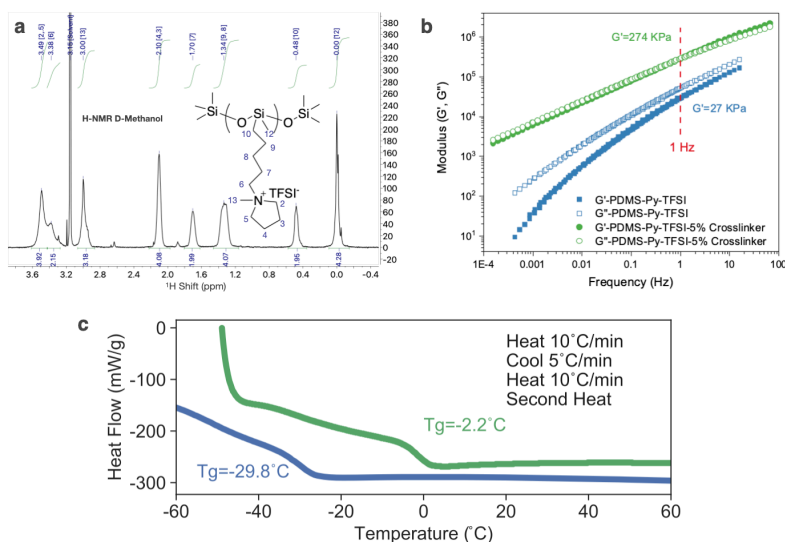


Figure XV.5.2 Characterization of the PDMS-PyTFSI polymer. (A) Proton NMR of the PDMS-PyTFSI polymer dissolved in protonated methanol. Each hydrogen containing functionality on the polymer is labeled with number corresponding to the numbering on top of each NMR peak signals. The integration value of the area under each peak is indicated at the bottom of each signal. (B) rheological frequency sweep of the PDMS PyTFSI polymer conducted at room temperature with 1% strain on the polymer. The open symbol stands for loss modulus (G'') and the filled symbol stands for storage modulus (G'). Green: PDMS-PyTFSI with 5% crosslinker, Blue: PDMS-PyTFSI. (C) glass transition (T_g) of the PDMS PyTFSI polymer with and without the crosslinker measured with differential scanning calorimetry (DSC). Green: PDMS-PyTFSI with 5% crosslinker, Blue: PDMS-PyTFSI.

To examine the stability of the PDMS-PyTFSI (not crosslinked) coating on the lithium metal anodes, a layer of polymeric coating was applied to the electrode surface via dip coating the lithium metal chip in a polymer THF solution (0.1 g/ml). The coated lithium metal chips were then assembled into Li||Li symmetric coin cell with 50 μ l of electrolyte, and the electrochemical impedance spectroscopy (EIS) was measured over 100 hours. Two of the most commonly used ether based (1M LiTFSI and 1 wt% LiNO₃ in DOL(1,3-Dioxolane)/DME(1,2-Dimethoxyethane)) and carbonate based (1M LiPF₆ in EC(Ethylene carbonate)/DEC (Diethyl carbonate) and 10% FEC(Fluoroethylene carbonate)) electrolytes were used in the system. To understand the changes in the interfacial impedance, control experiments with lithium chips that were just dipped in THF solvent and then assembled into the coin cells with the two electrolytes were also performed. Based on the interfacial impedance data shown in Figure XV.5.3, we can see that the interfacial impedance increased overtime in both ether and carbonate-based electrolytes. For the case of carbonate electrolyte, a layer of PDMS-PyTFSI coating on the lithium metal surface effectively reduced the increase of interfacial impedance. Over the 100 hours of measurement, the interfacial impedance of PDMS-PyTFSI coated lithium increases from 300 to 330 Ohms, while the uncoated bare lithium's interfacial impedance increases from 190 to 360 Ohms. The stable interfacial impedance value of the coated lithium metal in carbonate electrolyte shows that this polymer can effectively protect the lithium metal from further carbonate electrolyte corrosion while remaining on the electrode surface. For the case of ether-based electrolyte, the bare lithium metal's interfacial impedance increased to almost 2X the starting value at the first 20 hours of measurements. By applying a layer of polymeric coating on the surface, the interfacial impedance increases much slower over the periods of 100 hours, and eventually stabilizes at 1.5X the value of the starting impedance. Overall, the application of a PDMS-PyTFSI coating layer can limit the reaction between lithium metal and the electrolytes, and the coating is also stable on the electrode surface for long periods of time.

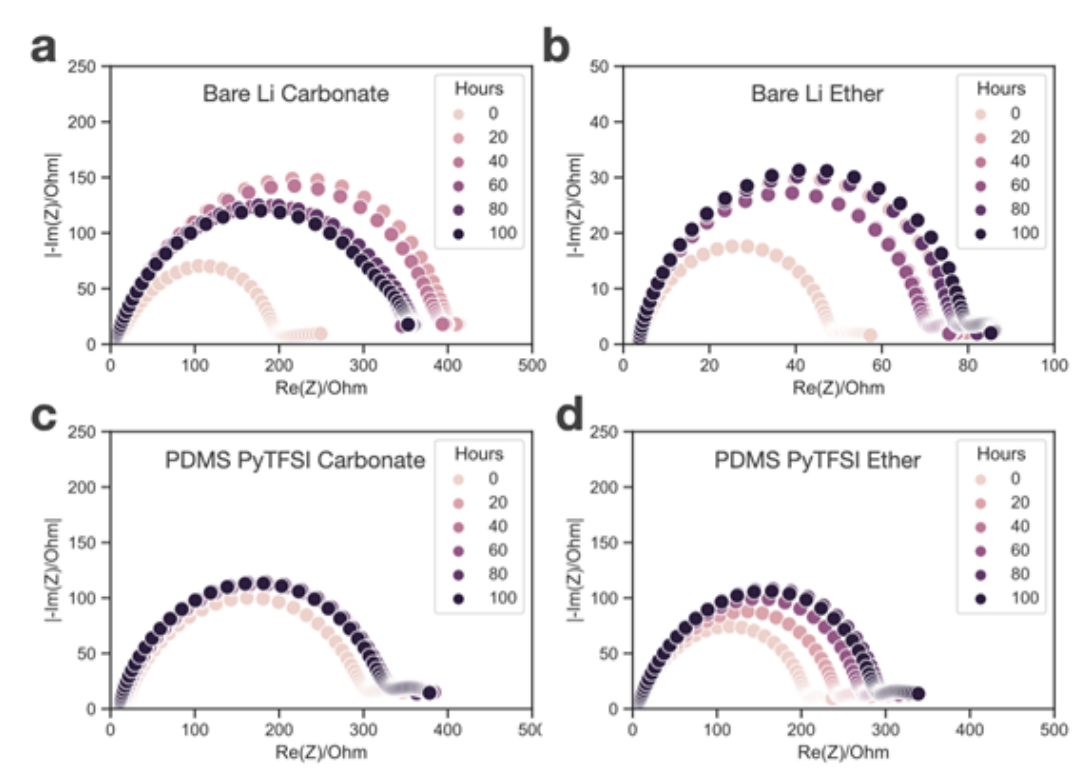


Figure XV.5.3 The interfacial impedance measured over 100 hrs on Li||Li symmetric cell with 50 μ l of electrolytes in between the two electrodes. The carbonate electrolyte is composed of 1M LiPF₆ in EC/DEC and 10% FEC, and the ether electrolyte is composed of 1M LiTFSI and 1 wt% LiNO₃ in DOL/DME. The absolute value of the imaginary part of the interfacial impedance (Z) and the real part of the Z was measured through electrochemical impedance spectroscopy (EIS) and plotted: bare lithium with (A) carbonate electrolyte; (B) ether electrolyte; PDMS PyTFSI coated lithium with (C) carbonate electrolyte; (D) ether electrolyte.

To examine the stability of the PDMS-PyTFSI coating on the lithium metal deposition morphology, a layer of polymer coating was applied to the Cu electrodes and Li||Cu half cells was assembled, with 50 μl of 1M LiTFSI and 1 wt% LiNO_3 in DOL(1,3-Dioxolane)/DME(1,2-Dimethoxyethane) electrolyte. We deposited 0.1 mAh/cm² Li on the Cu foil at the current density of 0.5 mA/cm² (first cycle).

Based on the SEM image shown in Figure XV.5.4, we observed that a layer of PDMS-PyTFSI polymer can effectively change the deposition morphology of the lithium metal. When the Cu electrode was not coated, the deposited lithium metal was presented as small spherical nucleus. When a layer of coating was present, the deposited lithium nuclei became bigger and flattened. Furthermore, we quantified the size distribution of deposited lithium nuclei, and we can see that Li deposition size increased from 2.2 μm to 3.4 μm upon the application of a coating layer. This series of characterization shows that the PDMS-PyTFSI coating can effectively shields the charging tips during lithium deposition and change the lithium deposition morphology. This results in more homogenous lithium deposition structures.

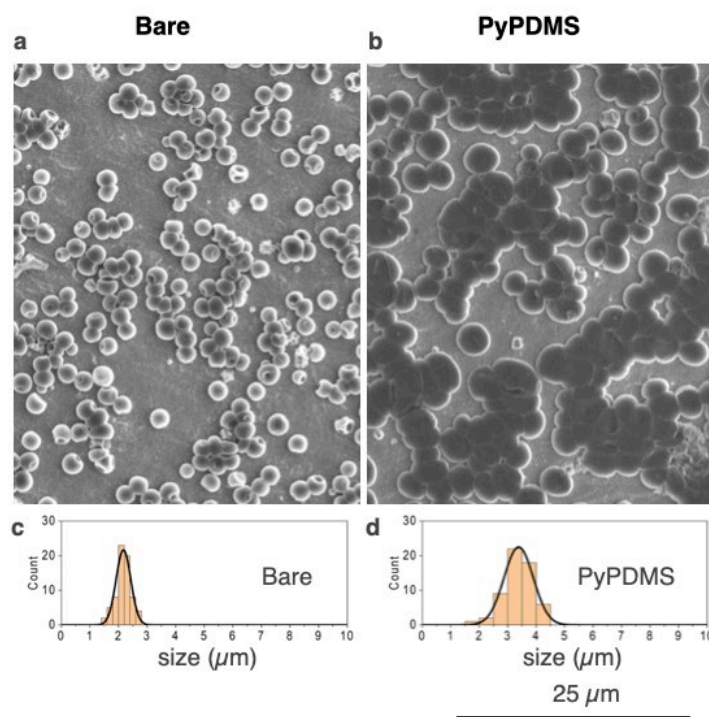


Figure XV.5.4 SEM images of lithium depositing on Cu foil: (A), bare Cu foil; (B), PDMS-PyTFSI coated Cu foil; size distribution of lithium nuclei under SEM: (C), bare Cu foil, (D) PDMS-PyTFSI coated Cu foil.

To examine the stability of the PDMS PyTFSI coating with lithium metal electrodes during long term cycling, a layer of polymer coating was applied to the Li electrodes and Li||Li symmetric cell was assembled, with 40 μl of three different types of electrolytes, as shown in Figure XV.5.5 below. We strip-and-plated 1 mAh/cm² Li at 1 mA/cm² current density for three different electrolytes, and we increased the current density to 2 mA/cm² for the FDMB electrolyte.

At 1 mA/cm² current density, the lithium metal coated electrodes showed stable cycling performance over 150 cycles in all three electrolytes (ether, carbonate, FDMB³). In DOL/DME electrolyte, the application of the coating slightly increased the overpotential. In EC/DEC electrolyte, the lithium electrodes without polymer coating demonstrated a soft shorting around 50 hrs of cycling, indicating non-stable cycling and lithium deposition behavior. For the lithium electrodes with the polymer coating in EC/DEC electrolyte, we observed stable voltage profile over cycles. In FDMB electrolyte, the uncoated lithium metal showcased increase in overpotential around 30 cycles. This is consistent with literature reported behavior, attributed to the formation

of resistive SEI layer on the lithium metal surface. With the layer of coating applied, the voltage profile was stabilized without increasing over cycles, showcasing more conductivity SEI layer was formed. Similar behavior was observed on the FDMB electrolyte at both 1 mA/cm² and 2 mA/cm² current density. This series of cycling performance shows that the PDMS-PyTFSI coating promotes the stable cycling behavior of lithium metal anodes in three different types of electrolytes.

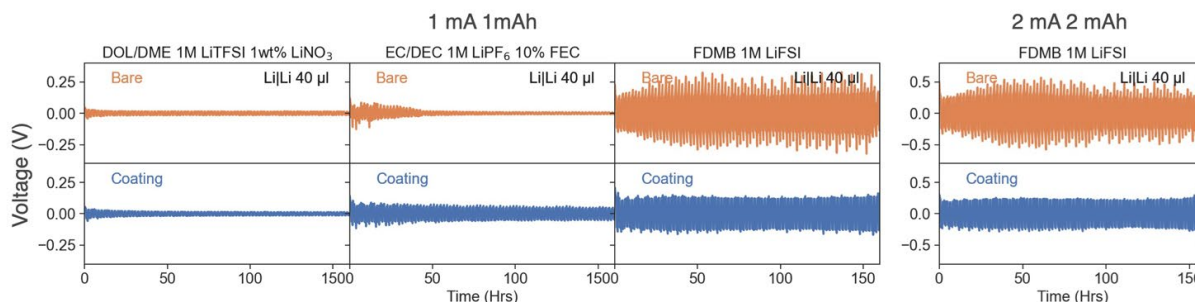


Figure XV.5.5 Li|Li cycling with polymer coating on the electrodes: the electrolyte composition and cell configurations are marked in the graph.

Conclusions

In all, in the past one year, we have made great progress in understanding how to design polymeric interface to promote stable operation of lithium metal anode. We showed a new lithium anode coating design and analyzed the polymer chemistry and mechanical property using NMR, differential scanning calorimetry (DSC) and rheology. We also examined the stability of the polymer in electrolyte and its ability to reduce the reaction in the lithium metal surface with impedance spectroscopy (EIS). The impact of the polymeric coating on lithium deposition morphology was characterized using scanning electron microscopy (SEM). The coated Li metal electrodes with the polymeric coating was cycled for 150 cycles at 1 and 2 mA/cm² current density, and stable cycling was achieved. Overall, through a series of materials characterization, we demonstrated a useful design strategy for polymer coating on lithium metal anode.

Key Publications

1. Z. Huang, S. Choudhury, H. Gong, Y. Cui, and Z. Bao " A Cation-Tethered Flowable Polymeric Interface for Enabling Stable Deposition of Metallic Lithium " *JACS* (2020) DOI: 10.1021/jacs.0c09649
2. Boyle, D.T., Huang, W., Wang, H., Li, Y., Chen, H., Yu, Z., Zhang, W., Bao, Z., Cui, Y. Corrosion of lithium metal anodes during calendar ageing and its microscopic origins. *Nat Energy* (2021).
3. H. Wang, W. Huang, Z. Yu, W. Huang, R. Xu, Z. Zhang, Z. Bao, Y. Cui, Efficient Lithium Metal Cycling over a Wide Range of Pressures from an Anion-Derived Solid-Electrolyte Interphase Framework, *ACS Energy Letters* 6 (2), 816–825.
4. J. Li, Y. Cai, H. Wu, Z. Yu, X. Yan, Q. Zhang, T.Z. Gao, K. Liu, X. Jia, Z. Bao, Polymers in Lithium-Ion and Lithium Metal Batteries, *Adv. Energ. Mater.*, published Jan. 25, 2021, doi.org/10.1002/aenm.202003239.
5. Sang Cheol Kim, Xian Kong, Rafael A. Vilá, William Huang, Yuelang Chen, David T. Boyle, Zhiao Yu, Hansen Wang, Zhenan Bao, Jian Qin, Yi Cui, "Potentiometric measurement to probe solvation energy and its correlation to lithium battery cyclability", *JACS*, doi:10.1021/jacs.1c03868, 2021.
6. Hansen Wang, Zhiao Yu, Xian Kong, William Huang, Zewen Zhang, David G. Mackanic, Xinyi Huang, Jian Qin, Zhenan Bao, and Yi Cui, "Dual-solvent Li-ion solvation enables high-performance Li-metal batteries", *Advanced Materials*, 2008619, 2021.

References

1. Cheng, X.-B. et al. Dendrite-Free Lithium Deposition Induced by Uniformly Distributed Lithium Ions for Efficient Lithium Metal Batteries. *Adv. Mater.* 28, 2888–2895 (2016).
2. Lopez, J. et al. Effects of Polymer Coatings on Electrodeposited Lithium Metal. *J. Am. Chem. Soc.* 140, 11735–11744 (2018).
3. Yu, Z. et al. Molecular design for electrolyte solvents enabling energy-dense and long-cycling lithium metal batteries. *Nat. Energy* 5, 526–533 (2020).

XVI Beyond Li-ion R&D: Solid-State Batteries

XVI.1 Improving the Stability of Lithium-Metal Anodes and Inorganic-Organic Solid Electrolytes (UC Berkeley)

Dr. Nitash P. Balsara

Department of Chemical and Biomolecular Engineering
University of California, Berkeley
Berkeley, CA 94720
E-mail: nbalsara@berkeley.edu

Tien Q. Duong, DOE Technology Development Manager

U.S. Department of Energy
E-mail: Tien.Duong@ee.doe.gov

Start Date: October 1, 2020

End Date: September 30, 2021

Project Funding: \$213,000

DOE share: \$213,000

Non-DOE share: \$0

Project Introduction

Polymer electrolytes offer increased stability against lithium metal anode batteries in comparison to more widely used liquid electrolytes. Nanostructured polymer electrolytes containing both soft, ion-conducting domains and rigid, nonconducting domains offer the opportunity to tune independently both mechanical and electrical properties. Such electrolytes are conveniently obtained by self-assembly of block copolymers. Most of the block copolymer electrolytes studied thus far comprise organic polymer chains for both the conducting and rigid domains. The team hopes to synthesize and study new organic-inorganic copolymer electrolytes that simultaneously have high transport properties and have greater stability against lithium in comparison to organic diblock copolymers. The project objective is to establish new hybrid electrolytes that will be stable against Li-metal anode.

Objectives

The objective of this project is to design organic-inorganic hybrid diblock copolymer electrolytes and to study their stability against lithium metal anodes. Acryloisobutyl polyhedral oligomeric silsesquioxane (POSS) covalently bonded to a chain is utilized as the non-conducting mechanically rigid block. The second block is a conventional polymer electrolyte, polyethylene oxide (PEO). The formation of different nanostructures will be studied by small angle X-ray scattering (SAXS) experiments. Electrochemical characterization of these polymers will include measurement of various transport parameters including conductivity, diffusion coefficient, and the transference number. The stability against lithium metal will be evaluated by cyclic voltammetry (CV), while its applications as an electrolyte will be evaluated and visualized using cycling X-ray tomography experiments on symmetric Li-polymer-Li cells. The combination of these approaches enables rational design of materials that exhibit improved stability against lithium metal.

Approach

First the team designed and synthesized new organic-inorganic hybrid copolymers by incorporating monomers that contain an inorganic POSS moiety. The electrolytes are formed by homogeneously mixing lithium salt to the copolymers. The self-assembled nanostructure formation was studied using SAXS techniques. The mechanical and electrochemical properties are performed before carrying out cycling X-ray tomography experiments. Finally, all the data are combined to analyze the performance of the electrolytes.

Results

Synthesis of POSS containing single-ion copolymers

Single-ion block copolymers containing covalently bound counter-ions can enable lithium metal anodes by eliminating concentration gradient. A series of organic-inorganic hybrid single-ion conductors, PEO-*b*-POSS-*r*-PSLiTFSI, were synthesized. Here PEO acts as an ion conducting block, POSS acts as mechanically rigid non-conducting block, and the polystyrene block acts as an ionic block in which the counter ion (sulfonyl(trifluoromethane sulfonyl) imide) is covalently bonded with the benzene ring of styrene.

The synthesis was carried out via nitroxide mediated copolymerization method as shown in scheme 1 (Figure VI.1.1). A PEO-based macroalkoxymine initiator was synthesized using the standard procedure. [1] In the next step, the macroinitiator was reacted with POSS acrylate and lithium-4-styrenesulfonyl(trifluoromethane sulfonyl) imide, in one step in dimethyl formamide at 120°C for 24 h to generate a random copolymer. After that reaction the polymer was precipitated from diethyl ether and then dialysed against deionized water for 72 h and dried to obtain the pure product. The composition of the polymer was determined by ¹H-NMR spectra and is shown in Table XVI.1.1.

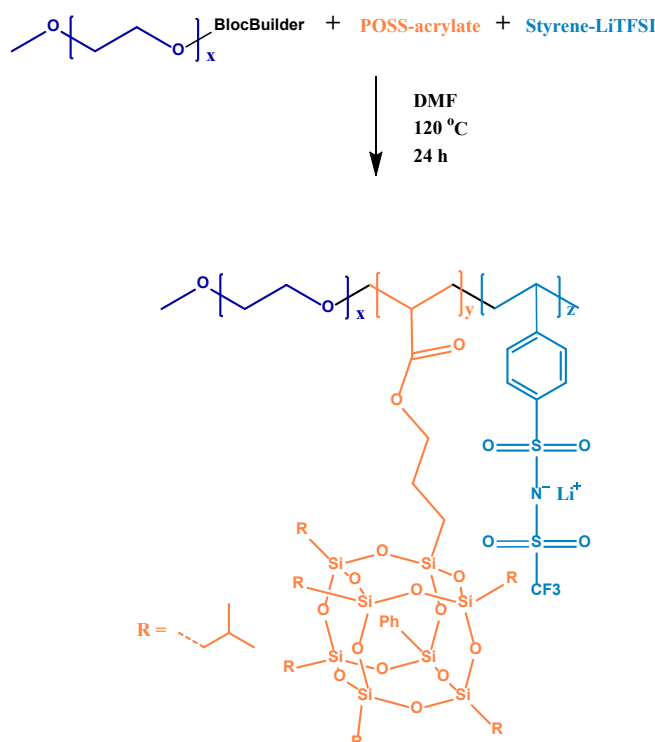


Figure XVI.1.1 Scheme 1. Synthesis of PEO-*b*-POSS-*r*-PSLiTFSI copolymer

Table XVI.1.1 Composition of the triblock copolymer PEO-*b*-POSS-*r*-PSLiTFSI. The compositions of POSS and PSLiTFSI were determined by ¹H-NMR spectra. The *r* values denote the concentration of Li ion in the polymer and is given by $r = [\text{Li}]/[\text{EO}]$.

PEO-POSS-PSLiTFSI	M _{PEO} (kg mol ⁻¹)	M _{POSS} (kg mol ⁻¹)	M _{PSLiTFSI} (kg mol ⁻¹)	<i>r</i>
5-2-2	5	1.9	2	0.055
5-2-4	5	1.9	4	0.11
5-2-11	5	1.9	11	0.31

Figure XVI.1.1a summarizes the temperature dependence of the ionic conductivity of the electrolytes measured using a stainless-steel symmetric cell setup. The ionic conductivity of the electrolytes decreases with increasing Li ion concentration. The current fraction ρ_+ was determined using Li symmetric cells following the Bruce and Vincent method [2] for two of the electrolytes with $r = 0.11$ and 0.31 . The values are 0.963 ± 0.04 and 0.96 ± 0.04 respectively, characteristic of the single ion conductors. The effective conductivity, given by $\kappa\rho_+$, is shown in Figure XVI.1.1b and compared with PEO/LiTFSI, $r = 0.06$ which exhibits current fraction of 0.115 ± 0.01 .

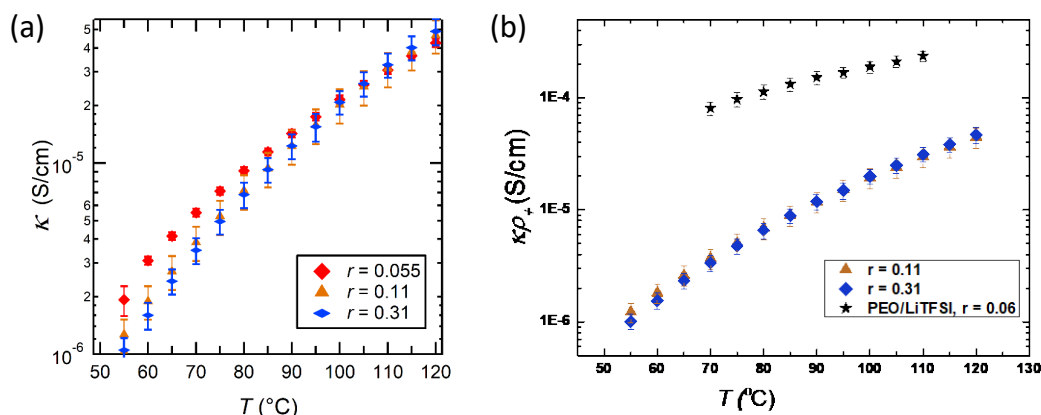


Figure XVI.1.2 (a) Temperature dependent conductivity κ is shown for three copolymers. (b) The effective conductivity $\kappa\rho_+$ is shown for two polymers with $r = 0.11$ and 0.31 and compared with PEO/LiTFSI, $r = 0.06$.

The non-linear mechanical property of two block copolymers were determined by creep experiments

Understanding the factors affecting the lithium dendrite growth could enable successful implication of lithium metal anodes. One of the approaches in mitigating dendrite growth is to use electrolytes with increased mechanical rigidity. [3] In this context, polymer-based electrolytes have been shown to provide mechanical rigidity against lithium dendrite growth during electrochemical lithium deposition. [4] In the present work, the rigidity of the copolymer is quantified in terms of storage modulus and yield stress.

The polymers used in this study are hybrid organic-inorganic diblock (PEO-POSS) and triblock (POSS-PEO-POSS) copolymers where the polyethylene oxide (PEO) is the ion conducting soft segment and polyhedral oligomeric silsesquioxane (POSS) is mechanically rigid segment. The composition of the copolymer is shown in Table XVI.1.2. Both copolymers have similar volume fraction of the conductive block (f_{EO}) and molecular weights.

Table XVI.1.2 Comparison of PEO-POSS and POSS-PEO-POSS diblock and triblock copolymers

PEO-POSS/POSS-PEO-POSS	Structure	MW of PEO (kg mol ⁻¹)	MW of POSS (kg mol ⁻¹)	f_{EO}
10-4	Diblock	10	3.8	0.76
2-10-2	Triblock	10	3.8	0.76

Figure XVI.1.2a shows the storage modulus of the neat copolymers measured at 90 °C. Both diblock and triblock copolymers exhibit similar storage modulus. The nonlinear mechanical properties of the copolymers were determined by creep experiments. In Figure XVI.1.2b, the creep compliance curves are shown for the triblock copolymer at various applied stress. The triblock copolymer exhibits linear viscoelastic properties at lower values of applied stress. At 14000 Pa, the slope of the compliance curve increases exponentially, indicating the onset of plastic deformation. The yield stress was calculated by plotting the slope of the creep

compliance curve as a function of the applied stress, shown in Figure XVI.1.2c. Figure XVI.1.2c demonstrates that the yield stress of the triblock copolymer is higher (13000 ± 1000 Pa) than the diblock copolymer (4500 ± 500 Pa), although both copolymers have comparable storage moduli.

Diblock and triblock copolymer electrolytes were prepared by mixing lithium bis(trifluoromethanesulfonyl)imide (LiTFSI) salt with the copolymers. The salt concentration of the electrolytes was $[\text{Li}]/[\text{EO}] = 0.1$. Lithium symmetric cells were fabricated by sandwiching the electrolytes between two lithium electrodes. All experiments were performed at 90°C . Cells were preconditioned for multiple cycles at low current density (0.02 mA cm^{-2}) in the positive and negative directions to stabilize the solid-electrolyte interface (SEI) at each lithium electrode. The cells were then polarized at a current density of 0.15 mA cm^{-2} . Figure XVI.1.2d shows that while the triblock copolymer electrolytes were able to sustain the current density, the diblock copolymer electrolyte showed signs of the dendrite growth after 1 hour. The observation of stable deposition in the triblock copolymer electrolyte while lithium dendrites short circuit the diblock copolymer electrolyte is attributed to the lower yield stress of the diblock copolymer.

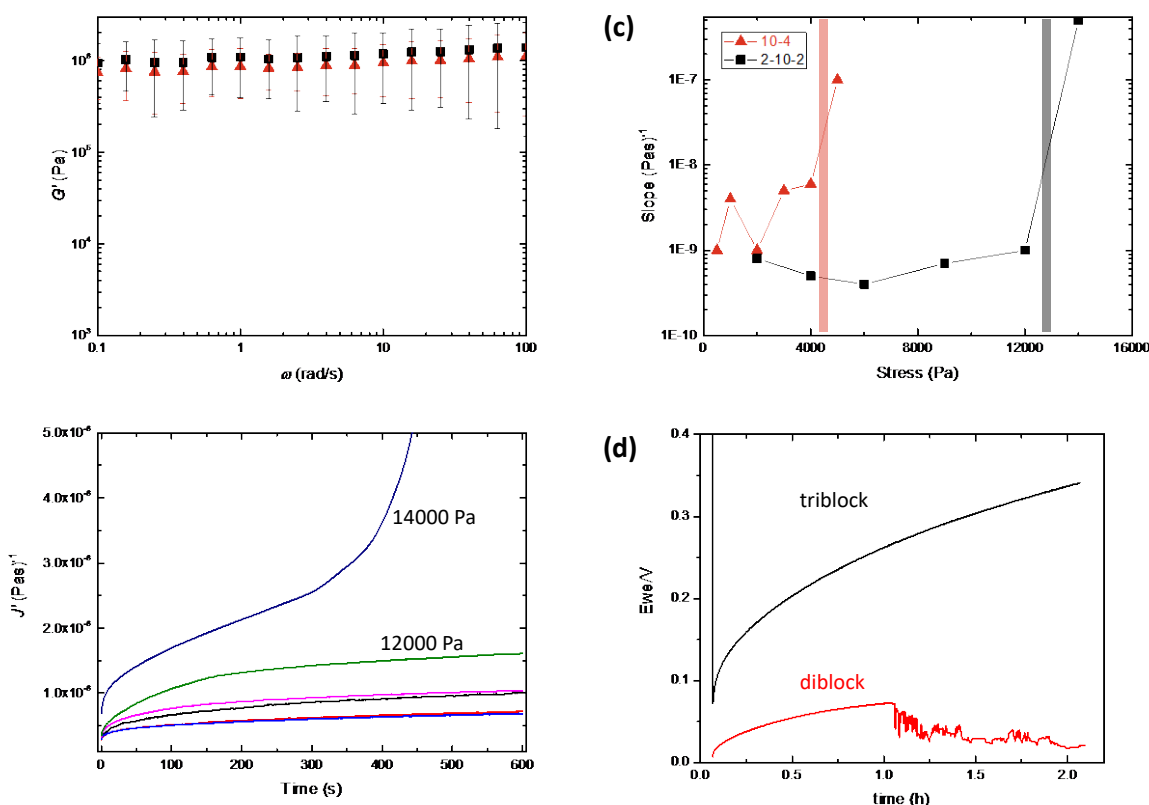


Figure XVI.1.3 (a) Storage modulus of the diblock (red triangle) and triblock (black square) copolymer (b) Creep compliance of the triblock at difference applied stress. Below 12000 Pa the polymers exhibit viscoelastic behavior. At 14000 Pa the slope of compliance increases sharply (c) Yield stress of the copolymers measured from the slope of the creep compliance curve (d) the electrolyte was subjected to 0.15 mA cm^{-2} current and the potential response was observed with time. The cells with diblock copolymer electrolytes failed within 1 h but the cells with triblock copolymer electrolyte was able to sustain the current. All data was collected at 90°C .

In situ X-ray scattering experiments on Li-polymer-Li symmetric cells to quantify polymer morphology in the presence of an applied field were conducted.

Block copolymer electrolytes are promising materials for lithium metal batteries, due to the combination of an ion conducting block—in this case, poly(ethylene oxide) (PEO)—and a mechanically rigid block to prevent

dendrite growth—in this case, polystyrene (PS). [5] The polymer used in this study has a PS molecular weight of 19 kg/mol and a PEO molecular weight of 20 kg/mol (SEO (19-20)), and contains a lithium salt, LiTFSI, with 0.16 Li ions per ethylene oxide monomer unit ($r = 0.16$). The electrolyte is lamellar at all relevant salt concentrations.

The goals of this study are to use small-angle x-ray scattering (SAXS) to characterize the morphology of the electrolyte as a function of position and time under an applied current. A schematic of the setup is shown in Figure XVI.1.3a. By designing the cell such that the beam is perpendicular to the direction of ion motion, different positions ranging between the two electrodes can be probed, and different azimuthal angles around the scattering pattern provide information about differently-oriented lamellar grains relative to the electrodes (Figure XVI.1.3b).

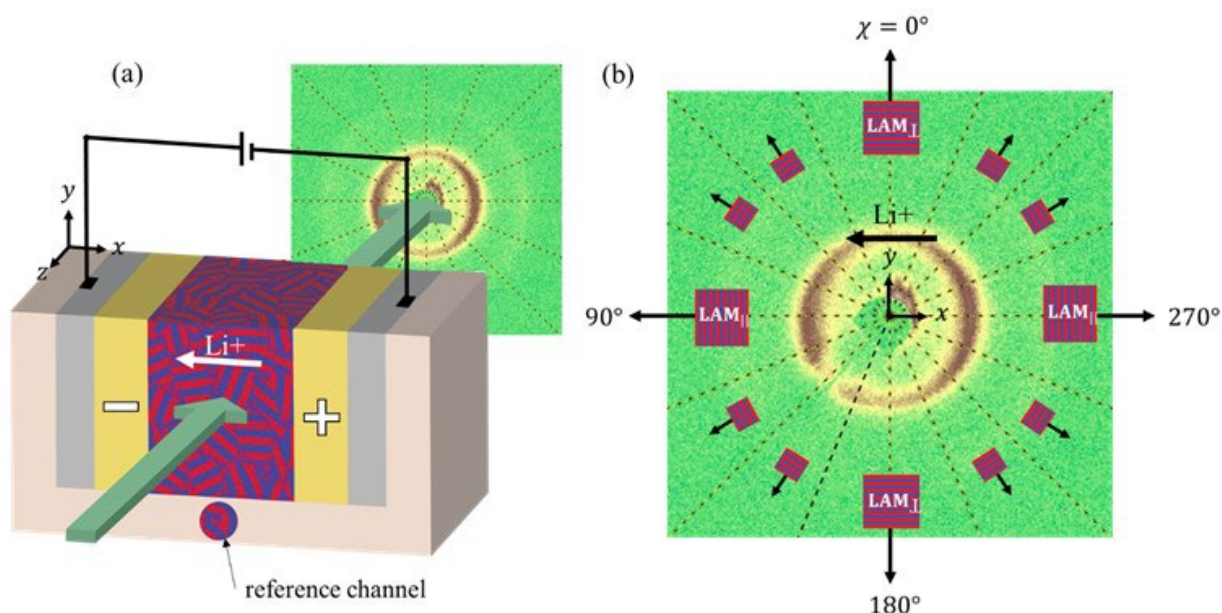


Figure XVI.1.4 (a) Schematic representation of the simultaneous polarization and SAXS experiment. An SEO/LiTFSI electrolyte with randomly oriented grains is sandwiched between two lithium electrodes with current passing parallel to the x -axis. X-rays pass parallel to the z -axis, perpendicular to the current. Scanning the beam along the x -axis allows for spatial resolution between the electrodes. A reference channel filled with electrolyte was placed next to the electrochemical cell. (b) Characteristic 2D SAXS pattern obtained from experiments. The pattern is divided into 16 sectors defined by the azimuthal angle, χ . Scattering data in each sector corresponds to lamellae oriented with the angle between the vector normal to the PEO/PS interfaces and the positive y -axis equal to χ . The cartoons in each sector show the lamellar orientation with normal vectors drawn.

Three cells were polarized at three different current densities: 0.926, 1.96, and 3.74 $\mu\text{A}/\text{cm}$, and their potential response is shown in Figure XVI.1.4a. By azimuthally averaging the SAXS patterns, the lamellar domain spacing, d , was calculated as a function of position, x/L , over time during cycling (Figure XVI.1.4b). As a salt concentration gradient builds up during polarization, [6] lamellae near the salt-rich electrode swell, increasing d , to accommodate additional salt, while lamellae near the salt-poor electrode shrink.

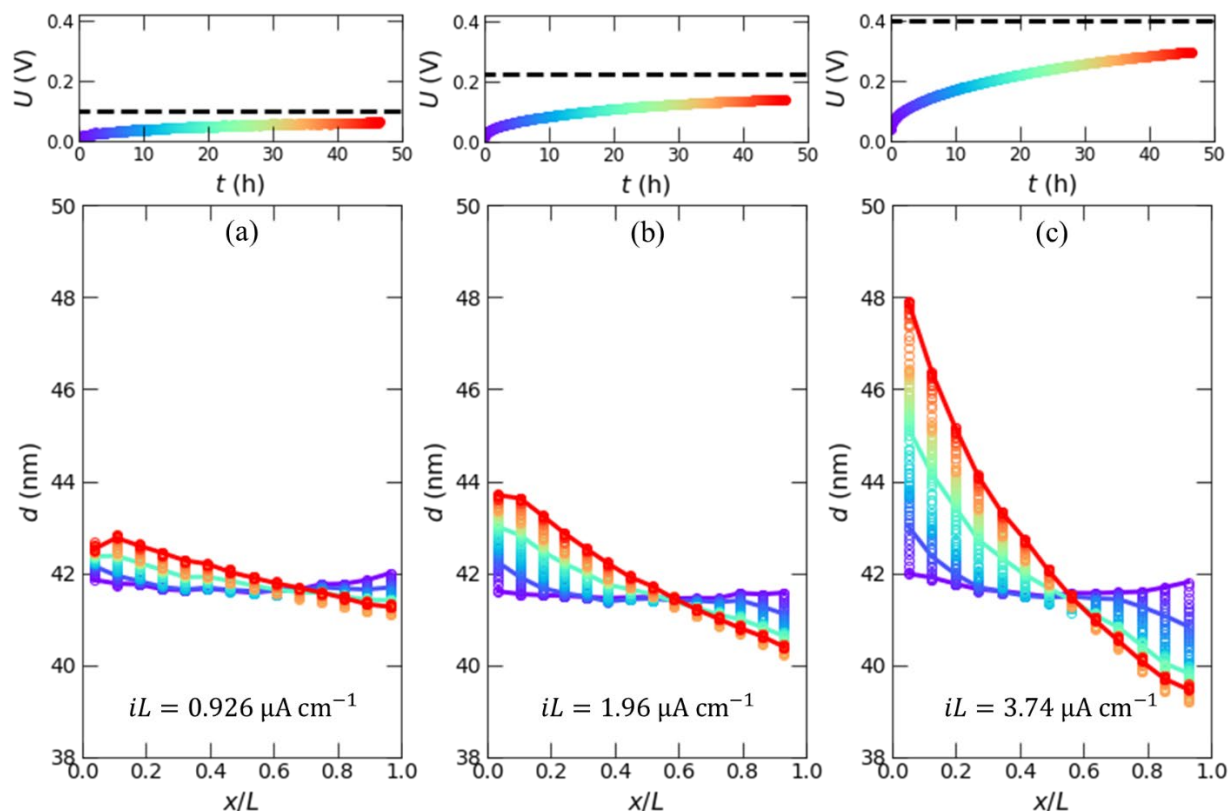


Figure XVI.1.5 Results from simultaneous polarization and SAXS experiments at three current densities: (a) The potential drop across the electrolyte, U , versus time, t , is plotted in the top panel of each figure. The dashed line represents the steady state potential (U_{ss}) predicted from concentrated solution theory. In the main panel, the domain spacing, d , is plotted versus normalized cell position, x/L . The color of each data set corresponds with the U versus t plot in the top panel. Purple data sets were obtained at the beginning of polarization ($t = 0$ h) and red data sets were obtained at the end of polarization ($t = 46.6$ h).

Figure XVI.1.4 shows the average domain spacing for lamellae of all orientations. However, lamellae oriented perpendicular and parallel to the electrodes (Figure XVI.1.3b) swell and contract to differing extents. Figure XVI.1.5a-b show the change in domain spacing, Δd , from the initial state to the end of polarization at 1.96, 3.74, and 11.1 $\mu\text{A}/\text{cm}$ as a function of azimuthal angle, χ , as defined in Figure XVI.1.3b. Each curve represents a different position within the cell, with the positions towards the center of the cell swelling or shrinking less than those near the electrodes, as shown in Figure XVI.1.4. The orientation dependence of the change in domain spacing shown in Figure XVI.1.5 illustrates that the lamellae oriented perpendicular to the electrodes, or parallel to the direction of ion transport, exhibit much smaller domain size changes during polarization. This shows that while lamellae parallel to the direction of ion transport form important channels to allow ions to traverse the cell, lamellae parallel to the electrodes may also play a crucial role in swelling and shrinking to accommodate the formation of salt concentration gradients, enabling the application of higher potentials and the achievement of faster charging.

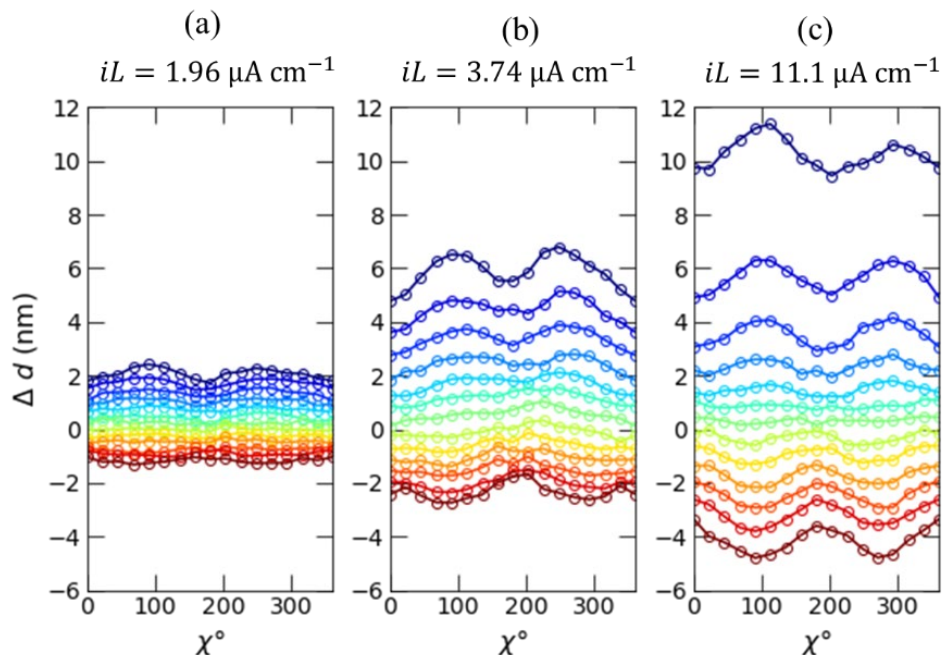


Figure XVI.1.6 Orientation dependence of lamellar distortion. The change in domain spacing, Δd , a function of azimuthal angle, χ , is plotted for each cell position for the cell polarized at (a) $iL = 1.96 \mu\text{A cm}^{-1}$ at $t = 46.7 \text{ h}$, (b) $iL = 3.74 \mu\text{A cm}^{-1}$ at $t = 46.7 \text{ h}$, and (c) $iL = 11.1 \mu\text{A cm}^{-1}$ at $t = 60.7 \text{ h}$. Each data set is based on the last scan taken at the end of each polarization. (d) Difference in domain spacing between LAM_{\perp} and LAM_{\parallel} as a function of normalized position, x/L , for the three data sets in (a), (b), and (c).

Quantification of dendrite growth in block copolymer electrolytes via X-ray tomography technique

Formation of nonplanar electrodeposition during charging is one of the main disadvantages in implementing lithium metal anode batteries. X-ray tomography technique is used to directly image plating and stripping of lithium protrusions during electrodeposition of symmetric lithium/polymer/lithium cells.

The electrolyte used in this study is a poly(styrene-*b*-ethylene oxide) (SEO) copolymer mixed with Lithium bis(trifluoromethanesulfonyl)imide (LiTFSI) salt. The symmetric cells were preconditioned at a current density of 0.02 mA cm^{-2} for 14 cycles. After preconditioning, the cells were polarized at a current density of 0.175 mA cm^{-2} till they short circuited due to growth of globular lithium protrusions. The cells are imaged at different time intervals before failure.

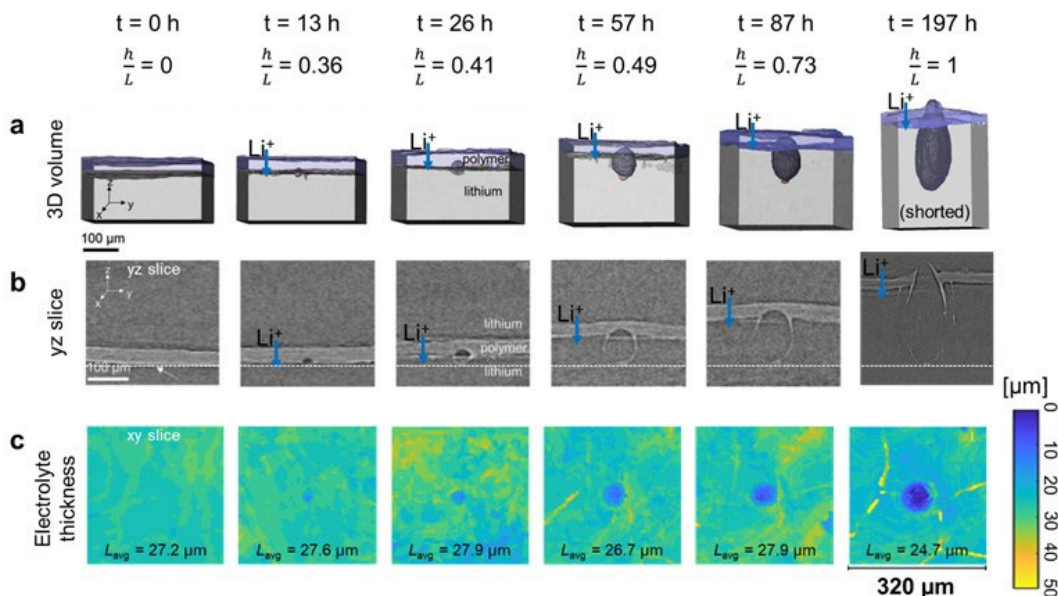


Figure XVI.1.7 a) Volume rendering of a lithium globule at different time intervals. The lithium globule is rendered in dark gray, while the electrolyte is rendered in purple, the bottom lithium in light gray, and the impurity particle in dark red. The top lithium electrode is transparent. Lithium is plated from the top to the bottom electrode. b) yz slice through the 3D reconstruction. The darker gray lithium sandwiches the lighter gray electrolyte. The approximate location of the original electrode-electrolyte interface is marked with the dashed white line. c) Maps of electrolyte thickness, or interelectrode distance, in the xy plane. The first five panels of Figure 1a and 1b were previously published in K. J. Harry, K. Higa, V. Srinivasan, and N. P. Balsara, *J. Electrochem. Soc.*, 163, 2216–2224 (2016).

The Local current density maps for both electrodes of a lithium symmetric cell during the growth of a lithium globule on the bottom electrode are presented in Figure XVI.1.7.

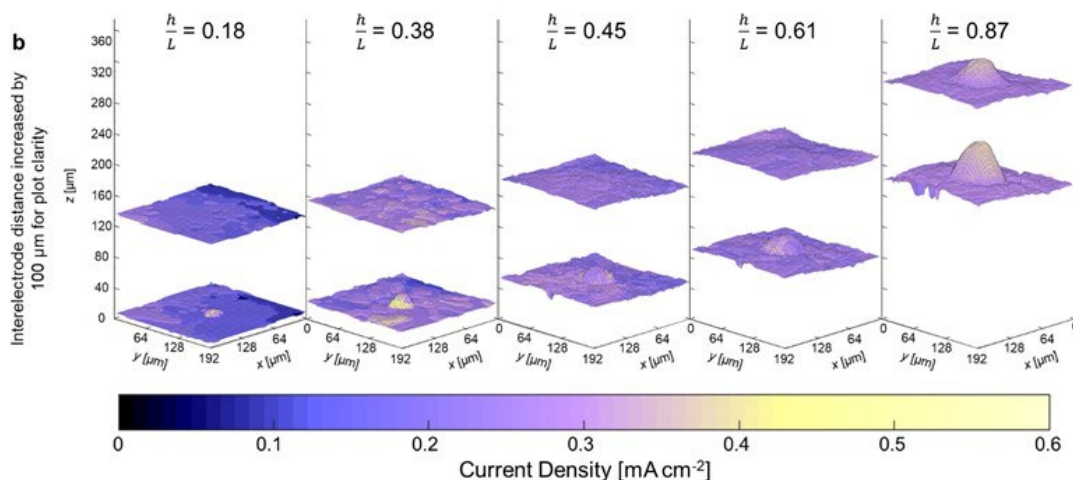


Figure XVI.1.8 Local current density maps for the top and bottom electrode during increasing time of growth for lithium globule on the bottom electrode. Each set of maps is labeled with the time point and normalized globule height corresponding to midway between the start and end points, where the start and end points are the two 3D renderings that were compared to calculate the plotted current density. The colormap indicates the calculated local current density at each x, y position. The plot represents an averaged 3D surface representing the interface between the electrode and electrolyte between the two time points used in the current density calculation. The z dimension represents the location of the interface, if $z = 0$ represents the initial position of the bottom electrode-electrolyte interface at $t = 0$. The plotted surfaces of the two electrodes were separated by an additional 100 μm for clarity.

Correlation functions were calculated to show that current density between the two parallel electrodes were not highly correlated until the interelectrode distance decreased to less than six μm at the protrusion, despite the initial interelectrode distance of 25 μm .

The nature of electrodepositions were compared between two organic-inorganic hybrid copolymer electrolytes, viz. poly(ethylene oxide)-*b*-poly(acryloisobutyl polyhedral oligomeric silsesquioxane) (PEO-POSS) diblock copolymer and POSS-PEO-POSS triblock copolymer containing LiTFSI salt. Both the copolymers have similar conducting phase volume fraction, molecular weight, and storage moduli but the yield stress of POSS-PEO-POSS is three times higher than PEO-POSS.

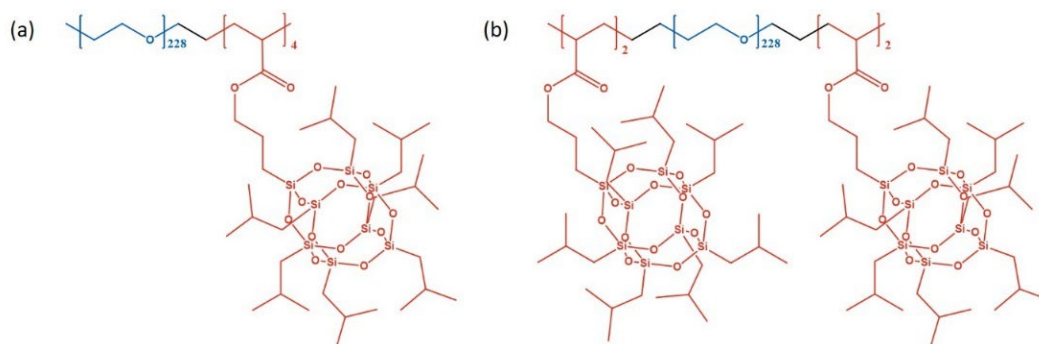


Figure XVI.1.9 Chemical structure of (a) PEO-POSS (b) POSS-PEO-POSS.

The cycle life of lithium/POSS-PEO-POSS/lithium cells are 50 times higher than that of cells with diblock copolymer. X-ray tomography images of the cycled symmetric cells reveal that dendrites are formed in the cells having diblock copolymer while globular protrusions are formed in case of the cells with triblock copolymer electrolytes.

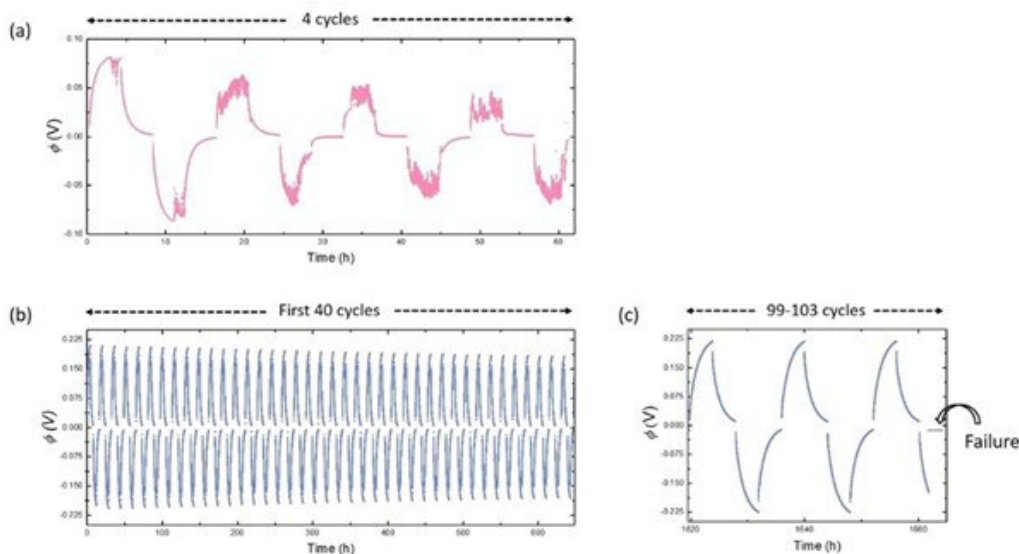


Figure XVI.1.10 (a) The voltage (Φ) versus time plot during cycling of the cell for PEO-POSS copolymer electrolyte. (b) Φ versus time plot for POSS-PEO-POSS electrolyte shown up to first 40 cycles. (c) Φ versus time plot for last 3 cycles before failure. The cells were cycled at 0.15 mA cm^{-2} current density for 4h in both positive and negative directions followed by 4h of rest. The cell failure was determined by the abrupt drop in the potential.

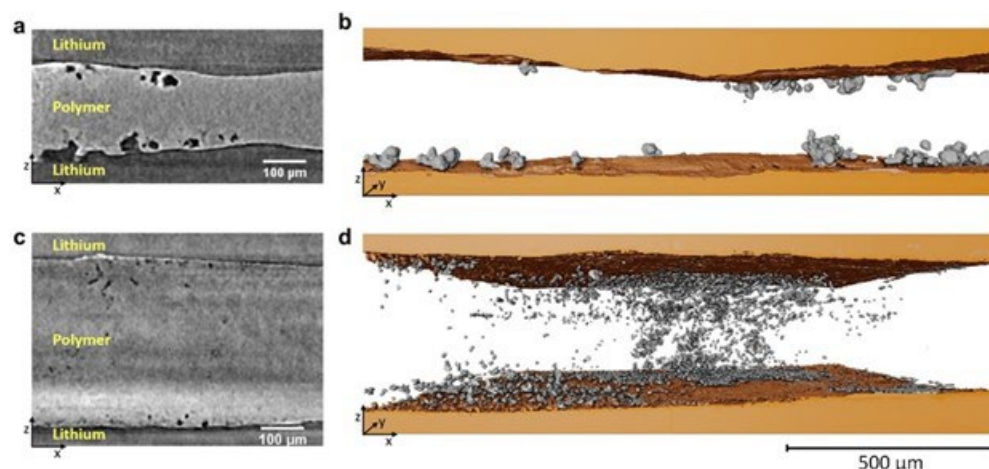


Figure XVI.1.11 Cross-sections through the cell are represented in the left side panels for (a) POSS-PEO-POSS after 40 cycles and (c) PEO-POSS after failure. Three dimensional (3D) visualizations of the dendrites are represented in the right-side panels, (b) POSS-PEO-POSS and (d) PEO-POSS. The protrusions are represented in grey, and the lithium electrodes are represented in orange.

Conclusions

In the present research, the stability of hybrid organic-inorganic hybrid copolymer electrolyte against lithium metal has been investigated. The major conclusions are summarized below:

1. A variety of organic-inorganic hybrid copolymers with covalently bonded single-ion chains were synthesized. Full electrochemical characterizations of these single ion copolymers were demonstrated.
2. The cell cycle lifetime of two analogous hybrid copolymer electrolytes of different architectures were compared. Furthermore, the cycle life was correlated with the mechanical property of the electrolytes, viz. yield stress.
3. The effect of yield stress of the copolymer electrolytes on the nature of electrodeposited lithium in a Li-polymer-Li cell during cycling were visualized using X-ray tomography technique.
4. Formation of the concentration gradient and its effect on the block copolymer nanostructure was studied. This study demonstrated the importance of orientation of gain structure in ion transport and formation of salt concentration hot-spot
5. Plating and stripping of a lithium protrusion in lithium metal symmetric cells over a series of time steps was imaged in 3D using X-ray tomography. The relationship between interelectrode distance and current density was established.

Key Publications

Publications

1. Dynamic Structure and Phase Behavior of a Block Copolymer Electrolyte under dc Polarization. Galluzzo, M. D.; Loo, W. S.; Schaible, E.; Zhu, C.; Balsara, N. P. *ACS Appl. Mater. Interfaces* **2020**, *12*, 51, 57421–5743
2. Sethi G. K.; Chakraborty S.; Zhu C.; Schaible E.; Villaluenga I.; Balsara N. P. *Gaint*, **2021**, *6*, 100055
3. Maslyn, J. A.; Frenck L.; Veeraraghavan, A.D.; Muller, A.; Ho, A. S.; Marwaha, N.; Loo, W. S.; Parkinson D, Y.; Minor, A.; Balsara, N. P. *Macromolecules*, **2021**, *54*, 4010–4022

4. Veeraraghavan, V. D.; Frenck, L.; Maslyn J. A.; Loo, W. S.; Parkinson, D. Y.; Balsara, N. P. *ACS Appl. Mater. Interfaces* **2021**, *13*, 27006–27018
5. Sethi, G.K.; Frenck, L.; Sawhney, S.; Chakraborty, S.; Villaluenga, I.; Balsara, N. P. *Solid State Ion.* **2021**, *368*, 115702
6. Galluzzo, M. D.; Grundy, L. S.; Takacs, C. J.; Cao, C.; Steinrück, H. G.; Fu, S.; Valadez, M. A. R.; Toney, M. F.; Balsara, N. P. *Macromolecules* **2021**, *54*, 7808–7821

Presentations

1. “Transient Structure of Block Copolymer Electrolytes under Dc Polarization”, Michael Galluzzo, U.C Berkeley Department of Chemical Engineering Colloquium, virtual, March 3rd, 2021.
2. “Impact of Frictional Interactions on Conductivity and Transference Number in Ether- and Perfluoroether-Based Electrolytes,” Lorena Grundy, American Physical Society March Meeting, virtual, March 17, 2021
3. “Effect of crystallization of the polyhedral oligomeric silsesquioxane block on self-assembly in hybrid organic-inorganic block copolymers with salt”, Gurmukh K Sethi, American Physical Society March Meeting, virtual, March 19, 2021

References

1. G. K. Sethi, X. Jiang, R. Chakraborty, W. S. Loo, I. Villaluenga, N. P. Balsara, *ACS Macro Lett.* **2018**, *7*, 1056.
2. P. G. Bruce, M. T. Hardgrave, C. A. Vincent, *J. Electroanal. Chem. Interfacial Electrochem.* **2002**, *271*, 27.
3. Monroe, C.; Newman, J. *Journal of The Electrochemical Society* **2005**, *152*, A396.
4. Frenck L. Sethi. G. K.; Maslyn J. A.; Balsara. N. P. *Frontiers in Energy Research* **2019**, *7*, 115.
5. Tu, Z.; Nath, P.; Lu, Y.; Tikekar, M. D.; Archer, L. A. *Acc. Chem. Res.* **2015**, *48*, 2947.
6. Doyle, M.; Fuller, T. F.; Newman, J. *Electrochim. Acta* **1994**, *39*, 2073

XVI.2 Lithium Thiophosphate Based Solid Electrolytes and Cathode Interfaces

Jagjit Nanda, Principal Investigator

Oak Ridge National Laboratory
1 Bethel Valley Road
Oak Ridge, TN 37831
E-mail: nandaj@ornl.gov

Tien Q. Duong, DOE Technology Development Manager

U.S. Department of Energy
E-mail: Tien.Duong@ee.doe.gov

Start Date: October 1, 2020

End Date: September 30, 2021

Project Funding (FY21): \$450,000

DOE share: \$450,000

Non-DOE share: \$0

Project Introduction

Advances in solid electrolytes (SEs) with superionic conductivity and stabilized electrode-electrolyte interfaces are key enablers for all solid-state batteries (SSBs) to meet the energy density and cost targets for next-generation batteries for electric vehicles. This project utilizes materials characterization and electrochemical methods to address key technical barriers associated with ion transport between sulfide-based SEs (e.g., β -Li₃PS₄) and high energy cathodes (e.g., LiMO₂ and FeS₂). Compared to their oxide counterparts, sulfide-based electrolytes offer several key advantages including: (i) exceptionally high ionic conductivities up to 10⁻² S/cm at room temperature (comparable to nonaqueous liquid electrolytes), (ii) availability of low temperature and inexpensive synthesis routes to produce glass, glass-ceramic, and crystalline structures, and (iii) soft mechanical properties which facilitates material processing. Among the drawbacks, sulfides SEs are moisture sensitive and have limited electrochemical stability windows which require engineering solutions to stabilize the Li/SE and cathode/SE interfaces. The present work investigates how various cell configurations and testing conditions impact the performance of Li metal SSBs containing sulfide-based SEs. Overall, this work aims to enable VTO's Battery500 goal of cell-level specific energies of 500 Wh/kg over 1,000 cycles.

Objectives

1. Develop solution-based synthesis routes for sulfide based solid-electrolytes and optimize conductivity and crystallinity.
2. Minimize interfacial resistance between sulfide SEs and cathodes via interfacial coatings, variable stack pressure and cathode composition.
3. Perform Raman microscopy, NMR, and electron microscopy to characterize bulk sulfide SE (β -Li₃PS₄) and cathode SE interfaces to investigate capacity loss and degradation mechanisms.
4. Select and optimize a few solid-state cathode compositions to demonstrate room-temperature cycling with LPS and/or argyrodite SEs. Stretch Goal: 50 cycles with < 20% capacity fade.

Approach

A key focus of this program is to develop solvent-mediated synthesis routes for sulfide-based SEs for high energy Li metal SSBs. Activities in FY21 focused on two Li₃PS₄-based SEs including β -Li₃PS₄ and amorphous composites containing Li₃PS₄+1 wt% PEO binder. Neutron scattering was used to probe how changes in short-range structure affect the Li⁺ conductivity of these glass-ceramic SEs. In addition to material synthesis and characterization, we also evaluated the cycling performance of SSBs containing sulfide-based SEs. Systematic

studies on how anode composition, stack pressure, and cathode composition impact the SSB performance are reported herein.

Results

1. Structure/Property Correlations for Glassy-Ceramic Sulfide SEs

Incorporating polymer binders while maintaining high Li^+ conductivity is one possible route to enable thin separators ($<30\text{ }\mu\text{m}$) for practical SSBs. In FY20, we reported the solvent-mediated synthesis of crystalline $\beta\text{-Li}_3\text{PS}_4$ and amorphous composites containing $\text{Li}_3\text{PS}_4 + 1\%$ poly(ethylene oxide) (PEO). These studies showed that the Li^+ conductivity is closely linked to the material's thermal processing history, and the presence of coordinated solvent reduces the Li^+ conductivity by several orders of magnitude. To supplement this original study, in FY21 we further evaluated the local bonding of $\beta\text{-Li}_3\text{PS}_4$ and amorphous $\text{Li}_3\text{PS}_4 + 1\%$ PEO SEs using neutron pair distribution function (nPDF) analysis. nPDF is powerful tool that allows one to precisely track the P-P, S-S, and P-S correlations for disordered glass-ceramics. Approximate distances between two atoms (P-P, S-S, and P-S) associated with several expected polyanionic structures are highlighted in Figure XVI.2.1a, and Figure XVI.2.1b shows each sample's reduced nPDF $[G(r)]$ which represents the probability of finding a neighboring atom at a distance r from a given atom. $\beta\text{-Li}_3\text{PS}_4$ exhibited a strong peak at $\sim 2.0\text{ }\text{\AA}$ (red line) which is consistent with the P-S bond length in PS_4^{3-} tetrahedra, the dominant polyanion in this structure. This finding is further supported by the peak near $3.3\text{ }\text{\AA}$ (black line) which corresponds to the distance between adjacent S atoms in PS_4^{3-} . In addition to the expected PS_4^{3-} tetrahedra, the $\beta\text{-Li}_3\text{PS}_4$ sample contained other P bonding environments (e.g., $\text{P}_2\text{S}_7^{4-}$) which indicates the presence of amorphous domains not detected by diffraction methods.

Compared to $\beta\text{-Li}_3\text{PS}_4$, the composites (heated at either 45 or 140°C under vacuum) contained more diverse P bonding environments (e.g., $\text{P}_2\text{S}_6^{4-}$ and $\text{P}_2\text{S}_7^{4-}$ indicated by the green and purple lines at $\sim 2.3\text{ }\text{\AA}$ and $\sim 3.5\text{ }\text{\AA}$, respectively), and the relative amount of these structures changed with thermal treatment. Notably, calcinating at 140°C coincided with decreased intensity of the $1.8\text{ }\text{\AA}$ peak and increased intensity of the $2\text{ }\text{\AA}$ peak. Here, the peak centered around $1.8\text{ }\text{\AA}$ (yellow line) is attributed to terminal P-S bonds (i.e., involving non-bridging S atoms) in $(\text{PS}_3)_n^{n-}$ chains. This assignment is supported by the trend in analogous phosphates wherein terminal P-O bonds in metaphosphate chains (PO_3^-) are typically $\sim 0.1\text{ }\text{\AA}$ shorter than in orthophosphates (PO_4^{3-}). These findings suggest that the $(\text{PS}_3)_n^{n-}$ chains are broken into isolated PS_4^{3-} units when annealing at 140°C .

Overall, these findings highlight the structural complexity of sulfide-based SEs prepared through solvent-mediated routes, and nPDF is an ideal tool to study the local bonding in these glass-ceramics. Due to the lower ionic conductivity of the amorphous composites compared to $\beta\text{-Li}_3\text{PS}_4$ (e.g., $8.7 \times 10^{-6}\text{ S/cm}$ and $1.2 \times 10^{-4}\text{ S/cm}$ at RT, respectively), the remainder of our work in FY21 focused on $\beta\text{-Li}_3\text{PS}_4$ (from here on denoted as LPS).

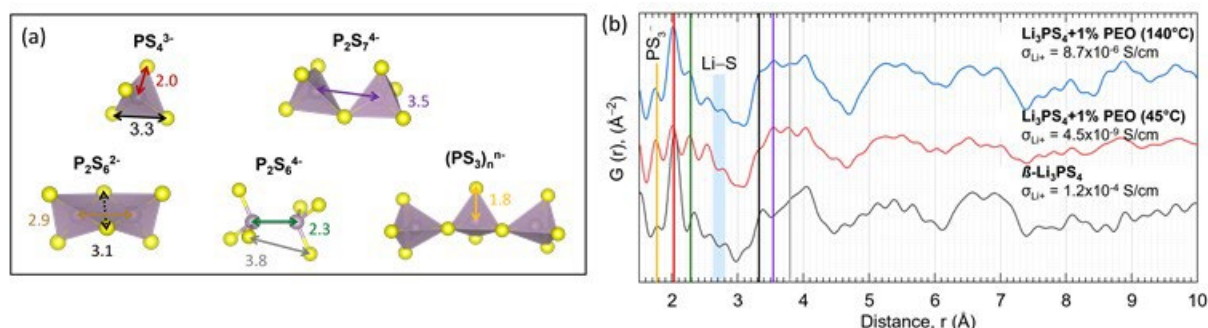


Figure XVI.2.1 (a) Various P-S polyanionic structures with approximate bond lengths (given in Å). (b) Neutron pair distribution function (nPDF) for $\beta\text{-Li}_3\text{PS}_4$ and $\text{Li}_3\text{PS}_4 + 1\%$ PEO samples measured at 300K. Vertical lines correspond to expected bond lengths described in (a). Li^+ conductivity values (σ_{Li^+}) for each sample were measured at room temperature in a blocking cell configuration.

2. Hot Pressed β - Li_3PS_4 Pellet Separators

Hot pressing represents one possible route to: (i) increase the density of sulfide-based SE separators and (ii) reduce the area specific resistance of electrode/SE interfaces. Our team established a hot-pressing setup inside an Ar-filled glovebox for densifying sulfide-based SE pellets at 25–250°C (see Figure XVI.2.2). Table XVI.2.1 summarizes the measured Li^+ conductivity (σ_{Li^+}) and activation energy (E_A) for various LPS samples prepared through a solvent-mediated route. In these experiments, two key processing variables were investigated including: (i) rinsing 0–4 times with THF to remove soluble species prior to calcination (the composition of these soluble species is unknown at this time) and (ii) pressing temperature. As shown in Table XVI.2.1, rinsing twice with THF increased the room temperature conductivity by a factor of 2, but additional rinses had no measurable impact on the conductivity. Similarly, a hot-pressed pellet exhibited a 2-fold higher conductivity compared to the same sample pressed at room temperature. These findings are a bit surprising since all pellets had the same density within experimental error (ca. $1.70 \pm 0.05 \text{ g/cm}^3$). Overall, the results in Table XVI.2.1 highlight how minor differences in processing conditions can have a significant impact on the properties of SE powders.

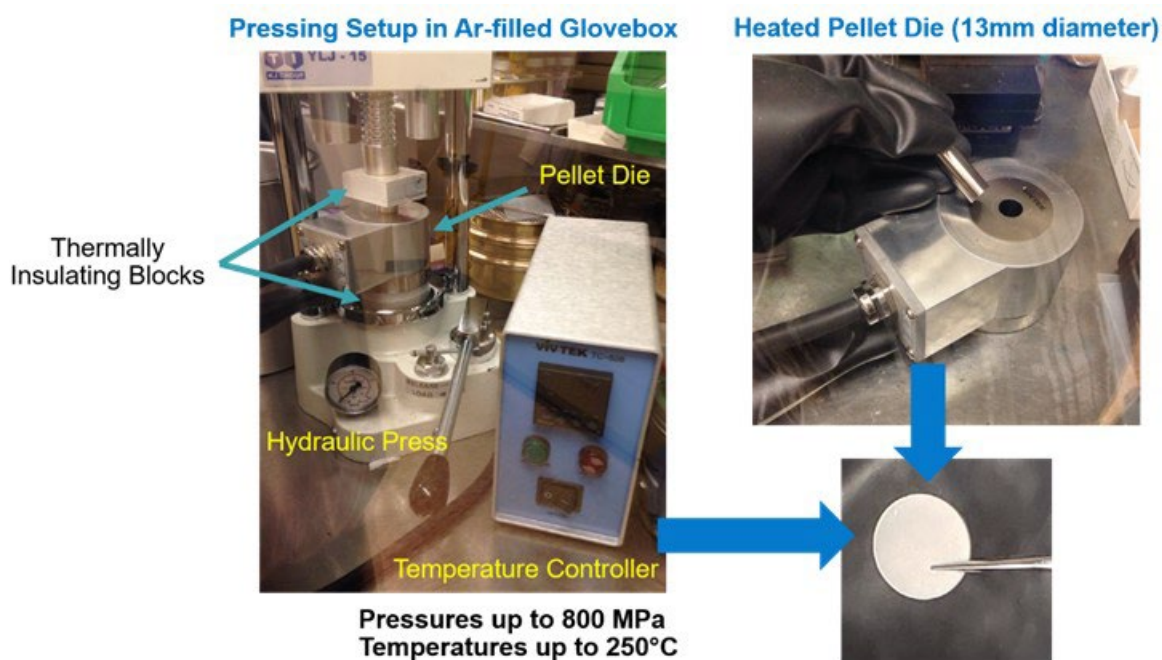


Figure XVI.2.2 Hot-pressing equipment inside an Ar-filled glovebox for processing sulfide-based SEs.

Table XVI.2.1 Li^+ conductivity (σ_{Li^+}) and activation energy (E_A) of LPS prepared through solvent-mediated synthesis routes. Samples were pressed at either room temperature or 240 °C. Dried samples were rinsed with THF 1–4 times prior to calcinating at 140 °C.

Sample Description	Pressing Temperature (°C)	σ_{Li^+} at RT (S/cm)	E_A (eV)
0 rinse, cold press	25	8.5×10^{-5}	0.37
2 rinse, cold press	25	1.5×10^{-4}	0.33
4 rinse, cold press	25	1.5×10^{-4}	0.38
4 rinse, hot press	240	3.0×10^{-4}	0.38

3. Effect of Anode Composition and Stack Pressure on SSB Performance

Indium anodes which alloy with Li during charging are commonly used in the SSB literature to avoid Li dendrite formation, but direct comparisons with cells containing Li metal are rarely reported. In the present study, a Li_xIn alloy was prepared by coulombically titrating indium metal in a SSB containing a Li auxiliary electrode and LPS separator. Figure XVI.2.3a shows the Li_xIn alloy had a constant open-circuit potential (E_{oc}) of 0.622 V vs. Li/Li^+ throughout the 2-phase In/LiIn region. The titration was stopped at $x = 0.169$ at which point the $\text{Li}_{0.169}\text{In}$ alloy was harvested from the cell for use in a full cell. This endpoint was selected to ensure the Li_xIn alloy could cycle moderate Li inventories (ca. $\pm 2 \text{ mAh/cm}^2$) while remaining in the desired 2-phase region with a well-known electrochemical potential.

Figure XVI.2.3b and Figure XVI.2.3c show galvanostatic cycling data for SSBs containing either a Li metal anode (ultra-high purity, vapor deposited on Cu foil) or $\text{Li}_{0.169}\text{In}$ anode. The cathode consisted of 60 wt% NMC811 ($6.6 \pm 0.8 \text{ mg/cm}^2$), 30 wt% LPS, and 10 wt% C, and an LPS pellet ($\sim 0.9 \text{ mm}$ thick) was used as the separator. Both cells exhibited high charge capacities $\sim 1.3 \text{ mAh/cm}^2$ (200 mAh/gNMC) during the first cycle, but the reversible capacity was low ($110\text{--}130 \text{ mAh/gNMC}$). The poor reversibility during the first cycle is due to oxidative decomposition of the LPS in the cathode. After 50 cycles, both cells exhibited significant capacity fade which is attributed to: (i) formation of a resistive cathode/electrolyte interface and/or (ii) degradation of solid-solid contacts in the cathode. Overall, these results demonstrate that replacing Li metal with a Li_xIn alloy had little impact on SSB performance which provides very strong evidence that cathode design and interface is the major bottleneck for $\text{Li}|\text{LPS}|\text{NMC}$ cells.

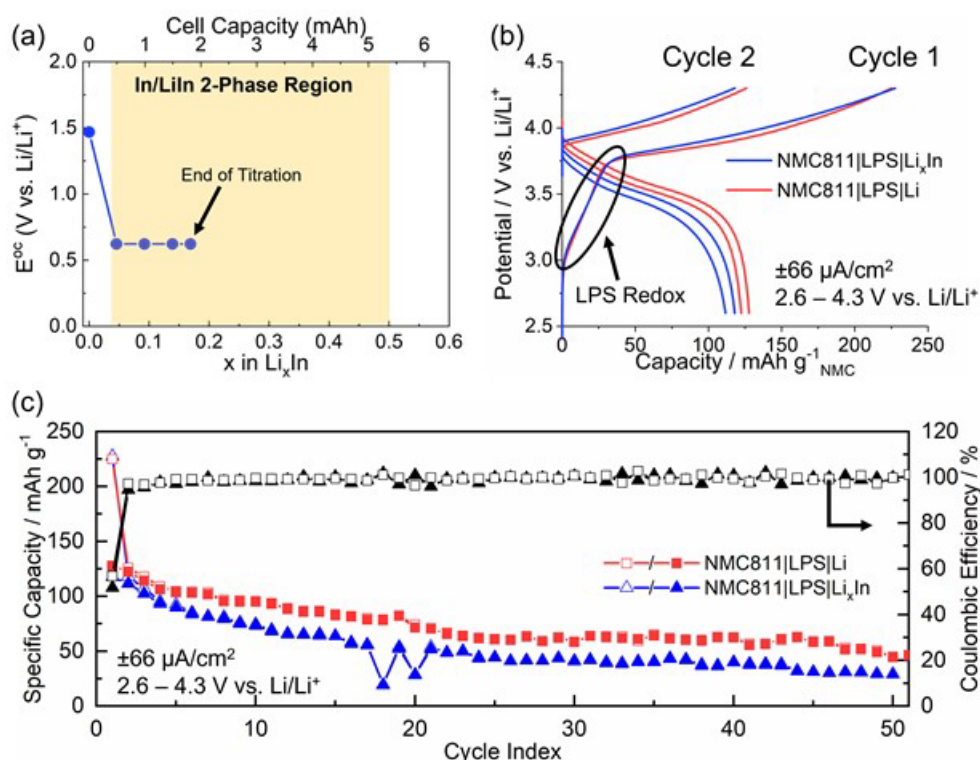


Figure XVI.2.3 (a) Open-circuit potential (E_{oc}) of a Li_xIn alloy prepared by coulombically titrating In metal in a $\text{Li}|\text{LPS}|\text{In}$ SSB at $-79 \mu\text{A/cm}^2$ at room temperature. (b-c) Electrochemical characterization of SSBs containing an NMC811 cathode, LPS separator, and either a Li metal or $\text{Li}_{0.169}\text{In}$ anode tested at room temperature with a stack pressure of 5 MPa. (b) Galvanostatic charge/discharge curves for the first 2 cycles and (c) long-term cycling performance. In (b-c), the cathode potential in the Li_xIn -containing SSB was referenced vs. Li/Li^+ by adding 0.622 V to the measured cell potential.

One means to encourage stable solid-solid contacts during SSB cycling is to utilize high stack pressures ($>1 \text{ MPa}$). Furthermore, some studies have suggested that applying very high pressures (tens of MPa) extends the

oxidative stability of sulfide-based SEs beyond 5 V vs. Li/Li^+ . Motivated by these prior investigations, our team evaluated how external stack pressure impacts the cycling performance of pellet-type SSBs containing vapor deposited Li metal anodes ($\sim 2.5 \text{ mAh/cm}^2$ on Cu foil), LPS separators ($\sim 0.9 \text{ mm}$ thick), and composite NMC811+LPS+C cathodes ($60 \text{ wt.}\%$ NMC, $6.6 \text{ mg}_{\text{NMC}}/\text{cm}^2$). Figure XVI.2.4a and Figure XVI.2.4b show galvanostatic voltage profiles for SSBs tested under stack pressures of 5 and 50 MPa, respectively. Both cells had an open-circuit potential of $2.41 \pm 0.01 \text{ V}$ and exhibited a sloping voltage profile $\sim 2.6\text{--}3.7 \text{ V}$ during the first charge due to oxidative decomposition of LPS described previously. These results clearly demonstrate that using high stack pressures has negligible impact on the thermodynamic stability of LPS and extent of LPS decomposition ($\sim 0.30 \text{ mAh/cm}^2$ for both cells). Surprisingly, the cell tested at 50 MPa had a slightly lower discharge capacity (113 mAh/g vs. 128 mAh/g at 5 MPa), indicating that mechanical confinement does not necessarily promote better active material utilization. During extended cycling (Figure XVI.2.4c), both cells exhibited gradual capacity fade, presumably due to formation of a resistive cathode/electrolyte interface and/or loss of solid-solid contact.

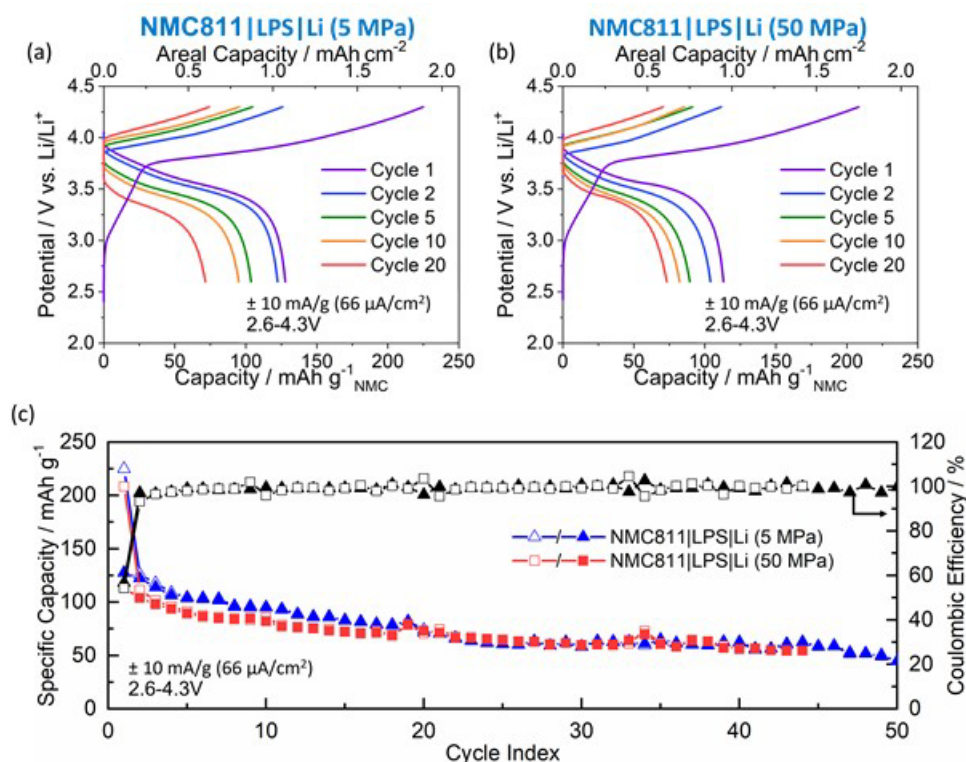


Figure XVI.2.4 Galvanostatic cycling performance of SSBs containing vapor deposited Li metal anodes, LPS separators, and composite NMC cathodes. (a-b) Voltage profiles for cells tested using stack pressures of (a) 5 MPa and (b) 50 MPa. (c) Long-term cycling performance.

4. Solid-State Cathode Design

Application of thin inorganic coatings to the active material is one common strategy to stabilize the cathode/electrolyte interface in SSBs. In this work, we evaluated the impact of a LiNbO_3 (LNO) coating on the performance of $\text{Li}|\text{LPS}|\text{NMC}+\text{C}+\text{LPS}$ SSBs. Figure XVI.2.5a shows voltage profiles for NMC811 cathodes with/without a 1 wt.% LNO coating. Interestingly, the LNO coating had little impact on cathode's capacity or cyclability. To investigate the redox properties of the SE phase in these composite cathodes, LPS was blended with carbon powder and characterized in $\text{Li}|\text{LPS}|\text{LPS}+\text{C}$ SSBs. The LPS loading in this control experiment ($3.3 \text{ mg}_{\text{LPS}}/\text{cm}^2$) was identical to that in the NMC-based cathodes. As shown in Figure XVI.2.5a, the LPS exhibited a sloping voltage profile which matched the feature $\sim 3.0\text{--}3.5 \text{ V}$ observed in the NMC cathodes. LPS oxidation was completely irreversible, and the SE had negligible redox activity during subsequent cycles. Overall, the results in Figure XVI.2.5 demonstrate that the performance of NMC+LPS+C cathodes is

significantly hindered by decomposition of LPS at high voltages. Furthermore, applying interfacial coatings directly on the active material does not address the poor oxidative stability of LPS, especially when the composite cathode contains high surface area carbon additives which exacerbate SE decomposition.

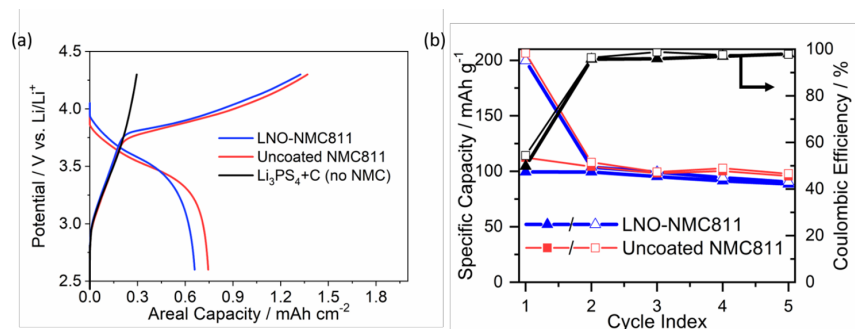


Figure XVI.2.5 Electrochemical characterization of SSBs containing a Li anode, LPS separator, and NMC811 cathodes with/without an LNO coating (1 wt.%) showing (a) first cycle charge/discharge curves and (b) capacity and coulombic efficiency over 5 cycles. In (b) open/closed symbols represent charge/discharge capacities, respectively. All cells were cycled at a current density of $\pm 66 \mu\text{A}/\text{cm}^2$.

Conclusions

Activities in FY21 explored structure/function correlations for sulfide-based SEs and evaluated cycling performance of Li metal SSBs. Neutron pair distribution function analysis studies showed that the local structure has a dramatic impact on the Li⁺ conductivity of SEs produced through solvent-mediated routes. More specifically, structures with high degrees of P-S coordination (e.g., PS₄³⁻ and P₂S₇⁴⁻) correlate with higher Li⁺ mobility compared to other polyanions (e.g., (PS₃)_nⁿ⁻ chains and P₂S₆⁴⁻). In addition to these structural studies, we also report the cycling performance of pellet-type SSBs containing β -Li₃PS₄ (LPS) separators and various composite cathodes. By systematically varying the anode composition (i.e., ultra-high purity vapor deposited Li metal vs. Li_xIn alloy), stack pressure, and cathode composition, we determined that cathode design is a major bottleneck for Li|LPS|NMC solid-state cells. Our results show that: (i) using high surface area carbon in composite cathodes exacerbates irreversible capacity losses due to oxidative decomposition of LPS and (ii) applying large external pressures (up to 50 MPa) does not necessarily ensure formation of robust solid-solid contacts. Unlike high voltage NMC cathodes, SSBs containing conversion cathodes with moderate operating voltages (i.e., FeS₂, 1-3 V vs. Li/Li⁺, results not shown here) exhibited stable performance over 50 cycles, and future work will optimize the active material particle size and carbon distribution to enable higher active material utilization. While the cathode represents a major bottleneck for SSBs, we emphasize that interfacial engineering solutions are still needed to enable stable Li plating/stripping at high rates ($>1 \text{ mA}/\text{cm}^2$) for practical SSBs.

To improve the performance of SSBs containing sulfide-based SEs, studies in FY22 will focus on: (i) replacing LPS with halide-containing SEs (e.g., Li₆PS₅Cl_xBr_{1-x}) with better oxidative stability, (ii) applying cathode coatings to promote more stable cathode/SE interfaces, (iii) optimizing the performance of high-capacity conversion cathodes (e.g., FeS₂ and FeF₂), and (iv) developing tape casting processes to produce thin, freestanding sulfide-based SE separators ($<50 \mu\text{m}$ thick) which will be incorporated into single layer pouch cells.

Key Publications

1. "Investigation of Complex Intermediates in Solvent Mediated Synthesis of Thiophosphate Solid-State Electrolytes" F. M. Delnick, G. Yang, E. C. Self, H. Meyer III, J. Nanda, *The Journal of Physical Chemistry C* **2020**, 124, 27396–27402.

2. “Anomalously High Elastic Modulus of a Poly(ethylene oxide)-Based Composite Electrolyte” G. Yang, M. L. Lehmann, S. Zhao, B. Li, S. Ge, P-F. Cao, F. M. Delnick, A. P. Sokolov, T. Saito, J. Nanda, *Energy Storage Materials*, **2020**, 35, 431–442.
3. “Investigation of Glass-Ceramic Lithium Thiophosphate Solid Electrolytes Using NMR and Neutron Scattering” E. C. Self, P.-H. Chien, L. F. O’Donnell, D. Morales, J. Lieu, T. Brahmabhatt, S. Greenbaum, J. Nanda, *Materials Today Physics* **2021**, 21, 100478.

Presentations

4. “Solvent-Mediated Synthesis of Amorphous Li₃PS₄/PEO Composite Solid Electrolytes with High Li⁺ Conductivity” E. C. Self, *MRS 2020 Fall Meeting*, November 2020 (virtual presentation).
5. “Composite Cathodes for All-Solid-State Batteries Containing Lithium Thiophosphate Separators” E. C. Self, *240th Meeting of the Electrochemical Society*, October 2021 (virtual presentation).
6. “Next Generation Materials and Systems for Electrochemical Energy Storage, Interdisciplinary Topics in Materials Science (ITAM)” July 27–29th 2021 (Invited-virtual)

Acknowledgements

This research is sponsored by the United States Department of Energy through the Office of Energy Efficiency and Renewable Energy (EERE) and Vehicle Technologies Office (VTO, Program Manager: Tien Duong). ORNL team members include Drs. Ethan Self, Frank Delnick, Guang Yang, Wan-Yu Tsai, and Mr. Teerth Brahmabhatt. Prof. Steve Greenbaum, Dr. Lauren O’Donnell, and Mr. Daniel Morales (Hunter College, funded collaborators) performed ssNMR measurements and data analysis (results not reported here). The team also thanks Drs. Jue Liu and Po-Hsiu Chien (ORNL) for their technical contributions on the neutron scattering measurements and Dr. Andrew Westover (ORNL) for providing the vapor deposited Li metal anodes.

XVI.3 Advancing Solid-Solid Interfaces in Li-ion Batteries (Argonne National Laboratory)

Sanja Tepavcevic, Principal Investigator

Argonne National Laboratory
9700 South Cass Avenue
Lemont, IL 60439
E-mail: sanja@anl.gov

Larry A. Curtiss, Principal Investigator

Argonne National Laboratory
9700 South Cass Avenue
Lemont, IL 60521
E-mail: curtiss@anl.gov

Tien Q. Duong, DOE Technology Development Manager

U.S. Department of Energy
E-mail: Tien.Duong@ee.doe.gov

Start Date: October 1, 2019

End Date: September 30, 2021

Project Funding (FY21): \$910,000

DOE share: \$910,000

Non-DOE share: \$0

Project Introduction

One of the most important technological advances in sustainable energy harvesting and storage is the development of Li-ion battery technology. However, many challenges must be resolved in order to fully implement this technology, including: (i) development of high energy density cathode and anode materials (activity/cyclability); (ii) enhancement in the stability of electrode materials and the corresponding electrolytes; (iii) improvement in the selectivity of electrochemical interfaces, e.g., minimizing undesired side reactions at electrode surfaces; and (iv) eliminating many of the safety issues related to the high flammability of organic solvents and Li dendrite formation on the anode electrode. The focus of much research in the field of Li energy storage is centered on the development of methods that can enable Li metal anodes (required for high energy density Li-ion batteries) without dendrite formation and parasitic electrode-electrolyte interactions, as well as the replacement of flammable organic solvents with solid electrolytes.

Today, two methods have been introduced to address the safety/performance issues. The first method relies on the hypothesis that by shielding the Li metal anode with various types of “thin membranes” (either polymers or ceramics) Li dendrite formation will be significantly reduced relative to the bare Li anode along with the harmful side reactions. The second method regards the development of an all-solid-state battery, composed of Li ion conductive solid electrolytes that connect metal Li anodes with high energy cathodes. “Hard” ceramic solid-state electrolytes have been developed with suitable ionic conductivities, but the stability of these materials must be improved to allow facile Li transport across the electrolyte while inhibiting dendrite formation. “Soft” polymer materials help to inhibit dendrite formation, none have ionic conductivities as high as liquid electrolytes (0.1 S cm^{-1}). Overall, both methods need further development to move Li-ion battery technology forward. Advances will require the application of knowledge, concepts, and tools from a variety of fields including materials science, physics, engineering, theory, and, in particular, interfacial electrochemistry.

Objectives

The project objectives are multifaceted, including the development of a mechanically / chemically stable and Li ion conductive ($\geq 2 \times 10^{-4} \text{ S/cm}$ at 298K) solid electrolyte for a solid-state battery. The battery consists of a metal Li anode, a transition metal oxide cathode, and a nonflammable crystalline / amorphous solid electrolyte that operates at cathode potentials $> 5\text{V}$ (denoted as a SLi-SEL-SC system). We will develop and exploit a

variety of ex-situ and in-situ experimental methods, including highly surface sensitive / electrochemical probes, as well as computational techniques, to explore, optimize, and explain bulk and interfacial properties of the selected materials. The results will serve to unravel many of the puzzling bulk and interfacial properties of $S_{Li-SEL-Sc}$ systems, including various types of ceramic and glass materials.

Approach

Our approach is to use the interdisciplinary, atomic-/molecular-level insight obtained from integrating both experimental- and computational-based methodologies to define the landscape of parameters that control interfacial properties for new generations of Li-ion solid-solid battery systems. Our strategy will involve transferring the knowledge gained from well-characterized thin film materials to real-world materials. This strategy forms a closed loop in the sense that the knowledge gained from the model systems is used to design the more complex, real-world materials and vice-versa. The work will focus on utilizing existing in-house synthesis and characterization methods to enable the rapid transition from fundamental science to realistic cell.

Results

Kinetic versus Thermodynamic Stability of LLZO in Contact with Metallic Li $Li_7La_3Zr_2O_{12}$ (LLZO) garnet-based oxides are a promising class of solid electrolytes used as the separator in all-solid-state batteries (ASSBs). While LLZO is considered to have a wide electrochemical stability window, its intrinsic stability in contact with lithium metal and the question of reaction kinetics remains largely unaddressed, as many measurements and theoretical insights rely on analysis of the thermodynamic ground state of the system to determine stability. This indicates that more precise knowledge of interfacial stability is needed to advance the understanding of lithium metal electrode kinetics and dendrite growth in LLZO-based solid-state batteries. Determining the critical link between chemical reactivity and electrochemical performance is essential to enable next-generation ASSBs.

To develop such insights, we have utilized a variety of different *in situ* and *operando* x-ray photoelectron spectroscopy (XPS) techniques—i.e., magnetron sputtering, electron beam evaporation, and electrochemical deposition – coupled with electrochemical measurements to investigate in detail the factors impacting the interfacial stability of Al-doped LLZO in contact with lithium metal (Figure XVI.3.1). The extent of oxygen deficient interphase (ODI) formation is found to depend on the energetics of Li metal as it arrives at the LLZO surface, with electrochemical and sputter deposition intrinsically leading to the reduction of Zr^{4+} and resulting in ODI layer formation. Lower energy e-beam evaporation does not result in any reduction of Zr^{4+} , even when Li is deposited at elevated temperatures; however, subsequent irradiation of e-beam-deposited Li by energetic Ar^+ species (data not shown) is able to reproduce the extent of ODI formation observed from electrochemical and sputter deposition. These results support the hypothesis that there is a kinetic barrier to LLZO reduction by Li, as the application of sufficient overpotential to electrochemically nucleate and grow Li metal provides sufficient energy to drive Zr^{4+} reduction at the Li|LLZO interface. Therefore, it can be concluded that the formation of an ODI is dependent on the lithium energy during the deposition process and that under further electrochemical cycling conditions, ODI formation is expected to occur. Despite the presence of a kinetic barrier to reduction, electrochemical impedance measurements of Li|LLZO|Li coin cells (data not shown) reveal an identical response whether or not the ODI is present, indicating that interphase formation does not impede the charge transfer kinetics of Li ions across the Li|LLZO interface and likely explaining the favorable electrochemical performance of LLZO-based ASSBs. However, a possible link between the formation of the ODI layer in LLZO and dendrite nucleation will be considered in future work. Overall, these results highlight the additional complexities governing the reactivity of solid-state interfaces in ASSBs and underscore the importance of *operando* characterization of interfacial stability to design more robust, high-performance protection strategies for solid electrolytes in contact with reactive electrodes.

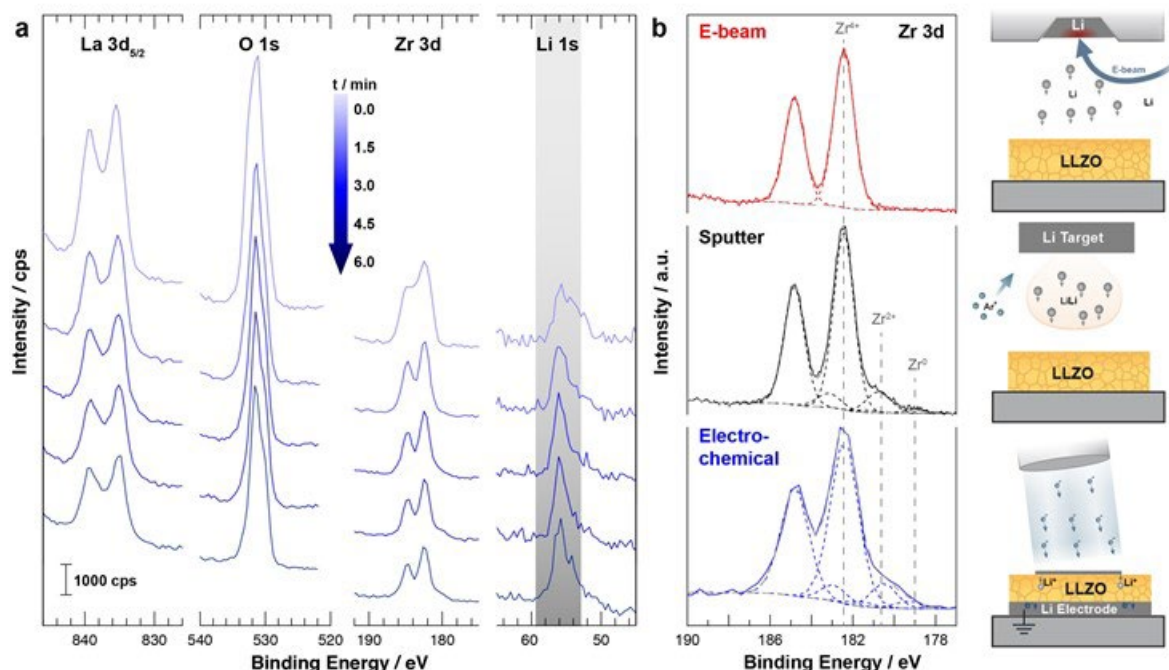


Figure XVI.3.1 (XPS measurement of in-situ electrochemical Li deposition) (a) Operando XPS measurements of individual core-level spectra during electrochemical deposition of Li showing their evolution with increasing Li deposition time. All core-level spectra are plotted on the same absolute scale in counts per second except Li 1s spectra, which are magnified by 10× for clarity. (b) Zr 3d core-level spectra comparing the extent of Zr⁴⁺ reduction as a function of the deposition technique.

Impact of Al/Ga Dopants on Chemical Reactivity of LLZO with Metallic Li Al³⁺ and Ga³⁺ dopants, when inserted into bulk LLZO, are directly substituting onto the lithium sublattice of interconnected tetrahedral and octahedral sites and show relatively little difference in formation energy with respect to defects on the lithium sublattice. This has led to the belief that both dopants are chemically similar in LLZO, making the choice of dopant a matter of preference and availability. An investigation into the phase transformation, dopant clustering, and diffusivity effects of Al³⁺ and Ga³⁺ doping was initiated. A series of modeling experiments have been initiated using density functional theory (DFT) calculations as uniquely suitable for modeling the oxidation/reduction of ionic species as they are moved closer to or further from the lithium metal interface. Example simulation cells of the Li|LLZO interface are shown in Figure XVI.3.2a. Single ions of Al³⁺/Ga³⁺ dopants were inserted into the simulation cell and optimized with lowest energy configurations arising when the dopant is on tetrahedral sites. The oxidation/reduction potential of LLZO was assessed by looking for changes in the density of states (DOS) for electrons in the structures shown in Figure XVI.3.2b. Substitutions of Al³⁺/Ga³⁺ in the bulk of LLZO show there is no change with respect to the location of the Fermi energy or width of the band gap, indicating that the substitution of Al³⁺/Ga³⁺ does not form electronically conducting states. However, when interfaced with lithium metal, the metallic lithium states fall between the valence and conduction bands of LLZO, shifting the DOS to the left and raising the Fermi energy closer to the conduction band of LLZO. In line with our previous experimental studies, a thin layer of Li metal was deposited on the Ga-LLZO surface by e-beam evaporation. XPS measurements (Figure XVI.3.2c) show Ga³⁺ is reduced to Ga⁰ and possibly forms a Ga-Li alloy at the interface. Raman measurements (Figure XVI.3.2d) show that the cubic phase of pristine Ga-LLZO is maintained, and no tetragonal or impurity phases—which might result from continuous reaction with Li⁰—are not detected. Additionally, no mixed conducting interphase due to electronic and ionic conduction was detected in conductive atomic force microscopy (data not shown). Electrochemical impedance spectroscopy (EIS) shows that with prolonged contact between Li and Ga-LLZO, interfacial resistance decreases but charge transfer resistance increases due to the chemical reactions at the Li|Ga-LLZO interface (Figure XVI.3.2e). Thus, interfacial reactions with dopant atoms can drastically impact overall cell performance.

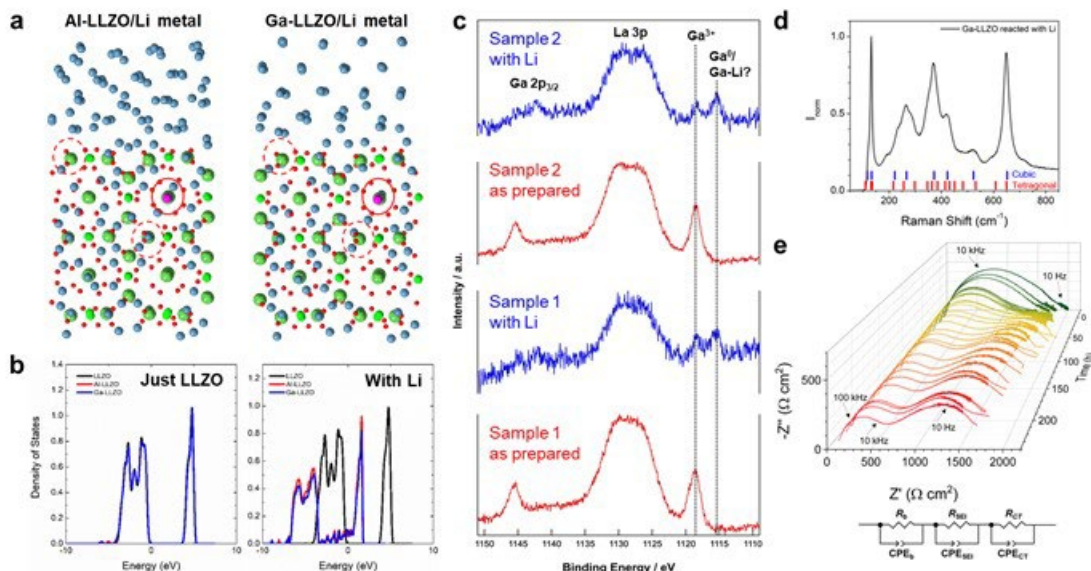


Figure XVI.3.2 (a) Simulation cell showing three possible dopant locations in the LLZO near the surface. The optimized dopant locations for Al³⁺ and Ga³⁺ are circled in solid red lines. (b) Density of states for doped and undoped bulk LLZO (left) and Li⁰|LLZO interface (right) shifted to the Fermi level at zero. (c) XPS measurements of Ga-LLZO samples before and after Li metal deposition. (d) Raman spectrum of Ga-LLZO reacted with Li metal. (e) EIS spectra and circuit of Ga-LLZO in a Li|Li symmetric cell at open circuit.

Controlling Grain Boundary Chemistry of LLZO Cubic LLZO generally densifies at temperatures above 1200 °C via solid-state sintering, but this rather high sintering temperature can cause volatilization of Li and can lead to a phase transition back to the less conductive tetragonal phase. Presence of pores left from an unsatisfactory sintering procedure can reduce ionic transport as well as degrade mechanical properties of the solid electrolyte. Grain boundaries between crystals in the electrolyte can limit performance through 1) adding more resistance to the overall cell by presenting a barrier to Li⁺ transport and 2) generally having higher electrical conductivity, thus generating favorable pathways for Li dendrite formation. This second point can be worsened by dopant segregation to the grain boundaries. It is important, therefore, to control grain boundary chemistry to prevent these issues and increase the ionic conductivity and critical current density of the solid electrolyte. One useful and straightforward route to optimization of the densification procedure is grain boundary engineering with sintering aids. Sintering aids such as Li₃BO₃ (LBO) are used during the annealing and sintering procedures to lower the temperature needed for LLZO grain growth. During sintering, LBO forms a liquid phase at temperatures below 1000 °C and enhances the densification of LLZO grains. Since LBO itself is a moderate Li⁺ conductor (~10⁻⁶ S/cm at room temperature), it should still allow high conductivity in the electrolyte. As a result, this improved densification procedure can lower sintering temperature and minimize the negative impacts of grain boundaries. SEM analysis of sintered Al-doped LLZO and Al-doped LLZO with 15 vol % LBO provided direct evidence that LBO not only decreases the temperature required for sintering but also segregates to grain boundaries and surfaces of the primary grains. This microstructure is expected to influence the electrochemical properties of the electrolyte and its ability to cycle with Li metal. To confirm the spatial distribution of LBO in the LLZO electrolyte, we used Raman microscopy. Mapping of LBO on the pellet surface shows clear segregation of LBO outside of large 5-10 μm LLZO grains (Figure XVI.3.3a). LBO is found in grain boundaries and triple junctions along with discrete crystals embedded in the electrolyte or as surface particles. This suggests that grain boundary modification with LBO is possible by simple inclusion as sintering aid.

EIS was used to determine how LBO impacts overall conductivity in the electrolyte. Figure XVI.3.3b shows Nyquist plots of Al-doped LLZO with and without 15 vol % LBO doping. Quantitative fits show that combined bulk and grain boundary impedance (10 MHz-10 kHz) increases for the doped sample (19.9 kΩ cm²) compared to the undoped sample (15.8 kΩ cm²). This agrees with expectations that adding a poorer

conductor in between grains will increase resistance, although it appears in this case only by $\sim 25\%$. More apparent is the change in interfacial/charge transfer resistance (10 kHz–100 Hz), which is almost two orders of magnitude higher for the undoped sample ($2.4 \text{ M}\Omega \text{ cm}^2$ vs. $45 \text{ k}\Omega \text{ cm}^2$). This result may be due to the surface impurities present on each sample, with Li_3BO_3 protecting LLZO from air and having moderate Li^+ conductivity itself. This demonstrates the benefits of using LBO as sintering aid and grain boundary modifier in LLZO processing.

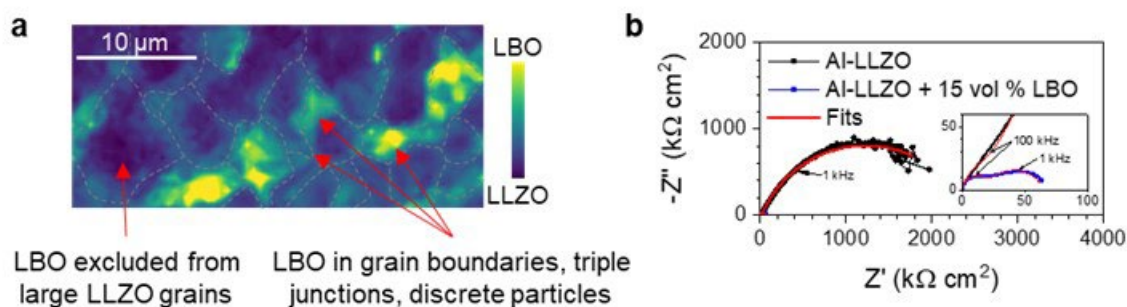


Figure XVI.3.3 (a) Raman mapping of LBO content within an Al-LLZO pellet synthesized with 15 vol % LBO. Dotted lines in the image are drawn to guide the eye around LBO in grain boundaries. (b) EIS spectra of Al-LLZO pellets in Li | Li symmetric cells sintered without and with 15 vol % LBO.

Development of Large-Scale LLZO Composite Electrolytes from Ultrafine-Grain Nanofibers

Conventional LLZO syntheses generate precursor green powders and require high sintering and long sintering times of >24 hours. With roll-to-roll technology that is scalable, an electrospinning approach reduces processing steps, shortens manufacturing time, and increases production energy efficiency leading to a novel and cost-effective manufacturing pathway to synthesize large-area solid-state electrolytes. Using electrospinning methods, we obtained cubic LLZO, even without doping elements usually needed to stabilize the cubic phase. During annealing, the electrospun polymers are removed as CO_2 gas while the crystalline LLZO fibers are formed through nucleation and grain coalescence. By adjusting the annealing conditions, LLZO fibers with various grain sizes and morphologies can be achieved. Figure XVI.3.4a shows the roll-to-roll (R2R) electrospinning tool for nanofiber LLZO fabrication along with nanofiber characterization showing cubic LLZO. During the subsequent slot-die coating process (Figure XVI.3.4b), LLZO fibers are mixed with a LiTFSI-doped poly (ethylene oxide) (PEO) solution, and the well-dispersed slurry is then coated on a fast-moving web to form a thin membrane. By accurately controlling coating parameters, uniform membranes of designed thickness (≤ 20 – $150 \mu\text{m}$) can be obtained. Figure XVI.3.4c presents cross-sectional SEM images of a coated membrane. While traditional drop-cast membranes are heterogenous and porous, slot-die coated samples are dense, uniform, and show good ductility and uniform fiber distribution in the polymer. Ideally, interconnected LLZO nanofiber network “scaffolds” are the basis of the composite while the polymer increases flexibility and interfacial contact with anode and cathode. High LLZO loadings are required to achieve this percolation network and high room-temperature conductivity, thus our future focus is on increasing LLZO content and network distribution.

Electrochemical Reactivity of Composite with Metallic Li We tested three composite compositions with LLZO loadings at 41, 50, and 56 wt% LLZO. Symmetric Li||Li cells were used to test the electrolytes’ performance with galvanostatic cycling and impedance measurements. Figure XVI.3.4d shows cycling of three samples from 0.05 mA/cm^2 up to 4.0 mA/cm^2 with capacities up to 4 mAh/cm^2 . All cells show a general decrease in polarization voltage with increased cycling over time. Figure XVI.3.4e shows that this is due to large decreases in interfacial impedance, as repeated stripping and plating provides better contact between the Li electrode and composite electrolyte. Impedance also shows that as LLZO content increases, more high-frequency impedance is resolved, likely due to the contribution of LLZO to overall ionic conductivity. No dendrites were seen in cross-sections of the cycled electrolytes, indicating high-rate capabilities are possible with these mechanically strong composite electrolytes.

Conclusions

In this work, we investigated the various aspects of LLZO reactivity and use in ASSBs. Controlled Li deposition methods revealed a kinetic barrier to LLZO reduction and interface decomposition via Zr^{4+} reduction. Substitutions of Al^{3+}/Ga^{3+} in the bulk of LLZO show there is no change with respect to the location of the Fermi energy or width of the band gap, indicating that the substitution of Al^{3+}/Ga^{3+} does not form of electronically conducting states. In the case of Ga-doped LLZO, reduction of Ga^{3+} to Ga^0 species is chemically unique to this dopant and increases charge transfer resistance against Li anodes over time. Disadvantages from LLZO synthesis can be limited by using the sintering aid Li_3BO_3 , which segregates to grain boundaries and surfaces of the primary grains/particles and lowers sintering temperature. Furthermore, LBO samples demonstrate lower interfacial and charge transfer impedance that will increase the ionic conductivity and critical current density of the solid electrolyte. LLZO nanofibers can be produced efficiently in a roll-to-roll manufacturing process and incorporated into composite polymer electrolytes at high LLZO loading. Ongoing work will optimize ink composition, mechanical fluidic properties, and coating process parameters to ensure dense and low-defect membranes with good LLZO fiber percolation networks. Initial electrochemical tests reveal these electrolytes can achieve $\geq 3 \text{ mA/cm}^2$ at $\geq 3 \text{ mAh/cm}^2$.

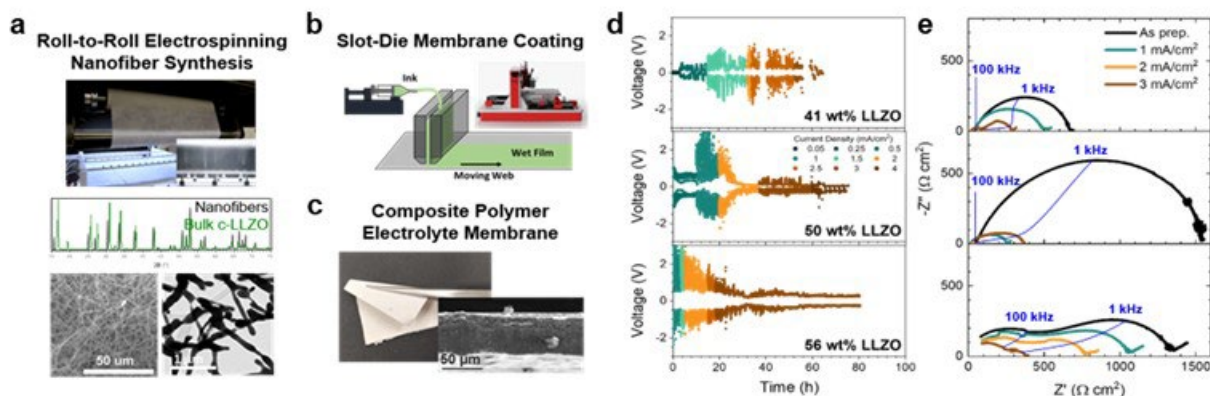


Figure XVI.3.4 (a) Roll-to-roll nanofiber fabrication by electrospinning; XRD pattern showing cubic LLZO fibers; SEM and TEM of nanofibers. (b) Schematics of slot-die coating; inset bench scale coater. (c) Photo and cross-section SEM of slot-die coated LLZO nanofiber-PEO membrane. (d) Symmetric Li | Li cycling of composites with different LLZO loadings at 60 °C. (e) EIS spectra of the corresponding cells from (d) before and after cycling.

Key Publications

Patents

1. **SOLID-STATE NANOFIBER POLYMER MULTILAYER COMPOSITE ELECTROLYTES AND CELLS.** Filed on 9-30-2021 as application 17/490,956.

Publications

1. **Kinetic versus Thermodynamic Stability of LLZO in Contact with Lithium Metal** Justin Connell, Till Fuchs, Hannah Hartmann, Thorben Krauskopf, Yisi Zhu, Joachim Sann, Regina Garcia-Mendez, Jeff Sakamoto, Sanja Tepavcevic, Jürgen Janek. *Chem. Mater.* 2020, 32, 23, 10207–10215.
2. **Increasing Ionic Conductivity of Poly (ethylene oxide) by Reaction with Metallic Li** Liu, P., Counihan, M.J., Zhu, Y., Connell, J.G., Sharon, D., Patel, S.N., Redfern, P.C., Zapol, P., Markovic, N.M., Nealey, P.F., Curtiss, L.A., Tepavcevic, S. (2021), *Adv. Energy Sustainability Res.* 2100142.
3. **Advancing Cycling Capabilities of Composite Polymer Electrolytes with LLZO Nanofiber** Michael Counihan, Devon Powers, Justin Connell, Yuepeng Zhang, Sanja Tepavcevic. *In Preparation.*

4. **Modifying Grain Boundary and Interfacial Chemistry in a Garnet Solid Electrolyte with Li_3BO_3 Sintering Additive** Zachary Hood, Michael Counihan, Sanja Tepavcevic. *In preparation*.

Presentations

1. Sanja Tepavcevic, et al, **Role of Dopants in Advancing Solid-Solid Interfaces in Li-ion Batteries**, Solid Power ANL Visit, July 21, 2021 (virtual).

Acknowledgements

The PIs are grateful to our collaborators, Justin G. Connell, Peter Zapol, John W. Freeland, Dillon D. Fong, and Nenad M. Markovic for data collection, analysis, and their valuable contributions to the project. We also thank Jeff Sakamoto (UM), Zachary Hood and Yuepeng Zheng (AMD, ANL) for materials synthesis and characterization.

XVI.4 Lithium Dendrite-Free Solid Electrolytes for High Energy Lithium Batteries (University of Maryland, College Park)

Chunsheng Wang, Principal Investigator

University of Maryland, College Park
Room 3236 Jeong H. Kim Engineering Building
College Park, MD 20742
E-mail: cswang@umd.edu

Duong Tien, DOE Technology Development Manager

U.S. Department of Energy
E-mail: Tien.Duong@ee.doe.gov

Start Date: October 1, 2020

End Date: September 30, 2021

Project Funding (FY21): \$300,000

DOE share: \$300,000

Non-DOE share: \$0

Project Introduction

The development of all solid-state Li metal batteries (ASSLBs) using nonflammable inorganic or organic solid-state electrolytes (SSEs) was reckoned as the promising direction due to their enhanced safety and high energy density. However, lithium dendrite growth during charge/discharge cycles still limits the use of all solid-state batteries.

In our project, a criterion for lithium dendrite suppression that is developed through systematical investigation on thermodynamics and kinetics of lithium dendrite growth was proposed to guide the SSE design and Li/SSE interface modification. $\text{Li}_7\text{N}_2\text{I-LiOH}$ and Li_3YCl_6 solid electrolyte with high ionic conductivity and low electronic conductivity was used to validate the criterion for lithium dendrite suppression and achieve the project objective. Different surface modifications were also explored to enhance the dendrite suppression capability of SSEs.

Objectives

The objective of this project is to research, develop, and test Li-metal-based batteries that implement solid Li-ion conductors (LICs) equipped with $\text{Li}_7\text{N}_2\text{I-LiOH}$ SSE capable of achieving cell performance of 350 Wh/Kg energy density for 1000 cycle life with a cost of $\leq \$100/\text{kWh}$. To achieve these, the team will 1) establish the relationship among interface energy, lithium plating/stripping overpotential, interface resistance, SSE stability with lithium, and critical current density (CCD). 2) The dendrite suppression criterion will be developed based on the relationship. 3) The dendrite suppression capability for the $\text{Li}_7\text{N}_2\text{I-LiOH}$ pellet will be evaluated by testing the CCD. 4) The $\text{Li}_7\text{N}_2\text{I-LiOH}$ electrolytes and $\text{Li}_7\text{N}_2\text{I-LiOH/Li}_3\text{YCl}_6$ bi-layer electrolytes will be used to validate the developed dendrite suppression criterion and support Nickel Manganese Cobalt oxides (NCM) cathodes. 5) New engineering methods would be developed to suppress the Li dendrite to realize ASSLB.

Approach

The dendrite suppression criterion will be developed based on the Butter-Volmer model and total energy analysis. The dendrite suppression criterion will also be validated by using $\text{Li}_3\text{N-LiF}$, $\text{Li}_7\text{N}_2\text{I-LiOH}$ and $\text{Li}_7\text{N}_2\text{I-LiOH/Li}_3\text{YCl}_6$ bi-layer electrolytes that are stable against Li metal together with high ionic conductivity and high interface energy against Li. New interface engineering methods will be explored based on the learned mechanisms on $\text{Li}_{6.5}\text{La}_3\text{Zr}_{1.5}\text{Ta}_{0.5}\text{O}_{12}$ (LLZTO) electrolyte.

Results

Reducing the interface resistance and suppressing Li dendrite by interface modification. $\text{Li}|\text{LLZTO}|\text{Li}$ cells with different interface modifications were assembled. The LLZTO pellets are from the same batch with the same thicknesses and diameters. As shown in Figure XVI.4.1a-c, the $\text{Li}|\text{LLZTO}|\text{Li}$ cells that were modified by carbon,

Bi, and AgF showed critical overpotentials (COP) of 0.18, 0.16, and 0.15 V, respectively. The COP varies within a small region between 0.15–0.18 V. We proposed that the COP rather than CCD should be used as a criterion for the Li dendrite suppression capability of SSEs because (1) the COP is an intrinsic property of the solid electrolyte materials, while CCD is an engineering parameter associating with COP, electrolyte thickness, interface resistance, as well as ionic/electronic conductivity; (2) COP represents the maximum resistance for Li dendrite growth which associates with the electronic conductivity, density, mechanical strength, and interfacial energy.

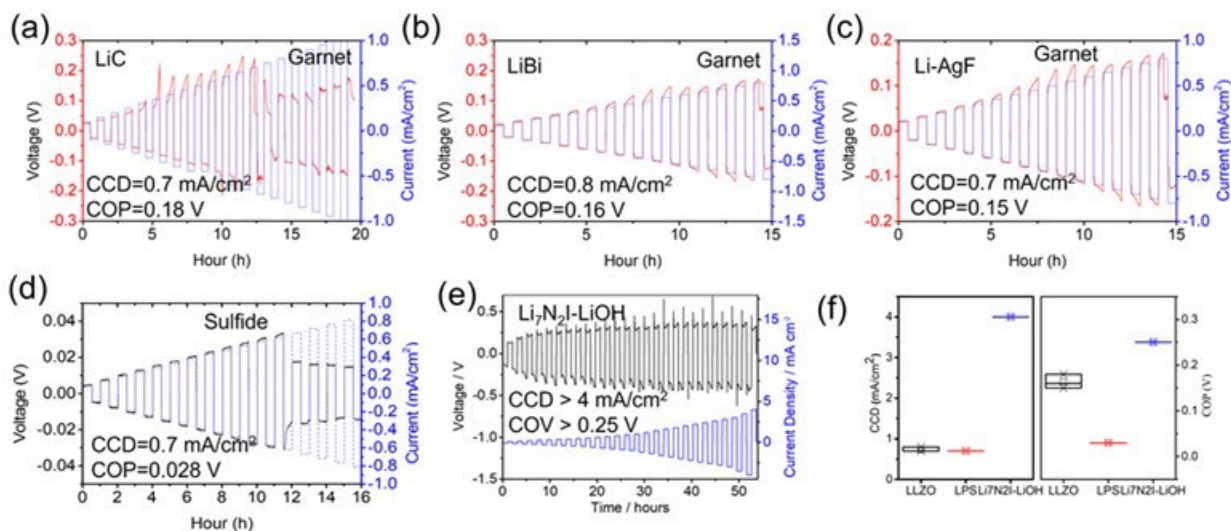


Figure XVI.4.1 CCD and COP determined by the plating/stripping measurement with step-increased current. Li plating/stripping behaviors for different surface modifications with (a) graphite, (b) Bi and (c) AgF for Li|LLZTO|Li cell and (d) Li|Li₆PS₅Cl|Li and (e) Li|Li₇N₂I-LiOH|Li cells at a step-increased current. The determined CCD and COP are listed in the figures. (f) The box chart for the determined CCD and COP of different SSEs.

Moreover, CCD of a typical sulfide SSE Li₆PS₅Cl was also determined as 0.7 mA/cm² (Figure XVI.4.1d), which is similar to the reported value. The corresponding COP of Li₆PS₅Cl SSEs is about 0.03 V. Although CCD of the two electrolytes (Li₆PS₅Cl and LLZTO) are close to each other (0.7–0.8 mA/cm²), the COPs of sulfide electrolytes (0.03 V) are much lower than those of LLZTO electrolytes (0.15–0.18 V) due to the less-stability of the sulfide electrolytes. The side reactions between Li and sulfide electrolytes result in cracks and new interphase formation with low interface energy against Li metal.

The COP of Li₇N₂I-LiOH pellets with similar size and thickness as those of oxides and sulfides was also investigated. As shown in Figure XVI.4.1e, the COP of Li₇N₂I-LiOH is > 0.25 V, which is higher than the COPs of LLZTO. This may originate from the intrinsic stability of Li₇N₂I-LiOH against lithium metal. Figure XVI.4.1f shows the box chart for the determined CCDs and COPs of Li₇N₂I-LiOH, LLZTO and LPS electrolytes. The COPs of Li₇N₂I-LiOH, LLZTO and LPS electrolytes reflect the stability of these electrolytes against Li, reconfirming that COP is a good indicator to reveal the intrinsic dendrite suppression capability of solid-state electrolytes.

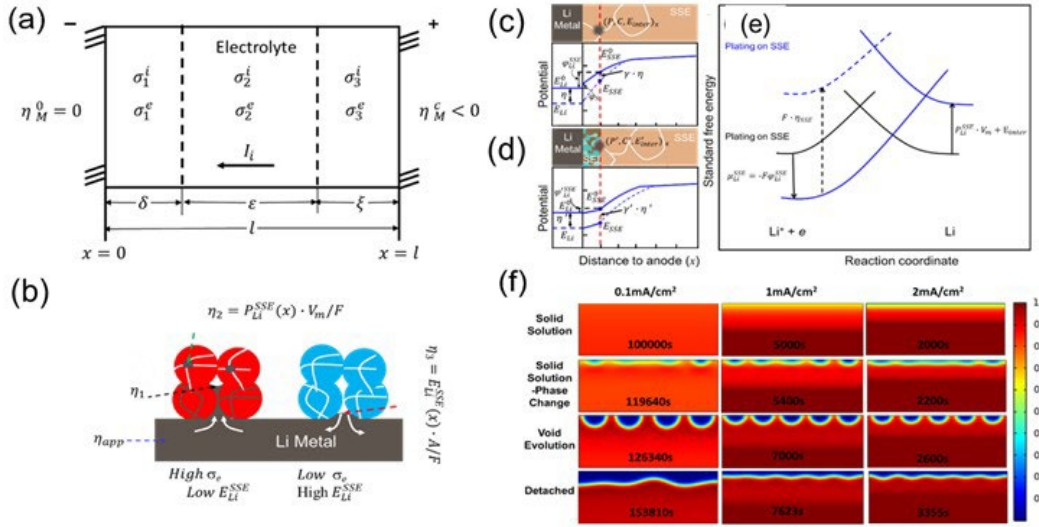


Figure XVI.4.2 Thermodynamic and kinetics analysis for solid state battery. (a) Thermodynamic model of SSE for Li dendrite growth, where σ_i , σ_e are ionic conductivity and electronic conductivity; $\nabla\eta_i$, $\nabla\eta_e$ are electrochemical potential gradients of ions and electrons, δ , ϵ and ξ (subscripts 1, 2 and 3) represent the areas for near anode, bulk SSE and near cathode. (b) Kinetics of Li dendrite growth in SSEs. Li dendrite growth in stable SSE which is not dense and has different electronic conductivity and interface energy, P_{Li}^{SSE} is the stress of Li nucleation site; E_{Li}^{SSE} is the interface energy of SSE against Li, V_m is the Li molar volume, and A is the interface area, F is the faraday constant. (c-d) 1D battery model near anode and their corresponding spatially dependent potential distribution in (c) stable and (d) unstable SSE. (e) Effects of a potential change on the standard free energy of activation for oxidation and reduction on Li metal (black lines) and SSE (blue lines). At the distance to anode of x , the stress, concentration of species i , and interface energy against Li metal are defined as $P(x)$, $C_i(x)$, and $E_{inter}(x)$ respectively. (f) Li metal diffusion kinetics at different applied current densities simulated by the phase-field model.

Investigation of thermodynamics and kinetics of Li deposition process. Using the model in Figure XVI.4.2a, we developed the Li dendrite formation criterion in LLZTO and LPS.

Consider a simple ionic solid where the conduction cations have a charge of +1, giving the equilibrium reaction:



Based on basic electrochemical principles and reasonable assumptions, we can get:

$$\frac{\Delta\eta_M^\delta}{F} = \frac{A \left[\frac{\Delta\eta_M^c}{F} + \frac{\sigma_2^i}{\sigma_3^i} V_T \right]}{1 + A} \quad (2)$$

where F is Faraday's constant, V_T and A are voltage and area, defined as $-\int_0^l \left(\frac{\nabla\eta_e}{F} \right) dx$ and $\frac{\delta}{l-\delta} \frac{\sigma_3^i}{\sigma_1^i}$ respectively.

Ionic conductivity (σ_i) is defined under Ohmic current flow. According to equation (2), we can find that the critical overpotential $\Delta\eta_M^c$ for the cell will be affected by not only the Li|SSE interface but also the cathode|SSE interface. To suppress Li dendrite, a stable SSE is needed. If unstable, the interphase should have a high ionic conductivity and a low electronic conductivity.

Apart from the thermodynamic analysis of the SSEs, kinetics are also important for the stable operation of the all-solid-state battery. The Li dendrite growth in SSEs depends on driving force (applied Li plating potential, $\Delta\eta_M^\delta$) and resistance (critical Li plating overpotential in SSE, $\Delta\eta_M^c$). The $\Delta\eta_M^c$ is determined by the property of SSEs, including thermodynamic stability, ionic conductivity, electronic conductivity, porosity, interface energy and mechanical strength. Once the $\Delta\eta_M^\delta$ exceeds the $\Delta\eta_M^c$, Li dendrites begin to grow. To suppress Li dendrite growth in SSEs, η_1 (also $\Delta\eta_M^\delta$) in Error! Reference source not found. **b** needs to be reduced by

increasing the ionic conductivity and reducing electronic conductivity and surface resistance. Meanwhile, the $\Delta\eta_M^c = \eta_2 + \eta_3$ of SSEs should be increased by enhancing the local stress [ENREF 1](#) and interface energy of SSEs. For the electrolytes which are not dense, the Li infiltration into porous SSEs behaves like an incompressible work fluid, driven by the chemical potential/pressure gradient and interface energy of Li/SSEs. [ENREF 2](#) The dendrite can easily propagate in the SSEs with high electronic conductivity and low interface energy. However, for the SSEs which are electronic insulators with a high interface energy, the nucleation and growth should be suppressed.

To analyze the kinetics for the solid-state battery, the Butler-Volmer equation based on the energy analysis and phase-field model was modified for the SSE and Li metal anode, respectively. Figure XVI.4.2c-e shows the 1D model near the anode based on the Butler-Volmer equation and its corresponding spatially dependent potential distribution. According to the Butler-Volmer model, the Li plating current on Li metal (Figure XVI.4.2e black lines) is related exponentially to the overpotential η . That is,

$$i_{Li} = F A k^0 [C_{Li^+}(0, t) e^{-\alpha f \eta} - C_{Li}(0, t) e^{(1-\alpha) f \eta}] \quad (3)$$

where, A , k^0 , α , and f are the frequency factor, standard rate constant, transfer coefficient and F/RT (R is gas constant and T is temperature). Accordingly, the potential in SSE will change from E_{SSE}^0 to E_{SSE} , resulting in an overpotential $\eta_{SSE} = E_{SSE} - E_{SSE}^0 = \gamma \cdot \eta$ in SSE (Figure XVI.4.2e blue dashed lines), where γ is the overpotential transfer coefficient which is related to the electronic conductivity of the SSE. Moreover, the stress P and interface energy E_{inter} in the SSE will raise an opposite overpotential for Li deposit. The stress P is linear with the overpotential by $\eta_{stress} = P \cdot V_m / F$, where V_m is the molar volume of Li metal. Thus, the Li plating current in SSE i_{SSE} is

$$i_{SSE} = F A k^0 [C_{Li^+}(x, t) e^{-\alpha f (-\mu_{Li}^{SSE}(x) + \gamma \cdot \eta)} - C_{Li}(x, t) e^{[(1-\alpha) f (-\mu_{Li}^{SSE}(x) + \gamma \cdot \eta) + P_{Li}^{SSE}(x) \cdot V_m + E_{inter}]}] \quad (4)$$

Consider the dendrite free situation, the i_{SSE} should be infinitely close to 0, thus,

$$C_{Li}(x, t) = C_{Li^+}(x, t) e^{[(1-\alpha) f (-\mu_{Li}^{SSE}(x) + \gamma \cdot \eta) + P_{Li}^{SSE}(x) \cdot V_m + E_{inter}]} \quad (5)$$

based on the equation, the summation of the overpotential should be as positive as possible to avoid the dendrite formation, requiring low electronic conductivity, high density and mechanical strength, and high interfacial energy.

Recent findings demonstrated that the kinetics of Li diffusion in Li metal anode plays a critical role in Li dendrite growth for all-solid-state batteries. Figure XVI.4.2f shows the Li metal stripping process at an applied current density. At a stripping current of 0.1 mA/cm², a solid-solution Li diffusion process takes place with the decrease in density of Li metal at Li/SSE interface. After 119,640 seconds, some voids can be observed because of the phase transformation. At the time of 126,340 second, apparent voids formed on the Li/SSE interface and the Li anode completely detach from the SSE after 153,810 seconds. The morphology evolution of the Li metal results in a rapid increase of polarization during the stripping process. At a large current density of 1.0 and 2.0 mA/cm², the detachment between the Li metal and SSE are much earlier than that at 0.1 mA/cm². These results indicate that the kinetics for Li metal diffusion is very important for achieving a high COP and CCD.

Tuning the lithiophobicity of the interface to reduce interfacial resistance and suppress Li dendrite formation in LLZTO electrolyte. Different from all previous metal/metal oxide coatings on garnet or Li alloy anodes that form lithiophilic interlayer, Li-Sr/SrO-Li₂O is a lithiophilic/lithiophobic bifunctional layer (Figure XVI.4.3a-e). This interlayer was demonstrated to simultaneously reduce the interfacial resistance and suppresses lithium dendrite. The optimized Li-Sr | garnet | Li-Sr symmetric cell can be cycled for 1,000 cycles under 0.5 mA/cm² (Figure XVI.4.3f) with a critical current density of 1.3 mA/cm² at room temperature (Figure XVI.4.3g). The good stability of the lithiophobic SrO doped Li₂O interphase prevents the garnet from reducing and suppresses Li dendrite, which distinguishes it from all reported alloy electron-conducting interlayers. Therefore, the

bifunctional lithiophilic/lithiophobic interlayer provides a new strategy for high-performance garnet solid-state lithium batteries (Figure XVI.4.3h).

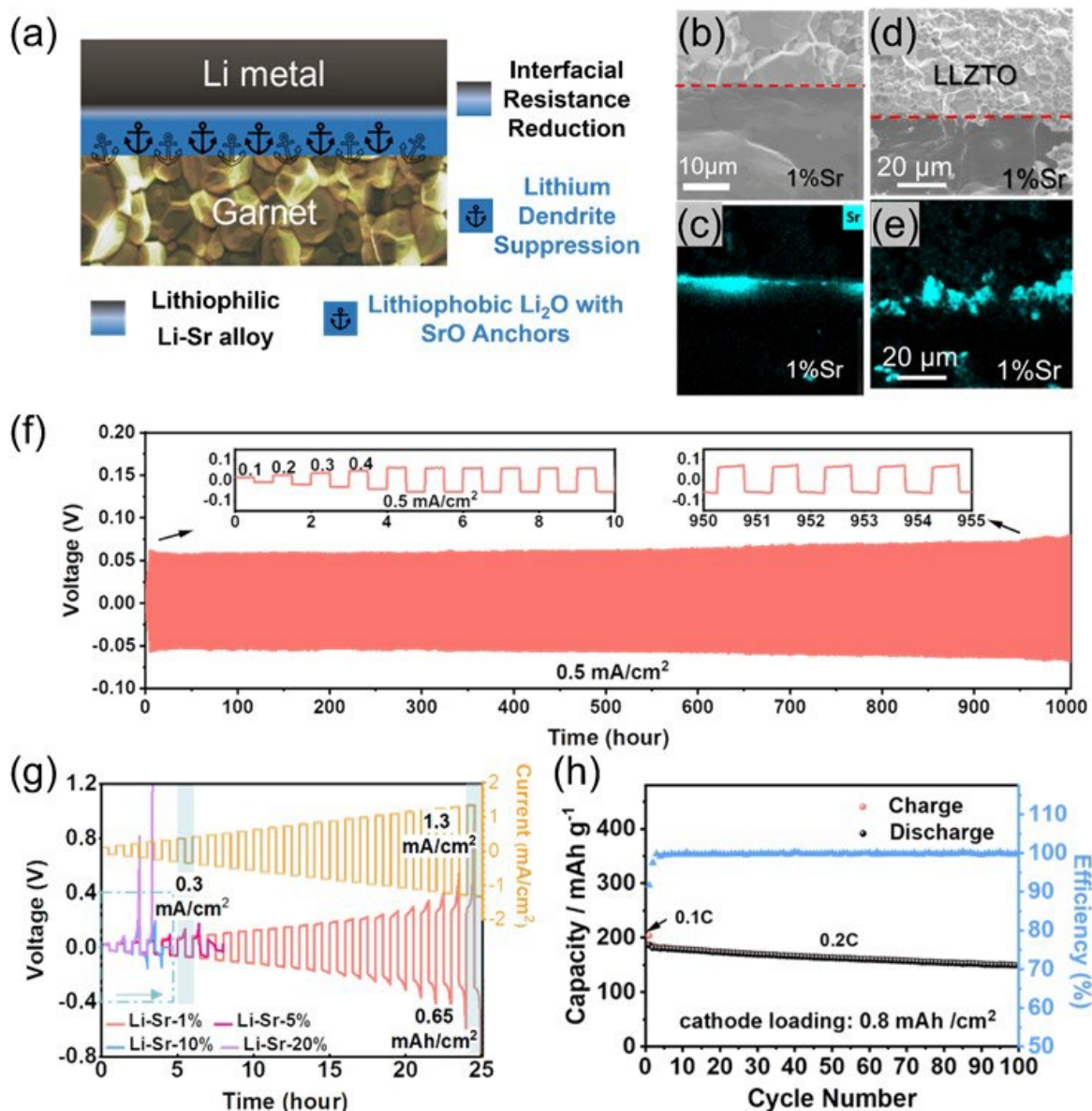


Figure XVI.4.3 The interface design to reduce surface resistance and suppress Li dendrite in LLZTO electrolyte. (a) Schematic diagram of the bifunctional lithiophilic/lithiophobic interlayer. Cross-section morphology and Sr elemental mapping of the electrode interface with the LLZTO pellet before (b-c) and after (d-e) cycling showing a stable Sr segregation right on the interface. The red dash lines mark the interfaces. (f) Long-term cycling performance of Li-Sr | LLZTO | Li-Sr symmetric cell at 0.5 mA/cm². Inset is the magnification of the voltage profiles of 1-10 cycles and 950-1000 cycles. (g) The Li plating/stripping behavior for the cells at a step-increased current for 0.5 h. (h) The cycle performance for proof-of-concept Li-Sr | LLZTO | LiNi_{0.8}Mn_{0.1}Co_{0.1}O₂ (NMC811) cells at 0.2 C with cathode loading of 0.8 mAh / cm² (0.1 C for the first cycle for activation).

Development of thermodynamic Stable $\text{Li}_7\text{N}_2\text{I}$ electrolytes for Li dendrite suppression. $\text{Li}_7\text{N}_2\text{I}$ electrolyte was prepared by sintering a mixture of Li_3N and LiI at 550 °C. Multi-walled Carbon Nanotube (MWCNT) was purchased from Sigma Aldrich and fully dried before use. Fine $\text{Li}_7\text{N}_2\text{I}$ powder was carefully mixed with 5 wt% MWCNT to use as the interface between $\text{Li}_7\text{N}_2\text{I}$ electrolyte and Li anode. The Li-Li symmetry cell was first pre-cycled at a low current density of 0.1 mA/cm² to fully activate the interface. As can be seen in Figure

XVI.4.4a, the cell voltage of Li symmetric cell gradually decreases from 0.3 V and finally stabilizes at ~ 0.07 V. The stable cycling of the symmetric cell is due to the introduction of ionic/electronic conducting interface. We further studied the CCD of the $\text{Li}_7\text{N}_2\text{I}$ with the designed interface in Li symmetric cells (Figure XVI.4.4b). The cell voltage increases with the current density. Finally, a record-breaking high CCD of $> 4.0 \text{ mA/cm}^2$ at a capacity of 4.0 mAh/cm^2 can be gotten before short-circuit occurs. On the other hand, the total resistance of the Li symmetric cell based on electrochemical impedance spectroscopy (EIS) decreases from $2500 \Omega \text{ cm}^2$ (Figure XVI.4.4c) to $800 \Omega \text{ cm}^2$ (Figure XVI.4.4d) during the pre-cycling at 0.1 mA cm^{-2} . This process can effectively activate the interface and is essential to fully unleash the Li dendrite suppression capability of the interface. The Li dendrite suppression capability of the electrolytes with the designed electronic/ionic mixed-conducting interface was demonstrated by a high CCD. Although the total resistance of the Li symmetric cell is significantly reduced after cycling (Figure XVI.4.4e), the EIS profile shows an obvious diffusion region at a low frequency of 0.1 Hz , which indicates the cell has not been shorted by Li dendrite formation.

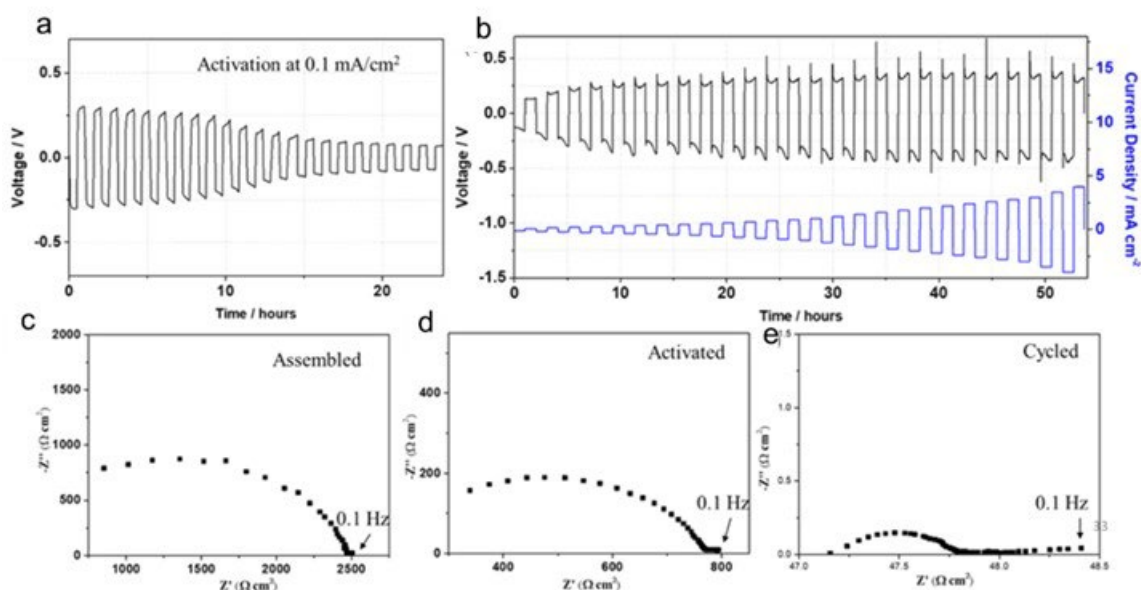


Figure XVI.4.4 Li plating/stripping behavior of the $\text{Li}_7\text{N}_2\text{I}$ -5% MWCNT protected $\text{Li}_7\text{N}_2\text{I}$ electrolyte in Li symmetric cell configuration at room temperature. (a) Galvanostatic cycling of the Li symmetric cell at a current density of 0.1 mA cm^{-2} . (b) Voltage profiles of the cell under step-increased current densities from 0.2 to 4.0 mA cm^{-2} for Li plating/stripping with a fixed time of 1 h. (c-e) Nyquist plots of the symmetric cell under different conditions: (c) before cycle (d) after activation, and (e) after cycled at 4 mAh cm^{-2} for 600 cycles.

Conclusions

1. We determined the critical overpotential of $\text{Li}_7\text{N}_2\text{I}$ -LiOH, LPS, and LLZO electrolytes.
2. We developed both thermodynamic and kinetic models for the Li dendrite suppression criterion in solid-state electrolytes.
3. A bifunctional lithiophilic/lithiophobic interlayer rich of Li-Sr/SrO-doped- Li_2O was proposed to suppress Li dendrite formation for garnet electrolytes.
4. High CCD was demonstrated by $\text{Li}_7\text{N}_2\text{I}$ -LiOH electrolyte with ionic-electronic mix conducting interface.

Key Publications

1. T. Deng, X. Ji, L. Zou, O. Chiekezi, X. Fan, L. Cao, T. R. Adebisi, H. Chang, H. Wang, B. Li, X. Li, C. Wang, D. Reed, J.-G. Zhang, V. Sprenkle, C. Wang, X. Lu, Interfacial engineering enabled practical low-temperature sodium metal battery, *Nat. Nanotechnol.*, **2021**, in press.
2. X. He, X. Ji, B. Zhang, N. Rodrigo, S. Hou, K. Gaskell, T. Deng, H. Wan, S. Liu, J. Xu, B. Nan, B. Lucht, C. Wang, Tuning interface lithiophobicity for lithium metal solid-state batteries, *ACS Energy Lett.*, **2021**, accept.
3. H. Wan, B. Zhang, S. Liu, J. Zhang, X. Yao, C. Wang, Understanding LiI-LiBr Catalyst Activity for Solid State Li₂S/S Reactions in an All-Solid-State Lithium Battery, *Nano Lett.* 2021, 21, 8488–8494.
4. H. Wan, S. Liu, T. Deng, J. Xu, J. Zhang, X. He, X. Ji, X. Yao, C. Wang, Bifunctional Interphase-Enabled Li₁₀GeP₂S₁₂ Electrolytes for Lithium-Sulfur Battery, *ACS Energy Lett.*, 2021, 6, 862–868.
5. X. Ji, S. Hou, P-F. Wang, X. He, N. Piao, X. Fan, C. Wang, Solid-State Electrolyte Design for Lithium Dendrite Suppression, *Adv. Mater.* 2020, 2002741.

Acknowledgments

We acknowledge the financial support from the Department of Energy (DOE) under Award number DEEE0008856.

XVI.5 All Solid-State Batteries Enabled by Multifunctional Electrolyte Materials (Solid Power, Inc.)

Pu Zhang, Principal Investigator

Solid Power Inc.

486 South Pierce Avenue, Suite E

Louisville, CO 80027

E-mail: pu.zhang@solidpowerbattery.com

Tien Q. Duong, DOE Technology Development Manager

U.S. Department of Energy

E-mail: Tien.Duong@ee.doe.gov

Start Date: October 1, 2019

End Date: September 30, 2022

Project Funding: \$422,290

DOE share: \$337,892

Non-DOE share: \$84,398

Project Introduction

Solid Power is teaming with University of California San Diego (Prof. Shirley Y. Meng) to develop a high energy, long life, low cost, and safe all-solid-state-battery (ASSB). The battery is enabled by a multifunctional solid-state electrolyte (SSE). The project will enable scalable production of large format solid state batteries required by the vehicle market and building domestic battery manufacturers as leaders in the global vehicle ASSB production.

Objectives

The project objective is to develop Li-metal solid batteries enabled by multifunctional SSEs for EV application. The ultimate goal is scalable production of large-format ASSBs able to deliver ≥ 350 Wh/kg specific energy, ≥ 1000 cycle life, and $\leq \$100/\text{kWh}$ cost.

Approach

The project will develop a high-performance Li-metal all-solid-state cell enabled by a multifunctional SSE. The new SSE will: (1) have high conductivity (up to 10 mS/cm), (2) be stable against lithium metal and high-voltage cathode (0–4.5 V), (3) promote uniform lithium plating (enabling $> 2C$ charge rate), and (4) be compatible with large-scale manufacturing processes. The specific cell chemistry to be demonstrated will be the SSE with Li-metal anode and high-nickel-content Li-metal oxide cathode. The all-solid-state cell will be assembled by scalable roll-to-roll processes developed by Solid Power.

Results

1. SSE material optimization

Solid Power's halogenated LPS material was used as a starting point. Li_2S , P_2S_5 , a halogen and other selected dopants were mechanically milled to form glassy sulfide electrolytes. A subsequent heat-treatment was conducted to obtain glass-ceramic solid electrolytes. The multifunctional SSE materials have been optimized for high conductivity and stability in Year 2. The optimized electrolyte has shown a Li ionic conductivity of 6 mS/cm at 25°C and a critical current density (CCD) of 20 mA/cm² at 70°C. The progress of the electrolyte development within the project is shown in Figure 1.

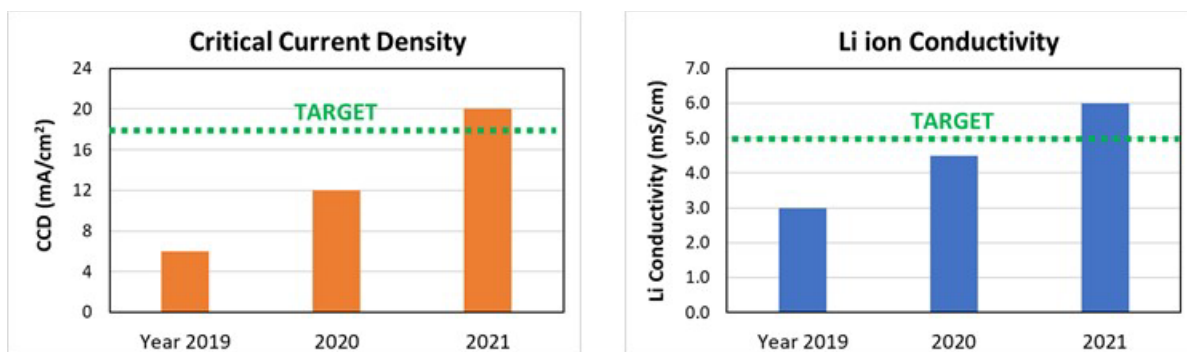


Figure XVI.5.1 The electrolyte development progress: CCD at 70 °C and Li ion conductivity at 25 °C

2. SSE separator development

The SSE separator coating process has been developed at pilot scale. A separator slurry was prepared by mixing the SSE powder, a binder, and a solvent by using a planetary mixer. The slurry was then cast on a carrier film on a slot-die coater. A roll-to-roll separator (≥ 100 m and ≤ 60 μ m) has been demonstrated.

3. Full cell demonstration

A single layer pouch cell (at 6 mAh) was assembled for performance demonstration. The cell contained a NMC 622 composite cathode (at 3 mAh/cm²), a thin Li metal anode, and a SSE separator. When tested at C/5 - C/5, 2.8 – 4.2V, and ambient temperature ($\sim 25^\circ\text{C}$), the cell shows 90% capacity retention after 500 cycles (in Figure 2). It should be noted that the capacity fluctuation was due to the ambient temperature change.

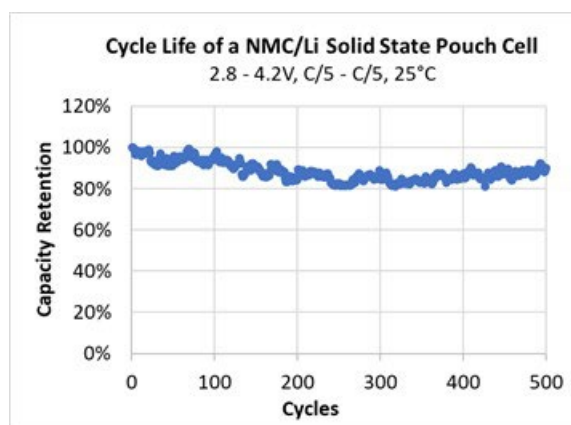


Figure XVI.5.2 Cycle life of an NMC/Li metal solid state pouch cell with the multifunctional SSE at 25 °C

Conclusions

Multifunctional SSE materials have been developed and optimized with high conductivity and stability. SSE separator films have been coated by using a roll-to-roll process. All-solid-state NMC-Li pouch cells containing the developed SSE have been assembled the cell cycle life of > 500 at 100% DOD has been demonstrated.

XVI.6 Development of Thin, Robust, Lithium-Impenetrable, High-Conductivity, Electrochemically Stable, Scalable, and Low-Cost Glassy Solid Electrolytes for Solid State Lithium Batteries (Iowa State University)

Steve W. Martin, Principal Investigator

Iowa State University
528 Bissell Rd
Ames, IA, 500116
E-mail: swmartin@iastate.edu

Tien Q. Duong, DOE Technology Development Manager

U.S. Department of Energy
E-mail: Tien.Duong@ee.doe.gov

Start Date: October 1, 2019
Project Funding: \$414,587

End Date: September 30, 2022
DOE share: \$331,254

Non-DOE share: \$83,333

Project Introduction

The development of thin, < 50 microns, mixed oxy-sulfide-nitride (MOSN) mixed glass former (MGF) glassy solid electrolyte (GSE) films that yield superior performance in a safer, lower-cost, and Li-dendrite impenetrable form will be used to develop new solid-state lithium batteries (SSLBs). It is expected that high rate and long cycle life SSLBs can be achieved using thin-film MOSN GSEs. The new GSEs in SSLBs are anticipated to increase the energy density (anode basis) from ~ 300 mAh/g to ~ 4,000 mAh/g, enabling replacement of internal combustion engines in both light and heavy-duty vehicles. Each 20% reduction in the ~ 1.6 billion liters of gasoline used per day in the United States would reduce CO₂ emissions by ~ 4 billion kg CO₂ per day. The team will also increase scientific and engineering knowledge of thin-film GSEs in SSLBs.

Objectives

The objective of this project is to develop new high Li⁺-conducting MOSN GSE thin-films, < 50 μm, that are impermeable to lithium dendrites, scalable through low-cost glass manufacturing, chemically and electrochemically stable, and will enable low-cost, high-energy-density SSLBs. It is expected that the SSLBs constructed from these new MGF MOSN GSEs will meet and exceed all program objectives: useable specific energy @ C/3 ≥ 350 Wh/kg, calendar life 15 years, cycle life (C/3 deep discharge with < 20% energy fade) 1,000, and cost ≤ \$100/kWh.

Approach

The MOSN MGF GSEs have been prepared and optimized in previous work in bulk glass form and exhibit high ionic conductivity and the necessary thermal stability to be successful in drawing into a thin film. In this project, the glass chemistry has been further improved to further optimize thermal stability and electrochemical properties. Optimized glass chemistries have been cast into large preforms, 10 cm x 30 cm x 1 cm and will be drawn into meters-long thin-films, 50 μm x 5 cm, for use at the cell level.

Results

Compositional optimization of MOSN MGF GSEs: Our previous research on MOSN MGF GSEs showed high conductivities near 10⁻³ S/cm at 25°C and good thermal stability against crystallization during cooling, assessed through the measuring the glass transition (T_g) and crystallization (T_c) temperatures and by calculating the working range ($\Delta T = T_c - T_g$). Further work on these glasses showed good stability against lithium metal in the voltage range from 0–5 V vs. Li/Li⁺, along with stable cycling at low current densities for greater than 100 cycles. Considering the strong properties of our MOSN MGF GSEs, known as ISU-5,

ISU-6, and ISU-7, a preform was cast of ISU-6 and a draw was attempted. While the glass was drawn into a thinner glass, crystallization occurred. As such, further methods were utilized to characterize and optimize the glass compositions. Several of the compositions developed and optimized this year are summarized in Table XVI.6.1 along with relevant thermal and electrical properties. It can be seen that while the conductivity of the ISU series has decreased slightly below the 10^{-3} S/cm, we have seen a significant increase in the working range of these glasses, with analysis indicating that we will be able to draw a MOS GSE into thin films.

Several glass compositions were investigated at the same time to determine the best dopant strategies to optimize the GSE composition. Work was conducted on the ISU-7 series to incorporate nitrogen into the GSE, which is believed to present several benefits, including higher conductivity, increased stability in air and against Li metal, and increase working range. Doping of LiPON into the GSE has been shown to introduce nitrogen into the GSE through XPS analysis. The doping of aluminum into the MOS GSE of the ISU-8 series was believed to potentially increase the ionic conductivity of the GSE while also increasing its resistance to crystallization. While the working ranges increased with addition of aluminum, the ionic conductivity did not increase and actually tended to decrease. The doping of lithium metasilicate, Li_2SiO_3 , was conducted to further increase the crystallization resistance of the MOS GSE. Future work will be done to continue to explore new compositions and further characterize the compositions previously studied.

Table XVI.6.1 Chemical composition and selected properties of various MOS glasses.

Sample ID	Working range, °C	Conductivity at 25 °C, mS/cm
ISU-5	75	1.1
ISU-6	110	0.7
ISU-7-1, -2, -3	104-120	0.32-0.53
ISU-8-1,-2	75-130	0.38-0.63
ISU-9-1	80-150	TBD

Optimization of processing conditions for the production of thin-film MOS MGF GSE ribbons: Several advancements have been made in the drawing of thin-film MOS MGF GSE ribbons. In order to easily test the drawing process, LiPO_3 glass was cast into a 200 g preform, annealed, and loaded into the draw tower. The preform was heated to between 315-330°C in order to generate films of around 50 μm in thickness. Following the success of the LiPO_3 drawing several attempts were made to draw thin films of the ISU-6 composition. During the process, it was determined that longer annealing times were needed to fully relieve stress in the preform prior to drawing, and slower heating rates were necessary to prevent thermal shocking the preform during the drawing process. Films of ISU-6 were drawn down to thicknesses around 250 μm , however; a third impedance arc was found in electrochemical impedance spectroscopy which is believed to be due to crystallites that formed during the draw process. This is further corroborated by the cloudy nature of the drawn thin-film. Due to the formation of crystallites during the draw process, further characterization of small-scale batches was required to determine the viscosity and crystallization behavior of the glass.

Characterization of the viscosity behavior can be done through application of the MYEGA model for viscosity, which utilizes parameters that can be determined through simple differential scanning calorimetry (DSC) experiments rather than challenging liquid viscosity measurements [1]. Furthermore, by conducting several DSC experiments at varying heating rates, a crystallization temperature at low heating rates $\sim 0.5^\circ\text{C}/\text{min}$ can be extrapolated and used as a maximum temperature for film drawing without crystallization occurring. By combining this crystallization experiment with the MYEGA model, a plot such as that in Figure XVI.6.1 can be developed. From this plot, it can be seen that ISU-6 possesses similar viscosity and crystallization behaviors to LiPO_3 and should be a viable MOS GSE composition for use in drawing. DSC scans of the large preform

used for previous film drawing attempts has shown a significant decrease in working range, indicating a change in the bulk glass properties which may have led to the reduced resistance to crystallization. A new preform is in the process of being made through a different means of synthesis to retain the properties exhibited in small-scale testing.

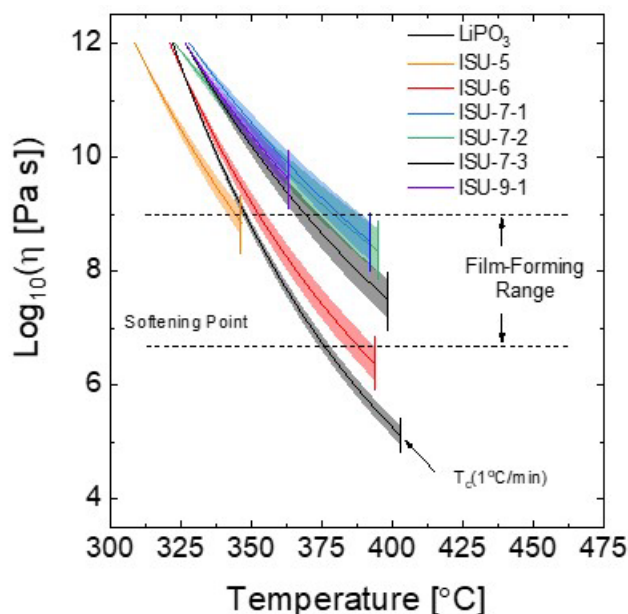


Figure XVI.6.1 Viscosity plot showing expected viscosity behavior of various glass compositions over a range of temperatures above the glass transition temperature with the cutoff point being the crystallization temperature at 1 °C/min heating rate.

Fabricate and test ASSLBs utilizing GSEs in small-area planar format: Continuing work conducted in FY 2020, several samples of poorly conducting ($\sim 10^{-9}$ S/cm) 50 μm thin-film LiPO_3 were fabricated into symmetric cells and subjected to galvanostatic cycling at different operating temperatures. Following 100 cycles at room temperature and 1 $\mu\text{A}/\text{cm}^2$ current density, the temperature was increased to 60°C where stable overpotentials were exhibited as shown in Figure XVI.6.2 (A). When the temperature was further increased to 90°C, stable overpotentials were seen for both low and increasing current densities as shown in Figure XVI.6.2 (B) and (C), prior to the cell shorting due to expected mechanical fracture of the GSE film at 65 $\mu\text{A}/\text{cm}^2$ seen in Figure XVI.6.2 (D). These results show that thin-film glasses can be easily fabricated into symmetric cells and can be mechanically robust enough to cycle for greater than 300 cycles prior to shorting. Future work in FY 2022 will be on extending this test into the MOS GSE thin-films.

Full cell studies were started during this fiscal year, beginning with commercially available cathode materials such as LiFePO_4 . To begin testing, a hybrid cell design was utilized with a small amount of liquid electrolyte applied to the cathode of the cell to help create a more intimate interface between the thicker (~ 1 mm) GSE and the cathode. For the anode, a lithium metal foil was applied dry directly to the surface of the GSE. Preliminary experiments of this cell design show good reversibility as shown in Figure XVI.6.3 (A). While the reversibility is good, there is high polarization exhibited and the polarization tends to increase with further cycles, indicating either the formation of an unstable interfacial layer, or a decomposition reaction between the GSE and the liquid electrolyte.

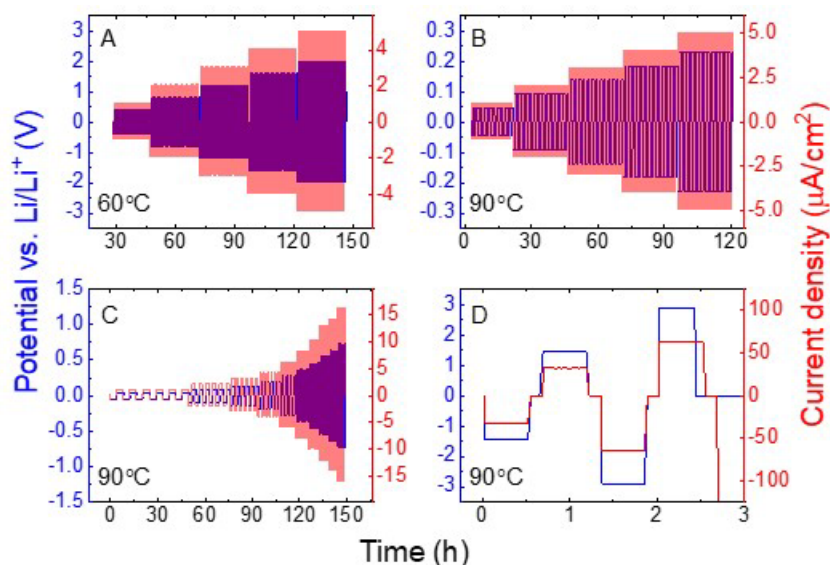


Figure XVI.6.2 Galvanostatic cycling of a 50 μm thin-film LiPO_3 at (A) 60°C (B) 90°C with lower current densities (C) 90°C under a critical current density experiment (D) 90°C with short circuiting exhibited at a current density of 65 $\mu\text{A}/\text{cm}^2$. Adapted from [2].

In addition to these hybrid cells, composite cathodes have been prepared through milling of MOS GSE, conductive carbon, LiFePO_4 active material, and binding material to create all-solid-state cells. Pellets of this composite cathode have been pressed and tested, but poor contact between the solid-state cathode and the GSE have led to poor performance with high polarization and low rates. A second, highly-scalable method has been developed through deposition of these composite cathodes directly onto the surface of the GSE, improving the interfacial contact. Using styrene butadiene as a binder and a xylene solvent, a slurry dispersion is able to be created containing the active material, the conductive carbon, and the ionically conductive GSE. As can be seen in Figure XVI.6.3 (B), cycling of this cathode design at 60°C with a lithium foil anode shows good capacity and decent reversibility. Increasing the temperature to 60°C helps to reduce the polarization effects present from resistance of the thicker GSE. Future efforts will be conducted to further improve the capacity and cyclability of the slurry deposited cathode.

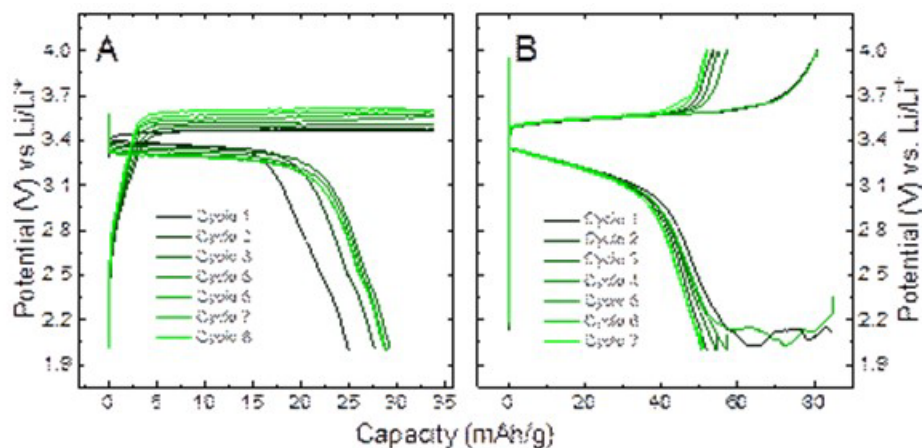


Figure XVI.6.3 Preliminary cycling results for (A) a hybrid full cell utilizing a MOS GSE with a Li foil anode and a LiFePO_4 cathode and (B) an all-solid-state full cell utilizing a MOS GSE with a Li foil anode and an LiFePO_4 composite cathode deposited directly onto the surface of the GSE, cycled at 60°C.

Conclusions

In FY 2021, we have continued the optimization and characterization of our MOS GSEs, including determining their viscosity and crystallization behaviors in order to allow us to draw thin-film GSE for use in all-solid-state batteries. Along with this, symmetric cells were made using poorly conductive thin-film LiPO_3 in order to test the proof-of-concept that thin-film GSEs are a viable method of generating thin conductive separators. We published the first study on a drawn thin-film glassy electrolyte, showing stable cycling and potential for future research. Thin-film MOS GSEs were drawn, but crystallization of the glass during the drawing process was experienced. Current work is being done to refine the glass composition to match the small-scale batches, which our analysis indicates will allow for successful thin-film drawing without significant crystallization during the draw. At the same time, preliminary investigations into full cell studies using our MOS GSE was conducted. Several cell designs have been tested, including direct slurry deposition onto the surface of the MOS GSE. Further research is being done to optimize the cathode composite powder and the slurry deposition process to decrease the polarization during cycling and to further improve the capacity of the full cell.

Key Publications

1. Joyce, Adriana, Steven Kmiec, and Steve W. Martin. 2021. "Glass transition temperature studies of planetary ball milled glasses: Accessing the rapidly cooled glassy state in $\text{Na}_4\text{P}_2\text{S}_7\text{-xOx}$, $0 \leq x \leq 7$, Oxy-thio phosphate glasses." *Journal of Non-Crystalline Solids* 551:120462. doi: <https://doi.org/10.1016/j.jnoncrysol.2020.120462>.
2. Wheaton, Jacob, Steven Kmiec, Devon Schuler, Christopher Sorensen, and Steve W. Martin. 2021. "Electrochemical Behavior of Drawn Thin-Film Vitreous Lithium Metaphosphate." *ACS Applied Energy Materials*. doi: 10.1021/acsaem.1c01809.
3. Zhao, Ran, Guantai Hu, Steven Kmiec, Ryan Gebhardt, Alison Whale, Jacob Wheaton, and Steve W. Martin. 2021. "New Amorphous Oxy-Sulfide Solid Electrolyte Material: Anion Exchange, Electrochemical Properties, and Lithium Dendrite Suppression via In Situ Interfacial Modification." *ACS Applied Materials & Interfaces* 13 (23):26841-26852. doi: 10.1021/acsaami.0c22305.

References

1. Mauro, John C., Yuanzheng Yue, Adam J. Ellison, Prabhat K. Gupta, and Douglas C. Allan. 2009. "Viscosity of glass-forming liquids." *Proceedings of the National Academy of Sciences* 106 (47):19780. doi: 10.1073/pnas.0911705106.
2. Wheaton, Jacob, Steven Kmiec, Devon Schuler, Christopher Sorensen, and Steve W. Martin. 2021. "Electrochemical Behavior of Drawn Thin-Film Vitreous Lithium Metaphosphate." *ACS Applied Energy Materials*. doi: 10.1021/acsaem.1c01809.

Acknowledgements

We would like to acknowledge collaboration with the Materials Analysis and Research Laboratory at Iowa State University, particularly Dr. Dapeng Jing, for help with collection of XPS spectra. We would also like to thank Dr. Sara Cady of the Chemical Instrumentation Facility at Iowa State University for her help on conducting MAS NMR experiments.

XVI.7 Physical and Mechano-Electrochemical Phenomena of Thin Film Lithium-Ceramic Electrolyte Constructs (University of Michigan)

Jeff Sakamoto, Principal Investigator

University of Michigan
Mechanical Engineering
2350 Hayward Avenue
Ann Arbor, MI 48109
E-mail: jeffsaka@umich.edu

Tien Q. Duong, DOE Technology Development Manager

U.S. Department of Energy
E-mail: Tien.Duong@ee.doe.gov

Start Date: October 1, 2019
Project Funding: \$1,250,000

End Date: September 30, 2022
DOE share: \$1,000,000

Non-DOE share: \$250,000

Project Introduction

While a small number of solid electrolytes exhibit high ionic conductivity ($\sim 1 \text{ mS cm}$ at 298K), few are stable against Li metal. The garnet-type solid electrolyte, based on the nominal formula $\text{Li}_7\text{La}_3\text{Zr}_2\text{O}_{12}$ (LLZO), is unique in that it is a fast ion conductor and—as we demonstrated in our recent project (DE-EE-00006821)—is stable against Li. Moreover, our former project successfully demonstrated a decrease in Li-LLZO interface resistance from 12,000 to 2 Ohms cm^2 and stable cycling at 1 mA cm^2 for 100 cycles (+ - 15 μm Li per cycle). Although the past project (DE-EE-00006821) demonstrated LLZO is a viable solid electrolyte for enabling batteries using metallic Li, the studies used thick pellets (1mm) and thick anodes ($\sim 500 \mu\text{m}$). To achieve commercial relevance, performance must be demonstrated using substantially lower LLZO and Li thickness in the range of < 30 microns and 20 microns, respectively.

Objectives

The objective of this project is to understand the underpinning mechanisms that comprise these knowledge gaps to advance LLZO thin film technology. At the University of Michigan (UM), **Sakamoto-Dasgupta-Siegel** have an established history of research with LLZO, batteries, solid-state batteries, computation related to batteries, interface engineering, and the manufacturing research of batteries.

Approach

The approach to achieve the project objectives is to use LLZO as a model system to study the mechano-electrochemical phenomena the control the stability and kinetics of the Li-solid electrolyte interface. In collaboration with Zakuro, Inc., the physical and mechano-electrochemical behavior of thin film LLZO and thin Li are studied. In the initial stages, thin Li, made through *in situ* plating, is used together with conventional lab-scale thick LLZO pellets. In the latter stages of the project, thin Li is used together with thin LLZO.

Results

Three separate but related studies primarily comprise the progress in FY 2021. Two of the three studies were accepted in peer-reviewed journals and the third will be submitted in Q1 FY 2022. First, a perspective article was published in FY 2021 that included substantial input from automotive manufacturers from Ford, Toyota, and Daimler-Benz. The outcomes from this article can provide guidance for EV solid-state battery research and development. Second, owing to the focus on the behavior of thin Li electrodes, a study was completed correlating the effect of Li thickness with the mechanical behavior of Li-LLZO-Li cells. Third, the middle and later phases of this project are to use *in situ* plating to form thin (< 20 micron) electrodes. Thus, an *operando*

study was completed to correlate Li plating conditions with electrode areal and thickness uniformity. Several novel insights resulted from the *operando* visualization platform. Summaries of the three studies are provided below.

1. Perspective on Solid-state Battery Technology for EVs

Owing to the potential to achieve $>1000 \text{ Wh L}^{-1}$, improve safety, and reduce cost compared to Li-ion, there is significant interest in commercializing solid-state batteries. However, solid-state batteries are currently not competitive with Li-ion on either a cost or performance basis and are not yet widely available on a commercial scale. Due to the solid nature of the individual components, solid-state batteries possess a unique set of design criteria that are dictated by the combination of their electrochemical, mechanical, and thermal properties. While significant scientific progress has been made in the past decade, in order to achieve commercial success, these criteria must be considered at each stage of the battery design, from the materials to the systems level.

Our perspective article¹ provides an overview of the couplings between the material properties of each component and how these links play a role in solid-state battery design, manufacturing, and operation (Figure XVI.7.1). Of the many industries that may benefit from solid-state batteries, automakers currently provide the largest impetus for their development due to the strict requirements for performance, safety, and costs for electric vehicles. Therefore, this perspective offers specific insight into the challenges facing solid-state batteries for electric vehicles, with input from three global automakers to provide targeted guidelines for continued solid-state battery research and development.

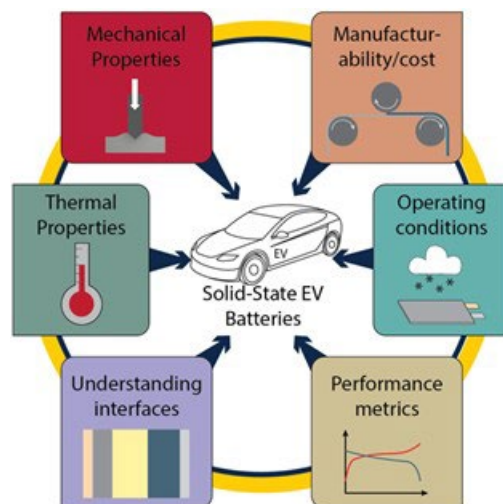


Figure XVI.7.1 Our Perspective¹ article accepted in Joule provides insight into the technological status of solid-state batteries and provides a guide for future challenges and opportunities to work with OEMs to advance the technology readiness level (TRL).

Key aspects and challenges for solid-state batteries from academic and industrial perspectives

It is hoped that the guidelines proposed in the perspective will help to further the state-of-understanding of a range of phenomena discussed herein, leading to accelerated progress in the community. In addition to the many phenomena already mentioned, there remain many outstanding questions that if answered, could make dramatic impacts on the trajectory of these technologies. In summary, we offer a list of a subset of these questions that were most frequently discussed in our discussions with industry and the community:

1. How will the Li plating/stripping processes change with variable vehicle charging and driving (discharge) profiles and with changing temperatures? In particular, can the electrochemical response to variable current draws be linked to the intrinsic time-dependent mechanical properties of the Li metal? For example, interspersing occasional “fast charge events”, into the cycling protocol may be used to simulate the habit of EV customers who typically operate using low charge/discharge rates with the occasional fast charging to meet immediate demands. Lesser used techniques, like direct current internal resistance² (DCIR) measurements may provide additional insight on the battery behavior under these conditions. Furthermore, can the causes of Coulombic efficiency loss be identified and used to predict how these external factors affect the lifetime of the battery?
2. Can we improve manufacturability and costs of solid-electrolytes while maintaining high conductivity? This may include reducing the costs of extraction of rare-earth metals and other critical elements or minimization of time/energy intensive steps such as drying and densification.

- How can mechanical fatigue induced by cyclic strains in the cell be managed? These effects may be related to swelling induced by the growth and shrinkage of a Li metal anode, or by cyclic cathode strains.
- How can the rate capability of composite cathodes be increased to compete with SOA LIBs without requiring elevated temperatures?
- Can solid state batteries provide life-cycle benefits such as improved/simpler recycling of components, and reduced need for supply-limited or hazardous materials?

2. The effect of aspect ratio on the mechanical behavior of Li metal in solid-state cells

While tensile creep experiments have reliably determined the creep mechanism for Li metal, compressive creep experiments more accurately reflect the stress state of Li metal under stack pressure in a solid-state battery.³ In this study, the effects of the applied compressive stress and Li thickness on the strain and strain rate of Li metal coupled with

$\text{Li}_{6.5}\text{La}_3\text{Ta}_{0.5}\text{Zr}_{1.5}\text{O}_{12}$ SSE and a Ni current collector were evaluated. The degree of Li/LLZO adhesion was controlled for all symmetric cells by measuring the Li/LLZO

interfacial resistance using electrochemical impedance spectroscopy. All Li/LLZO interfacial resistances were measured to be $< 15 \Omega \text{ cm}^2$ and differences in interfacial resistance did not correlate with creep strain, suggesting good Li/LLZO adhesion for all tests. It was shown that as the Li thickness decreased, the effects of friction from the Li/LLZO and Li/Ni interfaces were amplified, resulting in lower creep strain for thinner Li foil samples (Figure XVI.7.2). At 1 MPa applied stress, the measured strain rate for all foil thicknesses was almost four orders of magnitude smaller than the steady-state strain rate predicted from tensile creep tests of Li. The frictional effects of the interfaces prevented the determination of a stress exponent, but it was seen that strain rates were a function of both Li metal thickness and applied stress, decreasing as the thickness and applied stress decreased. We propose that frictional effects from the Li/LLZO and Li/Ni interfaces induce regions of hydrostatic stress in Li metal, thereby lowering the volume of material free to deform, which becomes more pronounced at lower aspect ratios. Overall, the results of this study have implications for stack pressure requirements in solid-state batteries, where the mechanical behavior of the Li metal anode may change with aspect ratio during battery operation. The proposed hydrostatic stress state of Li is also of great importance to accurately model failure mechanisms on the $< 100 \mu\text{m}$ length scale, including SSE crack propagation during plating and Li void formation during stripping.

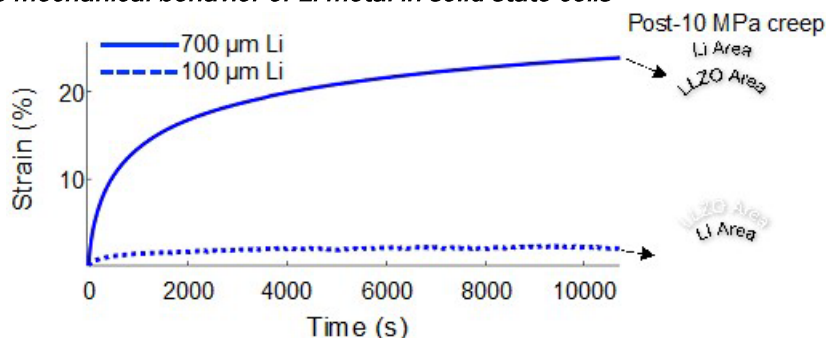


Figure XVI.7.2 Mechanical strain % vs time plot of Li-LLZO-Li cells consisting of thick (700 micron) and thin (100 micron) Li anodes. When Li was < 100 microns thick, negligible deformation occurred. This behavior suggests that Li-LLZO frictional or adhesion likely created hydrostatic stress in Li, thus limiting deformation when Li is thin (< 100 microns).

3. Understanding Coupled Electro-Chemo-Mechanics During *In Situ* Li Metal Anode Formation in Solid-State Batteries

Solid-state batteries (SSBs) could enable the use of Li metal anodes, giving a major advantage for energy density. Unfortunately, Li presents challenges in manufacturing stemming from the reactivity and the difficulty of fabricating thin Li films and high-quality Li/Electrolyte interfaces. Recently, *in situ*⁴ anode formation has shown promise for overcoming these challenges. In this approach, cells are assembled without an anode (“Anode-free”), and Li is plated out from the positive electrode after fabrication. This reduces the need for inert atmospheres, reduces cell complexity, and potentially lowers cost.

As the Li is plated out at the Li/Electrolyte interface, mechanical stresses evolve due to the volume changes in the cell. These stresses play an important role in the uniformity and quality of the resulting *in situ* formed Li electrode. The coupling between mechanics and electrochemistry also plays a key role in this process. This work utilizes *operando* 3D optical video microscopy to characterize electrode morphology evolution during *in situ* anode formation on one of the most promising solid electrolytes, $\text{Li}_7\text{La}_3\text{Zr}_2\text{O}_{12}$ (LLZO). These morphology changes are linked to corresponding electrochemical signatures in three regimes and linked to the mechanical stresses at the Li/LLZO interface. A mechanistic framework is built to understand these factors, which is then used to provide insight into the parameters that control uniformity and how systems can be designed to improve the resulting electrode properties. The role that stack pressure plays, and the importance of stack pressure uniformity are highlighted. The impacts of interfacial toughness, current collector properties, and cell geometry are discussed. Based on the mechanistic framework, improved areal Li coverage is demonstrated, providing insight for future works to enable *in situ* anode formation in a range of material systems and cell architectures. The details of this study will be published in a manuscript titled, “Understanding Coupled Electro-Chemo-Mechanics During *in Situ* Li Metal Anode Formation in Solid-State Batteries”, by Eric Kazyak, Michael Wang, Kiwoong Lee, Srinivas Yadavalli, Adrian J. Sanchez, M. D. Thouless, Jeff Sakamoto, and Neil P. Dasgupta.

Conclusions

The focus in the second year of this project was to study the mechano-electrochemical phenomena of thin Li electrodes integrated with relevant model LLZO solid electrolyte. In one study, new insight into the mechanical behavior of thin Li was found that could help guide efforts to understand the stability and kinetics of thin (< 20 micron) commercially-relevant Li electrodes in solid-state batteries. In another study, an *operando* visualization platform was used to better understand correlations between *in situ* Li plating conditions and Li areal and topographic homogeneity. Since the later stages of this project will exclusively use *in situ* plated Li, the outcomes of this study will be critical in achieving thin Li electrodes with uniform areal coverage and thickness. Lastly, a perspective study was completed together with input from key members of the EV automotive industry (Ford, Toyota, and Daimler-Benz). The article summarizes recent progress and suggests future research focal points to advanced and accelerate efforts to create viable and commercializable solid-state battery technology for EVs.

Key Publications

1. Wang, Michael J., Eric Kazyak, Neil P. Dasgupta, and Jeff Sakamoto. "Transitioning solid-state batteries from lab to market: Linking electro-chemo-mechanics with practical considerations." *Joule* (2021).
2. Haslam, Catherine G., Wolfenstine, Jeffrey B., and Sakamoto, Jeff. "The effect of aspect ratio on the mechanical behavior of Li metal in solid-state cells." *J. Power Sources* (2021).

References

1. Wang, Michael J., Eric Kazyak, Neil P. Dasgupta, and Jeff Sakamoto. "Transitioning solid-state batteries from lab to market: Linking electro-chemo-mechanics with practical considerations." *Joule* (2021).
2. Jong Hoon Kim, Seong Jun Lee, Jae Moon Lee, and Bo Hyung Cho. "A new direct current internal resistance and state of charge relationship for the Li-ion battery pulse power estimation." *7th International Conference on Power Electronics*, pp. 1173–1178(2007).
3. Haslam, Catherine G., Wolfenstine, Jeffrey B., and Sakamoto, Jeff. "The effect of aspect ratio on the mechanical behavior of Li metal in solid-state cells." *J. Power Sources* (2021).

4. Wang, Michael J., Eric Carmona, Arushi Gupta, Paul Albertus, and Jeff Sakamoto. "Enabling "lithium-free" manufacturing of pure lithium metal solid-state batteries through in situ plating." *Nature communications* 11, no. 1, pp. 1–9 (2020).

Acknowledgements

The PIs would like to acknowledge and also thank support from Patricia Smith (US Navy NSWC, Carderock). Adrienne Riggi served as the DOE NETL Program Manager for this project.

XVI.8 Low Impedance Cathode/Electrolyte Interfaces for High Energy Density Solid-State Batteries (University of Maryland, College Park)

Eric Wachsman, Principal Investigator

University of Maryland College Park
1206 Engineering Laboratory Building
University of Maryland
College Park, MD 20742
E-mail: ewach@umd.edu

Yifei Mo, Principal Investigator

University of Maryland College Park
1137 Engineering Laboratory Building
University of Maryland
College Park, MD 20742
E-mail: yfmo@umd.edu

Tien Q. Duong, DOE Technology Development Manager

U.S. Department of Energy
E-mail: Tien.Duong@ee.doe.gov

Start Date: October 1, 2019
Project Funding: \$1,250,000

End Date: February 23, 2023
DOE share: \$1,000,000

Non-DOE share: \$250,000

Project Introduction

All-solid-state batteries (ASSBs) using a ceramic fast Li-ion conductor as a solid-state electrolyte (SSE) have been proposed as a promising strategy to significantly increase the energy density of lithium batteries. Due to their high ion conductivity and excellent stability, Li-stuffed garnets exhibit the most promising physical and chemical properties for SSEs. However, the typical microstructure, thick ($>100\ \mu\text{m}$) bulk electrolyte and simple planar electrode/electrolyte interfaces, combined with poor electrode wetting of the garnet result in excessively high area specific resistances (ASRs) that severely limit achievable current density and cell energy density.

Recently, the University of Maryland PIs have pioneered thin garnet-based solid-state batteries that effectively address the interfacial impedance at the Li metal side. We have demonstrated the ability to overcome the solid-electrolyte/solid-electrode interfacial impedance using interfacial engineering [1] of solid-state garnet (e.g., $\text{Li}_7\text{La}_3\text{Zr}_2\text{O}_{12}$ LLZ) electrolytes under BMR contract DEEE0006860. Further, we have demonstrated Li-metal anodes with unique porous-dense-porous trilayer LLZ architectures achieving excellent stability and high current density ($10\ \text{mA}/\text{cm}^2$) for Li-cycling with no electrical shorting [2] successfully solving the high Li-garnet interfacial impedance that severely limited achievable current density. We have also developed state-of-the-art Li-metal solid-state batteries using this technology demonstrating high energy density ($\sim 300\ \text{Wh}/\text{kg}$) with both NMC high-voltage [3] and S high-capacity [4] cathodes using these trilayer garnet structures.

However, cycling rate in full cells is orders of magnitude lower than Li-symmetric cells as issues remain with regard to properties evolving at the cathode-electrolyte interface. Today's processing routes require temperatures of $\geq 1000^\circ\text{C}$ for the garnet, which unavoidably leads to enhanced ion diffusion at the interface, thereby raising the issues of material compatibility and the formation of possible interphases that influence the total cell resistance for desired cathode/electrolyte co-sintering. In addition, even with cathodes infiltrated into pre-sintered garnet structures major challenges still exist at the cathode interfaces for all-solid-state batteries,

including (1) high cathode interfacial resistance and (2) limited processing techniques that incorporate active cathode materials within the solid electrolyte.

Objectives

The project objective is to integrate computational and experimental research to develop and test Li-metal-based batteries that implement solid SSEs equipped with NMC cathodes integrated into the Li-metal/LLZ tri-layer architecture. Specifically, the team is achieving the following: (1) identify and demonstrate interfacial layers to achieve low-impedance and stable NMC/LLZ interfaces; (2) develop novel processing techniques to fabricate NMC/LLZ composite cathodes with low interfacial resistance; and (3) enable high-performance ASSBs with an energy density of 450 Wh/kg and 1400 Wh/L and negligible degradation for 500 cycles.

Approach

In this new project, the team is building on their demonstrated expertise with garnet electrolytes and ASSBs to accomplish the following: (1) engineer interfaces to overcome high NMC/LLZ interfacial impedance and interfacial degradation; (2) develop processing and fabrication techniques to achieve high-loading NMC/LLZ composite cathodes with low resistance and high cyclability; and (3) integrate the NMC/LLZ cathodes into all-solid-state Li-metal/LLZ cells to achieve high-energy-density batteries.

Results

Thermochemical stability between LLZ and NMC

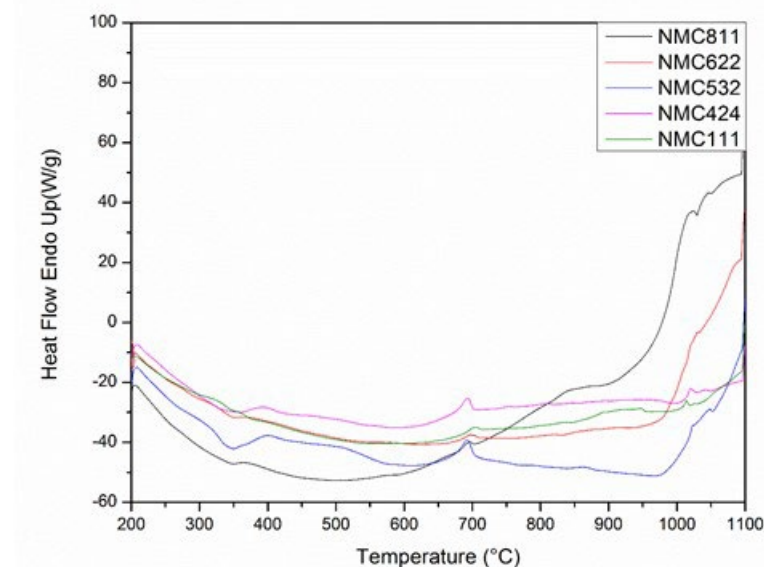


Figure XVI.8.1 DSC curves of 50/50 w/w mixtures of LLZTO with NMCs of various compositions.

The reactivity of NMCs with LLZTO was investigated by DSC of the powder mixture. All NMCs show an endotherm peak at 700°C (Figure XVI.8.1), corresponding to a kinetically slow reaction with garnet. Most notably, the scan for NMC811 shows a baseline that continues to increase after 700°C until another large endothermic peak beginning at 900°C emerges. This reaction above 900°C matches the XRD results indicating there is a strong reaction between NMC811 and LLZTO. Additionally, this large endothermic peak is similarly observable in the NMC622 and NMC532 samples but has a higher onset temperature with decreasing Ni content. This feature is not observable in the measured temperature range for lower Ni content NMCs. These results support the computational trend (below) that NMC and LLZTO react more strongly with increasing Ni content.

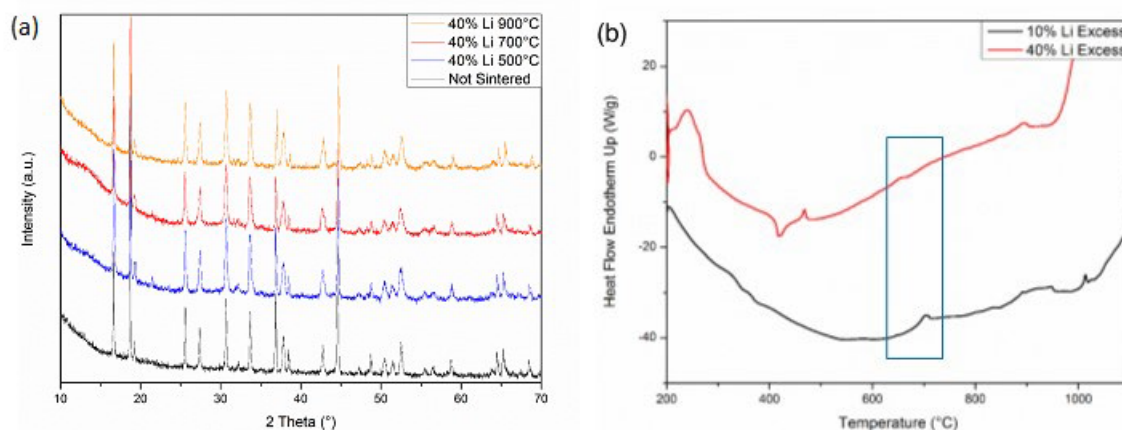


Figure XVI.8.2 (a) XRD and (b) DSC curves of 50/50 w/w mixtures of LLZTO (with 10mol% or 40 mol% excess Li) with NMC-111.

To investigate the effect of lithium content on the high temperature stability of NMC against LLZTO, LLZTO was synthesized with 10% and 40% molar excess Li and mixed with NMC-111 for XRD and DSC measurement. No new phases were detected by XRD in the mixtures with 40mol% excess Li even after sintering to 900 °C (Figure XVI.8.2a), indicating the reaction between the two materials detected previously was mainly caused by Li deficiency at high temperature. In the DSC curve (Figure XVI.8.2b), the endotherm peak detected at 700°C for the mixture with 10% excess Li LLZTO is missing for the mixture with 40% excess Li LLZTO, indicating the endotherm reaction is related to the loss of Li at high temperature.

Computations of promising coating materials to stabilize the LLZ-NMC interface

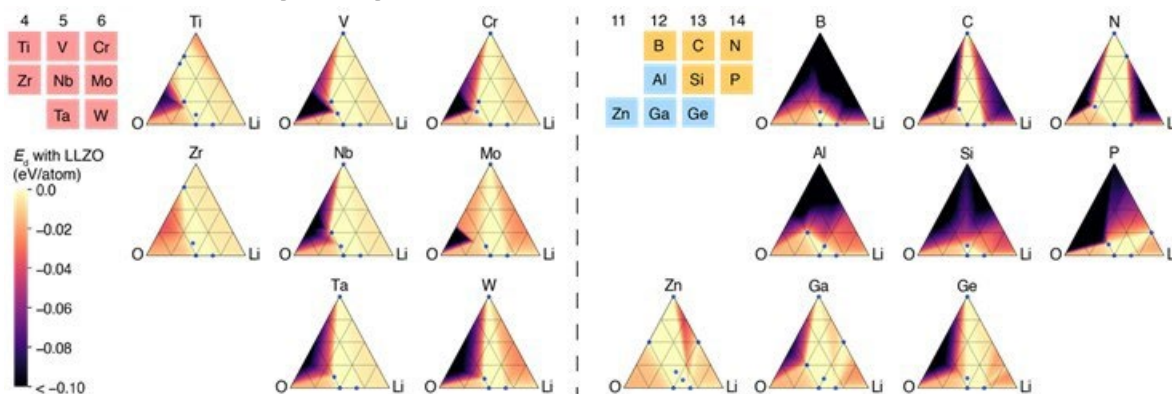


Figure XVI.8.3 Heatmaps of chemical stability (E_d) of Li-M-O (M = B, C, N, Al, Si, P, Ti, V, Cr, Zr, Nb, Mo, Zn, Ga, Ge, Ta, or W) with LLZO. Known compounds that are stable with LLZO are marked with blue points.

Using demonstrated thermodynamic analyses for interface stability based on first-principles computation, we studied the trends in stability with LLZO and NMC throughout the entire Li-M-O ternary composition space, in order to identify all compositions that are stable with LLZO as promising coating. The decomposition energy E_d of each composition with LLZO is illustrated by a heatmap of Li-M-O Gibbs ternary diagram (Figure XVI.8.3). Li-M-O systems with different cations M exhibit significantly different stability with LLZO. We extended our analysis to other Li-M-O systems for cations M = B, C, N, Al, Si, P, Ti, V, Cr, Zr, Nb, Mo, Zn, Ga, Ge, Ta, or W, which are commonly considered and used for coatings (Figure XVI.8.3). Many systems with nonmetal M such as B, Al, Si, P only have one or two ternary Li-M-O compositions (in addition to Li_2O and Li_2O_2) stable with LLZO, leading to a narrow compositional space with good LLZO stability. The transition metal elements V, Cr, Nb, Ta, Zn, Ga, Ge and nonmetals C and N are stable with garnet, and a wider Li-M-O compositional space of ternary Li-M-O oxides have good stability with LLZO. For cations M = Ti and Zr, the M metal exhibits minor reactions with LLZO, but the binary oxides M-O are stable with LLZO, leading

to a wide compositional space stable with LLZO. Notably, for the Li-Zn-O system, Zn metal, ZnO oxide, and LiZn alloy are stable with LLZO. Thus, this system has the widest composition space stable with LLZO, and so should be a promising system for garnet coatings as has been demonstrated in experiments. In general, one shall select within this stable compositional space for garnet coatings, as the compositions outside react exothermically with LLZO and may cause side reactions and interfacial degradation. Our Li-M-O heatmaps of the stability with LLZO provide guiding maps for selecting compositions for garnet coating layers.

In addition, we also analyzed the stability of the entire Li-M-O composition space with NMC (Figure XVI.8.4). Our analyses found that the only Li-M-O compositions stable with the cathode are along the tie-line of Li_2O and M-O metal oxides, and the cathode stability is generally good for O-rich compositions. We identify the coating layer stable with both SE and cathode, by combining the heatmaps and stable regions of Li-M-O with LLZO and those with NMC cathode. The materials compositions along the tie-line of Li_2O to M-O oxides, including multiple ternary oxides, show decent stability with both LLZO and NMC. In summary, we have successfully achieved our milestone of identifying promising coating materials determine appropriate compositions to stabilize the LLZO-NMC interface.

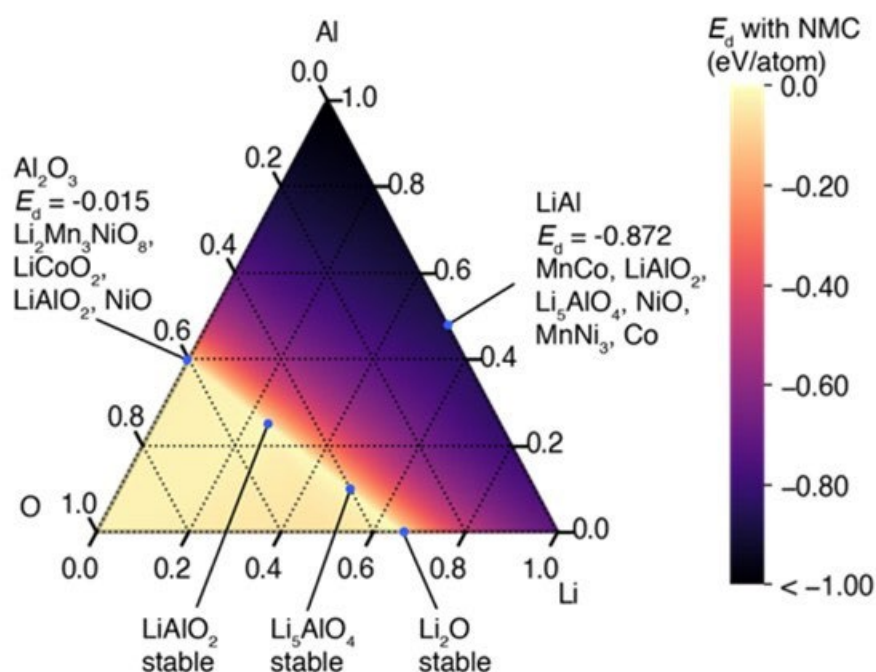


Figure XVI.8.4 Heatmap of the decomposition energy of Li-Al-O compositions with NMC 111.

Thermochemical stability between LLZ and infiltrated NMC and the effect of interfacial coating layers

Co-sintering of garnet trilayer structures with NMC622 filling into the porous layers was carried out at 500°C, 700°C, and 800°C for 3hrs on both uncoated and atomic layer deposition (ALD) coated structures under Ar atmosphere. Al_2O_3 and ZnO were used as the coating layer. These samples were then assembled into symmetric cells and EIS was performed to observe the effect of the ALD layer on the impedance of these cells.

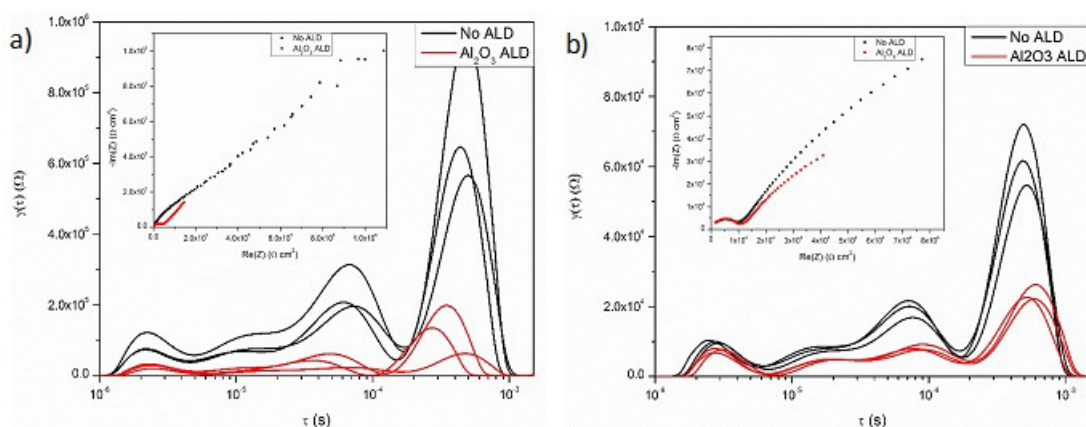


Figure XVI.8.5 Nyquist plot (inset) and DRT Analysis for symmetric NMC622|LLZO|NMC622 cells with and without Al₂O₃ coating co-sintered at (a) 700 °C and (b) 800 °C.

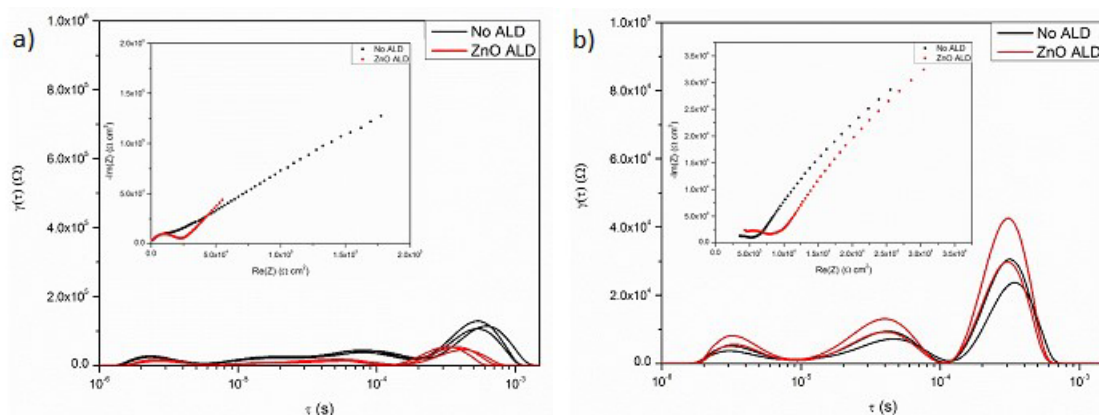


Figure XVI.8.6 Nyquist plot (inset) and DRT Analysis for symmetric NMC622|LLZO|NMC622 cells with and without ZnO coating co-sintered at (a) 700 °C and (b) 800 °C.

As shown by the EIS Nyquist plots and Distribution of Relaxation Times (DRT) analysis in Figure XVI.8.5, Al₂O₃ coating can significantly reduce the overall interfacial impedance at above 700 °C. Whereas, ZnO coating can only reduce the overall interfacial impedance at 700 °C but essentially had no effect at 800 °C (Figure XVI.8.6). These results indicate that Al₂O₃ is better than ZnO at improving the interfacial impedance.

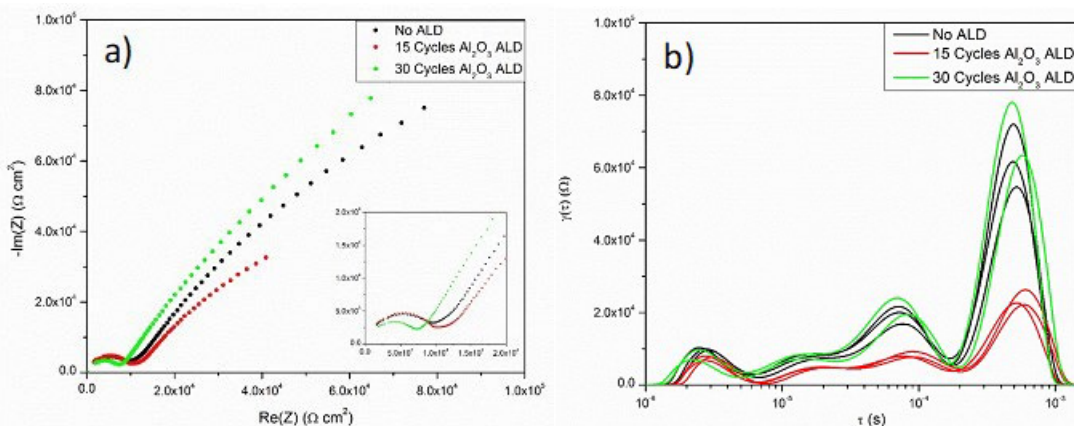


Figure XVI.8.7 a) Nyquist plot and b) DRT plot for symmetric NMC622|LLZO|NMC622 cells co-sintered at 800 °C comparing uncoated and Al₂O₃ ALD coated samples.

To determine the effect of the interlayer thickness on its ability to improve the interfacial impedance of NMC symmetric cells, samples were coated with different thicknesses of ALD alumina and co-sintered at 800°C. Figure XVI.8.7 demonstrates that the 3nm (15 cycles of ALD) interlayer has a 4x reduction in the ASR, whereas the 6nm (30 cycles) interlayer appears to have similar ASR to the uncoated samples.

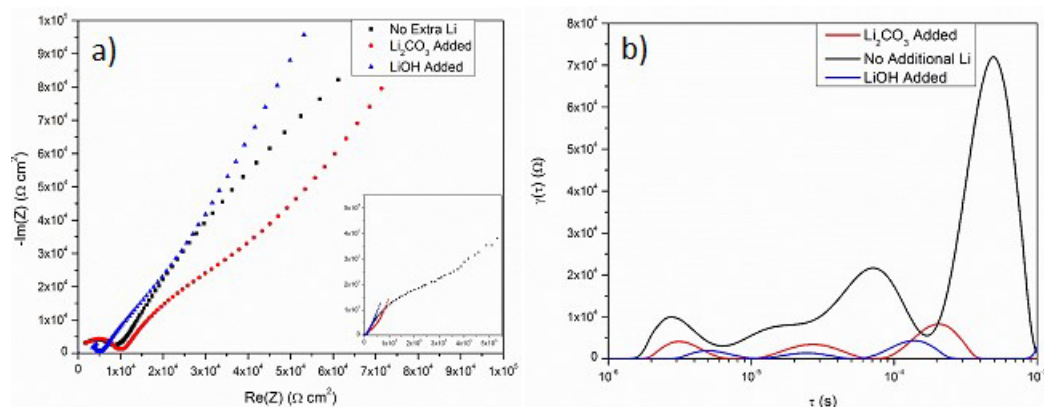


Figure XVI.8.8 a) Nyquist plot and b) DRT plot for symmetric NMC622|LLZO|NMC622 cells co-sintered at 800°C comparing samples with and without extra Li from various sources.

Due to previous computational and DSC results indicating that adding additional Li would prevent the reaction of NMC and LLZTO, symmetric NMC cells were co-sintered at 800°C with additional lithium from either LiOH or Li₂CO₃ as the source in a molar ratio of 1:3 (Li:NMC). Figure XVI.8.8 shows the EIS results for these experiments, demonstrating a more than 10X reduction of the ASR, regardless of Li source. This achieves the 10X ASR reduction milestone and confirms the predicted results that increasing the amount of available Li would reduce the reaction of NMC and LLZTO. Furthermore, this reduction can be integrated with the ALD interlayers for even greater reduction in interfacial impedance (Figure XVI.8.9). Given the previous results showing that the 6nm interlayer had higher ASR than the 3nm interlayer, this suggests that the thicker interlayer was not sufficiently lithiated since the ionic conductivity of lithiated alumina is several orders of magnitude higher than that of unlithiated alumina.

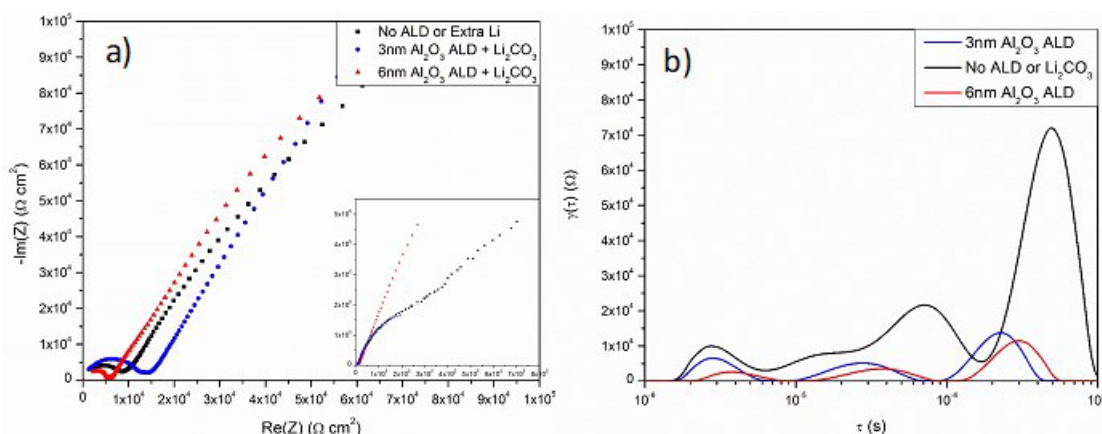


Figure XVI.8.9 a) Nyquist plot and b) DRT plot for symmetric NMC622|LLZO|NMC622 cells co-sintered at 800°C comparing various thicknesses of Al₂O₃ coated samples, all with the same amount of extra Li added.

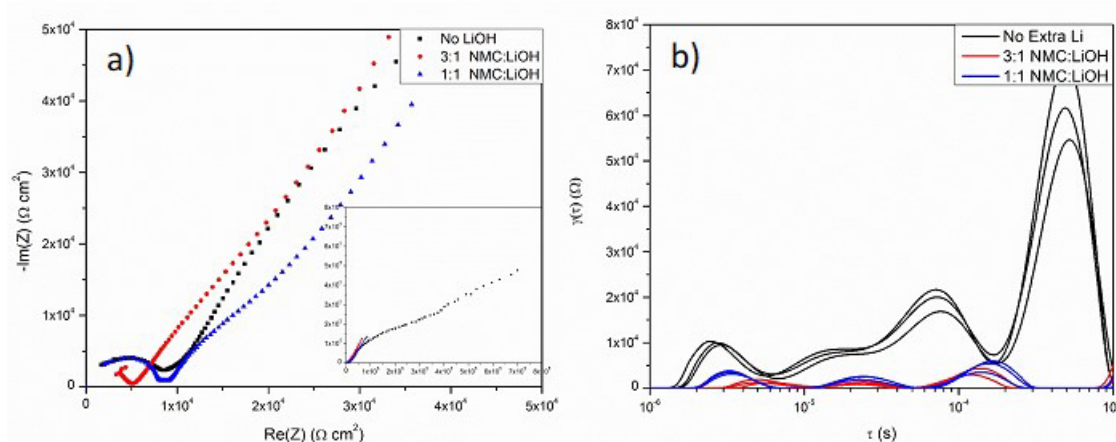


Figure XVI.8.10 a) Nyquist plot and b) DRT plot for symmetric NMC622|LLZO|NMC622 cells co-sintered at 800 °C comparing samples where the extra Li ratio was increased from 1:3 Li:NMC to 1:1.

Finally, the amount of extra Li was increased to get a sense for how much additional Li is beneficial to NMC/LLZTO co-sintering. The Li:NMC ratio was increased to 1:1. The Nyquist and DRT plots (Figure XVI.8.10) show that both ratios significantly decrease the ASR when compared to samples without extra Li.

Conclusions

The reactivity of NMC with LLZTO increases with increasing Ni content. The reaction is mainly caused by Li deficiency at high temperature. First-principles computation was used to study the trends in stability with LLZO and NMC throughout the entire Li-M-O ternary composition space, identifying M=Zn and Al as potential coating materials for stabilizing the NMC/LLZO interface. EIS measurement on NMC/trilayer LLZO/NMC symmetric cells found that Al_2O_3 is better than ZnO at improving the interfacial impedance. Moreover, increasing the amount of available Li during co-sintering can dramatically reduce the reaction of NMC and LLZTO achieving a 10X reduction in interfacial ASR.

Key Publications

Patent

1. Yaoyu Ren & Eric D. Wachsman, "Interlayer for Solid Cathode-Electrolyte Interface," Invention Disclosure

Papers

1. Adelaide M. Nolan, Eric D. Wachsman & Yifei Mo, "Computation-Guided Discovery of Coating Materials to Stabilize the Interface Between Lithium Garnet Solid Electrolyte and High-Energy Cathodes," *Energy Storage Materials*, 41, 571–580, (2021)
2. Neumann, T. R. Hamann, T. Danner, S. Hein, K. Becker-Steinberger, E. D. Wachsman, and A. Latz, "Effect of the 3D Structure and Grain Boundaries on Lithium Transport in Garnet Solid Electrolytes," *ACS Applied Energy Materials*, 4, 4786–4804 (2021)
3. Adelaide M. Nolan, Darshana Wickramaratne, Noam Bernstein, Yifei Mo*, Michelle D. Johannes*, "Li⁺ Diffusion in Amorphous and Crystalline Al_2O_3 for Battery Electrode Coatings", *Chemistry of Materials*, 33, 19, 7795–7804 (2021)
4. Menghao Yang, Yifei Mo*, "Interfacial Defect of Lithium Metal in Solid-State Batteries", *Angewandte Chemie Int. Ed.*, 60, 21494, (2021)

5. Menghao Yang, Yunsheng Liu, Adelaide M. Nolan, Yifei Mo*, "Interfacial Atomistic Mechanisms of Lithium Metal Stripping and Plating in Solid-State Batteries", *Advanced Materials*, 33, 2008081 (2021)

Presentations

1. E. D. Wachsman, "A Solid Transformation of Energy Storage," World Conference on Solid Electrolytes for Advanced Applications, virtual, October 25–27, 2021, Invited
2. Y. Mo, "Interfacial Failure of Lithium Metal in Solid-State Batteries: Insight from Large-Scale Atomistic Modeling", the International Battery Materials Association (IBA) 2021 Annual meeting in Xiamen, China (virtual) (10/2021) (Invited)
3. Y. Mo, "Interfacial Failure of Lithium Metal in Solid-State Batteries : Insight from Large-Scale Atomistic Modeling", World Conference on Solid Electrolytes for Advanced Applications (virtual) (10/2021) (Invited)
4. Y. Mo, "Interfacial Failure of Lithium Metal in Solid-State Batteries: Insight from Large-Scale Atomistic Modeling", Beyond Lithium Ion XIII, Argonne National Laboratory (virtual) (06/2021) (Invited)
5. Y. Mo, "Computation Accelerated Design of Materials and Interfaces for Solid-State Batteries", Phonon Science Seminar, SLAC (virtual) (05/2021) (Invited)
6. Nolan, Y. Mo, "Computation-Guided Discovery of Materials for Stabilizing Interfaces in High-Energy Solid-State Lithium-Ion Batteries", MRS Spring Meeting, Seattle WA (04/2021)

References

1. A.M. Nolan, Y. Zhu, X. He, Q. Bai, Y. Mo, "Computation-Accelerated Design of Materials and Interfaces for All-Solid-State Lithium-Ion Batteries", *Joule*, 2, 2016–2046 (2018)
2. X. He, Y. Zhu, Y. Mo, "Origin of Fast Ion Diffusion in Super-Ionic Conductors", *Nature Communications*, 8, 15893 (2017)
3. X. Han, Y. Gong, X. He, G.T. Hitz, J. Dai, Y. Mo, V. Thangadurai, E.D. Wachsman, L. Hu "Negating Interfacial Impedance in Garnet-Based Solid-State Li-Metal Batteries", *Nature Materials*, 16, 572 (2017)
4. W. Luo, Y. Gong, Y. Zhu, K. Fu, J. Dai, S. Lacey, C. Wang, B. Liu, X. Han, Y. Mo, E.D. Wachsman, L. Hu "Transition from Super-lithiophobicity to Super-lithiophilicity of Garnet Solid-State Electrolyte", *Journal of the American Chemical Society*, 138, 12258–12262 (2016)

Acknowledgements

We greatly thank Office of Energy Efficiency & Renewable Energy, Department of Energy for funding this project, without which we could not have achieved the significant progress detailed in this report.

XVI.9 Molecular Ionic Composites: A New Class of Polymer Electrolytes to Enable All Solid-State and High Voltage Lithium Batteries (Virginia Polytechnic Institute and State University)

Louis A. Madsen, Principal Investigator

Department of Chemistry
Virginia Tech
319 Davidson Hall
1040 Drillfield Drive
Blacksburg, VA 24061
E-mail: lmadsen@vt.edu

Feng Lin, Principal Investigator

Department of Chemistry
Virginia Tech
323 Davidson Hall
1040 Drillfield Drive
Blacksburg, VA 24061
E-mail: fenglin@vt.edu

Tien Q. Duong, DOE Technology Development Manager

U.S. Department of Energy
E-mail: Tien.Duong@ee.doe.gov

Start Date: January 1, 2021

End Date: December 31, 2021

Project Funding: \$421,232

DOE share: \$343,183

Non-DOE share: \$78,049

Project Introduction

Based on a newly discovered class of solid polymer electrolyte materials, which we term molecular ionic composites (MICs), we are developing Li solid electrolytes targeted for use in transportation applications. MICs form a mechanically stiff (~ 1 GPa modulus), electrochemically stable, and highly thermally stable matrix that can resist dendrite formation with metal anodes, allow high voltage operation, provide robust safety against fire, and enable fast charging/discharging over a wide temperature range. The component molecules in MICs are inexpensive and MICs can be processed to yield a large area format at room temperature and generally in ambient atmosphere. Our team is advancing this class of polymer electrolytes to promote uniform lithium plating, inherent safety, and low reactivity against both lithium metal anodes and high voltage layered oxide cathodes.

Objectives

Based on a newly discovered class of solid polymer electrolyte materials, that is, molecular ionic composites (MICs), the overall objective is to develop solid-state lithium conductors targeted for use in transportation applications. MICs form a mechanically stiff, electrochemically stable, and thermally stable matrix. Specific objectives include the following: (1) development of robust MIC electrolyte thin films (~ 20 μm) to serve as simultaneous nonflammable separators and dendrite-blocking Li^+ conductors, (2) electrochemical quantification of key performance metrics including electrolyte stability, interfacial reactions, and suitability/compatibility with a range of electrode materials, and (3) comprehensive investigation of ion transport mechanisms and electrode-electrolyte interfacial reactivity under practical operating conditions using NMR and synchrotron X-ray analyses.

Approach

MICs rely on a unique polymer that is similar to Kevlar® in its strength, stiffness, and thermal stability, but with densely spaced ionic groups that serve to form an electrostatic network that permeates mobile ions in the MIC. The team can tailor the ion concentrations and types to yield MIC electrolyte films that are electrochemically compatible with Li-metal anode as well as a range of high-voltage layered cathodes. The team is searching the composition space of lithium salts, electrochemically compatible ionic liquids, and polymer (PBDT) molecular weight to determine best composition windows for MIC electrolytes. The team is also investigating best methods for casting thin films in terms of temperature, solvent/evaporation conditions, and control over the initial liquid crystalline gel formation point. Concurrently, the team is testing MIC films in various electrochemical cells, quantifying transport and structural/morphology parameters with NMR and X-ray techniques, and measuring key mechanical (dynamic mechanical thermal analysis, stress-strain) and thermal (DSC, TGA) properties.

Results

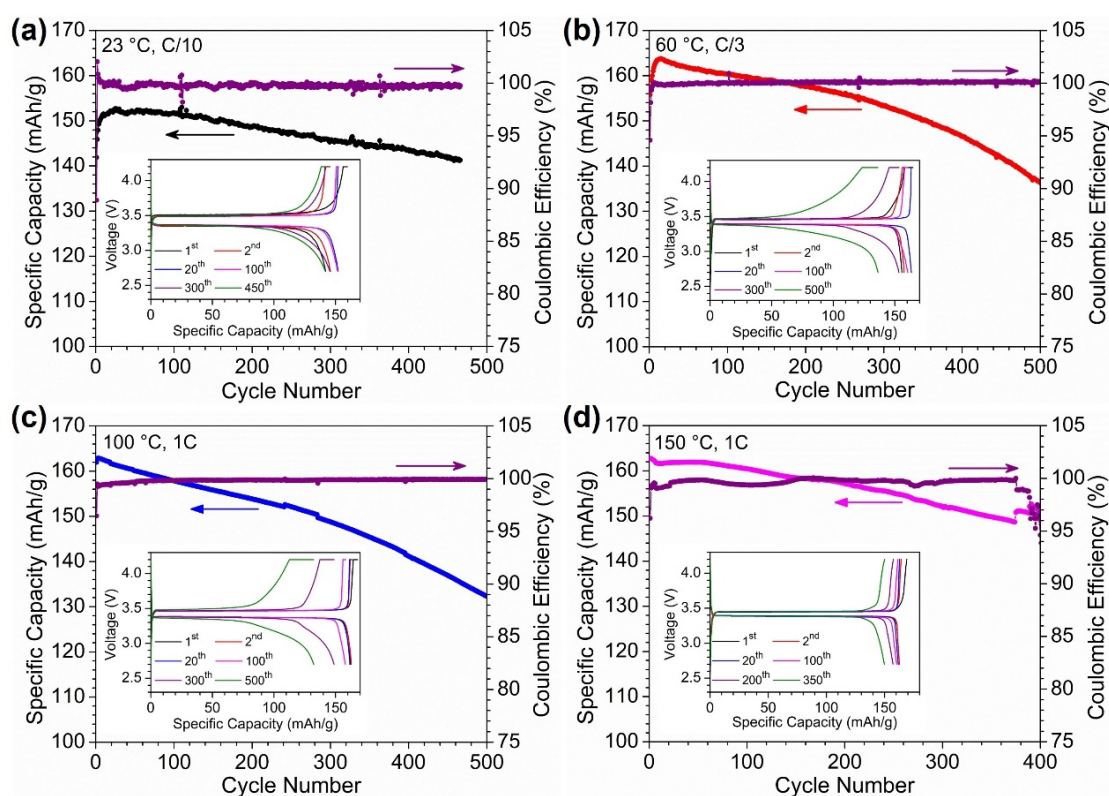


Figure XVI.9.1 Li/MIC/LiFePO₄ coin cells demonstrate strong cycling stability over a temperature range from 23 °C to 150 °C. Li/MIC/LiFePO₄ cycled at (a) 23 °C at C/10, (b) 60 °C at C/3, (c) 100 °C at 1C, and (d) 150 °C at 1C. Inset figures are the voltage profile for selected cycles under each cycling condition.

The team performed a systematic study of the long-term cycling stability of Li/MIC/LiFePO₄ cells at elevated temperatures. As shown in Figure XVI.9.1, the cells can be successfully cycled at 23 °C, 60 °C, 100 °C, and 150 °C with slow capacity decay during cycling. For example, when cycled at 150 °C and 1C rate, the cell shows a discharge capacity retention of 91% after 374 cycles. This clearly demonstrates that the solid electrolyte used here, which is a MIC material with only 10 wt% PBDT, is both mechanically and electrochemically stable at 150 °C to enable successful cycling of LiFePO₄ batteries. From what appears in the literature, this MIC electrolyte appears to be the highest temperature polymer-based gel used as a solid electrolyte for lithium metal battery cycling. Furthermore, this study also directly confirms the excellent

cycling stability of LiFePO_4 as a cathode material at high temperature. This makes LiFePO_4 an ideal cathode material when constructing lithium batteries for wide-temperature-range applications.

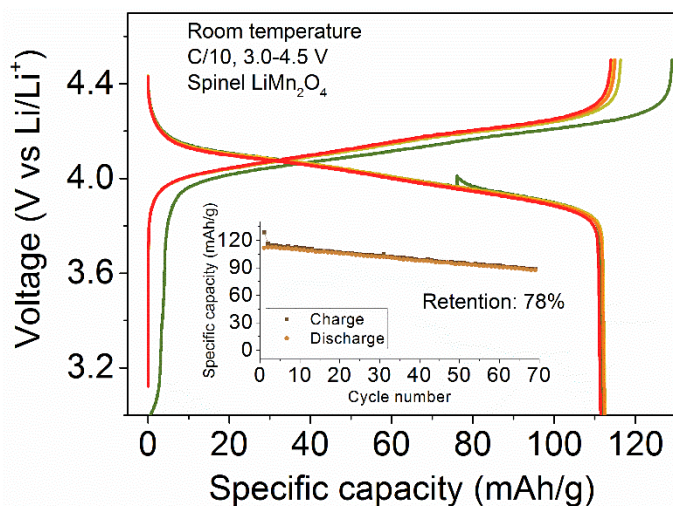


Figure XVI.9.2 Charge/discharge profiles of the cell built with a spinel LiMn_2O_4 cathode, MIC electrolyte and Li metal anode. The cell was cycled at C/10 in the range 3.0–4.5 V at room temperature. The inset shows the specific capacity as a function of the cycle number.

In addition, the team has utilized another promising cathode material, LiMn_2O_4 , to explore its compatibility with the MIC electrolyte. The positive electrode was cast onto Al foil with a homogenous slurry containing LiMn_2O_4 , carbon black, and PVDF in a mass ratio of 90:5:5. The cells were assembled with the positive electrode, MIC electrolyte, and Li metal anode into CR2032 coin cells. The team has first evaluated the cell performance at room temperature (Figure XVI.9.2). The discharge capacity of the cell can reach 112 mAh/g at C/10. The charge and discharge profiles overlap well in the first several cycles. After 70 cycles, a capacity retention of 78% was achieved. These results indicate that the MIC electrolyte shows compatibility with the spinel LiMn_2O_4 , which suggests the promise of integrating MICs into batteries with alternative cathode materials.

The team has also focused on (1) refining synthetic conditions and chemical compositions for fast Li^+ transport, (2) expanding the parameter spaces for film formation, (3) developing advanced NMR characterizations to understand MIC film microstructure, and (4) exploring our rigid-rod charge polymer (PBDT) as an electrode binder to possibly replace the ubiquitously used polymer PVDF.

Figure XVI.9.3 shows a new ionic liquid the team is incorporating into MIC electrolytes. This electrolyte composition forms a uniform film and exhibits an ionic conductivity of 1.0 mS/cm at room temperature, which is a factor of two higher than our previously optimized composition using 100% TFSI anions. The teams are also constructing membranes with $\text{Pyr}_{13}\text{FSI}$ ionic liquid and LiFSI salt, as described further below.

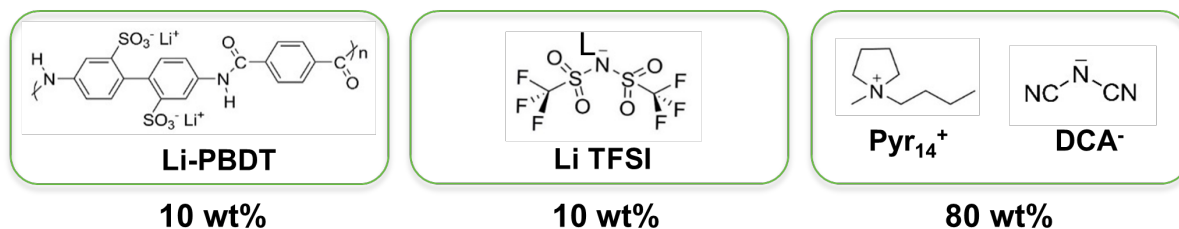


Figure XVI.9.3 New example composition of MIC electrolytes incorporating the DCA⁻ anion for faster Li^+ transport. The team is also working with the FSI⁻ anion and mixed systems to modulate morphology and phase segregation of different ions.

The team has made another exciting discovery when attempting ion exchange after initial MIC formation. This ion exchange step provides an alternate to single-step film casting to enable a wider parameter space for ion type incorporation. When starting with a MIC composed of PBDT and the ionic liquid $C_{2}mimBF_4$, and then ion exchanging by immersion in $Pyr_{13}FSI + LiFSI$, a highly Li^+ -dense nanocrystalline grain boundary phase condensed during the exchange process. The resulting materials, with structure depicted in Figure XVI.9.4, show enhanced conductivity ($> 1 \text{ mS/cm}$) and high Li^+ transference number (~ 0.5) while maintaining high elastic modulus ($> 200 \text{ MPa}$) and non-flammability. The team has undertaken $Li|Li$ symmetric cell cycling and a host of other tests, which are showing promising results for electrochemical stability ($\sim 4.5 \text{ V}$) and interfacial resistance ($\sim 30 \text{ Ohm-cm}^2$).

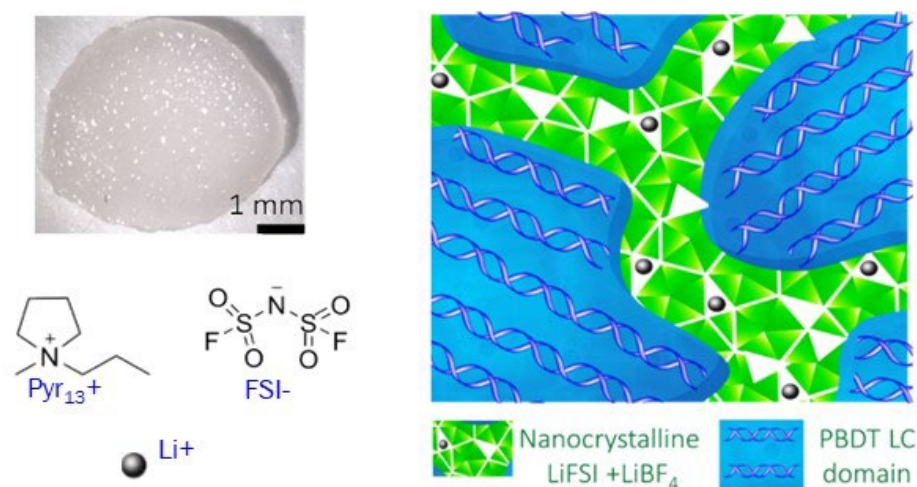


Figure XVI.9.4 New MIC membrane composition and internal structure. The image at upper left shows ion-exchanged electrolyte with iridescent appearance. At lower left are the chemical structures of new ions incorporated via ion exchange. The illustration at right shows liquid crystalline (LC) PBDT grains in blue, which provide a template for and scaffold to support the highly defective and conductive nanocrystalline phase containing $LiFSI$ and $LiBF_4$.

Figure XVI.9.5 shows two examples of the solid-state (SS) NMR spectroscopy experiments employed to understand the new MIC/nanocrystal material presented in Figure XVI.9.4. above. 7Li SSNMR integration shows that all lithium is found in a single, locally anisotropic environment, in agreement with all Li^+ residing in the condensed nanocrystalline phase. ^{19}F SSNMR spectral integration and referencing with pure $LiBF_4^-$ and $LiFSI$ spectra (not shown) allows assignment of anion environments/phases and quantification of relative abundances.

To improve the Li^+ transport dynamics, the team has prepared solid MIC electrolytes with new compositions of Li salts and ionic liquids, including mixtures of different anions such as dicyanamide (DCA), bis(fluorosulfonyl)imide (FSI), and bis(trifluoromethanesulfonyl)imide (TFSI). Most notably, a MIC composed of PBDT, $LiTFSI$, and $Pyr_{13}FSI$ with a mass ratio of 10:10:80 wt% demonstrates substantial improvement in ion diffusion and cycling capability (as compared to our previous benchmark material $PBDT:LiTFSI:Pyr_{14}TFSI$). Here we present NMR diffusion data and lithium symmetric cell cycling test results for this new $Pyr_{13}FSI$ -based MIC using $LiTFSI$ as the salt additive.

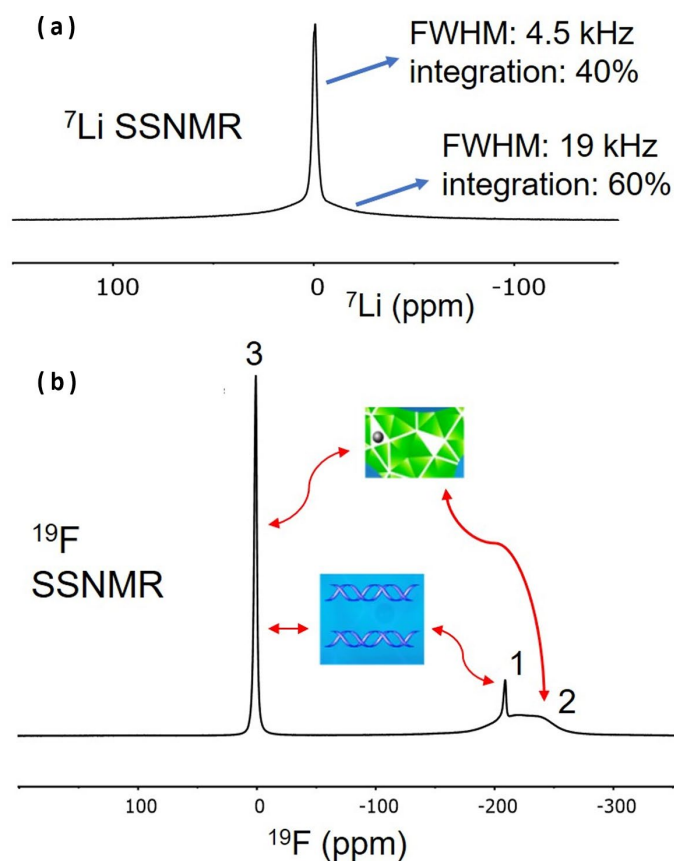


Figure XVI.9.5 Solid-state ^7Li and ^{19}F NMR of new MIC-nanocrystal system. (a) ^7Li SSNMR showing that all lithium is found in a single, locally anisotropic environment. The narrow central peak arises from the central transition of the spin-3/2 ^7Li energy level structure. The broad peak originates from the NMR quadrupolar satellite transitions, and this peak shape arises from the superposition of an isotropic distribution of crystallite orientations. The 4:6 integration ratio of these two components confirms that only one type of environment for Li^+ exists in this material, and the fact that the broad peak is observed confirms that the local environment is anisotropic, as expected for a nanocrystalline phase. (b) ^{19}F SSNMR identifying the different anions in the material (FSI^- and BF_4^-) and informing on their abundances and phase locations.

Peak 1 is mobile BF_4^- found in the PBDT liquid crystalline (LC) phase. Peak 2 is solid-like BF_4^- found in the nanocrystalline grain boundary phase. Peak 3 is FSI^- anion found in both phases and is narrow due to the internal ^{19}F dynamics in this anion, even though $\approx 12\%$ of each anion are in the LC phase and $\approx 88\%$ in the nanocrystalline phase.

PFG NMR diffusometry experiments enable measurement of diffusion coefficients for the large mobile ions in the new MIC material and comparison with the previous MIC material. Figure XVI.9.6 shows these diffusion coefficients as a function of temperature for the $\text{Pyr}_{13}\text{FSI}$ -based compared to the $\text{Pyr}_{14}\text{TFSI}$ -based MIC. At room temperature, the cations and anions in the $\text{Pyr}_{13}\text{FSI}$ -based MIC have a larger diffusion coefficient compared to the original $\text{Pyr}_{14}\text{TFSI}$ -based MIC by a factor of 3 and 4, respectively. The activation energies of diffusion further complement this, where the cation (Pyr_{13}^+) and anions (FSI^- and TFSI^-) in the new $\text{Pyr}_{13}\text{FSI}$ -based MIC were found to have a smaller activation energy of diffusion (both ≈ 25 kJ/mol) than the activation energy (≈ 37 kJ/mol) for the cation (Pyr_{14}^+) and anion (TFSI^-) in the original $\text{Pyr}_{14}\text{TFSI}$ -based MIC. The team is currently undertaking diffusion measurements over a wider temperature range and attempting to measure Li^+ diffusion as well. These results support substantially faster Li^+ transport in these new compositions of the solid MIC electrolytes.

The current symmetric $\text{Li}|\text{Li}$ cycling data for the new membranes incorporating $\text{Pyr}_{13}\text{FSI}$ (Figure XVI.9.6) further agree with the transport data observed. As previously reported, the $\text{Pyr}_{14}\text{TFSI}$ -based MIC was shown to have a limiting current density of between 0.15 and 0.20 mA/cm^2 at room temperature with a charge and discharge time of 0.5 h, respectively. Here, the new composition consistently shows a higher limiting current density under the same experimental conditions. Figure XVI.9.6 shows a lithium symmetric cell cycled at various current densities using the $\text{Pyr}_{13}\text{FSI}$ -based MIC with LiTFSI salt. The MIC electrolyte can reach a current density of at least 0.45 mA/cm^2 .

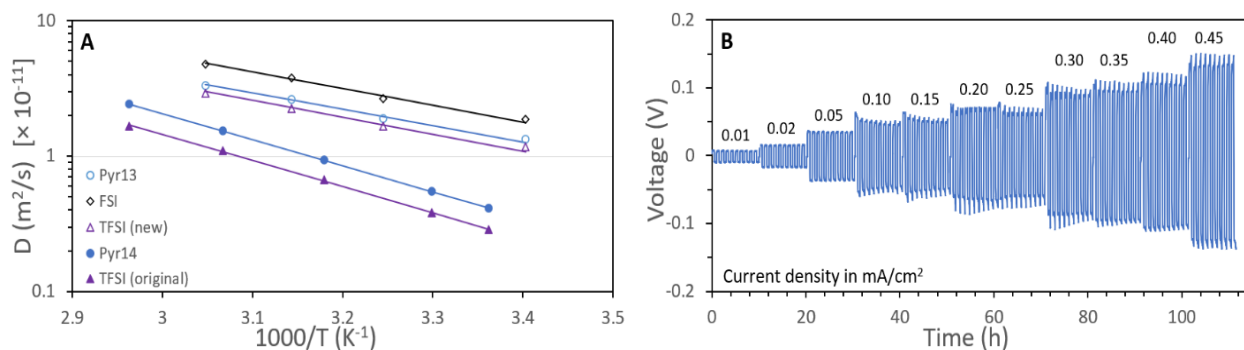


Figure XVI.9.6 (A) Temperature-dependent diffusion coefficients (via NMR) for the cations and anions in the new Pyr₁₃FSI-based MIC (hollow symbols) and original Pyr₁₄TFSI-based MIC (filled symbols). These new electrolytes are composed of 10:10:80 wt% PBDT:LiTFSI:IL. Activation energy of diffusion was derived using an Arrhenius fitting, where the measured ions in the Pyr₁₃FSI-based MIC have a substantially lower activation energy of diffusion compared to the measured ions in the Pyr₁₄TFSI-based MIC. These results are consistent with and support faster Li⁺ transport in the Pyr₁₃FSI-based MIC. (B) Voltage profile of a symmetric cell cycled at 23 °C, with stepwise increases in current density every 10 cycles. Each cycle consisted of charge and discharge times of 0.5 h, respectively. The electrolyte used is composed of a 10:10:80 wt % PBDT:LiTFSI:Pyr₁₃FSI MIC membrane. Under these conditions, the limiting current density reaches 0.45 mA/cm^2 . Multiple symmetric cells tested show consistent results. This is an improved limiting current density by at least a factor of 2 from the previous Pyr₁₄TFSI-based MIC, which showed a limiting current density below 0.2 mA/cm^2 under the same charge/discharge conditions. This cycling performance is consistent with the lower activation energy and faster diffusion coefficients of this MIC membrane compared to the original composition.

The team has also established in-house polymer synthesis capabilities. This will allow the team to make larger quantities of the rigid-rod PBDT polyanions for our future cell fabrication and systematic electrochemical measurements. The team also plans to use this as an avenue to explore optimal molecular weight by tailoring synthesis parameters, e.g., degree of polymerization. This synthetic flexibility in-house can enable different molecular weight and polydispersity of the polymer (via both time and temperature). The resulting polymers will be used to investigate the mass production of all solid-state batteries via an in-house-developed continuous process with an interface-less design. The team has also started optimization of the catholyte design. Specifically, we are tailoring the mass ratio and volume fraction of different cathode components, with the target of optimizing both ionic and electronic transport in the composite cathode. To date, the team has established different methods of formulating and processing composite cathodes and will investigate how different processing conditions may influence the composite cathode performance.

The research team is now capable of synthesizing rigid rod polymer poly(2,2'-disulfonyl-4,4'-benzidine terephthalamide) (PBDT), which is an essential component of the molecular ionic composites (MICs). Figure XVI.9.7 shows the reaction scheme for the synthesis. Our recent synthetic abilities combined with our analytical expertise provided the avenue to tailor the properties of the PBDT polymer for the development of all solid-state batteries at the fundamental level. The synthesis of sulfonated aramids, Na-PBDT and Li-PBDT, are based on an interfacial polycondensation procedure. This recent progress on the synthesis of PBDT polymer is further accelerating research toward the mass production (lab scale) of all-solid-state batteries by more amply supplying PBDT polymer.

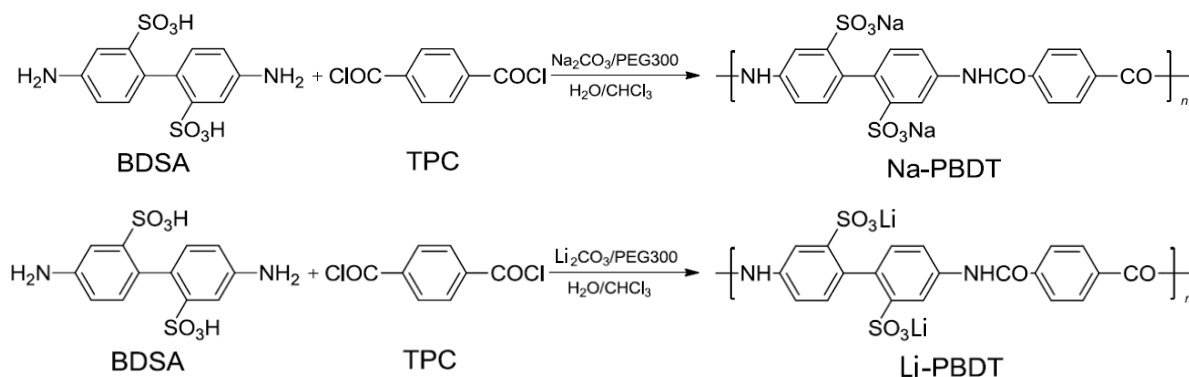


Figure XVI.9.7 Synthetic routes to produce Na-PBDT and Li-PBDT from commonly available starting materials.

The poor contact of the electrode-electrolyte interface is a key factor that undermines the electrochemical performance of solid-state batteries. To enhance the ionic conductivity and electronic conductivity in the system, microstructural engineering of composite electrodes is critical. Herein, with a solvent-assistant process, team members can introduce MIC solution upon preparing the composite electrodes and develop a novel catholyte electrode. Figure XVI.9.8 shows the flat and homogenized electrode morphology in both surface (A) and cross-section (B) without bare particles exposed to the ambient environment, which can potentially improve the solid-solid contact in the interfacial region and build a more uniform ionic percolation network. The team expects that the solid-state batteries using such catholyte electrodes will have higher specific capacity and more stable cycle life. Currently, the team is evaluating the battery performance of these electrodes and has established research plans to further optimize the ratio between different cathode components.

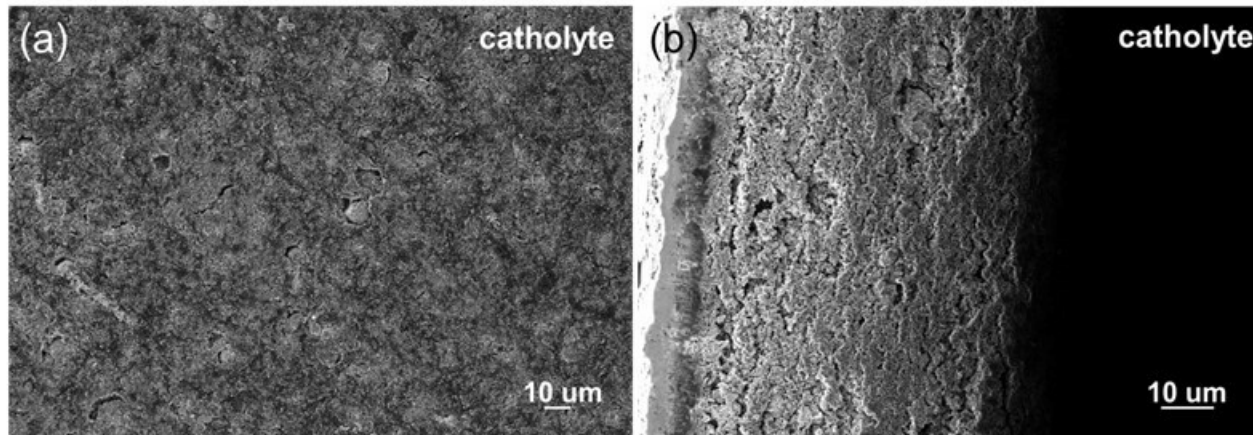


Figure XVI.9.8 (A) Top surface and (B) cross-section of the as-prepared composite cathode with the MIC solid electrolyte as the catholyte.

We have also made progress toward elucidating the ionic distribution inside the MIC electrolyte via sulfur K-edge X-ray absorption spectroscopy at the Brookhaven National Laboratory Synchrotron Light source. In our preliminary results, we established a baseline to analyze the sulfur element in a MIC electrolyte, which will further enrich our fundamental understanding of MIC-electrolyte-based all-solid-state batteries. Synchrotron X-ray absorption spectroscopy (XAS) serves as a powerful tool to probe the MIC electrolyte in an elementally selective way and provides valuable information on the local environment and the oxidation state of specific atoms in our MIC electrolyte. Tender energy X-ray absorption spectroscopy showed good results on XANES and XAFS without beam damage to the MIC electrolyte (Figure XVI.9.9). With our team's extensive expertise in developing codes and methods to analyze synchrotron imaging data, we envision that XAS experiments as

well as other complementary analysis methods on our novel electrolyte material will lay a foundation for improving the design principles for new MIC electrolytes.

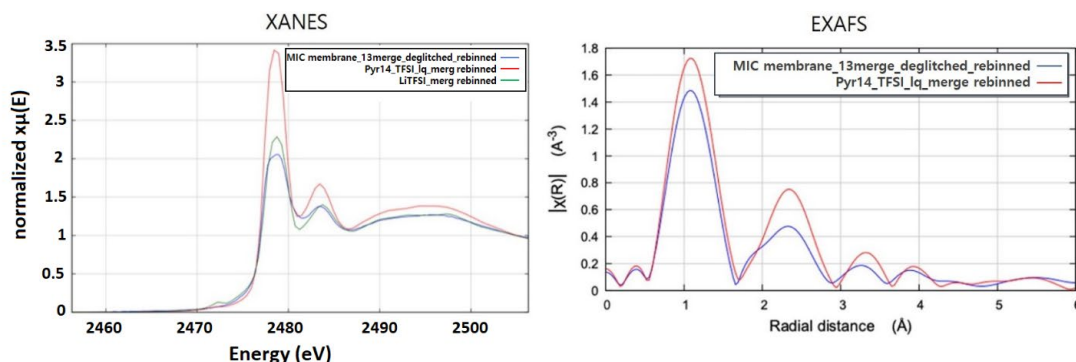


Figure XVI.9.9 Preliminary results of S K-edge XAS data. The EXAFS data has been obtained for the polymer membrane and ionic liquid samples without beam damage.

Conclusions

In summary, the team at Virginia Polytechnic Institute and State University has made significant progress in year 2 of the project. The team has established in-house synthesis capabilities for different components of MICs. The team has evaluated and confirmed the compatibility of MIC electrolytes with different cathode materials, including olivine, layered, and spinel structures. As the first testing platform, the LiFePO_4 has demonstrated exceptional performance over a wide temperature range. The team has also found that MIC electrolytes can enable high-voltage cycling of NMC cathodes. Currently, the team is working to optimize the cycling conditions and cell testing environments. As part of this new electrolyte development, the team has discovered several different chemical compositions that have different conduction mechanisms, which opens doors for new electrolyte innovations. Interfacial stability is a key to performance stabilization, and thus the team has established a workflow to perform post-mortem analysis of electrolytes and electrodes. Meanwhile, the team has started operando experiments to investigate ion speciation at the electrode-electrolyte interface. Going forward, the team plans to incorporate newly developed MIC compositions in full-cell testing. Furthermore, we have developed a path to perform a continuous process to manufacture stack-structured full cells, to achieve interface-less battery design.

Key Publications

1. Deyang Yu, Xiaona Pan, Joshua E. Bostwick, Curt J. Zanelotti, Linqin Mu, Ralph H. Colby, Feng Lin, and Louis A. Madsen. "Room temperature to 150 °C lithium metal batteries enabled by a rigid molecular ionic composite electrolyte." *Advanced Energy Materials* **2021**, 11, 2003559.
2. Deyang Yu, Curt J. Zanelotti, Ryan J. Fox, Theo J. Dingemans, and Louis A. Madsen. "Solvent-cast solid electrolyte membranes based on a charged rigid-rod polymer and ionic liquids." *ACS Applied Energy Materials* **2021**, 4, 6599–6605.
3. Ying Wang, Curt J. Zanelotti, Xiaoen Wang, Robert Kerr, Liyu Jin, Wang Hay Kan, Theo J. Dingemans, Maria Forsyth, and Louis A. Madsen. "Solid-state rigid-rod polymer composite electrolytes with nanocrystalline lithium-ion pathways." *Nature Materials* **2021**, 1255–1263.
4. Deyang Yu, Xiaona Pan, Curt J. Zanelotti, Feng Lin, and Louis A. Madsen. "Room temperature to 150 °C lithium metal batteries enabled by a "molecular ionic composite" solid electrolyte" PRiME and International Meetings, the Electrochemical Society (October 4, 2020)
5. Feng Lin. "Investigating structural defects and solid–liquid interfaces in electrochemical energy materials" –Invited Seminar Speaker (slides about this project were included), Department of Materials Science and Engineering, University of Maryland (Feb 5, 2021), College Park, MD, USA

Acknowledgements

The team acknowledges collaborations with T. J. Dingemans' group at University of North Carolina (UNC) Chapel Hill in which they are forming composites based on PBDT polymer with carbon materials such as graphene oxide and are beginning to develop new charged rigid-rod polymers that build on PBDT. The team also acknowledges collaborations with Prof. R. H. Colby at PSU on shear rheology and broadband dielectric spectroscopy to understand mechanical properties and conduction mechanisms. The team also acknowledges collaborations with Dr. D. Nordlund and Dr. Y. Liu at SLAC National Accelerator Laboratory (SLAC), and Seong-Min Bak of Brookhaven National Lab, for conducting synchrotron X-ray studies on MIC films and composite electrodes. The team also appreciate the collaboration with Prof. Y. Yao at University of Houston for establishing the solid-state battery testing platform.

XVI.10 Hot Pressing of Reinforced All-solid-state Batteries with Sulfide Glass Electrolyte (General Motors LLC)

Thomas A. Yersak, Principal Investigator

General Motors LLC
GM Global Research and Development
30470 Harley Earl Boulevard
Warren, Michigan 48092
E-mail: thomas.yersak@gm.com

Tien Q. Duong, DOE Technology Development Manager

U.S. Department of Energy
E-mail: Tien.Duong@ee.doe.gov

Start Date: October 1, 2019
Project Funding: \$1,250,000

End Date: June 30, 2023
DOE share: \$1,000,000

Non-DOE share: \$250,000

Project Introduction

The performance of all-solid-state batteries (ASSBs) with sulfide solid-state electrolytes (SSEs) is limited because they are 10 - 20% porous. Porosity limits energy density of the composite cathode and provides a conduit for Li-metal deposits through the separator if operating specifications (*i.e.*, current density, operating temperature, and pressure) are not strictly controlled. This project intends to demonstrate that hot press cell processing and appropriately formulated sulfide glass SSEs can eliminate porosity to enable Li-NCM ASSBs with energy density of ≥ 350 Wh/kg.

Objectives

The objective of this project is to research, develop, and test Li-NCM ASSBs capable of achieving program performance metrics by implementing appropriately formulated sulfide glass SSEs and hot press cell processing in a dry room environment. In the composite cathode, hot pressing eliminates porosity to increase energy density by enabling thick composite cathodes with high active material loading. In the separator, hot pressing eliminates porosity that may otherwise provide a conduit for Li metal deposits to short the cell. Unfortunately, hot press cell processing may cause a deleterious side-reaction between sulfide SSE and NCM active material even though sulfide SSEs are kinetically stable versus NCM at room temperature. For this reason, work conducted during this project's first budget period focused on enabling the hot press processing of composite cathodes with the objective of demonstrating a reversible capacity of > 120 mAh/g after hot pressing. Having established adequate thermal stability of the NCM/SSE interface, the second budget period now focuses on separator SSE development.

Approach

The sulfide SSE used in the composite cathode, otherwise known as the catholyte, will dictate the processing specifications for ASSB hot pressing. Thermal stability can be achieved by NCM passivation and proper catholyte formulation. Work conducted during this project's first budget period systematically evaluated different NCM coatings, catholyte formulations, and hot press cell processing conditions (*i.e.*, temperature, time, and pressure). Having established the feasibility of hot-pressed composite cathodes, work transitioned to this project's second budget period, which is focused solely on the separator. Separator glass electrolyte compositions are being systematically studied for processability and compatibility with secondary electrolyte phases. The functional characteristics of process glass electrolyte separators such as ionic conductivity and critical current density will then be determined. In the final budget period of this project, full ASSB stacks will be hot-pressed to realize thickness targets for cathode-supported separators.

Results

Our results are presented in three separate sections. The first section will detail the feasibility of hot-pressing composite cathodes. We report on the fundamental principles dictating the thermal stability of sulfide SSEs versus NCM cathode materials and report on the electrochemical performance of hot-pressed composite cathodes. The second and third sections detail the development of cathode-supported hot-pressed sulfide glass separators. In section two we present a glass formulation amenable to hot pressing. In section three we provide an update on the compatibility of this glass formulation versus secondary electrolyte phases intended to improve critical current density at reasonable stack pressures.

Hot-Pressed Composite Cathodes

This study demonstrates the feasibility of a hot-pressed cathode/separator cell stack to improve the energy density of all-solid-state batteries in two ways. First, hot pressing substantially reduces porosity in both the cathode composite and the separator. All-solid-state batteries made with sulfide solid-state electrolyte are often processed at room temperature with binders. As such, cell stacks are assembled from green tapes with porosity ranging from 15% to 30%. Porosity is dead space that must be eliminated to realize the theoretical limit of all-solid-state battery energy density. Second, hot pressing a cathode/separator stack provides a proof-of-concept demonstration of cathode-support for consolidated, reinforced glass separators. The thickness of the aforementioned consolidated, reinforced separators [1],[2] needs to be reduced from 100 μm to less than 30 μm to meet energy density targets [3]. Since it is extremely difficult to process standalone films with thickness less than 100 μm , cathode-support is the best way to achieve a separator thickness of 30 μm .

The consolidation and electrochemical function of hot-pressed $\text{LiNi}_x\text{Co}_y\text{Mn}_z\text{O}_2$ (NCM) cathode composites was assessed as a function of active material and sulfide solid-state electrolyte compositions. Specifically, $\text{LiNi}_{0.85}\text{Co}_{0.10}\text{Mn}_{0.05}\text{O}_2$ (NCM85105) and $\text{LiNi}_{0.6}\text{Co}_{0.2}\text{Mn}_{0.2}\text{O}_2$ (NCM622) were studied in combination with either glassy $\text{Li}_7\text{P}_3\text{S}_{11}$, glassy Li_3PS_4 , or $\beta\text{-Li}_3\text{PS}_4$ solid-state electrolytes. Several phenomena were characterized to understand the effect that hot pressing has on NCM and sulfide solid-state electrolyte (SSE). Specifically, we studied the consolidation of SSE, the devitrification of glass SSE, the thermal stability of the buried NCM/SSE interface, and the microcracking of high Ni content NCM during stack assembly. It was determined that cathode composites made with NCM622 and Li_3PS_4 maintained the best electrochemical function after hot pressing (Figure XVI.10.2). This result is attributed to NCM622's resistance to microcracking (Figure XVI.10.1) and the inherent stability of Li_3PS_4 's fully de-networked local structure. The results of this study confirm the feasibility of cathode-support for consolidated, reinforced glass separators.

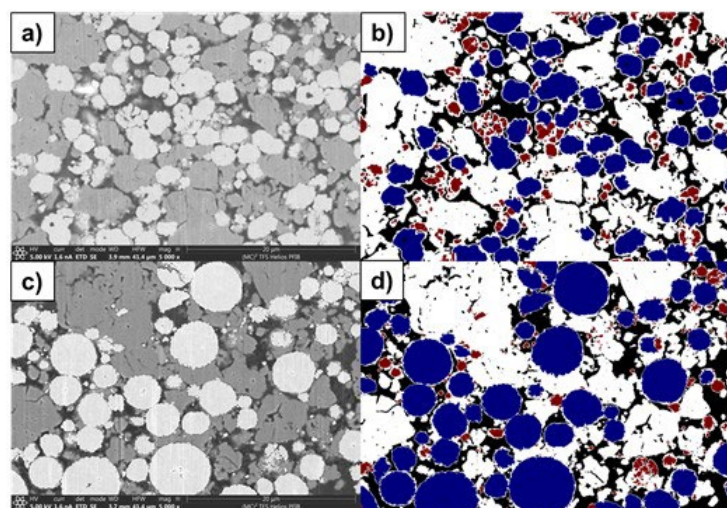


Figure XVI.10.1 NCM microcracking analysis using PFIB and digital image analysis software. a) PFIB SEM image of a NCM85105/ $\beta\text{-Li}_3\text{PS}_4$ cathode composite cross section and b) the corresponding processed image. c) PFIB SEM image of a NCM622/ $\beta\text{-Li}_3\text{PS}_4$ cathode composite cross section and d) the corresponding processed image. The color scheme for the processed images is as follows: white = SSE particle, black = pore, blue = intact NCM particle, and red = damaged NCM particle.

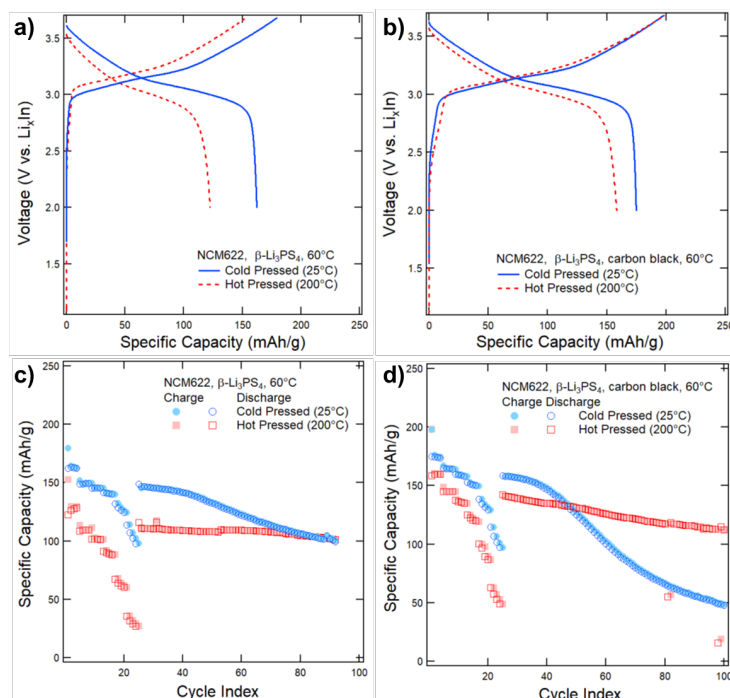


Figure XVI.10.2 Cycling data for NCM622/β-Li₃PS₄ cold-pressed (blue) and hot-pressed (red) cathode composites cycled at 60°C. a) First cycle voltage profiles for cathode composites without carbon black additive. b) First cycle voltage profiles for cathode composites with carbon black additive. c) Cyclic capacity of cathode composites without carbon black additive. d) Cyclic capacity of cathode composites with carbon black additive.

Glass Electrolyte Process Rheology

The process rheology of glass electrolytes was assessed to improve separator densification during hot pressing. We studied the binary 70Li₂S·30P₂S₅ and the ternary 70Li₂S·(30-x)P₂S₅·xA glass compositions, where A represents a third glass component. We assessed process rheology by measuring porosity and the change in sample diameter after hot pressing. Determination of optimal process variables was implemented with a half-factorial design of experiment with 2 levels (high and low), 4 variables (temperature, pressure, holding time, and composition), and 2 repetitions per combination as shown in Table XVI.10.1. A picture of samples after processing are provided in Figure XVI.10.3 and it is evident that ternary glass samples deform more than samples composed of binary 70Li₂S·30P₂S₅. The ternary glass composition decreases both the time and nominal pressure required to achieve adequate consolidation thus improving the manufacturability of hot-pressed separators.

To understand the ternary phase's improved process rheology, we investigated the glasses with both X-ray diffraction (XRD) and differential scanning calorimetry (DSC). Figure XVI.10.4 presents the diffraction spectra of both binary and ternary glasses after hot pressing and the spectra are indexed to the reflections of Li₇P₃S₁₁ (pdf #04-014-8383). The binary glass devitrified during hot pressing while the ternary glass remained largely amorphous. It is well known that the viscosity of glasses increases substantially upon devitrification as crystallites grow and physically interact. We therefore attribute the superior processability of the ternary glass to its more sluggish crystallization kinetics. To confirm this suspicion, we conducted DSC experiments on both the binary and ternary glasses. The binary glass had a crystallization onset of 272.79 °C while the ternary glass had a higher crystallization onset of 294.25 °C at a heating rate of 10 K/min. Additionally, we also measured the time required to complete full crystallization. It took the ternary glass 24 minutes to fully devitrify at 250°C while the binary glass fully crystallized in only 14.5 minutes at a lower temperature of 232.5 °C.

Table XVI.10.1 Summary of process rheology for half-factorial design of experiments.

Temperature (°Celsius)	Pressure (metric tons)	Time (min)	Composition	Nature of material	Δ Thickness	Δ Diameter
230	5	5	70-25-5	Glass	-28.00%	29.76%
240	1	10	70-30	Crystalized	-3.37%	4.26%
230	5	10	70-30	Crystalized	-15.73%	17.59%
240	1	5	70-25-5	Glass	-73.50%	79.00%
240	5	5	70-30	Crystalized	-11.93	12.58%
230	1	10	70-25-5	Glass	-39.60	42.78
230	1	5	70-30	Crystalized	-20.23%	14.99%
240	5	10	70-25-5	Glass	-74.01%	117.58%



Figure XVI.10.3 Pictures of binary and ternary glass samples after hot pressing trials. All samples contained 3 wt.% bulk Kevlar fiber to improve strength and handleability.

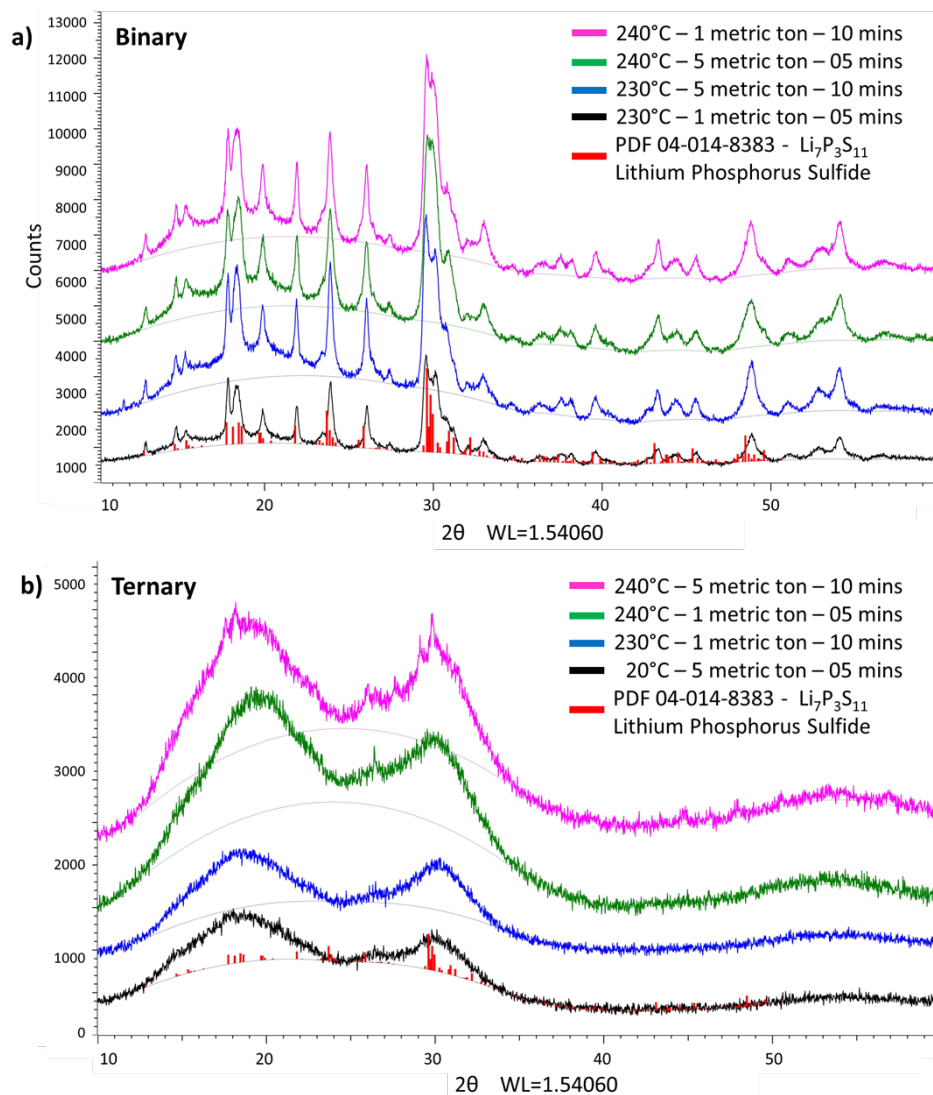


Figure XVI.10.4 XRD spectra for a) binary and b) ternary glass samples after hot pressing trials. Spectra are indexed to reflections for $\text{Li}_7\text{P}_3\text{S}_{11}$ (red bars, pdf 04-014-8383).

Glass Electrolyte Compatibility with Secondary Electrolyte Phase

We evaluated the solubility of glass electrolytes in solvate ionic liquids (SILs). The SILs were prepared by combining lithium bis(trifluoromethanesulfonyl)imide (LiTFSI) and triethylene glycol dimethyl ether (triglyme, G3) in a molar ratio of either 1:1 ($\text{Li}(\text{G3})\text{TFSI}$) or 1:4 ($\text{Li}(\text{G3})_4\text{TFSI}$). We evaluated the solubility of glass electrolytes with composition $70\text{Li}_2\text{S} \cdot (30-x)\text{P}_2\text{S}_5 \cdot xA$ ($x = 0, 2, 5$), where A represents a third glass component. These are the same glass compositions evaluated for process rheology. SSEs were prepared by ball-milling or melt quench methods as reported in previous work [1],[4].

Solubility tests were conducted by immersing SSE chunks in SILs and observing the color of the solution over time. Figure XVI.10.5 provides pictures of samples after soaking in SIL for 7 days. We observe that the solution remains clear for SSEs soaked in equimolar complex of $\text{Li}(\text{G3})\text{TFSI}$, however, the solutions became turbid and dark for SSEs soaked in $\text{Li}(\text{G3})_4\text{TFSI}$. The mass change of the SSEs was measured by filtering the solutions and drying the remaining solids at 60°C . The results are provided in Table XVI.10.2. No mass loss was observed for samples soaked in $\text{Li}(\text{G3})\text{TFSI}$, while significant mass loss was observed for samples soaked in $\text{Li}(\text{G3})_4\text{TFSI}$. The different behaviors between $\text{Li}(\text{G3})\text{TFSI}$ and $\text{Li}(\text{G3})_4\text{TFSI}$ can be addressed by the strong

complexation of G3 with Li salts in the salt–solvent complex significantly weakens the donor ability of oxygen. Oxygen in G3 would normally attack the electropositive elements (e.g., P) of the sulfide SSEs by nucleophilic attack. It is also worth noting that the solubility of glasses decreases as the content of the third glass component, *A*, increases. This could be due to a substitution of S for an element in *A*, which introduces higher steric hindrance and lowers the reactivity of the P site. UV-Vis spectroscopy was conducted to corroborate the data outline above and the data are provided in Figure XVI.10.6. The results of UV–Vis molecular absorption spectroscopy also confirm the insolubility of ternary glass compositions due to minimal absorbance above 350 nm wavelength. We conclude that solubility of SSE in SIL is reduced by increasing the salt content and by increasing the content of third glass component *A*.

Table XVI.10.2 Mass of SSEs before and after dissolving in glyme-based solvate ionic liquids (SILs) for 7 days.

Composition		Mass Before (g)	Mass After (g)	Mass Loss (%)
Li(G3)TFSI	70-30	0.0562	0.0561	0.18
	70-28-2	0.0345	0.0346	-0.29
	70-25-5	0.0396	0.0396	0.00
Li(G3) ₄ TFSI	70-30	0.0694	0.0522	24.78
	70-28-2	0.0240	0.0201	16.23
	70-25-5	0.0340	0.0331	2.65

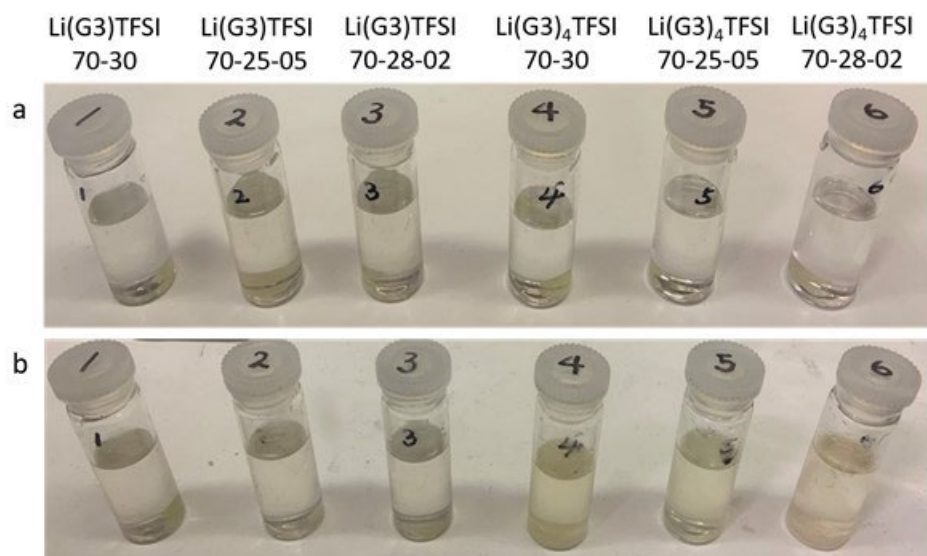


Figure XVI.10.5 Solubility of SSEs with glyme-based solvate ionic liquids (SILs). a) Photographic images of as-prepared mixtures of SSE chunks with the liquids (Li(G3)TFSI and Li(G3)₄TFSI) and b) after being kept for 7 days.

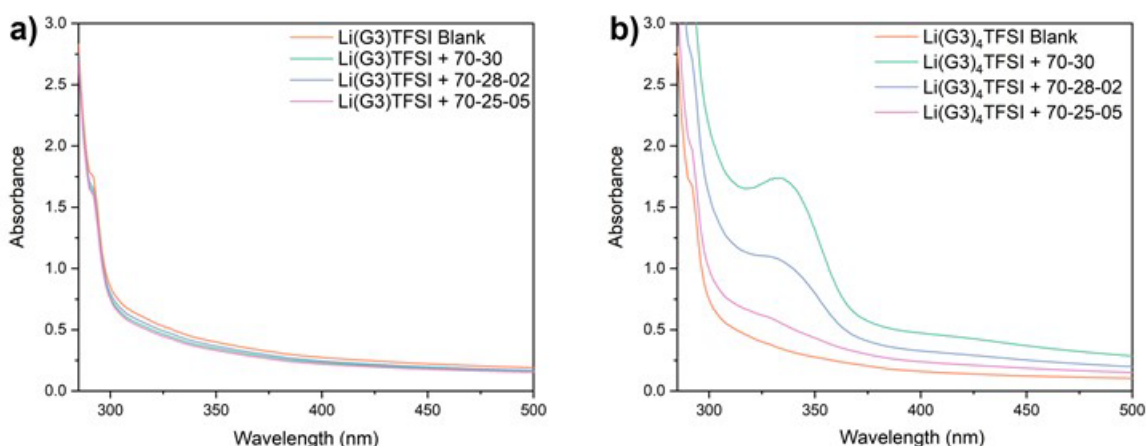


Figure XVI.10.6 UV-Vis molecular absorption spectroscopy results for SSE in a) Li(G3)TFSI and b) Li(G3)₄TFSI.

Conclusions

We conclude that hot pressing of electrochemically functional cathode composites is feasible provided that the cathode active material and SSE are properly chosen. While this study focused on Li-P-S sulfide SSEs, there are other classes of SSE that may provide better thermal stability and better process rheology. More importantly, this study suggests that cathode-support is a viable pathway towards reducing the thickness of consolidated, reinforced separators. Current work therefore investigates the process rheology of sulfide glasses. To date we have investigated the process rheology of ternary glasses and the compatibility of ternary glasses with SILs. We conclude that a third glass component, *A*, improves both process rheology and compatibility with SIL. Work is underway to demonstrate cathode support of hot-pressed separators.

References

1. Yersak, T., Salvador, J. R., Schmidt, R. D., Cai, M. (2019) Hot pressed, fiber-reinforced (Li₂S)₇₀(P₂S₅)₃₀ solid-state electrolyte separators for Li metal batteries. *ACS Applied Energy Materials*, 2(5): 3523–3531.
2. Yersak, T., Salvador, J. R., Schmidt, R. D., Cai, M. (2021) Hybrid Li-S pouch cell with a reinforced sulfide glass solid-state electrolyte film separator. *International Journal of Applied Glass Science*, 12(1): 124–134.
3. Berg E. J.; Trabesinger S. (2018) Viability of Polysulfide Retaining Barriers in Li-S Battery. *Journal of the Electrochemical Society*, 165(1): A5001–A5005.
4. McGrogan, F.P., et al., Compliant Yet Brittle Mechanical Behavior of Li₂S–P₂S₅ Lithium-Ion-Conducting Solid Electrolyte. *Advanced Energy Materials*, 2017. 7(12): p. 1602011.

Acknowledgements

The PI (Thomas A. Yersak) and co-PI (James R. Salvador) would like to provide recognition to our NETL manager, Adrienne L Riggi. Special thanks are also given to Dr. Fang Hao, Dr. Chansoon Kang, Dr. Yubin Zhang, and Dr. Hernando Jesus Gonzalez Malabet for their important contributions to the project.

XVI.11 Developing Materials for High-Energy-Density Solid State Lithium-Sulfur Batteries (Penn State University)

Donghai Wang, Principal Investigator

Penn State University
134 Energy & Environmental Laboratory
University Park, PA 16802
E-mail: dwang@psu.edu

Tien Q. Duong, DOE Technology Development Manager

U.S. Department of Energy
E-mail: Tien.Duong@ee.doe.gov

Start Date: January 1, 2021

End Date: December 31, 2021

Project Funding: \$413,415

DOE share: \$330,113

Non-DOE share: \$83,302

Project Introduction

Lithium-sulfur (Li-S) all-solid-state battery (ASSB) is a promising candidate to replace existing Li-ion batteries for application in electric and plug-in hybrid electric vehicles (EVs and PHEVs) due to its high energy density and superior safety. Moreover, recent advances in improving ionic conductivities ($\approx 10^{-2} \text{ S cm}^{-1}$) of sulfide-based solid-state electrolytes (SSEs) put us one step closer to the practical application of Li-S ASSBs [1]. In Li-S ASSBs, the polysulfide shuttling and self-discharges in liquid-type Li-S batteries could be fundamentally resolved [2]. Furthermore, as added benefits, sulfide-based SSEs possess improved safety due to the absence of flammable organic electrolytes [3],[4]. However, despite those encouraging characteristics of ASSBs, there are technological challenges such as low sulfur utilization and increased interfacial resistance due to poor contact, large volume expansion of sulfur upon cycling and unoptimized microstructure of sulfur-carbon-SSEs composites in the solid cathode, poor charge/discharge rate due to the low conductivity of SSEs, and SSEs' chemical instability against moisture and lithium/lithium alloy anodes. The challenges are fundamentally attributed to the properties of the solid materials and their interfaces in electrodes.

In brief, we shall address the following three problems of Li-S ASSBs in this project. First, we aim to construct electron and ionic transport pathways in the cathode to improve sulfur utilization upon cycling and boost overall energy density. Second, we target generating a favorable interface between carbon-sulfur composite and solid-state electrolytes with novel solid additives or approaches. Third, we plan to develop new sulfide-based solid electrolytes with high ionic conductivity and improved stability against moisture and lithium alloys for all.

Objectives

The project objectives are to develop materials involving advanced S-C composite materials, solid additives, and sulfide-based SSEs and acquire knowledge for Li-S ASSBs. Li-S ASSBs with high areal sulfur loading ($\geq 5 \text{ mg cm}^{-2}$) and high sulfur content ($\geq 50 \text{ wt\%}$ in cathode), pairing with lithium or lithium alloy anode, shall deliver a high initial specific capacity of over 1200 mAh g^{-1} at high charge/discharge rate ($> 0.3 \text{ C}$) for 500 cycles with over 80% capacity retention. The out-year goals are as follows: (1) develop new S-C materials, new cathode additives, and cation-doped solid electrolytes (ionic conductivity above 2 mS cm^{-1} at room temperature), (2) conduct characterization and performance tests on both material and electrode levels. The Go/No-Go Decision will be a demonstration of all-solid-state sulfur cathodes with over 1000 mAh g^{-1} discharge capacity at 0.3 C discharge rate and 50 wt\% sulfur content for 50 cycles at 60°C .

Approach

The project goal will be accomplished by developing new materials and the in-depth characterization of the sulfur cathode. Specifically, approaches to realize the project objectives include: (1) development of new

carbon material with unique structure, high surface area, and large pore volume; (2) development of new S-C materials to facilitate electron/ion transport; (3) development of novel additives to tune interfacial behavior among components in the cathode; (4) development and optimization of new SSEs through cation and anion doping with superior properties such as high ionic conductivity, reasonable moisture stability, and compatibility with lithium metal anode; and (5) diagnostics, characterization, and cell tests on the developed new material or advanced sulfur cathode.

Results

In this budget period, we mainly focused on the following three aspects: (1) development of sulfide-based SSEs with high ionic conductivity; (2) development of advanced hybrid materials for sulfur cathode; (3) development of solid additives for the sulfur cathode. Meanwhile, we were working on developing novel characterization techniques for the Li-S ASSBs to acquire knowledge of the electrochemical system. In the following part, we shall elucidate our accomplishments that have been achieved so far.

1. Sulfide-based SSEs development

SSE plays a critical role in determining the performance of Li-S ASSBs. An ideal SSE should possess the following properties: (1) high ionic conductivity ($>3 \text{ mS cm}^{-1}$) at room temperature; (2) good compatibility with lithium metal anode; (3) good formability; (4) good moisture stability. In this budget period, we developed two sulfide-based SSEs for Li-S ASSBs, namely, SSE-1 and SSE-2.

SSE-1 was synthesized via a facile liquid-phase synthesis method. The cold-pressed SSE-1 pellet exhibited a high ionic conductivity of 4.01 mS cm^{-1} at 25°C and low activation energy of 0.212 eV (Figure XVI.11.1a). Moreover, a high ionic conductivity of 6.09 mS cm^{-1} at 25°C was recorded for the hot-pressed SSE-1 pellet (Figure XVI.11.1b). Such high ionic conductivity meets our proposed milestone for synthesizing new anion-doped solid electrolytes in budget period 2. Notably, it is among the highest ionic conductivity so far in reported literature for liquid-phase synthesized sulfide-based SSEs, and this liquid-phase synthesis method is suitable for industrial production in large quantities.

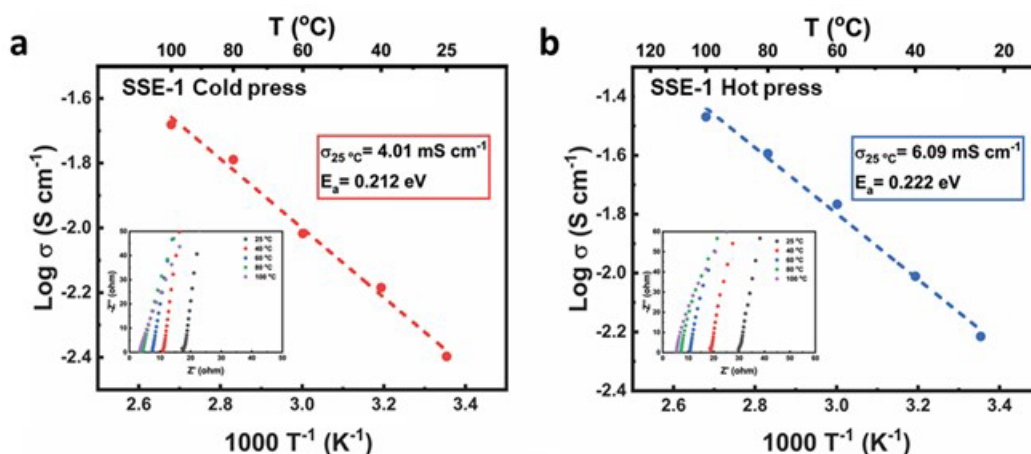


Figure XVI.11.1 The Arrhenius plot and Nyquist impedance plot for (a) cold-pressed and (b) hot-pressed SSE-1 from 25 to 100°C .

The morphology of SSE-1 was also reviewed by scanning electron microscopy (SEM) and transmission electron microscopy (TEM). The SEM and energy-dispersive X-ray spectroscopy (EDS) mapping images show that the as-synthesized SSE-1 powders are aggregates of $\sim 5 \mu\text{m}$ small particles with sulfur and phosphorous elements uniformly distributed throughout the particles (Figure XVI.11.2a-c). Furthermore, scanning transmission electron microscope (STEM) and TEM images of the SE particles uncovered that the $5\text{-}\mu\text{m}$ particles observed in the SEM images consist of smaller nanoparticles below 500 nm (Figure XVI.11.2d-e). Moreover, both diffraction spots and diffraction rings are observed in the selected area electron diffraction (SAED) pattern image (Figure XVI.11.2f), suggesting that LPB is composed of crystalline and

amorphous phases. The structure of SSE-1 was further scrutinized using the X-ray diffraction (XRD) technique. In Figure XVI.11.3, diffraction peaks associated with the crystalline cubic argyrodite phase were observed. Besides, some unknown peaks were also noticed, which are attributed to the impurities in the prepared SSE-1. Together, these results show that SSE-1 is an argyrodite glass-ceramic sulfide SSE.

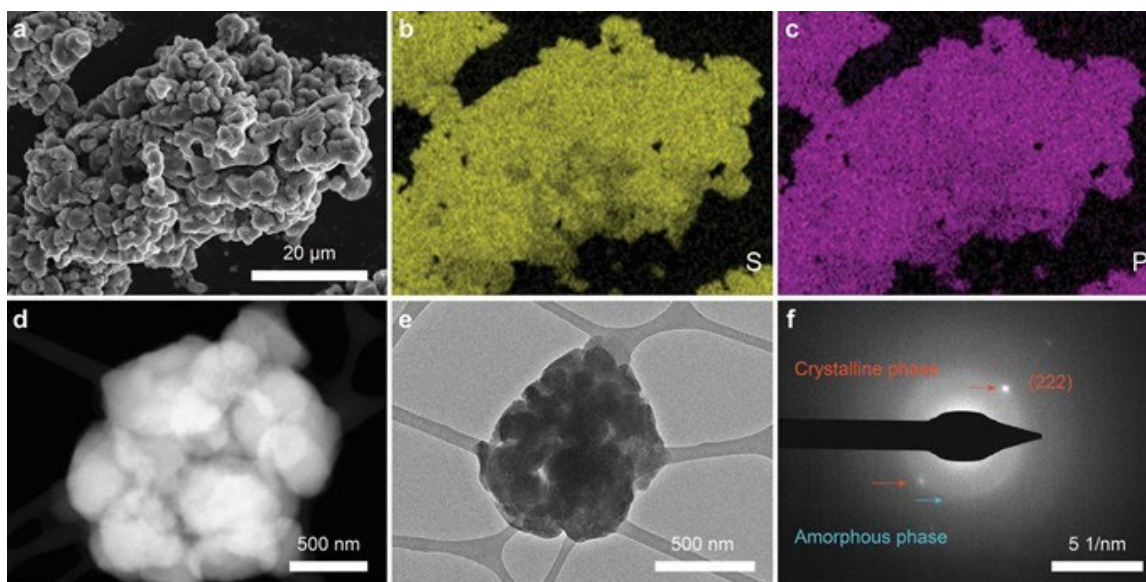


Figure XVI.11.2 The Arrhenius plot and Nyquist impedance plot for (a) cold-pressed and (b) hot-pressed SSE-1 from 25 to 100 °C.

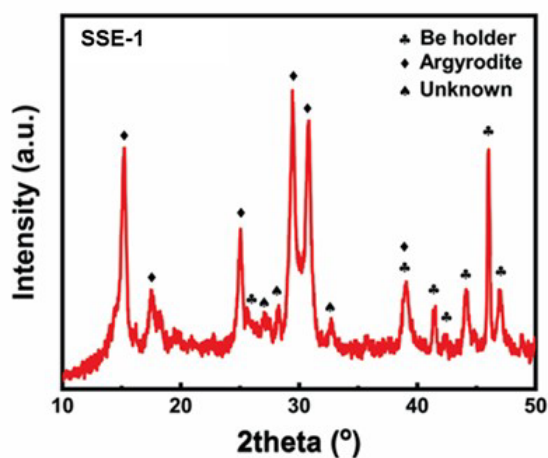


Figure XVI.11.3 XRD patterns of SSE-1.

The compatibility of the SSE-1 with lithium metal was also investigated using Li/SSE-1/Li symmetric cells. The cell was cycled at different current densities from 0.1 mA cm⁻² to 1.0 mA cm⁻² under 6 ~ 8 MPa at room temperature. The cycling voltage profile as a function of time is depicted in Figure XVI.11.4a. The cell cycled stably without short-circuiting until the current density reached above 1 mA cm⁻², demonstrating that the critical current density is 1 mA cm⁻². To gain an in-depth understanding of the evolution of the SEI layer, both areal total resistance (R_t) and areal interfacial resistance (R_{int}) were calculated and illustrated in Figure XVI.11.4b. During the first few cycles at 0.1 mA cm⁻², the voltage polarization, total resistance, and interfacial resistance gradually increased due to the growth of the SEI layer. After the current density increased to 0.25 mA cm⁻², the evolution of the SEI layer stabilized with a low interfacial resistance of 6 ~ 7 Ω cm², which

remains almost constant even at 1 mA cm^{-2} . This result demonstrates the formation of a low-resistance metastable SEI layer at the Li/SSE-1 interface.

Further analysis of the solid electrolyte interface (SEI) layer by X-ray photoelectron spectroscopy (XPS) (Figure XVI.11.4c-h) revealed that this low-resistance SEI layer was mainly composed of Li_2S . High-resolution XPS spectra of Li 1s, P 2p, and S 2p were collected for the original SSE-1 (Figure XVI.11.4c-e) and the lithium/SSE-1 interface at the Li metal (Figure XVI.11.4f-h) surface. On the surface of the SE pellet, with peaks sitting at their original position, there is no sign of SSE-1's decomposition. On the lithium metal surface, a peak corresponding to Li^0 metal was observed at $\sim 54.8 \text{ eV}$ in Li 1s spectra. Unlike the Li/SSE interface of other sulfide-based SEs like $\text{Li}_{10}\text{GeP}_2\text{S}_{12}$, where the SEI layer is as thick as over tens of nanometers and sputtering is required to uncover the full information of the SEI layer, the direct observation of Li^0 shows that the SEI layer at Li/SSE-1 is relatively thin. It indicates that further reduction of SSE-1 is retarded after forming the metastable SEI layer. In the P 2p spectra of SEI on Li, only one pair of doublet peaks attributed to SSE-1 were observed at ~ 131.8 and $\sim 132.6 \text{ eV}$ with weak intensity, while any peak associated with Li_3P from the reduction of the SE was not observed. In the S 2p spectra of SEI on Li, the formation of Li_2S was confirmed by the presence of doublet peaks of Li_2S at ~ 160 and $\sim 161 \text{ eV}$. Together, the results demonstrated the formation of a Li_2S -rich, thin, and stable SEI layer at the Li/SSE-1 interface, making SSE-1 stable against lithium metal anode.

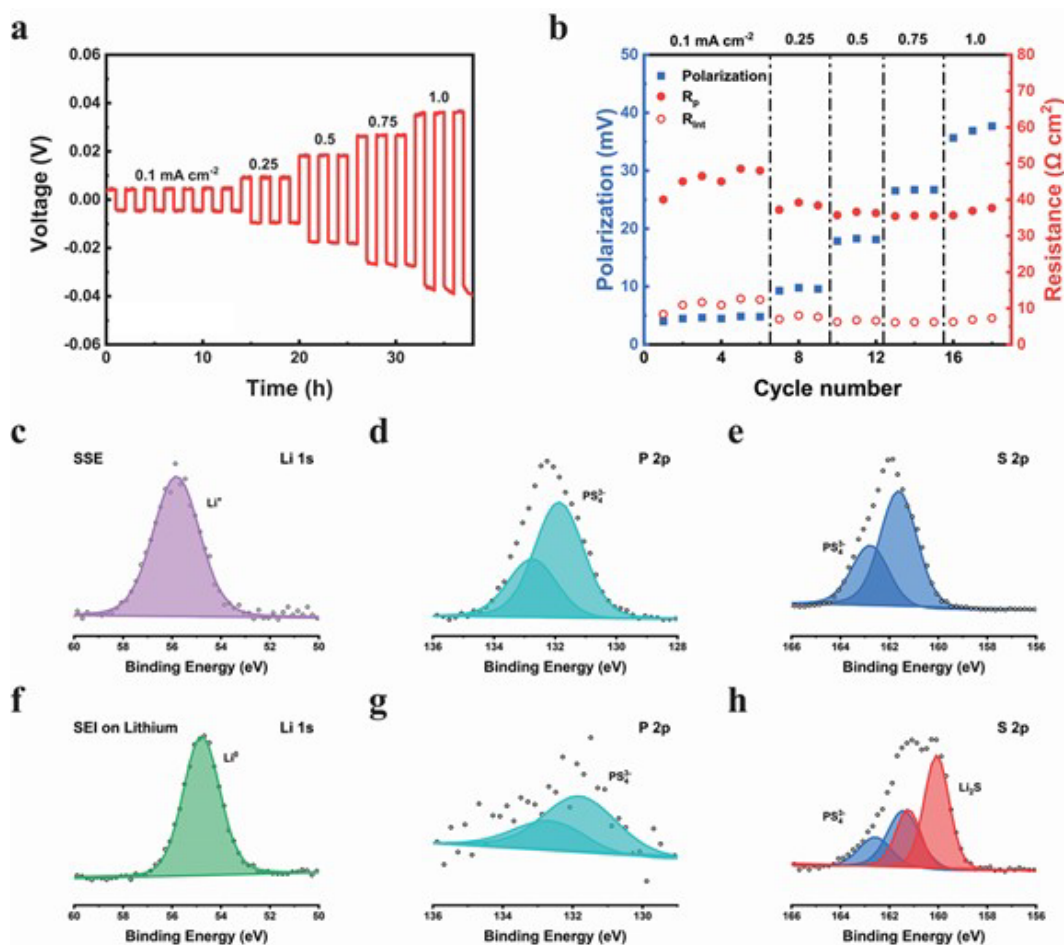


Figure XVI.11.4 (a) Cycling of a Li/SSE-1/Li symmetric cell at different current densities under room temperature. (b) Evolution of voltage polarization, total resistance, and interfacial resistance upon cycling. (c-h) XPS spectra of (c-e) original SSE-1 and (f-h) SEI layer on lithium at the Li/SSE-1 interface.

The electrochemical performance of Li-S ASSBs using SSE-1 was further evaluated at 60°C . Sulfur cathode with an ultrahigh sulfur content of $\sim 59.5 \text{ wt\%}$ of sulfur was fabricated. As shown in Figure XVI.11.5a, the Li-

S ASSBs using SSE-1 (S-C-SSE-1) delivered a high discharge specific capacity of $\sim 1092.5 \text{ mAh g}^{-1}$ at 0.1 C ($1 \text{ C} = 1675 \text{ mAh g}^{-1}$), much higher than that of the sulfur cathode using Li_3PS_4 SSE (S-C-LPS cathode, $\sim 510.2 \text{ mAh g}^{-1}$). The rate performance of Li-S ASSBs was evaluated as well (Figure XVI.11.5b). Compared with the S-C-LPS cathode, the S-C-SSE-1 cathode presented much higher discharge capacities of 1144.6, 1024, 907.8, and 663 mAh g^{-1} at 0.1, 0.3, 0.5, and 1 C, respectively. The superior performance of the S-C-LPB cathode at 0.1 C is equivalent to a high cathode-level energy density of $1318.7 \text{ Wh kg}^{-1}$ with a high average discharge voltage of 1.935 V (vs. Li/Li^+ , or 1.315 V vs. Li-In/Li^+). The improvement in the electrochemical performance of the S-C-SSE-1 cathode compared with the S-C-LPS cathode is attributed to the high ionic conductivity of SSE-1 than Li_3PS_4 .

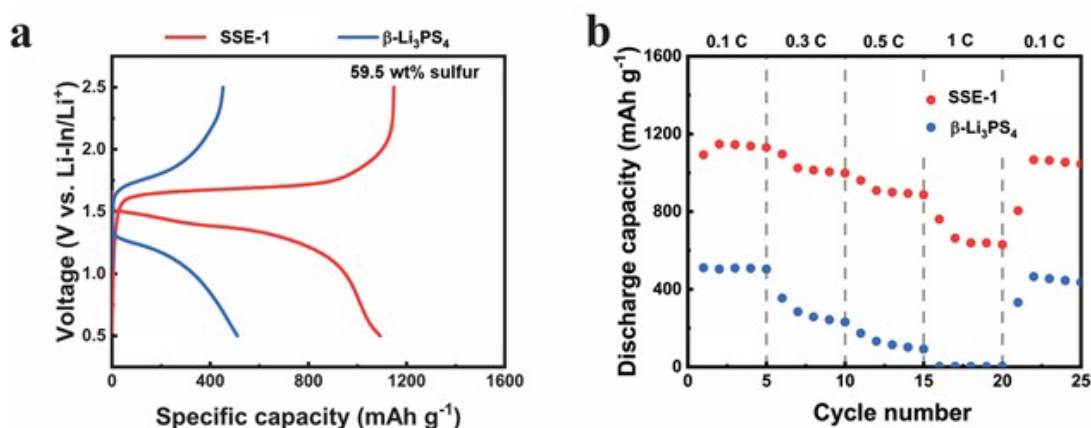


Figure XVI.11.5 Electrochemical evaluation of Li-S ASSBs at 60 °C. (a) Galvanostatic discharge-charge curves at 0.1 C. (b) Rate performance of Li-S ASSBs. Areal sulfur loading is between 2 and 3 mg cm^{-2} . Li-In alloy is used as the anode.

In addition, SSE-2, a cation-doped solid electrolyte (M_xS_y), has also been developed via mechanical ball milling and used for the fabrication of Li-S ASSBs. Compared with the sulfur cathode using conventional $75\text{Li}_2\text{S} \cdot 25\text{P}_2\text{S}_5$ solid electrolytes (S-C-LPS), the sulfur cathode ($\sim 50\text{wt}\%$ sulfur content) using SSE-2 (S-C-SSE-2) shows an improved discharge capacity at 0.1 C as shown in the charge-discharge curves in Figure XVI.11.6a. Moreover, their rate performances from 0.1 C to 1 C have also been evaluated as well. The S-C-SSE-2 cathode exhibited higher discharge specific capacity than the S-C-LPS cathode at all rates. In detail, the S-C-SSE-2 cathode delivered high discharge specific capacities of 1430.3, 1275.1, 934.1, and 629.7 mAh g^{-1} , at 0.1, 0.2, 0.5, and 1 C, respectively (Figure XVI.11.6b). Furthermore, the cycling performance of the S-C-SSE-2 cathode was evaluated at 2C under constant current constant voltage (CCCV) mode with a cutoff current of 0.1 C at 2.5 V. The cell cycled stably for over 1000 cycles with a capacity retention of 97.6 % based on the discharge capacity at the 2nd cycle (Figure XVI.11.7).

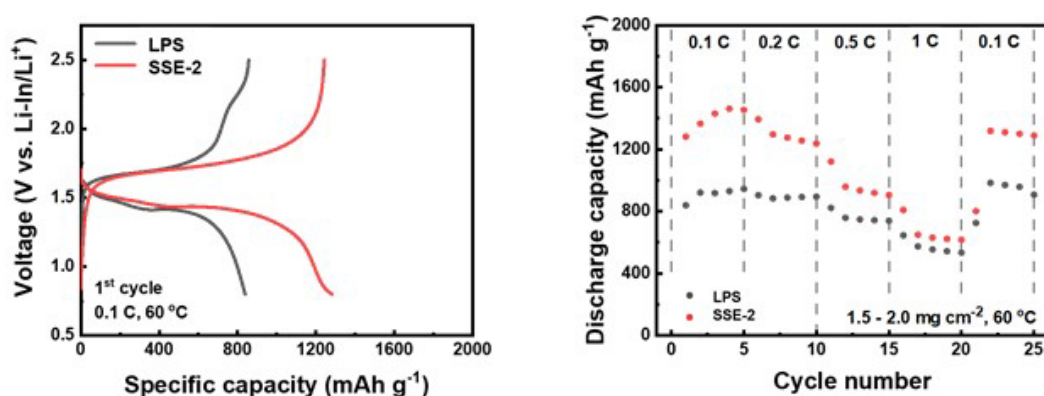


Figure XVI.11.6 (a) Charge-discharge curves and (b) rate performance of S-C-LPS cathode and S-C-SSE-2 cathode. The cells were tested between 0.8 and 2.5 V at 60 °C.

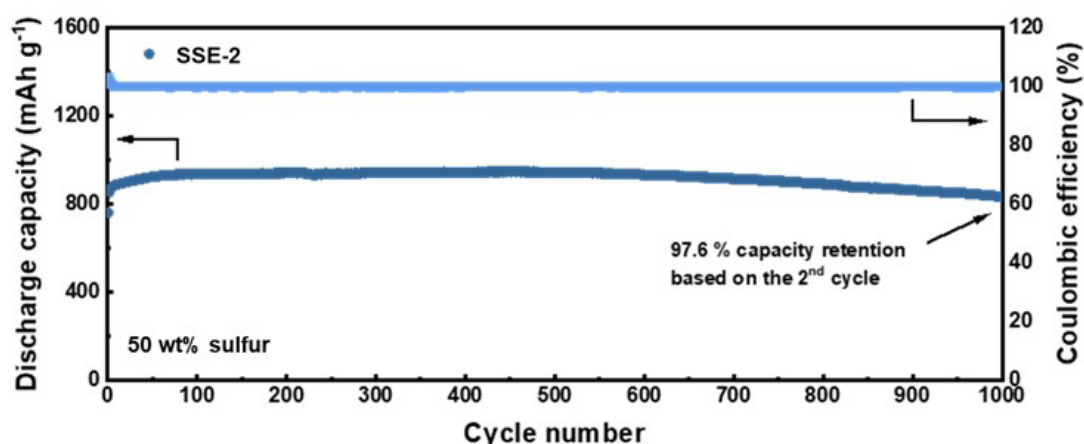


Figure XVI.11.7 Cycling performance of Li-S ASSB using SSE-2 at 60 °C.

2. Advanced hybrid materials for sulfur cathode

Fabricating sulfur cathode with efficient ion and electronic transport is the key to realizing high-performance Li-S ASSBs with high energy density. Therefore, we optimized the cathode preparation conditions and compositions. Moreover, we designed and developed novel advanced hybrid materials for sulfur cathodes. As a result, the developed cathode with a sulfur content of ~ 50 wt% and an areal sulfur loading of ~ 2.055 mg cm⁻² cycled stably for over 100 cycles at room temperature (Figure XVI.11.8). After 100 cycles, the discharge specific capacity is still over 1100 mAh g⁻² under a current of 0.1 A/g_{cathode} (~ 0.12 C). Such superior performance meets the requirement for the project progress cell demonstration target of Go/No Go decision for the budget period 2.

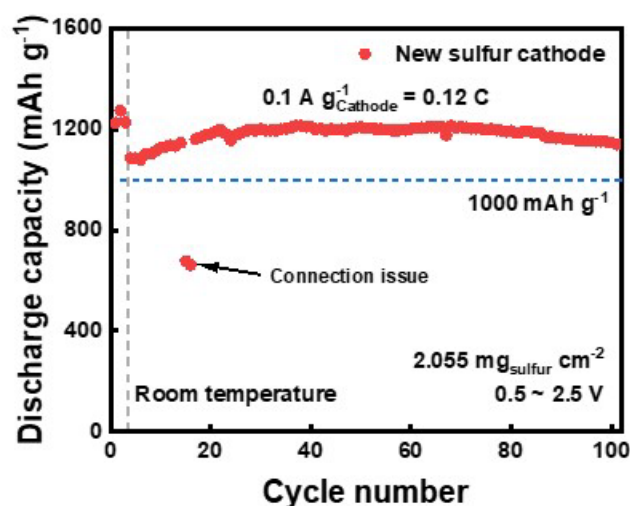


Figure XVI.11.8 Cycling performance of Li-S ASSB using new sulfur cathode at room temperature.

3. Solid additives for sulfur cathodes

Last year, we found that the electrochemically active molecules (EAMs) solid additives could impact charge/discharge behavior and improve cathode performance. Based on our previous findings, we further optimized the preparation procedures and reduced the content of solid additives to below 3 wt%. As a result, the developed sulfur cathode with a high sulfur content of ~ 50 wt% and a moderate sulfur loading of ~ 1.51 mg cm⁻² demonstrated a high discharge capacity of over 1400 mAh g⁻¹ at 0.05 C. After being cycled at 0.3 C for 50 cycles, the cell still showed high discharge capacity of over 1000 mAh g⁻¹. This result fulfills the requirements of EAMs additives demonstration milestone in budget period 2. Notably, 75Li₂S·25P₂S₅ glass SSE with ionic conductivity of ~ 0.4 mS cm⁻¹ at 25°C was used in the sulfur cathode and as the electrolyte membrane. Further improvement of the performance is feasible by using other SSE with higher ionic conductivity.

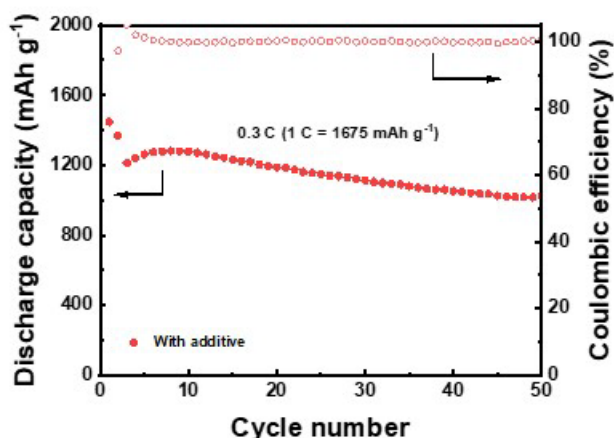


Figure XVI.11.9 Cycling performance of Li-S ASSB using solid additives (< 3 wt%) in the sulfur cathode. The cell was tested at 60°C.

4. Advanced characterization techniques

Developing new characterization techniques is crucial for acquiring knowledge of Li-S ASSBs and providing guidance for material design and cell fabrication. Last year, we developed a tool for the ex-situ characterization of Li-S ASSBs using computed tomography (CT). This year, we optimized our cell design and fabricated a new tool for the in-situ characterization of Li-S ASSBs. Hopefully, this new technique shall help us better understand the evolution of the system and contribute to the whole project. In addition, we also worked on ex-situ SEM, transmission electron microscopy (TEM), and other characterization techniques for our research. By developing these characterization techniques, we gained a better understanding of the electrode morphology evolution and cathode materials evolution upon cycling.

Conclusions

In conclusion, we have accomplished our goals and Go/no Go target for the budget period 2 and obtained the following four main achievements: 1) We synthesized a glass-ceramic argyrodite SSE via a facile liquid-phase method with high ionic conductivity of $\sim 6.09 \text{ mS cm}^{-1}$ at 25°C , and good electrochemical stability against lithium metal anode. 2) We developed an advanced cation-doped solid electrolyte that enabled higher sulfur utilization and stable cycling of Li-S ASSBs for over 1000 cycles. 3) We developed a novel hybrid sulfur cathode that cycled stably at room temperature for over 100 cycles with discharge specific capacity above 1000 mAh g^{-1} . 4) We further reduced the amount of solid additive content to below 3 wt% in the cathode while maintaining the high sulfur utilization of sulfur cathodes. 5) We developed in-situ electrochemical cells for CT technique and ex-situ SEM and TEM characterization techniques to investigate the evolution of Li-S ASSBs during cycling.

Key Publications

1. Wang, Daiwei, Li-Ji Jhang, Meng Liao, Shiyao Zheng, Atif AlZahrani, Tianhang Chen, Yue Gao, Donghai Wang. "Mixed ionic-electronic conductive lithium thiophosphate solid electrolyte for all-solid-state lithium-sulfur batteries with high sulfur utilization." *In preparation*.
2. Wang, Daiwei, Li-Ji Jhang, Rong Kou, Meng Liao, Shiyao Zheng, Heng Jiang, Guo-Xing Li, Kui Meng, Donghai Wang, "High-Energy All-Solid-State Lithium-Sulfur Batteries with High Sulfur Content Enabled by A Low-Density Nanostructured Lithium Thiophosphate Solid Electrolyte." *In preparation*.

References

1. Kamaya, Noriaki, Kenji Homma, Yuichiro Yamakawa, Masaaki Hirayama, Ryoji Kanno, Masao Yonemura, Takashi Kamiyama, Yuki Kato, Shigenori Hama, Koji Kawamoto, and Akio Mitsui. 2011. "A lithium superionic conductor." *Nature Material* 10: 682–686.
2. Hayashi, Akitoshi, Takamasa Ohtomo, Fuminori Mizuno, Kiyoharu Tadanaga, and Masahiro Tatsumisago. 2003. "All-solid-state Li/S batteries with highly conductive glass-ceramic electrolytes." *Electrochemistry Communications* 5, no. 8 (August): 701–705.
3. Inoue, Takao, and Kazuhiko Mukai. 2017. "Are All-Solid-State Lithium-Ion Batteries Really Safe? – Verification by Differential Scanning Calorimetry with an All-Inclusive Microcell." *ACS Applied Materials & Interfaces* 9, no. 2 (January): 1507–1515.
4. Tatsumisago, Masahiro, Motohiro Nagao, and Akitoshi Hayashi. 2013. "Recent development of sulfide solid electrolytes and interfacial modification for all-solid-state rechargeable lithium batteries." *Journal of Asian Ceramic Societies* 1, no. 1 (March): 17–25.

Acknowledgements

The work was supported by the Department of Energy, Office of Energy Efficiency and Renewable Energy (EERE), Vehicle Technology Office, under Award Number DE-EE0008862. We appreciate the support from Colleen Butcher at National Energy Technology Laboratory and Patricia Smith from DOE.

XVI.12 Developing an *In-situ* Formed Dynamic Protection Layer to Mitigate Lithium Interface Shifting: Preventing Dendrite Formation on Metallic Lithium Surface to Facilitate Long Cycle Life of Lithium Solid State Batteries (University of Wisconsin-Milwaukee)

Deyang Qu, Principal Investigator

University of Wisconsin-Milwaukee
3200 North Cramer Street
Milwaukee, WI 53211
E-mail: qud@uwm.edu

Tien Q. Duong, DOE Technology Development Manager

U.S. Department of Energy
E-mail: Tien.Duong@ee.doe.gov

Start Date: October 18, 2019

End Date: October 17, 2022

Project Funding: \$415,851

DOE share: \$340,681

Non-DOE share: \$85,170

Project Introduction

The next-generation battery innovations for EV without ICE will have to enable the vehicle to drive for long distances. Marginal improvements of state-of-art Li-ion technology cannot meet this challenge. Any “beyond Li-ion” technologies, which aim to achieve cell performance targets of $\geq 350\text{Wh/Kg}$, over 1000 cycles at C/3 rate, 15 year shelf life and $< \$100/\text{KWh}$ cost, will need a metallic Li anode ($\sim 3862\text{mAh/g}$). Applications of Li anodes in batteries are hindered by the dendrite formation during the battery operation leading to serious safety issues. Previous efforts to suppress the dendrite formation on lithium metal anodes by altering the electrolyte, modifying the Li surface, or optimizing the cell structure fell short because they did not solve the root causes of the dendrite formation during the interface shift of Li anodes during cycling. We propose to investigate interface shift, surface homogeneity and surface Li^+ concentration. Our work will focus on creating a dynamic protection layer during the interface shift to prevent dendrite formation throughout the battery operation, potentially enabling the commercialization of a safe metallic Li battery with a long cycle life. This is particularly important in a solid-state-electrolyte battery, since the interfacial changes between the Li anode and the electrolyte could create a physical gap which hinders the electrochemical reaction.

Objectives

The objectives of this project are to research, develop, and test lithium metal-based batteries that implement solid lithium-ion conductors equipped with a formed dynamic protection layer. The proposed project aims to enable safe, long cycle Li anodes achieving cell performance targets of 400Wh/Kg , over 100 cycles, 15-year shelf life and $< \$100/\text{KWh}$ cost.

Our efforts are to contribute an *in-depth* understanding of the Li interface and dendrite growth prevention to the field of Li metal batteries, which will pave the way for the eventual development of high energy density, low cost and long-lasting Li batteries. This advancement could be a crucial selling point for the greater adoption of electric vehicles (EV). This project will make possible the translation of fundamental research into the practical implementation of high energy Li anodes, enabling the eventual achievement of the cell performance targets.

Approach

The novelty of our approach is that we intend to mitigate the dendrite problem by creating a dynamic protection layer during the interface shift to prevent dendrite formation throughout the battery operation. Four

approaches will be explored: 1) Surface with homogeneous activity; 2) Artificial interface to “alloy” Li dendrites; 3) Dissolution and re-deposition of Li through re-distribution of Li-carrier complex; 4) Control local Li concentration.

Results

The challenge due to the COVID-19 pandemic remained throughout the FY 2021. The university only reopened fully on September 2021. But we managed to compete all milestones of FY 2021.

Based on our achievements in FY 2020, the Li anode with different dynamic surface protection layers were put in test in full solid state Li batteries. During FY 2021, we made major progress in the following areas:

1. Optimized and finalized test cell for a full solid state Li battery.
2. Continuing optimize the *in-situ* electrochemical optical cell for cross-section view.
3. Developed and demonstrated a long cycle 4.0 V full solid state Li battery.

Figure XVI.12.1(A) shows the two electrochemical cells for performance tests (right) and *in-situ* electrochemical optical cell for the observation of dendrite growth. The examples of dendrite observation are shown in (B).

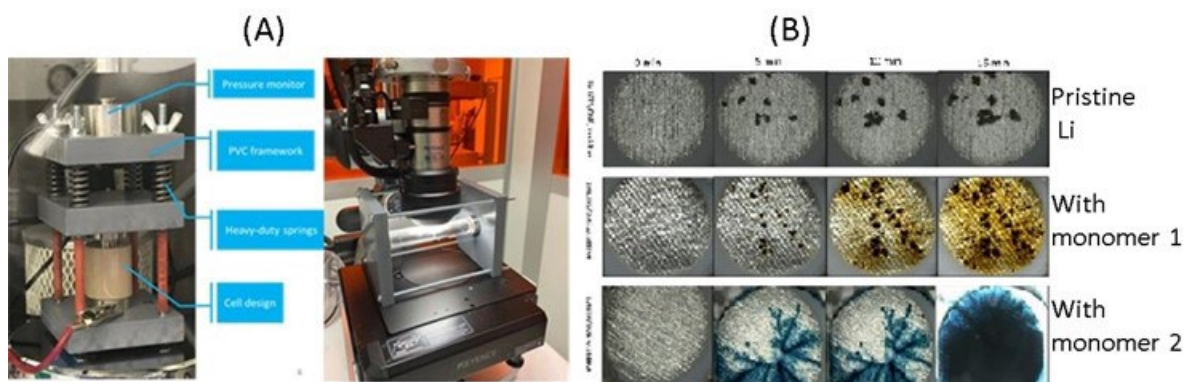


Figure XVI.12.1 (A) Full cell for full SS battery testing (left); in-situ optical cell (right); (B) comparison of pristine Li and Li anodes with formation of dynamic protective layers.

The most popular inorganic SEs are lithium thiophosphates which are good ionic conductors. However, the inherent instability at high potentials limits their application in the 4V batteries. Halide-based electrolytes have attracted ever-rising interest lately. Halides exhibit combined advantages of sulfides and oxides, including easy processability and (electro)chemical stability toward high-voltage cathodes. However, the poor reduction stability of halides in contact with lithium metal remains an open challenge. To tackle the problem, Li-Y alloys (Y=In, Sn, Ge) or metallic In to replace Li metal as anode, which sacrifices the cell overall energy density by lowering the operating potential.

In FY 2021, we constructed a kinetically stable interface by inserting an argyrodite buffer layer between Li metal and Li_3YCl_6 layer, a representative halide electrolyte. Argyrodite ($\text{Li}_6\text{PS}_5\text{Cl}$) was selected due to its fast ionic conduction, soft mechanical property, and more importantly, its ability to produce a kinetically stable interface in contact with Li metal. We demonstrate Li/Li symmetric cell with a polarization potential as low as 100 mV and a stable plating/stripping behaviour over 1000 h at 0.2 mA cm^{-2} , 0.2 mAh cm^{-2} . Moreover, $\text{LiNi}_{0.8}\text{Co}_{0.1}\text{Mn}_{0.1}\text{O}_2/\text{Li}$ full solid-state cell delivers a record-breaking high initial Coulombic efficiency of $> 87\%$. To the best of our knowledge, this is the first case to employ Li metal as anode in halide-based all-solid-state batteries.

To analyse the reaction products at the Li/LYCl interface, Li pieces and the as-synthesized white LYCl powder were hand-ground at a molar ratio of 3:1 (Figure II.9.L.2a), according to the stoichiometry of the idealized net reaction equation $\text{Li}_3\text{YCl}_6 + 3\text{Li} \rightarrow 6\text{LiCl} + \text{Y}^0$. After 20 minutes of grinding, the reaction product turned out to be black powder and the shiny lithium pieces became completely consumed (Figure XVI.12.2b). The corresponding X-ray diffraction (XRD) patterns are shown in Figure XVI.12.2c. Strong diffraction peaks attributed to LiCl were detected as labelled. The signal of yttrium metal is not significant, mainly caused by the low volume fraction of Y^0 compared to LiCl. In addition, Y^0 can immediately react with other species to form Y_2O_3 or $\text{Y}_2(\text{CO}_3)_2$ species. Therefore, a fast-growing and mixed ion/electron conducting interface is formed one way or another. Similarly, the reaction products at the $\text{Li}_6\text{PS}_5\text{Cl}/\text{Li}$ interface were investigated by mixing $\text{Li}_6\text{PS}_5\text{Cl}$ (LPSCl) powder and Li pieces at a molar ratio 1:8 (Figure XVI.12.2d), according to the net interfacial reaction $\text{Li}_6\text{PS}_5\text{Cl} + 8\text{Li} \rightarrow 5\text{Li}_2\text{S} + \text{Li}_3\text{P} + \text{LiCl}$. Lithium residues can still be observed from the greyish reaction products after 20 minutes (Figure XVI.12.2e). The XRD pattern (Figure XVI.12.2f) generally remain unchanged with only one additional peak assigned to Li_2S as labelled. The signal is rather weak, implying the reaction is self-limited and the reaction layer is rather thin. The dominant decomposition product, Li_2S , is an ionic conductor with low electronic conductivity, leading to a formation of a resistive interfacial layer. Regarding the other two decomposition products, Li_3P is a fast Li-ion conductor ($\sim 10^{-4} \text{ S cm}^{-1}$) and LiCl is less ionic conductive. Importantly, LiCl displays high interface energy against lithium, which can significantly suppress dendrite growth. Overall, a kinetically stable and ionic conducting interface can be expected between Li and LPSCl, just like the SEI layer formed in liquid electrolytes.

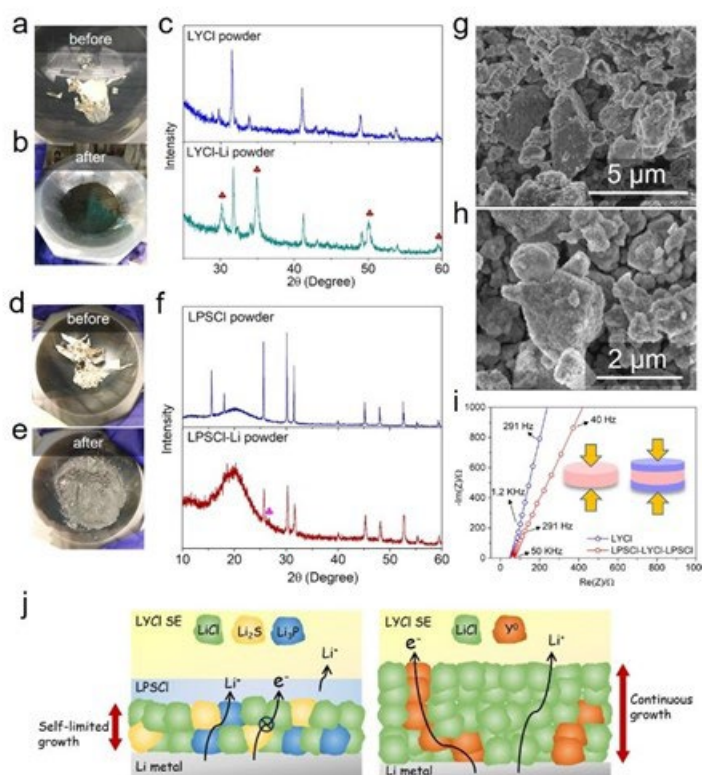


Figure XVI.12.2 Pictures of Li metal pieces and LYCl powder a) before and b) after hand grinding; c) corresponding XRD patterns of the reaction products. Pictures of Li metal pieces and LPSCl powder d) before and e) after grinding; f) corresponding XRD of the reaction products. SEM images of g) LPSCl and h) LYCl powder. i) Ionic conductivity measurement of LYCl pallet and LPSCl/LYCl/LPSCl composite pallet at room temperature. j) Schematic illustration showing the Li/LPSCl/LYCl design (left) and Li/LYCl design (right).

To verify the feasibility of LPSCl buffer layer, Li plating/stripping behaviour of symmetric cell was measured under various conditions. Long-cycling protocol is carried out to study the accumulative effect at the interface

during long-term operation (Figure XVI.12.3a). Li/LYCl/Li cell (control group) displayed an initial overpotential of ~ 600 mV and reach ~ 1500 mV after 60 h at a current of 0.2 mA cm^{-2} and capacity of 0.2 mAh cm^{-2} . The increased polarization indicated a build-up of reaction products that hinder the charge transfer at the Li/LYCl interface. Shorting was not observed throughout the process, since the as-formed thick and dense interlayer can act as a mechanical barrier to prevent lithium creeping through SE pallet. The electrochemical impedance spectra (EIS) evolution was also monitored during steady state (without charge/discharge) and after cycling (Figure XVI.12.3b). Typically, the high frequency region indicates the bulk conduction of SE while the low frequency region stands for the Li/SE interface. The overall impedance only increased slightly during rest, maybe attributed to the presence of a native contamination layer (composed of impurities like insulating Li_2O , Li_2CO_3 , etc.) on lithium surface. After cycling, the bulk contribution did not vary significantly while the resistance assigned to the interface dramatically increased to ~ 32000 ohms, more than three times higher compared to the steady state. After disassembling the cell, black reaction spots and cracks can be observed unevenly distributed on the lithium substrate. The fast interface evolution and the propagation of cracks were the primary cause for chemomechanical degradation and impedance increase. Figure XVI.12.3c shows the cycling performance of Li/LPSCI/LYCl/LPSCI/Li symmetric cell at the same testing condition. 25 mg LPSCI was screened out for the following study since it offered the best protection. The Li plating/stripping slightly increases from 50 mV to 100 mV over 1000 h (Figure XVI.12.3d). As shown in Figure XVI.12.3e, the corresponding impedance increases from 374 ohms to 379 ohms after cycling for 60 h, implying a formation of stable SEI layer and the layer would not cause a too high interface impedance.

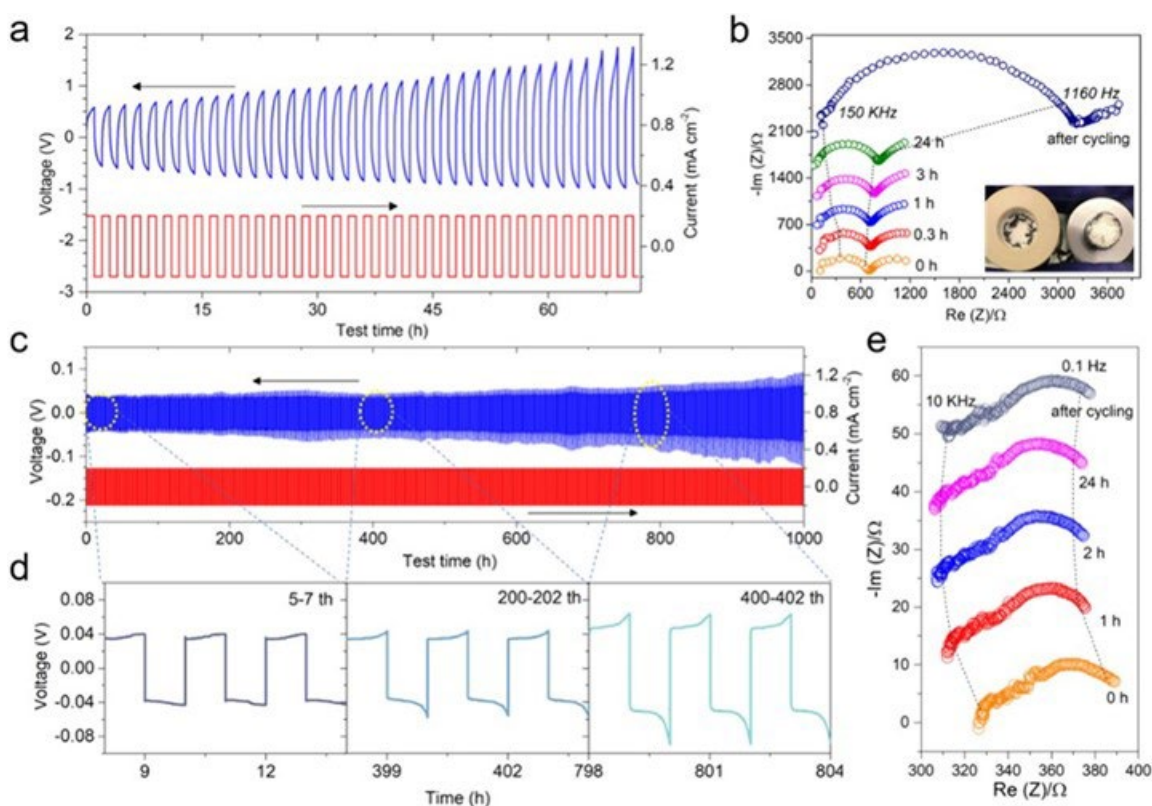


Figure XVI.12.3 a) Voltage and current profile of Li/LYCl/Li cell at 0.2 mA cm^{-2} , 0.2 mAh cm^{-2} . b) Corresponding EIS spectra during rest and after 60 h cycling. c) Voltage and current profile of Li/LPSCI/LYCl/LPSCI/Li cell at 0.2 mA cm^{-2} , 0.2 mAh cm^{-2} ; d) the details indicated by the areas marked by the yellow dashes. e) Corresponding EIS spectra during rest and after 60 h cycling.

The high oxidation stability of halide SEs allows the use of commercial 4V-class LiMO_2 ($\text{M}=\text{Ni}, \text{Co}, \text{Mn}, \text{Al}$) cathodes without any protective coating layer. To investigate full cell performance, cathode composite was made by hand grinding LYCl SE, bare $\text{LiNi}_{0.8}\text{Co}_{0.1}\text{Mn}_{0.1}\text{O}_2$ (NCM-811) powder, and conductive carbon at a weight ratio of 60:30:10. The charge/discharge voltage profiles of NCM-811/LYCl/Li full cell and NCM-

811/LYCl/LPSCl/Li full cell were compared in Figure XVI.12.4a-b. The current density is 0.1 mA cm^{-2} and the loading of NMC-811 is 6 mg cm^{-2} . At the initial cycle, NCM-811/LYCl/Li full cell exhibited a high charging capacity of 255 mAh g^{-1} and a low Coulombic efficiency (CE) of 65%. In the following cycles, the electrochemical polarization continuously increased. At the 12th cycle, the charging curve showed a long voltage plateau at 4.05 V and failed to reach the upper cut-off voltage of 4.3 V. This could be caused by continuous reaction between freshly deposited lithium and LYCl during delithiation process. By contrast, the NCM-811/LYCl/LPSCl/Li full cell delivered a capacity of 181 mAh g^{-1} and 183 mAh g^{-1} for the first two cycles, with a CE of 87% and 98%, respectively (Figure XVI.12.4b). As marked in the blue circle, no additional slope occurs prior to reaching the charge plateau, indicating no formation of space charge layer at the NCM-811/LYCl interface. A higher active material content leads to an even higher ICE of 89%. Typical curves representing the three-phase transition process of NCM-811 material can be clearly observed from dQ/dV curves (insert Figure XVI.12.4b) and CV profiles (Figure XVI.12.4c). The EIS evolution of full cell during one charge/discharge cycle (Figure XVI.12.4d) validates high interfacial stability of both LYCl/NCM-811 interface and LPSCl/Li interface. The full cell displayed stable cycling with a capacity retention of 91 % and a high CE of 99.7 % after 100 cycles (Figure XVI.12.4e). Figure XVI.12.4f displayed the rate capability and a reversible discharge capacity of 90 mAh g^{-1} was achieved at 1C rate.

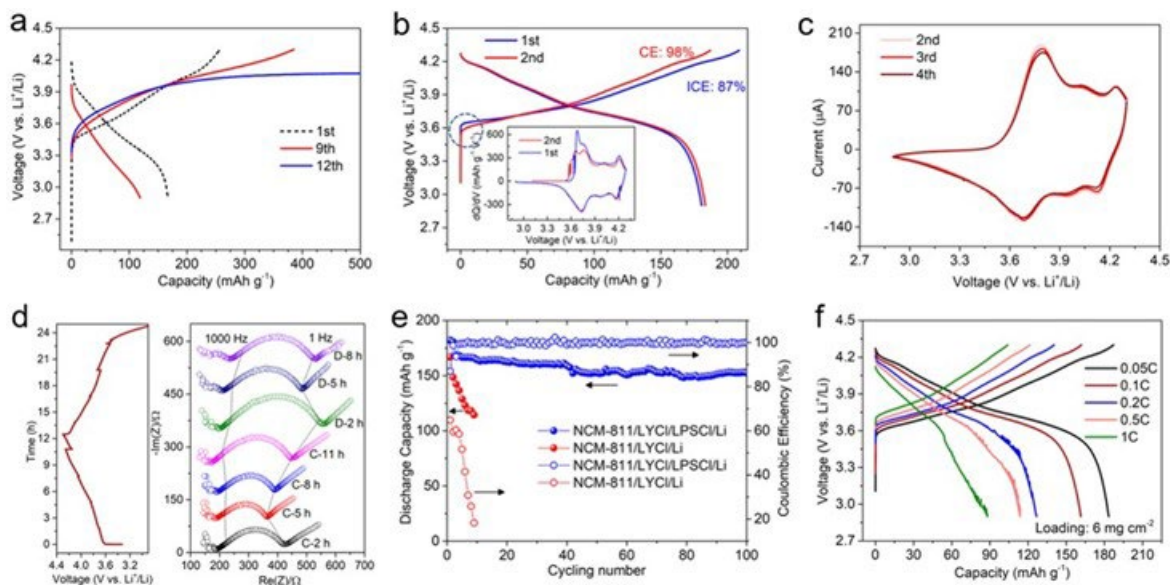


Figure XVI.12.4 a) Charge/discharge profiles of NCM-811/LYCl/Li cell at 0.1 mA cm^{-2} . Electrochemical performance of NCM-811/LYCl/LPSCl/Li cell: b) initial two charge/discharge profiles at 0.1 mA cm^{-2} (corresponding dQ/dV curves shown insert); c) CV profiles at 0.02 mV s^{-1} ; d) impedance evolution during one charge/discharge cycle. e) cycling performance at 0.1 mA cm^{-2} ; f) rate capability from 0.1 C to 1 C.

The thickness of LYCl pallet and LYCl/LPSCl pallet before cycling is measured to be $\sim 431 \text{ }\mu\text{m}$ (Figure XVI.12.5a) and $\sim 495 \text{ }\mu\text{m}$ (Figure XVI.12.5b), respectively. Thus, the LPSCl layer can be roughly estimated as $\sim 64 \text{ }\mu\text{m}$. According to the cross-sectional SEM image shown in Figure XVI.12.5c, after cycling, the thickness of LPSCl is about $70 \text{ }\mu\text{m}$, which is almost the same compared to before cycling. As indicated in Figure XVI.12.5d, the surface morphology of LYCl shows clear microcracks after cycling. By contrast, the LPSCl surface (Figure XVI.12.5e) is much smoother and exhibits no cracks throughout cycling, proved to be a good buffer layer. This should be ascribed to the ductile nature of sulfides, which can withstand higher local strain compared to halide electrolytes. Moreover, the intactness of LPSCl layer also indicates the decomposition reaction at the LPSCl/Li interface is well constrained, reflecting a self-limiting nature. As shown in Figure XVI.12.5f-i, a larger view of the LYCl/LPSCl interface after cycling is studied by SEM-EDS analysis. A clear transition region is presented by the distinguished difference of element distribution of sulfur, yttrium, and chloride (please ignore the small region in the upper middle area caused by powder contamination during

sample preparation process). This unveils no chemical reaction or elemental diffusion occurred at the LYCl/LPSCl interface during cycling. As shown in Figure XVI.12.5j-m, a distinct LPSCl/Li metal interface was maintained after cycling, with no lithium dendrites or decomposition-induced thick SEI formation.

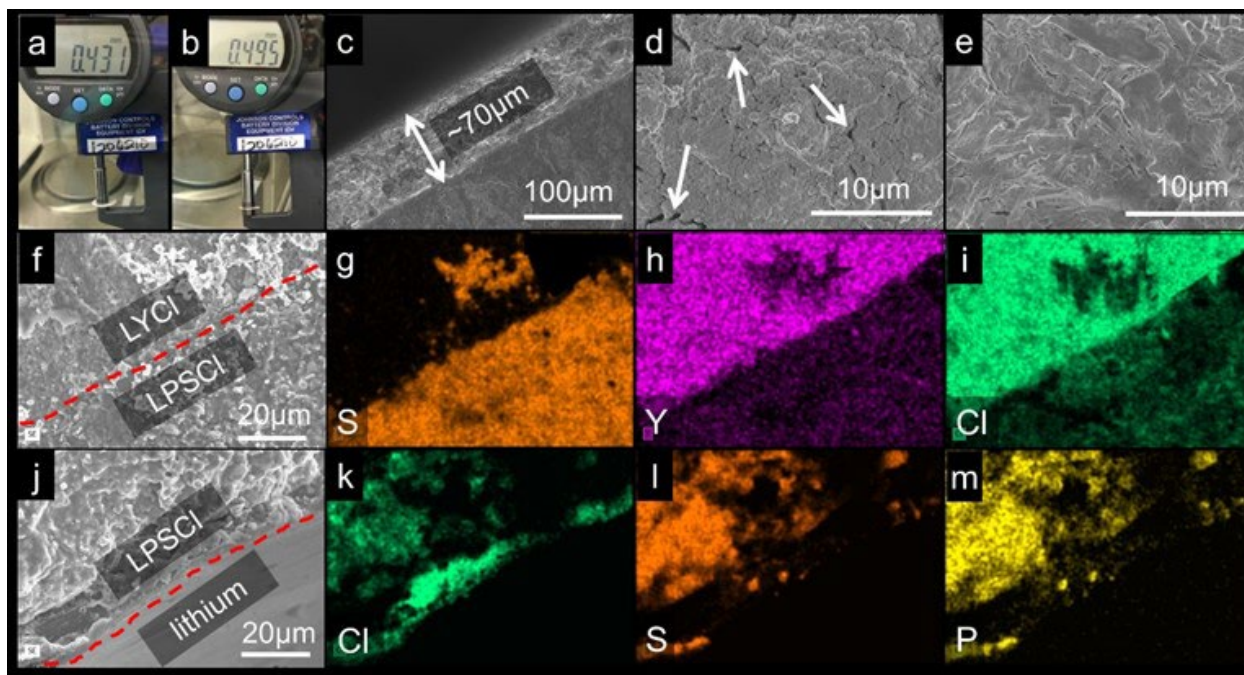


Figure XVI.12.5 Thickness measurement of the cold pressed a) LYCl pallet and b) LPSCl-LYCl pallet before cycling; after cycling: c) cross-sectional SEM image of the LPSCl-LYCl layer, top-view SEM images of d) LYCl surface and e) LPSCl surface; f) cross-sectional SEM image and g-i) elemental mapping analysis of the LYCl/LPSCl interface; j) cross-sectional SEM image and k-m) elemental mapping analysis of the LPSCl/lithium interface.

Conclusions

Using the optimized test cell, for the first time, protected lithium metal was employed as anode in a halide-based all-solid-state battery. Argyrodite was selected as protection layer, due to its capability to form kinetically stable SEI layer in contact with Li and also form good hetero contact with halide electrolyte. The $\text{LiNi}_{0.8}\text{Co}_{0.1}\text{Mn}_{0.1}\text{O}_2/\text{Li}$ full cell displayed remarkably improved Coulombic efficiency and cycling stability. In practice, this offers a universal strategy to apply the class of halide-based electrolytes in all-solid-state lithium.

Key Publications

1. Weixiao Ji, Dong Zheng, Xiaoxiao Zhang, Tianyao Ding, Deyang Qu, “Kinetically Stable Anode Interface for Li_3YCl_6 -based All-Solid-State Lithium Batteries” *J. Mat. Chem. A* 9(2021)15012–15018.

Acknowledgements

The PI and his staff researchers are grateful to Patricia Smith, Colleen Butcher and Tiffany Zachry for their guidance and supports. Such helps were extremely important to the success of our research during the pandemic of COVID.

XVI.13 Composite Solid Ion Conductor with Engineered Lithium Interface (Wildcat Discovery Technologies)

Dee Strand, Principal Investigator

Wildcat Discovery Technologies
6255 Ferris Square, Suite A
San Diego, CA 92121
E-mail: dstrand@wildcatDiscovery.com

Gang Cheng, Principal Investigator

Wildcat Discovery Technologies
6255 Ferris Square, Suite A
San Diego, CA 92121
E-mail: gcheng@wildcatdiscovery.com

Tien Q. Duong, DOE Technology Development Manager

U.S. Department of Energy
E-mail: Tien.Duong@ee.doe.gov

Start Date: October 1, 2019

Project Funding: \$1,529,792

End Date: September 30 2021

DOE share: \$1,223,833

Non-DOE share: \$305,959

Project Introduction

Successful widespread commercialization of electric vehicles is contingent upon development of safe high energy density batteries capable of long cycle life. Lithium metal affords the highest theoretical capacity (3,860 mAh/g) and lowest electrochemical potential (-3.04V vs SHE), which offers the highest specific energy density of anode materials today. While Li-ion batteries are capable of delivering energy densities of 400-600 Wh/kg, the development of lithium metal batteries – such as Li-S and Li-air may boost this number up to 650 and 950 Wh/kg, respectively. However, significant progress towards the passivation of lithium metal must occur before the energy density benefit can be realized. Issues with lithium dendrite formation, anode volume expansion, and continuous solid electrolyte interphase (SEI) build-up often result in significant safety concerns, high cell resistance, and poor cycle life. The intrinsic high reactivity between lithium metal with conventional lithium ion electrolytes (organic carbonate-based solvents) makes it extremely difficult to overcome these problems. In this project, Wildcat seeks to perform focused, fundamental research and development on composite polymer/ceramic electrolytes and protected lithium metal anodes to develop an all solid state lithium metal battery that achieves the DOE requirements to enable commercialization. Wildcat will leverage its high throughput battery platform and explore a broad composite electrolyte compositional space. Additionally, Wildcat will screen thousands of inorganic and organic coatings for lithium metal protection using in situ liquid methods and translate the best results to all solid cells.

Objectives

The project objective is to develop a composite polymer/ceramic electrolyte and protected lithium metal anode for an all-solid-state lithium metal battery that achieves the DOE requirements for performance and that enables the potential commercialization of this technology. Successful widespread commercialization of electric vehicles is contingent upon development of safe high energy density batteries capable of long cycle life. Lithium metal affords the highest theoretical capacity (3,860 mAh/g) and lowest electrochemical potential (-3.04V vs SHE) and offers the highest specific energy density of anode materials today. However, significant progress towards the passivation of lithium metal must occur before the energy density benefit can be realized. The intrinsic high reactivity between lithium metal with conventional lithium-ion electrolytes (organic carbonate-based solvents) makes it extremely difficult to overcome these problems. The proposed composite polymer/ceramic electrolyte and a protected lithium metal anode will enable an all-solid-state lithium metal

battery. It is expected that the outcomes from this effort will deliver a safe all solid-state lithium metal pouch cell with over 350 Wh/kg and over 1,000 cycles (C/3) with the cost estimate below \$100/kWh.

Approach

The project approach involves (1) identifying a suitable combination of solid ion conductor, polymer, and additive that minimizes overall interfacial impedance between the polymer electrolyte and solid ion conductor, and (2) identification of stable Li-metal protection agent or combination of agents that show enhanced cycling performance (relative to a non-protected system) using the down-selected cell architectures.

Results

Development of Composite Electrolyte

At the beginning of 2021, the main efforts to improve the composite electrolyte were in the following three areas: 1) development of high voltage polymer stable at $>4.3\text{V}$ vs. Li; 2) improvement of ionic conductivity of Composite Solid Electrolyte (CSE) membrane; 3) development of high ceramic loading ($>75\text{wt}\%$) CSE membrane with good processibility.

1. Development of high voltage polymer composite electrolyte

In terms of the HV stability, Wildcat screened different polymer types and Figure XVI.13.1A shows linear sweep voltammetry (LSV) plots for down-selected candidates. The LSV plots show that the PVDF-polymer with and without the inorganic ceramic has the best HV stability. The PEO based composite electrolyte shows residual current due to reactivity starting around 3.4V and then higher currents above 4.3V . Based on this work, we continued to develop the composite ceramic polymer electrolyte with PVDF instead of PEO. After testing the voltage stability, we also screened different concentrations of the lithium salt (Figure XVI.13.1B). As the salt concentration is increased to $32\text{wt}\%$ for the PVDF polymer composite system the highest ionic conductivity is obtained, reaching values similar to that of the LATP control. Further work is currently underway to improve the ionic conductivity using coupling agents to minimize the interfacial impedance between the ceramic and PVDF polymer. Next, we investigated several different compositions of the PVDF polymer based composite electrolyte for their electrochemical and mechanical properties. Figure XVI.13.2A shows that as the polymer concentration is increased, the ionic conductivity of the composite electrolyte is decreased, while maintaining the same ceramic loading content. Alternatively, Figure XVI.13.2B shows that as the polymer concentration increases, the shear modulus of the films improves. The results suggest that there is an interplay between the ionic conductivity and the mechanical properties of the composite solid electrolyte material.

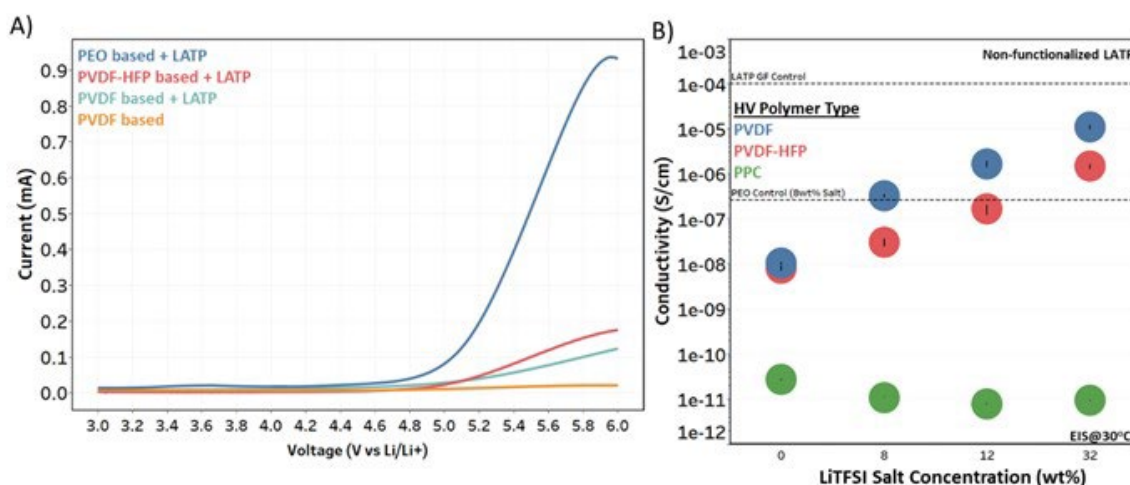


Figure XVI.13.1 A) Linear sweep voltammograms of different polymer based composite electrolytes, and B) ionic conductivity (30oC) results for various HV polymers with increasing salt concentration.

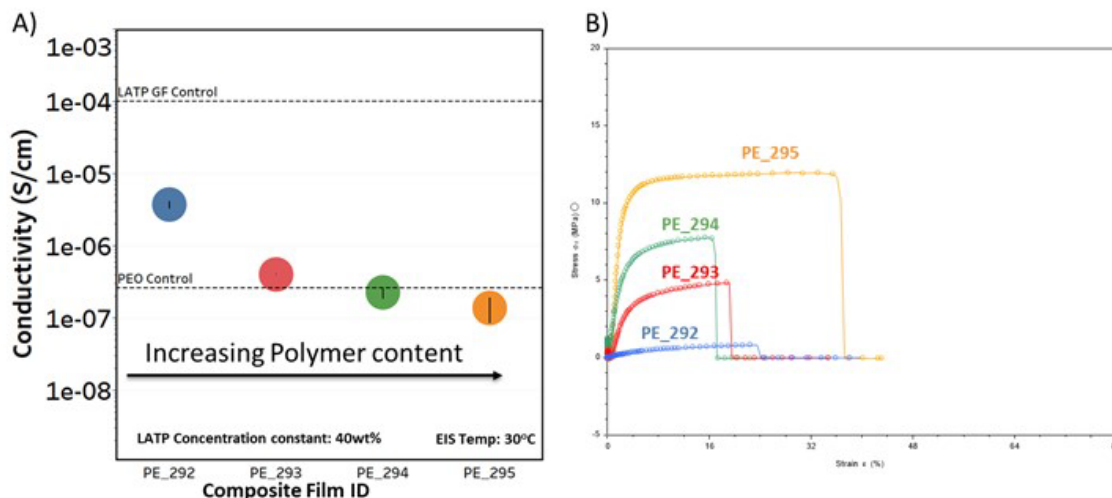


Figure XVI.13.2 A) Ionic conductivity (30°C) as a function of increasing PVDF polymer content and B) representative shear modulus plots

In the previous full cell integration study, it was found that the charge performance can be improved by varying the PVDF type (i.e., chain length, functionality, branching, etc.). Based on those results, this was further investigated. Different polymers were tested to determine the composite ceramic-polymer electrolyte conductivity as well as full cell performance integration. Figure XVI.13.3A shows room temperature ionic conductivity for 5 different PVDF polymer types. These types vary in chain length and functionality. While the results do not show significant improvement in ionic conductivity, the composite polymer-ceramic electrolytes processability and performance in full cell performance varied greatly which is shown in Figure XVI.13.4(a). For the full cell test, composite electrolyte containing PVDF-A had initially better charge rate performance while composite electrolyte PVDF-C had better initial cycling performance. Based on processability as well as their initial promising full cell performance, we decided to take two of the polymer types (Type A and C) and varied the weight percent ratio to see if we can further improve full cell performance. We also checked their ionic conductivity which is shown in Figure XVI.13.3B and selected the one with best ionic conductivity for the full cell test.

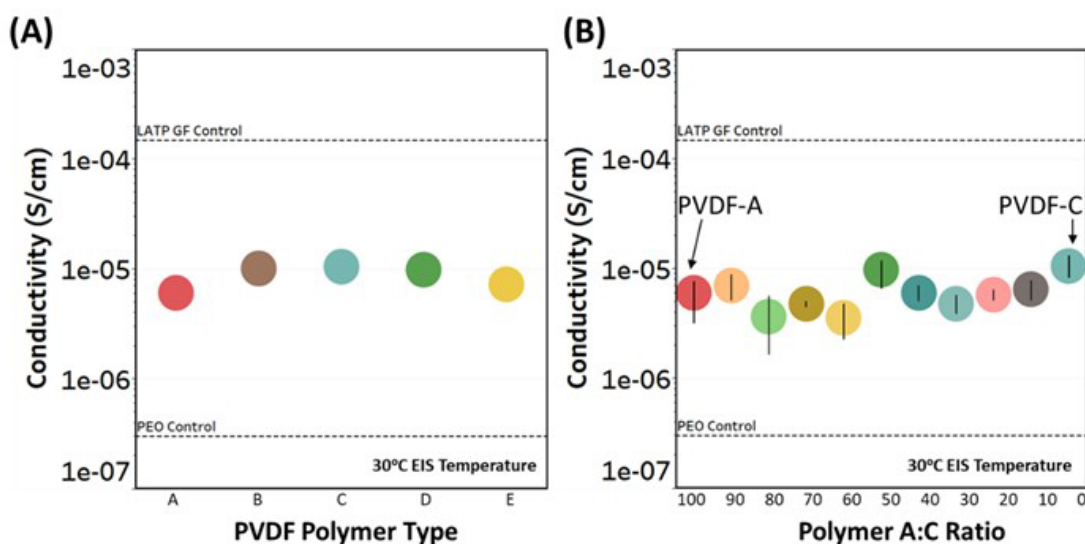


Figure XVI.13.3 (A) Electrochemical impedance spectroscopy data for different PVDF polymer types in the composite ceramic-polymer electrolyte and (B) Electrochemical impedance spectroscopy data for various ratios for blended PVDF types A and C.

As we investigated different type of PVDF polymers for their impact on ionic conductivity of ceramic-polymer composite as well as their full cell performance. We also investigated interaction between Li salt and promising type of PVDF polymers aiming to further improve the ionic conductivity of ceramic-polymer composite electrolyte (1.6×10^{-7} S/cm at 30°C).

Various approaches have been tried to improve the ionic conductivity of the polymer electrolyte. Figure XVI.13.4a shows the conductivity of 9 different polymers that have the same salt/polymer weight ratio (32:68) and the same polymer component (PVDF-A). Different colors represent different lithium salts in the formulations. The specific lithium salt showed a large impact on the polymer conductivity. Five Li salts showed much improved conductivity over LiTFSI, which is the salt used in the previous baseline polymer electrolyte. As a result, we identified several promising salt such as LiFSI, LiOTf, LiClO₄, showing 5-10 times higher conductivity than LiTFSI. The results suggest that anion of the Li salt could significantly impact how Li⁺ interacts with polymers by changing the crystallinity of the polymer, which could result in a very different Li⁺ pathway within the polymer phase.

Organic or inorganic fillers had been widely used to alter crystallinity of polymer in many industrial applications. Another approach taken was to investigate several PVDF copolymers with different crystallinities, possibly improving the ionic conductivity of polymer electrolyte. Figure XVI.13.4b shows the results of this approach. When we replace the homopolymer PVDF to PVDF-HFP copolymer with the same exact weight ratio of LiFSI (32wt%LiFSI/68wt%polymer), the ionic conductivity of copolymer is almost 100 times higher ($\sim 1.8 \times 10^{-5}$ S/cm). However, introduction of other organic or inorganic fillers did not show significant beneficial effects as expected.

We also investigated on the salt/polymer ratio effect on the polymer electrolyte conductivity, shown as Figure XVI.13.4c. We down selected the most promising polymer electrolytes in earlier studies for this study. As expected, the higher salt concentration, the higher polymer conductivity. It is worth to noting that the resulting polymer electrolyte still showed good processibility and film quality even in the presence of up to 50wt% of LiFSI.

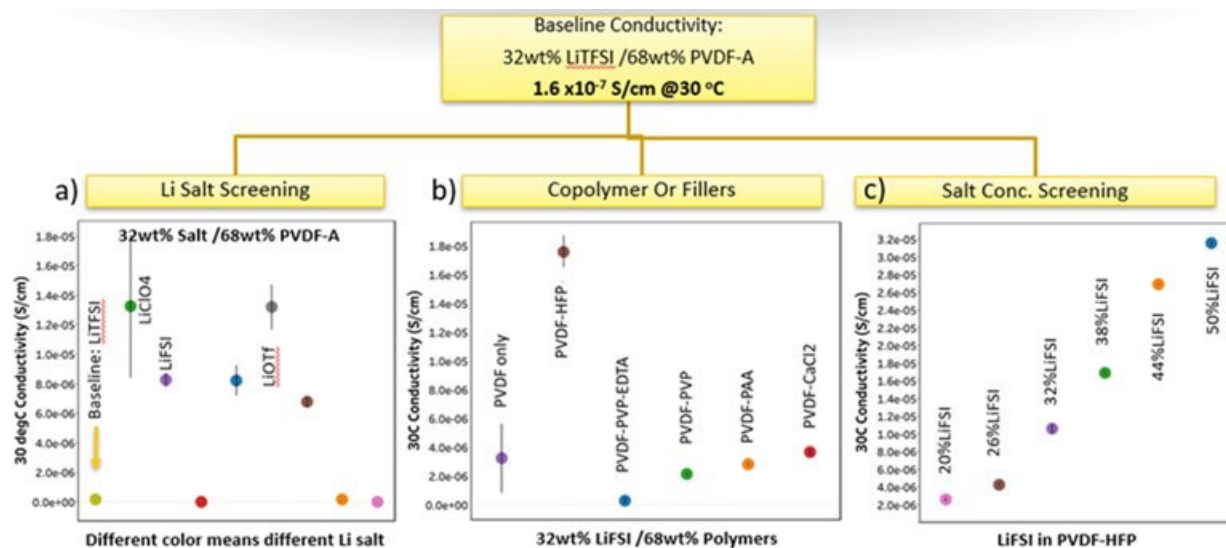


Figure XVI.13.4 Screening of various polymer electrolyte using Stainless Steel/Stainless Steel blocking electrode. a) Li salt screening; b) copolymer or filler screening; c) salt concentration screening.

Over the last quarter, we developed methods to fabricate composite polymer/ceramic electrolyte with high weight % (>75) of LLZTO powders which is so called “polymer in ceramics” composite electrolyte. The LLZTO ceramic particles serve as the primary phase to provide the bulk ionic conductivity and mechanical strength. The small portion of polymer electrolyte provides flexibility of the resulting composite electrolyte.

Because the intrinsic properties and surface modification of LLZTO play a crucial role in the final conductivity of the composite electrolyte, Wildcat team revisited the LLZTO synthesis and developed an improved synthesis method to better control the particle size of LLZTO.

As our previous LLZTO synthesis produced a large particle size with low yield, we wanted to develop a more efficient synthetic procedure to obtain uniform small particle size with high yield. After systematic evaluation of the amount of Li source material (Figure XVI.13.5a) and sintering condition, we developed a one-step annealing process to produce much smaller LLZTO particles with good batch to batch reproducibility. The XRD pattern in Figure XVI.13.5b shows all the identified peaks can be perfectly indexed to the standard pattern of cubic garnet structure, indicating high purity of the LLZTO powder. SEM images in Figure XVI.13.5c reveal most of the particles of the LLZTO powder are smaller than 2 μm , with the majority at the nanoscale. Compared to the previous LLZTO powder ($\sim 20\ \mu\text{m}$), the smaller particle size significantly increases the active surface area that is needed to create interactions between polymer and ceramic powders. With the simplified annealing and mixing procedure, the new process can provide over 1kg of LLZTO powder per day based on current setup and can be scaled up easily in the future.

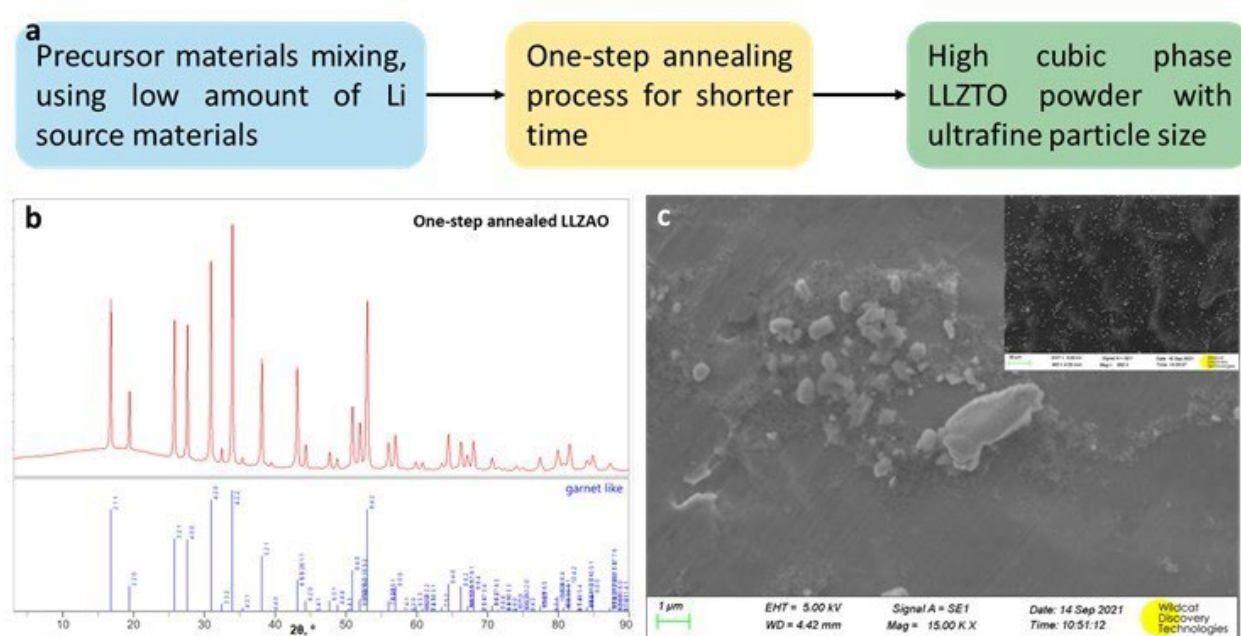


Figure XVI.13.5 Synthesis of ultrafine LLZTO powder. a. Flow chart of LLZTO synthesis process. b. XRD pattern of one-step sintered LLZTO, in consistent with standard cubic garnet structure. c. SEM image LLZTO powder, revealing the particle size lower than 2 μm .

Although LiFSI provides higher ionic conductivity than LiTFSI in PVDF based polymer electrolyte, the benefit of higher ionic conductivity was not observed in all solid-state cell possibly due to higher interfacial resistance. Indeed, we did observe higher overpotential in Li//CSE//Li symmetric cells when using LiFSI/polymer electrolyte. Therefore, we finally selected LiTFSI as the Li salt to fabricate high ceramic loading solid composite electrolyte.

After studying various of mixing methods as well as composition of mixing solvents, we found that polymer electrolyte films can be easily made by mixing specific PVDF powders and LiTFSI powder in specific solvents. The resulting slurry can be directly casted on glass plates to yield the white-colored semi-transparent film after the solvent is evaporated (Figure XVI.13.6a). To optimize the formulation, Wildcat studied different concentrations of LiTFSI in the polymer. As shown in Figure XVI.13.6b, the optimal LiTFSI/polymer ratio in this case is 3, which offers ionic conductivity around $2 \times 10^{-4}\ \text{S/cm}$. As we further increase the ratio of LiTFSI/polymer, gel formation occurs. Higher ratios can possibly be achieved without gel formation if different types of mixing solvents are used. To exclude the possible effect of solvent contribution to the Li^+

conductivity, the polymer electrolyte was further dried using an aggressive drying process (72h at 70 °C under vacuum). However, the conductivity remains at 10^{-4} S/cm. The slightly decreasing conductivity is likely due to the polymer structure damage caused by aggressive drying conditions.

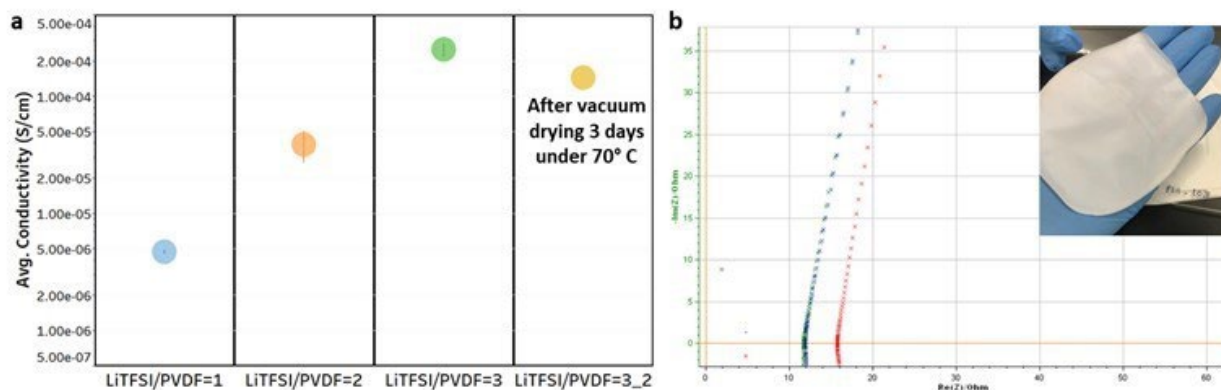


Figure XVI.13.6 High lithium salts concentration for polymer electrolyte. a. Impedance spectra and Digital image of prepared free-standing polymer electrolyte with optimized condition. b. Conductivity comparison between polymers with different formula and drying time.

The motivation on designing “polymer in ceramics” composite electrolyte is to increase the mechanical strength to suppress Li dendrite growth. However, as the amount of LLZTO ceramics in the composite electrolyte increases ($>75\text{wt}\%$), the composite electrolyte often turns into powder. To overcome this challenge, Wildcat developed a dry mixing method to produce a thin film by introducing small amount of film forming additive (Figure XVI.13.7a). The low concentration of film forming additive does not negatively affect ionic conductivity but significantly improves the flexibility of the solid composite electrolyte membrane. Following this strategy, Wildcat successfully fabricated stand-alone solid composite electrolyte membranes with thickness of $50\text{ }\mu\text{m}$ (Figure XVI.13.7b). The Li^+ diffusion pathway in the composite electrolyte was achieved due to surface reactions between polymer electrolyte and LLZTO particles, leading to the high ionic conductivity. The composition of the LLZO-LiTFSI-PVDF was then investigated to approach optimal room-temperature conductivity. If the LiTFSI/PVDF mass ratio is increased to specific values, the highest ionic conductivity of $8 \times 10^{-4}\text{ mS/cm}$ was obtained (Figure XVI.13.7c) at room temperature.

Furthermore, we studied the lithium-ion conductivity temperature. A major factor influencing the ionic conductivity at different temperatures is the activation energy for faster ion mobility because it corresponds to the energy barrier for ionic conduction. The activation energies E_a for the conduction were evaluated using the equation

$$\sigma_T = \sigma_0 \exp\left(-\frac{E_a}{k_B T}\right)$$

where σ_T is the total conductivity, σ_0 is the pre-exponential parameter, T is absolute temperature, E_a is the activation energy and k_B is the Boltzmann constant. The E_a for conduction (Figure XVI.13.7e), is then calculated from the slope of an Arrhenius plot. The E_a of our composite electrolyte is only 0.11 eV , which is much lower than most solid-state electrolytes ($0.2 \sim 0.3\text{ eV}$), which means that the ionic conductivity of our composite electrolyte is much less temperature dependent. Shown in Figure XVI.13.7d, the ionic conductivity of our solid composite electrolyte could still reach up to $4 \times 10^{-4}\text{ mS/cm}$ even at 0°C .

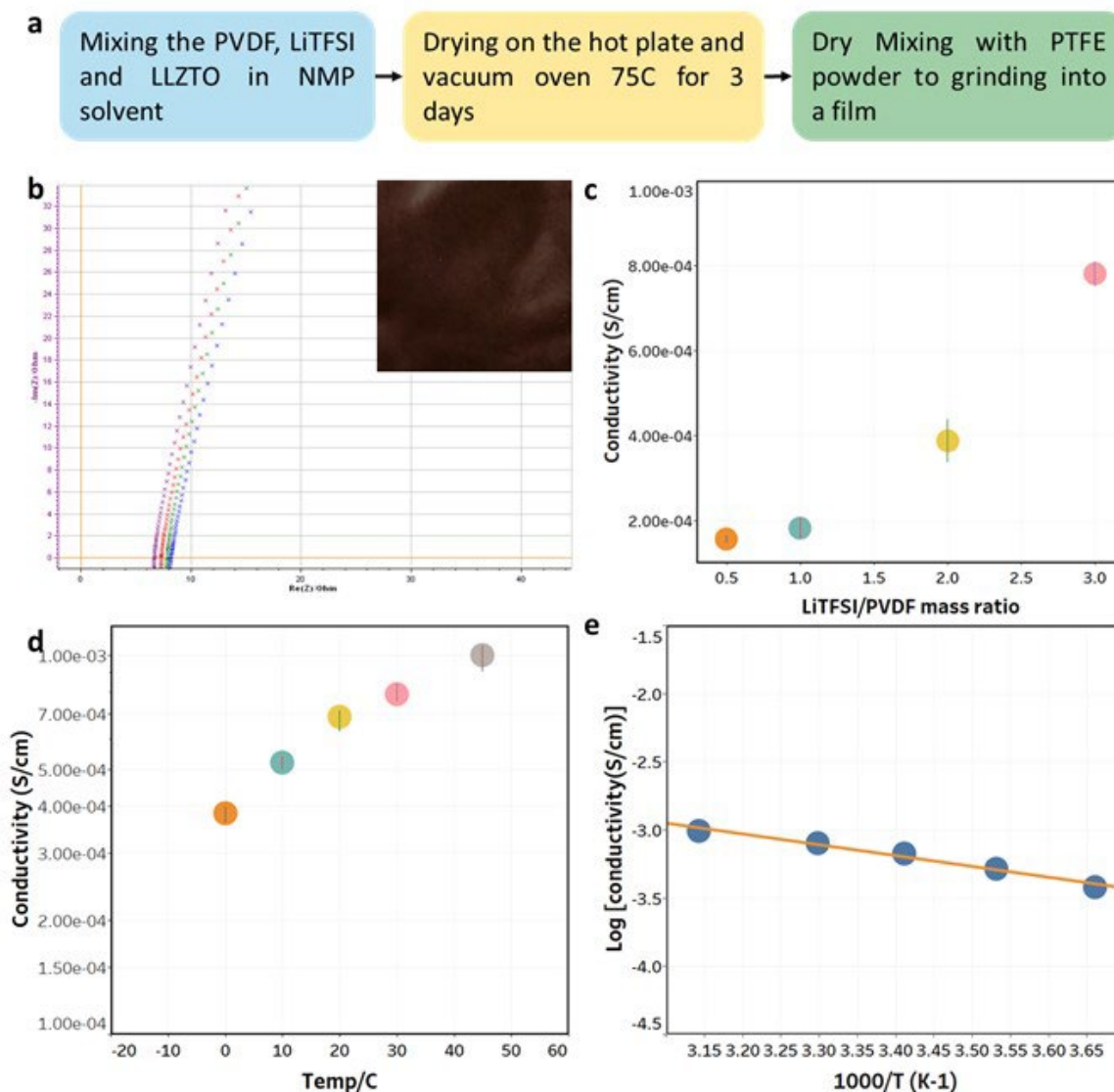


Figure XVI.13.7 Composite electrolyte conductivity. a. Flow chart of composite electrolyte film preparation. b. Impedance spectra and digital photo of prepared composite electrolyte film with optimized formulation. c. The effect of LiTFSI/PVDF mass ratio on the room-temperature conductivity. d. The composite electrolyte conductivity under different temperature. e. Arrhenius plot of composites electrolyte, revealing the low activation energy of ~0.11 eV.

In the future, Wildcat will continue to develop high ceramic % composite solid electrolyte and integrate it into all solid-state battery using protected Li metal as anode.

Li Metal Screening

During the last year of the project Wildcat focused on 1) demonstrating enhanced Li/Li cell cycling using liquid electrolyte and 2) investigating the interface between lithium metal and solid-state electrolyte materials, mainly on LATP based polymer composite. Based on the liquid electrolyte screening results, several promising artificial SEIs for Li metal had been applied to Li//SSE(LATP based)//Li cell testing shown as Figure XVI.13.8. As a result, several promising artificial SEIs identified in liquid electrolyte also showed lower interfacial resistance comparing to the baseline cell (dark blue, no lithium metal treatment).

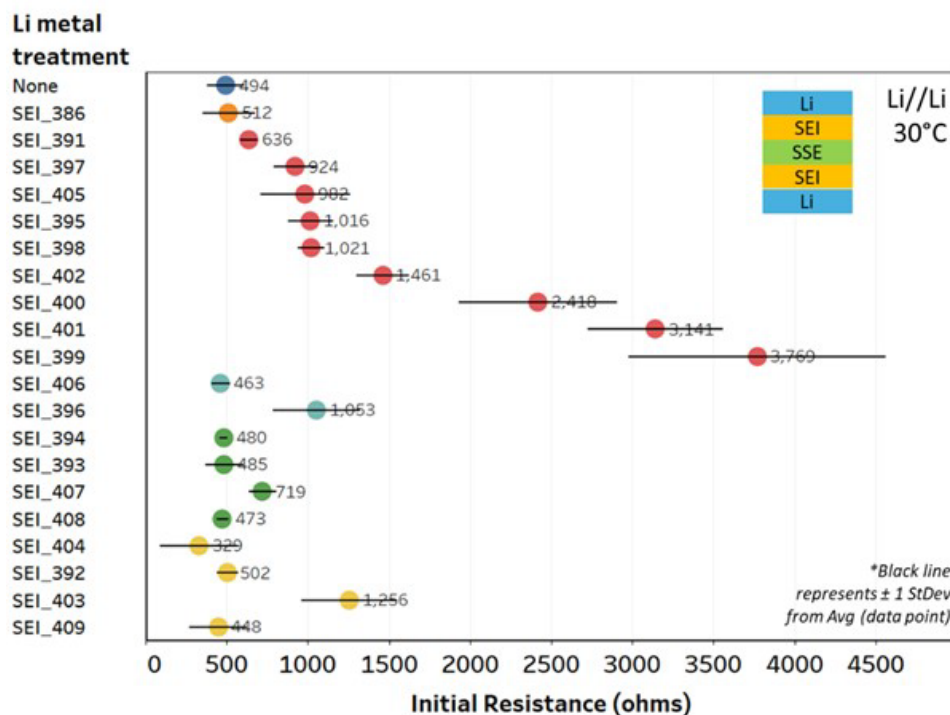


Figure XVI.13.8 EIS of Li/Li symmetric cells using an SSE composite electrolyte with and without Li metal protection. The cell format is shown in the top right. The average of multiple cells is shown as a colored circle, the average resistance labeled and the black line represents ± 1 standard deviation from the average. The various colors represent various families of additives tested (legend not shown).

With the focus on SSE composite electrolyte shifting towards LLZTO based solid composite electrolyte, we used the previously developed Li/SSE/Li symmetric cell to revisit some of artificial SEIs using LLZTO/PVDF based solid composite electrolyte. In a Li/Li symmetric cell format, lithium metal protection treatments were initially screened using EIS immediately after a cell is built (analysis and interpretation of the collected EIS were shown in an earlier quarterly report). Figure XVI.13.9 shows the initial resistance of Li/Li cells using various families of protection additives (salts, organics, etc.) represented in different colors and various types of SSE (PVDF, etc.) represented in different shapes (the legends for these are not included). The baseline system (labeled as “None”) shows a range of resistance from ~250 to 1250 ohms depending on the SSE used in the cell. The relatively wider range of cell resistance suggests that the untreated Li surface presents great challenges in batteries due to its inhomogeneous nature. Depending on the protection method, the repeatability of the interfacial resistance varies (look at the size of the black error bar) - for the better performing protection additives (see ones with lower initial resistances) the repeatability of the system is good while it is worse for higher resistance systems. In the past, we have evaluated over 500 different conditions of Li surface treatment by introducing various of reactive additives onto the Li surface. The protection additives in the green family showed significantly reduced resistances compared to other systems and the baseline system. This system was further explored (ratio of additives changed, etc.) to optimize its performance. Using an optimized additive system, the initial resistance of this system was measured at ~50 ohms compared to the baseline system with an average of ~700 ohms using the same SSE. This reduced resistance should directly translate to systems where current is passed between the Li metal electrodes.

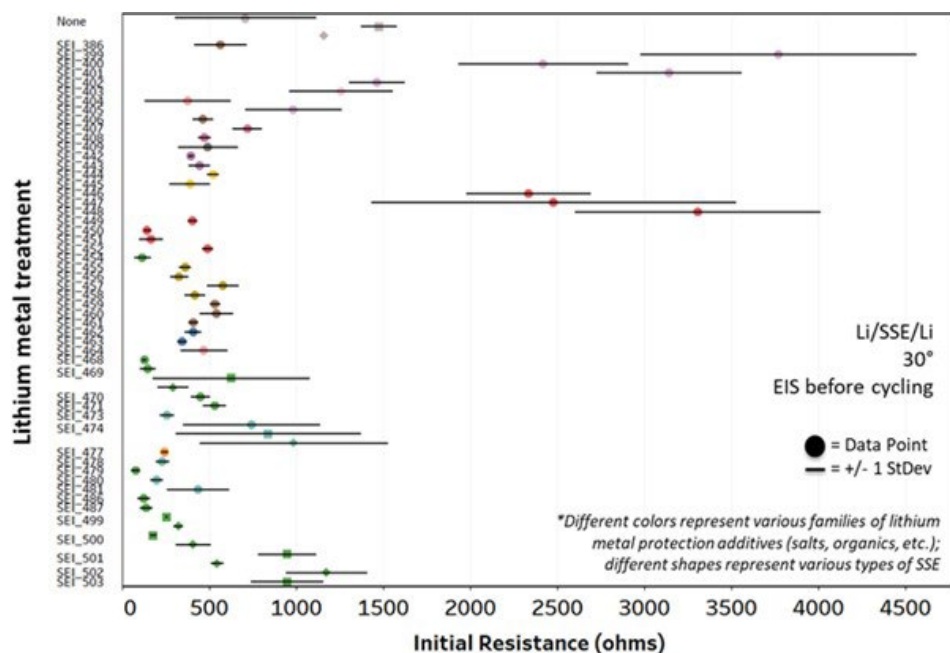


Figure XVI.13.9 Screening of protected lithium metal anodes using Li/Li symmetric cells. The different colors represent various families of lithium metal protection additives (salts, organics, etc.) and the different shapes represent various types of SSE used in the cell.

After the initial resistance is collected in the cells, they are subjected to cycling at 25°C using a plating/stripping current density of 1.0mA/cm² for one hour. Figure XVI.13.10 shows the plating/stripping voltage profile for a representative protected lithium metal anode (SEI_469 from Figure XVI.13.9) and the baseline system using the same SSE. The protected lithium metal anode shows flat voltage profiles and relatively low overpotentials (~10-20 mV) even after cycling for 300 hrs. In contrast, the baseline system shows dramatic and sporadic increases in voltage that occur throughout the cycling. These are likely indicative of lithium metal dendrite formation which causes hard/soft shorts to occur in the Li/Li symmetric cell system. With the promising results in Li//SSE//Li symmetric cycle life testing, the protected Li metal anode is being tested in Li//SSE//NMC all solid full cells next.

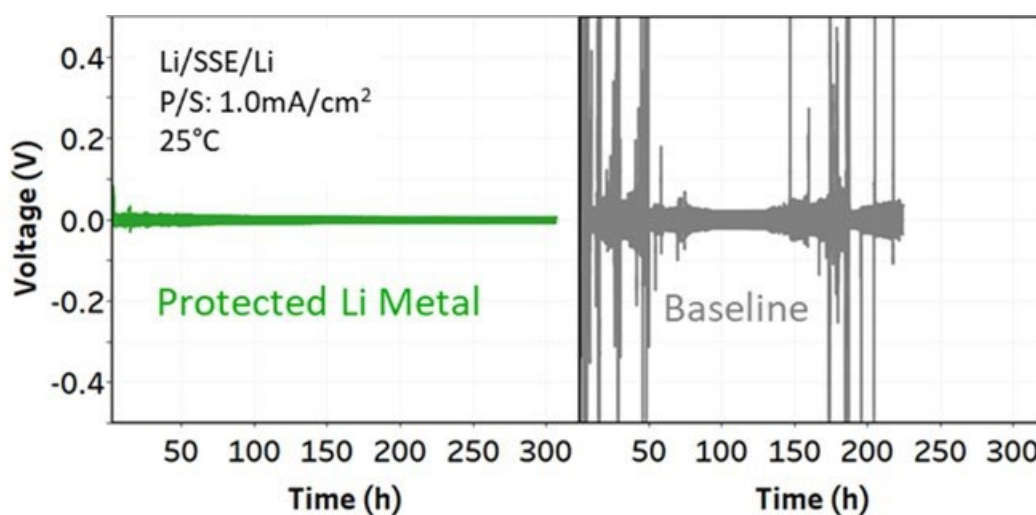


Figure XVI.13.10 Long-term Li/Li symmetric cell cycling. The protected lithium metal anode (green) shows minimal overpotential with no indication of dendrite formation or soft/hard shorts. The baseline (non-protected) system shows consistent voltage spikes indicative of soft/hard shorts caused by dendrite growth.

Catholyte Development & All Solid-State Full Cell Performance Demonstration

At the beginning of FY21, Wildcat began screening the integration of the solid electrolyte components into the cathode composite film. The goal of the work is to minimize the cathode/ceramic polymer electrolyte interface. Figure XVI.13.11 shows a schematic comparing the material compositions of a conventional cathode and a catholyte – which includes the components from the ceramic polymer electrolyte. The use of a catholyte instead of a conventional cathode not only lowers the interfacial resistance, but also increases the accessible sites for Li^+ ions in the electrode and therefore, enhances the electrochemical performance of the solid-state battery to a greater extent. In this context, Wildcat has begun testing several combinations of catholyte materials and the mixing conditions used to prepare them. As for the catholyte composition, although we would start by integrating this down-selected composite electrolyte with the cathode active material, we also intend to screen several other combinations of polymer, ceramic SSE, and salt with the NMC active material. For the purpose of maintaining the energy density advantage expected of all-solid-state batteries, it is desirable to have the cathode loading high (> 60 wt.%) and the electrolyte wt. % (< 30 wt.%) low in the catholyte. However, to also obtain a reasonably good capacity retention, it is important to have an electrolyte loading that is high enough to mimic the intimate contact and accessibility seen in liquid electrolyte cells. Wildcat tested a wide range of solid electrolytes (5 – 50 wt.%) wt.% in the catholyte to determine the optimal amount that balances energy density and capacity retention of the all-solid-state full cells.

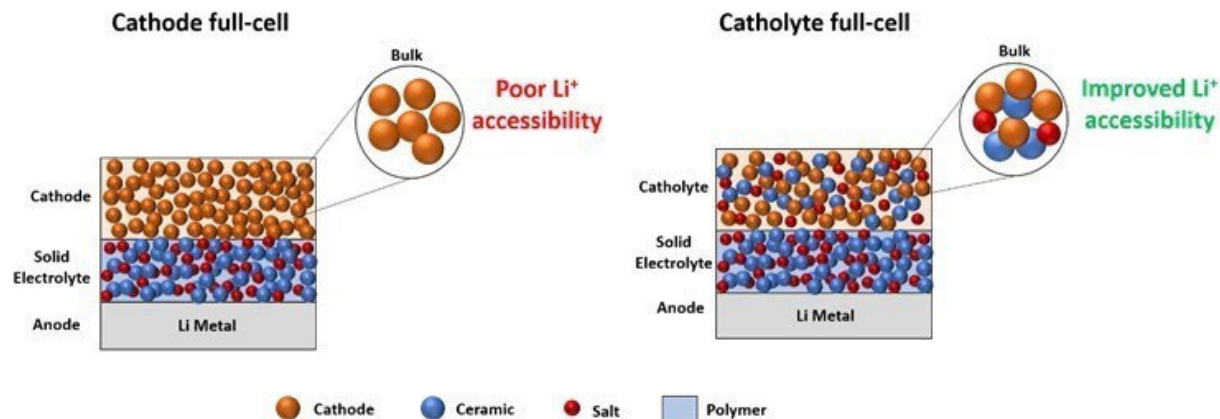


Figure XVI.13.11 Schematic comparing the structures of cathode and catholyte full cells and the possible extents of their Li^+ accessibilities.

Wildcat started evaluating catholyte compositions using its high-throughput platform and integrating them with the state-of-the-art solid-state electrolyte (SSE) and the optimal protected Li-metal from Thrust 1 and Thrust 2, respectively. After evaluating several different SSE/catholyte compositions using protected Li-metal from Thrust 2, Wildcat has successfully developed all-solid-state full cells that are capable of fully charging up to 4.3 V vs. Li^+/Li . Figure XVI.13.12a shows the Cycle-1 voltage traces of the all-solid-state full cells with different composite SSEs each featuring a different PVdF. For comparison, the voltage trace of a control cell with an identical catholyte and a liquid electrolyte (1M LiPF_6 in 1:1 EC:DMC) is also shown. The voltage traces of the liquid-electrolyte cell and the all-solid-state cells with PVdF A, C, and D look similar, indicating that the all-solid-state cells work as well as conventional Li-ion cells with a liquid electrolyte. Out of the several SSE compositions that Wildcat evaluated in this preliminary screening effort, one of the SSE types — with PVdF A — showed a promising cycling performance of about 84.2% capacity retention at the end of 20 cycles running at a rate of 0.1C (Figure XVI.13.12b).

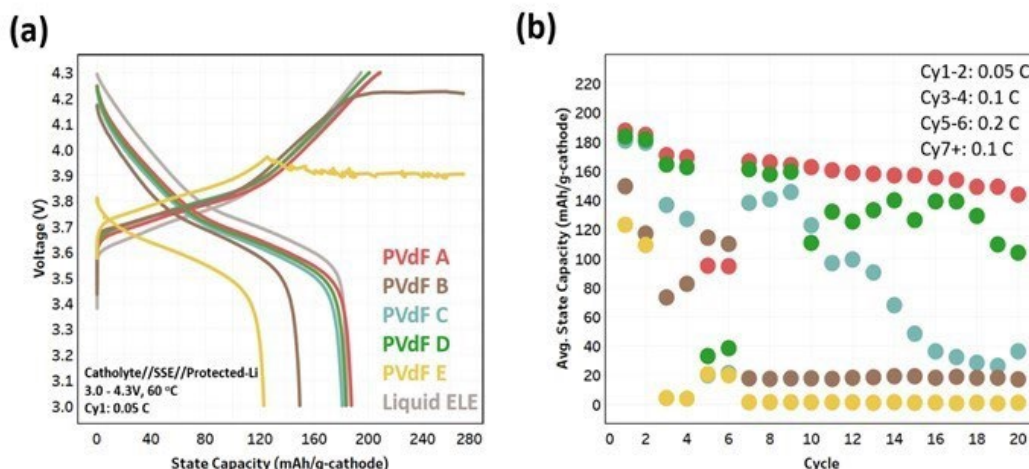


Figure XVI.13.12 Performance of all-solid-state full cells. (a) Cycle-1 voltage traces of all-solid-state Li//NMC full cells with different PVdF types in the composite SSE. A control cell with an identical catholyte and a liquid electrolyte ("Liquid ELE") is also shown. (b) Specific capacities of the all-solid-state full cells with different PVdFs in SSE up to 20 cycles.

With the promising PVdF polymer type which is PVdF A and two different ceramic materials, denoted by SSE A and SSE B. All-solid-state full cells were built with these two composite SSEs, the optimized catholyte selected from previous quarter, and the protected Li-metal from Thrust 2. The full cells were cycled in the voltage range 3.0 – 4.3 V at a temperature of 60°C. Figure XVI.13.13a shows the cycle life plots of the all-solid-state full cells. The initial discharge capacities of the full cells with SSE A and SSE B were 206 mAh/g and 213 mAh/g respectively, which were comparable to the values obtained in a liquid electrolyte cell. After a series of rate capability test steps carried out at 0.1C and 0.2C, the cycle life test step was started at 7th cycle. At the end of 80 cycles, the discharge capacities were 137 mAh/g and 157 mAh/g, corresponding to capacity retention values of 71.7 % and 76.2 %. Figure XVI.13.13b shows the voltage traces of the full cells built with the two different SSE types at 1st, 20th, and 60th cycles. The voltage traces at all cycles showed smooth and full charge profiles up to 4.3 V demonstrating the cyclability of the all-solid-state full cells.

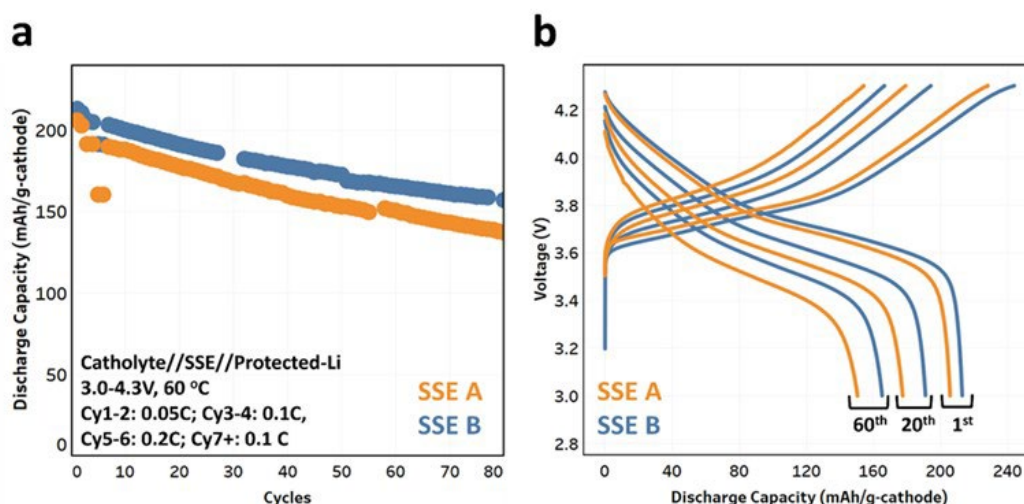


Figure XVI.13.13 Performance of all-solid-state full cells. (a) Cycle life plot of all-solid-state Li//NMC full cells with different SSE types. (b) Voltage traces of Cycles 1, 20, and 60 of all-solid-state full cells with different SSE types.

The additional effort has been made to further improve all solid-state battery using the SSE B composite electrolyte based on 45wt% of LLZTO with 1×10^{-5} s/cm ionic conductivity. Two different versions of the SSE composite SSE

B were made and labeled ‘SSE B – Gen 1’ and ‘SSE B – Gen 2’ to indicate that they differ only in the synthesis approach. To be more specific, SSE B – Gen 1 was using LLZTO made by old synthesis method and SSE B – Gen 2 was using the LLZTO with reduced particle size made by newly developed method. All-solid-state full cells were built with these two composite SSEs, the optimized catholyte, and the protected Li-metal from Thrust 2. These full cells were cycled in the voltage range 3.0 – 4.3 V at a temperature of 60°C. Figure XVI.13.14a and Figure XVI.13.14b show the cycle life plots of the all-solid-state full cells. After a series of rate capability test steps carried out at 0.1C and 0.2C, the cycle life test step was started at 7th cycle at the rate of 0.1C. At the end of 50 cycles, the discharge capacities were 148 mAh/g and 163 mAh/g, corresponding to capacity retention values of 83.7 % and 90.6 %. The optimized SSE candidate, SSE B – Gen 2 shows an improvement in the capacity retention by 7% over SSE B – Gen 1. Figure XVI.13.14c shows the voltage traces of the full cells built with the two different SSE composites at 1st and 50th cycles. The voltage traces at all cycles showed smooth and full charge profiles up to 4.3 V demonstrating the good high voltage stability and good cyclability of the all-solid-state full cells.

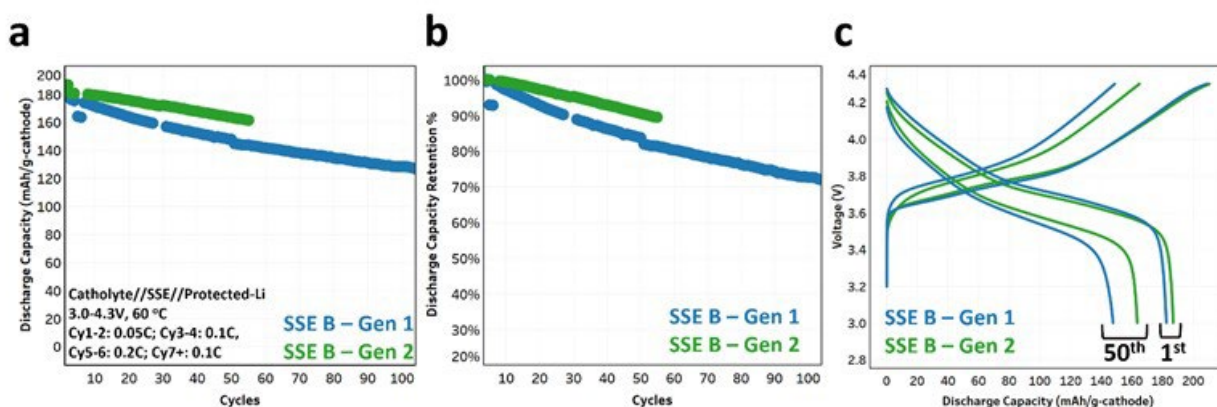


Figure XVI.13.14 Performance of all-solid-state full cells. (a) Cycle life plot of all-solid-state Li//NMC full cells with two different SSE types; Cycling conditions are provided in the inset. (b) Capacity retention plot, (c) Voltage traces of Cycles 1 and 50 of all-solid-state Li//NMC full cells with the two different SSE types.

In summary, over the course of the project, Wildcat has developed and optimized each component of an all-solid-state cell namely, the solid-state electrolyte composite, catholyte/cathode, and the Li-metal anode coupled with a custom-built protection layer. Upon optimization, Wildcat successfully assembled these components and demonstrated an all-solid-state full cell that exhibited a capacity retention of 91% at the end of 50 cycles. With the largely improved ionic conductivity of solid composite electrolyte recently developed recently, it is reasonable to expect that better cycle life can be achieved not only at elevated temperature but also at lower temperatures and higher cycling rate.

Conclusions

Based on the fundamental learnings from FY20 and Wildcat high throughput battery platform, Wildcat made a great progress on all three Thrusts during FY21, proving that our three prong approaches worked well. For composite solid electrolyte, we successfully improved the ionic conductivity over 10 times from 1×10^{-5} S/cm last year while increasing ceramic content from 45wt% to more than 75wt% with good processability. For protected Li metal anode, we successfully identified chemical passivation reagents that can lower the initial interfacial resistance between SSE and Li metal surface while preventing soft shorts during long-term cycling in Li//SSE//Li symmetric cells. We also demonstrated its application in all solid-state full cells with good long-term cycling performance at elevated temperature. Catholyte development is critical to demonstrate all solid-state full cell performance. Even though, it is not stated in the original scope of the work, Wildcat quickly developed a working catholyte composition based on the optimized SSE composition. With several initial attempts, we were able to achieve 91% retention at 50 cycles with close to theoretical reversible initial capacity. With the continuing improved ionic conductivity of our SSE, we believe that we can achieve even better cycling performance at lower temperature and faster cycling rate.

XVI.14 Fundamental Understanding of Interfacial Phenomena in Solid-State Batteries (General Motors)

Xingcheng Xiao, Principal Investigator

General Motors Research and Development Center
30470 Harley Earl Boulevard
Warren, MI 48092
E-mail: xingcheng.xiao@gm.com

Tien Q. Duong, Technology Development Manager

U.S. Department of Energy
E-mail: Tien.Duong@ee.doe.gov

Start Date: October 1, 2019
Project Funding: \$1,333,325

End Date: March 30, 2023
DOE share: \$1,000,000

Non-DOE share: \$333,325

Project Introduction

Solid-state batteries (SSBs) are considered the next generation battery technology for resolving the intrinsic limitations of current lithium-ion batteries, such as poor abuse tolerance, insufficient energy density, and short cycle life. However, the main hurdle for SSB in electric vehicle (EV) applications is the complexity caused by material interfaces, such as Li metal/solid electrolyte (SE) and SE/cathode interfaces, leading to increased impedance and shortened cycle life. Although interfaces in SSBs are one of the key factors, a clear understanding of their properties and functions is still unavailable, partly due to the difficulty in characterizing buried solid-solid interfaces and interphases formed during battery cycling.

Objectives

The project objective is to develop a comprehensive set of in situ diagnostic techniques combined with atomic/continuum modeling schemes to investigate and understand the coupled mechanical/chemical degradation associated with dynamic interfacial phenomena in SSBs. Specifically, in situ observations and characterizations of lithium plating-stripping processes, lithium dendrite formation, interphase formation, and the induced interfacial stresses, as well as the mechanical and electrochemical properties of interfaces and interphases, are paramount. The study will provide useful guidelines for optimizing cell structure design and engineering interfaces and interphases to enable SSBs. In addition, it will establish a critical guideline to design safe and durable SSBs with energy density > 500 wh/kg for EV applications.

Approach

The multiscale in situ diagnostic tools, including AFM, nanoindentation, dilatometer, stress sensors, and pressure cells, will be used to investigate mechanical behavior and microstructure evolution at interface/interphase during lithium plating and stripping. The information (along with Li-ion transport properties and microstructure evolution obtained using the advanced spectroscopic ellipsometry, and in situ TEM) will be correlated with electrochemical performance toward high cycle efficiency and dendrite-free SSBs. The goal of this understanding is to develop strategies for surface and interface engineering, apply them to commercially available SEs (including powder, pellets, and foils), and assemble SSBs for further validation and optimization, eventually extending cycle life for EV application.

Results

Validating Curvature Increase During Galvanostatic Plating Using LLZO Solid Electrolyte

We further verified that the linear increase in curvature is associated with lithium metal penetration within the LLZO solid electrolyte, an additional experiment with 12-hour plating was carried out. In this experiment, the electrochemical measurements were interrupted with OCV holds between plating and stopped without a short-circuit after observing a similar buildup in curvature. The results are shown in Figure XVI.14.1a. After plating

at 0.02 mA/cm^2 , 10 hours of OCV hold was added. During the OCV, the curvature shows a small relaxation, followed by further increase in curvature. The initial relaxation is likely associated with inelastic properties of plated lithium, relaxing via plastic flow.

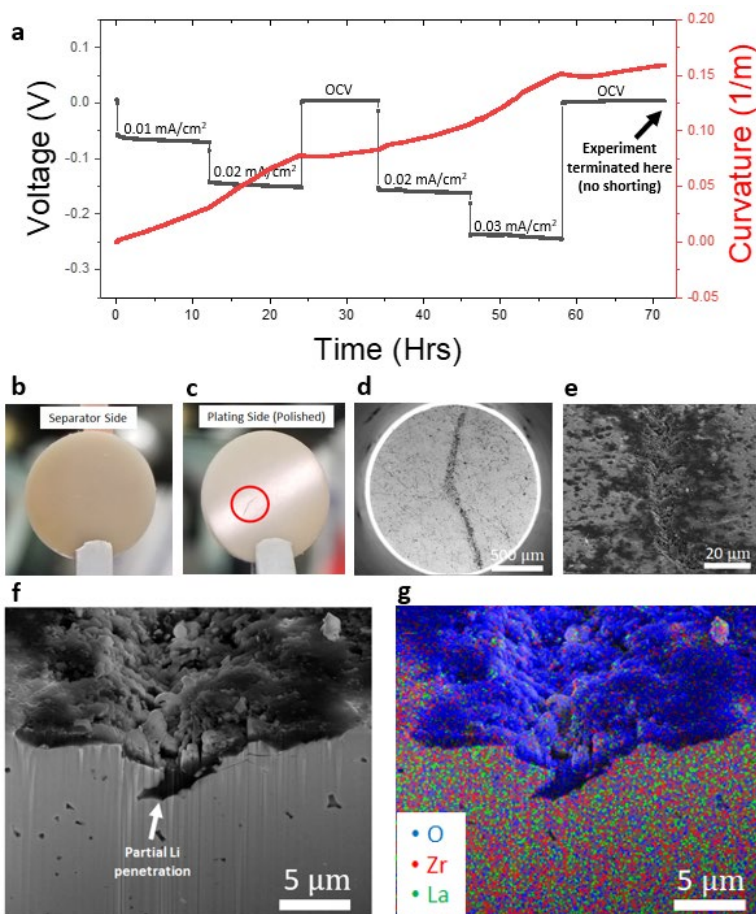


Figure XVI.14.1 a) Voltage & curvature vs. time of the LLZO/quartz electrode. Black and red lines indicate voltage and curvature profile, respectively. b-c) separator and plating side of the LLZO pallet after the experiment. On the plating side, a small crack is observed. d-e) observed crack in the SEM. f) FIB cut on the crack reveals a partial lithium metal penetration through the solid electrolyte. g) EDS mapping of the FIB cut cross-section. Blue, red, and green dots indicate signatures of Oxygen, Zirconium, and Lanthanum, respectively.

After the experiment was stopped without short-circuiting, the cell was then taken apart with similar methods, and the residual lithium metal on LLZO was removed by lightly polishing. As shown in Figure XVI.14.1c, there is an apparent crack observed on the plating side of the LLZO pallet. No cracks were observed on the separator side in Figure XVI.14.1b. This crack was then observed directly in the SEM, as shown in Figure XVI.14.1d and Figure XVI.14.1e. The cross-sectional image of the crack was obtained by Focused Ion Beam (FIB) milling, which is shown in Figure XVI.14.1f. Here, partial lithium metal penetration beneath the crack is clearly shown and supported by the EDS map shown in Figure XVI.14.1g. The Oxygen signature in the map indirectly supports mapping of lithium metal, as the signal is most likely associated with the atmosphere-reacted plated lithium metal due to the sample being briefly exposed to the air during the transfer to the SEM/FIB.

The experiment in Figure XVI.14.1 further validates that the increase in curvature prior to short-circuit is associated with stress build up due to lithium metal penetration through the LLZO solid electrolyte. The curvature evolution, formation of crack, and the partial penetration observed all point towards the idea that the cracks formed like the ones Figure XVI.14.2c are the main source of curvature evolution during plating. If this

is true, then there must exist some anisotropy in curvature values at different orientation relative to the crack location. To test this hypothesis, curvature measurements at different angle orientations were carried out at the end of the experiment in Figure XVI.14.2a by rotating the sample in 45 degrees increments and taking curvature measurement in each angle. As shown in Figure XVI.14.2, there is a significant anisotropic trend in curvature at different orientations. The crack shown here is nearly parallel to the 45-degree orientation, which indicate that the curvature values at 45 degrees, 225 degrees should exhibit the least amount of curvature. Furthermore, the angle orientations which are perpendicular to the crack orientation should experience the largest stress and hence the largest value of curvature. The results shown in Figure XVI.14.2b clearly indicates that the angle orientations which are approximately perpendicular to the crack orientation (at 135 degrees and 315) show the largest value of curvature. This serves as an additional validation for how crack formation at the interface due to lithium metal penetration generates the dominate stress experienced in the overall cell.

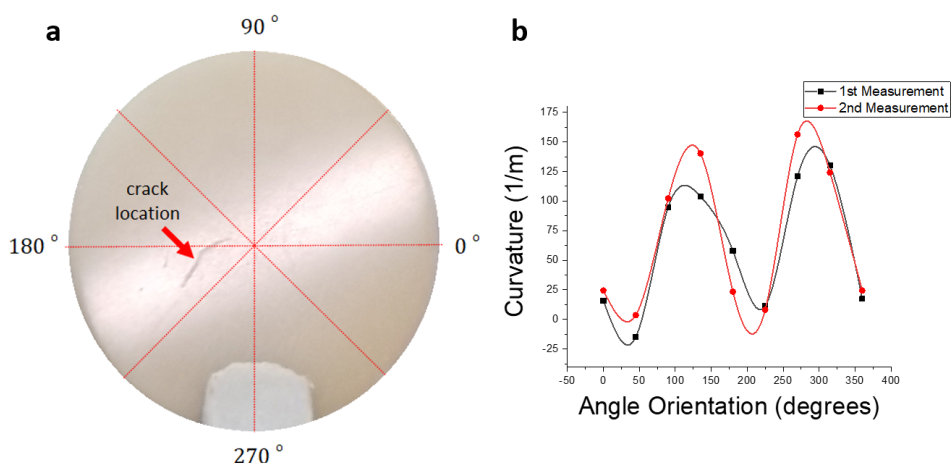


Figure XVI.14.2 a) Visual representation of the laser orientation angles relative to the crack location after the experiment shown in Figure II.9.N.1a. The data from Figure II.9.N.1a was measured with the laser orientation angle of 0 degrees. b) Measured curvature values vs. laser orientation angle after the experiment shown in Figure II.9.N.1a. The curvature values were measured in 45 degrees increment relative to the original laser orientation (0 degrees).

Incorporated Li creep into the kinetic Monte Carlo model to study the impact of coating, stress, and delithiation rate on the Li-surface morphology

Our previously developed multiscale simulation framework has shown the interfacial properties (such as lithiophobic Li/LiF and lithiophilic Li/Li₂O) plays an important role in maintaining smooth Li surface during delithiation. The goal of this quarter is to extend the kinetic Monte Carlo (KMC) simulations to incorporate the impact of compressive stack stress on delithiation. We consider the mechanical stress creates a bias for Li to hop toward the Li/SE interface. The elastic deformation has negligible impact on Li hopping. Our DFT calculations of Li vacancy formation energy under a compressed strain (with the corresponding stress from 14 to 400 MPa) showed neglectable differences. The elastic strain energy is on the order of 10⁻⁶ eV, which had little impact on Li hopping barriers.

Under the stacking pressure, Li creep cannot be neglected given the low melting point of Li (454 K). In the stripping process, creep effects will push the Li atoms in the bulk towards the interface to fill the voids generated due to the stripped Li atoms. Thus, we converted the Li creep induced Li flux toward the interface as a bias energy for Li hopping and derived the formula for change in forward and backward hopping processes. Considering a Li anode with a thickness L of 100 microns and a strain rate $\dot{\epsilon}$ of 0.01 at 300 K, the bias energy is $E_p = 0.55$ eV. With the bias, all the forward rate constants are increased by at least a factor of 2 while the backward rate constants are decreased by more than 4 magnitudes. Figure XVI.14.3 compares the simulated structures for Li/Li₂O (Figure XVI.14.3a, Figure XVI.14.3b) and Li/LiF (Figure XVI.14.3c, Figure XVI.14.3d) with ($E_p = 0.55$ eV) and without bias ($E_p = 0$ eV). In the Li/Li₂O interfaces, most vacancies are far away from the interface (deeply in the bulk) with a single vacancy in the bulk/interface transition region

after imposing the bias (Figure XVI.14.3a). In contrast, the systems without (Figure XVI.14.3b) bias show several vacancies trapped near the interface and a few vacancies randomly distributed in the transition region. In the Li/LiF interfaces, the difference is more obvious. All the vacancies are localized in the bulk in the biased model, but all are trapped in the model without bias. Thus, our model can capture the impact of stack stress on Li diffusion and filling the void generated during diffusion.

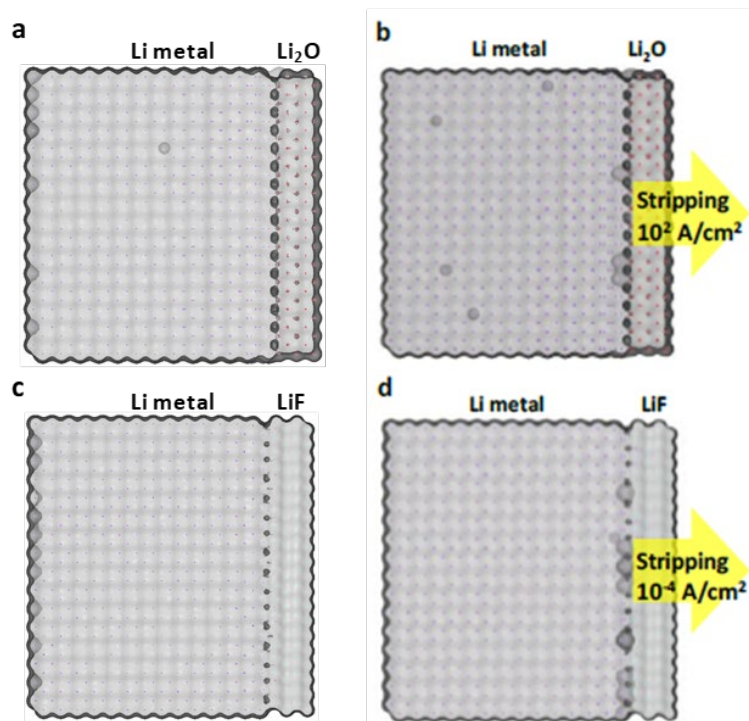


Figure XVI.14.3 KMC simulations of the stripping process. (a) and (c), Under stress bias, $E_p = 0.55$ eV, $\epsilon' = 0.01$) the Li surface during delithiation is smooth at both interfaces. Without the stress, (b) the Li surface is smooth with Li_2O layer but (d) has trapped vacancies with LiF layer.

Investigated the effect of pressure on the interface between lithium lanthanum zirconium oxide (LLZO) and lithium metal electrodes

The effect of external pressure on the interfacial resistance between Ta doped LLZO solid electrolyte and lithium metal electrodes were investigated using electrochemical impedance spectroscopy (EIS). Prior to electrochemical cycling, a lithium metal symmetric pouch cell was placed in a homemade pressure device. An external pressure of 1.81 MPa was then applied for less than 1 minute, and an EIS measurement was taken to record the contact resistance while under this max pressure. The external pressure was then removed. After removing the pressure, EIS measurements were taken as a function of time to study the cell's response. An intriguing new observation was seen upon removing the external pressure. The interfacial resistance continued to decrease even without the driving force of stack pressure. As seen in Figure XVI.14.4, the interfacial resistance decreases over the course of 7 days after the initial pressure of 1.81 MPa was removed.

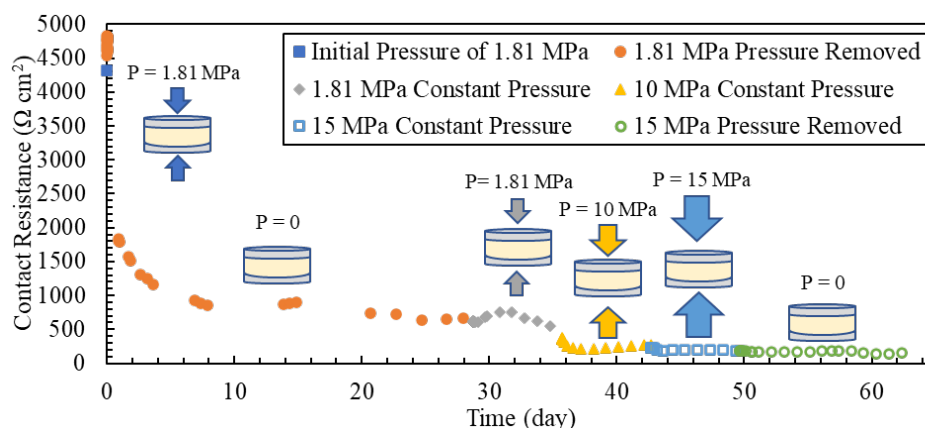


Figure XVI.14.4 Contact resistance vs. time plotted out under various pressure conditions. The initial pressure of 1.81 MPa was applied at time zero.

We proposed that after the pressure is removed, the interfacial resistance decreased further as a result of the power-law creep of lithium metal which increased its contact area with the LLZTO as schematically shown in Figure XVI.14.5. The dislocations formed during the initial application of pressure and start to move once pressure is removed because of the back-stress in the dislocation substructures. The dislocations find their way to the surface, reducing stress and creating more contact area with LLZTO. In addition to the driving force due to creep, growing the contact area between lithium and LLZTO is energetically favorable since LLZTO is lithiophilic. We propose that the lithium metal continues to flow even after the pressure is removed to reduce surface energy of lithium metal and LLZTO, as well as the strain energy in the dislocation substructure. However, this proposal should be examined in the future.

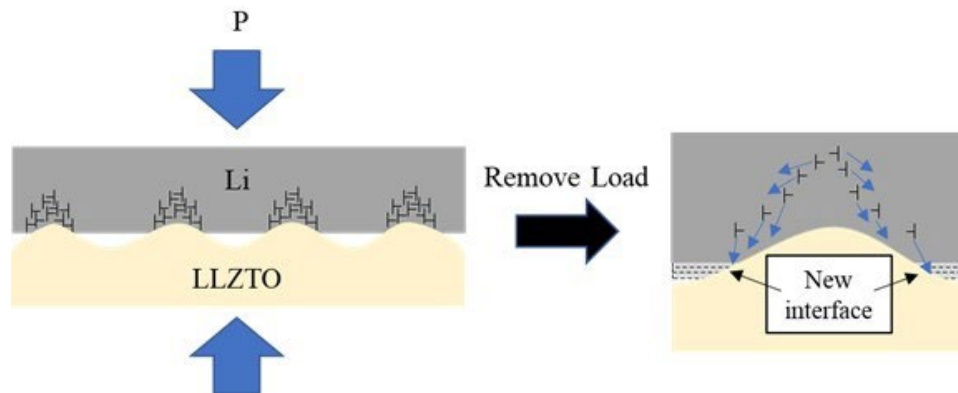


Figure XVI.14.5 Conceptual diagrams depicting the cross section of lithium and LLZTO interface. The formation of dislocation substructures, and the movement of dislocations after removing the external pressure causing an increase in the contact area with LLZTO.

Micro-CT to understand the interface reaction between solid electrolyte and Li metal

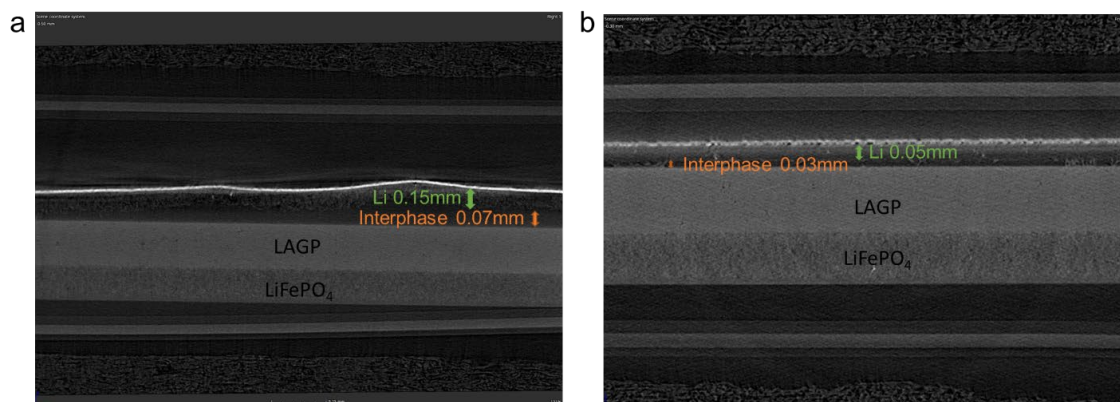


Figure XVI.14.6 CT scan of the cross-section of Li/LAGP/LiFePO₄ cell. (a) Li/LAGP/LiFePO₄ cell with control lithium electrode. (b) Li/LAGP/LiFePO₄ cell with coated lithium electrode.

LAGP is short for $\text{Li}_{1.5}\text{Al}_{0.5}\text{Ge}_{1.5}(\text{PO}_4)_3$ and it possesses a lithium-ion conductivity of 5×10^{-4} S/cm at room temperature. However, the Ge is easily reduced by lithium metal and this reaction is not self-limiting since the side-reaction product is a mixed electronic and ionic conductive phase. A computerized tomography (CT) scan can construct a three-dimensional (3D) image of the object non-destructively. Without any air exposure, the interfacial property of the solid-state cell is revealed. As shown in Figure XVI.14.6, the coated sample shows a much stable interphase. The control lithium electrode shows a bumpy structure while the coated lithium electrode is flat. In addition, the control lithium has a thickness around 0.15 mm, which is a three-time increase compared with pristine lithium metal (0.05 mm). As a contrast, the coated lithium still maintains the same thickness as before. The increased thickness of control lithium electrode can be either caused by the unintimate solid-solid contact or the side reaction occurred within the lithium foil. An interphase with a distinct dark color is formed between solid state electrolyte (LAGP) and lithium electrode, and this thickness can directly represent the side reaction level. In the control lithium electrode, the interphase layer caused by the side reaction is 0.07 mm, which is 2.33 times higher than the coated sample (0.03 mm). As a result, with coating, the side reaction between lithium electrode and LAGP is largely depressed, and a good cycle life is reached.

Conclusions

- An additional experiment further validated that the dramatic increase in curvature during galvanostatic plating on LLZO solid electrolyte is closely associated with lithium metal penetration along the grain boundaries. Interrupting the experiment prior to short circuiting showed partially penetrated lithium metal through the LLZO surface, and the anisotropic curvature at different angle orientation further confirmed that the penetration site contributes largely to the overall curvature evolution.
- Multiscale modeling has been further developed to understand the interfacial mechanical properties and ion transport properties. Atomistic model (DFT + KMC) revealed a lithiophilic coating on Li is preferred not only for interface adhesion, but also for preventing dendrites. COMSOL model revealed that the interface reaction layer causes more significant stress than Li diffusion induced stress.
- The irreversible decrease of interfacial resistance can be understood by a gradual reduction of the total energy of the system, including strain energy and interfacial energy. Under external pressure exceeding ~ 25 MPa, however, lithium can be squeezed into LLZTO, fracturing the ceramic solid electrolyte. These observations can help improve the understanding of lithium metal creep and the interactions between garnet-type solid electrolytes and lithium metal.

- The interlayer engineering efforts have been initiated and liquid metal as an interlayer could maintain the intimate contact between the electrode and solid electrolyte to reduce the impedance. Long term cycle tests are needed to further validate the benefits from soft liquid metal.

Key Publications

1. Andrew Meyer, Xingcheng Xiao, Mengyuan Chen, Ambrose Seo, and Yang-Tse Cheng, A Power-Law Decrease in Interfacial Resistance Between $\text{Li}_7\text{La}_3\text{Zr}_2\text{O}_{12}$ and Lithium Metal After Removing Stack Pressure. *J. Electrochem. Soc.* 2021(168), 100522
2. Min Feng, Jie Pan, and Yue Qi, Impact of Electronic Properties of Grain Boundaries on the Solid Electrolyte Interphases (SEIs) in Li-ion Batteries, *J. Phys. Chem. C* 2021(125), 29, 15821–15829
3. Chi-Ta Yang and Yue Qi, Maintaining a Flat Li Surface during the Li Stripping Process via Interface Design, *Chemistry of Materials* 2021, 33 (8), 2814–2823
4. Michael W. Swift, James W. Swift & Yue Qi, Modeling the electrical double layer at solid-state electrochemical interfaces, *Nature Computational Science* 2021(1), 212–220
5. Xingcheng Xiao, Mengyuan Chen, Methods for Forming Ionically Conductive Polymer Composite Polymer Interlayers in Solid-state Batteries, GM Ref. No. P054138-US-NP, US patent application filed
6. Mengyuan Chen, Xingcheng Xiao, Composite Interlayers for Solid State Batteries and the Method of Making Same, GM Ref. No. P054203-US-NP, US patent application filed
7. Xingcheng Xiao, Mengyuan Chen, Qinglin Zhang, Mei Cai, A solution-based approach to protect lithium metal electrode, GM Ref. No. P053352-US-NP, US patent application filed

Acknowledgements

The PI and co-PIs (Profs. Brian W. Sheldon, Yue Qi, Yang-Tse Cheng, and Ambrose Seo) would like to thank financial support from the Assistant Secretary for Energy Efficiency and Renewable Energy, Office of Vehicle Technologies, Advanced Battery Materials Research (BMR) programs of the U.S. Department of Energy (DOE) under contract no. DE-EE0008863. They also would like to thank Tien Duong, Tricia Smith, and Adrienne Riggi at DoE for program management, and all the students and postdocs involved in this project Mengyuan Chen, Yifan Zhao (General Motors), Juny Cho, Min Feng (Brown University), and Andrew Meyer (University of Kentucky).

XVI.15 Multidimensional Diagnostics of the Interface Evolutions in Solid-State Lithium Batteries (University of Houston)

Yan Yao, Principal Investigator

University of Houston
4800 Calhoun Road
Houston, TX 77004
E-mail: yyao4@uh.edu

Tien Q. Duong, DOE Technology Development Manager

U.S. Department of Energy
E-mail: Tien.Duong@ee.doe.gov

Start Date: October 1, 2019
Project Funding: \$1,250,000

End Date: March 31, 2023
DOE share: \$1,000,000

Non-DOE share: \$250,000

Project Introduction

The failure of a solid-state Li battery may be briefly attributed to two main causes: interfacial resistance increase and Li dendrites growth. The former may be further attributed to electrolyte decomposition and interfacial void formation (*i.e.*, loss of physical contact). Electrolyte decomposition happens in two ways: oxidative decomposition at the cathode active material–electrolyte interface and reductive decomposition at the Li (including dendrites)–electrolyte interface. Void formation occurs at the same two interfaces. The complex origins of battery failure call for multidimensional diagnostics utilizing not one but a combination of tools that can quantify the formed void and dendrites, identify the chemical and mechanical natures of the Li dendrites and electrolyte decomposition products, and *in situ* monitor the evolution of the processes. The tools also need to cover a sufficiently large scale (up to $\sim 100\ \mu\text{m}$), have spatial resolutions of a few nanometers, and be sensitive enough to detect subtle changes in chemical and mechanical properties. These considerations lead us to a toolset of FIB-SEM tomography, ToF-SIMS, and nanoindentation (inside SEM chamber, *i.e.*, in-SEM nanoindentation) and atomic force microscopy (AFM; inside SIMS chamber, *e.g.*, in-SIMS AFM)-based stiffness mapping for structural, chemical, and mechanical characterizations, respectively. We will acquire detailed information of interfaces and dendrites evolutions including but not limited to (1) real-time visualization of Li dendrites growth within the whole thickness of electrolyte layer, (2) chemical composition, mechanical property, and evolution of electrolyte decomposition products, including intermediate and metastable ones, at both cathode and anode interfaces, (3) potential correlation of the induction and propagation of Li dendrites with electrolyte decomposition, and, (4) quantitative correlation between electrolyte decomposition, void formation, and cell performance. These in-depth understandings will allow us to effectively predict and optimize the physical and chemical changes of components within solid-state Li batteries during charge and discharge.

Objectives

The project objective is to develop a platform in combination of FIB-SEM tomography, ToF-SIMS, and in-SEM nanoindentation-based stiffness mapping for structural, chemical, and mechanical characterizations in solid-state Li batteries. Assessment of the influence of cell design and testing conditions (external pressure, current density, temperature) on the evolutions of interfaces will be performed.

Approach

Space- and time-resolved structural, chemical, and mechanical characterizations of the cathode–electrolyte and anode–electrolyte interfaces will be performed on all-solid-state Li batteries using FIB-SEM, ToF-SIMS, in-SEM nanoindentation. Tasks include (1) development of solid-state cell thin stacks and test-cell configurations that are suitable for in-situ characterizations, (2) quantitative characterization and in-situ tracking of interfacial voids formation within composite cathode and electrolyte layer; (3) identification and in-situ tracking of the

chemical composition, spatial distribution, and mechanical properties of electrolyte decomposition products at the Li- and cathode-electrolyte interfaces; (4) visualization, chemo-mechanical properties detection, and in-situ tracking of Li dendrites grown within solid electrolyte layer.

Results

Performance optimization of thin solid-state cells continued this year. Our previous thin cells were most successful when lithium-indium anodes were used. For example, we have reported on an NMC|LPSCI|Li-In full cell with a combined 100- μm thickness and stable capacity over 50 cycles (Figure XVI.15.1a). Our original goal for the project, however, is to use lithium as the anode for practical higher-energy cells. Direct use of lithium metal in our thin cells leads to fast short-circuiting, probably as the result of both lithium creeping and dendrite formation. Several methods have been attempted to adapt lithium metal to the cells. One of them is to use an interlayer ($\leq 10\text{ }\mu\text{m}$ thick) between the electrolyte and the lithium anode, a physical barrier that prevents any creeping lithium or dendrite to penetrate the thin electrolyte layer. A cell based on lithium anode and an added interlayer is shown in Figure XVI.15.1b, which shows an increased cell voltage versus a Li-In-based cell. The suppression of lithium is so successful that the cell has survived 200 cycles without shorting, even though the electrolyte layer is less than 50 microns thick. The relatively low specific capacity was due to the experimental cathode recipe we employed for the demo, which was not part of the requirement for the use of interlayer and lithium anode. Other effective methods are also being developed and will be used in conjunction with the interlayer.

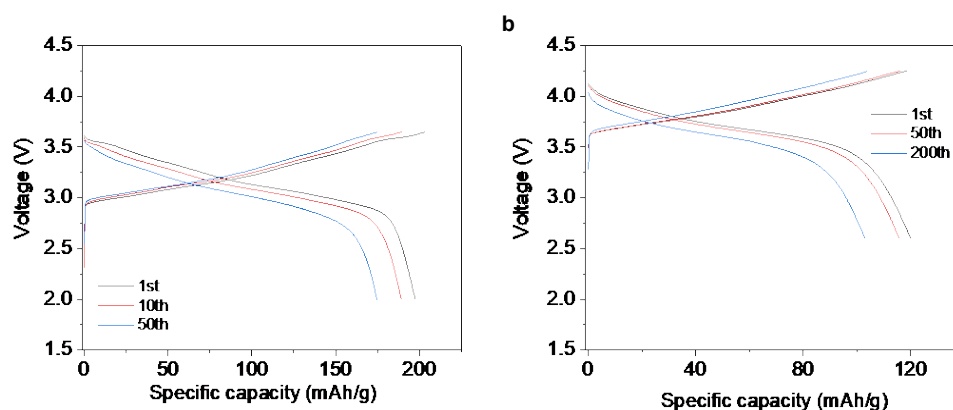


Figure XVI.15.1 Charge-discharge profiles of NMC|LPSCI|Li-In (a) and NMC|LPSCI|interlayer|Li thin cells.

We have applied multidimensional diagnostic techniques to evaluate the cell components that we have developed for thin solid-state NMC-Li cells fabrication. The many methods available today to prepare thin cathode and electrolyte layers can be categorized into dry methods, which use insoluble binders such as polytetrafluoroethylene (PTFE), and wet methods, where soluble binders like nitrile butadiene rubber (NBR) are used. Depending on the methods used and the degree of optimization, composites with apparently similar composition show major difference in performance. Structural and chemical characterization techniques at the suitable resolution and sensitivity will provide insights into the difference of two processes, thus providing feedback and guidance on the fabrication process.

Here we compare two NMC-LPSCI-binder cathodes, one fabricated with a dry method using PTFE binder, the other with wet method using NBR binder. Since the solvents used in the wet method are known to affect the conductivity of LPSCI, an additional control sample was fabricated with dry method using PTFE binder and LPSCI treated with the same solvents that are used in the wet method. SEM shows the PTFE binder is fiber-like and distributes on the NMC and LPSCI particle surface (Figure XVI.15.2a), while NBR is more homogeneously blended with the particles with no individual binder domain (Figure XVI.15.2b). ToF-SIMS offers the opportunity to visualize light elements with good resolution. Fragments F^- and C_3H_5^+ , respectively representing PTFE and NBR binders, are mapped to quantify the distribution of each component in these

electrode composites. The PTFE fibers are clearly visible in Figure XVI.15.2c, as well as the homogeneous NBR in Figure XVI.15.2f. The presence of PTFE does not correlate much with the NMC (Figure XVI.15.2d) and LPSCl (Figure XVI.15.2e) particles. In contrast, the amount of NBR shows good alignment with NMC particle (Figure XVI.15.2h) and slightly less so with LPSCl particles (Figure XVI.15.2i), an indication of NBR enrichment on inorganic particle surface.

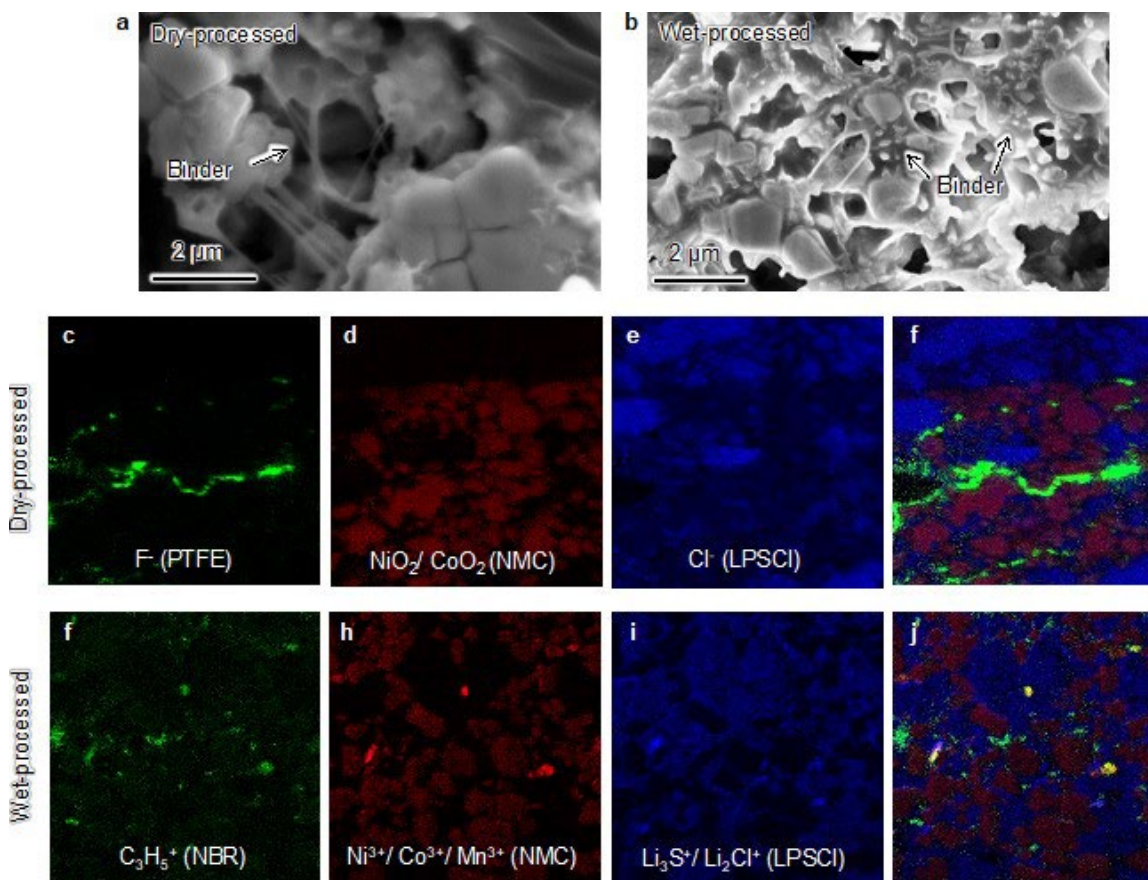


Figure XVI.15.2 Characterization of NMC cathode composites processed with different methods. a and b, SEM images of cathodes containing PTFE (a) and NBR (b) binders processed with dry and wet methods, respectively. c–j, ToF-SIMS mapping (30 μm \times 30 μm) of F (c, f), transition metals (d, h), Cl (e, i) and the combined view of the three (r, j).

The electrochemical properties of the cathodes were then characterized both at the electrode level and cell level. The ionic conductivity of the cathode was measured with both AC and DC methods and the results are shown in Figure XVI.15.3a. Both electrodes made with solvent-treated LPSCl show decreased ionic conductivity compared with the one made with pristine LPSCl (green circle). What is notable is the lower conductivity of electrode one containing NBR binder (blue up triangle) than that with PTFE (magenta down triangle), which can be explained by the binder distribution revealed in the ToF-SIMS mapping: the NBR binder enriched on both the NMC and LPSCl surfaces could serve as an ionic (and possibly also electrical) insulator. While the soluble binder has the advantage of being uniformly dispersed in the composite, it also provides comprehensive passivation of active particles and induces undesirable performance reduction. Indeed, cells with dry-process cathode show greater rate capability in NMC-Li full cells (Figure XVI.15.3b).

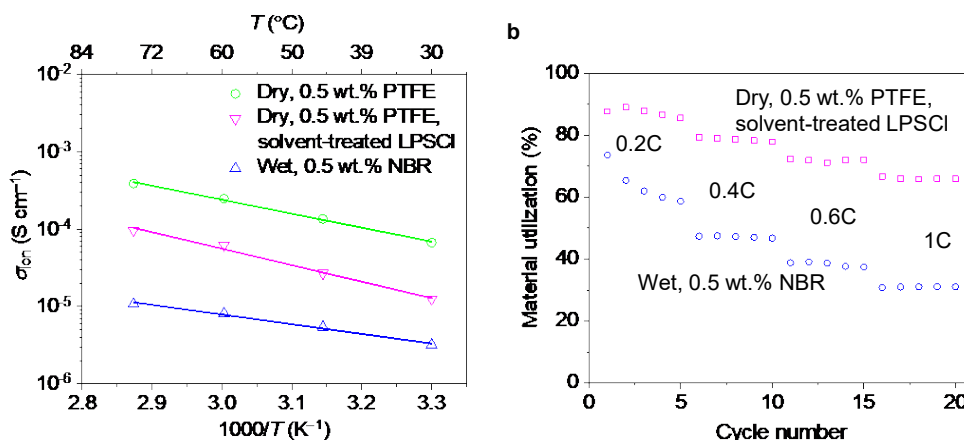


Figure XVI.15.3 Characterization of NMC cathode composites processed with different methods. a and b, SEM images of cathodes containing PTFE (a) and NBR (b) binders processed with dry and wet methods, respectively. c–j, ToF-SIMS mapping (30 μm \times 30 μm) of F (c, f), transition metals (d, h), Cl (e, i) and the combined view of the three (r, j).

To understand the underlying capacity fading mechanism in solid-state batteries, it is important to conduct in-operando investigations with high spatial resolution during charging-discharging process. To achieve this goal, we have designed and fabricated a nano-cell made from a ~ 300 μm thin-cell combined with Ar-beam polishing as shown in Figure XVI.15.4a. After polishing a cross-section, 30 keV focused Ga ion beam was employed in a SEM/FIB system (detailed fabrication process is described below) to lift out a lamella for nano-cell fabrication. The nano-cell comprising anode, electrolyte and cathode is hundreds of nanometers in thickness and ~ 130 μm in length (Figure XVI.15.4d). Since the electrochemical reactions would occur at or near sample surface when the sample is at the length scale of a few hundreds of nanometers, such a design could enable direct observation of microstructural change at high spatial resolution.

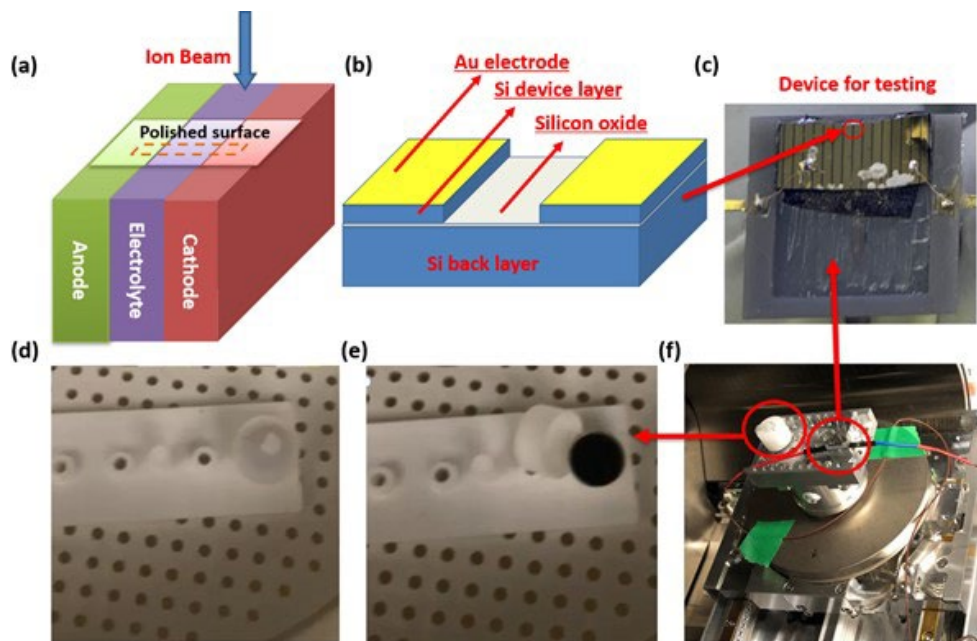


Figure XVI.15.4 (a) Schematic illustration of nano-cell fabrication from the polished thin-cell sample, (b) schematic illustration of the micro-fabricated device for nano-cell testing, (c) optical image of the micro-fabricated device for charging-discharging experiments, (d) optical image of the closed pop-up SEM stub, (e) optical image of an opened pop-up SEM stub, (f) the complete in-operando experimental configuration inside an SEM/FIB system.

Figure XVI.15.4b shows a micro-fabricated chip for charging-discharging the nano-cell. Au electrodes were deposited on a SOI wafer. The SiO₂ layer serves as the insulating layer under the 10- μ m thick Si device layer. A 100- μ m-wide gap between the electrodes was formed by the standard etching process. Since the nano-cell was suspended, both the top and bottom surfaces of the sample could be fine-polished by FIB. Figure XVI.15.4c shows a picture of a nano-cell mounted on a 3D-printed chip carrier. Additionally, to protect the air-sensitive thin-cell sample, a pop-up SEM stub was machined for sample transfer between the glovebox and the SEM/FIB. Figure XVI.15.4d shows a picture of the closed stub with Ar sealed inside. The cap on the stub automatically pops up when the environment is pumped to vacuum as shown in Figure XVI.15.4e, simulating the scenario in a SEM/FIB chamber and demonstrating the effectiveness of the pop-up stub design. Figure XVI.15.4f shows the experimental setup inside a SEM/FIB including a thin-cell sample placed in a pop-up stub and the micro-fabricated chip carrier ready for charging-discharging experiments.

The nano-cell fabrication process is described in Figure XVI.15.5. First, the as-prepared thin-cell was polished by Ar-ion beam polisher to expose a cross section. The NMC cathode/LPSCI solid electrolyte/Li₄Ti₅O₁₂ anode can be clearly visualized in Figure XVI.15.5a. A ~ 2 μ m thick lamella was cut out by focused ion beam (30 keV, 21 nA) along the area outlined by the dash line. An in-SEM EasyliftTM manipulator was employed to lift out the lamella (~ 130 μ m long, ~ 30 μ m wide) as shown in Figure XVI.15.5b, and then transferred the lamella onto the micro-fabricated chip. The connections between the nano-cell and the chip were formed by Pt deposition. Both surfaces of the lamella were polished to reduce the lamella thickness and remove the surface redeposition. Figure XVI.15.5c reveals the morphologies.

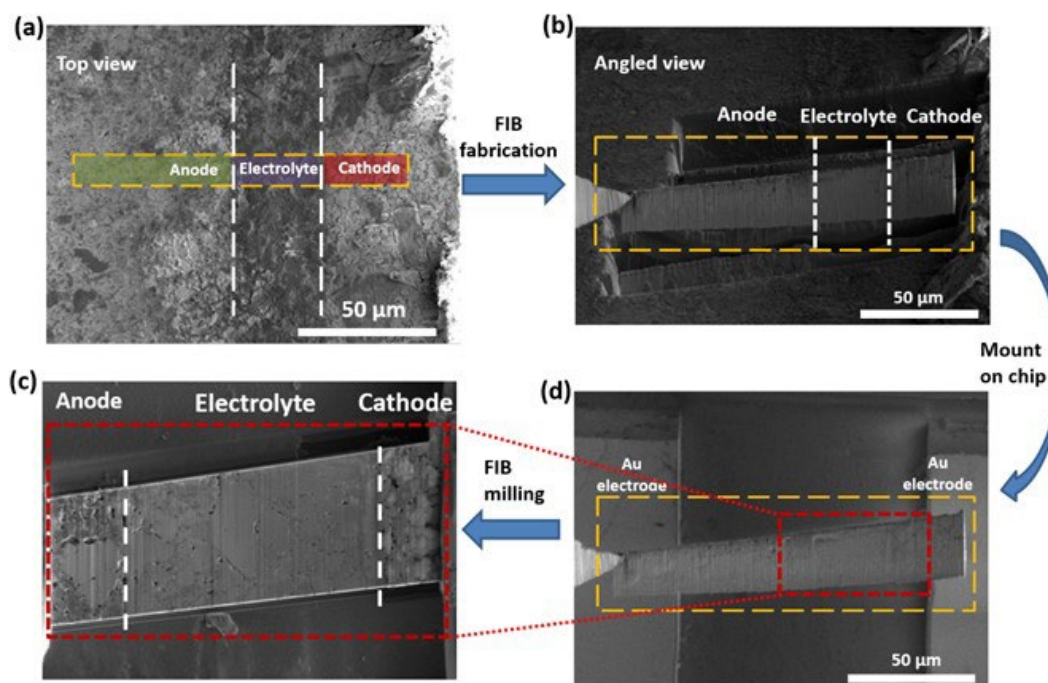


Figure XVI.15.5 Nano-cell fabrication process. (a) SEM image of the polished surface of a thin-cell, (b) SEM image of a laminated thin layer prepared by FIB, (c) SEM image of the nano-cell, clearly showing the anode/electrolyte/cathode configuration. (d) SEM image of the nano-cell bridging the gap of two Au electrodes for electrochemical tests.

We have then optimized the fabrication process of nano-cells and improved yields. We can now fabricate nano-cells with a variety of configurations and carry out select in situ measurement and characterization on them. Figure XVI.15.6 shows some examples of such capability we developed. Characterization of a LPSCI electrolyte in the nano-cells is done on a strip of LPSCI connected to Au electrodes via Pt contacts (Figure XVI.15.6a). Electrochemical impedance spectroscopy measurement of the Pt|LPSCI|Pt symmetrical cell shows an ionic conductivity of 1.7×10^{-3} S/cm. This result is line with the value of the same electrolyte obtained from bulk cells (1.1×10^{-3} S/cm), indicating chemical integrity of the electrolyte, good contact between cell

components, and overall successful demonstration of the cell configuration. An NMC|LPSCI|Li₄Ti₅O₁₂ full cell was similarly fabricated (Figure XVI.15.6c). Cyclic voltammogram shows noisy current response, and redox waves are not clearly isolated from the background (Figure XVI.15.6d). This is not necessarily a flaw of the fabricated cell, but due to the extremely small current reaching the detection limit of our potentiostat. An incoming potentiostat with low-current detection capability will be used in future electrochemical measurement. That the current not properly recorded did not prevent cell operation and structural characterization.

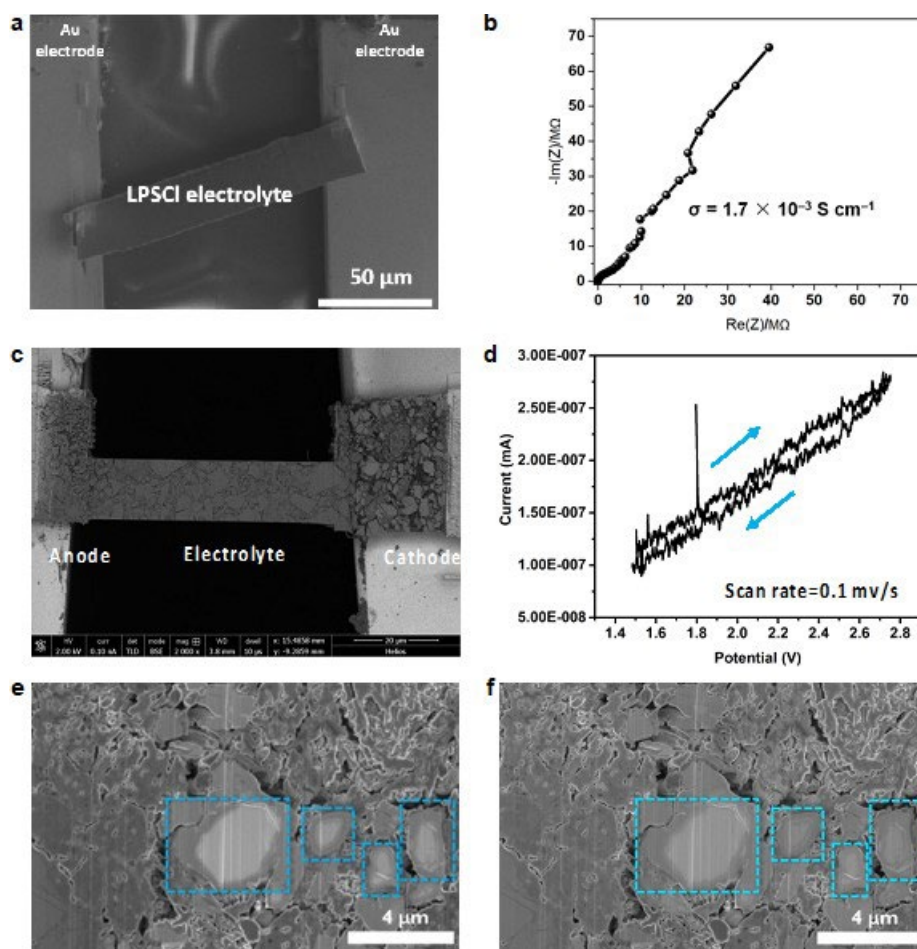


Figure XVI.15.6 Electrochemical and structural characterization of nano-cells. a and b, Structure (a) and impedance measurement (b) of a Pt|LPSCI|Pt symmetrical cell. c and d, Structure (c) and cyclic voltammogram (d) of an NMC|LPSCI|LTO full cell. e and f, In situ observation of the full cell before (e) and after (f) cycling.

An example of in situ SEM observation of the nano-cell electrodes is shown in Figure XVI.15.6e and f. Highlighted in squares are NMC particles which show gradients within the particle. The different greyscale could be reflective of local composition and/or crystallinity differences. Before cycling, the brighter and darker regions are distinctively separated by sharp lines (Figure XVI.15.6e). The distinction gradually lost upon cycling, with some smaller particles appear almost uniform (Figure XVI.15.6f). Interpretation of such transformation will be made possible once current response information is obtained from cyclic voltammogram. Other chemical and structural characterization methods are also being implemented to the nano-cell platform.

As a part of our ongoing multiscale structural investigations, we have improved our micro-cell setup to be ready for operando observations. Figure XVI.15.7 shows the operando SEM observation of a solid-state micro-cell with NMC cathode, LPSCI electrolyte, lithium anode, and an interlayer of Ag–C to mitigate lithium

dendrite formation. In this example, we focused on the morphology evolution of the electrolyte–anode interface which is highlighted in Figure XVI.15.7a. Figure XVI.15.7b–d show the temporal evolution of the interface during the discharge of the cell. A representative structural feature in the lithium anode is highlighted in the bottom part of Figure XVI.15.7b. As discharge proceeds, the feature is seen moving toward the interface, a clear indication of the bulk consumption of the lithium layer near the interface. No notable change is found in the electrolyte layer (the upper half of the images) and the interlayer in the middle. A gap forms between the Ag–C interlayer and lithium shortly after the start of the discharge (Figure XVI.15.7c), and the morphology of the gap continuously changes throughout the discharge, ending in a totally different appearance in Figure XVI.15.7d.

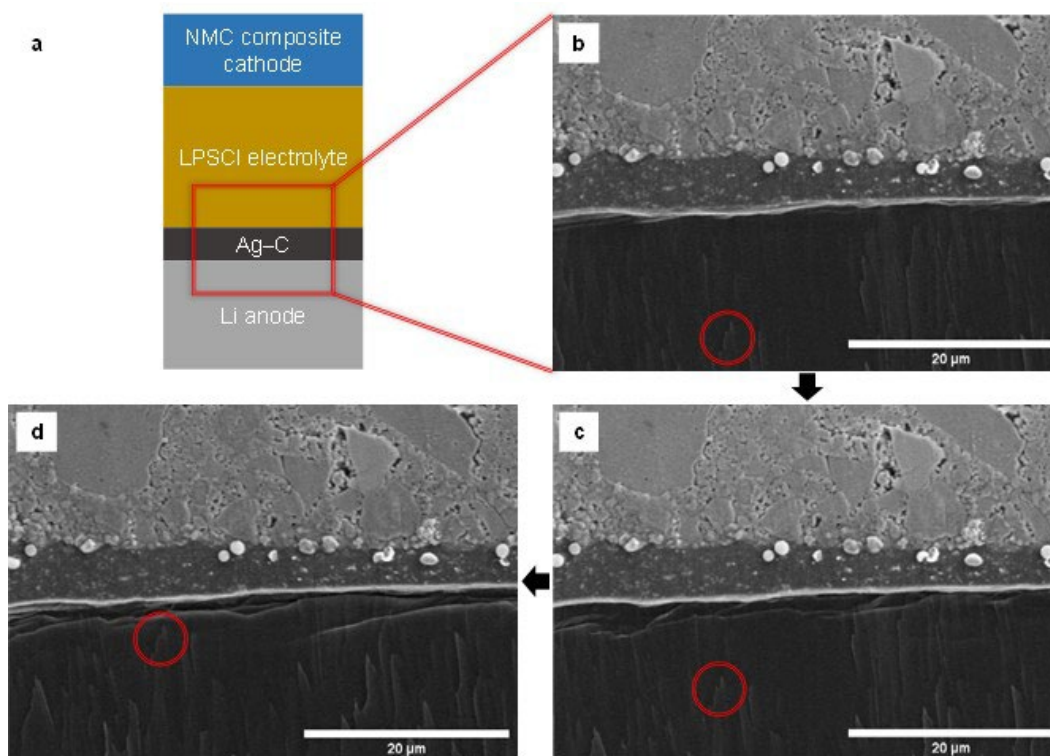


Figure XVI.15.7 Structure (a) and in operando morphology characterization (b–d) of an NMC|LPSCI|Ag–C|Li micro-cell during discharge. The imaging area in Figure a is highlighted with a rectangle. A moving structural feature in Figure b–d is highlighted with a circle.

We have also monitored the morphology evolution during the charge process (Figure XVI.15.8). In particular, we want to highlight an area where the contact between the electrolyte (the top, lighter layer in Figure XVI.15.8a) and the interlayer (the middle, darker layer) is not intimate. A line crack quickly propagate into a gap as charging starts (Figure XVI.15.8b). As charging continues, the gap becomes wider, and bright particles pop up from the interlayer throughout the thickness of the layer (Figure XVI.15.8c). The bright particles are most likely lithium metal. Toward the end of the charge, lithium fibrils grow out of the further-widened gap (Figure XVI.15.8d), at which point the cell short-circuits. It appears that the initial crack is what leads to the eventual cell failure.

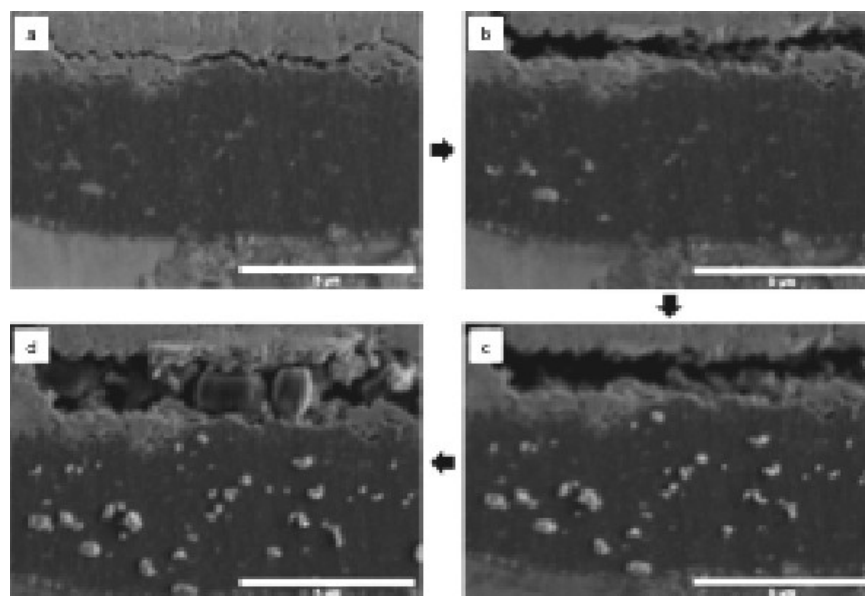


Figure XVI.15.8 In operando morphology characterization of an NMC|LPSCl|Ag-C|Li micro-cell during charge.

Conclusions

We have demonstrated high capacity and cycling stability in solid-state lithium batteries consisting of cast cathode, cast thin electrolyte, and lithium anode after a series of optimization. A nano-cell setup is developed to serve as a platform for investigating the evolution of structural and chemical properties with high spatial and chemical resolution. A micro-cell setup is advanced to allow for in operando observation during cell operation. These platforms allow us to probe the failure mechanism of solid-state cells from multiple angles. Clearly many potential factors governing the longevity of the cells are involved from the limited examples we presented herein. The relationship between the interfacial contact and cell performance is therefore a focus of our future study.

Key Publications

1. Fang Hao, Yanliang Liang, Ye Zhang, Zhaoyang Chen, Jibo Zhang, Qing Ai, Hua Guo, Zheng Fan, Jun Lou, Yan Yao*, High-Energy All-Solid-State Organic–Lithium Batteries Based on Ceramic Electrolytes, *ACS Energy Letters* **2020**, 6, 201–207.
2. Jibo Zhang, Zhaoyang Chen, Qing Ai, Tanguy Terlier, Fang Hao, Yanliang Liang, Hua Guo, Jun Lou, Yan Yao*, Microstructure engineering of solid-state composite cathode via solvent-assisted processing *Joule* **2021**, 5, 1845–1859.
3. Benjamin Emley, Yanliang Liang*, Rui Chen, Chaoshan Wu, Miao Pan, Zheng Fan, Yan Yao*, On the quality of tape-cast thin films of sulfide electrolytes for solid-state batteries, *Materials Today Physics* **2021**, 18, 100397.
4. Chaoshan Wu, Jiatao Lou, Jun Zhang, Zhaoyang Chen, Akshay Kakar, Benjamin Emley, Qing Ai, Hua Guo, Yanliang Liang, Jun Lou, Yan Yao*, Zheng Fan*, Current status and future directions of all-solid-state batteries with lithium metal anodes, sulfide electrolytes, and layered ternary oxide cathodes. *Nano Energy* **2021**, 106081.

Acknowledgements

We thank our UH team members Prof. Zheng Fan and Prof. Yanliang Liang and our collaborators Prof. Jun Lou and Prof. Hua Guo at Rice University. We appreciate the support from Tien Duong, DOE Technology Development Manager, and Mr. Walter Parker and Ms. Colleen Butcher at NETL for project management.

XVI.16 First-Principles Modeling of Cluster-Based Solid Electrolytes (Virginia Commonwealth University)

Puru Jena, Principal Investigator

Virginia Commonwealth University
Department of Physics, Virginia Commonwealth University
701 West Grace Street
Richmond, VA 23284
E-mail: pjena@vcu.edu

Hong Fang, Principal Investigator

Virginia Commonwealth University
Department of Physics, Virginia Commonwealth University
701 West Grace Street
Richmond, VA 23284
E-mail: hfang@vcu.edu

Tien Q. Duong, DOE Technology Development Manager

U.S. Department of Energy
E-mail: Tien.Duong@ee.doe.gov

Start Date: October 1, 2019

End Date: October 31, 2022

Project Funding: \$991,335

DOE share: \$793,040

Non-DOE share: \$198,295

Project Introduction

The current modeling schemes to develop advanced solid electrolytes are focusing on materials in which the building blocks are individual atoms. Our theoretical approach is a paradigm shift in solid electrolyte design. Instead of atoms, we focus on clusters as the building blocks and model these solid electrolytes and their interfaces with electrodes, especially Li-metal anode, for their successful implementation in solid-state batteries. The advantage of using the cluster-ions to replace elemental-ions is that the size, composition, and shape of the former can be tailored to achieve higher superionic conductivity, electrochemical stability, and charge transfer across solid-solid interfaces than conventional materials. Specifically, our proposed project includes: (1) Developing cluster-based solid electrolytes, where the halogen components are replaced by cluster-ions that mimic the chemistry of halogens but are characterized by additional degrees of freedom, including the size, shape, and composition. (2) Providing a fundamental understanding of the ionic conduction mechanism in the newly-developed cluster-based solid electrolytes; (3) Modeling the interfacial properties (i.e., structural, chemical and transport) between the cluster-based solid electrolytes and electrodes at the atomic level. For the cluster-based solid electrolytes incompatible with the Li-metal anode or cathode materials, potential candidates for interfacial coatings will be identified and studied. (4) Providing a theoretical framework towards optimizing critical parameters, such as current density, kinetic and mechanical stability, that will guide experimentalists to attain desired cathode-electrode interface for cluster-based solid electrolytes.

Objectives

The objective of the project is to use cluster-ions, which are stable atomic clusters that mimic the chemistry of individual atoms, as the building blocks of new solid electrolytes (SEs) for Li-ion batteries and the corresponding battery system. The advantages of using cluster-ions to replace elemental ions is that the size, shape, and composition of the former can be tailored to achieve higher superionic conductivity, electrochemical stability, and charge transfer across the solid-solid interfaces than the conventional materials. More specifically, the goal is to develop superior SEs based on cluster-ions and to model these SEs and their interfaces with electrodes, especially with the Li-metal anode, for successful integration into high performance SSBs for EVs. The team will model and screen cluster-based SEs that, compared to conventional SEs, have

low activation energies, practical room-temperature ionic conductivities, wide electrochemical stability windows, and desired mechanical properties that, for example, can inhibit the Li-metal anode dendrite growth. They will provide a fundamental understanding of the ionic conduction mechanism in the newly developed, cluster-based SEs and identify means to further improve property metrics via chemical and defect engineering. The team will model the interfacial properties, such as the structural, chemical, electrochemical, and ion/charge transfer properties, between the cluster-based SEs and electrodes at the atomic level, as well as find the interfacial coating materials with desired properties. Based on accumulated data from modeling, they will establish links between the basic parameters of the cluster-ions and the bulk/interface properties, which can directly guide experiments. Meanwhile, the team will work closely with experimentalists in the BMR Program to complement the project's theoretical efforts and to guide them in focused development of the predicted cluster-based SEs and the interfaces.

Approach

1. *Developing new cluster-based solid electrolyte materials using selected cluster-ions from the established database of clusters.*

The possible crystal structures of the newly developed materials will be determined using structure prediction techniques, such as the particle swarm optimization and the evolutionary algorithm [1],[2]. The most stable phases that contain the cluster-ion from the search will be considered as the initial structures, subject to further investigation. Each cluster-based solid electrolyte material with the determined crystal structure will be fully optimized (for both the ion positions and lattice parameters) to its energy minimum using DFT calculations [3],[4]. The lattice dynamic stability of the structure will then be tested by phonon calculations based on the optimized structure; absence of imaginary frequency would define a stable structure. The formation energy of the lattice-dynamically stable cluster-based solid electrolyte material will be calculated. Its thermodynamics stability will be investigated by calculating the pair correlation function and the position correlation function using the structural data from MD simulations at different temperatures. For each cluster-based solid electrolyte that is thermally stable, possible defects involving Li^+ in the material will be studied by calculating their formation and binding energies. Next, for each cluster-ion based solid electrolyte, a supercell system with the relevant defect will be subjected to MD simulations with constant volume at different temperatures. MSD of the Li-ions will be calculated using our own programs. The diffusion coefficients and the ionic conductivity at different temperatures will be calculated from the MSD using the Nernst-Einstein relation. The room temperature ionic conductivity and the activation energy of the material will be obtained by fitting to the Arrhenius relationship. The relevant electronic properties, including the bandgap, the band edges and the electronic conductivity will be calculated using DFT. The hybrid functional (e.g., HSE [5]) or meta-GGA (e.g., mBJ [6]) will be applied. All the obtained results from the above process will be collected into a database.

2. *Modeling the ionic conduction mechanism in the cluster-based solid electrolyte materials.*

To study the ionic conduction mechanism, we first investigate the channel size inside the solid electrolyte for Li^+ migration, created by different cluster-ions. Next, the migration routes of Li^+ in the presence of the chosen defect will be studied. Given the non-spherical nature of the cluster-ion, there are a number of inequivalent migration routes. The energy barrier for each of these will be calculated using the NEB method. The effect of the changing orientation of the cluster-ions on the ionic conductivity of the material will be studied.

3. *Modeling and optimizing the chemical mixing and doping in the cluster-based solid electrolyte materials.*

Different phases with mixed halides and clusters will be created via chemical mixing. Their structures with different ratio will be fully optimized using DFT energy calculations. Each optimized system will then be investigated using DFT calculations and MD simulations. The ratio that can enable the highest ionic conductivity while maintaining merits in other aspects will be recorded in the database.

4. Modeling and optimizing the defect formation and concentration.

Models will be built for the cation-doped cluster-based solid electrolyte systems with supercells that contain different concentrations of the Li-vacancy defects. The structure of these systems will first be energetically optimized using DFT calculations. Then, the structures will be studied using MD simulations at fixed temperature. The ionic conduction properties of the resulting structures will be investigated. The defect concentration that can entail the highest ionic conductivity in the cluster-based solid electrolyte will be revealed.

5. Modeling the electrolyte-electrode interfaces.

Given that many of the cluster-based solid electrolytes material are metastable, the possible equilibrium phases at the interfaces when the solid electrolyte is in contact with the electrode will be first identified by building lithium grand potential diagrams at different battery voltages (modeled by the lithium chemical potential) using the crystal data from the material database, e.g., the Materials Project [7]. Next, DFT calculations and MD simulations will be conducted to study the stability, electronic and ionic conduction properties of the obtained equilibrium phase at the interface. The interface between the cluster-based solid electrolyte and the equilibrium phase, or between the equilibrium phase and the electrode will be modeled using stacked slabs of the active materials. The local bonding reconstruction and charge transfer, as well as possible amorphization of the interface will then be studied using MD simulations.

6. Modeling and optimizing the interface between the cluster-based solid electrolyte and the identified coating materials.

Possible alloying phases between the cluster-based solid electrolyte and the coating material will be investigated using the cluster expansion method [8],[9]. The alloys that appear on or near the built convex hull will be selected as the stable phases and their relevant properties, e.g., the ionic conductivity, will be studied using DFT calculations and MD simulations.

7. Establishing links between the key parameters of the cluster-ion and the bulk and interfacial properties of the cluster-based solid electrolyte materials.

With the data accumulated in our database, links between the key parameters (such as the size, shape, composition, charge distribution, and electron affinity) of the cluster-ion and the cluster-based solid electrolyte as well as its interfaces can now be drawn by using machine learning techniques. The established links aim to guide experiments in terms of which cluster-ions to choose that can entail high-performance cluster-based solid electrolytes and interfaces with the electrodes, especially with the Li-metal anode. The PI and team at VCU will work in close collaboration and coordination (unfunded) with VTO-BMR (Vehicle Technology Office's Battery Materials Research) Program PIs working at multiple DOE National Laboratories on solid electrolyte modeling and interfaces and specifically with experimental groups working on synthesis and interfacial characterization of Li-based solid electrolytes.

Results

1. Complete development of new cluster-based solid electrolyte (SE) materials with a database. (Q1, FY 2021; Completed, December 31, 2020)

The database (Figure XVI.16.1) contains the chemical compositions of the SE materials, their physical properties (e.g., lattice dynamics and electronic structures), their activation energies and ionic conductivities at different temperatures, as well as the fast-ion transport mechanism. In addition, we have added to the database a few nonstoichiometric configurations of selected SE materials which exhibit very high ionic conductivities at room temperature. We have also written programs (coded in Python and Fortran) to systematically find and characterize the topology of each SE, long-lived long-distance Li-ion transitions, as well as Li-ion and cluster-ion dynamics. A fundamental mechanism has been uncovered from the analysis to explain the fast-ion transport in the SE.

Data_1 Cluster-ion based structures studied as candidates for electrolytes of lithium superionic conductors. A well-known typical argyrodite solid electrolyte $\text{Li}_6\text{PS}_5\text{Cl}$ is listed for comparison. "EA" stands for electron affinity of the cluster-ion. Band gaps are in eV. "Z" stands for the number of formula units in the unit cell. "S" means lattice dynamically stable and "INS" means instable. "C" means electrically conductive. "IC" means the calculated ionic conductivity at room temperature. " E_a " means the activation energy.

Material	Structure Identified	Z	Lattice Dynamics	Bandgap	IC (mS/cm)	E_a (eV)
$\text{Li}_6\text{PS}_5\text{Cl}$	○	4	S	3.4 (HSE)	0.25×10^{-3}	0.647
$\text{Li}_{6.25}\text{PS}_{5.25}\text{Cl}_{0.75}$	Nonstoichiometric $\text{Li}_6\text{PS}_5\text{Cl}$ with Li-excess actually synthesized in the experiment				14	0.210
$\text{Li}_6\text{PS}_5(\text{CN})$	○	1	S	3.22 (HSE) 2.14 (mBJ)	0.18	0.353
$\text{Li}_6\text{PS}_5(\text{OH})$	●	1	S	4.37 (HSE) 3.18 (mBJ)	82	0.166
$\text{Li}_{6.25}\text{PS}_{5.25}(\text{OH})_{0.75}$	Nonstoichiometric configuration with Li-excess				51	0.183
$\text{Li}_6\text{PS}_5(\text{SCN})$	○	1	S	3.40 (HSE) 2.22 (mBJ)	1.9	0.201
$\text{Li}_{6.25}\text{PS}_{5.25}(\text{SCN})_{0.75}$	Nonstoichiometric configuration with Li-excess				10	0.197
$\text{Li}_6\text{PS}_5(\text{BH}_4)$	○	1	S	3.47 (HSE) 2.25 (mBJ)	0.20	0.333
$\text{Li}_{6.25}\text{PS}_{5.25}(\text{BH}_4)_{0.75}$	Nonstoichiometric configuration with Li-excess				177	0.108
$\text{Li}_6\text{PS}_5(\text{BF}_4)$	○	1	S	3.50 (HSE) 2.41 (mBJ)	0.15	0.323
$\text{Li}_6\text{PS}_5(\text{CB}_6\text{H}_7)$	○	1	S	4.39 (HSE) 3.21 (mBJ)	296	0.090
$\text{Li}_6\text{PS}_5(\text{CB}_4\text{H}_5)$	○	4	S	2.66 (mBJ)	235	0.112
$\text{Li}_6\text{PS}_5(\text{B-H})$	●	4	S	2.32 (mBJ)	melting	
$\text{Li}_6\text{PS}_5(\text{CB}_7\text{H}_6)$	○	1	S	4.20 (HSE) 3.05 (mBJ)	78	--
$\text{Li}_6\text{PS}_5(\text{B}_6\text{H}_6)$	●	1	S	C	11	0.254
$\text{Li}_6\text{PS}_5(\text{CB}_7\text{H}_8)$	○	1	INS	--	--	--
$\text{Li}_6\text{PS}_5(\text{B}_8\text{H}_8)$	●	8	INS	--	--	--
$\text{Li}_6\text{PS}_5(\text{B}_9\text{H}_9)$	○	8	INS	--	--	--
$\text{Li}_6\text{PS}_5(\text{CB}_8\text{H}_9)$	●	1	S	2.99 (HSE) 1.85 (mBJ)	103	0.101
$\text{Li}_6\text{PS}_5(\text{CB}_9\text{H}_9)$	○	2	S	3.96 (HSE) 2.87 (mBJ)	310	0.051

○ The cluster-ion remains in the lowest-energy structure.
 ● The cluster-ion partially reacts with PS_4^{3-} in the lowest-energy structure. One hydrogen in B_nH_n is replaced by S and $\text{B}_n\text{H}_{n-1}\text{S}^{2-}$, HS^- and PS_3^{3-} are formed in the structure.
 — The cluster-ion is highly distorted or disintegrated in the lowest-energy structure.

Data_2 Cluster-ion based structures studied as candidates for electrolytes of lithium superionic conductors. "EA" stands for electron affinity of the cluster-ion. Band gaps are in eV. "Z" stands for the number of formula units in the unit cell. "S" means lattice dynamically stable and "INS" means instable. "C" means electrical conducting. "IC" is the calculated ionic (Li^+) conductivity at room temperature. " E_a " is the activation energy.

Material	Tolerance Factor	Z	Lattice Dynamics	Bandgap	IC (mS/cm)	E_a (eV)
$\text{Li}_3\text{O}(\text{SCN})$	1.015	1	S	2.50	11	0.224
$\text{Li}_3\text{S}(\text{SCN})$	0.844			3.08	62	0.142
$\text{Li}_3\text{S}(\text{CB}_6\text{H}_7)^a$	1.157	1	S	2.97	928 (800 K)	--
$\text{Li}_3\text{S}(\text{CB}_4\text{H}_5)$	1.157	1	S	3.34	531 (600 K)	--
$\text{Li}_3\text{S}(\text{B}_7\text{H}_7)$	1.164	1	S	C	9.8	0.214
$\text{Li}_3\text{S}(\text{CB}_5\text{H}_6)$	1.170	1	S	3.52	0.0	--
$\text{Li}_3\text{S}(\text{B}_6\text{H}_6)^a$	1.179	8	S	3.45	412 (500 K)	--
$\text{Li}_3\text{S}(\text{CB}_7\text{H}_8)^a$	1.182	1	S	2.86	1185 (800 K)	--
$\text{Li}_3\text{S}(\text{B}_8\text{H}_8)$	1.197	1	S	C	30	0.143
$\text{Li}_3\text{S}(\text{B}_5\text{H}_5)$	1.202	8	S	1.40	0.38	0.360

^a Calculations show that these materials exhibit little fast-ion conductivities at room temperature. In each of these cases, the Li^+ conductivity corresponds to the value at the simulated temperature specified in the parenthesis. The activation energy from the Arrhenius relationship is, therefore, unavailable.

Figure XVI.16.1 Studied cluster-based solid electrolytes in the established database.

2. Structural studies of the chemically mixed systems containing both cluster-ions and elemental ions. (Q2, FY 2021; Completed, March 31, 2021)

The structures of the cluster-based solid electrolyte materials with different halogen-substitution concentrations have been first identified based on a periodic electrostatic model and then further optimized using density functional theory (DFT). For each cluster-based solid electrolyte in the previously developed database, given a specified concentration of halogen in the material, all possible substitutional configurations in the range of 0 to 100% with a 12.5% step size are considered.

Data_1 Calculated room-temperature ionic conductivity (IC in mS/cm) and activation energy (E_a in eV) of the studied halogen-cluster mixed solid electrolytes (SE). The values of the original cluster-based SE (with $x = 0$) are colored in blue. The chemically-mixed cases with comparable or improved values are colored in red.										
x	$\text{Li}_6\text{PS}_5(\text{BF}_4)_{1-x}\text{Cl}_x$		$\text{Li}_6\text{PS}_5(\text{BH}_4)_{1-x}\text{Cl}_x$		$\text{Li}_6\text{PS}_5(\text{OH})_{1-x}\text{Cl}_x$		$\text{Li}_6\text{PS}_5(\text{CN})_{1-x}\text{Cl}_x$		$\text{Li}_6\text{PS}_5(\text{SCN})_{1-x}\text{Cl}_x$	
	IC	E_a	IC	E_a	IC	E_a	IC	E_a	IC	E_a
0	0.15	0.323	0.18	0.336	82	0.166	0.18	0.353	1.9	0.201
0.125	0.018	0.406	5.17	0.206	68.2	0.167	1.15	0.29	4.14	0.221
0.25	0.021	0.407	0.64	0.299	99.6	0.154	0.34	0.336	0.0048	0.47
0.375	2.4×10^{-4}	0.595	10.5	0.177	13	0.25	0.234	0.351	1.06	0.302
0.5	0.115	0.359	0.014	0.457	4.23	0.3	1.65	0.272	6.42	0.218
0.625	4.4×10^{-5}	0.647	0.215	0.339	6.35	0.283	0.83	0.305	7.14	0.222
0.75	0.0028	0.493	100.4	0.118	10.2	0.256	0.79	0.309	1.36	0.288
0.875	0.415	0.326	0.043	0.416	31.5	0.208	0.74	0.299	5.58	0.226
1	2.5×10^{-4}	0.647	2.5×10^{-4}	0.647	2.5×10^{-4}	0.647	2.5×10^{-4}	0.647	2.5×10^{-4}	0.647

Data_2 Calculated room-temperature ionic conductivity (IC) and activation energy (E_a) of the studied multi-valence metal doped cluster-based solid electrolytes (SE). The ionic radii of Li^+ , Mg^{2+} , Al^{3+} and Ga^{3+} are 0.90, 0.86, 0.68 and 0.76 Å, respectively. The values of the original cluster-based SE (without doping) are colored in blue. The cation-doped cases with comparable or improved values are colored in red.		
SE	IC (mS/cm)	E_a (eV)
$\text{Li}_6\text{PS}_5(\text{BF}_4)$	0.15	0.323
$\text{Li}_{5.75}\text{Mg}_{0.125}\text{PS}_5(\text{BF}_4)$	0.14	0.319
$\text{Li}_{5.625}\text{Al}_{0.125}\text{PS}_5(\text{BF}_4)$	0.008	0.429
$\text{Li}_{5.625}\text{Ga}_{0.125}\text{PS}_5(\text{BF}_4)$	0.023	0.394
$\text{Li}_6\text{PS}_5(\text{BH}_4)$	0.20	0.333
$\text{Li}_{5.75}\text{Mg}_{0.125}\text{PS}_5(\text{BH}_4)$	0.005	0.485
$\text{Li}_{5.625}\text{Al}_{0.125}\text{PS}_5(\text{BH}_4)$	8.0	0.189
$\text{Li}_{5.625}\text{Ga}_{0.125}\text{PS}_5(\text{BH}_4)$	0.40	0.338
$\text{Li}_6\text{POS}_4(\text{SH})$	82	0.166
$\text{Li}_{5.75}\text{Mg}_{0.125}\text{POS}_4(\text{SH})$	20	0.222
$\text{Li}_{5.625}\text{Al}_{0.125}\text{POS}_4(\text{SH})$	37	0.197
$\text{Li}_{5.625}\text{Ga}_{0.125}\text{POS}_4(\text{SH})$	40	0.191
$\text{Li}_6\text{PS}_5(\text{CN})$	0.18	0.353
$\text{Li}_{5.75}\text{Mg}_{0.125}\text{PS}_5(\text{CN})$	6.3	0.228
$\text{Li}_{5.625}\text{Al}_{0.125}\text{PS}_5(\text{CN})$	0.44	0.339
$\text{Li}_{5.625}\text{Ga}_{0.125}\text{PS}_5(\text{CN})$	1.2	0.300
$\text{Li}_6\text{PS}_5(\text{SCN})$	1.9	0.201
$\text{Li}_{5.75}\text{Mg}_{0.125}\text{PS}_5(\text{SCN})$	3.1	0.208
$\text{Li}_{5.625}\text{Al}_{0.125}\text{PS}_5(\text{SCN})$	0.11	0.335
$\text{Li}_{5.625}\text{Ga}_{0.125}\text{PS}_5(\text{SCN})$	0.08	0.350

Figure XVI.16.2 Chemically-mixed and cation-doped cluster-based solid electrolytes in the established database.

3. Characterizations of the chemically mixed systems. (Q3, FY 2021; Completed, June 30, 2021)

Based on the ground-state structures (as demonstrated in Figure XVI.16.1) obtained in the last period study for different chemical mixing concentrations (in the range of 0 to 100% with a 12.5% step size), the ionic

conductivities and activation energies of 35 new solid electrolytes (SEs) have been studied and characterized. The ionic conductivity (e.g., at RT) and the activation energy of the chemically-mixed system do not change monotonically with the increasing halogen concentration. Therefore, for each studied system, there exists an optimal halogen concentration that can entail the best fast-ion diffusion properties. In general, the calculated ionic conductivity and the activation energy of the chemically-mixed systems are in the same order or better than those of the corresponding cluster-based systems (Figure XVI.16.2). This is accompanied by the great reduction of the activation energy of the system.

4. Structural and elemental optimization of the cation-doped cluster-based solid electrolytes. (Q4, FY 2021; Completed, September 30, 2021)

Based on the cluster-based solid electrolytes in our database, the cation-doped systems, $\text{Li}_{5.75}\text{M}_{0.125}\text{PS}_5\text{X}$ ($\text{M} = \text{Mg}^{2+}$) and $\text{Li}_{5.625}\text{M}_{0.125}\text{PS}_5\text{X}$ ($\text{M} = \text{Al}^{3+}/\text{Ga}^{3+}$; $\text{X} = \text{BF}_4^-, \text{BH}_4^-, \text{OH}^-, \text{CN}^-$ and SCN^-), are modeled and studied. Multi-valence metal elements, including Mg^{2+} , Al^{3+} and Ga^{3+} , are selected due to their compatible ionic radii (0.86, 0.68 and 0.76 Å, respectively) with that Li^+ (0.9 Å).

5. Complete modeling and optimizing the chemical mixing and cation doping for the cluster-ion based solid electrolyte materials with enriched database. (Q4, FY 2021; Completed, September 30, 2021)

The chemically-mixed and cation doped systems together with their key properties are added into our database of cluster-based solid electrolytes, as shown in Figure I.1.A.2. It is found that, in most cases, both the chemical mixing and the cation doping can significantly improve the ionic conduction properties of the cluster-based solid electrolytes.

Conclusions

The major conclusions are:

1. The newly developed cluster-based solid electrolyte materials show good properties in terms of their high room-temperature ionic conductivities as well as low activation energies. Based on each of them, a number of nonstoichiometric (e.g., with Li-excess) new solid electrolytes have been developed which exhibit even better properties.
2. Besides creating nonstoichiometric configurations, chemically mixing with both the cluster-ion and halogen is another viable way to significantly improve the properties of the cluster-based solid electrolytes.
3. Doping with selected multi-valence cations can further improve the properties of the cluster-based solid electrolytes.

Key Publications

1. H. Fang, P. Jena, J. Nanda, D. Mitlin et al., Heavily Tungsten Doped Sodium Thioantimonate Solid State Electrolytes with Exceptionally Low Activation Energy for Ionic Diffusion, *Angew. Chem.* DOI: 10.1002/anie.202110699, 2021, Accepted.
2. H. Fang and P. Jena, Advanced lithium superionic conductors enabled by local interatomic deformation. *Nature Communications*, 2021, Under revision.
3. H. Fang, P. Jena, Y. Wu et al., Antiperovskite K_3OI for K-Ion Solid State Electrolyte, *J. Phys. Chem. Lett.* 12, 7120, 2021.
4. H. Fang, P. Jena, J. Nanda, D. Mitlin et al., Structure and Interface Modification Strategies in Emerging Inorganic Solid-State Electrolytes (SSEs) for Lithium, Sodium and Potassium Batteries, *Joule*, 2021, Accepted.

5. Collaboration with the Dr. J. Nanda's Oak Ridge National Laboratory group: Synthesis and Design Rules for Protiated Antiperovskites, 2021, Under revision.
6. Quarterly Research Performance and Progress Reports (4), DOE BMR Quarterly reports (4), and Annual Merit Review report.

References

1. Y. Wang, J. Lv, L. Zhu, Y. Ma, CALYPSO: A Method for Crystal Structure Prediction, *Comput. Phys. Commun.* **2012**, 183, 2063.
2. A. R. Oganov, C. W. Glass, Crystal Structure Prediction Using Evolutionary Algorithms: Principles and Applications, *J. Chem. Phys.* **2006**, 124, 244704.
3. S. J. Clark, M. D. Segall, C. J. Pickard, P. J. Hasnip, M. J. Probert, K. Refson, M. C. Payne, First Principles Methods Using CASTEP, *Zeitschrift fuer Kristallographie.* **2005**, 220, 567.
4. G. Kresse, J. Furthmüller, Efficiency of Ab Initio Total Energy Calculations for Metals and Semiconductors Using a Plane-Wave Basis Set, *Int. J. Comput. Mater. Sci. Eng.* **1996**, 6, 15.
5. A. V. Krukau, O. A. Vydrov, A. F. Izmaylov, G. E. Scuseria, Influence of the Exchange Screening Parameter on the Performance of Screened Hybrid Functionals, *J. Chem. Phys.* **2006**, 125, 224106.
6. J. Sun, A. Ruzsinszky, J. P. Perdew, Strongly Constrained and Appropriately Normed Semilocal Density Functional, *Phys. Rev. Lett.* **2015**, 115, 036402.
7. A. Jain, S. P. Ong, G. Hautier, W. Chen, W.D. Richards, S. Dacek, S. Cholia, D. Gunter, D. Skinner, G. Ceder, K.A. Persson, The Materials Project: A Materials Genome Approach to Accelerating Materials Innovation, *APL Materials.* **2013**, 1, 011002.
8. A. V. D. Walle, G. Ceder, Automating First-Principles Phase Diagram Calculations, *J. Phase Equilib.* **2002**, 23, 348.
9. A. V. D. Walle, M. Asta, G. Ceder, The Alloy Theoretic Automated Toolkit: A User Guide, *Calphad.* **2002**, 26, 539.

XVI.17 Predictive Engineering of Interfaces and Cathodes for High-Performance All Solid-State Lithium-Sulfur Batteries (University of Louisville)

Badri Narayanan, Principal Investigator

University of Louisville
332 Eastern Parkway
Louisville, KY 40292
E-mail: badri.narayanan@louisville.edu

Tien Q. Duong, DOE Technology Development Manager

U.S. Department of Energy
E-mail: Tien.Duong@ee.doe.gov

Start Date: October 1, 2019
Project Funding: \$1,250,000

End Date: September 30, 2022
DOE share: \$1,000,000

Non-DOE share: \$250,000

Project Introduction

All solid lithium-sulfur battery (ASLSB) is a promising next-generation energy storage technology due to its high theoretical capacity (~ 1675 Ah/kg; ~ 5 -6 times higher than state-of-the-art Li-ion batteries), high promised energy density (400 Wh/kg), safety, no polysulfide-shuttling, and natural abundance of sulfur. Sulfide (Li_2S - P_2S_5) solid electrolytes (SSEs) possess high Li-ion conductivity ($\sim 10^{-3}$ S/cm), good elastic stiffness (~ 30 GPa), good stability against Li metal, and low flammability. Such a collection of unique properties make them promising for use in long-lived, safe, high-capacity Li-S batteries for all-electric transportation. Despite this promise, ASLSBs (even using SSEs) remain far from commercialization due to unresolved issues at the electrode-electrolyte interfaces, including (a) poor contact, and high resistance to Li^+ ion transport across the cathode/SSE interface, (b) poor ionic/electronic conduction within the cathode, and (c) dendrite growth at the Li/SSE interface. Most of these daunting challenges arise primarily from a lack of fundamental understanding of electrochemical/chemical and transport processes that occur at electrode/electrolyte interfaces, especially at atomic to mesoscopic scales.

Here, we propose to bridge this knowledge gap and address the interfacial issues by developing highly accurate materials models at atomic-to-mesoscopic length/time scales using data-centric and machine learning methods. Successful development of these models will significantly advance the current state-of-the-art in fundamental understanding of reaction chemistry, kinetics, charge transfer, and dendrite growth at electrified solid-solid interfaces. Multi-scale simulations based on the newly developed models, alongside our wet-chemistry synthesis and advanced characterization will unravel novel strategies to mitigate interfacial resistance, enable precise control over the composition/morphology of solid electrolyte interphase (SEI) and design cathodes with high sulfur loading. Broadly, fundamental knowledge gained by this work will enable development of high-performance ASLSBs that meet DOE targets of specific energy (350 Wh/kg @C/3), sulfur loading (> 6 mg/cm²), and high cycle life (1000).

Objectives

The primary goal of this project is to leverage data-driven methods and ML strategies to develop accurate multi-physics models for all-solid-state Li-S battery (ASLSB) materials that can capture electrochemical and transport phenomena over atomic-to-mesoscopic length/timescales; these models will be rigorously validated by synthesis and advanced characterization experiments. The team will leverage the predictive power of these models, alongside synthesis/characterization experiments and battery fabrication to address longstanding issues at the electrode/electrolyte interfaces in ASLSBs. The project's proposed technology involves the following: (1) halide-doped solid sulfide electrolytes that can concurrently provide high Li^+ ion conductivity and suppress dendrite growth; (2) novel mesoporous cathode composed of interconnected carbon nano-cages co-infiltrated

with sulfur and sulfide electrolyte, which hold potential to allow high sulfur loading and optimal ion/electron pathways; and (3) functionalization of sulfide electrolyte with ionic liquids to improve physical contact and minimize impedance at the cathode/electrolyte interface.

Approach

The project brings together innovative solutions in multi-scale materials modeling, electrolyte synthesis, fabrication of cathode architecture, and electrolyte functionalization to overcome the issues at electrode-electrolyte interfaces in ASLSBs. The central idea is to employ a data-driven and ML-based approach to develop accurate multi-physics battery models at atomic-to-mesoscopic scales. This approach overcomes critical problems with existing model development methods by foregoing need for pre-defined functional forms, introducing deep-learning technique to describe reactivity, and employing optimization methods that do not require human intuition. Multi-scale simulations based on the newly developed models will provide insights into electrochemical phenomena at electrode/electrolyte interfaces.

Results

1. Fundamental understanding of the atomic-scale processes at cathode-electrolyte interface

Solid sulfide electrolyte (SSE) materials comprise of networks of several P-S anion motifs surrounded by Li ions. For example, Li_7PS_6 , $\text{Li}_4\text{P}_2\text{S}_6$, Li_2PS_3 , and $\text{Li}_7\text{P}_3\text{S}_{11}$ electrolyte systems comprise of PS_4^{3-} , $\text{P}_2\text{S}_6^{2-}$, PS_3^- and $\text{P}_2\text{S}_7^{4-}$ motifs, respectively. We employed *ab initio* molecular dynamics (AIMD) simulations to understand the effect of P-S motifs on the reactivity of cathode/electrolyte interfaces. We considered cathodes at two extreme states of charging, namely (a) fully charged: S_8 (cubic, *Fddd*), and (b) fully discharged: Li_2S (face-centered cubic). We chose three different SSE compositions for this study, Li_7PS_6 , $\text{Li}_4\text{P}_2\text{S}_6$, Li_2PS_3 containing PS_4^{3-} , $\text{P}_2\text{S}_6^{2-}$, and PS_3^- motifs, respectively. For all the cases, we investigated the interface between the cathode (Li_2S and S_8) and SSE oriented such that their crystallographic [001] directions are aligned normal to the interface (Figure XVI.17.1)

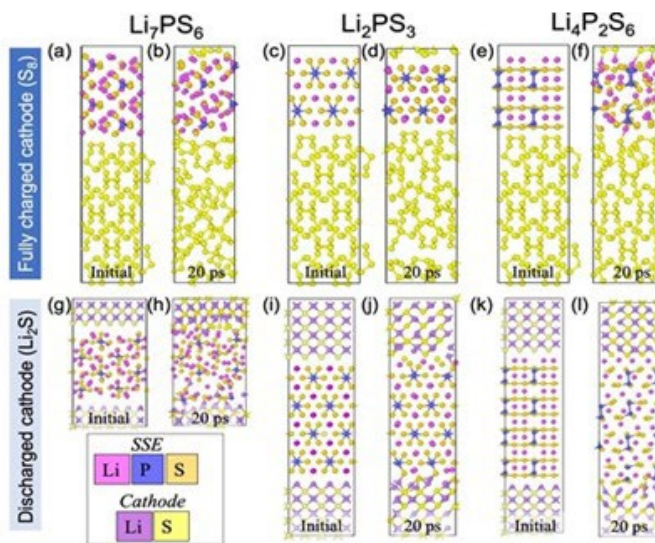


Figure XVI.17.1 Structural evolution of cathode/electrolyte interface obtained from AIMD simulations under ambient conditions. The atomic-scale structure of interface between $\text{S}_8(001)$ (i.e., fully charged cathode) and electrolytes with varying P-S motifs (a,b) $\text{Li}_7\text{PS}_6(001)$ (PS_4), (c,d) $\text{Li}_2\text{PS}_3(001)$ (PS_3), and (e,f) $\text{Li}_4\text{P}_2\text{S}_6(001)$ (P_2S_6). Corresponding interfaces with $\text{Li}_2\text{S}(001)$ (i.e., fully discharged cathode) are shown for (g,h) $\text{Li}_7\text{PS}_6(001)$, (i,j) $\text{Li}_2\text{PS}_3(001)$, and (k,l) $\text{Li}_4\text{P}_2\text{S}_6(001)$. In all panels, Li, P, and S atoms belonging to SSE are depicted as magenta, blue, and tan spheres respectively, while the Li and S in cathode are shown in dark purple and yellow colors.

AIMD simulations showed four distinct atomic processes at the cathode/SSE interface, namely: (a) breaking of PS_4^{3-} , $\text{P}_2\text{S}_6^{2-}$ and PS_3^- structural units, (b) breaking of sulfur (S_8) rings, (c) polymerization of PS_4^{3-} to form $\text{P}_2\text{S}_6^{2-}$ structural units (d) formation of new Li-S bonds at the interface. Regardless of the type of motifs, SSEs

react more with the fully discharged state of cathode (Li_2S) as compared to the fully charged state (i.e., S_8). Importantly, the nature of the motifs strongly governs the extent and type of interfacial reactions. At the interface with fully charged cathode (S_8), Li_7PS_6 and Li_2PS_3 do not decompose (Figure XVI.17.1(a-d)). Note, the PS_3^- motifs in Li_2PS_3 polymerize to form new $\text{P}_2\text{S}_6^{2-}$ motifs system (Figure XVI.17.1(c,d)). On the other hand, $\text{Li}_4\text{P}_2\text{S}_6$ exhibits decomposition reactions involving (a) ring opening of S_8 rings in the cathode via Li of SSE, and (b) conversion of $\text{P}_2\text{S}_6^{2-}$ to form P_2S_5 (Figure XVI.17.1(e,f)). Interfaces of the SSEs with Li_2S are found to be more reactive than that with S_8 , due to the presence of Li atoms in Li_2S . The PS_4^{3-} motifs (present in Li_7PS_6) decompose to form reduced species, namely, PS_3 , PS_2 , and PS . During the 20 ps of AIMD, $\sim 25\%$ of PS_4^{3-} gets decomposed ($\sim 12.5\%$ forms PS_3^- and remaining 12.5% forms PS) (Figure XVI.17.1(g,h)). For the interface of Li_2PS_3 with Li_2S , initially polymerization reaction takes place due to which all the PS_3^- motifs are converted to $\text{P}_2\text{S}_6^{2-}$ motifs. During 20 ps of AIMD, $\sim 37.5\%$ of $\text{P}_2\text{S}_6^{2-}$ motifs break into P_2S_5 . In this case, $\text{P}_2\text{S}_6^{2-}$ motif exposed to both S and Li side of Li_2S undergoes decomposition (Figure XVI.17.1(i,j)). On the other hand, only $\sim 12.5\%$ $\text{P}_2\text{S}_6^{2-}$ motifs are broken to form P_2S_5 at the interface between $\text{Li}_4\text{P}_2\text{S}_6$ and Li_2S (Figure II.9.Q.1 (k,l)). In all the three cases, the S atoms released from the decomposition of PS_4^{3-} and $\text{P}_2\text{S}_6^{2-}$ motifs moves towards the cathode to form new $\text{Li}_{(\text{cathode})}\text{-S}_{(\text{SSE})}$ bonds.

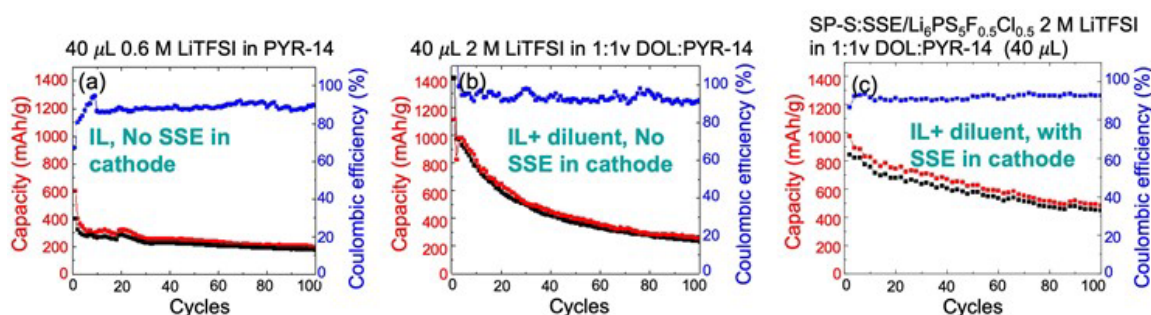


Figure XVI.17.2 Electrochemical performance during cycling of Li-S batteries made up of super P/C-S cathode, $\text{Li}_6\text{PS}_5\text{F}_{0.5}\text{Cl}_{0.5}$ SSE and Li anode with 0.04 mL of functionalizing liquid containing (a) 0.6 M of LiTFSI in PYR (b) 2M LiTFSI in PYR:DOL (1:1) using DOL diluent, and (c) 2M LiTFSI in PYR:DOL (1:1) using DOL diluent along with SSE incorporated in the cathode. Note the batteries in panels (a) and (b) do not have any SSE in the cathode. The left axis corresponds to discharge capacity, while the right axis shows the Coulombic efficiency. The batteries are cycles at a rate of C/20

In the last year, we had computationally identified $\text{Li}_6\text{PS}_5\text{F}_{0.5}\text{Cl}_{0.5}$ to be the best composition for SSE with most optimal combination of high Li-ion conductivity and stability against Li-metal anode. However, our battery fabrication experiments showed that ASLSBs with Li-anode, mesoporous carbon cathode (super-P or with carbon nano-cages), and $\text{Li}_6\text{PS}_5\text{F}_{0.5}\text{Cl}_{0.5}$ SSE showed low discharge capacity and did not charge due to poor interfacial contact on the cathode side. We found that the interfacial resistance on the cathode side can be reduced significantly by coating a mesoporous carbon cathode hosting sulfur with a concentrated solution of LiTFSI salt in N-butyl-N-methyl pyrrolidinium (PYR-14) ionic liquid (IL) (Figure XVI.17.2(a)). Although the IL enhances cycle life of solid-state Li-S batteries (with $\text{Li}_6\text{PS}_5\text{F}_{0.5}\text{Cl}_{0.5}$ electrolyte, Li anode, and mesoporous carbon cathode, the initial discharge capacity remains low (~ 600 mAh/g). This is possibly due to the high viscosity of LiTFSI-PYR14 IL, which inhibits reaction kinetics (Figure XVI.17.2(a)). To mitigate this issue, we diluted the LiTFSI-PYR14 with 1,3 dioxolane (DOL). Indeed, addition of DOL significantly increases the initial discharge capacity significantly to ~ 1100 mA/h (Figure XVI.17.2(b)). We systematically analyzed the effect of (a) concentration of LiTFSI, (b) relative fractions of PYR-14 and DOL, and (c) volume of liquid for coating. We found that functionalizing the cathode with a 0.04 mL solution containing 2M LiTFSI in 1:1 (volume) PYR:DOL gives the most optimal performance with $\text{Li}_6\text{PS}_5\text{F}_{0.5}\text{Cl}_{0.5}$ electrolyte, Li anode, and Super-P cathode (note we operated under low sulfur loading ~ 0.7 mg/cm²). Using half the volume of functionalizing liquid (i.e., 0.02 mL) yields similar capacities (~ 1100 mAh/g (cycle 1); ~ 300 mAh/g (cycle 100)) but slightly lowers Coulombic efficiency ($\sim 85\%$ and $\sim 90\%$ at 0.02 mL and 0.04 mL liquid respectively). We also tested the rate capability of the batteries. At both C/20 and C/10, initial discharge capacity is ~ 1100 mAh/g, which fades to ~ 300 mAh/g after 100 cycles. The charging profiles exhibit long plateaus ~ 2.1 V indicative of formation of long chain polysulfides. Capacity retention of the Li-S batteries can be further enhanced by

incorporating SSE in the C-S cathode to ~480 mAh/g after 100 cycles albeit with a slightly lower diminished Coulombic efficiency (Figure XVI.17.2(c)).

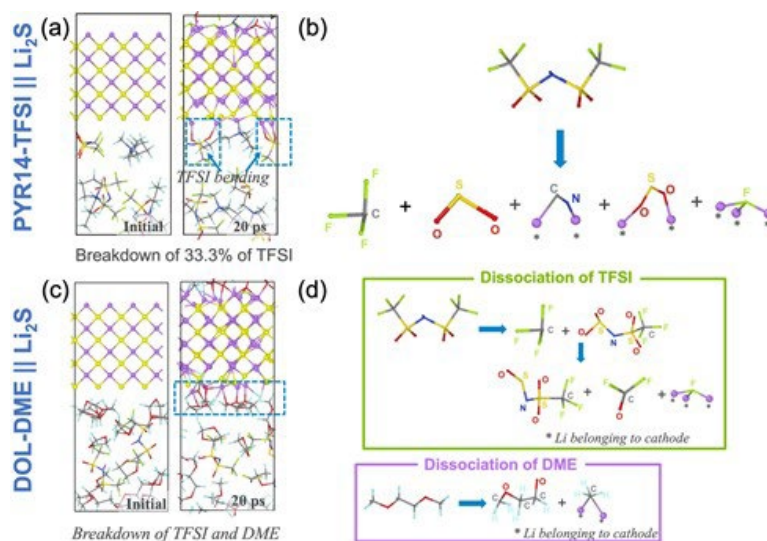


Figure XVI.17.3 Decomposition reactions of (a,b) PYR₁₄-TFSI IL, and (c,d) LiTFSI in DOL-DME near the cathode in its fully discharged state (Li₂S) obtained from ab initio molecular dynamics simulations under ambient conditions. In both panels (a,c), we show the atomic snapshots of the interface in the beginning and end of AIMD trajectory, while the key reactions are summarized in panels (b,d). Note, both Li₂S and Li₆PS₅F_{0.5}Cl_{0.5} are oriented such that their crystallographic [001] directions are aligned normal to the interface. In all cases, TFSI⁻ anion dissociates resulting in Li-F bonds. PYR and DOL do not dissociate as opposed to DME.

AIMD simulations revealed the effect of two types of functionalizing liquid, namely (a) ionic liquid ([PYR₁₄][TFSI]), and (b) glyme (2M LiTFSI in DOL:DME = 1:1 by volume) on the interfacial reactions with representative SSE (Li₆PS₅F_{0.5}Cl_{0.5}) and cathode (Figure XVI.17.3). Both [PYR₁₄][TFSI] and DOL-DME do not react with SSE (Li₆PS₅F_{0.5}Cl_{0.5}). Notably, the ethereal oxygen of DOL and DME coordinate with Li of SSE at DOL-DME || SSE interface without any decomposition; in contrast, the PYR₁₄ does not coordinate with the SSE. Similarly, no decomposition reactions were observed between the functionalizing liquid ([PYR₁₄][TFSI] or DOL-DME) and the cathode in the fully charged state (S8). Detailed analysis of our AIMD trajectories show that both [PYR₁₄][TFSI] and DOL-DME react with the cathode in its fully discharged state (i.e., Li₂S) via breakdown of the TFSI anions facilitated by the Li atoms in Li₂S (Figure XVI.17.3). However, the extent of decomposition, and the reaction products are strongly dependent on the nature of the functionalizing liquid. At the interface between [PYR₁₄][TFSI] and Li₂S-cathode, ~33.3% of [TFSI] dissociate to form -CF₃, -SO₂, and -CN species (Figure XVI.17.3(a)), consistent with previous AIMD studies on interface between [PYR₁₄][TFSI] and Li-metal [1]. The [PYR₁₄] cations remain stable throughout the simulation time (20 ps). On the other hand, at the DOL-DME || Li₂S interface, ~50% of the [TFSI] anions dissociate forming -CF₂O and -SO-N-SO₂-CF₃ species (Figure XVI.17.3(b)). Additionally, ~20% of DME break down forming -O-CH₂-CH₂-O-CH₃ and -CH₃ species. Interestingly, DOL does not dissociate against Li₂S – making it a better diluent than DME, consistent with our experiments. In both the cases ([PYR₁₄][TFSI] and DOL-DME with Li₂S-cathode), the F atoms obtained from the dissociation of [TFSI] bind with Li of the cathode to form new Li-F bonds, which could enhance interfacial stability.

2. Extend the Reactive Interatomic Potential Models Developed to Include Cathode Materials and The Interfaces

We extended the Tersoff+Qeq interatomic potential (developed in Year 1) to account for electrode/electrolyte interfaces with reasonable success. This classical potential was found to perform well for Li | SSE, and Li₂S | SSE interfaces. Note that Tersoff+Qeq predicted these interfaces to be more reactive than that shown by AIMD simulations, which raised concerns on its suitability for investigating long-time dynamics associated with these interfaces. More importantly, classical molecular dynamics (CMD) simulations with Tersoff+Qeq

on the $S_8(001)/LiPS(001)$ interface exhibits an anomalous behavior—most of the S_8 rings in the cathode open, in stark contrast to previous AIMD reports, wherein, S_8 structure remains largely unperturbed. Careful analysis of the CMD trajectories indicated that this spurious behavior is an artifact of the inherent inability of the Tersoff+Qeq potential in treating the dihedral interactions within S_8 rings, and long-range dispersive forces between S_8 rings. To address this issue, we added dihedral terms to our Tersoff + Qeq potential; the overall potential has the same formalism as the reactive force field (ReaxFF) developed by Adri van Duin [2]. We employed our in-house machine learning based FF development framework [3]–[7] to optimize the ReaxFF parameters by employing the large first principles dataset (containing ~15,000 training properties) including atomic structures, energies, atomic charges for numerous configuration, equation of state of various condensed phases, elastic properties, surface properties, and interfacial structure/energy/charges. The Tersoff+Qeq potential was used as a starting point for the fitting process. Indeed, our newly developed ReaxFF potential. Our newly developed ReaxFF can accurately predict (a) lattice parameters (within ~1% of DFT), (b) heat of formation (~within 15 meV/atom of DFT), and (c) elastic constants (within ~20% of DFT). Additionally, the predicted interfacial energies for various Li | SSE, S_8 | SSE, and Li_2S | SSE are within 0.2 J/m² of DFT values; while the atomic charges in the interface are close to Bader charges predicted by DFT calculations.

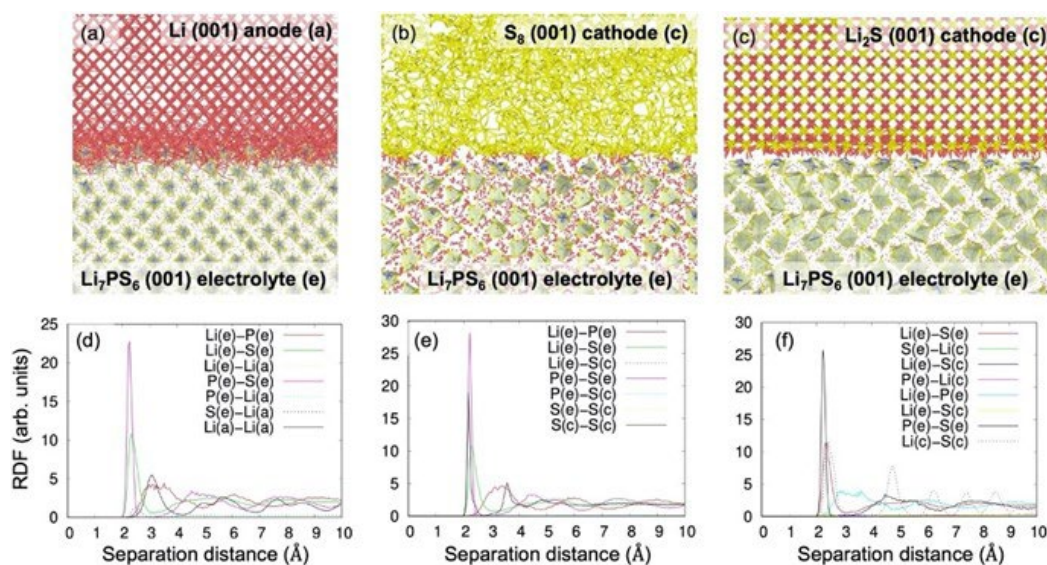


Figure XVI.17.4 Equilibrated interface structures obtained from ReaxFF-CMD simulations under ambient conditions. (a) Li(001)/LiPS(001), (b) $S_8(001)/LiPS(001)$, and (c) $Li_2S(001)/LiPS(001)$ interfaces. The lithium, sulfur, and phosphorus atoms are shown in red, yellow, and green colors. The PS_4^{3-} tetrahedra are shown in green. Radial distribution functions (RDF) $g(r)$ for selected atom pair types for each interface are shown in the bottom row. The labels (e), (c), (a) identify the atoms that belong to electrolyte, cathode, and anode

To assess the performance of newly developed set of ReaxFF parameters in describing interfacial processes, we ReaxFF-CMD simulations for three different interfaces containing Li_7PS_6 (LiPS) solid electrolyte (SE), namely: Li(001)/LiPS(001), $S_8(001)/LiPS(001)$ and $Li_2S(001)/LiPS(001)$. Our computational supercell for Li(001)/LiPS(001) interface, is composed of 16,000 atoms in Li anode and 15,680 atoms in the SSE. Similarly, in $S_8(001)/LiPS(001)$, the cathode is composed of 7,680 S atoms and the SSE is built with 19,712 atoms. Finally, the $Li_2S(001)/LiPS(001)$ consists of 9,360 atoms in Li_2S electrode and 8,960 atoms in SSE. All the interfaces are constructed such that the epitaxial strain of < 1%. Before performing MD simulations, the interface structures are optimized using the conjugate gradient algorithm. After minimization, we performed the equilibration run within a canonical ensemble (NVT) under ambient conditions for 0.1 ns with a timestep of 1 fs (Figure XVI.17.4)

Direct visualization of the CMD-ReaxFF simulations show that PS_4^{3-} motifs in the Li_7PS_6 SSE undergo reductive decomposition against Li metal to form $LiPS_x$ compounds at the anode/SSE interface as indicated by

formation of new bonds between Li of the anode and P/S atoms of SSE (Figure XVI.17.4(a)). The formation of these new Li-P and Li-S bonds is evidenced by appearance of new peaks in the RDF for Li(a)-P(e) at ~ 2.6 Å, and Li(a)-S(e) at ~ 2.1 Å (Figure XVI.17.4(c)). Such reductive decomposition of SSE against Li metal is consistent with previous AIMD simulations [8]. On the other hand, no new peaks are observed in the RDF for S(c) – Li (e) pairs in the equilibrated $S_8 | Li_7PS_6$, and the S_8 rings remain largely intact (Figure XVI.17.4(b,e)). This suggests that no reactions occur at the $S_8 | Li_7PS_6$ interface, consistent with our AIMD simulations (Figure XVI.17.1(a,b)). Notably, the newly developed ReaxFF completely eliminates spurious opening of S_8 rings and their polymerization -- the artifacts of the Tersoff+Qeq potential. Similarly, few Li-S bonds form across the interface between Li_2S and Li_7PS_6 as shown by a small peak in the Li(c)-S(e) RDF at ~ 2.1 Å (Figure XVI.17.4(c,f)), consistent with our AIMD trajectory (Figure XVI.17.1(g,h)). Clearly, the newly developed ReaxFF is capable of treating the electrode/electrolyte interfaces in the Li-P-S system accurately. In addition, the newly developed ReaxFF also captures the Li-ion conductivity in sulfide electrolyte in good agreement with experiments. For instance, the room temperature conductivity of Li_7PS_6 predicted by ReaxFF (9×10^{-6} S/cm) lies within previously reported experimental values (10^{-6} to 10^{-5} S/cm) [9]. We are currently employing ReaxFF-CMD simulations to understand the effect of grain boundaries and extended defects on Li-ion conduction in SSEs. Such an understanding promises to unravel new pathways to engineer morphology of SSEs to control Li-ion conduction.

3. Fabrication of Battery with Optimized Cathode at high S-loading, SSE, and Li anode

To achieve high S-loading (> 4 mg/cm²), we employed two strategies, namely (a) water-based binder chemistry, and (b) engineering cathode architecture (using carbon nano-cages to host S or SSE)—both alongside using porous aluminum collectors.

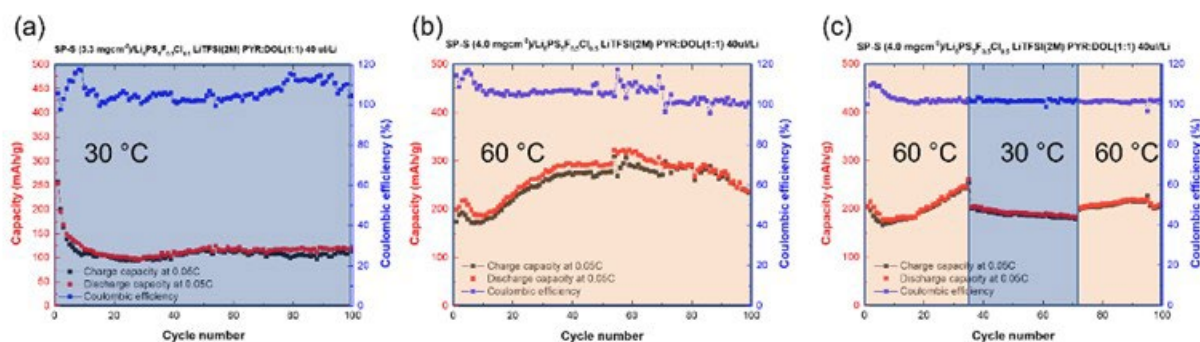


Figure XVI.17.5 Performance of battery with super-P cathode at high S-loading (4 mg/cm²) functionalized with 40 μ L functionalizing liquid containing 2M LiTFSI in PYR₁₄:DOL (1:1), $Li_6PS_5F_{0.5}Cl_{0.5}$ SSE and Li anode cycled at (a) 30 °C, (b) 60 °C, and (c) temperatures alternating between 60 °C and 30 °C. All batteries are cycled at C/20 rate.

We first used a cathode architecture consisting of Super P-S (1:3) 88 wt%, CNT 8 wt%, CMC 4 wt%. Figure XVI.17.5 compares the electrochemical performance of batteries with Super P-S cathode with 4.0 mg/cm² sulfur loading, $Li_6PS_5F_{0.5}Cl_{0.5}$ SSE and Li anode with 40 μ L functionalizing liquid containing 2M LiTFSI in PYR₁₄:DOL(1:1) at 30 °C and 60 °C. At 30 °C, the battery shows an initial discharge capacity of ~ 250 mAh/g, which fades away quickly (within first 10 cycles) to ~ 100 mAh/g. However, after this initial fade, the capacity remains steady at ~ 100 mAh/g, even after 100 cycles (Figure XVI.17.5(a)). Interestingly, cycling tests at 60 °C showed an increase in capacity from an initial value of ~ 200 mAh/g to ~ 250 mAh/g at 100 cycles (Figure XVI.17.5(b)). This anomalous behavior is likely due to the temperature-induced lowering in viscosity of functionalizing IL, and the consequent favorable reaction kinetics. This hypothesis is supported by our electrochemical tests alternating between 30 °C and 60 °C (Figure XVI.17.5(c)). Over the initial 30 cycles when the battery is cycled at 60 °C, we observe a steady increase in capacity; followed by a capacity fade when the temperature is lowered to 30 °C (cycles 35–72); and a slight increase in capacity when the temperature is subsequently increased to 60 °C. A detailed spectroscopic analysis of the interfaces is currently ongoing to understand the effect of temperature on the interfacial reactions.

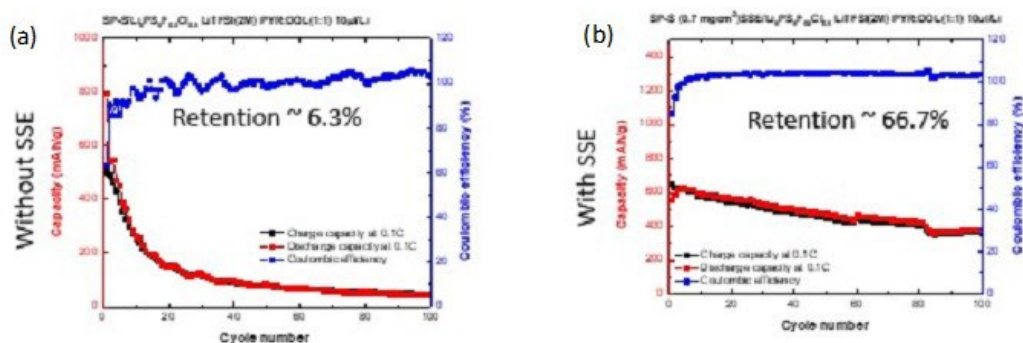


Figure XVI.17.6 Electrochemical performance of battery consisting of Super P-S cathode with 0.7 mg/cm² loading functionalized with 10 μ L functionalizing liquid containing 2M LiTFSI in PYR14:DOL (1:1), Li₆PS₅F_{0.5}Cl_{0.5} SSE and Li anode (a) without any SSE in cathode, and (b) when SSE is drop casted onto the cathode.

To make rapid advances in solid-state lithium sulfur batteries, it is crucial to minimize the amount of functionalizing liquid. Incorporating SSE in the cathode on the battery performance can provide ion conduction pathways and enable much lower amounts of functionalizing liquid. To optimize the process of incorporating SSE in the cathode, we first fabricated batteries with low sulfur loading \sim 0.7 mg/cm² and low amount of functionalizing liquid (10 μ L) (Figure XVI.17.6). Indeed, we observe that in the absence of any SSE in the cathode, the scarcity of IL functionalization drives a rapid capacity fade from an initial value of \sim 800 mAh/g to \sim 50 mAh/g, yielding a poor capacity retention (\sim 6%) (Figure XVI.17.6(a)). Upon drop casting a 100 μ L of solution of SSE in anhydrous ethanol (10 wt%) on to the cathode, the capacity retention improves dramatically, yielding a capacity of \sim 400 mAh/g after 100 cycles (Figure XVI.17.6(b)). This clearly suggests that incorporating SSE into the cathode provides an excellent route to reduce the amount of functionalizing liquid. However, it is challenging to extend this technique to high S-loading owing to the need for water-based binders at high S-loading.

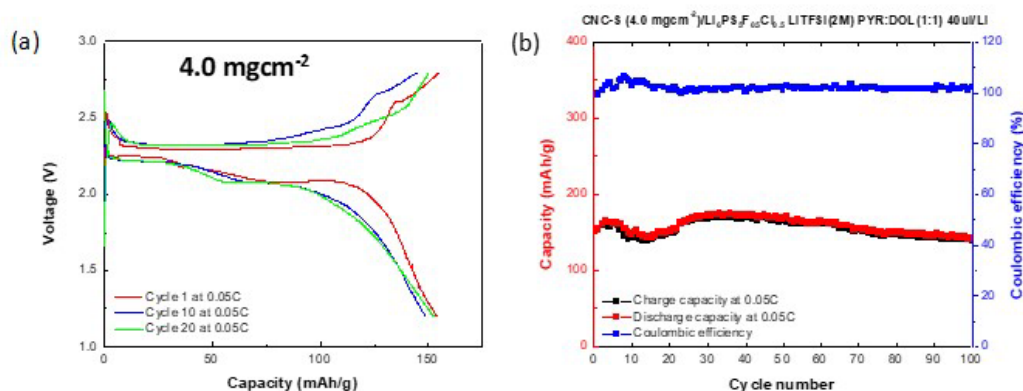


Figure XVI.17.7 Performance of battery with CNC-S cathode at high S-loading (4 mg/cm²) functionalized with 40 μ L functionalizing liquid containing 2M LiTFSI in PYR14:DOL (1:1), Li₆PS₅F_{0.5}Cl_{0.5} SSE and Li anode cycled at 60°C at C/20 rate. (a) Charge-discharge curve at 1, 10 and 20 cycles. (b) Charge/discharge capacity (shown in black/red) and Coulombic efficiency (shown in blue) during battery cycling.

An effective way to concomitantly achieve good SSE incorporation and high S-loading is to employ mesoporous cathode architectures made up of interconnected carbon nanocages (CNCs). Such a network can provide necessary electronic conductivity; additionally, the size of the hollow CNCs can be tuned to achieve desired S-loading and incorporation of SSE. We prepared a cathode consisting of CNC-S (1:3) 85 wt%, CNT 10 wt%, CMC 5 wt% and coated on Aluminum current collector using the doctor blading technique. Figure 4 shows the performance of a battery with CNC-S cathode with 4.0 mg/cm² sulfur loading and functionalized with 40 μ L 2M LiTFSI in PYR:DOL (1:1), Li₆PS₅F_{0.5}Cl_{0.5} SSE and Li anode at 60°C. It showed an initial

discharge capacity ~ 150 mAh/g with a slight decrease of the capacity in the first 10 cycles. Then the capacity started to increase again and retained its value at ~ 140 mAh/g after 100 cycles (Figure XVI.17.7). Although these results show promise, further engineering of ionic/electronic conductivity of cathode is essential to improve the battery performance. Currently, we are exploring several strategies including (a) adding more CNT to improve electronic conductivity of cathode, (b) engineering porosity of the cathode, (c) adding SSE into cathode to improve its ionic conductivity and minimizing the amount of functionalizing ionic liquid.

Conclusions

AIMD simulations revealed that the extent of decomposition of sulfide electrolytes, and the reaction pathways at the cathode side are strongly dictated by the PS_x motifs in the electrolyte. Electrolytes with PS_3 and P_2S_6 motifs (e.g., Li_2PS_3 , $\text{Li}_4\text{P}_2\text{S}_6$) are less susceptible to decomposition as compared to those with PS_4 motifs (e.g., Li_7PS_6). Our battery fabrication efforts showed that interfacial resistance across cathode/electrolyte interface in solid-state Li-S batteries (with $\text{Li}_6\text{PS}_5\text{F}_0.5\text{Cl}_{0.5}$ electrolyte, Li anode, and Super-P cathode) can be alleviated significantly by functionalizing with an ionic liquid (LiTFSI salt in N-butyl-N-methyl pyrrolidinium (PYR-14)). This, in turn, can enable stable cycling of solid-state, albeit with a somewhat low initial discharge capacity (~ 600 mAh/g) owing to high viscosity of IL.

Both initial discharge capacity, and cycle life can be significantly enhanced by diluting IL with 1,3 dioxalane (DOL). We found that a 0.04 mL solution containing 2M LiTFSI in 1:1 (volume) PYR:DOL gives the most optimal performance with $\text{Li}_6\text{PS}_5\text{F}_0.5\text{Cl}_{0.5}$ electrolyte, Li anode, and Super-P cathode (at low S-loading of 0.7 mg/cm²)—1100 mAh/g initial discharge capacity, with a retention of 400 mAh/g after 50 cycles (@C/20) with excellent Coulombic efficiency. Adding SSE to the Super-P cathode improves capacity retention to 480 mAh/g but with a slightly diminished Coulombic efficiency. AIMD simulations elucidated the interactions between the salt anion (TFSI-), cation of the functionalizing ionic liquid (PYR14), and Li/S at the cathode/electrolyte interface. We find that PYR14 cations stay intact, while the TFSI- anions break down at the interface with cathode in the fully discharged state (Li_2S) via interaction with Li to form $-\text{CF}_3$, $-\text{SO}_2$, Li-F, and Li-CN complexes at the interface. In terms of diluents, dimethoxyether (DME) also dissociates at cathode, while dioxalane (DOL) remains intact. This indicates that DOL is a better diluent than DME, consistent with our XPS characterization experiments.

To enable large-scale atomistic simulations of battery interfaces, we extended our reactive interatomic potential to accurately describe dynamics in cathodes as well as electrode/electrolyte interfaces using in-house automated FF development tools based on ML. In particular, we added (a) dihedral interaction terms to capture the ring structure of S_8 , and (b) long-range dispersive forces—using ReaxFF formalism—which are vital for the predictive power of the newly developed reactive interatomic potential. Our newly developed ReaxFF can accurately predict (a) lattice parameters (within $\sim 1\%$ of DFT), (b) heat of formation (\sim within 15 meV/atom of DFT), (c) elastic constants (within $\sim 20\%$ of DFT), and (d) lithium-ion conduction in sulfide electrolytes. Additionally, the predicted interfacial energies for various $\text{Li} \mid \text{Li}_7\text{PS}_6$, $\text{S}_8 \mid \text{Li}_7\text{PS}_6$, and $\text{Li}_2\text{S} \mid \text{Li}_7\text{PS}_6$ are within 0.2 J/m² of DFT values; while the atomic charges in the interface are close to Bader charges predicted by DFT calculations. Additionally, the atomic-scale interfacial processes predicted by ReaxFF-MD simulations are consistent with our *ab initio* molecular dynamics (AIMD) simulations, and previous experiments.

Finally, innovations in water-based binder chemistry, and use of porous Al collectors enabled us to achieve cathodes with high S-loading (up to 4.8 mg/cm²).

Key Publications

1. R. Kempaiah, H. Chan, S. Srinivasan, S. Sankaranarayanan, B. Narayanan,* and A. Subramanian*, “Impact of Stabilizing Cation on Lithium Intercalation in Tunneled Manganese Oxide Cathodes”, *ACS Applied Energy Materials* Article ASAP DOI: 10.1021/acsaem.1c01598 (2021) *Corresponding Authors

2. (Invited) B. Narayanan, “Computational Modeling of Battery Materials”, Book Chapter in Encyclopedia of Energy Materials, Elsevier, *In Press*.
3. W. Arnold, V. Shreyas, Y. Li, J. Jasinski, A. Thapa, G. Sumanasekera, A. T. Ngo, B. Narayanan,* H. Wang*, “Novel Fluoride Doped Lithium Argyrodite Solid Electrolytes from Solvent-based Synthesis” Submitted to *Journal of Materials Chemistry A*
4. V. Shreyas, S. Gupta, W. Arnold, H. Wang*, and B. Narayanan*, “Structure and lithium superionic conduction in lithium argyrodites with multiple halogen dopants”, Submitted

References

1. Merinov, B.V., et al., Interface Structure in Li-Metal/[Pyr14][TFSI]-Ionic Liquid System from ab Initio Molecular Dynamics Simulations. *The Journal of Physical Chemistry Letters*, 2019. 10(16): p. 4577–4586.
2. Senftle, T.P., et al., The ReaxFF reactive force-field: development, applications and future directions. *NPJ Computational Materials*, 2016. 2: p. 15011.
3. Cherukara, M., et al., Ab Initio-Based Bond Order Potential to Investigate Low Thermal Conductivity of Stanene Nanostructures. *Journal of Physical Chemistry Letters*, 2016. 7(19): p. 3752–3759.
4. Narayanan, B., et al., Describing the Diverse Geometries of Gold from Nanoclusters to Bulk-A First-Principles-Based Hybrid Bond-Order Potential. *Journal of Physical Chemistry C*, 2016. 120(25): p. 13787–13800.
5. Narayanan, B., et al., Development of a Modified Embedded Atom Force Field for Zirconium Nitride Using Multi-Objective Evolutionary Optimization. *The Journal of Physical Chemistry C*, 2016. 120(31): p. 17475–17483.
6. Chan, H., et al., Machine Learning Classical Interatomic Potentials for Molecular Dynamics from First-Principles Training Data. *The Journal of Physical Chemistry C*, 2019.
7. Chan, H., et al., Machine learning coarse grained models for water. *Nature Communications*, 2019. 10(1): p. 379.
8. Cheng, T., et al., Quantum Mechanics Reactive Dynamics Study of Solid Li-Electrode/Li6PS5Cl-Electrolyte Interface. *ACS Energy Letters*, 2017. 2(6): p. 1454–1459.
9. Deiseroth, H.-J., et al., Li7PS6 and Li6PS5X (X: Cl, Br, I): Possible Three-dimensional Diffusion Pathways for Lithium Ions and Temperature Dependence of the Ionic Conductivity by Impedance Measurements. *Zeitschrift für anorganische und allgemeine Chemie*, 2011. 637(10): p. 1287–1294.

Acknowledgements

This project involves three co-investigators: Dr. Hui Wang, Dr. Gamini Sumanasekera, and Dr. Jacek Jasinski at the University of Louisville. A part of this work was performed in collaboration with Prof. Anh Ngo (University of Illinois-Chicago, Argonne National Laboratory), Prof. Subramanian Sankaranarayanan (University of Illinois-Chicago, Argonne National Laboratory), and Prof. Arunkumar Subramanian (University of Illinois-Chicago). This research used resources of the National Energy Research Scientific Computing Center; a DOE Office of Science User Facility supported by the Office of Science of the U.S. Department of Energy under Contract No. DE-AC02-05CH11231. Use of the Center for Nanoscale Materials was supported by the U. S. Department of Energy, Office of Science, Office of Basic Energy Sciences, under Contract No. DE-AC02-06CH11357. We also acknowledge generous computer time allocations at the Laboratory Computing Resource Center at Argonne National Laboratory.

XVI.18 Design of Strain Free Cathode – Solid State Electrolyte Interfaces Using Chemistry-Informed Deep Learning (ANL)

Hakim Iddir, Principal Investigator

Argonne National Laboratory
9700 South Cass Avenue
Lemont, IL 60439
E-mail: Iddir@anl.gov

Duong Tien, DOE Technology Development Manager

U.S. Department of Energy
E-mail: Tien.Duong@ee.doe.gov

Start Date: October 1, 2019
Project Funding: \$300,000

End Date: September 30, 2022
DOE share: \$300,000

Non-DOE share: \$0

Project Introduction

Structure-property relationships are at the heart of most fundamental scientific approaches. However, the link between structure and property remains a challenge in the materials science of complex systems, such as the oxides that form battery components. **In particular, the chemical and mechanical stability of the cathode-SSE interface presents a challenge to the development of solid-state batteries.** High performance Density Functional Theory (DFT) calculations provide the necessary framework to understand such systems. Unfortunately, given the limited number of atoms and time scales accessible by the method and the myriad calculations required to achieve satisfactory results, the computational cost of simulating all the possible configurations of a multicomponent oxide is prohibitive. In this work, we augment the DFT data with Machine Learning (ML)—especially deep learning—techniques that allow us to access large system sizes and longer time scales necessary to build thermodynamic models. We focus on understanding the nature of benchmark $\text{Li}_{1-x}\text{Ni}_{1-x-y-z}\text{Mn}_x\text{Co}_y\text{M}_z\text{O}_2$ structures (M dopant, $\alpha, x, y, z < 1$), their volume change with Li content, nature and concentration of the dopants, as well as the chemical stability of the SSE-cathode interface. The DFT and ML approach will provide new cathode compositions that will reduce the strain of the SSE-cathode interface and hence improve its mechanical and chemical stabilities.

Objectives

In this project we aim at developing a methodology that will allow us to explore and expand the configurational space using High-Performance Computing (HPC) approaches in a systematic and efficient way. The methodology will encompass, DFT, Ab-Initio Molecular Dynamics (AIMD), Molecular Dynamics, and ML. The methodology will also take advantage of the variety of software already developed at Argonne and at other DOE laboratories, such as BALSAM to automate, manage and control the large number of calculations needed to achieve our goal.

Approach

All calculations will be performed by spin-polarized DFT as implemented in the Vienna Ab Initio Simulation Package (VASP). [1],[2] To make sure all the oxidation state of ions are correct, after geometry optimization within the DFT+U framework, electronic relaxation will be performed using a single point calculation with the hybrid functional HSE06.[3] For production calculations we will use the MPI parallelized version of VASP.

Exploration of the potential energy surface (PES) is needed to predict the structure of solid materials and interfaces. Such calculations are infeasible using MD or DFT calculations alone. Thankfully, the PES of a system can be represented by the sum of the energies of the local neighborhoods surrounding each atom. This enables the use of ML surrogate models trained with DFT calculations to capture the energies in local neighborhoods. The input to the ML surrogate must be a unique representation of the system under study.

Consequently, the local environment of each ion is described using a local environment descriptor that renders the atomic configuration invariant to rotations, translations, and permutations of the atoms. In recent years, several different descriptors have come to prominence with advantages and disadvantages. Once the ML surrogate is trained, the total energy and forces over all the ions of any structural configuration can be determined. Such information can be used for atomistic simulations, namely, MD and Monte Carlo (MC).

In this project, we propose to use the open-source DeepMDkit python/C++ package to construct the ML PES and force fields. The promise of DeepMDkit in this work is to provide near-DFT accuracy at orders of magnitude lower computational expense, comparable to traditional molecular dynamic simulations. Efficiency in training is facilitated through integration with TensorFlow and MPI/GPU support.

One of the challenges of the development of a ML PES is achieving accurate predicted forces and energies across the entire configurational space, while minimizing the total number of calculations required for training. In recent years, active learning has been highlighted for its ability to target training examples most likely to improve the model quality or to achieve some other objective (i.e., maximizing a predicted material property). DP-GEN, an open source python package based on DeepMDkit, implements a similar active learning scheme with HPC support, and has been employed to construct a ML PES with accuracy approaching DFT and sometimes exceeding embedded atom potential for experimentally measured properties of interest.^[4] In this work, we propose to leverage DeepMDkit and DP-GEN to efficiently generate ML-PESs for cathode-electrolyte systems including a variety of dopants.

Results

One of the main challenges of Ni rich cathodes in solid state electrolyte batteries is the mechanical strain produced at the cathode-electrolyte interface. In Ni-rich cathodes, the phase transformation at high state of charge is the main component of the total volume change. Hence, the atomistic models must be able to capture the key processes involved in the phase transformation. We have set up a methodology to understand the thermodynamics and lattice parameters of Lithium Nickel Oxide (Li_xNiO_2) from machine learning and molecular dynamics.

We used the machine learning interatomic potential framework DeepMDkit^[5] to construct an interatomic potential for modeling the thermodynamic properties and lattice parameters from room temperature up to 400 K. A bootstrapping scheme where an ensemble of five potentials was fit with different re-samplings of the training datasets was employed to obtain uncertainty estimates for the energies and forces.

Using this potential, we evaluated the phase stability of the H2-rich and H3-rich phases of Li_xNiO_2 to check if they can coexist. As a first step, we determined the enthalpy of each of the H2-rich and H3-rich phases obtained at 250, 298, 350, and 400 K from isobaric isothermal (*npt*) ensemble molecular dynamics simulations in LAMMPS with the DeepMDkit potential. Applying a Bayesian automated weighting scheme^[6], we found that a linear model for the enthalpy was most supported by the data collected. With the machine learning force field, the Gibbs free energy of each phase modeled by the hybrid computational cells (*O1*-rich and *O3*-rich) and composition were each computed with respect to the reference Gibbs free energy of an Einstein solid using the adiabatic switching method.

Shown in Figure XVI.18.1 are the mean Gibbs free energies with their 95th confidence interval each. The uncertainty of the mean prediction (half-width of the 95th confidence interval) for the Gibbs free energy ranges from 25 meV/f.u. to 40 meV/f.u. Nonetheless, compared pair-wise, the energy differences between the same potentials for each composition and phase is also of the order of 25 meV/f.u. or less. These results show that there is uncertainty in whether *O1*-rich or *O3*-rich stacking is thermodynamically preferred.

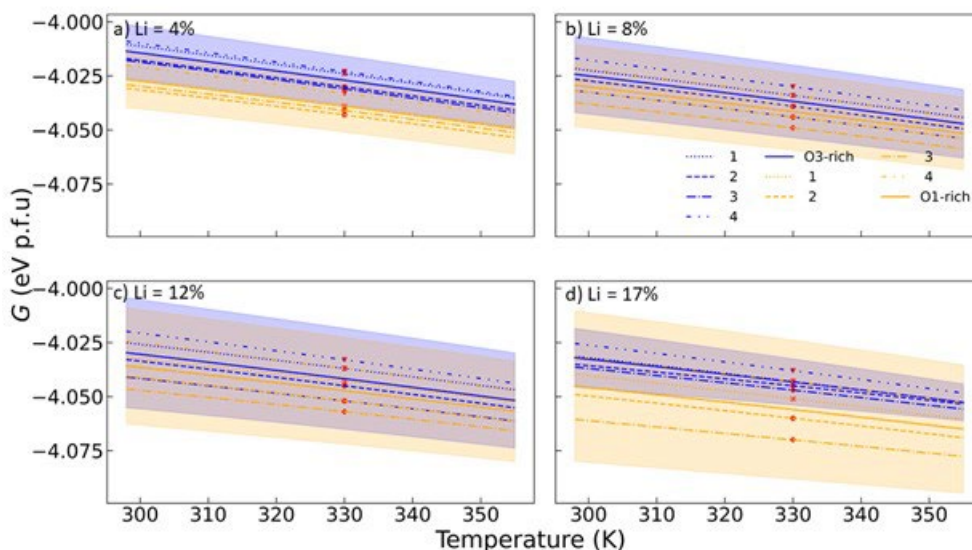


Figure XVI.18.1 Gibbs free energies for the H3 (O3-rich, in blue) and H3/H4 (O1-rich, in orange) phases for a) 4% Li b) 8% Li c) 12% d) 17% for 4 potentials from the ensemble. 95th confidence intervals are indicated by the shaded region and were determined from a Student's t-distribution fit.

It is critical to include Van der Waals (VDW) forces to model the collapse of Li_xNiO_2 as x approaches zero. The SCAN functional, which includes some VDW forces, has some binding energy between layers and significantly smaller c lattice constants. The SCAN+rVV10 functional includes a more complete description of the VDW forces and predicts a larger binding energy and c lattice constants close to experiment.

We have shown before that the volume collapse at very low Li content can be simulated using density functional theory (DFT), using the Hubbard U correction when considering the Van der Waals interactions appropriately using the XC functional optB86b-vdW. However, we have concluded that at this level of theory it is not possible to discriminate between the O1 and O3 phases of NiO_2 because the energies (internal and free energies) are within the accuracy of the methods, including the state-of-the-art Random Phase Approximation (RPA). It is important to notice that the c lattice parameter is the same for both cases, indicating that the collapse of the volume at high state of charge does not depend on the oxygen stacking sequence. This result is very important for the understanding of volume change of high-Ni cathodes at high SOC and for the continuation of this project. However, any gliding could have consequences on the formation of cracks and possibly change the properties of the top surface layers.

Slab model calculations were set up to understand elemental segregation in Ni-rich materials. The segregation to the most common surface has been studied as a first step to understand which ions would interact with the cathode solid electrolyte at the interface. Our results show a trend where Co atoms preferentially segregate to the surfaces of the (104) and (012) facets. This contrasts with our previous findings for NMC111, where the segregation of Co was only found for the (104) facet. These results are being incorporated in our SSE-NMC811 interface models currently under study.

To understand the effect of composition and dopants on the volume change in Ni-rich materials, a simulation cell was set up to model the delithiation process of $\text{Li}_x(\text{Ni}_{0.8}\text{Mn}_{0.1}\text{Co}_{0.1})\text{O}_2$ (NMC811) (see Figure XVI.18.2a). The supercell with a space group R-3m has 27 MO_2 units ($\text{M}=\text{Ni}, \text{Co}, \text{Mn}$) distributed in three layers. Each composition was generated by randomly shuffling the Li ions in all the available octahedral Li sites. Symmetry equivalent structures were discarded using the recipe from Lonie et. Al.^[7] Preliminary results are shown in Figure XVI.18.2b.

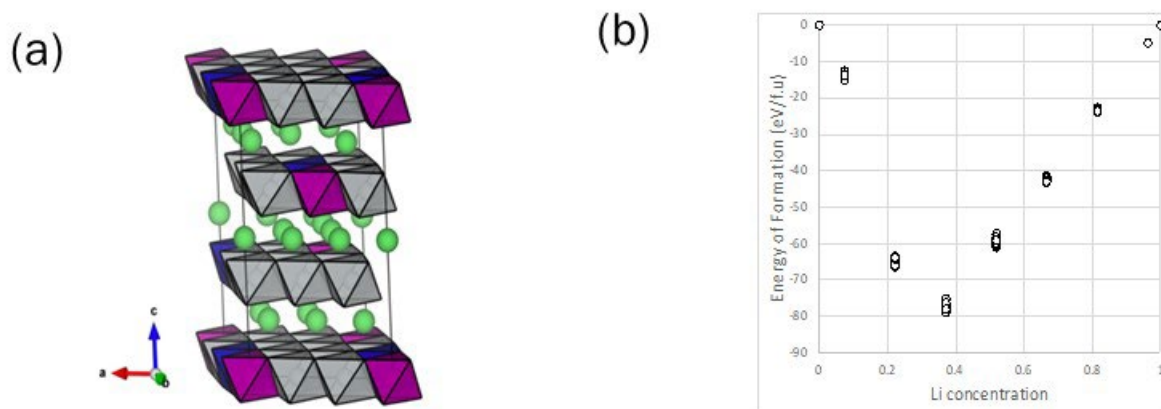


Figure XVI.18.2 (a) Sample $\text{Li}_x(\text{Ni}_{0.8}\text{Mn}_{0.1}\text{Co}_{0.1})\text{O}_2$ supercell model for $x = 0.33$ with randomly distributed Li ions in the Li layer. Grey octahedrons represent Ni site, purple octahedrons represent Mn sites, blue octahedron represent Co sites and green spheres represent Li ions. (b) DFT computed $\text{Li}_x(\text{Ni}_{0.8}\text{Mn}_{0.1}\text{Co}_{0.1})\text{O}_2$ energy of formation.

Effect of dopants on Ni-rich cathode volume change upon delithiation

We are modeling mitigation strategies to avoid excessive strain caused by the collapse of the lattice upon delithiation, using $\text{LiNi}_{0.8}\text{Mn}_{0.1}\text{Co}_{0.1}\text{O}_2$ (NMC811) as a benchmark material. We focus on dopants that substitute Co ions first. We have developed software to automatically dope and generate configurations under constraints to limit the search space (to more than 60 million configurations). The computational workflow is shown by the schematic in Figure XVI.18.3. Over an undergraduate summer internship program, we trained an intern to perform a test of this workflow on Nb- and Al-doped NMC (432 atom cell) on a subset of 700,000 configurations for a dopant composition of 1 Nb or 1 Al substituting for 1 cobalt and found that Al-doped NMC mitigated the volume change slightly better than Nb-doped NMC.

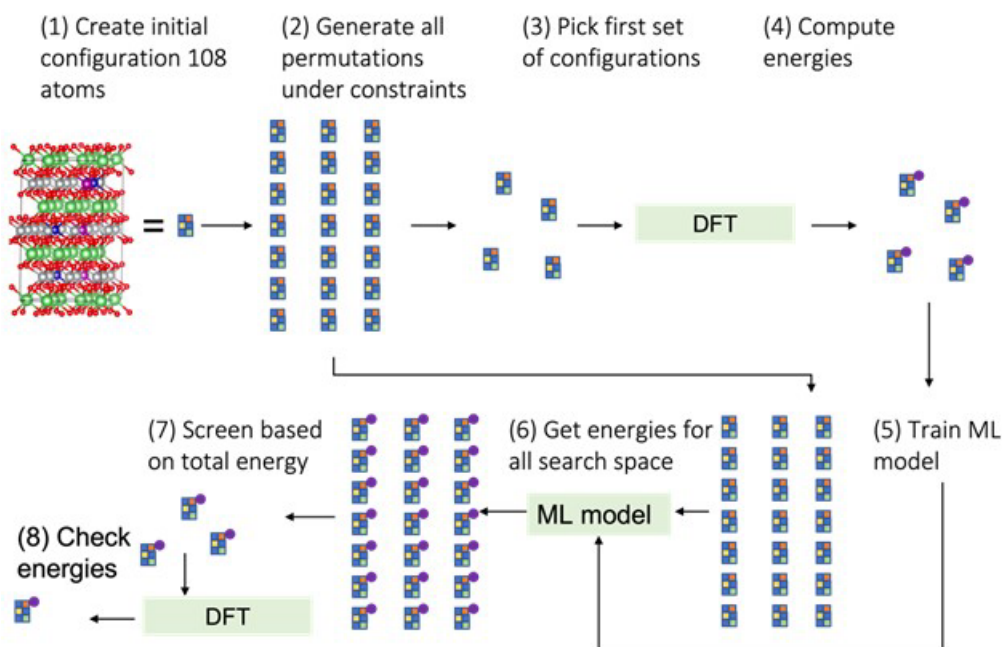


Figure XVI.18.3 Schematic of workflow to get the lowest energy configurations of fully lithiated doped NMC811

Cells with the lowest energy configurations will be delithiated to $\sim 4\%$ Li content and the distribution of Li within the material will be tested in a similar fashion. Finally, the volume change and other properties will be

computed. The effect of temperature will be considered using molecular dynamics simulations with the machine learning potential.

It is important to highlight that, given the large number of dopants planned for the screening, the GGA+U approach presents new challenges, such as finding the most appropriate U values for dopants, that are not always available. Hence, we set up and tested a DFT procedure using the novel “R²SCAN”^[1] plus Van der Waals corrections D3/D4. This is a regularized variant of the strongly constrained and appropriately normed semi-local density functional “SCAN” that includes semi-classical London dispersion corrections. It has the speed of generalized gradient approximations while approaching the accuracy of hybrid functionals. We found that if we start from a previously optimized geometry and wavefunction using the functional optB86b-vdW the convergence of the R²SCAN-D3 simulation is reliable and fast. Also, we are taking advantage of the GPU nodes on Argonne’s LCRC Swing cluster to speed up the calculations.

Cathode solid electrolyte interfaces analysis

To understand the strain issues in solid state Li-ion batteries, we built simulation cells with minimum initial strain between the materials. Using a proprietary software, we generated a total of 2517 interfaces between LZO/LLZO and LNO/NMC cathodes. The interfaces span a variety of conditions, including cathode facets (104)/(012)/(001), planar (ab) strain, buffer space between materials, vacuum space surrounding the materials and slab thickness. A representative model interface is shown in Figure XVI.18.4 DFT simulations are running in our available computational clusters at Argonne’s LCRC (Bebop/Swing) and NREL HPC facilities (Eagle/Swift). Software that automates the workflow, including the ML training, has been developed within our group.

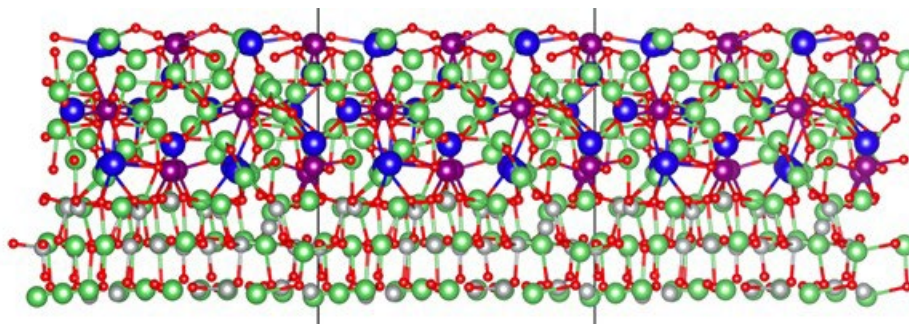


Figure XVI.18.4 Representative LiNiO₂-LLZO interface model. Green, grey, red, blue, and purple spheres represent Li, Ni, O, La and Zr respectively.

Conclusions

A machine learning methodology was developed and tested to investigate the effect of Li content and dopants on the volume change in Ni—rich cathode materials. The results obtained using state-of-the-art DFT methods show that the volume collapse at high state of charge is mostly independent of the oxygen stacking sequence. Preliminary data suggests that Al-doped NMC mitigates the volume change slightly better than Nb-doped NMC. Elemental segregation of Co to (012) and (104) facets is predicted for NMC811 composition. DFT calculations on NMC811-LLZ and NMC881-LLZO interface models with minimum strain are being used to generate ML potentials that will include interactions between NMC and LLZO components at the interface.

Key Publications

1. Gabriel, Joshua, Juan Garcia, Noah Paulson, John Low, Marius Stan and Hakim Iddir. "Machine Learning Force Fields for high Nickel Li ion cathodes." Abstract of presentation at the 2021 AIChE Midwest Regional Virtual Conference, March 17, 2021 – March 18, 2021.
2. Paulson, N.H., “Deep-Learned Interatomic Potentials to Simulate Volume Change in Cathode Materials” NREL Machine Learning for Batteries Virtual Workshop, March 23, 2021.

3. Juan Garcia, Joshua Gabriel, Noah Paulson, John Low, Marius Stan, Hakim Iddir. Insights from computational studies on the anisotropic volume change of Li_xNiO_2 at high state of charge ($x < 0.25$) (under revision JPCC).
4. Alex Tai, Joshua Gabriel, Noah Paulson, Juan Garcia, John Low, Hakim Iddir, **Exploring Solid State Cathode Materials Space** (2021 NAISE Undergraduate Interns Symposium - (US, 08/01/21–08/16/21))

References

1. Kresse, G.; Furthmüller, J. Efficiency of Ab-Initio Total Energy Calculations for Metals and Semiconductors Using a Plane-Wave Basis Set. *Comput. Mater. Sci.* 1996, 6 (1), 15–50.
2. Kresse, G.; Hafner, J. Ab Initio Molecular Dynamics for Liquid Metals. *Phys. Rev. B* 1993, 47 (1), 558–561.
3. Heyd, J.; Scuseria, G. E.; Ernzerhof, M. Hybrid Functionals Based on a Screened Coulomb Potential. *J. Chem. Phys.* 2003, 118 (18), 8207–8215.
4. Zhang, L.; Han, J.; Wang, H.; Saidi, W.; Car, R.; E, W. End-to-End Symmetry Preserving Inter-Atomic Potential Energy Model for Finite and Extended Systems. In *Advances in Neural Information Processing Systems 31*; Bengio, S., Wallach, H., Larochelle, H., Grauman, K., Cesa-Bianchi, N., Garnett, R., Eds.; Curran Associates, Inc., 2018; pp 4436–4446.
5. Wang, H.; Zhang, L.; Han, J.; E, W. DeePMD-Kit: A Deep Learning Package for Many-Body Potential Energy Representation and Molecular Dynamics. *Comput. Phys. Commun.* 2018, 228, 178–184.
6. Paulson, N. H.; Zomorodpoosh, S.; Roslyakova, I.; Stan, M. Comparison of Statistically-Based Methods for Automated Weighting of Experimental Data in CALPHAD-Type Assessment. *Calphad* 2020, 68, 101728.
7. Lonie, D. C.; Zurek, E. Identifying Duplicate Crystal Structures: XtalComp, an Open-Source Solution. *Comput. Phys. Commun.* 2012, 183 (3), 690–697. <https://doi.org/10.1016/j.cpc.2011.11.007>.
8. Kirkwood, J. G. Statistical Mechanics of Fluid Mixtures. *J. Chem. Phys.* 1935, 3 (5), 300–313.
9. Baskes, M. I.; Muralidharan, K.; Stan, M.; Valone, S. M.; Cherne, F. J. Using the Modified Embedded-Atom Method to Calculate the Properties of Pu-Ga Alloys. *JOM* 2003, 55 (9), 41–50.

Acknowledgements

This work is performed by the Strain-Free project team: Juan Garcia, Joshua Gabriel, Marius Stan, Noah Paulson, John Low from Argonne National Laboratory, using the computational resources at NREL and ANL (LCRC).

XVI.19 Enabling continuous production of defect-free, ultrathin sulfide glass electrolytes for next generation solid state lithium metal batteries (ANL)

Tim Fister, Principal Investigator

Argonne National Laboratory
9700 South Cass Avenue
Lemont, IL 60439
E-mail: fister@anl.gov

Simon Thompson, DOE Technology Development Manager

U.S. Department of Energy
E-mail: Simon.Thompson@ee.doe.gov

Start Date: October 1, 2020
Project Funding: \$167,000

End Date: September 30, 2023
DOE share: \$167,000

Non-DOE share: \$0

Project Introduction

Sulfide glass materials are one of the most appealing candidates for solid state batteries due to their superior performance using relatively inexpensive raw materials. Glass materials prepared from a melt, unlike ball milled sulfides or polycrystalline electrolytes, also lack the void space and grain boundaries that are often weak points for lithium dendrites or decomposition species. In practice these glasses are not entirely defect free and can have isolated defects such as bubbles or crystalline inclusions formed during manufacture and processing. Recent advances from PolyPlus have demonstrated the ability to draw glasses to thicknesses approaching 10-20 microns. These thicknesses produce a flexible glass that is compatible with roll-to-roll manufacturing, but impurities become an even more negative design parameter in this regime.

Objectives

The goal of this project is to identify the source of defects in sulfide glasses and understand their impact on the mechanical and electrochemical stability of the solid electrolyte. Understanding the distribution, size, and composition of these defects, and identifying ways to mitigate them, is a critical requirement for achieving ultrathin glass sheets necessary for a roll-to-roll manufacturer to build them into cylindrical format cells.

Approach

This project focuses on sulfide glasses developed and produced at PolyPlus and uses advanced synchrotron and optical methods at Argonne National Laboratory to identify and analyze defects in glass samples ranging from 20-1000 μm in thickness. Analytical methods developed in this project will focus on buried defects within the glass and reactions that form at the surface and electrode interface, both from processing and electrochemical treatments, as illustrated in Figure XVI.19.1.

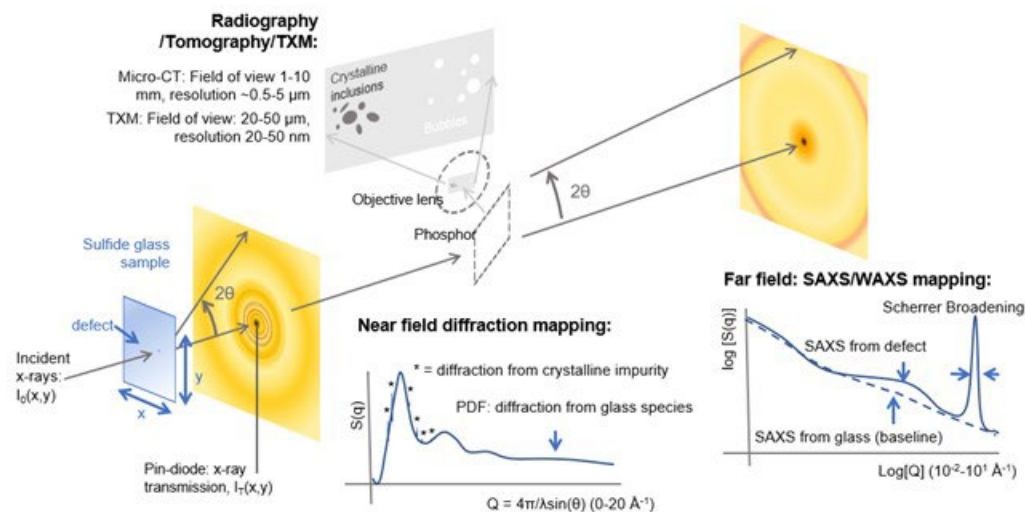


Figure XVI.19.1 Schematic of multimodal synchrotron analysis of sulfide glass samples.

During the first two quarters of this project, Argonne and PolyPlus established protocols for transferring samples between each location and developed sample holders with sealed glass windows compatible for both optical and x-ray characterization. Preliminary x-ray diffraction (XRD) and pair distribution function (PDF) measurements were mapped over the entire volume of several preliminary glass samples provided by PolyPlus. These feasibility measurements showed that these techniques are uniquely sensitive to the atomic structure of the glasses and that the x-rays were easily capable of measuring 100 μm thick glass samples and will be able to resolve structure in the final ultrathin samples.

Results

A sealed holder for the air sensitive samples using a KF-flanged assembly was developed for shipment between PolyPlus and ANL/APS (Figure XVI.19.2). The holders can be mounted on the beamline enabling powder XRD and PDF measurements and are compatible with optical characterization by Raman scattering or Digital Holographic Microscopy (DHM).

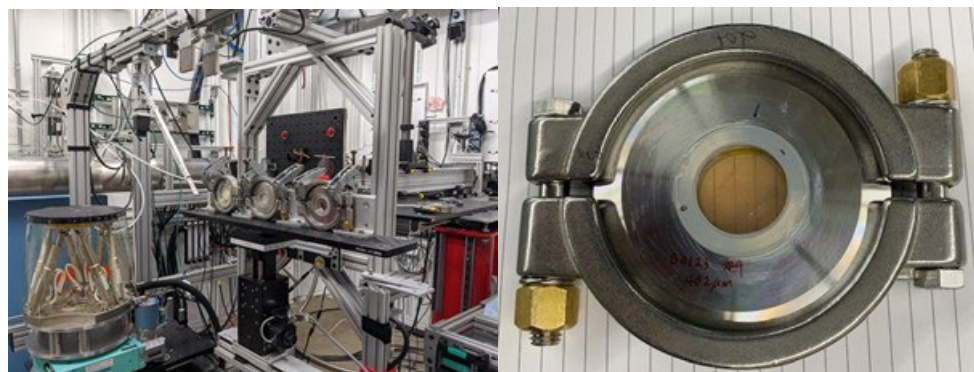


Figure XVI.19.2 Sealed holders mounted at beamline 11-ID-B for PXRD and PDF studies, allowing mapping of the samples. Note that the transparency of the sulfide glass allows for optical characterization of the buried electrode/electrolyte interface in later phases of the project.

First generation holders used polycarbonate windows but were found to have long-term issues with water permeation through the plastic as well as thickness variability, which affected the x-ray data analysis. Subsequent holders use thin glass (borosilicate) cover slips instead, which are more uniform and has better sealing properties.

The first APS experiments focused on x-ray scattering from the sulfides in both the XRD and PDF regimes, as illustrated in Figure XVI.19.3. PDF data was measured to high x-ray momentum transfer (q) to reach high real space resolution in the PDF. Data were corrected for Compton scattering and background from the windows and air scatter. Diffraction was measured at lower q , with high angular resolution to resolve sharper Bragg features from crystalline impurities. Note that Bragg features were typically much smaller than the bulk x-ray scattering from the glass.

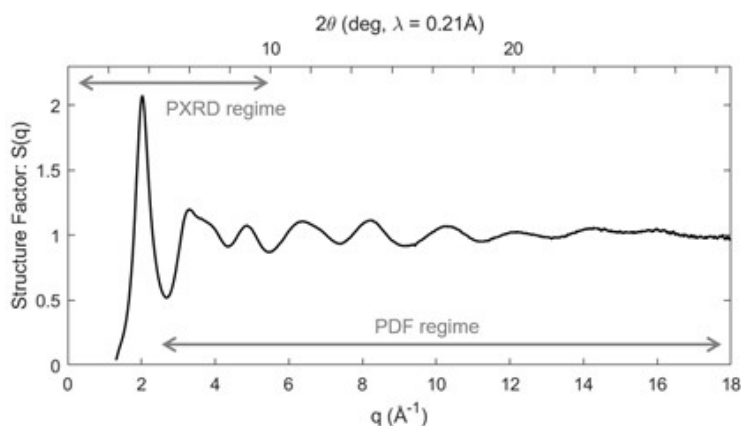


Figure XVI.19.3 Data taken from 400 μm -thick sulfide glass from PolyPlus. Data has been corrected for background scatter processes and normalized by atomic scattering factors to get the overall structure factor. Higher q -resolution data collected at low q was used to screen for impurity phases, while data taken to high q was used to compute the PDF of the glass itself.

Initial glass samples were largely phase-pure, with a small number of crystalline impurities. Data collected in the Bragg regime were fit to phases from the glass and the polycarbonate (PC) window species and deviations from this linear combination were screened for impurity peaks. An example of this phase analysis is shown in Figure XVI.19.4, with an example of a spectrum containing impurity peaks.

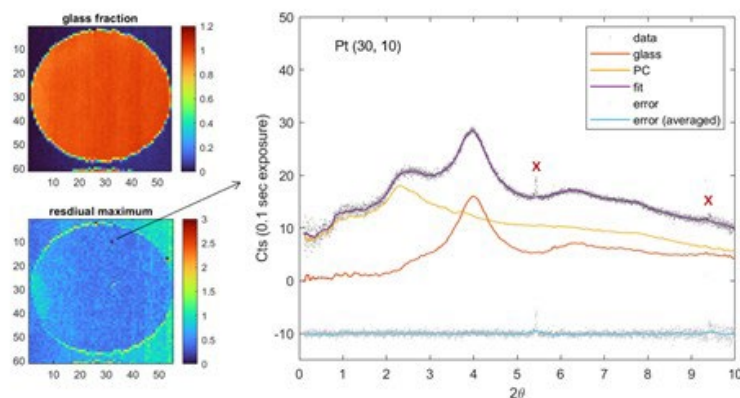


Figure XVI.19.4 Maps of the glass fraction and deviations from a simple two-phase model of glass and polycarbonate (PC) were constructed from 3600 diffraction patterns for each sample. While the first samples were found to have maps containing $<1\%$ impurities, an example of one point with weak impurity Bragg peaks (labeled "x") is shown.

While early data suggest that impurities are low concentration or non-crystalline, the PDF of the glass itself was found to be sensitive to composition and processing parameters. The reduced PDF, $G(r)$, was calculated using the structure factor of the glass, $G(r) = 2/\pi \int q[S(q) - 1] \sin(qr) dq$. From this the overall PDF of the glass, $g(r)$, was calculated using $g(r) = G(r)/4\pi r \rho_0 + 1$, where ρ_0 is the average number density within the glass. This correlation function represents the radial number density with the glass. Despite not having the long-range order associated with crystalline materials, PDF was found to be sensitive to changes within the local structure of the glass, as shown in Figure XVI.19.5.

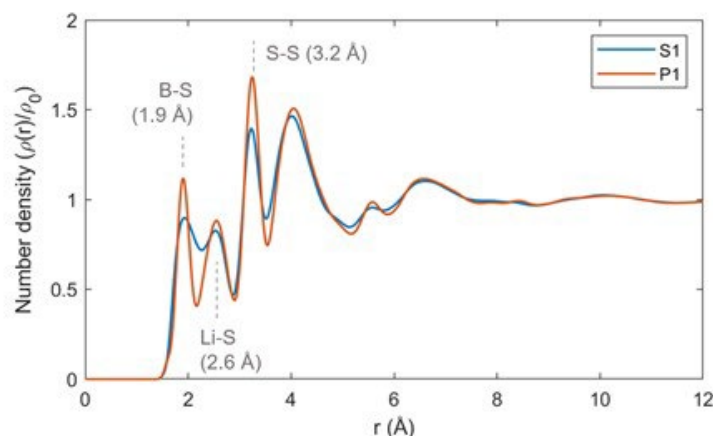


Figure XVI.19.5 Examples of real-space PDF data taken from two glass samples (S1 and P1). Peaks due to different chemical bonds are labeled.

Given the low concentration of crystalline impurities, principal component analysis of the PDF maps, analogous to XRD maps shown in Figure XVI.19.3, will be developed to screen for noncrystalline impurities or phase heterogeneity in the sulfide glass itself. Raman spectroscopy will also be incorporated into the setup shown in Figure XVI.19.2, providing simultaneous x-ray and optical characterization of the samples at APS.

Interfacial characterization of the glass materials will be emphasized in the coming year of this project. This will include optical analysis of features within the glass and at an electrode/glass interface using digital holographic microscopy. Changes in composition near the surface of the glass will also be evaluated using glow discharge optical emission spectroscopy (GDOES). Preliminary data (Figure XVI.19.6) was taken on the same glass samples and showed the elemental sensitivity on elements as light as Li, although the setup requires further optimization including minimized re-deposition, calibration standards for each element, and sputtering rate.

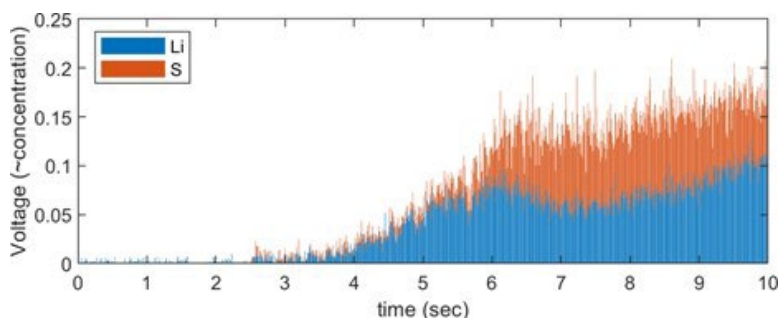


Figure XVI.19.6 Preliminary GDOES depth profiling of Li and S species during first 10 sec of sputtering.

Conclusions

- Initial sulfide glasses were produced by PolyPlus and evaluated at Argonne and analyzed at the Advanced Photon Source.
- X-ray scattering (XRD and PDF) was used to compare the local structure of each glass and identify location of crystalline defects.
- Initial GDOES measurements show sensitivity to composition gradients at the surface or interface of glass samples.

XVI.20 Scaling-Up and Roll-to-Roll Processing of Highly Conductive Sulfide Solid-State Electrolytes

Dongping Lu, Principal Investigator

Pacific Northwest National Laboratory
902 Battelle Boulevard
Richland, WA 99354
E-mail: dongping.lu@pnnl.gov

Simon Thompson, DOE Technology Development Manager

U.S. Department of Energy
E-mail: Simon.Thompson@ee.doe.gov

Start Date: October 1, 2020

End Date: September 30, 2023

Project Funding: \$500,000

DOE share: \$500,000

Non-DOE share: \$0

Project Introduction

All-solid-state lithium batteries (ASSLBs) have the potential to achieve higher energy and power densities, extending the range of electric vehicles and reducing charging time simultaneously. Some inorganic solid-state electrolytes (SSEs) possess high Li^+ transference number (~ 1.0), low activation energy (< 0.3 eV), and conductivities even higher than conventional liquid electrolytes. More importantly, safety of SSEs generally surpasses organic liquid electrolytes. Another feature of SSEs is their superior dimensional stability, which could enable the battery design to handle both extremely high and low electrochemical potentials at the cathode (e.g., NMC811) and anode (e.g., Li), respectively. This makes it possible to use different electrolytes in an individual cell and even electrode, which provides more flexibility in the development of next-generation Li battery technologies. Although oxide systems are intrinsically more stable than sulfide systems, sulfides are arguably more viable for bulk-type ASSLBs. This stems from sulfides' low material density and low elastic modulus which allows intimate contact with active materials. A series of sulfide-based SSEs have been developed and displayed extremely high ionic conductivities ($> 10^{-2}$ S/cm). Demonstrations of stable cycling of coated LiCoO_2 and NMC with sulfide-based SSEs prove their viability for high-energy cathode if protection layers are applied on the cathode particles.

While expectations for sulfide SSEs are high, there are significant materials and processing challenges that need to be addressed. First, what SSEs are suitable for reductive Li metal anode and retain practical processing? For this aspect, SSEs need to meet two critical requirements. 1) Being self-limited passivation against Li metal. Despite high conductivity, LGPS and its derivatives can be reduced to electronically conducting metal (e.g., Ge) or an alloy (e.g., Ge-Li) upon contact with Li metal. 2) High moisture stability. One drawback of phosphorus-containing sulfide-based SSEs is its extreme sensitivity to moisture and easy release of H_2S gas. It has been shown that $\text{P}_2\text{S}_7^{4-}$ ions hydrolyze much more readily than PS_4^{3-} ions. Based on those requirements, new sulfide SSEs should be built solely on the PS_4^{3-} polyanion units without use any metal or semiconductor elements. Second, despite superior conductivity and favorable mechanical properties, deployment of sulfide SSEs in practical ASSLBs is limited by processability due to the high reactivity against moisture. Air exposure not only deteriorates the ion transport properties but also causes safety hazards, namely toxic H_2S gas. Solid-state reactions and processing of sulfide SSE have been demonstrated at lab scales by using ball milling with operation under inert atmosphere or in the glove box, which is arguably not scalable for mass production. Solvent-assisted mechano-chemical synthesis has been studied in recent years and proven to be more controllable and scalable compared to solid-state methods. However, the selection of solvent affects not only the quality of SSE but also the processability and cost of the process. A new synthesis approach and equipment design dedicated to the mass production of sulfide SSE are essentially needed. The third grand challenge faced by the production of ASSLBs is developing a feasible processing method that can be used for efficient fabrication of ultrathin and highly conductive solid separator or cathode film. Currently, most of the

ASSBs were evaluated on a lab-scale using binder-free electrolyte pellets, which need to be very thick (>100 microns) and are not realistic because of the poor processability of large-area film and significant sacrifice of cell-level energy. Dry processing is desirable in considering sulfides' moisture sensitivity and chemical instability. However, without the assistance of any solvent, efficient homogenization of the SSE powder and polymeric binder is very challenging in achieving a high-quality film with very lean amount of binder (<1 wt.%). The wet slurry coating process requires a small amount of polymeric binder but enough solvents to form a uniform slurry. However, the severe reactivity between sulfides and common organic solvents restricts the choices of solvents. Chemical compatibility of SSE, polymeric binder, and the solvent is key to the wet processing of sulfides. A modified high throughput roll-to-roll processing by using a very lean amount of binder and the compatible solvent is necessary for the large production of sulfide-based ASSLBs.

This project aims to identify and address key technical barriers in scale-up synthesis and processing of highly conductive SSEs by leveraging PNNL's patent-pending SSEs ($\text{Li}_7\text{P}_2\text{S}_8\text{X}$, X=Cl, Br, or I), Ampcera Inc.'s environmentally friendly manufacturing capability, and UW's roll-to-roll processing.

Objectives

1. Development of novel sulfide SSEs with room-temperature Li^+ conductivity > 5 mS/cm.
2. Realize low Li/SSE interfacial resistance <5 Ωcm^2 .
3. Scalable production pathway of sulfide SSEs at 1 metric ton/year.
4. High throughput roll-to-roll processing of highly conductive (>1 mS/cm) and ultra-thin solid film (10–30 μm).

Approach

1. Solvent-assisted mechano-chemical synthesis of highly conductive sulfide SSEs with screened compatible solvents.
2. Appropriate halogen doping to enhance ionic conductivity of the $\text{Li}_7\text{P}_2\text{S}_8\text{X}$ (X=Cl, Br, or I) SSEs.
3. Improve Li/SSE critical current density through reducing the Li/SSE interfacial resistance at different temperature.
4. Validate synthesis protocol through up-scaling production.

Results

1. Solvent-assisted mechano-chemical synthesis of highly conductive sulfide SSEs

The $\text{Li}_7\text{P}_2\text{S}_8\text{X}$ (X=Cl, Br, or I) SSEs with high ionic conductivities have been synthesized by solvent-assisted mechano-chemical reactions. The selection of compatible solvents is a key to achieving high ionic conductivity for a given composition. Figure XVI.20.1 shows the electrochemical impedance spectra of $\text{Li}_7\text{P}_2\text{S}_8\text{Br}_{0.5}\text{I}_{0.5}$ synthesized using solvents with different polarities as well as the corresponding ionic conductivities at 20 °C. It is found that the lower polarity of the solvents, the higher the ionic conductivity of the synthesized products. $\text{Li}_7\text{P}_2\text{S}_8\text{Br}_{0.5}\text{I}_{0.5}$ synthesized with cyclohexane (polarity of 0) showed the highest ionic conductivity of 5.9 mS/cm, compared to the one synthesized by toluene (with moderate polarity of 2.4) of 5.0 mS/cm and the one by acetonitrile (with high polarity of 5.8) of 0.8 mS/cm. Study through Scanning Electron Microscopy/Energy Dispersive Spectroscopy (SEM/EDS), X-ray photoelectron spectroscopy (XPS), and Mass spectrometry (MS) revealed that solvent polarity determines the solubility of Li halides and thus their recrystallization and distribution in the precursor mixture after removing the solvents, which has a direct effect on the phase purity of the SSEs after the heat treatment. This is different to the synthesis of conventional sulfide electrolytes like Li_xPS_y , where highly polar solvents like acetonitrile or tetrahydrofuran are applicable. Synthesis of 4 grams/batch of $\text{Li}_7\text{P}_2\text{S}_8\text{Br}_{0.5}\text{I}_{0.5}$ has been realized by the mechanochemical synthesis followed by low-

temperature heat treatment. The obtained $\text{Li}_7\text{P}_2\text{S}_8\text{Br}_{0.5}\text{I}_{0.5}$ showed a high ionic conductivity of >5 mS/cm at room temperature.

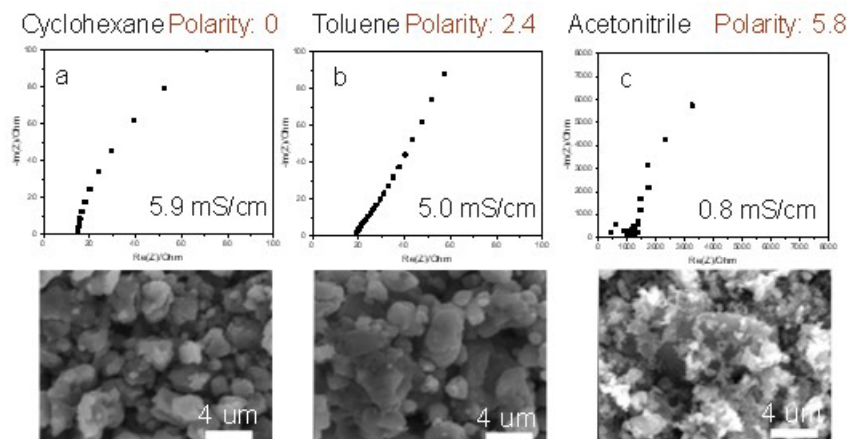


Figure XVI.20.1 Electrochemical impedance spectra and SEM images of $\text{Li}_7\text{P}_2\text{S}_8\text{Br}_{0.5}\text{I}_{0.5}$ synthesized with solvent of (a) cyclohexane, (b) toluene, and (c) acetonitrile.

2. Effects of halogen doping on ionic conductivity of $\text{Li}_7\text{P}_2\text{S}_8\text{X}$ ($\text{X}=\text{Cl}, \text{Br}, \text{or I}$)

Effects of the Br/I ratio on the structure and transport properties of $\text{Li}_7\text{P}_2\text{S}_8\text{Br}_{1-x}\text{I}_x$ ($0 \leq x \leq 1$) were studied. Powder X-ray diffraction (XRD) patterns of the prepared $\text{Li}_7\text{P}_2\text{S}_8\text{Br}_{1-x}\text{I}_x$ ($0 \leq x \leq 1$) are compared in Figure XVI.20.2a. Diffraction peaks of Beryllium (Be) from the sample holder were used as an internal reference. XRD peaks centered at 28.2° and 32.6° were detected in $\text{Li}_7\text{P}_2\text{S}_8\text{Br}$ ($x=0$) and ascribed to a Br-dominated phase. With the increase of I/Br ratio, the Br-dominated phase became less and completely disappeared when I concentration approached 0.5. Beyond that, two new peaks, centered at around 21° and 31° , showed up in $\text{Li}_7\text{P}_2\text{S}_8\text{Br}_{1-x}\text{I}_x$ ($x > 0.5$), suggesting the formation of an I-dominated phase. No clear evidence of either Br-dominated or I-dominated phase was detected in $\text{Li}_7\text{P}_2\text{S}_8\text{Br}_{0.5}\text{I}_{0.5}$, indicating a relatively pure phase was obtained when Br/I=1 ($x=0.5$). Figure XVI.20.2b shows room temperature Li^+ conductivity of $\text{Li}_7\text{P}_2\text{S}_8\text{Br}_{1-x}\text{I}_x$ ($0 \leq x \leq 1$) as a function of x at 20°C . When $x=0$, the as-prepared Br-dominated phase ($\text{Li}_7\text{P}_2\text{S}_8\text{Br}$) possessed a conductivity σ of 1.9 mS/cm. With the increase of I concentration, the ionic conductivity of $\text{Li}_7\text{P}_2\text{S}_8\text{Br}_{1-x}\text{I}_x$ increased and reached a maximum value of 5.9 mS/cm with $x=0.5$. If $x > 0.5$, a decreasing trend was observed from 4.4 mS/cm for $\text{Li}_7\text{P}_2\text{S}_8\text{Br}_{0.2}\text{I}_{0.8}$ to 3.6 mS/cm for $\text{Li}_7\text{P}_2\text{S}_8\text{I}$. The peak ionic conductivity (5.9 mS/cm) of the $\text{Li}_7\text{P}_2\text{S}_8\text{Br}_{0.5}\text{I}_{0.5}$ is believed to be related to high phase purity and unique structure of the compound when $x=0.5$, which is under our study.

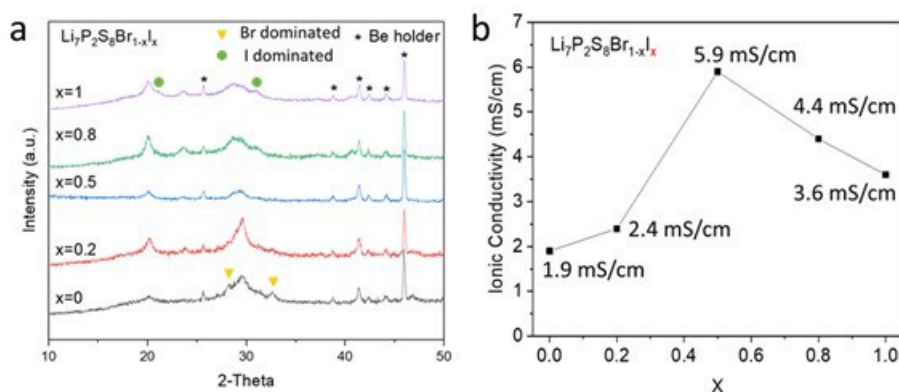


Figure XVI.20.2 (a) XRD patterns and (b) ionic conductivities of $\text{Li}_7\text{P}_2\text{S}_8\text{Br}_{1-x}\text{I}_x$ ($0 \leq x \leq 1$) at 20°C

3. Effects of halogen doping on Li/SSE critical current density

The capability of the $\text{Li}_7\text{P}_2\text{S}_8\text{Br}_{1-x}\text{I}_x$ ($0 \leq x \leq 1$) in suppressing Li dendrite penetration and its correlation with halogen content were studied by galvanostatic cycling of Li/SSE/Li symmetric cells at step-increased current densities at 20 °C. Figure XVI.20.3a–e shows the voltage-time profiles of Li/ $\text{Li}_7\text{P}_2\text{S}_8\text{Br}_{1-x}\text{I}_x$ /Li ($0 \leq x \leq 1$) with different contents of LiI. Generally, the voltage polarization increases with current densities (step size of 0.1 mA/cm^2) for SSEs at all compositions. After cycling at elevated current densities, the Li-Li symmetric cells experience a voltage drop eventually, which is due to the internal short circuit caused by Li dendrite penetration through the SSE membrane. The current density after which voltage starts to drop is called critical current density (CCD), and the magnitude of the CCD is used to evaluate the quality of Li/SSE interface or capability of SSE for dendrite suppression. Figure XVI.20.3f compares the CCDs for the SSEs with different LiI contents at 20 °C. Without any LiI, the CCD of the $\text{Li}_7\text{P}_2\text{S}_8\text{Br}$ is as low as 0.3 mA/cm^2 . With the increase of the LiI content, the CCD increases and reaches the maximum value of 1.4 mA/cm^2 at $x=0.5$ ($\text{Li}_7\text{P}_2\text{S}_8\text{Br}_{0.5}\text{I}_{0.5}$), and then decreases to 1.1 mA/cm^2 at $x=0.8$ and 0.8 mA/cm^2 at $x=1$. The observed peak CCD at $x=0.5$ is related to both the high ionic conductivity of the electrolyte and unique solid electrolyte interface (SEI) properties contributed by the rich I when contacting with Li, which was proved by SEM/EDS, XPS, and Time-of-flight Secondary Mass Spectrometry (ToF-SIMS) analysis.

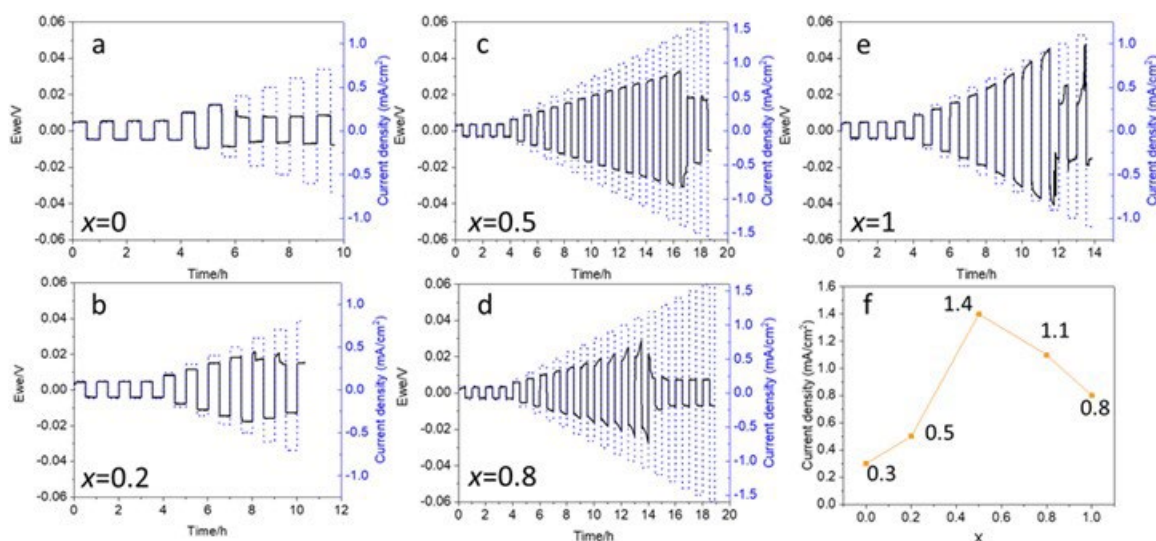


Figure XVI.20.3 Galvanostatic cycling of the Li-Li cells at step-increased current densities at 20 °C with $\text{Li}_7\text{P}_2\text{S}_8\text{Br}_{1-x}\text{I}_x$ ($0 \leq x \leq 1$) electrolytes, where (a) $x = 0$, (b) $x = 0.2$, (c) $x = 0.5$, (d) $x = 0.8$, and (e) $x = 1$. The time for each charge and discharge is 0.5 h. The step size for the current increase is 0.1 mA/cm^2 . (f) The critical current densities versus the composition of the sulfide-based solid-state electrolytes.

4. Effects of halogen doping on Li/SSE interface

Li metal is highly reductive and reacts with sulfide-based SSEs spontaneously, building up a resistant SEI layer. This causes high cell internal resistance, nonuniform Li plating/stripping, and even early cell failure. It is found in this study that different from other sulfides like Li_3PS_4 , Li/ $\text{Li}_7\text{P}_2\text{S}_8\text{Br}_{0.5}\text{I}_{0.5}$ /Li cell shows stable long-term cycling performance both at 20 °C and elevated temperatures, indicating that $\text{Li}_7\text{P}_2\text{S}_8\text{Br}_{0.5}\text{I}_{0.5}$ is compatible with Li metal. Accordingly, Li/SSE interfacial stability was studied and correlated to the halogen doping type and content. We investigated interfaces of $\text{Li}_7\text{P}_2\text{S}_8\text{Br}/\text{Li}$, $\text{Li}_7\text{P}_2\text{S}_8\text{Br}_{0.5}\text{I}_{0.5}/\text{Li}$, and $\text{Li}_7\text{P}_2\text{S}_8\text{I}/\text{Li}$ by monitoring the impedance evolutions of the corresponding Li/SSE/Li symmetric cells for 24 h. The Nyquist plots of Li/Li cells with equivalent circuit fitting are shown in Figure XVI.20.4. A clear semicircle was detected in the initial EIS spectra of $\text{Li}_7\text{P}_2\text{S}_8\text{Br}$ at 20 °C. It is ascribed to the grain boundary resistance of the SSE rather than interfacial resistance due to the short contacting time between $\text{Li}_7\text{P}_2\text{S}_8\text{Br}$ and Li. By contrast, no semicircle was detected for $\text{Li}_7\text{P}_2\text{S}_8\text{Br}_{0.5}\text{I}_{0.5}$ and $\text{Li}_7\text{P}_2\text{S}_8\text{I}$ at 0 h, indicating a negligible grain boundary resistance, which was mainly due to the solid-wetting agent LiI moving to the grain boundaries and enhancing the Li conduction across grain boundaries. After 24 h testing, the overall resistance of Li/ $\text{Li}_7\text{P}_2\text{S}_8\text{Br}/\text{Li}$ cell increased from 37.2 to

$42.5 \Omega \text{ cm}^2$, corresponding to the deterioration of $\text{Li}_7\text{P}_2\text{S}_8\text{Br}/\text{Li}$ interface. Thereby, the half of such a change could be considered as areal interfacial resistance (AIR) at $\text{Li}_7\text{P}_2\text{S}_8\text{Br}/\text{Li}$, which was $2.65 \Omega \text{ cm}^2 \text{ h}$ for $\text{Li}_7\text{P}_2\text{S}_8\text{Br}$ after 24h. The evolution of overall resistance and AIR along with time are shown in Figure XVI.20.4d and e. In contrast to $\text{Li}_7\text{P}_2\text{S}_8\text{Br}$, the AIR of $\text{Li}_7\text{P}_2\text{S}_8\text{Br}_{0.5}\text{I}_{0.5}/\text{Li}$ and $\text{Li}_7\text{P}_2\text{S}_8\text{I}/\text{Li}$ after 24 h were only 1.09 and $1.08 \Omega \text{ cm}^2$, respectively. Moreover, both SSEs with LiI ($\text{Li}_7\text{P}_2\text{S}_8\text{Br}_{0.5}\text{I}_{0.5}$ and $\text{Li}_7\text{P}_2\text{S}_8\text{I}$) showed an exceptionally stable and low AIR, indicating that the presence of LiI facilitates building a Li metal compatible interface. Chemical reactions between Li thiophosphates and Li metal are believed to be more severe at elevated temperatures, which potentially leads to a quick increase of AIRs.

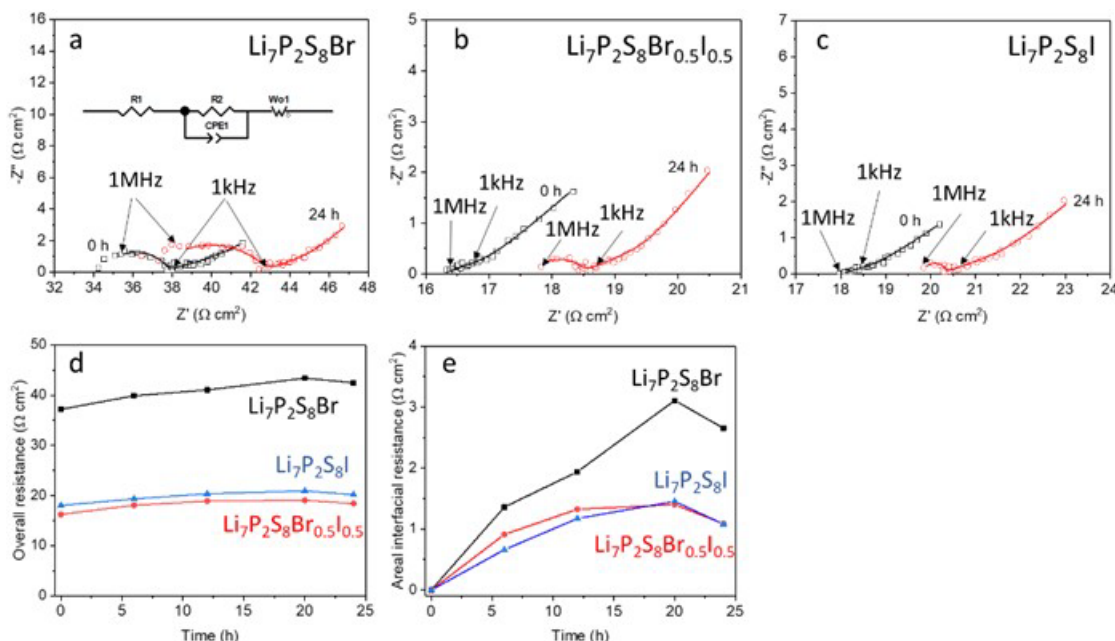


Figure XVI.20.4 Nyquist plots of (a) $\text{Li}/\text{Li}_7\text{P}_2\text{S}_8\text{Br}/\text{Li}$, (b) $\text{Li}/\text{Li}_7\text{P}_2\text{S}_8\text{Br}_{0.5}\text{I}_{0.5}/\text{Li}$, and (c) $\text{Li}/\text{Li}_7\text{P}_2\text{S}_8\text{I}/\text{Li}$ cell with equivalent circuit fitting at 20 °C. Evolution of overall resistance (d) and areal interfacial resistance (e) of each cell with time at 20 °C.

Conclusions

- $\text{Li}_7\text{P}_2\text{S}_8\text{Br}_{1-x}\text{I}_x$ ($0 \leq x \leq 1$) SSEs were developed by solvent assisted chemo-mechanical synthesis followed by a low-temperature heat treatment. High room-temperature ionic conductivity $>5 \text{ mS/cm}$ was realized by using the screened compatible solvents.
- $\text{Li}_7\text{P}_2\text{S}_8\text{Br}_{0.5}\text{I}_{0.5}$ has the highest ionic conductivity (5.9 mS/cm) among $\text{Li}_7\text{P}_2\text{S}_8\text{Br}_{1-x}\text{I}_x$ ($0 \leq x \leq 1$) and highest critical current density of 1.4 mA/cm^2 at 20 °C in Li/Li symmetric cells.
- Both SSEs with LiI ($\text{Li}_7\text{P}_2\text{S}_8\text{Br}_{0.5}\text{I}_{0.5}$ and $\text{Li}_7\text{P}_2\text{S}_8\text{I}$) show an exceptionally stable and low areal interfacial resistance in contacting Li metal (1.09 and $1.08 \Omega \text{ cm}^2$, respectively), indicating unique role of I-rich SEI in promoting stable and low-resistance Li/SSE interface.
- Synthesis of $\text{Li}_7\text{P}_2\text{S}_8\text{Br}_{0.5}\text{I}_{0.5}$ at 4 g/batch is successfully achieved and the room-temperature ionic conductivity is 5.9 mS/cm in cold pressed pellet.

Key Publications

- Zhaoxin Yu, Dongping Lu, Jie Xiao, Jun Liu. "Air-stable solid-state electrolyte", U.S. Application No. 17/507,432. 2021
- Zhaoxin Yu, Dongping Lu, Jie Xiao. "Lithium Compatible Sulfide Solid-state Electrolytes", U.S. Application NO. 63/145,063. 2021

3. Jianbin Zhou, Ying Chen, Zhaoxin Yu, et al. “Wet-chemical synthesis of $\text{Li}_7\text{P}_3\text{S}_{11}$ with tailored particle size for solid state electrolytes”, *Chemical Engineering Journal*, 2021, 429, 132334.
4. Zhaoxin Yu, Kiseuk Ahn, Jie Xiao, Jun Liu, Dongping Lu, “Enabling Highly Conductive and Flexible Solid-state Electrolyte Film for All-solid-state Li-ion Battery”, MRS Spring Meeting, 2021

Acknowledgements

Zhaoxin Yu (PNNL), Hui Du (Ampcera Inc.), and Jun Liu (University of Washington)

XVII Beyond Li-Ion R&D: Lithium Sulfur Batteries

XVII.1 A Novel Chemistry: Lithium-Selenium and Selenium-Sulfur Couple (ANL)

Khalil Amine, Principal Investigator

Argonne National Laboratory
9700 South Cass Avenue
Lemont, IL 60439
E-mail: amine@anl.gov

Tien Q. Duong, DOE Technology Development Manager

U.S. Department of Energy
E-mail: Tien.Duong@ee.doe.gov

Start Date: October 1, 2020

End Date: September 30, 2021

Project Funding (FY21): \$500,000

DOE share: \$500,000

Non-DOE share: \$0

Project Introduction

Lithium/sulfur (Li/S) batteries have attracted extensive attention for energy storage applications due to the high theoretical energy density (2600 Wh kg^{-1}) and earth abundance of sulfur.[1] Recently, selenium and selenium-sulfur systems have also received considerable attention as cathode materials for rechargeable batteries because of the high electronic conductivity (20 orders of magnitude higher than sulfur) and high volumetric capacity (3254 mAh cm^{-3}) of selenium.[2] Selenium-sulfur (Se-S) mixtures are miscible in a wide concentration range, and many Se-S composites can be prepared, including Se_5S , Se_5S_2 , Se_5S_4 , SeS , Se_3S_5 , SeS_2 , SeS_7 , and even materials with a small amount of Se such as SeS_{20} . [2] These Se-S composites offer higher theoretical specific capacities than Se alone and improved conductivity compared to pure S. However, similar to Li/S batteries, two major obstacles resulting from lithium polysulfides/polyselenides (LiPSs/LiPSes) shuttle and lithium dendrite formation remain huge challenges for long-life Li/Se-S batteries.[3] The former is due to the dissolution and migration of polysulfides/polyselenides intermediates in the conventional ether-based electrolytes, which could induce severe parasitic reactions with Li metal and hence formation of porous or mossy Li metal. The latter is originated from the parasitic reactions of lithium metal with the electrolytes, leading to the formation of fragile solid electrolyte interphase (SEI) on Li metal, further uncontrolled lithium dendrite growth and eventually dead lithium. These parasitic reactions are the direct cause for the rapid capacity fade and poor coulombic efficiency of Li/S and Li/Se-S batteries.

Via advanced diagnostic tools including synchrotron X-ray probes and computational modeling, the team led by Dr. Khalil Amine at Argonne National Laboratory (ANL) is focusing on the development of rational cathode structure designs and exploration of novel electrolytes to effectively eliminate these parasitic reactions and simultaneously suppress the shuttle effect and lithium dendrite formation during long-term cycling.

Objectives

The objective of this project is to develop novel Li/Se-S batteries with high energy density (500 Wh kg^{-1}) and long life (>500 cycles) along with low cost and high safety.

Approach

To prevent the dissolution of polysulfides and increase the active material utilization, S or Li_2S is generally impregnated in a conducting carbon matrix. However, this approach makes it difficult to increase the loading density of practical electrodes. It is proposed here to solve the above barriers by the following approaches: (1) partial replacement of S with Se, (2) confinement of the Se-S in a porous conductive matrix with high pore

volume, and (3) exploration of advanced electrolytes that can suppress shuttle effect and lithium dendrite growth.

Collaboration

- Cathode materials and electrolytes development (Dr. Guiliang Xu at CSE of ANL)
- Synchrotron X-ray characterization (Dr. Yang Ren and Dr. Chengjun Sun at APS of ANL)
- Computational modeling (Dr. Lei Cheng at MSD of ANL)

Results

1. Building in-house Li/S pouch cell fabrication line and demonstration of > 100 mAh pouch cells performance using Se-doped sulfur cathode and fluorinated ether-based electrolytes

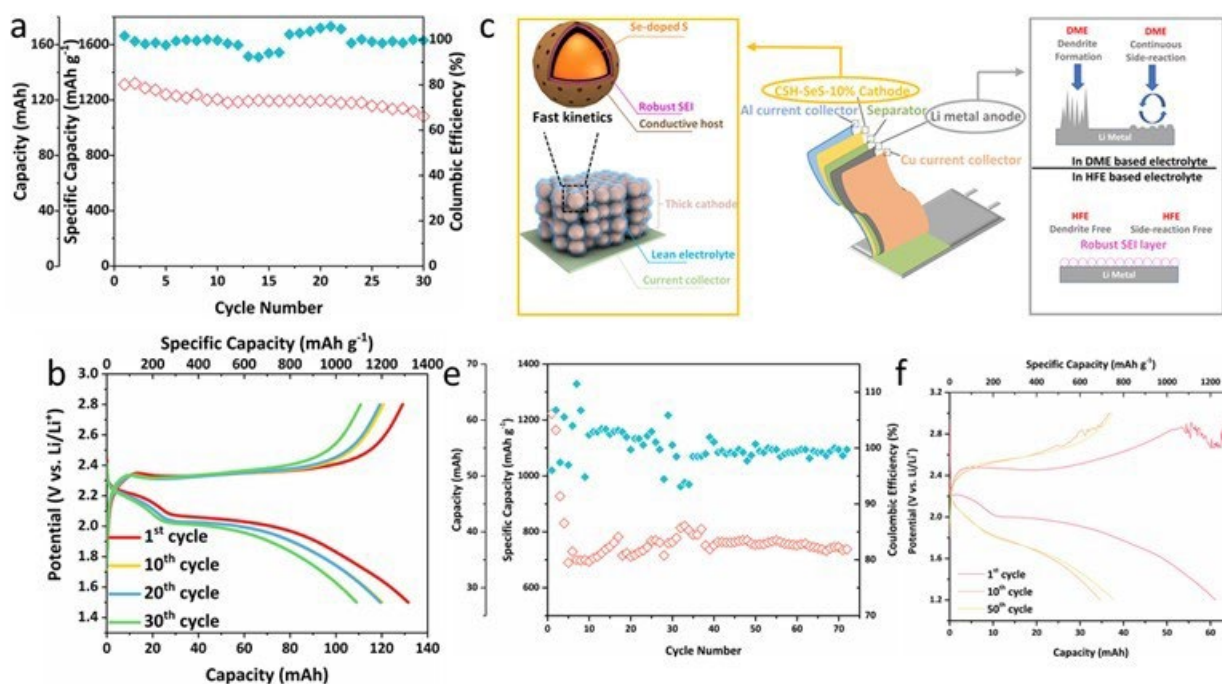


Figure XVII.1.1 (a) Cycling performance and (b) charge/discharge curves of Li/Se-S pouch cell with 100 mg Se-S loading at 200 mA g⁻¹ with a E/S ratio of 10. (c) The effectiveness of the combination of cathode design, Se doping, and fluorinated electrolyte in achieving a shuttle- and dendrite-free Li/S pouch cell under thick-cathode and low-E/S ratio conditions. (d) Cycling performance and (e) charge/discharge curves of Li/Se-S pouch cell with 50 mg Se-S loading at 200 mA g⁻¹ with a E/S ratio of 5.

Currently, most of the reported Li/S batteries were evaluated in coin cells only, while the performance in practical pouch cells showed disappointingly lower specific energy and shorter cycle life. In FY21, we have built an in-house Li/S and Li/Se-S pouch cell assembly and testing line to evaluate the concept of selenium-doped sulfur (core-shell structure) cathodes and fluorinated ether-based (HFE) electrolytes under different electrolytes/Se-S (E/S) ratio. Figure XVII.1.1a and Figure XVII.1.1b present the cycling performance and voltage profiles of the as-assembled Li/Se-S pouch cell (~120 mAh) with 100 mg Se-S loading in the HFE-based electrolyte, respectively. As shown, with an E/S ratio of 10, this cell delivered an initial specific capacity of 1312 mAh g⁻¹ at 200 mA g⁻¹. After 30 cycles, it still maintained 1103 mAh g⁻¹, corresponding to a high-capacity retention rate of 84.07%. The good cycle performance together with the high Coulombic efficiency (> 98.5%) of the pouch cell in HFE-based electrolyte serves as good support for our concept. Figure XVII.1.1c presents a schematic of the underlying mechanism of the Li/Se-S system in different electrolytes. In the conventional dimethoxyethane (DME)-based electrolyte, the severe loss of active material caused by the shuttling of highly soluble LiPSs/LiPSes leads to the fast capacity decay. Meanwhile, the parasitic reactions

between Li metal and DME-based electrolyte molecules leads to dendrite formation and low Coulombic efficiency, resulting in poor cycling stability and severe safety concern. By contrast, in the case of HFE-based electrolyte, a layer of robust SEI can in situ form on the surface of both Se-S cathode and Li metal, which can simultaneously prevent the dissolution of polysulfides and eliminate the parasitic reactions between Li metal and electrolyte molecules, significantly improving the cycling stability and Coulombic efficiency.

In order to further increase the specific energy, we further tested the Li/Se-S pouch cell under a lower E/S ratio to 5. As shown in Figure XVII.1.1d and Figure XVII.1.1e, under a lower E/Se-S ratio, despite the pouch cell and still maintain a relatively stable cycle life, but the specific capacity was decreased to around 800 mAh/g. Meanwhile, the voltage curves shown in Figure XVII.1.1e exhibited a larger voltage polarization than that under a higher E/S ratio. This is because of reduced reaction kinetics by the low E/Se-S ratio. Further development on the optimization of Li/S pouch cells under low E/S ratio will be explored in the next year.

2. Development of macroporous carbon with double-end binding sites for high-energy Li/S batteries

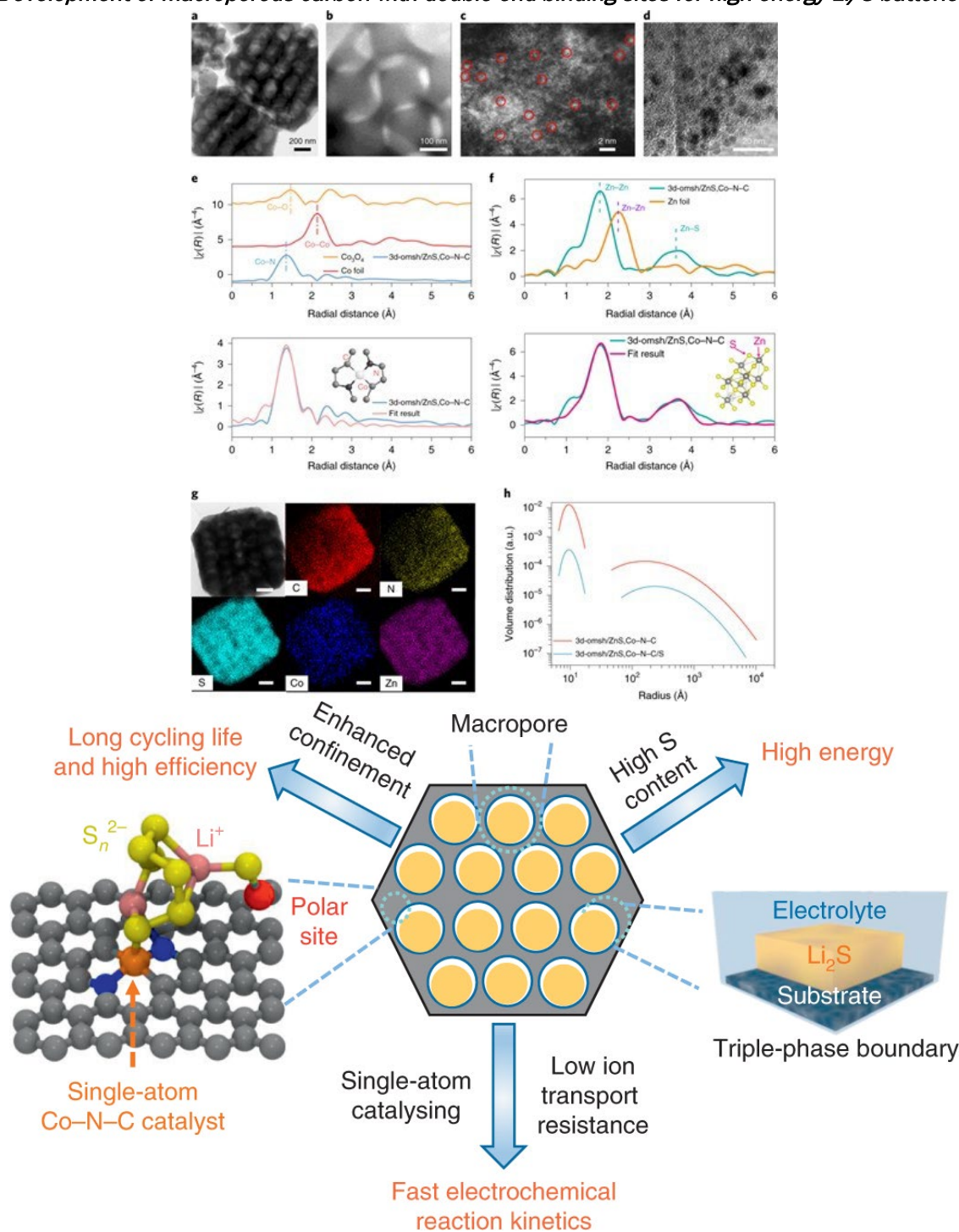


Figure XVII.1.2 (a,b) TEM images of the 3d-omsh/ZnS,Co-N-C. (c) High-angle annular dark-field TEM image of the SAC sites (marked by the red circles) inside the 3d-omsh/ZnS,Co-N-C. (d) TEM image of the polar binding sites inside the 3d-omsh/ZnS,Co-N-C. (e) Co K-edge EXAFS of the 3d-omsh/ZnS,Co-N-C with the reference Co foil and Co₃O₄ (top), and the fitting result using the Co-N-C model (bottom), as shown in the inset. χ , absorption coefficient; R, average distance of neighboring atoms from atoms emitting photoelectrons. (f) Zn K-edge EXAFS of the 3d-omsh/ZnS,Co-N-C with the reference Zn foil (top), and the fitting result using the ZnS model (bottom), as shown in the inset. (g) TEM image of the 3d-omsh/ZnS,Co-N-C/S cathode and the corresponding EDS element mapping of C, N, S, Co and Zn. The scale bars are 200 nm. (h) SAXS simulation on the pore size distributions of 3d-omsh/ZnS,Co-N-C and 3d-omsh/ZnS,Co-N-C/S using spherical shape model.

In FY21, we have further designed and synthesized a novel catalytic cathode host by embedding polar ZnS nanoparticles and Co-N-C single-atom catalyst (SAC) double-end binding (DEB) sites into a highly oriented macroporous conductive framework. The three-dimensional (3D) ordered macroporous sulfur host with DEB sites (denoted as '3d-omsh/ZnS,Co-N-C') was synthesized by connecting $\text{Zn}^{2+}/\text{Co}^{2+}$ ions with 2-methylimidazole linkers inside a 3D template. Transmission electron microscopy (TEM) images (Figure XVII.1.2a & Figure XVII.1.2b) clearly confirmed the 3d-omsh/ZnS,Co-N-C's ordered and interconnected macroporous structure with a pore diameter of ~ 180 nm. Furthermore, single-atom spots were identified from a scanning TEM high-angle annular dark-field image of 3d-omsh/ZnS,Co-N-C (highlighted by red circles in Figure XVII.1.2c), indicating the existence of SAC inside the host material. Uniformly distributed polar ZnS nanoparticles were found (Figure XVII.1.2d), which can pair with Co-N-C SAC to form the DEB sites.

Moreover, the Co K-edge extended X-ray absorption fine structure (EXAFS) of 3d-omsh/ZnS,Co-N-C (Figure XVII.1.2e) shows a weaker peak with much lower radial distance than the reference Co foil, indicating that atoms such as carbon and nitrogen are distributed around the Co atom. The Co-Co peak (2.14 \AA), which is evident for the standard Co foil, is undetectable in the 3d-omsh/ZnS,Co-N-C. The Co K-edge EXAFS of the 3d-omsh/ZnS,Co-N-C peak fits the model of two carbon and two nitrogen atoms surrounding the Co atom. In the case of the Zn K-edge EXAFS (Figure XVII.1.2f), we observed a stronger signal than that of the Zn-Zn (2.24 \AA) in the Zn foil, which is assigned to Zn-S (3.65 \AA). A good fit of the Zn K-edge EXAFS result using the ZnS model further confirmed the existence of ZnS in the 3d-omsh/ZnS,Co-N-C host material. The TEM EDS elemental mapping (Figure XVII.1.2g) confirmed that sulfur was successfully encapsulated into the macroporous chambers of the 3d-omsh/ZnS,Co-N-C. Moreover, the homogeneous distribution of Co, N, C and Zn confirms the uniform distribution of DEB sites inside the cathode. Small-angle X-ray scattering (SAXS) characterization (Figure XVII.1.2h) revealed that about 85% of the macropores was filled by sulfur after sulfur encapsulation.

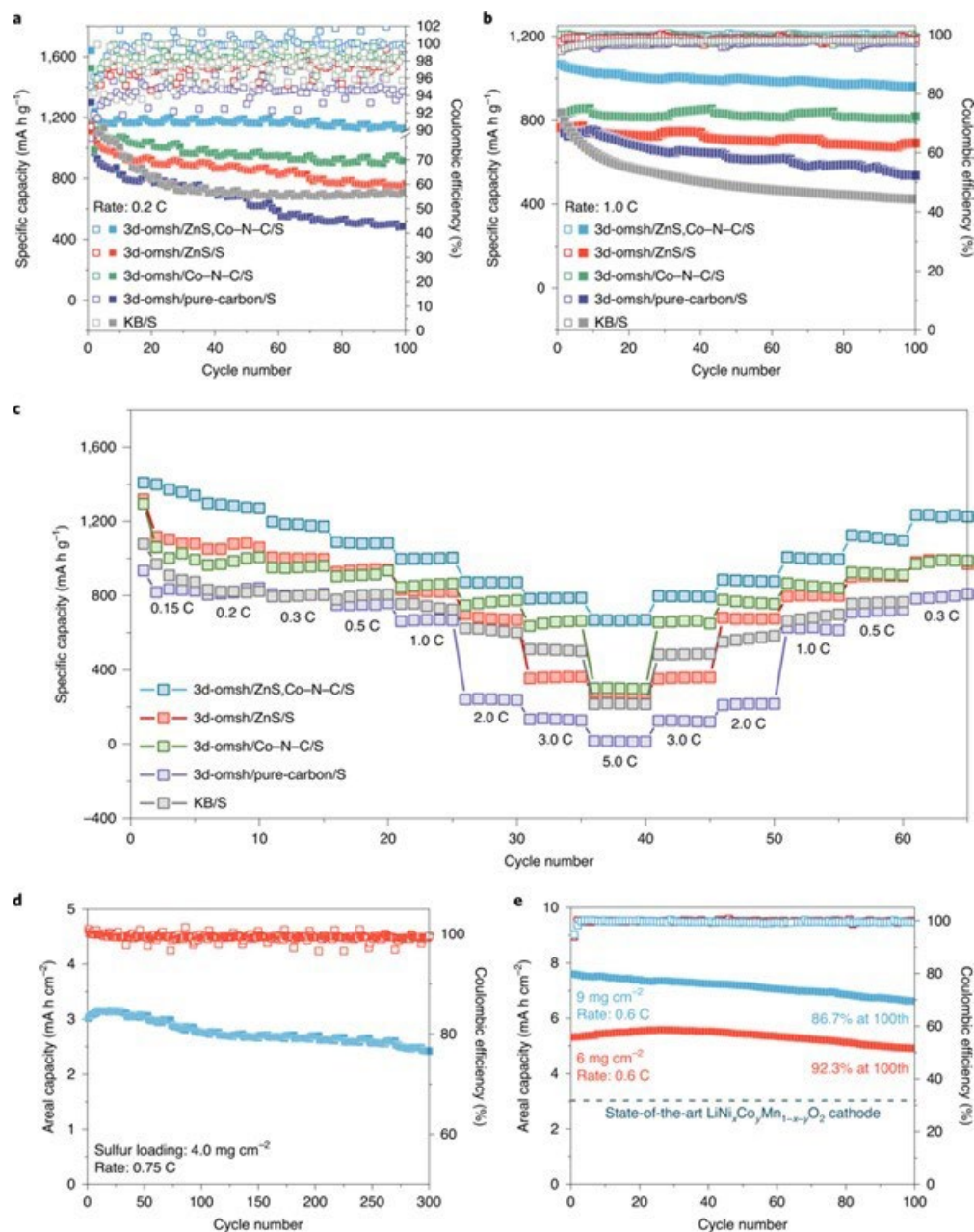


Figure XVII.1.3 (a,b) Cycling performance of various sulfur cathodes at 0.2 C (a) and 1.0 C (b). (c) Rate capability of various sulfur cathodes. (d,e) Cycling performance of the 3d-omsh/ZnS,Co-N-C/S cathode with high areal sulfur loading: 4 mg cm⁻² for 300 cycles at 0.75 C (d) and 6 mg cm⁻² and 9 mg cm⁻² for 100 cycles at 0.6 C (e). 1C equals to 1675 mA g⁻¹.

We have evaluated the electrochemical performance of S/3d-omsh/ZnS,Co-N-C composite. The electrolyte is conventional DME-based electrolytes. The E/S ratio for all the cells were controlled at 10 $\mu\text{L mg}^{-1}$. To demonstrate the effectiveness of our DEB sites concept in immobilizing and catalyzing polysulfides, we prepared and tested the following sulfur cathode materials for comparison: Ketjenblack (denoted as KB/S), 3d-omsh without ZnS/Co-N-C DEB sites (denoted as 3d-omsh/pure-carbon/S), 3d-omsh with only ZnS polar sites (denoted as 3d-omsh/ZnS/S) and 3d-omsh with only Co-N-C single-atom catalyst sites.

As shown in Figure XVII.1.3a, the 3d-omsh/ZnS,Co-N-C/S cathode exhibited a higher capacity retention rate (93.86%) and Coulombic efficiency (100%) after cycling at 0.2 C for 100 cycles, compared with KB/S (60.25% and 97%, respectively), 3d-omsh/pure-carbon/S (54.70% and 94%), 3d-omsh/ZnS/S (69.22% and

97%) and 3d-omsh/Co-N-C/S (83.15% and 98%). At 1.0 C, the 3d-omsh/ZnS,Co-N-C/S cathode still demonstrated the best performance among the five samples (Figure XVII.1.3b). The rate capability test (Figure XVII.1.3c) further showed that the 3d-omsh/ZnS,Co-N-C/S cathode presents the highest specific capacity among the five samples under all testing rates (0.15 C to 5.0 C). We have further evaluated the electrochemical performance of the sulfur/3d-omsh/ZnS,Co-N-C composite under high areal S loading. At a higher areal sulfur loading to 4.0 mg cm^{-2} (Figure XVII.1.3d), the 3d-omsh/ZnS,Co-N-C/S exhibits an initial areal capacity of $3.07 \text{ mA h cm}^{-2}$ and can maintain a reasonable areal capacity of $2.41 \text{ mA h cm}^{-2}$ with minimal voltage polarization after 300 cycles at 0.75 C, demonstrating good cycle stability. Moreover, the coulombic efficiency are all maintained at $\sim 100\%$, indicating low shuttle effect. We further increased the areal S loading to extreme high areal S loading of 6 mg cm^{-2} and 9 mg cm^{-2} (Figure XVII.1.3e). After cycling at 0.6 C for 100 cycles, these cathodes can still deliver 4.9 mA h cm^{-2} and 6.5 mA h cm^{-2} , respectively.

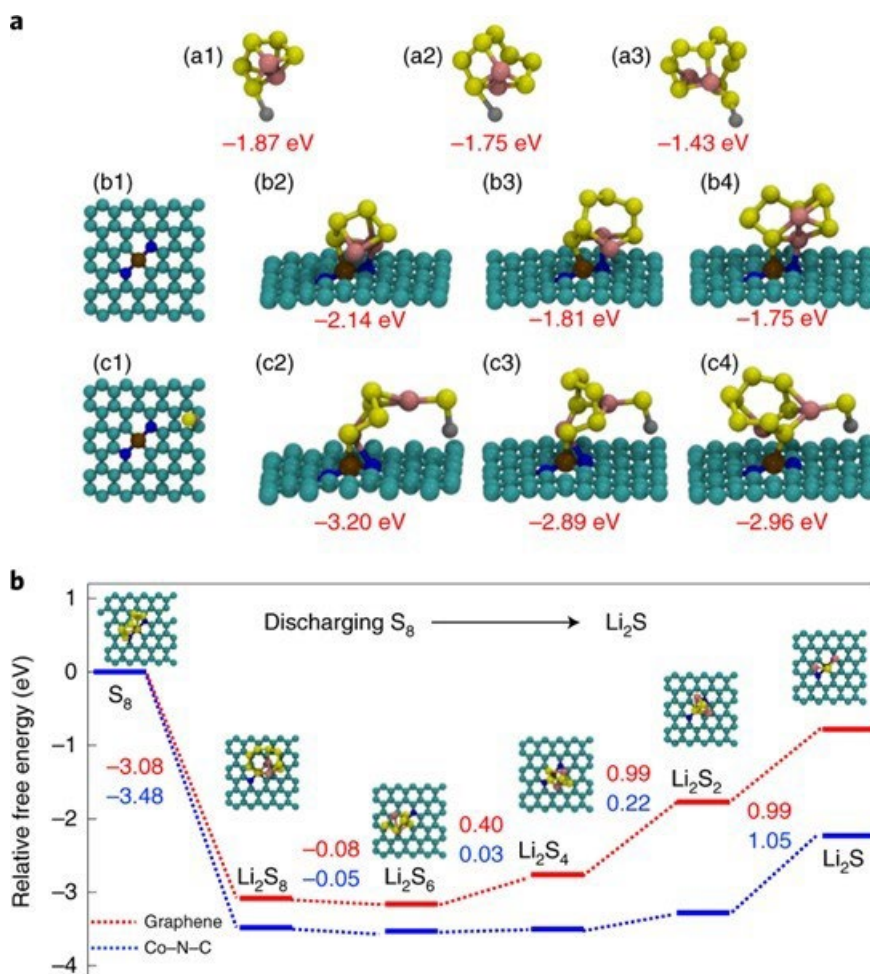


Figure XVII.1.4 (a) Optimized configurations of Li_2S_4 , Li_2S_6 and Li_2S_8 absorption on ZnS (a1-a3), the Co-N-C surface (b1-b4) and the ZnS,Co-N-C surface (c1-c4). The yellow, pink, silver, brown, blue and cyan balls denote the S, Li, Zn, Co, N and C atoms, respectively. (b) Relative free energy for the discharging process from S_8 to Li_2S on the bare graphene and Co-N-C surfaces. The optimized structures of the intermediates on the Co-N-C surface are shown as the insets. Same colour coding for atomic structure as in (a).

We further conducted computational modeling to understand the interaction between lithium polysulfides (LiPSs) and our ZnS/Co-N-C double-end binding host. The dimension of the rectangular graphene layer was chosen to be $12.30 \text{ \AA} \times 12.78 \text{ \AA}$ with 60 carbon atoms. Three carbon atoms on the graphene surface were replaced by one Co and two N atoms to form the Co-N-C surface shown in Figure XVII.1.4 (b1). ZnS was placed near the CoN site to explore the synergistic effect between the two sites. This ZnS,Co-N-C surface is

shown in Figure XVII.1.4 (c1). The lithium polysulfide clusters were then placed on different positions of the graphene and the Co-N-C surface to explore the most stable adsorption structure. Figure XVII.1.4a shows the optimized configurations of LiPSs with polar ZnS, Co-N-C SAC, and ZnS,Co-N-C surfaces, in which Li^+ binds with S atoms in the case of polar ZnS (a1-a3), and S_n^{2-} binds with cobalt and nitrogen in the case of the Co-N-C SAC surface (b1-b4), while Li^+ and S^{2-} bind with the S and Co atoms on the ZnS,Co-N-C surface. The calculated results show that the binding energies of Li_2S_4 , Li_2S_6 and Li_2S_8 on the ZnS,Co-N-C surface are -3.20, -2.89 and -2.96 eV, respectively, which are all higher (~ 1 eV higher) than the former SEB surface condition due to the synergistic effect of Co-N-C SAC and polar ZnS. Such enhanced binding strength towards LiPSs can suppress the dissolution and migration of LiPSs from the cathode.

To gain an in-depth understanding of the Co-N-C SAC surface in enhancing the electrochemical reaction kinetics, the whole reaction involving the formation of Li_2S from S_8 was considered. Figure XVII.1.4b shows the relative free energy landscape for the discharging process from S_8 to Li_2S on the bare graphene and Co-N-C surface. The optimized structures of the intermediates on the Co-N-C SAC substrates are shown in the insets. The data clearly show that the discharging process is more thermodynamically favourable on the Co-N-C SAC surface compared to the graphene surface. Specifically, the reaction energy from solid S_8 to liquid Li_2S_8 on the Co-N-C SAC surface is more exothermic than that on the graphene surface. The last two steps—from Li_2S_4 to Li_2S_2 and from Li_2S_2 to Li_2S —exhibit larger energy barriers (~ 1.98 eV) compared to the other steps on both substrates, suggesting that the $\text{Li}_2\text{S}_2/\text{Li}_2\text{S}$ precipitation process is the rate-limiting step during discharging. Nevertheless, on the Co-N-C SAC surface, the energy barrier of the endothermic precipitation process is effectively lowered (1.27 eV). This finding indicates that the $\text{Li}_2\text{S}_2/\text{Li}_2\text{S}$ precipitation process is thermodynamically more favourable on the Co-N-C SAC surface because it demonstrates stronger binding strength towards LiPSs, which can effectively adsorb the dissolved LiPSs. Moreover, the Co-N-C SAC is electronically conductive, which can thus provide fast electron transfer between Co atoms of SAC and S atoms of LiPSs and further facilitate the weakening of the Li-S bonds of LiPSs. Thus, SAC can significantly decrease the reduction barrier of LiPSs, facilitate the Li_2S precipitation and improve the reaction reversibility.

Conclusions

In summary, we have built an in-house Li/S pouch cells assembly and testing line, which enable us to evaluate the electrochemical performance of our cathodes and electrolyte design in the practical pouch cells up to 1Ah. We have further reported a novel macroporous carbon with double-end binding sites for high-energy Li/S batteries. The Co-N-C SAC site and the ZnS polar site can effectively immobilize the LiPSs by binding with the negatively charged end S_n^{2-} and positively charged end Li^+ , respectively, leading to almost zero shuttle effect and no Li metal corrosion. The ordered macropores can attain both high S accommodation (high specific energy) and fast ion transport, which can facilitate the formation of triple-phase boundaries and avoid ‘dead sulfur’. The sufficient triple-phase boundaries, combined with the excellent immobilization and catalytic effect of the DEB sites, can further boost the electrochemical S redox kinetics. Improvement on the performance of Li/S batteries under lean electrolytes conditions ($E/S < 3 \mu\text{L mg}^{-1}$) would be the primary goal for the next year.

Key Publications

Publications

1. Zhao, C.; Xu, G. L.(*) ; Yu, Z.; Zhang, L.; Hwang, I.; Mo, Y.-X.; Ren, Y.; Cheng, L.; Sun, C. -J.; Ren, Y.; Zuo, X.; Li, J.-T.; Sun, S.-G.; Amine, K.(*) and Zhao, T.(*). A high-energy and long-cycling lithium-sulfur pouch cell via a macroporous catalytic cathode with double-end binding sites. *Nature Nanotechnology*, 2020, 16, 166-173.
2. Lee, B. J.; Kang, T. H.; Zhao, C.; Park, H. Y.; Kang, J.; Jung, Y.; Liu, X.; Li, T.; Xu, W.; Zuo, X. B.; Xu, G. L.(*) ; Amine, K.(*) ; Yu, J. S.(*) A redox-active interlayer for high-energy and long-cycling lithium-sulfur batteries. *Nature Communications*, 2021, under revision.

Presentation

1. Guiliang Xu and Khalil Amine, New Cathode and Electrolytes Strategies to Enable High-Energy Li-S Batteries. 239th ECS meeting with the 18th International Meeting on Chemical Sensors (IMCS), Oral presentation, May 30-June 3, 2021.
2. Guiliang Xu and Khalil Amine, Stabilization of Advanced cathode and Anode to make Better batteries. Battery & Electrification Summit, invited talk, June 16th, 2021.

References

1. Z.W. Seh, Y. M. Sun, Q. F. Zhang, and Y. Cui. “Designing High-Energy Lithium-Sulfur Batteries.” *Chemical Society Reviews* 45, no. 20 (2016): 5605-34. DOI:10.1039/c5cs00410a.
2. A. Abouimrane, D. Dambournet, K. W. Chapman, P. J. Chupas, W. Weng, and K. Amine. “A New Class of Lithium and Sodium Rechargeable Batteries Based on Selenium and Selenium-Sulfur as a Positive Electrode.” *Journal of the American Chemical Society* 134, no. 10 (2012): 4505–08. DOI: 10.1021/ja211766q.
3. Y. Cui, A. Abouimrane, J. Lu, T. Bolin, Y. Ren, W. Weng, C. Sun, et al. “(De)Lithiation Mechanism of Li/SeS_x (X = 0-7) Batteries Determined by in Situ Synchrotron X-Ray Diffraction and X-Ray Absorption Spectroscopy.” *Journal of the American Chemical Society* 135, no. 21: 8047-56. DOI: 10.1021/ja402597g.

Acknowledgements

Support from Tien Duong of the U.S. DOE’s Office of Vehicle Technologies Program is gratefully acknowledged. I would like to thank Dr. Guiliang Xu at ANL for the major contribution to this project.

XVII.2 Development of High Energy Lithium-Sulfur Batteries (PNNL)

Dongping Lu, Principal Investigator

Pacific Northwest National Laboratory
902 Battelle Boulevard, Richland, WA 99354
E-mail: dongping.lu@pnnl.gov

Jun Liu, Co-Principal Investigator

Pacific Northwest National Laboratory
902 Battelle Boulevard, Richland, WA 99354
E-mail: jun.liu@pnnl.gov

Tien Q. Duong, DOE Technology Development Manager

U.S. Department of Energy
E-mail: Tien.Duong@ee.doe.gov

Start Date: October 1, 2015

End Date: September 30, 2021

Project Funding (FY21): \$275,000

DOE share: \$275,000

Non-DOE share: \$0

Project Introduction

Lithium-sulfur (Li-S) battery has a high theoretical energy and low cost, making it one of the most promising battery technologies to meet the DOE target of < \$80/kWh for vehicle electrification. Despite advances in Li-S battery, deployment of the technology is still hindered by the low practical energy and limited cycle life. Achieving a high energy in Li-S cell is feasible only through the simultaneous integration of a high-loading S cathode, thin Li anode, and most importantly a very lean amount of electrolyte. However, a simple combination of these parameters in a high-energy cell often leads to both a low reversible capacity and very limited cycling life. Fundamental mechanisms of the cell failure at realistic conditions remain unclear. Our study of high-energy Li-S pouch cell proved 1) electrolyte amount has a nearly linear correlation with the cumulative cell capacity (or lifespan); and 2) electrolyte diffusion/ redistribution is hindered by the high tortuosity sulfur electrodes, which leads to the reaction heterogeneity and accelerated cell-failure. To improve cell cycle life and maintain high energy density of the cell at the same time, new designs and understanding of materials and electrode architectures are needed. Rational designs are required to increase effective electrolyte supply, facilitate electrolyte distribution, reduce electrolyte consumption, and maintain a durable Li-ion conduction network under realistic cell operation conditions. First, reducing electrode porosity is critical to conserving more electrolyte for cell cycling. For a given areal capacity, sulfur cathodes are much thicker and more porous (>60%) compared to the dense NMC cathodes due to the use of low density and porous S/C materials. This severely diminishes cell energy while also requiring more electrolyte for pore filling. However, reducing electrode porosity proves challenging if using the materials designed for highly porous cathodes. This is because the electrodes featuring low porosity and high tortuosity have slow electrolyte diffusivity, reducing the sulfur reaction kinetics and utilization rate. Therefore, a clear understanding of the effect that electrode porosity/tortuosity has on the electrolyte transport, sulfur reaction kinetics and cell life is critical for the rational design of materials and electrode architectures. Approaches that reduce the tortuosity in a low-porosity cathode are required to ensure the quick electrode wetting. Second, Li-ion conduction pathways should be maintained by either developing stable electrolytes/additives or through building quasi-solid Li⁺ conduction networks. So far, ether-based liquid solutions combined with LiNO₃ additive remain the most viable option for Li-S electrolytes. However, consumption and depletion occur quickly upon chemical and electrochemical reactions. The “non-solvating” electrolytes, localized concentrated electrolytes, and solid electrolytes received widespread attention for prolonging the cycle life of the Li metal batteries. These electrolytes may also be helpful in Li-S cells but need an optimal electrode architecture that can take advantages of novel electrolytes.

The objective of this project is to develop high-energy Li-S batteries with a long lifespan. Our research in FY21 focus on the fundamentals of materials and electrode design to realize operation of low porosity electrodes at very lean electrolyte conditions based on our developed materials and electrolytes (U.S. Patent No. 9577250 and U.S. Pat. App. No. 15/334240).

Objectives

- Realize S utilization rate $>1000 \text{ mAh/g}$ in highly dense (porosity $\leq 40\%$) and high-loading ($> 4 \text{ mg/cm}^2$) S electrodes through optimization of materials and electrode architectures.
- Realize scale-up preparation of the high-loading and dense sulfur electrodes with high areal capacity.

Approach

1. Optimize electrode architecture to realize discharge capacity of $>1000 \text{ mAh/g}$ in high loading S electrode ($>4 \text{ mg S/cm}^2$) at very low porosity ($< 40\%$).
2. Build an electrode model to understand the effects of electrode porosity and tortuosity on the electrolyte transport and S reaction kinetics.
3. Enable a quasi-solid electrolyte networks by introducing polymer solid electrolytes into the low porosity electrodes, and realize cell operation at an extremely low E/S.
4. Identify compatible binder and solvent combinations to enable facile processing of the dense electrodes.

Results

1. Effects of cathode particle size on sulfur utilization and cell cycling of high-loading sulfur electrodes ($>4 \text{ mg S/cm}^2$)

High sulfur utilization rate ($>1000 \text{ mAh g}^{-1}$) was realized in dense electrodes with the porosity as low as $\sim 40\%$; effects of cathode particle size on sulfur reactions were studied at various porosities and electrolyte conditions by using small particle cathodes (SPC, particle size $< 20 \text{ }\mu\text{m}$) and large particle cathodes (LPC, particle size $> 90 \text{ }\mu\text{m}$) as examples. The cathode materials (Integrated Ketjen Black, IKB) with different particle sizes were synthesized at PNNL. Figure XVII.2.1a-f compare the capacity retentions of SPC and LPC at an electrolyte/sulfur (E/S) ratio of $10 \text{ }\mu\text{L mg}_s^{-1}$. Reducing porosity has different impacts on sulfur electrodes composed of large or small particles. Although SPCs and LPCs have similar 1st discharge capacities at each level of porosity, LPCc demonstrates much higher capacity and better capacity retention for the subsequent cycles. The LPC electrode shows improved cycling stability when the porosity decreased from 62% to 53%. Even at a very low porosity of 45%, it still maintains similar performance as those at 62% porosity. It is important to notice that for LPC, most of the capacity loss occurs in the second discharge process and then it becomes very stable in the following cycles (Figure XVII.2.1d-f). On the contrary, clear detrimental effects were detected in SPCs as the porosity decreasing. Also, the capacity loss of SPC in first five cycles drastically increases when the porosity is reduced from 62% to 45%. Another important observation is that particle size has a direct impact on the Coulombic Efficiency. As shown in Figure XVII.2.1d-f, at each porosity, the LPC electrode always shows relatively higher Coulombic Efficiency in the first and subsequent cycles if compared with SPC electrodes. This is consistent with capacity retention observed in SPC and LPC and could be ascribed to the longer diffusion path of the LPC particles. Under lean electrolyte conditions ($\text{E/S}=4 \text{ }\mu\text{L mg}_s^{-1}$), at a relatively high porosity of 62%, the SPC electrodes have almost identical reversible capacity and capacity retention with those of LPC electrodes. Performance difference between the SPC and LPC becomes more obvious with reduction of electrode porosity. At a porosity of 53%, deteriorated polarization and capacity decay were observed in SPC. At a very low porosity of 45%, the first discharge capacity drops to 451 mAh g^{-1} . In opposite, LPC at 45% porosity can still deliver a promising specific capacity of 1001 mAh g^{-1} and 90.8% capacity retention after 30 cycles.

2. Understanding of electrode porosity and tortuosity on the electrolyte transport and polysulfide diffusion

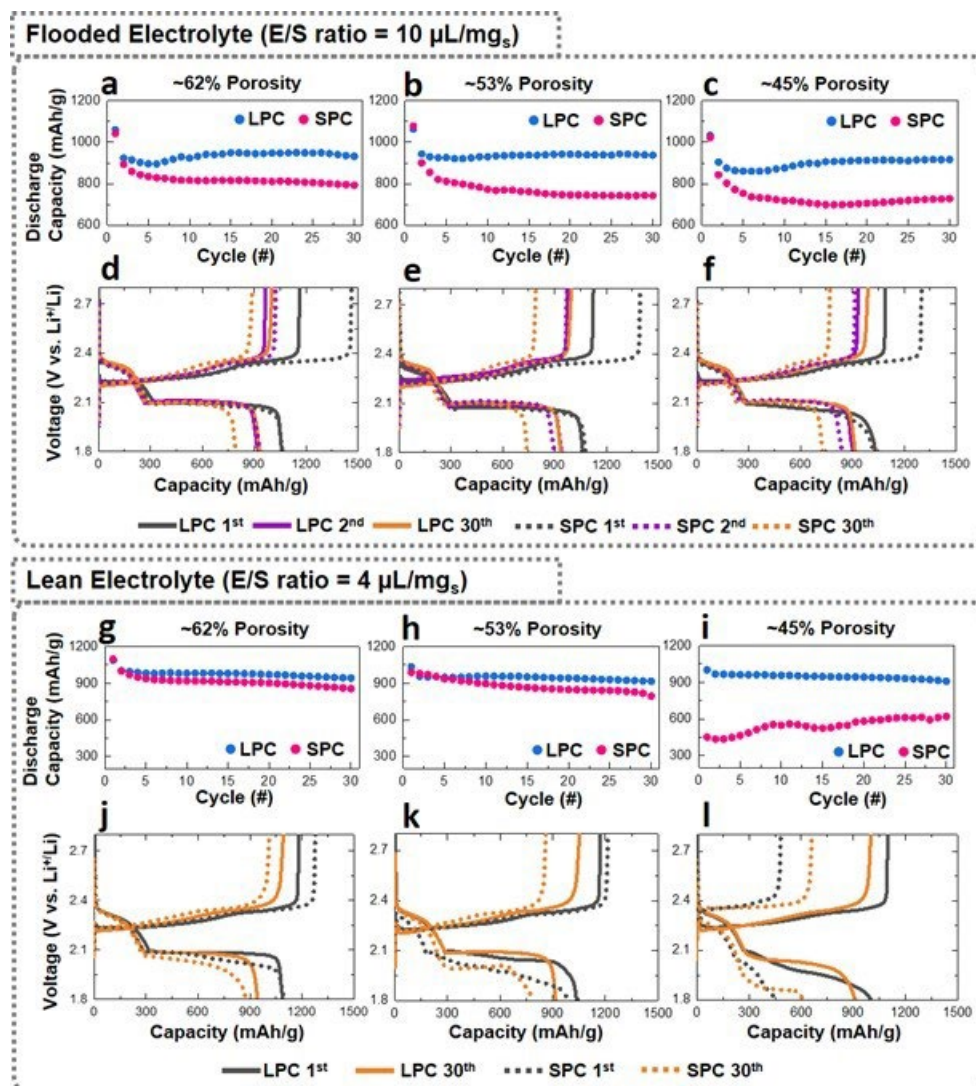


Figure XVII.2.1 Electrochemical performances of SPC and LPC Electrodes (4 mg S/cm^2) under flooded ($\text{E/S ratio} = 10 \text{ } \mu\text{L/mg}_s$) and lean ($\text{E/S ratio} = 4 \text{ } \mu\text{L/mg}_s$) electrolyte conditions. Capacity retention (a-c) and corresponding discharge/charge curves (d-f) of SPC and LPC under flooded electrolyte condition at 0.1 C ($1 \text{ C} = 1000 \text{ mA/g}$); Capacity retention (g-i) and corresponding discharge/charge curves (j-l) of SPC and LPC under lean electrolyte condition.

The S/C composite holds the largest mass/volume ratio in the sulfur cathode, so its property dictates an electrode's architecture. To identify optimal particle size for prompt electrode wetting, electrode models with different particle sizes were built, and computational fluid dynamics (CFD) simulations were conducted using STAR-CCM+. The multiphase flow simulations using volume of fluid (VOF) is applied to study the electrolyte wetting process in a LPC and SPC electrodes. When adding electrolyte on the top of electrodes, gravity is the main driving force to initiate the electrolyte infiltration, and the wetting process can be dictated by the competing effect between gravity and pore scale capillary pressure. Figure XVII.2.2a demonstrates the initial state of the LPC and SPC, in which the blue and black colors represent the electrolyte and void space in the electrode, respectively. By conducting a transient flow simulation, the temporal evolution of the LPC and SPC wetting can be monitored. The steady state electrolyte distribution inside the electrode is illustrated in Figure XVII.2.2b. It is clear that with the same electrolyte volume and electrode porosity in the initial state,

LPC shows better wetting, and the electrolyte can be uniformly distributed in the deeper part of electrode. As for SPC, within the same simulation period, electrolyte can hardly penetrate the porous electrode, leading most of the particles unwetted. The wetted area of particles (A_w) is computed and normalized by the total area of the particles' outer surfaces (A_p). When plotting the evolution of normalized wetted area with time, the A_w/A_p (%) not only quantifies the net degree of wetting but also indicates the electrolyte infiltration speed in different electrodes. As shown in Figure XVII.2.2c, in LPC, the A_w/A_p quickly increases once the electrolyte infiltration starts, and more than 40% of the outer surfaces can be wetted after achieving steady state, suggesting both faster infiltration speed and a high degree of wetting. In contrast, the A_w/A_p curve for SPC shows a plateau behavior at the beginning of infiltration process, which means the electrolyte infiltration experiences high capillary pressure developed in the small pores in SPC. Although the normalized wetted area reaches steady state, the wetting degree is significantly lower than that of LPC. It is also important to notice the slow electrolyte infiltration can be improved by increasing the electrolyte volume. As shown in Figure XVII.2.1c and d, when the electrolyte volume is doubled (denoted as flooded electrolyte), the gravitational force overwhelms the pore scale capillary pressure, subsequently the wetting degree and absorbed electrolyte are increased in both SPC and LPC electrodes. This clearly demonstrates how a flooded electrolyte condition obscures the wetting issues of sulfur cathodes under lean electrolyte conditions. The VOF flow simulations suggest the LPC composed of large particles has faster electrolyte infiltration and better wettability compared to the corresponding ones for SPC.

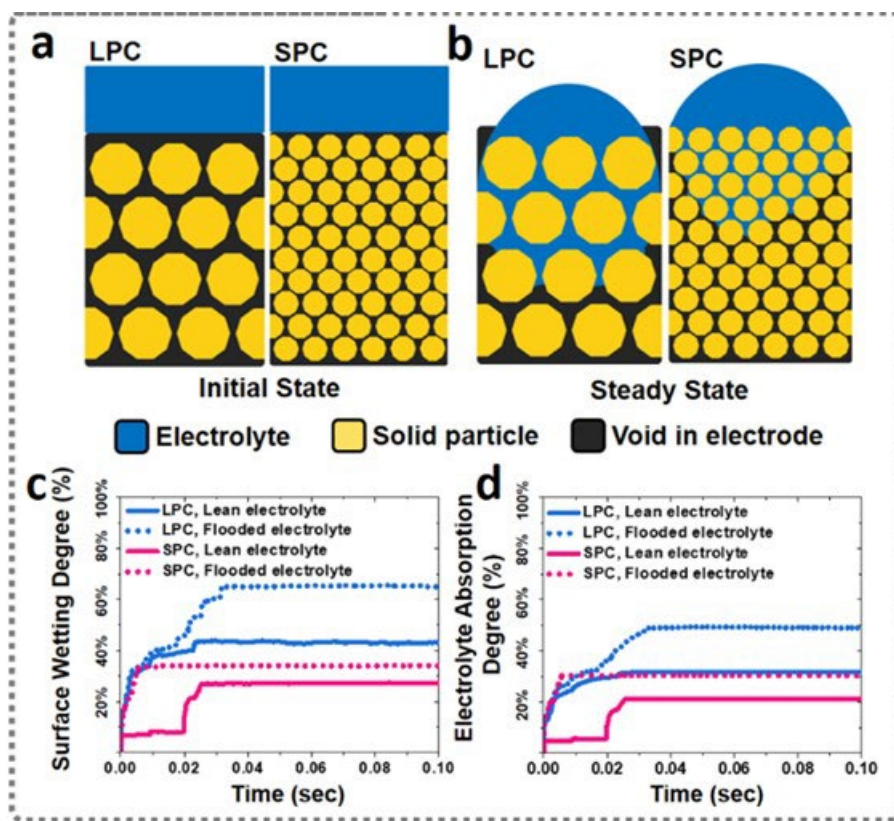


Figure XVII.2.2 Simulations of electrolyte infiltration in different electrode structure: (a) initial state and (b) steady state of electrolyte infiltration in LPC and SPC, (c) surface wetting degree and (d) electrolyte absorption degree in LPC and SPC at steady state.

3. Polymer enhanced Li-ion conduction network in dense S electrode

To reduce the volume of pore-filling electrolyte, the electrode porosity should be further reduced. However, in practice, further reducing the porosity of high-loading electrode is hindered by poor electrode wetting and low sulfur utilization rate. Electrodes featuring low porosity have slow electrolyte diffusivity, limiting reaction

kinetics and sulfur utilization rate. Therefore, approaches that can promote electrolyte infiltration and distribution in a dense cathode are critical to increase effective electrolyte supply particularly at low E/S ratio.

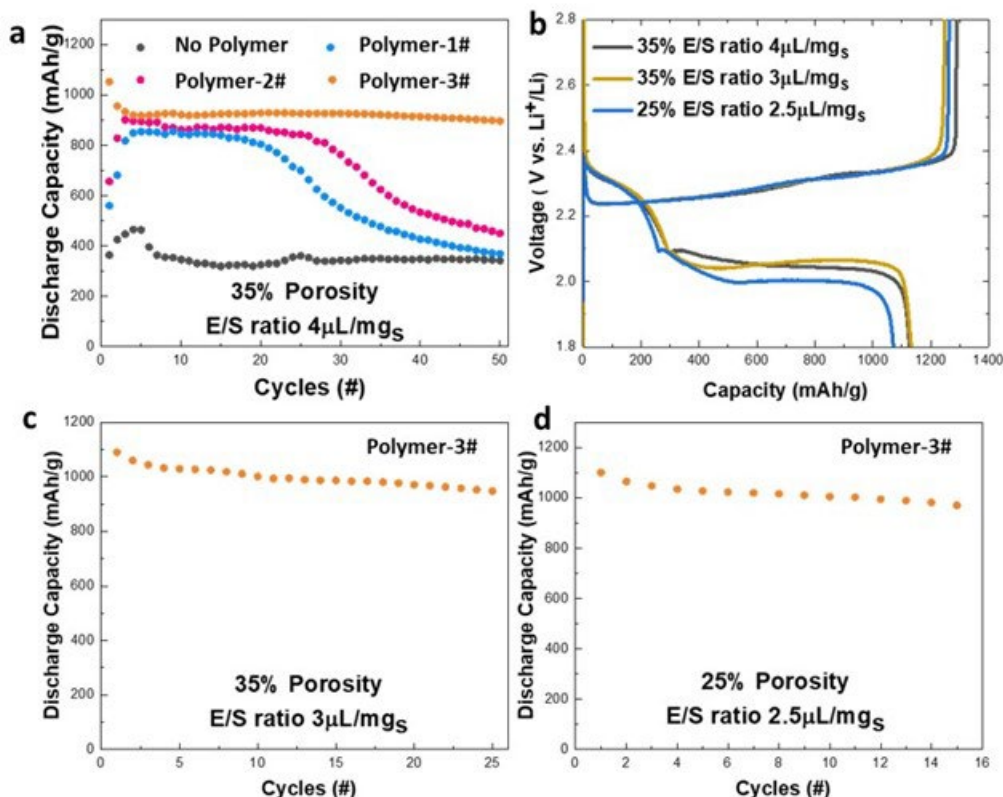


Figure XVII.2.3 Electrochemical performances of low-porosity sulfur electrodes with polymer/liquid electrolyte design. (a) Effects of polymer on sulfur utilization rate and cycling stability with electrode porosity of 35% and E/S ratio=4 $\mu\text{L}/\text{mg}$, (b) charge/discharge curves of polymer integrated electrodes at various porosities and E/S ratio. (c) Cycling performance of 35% porosity electrode and E/S ratio=3 $\mu\text{L}/\text{mg}$. (d) Cycling performance of 25% porosity electrode at E/S=2.5 $\mu\text{L}/\text{mg}$. (4 $\text{mg}_\text{S}/\text{cm}^2$, 0.1C for both charge and discharge)

Our strategy is to build up a hybrid Li-ion conduction network in the dense electrodes by using appropriate polymer additives. The selected polymer can be introduced into electrodes either through pre-coating of cathode materials or during the slurry making. After electrode drying and calendaring, the polymeric components will stay between the electrode particles. High affinity of the polymer with liquid electrolytes helps to facilitate uniform electrolyte infiltration in the low-porosity electrodes. After electrode wetting, interactions between the polymer and liquid electrolytes cause partial solidification or gelation of the liquid electrolytes, which in turn confines liquid electrolyte inside the electrode and suppresses free shuttling of soluble lithium polysulfides. We studied the effects of polymer property on cell performance by using high-loading electrodes (4 mg/cm^2) at lean electrolyte conditions. The presence of a polymer component improves sulfur utilization in low-porosity electrode and the effectiveness is dependent on the polymer properties. For the electrode at a porosity of 35% without polymer, high polarization and very limited capacity were observed at lean electrolyte conditions (E/S=4 $\mu\text{L}/\text{mg}$) due to the blocked electrode wetting (Figure XVII.2.3a). Introducing polymer into the electrodes significantly improved the sulfur utilization rate, particularly for the polymer-3#. The electrode delivered a high initial specific capacity of >1000 mAh/g and maintained stable cycling of over 50 cycles. To validate the effectiveness of the approach, the electrode porosity was further decreased to 25% and the E/S was lowered to 2.5 $\mu\text{L}/\text{mg}$. As shown in Figure XVII.2.3b, the 35% electrodes have almost identical discharge capacities at E/S of 4 and 3 $\mu\text{L}/\text{mg}$. Even at harsh conditions of 25%

porosity and E/S of 2.5 $\mu\text{L}/\text{mg}$, the electrode is still able to deliver a capacity $>1000 \text{ mAh/g}$. Benefits of decreasing electrode porosity not only include an increase in cell energy density, but also extending cell cycling at lean electrolyte conditions. As shown in Figure XVII.2.3c and d, the electrode can be cycled at E/S ratio of 3 and 2.5 $\mu\text{L}/\text{mg}$ in coin cells, while the cells using porous electrodes always fail under the similar conditions. This strategy is transferrable to practical Li-S pouch cell fabrication.

4. Binder and solvent combinations to enable the large processing of the dense electrodes.

To realize facile preparation of sulfur electrodes with both high mass loading and low porosity, a lubricant-assisted rolling method was developed by using the polytetrafluoroethylene (PTFE) as binder. As illustrated in Figure XVII.2.4a, a uniformly mixed paste of S/C, Super P conductive additive, and PTFE binder was prepared with the assistance of lubricant (isopropanol, IPA). The paste was rolled into electrode film at different thickness and vacuum dried into free-standing electrodes (Figure XVII.2.4c) (denoted as the G2 electrode). This modified rolling processing prevents electrode cracking and cohesive failure issues as observed in conventional thick sulfur electrodes processed by slurry coating of S/C materials and binders (G1). The electrodes fabricated through the lubricant-assisted rolling method have controllable S loading and thickness to fit the need of different cell designs. Scanning electron microscopy (SEM) characterization indicates that the surface of the G2 electrode is flat, uniform, and very compact (Figure XVII.2.4d). Long and thin fibers are observed across the electrode uniformly and are ascribed to the deformed PTFE binder (Figure XVII.2.4e). The cross-sectional observation via plasma focused ion beam-scanning electron microscopy (PFIB-SEM) reveals that the G2 electrode has a hierarchical structure composed of long slits (length $>10 \mu\text{m}$), medium pores (1–10 μm), and small pores ($<1 \mu\text{m}$) (Figure XVII.2.4f and g). This is because the IPA functions as a lubricant and liquid template for the formation of the hierarchically porous architecture. Compared to conventional slurry casted electrodes (e.g., G1), G2 electrode has the significant advantage of high press density. For a pristine G2 with a S loading of 4.3 mg cm^{-2} , the corresponding electrode thickness is only 55 μm , yielding a high electrode density of 1.1 g cm^{-3} (porosity 47.6%). Compared with the reported literature results, a remarkable improvement in electrode density has been achieved by this process. More importantly, with assistance of the IPA lubricant, the PTFE binder is deformed into long binder fibers and distributed evenly inside the electrode. So, the binder content in G2 can be reduced to an extremely low level of 1 wt% without sacrificing the electrode quality, boosting S content to $>80 \text{ wt\%}$ in the whole electrode. Using dense G2 electrodes with S loadings $>7 \text{ mg cm}^{-2}$, high areal capacities of $>9 \text{ mAh cm}^{-2}$ were achieved. This facile electrode processing method enables the large-scale fabrication of dense and high-loading electrodes by a very lean amount of binder. In addition, additional polymer or organic based Li-ion conductors can be integrated into the electrode architecture by using this method, improving sulfur utilization rate and reaction kinetics.

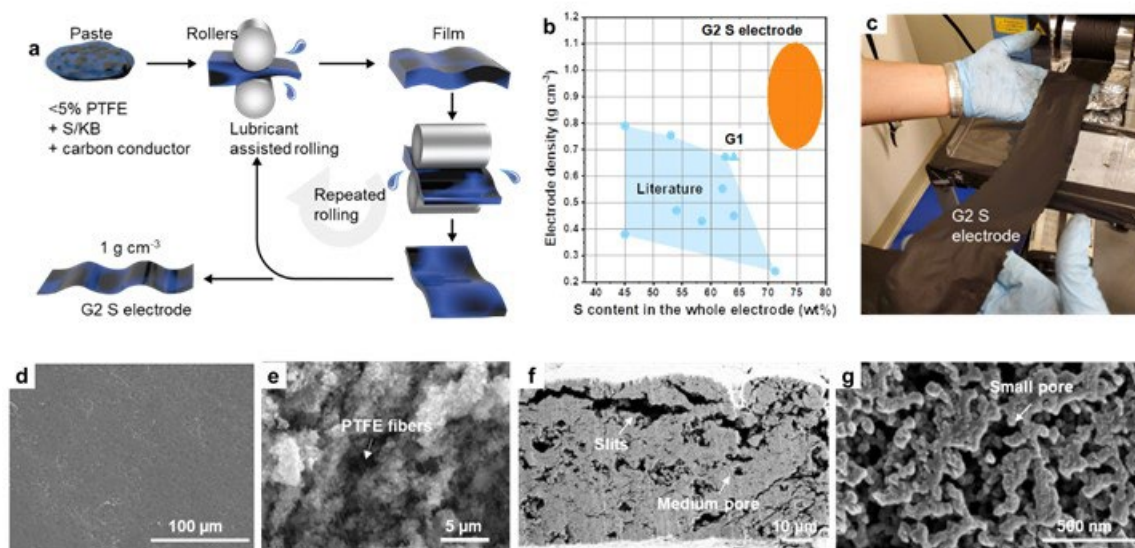


Figure XVII.2.4 Preparation of the dense S electrode. (a) Schematic illustration of the preparation process of the G2 electrode. (b) Comparison of electrode density and S content in whole electrode between the G1, G2, and literature results. If electrode density was not directly reported, it was calculated by “S loading/(S content \times electrode thickness)”. (c) Photo of the free-standing G2 electrode. (d-g) Scanning electron microscope (SEM) images of the G2 electrode: (d) surface, (e) cross-section (without milling), and (f, g) high-resolution images of the milled cross-section.

Conclusions

1. High sulfur utilization rate ($>1000 \text{ mAh/g}$) was realized in dense electrodes with porosities as low as $\sim 40\%$; effects of cathode particle size on sulfur reactions were studied at various porosities and electrolyte conditions.
2. Effects of the electrode porosity/tortuosity on electrolyte transport and polysulfide diffusion were studied by computational fluid dynamics (CFD) and multi-phase volume of fluid (VOF) simulations.
3. Introduction of functional polymer into the dense electrode architecture enables operation of sulfur electrodes at extremely low porosity of 25% and very lean electrolyte conditions ($E/S \leq 3 \text{ } \mu\text{L/mg}$).
4. A lubricant-assisted rolling method was developed to prepare dense sulfur electrodes with a density $>1 \text{ g/cm}^3$ and with S loadings $>7 \text{ mg/cm}^2$.

Key Publications

1. Feng S., Shi L., Anderson C., Lin Y., Xiao J., Liu J., and Lu D., Rational Design of Sulfur Cathode for High-energy Lithium-sulfur Batteries, 2021 Virtual MRS Spring Meeting & Exhibit, April 17–23, 2021.
2. Yu Z., Ahn K., Xiao J., Liu J. and Lu D., Enabling Highly Conductive and Flexible Solid-state Electrolyte Film for All-solid-state Lithium-sulfur Batteries, 2021 Virtual MRS Spring Meeting & Exhibit, April 17–23, 2021.
3. Shi L., Niu C., Anderson C., Feng S., Liu D., Lu D., Xiao J., and Liu J., Reaction Heterogeneity in High-Energy Lithium-Sulfur Pouch Cells, 2021 Virtual MRS Spring Meeting & Exhibit, April 17–23, 2021.

Acknowledgements

Shuo Feng, Lili Shi, Rajesh Kumar Singh, Jie Bao, Zhijie Xu, Jie Xiao and Ji-Guang Zhang (PNNL); Peter Khalifah (BNL); Zhao Liu, Adam Stokes (Thermo Fisher Scientific); Wen-Qing Xu (II-VI Incorporated)

XVII.3 Nanostructured Design of Sulfur Cathodes for High Energy Lithium-Sulfur Batteries (Stanford University)

Yi Cui, Principal Investigator

Stanford University

Department of Materials Science and Engineering, Stanford University
Stanford, CA 94305

E-mail: yicui@stanford.edu

Tien Q. Duong, DOE Technology Development Manager

U.S. Department of Energy

E-mail: Tien.Duong@ee.doe.gov

Start Date: October 1, 2017

End Date: September 30, 2021

Project Funding: \$500,000

DOE share: \$500,000

Non-DOE share: \$0

Project Introduction

Lithium-sulfur (Li-S) batteries are regarded as next-generation high-energy storage devices for portable electronics, electric vehicles, and grid-scale storage due to their high theoretical energy density (2500 Wh kg⁻¹). The practical applications of Li-S batteries are found to be hampered by the low electronic and lithium-ion conductivity of sulfur and lithium sulfide (Li₂S), polysulfides shuttling, and poor stability of lithium metal anodes. Recently, there is a new direction to address the problems of Li-S chemistry by replacing flammable liquid electrolytes with solid-state electrolytes for achieving high energy density and safe Li-S batteries. However, several intrinsic issues of conversion chemistry between sulfur and Li₂S in all-solid-state Li-S batteries (ASSLSBs) still need to be addressed, such as the insulating properties of sulfur and Li₂S, and interfacial parasitic reactions toward the anode side. Particularly, we want to point out that the hypothesis that solid polymer electrolytes (SPEs) suppress polysulfides dissolution is found to be incorrect, recent studies show that significant polysulfides dissolution occurs in SPEs. In this project, we apply the concept of nanoscale encapsulation in solid polymer based ASSLSBs. We use a thin (~20 nm) layered titanium disulfide (TiS₂) encapsulation to inhibit polysulfides dissolution into SPEs in all-solid-state Li₂S-Li batteries. Using in situ optical cell measurement and density functional theory calculations, we find that the intimate TiS₂ coating on Li₂S cathode enables simultaneous polysulfide entrapment and catalytic Li₂S oxidation. A high cell-level energy density of 427 Wh kg⁻¹ (excluding the current collectors) is realized by integrating TiS₂ coated Li₂S cathodes (Li₂S@TiS₂) with ultrathin polyethylene oxide-based polymer solid-state electrolytes (10~20 μm). The Li₂S@TiS₂ cathodes show excellent stability over 150 charge/discharge cycles at 0.8 C at 80 °C. This study provides a general route to avoid polysulfide shuttling in polymer-based electrolytes and expedites the design of Li-S cell with high-energy density.

Objectives

The charge capacity limitations of conventional transition metal oxide cathodes are overcome by designing optimized nano-architected sulfur cathodes. This study aims to enable sulfur cathodes with high capacity and long cycle life by developing sulfur cathodes from the perspective of nanostructured materials design, which will be used to combine with lithium metal anodes to generate high-energy Li-S batteries. In situ optical microscopy combined with ex situ analyses are used to investigate the polysulfide dissolution behavior in SPEs. We propose that some of the material design improvements originally developed in liquid electrolytes can be incorporated to solid-state electrolytes with excellent outcomes. The concept of nanoscale encapsulation will be applied in solid polymer based ASSLSBs in this study. Novel sulfur nanostructures with multi-functional coatings are designed and fabricated to overcome issues related to volume expansion, polysulfide dissolution, and the insulating nature of sulfur in ASSLSBs. The batteries with nanoscale TiS₂ coating deliver better reversible capacity, faster reaction kinetics, and longer cycling life as compared to bare sulfur cathodes.

Approach

The approaches refer to three main parts: (I) advanced nanostructured sulfur cathodes design and synthesis, including (1) develop novel sulfur nanostructures with multi-functional coatings for the confinement of sulfur/lithium polysulfides to address the issues of active materials loss and low conductivity; (2) develop/discover optimal nanostructured materials that can capture the polysulfide dissolved in the electrolyte; (3) develop space efficiently packed nanostructured sulfur cathode to increase the volumetric energy density and rate capability; (4) identify the interaction mechanism between sulfur species and different types of oxides/sulfides, and find the optimal material to improve the capacity and cycling of sulfur cathode. (II) Structure and property characterization, including (1) ex-situ scanning electron microscopy; (2) in situ optical microscopy. (III) Electrochemical testing including (1) coin cells; (2) A set of electrochemical techniques.

Results

To study the dissolution behavior of intermediate polysulfides in solid polymer based ASSLSBs, a home-made in situ optical cell (Figure XVII.3.1a) are fabricated by using lithium sulfide (Li_2S) or TiS_2 coated Li_2S ($\text{TiS}_2@\text{Li}_2\text{S}$) as the working electrode, lithium metal as the counter electrode, and polyethylene oxide/lithium bis(trifluoromethanesulfonyl)imide (PEO/LiTFSI) as the electrolytes. All the components are sealed between a glass substrate and a piece of transparent cover glass slide to enable *in situ* optical observation and heated at 60 °C (Figure XVII.3.1b).

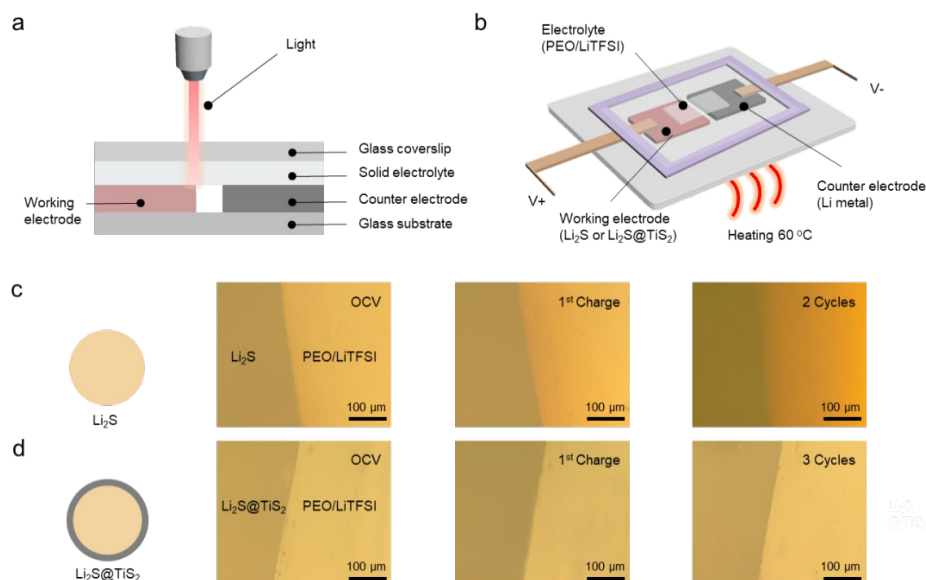


Figure XVII.3.1 Polysulfides entrapment in $\text{Li}_2\text{S}@\text{TiS}_2$ cathodes. (a) Schematic of the setup for in situ optical observation. A thin gap (1–2 mm) between the working electrode and the counter electrode is designed to avoid short-circuiting. (b) Illustration of the electrochemical cell assembled with bare Li_2S working electrode or $\text{Li}_2\text{S}@\text{TiS}_2$ working electrode, PEO/LiTFSI electrolyte, and lithium metal counter electrode. The entire cell is heated to 60 °C. The open circuit voltage of as-prepared cell is 2.5 V. The cell is first charged to 3.8 V at a constant current of 5 μA and then discharged to 1.6 V at a current of -2 μA . The in situ OM imaging shows the working electrode/electrolyte interface for (c) bare Li_2S electrode and (d) $\text{Li}_2\text{S}@\text{TiS}_2$ electrode.

Figure XVII.3.1c and Figure XVII.3.1d show the evolution of the interface between the working electrode and the solid-state PEO/LiTFSI electrolyte during the cycling process. Before charging, the interface can be clearly observed and the pure PEO/LiTFSI electrolyte part shows pale yellow color by optical microscopy (OM) imaging at open circuit voltage. For optical cells with bare Li_2S electrodes, only after the first charging process, the color of PEO/LiTFSI electrolyte gradually changes from a pale-yellow color to red brown starting from the interface between the working electrode and the electrolyte. The red-brown coloration fully spreads over the whole PEO/LiTFSI electrolyte after only two cycles, suggesting that polysulfides are dissolving into the PEO/LiTFSI electrolyte (Figure XVII.3.1c). In contrast, no obvious color change of the PEO/LiTFSI

electrolyte is observed in optical cells with $\text{Li}_2\text{S}@\text{TiS}_2$ electrodes after three cycles (Figure XVII.3.1d). All the results show that polysulfides form and dissolve into PEO/LiTFSI electrolytes from bare Li_2S electrodes during cycling, while $\text{Li}_2\text{S}@\text{TiS}_2$ electrodes can effectively trap polysulfides by a structurally intact encapsulation layer, thereby avoiding polysulfides dissolution into SPEs.

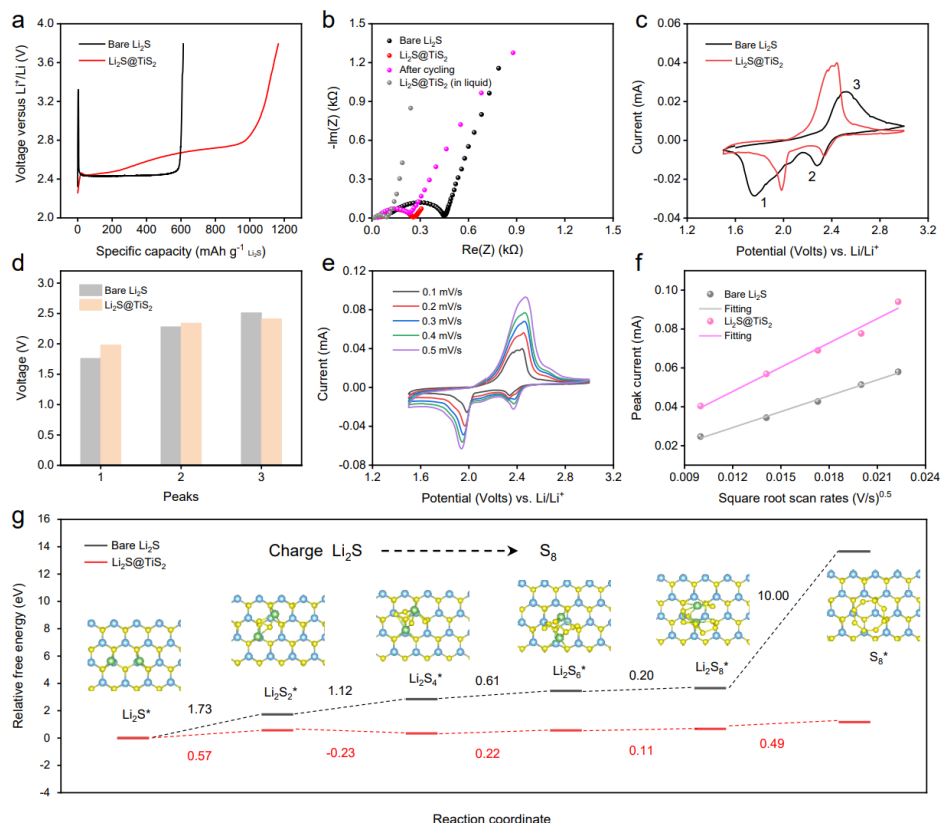


Figure XVII.3.2 TiS_2 enhanced Li_2S oxidation reaction kinetics in all-solid-state Li-S batteries (ASSLSBs). (a) First cycle charge voltage profiles of $\text{Li}_2\text{S}@\text{TiS}_2$ and bare Li_2S cathodes. (b) Electrochemical impedance spectra of ASSLSBs using bare Li_2S and $\text{Li}_2\text{S}@\text{TiS}_2$ cathodes, and the liquid system data adapted from Nat. Commun. 5, 5017 (2014). (c) Cyclic voltammetry (CV) curves and (d) corresponding peak potentials of $\text{Li}_2\text{S}@\text{TiS}_2$ and bare Li_2S electrode. (e) CV curves of the $\text{Li}_2\text{S}@\text{TiS}_2$ electrode at various scan rates (0.1 mV s^{-1} , 0.2 mV s^{-1} , 0.3 mV s^{-1} , 0.4 mV s^{-1} , and 0.5 mV s^{-1}). (f) Plots of CV peak current for the anodic oxidation process (peak 3: $\text{Li}_2\text{S} \rightarrow \text{S}_8$) versus the square root of the scan rates. All the cells are tested at 60°C . (g) Energy profiles for the oxidation of bare Li_2S and Li_2S on TiS_2 . The optimized geometries of TiS_2 with adsorbates (Li_2S^* , Li_2S_2^* , Li_2S_4^* , Li_2S_6^* , Li_2S_8^* , and S_8^*) are shown in the insert (Ti: blue; S: yellow; Li: green).

In addition to the function of trapping polysulfides, we would like to study whether TiS_2 coating could play a crucial role in promoting Li_2S oxidation kinetics in solid-state electrolytes. Coin cells (type 2032) are assembled using Li_2S composite cathodes, SPEs, and lithium metal anodes. Due to the large charge transfer resistance and intrinsic poor electronic conductivity of Li_2S , the as-assembled unencapsulated Li_2S cells show a high energy barrier of 3.3 V at the initial charge cycle for activation (Figure XVII.3.2a) and a large charge transfer resistance at open-circuit voltage (Figure XVII.3.2b). It indicates that the oxidation reaction may only occur at the localized regions of the active particles directly interfacing electron and ion transfer channels, thus resulting in a much lower specific capacity than the theoretical value. After TiS_2 coating, the initial activation energy barrier significantly decreases below 2.5 V (Figure XVII.3.2a). This is direct evidence that TiS_2 coating facilitates Li_2S oxidation reaction. Moreover, owing to the high conductivity of TiS_2 , the impedance spectrum of the as-assembled $\text{Li}_2\text{S}@\text{TiS}_2$ cells also show a smaller semicircle in the high frequency region compared with bare Li_2S cells, indicating a reduced charge-transfer resistance (Figure XVII.3.2b). The charge transfer

resistance is comparable with that in the liquid system and further decreases after 10 cycles, which indicates the formation of a stable TiS_2 interface allowing fast charge transfer during cycling.

Cyclic voltammetry (CV) evaluation on the as-assembled cells provides additional evidence for the catalytic effect of TiS_2 in ASSLSBs. When compared to bare Li_2S electrodes, the $\text{Li}_2\text{S}@\text{TiS}_2$ electrodes demonstrate a lower oxidation potential and higher reduction potential (Figure XVII.3.2c and Figure XVII.3.2d), suggesting that the TiS_2 coating significantly reduces the electrode polarization by catalyzing Li-S redox reactions. Additionally, the CV curves of as-prepared electrodes at various scan rates are used to study the electrode kinetics with respect to the lithium-ion diffusion coefficient, as shown in Figure XVII.3.2e. The CV peak current versus the square root of the scan rates for both $\text{Li}_2\text{S}@\text{TiS}_2$ and Li_2S electrodes (Figure XVII.3.2f) shows a linear relationship. Notably, the slope of $\text{Li}_2\text{S}@\text{TiS}_2$ curve is larger than that of the bare Li_2S . According to the classical Randles-Sevcik equation for a diffusion-limited process, a larger slope of the curve for $\text{Li}_2\text{S}@\text{TiS}_2$ electrode indicates a faster lithium diffusion within the $\text{Li}_2\text{S}@\text{TiS}_2$ electrode compared to the bare Li_2S electrode, which further facilitates sulfur transformation reactions. To attain an in-depth understanding of the catalytic effect of TiS_2 coating for the improved charge reaction kinetics in ASSLSBs, the overall reaction mechanism for Li_2S oxidation is simulated theoretically. First-principles calculations propose detailed energetics and kinetics of reaction steps for the TiS_2 modulated Li_2S oxidation. As shown in Figure XVII.3.2g, TiS_2 modulated Li_2S oxidation becomes the energetically favored reaction, which results in the enhanced electrochemical performance of Li-S batteries.

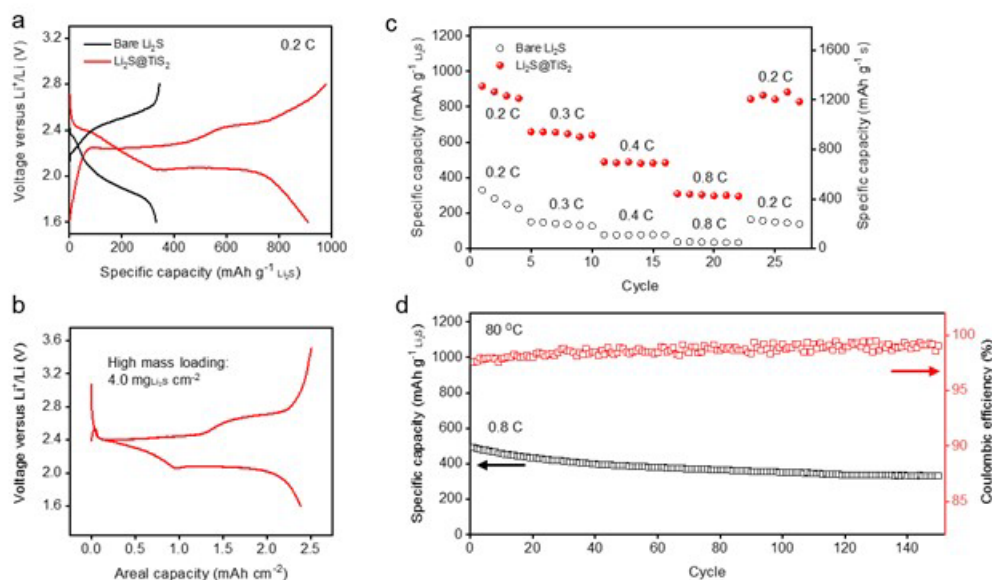


Figure XVII.3.3 **Electrochemical performance of $\text{Li}_2\text{S}@\text{TiS}_2$ cathodes and bare Li_2S cathodes in ASSLSBs.** (a) Charge-discharge voltage profiles of $\text{Li}_2\text{S}@\text{TiS}_2$ and bare Li_2S cathodes at 0.2 C at 60 °C. (b) Voltage profile and areal capacity of $\text{Li}_2\text{S}@\text{TiS}_2$ cathode with a high mass loading ($4.0 \text{ mgLi}_2\text{S cm}^{-2}$) at a current density of 0.04 mA cm^{-2} at 60 °C. (c) Rate performance of $\text{Li}_2\text{S}@\text{TiS}_2$ and bare Li_2S cathodes at various charging rates, cycled at 60 °C, within a potential window of 1.6–2.8 V versus Li^+/Li . (d) Cycling performance and Coulombic efficiency of $\text{Li}_2\text{S}@\text{TiS}_2$ cathode at 0.8 C for 150 cycles at 80 °C.

We further prove the catalysis efficacy and polysulfide capture of nanoscale encapsulation in ASSLSBs by testing the electrochemical performance of $\text{Li}_2\text{S}@\text{TiS}_2$ cathodes in solid polymer electrolytes (SPEs). As-assembled cells are constructed for galvanostatic cycling tests from 1.6 to 2.8 V. A specific capacity as high as $\sim 910 \text{ mAh g}^{-1}$ Li_2S at 0.2 C is realized by $\text{Li}_2\text{S}@\text{TiS}_2$ cathodes, which is more than twice higher than that of the bare Li_2S one ($\sim 330 \text{ mAh g}^{-1}$) (Figure XVII.3.3a). Additionally, the $\text{Li}_2\text{S}@\text{TiS}_2$ cathode with a high mass-loading of Li_2S is fabricated and tested in ASSLSBs, obtaining an areal capacity of 2.4 mA h cm^{-2} at 60 °C (Figure XVII.3.3b), which corresponds to a high cell-level energy density of 427 W h kg^{-1} . The energy density is calculated from the average discharge voltage (2.1 V), cell capacity (2.4 mA h cm^{-2}), and total mass of the

cathode ($8.6 \text{ mg}\cdot\text{cm}^{-2}$, excluding the current collector), the solid electrolyte ($1.2 \text{ mg}\cdot\text{cm}^{-2}$), and the anode ($2 \text{ mg}\cdot\text{cm}^{-2}$).

In addition, the rate performance of as-prepared cathodes is investigated by cycling cells at different C-rates (Figure XVII.3.3c). For the bare Li_2S cathode, significant capacity fading (from $330 \text{ mAh}\cdot\text{g}^{-1}$ to $226 \text{ mAh}\cdot\text{g}^{-1}$) is observed during four cycles at 0.2 C, with capacity severely decreasing to $38.5 \text{ mAh}\cdot\text{g}^{-1}$ at a higher rate of 0.8 C. Comparatively, the $\text{Li}_2\text{S}@ \text{TiS}_2$ cell, benefiting from the effective TiS_2 enhanced oxidation kinetics, shows a much better rate capability, achieving a discharge capacity of $660 \text{ mAh}\cdot\text{g}^{-1}$, $488 \text{ mAh}\cdot\text{g}^{-1}$, and $309 \text{ mAh}\cdot\text{g}^{-1}$ based on Li_2S at 0.3 C, 0.4 C, and 0.8 C, respectively. Moreover, the $\text{Li}_2\text{S}@ \text{TiS}_2$ cell exhibits stable cycling performance after charge/discharge cycling at 0.8 C at 80°C . After an initial discharge capacity of $490 \text{ mAh}\cdot\text{g}^{-1}$ at 80°C , the $\text{Li}_2\text{S}@ \text{TiS}_2$ cells retain 79%, 71%, and 68% of their initial capacity after 50, 100, and 150 cycles, respectively (Figure XVII.3.3d). Average Coulombic efficiency after 150 cycles is calculated to be 98.6%, which shows little shuttle effect owing to efficient polysulfides trapping by TiS_2 encapsulation. All the above results show that TiS_2 encapsulation enables polysulfides entrapment and enhances oxidation kinetics to achieve high performance ASSLSBs.

Conclusions

In all, in the past one year, we have made great progress in developing high energy density all-solid-state Li-S batteries. We demonstrate that the nanoscale encapsulation concept based on $\text{Li}_2\text{S}-\text{TiS}_2$ core-shell particles, originally developed in liquid electrolytes, is very effective in solid polymer electrolytes. Using in situ optical cell measurement, we find that polysulfides form and are well trapped inside individual particles by the nanoscale TiS_2 encapsulation. This TiS_2 encapsulation layer also functions to catalyze the oxidation reaction of Li_2S to sulfur, even in solid-state electrolytes, proved by both experiments and density functional theory calculations. A high cell-level specific energy of $427 \text{ W}\cdot\text{h}\cdot\text{kg}^{-1}$ at 60°C (including the mass of the anode, cathode, and solid-state electrolyte, but excluding the current collector and packaging) is achieved by integrating TiS_2 encapsulated Li_2S cathode with ultrathin polyethylene oxide-based solid polymer electrolyte ($10\sim 20 \mu\text{m}$) and lithium metal anode. The solid-state cells show excellent stability over 150 charge/discharge cycles at 0.8 C at 80°C .

Key Publications

1. Xin Gao, Xueli Zheng, Jingyang Wang, Zewen Zhang, Xin Xiao, Jiayu Wan, Yusheng Ye, Lien-Yang Chou, Hiang Kwee Lee, Jiangyan Wang, Rafael A. Vila, Yufei Yang, Pu Zhang, Lin-Wang Wang, and Yi Cui* Incorporating the nanoscale encapsulation concept from liquid electrolytes into solid-state lithium-sulfur batteries. *Nano Lett.* 2020, 20, 5496.

XVII.4 Mechanistic Investigation for the Rechargeable Li-Sulfur Batteries (BNL)

Enyuan Hu, Principal Investigator

Chemistry Division
Bldg. 555, Brookhaven National Laboratory
Upton, NY 11973
E-mail: enhu@bnl.gov

Deyang Qu, Principal Investigator

University of Wisconsin Milwaukee
3200 North Cramer Street
Milwaukee, WI 53211
E-mail: qud@uwm.edu

Tien Q. Duong, DOE Technology Development Manager

U.S. Department of Energy
E-mail: Tien.Duong@ee.doe.gov

Start Date: September 1, 2020

End Date: August 30, 2021

Project Funding (FY21): \$160,000

DOE share: \$160,000

Non-DOE share: \$0

Project Introduction

Rechargeable lithium-sulfur (Li-S) batteries have received extensive attentions as a promising candidate of next-generation batteries to replace state-of-art Li-ion batteries in EV applications. Due to its high theoretical energy density ($1672\text{mAh}\cdot\text{g}^{-1}$), safety, and low cost, the practical gravimetric energy density of a Li-S battery could potentially be 2–3 times higher than that of a state-of-art Li-ion battery. However, many obstacles remain to be overcome before the full potential of a rechargeable Li-S battery could be unlocked. Those traditional technical barriers include high self-discharge, low efficiency, low active material utilization and low cycle life. Most of challenges on the sulfur side are related to the polysulfide dissolution and the change of conductivity during cycling, while dendrite growth and “dead” Li formation on Li anode still remain as major technical difficulties.

In the past few years, we have successfully developed the MS-HPLC essays for the quantitative and qualitative identification of dissolved polysulfide ions in various electrolyte. Couple with *in-situ* electrochemical method, the change of the dissolved polysulfides during the battery operation can be determined. The mechanisms for the sulfur redox reaction which including the equilibrium between dissolved polysulfide ions and element sulfur were revealed. So, the continuous decay of the capacity during cycling, “shuttle-effect” and high self-discharge during the storage became better understood. We also developed an *in-situ* electrochemical–microscopic technique for the real-time investigation of Li anode during cycling. Taking the advantages of the advancements of *in-situ* diagnostic technologies, the effectiveness of many potential inhibitors was investigated, the stability of cell components in polysulfide electrolyte was also studied, new anode materials were explored and polymerized sulfur compounds were synthesized and tested.

Although the mechanism and behaviors of the dissolved polysulfide ion in the electrolyte were very well understood from our previous investigation, the reaction mechanism of the polysulfides and sulfur in the cathode side in solid phase has not been thoroughly studied yet, especially the sulfur redeposition and distribution during charging. Collaborating between UWM and BNL, we will start investigating the sulfur redox reaction in the solid phase taking the advantage of synchrotronic techniques in BNL and electrochemical analytical techniques in UWM.

In FY2021, the interim goal is to develop a Li-sulfur battery with sulfur containing cathode of 600-800 mAh/g capacity with the mitigation of the “shuttle effect”.

In this collaborative project firstly, we will continue to synthesize cross-linked polymerized sulfur compounds, in which sulfur is attached to the conductive backbone with covalent bonds, therefore the polysulfides can be immobilized within the matrix; secondly, we will investigate the sulfur redox reaction mechanism in the solid phase; thirdly, we will develop engineering process for high sulfur loading electrodes.

In addition, we will continue to engage in the fundamental in-situ electrochemical investigations of the sulfur redox mechanisms in order to guide the material and engineering designs. We will also continue optimize the alternative electrode fabrication processes.

Objectives

The primary objectives were:

- To continue conducting fundamental research on the mechanism of the sulfur redox reaction especially those on the interplay of the dissolved polysulfides in electrolyte and those in the solid phase in cathode during charging.
- To continue developing the polymeric sulfur electrode, adequate anode and corresponding electrolyte to achieve high energy density, long cycle life Li-S batteries. We will focus on the overall dissolution of polysulfide in an electrolyte and effectiveness of polymeric sulfur electrodes.
- To develop the alternative anode materials having low reactivity with dissolved polysulfide ions.
- To continue develop and optimize creative electrode making processes to improve processability and aerial capacity, e.g., dry process and thick electrodes.

The ultimate goal for the project is to develop a practical rechargeable Li-S battery to meet the requirements

Approach

1. Synthesis of polymer sulfur composite materials to limit the polysulfide dissolution especially the dissolution of long-chain polysulfide.
2. *In-situ* High Performance Liquid Chromatography (HPLC)/Mass Spectroscopy (MS)-Electrochemical method was developed during the course of this project. It is the first and arguably the only reliable quantitative and qualitative analytical tool to monitor the change of polysulfide ions during the electrochemical and chemical reactions in real time.
3. *Ex-situ* X-ray diffraction (XRD) and X-ray photoelectron spectroscopy (XPS) to investigate the surface of the sulfur cathode and Li anode to elucidate the surface changes during the Li-S battery operation.
4. Theoretical modeling of the interaction between polysulfide ions with polymer backbone and solvent molecules.

Results

Polymeric Sulfur Cathodes: By means of the in-situ HPLC diagnostic technique, we revealed that the short chain-length polysulfide ions e.g., S_4^{2-} and S_3^{2-} are much less reactive with Li than the longer chain polysulfide ions, the results were reported in the last year's report. To mitigate the problem caused by the soluble long-chain polysulfides in a Li-S battery, sulfur/organic polymer materials were synthesized as alternative cathode materials instead of elemental sulfur (S_8). Based on the polymerization temperature, the sulfur/organic polymer materials can be divided into two groups: high temperature (HT) materials and low temperature (LT) materials. There were only one discharge and one recharge plateau for a HT Sulfur polymer, which is different from that

of an elemental S cathode typically with two discharge and recharge plateaus. Also, in addition to the widely used ether-based electrolytes, carbonate-based electrolytes, which are proved to be incompatible with traditional Li-S battery based on elemental sulfur (S_8), can be used in the Li-S batteries with HT S polymer cathodes. We hypothesize that there were no long-chain soluble polysulfide intermediates formed during the discharge and charge of the HT Sulfur polymer. Compared with the HT S polymer materials, the LT S polymer materials have two distinguishable advantages: low cost and high S contents. Many bio-derived chemicals and industrial by-products can be used as the organic monomers in the low temperature polymerization process. The S content in a LT S polymer could reach up to 90 wt%, while the S content in HT S polymers was typically under 50 wt%. As tabulated in Figure XVII.4.1, We synthesized and tested three different S/organic polymer materials prepared through inverse vulcanization with different compositions and different organic monomers, and PAN based sulfur co-polymer with 10 different S: PAN ratios. The monomers are shown in Figure XVII.4.1. By using the well-developed chromatographic method, the battery performance was investigated against S polymer materials.

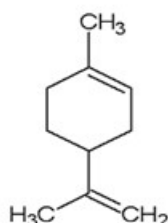
Table XVII.4.1 Composition of sulfur/organic polymers

Sample	S8 (%)	PAN (%)	DCPD(%)	Limonene(%)	EGDMA(%)
SP1	50	-	25	25	-
SP2	50	-	5	-	45
SP3	50	-	25	-	25
S/PAN	10 different ratios				

DCPD (dicyclopentadiene):



Limonene:



EGDMA(ethylene glycol dimethacrylate)

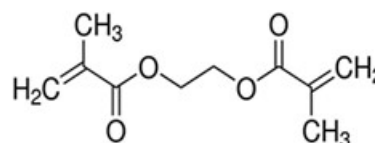


Figure XVII.4.1 Chemical structure of monomers used in the synthesis

As shown in Figure XVII.4.2(A), the diffraction patterns of crystalline S_8 were not observed in the XRD. The endothermic peaks at 104.6, 119.9, and 168.9 °C were not observed in the DSC either (Figure XVII.4.2(B)). The peaks were associated with the transition of a S_8 from orthorhombic state to monoclinic state, the melting of monoclinic sulfur, and the λ transition of liquid sulfur, respectively. Evidentially, no apparent decomposition of the S polymers was observed after mechanical grinding, since S_8 was one of the products of decomposition. The content of extractable S in the polymers was also measured by a solvent (DME) extraction. Interestingly, elemental S was clearly detected in the extractant as shown in Figure XVII.4.2(C). But the extracted elemental S only represented less than 2 % (w_i) of the S polymer as tabulated in Table XVII.4.1 which indicated most of the S was in a stable polymeric form.

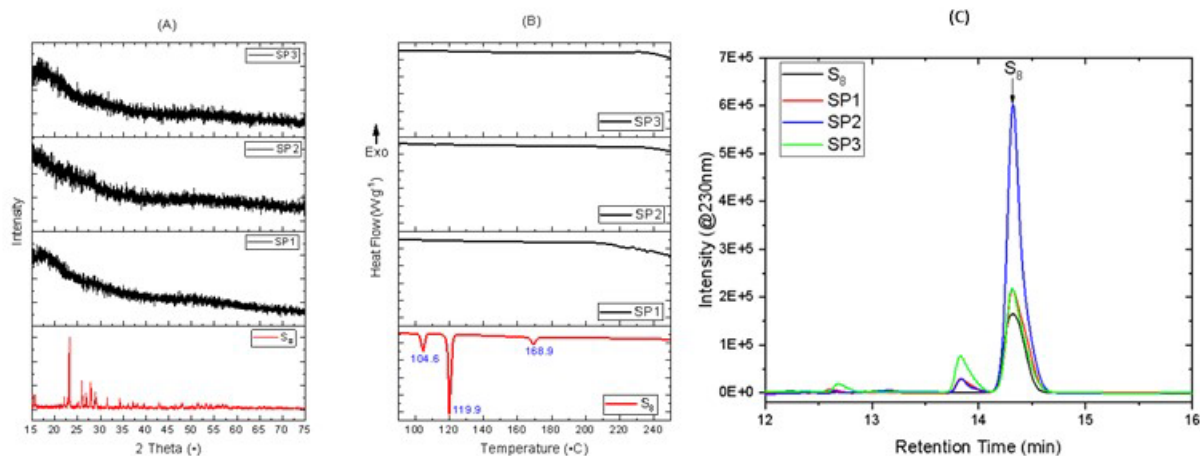


Figure XVII.4.2 XRD patterns (A) and DSC curves (B) of elemental sulfur and three sulfur/organic polymers (C) relative abundance of S₈ in the polymeric sulfurs.

The galvanostatic discharge and charge profiles for the Li-S polymer batteries are shown in Figure XVII.4.3(A-C). There were two discharge plateaus and two charge plateaus for the three Li-S polymer batteries. The results were consistent with those of the Li-S polymer batteries in ether-based electrolytes reported in the literature. The discharge and recharge curves were very similar with those of traditional Li-S battery as shown in Figure XVII.4.3(D). Figure XVII.4.4(E) shows the distribution of the polysulfide ions in the electrolytes of the Li-S polymer batteries and Li-S battery at 20% depth of discharge. The electrolytes were recovered from the separators of those batteries. All polysulfide ions, S₃²⁻, S₄²⁻, S₅²⁻, S₆²⁻, S₇²⁻, S₈²⁻ and S₈ can be observed.

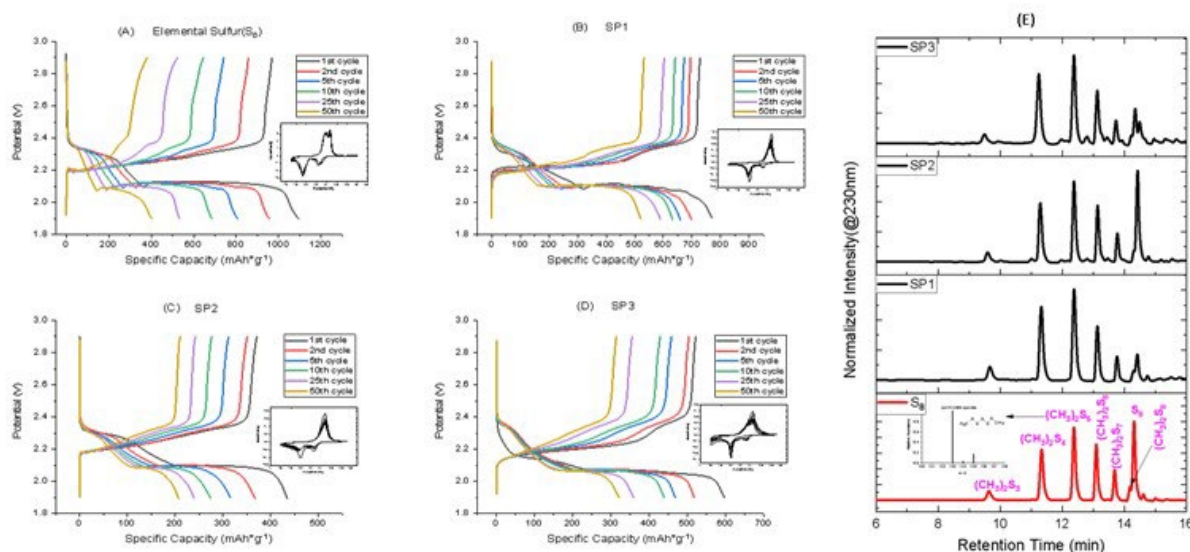


Figure XVII.4.3 The discharge/charge profiles and CVs of a Li-Sulfur battery (A), and three Li-Sulfur polymer batteries (B, C, D); The HPLC of dissolved polysulfide distribution in the electrolyte at 20% DoD.

Compared with a traditional Li-S battery, the initial specific capacities of three Li-S polymer batteries were lower than that of traditional Li-S battery, however the capacity retention of all three Li-sulfur polymer batteries were better than that of traditional Li-S battery. Based on a recently proposed mechanism and qualitative HPLC analysis, the different cycle stabilities of three Li-sulfur polymer batteries are ascribed to the different capabilities of retaining the long-chain polysulfides and elemental sulfur within the different polymer structures or the distribution of dissolved polysulfide ions in the electrolyte.

PAN based polymeric sulfur materials are considered as HT polymer sulfur. Figure XVII.4.4 shows the initial 10 cycles of the S-polymers made with different S₈ to PAN ratios. Two things can be observed in this study. First, the first discharge curves were always different to the subsequent ones except the one with very low sulfur content. It seems that electrochemical formation is necessary for the chemically synthesized compounds after high temperature treatment. Second, up to 4:1 S₈:PAN ratio, there is little elemental sulfur in the synthesized compounds. But beyond the level of the saturation ratio, e.g., 8:1 S₈:PAN ratio, a clear two-step discharge curve was evident the existence of long-chain polysulfides or elemental sulfur.

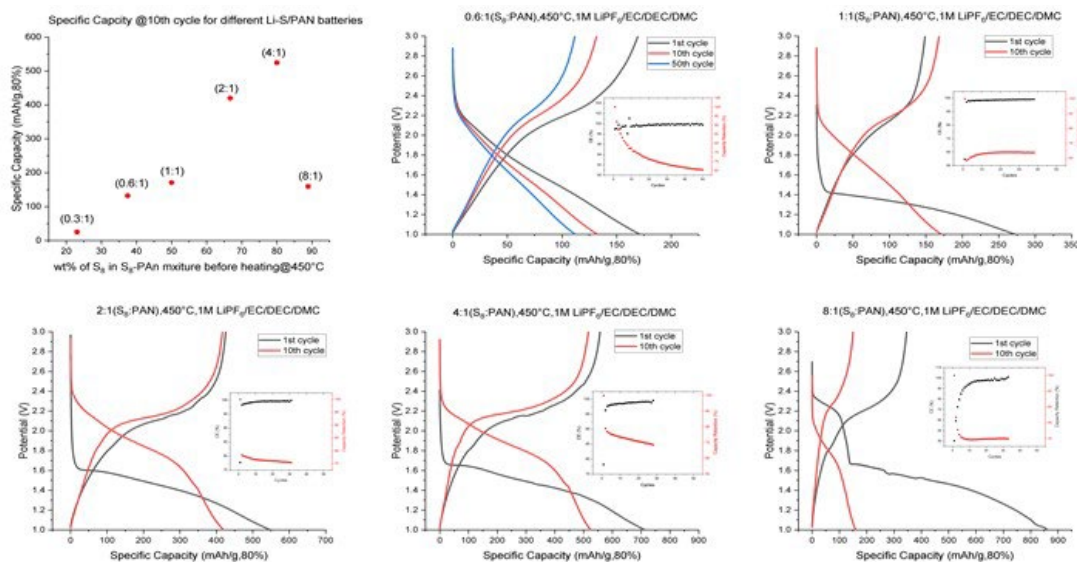


Figure XVII.4.4 The comparison of multiple discharge and recharge curves of S-PAN cathode made with various sulfur to PAN ratios.

Figure XVII.4.5 shows the impact of electrolyte on the cycleability of the S-polymer cathode. Interestingly, the S-polymer worked in carbonate electrolyte, where elemental sulfur cathode does not. It was hypothesized that sulfide free radicals can react with carbonate solvents. It appears sulfide free radicals may not be formed or become stabilized in the polymeric structure. Figure XVII.4.5 also shows that the sulfur PAN cathode does not cycle well in ether-based electrolyte, which is the traditional electrolyte system for elemental sulfur cathode. The evidence showed that after the first cycle, the high-voltage plateau started to show up, which is the evident the formation of soluble long-chain polysulfide ions.

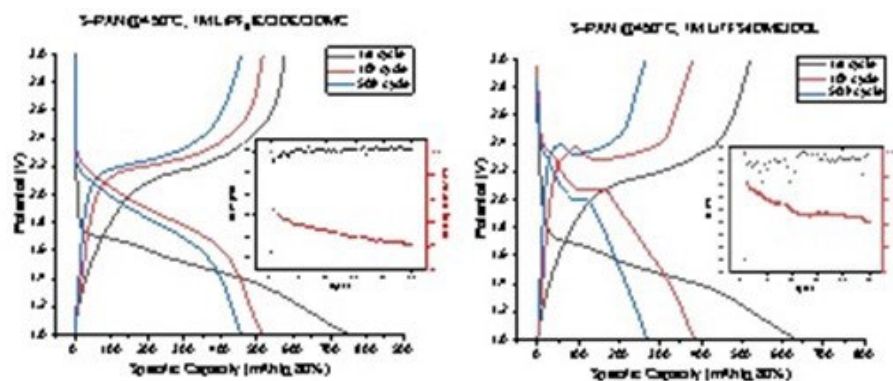


Figure XVII.4.5 The comparison of S-PAN cathodes cycled in either and carbonate-based electrolytes.

We performed a full-atomistic MD simulation to unravel the binding effectiveness between tetra-sulfides and polymer backbones PNB, LEB, PEDOT and PPY with the effect of a 1:1 (v/v) mixture of DOL/DME when

considering the ratio between sulfur and binder in a real Li-S cell. The simulations in solvent demonstrate that the end group 2 of PNB can effectively bind one Li_2S_4 cluster or 2 out of 43 Li_2S_4 molecules with the effect of the solvent mixture through non-bonded interaction. Therefore, PNB, LEB, PEDOT and PPY seem to be ineffective in binding polysulfides through non-bonded interaction, especially when the concentration of polysulfide/binder in a local domain of the cathode is as low as that in the simulations. Based on that, polymers with the functional group (i.e., end group 2 of PNB) are suggested to be further studied in order to get effective backbones.

Figure XVII.4.6(a)-(h) show the structures of the simulation frames. It can be observed that Li^+ and S_4^{2-} form a cluster in each system; and the interaction between the cluster and each polymer results in a twisted and/or bended conformation of the polymer chain; in other words, the whole polymer chains are involved in the interaction rather than only the involving three units. Fig. 1(i) and (j) show the S_4^{2-} -polymer and Li_2S_4 -polymer interaction energies; respectively. The Li^+ in the clusters contributes to the attractive interaction mainly through electrostatic interaction, while S_4^{2-} makes the contribution mainly by the vdW interaction. Figure XVII.4.6(e) shows that an end of the PNB chain is dangling, indicating that the end of PNB has weaker binding effect with Li_2S_4 .

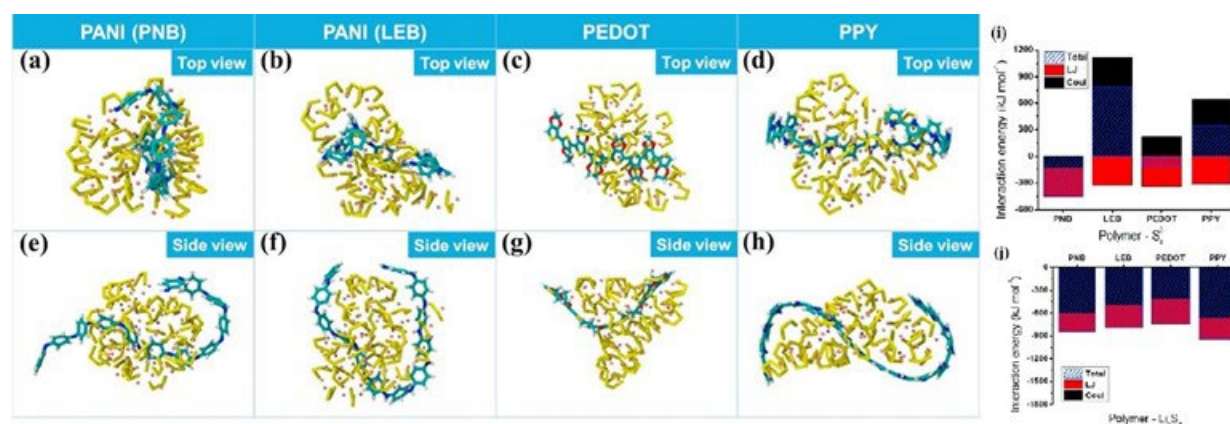


Figure XVII.4.6 (a)–(h) Structure, (i) polymer- S_4^{2-} interaction energy, and (j) polymer- Li_2S_4 interaction energy of the self-assembled multiple S_4^{2-} , Li^+ and single polymer chain. Columns with heights equal to the value of the interaction energy components are stacked up, where the summation is the total interaction energy corresponding to each polymer.

The constructed MD models have a potential to be extended to study binding effectiveness between polysulfides and polymers under other influencing factors, such as side groups of polymer backbones and doped states of conductive polymers. Since the solvent environment has considerable impact on the binding effectiveness between tetra-sulfides and polymer backbones, it is suggested to use the explicit solvation models, similar to the ones built in this work, to predict how other influencing factors affect binding effectiveness between polysulfides and polymers, which will contribute to the existing demand for guiding binder design and rational experiments for Li-S technology as well as propel the advancement of MD modeling methodology for understanding properties and performance of polymer materials in energy storage systems.

Conclusions

We provided initial experimental and theoretical evidence demonstrating that the polymeric sulfur compounds which have better ability to restrain both elemental sulfur and long-chain polysulfides within the cathode can retain the cycle capacity of a Li-S battery. The shuttle-effect can be mitigated by forming short-chain polysulfide ions, which are much less reactive than longer chain polysulfide ions.

Key Publications

1. Yihan Xu, Dong Zheng, Weixiao Ji, Nidal Abu-Zahra, Deyang Qu, "A Molecular Dynamics Study of the Binding Effectiveness between Undoped Conjugated Polymer Binders and Tetra-sulfides in Li-S Batteries", *Composite Part B: Engineering* 206(2021)108531.

XVII.5 New Electrolyte Binder for Lithium Sulfur Battery (LBNL)

Gao Liu, Principal Investigator

Lawrence Berkeley National Laboratory
Berkeley, CA 94720
E-mail: gliu@lbl.gov

Tien Q. Duong, DOE Technology Development Manager

U.S. Department of Energy
E-mail: Tien.Duong@ee.doe.gov

Start Date: October 1, 2020

End Date: September 30, 2023

Project Funding (FY21): \$420,000

DOE share: \$420,000

Non-DOE share: \$0

Project Introduction

A strong demand for low-cost and high-energy-density rechargeable batteries has spurred lithium-sulfur (Li-S) rechargeable battery research. First, sulfur is an abundant and low-cost material. Second, the Gibbs energy of the lithium (Li) and sulfur reaction is approximately 2,600 Wh/kg, assuming the complete reaction of Li with sulfur to form Li_2S , more than five times the theoretical energy of transition metal oxide cathode materials and graphite coupling. With these advantages, Li-S batteries could be both high energy density and low cost, satisfying demand in energy storage for transportation application. The major obstacle is the loss of sulfur cathode material as a result of polysulfide dissolution into common electrolytes, which causes a shuttle effect and significant capacity fade. The polysulfide shuttle effect leads to poor sulfur utilization and fast-capacity fade, which have hindered widespread use of rechargeable Li-S batteries. This proposed work of new electrolyte development in understanding the thermodynamics and kinetics of polysulfide dissolution and precipitation will yield new approaches for electrolytes of Li-S rechargeable batteries.

Objectives

This project aims to develop new electrolytes and additives for Li-S battery. The properties of the ideal electrolyte for sulfur electrode would be high ion conductivity, stable towards polysulfide, and promoting the polysulfide affiliation with the electrode substrate to prevent polysulfide dissolution. The first objective is to understand the electrode substrate interaction with the polysulfides in different electrolytes. This will lead to better understandings of the polysulfide nucleation and precipitation mechanisms in common electrolytes. The second objective is chemically modifying the structures of the solvent and salt electrolyte molecules to increase electrolyte stability and ionic conductivity and to prevent polysulfide dissolution and promote polysulfides precipitation.

Approach

This project aims to develop new electrolytes and additives for Li-S battery. The properties of the ideal electrolyte for sulfur electrode would be high ion conductivity, stable towards polysulfide, and promoting the polysulfide affiliation with the electrode substrate to prevent polysulfide dissolution. The project is designed to first understand the electrode substrate interaction with the polysulfides in different electrolytes. This will lead to better understandings of the polysulfide nucleation and precipitation mechanisms in common electrolytes. The second stage of the project will focus on chemically modifying the structures of the solvent and salt electrolyte molecules to increase electrolyte stability and ionic conductivity and to prevent polysulfide dissolution and promote polysulfides precipitation.

Results

New approach is developed using the amphiphilic hydrofluoroethers (HFE) electrolyte to improve the sulfur (S) electrode cycling and to stabilize lithium metal. Lithium anode corrosion and dendrite formation can be significantly reduced in the electrolyte with the presence of this fluoro-based amphiphilic electrolyte and with

highly concentrated salt solution, leading to high coulombic efficiency. Our HFE molecules are designed to have a bi-functional, amphiphilic structure consisting of a fluorocarbon moiety and an ethylene oxide (EO) moiety on each end, respectively. The molecular structure in this study is 1,1,1,2,2,3,3,4,4-nonafluoro-6-(2-methoxyethoxy)hexane (F_4EO_2). The salt is 0.5M LiTFSI. The base solvent is 1,1,2,2-tetrafluoroethyl-2,2,3,3-tetrafluoropropyl ether (TTE) with F_4EO_2 :TTE weight ratio of 1:5. The EO moiety is lithiophilic and incompatible with fluorinated solvents, therefore is able to coordinate with Li^+ , while the fluorocarbon moiety is lithiophobic but fluorophilic, which is associated with fluorinated TTE solvent. This structure feature results in the formation of micelle-like molecular complexes with lithium salts concentrated in the EO cores, which are dispersed by the TTE solvent. In order to improve the compatibility of the electrolyte with the S electrode, a small amount of dioxolane (DOL) is added to the micelle electrolytes. The DOL dissolves polysulfides, but at a controlled amount, the DOL acts to facilitate Li_2S_x formation to significantly improve the utilization of the S materials. However, the polysulfides shuttle effects also increases at the addition of DOL. To curb the shuttle effect, additional LiTFSI is added to saturate the electrolyte to prevent the lithium polysulfides dissolution as well as to further stabilize the lithium metal electrode. By balancing the DOL amount and LiTFSI salt concentration, a Li-S cell operated above 1200 mAh/g at over 99.5% coulombic efficiency is achieved as shown in Figure XVII.5.1.

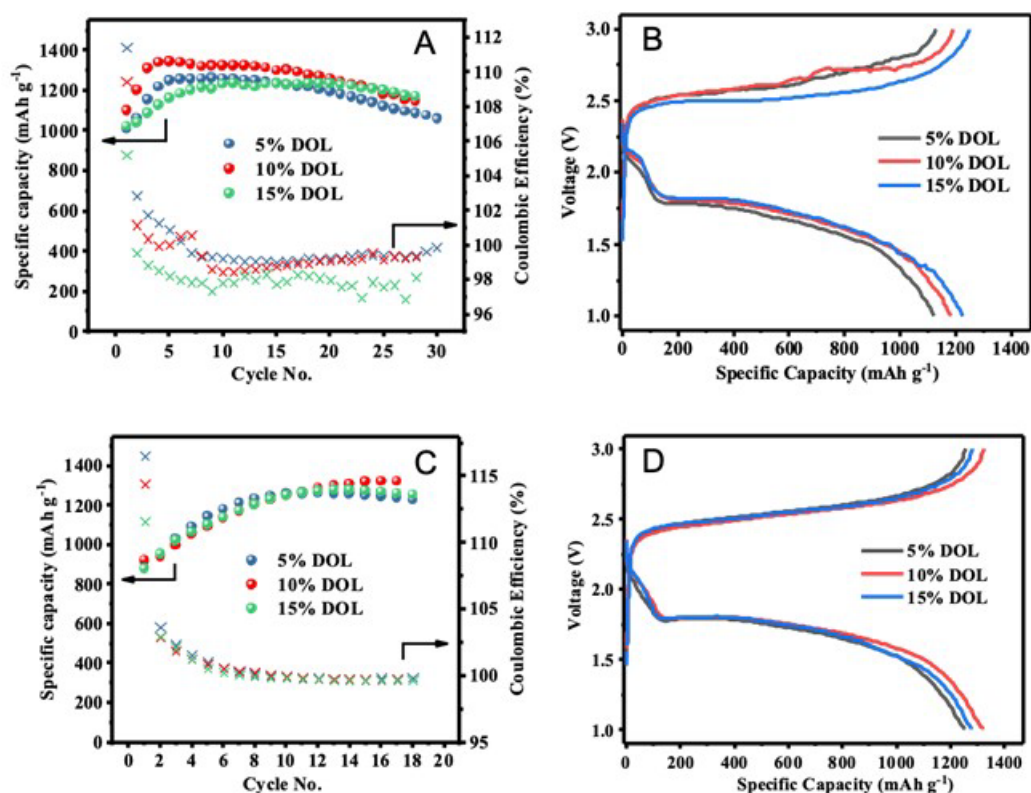


Figure XVII.5.1 Li-S battery recycling with different amount of DOL added. A. The capacity and coulombic efficiency vs. cycle numbers of the Li-S cell with the DOL additives at 5, 10, 15% by weight. B. The voltage and capacity profile of the Li-S cell at the 25th cycle (of Figure 1A) with the DOL additive at 5, 10, 15% by weight. C. The capacity and coulombic efficiency vs. cycle numbers of the Li-S cell with the DOL additives at 5, 10, 15% by weight, and saturated with LiTFSI salt. D. The voltage and capacity profile of the Li-S cell at the 15th cycle (of Figure 1C) with the DOL additive at 5, 10, 15% by weight, and saturated with LiTFSI salt.

The micelle-based electrolyte was made by dissolving LiTFSI salt in F_4EO_2 fluorinated ether molecules blended with solvent TTE. This study is focused on 0.5M and 1.0M LiTFSI concentration electrolyte which were made by using 1:5 and 1:2.5 F_4EO_2 /TTE volume ratio respectively. A key property of the electrolyte system is transference number aside from ionic conductivity. Bruce-Vincent method is a convenient

electrochemical approach to investigate electrolyte transport property which measures transference number.² The measurement was conducted on Li-Li symmetrical cell which the analyte electrolyte was sandwiched by two identical piece of Li electrodes. The cell was first run two cycles of Li plating/stripping at 0.4 mA/cm² for 1h per cycle for the stable SEI formation. Next, impedance of the cell was measured with the frequency range of 300 kHz–100 mHz. The initial current i_T was then measured once a small DC polarization ($\Delta V = 10\text{mV}$) was applied. After 40 hours of polarization, the steady current i_0 was reached and immediately recorded. Finally, the impedance of the cell was measured again with the same frequency range. The transference number of t_{Li^+} can then be expressed by the following equation:

$$t_{\text{Li}^+} = \frac{i_0(\Delta V - i_T R_T)}{i_T(\Delta V - i_0 R_0)}$$

Where R_0 and R_T are the initial and steady state resistance of passive layers (R_{SEI}) which can be extracted from the impedance measurement. Figure XVII.5.2a and Figure XVII.5.2b below show the i - t curve of polarization process and Nyquist plot of impedance measurement prior and post polarization for 0.5M LiTFSI in F₄EO₂/TTE (v/v, 1:5) electrolyte. These two plots demonstrate the selection of important data points of i_0 , i_T and R_0 , R_T . Figure XVII.5.1c reveals transference number as a function of LiTFSI electrolyte with 0.5M–2.0M concentrations. The number plotted is the average of three repeated tests with error bars included on the plot. As you can tell, the transference number of Li⁺ was ~ 0.8 through all concentrations which is higher than conventional liquid electrolyte systems.

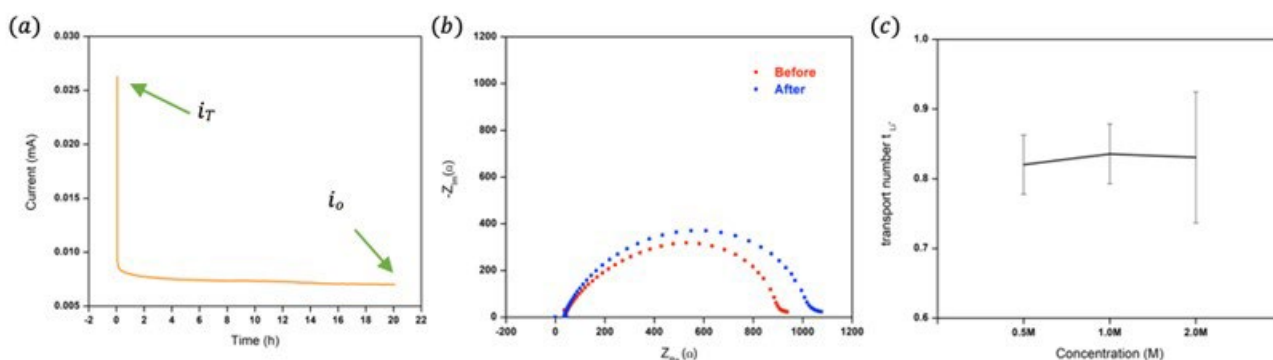


Figure XVII.5.2 0.5M LiTFSI in F₄EO₂/TTE (v/v,1:5) electrolyte: (a) i - t curve of DC polarization process. (b) Impedance of the cell before and after polarization. (c) The transference number of LiTFSI in F₄EO₂/TTE electrolyte as a function of concentration with error bars from multiple tests.

Polysulfides are intermediate species formed from lithiation and de-lithiation process of the sulfur (S) electrode. The long-chain polysulfides (Li_2S_m , $m = 4-8$) are extremely soluble in the conventional ether-based electrolyte in Li-S battery. Thus, S electrode experiences the transformation of solid sulfur to solid Li_2S with the formation of polysulfides which have been only observed in the liquid form during cycling. By preparing electrolyte saturated with S and Li_2S at various polysulfides composition and measuring the overall concentration of sulfur species, we are able to quantify the solubility of polysulfides in our fluorinated micelle electrolyte.

The elements C, H, N, S (weight %) were detected by the ThermoFisher Flash Smart Elemental analyzer. Various polysulfides solutions were prepared by adding and mixing Li_2S , S in 1.0M LiTFSI F₃EO₂/TTE electrolyte (0.3 ml, accurately measured by micro-pipet) based on stoichiometric ratio. The total concentration of S added is fixed at 5M for all samples. In order to overcome the slow kinetic of dissolution process, the solution was stirred at elevated temperature (60°C) for two days and followed by continuously stirring at R.T. for another two days. The solution was syringe filtered ($<0.45\mu\text{m}$ pore sizes) to remove the undissolved solids. The clear supernatant sample was analyzed. The weight percentage of C, H, N, S elements was measured and used to calculate the polysulfide concentration in the electrolyte. The X-axis of molecular formula label of

Li_nS_m is nominal based on the ratio of Li and S element in the Li_2S and S starting materials (Figure XVII.5.3). The measurement shows very limited solubility of polysulfide up to Li_2S_6 in the electrolyte. Even at Li_2S_8 , the solubility of polysulfide in the F_3EO_2 /TTE electrolyte are significantly below the solubility of polysulfide in DOL based electrolyte, noted that solubility of S species is above 6M for a typical ether solvent electrolyte. The finding indicates polysulfide dissolution was effectively suppressed in our fluorinated ether electrolyte; the result agrees with electrochemical performance.

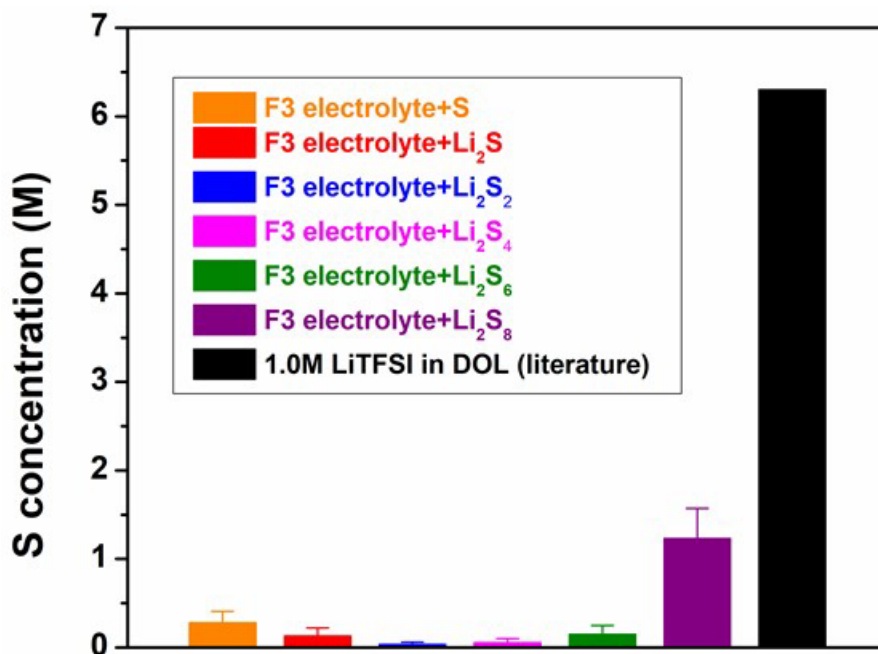


Figure XVII.5.3 The S concentration detected from the supernatant of the electrolyte solution saturated by Li_2S , S, and all types of polysulfides (Li_2S_m , $m = 2, 4, 6, 8$) respectively. The error bar was calculated based on Gaussian distribution analysis. In comparison, the S concentration of 1.0M LiTFSI in DOL is 6.3M based on the literature.

Sulfur electrode design and lithium metal anode stabilization are other important aspects to ensure proper operation of the Li-S cells. The electrolyte is one of the determining factors to the morphology and composition of sulfur electrodes. When electrolyte solvents of high polysulfide solubility are chosen such as DOE/DME, sulfur electrode needs to have high porosity and larger pore sizes to allow reversible S and Li_2S dissolution and precipitations. The larger pore sizes facilitate polysulfide transportation and precipitation during electrochemical process, especially at high current density operation. However, when an electrolyte of very low polysulfides solubilities is used, high porosity is important to accommodate volume change of the S to Li_2S transformation, but larger pore sizes are no longer critically required. Here, we demonstrate a performance characteristic of a dissolved polysulfide solutions in a traditional sulfur electrode design, when different concentration of LiNO_3 is used to stabilize the Li metal surface. It is known that LiNO_3 additive in the electrolyte can suppress the shuttling effect and enhance cycling stability of the Li metal electrode, since it can form the good SEI layer on lithium anode and help to capture Li_2S_x on the cathode, decreasing of the excessive electrolyte decomposition and lithium-polysulfide migration to the anode, respectively. In addition, the LiTFSI-based electrolyte shows high conductivity and TFSI⁻ anion also can help to form stable SEI layer on the anode. Consequently, the 1.0 M LiTFSI in DME:DOL (1/1, v/v) with 1% LiNO_3 (~0.15 M) has become the standard electrolyte for the Li-S batteries. However, the generated-SEI layer on Li anode could be unstable, and the LiNO_3 is continue consumed during the cycling process, along with the electrolyte decomposition by exposing to Li metal, leading to overall decreasing of batteries performance. The alternative approach of amphiphilic hydrofluoroethers electrolyte could prevent polysulfide dissolution and stabilizing Li metal anode. In the DOE/DME (1/1, v/v) based electrolyte, the molar ration of LiTFSI and LiNO_3 should be varied in order to obtain optimized composition in term of its high conductivity, stable SEI layer and sulfur utilization to

compare the cell performance results based on amphiphilic hydrofluoroether electrolyte. Herein, the LiNO_3 concentration is fixed at 0.6 M first, and then the LiTFSI concentration are varied from 0.2 - 0.8 M in DOL/DME (1/1, v/v) system. From Figure XVII.5.4A, it is observed that the Li-S cells with high LiTFSI concentration electrolytes such as 0.6 and 0.8 M LiTFSI exhibit low specific capacity. The low capacity of the cell with 0.2 M LiTFSI electrolyte could be because of its lower conductivity compared to other electrolytes. The 0.4 M LiTFSI - 0.6 M LiNO_3 electrolyte having a low capacity in early cycling state shows higher capacity compared to the commercial electrolyte 1.0 M LiTFSI with 1% LiNO_3 (~0.15 M) after 30 cycles and starts to decay in capacity after 70 cycles, which might be attributed to the exhaustion of LiNO_3 portion in the electrolyte. Although the 0.6 and 0.8 M LiTFSI showed low capacity, high coulombic efficiencies are observed for these electrolytes compared to the others, as shown in Figure XVII.5.4B. In a dissolved polysulfides electrolyte system (such as DOE/DME), the stabilization of Li metal electrode is another very important factor for achieving acceptable Li-S battery electrochemical performance.

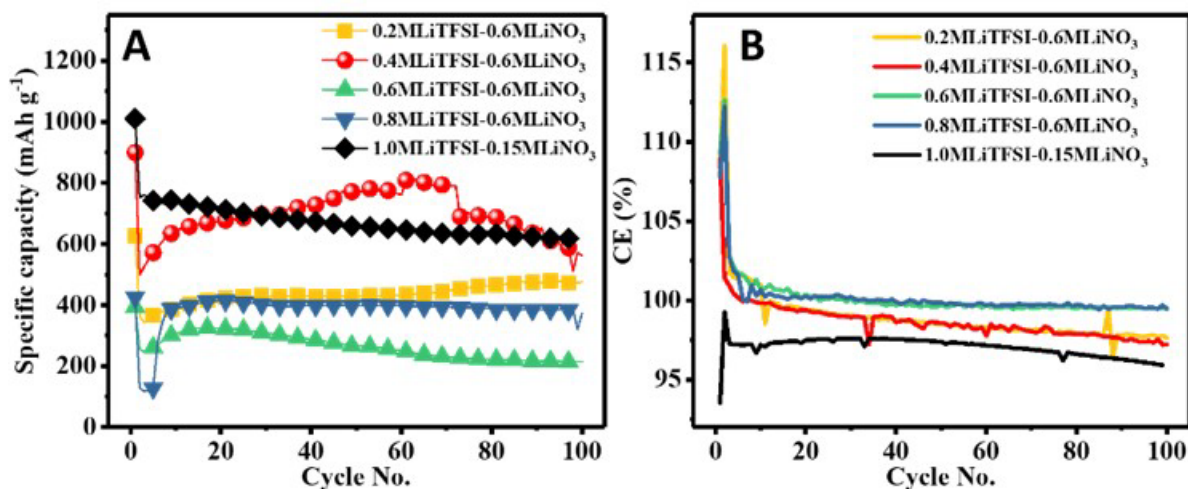


Figure XVII.5.4 (A) Cycling performance of lithium-sulfur cells with different LiTFSI concentrations with 0.6M LiNO_3 in DOL/DME (1/1, v/v) and (B) Coulombic efficiency evolution during the cycling test.

Conclusions

In this annual report, we included our recent effort on enabling Li-S battery on two main thrusts related to the new electrolyte development. The first thrust continues our work on the novel strategy to suppress polysulfide dissolution in Li-S cells utilizing fluorinated ether with an amphiphilic additives (one lithiophilic section and one lithiophobic section) similar to that of amphiphilic surfactants. The electrolyte used in this work was made by LiTFSI dissolved in HFE solvent at various concentrations with dilution of 1,1,2,2-tetrafluoroethyl-2,2,3,3-tetrafluoropropyl ether (TTE) solvent. Lithium salts dissolution follows a special solvation mechanism where dissociated lithium ions are readily coordinated with donating groups to form micelle-like complex, which was verified by small angle X-ray scattering. Superior cycling stability and higher coulombic efficiency was observed for Li-S cells fabricated with micelle electrolyte compared to those using benchmark DME/DOL electrolyte. Small amount of DOL was used as a co-additive to the amphiphilic electrolyte to further adjust the polysulfide dissolution and precipitation properties in the electrolyte to achieve both high sulfur utilization and electrode stability. The high coulombic efficiency indicates good chemical compatibility of amphiphilic electrolyte with sulfur electrode. In the second thrust, a high loading porous electrode architecture was tested to gauge the limit of sulfur loading. In turns, the high loading sulfur electrode also affect the lithium metal cyclability. Combining the effort of two thrusts, we are planning to develop practical high-loading Li-S battery system with tailored electrode architecture and novel fluorinated micelle electrolyte in the future.

Key Publications

1. G. Liu, Novel Electrolyte Additives for Lithium-Sulfur Rechargeable Battery, PCT Patent application, 2021, USPTO application no. PCT/US20/58064.

2. Park, H.; Tamwattana, O.; Kim, J.; Buakeaw, S.; Hongtong, R.; Kim, B.; Khomein, P.; Liu, G.; Meethong, N.; Kang, K., Probing Lithium Metals in Batteries by Advanced Characterization and Analysis Tools. *Adv. Energy Mater.* **2021**, *11* (15), 18.
3. Jia, L. J.; Wang, J.; Ren, S. Y.; Ren, G. X.; Jin, X.; Kao, L. C.; Feng, X. F.; Yang, F. P.; Wang, Q.; Pan, L. D.; Li, Q. T.; Liu, Y. S.; Wu, Y.; Liu, G.; Feng, J.; Fan, S. S.; Ye, Y. F.; Guo, J. H.; Zhang, Y. G., Unraveling Shuttle Effect and Suppression Strategy in Lithium/Sulfur Cells by In Situ/Operando X-ray Absorption Spectroscopic Characterization. *Energy Environ. Mater.* **2021**, *4* (2), 222–228.
4. He, X.; Liu, Z. M.; Gao, G. P.; Liu, X. T.; Swietoslawski, M.; Feng, J.; Liu, G.; Wang, L. W.; Kostecki, R., Revealing the working mechanism of a multi-functional block copolymer binder for lithium-sulfur batteries. *J. Energy Chem.* **2021**, *59*, 1–8.
5. Y. Zhao, C. Fang, G. Zhang, D. Hubble, A. Nallapaneni, C. Zhu, Z. Zhao, Z. Liu, J. Lau, Y. Fu, G. Liu, "A Micelle Electrolyte Enabled by Fluorinated Ether Additives for Polysulfide Suppression and Li Metal Stabilization in Li-S Battery", *Front. Chem.* 2020, *8*, 484.
6. H. Zhong, Y. Zhao, T. Zhang, G. Liu, "Controlled Lithium Deposition on Alq₃ Coated Substrate", *Batteries & Supercaps*, 2020, *3*, 1–9.

References

1. Li, Z. H.; Fang, C.; Qian, C.; Zhou, S. D.; Song, X. Y.; Ling, M.; Liang, C. D.; Liu, G., Polyisoprene Captured Sulfur Nanocomposite Materials for High-Areal-Capacity Lithium Sulfur Battery. *ACS Appl. Polym. Mater.* 2019, *1* (8), 1965–1970.
2. Fang, C.; Zhang, G. Z.; Lau, J.; Liu, G., Recent advances in polysulfide mediation of lithium-sulfur batteries via facile cathode and electrolyte modification. *APL Mater.* 2019, *7* (8), 7.
3. Yang, C. A.; Du, Q. K.; Li, Z. H.; Ling, M.; Song, X. Y.; Battaglia, V.; Chen, X. B.; Liu, G., In-situ covalent bonding of polysulfides with electrode binders in operando for lithium-sulfur batteries. *Journal of Power Sources* 2018, *402*, 1–6.
4. Borchert, H.; Shevchenko, E. V.; Robert, A.; Mekis, I.; Kornowski, A.; Grübel, G.; Weller, H., Determination of Nanocrystal Size: A Comparison of TEM, SAXS, and XRD Studies of Highly Monodisperse CoPt₃ Particles. *Langmuir* 2005, *21*, 1931–1936.
5. Yin, Y. X.; Xin, S.; Guo, Y. G.; Wan, L. J., Lithium-sulfur batteries: electrochemistry, materials, and prospects. *Angew. Chem., Int. Ed. Engl.* 2013, *52* (50), 13186–13200.
6. Zhang, X.-Q.; Cheng, X.-B.; Chen, X.; Yan, C.; Zhang, Q., Fluoroethylene Carbonate Additives to Render Uniform Li Deposits in Lithium Metal Batteries. *Advanced Functional Materials* 2017, *27* (10).
7. Y. Guo, H. Li, T. Zhai, Reviving Lithium-Metal Anodes for Next-Generation High-energy Batteries eneration, *Adv Mater.* 2017, 29.
8. H. Ye, Z. J. Zheng, H. R. Yao, S. C. Liu, T. T. Zuo, X. W. Wu, Y. X. Yin, N. W. Li, J. J. Gu, F. F. Cao, Y. G. Guo, Guiding Uniform Li Plating/Stripping through Lithium-Aluminum Alloying Medium for Long-Life Li Metal Batteries, *Angew Chem Int Ed Engl.* 2019, *58*, 1094–1099.
9. Y. Hamon, T. Brousse, F. Jousse, P. Topart, P. Buvat, D. M. Schleich, Aluminum negative electrode in lithium-ion batteries, *J. Power Sources.* 2001, *97*, 185–187.

10. H. Wu, Y. Cao, L. Geng, C. Wang, In Situ Formation of Stable Interfacial Coating for High Performance Lithium Metal Anodes, *Chem. Mater.* 2017, 29, 3572–3579.

Acknowledgements

Dr. Thanh-Nhan Tran, Dr. Yangzhi Zhao, Dr. Chen Fang performed experimental work, and analyzed data.

XVIII Beyond Li-ion R&D: Lithium-Air Batteries

XVIII.1 Rechargeable Lithium-Air Batteries (PNNL)

Ji-Guang Zhang, Principal Investigator

Pacific Northwest National Laboratory
902 Battelle Boulevard
Richland, WA 99354
E-mail: jiguang.zhang@pnnl.gov

Wu Xu, Co-Principal Investigator

Pacific Northwest National Laboratory
902 Battelle Boulevard
Richland, WA 99354
E-mail: wu.xu@pnnl.gov

Tien Q. Duong, DOE Technology Development Manager

U.S. Department of Energy
E-mail: Tien.Duong@ee.doe.gov

Start Date: October 1, 2015

End Date: September 30, 2021

Project Funding (FY21): \$200,000

DOE share: \$200,000

Non-DOE share: \$0

Project Introduction

It is well known that the state-of-the-art (SOA) lithium (Li)-ion batteries are a mature technology and may reach their practical limit on specific energy ($\sim 300\text{--}350\text{ Wh kg}^{-1}$) soon. Therefore, a worldwide effort has been made to explore new battery chemistries that may far exceed the specific energies of Li-ion batteries. Among the alternative energy storage systems, Li-air batteries (LABs) or Li-oxygen batteries (LOBs) have caught worldwide research interest since the first report of a nonaqueous Li-air battery in 1996 due to their extremely high theoretical specific energy density ($\sim 5,200\text{ Wh kg}^{-1}$ when only the weights of Li and O_2 are included). However, before the commercialization of LABs, considerable challenges need to be overcome. These challenges include electrolyte instability, high overpotential, and severe corrosion of Li metal anodes. These problems cause poor round-trip efficiency and short cycle life in the state-of-the-art LOBs. To enable ultrahigh-energy-density LBS suitable for electric vehicle applications, it is critical to develop electrolytes that are more stable against reactive oxygen species and Li metal anodes, design alternative catalysts and carbon-based or carbon-free air electrodes that are stable against side reaction, stabilize Li metal anodes, and seek new insights into the mechanisms of oxygen reduction reaction (ORR) and oxygen evolution reaction (OER).

Objectives

The objective of this project is to develop rechargeable LOBs with long-term cycling stability through in-depth research on more stable electrolytes and highly efficient catalysts for air electrodes, protection of Li metal anode (LMA), and deeper understanding on the ORR and OER mechanisms behind the electrochemical performance of LOBs. In FY 2021, we will further improve the cycle life and safety of LOBs using novel polymeric colloidal localized high concentration electrolytes (PC-LHCEs), binder-free catalysts with a robust artificial solid electrolyte interphase (SEI) layer, and synthesis of stable solvents. The fundamental mechanism behind the enhanced stability of LABs using these new materials will also be investigated.

Approach

- Develop highly stable electrolytes, including novel PC-LHCEs with an optimized surface protection (PEO-based gel polymer (PG) coating) for LMA. Test electrochemical performance of $\text{Li}||\text{Li}$

symmetric cells with these electrolytes and conventional ether (tetraglyme, G4) based electrolytes to evaluate the stability of the electrolyte itself and the artificial SEI layer.

- Develop effective catalysts to prevent the irreversible parasitic reactions at both cathode and anode.
- Develop novel electrode with three-dimensionally ordered macroporous (3DOM) structure to improve the cycle life of LOBs.

Results

Significant progress has been made in protection and modification of electrodes (both carbon-based air electrode and LMA) and optimization of dual catalysis for Li-O₂ batteries in FY21. The details are described below.

1. Optimization of cell components for long-term cycling of Li-O₂ batteries

The effect of polymer-supported solid electrolyte interface (PS-SEI) layer (generated on Li metal surface) on the cycling stability of LOBs was investigated. Fig. II.11.A.1a shows the cross-sectional morphology (measured by scanning electron microscopy (SEM)) and composition (measured by energy-dispersive X-ray spectroscopy (EDX)) of SEI layer generated via the electrochemical pretreatment of the un-coated LMA under Ar atmosphere (noted as PLi). The similar characteristics for the SEI layer generated on polymer coated LMA under oxygen atmosphere (noted as PPG5 for LMA coated with 5% PEO-based gel polymer solutions) via the same electrochemical pretreatment are shown in Fig. II.11.A.1b. The SEM images exhibit largely different morphologies between PPG5 and PLi. The PLi has a mosaic type SEI layer consisting of the packed particulate components with some submicron sized cracks (Fig. II.11.A.1a), while PPG5 has a continuous film-like SEI layer without cracks or particle boundaries. PLi has a non-uniform thickness (0.31 – 1.63 μm) with an uneven surface while PPG5 have uniform thickness with smooth surfaces. The EDX maps of carbon (C, green) and O (red) clearly reveal the uniformity of the surface layers.

Electrochemical impedance spectroscopy (EIS) was used to investigate impedance of LOBs with LMA treated under different conditions and at selected cycles. The right side of Fig. II.11.A.1a and 1b compares EIS of LOBs with PLi and PPG5 LMAs at 10th, 30th and 50th cycles. The cells were tested with a current density of 0.2 mA cm⁻² under a capacity limited protocol of 1.0 mAh cm⁻² and voltage range of 2.0 – 5.0 V operated at 25°C. The impedance of LOB with the uniform and robust PS-SEI layer PPG5 was much smaller (Figure XVIII.1.1b, 117 Ω) than those with non-uniform SEI layer (Figure XVIII.1.1a, 278 Ω) formed without a polymer support after 50 cycles. These results indicate that the cell resistance is directly related to the properties of SEI layer. It is also consistent with the observation that the LOB with LMA protected by PS-SEI layer (PPG5) exhibit a cycle life twice as long as those without PS-SEI layer (PLi) as shown below.

The suitable lithium salt in tetraglyme solvent (G4) with the PS-SEI layer and the effect of concentration of redox mediator (RM), (2,2,6,6-tetramethylpiperidin-1-yl) oxidanyl (TEMPO) on the cell impedance were further investigated to enhance the long-term cyclability of LOBs. Figure XVIII.1.1c shows that the LOBs with lithium bis(trifluoromethanesulfonyl)imide (LiTFSI) salt is more stable than those using lithium trifluoromethanesulfonate (LiTf). Figure XVIII.1.1d shows that the cell overpotential significantly decreases with 0.1M TEMPO in 1M LiTf/G4 electrolyte and the cell can be operated in a narrow cut-off voltage range (2.0 – 4.5 V). In contrast, the cell using 1M LiTf salt needs to operate in a voltage range of 2.0 – 5 V to reach the same capacity. EIS analysis was used to investigate the effect of TEMPO concentrations on the performance of LOBs. It is found that the LOBs with LiTFSI based electrolytes have much lower solution resistance (R_s , Figure XVIII.1.1e) than those with LiTf based electrolyte (Figure XVIII.1.1f) and the cell impedance increases with increasing concentration of TEMPO in the electrolytes (Figure XVIII.1.1e). Since the TEMPO molecules may have side reactions with Li metal surface, LOBs with PPG5 protected LMA were used with TEMPO containing electrolyte (1M LiTFSI/G4). Even after the pre-charging step to generate PS-SEI layer, the cell with LiTFSI based electrolyte exhibits a lower solution resistance (28 Ω) than those with the LiTf based electrolyte (67 Ω) (Figure XVIII.1.1f).

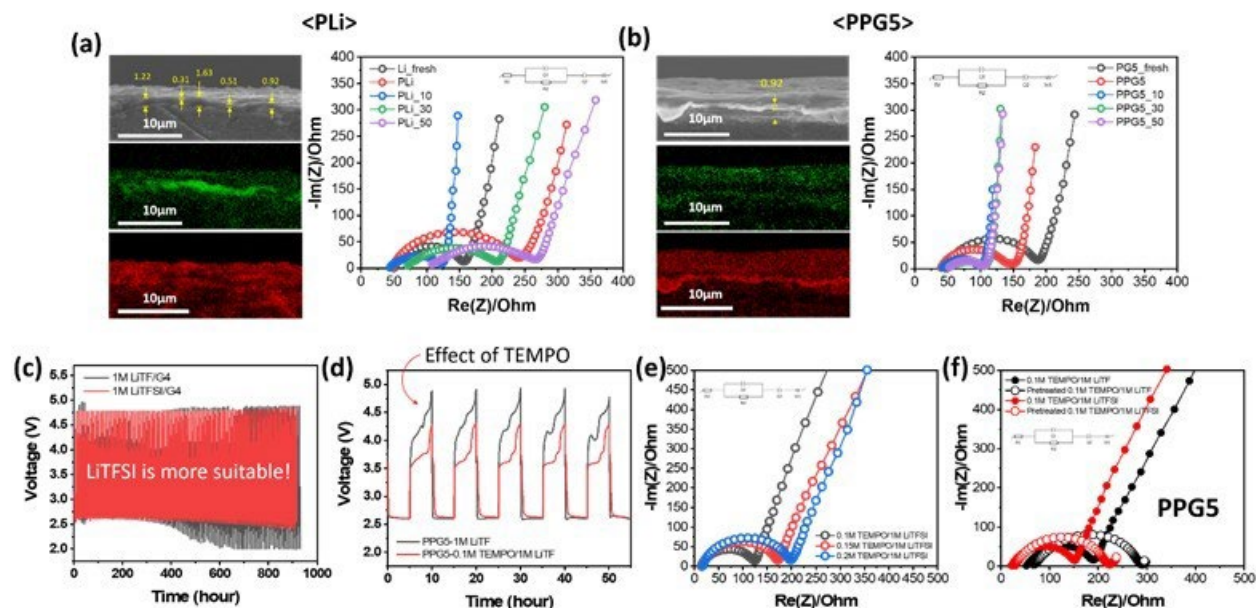


Figure XVIII.1.1 (a and b) Cross-sectional images, oxygen- and carbon-EDX maps of Li metal surface with PPG5 (PEO-based gel polymer (PG) coating and electrochemical pre-treatment under O₂) and with PLi (without PG coating but with electrochemical pre-treatment under Ar). (c) Charge/discharge curves of LOBs with different lithium salts and (d) with and without 0.1M TEMPO. (e) EIS of fresh LOBs with different concentration of TEMPO in the LiTFSI based electrolytes. (f) EIS of LOBs with different lithium salts and PPG5 layer before and after pretreatment step.

2. The effect of dual catalysis with PS-SEI layer on the stability of Li-O₂ batteries

The concentration of TEMPO redox mediator in 1 M LiTf/G4 electrolyte was optimized for long-term cycling of LOBs in a cut-off voltage range of 2.0 – 4.5 V. LOBs using pristine LMA and PS-SEI layer coated LMA with different TEMPO concentrations (0.1 M, 0.15 M and 0.2 M) in 1 M LiTf/G4 electrolyte were investigated. Figure XVIII.1.2a shows that LOBs using PS-SEI layer coated LMA demonstrate much better cycling stability (105, 123 and 115 cycles, respectively) than those using pristine Li anode cell (54 cycles) because TEMPO molecules lead to serious parasitic side reactions with Li metal, but the PS-SEI layer can protect Li metal against such side reactions (Figure XVIII.1.2b). We found that increasing TEMPO concentration leads to lower cell resistance after 10 cycles (Figure XVIII.1.2c), but too much TEMPO may cause some solubility issue in 1 M LiTf/G4 electrolyte. Through the protection effect of uniform and robust PS-SEI layer on LMA, even higher TEMPO concentration works properly during the long-term operation of LOBs. It is also found that LiTFSI based electrolytes lead to better cycling stability (123 cycles) compared to LiTf based Li-O₂ cell (106 cycles) (Figure XVIII.1.2d). We further combined the solid catalyst (ruthenium oxide, RuO₂) generated on single walled carbon nanotube (SWCNT) air electrode with TEMPO as soluble catalyst in LOBs. The dual-catalyst system reduced impedance of fresh LOB (Figure XVIII.1.2e) with LiTFSI/G4 electrolyte and PS-SEI layer. In addition, dual catalyst also leads to a lower oxidation voltage of 3.7V (Figure XVIII.1.2f) due to oxidation of two different catalysts at around 3.7 V with a good utilization of TEMPO, as illustrated in Figure XVIII.1.2g.

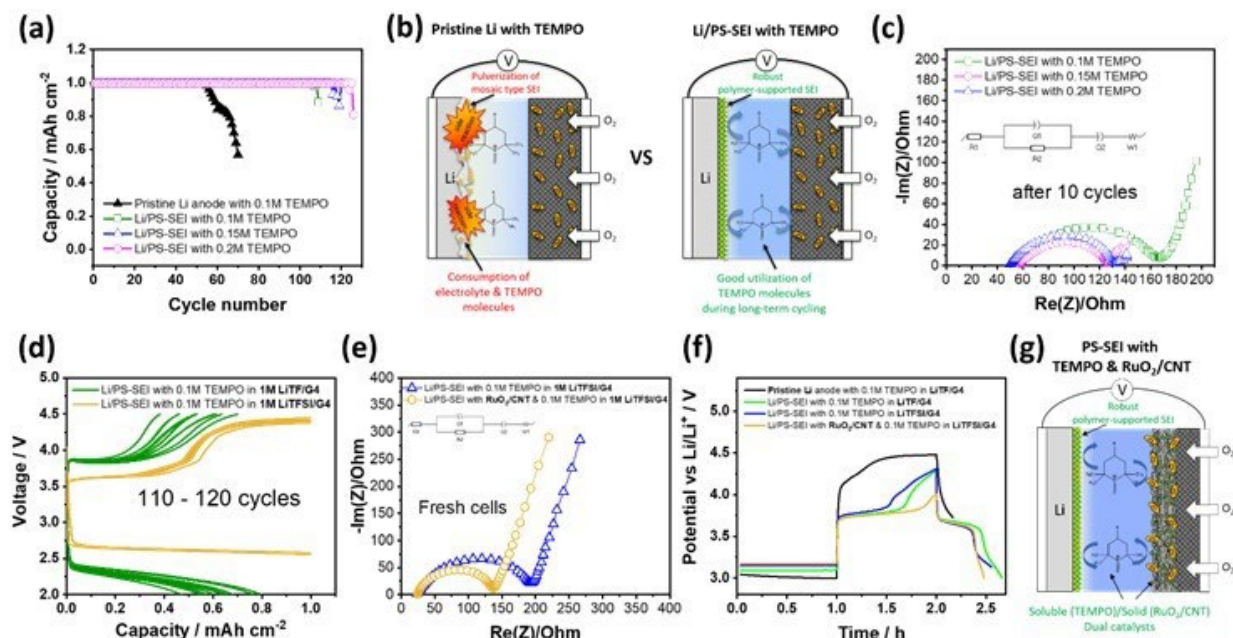


Figure XVIII.1.2 (a) Cycling stability of pristine Li anode with 0.1 M TEMPO and Li/PS-SEI anodes with different TEMPO concentrations (0.1, 0.15 and 0.2 M) in 1 M LiTf/G4 and (b) schematic illustration of the effect of PS-SEI layer operating with TEMPO as redox mediator. (c) EIS Nyquist plots of the corresponding cells after 10th cycle at a current density of 0.2 mA cm⁻² under a capacity limited protocol of 1.0 mAh cm⁻² in the operation voltage range of 2.0 – 4.5 V operated at 25 °C. (d) Charge/discharge curves (110th – 120th) of Li-O₂ batteries with two different lithium salts (LiTf or LiTFSI) in G4 solvent with PS-SEI layer and 0.1 M TEMPO. (e) EIS of fresh Li-O₂ batteries with 0.1 M TEMPO in the LiTFSI based electrolytes and GDL carbon or RuO₂/CNT electrodes. (f) Charge profiles of pristine Li anode in 1 M LiTf/G4 with 0.1 M TEMPO, Li/PS-SEI in 1 M LiTf/G4 with 0.1 M TEMPO, Li/PS-SEI in 1 M LiTFSI/G4 with 0.1 M TEMPO and Li/PS-SEI with RuO₂/CNT electrode in 1 M LiTFSI/G4 with 0.1 M TEMPO, respectively. (g) Schematic illustration of the synergy effect of dual-catalysis with PS-SEI layer in Li-O₂ cell.

3. Development of 3DOM carbon electrode with dual-catalyst for Li-O₂ batteries

The dual-catalyst (soluble: TEMPO and solid: ruthenium oxide (RuO₂) or ruthenium (Ru) metal, Figure XVIII.1.3a) was used to reduce cell overpotential with a Li anode protection PS-SEI and improve the long-term cycle life of LOBs. LOBs with dual-catalyst and PS-SEI protected LMA lead to much higher open circuit voltage (OCV, 3.18V) and smaller cell impedance (137 Ω) than those without dual-catalyst (2.79V and 193 Ω, Figure XVIII.1.3b). The LOBs with dual-catalyst also show much better cycling stability (180 cycles, Figure XVIII.1.3c) than those with single catalyst (130 cycles) in the cut-off voltage range of 2 to 5 V because a robust PS-SEI layer can preserve the activity of dual-catalyst and stabilize LOBs for long-term operation. To further improve the activity of dual-catalyst and extend the cycle life of LOBs, a three-dimensionally ordered macroporous (3DOM) structure was generated in the SWCNT air electrode by a templating method (Figure XVIII.1.3d). It is found that the 3DOM structure leads to higher OCV (3.36 V) compared to non-3DOM air electrode (3.18 V) (Figure XVIII.1.3e). The LOB with dual-catalyst combined with a 3DOM air electrode also exhibits much lower charge voltage profiles than those with dual catalyst and regular air electrode even after 100 cycles (Figure XVIII.1.3f).

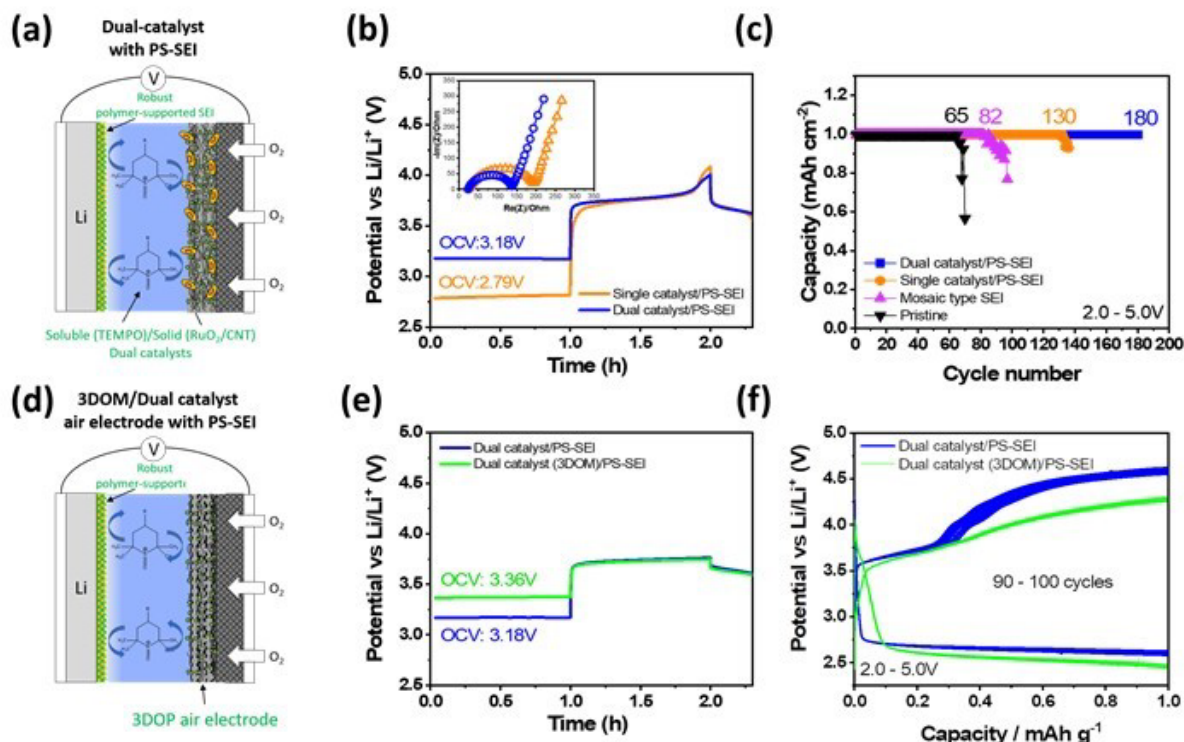


Figure XVIII.1.3 (a) Schematic illustration of the synergy effect of dual-catalysis with PS-SEI layer in Li-O₂ cell. (b) EIS Nyquist plots (inlet) of fresh Li-O₂ cells with single and dual catalysts and their charge curves during pre-charging to 5 V. (c) Cycling stability of pristine Li anode, Li/mosaic type SEI, Li/PS-SEI with 0.1 M TEMPO and Li/PS-SEI with 0.1 M TEMPO and ruthenium oxide fixed on the SWCNT air electrode at a current density of 0.2 mA cm⁻² under a capacity limited protocol of 1.0 mAh cm⁻² in the operation voltage range of 2 – 5 V operated at 25 °C. (d) Schematic illustration of the three-dimensionally ordered macroporous (3DOM)/SWCNT air electrode with dual-catalyst and PS-SEI layer in Li-O₂ cell. (e) Charge curves of Li-O₂ cells with dual-catalyst/PS-SEI layer and 3DOM/dual catalyst with PS-SEI layer during pre-charging to 5 V. (f) Charge-discharge profiles of Li-O₂ cells with dual-catalyst/PS-SEI and 3DOM/dual-catalyst with PS-SEI layer at a current density of 0.2 mA cm⁻² under a capacity limited protocol of 1.0 mAh cm⁻² in the operation voltage range of 2 – 5 V operated at 25 °C.

The interconnected 3DOM structure (Figure XVIII.1.4b) was generated in single-walled carbon nanotubes with ruthenium catalysts (Ru/SWCNTs) by a template method. The Ru/SWCNTs air electrode with no macroporous structure was also investigated as a reference (Figure XVIII.1.4a). After discharging step, the interconnected pore in 3DOM structure is still maintained (2nd image in Figure XVIII.1.4b) even after formation/growth of discharge products. In contrast, the mesopores of non-3DOM air electrode are completely blocked with the deposited/grown discharge products (2nd image in Figure XVIII.1.4a). The cross-sectional views of two air electrodes also show the consistent results (4th images in Figure XVIII.1.4a and Figure XVIII.1.4b). The accumulation of solid discharge products leads to clogging pores, cell impedance increases by blocking access for electrolyte. EDX-line profiles indicate that the 3DOM structure (Figure XVIII.1.4d) allows uniform formation of the discharge products throughout the active layer while the non-3DOM electrode (Figure XVIII.1.4c) does not efficiently utilize active phase inside of air electrode because of the blocking pores. EIS Nyquist plots of two air electrodes after discharge (Figure XVIII.1.4e) also demonstrated that the 3DOM electrode leads to lower cell impedance due to the lower electrode/electrolyte interfacial resistance even with the accumulation of discharge products. The LOBs with 3DOM air electrode (red) exhibits better cycling stability (140 cycles) than the cell with Ru/SWCNTs air electrode without 3DOM structure (green, 115 cycles) in the cut-off voltage range of 2.0 to 4.5 V (Figure XVIII.1.4f). Therefore, in-depth study on the pore structure control of the air electrodes is one of the critical approaches to improve electrochemical reversibility and long-term cyclability of LOBs.

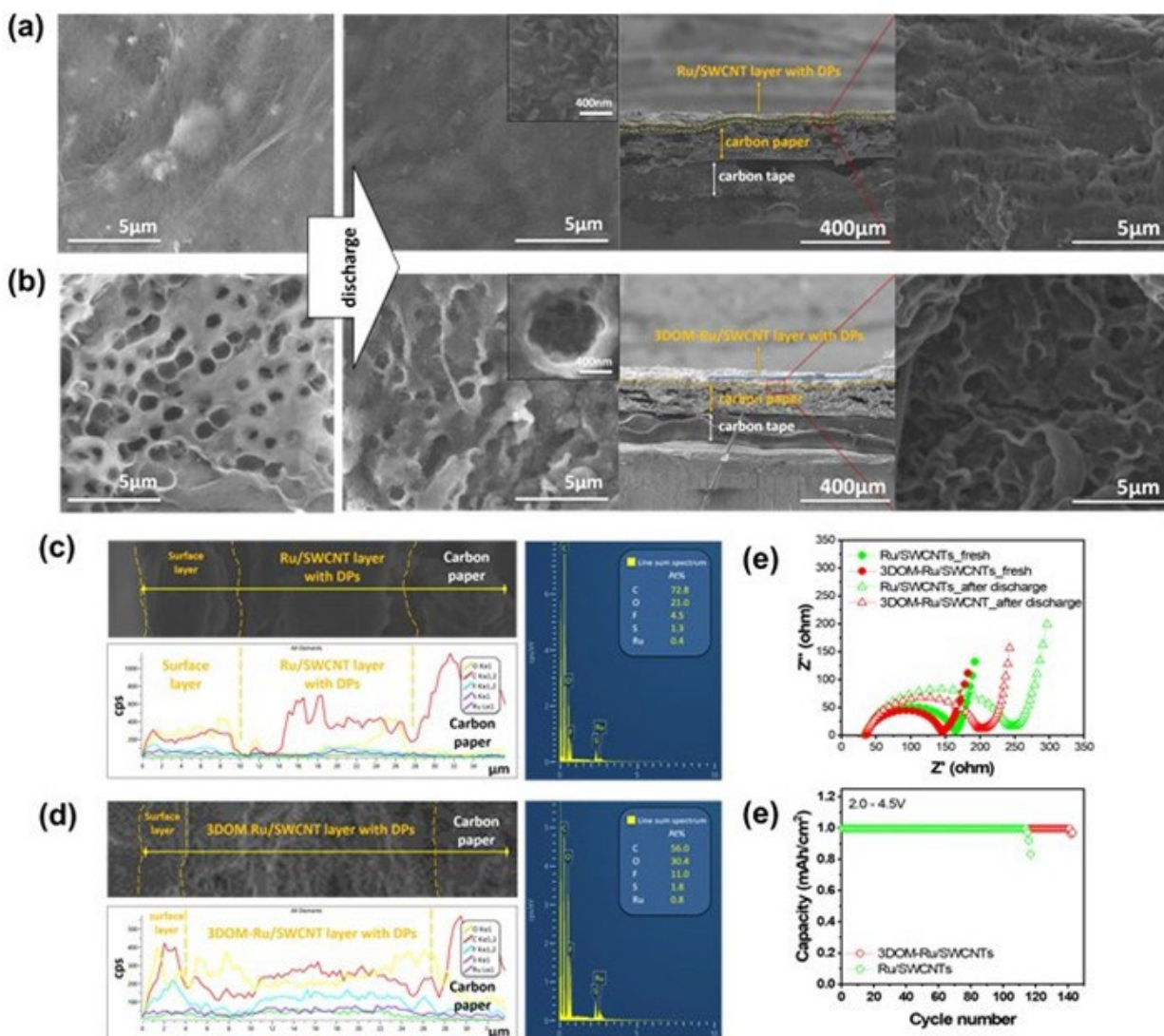


Figure XVIII.1.4 Top and cross-sectional views of SEM images of (a) Ru/SWCNTs (non-3DOM) and (b) three-dimensionally ordered macroporous (3DOM)-Ru/SWCNTs air electrodes before (fresh) and after 1st discharge at a current density of 0.2 mA cm⁻² under a capacity limited protocol of 1.0 mAh cm⁻² in the operation voltage range of 2.0 – 4.5 V operated at 25 °C. EDX line-profiles and spectra scanned through cross-sectional views of (c) Ru/SWCNTs and (d) 3DOM-Ru/SWCNTs air electrodes after 1st discharge, (e) EIS Nyquist plots before (fresh) and after 1st discharge to 2.0 V and (f) cycling stability of Li-O₂ cells with (green) Ru/SWCNTs and (red) 3DOM-Ru/SWCNTs air electrodes at a current density of 0.2 mA cm⁻² under a capacity limited protocol of 1.0 mAh cm⁻² in the operation voltage range of 2.0 – 4.5 V operated at 25 °C.

Conclusions

- LOBs with LiTFSI based electrolyte exhibit lower solution resistance, better TEMPO utilization, and better cycling stability than those with LiTf based electrolyte.
- Dual-catalyst (solid catalyst: RuO₂ and mobile catalyst: TEMPO) reduces the pre-charging voltage and cell resistance of LOBs.
- 3DOM structure in the air electrode can effectively reduce the blocking of air electrode during cycling of LOBs. It also leads to uniform deposition/growth of discharge products (DPs) during the discharging step, reduce the over voltage and cell impedance, therefore extend the cycle life of Li-O₂ batteries.

Key Publications

1. H. S. Lim, W. J. Kwak, S. Chae, S. Wi, L. Li, J. Hu, J. Tao, C. Wang, W. Xu*, J. G. Zhang*, “A Stable SEI Layer Formed by Electrochemical Pretreatment of Gel Polymer Coating on Li Metal Anode for Lithium-Oxygen Batteries”, *ACS Energy Letters* 2021, **6** (9), 3321–3331.
DOI: [10.1021/acsenergylett.1c01144](https://doi.org/10.1021/acsenergylett.1c01144)

Acknowledgements

Key contributors include Drs. Hyung-Seok Lim and Won-Jin Kwak.

XVIII.2 Lithium-Air Batteries (ANL)

Khalil Amine, Principal Investigator

Argonne National Laboratory
9700 South Cass Avenue
Lemont, IL 60439
E-mail: amine@anl.gov

Tien Q. Duong, DOE [Technology Development Manager]

U.S. Department of Energy
E-mail: Tien.Duong@ee.doe.gov

Start Date: October 1, 2019

End Date: September 30, 2024

Project Funding (FY21): \$500,000

DOE share: \$500,000

Non-DOE share: \$0

Project Introduction

Lithium-oxygen batteries are of much interest because they offer, in principle, ten times the energy density of conventional lithium-ion systems. The inherent energy potential of lithium metal approaches that of gasoline, but there are challenges that remain to be able to unlock this potential. While today's lithium-ion batteries may provide acceptable power for hybrid electric vehicles and all-electric vehicles, they do not as yet provide sufficient energy for driving distances desired by consumers. A breakthrough in Li-oxygen battery technology would significantly increase the possibility of extending the electric range of these vehicles with the added advantages of reducing battery cost and weight.

The successful implementation of non-aqueous Li-air cells has been hampered because of severe materials problems that have limited electrochemical performance. These include (1) the non-aqueous electrolytes can be unstable under both the charge and discharge conditions, thereby seriously limiting cycle life; (2) during discharge, the solid and insoluble Li_2O_2 and/or other lithium oxide products are deposited on the surface or within the pores of the carbon cathode, thereby passivating the surface as well as clogging the pores and restricting oxygen flow; (3) degradation of the lithium anode due to oxygen crossover destroys the integrity and functioning of the cell; and (4) commonly used transition metal cathode catalysts, do not access the full capacity of the oxygen electrode or enable sufficiently high rates.

The team led by Dr. Khalil Amine at Argonne National Laboratory is working on problems that limit the electrochemical performance of the Li-oxygen battery, including the stability of the organic electrolytes, development of new cathode catalysts, and new electrolytes. This effort will lead to the development of a reversible lithium oxygen battery that provides much higher energy density than state-of-the-art lithium-ion batteries for electric vehicles

Objectives

This project will develop new cathode materials and electrolytes for Li-air batteries for long cycle life, high capacity, and high efficiency. The goal is to obtain critical insight that will provide information on the charge and discharge processes in Li-air batteries to enable new advances to be made in their performance. This will be done using state-of-the-art characterization techniques combined with state-of-the-art computational methodologies to understand and design new materials and electrolytes for Li-air batteries.

Approach

The project is using a joint theoretical/experimental approach for design and discovery of new cathode and electrolyte materials that act synergistically to reduce charge overpotentials and increase cycle life. Synthesis methods, in combination with design principles developed from computations, are used to make new cathode architectures. Computational studies are used to help understand decomposition mechanisms of electrolytes

and how to design electrolytes with improved stability. The new cathodes and electrolytes are tested in Li-O₂ cells. Characterization, along with theory, is used to understand the performance of materials used in the cell and to make improved materials.

Results

In this project, we have developed new cathodes for high energy efficiency and long cycle life and investigated the effects of the anion and cation additives in Li-O₂ batteries.

1. Carbon source has a large impact on the performance of Li-O₂ batteries

A reasonable pore architecture design and a good catalytic capability of the cathode are considered to be the key to solve this problem. Biomass carbon materials with unique nanostructures have been employed as porous cathode materials with certain catalytic properties. However, the current synthesis methods of carbon materials are always limited to a specific biomass raw material that is not favorable to its large-scale practical application. What is worse, owing to the fact that carbon materials synthesized so far are mostly concave cylindrical-like pore structures that are easily blocked by the discharge products, the internal micro- and mesoporous structures and the active reaction sites are not all effectively involved in the electrode reaction and thus result in the termination of discharge.

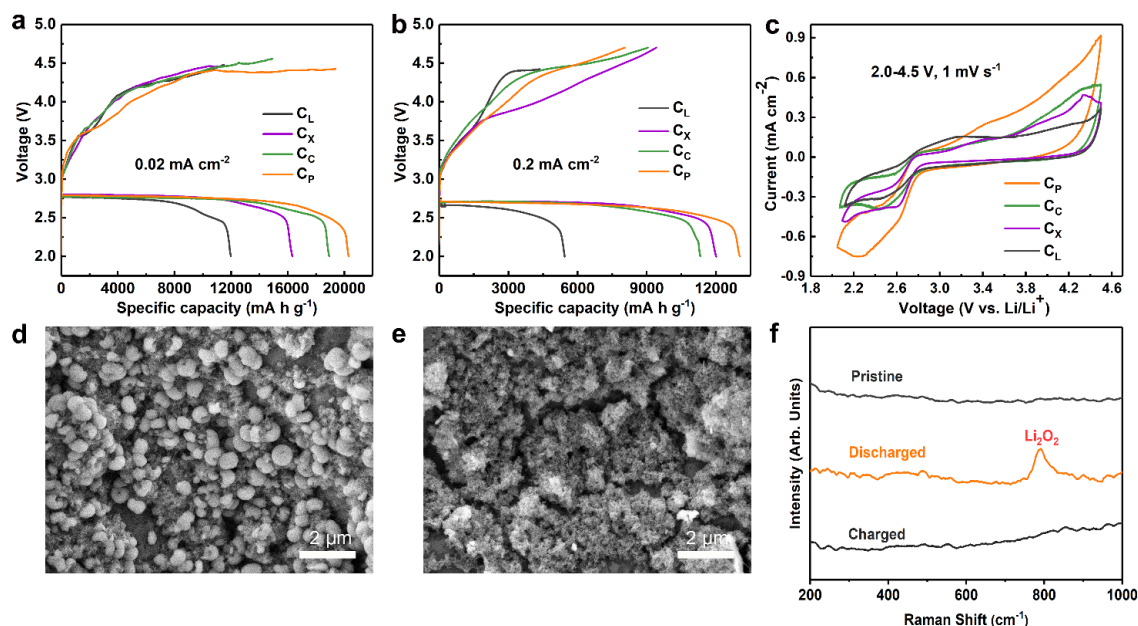


Figure XVIII.2.1 Initial full discharge-charge voltage profiles of CL, CX, CC and CP cathode at a current density of (a) 0.02 mA cm⁻² and (b) 0.2 mA cm⁻²; (c) CV curves of CL, CX, CC and CP electrodes within a voltage window of 2.0-4.5 V at a scanning rate of 1 mV s⁻¹; SEM images of CP cathode after first discharge (d) and charge steps (e) at a current density of 0.02 mA cm⁻²; (f) Raman spectra of CP cathode at different stages: pristine, and after first discharge and charge steps.

A series of carbon source was explored (lignin, xylan, cellulose, and pomelo peel) defined as CL, CX, Cc and Cp, respectively. The electrochemical properties of four carbon materials are tested (Figure XVIII.2.1 a-b). At a current density of 0.02 mA cm⁻², C_X, C_C and C_P deliver an excellent specific capacity of 16320, 18931 and 20300 mA h g⁻¹, respectively, which is higher than 11985 mA h g⁻¹ of C_L. When the current density is increased to 0.2 mA cm⁻², four carbon materials, except C_L, still keep a specific capacity exceed 11300 mA h g⁻¹ with a decreased discharge voltage platform of about 70 mV only, particularly, the specific discharge capacity of C_P is still as high as 13030 mA h g⁻¹. The remarkable specific capacity of C_P is beyond almost all the cathode materials in nonaqueous system that have been reported according to the results of the literature search. The cyclic voltammetry (CV, Figure XVIII.2.1 c) curves demonstrate that C_P has the highest ORR (oxygen reduction reaction) onset potential and the lowest OER (oxygen evolution reaction) onset potential,

and also the highest ORR and OER peak currents, indicating a good catalytic performance of C_P for both ORR and OER processes.

The electrochemical reaction process was preliminary investigated. SEM images of C_P cathode after first discharge and charge steps indicate an excellent reversibility of the cathode reaction (Figure XVIII.2.1 d-e, respectively), and Raman result has verified the formation and complete decomposition of Li_2O_2 (Figure XVIII.2.1 f).

2. The specific pore structure has large impact on Li-O₂ batteries

The source of the performance difference can be traced to the pore structure. As seen in Figure XVIII.2.2 a-b, C_P , C_C , and C_X have a hierarchical pore structure where the pore size distribution contains micropores and mesopores, while the pore type of C_L is mainly microporous. C_L shows the highest specific surface area, but its pore volume and average pore diameter are significantly smaller than those of the other three carbons. Sorption isotherms of C_P , C_C and C_X are classified into a type H3 hysteresis loop, indicating that their pores are assemblage of non-rigid slit-shaped pore structures. Whereas, the hysteresis curve of C_L belongs to the H4 type. This material contains concave cylindrical-like micropores and mesopores. In the case of concave cylindrical-like pores, discharge products would close the openings on the surface, block the mass transfer inside the pore, and deactivate the inner surface reactive sites. Conversely, with an open slit-shaped pore structure, porous carbon can fully expose the reactive sites, and the non-rigid open pore can transport reactive ions and gases quickly. Besides the pore structure, surface properties were also investigated. C_L , C_X , C_C and C_P all have a fairly high C/O ratio of 14.7, 19.4, 16.5 and 17.94, respectively (Figure XVIII.2.2 c). With a relatively low concentration of oxygenic groups and structure defects on the surface, the side reactions associated with carbon decomposition can be minimized, and the electric conductivity can also be enhanced (Figure XVIII.2.2 d). Therefore, fast reaction kinetics and ultra-high specific capacity are achieved.

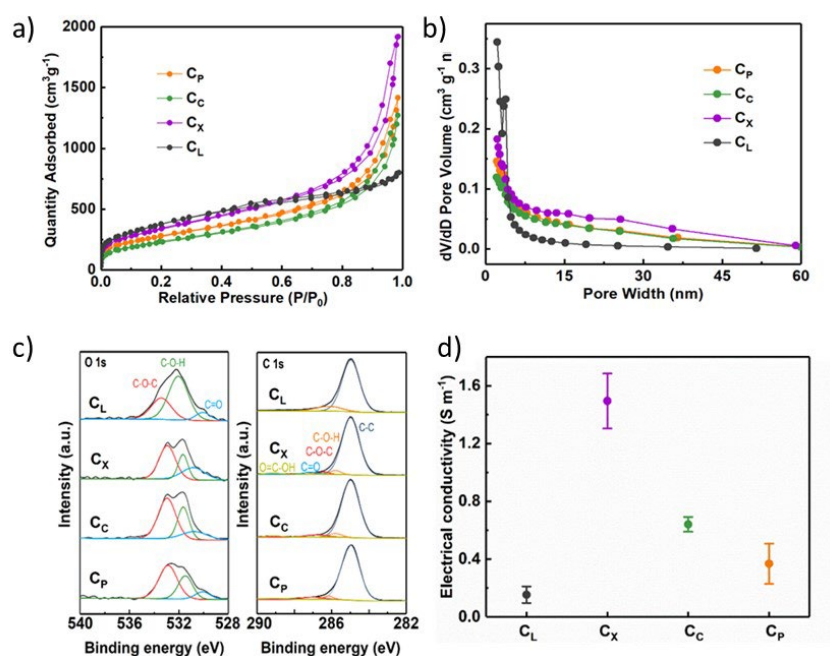


Figure XVIII.2.2 (a) Nitrogen adsorption-desorption isotherms, (b) pore-size distributions of C_L , C_X , C_C and C_P . (c) O 1s and C 1s XPS scan and (d) electric conductivity of C_L , C_X , C_C and C_P , respectively.

3. Surface optimized Pt₃Ni catalyst ORR and OER

Numerous functional catalysts have been developed for lithium oxygen ($Li-O_2$) batteries, among which precious metal catalysts have shown good catalytic performance for Li_2O_2 formation and decomposition. However, it could not only decompose Li_2O_2 , but also catalyze the degradation of the ether-based solvent in

the electrolyte, leading to an unstable cell environment and poor cycle life. Using Pt_3Ni as a model catalyst, the effect of different surface properties on the catalytic performance was explored. Three Pt_3Ni nanoparticle-based catalysts were prepared by a wet chemical synthesis method with Pt loading of 15:85 ratio in mass with carbon black. Sample 1 is the as synthesized Pt_3Ni nanoparticles where the surface is covered by organic compounds (Figure XVIII.2.3 a). Sample 2 is further annealed at a temperature of 185°C in air, where the surface contains a layer of NiO (Figure XVIII.2.3 b). Sample 3 is the as-synthesized Pt_3Ni treated in perchloric acid to achieve a Pt outer surface layer (Figure XVIII.2.3 c). The three catalysts all have a Pt_3Ni core but different surfaces.

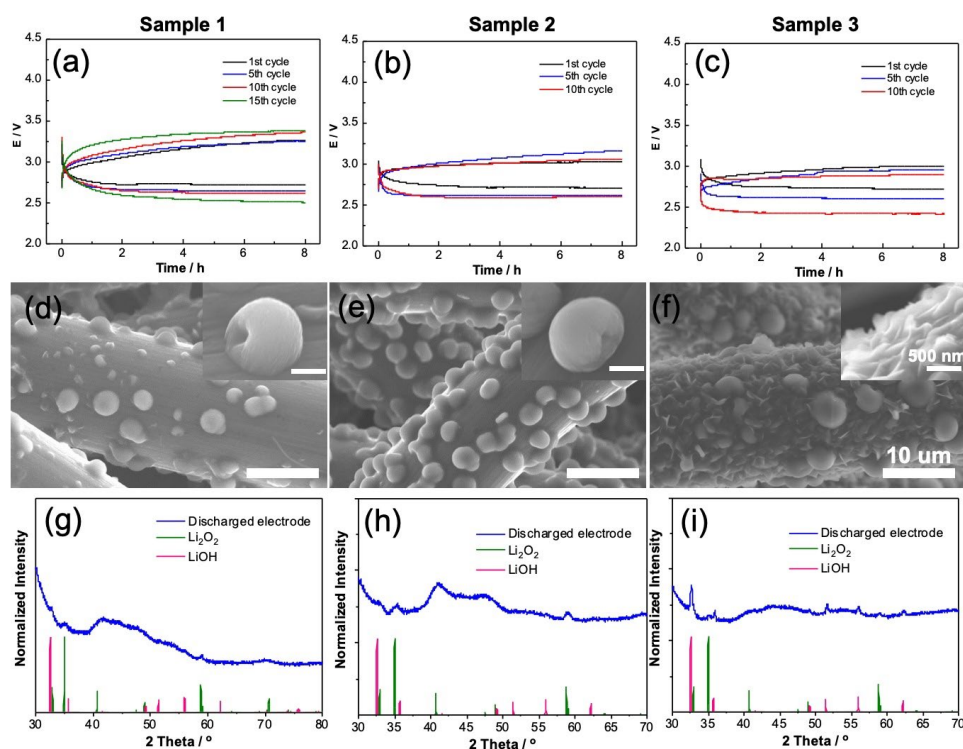


Figure XVIII.2.3 Voltage profiles of Li-O₂ batteries with (a) sample 1, (b) sample 2, and (c) sample 3. SEM images of the discharged cathodes for (d) sample 1, (e) sample 2, and (f) sample 3. The scales are labeled the same for the images. XRD of the discharged cathodes for (g) sample 1, (h) sample 2, and (i) sample 3.

We applied the three catalysts in Li-O₂ batteries and different electrochemical performance and discharge products were achieved. After discharge, the cell with sample 1 as the cathode catalyst has Li_2O_2 as the major discharge product, with the presence of a small amount of LiOH, supported by SEM and XRD (Figure XVIII.2.3 e and g). The cell with $\text{Pt}_3\text{Ni}/\text{NiO}$ shows a discharge product of Li_2O_2 (Figure XVIII.2.3 e and h), while the product in the cell with $\text{Pt}_3\text{Ni}/\text{Pt}$ is mainly LiOH (Figure XVIII.2.3 f and i).

4. Metal-free catalyst derived from cathode coating

As seen in the cryogenic-transmission electron microscopy shown in Figure XVIII.2.4 a, the catalytic layer can be found deposited neatly over the surface of carbon paper. This layer is derived from the lithiation of carbon paper in ether electrolyte (lithiation voltage profile shown in Figure XVIII.2.4 b), akin to the solid-electrolyte interphase formation process. Directly applying the cathode with this catalytic layered yielded exceptionally low overpotential. Figure XVIII.2.4 c-d compares the voltage profile at various cycles of cell using a pristine carbon paper with and without the catalytic layer, respectively. When the catalytic layer is present, the charge potential maintains well below 3.75 V vs Li⁺/Li while the pristine carbon paper experienced charge potentials well above 4.2 V vs Li⁺/Li. Furthermore, the impact of the substrate selection was explored. Different types of carbon-based substrate (carbon nanotube, carbon black, graphite, and carbon paper) were used to form the

catalytic layer, revealing varying degrees of impact on the final cell performance. The charge potential was observed to be the highest in the carbon paper system followed by carbon nanotube, carbon black, and graphite. The cause of this trend and the overall functioning mechanism offered by this novel metal-free catalytic layer is currently under study.

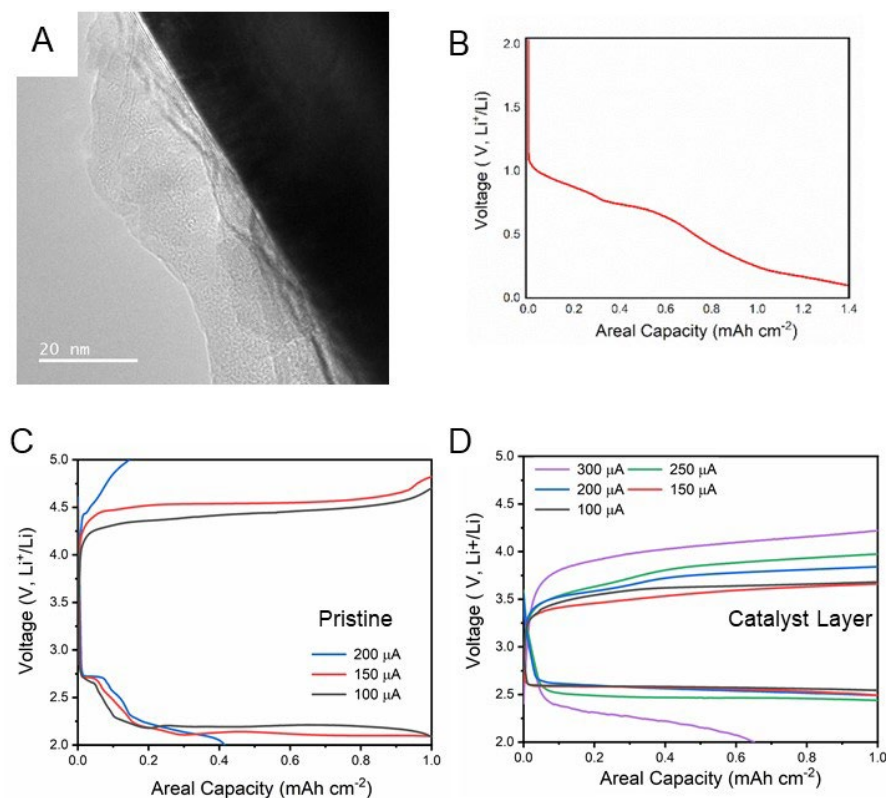


Figure XVIII.2.4 A) Cryogenic transmission electron microscopy of catalytic layer formed in ether-based electrolyte over carbon nanotube. B) Voltage profile of catalytic layer formation process. Rate performance of Li-O₂ assembled using C) pristine carbon paper and D) with catalytic layer formed over the carbon paper.

Conclusions

In the project, we have developed multiple effective cathode materials to achieve long cycle life and high energy efficiency of the lithium oxygen batteries. A novel carbon nanosphere material with an open hierarchical pore structure has been synthesized through a hydrolysis and carbonization process. The relationship between pore structure/surface properties and electrochemical performance in Li-O₂ batteries has been clearly revealed. Particularly, benefiting from an open slit-shaped structure exposing a large portion of active sites to the surface, the porous carbon based Li-O₂ batteries deliver a super-high discharge capacity and long-cycle life. Secondly, the impact of surface chemistry of Pt₃Ni was investigated. Different surface modifications were developed to achieve different surface components based on the Pt₃Ni nanoparticles. Large variation in the nature (composition and morphology) of the discharge products was observed. Finally, a novel metal-free catalyst was developed. The new catalyst is a thin organic/inorganic layer derived from the reduction of electrolyte compounds from a conditioning step. Outstanding performance was achieved with this method with respect to overpotential and cycle life.

Key Publications

1. Bi, X.; Li, J.; Dahbi, M.; Alami, J.; Amine, K.; Lu, J.; Understanding the role of Lithium iodide in Lithium oxygen batteries. *Advanced Materials* 2021, DOI: 10.1002/adma.202106148.

2. Bi, X.; Li, M.; Liu, C.; Yuan, Y.; Wang, H.; Key, B.; Wang, R.; Shahbazian-Yassar, R.; Curtiss, L. A.; Lu, J.; Amine, K. Cation Additive Enabled Rechargeable LiOH-Based Lithium–Oxygen Batteries. *Angew. Chem. Int. Ed.* 2020, 59, 22978.
3. Ma, Z.; Cano, Z. P.; Yu, A.; Chen, Z.; Jiang, G.; Fu, X.; Yang, L.; Wu, T.; Bai, Z.; Lu, J. Enhancing Oxygen Reduction Activity of Pt-based Electrocatalysts: From Theoretical Mechanisms to Practical Methods. *Angew. Chem. Int. Ed.* 2020, 59, 18334.
4. Zhao, T.; Yao, Y.; Yuan, Y.; Wang, M.; Wu, F.; Amine, K.; Lu, J. A universal method to fabricating porous carbon for Li-O₂ battery. *Nano Energy* 2021, 82, 105782.
5. Plunkett, S. T.; Zhang, C.; Lau, K. C.; Kephart, M. R.; Wen, JG, Chung, D. Y., Phelan, D., Ren, Y., Amine, K., Al-Hallaj, S., Chaplin, B. P., Wang, H.-H., Curtiss, L. A., Electronic Properties of Ir₃Li and Ultra-Nanocrystalline Lithium Superoxide Formation, *Nano Energy* 2021, 90, 106549.
6. Peng, X.; Li, T.; Zhong, L.; Lu, J. Flexible metal–air batteries: An overview. *SmartMat* 2021, 2, 123.
7. Li, J.; Bi, X.; Amine, K.; Lu, J. Understanding the Effect of Solid Electrocatalysts on Achieving Highly Energy-Efficient Lithium–Oxygen Batteries. *Adv. Energy & Sustainability Res.* 2021, 2, 2100045.
8. Bi, X.; Lu, J.; Amine, K. UChicago Argonne LLC, 2021. Rechargeable Lithium-Hydroxide Based Non-Aqueous Lithium Oxygen Batteries. U.S. Patent Application 16/545,127.
9. Lu, J.; Amine, K.; Guo, YY; Zeng, XQ; Bi, XX. UChicago Argonne LLC, 2021. Cathode for alkaline earth air batteries. US Patent App. 16/856,302.

XVIII.3 Lithium Oxygen Battery Design and Predictions (ANL)

Larry A. Curtiss, Principal Investigator

Argonne National Laboratory
9700 South Cass Avenue
Lemont, IL 60439
E-mail: amine@anl.gov

Amin Salehi, Principal Investigator

University of Illinois at Chicago
Department of Mechanical and Industrial Engineering
842 West Taylor Street
Chicago, IL 60607
E-mail: salehikh@uic.edu

Anh Ngo, Principal Investigator

Argonne National Laboratory
9700 South Cass Avenue
Lemont, IL 60516
E-mail: curtiss@anl.gov

Tien Q. Duong, DOE Technology Development Manager

U.S. Department of Energy
E-mail: Tien.Duong@ee.doe.gov

Start Date: October 1, 2019	End Date: September 30, 2022	
Project Funding (FY21): \$1,550,000	DOE share: \$1,550,000	Non-DOE share: \$0

Project Introduction

Lithium (Li)-oxygen (O₂) batteries are considered as a potential alternative to Li-ion batteries for transportation applications due to their high theoretical specific energy. The high energy density of Li-O₂ batteries is made possible because of the formation of the Li₂O₂ product, which can store significantly higher amounts of energy compared to other energy storage systems because of the Li-O bonds. However, the challenge is that the decomposition of Li₂O₂ during the charge process requires charge transfer, which is difficult because of the large band gap of solid Li₂O₂ likely covering catalytic sites. This leads to a sluggish charge process requiring higher potentials for Li₂O₂ decomposition, which in turn reduces the energy efficiency of the battery and puts the electrolyte at risk of degradation. Additionally, the charge potential can depend on the morphology and size of Li₂O₂ product. The major issues with the existing Li-O₂ systems include degradation of the anode electrode, reactions with air components, clogging of the cathode, and electrolyte instability. These issues are being addressed in this project.

Objectives

The objective of this work is to develop new materials for Li-O₂ batteries that give longer cycle life and improved efficiencies in an air environment as well as high charge rates. New electrolytes blends and additives are being investigated that can reduce clogging and at the same time can promote the cathode functionality needed to reduce charge overpotentials and increase discharge/charge rates. The cathode materials are based on two-dimensional transition metal dichalcogenides (TMDCs) that we have found to be among the best oxygen reduction and evolution catalysts. New high entropy alloys are also being investigated. The objective is to design and predict new electrolytes that work with these catalysts to give longer cycle life, high charge rates, good efficiencies, and high capacities needed to make scale up possible for these types of batteries.

Approach

The experimental strategy is to use new cathode materials based on 2-dimensional transition metal dichalcogenides (TMDCs) and high entropy alloys that are among the best oxygen reduction and evolution catalysts. These cathode materials will be combined with new electrolyte blends and additives that can work in synergy to reduce charge potentials and increase the stability of the Li-air system. Density functional theory and ab initio molecular dynamics simulations are used to gain insight at the electronic structure level of theory of the electrolyte structure and function both in the bulk and at interfaces with the cathode, anode, and discharge product. Classical molecular dynamics are used to obtain understanding at longer length and time scales of processes occurring in the electrolyte and growth mechanisms of discharge products. Computations play a key role in the design and predictions of new electrolytes as well as characterization for understanding.

Results

Conductive copper tetrahydroxyquinone (Cu-THQ) metal organic framework as a catalyst

Metal organic frameworks have been investigated for Li-O₂ batteries, but all studies have used added carbons for conductivity. We have investigated the effect of adding conductivity directly to the metal organic framework (MOF) instead of combining the MOFs with carbons to make them conductive. This has the advantage of providing active sites situated within the pores as opposed to being located away from the pores in the carbon part of the composite. MOFs have been used in Li-O₂ batteries because of their high surface area. Including conductivity in the framework has enabled us to achieve high charge rates for extended cycles and low charge potentials.

A bulk conductive copper tetrahydroxyquinone (Cu-THQ) MOF with an electrical conductivity of $\sim 1.5 \times 10^{-7}$ S cm⁻¹ was exfoliated into 2D nanoflakes via a liquid-phase exfoliation technique. This prepared Cu-THQ cathode was used in combination with an electrolyte combination comprised of a lithium nitrate (LiNO₃) salt and a bifunctional indium bromide (InBr₃) redox mediator (RM) in tetraethylene glycol dimethyl ether (TEGDME) solvent. To evaluate the battery performance of this system, a constant current density of 1 A/g was applied within a potential range of 2.5-4.0 V vs. Li/Li⁺ under two limiting capacities of 1000 mAh/g and 2000 mAh/g. Figure XVIII.3.1 (left) shows the obtained charge-discharge profiles for the battery with the increased capacity of 2000 mAh/g and current density of 1 A/g. A potential gap of 0.92 V was observed at the first cycle which remained stable, with only a slight increase reaching 1.0 V at the end of cycling. Figure XVIII.3.1 (right) shows the results obtained under 2000 mAh/g limiting capacity and doubled current density of 2 A/g. The battery operates for 100 cycles before reaching the discharge cut-off potential. Under this condition, the potential gap increased from 1 V at the 1st cycle to 1.31 V at the 100th cycle. Considering the significantly high current density rates and extended capacity values, the charge profile remains stable throughout the cycling of these batteries with a low potential of <3.69 V. In addition, our results show an efficient battery operation with a low charge potential of 3.64 V and an extended lifetime of 300 cycles with the capacity of 1000 mAh/g, under the current density of 1 A/g (not shown).

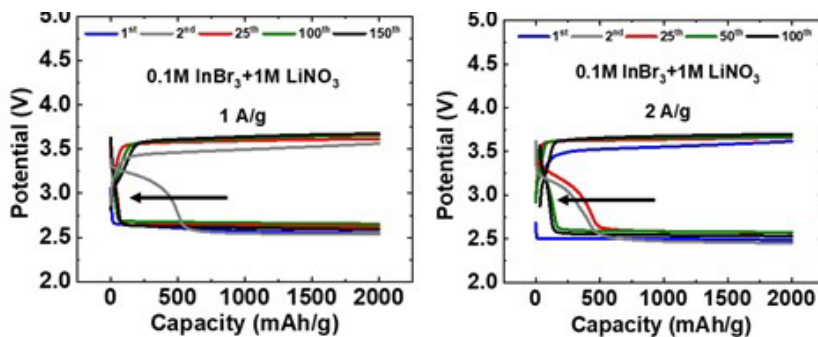


Figure XVIII.3.1 Li-O₂ battery voltage profiles for cathode based on Cu-THQ MOF with current densities of 1 A/g (left) and 2 A/g (right)

In summary, we have found that the conductive MOF and the InBr_3 RM produces conductive amorphous Li_2O_2 rather than insulator crystalline structure that facilitates the growth and decomposition of discharge products. Our results show an efficient battery operation with a low charge potential of 3.64 V and an extended lifetime of 300 cycles with the capacity of 1000 mAh/g, under the current density of 1 A/g. Furthermore, this system exhibits a very stable and reduced charge potential of ≤ 3.69 V and cycle life of 150 and 100 with the specific capacity of 2000 mAh/g and current density values of 1 A/g and 2 A/g, respectively. The performance of this Li-O₂ battery with a conductive MOF framework is much improved over previous studies that used MOF composites with carbons added to provide a conductivity to the cathode.

Binary transition metal dichalcogenide alloy catalyst

In other work we have used a new binary transition metal dichalcogenide (TMDC) alloy, $\text{Nb}_{0.5}\text{Ta}_{0.5}\text{S}_2$, that we have synthesized as a cathode to improve charge/discharge rates. We used this TMDC alloy because it has a work function (3.8 eV) much lower than most noble metals (e.g., 5.4 eV for Au nano particles) as well as MoS_2 (4.5 eV) that we previously have used. Due to its low work function, effective electron transfer between the $\text{Nb}_{0.5}\text{Ta}_{0.5}\text{S}_2$ metal edge and O_2 facilitates both oxygen reduction and evolution reactions (ORR and OER) occurring during discharge and charge processes. This material also shows excellent structural stability when operated at high current densities. The $\text{Nb}_{0.5}\text{Ta}_{0.5}\text{S}_2$ alloy was synthesized with the desired stoichiometry of $x=0.5$ through a chemical vapor transport (CVT) method followed by a liquid phase exfoliation technique to produce nanoflakes with an average size of ~ 220 nm.

The $\text{Nb}_{0.5}\text{Ta}_{0.5}\text{S}_2$ cathode was used with an electrolyte based on a 9:1 ratio of DMSO/IL solvents with three salts (LiCl , LiClO_4 , and KMnO_4) in the Li-O₂ cell with dry air. Figure XVIII.3.2a-b show the discharge and charge profiles of the battery operating in a dry air environment tested up to 250 and 100 cycles, with the cut-off potential of 2.5V-4.5V and the current density of 0.1 (1000 mA/g) and 0.5 mAcm^{-2} (5000 mA/g), respectively. The discharge plateaus are stable without any evidence of capacity loss of Li_2O_2 . At 0.5 mAcm^{-2} and 5000 mAhg^{-1} specific capacity the battery did not fail until 130 cycles before a sudden drop in the discharge potential was observed. Figure XVIII.3.2c demonstrates the battery results with the current density of 1 mAcm^{-2} (5000 mA/g) and a specific capacity of 10,000 mAhg^{-1} that ran up to 34 cycles.

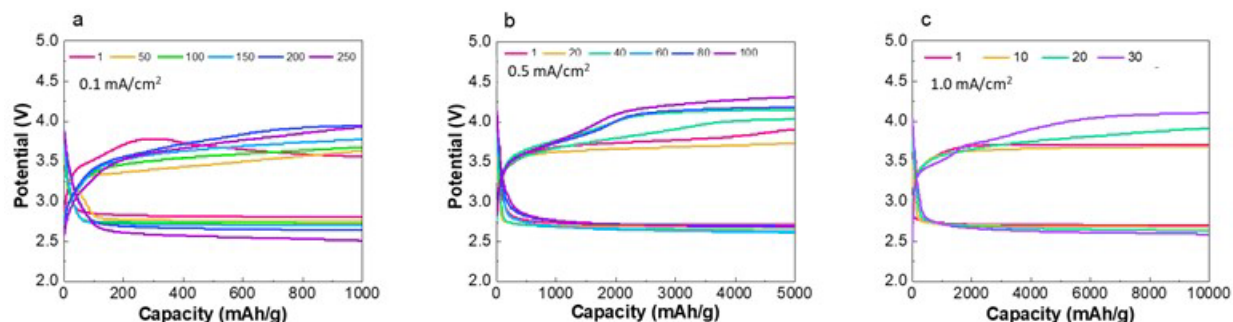


Figure XVIII.3.2 Discharge-Charge voltage profile of Li-O₂ battery with $\text{Nb}_{0.5}\text{Ta}_{0.5}\text{S}_2$ as the cathode catalyst (a-c) current density of 0.1, 0.5 and 1 mAcm^{-2} , respectively.

In summary, we have provided evidence that fast charge and discharge rates are possible in Li-O₂ batteries using a new binary transition metal dichalcogenide alloy, $\text{Nb}_{0.5}\text{Ta}_{0.5}\text{S}_2$, for the cathode. We used this TMDC alloy because it has a work function (3.8 eV) much lower than most noble metals (e.g., 5.4 eV for Au nano particles) as well as MoS_2 (4.5 eV) that we previously have used. Due to its low work function, effective electron transfer between the $\text{Nb}_{0.5}\text{Ta}_{0.5}\text{S}_2$ metal edge and O_2 facilitates both oxygen reduction and evolution reactions (ORR and OER) occurring during discharge and charge processes.

New redox mediator

We investigated the use of a new redox mediator for use in conjunction with the $\text{Nb}_{0.5}\text{Ta}_{0.5}\text{S}_2$ catalyst. The new redox mediator is KMnO_4 in a DMSO/IL electrolyte with the ionic liquid (IL) being 1-ethyl-3-

methylimidazolium tetrafluoroborate (EMIM-BF₄). During the electrolyte preparation, there is a reaction between KMnO₄ and DMSO resulted in the formation of colloidal MnO₂ particles and K₂MnO₄ with some remaining unreacted KMnO₄ in the resulting electrolyte. The manganate anion, MnO₄²⁻ has an oxidation potential of ~3.5 V (vs Li/Li⁺) and, thus, can serve as a redox mediator with the resulting permanganate anion, MnO₄⁻ serving as an oxidizer for the decomposition of the solid lithium peroxide.

This process results in the decomposition of the Li₂O₂ and release of O₂. The feasibility of the first step of the decomposition reaction has been studied by ab initio molecular dynamics (AIMD) simulations where the KMnO₄ extracts a Li from Li₂O₂ as shown in Figure XVIII.3.3. The results of the simulation indicate that the Li migrates from the Li₂O₂ surface without any barrier in the presence of KMnO₄. The final state has an energy lower than the initial state by 1.4 eV. In a previous similar study for the redox mediator of LiI, the LiI₃ has a barrier of ~0.5 eV for the first step in the decomposition of Li₂O₂. In that case, the oxidizer reaction is LiI₃ + Li₂O₂ → 3LiI + O₂. In addition, we have carried out DFT calculations based on cluster representations of Li₂O₂. In those calculations the thermodynamics for the reaction of KMnO₄ (or LiMnO₄) to decompose Li₂O₂ clusters are very favorable energetically, in agreement with the AIMD calculations.

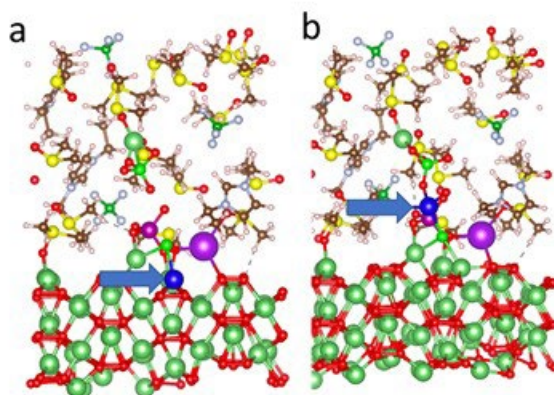


Figure XVIII.3.3 (a) DFT simulation of DMSO/IL electrolyte on a Li₂O₂ surface with KMnO₄ shows Li (blue) initially located at interface Li₂O₂; (b) after optimization the Li ion migrates from Li₂O₂ surface to electrolyte without any barrier and the final structure has an energy lower than the initial state by 1.4 eV.

The redox mediator property of the KMnO₄ additive is evident from a comparison of experimental results with an electrolyte with no KMnO₄ additive. For example, the charge potential for a cell with the KMnO₄ electrolyte at 0.1 mA.cm⁻² (1000 mAh.cm⁻² capacity) is 3.55 V (at the end of the 20th cycle) compared to 4.25 V for a cell with a LiTFSI salt as shown in Figure XVIII.3.2 under the same conditions. The KMnO₄ electrolyte has a similar charge potential as one with an LiI additive, a well-studied redox mediator, (3.55 V vs 3.50 at 0.1 mA.cm⁻² after 20 cycles and 3.75 V vs 3.85 V at 0.5 mA.cm⁻² after 20 cycles). When the cell is run with the KMnO₄ redox mediator at the higher rates of 0.5 and 1 mA.cm⁻² and higher capacities a second plateau at a higher voltage starts appearing at 20-40 cycles, which also appears for the LiI cell, but at less cycles. It is not clear what causes the second plateau, but a different mechanism may govern the charge process.

Anode protection

The chemical reaction of KMnO₄ with DMSO also results in a protective coating on the Li anode that enables a long cycle life for the battery. We investigated properties of the LiMnO_x coating formed on the Li anode from the electrolyte. The long-term performance of the Li anode was studied with a Li|Li symmetrical cell using electrolytes with and without the colloidal MnO₂ electrolyte at two different fixed capacities of 0.5 and 1 mA.h.cm⁻² and current densities of 0.5 and 1 mA.cm⁻², respectively. Results indicate stable and long cycling performance (~1400 hours) with low overpotentials, 25mV and 50mV for 0.5 mA.cm⁻² and 1 mA.cm⁻², respectively. The cells without the protective coating fail at a relatively early stage <200 hours with high overpotentials (150mV and 200mV) for 0.5 mA.cm⁻² and 1 mA.cm⁻², respectively. The conductivity of the SEI

(accounting for two SEI layers in the symmetric Li|Li cells) was found to be $0.814 \pm 0.001 \times 10^{-3}$ S/cm, with activation energy of 0.65 ± 0.04 eV. The rate capability of symmetrical Li|Li cells at different current densities of $0.1 \text{ mA}\cdot\text{cm}^{-2}$ to $5 \text{ mA}\cdot\text{cm}^{-2}$ was investigated. The overpotential for 3 and $5 \text{ mA}\cdot\text{cm}^{-2}$ is 161mV and 220mV, respectively.

We also investigated the reaction of a lithium surface with MnO_2 . To understand the chemistry and interactions between the MnO_2 and Li we have performed an AIMD simulation of an $\alpha\text{-MnO}_2/\text{Li}$ interface. This AIMD simulation reveals mixing between Li and MnO_2 , as shown in Figure XVIII.3.4. The radial distribution function for the Li-Mn and Li-O bonds reveals the formation of these bonds in the interface region. Similarly, the coordination numbers of the Li with respect to Mn and O show about a factor of 2 between the number of Li-Mn and Li-O bonds near the interface (up to 3 Å of radius) suggesting that the composition of the interface is more likely to be composed of LiMnO_2 similar to experiment. Additionally, the number of atoms near the interface region (within 2 Å) gives a $\sim 1:1:2$ ratio for the Li:Mn:O. We have also studied the dynamics of this interface by calculating the mean square displacement (MSD) of each species as well as their corresponding diffusion coefficients (D). The simulation reveals that the diffusion coefficient of Mn and O atoms are similar within this system with values of $1.35 \times 10^{-5} \text{ cm}^2\cdot\text{s}^{-1}$ and $1.27 \times 10^{-5} \text{ cm}^2\cdot\text{s}^{-1}$, respectively, while Li has a D value of $3.45 \times 10^{-5} \text{ cm}^2\cdot\text{s}^{-1}$. This suggests that there will be favorable Li transport within the MnO_2 layer consistent with the findings of the excellent rate-capability of symmetrical Li|Li cell.

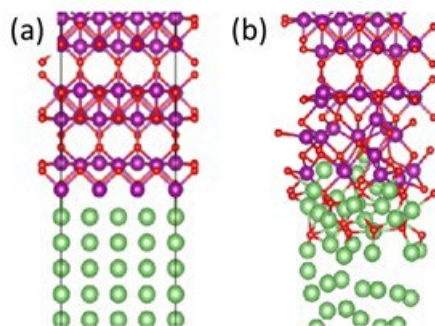


Figure XVIII.3.4 Density functional calculations of an Li interface with MnO_2 : (a) initial structure of $\alpha\text{-MnO}_2/\text{Li}$ interface, (b) final structure of the $\alpha\text{-MnO}_2/\text{Li}$ interface showing LiMnO_x interlayer. The purple, red and green spheres represent the Mn, O and Li atoms, respectively.

Conclusions

Two promising Li-O₂ batteries with new materials were developed and reported on. The first is based on a conductive MOF and a InBr_3 redox mediator. It produces conductive amorphous Li_2O_2 as a discharge product rather than an insulator crystalline structure. This facilitates the growth and decomposition of discharge products. Our results show an efficient battery operation with a low charge potential of 3.64 V and an extended lifetime of 300 cycles with the capacity of 1000 mAh/g, under the current density of 1 A/g. The performance of this Li-O₂ battery with a conductive MOF framework is much improved over previous studies that used MOF composites with carbons added to provide a conductivity to the cathode. The second battery system is based on a new alloy catalyst and a new electrolyte. In this work, fast charge and discharge rates are found to be possible in Li-O₂ batteries using a new binary transition metal dichalcogenide alloy, $\text{Nb}_{0.5}\text{Ta}_{0.5}\text{S}_2$, for the cathode. Due to its low work function, effective electron transfer between the $\text{Nb}_{0.5}\text{Ta}_{0.5}\text{S}_2$ metal edge and O₂ facilitates both oxygen reduction and evolution reactions occurring during discharge and charge processes. The new electrolyte used in this system based on a KMnO_4 additive provides a new class of redox mediators and a new protective coating for the lithium anode. Both functions add to the improved performance of the battery.

Key Publications

1. “Lowering Charge Potentials with Negligible Capacity Loss in High-Rate Lithium Oxygen Batteries,” Alireza Ahmadiparidari, Shadi Fuladi, Leily Majidi, Samuel Plunkett, Erik Sarnello, Zahra Hemmat,

Sina Rastegar, Saurabh Misal, Paul C Redfern, Jianguo Wen, Tao Li, Anh T. Ngo, Fatemeh Khalili-Araghi, Larry A. Curtiss, Amin Salehi-Kojin, *Journal of Power Sources*, **491**, 229506 (2021).

2. “A Lithium-Oxygen Battery that Operates in Dry Air with a Bifunctional InX_3 (X=Br,I) Electrolyte Additive,” Sina Rastegar, Zahra Hemmat, Chengji Zhang, Samuel Plunkett, J. G. Wen, Naveen Dandu, Tomas Rojas, Leily Majidi, Saurabh Misal, Anh T. Ngo, Larry A. Curtiss, Amin Salehi-Khojin, *ACS Applied Materials and Interfaces*, **13 (4)**, 4915–4922 (2021).
3. “High Performance Air Breathing Flexible Lithium–Air Battery,” Ahmad Jaradat, Chengji Zhang, Sachin Kumar, Singh, Junaid, Ahmed, Alireza, Ahmadiparidari, Leily Majidi, Sina Rastegar, Zahra Hemmat, Shuxi Wang, Anh T. Ngo, Larry A. Curtiss, Matthew Daly, Arunkumar Subramanian, Amin Salehi-Khojin, *Small*, **17(42)** 2102072 (2021).

XIX Beyond Li-ion R&D: Sodium-Ion Batteries

XIX.1 An Exploratory Studies of Novel Sodium-Ion Battery Systems (BNL)

Xiao-Qing Yang, Principal Investigator

Chemistry division, Brookhaven National laboratory
Bldg. 555, Brookhaven National Laboratory
Upton, NY 11973
E-mail: xyang@bnl.gov

Enyuan Hu, Principal Investigator

Chemistry division, Brookhaven National laboratory
Bldg. 555, Brookhaven National Laboratory
Upton, NY 11973
E-mail: enhu@bnl.gov

Tien Q. Duong, DOE Technology Development Manager

U.S. Department of Energy
E-mail: Tien.Duong@ee.doe.gov

Start Date: October 1, 2020

End Date: September 30, 2021

Project Funding: \$320,000

DOE share: \$320,000

Non-DOE share: \$0

Project Introduction

The next generation of rechargeable battery systems with higher energy and power density, lower cost, better safety characteristics, and longer calendar and cycle life need to be developed to meet the challenges to power electrified vehicles in the future. Na-ion battery systems have attracted more and more attention due to the more abundant and less expensive nature of Na resources. However, building a sodium battery requires redesigning battery technology to accommodate the chemical reactivity and larger size of sodium cations. Since Na-ion battery research is an emerging technology, new materials to enable Na electrochemistry and the discovery of new redox couples and the related diagnostic studies of these new materials and redox couples are quite important. This project uses the synchrotron based in situ x-ray diagnostic tools developed at BNL to evaluate the new materials and redox couples, to explore in-depth fundamental understanding of the reaction mechanisms aiming to improve the performance of these materials and provide guidance for new material developments. This project also focuses on developing advanced diagnostic characterization techniques for these studies. The synchrotron based in situ X-ray techniques (x-ray diffraction, x-ray pair distribution function, or PDF, and x-ray absorption XAS) will be combined with other imaging and spectroscopic tools such as transmission electron microscopy (TEM), scanning transmission electron microscopy (STEM), mass spectroscopy (MS), transmission x-ray microscopy (TXM), as well as neutron diffraction (ND) and neutron PDF (NPDF). In FY2019, this BNL team has performed several successful experimental studies at various beamlines of National Synchrotron Light Source II (NSLSII) such as (HXN) beamline, x-ray Powder diffraction (XPD), and ISS beamlines. By collaborating with Dr Huoling Xin, this team also has carried out studies using the 3d TEM tomography and STEM, EELS on the new cathode materials for Na-ion batteries. The BNL team has been closely working with top scientists on new material synthesis at ANL, LBNL, SLAC, and PNNL, with U.S. industrial collaborators.

Objectives

The primary objective of this project is to develop new advanced in situ material characterization techniques and to apply these techniques to support the development of new cathode, anode, and electrolyte materials with high energy and power density, low cost, good abuse tolerance, and long calendar and cycle life for the next

generation of Sodium-ion batteries (SIBs) to power plug-in hybrid electric vehicles (PHEV) and electric vehicles (EV). The diagnostic studies have been focused on issues relating to capacity retention, thermal stability; cycle life and rate capability of advanced Na-ion and beyond Li-ion batteries

Approach

- This project has used the synchrotron based in situ x-ray diagnostic tools developed at BNL to evaluate the new materials and redox couples to enable a fundamental understanding of the mechanisms governing the performance of these materials and provide guidance for new material and new technology development regarding Na-ion battery systems. These techniques include:
- Using nano-probe beamline at NSLSII to study the elemental distribution of new solid electrolyte materials for Na-ion batteries
- Using transmission x-ray microscopy (TXM) to do multi-dimensional mapping of cathode materials of Na-ion batteries
- Using A combination of time resolved X-ray diffraction (TR-XRD) and mass spectroscopy (MS), together with in situ soft and hard X-ray absorption (XAS) during heating to study the thermal stability of the cathode materials for Na-ion batteries
- Design and carry out three-dimensional (3D) STEM tomography experiments to study new cathode materials for Na-ion batteries at pristine state and after multiple cycling.

Results

In FY2021, BNL has been focused on the development of new diagnostic techniques to study and improve the performance of sodium-ion batteries. These techniques have been applied to the study two new P2 types layered cathode materials for sodium-ion batteries: $\text{Na}_{0.67}[\text{Mn}_{0.66}\text{Ni}_{0.33}]\text{O}_2$ (MN) and Sb-substituted MN, $\text{Na}_{0.67}[\text{Mn}_{0.61}\text{Ni}_{0.28}\text{Sb}_{0.11}]\text{O}_2$ (MNS). In order to verify the element and valence distribution in MNS, transmission X-ray microscopy (TXM) combined with XANES spectroscopy was collected by using synchrotron-based imaging techniques. The two-dimensional (2D) XANES mapping for the oxidation states of Mn and Ni are shown in Figure XIX.1.1c and Figure XIX.1.1d respectively using the energy levels (color coded) near their K-edges. The results were collected at the same region of the sample by scanning the energies across the Mn K-edge (6539 eV) and Ni K-edge (8333 eV) separately in sequence. Figure XIX.1.1d shows the uniform spatial distribution of Ni^{2+} , but Mn has slightly lower valence state than Mn^{4+} in Figure XIX.1.1c. The 2D XANES obtained from TXM shows that $\text{Mn}^{3.7+}$ and Ni^{2+} are uniformly distributed throughout the bulk of pristine MNS sample with little variation of Mn. The magnitudes of the Fourier transformed extended X-ray absorption fine structure (FT-EXAFS) spectra and their least square fit are shown in Figure XIX.1.1e, and Figure XIX.1.1f, reflecting the local environment around Mn and Ni in MNS and MN. The first peak at $R=1.5\text{-}1.6\text{ \AA}$ in Figure XIX.1.1e and 1f represents the formation of six coordination in the nearest MnO_6 and NiO_6 octahedra, respectively. The Mn-TM₆ and Ni-TM₆ hexagon contribute to the second peaks around 2.6 \AA on *a-b* plane in the second coordination shell respectively. It should be noted that the FT-EXAFS spectra are not phase corrected, and the bond length shown in Figure XIX.1.1e and Figure XIX.1.1f are about $0.3\text{-}0.4\text{ \AA}$ shorter than the actual bond lengths.

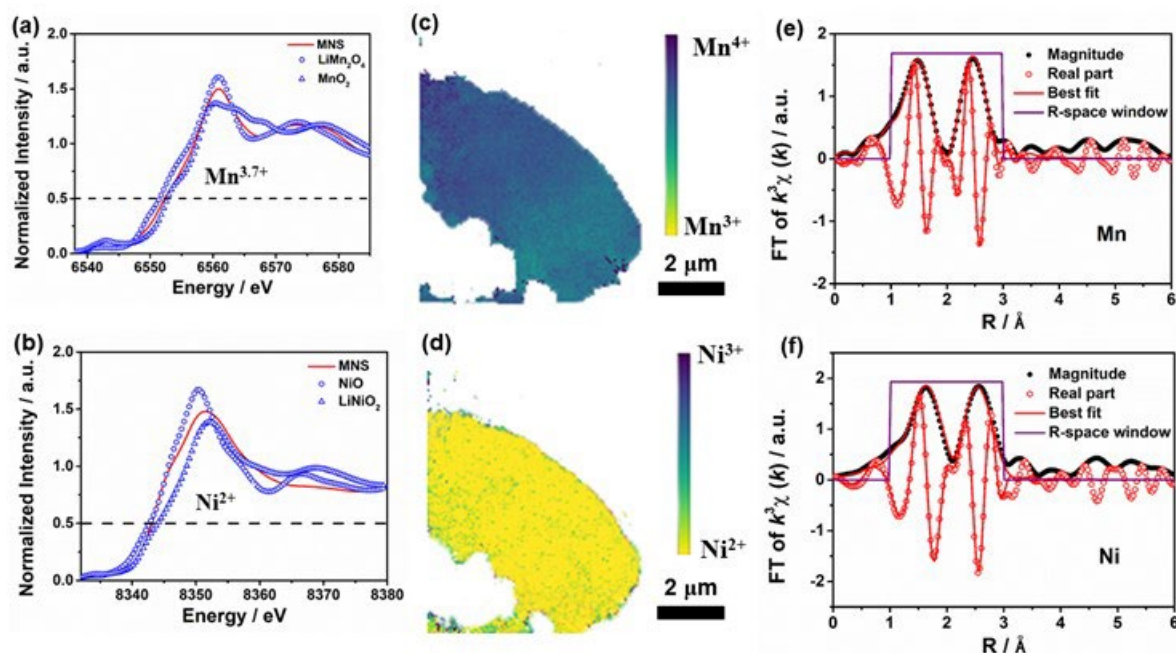


Figure XIX.1.1 XANES spectra of the a) Mn and b) Ni K-edges of pristine MNS and standard metal oxide references. The two-dimensional (2D) XANES mapping of c) Mn and d) Ni in MNS. The least-square fits of the calculated FT-EXAFS phase and amplitude functions to the experimental EXAFS spectra for Mn e) and Ni f) in MNS.

The new diagnostic techniques developed at BNL have been applied to the study of a new P2 types layered cathode material for sodium-ion battery: Sb-substituted MN, $\text{Na}_{0.67}[\text{Mn}_{0.61}\text{Ni}_{0.28}\text{Sb}_{0.11}]\text{O}_2$ (MNS). Figure XIX.1.2a to Figure XIX.1.2f show the XANES evolutions for the K-edge of Mn and Ni in MNS during the first charge, first discharge and second charge, respectively, while Figure XIX.1.2g and Figure XIX.1.2h present the change of the edge energy. The charge compensation of MNS during cycling is summarized in Figure XIX.1.2i. Mn and Ni ions in MNS dominate different voltage regions for charge compensation. In the first charge process, the specific capacity of 99 mAh g^{-1} is mainly contributed by $\text{Ni}^{2+}/\text{Ni}^{3+}$ and $\text{Mn}^{3.7+}/\text{Mn}^{4+}$. During discharge, Ni ions are reduced in the voltage from 4.2 to 2.3 V. Afterwards, Mn ions are reduced in the voltage range from 2.3 V to 1.8 V. Correspondingly, a total number of 0.58 Na^+ per MNS are intercalated during discharge process, accompanying with Mn and Ni redox reactions. In the second charge process, the valence states of Mn and Ni undergo reversed changes to the first discharge process, suggesting a highly reversible valence state changes of Mn and Ni in MNS.

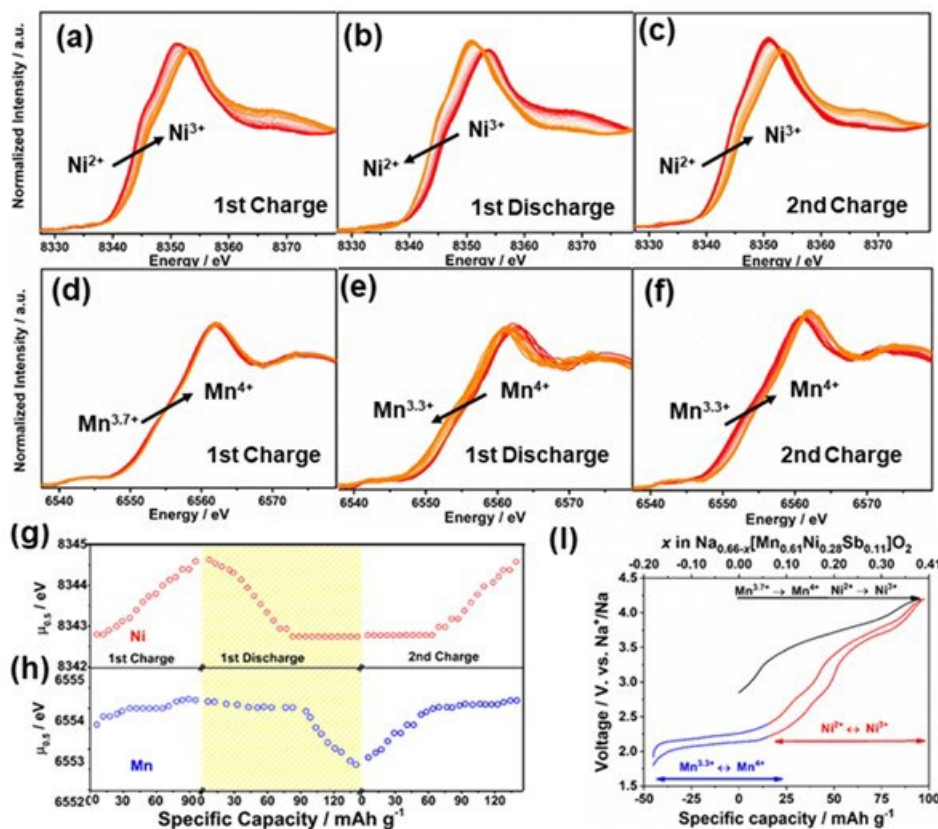


Figure XIX.1.2 In situ XAS spectra for MNS. a-c) Ni and d-f) Mn K-edge XANES of MNS at various stages during the first charge/discharge and second charge processes, respectively. The edge energy evolution at half edge-step ($E_{0.5}$) for g) Ni and h) Mn in $\text{Na}_{0.67}[\text{Mn}_{0.61}\text{Ni}_{0.28}\text{Sb}_{0.11}]\text{O}_2$ at different states. i) Charge compensation of different elements contribution during charge and discharge.

Advanced diagnostic techniques developed by BNL has been successfully applied to the investigation and improvement of the new high-capacity and high-C rate multi-component sodium cathode materials NaMnFeCoNiO_2 (NMFCN). Figure XIX.1.1 shows the Ni K-edge 2D-X-ray near edge spectrum (XANES) mapping of the pristine material. Figure XIX.1.3a shows the thickness map of pristine particles. Figure XIX.1.3b and Figure XIX.1.3d show the component mapping Ni^{2+} and Ni^{3+} throughout the region of interest, which indicate that Ni predominantly exist as Ni^{3+} rather than Ni^{2+} in the pristine state. Figure XIX.1.3c shows the spectrum integrated from the whole field of view shown in Figure XIX.1.3a, which confirms that the averaged valence state of Ni is closer to Ni^{3+} . The 2D XANES result is consistent with the cyclic voltammetry (CV) test result shown in Figure XIX.1.3e, where no $\text{Ni}^{2+}/\text{Ni}^{3+}$ redox is observed in the first charging process.

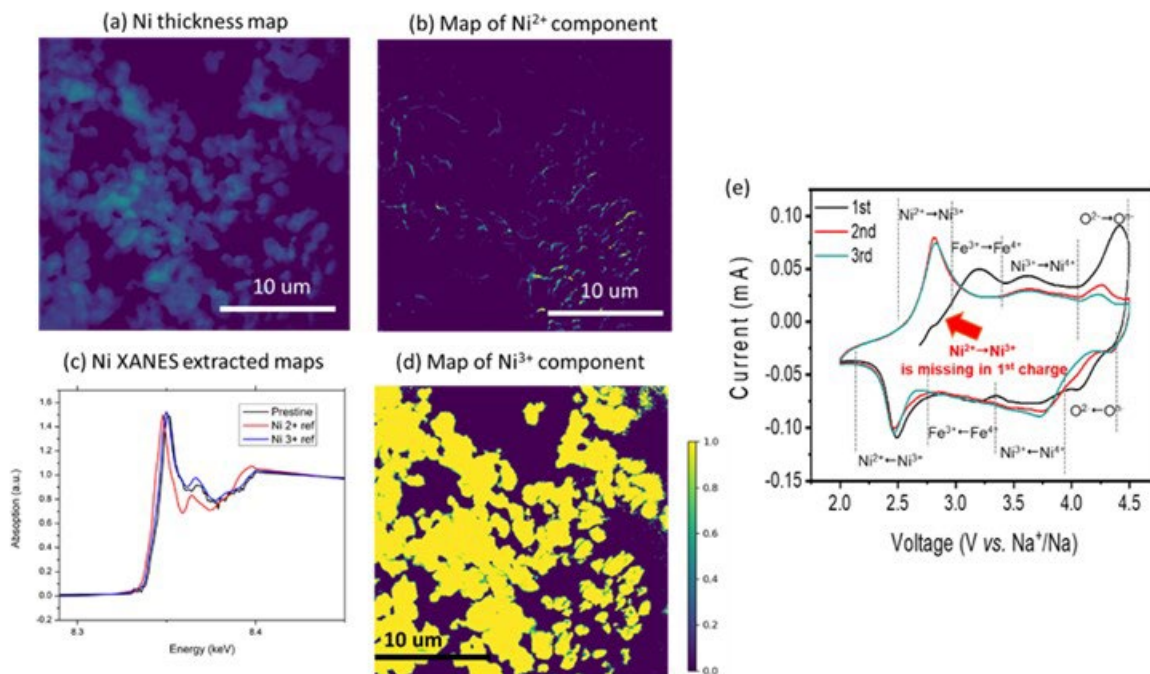


Figure XIX.1.3 2D-XANES mapping of pristine NaMnFeCoNiO₂ and cyclic voltammetry test. (a) Ni thickness map; (b) Ni²⁺ composition map; (c) Ni XANES integrated from the field of view in (a); (d) Ni³⁺ composition map; (e) CV test for the 1st, 2nd and 3rd electrochemical cycles.

Advanced diagnostic techniques developed by BNL has been successfully applied to the investigation and improvement of the new high-capacity and high-C rate multi-component sodium cathode materials P2-Na_xMg_{0.2}[Fe_{0.2}Mn_{0.6}□_{0.2}]O₂ (MFM-2). Figure XIX.1.4 shows the K-edge X-ray near edge spectrum (XANES) of Mn (a-c) and Fe (d-f) for MFM-2 at various charge/discharge states during the first cycle and second charging. During the first charge process, Mn K-edge continuously shifts to higher energy range toward MnO₂ reference, suggesting that the valence of Mn changes from the initial +3.8 to +4. Meanwhile, Fe K-edge also moves from the initial position to higher energy during the entire procedure, indicating Fe is oxidized from +3 to +3.5. Based on the valence change of Mn and Fe upon charging, the specific capacity contributed by the oxidation of Mn and Fe can be estimated to be 33.1 mAh g⁻¹ (Mn^{3.8+/4+}) and 27.6 mAh g⁻¹ (Fe^{3+/3.5+}), respectively. However, the total specific capacity in the initial charge up to 4.5 V is 124.1 mAh g⁻¹, which is much higher than the total contribution from Mn^{3.8+/4+} and Fe^{3+/3.5+}. Previous studies have revealed that oxygen could contribute to the charge compensation in Mn-based layered cathode materials, where oxygen ions were partially oxidized during charge in the high voltage region. Therefore, it is very possible that the extra capacity for MFM-2 cathode during charge comes from oxygen redox.

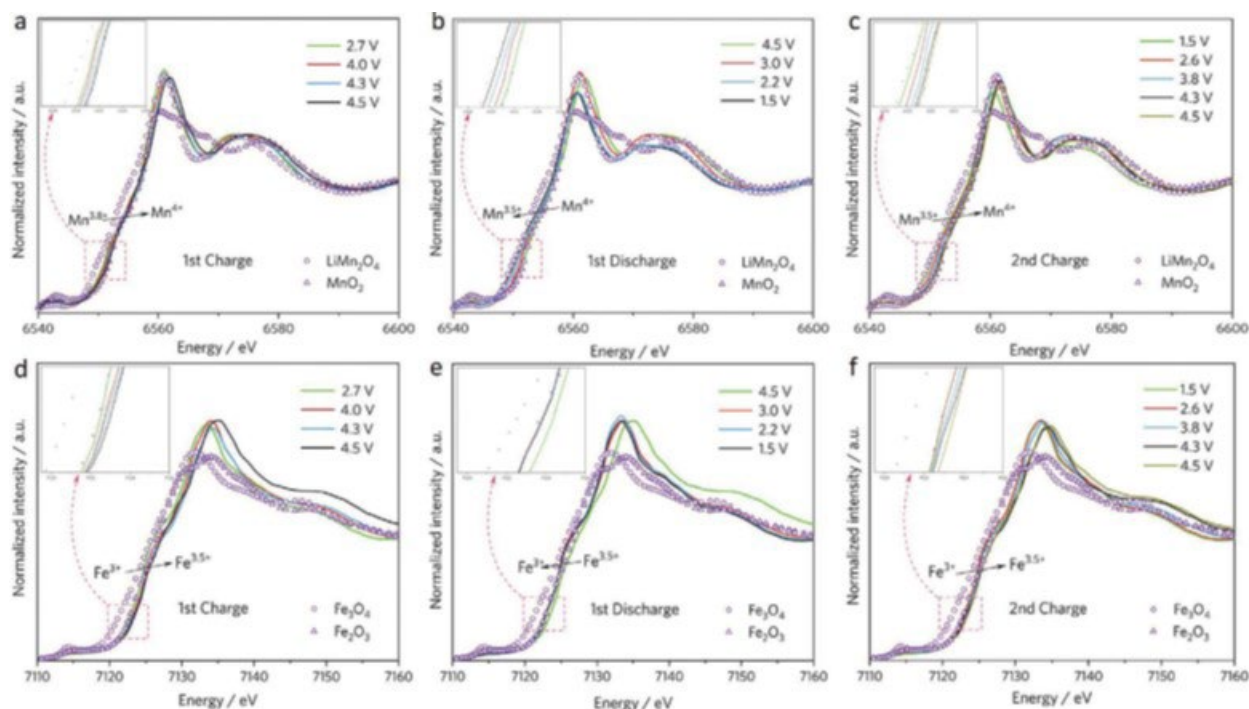


Figure XIX.1.4 The K-edge X-ray near edge spectrum (XANES) of Mn (a-c) and Fe (d-f) for P2-Na_xMg_{0.2}[Fe_{0.2}Mn_{0.6}□_{0.2}]O₂ (MFM-2) at various charge/discharge states during the first cycle and second charging.

Conclusions

This project, “Exploratory Studies of Novel Sodium-Ion Battery Systems (BNL)”, has been successfully completed in FY2021. All milestones have been completed. The publication records are very good. Extensive collaboration with other national Labs, US universities and international research institutions were well established.

Key Publications

Publications

1. Kang Ho Shin, Sul Ki Park, Puritut Nakhanevej, Yixian Wang, Pengcheng Liu, Seong-Min Bak, Min Sung Choi, David Mitlin, and Ho Seok Park, “Biomimetic composite architecture achieves ultrahigh rate capability and cycling life of sodium ion battery cathodes”, *Appl. Phys. Rev.* 7, 041410 (2020); DOI: ; 10.1063/5.0020805, Publication Date: December 08, 2020.
2. Biwei Xiao, Yichao Wang, Sha Tan, Miao Song, Xiang Li, Yuxin Zhang, Feng Lin, Kee Sung Han, Fredrick Omenya, Khalil Amine, Xiao-Qing Yang, David Reed, Yanyan Hu, Gui-Liang Xu, Enyuan Hu*, Xin Li*, Xiaolin Li*, “Vacancy-Enabled O3 Phase Stabilization for Manganese-rich Layered Sodium Cathodes”, *Angewandte Chemie*, DOI: 10.1002/anie.202016334, Publication Date (web): January 21, 2021
3. Cui, J.; Zheng, H.; Zhang, Z.; Hwang, S.; Yang, X.-Q.; He, K., “Origin of anomalous high-rate Na-ion electrochemistry in layered bismuth telluride anodes” *Matter* 2021. DOI:10.1016/j.matt.2021.01.005, Publication Date (web): February 1st, 2021.
4. Ding-Ren Shi, Tian Wang, Zulipiya Shadike, Lu Ma, Xiao-Qing Yang, Shu-Fen Chu, Zhi-Wei Zhao, Zhang-Quan Peng and Zheng-Wen Fu *, “Anionic redox reaction triggered by trivalent Al³⁺ in P3-Na_{0.65}Mn_{0.5}Al_{0.5}O₂”, *Chem. Commun.*, 2021, DOI: 10.1039/D1CC00373A, Publication Date (web): February 17, 2021.

5. Qin-Chao Wang,* Zulipiya Shadike, Xun-Lu Li, Jian Bao, Qi-Qi Qiu, Enyuan Hu, Seong-Min Bak, Xianghui Xiao, Lu Ma, Xiao-Jing Wu, Xiao-Qing Yang* Yong-Ning Zhou*, “Tuning Sodium Occupancy Sites in P2-Layered Cathode Material for Enhancing Electrochemical Performance”, *Advanced Energy Materials*, 2021, DOI: 10.1002/aenm.202003455, Publication Date (web): February 24, 2021.
6. Xun-Lu Li, Tian Wang, Yifei Yuan, Xin-Yang Yue, Qin-Chao Wang, Jun-Yang Wang, Jun Zhong, Ruo-Qian Lin, Yuan Yao, Xiao-Jing Wu, Xi-Qian Yu, Zheng-Wen Fu, Yong-Yao Xia, Xiao-Qing Yang, Tongchao Liu, Khalil Amine, Zulipiya Shadike*, Yong-Ning Zhou,* and Jun Lu*, “Whole-Voltage-Range Oxygen Redox in P2-Layered Cathode Materials for Sodium-Ion Batteries”, *Advanced Materials*, 2021, DOI: 10.1002/adma.202008194, Publication Date (web): March 1st, 2021.
7. Xun-Lu Li, Jian Bao, Zulipiya Shadike, Qin-Chao Wang, Xiao-Qing Yang, Yong-Ning Zhou,* Dalin Sun,* and Fang Fang*, “Stabilizing Transition Metal Vacancy Induced Oxygen Redox by Co²⁺/Co³⁺ Redox and Sodium-Site Doping for Layered Cathode Materials”, *Angew. Chem. Int. Ed.* 2021, DOI: 10.1002/anie.202108933, Publication date: August 10, 2021.

Presentations

1. Enyuan Hu, “Oxygen redox in P3 Cu-based sodium battery cathode”, presented at 2021 Virtual MRS Spring Meeting and Exhibit, April 17–23, 2021. Invited
2. Zulipiya Shadike, Tian Wang, Ding-Ren Shi, Enyuan Hu, Zheng-Wen Fu and Xiao-Qing Yang*, “Anionic Redox Chemistry in Layered Chalcogenide Cathode Materials for Sodium Batteries”, presented at 2021 Virtual MRS Spring Meeting and Exhibit, April 17–23, 2021. Invited

XIX.2 Development of Advanced High-energy and Long-life Sodium-Ion Battery (ANL)

Khalil Amine, Principal Investigator

Argonne National Laboratory
9700 South Cass Avenue
Lemont, IL 60439
E-mail: amine@anl.gov

Christopher S. Johnson, Principal Investigator

Argonne National Laboratory
9700 South Cass Avenue
Lemont, IL 60439
E-mail: cjohnson@anl.gov

Tien Q. Duong, DOE Technology Development Manager

U.S. Department of Energy
E-mail: Tien.Duong@ee.doe.gov

Start Date: January 1, 2019

End Date: September 30, 2021

Project Funding (FY21): \$700,000

DOE share: \$700,000

Non-DOE share: \$0

Project Introduction

Considering the natural abundance and low cost of sodium resources, sodium-ion batteries (SIBs) have received much attention for large-scale electrochemical energy storage. [1] However, the larger ionic radius of Na^+ (1.02 Å) than Li^+ (0.67 Å) brings more challenges on the development of good Na-host materials with optimal electrochemical properties. On one hand, despite most SIBs cathode materials are either imitating or duplicating from lithium analogues, there are significant differences in the intercalation chemistries between sodiation and lithiation. The layered oxides cathodes deliver very high energy density, but undergo more complex phase transition during charge/discharge, resulting in severe capacity fade during prolonged cycling. [2] On the other hand, the absence of suitable anode materials has obstructed progress in the development of SIBs. Two of the most promising anode materials, graphite and silicon have limited sodium storage capability. Hard carbon can demonstrate reversible sodiation/de-sodiation, but the capacity is lower than 300 mAh g⁻¹, significantly limited the energy density of SIBs. [3],[4] Alloying anode materials such as phosphorus can deliver high capacity, but suffer from huge volume changes and severe parasitic reactions with the electrolytes, resulting in rapid capacity degradation during long-term cycling. [5]

Via advanced diagnostic tools including synchrotron X-ray probes and computational modeling, the team led by Dr. Khalil Amine and Dr. Christopher S. Johnson at Argonne National Laboratory (ANL) is focusing on the development of rational cathode materials, anode materials and electrolytes to develop long life and high energy SIBs with low cost and high safety.

Objectives

The project objective is to develop high-energy SIBs with long life, low cost and high safety. The energy density target is 200 Wh kg⁻¹ and/or 500 Wh L⁻¹, wherein the anode capacity and cathode capacity targets are 600 mAhg⁻¹ and 200 mAhg⁻¹, respectively.

Approach

In a team approach, the Na-ion battery group will create a versatile Na-ion battery chemistry with beneficial advantages such as low cost, safety, recycling, and sustainability of materials used. The team will work in a synergistic way so that the final design is the culmination of advances in phosphorus carbon composites mated

with optimized lead or other highly dense metalloids, such as tin and/or antimony and derivatives thereof, for the recyclable anode. Synthesis and optimization of such blended composite anodes will be conducted in parallel to diagnostic characterization of structures, phase formation, and cycling stability. Cathode work will involve (1) gradient cathodes consisting of Fe-Mn compositions, and (2) intergrowths of layer stacking sequenced oxides. If resources allow, the team also will attempt to stabilize cathode surfaces using ALD methods, particularly for the benefit of staving off dissolution of manganese and iron/electrolyte reactivity.

Results

Development of high-performance and low-cost phosphorus anode by Sb doping

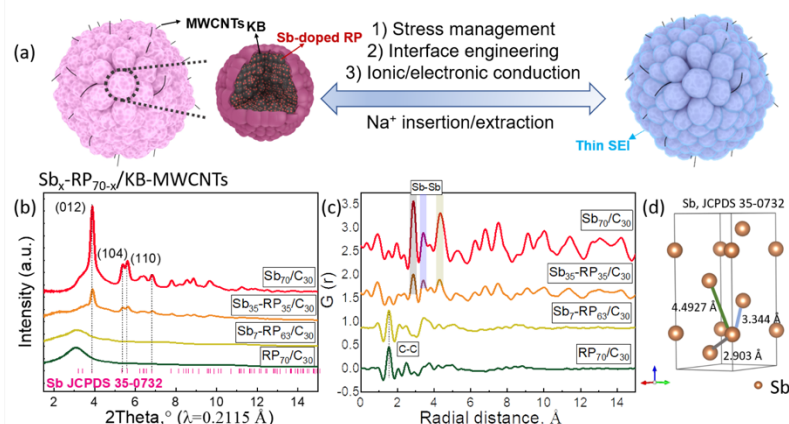


Figure XIX.2.1 (a) Schematic illustration of the structure of hierarchical micro/nanostructured $\text{Sb}_x\text{-RP}_{70-x}/\text{C}_{30}$ composite before and after cycling. (b) High-resolution XRD and (c) PDF data for $\text{Sb}_x\text{-RP}_{70-x}/\text{C}_{30}$ composite. (d) Crystal structure of standard Sb (JCPDS 35-0732) with interatomic Sb-Sb distance index.

Red phosphorus (RP) possesses a high theoretical specific capacity but suffers from large volume change, low electronic conductivity, and unstable solid-electrolyte interphase (SEI). In FY20, we have developed a hierarchical micro/nanostructure RP/Ketjenblack composite to achieve stable cycle life. In FY21, we further adopted Sb doping to improve the reversible capacity and rate performance. As shown in Figure XIX.2.1a, a series of $\text{Sb}_x\text{-RP}_{70-x}/\text{C}_{30}$ composites were synthesized using high-energy ball-milling (HEBM) process by tuning the weight ratio ($x=0, 7, 35$, and 70) between Sb and RP. X-ray diffraction (XRD) characterization (Figure XIX.2.1b) show that both $\text{RP}_{70}/\text{C}_{30}$ and $\text{Sb}_7\text{-RP}_{63}/\text{C}_{30}$ composites exhibit amorphous structures, indicating that both RP and $\text{Sb}_7\text{-RP}_{63}$ have very small particle sizes and are homogeneously distributed in the carbon matrix after HEBM. In contrast, the $\text{Sb}_{70}/\text{C}_{30}$ and $\text{Sb}_{35}\text{-RP}_{35}/\text{C}_{30}$ composites show obvious Sb diffraction peaks with slight peak broadening, indicating the formation of individual Sb nanocrystalline particles in the composites. Pair distribution function (PDF) was further conducted on the $\text{Sb}_x\text{-RP}_{70-x}/\text{C}_{30}$ composites. The results in Figure XIX.2.1c show that both $\text{Sb}_{70}/\text{C}_{30}$ and $\text{Sb}_{35}\text{-RP}_{35}/\text{C}_{30}$ present clear oscillations and characteristic PDF peaks at 2.9, 3.3, and 4.49 Å, matching well with the interatomic distance of the Sb-Sb bond as indexed in Figure XIX.2.1d. In contrast, the $\text{RP}_{70}/\text{C}_{30}$ and $\text{Sb}_7\text{-RP}_{63}/\text{C}_{30}$ only show oscillations in the low radial distance range (<6 Å), which confirms their amorphous structure and reveals that the coherent domain size of RP and Sb are both smaller than 6 Å. In the case of $\text{Sb}_7\text{-RP}_{63}/\text{C}_{30}$, not any interatomic distance of Sb-Sb pairs can be observed, which indicates that the Sb exists as an atomic-level dopant in the RP. In short, a low concentration of Sb could lead to formation of Sb-doped RP, while a high concentration of Sb would result in the formation of Sb/P mixtures.

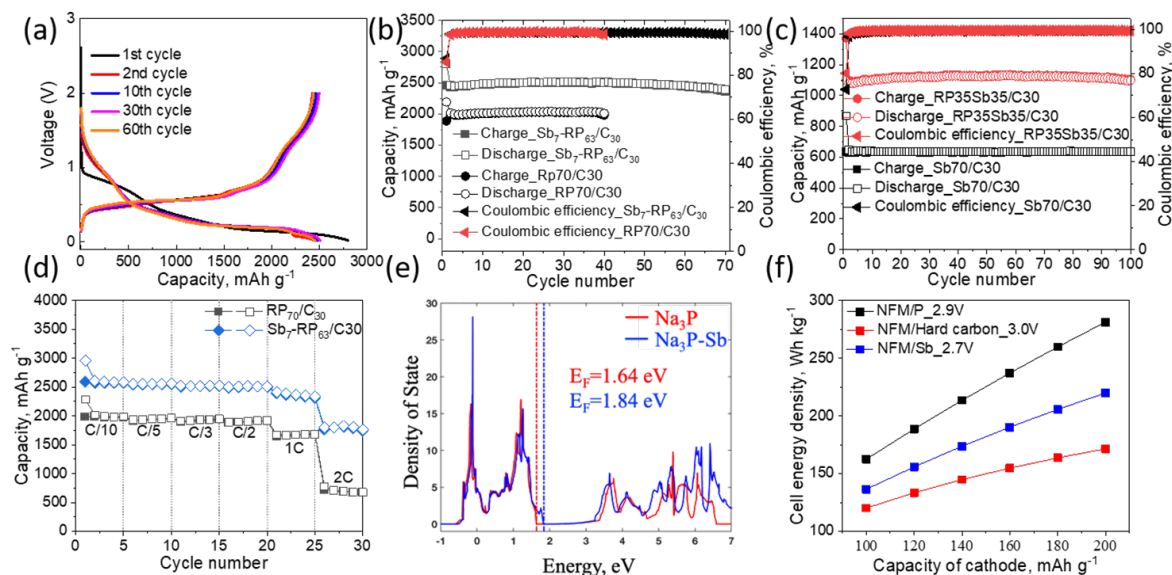


Figure XIX.2.2 (a) Charge/discharge curves of Sb₇-RP₆₃/C₃₀ anode at C/3. and (b) cycling performance of Sb₇-RP₆₃/C₃₀ anode at C/3 and RP₇₀/C₃₀ anode at C/10. (c) Cycling performance of Sb₃₅-RP₃₅/C₃₀ and Sb₇₀/C₃₀ anode at C/3. (d) Rate performance of Sb₇-RP₆₃/C₃₀ and RP₇₀/C₃₀ anode. Open and solid symbols represent discharge and charge capacities, respectively. (e) The density of states distribution of valence electrons for Na₃P and Sb-doped Na₃P. (f) Estimated cell energy density of sodium-ion batteries with different anode materials using BatPaC.

All the Sb_x-RP_{70-x}/C₃₀ composites demonstrated excellent cycle stability, while the concentration of Sb significantly affected their specific capacity, average working voltage and rate performance. Figure XIX.2.2a shows the voltage profiles of the Sb₇-RP₆₃/C₃₀ anode at C/3 within 0.02-2.0 V in the conventional carbonate-based electrolytes. Two sloping regions can be observed at about 1.0-0.5 V and below 0.5 V during the sodiation process, corresponding to the sodiation process from P to Na_xP and eventually Na₃P. In the desodiation process, the charge curves consist of a sloping region at 0.02-0.4 V and an inclined plateau at 0.4-1.0 V followed by a sloping region up to 2.0 V. The initial discharge and charge capacities of Sb₇-RP₆₃/C₃₀ at C/3 were measured to be 2801.3 and 2456.1 mAh g⁻¹, manifesting a high ICE of ~ 88% and an extremely high phosphorus utilization of 95%. The initial irreversible capacity loss (~12%) was mainly attributed to the decomposition of electrolytes to form the SEI on the surface of Sb₇-RP₆₃/C₃₀.

Sb₇-RP₆₃/C₃₀ demonstrates superior cycle stability (Figure XIX.2.2b), which can still maintain an ultrahigh reversible capacity of 2356.3 mAh g⁻¹ (i.e., 1650 mAh g⁻¹_{composite}) and a high capacity retention of 96% after 70 cycles. The areal P loading was controlled at around 0.6-0.8 mg cm⁻², resulting in an areal capacity loading up to ~ 2 mAh cm⁻². The tap density of Sb₇-RP₆₃/C₃₀ composite was measured to be ~0.7 cc g⁻¹, which thus leads to a high volumetric capacity of 1155 mAh cc⁻¹ (1650 mAh g⁻¹_{composite} × 0.7 cc g⁻¹) based on the mass of Sb₇-RP₆₃/C₃₀ composite (i.e., 1650 mAh cc⁻¹ Sb₇-RP₆₃).

As a comparison, the RP₇₀/C₃₀ without Sb doping also demonstrates a high ICE of 86% and good cycle stability within 40 cycles at C/10 (Figure XIX.2.2b). However, its reversible capacities (~2000 mAh g⁻¹) are lower than that of Sb₇-RP₆₃/C₃₀, which clearly illustrates that Sb doping can further boost the electronic transport of RP₇₀/C₃₀. As further shown in Figure XIX.2.2c, Sb₇₀/C₃₀ and Sb₃₅-RP₃₅/C₃₀ can also deliver a highly reversible capacity of ~ 632 and 1100 mAh g⁻¹ within 100 cycles at C/3, respectively. Despite the excellent cycle stability, increasing the content of Sb in the Sb_x-RP_{70-x}/C₃₀ lead to decreased specific energy compared to atomic-level Sb doping in Sb₇-RP₆₃/C₃₀. Thus, it is essential to improve the electrochemical performance of an RP-based anode by atomic-level Sb doping.

Among various phase structures in the sodium layered oxides cathodes, O3 phase represents the structure with highest Na content and could thus deliver higher specific capacity and bypass the Na deficient of P2 cathodes. However, its formation mechanism remains elusive. In FY21, we have used in situ high-energy X-ray diffraction (HEXRD) to probe the solid-state synthesis of O3 sodium layered oxide cathodes. Figure XIX.2.3a show the 2D contour plot of in situ HEXRD patterns during the formation process of O3 $\text{NaNi}_{0.4}\text{Mn}_{0.4}\text{Co}_{0.2}\text{O}_2$ as a control cathode. We decided that this control work will be used to compare trivalent Co with trivalent Fe

reactivity and its nature of Na intercalation. The ultimate goal is to create a Fe-Mn based layered oxide cathode with an O3 phase.

The Co-containing control starting material was a mixture of $\text{Ni}_{0.4}\text{Mn}_{0.4}\text{Co}_{0.2}(\text{OH})_2$ and 5% excess mole of NaOH. As clearly shown, the major reactions started to occur at around 150°C and 350°C, respectively. Therefore, the formation process of O3 $\text{NaNi}_{0.4}\text{Mn}_{0.4}\text{Co}_{0.2}\text{O}_2$ can be classified into three regions according to their phase composition: 25–185°C (region I, starting material), 185–500°C (region II, intermediates), and 500–875°C (region III, final product). The Rietveld refinement in Figure XIX.2.3b and Figure XIX.2.3c showed that the starting material can be well indexed as $\text{Ni}(\text{OH})_2$ and NaOH; while the XRD pattern of the intermediate product at 350°C is consisting with that of P3- $\text{Na}_{0.8}\text{Ni}_{0.4}\text{Mn}_{0.4}\text{Co}_{0.2}\text{O}_2$. Upon further reaction beyond 500°C, more Na^+ was inserted into the layered structure and hence the structure of O3 phase started to evolve. Therefore, a high temperature of > 800°C is required to synthesize high-purity O3 phase. More detailed analysis on the changes of lattice parameter, $\text{Li}^+/\text{Ni}^{2+}$ mixing, and crystalline size as a function of temperature will be made in the future to obtain the optimal heating temperature and holding time.

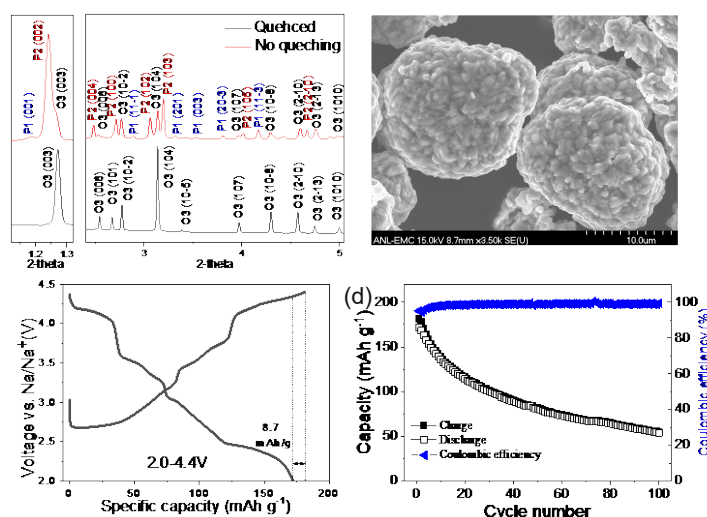


Figure XIX.2.4 (a) HEXRD patterns of samples with/out quenching. (b) SEM images of O3 $\text{NaNi}_{0.4}\text{Mn}_{0.4}\text{Co}_{0.2}\text{O}_2$. (c) The 1st charge/discharge curve and (d) the corresponding cycling performance of O3 $\text{NaNi}_{0.4}\text{Mn}_{0.4}\text{Co}_{0.2}\text{O}_2$ cathode at C/10.

From the in situ HEXRD results, we found that quenching is necessary to maintain the O3 phase structure during cooling. With a slow cooling under air atmosphere, the obtained material exhibited a mixed phase of P1/P2/O3 (Figure XIX.2.4a), which might be probably due to the surface reconstruction induced by slow cooling and thus lead to the formation of Na-deficient phase such as P1 and P2. In sharp contrast, the quenched sample exhibited high purity O3 phase. The morphologies of the quenched cathode are shown in Figure XIX.2.4b, which exhibited characteristic conventional polycrystalline features. The electrochemical performance of the quenched $\text{NaNi}_{0.4}\text{Mn}_{0.4}\text{Co}_{0.2}\text{O}_2$ cathode was evaluated by using coin-cells with sodium metal as reference and counter electrode. Figure XIX.2.4c shows the first charge/discharge curves within 2.0–4.4 V at 0.1C, which exhibited the characteristic features of O3 phase with multiple-step voltage plateaus. The 1st charge and discharge capacity were measured to be as high as 180.6 mAh/g and 171.9 mAh/g, leading to a low initial irreversible capacity loss of only 8.7 mAh/g and a high initial Coulombic efficiency of 95%. This is extremely important for the practical application of sodium layered cathode. In addition, it exhibited an average working voltage of ~ 3.5 V. These results can lead to a high energy density of ~ 600 Wh/kg based on the material level. This is comparable with LiFePO_4 cathode and LiCoO_2 cathode. However, upon further charge/discharge, the capacity exhibited a continuous decrease. After 100 cycles, the reversible capacity was only ~ 50 mAh/g, resulting in a low capacity retention of 30% (Figure XIX.2.4d). We will conduct advanced characterization, particularly with electrolyte optimization, during charge/discharge to understand the

degradation mechanism and develop corresponding strategies to stabilize O3 cathode during prolonged cycling.

Chemical compatibility of Fe-based cathodes with carbonate electrolytes

Iron (Fe) potentially is the most attractive transition metal constituents that can be envisioned in LIB cathode compounds as they are abundant, non-toxic, environmentally benign, and light in weight. However, the reversible operation of $\text{Fe}^{3+}/\text{Fe}^{4+}$ redox, which would provide a higher operating voltage and subsequently a higher specific energy density, has not been successful in lithium-ion batteries yet. The inactivity of $\text{Fe}^{3+}/\text{Fe}^{4+}$ redox in layered lithium transition metal oxides has been largely attributed to the structural instability where Fe^{3+} readily migrates to lithium sites during cycling resulting in a significant cation disorder in the layered structure. In contrast, layer structured $\text{NaFe}_{1-x}\text{M}_x\text{O}_2$ supports reversible $\text{Fe}^{3+}/\text{Fe}^{4+}$ redox reaction because the large size difference between sodium and iron effectively suppresses Na/Fe cation mixing stabilizing the layered structure. Nevertheless, the reversibility of the $\text{Fe}^{3+}/\text{Fe}^{4+}$ operation in layered oxides is still unsatisfactory and requires further improvement. Herein, we have investigated the effect of different electrolytes on the chemical stability of Fe^{4+} species in charged $\text{Na}_{1-x}\text{FeO}_2$ cathode. Sodium iron oxide (NaFeO_2) is the prototype material which first needs to be best understood properly in order to implement iron redox chemistry in SIB.

The initial charge-discharge of the Na/NaFeO₂ cells was conducted in various electrolyte compositions: 1M NaClO₄/PC, 1M NaPF₆/PC, 1M NaPF₆/PC+FEC, 1M NaPF₆/EC+DEC. The cell with 1M NaClO₄/PC electrolyte shows the highest charge capacity but the lowest discharge capacity among the tested electrolytes; the initial Coulombic efficiency (1st-CE) is only 64%. The 1st-CE was improved by replacing NaClO₄ with NaPF₆. The 1M NaPF₆/PC with 2% FEC additive shows the highest 1st-CE (91%). Figure XIX.2.5 displays the performance degradation after aging the charged $\text{Na}_{1-x}\text{FeO}_2$ electrodes in different electrolytes. The aging cycle was performed applying a series of charge (C1) – aging for 10 days at OCV (aging@SOC) – discharge (D'1) – charge (C'2) – discharge (D'2) steps. In Figure XIX.2.5a, the discharge capacity for the 1M NaClO₄/PC cell significantly decreases after the aging@SOC step (D1 = ~90 mAh/g vs. D'1 = ~40 mAh/g). The subsequent C'2 and D'2 capacities show even lower values indicating an irrecoverable degradation to the cell. In Figure XIX.2.5b, the 1M NaPF₆/PC cell shows similar degradation after the aging@SOC step (D1 = ~90 mAh/g vs. D'1 = ~40 mAh/g). However, the average discharge voltage of the D'1 curve is higher than that for the 1M NaClO₄/PC cell. Furthermore, the cell performance partially recovers in the subsequent C'2-D'2 steps (D'2 = 60 mAh/g). The aging stability significantly improves when 2% FEC is added to 1M NaPF₆/PC electrolyte (Figure XIX.2.5c; D1 = 90 mAh/g vs. D'1 = ~85 mAh/g).

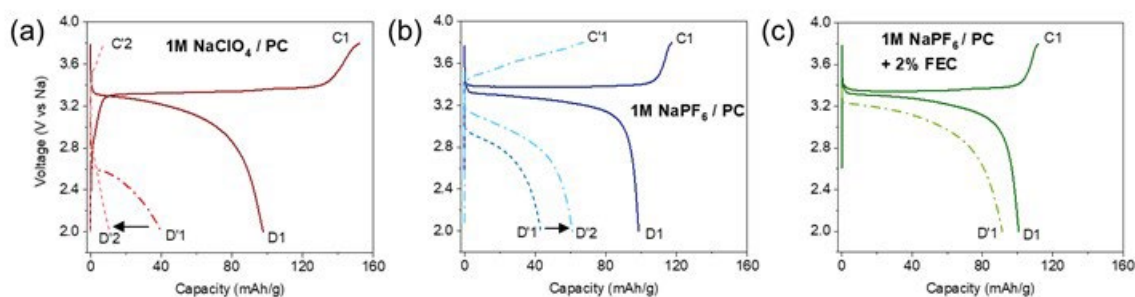


Figure XIX.2.5 Comparison of performance degradation of Na/NaFeO₂ cell after resting at the end of 1st charge for 10 days in (a) 1M NaClO₄/PC, (b) 1M NaPF₆/PC, and (c) 1M NaPF₆/PC with 2% FEC electrolytes. Continuous cycle (C1 – D1) vs. aging cycle (C'2 – OCV storage for 10 days – D'1 – C'2 – D'2).

Although the potential benefit of FEC to sodium metal anode cannot be ruled out, we've performed further evaluation focused on the effect of FEC on cathodes. Figure XIX.2.6a compares the SEM morphology of the $\text{Na}_{1-x}\text{FeO}_2$ electrodes. The electrode aged with FEC shows a more uniform surface morphology. The electrode surface aged without FEC appears to have built up thicker surface layers. The inset images display the

separators (interfaced against the cathode) harvested from the aged cells. The clean separator collected from the FEC-containing cell contrasts with the significantly discolored separator harvested from the FEC-free cell. Figure XIX.2.6b also shows that the FEC-containing cell has a lower leakage current during the constant voltage hold at 3.8 V vs. Na. Figure XIX.2.6c exhibits that the cathode impedance of the FEC-free cell continuously increases during the aging period, whereas, despite a thicker CEI on the cathode surface, the FEC effectively suppresses the impedance rise. Ex situ XRD data show that the lattice parameters and peak intensities of the $\text{Na}_{1-x}\text{FeO}_2$ electrode aged in the FEC-free cell gradually recover the values for pristine NaFeO_2 (Figure XIX.2.6d). This observation suggests that the degradation during the aging@SOC step is associated with self-discharge of the $\text{Na}_{1-x}\text{FeO}_2$ (spontaneous reduction of Fe^{4+} to Fe^{3+} and associated sodium insertion). The beneficial effect of FEC in forming thinner and denser fluorinated passivation layer which can protect the oxidized $\text{Na}_{1-x}\text{FeO}_2$ surface against the continuous electrolyte oxidation is further confirmed by XPS analysis (data not shown).

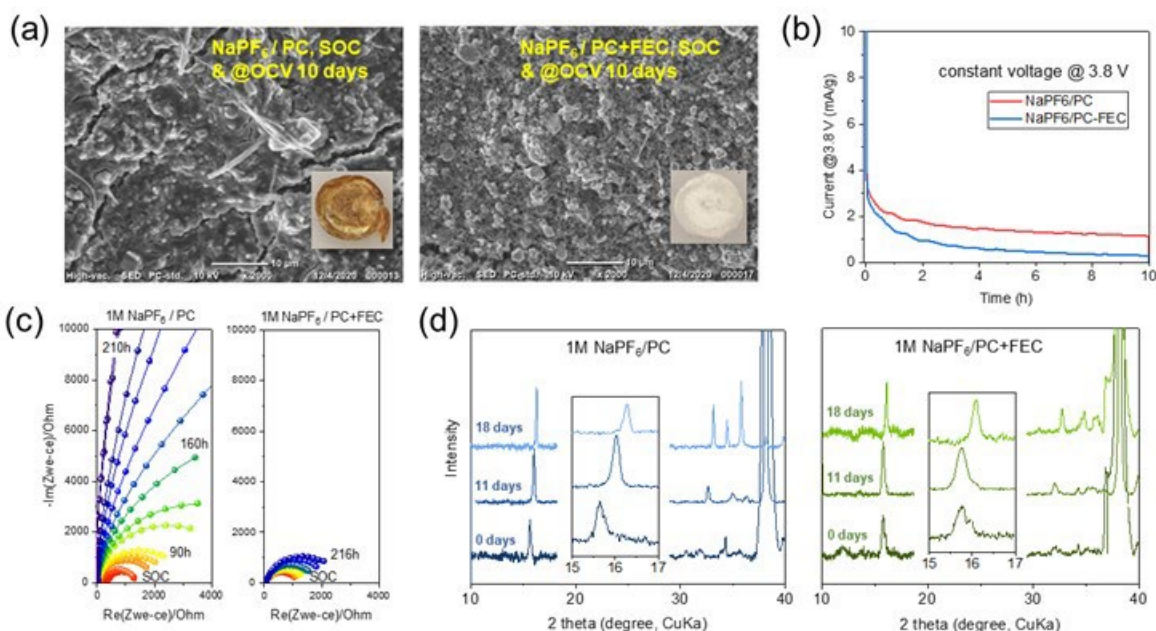


Figure XIX.2.6 The effect of FEC additive on stabilizing the charged $\text{Na}_{1-x}\text{FeO}_2$ electrode in 1M NaPF_6/PC electrolyte. (a) SEM morphology (inset image showing the surface of harvested separator), (b) leakage current at 3.8 V, (c) cathode EIS as a function of SOC resting time, (d) ex situ XRD of harvested $\text{Na}_{1-x}\text{FeO}_2$ electrodes.

High voltage performance of $\text{NaFe}_x(\text{Mn}_{0.5}\text{Ni}_{0.5})_{1-x}\text{O}_2$ cathodes

Since the first report on the reversible sodium cycling of $\text{NaFe}_{1/3}\text{Mn}_{1/3}\text{Ni}_{1/3}\text{O}_2$ in 2012,^[6] the O3-type layered $\text{Na}(\text{Fe},\text{Mn},\text{Ni})\text{O}_2$ cathodes have been of great interest because of their high theoretical capacity, decent cycle stability, and utilization of abundant, low-cost raw materials. Although the following comparative studies of the $\text{NaFe}_x(\text{Mn}_{0.5}\text{Ni}_{0.5})_{1-x}\text{O}_2$ system have suggested different optimum compositions depending on the research groups, there is a consensus that the Fe content should not be higher than 50% for a good cycle performance.^{[7],[8],[9]} Building on these results, Ma et al. have demonstrated prototype sodium-ion battery (SIB) full cells comprising the $\text{NaFe}_{1/3}\text{Mn}_{1/3}\text{Ni}_{1/3}\text{O}_2$ cathode and hard carbon anode couple and continuous effort to commercialize sodium-ion batteries based on the $\text{Na}(\text{Fe},\text{Mn},\text{Ni})\text{O}_2$ cathode.^[10] Nevertheless, these developments of $\text{Na}(\text{Fe},\text{Mn},\text{Ni})\text{O}_2$ cathodes have focused on optimizing the performance within a moderate desodiation range, for example, below 4.0 V vs. Na. To better understand the mechanism by which the $\text{Fe}^{3+/4+}$ redox center affects the stability of the $\text{Na}(\text{Fe},\text{Mn},\text{Ni})\text{O}_2$ cathode, we have synthesized the morphology controlled $\text{NaFe}_x(\text{Mn}_{0.5}\text{Ni}_{0.5})_{1-x}\text{O}_2$ particles ($x = 0, 1/3, 1/2, 2/3$, and 0.8) by solid-state reaction of Na_2CO_3 , Fe_3O_4 , and $(\text{Mn}_{0.5}\text{Ni}_{0.5})(\text{OH})_2$ precursors. The synthesized oxide particles have secondary particle morphology (average particle size $\sim 10\ \mu\text{m}$) of spherically aggregated primary particle granules. The XRD data

showed highly crystalline single-phase materials with the α -NaFeO₂ layered structure and the linear relationship between the transition metal composition and lattice parameter confirmed the solid-solution of transition metal cations.

Figure XIX.2.7 shows the initial charge and discharge profiles of the NaFe_x(Mn_{0.5}Ni_{0.5})_{1-x}O₂ cathodes. NaMn_{0.5}Ni_{0.5}O₂ (i.e., Fe₀) exhibits several voltage steps corresponding to the phase transitions and Na-vacancy orderings. Fe substitution removes the voltage steps making the voltage profile smoother indicating a solid-solution type voltage response. It is presumed that the substituted Fe perturbs the charge ordering in the transition metal layers suppressing coordinated layer gliding and Na-vacancy ordering during the electrochemical (de)sodiation process. Fe substitution also increases the initial polarization and average operation voltage. The electrochemical property of the high Fe-content samples, such as Fe_{2/3} and Fe_{0.8}, resembles that of pure NaFeO₂. In Figure XIX.2.7f, the Fe_{1/2} sample shows good capacity retention when cycled between 3.8 and 2.0 V vs. Na. The high voltage charging of the cathode (i.e., 4.3 V cut-off) significantly degrades the cycle performance, as expected. However, after the rapid capacity drop during the first ~10 cycles, the cycle performance gradually improves, and the Fe_{1/2} cathode exhibits better capacity retention than the Fe₀ electrode. It is not yet clear though whether the comparable (or even better) high-voltage cycle performance of the morphology controlled Fe_{1/2} cathode is simply due to the lower chemical stress (i.e., lower specific capacity) or the optimized physico-chemical properties of our sample. Overall, our preliminary structure and electrochemistry data collected on the morphology controlled NaFe_x(Mn_{0.5}Ni_{0.5})_{1-x}O₂ materials corroborate the general performance trends that have been reported in the literature. In addition, the relatively decent cycle performance of the Fe_{1/2} electrode requires revisiting the NaFe_x(Mn_{0.5}Ni_{0.5})_{1-x}O₂ cathode system. Studies are ongoing to elucidate the structural and electrochemical mechanisms behind the effect of Fe substitution in the layered cathodes.

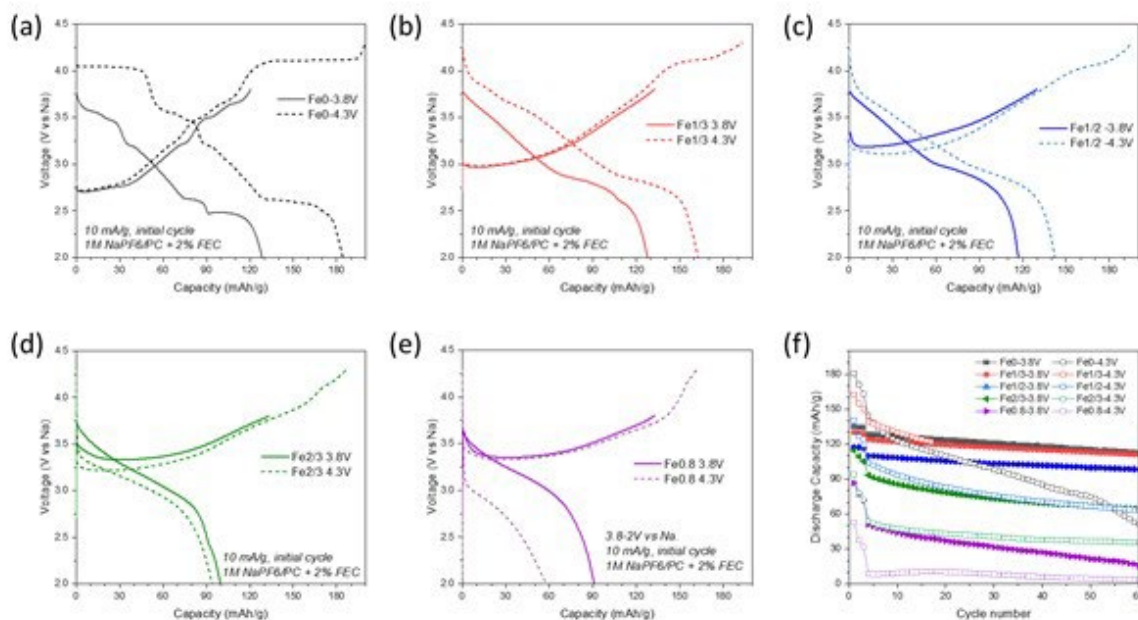


Figure XIX.2.7 (a-e) Initial voltage profiles and (f) cycle performance of the NaFe_x(Ni_{1/2}Mn_{1/2})_{1-x}O₂ cathodes ($x = 0, 1/3, 1/2, 2/3$, and 0.8). Three formation cycles with 10 mA/g current density were followed by regular cycles with 30 mA/g.

Conclusions

This sodium-ion battery (SIB) research conducted in FY'21 by Amine and Johnson research groups focused on development of Sb-doped high-performance red phosphorus (P) anodes and synthesis and characterization of sodium layered oxide cathodes with the intent to deliver a cell energy density chemistry of 200 Wh/kg for transportation applications. While much has been learned about the electrode materials, there is room for

improvement in the layered oxide cathodes' capacities and cycle life. In particular the investigation into electrolyte development and optimization is necessary in order to create iron redox stability in cell environment. Structural tuning of layered oxide cathodes per layer stacking sequences defects, and choice of transition metals, dopants and coatings also must be understood. In short, the ability of SIB to compete with LIB in EVs will be predicated on cost, safety and battery supply and ease of use. We intend to position the technology strategically within the suite of energy storage options available to the community and for use in the field.

Key Publications

Patent

1. Guiliang Xu, Xiang Liu and Khalil Amine. Electroactive materials for secondary batteries. US20210320292A1.

Publication

1. Xu, G. L. (*); Liu, X.; Zhou, X.; Zhao, C.; Hwang, I.; Daali, A.; Ren, Y.; Sun, C. J.; Chen, Z.; Liu, Y. (*); Amine, K. (*). Beyond phase transition and parasitic reactions: native lattice strain induced structural earthquake in layered oxide cathodes. *Nature Commun.* 2021, under revision.
2. Liu, X.; Zhou, X.; Liu, Q.; Diao, J.; Zhao C.; Li, L. (*); Liu, Y. (*); Xu, W.; Daali, A.; Harder, R.; Robinson, I. K.; Dhahi, M.; Alami, J.; Chen, G.; Xu, G. L. (*); Amine, K. (*). Multiscale understanding of surface structural effects on high-temperature operational resiliency of layered oxide cathodes. *Adv. Mater.* 2021, 2107326.
3. Liu, X.; Xiao, B.; Daali, A.; Zhou, X.; Yu, Z.; Li, X.; Liu, Y.; Yin, L.; Yang, Z.; Zhao, C.; Zhu, L.; Ren, Y.; Cheng, L.; Ahmed, S.; Chen, Z.; Li, X. (*); Xu, G. L. (*); Amine, K. (*). A stress/interface-compatible red phosphorus anode for high-energy and durable sodium-ion batteries. *ACS Energy Lett.* 2021, 21, 8, 547–556.
4. Xiao, B.; Liu, X.; Chen, X.; Lee, G. H.; Song, M.; Yang, X.; Omenya, F.; Reed, D.; Sprenkle, V.; Ren, Y.; Sun, C. J.; Yang, W.; Amine, K.; Li, X. (*); Xu, G. L. (*); Li, X. (*). Uncommon behavior of Li doping suppresses oxygen redox in P2-type Manganese-rich sodium cathodes. *Adv. Mater.* 2021, 2107161
5. Xiao, B.; Wang, Y.; Tan, S.; Li, X.; Zhang, Y.; Lin, F.; Han, K. S.; Omenya, F.; Amine, K.; Reed, D.; Hu, Y.; Xu, G. L. (*); Hu, E. (*); Li, X. (*); Li, X. (*). Vacancy-enabled O3 phase stabilization for manganese-rich layered sodium cathodes. *Angew. Chem. Int. Ed.* 2021, 60, 8258–8267.
6. Xiao, B.; Liu, X.; Song, M.; Yang, X.; Omenya, F.; Feng, S.; Sprenkle, V.; Amine, K.; Xu, G.-L.; Li, X.; Reed, D. A General strategy for batch development of high-performance and cost-effective sodium layered cathodes. *Nano Energy*, 2021, 106371.
7. Deng, C.; Gabriel, E.; Skinner, P.; Lee, S.; Barnes, P.; Ma, C.; Gim, J.; Lau, M. L.; Lee, E. (*); Xiong, H. (*). Origins of irreversibility in layered $\text{NaNi}_x\text{Fe}_y\text{Mn}_z\text{O}_2$ cathode materials for sodium ion batteries. *ACS Appl. Mater. Interfaces*, 2020, 12, 51397–51408.

Presentation

1. (Invited talk) Guiliang Xu and Khalil Amine. Development of Layered Oxides Cathodes and Phosphorus Anode for High-Energy and Low-Cost Sodium-Ion Batteries. 2021 MRS Fall.
2. Jehee Park, Electrolyte engineering to improve cathode-electrolyte interface of $\text{Na}_{1-x}\text{FeO}_2$ cathode for sodium ion batteries. ECS Meeting, Oct. 10–14, 2021.

References

1. N. Yabuuchi, et al., *Chemical Reviews* 114 (2014):11636–11682.
2. M. Han, et al., *Energy & Environmental Science* 8 (2015):81–102.
3. Y. Wen, et al., *Nature Communications* 5 (2014): 4033.
4. S. Huang, et al., *Adv. Mater.* 30 (2018):1706637.
5. H. Kang, et al., *Journal of Materials Chemistry A* 3 (2015):17899–17913.
6. C. Johnson, et al., *Electrochem. Commun.* 18 (2012):66–69.
7. N. Yabuuchi, et al., *J. Electrochem. Soc.* 160 (2013):A3131–A3137.
8. D. Yuan, et al., *ACS Appl. Mater. Interfaces* 7 (2015):8585–8591.
9. Y.-K. Sun, et al., *J. Power Sources* 324 (2016): 106–112.
10. Z.-F. Ma, et al., *J. Alloys Compounds* 724 (2017): 465–473.

Acknowledgements

Support from Tien Duong of the U.S. DOE's Vehicle Technologies Office is gratefully acknowledged. We would like to thank Dr. Guiliang Xu and Dr. Eungje Lee at ANL for the major contribution to this project.

XIX.3 High Capacity, Low Voltage Titanate Anodes for Sodium-Ion Batteries (LBNL)

Marca Doeff, Principal Investigator

Lawrence Berkeley National Laboratory
1 Cyclotron Road
Berkeley, CA 94720
E-mail: mmdoeff@lbl.gov

Tien Q. Duong, DOE Technology Development Manager

U.S. Department of Energy
E-mail: Tien.Duong@ee.doe.gov

Start Date: January 1, 2019

End Date: September 30, 2021

Project Funding (FY21): \$200,000

DOE share: \$200,000

Non-DOE share: \$0

Project Introduction

Cost and supply security issues with lithium [1] are compelling reasons to develop sodium-ion batteries as potential alternatives to the better-known lithium-ion analogs. Identification of a suitable anode material for sodium-ion cells remains the critical challenge to further progress, as graphite (the anode material used in lithium-ion batteries) does not intercalate sodium to an appreciable extent. Recently, several sodium titanates [2],[3],[4] have been found to undergo reversible sodium intercalation processes at potentials much lower than 1 V vs. Na⁺/Na, making them attractive candidates for use as anodes in sodium ion systems. These materials have stepped layered structures but show very different electrochemical behaviors depending on composition and step size. Work on this project is directed towards understanding these differences through an array of synthetic, electrochemical, and structural characterization techniques, and overcoming practical impediments to their use, such as the high first cycle coulombic inefficiencies that are currently observed. The ultimate goal of the project is to produce a 200–250 mAh/g anode that cycles reversibly. Such a material would be an enabling technology for a practical high-energy sodium ion battery.

Objectives

The planned work is conceived to overcome the main obstacle to the practical realization of sodium-ion batteries, the lack of a suitable anode material. Experiments are designed to improve the practical reversible capacities and overcome the high first cycle coulombic inefficiencies of promising low voltage sodium titanates, as well as to assess the stabilities of the sodiated (partially and fully discharged) products of the electrochemical reactions. Some effort is devoted to consideration of electrolytes and understanding of the electrolyte/anode interface, which must go hand-in-hand with anode development. The ultimate goal is to produce a high capacity (200-250 mAh/g), stable, and reversible low voltage anode material suitable for use in a sodium-ion battery configuration.

Approach

Candidate stepped layered titanates are synthesized by appropriate routes (hydrothermal, solid-state routes, etc.). Materials are then characterized electrochemically and physically. Structure-function relationships are built to correlate the effect of changing structure (for example, step size) on electrochemical properties.

Synchrotron methods such as soft and hard X-ray absorption spectroscopy and XPS are used to probe electronic structures and particle surfaces of pristine and cycled materials. Various electrolytic solutions are prepared from commercially available materials and studied in cells to understand the effect on coulombic efficiency.

Results

Work in FY2021 was focused on completing characterization of the promising nonstoichiometric lepidocrocite-type titanate, $\text{Na}_{0.74}\text{Ti}_{1.815}\text{O}_4$, made by ion-exchange from the Cs-containing analog. The structure is shown in Figure XIX.3.1, along with high-resolution transmission electron micrographs (HRTEM), selected area electron diffraction (SAED) patterns, a refined synchrotron XRD pattern, and elemental mapping. This electrode delivers up to 230 mAh/g at an average potential of 0.6 V during the second discharge in a sodium half-cell.

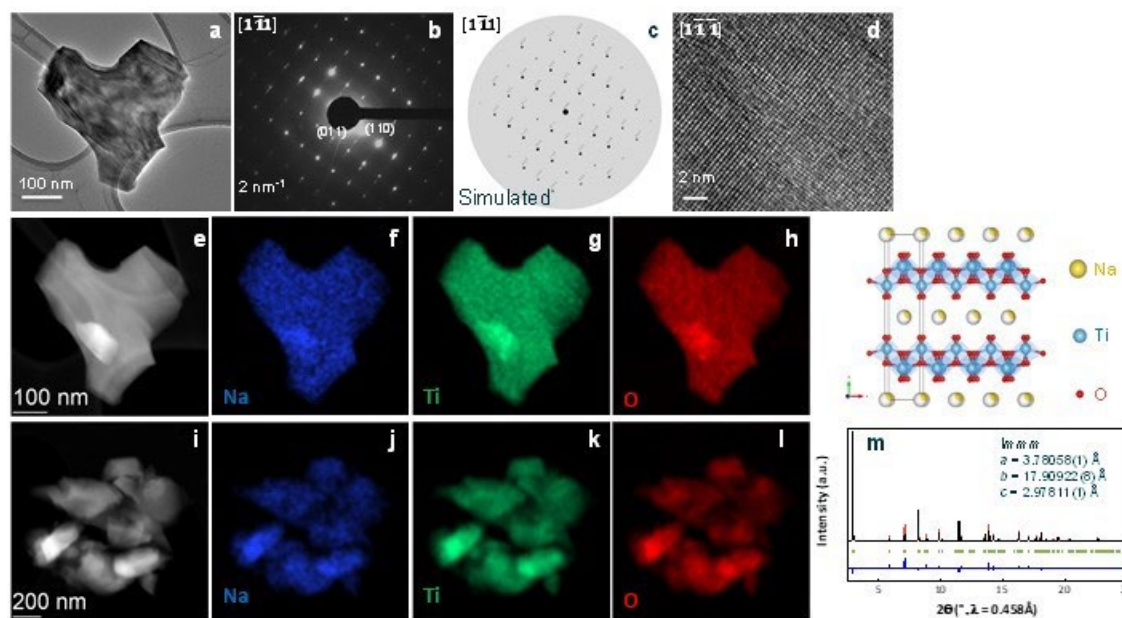


Figure XIX.3.1 a. HRTEM image of a single $\text{Na}_{0.74}\text{Ti}_{1.815}\text{O}_4$ particle, and the corresponding experimental (b) and simulated (c) SAED patterns. Crystal structure model derived from Rietveld refinement of the synchrotron XRD pattern of $\text{Na}_{0.74}\text{Ti}_{1.815}\text{O}_4$ was used in the SAED simulations. d. HRTEM image showing the lattice fringes directing along the zone axis $[1\bar{1}\bar{1}]$. TEM image (e) and element mapping images for Na (f), Ti (g) and O (h) of a single $\text{Na}_{0.74}\text{Ti}_{1.815}\text{O}_4$ particle. TEM image (i) and element mapping images for Na (j), Ti (k) and O (l) of $\text{Na}_{0.74}\text{Ti}_{1.815}\text{O}_4$ particles. (m) Rietveld refinement of the synchrotron XRD pattern of $\text{Na}_{0.74}\text{Ti}_{1.815}\text{O}_4$, the top panel shows a schematic representation of the crystal structure of $\text{Na}_{0.74}\text{Ti}_{1.815}\text{O}_4$ comprising of TiO_6 octahedra (blue) and Na ions (yellow spheres).

An analysis of the electrochemical characteristics indicates that the main redox process is (de)interaction of sodium into/from the structure, although some surface processes contribute to the capacity at higher potentials [5]. This is supported by ex situ XRD and Raman spectroscopy, showing reversible changes in the structure as a function of state-of-charge (Figure XIX.3.2). The structure is well-maintained over 67 cycles (Figure XIX.3.3), although some capacity fading is exhibited. Cell impedance rise (Figure XIX.3.3b) is primarily responsible for the losses. An analysis of the cycling data shows that losses are greater in the region above 1.0V vs Na^+/Na than below this limit, suggesting that the surface adsorption processes are less reversible than intercalation.

The cycling behavior and shape of the voltage profile differ depending on the history of exposure of the electrode material to air. Somewhat surprisingly, air-exposed electrodes cycle better than those from which air was strictly excluded during processing, although 1st cycle coulombic efficiencies are worse.

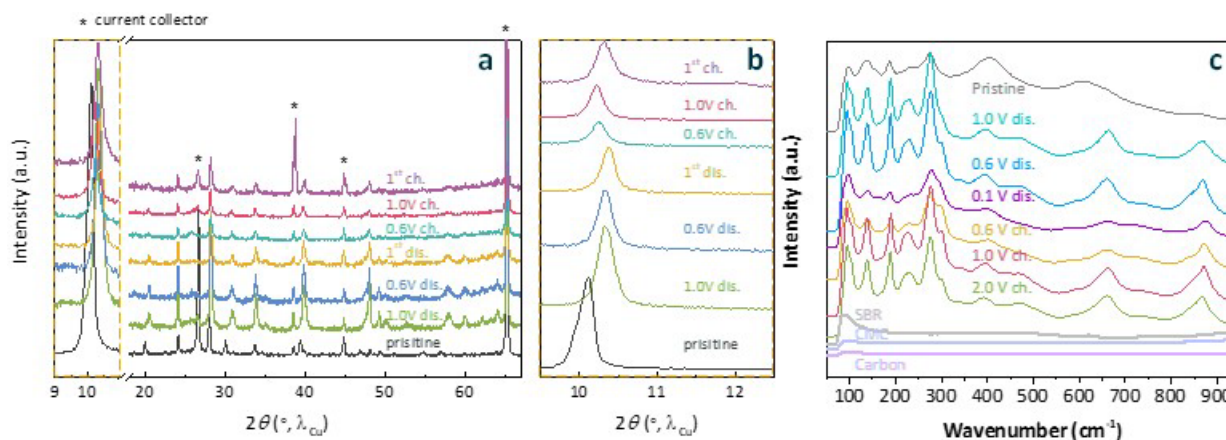


Figure XIX.3.2 Laboratory X-ray diffraction patterns of $\text{Na}_{0.74}\text{Ti}_{1.815}\text{O}_4$ electrodes in the pristine state and cycled to the annotated voltages in the first electrochemical cycle. **b.** Magnified plot of the dashed rectangle area in Figure XIX.3.2a. **c.** Ex-situ Raman spectra of $\text{Na}_{0.74}\text{Ti}_{1.815}\text{O}_4$ electrodes in the pristine state and cycled to the annotated voltages in the first electrochemical cycle.

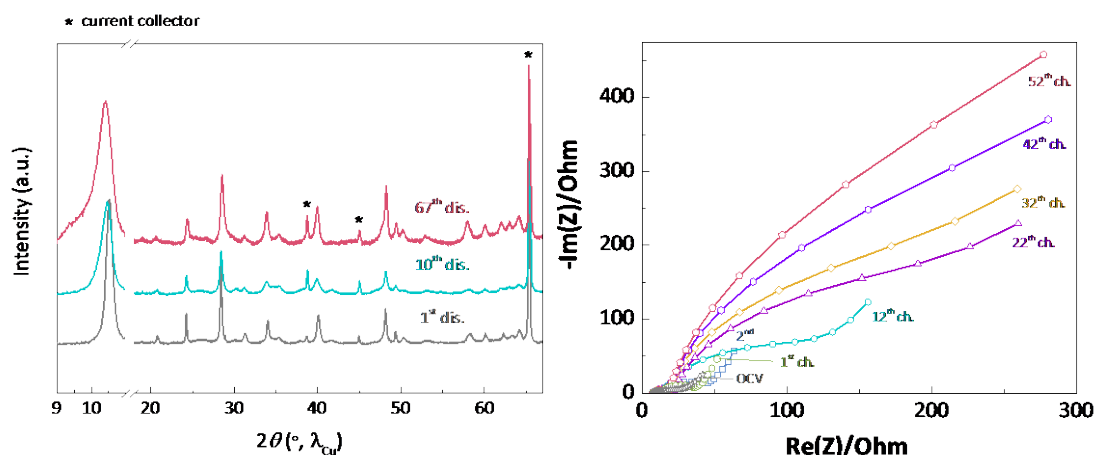


Figure XIX.3.3 Laboratory X-ray diffraction patterns of $\text{Na}_{0.74}\text{Ti}_{1.815}\text{O}_4$ electrodes collected at the end of discharge for annotated cycles. **b.** Nyquist plots of a $\text{Na}/\text{Na}_{0.74}\text{Ti}_{1.815}\text{O}_4$ cell showing impedance data at the open circuit voltage (OCV) and at the end of charge for annotated cycles.

The first cycle coulombic efficiency is also strongly dependent on the electrolyte and binder used; the best result of 81% was obtained with 0.5M sodium tetraphenylborate in DEGDME for the air-excluded electrode using a CMC binder, although a binder-free configuration gave 95%.

Ti-L edge soft X-ray absorption spectra were obtained on both the air-exposed and air-excluded powders. There are slight differences, suggesting that air exposure slightly reduces titanium on the surface (not shown). We speculate that air exposure results in the formation of hydroxyl groups at defect sites and results in titanium reduction. The modification of the defect sites appears to result in better reversibility for the capacitive component of the redox chemistry, resulting in better overall capacity retention.

The material discussed above was dried after ion-exchange at a temperature of 60°C. Drying temperature is expected to affect surface properties of the titanate material (for example, it may be possible to anneal away defects, which may affect the surface adsorption properties). Samples of $\text{Na}_{0.74}\text{Ti}_{1.815}\text{O}_4$ were dried at various temperatures from 60°C–800°C to understand the effect of temperature upon bulk and surface structure. Ex situ XRD patterns for the heat-treated samples are shown in Figure XIX.3.4a. $\text{Na}_{0.74}\text{Ti}_{1.815}\text{O}_4$ slowly transforms into a new, structurally related phase above 175°C in air, which is stable to about 700°C. Above this temperature, it decomposes to form $\text{Na}_2\text{Ti}_6\text{O}_{13}$. The identity of the new phase is not yet known, although it

may be a C-type structure, caused by the shifting of the corrugated titanate layers with respect to one another. This has also been observed in a related material, $\text{Na}_{0.8}\text{Ti}_{1.73}\text{Li}_{0.27}\text{O}_4$, upon heating [4].

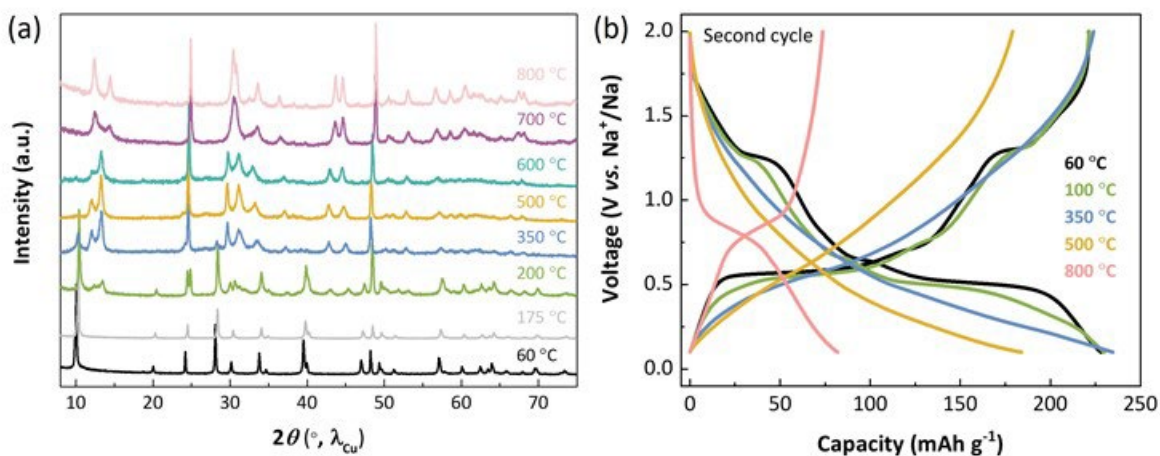


Figure XIX.3.4 (a) Ex situ XRD patterns of $\text{Na}_{0.74}\text{Ti}_{1.815}\text{O}_4$ dried to the indicated temperatures, showing evolution into a related layered phase. (b) Second cycle profiles of materials dried to the indicated temperatures.

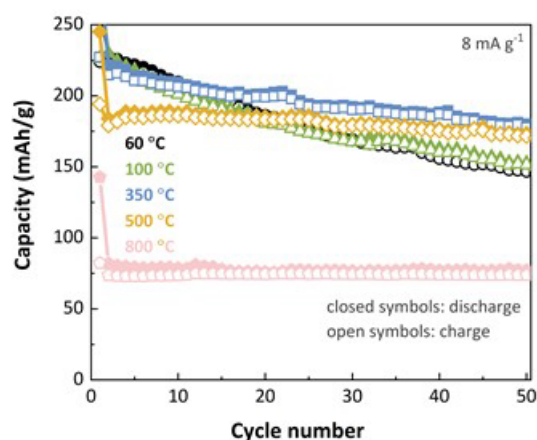


Figure XIX.3.5 Cycling of sodium half-cells containing $\text{Na}_{0.74}\text{Ti}_{1.815}\text{O}_4$ dried to different temperatures.

The effect of drying temperature on the electrochemical properties is shown in Figure XIX.3.4b. The prominent plateaus observed near 1.25V and 0.6V in the cells with the 60°C-treated material are much less evident or disappear entirely in cells with samples heated to moderately higher temperatures. The average potentials of the discharge profiles also decrease (to account for this, different lower voltage limits were used), but overall capacities are not significantly affected. The capacity retention is significantly improved for the cells containing materials heated to 500°C (Figure XIX.3.5). Heating to 800°C leads to a drastic decrease in capacity and increase in average potential for cells containing this material, consistent with decomposition to $\text{Na}_2\text{Ti}_6\text{O}_{13}$. An array of characterization techniques is underway to understand the surface and bulk structural changes that occur as $\text{Na}_{0.74}\text{Ti}_{1.815}\text{O}_4$ is heated, and how they affect the electrochemistry. Figure XIX.3.6 shows Ti K-edge hard X-ray absorption spectroscopy carried out on the heated $\text{Na}_{0.74}\text{Ti}_{1.815}\text{O}_4$ samples. The titanium oxidation state in the bulk of all materials is +4, but the pre-edge region and the EXAFS data reveal subtle structural differences that occur upon heating. This data is currently under analysis.

Figure XIX.3.7 shows Ti K-edge hard XAS data for pristine, discharged, and charged electrodes with a comparison to several reference materials. The Ti shift to lower energy upon discharge is consistent with bulk

reduction of titanium to the trivalent state as sodium is inserted into the structure. The reverse occurs upon cell charge. EXAFS analysis indicates that Ti-O bonds lengthen as titanium is reduced.

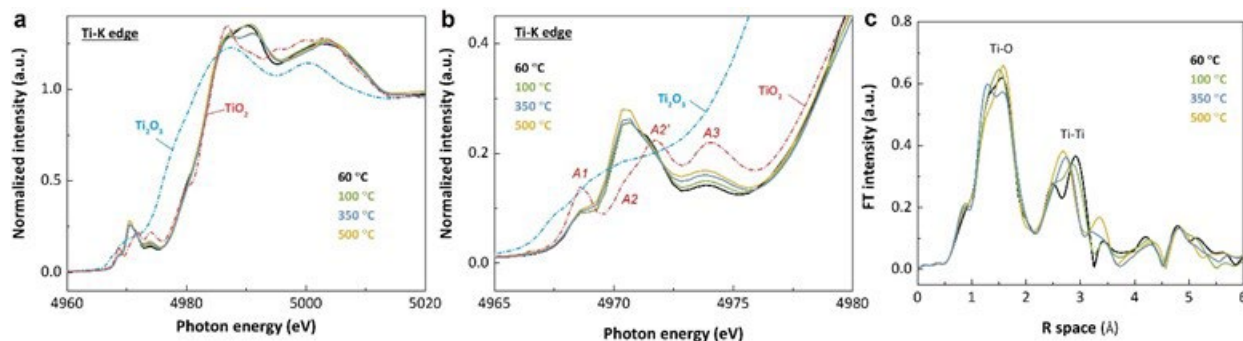


Figure XIX.3.6 a) Ti K-edge XAS spectra on heated $\text{Na}_{0.74}\text{Ti}_{1.815}\text{O}_4$ powders and reference materials, b) pre-edge features, c) Fourier-transformed Ti K-edge EXAFS spectra.

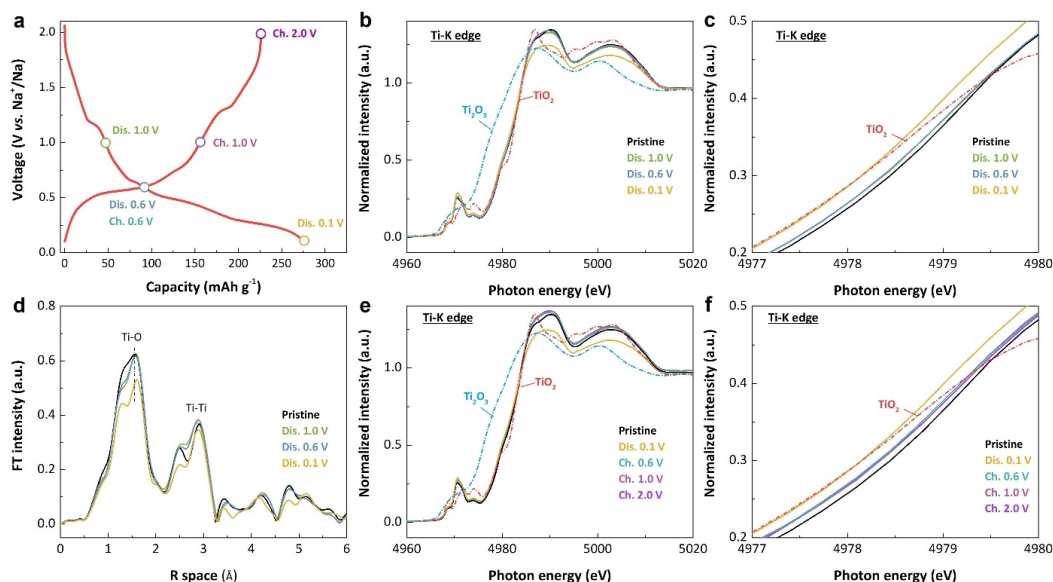


Figure XIX.3.7 a) first cycle of a cell containing $\text{Na}_{0.74}\text{Ti}_{1.815}\text{O}_4$ heated to 60°C with points indicated where data was taken. b) Ti K-edge spectra of discharged electrodes with reference materials included and e) charged electrodes. c) expansion of region showing shifts in the Ti K-edge for discharged electrodes and f) for charged electrodes, d) Fourier-transformed Ti K-edge data.

$\text{Na}_{0.74}\text{Ti}_{1.815}\text{O}_4$ (60°C)/ $\text{Na}_3\text{V}_2(\text{PO}_4)_3$ (NTO/NVP) cells were assembled and cycled using 1M NaPF_6 in EC/DEC electrolyte (Figure XIX.3.8). Improved results were obtained when the anode was pre-cycled prior to incorporation in the full cell, which minimized losses associated with SEI formation.

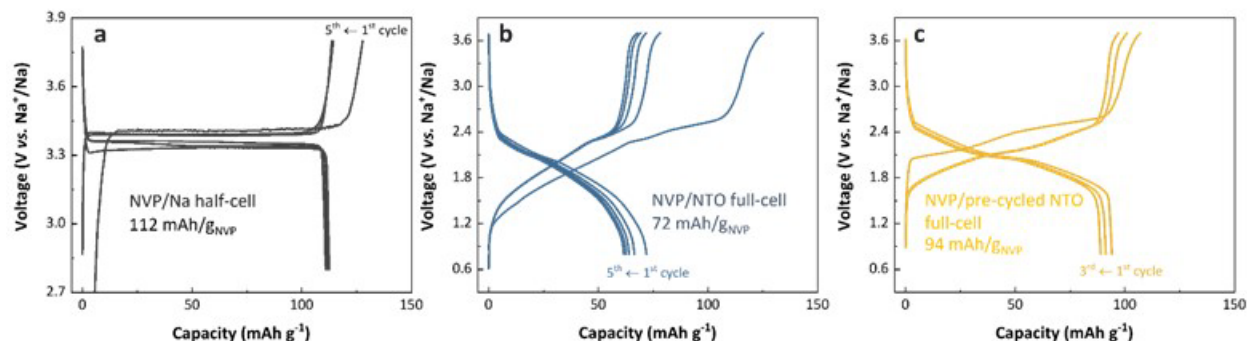


Figure XIX.3.8 Cycling profiles of (a) an NVP/Na half cell (b) a NVP/NTO full cell, and (c) a NVP/NTO full cell where the NTO anode was pre-cycled to reduce losses from SEI formation. All the cells were cycled at a current rate of C/10 calculated based on NVP. The capacity is normalized based on NVP. The N/P ratio is ~1.0–1.04.

Conclusions

The non-stoichiometric lepidocrocite structured titanate, $\text{Na}_{0.74}\text{Ti}_{1.815}\text{O}_4$, is a promising material for use as an anode in Na-ion cells, based on the high initial capacities that are obtained, and the low average potential vs. Na^+/Na . The redox mechanism is primarily reductive intercalation, although some surface processes appear to contribute capacity. The voltage characteristics can be modified by heating the material to moderately high temperatures, resulting in a lower average potential and improved capacity retention. The bulk and surface structural changes that occur upon heating are currently under investigation. Full cells with NVP cathodes have been assembled and cycled with this anode material. Future work is planned on investigating the effect of changing the interlayer species on the electrochemical properties.

Key Publications

1. Yin, W., Alvarado, J., Barim, G., Scott, M.C., Peng, X. and Doeff, M., “A Layered Nonstoichiometric Lepidocrocite-type Sodium Titanate Anode Material for Sodium-Ion Batteries” *MRS Energy & Sustainability* (2021) DOI: 10.1557/s43581-021-00008-6.

References

1. Vaalma, C., Buchholz, D., Weil, M., and Passerini, S., “A Cost and Resource Analysis of Sodium-Ion Batteries” *Nature Rev. Mater.* 3, (2018): article number 18013.
2. Senguttuvan, P., Rousse, G., Seznec, V., Tarascon, J.-M., and Palacin, M. R., “ $\text{Na}_2\text{Ti}_3\text{O}_7$; The Lowest Voltage Every Reported Oxide Insertion Electrode for Sodium Ion Batteries” *Chem. Mater.*, 23, (2011): 4109–4111.
3. Shirpour, M., Cabana, J., and Doeff, M., “New Materials based on a Layered Sodium Titanate for Dual Electrochemical Na and Li Intercalation Systems” *Energy & Environ. Sci.*, 6, (2013): 2538–2547.
4. Shirpour, Mona, Cabana, Jordi, and Doeff, Marca “Lepidocrocite-type Layered Titanate Structures: New Lithium and Sodium Ion Intercalation Anode Materials”, *Chem. Mater.* 26, (2014): 2502–2512.
5. Yin, W., Alvarado, J., Barim, G., Scott, M.C., Peng, X. and Doeff, M., “A Layered Nonstoichiometric Lepidocrocite-type Sodium Titanate Anode Material for Sodium-Ion Batteries” *MRS Energy & Sustainability* (2021) DOI: 10.1557/s43581-021-00008-6.

Acknowledgements

We acknowledge the contributions of Prof. M.C. Scott and Dr. Xinxing Peng for microscopy work.

XIX.4 Electrolytes and Interfaces for Stable High-Energy Sodium-ion Batteries (PNNL)

Ji-Guang Zhang, Principal Investigator

Pacific Northwest National Laboratory
902 Battelle Boulevard
Richland, WA 99354
E-mail: jiguang.zhang@pnnl.gov

Phung M. Le, Principal Investigator

Pacific Northwest National Laboratory
902 Battelle Boulevard
Richland, WA 99354
E-mail: jiguang.zhang@pnnl.gov

Tien Q. Duong, DOE Technology Development Manager

U.S. Department of Energy
E-mail: Tien.Duong@ee.doe.gov

Start Date: October 1, 2018

End Date: September 30, 2021

Project Funding (FY21): \$430,000

DOE share: \$430,000

Non-DOE share: \$0

Project Introduction

The sodium (Na)-ion battery (NIB) is a potential alternative energy source for electric vehicles and grid applications due to the low cost and the natural abundance of sodium. The performance of NIBs largely depends on the development of electrode materials and electrolytes. In recent years, a series of potential electrode materials have been developed. However, a fundamental understanding of the electrochemistry of NIBs, especially the stability of the electrode-electrolyte interface in these batteries, is still not well established. For example, though many attractive attributes of high-capacity alloy anode materials with 3D porous structure have been reported to have extended cycle life, their practical low initial coulombic efficiency (ICE) and low volumetric energy density represent a significant deficiency for practical application of these electrode materials to NIBs. There are two main challenges directly related to the low energy and limited cycle life of the state-of-the-art NIBs. One is the larger size of Na^+ ions and the lower cell operating voltage of NIBs as compared to LIBs, which lead to intrinsically sluggish kinetics and lower energy density. The other is the unstable solid electrolyte interphase (SEI) formed on electrode material that leads to poor utilization of electrode materials, fast capacity fading, and safety concerns due to continuous decomposition of flammable electrolytes. Therefore, designs of advanced electrodes that can host more Na^+ ions and electrolytes that can maximize the reversible Na storage capacity in electrodes with a stabilized interface and good efficiency are greatly needed. The fundamental understanding on the nature of the dynamic interface between electrode and electrolyte is also critical to guide the further development of NIBs with higher energy density and cycling stability.

Objectives

1. Optimize synthesis condition of high-capacity anode ($> 450 \text{ mAh g}^{-1}$). Carbon sources with different nanostructures and graphitization conditions will be investigated.
2. Develop high voltage electrolytes ($\geq 4.2\text{V}$) to form stable SEI/CEI layers on both high-capacity carbon anodes and high voltage cathodes. Full cells will be used in this investigation to improve energy density and cycling stability of NIBs.

3. Characterize CEI/SEI interphase properties in optimized electrolyte to probe the mechanism of high voltage cycling stability of NIBs.
4. Develop electrolytes compatible with conventional polymer separators to replace glass fiber separator typically used in NIBs. This will accelerate the practical application of NIBs.

Approach

1. Optimize the electrolyte components and concentrations to develop innovative electrolytes and additives with improved electrochemical and physical properties. Phosphate-based localized high concentration electrolytes (LHCE) will be optimized to improve the cycling performance of NIB.
2. Use in situ and ex situ spectroscopy methods to unravel the origin of the SEI/CEI layer at the dynamic interface, providing guidance for the electrolyte and interface design and enabling high capacity and long life of Na-ion batteries.

Results

1. Optimize synthesis condition of high-capacity anode ($> 450 \text{ mAh g}^{-1}$)

A novel carbon anode with a record specific capacity has been developed by CVD coating of soft carbon (using acetylene precursor) on two porous carbon precursors with 1 and 2 nm of pore size, respectively. Table XIX.4.1 summarizes the preparation conditions, physical and electrochemical properties of the anode samples prepared by this approach. With the same porous carbon precursor, the desodiation capacity and 1st efficiency of the final electrode material increase with the increasing CVD deposition temperature. The difference on pore size of precursor does not affect the 1st discharge capacity (489 mAh g^{-1} for AC-4b vs 487 mAh g^{-1} for PC-4b) although AC-4b sample exhibits lower sodiation potential than those of PC-4b (Figure XIX.4.1a). However, the capacity retention of AC-4b at high rate is much poor than those of PC-4b as shown in Figure XIX.4.1b. This is because the sodiation potential of AC-4b is too close to the cut-off potential (5 mV) and the sodiation step is consequently interrupted even at small polarization.

Table XIX.4.1 Effect of synthesis conditions on the physical/electrochemical properties of carbon anode

Sample	Pore size of carbon precursor (nm)	CVD temperature ($^{\circ}\text{C}$)	Helium true density (g cm^{-3})	Porosity (%)	1st desodiation capacity (mAh g^{-1}) (5 mV – 2 V)	1st Coulombic efficiency (CE) (%)
AC-2b	1	800	1.29	42.9	444	83
AC-3b	1	900	1.51	33.2	460	87
AC-4b	1	920	1.49	34.1	489	88
PC-4b	2	920	1.48	34.5	487	85

The carbon anode (PC-4b) with record capacity and excellent rate capability has been further evaluated in sodium full-cells with NaNMC ($\text{O}_3\text{-NaNi}_{0.68}\text{Mn}_{0.2}\text{Co}_{0.10}\text{O}_2$) cathode (85 wt% active material: 8 wt% super P carbon: 7 wt% PVDF binder) and compared with the baseline cells with the commercial Kuraray carbon (type 2, particle size $\sim 9 \mu\text{m}$). A localized high concentration electrolyte (NaFSI-TEP/TTE (1:1.5:2 in molar ratio)) is used to improve the cycling stability of the cells. The cells with PC-4b anode demonstrates an initial discharge capacity of $\sim 440 \text{ mAh g}^{-1}$ with the 1st CE of 79% while the cells with Kuraray hard carbon anode only delivers a reversible capacity of 202 mAh g^{-1} and a lower 1st CE value of 69% (Figure XIX.4.2a). Full-cell using PC-4b anode exhibit a capacity of twice as much as those using Kuraray hard carbon anode (Figure XIX.4.2b). After 400 cycles, PC-4b based full-cell still retain a capacity of 70% as compared to 65% capacity retention for the cells with Kuraray carbon anode.

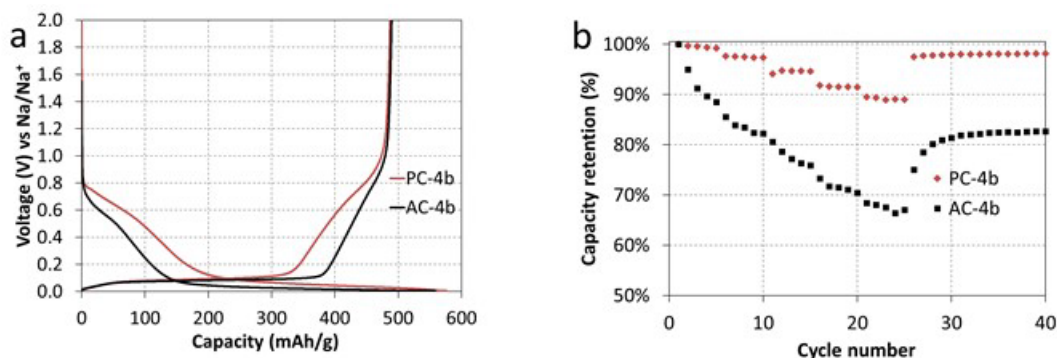


Figure XIX.4.1 (a) 1st cycle voltage profile and (b) rate performance of PC-4b and AC-4b in sodium half-cell performed in a potential range 5 mV to 2 V with 1 M NaPF₆ in EC/DMC (1:1 in weight) as electrolyte.

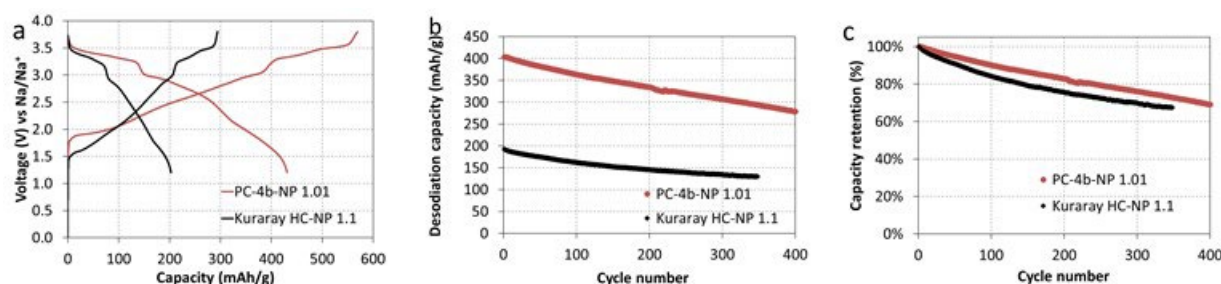


Figure XIX.4.2 (a) Voltage profile, (b) Cycling reversible discharge capacity and (c) CE of PC-4b | NMC full-cell (N/P=1.01) compared to Kuraray HC | NMC full cells (N/P=1.1), using NaFSI-TEP/TTE electrolyte (1:1.5:2 in molar ratio). Both pristine cathode and anode are used without any pretreatment or presodiation. The operating voltage window is 1.2V–3.8V and the 1st formation C rate is 0.1C and cycling C rate afterward is 0.33C.

2. Develop high voltage electrolytes ($\geq 4.2V$) to form stable SEI/CEI layers on both high-capacity carbon anodes and high voltage cathodes.

To realize high energy density of NIBs, their electrolytes need to be stable at high voltage so a high voltage cathode can be fully utilized. Ideally, these electrolytes should also be nonflammable to ensure the safe operation of NIBs. Recently, a nonflammable high-concentrated-electrolyte (HCE) using triethylphosphate (TEP) as solvent has been developed. This electrolyte is compatible with high voltage cathode NaNi_{0.68}Co_{0.1}Mn_{0.22}O₂ (NaNMC). Figure XIX.4.3a and b shows the long-term cycling performance and coulombic efficiency (CE) of Na||NaNMC half-cell with a HCE electrolyte (NaFSI: TEP = 1: 1.5 in mole ratio). The similar cells with a 1M NaPF₆/PC electrolyte were used as a reference. The cell with HCE electrolyte exhibits excellent CE (near 100%) at a high voltage of 4.2 V. After 500 cycles, these cells still retain 78 %, 85 %, and 81 % capacity at a rate of 0.2 C, 0.33 C, and 0.5 C, respectively. In contrast, the cell with conventional electrolyte retains only ~ 50% capacity in 100 cycles. Its CE also shows significant fluctuation which indicates an unstable interphase. Figure XIX.4.3c shows the voltage profiles of these cells in selected cycles. At 0.33 C rate, the initial and 500th cycle discharge capacity were 181.2 and 146.9 mAh g⁻¹ for HCE based cell compared to 161.9 and 30 mAh g⁻¹ for conventional electrolyte-based cell. The superior performance of NIBs using HCEs could be attributed to the highly stable cathode electrolyte interphase (CEI) which prevents further electrolyte oxidation at high potential when they are in contact with NaNMC electrode.

The performance of the new electrolyte developed in this work is also evaluated in full cells using hard carbon anode coupled with NaNMC cathode and cycled in both HCE and baseline electrolyte. The full-cell using HCE electrolyte shows stable performance in 100 cycles with initial discharge capacity of 183.5 mAh g⁻¹ and capacity retention of 86 % at 0.2 C compared to 168.8 mAh g⁻¹ and 68 % capacity retention when baseline electrolyte is used (Figure XIX.4.4a-b). In addition, the rate capability of full cells using HCE is also much better than those of using baseline electrolyte (Figure XIX.4.4c). The excellent compatibility between HCE

electrolyte versus cathode and anode material will be further studied by advanced characterization tools to have a better understanding on the role of interphase in cycling performance of NIBs.

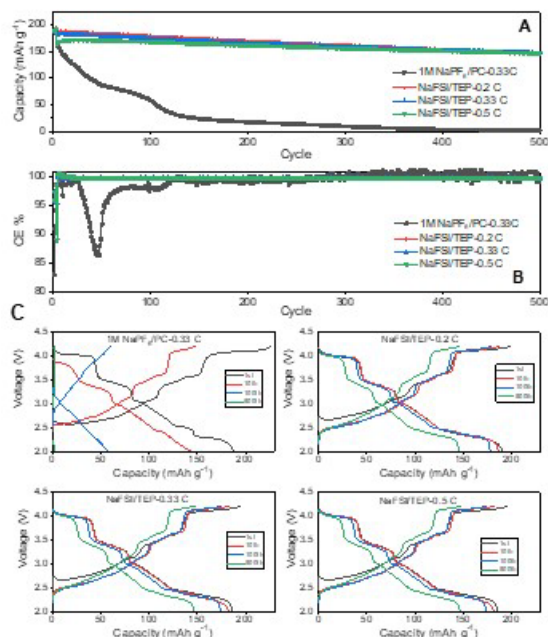


Figure XIX.4.3 Performance of Na||NaNCM half-cells using HCE and baseline electrolyte: A) Cycling capacity; B) Coulombic efficiency and C) Voltage profiles.

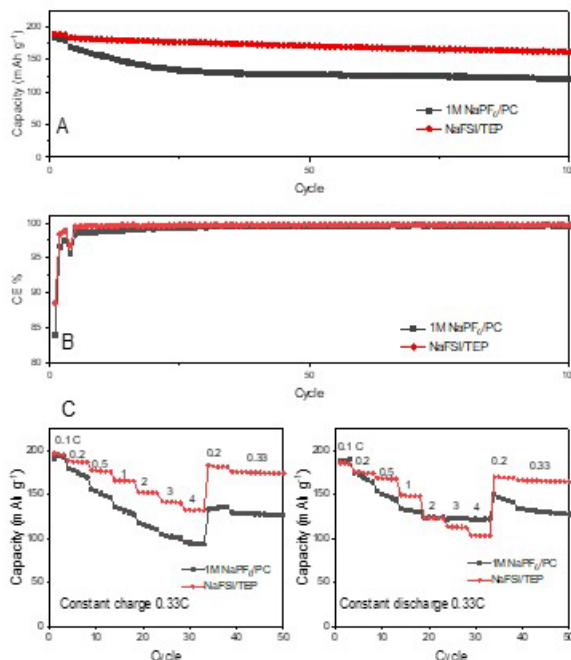


Figure XIX.4.4 Performance of HC||NaNCM full cell using HCE and baseline electrolyte: A) Cycling stability at 0.2C; B) Coulombic efficiency, and C) rate capability.

3. Characterize CEI/SEI interphase properties in optimized electrolyte to probe the mechanism of high voltage cycling stability of NIBs

To understand the mechanism behind the stable electrochemical performance of 4.2 V hard carbon|| $\text{NaNi}_{0.68}\text{Mn}_{0.22}\text{Co}_{0.10}\text{O}_2$ (NaNCM) cells in advanced nonflammable high-concentrated-electrolyte (HCE, NaFSI: TEP = 1: 1.5 in mole ratio) compared with baseline electrolyte (BE: 1 M NaPF_6/PC), the compositions of electrode/electrolyte interphases were analyzed by X-ray photoelectron microscopy (XPS). The results of XPS analysis on cathode electrolyte interphase (CEI) layer formed on cycled NaNCM cathode surface is shown in Figure XIX.4.5. In C 1s spectra of CEI formed in BE, the main species are C-C/C-H, C-O, C=O, CO_3 and PVDF as shown in Figure XIX.4.5a. In contrast, for the CEI layer formed in HCE, additional C-SO_x peak from NaFSI salt decomposition can be clearly identifies as shown in Figure XIX.4.5d. The F 1s spectra of CEI layers formed in both electrolytes contain NaF and C-F/P-F/S-F peaks. The P 2p and S 2p spectra typically represent the contributions from inorganic components derived from the conductive salts (NaPF_6 or NaFSI). The intensity of S 2p spectrum in NaFSI-TEP electrolyte was higher than P 2p spectrum in $\text{NaPF}_6\text{-PC}$ electrolyte, indicating more salt has been decomposed to form CEI layer when HCE was used. The XPS analysis revealed that the use of high concentration NaFSI-TEP electrolyte can effectively suppress dissolution of transition metal in cathode, which is a significant advantage of this electrolyte. Figure XIX.4.5g indicates that the atomic ratio of Mn in the CEI layer formed in NaFSI-TEP electrolytes is much less (0.46% vs. 2.18%) than those formed in $\text{NaPF}_6\text{-PC}$ electrolyte. Similarly, the atomic ratio of Ni in the CEI layer formed in NaFSI-TEP is also much less (0.11% vs. 0.35%) than those formed in $\text{NaPF}_6\text{-PC}$ electrolyte. This is consistent with Figure XIX.4.5h and i that show much less transition metals were found in cycled NaFSI-TEP than in $\text{NaPF}_6\text{-PC}$ electrolyte. These results clearly indicate that the inorganic-rich CEI layer formed in NaFSI-TEP electrolyte can effectively suppress the dissolution of transition metal, stabilize cathode/electrolyte interphase, therefore improve electrochemical performance of NIBs.

The XPS spectra and atom ratio of cycled hard carbon anode in two electrolytes were also summarized in Figure XIX.4.6. The organic species (C 1s) were similar in two electrolytes. However, the XPS spectra were different for inorganic elements, including P 2p from NaPF₆ salt, N 1s and S 2p from NaFSI salt decomposition. In NaFSI-TEP electrolyte, the intensity of N 1s and S 2p peaks from NaFSI salt decomposition were much higher than P 2p peak from NaPF₆ salt decomposition in NaPF₆-PC electrolyte. Briefly, in NaPF₆-PC electrolyte, the SEI components with inorganic and organic hybrid species were derived from both PC solvent and NaPF₆ salt decomposition. However, in NaFSI-TEP electrolyte, more NaFSI salt decomposition forms N, S based inorganic SEI components, which can ensure a robust SEI layer and excellent cycling stability of hard carbon.

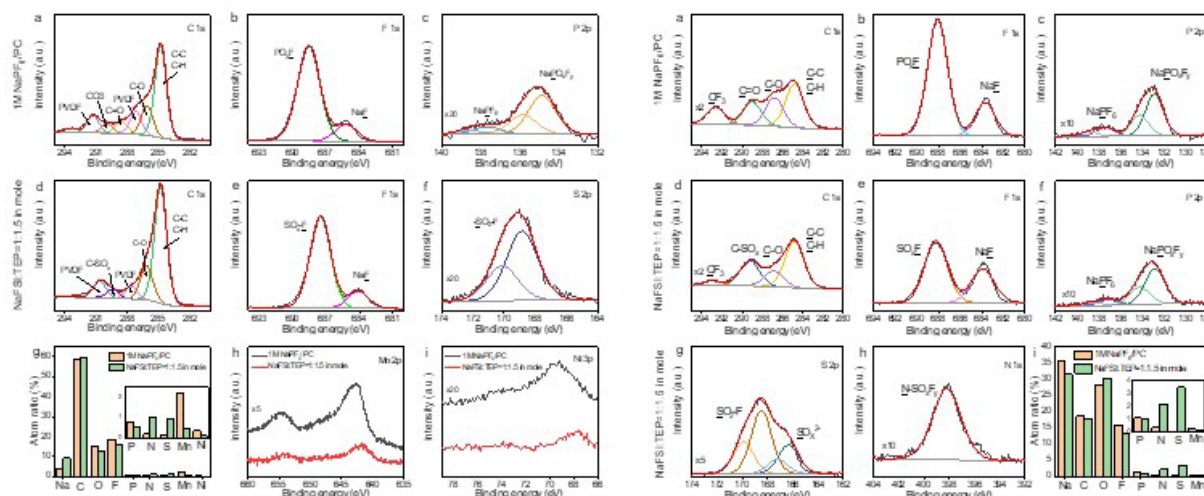


Figure XIX.4.5 XPS spectra of SEI components on cycled NaNCM surface. a, d) C 1s spectra, b, e) F 1s spectra, c) P 2p spectra and f) S 2p spectra in NaPF₆-PC electrolyte (a-c) and NaFSI-TEP electrolyte (d-f). g) Atomic composition of SEIs in two electrolytes. h, i) Mn 2p and Ni 3p spectra in two electrolytes.

Figure XIX.4.6 XPS spectra of SEI components on cycled hard carbon surface. a, d) C 1s spectra, b, e) F 1s spectra, c, f) P 2p spectra, g) S 2p spectra and h) N 1s spectra in NaPF₆-PC electrolyte (a-c) and NaFSI-TEP electrolytes (d-h). i) Atom ratios of SEI in two electrolytes.

4. Develop electrolytes that are compatible with conventional polymer separators

Wettability issue is a significant concern in developing the sodium-based electrolytes that usually exhibit a higher polarity compared to those of Li-ion analogues. The typical separators (PE or PP) commonly used in Li ion batteries have a poor wettability with most of sodium-ion electrolytes using carbonate solvents (such as 1M NaPF₆ in propylene carbonate (PC)) reported in literature. As a result, glass fiber must be used in most of previous studies on NIBs except when ether or ester-based electrolytes were used. On the other hand, most of electrolyte used for NIBs are flammable. To address these problems, a new electrolyte based on tris(2,2,2-trifluoroethyl) phosphate (TFP) solvent has been developed. This electrolyte is not only compatible with PE separator, but is also non-flammable and stable in a high voltage NIB. Therefore, it has a great potential for large-scale applications.

To investigate the compatibility of TFP based sodium electrolyte with PE separator, the performances of high voltage (4.2V) NaNCM||HC full cells using TFP based electrolytes were systematically studied. As a comparison, similar cells with the carbonate-based electrolyte (1 M NaPF₆/EC:EMC (3:7 in vol)) were also studied as a baseline with PE separator. All cells have been cycled three cycles at a low rate of 0.05 C (1 C = 200 mAh g⁻¹) to stabilize SEI layers prior to long term cycling at 0.2 C. Figure XIX.4.1 compares the electrochemical performance of these cells during long-term cycling. In carbonate-based electrolyte, the full cell exhibits fast capacity decay with only 33.5% capacity retention (169 mAh g⁻¹ for 4th cycle, 56.6 mAh g⁻¹ for 200th cycle) after 200 cycles (Figure XIX.4.7a). The average CE of this cell during long cycling is relatively low (< 99.2%), indicating continuous side reactions due to unstable electrode/electrolyte interphases,

poor compatibility between electrolyte and electrodes, and limited high voltage stability, which is consistent with the poor oxidation stability of the electrolyte (Figure XIX.4.7b). In contrast, the full cell with 1 M NaFSI/TFP electrolyte shows much better cycling performance with 80.4% capacity retention (164.8 mAh g⁻¹ for 4th cycle, 132.5 mAh g⁻¹ for 200th cycle) after 200 cycles at 0.2 C. Moreover, NaFSI/TFP was further modified to improve its ionic conductivity and reduce its viscosity by adding optimized amount of DMC in the electrolyte to form the advanced electrolyte (named NaFSI/DMC:TFP). The cell with NaFSI/DMC:TFP electrolyte has demonstrated the best performance among three HC||NaNMC cells investigated in this work as shown in Figure XIX.4.7a. A high-capacity retention of 92.4% (162 mAh g⁻¹ for 4th cycle, 149.7 mAh g⁻¹ for 200th cycle) after 200 cycles with an excellent cycling CE of >99.9% (Figure XIX.4.7b) has been achieved.

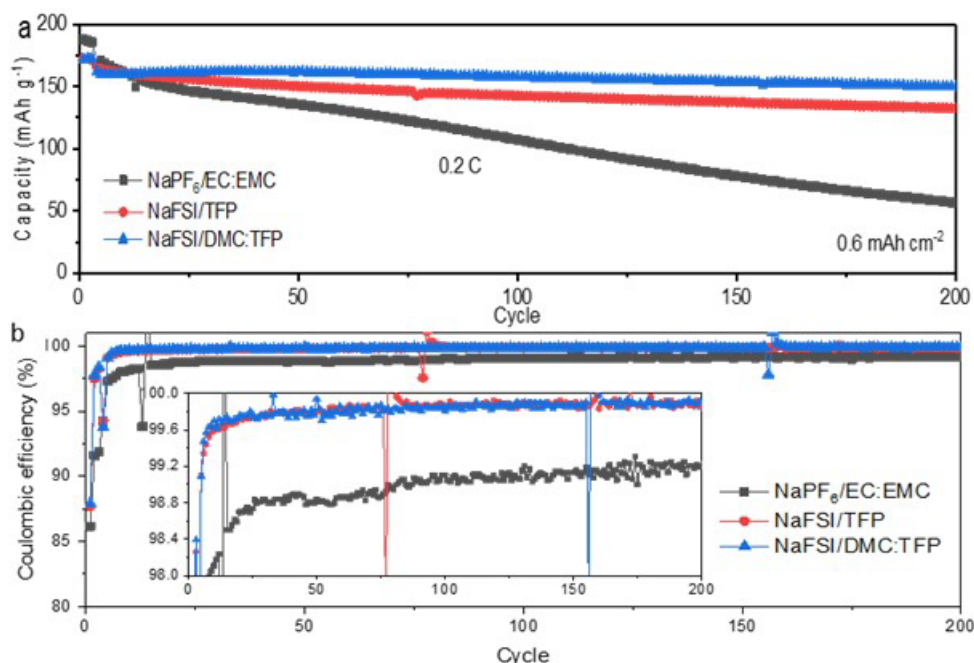


Figure XIX.4.7 Electrochemical performance of HC||NaNMC full cells: Discharge capacity (a) and CE (b) of HC||NaNMC full cells using different electrolytes cycled at 0.2 C in a voltage range 1.2 – 4.2 V after three formation cycles at 0.05 C. The cathode loading is 0.6 mAh cm⁻².

Conclusions

- Developed a high-capacity carbon anode with a capacity of 489 mAh g⁻¹ which is 80 % higher than those of the commercial hard carbon (KURANODE).
- Identified relationship between the composition of the SEI/CEI layers and electrochemical performance of NIBs. The inorganic component of CEI/SEI layers formed in HCE (NaFSI-TEP) can effectively suppress dissolution of transition metal in cathode, minimize the interactions between hard carbon anode and electrolyte, therefore leads to excellent cycling stability of NIBs.
- Non-flammable high voltage electrolyte (>4.2 V) based on phosphate (TEP) and fluorinated phosphate (TFP) have been developed for NaNi_{0.68}Mn_{0.22}Co_{0.10}O₂ (NaNMC) cathode material. TFP based sodium electrolytes is compatible with PE separator. HC||NaNMC full cell using optimized NaFSI/DMC:TFP electrolyte demonstrates a high-capacity retention 92.4% (162 mAh g⁻¹ for 4th cycle, 149.7 mAh g⁻¹ for 200th cycle) after 200 cycles with an excellent cycling CE of > 99.9% and a capacity retention of 82.5% after 200 cycles with a final CE of 99.93%.

Key Publications

1. P. M Le, T. D Vo, H. Pan, Y. Jin, Y. He, X. Cao, H.V Nguyen, M. H Engelhard, C-M. Wang, J. Xiao, J.-G. Zhang*. “Excellent cycling stability of sodium anode enabled by a stable solid electrolyte interphase formed in ether-based electrolytes,” *Advanced Functional Materials*, 2020, 30, 2001151.
2. Yan Jin, Yaobin Xu, Phung M. L. Le, Thanh D. Vo, Quan Zhou, Xingguo Qi, Mark H. Engelhard, Bethany E. Matthews, Hao Jia, Zimin Nie, Chaojiang Niu, Chongmin Wang, Yongsheng Hu, Huilin Pan,* and Ji-Guang Zhang*, “Highly Reversible Sodium Ion Batteries Enabled by Stable Electrolyte-Electrode Interphases”, *ACS Energy Letters*, 2020, 5, 3212.
3. Yan Jin, Phung L.M. Le, Ran Yi, Thanh D. Vo, Ji-Guang Zhang. “Phosphate Electrolyte Design for Highly Reversible Sodium Ion Batteries”, Presented by Yan Jin in 239th ECS Meeting, May 2021.

Acknowledgements

Key contributors include Dr. Yan Jin, Thanh Vo, and Dr. Ra

XX Beyond Li-ion R&D: Battery500

XX.1 Battery500 Innovation Center (PNNL)

Jun Liu, Principal Investigator

Pacific Northwest National Laboratory
902 Battelle Boulevard
Richland, WA 99354
E-mail: jun.liu@pnnl.gov

Yi Cui, Principal Investigator

Stanford University/SLAC
450 Serra Mall
Stanford, CA 94305
E-mail: yicui@stanford.edu

Tien Q. Duong, DOE Technology Development Manager

U.S. Department of Energy
E-mail: Tien.Duong@ee.doe.gov

Start Date: October 1, 2020

End Date: September 30, 2021

Project Funding (FY21) : \$8,000,000

DOE share: \$8,000,000

Non-DOE share: \$0

Project Introduction

Lithium (Li)-ion batteries play a critical role in modern day technologies, but their specific energy (Wh/kg) and energy density (Wh/L) are approaching the maximum practically achievable values based on existing technology with the conventional cathode and anode materials. The large-scale deployment of electric vehicles and ever-increasing demand of modern technologies require further increase in cell energy and cost reduction. Rechargeable Li-metal batteries are regarded as “Holy Grail” of high-energy-density systems because Li metal has an ultrahigh theoretical specific capacity (3860 mAh/g), an extremely low redox potential (-3.040 V vs. standard hydrogen electrode), and a very low gravimetric density (0.534 g/cm³). However, the practical application of Li metal anode (LMA) still faces several big challenges, including safety concerns due to Li dendrite growth, limited cycle life because of low Li Coulombic efficiency (CE), and infinite volume change during Li stripping and redeposition if a two-dimensional (2D) flat Li foil is used. In addition, developing the next generation rechargeable Li metal batteries with a specific energy higher than 300 Wh/kg, up to 500 Wh/kg, is still a significant challenge. Many groups are focusing on the fundamental breakthroughs in electrode materials and control the unnecessary side reactions in such new battery concepts. Solid-state Li batteries using solid electrolytes have recently received wide attention due to the inherent high safety and decent energy. There have been intense efforts to improve the bulk conductivity, interfacial charge transport and stability for the manufacturing of the solid-state cells. A very desirable strategy is to take advantage of the electrode materials that are commercially or nearly commercially available and introduce the least perturbation to the cell configuration and manufacturing process of the current technologies. Based on these considerations, two battery chemistries, high nickel content lithium nickel-manganese-cobalt oxide (high-Ni LiNi_xMn_yCo_zO₂ (NMC), Ni>60%), coupled with LMA, and Li-sulfur (S) chemistry, with the potential to achieve a specific energy higher than 500 Wh kg⁻¹ are selected for this Battery500 innovation center project.

Objectives

The Battery500 Consortium aims to develop commercially viable Li battery technologies with a cell level specific energy of 500 Wh/kg through innovative electrode and cell designs that enable the extraction of the

maximum capacity from advanced electrode materials. In addition, the project aims to be able to achieve 1000 cycles for the developed technologies.

Approach

The Battery500 Consortium will utilize first class expertise and capabilities in battery research in the United States and develop an integrated and multidisciplinary approach to accelerate the development and deployment of advanced electrode materials in commercially viable high energy batteries. The LMA combined with compatible electrolyte systems and two types of cathodes—one high-Ni NMC and another S—will be studied and developed to reach high specific energy. The project focus is to design novel electrode and cell architectures to meet the 500 Wh/kg goal. The Consortium will work closely with R&D companies, battery/materials manufacturers and end-users/OEMs to ensure that the developed technologies are aligned with industry needs and can be transferred to production. The out-year goals for FY2020 include: (1) Deliver pouch-cell design and pouch-cell parameters for over 400 Wh/kg pouch cells; (2) Develop new 3D anode structures; test and validate such using coin-cell standard protocols; (3) Fabricate and test 350 Wh/kg Li-S pouch cells with over 50 stable cycles; and (4) Fabricate and test a pouch cell capable of 400 Wh/kg and 100 cycles. All these goals have been successfully achieved in FY2021.

Results

1. Keystone project 1: Materials and interfaces

In FY2021, **Stanford University** team has further developed a rationally designed electrolyte solvent ether molecule, FDMB, which is very stable relative to Li metal and to high voltages such as found in high-Ni NMC. The results are shown in Figure XX.1.1. The upper figure shows the excellent behaviour of the electrolyte using LiFSI salt in FDMB compared with that of using LiFSI in DMB and DME as well as of LiPF₆ salt in a carbonate electrolyte. The coulombic efficiency of this new electrolyte in Li||NMC532 cell is over 99.98%. The lower figure shows the excellent behaviour for a range of high-Ni NMCs, 811, 622 and 532.

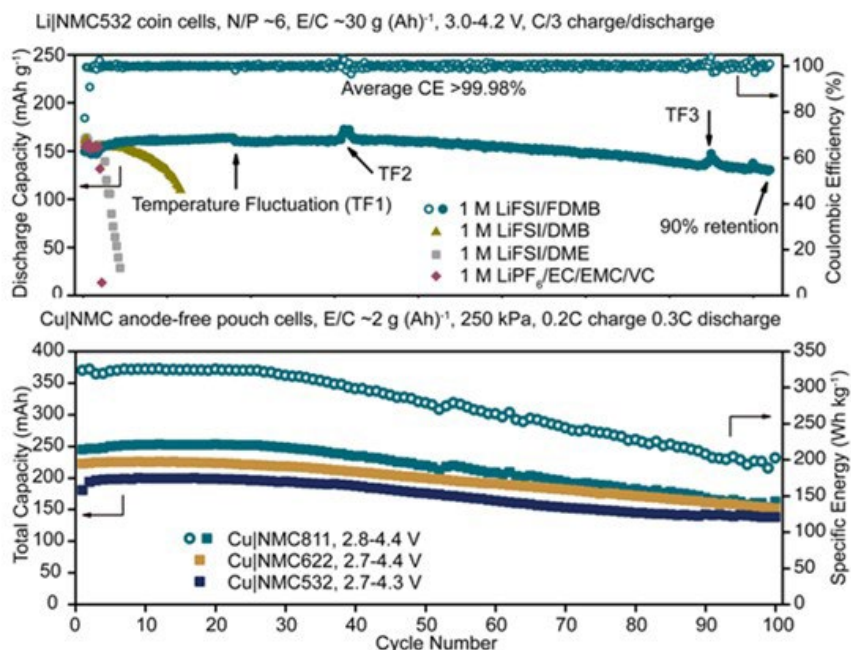


Figure XX.1.1 Behavior of the new FDMB ether electrolyte, showing (upper) relative to other electrolytes, and (b) for three high Ni NMC cathodes.

Researchers at **Binghamton** studied a Li-free niobium oxide treatment of 811 NMC cathode to determine the impact of coating and lattice substitution. Using a Li-free treatment allowed for the removal of any surface

carbonate species forming Li-Nb-O species. This treatment at a 1% Nb level decreased the first cycle loss as shown in Figure XX.1.2a; it was found that the Nb was predominantly on the surface and in the surface layers when heated at 400 and 500 °C, whereas at higher temperatures it diffuses into the bulk of the material. For the latter, the impact is much less on the 1st cycle. The rate capability is also improved by this surface treatment (Figure XX.1.2b). However, the long-term cyclability is improved when the niobium substitutes in the lattice as shown in Figure XX.1.2c. These studies will be repeated using the newly adopted LHCE electrolyte system.

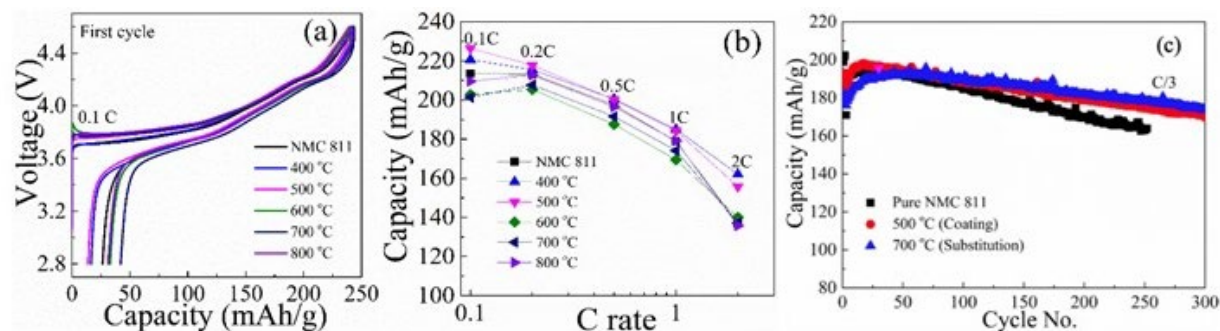


Figure XX.1.2 Impact of a NbO₅ treatment of NMC 811. (a) Reduction of 1st cycle loss by surface treatment, 400 and 500 °C; (b) Improved rate capability of surface treated material; and (c) bulk treated material shows the highest capacity retention. (a) and (b) charge to 4.6 V; (c) charged to 4.4 V.

Researchers at **UT Austin** have synthesized the very high-Ni cathode LiNi_{0.94}Co_{0.06}O₂ (NC) and provided samples to the team. They found that a phosphoric acid treatment protected the surface from residual lithium formation on long standing in an air environment. The H₃PO₄ scavenges residual lithium species from the surface, as shown in Figure XX.1.3. The H₃PO₄-treated samples (PNC) maintain good morphology after exposure to also show a thinner rock-salt layer (~ 3 nm) after long-term cycling than the untreated samples (~ 15 nm), as indicated by TEM. Treatment with ¹⁸O isotope-labeled H₃PO₄ reveals the protection of the cathode surface by the formation of Li₃PO₄, as indicated by TOF-SIMS. Collaborators at **PNNL** have found that their new LHCE works very well with this high-Ni cathode at 1C rate, as shown in Figure XX.1.4; its behavior is much better than that in the former carbonate baseline electrolyte.

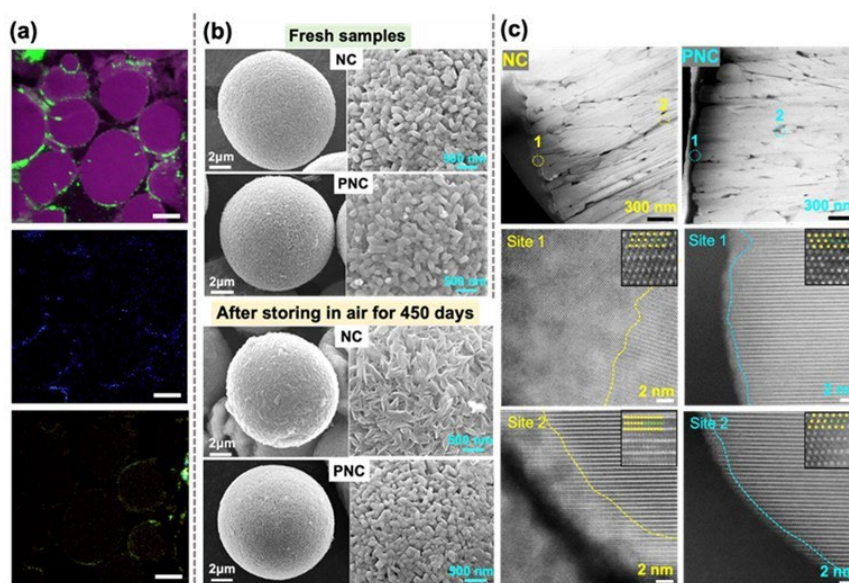


Figure XX.1.3 H₃PO₄ scavenges residual lithium and protects the surface with Li₃PO₄ as revealed by TOF-SIMS with ¹⁸O labeling. The H₃PO₄-treated sample (PNC) forms a thinner rock-salt layer (~ 3 nm) than the untreated sample (NC) (~ 15 nm). The purple and green colors in the top of (a) represent, respectively, ¹⁶O- and ¹⁸O- species, the blue color in the middle of (a) represents P¹⁸O₂⁻ species, and the green color in the bottom of (a) represents Li₂¹⁸O⁺ species. The scale bar in (a) is 10 μm.

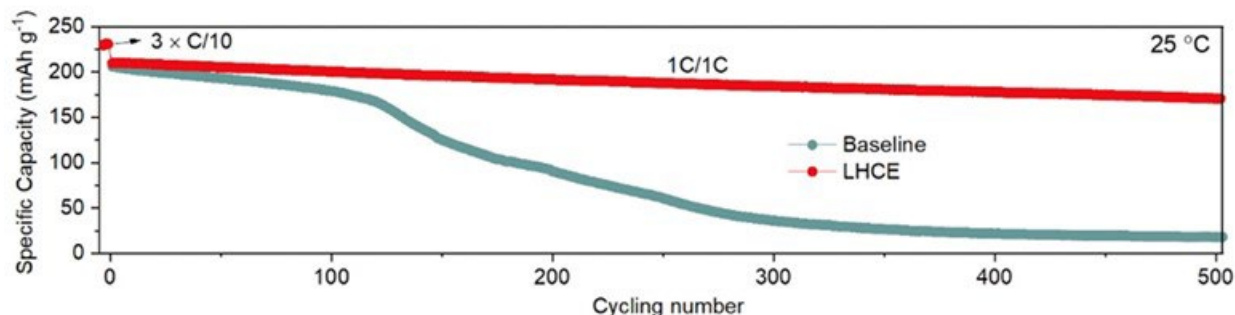


Figure XX.1.4 Cycling of Li || LiNi_{0.94}Co_{0.06}O₂ cells in the prior baseline electrolyte compared with that in LHCE.

Binghamton also worked with **Stanford** and **PNNL** to determine the electrochemical and thermal stabilities of the advanced next-generation electrolytes, which are much more effective in Li metal cells compared to carbonate-based electrolytes. In these initial experiments, the electrolytes were pushed to their limits to determine those limits in order to optimize the testing regimes for future in-depth studies. As shown in Figure XX.1.5, all electrolytes are stable up to around 4.4 V and up to 60°C. The 1 M LiFSI/FDMB was as stable as the baseline carbonate electrolyte, only showing side reactions at 60°C above 4.4 V. The M47 LHCE showed side reactions at both 45°C and 60°C above 4.5 V, and at 30°C above 4.6 V as expected. Longer term testing is now underway within their stability ranges at 4.4 V and 30°C, which is within the stability limits of these next generation electrolytes.

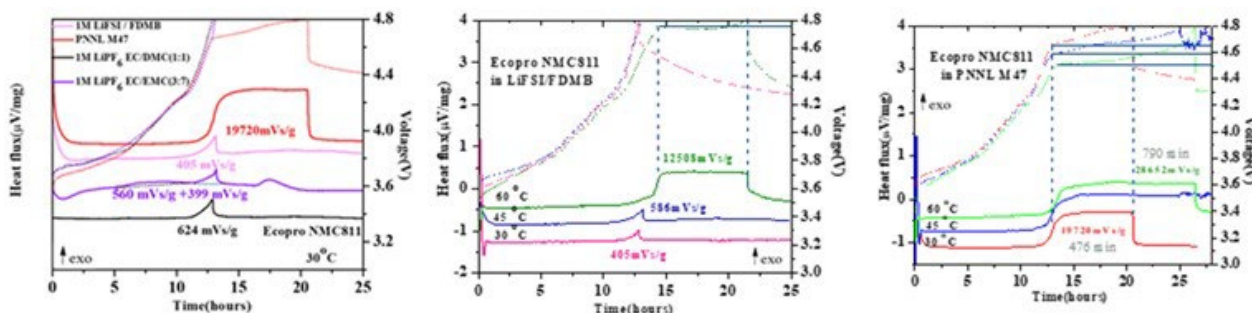


Figure XX.1.5 Operando DSC studies comparing the 2020 carbonate electrolyte with the next generation LiFSI ether-based FDMB and M47 electrolytes.

UW employed the solid electrolyte LATP as the coating material for Al-NMC811 cathode by radio-frequency magnetron sputtering approach. The direct coating on the cathode surface effectively reduces the side reaction without disrupts the inter-particle electronic/ionic pathways and hence improves the electrochemical performance of Al-NMC811. After sputtering for 8 hours, the grey surface of the Al-NMC811 turns blue (Figure XX.1.6a) and the surface morphology of the Al-NMC811 becomes smoother (Figure XX.1.6b and Figure XX.1.6c). These results suggest that a thin film has been smoothly coated on the surface of the Al-NMC811 electrode. Figure XX.1.6d-g exhibit the initial charge-discharge curves at 0.1C (1 C = 1.4 mAh cm⁻²) between 2.8 V and 4.4 V for Li metal cells. The LATP-coated Al-NMC811 shows a similar initial capacity and Coulombic efficiency (CE) to those of pristine Al-NMC811 cathode (Figure XX.1.6d). After 320 cycles at C/3, the LATP-coated Al-NMC811 shows higher reversible capacity (163.2 mAh g⁻¹) and capacity retention (81.0%) than those of the pristine Al-NMC811 (151.8 mAh g⁻¹ and 75.3%). (Figure XX.1.6e and Figure XX.1.6f display the dQ/dV curves of pristine and LATP-coated Al-NMC811 electrodes at selected cycles. At the 150th cycle, the voltage hysteresis of pristine Al-NMC811 in the high-voltage region is 87 mV, larger than that for the LATP-coated Al-NMC811 (75 mV). At the 250th cycle, the voltage hysteresis of pristine Al-NMC811 increases by 107 mV while only a 76 mV increase in hysteresis is found for the LATP-coated Al-NMC811. This result indicates that LATP direct coating on Al-NMC811 electrode helps reduce polarization increase and enhance the electrochemical performance.

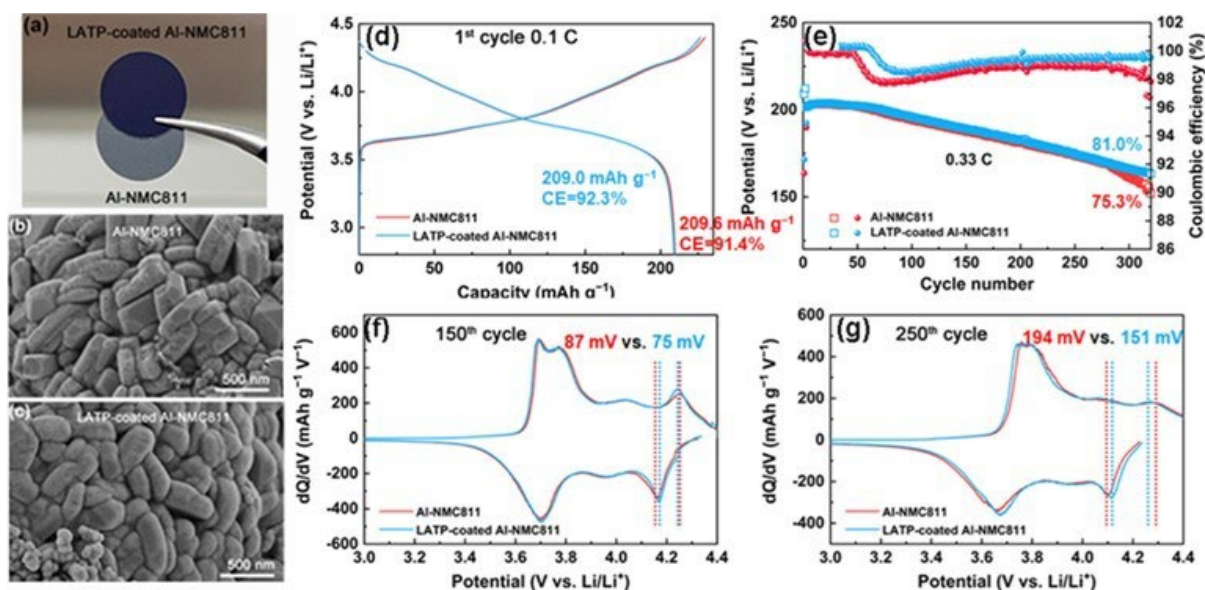


Figure XX.1.6 (a) Photo images of Al-NMC811 and LAMP-coated Al-NMC811 electrodes. SEM images of (b) Al-NMC811 and (c) LAMP-coated Al-NMC811 electrodes. (d) Initial charge-discharge curves and (e) cycling performance of pristine and LAMP-coated Al-NMC811 electrodes. The dQ/dV curves of (f) the 150th cycle and (g) the 250th cycle of pristine and LAMP-coated Al-NMC811 electrodes.

PNNL team investigated the calendar life of Li||NMC811 coin cells consisted of a NMC811 cathode (4.2 mAh cm⁻²), a thin Li foil (50 μm) and the TFE0-based LHCE. The electrolyte amount was controlled at an electrolyte/capacity (E/C) ratio of 7 g (Ah)⁻¹. All cells were stored in 25°C temperature chambers and charged and discharged between 2.8 and 4.4 V at C/10 rate, where 1C = 4.2 mA cm⁻². For the calendar life tests, cells were firstly cycled twice in the voltage range of 2.8-4.4 V at C/10 rate and then charged to the target states-of-charge (SOCs). As shown in the Figure XX.1.7a-Figure XX.1.7c, three SOC conditions, i.e., fully discharged state (0% SOC, rest after formation cycles), half charged state (50% SOC, with a specific capacity of 97 mAh g⁻¹ charged at CC mode), and fully charged state (100% SOC, where cells were charged to 4.4 V at CC mode followed with an additional CV step), were selected for this study. The self-discharge capacity and the recoverable capacity of the cells were measured after selected storage periods (1 day, 1 week, 2 weeks, 3 weeks, 4 weeks, 2 months, 3 months, 6 months, 9 months, and 18 months) at 25°C. At each scheduled time, cells at fully discharged state were charged and discharged at C/10 for 1 cycle to check the recoverable capacity as shown in Figure XX.1.7d. For the cells charged to 50% or 100% SOC, they were first fully discharged at C/10 to check the capacity loss (or self-discharge) during the selected rest period, and then charged back to the target SOC as shown in Figure XX.1.7e and Figure XX.1.7f, respectively. The last curve (18-month storage) in Figure XX.1.7e shows the discharge profile of a separate sample stored at 50% SOC for 18-months without intermediate steps. The self-discharge rate is defined as the capacity loss during the rest period divided by the storage time since the beginning of the last rest period. After 9 months storage, the capacity recovery reduced slightly, indicating the calendaring degradation accelerated in this period. When the storage time further prolonged to 18 months, 181.9 mAh g⁻¹ (i.e., 89.6% of initial capacity) can still be recovered. This result clearly demonstrates that great capacity recovery can be achieved in high voltage Li||NMC811 cells using the TFE0-based LHCE. For the cells stored at 50% SOC, the self-discharge rates are between 0.31- 0.82%/day during different storage periods with an average self-discharge rate of 0.42%/day for the whole storage time. For the cells stored at 100% SOC, the self-discharge rates are between 0.23 - 0.86%/day during different time periods with an average self-discharge rate of 0.26%/day. The slight variation of the self-discharge rates may come from the systematic error of the Land Battery Tester System used, which could be reduced in the long storage time. A fully charged battery would lose only 2.5% (5.7 mAh g⁻¹) of its initial capacity (227.5 mAh g⁻¹) for 1 week storage. In addition, a fully charged cell can still retain more than

half of the capacity (114.0 mAh g^{-1} of its previous charged capacity (216.8 mAh g^{-1}) after 9-month storage which is excellent for practical applications such as electrical vehicles.

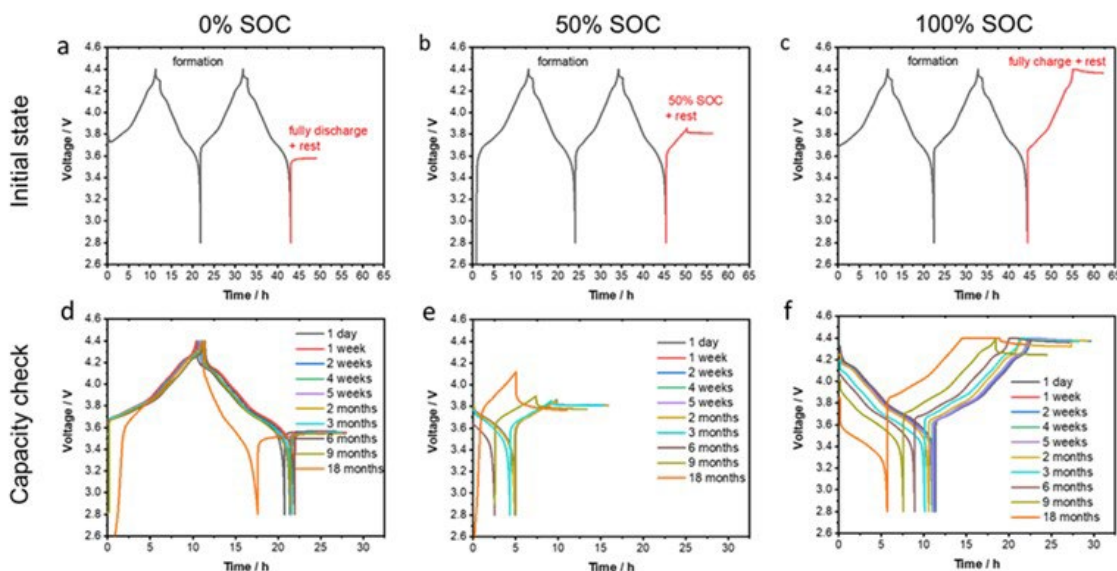


Figure XX.1.7 Electrochemical performances of cells at different states of charge (SOCs) at 30 °C. (a-c) Voltage profiles of the cells during the formation process and rest conditions, (a) the cell rested at fully discharged state (0% SOC), (b) the cell rested at half charged state (50% SOC), and (c) the cell rested at fully charged state (100% SOC). (d-f) Voltage profiles of the cells after different storage periods at different SOC, (d) 0% SOC, (e) 50% SOC, and (f) 100% SOC.

BNL team applied synchrotron X-ray fluorescence (XRF) mapping to understand the transition metal (TM) dissolution at high voltage charging and consequent deposition on the Li metal anode. This is closely related to the Battery500 goal of further increasing the cell energy density which can be realized by increasing the charging voltage. However, high voltage can lead to serious transition metal (TM) dissolution on the cathode side, followed by TM migration through electrolyte and deposition on Li metal anode, resulting in surface/interphase degradation and cell capacity fade. XRF mapping images with a spatial resolution around 30 μm were collected from the Li metal anodes recovered from both baseline electrolyte and electrolyte that contains a new phosphorus-based additive after 90 cycles. As the fluorescence intensity can be directly related to the TM concentration, the deposited TM on Li anode surface can also be mapped quantitatively as shown in Figure XX.1.8a, in which the concentrations of Ni, Mn, and Co are represented by the color scale bar with the unit in $\mu\text{g mm}^{-2}$. Several interesting findings are noted: Firstly, there are substantial inhomogeneities across the electrode, which apply to electrodes harvested from both baseline and additive-containing electrolytes. TM concentration in one area can be higher than another area by an order of magnitude. Such inhomogeneities demonstrated the necessity of considering TM dissolution in the length-scale of electrode-level instead of just at nanometric level and such electrode level study has never been explored so far. Secondly, among all three TMs, Ni experiences the most severe dissolution. This is completely different from the widely accepted belief that Mn is the most dissolved element among Ni, Mn, and Co. One possible reason for such difference is that the entire electrode was evaluated in this work, while previous work usually only focused on a randomly selected spot that may not be representative, considering the high inhomogeneities of the deposition cross the electrode. Thirdly, the additive can very effectively suppress TM dissolution as shown in Figure XX.1.8b. On average, the deposited TM is reduced by $\sim 70\%$ when the additive is present.

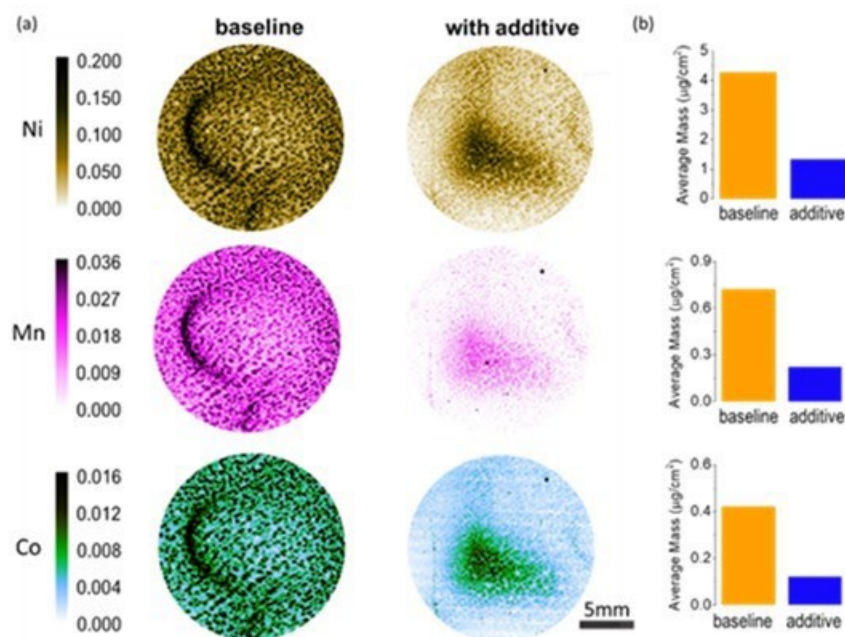


Figure XX.1.8 Electrode-level quantification of the deposited transition metal on Li anode. (a) XRF mapping of the Li anode with spatial resolution around $30\text{ }\mu\text{m}$. The unit of the color scale bar is $\mu\text{g mm}^{-2}$. (b) Average deposited transition metal mass per unit area for the three transition metals. In both (a) and (b), comparisons are made between the baseline electrolyte and the 'with additive' electrolyte.

The **Binghamton** team worked with **PNNL** and **Stanford University** to determine the electrochemical and thermal stabilities of their novel electrolytes. Besides the previously reported LiFSI/FDMB and M47 LHCE electrolytes, two additional electrolytes, T3 and ED2 from PNNL, were studied at the same conditions. The isothermal calorimetry experiments were performed at 30°C , 45°C and 60°C with charging to 4.8 V at C/10 rate ($1\text{C} = 200\text{ mAh g}^{-1}$). The results of the four ether-based electrolytes are compared to the baseline carbonate electrolyte in Figure XX.1.9. All electrolytes are stable up to around 4.4 V and even up to 60°C . However, differences between the electrolytes can be clearly observed when charged above 4.4 V . T3 was as stable as the baseline carbonate electrolyte at each temperature without any obvious side reaction. The 1 M LiFSI/FDMB showed similar stability as T3 and the carbonate electrolyte at 30°C and 45°C , but began to show side reactions above 4.6 V at 60°C , associated with a large heat release. Meanwhile, the stabilities of M47 LHCE and ED2 were lower than the other electrolytes, where apparent side reactions were observed at all three temperatures above 4.5 V . Comparatively, the M47 LHCE had much more heat release than ED2, indicating the worst thermal stability among these five electrolytes. Interestingly, the heat flux of the ED2 electrolyte decreased with increasing temperature, which is contrary to other electrolytes. Overall, the ether-based electrolytes were less stable than the carbonates under the extreme conditions of these tests, but all are stable at 30°C for charging voltages up to 4.4 V where long term tests are now underway. In the end a compromise must be reached between electrolyte stability under extreme conditions and ability to plate lithium with near 100% efficiency.

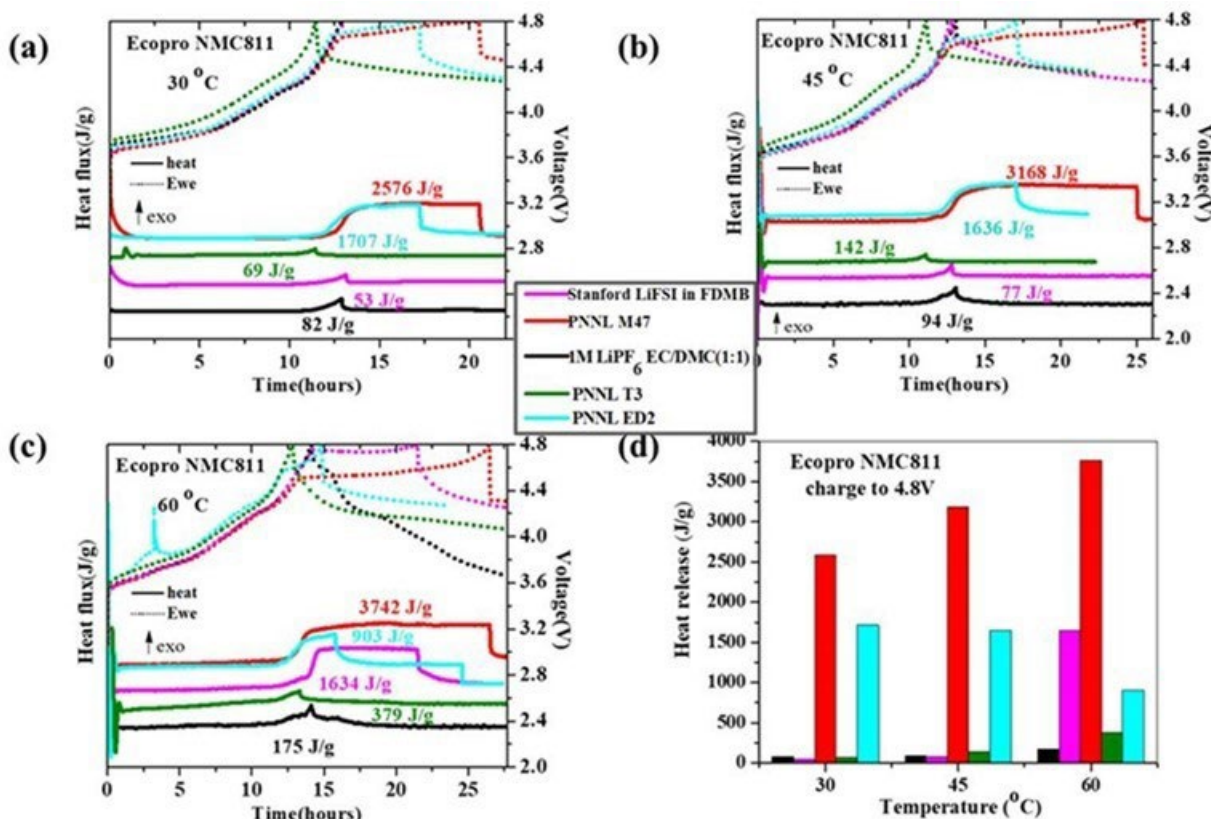


Figure XX.1.9 Operando DSC measurements (dotted curves for electrochemical test and solid curves for the measured heat flux) of novel ether-based M47, ED2, T3, 1 M LiFSI/FDMB electrolytes and traditional carbonate electrolyte (1M LiPF₆ in EC/DMC (1:1)) for NMC 811 charged to 4.8 V while held at (a) 30°C, (b) 45°C and (c) 60°C isothermally. (d) Summary of total heat release.

The **UT Austin** team benchmarked an undoped, pure-nickel LiNiO₂ (LNO) cathode with carbonate and LHCE electrolytes to highlight the remarkable performance enabled by advanced electrolytes. Figure XX.1.10a shows the cycling performance of LNO cathodes in lithium-metal pouch cells with a typical carbonate electrolyte (LP57, 1 M LiPF₆ in 3 : 7 EC : EMC with 2% VC) as well as with the baseline localized high concentration electrolyte (LiFSI-1.2DME-3TTE). After 200 cycles, the cell with LHCE showed a more than 5-fold improvement in capacity retention. When the cathodes from these cells were harvested and assembled into new cells, most of this capacity difference remained, indicating that the capacity loss during cycling was mostly associated with the cathode itself (Figure XX.1.10b). The improved capacity retention of LNO in the LHCE electrolyte can be attributed to several factors, including formation of a more robust cathode-electrolyte interphase (CEI). Figure XX.1.10c shows the X-ray photoelectron spectroscopy (XPS) data for the cathodes cycled in each electrolyte. The cathode cycled in LHCE shows the presence of sulfur and nitrogen species, which can be attributed to the decomposition of the lithium salt, lithium bis(fluorosulfonyl)imide. Similarly, an increase in fluorine concentration and the presence of lithium fluoride can be attributed to salt decomposition as well as to decomposition of the fluorinated solvent. Lithium fluoride is known to be an effective CEI component, contributing to the improved stability of LNO in LHCE. In addition to improved surface stability, LNO in LHCE is also subject to reduced microcracking relative to the same cathode in carbonate electrolyte. Figure XX.1.10d shows the cross-sectional scanning electron microscopy (SEM) images of the LNO cathodes after 200 cycles. The cathode particles, which were cycled in LHCE, show some small number of cracks, typical also of pristine cathode material. Meanwhile, the particles cycled in LP57 show many microcracks. While 200 cycles are not enough for complete particle pulverization, *i.e.*, destruction of the secondary particle structure, microcracks can disrupt the ion or electron conduction pathway and allow for electrolyte penetration

and increased surface reactivity. The findings demonstrate that the viability of high-nickel cathodes, and their degradation mechanisms should be re-evaluated in light of using advanced electrolytes, such as LHCE.

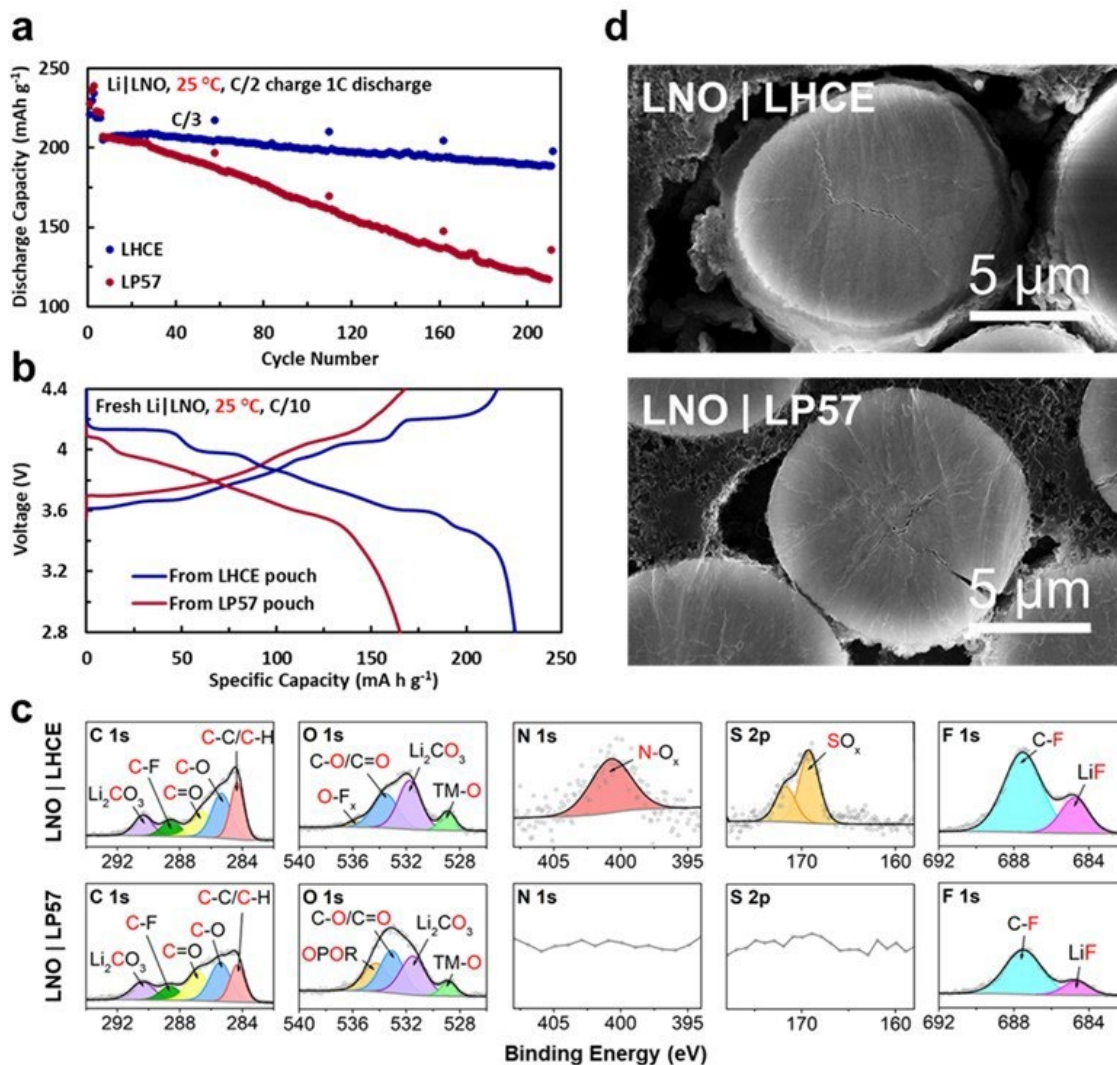


Figure XX.1.10 (a) Cycling performances of lithium-metal pouch cells with LNO cathodes at C/2 charge and 1C discharge rate, with C/3 rate every 50 cycles. (b) Charge-discharge curves of fresh coin cells assembled using the cathodes recovered from the cyclic pouch cells. (c) Cross-sectional SEM images of LNO cathodes recovered from cyclic pouch cells after 200 cycles in LHCE (top) and carbonate electrolyte (bottom). (d) XPS data of LNO cathodes recovered from cyclic pouch cells after 200 cycles in LHCE (top) and carbonate electrolyte (bottom). Spectra were normalized across samples for each element.

The PNNL team developed an ionic conductive double-layer coating for lithium-metal anode protection to improve the battery performance. The protective double layer consists of a top layer based on a cross-linkable polymer and a bottom layer of polyethylene oxide (PEO)-based polymer electrolyte. PEO is well known to be stable with Li metal and to have a high donor number for Li ion as well as high chain flexibility, which are important for promoting ion transport in the protection layer. However, it needs to be covered by durable materials to preserve its integrity because PEO can swell and even dissolve in liquid electrolytes. For this reason, the cross-linkable polymer is selected as the top layer (TL) to maintain the integrity of the PEO-based layer that directly covers the Li-metal surface. The cycle life of Li||Li symmetric cells composed of a thin Li anode (50 μm) and 75 μL of DME-LHCE (LiFSI-1.2DME-3TTE) electrolyte was investigated at a current density of 1 mA cm⁻² and a capacity of 1 mAh cm⁻², as shown in Figure XX.1.11a. Bare Li shows a short circuit failure at around 960 h. The top layer coated Li (TL@Li) and double layer coated Li with pure PEO in

the bottom layer (DL-0@Li) have a longer cyclability, but lead to a higher polarization than bare Li. To reduce the polarization during cycling, an additive was added to the double layer. The double layer with the additive-coated Li (DL-3@Li) exhibits a long cycling lifespan for 1,000 h without significant increase in polarization. Based on this result, DL-3@Li was selected as the optimum protection layer for the Li-metal electrode. The coating layer morphology was checked by SEM using a DL-3 coated Cu foil, which was prepared by the same process as DL-3@Li. As shown in Figure XX.1.11b, the total thickness of the coating layer is ~ 630 nm, including ~ 180 nm of top layer and ~ 450 nm of bottom layer. The thickness of DL-3 coated on Li is similar to that coated on Cu foil. In addition, DL-3@Li delivers a stable deposition/stripping behavior with a slightly improved average coulombic efficiency (CE) value compared to the bare Li (Figure XX.1.11c). Furthermore, in Li||NMC622 coin cells consisting of a NMC622 cathode (4.2 mAh cm^{-2}), a thin Li foil ($50 \mu\text{m}$) and $75 \mu\text{L}$ DME-LHCE, the Li||NMC622 cell using DL-3@Li exhibits a higher capacity retention of 92.4% after 220 cycles at a current density of 2.1 mA cm^{-2} (*i.e.*, C/2 rate) compared to those using bare Li (74.6%) (Figure XX.1.11d). To understand the mechanism behind the improved electrochemical performance, SEM images of Li-metal electrodes extracted from the cycled coin cells are compared in Figure XX.1.11e. The cycled DL-3@Li exhibits a flat and smooth surface without Li dendrites while the bare Li anode shows a rough and porous surface with massive dendritic Li. This result demonstrates that uniform Li deposition and controlled side reactions can be achieved on Li metal at a high current density after DL-3 coating.

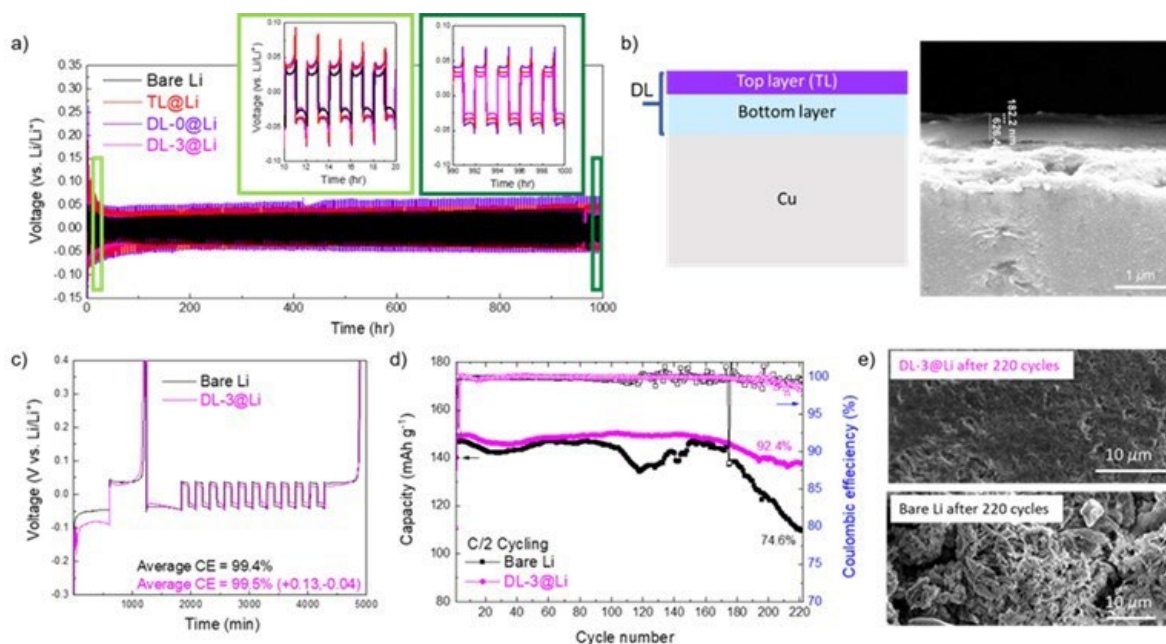


Figure XX.1.11 (a) Voltage profiles of Li metal deposition/stripping in Li||Li symmetric cells (1 mAh cm^{-2}) at a current density of 1 mA cm^{-2} . (b) Schematic illustration and cross-sectional SEM image of DL-3@Cu. (c) Average CEs of Li||Cu cells using bare Li and DL-3@Li. (d) Cycling performances of Li||NMC622 cells (4.2 mAh cm^{-2}) at high rate (C/2, $1\text{C} = 4.2 \text{ mA cm}^{-2}$) in the voltage range of 2.8 – 4.4 V at 25°C . (e) Surface SEM images of bare Li and DL-3@Li after 220 cycles.

The **Stanford University** team has developed a family of rationally designed electrolyte solvent ether molecules: FDMB, FDMP, FDMH, and FDMO; all of which are very stable relative to Li metal and to high-voltage cathodes, such as high-Ni NMC. However, there is a balance between electrode stability and reasonable ionic conduction. The molecular structures, design logic, and battery performance are shown in Figure XX.1.12. Generally, longer fluorinated chains result in higher stability, yet lower ionic conductivity; therefore, a balance needs to be achieved (Figure XX.1.12a-b). After screening different electrolyte recipes, the team has identified 1 M LiFSI/1DME/6FDMH (by volume) as the best electrolyte even compared to previously reported 1 M LiFSI/FDMB (Nature Energy, 2020, 5, 526-533). The 1 M LiFSI/1DME/6FDMH electrolyte showed a replicable 99.4% Li metal CE and high oxidative stability, enabling 120 cycles in an anode-free Cu||NMC811 pouch cell (Figure XX.1.12c-e).

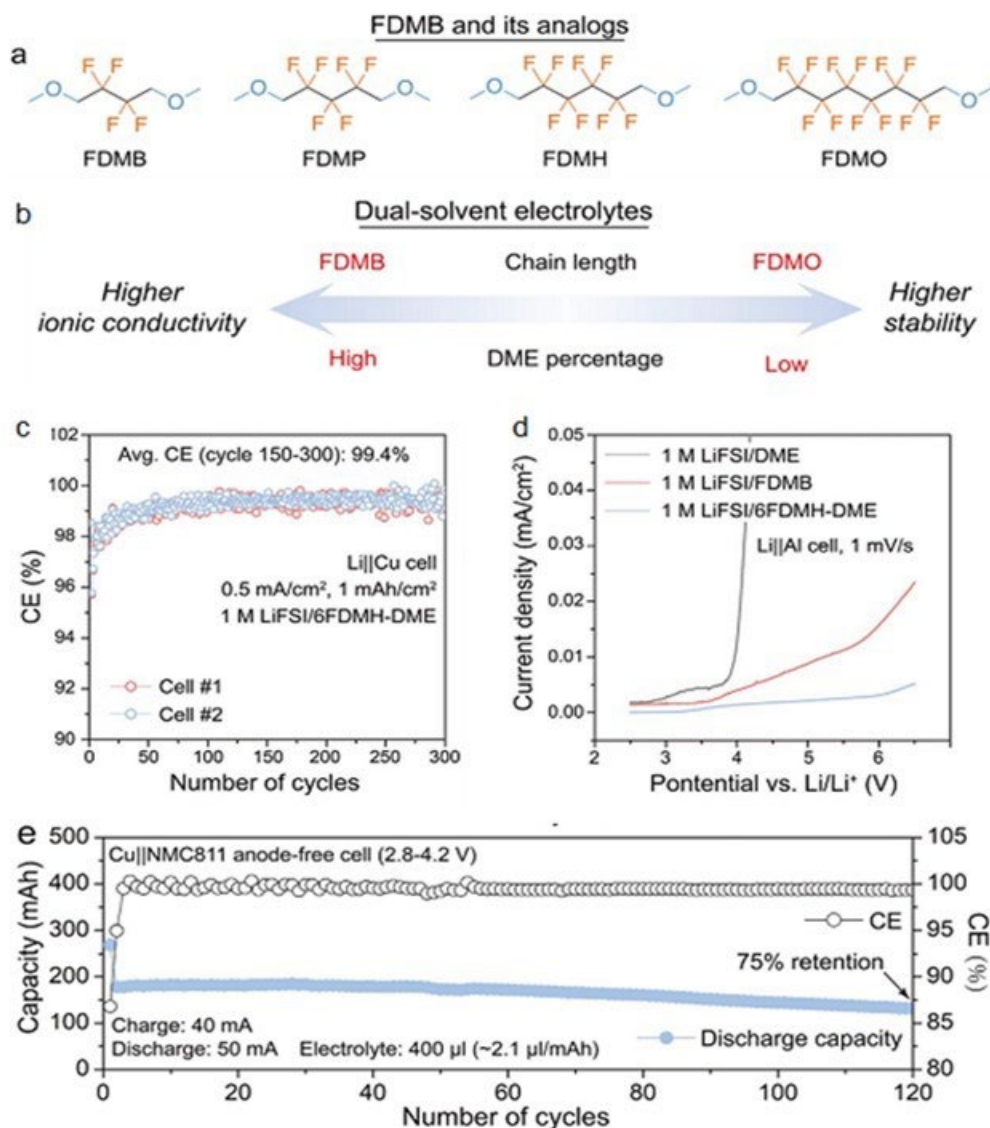


Figure XX.1.12 (a,b) Molecular structures and design logic of FDMB and its analogs. (c) Long cycling CE of Li||Cu half cells. (d) LSV showing the high-voltage stability of developed electrolytes. (e) Anode-free pouch cell performance using the best electrolyte, 1 M LiFSI/1DME/6FDMH.

2. Keystone project 2: Electrode architectures

Analysis of Sulfurized Polyacrylonitrile Meng's group at UCSD used UCSD STEM EELS to probe the bonding environment evolution of Nitrogen (N), Sulfur (S) and Carbon (C) in Sulfurized Polyacrylonitrile (SPAN) cathode at the pristine, 1-cycle discharged and charged states. It was found that all three elements were actively participating in the electrochemical reaction. The 10-cycled SPAN sample was studied by STEM EDS to see whether long term cycling would affect the structure as well as the elemental distribution in the SPAN particles. The pristine SPAN particles were studied as the baseline reference. The elemental distribution of S, C and N were obtained by STEM EDS (Figure XX.1.13a-d). It was shown that the SPAN particles have a diameter about 500 nm and all three elements are uniformly distributed in the whole particle. The 'U' shape C signal comes from the lacey carbon supportive film on the TEM grid. There is no evidence of S clusters in all the SPAN particles, which further confirms that S element is bonded to the SPAN polymer backbone and elemental S particle does not exist in the sample. The SPAN particles at discharged state after 10 cycles were studied to see if there would be any significant redistribution of elements after cycling. It is still under debate

whether the S element is detached from the SPAN polymer after cycling. By studying the elemental distribution in the SPAN particles by STEM EDS after 10 cycles, we can gain some useful insights about how the elements, especially S, are participating in the electrochemical reaction. The cycled sample lamella is prepared by Cryo-FIB, which thinned the samples to ~ 100 nm to make sure that thickness was strictly controlled across different samples. Figure XX.1.13e shows the morphology of the 10-cycle discharged SPAN particles, which still have a diameter about 500 nm. Overall, the structure of the SPAN did not change much compared to the pristine one. As shown in Figure XX.1.13f-h, there was not much redistribution of C and N elements in the sample, which could suggest that the SPAN polymer backbone is still intact after the cycling. Although a small portion of the S started to accumulate on the surface of the particle, most of the S was still uniformly distributed in the whole particle. The result shows that while a small portion of S would leave the SPAN particle after cycling, the most of S would still stay in the SPAN particle, which could be evidence of the ultra-stability of the SPAN cathode. Similar results were observed in the SPAN sample at charged state after 10-cycles. Figure XX.1.13i shows the morphology of the 10-cycle charged SPAN particles, which also did not change much compared to the pristine and discharged ones. As shown in Figure XX.1.13h, all three elements were still uniformly distributed in the SPAN particles. The results shown in Figure XX.1.13 suggest that the electrochemical reaction of SPAN will not create a large-scale elemental redistribution. Most importantly, the S element did not segregate much and form clusters after cycling, which could be a main reason for the stability of SPAN/Li electrochemical reaction.

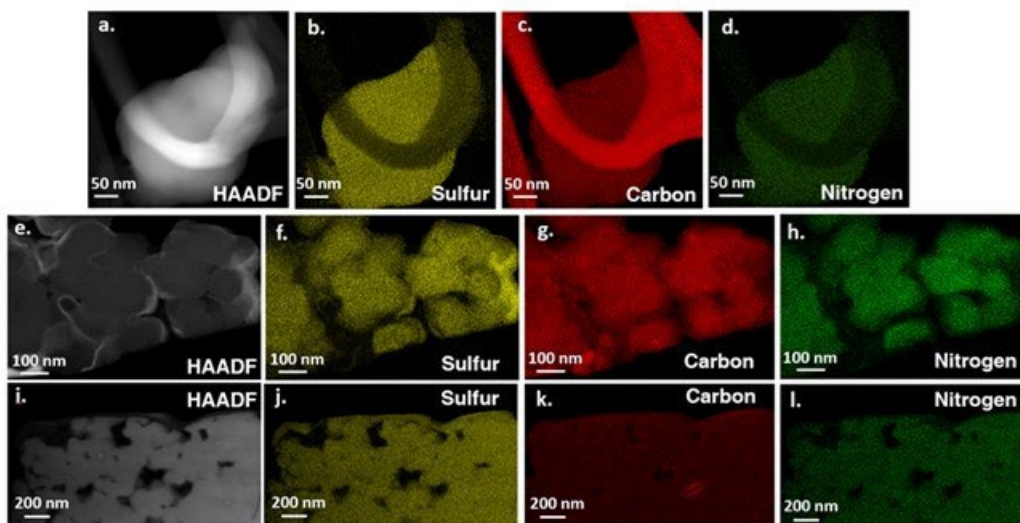


Figure XX.1.13 STEM EDS mapping of a-d) Pristine SPAN; e-h) 10-cycle discharged SPAN; i-l) 10-cycle charged SPAN

The PNNL team further evaluated the Li||SPAN cells with two electrolytes, LHCE (LiFSI-1.2DME-3TTE, by mol.) and baseline electrolyte [LiPF₆/carbonate (1 M LiPF₆ in EC-EMC (3:7 by vol.) + 2 wt.% VC)], about the high-temperature (HT, 60°C) cycling stability, room temperature discharge rate capability as well as low-temperature (LT) discharge performance. The SPAN electrode had an areal capacity loading of about 6 mAh cm⁻² and was obtained from the UCSD team. As shown in Figure XX.1.14a, the Li||SPAN cell with LiPF₆/carbonate exhibits an abrupt capacity drop after about 10 cycles. In contrast, the cell with LHCE maintains an available capacity of 6.4 mAh cm⁻² after 100 cycles at C/5, corresponding to a high-capacity retention of 92.1%. From Figure XX.1.14b, the cell using LHCE exhibits superior discharge rate capability up to 3C and zero capacity loss when the discharge rate is set back to C/5 after the high-rate discharge. In contrast, the cell with LiPF₆/carbonate shows fast capacity decay after 5 cycles at C/5 and limited reversible capacity after 20 cycles at different discharge rates. Figure XX.1.14c and Figure XX.1.14d present the charge/discharge curves of Li||SPAN cells with LiPF₆/carbonate and LHCE, respectively under various discharge temperatures (from 25 to -30°C). Obviously, the LHCE enables higher capacity retentions and average voltage outputs as well as better capacity recovery (Figure XX.1.14d) than the LiPF₆/carbonate

(Figure XX.1.14c), where the reversible capacities at -20 and -30°C can be maintained at 4.86 and 4.68 mAh cm⁻², corresponding capacity retentions of 81.3% and 78.3%, respectively. When the temperature is back to 25°C, only 2% capacity is lost compared the initial discharge capacity of 5.98 mAh cm⁻² at 25°C. The much-improved HT cycling stability, rate capacity and LT discharge performance in cells using LHCE suggest that the electrode/electrolyte interface layers are more conductive than those with LiPF₆/carbonate, thus benefiting superior Li⁺ ion transfer kinetic.

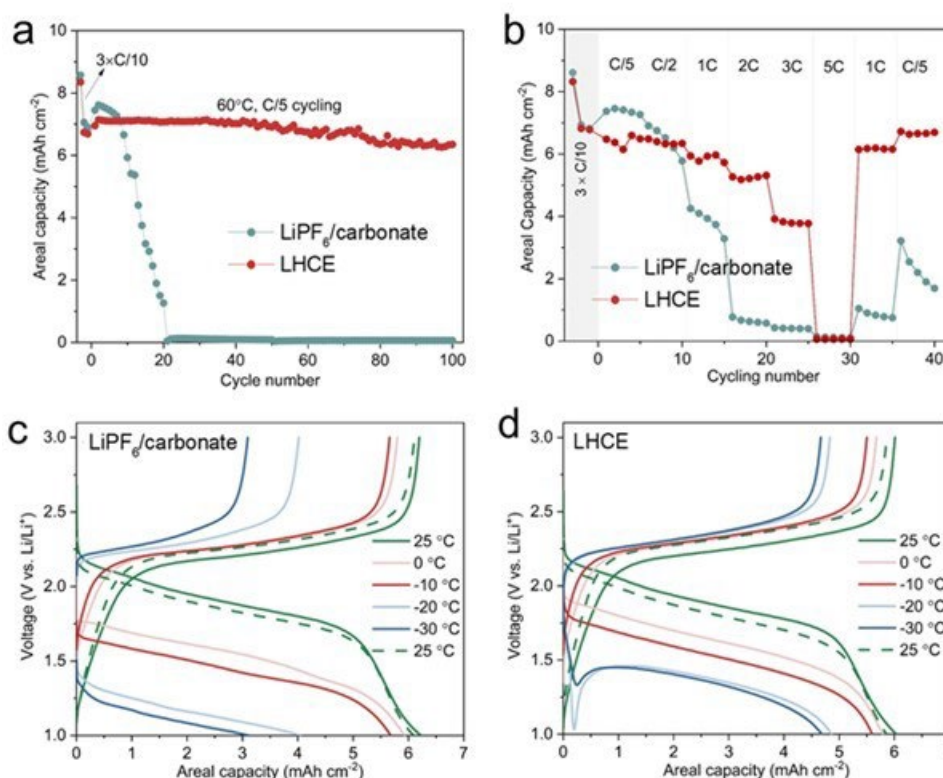


Figure XX.1.14 Electrochemical performances of Li | SPAN batteries with LiPF₆/carbonate and LHCE between 1.0–3.0 V. (a) Cycling stability under 60 °C. (b) Cell discharge rate capability tests at 60 °C after 3 formation cycles at 25 °C, with a constant charge rate of C/5 and different discharge rates from C/5 to 5C. (c, d) Low-temperature discharge tests at C/5 with (c) LiPF₆/carbonate and (d) LHCE, where the operating temperature for all charging process was 25 °C while the discharging was conducted at 25, 0, -10, -20, and -30 °C, respectively, and then back to 25 °C. In all cell tests in (a–d), 1C = 6.0 mA cm⁻².

Identification of LiH and crystalline LiF in the solid-electrolyte-interphase (SEI) on lithium metal anode by BNL team. In collaboration with PNNL group, BNL applied synchrotron X-ray diffraction to understand the chemical composition of lithium metal anode interphase. Two particular goals are 1). to resolve the controversy over if LiH is a significant component or not in SEI and 2). to understand why LiF, an ionic insulator in bulk phase could be a favored solid-electrolyte-interphase (SEI) component. SEI samples are collected from lithium metal anodes which are cycled in a series of electrolytes using the same salt of lithium bis(fluorosulfonyl) imide (LiFSI) but different solvents (including propylene carbonate (PC), dimethyl carbonate (DMC), and 1,2-dimethoxyethane (DME)). As Figure XX.1.15a shows, LiH is detected in all the SEI samples, regardless of the solvents used or the salt concentration employed. The identity of LiH is confirmed based on the fact that this phase has a face-centered-cubic structure with lattice parameter of 4.084 Å (Figure XX.1.15b), in full agreement with literature report about the LiH phase. Larger amount of LiF was detected in the SEI of high concentration electrolytes, regardless of the solvents used. This is consistent with current understanding that anion decomposition dominates in high concentration electrolyte with LiF being the major decomposition products. Interestingly, detailed fitting of the XRD patterns indicate that the LiF in SEI differ from the bulk LiF in two aspects: the former has a larger lattice parameter and a much smaller grain size

(< 3nm), both of these features are favorable for Li ion transport. To emphasize this discovery, LiF in SEI is denoted as LiF_(SEI) in Figure XX.1.15. The unique properties of LiF_(SEI) may explain why it is a favored component in lithium metal anode SEI.

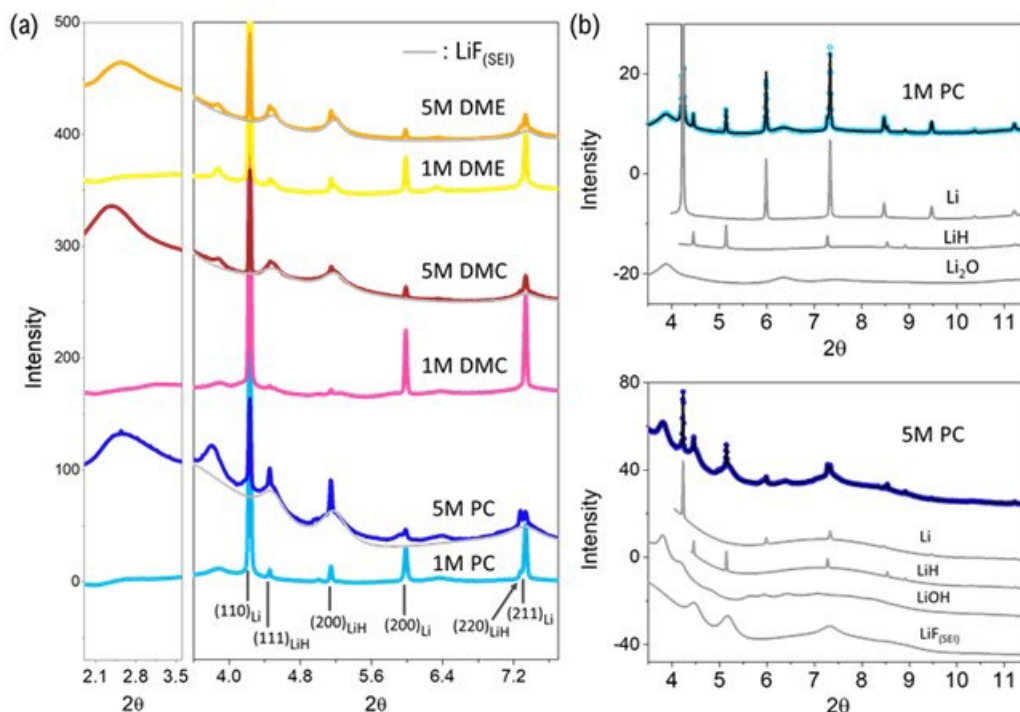


Figure XX.1.15 (a) SEI XRD of low and high concentration electrolytes using LiFSI as salt and PC, DMC, and DME as solvents. The light grey pattern belongs to SEI-LiF (denoted as LiF_(SEI)). The wavelength used is 0.18323 Å. (b) Rietveld refinement of SEI XRD data of low and high concentration LiFSI in PC. Contributions of individual phase to the XRD pattern are also shown. Open circles, experimental data; black lines, calculated data.

Pressure Tailored Lithium Metal Deposition by UCSD team. It is qualitatively believed that increased uniaxial stack pressure can help to alleviate Li dendrite formation and improve Coulombic efficiency (CE) and cycling performance of Li metal batteries. Quantitatively understanding the role of stack pressure on Li nucleation, growth and dissolution, and the pressure-morphology-performance relationship will open new opportunities in our efforts in solving problems regarding Li metal anodes in high-energy Li metal batteries. UCSD team used a customized split cell with a load cell (Figure XX.1.16a) to precisely control the uniaxial stack pressure applied to the battery during cycling. The pressure was set as the on-set value for the electrochemical performance testing. Figure XX.1.16b shows the first cycle CE of Li-Cu cells as a function of applied stack pressure under different current densities from 1, 1.5, to 2 mA/cm², using an ether-based electrolyte. At 0 kPa, the CE was the lowest among all current densities. When the stack pressure is slightly increased to ~35 kPa, the CE increased for all current densities while the CE at 2 mA/cm² jumped to 92%. At 350 kPa, the CE was boosted to 98%, 97% and 96% at 1, 1.5 and 2 mA/cm², respectively. Increasing the stack pressure above 350 kPa did not further improve the CE. Figure XX.1.16c shows the electrochemically deposited Li at a high current density of 2 mA/cm² after high loading of 4 mAh/cm² deposition exhibits metallic silver color. We then used cryo-FIB-SEM to examine the deposited Li morphology under four representative pressures: 70, 140, 210 and 350 kPa. A high current density of 2 mA/cm² was applied for the one-hour Li deposition (2 mAh/cm²) morphological study. The Li deposits become notably close-packed with increased pressure from 70 kPa to 350 kPa (Figure XX.1.10d-g). The cross-section evolution is even more noticeable. As shown in Figure XX.1.10h-k, along with the increased stack pressure, the electrode thickness obviously decreased. Especially, the cross-section morphology at 350 kPa (Figure XX.1.10k) shows that the Li deposits form perfect columnar structures with large granular diameter of ~4 μm, near-theoretical thickness

($9.64\ \mu\text{m}$, $2\ \text{mAh}/\text{cm}^2$) of $\sim 10\ \mu\text{m}$ and minimum electrode-level porosity, indicating that stack pressure can be used to precisely control the Li deposition morphology.

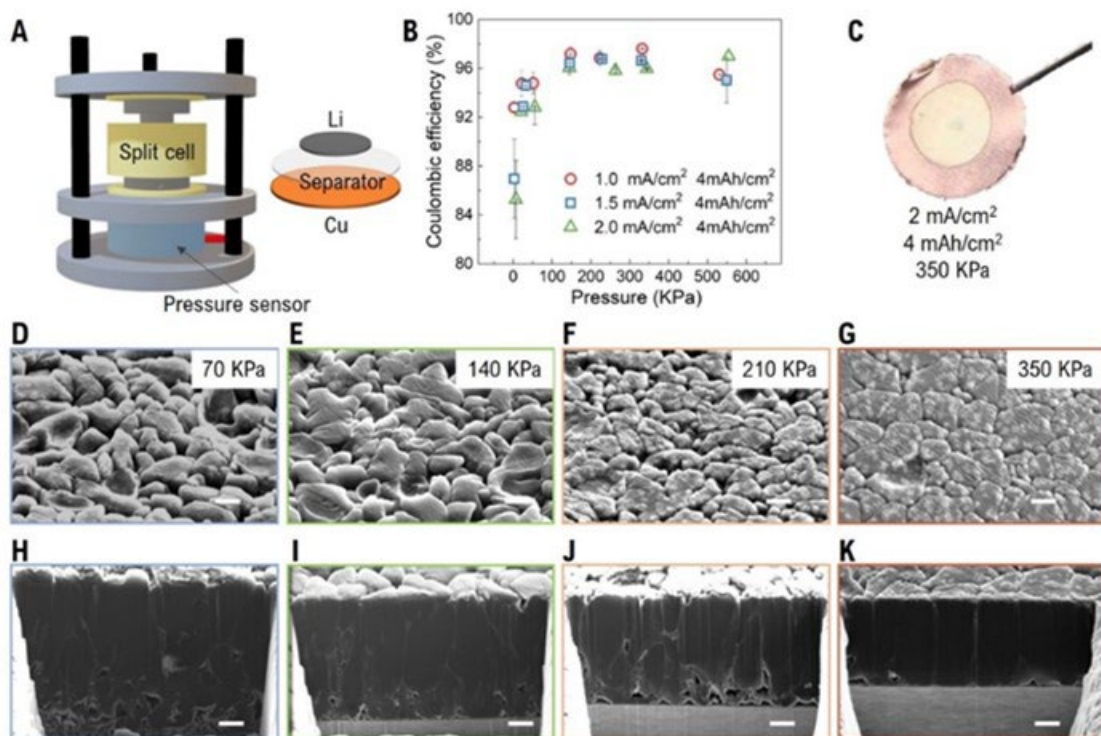


Figure XX.1.16 (a) the pressure experiment set-up. (b) pressure vs. Coulombic efficiency under various current densities. (c) Optical image of deposited Li under high current density ($2\ \text{mA}/\text{cm}^2$), high loading ($4\ \text{mAh}/\text{cm}^2$), and optimized pressure conditions (350 kPa). (d-g) top view and (h-k) cross-section of Li deposited under various pressure at $2\ \text{mA}/\text{cm}^2$ for 1 hour. (d, h) 70 kPa, (e, i) 140 kPa, (f, j) 210 kPa, (g, k) 350 kPa. Scale bar is $2\ \mu\text{m}$

Development of one- and two-dimensional models for Li deposition growth with mass conservation by UW/UT team. The UW/UT team has been developing one- (1D) and two-dimensional (2D) models to capture the movement of Li during plating/stripping when it is cycled at various rates. In this quarter, it was observed that the imperfect mass conservation in previous treatment is too significant to be ignored, especially for repeated charge/discharge cycles. The improper formulation for mass conservation in electrochemical models involving moving boundaries, if ignored, might lead to erroneous results for the variables of interest in a battery, and in turn affect the accuracy of predictions for battery degradation and cycle life. Figure XX.1.17 shows comparative results obtained after a careful implementation of an improved mass conservation formulation at the moving boundary at the electrode-electrolyte interface where an advective flux term has been included in the interface boundary condition based on the mass jump condition at moving interfaces. The 1D transport model example has been chosen as a base case to demonstrate and emphasize on the importance of electrode-electrolyte interface mass balance and has also been incorporated into 2D models. Both the 1D and 2D models have been implemented in an efficient form – for example, 100 cycles of charge/discharge curves take less than a minute of CPU time.

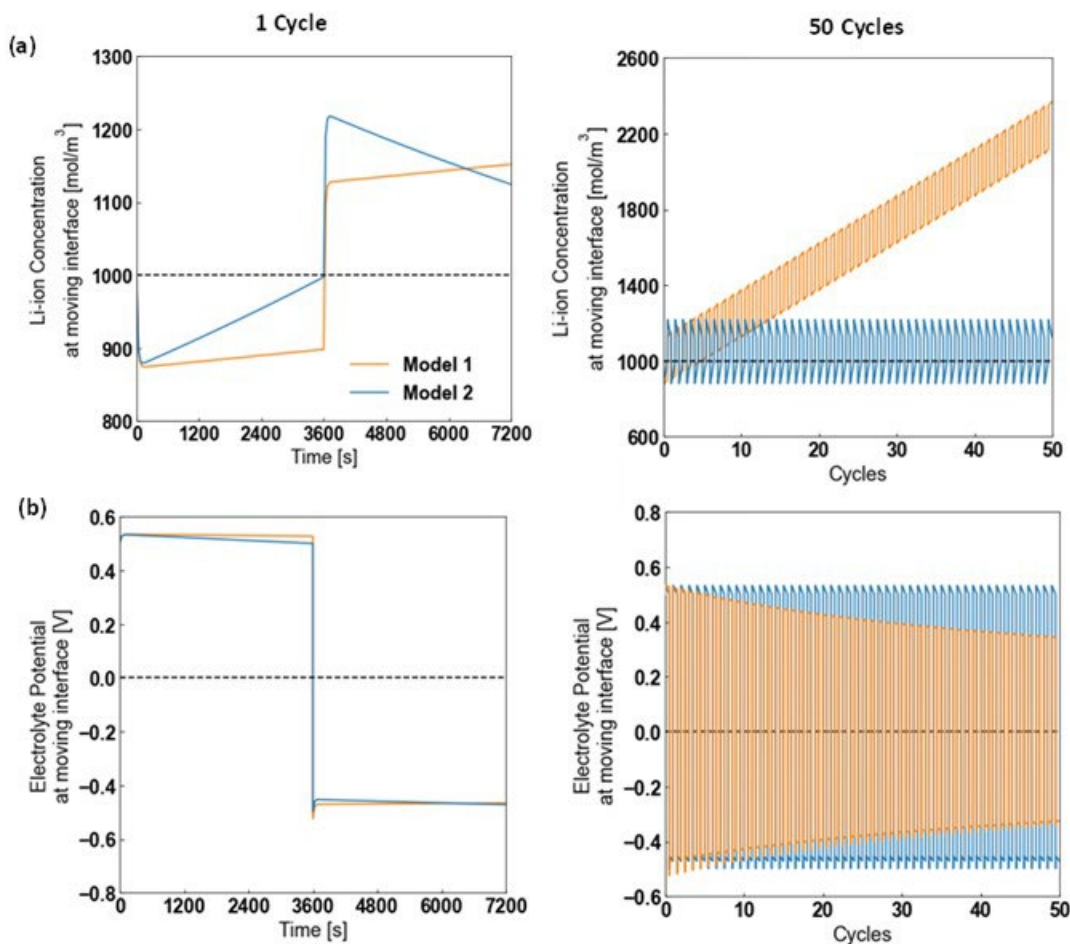


Figure XX.1.17 Comparative results for electrolyte (a) concentration and (b) potential over 50 cycles for the original model without advective flux (Model 1) and modified model with advective flux (Model 2) at moving interface at $x = 0$.

Controlling the Chemical Corrosion of Li Metal Anodes by UCSD team. Although extensive studies have been performed trying to prolong the cycling life of Li metal anode, the lack of comprehensive understanding of chemical stability between Li metal and liquid electrolytes, which causes the corrosion of Li metal, has prevented it from having an extended calendar life. The UCSD team designed experiments to study the trend of Li corrosion in liquid electrolyte. First, 0.318 mAh of Li was plated onto a copper (Cu) substrate at a rate of 0.5 mA cm⁻² in a coin cell setup with a high concentration “Bisalt” electrolyte (4.7 M LiFSI + 2.3 M LiTFSI in DME) and carbonate solvent based “Gen 2” electrolyte (1.2 M LiPF₆ in EC-EMC). After plating, the deposited Li metal with the Cu substrate was kept in coin cell with the corresponding electrolytes while the cell was under the open circuit condition (without linked to a cycler). After a certain period of storage time, the cells were disassembled, and the Titration Gas Chromatography (TGC) method was used to quantify the mass of metallic Li⁰ remaining on the Cu substrate. The Li mass retention (%) as a function of storage time is shown in Figure XX.1.18a and Figure XX.1.18d. For Li plated in both Bi-salt and Gen 2 electrolytes, there was a sudden drop of Li⁰ mass in the first 24 hours of resting. After that, the corrosion rate of Li plated in Bisalt electrolyte slowed down, which resulted in a 26.0% loss of Li⁰ mass after 5 weeks of resting. However, a more drastic loss of Li⁰ mass was observed in the Gen 2 electrolyte. The continuous corrosion of Li caused a 60.8% loss of Li⁰ mass after 5 weeks of resting. The morphological study by Cryo-FIB/SEM further confirms the corrosion trend obtained by TGC. The Li morphology in Bisalt electrolyte did not experience a significant change after 5 weeks of resting under open circuit Figure XX.1.18b, Figure XX.1.18c). The Li retained mostly its granular shape even after the resting period, although there was a decrease of Li thickness from 1.16 μm to 0.92 μm. As expected, a sharp change in the morphology of Li plated in the Gen 2 electrolyte was observed by Cryo-

FIB/SM (Figure XX.1.18e, Figure XX.1.18f). The freshly deposited Li in Gen 2 electrolyte exhibited a whisker-like morphology, while the corroded Li showed a porous and powder-like morphology. There was also a substantial decrease of Li thickness from 2.93 μm to 1.02 μm , which again agreed with the loss of Li^0 mass quantified by TGC. The two fundamentally different electrolyte systems, Bisalt (high concentration ether-based electrolyte) and Gen 2 (conventional carbonate-based electrolyte), showed two drastically different corrosion trends: Bisalt showed a fast corrosion during the first 24 hours, but stabilized quickly afterward, while Gen 2 showed a continuous corrosion rate throughout the 5 weeks of resting period. Based on the results so far, there might be two possible reasons for the difference in the corrosion trends from the two electrolytes: 1) Li metal surface chemistry; 2) Li metal porosity. More research work will be performance to study which parameters has the most significant impact on the Li corrosion rate.

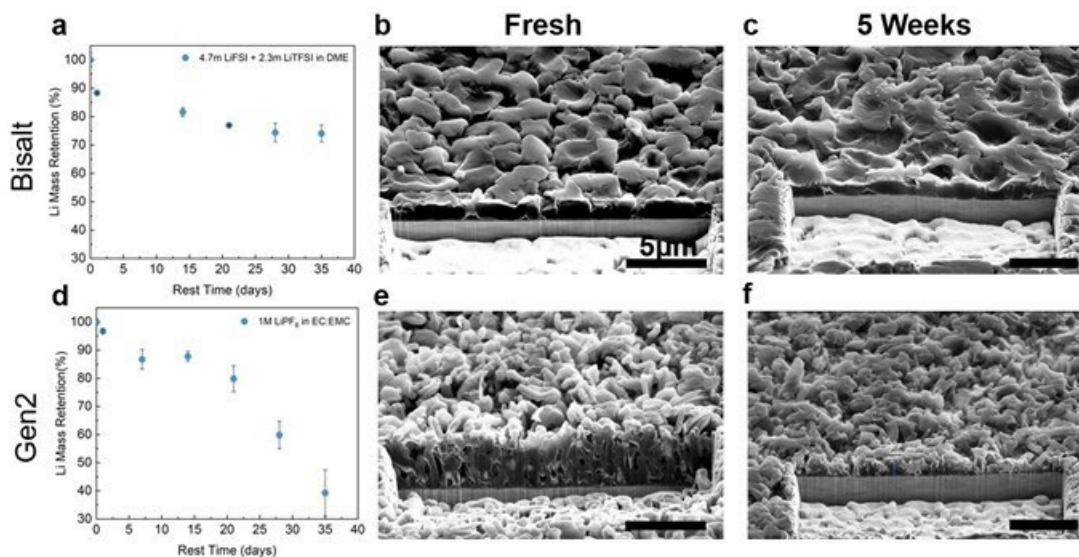


Figure XX.1.18 a-c) The trend of Li metal corrosion in high concentration “Bisalt” electrolyte: a) the Li^0 mass retention (%) as a function of resting time; The SEM images of the Li morphology b) before and c) after 5 weeks of resting. d-f) The trend of Li metal corrosion in carbonate solvent based “Gen 2” electrolyte (1 M LiPF_6 in EC-EMC): d) the Li^0 mass retention (%) as a function of resting time; The SEM images of the Li morphology e) before and f) after 5 weeks of resting. Total amount of 0.318 mAh of Li is plated at a rate of 0.5 mA cm^{-2} in all samples.

UCSD team has systematically investigated the effect of binders on the cycling performance of high areal capacity SPAN cathodes ($> 6 \text{ mAh cm}^{-2}$) with different porosities. The cycling stability of the SPAN electrode with a porosity of 50% using a PVDF binder was tested first. In order to mitigate the effect of Li degradation on the cell cycling performance, a 1.8 M LiFSI in DEE/BTFE electrolyte was used for the test. The Li||SPAN cell shows a rapid capacity fading from 650 mAh g^{-1} to 400 mAh g^{-1} within 60 cycles when the electrode loading was 10 mg cm^{-2} . The corresponding voltage profiles indicate a fast polarization increase (Figure XX.1.19a and Figure XX.1.19d). Their previous studies revealed that the mechanical failures of cracking, delamination, and volume change are likely the root cause of the rapid capacity fading of the 10 mg cm^{-2} SPAN electrode. Optimizing the polymer binder is a practical approach to improve the electrode mechanical integrity. As a comparison, the 6 mAh cm^{-2} SPAN cathode using a CMC binder exhibited stable cycling. It maintained 94.5% of its capacity (based on the 3rd cycle) at the 60th cycle, while the PVDF electrode at the 60th cycle only delivered capacity retention of 66.7% (Figure XX.1.19a). Another critical step towards high energy density Li||SPAN battery is to reduce the cathode porosity. Because lower porosity electrode requires less electrolyte, resulting in higher cell level energy density. The binder plays a key role at low porosity because the SPAN electrode will expand outwardly due to the limited spaces inside, which will apply significant stress on the binder skeleton. SPAN cathodes with 40% and 30% porosity were tested and the results are shown in Figure XX.1.19b and Figure XX.1.19c. The capacity of PVDF-based electrodes quickly decays from 600 to $< 150 \text{ mAh g}^{-1}$ within 10 cycles. In contrast, the 30% and 40% porosity SPAN electrodes using CMC binder

were able to maintain high-capacity retention of 95.1% and 94.4%, respectively (Figure XX.1.19e and Figure XX.1.19f), clearly demonstrating the benefits of using CMC for high areal loading, low porosity SPAN cathodes. This work proves the importance of binder on low porosity thick SPAN cathodes and paves the road for high energy density Li||SPAN cell.

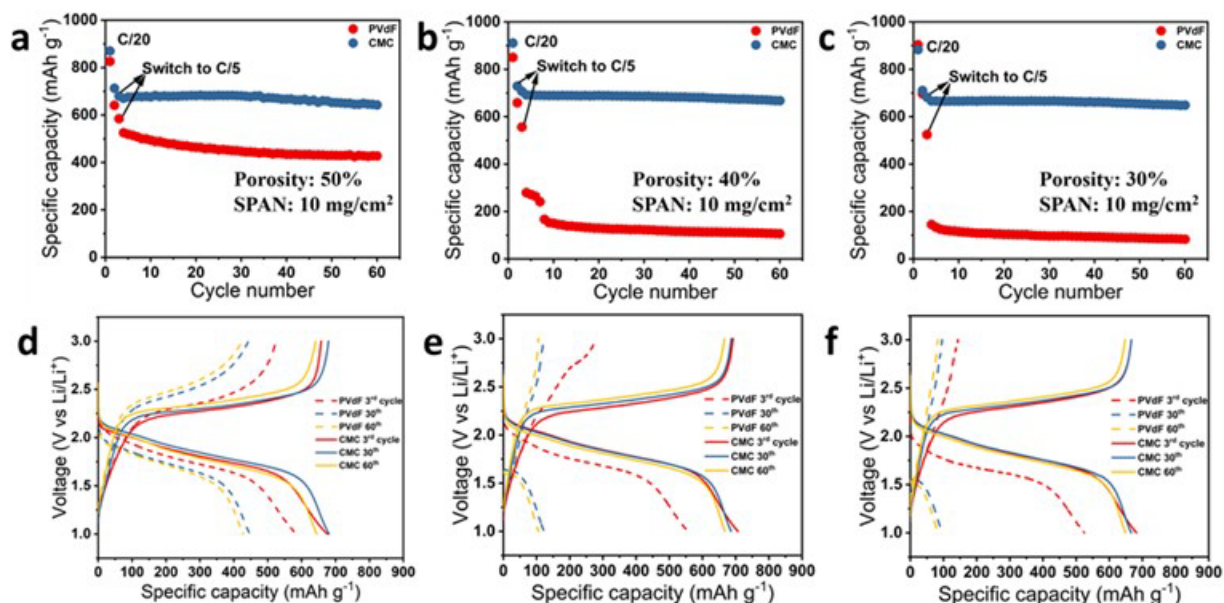


Figure XX.1.19 Comparison of the cycling performance of high areal capacity SPAN electrodes. a) 50% cathode porosity, b) 40% cathode porosity, c) 30% cathode porosity. Voltage profiles of Li||SPAN cells with d) 50% cathode porosity, different binder, e) 40% cathode porosity, different binder, f) 40% cathode porosity, different binder. The mass loading of the SPAN cathode is 10 mg cm⁻². The cell was cycled under C/20 rate for two formation cycles and then cycled under C/5 rate.

3. Keystone project 3: Cell fabrication, testing and diagnosis

The PNNL pouch cell team prepared and evaluated multiple high energy cells using either a bare Cu current collector or thin Li anode and a NMC622 cathode. Three of the cells were comprised of a Li metal anode (denoted as Cell 1-3) and one with Li-free Cu anode (denoted as Li-free cell). The charge-discharge cycling data and charge retention curves were analyzed by INL team using detailed electrochemical analytic diagnosis (eCAD) analysis. The eCAD analyses and the results are reported in Figure XX.1.20 as a summary report of the NMC622 cathode active material's utilization and the impact on charge retention and cycle life. Figure XX.1.20a shows the NMC622 utilization efficiency $\epsilon_{C/n}$ at C/3 cycling as a function of cycle number. The utilization efficiency $\epsilon_{C/n}$ was calculated according to

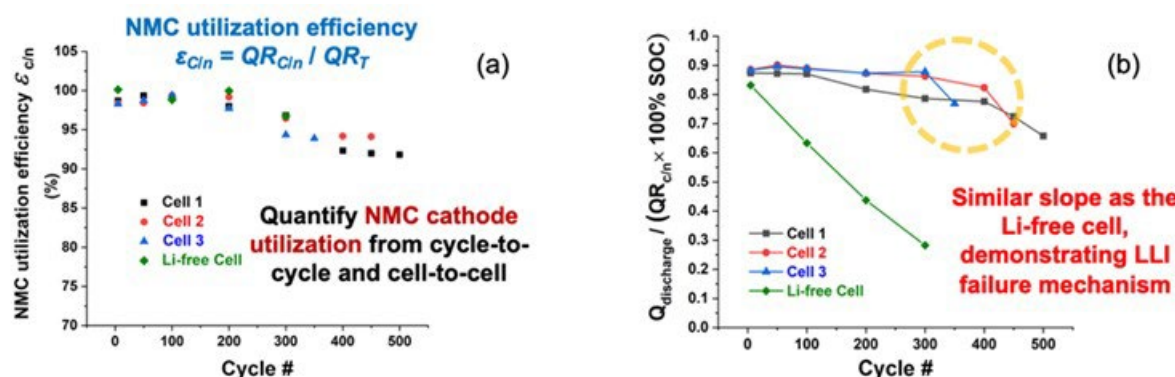
$$\epsilon_{C/n} = QR_{C/n} / QR_T \quad (2)$$

where QR is the "capacity ration" expressed as mAh g⁻¹ %SOC⁻¹. $QR_{C/n}$ is the capacity ration measured at C/n rate, and QR_T is the theoretical capacity for the NMC composition. A reliable way to obtain the $QR_{C/n}$ is shown in Figure XX.1.21. The capacity ration QR can be calculated by a general equation as

$$QR = \Delta Q / \Delta SOC \quad (3)$$

In Figure XX.1.21 several discharge curves as a function of cycle number were transformed into IR-free voltage vs. SOC profiles using the eCAD method, and they are aligned with a universal pseudo-OCV vs. SOC curve that represents the proper OCV vs. Li content in NMC622. The region highlighted by the blue dashed circle shows that the IR-free voltage vs. SOC profiles from the C/3 polarization aligned very well with the universal pseudo-OCV vs. SOC curve, implying the SOC and Li content in NMC correlated very well. In this region we can arbitrarily select two points A and B to illustrate how QR and $\epsilon_{C/n}$ can be derived. For $QR_{C/n}$ we

can determine the capacity difference $\Delta Q_{C/n}$ between A and B from the capacity measurements in the discharge curve, while the eCAD analysis shall give the ΔSOC . Thus, $QR_{C/n}$ can be derived from Eq. (3). Likewise, we can calculate the ΔQ_T between A and B from the Li content and Faraday's law and use the same ΔSOC to calculate the QR_T . The utilization efficiency $\varepsilon_{C/n}$ can readily be obtained by Eq. (2) as exhibited in Figure XX.1.20a. The results shown in Figure XX.1.20a are quite informative. Despite the cell design differences, the NMC $\varepsilon_{C/n}$ values among the four are rather consistent, sharing the same trend. The NMC utilization can hold up well in the first 200 cycles. The variations in kinetics, including mass transport in different porous electrode structures, do not affect the NMC utilization during this period, indicating the NMC utilization is mostly governed by the NMC's bulk property itself. After 200 cycles, the utilization began to decrease by 6-8 % across the four designs, again consistently. We shall infer that this is likely due to the change in the charge retention ability internally by NMC lattice structure. The capacity variations among them that are exceeding the internal effect by NMC identified above, must then come from the transport properties in the porous media and the kinetic polarization hindrance at the interface. Figure XX.1.20b compares the measured capacity $Q_{C/3}$ versus the one determined from the capacity ration obtained from the highlighted region in Figure XX.1.21, as $QR_{C/3} \times 100\% \text{SOC}$. The ratio of $Q_{C/3} / (QR_{C/3} \times 100\% \text{SOC})$ shall represent the utilization loss due to kinetic origins outside the NMC bulk or those that come from the transport properties in the porous media and the kinetic polarization hindrance at the interface. Such an identification and separation of the kinetic effects by careful quantification of the NMC utilization in the polarization shall provide valuable information for cell design improvements and for gap analysis of kinetic issues to improve performance.



- Besides material's and electrode's thermodynamic and kinetic attributes to the NMC's utilization as displayed in the capacity fade, we can further observe cell balance issues associated with electrode cross-talks and Li inventory depletion.

Key Concept — All identified and verified impacts on cell performance from material to cell can provide proper feedback to improve cell design and performance to achieve the Battery500 goals in a tangible manner.

Figure XX.1.20 Electrochemical Analytic Diagnosis (eCAD) characterizations to analyze cell performance based on cathode active material's utilization and cell degradation due to Li inventory loss at the Li anode. (a) The NMC622 cathode utilization variations as a function of cycle number among four different cells of design. (b) The capacity retention presented as a function of the ratio of capacity Q vs. capacity ration QR under the same test protocol at C/3.

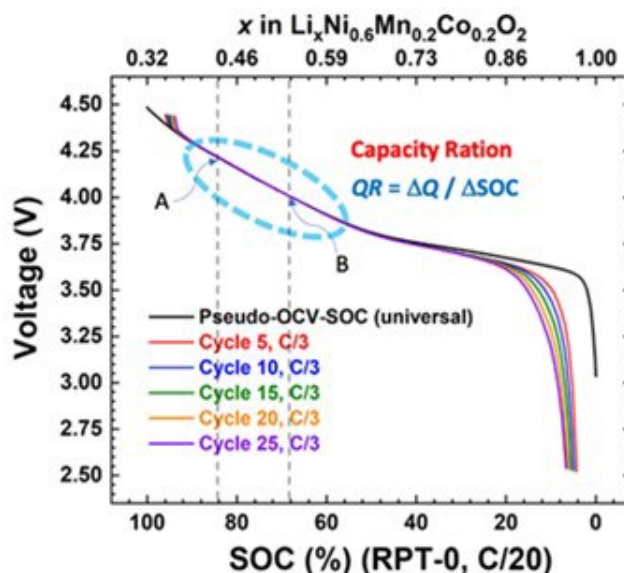


Figure XX.1.21 IR-free voltage vs SOC profiles derived using the eCAD method to show the OCV vs Li content in the NMC.

INL team in Keystone 3 focused on understanding the impact of early cycling conditions on cycling life and the role of different porous host design on Li. It was observed that the cycling performance of Li||NMC811 cells, operating at 25°C during aging, varied when the temperature during formation cycles was changed from 10°C, 25°C to 45°C. It is suspected that the external temperature can be utilized to alter the composition and structure of early-formed SEI during the formation cycles. Three different electrolytes were used as shown in Figure XX.1.22a, each with different formation cycle temperature as the superior performer. With a carbonate-based electrolyte (1.6 M LiPF₆ in 3:7 wt.% EC:EMC + 10 wt.% VC), high-temperature (45°C) formation cycles benefit extended cycling before rapid capacity fade, maintaining over 175 mAh/g for 58 cycles. However, a high-concentration ether electrolyte (HCE, 4 M LiFSI in DME) operated best when low temperature (10°C) was used for formation cycles, maintaining over 200 mAh/g for over 80 cycles. A localized high-concentration electrolyte (LHCE, 1:1.2:2 mol% LiFSI:DME:TFEO) performed best in the middle temperature (25°C), maintaining over 180 mAh/g for over 135 cycles with a Coulombic efficiency above 99%. The capacity during the formation cycles was lower for 10°C cells, followed by 25°C and 45°C, respectively, among all the electrolytes. It appears that the difference in performance during aging cycles is based upon the composition and morphology of the SEI and is not dependent upon the cycling behavior during those formation cycles. Raman spectra of ether-based electrolytes were observed at different temperatures (Figure II.13.A.22.b). It was seen that as the concentration of LiFSI in DME was increased, the number of contact-ion pairs (CIPs, single Li⁺-FSI⁻ coordination) and aggregate clusters (AGGs, multiple Li⁺ coordinating to one FSI⁻) increased, evidenced by an 11 cm⁻¹ blue shift. At the low concentration (LCE, 1M LiFSI in DME), solvent separated ion pairs (SSIPs, Free FSI⁻) are much more prevalent. When the TFEO diluent is incorporated to produce the LHCE, an even greater blue-shift is seen (22 cm⁻¹ from HCE peak), thus showing that AGG concentration is much higher. Comparing Li⁺ coordination with the FSI⁻ anion (CIPs and AGGs) and coordination with the solvent (Li⁺-DME), shifts in increased aggregates for HCE and LHCE also demonstrated reduced coordination between Li⁺ and DME. Therefore, the utility of the LHCE electrolyte is shown to make a salt-derived SEI more viable than in LCE or even HCE.

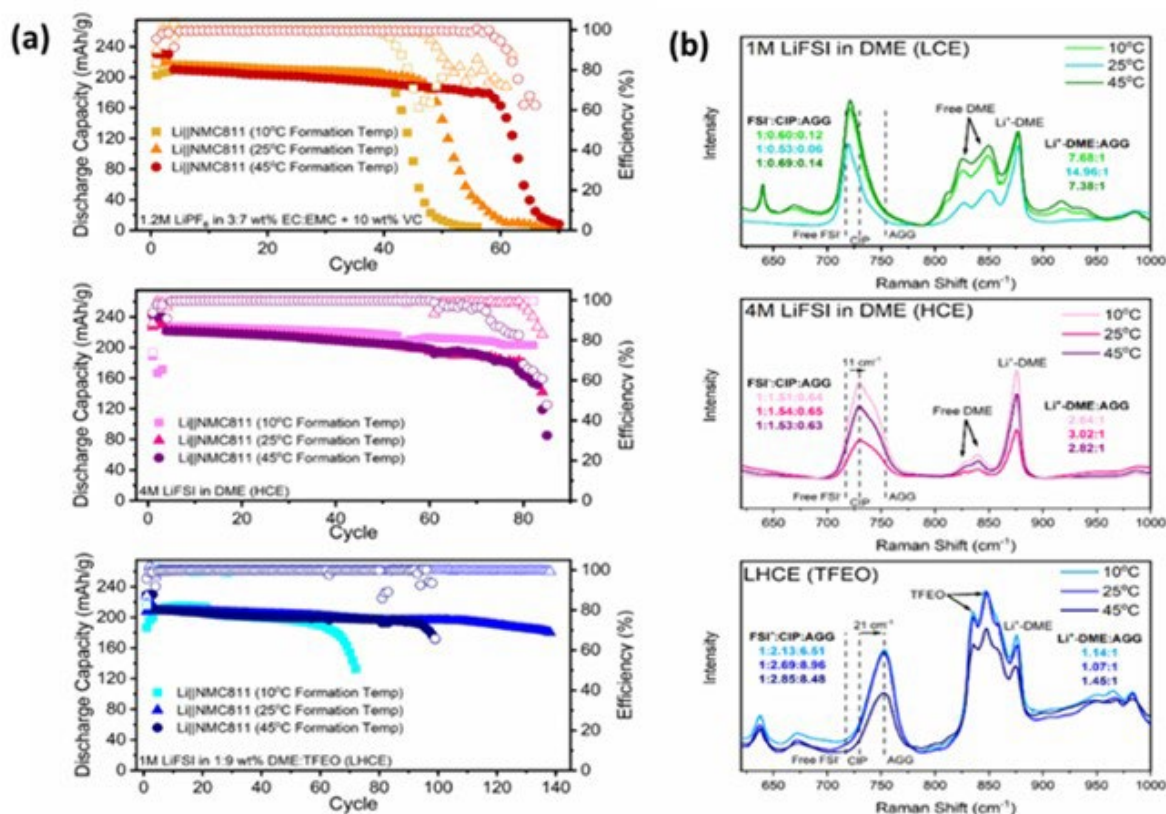


Figure XX.1.22 (a) Cycling performances of Li||NMC811 cells for different electrolytes, operating at 25°C during aging, varied when the temperature during formation cycles was changed from 10°C, 25°C to 45°C; (b) Raman spectra of ether-based electrolytes (LCE, HCE and LHCE) at different temperatures.

The INL and PNNL teams worked together to compare the results between cycle aging and calendar aging using the Battery500 FY2020 cell design. Comparison was made on 350 Wh kg⁻¹ pouch cells cycle-aged (using a standard C/10 charge and C/3 discharge) and calendar-aged (cells kept at 80% SOC for 14 days between reference performance tests (RPTs)). The results are shown in Figure XX.1.23. Both sets of cells show comparable loss of Li inventory to SEI growth during aging. The cells which were maintained at rest for 14 days also showed negligible fade over the course of the aging though polarization did increase over the life of the cell resulting in a progressively lower SOC during the rest period. A key contributor of this shift was due to the cycles the cells underwent as part of the RPT. Based on these results, new evaluation methods and analysis protocols have been developed to decouple the impact of combined cycle and calendar aging effects.

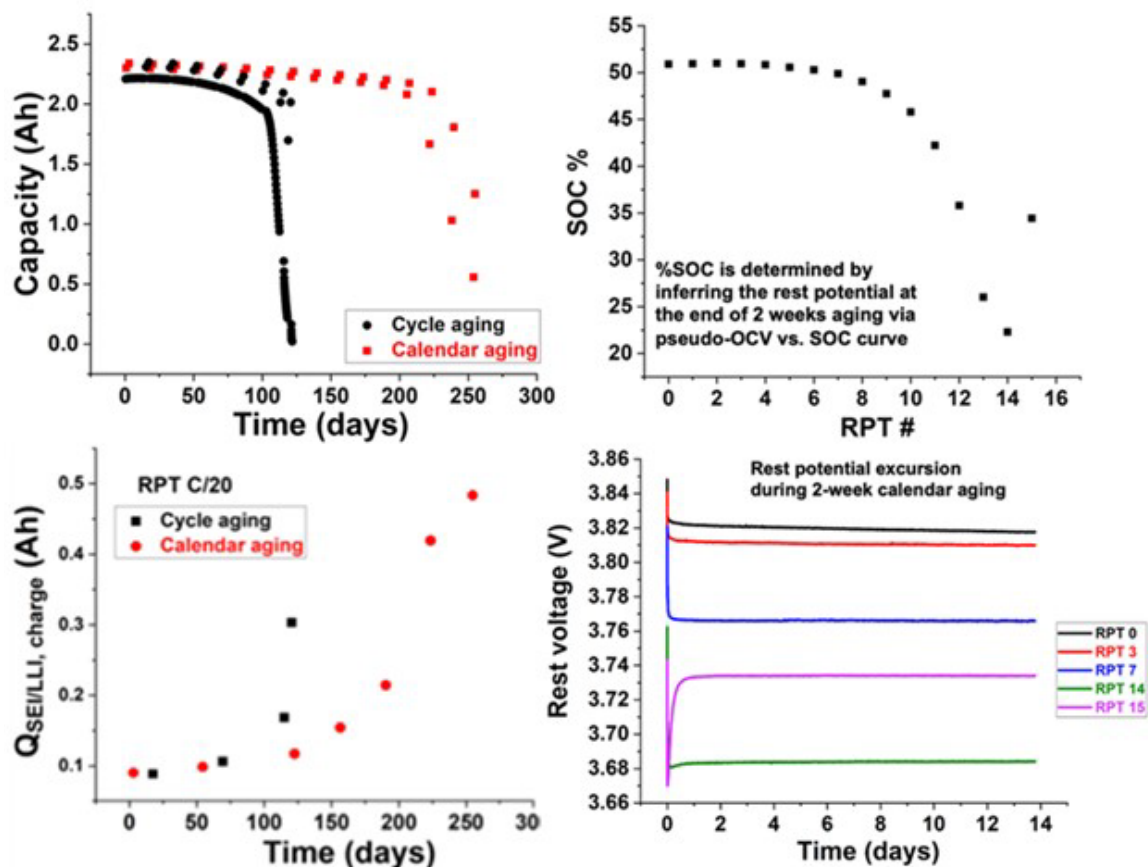


Figure XX.1.23 Comparison of calendar and cycle life aging for LMBs.

PNNL team carried out studies on balancing the interfacial reactions by tuning the thickness of Li anode. Although the addition of extra Li in the pouch cell initially shows stable cycling, serious polarization still occurs due to the accumulation of an insulating SEI. To mitigate this problem, 350 Wh kg⁻¹ pouch cells with two thinner Li foils (50 μ m and 20 μ m) were fabricated and investigated. For the 50 μ m Li cell, the N/P ratio is 2.5:1. Similar long stable cycles are observed for the first 400 cycles (Figure XX.1.23a), maintaining almost 100% CE. However, after 400 cycles, the cell energy and capacity begin to drop rapidly, and the CE decreases quickly. This sudden capacity drop is similar to that observed in the 100 μ m Li pouch cell. Minimum polarization is seen during the first 400 cycles (Figure XX.1.24d), beyond which IR drop and ohmic polarization increase drastically. These results indicate that a 50 μ m Li anode is enough for the compensation of the Li loss in early cycles, but the resistive SEI build-up still accelerates during later cycling and causes sudden cell death. The most interesting result is obtained when the thickness of Li is further reduced to 20 μ m (thin-Li cell, the N/P ratio is 1:1). The stable cycling of the 350 Wh kg⁻¹ pouch cell is extended to over 600 cycles with a cell capacity retention as high as 76% (Figure XX.1.24e). The CE remains at almost 100% until reaching 600 cycles. Although the CE is artificially inflated due to the presence of excess Li in the cell, the extended long-term cycle life implies a good balance between a timely supply of Li while minimizing the accumulation of ineffective SEI layers. The charge-discharge curves of this thin-Li pouch cell remain very stable, as shown in Figure XX.1.24f. Different from the Li-free-anode and thick-Li pouch cells, no obvious voltage shift (that is, polarization) is found in the well balanced 20 μ m Li cell throughout the entire 600 cycles. The cell-level energy density of this 350 Wh kg⁻¹ pouch cell with 20 μ m Li maintains was 71% after 600 cycles. This result suggests SEI build-up is greatly reduced in the thin-Li cell. The changes in SEI structures are also confirmed by preliminary impedance measures. After extensive cycling, the thin-Li pouch cell has the smallest interfacial charge transfer resistance, followed by the 50 μ m and 100 μ m Li pouch cells. The results of this work were published on *Nature Energy* (2021) (<https://doi.org/10.1038/s41560-021-00852-3>).

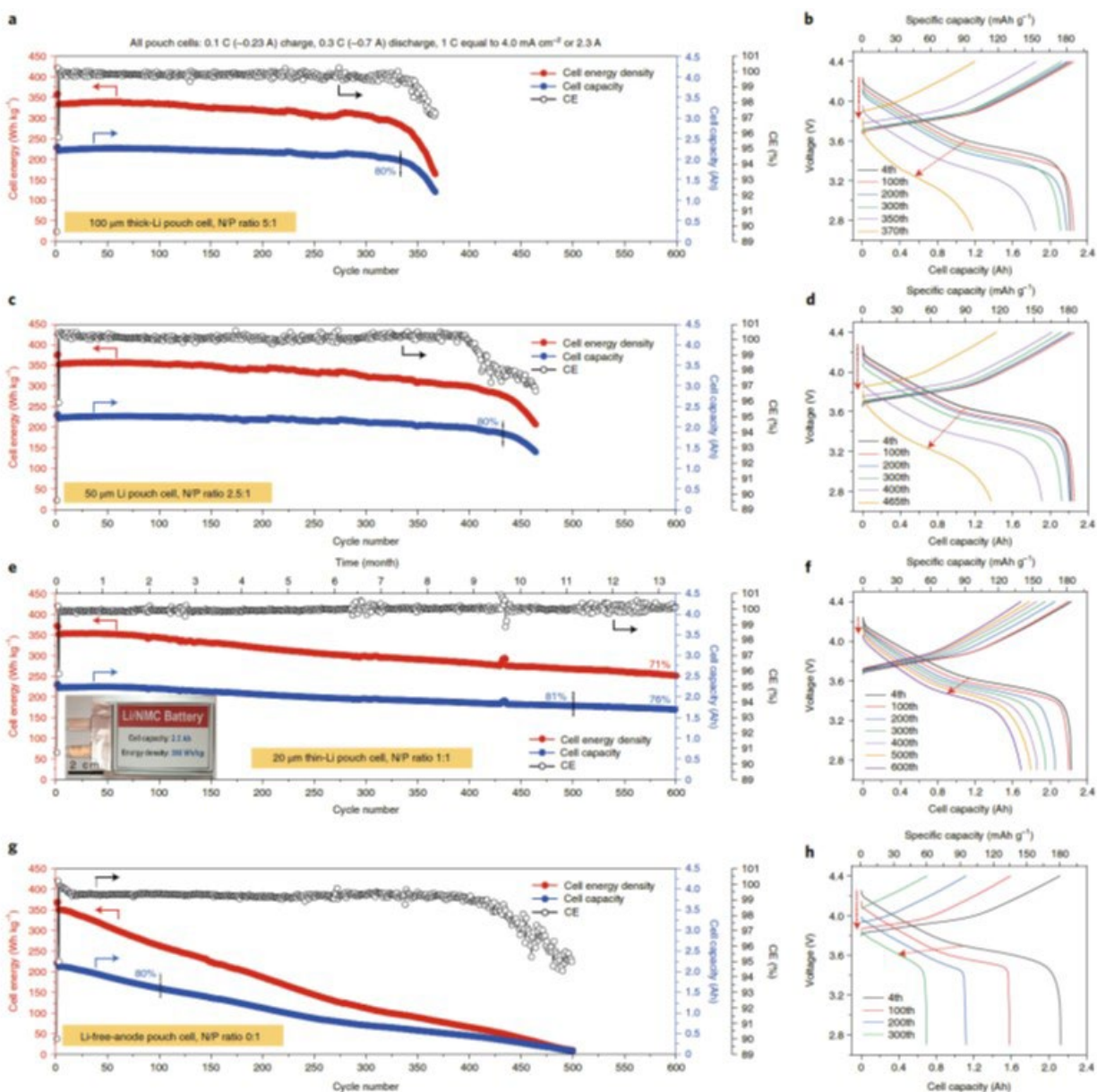


Figure XX.1.24 Electrochemical performances of four types of 350 Wh kg⁻¹ Li || NMC622 pouch cells at 2.0 Ah level. **a,b**, Cell-level energy density, cell capacity, CE and charge-discharge curves of the pouch cell with 100 μm thick-Li in the anode; the N/P ratio is 5:1. **c,d**, Cycling performance and charge-discharge curves of the 50 μm Li pouch cell; the N/P ratio is 2.5:1. **e,f**, Cycling performance and charge-discharge curves of the 20 μm thin-Li pouch cell; the N/P ratio is 1:1 and the E/C ratio is 2.4 g Ah⁻¹. **g,h**, Cycling performance and charge-discharge curves of the Li-free-anode pouch cell, Cu || NMC622; the N/P ratio is 0:1. All pouch cells were cycled at 0.1 C for two initial formation cycles, and then charged at 0.1 C (the electric current is ~0.23 A) and discharged at 0.3 C (the electric current is ~0.7 A) in subsequent cycles (1 C equals 4.0 mA cm⁻² or corresponds to 2.3 A, from 2.7 V to 4.4 V, 25 °C). The arrows indicate the voltage changes during the charge-discharge processes. During the long testing of more than 13 months, these pouch cells suffered two power outages and one period of oven maintenance, so some cycling behaviors show fluctuations. Note that the cell energy density is calculated based on the total weight of the whole pouch cell, including all active and inactive parts in the pouch cell.

Conclusions

This project has been successfully completed in FY2021. All milestones have been completed. The publication records are very good: 3 US patent applications were filed by the Battery500 team member institutions. **47 peer reviewed papers** were published, and more than **113 invited** presentations were delivered in FY2021.

Extensive collaboration within the consortium, between the consortiums and seedling teams, as well as with other national Labs and US universities has been well established and achieved very fruitful results.

Key Publications

Patents

1. Provisional patent on niobium oxide treatment of NMC materials has been filed by **Binghamton University**.
2. Jihui Yang, Yao Liu, Xianyong Wu, Xiaoyu Jiang, and Jun Liu, “High Energy Li Batteries with Lean Lithium Metal Anodes and Methods for Prelithiation”, Patent Application PCT/US2021/039491, filed 6/29/2021, by **University of Washington**.
3. Xiaodi Ren, Wu Xu, Ji-Guang Zhang, High Efficiency Electrolytes for High Voltage Battery Systems, US Patent No. 11,094,966 granted on 8/17/2021 to **Pacific Northwest National Lab. (PNNL)**

Publications

1. Fengxia Xin and M. Stanley Whittingham*, “Challenges and Development of Tin Based Anode with high Volumetric Capacity for Li-ion Batteries”, *Electrochem. Energy Reviews*, 2020, 3, 643-655. DOI: 10.1007/s41918-020-00082-3. Publication date: October 1st, 2020.
2. Zhuojun Huang, Snehashis Choudhury*, Huaxin Gong, Yi Cui*, Zhenan Bao*, “A Cation-tethered flowable polymeric interface for enabling stable deposition of metallic lithium ” *J. Am. Chem. Soc.*, 2020, 142(51), 21393–21403. DOI: 10.1021/jacs.0c09649. Publication date: December 14th, 2020.
3. Ningshengjie Gao, Alexander W. Abboud, Gerard S. Mattei, Zhou Li, Adam A. Corrao, Chengcheng Fang, Boryann Liaw, Y. Shirley Meng, Peter G. Khalifah, Eric J. Dufek, Bin Li*, “Fast diagnosis of failure mechanisms and lifetime prediction of Li metal batteries”, *Small Methods*, 2020, 2000807. DOI:10.1002/smt.202000807. Publication date (web) online: November 3, 2020.
4. Ji-Guang Zhang*, Wu Xu, Jie Xiao, Xia Cao, Jun Liu, “Lithium Metal Anodes with Nonaqueous Electrolytes”, *Chemical Reviews*, 2020, 120(24), 13312–13348. DOI:10.1021/acs.chemrev.0c00275, Publication date: November 11th, 2020.
5. Xiaodi Ren[#], Xianhui Zhang[#], Zulipiya Shadike, Lianfeng Zou, Hao Jia, Xia Cao, Mark H. Engelhard, Bethany E. Matthews, Chongmin Wang, Bruce W. Arey, Xiao-Qing Yang, Jun Liu, Ji-Guang Zhang*, Wu Xu*, “Designing Advanced In-Situ Electrode/Electrolyte Interphases for Wide Temperature Operation of 4.5-V Li||LiCoO₂ Batteries”, *Advanced Materials*, 2020, 32(49), 2004898. DOI: 10.1002/adma.202004898, Publication date: November 4th, 2020.
6. Xiaodi Ren[#], Peiyuan Gao[#], Lianfeng Zou, Shuhong Jiao, Xia Cao, Xianhui Zhang, Hao Jia, Mark H. Engelhard, Bethany E. Matthews, Haiping Wu, Hongkyung Lee, Chaojiang Niu, Chongmin Wang, Bruce W. Arey, Jie Xiao, Jun Liu, Ji-Guang Zhang*, Wu Xu*, “The Role of Inner Solvation Sheath within Salt-Solvent Complexes in Tailoring Electrode/Electrolyte Interphases for High-Voltage Lithium Metal Batteries”, *Proceedings of the National Academy of Sciences of the United States of America (PNAS)*, 2020, 117(46), 28603–28613. DOI:10.1073/pnas.2010852117, Publication date: November 17th, 2020.
7. Caitlin D. Parke, Akshay Subramaniam, Suryanarayana Kolluri, Daniel T. Schwarz, and Venkat R. Subramanian*, “An Efficient Electrochemical Tanks-in-Series Model for Lithium Sulfur Batteries”, *Journal of The Electrochemical Society*, 2020, 167, 163503. Publication Date: December 3, 2020.
8. Maitri Uppaluri, Akshay Subramaniam, Lubhani Mishra, Vilayanur Viswanathan, and Venkat R. Subramanian*, “Can a Transport Model Predict Inverse Signatures in Lithium Metal Batteries

Without Modifying Kinetics?”, *Journal of The Electrochemical Society*, 2020, 167, 160547.
Publication Date: December 29, 2020

9. Zhuo Li, Liang Yin, Gerard S. Mattei, Monty R. Cosby, Byoung-Sun Lee, Zhaohui Wu, Seong-Min Bak, Karena W. Chapman, Xiao-Qing Yang, Ping Liu, and Peter G. Khalifah*, “Synchrotron Operando Depth Profiling Studies of State-of-Charge Gradients in Thick $\text{Li}(\text{Ni}_{0.8}\text{Mn}_{0.1}\text{Co}_{0.1})\text{O}_2$ Cathode Films”, *Chem. Mater.*, 2020, **32**, 6358–6364. DOI: 10.1021/acs.chemmater.0c00983. Publication date: July 5th, 2020 (This paper should be reported in FY2020 APR report, but we missed it in our FY2020 APR report).
10. Solomon T. Oyakhire, William Huang, Hansen Wang, David T. Boyle, Joel R. Schneider, Camila de Paula, Yecun Wu, Yi Cui*, Stacey F. Bent*, "Revealing and Elucidating ALD-Derived Control of Lithium Plating Microstructure", *Advanced Energy Materials*, 2020, 10(44), 2002736. DOI: 10.1002/aenm.202002736. Publication date (Web): October 11, 2020.
11. Fengxia Xin, Hui Zhou, Yanxu Zong, Mateusz Zuba, Yan Chen, Natasha A. Chernova, Jianming Bai, Ben Pei, Anshika Goel, Jatinkumar Rana, Feng Wang, Ke An, Louis F. J. Piper, Guangwen Zhou, and M. Stanley Whittingham, “What is the Role of Nb in Nickel-Rich Layered Oxide Cathodes for Lithium-Ion Batteries?”, *ACS Energy Letters*, 2021, 6, 1377–1382. DOI: 10.1021/acsenenergylett.1c00190. Publication Date: March 18, 2021
12. M. Stanley Whittingham, “Solid-state ionics: The key to the discovery and domination of lithium batteries: some learnings from β -alumina and titanium disulfide”, *MRS Bulletin*, 2021, 6, 168–173. DOI: 10.1557/s43577-021-00034-2. Publication Date: February 12, 2021
13. Jiangtao Hu, Qinchao Wang, Bingbin Wu, Sha Tan, Zulipiya Shadike, Yujing Bi, M. Stanley Whittingham, Jie Xiao, Xiao-Qing Yang, Enyuan Hu, “Fundamental Linkage Between Structure, Electrochemical Properties and Chemical Compositions of $\text{LiNi}_{1-x-y}\text{Mn}_x\text{Co}_y\text{O}_2$ Cathode Materials”, *ACS Applied Materials & Interfaces*, 2021, 13, 2622–2629. DOI: 10.1021/acsaami.0c18942. Publication Date: January 07, 2021
14. Yao Liu, Xianyong Wu, Chaojiang Niu, Wu Xu, Xia Cao, Ji-Guang Zhang, Xiaoyu Jiang, Jie Xiao, Jihui Yang, M. Stanley Whittingham, and Jun Liu*, “Systematic Evaluation of Carbon Hosts for High-Energy Rechargeable Lithium-Metal Batteries”, *ACS Energy Letters*, 2021, 6, 1550–1559. DOI: 10.1021/acsenenergylett.1c00186. Publication Date: March 29, 2021.
15. Zulipiya Shadike, Hongkyung Lee, Oleg Borodin, Xia Cao, Xiulin Fan, Xuelong Wang, Ruqian Lin, Seong-Min Bak, Sanjit Ghose, Kang Xu, Chunsheng Wang, Jun Liu, Jie Xiao*, Xiao-Qing Yang* and Enyuan Hu*, “Identification of LiH and nanocrystalline LiF in the solid–electrolyte interphase of lithium metal anodes”. *Nature Nanotechnology*, (2021). DOI: 10.1038/s41565-020-00845-5, Publication Date (web): January 28, 2021.
16. Xia Cao[#], Peiyuan Gao[#], Xiaodi Ren, Lianfeng Zou, Mark H Engelhard, Bethany E Matthews, Jiangtao Hu, Chaojiang Niu, Dianying Liu, Bruce W Arey, Chongmin Wang, Jie Xiao, Jun Liu, Wu Xu*, Ji-Guang Zhang*, “Designing Rules of Diluents in Localized High-Concentration Electrolytes for High-Voltage Lithium Metal Batteries.” *Proceedings of the National Academy of Sciences of the United States of America*, 2021, 118(9), e2020357118. DOI:10.1073/pnas.2020357118. Publication date: March 2, 2021.
17. Ju-Myung Kim[#], Xianhui Zhang[#], Ji-Guang Zhang, Arumugam A. Manthiram, Y. Shirley Meng, Wu Xu*, “A review on the stability and surface modification of layered transition-metal oxide cathodes”, *Materials Today*, 2021, DOI:10.1016/j.mattod.2020.12.017. Publication date: February 27, 2021.

18. Xianhui Zhang, Lianfeng Zou, Zehao Cui, Hao Jia, Mark H. Engelhard, Bethany E. Matthews, Xia Cao, Qiang Xie, Chongmin Wang, Arumugam A. Manthiram, Ji-Guang Zhang, Wu Xu*, “Stabilizing Ultrahigh-Nickel Layered Oxide Cathodes for High-Voltage Lithium Metal Batteries”, *Materials Today*, 2021, DOI:10.1016/j.mattod.2021.01.013. Publication date: February 27, 2021.
19. Xia Cao, Hao Jia, Wu Xu, Ji-Guang Zhang*, “Localized high-concentration electrolytes for lithium batteries”, *Journal of the Electrochemical Society*, 2021, 168(1), 010522. DOI:10.1149/1945-7111/abd60e. Publication date: January 14, 2021.
20. Jayse Langdon, Arumugam A. Manthiram, “A perspective on single-crystal layered oxide cathodes for lithium-ion batteries”, *Energy Storage Materials*, 2021, 37, 143-160. DOI: 10.1016/j.ensm.2021.02.003. Publication date (web): February 4, 2021.
21. Jayse Langdon, Arumugam A. Manthiram, “Crossover Effects in Batteries with High-Nickel Cathodes and Lithium-Metal Anodes”, *Advanced Functional Materials*, 2021, 2010267. DOI: 10.1002/adfm.202010267. Publication date (web): February 17, 2021.
22. Zehao Cui, Qiang Xie, Arumugam A. Manthiram, “Zinc-Doped High-Nickel, Low-Cobalt Layered Oxide Cathodes for High-Energy-Density Lithium-Ion Batteries”, *Applied Materials and Interfaces*, 2021, 13, 15324–15332. DOI: 10.1021/acsami.1c01824. Publication date (web): March 24, 2021.
23. Caitlin D. Parke, Akshay Subramaniam, Venkat R. Subramanian*, and Daniel T. Schwartz, “Realigning the Chemistry and Parameterization of Lithium-Sulfur Battery Models to Accommodate Emerging Experimental Evidence and Cell Configurations”, *ChemElectroChem*, 2021, 8(6), 1098-1106. DOI: 10.1002/celec.202001575, Publication date: February 26th, 2021.
24. Linnette Teo, Venkat R. Subramanian*, and Daniel T. Schwartz, “Dynamic Electrochemical Impedance Spectroscopy of Lithium-ion Batteries: Revealing Underlying Physics through Efficient Joint Time-Frequency Modeling”, *Journal of The Electrochemical Society*, 2021, 168(1), 010526. DOI: 10.1149/1945-7111/abda04, Publication date: January 18th, 2021.
25. Gerard S. Mattei, Zhuo Li, Adam A. Corrao, Chaojiang Niu, Yulun Zhang, Boryann Liaw, Charles C. Dickerson, Jie Xiao, Eric J. Dufek, Peter G. Khalifah, “High-energy lateral mapping (HELM) studies of inhomogeneity and failure mechanisms in NMC622/Li pouch cells.” *Chemistry of Materials*, 2021. <https://doi.org/10.1021/acs.chemmater.0c04537>. Publication date: February 21, 2021.
26. Yulun Zhang, Ruby Nguyen, Boryann Liaw, “Status and gaps in Li-ion battery supply chain: Importance of quantitative failure analysis.” *Proceedings of the IEEE*, Special Issue on Electric and Hybrid Vehicles (Invited). DOI:10.1109/JPROC.2020.3047880. Publication date: January 21, 2021.
27. John Holoubek, Haodong Liu, Zhaohui Wu, Yijie Yin, Xing Xing, Guorui Cai, Sicen Yu, Hongyao Zhou, Tod A. Pascal, Zheng Chen, Ping Liu, “Tailoring Electrolyte Solvation for Li Metal Batteries Cycled at Ultra-Low Temperature”, *Nature Energy*, 2021, 6, 303–313, DOI: 10.1038/s41560-021-00783-z, Publication date: February 25, 2021.
28. David T. Boyle, William Huang, Hansen Wang, Yuzhang Li, Hao Chen, Zhiao Yu, Wenbo Zhang, Zhenan Bao & Yi Cui, “Corrosion of lithium metal anodes during calendar ageing and its microscopic origins”, *Nature Energy*, 2021, DOI: 10.1038/s41560-021-00787-9, Publication Date: March 22nd, 2021.
29. Hansen Wang, William Huang, Zhiao Yu, Wenxiao Huang, Rong Xu, Zewen Zhang, Zhenan Bao*, and Yi Cui*, “Efficient Lithium Metal Cycling over a Wide Range of Pressures from an Anion-Derived Solid-Electrolyte Interphase Framework”, *ACS Energy Letters*, 2021, 6, 816–825, DOI: 10.1021/acsenenergylett.0c02533, Publication Date: February 3, 2021.

30. Ben Pei, Hui Zhou, Anshika Goel, Mateusz Zuba, Hao Liu, Fengxia Xin, and M. Stanley Whittingham*, “Al Substitution for Mn during Co-Precipitation Boosts the Electrochemical Performance of $\text{LiNi}_{0.8}\text{Mn}_{0.1}\text{Co}_{0.1}\text{O}_2$ ”, *Journal of the Electrochemical Society*, 2021, **68**, 050532. DOI: 10.1149/1945-7111/ac0020, Publication Date (web): May 19, 2021.
31. Ruoqian Lin*, Seong-Min Bak*, Youngho Shin, Rui Zhang, Chunyang Wang, Kim Kisslinger, Mingyuan Ge, Xiaojing Huang, Zulipiya Shadike, Ajith Pattammattel, Hanfei Yan, Yong Chu, Jinpeng Wu, Wanli Yang, M. Whittingham, Huolin Xin*, and Xiao-Qing Yang*, “Hierarchical nickel valence gradient stabilizes high-nickel content layered cathode materials”, *Nature Communications*, 2021, **12**, 2350. DOI: 10.1038/s41467-021-22635w, Publication date: April 20, 2021.
32. Hui Zhou, Ben Pei, Qinglu Fan, Fengxia Xin and M. Stanley Whittingham*, “Can Greener Cyrene Replace NMP for Electrode Preparation of NMC 811 Cathodes?”, *Journal of the Electrochemical Society*, 2021, **168**, 040536, Publication Date (web): April 27, 2021.
33. Biyi Xu, Xinyu Li, Chao Yang, Yutao Li, Nicholas S Grundish, Po-Hsiu Chien, Kang Dong, Ingo Manke, Ruyi Fang, Nan Wu, Henghui Xu, Andrei Dolocan, John B Goodenough*, “Interfacial chemistry enables stable cycling of all-solid-state Li metal batteries at high current densities”, *Journal of the American Chemical Society*, 2021, **143**(17), 6542-6550. DOI: 10.1021/jacs.1c00752. Publication date (web): April 27, 2021.
34. Ruyi Fang, Biyi Xu, Nicholas S. Grundish, Yang Xia, Yutao Li, Chengwei Lu, Yijie Liu, Nan Wu, John B. Goodenough*, “ Li_2S_6 -integrated PEO-based polymer electrolytes for all-solid-State Lithium-metal batteries”, *Angewandte Chemie International Edition*, 2021. DOI: 10.1002/ange.202106039. Publication date (web): June 30, 2021.
35. Hongyao Zhou, Haodong Liu, Xing, Zijun Wang, Sicen Yu, Gabriel M. Veith, and Ping Liu*, “Quantification of ion transport mechanism in protective polymer coatings on lithium metal anodes”, *Chemical Sciences*, 2021, **12**, 7023-7032, DOI: 10.1039/D0SC06651F, Publication date (web): April 12, 2021.
36. Ruoqian Lin, Rui Zhang, Chunyang Wang, Xiao-Qing Yang, and Huolin L. Xin*, “TEM mageNet training library and AtomSegNet deep-learning models for high-precision atom segmentation, localization, denoising, and deblurring of atomic-resolution images”, *Scientific Report*, 2021, **11**, 5386. DOI: 10.1038/s41598-021-84499-w. Publication Date (web): March 08, 2021.
37. Bingyu Lu, Edgar Olivera, Jonathan Scharf, Mehdi Chouchane, Chengcheng Fang, Miguel Ceja, Lisa E. Pangilinan, Shiqi Zheng, Andrew Dawson, Diyi Cheng, Wurigumula Bao, Oier Arcelus, Alejandro A. Franco, Xiaochun Li, Sarah H. Tolbert,* and Ying Shirley Meng*, “Quantitatively Designing Porous Copper Current Collectors for Lithium Metal Anodes”, *ACS Applied Energy Materials*, 2021. DOI: 10.1021/acsaem.1c00438, Publication Date (web): June 18, 2021.
38. Chaojiang Niu, Dianying Liu, Joshua A. Lochala, Cassidy S. Anderson, Xia Cao, Mark E. Gross, Wu Xu, Ji-Guang Zhang, M. Stanley Whittingham, Jie Xiao*, and Jun Liu, “Balancing interfacial reactions to achieve long cycle life in high-energy lithium metal batteries”, *Nature Energy*, 2021, DOI: 10.1038/s41560-021-00852-3, Publication Date (web): June 28, 2021.
39. Corey Efaw, Bingyu Lu, Yuxiao Lin, Gorakh Pawar, Parameswara Chinnam, Michael Hurley, Eric Dufek, Ying Shirley Meng, Bin Li*, “A closed-host bi-layer dense/porous solid electrolyte interphase for enhanced lithium-metal anode stability”, *Materials Today*, 2021. DOI: 10.1016/j.mattod.2021.04.018, Publication Date (web): May 19, 2021.

40. Sang Cheol Kim, Xian Kong, Rafael A. Vilá, William Huang, Yuelang Chen, David T. Boyle, Zhiao Yu, Hansen Wang, Zhenan Bao, Jian Qin, Yi Cui*, “Potentiometric measurement to probe solvation energy and its correlation to lithium battery cyclability”, *Journal of the American Chemical Society*, 2021. doi:10.1021/jacs.1c03868. Publication Date (web): June 29, 2021.
41. Hansen Wang, Zhiao Yu, Xian Kong, William Huang, Zewen Zhang, David G. Mackanic, Xinyi Huang, Jian Qin, Zhenan Bao*, and Yi Cui*, “Dual-solvent Li-ion solvation enables high-performance Li-metal batteries”, *Advanced Materials*, 2021, **33** (25), 2008619. Publication Date (web): May 9, 2021.
42. Chaojiang Niu, Dianying Liu, Joshua A Lochala, Cassidy S Anderson, Xia Cao, Mark E Gross, Wu Xu, Ji-Guang Zhang, M. Stanley Whittingham, Jie Xiao and Jun Liu “Balancing Interfacial Reactions to Achieve Long Cycle Life in High Energy Lithium Metal Batteries”, *Nature Energy*, 2021, 6: 723-732. DOI: 10.1038/s41560-021-00852-3. Publication Date: June 28, 2021.
43. Qiang Xie, Zehao Cui, Arumugam A. Manthiram, “Unveiling the Stabilities of Nickel-Based Layered Oxide Cathodes at an Identical Degree of Delithiation in Lithium-Based Batteries”, *Advanced Materials*, 2021. DOI: 10.1002/adma.202100804. Publication date (web): July 05, 2021.
44. Sang Cheol Kim, Xian Kong, Rafael A. Vilá, William Huang, Yuelang Chen, David T. Boyle, Zhiao Yu, Hansen Wang, Zhenan Bao, Jian Qin, Yi Cui*, “Potentiometric measurement to probe solvation energy and its correlation to lithium battery cyclability”, *Journal of the American Chemical Society*, 2021. doi:10.1021/jacs.1c03868. Publication Date (web): June 29, 2021.
45. Yuchi Tsao, Huaxin Gong, Shucheng Chen, Gan Chen, Yunzhi Liu, Theodore Z. Gao, Yi Cui, Zhenan Bao, “A Nickel-Decorated Carbon Flower/Sulfur Cathode for Lean-Electrolyte Lithium–Sulfur Batteries”, *Advanced Energy Materials*, 2021, 11, 2101449. Publication Date (web): August 4, 2021.
46. Zhaohui Wu, Seong-Min Bak*, Zulipiya Shadike, Sicen Yu, Enyuan Hu, Xing Xing, Yonghua Du, Xiao-Qing Yang, Haodong Liu*, and Ping Liu, “Understanding the Roles of the Electrode/Electrolyte Interface for Enabling Stable Li||Sulfurized Polyacrylonitrile Batteries”. *ACS Appl. Mater. Interfaces* 2021, 13, 31733–31740, Publication date: July 2, 2021.
47. Lubhani Mishra, Akshay Subramaniam Taejin Jang, Krishna Shah, Maitri Uppaluri, Scott A. Roberts, and Venkat R. Subramanian, “Perspective – Mass Conservation in Models for Electrodeposition/Stripping in Lithium Metal Batteries”, *J. Electrochem. Soc.*, 168, 092502 (2021). DOI: 10.1149/1945-7111/ac2091. Published, September 6, 2021.

Invited Presentations

1. Bay Area Battery Summit 2020, CA, November 18th, 2020.
2. M. Stanley Whittingham, “Past, Present and Future Directions of Battery Energy Storage” Microsoft, Jun Liu, “Status of Battery500 Consortium”, The Electrochemical Society PRiME Virtual Meeting, October 4–9, 2020.
3. M. Stanley Whittingham, “We Owe Future Generations a Cleaner and Sustainable World”, STS Kyoto Climate Change Forum, October 6th, 2020.
4. M. Stanley Whittingham, “Battery Energy Storage Past, Present and Future Directions”, BU with IIT Madras and IIT Roper, October 6th, 2020.
5. M. Stanley Whittingham, “The Origins of the Lithium Battery and Future Challenges/Opportunities”, Tobin Marks Lecture in Discovery Chemistry, U. Maryland, October 13th, 2020.

6. M. Stanley Whittingham, “Li-Ion Battery Storage with Renewable Energy: A Solution to Cleaning the Environment and Mitigating Global Warming”, World Laureates Forum on Science and Technology for the Common Destiny of Mankind, Shanghai, China, October 29th, 2020.
7. M. Stanley Whittingham, “The Origins of the Lithium Battery and Future Challenges/Opportunities” MSE Seminar, Imperial College, London, November 4th, 2020.
8. M. Stanley Whittingham, “The Origins of the Lithium Battery and Future Challenges/Opportunities” NIST, November 4th, 2020.
9. M. Stanley Whittingham, “Pushing the Limits of Intercalation Reactions: Two Li vs Higher Ni NMC” IBA, Bled, Slovenia, November 17th, 2020.
10. M. Stanley Whittingham, “Li-Ion Batteries: The Journey from an Idea to Commercialization to Domination” Richmond, WA (on-line), November 24th, 2020.
11. M. Stanley Whittingham, “How I Created a Rechargeable World” European Battery Association, Berlin, Germany, November 25th, 2020.
12. M. Stanley Whittingham, “Energy Storage: Key for a Greener Economy” International Green Energy Summit (on-line), December 4th, 2020.
13. M. Stanley Whittingham, “Energy Storage: Present Status, Future Challenges and Key Role in a Greener Economy” American Chemical Society: Advancing Energy Conversion, Capture and Storage (on-line), December 4th, 2020.
14. Zhenan Bao, “Molecular design for electrolyte solvents and artificial SEI for stable lithium-metal anodes”, Storage X International Virtual Symposium, November 13, Stanford University.
15. A. Manthiram, “Intercalation Chemistry of Oxides,” Pacific Rim Meeting on Electrochemical and Solid State Science (PRiME), Honolulu, HI, October 4 – 9, 2020.
16. A. Manthiram, “Next Generation Battery Technologies,” Thermo Fisher – UT Austin Battery Seminar, Austin, TX, October 14, 2020
17. A. Manthiram, “High-Energy Cobalt-free Lithium-ion Batteries,” Towards Extreme Fast Charging and High Energy Batteries, CBMM Webinar Series, Austin, TX, October 20–22, 2020.
18. A. Manthiram, “Pairing Lithium-metal Anode with High-nickel NMC and Sulfur Cathodes: Fundamental Understanding and Engineering Solutions,” 2020 Fall Meeting of the Materials Research Society, Boston, MA, November 28 – December 4, 2020.
19. A. Manthiram, “Near-term and Long-term Perspective of Electrical Energy Storage,” Northeastern University, Boston, MA, December 9, 2020.
20. Liaw, et al., “Quantitative cell qualification to enable long life rechargeable Li metal batteries.” International Battery Association meeting 2020 (Virtual IBA-2020), November 17–18, 2020.
21. Y. Zhang, B. Liaw*, E.J. Dufek, B. Li, “How well cathode materials are being used in rechargeable Li batteries?” PRiME 2020, the 238th Electrochemical Society meeting, A-01-0034, Symposium of Intercalation Chemistry for Electrochemical Energy Storage Technologies: In Honor of M. Stanley Whittingham. October 4–9, 2020.

22. Liaw, “INL’s battery diagnostic and prognostic approach for failure mode and effect analysis (FMEA)—Identify cell quality through better qualification,” Battery Safety Council Forum 9 (virtual meeting), November 17–18, 2020.
23. MF Toney, “Ion Transport in Electrolytes”, BESSY III Expert Workshop - Energy Storage and Batteries, Nov 4, 2020
24. MF Toney, “Challenges and opportunities in electrochemical energy storage technologies”, PETRA IV Workshop, Materials and Processes for Energy and Transport Technology, Oct 21, 2020
25. Seongmin Bak, Zulipiya Shadike, Lili Shi, Haodong Liu, Ping Liu, Paul Northrup, Yonghua Du, Yong S. Chu, Dongping Lu, Jie Xiao, and Xiao-Qing Yang, “Direct Observation of the Sulfur-Based Chemical Species in Li-S Batteries by Spatially-”presented at ECS Prime 2020, October 4–9, 2020, Invited.
26. Ruoqian Lin, Seongmin Bak, Youngho Shin, Zulipiya Shadike, Qinchao Wang, Sha Tan, Enyuan Hu, Xiao-Qing Yang*, “Multi-dimensional Multi-scale Diagnostic Study on Layered Cathode Materials”, presented at ECS Prime 2020, October 4–9, 2020.
27. Zulipiya Shadike, Seong-Min Bak, Enyuan Hu, Sha Tan, Qin-Chao Wang, Ruoqian Lin and Xiao-Qing Yang*, “Probing the in-situ Surface Chemistry of $\text{LiNi}_{0.94}\text{Co}_{0.06}\text{O}_2$ and $\text{LiNi}_{0.92}\text{Co}_{0.06}\text{Al}_{0.02}\text{O}_2$ Cathode Materials using Synchrotron-based Ambient-Pressure XPS”, presented at ECS Prime 2020, October 4–9, 2020.
28. Peter Khalifah, “Clockwork inside cathodes – unparalleled insights into defects and inhomogeneities”, 2nd Battery and Energy Storage Conference (AIChE), October 2020.
29. Wu Xu*, Xiaodi Ren, Xia Cao, Peiyuan Gao, and Ji.-Guang Zhang. "Designing New Electrolytes for High-Energy Lithium Metal Batteries", PRiME 2020 (ECS, ECSJ, & KECS Joint Meeting), October 8, 2020, Virtual, United States.
30. J. Xiao, “Integrating Materials Science, Electrochemistry and Engineering in Energy Storage Technologies”, Materials Today Award Presentation, December 14, 2020
31. J. Xiao, “Electrochemistry in Rechargeable Lithium Metal Batteries”, The Electrochemical Society Webinar, November 11, 2020.
32. J. Xiao, “Integrating Materials Science, Electrochemistry and Engineering in Energy Storage Technologies”, The Electrochemical Society PRiME Virtual Meeting, October 4, 2020.
33. J. Xiao, “Battery 500 Consortium: Understanding and Addressing the Fundamental Challenges in Rechargeable Lithium Metal Batteries”, 20th Annual Advanced Automotive Battery Conference (AABC) Virtual, November 3rd, 2020.
34. Xia Cao*, Wu Xu and Ji-Guang Zhang, “Enhanced Electrode/Electrolyte Interphases in Fluorinated Orthoformate Electrolytes for Stable High-Voltage Lithium Metal Batteries, The Electrochemical Society PRiME Virtual Meeting, October 6, 2020.
35. Y. Shirley Meng, invited talk, “Advanced Diagnostic Tools for Characterizing Lithium Metal and Solid-State Batteries”, 2020 MRS (co-hosted by ThermoFisher Scientific), Oct. 27th, 2020
36. Y. Shirley Meng, invited talk, “Advanced Diagnostic Tools for Characterizing Lithium Metal and Solid-State Batteries”, 8th International Renewable Sustainable Energy Conference, Nov. 25th – 28th, 2020

37. Ping Liu, invited talk, “High Coulombic Efficiency Electrolyte Enables Li||Span Batteries with Superior Cycling Performance”, 2020 ECS PRiME, Oct 4th -9th, 2020.
38. M. Stanley Whittingham, “The Origins of the Lithium Battery and Future Challenges/Opportunities”, Global Young Scientists Summit, Singapore, January 13th, 2021.
39. M. Stanley Whittingham, “The Lithium Battery, From a Dream to Domination of Energy Storage” Clarkson University and ECS Section, January 29th, 2021.
40. M. Stanley Whittingham, “The Lithium Battery: From a Dream to Readiness to Take on Climate Change – Opportunities and Challenges”, PSI Swiss Battery Days, Switzerland, February 16th, 2021.
41. M. Stanley Whittingham, “The Lithium Battery: From a Dream to Readiness to Take on Climate Change – Opportunities and Challenges”, Chey Institute, Seoul, February 18th, 2021.
42. M. Stanley Whittingham, “The Lithium Battery: From a Dream to Readiness to Take on Climate Change – Opportunities and Challenges”, North Carolina State U., February 19th, 2021.
43. M. Stanley Whittingham, Director’s Lecture, “Li-Ion Batteries: From an Idea to Readiness to Take on Climate Change – Opportunities and Challenges”, Argonne National Laboratory 75th Anniversary – Energy Storage for a Changing World, February 23rd, 2021.
44. M. Stanley Whittingham, “The Lithium Battery, From a Dream to Domination of Energy Storage”, Brazilian Chemical Society, February 24th, 2021.
45. M. Stanley Whittingham, “The Lithium Battery, From a Dream to Domination of Energy Storage”, Netherlands Student Meeting, Utrecht, March 4th, 2021.
46. M. Stanley Whittingham, “Li-Ion Batteries: From an Idea to Readiness to Take on Climate Change – Opportunities and Challenges”, Forum on Clean Energy, Hong Kong, March 10th, 2021.
47. M. Stanley Whittingham, Sir Jerry Price Lecture, “Li-Ion Batteries: From an Idea to Readiness to Take on Climate Change – Opportunities and Challenges”, CSIRO, Melbourne, Australis, March 10th, 2021.
48. M. Stanley Whittingham, “Li-Ion Batteries: From an Idea to Readiness to Take on Climate Change – Opportunities and Challenges”, ICDD, Philadelphia, March 12th, 2021.
49. M. Stanley Whittingham, “Li-Ion Batteries: From an Idea to Readiness to Take on Climate Change – Opportunities and Challenges”, BU-IIT Ropar Webinar Series, March 16th, 2021.
50. M. Stanley Whittingham, “The Lithium Battery, From a Dream to Domination of Energy Storage”, Chemical Engineering, IST Lisbon, March 18th, 2021.
51. M. Stanley Whittingham, “Li-Ion Batteries: From an Idea to Readiness to Take on Climate Change – Opportunities and Challenges”, CIBF, Shenzhen, China, March 19th, 2021.
52. M. Stanley Whittingham, “Li-Ion Batteries: From an Idea to Readiness to Take on Climate Change – Opportunities and Challenges”, Cambridge, England, March 22nd, 2021. M. Stanley Whittingham
53. M. Stanley Whittingham, “Li-Ion Batteries: From an Idea to Readiness to Take on Climate Change – Opportunities and Challenges”, Int. Workshop on Nanocatalysts and Green Energy, Chinese Academy of Sciences, March 27th, 2021.

54. W. Xu, “Developing New Electrolytes for Lithium Metal Batteries”, Materials Engineering Program Virtual Seminar, Department of Electrical and Computer Engineering, University of Houston, Houston, Texas, February 12, 2021.
55. A. Manthiram, “Next Generation Battery Technologies,” *2021 Center for Research in Extreme Batteries (CREB) Biannual Winter Meeting, Army Research Laboratory and University of Maryland*, College Park, MD, January 15, 2021 (invited).
56. A. Manthiram, “Next Generation Battery Technologies,” *Columbia University*, New York, NY, February 5, 2021 (invited).
57. A. Manthiram, “Battery Technologies for Renewable Energy Storage and Vehicle Electrification,” *Tata Institute of Fundamental Research*, Mumbai, India, February 15, 2021 (invited).
58. A. Manthiram, “Sustainable Battery Chemistries for Electrical Energy Storage,” NanoBioLab Symposium 2021 Webinar, Singapore’s Agency for Science, Technology, and Research (A*STAR), Singapore, February 23, 2021 (invited).
59. A. Manthiram, “Sustainable Battery Chemistries for E-Mobility,” *SRM Institute of Science and Technology*, Chennai, India, March 25-27, 2021 (invited keynote talk).
60. J. Xiao, “Electrochemical Energy Storage: From Materials Science to Prototype Batteries and Manufacturing”, Virtual Materials Science and Engineering (MSE) seminars, University of Houston, March 26th, 2021.
61. Y. Zhang, B. Liaw,* E. J. Dufek, B. Li, “First Cycle Capacity Loss of Li–NMC 811 Cells — A Close Look from Electrochemical Diagnostic Analysis.” A special seminar presented to GM Warren Technical Center, March 2, 2021.
62. Y. Zhang, B. Liaw*, E. J. Dufek, B. Li, “Tracking Rechargeable Li Battery Cell Degradation Through Quantifiable Capacity Fade Modes from Formation to Cycle Aging.” Presented in 2021 IAPG Chemical Working Group (CWG) Safety Panel Virtual Meetings, February 19, 2021.
63. Michael Toney, “Quantifying capacity losses due to solid-electrolyte interface formation”, American Physical Society March Meeting, Mar 18, 2021.
64. Michael Toney, “Advances in operando X-ray characterization of batteries” at the Advanced Photon Source “Bright future for in situ and operando structural science at APS-U”. January 15, 2021.
65. M. Stanley Whittingham, “The Lithium Battery, From a Dream to Domination of Energy Storage”, Morocco, April 7th, 2021.
66. M. Stanley Whittingham, “My Journey to the Nobel Prize”, GEM, UAE, April 15th, 2021.
67. M. Stanley Whittingham, Stoffer Lecture “Li-Ion Batteries: From an Idea to Readiness to Take on Climate Change – Opportunities and Challenges”, Chemistry Seminar, MST, April 16th, 2021.
68. M. Stanley Whittingham, “Batteries for Energy Storage to Green the Environment - Is there another battery alternative?”, Earth Day, Materials Research Society Spring Meeting, April 22nd, 2021.
69. M. Stanley Whittingham, “Smart Cities and New Green Solutions”, Nobel Prize Summit – Our Planet, Our Future (National Academy and Nobel Prize Institute), April 28th, 2021.
70. M. Stanley Whittingham, “Webinar #1: Battery Energy Storage Systems 101”, NYSERDA Presents: Battery Energy Storage Systems – Key Considerations for Local Governments May 5th, 2021.

71. M. Stanley Whittingham, “Perspective on Lithium Battery Origins & Future Challenges/Opportunities”, Israel Electrochemical Society, ISEL2021. June 16th, 2021.
72. M. Stanley Whittingham, “Overview of Li Battery R&D”, LGES Innovation Forum, June 20th, 2021.
73. M. Stanley Whittingham, “Storage is Ready to Take-on Climate Change”, Lindau Nobel, June 29th, 2021.
74. Venkat R. Subramanian, “Model-based Battery Management System for current and next-generation lithium batteries”, Mexican Energy Storage Network, May 21st, 2021
75. T. Jang, L. Mishra, K. Shah, P. Mittal, A. Subramaniam, M. P. Gururajan, S. A. Roberts, and V. R. Subramanian, “Robust 2D simulation of morphological evolution in lithium metal batteries”, 239th ECS Meeting, 30th May – 3rd June 2021.
76. A. Manthiram, “Sustainable Battery Chemistries for Electrical Energy Storage,” Platinum Seminar Series, Monash University, Melbourne, Australia, June 2, 2021.
77. A. Manthiram, “Low- and Zero-cobalt Layered Oxide Cathodes for Lithium-ion Batteries,” 239th Electrochemical Society Meeting, Chicago, IL, May 30 – June 3, 2021.
78. A. Manthiram, “Sustainable Battery Technologies for Renewable Energy Utilization and Vehicle Electrification,” Distinguished Lecture Series Organized by Phi Lambda Upsilon Student Organization, Kansas State University, Manhattan, KS, April 15, 2021.
79. Y. Shirley Meng, “Advanced Diagnostic Tools for Characterizing Lithium Metal Batteries and Solid- State Batteries”, EMRS European Materials Research Society, May 31st, 2021
80. Ping Liu, “Advances in Pyrolyzed Polymeric Sulfur Cathodes for Low-Cost Lithium Metal Batteries”, 239th ECS Meeting, May 30 – June 3, 2021.
81. Ping Liu, “Li-S batteries with pyrolyzed polymer sulfur cathodes”, NDIA - Lithium Sulfur Battery Symposium, June 8, 2021
82. Ping Liu, “Going beyond today’s lithium-ion batteries”, SAE Battery Summit, June 15 – 16, 2021.
83. Enyuan Hu, “Resolving the Controversy over the Elusive Components in Solid Electrolyte Interphase on Li Metal Anode”, Materials Research Society 2021 Spring Meeting, April 23, 2021.
84. J. Xiao, “From Fundamental Research to Technology Transfer”, Virtual Seminar, DOE OTT Entrepreneurship Program, June 24th, 2021.
85. J. Xiao, “From Reproducible Coin Cells to Pouch Cell Design and Fabrication”, Department Seminar, University of Washington, June 2nd, 2021.
86. J. Xiao, “A Top-down approach to understand and address fundamental challenges in rechargeable lithium metal batteries”, MRS Spring Meeting (Virtual), April 21, 2021.
87. P. Khalifah, “High-throughput diffraction mapping of Li metal pouch cell batteries”, Beyond Li-Ion XIII, Argonne National Laboratory, IL, June 9 – 11, 2021.
88. W. Xu. "Liquid Electrolytes for High-Voltage Lithium Metal Batteries", Virtual Seminar at Department of Mechanical Engineering, Massachusetts Institute of Technology, April 13, 2021.

89. X. Ren, X. Zhang, H. Jia, X. Cao, J. Zhang, and W. Xu. "Building Advanced Electrode/Electrolyte Interphases for Stable Operation of High-Voltage Lithium Metal Batteries", 2021 ACS Spring, Virtual, United States, April 12, 2021.
90. M. Li, C. Fang, Y. Zhang, B. Lu, Y.S. Meng, G. Pawar, Y. Lin, B. Liaw*, "Can fast charging rechargeable lithium batteries be a reality?" Symposium A02 – LIBs Fast Charging, 239th Electrochemical Society Meeting, May 30–June 3, 2021.
91. M. Stanley Whittingham, "The Creation of a Rechargeable World", BMW Supervisors, July 14th, 2021.
92. M. Stanley Whittingham, "The Lithium Battery: The Origins to Domination - The Role of Structure and Disorder". Denver X-Ray conference, August 5th, 2021.
93. M. Stanley Whittingham, "Energy Storage to Ameliorate Global Warming :The Lithium Battery and it's Journey to Domination", Nottingham, Roosevelt Memorial UK, 2021.
94. M. Stanley Whittingham, "The Lithium Intercalation Battery: Its Origin, Future Challenges and the Role that Characterization Play", LBNL-ALS, August 11th, 2021.
95. M. Stanley Whittingham, "Lithium Batteries: Future Trends and the Energy/Safety Tradeoff", UL August 11th, 2021.
96. M. Stanley Whittingham, "The Lithium Battery, from a Dream to Readiness to Take on Climate Change – Materials Opportunities and Challenges", MRS Serbia, Yucomat, August 30th, 2021.
97. M. Stanley Whittingham, "The Lithium Battery, from a Dream to Readiness to Take on Climate Change – Materials Opportunities and Challenges", Alfred University Seminar, September 2nd, 2021.
98. M. Stanley Whittingham, "The Lithium Battery, from a Dream to Readiness to take on Climate Change – Opportunities and Challenges for Chemists", Italian Chemical Society Opening Plenary, September 14th, 2021.
99. M. Stanley Whittingham, "The Critical Role that Energy Storage Plays in Reducing the Carbon Footprint of Cities", CIIF-WLA – Build Low Carbon Cities, Shenzhen, China, September 14th, 2021.
100. M. Stanley Whittingham, "The Lithium Battery, from a Dream to Readiness to Take on Climate Change – Materials Opportunities and Challenges", Cambridge University, UK, September 30th, 2021.
101. Ying Shirley Meng, Award Talk, Faraday Medal of Royal Chemical Society, United Kingdom, Virtual, September 6, 2021
102. Ying Shirley Meng, Keynote Address, XRD Workshop Hosted by Benha University, Egypt, Virtual Conference, August 23rd, 2021
103. Ying Shirley Meng, Keynote, Singapore Section, Electrochemical Society Chapter Talk, July 7th, 2021.
104. Ping Liu, invited, "Development of next generation batteries: performance and safety", John Deere, August 2021.
105. Ping Liu, invited, "Automotive & Battery Safety Conference", September 27, 2021.

106. A. Manthiram, “Sustainable Battery Chemistries for E-Mobility and Renewable Energy Storage,” *TUBA World Conference on Energy Science and Technology (TUBA WCEST-2021)*, August 8 – 12, 2021
107. A. Manthiram, “Sustainable Next-generation Battery Chemistries,” Battery Safety Science Symposium: Advancing Safer Energy Storage through Science, August 11, 2021.
108. A. Manthiram, “Sustainable Battery Chemistries for Electrical Energy Storage,” MateriAIZ Seminar Series, Arizona State University and University of Arizona, Phoenix, AZ, August 27, 2021.
109. A. Manthiram, “Sustainable Battery Chemistries for Energy Storage,” 50 Global Leaders of Energy Storage and E-Mobility Convention, ETN, Virtual, India, September 15, 2021.
110. A. Manthiram, “Sustainable Battery Chemistries for Energy Storage,” Indian Oil R&D Golden Jubilee Webinar Series, Virtual, Indian Oil, India, September 17, 2021.
111. J. Xiao, “Electrochemical Energy Storage: From Materials Science to Prototype Batteries and Cell Manufacturing”, Shell, July 6th, 2021.
112. J. Xiao, “From Materials Science to Prototype Batteries and Cell Manufacturing”, Molecular Foundry 2021 Annual User Meeting, LBNL, August 20, 2021.
113. J. Xiao, “Electrochemistry in Energy Storage Research”, Oregon Center for Electrochemistry Conference, University of Oregon, September 24, 2021.

(This page intentionally left blank)

